M. Y. H. Bangash

Shock, Impact and Explosion

Structural Analysis and Design

Shock, Impact and Explosion

M.Y.H. Bangash

Shock, Impact and Explosion

Structural Analysis and Design

Springer

Prof. Dr. M.Y.H. Bangash
Emeritus Professor of Aerospace
and Nuclear Structures
Consulting Engineer
39 Wontner rd.
SW177QT London
United Kingdom

The Late Mr. Hassan Jan Khan was the author's secondary school teacher in mathematics at Hangu in the N.W.F.P. of Pakistan. His love and enthusiasm for classical mathematics needed no bounds. His admiration for wellknown mathematicians, including Ramanujan and Goate, could not be hidden but to translate them into "the after class short stories." This remarkable man living in rugged mountains of Hindukush did have the vision for the importance of maths. When I heared about his sad demise from his son Professor M. Qasim Jan, the Vice-Chancellor of the Quaid-i-Azam University at Islamabad, I am more than happy to dedicate this book in the name of my this wonderful teacher who inculcated the spirit of mathematics.

M.Y.H. BANGASH

Preface for Previous Title: Impact and Explosion – Analysis and Design

The dynamics of impact and explosion are an important consideration in the design of conventional structures in general, and sensitive and unconventional structures in particular. Accidents causing damage and explosion are a matter of growing concern in many areas such as nuclear, chemical, civil, mechanical, electrical, offshore, gas, aeronautical and naval engineering. This book provides, in Chap. 1, a comprehensive, illustrated survey of accidents and explosions, including those caused by aircraft, missiles, bombs, detonators, sea-going vessels, cars, lorries, trains, etc. Gas and nuclear explosions are also covered.

Engineering modelling of impact and explosion requires a great deal of data as an input. This input is needed so that a comprehensive analysis can be carried out on the design of structures. Chapter 2 gives a comprehensive treatment of various types of impact and explosion. Tables and examples are given for tornado-generated, plant-generated and military missiles, and civilian and military aircraft. The impactors included may be categorized as follows:

Environmental	Jet fluids, snow/ice, falling stones/boulders, trees, poles, pylons and various types of dropped weights
Military/naval	Tanks, tankers, ships, carriers, hydrofoils and hovercrafts
Civilian	Cars, lorries, trains, earth movers and bulldozers

Data on explosion cover bombs, shells, grenades, explosives, gas leaks, chemical dusts and nuclear and underwater detonations. Tables and graphs are provided to act as inputs to various engineering problems. Both Chaps. 1 and 2 will familiarize the reader with the range of types of missiles/impactors and explosions and their disastrous effects in terms of human lives and structural damage.

The modelling of shock impact and explosion remains one of the most difficult tasks. It involves structural dynamics, load–time relationships, impactor–target interaction, material properties including strain-rate effects and

solution/convergence procedures. Before the reader is introduced to numerical models and design/protection techniques, it is essential to emphasize the importance of knowing basic structural dynamics, which is the theme of Chap. 3. This chapter covers all areas of basic structural dynamics, such as elastic and elasto-plastic systems, degrees of freedom, fundamental vibrations, forced vibrations and impact/impulsive loads versus vibrations, and includes tables and graphs covering numerical data with typical examples.

The reader is then in a position to study the dynamics of impact and explosion. Chap. 4 provides an extensive treatment of impact dynamics. It includes vehicle collision mechanics and impact due to dropped weights, water jets, snow/ice, ocean waves, missiles and aircraft. Empirical models are introduced for non-deformable and deformable missiles. Materials considered are steel, concrete, bovine, soil/rock and composites. A special section covers impact on water surfaces. A simplified analysis for load–time relationship is presented. Tables, graphs and line diagrams are used to evaluate parameters and coefficients in the numerical analysis.

The dynamics of explosion, as introduced in Chap. 2, is considered in depth in Chap. 5. Apart from discussing various numerical parameters and major assumptions, this chapter includes detailed analysis and numerical modelling for explosions occurring in air, underground and underwater. Prominent among them are explosions due to nuclear detonations, gas leaks, dust bombs and explosives. Blast loads and their overpressures are fully discussed.

Chapter 6 gives formulations for the dynamic finite-element analysis of shock, impact and explosion. Various boundary conditions are discussed. A step-by-step analysis suggests only the use of higher-order elements representing various materials alone or in combination. Material strain rates, dynamic material modelling simulation and solution techniques are fully discussed. On the other hand, the analysis is flexible enough to include linear, non-linear, plasticity and cracking criteria under shock, impact and explosion conditions.

Chapter 7 covers impact and blast load design. Case studies are chosen from various engineering disciplines. Each case study is supported by a brief introduction to the background of the relevant areas. Care is taken to include those case studies that are supported by experimental test results and/or site monitoring. This then gives a degree of validation to the analytical results. The major case studies chosen are from the following disciplines: building, civil, mechanical, naval, aerospace, offshore, defence, nuclear, transportation and underwater facilities. Final design recommendations are made for each case study. The text gives a comprehensive bibliography for those who wish to carry out further research in depth.

Shock, Impact and Explosion – Analysis and Design will be of use to research and practising engineers, designers, technologists, mathematicians and specialists in computer-aided techniques of structures under transient loads in various engineering disciplines as identified earlier in this text. It will

also be of use to non-engineering specialists involved in the manufacture and application of various impactors and explosive induced structures and their protection.

London, UK   *M.Y.H. Bangash*
1993

Preface for Shock, Impact and Explosion

The Preface given here can be treated as an extension to the earlier preface given in this text under 'Impact and Explosion – Analysis and Design'. The statement given therein must therefore be valid for this new text. This book gives additional materials on the individual subjects of importance. Chap. 1 on accidental survey has been improved upon. This now gives an up-to-date data on accidents. Chap. 2 gives additional materials on impactors, aircraft and missiles. Very recent data have been incorporated on aircraft, missiles and their collisions and crashes. Many new items are included, which are based on advanced research and recent events. Chap. 3 gives an updated version of basic structural dynamics. Examples and mini-case studies are included to explain and support the understanding of basic dynamics. Chap. 4 is devoted to impact dynamics. The subject has been extended by including more advanced materials, data, charts, tables and examples. Explosion and blast effects are extremely difficult to evaluate and correlate with site monitoring data. Chap. 5 has tried to reach the audience and find some valuable answers to the complicated problems. Many advanced materials on dynamic finite element concerning shock, impact and explosion are included in Chap. 6. Criteria for solution procedures are examined. Useful problems are solved with the help of computer programs compiled under Program ISOPAR in the Appendices.

Chapter 7, as before, deals with numerous case studies. Many additional case studies are included apart from revising some existing case studies. Sections and their contents are slightly changed to bring about a uniformity concerning the subject matter. Section A covers steel and composites. A modification is proposed to A.1 on steel structures. Section B, which is devoted to concrete structures, has been modified. Topics like steel–concrete composite structures and steel fibre-reinforced concrete panels or slabs have been added with detailed results and conclusions. More sophisticated approach on masonry structures with proven results are now given in Section C. Sections D, E, F, G, H, I, J, K, and L have been revised to cater for the new advancement in research, practice and site monitoring techniques. Section I is devoted

to underground and underwater explosion and their effects. An effort has been made to correlate results with experimental and site monitoring data. Section J is entirely devoted to shock, impact and explosion on bridges. A comprehensive analytical and codified method is referred to in this section. Results and discussions are given with every section. Section K is entirely earmarked for the analysis of luggage container under explosion. The results are fully described and are meaningful. Section L is devoted to buildings under impact and explosion. Since the author has published a well-known book *Explosion-Resistant Buildings*, Springer, 2005, some latest results on the Twin Tower collapse are included. This section also covers collision and provides analysis and results between adjacent buildings. Apart from existing computer subroutines, many more are given to cover for the analysis of all the aspects of this volume. More references are added for the readers who wish to carry out research and design of individual structures subject to shock, impact and explosion.

London, UK   *M.Y.H. Bangash*
2008

Contents

Acknowledgements

The author is indebted to many individuals, institutions, organizations and research establishments, mentioned in the text, for helpful discussions and for providing useful practical data and research materials.

The author owes a special debt of gratitude to his family who, for the third time, provided unwavering support.

The author also acknowledges the following private communications:

Definition of Terms

Acceleration: The change of velocity as a function of time.

Ambient pressure: The atmospheric pressure acting at a given altitude.

Angle of incidence: The angle formed by the line which defines the shock propagation and between the centre of explosion and the point on the structure.

Attenuation: The decrease in intensity of a blast wave as a result of absorption of energy.

Barrier: A protective structure.

Blast door: A protective closure for personnel and/or vehicles.

Blast effect (or blast output): The blast pressures and impulse produced by an explosion.

Blast loads: The forces, associated with the pressure output, or pressure acting on structures.

Blast shield: A protective closure device for ventilation openings.

Blast valve: A mechanical and electrical protective closure device for ventilation openings.

Blast wave: A pulse of air in which the pressure increases sharply at the front and is accompanied by blast winds, propagated from an explosion. See **Shock wave**.

Burst: An explosion located on or close to the structure or at a distance away from the structure.

Casing (or container): A metal or any other covering which partially or fully encloses an explosive.

Charge weight (or charge):

  Actual: The total weight of an explosive.

  Effective: The net weight of an explosive involved in the detonation process.

  Equivalent: The weight of a spherical TNT charge which will produce the same blast effects as the explosive under consideration.

Cubicle: An area which is partially or fully enclosed by blast-resistant walls and roof.

Deflagration: Rapid and violent burning.

Degree of freedom: The number of independent displacement variables needed to specify the configuration of a dynamic system.

Degree of protection: A scale which is used to measure the required protection.

Detonation:

   Simultaneous: A detonation of separated quantities of explosives or ammunition occurring very nearly at the same time.

   Mass: Similar to a simultaneous detonation except that the explosives involved are of large quantity.

Direct spalling: The dynamic disengagement of the concrete surface of a structural component.

Donor explosive: The explosive contained in the explosion protective system, called a donor system.

Drag coefficient: The drag pressure divided by the dynamic pressure; it is dependent upon the shape of the structure.

Drag loading (or drag pressure): The force on a structure due to the transient winds accompanying the passage of a blast wave.

Ductile mode: The response of a structural element to attain relatively large inelastic deflections without complete collapse.

Ductility factor: The ratio of the maximum deflection to the equivalent maximum elastic deflection of the structure.

Duration: The interval between the time of arrival of the blast wave and the time for the magnitude of the blast pressures to return to ambient pressure.

Dynamic increase factor: The ratio of the dynamic to static stresses of a material.

Effective mass: The mass of an equivalent single-degree-of-freedom system.

Elastic range: The response range of an element in which its deflections will essentially return to zero after removal of the load.

Elastic rebound: The elastic displacement of an element occurring in an opposite direction to that of the blast load.

Elasto-plastic range: The response range of an element which occurs after the formation of the first yield line.

Element (member): A component of a structure.

Equivalent dynamic system: A system which consists of a number of concentrated masses joined together by weightless springs and subjected to time-dependent concentrated loads.

Explosions:

   Unconfined: An explosion (air or surface burst) occurring exterior to a structure.

   Confined: An explosion occurring within or immediately next to a structure which is subdivided into several vents.

Multiple: Two or more explosions to be cumulative on the response of the structure.

Explosive: A chemical compound or mechanical mixture subjected to heat, friction and detonation (undergoes a very rapid chemical change) which exerts pressure in the surrounding medium.

Explosive protection system: A storage or a manufacturing facility containing potentially explosive material.

Fragment shield: A device which is composed of steel plates or other mass material which can be attached to or placed a short distance from a protective barrier.

Ground shock:
    Air-induced: Ground motions induced by a blast wave travelling over the ground surface and generating stress waves into the ground.
    Direct-transmitted: Ground motions induced in the ground in the immediate vicinity of the explosion, where it is then dispersed to areas of lower pressure level directly through the ground.

Haunch: A concrete fillet between two intersecting structural elements.

Impulse/impact: Sudden time-dependent load.

Impulse capacity:
    Flexural: The flexural impulse capacity responding in the ductile mode is the area under the resistance–time curve.
    Brittle: The impulse capacity (momentum) of the post-failure fragments must be added to the flexural impulse capacity.

Interior pressure: The pressures from an explosion within a barrier type structure which are amplified due to their multiple reflections.

Kinetic energy: The energy the structural element has by virtue of its motion (translational and/or rotational).

Lacing reinforcement: Continuous, bent diagonal bars which tie together the straight flexural reinforcing bars on each face of an element.

Load factor: The design factor (numerically equal to the resistance factor) by which the total load applied to a structure is multiplied to obtain the equivalent concentrated load for the equivalent single-degree-of-freedom system.

Load-mass factor: Mass factor divided by the load factor.

Mach front or mach stem: The shock front formed by the interaction of the incident and the reflected shock fronts accompanying an air burst.

Magazine: Any structure specifically designated for the storage of explosives, ammunition and loaded ammunition components.

Mass: The weight of a structural component divided by the acceleration due to gravity.

Mass factor: The design factor by which the total distributed mass of a structural element is multiplied to obtain the equivalent lumped mass of the equivalent single-degree-of-freedom system.

Mode of vibration: The dynamic deflection shape of a structure or its components produced by a specific loading.

Modular ratio: The ratio of the modulus of elasticity of structural steel to that of concrete.

Modulus of elasticity: The ratio of stress to strain in the elastic range of response of a structure.

Moment of inertia: The summation of the second moment of the area of a structure about its neutral axis.

Momentum: The product of the mass and velocity of an impactor or structural component.

Multiple reflections: The amplification of the blast wave pressures, produced by a partially confined explosion on various interior surfaces of a structure.

Natural frequency: The number of variations in one second a structure completes in its fundamental mode of vibration.

Natural period of vibration: The time interval during which a structure completes one vibration in its fundamental mode.

Normal distance: The distance measured between the centre of an explosion and a given location of the surface of a structure.

Partial failure: The failure of one or more supports of a structural element resulting in a loss of strength and a reduction in the resistance.

Penetration: A partial perforation but not extending to the other side.

Perforation: A complete penetration or hole from one side to another.

Phase:
  Positive: A period beginning with the arrival of the shock wave and ending with the two positive shock pressures at the level of the ambient pressure.
  Negative: A period from the ambient pressure, described in the 'positive case', to the ending of the negative shock pressures by returning back to the ambient value.

Post-failure fragments: Fragments formed upon failure of a structural element.

Post-ultimate range: The response occurring between partial and incipient failure of the structure.

Potential energy: The strain energy which results from the straining of an element produced by the blast loads.

Primary fragments: Fragments formed from casings, containers and other objects.

Propagation of explosion: A time-dependent movement of the explosion caused by a source.

Protective structure: A structure which is designed to provide protection.

Reflection factor: The ratio of the peak reflected pressure to its corresponding incident pressure.

Resistance: The sum of the internal forces in a structural element whose function is to resist movement of the mass produced by the blast loads. These forces occur at elastic, elasto-plastic, post-ultimate, rebound and ultimate conditions.

Resistance factor: Design factor multiplied by the structural resistance.

Safety distance: A distance at which the explosive can be placed and after detonation causes no destruction or risk of any kind to living beings and their facilities.

Safety factor: A factor used in design to account for unknown factors.

Scabbing: The dynamic disengagement of the concrete surface of an element resulting from a tension failure in the concrete normal to its free surface.

Separation distance: A minimum distance between possible explosions and a facility.

Shelter: A structure which encloses or nearly encloses the receiver system and is used to provide full protection.

Shock front: The sharp boundary between the pressure disturbance created by an explosion and the ambient atmosphere.

Shock wave: A continuously propagated pressure pulse in the surrounding medium produced by an explosion.

Slant distance: The distance between the centre of an explosion and a location on the ground.

Spalling: See **Direct spalling.**

Structural motion: The motion or dynamic displacement of a structure (with velocity and acceleration) caused by an impact or blast or both.

Time:

   Arrival: The finite time interval required for the blast wave to travel from the centre of an explosion to any particular location of the structure.

   Clearing: The finite time interval required for the blast pressures acting on a structure to reduce to some specified intensity.

   Response: The finite time interval required for the maximum deflection of a structure.

   Rise: The finite time interval required for the blast pressures acting on a structure to increase from zero to a maximum value.

TNT equivalent: A measure of the energy released in the explosion of a given quantity of material which would release the same amount of energy when exploded.

Total collapse: The condition of a structural element in which it completely loses its ability to resist the applied blast loads.

Triple point: The intersection of the incident and mach shock fronts accompanying an air burst.

Velocity: A distance travelled in a specific time; area under a distance–time curve.

Work: Force multiplied by distance.

Yield: Weapon detonation capacity.

Notation

A	Constant
A	Projected area, hardening parameter
A_0	Initial surface area
A_{ST}	Surface area of the enclosure
A_{V}	Vent area
$\bar{A}$	Normalized vent area
a	Radius of the gas sphere
a_0	Loaded length, initial radius of gas sphere
B	Burden
$[B]$	Geometric compliance matrix
BG	Blasting gelatine
b	Spaces between charges
b_1	Distance between two rows of charges
$C_{\mathrm{D}}, C_{\mathrm{d}}$	Drag coefficient or other coefficients
C_{d}'	Discharge coefficient
C_{f}	Charge size factor, correction factor
C_{l}	A coefficient which prevents moving rocks from an instant velocity
$[C_{\mathrm{in}}]$	Damping coefficient matrix
C_{p}	Specific heat capacity at constant pressure
C_{r}	Reflection coefficient
C_{v}	Specific heat capacity at constant volume
$c_{\mathrm{a}}, c_{\mathrm{l}}, c_{\psi}, c_{\theta}$	Coefficients for modes
D	Depth of floater, diameter
$[D]$	Material compliance matrix
D_{a}	Maximum aggregate size
D_{i}	Diameter of ice
D_{p}	Penetration depth of an infinitely thick slab
DIF	Dynamic increase factor

d	Depth, diameter
d_0	Depth of bomb from ground surface
E	Young's modulus
E_b	Young's modulus of the base material
ΔE_{er}	Maximum energy input occurring at resonance
E_{ic}	Young's modulus of ice
E_K	Energy loss
E_{na}	Energy at ambient conditions
E_{ne}	Specific energy of explosives
E_R	Energy release
E_t	Tangent modulus
e	Base of natural logarithm
e	Coefficient of restitution, efficiency factor
F	Resisting force, reinforcement coefficient
F_{ad}	The added mass force
$F_1(t)$	Impact
$F(t)$	Impulse/impact
F_s	Average fragment size, shape factor
f	Function
f	Frequency (natural or fundamental), correction factor
f_a	Static design stress of reinforcement
f_c	Characteristic compressive stress
f_c'	Static ultimate compressive strength of concrete at 28 days
f_{ci}^*	Coupling factor
f_d	Transmission factor
f_{dc}'	Dynamic ultimate compressive strength of concrete
f_{ds}	Dynamic design stress of reinforcement
f_{du}	Dynamic ultimate stress of reinforcement
f_{dyn}	Dynamic yield stress of reinforcement
f_{TR}^*	Transitional factor
f_u	Static ultimate stress of reinforcement
f_y	Static yield stress of reinforcement
G	Elastic shear modulus
G_a	Deceleration
G_f	Energy release rate
G_m, G_s	Moduli of elasticity in shear and mass half space
g	Acceleration due to gravity
H	Height
H_s	Significant wave height
HE	High explosion
HP	Horsepower
h	Height, depth, thickness

I	Second moment of area, identification factor
$[I]$	Identity matrix
I_1	The first invariant of the stress tensor
i_p	Injection/extraction of the fissure
J_1, J_2, J_3	First, second and third invariants of the stress deviator tensor
J_F, J	Jacobian
K	Vent coefficient, explosion rate constant, elastic bulk modulus
$[K_\mathrm{c}]$	Element stiffness matrix
K_p	Probability coefficients
K_s	Stiffness coefficient at impact
K_TOT	Composite stiffness matrix
K_W	Reduction coefficient of the charge
K_σ	Correction factor
KE	Kinetic energy
k_cr	Size reduction factor
k_r	Heat capacity ratio
k_t	Torsional spring constant
L	Length
L'	Wave number
L_i	Length of the weapon in contact
$\ln, \log_\mathrm{e}$	Natural logarithm
l_x	Projected distance in x direction
M	Mach number
$[M]$	Mass matrix
M'	Coefficient for the first part of the equation for a forced vibration
${}^*M_\mathrm{A}$	Fragment distribution parameter
M_p	Ultimate or plastic moment or mass of particle
m	Mass
N	Nose shaped factor
N_c	Nitrocelluloid
N_f	Number of fragments
N'	Coefficient for the second part of the equation for a forced vibration
NG	Nitroglycerine
n	Attenuation coefficient
P_i	Interior pressure increment
P_m	Peak pressure
P_u	Ultimate capacity
PE	Potential energy

PETN	Pentaerythrite tetra-nitrate
p	Explosion pressure
p_a	Atmospheric pressure
p_d	Drag load
p_df	Peak diffraction pressure
p_gh	Gaugehole pressure in rocks
p_pa	Pressure due to gas explosion on the interface of the gases and the medium
p_r	Reflected pressure
p_ro	Reflected overpressure
p_s'	Standard overpressure for reference explosion
p_so	Overpressure
p_stag	Stagnation pressure
Q_sp	Explosive specific heat (TNT)
q_do	Dynamic pressure
R	Distance of the charge weight gas constant, Reynolds number, Thickness ratio
R'	Radius of the shock front
$\{R(t)\}$	Residual load vector
R_T	Soil resistance
R_vd	Cavity radius for a spherical charge
$R_\mathrm{w}, r_\mathrm{s}$	Radius of the cavity of the charge
r	Radius
$r_\mathrm{o}, r_\psi, r_\phi$	Factors for translation, rocking and torsion
S_i	Slip at node i
S_{ij}	Deviatoric stress
S_L	Loss factor
$S_{\eta\eta}(f)$	Spectral density of surface elevation
s	$\pm i\omega t$ or distance or wave steepness, width, slope of the semi-log
T	Temperature, period, restoring torque
T_a	Ambient temperature
T_d	Delayed time
T_i'	Ice sheet thickness
T_ps	Post shock temperature
$[T'']$	Transformation matrix
TR	Transmissibility
t	Time
t_A	Arrival time
t_av	Average time
t_c	Thickness of the metal
t_d	Duration time
t_exp	Expansion time

t_i	Ice thickness
t_p	Thickness to prevent penetration, perforation
t_{sc}	Scabbing thickness, scaling time
t_{sp}	Spalling thickness
U	Shock front velocity
u	Particle velocity
V	Volume, velocity
V'	Velocity factor
V_{Rn}	Velocity at the end of the nth layer
v_b	Fragment velocity or normalized burning velocity
v_{bT}	Velocity affected by temperature
v_c	Ultimate shear stress permitted on an unreinforced web
v_{con}	Initial velocity of concentrated charges
v_f	Maximum post-failure fragment velocity
v_{in}, v_0	Initial velocity
v_l	Limiting velocity
v_m	Maximum mass velocity for explosion
v_p	Perforation velocity
v_{pz}	Propagation velocities of longitudinal waves
v_{RZ}	Propagation velocities of Rayleigh waves
v_r	Residual velocity of primary fragment after perforation or $\sqrt{E/\rho}$
v_s	Velocity of sound in air or striking velocity of primary fragment or missile
v_{so}	Blast-generated velocity at initial conditions
v_{su}	Velocity of the upper layer
v_{sz}	Propagation velocities of transverse waves
v_{szs}	Propagation velocity of the explosion
v'_{xs}	Initial velocity of shock waves in water
v_z	Phase velocity
v_{zp}	Velocity of the charge
W	Charge weight
$W^{1/3}, Y$	Weapon yield
W_t	Weight of the target material
w_a	Maximum weight
w_f	Forcing frequency
X	Amplitude of displacement
$\dot{X}$	Amplitude of velocity
$\ddot{X}$	Amplitude of acceleration
X_f	Fetch in metres
$X(x)$	Amplitude of the wave at a distance x
X_0	Amplitude of the wave at a source of explosion

x	Distance, displacement, dissipation factor
x	Relative distance
$\dot{x}$	Velocity in dynamic analysis
$\ddot{x}$	Acceleration in dynamic analysis
$\{x\}^*$	Displacement vector
x_{cr}	Crushed length
x_{i}	Translation
x_n	Amplitude after n cycles
x_{p}	Penetration depth
x_{r}	Total length
Z	Depth of the point on the structure
α	Cone angle of ice, constant for the charge
$\alpha_{\mathrm{a}}, \alpha_{\mathrm{l}}, \alpha_{\psi}$	Spring constants
α_{B}	Factor for mode shapes
α'	Angle of projection of a missile, constant
$\bar{\alpha}$	Constant
β	Constant for the charge, angle of reflected shock
$\bar{\beta}$	Constant
γ	Damping factor, viscosity parameter
γ_{f}	$\omega_{\mathrm{f}}/\omega$
δ	Particle displacements
$\overline{\delta}$	Pile top displacement
δ_{ij}	Kronecker delta
$\delta_{\mathrm{m}}, \delta'_{\mathrm{m}}, \delta''_{\mathrm{m}}$	Element displacement
δ_{ST}	Static deflection
δt	Time increment
ε	Strain
$\dot{\varepsilon}$	Strain rate
ε_{d}	Delayed elastic strain
η	Surface profile
θ	Deflection angle
θ_{g}	Average crack propagation angle
λ	A constant of proportionality
μ_{f}	Jet fluid velocity
ν	Poisson's ratio
ρ_{a}	Mass density of stone
ρ_{w}	Mass density of water
σ	Stress
σ_{c}	Crushing strength
σ_{cu}	Ultimate compressive stress
σ_{f}	Ice flexural strength
$(\sigma_{\mathrm{nn}})^{\mathrm{c}}$	Interface normal stress
$(\sigma_{\mathrm{nt}})^{\mathrm{c}}$	Interface shear stress
σ_{pi}	Peak stress

σ_t	Uni-axial tensile strength
τ_o	Crack shear strength
ϕ	Phase difference
ψ	Circumference of projectile
ω	Circular frequency
l, m, n, p, q, r, s, t	Direction cosines
$X, Y, Z; x, y, z$	Cartesian co-ordinates
(ξ, η, ζ)	Local co-ordinates

Conversion Tables

Weight

1 g	= 0.0353 oz	1 oz	= 28.35 g
1 kg	= 2.205 lbs	1 lb	= 0.4536 kg
1 kg	= 0.197 cwt	1 cwt	= 50.8 kg
1 tonne	= 0.9842 long ton	1 long ton	= 1.016 tonne
1 tonne	= 1.1023 short ton	1 short ton	= 0.907 tonne
1 tonne	= 1000 kg	1 stone	= 6.35 kg

Length

1 cm	= 0.394 in	1 in	= 2.54 cm = 25.4 mm
1 m	= 3.281 ft	1 ft	= 0.3048 m
1 m	= 1.094 yd	1 yd	= 0.9144 m
1 km	= 0.621 mile	1 mile	= 1.609 km
1 km	= 0.54 nautical mile	1 nautical mile	= 1.852 km

Area

$1\,cm^2$	= 0.155 in^2	$1\,in^2$	= 6.4516 cm^2
$1\,dm^2$	= 0.1076 ft^2	$1\,ft^2$	= 9.29 dm^2
$1\,m^2$	= 1.196 yd^2	$1\,yd^2$	= 0.8361 m^2
$1\,km^2$	= 0.386 sq mile	1 sq mile	= 2.59 km^2
1 ha	= 2.47 acres	1 acre	= 0.405 ha

Volume

$1\,cm^3$	= 0.061 in^3	$1\,in^3$	= 16.387 cm^3
$1\,dm^3$	= 0.0353 ft^3	$1\,ft^3$	= 28.317 dm^3
$1\,m^3$	= 1.309 yd^3	$1\,yd^3$	= 0.764 m^3
$1\,m^3$	= 35.4 ft^3	$1\,ft^3$	= 0.0283 m^3
1 litre	= 0.220 Imp gallon	1 Imp gallon	= 4.546 litres
$1000\,cm^3$	= 0.220 Imp gallon	1 US gallon	= 3.782 litres
1 litre	= 0.264 US gallon		

Density

$1 \, \text{kg/m}^3 = 0.6242 \, \text{lb/ft}^3$ $1 \, \text{lb/ft}^3 = 16.02 \, \text{kg/m}^3$

Force and pressure

1 ton $= 9964 \, \text{N}$
$1 \, \text{lbf/ft}$ $= 14.59 \, \text{N/m}$
$1 \, \text{lbf/ft}^2$ $= 47.88 \, \text{N/m}^2$
$1 \, \text{lbf in}$ $= 0.113 \, \text{Nm}$
1 psi $= 1 \, \text{lbf/in}^2 = 6895 \, \text{N/m}^2 = 6.895 \, \text{kN/m}^2$
$1 \, \text{kgf/cm}^2 = 98070 \, \text{N/m}^2$
1 bar $= 14.5 \, \text{psi} = 10^5 \, \text{N/m}^2$
1 mbar $= 0.0001 \, \text{N/mm}^2$
1 kip $= 1000 \, \text{lb}$

Temperature, energy, power

$1 °\text{C} = 5/9(°\text{F} - 32)$ 1 J $= 1$ milli-Newton
$0 \, \text{K} = -273.16 °\text{C}$ 1 HP $= 745.7$ watts
$0 °\text{R} = -459.69 °\text{F}$ 1 W $= 1 \, \text{J/s}$
                                1 BTU $= 1055$ J

Notation

lb = pound weight   °R = Rankine
lbf = pound force   °F = Fahrenheit
in = inch   oz = ounce
cm = centimetre   cwt = one hundred weight
m   = metre   g   = gram
km = kilometre   kg = kilogram
d   = deci   yd = yard
ft   = foot   HP = horsepower
ha = hectare   W   = watt
s   = second   N   = Newton
°C = centigrade = Celsius   J   = Joule
K   = Kelvin

1

Accident Survey

1.1 Introduction

This chapter surveys impact and explosion in various fields ranging from the domestic environment to military warfare. It covers hurricane and tornado disasters, aircraft accidents and explosions in cars, houses and military establishments. Cases of impact on the ground, in water and in the air are given. The work is supported by numerous tables and photographs.

1.2 Wind, Hurricane and Tornado Generated Missiles

Wind, gales, hurricanes and tornadoes have caused disasters in a number of countries. There is always one country somewhere affected by them at any given time in any year. The great hurricane of 1987 (120 miles h^{-1}) in England and severe gales in 1990 (100 miles h^{-1}), hurricane "Hugo" (138 miles h^{-1}) and many others have caused death and damage. The extent of the damage to structures ran hundreds of thousands. Cars and boats were lifted into the air and dropped on other vehicles, others were damaged by structural missiles from nearby buildings or by falling trees. The storms caused widespread flooding, uprooted trees, damaged buildings, bridges and pylons and stressed air-sea rescue services to the limit as ships foundered in huge seas.

In Charleston, South Carolina, USA, where sea water was swept 10 miles inland, a 16 m (50 ft) yacht hit the side of a car parked in a downtown area. The same hurricane "Hugo", as shown in Fig. 1.1, continued to ravage Puerto Rico, forcing three planes at the airport to be twisted by multiple and repeated impacts. The costs in all three incidents ran into billions and many thousands were killed or injured. Missiles were ejected from a school building after the passage of hurricane "Hugo". In October 1989, hurricane-force winds in the UK caused an 18.3 m (60 ft) steel chimney to collapse on a car. The same hurricane caused two cars to collide in France, and in other Western countries 170 vehicles collided and 27,500 houses, buildings, bridges and other structures
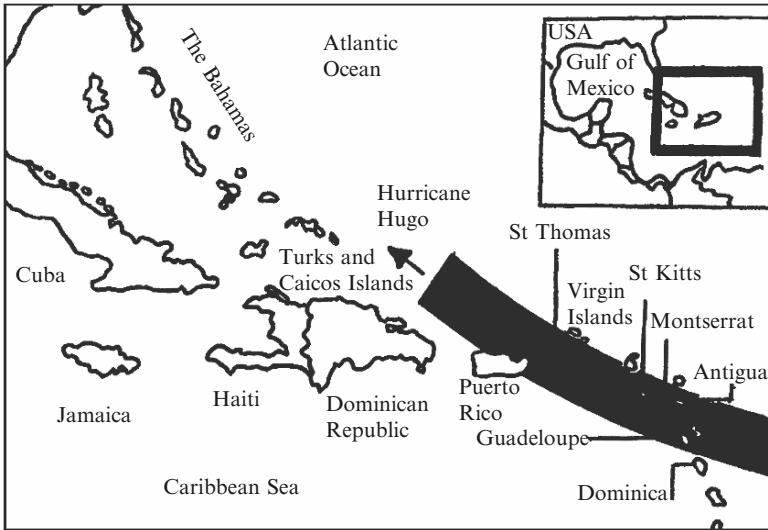
Fig. 1.1. The direction taken by hurricane "Hugo"

were damaged and many building components were ejected as missiles with speeds ranging from $5\,\mathrm{miles\,h^{-1}}$ to $1{,}500\,\mathrm{miles\,h^{-1}}$. Table 1.1 gives useful data on hurricanes, tornadoes, typhoons, blizzards and storms.

1.2.1 Wind Storm Statistics

Wind storms come within the natural disasters normally designated under hydro meteorological disasters. Table 1.2 gives data on the basis of particular contents.

1.3 Impact and Explosion at Sea

Much can be said on the subject of impact and explosion at sea. As for other incidents or accidents, it is extremely difficult to keep records of their daily or monthly occurrence. In December 1989, the 13,141 tonne North Sea ferry *Hamburg* collided with the 10-year-old roll-on roll-off cargo vessel *Nordec Stream* (8,026 tonnes) at the mouth of the River Elbe, about 25 miles off the coast of West Germany. The number of casualties was lower. In the same period two helicopters were lost, one of them was on traffic and weather surveillance duties and the other was the North Sea Chinook helicopter carrying platform workers. In November 1988, the 3,500 tonne Swedish vessel *SAMO* smashed into the 120-year-old 250 m swing bridge near Goole. Heavy iron girders on one of the approach spans were buckled. Two of the bridge's five approach spans were pushed up to 10 m out of line, leaving just 50 mm of pier support to prevent one 30 m section falling into the river. The costs

Table 1.1. Hurricanes, tornadoes, typhoons, blizzards and storms in the USA and other countries

Date	Place	Deaths
Notable Tornadoes in the USA		
18/3/1925	Montana, Illinois, Indiana	689
12/4/1927	Rock Springs, Texas	74
9/5/1927	Arkansas, Poplar Bluff, Missouri	92
29/9/1927	St Louis, Missouri	90
6/5/1930	Hill & Ellis Co, Texas	41
21/3/1932	Alabama (series of tornadoes)	268
5/4/1936	Mississippi, Georgia	455
6/4/1936	Gainesville, Georgia	203
29/3/1938	Charleston, S Carolina	32
16/3/1942	Central to NE Mississippi	75
27/4/1942	Rogers & Mayes Co, Oklahoma	52
23/6/1944	Ohio, Pennsylvania, W Virginia Maryland	150
12/4/1945	Oklahoma, Arkansas	102
9/4/1947	Texas, Oklahoma, Kansas	169
19/3/1948	Bunker Hill & Gillespie, Illinois	33
3/1/1949	Louisiana, Arkansas	58
21/3/1952	Arkansas, Missouri, Tennessee (series)	208
11/5/1953	Waco, Texas	114
8/6/1953	Michigan, Ohio	142
9/6/1953	Worcester and vicinity, Massachusetts	90
5/12/1953	Vicksburg, Mississippi	38
25/5/1955	Kansas, Missouri, Oklahoma, Texas	115
20/5/1957	Kansas, Missouri	48
4/6/1958	Northwestern Wisconsin	30
10/2/1959	St Louis, Missouri	21
5 to 6/5/1960	SE Oklahoma, Arkansas	30
11/4/1965	Indiana, Illinois, Ohio, Michigan, Wisconsin	271
3/3/1966	Jackson, Mississippi	57
3/3/1966	Mississippi, Alabama	61
21/4/1967	Illinois, Michigan	33
15/5/1968	Midwest	71
23/1/1969	Mississippi	32
21/2/1971	Mississippi delta	110
26 to 27/5/1973	South midwest (series)	47
3 to 4/4/1974	Alabama, Georgia, Tennessee, Kentucky, Ohio	350
4/4/1977	Alabama, Mississippi, Georgia	22
10/4/1979	Texas, Oklahoma	60
3/6/1980	Grand Island, Nebraska (series)	4
2 to 4/3/1982	South midwest (series)	17
29/5/1982	S Illinois	10
18 to 22/5/1983	Texas	12
28/3/1984	N Carolina, S Carolina	67
21 to 22/4/1984	Mississippi	15

(*continued*)

Table 1.1. (continued)

Date	Place	Deaths
26/4/1984	Series Oklahoma to Minnesota	17
31/5/1985	New York, Pennsylvania, Ohio, Ontario (series)	90
22/5/1987	Saragosa, Texas	29

Hurricanes (H), typhoons (T), blizzards and other storms

11 to 14/3/1888	Blizzard, eastern USA	400
Aug–Sept 1900	H, Galveston, Texas	6,000
21/9/1906	H, Louisiana, Mississippi	350
18/9/1906	T, Hong Kong	10,000
11 to 22/9/1926	H, Florida, Alabama	243
20/10/1926	H, Cuba	600
6 to 20/9/1928	H, S Florida	1,836
3/9/1930	H, Dominican Republic	2,000
21/9/1938	H, Long Island, New York, New England	600
11 to 12/11/1940	Blizzard, USA, northeast, midwest	144
15 to 16/10/1942	H, Bengal, India	40,000
9 to 16/9/1944	H, N Carolina to New England	46
22/10/1952	T, Philippines	300
30/8/1954	H ("Carol"), northeast USA	68
5 to 18/10/1954	H ("Hazel"), eastern USA, Haiti	347
12 to 13/10/1955	H ("Connie"), Carolinas, Virginia, Maryland	43
7 to 21/8/1955	H ("Diane"), eastern USA	400
19/9/1955	H ("Hilda"), Mexico	200
22 to 28/9/1955	H ("Janet"), Caribbean	500
1 to 29/2/1956	Blizzard, Western Europe	1,000
25 to 30/6/1957	H ("Audrey"), Texas to Alabama	390
15 to 16/2/1958	Blizzard, Western Europe	171
17 to 19/9/1959	T ("Sarah"), Japan, S Korea	2,000
26 to 27/9/1959	T ("Vera"), Honshu, Japan	4,466
4 to 12/9/1960	H ("Donna"), Caribbean, eastern USA	148
11 to 14/9/1961	H ("Carla"), Texas	46
31/10/1961	H ("Hattie"), British Honduras	400
28 to 29/5/1963	Windstorm, Bangladesh	22,000
4 to 8/10/1963	H ("Flora"), Caribbean	6,000
4 to 7/10/1964	H ("Hilda"), Louisiana, Mississippi, Georgia	38
30/6/1964	T ("Winnie"), N Philippines	107
5/9/1964	T ("Ruby"), Hong Kong and China	735
11 to 12/5/1965	Windstorm, Bangladesh	17,000
1 to 2/6/1965	Windstorm, Bangladesh	30,000
7 to 12/9/1965	H ("Betsy"), Florida, Mississippi, Louisiana	74
15/12/1965	Windstorm, Bangladesh	10,000
4 to 10/6/1966	H ("Alma"), Honduras, southeast USA	51
24 to 30/9/1966	H ("Inez"), Caribbean, Florida, Mexico	293
9/7/1967	T ("Billie"), southwest Japan	347
5 to 23/9/1976	H ("Beulah"), Caribbean, Mexico, Texas	54

Table 1.1. (continued)

Date	Place	Deaths
12 to 20/12/1967	Blizzard, southwest USA	51
18 to 28/11/1968	T ("Nina"), Philippines	63
17 to 18/8/1969	H ("Camille"), Mississippi, Louisiana	256
30/7 to 5/8/1970	H ("Celia"), Cuba, Florida, Texas	31
20 to 21/8/1970	H ("Dorothy"), Martinique	42
15/9/1970	T ("Georgia"), Philippines	300
14/10/1970	T ("Sening"), Philippines	583
15/10/1970	T ("Titang"), Philippines	526
13/11/1970	Cyclone, Bangladesh	3,000,000
1/8/1971	T ("Rose"), Hong Kong	130
19 to 29/6/1972	H ("Agnes"), Florida to New York	118
3/12/1972	T ("Theresa"), Philippines	169
June–Aug 1973	Monsoon rains in India	1,217
11/6/1974	Storm Dinah, Luzon Island, Philippines	71
11/7/1974	T ("Gilda"), Japan, South Korea	108
19 to 20/9/1974	H ("Fifi"), Honduras	2,000
25/12/1974	Cyclone levelled Darwin, Australia	50
13 to 27/9/1975	H ("Eloise"), Caribbean, northeast USA	71
20/5/1976	T ("Olga"), floods, Philippines	215
25 and 31/7/1977	T ("Thelma"), T ("Vera"), Taiwan	39
27/10/1978	T ("Rita"), Philippines	c.400
30/8 to 7/9/1979	H ("David"), Caribbean, eastern USA	1,100
4 to 11/8/1980	H ("Allen"), Caribbean, Texas	272
25/11/1981	T ("Irma"), Luzon Island, Philippines	176
June 1983	Monsoon rains in India	900
18/8/1983	H ("Alicia"), southern Texas	17
2/9/1984	T ("Ike"), southern Philippines	1,363
25/5/1985	Cyclone, Bangladesh	10,000
26/10 to 6/11/1985	H ("Juan"), southeast USA	97
25/11/1987	T ("Nina"), Philippines	650
5/1/2007 to 2/1/2008	Tsunami, Hurricanes etc. U.S.A, Indian Ocean	51,000

exceeded £2.2 million. On 21 October 1988, the 6,300 tonne Greek cruiser *Jupiter* collided with an Italian oil tanker less than 1 mile out of Piraeus harbour at 14.30 GMT. A 3 m hole was created. People were injured. The impact/collision occurred at the side of the ship. After all possible lives had been saved, the ship was allowed to sink.

The collision between the cruise boat *Marchioness*, a 26.6 m long luxury vessel, and the Thames sand dredger *Bowbelle*, 1,880 tonnes and 76 m long, occurred on 20 August 1989. The accident happened at the point where the Thames passes through the heart of the city of London. Both were travelling down river, eastwards when the collision took place near Cannon Street Rail Bridge. The cruise boat *Marchioness*, carrying between 110 and 150 passengers, sank within minutes. A number of causalities were reported within 24 h of the collision. The *Marchioness* was brought to the surface by two cranes mounted on platform barges.

Table 1.2. Wind statistics based on individual contents

Wind storms (1994–2006)						
Africa		*America*		*Asia*		
Eastern	150	Caribbean	169	Eastern		295
Middle	50	Central	153	South-Central		290
Northern	70	Northern	152	South-East		283
Southern	75	Southern	24	Western		160
Western	85					
Total	430	Total	508	Total		1,028
	Europe			*Oceania*		
Eastern		92	Australia-New Zealand		100	
Northern		56	Melanesia		65	
Southern		169	Micronesia		50	
Western		432	Polynesia		40	
Total		749	Total		255	

In the last five decades, the total number of explosions which have occurred in sea-going vessels, including pleasure boats, merchant ships, warships, submarines and others, is around 100,000. In the two World Wars alone the number is 51% of this total value and does not include war damage. The human loss runs into hundred thousands. Table 1.3 gives a list of important sea-going vessels destroyed either by collision or by explosions, excluding war-damaged ones.

1.4 Car Collisions and Explosions

Car accidents statistics vary from country to country, taking into consideration both cars hitting other cars and other objects. Table 1.4 provides useful information on car accidents in chosen countries over a number of years. It is interesting to note that, owing to an increase in terrorist activity in 1980–1989, the number of cars blown up by bombs placed underneath or nearby reached 170,000 in 150 countries of the world. The greater part of this total was contributed by Beirut, Afghanistan, Indian Punjab, Northern Ireland and some South American countries.

1.5 Train Collisions and Impacts

Trains are subject to accidents. They collide with both one another and other objects. The causes are numerous, mostly signal failure, derailment and human error. Trains can also be subject to missile and rocket attack and can be destroyed by bombs and other detonators. Even trees and other heavy objects such as boulders, pylons and short-span bridge deck components can crash into them. Trains have collided with public vehicles at level crossings on a number

Table 1.3. Impacts, collisions and explosions of sea-going vessels

Date	Vessel/location	Deaths
March 1854	*City of Glasgow*; British steamer missing in North Atlantic	480
27/9/1854	*Arctic*; US (Collins Line) steamer sunk in collision with French steamer *Vesta* near Cape Race	285–351
23/1/1856	*Pacific*; US (Collins Line) steamer missing in North Atlantic	188–286
23/9/1858	*Austria*; German steamer destroyed by fire in North Atlantic	471
27/4/1863	*Anglo-Saxon*; British steamer wrecked at Cape Race	238
27/4/1865	*Sultana*; a Mississippi River steamer blew up near Memphis, Tennessee, USA	1,450
27/10/1869	*Stonewall*; steamer burned on Mississippi River below Cairo, Illinois, USA	200
25/1/1870	*City of Boston*; British (Inman Line) steamer vanished between New York and Liverpool	177
19/10/1870	*Cambria*; British steamer wrecked off Northern Ireland	196
7/11/1872	*Mary Celeste*; US half-brig sailed from New York for Genoa; found abandoned in Atlantic 4 weeks later in mystery of sea; crew never heard from; loss of life unknown	
22/1/1873	*Northfleet*; British steamer foundered off Dungeness, England	300
1/4/1873	*Atlantic*; British (White Star) steamer wrecked off Nova Scotia	585
23/11/1873	*Ville du Havre*; French steamer sunk after collision with British sailing ship *Loch Earn*	226
7/5/1875	*Schiller*; German steamer wrecked off Scilly Isles	312
4/11/1875	*Pacific*; US steamer sunk after collision off Cape Flattery	236
3/9/1878	*Princess Alice*; British steamer sank after collision on Thames River, Canada	700
18/12/1878	*Byzantin*; French steamer sank after Dardanelles collision	210
24/5/1881	*Victoria*; steamer capsized in Thames River, Canada	200
19/1/1883	*Cimbria*; German steamer sunk in collision with British steamer *Sultan* in North Sea	389
15/11/1887	*Wah Yeung*; British steamer burned at sea	400
17/2/1890	*Duburg*; British steamer wrecked, in the China Sea	400
19/9/1890	*Ertogrul*; Turkish frigate foundered off Japan	540
17/3/1891	*Utopia*; British steamer sank in collision with British ironclad *Anson*, off Gibraltar	562
30/1/1895	*Elbe*; German steamer sank in collision with British steamer, *Craithie*, in North Sea	332
11/3/1895	*Reina Regenta*; Spanish cruiser foundered near Gibraltar	400
15/2/1898	*Maine*; US battleship blown up in Havana Harbor, Cuba	260
4/7/1898	*La Bourgogne*; French steamer sunk in collision with British sailing ship *Cromartyshire* off Nova Scotia	549
26/11/1898	*Portland*; US steamer wrecked off Cape Cod	157

Table 1.3. (continued)

Date	Vessel/location	Deaths
15/6/1904	*General Slocum*; excursion steamer burned in East River, New York City, USA	1,030
28/6/1904	*Norge*; Danish steamer wrecked on Rockall Island, Scotland	620
4/8/1906	*Sirio*; Italian steamer wrecked off Cape Palos, Spain	350
23/3/1908	*Matsu Maru*; Japanese steamer sunk in collision near Hakodate, Japan	300
1/8/1909	*Waratah*; British steamer, Sydney to London, vanished	300
9/2/1910	*General Chanzy*; French steamer wrecked off Minorca, Spain	500
25/9/1911	*Liberté*; French battleship exploded at Toulon	285
5/3/1912	*Principe de Asturias*; Spanish steamer wrecked off Spain	500
14 to 15/4/1912	*Titanic*; British (White Star) steamer hit iceberg in North Atlantic	1,503
28/9/1912	*Kichemaru*; Japanese steamer sank off Japanese coast	1,000
29/5/1914	*Empress of Ireland*; British (Canadian Pacific) steamer sunk in collision with Norwegian collier in St. Lawrence River, Canada	1,014
7/5/1915	*Lusitania*; British (Cunard Line) steamer torpedoed and sunk by German submarine off Ireland	1,198
24/7/1915	*Eastland*; excursion steamer capsized in Chicago River, USA	812
26/2/1916	*Provence*; French cruiser sank in the Mediterranean	3,100
3/3/1916	*Principe de Asturias*; Spanish steamer wrecked near Santos, Brazil	558
29/8/1916	*Hsin Yu*; Chinese steamer sank off Chinese coast	1,000
6/12/1917	*Mont Blanc, Imo*; French ammunition ship and Belgian steamer collided in Halifax Harbor, Canada	1,600
25/4/1918	*Kiang-Kwan*; Chinese steamer sank in collision off Hankow	500
12/7/1918	*Kawachi*; Japanese battleship blew up in Tokayama Bay	500
17/1/1919	*Princess Sophia*; Canadian steamer sank off Alaskan coast	398
17/1/1919	*Cheonia*; French steamer lost in Straits of Messina, Italy	460
9/9/1919	*Valbanera*; Spanish steamer lost off Florida coast, USA	500
18/3/1921	*Hong Kong*; steamer wrecked in South China Sea	1,000
26/8/1922	*Nitaka*; Japanese cruiser sank in storm off Kamchatka, USSR	300
25/10/1927	*Principessa Mafaida*; Italian steamer blew up off Parto Seguro, Brazil	314
12/11/1928	*Vestris*; British steamer sank in gale off Virginia, USA	113
8/9/1934	*Morro Castle*; US steamer, Havana to New York, burned off Asbury Park, New Jersey, USA	134
23/5/1939	*Squalus*; US submarine sank off Portsmouth, New Hampshire, USA	26
1/6/1939	*Thetis*; British submarine sank in Liverpool Bay, England	99

Table 1.3. (continued)

Date	Vessel/location	Deaths
18/2/1942	*Truxtun* and *Pollux*; US destroyer and cargo ship ran aground and sank off Newfoundland	204
2/10/1943	*Curacao*; British cruiser sank after collision with liner *Queen Mary*	338
17 to 18/12/1944	Three US Third Fleet destroyers sank during typhoon in Philippine Sea	790
19/1/1947	*Himera*; Greek steamer hit a mine off Athens	392
16/4/1947	*Grandcamp*; French freighter exploded in Texas City Harbor, starting fires	510
Nov 1948	Chinese army evacuation ship exploded and sank off South Manchuria	6,000
3/12/1948	*Kiangya*; Chinese refugee ship wrecked in explosion south of Shanghai	1,100+
17/9/1949	*Noronic*; Canadian Great Lakes cruiser burned at Toronto dock	130
26/4/1952	*Hobson* and *Wasp*; US destroyer and aircraft carrier collided in Atlantic	176
31/1/1953	*Princess Victoria*; British ferry sunk in storm off Northern Irish coast	134
26/9/1954	*Toya Maru*; Japanese ferry sank in Tsugaru Strait, Japan	1,172
26/7/1956	*Andrea Doria* and *Stockholm*; Italian liner and Swedish liner collided off Nantucket	51
14/7/1957	*Eshghabad*; Soviet ship ran aground in Caspian Sea	270
8/7/1961	Portuguese ship ran aground off Mozambique	259
8/4/1962	*Dara*; British liner exploded and sank in Persian Gulf	236
10/4/1963	*Thesher*; US Navy atomic submarine sank in North Atlantic	129
10/2/1964	*Voyager, Melbourne*; Australian destroyer sank after collision with Australian aircraft carrier *Melbourne* off New South Wales	82
13/11/1965	*Yarmouth Castle*; Panamanian registered cruise ship burned and sank off Nassau	90
29/7/1967	*Forrestal*; US aircraft carrier caught fire off North Vietnam	134
25/1/1968	*Dakar*; Israeli submarine vanished in Mediterranean Sea	69
27/1/1968	*Minerve*; French submarine vanished in Mediterranean Sea	52
May 1968	*Scorpion*; US nuclear submarine sank in Atlantic near Azores	99
2/6/1969	*Evans*; US destroyer cut in half by Australian carrier *Melbourne*, South China Sea	74
4/3/1970	*Eurydice*; French submarine sank in Mediterranean near Toulon	57
15/12/1970	*Namyong-Ho*; South Korean ferry sank in Korea Strait	308
1/5/1974	Motor launch capsized off Bangladesh	250

Table 1.4. Data on car accidents (in thousands) in a number of countries

Year	UK	USA	France	Gulf	Indian subcontinent	Year	UK	USA	France	Gulf	Indian subcontinent
1926	124	110	110			1958	237	161	75	35	13
1927	134	135	135			1959	261	139	90	10	15
1928	148	131	155			1960	272	151	110	11	16
1929	152	131	131			1961	270	310	115	50	15
1930	157	–	–			1962	264	333	110	30	11
1931	181	161	133			1963	272	353	100	40	13
1932	184	131	115			1964	292	164	95	60	15
1933	192	133	115			1965	299	325	99	50	16
1934	205	100	100			1966	292	210	75	30	15
1935	196	75	125			1967	277	255	80	31	17
1936	199	35	110			1968	264	235	90	25	30
1937	196	40	115			1969	262	211	79	26	31
1938	196	–	–			1970	267	219	81	–	–
1939	–	–	–			1971	259	300	130	17	40
1940	–	–	–			1972	265	295	133	16	43
1941	–	–	131			1973	262	330	135	15	45
1942	–	–	–			1974	244	250	170	13	45
1943	–	–	–			1975	246	275	145	20	39
1944	–	115	171			1976	259	310	110	15	41
1945	–	–	–			1977	266	350	109	13	45
1946	–	–	–			1978	265	360	107	12	47
1947	–	131	–			1979	255	159	95	10	50
1948	–	–	–			1980	252	290	97	9	51
1949	147	100	116			1981	248	–	–	–	–
1950	167	150	–			1982	256	245	99	11	47
1951	178	100	89	15	30	1983	243	235	101	20	39
1952	172	75	75	20	15	1984	253	215	105	21	40
1953	186	85	61	15	15	1985	246	159	95	30	35
1954	196	91	65	31	10	1986	248	110	96	32	25
1955	217	110	39	15	9	1987	239	100	93	40	30
1956	216	130	45	71	11	1988	247	90	92	30	25
1957	219	135	79	75	12						

of occasions. Hundreds of such cases have occurred. Recent ones are included for the reader's perusal. In the month of October 1989, 10 people were killed and 65 injured when the first 10 bogies of the Howrah bound Indian Toofan Express were derailed. The bogies were badly damaged and came in contact with live wires after severe impact with electricity poles. Eight bogies were overturned and one fell into a ditch. In August 1989 a train in Mexico was derailed and fell into the river, causing 100 deaths. It is a classical example of an object impacting a water surface.

In May 1989, 75 deaths were reported in the Karnataka Express accident in India caused, presumably, by mechanical defects of one of the coaches. The train was on its way from Bangalore to Delhi. The 30 tonne locomotives were pulling 20 coaches (a 10,000 tonne load) along a steel track at a speed exceeding $100 \, \text{km h}^{-1}$. After derailment and impact, the wreckage of the express train is shown in Fig. 1.2. The past few years have been grim ones for the Indian railways. This accident is one of three major tragedies in three years. The other two occurred in Mancherial (Andhra Pradesh) and Perumon in Kerala in July 1988, causing 55 and 105 deaths, respectively. The size and scope of the operations of the Indian railways are awesome. Accidents are due
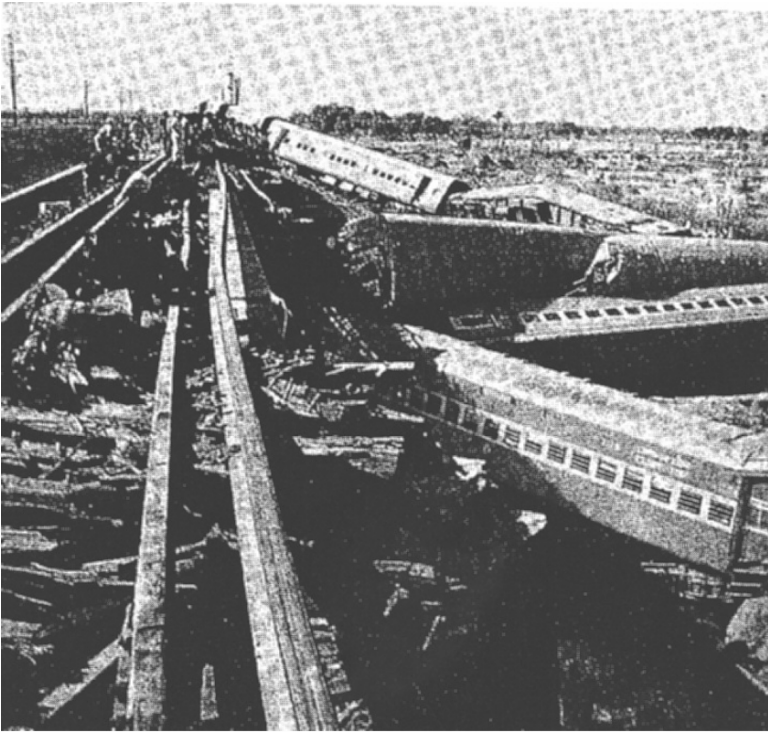
Fig. 1.2. Karnataka express train derailment and impacting objects. (courtesy of the Front Line, India)

Bournemouth
train

Basingstoke
train

Haslemere train
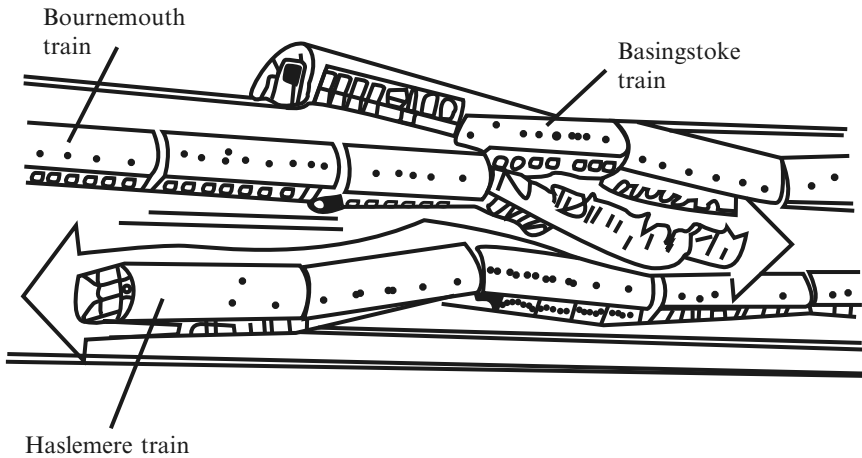
Fig. 1.3. The Clapham train disaster

to lack of administration and to an overwhelming increase in traffic – around 13,000 trains carry 10.3 million people daily through all manner of terrain and in all kinds of weather.

The Clapham (London) disaster is well remembered. This accident happened on 12 December 1988. The cause of the crash was established as faulty wiring on signaling equipment. The Basingstoke, Bournemouth and Haslemere trains were involved. The Bournemouth train ran into the back of the Basingstoke train. As illustrated in Fig. 1.3 the on-coming Haslemere train prevented worse carnage by absorbing the impact of the Bournemouth carriages and preventing some of them from overturning. In one year alone, more than 800,000 accidents were reported in 120 countries.

On March 1989, two London-bound trains collided outside Purley station. The bogies acted as an impactor on a nearby house, causing serious damage to the house lying under the embankment. On the same day a rail crash in Glasgow (Scotland) at the junction between a branch line and a main line resulted in injuries to a number of people. There has been a spate of accidents since 1984.

In England, 15 people were injured when two express trains collided outside Newcastle upon Tyne Central station on 30 November 1988; in the same month a driver was killed and 18 passengers hurt when a commuter train crashed at St. Helens, Merseyside.

In October 1987, four people died when a train fell into the swollen River Towey, in Wales, after a bridge collapsed. Fourteen were injured in the same month when two trains collided at Forest Gate on London's Liverpool Street Line.

On 26 July 1986, nine people died when a passenger train hit a van on a level crossing at Lockington, Yorkshire, UK. In September 1986, 60 people

were hurt and one killed in a collision between two express trains at Colwich, Staffordshire, UK. In December 1984, two people were killed when a passenger train hit a tanker train in Salford, UK.

Other major accidents have included 49 killed at Hither Green, southeast London, in November 1967, 90 killed at Lewisham, southeast London, in December 1965 and 112 killed at Harrow, northwest London, in October 1952.

Britain's worst rail crash was on 22 May 1915 when a troop train and a passenger train collided at Gretna Green, killing 227 people.

Another example of impact and direct collision occurred on the London – Bristol railway line when a passenger train overturned after hitting a derailed stone-quarry train near Maidenhead, Berks, England.

Later in the morning a mail van crashed into the parapet, sending masonry tumbling onto the tracks. The Paddington – Penzance train was too close to stop and ran into the same rubble.

The worst train disaster in Europe occurred on 12 December 1917 at Modane, France, killing 543 passengers.

In 1972, 60 people died in a crash near the Punjab town of Liaquatpur. In the nation's worst rail disaster, 225 people were killed and about 400 injured in Southern Pakistan, when a crowded passenger express train ploughed into a stationary freight train, destroying seven packed carriages. The collision occurred on 3 January 1990. The 16-carriage Zakaria – Bahauddin express with 1,500 passengers, was travelling at $635 \, \text{miles h}^{-1}$ when it smashed into the freight train. Trains in Pakistan, as in India, are always overcrowded and rail traffic has increased rapidly without a corresponding increase in investment.

Many rail accidents have occurred in the past, the ones described here are exceptional and recent. Table 1.5 gives a historical view of US train accidents.

1.6 Aircraft and Missile Impacts, Crashes and Explosions

Aircraft crashes are not uncommon. They happen for various reasons which will be elucidated later on in this section. To begin with, a few recent crashes, with and without explosions, will be discussed.

On 19 October 1988, the first Indian Airlines Boeing 737 aircraft, on routine flight from Bombay to Ahmedabad, inexplicably crashed into a stream 4 km short of the airport. It killed all but five of the 134 passengers. A chronological breakdown of the flight is given in Fig. 1.4. One hour later and 3,000 km away, a Vayudoot Fokker slammed into a hill near Guwahati, killing all 34 passengers. In the same year, two high-tech 2000S two trisonic MIG-25s and two Soviet-built transport AN-12 and AN-32 aircraft crashed while on various missions. Table 1.6 lists information on notable aircraft disasters. Table 1.7 summarizes accident data for various aircraft until the end of 2006.

If the aircraft does not break up in the air, it generally hits the ground at a certain angle. A typical example of a tangled wreckage of a Gulfstream Turbo

Table 1.5. Notable US train disasters

Date	Location	Deaths
29/12/1876	Ashtabula, Ohio	92
11/8/1880	Mays Landing, New Jersey	40
10/8/1887	Chatsworth, Illinois	81
10/10/1888	Mud Run, Pennsylvania	55
30/7/1896	Atlantic City, New Jersey	60
23/12/1903	Laurel Run, Pennsylvania	53
7/8/1904	Eden, Colorado	96
24/9/1904	New Market, Tennessee	56
16/3/1906	Florence, Colorado	35
28/10/1906	Atlantic City, New Jersey	40
30/12/1906	Washington DC	53
2/1/1907	Volland, Kansas	33
19/1/1907	Fowler, Indiana	29
16/2/1907	New York	22
23/2/1907	Colton, California	26
20/7/1907	Salem, Michigan	33
1/3/1910	Wellington, Washington DC	96
27/10/1925	Victoria, Missouri	21
5/9/1926	Waco, Colorado	30
24/8/1928	IRT subway, Times Square, New York	18
19/6/1938	Saugus, Montana	47
12/8/1939	Harney, Nevada	24
19/4/1940	Little Falls, New York	31
31/7/1940	Cuyahoga Falls, Ohio	43
29/8/1943	Wayland, New York	27
6/9/1943	Frankford Junction, Philadelphia, Pennsylvania	79
16/12/1943	Between Rennert and Buie, N Carolina	72
6/7/1944	High Bluff, Tennessee	35
4/8/1944	Near Stockton, Georgia	47
14/9/1944	Dewey, Indiana	29
31/12/1944	Bagley, Utah	50
9/8/1945	Michigan, North Dakota	34
25/4/1946	Naperville, Illinois	45
21/3/1910	Green Mountain	55
25/8/1911	Manchester, New York	29
4/7/1912	East Corning, New York	39
5/7/1912	Ligonier, Pennsylvania	23
5/8/1914	Tipton Ford, Missouri	43
15/9/1914	Lebanon, Missouri	28
29/3/1916	Amherst, Ohio	27
28/9/1917	Kellyville, Oklahoma	23
20/12/1917	Shepherdsville, Kentucky	46
22/6/1918	Ivanhoe, Indiana	68
9/7/1918	Nashville, Tennessee	101
1/11/1918	Brooklyn, New York	97

Table 1.5. (continued)

Date	Location	Deaths
12/1/1919	South Byron, New York	22
1/7/1919	Dunkirk, New York	12
20/12/1919	Onawa, Maine	23
27/2/1921	Porter, Indiana	37
5/12/1921	Woodmont, Pennsylvania	27
5/8/1922	Sulpher Spring, Missouri	34
13/12/1922	Humble, Texas	22
27/9/1923	Lockett, Wyoming	31
16/6/1925	Hackettstown, New Jersey	50
18/2/1947	Gallitzin, Pennsylvania	24
17/2/1950	Rockville Centre, New York	31
11/9/1950	Coshocton, Ohio	33
22/11/1950	Richmond Hill, New York	79
6/2/1951	Woodbridge, New York	84
12/11/1951	Wyuta, Wyoming	17
25/11/1951	Woodstock, Alabama	17
27/3/1953	Conneaut, Ohio	21
22/1/1956	Los Angeles, California	30
28/2/1956	Swampscott, Massachusetts	13
5/9/1956	Springer, New Mexico	20
11/6/1957	Vroman, Colorado	12
15/9/1958	Elizabethport, New Jersey	48
14/3/1960	Bakersfield, California	14
28/7/1962	Steelton, Pennsylvania	19
28/12/1966	Everett, Massachusetts	13
10/6/1971	Salem, Illinois	11
30/10/1972	Chicago, Illinois	45
4/2/1977	Chicago, Illinois (elevated train)	11
4/1/1987	Essex, Maryland	16

Commander impacting the ground. Table 1.8 is an extensive list of aircraft disasters due to ground impact.

At Ramstein Airshow in Germany (12 August 1988), during the ill-fated Freccie tri-colour display, the two sets of aircraft interlocked as they formed the heart-shaped loop in a manner shown in Fig. 1.5. The letter scheme gives the step-by-step revelation of the disaster. Such mid-air collisions have occurred in the past. A total of 1,476 aircraft were involved in such collisions from 19 December 1946 to September 1989. Table 1.9 gives data on mid-air collisions of some of the well known aircraft. Bird strikes of aircraft, according to the research carried out at Rutgers University, New Jersey, USA, are related to the jet noise. Table 1.10 lists the number of aircraft subject to bird strikes over a 10-year period or so.

On 8 June 1989, a MIG-29 at the Paris airshow hit the ground 90 m (300 ft) from the crowd. A sheet of flame shot from the starboard engine,

IC 113's FLIGHT TO DISASTER
(OCT 19, '88)

5.55 am
IC 113 with 134 people on board departs from Bombay 10 minutes late.

6.35 am
Captain O.M. Dalaya radios Ahmedabad control tower and says : "We are approaching".

6.41 am
Control tower gives clearance to IC 113 to descend. 'Fasten seat belts' sign switch on inside the aircraft.

6.47 am
Dalaya radios tower and says "I am outbound" meaning he is commencing the standard P-loop turn to line aircraft with runway.

6.50 am
Dalaya radios tower : "I am inbound. Will call when runway in sight."

6.52 am
Control tower radios Dalaya saying : "IC 113 where are you ? Request position." But gets no reply.

6.55 am
Eyewitnesses see aircraft looming overhead, hit high tension wires and clip trees before crashing.

7.45 am
Fire brigade reaches spot and begins rescue operations.

Control Tower

Ahmedabad Airport

1,700 feet

500 feet

4 km

Normal Flight Path.

Fig. 1.4. Indian Airlines IC 113's flight route (courtesy of India Today and Front Line, India)

Table 1.6. Notable aircraft disasters

Date	Aircraft	Site of accident
6/5/1937	German zeppelin Hindenburg	Burned at mooring, Lakehurst, New Jersey, USA
23/8/1944	US Air Force B-24	Hit school, Freckelton, England
28/7/1945	US Army B-25	Hit Empire State building, New York City, USA
30/5/1947	Eastern Airlines DC-4	Crashed near Port Deposit, Michigan, USA
20/12/1952	US Air Force C-124	Fell burned, Moses, Lake Washington, USA
3/3/1953	Canadian Pacific Comet Jet	Karachi, Pakistan
18/6/1953	US Air Force C-124	Crashed, burned near Tokyo
1/11/1955	United Airlines DC-6B	Exploded, crashed near Longmont, Colorado, USA
20/6/1956	Venezuelan Super-Constellation	Crashed in Atlantic off Asbury Park, New Jersey, USA
30/6/1956	TWA Super-Constellation, United DC-7	Collided over Grand Canyon, Arizona, USA
16/12/1960	United DC-8 jet, TWA Super-Constellation	Collided over New York City, USA
16/3/1962	Flying tiger Super-Constellation	Vanished in Western Pacific
3/6/1962	Air France Boeing 707 jet	Crashed on take off from Paris, France
22/6/1962	Air France Boeing 707 jet	Crashed in storm, Guadeloupe, West Indies
3/6/1963	Chartered Northwest Airlines DC-7	Crashed in Pacific off British Columbia, Canada
29/11/1963	Trans-Canada Airlines DC-8F	Crashed after take off from Montreal, Canada
20/5/1965	Pakistani Boeing 720-B	Crashed at Cairo airport, Egypt
24/1/1966	Air India Boeing 707 jetliner	Crashed on Mont Blanc, France/Italy border
4/2/1966	All-Nippon Boeing 727	Plunged into Tokyo Bay
5/3/1966	BOAC Boeing 707 jetliner	Crashed on Mount Fuji, Japan
24/12/1966	US military chartered CL-44	Crashed into village in South Vietnam
20/4/1967	Swiss Britannia turboprop	Crashed at Nicosia, Cyprus
19/7/1967	Piedmont Boeing 727, Cessna 310	Collided in air, Hendersonville, North Carolina, USA
20/4/1968	South African Airways Boeing 707	Crashed on take off, Windhoek, Southwest Africa
3/5/1968	Braniff International Electra	Crashed in storm near Dawson, Texas, USA
16/3/1969	Venezuelan DC-9	Crashed after take off from Maracaibo, Venezuela
8/12/1969	Olympia Airways DC-6B	Crashed near Athens, Greece, in storm
15/2/1970	Dominican DC-9	Crashed into sea on take off from Santo Domingo, Dominican Republic

(*continued*)

Table 1.6. (continued)

Date	Aircraft	Site of accident
3/7/1970	British chartered jetliner	Crashed near Barcelona, Spain
5/7/1970	Air Canada DC-8	Crashed near Toronto International Airport, Canada
9/8/1970	Peruvian turbojet	Crashed after take off from Cuzco, Peru
14/11/1970	Southern Airways DC-9	Crashed in mountains near Huntington, West Virginia, USA
30/7/1971	All-Nippon Boeing 727 and Japanese Air Force F-86	Collided over Morioka, Japan
4/9/1971	Alaska Airlines Boeing 727	Crashed into mountain near Juneau, Alaska
14/8/1972	East German Illyushin-62	Crashed on take off, East Berlin, Germany
13/10/1972	Aeroflot Illyushin-62	East German airline crashed near Moscow
3/12/1972	Chartered Spanish airliner	Crashed on take off, Canary Islands
29/12/1972	Eastern Airlines Lockhead Tristar	Crashed on approach to Miami International Airport
22/1/1973	Chartered Boeing 707	Burst into flames during landing, Kano Airport, Nigeria
21/2/1973	Libyan jetliner	Shot down by Israeli fighter planes over Sinai, Egypt
10/4/1973	British Vanguard turboprop	Crashed during snowstorm at Basel, Switzerland
3/6/1973	Soviet supersonic TU-144	Exploded in air near Goussainville, France
11/7/1973	Brazilian Boeing 707	Crashed on approach to Orly airport, Paris
31/7/1973	Delta Airlines jetliner	Crashed, landing in fog at Logan Airport, Boston, USA
23/12/1973	French Caravelle jet	Crashed in Morocco
3/3/1974	Turkish DC-10 jet	Crashed at Ermenonville near Paris, France
23/4/1974	Pan American 707 jet	Crashed in Bali, Indonesia
1/12/1974	TWA-727	Crashed in storm, Upperville, Virginia, USA
4/12/1974	Dutch chartered DC-8	Crashed in storm near Colombo, Sri Lanka
4/4/1975	Air Force galaxy C-5B	Crashed near Saigon, South Vietnam, after take off
24/6/1975	Eastern Airlines 727 jet	Crashed in storm, JFK Airport, New York City, USA
3/8/1975	Chartered 707	Hit mountainside, Agadir, Morocco
10/9/1976	British Airways Trident, Yugoslav DC-9	Collided near Zagreb, Yugoslavia
19/9/1976	Turkish 727	Hit mountain, southern Turkey
13/10/1976	Bolivian 707 cargo jet	Crashed in Santa Cruz, Bolivia

Table 1.6. (continued)

Date	Aircraft	Site of accident
13/1/1977	Aeroflot TU-104	Exploded and crashed at Alma-Ata, Central Asia
27/3/1977	KLM 747, Pan American 747	Collided on runway, Tenerife, Canary Islands
19/11/1977	TAP Boeing 727	Crashed on Madeira
4/12/1977	Malaysian Boeing 737	Hijacked, then exploded in mid-air over Straits of Johore
13/12/1977	US DC-3	Crashed after take off at Evansville, Indiana, USA
1/1/1978	Air India 747	Exploded, crashed into sea off Bombay, India
25/9/1978	Boeing 727, Cessna 172	Collided in air, San Diego, California
15/11/1978	Chartered DC-8	Crashed near Colombo, Sri Lanka
25/5/1979	American Airlines DC-10	Crashed after take off at O'Hare International Airport, Chicago, USA
17/8/1979	Two Soviet Aeroflot jetliners	Collided over Ukraine
31/10/1979	Western Airlines DC-10	Skidded and crashed at Mexico City Airport
26/11/1979	Pakistani Boeing 707	Crashed near Jidda, Saudi Arabia
28/11/1979	New Zealand DC-10	Crashed into mountain in Antarctica
14/3/1980	Polish Illyushin 62	Crashed making emergency landing, Warsaw, Poland
19/8/1980	Saudi Arabian Tristar	Burned after emergency landing, Riyadh, Saudi Arabia
1/12/1981	Yugoslavian DC-9	Crashed into mountain in Corsica
13/1/1982	Air Florida Boeing 737	Crashed into Potomac River after take off
9/7/1982	Pan-Am Boeing 727	Crashed after take off in Kenner, Louisiana, USA
11/9/1982	US Army CH-47 Chinook helicopter	Crashed during air show in Mannheim, Germany
1/9/1983	South Korean Boeing 747	Shot down after violating Soviet airspace
27/11/1983	Colombian Boeing 747	Crashed near Barajas Airport, Madrid, Spain
19/2/1985	Spanish Boeing 727	Crashed into Mount Oiz, Spain
23/6/1985	Air India Boeing 747	Crashed into Atlantic Ocean, south of Ireland
2/8/1985	Delta Airlines jumbo jet	Crashed at Dallas Fort Worth International Airport, USA
12/8/1985	Japan Airlines Boeing 747	Crashed into Mount Ogura, Japan
12/12/1985	Arrow Air DC-8	Crashed after take off in Gander, Newfoundland
31/3/1986	Mexican Boeing 727	Crashed northwest of Mexico City
31/8/1986	Aeromexico DC-9	Collided with Piper PA-28 over Cerritos, California, USA

Table 1.7. Accident data for a number of aircraft prior to 1988

Type	Total number
Airbus	24
Boeing 707/720 series	122
Boeing 727	157
Boeing 737	120
Boeing 747	100
Boeing 757	3
DHC-4	8
Douglas DC-3/C47	213
Douglas C54/DC-4	32
Douglas DC-7	7
Douglas DC-8	74
Douglas DC-9	105
Douglas DC-10	70
Fairchild	10
Fokker/Fairchild	
F-27	98
F-28	24
Gulfstream	15
Hawker Siddeley Trident	51
Hawker Siddeley BAe 748 series	71
Jetstream	13
Lockheed L-188 Electra	25
Lockheed L-382B Hercules	20
Lockheed L-18 Lodest	21
Lockheed L-1011 Tristar	33
Lockheed Volga	10
Miscellaneous	313
Sovict aircraft, Illusion	97
Vickers Vicount	40

indicating compressor failure. The aircraft rolled over to its right and plunged downwards.

The British Midland Boeing 737–400 is one of the world's newest and most sophisticated passenger aircraft. It was fresh from Boeing's Seattle factory, with only 518 flying hours on the clock. It was the latest version of the world's most popular jetliner. Either of the 10 tonne CFM56-3C power plants could have held the plane aloft as long as fuel lasted. At around 400 m from the airport, while travelling at approximately 150 miles per hour, the two engines were in trouble and the plane crashed on the M1 motorway and hit trees as it limped into East Midlands airport, with a loss of 44 lives.

The engine on the crashed 737–400s, a CFM56–3, is fitted to all Boeing 737–300s, which are operated by 39 airlines or aircraft leasing companies worldwide.

Table 1.8. Aircraft impact at ground level

Date	Aircraft	Location
15/1/1976	DC-4	Bogota, Colombia, South America
20/1/1976	HS748	Loja, USA
1/6/1976	TU-154	Malabo
1/8/1976	Boeing 707	Mehrabad, Iran
7/8/1976	Falcon	Acapulco, Mexico
19/9/1976	Boeing 727	Isparta, Italy
22/9/1976	DHC-6	Mosher, Iran
26/9/1976	Gulfstream	Hot Springs, USA
4/10/1976	DC-7C	Mount Kenya
23/11/1976	YS-11A	Greece
30/11/1976	DC-3	Victoria, Australia
30/12/1976	DC-4	Trujillo
6/1/1977	Gates Lear	Palm Springs, USA
14/1/1977	DHC-6	Terrace airport, British Columbia, Canada
18/1/1977	Gates Lear	Sarajevo, Yugoslavia
29/3/1977	DHC-6	Bainaha Valley, Indonesia
5/4/1977	DC-3	Edavli, India
10/4/1977	DC-3	Colombia, South America
13/5/1977	AN-12	Aramoun, Lebanon
20/7/1977	DC-3	Ethiopia
7/8/1977	DHC-6	El Bolson, Argentina
4/9/1977	Viscount	Cuenca, Ecuador
6/9/1977	DHC-6	Alaska, USA
23/10/1977	DC-3	Manidar, Iran
21/11/1977	BAC 1–11	San Carlos de Bariloche, Argentina
11/12/1977	He111	Cercedilla, Spain
13/12/1977	DC-3	Evansville, USA
18/12/1977	DC-8	Salt Lake City, USA
29/12/1977	Viscount	Cuenca, Ecuador
28/1/1983	DC-3	Cerro Grenada, Colombia, South America
14/8/1978	C-46	Tota, Colombia, South America
27/8/1978	DC-6	Muscat, Oman
9/9/1978	–	Mexico City, Mexico
21/11/1978	DC-3	Rubio, Venezuela
4/12/1978	DHC-6	Steamboat Spring, USA
28/1/1979	F-27	Rodez, France
28/1/1979	DHC-6	Alaska, USA
6/3/1979	F-28	Ngadirejo Sukapur, Indonesia
23/4/1979	Viscount	Ecuador
11/7/1979	F-28	Mount Sebayat, Indonesia
26/7/1979	Boeing 707	Rio de Janeiro, Argentina
4/8/1979	HS748	Panvel, India
29/8/1979	DHC-6	Frobisher Bay, North-Western Territory
14/9/1979	DC-9	Cagliari, Italy
14/9/1979	DC-7C	Klamath Falls, USA

(continued)

Table 1.8. (continued)

Date	Aircraft	Location
21/11/1979	Arava	Navarino Island, Chile
28/11/1979	DC-10	Mount Erebus, Antarctica
19/12/1979	DC-4	Cerro Toledo, Colombia, South America
19/12/1979	DHC-6	Colombia, South America
23/12/1979	F-28	Ankara, Turkey
21/1/1980	Boeing 727	Teheran, Iran
22/1/1980	DHC-6	Kenai, Alaska, USA
23/1/1980	CASA 212	Cemonyet, Indonesia
12/4/1980	Boeing 727	Florianopolis, Brazil
24/4/1980	B-26 Invader	Slave Lake, Alberta
25/4/1980	Boeing 727	Tenerife
2/6/1980	F-27	Yacuiba, Bolivia
8/6/1980	Yak-40	Southern Angola
12/6/1980	Yak-40	Tadzhikistan
1/8/1980	DC-8	Mexico City
13/8/1980	Lear 35	Majorca
28/8/1980	CASA 212	Bursa, Turkey
24/11/1980	DC-3	Medellin, Colombia
18/1/1981	Skyvan	Guyana
20/1/1981	Beech 99	Spokane, Washington, USA
6/4/1981	DC-3	Laguna Soliz, South America
20/5/1981	Convair 440	Oaxaca, Mexico
24/7/1981	DHC-6	Madagascar
19/8/1981	HS748	Mangalore, India
26/8/1981	Viscount	Florencia, Colombia, South America
2/9/1981	EMB110 Bandeirante	Paipa, Colombia, South America
1/10/1981	Learjet	Felt, Oklahoma, USA
9/11/1981	DC-9	Acapulco, Mexico
1/12/1981	DC-9	Ajaccio, Corsica
18/12/1981	DHC-6	Lorica, Colombia, South America
11/1/1982	Learjet	Narssarssuma
9/2/1982	DC-3	Panay Island, Philippines
19/2/1982	DC-6	Cuginamarca, Colombia, South America
26/3/1982	Viscount	Qeuate, Colombia, South America
26/4/1982	Trident	Guilin, China
19/5/1982	Citation	Kassel
8/6/1982	Boeing 727	Fortaleza, Brazil
25/8/1982	CV440	Del Norte, Colorado
1/9/1982	DHC-4	Valladolid
12/10/1982	DC-3	Graskop, South Africa
29/11/1982	AN-26	ME Bibala, Angola
29/11/1982	DHC-6	Villavicencio
7/12/1982	Metro	Pueblo
3/1/1983	Challenger	Hailey, Idaho, USA
11/1/1983	DC-8	Detroit, USA

Table 1.8. (continued)

Date	Aircraft	Location
16/1/1983	DC-3	Bay City, USA
22/2/1983	Boeing 737	Manaus Airport
10/3/1983	–	Uruzgan
14/3/1983	Boeing 707	North of Sabha City, Indonesia
30/3/1983	Learjet 25	Newark, New Jersey, USA
6/4/1983	Learjet 35	Indianapolis, USA
16/4/1983	HS748	Khartoum, Sudan
23/6/1983	Lockheed 18	Millhaven, Georgia
1/7/1983	IL-62	Labe, Guinea
11/7/1983	Boeing 737	Cuenca, Ecuador
27/8/1983	Hercules	Dundo, Angola
7/10/1983	EMB-110	Uberaba
27/11/1983	Boeing 747	Madrid, Spain
18/12/1983	Airbus A300	Kuala Lumpur, Malaysia
24/1/1984	CASA C212	Lokon Mountain, Indonesia
3/4/1984	DHC-6	Quthing, Lesothe
5/5/1984	Beech 200	Poza Rica, Mexico
28/6/1984	Bandeirante	Macae, Brazil
15/8/1984	DC-3	Pass Valley, Indonesia
11/10/1984	DHC-6 Twin Otter	Mealy Mountain, USA
19/11/1984	Bandeirante	Inverness, Scotland
20/11/1984	DHC-6 Twin Otter	En route
22/12/1984	DHC-6	Bhojpur, India
1/1/1985	Boeing 727	La Paz, Bolivia
22/1/1985	Bandeirante	Buga, Colombia, South America
22/2/1985	DHC-6	Andes, Colombia, South America
18/2/1985	Boeing 727	Mount Oiz, Bilbao, South America
28/2/1985	F-28	Florencia, Colombia, South America
11/4/1985	HS125	Salta, Uruguay
15/4/1985	Boeing 737	Phuket, Thailand
22/4/1985	DC-6	Fitoy, France
21/5/1985	Citation 501	Harrison, Arkansas
27/5/1985	CV580	Oro Negro, Venezuela
19/6/1985	Merlin	Rock Springs, Texas
12/8/1985	Boeing 747	Mount Ogura, Japan
29/8/1985	Aeritalia G222	Sardinia
11/10/1985	DHC-6	Homer City, Pennsylvania, USA
22/10/1985	Learjet 24D	Juneau, Alaska, USA
18/1/1986	Caravelle	Santa Elena, Guatemala
20/3/1986	Casa 212	Manado, Northern Sulawesi, Indonesia
31/3/1986	Boeing 727	–
27/4/1986	DHC-6	Sarevena, Indonesia
12/6/1986	DHC-6	Port Ellen, Islay, Scottish Highlands
22/6/1986	DHC-6	Dembidollo, Ethiopia
19/7/1986	DC-6	Mont de la Plage

<div align="right">(continued)</div>

Table 1.8. (continued)

Date	Aircraft	Location
22/7/1986	MU-300 Diamond 1A	Sado Island
19/9/1986	EMB 120 Brasilia	Sao Jose dos Campos, Brazil
30/9/1986	DHC-6	Northern Sulawesi, Indonesia
2/10/1986	Falcon 10	Haenertsburg
3/10/1986	Skyvan	Manado
19/10/1986	TU-134A	Komatipoort, Swaziland
5/2/1987	Learjet 55	Jakiri, Cameroon
17/2/1987	Beech 200	Fukuoka, Japan
27/3/1987	Learjet 24	Eagle, Colorado, USA
19/5/1987	DHC-6	El Trompillo, Santo Cruz, Bolivia
21/6/1987	F-27	Pansauk, Burma
26/6/1987	HS748	Mount Ugo, Philippines
17/7/1987	Beech 200	Lake Tahoe, California, USA
11/10/1987	F-27	Turen Taung, China
15/10/1987	ATR42	Mount Crezzo
19/10/1987	Beech 200	Leeds/Bradford, UK
13/12/1987	SD3-60	Iligan, Philippines
4/1/1988	Boeing 737	Izmir, Turkey
18/1/1988	C-46	Colorado Mountain, USA
18/1/1988	IL-18	Chongging, China
26/2/1988	Boeing 727	Northern Cyprus
17/3/1988	Boeing 727	Cucuta Camilo Daza, Colombia, South America
19/4/1988	Let L-410 Turbolet	Bagdarin, Iran
6/5/1988	DHC-7	Bronnoysund
24/5/1988	DC-6	–
24/5/1988	Learjet 35A	West Patterson, New Jersey, USA
16/6/1988	F-27	Northern Burma
17/6/1988	DHC-6	Tau, Samoa, Indonesia
14/7/1988	DHC-6	Battle Creek Mountain, Oregon, USA
31/8/1988	Bandeirante	Cerro de la Calera, Mexico
18/9/1992	Airbus PIA	Katmandu, Nepal
4/10/1992	Boeing 747-200F	Amsterdam, The Netherlands
Accidents due to tyre burst at ground level		
11/3/1978	L-188	Fort Myers, USA
22/12/1980	L-1011	State of Qatar
27/6/1983	L-1011	London, Gatwick, UK
16/11/1983	Boeing 727	Miaimi, Florida, USA
3/5/1987	A-300	Athens, Greece

Since 1984, when they first came on line, Boeing has delivered 488 737–300s with CFM56–3 engines to many prestigious airlines, including Air Europe, KLM, Lufthansa and Sabena.
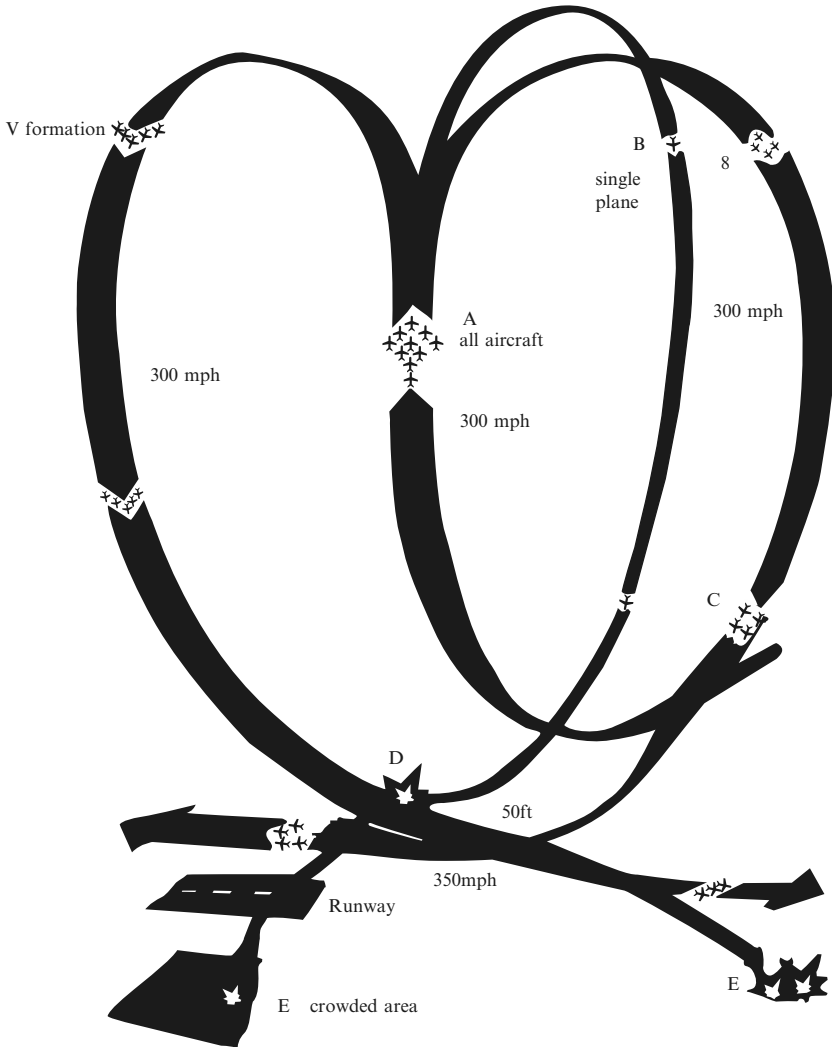
Fig. 1.5. Heart-shaped formation by jets. C – two formations aimed to complete the heart shape by passing each other in opposite directions. D – two groups of five planes just passed the group of four planes flying too low. E – Straight ahead, a solo plane changed direction

The same CFM56–3 engine prototype, developed jointly by Snecma, a French company, and General Electric, USA, is also fitted to 737–400s – the crashed British Midland aircraft. Until the crash, 18 of these were flying, including two leased by British Midland, one by Air UK Leisure and one by Dan Air. All three companies grounded their 737–400s.

Such structural and other failures have occurred in the past and are listed earlier in this text.

Table 1.9. Mid-air collisions

Date	Aircraft	Location	Date	Aircraft	Location
18/3/1976	DC-8 / AN24	Havana, Cuba	7/3/1984	Beech 200	Benson, Carolina, USA
10/9/1976	Trident / DC-9	Zagreb, Yugoslavia	18/4/1984	Bandeirante / Bandeirante	Imperatriz, Brazil
9/4/1977	Nord 262 / Cessna 195	Reading, USA	3/5/1985	TU-134 / AN-2	Kvov, USSR
1/3/1978	F-28 / Trainer	Kano, Nigeria	12/8/1985	Beech 200 / Cessna U206F	Quinlan, Texas, USA
18/5/1978	Falcon 20 / Cessna 150	Memphis, USA	22/9/1985	Learjet 35A / Ultralight	Auburn, Alabama, USA
25/9/1978	Boeing 727 / Cessna 721	San Diego, USA	10/11/1985	Falcon 50	Cliffside Park, New Jersey, USA
17/2/1979	Boeing 707 / F-5	Over Taoyaun, Taiwan	5/3/1986	Learjet 35 / Learjet 24D	San Clemente Island
11/8/1979	TU-134 / TU-134	Dneprodzerkinsk, Ukraine	18/6/1986	DHC-6 / Bell 206	Grand Canyon, USA
6/8/1980	F-27 / Cessna 172	Bridgeport, Texas, USA	31/8/1986	DC-9 / PA28	Los Angeles, USA
17/4/1981	Jetstream / Cessna	Loveland, Colorado, USA	15/1/1987	Metro II / Mooney M20C	Salt Lake City, USA
18/7/1981	TU-206 / CL-44	Yerevan, USSR	16/6/1987	B737 / J-6	Fuzhou, China
19/1/1982	Swearingen SA226T	Rockport, Texas, USA	4/8/1987	DHC-6 / Cessna 172	Palmdale, California, USA
6/11/1982	Learjet 24 / Learjet 25	Elizabeth City, North Carolina, USA			

Table 1.10. Bird strikes

Date	Aircraft	Location
1/1/1976	DC-10	Kastrup
25/1/1976	Boeing 747	Istanbul, Turkey
6/2/1976	Lear	Palese airport
12/11/1976	Falcon	Naples, Italy
11/7/1977	Boeing 747	Tokyo, Japan
16/8/1977	Gates Lear	Baton Rouge, USA
18/1/1978	DC-9	Hamburg, Germany
18/2/1978	Boeing 747	Lyon, France
20/2/1978	Boeing 707	Sharjah
4/4/1978	Boeing 737	Gosselies, Belgium
25/7/1978	CV580	Kalamazoo, USA
26/7/1978	DC-3	Guatemala
26/5/1979	Boeing 727	Patna, India
19/10/1979	Merlin	Palo Alto, California
8/7/1980	Airbus A300	Lyon, France
–/10/1980	Yak-40	USSR
20/11/1980	Falcon	Kansas City, USA
7/4/1981	Learjet	Cincinnati, Ohio, USA
18/4/1981	YS-11	Sand Point, Alaska
1/9/1981	Fokker F26	Ornskoldsvit, Sweden
2/2/1982	Beech 200	Nairobi, Nigeria
15/2/1982	HS 125	Curitiba
17/8/1983	Lear 25	Wilmington, USA
1/10/1983	TU-134	Krasnodar
6/11/1983	CV580	Sioux Falls, USA
19/9/1984	Boeing 727	Kimberley, South Africa
6/11/1984	Boeing 737	Lasham
11/7/1985	Boeing 727	Bellevue, Nebraska, USA
7/12/1985	Boeing 737	Dublin, Eine
20/7/1986	Boeing 737	Wabush, Newfoundland, Canada
5/3/1987	Bandeirante	Norfolk, Nebraska, USA

In August 1989, a British tornado fighter bomber and two West German Air Force alpha jets collided during low flying exercises near the north German coast. Eye-witness said the tornado crashed in fields only 500 m from a village school. Similar cases of mid air collisions are given in Table 1.8.

On 19 November 1988, a MIG-21 belonging to the Indian Air Force crashed. The jet hit the houses near Nazamgarh in West Delhi (India).

On 1 December 1988, PA103, the Pan Am 747 which crashed in Scotland, was one of the oldest jumbo jets still flying. It was 15th out of 710 jumbo jets built by Boeing in Seattle and was delivered to Pan Am in February 1970. It had flown for 72,000 h and had completed 16,500 take-off and landing cycles, well below the 50,000 cycles that is considered high for a commercial jetliner. The town of Lockerbie suffered a direct hit. Forty houses were destroyed when

the wreckage fell. The 747 engines, acting as missiles, landed on two rows of houses, completely destroying them. A fireball 91 m (300 ft) high lit up the sky as the aircraft blew up. Houses 10 miles east of Dumfries and 15 miles north of the Scottish border simply disappeared in the explosions. Others were set ablaze or had their roofs blown off. On impact, pieces of wreckage carved a hole in the A47 road, blocking the route through the town, and cars driving past were set on fire. Eye-witnesses reported that the doomed aircraft fell from the sky, hit, in trailing flames, a small hill east of Lockerbie and broke up, somersaulting across the main A47 London–Glasgow road before crashing into houses. One section hit a petrol station while other parts of the wreckage were scattered over 10 miles.

The Boeing corporation has manufactured 740 of the 747 aircraft since 1969, of which 13 have crashed:

1. November 1974, a Lufthansa 747 crashed at Nairobi, 59 people died, pilot error was blamed.
2. June 1975, an Air France 747 crashed at Bombay and burnt on the tarmac, no fatalities.
3. May 1976, an Iranian Air Force 747 crashed at Madrid, 17 people died.
4. March 1977, Pan Am and KLM 747s collided in fog at Tenerife Airport.
5. January 1978, an Air India 747 overstretched on landing at Bombay and crashed into the water, 213 people died.
6. November 1980, a Korean Air 747 overstretched on landing at Seoul and crashed into water, 14 fatalities.
7. August 1983, a Pan Am 747 misjudged the landing at Karachi, no fatalities.
8. September 1983, a Korean Air 747 was shot down near the Soviet Union, 269 fatalities.
9. November 1983, an Avianca 747 landed short at Madrid, 183 people died.
10. June 1985, an Air India 747 was blown up off the Irish coast, 329 people died.
11. August 1985, a Japan Air Lines 747 crashed near Tokyo, 524 died.
12. November 1987, a South African Airways 747 crashed near Mauritius, 160 died; the cause was believed to be a chemical or explosives leak in the cargo hold.

Table 1.11 gives additional information on in-flight accidents caused by bombs hidden on aircraft.

On 20 September 1989, a US Air Boeing 737–400 crashed on take off at La Guardia Airport, New York, into the East River. This was a tyical example of an impact on a water surface. The plane broke into three after hitting the water. Many such accidents have occurred. Table 1.12 lists aircraft disasters which involved water impact within the last decade or so. The total number of aircraft involved in this type of accident since 1946 is 610.

Table 1.11. In-flight accidents due to secretion of bombs on aircraft

Date	Aircraft	Location	Date	Aircraft	Location
7/5/1949	DC-3	Philippines	20/11/1971	Caravelle	Formosa Strait
9/9/1949	DC-3	Quebec, Canada	26/1/1972	DC-9	Hermsdorf, Germany
13/4/1950	Viking	Hastings, UK	25/5/1972	Boeing 727	Panama/Miami
24/9/1952	DC-3	Mexico	15/6/1972	CV880	Pleiku
11/4/1955	L-749A	South China Sea	16/8/1972	Boeing 707	Rome/Tel-Aviv
1/11/1955	DC-6B	Longmont, USA	15/9/1972	F-27	Over Philippines
25/7/1957	CV240	Daggett	19/3/1973	DC-4	Ban Me Thuot, South Vietnam
19/12/1957	Armagnac	Central France	8/9/1974	Boeing 707	Ionian Sea
8/9/1959	DC-3	Mexico	15/9/1974	Boeing 727	Vietnam
6/1/1960	DC-6B	Bolivia	3/6/1975	BAC 1–11	Manila, Philippines
28/4/1960	DC-3	Venezuela	1/1/1976	Boeing 720B	Al Qaysumah, Egypt
22/5/1962	Boeing 707	Unionville, USA	6/10/1976	DC-8	Off Barbados
8/12/1964	C47	Bolivia	18/8/1978	BAC 1–11	Philippines
8/7/1965	DC-6B	British Columbia, Canada	7/9/1978	HS748	Colombo, Ceylon
22/11/1966	Dakota	Meijah/Aden	26/4/1979	Boeing 737	Trivandrum/Madras, India
29/6/1967	DC-6	Baranquilla/Bogota	15/11/1979	Boeing 727	Chicago/Washington, USA
12/10/1967	Comet 4B	100 miles east of Rhodes	9/9/1980	Boeing 727	Sacramento, California, USA
11/12/1967	Boeing 727	Chicago/San Diego, USA	21/12/1980	Caravelle	Riohaea, Colombia, South America
19/11/1968	Boeing 707	Over Gunnison, USA	11/8/1982	Boeing 747	Hawaii, USA
5/9/1969	HS748	Zamboanga, Africa	10/3/1984	DC-8	Ndjamena, Chad
22/12/1969	DC-6B	Nha Trang, Vietnam	23/1/1985	Boeing 727	Santa Cruz, Bolivia
21/2/1970	CV990	Wuerenlingen, Germany	2/4/1986	Boeing 727	Corinth, Greece
21/2/1970	Caravelle	Frankfurt, Germany	26/10/1986	A300–600	Kochi, Shikoku
14/3/1970	AN-24	Alexandria, Egypt	25/12/1986	Boeing 737	Arar, Saudi Arabia
21/4/1970	HS748	En route, France			
2/6/1970	F-27	En route, France			
26/8/1970	AN-24	En route, France			

Table 1.12. Aircraft impact on water

Date	Aircraft	Location	Date	Aircraft	Location
14/1/1976	Sabreliner	Recife, Brazil	8/5/1978	Boeing 727	Pensocola, USA
4/2/1976	DC-6	Santa Marta	12/5/1978	CV440	Shippingport, USA
2/4/1976	DC-3	Puerto Asis	22/7/1978	C46	Opalocka, USA
28/7/1976	IL-18	Bratislava	2/9/1978	DHC-6	Vancouver, Canada
16/9/1976	C46	Caribbean	21/9/1978	DC-3	Mantanzas, Cuba
6/10/1976	DC-8	Off Barbados	1/10/1978	DC-3	FT Walton Beach, Florida, USA
5/11/1976	DC-3	En route	5/11/1978	DC-3	Mediterranean
22/11/1976	Skyvan	Das Island	18/11/1978	DHC-6	Marie Galante
16/12/1976	DHC-6	Juan de Fuca	29/11/1978	CV240	Miami, USA
8/2/1977	C46	San Juan, Puerto Rico	23/12/1978	DC-9	Palermo, Sicily, Italy
1/3/1977	DC-3	Aden	30/1/1979	Boeing 707	Pacific
6/5/1977	C46	Off Hollywood, Florida, USA	17/2/1979	F-27	Auckland, New Zealand
28/5/1977	Yak 40	Genoa, Italy	10/3/1979	Nord 262	Los Angeles, USA
30/6/1977	L188	San Joe Maiquetia	17/3/1979	DHC-4	Barbados
17/7/1977	YS-11A	off Macton Island	17/5/1979	DC-4	Gulf of Mexico
25/7/1977	HFB320	Adjivou, Ivory Coast	11/6/1979	DC-3	Selwey River, Idaho
24/8/1977	C46	Guadeloupe	14/6/1979	DC-4	Eagle Lake, Maine
2/9/1977	CL-44	Hong Kong	7/7/1979	Lockheed	Aruba
7/11/1977	Sabre 40	New Orleans	20/7/1979	DC-6	Kingston, Jamaica
19/11/1977	Learjet	Gunabara Bay, Brazil	31/7/1979	HS748	Sumburgh
18/12/1977	Caravelle	Funchal, Madeira	11/8/1979	Lear	Athens/Jeddah
1/1/1978	Boeing 747	Bombay, India	3/9/1979	Corvette	Nice, France
2/1/1978	DC-3	Rio Grande, Brazil	11/9/1979	Boeing 707	Taoyuan, Taiwan
22/2/1978	Lear 35	Rome/Palermo, Italy	1/11/1979	DHC-6	Big Trout Lake, Canada
3/3/1978	HS748	Macuto, Venezuela	4/3/1980	Lear 25	Port au Prince
23/3/1978	DC-3	Off Grand Turk	14/3/1980	IL-62	Warsaw, Poland
1/4/1978	CV240	Unguia, Colombia, South America			

Date	Aircraft	Location	Date	Aircraft	Location
13/5/1980	IL-14	Off Varadero, Cuba	5/8/1984	F-27	Zia, Dhaka, Bangladesh
19/5/1980	Gates Lear	Gulf of Mexico	7/8/1984	F-27	Rio de Janerio, Argentina
27/6/1980	DC-9	Off Palermo, Sicily, Italy	18/8/1984	DHC-6 Twin Otter	Tuktoyaktu, Canada
7/8/1980	TU-154	Nouadhibou	5/10/1984	Citation	Off Skiathos, Greece
12/9/1980	Boeing 727	Corfu airport	13/10/1984	Catalina PBT-6A	Brownsville, Texas, USA
12/9/1980	DC-3	Freeport, Bahamas	23/10/1984	DHC-4	Sable Island, Canada
15/9/1980	DC-6B	Haiti	31/10/1984	DC-3	Davao/Manila, Philippines
3/10/1980	DC-3	En route	10/11/1984	Learjet 24F	St. Thomas, Virgin Islands
28/11/1980	DC-6	Bimini, Bahamas	23/6/1985	Boeing 747	Atlantic, southwest of Ireland
28/3/1981	DC-4	St. Croix, Virgin Islands	27/6/1985	DC-10	San Juan, Puerto Rico
12/4/1981	DC-3	Mediterranean	17/9/1985	Merlin III	Gulf of Mexico
7/5/1981	BAC 1-11	River Plate Estuary	10/10/1985	IAI 1124 Westwind	Sydney, Australia
10/6/1981	Swearingen SA226T	Cameron, La	25/12/1985	DC-3	Cumana, Venezuela
17/6/1981	DC-3	Miraflores	16/2/1986	Boeing 737	Pescadores Islands, Taiwan
26/10/1981	Constellation	St. Thomas, Virgin Islands	22/7/1986	DC-3	San Juan, Puerto Rico
17/1/1982	Convair 440	Honolulu, Hawaii, USA	3/8/1986	DHC-6	Kingstown, St. Vincent
23/1/1982	DC-10	Boston, USA	9/9/1986	Merlin 3	McLainstow, Grand Bahamas
9/2/1982	DC-8	Tokyo, Japan	9/10/1986	DC-7	Dakar, Africa
11/3/1982	DHC-6	East of North Cape	28/10/1986	G73 Mallard	St. Croix
6/5/1982	Learjet	Savannah, Georgia, USA	23/12/1986	DC-4	Pacific Ocean
9/5/1982	DHC-7	Aden	7/2/1986	Bandeirante	East coast of Papua New Guinea
10/9/1982	Boeing 707	Khartoum, Sudan	31/8/1987	Boeing 737	Phuket, Africa
13/2/1983	Learjet 35A	Strait of Malacca	11/10/1987	Falcon 20	Keflavik, Africa
6/6/1983	Fairchild Packet	Taiwan Strait	28/11/1987	Boeing 747	Mauritius
8/12/1983	Citation	Stornoway			
28/2/1984	DC-10.30	New York, USA			
15/5/1984	Learjet 35	Ushuaia, Argentina			
4/8/1984	BAC 1-11	Tacloban airport, Philippines			

Table 1.13. Aircraft crashes due to electrical and power plant unit failures

Cause of crash	Number of aircraft
Aquaplaning/hydroplaning	33
Electrical system failure or malfunction	120
Failure of power units	550
Malfunction of flying control system	210
Fuel contamination, exhaustion	95
Instrumentation misreading/malfunction	33
Airframe failure	89
Doors and windows opening or failing flight	88
Inflight smoke/fire	220
Ground fire/missiles, dog fights	18,370

Crashes have occurred for other reasons, including failures in electrical and power plant units. The number of aircraft crashed since 1940 can be assessed from the data given in Table 1.13.

In war and in peace, an air force may intrude physically or send missiles into the airspace of other countries. Examples include the American missiles hitting the Libyan Air Force planes over the Mediterranian and the Iranian civilian plane in the Gulf, in 1989.

On 19 August 1981, a pair of US Navy F14 jet fighters shot down two attacking Soviet-built Libyan SU 22s about 60 miles from the Libyan coast. According to the Pentagon, the F14 pilots apparently saw the two Libyan jets about 5 miles away. Rather than turn away, one Libyan jet fired a Soviet-made Atoll air-to-air missile at the two F14s, while the other jet appeared to be moving into position to fire. The Atoll missed its target. Each US F14 then fired a Sidewinder missile, destroying both Libyan aircraft.

Since 1940, the number of missiles used has reached 300,000 plus. On 5 September 1989, a Pakistan Air Force F16 and a Norwegian F16 crashed. The Norwegian one was stolen by a Belgian technician. The plane left a crater.

Aircraft are also subject to hail impact or ice/snow accretion. Tables 1.14 and 1.15 list aircraft damaged by hail impact and ice/snow accretion, respectively. The total number of aircraft damaged by ice/snow accretion since 1946 is around 250.

A great deal of care is exercised to ensure that aircraft do not over-run or veer off the runway. Nevertheless, this has been a problem. Since 1946 there have been around 1,100 accidents of this type. Table 1.16 gives information on aircraft impact due to over-running or veering off the runway.

Other types of aircraft accidents include aircraft hitting ground vehicles, seagoing vehicles and sea birds, but these data are extremely difficult to find and consequently have not been included here. Insufficient information is available on crashes and missile/target interaction in some former communist countries.

Table 1.14. Aircraft damaged by hail impact

Date	Aircraft	Location
7/9/1946	DC-4	Chicago, USA
28/6/1947	York	Central France
14/9/1947	DC-6	Monclova
25/5/1948	DC-6	Midland, UK
12/6/1948	DC-3	Harrisburg, USA
25/5/1949	DC-6	Guadalupe
29/4/1950	DC-6	En route
27/6/1951	C54A-DC	Pueblo
19/7/1951	L-749	Richmond, USA
2/6/1952	L-049	Des Moines, USA
23/5/1954	L-049	Tucumcari, Africa
19/7/1956	Viscount	Chicago, USA
8/4/1957	Viscount	Norfolk, UK
26/9/1957	DC-4	En route
27/5/1959	Viscount	En route
1/11/1963	Caravelle	En route
9/5/1965	Boeing 707	Mineral Wells, USA
5/7/1965	Boeing 707	Texarkana
17/7/1971	DC-9	Venice, Italy
19/7/1971	DC-8	Haneda
21/3/1972	Boeing 720	Riyadh, Saudi Arabia
18/6/1975	Boeing 747	Over Greece
3/8/1975	DC-9	Buffalo, USA
17/7/1976	Boeing 747	Tokyo
4/4/1977	DC-9	New Hope, USA
31/7/1981	Boeing 727	Paris, France
22/9/1983	DC-3	South Africa
6/10/1983	BAC 1–11	Ezeiza, Argentina

The Lockheed C-130 has been in continuous production since 1954 and an average of three Hercules are produced every month. More than 1,800 have so far been produced. It is a needle-nosed, thin-winged aircraft with a huge belly and has a superb web of control systems redundancy such that they simply do not fail. The power levers, engines and utility systems have never let down the aircraft in great sweeping rises and long cruising flights. On 17 August 1988, a C-130 crashed and exploded near the Bahawalpur desert in Pakistan. The President and many Pakistani generals and US diplomats were killed. Normal weather conditions were reported. It is estimated that the angle of impact was around 30° to the vertical. The US/Pakistani report gives the height of fall as around 3,000 m. According to eye-witnesses, an explosion did occur and the report suggested the crash could have occurred due to the sudden death of the crew and passengers. The theory of the crash rests on the poisonous gas PTN (pentaerythrite tetra-nitrate), a gas explosive contained in a special flask which opens under pressure at a certain altitude, generally around 3,000 m.

Table 1.15. Aircraft damaged by ice/snow accretion

Date	Aircraft	Location
4/1/1977	Boeing 737	Frankfurt, Germany
13/1/1977	DC-8	Anchorage, USA
14/1/1977	Boeing 737	Frankfurt, Germany
15/1/1977	Viscount	Bromma airport
26/1/1977	Boeing 737	Oslo, Norway
31/1/1977	Chase C122	Anchorage, USA
21/2/1977	L-18	Truckee, USA
20/2/1978	Boeing 737	Hannover, Germany
7/3/1978	HS125	Dusseldorf, Germany
2/12/1978	DC-3	Des Moines, USA
4/12/1978	DHC-6	Steamboat Springs, Colorado, USA
4/12/1978	Gates Lear	Anchorage, USA
7/12/1978	Trident	Bovingdon
19/1/1979	Gates Lear	Detroit, USA
12/2/1979	Nord 262	Clarksburg, West Virginia, USA
19/11/1979	Citation	Castle Rock, Colorado, USA
23/11/1979	Twin Pioneer	Anchorage, USA
2/3/1980	B-26 Invader	California, USA
25/12/1980	Howard 500	Toronto, Canada
16/1/1981	DC-6B	Gambell, Alaska, USA
16/12/1981	Boeing 727	Gander, Newfoundland, Canada
13/1/1982	Boeing 737	Washington DC, USA
11/1/1983	Sabreliner	Toronto, Canada
12/3/1983	Metro II	–
21/12/1983	Beech 200	Detroit, USA
21/12/1983	Learjet 25	Kansas City, USA
13/1/1984	F-27	New York, USA
8/1/1985	SA227AC	Covington, Kentucky, USA
5/2/1985	DC-3	Charlotte, North Carolina, USA
5/2/1985	DC-9	Philadelphia, USA
11/2/1985	Jetstream 31	Macon, Georgia, USA
13/2/1985	SA226TC Metro II	Berkeley, Missouri, USA
12/3/1985	DHC-6	Bartar Island, Alaska, USA
15/12/1985	DC-3	Dillingham, Alaska, USA
15/12/1986	AN24	Lanzhou, China
18/1/1987	F-27	Castle Donington race track

1.6.1 Recent Investigations with NTSB Participation

The National Transportation Safety Board (NTSB) is the independent agency of the United States Government responsible for the investigation of transportation accidents. The NTSB participates in the investigation of aviation accidents and serious incidents outside the United States in accordance with the Chicago Convention of the International Civil Aviation Organization (ICAO) and the Standards and Recommended Practices (SARPS) provided in Annex 13 to the Convention.

Table 1.16. Aircraft impact due to over-running or veering off the runway

Date	Aircraft	Location
17/11/1977	Boeing 747	JFK airport, New York, USA
19/11/1977	Boeing 727	Funchal, Maderia, Spain
19/11/1977	Gates Lear	Rio de Janeiro, Argentina
5/1/1978	DHC-6	Leadville, USA
9/1/1978	Falcon	Riviere du Loup, Canada
24/1/1978	CV440	San Remon, Bolivia
24/1/1978	Boeing 737	Miri, Malaysia
12/2/1978	Boeing 737	Cranbrook, Canada
15/2/1978	HS748	Mirgan, Canada
28/2/1978	Sabreliner	International Falls, USA
1/3/1978	DC-10	Los Angeles, USA
3/3/1978	DC-8	Santiago de Compostela, Spain
30/3/1978	Gates Lear	Burbank, USA
4/4/1978	Boeing 737	Gosselies, Belgium
20/4/1978	CV580	Cleveland, USA
20/5/1978	Sabre 60	Sao Paulo, Brazil
25/5/1978	CV880	Miami, USA
8/6/1978	DC-3	Nashville, USA
26/6/1978	DC-9	Toronto, Canada
28/6/1978	IAI 1121	Aspen, Colorado
9/7/1978	BAC 1–11	Rochester, New York, USA
25/7/1978	DC-3	Pikangikum, Canada
31/7/1978	FH227	Chub Bay, Bahamas
29/8/1978	Boeing 747	Delhi, India
6/9/1978	CV880	Managua, Nicaragua
18/9/1978	DC-3	Komakuk, North-Western Territory
20/9/1978	DC-10	Monrovia, Liberia
7/10/1978	DC-3	Belo Horizonte, Brazil
15/10/1978	DC-3	Soddo, Ethiopia
24/10/1978	Lear 24D	Las Vegas, USA
25/10/1978	DC-3	Degahabour, Ethiopia
3/11/1978	Lear 24	Dutch Harbour, Alaska
14/11/1978	TU154	Stockholm, Sweden
17/12/1978	Boeing 737	Hyderabad, India
26/12/1978	Lear 26	Sao Paulo, Brazil
15/1/1979	Jetstream	Missoula, Montana, USA
21/7/1979	DC-3	Williamson, USA
22/1/1979	Jetstar	Concord, USA
23/1/1979	Boeing 707	Stansted, UK
26/1/1979	HS125	Taos, New Mexico, USA
29/1/1979	DHC-6	Eastmain airport, Canada
9/2/1979	DC-3	Hau Hau, Indonesia
15/2/1979	Boeing 747	Chicago, USA
3/3/1979	IAI 1124	Aspen, Colorado, USA
18/3/1979	DHC-6	Akiachak, Alaska, USA

(continued)

Table 1.16. (continued)

Date	Aircraft	Location
26/3/1979	IL-18	Luanda, Angola
1/4/1979	DHC-4	Bethel, Alaska
11/4/1979	Lockheed Vega 37	Belle Glade, Florida, USA
16/4/1979	Boeing 747	Frankfurt, Germany
23/4/1979	Boeing 727	Tunis
26/4/1979	Boeing 737	Madras, India
7/5/1979	DC-3	Sta Elena Peten, Guatemala
15/5/1979	DC-4	Mesa, Arizona, USA
6/6/1979	DC-6	Charleston, West Virginia, USA
21/6/1979	Constellation	Riviere Loup, Canada
21/6/1979	HS748	Mangalore, India
27/7/1979	DC-3	Bettles, Alaska, USA
31/7/1979	HS748	Sumburgh, Germany
16/9/1979	DHC-6	Resolute, North-Western Territory
7/10/1979	DC-8	Athens, Greece
25/10/1979	Viscount	Kirkwall, Orkney Islands
4/11/1979	Boeing 720	Multan, Pakistan
10/12/1979	HS125	Sassandra, Spain
5/1/1980	Lodestar	Palmyra Island
27/1/1980	Boeing 720	Quito, Ecuador
30/1/1980	FH227	Shingle Point, Yukon, China
31/3/1980	AN-24	Bessau
22/4/1980	DHC-6	Koartac, Canada
19/5/1980	Boeing 737	Dar-es-Salaam, Tanzania
4/6/1980	Boeing 707	Bangkok, Thailand
9/6/1980	Caravelle	Atlanta, USA
16/6/1980	Metro	Birmingham, Alaska, USA
21/6/1980	HS748	Chiang Rai, Thailand
30/6/1980	DC-3	Robb Lake, Canada
1/8/1980	DC-3	Smyrna Beach, Florida, USA
7/8/1980	Viscount	Leeds/Bradford, UK
2/9/1980	IAI 1124	Iowa City, USA
3/9/1980	Packet	Goodnews, Alaska, USA
6/9/1980	DHC-6	Seal River, Canada
10/9/1980	Learjet	Atlanta, USA
12/9/1980	Boeing 727	Corfu airport, Greece
16/9/1980	Learjet	Waukegan, Illinois, USA
22/9/1980	CV240	Okeechobee, Florida, USA
4/10/1980	Learjet	Aspen, Colorado, USA
28/10/1980	DC-10	Waukegan, Illinois, USA
11/11/1980	Boeing 727	Newark, New Jersey, USA
21/11/1980	Boeing 727	Yap Island, USA
5/12/1980	Metro	Moncton, Canada
12/1/1981	DC-10	Ujung, Pedang, China
17/1/1981	Boeing 737	Antwerp, Belgium

Table 1.16. (continued)

Date	Aircraft	Location
21/1/1981	Citation	Bluefield, West Virginia, USA
13/2/1981	Boeing 737	Madras, India
17/2/1981	Boeing 737	Santa Ana, California, USA
29/3/1981	Jetstar	Luton Airport, UK
13/5/1981	HS125	Semerang, Indonesia
15/5/1981	IL-18	Gdansk, Poland
23/5/1981	Short SC7 Skyvan	Alexander Lake, Alaska, USA
5/6/1981	F-27	Gilgit airport, Pakistan
1/8/1981	DHC-6	Sugluk, Canada
17/8/1981	Boeing 727	Fort Lauderdale, USA
19/8/1981	HS748	Mangalore, India
27/8/1981	DC-3	Dire Dawa, Arabian Desert
7/9/1981	Packet	Dahi Creek, Alaska, USA
15/9/1981	Boeing 747	Manila, Philippines
19/9/1981	HS748	Ndola
23/10/1981	Boeing 707	Tokyo, Japan
23/10/1981	C46	El Tiboy, Bolivia
31/10/1981	DHC-6	Bafoussam
7/12/1981	Airbus A300	Porto Alegre, Brazil
30/12/1981	C-46	San Juan, Puerto Rico
7/1/1982	IAI 1121	–
23/1/1982	DC-10	Boston, USA
3/2/1982	DC-10	Philadelphia, USA
12/2/1982	Howard 500	Fort Lauderdale, Florida, USA
15/2/1982	HS125	Curitiba, Spain
17/2/1982	Boeing 727	Miami, USA
17/2/1982	Boeing 737	Los Angeles, USA
12/3/1982	Citation	Chino, California, USA
24/3/1982	Boeing 707	Marana, Arizona, USA
5/4/1982	Swearingen SA226TC	Fort Wayne, Texas, USA
4/5/1982	L-1011	Santo Domingo
5/5/1982	Metro	Fort Wayne, Texas, USA
7/5/1982	DC-3	Calgary, Canada
12/5/1982	Boeing 727	Barcelona, Spain
18/5/1982	Gulfstream 1	Gillette, Wyoming, USA
24/5/1982	Learjet	Uberaba, Brazil
29/5/1982	DC3A	Sandwich, Illinois, USA
9/6/1982	F-27	Brisbane, Australia
22/6/1982	Boeing 707	Bombay, India
11/7/1982	HS748	Jolo, Brazil
1/8/1982	F-27	Kasese, Uganda
26/8/1982	Boeing 737	Ishigaki Island
6/9/1982	Boeing 737	Luxor, Egypt
13/9/1982	DC-10	Malaga, Spain
17/9/1982	DC-8	Shanghai, China

(continued)

Table 1.16. (continued)

Date	Aircraft	Location
29/9/1982	IL-62	Luxembourg
13/10/1982	HS125	Atlanta, USA
6/12/1982	Learjet	Paris, France
10/12/1982	HS748	Mande Sulawesi, Indonesia
17/12/1982	Metro	Montreal, Canada
20/12/1982	Metro III	Gillette, USA
7/1/1983	Boeing 727	Teheran, Iran
9/1/1983	Convair 580	Brainerd, France
10/1/1983	HS125	Paris, France
19/1/1983	IAI 123	Harrisburg, USA
6/2/1983	Learjet 24	St. Paul Island, Alaska, USA
11/2/1983	Merlin	Houston, USA
27/2/1983	Trident	Fuzhou, China
8/3/1983	Convair 580	Canada
13/3/1983	F-27	Sao Jose de Rio Preto, Brazil
19/4/1983	HS125	Gaspe, USA
2/6/1983	F-28	Branti, Italy
26/6/1983	HS125	Houston, Texas, USA
4/7/1983	HS748	Kasama
12/7/1983	Sabreliner	Flushing
16/7/1983	Gulfstream	Blountville, Tennessee, USA
4/8/1983	Boeing 747	Karachi, Pakistan
13/8/1983	DC-8	Sanaa, Yemen
24/8/1983	F-27	Calcutta, India
20/9/1983	Learjet	Massena
23/9/1983	Guarani II	Argentina
11/10/1983	Boeing 747	Frankfurt, Germany
18/10/1983	Boeing 747	Hong Kong
25/10/1983	DC-8	Norfolk, Virginia, USA
9/12/1983	HS125	Portland, USA
17/12/1983	EMB-110	Sao Pedro de Xingu, China
22/12/1983	Learjet	Eagle, Colorado, USA
16/1/1984	DC-3	Kissidouglas
27/1/1984	F-28	Pangkal, Indonesia
30/1/1984	Learjet 24	Santa Catalina, California, USA
4/2/1984	Canadair CL600	Little Rock, Arkansas, USA
6/2/1984	Sabreliner	St. Hubert, Canada
11/2/1984	Boeing 737	Tegal airport
22/2/1984	Bandierante	Cordova, Spain
28/2/1984	DC–10–30	New York, USA
28/2/1984	Citation I	Fitchburg, USA
2/3/1984	Beech 200	Vermil, USA
5/3/1984	HS748	Hyderabad, India
2/4/1984	Challenger	–
28/4/1984	DC-6	Arizona, USA

Table 1.16. (continued)

Date	Aircraft	Location
16/5/1984	Lockheed L382 Hercules	Palmerala, Honduras
16/6/1984	IL-18	Sanaa, Yemen
17/6/1984	Boeing 727	Pearson airport, Canada
24/6/1984	Boeing 707	Chicago, USA
7/7/1984	Citation I	Gualala, California, USA
21/7/1984	DHC-6 Twin Otter	Tau
28/7/1984	Learjet 25B	Waterville, USA
4/8/1984	BAC 1–11	Tacloban
7/8/1984	F-27	Rio de Janerio, Argentina
12/8/1984	DHC-6	Back Bay, USA
18/8/1984	HS748	Surabaya, Indonesia
24/8/1984	AN-12	Addis Ababa, Ethiopia
5/9/1984	Twin Otter	Newcastle, UK
7/5/1986	Learjet 24	Hollywood, Florida, USA
20/5/1986	Metro II	Hutchinson, Kansas, USA
21/5/1986	F-28	Puerto Asis, Colombia, USA
8/6/1986	Hercules	Dondo, Angola
20/7/1986	Boeing 737	Wabush, Newfoundland
25/7/1986	F-27	Tabou, Ivory Coast
26/7/1986	F-27	Sumbe, Angola
27/7/1986	Boeing 747	Changi, China
27/7/1986	Beech 200	Farmingdale, New York, USA
2/8/1986	HS 125	Bedford, Indiana, USA
6/8/1986	Learjet 55	Rutland, Vermont, USA
16/8/1986	Caravelle	Calabar, Nigeria
11/9/1986	Riley Heron	Vanua Mbalvu
29/9/1986	Sabreliner	Liberal, Kansas, USA
29/9/1986	A300	Madras, India
19/10/1986	DC-9	Copenhagen, Denmark
21/10/1986	Skyvan	Nightmute, Alaska
25/10/1986	Boeing 737	Charlotte, North Carolina, USA
30/10/1986	Boeing 727	Aeroparque, Buenos Aires
1/11/1986	Learjet 24	Lake Tahoe, California, USA
27/11/1986	Caravelle	Arauca
29/11/1986	DHC-6	San Juan, Puerto Rico
17/12/1986	SA226TC	Lidkoeping/Hovby
26/12/1986	B727	Istanbul, Turkey
3/1/1987	Metro II	Lidkoeping/Hovby
10/1/1987	DC-10	Ilorin, Nigeria
10/1/1987	Metro III	Yuma, Arizona, USA
14/1/1987	Learjet 35A	Lugano, Italy
27/1/1987	F-27	Varginha, Belgian Congo
25/2/1987	Sabreliner	East Alton, Illinois, USA
26/2/1987	Learjet 35	Centennial airport, Englewood, Colorado, USA
23/3/1987	CV580	Dallas, USA

(continued)

Table 1.16. (continued)

Date	Aircraft	Location
11/4/1987	Boeing 707	Manaus
6/5/1987	Catalina	Gander
26/5/1987	Jetstream	New Orleans, USA
20/6/1987	Falcon 20	Seletar, Singapore
21/6/1987	Blenheim	Denham, Germany
16/7/1987	Jet Commander	Jackson, Mississippi, USA
24/7/1987	BAe748	Jakarta
25/7/1987	Bandeirante	Santo Angelo
22/8/1987	Boeing 767	Scott AFB
24/8/1987	Merlin IIA	Riveire Madeline
8/9/1987	A310	Port Harcourt
19/9/1987	A300	Manila
21/9/1987	A300	Luxor, Egypt
23/9/1987	TU154	Moscow, Domodedovo
6/10/1987	Jetstream 31	Kennewick
28/10/1987	CV640	Bartlesville, Oklahoma, USA
13/12/1987	B737–300	Belo Horizonte

If an accident or serious incident occurs in a foreign state involving a civil aircraft of U.S. Registry, a U.S. operator, or an aircraft of U.S. design or U.S. manufacture, where the foreign state is a signator to the ICAO Convention, that state is responsible for the investigation. In accord with the ICAO Annex 13 SARPS, upon receipt of ICAO Notification of the accident or serious incident, the NTSB designates a U.S. Accredited Representative and appoints advisors to carry out the Obligations, receive the Entitlements, provided Consultation, and receive Safety Recommendations from the state of occurrence.

If an accident or serious incident occurs in a foreign state not bound by the provisions of Annex 13 to the ICAO Convention, or if a foreign state delegates all or part of an investigation by mutual consent to the NTSB, or if the accident or serious incident involves a public aircraft, the conduct of the investigation shall be in consonance with any agreement entered into between and the United States and the foreign state.

The official source for information on any ICAO aircraft accident or serious incident investigation rests with the state of occurrence. The data presented on this page is provided by the U.S. Accredited Representative and is intended only for informational purposes as a record of US participation for each specific event. Every attempt is made to confirm the information with the investigating authority of the state of occurrence prior to its appearance. However, for the most current official information, a hyperlink to the appropriate Web site of the foreign state is provided when available.

1.6.1.1 Aviation Accidents from More than 10 Years Ago

Note: only major reports are listed here – see Accident synopses for descriptions of all accidents in database

NTSB Home | Availability | Recent Accidents

Recent publications are available online in the Adobe Portable Document Format (PDF), which requires the free Acrobat Reader from Adobe for viewing. IMPORTANT: some PDF publications are quite large – see the summary description for each document to obtain file size.
(Questions/Problems/Tips)

Aircraft Accident Report: Uncontrolled Descent and Collision with Terrain, United Airlines Flight 585, Boeing 737-200, N999UA, 4 miles South of Colorado Springs Municipal Airport Colorado Springs, Colorado, 3 March 1991
NTSB Report Number: AAR-01-01, adopted on 3/27/2001 [Summary | PDF Document]
NTIS Report Number: PB2001-910401

Uncontrolled Descent and Collision With Terrain, USAir Flight 427, Boeing 737-300, N513AU Near Aliquippa, Pennsylvania, 8 September 1994
NTSB Report Number: AAR-99-01, adopted on 3/24/1999 [Summary | PDF Document]
NTIS Report Number: PB99-910401

Aircraft Accident Report: In-Flight Fire and Impact With Terrain Valujet Airlines Flight 592 DC-9-32, N904VJ Everglades, Near Miami, Florida, 11 May 1996
NTSB Report Number: AAR-97-06, adopted on 8/19/1997 [Summary | PDF Document]
NTIS Report Number: PB1997-910406

Aircraft Accident Report In-Flight Loss of Control and Subsequent Collision with Terrain CESSNA 177B, N35207 Cheyenne, Wyoming, 11 April 1996
NTSB Report Number: AAR-97-02, adopted on 3/11/1997 [Summary | PDF Document]
NTIS Report Number: PB97-910402

Aircraft Accident Report Wheels-Up Landing Continental Airlines Flight 1943 Douglas DC-9 N10556 Houston, Texas, 19 February 1996
NTSB Report Number: AAR-97-01, adopted on 2/11/1997 [Summary | PDF Document]
NTIS Report Number: PB97-910401

Ground Spoiler Activation in Flight/Hard Landing, Valujet Airlines Flight 558 Douglas DC-9-32, N922VV Nashville, Tennessee, 7 January 1996
NTSB Report Number: AAR-96-07, adopted on 11/11/1996 [Summary | PDF Document]
NTIS Report Number: PB96-910407

In-flight Loss of Propeller Blade Forced Landing, and Collision with Terrain Atlantic Southeast Airlines, Inc., Flight 529 Embraer EMB-120RT, N256AS, Carrollton, Georgia, 21 August 1995
NTSB Report Number: AAR-96-06, adopted on 11/26/1996 [Summary | PDF Document]
NTIS Report Number: PB96-910406

Collision with Trees on Final Approach American Airlines Flight 1572, McDonnell Douglas MD-83, N566AA, East Granby, Connecticut, 12 November 1995
NTSB Report Number: AAR-96-05, adopted on 11/13/1996 [Summary | PDF Document]
NTIS Report Number: PB96-910405

Runway Departure During Attempted Takeoff, Tower Air Flight 41 Boeing 747-136, N605FF, JFK International Airport, New York, 20 December 1995
NTSB Report Number: AAR-96-04, adopted on 12/2/1996 [Summary | PDF Document]
NTIS Report Number: PB96-910404

Uncontained Engine Failure/Fire Valujet Airlines Flight 597 Douglas DC-9-31, N908VJ, Atlanta, Georgia, 8 June 1995
NTSB Report Number: AAR-96-03, adopted on 7/30/1996 [Summary | PDF Document]
NTIS Report Number: PB96-910403

In-flight Icing Encounter and Loss of Control Simmons Airlines, d.b.a. American Eagle Flight 4184 Avions de Transport Regional (ATR) Model 72-212, N401AM, Roselawn, Indiana, 31 October 1994; Volume 1: Safety Board Report (Revision 9/13/02)
NTSB Report Number: AAR-96-01, adopted on 7/9/1996 [Summary | PDF Document]
NTIS Report Number: PB96-910401

In-flight Icing Encounter and Loss of Control Simmons Airlines, d.b.a. American Eagle Flight 4184 Avions de Transport Regional (ATR) Model 72-212, N401AM, Roselawn, Indiana, 31 October 1994; Volume II: Response of Bureau Enquetes
NTSB Report Number: AAR-96-02, adopted on 7/9/1996 [Summary | PDF Document]
NTIS Report Number: PB96-910402

Uncontrolled Collision with Terrain Flagship Airlines, Inc., dba American Eagle Flight 3379, BAe Jetstream 3201, N918AE Morrisville, North Carolina, 13 December 1994
NTSB Report Number: AAR-95-07, adopted on 10/24/1995
NTIS Report Number: PB95-910407

Runway Collision involving Transworld Airlines Flight 427 and Superior Aviation Cessna 441 Bridgeton, Missouri, 22 November 1994
NTSB Report Number: AAR-95-05, adopted on 8/30/1995
NTIS Report Number: PB95-910405

Uncontrolled Collision with Terrain Air Transport International Douglas DC-8-63, N782AL Kansas City International Airport Kansas City, Missouri, 16 February 1995

NTSB Report Number: AAR-95-06, adopted on 8/30/1995
NTIS Report Number: PB95-910406

Crash during Emergency Landing Phoenix Air Learjet 35A, N521PA Fresno, California, 14 December 1994
NTSB Report Number: AAR-95-04, adopted on 8/1/1995
NTIS Report Number: PB95-910404

Flight into Terrain during Missed Approach USAir 1016, DC-9-31, N954VJ Charlotte/Douglas International Airport Charlotte, North Carolina, 2 July 1994.
NTSB Report Number: AAR-95-03, adopted on 4/4/1995
NTIS Report Number: PB95-910403

Controlled Collision with Terrain Transportes Aereos Ejecutivos, S.A. (TAESA) Learjet 25D, XA-BBA Dulles International Airport Chantilly, Virginia, 18 June 1994.
NTSB Report Number: AAR-95-02, adopted on 3/7/1995
NTIS Report Number: PB95-910402

Runway Overrun Following Rejected Takeoff, Continental Airlines Flight 795 McDonnell Douglas MD-82, N18835 LaGuardia Airport Flushing, New York, 2 March 1994.
NTSB Report Number: AAR-95-01, adopted on 2/14/1995
NTIS Report Number: PB95-910401

Impact with Blast Fence upon Landing Rollout Action Air Charters Flight 990 Piper PA-31-350, N990RA Stratford, Connecticut, 27 April 1994.
NTSB Report Number: AAR-94-08, adopted on 12/13/1994
NTIS Report Number: PB94-910410

Stall and Loss of Control on Final Approach, Atlantic Coast Airlines, Inc./ United Express Flight 6291 Jetstream 4101, N304UE Columbus, Ohio, 7 January 1994.
NTSB Report Number: AAR-94-07, adopted on 10/6/1994
NTIS Report Number: PB94-910409

Overspeed and Loss of Power on both Engines During Descent and Power-Off Emergency Landing Simmons Airlines, Inc., d/b/a American Eagle Flight 3641, N349SB False River Air Park, New Roads, LA, 1 February 1994.
NTSB Report Number: AAR-94-06, adopted on 9/27/1994
NTIS Report Number: PB94-910408

Controlled Collision with Terrain Express II Airlines, Inc./Northwest Airlink Flight 5719 Jetstream BA-3100, N334PX Hibbing, Minnesota, 1 December 1993.
NTSB Report Number: AAR-94-05, adopted on 5/24/1994
NTIS Report Number: PB94-910407

Uncontrolled Collision with Terrain American International Airways Flight 808, Douglas DC-8-61, N814CK U.S. Naval Air Station Guantanamo Bay, Cuba, 18 August 1993.
NTSB Report Number: AAR-94-04, adopted on 5/10/1994
NTIS Report Number: PB94-910406

Controlled Flight into Terain Federal Aviation Administration Beech Super King Air 300/F, N82 Front Royal, Virginia, 26 October 1993.
NTSB Report Number: AAR-94-03, adopted on 4/12/1994
NTIS Report Number: PB94-910405

Pine Bluff, AR–April 29, 1993
NTSB Report Number: AAR94-02*, adopted on 3/15/1994
NTIS Report Number: PB94-910404

In-Flight Turbulence Encounter and Loss of Portions of the Elevators, China Airlines Flight C1-012 McDonnell Douglas MD-11-P Taiwan Registration B-150 about 20 miles East of Japan, 7 December 1992.
NTSB Report Number: AAR-94-02, adopted on 2/15/1994
NTIS Report Number: PB94-910403

Runway Departure Following Landing American Airlines Flight 102 McDonnell Douglas DC-10, N139AA Dallas/Fort Worth International Airport, Texas, 14 April 1993.
NTSB Report Number: AAR-94-01, adopted on 2/14/1994
NTIS Report Number: PB94-910402

Shelton, NE–April 28, 1993
NTSB Report Number: AAR94-01*, adopted on 1/19/1994
NTIS Report Number: PB94-910401

In-Flight Loss of Propeller Blade and Uncontrolled Collision with Terrain Mitsubishi MU-2B-60, N86SD Zwingle, Iowa, 19 April 1993.
NTSB Report Number: AAR-93-08, adopted on 11/16/1993
NTIS Report Number: PB93-910409

Inadvertent In-Flight Slat Development China Eastern Airlines Flight 583 McDonnell Douglas MD-11, B-2171 950 Nautical Miles South of Shemya, Alaska, 6 April 1993.
NTSB Report Number: AAR-93-07, adopted on 10/27/1993
NTIS Report Number: PB93-410408

In-Flight Engine Separation Japan Airlines, Inc., Flight 46E Boeing 747-121, N473EV Anchorage, Alaska, 31 March 1993.
NTSB Report Number: AAR-93-06, adopted on 10/13/1993
NTIS Report Number: PB93-410407

Midair Collision Mitsubishi MU-2B-60, N74FB, and Piper PA-32-301, N82419 Greenwood Municipal Airport Greenwood, Indiana, 11 September 1992.
NTSB Report Number: AAR-93-05, adopted on 9/13/1993
NTIS Report Number: PB93-910406

Aborted Takeoff Shortly After Liftoff Trans World Airlines Flight 843 Lockheed L-1011, N11002 John F. Kennedy International Airport Jamaica, New York, 30 July 1992.
NTSB Report Number: AAR-93-04, adopted on 3/31/1993
NTIS Report Number: PB93-910404

Controlled Collision with Terrain GP Express Airlines, Inc., Flight 861 A Beechcraft C99, N118GP Anniston, Alabama, 8 June 1992.

NTSB Report Number: AAR-93-03, adopted on 3/2/1993
NTIS Report Number: PB93-910403

Takeoff Stall in Icing Conditions USAIR Flight 405, FOKKER F-28, N485US LaGuardia Airport, Flushing, New York, 22 March 1992
NTSB Report Number: AAR-93-02, adopted on 2/17/1993
NTIS Report Number: PB93-910402

Block Island, RI–December 28, 1991
NTSB Report Number: AAR-93-01*, adopted on 4/27/1993
NTIS Report Number: PB93-910405

NTSB Report Number: AAR-93-01, adopted on 2/2/1993
NTIS Report Number: PB93-910401

United Airlines Flight 585, Boeing 737-291, N999UA, Uncontrolled Collision with Terrain for Undetermined Reasons, 4 miles South of Colorado Springs, Colorado, 3 March 1991. Revised report and probable cause issued as "NTSB/AAR-01/01"
NTSB Report Number: AAR-92-06, adopted on 12/8/1992
NTIS Report Number: PB92-910407

Air Transport International, Inc., Flight 805 Douglas DC-8-63, N794AL Loss of Control and Crash Swanton, Ohio, 15 February 1992.
NTSB Report Number: AAR-92-05, adopted on 11/19/1992
NTIS Report Number: PB92-910406

Britt Airways, Inc., d/b/a Continental Express Flight 2574 In-Flight Structural Breakup EMB-120RT, N33701 Eagle Lake, Texas, 11 September 1991.
NTSB Report Number: AAR-92-04, adopted on 7/21/1992
NTIS Report Number: PB92-910405

Atlantic Southeast Airlines, Inc. Flight 2311 Uncontrolled Collision with Terrain an Embraer EMB-120, N270AS Brunswick, Georgia, 5 April 1991.
NTSB Report Number: AAR-92-03, adopted on 4/5/1991
NTIS Report Number: PB92-910403

Explosive Decompression – Loss of Cargo Door in Flight, United Airlines Flight 811 Boeing 747-122, N4713U Honolulu, Hawaii, 24 February 1989. Revised
NTSB Report Number: AAR-92-02, adopted on 3/18/1992 [Summary]
NTIS Report Number: PB92-910402

Rome, GA–December 11, 1991
NTSB Report Number: AAR92-01*, adopted on 7/8/1992
NTIS Report Number: PB92-910404

L'Express Airlines, Inc., Flight 508 Beech C99, N7217L Weather Encounter and Crash near Birmingham, Alabama, July 10, 1991.
NTSB Report Number: AAR-92-01, adopted on 3/3/1992
NTIS Report Number: PB92-910401

Ryan intl Airlines DC-9-15, N565PC Loss of Control on Takeoff Cleveland-Hopkins intl Airport Cleveland, OH, 17 February 1991.

NTSB Report Number: AAR-91-09, adopted on 11/16/1991
NTIS Report Number: PB91-910410

Runway Collision of USAIR Flight 1493, Boeing 737 and Skywest Flight 5569 Fairchild Metroliner, Los Angeles, California, 1 February 1991.
NTSB Report Number: AAR-91-08, adopted on 10/22/1991
NTIS Report Number: PB91-910409

Fuel Farm at Stapleton International Airport Denver, Colorado, 25 November 1990.
NTSB Report Number: AAR-91-07, adopted on 10/1/1991
NTIS Report Number: PB91-910408

Aircraft Accident/Incident Summary Report: Midair Collision involving Lycoming Air Services Piper Aerostar PA-60 and Sun Company Aviation Department Bell 412, Merion, PA, 4 April 1991
NTSB Report Number: AAR91-01*, adopted on 9/17/1991
NTIS Report Number: PB91-910407

Unstabilized Approach and Loss of Controll NPA, Inc. dba United Express Flight 2415 British Aerospace BA-3101, N410UE, Tri-Cities Airport Pasco, Washington, 26 December 1989.
NTSB Report Number: AAR-91-06, adopted on 11/4/1991
NTIS Report Number: PB91-910406

NW Airlines, Inc., Flights 1482 and 299 Runway Incursion and Collision Detroit Metropolitan/Wayne County Airport Romulus, Michigan, 3 December 1990.
NTSB Report Number: AAR-91-05, adopted on 6/25/1991
NTIS Report Number: PB91-910405

Avianca, The Airline of Columbia, Boeing 707-321B, HK 2016, Fuel Exhaustion, Cove Neck, New York, 25 January 1990.
NTSB Report Number: AAR-91-04, adopted on 4/30/1991
NTIS Report Number: PB91-910404

Runway Collision of Eastern Airlines Boeing 727, Flight 111 and EPPS Air Service, Atlanta Hartsfield intl. Arpt. Atlanta, Georgia, 18 January 1990.
NTSB Report Number: AAR-91-03, adopted on 5/29/1991
NTIS Report Number: PB91-910403

Markair, Inc., Boeing 737-2X6C, N670MA Controlled Flight into Terrain, Unalakleet, Alaska, 2 June 1990.
NTSB Report Number: AAR-91-02, adopted on 1/23/1991
NTIS Report Number: PB91-910402

Grand Canyon Airlines Flight Canyon 5 DeHavilland Twin Otter, DHC-6-300, N75GC Grand Canyon National Park Airport Tusayan, Arizona, 27 September 1989.
NTSB Report Number: AAR-91-01, adopted on 1/8/1991
NTIS Report Number: PB91-910401

Issue 1 of 1989
NTSB Report Number: AAB-90-01, adopted on 12/18/1990
NTIS Report Number: PB90-916901

United Airlines Flight 232 McDonnell Douglas DC-10-10 Sioux Gateway Airport, Sioux City, Iowa, 19 July 1989
NTSB Report Number: AAR-90-06, adopted on 11/1/1990 [Summary]
NTIS Report Number: PB90-910406

Aloha Island Air, Inc., Flight 1712 DeHavilland Twin Otter, DHC-6-300, N707PV, Halawa Point, Molokai, Hawaii, 28 October 1989.
NTSB Report Number: AAR-90-05, adopted on 9/25/1990

USAIR Flight 105 Boeing 737-200, N283AU Kansas International Airport, Missouri, 8 September 1989.
NTSB Report Number: AAR-90-04, adopted on 9/11/1990
NTIS Report Number: PB90-910404

USAIR, Inc., Boeing 737-400 LaGuardia Airport Flushing, New York, 20 September 1989.
NTSB Report Number: AAR-90-03, adopted on 7/3/1990
NTIS Report Number: PB90-910403

Evergreen International Airlines McDonnell Douglas DC-9-33F, N931F Saginaw, Texas, 18 March 1989.
NTSB Report Number: AAR-90-02, adopted on 4/23/1990
NTIS Report Number: PB90-910402

United Airlines Flight 811 Boeing 747-122, N4713U Honolulu, Hawaii, 24 February 1989. SEE AAR-92-02 THIS IS SUPERSEDED
NTSB Report Number: AAR-90-01, adopted on 4/16/1990
NTIS Report Number: PB90-910401

Kenai, AK–December 23, 1987
NTSB Report Number: AAR89-03*, adopted on 9/30/1989
NTIS Report Number: PB89-910407

Delta Air Lines, Inc., Boeing 727-232, N473DA, Dallas-Fort Worth International Airport, Texas, 31 August 1988.
NTSB Report Number: AAR-89-04, adopted on 9/26/1989
NTIS Report Number: PB89-910406

Title: Belleville, II–August 22, 1987 Pensacola, FL–27 December 1987
NTSB Report Number: AAR89-02*, adopted on 6/30/1989
NTIS Report Number: PB89-910405

Aloha Airlines, Flight 243, Boeing 737-200, N73711, Near Maui, Hawaii, 28 April 1988.
NTSB Report Number: AAR-89-03, adopted on 6/14/1989 [Summary]
NTIS Report Number: PB89-910404

Kansas City, MO–April 13, 1987
NTSB Report Number: AAR89-01*, adopted on 3/31/1989
NTIS Report Number: PB89-910403

Horizon Air, Inc., DeHavilland DHC-8 Seattle-Tacoma International Airport Seattle, Washington, 15 April 1988.

NTSB Report Number: AAR-89-02, adopted on 3/6/1989
NTIS Report Number: PB89-910402

Trans-Colorado Airlines, Inc., Flight 2286 Fairchild Metro III, SA227 AC, N68TC, Bayfield, Colorado, 19 January 1988.
NTSB Report Number: AAR-89-01, adopted on 2/4/1989
NTIS Report Number: PB89-910401

Travis AFB, CA–8 April 1987
NTSB Report Number: AAR88-03*, adopted on 12/31/1988
NTIS Report Number: PB88-910414

Ryan Air Service, Inc. Flight 103, Beech Aircraft Corporation 1900C, N401RA, Homer, Alaska, 23 November 1987.
NTSB Report Number: AAR-88-11, adopted on 12/20/1988
NTIS Report Number: PB88-910413

Avair Inc. Flight 3378 Fairchild Metro III, SA227 AC, N622AV, Cary, NC, 19 February 1988.
NTSB Report Number: AAR-88-10, adopted on 12/13/1988
NTIS Report Number: PB88-910412

In-Flight Fire, McDonnell Douglas DC-9-83, N569AA, Nashville, Tennessee, 3 February 1988.
NTSB Report Number: HZM-88-02, adopted on 9/13/1988
NTIS Report Number: PB88-917006

Continental Airlines, Inc., Flight 1713 McDonnell Douglas DC-9-14, N626TX, Stapleton International Airport, Denver, Colorado, 15 November 1987.
NTSB Report Number: AAR-88-09, adopted on 9/27/1988 [Summary]
NTIS Report Number: PB88-910411

Fischer Bros. Aviation, Inc. dba NW Airlink, Flight 2268 Construcciones Aeronautics, S.A. (CASA) C-212-CC, N160FB, Detroit Metropolitan Wayne County Airport, Romulus, Michigan, 4 March 1987.
NTSB Report Number: AAR-88-08, adopted on 9/14/1988
NTIS Report Number: PB88-910410

Executive Air Charter, Inc. dba American Eagle, Flight 5452 CASA C-212, N432CA, Mayaguez, Puerto Rico, 8 May 1987.
NTSB Report Number: AAR-88-07, adopted on 8/2/1988
NTIS Report Number: PB88-910409

Air New Orleans, DBA Continental Express Flight 962, British Aerospace 3101 (Jetstream 31) N331CY, New Orleans intl Arpt., Kenner, Louisiana, 26 May 1987.
NTSB Report Number: AAR-88-06, adopted on 5/31/1988
NTIS Report Number: PB88-910408

Copperhill, TN–22 February 1986
NTSB Report Number: AAR88-02*, adopted on 3/30/1988
NTIS Report Number: PB88-910407

Northwest Airlines, Inc., McDonnell Douglas DC-9-82, N312RC, Detroit Metropolitan Wayne County Airport, Romulus, Michigan, 16 August 1987.

NTSB Report Number: AAR-88-05, adopted on 5/10/1988 [Summary]
NTIS Report Number: PB88-910406

Joe Foster Excavating, Inc., Bell 206B, N49606, In-Flight Collision with Trees, Alamo, California, 3 August 1986.
NTSB Report Number: AAR-88-04, adopted on 5/2/1988
NTIS Report Number: PB88-910405

Midair Collision of Skywest Airlines Swearingen Metro II, N163SW and Mooney M20, N6485U, Kearns, UT, 15 January 1987.
NTSB Report Number: AAR-88-03, adopted on 3/15/1988
NTIS Report Number: PB88-910404

Modena, Pennsylvania–17 March 1986 Redwater, Texas–4 April 1986
NTSB Report Number: AAR88-01*, adopted on 3/30/1988
NTIS Report Number: PB88-910403

Midair Collison of Cessna-340A, N8716K, and North American SNJ-4N, N71SQ, Orlando, Florida, 1 May 1987
NTSB Report Number: AAR-88-02, adopted on 2/16/1988
NTIS Report Number: PB88-910402

Midair Collision of U.S. Army U-21A, Army 18061, and Sachs Electric Company Piper PA-31-350, N60SE, Independence, Missouri, 20 January 1987.
NTSB Report Number: AAR-88-01, adopted on 2/3/1988
NTIS Report Number: PB88-910401

Newark, New Jersey–13 November 1986
NTSB Report Number: AAR87-04*, adopted on 12/30/1987
NTIS Report Number: PB87-910413

North Star Aviation, Inc. PA-32 RT-300, N39614 and Alameda Aero Club Cessna 172, N75584, Oakland, California, 31 March 1987.
NTSB Report Number: AAR-87-09, adopted on 10/27/1987
NTIS Report Number: PB87-910412

Des Moines, Iowa–25 November 1985 Chicago, Illinois–10 August 1986
NTSB Report Number: AAR87-03*, adopted on 9/30/1987
NTIS Report Number: PB87-910411

Piedmont Airlines Flight 467 Boeing 737-222, N752N, Charlotte Douglas intl Airport, Charlotte, NC, 25 October 1986.
NTSB Report Number: AAR-87-08, adopted on 9/1/1987
NTIS Report Number: PB87-910410

Collision of Aeronaves De Mexico, S.A. McDonnell Douglas DC-9-32, XA-JED and Piper PA-28-181, N4891F, Cerritos, California, 31 August 1986.
NTSB Report Number: AAR-87-07, adopted on 7/7/1987 [Summary]
NTIS Report Number: PB87-910409

Unalaska, Alaska–September 25, 1985 Jenkinsburg, GA–September 29, 1985 Boston, Massachusettes–Dec. 15, 1985 DeKalb, Texas, 31 December 1985 Erie, Pennsylvania–21 February 1986
NTSB Report Number: AAR87-02*, adopted on 6/30/1987
NTIS Report Number: PB87-910408

Table 1.17. Aircraft accidents

Event date	Probable cause release	Location	Make/model	Registration number	Event severity
28/8/1983		Angola/Dundo, Angola	Lockheed 382G	N17ST	Fatal (7)
4/8/1983			Boeing 747 − 121	N738PA	Non-fatal
13/3/1987		Calgary, Canada	Boeing 747 − 247	N2819W	Non-fatal
14/2/1987		Durango, Mexico	Boeing 707 − 323B	N712PC	Fatal (1)
23/5/1986		Sydney, Australia	Boeing 747SP-21	N531PA	Non-fatal
2/4/1986		Athens, Greece	Boeing 727 − 231	N54340	Fatal (4)
12/12/1985		Gander, Canada	Douglas DC-8-63	N950JW	Fatal (256)
26/11/1985		Cat Cay, Bahamas	Grumman G-73	N51151	Non-fatal
8/5/1985		Guadalupe, Dominica	Cessna 402C	N2712L	Non-fatal
1/1/1985		La Paz, Bolivia	Boeing 727 − 225	N819EA	Fatal (29)
19/11/1984		Nassau, Bahamas	Douglas DC-8	N1234	Incident
9/3/1984		Seoul, Republic of Korea	Cessna 150L	N6764G	Fatal (2)
3/11/1988		Svarstad, Norway	Schweizer 269C	LNOTK	Unavailable
29/9/1988		Alajuela, Costa Rica	Boeing 757	N523EA	Non-fatal
21/5/1988		Kingston, Jamaica	Bell 222UT	H-18	Unavailable
4/4/1988		Freeport, Bahamas	Cessna 421A	N42A	Fatal (5)
9/1/1988		Snaefellsnes, Iceland	Piper PA-28-180	N9120B	Fatal (1)
27/12/1987		St. Barthelemy, West Indies	Cessna 402	N8209Q	Fatal (1)
7/11/1987		Tijuana, Mexico	McDonnell Douglas DC-10-15	N1003N	Incident
28/9/1987		Freeport, Bahamas	Embraer EMB 110-P-2	N876AC	Fatal (1)
16/8/1987		Frankfurt, Germany	Boeing B 767 200ER	N332AA	Incident
1/5/1987		St. Johns, Canada	Cessna P206 S/N P206-0009	N2509X	Fatal (6)
16/12/1988		Cuatro Cienegas, Mexico	Learjet 24B	N234CM	Fatal (2)
18/3/1991		Treasure Cay, Bahamas	Cessna 402C	N5785C	Fatal (5)
5/5/1990		Guatemale City, Guatemala	Douglas DC-6B	N84BL	Fatal (27)
2/12/1989		George Town, Bahamas	Douglas DC-6B	N371	Non-fatal

Date	Location	Aircraft	Registration	Outcome
21/10/1989	Tegucigalpa, Honduras	Boeing 727 – 224	N88705	Fatal (131)
7/6/1989	Paramaribo, Suriname	McDonnell Douglas DC-8-62	N1809E	Fatal (174)
12/4/1989	Santo Domingo, Dominican Republic	Beech A80	HI563	Unavailable
19/2/1989	Puchong Malaysi, Malaysia	Boeing 747 – 200	N807FT	Fatal (4)
8/2/1989	Santa Maria, Portugal	Boeing 707	N7231T	Fatal (144)
21/12/1988	Lockerbie, United Kingdom	Boeing 747 – 121	N739PA	Fatal (270)
21/12/1992	Faro, Portugal	McDonnell Douglas DC-10-30F	PH-MB	Fatal (56)
21/12/1992	Quito, Ecuador	Piper PA-34-200T	HCBHK	Fatal (5)
10/12/1992	Quito, Ecuador	Rockwell Sabreliner 75A	AE402	Fatal (10)
6/6/1992	Tucuti, Panama	Boeing 737 – 204	HP120	Fatal (47)
2/2/1992	Kafoutine, Senegal	Convair 640	N862FW	Fatal (30)
20/1/1992	Strasburg, France	Airbus Industrie A320	FGGED	Fatal (87)
29/12/1991	Taipei, Taiwan	Boeing 747 – 200F	B198	Fatal (5)
27/12/1991	Stockholm, Sweden	McDonnell Douglas MD-81 (DC-9-81)	OYKHO	Unavailable
12/12/1991	Nakina, Ontario, Canada	Boeing B-747-121	N475EV	Incident
11/10/1991	Grand Cayman Is, Cayman Island	Boeing 737 – 300	VRCCW	Incident
1/2/1995	San Paulo, Brazil	Boeing 737 – 200	PPSMV	Non-fatal
11/1/1995	Maria La Baja, Colombia	McDonnell Douglas DC-9-14	HK383	Fatal (52)
21/12/1994	Coventry, Algeria	Boeing B737-2D6C	7TVEE	Fatal (5)
9/8/1994	Salama, Guatemala	Bell UH-1B	TGHUY	Fatal (5)
8/5/1994	Maiquetia, Venezuela	McDonnell Douglas DC9-34	YV37C	Incident
4/4/1994	Seville, Spain	Learjet 55	IKILO	Non-fatal
1/3/1994	Narita, Japan	Boeing 747	N637U	Non-fatal
18/8/1993 / 10/5/1994	Guantanamo Bay, Cuba	Douglas DC-8-61	N814CK	Non-fatal
19/6/1993	Aruba, Aruba	Cessna 421A	N421RK	Non-fatal
5/4/1993	Guatemala City, Panama	Boeing 767 – 251	N767TA	Non-fatal

1.6.1.2 Aviation Accidents from the Past 10 Years

Note: only major reports are listed here – see Accident Synopses for descriptions of all accidents in database

---

Aircraft Accident Brief: Departure From Controlled Flight, Learjet 24B, N600XJ, Helendale, California, 23 December 2003
NTSB Report Number: AAB-06-04 [Full Text]

Aircraft Accident Brief: Controlled Flight Into Terrain, Learjet 35A, N30DK, San Diego, California, 24 October 2004
NTSB Report Number: AAB-06-05 [Full Text]

Aircraft Accident Report: Crash During Approach to Landing, Air Tahoma, Inc., Flight 185, Convair 580, N586P, Covington, Kentucky, 13 August 2004
NTSB Report Number: AAR-06-03, adopted on 5/2/2006 [Summary | PDF Document]
NTIS Report Number: PB2006-910403

Aircraft Accident Brief: Crash During Takeoff in Icing Conditions, Canadair, Ltd., CL-600-2A12, N873G, Montrose, Colorado, 28 November 2004
NTSB Report Number: AAB-06-03 [Full Text]

Aircraft Accident Report: Controlled Flight into Terrain, Era Aviation, Sikorsky S-76A++, N579EH, Gulf of Mexico About 70 Nautical Miles South-Southeast of Scholes International Airport, Galveston, Texas, 23 March 2004
NTSB Report Number: AAR-06-02, adopted on 3/7/2006 [Summary | PDF Document]
NTIS Report Number: PB2006-910402

The brief number below is not being used.
NTSB Report Number: AAB-06-02

Aircraft Accident Report: Collision with Trees and Crash Short of Runway, Corporate Airlines Flight 5966, British Aerospace BAE-J3201, N875JX, Kirksville, Missouri, 19 October 2004
NTSB Report Number: AAR-06-01, adopted on 1/24/2006 [Summary | PDF Document]
NTIS Report Number: PB2006-910401

Aircraft Accident Brief: Controlled Flight Into Terrain, Beech King Air 200, N501RH, Stuart, Virginia, 24 October 2004
NTSB Report Number: AAB-06-01, adopted on 2/7/2006 [Full Text | PDF Document]
NTIS Report Number: PB2006-104812

Aircraft Accident Report: Crash During Landing, Executive Airlines Flight 5401, Avions de Transport Regional 72-212, N438AT, San Juan, Puerto Rico, 9 May 2004
NTSB Report Number: AAR-05-02, adopted on 9/7/2005 [Summary | PDF Document]
NTIS Report Number: PB2005-910402

Aircraft Accident Report: Hard Landing, Gear Collapse Federal Express Flight 647, Boeing MD-10-10F, N364FE, Memphis, Tennessee, 18 December 2003
NTSB Report Number: AAR-05-01, adopted on 5/17/2005 [Summary | PDF Document]
NTIS Report Number: PB2005-910401

Aircraft Accident Report: In-Flight Engine Failure and Subsequent Ditching Air Sunshine, Inc., Flight 527, Cessna 402C, N314AB, About 7.35 Nautical Miles West-Northwest of Treasure Cay Airport, Great Abaco Island, Bahamas, 13 July 2003
NTSB Report Number: AAR-04-03, adopted on 10/13/2004 [Summary | PDF Document]
NTIS Report Number: PB2004-910403

Aircraft Accident Report: In-Flight Separation of Vertical Stabilizer American Airlines Flight 587, Airbus Industrie A300-605R, N14053, Belle Harbor, New York, 12 November 2001 (Spanish summary available)
NTSB Report Number: AAR-04-04, adopted on 10/26/2004 [Summary | PDF Document]
NTIS Report Number: PB2004-910404

Aircraft Accident Report: Collision With Trees on Final Approach Federal Express Flight 1478, Boeing 727-232, N497FE, Tallahassee, Florida, 26 July 2002
NTSB Report Number: AAR-04-02, adopted on 6/8/2004 [Summary | PDF Document]
NTIS Report Number: PB2004-910402

Aircraft Accident Brief: Uncontrolled Descent and Impact with Terrain, Eurocopter AS350-B2 Helicopter, N169PA, Meadview, Arizona, 10 August 2001
NTSB Report Number: AAB-04-02, adopted on 6/3/2004 [Full Text | PDF Document]

Aircraft Accident Brief: Loss of Control and Impact with Terrain, Canadair Challenger CL-604 Flight Test Airplane, C-FTBZ, Wichita, Kansas, 10 October 2000
NTSB Report Number: AAB-04-01, adopted on 4/14/2004 [Full Text | PDF Document]

Aircraft Accident Report: Loss of Pitch Control During Takeoff Air Midwest Flight 5481, Raytheon (Beechcraft) 1900D, N233YV, Charlotte, North Carolina, 8 January 2003
NTSB Report Number: AAR-04-01, adopted on 2/26/2004 [Summary | PDF Document]
NTIS Report Number: PB2004-910401

Aircraft Accident Report: Loss of Control and Impact With Terrain Aviation Charter, Inc., Raytheon (Beechcraft) King Air A100, N41BE, Eveleth, Minnesota, 25 October 2002
NTSB Report Number: AAR-03-03, adopted on 11/18/2003 [Summary | PDF Document]
NTIS Report Number: PB2003-910403

Aircraft Accident Report: Loss of Pitch Control on Takeoff, Emery Worldwide Airlines, Inc., McDonnell Douglas DC-8-71F, N8079U, Rancho Cordova, California, 16 February 2000
NTSB Report Number: AAR-03-02, adopted on 8/5/2003 [Summary | PDF Document]
NTIS Report Number: PB2003-910402

Aircraft Accident Report: In-Flight Electrical System Failure and Loss of Control, Jet Express Services, Raytheon (Beechcraft) Super King Air 200, N81PF, Near Strasburg, Colorado, 27 January 2001
NTSB Report Number: AAR-03-01, adopted on 1/15/2003 [Summary | PDF Document]
NTIS Report Number: PB2003-910401

Aircraft Accident Report: Loss of control and Impact with Pacific Ocean, Alaska Airlines Flight 261, McDonnell Douglas MD-83, N963AS, about 2.7 miles North of Anacapa Island, California, 31 January 2000
NTSB Report Number: AAR-02-01, adopted on 12/30/2002 [Summary | PDF Document]
NTIS Report Number: PB2002-910401

Aircraft Accident Brief: Schempp-Hirth Nimbus-4DM, N807BB, Minden, Nevada, 13 July 1999
NTSB Report Number: AAB-02-06, adopted on 9/27/2002 [Full Text | PDF Document]

Executive Airlines, British Aerospace J-3101, N16EJ, Bear Creek Township, Pennsylvania, 21 May 2000
NTSB Report Number: AAB-02-05, adopted on 8/26/2002 [Full Text | PDF Document]

Aircraft Accident Brief: Southwest Airlines Flight 1455, Boeing 737-300, N668SW, Burbank, California, 5 March 2000
NTSB Report Number: AAB-02-04, adopted on 6/26/2002 [Full Text | PDF Document]

Aircraft Accident Brief: Gulfstream III, N303GA, Aspen, Colorado, 29 March 2001
NTSB Report Number: AAB-02-03, adopted on 6/11/2002 [Full Text | PDF Document]

Aircraft Accident Brief: Cessna 335, N8354N near Hillsboro, Missouri, 16 October 2000
NTSB Report Number: AAB-02-02, adopted on 6/5/2002 [Full Text | PDF Document]

Aircraft Accident Brief: Egypt Air Flight 990 Boeing 767-366ER, SU-GAP, 60 Miles South of Nantucket, Massachusetts, 31 October 1999
NTSB Report Number: AAB-02-01, adopted on 3/13/2002 [Full Text | PDF Document]
NTIS Report Number: PB2002-910401

Aviation Accident Report: Runway Overrun During Landing, American Airlines Flight 1420, McDonnell Douglas MD-82, N215AA, Little Rock, Arkansas, 1 June 1999
NTSB Report Number: AAR-01-02, adopted on 10/23/2001 [Summary | PDF Document]
NTIS Report Number: PB2001-910402

Aircraft Accident Brief: Collision with Terrain of Big Island Air flight 58, near Volcano, Hawaii, 25 September 1999
NTSB Report Number: AAB-01-02, adopted on 9/26/2001 [Full Text | PDF Document]

Aircraft Accident Brief: Ground Impact of American Airlines 1340, Chicago, Illinois, 9 February 1998
NTSB Report Number: AAB-01-01, adopted on 5/14/2001 [Full Text | PDF Document]

Aviation Accident Report: In-flight Breakup Over the Atlantic Ocean Trans World Airlines Flight 800, Boeing 747-141, N93119, near East Moriches, New York, 17 July 1996
NTSB Report Number: AAR-00-03, adopted on 8/23/2000 [Summary | PDF Document]
NTIS Report Number: PB2000-910403

Aircraft Accident Brief: Crash of Sunjet Aviation, Learjet Model 35, N47BA, Aberdeen, South Dakota, 25 October 1999
NTSB Report Number: AAB-00-01, adopted on 11/28/2000 [Full Text | PDF Document]

Aircraft Accident Report: Crash During Landing Federal Express, Inc., McDonnell Douglas MD-11, N611FE, Newark International Airport Newark, New Jersey, 31 July 1997
NTSB Report Number: AAR-00-02, adopted on 7/25/2000 [Summary | PDF Document]
NTIS Report Number: PB2000-910402

Controlled Flight into Terrain Korean Air Flight 801, Boeing 747-300, HL7468, Nimitz Hill, Guam, 6 August 1997 DCA97MA058
NTSB Report Number: AAR-00-01, adopted on 1/13/2000 [Summary | PDF Document]
NTIS Report Number: PB2000-910401

In-Flight Icing Encounter and Uncontrolled Collision with Terrain, Comair Flight 3272, Embraer EMB-120RT, N265CA, Monroe, Michigan, 9 January 1997
NTSB Report Number: AAR-98-04, adopted on 11/4/1998 [Summary | PDF Document]
NTIS Report Number: PB98-910404

Aircraft Accident Report In-Flight Fire/Emergency Landing Federal Express Flight 1406 Douglas DC-10-10, N68055 Newburgh, New York, 5 September 1996
NTSB Report Number: AAR-98-03, adopted on 7/22/1998 [Summary | PDF Document]
NTIS Report Number: PB98-910403

Aircraft Accident Report Uncontrolled Impact with Terrain Fine Airlines Flight 101 Douglas DC-8-61, N27UA, Miami, Florida, 7 August 1997
NTSB Report Number: AAR-98-02, adopted on 6/16/1998 [Summary | PDF Document]
NTIS Report Number: PB98-910402

Uncontained Engine Failure Delta Air Lines Flight 1288 McDonnell Douglas MD-88, N927DA Pensacola, Florida, 6 July 1996
NTSB Report Number: AAR-98-01, adopted on 1/13/1998 [Summary | PDF Document]
NTIS Report Number: PB98-910401

Aircraft Accident Report Uncontrolled Flight Into Terrain ABX Air (Airborne Express) Douglas DC-8-63, N827AX Narrows, Virginia, 22 December 1996
NTSB Report Number: AAR-97-05, adopted on 7/15/1997 [Summary | PDF Document]
NTIS Report Number: PB97-910405

Aircraft Accident Report Runway Collision United Express Flight 5925 and Beechcraft King Air A90 Quincy Municipal Airport Quincy, IL, 19 November 1996 (Revision 9/5/00)
NTSB Report Number: AAR-97-04, adopted on 7/1/1997 [Summary | PDF Document]
NTIS Report Number: PB97-910404

Aircraft Accident Report Descent Below Visual Glidepath and Collision with Terrain Delta Air Lines Flight 554 McDonnell Douglas MD-88, N914DL LaGuardia, New York, 19 October 1996
NTSB Report Number: AAR-97-03, adopted on 8/25/1997 [Summary | PDF Document]
NTIS Report Number: PB97-910403

1.7 Explosions With and Without Impact

Explosions have occurred in the past and are occurring at the present and there is no guarantee that they will not occur in the future. Chemical explosives, bombs, grenades, rockets, missiles, fire and gases are generally involved. Cars, lorries, vans, trains, aircraft, sea-going vessels, houses, buildings, pylons, towers, bridges, dams, ammunition dumps and many other structures including bandstands have been damaged by explosions. Some typical examples of bandstands targeted by terrorists in the UK and elsewhere are the Regiment Band in the Grande Palace, Brussels (August 1979), the Royal Airforce Central Band in Uxbridge (January 1981) and the Royal Green Jacket Bandstand in Regent's Park, London (July 1982). Barracks have been targeted too, such as the Chelsea Barracks, London (October 1981), the Parachute Regiment Officers Mess, Aldershot, Surrey (February 1972) and the Duke of York Barracks in Chelsea, London (October 1974). The devastation at Inglis Barracks at Mill Hill in North London, UK (1989). The structure was

Table 1.18. Aircraft accident

Event date	Probable cause released	Location	Make/model	Register number	Event severity	Type of air carrier operation and carrier name (doing business as)
7/11/1995		Panama City, Panama	Boeing B727 – 224	N79750	Incident	
31/10/1995		Piedras Negras, Mexico	Cessna 208B	XASVM	Fatal (9)	
12/9/1995		Bereza, Belarus	Balloonbau Woerner GMBH	CARIB	Fatal (2)	
9/8/1995		San Vicente, El Salvador	Boeing 737 – 200	N125GU	Fatal (65)	
10/7/1995		Mexico City, Mexico	Aerospatiale AS355F	XBDDX	Fatal (3)	
27/6/1995		La Ramona, Dominican Republic	Convair CV-440	N356SA	Fatal (2)	
3/5/1995		Quito, Ecuador	Grumman G-1159	N409MA	Fatal (7)	
28/4/1995		Guatemala City, Guatemala	Douglas DC-8F-54	N43UA	Fatal (6)	
31/3/1995		Tegucigalpa, Honduras	Cessna 185-F	FAH12	Fatal (4)	
17/3/1995		Barranquilla, Colombia	McDonnell Douglas DC-9-15	HK354	Non-fatal	
20/12/1995		Buga, Colombia	Boeing B757	N651AA	Fatal (160)	SCHD Part121: Air Carrier AMR Corporation (D.B.A. American Airlines)
3/12/1995		Douala, Cameroon	Boeing B-737-200	TJ-CB	Fatal (72)	SCHD non-U.S. Commercial Cameroon Airlines
9/10/1996		Andros Island, Bahamas	Bell 407	N1117P	Non-fatal	Part 91: General Aviation
2/10/1996		Lima, Peru	Boeing B-757-23A	N52AW	Fatal (70)	SCHD Part 129: Foreign Aeroperu

(continued)

Table 1.18. (continued)

Event date	Probable cause released	Location	Make/model	Register number	Event severity	Type of air carrier operation and carrier name (doing business as)
3/4/1996		Dubrovnik, Croatia	Boeing CT-42A	-1149	Fatal (33)	Armed Forces
29/2/1996		Arequipa, Peru	Boeing 737 – 222	OB145	Fatal (123)	SCHD non-U.S. Commercial Compania de Aviacion Faucett (D.B.A. Faucett)
24/2/1996			Cessna 337	N5485S	Fatal (4)	Part 91: General Aviation
24/2/1996			Cessna 337	N2456S	Fatal (4)	Part 91: General Aviation
6/2/1996		Ensenada, Mexico	Cessna 550	XASLQ	Fatal (8)	Non-U.S. Commerical Aero Taxi el Chanilla
6/2/1996		Puerto Plata, Dominican Republic	Boeing 757 – 200	TCGEN	Fatal (189)	NSCH Part 129: Foreign Birgenair
20/11/1996		Moran, Spain	Bell 407	ECGJC	Non-fatal	NSCH Non-U.S. Commercial
22/10/1996		Manta, Ecuador	Boeing 707 – 323	N751MA	Fatal (34)	NSCH Part 121: Air Carrier Millon Air Inc. (D.B.A. Millon Air)
20/10/1996		Eel River Cross, Canada	Piper PA-31-350	N744W	Fatal (8)	NSCH Part 135: Air Taxi & Commuter
15/8/1997		Cuernavaca, Mexico	Bell 412HP	XCPFI	Fatal (8)	Non-U.S. non-commercial
8/6/1997		Nagoya, Japan	McDonnell Douglas MD-11	J8580	Non-fatal	SCHD Part 129: Foreign Japan Airlines
30/5/1997		Roque, Peru	Bell UH-1H	PNP30	Fatal (2)	Non-U.S. non-commercial
20/5/1997		La Carbonera, Mexico	Rockwell 1121B	N1121F	Fatal (4)	Part 91: General Aviation
26/3/1997		Mariquita, Colombia	Bell UH-1H	PN160	Fatal (2)	Non-U.S. non-commercial
15/3/1997		Lofssjon, Sweden	Bell 205A1	HSX	Fatal (1)	Non-U.S. Commercial Heliflug AB
5/2/1997		Santa Catarina, Mexico	Beech 23	N8723M	Fatal (1)	Part 91: General Aviation

Date	Location	Aircraft	Registration	Result	Description
19/12/1997		Boeing 737 – 300	9VTRF	Fatal (97)	Part 129: Foreign SILKAIR
16/12/1997	Fredericton, Canada	Canadair CL-600-2B19	CFSKI	Non-fatal	SCHD Non-U.S. Commercial Air Canada
13/12/1997	Fairchild Metro, Bolivia	Fairchild SA-226-TC	CP163	Fatal (10)	SCHD Part 129: Foreign
12/12/1997	La Vertiente, Bolivia	Fairchild SA-2226-TC	CP-1635	Fatal (10)	Non-U.S. Commercial Gonzalo Vargas Campero (D.B.A. Servicios Aereos Vargas Espana)
25/11/1997	La Palma, Panama	Bell UH-1H	N124	Fatal (9)	Non U.S. Commercial Servcio Aereo Nacional (SAN)
30/10/1997	Comox, Lake, Canada	Boeing 234	CFHFH	Fatal (2)	Non-U.S. non-commercial
14/10/1997	Neiva, Colombia	Ayres S2R-T65	PN259	Non-fatal	Non-U.S. non-commercial
10/10/1997	Nuevo Berlin, Uruguay	McDonnell Douglas DC-9-32	LVWEG	Fatal (75)	SCHD Part 129: Foreign Austral Airlines
6/9/1997		Boeing 737 – 200	HZ-AG	Non-fatal	Non-U.S. Commercial Saudi Arabian Airlines (D.B.A. Saudi Arabian Airlines)
21/8/1997	Arica, Peru	Bell 206L-1	N2246Q	Fatal (3)	Non-U.S. non-commercial
30/7/1998	Lorient, France	Cessna 177 RG	FGAJE	Fatal (15)	Non-U.S. non-commercial
27/7/1998	San Jose Del, Colombia	Ayres S2R-T34	N3090M	Fatal (2)	Part 91: General Aviation
18/7/1998	Nueva Colonia, Colombia	Bell UH-1H	159	Fatal (7)	Non-U.S. non-commercial
18/6/1998	Montreal, Canada	Swearingen METRO II	CGQAL	Fatal (13)	NSCH Part 129: Foreign Propair, Inc. (D.B.A. Propair)
20/4/1998	Bogota, Colombia	Boeing 727 – 200	HCBRI	Fatal (52)	SCHD Part 129: Foreign Tame Airlines (D.B.A. Tame Airlines)

Table 1.18. (continued)

Event date	Probable cause Released	Location	Make/model	Register number	Event severity	Type of air carrier operation and carrier name (Doing Business As)
18/3/1998		Taipai, Taiwan	Saab-Scania AB (Saab) 340	UNK	Fatal (13)	NSCH Part 129: Foreign Formosa Airlines (D.B.A. Formosa Airlines)
9/3/1998		Amport, United Kingdom	Robinson R22B	GBUTW	Fatal (1)	NSCH Part 129: Foreign
2/2/1998		Philippine Isla, Philippines	McDonnell Douglas DC-9-32	PC150	Fatal (104)	SCHD Part 129: Foreign CEBU Pacific Airline
9/1/1998		London, United Kingdom	Boeing 767-322ER	N653UA	Non-fatal	SCHD Part 121: Air Carrier United Airlines, Inc.
2/1/1998		Tampico, Mexico	Learjet 24	XARRK	Fatal (3)	Non-U.S. Commercial Unknown
17/1/1999		Jumla, Nepal	Cessna CE-208	UNK	Fatal (4)	SCHD Part 129: Foreign
16/12/1998		Las Mesitas, Honduras	Piper PA-31-310	YS14C	Fatal (2)	NSCH Part 129: Foreign
8/10/1998		Shannon, Ireland	Douglas MD-11	N805DE	Incident	SCHD Part 121 Air Carrier Delta Airlines, Inc.
5/10/1998		Mopzambique, Mozambique	Boeing 747SP	ZSSPF	Non-fatal	SCHD Part 129 Foreign
16/9/1998		Guadalajara, Mexico	Boeing 737 – 524	N20643	Non-fatal	SCHD Part 121: Air Carrier Continental Airlines
14/9/1998		MT Cook, New Zealand	Cessna 177	ZKDKL	Fatal (3)	NSCH Non-U.S. Commercial
10/9/1998		Shanghai, China	McDonnell Douglas MD-11	B2173	Incident	SCHD Part 129: Foreign China Eastern
2/9/1998		Nova Scotia, Canada	Douglas MD-11	HBIWF	Fatal (229)	SCHD Part 129: Foreign Swiss Air

Date	Location	Aircraft	Registration	Severity	Operator
23/8/1998	Melville Hall, Dominica	Cessna 402C	N2748J	Fatal (11)	NSCH Part 135: Air Taxi & Commuter
30/7/1998	Lorient, France	Beech 1900D	FGSJM	Fatal (15)	Non-U.S. Commercial Protheus Airline
10/8/1999	Monrovia, Liberia	Cessna 414	N373BC	Fatal (6)	Non-U.S. Commercial Gibalco Air Services
20/7/1999	Bluefields, Nicaragua	Cessna 208B	YNCED	Fatal (16)	Non-U.S. Commercial La Costena
17/5/1999	Cuenca, Ecuador	Bell 206L4	HCBYQ	Non-fatal	Non-U.S. Commercial ICARO S.A.
21/4/1999	Keelung, Taiwan	Kawasaki BK-117B-1	B5550	Fatal (3)	Non-U.S. non-commercial
15/4/1999	Shanghai, China	McDonnell Douglas MD-11	HL737	Fatal (3)	SCHD Part 129: Foreign Korean Air
14/4/1999	60 N. Jakarta, Indonesia	Bell 206B	PKDBC	Fatal (4)	Non U.S. non-commercial
14/4/1999		Learjet 55	UNK	Non-fatal	NSCH Part 129: Foreign IPP Jet OY
7/4/1999	Ceyhan Adana, Turkey	Boeing 737 – 400	TC-JEP	Fatal (6)	NSCH non-U.S. Commercial Turkish Air Lines
26/2/1999	Belo Horizonte, Brazil	Bell 407	PT-YVI	Fatal (2)	Non-U.S. non-commercial
18/1/1999	Paris, France	Cessna 550	HBVIT	Incident	Non-U.S. Commercial (D.B.A. TAG Aviation)
31/8/1999	BA, Argentina	Boeing 737 – 200	LVWRZ	Fatal (80)	SCHD Part 129: Foreign
24/8/1999	Hualien, Taiwan	McDonnell Douglas MD-90	B7873	Fatal (1)	SCHD Part 129: Foreign
23/8/1999	Hong Kong, China	McDonnell Douglas MD-11	UNK	Non-fatal	SCHD Part 129: Foreign China Airlines
14/9/1999	Gerona Spain, Spain	Boeing 757		Incident	NSCH Part 129: Foreign

Table 1.18. (continued)

Event date	Probable cause released	Location	Make/model	Register number	Event severity	Type of air carrier operation and carrier name (doing business as)
14/9/1999		Bucharest, Romania	Dassault Falcon 900	SXECH	Fatal (6)	NSCH Part 129: Foreign
3/9/1999		Linwood, United Kingdom	Cessna 404	GILGW	Fatal (8)	Non-U.S. non-commercial Airtour, Inc.
25/1/2000		Guadalajara, Mexico	Cessna 404	CAA91	Fatal (5)	Non-U.S. non-commercial
15/1/2000		Pavas, Costa Rica	Let 410 UVP-E	YSO9C	Fatal (4)	Non-U.S. Commercial Aviones Taxi Aereo S.A (D.B.A. Atasa)
14/1/2000		Chimore, Bolivia	Lockheed C-130B		Fatal (5)	Non-U.S. non-commercial
10/1/2000		Zurich, Switzerland	Saab-Scania AB (Saab) 340	HBAKK	Fatal (10)	SCHD Part 129: Foreign Cross Air
22/12/1999		Stansted, United Kingdom	Boeing 747 – 200F	HL745	Fatal (4)	SCHD Part 129: Foreign Korean Airlines Inc.
11/12/1999		Cali, Colombia	Bell UH-1H	PN169	Fatal (1)	Non-U.S. non-commercial
3/12/1999		Rangali, Maldives	Bell 212		Fatal (10)	Non-U.S. Commercial Maldavian Air Taxi (PTE) Ltd.
1/12/1999		Cabinda, Angola	Bell 206-L1	N5005B	Fatal (1)	Non-U.S. Commercial Petroleum Helicopters, Inc.
30/11/1999		Tepic, Mexico	Cessna 182S	5439	Fatal (3)	Non-U.S. non-commercial
9/11/1999		Uruapan, Mexico	Douglas DC-9-31	XATKN	Fatal (18)	Non-U.S. Commercial Transportes Aereos Ejecutivos (D.B.A. Taesa)
17/10/1999		Subic Bay, Philippines	McDonnell Douglas MD-11F	N581FE	Non-fatal	NSCH Part 121: Air Carrier
13/10/1999		Quetzaltenango, Guatemala	Bell 206L-1	TGAMA	Fatal (2)	Non-U.S. non-commercial

Date	Location	Aircraft	Registration	Status	Category
2/10/1999	Dhahran, Saudi Arabia	Bell 214ST	N704H	Fatal (12)	Part 91: General Aviation
23/8/2000		Robinson R-22	OYHFI	Fatal (2)	Non-U.S. non-commercial
11/8/2000	Cape Town, south Africa	Hughes 369HS	ZSHFE	Non-fatal	Non-U.S. non-commercial
4/8/2000	Burgersfort, south Africa	Bell 206B	ZSHKP	Fatal (2)	Non-U.S. non-commercial
25/7/2000	Paris-Gonesse, France	Aerospatiale Concorde Version 101	FBTSC	Fatal (113)	SCHD Part 129 Foreign Air France
20/7/2000	Nassau, Bahamas	Douglas DC-3	N54AA	Fatal (2)	NSCH Part 13: Air Taxi & Commuter
18/7/2000	NUUK, Greenland	Hughes 369D	OYHGF	Fatal (1)	Non-U.S. non-commercial
8/7/2000	Chulum Juarez, Mexico	British Aerospace Jetstream 3201	N912FJ	Fatal (19)	Non-U.S. Commercial Aereocari S.A. DE C.V. (D.B.A. Aereocari Airlines)
13/6/2000	Rio de Janeiro, Brazil	Boeing B737-200	PPSMC	Non-fatal	SCHD Part 129: Foreign
8/6/2000	San Juanito, Mexico	Bell 412	XATPH	Non-fatal	Non-U.S. Commercial
31/5/2000	Whyalla, Australia	Piper PA-31-350	VHMZK	Fatal (8)	Non-U.S. Commercial Whyalla Airlines
22/9/2000	Clearwater, Canada	De Havilland DHC-2T	CFOES	Non-fatal	Non-U.S. Commercial Air Service 1900 Ltd.
9/9/2000	Manta, Ecuador	Dornier DO-28D-2	HCBNT	Fatal (1)	Non-U.S. non-Commercial
5/9/2000	Jakarta, Indonesia	Boeing B-747-300	JA817	Non-fatal	Non-U.S. Commercial Japan Airlines
23/8/2000	Manama, Bahrain	Airbus Industrie A320		Fatal (143)	Non-U.S. Commercial Gulfair, Inc.
18/5/2000	Coban, Guatemala	Cessna 182P	TGJOR	Fatal (4)	Non-U.S. non-commercial
8/5/2000	Santa Cruz, Bolivia	Piper PA-23-250F	1430	Fatal (3)	Non-U.S. non-commercial

Table 1.18. (continued)

Event date	Probable cause released	Location	Make/model	Register number	Event severity	Type of air carrier operation and carrier name (doing business as)
2/5/2000		Lyon, France	Learjet 35A	GMURI	Fatal (2)	Non-U.S. Commercial Northern Executive Aviation (D.B.A. Same)
17/4/2000		Nevaj, Guatemala	Cessna TU206F	N59143	Fatal (7)	Non-U.S. non-commercial
14/4/2000		Guayaquil, Ecuador	Lockheed L-1011-385	N308GB	Non-fatal	NSCH Part 121: Air Carrier Arrow Air
2/4/2000		Guayaquil, Ecuador	Boeing 747-200F	N534MC	Non-fatal	NSCH Part 121: Air Carrier Atlas Air, Inc.
28/3/2000		Tingo Mar, Peru	Bell UH-1H		Non-fatal	Non-U.S. non-commercial
22/3/2000		Miazal, Ecuador	Helio 700	HCCAJ	Non-fatal	Non-U.S. non-commercial
21/3/2000		Toluca, Mexico	Bell 206L4	XCJCF	Fatal (6)	Non-U.S. non-commercial
21/2/2000		Prince George, Canada	Schweizer 269C	CGFJO	Non-fatal	Part 91: General Aviation
11/12/2000		Sumacal, Bolivia	Cessna U206G	CP-1721	Fatal (6)	Non-U.S. non-commercial
31/10/2000		Taipei, Taiwan	Boeing 747 – 400	9V-SPK	Fatal (83)	SCHD Part 129: Foreign Singapore Airlines Ltd.
14/10/2000		Ensenada, Mexico	Cessna 320E	N269WP	Fatal (6)	Part 91: General Aviation
6/10/2000		Reynosa, Mexico	Douglas DC-9-31	N936ML	Fatal (4)	Part 129: Foreign Aerovias de Mexico S.A. (D.B.A. Aeromexico)
30/9/2000		Carlos Tejedor, Argentina	Robinson R-44	LVWIF	Fatal (1)	Non-U.S. non-commercial
25/8/2001		Marsh Harbour, Bahamas	Cessna 402B	N8097W	Fatal (9)	NSCH Part 135: Air Taxi & Commuter
16/7/2001		Tulcan, Ecuador	Fokker F28	HC-BMD	Non-fatal	SCHD non-U.S. Commercial TAME Airlines

Date	Location	Aircraft	Registration	Fatalities	Operator
10/7/2001	La Paz, Bolivia	Cessna 208B	CP-2395	Non-fatal	SCHD non-U.S. Commercial Amaszonas Transportes Aereos
8/7/2001	La Fortuna, Paraguay	Robinson R-44	ZP-PHRA	Fatal (2)	Non-U.S. non-commercial
3/7/2001	San Ignacio, Bolivia	Cessna U206G	CP-1644	Fatal (2)	Non-U.S. non-commercial
25/6/2001	Guadalajara, Mexico	McDonnell Douglas MD-82	N491SH	Incident	SCHD Part 129: Foreign AeroMexico (D.B.A. AeroMexico)
18/5/2001	Puerto Princesa, Philippines	Bell 407	RP-C2345	Fatal (6)	NSCH non-U.S. Commercial JAKA Transportation
10/5/2001	Liverpool, United Kingdom	McDonnell Douglas MD-83	EC-FXI	Incident	SCHD Non-U.S. Commercial Spainair
4/5/2001	Coban, Guatemala	Cessna 182J	TG-CEG	Fatal (5)	NSCH non-U.S. Commercial Antonio Arevalo Posadas
3/3/2001	Bangkok, Thailand	Boeing 737 – 400	HS-TDC	Fatal (1)	SCHD Part 129: Foreign Thai Airways International Ltd
14/1/2002	Pekanbaru, Indonesia	Boeing 737 – 200	PK-LID	Non-fatal	SCHD non-U.S. Commercial Lion Airlines
4/1/2002	Birmingham, United Kingdom	Canadair challenger 604	N90AG	Fatal (5)	Non-U.S. non-commercial
10/12/2001	Mount Gambier, Australia	Beech 200C	VH-FMN	Fatal (1)	Non-U.S. non-commercial
28/11/2001	Quepos, Costa Rica	Cessna 208	HP-1405	Fatal (3)	SCHD non-U.S. Commercial Servicios Aereos Nacionales S.A. (D.B.A. Sansa)
4/11/2001	Maracaibo, Venezuela	Bell 206B	YV-OGEZ	Non-fatal	Non-U.S. non-commercial
8/10/2001	Milan, Italy	McDonnell Douglas MD-87	SE-DMA	Fatal (118)	SCHD non-U.S. Commercial Scandinavian Airlines System (D.B.A. Scandinavian Airlines System)

Table 1.18. (continued)

Event date	Probable cause released	Location	Make/model	Register number	Event severity	Type of air carrier operation and carrier name (doing business as)
8/10/2001		Milan, Italy	Cessna Citationjet 2	D-IEVX	Fatal (118)	Non-U.S. non-commercial
18/9/2001		Guatemala City, Guatemala	LET 410 UVP-E	TG-CFE	Fatal (8)	SCHD non-U.S. Commercial Atlantic Airlines S.A.
12/9/2001		Chichen Itza, Mexico	LET 410 UVP-E	XA-ACM	Fatal (9)	NSCH non-U.S. Commercial Aero Ferinco S.A. DE C.V.
9/6/2001		Tijuana, Mexico	Saab-Scania AB (Saab) 340B	XA-ACK	Non-fatal	SCHD non-U.S Commercial Aerolitoral Airlines
1/7/2002		Uberlingen, Germany	Tupolev TU 154	RA-85816	Fatal (71)	SCHD non-U.S. Commercial Bashkirian Airlines
25/5/2002		Makung Island, Taiwan	Boeing 747 – 200		Fatal (206)	SCHD non-U.S. Commercial China Airlines Ltd.
7/5/2002		Tunis, Tunisia	Boeing 737 – 500	SU-GBI	Fatal (14)	SCHD non-U.S. Commercial Egypt Air
27/4/2002		San Salvador, El Salvador	McDonnell Douglas DC-10-40F	N141WE	Non-fatal	NSCH Part 121: Air Carrier Centurion Air Cargo Inc.
24/4/2002		Catacamas, Honduras	Cessna TU 206G	N7344N	Fatal (6)	Non-U.S. non-Commercial
15/4/2002		Pusan, Republic of Korea	Boeing 767-200ER	B-2552	Fatal (138)	SCHD non-U.S. Commercial Air China
13/2/2002		Cackchila, Guatemala	Cessna U206	TG-SAC	Fatal (2)	NSCH non-U.S. Commercial
5/2/2002		Ishpingo, Ecuador	Bell 212	HC-CBN	Non-fatal	NSCH non-U.S. Commercial Aeromasters airways
17/1/2002		El Tigre, Colombia	Fairchild FH-227	HC-AYM	Fatal (26)	Non-U.S. non-commercial
16/1/2002		Solo (Java IS.) Indonesia	Boeing 737 – 300	PK-GWA	Fatal (1)	SCHD non-U.S. Commercial Garuda Indonesia

Date	Location	Aircraft	Registration	Fatality	Operator
16/7/2002	Villavicencio, Colombia	Gavilan 358	HK4217X	Non-fatal	NSCH non-U.S. Commercial SAER Air Charters S.A.
6/7/2002	Paris, France	Airbus Industrie A320-212	F-GFKS	Unavailable	SCHD non-U.S. Commercial Air France
1/7/2002	Uberlingen, Germany	Boeing 757-23F	A9C-DHL	Fatal (71)	SCHD non-U.S. Commercial DHL Airways Inc.
8/7/2003	Port Sudan, Sudan	Boeing 737 – 200	ST-AFK	Fatal (115)	SCHD non-U.S. Commercial Sudan Airways
6/3/2003	Tamanrassett, Algeria	Boeing 737-2T4	7T-VEZ	Fatal (102)	SCHD non-U.S. Commercial Air Algerie
24/1/2003	Busia, Kenya	Gulfstream Aerospace G-159	5Y-EMJ	Fatal (3)	NSCH non-U.S. commercial African Commuter Services Ltd.
17/1/2003	Quito, Ecuador	Fokker F28	HC-BMD	Non-fatal	SCHD non-U.S. Commercial Transportes Aereos Militares del Ecuador
9/1/2003	Chachapoyas, Peru	Fokker F-28 MK1000	OB-1396	Fatal (46)	NSCH non-U.S. Commercial Transportes Aereos Nacionales de la Selva
31/10/2002	Monterrey, Mexico	McDonnell Douglas DC 9-32	XA-AMF	Non-fatal	SCHD non-U.S. Commercial Aerovias de Mexico S.A.
12/9/2002	Atalaya, Peru	Cessna U206G	OB-1226	Fatal (6)	NSCH non-U.S. Commercial Aeropantanal EIR Limitada
30/11/2004	Solo City, Indonesia	McDonnell Douglas MD-82	PK-LMN	Fatal (25)	SCHD non-U.S. Commercial Lion Air
21/11/2004	Baotou, China	Bombardier CRJ-200	B3072	Fatal (55)	SCHD non-U.S. Commercial China Eastern Airlines
14/10/2004	Halifax, Canada	Boeing 747-244BC	9G-MKJ	Fatal (7)	NSCH non-U.S. Commercial MK Airlines

Table 1.18. (continued)

Event date	Probable cause released	Location	Make/model	Register number	Event severity	Type of air carrier operation and carrier name (doing business as)
28/7/2004		Rome, Italy	Boeing 767ER	5Y-QQQ	Non-fatal	SCHD Part 129: Foreign East African Safari Air
2/7/2004		Tocumen, Panama	Israel Aircraft Industries 1124	N280AT	Fatal (7)	NSCH Part 135: Air Taxi & Commuter
26/2/2004		Bosnia, Bosnia and Herzegovina	Beech 200	Z3-BAB	Fatal (9)	SCHD non-U.S. Commercial Macedonia Govt
3/1/2004		Sharm El Sheikh, Egypt	Boeing 737 – 300	SU-ZCF	Unavailable	NSCH non-U.S. Commercial
20/1/2005		Guerrero, Mexico	Piper PA-32RT-300	N2144C	Fatal (2)	Part 91: General Aviation
3/2/2005		Kabul, Afghanistan	Boeing 737 – 200	EX-037	Fatal (104)	SCHD non-U.S. Commercial Phoenix Aviation
6/7/2005		Rome, Italy	Erickson Air Crane Inc. S-64F	N236AC	Fatal (1)	Part 91: General Aviation
10/3/2005		Beijing, China	Boeing B757-200	B2850	Non-fatal	Part 91: General Aviation
6/3/2005		Veradero, Cuba	Airbus A310	CGPAT	Non-fatal	SCHD non-U.S. Commercial Shanghai Airlines
10/2/2005		Shanghai, China	McDonnell Douglas MD-902	B2116	Fatal (3)	NSCH non-U.S. Commercial Guangdong Ltd.
10/12/2005		Port Harcourt, Nigeria	McDonnell Douglas DC-9-31	5N-BFD	Fatal (107)	SCHD non-U.S. Commercial Sosoliso Airlines
19/11/2005		Moscow, Russia	Cessna	P4-OIN	Fatal (8)	Non-U.S. non-commercial
22/10/2005		Lagos, Nigeria	Boeing 737 – 200	5N-BFN	Fatal (117)	SCHD non-U.S. Commercial Bellview Airlines
10/8/2005		Tallinn, Estonia	Sikorsky S-76	OH-HCI	Fatal (14)	SCHD non-U.S. Commercial

Date	Location	Aircraft	Registration	Outcome	Category
6/8/2005	Palermo, Italy	ATR ATR-72-202	TS-LBB	Fatal (16)	SCHD non-U.S. Commercial Tuninter
2/8/2005	Toronto, Canada	Airbus Industrie A-340	F-GLZQ	Non-fatal	SCHD non-U.S. Commercial Air France
1/8/2005	Perth, Australia	Boeing 777 – 200	9M-MRG	Incident	SCHD non-U.S. Commercial Malaysian Airline System
30/7/2005	Zuria Mountains, Uganda	MIL Design Bureau Mi-172	AF 615	Fatal (13)	non-U.S. non-commercial
16/7/2005	Brasilito, Costa Rica	Pilatus PC-6	N908PL	Fatal (6)	Non-U.S. non-commercial
6/7/2005	Rome, Italy	Erickson Air-Crane Inc S-64F	N236AC	Fatal (1)	Part 91: General Aviation
10/3/2005	Beijing, China	Boeing B757-200	B2850	Non-fatal	SCHD non-U.S. Commercial Shanghai Airlines
6/10/2005	Winnipeg, Canada	Cessna 208B	C-FEXS	Fatal (1)	NSCH non-U.S. Commercial Morningstar Air Express
5/9/2005	Medan, Indonesia	Boeing B737-200	PK-RIM	Fatal (145)	SCHD non-U.S. Commercial Mandala Airlines
23/8/2005	Pucallpa, Peru	Boeing 737 – 200	OB-1809-P	Fatal (45)	SCHD non-U.S. Commercial Transportes Aereos de Selva (TANS) Peru
16/8/2005	Machiques, Venezuela	Boeing MD-82	HK-4374X	Fatal (160)	NSCH non-U.S. Commercial West Caribbean Airways
14/8/2005	Grammatikos, Greece	Boeing B737-300	5B-DBY	Fatal (121)	SCHD non-U.S. Commercial Helios Airways
30/5/2006	Grand Isle 43AA, GM	Bell 206L-3	N92MT	Incident	Part 91: General Aviation
29/5/2006	Minden NV	Hunter Comp Air 6	N6008N	Non-fatal	Part 91: General Aviation
29/5/2006	Skwentna AK	Robinson R44	N688JK	Non-fatal	NSCH Part 135: Air taxi & Commuter
28/5/2006	Muddy Gap, WY	Garlick Helicopters Inc OH-58C	N16JD	Non-fatal	Part 91: General Aviation

Table 1.18. (continued)

Event date	Probable cause released	Location	Make/model	Register number	Event severity	Type of air carrier operation and carrier name (doing business as)
28/5/2006		Berlin Center, OH	Hughes 269A	N69HU	Fatal (1)	Part 91: General Aviation
28/5/2006		Payson, AZ	Diamond Aircraft Industries HK 36 TTC	N637TT	Non-fatal	Part 91: General Aviation
28/5/2006		Payne Springs, TX	Robinson R44	N42KJ	Non-fatal	Part 91: General Aviation
26/5/2006		Edna, TX	Aviat A-1B	N166MA	Fatal (2)	Part 91: General Aviation
26/5/2006		Eagar, AZ	Piper PA-28-140	N6309W	Non-fatal	Part 91: General Aviation
26/5/2006		Oxnard, CA	Piper Pa-28-151	N4596X	Non-fatal	Part 91: General Aviation
4/5/2006		Bangalore, India	Boeing B727-200	9M-TGA	Incident	SCHD unknown
24/3/2006		Cuenca, Ecuador	Cessna 208B	HC-BXD	Fatal (5)	NSCH non-U.S. Commercial Atesa Aero Taxis Ecuatorianos S.A.
21/5/2006		Seoul, Republic of Korea	Cessna 210G	HL1027	Non-fatal	non-U.S. non-commercial
29/4/2006		San Javier, Spain	Piper PA-34-220T	EC-1YY	Fatal (1)	non-U.S. non-commercial
25/4/2006		Sarawak, Malaysia	Garlick UH-1H	N126AC	Non-fatal	non-U.S. non-commercial
19/4/2006		Shanghai, China	Boeing 777	N216UA	Non-fatal	SCHD Part 121: Air Carrier United Airlines Inc.
16/4/2006		Lady Smith, Canada	Lake LA-4-200	N2788P	Non-fatal	Part 91: General Aviation
14/4/2006		El Alto, Bolivia	Cessna 208B	CP-2413	Incident	NSCH non-U.S. Commercial Amaszonas
12/4/2006		Antioquia, Colombia	Piper PA-34-200T	HK-2387	Fatal (2)	NSCH non-U.S. Commercial Star
11/4/2006		Morelia, Mexico	Bell 407	XC-UPN	Non-fatal	non-U.S. non-commercial
9/4/2006		Propriano, France	Bell 206	F-GIVH	Non-fatal	NSCH Unknown

a two-storey, gaunt, Victorian redbrick dormitory and about a quarter of it was destroyed. The roof and the first floor of this section were blown up. Upstairs the steel joists protruded out from the walls of the dormitory, entangled together. Across the parade ground, a missile fired by the blast had made a neat hole in a window in the new gymnasium block. Also bearing witness to the blast load was the steel flag-pole knocked off vertical. A similar example is given by the buildings devastated by the terrorist bomb attack at the Royal Marines School of Music in Deal, UK. Table 1.19 lists explosions reported in Great Britain from 1966 onwards. Table 1.20 lists major explosions which have occurred in other countries.

The Ojheri disaster in Pakistan of the twin cities Islamabad and Rawalpindi can be considered the previous century's greatest disaster. It occurred on 10 April 1988 when an ammunition dump exploded. Rockets, shells and shrapnel caused wide-spread destruction to life and property in a 20 km radius. Streets were rapidly littered with exploded and unexploded ammunition, including anti-tank mortars, rockets, RPG7s, anti-tank wire-guided missiles, Bazooka warheads and white phosphorous filled smoke shells and many others. Dozens of live and dead rockets and bombs caused vast damage to property and vehicles and over 150 houses were raised to the ground. Thousands died as a result of panic and mayhem as rockets and missiles showered the cities.

A very high intensity of explosion occurred in the Ojheri ammunition depot. It is widely believed that this explosion involved premature functioning of the large volume of different types of ammunitions described earlier. From the very sketchy news reports that have appeared in the media, it appears that white phosphorous shells were stacked inside sheds in combination with other shells, bombs, rockets, etc. Some of the white phosphorous shells started leaking in the sheds, generating copious fumes of oxides which combined with atmospheric oxygen. The heat generated in the process increased the interior temperature to a level sufficient to ignite the propellant fuel of the rocket motors, which developed high forward thrust and behaved like jet-propelled projectiles flying in all directions with great acceleration. Concurrently, the intense pressure produced inside was instrumental in ejecting a large number of unexploded rounds that were thrown in the air in the form of missiles with no explosive potential.

Thousands of lives were lost and many people were injured. Eye-witnesses reported that shells used to land continuously for almost a month. Many adjacent areas were littered with unexploded land mines, thousands of rounds of bullets and some RPG launchers were even sighted. The Pakistani's claimed that the tragedy was purely due to an accident.

Another major explosion in a missile storage area occurred in the military industrial complex near Al-Hillah, 40 miles south of Baghdad, and was apparently heard in the Iraqi capital. The blast occurred on 17 August 1989 and it was reported that 700 bodies were recovered. The casualties appear to have included Egyptians and Iraqi military personnel and civilians. The explosions occurred in an area where longer-range versions of the Soviet-made Scud

Table 1.19. List of explosions in Great Britain

Date	Details
23/7/1966	Bomb found at Flawith, 23 July 1966
23/2/1967	Gelignite found attached to car
17/7/1967	Unexploded mortar bomb found in golf course bunker
27/7/1967	Missile found at Milford Haven
1/8/1967	Mystery bomb found at Sand Bay
2/9/1967	Unexploded bomb was found in scrap yard
7/12/1967	Home-made bomb thrown into art school
1/1968–2/1968	Unexploded mortars and bombs were found in Weston-Super-Mare, Dagenham and Falforth Farm
21/5/1968	Petrol bombs were found
23/4/1969	Home-made bombs damaged houses in Norbury, London
31/7/1969	Unexploded bomb found in Bryanston Square, London
5/5/1970	Anti-tank bombs found in Colchester
2/6/1970	Bomb exploded in Buckingham, killing a boy
1/7/1970	Petrol bombs thrown at Army Publications office, London
7/7/1970	Bomb thrown into a recruiting office in London
10/7/1970	Bomb thrown into a retired policeman's home in London
17/8/1970	Explosion in car in Charing Cross Road, London
18/8/1970	London offices of Iberia Airways damaged by explosion
28/8/1970	Bomb exploded in bus station in Gloucester
1/1971	Four bombs exploded in London
9/2/1971	Petrol bomb thrown at house of a company manager, Jersey
13/7/1971	Petrol bombs thrown into a lounge of a public house in Bedford
1/11/1971	London Territorial Army headquarters were damaged
1/12/1971	Fire bombs damaged Town Hall at Broadstairs
4/12/1971	Army explodes old bomb on M5 motorway
3/1/1972	Man rode 8 miles on a motor bike with a live bomb, Grimsby
3/1/1972	A home in Lincoln wrecked by explosion
5/1/1972	Blast damaged a public house in Tring
2/2/1972	Explosion at gasworks in Croydon
8/2/1972	A house in Hull damaged by blast
22/2/1972	A home in Roehampton wrecked by explosion
4/4/1973	Parcels exploded at Kilburn and Paddington sorting offices, London
3/7/1973	Blast from a gas cylinder in a house in Hackney, London
30/8/1973	Solihull town centre rocked by two explosions
3/9/1973	Fire bombs thrown at four houses in Hockley
10/9/1973	Three incendiary devices exploded in Manchester
15/9/1973	Two petrol bombs thrown into a house in Nottingham
3/1/1974	Two bombs damage a building in Birmingham
22/1/1974	Paint store blast stops a train at Brixton, London
26/1/1974	Bomb blast at gasworks, St. Helens
4/2/1974	Explosion wrecks a coach on M62 motorway
15/2/1974	Factory explosion in Ardeer
14/3/1974	Blast in chemical factory, Gosport
3/4/1974	Explosion at soda siphon factory, Tottenham, London

Table 1.19. (continued)

Date	Details
2/5/1974	Factory explosion at Isleworth
10/5/1974	Gas blast in home in Clements End
11/10/1974	Chemical plant explosion at Flixborough
16/10/1974	Dental workshop wrecked in Thetford
24/10/1974	Bomb damages a house near a school in Harrow
29/10/1974	A bomb exploded under a minister's car in Birmingham
30/10/1974	Blast demolishes telephone exchange at Sunderland
9/11/1974	Blast at dockyard, Chatham
11/11/1974	Blast wrecks a public lavatory near a tank range in Castlemartin
14/11/1974	Explosions outside a post office in Shepherds Bush, London
23/11/1974	Bombs blasted two Irish-owned premises in London
13/12/1974	Pillar-box exploded due to electrical fault in Marylebone, London
1/5/1977	Oxygen explosion shakes British Rail engineering workshop at Crewe
24/1/1977	Explosion wrecks flat in Blantyre
30/1/1977	Two explosions at chemical laboratory in Erith
3/1977	Blast in a school chemistry laboratory at Burgess Hill
5/4/1977	Gas cylinder explosion in Chessington
30/5/1977	Gas bottle explosion at Blackfriars Railway Bridge, London
21/9/1977	Explosion in a restaurant in Bristol
3/12/1977	Offshore explosion, North Yorkshire
6/1/1978	Bomb left outside charity offices in Horsham
14/3/1978	Caravan explodes in Saffron Walden
20/4/1978	Explosion in the basement of a sex shop in Soho, London
9/5/1978	Hackney flat severely damaged by a blast
12/5/1978	Blast destroys two homes in Glasgow
12/5/1978	Underground mine explosion at Ammenford
1/8/1978	Blast caused fire at a shop in Forest Gate, London
12/9/1978	Letter bomb arrived at the Iraqi Embassy in Queens Gate, London
7/10/1978	Bomb exploded in a car outside Orange Lodge Hall, Liverpool
7/10/1978	Parcel bomb delivered to a flat in Blackpool
22/10/1978	Explosion from compressor on board a Navy diving vessel at Falmouth
25/10/1978	Explosion on a housing estate in Kirby
22/11/1978	Home-made bomb exploded at Ashtead
14/1/1979	A row of Essex seaside houses wrecked by a gas explosion
25/2/1979	Brentwood scout camp partially destroyed by a blast
3/3/1979	Tower block wrecked by an explosion in Battersea, London
15/3/1979	Explosion in a house at Billingham-on-Tees
1/4/1979	Gas cylinder exploded in the basement of the Carlyle Hotel, Bayswater, London
6/4/1979	Council house destroyed by an explosion in South Norwood, London
6/4/–20/6/1979	Ten explosions at various places in London
21/5/1979	Explosion at an ammunitions factory in Birmingham

(*continued*)

Table 1.19. (continued)

Date	Details
9/6/1979	Four letter bombs exploded in two sorting offices in Birmingham
30/8/1979	Molotov cocktail thrown at Irish Embassy social club in Nottingham
18/12/1979	Explosion at a West End office, London
20/12/1979	Package exploded in a betting shop in Glasgow
19/2/1980	Explosion at a Boulby potash mine
20/8/1980	Oil tank exploded at Warrington
11/5/1981	Explosions and fire at an ethylene plant at Grangemouth
22/6/1981	Explosion at the Iraqi Embassy, London
22/7/1981	Fire bomb attack on an Asian family home in Middlesborough
1/10/1981	Device exploded in an Irish diplomat's car in Orpington
1/11/1981	Explosions in ice cream vendor's back garden, Luton
19/3/1982	Explosions in a Marine's camp at Otterburn.
1/8/1982	Bomb exploded outside Ashraq-AR-Awsat newspaper offices, London
23/12/1982	Explosion at a Labour club in Hornsey, London
7/1/1983	Army blows open Irishwoman's van, Hull
1/–12/1983	Letter bombs delivered to 25 places in London
11/7/1983	London flat extensively damaged by an incendiary device
11/12/1983	Woolwich barracks, London, blasted
14/12/1983	Device explodes in a telephone kiosk in Oxford
14/12/1983	Device blown up in Kensington, London, in a controlled explosion
15/12/1983	Briefcase blown open outside the Hilton Hotel, London
24/5/1984	Explosion wrecks the underground water treatment plant a water station in Lancashire
16/6/1984	Three blasts and a fireball in an empty oil tanker at Milford Haven
3/12/1984	Explosion in an electricity substation on Merseyside
20/4/1985	A luggage bomb exploded at Heathrow airport, London
21/10/1985	Blast in a block of flats in Edinburgh
26/11/1985	Bomb explosion at the Iranian Embassy, London
7/1/1986	Blast in a sewer under construction in Glasgow
22/2/1986	Blast at a fireworks factory in Salisbury
16/3/1986	Blast and fire at a chemical plant in Peterlee, Durham
4/4/–9/1986	Nine blasts in streets in London
22/7/1986	Blast in an old people's home in Berkshire
4/11/1986	Electronically-detonated bombs wrecked a public lavatory cubicle in Oxford
1/1987–7/1987	Six bomb blasts in London
21/7/1987	Army defused a fire bomb outside a police station in Wolverhampton
23/12/1987	Petrol bomb attack on council houses in Manchester
24/9/1988	RAF practice bomb safely detonated in Humberside
17/1/1989	A letter bomb was defused at the Israeli Embassy, London
24/2/1989	A power bomb was set off at Bristol University
23/3/1989	Lorry carrying detonators and explosives exploded at Fengate
3/2/2006	The total number of explosions is 105

Table 1.20. Notable explosions in the world

Date	Location	Deaths
31/10/1963	State Fair Coliseum, Indianapolis, USA	73
23/7/1964	Harbour munitions, Bone, Algeria	100
4/3/1965	Gas pipeline, Natchitoches, Louisiana, USA	17
9/8/1965	Missile silo, Searcy, Arkansas	53
21/10/1965	Bridge, Tila Bund, Pakistan	80
30/10/1965	Cartagena, Colombia	48
24/11/1965	Armory, Keokuk, Louisiana, USA	20
13/10/1966	Chemical plant, La Salle, Quebec, Canada	11
17/2/1967	Chemical plant, Hawthorne, New Jersey, USA	11
25/12/1967	Apartment building, Moscow	20
6/4/1968	Sports store, Richmond, Indiana, USA	43
8/4/1970	Subway construction, Osaka, Japan	73
24/6/1971	Tunnel, Sylmar, California, USA	17
28/6/1971	School, fireworks, Pueblo, Mexico	13
21/10/1971	Shopping centre, Glasgow, Scotland	20
10/2/1973	Liquefied gas tank, Staten Island, New York, USA	40
27/12/1975	Mine, Chasnala, India	431
13/4/1976	Munitions works, Lapua, Finland	45
11/11/1976	Freight train, Iri, South Korea	57
22/12/1977	Grain elevator, Westwego, Louisiana, USA	35
24/2/1978	Derailed tank car, Waverly Tennessee, USA	12
11/7/1978	Propylene tank truck, Spanish coastal campsite	150
23/10/1980	School, Ortuella, Spain	64
13/2/1981	Sewer system, Louisville, Kentucky, USA	0
7/4/1982	Tanker truck, tunnel, Oakland, California, USA	7
25/4/1982	Antiques exhibition, Todi, Italy	33
2/11/1982–2006	Salang Tunnel, Afghanistan	30,000
25/2/1984	Oil pipeline, Cubatao, Brazil	508
21/6/1984	Naval supply depot, Severomorsk, USSR	200+
19/11/1984	Gas storage area, northeast Mexico City	334
5/12/1984	Coal mine, Taipei, Taiwan	94
25/6/1985	Fireworks factory, Hallett, Oklahoma, USA	21
6/7/1986	Oil rig, North Sea	166
1/6/1988	Coalmine, Brocken, West Germany	−
4/6/1988	Freight train, Arzamar, USSR	−
27/6/1988	Commuter trains, Paris, France	−
3/7/1988	Commercial Iranian airline, Persian gulf	−
2/2/2006	Total number of blasts in Iraq recorded as 350,000 to 3.5 millions	

Table 1.21. Missiles in the Gulf countries

Country	Missile type	Range (miles)
Libya	M9 missile	410
Egypt	Scud B2	380
Israel	Jericho II	470
Syria	Spider SS23	320
Iran	Silkworm	280
Saudi Arabia	CSS-2 (DF-3)	1,550–1,875

B missile are produced, with a North Korean-manufactured supplementary fuel tank. In this field the team also developed the Badr-2000, which is the improved version of the Argentine Condor-2, ranging over 500 miles. In this area also it is believed that North Korean experts developed a technique of dismantling the warhead to rearrange the explosive charge. It is widely understood that this might be responsible for the blast which occurred at Al-Hillah, at the place chemical weapons are also produced, such as those widely used in the Gulf war. The place is in the striking range from other countries carrying different type of missiles. Table 1.21 gives such ranges.

Another disaster occurred in July 1988 at sea – on the Piper Alpha oil platform in the North Sea. The layout of this platform is shown in Fig. 1.6. Such platforms are designed to withstand the worst wave likely to hit them in 100 years. This may sound favorable, until compared with nuclear power stations or hazardous chemical plants which must be designed so that there is only a one in a million chance of catastrophic accident from all causes. Oil Platforms are inherently dangerous and it appears that, in cases such as the Piper Alpha and a few others, they were designed to far lower safety standards than would be permitted on land. A gas explosion caused the platform disaster. It was due to compressor failure and involved the shattering of a compressor casing by a broken piston.

Since the top was totally integral with the jacket, side blasts could have literally torn out supporting members. The temperature in such circumstances could easily reach 800°C. Steel designed to a typical $340\,\mathrm{N\,mm^{-2}}$ yield strength would be reduced to just $30\,\mathrm{N\,mm^{-2}}$ at the height of the fire at a temperature of 800°C. Collapse of deck equipment, such as the 100 tonne drilling derrick, might have caused additional damage. The blast may have been so large that it destroyed the local gas-detection systems triggering automatic shut down. Since there was a major pipe rupture too, it might have been caused by metal fatigue.

Since this accident, the platform top sides design has inevitably found itself under close scrutiny. Among many issues are the top sides layout location of accommodation modules, detection and shut-down systems, evacuation procedures and the effectiveness of inspection, regulations and guidelines. Overall, it was the worst disaster caused by gas explosions.
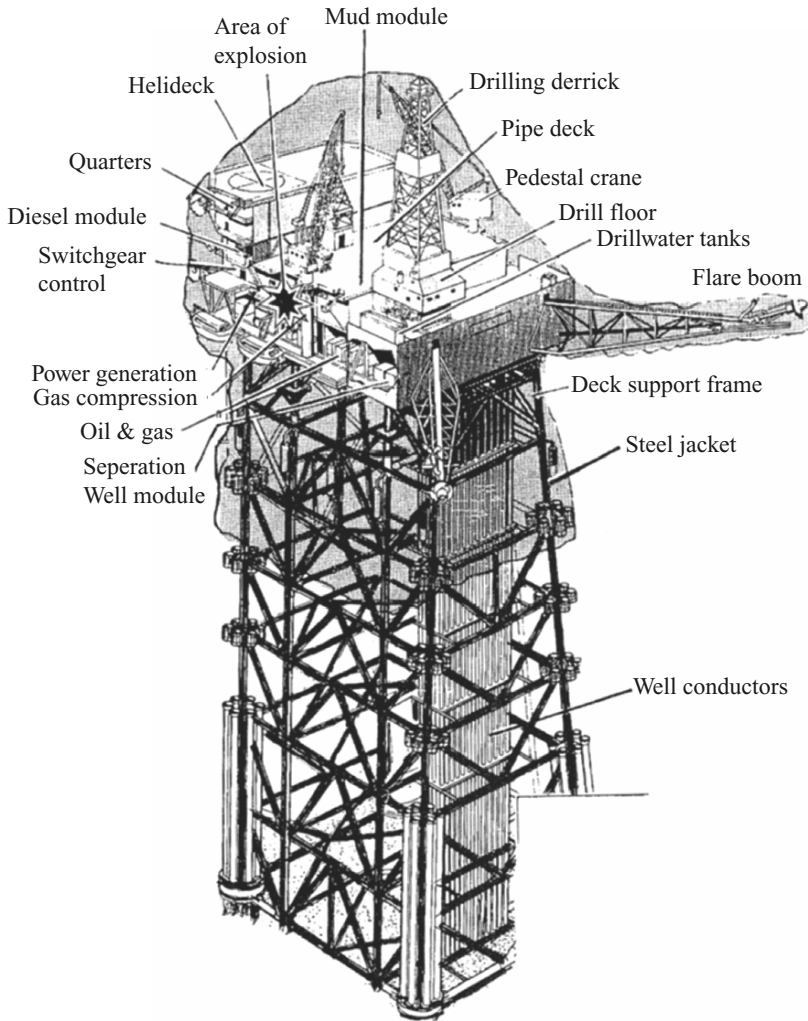
Fig. 1.6. The layout of the Piper Platform

Flats, houses, restaurants and public places where gas is abundantly used have been subject to explosions. In October 1971, the gas explosions in the town of Clarkston, Glasgow, Scotland, which killed 20 people, initiated a fundamental rethinking of building methods in the basements of large buildings. The disaster occurred because of the way shop basements were constructed in relation to the nearby gas main. The 20 shops in the terrace were built in 1965. As shown in Fig. 1.7 with the exception of shop 13, there was no access to the front basement of any shop, built in prestressed concrete, which had neither individual side walls nor a front wall – the only access, indeed, was through manholes at either end of the block. The front basements were half

Fig. 1.6a. The aftermath of Piper Alpha

filled with loose clay at an angle of 45° running back from the footpath. At 1 m down and about 1 m from the building line was a 100 mm gas pipe running under the pavement. Owing to dead and imposed loads on the roadway and footpath and insufficient support from loose soils underneath, the pipe must have buckled and finally cracked. The explosions in the first few shops were minor and their floors were less severely damaged. The gas se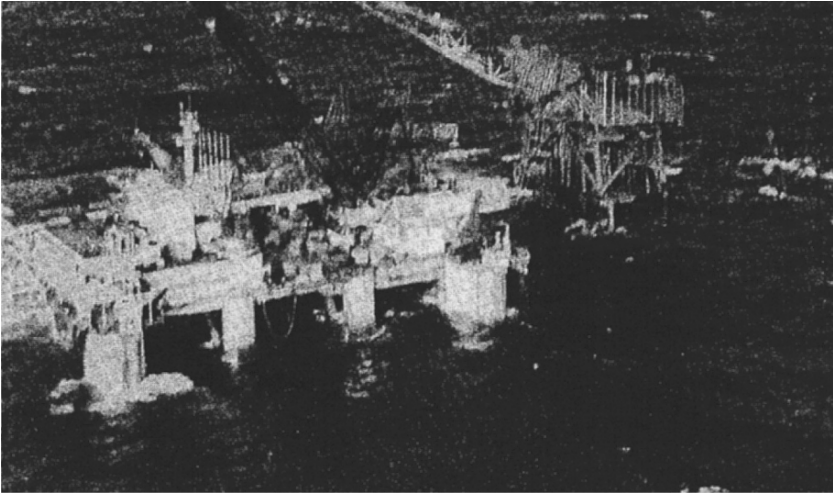eped backwards into what was a kind of "tunnel" running along the terrace formed by the front basements. The gas lay in huge pockets between concrete girders. A mixture of gas and air caused an explosion when it reached the pockets.

While the possibility of gas explosions in domestic buildings cannot be ruled out, attention was focused on this hazard only in 1968 when the Ronan Point disaster, London, occurred. As shown in Fig. 1.8. Ronan Point was a 22-storey block, 192 m high and 24 m × 18 m on plan. It was built using the Larssen and Nielsen system of pre-cast concrete panel construction. On 16 May 1968 at 5.45 am there was an explosion in flat 90, a one-bedroom flat on the southeast corner of the 18th floor. The explosion blew out the cladding which acted as non-load bearing walls of the kitchen and living room. As the floor slab collapsed, the flank panel walls and floors above fell, causing progressive collapse of the floor and wall panels in the corner of the block right down to the podium. Gas is believed to have leaked into the flat from a broken connection at the gas cooker. It is believed that the gas could have risen to the ceiling, mixed with air and thus formed a gas/air layer at the kitchen ceiling which gradually extended downwards until it flowed under the door lintel and accumulated in the flat.

Similar explosions occurred in Putney houses and in a three-storey house in Balham Market in London, UK. The former was caused by a gas leak and
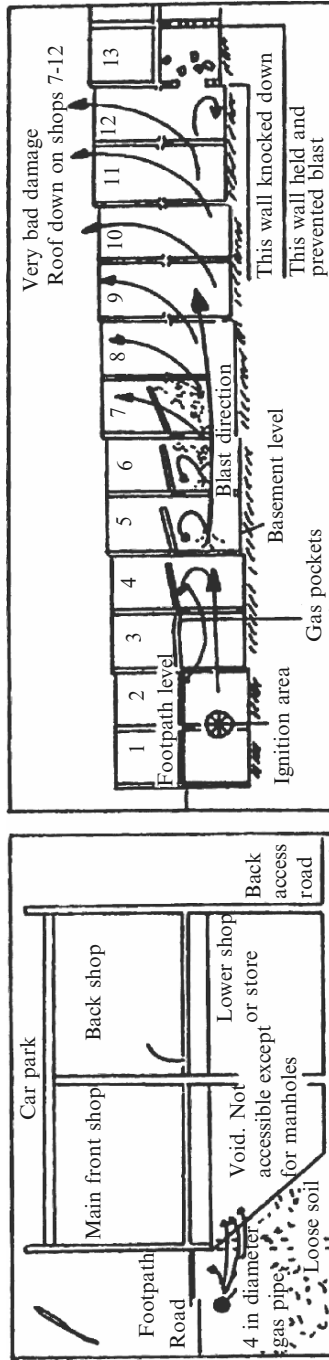
Fig. 1.7. Gas explosions in basements in Clarkston, Glasgow
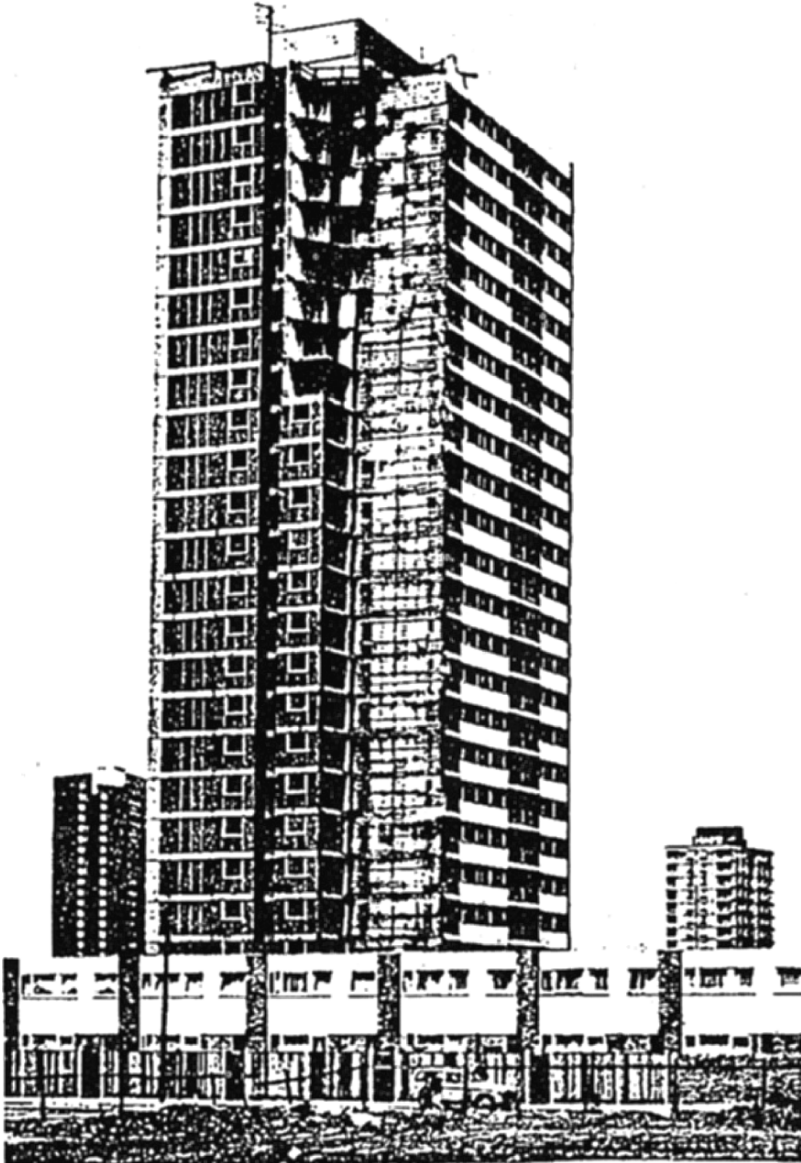
Fig. 1.8. Gas explosion at Ronan Point (courtesy of the British Ceramic Society U.K.)

the latter by a cigarette lit too close to a gas cylinder. A number of people were killed and injured.

At about 7.30 am on 4 October 1989 an explosion occurred in Guthrie Street in the centre of the old part of Edinburgh, Scotland, crumbling six flats to the ground and leaving part of their roof hanging precariously. All flanking

buildings remained standing, although one was later pulled down. The scale of damage caused by the explosion suggested a large build-up of gas, probably in the stairwwell of the building. Only the basement ceiling stayed in place. A fracture was found in the 200 mm cast iron pipe located above the main sewer which led in the direction of the flats in Guthrie Street. It is probable that the gas from this fracture reached the building and caused an explosion.

Table 1.22 records gas explosions in selected countries.

Table 1.22. Gas explosions in selected countries

| Country	No. of explosions	Country	No. of explosions
Afghanistan	50^a	Korea (North)	$131^{b,c}$
Albania	71	Korea (South)	$310^{b,c}$
Algeria	310^a	Kuwait	375^a
Argentina	536^b	Libya	30^{a-c}
Australia	590^b	Malaysia	51^{a-c}
Austria	115	Morocco	330^a
Bahrain	400^a	Netherlands	150^b
Bangladesh	58^a	New Zealand	–
Brazil	350^b	Nigeria	550^a
Bulgaria	$31^{b,c}$	Norway	150^b
Burma	370^b	Pakistan	$88^{a,b}$
Canada	318^b	Philippines	85^c
Chili	200	Poland	61^c
China	710^b	Portugal	$220^{b,c}$
Colombia	35	Qatar	90^b
Cuba	$20^{a,b}$	Saudia Arabia	210^a
Cyprus	30^b	Singapore	$110^{a,b}$
Egypt	$500^{a,b}$	South Africa	310^{a-c}
Fiji	10^b	Spain	$610^{b,c}$
Finland	200^b	Sri Lanka	69^b
France	250^b	Sudan	$75^{a,b}$
Germany	150^b	Sweden	$95^{b,c}$
Greece	350^b	Switzerland	50^b
Hong Kong	150^b	Syria	$161^{a,b}$
India	$1509^{b,c}$	Tunisia	175^a
Indonesia	170^b	Turkey	$310^{a,b}$
Iran	$10^{b,c}$	United Arab Emirates	400^a
Iraq	15^{a-c}	USA	$670^{a,c}$
Irish Republic	150^b	USSR	$1100^{b,c}$
Israel	40^b	Yugoslavia	$210^{b,c}$
Italy	$450^{b,c}$	Zaire	89^c
Japan	$310^{b,c}$	Zambia	120^b
Kenya	$70^{b,c}$	Zimbabwe	110^b

[a] Mostly gas cylinders
[b] Mostly domestic
[c] Mostly in mines or industry

1.8 Nuclear Explosions and Loss-of-Coolant Accidents

Nuclear explosions result from the very rapid release of a large amount of energy within a limited space. Nuclear explosions can be many thousands of times more powerful than the largest conventional detonations. In a nuclear explosion the temperatures are comparatively greater and the energy is emitted in the form of light and heat, referred to as *thermal radiation*. The measure of the amount of explosive energy is known as the *yield* and is generally stated in terms of the equivalent quantity of TNT. For example, a 1 kiloton (1,000 tonne) nuclear weapon is one which produces the same amount of energy in an explosion as does 1 kiloton of TNT. These effects are directly responsible for structural damage.

On 6 August 1945, at about 8.15 am, a new era was born amidst death and destruction as the US Air Force B-29 bomber banked away after dropping a 13.5 kiloton bomb on Hiroshima. On 9 August 1945, at about 12.01 pm, a similar bomb was dropped over Nagasaki, killing and maiming many hundred thousands of people. Figure 1.9 shows the nuclear fireball at Hiroshima. In these two cities the nuclear bomb damage was extensive. Everywhere debris was evidence to how a disaster occurred in Japan in split seconds. People from other areas witnessed the buckling of structural frames, collapsed roofs, caved-in walls, shattered panels and damage to windows, doors, vehicles, trains, etc. In this city light structures and residences were totally demolished by the blast. Industrial buildings were denuded of roofing and siding. Some robust
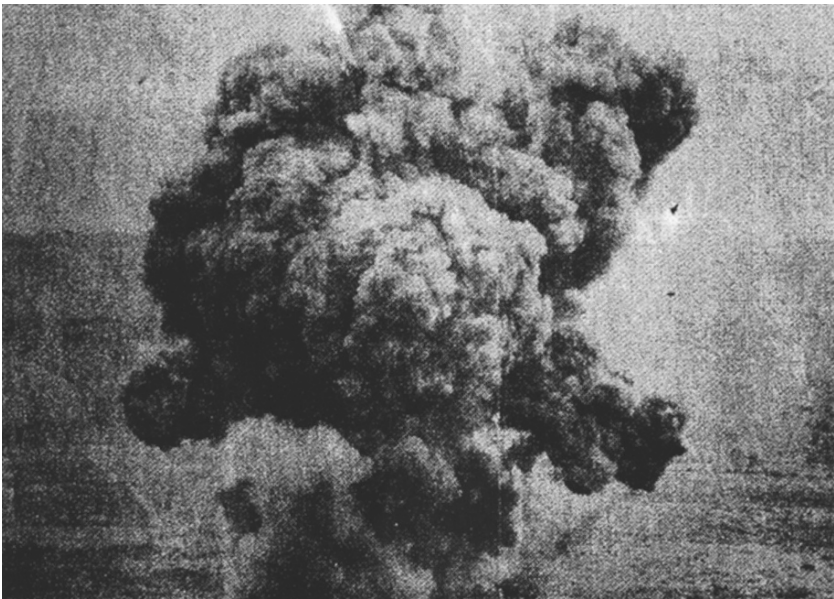

Fig. 1.9. Nuclear fireball at Hiroshima

buildings leaned away from ground zero. All masonry buildings were engulfed by the blast wave pressure and collapsed. Buildings and other structures at a distance away suffered damage. Underground pipes burst and much of the area was gutted by the sudden release of fire. A similar scene was witnessed in Nagasaki.

Other types of nuclear accident involve the nuclear reactors of commercial and military establishments. The loss-of-coolant accident at Three Mile Island (USA) and a similar one with fire at Chernobyl (USSR) received widespread media coverage.

A list of some notable nuclear accidents is given below.

- *7 October 1957.* A fire in the Windscale plutonium production reactor north of Liverpool, UK, spread radioactive material throughout the countryside.
- *3 November 1957.* A chemical explosion in Kasli, USSR, in tanks containing nuclear waste, spread radioactive material.
- *3 January 1961.* An experimental reactor at a federal installation near Idaho Falls, USA, killed three workers. The plant had high radiation levels but damage was contained.
- *5 October 1966.* A sodium cooling system malfunction caused a partial core meltdown at the Enrico Fermi demonstration breeder reactor near Detroit, USA. Radiation was contained.
- *21 January 1969.* A coolant malfunction from an experimental underground reactor at Lucens Vad, Switzerland, resulted in the release of a large amount of radiation into a cavern which was then sealed.
- *19 November 1971.* The water storage space at the Northern States Power Company's reactor in Monticello, USA, filled to capacity and spilled over, dumping about 50,000 gals of radioactive waste water into the Mississippi River.
- *22 March 1975.* A technician checking for air leaks with a lighted candle caused a fire at the Brown's Ferry reactor in Decatur, USA. The fire burned out electrical controls. The cost was $100 million.
- *28 March 1979.* The worst commercial nuclear accident in the USA occurred as equipment failures and human mistakes led to a loss of coolant and partial core meltdown at the Three Mile Island reactor in Middletown, USA.
- *7 August 1979.* Highly enriched uranium was released from a top-secret nuclear fuel plant near Erwin, USA.
- *11 February 1981.* Eight workers were contaminated when over 100,000 gal of radioactive coolant leaked into the containment building of the TVA's Suquohay 1 plant in Tennessee, USA.
- *25 April 1981.* Some 100 workers were exposed to radioactive material during repairs of a nuclear plant at Tsuruga, Japan.
- *25 January 1982.* A steam-generator pipe broke at the Rochester Gas & Electric Company's Ginna plant near Rochester, New York, USA. Small amounts of radioactive steam escaped into the air.

Table 1.23. Nuclear accidents in various countries in the years 1984–2006

Country	Number
Canada	1,500
China	1,200
France	2,800
Germany	3,100
India	1,700
Israel	1,100
Italy	800
Japan	350
Netherlands	150
Pakistan	5
Sweden	110
Switzerland	–
UK	1,750
USA	4,150
USSR	–

- *6 January 1986.* A cylinder of nuclear material burst after being improperly heated at a Kerr-McGee plant at Gore, USA.
- *April 1986.* A serious accident at the Chernobyl nuclear plant about 60 miles from Kiev in the Soviet Union caused the emission of clouds of radiation that spread over several other countries.

In 1986 and 1987, the number of accidents in US commercial nuclear power plants was 2,836 and 2,810, respectively. In the years 1984–2006, the accidents which occurred outside nuclear islands are listed in Table 1.23.

1.9 The Gulf War

The Gulf war between Iraq and the USA and its allies was a perfect example of the kind of precise, high-technology air war one would expect in this age. The full-scale war began on 16 January 1990. For weeks the dominant image of the battle was a grainy video clip. A tiny bomb headed for a tiny building or a tiny puff of smoke exploded across the screen. The scene made the war seem remote and bloodless. Looking at the aftermath, the world discovered a total destruction of the important zones of the country and a great tragedy to its people. The initial operation of the war was purely from the air. The USA-led coalition flew more than 10,000 sorties, targetting command-and-control centres, airfields and scud missile launchers.

The long-range attack was carried out from ships, submarines and aircraft. Cruise missiles, Stealth fighter bombers, electronic jamming, the Patriot system, "smart bombs" and night division devices all took part. The Tomahawk cruise missiles (range 780 miles), launched from naval ships and flying at the

speed of a commercial airline, used digital mapping technology to penetrate beneath Iraqi radar and strike within 18 m of their targets. The US Air Force F-117A Stealth fighters led the aircraft strike. The F-4G aircraft Wild Weasel launched missiles that homed in on the signals to knock out the emitting facility and so kept the Iraqis from co-ordinating their surface-to-air missiles (SAMs).

Some of the F-15E Eagle and F-16 Fighting Falcon attackers released their ordinance from as high as 600 m, well above the light calibre Iraqi flak. These fighters, as well as the US Navy's F/A-18 Hornets, also delivered laser-guided or other smart bombs to their targets. The B-52 bombers created havoc and with their carpet bombing destroyed much of the enemy's military arsenal and personnel. Tornado GR-1S aircraft with F-4G escorts took out airfields and radar equipment. AWACs were used to monitor attacks. Impacts/explosions could be witnessed between Patriot and Scud missiles (also known as SS-1 missiles). GBU-15(V)2 glide bombs (weight 2,450 lb, length 12.75 ft (3.9 m), also known as smart bombs) were focused on various targets.

1.10 Recent Air Crashes: Aircraft Impact at Ground Level

On 18 September 1992, a Pakistan International Airways Airbus crashed near Katmandu, Nepal. The jagged ridges were clouded. The aircraft passed only 2,500 ft (761.9 m) above the mountains. All 167 people on board were killed when the aircraft hit the mountains.

On 4 October 1992, an El Al jet cargo 747–220F plane from Schiphol airport crashed and impacted a block of flats in Amsterdam. One engine caught fire and both starboard engines fell off thus destabilizing the plane and preventing it from flying.

Both crashes are being investigated at the time of printing.

1.11 The Dust Explosion Hazard

Dust explosions have been a recognized threat to humans and property for a long time. One of the earliest comprehensive reports known is Count Morozzo's (1795) detailed analysis of an explosion in the flour warehouse of Mr. Giacomelli in Turin in 1785. It is interesting to observe that Morozzo also mentions even earlier incidents of violent combustion of clouds of flour in air.

However, at the time of Morozzo, the coal mining industry was not fully aware of the important part played by coal dust in the serious coal mine explosions, which had become quite common. Faraday and Lyell (1845) were probably some of the first scientists to realize the central role of coal dust in these explosions. In their report to Sir James Graham, they discussed the

fatal explosion in the Haswell coal mine near Durham, United Kingdom, on 28 September 1844. It was concluded that the primary event was a methane/air ("fire-damp") explosion initiated by a defective Davy lamp. However, the central role of the coal dust in developing the devastating main explosion was emphasized, based on a systematic analysis that is exemplary even today. In their report Faraday and Lyell stated:

> "In considering the extent of the fire for the moment of explosion, it is not to be supposed that fire damp is its only fuel; the coal dust swept by the rush of wind and flame from the floor, roof, and walls of the works would instantly take fire and burn, if there were oxygen enough in the air present to support its combustion; and we found the dust adhering to the face of the pillars, props, and walls in the direction of, and on the side towards the explosion, increasing gradually to a certain distance, as we neared the place of ignition. This deposit was in some parts half an inch, and in others almost an inch thick; it adhered together in a friable coked state; when examined with the glass it presented the fused round form of burnt coal dust, and when examined chemically, and compared with the coal itself reduced to powder, was found deprived of the greater portion of the bitumen, and in some instances entirely destitute of it. There is every reason to believe that much coal-gas was made from this dust in the very air itself of the mine by the flame of the fire-damp, which raised and swept it along; and much of the carbon of this dust remained unburned only for want of air."

During the 150–200 years that have passed since the days of Morozzo and Faraday, the phenomenon of dust explosions has become fully accepted as a serious industrial hazard. Furthermore, since that time, the expanding chemical and metallurgical industries have given birth to a steadily increasing number of new, finely divided combustible solid materials that have caused dust explosions to remain a significant hazard in many industries. As an important element in the constant efforts to fight the dust explosion hazard actual accidents are carefully investigated. In some countries, valuable statistical records are available, some of which are discussed in the following sections.

1.11.1 Dust Explosions in the United States, 1900–1956

The National Fire Protection Association published a report of important dust explosions in the United States from 1900 to 1956 (NFPA, 1957). The report gives informative details of a selection of 75 of the most serious and recent of the 1,123 explosions recorded. The selection covers a wide range of dusts from all the categories–wood, food and feed, metals, plastics, coal, paper, and chemicals. In addition, each of the 1,123 explosions is mentioned

briefly individually by specifying the date, location, dust involved, probable ignition source, number of fatalities and injuries, and material losses.

Table 1.24 gives an overall summary of the consequences of explosions involving various dust categories. The table illustrates some interesting differences. For example, the metal dust explosions, representing 7.1% of the total number of explosions, were responsible 16% of all the fatalities and 11.2% of all the injuries but only 3.2% of the material losses. The food and feed dust explosions also were responsible for higher percentages of fatalities and injuries than the 51.4% share of the number of explosions. Furthermore, food and feed caused by far the highest material loss per explosion. The pulverized coal dust explosions (not mining), on the contrary, caused lower percentages of fatalities, injuries and material losses than their share of the total number of explosions.

1.11.2 Dust Explosions in the Federal Republic of Germany, 1965–1985

Table 1.25 provides some data from the Federal Republic of Germany that can be compared directly with the older data from the United States in Table 1.26. There are interesting differences in the distribution of the number of explosion accidents on the various dust categories. This may reflect both a change with time, from the first to the second part of this century, and differences between the structure of the industry in the United States and the Federal Republic of Germany.

Table 1.26 shows how the involvement of various categories of plant items in the explosions varies with dust type. This reflects differences between typical processes for producing, storing, and handling the various categories of powders and dusts.

Table 1.27 provides an interesting correlation between the various plant items involved in the explosions and the probable ignition sources. Mechanical sparks are frequent ignition sources in dust collectors, mills, and grinding plants, whereas smoldering nests are typical when the explosion is initiated in silos, bunkers and dryers.

1.11.3 Recent Statistics of Grain Dust Explosion in the United States

Schoeff (1989) presented some statistical data that are shown in a slightly rearranged form in Table 1.28. The data for 1900–1956 are from the same source as the data in Table 1.3. The alarming trend is that the annual number of explosions seems to increase rather than decrease. The annual number of fatalities is also higher for the last period, 1979–1988, than for the previous one, 1957–1975. The annual number of injuries for the last period is higher than for both previous periods. From 1957–1975 to 1979–1988, the annual estimated damage to facilities seems to have increased more than what can be accounted for by inflation.

Table 1.24. Dust explosions in the United States, 1900–1956: fatalities, injuries, and material losses in a sample of 1,123 accidental explosions

Type of dust	Explosions		Fatalities			Injuries			Material losses	
	Number	%	Number	%	Per explosion	Number	(%)	Per explosion	Million $[a]	Per explosion
Wood and bark	162	14.5	38	5.6	0.23	160	9.0	0.99	11.4	0.070
Food and feed	577	51.4	409	60.5	0.71	1061	60.0	1.84	75.8	0.131
Metals	80	7.1	108	16.0	1.35	198	11.2	2.48	3.2	0.040
Plastics	61	5.4	44	6.5	0.72	121	6.8	1.98	3.7	0.061
Coal (not mines)	63	5.6	30	4.4	0.48	37	2.1	0.59	1.6	0.025
Paper	9	0.8	0	0.0	0.0	0	0.0	0.0	0.5	0.056
Others	171	15.2	47	7.0	0.27	193	10.9	1.13	4.3	0.025
All	1,123	100.0	676	100.0		1,770	100.0		100.5	

Source: Data from NFPA, 1957

[a] Numerical value in U.S. dollars at year of explosion, not inflated

Table 1.25. Dust explosions in the Federal Republic of Germany 1965–1980: fatalities and injuries in a sample of 357 explosions

Type of dust	Explosions		Fatalities			Injuries		
	Number	(%)	Number	(%)	Per explosion	Number	(%)	Per explosion
Wood	113	31.6	12	11.7	0.11	124	25	1.10
Food and feed	88	24.7	38	36.8	0.43	127	26	1.44
Metals	47	13.2	18	17.5	0.38	91	18.5	1.94
Plastics	46	12.9	18	17.5	0.39	98	20	2.13
Coal and peat	33	9.2	7	6.8	0.21	39	8	1.18
Paper	7	2.0	0	0.0	0.0	0	0	0.0
Others	23	6.4	10	9.7	0.43	13	2.5	0.56
All	357	100.0	103	100.0	0.43	492	100.0	0.56

Source: Beck, 1982

Table 1.26. Dust explosions in the Federal Republic of Germany 1965–1985: frequencies in percent of primary involvement of various plant items in a total of 426 dust explosions and in the explosions of various categories of dusts

Type of plant item	Total of 426 explosions			Wood and wood products	Coal and peat	Food and feed	Plastics	Metals
	Number	% of total	% change 80/85					
Silos and bunkers	86	20.2	0	35.9	23.1	22.9	2	2
Dust collecting systems	73	17.2	+2.9	18.0	5.1	9.5	13.5	45.6
Milling and crushing plants	56	13.0	−0.7	7.0	12.8	18.1	15.4	5.3
Conveying systems	43	10.1	0	4.7	5.1	26.7	17.3	2.0
Dryers	34	8.0	+0.4	10.2	2.0	7.6	9.6	2.0
Furnaces	23	5.4	+0.1	10.9	18.0	2.0	0	0
Mixing plants	20	4.7	+0.2	0	5.1	2.0	17.3	3.5
Grinding and polishing plants	19	4.5	0	3.9	0	0	2	22.8
Sieves and classifiers	12	2.8	−0.3	4.7	0	2.8	0	3.5
Unknown and others	60	14.1	−2.6	4.7	28.8	8.4	22.9	13.3
All	426	100.0	0	100.0	100.0	100.0	100.0	100.0

Source: Jeske and Beck, 1989

Table 1.27. Dust explosions in the Federal Republic of Germany 1965–1985: frequencies in percent of various types of ignition sources of explosions initiated in various plant items

Type of ignition source	All 426 explosions	Silos and bunkers	Dust collectors and separators	Mills and crushing plants	Conveying systems	Dryers	Mixing plants	Ginding plants	Sieves and classifiers
Mechanical sparks	26.2	16.3	41.1	60.0	25.6	0	15.0	89.5	16.7
Smoldering nests	11.3	27.9	11.0	0	2.3	29.4	0	0	8.3
Mechanical heating and friction	9.0	3.5	6.8	12.7	25.6	2.9	25.0	5.3	0
Electrostatic discharges	8.7	2.3	9.6	5.5	18.6	5.9	45.0	0	16.7
Fire	7.8	4.7	4.1	2	0	0	5.0	0	16.7
Spontaneous ignition (self-ignition)	4.9	2.3	2.7	0	4.7	14.7	0	0	8.3
Hot surfaces	4.9	11.6	0	3.6	2.3	23.5	0	0	0
Welding and cutting	4.9	5.8	2	0	4.7	2.9	5.9	0	0
Electrical machinery	2.8	2.3	2	0	0	0	0	0	0
Unknown and others	19.5	23.3	20.7	16.2	16.2	20.7	4.1	5.2	33.3
All	100.0	100.0	100.0	100.0	100.0	100.0	100.0	100.0	100.0

Source: Jeske and Beck, 1989

Table 1.28. Grain dust explosions in the United States: recent development

Loss category	1900–1956		1957–1975		1979–1988	
	Total	Per year	Total	Per year	Total	Per year
Number of explosions	490	8.6	192	10.1	202	20.2
Fatalities	381	6.8	68	3.6	54	5.4
Injuries	991	17.4	346	18.2	267	26.7
Estimated damage to facility (U.S. $ millions), not inflated	70	1.3	55	2.9	169	16.9

Source: Data from Schoeff, 1989

1.12 The Explosion in a Flour Warehouse in Turin on 14 December 1785

This is probably the most-frequently quoted of all dust explosions that occurred. However, only very rarely are details of Count Morozzo's (1975) fascinating account mentioned. It is therefore appropriate to start this sequence of case histories with the full original account of what wheat flour explosion in Mr. Giacomelli's bakery in Turin. The explosion was a comparatively minor one, but there is still much to learn from Count Morozzo's analysis. The considerations related to the low moisture content of the flour due to dry weather are important and still relevant. The same applies to the primary explosion causing a secondary explosion by entrainment of dust deposits.

1.13 Grain Dust Explosions in Norway

1.13.1 Wheat Grain Dust, Stavanger Port Silo, June 1970

The explosion, which was discussed by Astad and Mo (personal communications from A. Astad, director, Stavanger Port Silo, and A. Mo, Norwegian Grain Corporation, 1970), occurred in Norway's largest and newly built import grain silo in Stavanger on a hot, dry summer day. Fortunately, no persons were killed, but some workers suffered first degree burns. Although the extent of flame propagation was considerable, the material damage was moderate, due to the comparatively strong reinforced concrete structure of the buildings and the venting through existing openings.

The entire event lasted for a period of about 25–30 s, during which a sequence of six or seven distinct major explosions was heard. In the middle of this sequence was an interval of 10–12 s. The flame propagated a total distance of about 1,500 m, through a number of bucket elevators, horizontal conveyors, ducting filters and rooms in the building. Dust explosions occurred in six of the large cylindrical storage silos of total volume 2,000 m³ each in one large slightly smaller silo in seven of the slimmer intermediate silos of

capacities 400 or 1,000 m^3 in one 150 m^3 silo and in seven loading out-silos with capacities of 50 m^3 each. The six largest silos had no venting whereas the explosions in the large silo of slightly smaller volume and in all the intermediate and loading out silos were vented through 0.4 m^2 manholes, which had their covers flung open.

It is of interest to note that only one silo was damaged in the incident, namely one of the six unvented large storage silos, which had its roof blown up. It is therefore clear that the maximum explosion pressures in all the other 21 silos, vented and unvented were lower than about 0.2 bangs, which would be required to blow up the actual type of silo roof.

Almost all the windows except those in the offices were blown out as was a large provisional light wall at the top of the head house. The legs of all five bucket elevators (0.65 m × 0.44 m cross-section) were torn open from bottom to top. The dust extraction ducts were also in part torn open.

1.13.2 Wheat Grain Dust, New Part of Stavanger Port Silo, October 1988

The explosion was described by Olsen (personal communication from Olsen, 1989). Because of effective mitigation by explosion suppression and venting, both the extent of and damage caused by the explosion were minor. There were neither fatalities not injuries. The incident deserves attention, however, because the chain of events leading to the explosion initiation was identified and the incident illustrates that proper measures for explosion mitigation are effective.

The explosion occurred in a bucket elevator head immediately after termination of transfer of Norwegian wheat grain between two silo cells. At the moment of explosion the transport system was free of grain. In this new part of Stavanger Port Silo, the bucket elevator legs are cylindrical and mounted outdoors, along the wall of the head house. A number of vents are located along the length of the legs. The vent covers on the elevator legs involved were blown out, which undoubtedly contributed to reducing the extent of the explosion. There was no significant material damage either by pressure or by heat.

1.13.3 Grain Dust (Barley/Oats), Head House of the Silo Plant at Kambo, June 1976

This explosion, described by Storli (personal communication, Storli, Norwegian factory in reply to inspectorate, 1976), caused considerable material damage but due to fortunate circumstances, neither fatalities nor significant injuries. The dust involved was from Norwegian barley or oats.

The explosion probably started in a bucket elevator, initiated by burning or glowing material from an overheated hammer mill. The primary explosion developed into a secondary explosion in the head house itself, which pushed out most of the front wall of the head house.

1.13.4 Malted Barley Dust, Oslo Port Silo, July 1976

The explosion, described by Johansen (1976), occurred in an old silo building in the central harbor area of Oslo at about 7:30 on a dry summer morning. The material damage was extensive and much debris was thrown into the surroundings. However due to several fortunate circumstances there was neither loss of life nor severe injuries.

The dust involved was from malted barley of only 5–6% moisture content. The ignition source was not identified but the explosion probably started in a silo cell and propagated to other cells through the common dust extraction system. The primary explosions in the silo cells blew up the cell roofs which were part of the floor of the silo loft and gave rise to an extensive secondary explosion in the loft, blowing up the entire silo roof. The damage was so extensive that the entire building had to be demolished.

1.13.5 Malted Barley Dust, Oslo Port Silo, June 1987

The explosion, described by Johansen, Johansen and Mo (1987) occurred on a warm dry summer day during unloading of malted barley from a ship. There were neither fatalities nor injuries and no damage to the building apart from broken window panes and a broken silo cell roof.

1.14 A Dust Explosion in a Fish Meal Factory in Norway in 1975

The explosion, took place at the end of a hot, dry day in august 1975, in one of the many fish meal factories located along the Norwegian west coast. A young worker lost his life due to severe burns and another was injured. At the time of the explosion, the Norwegian factory inspectorate had just about realized its very first set of rules for fighting industrial dust explosions. Hence, the general appreciation of the dust explosion hazard in Norwegian industry was still meager.

The part of the factory involved in the explosion was the fish meal grinding plant, illustrated in Fig. 1.10. This plant was located in a 30 m tall building that also continued several fairly large storage and mixing silos. The three silos played a key role in the development of the explosion, were 12 m high with diameters of about 3 m the wooden floor of the loft of the building also served as the common roof of the three silos. Close to the top of the silos there were 0.1 m × 1 m open slots in the common wall between silos no. 1 and no. 2 and no. 2 and no. 3. The original purpose of the three silos was to store the production of fish meal accumulated during the night shift, allowing the screening operation to be limited to the day shift.

In addition to having a much larger specific surface area than the main fish meal product, in periods of hot and dry weather as on the day of the explosion, this fine dust would become quite dry. Because of the heat liberated
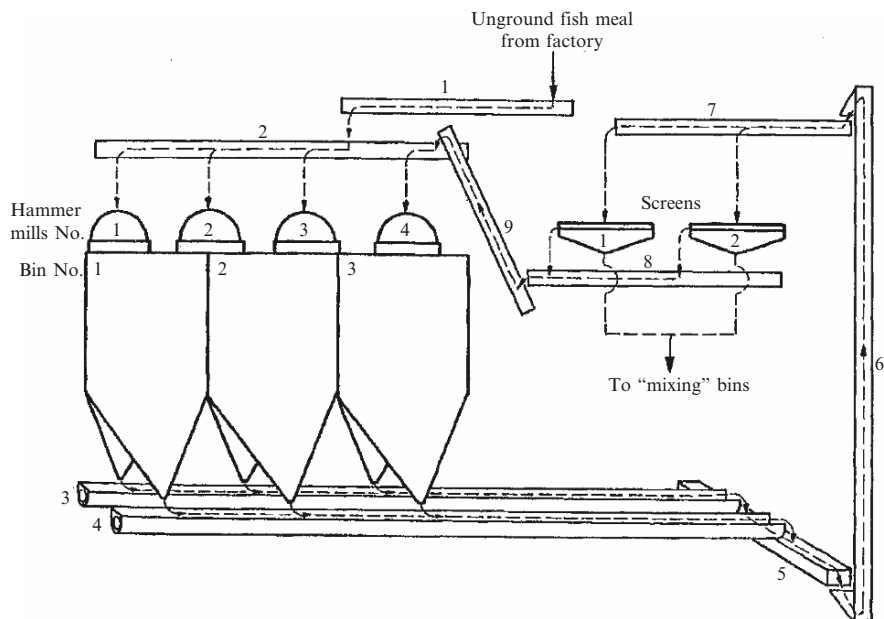
Fig. 1.10. The fish meal grinding plant afflicted with a dust explosion in 1975

by the production process itself, the temperature in the loft of the silo building would frequently be in the range 25–30°C. On the exceptionally hot day of the explosion, the temperature in the loft in the middle of the day was 45°C.

One particular feature of the screw conveyors of this plant was that the bolts fixing the crew blades to the shaft (bolts of lengths 110–120 mm and diameters 12–16 mm) broke fairly regularly, presumably as a result of material fatigue. In spite of frequent bolt failures, the plant made no provision for trapping tramp metal, such as broken bolts, before it reached the hammer mills. Neither were there any instructions for controlling the crews to replace defective bolts in advance. As a consequence, the entrance of broken bolts and other tramp metal into the hammer mills was a fairly frequent event. The presence of bolts in the mills created a most unpleasant noise, which warned the operators of the plant. The normal procedure for removal of bolts from the mill was to open the 250 mm × 180 mm door in the mill chute and wait until the foreign metal object eventually found its way out of the opening.

The explosion was also observed from the outside by two persons who just happened to pass by. One distinct and fairly strong explosion could be heard. This was followed by a large pyramidal flame lasting for 30–45 s and extending 4–5 m above the roof of the building. The explosion was sufficiently strong to blow out windows in the building even in other parts than the loft.

Hence the three key ingredients needed for generating a serious dust explosion were present: large enclosures that were empty apart from explosible dust clouds, large quantities of dust throughout the entire building and an ignition source.

1.15 Smoldering Gas Explosion in a Silo Plant in Stavanger, Norway, in November 1985

This accident, was not primarily a dust explosion but an explosion of combustible gases released from a solid organic material during self-heating in a silo cell. At first glance, such an event may seem out of place in the context of dust explosions. However, smoldering combustion is most often related to powders and dusts; therefore, the initial smoldering gas explosion, in most cases, entrains combustible dust and the explosion can easily develop into a normal dust explosion. The explosion occurred in a fairly modern reinforced concrete silo complex used to store various feedstuffs. Pellets of Canadian rape seed flour had been stored in one of the silos for some time, when it was discovered that the material in the bottom part of the silo had become packed to a solid mass and could not be discharged through the silo exit. Some time later, one week before the explosion, flames were observed in the silo. The fire brigade was called and covered the pellets in the silo with foam from above. Various unsuccessful attempts were then made at discharging the pellets mass at the silo bottom. During this phase there was considerable development of smoke, which mixed with the air, not only in the silo cell in question but also in the silo loft above the cells. It is probable that the smoke contained combustible gases, such as CO, and that the strong explosion, which occurred just after the top of the pellets had been covered with foam once more, was mainly a gas explosion. However, any dust deposits in the loft may also have been involved. The entire roof of the building was blown up, and debris was thrown into the surrounding area. The explosion probably started in a main dust filter, ining dust in the unloading screw at the filter bottom. Due to the buildup of explosion pressure in the filter, the airflow in the dust extraction duct to the filter was reversed, and the explosion propagated upstream to the silo cell to which the duct was connected. The resulting explosion in the silo cell blew up the part of the concrete floor of the loft that was also the roof of that particular silo cell, and a fairly strong explosion occurred in the loft. The explosion also propagated from the filter to a bucket elevator that was torn open which gave rise to a secondary explosion in the room. Furthermore, the explosion propagated to the truck loading station of the silo plant.

1.16 Four Grain Dust Explosions in the United States, 1980–1981

1.16.1 Inland Grain Terminal at St. Joseph, Missouri, April 1980

The explosion, which occurred in the middle of the day, killed one person and injured four. Material damage was estimated at US $2 million. The explosion probably started in a dust cloud in a silo cell used for the receipt and delivery of grain. The probable ignition source was an electric arc between the electric

wires of the lower-level indicator in the silo. Repeated filling and discharge of grain had pulled the level indictor from the wall and the electric arc occurred between the bare wires that had been pulled out of their conduit.

Severe structural damage occurred to almost all the silos in the head house and moderate damage to most of the head house structure. Most of the head house silo roofs were blown up, destroying the spout floor and the top of the cleaner floor. Rupture of the silos around the edge of the head house caused failures in the outside wall. The casings of all bucket elevators, steel as well as concrete had opened up in many places. A silo complex comprising 18 cells suffered severe explosion damage to the gangway connecting it to the head house, to the gallery, to the far end of the tunnel and to a small group of silos centered around an airshaft approximately one-third of the way along the gallery. At the location of the airshaft, the gallery wall and roof had been completely destroyed. Beyond this pinot the explosion damage to the gallery was still significant but not as severe. The exterior concrete silo walls had been extensively shattered in many places leaving only the reinforcing rods.

1.16.2 River Grain Terminal at St. Paul, Minnesota, 10 June 1980

The explosion occurred just before lunchtime. There was no fatalities, but 13 persons were injured. The material loss was estimated at about US $0.3 million. The probable cause of the explosion was that an electrician was repairing live electrical equipment in a truck-receiving cross tunnel, while the elevator was unloading grain trucks. The ignition source probably was electric arcing in an open electric junction box located within an explosible dust cloud.

The blast and flame front moved in one direction long the tunnel into the head house basement. There were open spouts to the bucket elevators, and with the secondary explosion in the basement initiated by the cross tunnel explosion, the explosion was carried into all the bucket elevators and the dust extraction systems. The building was of structural steel with non-supporting metal clad walls and this allowed rapid pressure relief by blowing out the wall panels. Therefore, the blast that went out of the head house and up one of the bucket elevators did not do much damage to the galleries.

A dust layer only 0.5 mm thick may propagate a dust flame when being entrained by the blast wave preceding a propagating dust flame. This experience has been transformed into a simple rule of thumb, saying that, if footprints are visible, the dust layer is unacceptably thick. During the explosion at St. Paul, the flame front and pressure wave from the primary cross-tunnel explosion also traveled into three tunnels under the grain storage tanks. However, these tunnels were clean, the blast was unable to pick up sufficient dust to sustain the flame propagation and the explosion dissipated. However, the pressure wave continued down the three tunnels, sweeping away objects in its path and finally damaging the aeration fans before venting itself to the atmosphere at the tunnel ends.

1.17 Two Devastating Aluminum Dust Explosions

1.17.1 Mixing Section of Premix Plant of Slurry Explosive Factory at Gullaug, Norway, in 1973

The main source of information concerning the original investigation of the accident is Berg. The explosion occurred during the working hours, just before lunch, while ten workers were in the same building. Five of these lost their lives, two were seriously injured, two suffered minor injuries, only one escaped unhurt. A substantial part of the plant was totally demolished.

The premix preparation plant building was completely destroyed. Debris was found up to 75 m from the explosion site. The explosion was followed by a violent fire in the powders left in the ruins of the plant and in adjacent storehouse for raw materials.

The explosion occurred when charging the $5.2\,m^3$ batch mixer. It appeared that about 200 kg of very fine aluminum flake, sulfur and some other ingredients had been charged at the moment of the explosion. The total charge of the formulation in question was 1,200 kg.

The upper part of the closed vertical mixing vessel was cylindrical and the lower part had the form of an inverted cone. The feed chute was at the bottom of the vessel. The mixing device in the vessel consisted of a vertical rubber-lined screw surrounded by a rubber-lined grounded steel tube. The powders to be mixed were transported upward by the screw and when emerging from the top outlet of the tube, they dropped to the surface of the powder heap in the lower part of the vessel, where they were mixed with other powder elements and eventually retransported to the top.

The final central concern of the investigators was identification of the probable ignition source. In the reports from 1973, it was concluded that the primary explosion in the tube surrounding the screw was probably initiated by an electrostatic discharge. However, this conclusion was not qualified in any detail. In more recent years, the knowledge about various kinds of electrostatic discharges has increased considerably. It now seems highly probable that the ignition source in the 1973 Gullaug explosion was a propagating brush discharge, brought about by the high charge density that could be accumulated on the internal rubber lining of the steel tube surrounding the screw because of the grounded electrically conducting backing provided by the steel tube itself. The discharge could then have occurred through a hole in the lining.

This explosion, which occurred in the early afternoon, caused neither fatalities nor injuries. The material loss was modest, estimated at US $0.03 million. The probable cause of the explosion was electrical welding on a bucket elevator. However, the ignition source was not the welding spot itself, but probably a hot spot in the casing of the elevator boot caused by poor electrical contact between the grounding clamp and the grounded elevator casing. The hotspot either ignited the corn in the elevator boot, which in turn ignited the corn dust cloud or the dust cloud was ignited directly by the hot spot.

The explosion was transmitted to a second bucket elevator and blast waves and flames propagated upward in the legs of both elevators, bursting the casings. Kauffman (1982) emphasized the essential role played by bucket elevators in 14 carefully investigated grain dust explosions in the United States. In 5 of the 14 accidents, the explosion originated in the bucket elevator. In six other accidents, bucket elevators were able to effectively amplify and propagate the explosion, although the combustion process did not originate there. Only in 3 of the 14 cases, the bucket elevators were not involved.

1.17.2 Large Export Grain Silo Plant at Corpus Christi, Texas, April 1981

In this catastrophic explosion, 9 persons lost their lives and 30 injured. The material loss was also substantial estimated at US $30 million.

The probable cause of ignition was smoldering lumps of sorghum that entered a bucket elevator together with the grain and ignited the dust cloud in the elevator. The sorghum was being unloaded from hopper-bottom railway cars. The grain had been stored in these cars for 30 days, and the weather had been quite warm. A fine screen had been put over the rail dump to prevent the larger lumps of the sorghum from entering the elevator. However, smaller lumps of smoldering sorghum nevertheless probably entered one of the operating bucket elevators and ignited the dust cloud there.

From this elevator the explosion propagated into the other elevators and eventually broke into the head house basement, through the dust control system, spout mixers, or the head house silos. It then traveled from the basement into a tunnel to the basement of a large concrete silo complex, where the combustion process entered the hooded conveyors and found more than sufficient dust to sustain the combustion process. As it traveled within this enclosure, the flame accelerated and generated a pressure wave moving ahead of it. Approximately halfway down the basement of the silo complex, the conveyor hoods blew up, throwing a large cloud of dust throughout the basement. The trailing flame front then arrived at this dust cloud and a very rapid combustion process developed. This explosion then vented itself in four different directions. It blew out the north basement wall, it went upward through the grain silo cells, westward through the dog house, and eastward back into the head house, which eventually exploded. The explosion then propagated further through the dust extraction system and into the hooded conveyors in the middle of the basement of the second large concrete silo complex, through which it was channeled to the railway dump area on the north and the shipping gallery on the south. The explosion in the basement of the second silo complex was vented through the basement windows.

1.18 Smoldering Gas Explosions in a Large Storage Facility for Grain and Feedstuffs in Tomylovo, Knibyshev Region, USSR

This extensive series of explosions were of the same nature as the smoldering gas explosion discussed in Sect. 2.6. The report of the event was provided by Borisov and Gelfand (personal communication from Borisov and Gelfand, USSR Academy of Science, Moscow, 1989).

The large storage facility for grain and feedstuffs consisted of four sections of 60 silo cells each, that is, 240 silo cells altogether. Each cell had a $3\,m \times 3\,m$ square cross-section and 30 m height. The first explosion occurred in December 1987 in a silo cell containing moist sunflower seed, which was not supposed to be stored in such silos due to the risk of self-heating. However, this had nevertheless been done and the resulting self-heating developed into extensive smoldering decomposition during which methane and carbon monoxide were produced and mixed with the air in the empty top part of the silo, above the powder bed surface. It is reasonable to believe that the primary explosion was in this mixture of explosive gas and air and that the ignition source was smoldering combustion when it penetrated to powder bed top surface. However, dust deposits on the internal silo walls and roof may well have become entrained by the initial blast and involved in the explosion. This was only the first of a large series of 20–30 subsequent explosions that took place in the same facility, in one silo cell after the other, during 1988 and 1989.

There are two main reasons for this continued explosion activity in the silo complex. The most important is the heat transfer from a silo cell in which smoldering combustion is taking place to the neighboring cells. Such heat transfer is facilitated by the large contact surface area between the cells provided by the square cross-section. Furthermore, the prefabricated construction elements used throughout the entire facility may have been comparatively poor heat insulators. The second main reason for the repeated explosions was that sunflower seed was not the only material in the facility that was not supposed to be stored there. Some of the silo cells contained buckwheat and whet grain of higher moisture contents than the maximum permissible limits for storage in such facilities.

At one stage, it was discussed whether the whole facility could be blown up to put an end to the problem. However, this was considered too hazardous. The final solution chosen was to just leave the entire facility to itself and await a natural termination of the problem over time.

In addition to obeying the rules specifying which materials can be stored in silos, systematic use of portable gas analyzers for early detection of hydrogen, methane and carbon monoxide in the silo cells was suggested as the best means for preventing similar accidents in the future.

1.19 Linen Flax Dust Explosion in Harbin Linen Textile Plant, Peoples Republic of China, in March 1987

1.19.1 Explosion Initiation and Development, Scenario 1

Figure 1.11 illustrates the 13,000 m² spinning section through which the explosion swept and the possible locations and sequence of the nine successive explosions that constituted the event according to Xu Bowen (1988) and Xu Bowen et al. (1988). These workers based their reconstruction of the explosion on three independent elements of evidence. Firstly they identified the location of the various explosion sites throughout the damaged plant. Second, they ranked the relative strengths of the local explosions by studying the extent and nature of the damage. Third, they arranged the various local explosions in time by means of the relative strengths of the nine successive explosions, identified by decoding the seismic recording of the event.

Figure 1.12a shows a direct tracing of the amplitude-modulated seismic signal actually recorded 17 km from the explosion site. Figure 1.12b shows the sequence of the nine energy pulse impacts on the Earth at the location of Harbin Linen Textile Plant, deduced from the signal in Fig. 1.12a. Figure 1.12c finally shows the theoretical prediction of the seismic signal to be expected from the sequence of explosions in Fig. 1.12b. The agreement between the (a) and (c) signals is striking, which supports the validity of the energy impact pulse train (b).
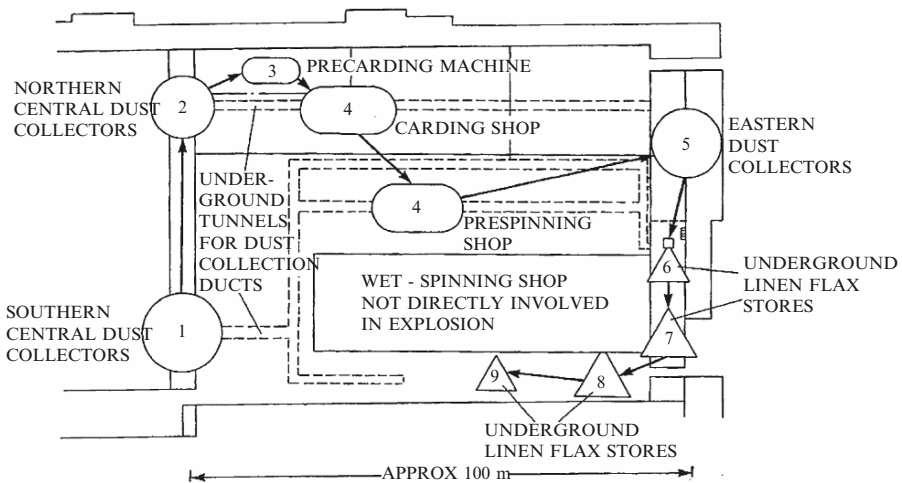

Fig. 1.11. The 12,000 m² spinning section of the Harbin Linen Textile Plant, Peoples Republic of China that was afflicted with a catastrophic dust explosion on March 15, 1987. Numbered *circles*, *ovals* and *triangles* indicate location and sequence of a postulated series of nine successive explosions (from Xu Bowen et al., 1988)
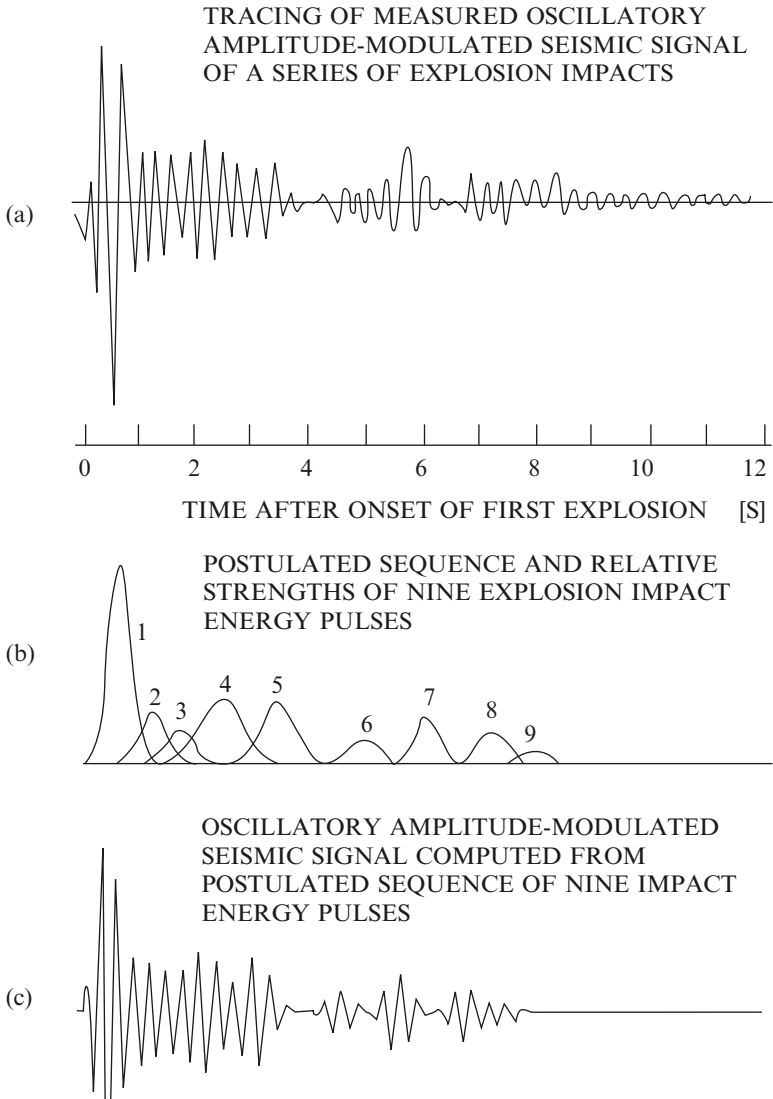
TRACING OF MEASURED OSCILLATORY
AMPLITUDE-MODULATED SEISMIC SIGNAL
OF A SERIES OF EXPLOSION IMPACTS

(a)

TIME AFTER ONSET OF FIRST EXPLOSION   [S]

POSTULATED SEQUENCE AND RELATIVE
STRENGTHS OF NINE EXPLOSION IMPACT
ENERGY PULSES

(b)

OSCILLATORY AMPLITUDE-MODULATED
SEISMIC SIGNAL COMPUTED FROM
POSTULATED SEQUENCE OF NINE IMPACT
ENERGY PULSES

(c)

Fig. 1.12. Sequence of nine impact energy pulses from nine successive explosions in
the Harbin Linen Textile Plant, Harbin, Peoples Republic of China, 15 March 1987,
postulated on the basis of a seismic record of the event (from Xu Bowen et al., 1988)

Table 1.29 summarizes the findings of Xu Bowen et al. (1988) that led to
the suggestions of the explosion development indicated in Fig. 1.12. Accord-
ing to this scenario the explosion was initiated in one of the nine units in the
central dust collector system. All nine units were connected by ducting. The
ignition sources were not identified and an electrostatic spark was considered

Table 1.29. Sequence, relative strengths and locations of nine successive dust explosions Harbin Linen Textile Plant, Harbin, Peoples Republic of China, 15 March 1987, postulated basis of damage analysis in the plant and a seismic recording of the explosion

Explosion number	Onset of explosion (s)	Selsmic energy (T erg)	Location of explosion in plant
1	0.0	50.7	Southern central dust collector
2	0.6	5.4	Northern central dust collector
3	1.2	2.5	Precarding machine
4	1.6	7.6	Carding and prespinning shops
5	3.0	6.8	Eastern dust collectors
6	4.8	1.4	
7	6.0	3.9	Underground linen flax stores
8	7.3	2.2	
9	8.2	0.45	

Source: Bowen et al., 1988

a possibility, a local fire or glow another. The initial flame was transmitted immediately to the next dust collecting unit and both units exploded almost simultaneously, giving rise to the first major impact pulse in Fig. 1.12b. The explosion the propagated through the other seven dust collecting units the central collecting plant (2) and into the precarding area, where the blast wave preceding the flame generated an explosible dust cloud in the room, which ignited the flame jet from the dust collectors (3). The room explosion propagated further to the re-distinct explosion (5) occurred. The final four explosion pulses were generated as explosion propagated further into the underground linen flax stores, where it finally terminated after having traveled a total distance of about 300 m the chain of nine explosions lasted for about 8 s.

1.19.2 Explosion Initiation and Development, Scenario 2

This alternative scenario originates from the investigation of Zhu Hailin (1988). He found evidence of an initial smoldering dust fire caused by a live 40 W electrical portable light lamp lying in a flax dust layer of 6–8 cm thickness in a ventilation room. Found evidence of flame propagation through the underground tunnels for the dust. On the basis of his analysis, Zhu suggested that the explosion was initiated in the eastern dust collectors (5 in Fig. 1.11) from which it transmitted to nine units of the central dust collecting plant (1 and 2 in Fig. 1.11) via the ducting in the underground tunnels. Severe room explosions were initiated when the ducting in the tunnel ruptured and the resulting blast dispersed large quantities of dust in the workrooms into explosible clouds that were subsequently ignited. From the eastern dust collectors, the explosion also propagated into the underground flax stores. It is

not unlikely that even this scenario could be developed further in such a way as to agree with the evidence from the seismic recording.

1.20 Fires and Explosions in Coal Dust Plants

1.20.1 Methane Explosion in 17,000 m^3 Coal Silo at Elkford, British Columbia, Canada, in 1982

The handling and storage of coal can, in addition to the dust explosion hazard, present a gas explosion risk, due to release of methane from some types of coal. An account of such an explosion was given by Stokes (1990).

The silo of height 48 m and diameter 21 m that exploded was used for storage and load out of cleaned, dried metallurgical coal. The capacity of the silo was 15,000 tonnes. Prior to the explosion, a methane detector had been installed in the roof of the silo. The detector activated a warning light in the silo control room when a methane concentration of 1% was detected and an alarm light was activated when detecting 2% methane. A wet scrubber was located in the silo head house to remove dust from the dust laden air in the silo during silo loading. A natural ventilation methane stack was also located in the silo roof to vent any build up of methane gas from the silo.

The explosion occurred early in the morning on 1 May 1982, devastating the silo roof, head house and conveyor handling system. Witnesses stated that a flash was noticed in the vicinity of the head hours, followed seconds later by an explosion that displaced the silo top structures. This was followed by an orange-coloured fireball that rolled down the silo walls and extinguished prior to reaching the base of the silo.

2

Data on Missiles, Impactors, Aircraft and Explosions

2.1 Introduction

This chapter introduces various types of missiles, impactors, aircraft and explosions. They include tornado-generated and windborne missiles, plant-generated missiles, missiles from jet fluid, snow/ice and rocks/boulders which have disintegrated under environmental conditions. Dropped weights are discussed together with other impactors such as trucks, lorries, cranes, tanks and naval vessels. Data exist on all popular types of available military missiles, rockets, civilian and military aircraft and helicopters. A brief introduction is given to types of explosions. The chemistry of bombs, shells, grenades, shrapnel and explosives is discussed. A full account is given of gas explosions, nuclear detonations, dust explosions and underwater explosions. Wherever possible, the reader is given full access to data which can act as an input for solving problems in specific areas. Great care is taken to ensure that, under a specific topic, sufficient data are available to compare known results. In addition, a comprehensive bibliography is provided for further in-depth studies.

2.2 Types of Conventional Missiles and Impactors

For impact analysis and design, missiles generated by tornadoes, hurricanes and wind can be anything from roof tiles and planks to cars, lorries, boats, etc. Because of mechanical faults or for other reasons, components have been ejected from parent structures with greater velocities and, acting as missiles, have had devastating effects on the workforce and on structures.

In combat situations, military missiles are always in action to destroy sensitive targets. Aircraft and helicopter crashes produce missile effects on vital installations on the ground or in the sea. The breakaway rotors, engines, wings and tails themselves act as high-speed missiles. Vehicles, ships, tankers and high-speed boats may collide with each other or with vital installations,

and consequently are a major hazard. Such impactors have caused damages worth millions of pounds.

On the environmental side, falling trees, high-speed water jets, ejecting stones from rocks during the penetration process, water waves, snow/ice loads impacting on structures and missiles generated by blasts and explosions due to gas leaks and nuclear detonations are part of a wider aspect of impact problems (covered in all sections of the bibliography). This section is, therefore, entirely devoted to data about missiles and impactors which can be used as an input for problem-solving exercises and for case studies.

2.2.1 Tornado- and Wind-Generated Missiles

Tornadoes occur frequently in certain parts of the world. They vary considerably in their width, length and maximum speed. Owing to their small path area, the chance of recording a tornado wind for a specific zone is remote. The length, width and area are generally considered to be those bounding the area of potential damage. A great deal of research has been carried out on tornadoes. If one includes all the reported tornadoes, the average area is between 1.0 and 1.1 square miles (2.6 and 2.8 km^2). The estimated maximum wind speeds of tornadoes also vary widely, from 70 miles h^{-1} (112 km h^{-1}) (hurricanes damaging roofs and trees), to an estimated 400 miles h^{-1} (640 km h^{-1}), causing complete destruction and generating land-based missiles with greater speeds. Various codes exist for estimating wind loads for different terrains and, where necessary, they are generally referred to in estimating the wind speed and its relation to the speed at which a missile is generated. The details of this topic are beyond the scope of this book. However, a comprehensive bibliography is given for those who wish to study this in greater depth.

The characteristics of tornado-generated missiles must be studied carefully. It is important to identify objects in the path of a tornado prior to them becoming airborne. These objects can range from small debris to full-scale structural components and vehicles. Tables 2.1 and 2.2 list data on tornado- and wind-generated missiles and their characteristics.

2.2.2 Plant-Generated Missiles

Plant-generated missiles, according to their origin, vary in size and weight and have a wide range of impact velocities. They are generated as a result of high-energy system rupture. Rotating machinery, on disintegration, generates potentially dangerous missiles. Several references are given on the general characteristics of potential turbine missiles and broken pipes from sections of pressurized piping in nuclear power plants [2.73–2.80]. Failure of large steam turbines in both nuclear- and fossil-fuelled power plants has occurred occasionally in the past due to metallurgical and/or design inadequacies, environmental and corrosion effects and failure of the overspeed protection systems. This has resulted in the loss of many mechanical items including

Table 2.1. Tornado- and wind-generated missiles and their characteristics: wood, steel and concrete building components

Missile type	Geometry			Velocity $(\mathrm{m\,s^{-1}})$	Weight (kg)
	Diameter (mm)	Length (m)	Impact area (m^2)		
Wooden plank	–	3.67	0.03	41.5	56.7
Wooden pole	200	3.67	0.03	5.73	94.8
Circular hollow sections in steel (average)	168.3	4.00	0.000026	70.2	60
Sign boards (average)	–	–	6.0	57.0	56
Steel I-beam light sections (average)	–	4.0	0.000032	40.5	100
Steel members channel sections (average)	–	3.0	0.000013	50.5	30
Steel members L-sections (average)	–	3.0	0.000015	45.5	36
Steel rafters T-sections (average)	–	3.0	0.000018	45.5	42
Steel rod	25	0.92	0.00049	75.6	3.63
Concrete lintels	–	3.0	0.025	60.5	1.80
Concrete sleepers	–	2.70	0.0031	75.0	0.20
Precast concrete beams or piles at delivery stage	–	9.0	0.09	60.5	19.44
Precast concrete wall panels	–	5.0	11.5	2.5	1380
Prestressed concrete pipes	400	–	–	–	1.100
	500	–	–	–	1.375
	600	–	–	–	1.650
	700	–	–	–	1.920
	800	–	–	–	2.200
	900	–	–	–	2.474
	1,676	6.0	0.032	–	4.608
Prestressed concrete poles	–	17.0	0.0019	30.5	65.7
		12.0	0.00080	50.1	14.46
		9.0	0.000025	65.2	9.65

Table 2.2. Tornado- and wind-generated missiles and their characteristics: basic data on cars and other road vehicles

Manufacturer vehicle	Length (m)	Width (m)	Height (m)	Wheel base (m)	Laden weight (kg)	Max. speed (miles h^{-1})
Alfa Romeo						
33 1.7 Sport Wagon Veloce	4.142	1.612	1.345	2.465	925	115
75 2.0i Veloce	4.330	1.630	1.350	2.510	1,147	124
164 3.0 V6	4.555	1.760	1.4	2.660	1,300	142
American Motors (USA)						
Jeep Wagoner limited	4.198	1.790	1.615	2.576	2,074	90
Aston Martin						
Lagonda	5.820	1.790	1.3	2.91	2,023	143
V8 Vantage Volante	4.39	1.86	0.1295	2.610	1,650	160
Vantage Zagato	4.39	1.86	0.1295	2.610	1,650	186
Audi (D)						
80 1.85	4.393	1.695	1.397	2.544	1,020	113
90 Quattro	4.393	1.695	1.397	2.546	1,270	125
100	4.792	1.814	1.422	2.687	1,250	118
100 Turbo Diesel	4.793	1.814	1.422	2.687	1,250	108
200 Avant Quattro	4.793	1.814	1.422	2.687	1,410	139
Austin						
Maestro 1.60 Mayfair	4.049	1.687	1.429	2.507	946	102
Metro 1.0 Mayfair 3-door	3.405	1.549	1.361	2.251	771	86
Montego Vanden Plas EFi Estate	4.468	1.710	1.445	2.570	1,111	110
Bentley (GB)						
Mulsanne	5.268	1.887	1.485	3.061	2,245	119
Mulsanne Turbo R	5.268	1.887	1.486	3.061	2,221	143
Bitler (D)						
Type III	4.450	1.765	1.395	–	1,300	140
BMW (D)						
320i Convertible	4.325	1.645	1.380	2.57	1,125	123
325i Touring	4.325	1.645	1.380	2.57	1,270	132
M 3	4.325	1.645	1.380	2.57	1,150	139
520i	4.72	1.751	1.412	2.761	1,400	126
735i	4.91	1.845	1.411	2.832	1,590	145
750i L	5.024	1.845	1.401	2.832	–	155
Z 1	3.921	–	–	2.45	110	140
Bristol (GB)						
Brigand Turbo	4.902	0.1765	1.4535	2.895	1,746	150
Buick (USA)						
Lesabre T-type Coupé	4.991	1.838	1.389	2.814	1,458	115
Cadillac (USA)						
Allanté Convertible	4.537	1.864	1.325	2.525	1,585	110

Table 2.2. (continued)

Manufacturer vehicle	Length (m)	Width (m)	Height (m)	Wheel base (m)	Laden weight (kg)	Max. speed (miles h^{-1})
Cadillac (USA)						
Allanté Convertible	4.537	1.864	1.325	2.525	1,585	110
Chevrolet (USA)						
Camaro IROC-2	4.775	1.850	1.270	2.565	1,525	130
Corvette Convertible	4.483	1.805	1.185	2.438	1,414	142
Chrysler (USA)						
le Baron Convertible	4.697	1.738	1.326	2.546	1,474	110
GS Turbo 2 Portofino	4.555	1.760	1.302	2.465	1,194	125
	–	–	–	–	–	150
Citroën (F)						
Ax 14 TRS	3.495	1.56	1.35	2.285	695	99
Bx 19 GTi 16v	4.229	1.657	1.365	2.655	1,093	130
Bx 25 GTi Turbo	4.660	1.77	1.36	2.845	1,385	126
Coleman Milne (GB)						
Grosvenor limousine	5.563	1.964	1.575	3.661	2,100	115
Dacia (R)						
Duster 4 × 4 GLX	3.777	1.6	1.74	2.4	1,180	70
Daihatsu (J)						
Charade LX Diesel Turbo	3.61	1.615	1.385	2.34	810	87
Charade GT ti	3.61	1.615	1.385	2.34	816	114
Fourtrak Estate EL TD	4.065	1.580	1.915	2.53	1,660	83
Daimler						
3.6	4.988	2.005	1.358	2.87	1,770	137
Dodge (USA)						
Daytonna Shelby 2	4.545	1.76	1.279	2.464	1,220	120
Ferrari						
F40	4.43	1.981	1.13	2.451	1,100	201
Mondial 3.2 Quattro valvole	4.58	1.79	1.26	2.65	1,430	143
Fiat						
Croma Turbo ie	4.495	1.76	1.433	2.66	1,180	131
Panda 4 × 4	3.378	1.485	1.46	2.159	761	83
Ford						
AC (GB)	3.962	1.816	1.168	2.477	907	140
Ford (D)						
Escort RS Turbo	4.046	1.588	1.348	2.4	1,017	124
Granada 2.4i GL	4.669	1.760	1.41	2.761	1,265	120
Scorpio 4 × 4 2.9i	4.669	1.766	1.453	2.765	1,385	126
XR3i Cabriolet	4.049	1.64	1.336	2.398	925	115
Ford (GB, B)						
Sierra Sapphire GLS 2.0EFi	4.468	1.699	1.359	2.609	1,060	115

Table 2.2. (continued)

Manufacturer vehicle	Length (m)	Width (m)	Height (m)	Wheel base (m)	Laden weight (kg)	Max. speed (miles h^{-1})
Ford (B)						
Sierra Ghia 4 × 4 Estate	4.511	1.694	1.359	2.612	1,315	119
Ford (USA)						
Taurus	4.785	1.796	1.795	2.692	1,299	105
Ginetta (GB)						
G32	3.758	1.651	1.168	2.21	753	135
Honda (J)						
Accord Aerodeck 2.0 EXL	4.335	1.651	1.335	2.6	1,147	110
Legend Coupé	4.755	1.745	1.37	2.705	1,395	132
Prelude 2.0L-16	4.460	1.695	1.295	2.565	1,145	128
Hyundai (J)						
Pony 1.5 GLS	3.985	1.595	1.38	2.38	890	96
Stellar 1.6 GSL	4.427	1.72	1.372	2.579	1,034	98
Isuzu (J)						
Trooper Turbo Diesel	4.38	1.65	1.8	2.3	1,655	78
Jaguar (GB)						
Sovereign 3.6	4.988	2.005	1.358	2.87	1,770	137
XJ6 2.9	4.988	2.005	1.38	3.87	1,720	117
Lada (Su)						
Riva Cossack	3.708	1.676	1.638	2.197	1,150	77
Samara 1300 SL	4.006	1.62	1.335	2.46	900	92
Lamborghini (I)						
Countach 5000s Quattro valvole	4.14	2.0	1.07	2.45	1,446	178
Lancia (I)						
Delta 1.6 GTie	3.895	1.62	1.38	2.475	995	115
Delta HF vitegrade	3.9	1.7	1.38	1.38	1,200	134
Thema 2.0ie Turbo Estate	4.59	1.755	1.433	2.66	1,150	139
Thema 8.32	4.59	1.755	1.433	2.66	1,400	139
Y10 Turbo	3.392	1.507	1.425	2.159	790	111
Land Rover (GB)						
One Ten Diesel Turbo	4.445	1.79	2.035	2.795	1931	73
Range Rover Vogue Turbo D	4.47	1.718	1.778	2.591	2,061	90
Lincoln (USA)						
Continental	5.21	1.847	1.412	2.769	1,645	112
Lotus (GB)						
Esprit Turbo	4.331	1.859	1.138	2.459	1,268	152
Maserati (I)						
Bi Turbo 228	4.46	1.865	1.33	2.6	1,240	151

Table 2.2. (continued)

Manufacturer vehicle	Length (m)	Width (m)	Height (m)	Wheel base (m)	Laden weight (kg)	Max. speed (miles h^{-1})
Mazda (J)						
121 1.3LX Sun Top	3.475	1.605	1.565	2.295	775	99
626 2.0 GLX Hatchback	4.515	1.69	1.375	2.575	1,196	111
626 2.0i GT Coupé	4.45	1.69	1.36	2.515	1,230	130
RX7	4.29	1.69	1.265	2.43	1,221	134
Mercedes Benz (D)						
190E 2.6	4.427	1.678	1.39	2.665	1,209	130
300CE	4.655	1.682	1.41	2.715	1,390	126
560 SEL	5.16	2.006	1.446	1.555	1,780	147
Mercury (USA)						
Topa 3 XR5	4.468	1.747	1.339	2.537	1,135	92
MG (GB)						
Maestro 2.0 EFi	4.05	1.69	1.42	2.51	975	114
Metro Turbo	3.403	1.563	1.359	2.251	840	110
Montego Turbo	4.468	1.71	1.42	2.565	1,079	125
Mitsubishi (J)						
Galant Sapporo	4.66	1.695	1.375	2.6	1,230	114
Starion 2000 Turbo	4.43	1.745	1.315	2.435	1,308	133
Mitsubishi Colt (J)						
Lancer 1500 GLX Estate	4.135	1.635	1.42	2.38	950	95
Morgan (GB)						
Plus 8	3.96	1.575	1.32	2.49	830	122
Nissan (J)						
Bluebird 1.6 LS	4.405	4.365	1.69	1.395	1,120	103
Prairie Anniversary II	4.09	1.655	1.6	2.51	1,070	95
Silvia Turbo ZX	4.351	1.661	1.33	2.425	1,136	124
Oldsmobile (USA)						
Trofeo	4.763	1.798	1.346	2.741	1,526	115
Panther (GB)						
Kallista 2.9i	3.905	1.712	1.245	2.549	1,020	112
Solo 2	4.344	1.78	2.18	2.53	1,100	150
Peugeot (F)						
205 GTi Cabriolet	3.706	1.572	1.354	2.421	884	116
205 GRD	3.706	1.572	1.369	2.421	895	96
Peugeot (GB)						
309 SRD	4.051	1.628	1.379	2.469	950	99
Plymouth (USA)						
Sundance	2.463	1.71	1.339	2.463	1,131	105
Pontiac (USA)						
Bonneville SSE	5.046	2.838	1.409	2.814	1,504	112

(*continued*)

Table 2.2. (continued)

Manufacturer vehicle	Length (m)	Width (m)	Height (m)	Wheel base (m)	Laden weight (kg)	Max. speed (miles h^{-1})
Porsche (D)						
911 Speedster	4.291	1.65	1.283	2.273	1,140	152
944 S	4.2	1.735	1.275	2.4	1,280	140
Reliant (GB)						
Scimitar 1800 Ti	3.886	1.582	1.24	2.133	889	124
Renault (F)						
Espace 2000–1	4.25	1.277	1.66	2.58	1,177	105
5 GTD	3.65	1.585	1.397	2.466	830	94
21 GTS	4.46	1.714	1.415	2.659	976	113
21 Turbo	4.498	1.714	1.375	2.597	1,095	141
Rolls-Royce (GB)						
Silver Spirit	5.27	1.887	1.495	3.06	2245	119
Rover (GB)						
216 Vanden Plas	4.16	1.62	1.39	2.45	945	107
820i	4.694	1.946	1.398	2.759	1,270	126
Saab (S)						
900 Turbo 16S Convertible	4.739	1.69	1.42	2.525	1,185	124
9000i	4.62	1.765	1.43	2.672	1,311	118
Seat (E)						
Ibiza 1.5 GLX 5-door	3.638	1.609	1.394	2.448	928	107
Malaga 1.5 GLX	4.273	1.65	1.4	2.448	975	103
Skoda (CS)						
130 Cabriolet LUX	4.2	1.61	1.4	2.4	890	95
Subaru (J)						
Justy 4 × 4	3.535	1.535	1.42	2.85	770	90
XT Turbo Coupé	4.49	1.69	1.335 1.370	2.465	1,139	119
Suzuki (J)						
Santana	3.43	1.46	1.69	2.03	830	68
Swift 1.3 GTi	3.67	1.545	1.35	2.245	750	109
Toyota (J)						
Celica 2.0 GTi Convertible	4.365	1.71	1.29	2.525	1,195	125
Corolla GTi	4.215	1.655	1.365	2.43	945	122
Space Cruiser	4.285	1.67	1.815	2.235	1,320	87
Supra 3.0i	4.62	1.745	1.31	2.595	1,550	135
TVR						
S Convertible	4.0	1.45	1.117	2.286	900	128
TVR (GB)						
9205 EAC Convertible	4.051	1.628	1.379	2.469	950	99

Table 2.2. (continued)

Manufacturer vehicle	Length (m)	Width (m)	Height (m)	Wheel base (m)	Laden weight (kg)	Max. speed (miles h^{-1})
Vauxhall						
Astra Cabriolet	2.463	1.71	1.339	2.463	1,131	105
Astra GTE 2.0ie 16v	5.046	2.838	1.409	2.814	1,504	112
Carlton CD 2.0i	4.291	1.65	1.283	2.273	1,140	152
Carlton GSi 3000	4.2	1.735	1.275	2.4	1,280	140
Senator 3.0i CD	3.886	1.582	1.24	2.133	889	124
Volkswagon (D)						
Golf GTi 16v	4.25	1.277	1.66	2.58	1,177	105
Jetta GTi 16v	3.65	1.585	1.397	2.466	830	94
Scirocco GTX	4.46	1.714	1.415	2.659	976	113
Volvo (NL)						
360 GLY	4.498	1.714	1.375	2.597	1,095	141
480 ES	5.27	1.887	1.495	3.06	2,245	119
Volvo (S)						
760 GLE	4.16	1.62	1.39	2.45	945	107
Yugo (YU)						
65A GLX	4.694	1.946	1.398	2.759	1,270	126

blades, disks and rotors or their respective fragments. These can act as either high-trajectory missiles, which are ejected upward through the turbine casing, or low-trajectory or direct missiles, ejected from the turbine casing, any of which may strike an essential industrial system. The generation of the latter missiles is the more probable. Table 2.3 lists characteristics of plant generated missiles.

2.2.3 Impact Due to Jet Fluid and Rock Blasting

Shaped-charge jets, jet fluids and rock blasting create rock fragments which are ejected with great velocities, known as ejecta velocities. Nearby structures can be subject to intense dynamic loading from such missiles. Sometimes it is difficult to assess individual break-up and to mitigate or control ejecta velocities. The work focuses primarily on the following two broad topics:

(1) Intensity of fragmentation or average fragment size resulting from the impulsive failure event and its relationship to material properties and loading conditions.
(2) Fragmentation size distribution, geometry and wave propagation.

Research has shown that the two topics are diverse and complex, especially when related to catastrophic failure conditions. After the examination of many cases studies [2.147–2.162]. Table 2.4 has been drawn up for soil/rock.

Table 2.3. Plant-generated missiles and their characteristics

Type of missile	Weight (kg)	Impact area (cm^2)	Impact velocity (m s^{-1})
Control rod mechanism or fuel rod	53	15.5	91.5
Disc 90° Sector	1,288	4,975	125
Disc 120° Sector	1,600	6,573	156
Hexagon head bolts			
1.4 cm dia	0.20	1.54	250
2.0 cm dia	0.30	2.30	230
2.4 cm dia	0.37	2.84	189
3.3 cm dia	0.42	3.22	150
6.8 cm dia	0.97	7.44	100
Turbine rotor fragments			
High trajectory			
Heavy	3,649	5,805	198
Moderate	1,825	3,638	235
Light	89	420	300
Low trajectory			
Heavy	3,649	5,805	128
Moderate	1,825	3,638	162
Light	89	420	244
Valve bonnets			
Heavy	445	851	79
Moderate	178	181	43
Light	33	129	37
Valve stems			
Heavy	23	25.0	27.5
Moderate	14	9.7	20.0
Other			
30 cm pipe	337.0	260.00	68
12 cm hard steel disc	1.6	113.0	140
Steel washers	0.0005	3.0	250
Winfrith test missile	15.6	176.0	240

Table 2.5 gives thrust force vs. penetration for a number of rocks. From these two tables, the size of the fragmental rock and its velocity can easily be estimated. If the fragment size and velocity are known, impact analysis can then be successfully carried out using various dynamic models given in this text.

2.2.4 Snow Load as an Impactor

Several researchers [2.279–2.340] have investigated snow/ice impact on structures. Several graphs have been plotted on failure pressure vs. aspect ratio.

Table 2.4. Soil/rock characteristics and ejecta velocities

Soil/rock type	$V_L \times 10^3$ (m s^{-1})	$V_c \times 10^3$ (m s^{-1})	ν	E (kPa cm^{-2} ×10^5)	G (kPa cm^{-2} ×10^5)	K (kPa cm^{-2} ×10^5)	σ_c (kPa cm^{-2} ×10^5)	τ (kPa cm^{-2})	σ_t (kPa cm^{-2})	ρ (g cm^{-2})
Sand	0.3–1.4	0.4–2.7	–	0.0032	–	–	50–60	–	–	1.4–2.0
Clay	0.8–3.5	1.0–8.30	–	0.0032	–	–	65–100	2.0 (average)	3.8	1.4–2.0
Limestone	6.2	1.00	0.26	2.16	0.85	1.70	448	105	70.0	2.41
Slate	7.0	3.30	0.24	10.20	3.85	6.50	455	70	50.0	2.45
Granite	5.30	3.31	0.21	6.10	2.55	3.80	1560	–	180.0	260.00
Shale	9.2	1.00								
Quartzite	7.3	3.70	0.25	9.30	3.80	7.90	1500	240	–	2.60
White marble	5.5	3.00	0.20	3.85	1.60	3.40	750	–	150.0	2.70
Black marble	6.0	3.28	0.33	5.75	2.20	7.00	755	350	–	2.80
Red marble	6.10	3.10	0.26	6.75	2.70	4.75	1,200	215	–	2.74
Gneiss	6.10	3.40	0.28	8.30	3.40	6.40	1,180	340	–	2.85
Dolomite	12.6	2.30	0.28	9.80	3.80	7.60	1,880	1,200	350.0	2.85
Coal	1.3	3.35	0.35	0.18	0.07	0.09	80	30	5.5	1.30

ρ, density; V_L, V_c, velocities in longitudinal and transverse directions; E, G, K, Young's modulus, modulus of rigidity and bulk modulus; σ_c, σ_t and τ, compressive stress, tensile stress and shear stress; ν, Poisson's ratio

Table 2.5. Thrust force of a fragment vs. penetration

Thrust force (kN)	Penetration ($cm\,min^{-1} \times 10^{-1}$)									
	Granite	Limestone	Basalt	Charcoal	Taconite	Shale	Sandstone	Quartzite	Gneiss	Dolomite
1.50	11	17	19	15	11	16	15	17	13	11
1.75	13	19	24	32	25	31	30	20	17	14
2.00	15	21	29	38	31	36	33	25	20	19
2.25	20	25	35	43	39	39	38	27	–	–
2.50	23	29	41	45	42	40	39	31	35	33
3.00	29	35	45	55	53	45	42	35	39	37
3.25	31	39	49	63	59	50	50	45	–	–
4.00	41	55	61	69	63	55	53	52	59	57
4.25	45	63	65	73	71	60	60	59	69	65
10.00	60	139	165	178	161	120	110	80	–	–
20.00	120	239	270	310	210	160	171	100	150	147
30.00	220	300	328	400	270	230	240	150	179	171
50.00	250	349	420	450	310	310	305	210	283	270
75.00	270	410	570	610	459	459	460	310	350	339
100.00	300	500	630	670	560	550	500	358	410	400
125.00	350	535	710	750	620	610	559	452	490	480
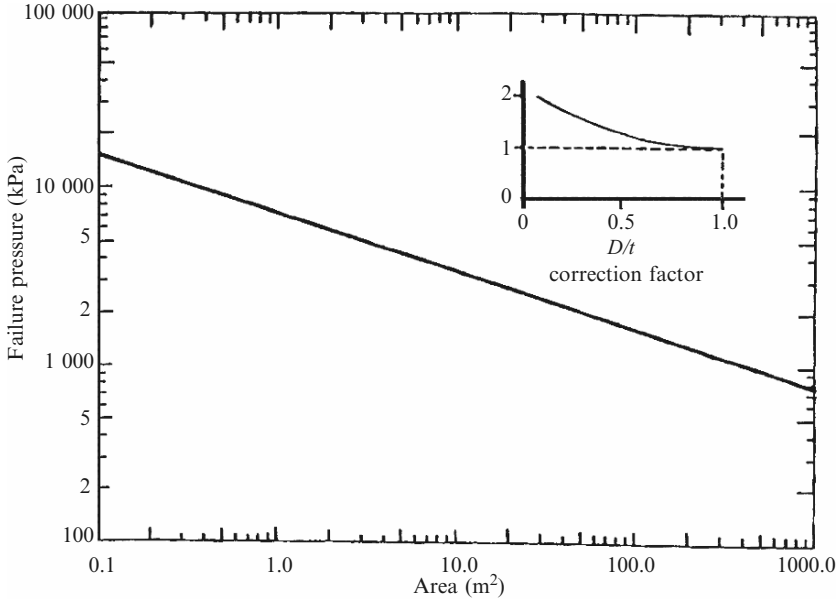
Fig. 2.1. Imperial ice-failure pressure curve

The aspect ratio is equal to the chord length or width D_i of the interaction zone divided by the average snow/ice thickness t_i in the zone. The impact forces are calculated using the contact factor and the shape factor. The modes of ice impact load on a floating or fixed structure are intrinsically the same, but with a difference in the time-history variations. Figures 2.1–2.5 show ice-failure pressure curves.

The total forces computed by various theories vary considerably. For a typical example of an 18.3 m diameter conical tower, Table 2.6 compares the results calculated in three different ways. The relevant data were $D_i = 18.3$ m; $t_i = 0.91$ m; Poisson's ratio $= 0.33$; $\sigma_c =$ crushing strength $= 0.7$ MPa; $E_{ice} = 7$ GPa; cone angle $\alpha = 45°$; free board $= 6.1$ m; coefficient of friction $= 0.15$.

Using Sinha theory [2.323–2.334] Fig. 2.4 shows the stress at the first crack and the strain rate of the snow/ice. Figure 2.5 gives a useful relationship between the unconfined compressive strength and the strain rate of the snow/ice.

2.2.5 Falling or Dropped Weights as Impactors

Falling or dropped weights can be anything from rock falls, trees, sign boards, cars, lorries, trucks, freight containers to sensitive heavy objects such as aircraft wings and engines or nuclear waste casks. Details about cars, lorries and trucks are given in this chapter. Rock falls have tragic effects due to their appalling speed. Figure 2.6 illustrates the gravity-induced descent of
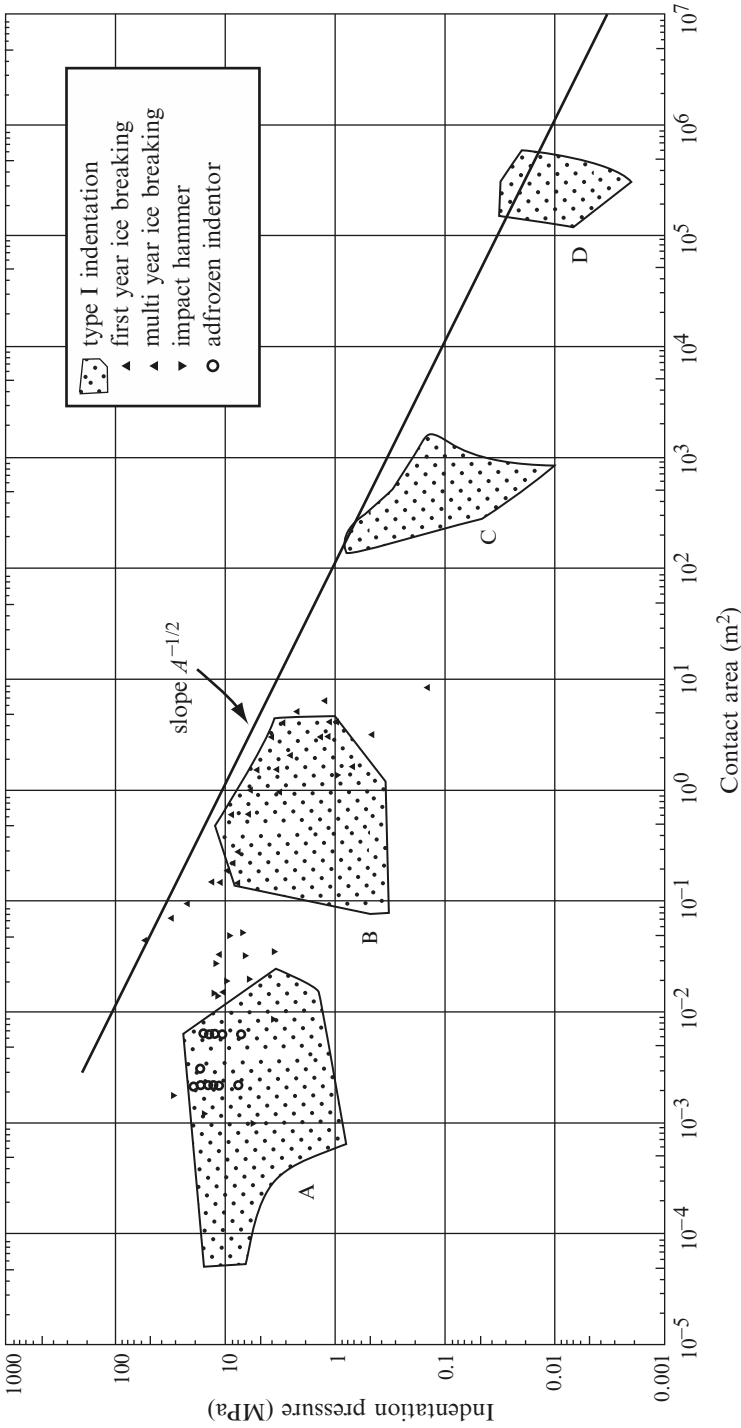
Fig. 2.2. Imperial ice-failure pressure curve. A, laboratory tests; B, medium-scale in situ tests, lighthouses and bridge piers; C, full-scale Arctic islands and structures; D, mesoscale models [2.329]

Flexural strength = 100 psi
(7.03 kg/cm^2)
Friction coefficient = 0.10
Ice thickness = 1.0 ft (30.5 cm)

indenter radius A
in ft   35.0
               30.0
               25.0
               20.0

               15.0

               10.0

               5.0
               1.0

Total vertical force (kips)
(tonnes)
Slope angle (degrees)

(a)

Flexural strength = 100 psi
(7.03 kg/cm^2)
Friction coefficient = 0.30
Ice thickness = 3.0 ft (91.5 cm)

indenter radius A
in ft
35.0
30.0
25.0
20.0
15.0
10.0
5.0
1.0

Total vertical force (kips)
(tonnes)
Slope angle (degrees)

Flexural strength = 100 psi
(7.03 kg/cm^2)
Friction coefficient = 0.10
Ice thickness = 1.0 ft (30.5 cm)

indenter
radius A in ft
35.0
30.0
25.0
20.0
15.0
10.0
5.0
1.0

Total horizontal force (kips)
(tonnes)
Slope angle (degrees)

(b)

Flexural strength = 100 psi
(7.03 kg/cm^2)
Friction coefficient = 0.30
Ice thickness = 3.0 ft (91.5 cm)

indenter
radius A in ft
35.0
30.0
25.0
20.0
15.0
10.0
5.0
1.0

Total horizontal force (kips)
(tonnes)
Slope angle (degrees)

Fig. 2.3. Vertical force (**a**) and horizontal force (**b**) vs. slope angle and indenter radius A for constant flexural strength, friction and ice thickness (kip = 1,000 lb)

rocks which are lying in a state of physical separation. Their free fall may be accompanied by rolling, bouncing or sliding or any combination thereof. The weights of these rocks vary from initially at least 1 kg to 50,000 kg over speeds in the range of $30\,\mathrm{m\,s^{-1}}$ to $100\,\mathrm{m\,s^{-1}}$. Again the definitions and constitutive
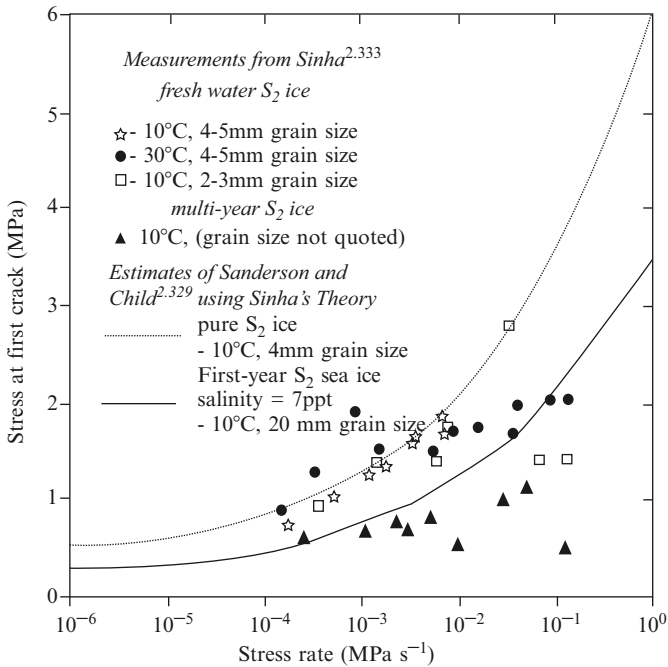
Fig. 2.4. Stress at first crack vs. strain rate [2.333]

details of various rocks are given in this chapter. With size and speed any category of rocks can cause a large impact load on buildings, railway lines and on vehicles passing on a nearby motorway.

The transport of goods in large re-usable boxes (containers) can be achieved using various cranes. These cranes vary in their capacity and in their operating speeds. The weights, heights and speeds at which cranes operate can certainly give an accurate assessment of the impact loads. On construction sites, different cranes operate for lifting weights. They are shear legs, derrick cranes, crawler-mounted cranes, self-propelled, rubber-tyred wheeled cranes, self-propelled telescopic-jib cranes and their truck-mounted versions, hoists, tower and gantry cranes. Figure 2.7 shows two types of derrick cranes. For impact analysis, the data for 7 and 10 tonne capacity derrick cranes are given in Table 2.7.

The *short and long crawler cranes* are of 30 and 80 tonne capacity. The hoisting speed is 40–50 m min^{-1} with a slowing speed of two revolutions per minute. The dragline bucket data and grabbing crane weights are given as 9,200 and 2975 kg, respectively. The *self-propelled telescopic-jib cranes* are of 4–10 tonne capacity with a travelling speed of 30 km per hour. The boom length is 6–8 m and width and height are approximately 2.75 m. The
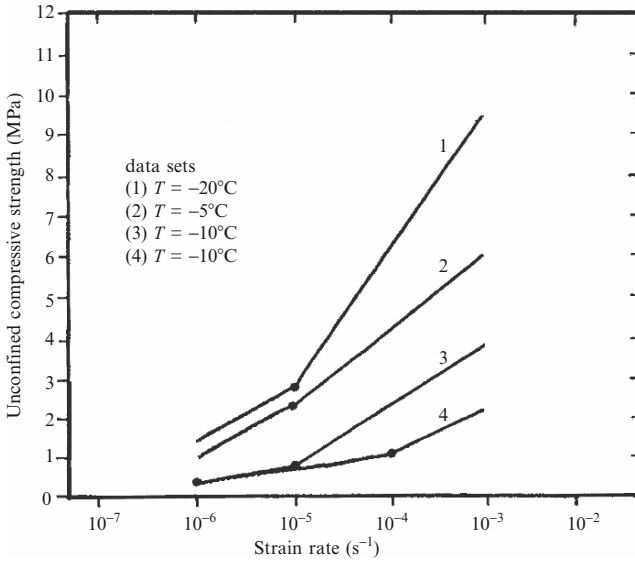
Fig. 2.5. Unconfined compressive strength vs. strain rate (API, 1987)

Table 2.6. A comparative study of three theories

Type of analysis	Breaking force (kN)	Riding-up force (kN)	Total force (kN)
Bercha and Danys [2.280]	1,558	–	1,558
Ralston [2.323–2.325]	1,964	1,196	3,160
Edwards and Croasdale [2.297]	922	900	1,822

truck-mounted jib crane has a capacity of between 30 and 50 tonnes and its travelling speed is up to 75 km h^{-1} with a maximum hoisting speed and slowing speed of 120 m min^{-1} and 0.3 revolutions per minute, respectively. For larger cranes of 40 tonne capacity, Table 2.8 lists useful data. Figure 2.8 illustrates a tower crane and various jib radii, loading capacities and other major parameters required for impact analysis are given in Table 2.9.

The containers vary in sizes and have either a closed or a removable top (Table 2.10). The most common sizes of containers are 6.10 m × 2.43 m × 2.43 m and 12.20 m × 2.43 m × 2.58 m. They may be loaded or unloaded at the dockside by either shipboard cranes or dockside gantries. They are provided with lifting facilities. Figure 2.9 shows the structural arrangement of a typical dry freight container.

Fig. 2.6. Rock falls
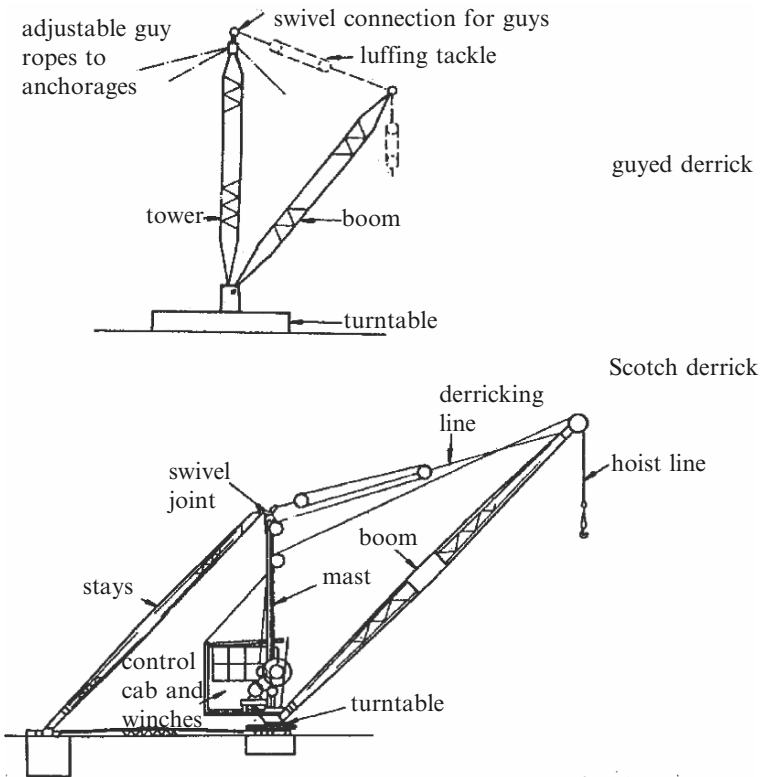
Fig. 2.7. Derrick cranes for dropped weights (courtesy of Crane Manufacturers'
Association, UK.)

Table 2.7. Comparative data for 7 and 10 tonne capacity derrick cranes

	Up to 7 tonne capacity	Ten tonne capacity and over
Hoisting speed–lifting design capacity $(\mathrm{m\,min^{-1}})$	30–35	10–15
Hoisting speed–lifting light load $(\mathrm{m\,min^{-1}})$	70	20–30
Derricking (luffing/speed) $(\mathrm{m\,min^{-1}})$	30	12–15
Slewing speed $(\mathrm{rev\,min^{-1}})$	1	0.3
Hoist motor (kW)	50	50
Slewing motor (kW)	10	30
Derricking motor (kW)	40	50
Travelling speed $(\mathrm{m\,min^{-1}})$	40	10
Travelling motor (kW)	20	60

Table 2.8. Data for cranes of 40 tonne capacity

Engine size	150–200 hp (112–150 kW)
Machine weight	20–40 tonnes
Max hoisting speed (single fall line)	50–60 m min^{-1}
Derricking (max to min)	25 s
Slewing speed	3 rev m^{-1}
Travelling speed	30 km h^{-1}
Turning radius	10 m
Road gradient: unladen	1 in 25
Boom length: four part	20 m
three part	14 m
Overall height	3 m
Overall width	2.5 m
Overall length	8 m

Spent fuel, low-level wastes, decommissioning waste, etc. are transported by rail, road and ship. The spent-fuel containers (casks or flasks) have safety problems which are similar to those of reactors. In order to contain high levels of spent-fuel radiation and decay heat emissions, the cask or flask must be safe against accidents. As shown in Fig. 2.10, the casks are usually made of carbon steel with stainless steel linings. They are usually cylindrical in shape, fitted with a lid. The lid is bolted to the body of the cylinder and sealed with O-rings. The external surface has fins for dissipating heat. During transportation, shock absorbers (made of stainless steel encased in balsa wood collars) are fixed to the ends. Sometimes additional lead linings are provided
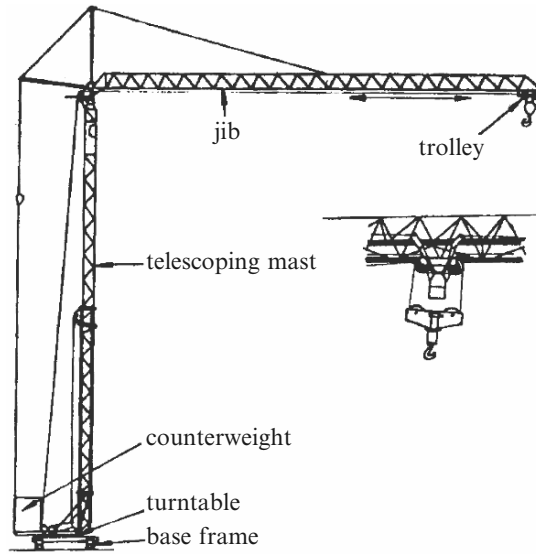
Fig. 2.8. Quick-assembly saddle-jib tower crane

to support or strengthen radiological shielding. Inside the container, the fuel elements are positioned in a basket. The CEGB (now Nuclear Electric, UK) has carried out drop tests on a full-scale magnox fuel flask. This flask, according to the International Atomic Energy Agency, Vienna (IAEA) regulations, must withstand the impact of a free fall from a height of 9 m on to a hard unyielding target followed by a 30 min totally enveloping fire at 800°C without leaking. CEGB also tested a similar container or flask in a high-speed impact test using a railway train. Data for the flask shown in Fig. 2.10 are listed in Table 2.11.

The data for aircraft engines are included in a study of aircraft impact data later on in this chapter.

2.2.6 Heavy Lorries, Trucks and Bulldozers as Impactors

Heavy lorries and trucks are in frequent use on many constructions sites, highways and in industrial areas. They are frequently involved in various incidents and accidents. It is, therefore, essential for the structural engineer to know the basic parameters such as payloads, masses/weights, speeds and dimensions. The standard lorries and trucks used in Britain and in the rest of Europe are given in Table 2.12 with their horsepower (HP) (kW), weights and payloads.

Trucks are described in terms of the total number of wheels and drive wheels. Thus a 4 × 4 truck has four wheels and four-wheel drive. An 8 × 4 truck has eight wheels, of which only four provide drive, thus leaving the other four as free wheels. The modern 300 tonnes rear dump truck is heavily used

Table 2.9. Tower cranes: relevant parameters for impact analysis (courtesy of the Crane Manufacturers' Association, UK)

Max jib radius (m)	11	16	18	20	22	25	27	30	35	35	35	40	55	60	65	80
Max capacity (tonnes)	0.45	1.5	1.5	1.7	2.0	3.0	3.0	4.0	6.0	8.0	8.0	8.0	12.0	20.0	20.0	63.0
Radius (m)	7.8	8.2	10.3	11.42	9.8	10.3	11.0	9.4	8.8	14.9	14.9	10.7	14.6	14.0	19.5	23.5
Min radius (m)	3.0	3.0	3.0	3.0	3.0	3.0	3.0	3.0	3.0	3.0	3.0	3.0	3.0	3.0	3.0	3.5
Track/wheel gauge (m)	2.0	2.32	2.8	3.2	2.8	2.8	3.2	3.8	4.5	6.0	6.0	5.0	6.0	8.0	8.0	12.5
Power supply (kW)	16.0	16.0	16.0	22.0	20.0	20.0	20.0	25.0	40.0	35.0	35.0	50.0	66.0	66.0	62.0	96.0
Max hook height (kW)	10.6	16.0	18.0	18.0	20.0	20.0	23.5	20.0	32.8	29.3	32.8	32.8	100.0	160.0	200.0	360.0

Table 2.10. Data for freight containers

	40 ft Dry cargo	40 ft Dry cargo hi-cube	40 ft Reefer	40 ft Tank	40 ft Open top	40 ft Half-high open top	20 ft Dry cargo	20 ft Dry cargo
Outside dimensions								
Length	40'	40'	40'	40'	40'	40'	20'	20'
Width	8'	8'	8'	8'	8'	8'	8'	8'
Height	8'	8'6"	8'6"	4'3"	8'6"	4'3"	8'	8'
Inside dimensions								
Length	39'7"	39'6"	37'10"		39'6"	39'6"	19'6"	19'7"
Width	7'9"	7'9"	7'4"		6'8"	7'9"	7'8"	7'10"
Height	7'4"	7'10"	7'1½"		7'6"	3'4"	7'4"	7'6"
Door opening								
Width	7'5¾"	7'6"	7'6"		7'6"	7'6"	7'5¾"	7'5¾"
Height	6'11¾"	7'5½"	7'5¾"		6'11"	3'4"	6'11¾"	6'11¾"
Construction	Aluminium	Aluminium	Aluminium	Stainless steel AISI 304	Aluminium	Aluminium	Aluminium	Plastic playwood
Internal cubic capacity	2,250 ft³	2,398 ft³	1,988 ft³	6,020 gal	2,296 ft³	1,020 ft³	1,096 ft³	1,151 ft³
Max load capacity (lb)	60,260 lb	60,950 lb	50,000 lb	51,600 lb	59,280 lb	45,000 lb	44,800 lb	40,650
Tare weight (lb)	6,400	6,940	10,700	9,260	7,750	6,660	4,500	4,500
Special features	End door opening	End door opening	Temp control meat rails	Bulk liquid; loading equipment supplied	End door opening; open top loading; swinging roof bows	End door opening; open top loading; swinging roof bows	End door opening	End door opening
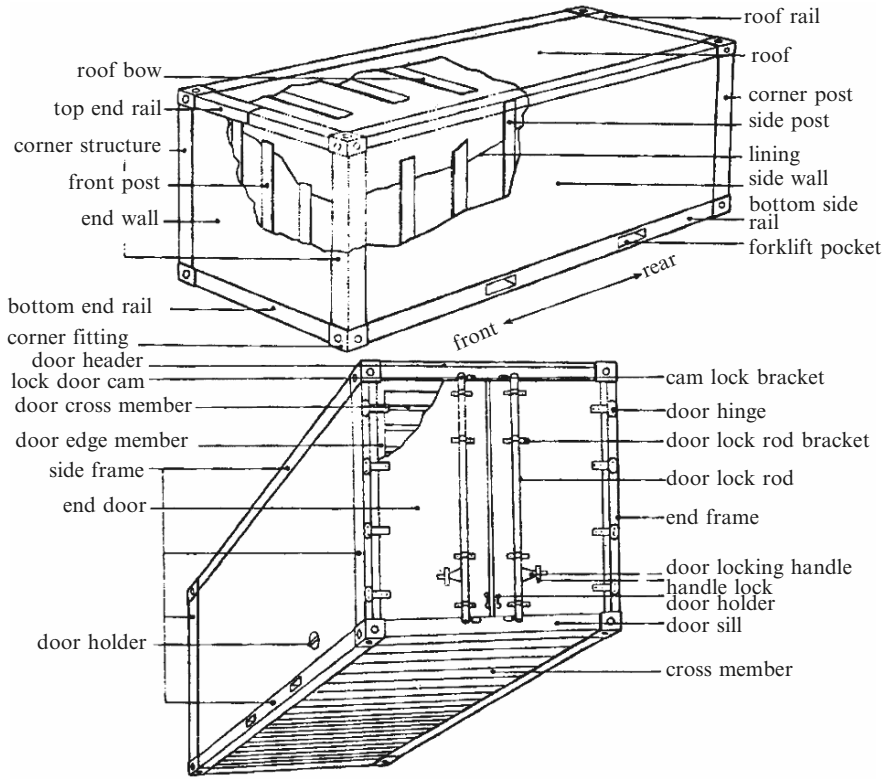
Fig. 2.9. A layout for a typical dry freight container [2.385]
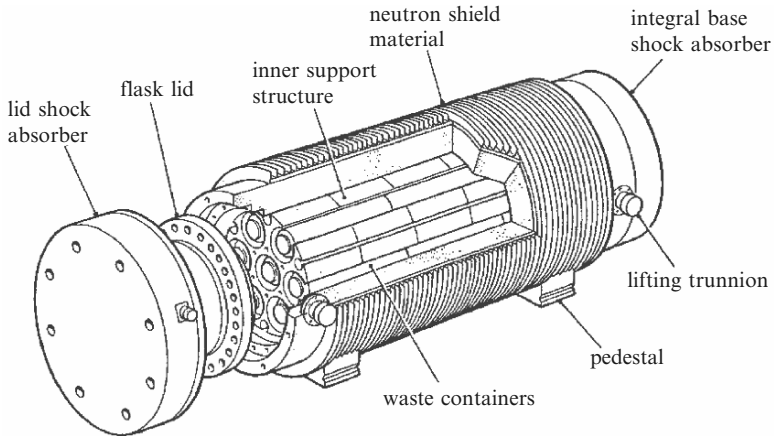
Fig. 2.10. A transport flask for vitrified waste (courtesy of the UK Atomic Energy Authority and CEGB)

Table 2.11. Data for the transport flask illustrated in Fig. 2.10

Description	Max external dimensions (m)	Max gross weight (t)
200 l drum	0.61 O/D × 0.863	0.75[a]
3 m³ box	2.15 × 1.5 × 1.3[a]	15[a]
12 m³ box for LLW	4.0 × 2.4 × 1.85[a]	60[a]
Freight container	6.0 × 2.44 × 2.59	24
500 l drum	0.8 O/D × 1.2	2[a]
3 m³ box	1.72 × 1.72 × 1.20	16
12 m³ box for ILW	4.0 × 2.4 × 1.85[a]	60
Transport container	2.46 × 2.46 × 2.48	70

[a] Approximated to the nearest dimension or weight

Table 2.12. Vehicle weights and payloads

	Gross vehicle HP (kW)	Capacity (m³)	Net weight empty (tonnes)	Payload (tonnes)
	60–350 (45–261)	30+	10	up to 16.26
	200–350 (150–261)	50+	20	up to 26
	156–1600 (112–1194)	6–70	6–120	up to 150
	200–3000 (150–2235)	6–120	10–250	up to 300
	100–400 (75–298)	70–130	4–10	up to 16.26
	200–400 (150–298)	120	20	up to 32.5
	100–200 (75–150)	10–15	20	up to 35

on site in quarrying operations. The standard truck load used for the bridge impact analysis in North America is given in Fig. 2.11. The average actual dimensions of tyres and trucks/containers and the rectangular wheel-load areas at the level surface are given in Tables 2.13 and 2.14.

Bulldozers are versatile machines and are used frequently for stripping soils, shallow excavation, maintenance of haul roads, opening up pilot roads, spreading, grading and ripping. The machine is assembled in two separate sections, comprising
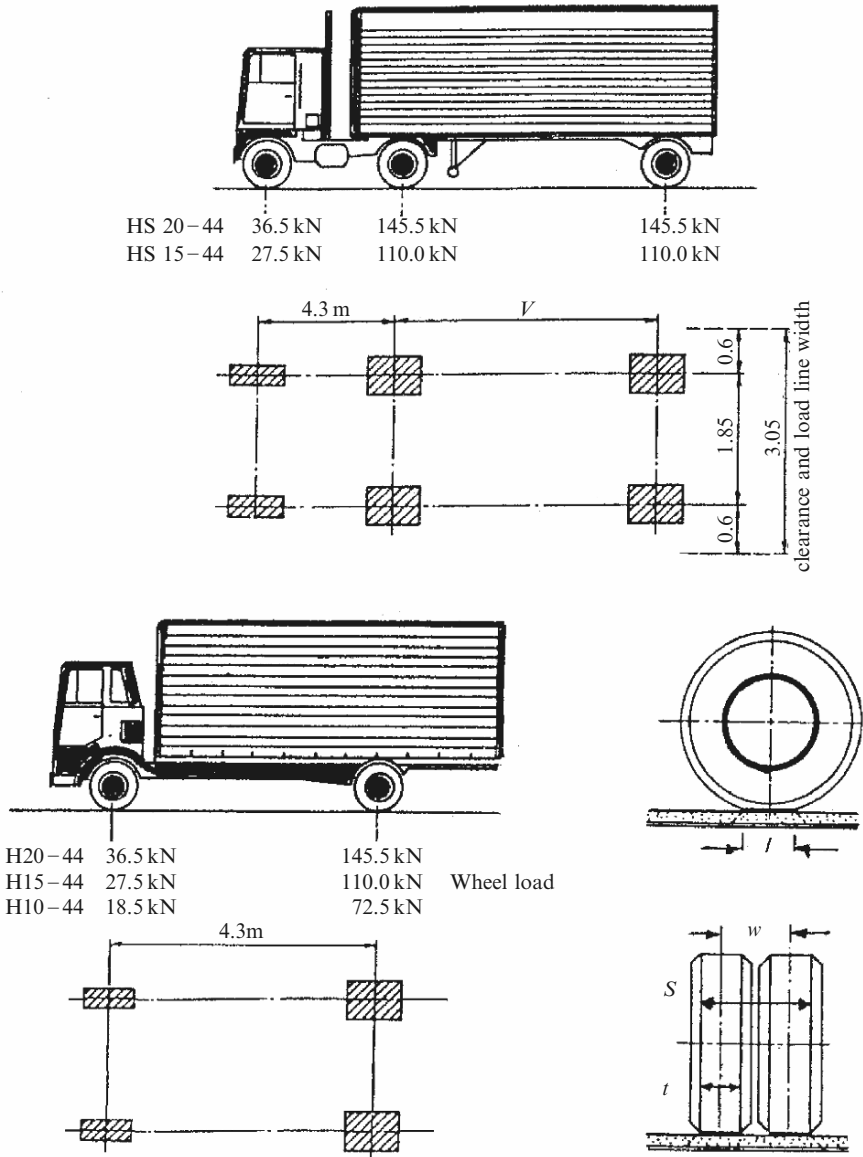
Fig. 2.11. Typical North American trucks (courtesy of the North American Trucks Association, New York)

(1) A base frame welded and attached with mountings for the dozer blade, the drive sprockets and rollers for the tracks;
(2) The superstructure carrying the engine, transmission, hydraulics cab and controls.

Table 2.13. Truck/container data

Type	L (m)	S (m)	H (m)	w_a (tonnes)
1A	12.190	2.435	2.435	30
1B	9.125	2.435	2.435	25
1C	6.055	2.435	2.435	20
1D	2.990	2.435	2.435	10
1E	1.965	2.435	2.435	7
1F	1.460	2.435	2.435	5

L, length; S, width; H, height; w_a, maximum weight

Table 2.14. Wheel dimensions vs. wheel loads

Nominal wheel loads (kN)	Wheel dimensions (mm)				
	t	l	a^c	W	S
36.5	178	226	40×10^3	290	467
54.5	201	274	55×10^3	325	526
73.0	254	279	71×10^3	412	666

a^c, actual contact area of one tyre at the top of the wearing surface (mm^2); t and l are given in Fig. 2.11
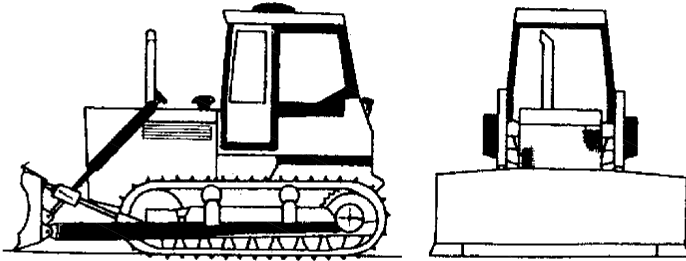
Fig. 2.12. A typical bulldozer

The attached blades can be U-blades, angled blades or push blades. A typical bulldozer is shown in Fig. 2.12. Data on engine sizes, weights and blade lengths and heights are given in Table 2.15. Since these bulldozers are brought on site via roads and are involved on sites for the construction of roads, runways, power stations, etc. they are treated as potential hazards. Many accidents have occurred, particularly during demolition work. Consequently it was thought necessary to list selected data on these machines.

2.2.7 Railway Trains

Railway trains are frequently involved in crashes with other trains, with vehicles at crossings or with other structural objects. The structural layouts of

Table 2.15. Data on bulldozers (Courtesy of the Federation of Master Builders, UK)

Engine size	hp	400	300	200	100–150
	kW	298	224	149	75–112
Machine weight	tonnes	35	25	16	10–12
Blade length	m	5	4.5	4.0	3.5
Blade height	m	1.8	1.5	1.2	1.0
Recommended operating speeds $km\,h^{-1}$					
Grading site roads			4–9		
Scarifying (eg, soil stabilization)			8–18		
Forming ditches			4–8		
Spreading			4–10		
Trimming and levelling			9–40		
Snow ploughing			8–20		
Self-transporting			10–40		

trains vary from country to country. Only the British and French systems will be discussed here. Comprehensive data are given in Tables 2.16–2.23. Where crash worthiness is to be checked for other engines and railway buggies, similar data are to act as an input for preliminary impact/crash analyses, typical views and cross-sections are given in Figs. 2.13 and 2.14.

2.3 Military, Air Force and Navy Missiles and Impactors

2.3.1 Introduction to Bombs, Rockets and Missiles

Different versions of bombs, rockets and missiles are available in the defence markets. Table 2.24 summarizes the characteristics of a number of shells and bombs. Figure 2.15 shows typical cartridges, high explosive shells, shrapnel shells, hand grenades and bombs as impactors. The chemistry of such bombs, shells and cartridges is described later on in this chapter. Advances in the manufacture of bombs have reached their acme. Some of the new ones are fully described in this chapter with appropriate specifications.

Different missile systems exist in a number of countries. The range capability determines their category. Missiles with a maximum range exceeding 550 km are classified *strategic* and those with ranges between 1,000 and 5,500 km are known as *intermediate missiles*. Missile systems with ranges less than 1,000 km are called *short-range* missile systems.

Certain symbols used in the explanatory notes for the missiles are defined as follows:

- ICBM Intercontinental ballistic missiles or strategic missile
- IRBM Intermediate range ballistic missile
- SRM Short-range missile

Table 2.16. Data on British railway systems

	Class 37		
Subclass	37/0	37/3	37/9
Former class codes	D17/1, Later 17/3	–	–
Number range	37 001–37 326	37 350–37 381	37 905–37 906
Former number range	D6600–D6999	From main fleet	From main fleet
Built by	EE & RSH Ltd	EE & RSH Ltd	EE Ltd
Introduced	1960–65	As 37/3/1988	As 37/9/1987
Wheel arrangement	Co–Co	Co–Co	Co–Co
Weight (operational)	102–108 tonnes	106 tonnes	120 tonnes
Height	3.89 m	3.89 m	3.89 m
Width	2.70 m	2.70 m	2.70 m
Length	18.74 m	18.74 m	18.74 m
Minimum curve negotiable	80.46 m	80.46 m	80.46 m
Maximum speed	129 km/h	129 km/h	129 km/h
Wheelbase	15.44 m	15.44 m	15.44 m
Bogie wheelbase	4.11 m	4.11 m	4.11 m
Bogie pivot centres	11.32 m	11.32 m	11.32 m
Wheel diameter (driving)	1.14 m	1.14 m	1.14 m
Brake type	Dual	Dual	Dual
Sanding equipment	Pneumatic	Pneumatic	Pneumatic
Route availability	5	5	7
Coupling restriction	Blue Star	Blue Star	Blue Star
Brake force	50 tonnes	50 tonnes	50 tonnes
Engine type	EE 12 CSVT	EE 12 CSVT	Ruston RK 270T
Engine horsepower	1,750 hp (1,304 kW)	1,750 hp (1,304 kW)	1,800 hp (1,340 kW)
Power at rail	1,250 hp (932 kW)	1,250 hp (932 kW)	–
Tractive effort	55,000 lb (247 kN)	55,000 lb (247 kN)	–
Cylinder bore	10 in (0.25 m)	10 in (0.25 m)	–
Cylinder stroke	12 in (0.30 m)	12 in (0.30 m)	–
Main generator type	EE 822/10G	EE 822/10G	Not fitted
Traction alternator type	Not fitted	Not fitted	GEC 564
Auxiliary generator type	EE 911/5C	EE 911/5C	Not fitted
Number of traction motors	6	6	6
Traction motor type	EE 538/1A	EE 538/1A	EE 538/1A
Gear ratio	53:18	53:18	53:18

Table 2.16. (continued)

	Class 37		
Fuel tank capacity	890 gal (4,046 l)	1,690 gal (7,682 l)	1,690 gal (7,682 l)
Cooling water capacity	160 gal (727 l)	160 gal (727 l)	–
Boiler water capacity	800 gal (3,637 l)	Not fitted	Not fitted
Lubricating oil capacity	120 gal (545 l)	120 gal (545 l)	–
Boiler fuel capacity	From main supply	Not fitted	Not fitted
Region of allocation	Eastern, Western, Scottish	Eastern, Western	Western

	Class 45	
Subclass	45/0	45/1
Former class codes	D25/1, later 25/1	D25/1, later 25/1
Number range	45,007–45,052	45 103–45 141
Former number range	D11–137	D11–137
Built by	BR Derby & Crewe	BR Derby & Crewe
Introduced	1960–62	As 45/1/1973–75
Wheel arrangement	1Co–Co1	1Co–Co1
Weight (operational)	138 tonnes	135 tonnes
Height	3.91 m	3.91 m
Width	2.70 m	2.70 m
Length	20.70 m	2.17 m
Minimum curve negotiable	100.58 m	100.58 m
Maximum speed	145 km h^{-1}	145 km h^{-1}
Wheelbase	18.18 m	18.18 m
Bogie wheelbase	6.55 m	6.55 m
Bogie pivot centres	9.95 m	9.95 m
Wheel diameter (driving)	1.14 m	1.14 m
	0.91 m	0.91 m
Brake type	Dual	Dual
Sanding equipment	Pneumatic	Pneumatic
Route availability	7	6
Coupling restriction	Not multiple fitted	Not multiple fitted
Brake force	63 tonnes	63 tonnes
Engine type	Sulzer 12LDA28B	Sulzer 12LDA28B
Engine horsepower	2,500 hp (1,862 kW)	2,500 hp (1,862 kW)
Power at rail	2,000 hp (1,490 kW)	2,000 hp (1,490 kW)

(*continued*)

Table 2.16. (continued)

	Class 45	
Tractive effort	55,000 lb (245 kN)	55,000 lb (245 kN)
Cylinder bore	11 in (0.27 m)	11 in (0.27 m)
Cylinder stroke	14 in (0.35 m)	14 in (0.35 m)
Main generator type	Crompton CG462A1	Crompton CG462A1
Traction alternator type	Crompton CAG252A1	Crompton CAG252A1
Auxiliary generator type	Not fitted AG252A1	Brush BL 100–30 Mk 11
Number of traction motors	6	6
Traction motor type	Crompton C172A1	Crompton C172A1
Gear ratio	62:17	62:17
Fuel tank capacity	790 gal (3,591 l)	790 gal (3,591 l)
Cooling water capacity	346 gal (1,572 l)	346 gal (1,572 l)
Boiler water capacity	190 gal (864 l)	190 gal (864 l)
Lubricating oil capacity	1,040 gal (4,727 l)	Not fitted
Boiler fuel capacity	From main supply	Not fitted
Region of allocation	Eastern	Eastern

	Class 47		
Subclass	47/0	47/3	47/9
Former class codes	27/2	27/2	–
Present number range	47 002–47 299	47 301–47 381	47901
Former number range	D1521–D1998	D1782–D1900	D1628 (47 046)
Built by	BR Crewe, Brush Ltd	BR Crewe, Brush Ltd	BR Crewe
Introduced	1962–5	1964–5	As 47/9/1979
Wheel arrangement	Co–Co	Co–Co	Co–Co
Weight (operational)	111–121 tonnes	114 tonnes	117 tonnes
Height	3.89 m	3.89 m	3.89 m
Width	2.79 m	2.79 m	2.79 m
Length	19.38 m	19.38 m	19.38 m
Minimum curve negotiable	80.46 m	80.46 m	80.46 m
Maximum speed	153 km h^{-1}	153 km h^{-1}	129 km h^{-1}
Wheelbase	15.69 m	15.69 m	15.69 m

Table 2.16. (continued)

	Class 47		
Bogie wheelbase	4.41 m	4.41 m	4.41 m
Bogie pivot centres	12.27 m	11.27 m	11.27 m
Wheel diameter (driving)	1.14 m	1.14 m	1.14 m
Brake type	Dual	Dual	Air
Sanding equipment	Not fitted	Not fitted	Pneumatic
Heating type	Steam	Not fitted	Not fitted
Route availability	6	6	6
Coupling restriction	Not fitted	Not fitted	Not fitted
Brake force	60 tonnes	60 tonnes	60 tonnes
Engine type	Sulzer 12LDA28C	Sulzer 12LDA28C	Ruston Paxman 12RK3CT
Engine horsepower	2,580 hp (1,922 kW)	2,580 hp (1,922 kW)	3,300 hp (2,455 kW)
Power at rail	2,080 hp (1,550 kW)	2,080 hp (1,550 kW)	2,808 hp (2,089 kW)
Tractive effort	60,000 lb (267 kN)	60,000 lb (267 kN)	57,325 lb (255 kN)
Cylinder bore	11 in (0.27 m)	11 in (0.27 m)	10 in (0.25 m)
Cylinder stroke	14 in (0.35 m)	14 in (0.35 m)	12 in (0.30 m)
Main generator type	Brush TG160–60 or TG172–50	Brush TG160–60 or TG172–50	Not fitted
Main alternator type	Not fitted	Not fitted	Brush BA 1101A
Auxiliary generator type	Brush TG69–20 or TG69–29	Brush TG69–20 or TG69–28	Not fitted
Auxiliary alternator type	Not fitted	Not fitted	Brush BAA602A
ETS generator	Not fitted	Not fitted	Not fitted
ETS alternator	Not fitted	Not fitted	Not fitted
Number of traction motors	6	6	6
Traction motor type	Brush TM64–68	Brush TM64–68	Brush TM64–68 Mk 1A
Gear ratio	66:17	66:17	66:17
Fuel tank capacity	765 gal (3,477 l)	765 gal (3,477 l)	765 gal (3,477 l)
Cooling water capacity	300 gal (1,364 l)	300 gal (1,364 l)	300 gal (1,364 l)
Boiler water capacity	1,250 gal (5,683 l)	Not fitted	Not fitted
Lubricating oil capacity	190 gal (864 l)	190 gal (864 l)	190 gal (864 l)
Boiler fuel capacity	From main supply	Not fitted	Not fitted
Region of allocation	Eastern, Midland, Scottish, Western	Eastern, Midland, Western	Western

(*continued*)

Table 2.16. (continued)

	Class 50	
Subclass	50/0	50/1
Former class codes	27/3	–
Number range	50,001–50,050	50,149
Former number range	D400–D449	50,049
Built by	EE (Vulcan Foundry) Ltd	Rebuilt Laira
Introduced	1967–8	Originally 1968, rebuilt 1987
Wheel arrangement	Co–Co	Co–Co
Weight (operational)	117 tonnes	117 tonnes
Height	3.95 m	3.95 m
Width	2.77 m	2.17 m
Length	20.87 m	20.87 m
Minimum curve negotiable	80.46 m	80.46 m
Maximum speed	161 km h^{-1}	129 km h^{-1}
Wheelbase	17.11 m	17.11 m
Bogie wheelbase	4.11 m	4.11 m
Bogie pivot centres	13.00 m	13.00 m
Wheel diameter (driving)	1.09 m	1.09 m
Brake type	Dual	Dual
Sanding equipment	Not fitted	Not fitted
Heating type	Electric–Index 61	Not available
Route availability	6	6
Coupling restriction	Orange square	Orange square
Brake force	59 tonnes	59 tonnes
Engine type	English Electric 16CSVT	English Electric 16CSVT
Engine horsepower	2,700 hp (2,014 kW)	2,450 hp
Power at rail	2,070 hp (1,540 kW)	1,890 hp
Tractive effort	48,500 lb (216 kN)	48,500 lb (216 kN)
Cylinder bore	10 in (0.25 m)	10 in (0.25 m)
Cylinder stroke	12 in (0.30 m)	12 in (0.30 m)
Main generator type	EE840–4B	EE840–4B
Traction alternator type	EE911–5C	EE911–5C
Auxiliary generator type	EE915–1B	EE915–1B
Number of traction motors	6	6
Traction motor type	EE538–5A	EE538–1A
Gear ratio	53:18	53:18

<div align="center">Table 2.16. (continued)</div>

	Class 50	
Fuel tank capacity	1,055 gal (4,797 litres)	1,055 gal (4,797 litres)
Cooling water capacity	280 gal (1,272 litres)	280 gal (1,272 litres)
Boiler water capacity	130 gal (591 litres)	130 gal (591 litres)
Region of allocation	Western	Western

<div align="center">Table 2.17. Data on British railway systems</div>

	Class 58	Class 59
Number range	58 001–58 050	59 001–59 004 JT26SS–55
Built by	BREL Doncaster, UK	General Motors Ltd, Illinois, USA
Introduced	1983–7	1986
Wheel arrangement	Co–Co	Co–Co
Weight (operational)	130 tonnes	126 tonnes
Height	3.91 m	3.91 m
Width	2.70 m	2.65 m
Length	19.13 m	21.40 m
Minimum curve negotiable	80.46 m	
Maximum speed	$129 \,\mathrm{km\,h^{-1}}$	$97 \,\mathrm{km\,h^{-1}}$
Wheelbase	14.85 m	17.269 m
Bogie wheelbase	4.18 m	4.14 m
Bogie pivot centres	10.80 m	13.25 m
Wheel diameter (driving)	1.12 m	1.06 m
Brake type	Air	Air
Sanding equipment	Pneumatic	Pneumatic
Heating type	Not fitted	Not fitted
Route availability	7	7
Multiple coupling restriction	Red diamond	Within type only
Brake force	62 tonnes	69 tonnes
Engine type	Ruston Paxman 12RK3ACT	EMD 645E3C
Engine horsepower	3,300 hp (2,460 kW)	3,300 hp (2,238 kW)
Power at rail	2,387 hp (1,780 kW)	
Tractive effort	61 800 lb (275 kN)	122,000 lb (573 kN)
Cylinder bore	10 in (0.25 m)	91/16 in (0.23 m)
Cylinder stroke	12 in (0.30 m)	10 in (0.25 m)
Main generator type	Brush BA1101B	EMD AR11 MLD D14A
Number of traction motors	6	6
Traction motor type	Brush TM73–62	EMD D77B

<div align="right">(continued)</div>

Table 2.17. (continued)

	Class 58	Class 59
Fuel tank capacity	985 gal (4,480 l)	919 gal (4,543 l)
Cooling water capacity	264 gal (1,200 l)	212 gal (962 l)
Lubricating oil capacity	110 gal (416 l)	202 gal (920 l)
Region of allocation	Midland	

Table 2.18. Data on British railway systems

	Class 81	Class 83
Former class code		AL3
Present number range	81 002–81 019	83 009–83 012
Former number range	E3001–E3023,	E3024–E3035,
	E3096–E3097	E3098–E3100
Built by	BRC & W Ltd	English Electric
Introduced	1959–64	1960–62
Wheel arrangement	Bo–Bo	Bo–Bo
Weight (operational)	79 tonnes	77 tonnes
Height (pantograph lowered)	3.76 m	3.76 m
Width	2.65 m	2.65 m
Length	17.22 m	17.52 m
Minimum curve negotiable	80.46 m	80.46 m
Maximum speed	129 km h^{-1}	64 km h^{-1}
Wheelbase	12.87 m	12.19 m
Bogie wheelbase	3.27 m	3.04 m
Bogie pivot centres	9.60 m	9.14 m
Wheel diameter	1.21 m	1.21 m
Brake type	Dual	Dual
Sanding equipment	Pneumatic	Pneumatic
Heating type	Electric–Index 66	Electric–Index 66
Route availability	6	6
Coupling restriction	Not multiple fitted	Not multiple fitted
Brake force	40 tonnes	38 tonnes
Horsepower (continuous)	3,200 hp (2,387 kW)	2,950 hp (2,200 kW)
(maximum)	4,200 hp (3,580 kW)	4,400 hp (3,280 kW)
Tractive effort (maximum)	50,000 lb (222 kN)	38,000 lb (169 kN)
Number of traction motors	4	4
Traction motor type	AEI 189	EE 532A
Control system	LT Tap changing	LT Tap changing
Gear drive	Alsthom Quill,	SLM flexible,
	single	single
	reduction	reduction
Gear ratio	29:76	25:76
Pantograph type	Stone-Faiveley	Stone-Faiveley
Rectifier type	Mercury Arc	Mercury Arc
Nominal supply voltage	25 kV ac	25 kV ac
Region of allocation	Scottish	Midland

Table 2.19. Data on British railway systems

	Class 85	Class 86
Subclass		86/4
Former class code	AL5	AL6
Present number range	85 002–83 040	86 401–86 439
Former number range	E3056–E3095	–
Built by	BR Doncaster	EE Ltd and BR Doncaster
Introduced	1961–4	As 86/4 1984/87
Wheel arrangement	Bo–Bo	Bo–Bo
Weight (operational)	83 tonnes	83 tonnes
Height (pantograph lowered)	3.76 m	3.97 m
Width	2.66 m	2.64 m
Length	17.19 m	17.83 m
Minimum curve negotiable	120.70 m	120.70 m
Maximum speed	129 km h^{-1}	161 km h^{-1}
Wheelbase	12.87 m	13.25 m
Bogie wheelbase	3.27 m	3.27 m
Bogie pivot centres	9.60 m	9.98 m
Wheel diameter	1.21 m	1.16 m
Brake type	Dual	Dual
Sanding equipment	Pneumatic	Pneumatic
Heating type	Electric–Index 66	Electric–Index 74
Route availability	6	6
Coupling restriction	Not multiple fitted	
Brake force	41 tonnes	40 tonnes
Horsepower (continuous)	3,200 hp (2,390 kW)	4,040 hp (3,014 kW)
(maximum)	5,100 hp (3,800 kW)	5,900 hp (4,400 kW)
Tractive effort (maximum)	50,000 lb (222 kN)	58,000 lb (258 kN)
Number of traction motors	4	4
Traction motor type	AEI 189	AEI 282AZ
Control system	LT Tap changing	HT Tap changing
Gear ratio	29:76	22:65
Pantograph type	Stone-Faiveley	Stone-Faiveley/AEI
Rectifier type	Germanium	Silicon semi-conductor

- SSM Surface-to-surface missile
- NSA Naval surface-to-air missile
- ADM Air defence missile
- AAM Air-to-air missile
- ASM Air-to-surface missile
- RO Rocket
- B Bomb
- Parameters L, length; S, span; d, diameter; w_L, weight; V, speed; R, range in miles (km); SG, self-guided; P_L, payload.

Table 2.20. Data on British railway systems

	Class 87		Class 91
Subclass	87/0	87/1	
Number range	87 001–87 035	87 101	91 001–91 050
Built by	BREL Crewe	BREL Crewe	BREL Crewe and GEC
Introduced	1973–4	1977	1988–90
Wheel arrangement	Bo–Bo	Bo–Bo	Bo–Bo
Weight (operational)	83 tonnes	79 tonnes	80 tonnes
Height (pantograph lowered)	3.99 m	3.99 m	3.75 m
Width	2.64 m	2.64 m	2.74 m
Length	17.83 m	17.83 m	19.40 m
Minimum curve negotiable	120.70 m	120.70 m	80.80 m
Maximum speed	177 km h^{-1}	177 km h^{-1}	225 km h^{-1}
Wheelbase	13.25 m	13.25 m	17.20 m
Bogie wheelbase	3.27 m	3.27 m	3.35 m
Bogie pivot centres	9.98 m	9.98 m	10.50 m
Wheel diameter	1.16 m	1.16 m	1.00 m
Brake type	Air	Air	Air (rheostatic)
Sanding equipment	Pneumatic	Pneumatic	Pneumatic
Route availability	6	6	
Coupling restriction	Within type and Class 86	Within type and Class 86	Fitted with TDM
Brake force	40 tonnes	40 tonnes	
Horsepower (continuous)	5,000 hp (3,730 kW)	4,850 hp (3,620 kW)	6,080 hp (4,530 kW)
(maximum)	7,860 hp (5,860 kW)	7,250 hp (5,401 kW)	6,310 hp (4,700 kW)
Tractive effort (maximum)	58,000 lb (258 kN)	58,000 lb (258 kN)	
Number of traction motors	4	4	
Traction motor type	GEC G412AZ	GEC G412BZ	GEC
Control system	HT Tap changing	Thyristor	Thyristor
Gear ratio	32:73	32:73	
Pantograph type	Brecknell Willis HS	Brecknell Willis HS	Brecknell Willis HS
Nominal supply voltage	25 kV ac	25 kV ac	25 kV ac
Region of allocation	Midland	Midland	Eastern

It is important to mention a few of the missiles. A typical example of the ICBM/IRBM is Patriot, a SAM, and three shoulder-mounted missiles, namely Stinger, Blow Pipe and Javelin missiles. Others are described in Tables 2.25–2.33. Figures 2.16 and 2.17 show major components of AT2 and M77 rockets. A typical Matra bomb described in the tables is shown in Fig. 2.18.

Table 2.21. Data on French railway systems

Class	Transmission	Rated power hp (kW)	w_a (kg)	V mph (km h^{-1})	V_{max} mph (km h^{-1})	Wheel dia (mm)	Total weight tonnes	L (mm)	First built
68,000	Electric	2,225 (1,660)	30,400	19 (30.6)	81 (130)	1,250	106	17,920	1963
68,500	Electric	2,205 (1,645)			81 (130)		105		1963
65,000	Electric	1,300 (970)	25,000		75 (120)	1,050	112	19,814	1956
			17,000						
72,000	Electric	3,020 (2,250)	36,400	34.7 (65)	100 (160)	1,140	110	20,190	1967
monomotor bogies (2 gears)				21.5 (34.5)	53 (85)				
			37,000						
63,000	Electric	480 (355)	17,000	6 (10)	50 (80)	1,050	68	14,680	1953
		585 (435)	17,000	8 (13)	50 (80)	1,050	68	14,680	1957
63,500	Electric	605 (450)	17,100	7.5 (12)	50 (80)	1,050	68	14,680	1956
66,000	Electric	1,115 (830)			75 (120)		70	14,898	1959
66,600	Electric	1,195 (890)			75 (120)		71	14,898	1962
67,000	Electric	1,930	20,600	26	56	1,150	80	17,090	1963
monomotor bogies (2 gears)		(1,440)		(42)	(90)				
			31,000	17.4 (28)	56 (90)				
67,400	Electric	2,045 (1,525)	29,000	23 (37)	87 (140)	1,250	83	17,090	1969
Y7100	Hydrodynamic	175	7,400		34 (54)	1,050	32	8,940	1958
Y7400	Mechanical	175			37 (60)	1,050	32	8,940	1963
Y8000 (2 gears)	Hydrodynamic	290	6,750	20 (32)	37 (60)	1,050	36	10,140	1977

w_a, max weight; V, speed; V_{max}, max speed; L, length

Table 2.22. Data on French railway systems

Class	Line current	Rate output hp (kW)	w_a (kg)	V mph (km h^{-1})	V_{max} mph (km h^{-1})	Wheel dia (mm)	Total weight (tonnes)	L (mm)	Year built
BB-8100	1,500 V dc	2,815 (2,100)	30,400	25.8 (41.5)	65 (105)	1,400	92	12,930	1949
BB-8500 (2 gear ratios)	1,500 V dc	3,940 (2,940)	20,100, 33,000	51.3 (82.5), 30.6 (49.2)	93 (140), 56 (90)	1,100	78	14,700–15,570	1963
BB-7200	1,500 V dc	5,845 (4,360)	30,000	60 (97)	112 (180)	1,250	84	17,480	1977
BB-9200	1,500 V dc	5,160 (3,850)	26,500	58 (93)	100 (160)	1,250	82	16,200	1957
BB-9300	1,500 V dc	(3,850)							1968
BB-9400	1,500 V dc	2,965 (2,210)	27,500	31 (50)	81 (130)	1,020	59	14,400	1959
CC-6500 (2 gear ratios)	1,500 V dc	7,910 (5,900)	29,347	38.5 (62)	62 (100), 137 (220)	1,140	115	20,190	1970
CC-7100	1,500 V dc	4,680 (3,490)	26,500	49.5 (79.5)	93 (150)	1,250	105	18,922	1951
BB-12000	25 kV, 50 Hz	3,310 (2,470)	36,000	29.5 (47.5)	75 (120)	1,250	83	15,200	1954
BB-13000	25 kV, 50 Hz	2,680 (2,000), 2,855 (2,130)	25,000	40.5 (65)	65 (105), 75 (120)	1,250	84	15,200	1954, 1956

BB-1600	25 kV, 50 Hz	5,540 (4,130)	31,500	53 (85)	100 (160)	1,250	84	16,200	1958
BB-15000	25 kV, 50 Hz	5,485 (4,360)	29,000	62 (100)	112 (180)	1,250	88	17,480	1971
BB-16500 (2 gear ratios)	25 kV, 50 Hz	3,460 (2,580)	33,000 19,200	51 (82) 30 (90)	93 (150) 56	1,100	74	14,400	1958
BB-17000 (2 gear ratios)	25 kV, 50 Hz	3,940 (2,940)	20,100 33,000	51.3 (82.5) 30.6 (49.2)	87 (140) 56 (90)	1,100	78	14,700–14,940	1964
CC-14100	25 kV, 50 Hz	2,495 (1,860)	43,000	17.7 (28.5)	37 (60)	1,100	126	18,890	1954
BB-20200 (2 current) (2 gear ratios)	25 kV, 50 Hz 15 kV, 162/3 Hz	3,940 (2,940) 2,225 (1,660)			56 (90) 93 (150)		80	14,490	1969
CC-21000 (2 current) (2 gear ratios)	25 kV, 50 Hz 1.5 kV dc	7,910 (5,900)			62 (100) 137 (220)		122	20,190	1969
BB-22200 (2 current)	25 kV, 50 Hz and 1,500 V dc	5,845 (4,360)	30,000	60 (97)	112 (180)	1,250	89	17,480	1977
BB-25100 (2 current)	25 kV, 50 Hz and 1,500 V dc	5,540 (4,130) 4,560 (3,400)	37,000	52 (83.5)	81 (130)	1,250	84	16,200	1963

Table 2.22. (continued)

Class	Line current	Rate output hp (kW)	w_a (kg)	V mph (km h^{-1})	V_{max} mph (km h^{-1})	Wheel dia (mm)	Total weight (tonnes)	L (mm)	Year built
BB-25200 (2 current)	25 kV, 50 Hz and 1,500 V dc	5,540 (4,130) 4,560 (3,400)	31,000	62 (99.5)	99 (160)	1,250	84	16,200	1964
BB-25500 (2 current) (2 gear ratios)	25 kV, 50 Hz and 1,500 V dc	3,940 (2,940)	20,100 33,600	51 (82) 30 (48)	93 (140) 56 (90)	1,100	78	14,700–15,570	1963
CC-40100 (4 current) (2 gear ratios)	25 kV, 50 Hz 15 kV, 162/3 Hz 3,000 V dc 1,500 V dc	6,000 (4,480) 6,000 (4,480)	14,500 20,200	95.4 (153.5) 68 (110)	149 (240) 99 (160)	1,080	108	22,030	1964

w_a, max weight; V, speed; V_{max}, max speed; L, length

Table 2.23. Data on French railway systems

Class	Cars per unit	Line voltage frequency	Motor cars per unit	Motored axles per motor car	Rated output (kW)	Max speed (km h^{-1})	Weight (tonnes)	Length of unit (mm)	Rate of acceleration under normal load	Year first built
Z5300	4	1.5 kV dc	1	4	1,180	130	154	102,800	0.7 m s^{-2} 0–50 km h^{-1}	1965
Z5600	4	1.5 kV dc	2	4	2,700	140	216	98,760	0.9 m s^{-2} 0–50 km h^{-1}	1982
Z7100	4	1.5 kV dc	1	2	940	130	139	94,170	0.47 m s^{-2} 0–50 km h^{-1}	1960
Z7300 Z7500	2	1.5 kV dc	1	4	1,275	160	103	50,200	0.5 m s^{-2} 0–50 km h^{-1}	1980
Z6100	3	25 kV, 50 Hz	1	2	615	120	113	74,450	0.45 m s^{-2} 0–40 km h^{-1}	1964
Z6300	3	25 kV, 50 Hz	1	2	615	120	105	60,100	0.5 m s^{-2} 0–40 km h^{-1}	1965
Z6400	4	25 kV, 50 Hz	2	4	2,350	120	189	92,430	1 m s^{-2} 0–50 km h^{-1}	1976
Z8100	4	1.5 kV dc, 25 kV, 50 Hz	2	4	2,500	140	212	104,160	0.9 m s^{-2} 0–50 km h^{-1}	1985
Z8800	4	25 kV, 50 Hz	2	4	2,800	140	224	98,760	0.9 m s^{-2} 0–50 km h^{-1}	1985
Z9500 Z9600	2	1.5 kV dc, 25 kV, 50 Hz	1	4	1,275	160	115	50,200	0.5 m s^{-2} 0–50 km h^{-1}	1982
Z11500	2	25 kV, 50 Hz, 25 kV, 50 Hz	2	4	1,275	160	115	50,200	NA	1987
TGV 23000	10	25 kV, 50 Hz 1.5 kV dc	2	12	6,450 3,100	270	418	200,190	0.5 m s^{-2} 0–50 km h^{-1}	1978
TGV 3300	10	25 kV, 50 Hz 162/3 Hz, 1.5 kV dc	2	12	6,450 3,100 2,800	270	419	200,190	0.5 m s^{-2} 0–50 km h^{-1}	1981

NA, not applicable
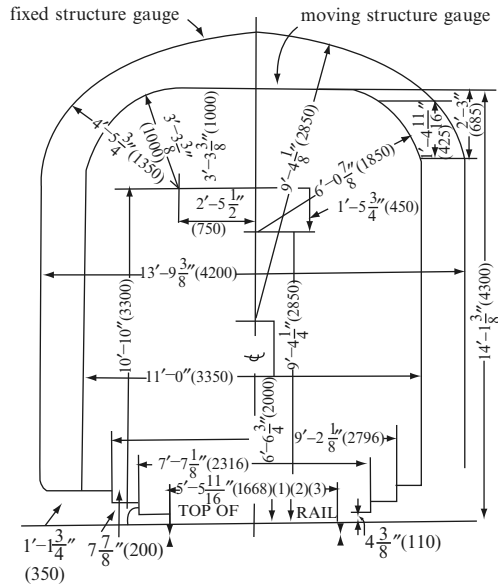
Fig. 2.13. A typical structural cross-section of a French train with circular heads
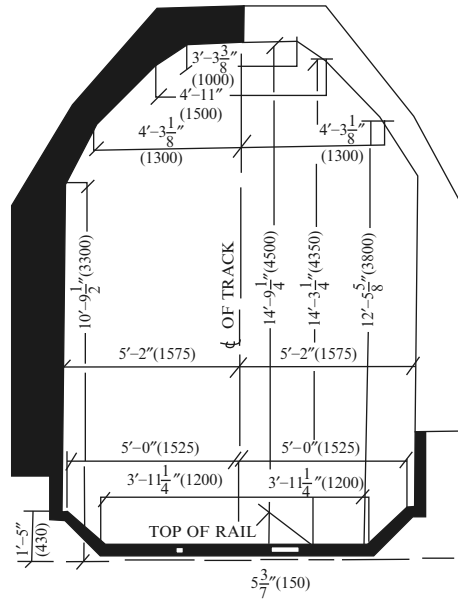
Fig. 2.14. A typical cross-section of a French Train with parabolic heads

2.3.1.1 Patriot: a SAM

In March 1972, Patriot was underway with modifications in radar, computer and guidance hardware. In July 1973, demonstration model fire control group

Table 2.24. Guns, shells and bombs

Types of shells and bombs	Manufacturer	Dimensions	w_L (kg)	Shape and guidance	R	V (m s^{-1})	Warhead (kg)	Mechanisms
Double base shot gun	International	$d = 1.25$ $t = 0.150$	–	Porous disc	Short	–	–	Guns
Single or double base rim fire	International	$d = 0.875$ $t = 0.10$	–	Porous disc	Short	–	–	Guns
Double base revolver	International	$d = 1.00$ $t = 0.125$	–	Porous disc	Short	–	–	Gun
Single base rifle	International	$d = 1.25$ $d = 0.375$ $t = 0.045$	–	Tubular	Short	–	–	Gun
GBU-15 HOBOS guided bomb	Rockwell International USA	$L = 3.75$ $MK84$ $S = 112$ $d = 46$ $(M11.8)$ $S = 132$ $d = 61$	$MK84$ 2,240 (1016) $M118$ 3,404	The forward guidance system is KMU-353 or 390 electro-optical with TV camera or target seeker optics	Medium	–	–	Free fall bomb from
Bofor	Sweden	–	0.120	5,500 kg guns	3.7 km	10,005	0.88	Trajectory fall
ZSU-23-4	USSR	$L = 654$ $d = 29.5$ 3,400 rounds	20.50	SPAA vehicles 4×3 automatic	Short	7,000	–	Gun
GBU-15(V)2 glide bomb (smart bomb)	USA	$L = 388$		Imaging infra-red	Short		1,111.0	

d, diameter (mm); t, web thickness (mm); L, length (cm); w_L, weight; S, span (cm); R, distance; V, velocity

(DMFCG) was tested. In January 1979, the programme was redesignated XMIM-104 Patriot. A full-scale development commenced in August 1979. First firing in CM electronic counter measures (ECM) was carried out in December 1976. A Patriot fire unit consists of a fire control section (FCS)

rifle cartridge

cap   powder   bullet

hand grenade

pin

explosive

detonator

percussion
cap   fuse

high explosive shell

fuse

explosive

driving band

shrapnel shell

fuse

shrapnel

driving
band

explosive
charge

aircraft bomb

fuse

explosive

fin

tail fuse
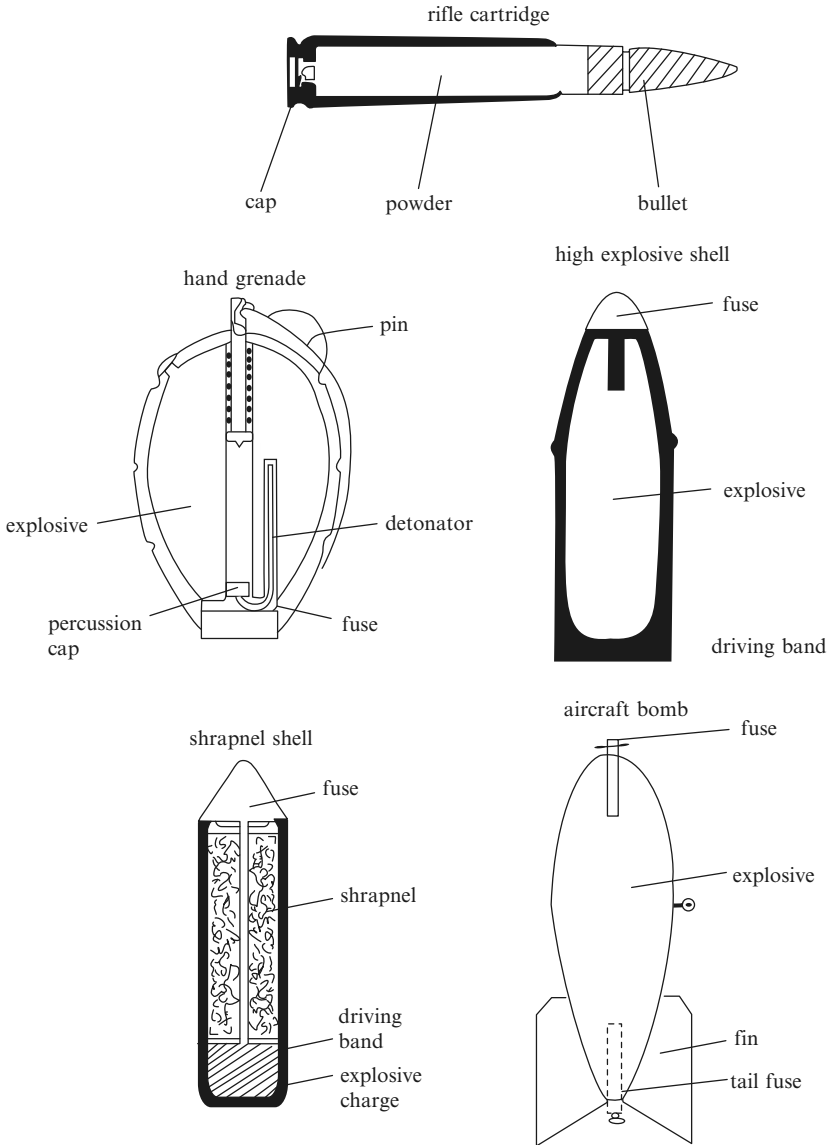
Fig. 2.15. Cartridges, high explosives, shrapnel shells and bombs as impactors (sketches and information from Dara Adam Khel, NWFP, Pakistan (Malik Zarak Khan))

liquefied liner is
propelled down tube
and penetrates
armour

bullet propels grenade
from end of the
rifle

SA-80 rifle

base
detonator

copper
liner
is
melted

tube

armour

exploding
fragments
inside vehicle

isometric view
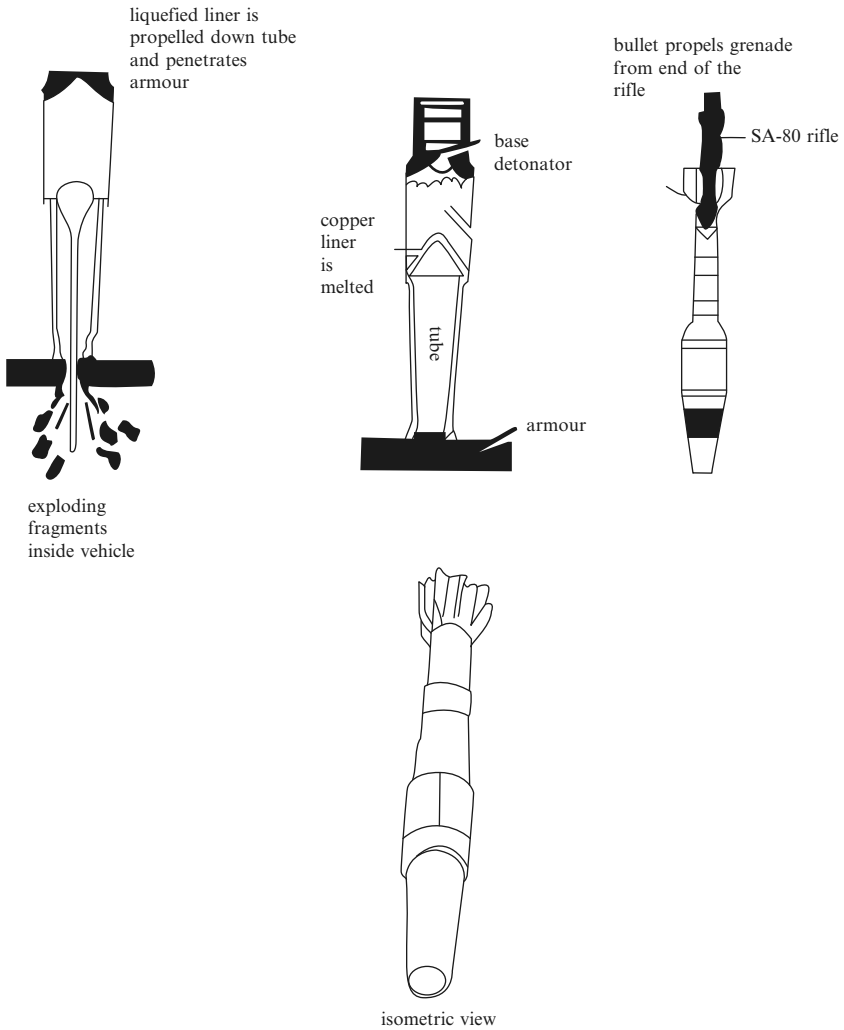
Fig. 2.15. (Continued)

and its launchers. The individual sections of the weapon from nose to tail are
given below:

(1) Nose radome
(2) Terminal guidance system
(3) Warhead section
(4) Propulsion system
(5) Control section.

The nose radome is fabricated from 12 mm thick slip-cast fused silica and
tipped with cobalt alloy; Fig 2.19 shows the layout. Below the silica a planar

Table 2.25. Missiles for Armed Forces (ICBM and IRBM) (China, USSR)

Types of missiles/rockets	Manufacturer/ country of manufacture	Dimensions	w_L lb (kg)	Power plant and guidance	R miles (km)	V mach	Warhead	Mechanisms
BGM-109 Tomahawk cruise missile (IRBM)	General dynamics/ Convair, San Diego, USA	$L = 5.56$ $S = 2.45$ $d = 0.53$	2200 (1,000) to 4,000 (1,814)	Williams Research F107 Turbofan 600 lb (272 kg) Thrust Guidance MD Tercom and Inertial	1,727 (2,780)	0.72 (550 mph/ 885 km h^{-1})	Thermo-nuclear 1000 lb (454 kg)	SG
CSS-2 CSS-3 (IRBM)	China	–		Liquid propellant Stage 2 Stage 3	(12,000)	0.8	Nuclear 2 Mt 1–5 Mt	SG
CSS-1 CSS-2 (IRBM) Sandal (IRBM)	China	–		Liquid propellant Two stages Two stages	(1,200) (2,700) (2,000)	0.7	Nuclear 20 kt 1–3 Mt 1 Mt	SG
SSBS S-3	France	–	–	Solid propellant Two stages	(3,000)	0.65	Nuclear 1.2 Mt	–
SS-N-20 Sturgeon (IRBM)	USSR	–	–	Solid propellant	(3,000)	0.65	Nuclear 1.2 Mt	–
UGM-73 Poseidon missile (IRBM)	Lockheed Missiles and Space Company, California, USA	$L = 10.36$ $d = 1.88$	65,000 (29,500)	Solid motor Thiokol as first stage; Hercules as second stage; guidance: inertial	3,230 (5,200)	10.0	Lockheed MIRV carrying 50 kt Rvs	Submarine launch
UGM-27 Polaris (ICBM) missile	Lockheed, California, USA	$L = 9.45$ $d = 1.37$	35,000 (15,850)	Aerojet solid motor with jetavator control as first stage; Hercules motor with liquid injection as second stage	2,875 (4,630)	10.0	MIRV 200 kt	Submarine launch

d, diameter (m); L, length (m); S, wingspan (m); w_L, launch weight; R, range; V, speed; SG, self-guided

Table 2.26. Missiles for Armed Forces (ICBM and ALCM) (USA, USSR)

Types of missiles/rockets	Manufacturer/ country of manufacture	Dimensions	w_L lb (kg)	Power plant and guidance	R miles (km)	V mach	Warhead	Mechanisms
AGM-86A air-launched cruise missile (ALCM)	Boeing, Aerospace, Seattle, USA	$L = 4.27$ $S = 289$ $d = 64$	1,900 (862)	Williams Research F107-WR-100 2 No shaft turbofans 600 lb (272 kg) thrust; McDonnell Douglas Tercom with inertial system	760 (1,200)	0.6 to 0.8	Thermo-nuclear 200 kt	B-52
LGM-30 Minuteman (ICBM) missile, located in Silos	Boeing Aerospace, Ogden, USA	$L = 18.2$ $d = 183$	Model II 70,116 (31,800) Model III 76,015 (34,475)	I-Stage: Triokol TU-120 (M55E), 2×10^5 lb (9×10^3 kg) thrust II-Stage: Hercules rocket 35×40^3 lb (16×10^3 kg) thrust III-Stage: Aerojet 35×10^3 lb (16×10^3 kg) thrust	II Stage: 7,000 (11,250) III Stage: 8,000 (12,875)	1500 mph	Thermo-nuclear 1–5 Mt II-Stage: AVCO MK 11C III-Stage: GE MK-12 MIRV	SG
RS-12/SS13 Savage (ICBM)	USSR	–	–	Solid fuel propellant; three stages	(9,400)	0.8	Nuclear 750 kt	SG
RS-16/SS17 (ICBM)	USSR	–	–	Liquid cold launch; two stages	(11,000) (10,000)	0.8	3.6 Mt mode 2 or MIRV 4 × 200 kt	SG
RS-20/SS18 (ICBM)	USSR	–	–	Liquid propellant; two stages	(10,000)	1.0	5–10 Mt mode 2	
SS-23 Scalpel (ICBM)	USSR	–	–	Solid cold launch propellant; three stages	(10,000)	1.0	Nuclear MIRV 8–10 ×300–500 kt	Rail; mobile
SS-25 Sickle (IRBM)	USSR	–	–	Solid cold launch propellant; three stages	(10,500)	1.0	Nuclear 550 kt	

L, length (m); S, wingspan (cm); d, diameter (cm); w_L, launch weight; R, range; V, speed; SG, self-guided

Table 2.27. Missiles for Armed Forces (SRM, SCUD, RBS, HJ) (USSR, France, UK, USA, China, Sweden)

Types of missiles/rockets	Manufacturer/ country of manufacture	Dimensions	w_L lb (kg)	Power plant and guidance	R (km)	Warhead	Mechanisms
M Type (SRM)	China	L = 910	6,200	Solid propulsion; inertial	600	Nuclear	SSM
Frog-7 (SRM)	France	L = 910 d = 85	2,300	Solid propulsion	70	Nuclear	SSM
SS-1C Scud B	USSR	L = 1125 d = 85	6,370	Storable liquid; inertial	280	Nuclear	
SS-23 Spider (SRM)	USSR	L = 605 d = 100	3,500	Solid propulsion; inertial	525 miles	Nuclear	SSM
Exocet MM 10	France	L = 578 S = 100 d = 35	850	Solid propulsion; two stages: inertial and active radar homing	70	165 kg Conventional	SSM ship
RBS 15	Sweden	L = 435 d = 50	(600)	Turbojet and boosters	150	Conventional	SSM ship
Arrow 8 (HJ-8)	China	L = 99.8 S = 47 d = 10.2	(11.3)	Solid propulsion; wire-guided	0.1 to 3	Heat	SSM anti-tank
Spandrel	USSR	L = 100 d = 16	(12–18)	Solid propulsion; semi-automatic	4	Heat	SSM anti-tank
Vigilant	UK	L = 107 S = 28 d = 11	(14)	Solid propulsion; two stages: wire manual or auto	1.375	Heat 6 kg	
Dragon 1 M 47	USA	L = 74 S = 33 d = 13	(13.8)	Multiple solid propulsion; wire manual	1.0	Heat	SSM anti-tank

L, length (cm); d, diameter (cm); S, wingspan (cm); w_L, launch weight; R, range

Table 2.28. Missiles for Armed Forces (BGM, M, MK, RGM, etc.) (USA, France, Israel)

Types of missiles/rockets	Manufacturer/ country of manufacture	Dimensions	w_L lb (kg)	Power plant and guidance	R (km)	Warhead	Mechanisms
TOW 2 (BGM-71 D)	USA	$L = 140$ $d = 15$	(21.5)	Solid propulsion; wire manual or auto	3.75	Heat conventional	SSM anti-tank
Copperhead (M712)	USA	$L = 137$ $d = 15$	63.5	Cannon launched; laser homing	16	Heat 6.4 kg	SSM anti-tank
Gabriel	Israel	L S d		Two stage solid		Conventional	SSM shipborne
MK I		335 135 34	430	propulsion; auto	18	100 kg	
MK II		341 135 34	430	pilot/command	36	100 kg	
MK III		381 135 34	560		36+	150 kg	
MK IV		381 135 34	560	Turbojet propulsion; inertial and active radar homing	200		
SS-N-3 Shaddock (SRM)	USSR	$L = 1,020$ $d = 86$	4,700	Solid boosters; internal turbojet radio command	460–735	Nuclear and conventional	SSM shipborne
Harpoon (RGM-84A)	USA	$L = 384$ $S = 830$ $d = 34$	519	Solid booster turbojet cruise; inertial and radar	90	Conventional	SSM shipborne
Deadeye 5	USA	$L = 384$ $d = 12.7$	47.5	Solid propulsion; laser homing	24	–	Guided projectile, shipborne
Crotale	France	$L = 290$ $S = 54$ $d = 15$	80	Solid propulsion; radio command	18	15 kg Conventional	NSA
Sadral	France	$L = 180$ $d = 16$	17	Solid propulsion; infra-red homing	0.3–6	3 kg Heat conventional	NSA

L, length (cm); d, diameter (m); S, wingspan (cm); w_L, launch weight; R, range

Table 2.29. Missiles for Armed Forces (mixed) (Israel, USSR, France, Italy)

Types of missiles/rockets	Manufacturer/ country of manufacture	Dimensions	w_L lb (kg)	Power plant and guidance	R (km)	Warhead	Mechanisms
Barak missile	Israel Aircraft Industries (IAI)	$L = 217$ $d = 17$	(86)	Semi-active radar-homing missile with disposable launch canister, manually fitted to an 8-round launcher based on the MBT TCM-30 twin 30 mm anti-aircraft gun mounted	10	Conventional 2 nuclear 7 kg	NSA small patrol boats
SA-N-3 Goblet	USSR	$L = 620$ $S = 150$ $d = 33.5$	550	Solid propulsion; semi-active homing	55	80 kg Conventional	NSA
SA-N-4	USSR	$L = 320$ $d = 21$	190	Solid propulsion; semi-active homing	14.8	50 kg	NSA
Roland 3	France and Italy	$L = 260$ $S = 50$ $d = 27$	85	Solid propulsion and command	8	9 kg Conventional	ADM
SA-4 Ganef (SRM)	USSR	$L = 880$ $S = 290$	100,000	Ramjet and solid boosters; radio command	70	135 kg	ADM
SA-10 Grumble MM 10	USSR	$L = 700$ $S = 10$ $d = 45$	1,500	Solid propulsion	100	Nuclear	ADM
SA-12 Gladiator	USSR	$L = 750$ $S = 350$ $d = 50$	2,000	Solid propulsion; semi-active radar	80	150 kg Conventional	ADM
SA-13 Gopher (HJ-8)	USSR	$L = 220$ $S = 40$ $d = 12$	55	Solid propulsion; infra-red homing	10	4 kg Conventional	ADM

L, length (cm); d, diameter (cm); S, wingspan (cm); w_L, launch weight; R, range

Table 2.30. Missiles for Armed Forces (medium type) (UK, USA, China, France)

Types of missiles/rockets	Manufacturer/ country of manufacture	Dimensions	w_L lb	Power plant and guidance	R (km)	Warhead	Mechanisms
Blood hound	UK	$L = 846$ $S = 283$ $d = 55$	–	Ramjet and solid boosters; semi-active radar homing	80	Conventional	ADM
Blow Pipe	UK	$L = 139$ $S = 270$	20.7	Solid propulsion; radio command	Any short distance 3	Conventional	ADM, shoulder-fixed
Javelin	UK	$L = 140$ $d = 8$	–	Solid propulsion; Saclos	4+	Conventional	ADM, shoulder-fixed
Hawk MIM-23B	USA	$L = 503$ $S = 119$ $d = 36$	627.3	Solid propulsion; semi-active homing	40	Conventional	ADM
Stinger FIM-92A	USA	$L = 152$ $S = 14$ $d = 7$	15.8	Solid propulsion; infra-red homing	Short range 3	Conventional	ADM
MIM Hercules	USA	$L = 1210$ $d = 80$	4,858	Solid propulsion; command	140	Nuclear and conventional	ADM
L-5B	China	$L = 289$ $S = 66$ $d = 13$	85	Solid propulsion; infra-red	5	Conventional	AAM
L-7	China	$L = 275$ $S = 66$ $d = 16$	90	Solid propulsion; infra-red	5	Conventional	AAM
Mistrel	France	$L = 180$ $d = 9$	18	Solid propulsion; infra-red	3	3 kg Conventional	AAM
Super 530	France	$L = 354$	250	Solid propulsion	25	30 kg	AAM

L, length (cm); S, wingspan (cm); d, diameter (cm); w_L, launch weight; R, range

Table 2.31. Missiles for Armed Forces (missiles and rockets) (France, USA, USSR)

Types of missiles/rockets	Manufacturer/ country of manufacture	Dimensions	w_L lb (kg)	Power plant and guidance	R	Warhead	Mechanisms
550 Magic	France	$L = 275$ $S = 66$ $d = 16$	–	Solid propulsion; infra-red	5 km	Conventional	AAM
AIM-9 Sidewinder	Naval Weapon Centre, Philco-Ford, Ford Aero-Space, General Electric, USA	$L = 283$ to 2.91 $S = 56$ to 64 $d = 12.7$	up to 190 (86)	Rocket dyne, Thiokol, Bermite or Naval propellant; Single Grain solid MK 17, 36, 86; guidance: 9E to 9L, high power servo-system, AM/ FM IR conical scan head or Raytheon track via missile	2.5+ miles cruise 6.0 miles max	XM 248 high explosive (150 lb)	AAM (F-16,F-20, F-5E aircraft)
Alamo AA-10	USSR	$L = 400$ $S = 70$ $d = 19$	200	Solid propulsion; semi-active or infra-red	30 km	Conventional	AAM
AMBAAAM	USA	$L = 357$ $S = 63$ $d = 18$	150	Solid propulsion; command and inertial	12 km	Conventional	AAM
Falcon	USA	$L = 213$ $S = 639$ $d = 29$	115	Solid propulsion; semi-active radar	8 km	Conventional	AAM
Phoenix	USA	$L = 396$ $S = 92$ $d = 38$	454	Solid propulsion; semi-active radar	150 km	Conventional	AAM
Sparrow AIM-7M	USA	$L = 366$ $S = 102$ $d = 20$	227	Solid propulsion; infra-red	140 km	Conventional	AAM

L, length (cm); S, wingspan (cm); d, diameter (cm); w_L, launch weight; R, range

Table 2.32. Missiles for Armed Forces (mixture ASM and rockets) (China, USSR, USA)

Types of missiles/rockets	Manufacturer/country of manufacture	Dimensions			w_L lb (kg)	Power plant and guidance	R	V mach (mph)	Warhead	Mechanism
		L	S	d						
C-601	China	738	280	92	2,440	Liquid propulsion	100 km	–	400 kg	ASM
HY-4		736	280	76	1,740	Turbofan propulsion	150 km	–	to	ASM
C-801		480	165	55	1,025	Solid propulsion All active radar	150 km	–	500 kg Conventional	ASM
		L	S	d						
S-9	USSR	600	150	50	750	Solid propulsion; semi-active laser	150 km	–	Conventional	ASM
S-10		350	90	30	300					
AS-11	USSR	L = 350 S = 90 d = 30			300	Solid propulsion; infra-red	300 km min	–	Conventional	ASM
Sea Eagle	UK	L = 414 S = 120 d = 40			600	Turbofan inertial; active radar	110 km	–	Conventional	ASM
AGM-65 Maverick	Hughes Aircraft, Tulson, USA	L = 246 S = 71 d = 44.5			462 (210)	Thiokol TX-481 solid motor; AGM-65C laser guidance	8 miles (13 km) to 14 miles (22.5 km)	6–10	Mk 19 113 kg	ASM
AGM-69A SRAM	Boeing Aerospace, Seattle, USA	L = 4,127 S = 89 d = 44.5			2,230 (1,010)	LPC (Lockheed Company) propulsion two-pulse solid motor; guidance: inertial	High 105 miles (170 km); low 35 miles (56 km)	(200)	Conventional Nuclear 170 kt	ASM Rocket
ASLAM Missile MK III MK IV	McDonnell Douglas, USA	L = 4,127 S = 89 d = 44.5			2,700 (1,200)	Internal rocket/ramjet; guidance: inertial with Tercom		6–10	170 kt Nuclear and conventional	ASM

L, length (cm); S, wingspan (cm); d, diameter (cm); w_L, launch weight; R, range

Table 2.33. Missiles for Armed Forces (ADM and NSA types) (UK, USA)

Types of missiles/rockets	Manufacturer/ country of manufacture	Dimensions	w_L lb (kg)	Power plant and guidance	R miles (km)	V mach (mph)	Warhead	Mechanisms
MGM-31A Pershing missile	Martin, Orlando, USA	$L = 10.51$ $S = 202$ $d = 101$	10,150 (4,600)	2 No. Thiokul solid motors; first stage – M105, second stage – M106; guidance: inertial	100 (160) to 520 (840)	8	Nuclear 400 kt	Mobile tactical system, ADM/SSM
MGM-51C Shillelagh missile	Ford, New Post Beach, USA	$L = 1.14$ $S = 29$ $d = 15.2$	60 (27)	Amoco single-stage solid jetavators; guidance: optical tracking and infra-red command link	3.0	(800)	Octal-shaped charge 15 lb (6.8 kg)	Battle tank, ADM/SSM
BGM-71 TOW missile	Hughes Aircraft, Culver City, USA	$L = 1.17$ $S = 34$ $d = 14.7$	42 (19)	Quad boost motor for recoil-less launch; guidance: with optical sighting and trailing wire	up to (3.75)	(620)	Shaped charge containing 5.3 lb (2.4 kg) high explosive	Vehicles, aircraft, ADM/SSM
Sea Dart missile	British Aerospace, UK	$L = 4.4$ $d = 42$	(550)	Marconi radar 805 SW tracker with type 909 illuminator; guidance: semi-active	(30)	–	Conventional and nuclear	NSA patrol boats and ships

Sea Wolf missile	British Aerospace, UK	$L = 1.9$ $d = 18$	(82)	GWS 25 – Marconi radar (805547) search, tracking radars, Ferranti fire-control computer; guidance: radio command	(30)	–	Conventional and nuclear	NSA/SSM boats and ships
Sea Cat missile	Short Brothers, Belfast, UK	$L = 1.47$ $d = 19$	(63)	Radio command guidance with optical remote TV and radar aided tracking	(30)	–	Conventional and nuclear	NSA/SSM boats and ships
Raytheon/Martin XMIM-104A Patriot missile	Martin Orlando Division, USA	$L = 5.31$ $S = 87$ $d = 41$	3740 (1696)	Thiokol TX-486 single-thrust solid motor	30 (48)	3–5	Nuclear and conventional	Advanced Mobile System SAM

L, length (m); S, wingspan (cm); d, diameter (cm); w_L, launch weight (cm); R, range; V, speed

folding fins
(same)

fin restraint/
release (same)

solid propellant
motor (same)

aerodynamic fairing

mine
distribution
canister

filler block

distribution
unit bay

warhead/motor
interface

bladder

gas generator

sabots (4)

signal distribution
system

FLSC
opening
system

mine
distribution
canisters
(7 per warhead)

filler blocks

3.5:1
ogive
nose

combined
fuse/mine
programming
connector and
external
harness

remote
settable
fuse

Fig. 2.16. Major components of AT2
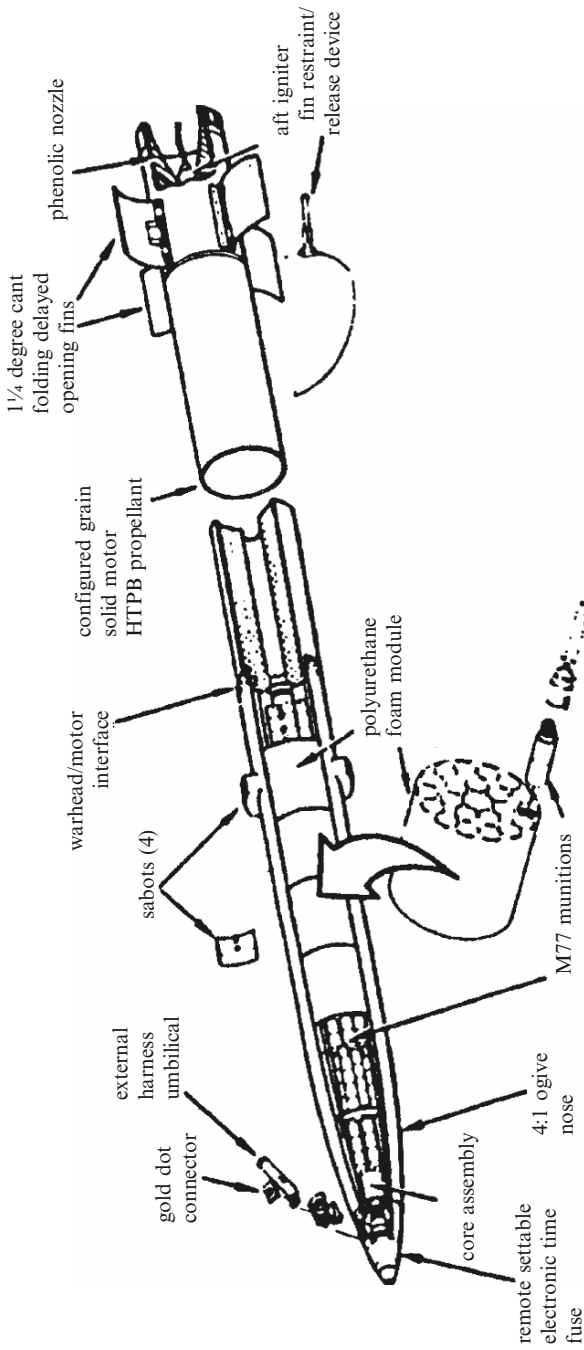
Fig. 2.17. Major components of M77 rockets

phenolic nozzle

aft igniter

fin restraint/
release device

1¼ degree cant
folding delayed
opening fins

configured grain
solid motor
HTPB propellant

warhead/motor
interface

sabots (4)

polyurethane
foam module

M77 munitions

external
harness
umbilical

gold dot
connector

core assembly

4:1 ogive
nose

remote settable
electronic time
fuse
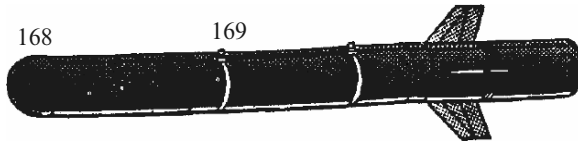
Fig. 2.18. 168 Matra Durandal, 430 lb (195 kg) penetration bomb (courtesy of United States Defense and Ministry of Defence Industry of France)
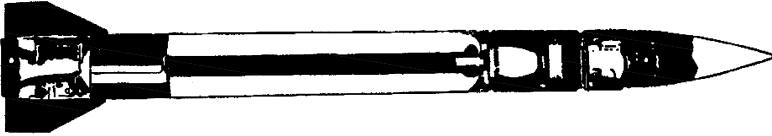
Fig. 2.19. Patriot: a SAM

seeker antenna, glimbal system and inertial platform are mounted. Behind these lie two units: the guidance system (TGS) and modular mid-course package (MMP). The latter, containing navigation electronics and computer, is located in the warhead section. Also in the warhead section, separate places are earmarked for the inertial sensor assembly, signal data converter, high explosive and safety devices.

Two external conduits on the propulsion section carry signals from the guidance electronics back to the aft-mounted control system. The Thiokol TX-486 rocket motor supports the operation of this missile.

Each Patriot XM-901 launcher carries a maximum of four rounds remotely operated from the ECS and is mounted on a wheeled semi-trailer and towed by a wheeled tractor.

2.3.1.2 Stinger Missile

The Stinger missile system is designed to provide superior defence. This portable, shoulder-fired system can easily be deployed in any combat situation. With the introduction of the reprogrammable microprocessor (RMP), the Stinger has been able to meet the demand for sophisticated land, air or sea-based defence. Figure 2.20 shows the guidance and warhead layout of the Manpad Stinger. The system is based on a target-adopted guidance (TAG) technique which biases missile orientation toward vulnerable portions of the airframe with consequent maximum lethality. The superior lethality is derived from hit-for-kill accuracy, warhead lethality and kinetic energy. The force of impact of the Stinger on the target is equivalent to that of a medium sized vehicle travelling on a road at 60 miles per hour. Recently advanced Stinger configurations employ a rosettepattern image scanning technique, as shown in Fig. 2.20. This capability allows the missile effectively to discriminate between targets, flares and background clutter within detectable ranges, which prevents launches against false targets.
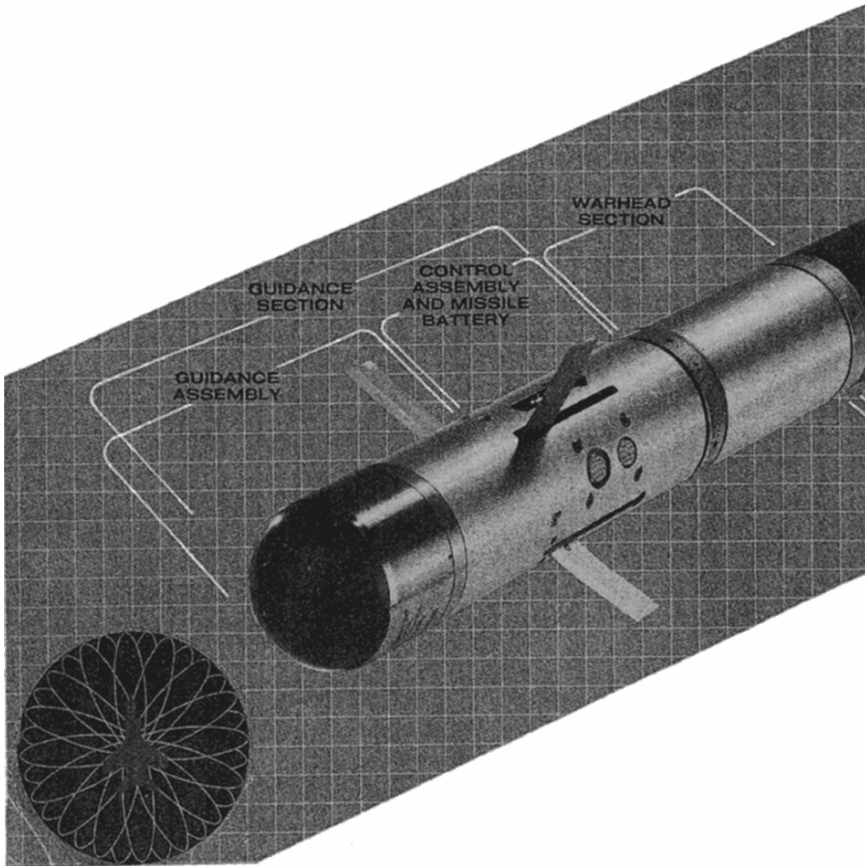
Fig. 2.20. Stinger missile (courtesy of General Dynamics of USA)

The missile has a flight motor, launch motor and an accurate propulsion system. The missile is issued as a certified round of ammunition requiring no field maintenance or associated logistical costs. The next generation of Stinger is Stinger-Post and Stinger-RMP.

2.3.1.3 Shorts' Javelin Missile and Blow-Pipe Missile

Javelin is a guided missile system for use as a self-defence weapon against low-flying attacking aircraft. It employs a semi-automatic command to line of sight (SACLOS) guidance system consisting of a stabilized tracking system and an auto-guidance system. A miniature television camera, aligned with the operator's stabilized sightline, detects the missile by means of its flares and computes automatically the necessary guidance demands. The system includes compensations for cross-winds, low-level targets and automatic generation of a "lead angle" for launching the missile ahead of the crossing target. It is

the improved version of the Blow-Pipe missile. As shown in Fig. 2.21 the missile structure consists of a nose section, a body tube assembly and a wing assembly.

The nose section consists of a rotary nose portion and the control surfaces actuator connected by a two-row ballrace. The rotary nose portion supports the four control surfaces and contains the fuse and cordite blast start roll position gyroscope. Four spike aerial elements on the control surface actuator form the aerial system for the missile receiver.

The body tube assembly consists of a forward sleeve and three tubular body casings. The sleeve joins the assembly to the nose section. The forward body casings house the guidance and control electronics, the warhead and the ignition, safety and arming units (ISAU). The centre and the rear body casings house the two-stage rocket motor and flares.

The wing assembly consists of four swept-back wings arranged in cruciform configuration on a central tube.

The control of the missile is by a twist-and-steer system using the control surfaces on the nose section. The role control surface (ailerons) rotate the nose independently of the missile body. Figure 2.21 shows the control unit.

Figure 2.22 shows the Blow-Pipe missile.

The following technical characteristics apply for the Javelin missile.

Operational use
$L = 1.394$ m, $d = 19.7$ cm, $w_L = 34$ lb (15.4 kg)
Dimensions of the aiming unit: 408 mm × 342 mm × 203 mm,
$w_L = 19.7$ lb (8.9 kg)

Field use
$L = 1.454$ m, $d = 23.5$ cm, $w_L = 41.9$ lb (19 kg)
Dimensions of the aiming unit: 482.6 mm × 431.8 mm × 271.8 mm,
$w_L = 22.3$ lb (10.1 kg)

Altitude: 1,500 ft (4,500 m)
Range: <500 m minimum
　　　　>500 m maximum

2.3.1.4 Anti-Armour Weapons: First Generation

Introduction

Often regarded as one of the most difficult targets to detect and destroy, the modern tank is now equipped with hi-tech armour in a bid to survive.

During the Second World War, "tank-busting" specialised art, usually requiring the use of heavier caliber cannon than was carried by run-of-the-mill fighter bombers. The conflict saw the development of a number of highly specialised tank-killers, from the German Henschel Hs 129 to the 40-mm cannon-armed
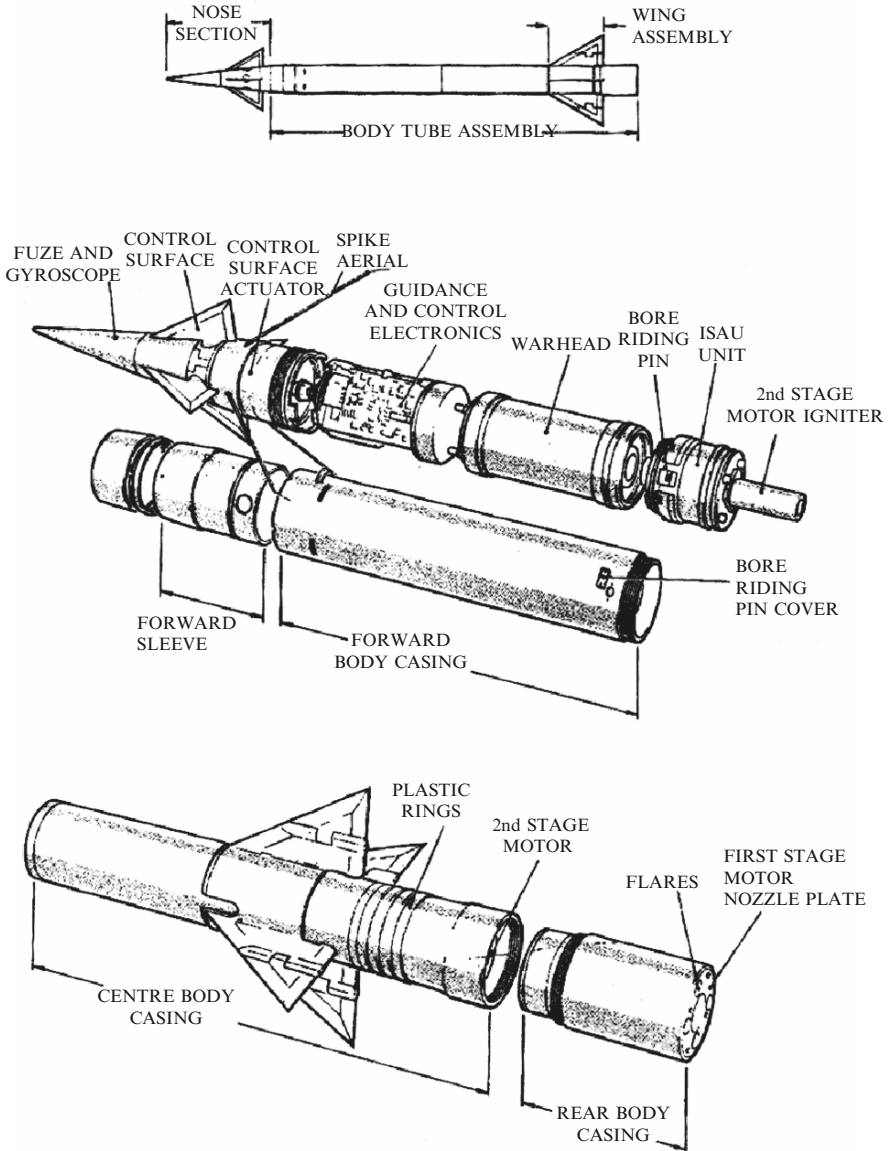
Fig. 2.21. A Javelin missile (courtesy of shorts Brothers, Belfast)

version of the Hurricane. But "ordinary" fighter bombers, armed with nothing more lethal than 20-mm cannon and unguided rockets, played their part in anti-tank operations, exemplified by the role of RAF Typhoon and Tempest squadrons in the wake of D-Day. Developments in tank armour have made it
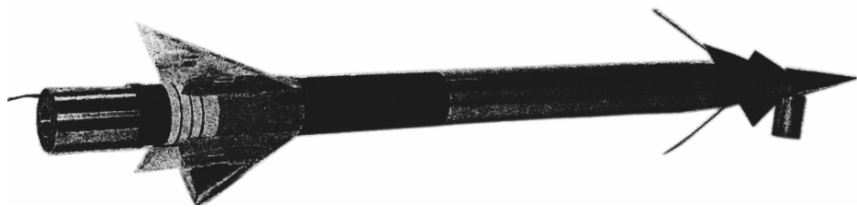
Fig. 2.22. A Blow-Pipe missile (courtesy of Shorts Brothers, Belfast)

progressively less likely that standard 20-mm caliber cannon rounds or simple unguided rockets will guarantee a tank kill, while the development of mobile AAA and SAM systems has forced anti-tank aircraft to attack their targets from greater stand-off ranges. This has necessitated the development of specialised new weapons, and of new tactics to exploit them fully. Helicopters have steadily gained in importance as anti-armour platforms since, although they lack the high speed capability of fixed-wing fighter bombers, they are in some ways less vulnerable over the battlefield, being able to take fuller advantage of terrain masking and to sit in ambush behind buildings or trees, popping up only to engage an enemy target.

The last gunfighter. The humble cannon remains a potent anti-armour tool, albeit in a highly specialised form. Aircraft such as the Fairchild A-10 Thunderbolt II, AH-64 Apache and Mil Mi-24P "Hind-F" employ heavy-calibre 30-mm cannon as anti-armour weapons, although all rely upon a sophisticated array of guided missiles as their primary armament.

The first generation of anti-tank missiles – or anti-tank guided missiles (ATGMs) to use the current term – tended to employ line-of-sight guidance, usually with radio commands passed to the missile via steering wires. Missiles often incorporated a tracking flare to allow the operator to see the weapon in his sight, thus enabling him to steer it more accurately. Such weapons had only a relatively limited stand-off range and forced the launch aircraft to remain exposed throughout the missiles' flight time. Moreover, early weapons (such as the French AS-11) which had to be physically steered to the target, imposed a high workload on the operator. Refinements to the wire-guided missile resulted in weapons with semi-automatic command to line-of-sight (SACLOS) guidance, where the operator only had to keep his sight crosshairs centered on the target, with the missile being steered by computer to wherever the sight was pointing. Wire-guided missiles had the benefit of relative invulnerability to enemy EW (they were effectively unjammable) and did not necessitate the careful allocation of different guidance frequencies (or laser pulse codes) to each missile and each helicopter within a force. Wire-guided missile development culminated in the Hughes BGM-71 TOW, which remains in widespread use.

The principal drawback of the wire-guided missile is the limitation it places on defensive manoeuvring by the launch aircraft. The use of fire-and-forget

Helicopters have brought a new dimension to the battlefield, but for those unable to afford expensive dedicated attack models, the BO 105 is a highly capable alternative.

Recent advances in armour technology have been countered by the capabilities of the latest ATGMs. Here, a retired tank is about to be destroyed by a TOW test round. TOW has matured into a devastating ATGM.

Hellfire missile

In its laser-guided AGM-114A, B, C and K forms, the Hellfire missile has proved to be a devastating ATGM. Laser designation is provided by the Apache launch aircraft, an OH-58D scout helicopter or by a third party on the ground.

AH-64 Apache

1 Missile platform While the small and nimble OH-58D scout moves forward to acquire the target, the Apache waits in hiding. With its load of Hellfire, the Apache is both a highly valuable and comparatively large target for enemy defences and so pops up to fire its missiles at the very last moment.

Lock-on

Ground-based laser designation

2 Launch After launch, the Hellfire climbs above the battlefield so that its laser seeker can obtain a clear view of the target area. The seeker recognises and locks on to the laser 'sparkle' provided by the designating system.

Target

3 Laser designation With its mast-mounted sight and powerful laser designator, the small OH-58D is able to move in close to the enemy and designate from a hidden position.

OH-58D Kiowa Warrior

Plate 2.1. Anti-Armour Weapons

missiles allows the launch aircraft to pop up (or even sometimes to fire from cover) and then "scarper" before the enemy can retaliate. Weapons like the original laser-guided AGM-65 Maverick or the AGM-114 Hellfire can be used in this way, as long as the designator (on the ground or in the air) keeps illuminating the target. In many recent conflicts, standard laser-guided bombs, dropped from medium altitude, have been used against tanks.

Tank killing. Laser-guided bombs can be sent directly into a tank's vulnerable top surfaces, where the bombs' kinetic energy is sufficient to penetrate armour or where the very large explosive charge can be enough to disable

the vehicle, kill its crew and often blow the turret clean off. Weapons using millimetre wave (MMW) radar or imaging infra-red (IIR) can also be used in the fire-and-forget mode, and have the added advantage of not relying on third party target designation.

The future lies with the new generation of the semi-autonomous stand-off weapons which fly to the target area, where they release large numbers of independent sub-munitions, each with its own smart seeker.

One of the most difficult problems facing the designers of anti-tank weapons is how to penetrate modern armour GAU-8/A cannon rounds incorporate depleted uranium to give maximum density, while missile warheads use a variety of strategies. Dual tandem warheads can counteract the use of explosive reactive armour, by firing a small precursor charge which activates the tank's explosive reactive armour, before the second primary charge penetrates the tank's relatively soft inner skin. Hellfire's warhead includes a narrow cone of copper, which is transformed into a jet of liquid metal on impact. This has the capability to penetrate the thickest armour. Other missiles are designed not to penetrate armour but to cause pieces of the tank's own armour or equipment to break off inside the tank, turning the interior into a maelstrom of flying shrapnel.

Anti-Armour Weapons: Second Generation (Plates 2.1 to 2.2)

Modern air-launched anti-armour weapons, such as TOW and Hellfire, have proved their ability to destroy virtually any target on the battlefield. The efforts of weapons' designers are now concentrated on attempts to destroy multiple targets with a single weapon – at a stand-off range that keeps the shooter well out of harm's way.

Though huge progress has been made since the earliest attempts at building guided anti-armour weapons, the majority of those in use today remain "point-and-shoot" systems, which require some element of visual contact with the target. The AGM-114K, the radar-guided Longbow Hellfire, does allow the shooter to stay hidden throughout the engagement but even this (extremely expensive) missile is a "one shot/one kill" weapon.

For over 30 years, research has been conducted into combining affordable tank-killing munitions with autonomous seekers – allowing a weapon to find and destroy a target successfully with no human intervention. Combining an array of such weapons within a single cluster bomb would give one aircraft immense killing power. Fitting them to a powdered, or gliding, dispenser would add stand-off range that would keep the launch aircraft well out of range of the engagement envelope of defensive SAMs or AAA.

The USAF is now preparing to field the first such weapons. Chief among these is the CBU-97/B SFW (Sensor Fused Weapon) System, developed by Textron. SFW uses the basic SUU-64/B Tactical Munitions Dispenser (TMD), or cluster bomb, to carry ten revolutionary new BLU-108/B submunitions. Each of these is in turn fitted with four Skeet "smart" warheads which have

This live SFW test was conducted against representative Soviet-type armoured vehicles, including T-62 tanks. Note the BLU-108B submunitions, descending on their parachutes, and the heavy black smoke plumes from the individual Skeet projectile rocket motors.
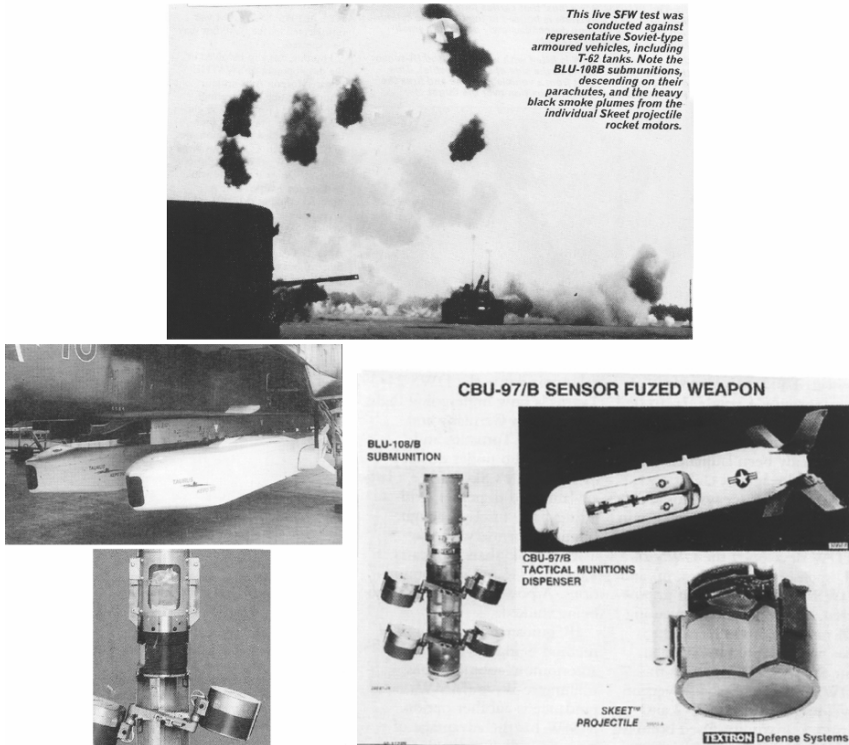
Above: The SFW uses a standard US bomb, and looks unremarkable from the outside. It is the sophisticated contents of the bomp that make this weapon so deadly - and so expensive.

Left: The German/Swedish developed Taurus stand-off dispenser can be armed with anti-armour bomblets, In July 1998 the Taurus system gained its first export order, from Greece.

Plate 2.2. Anti-armour: second generation weapons

individual infra-red sensors. The CBU-97 can be dropped at any height from 600 ft (182 m) up to 20,000 ft (6,100 m) – but will perform better at higher altitudes. Once the SFW is dropped, the BLU-108/Bs are ejected and deploy their own miniature parachutes to descend slowly over the target area. A small rocket spins each submunition which then spins out its four Skeets. As a result, the IR sensor on each Skeet turns in a circular search pattern, looking for the signature of a "live" target. When it finds one, a small onboard rocket is fired to give it terminal velocity. The Skeet has a self-forging explosively formed penetrator (EFP) warhead which forms an ultra-high speed jet of molten metal (from solid disc of copper) to destroy any tank.

Because it is a guided weapon, SFW is far more effective than conventional cluster bombs, but to improve its accuracy even further the USAF is modifying them to WCMD (Wind-Corrected Munitions Dispenser) standard. This add a pop-out "flying tail" to the CBU-97/B that guides the bomb towards the

intended target and corrects for drift caused by winds at high altitude. In its
final operation test, an F-16 dropped four live SFWs (160 Skeets) in a single
pass against an armoured column of 24 vehicles from 600 ft (182 m) – with
hits on 11 vehicles.

Britain also had a programme to develop an IR-guided submunition, similar to the SFW, dubbed Damocles. This was a joint UK/German project
aimed at fielding a cluster bomb containing four parachute-stabilised anti-
armour bomblets. These would be fitted with an IR sensor, laser rangefinder
and self-forging warhead, but the status of this programme is uncertain.
Confusingly, a US-developed advance guided submunition programme is also
named Damocles. The US Damocles is intended for use with ground-based
Multiple Launch Rocket System (MLRS) and JSOW.

It is also planned to integrate the SFW with the USAF/USN AGM-145
JSOW (Joint Stand-Off Weapon). JSOW is an unpowered, gliding dispenser
system which has a range of up to 18.6 miles (30 km) when launched from
altitude. Six BLU-108/Bs can be carried by each AGM-145, which can also
carry 145 (unguided) BLU-97 Combined Effects Bomblets which are also very
effective against tanks.

The USAF is now developing the LOCAAS (low cost autonomous attack
system) together with Lockheed Martin. This air-launched dispenser, in
powered and unpowered versions, uses a laser radar to find targets, and
attacks them with bomblets and mines. LOCAAS has already been launched
successfully against tank targets.

Many dispenser systems are under development elsewhere in the world. In
Germany, LFK and TDW developed the DWS 24 (Dispenser Weapon System)
and DWS 39. DWS 24 is an unpowered, glide dispenser containing 24 mines
and bomblets which has been adopted by Sweden for the JAS 39 Gripen
(as the DWS 39). The Swedish version will use the Bofors MJ-2 anti-armour
proximity-fused bomblet (among others) and will eventually be integrated
with the Bofors BONUS sensor-fused munitions which has a dual-band IR-
seeker with an EEP warhead, and uses folding metallic aerofoils to remain
soft. A version of the DWS 24 has been successfully tested by the US as the
AFDS (autonomous free-flight dispenser system), a low cost export orientated
weapon, primarily for the F-16. AFDS could be fitted with 12 BLU-108/B
SFWs or 200 BLU-97/B bomblets.

DWS 24 also forms the basis for the joint Swedish-German Bofors/LFK
KEPD 350 Taurus powered dispenser, with GPS and IR guidance. KEPD 350
has a range of 217 miles (350 km) and has been proposed in several versions. It
a future weapons option for Germany's Eurofighters and can be fitted with the
same anti-armour submunitions as the DWS 24/39. Taurus is now undergoing
flight tests both in Germany and Sweden on Tornados and Viggens. Also
under development, is Italy's Skyshark – a large air-launched dispenser, with
a lifting-body fuselage design. Intended for use with the Tornado, Skyshark
can carry 1,642 lb (745 kg) of submunitions. A powered version is also being
studied.

IR guidance is not the only method being developed for autonomous submunitions-millimetre-wave (MMW) radar guidance is another option. MMW has the advantage of being able to find "cold" targets – vehicles that have been stationary for some time and might be invisible to an IR sensor. On the other hand, the radar return on a tank may be similar to that of a large rock and substantial technical sophistication is needed to discriminate between the two. The UK's Hunting Engineering has developed the SADARM (sensor and destroy armour) system, which adds a dual-mode IR and MMW radar seeker to bomblets developed by the USA's Alliant TechSystems. SADARM has been combined with the German DWS 24 glide dispenser, which can hold 16 of these submunitions, and is suitable for high-speed low-level attacks. This new weapon was named SWARM 2000 (smart weapon anti-armour) and offered to the RAF in 1996. SWAARM was not selected by the RAF but may be exported.

Hunting was also involved in the development of SWATHE (smart weapon anti-armour thorn-hunting engineering), based on the proven BL755 cluster bomb, but fitted with four terminally guided sub-munitions (TGSMs). Each TGSM was fitted with a MMW seeker and flip-out wings, allowing it to glide while looking for a target. The bomblet could then climb and dive onto the top of the target vehicle. SWATHE was renamed TAAWS (thomson-thorn advance anti-armour weapon system) but it too failed to win British orders. For its next generation anti-armour weapon the RAF will rely on the Brimstone missile, an MMW-guided development of the Hellfire. The RAF will acquire a powered stand-off weapon in the form of single-warhead MATRA/BAE Storm Shadow, which it does not yet plan to use as an anti-armour system.

Storm Shadow won the UK's CASOM (conventionally armed stand-off missile) competition in July 1996 and is based on the original MATRA APACHE (Armée Propulsé À Charges Ejectables, powered dispenser weapon) stand-off missile. APACHE does come with an anti-armour option (APACHE-MAW), which was being developed with Germany. However, Germany withdrew from the programme in 1998 and now appears to have opted for the Taurus system.

Anti-Armour Weapons. Steadily improved over the years from its combat debut in the 1950s, the anti-tank missile is an effective and, in some cases, relatively cheap method of wrecking havoc on an armoured column.

Anti-Armour Missiles. This series of diagrams illustrates the first generation of anti-armour weapons, which have been in the front line service with armies around the world since the early 1970s. Many have been fired in anger.

AGM-114A Hellfire (USA) (Fig. 2.23). Intended as an air-to-surface missile (optimised for the anti-tank role), Hellfire employs semi-active laser guidance. The missile itself is able to home in on reflections from tanks laser-illuminated by either aerial or ground-based designators. With a length of 5 ft 6 in (167 cm) and a range of 3.69 miles (5,945 m) the 20-lb (9.1 kg) shaped-charge HE warhead is powerful enough to penetrate all current armour. Hellfire is also utilised by the US Navy and USMC, the type being designated

AGM-114A Hellfire
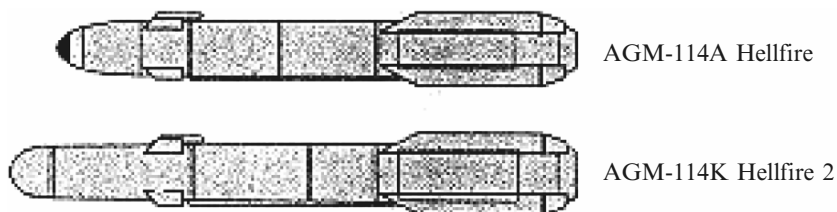
AGM-114K Hellfire 2

Fig. 2.23. Hellfire missiles
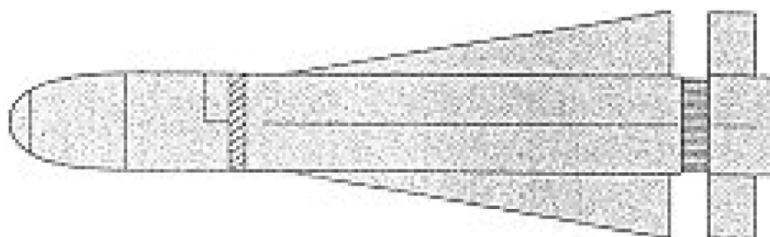
Fig. 2.24. AGM-65 Maverick

AGM-114B for attacks against surface vessels. Sweden has also developed a variant of the missile known as RBS 17. this is used for coastal defence purposes by the Swedish Army. This example is larger and heavier than the US version and is fitted with a delayed-action blast fragmentation warhead suitable for attacks on landing craft and assault hovercraft. In addition, the Longbow Hellfire has been developed. Based on the AGM-114K Hellfire 2 which was developed following the Gulf War experience, the AGM-114L Hellfire employs millimetre wave radar guidance.

AGM-65 Maverick (USA) (Fig. 2.24). Introduced in 1972 as a USAF air-to-surface missile, the Maverick consists of a substantial cylindrical body 68 ft 2 in (2.49 m) in length, attached to a cruciform arrangement of swept low-aspect-ratio delta wings. The AGM-65 series is the smallest fully guided air-to-surface missile family in the US inventory, and at present is NATO's most important weapon of the type, largely because in all its versions it is a fire-and-forget design. The AGM-65A in its initial TV imaging version suffered the disadvantage of low magnification for its nose-mounted camera, forcing the pilot of the launch aircraft to fly close to the target to secure lock on before missile launch.

As.11 (France) (Fig. 2.25). Derived from the SS.11 ground-launch tank missile, the AS.11 is one of the oldest missiles still in operation. Originally developed by Nord-Aviation during 1953-5 as Type 5210, it has been slightly improved over the years, notably by the introduction of the AS.11B1 with transistorised circuits and optional TCA semi-automatic IR-based guidance in 1962. It stayed in production at Aérospatiale (into which Nord merged) until late 1980, with deliveries exceeding 179,000 of all versions. The AS.11 has four swept rectangular wings on a body measuring 3 ft 9 in (1.21 m) in
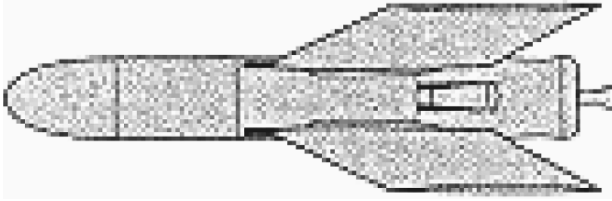
Fig. 2.25. AS-11 Missile (France)

Fig. 2.26. AT-X-16 Missile (Russia)

Fig. 2.27. AT-6/AT-9 Spiral (Russia)

length. The missile weighs 66.1 lb (30 kg), and a booster providing a 20 s burn gives a range of 1.8 miles (3 km). The AS.11 has served with Bahrain, Iran, Libya, Sweden, the UK and the USA.

AT-X-16 (9M120M/9M121 Vikhr-M) (Russia) (Fig. 2.26). A medium-range, laser-guided, tube-launched anti-tank missile, the AT-X-16 was first seen in the West in 1992. Nothing is known of the missile's development, but it is believed to be an improved variant of AT-12 with an extended range. The missile measures 9.18 ft (2.8 m) in length and weighs 99 lb (45 kg). Reports suggest that the AT-X16, often seen mounted on the canisters on the pylons of the Ka-50 Werewolf attack helicopter, can penetrate armour to a depth of more than 39 in (1,000 mm). The warhead on the missile is believed to weigh around 17.6 lb (8 kg). Fitted with both impact and sophisticated fuses, the AT-X-16 is believed to be in full-scale production and is currently being offered for export.

AT-6/AT-9 "Spiral" (9M114 Kokon/Shturm) (Russia) (Fig. 2.27). First identified in 1977, it was originally believed that this tube-launched system used the same missile as the AT-4 and AT-5 but, by 1980, Western observers had realised that it was a completely new weapon. Unlike other Russian anti-tank missiles, it has been identified only in air-launched applications, carried by such types as the Mi-24 "Hind-E", Mi-28 "Havoc" and Ka-29 "Helix-B", with a body length of 6 ft (1.83 m), the "Spiral" is fitted with a series of flares to aid optical guidance of the missile, although a laser if fitted for range-finding. The missile has been tested in air-to-air mode against helicopter
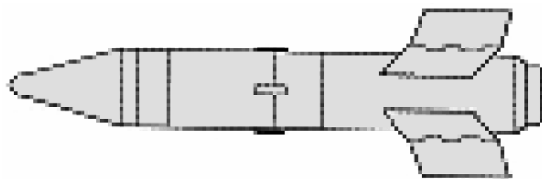
Fig. 2.28. AT-3 Sagger (Russia)

Fig. 2.29. AT-12 Swinger (Russia)

targets, where a range of 3.7 miles (6 km) is possible. Entering service in 1978, exports to Libya, Poland and Slovakia commenced in 1990.

AT-3 "Sagger" (9M14 Malyutka) (Russia) (Fig. 2.28). Developed as a helicopter-launched medium-to-long-range anti-tank missile, the "Sagger" achieved notoriety during the Yom Kippur War of 1973 when the Egyptian soldiers used it as a man-infantry anti-tank weapon to inflict unprecedented casualties to the Israeli battle tank force. First seen by the West in a Moscow parade in May 1965, the missile has a length of only 2 ft 10 in (0.98 m) with a hollow-charge warhead of 6.6 lb (3 kg). "Sagger" was subsequently seen on many army platforms of the former Warsaw Pact, although air-launching from a helicopter proved to be the most versatile method of delivery. Mi-8 "Hips" and Mi-24 "Hind-As" were often seen with the missile mounted on pylons on either side of the fuselage. The missile has no aerodynamic controls and instead is stirred by jet deflection. A tracking flare is attached beside the body and it is claimed that an operator can stir the missile successfully to 1,100 yards (1,000 m) with unaided eyesight, and three times this distance with the magnifying sight used in helicopters.

AT-12 "Swinger" (9M120 Vikhr/Ataka) (Russia) (Fig. 2.29). The laser-guided short-range "Swinger" anti-tank missile was first seen publicly at the 1991 Dubai Air Show with the Russian name Vikhr. Little is known of the missile's development, although export models are described as laser beam riding capable. With a body length of 5 ft 5 in (1.7 m), the "Swinger's" warhead can penetrate up to 31.4 in (800 mm) of armour. Principal air launching platforms are the Ka-50 "Hokum" and Su-25 "Frogfoot". Most recently a ship-based variant has been proposed based on the helicopter variant.

Hongjian 8 (HJ-8) (China) (Fig. 2.30). With a length of 3 ft 3 in (1 m) this long-range tactical anti-tank missile is China's most advanced battlefield weapon. Dubbed "Red-Arrow 8" by the West, the HJ-8 has only been seen in the surface-launch mode although air-launch is also a possibility for the

Fig. 2.30. Hongjian 8 (China)
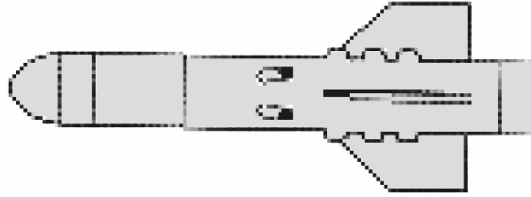
BGN-71 TOW
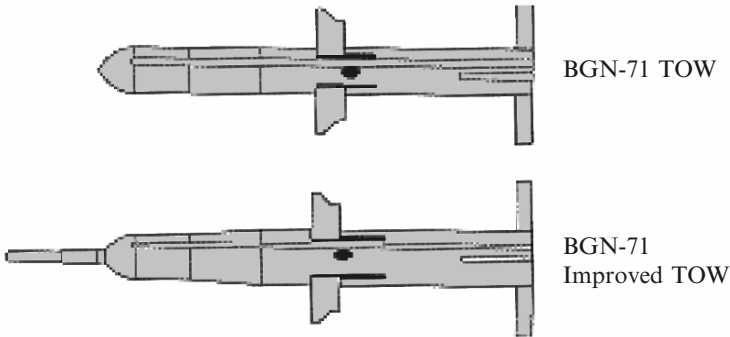
BGN-71
Improved TOW

Fig. 2.31. BGN-71 TOW (USA)

weapon. Optically-tracked and wire-guided with semi-automatic command-to-line-of-sight guidance the HJ-8 present a formidable foe to any armoured column. The likely armour penetration of the unrevealed hollow-charge HE warhead is estimated at 31.5 in (800 mm). In many respects the missile bears a striking similarity to the Franco-German Euromissile Milan and this similarity has led to claims of espionage by some Western commentators who believe Chinese intelligence officers obtained data through a third party.

BGN-71 TOW (USA) (Fig. 2.31). TOW (Tube-launched, Optically tracked, Wire-guided) is the West's most important anti-tank weapon, and is a heavy-weight model designed for vehicle- or helicopter-borne launchers. It has proved its capabilities in several conflicts in the Middle East and in Vietnam, with operators such as Israel, the United States, Kuwait and Iran. Entering service in 1970, the initial version featured a 5.3 lb (2.4 kg) explosive warhead, able to penetrate 23.62 in (600 mm) of armour, mounted in a 3 ft 8 in long body. This model has a range of 1,100 yards (1,000 m), this being restricted by the length of its guidance wires. The Improved TOW, introduced in early 1980, offered a larger diameter warhead with LX-14 explosive, greater range, and a telescoping 15 in (381 mm) nose probe that extends in flight to ensure a perfect stand-off distance for the denotation of the shaped-charged warhead, which is able to penetrate the latest Soviet armour. Introduced in 1983, the TOW 2 has become the standard US weapon for attacking the latest
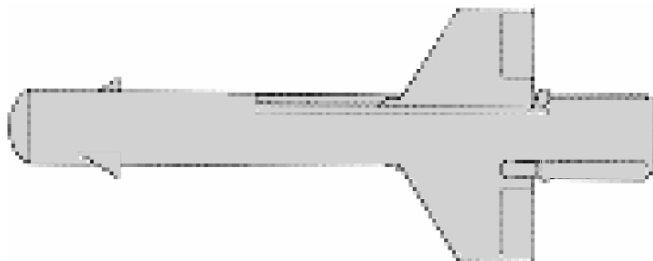
Fig. 2.32. AT-2 Swatter (Russia)

generation of main battle tanks at long range. It features a warhead increased to 13.2 lb (6 kg), and a longer nose probe measuring 21.25 in (540 mm) ensuring optimum stand-off distance for penetration of 31.5 in (800 mm) of armour. This improved variant can fired from the original analog-electronic launcher, or it can be used from an improved digital-electronics launcher and used in conjunction with a thermal as well as an optical sight.

AT-2 "Swatter" (9M17 Skorpion) (RUSSIA) (Fig. 2.32). This type was introduced in the mid-1960s with the Soviet designation PUR-62 Falanga and is known in the West as the "Swatter-A" ground-launched anti-tank missile. With a length of only 2 ft 9 in (902 mm) and a hollow-charge HE warhead, the "Swatter" is guided to its target by simple radio-guidance (with all that system's vulnerability to countermeasures), the signal being passed to the four rear wings which have roll-control elevons. Able to penetrate 18.9 in (480 mm) of armour, the missile is somewhat outdated on the modern battlefield, but because of the very large number deployed it is still seen mounted on Mi-8 "Hip-Es" and Mi-24 "Hind-As".

HOT (France/Germany) (Fig. 2.33). Entering service in the early 1970s, the HOT (Haute subsonique, Optiquement téléguide, tire d'un Tube, or high-subsonic optically-guided tube-launched) missile is a joint development between France and Germany. Measuring 4 ft 2 in (1,275 mm) long with a warhead comprising 13.2 lb (6 kg) of hollow-charge HE, HOT is designed to be fired from armoured vehicles or helicopters. The primary disadvantage of the type is its modest speed, which means that the missile takes some 17 s to reach its maximum range of 2.64 miles (4,250 m), even when launched from a helicopter, which thus has to be exposed for this time. An improved version of the basic weapon known as the HOT 2 is also faster than its predecessor. A further development is the improved HOT 2T which is able to penetrate the latest Explosive Reaction Armour.

ZT3/ZT35 Swift (South Africa) (Fig. 2.34). Revealed in 1990 by South Africa, the Swift is intended as a short-range, laser-command-guided anti-armour weapon powered, as are most similar types, by a solid propellant motor, and armed with an HE armour-penetrating warhead. The Swift bears a striking resemblance to the basic US-designed TOW missile. Used operationally in 1987 during the fighting in Angola, the Swift has a range of over
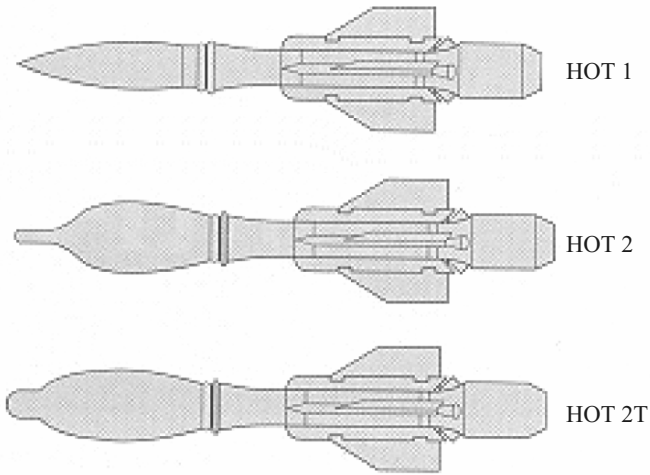
Fig. 2.33. Subsonic Tube Missiles (France/Germany)
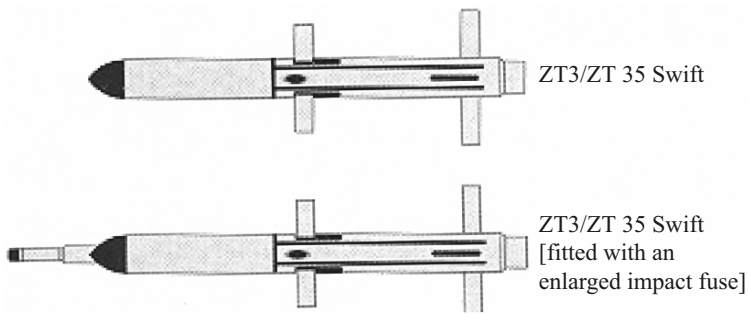
Fig. 2.34. Swift Missiles (South Africa)
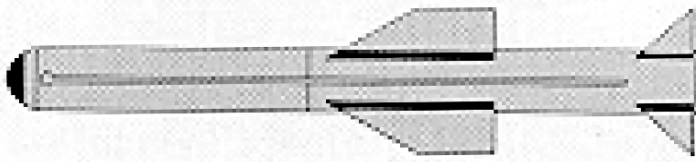
Fig. 2.35. ATGW-3LR Trigat (France, Germany, UK)

2.5 miles (4 km). The latest version is fitted with a 9.8 in (250 mm) long probe which allows stand-off detonation in order to defeat the latest reactive armour. South Africa has developed a quadruple launcher for the missile which is able to be attached to the stub wings of the Rooivalk attack helicopter.

ATGW-3LR Trigat (France/Germany/UK) (Fig. 2.35). A short-range infra-red-guided missile, Trigat was developed by France, Germany and the

UK, with Belgium and the Netherlands joining later. The first test-firing, of the medium-range variant, was carried out in August 1991. The other two variants currently under development are a medium-range, portable, ground-launchable (from vehicle) version, and a long-range helicopter model. The intended helicopter launch platform is Eurocopter's Tiger (PAH-2/HAC). Intended to enter service in 1999, the missile has been delayed and is not likely to enter service until 2001.

2.3.1.5 Laser-Guided Bombs

Used operationally for the first time in Vietnam, the laser-guided bomb has become the standard weapon for precision strikes with minimum collateral damage.

It is one of the classic images from the Gulf War: a ghostly IR television image showing cross-hairs neatly centred over a building, hardened aircraft shelter (HAS), or bridge. Seemingly from nowhere, a sinister dark shape streaks across the bottom of the screen, heading inexorably towards the target. Within milliseconds, there is a blinding flash, and the target is destroyed. One bomb, one hit.

Deployed in huge numbers during the 1991 Gulf War, the LGB was the principal precision-guided weapon of many of the coalition air forces. During the war, LGB strikes and the Lockheed F-117A Nighthawk became symbols of US air power.

GBU-27A/B and GBU-27/B Laser-Guided Bombs

Unique to the F-117A, the GBU-27 LGB came with the F-117A's 1984 WSCS upgrade effort and employs the more recent-technology Paveway III guidance kit. The weapon is based on the GBU-24 in general use, but has clipped front canards and rear fins based on the Paveway II, rather than Paveway III, configuration. The version that uses a Mk 84 warhead is designated GBU-27/B and the one equipped with the BLU-109B warhead is known as the GBU-27A/B.

GBU-27/A and GBU-27/B Guidance Modes. The GBU-27 offers two guidance modes, each optimised to achieve the best penetration angle for horizontially or vertically orientated targets. For a horizontal target, such as a bunker, the GBU-27 flies on a commanded pitch down pathway so that it strikes the target in an attitude which is as near vertical as possible. The trajectory for a vertical target, such as a high-rise building, is essentially the ballistic path. In early development trials, on the second occasion when a Senior Trend aircraft dropped a GBU-27, the bomb hit a target barrel and split it in half. This was testimony to bombing accuracy and produced a memento which has been kept by the "Skunk Works".

Penetration Warhead. The BLU-109 penetration warhead fitted to the GBU-27/B and GBU-10G/H/J LGBs has a thick 4,340 steel alloy case, a low

GRUMMAN F-14 TOMCAT
Air-to-air missile load-out configurations

The tomcat carries different mixes of weapons which depend on the type of threat envisaged and thus the type of mission flown. AIM-9s are carried on the wing glove pylons only, while AIM-7s are carried semi-recessed under the fuselage. AIM-54s are carried in tandem pairs on special pallets which fit to the underbelly attachment points. Stations 1 B and 8 B (port and starboard wing glove main weapon stations, respectively) can carry all three missile types.

Standard intercept
4 × AIM-54C Phoenixes
2 × AIM-7M Sparrows
2 × AIM-9M Sidewinders
2 × fuel tanks

Medium-/short-range intercept
4 × AIM-7M Sparrows
4 × AIM-9M Sidewinders
2 × fuel tanks

Mixed intercept
1 × AIM-54C Phoenix
3 × AIM-7M Sparrows
2 × AIM-9M Sidewinders
2 × fuel tanks

Hughes AIM-54 Phoenix

The Tomcat's primary weapon is the AIM-54 Phoenix Long-range missile, the first air-to-air weapon specifically designed to simultaneously take down multiple incoming targets, including bombers, fighters and even missiles. All variants of the missile use active radar homing and mid-course guidance, and therefore require that the target be 'painted' by the fighter's onboard AWG-9 weapon system. Once it gets within about 14 miles (23 km), the Phoenix missile's own DSQ-26 active radar takes over for the final thrust to target. The Phoenix can be launched from all stations from V_{Min} to Mach 1.6, up to 50,000 ft (15243 m) and from 0-6.5g. The current version is the upgraded AIM-54C with a new solid state transmitter/receiver for the seeker head, improved target discrimination, and improved electronic counter-countermeasures (ECCM) capability.

Stations 8A & 8B
Station 7, fuel tank only
Station 6
Station 5 Alternate
Station
tank
Station 1A & 1B
Station 5
Station 4 Alternate
STATION:
AIM-54C Phoenix
AIM-7M Sparrow
AIM-9M Sidewinder

Plate 2.3. Air-to-air weapons

Comparative weapon ranges

AIM-9L/M Sidewinder
Launch weight: 192 lb (87 kg)
Range: 5 miles (8 km)

AIM-54C Phoenix
Launch weight: 1021 lb (463 kg)
Range: 93 miles (150 km)

M61A1 cannon
Effective range: approx. 1 mile (1.6 km)

AIM-7M Sparrow
Launch weight: 507 lb (230 kg)
Range: 28 miles (45 km)

Unrivalled weapons mix
The Tomcat's mix of air-to-air weapons allows it to engage any target at any altitude from a few hundred feet to over 100 miles, perhaps its closest rival is the Russion MiG-31M, but this aircraft has only been seen carrying long-range R-37 and medium-range R-77 AAMs. It seems unlikely that the MiG-31M will enter service, leaving the Tomcat unrivalled as along intercepter.

Plate 2.4. Lockheed F-117 with compliments of Lockheed, USA

Raytheon AIM-7 Sparrow. At medium range, the Tomcat uses the AIM-7 Sparrow semi-active homing missile. This requires a target to be constantly illuminated by the continuous wave tube transmitter within the Tomcat's AWG-9 radar in order to home onto its target. Only one AIM-7 can be guided at a time, so only one target can be engaged at once. Early Tomcats used the AIM-7F-2 model, which was followed by the AIM-7F with solid state electronics. The current version is the AIM-7M, which gained IOC in 1987. This has a monopulse seeker which is much tougher to detect and to jam, and is thus more effective in an electronic warfare environment. It also introduced digital signal processing.

Ford Aerospace AIM-9 Sidewinder. For closer-range combat, the F-14 uses infra-red (IR) homing AIM-9 Sidewinder. Early F-14s carried AIM-9H/J models, which were followed by the "all aspect" AIM-9L in 1979. Most importantly, this was able to engage a head-on target, freeing the launch aircraft from the need to manoeuvre into its opponent's "six". The L introduced a DBFF (Directional Blast Fragged Fuse), rigged to detonate to blow outward toward the target, and also fitted to late AIM-54s and AIM-7s. The current version is the AIM-9M which entered production in 1982. This has better capability to discriminate between a target and IR decoy flares. The AIM-9L/M can be fired over a wide envelope, from V_{MIN} to Mach 2, without altitude restrictions, between 1 and 7 g.

General Electric M61A1 Vulcan 20-mm cannon. The final air-to-air weapon fielded by the F14 is the 20 mm General Electric M61A1 Vulcan cannon (frequently called the "Gatling gun"). The cannon is 74 in (1.88 m) long and weighs 265 lb (120 kg), and is installed on the lower left of the aircraft below the front cockpit. It has 678 rounds of ammunition, and is capable of firing up to 6,000 rounds per minute, using a linkless feed system. The six rifled barrels rotate anti-clockwise. Having six barrels reduce wear and helps dissipate heat, thereby making possible a higher rate of fire. Boresighting the gun is achieved using a built-in laser device and a collimating lens attached to the gun barrel. The cannon bay is cooled using Ram air, with the intake opening automatically when the trigger is actuated, closing 10 s after the trigger is released.

explosive/weight ratio (30%) and a tail-mounted FMU-143 fuse to ensure that it explodes after punching through a hardened structure, thereby destroying the contents. It can penetrate up to 6 ft (1.83 m) of reinforced concrete. The bomb is designed to be dropped from medium altitude, although its short wings degrade some of its stand-off capability.

In order to knock out high-value, hardened targets, the F-117A relies on the deadly accuracy of the laser-guided bomb. Four main versions are used, consisting of combinations of two warhead types and two seeker heads. The Nighthawk is also capable of carrying B61 free-fall nuclear bombs and, allegedly, the AGM-88 HARM anti-radar weapon.

Anti-Ship Missiles

Anti-ship missiles have made their mark in recent years, rising to prominence during the Falklands War with Argentine Exocet attacks, and again grabbing the headlines during the Iran–Iraq tanker wars. Today, a wide variety is in use, from long-range supersonic missiles for destroying large surface vessels, to shorter-range weapons for littoral (coastal) work.

Now termed anti-surface unit warfare (ASUW), the task of destroying enemy shipping has always been an important part of the military aircraft's repertoire. Until late in World War II, air-dropped torpedoes or free fall bombs were the principal weapons, but the fielding of guided missiles by the Luftwaffe in the latter part of the conflict heralded the arrival of the anti-ship missile (AShM). While torpedoes can still employed by large maritime patrol aircraft, AShMs have largely assumed the role, although a well-aimed (or precision-guided) bomb is still a valuable anti-shipping tool.

Missiles used to attack ships initially utilised some form of visual guidance, later enhanced by TV and datalinks. Today, the improvement in radar tech-nology means that most dedicated AShMs feature active radar guidance in the terminal phase, having approached the target in radar-silent mode using inertial guidance. An important and growing are is the use of passive seekers which home in on the target's radar emissions.

Lockheed F-117
LASER-GUIDED BOMB

Anatomy of a laser-guided bomb
Many types of laser-guided bomb (LGB) have been developed, but most follow the
fundamental principle of fitting a free-fall "dumb" bomb with aerofoil surfaces and
a guidance system. Hence, LGBs are far more expensive than "dumb" bombs and
are reserved for high-priority targets.
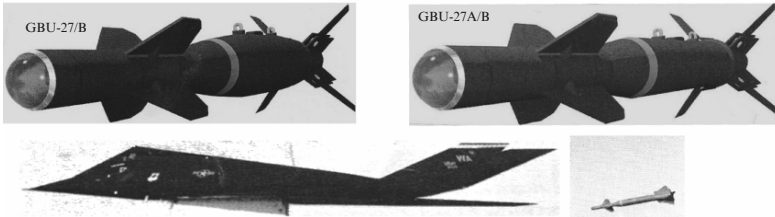
Guidance
A scanning detector and laser energy receiver mounted in the nose of the weapon
pick up the "splash" of laser light reflected off the target by the laser designator.
Some problems were encountered during the Gulf War when drifting clouds of thick
smoke confused guidance systems.

Canards
These forward surfaces
are deflected under com-
puter control, steering
the weapon in flight.

Warheads
Since the forward section of the
LGB is "bolted on" to a dumb
weapon, the warhead is housed
to the rear of the canards.

Wings
Mounted aft, they are
the principal lifting
surfaces.

Plate 2.5. F-117 Nighthawk Weapons
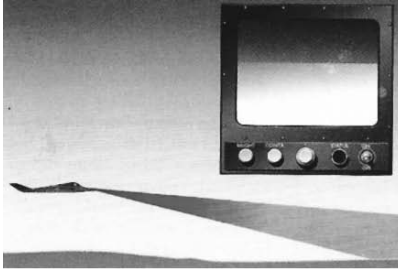
1 Target search: The F-117A uses a Forward-Looking Infra-Red (FLIR) sensor mounted in the nose to acquire its target. The FLIR has a zoom function, which allows early target identification and lock-on. The target image is presented on a display in the cockpit.
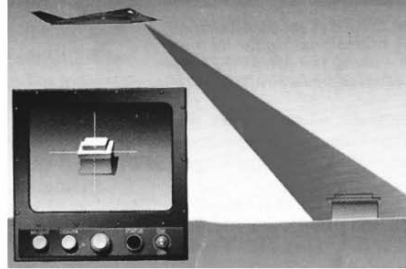
2 Lock-on: As the downward angle increases, the target and lock-on is handed over to the DLIR (Downward-Looking Infra-Red) sensor. This enables the F-117A to lock on to and keep the target in view even when directly overhead.
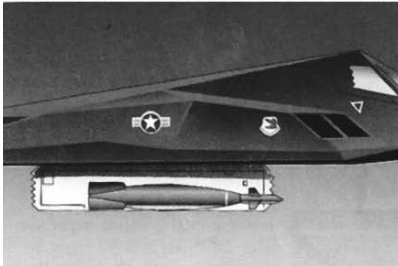
3 Bomb deployment: The pilot uses the target image to fine-tune the lock-on before initiating weapon release. Just before the drop point the weapons bay doors snap open, allowing the GBU-27A/B laser-guided bomb to drop into the slipstream.
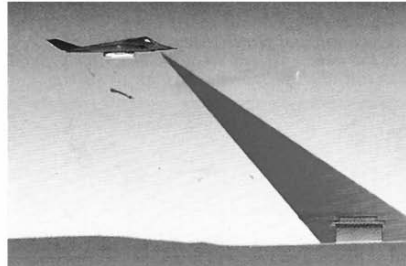
4 Doors close: Dropping nose down, the LGB follows a free-fall ballistic glide path. When clear of the bomb-bay the doors are closed rapidly, since leaving them open greatly increases the F 117A's radar signature.
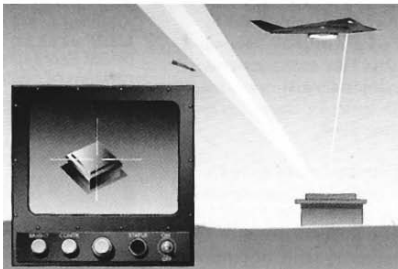
5 Designation: The F-117 can make attacks independently of other laser designation aircraft. A bore-sighted laser designator in the DLIR turret fires a burst of coded laser energy at the locked-in aimpoint at some instant during the bomb's trajectory.
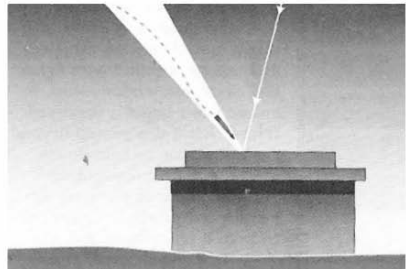
6 Homing in: The laser energy reflects upwards in a cone-shaped 'basket'. Once inside the cone, the homing sensor in the bomb's nose is programmed to seek the most intense area of the laser 'sparkle', steering the bomb directly into the point of aim.

Plate 2.5A. Laser-Guided Bomb Attack Profile: F-117A Nighthawk with compliments of Lockheed U.S.A

During the 1980s, the accent was on a blue-water (open ocean) Cold War scenario, in which high numbers of large anti-ship missiles would be launched against heavily-defended capital ship targets from long stand-off ranges. With the ending of the Cold War and consequent change in the nature of global threats, the emphasis is now shifting to smaller, more versatile weapons that can be employed in coastal waters against small vessels.

Today's sea-skimming anti-ship missile is a complicated and expensive weapon, but it is a highly effective means of stopping or even sinking a modern warship.

Sea Eagle was developed by British Aerospace Dynamics (now part of Matra/BAe) in answer to a requirement for a successor to the Martel Missile. With a maximum range of over 50 nm (58 miles; 93 km), the missile was developed for blue-Jaguars and Sea Kings) and Saudi Arabia (carried by Tornados). Since the retirement of the Buccaneer, the missile is the primary anti-ship weapon of the RAF's Tornado GR.Mk 1B.

Among the more sophisticated of anti-ship missiles, the Sea Eagle uses advanced navigation and radar systems to maintain a very low-level approach. This aims to keep the missile below water (open ocean) operations against large Soviet warships, with attacks being made by large numbers of missiles simultaneously. Originally carried by RAF Buccaneers and RN Sea Harriers, the missile has also been bought by India, the ship's radar coverage until it is close to the vessel. The effectiveness of the missile is greatly enhanced by the provision of accurate target data from the launch aircraft or from maritime patrol aircraft, but it does have an impressive search capability of its own. However, it does not have any target discretion, and attacks the first ship it sees when it turns on its radar.

2.3.1.6 Air-to-Air Missiles

AIM-9 Sidewinder

No weapon system has ever been more cost-effective than the Sidewinder. The weapon has its origins in the late 1940s, when the US Navy realised that gun armed fighters would have difficulty in making effective interceptions against the new jet powered bombers soon to enter service, which were just as fast as the fighters of the time.

The sidewinder was developed between 1950 and 1954 by a small team at the US Naval Ordnance Test Station, China Lake, California. Led by Dr. W. B. Maclean, they spent less than one-thousandth of the annual cost of the still-unfinished process of developing its replacement and fired the first Sidewinder round successfully on 11 September 1953.

In May 1956 the Sidewinder I entered Fleet service. Originally given the designation AAM-N-7, the Sidewinder acquired its more familiar tri-service AIM-9 designation in 1962.

No fewer than 80,900 were made of the first production version, the AIM-9B, and for more than 40 years progressively improved Sidewinders have been virtually the standard close-range AAMs (air-to-air missiles) of the non-communist world (and for much of that time the standard communist weapon (the K-13, AA-2 "Atoll") was a direct copy!).

The Sidewinder is characterised by its simplicity and cheapness. With only 20 moving parts, and costing around $3,000 in 1960, it is basically a metal
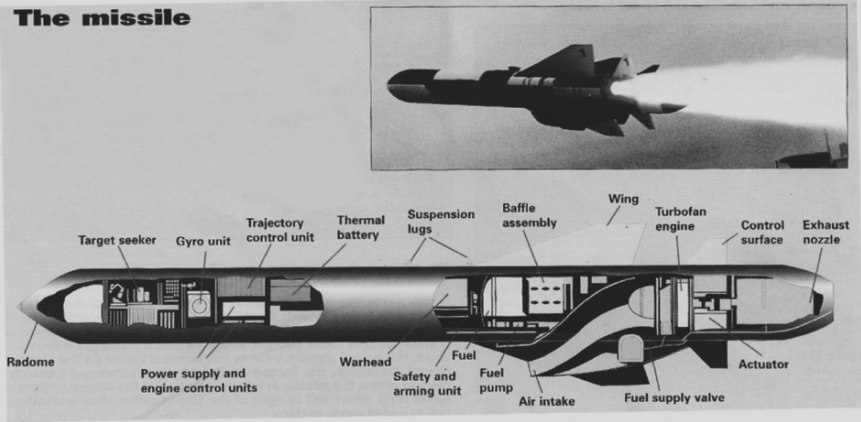
Plate 2.6. Anti-ship Missiles (with compliments of BAe systems)

This series of diagrams depicts the dedicated AShMs in common service. In addition, to these, there are also several general air-to-surface missiles, such as the AGM-88 HARM, which are commonly employed in an anti-ship role.
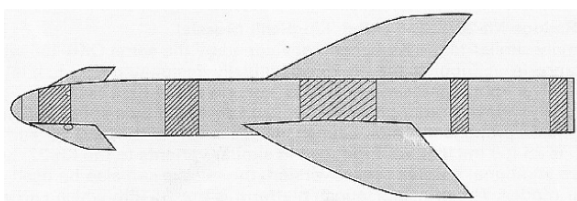
Kongsberg AGM-119 Penguin (Norway). At 9 ft 8 in (2.96 m) long in its Penguin 2 Version, this Norwegian weapon is one of the smaller AShMs, but it is also highly versatile. It employs a passive IR terminal seeker and inertial midcourse guidance, with a number of pre-programmed modes available. The Penguin 2 Mod 7 (AGM-119B) is the helicopter-launched version with folding wings, acquired by the US Navy and others for carriage by SH-2s and SH-60s, while the Penguin 3 (AGM-119A) is a fixed-wing version used by the Royal Norwegian Air Force F-16s.
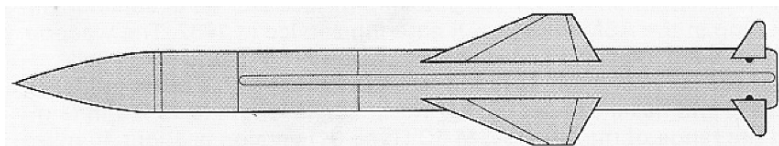
Aérospatiale Exocet (France). The air-launched AM39 version of this well-known missile measures 15 ft 5 in (4.70 m) in length, has a 364 lb (165 kg) shaped charge warhead, a range of around 31 miles (50 km) and is in use with a number of countries. It is carried by several fixed-wing aircraft, mostly of French origin, plus the SEA King, Super Puma and Super Frelon helicopters. The missile employs inertial guidance for mid-course navigation at sea-skimming height before active radar takes over for the terminal phase.

Boeing (McDonnell Douglas) AGM-84 Harpoon (USA). The turbofan-powered Harpoon entered service in 1977 and has since established itself as the AShM of choice for many air arms, including the USAF, and US Navy. As a result, it has been cleared for carriage by a wide variety of aircraft ranging from the B-1 and B-52 strategic bombers, through Nimrod, P-3 and Fokker 50 maritime patrollers to tactical jets such as the F-16 and F/A-18. The standard Harpoon is 12 ft 8 in (3.85 m) long, has a 490 lb (222 kg) warhead and a range of around 60 miles (96 km). Successive variants have significantly enhanced the capabilities of the missile, including a reattack capability in the latest. The Harpoon also forms the basis for the land-attack AGM-84E SLAM and AGM-84H SLAM-ER.

Plate 2.6A. Current anti-ship missiles

tube of 127 mm (5 in) diameter and 2.7 m (9 ft) long, most of which is filled by a rocket motor which blasts it rapidly to about Mach 1.7 in early models, later increasing to Mach 2.5. The tube also contains a warhead (which varies with the model of missile) and is stabilised by four tailfins fitted with "rollerons", small slipstream driven flywheels at the tip of each fin, designed to provide a gyro effect.

The vital guidance function is provided by the nose section, typically about 30 in (0.75 m) long. At the tip is a gyro-stabilised telescope which picks up infra-red (IR) radiation (basically heat) from a target and concentrates it on to an IR sensitive cell. This converts the heat into an electric current which controls four pivoted fins around the guidance/control section. These fins steer the missile, keeping it on target.

No guided AAM has ever been easier to integrate with a fighter, because the Sidewinder has never needed airborne radar (except in the rare AIM-9C version) and requires only a special launch rail and simple wiring to the launch pylons.

2.3.1.7 Lethal Sead – AGM-88 HARM

In order to counter the increasing risk to combat aircraft from modern surface-to-air missile systems, the US has developed the powerful AGM-88 HARM.

In the late 1950s, the US Navy began the development of specialised anti-radar missiles (ARMs). Their purpose was to home in on enemy radar transmitters, improving the survivability of attack aircraft in the face of modern air defences. ARMs worked by denying the enemy access to his own radar data, either by forcing him to cease all radar emissions, or by destroying the radar's antenna.

The first tactical ARM to enter production was the Texas Instruments AGM-45A Shrike, which was used extensively in Vietnam, in the Middle East and briefly in the Falklands. It was not altogether satisfactory, however, since at that time the computer revolutions was barely under way and there was no method of building a memory into the missile. Thus, it was easily fooled if the radar under attack was turned off.

Shrike was followed by the AGM-78, which was a variant of the US Navy's RIM-66 Standard surface-to-air missile. More sophisticated than the Shr, it was also five times more expensive and three times larger.

In the light of combat experience over Vietnam, work began on the development of the definitive supersonic High-speed Anti-Radiation Missile or HARM, in 1969. Immense technical difficulties meant that development was slow and initial production rounds of what was designated AGM-88 were not delivered until 1983. Weighing approximately 800 lb (363 kg) at launch, the AGM-88 uses its high speed to reach and destroy an enemy transmitter before its operators have had time to shut it down.

Multi-mode HARM. HARM has been cleared for carriage on a wide variety of combat aircraft, and is the primary armament of the USAF's "Wild Weasel"
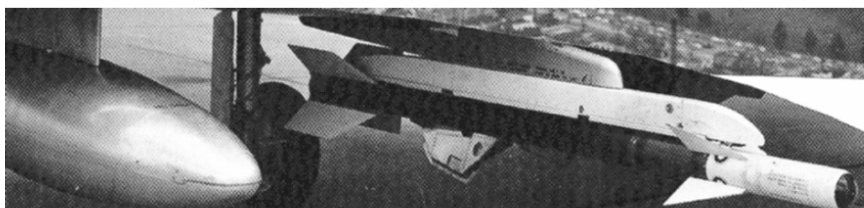
Plate 2.7. AIM-9 Sidewinder

teams. HARM has been fired by the F-4 Phantom II, the F-16 Fighting Falcon, the F/A-18 Hornet, the A-6 Intruder, the EA-6 Prowler, the A-7 Corsair II and the European Panavia Tornado.

Three modes of employment are available to the missile. In the long-range stand-off mode, three specific targets are programmed into the missile on the ground. When electromagnetic radiation from one of these targets is detected, it is launched in the direction of the threat emitter. The enemy radar must remain transmitting if the missile is to continue homing in.

In the self-protection mode the missile is launched against radars detected by the carrier-aircraft's own RWR (radar warning receiver), while the target of opportunity mode uses the HARM's seeker to cue and launch the missile against a previously unknown threat.

In addition to its multi-mode capabilities, AGM-88 is also available in three variants. AGM-88A is the least versatile model, since its seeker must be reprogrammed in the US, giving the weapon little flexibility in the field.

AIM-54 Phoenix

Early development. The AIM-54A was a revised version of a missile that had been under test for almost 10 years, and whose conception occurred in the mid-1950s. It originated from the Bendix XAAM-M-10 Eagle, a two-stage missile developed for the US Navy's Douglas F6D-1 Missileer fleet interceptor proposal, and the later, infra-red homing. Hughes GAR-9/AIM-47, which was developed for the USAF's abandoned F-108 Rapier interceptor and experimental Lockheed YF-12A programmes.

Missile Testing. The full six-shooting capability of the F-14/AWG-9/AIM-54 weapon system has been demonstrated only once! On 22 November 1973 an F-14 fired six Phoenix missiles in 38 seconds, while flying at Mach 0.78 at 24,800 ft (7,678 m) over Point Mugu, California. Its six drone targets were operating at speeds of between Mach 0.6 and 1.1. Although one missile failed and a second was released against a drone which lost augmentation (causing the AWG-9 to break lock), the four remaining missiles scored direct hits or passed within "lethal distance". The AIM-54A was deployed in 1974 and remained basically unchanged for several years.

Modern Russian AAMs

Despite the new generation of Russian AAMs now equipping its fighters, those developed by Soviet engineers in the 1950s and 1960s are still to be seen in modified form, mounted under the wings of the older generation of Russian fighters.

The USSR lagged behind the USA in the development of guided air-to-air missiles, partly because of a generally less advanced technological base, and perhaps partly because the heavy cannon armament of its fighters was more effective than the 0.50 in (12.7 mm) machine-guns (and occasional 20 mm cannon) fitted to contemporary US fighters. Thus, while the first radar-equipped USAF fighters tended to augment or replace their gun armament (initially with pods of high-velocity unguided rockets), the first radar-equipped Soviet fighters (then MiG-17P "Fresco" and MiG-17PF) to enter service retained their cannon armament, as did the first radar-equipped MiG-19 "Farmer" version, the MiG-19P.

The first missile-armed Russian interceptor was the MiG-17PFU, which was equipped with the RP-1U version of the MiG-17P's Izumrud (Emerald) radar. The aircraft retained a single 23 mm cannon, but introduced underwing launch rails for K-5/RS-1U (AA-1 "Alkali") beam-riding missiles. The same type of weapon was carried by the MiG-19PM, which dispensed with cannon armament entirely. Interestingly, the interceptors equipped to carry the RS-1U could also carry single ARS-160 or ARs-212M unguided rockets. However, these were a far cry from US air-to-air rockets, which relied on putting a "box of destruction" into an area of sky, rather than on a single unguided weapon hitting its target. Much closer to the US "Mighty Mouse" AAM in concept were the retractable packs of ARS-57M or TRS-85 rockets used on the Yak-27 and designed to be carried by the mixed-power plant Yak-27V interceptor.

Whereas, in the USA, a single missile type tended to be deployed on a relatively wide range of aircraft, Russian missiles were more narrowly applied. The early Russian missiles tended to be closely associated with a specific type of radar, and to be used only by aircraft with that type of radar.

Following the beam riding RS-1U and RS-2U, Russian missiles tended to switch to semi-active radar homing as their preferred method of guidance,

AGM-88 HARM

In the light of combat experience over Vietnam with the less capable AGM-45 and AGM-78, high-speed, accuracy and an onboard memory were all incorporated into the AGM-88.

Launch rail attachment
Lugs on the missile body attach it to the special LAU-118 launch rail. This rail forms an interface between the missile and the pylon of the launch aircraft. It is also compatible with the AGM-45 Shrike.

Warhead
A 145-lb (66-kg) high-explosive blast-fragmentation warhead gives HARM its destructive power. Metal fragmentation cubes spread out when the warhead explodes, causing maximum damage to the target. The AGM-88C introduced heavier tungsten-alloy cubes, to replace the steel cubes of earlier models.
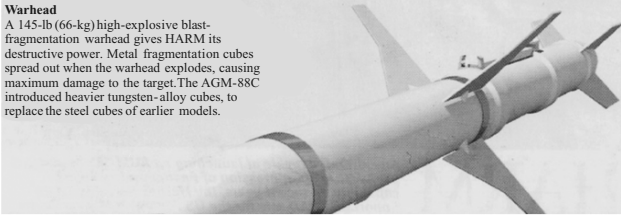
SPECIFICATION
Texas Instruments AGM-88 HARM
Type: medium-range fire-and-forget anti-radiation missile
Length: 13 ft 8¾ in (4.17 m)
Diameter: 10 in (25.4 cm)
Wing span: 3 ft 8½ in (1.13 m)
Launch weight: 800 lb (363 kg)
Warhead: 145-lb (66-kg) HE blast-fragmentation
Fuse: proximity and laser height sensing
Guidance: passive broad-band radar seeker programmable to specific hostile rader characteristics
Propulsion: single-stage, dual-thrust solid-propellant rocket
Performance: speed Mach 3+
Normal range: about 15½ miles (25 km)
Maximum range: up to 50 miles (80 km) when launched from altitude
Minimum range: estimated at 4 miles (6 km)
Users: United States, Germany, Israel, Italy.

Plate 2.8. AGM-88 Harm with Allack profile

AIM-54C Phoenix
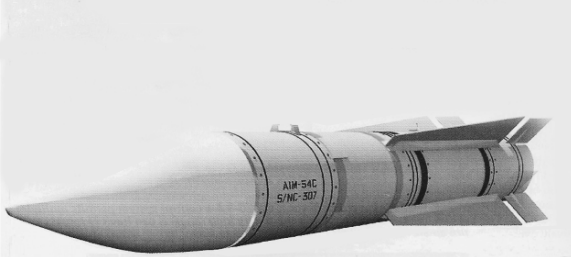
SPECIFICATION
AIM-54C Phoenix
Type: long-range air-to-air missile
Powerplant: one Rocketdyne Mk 47 or Aerojet Mk 60 long-burning solid propellant rocket motor
Performance: maximum speed approximately Mach 5.0 at high altitude; range 96 miles (150 km)
Launch weight: 1021 lb (463 kg); (AIM-54A) 977 lb (443 kg)
Dimensions: wing span 3 ft (0.92 m); length 13 ft (3.96 m); body diameter 1 ft 3 in (0.38 m)
Warhead: 132-lb (60-kg) high-explosive continuous rod, annular blast fragmentation
Fusing: optional impact, Downey Mk 334 proximity or Bendix infra-red
Guidance: continuous wave monopulse semi-active, mid-course updates, terminal active rader with 'home-on-jam' capability

Plate 2.9. AIM-54C with Long-range Engagement

although most were produced in IR-homing versions as well, allowing fighters to gain high kill probabilities by ripple firing one of each. This meant that those aircraft that carried only two missiles could effectively deal with just one target, but the practise continues to this day.

By comparison with their Western contemporaries, Russian missiles tended to be crude, large and heavy. Although this reduced their range, it tended to mean that larger, more lethal warheads were used and it may have made the missiles more robust. As far as is known, the USSR never developed a weapon as crude or with as powerful a warhead as the McDonnell Douglas astronautics AIR-2A Genie, which was unguided but which made up for the inaccuracy inherent in this approach by using a nuclear warhead.

While there can be no doubt that early Russian AAMs were of limited effectiveness and dubious reliability, their Western contemporaries were seldom as effective as brochure figures might suggest, as became apparent in Vietnam, where even the advanced AIM-7 proved to have a poor kill probability. Because Russian first generation AAMs tended to be fitted to PVO interceptor aircraft types (which tended not to be exported), little was known

Modern Russian AAMs

This MiG-29 is in full operational configuration for the air defence role, with 'Archer' AA-11 missiles inboard and AA-11 'Archers' on centre and outboard pylons.

Pictured flying over the Baltic, this Sukhoi Su-15 'Flagon' is armed with AA-3 'Anabs' (R-8s). This combination of missiles and aircraft was to lead to the destruction of the Korean Airlines 747 in September 1983.

Plate 2.10. Aircraft loaded with AAMS
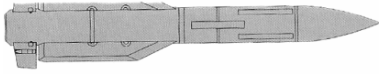
R-33 (AA-9 'Amos')

The most striking thing about the MiG-31's AA-9 'Amos' is its appearance, the missile showing every sign of being a straight copy of the AIM-54 Phoenix carried by the F-!4 Tomcat. The Phoenix was almost certainly compromised following the fall of the Shan in Iran, and it has been widely reported that Phoenix rounds were delivered to the USSR by the new revolutionary regime.It is perhaps surprising that suggested performance figures for the AA-9 give it a capability in broadly the same league as the much smaller AIM-7, with simple semi-active radar homing.

It seems inconceivable that such a large weapon could have such a short range. It is therefore probable that the missile has much the same absolute range as the AIM-54, but that this range is beyond the aircraft's ability to illuminate a target for the weapon's semi-active radar homing (SARH) seeker. The missile could perhaps theoretically reach a long-range target, but seeker limitations may mean that this absolute reach cannot be exploited without third party targeting, or without using inertial guidance to reach the target's approximate position, and a nuclear warhead to 'take out' minor navigational errors.

R-77 (AA-12 'Adder')

The R-77, originally known in the west as 'Amraamskii', is being offered for export with upgraded MiG-29s and Su-27 variants, although it was designed for use by the stillborn 'fifty generation' Soviet fighters such as the MiG 1.42. This might explain why the missile uses cruciform lattice tailfins which may be folded, allowing carriage internally or semi-conformally.

Bigger (37 lb/17 kg heavier,and with a larger diameter) than the Western AIM-120 AMRAAM, the R-77 may be assumed to carry more fuel (which may itself be more powerful) than the Western missile, and to have a larger seeker antenna (implying a greater lock-on range). Simulated engagements between Malaysian AIM-7 armed F/A-18Ds and R-77 armed MiG-29s revealed that the F/A-18s launched their weapons at 28-31 miles (45-50 km) from the target, while the MiGs launched theirs at a distance of 34-37 miles (55-60 km). The R-77 manufacturer, Vympel, claims a maximum range of 62 miles (100 km) (the AIM-120 has a claimed maximum range of only 46 miles/75 km) Moreover, there are at least two extended-range versions of the R-77, one with a solid-fuel ramjet engine giving a maximum range of 99 miles/160 km, the other with a larger diameter long-burn booster and perhaps with passive radar homing capability.

R-27 (AA-10 'Alamo')

Developed as the primary BVR armament for the MiG-29 and Su-27, the R-27 appears to be derived from the MiG-23's R-23, with a similar (and perhaps common) airframe. The missile has a revised control surface arrangement, with moving trapezoidal fins forward and fixed fins aft. It almost certainly has entierly new 'internals' with new seekers, warheads, fuses, and perhaps even motors.

Available in a number of versions,with long-range boosters and with infra-red (IR) and SARH, the missile is effective and deadly. However, extensive testing of the weapon during combat evaluation of former East German MiG-29 'Fulcrums' suggests that it is broadly equivalent to the late Sparrow in performance and range, with a rather less user-friendly launch sequence.

R-37

The R-37 has been spotted under a number of MiG-31M prototypes and development aircraft at Akhtubinsk, and appears to have reached an advanced stage of development although, with the cancellation of the MiG-31M, its future must be in doubt. Clearly based on the R-33, the R-37shares a common airframe, but has revised control surfaces and almost certainly features a revised or new seeker head, fusing, motor and warhead. Improvements to the original R-33 may have resulted in a weapon which is finally broadly equivalent to the AIM-54 Phoenix, from which the original R-33 appears to have been derived.

Plate 2.10A. Major Missiles

about them and they tended not to be used in the various proxy wars fought during the Cold War. One of the few occasions during which such a missile was seen in action occurred when a PVO Su-15 "Flagon" (armed with R-8s) shot down a Korean Airlines Boeing 747, the two missiles fired cutting the giant airliner into many pieces.

2.4 Data on Civilian and Military Aircraft, Tanks and Marine Vessels

2.4.1 Civilian Aircraft

Civilian aircraft normally in service include Concorde, Airbus, Boeing, Antonov, BAC, Tri-Star, DC Series, Ilyushin and Tupolov.

Table 2.34. Basic parameters of Concorde

	Power plant
	$4 \times 38{,}050$ lb (169 kN) Rolls-Royce/Sneema Olympus 593 Mk60 two-spool turbojet
S (m)	25.61
L (m)	62.10
H (m)	12.19
A_{w} (m^2)	358
P_{L} (kg)	11,340
V (km h^{-1})	2,150
w_{a} (kg)	186,800

S, span; L, length; H, height; A_{w}, wing area; P_{L}, payload; V, speed; w_{a}, weight at take-off or landing

2.4.1.1 British Aerospace/Aerospatiale Concorde

Figure 2.24a, b shows a photograph and a cut-away drawing of the aircraft Concorde 206, respectively. The aircraft has a variable geometry drooping nose linked with an A-frame and guide rails. The fuselage is situated close to the delta wing. Fuel is carried in the fin as well as in tanks which are located in the wings. This fuel can automatically be transferred between tanks at supersonic speed in order to maintain the centre of gravity of the aircraft. Table 2.34 lists basic data.

2.4.2 Boeing 737

2.4.2.1 Introduction

Boeing started serious studies of a new twin-engine, 100 seat airliner in 1964. its model 727 tri-jet was already proving to be very successful, but rivals Douglas and BAC had launched smaller jets (the DC-9 and One-Eleven, respectively) at around the same time and were now enjoying good sales. Douglas was already talking about a new, stretched, version of its DC-9 which would be almost as big as the 727 and would certainly steal even more market share from Boeing. Of the four big US airliners, Delta had bought DC-9s and American had ordered One-Elevens – leaving United and Eastern still in the market. The major European airlines were also waking up to the possibilities of the smaller twin-jet airliners, though most of them wanted aircraft that were slightly larger than those on offer.

Studies of what would today be termed a "regional airliner" had begun at Boeing in 1962, but it was not until November 1964 that the Model 737 emerged as a firm project. At that time, Boeing designers had conceived

an aircraft approximately 85 ft (25.9 m) in length, with a wingspan of 75 ft (22.86 m). Versions of the Pratt & Whitney JT8D engine were slated to power the new aircraft which would have a maximum take of weight of 79,000 lb (35,834 kg). The Boeing aircraft rejected the rear-engine configuration of its rivals in favour of a low winged design with under-wing engines. Adopting this configuration allowed the airframe to be lighter, but crucially permitted many common parts and structures to be incorporated from the Model 727 production line.

The 737 had its engines fitted snugly against the wings, not in pods on pylons as on the 707 and the 747. This allowed the aircraft to be lighter and also kept the cabin floor as close to the ground as possible. The 737 had a wider cabin (with six-abreast seating) than the DC-9 or One-Eleven. The design was undergoing constant revision and under pressure from the market, began to grow in size. On 19 February 1965 the 737 received its formal go-ahead with a launch order from Germany's Lufthansa for 21 aircraft. This was a much lower figure than Boeing had ever received in order to launch an aircraft project – and the first time that a Boeing programme had gone ahead without a firm commitment from a US airline. Lufthansa, already a 727 operator had told Boeing that if it did not offer the 737 as a firm project, then the airline would buy the DC-9 instead. Faced with the loss of its most important European customer, Boeing felt it had to agree.

Fuselage Stretches

The aircraft that was delivered to Lufthansa became known as the 737 Series 100 (737-100) and was larger than originally planned. It was 94 ft (28.65 m) long and had a maximum take-off weight of 97,000 lb (43,999 kg). This growth, however, was not enough and to win the 737's next critical order, from United Airlines, the design had to change again. United demanded a longer version of the 737, with a 6 ft 6 in (2.01 m) fuselage stretch. This allowed the 737 to accommodate two extra rows of seats, and with these changes in place United ordered 40 aircraft in 1965, with options on another 30.

This revised design was the 737-200 and it would prove to be the definitive 737 for the next 20 years. But before this aircraft could write itself into the history books, the 737 encountered some serious teething troubles.

The prototype 737 made its first flight on 9 April 1967 with first deliveries set for just nine months later. The aircraft proved to be much more "draggy" in the air then its designers had anticipated, and the engine nacelle fairings had to be completely redesigned. A problem also arose with the thrust reversers, which were too close to the wing trailing edge, and so the rear of the engine nacelles had to be extended by 40 in (102 cm). These problems seriously affected the 737-100s sales and only 30 of this version were built. However, the 737s troubles had been cured by the time the 737-200 was ready for airline service.

The 737-200 was a far more economical version of the aircraft to operate – chiefly because of its improved passenger capacity, but also because of its higher fuel load and improved Pratt & Whitney JT8D-7 engines. The 737-200 could be powered by 14,500 lb (64.5 kN) JT8D-7/9As, 15,500 lb (69 kN) JT8D-9/-15/-15As and the 16,000 lb (71.2 kN) JT8D-17/-17A. This array of engines was required to cope with the 737s range of take-off weights which stretched from 10,000 lb (45,360 kg) to 128,100 lb (58,106 kg). With 115 passengers, a 737-200 had a typical range of 1,800 nm (2,066 miles; 3,325 km).

After the first 280 aircraft had been delivered, Boeing introduced the Advanced 737-200 which became the main production version from May 1971 onwards. This aircraft had an aerodynamically refined wing with many changes made to the engine nacelle fairings, leading-edge, trailing-edge, slats and flaps. The first Advanced 737-200 flew on 15 April 1971 and it was this version which took the lion's share of 737-200 sales.

Boeing built a military version of the Advanced 737-200, the T-43A, which served with the USAF primarily as a navigation trainer. The distinctive aircraft had only nine cabin windows and two cabin doors. They had a strengthened floor to carry the required avionics consoles and view ports in the cabin roof for sextant alignment/astro navigation training. A total of 19 aircraft was delivered between 1973 and 1974 and several were later adapted to serve as VIP and staff transport.

Another military development of the 737-200 was a maritime patrol/surveillance version fitted with a Motorola SLAMMR 9side-looking airborne multi-mission radar), which was announced in 1981. Three of these aircraft were delivered to Indonesia in 1982/1983.

Rough-field operation. Boeing developed a rough-field kit for the 737, allowing the aircraft to operate from unpaved runways. On these aircraft, the underfuselage surface was given a protective coating to reduce gravel damage and the antennas were all strengthened to avoid being broken off. The landing gear and flaps sections were also given reinforced protection and the main landing gear tyres were increased in size. A deflector plate was fitted to the nose gear, which did not retract into the wheel well but remained outside flush with the fuselage. An air blower was fixed to the front of each engine inlet, to bleed off engine pressure and to reduce the chances of debris being sucked into the (low slung) engines. This kit was fitted by several 737 operators, particularly in Africa and Alaska.

Cargo versions of the 737-200 were also developed by Boeing, allowing the aircraft to be operated in all-freight or Combi (with passengers and freight on the same deck) layouts. An 84.5 in × 134 in (214.6 cm × 340 cm) cargo door was fitted to the front forward fuselage and the aircraft was given reinforced floor, with cargo-handling equipment, restraint netting, etc. Two versions were offered, the 737-220C which used conventional non-palletised seats (taking approximately 5.7 man-hours to convert from freighter to passenger configuration), and the "quick change", 737-200QC with palletised seating that could be removed/refitted in just 0.92 man-hours.
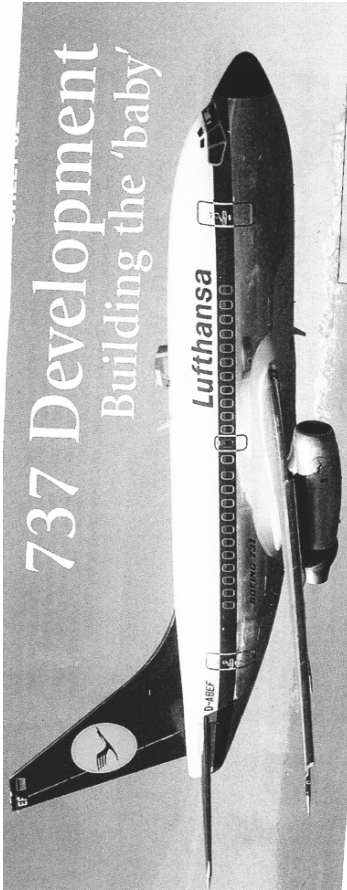
Lufthansa was the launch customer for the 737, initially ordering 21 of the short-body Series 100. The airline added a further 737-100, and later signed up for a large batch of the definitive early-generation Series 200.

An unusual military application of the 737 is its used by Indonesia as a maritime patroller. The three modified 737-2X9s carry side-looking radar above the rear fuselage.

Boeing was a late-comer to the small medium-range jet airliner market and the success of its first design, the Model 737, was once far from assured. Despite its initial troubles, however, the 737 would go on to be the best-selling jet airliner in histroy.

Plate 2.11. Boeing 737 Aircraft

The 747 quickly established itself on the world's long-haul routes, but the early years were anything but trouble-free. Hijacking became fashionable in the early 1970s, and the big Boeing suffered its share of trouble. The most serious episodes occurred on 6 September 1970 and 24 July 1973, both resulting in aircraft being blown up by Palestinian guerrillas. The first, Pan Am's *Clipper Fortune*, on a flight from Amsterdam to New York, was re-routed to Cairo, and the second, a Japan Airlines 747, met its end at Benghazi.

747 Upgrades. As early as June 1968, Boeing had announced the availability of a heavier model with improved payload and range which as the 747-200B, entered passenger service with KLM in February 1971. Combi and all freighter versions, designated the 747-200C and 747-200F, respectively were also built. More powerful Pratt & Whitney engines brought higher take-off weights and General Electric CF6-50 and Rolls-Royce RB211 engines also became available.

Northwest Airlines was the first airline to receive the newest member of the 747 family, the −400 series. The airline was a natural recipient of the new aircraft, as much of its business is conducted across the Pacific, where the additional range of the −400 is useful.

Pan Am and Boeing collaborated on a number of projects and the 747 represents their greatest success. Pan AM was the first airline to order the 747 and even by that stage had been intrinsically involved in the design. However, Pan Am suffered financial problems in the 1980s and eventually ceased trading.

2.4.2.2 Power Plants, Accommodation and Records

Power-plant. Depending on which airline it flies with, the 747-200 carries either four Pratt and Whitney JT9D-7R4G2 turbofans rated at 54,750 lb (243.5 kN) thrust, General Electric CF6-50E2 turbofans at 52,500 lb (233.5 kN) thrust or Rolls Royce RB.211-524D4-B turbofans at 53,110 (236.2 kN) thrust.

Accommodation. The 747-200B has a cabin length of 187 ft (57 m) and a width of 20 ft $1\frac{1}{2}$ in (6.13 m). The basic layout of the aircraft provides seating for 48 first-class and 3347 economy-class passengers (including a 16 passenger upper deck lounge). Alternatively, 447 passengers can sit nine-abreast in one class conditions, or 500 passengers can sit 10-abreast, with 32 on the upper deck. The aircraft is flown by a flight crew of three.

Records. On 12 November 1970, a test 747-200B set a new heavyweight record by taking off at a gross weight of 820,700 lb (372,261 kg). An even more remarkable fact is that the cabin of the 747 is longer than the distance covered by the Wright brothers.

Plate No. 2.12 A, B and c give briefing and the "cut away" of the Boeing 747-200, clearly establishing specification of Boeing 747-200B.

Boeing 747
Briefing

Plate **2.12.** PaAs Layouts

Cathay Pacific Airways, Hong Kong's flag carrier, has its origins in ad hoc charter flights undertaken by American, Roy Farrell, in 1946, who began operating out of Shanghai using a refurbished C-47. The airline has come a long way since then, and now boasts sixty 747s of various marks among its vast fleet of airliners. Resplendent in its new brushwing livery is this 747-200, which is one of seven examples in operation. Serving alongside the standard passenger examples are four -200F freighters.

Boeing 747-200

Cutaway key
1 Radome
2 Weather radar scanner
3 Forward pressure bulkhead
4 Radar scanner mounting
5 Nose visor cargo door
6 First-class passenger cabin
7 32 seats (typically) in forward cabin
8 Nose visor hydraulic jack
9 Visor hinge fixing
10 Rudder pedals
11 Control column
12 Instrument panel shroud
13 Curved windscreen panels
14 Co-pilot's seat
15 Flight engineer's control panel
16 Cockpit doorway
17 Observers' seats (2)
18 Captain's seat
19 Cockpit floor level
20 First-class bar unit
21 Window panel
22 Nose undercarriage wheel bay
23 Nose wheel doors
24 Twin nosewheels, forward retracting
25 Steering hydraulics jacks
26 Under floor avionics equipment racks
27 Circular staircase between decks
28 Upper deck crew door, port and starboard
29 Cockpit air conditioning ducting
30 First-class galley
31 First-class toilet
32 Plug-type forward cabin door, No. 1
33 First- class passenger seating
34 Cabin-dividing bulkhead
35 Upper deck window panel
36 Upper deck toilet
37 Anti-collision light
38 Cabin roof construction
39 Uppeer deck galley
40 Upper deck passenger seating, up to 32 seats

41 Air-conditioning supply ducts
42 Forward fuselage frame construction
43 Baggage pallet containers
44 Forward underfloor freight compartment
45 Air conditioning system ram air intake
46 Wing root fairing
47 Ventral air conditioning plant, port and starboard
48 No. 2 passenger door, port and starboard
49 Lower deck forward galley
50 Upper deck galley
51 Meal trolley elevators
52 Communications aerial
53 Forward tourist-class cabin, typically 141 seats
54 Fuselage frame and stringer construction
55 Cabin floor beam construction
56 Centre-wing section skin/stringer panel
57 Fresh water tanks
58 Wing spar bulkhead
59 Wing centre-section fuel tank, capacity 17,000 US gal (64345 litres)
60 Front spar attachments fuselage main frame
61 Air-conditioning cross-feed ducts
62 Air distribution duct
63 Risers to distribution ducts
64 Wing centre spar attachment main frame

65 Satellite navigation aerial
66 Fuselage skin panelling
67 Starboard wing inboard fuel tank, capacity 12,300 US gal (46555 litres)
68 Fuel pumps
69 Engine bleed air supply duct
70 Krüger flap operating jacks
71 Inboard Krüger flap
72 Starboard inner engine nacelle
73 Inboard engine pylon
74 Leading edge Krüger flap segments
75 Krüger flap drive shaft

76 Ventral refuelling panel
77 Krüger flap motors
78 Starboard wing outboard fuel tank, capacity 4,420 US gal (16,730 litres)
79 Starboard outer engine nacelle
80 Outboard engine pylon
81 Outboard Krüger flap segments
82 Krüger flap drive mechanism

83 Extended-range fuel tank, capacity 800 US gal (3028 litres)
84 Surge tank
85 Wingtip fairing
86 Starboard navigation light
87 VHF aerial boom
88 Fuel vent
89 Static dischargers
90 Outboard, low-speed, aileron
91 Outboard spoilers
92 Outboard slotted flaps
93 Flap drive mechanism
94 Inboard, high-speed, aileron
95 Trailing edge beam
96 Inboard spoilers/lift dumpers
97 Inboard slotted flap
98 Flap screw jack
99 Centre fuselage construction
100 Pressure floor above starboard wheel bay
101 Wing-mounted main undercarriage wheel bay

102 Central flap drive motors
103 Undercarriage mounting beam
104 No. 3 passenger door, port and starboard
105 Fuselage-mounted main undercarriage wheel bay
106 Hydraulic retraction jack
107 Wheel bay pressure bulkhead
108 Cargo net
109 Rear underfloor freight hold
110 Freight and baggage container, LD-1
111 Cargo loading deck
112 Roller conveyor floor tracks
113 Cabin wall trim panelling
114 Rear cabin air supply duct
115 Control cable runs
116 Rear fuselage frame and stringer construction
117 Upper deck freight containers, M1
118 Rear toilet compartments
119 Fin root fairing
120 Starboard tailplane
121 Static dischargers
122 Starboard elevators
123 Fin leading-edge construction
124 Fin spar construction
125 Fin tip fairing
126 VOR aerial
127 Static dischargers
128 Upper redder segment
129 Lower rudder segment
130 Rudder hydraulics jacks
131 Tailcone fairing
132 APU exhaust
133 Auxiliary Power Unit (APU)
134 Port elevator inner segment
135 Elevator outer segment
136 Static dischargers
137 Tailplane construction

Plate 2.12A. Designation's for Boeing 747-200 with compliments Boeing CO, Washington, USA

2.4.3 Boeing 767-200ER

Plate No. 2.13 gives passenger, cargo, engines specification, fuel capacity, take-off weight, cruise speed and basic dimensions of this aircraft. This aircraft has been used as an impactor to be crashed on World Trade Centre at New York of 9/11, disaster scenario in 2001.

SPECIFICATION

Boeing 747-200B
(unless otherwise noted)

Dimensions

Length overall: 231 ft 4 in (70.51 m)
Length of fuselage: 225 ft 2 in
(68.63 m)
Wingspan: 195 ft 8 in (59.64 m)
Wingarea: 5,500 sq ft (511 m²)
Wing aspect ratio: 6.96
Wing chord at root: 54 ft 4 in (16.56 m)
Wing chord at tip: 13 ft 4 in (4.06 m)
Tailplane span: 72 ft 9 in (22.17 m)
Horizontal tail area: 1,470 sq ft
(136.6 m²)
Aireron area: 222 sq ft (20.6 m²)
Elevator area: 350 sq ft (32.5 m²)
Fin area (total): 830 sq ft (77.1 m²)
Rudder area: 247 sq ft (22.9 m²)
Height overall: 63 ft 5 in (19.33 m)
Cabin volume: 27,860 cu ft (789 m³)
Cabin length(total): 187 ft (57.00 m)
Cabin width: 63 ft 5 in (19.33 m)
Cabin height: 8 ft 4 in (2.54 m)
Maximum usable floor area:
3,529 sq ft (327.9 m²)

Power plant

Four 52,500 lb st (238.1 kN) General
Electric CF6-50E2 or 54,750 lb st
(243.5 kN) Pratt & Whitney
JT9D-&74G2 or 53,110 lb st (236.2 kN)
Rolls-Royce RB.211-524D4-B turbofans
747-100B: four 46,950 lb st (208.8 kN)
Pratt & Whitney JT9D-7A turbofans
747-200B Combi: similar engines to
the standard -200 passenger variant
747-200C Convertible: four
50,000 lb st (222.4 kN) Pratt & Whitney
JT9D-7FW or 50,100 lb st (222.8 kN)
Rolls-Royce RB.211-524B turbofans

Weight

Empty weights: 375,500 lb
(170320 kg) or 385,500 lb (174860 kg);
747-100B 371,000 lb (168280 kg);
747-200B Combi 375,500 lb
(170320 kg) or 385,500 lb (174860 kg);
747-200C 358,000 lb (162385 kg) or
369,000 lb (167380 kg)
Maximum take-off weights:
800,000 lb (362875 kg);
747-100B 710,000 lb (322051 kg);
747-200B Combi 800,000 lb (362875 kg)

Fuel load

Total fuel capacity: 42,832 Imp gal
(194715 litres); **747-100B**
39,584 Imp gal (179953 litres)

Performance

Maximum level speed: 523 kt
(602 mph; 969 km/h); **747-100B** 552 kt
(601 mph; 967 km/h)
Cruising ceiling: 45,000 ft (13715 m)

Range

Range with maximum payload:
5,450 nm (10100 km); **747-100B**
4,500 nm (8339 km)

Interior specifications

Cabin: Normal operating crew of three,
on flight deck above level of main deck.
Observer station and provision for
second observer
Passenger capacity: Basic
accomandation for 385 passangers: 48
first-class (includes 16-passenger upper
deck lounge) and 337 economy class.
Alternative layouts seat 447 economy
class passangers nine-abreast or 500
10-abreast, with 32 on the upper deck.

Plate 2.12B. Designation's and specification's for Boeing 747-200B

2.4.4 Boeing 777

2.4.4.1 Introduction

A final agreement between Boeing and JADC, signed on 21 May 1991, made the Japanese companies risk-sharing partners for 20% of the entire 777 programme. This unprecedented move; along with sizeable subcontractors which were issued to companies around the world, allowing Boeing to use the very best manufacturers at each stage of production.

Multiple roles for Boeing's 747

747-123 NASA-owned modified Shuttle Transporter

747-100/200B 452-516 passengers

747-200F Freighter

747SP (Special Performance) 288-331 passengers

E-4B Airborne Command Post

747-300 400-509 passengers 624-passenger high density option

747-400 412-509 passengers
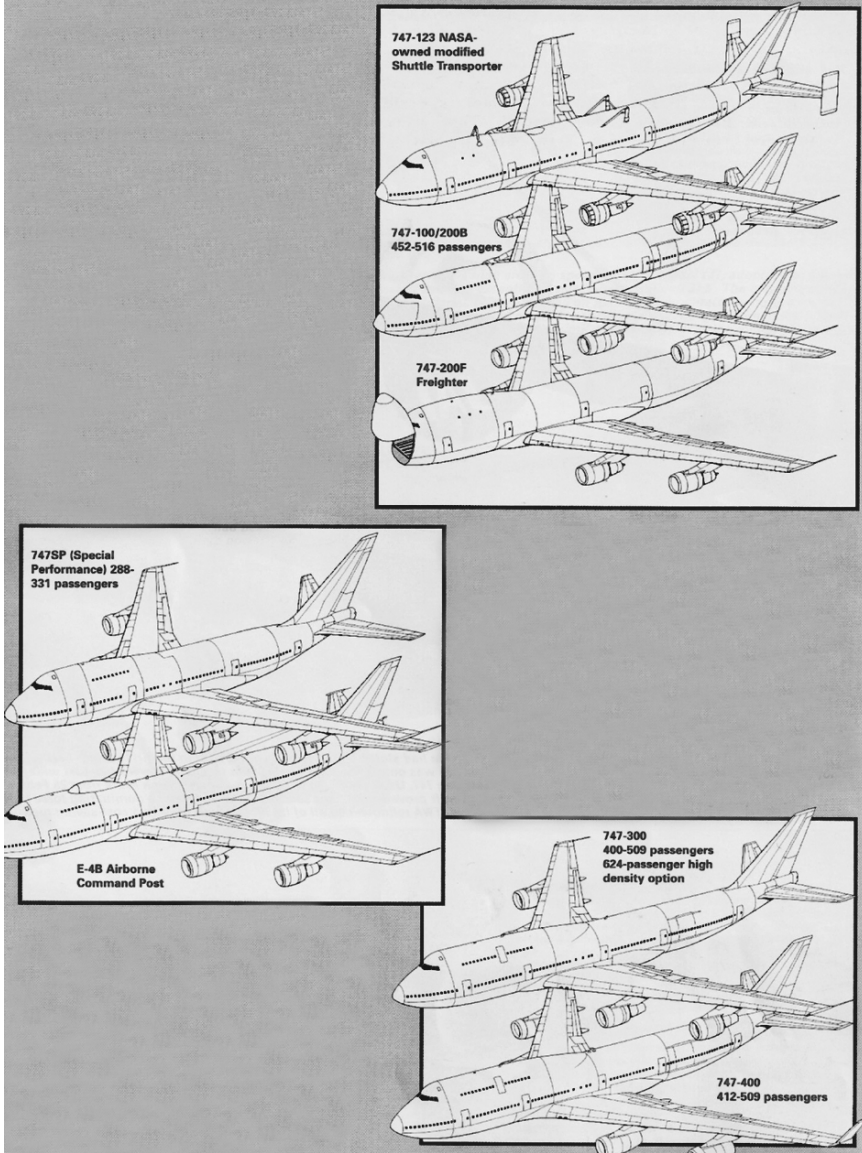
Plate 2.12C. Multiple role data
Specifications:
In January 1974, the National Aeronautics and Space Administration (NASA) obtained a 747-123 from American Airlines. After using it for wake vortex investigation, it was sent to Boeing in 1976 for modification as a carrier for the then forthcoming Space Shuttle, and was subsequently designated the Shuttle Carrier

Plate 2.12C. (Continued) Aircraft (SCA), receiving the callsign 'NASA 905'. The aircraft was stripped of all airline equipment, but the original American Airlines red, white and blue striping was retained. The fuselage was reinforced to support the weight of the 150,000-lb (68,038-kg) shuttle, and removable end fins were added to the tailplane to improve directional stability when carrying the shuttle. The JT9D-3A engines were modified to JT9D-7AH standard to increase the take-off thrust to 46,900 lb (208.6 kN). The shuttle is mounted on top of the SCA having been suspended from an overhanging gantry, after which the SCA is wheeled into place beneath it. The shuttle is then lowered into the cradles on top of the SCA.

Equipped with a fuselage loading door in Combl configuration, the 747-100 and -200 often fly with a mixed load of passengers and cargo on the same deck, while the 747-200F was presented as a dedicated freighter with an upward hinging nose door. From the outset, Boeing had intended to offer a 747F, but this plan had been temporarily shelved. However, as more powerful engines became available, the 747F became reality, and the 747-200F first flew on 30 November 1971. It had a new fuselage with no side windows, and a strong cargo floor fitted with a computer-controlled mechanised system for handling containers and pallets.

One variant to emerge in the mid-1970s was the SP (Special Performance) for long-range flights. The 747SP was an almost total redesign. The objective was to carry fewer passengers, but to operate from short, or hot-and-high, runways and yet still fly extremely long distances. The whole appearance was altered by reducing the length of the fuselage by 47 ft 1 in (14.3 m), to seat 288-331 passengers. Because of the reduced tail moment arm, the tail had to be made larger and the tailplane span was increased by 10 ft (3.04 m). The tail fin was fitted with a double-hinged rudder. Pan Am took delivery of the first SP on 5 March 1976, and this aircraft soon made a flight around the world (New York-Delhi-Tokyo-New York) in only 40 hours.

The E-4B Airborne Command Post, which is based on the 747-200 variant, would become the USA's operations centre in the event of a nuclear exchange. Fitted with a comprehensive suite of communications equipment, including SHF satellite communication facilities, the E-4B is able to remain aloft for at least 72 hours, during which time it can receive fuel through a nose-mounted flight refuelling receptacle.

First offered as a conversion option on existing 747-200s, the Series 300 features an increased upper deck area in an enlarged fairing; this not only offers greater capacity, but also increases maximum cruising speed. An option on the -300m Combi variant is a rear cargo door to allow a larger payload to be carried. The latest version of Boeing's remarkable 747 is the 747-400. A considerably improved model compared to its predecessors, the -400 has extended wings with winglets, and increased volume fuel tanks, with the resulting improvement in range. The aircraft can be operated by a two-man crew due to its advanced multi-functional cockpit displays. The first 747-400 was rolled out on 26 January 1988. Orders for the new aircraft exceeded 200, with most major operators adopting the airliner for their long-haul routes.

Boeing 767-200ER

General Specifications

Passengers	
Typical 3-class configuration	181
Typical 2-class configuration	224
Typical 1-class configuration	up to 255
Cargo	2,875 cubic feet (81.4 cubic meters)
Engines' Maximum Thrust	
Pratt & Whitney PW4062	63,300 pounds (28,713 kilograms)
General Electric CF6-80C2B7F	62,100 pounds (28,169 kilograms)
Maximum Fuel Capacity	23,980 U.S. gallons (90,770 liters)
Maximum Takeoff Weight	395,000 pounds (179,170 kilograms)
Maximum Range	6,600 nautical miles
Typical city pairs: New York-Beijing	12,200 kilometers
Typical Cruise Speed	0.80 Mach
at 35,000 feet	530 mph (850 km/h)
Basic Dimensions	
Wing Span	156 feet 1 inch (47.6 meters)
Overall Length	159 feet 2 inches (48.5 meters)
Tail Height	52 feet (15.8 meters)
Interior Cabin Width	15 feet 6 inches (4.7 meters)

Plate 2.13. Aircraft Information with compliments of FEMA 2007 Washington D.C.

Representatives of JADC's constituent companies and two important Japanese Aircraft Manufacturing Co. Limited and ShinMaywa Industry Co. Limited, were soon based in Seattle, Washington, alongside their Boeing colleagues.

Other subcontractors play a less major, but nonetheless important role in 777 manufacture. Much of the aircraft's primary flight control and avionics systems are British-designed and built, while the unique main undercarriage units are a product of collaboration between Menasco and Messier-Bugatti.

2.4.4.2 Digital Design

Making full use of new digital design and definition techniques, the 777 took shape with virtually no paper drawings. It became the first airliner to be 100% digitally defined and pre-assembled, using the Dassualt/IBM-developed CATIA CAD/CAM (computer-aided design and computer-aided manufacturing) software system. This powerful tool allows parts and systems to be viewed in three-dimensions, with misalignments and errors easily corrected on a computer screen, ensuring enhanced accuracy and fewer production changes. It also eliminated the need for costly full-scale mock ups.

Boeing also tackled the 777 programme from a multi-disciplinary perspective, establishing 238 design/build teams which, via access to a common database, were able to work concurrently from concept to completion. But Boeing took this process a step further by making suppliers and airline customers an integral part of the design teams, giving both unprecedented access to the design process from an early stage. This "working together" concept considerably reduced post-engineering changes and provided fewer "in-service" surprises and enhanced reliability. It also ensured that customer airlines were receiving exactly the aircraft they required.

Testing and validation of aircraft systems installation was undertaken in a purpose-built Flight Controls Test Rig and Systems Integration Laboratory (SIL), identifying and potentially expensive problems.

Boeing carries out all 777 final assembly and flight testing. The barrel sections of the airliner's mid – and rear-fuselage are built by JADC in Japan. A hoist holds the Boeing-built wings which are united with the Japanese-built centre section.

2.4.4.3 Specifications

- Long range Twin Turbofan
- Power-plant – 2nd 400.8 kN. Pratt & Whitney PW4090 Turbofan
- Performance – Maximum cruising speed   Mach 0.87
                  – Economic cruising speed   Mach 0.83
- Average Speed – 256 km h^{-1}
- Take off run – Maximum 2,469 m range with 375 passengers
                  – Weights (operating)   135,580 kg
                  – Maximum take-off   229,520 kg
                  – Maximum Payload   54,930 kg
- Dimensions – Wingspan   60.93 m
                  – Length   62.78 m
                  – Height   161.51 m
                  – Wing Area   427.8 m^2
                  – Accommodation   440 Passengers

Boeing 777
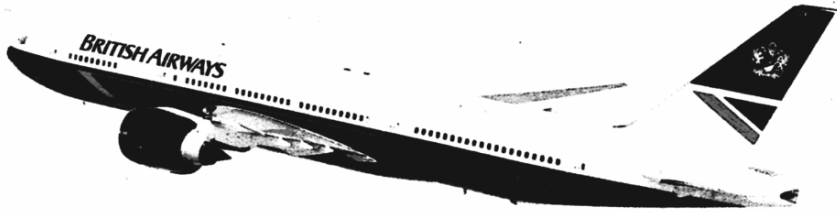
British Airways has remained faithful to Boeing, by purchasing the 777 in the face of stiff competition from Airbus. The American manufacturer has produced one of the most capable airliners on the market, allowing it to compete head on with both the twin-engined Airbus A330 and four-engined A340.

Structural breakdown

Boeing sources 777 structural components from companies in the US and from abroad. US subcontractors include Kaman, Northrop Grumman and Rockwell, while international suppliers include Aerospace Technologies, Alenia, EMBRAER, Hawker de Havilland, Korean Air, Shorts and Singapore Aerospace.
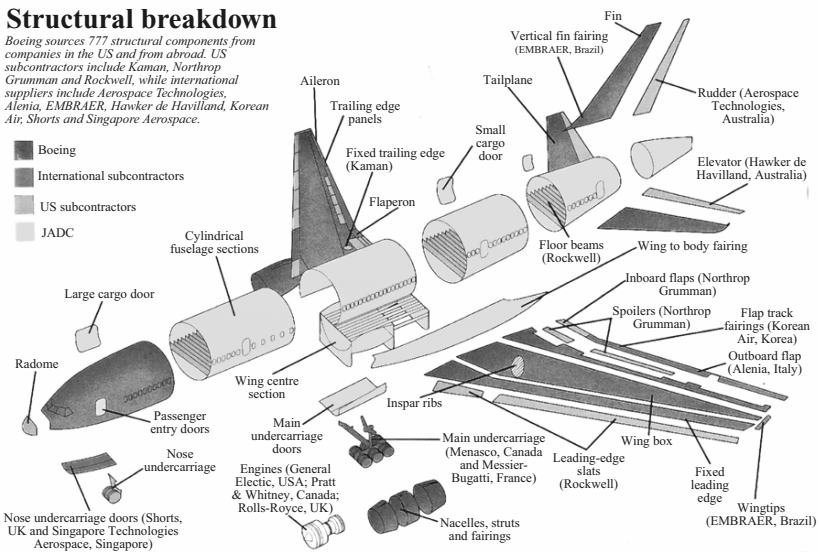
Plate 2.14. Boeing 777 with designated parts with compliments from Boeing Co Washington USA

2.5 Military Aircraft

2.5.1 British Aerospace Tornado Interdictor Strike (IDS) and Air Defence Variant (ADV)

The multi-role combat aircraft Tornado is proof that multi-national collaboration in technology at the frontiers of science is not only possible but can be successful in meeting the requirements of the world's airforces. The aircraft been produced in various batches since August 1974. Figure 2.36 shows a Tornado aircraft GR Mk 1 from 9 Squadron RAF Honington carrying
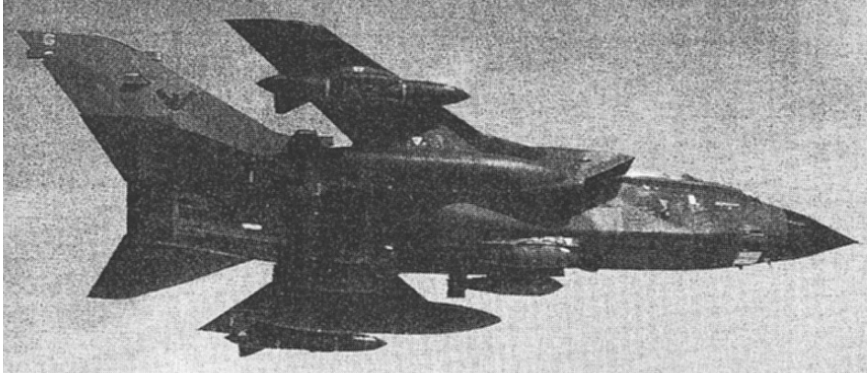
Fig. 2.36. Royal Airforce Tornado GR Mk 1 with four MK13/15 bombs (courtesy of British Aerospace UK)

four 1,000 lb (454.74 kg) bombs, two full tanks and two ECM pods. Figure 2.37 shows the cut-away diagram of a Tornado IDS giving intimate details of the airframe, weaponry and internal structural, mechanical and avionic systems.

The IDS Tornado is designed primarily to fly at trans-sonic speeds, hugging the ground at a very low level and striking the targets in all weathers. With wings at the optimum sweep angle, it is highly manoeuvrable and possesses long-range capability. The wings are fully swept under speed performance, at both high altitude and low level. Relevant data are given in Table 2.35.

2.5.2 Northrop F-5E and F-20 Tigershark

Both the F-5E and the F-20 are combat aircraft. The acceleration time of these aircraft varies from $900 \, \text{miles} \, \text{h}^{-2}$. Figures 2.38 and 2.39 illustrate the F-5E in full combat form and the layout, respectively. Figures 2.40 and 2.41 show the F-20 in full combat form and the layout, respectively.

Relevant data on the F-5E and F-20 aircraft are listed in Table 2.36.

2.5.3 General Dynamics F-16

This is the most important combat aircraft and is known as the "fighting falcon". Various versions have been developed under the Multi-national Staged Improvement Programme (MSIP). This programme was accomplished in three stages:
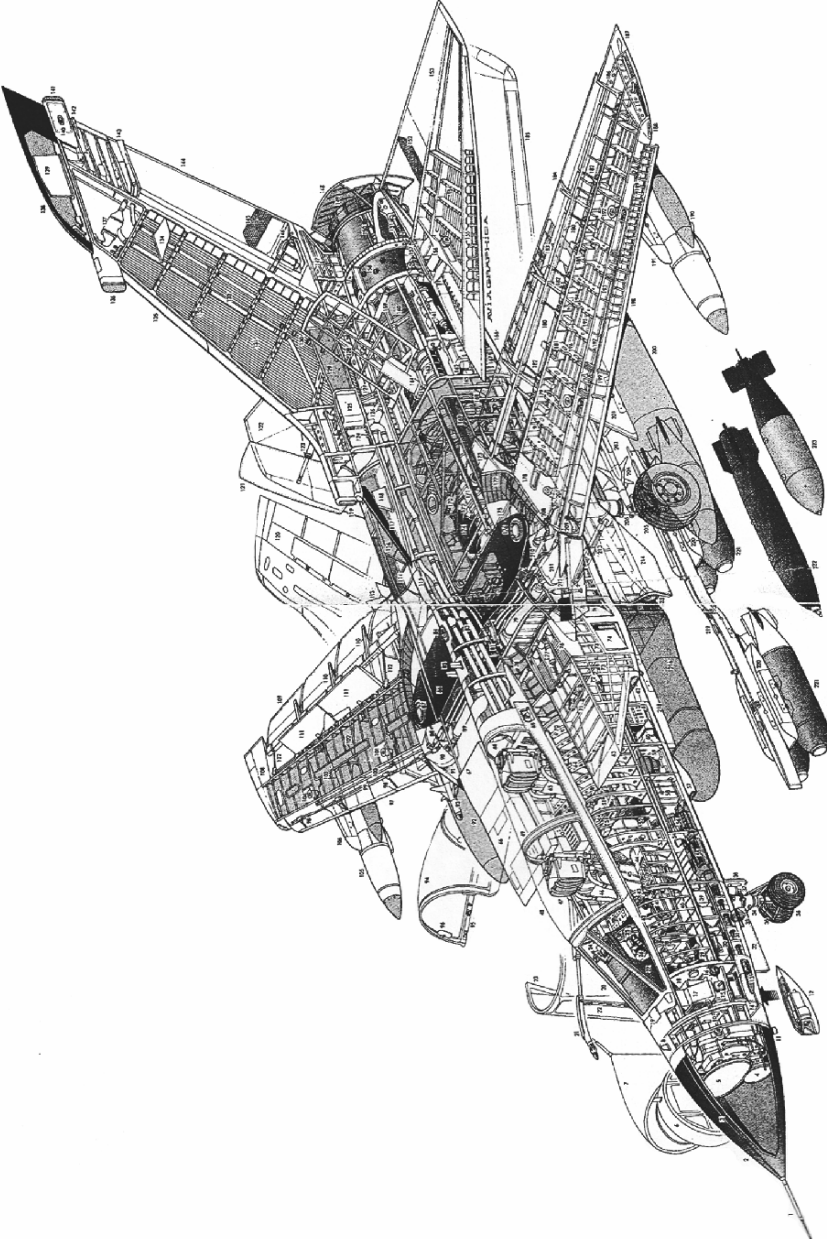
Fig. 2.37. A cut-away diagram of a Panavia Tornado GR Mk 1

Table 2.35. Data on the Tornado IDS and ADV aircraft

Power plant		
	Interdictor Strike (IDS)	Air Defence Variant (ADV)
	Turbo-Union RB 199–34R (101 or 103) after burning turbofan MK 8,090 lb (3,670 kg) to 15,950 lb (7,253 kg) after burning thrust	As for IDS, with MK 104
S (m)	8.60 max swept	8.60 at 67° sweep
	13.90 max unswept	13.90 at 25° sweep
L (m)	16.67	18.68
H (m)	5.95	5.95
A_w (m^2)	–	–
P_L (kg)	9,000	9,000
V (Mach)	Mach 2 at high level	Mach 2.2
	Mach 1 at low level	
w_a (kg)	28,000	28,000
Armament	4 × MK 13/15 1,000 lb (454.74 kg) bombs	
	2 AIM-9L missiles	
	8 MK 83 retarded bombs	
	2 CBLS-200 practice bomb containers	
	4 Kormoram ASM	
	8 × BL755 cluster bombs	

S, span; L, length; H, height; A_w, wing area; P_L, payload; V, speed; w_a, weight at take-off or landing

Stage I	F-16A+/B+	Early wiring and structural provisions for the incorporation of future systems. Production deliveries began in November 1981 and ended in March 1985.
Stage II	F-16C/D	Core avionic cockpit and airframe provisions to accommodate emerging systems. Production deliveries began in July 1984.
Stage III	F-16A/B/C/D	Installation of advanced systems as these became available.

The F-16C/D versatility is increased with the common engine bay which permits the installation of either the F100-PW-220 or F110-GE-100 improved engine or future derivatives of these. The US Navy has the F-16N, a single-plate fighter which is a derivative of the F-16C multi-role fighter and is powered by the F110-GE-100 engine and has the growth potential to simulate the next generation of threat fighters. It is equipped with the AIM-9 series of Sidewinder missiles and ACMI/TACTS pods. A two-seater fighter/trainer aircraft is known as the TF-16N for the navy and the F-16D for the airforce. Figures 2.42 and 2.43 show the F-16C and F-16N versions of the aircraft with the AIM-9 series of Sidewinder missiles. Figure 2.44 shows a typical cut-away diagram of the F-16 aircraft.

Relevant data on the F-16 series of aircraft are listed in Table 2.37.

Fig. 2.38. The Northrop F-5E in full combat form (courtesy of Northrop)
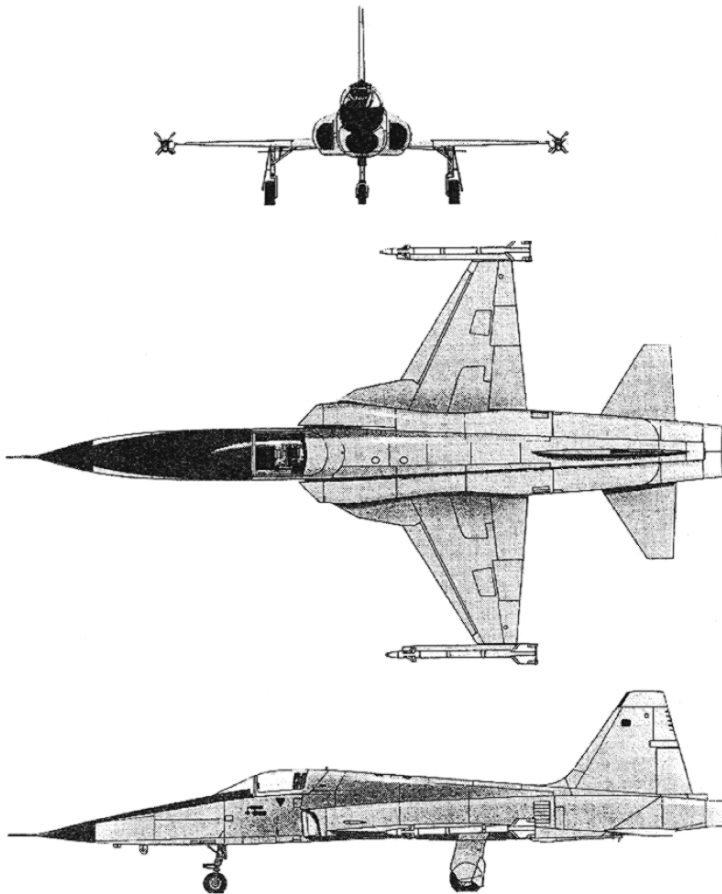
Fig. 2.39. The layout of the Northrop F-5E (courtesy of Northrop)

Fig. 2.40. The Northrop F-20 Tigershark in full combat form (courtesy of Northrop)
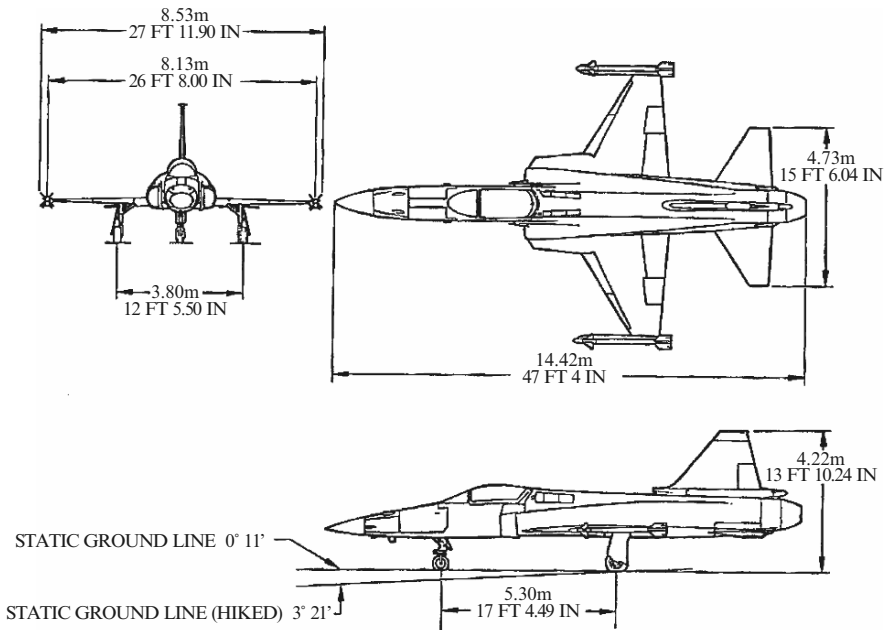
Fig. 2.41. The layout of the F-20 Tigershark (courtesy of Northrop)

Table 2.36. Basic parameters for the F-5E and F-20 aircraft

	Power plant	
	Engine 2GEJ 85–21	Engine GEF404-GE100
	5,000 lb (2,268 kg) thrust each	1,800 lb (8,164 kg) thrust each
S (m)	7.98 with missiles	8.5 with missiles
	8.53 without missiles	
L (m)	14.45	14.42
H (m)	4.07	4.10 (4.73 with wheels)
A_w (m^2)	28.1	27.5
P_L (kg)	6,350	7,263
V (miles h^{-1})	850	1,300
w_a (kg)	11,213.8	12,700
Armament	Air-to-air	2 No. 20 mm guns and AIM 9
		Sidewinder missiles
	Air-to-ground	2 No. 20 mm guns and 9 bombs of 3,020 kg

S, span; L, length; H, height; A_w, wing area; P_L, payload; V, speed; w_a, weight at take-off or landing

2.5.4 General Dynamics F-111

This is an early version of the fighter plane which is still in service and shall be phased out in the very near future. It is a two-seater, all-weather attack bomber and the well known versions are the F-111A, F-111F and EF-111A, made initially by Grumman Aerospace and then taken over by General Dynamics. Data on the aircraft are given in Table 2.38.

2.5.5 British Aerospace Jaguar

The Jaguar GR.1 and T.2, A and E were developed jointly by British Aerospace (BAe) and Dessault-Breguet of France. Figure 2.45 shows two Jaguars of the Indian Air Force in combat form. A cut-away diagram of the Jaguar showing the laser ranger on the marked target seeker behind a chisel nose is shown in Fig. 2.46 All versions have nose radar, a refuelling probe and the option of the overwing pylons for light dog fight missiles such as the air-to-air Matra 550 Magic. Data are listed in Table 2.39.

2.5.5.1 Avions Marcel Dassault Aircraft

The major aircraft designed by Marcel Dassault are the Estendard, the Breguet F1 and the Mirage 3, 5, 2000 and 4000. The Mirage 2000 is designed to take full advantage of the Mirage F/3/5 and the F1 and is a multi-role, medium-size, single-seat combat aircraft with a variable camber delta wing, as shown in Fig. 2.47. The Mirage 2000B is a two-seater, designed for the same
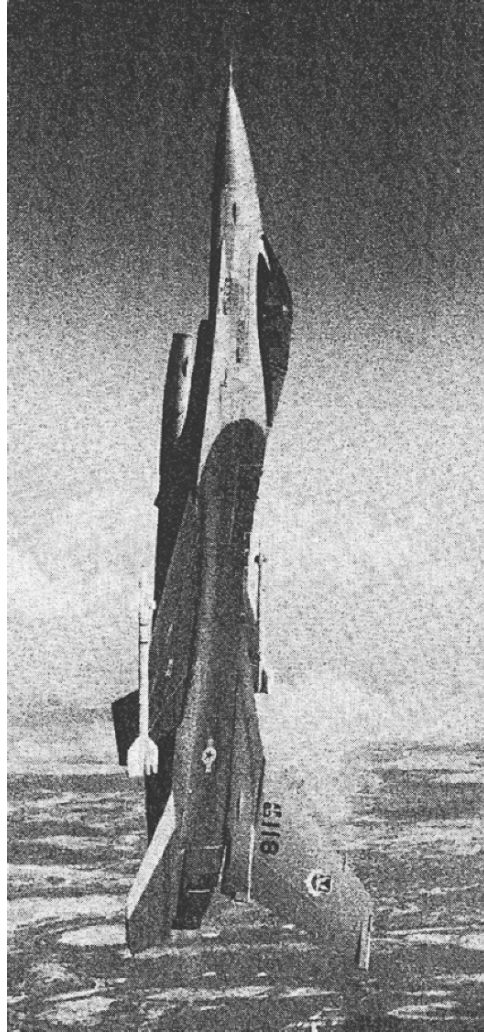
Fig. 2.42. F-16C Aircraft in full combat form (courtesy of General Dynamics)

operational capabilities as the single-seater Mirage 2000. The Mirage 4000 is a twin-engine aircraft and is a logical follower of the Mirage 2000, benefitting from various research work on advanced aerodynamics.

With regard to size, the Super Mirage 4000 ranks between the Grumman F14 Tomcat and the McDonnell Douglas F18 Hornet. Its twin SNECMA 53 engines, in the 10 tonne thrust class (22,000 lb), provide a thrust/weight ratio greater than 1.0, ensuring performance figures above those of all currently known aircraft in the same class.
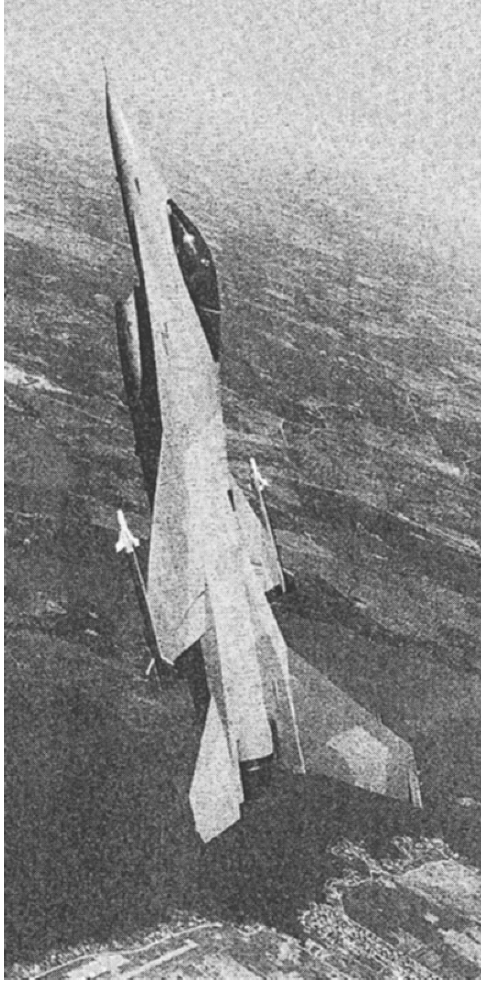
Fig. 2.43. F-16N aircraft in full combat form (courtesy of General Dynamics)

In contrast with the F14, F15, Tornado or MIG 23 of the same category, with either a variable-geometry wing or a separate tailplane, the Super Mirage 4000 profits from reduced drag, combined with the simple and compact design of the pure delta wing configuration Figs. 2.48 and 2.49.

Relevant data on the Dassault aircraft are given in Table 2.40.

2.5.6 McDonnell Douglas F/A-18 Hornet

The F/A-18 Hornet is a multi-role, high-performance, tactical aircraft Fig. 2.50, which can perform fighter strike or intercept missions. The twin-engine, multi-mission aircraft is capable of operating from both aircraft carriers and short
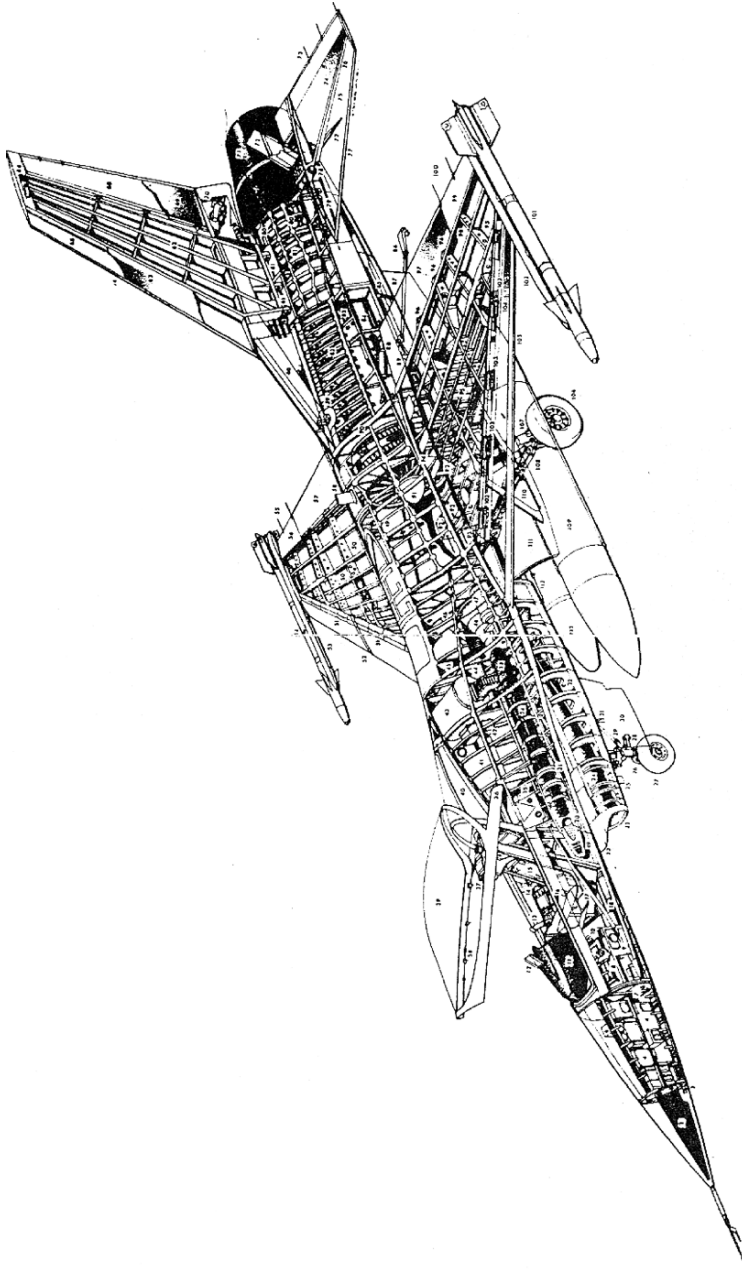
Fig. 2.44. A cut-away diagram for the F-16 aircraft (courtesy of General Dynamics)

Table 2.37. Data on the F-16 series of aircraft

	F-16A and F-16B	F-16C and F-16D	F-16N	TF-16N
Power plant	Pratt and Whitney turbofan two shaft 24,000 lb (10,885 kg) thrust F100-PW-100	F100-PW-200 F100-PW-220 F110-GE-100 25,000 lb (11,340 kg) thrust	F110-GE-100 25,000 lb (11,340 kg) thrust	F110-GE-100 25,000 lb (11,340 kg) thrust
S (m)	9.45 10.01 (with Sidewinder)	9.45 10.01 (with Sidewinder)	9.895 (without Sidewinder)	
L (m)	14.52	15.03	15.10	
H (m)	5.01	5.09	5.10	
A_{w} (m^2)	27.87	27.87	27.87	
P_{L} (kg)	33,000 lb (14,969 kg)	37,500 lb (16,781 kg)	37,500 lb (16,781 kg)	
V (miles h^{-1})	1,300	1,300	1,300	
w_{a} (kg)	12,000 lb (5,443 kg)	12,430 lb (5,638 kg)	17,278 lb (7,836 kg)	

S, span; L, length; H, height; A_{w}, wing area; P_{L}, payload; V, speed; w_{a}, weight at take-off or landing

Table 2.38. Data on the General Dynamics F-111

	Power plant
	Pratt and Whitney two shaft turbofans, thrust range 18,500 lb (8,390 kg) to 20,350 lb (9,230 kg)
S (m)	10.35±
L (m)	22.4
H (m)	5.22
A_{w} (m^2)	35.75
P_{L} (kg)	20,943
V (km h^{-1})	1,450
w_{a} (kg)	41,400–54,000

S, span; L, length; H, height; A_{w}, wing area; P_{L}, payload; V, speed; w_{a}, weight at take-off or landing

bases. It is designed to replace the F-4 fighter and A-7 attack aircraft. It is a superior fighter with attack capabilities which include close-in and beyond-visual-range, all-weather and day/night strike.

Data on the F/A-18 are listed in Table 2.41.
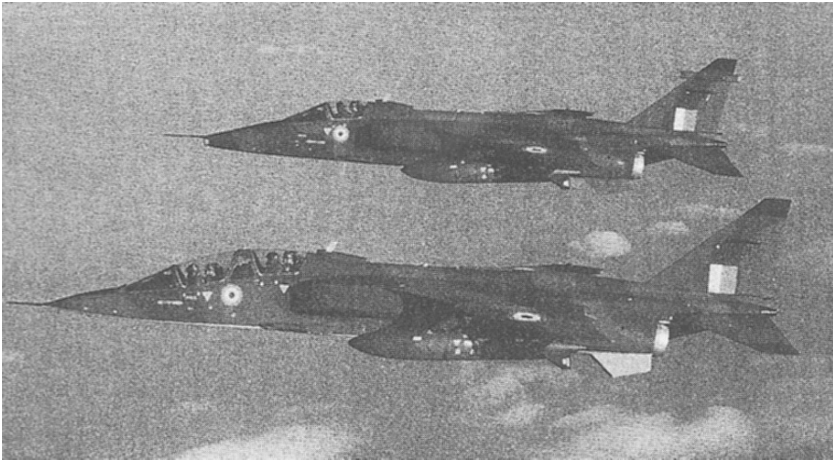
Fig. 2.45. Two jaguar Internationals of the Indian Air Force comprising of a single-seater strike and a two-seater trainer (courtesy of British Aerospace, Warton Division)

2.5.6.1 Grumman F-14 Tomcat

The F-14A Tomcat represents the culmination of the US Navy's efforts for a total air superiority of fighters through the use of an advanced airframe with a variable sweep wing and a long-range weapon system. Some technical changes, including engine thrusts, have been introduced in the F-14B, C and D versions. Figure 2.51 shows the F-14A in full combat form armed with two AIM-54A Phoenix missiles, two AIM-7F Sparrow missiles and two AIM-9G Sidewinders while Fig. 2.52 shows a F-14D. Figure 2.53 illustrates the wing and gloves movement of the F-14. Data for the Tomcat are shown in Table 2.42.

2.5.7 Soviet Union MIG Aircraft

The MIG aircraft in operation with a number of world air forces are the MIG-17 (Hip-H), MIG 19–195, MIG-5F, MIG-19PM (NATO name "Farmer"), MIG-23BN (Flogger H), MIG-23MF (Flogger G), MIG-23CKD (Flogger J), MIG-24 (Hind D), MIG-25R (Foxbat B) and the MIG-29CKD (Fulcrum). The MIG-23 is further accommodated with a 23 mm GSH-23 twin-barrel gun on the ventral central line plus various mixes of air-to-air missiles of 2 No. infra-red AA-7 "Apexes" and infra-red or radar-homing AA-8 "Aphids". Table 2.43 is a comparative study of various MIG aircraft.

It is interesting to note that the MIG-25 has four underwing pylons, each carrying one AA-6 air-to-air (two radar and two infra-red) missiles with VO guns employed. On the other hand, the MIG-27 has a 23 mm barrel Gatling-type gun in a belly. Seven external pylons are provided for a wide range

Jaguar International Specification

Power Plant: Two Rolls-Royce/Turbomeca RT172-26 Adour 804 turbofans each rated at 5,320 lb st (2410 kgp) dry and 8,040 lb st (3 645 kgp) with reheat, or RT172-58 Adour 811 rated at 5,500 lb st (2 504 kgp) dry and 8,400 lb st (3811 kgp) with reheat, static at sea level. Total internal fuel capacity, 924 Imp gal (4 200 l); provision for three external drop tanks of 264-Imp gal (1 200-l) capacity each.

Performance: (At typical weights for representative tactical missions) Take-off distance to 50 ft (15,2 m), 3,085 ft (940 m); max speed, Mach 1.1 at low level, Mach 1.6 = 1,055 mph (1,698 km/h) at high altitude; range (with external fuel) LO-LO-LO, 564 mls (907 km), Hi-Lo-Hi, 875 mls (1 408 km); ferry range (without in-flight refueling), 2,190 mls (3 524 km); landing distance from 50 ft (15,2 m), 2,575 ft (785 m).

Weights: Typical empty weight, 15,432 lb (7000 kg); normal take-off, 24,000 lb (11 000 kg); max take off, 34,000 lb (15 500 kg), max external load, 10,000 lb (4540 kg).

Dimensions: Span, 28 ft 6 in (8,69 m); length (including nose probe), 55 ft 2' in (16,83 m); length overall (two-seat variants), 57 ft 6? in (17,53 m); height overall, 16 ft 0' in (4,89 m); aspect ratio, 3·1; wing sweepback, 40 deg at quoter chord; undercarriage track, 7ft 11 in

(2,40 m); wheelbase, 18 ft 8 in (5,69 m); gross wing area, 260-3b sq ft (24,18 m²)

Armament: Two 30-mm DEFA 553 or Aden cannon in lower front fuselage. One external stores attachment point on fuselage centerline and four underwing attachment points, to carry
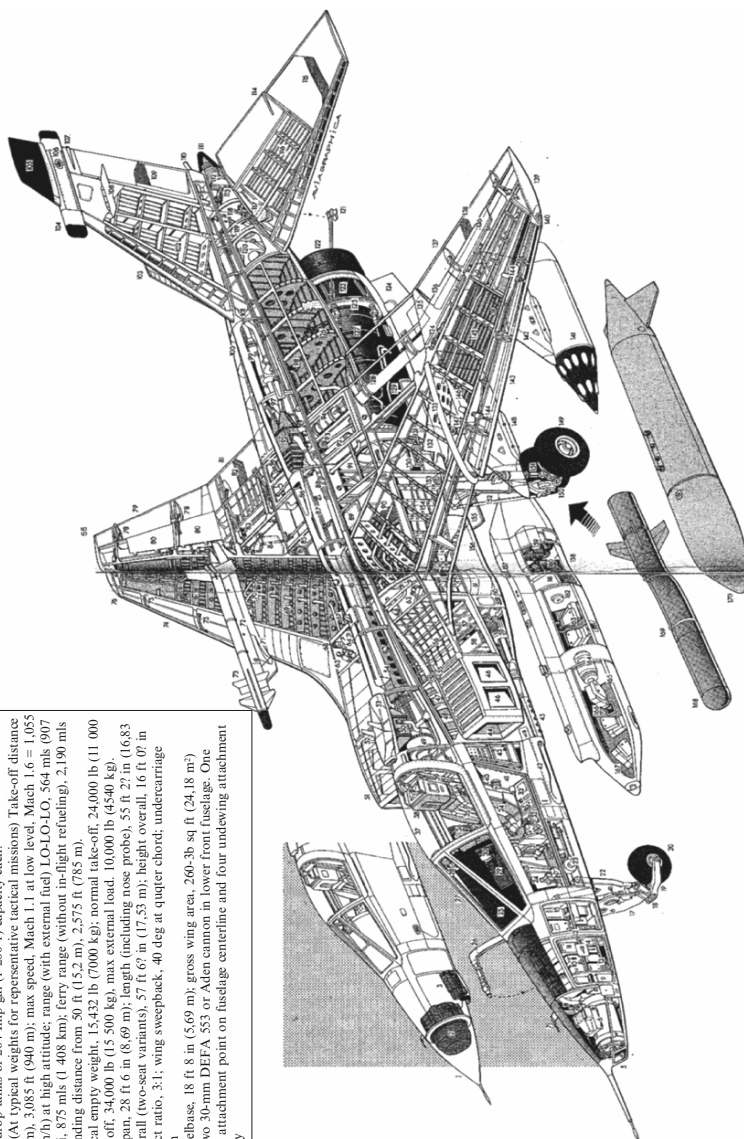
Fig. 2.46. A cut-away diagram of a Jaguar equipped with missiles and bombs (courtesy of British Aerospace, Warton Division)

Table 2.39. Data on the British Aerospace Jaguar

	Power plant
	2 No. Rolls-Royce Turboméca Adour two shaft turbofans 7,305 lb (3,313 kg) to 8,000 lb (3,630 kg) thrust
S (m)	8.69
L (m)	15.4–16.42
H (m)	4.92
A_{w} (m^2)	–
P_{L} (kg)	6,800
V (km h^{-1})	1,450
w_{a} (kg)	1,550

Armament and other data
    2 No. 30 mm DFA 553 each with 150 rounds
    5 No. pylons with total external loads of 4,536 kg with guns
    2 No. 30 mm Aden for its T-2 model
    Matra 550 Magic air-to-air missiles

Jaguar A and B and EMK 102 Adour ⎫
engines   ⎪
Jaguar S MK 104 s ⎫   ⎪ Using digital quadruplex fly-by-wire
    MK 108 ⎬ Adour engines ⎬ control system
Jaguar Act   ⎪
Jaguar FBW   ⎭

S, span; L, length; H, height; A_{w}, wing area; P_{L}, payload; V, speed; w_{a}, weight at take-off or landing
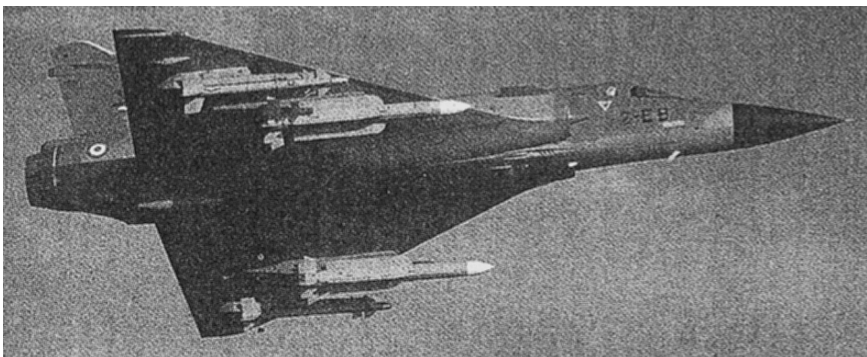
Fig. 2.47. The Dassault Mirage 2000 (courtesy of AMD, France)
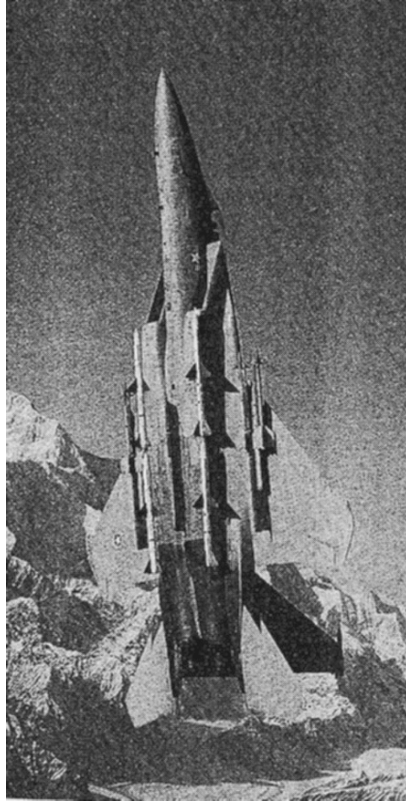
Fig. 2.48. McDonnell Douglas F-15 in a vertically accelerated position, with missiles (courtesy of McDonnell Douglas)

of ordnance including guided missiles AS-7 "Kerry" and tactical nuclear weapons. All ECM are internal. The pylons on the outer wing are piped but not fixed drop tanks. Since they do not pivot, they can only be loaded when the wings remain unswept.

2.5.8 Other Important Fighter/Bomber Aircraft

Data are included in this section for the well-known combat aircraft Rockwell B-1 bomber, Russian Sukhoi (SU), Chinese F-6 and F-7, Saab 37 Viggen and BAe Harrier. These well proved aircraft are operational with many air forces in the world. Their layouts and performances are similar to the combat aircraft described earlier. Slight variations exist in the engine capacities, dimensions, payloads and maximum and minimum speeds. Comparative data are listed in Table 2.44.
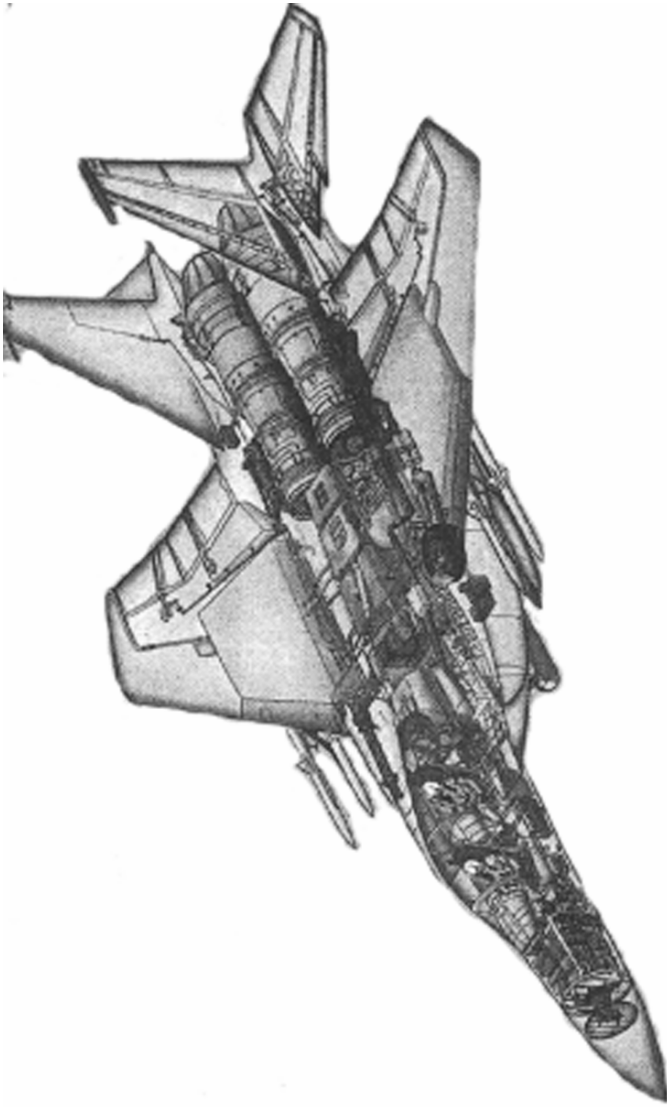
Fig. 2.49. A cut-away diagram of the F-15E (courtesy of McDonnell Douglas)

Table 2.40. Data on the F-15

	Power plant
	2 No. Pratt and Whitney F-100-PW-220 each with 24,000 lb thrust
S (m)	13.05
L (m)	19.45
H (m)	5.64
A_w (m^2)	–
P_L (kg)	7,000
V (km h^{-1})	2,500
w_a (kg)	20,000
Armament	4 AIM-9L/M infra-red-guided Sidewinder missiles; 4 AIM-7F/M radar-guided Sparrow missiles; eight advanced medium-range air-to-air missiles (AMRAAMs); M-61 20 mm Gatling gun with 940 rounds of ammunition. Accommodates a full range of air-to-ground ordnance.

S, span; L, length; H, height; A_w, wing area; P_L, payload; V, speed; w_a, weight on take-off or landing
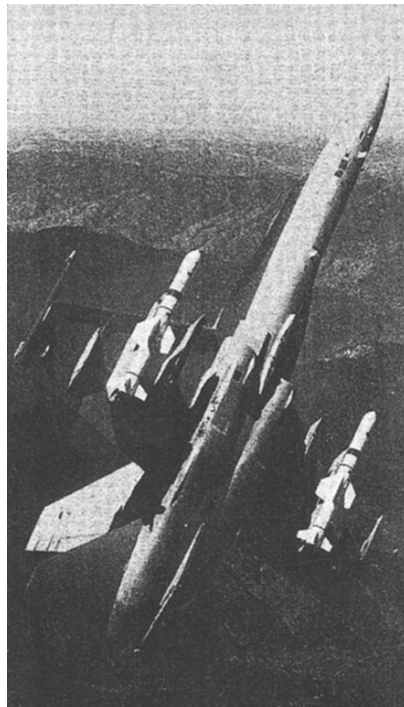
Fig. 2.50. F/A-18 Hornet with Harpoon missiles (courtesy of McDonnell Douglas)

Table 2.41. Data on the F/A-18 Hornet

	Power plant
	2 No. F404-GF-400 low bypass turbofan engines each in 1,600 lb (70.53 kN) thrust and with a thrust/weight ratio of 8:1
S (m)	11.43
L (m)	17.06
H (m)	4.7
A_w (m^2)	37.2
P_L (kg)	–
V (km h^{-1})	2,700
w_a (kg)	24,402
Armament	Up to 7,711 kg maximum on nine stations: two wing-tips for Sidewinder heat-seeking missiles; two outboard wings for air-to-ground ordnance; two inboard wings for Sparrow radar-guided missiles, air-to-ground, or fuel tanks; two nacelle fuselage for Sparrow missiles or sensor pods; one centreline for weapons, sensor pods or tank. Internal 20 mm cannon mounted in nose

S, span; L, length; H, height; A_w, wing area; P_L, payload; V, speed; w_a, weight at take-off or landing
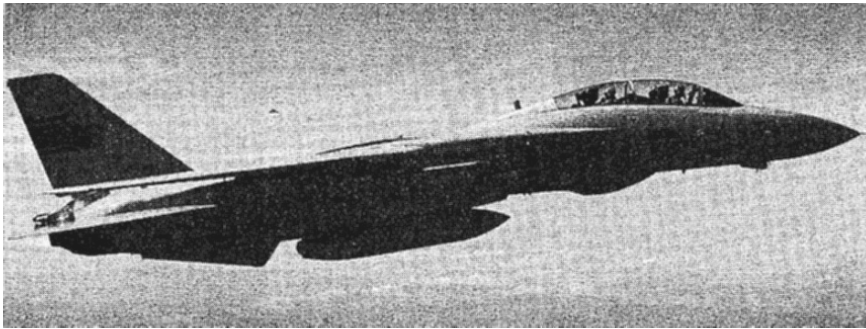
Fig. 2.51. The F-14A in combat form (courtesy of Grumman Corporation, USA)

2.5.8.1 Lockheed F-117 Nighthawk

Introduction

The extraordinary shape, revolutionary radar-defeating features and a top secret, yet highly glamorous development have combined with a star appearance in Desert Storm to make the Lockheed F-117 best known warplane in the world. It is able to penetrate hostile airspace and strike vital targets without being detected by radar defences.
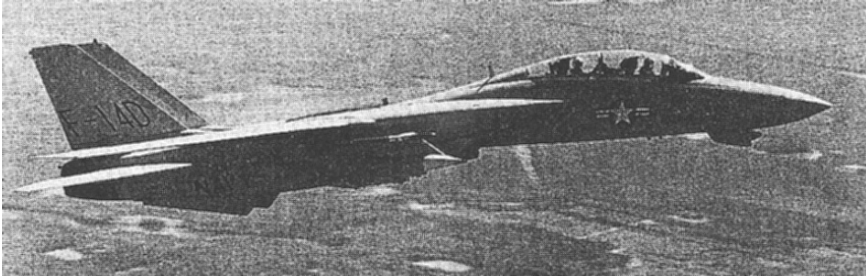
Fig. 2.52. The F-14D in combat form (courtesy of Grumman Corporation, USA)

Fig. 2.53. The F-14 with wing and glove movement (courtesy of Grumman Corporation, USA)

The F-117 was a mystery and to some a miracle, when revealed to the public a decade ago. Now, it is an aging warplane with a specialised purpose. When it emerged from a shroud of secrecy, the F-117 (Plate No. 2.15) was hailed as marking a scientific breakthrough because of its ability to do just one thing. Today, critics are insisting that this once revolutionary warplane is old, slow, and costly, given its ability to do only one task. But even though it has little versatility, the F-117 performs its one mission with such drama, and so superbly, that the retirement talk is almost certainly highly premature.

The F-117 is the first operational warplane to employ low observable (LO), or stealth, technology to reduce its vulnerability to radar detection. Though called a fighter, the F-117 is not intended for air-to-air combat. Its purpose is to deliver ordnance in a dense threat environment against targets of extremely high value. The Lockheed F-117 emerged from a Cold War "black" program where it was developed in conditions of unprecedented secrecy.

The mission of the F-117 is unique: to attack small, well-protected targets which are, in Pentagon jargon, highly leveraged. This means that their

Table 2.42. Data for the Grumman F-14 Tomcat

Power plant	
F-14A	F-14B,C
$2 \times 20{,}900$ lb (9,480 kg)	$2 \times 28{,}090$ lb (12,741 kg) thrust
thrust Pratt and Whitney	Pratt and Whitney F401–400
TF30–1412A	

Two shaft after-burning turbofans

S (m)	11.630	(68° sweep)	safely landing
	19.54	(20° sweep)	
L (m)	18.89		
H (m)	4.88		
A_{w} (m^2)	–		
P_{L} (kg)	17,010		
V	Mach 2.3 or 1,564 mph maximum speed, 400–500 km/h cruise speed, 125 km h^{-1} approaching speed		
w_{a} (kg)	27,216		
Armament	AIM-54 Phoenix missiles		
	AIM-7 Sparrow missiles		
	AIM-9 Sidewinder missiles		
	M61–A1 Vulcan 20 mm cannon		

S, span; L, length; H, height; A_{w}, wing area; P_{L}, payload; V, speed; w_{a}, weight at take-off or loading

destruction will damage an enemy out of proportion to their intrinsic value. A typical assignment would be to "decapitate" an enemy's command, control, communications and intelligence (C^3I) structure by attacking it by surprise with precision-guided bombs. (Plate No. 2.16 shows the view of this stealth aircraft as seen on a plane). Other F-117 targets might be nuclear storage sites, critical bridges and tunnels, or key leadership headquarters.

The wedge-shaped, V-tailed F-117 employs radar absorbent composite materials on its external surfaces. In addition, it has angular features which contribute to its low-observable characteristics by reducing the aircraft's radar cross-section (RCS). Use of radar absorbent materials should make the aircraft appear dim to a radar while the angular shape should cause it to "glitter" irregularly, without giving any solid return signal as its aspect angle varies.

The angular shape results from a technique known as faceting which applies computer technology to aircraft design and in this instance produced radical use of "chisel-edge" leading surfaces and sharp fuselage angles, eliminating curved surfaces in order to diffuse radar returns. The skin panels of the airframe are divided into many small, perfectly flat surfaces which reflect at a variety of angles all signals from probing hostile ground or airborne radars.

The stealth qualities of the aircraft are enhanced by engine exhaust nozzles located atop the fuselage along the wing root just ahead of the tail surfaces.

Table 2.43. Comparative data for MIG aircraft

	MIG-19 (Mikoyan)	MIG-21	MIG-23 (Flogger)	MIG-25 (Foxbat)	MIG-27	MIG-29
Power Plant (Engines)	*Single-seater* $2 \times 6,700$ lb (3,040 kg) to $2 \times 7,165$ lb (3,250 kg) Kimov RD-9B turbojets	*Single-seater* Range turbojet $11,240$ lb (5,100 kg) to $14,500$ lb (6,600 kg) Tumansky single shaft	*Single-seater* $17,640$ lb (8,000 kg) to $25,350$ lb (11,500 kg) thrust, 1 Tumansky turbofan	*Single-seater* $27,000$ lb (12,250 kg) thrust, 2 Tumansky R-266 after-burning turbojets	*Single-seater* $17,640$ lb (8,000 kg) to $25,350$ lb (11,500 kg) thrust, 1-Tumansky after-burning turbofan	—
S (m)	9.00	7.15	8.7 (72° sweep) 14.4 (16° sweep)	14.0 Foxbat A	8.7 (72° sweep) 14.4 (16° sweep)	
L (m)	13.08 (S-5F)	14.35	16.15	22.3 (Foxbat A) 22.7 (Foxbat R) 23.16 (Foxbat U)	16.15	
H (m)	4.02	4.50	3.96	5.60	4.60	
A_w (m²)	–	–	–	–	–	
P_L (kg)	3,760	4,600	7,050	14,970	9,900	
V (max)	Mach 1.3 or $1,480$ km h⁻¹ (920 mph)	Mach 2.1 or $2,070$ km h⁻¹ (1,285 mph)	Mach 1.1 or $1,350$ km h⁻¹ (840 mph)	Mach 3.2 or $3,380$ km h⁻¹ (2,100 mph)		
w_a (kg)	9,500	9,800	15,000	34,930	17,750	

S, span; L, length; H, height; A_w, wing area; P_L, payload; V, speed; w_a, weight at take-off or landing

Table 2.44. Comparative data of some important combat aircraft

Type	Power plant	S (m)	L (m)	H (m)	P_L (kg)	V mach (mph)	w_a (kg)
BAe Harrier GR-3 model T-Mark 4 model (AV-8A, TAV-8A) FRS-I model Single-seater Two-seater	1 × 21,500 lb (9,752 kg) thrust Rolls-Royce Pegasus 103 two shaft turbofan (US designation F-402)	7.7	13.87 17.0 (GR-3)	3.43	6,260	1.2 (860)	11,793
F-6 Shenyang (or NATO's name FANTAN 'A') Single-seater	2 × Axial turbojets MD manufactured	10.2	15.25	3.35	4,500	1.0 (760)	10,700
Rockwell B-1 Four-seater	4 × 30,000 lb (13,610 kg) General Electric F101-100 two shaft augmented turbofans	41.4	45.6	10.24	115,670	0.85 (646)	179,170
Saab 37 AJ, JA Viggen SF, SH, SK versions Single-seater	1 Svenska flying motor RMB; Pratt and Whitney two shaft 25,970 lb (11,790 kg) to 28,086 lb (12,750 kg) thrust	10.6	AJ: 10.6 JA: 16.3	5.6	4,500	2.0 (1,320)	16,000
SU-9 Fishpot B SU-11 Fishpot C Single-seater	1 Lyulka single shaft turbojet; 19,840 lb (9000 kg) thrust (SU-9) and 22,040 lb (10,000 kg) thrust (SU-11)	8.43	SU-9: 18.5 SU-11: 17.4	4.9	4,540	0.95 (1,195)	13,610
SU-15 (Flagen A to E models) Single-seater	2 × Tumonsky R-25 turbofans; 16,530 lb (7,500 kg) thrust after burner	9.5 D Model	21.50	5.0	10,100 (D) 5,100 (A)	2.3 (1,520)	21,000 (D) 16,000 (A)
SU-17, SU-20 and SU-22 models Single-seater	(17) 1-Lyulka AL-21 F-3 thrust single shaft 17,200 lb (7,800 kg) (20–22) AL-7F 22,046 lb (10,000 kg)	14 (28° sweep) 10.6 (62° sweep)	18.75	4.75	9,000	1.05 (798) to 2.17 (1,432)	19,000

S, span; L, length, H, height; P_L, payload; V, speed; w_a, weight at take-off or landing

F-117A Nighthawk 85-0835/HO of 49th FW (USAF)
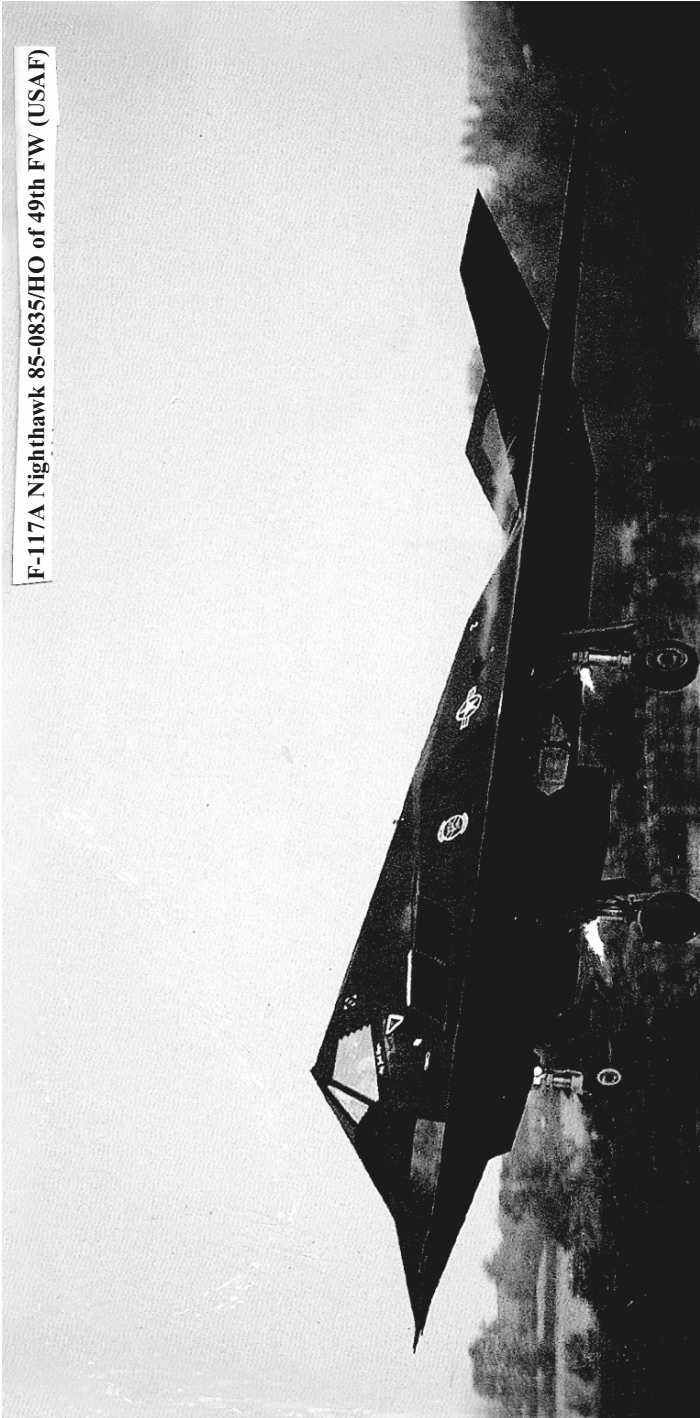
Plate 2.15. F-117A Nighthawk Stealth Aircraft
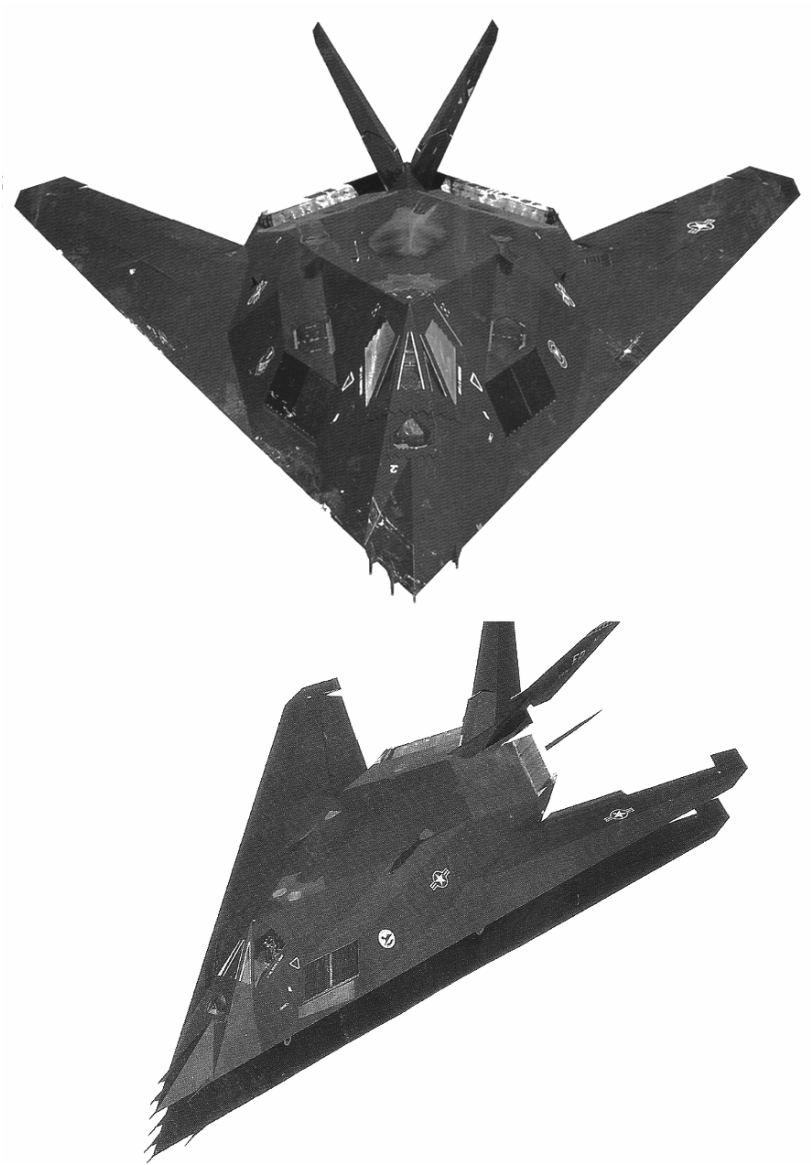
Plate 2.16. Black Bird

The exhaust bleeds over the aft fuselage to screen the heat emissions from detection below.

Stealth Pilot (Plate No. 2.15). The pilot of an F-117 occupies a small cockpit which features a windshield arrangement with a separate panel in front and two different-sized windows on each side. The pilot has a conventional head-up display for flight information and infra-red imagery, with an up-front control panel beneath it for radio and display mode selections. On the main panel are, standard MFDs (malfunction displays) installed either side of a large monochrome CRT screen.

The F-117 was regarded by US was planners as a "silver bullet". In other words, only a few existed and they were to be used against high-value assets (HVAs), the Pentagon's term for the enemy's leadership structure, communications and transportation assets. With its clandestine "Stealth Fighter" operational, the USAF now had a war plane which had settled into service and was beginning to mature, although few people outside the programme knew of the F-117.

On the night of 19 December 1989, two F-117s were launched to support a Special Operations "snatch" of Noriega. The "Snatch" was later called off as the aircraft approached Panamanian airspace, and the nature of the target was changed. Two more F-117s flew a bombing mission intended to "stun and confuse" Panamanian Defence Forces (PDF) at Rio Hato, with another two F-117s flown as back-ups. Their target was a large open field alongside a barracks housing 200 elite PDF troops, rather than the barracks itself.

The six F-117s flew from Tonopah and refuelled five times during the round trip to Panama. The two Rio Hato F-117s dropped two 2,000 lb (907k-27A/B bombs with BLU-109B/I-2000 warheads, both of which exploded several hundred feet away from their intended target. Lead pilot for this attack was Major Greg Feest, who later dropped the first bomb on Baghdad. Four of the six F-117s returned to Tonopah with their bombs on board.

Specification

F-117A Nighthawk:

Dimensions

Length overall:	65 ft 11 in (20.08 m)
Wing Span:	43 ft 4 in (13.20 m)
Wing aspect ratio:	1.65
Wing area (estimated):	1,140 sq ft^{-1} (105.9 m^2)
Wing sweepback angle:	67°30′
Ruddervator sweep angle:	about 65°
Overall height:	12 ft 5 in (3.78 m)
Wheel track (estimated):	18 ft 7 in (5.66 m)
Wheel base (estimated):	18 ft 7 in (5.66 m)
Maximum wing loading:	46.0 lb sq ft^{-1} (225 kg m^{-2})
Frontal radar cross-section (estimated):	0.1 sq ft (0.009 m^2)

Power-Plant
Two General Electric F404-GE-F1D2 non-afterburning turbofans each rated
at 10,800 lb (48.04 kN) maximum thrust.

Weights

Empty operating:	29,000 lb (13,154 kg)
Normal maximum take-off:	52,000 lb (23,814 kg)
Maximum overload take-off:	64,400 lb (24,494 kg)

Fuel and Load

Total fuel load:	18,000 lb (8,165 kg) of P-4 fuel
Total fuel capacity:	2.769 US gal

Performance
Applies to ISA conditions unless
(otherwise stated)

Maximum level speed:	561 kt, 1,040 km h^{-1}
Normal maximum operating speed:	Mach 0.9 at optimum altitude
Normal cruising speed:	Mach 0.81, 562 mph, 904 km h^{-1} at 60,000 ft (9,144 m)
Undercarriage limiting speed:	800 kts (345 mph, 556 km h^{-1})
Service ceiling:	38, 600 ft (11,765 m)
Rotation speed:	152–195 kts (175–225 mph; 282–361 km h^{-1}) at 38,000–54,000 lb (17,237–24,494 kg) all-up weight (AUW)
Lit-off speed:	173–208 kts (199–240 mph; 321–385 km h^{-1}) at 38,000–54,000 lb (17,237–24,494 kg) AUW
Minimum take off distance:	2,500–2,800 ft (762–853 m)
Minimum take-off distance at maximum take-off weight:	5,400–6,200 ft (1,654–1,890 m)
Approach speeds:	143–185 kts (165–213 mph; 265–343 km h^{-1}) at 30,000–50,000 lb (13,608–22,680 kg) landing weight
Approach angle of attack:	9.5°
Minimum landing distance (from 50 ft/15 m) with brake parachute:	4,850 ft (1,478 m)
Minimum landing roll with brake parachute:	2,790 ft (850 m)

Range

Unrefuelled combat radius with 4,000 lb (1,814 kg) weapons load, normal diversion fuel and reserves:	465 nm (535 miles; 862 km) at 30,000 ft (9,144 m)

g limit

Maximum:	+7.0

Armament

Maximum weapons load:	5,000 lb (2,268 kg)
Weapon stations:	Internal weapons bay with two stations each stressed for a 2,000 lb (907 kg) weapon.
Internal weapons bay length:	15 ft 5 in (4.70 m)
Internal weapons bay width:	5 ft 9 in (1.75 m)
Operational weapons (primary):	Up to two laser-guided bombs (LGBs) comprising 496 lb (225 kg) GBU-12, 1,984 lb (900 kg) (approximate weight) GBU-10 or 2,169 lb (984 kg) GBU-27A/B: latter two LGBs fitted with either Mk 84 Paveway II or BLU-109B (Lockheed designation I-2000) Paveway III penetration warheads; other stores may include AGM-88 HARM anti-radar missiles.
Probable nuclear strike weapons:	B61 free-fall nuclear bomb weighing 719–765 lb (326–347 kg); F-117A has known nuclear capability and nuclear strike role.
Training/utility stores:	500 lb (227 kg) Mk 82 free-fall general-purpose bombs dropped during early development; SUU-20 practise bomb and rocket dispenser with six BDU-33 bomb training shapes (no rockets carried)

Main features and Cut out diagram

Plate No. 2.17 shows the main feature of the F-117A identifying various zones and parts. Plate No. 2.18 show the cut away, key parts of the plane giving salient features of the inside and outside components integrated to make the plane.

2.6 Lockheed SR-71 Blackbird

2.6.1 Introduction

Missions from Kadena took the 9th SRW all over the Far East. This aircraft, 64-17978, was the first of three to be deployed in the initial phase, leaving Beale for Okinawa on 8 March 1968. After flying some 300 h from the detachment, '978 returned to Beale in September, having acquired the reputation of being a very reliable aircraft'.

F-117 Nighthawk
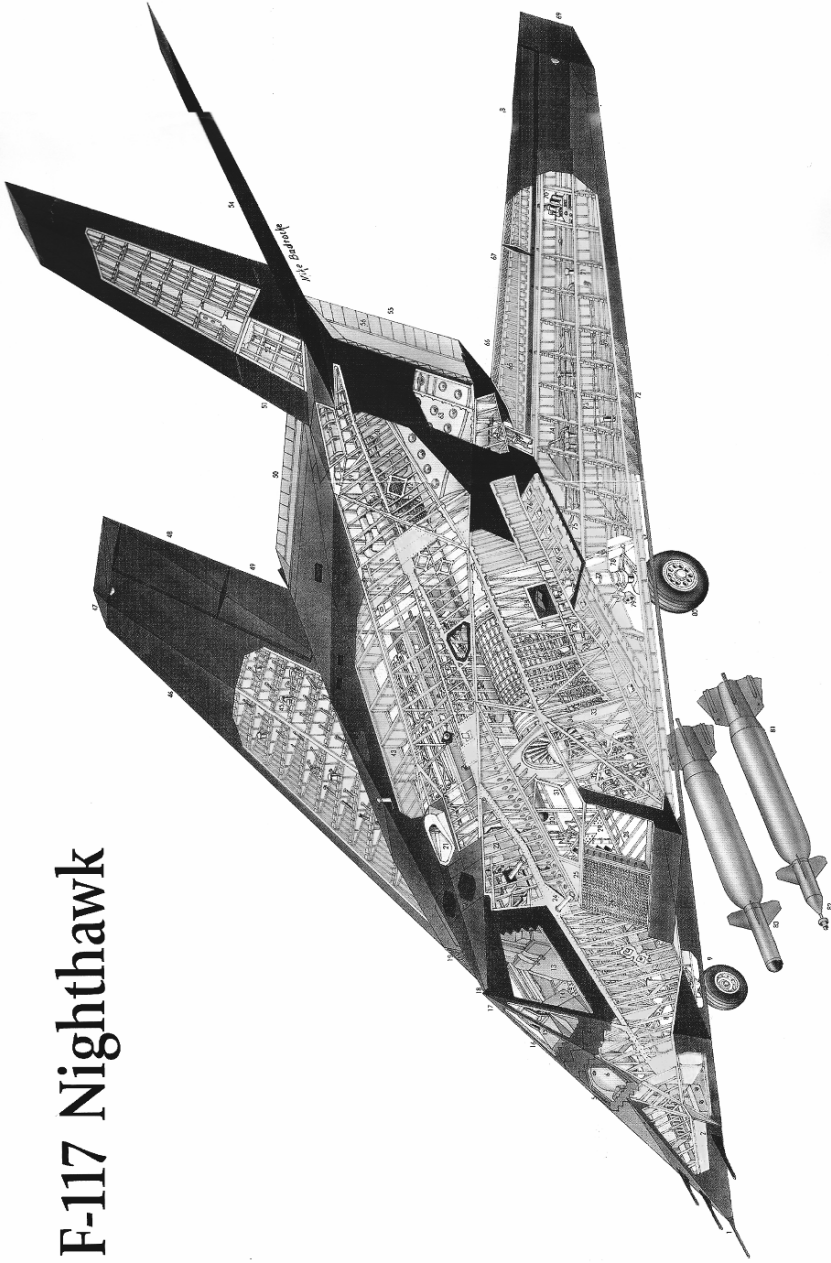
Plate **2.17.** F-117 Nighthawk with compliments from Lockheed Co.
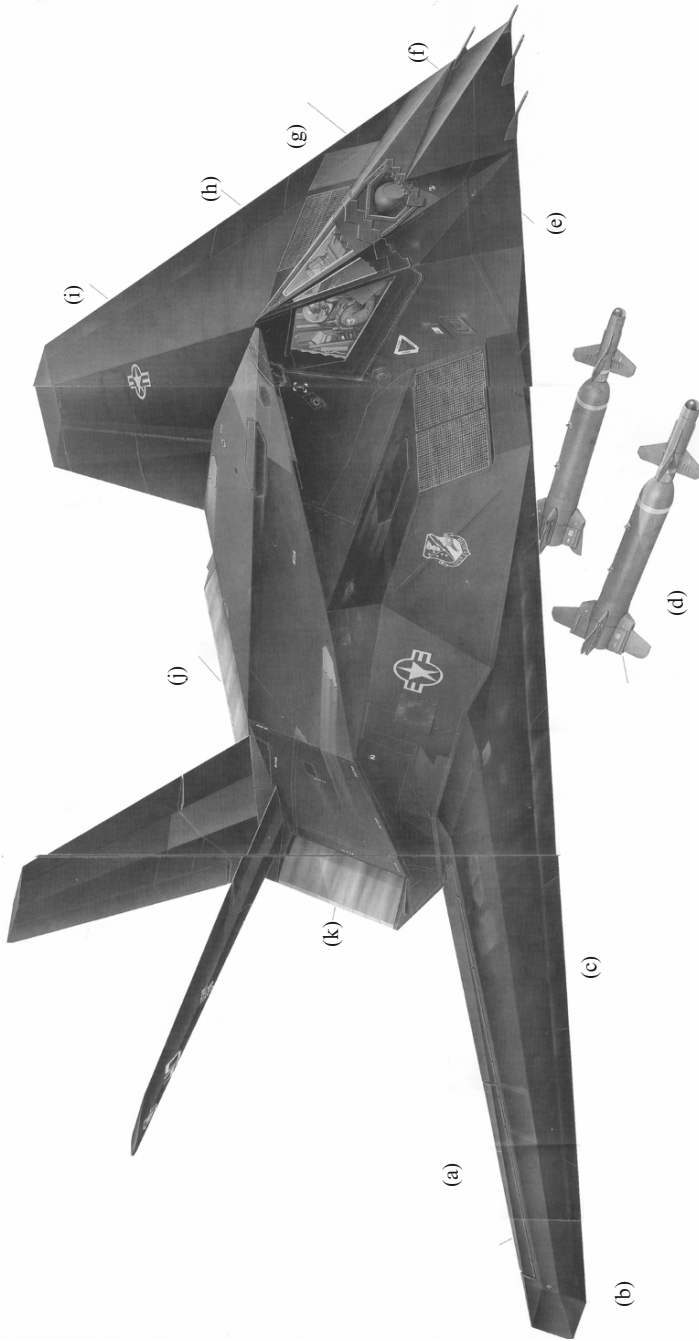
Plate 2.18. Nighthawk with missiles with compliments Lockheed Co, USA

The F-117 was designed and devoloped by the renowned Lockheed"Skunk Works"at Palmdale, California. Adhering to true "Skunk Works"philosophy, the manufacturer delivered a total of 59 production F-117A Nighthawks to the US Air Force, on time and within a surprisingly low budget for such a sophisticated aircraft.

Above: Nighthawk pilots from an elite within an elite. They have come from a variety of backgrounds, mainly from the USAF's fighter and attack fast jet communities, but have also included former SAC bomer pilots. Undergoing a selection procedure which is almost as rigorous as that for SR-71 aircrew, F-117 pilots are chosen as much for their flying skills as for such intangible qualities as stability of temperament. Maintaining the close military links between the US and the UK, Royal Air Force pilots have been the only non-US aircrew permitted to fly the F-117; at least four RAF pilots have so far achieved operational status on the"Black Jet".

An extraordinary shape, revolutionary radar-defeating features and a top secret, yet highly glamorous development have combined with a star-combat appearance in Desert Storm to make the Lockheed F-117 Nighthawk the best-known warplane in the world. Able to penetrate hostile airspace without being seen by radars or infra-red sensors, the F-117 can use its sophisticated target acquisition and designation system to score strikes against vital targets with pinpoint accuracy.

Plate 2.18A. Nighthawk with different phases with compliments from Lockheed U.S.A

F-117 "Stealth Fighter" weapons system
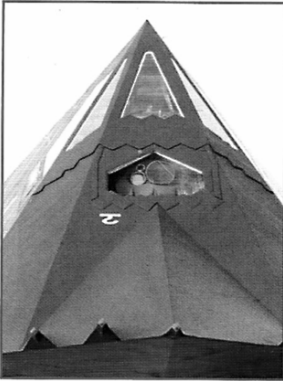
Above: The nose-mounted FLIR sensor is used to search for and acquire the target. The turret cover has serrated edges to reduce radar cross-section and is covered in a fine mesh which acts like a flat surface when illuminated by radar. As a back-up the upper nose turret also has a boresighted laser designator. Both FLIR and DLIR turrets are interchangeable.

F-1174 top view
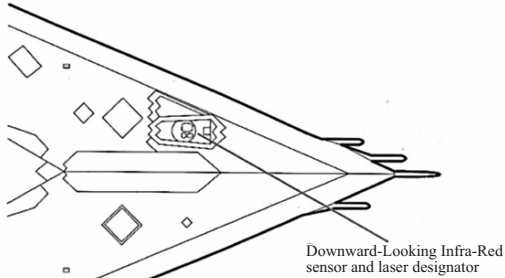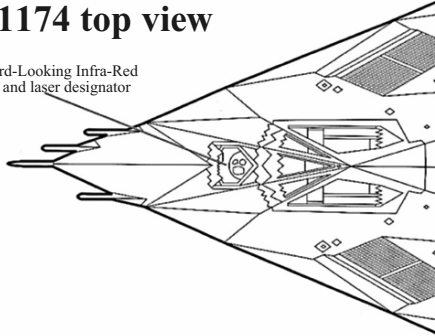
Forward-Looking Infra-Red
sensor and laser designator

F-117A underside view

Downward-Looking Infra-Red
sensor and laser designator

Plate 2.18B. F-117 Weapons system defacts

Kadena, Okinawa was the site for the SR-71's first overseas operational deployment when it took over from the CIA A-12. The 9th SRW began missions in August 1974 and operated as such until the aircraft's retirement in 1990. During the early years of the SR-71 programme, Kadena was the most important operating location for the aircraft due to its proximity to Vietnam, Korea, China and the Soviet Far East. For more than 20 years, the "Habus" of OL-8 kept a watchful eye over manoeuvres in the Sea of Japan.

Most SR-71 missions involved at least one refuelling. The standard procedure was to launch the tanker(s) ahead of the SR-71, which followed the tanker and topped up its tanks after taking-off, having climbed to around 26,000 ft (7,925 m). Aircraft 64-17974, Ichi Ban, wears the "Habu" mission marks given to those aircraft flying from Kadena. This aircraft would eventually carry no fewer than 50 mission markings before such items were banned by the USAF.

2.6.2 Limited Numbers

Although 32 SR-71s were built, only about ten were in use at any one time – two each at the permanent detachments and five or six at Beale, including a pilot-training SR-71B. In addition a single aircraft was based at Palmdale for test and development work. Eleven are known to have been written off in accidents, the others being held in storage. Aircraft were rotated in and out of storage to equalise flying hours in the fleet.

The appropriately-numbered 1st strategic Reconnaissance Squadron (SRS) flew this extraordinary two-seat aircraft. Its potential pilots had to have 1,500 hours of jet time and candidate Reconnaissance Systems Operators (RSOs) were already experienced military navigators. They had to pass rigorous physical examinations, searching interviews and numerous background security checks.

The SR-71A's unique high speed, ceiling and the rapid temperature changes that it encountered during flight made reconnaissance sensors as well as the aircraft's unique astro-inertial navigation system. After about eight flights, the trainee pilot was joined in an SR-71A by the trainee RSO, and they flew together from then on as a permanent team, working up to mission-ready status.

The SR-71's record for achievement is untouchable by any known aircraft on the drawing board today: 53,490 total flight hours; 17,300 missions flown (of which 3,551 were operational reconnaissance missions flown over North Korea, North Vietnam, the Middle East, South Africa, Cuba, Nicaragua and Libya); 11,008 h flown in support of operational missions; 25,862 h spent in flight refuelling, mostly by KC-135Qs; and an unbelievable 11,675 flight hours at or above Mach 3.0.

But despite these outstanding achievements, the spiralling costs of supporting the Blackbird missions was deemed too expensive by the Air Force Chief of Staff, General Larry Welch. In 1989 he ordered the retirement.

Drone operations. Denied the use of manned over-flights of the Communist bloc, Lockheed engineers developed a tri-sonic reconnaissance drone. Being highly complex, operation of the drone was fraught with danger and would ultimately cost the life of one of the test pilots. Without the D-21 drone,

the M-21 had the same phenomenal performance as the standard A-12 but with the extra payload, it became very sluggish. Eventually when the drone's intake and exhaust covers were discarded, the Marquardt ramjet was used to augment the thrust from the M-21's J58 engines.

Construction began in building 199 at Burbank and by June 1963, a D-21 had been mated to it mother ship. The launch platform was to be a modified A-12, designated as the M-21, two of which, bearing serial numbers 60-6940 and 60-6941, were retrofitted to perform the task. Built primary from titanium, the D-21 had a range of 1,250 nm (1,438 miles; 2,315 km), cruised at Mach 3.3 and possessed an altitude capacity of 90,000 ft (27,432 m). it was powered by a Marquardt RJ-43-MA-11 ramjet and once released from the M-21 by a Launch Control Officer (LCO) sitting in what had been the aircraft's Q-bay, the drone flew its sortie independently. Programmed into the D-21 internal navigation system (INS) were the desired track, flight profile, camera "on" and "off" points and bank angles, allowing it to satisfactorily execute the perfect photo-recce sortie. Having completed its camera run, the drone's INS would send signals to the auto-pilot system to bring the vehicle down to its ocean collection point. The entire palletised camera unit would then be ejected and allowed to parachute to the ground. As the drone continued its descent, it would be blown apart by a barometrically activated explosive charge. The camera unit, containing its valuable film, would be retrieved by an HC-130 Hercules equipped with a Mid-air recovery System (MARS), and flown to a base for processing and analysis.

First flight. The first flight of this so-called "Mother-Daughter" combination took place at Groom Dry Lake on 22 December 1964. Take-off time was delayed due to the late arrival of senior Lockheed executives, who had already attended the maiden flight of the SR-71 at Palmdale earlier that day.

Monumental problems were encountered concerning platform and systems integration. By 1966, the programme had progressed to the point where vehicle separation was to be performed. The mission profile for this crucial stage called for Lockheed test pilot Bill Park (who piloted all the M-21 at Mach 3.2 and commence a slight pull up at 72,000 ft (21,945 m) to maintain a steady 0.9 g on the highly sensitive g meter fitted to the M-21, then push over. With controllability checks on the D-21 completed and its ramjet burning, (in the LCO position) initiated vehicle separation.

Plate No. 2.20 and 2.21 show SR-71A Blackbird photo with instrument indictors and a cut-away with specifications, respectively. NASA still has a few kept owing North Korea and Iran nuclear plans.

2.7 Northrop Grumman B-2 Spirit

2.7.1 Introduction

An aircraft like no other, the B-2 was designed to penetrate Soviet airspace and destroy the ballistic forces of the Soviet Strategic Rocket Forces.
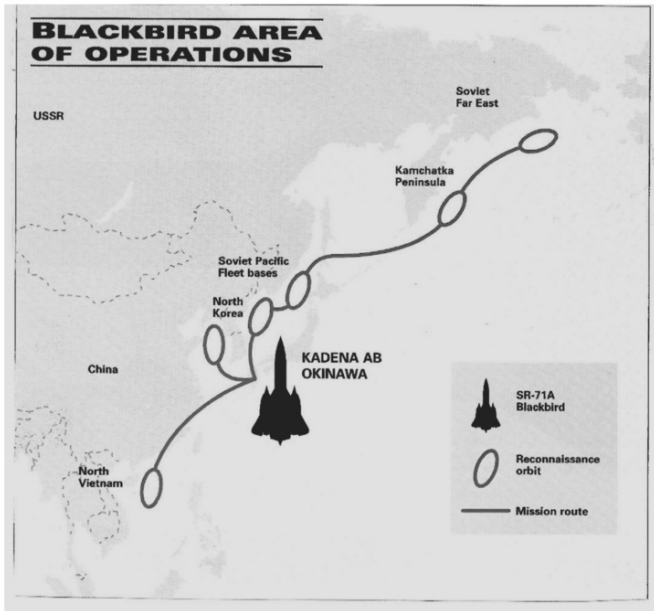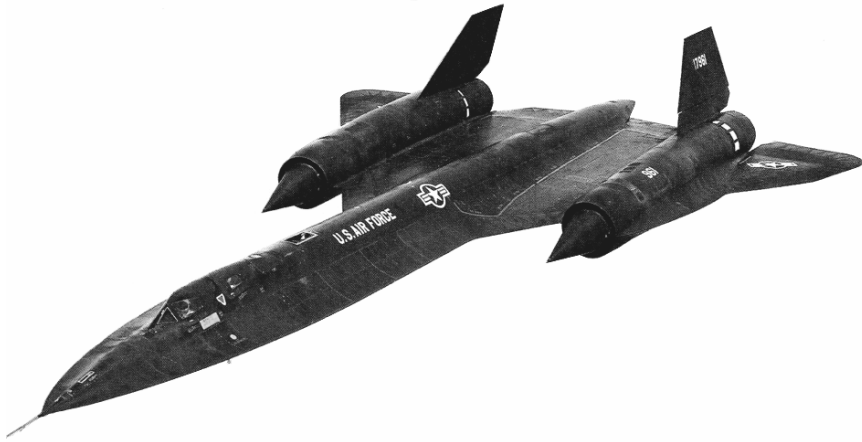
Plate 2.19. Lockheed SR-71 Blackbird

Developed in great secrecy, the Northrop Grumman B-2 flying wing was designed as a "stealthy" or radar-evading bomber for the Cold War mission of attacking Soviet strategic targets with nuclear bombs and stand-off weapons. The B-2 began as "black" programme, known in its infancy as Project Senior C.J and later as the ATB (Advanced Technology bomber). In its early days, USAF leaders believed that the service's top priority was the B-1B bomber and only a handful even knew of the B-2 project. To the latter group, the

SPECIFICATION

SR-71A Blackbird

Dimensions

Length overall:
103 ft 10 in (31.65 m)
Length overall (including probe):
107 ft 5 in (32.74 m)
Wing span: 55 ft 7 in (16.94 m)
Wing area: 1,605 sq ft (149.10 m²)
Moving vertical tail area: 70.2 sq ft (6.52 m²)
Height: 18 ft 6 in (5.64 m)
Wheel track: 16 ft 8 in (5.08 m)
Wheel base: 37 ft 10 in (11.53 m)

Powerplant

Two Pratt & Whitney J58 afterburning bleed turbojets, each rated at 32,500 lb (144.57 kN) of thrust with afterburning

Weights

Empty: 67,500 lb (30617 kg)
Maximum take-off: 172,000 lb (78017 kg)

Fuel and load

Total fuel capacity: 12,219 US gal (46254 litres)
Internal sensor payload (approximate): 2,770 lb (1256 kg)

Performance

Design maximum speed: Mach 3.2-3.5 at 80,000 ft (24385 m) (limited by structural integrity of windscreen)
Maximum speed: Mach 3.35 at 80,000 ft (24385 m)
Maximum cruising speed: Mach 3.35 at 80,000 ft (24385 m)
Maximum sustained cruising speed: Mach 3.2 or approximately 2,100 mph (3380 km/h) at 80,000 ft (24385 m)
Maximum altitude (approximate): 100,000 ft (30480 m)
Operational ceiling: 85,000 ft (25908 m)
Take-off run at 140,000-lb (63503-kg) gross weight: 5.400 ft (1646 m)
Landing run at maximum landing weight: 3,600 ft (1097 m)

Range

Maximum unrefuelled range at Mach 3.0: 3,250 miles (5230 km)
Operational radius (typical): 1,200 miles (1931 km)
Maximum unrefuelled endurance at Mach 3.0: 1 hour 30 minutes

Blackbird

Briefing

The inability of surveillance satellites to provide the specific, targetted reconnaissance required by US military commanders saw the brief resurrection of the SR-71, although the type has now once more been retired by the USAF.

Plate 2.20. Parts Details and Specification
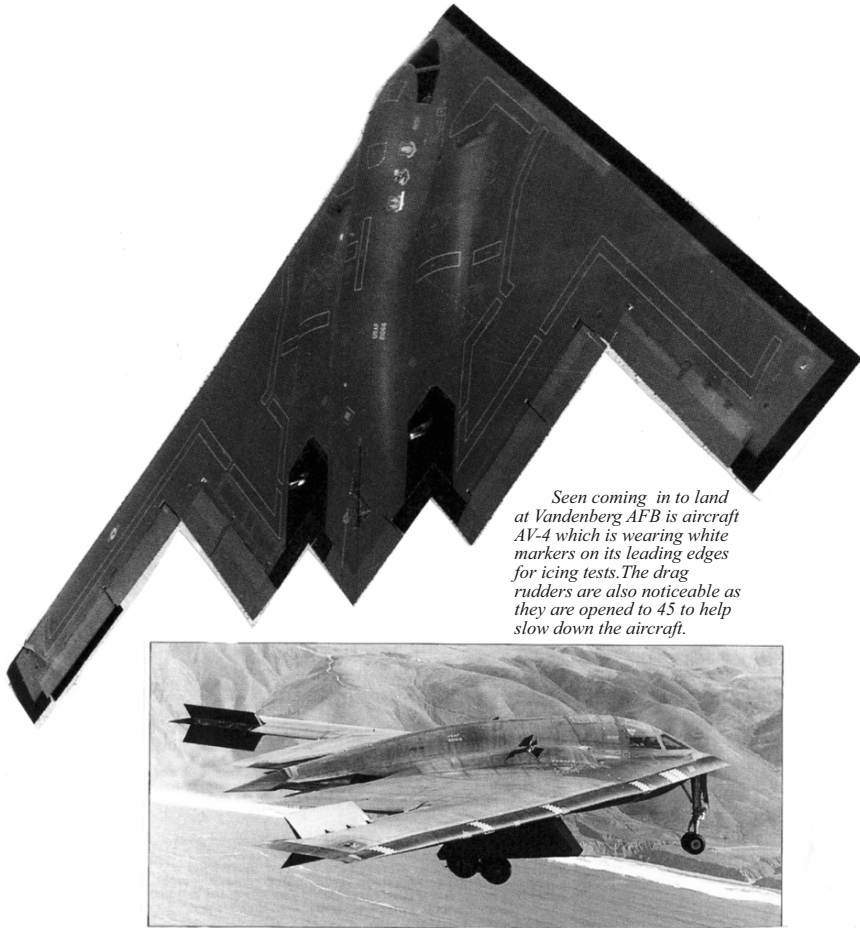
Seen coming in to land at Vandenberg AFB is aircraft AV-4 which is wearing white markers on its leading edges for icing tests.The drag rudders are also noticeable as they are opened to 45 to help slow down the aircraft.

Plate 2.21. Northrop Grumman B-2 Spirit "Stealth Bomber"

B-1B was an "interim" weapon awaiting the B-2; at the height of the Cold War, the USAF expected to procure no fewer than 132 examples of the B-2.

Drawing heavily on it previous flying wing designs, Northrop was aided extensively by Boeing, Vought and General Electric using a three-dimensional computer aided design and manufacturing system to create the B-2's unique "blended wing/double – W" shape. Nine hundred new manufacturing processes had to be developed for the programme as well as the use of rugged, high temperature composite materials, ultrasonic cutting machinery, automated tooling via the 3D database and laser sheraography inspection. Northrop is responsible for building the forward and mid-fuselage sections, aluminium,

titanium and composite parts and the cockpit, while Boeing builds the aft centre and outboard sections.

Graphite/epoxy composites are extensively used on the B-2 to provide a radar-absorbent honey-comb structure. To reduce infra-red signature, the four prototypes but by 1991, this had been cut back to 76 aircrafts. After the original six aircraft were ordered in 1982, three more were funded while the B-2 was still a "black" project. In 1989, money was allocated for a further three, followed by two in 1990 and two in 1991. Congress then froze acquisition at 16 (15 for the USAF). The USAF claimed that it could not provide effective operational capability with fewer than 20 aircraft and five more were subsequently approved by 1993. This approval came with the caveat that the type's LO problems should be rectified before any production occurred.

The first aircraft for the USAF (88-0329/'WM', *Spirit of Missouri*) was delivered to the 509th BW at Whiteman AFB, MO, on 17 December 1993, exactly 90 years to the day after the Wright brothers' first flight. This was the eighth B-2 (AV-8) the first aircraft to production standard. It proceeded into the air AV-7, which was still undergoing extensive electromagnetic and emission-control tests.

Currently, work is being done to ensure that the 394th will join the already operational 393rd Bomb Squadron. At present, the USAF operates 19 B-2As, which include aircraft assigned to training, operations, testing and maintenance, as well as those in reserve or under modification.

2.7.1.1 Unstealthy B-2

In August 1997, a highly publicised report by the general accounting office (GAO) highlighted a number of shortcomings in the B-2. Most notable of these was the fact that the B-2's "stealthy" qualities were degraded by excessive moisture, and thus the aircraft required extensive field maintenance. In short, the B-2 could not operate in the rain as it should do. The maintenance time for each flight hour has also risen from the projected 50 hours to 124 h. All B-2s will now have to fly operational missions from Whiteman AFB, generally on a non-stop basis and supported by tankers.

Another, less critical, problem encountered with the B-2 was its lack of a name in accordance with USAF tradition, the official name of Spirit is never heard around the aircraft. The name "Beak" (in similar vein to the one-syllable "Buff" for the B-52, and "Bone" for the B-1) is used by some as a nickname due to the B-2's beak-like nose, but this has not achieved universal status. Neither has *"Voron"* (Russian for raven), the callsign for B-2 test flights. Many crews simply refer to it as "the jet" and there is no doubt to those at Whiteman as to what that means.

B-2A Spirit Briefing and Design. Plate No. 2.22 gives a technical summary of identifying several parts of the aircraft. Plate No. 2.23 indicates the "cutaway" diagram of Northrop Grumman B-2A stealth aircraft.

SPECIFICATION

B-2A Spirit

Dimensions

Length: 69 ft (21.03 m)
Height: 17 ft (5.18 m)
Wingspan: 172 ft (52.43 m)
Wing aspect ratio: 5.92
Wing area: 5000 sq ft (464.5 m²) plus
Wheel track: 40 ft (12.2 m)

Powerplant

Four General Electric F118-GE-100
non-afterburning turbofans each
rated at 19,000 lb (84.5 kN)

Weights

Empty: 153,700 lb (69717 kg)
Normal take-off: 336,500 lb
(152635 kg)
Maximum take-off: 376,000 lb
(170550 kg)
Maximum wing loading:
75.20 lb/sq ft (367.2 kg/m²)
Maximum power loading:
5.43 lb/lb st (554 kg/kN)

Fuel and load

Internal fuel capacity: 180,000 lb
(81635 kg)
Maximum weapon load: 40,000 lb
(22700 kg)

Performance

Cruising speed at high altitude:
Mach 0.85 or 416 kt (475 mph; 900 km/h)
Cruising speed at low altitude:
Mach 0.8 or 530 kt (610 mph; 980 km/h)
Approach speed: 140 kt (161 mph,
259 km/h)
Service ceiling: 50,000 ft plus (15240 m)
Range with one flight refuelling:
10,000 nm (11,515 miles ; 18532 km)
**Range unrefuelled with 8 SRAM
and 8 B83:** 4,410 nm (5075 miles;
8167 km)

Armament

Two side-by-side weapons bays in the
lower centrebody house Boeing rotary
launcher assemblies (RLA) which are
detachable and each house eight large
stores. Total capacity is 16 AGM-129
ACMs or 16 AGM-69 SRM IIs.
Designed with a nuclear mission in
mind, the B-2 can carry 16 B83 or
16 B61 freefall nuclear bombs. For
conventional missions, 80 Mk 82 500-lb
(227-kg), 16 Mk 84 2,000-lb (908-kg)
bombs, 36 CBU-87, -89, -97 and -98
cluster bombs, 80 Mk 36 560-lb
(254-kg) or Mk 62 sea mines, 36 M117
750-lb (340-kg) fire bombs, 8 GAM-11
deep penetration bombs, 16 GAM-84s,
or 16 JDAMs, can be carried.

SHEET 03

NORTHROP GRUMMAN B-2 SPIRIT

B-2A Spirit Briefing

AV-1 and AV-2 prepare for an early morning launch at
Edwards South Base. Testing for the B-2 was centred at South
Base where a secure and purpose-built home for the aircraft
was set up. It is now named the Birk Flight Test facility in
honour of Colonel Frank Birk, the former B-2 director who was
killed in air crash.
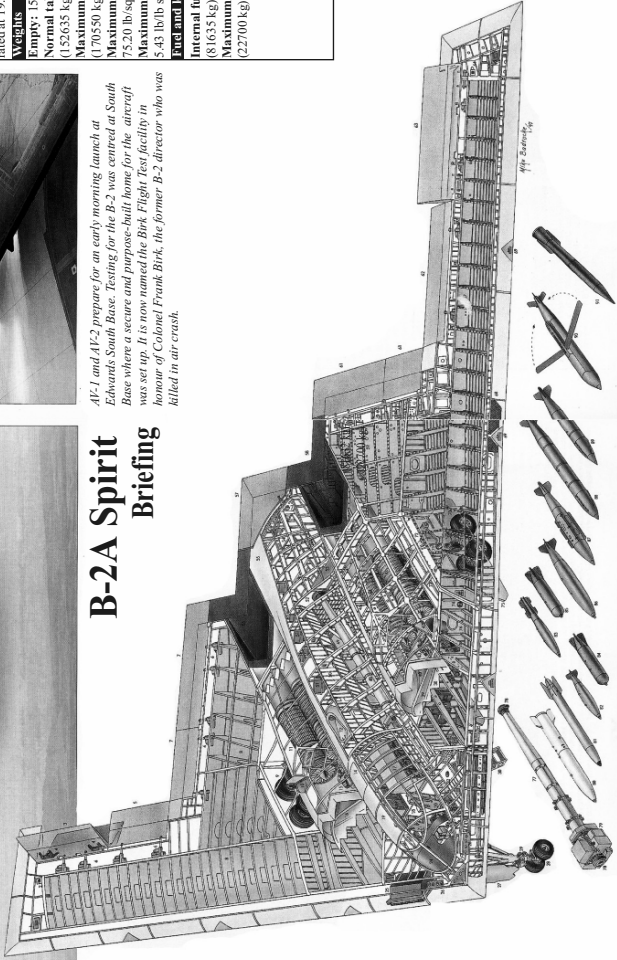
Plate **2.22**. B-2A Spirit

B-2A Spirit

This Northrop Grumman B-2A Spirit is one of those which presently operate with the 393rd Bomb Squadron as part of the 509th Bombardment Wing at Whiteman AFB. The 393rd will be followed by a further squadron; the 394th which is currently a conversion training unit and uses borrowed T-38As and B-2s or training purposes. When the 509th Wing is fully formed, it will be potentially the most powerful air force wing in existence, theoretically able to strike with impunity at targets anywhere in the world.
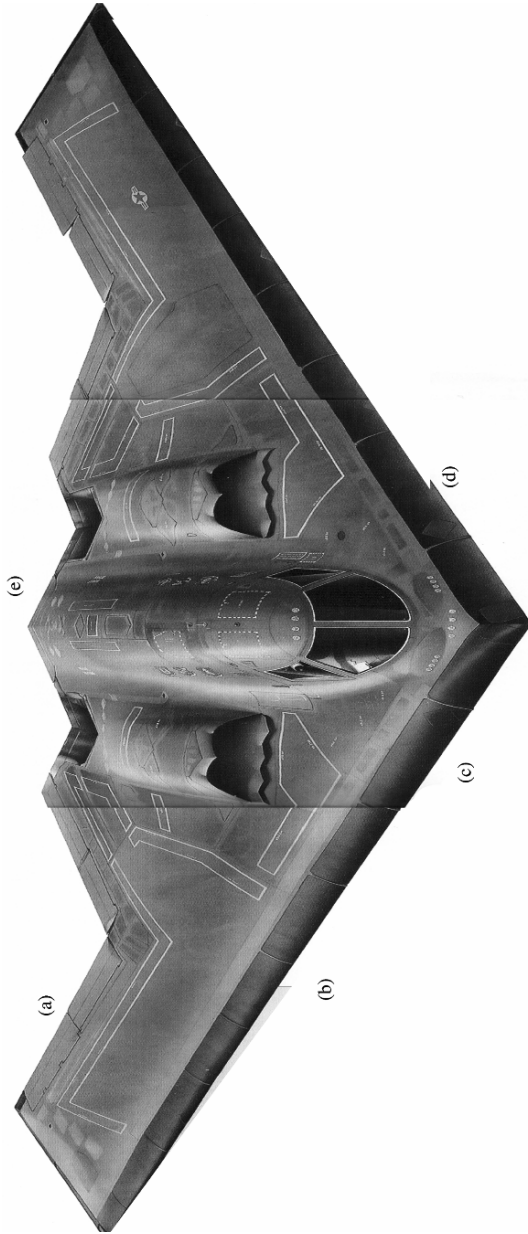
Plate 2.23. B-2A Spirit

2.8 Grumman F-14 Tomcat

2.8.1 Introduction

While the US Navy has always regarded the Tomcat primarily as an interceptor, the aircraft's potential as a bombing and tactical reconnaissance platform was clear from the very beginning of its career.

Grumman's F-14 Tomcat has long been regarded as one of the most capable fighters produced over the last 25 years. Entering US Navy service in September 1974, the F-14 was intended to fulfil the air-to-air role by providing offensive and defensive intercept missions, day or night, over the carrier battle group – a role that it continues to fulfil to this day.

Tightening purse strings from the White House during the 1990s following the collapse of the Soviet Union resulted in the US Navy losing a number of dedicated carrier-based reconnaissance and strike aircraft. As the F-14 had already built itself an enviable reputation in fleet service as an interceptor, US Navy chiefs had already begun a programme early in the 1980s to expand the capabilities of the aircraft.

Tarps. The F-14 has proved highly capable of performing reconnaissance missions. Normally this duty is assigned to one or two squadrons within a carrier air wing, which each have three F-14s tasked with recce duties. Specially modified for the role, the Tomcats are equipped with a TARPS (Tactical Air Reconnaissance Pod System) which attaches to the rear left AIM-54 fuselage station.

Within the 17.3 ft (5.27 m) TARPS pod are two cameras and an infrared line scanner. The first of these is a KS-87B conventional frame camera, while mounted mid-way along the pod is a KA-99 low altitude panoramic camera. Also located here is an AN/AAD-5A infra-red line scanner, which allows reconnaissance missions to be performed under all weather conditions, day or night.

"*Bombcat*". The Tomcat plates 2.24 and 2.25 was initially specified to have a limited ground-attack capability, although the ground-attack role was abandoned early in the F-14's career. However, the 1990s found the US Navy again needing more strike aircraft and the "Bombcat" was revived. The selection of air-to-ground weapons, delivery mode and desired impact performance is accomplished by the RIO (Radar Intercept Officer), but the release of air-to-ground weapons is exclusively pilot initiated. Various combinations of missiles or bombs can be carried, up to a maximum external weapons load of 14,500 lb (6,577 kg).

To accommodate the variety of weapons, a system of pre-loaded weapons rails was devised; this method greatly reduces weapons loading time. Individual rails can carry either an AIM-54 or a 30 inch (76.2 cm) bomb rack. A built-in hoist mechanism within the hardpoint lifts the rail into place.

Air-to-ground armament can include 10 Mk 82,500 lb (226 kg) bombs, plus two AIM-9 AAMs for self defence. Other combinations can include Mk 84 bombs and two AIM-54 AAMs.

F-14A Tomcat 160660/NL-200 of VF-111(USN)
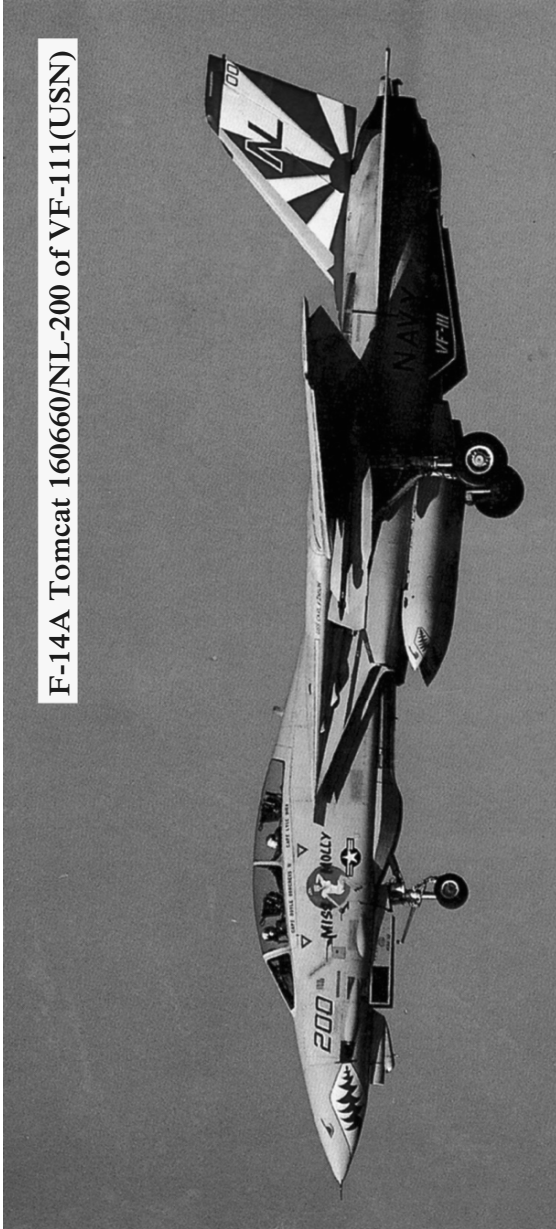
Plate 2.24. F-14 Tomcat multiple Aircraft

Once equipped solely with air-to-air missiles, the F-14 Tomcat has seen its combat role alter dramatically in recent years. As the US Navy cut back its carrier force in the late 1980s and early 1990s, so began the drive to make its available aircraft more 'multirole'. The 'Bombcat' programme initially gave the Tomcat the capability to drop 'dump' bombs - such as the Mk 80 series bombs and Mk 20 cluster bombs. By 1990, attack-capable Tomcat squadrons were being fielded, but the aircraft were not yet integrated into regular Navy operations. By 1994, the 'Bombcats' had finally gained laser-guided bomb (LGB) capability and, in 1995, Tomcats from VF-41 made the first combat bomb drops by an F-14, using LGBs over Bosnia. Now the F-14 is being integrated with the LANTIRN system, giving it true all-weather, day/night precision attack capability.

TARPS (Desert Storm)
1 × AN/ALQ-167 ECM pod
1 × Expanded Chaff Adaptor
1 × TARPS pod
2 × AIM-7M Sparrows
2 × AIM-9M Sidewinders
2 × Fuel tanks

'Bombcat' multi-role (F-14D)
4 × Mk 84AIR
1 × AIM-54C Phoenix
1 × AIM-7M Sparrow
2 × AIM-9M Sidewinders
2 × Fuel tanks

LANTIRN 'Bombcat'
2 × GBU-16 Paveway II
2 × AIM-7M Sparrows
2 × AIM-9M Sidewinder
1 × LANTIRN pod
2 × Fuel tanks
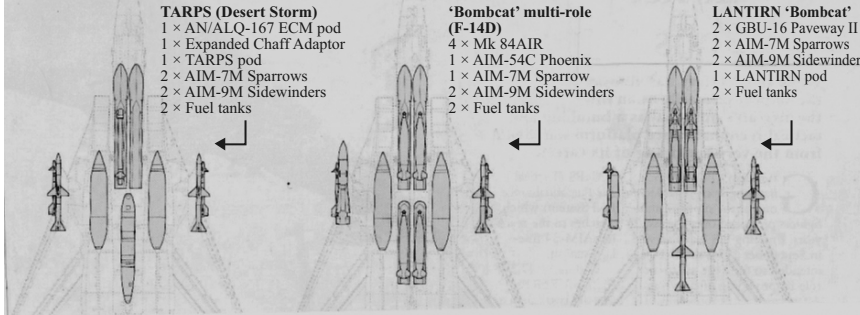
Plate 2.25. Tomcat Weapon Loads

Introduced in mid-1996, the LANTIRN targeting pod allows the F-14 (Plate 2.25) to use precision-guided munitions such as GBU-12s and GBU-16s, a typical precision strike mission would use two of these laser-guided bombs.

2.9 McDonnell Douglas F-15 Eagle

2.9.1 Introduction

Developed as fighter with a wide margin of performance and technological superiority over its rivals, the F-15 has held the position of being the world's

premier fighter for more than 20 years. It has also been developed into a highly successful strike platform.

The history of the F-15 dates back to the late 1960s, when a far-reaching specification known as F-X was laid down by the US Air Force. This, in essence, required the basic F-4 weapons load (four Sparrows, four Sidewinders plus a 20 mm Vulcan cannon) to be repackaged into an aircraft optimised for air combat. The eventual result was the F-15 Eagle, which marked a major advance in virtually all areas.

Range and manoeuvrability were markedly improved; while the aircraft's APG-63 radar ushered in a new era of looking down/shoot-down capability. The cockpit was designed to enable the single pilot to extract the maximum fighting capability fro the impressive systems, utilising then-novel concepts such as head-up display and HOTAS 9 hands on throttle and stick controls. The airframe was stressed for sustained high-g turning, while the F100 turbofans were fuel-efficient yet awesomely powerful. From the F-15C/D model onwards, the pilot could in theory also slam the throttles from idle to full without fear of compressor stall (although, in reality, the F100 proved very troublesome in the early days of the F-15). Similarly, the F-15 had a "carefree" handling system which automatically limited control inputs from the pilot at the outer edges of the flight envelope to prevent departures.

Reaching service status in November 1974, the F-15A (and the equivalent F-15B two-seater) immediately demonstrated a dramatic improvement in combat power over the F-4E Phantom which was at the time, the USAF's mainstream fighter.

2.9.2 Multi-Role Fighter

In USAF service the F-15's repertoire was rapidly expanded to embrace all areas of the fighter role. Its rapid-reaction time, excellent radar and high speed/climb performance allowed it to perform the dedicated interceptor role with ease, and F-15s stood "Zulu" ground alert in Korea and Germany, as well as back home. Occupying most F-15s was and is the air superiority role, Eagles flying sweep, CAP and escort roles.

Continuing development of the Eagle saw the introduction of the F-15C/D in 1980, initial deliveries of which went to units in West Germany and Okinawa.

The C/D introduced several new features, notably increased g capability, additional internal fuel and the ability to carry conformal fuel tanks along the fuselage sides. In addition to the re-equipment of some UASF units, F-15C/Ds also went to Israel.

Bird of Prey. Problems were initially encountered with the Eagle's Pratt 7 Whitney F100-PW-100 engine, and the X-band Hughes APG-63 coherent pulse-Doppler radar, both of which had been designed specifically for the F-15. These have been overcome during the Eagle's service career.

The F-15A has a sophisticated avionics system, with the main radar being supplemented by an AN/ALR-56 RWR, and an AN/ALQ-128 EW warning system. These are backed up by a Northrop AN/ALQ-135 countermeasures set. Lessons learned in Vietnam proved that good pilot visibility was essential and to this end the F-15 pilot sits high up and well forward on a McDonnell Douglas Escapac IC-7 ejection seat.

Data on F-15 Eagle. Plate No. 2.26–2.27 give briefings about F-15E Eagle profile with armour such as laser guided bombs, Amraam missiles, wings, power-plant, radar, Air-to-ground weapons and cut away identifying various parts together with complete specifications.

2.10 McDonnell Douglas F/-18 Hornet

2.10.1 Introduction

Today's F/A-18 Hornet owes its origin to Northrop, which in the 1950s and 1960s excelled in the lightweight fighter (LWF) business. The P-530 Cobra of 1966 was the best-known of these LWFs. A few USAF veterans of combat against the light and simple MiG-17 believed in a Cobra-like machine, but the USAF had no requirement for it and decided in 1969 to buy the costly F-15 Eagle.

In the late 1960s Northrop designers revised and redesigned the Cobra. They kept it simple but introduced new features such as a HOTAS (hands on throttle and stick) cockpit, which enabled the fighter pilot to keep his eyes up, out of the cockpit. By 1971, the future of the F-15 was secure and supporters of the LWF finally managed to persuade Congress to fund an LWF technology demonstration programme with flying prototypes from two manufacturers. On 13 April 1972 Northrop and General Dynamics were awarded contracts to build two prototypes. Fourteen days later, the US Secretary of Defence dropped a bombshell, announcing that he felt it "appropriate to consider full-scale development and eventual production of an Air Combat Fighter", which would provide an alternative to "high-cost tactical aircraft while maintaining a credible tactical air force". This effectively turned the Northrop and General Dynamics aircraft into competing prototypes of a new USAF Air Combat Fighter (ACF) and caused a storm of controversy. While the LWF was an experimental machine it was welcomed by the USAF, but as a production aircraft it could only threaten the future production of the all-important F-15 Eagle. Objections were overruled and the LWF evaluation became the ACF competition.

Plate 2.26. McDonnell Douglas F-15 Eagle

2.10.2 Fighter Prototypes

Plate No. 2.29 shows, F/A-18A Hornet with AGM-88A HARM radar and cannon, cockpit equipment, Mk 20 Rockeye II, Flir pods, fly-by-wire controls, AIM-7M Sparrow, complete briefing on its "cut-away" together with detailed specifications.

F-15 Eagle

SPECIFICATION

F-15E

Dimensions

Length: 63 ft 9 in (19.43 m)
Height: 18 ft 5½ in (5.63 m)
Wingspan: 42 ft 9 ¾ in (13.05 m)
Wing aspect ratio: 3.01
Tailplane span: 28 ft 3 in (8.61 m)
Wheel track: 9 ft ¼ in (2.75 m)
Wheelbase: 17 ft 9½ in (5.42 m)

Powerplant

Original F-15E had powerplant of F-15C/D, but with option of General Electric F110-GE-129. Aircraft from 135 onwards (90-0233), built from August 1991, have two Pratt and Whitney F100-PW-229s rated at 29,000 lb st (129 kN)

Weights

Empty operating: 31,700 lb (14379 kg)
Normal take off: 44,823 lb (20331 kg)
Maximum take-off: 36,741 lb (81000 kg)

Fuel and load

Internal fuel: 13,123 lb (5952 kg)
External fuel: 21,645 lb (9818 kg)
Maximum weaponload: 24,500 lb (11113 kg)

Performance

Maximum level speed: Mach 2.5
Maximum combat radius: 685 nm (790 miles; 1270 km)
Maximum combat range: 2,400 nm (2,765 miles; 4445 km)

Armament

One 20-mm M61A-1 six-barrel gun, with 512 rounds, in starboard wingroot. Wing pylons for AIM-9 Sidewinder, AIM-120 AMRAAM, and AIM-7 Sparrow. Single or triple rail launchers for AGM-65 Maverick on wing pylons. A wide range of guided and unguided weapons including Mk 20 Rockeye, Mk 82, MK 84, BSU-49 and -50 GBU-10, -12, -15, and -24; CBU-52, -58, -71, -87, -89, -90, and -93; LAU-3A rockets; B57 and B61 nuclear weapons

F-15Es Serve with two overseas commands USAFE and PACAF. Like the 21st Composite Wing (previously US AFB 43th TW, PACAF) of Wing operates a mix of F-15Cs and E-15Es, the latter flying with the 90th FS 'Pair o' Dice.' Here the wing commander leads aircraft from the three Eagle squadrons through the Alaskan mountain from the unit's base at Elmendorf AFB

Plate 2.27. F-15 Eagle and major specifications

F-15E Eagle

Able to carry virtually any payload in any weather the F-15E, with its LANTRIN and APG-70, is a formidable ground-attack vehicle which can deliver unguided weapons with exceptional accuracy while demonstrating the ability to drop Precision-Guided Munitions (PGMs) in pinpoint attacks. The F-15 can also take care of itself in hostile airspace, having a powerful integral defence system and an air-to-air capability as good as that of most modern fighters. However, a major drawback is that the F-15E comes at a tremendous price, half as much again as the latest F-16C.

This aircraft is from the 48th Fighter Wing, based at Lakenheath, UK, from where the 48th FW has deployed aircraft to both the Middle East and the former Yugoslavia as part of multinational peacekeeping forces. Aircraft operating out of Incirlik in Turkey enforce the Northern Iraqi 'No-Fly Zone' while, over Bosnia, 48th FW aircraft have flown from Aviano, Itlay. F-15Es from the 48th have been used to attack runways, SAM sites and aircraft defences of the Serb military which had constantly defined UN and NATO warnings to cease hostile action.
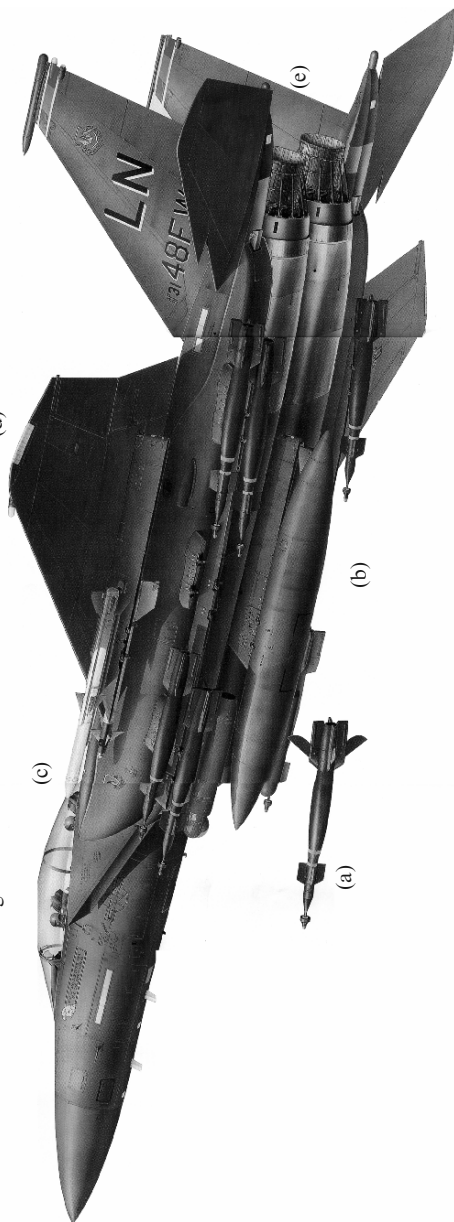
Plate 2.28. F-15E Eagle fully loaded

(a) **Laser-guided bomb**
    The Paveway LGB is the main precision-guided munition of the F-15E. There are four options
    currently available: the 500 lb (227 kg) GBU-12 shown here, of which eight is the normal load, the
    2,000 lb (907 kg) GBU-10 and GBU-24, of which four are carried, and the 4,700 lb (2,132 kg) GBU-
    2B, usually carried singly with a "dumb" Mk 84 to counterbalance it. The LGB consists of three
    sections.

(b) **Radar**
    The remarkable Hughes APG-70 radar of the F-15E is based on the APG-63 which was fitted to
    all pre-MultiStage Improvement Program (MSIP) fighter Eagles. In addition to its SAR mode for
    high-resolution ground-mapping, the APG-70 offers a wide range of general mapping and air-to-air
    modes, operating across a number of frequencies in the l/J-bands.

(c) **AMRAAM missile**
    Developed by Hughes, the AIM-120 is one of three AAMs currently available to the F-15E for air
    combat and, despite having a range against head-on targets of about 30 miles (50 km) more than
    the AIM-7 Sparrow, it can be carried on the shoulder launch rails, leaving the lower Conformal Fuel
    Tank (CFT) positions free for offensive stores carriage.

(d) **Wings**
    The wing is based on an exceptionally strong torque box made of integrally-machined skins and
    ribs in light alloy and titanium, to which are attached wingtip sections, flaps and ailerons made of
    aluminium honeycomb. Set at zero incidence, the wing features $1°$ of anhedral to destabilise it in
    the rolling plane, and has a NACA 64A aerofoil section throughout.

(e) **Powerplant**
    The Pratt & Whitney F100 is a highly reliable turbofan with high thrust-to-weight ratio. It has
    powered all F-15s and all the early F-16s. Only in the later F-16s has it been challenged by the F110.
    The F100 is a two-stage axial turbofan, at the heart of which is a smokeless annular combustor with
    24 airblast nozzles and continuous capacitor discharge ignition.

Plate 2.28A. F-15E Eagle

2.11 Lockheed C-130 Hercules

2.11.1 Introduction

Lockheed first flew its YC-130 in 1954, 3 years after its specification had been
issued by the USAF. Since then, its avionics and systems have been upgraded,
but the basic design has remained faithful to that first prototype.

The C-130 is rare in engineering terms, in that its basic design was right
from the very beginning and in fact remains relatively unchanged in almost
50 years. The C-130 owes its configuration to the humble Laister–Kauffman
CG-10 Trojan Horse assault glider which was able to land on rough tactical
airstrips. This glider was ultimately cancelled for political reasons, however
in favour of the Chase CG-14, which resulted in the C-123 provider.

During World War II, a number of transport types were used, although
most had shortcomings. The C-46 and C-47 did not have a level floor, an
obvious problem when loading cargo, while the floor of the C-54 was level
but was 11 ft (3.40 m) off the ground. In this era, aircraft designers were more
interested in an aircraft's aerodynamic properties than in its ease of cargo
handling.

Specialised cargo-haulers like the Curtiss C-76 Caravan and Budd RB-1
Conestoga were never built in sufficient numbers, while the more success-
ful C-82 did not have sufficient range and was limited by what it could carry.

Air-to-ground weapons of the F-15E

McDonnell Douglas's F-15, in particular the F-15E, can carry a formidable array of weaponry on its many pylons. The use of the LANTIRN system enables the F-15E to hit ground targets by day and night, while precision-guided weapons give the aircraft a fearsome surgical strike capability

AGM-65 MAVERICK
The Maverick missile, in service since the 1960s, gives the F-15E a potentially lethal tank-busting capability.

CBU-87
Cluster bombs allow a larger number of soft targets to be hit simultaneously across a wide area.
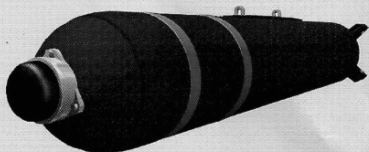
FREE-FALL BOMBS
F-15s can carry a wide range of unguided air-to-ground weapons including nuclear bombs. When combined with the LANTIRN pod on the F-15E, these weapons can be delivered with extreme accuracy.

B61
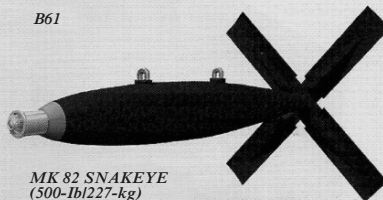
MK 82 SNAKEYE
(500-lb/227-kg)

MK 82 (1,000-lb/454-kg)

PRECISION-GUIDED MUNITIONS
A number of different guided bombs can be carried by the F-15E. These TV-(GBU-15) or laser-guided weapons can be used against hardened targets such as bunkers, and proved devastating during the GulfWar.
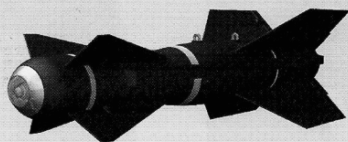
GBU-28

GBU-15
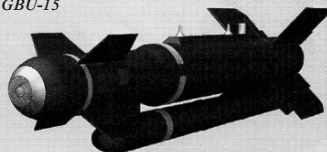
GBU-24

AGM-130
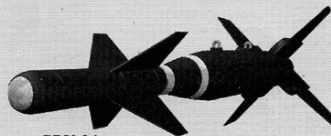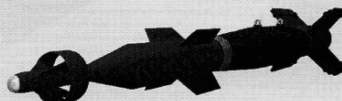
GBU-12

Plate 2.28B. Air to Ground missiles with compliments of McDonnell Douglas U.S.A

F/A-18A Hornet

This F/A-18A belonged to US Marine Corps fighter/attack squadron VMFA-314 "Black Knights", which was deployed aboard USS *Coral Sea* (CV-43) and engaged in attacks on Libyan SAM sites during Operations El Dorado Canyon and Prairie Fire in 1986. The unit's usual "VW" tailcode was replaced by "AK", denoting its inclusion within Carrier Air Wing 13 (CVW-13) aboard the *Coral Sea*. Other types included in CVW-13 were A-6E and KA-6D Intruders, EA-6B Prowlers, E-2C Hawkeyes and SH-3 Sea King helicopters.
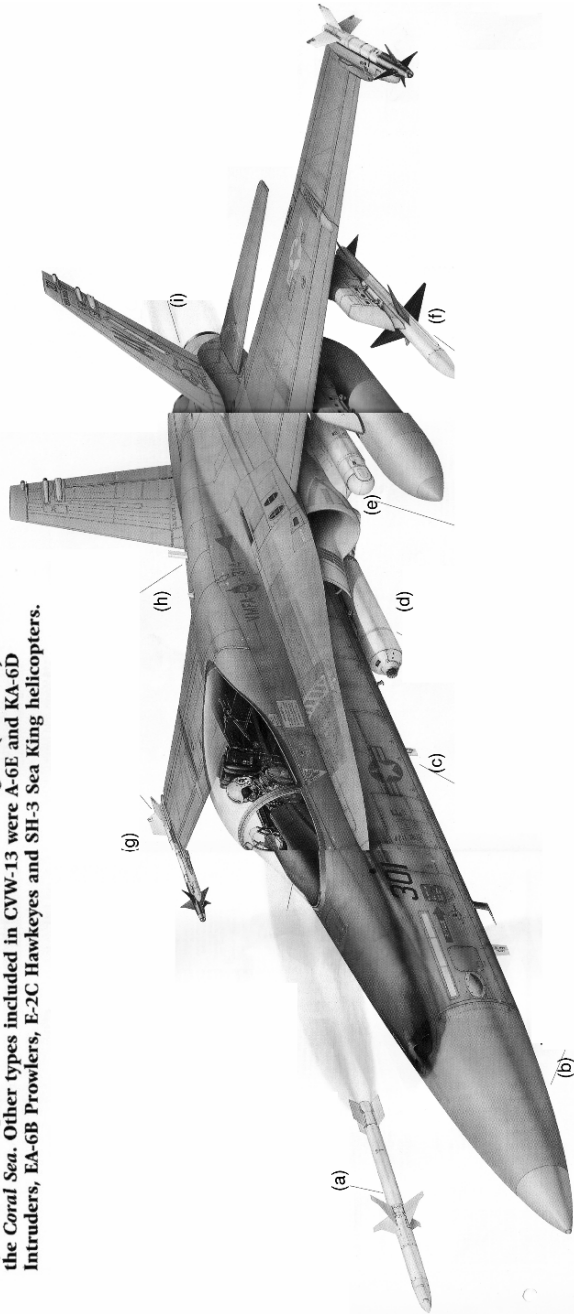
Plate 2.29. F/A-18A Hornet photo provided by McDonnell Douglas U.S.A

(a) **AGM-88A HARM**
Designed to replace the Shrike and Standard ARMs, the HARM (High-speed Anti-Radiation Missile) offered higher speed, faster reaction, longer range and a more destructive warhead.

(b) **Radar and cannon**
The F/A-18A, two-seat B and early-production C-model aircraft were fitted with a Hughes AN/APG-65 multi-mode radar set; later F/A-18C, D, E and F-model machines have the more capable APG-73, which boasts faster processing and a larger memory.

(c) **Cockpit equipment**
With one of the most coveted seats in US naval aviation, the F/A-18 had the most advanced cockpit in service when it appeared. Three monochrome CRTs (cathode ray tubes) and HOTAS (hands on throttle and stick) controls – the latter allowing head-up operation – were among its features.

(d) **Mk 20 Rockeye II**
The most commonly used version of the Mk 7 sub-munitions dispenser, the Rockeye II is an anti-armour weapon containing 247 Mk 118 shaped charge bomblets.

(e) **FLIR pods**
Useful night/all-weather capability is available with the AN/AAS-38 NITE Hawk forward-looking infra-red (FLIR) pod, AAS-38A NITE Hawk FLIR-LTD/R (which adds a laser designating and ranging capability) or AAS-38B (with laser spot tracker). One of these occupies the port shoulder Sparrow/AMRAAM station when carried.

(f) **AIM-7M Sparrow**
An ageing design first introduced by the US Navy in 1951, the AIM-7 AAM has been progressively updated over the intervening 40 years to meet the ever-changing, medium-range beyond-visual-range (BVR) threat.

(g) **Wingtip launch rail**
This is usually used to carry an AIM-9M Sidewinder heating-seeking air-to-air missile (AAM). Like the AIM-7 Sparrow, the AIM-9 was developed, originally for the US Navy, in the early-1950s.

(h) **Powerplant**
For the initial versions of the F/A-18. General Electric developed the F404 afterburning low-bypass turbofan, rated at 16,000 lb or 17,700 lb (71.2 or 78.3 kN) thrust, with afterburning, depending on the variant. Derived from the YJ101 engine in the YF-17, the powerplant has proved reliable and fuel-efficient. Fuel is fed from four main tanks in the aircraft's spine, which hold 1,400 US gal (5,300 l) in total. External fuel may be carried in 330 US gal (1,249-l) drop tanks on wing pylons. For the redesigned F/A-18E/F, a more powerful F404 derivative has been developed. The F414, producing close to 100 kN with a new afterburner, is closely related to the F412 turbofan intended for the ill-fated A-12 Avenger II.

Plate 2.29A. (Continued)

However, these aircraft set a trend for level, low floored, easily accessible and rough field capable aircraft. Despite this the USAF preserved with other designs like the low-wing, front-loading C-124 Globemaster. Eventually the decision was made by both the USAF and commercial operators, to develop a "flying truck" designed as such from the beginning.

SPECIFICATION

F/A-18A Hornet

Dimensions

Length: 56 ft 0 in (17.07 m)
Height: 15 ft 3½ in (4.66 m)
Wing span: 37 ft 6 in (11.43 m); 40 ft 4¾ in (12.31 m) with tip-mounted AAMs; 27 ft 6 in (8.38 m) with wings folded.
Wing chord: 13 ft 3 in (4.04 m) at root; 5 ft 6 in (1.68 m) at tip
Wing aspect ratio: 3.5
Wing area: 400 sq ft (37.16 m²)
Leading-edge flap area: 48.8 sq ft (4.50 m²)
Trailing-edge flap area: 61.9 sq ft (5.75 m²)
Tailplane span: 21 ft 7¼ in (6.58 m)
Tailplane area: 88.1 sq ft (8.18m²)
Fin area: 104.2 sq ft (9.68 m²)
Distance between fin tips: 11 ft 9½ in (3.60 m)
Rudder area (total): 15.6 sq ft (1.45 m²)
Wheel track: 10 ft 2½ in (3.11 m)
Wheelbase: 17 ft 9½ in (5.42 m)

Power plant

Two General Electric F404-GE-400 turbofans each rated at 16,000 lb st (71.17 kN) with afterburning or, in aircraft built from early-1992, F404-GE-402 turbofans each rated at 17,700 lb st (78.73 kN) with afterburning.

Weights

Empty: 23,050 lb (10455 kg)
Take-off: 33,585 lb (15234 kg) on a fighter mission or 48,253 lb (21888 kg) on an attack mission
Maximum take-off: about 56,000 lb (25401 kg)

Fuel and load

Internal fuel: 10,860 lb (4926 kg)
External fuel: up to 6,732 lb (3053 kg) in three 330-US gal (1250-litre) drop tanks
Maximum ordnance load: 15,500 lb (7070 kg) on nine external stores stations.

Performance

Maximum level speed: 'clean' at high altitude more than 1,033 kt (1,190 mph; 1915 km/h)
Maximum rate of climb at sea level: 45,000 ft (13715 0 m) per minute
Combat ceiling: about 50,000 ft (15240 m)
Take-off run: less than 1,400 ft (427 m) at maximum take-off weight
Approach speed: 134 kt (154 mph; 248 km/h)
Acceleration: from 460 kt (530 mph; 850 km/h) to 920 kt (1060 mph; 1705 km/h) at 35,000 ft (10670 m) in under two minutes

Range

Ferry range: more than 1,800 nm (2,073 miles; 3336 km) with drop tanks
Combat radius: more than 400 nm (460 miles; 740 km) on a fighter mission, or 575 nm (662 miles; 1065 km) on an attack mission, or 290 nm (340 miles; 537 km) on a hi-lo-hi interdiction mission

Armament

Gun: M61A1 Vulcan 20-mm cannon with 570 rounds
Air-to-air missiles: AIM-120 AMRAAM, AIM-7 Sparrow, AIM-9 Sidewinder
Precision-guided munitions: AGM-65 Maverick; AGM-84 Harpoon; AGM-84E SLAM; AGM-88 HARM; AGM-62 Walleye EO- (Electro-Optic) guided bomb; AGM-123 Skipper; GBU-10/12/16 laser-guided bombs
Unguided munitions: B57 and B61 tactica nuclear bombs; Mk 80 series general-purpose bombs; Mk 7 dispenser (including Mk 20 Rockeye II, CBU-59, CBU-72 FAE, CBU-78 Gator mine dispenser); LAU-97 2nm FFAR pods

Radar

Hughes AN/APG-65 or AN/APG-73
Effective radar range: more than 100 nm (115 miles; 185 km)

F/A-18C Hornet

generally similar to F/A-18A except

Weights

Take-off: 36,710 lb (16652 kg) for a fighter mission or 51,900 lb (23541 kg) on an attack mission

F/A-18D Hornet

Two-seat, multi-role, attack fighter and trainer generally similar to the F/A-18A/C Hornet except

Weights

Normal take-off: 33,585 lb (15234 kg) on the fighter mission
Maximum take-off: 47,000 lb (21319 kg) for an attack mission

Fuel and load

Internal fuel reduced by less than six per cent to accommodate second seat

Range

Ferry range: 1900 nm (2,187 miles; 3520 km) with internal and external fuel
Combat radius: 550 nm (634 miles; 1020 km)

A VMFA-323 Hornet demonstrates a possible attack load of eight 500-lb (227-kg)Mk 82 'iron' bombs and a pair of AIM-9 AAMs. F/A-18s flew the bulk of USN/USMC missions during Operation Desert Storm. The Hornet first saw combat during the Libyan confrontation in 1986,when the type flew ship-to-shore strike and defence suppression missions. Since desert Storm in 1991, Bosnian peacekeeping duties have also kept these aircraft busy, especially in their F/A-18D form.

F/A-18 Hornet

Plate 2.30. Parts Details with specifications

2.11.2 Design

Starting from the premise that the design of the airframe remains adequate, the Lockheed designers instead decided to improve the C-130's mission effectiveness. The heart of these improvements is the new mission computer, which is connected to electronically operated propellers and engine, 1553B databus architecture and digital avionics. The result of this is a transformed two-seater cockpit that is without the traditional air engineer and navigator, though the flight deck does provide a third set for an additional crew member if needed. The mission computer provides increased navigational capability and better situational awareness. A references made to Plate 2.31.

2.11.3 Performance

The performance of the new aircraft is also suitably increased; the C-130J can climb to 29,000 ft (8,839 m) in just under 20 min and can go on to reach 35,000 ft (10,668 m) in doing so, the C-130J uses less fuel than the old C-130E/H and overall the C-130J can boast a 40% greater range, 40% higher cruising ability, 50% decrease in time-to-climb, 21% increase in maximum speed and a 41% shorter maximum effort take-off run than its predecessors. This improved performance results directly from the C-130J's new propulsion system. Four Rolls-Royce Allison AE2100D3 turboprops, each rated at 4,591 shp (3,425 kW), are allied to new, more efficient Dowty R391 six-bladed, composite propellers which generate up to 30% more thrust while using some 15% less fuel. It is these propellers that are one of the most notable new features on the C-130J.

The Lockheed design team had quickly settled upon turboprop engines and selected for Allison T56-A-1As, each capable of 3,750 shp (2,800 kW). These power-plants, linked to variable-pitch constant speed Curtiss Turboelectric propellers, gave the new transport a cruising speed of 360 mph (579 km h^{-1}). This was only slightly slower than that of the sleek passenger aircraft of the day such as the L-1649 Starliner or Viscount.

For cargo-loading purposes, the aft cargo door opens directly upwards and the ramp comes straight down. The height restriction of 76 in (1.93 m) is generous and allows easy cargo-loading. When the ramp is closed, the C-130 can be fully pressurised at around 28,000 ft (8,668 m) and the ramp itself can store 5,000 lb (2,276 kg) of cargo. When loading and unloading in a confined area, the "Herk" can turn itself in 170 ft (52 m) with the nose gear canted to its maximum of 60°, whereas the DC-6A cargo carriers being used by Flying Tiger Lines and Slick Airways were carrying a maximum permissible payload of 32,000 lb (15,515 kg). Lockheed's sales team believed that US domestic air freight business would quadruple by 1960 and that a vast civilian "air trucking" business lay just around the corner. It seemed certain that if the YC-130 succeeded, it would become an important part of the civil scene.
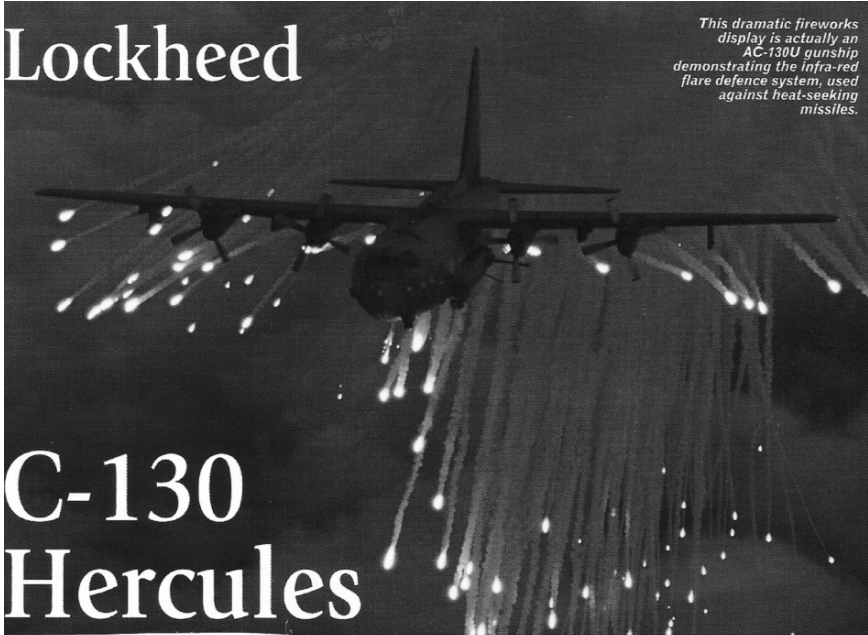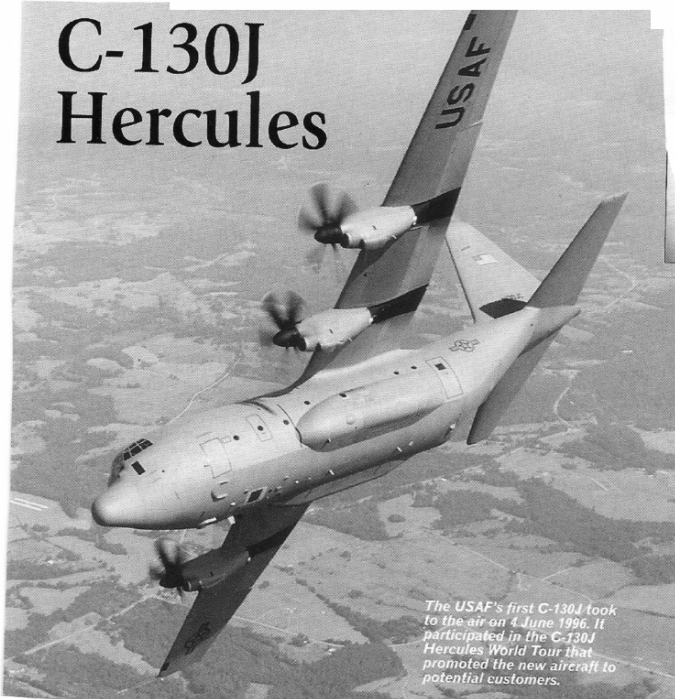
Plate 2.31. C-130 Hercules

2.11.4 Into service

The first YC-130 to fly was actually the second aircraft built and it took to the air from Burbank on 23 August 1954; first flight of a production C-130A was made at Marietta on 7 April 1955. The USAF received its first C-130A on 9 December 1956 and it joined the Tactical Air Command's 463rd Troop Carrier Wing at Ardmor AFB. Oklahoma. The "Roman" nose on early models, which fell straight down following the profile of the windscreen, was soon replaced by a "Pinocchio" nose housing an AN/APN-59 radar. The vertical tail outline, once rounded at the top, was squared off to mount a rotating red anticollision light. With early production models, a shift was made to an Aeroproducts propeller, still an interim model with three blades. The first flight made using this propeller was by the sixth C-130A on 26 November 1955. In August 1957, Lockheed and the USAF jointly announced the development of the C-130B which incorporated more powerful Allison T56-A-7A engines rated at 4,050 shp (3,020 kW) and increased tankage in the wings inboard of the engines. Its strengthened structure and undercarriage permitted operation at a take-off weight of 135,000 lb (61,235 kg), compared with the 124,000 lb (56,245 kg) of the C-130A. (Plate 2.31).

The second change of propellers saw the C-130B flying with four-bladed 13.5 ft (4.17 m) Hamilton Standard hydromatic 54H60-39 propellers to replace the three-bladed unit, thus reducing tip speed. The Hamilton Standard propeller was much later retrofitted to the surviving early "Herks".

The first C-130B was rolled out in September 1958 and made its first flight two months later. This model remained in service until the 1990s and was the only version of the aircraft not to be equipped with external fuel tanks.

The Hercules soon found itself in service around the world, the first overseas customer being Australia which purchased a total of 11 C-130As and has gone on to acquire others since. Britain and more than 50 other nations have received later versions of the C-130. The civilian variant of the Hercules, the L-100 and its subsequent derivatives, has also seen service with world-wide freight haulers and organisations which have included the CIA's shadowy airline Air America.

Plate No. 2.32–2.34 give AC-130H spectre layout indicating sensors, crew stations, forward armament, after weapons, observer station, variants and details, AC-130 briefing with a "cut-away" indicating aircraft elements and complete specifications.

2.12 Mikoyan MIG-23/27 "Flogger"

2.12.1 Introduction

In service in huge numbers with the Russian air forces and with virtually all of its former client states, the MiG-23/27 is one of the most widely operated

SPECIFICATION

C-130H (AC-130H/U similar)

Dimensions

Wingspan: 132 ft 7 in (40.41 m)
Wing aspect ratio: 10.07
Wing area: 1,745 sq ft (162.12m²)
Tailplane span: 52 ft 8 in (16.05 m)
Tailplane area: 381 sq ft (35.40m²)
Length overall: 97 ft 9 in (29.79m)
Height overall: 38 ft 3 in (11.66 m)
Wheelbase: 32 ft 1 in (9.77 m)
Wheel track: 14 ft 3 in (4.35 m)

Powerplant

Four Allsiuon T56-A-15 turboprops, each rated at 4,508 shp (3362 kW), driving a Hamilton Standard 54H60 four-bladed constant-speed, reversible-pitch, fully-feathering propeller

Weights

Operating empty (C-130H): 76,469 lb (34686 kg)
Maximum take-off: 155,000 lb (70305 kg)
Maximum overload: 175,000 lb (79380 kg)

Fuel and load

Maximum internal fuel capacity: 6,820 US gal (5,679 Imp gal;

25816 litres)
Underwing tank capacity (combined): 2,800 US gal (2,332 Imp gal; 10600 litres)
Maximum payload (C-130H): 49,818 lb (22597 kg)

Performance

Maximum cruising speed: 315 kt (362 mph; 583 km/h)
Economical cruising speed: 300 kt (345 mph; 556 km/h)
Maximum rate of climb: 1,800 ft (548 m) per minute
Time to 20,000 ft (6100 m): 22 minutes
Service ceiling: 18,000 ft (5485 m)
Take-off run: 4,000 ft (1220 m)
Landing run: 1,500 ft (457 m)

Range

2,238 miles (3600 km) with 40,000-lb (18144-kg) payload

Armament

One single-round loaded M102 105-mm Howitzer and one clip-fed Bofors L-60 40-mm cannon (AC-130H/U); two belt-fed 20-mm M61 Vulcan cannon (AC-130H) or one belt-fed 25-mm GAU-12 rotary cannon (AC-130U)

AC-130

Briefing

The gunship concept was developed for the war in Southeast Asia. AC-130s were the most powerful and best-equipped of the gunship types, and were used principally on night interdiction sorties over the Ho Chi Minh Trail.

Plate 2.32. AC-130 Aircraft (with compliments from Lockheed Inc. U.S.A)

Mikoyan

MiG-23/27 'Flogger'

Plate 2.33. MiG-23/27 Variants

'Flogger' at war

This MiG-23MLD 'Flogger-K' was used by Major Anatoly Stipanjk during his squadron's deployment to Afghanistan in 1986. The aircraft carried mission markings in the form of small white stars below the cockpit. Sometimes, individual stars were initialled by the pilot responsible for each mission.

Missile threat

'Flogger-Gs' in Afghanistan carried flare/chaff launchers mounted on the upper fuselage. These were used to decoy IR-guided, shoulder-launched anti-aircraft missiles, such as the American Stinger, fired by rebel forces.

Hero of the Soviet Union

'Flogger' pilot Col Anatolij Levchenko flew 188 missions during the war in Afghanistan, his last being on 27 December 1986. Having attacked traffic on the Salang Pass, his aircraft was hit by AAA. Unable to eject, he dived into the enemy gun position, subsequently destroying it, and enabling the rest of his squadron to escape. Levchenko was posthumously awarded Russia's highest honour.
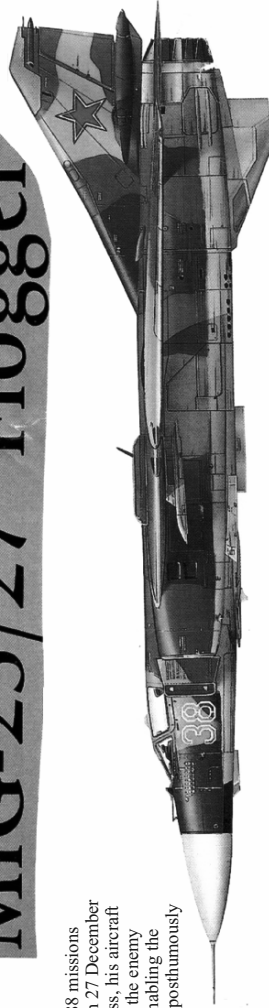
Air-to-air combat

With the Mujahideen lacking any air force, most 'Floggers' served as ground-attack aircraft. However, when attacking rebel camps in Pakistan, aerial engagements with PAF F-16s resulted in the loss of at least two examples.

MiG-23ML 'Flogger-G'

This MiG-23 wears the colours of the Syrian Air Force, which acquired large numbers of the type. For many years, the MiG-23ML was thought to be a sound but basic aircraft, but, with the end of the Cold War, Western analysts found that it was a surprisingly effective aircraft able to outperform many supposedly 'superior' Western types, notably in terms of straight-line acceleration.

Radar

The MiG-23ML's radar marks a major improvement over that of the MiG-23MF, with a range of 56 miles (90 km) rather than 37 miles (60 km) and improved look-down and jamming capabilities. The radar 'picture' is displayed in the pilot's head-up display.

Engine intakes

The rectangular-section air intakes incorporate huge variable intake ramps whish also act as splitter plates. They stand proud from the fuselage and its sluggish boundary layer airflow.

Armament

This MiG-23ML carries a pair of R-23 (AA-7 'Apex') missiles under the wing glove and two pairs of IR-homing R-60 AA-8 'Aphids' under the fuselage. A GSh-23L twin-barrelled cannon is housed in a GP-9 gun pack under the fuselage.

Cockpit

Giving the pilot a good view of his 'six' was not a priority when the MiG-23 was designed. Rear-view mirrors remedy some of the problems, but nothing can alter the poor view downwards.

Plate 2.34. MiG-23ML 'Flogger-G'

jet fighters ever. The key to its enduring success lies in its basic design configuration, which offers a unique blend of robustness, performance and versatility.

Development of the MiG-23 began in the early 1960s, when the Mikoyan-Gurevich OKB began studies for a replacement for its MiG-21 "Fishbed" tactical fighter. Aware of the shortcomings of the MiG-21, the Design Bureau wanted to produce a fighter with greater payload, range and fire power and with more sensors to give freedom from the constraints of tight ground-controlled interception (GCI). The new aircraft was to be faster and able to climb more rapidly than the "Fishbed". The new fighter would therefore have to be larger and heavier, but this would result in the aircraft having exceptionally long take-off run. Mikoyan engineers studied many alternative approaches to the problem of producing a STOL fighter.

Variable geometry. The variable-geometry (VG) wing had been recognised by MiG OKB as the best way of overcoming the primary shortcomings of the "Fishbed", i.e. short range and a small weapons load. Fully spread, the VG wing offered a shorter take-off/landing roll while enabling the aircraft to carry a heavier weapon load. In the fully-swept position, the wing allowed for a high top speed and good supersonic handling characteristics. There were disadvantages to the VG wing, however as the construction of the wing sweep mechanism required a larger fuselage and was relatively heavy. These factors, together with the importance of the position to be held by the new aircraft within the Soviet air force, resulted in two parallel designs being developed simultaneously by Mikoyan.

Although both designs utilised similar fuselages, the first design, designated 23-01 (and later MiG-23PD), utilised a fixed delta wing and was powered by a single main engine (a Tumanskii R-27-300), with two lift "sustainer" engines (actually Koliesov RD-36-35s) located in the centre fuselage for take-off and landing. The aircraft accomplished its first flight on 3 April 1967 and was exhibited at the Domododevo air show in July of that year, where the new design was designated "Faithless" by Western observers.

Having accomplished only 14 flights, Mikoyan realised that the lift-jet concept was flawed and the programme was quickly terminated. While this design was being developed, a second design team were constructing 23-11, which was intended to be a VG version of the 23-01. However, only the nose section, empennage design and turbojet powerplant (Tumanskii's R-27F-300) were common to the two aircraft. Following the failure of earlier design, the 23-11 was given the highest priority within the Soviet government, with the result that the aircraft accomplished its first flight on 10 April 1967, a little over 2 years since VG design had first been studied. Within weeks of its maiden flight, the new design was displayed to the public at Domododevo, where NATO assigned it the name "Flogger". Basic flight trials ended in July 1968, after 98 highly successful flights, resulting in the "Flogger" being quickly ordered for frontline squadrons.

2.12.2 Fledgling "Floggers"

The first variant to enter operational squadron service was the MiG-23S, which was intended to utilise the advanced Sapfir radar (hence the "S" affix) and a more powerful variant of the Tumanskii turbojet. However, development of the radar was not completed by the time the aircraft entered service, resulting in early "Floggers" being equipped with the far less capable "Jay Bird" radar adopted from the MiG-21s. in a single stroke, the capabilities of the new aircraft were comprised for the "Flogger" completely lacked any BVR capability.

2.12.2.1 MiG-23S/M/MF/MS "Flogger-A/B/E"

During the 1960s, the need for a MiG-21 replacement was conceived and Mikoyan-Gurevich began design work on the MiG-23. The authorities were determined that the increased size and weight of the new fighter would not impose longer take-off distances. A series of trials confirmed that the variable-geometry Model 23-11 represented the most effective configuration and this was ordered into production as the MiG-23S with a powerful 22,046 lb st (98.1 kN) R-27F2M-300 engine. Initially, an RP-22 "Jay Bird" radar (like that of the MiG-21S) was installed giving a very recognisable short radome and removing BVR capability. The aircraft was also fitted with a TP-23 IRST. Fifty were built between mid 1969 and the end of 1970 and were used for operational trials before production switched to the MiG-23M, dubbed "Flogger-B" by NATO. This featured the pulse-Doppler Sapfir-23 ("High Lark") radar and new fire control system and autopilot. The MiG-23M could fire the R-23 (AA-7 "Apex") semi-active radar-homing missile. A new 27,557 lb st (122.63 kN) Soyuz (Tumanskii) R-29-300 (with shorter jetpipe) was fitted, while at the same time the aircraft's horizontal tail surfaces were moved aft, giving a very different appearance. A fourth fuel tank was added in the rear fuselage. A new type 1 wing, with an extended leading edge, was introduced, having a pronounced "dogtooth" inboard. Leading-edge slats were deleted (type 2 wing), then reintroduced in 1973 with the Type 3 wing.

MiG-23 Ms were delivered to Frontal Aviation as MiG-21 replacements, operating mainly in the battlefield air superiority role, but with an important secondary ground attack capability. Others went to the IA-PVO, where they augmented MiG-21s, Su-9s, Su-11s and Su-15s in the air defence role. Two downgraded export versions of the MiG-23M were produced, the second gaining the new reporting name "Flogger E". The MiG-23Ms was substantially downgraded version with MiG-21 type "Jay Bird" radar in a short radome, with no BVR missile capability. The MiG-23MF was less radically sanitised and retained the "High Lark" fire control radar, AA-7 "Apex" missile

capability and "Flogger B" reporting name of the MiG-23M and was delivered to Russia's Warsaw Pact allies, then later to Syria, Angola, Iraq, India and Libya.

2.12.2.2 MiG-23B/BK/BM/BN "Flogger-F-H"

In 1969, Mikoyan began studies of a cheap, mass-produced attack aircraft. However instead of a new aircraft, economics constraints forced Mikoyan to examine the possibility of using a derivative of the MiG-23S, whose supersonic dash capability was felt to be a useful bonus. Mikoyan allocated a new designated (Model 32) but the air force – perhaps feeling that funding for a new aircraft would be harder to obtain retained the MiG-23 designation.

The original MiG-23 had been developed as a multi-role tactical fighter and with its rugged airframe, strong undercarriage, powerful engine and variable geometry wing it has the ability to operate from primitive, semi-prepared airstrips. It was extremely suitable for conversion or adaptation to the fighter bomber role. The basic MiG-23B (32-24) was based on the airframe of the MiG-23S but with a new more sloping nose that gave the pilot an improved view forward and downward and with a 112.78 kN (25,353 lb st) Lyul'ka AL-21F-300 powerplant in a shortened rear fuselage. Also like the MiG-23M, the new ground attack variant featured the No. 2 wing and was later fitted with Armour was scabbed on to the sides of the forward fuselage to protect the pilot and the fuel tanks were fitted with an inert gas-injection fire protection system. A missile illuminator and a TV camera were housed in bullet-like fairings on the wingroot glove. Some 24 MiG-23Bs were built before production switched to an improved variant. The MiG-23BN (32-23) featured an upgraded PrNK Sokol 23N nav/attack system and was powered by a slightly derated version of the Soyuz (Tumanskii) R-29B-300 engine. The MiG-23BN was intended to have been the first attack version, but was delayed by equipment and engine problems. It introduced the leading-edge bullet fairings on the fixed wing gloves that are usually associated with the AS-7 "Kerry" ASM. The MiG-23B and MiG-23BN share the NATO reporting name "Flogger-F".

Plate No. 2.35–2.36 give the layout of the aircraft MiG-23/27 with complete briefings, "cut-away" diagram and specification.

2.13 Sukhoi SU-25 "Frogfoot"

2.13.1 Introduction

Built in relatively small numbers and equipping only a handful of Frontal Aviation regiments, the Su-25 is an effective and popular close air support aircraft, which has seen extensive action in Afghanistan. In recent years, a host

MiG-27L 'Flogger-J'

Plate 2.35. MiG-23/27 Variants

Indian's Mig-27/s were designated MiG-27L (Model 32-29L) by Milkoyan itself, although they are acknowledged to be an export version of the MiG-27M (Model 32-29) 'Flogger -J2'. In fact, so much equipment is missing (by comparison with full-standard Soviet MiG-27Ms) that the aircraft is effectively equivalent to the earlier MiG-27D (Model 32-27) 'Flogger-J'. A mid-life avionics upgrade dramatically increased the capability of these aircraft, adding a similar Smiths/Sagem DARIN nav/attack system to that fitted to Indian Jaguars. Indian participation in the MiG-27L programme has been significant; the first aircraft were assembled from Soviet-supplied kits at Hindustan Aeronautics Ltd's Nasik plant, but under Phase Two of the programme major Indian sub-assemblies were incorporated, with further, smaller components added during Phase Three. Phase Four introduced local airframe manufacture, with locally-built engines and some indigenous systems. The Indian

SPECIFICATION

MiG-27 'Flogger-D'

Dimensions

Wingspan (spread): 45 ft 9¾ in (13.97 m)
Wingspan (swept): 25 ft 6¼ in (7.78 m)
Wing aspect ratio (spread): 5.22
Wing aspect ratio (swept): 1.77
Tailplane span: 18 ft 10¼ in (5.75 m)
Wing area (spread): 402.05 sq ft (37.35 m²)
Wing area (swept): 367.71 sq ft (34.16 m²)
Length (including probe): 56 ft¼ in (17.08 m)
Wheel track: 8 ft 8¾ in (2.66 m)
Wheel base: 18 ft 11¼ in (5.77 m)
Height: 16 ft 5 in (5.00 m)

Powerplant

One Soyuz/khachaturovR-29B-300 trbojet rated at 17,625 lb st (78.40 kN) dry and 25,335 lb st (112.77 kN) with afterburning

Weights

Empty equipped: 26,252 lb (11908 kg)
normal take-off: 39,903 lb (18100 kg)
Maximum take-off: 44,753 lb (20300 kg)

Fuel and load

Internal fuel: 10,053 lb (4560 kg), or 1,188 Imp gal (5400 litres)
External fuel: Up to three 174-Imp gal (790-litre) drop tanks
Maximum weaponload: 8,818 lb (4000 kg)

Performance

Maximum level speed 'clean' at 26,245 ft (8000 m): 1,170 mph (1885 km/h)
Maximum level speed 'clean' at sea level: 839 mph (1350 km/h)
Maximum rate of climb at sea level: 39,370 ft (12000 m) per minute
Service ceiling: 45,930 ft (14000 m)
Take-off run at maximum take-off weight: 3,117 ft (950 m)
Landing run at normal landing weight (without brake 'chute): 4,265 ft (1300 m)
Landing run at normal landing weight (with brake 'chute): 2,953 ft (900 m)

Range

Combat radius: 335 miles (540 km) on a lo-lo-lo attack mission with two Kh-29 ASMs and three drop tanks, or 140 miles (225 km) with two Kh-29 ASMs

Armament

One 23-mm GSh-23L twin-barrelled cannon in underfuselage pack; two bomb or JATO hardpoints either side of rear fuselage, plus five further hardpoints for the carriage of tactical nuclear bombs; Kh-23 (AS-7 'Kerry') and Kh-29 (AS-14 'Kedge') ASMs; 9⅞-in (240-mm) S-24 rockets, 2¼-in (57-mm) UB-32 or UB-16 rocket packs; 22 110-lb (50-kg) or 220-lb (100-kg) bombs, or nine 551-lb (250-kg) bombs, or eight 1,102-lb (500-kg) bombs; napalm containers or R-3S/K-13T (AA-2D 'Aphid') and R-13M AAMs

MiG-23ML 'Flogger-G'

The variable wing of the MiG-23 was never as simple as some Western analysts have assumed.The wing was designed on the leading and trailing edges and wing-sweep angles were fully and continuously variable from 16' to 72' although the three most-used values (16' to 45' and 72' although the three most-used values (16' to 45' and 72') are chosen to act as easily selected 'steps' and provide the best handling characteristics. This Bulgarian Flogger-b' is seen with its wings in the maximum forward sweep of position 16' for speed maneuvers. The aircraft carries empty dual AA-8 'Aphid' missile rails on the fuselage pylons.
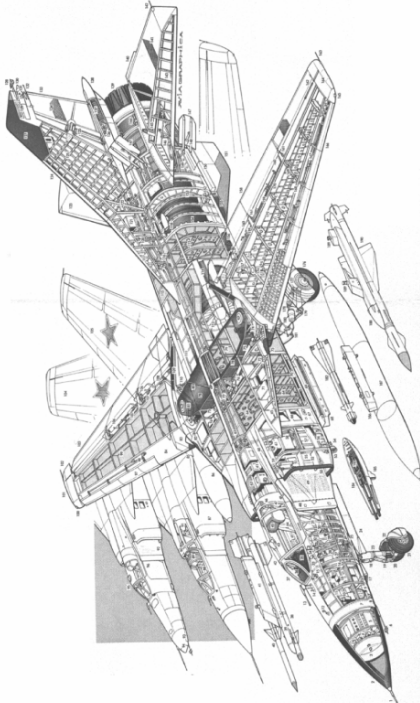
Plate 2.36. MiG-23/27 Flogger

of new variants has emerged, although few have entered large-scale production. A reference is made to Plate No. 2.37.

VVS USSR (Soviet Air Force) was a pioneer in the development and wide use of specialised ground attack aircraft to support its ground forces on the battlefield. After the end of World War II, units equipped with the well-known Il-2 Stormovik and its successor, the Il-10, were disbanded and new designs were ordered. The Soviet order of battle in the 1950s and 1960s was based on fighter-bomber units able to deliver not only conventional ordnance, but also tactical nuclear weapons. Typical of the aircraft based on this philosophy were the Su-7 "Fitter" and its variants, supplemented by the MiG-15 and MiG-17

Far removed from its single-seat attack cousin, the Su-25UTG was intended to train Soviet pilots in basic carrier operations, but these were never conducted at the proper level.

As it catches the wire aboard the carrier Admiral kuznetsov, *one of the 10 Su-25UTGs is brought to a halt. Following the collapse of the Soviet Union, five example were given to the Ukraine.*

Plate 2.37. Su-25 Frogfoot

fighter bomber versions, equipping regiments specialised for battlefield ground support.

In the early 1960s, project discussions on the need for a new ground attack aircraft were held. The reasons behind these talks were the emergence of new data from Southeast Asia and the other localised conflicts, the WarPac Dnieper' 67 exercise, analyses of the new USAF A-X attack aircraft project (resulting in the development of the A-10 thunderbolt), and the requirement for better damage resistance and survivability. General I.P. Pavlovskiy, Commander of Army, was the leading person in these discussions and he managed to persuade the highest authorities about the necessity for new ground attack aircraft. The Ministry of Air Industry issued the official proposals to LSSh "Stormovik" in March 1969 and four construction bureaux – Mikoyan, Yakovlev, Ilyushin and Sukhoi OKB – took part in the competition.

The latter submitted its T8 project as a private venture by a group of designers. Its design did not comply with the thinking of the period, which had produced aircraft such as the MiG-23/27 "Flogger". However, the design proved successful enough to win the competition, although continued development of the T8 would be needed before the aircraft could enter front-line units. Sukhoi was keen to test its new aircraft under combat conditions and two T8 prototypes took part in Operation Romb-1, which involved gun and weapon trials in Afghanistan in April/March 1980. The state acceptance trials were finished by another member of the early T8 prototypes batch at air base Mary in Turkmenistan. With final trials protocol coming to an end, recommendation to put the new aircraft into production – under the designation of Su-25 – was agreed in March 1981. The new aircraft had been initially detected in the West by a US satellite in 1977, where upon it was designated "Frogfoot" by the ASCC.

2.13.2 Future "Frogfoots"

Following the introduction of the single-seat Su-25 K "Frogfoot – A" and its tandem two-seat operational trainer derivative, Su-25UB "UBK Frogfoot-B", Sukhoi has proposed a huge number of variations of these baseline models. The first of these was the Su-25BM, which utilised the basic airframe of the "Frogfoot-A". This model was developed as a target-tug following the attachment of a "Kometa" (Comet) pod to the fuselage. Although successful, only 50 examples were purchased by the VVS and the type's close resemblance to the standard "A" variant frequently resulted in this ordinary attack missions.

Following the development of three Russian aircraft-carriers, Sukhoi developed the Su-25UTG/UBP. This utilised the two-seat fuselage and the remaining examples are used as land-based trainers following the cancellation of the carrier programme. By far the most capable variant yet developed utilising the Su-25 airframe is the Su-25T, which makes use of the two-seat fuselage,

but is fitted for single – pilot configuration only. The rear space is used for extra avionics; the nose of the aircraft houses improved Shkval avionics and a larger fuselage-mounted cannon is installed. The greatest improvement is seen in the cockpit, which is equipped with MFDs; the Su-25T is thus able to deliver the latest air-to-ground weapons such as the Kh-35 and Kh-58 guided missiles.

A further improvement of this variant is the Su-25TM (Su-39), of which eight have been delivered for state acceptance trials. Bulgaria and Slovakia are interested in obtaining this example. Despite Sukhoi's introduction of other types such as the impressive Su-27, the 700 or so "A" models built look set to remain a potent attack aircraft well into the next century.

2.14 Sukhoi Su-27 "Flanker"

2.14.1 Introduction

The side-by-side seating Su-27 variants are radical developments of the original "Flanker" interceptor, and their evolution has been shrouded in confusion and not a little mystery. What is clear is that they promise a deadly combination of long-range "reach" and powerful attack "punch". A reference is made to Plate No. 2.38 and 2.39.

Although Sukhoi's Su-27 has always had a secondary ground-attack capability, Sukhoi chose to develop a dedicated two-seat attack version of the "Flanker". This radically rebuilt aircraft was dubbed the Su-27IB (Istrebitel Bombardirovschik/fighter-bomber) and had the bureau designated T10V-1.

The prototype, which first flew on 13 April 1990, was converted from an Su-27UB trainer, with a new side-by-side armoured cockpit section (including the nose gear) grafted onto the existing fuselage. The Su-27IB has a distinctive long, flattened nose, which led to the nickname "playpus". The aircraft is also fitted with small canards on the long chines running back to the leading edge of the wing.

2.14.2 Production Variants

The full standard Su-34 (Bureau designation T10V-2) is fitted with 12 hardpoints and can carry up to 17,640 lb (8,000 kg) of weapons. It is cleared to carry virtually the full range of Russian air-to-surface ordnance. This could include a total of 34,100 kg (220 lb) AB-100 bombs under various pylons, or a triple cluster of 250 kg (550 lb) AB-250s under each hardpoint for a total of 22 bombs or 12,500 kg (1,100 lb) AB-500 bombs. Alternatively, the Su-34 can carry up to seven KMGU cluster bomb dispensers, a variety of unguided or laser-guided rockets or a number of precision-guided missiles, such as the KAB-500 or the KAB-1500.

Su-27 'Flanker'

Su-27UB 'Flanker-C'

Electrics
The electrical system is driven by two integral AC generators, each producing 115 V at 400 Hz. They are backed up by a pair of nickel cadmium batteries. DC is supplied at 27 volts.

Tailfins
Compared to those of single-seat Su-27s, the Su-27UB's tailfins are of increased height, with an extra section added at the base of the rudder. Ram air inlets are located at the bottom of each leading edge, the port inlet being lower and larger.

This Su-27UB 'Flanker-C' of the 234th 'Proskurovskii' Guards Fighter Regiment at Kubinka wears the striking per-1997 colour scheme of the 'Russian Knights' areobatic demonstration team. This added a white forward fuselage and red leading edges to the basic camouflage, with the tailfins decorated with the VVS flag and the undersides, variegated from dark blue (aft) to white.

Plate 2.38. Su-27 Flanker

Sukhoi Su-27IB

The Su-27IB (known to the Bureau as the T10V-1) was unveiled in the early 1990s under the guise of a side-by-side two-seat trainer, for carrier operations. It was given the spurious designation 'Su-27KU'. Sukhoi repeatedly denied the Su-27IB

designation, as that pointed to the aircraft's true combat role, and made strenuous efforts to conceal all documentation that referred to the 'Su-27IB'. For example, at the 1992 Minsk-Maschulische, a display board describing the aircraft as the Su-27IB was covered before photographers could reach it.

Today, Sukhoi is now more open about the aircraft's role and has attempted to split the Su-27IB into dedicated land attack (Su-34) and maritime attack (Su-32FN) variants. The aircraft seen here, 'Blue 42', was the Su-27IB prototype which first flew on 13 April 1990 – the first of a new breed of larger attack 'Flankers'.

Canard foreplanes

Canards were first flown on the T10-24 (Su-27K) during May 1985 and were later included on several 'Flanker' variants, including the Su-27IB. These foreplanes increase take-off performance by generating extra lift forward of the centre of gravity, but are also used as control surfaces in their own right.

Nose shape

The Su-27IB has an entirely new nose section grafted on at the wing leading edge. The cockpit is provided with side-by-side seats and has been moved forward to give a better view over the broad, flat nose, to which the aircraft owes its 'platypus' nickname. Chines flow back to join the leading edge root extensions on each side. When a radar is fitted (to production-standard aircraft), it is probably only carried in the very forward portion of the nose.

Armament

This aircraft is seen carrying IR-guided R-73 (AA-11 'Archer') air-to-air missiles (AAMs) outboard and longer-range radar-guided R-77 (AA-12 'Adder') AAMs inboard. Underwing it carries a Kh-29L/AS-14 'Kedge' (port) and Kh-29T (starboard) with two KAB series LGBs inboard and two Kh-31 (AS-14 'Krypton') air-to-surface missiles (ASMs) under each intake.

Tailfins

The Su-27IB has the same increase height tailfins as those of the Su-27UB but, surprisingly, lacks its massive forward ventral fins, despite 'keel' area.

Cockpit access

Access to the new side-by-side cockpit is via a ladder in the nosewheel bay, although the panels above the cockpit look similar to the opening cockpit panels of the Su-24 'Fencer'.

Su-27K Briefing

Plate 2.39. Sukhoi Su-27

2.14.3 Long-Range Strike

Although the su-34 might be considered to be a replacement for the air force's Su-24s in the tactical strike role, it may also replace Tupolev's Tu-16 and Tu-22 m in some roles, such as that of a long-range stand-off missile carrier. The su-3 has already been proposed as a potential launch platform for the Novator ASM-MS Alfa long-range hypersonic cruise missile.

2.14.4 Maritime Role

When Sukhoi first presented the Su-34 ("45", the T10V-5 which had first flown on 28 December 1994) AT THE 1995 Paris Air Show, it did so using the surprise designation Su-32FN. The aircraft was described as an all-weather, 24-h maritime strike aircraft, equipped with the Sea Snake sea-search and attack radar. An (unlikely) anti-submarine capability was even attributed to the aircraft, when Sukhoi stated that it could carry up to 72 sonobuoys and be fitted with a MAD system in the tail "sting". The Su-32FN is certainly capable of carrying all existing Russian anti-ship/air-to-surface missiles. The Su-32FN returned to Paris in 1997 when another aircraft ("44") took part in the flying display for the first time. It is unclear how many Su-27IB/Su-34/Su-32FN aircraft have been built to date, but it is probably less than six.

The three T10s were followed by a batch of T10 K (Su-27 K) prototypes, each of which differed slightly from the others. The first Su-27 K prototype (TK 10K-1, coded "37") followed the t10-24 and made its maiden flight on 17 August 1987. Between five and eight subsequent prototypes were built to a standard which approximated more closely to the intended production configuration. All featured twin nosewheels, wing and tailplane folding, and double-slotted trailing-edge flaps. A reference is made to Plate 2.39 for Su27 performance.

2.14.5 Carrier Trails

Carrier landing trials began on 1 November 1989, when Victor Pugachev landed the second Su-27 K aboard the carrier Tbilisi, becoming the first Russian pilot to land a conventional aircraft aboard the carrier. The second prototype (T10-39) was the first full-standard Su-27K, fitted with all "naval" features. Takhtar Aubakirov (in the MiG-29K) made the first ski-jump take-off from the Tbilisi and was followed by Pugachev in the Su-27K.

Russian naval pilots began carrier operations on 26 September 1991. Service trials were highly with the Russian navy, both the AEW aircraft and MiG-29K programmes were abandoned. If only one fixed-wing type was to be procured for the new carrier, logic would have dictated that it should be the multi-role MiG-29K. However, the political influence of Sukhoi's chief designer, Mikhail Simonov, was such that the Sukhoi aircraft was selected for production and service, and the Russian navy was forced to accept the aircraft's (and thus the carrier's) more limited role.

The Su-27 K does enjoy some significant advantages over the MiG-29 K, primarily exceptional range performance. Before entering service, the production Su-27K was redesignated Su-33 by the OKB, but the aircraft remains a navalised version basic IA-PVO interceptor, with the same basic "Slot Back" radar and with only a very limited ground-attack capability. It is uncertain whether the AV-MF uses the Su-33 designation.

2.14.6 First Operation Cruise

The Kuzentsov's first truly operational deployment took place in early 1996, when it spent two months in the Mediterranean. The ship's complement included the Su-27 K-equipped 1st Squadron of the Severomorsk Regiment. Although a production batch of 18 Su-27Ks has reportedly been built, the Kuznetsov's complement included the last Su-27 K prototype in addition to at least ten production Su-27 Ks.

Despite the apparent abandonment of the MiG-29 K, sources suggest that production of this aircraft is still under consideration. If it does enter service, the Russian navy will have obtained its originally favoured aircraft mix, and the carrier will be a more versatile weapon. A more advanced carrier-borne Su-27 (reported to have been designated Su-27 KM, or T10 KM) based on the Su-27 M has been proposed, but has not materialised in the light of the massive drawdown in Russia's armed forces following the end of the Cold War. However, it remains possible that the existing Su-27 Ks could be usefully upgraded to improve their capabilities. Incorporating the modifications of the Su-27SM mid-life upgrade would add a Zhuk radar and would give compatibility with the R-77 (RVV-AE "AMRAAMski") missile and a wide range of advanced air-to-surface precision-guided weapons, and uprated AL-31FM or AL-35 turbofan engines.

2.14.7 Su-27 K Armament Options

Service Su-27 Ks have been seen carrying the usual IA-PVO load-out of R-27 (AA10 "Alamo") and R-73 (AA-11 "Archer") AAMs, although the extra pair of underwing hardpoints actually allows the carriage of two additional R-27s, bringing the beyond-visual-range (BVR) armament to eight missiles. The R-27 is available in a number of versions, and those carried by the Su-27 K include the R-27EM which has improved only 10 ft (3 m) above the water. The aircraft will be among the first to receive the R-27 AE which will introduce active radar terminal homing.

Service Su-27 Ks have also been seen carrying an unusual centreline pod, provisionally identified as a reconnaissance pod, or an equipment pod associated with some kind of carrier landing system. Alternative stores may include a centreline fuel tank, or a UPAS buddy inflight-refuelling store. A range of unguided bombs and rockets (podded and large-calibre single rounds)

and the Kh-31 (AS-17 "Krypton") ASM can be carried underwing. None of these alternative stores has been photographed under production Su-27 Ks, which seem to fulfil a pure fleet air defence role. One weapon frequently ascribed to the Su-27 K is the gigantic Kh-41, an air-launched version of the 3M80 "Moskit" anti-ship missile, sometimes known under the codename ASM-MSS.

Plate No. 2.40–2.41 gives Su-27 Flanker B layout along with armament and various systems together with a "cut-away" of the aircraft identifying various zones. A complete specification of this aircraft is given there in.

2.15 Mikoyan MIG-25 "Foxbat"

2.15.1 Introduction

The MiG-25 "Foxbat" became a great symbol of the Soviet Cold War threat. The large family of variants remains of potent force within the former Soviet Union, despite the aircraft's 30-year old design. A reference is made to Plate No 2.42 for this super fighter.

The MiG-25 was developed as a panic response to the American North American XB-70 Valkyrie strategic bomber, whose Mach 3 performance and very high-altitude capability threatened to present Soviet air defences with almost insoluble problems. When development of the Valkyrie was halted in 1961, work on the MiG-25 was well advanced, and the USSR continued with the project, perhaps knowing that a Mach-3 capable reconnaissance aircraft, the Lockheed A-12 (later SR-71), was about to begin flight tests.

In designing an aircraft for sustained flight at Mach 3, the biggest problem facing the design bureau was the so-called heat barrier. Those parts of the airframe that had to withstand the greatest heat, such as the nose and leading edges had to be of titanium construction, but many other areas that could theoretically have been made of riveted aluminium – such as the wing skins – had to be of welded steel because no suitable heat-resistant sealant could be found, and because there was a shortage of skilled riveters. Eventually, 80% of the aircraft was of tempered steel, 11 percent of aluminium alloys and nine percent of titanium.

Development of the Ye-155P (the original MiG-25 designation) interceptor was approved in February 1962, and the prototype made its maiden flight on 9 September 1964. The aircraft was powered by a pair of 22,500 lb (100 kN) Mikulin (later Tumanskii) R-15B-300 turbojets with a life of 150 h, and was fitted with a Smertch-A radar, known to NATO as "Fox Fire", the radar had a detection range of 54 mm (62 miles, 100 km). The aircraft carried two R-40 air-to-air missiles, in mixed pairs of R-40R and R-40T semi-active radar – and IR-homing versions. Look-down capability was virtually non-existent.

SUKHOI SU-27 'FLANKER' . BRIEFING

Su-27 'Flanker-B'

'Blue 24' was one of the Su-27s allocated to the 582nd Guards Fighter Regiment of the 4th Air Army (Chojna in western Poland, the 582nd was one of two Poland-based Su-27 units withdrawn to Russia during 1992 as part of the general withdrawal of Russian forces from Europe. Some of the Chojna-based Su-27s came from an early production batch and featured dark green radomes and dielectric panels. They were changed to white for later 'Flankers'.,

Short-range missile engagement

For close-range engagements, the Su-27 can carry up to four Vympel R-73 (AA-11 'Archer') infra-red-homing dogfight missiles on wingtip and outboard underwing pylons. Developed as a replacement for the R-13M (AA-2 'Atoll'), the R-73 is the first of a new generation of close-range AAMs, having a new level of agility and being capable of off-axis launch from all aspects. Until the advent of the Israeli Rafael Python 4, the R-73 was widely viewed as being the world's most capable and sophisticated IR-guided AAM. The missile owes its manoeuvrability to a combination of fixed rear fins, and deflectors for the rocket nozzle. Four AoA sensors are mounted ahead of the forward fins. There are two variants, the RDM-1 (with 19-mile/30-km range) and the RDM-2 (11 lb/5 kg higher weight and 6.2 miles/10 km greater range). Both variants have a 16-lb (7.4-kg) expanding rod warhead and can manoeuvre at up to 12 g. They can be fired at targets at 45° or 60° respectively, off the axis of the Su-27's nose.

Aircraft markings

This aircraft carries seven red stars under the cockpit, possibly denoting exercise 'kills' or live missile firings. The 'dart and pentagon device below these is an excellence award, applied to individual aircraft in recognition of their condition as a reward to the crew chief. The excellence award is not, as has often been said, in any way equivalent to American outstanding units citations.

Frontal Aviation role

Although designed primarily as an interceptor for the I-A-PVO), the Su-27 has also been delivered in significant numbers to Frontal Aviation units. The involvement of the PVO in the abortive coup against President Gorbachev undermined the organisation and led to forces (WS), which stayed loyal. Frontal Aviation uses the Su-27 primarily as part of a high/low mixed fighter force c1necost in which the heavyweight, long-range 'Flankers' are targeted against high value enemy aircraft 9tankers, AWACS platforms) further behind the front line, and also by long-range escort for strike and attack aircraft.

'Flankers' have been exported to relatively few countries, China, Vietnam and India are confirmed operators, with former Soviet client states in the Middle East being viewed as other potential customers. Outside of Russia, the Ukraine (illustrated) remains the largest Su-27 operator, inheriting two Su-27 regiments when the USSR split apart. Su-27s are also operated by other former Soviet republics.

Combat persistence

One area where the Su-27 excels is its ability to engage many targets during the same mission. With a typical combat load of six R-27 medium–long-range missiles, four short-range R-73s and an internal cannon, the Su-27 can engage several targets before having to return to base and refuel. The internal 30-mm cannon is the same highly-accurate GSh-30-1 as is carried by the MiG-29 'Fulcrum'. Combat capability is boosted significantly by the integration of a pilot's helmet-mounted weapon cueing system.

Colours and markings

All operational service Su-27s seen in the west have worn an effective (if unusual) three-tone air superiority blue–grey camouflage scheme. Some reports suggest that a handful os aircraft were delivered in a fighter-bomber scheme of green and brown. Dielectric areas are usually in green or white. Despite the break-up of the USSR's traditional red star as a national marking, with use of the pre-revolutionary tricolour so far confined to factory demonstrators and civil aircraft. Su-27s operated by other republics, such as the Ukraine, have recved new national markings.

Flight control system

The Su-27 has often been simplistically described as having fly-by-wire (FBW) flight control system. This is only partially true. The aircraft is statically unstable only in pitch, since this is all that is necessary to achieve the benifits of high manoeuvrability, low drag, high lift and superior control system controls the aircraft in pitch but provides only stability augmentation to the mechanical lateral and yaw control circuits. The control system consists of four computers, each 'fed' from a separate air data source, with quadruply-redundant transducers and signal paths. The control system limits the aircraft to +8.5/-2.5 g and to 28 units of Alpha, but these are 'soft' limits, which can be overridden by the pilot either by switching off the limiter switches or by using extra pressure (about 33lb/15 kg) to 'pull through' the stick stops.

Long-range missile armament

The Su-27's primary armament is th Vympel R-27, known to NATO as the AA-10 'Alamo'. This is a family of missiles with long-and short-range IR-homing and semi-active radar homing variants, which entered production in 1982 for use on the MiG-29 and Su-27, in place of the R-23 (AA-7 'Apex') and earlier missiles used on previous fighters. The Su-27 carries R-27s on its inboard underwing pylons, on pylons below the engine intake ducts, and in tandem between the engine nacelles. The basic semi-active radar homing (SARH) R-27R ('Alamo-A') is usually carried between the nacelles (as seen here) or underwing, as is the Ir-homing R-27T ('Alamo-B). IR-homing R-27s are seen under the wing of this aircraft. Long-range versions of both SARH-and R-homing variants have been produced, under the designations R-27RE and R-27TE ('Alamo-C' and '-D') with a boost sustain motor. They can be recognised by their increased body length and a slightly 'fattened' rear fuselage, and on the Su-27 are usually carried under the intakes. A further variant carried by later production Su-27s is the R-27EM with an improved SARH seeker for use against low-flying and sea-skimming missiles.

Sukhoi OKB insignia

Many Su-27s still carry this insignia on their tailfins,and the same badge has also been seen on Su-17s, Su-24s and Su-25s. Variously described as a 'winged helmet, or more correctly as a 'winged archer', the badge is the old Sukhoi OKB logo; it has since been largely replaced by a simple triangle containing the Cyrillic equivalents of the letters 'Su' (Су).

Sheet 02

Despite the limitations of its radar, even the basic Su-27 remains a highly capable interceptor, with superb manoeuvrability. Early Su-27s (identifiable by their green radomes) remain in widespread service. This example is an aircraft from the test centre at Akhtubinsk and carries a weapon load of two R-27 and two R-73 missiles, identifiable as drill rounds from thier black bands.

Defensive systems

The Su-27 is protected by an L-006 (SPO-15) 'Beryoza' Passive radar warning receiver system, with antennas on the trailing edges of the tailfins. This gives 360° coverage and classifies, priorities and displays threats using a built-in thread library, and indicates bearing, range and system type. The aircraft also has a Patrol IFF set and an SO-69 transponder. The internal pallud electronic countermeasures (ECM) system can be used in the rear hemisphere only when the Su-27's own onboard radar is in use. The 'Flanker' also has provision for the L-005 (Sothsiya-S) ECM system, carried in large wingtip pods. Other active countermeasures comprise a comprehensive APP-50 chaff/flare dispenser 32 chaff/flare launchers, each containing three chaff or flare cartridges for a total of 96.

Tailcone and engine nacelles

The long tailcone projecting aft from between the engine nacelles reduces drag and serves as an invaluable location for the twin barking parachutes and a variety of other equipment items. Perhaps most obviously, there are 32 groups of chaff/flare dispensers above the tailcone, each containing three launchers. The engine nacelles are anchored beneath the mid fuselage. They are of semi-monnococue stressed-skin construction, reinforced by stringers and bulkhead frames. The whole rear end of each nacelle is of unpainted welded titanium alloy, the high quality welds showing clear signs that sophisticated computer-controlled welding equipment is used in thier construction.

Plate 2.40. Su-27 Flanker-B with compliments (Russian Aircraft Industry) Sukhoi Groups

Su-27 'Flanker'

SPECIFICATION

Su-27P 'Flanker-B'

Dimensions

Fuselage length (including probe): 72 ft 0 in (21.94 m)

Wing span over tip missile launch rails: 48 ft 3 in (14.70 m)

Wing aspect ratio: 7.76

Tailplane span: 32 ft 5 in (9.88 m)

Wing area: 667.8 sq ft (62.01 m²)

Horizontal tail area: 131.75 sq ft (12.24 m²)

Total fin area: 165.76 sq ft (15.40 m²)

Distance between fin tips: 14 ft 1¼ in (4.30 m)

Overall height: 19 ft 6 in (5.93 m)

Wheel track: 14 ft 3 in (4.34 m)

Wheelbase: 19 ft 4 in (5.88 m)

Maximum wing loading: 93.4 lb/sq ft (456.2 kg/m²)

Powerplant

Two saturn Lyul'ka AL-31F afterburning turbofans each rated at 16,755 lb st (74.53 kN) dry and 27,558 lb st (122.59 kN) with after burning

Weights

Empty operating: 36,112 lb (16380 kg)

Normal take-off: 50,705 lb (23000 kg)

Maximum take-off: 162,391 lb (28300 kg)

Fuel and load

Internal fuel: (normal) 11,620 lb (5270 kg), (maximum) 20,723 lb (9400 kg) or 2,640 Imp gal (12000 litres) in three main fuselage tanks, with additional tanks in outer wing panels; the basic Su-27 has no provision for inflight refuelling or for the carriage of external fuel tanks (but see under individual varient briefings for exceptions)

Maximum theoretical weapon load: 17,636 lb (8000 kg)

Normal weapon load: 8,818 lb (4000 kg)

g limits

8-9 at basic design gross weight

Performance

Maximum level speed at sea level (estimated): 743 kt (850 mph; 1370 km/h)

Maximum level speed 'clean' at altitude: 1,236 kt (1,418 mph; 2280 km/h)

Limiting Mach No.: 2.35

Absolute ceiling: 60,700 ft (18500 m)

Practical service ceiling (estimted): 58,070 ft (17700 m)

Take-off run: 1,640 ft (500 m) or 1,476 ft (450 m)

Landing roll: 1,968 ft (600 m) or 2,297 ft (700 m)

Landing speed: 121-124 kt (140-143 mph; 225-230 km/h)

Range

Maximum range: 1,987 nm (2,285 miles; 3680 km) at altitude, 740 nm (851 miles; 1370 km) at low level

Radius of action (high-altitude): 590 nm (677 miles; 1090 km)

Radius of action (low-altitude): 227 nm (261 miles; 420 km)

Armament

detailed separately, sheets 11 & 17

Note: This specification should be treated with some caution. Sukhoi has released widely differing performance figures on different occasions (and even releases different dimensions for the same aircraft), while rarely specifying the loads carried for particular range or performance figures.

Plate 2.41. Su-27 Flanker with structural parts and specifications

Mikoyan
MiG-25 'Foxbat'
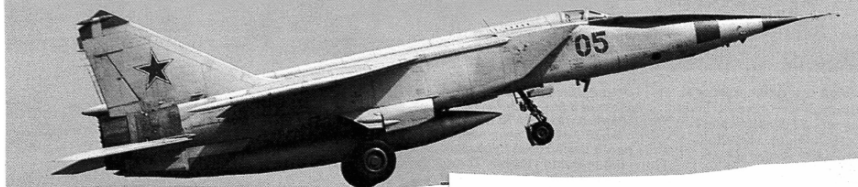
Soviet Superfighter

*Mikoyan employed models to explore numerous
configurations that would allow a fighter to travel at Mach 3.
Prior to the aircraft entering service, the six design team
members were awarded the Lenin prize for their achievements.*
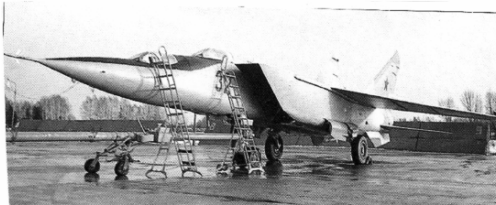
*The MiG-25PU 'Foxbat-C' is a highly valued type. Serving
as trainers, familiarisation aircraft and weather recce ships, the
two-seaters see more flying hours than any other MiG-25 version.*

Plate 2.42. MIG-25 Foxbat

Performance was up to expectations and, in March 1965 – under the cover designation Ye-266 – an early aircraft was used to establish several performance records which were countered by the US YF-12 in May 1965. Between 1965 and 1977, the Ye-266 and another early variant, the Ye-266M, eventually made 21 FAI-notified record-breaking flights, setting nine records which remained unbroken until 1994.

Production began in 1969, but the aircraft did not enter full air force service until 1973, having been plagued by engine problems. Even in service the MiG-25 was subject to severe operating limitations.

Normal armament comprises two R-40 (AA-6 "Acrid") and four R-60 (AA-8 "Aphid") AAMS. The PD/PDS upgrade has restored the MiG-25's viability and some are expected to serve on into the next millennium.

2.15.2 Mach 3 Spyplane

Although the MiG-25 was originally designed as an interceptor, it had obvious potential as a reconnaissance platform. The prototype recce aircraft, the Ye-155R-1, made its maiden flight 6 months before the prototype fighter, 6 March 1964. As the MiG-25R, the reconnaissance version passed its state acceptance test in 1969, and series production began in April of that year. The MiG-25R had five camera ports in the nose (one vertical and four oblique), with small square flush antennas further forward on the nose.

The original MiG-25R was replaced on the production line by the MiG-25RB "Foxbat-B" in 1970, this type remaining in production until 1982. The MiG-25RB was a dual-role reconnaissance bomber, with a Peeling automatic bombing system, as well as having the Soviet Union's first operational inertial navigation system. Camera-equipped MiG-25RBs were exported to Algeria, Bulgaria, India, Iraq, Libya and Syria.

The basic MiG-25RB also formed the basis of a model dedicated to Elint duties, with its optical sensors replaced by a variety of passive receivers and active SLAR systems. This example received the NATO reporting name "Foxbat-D". The first "camera-less" reconnaissance "Foxbat" was the MiG-25RBK, in which the usual flush antennas and cameras were removed and replaced by a large dielectric panel, housing the new Kub SLAR, on each side of the cock-pit. The MiG-25RBK entered service in 1972 and remained in production until 1980.

The final reconnaissance variant was the MiG-25RBF, which is described either as an RB brought up to RKB standards, or as a new production aircraft which replaced the RBK on the production line, it has expanded jamming capability. Unusually, the reconnaissance "Foxbat" has its own dedicated two-seat trainer, designated MiG-25RU – this variant has no operational equipment.

2.15.3 SAM Suppression

Having closely followed the development of dedicated "Wild Weasel" aircraft by the US in the final stages of the Vietnam War and in the immediate post-war period, Mikoyan developed the M-G-25BM. Developed in 1972 and known as the "Foxbat-F" by NATO, the MiG-25BM was adapted to carry four Kh-85 (AS-11 "Kilter") anti-radiation missiles. The aircraft are believed to be equipped with a sophisticated avionics package including a Sych-M ("Little Owl") radar. The MiG-25BMs observed in service have their noses painted to represent the radomes of the fighter MiG-25s. Fewer than 100 MiG25BMs were built between 1982 and 1985 and all were delivered to Frontal Aviation units in East Germany and Poland, the aircraft has not been offered for export and remains extremely secret.
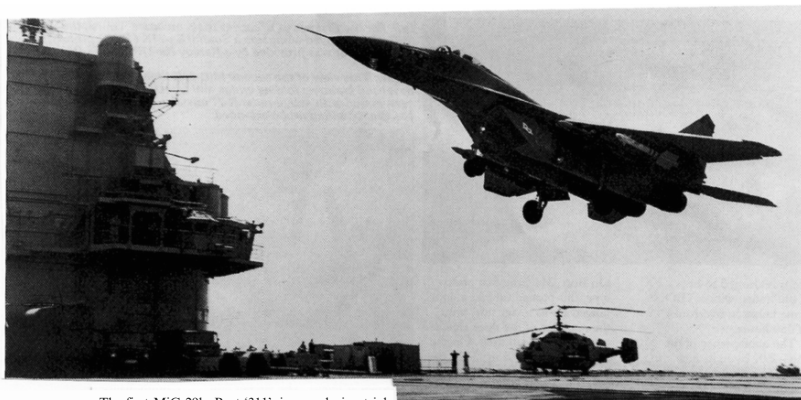
The first MiG-29k, Bort '311', is seen during trials aboard Tbilisi. These included landing aboard with R-73 and R-77 missiles, the main air-to-air weapons of the type. The aircraft bore the brunt of the carrier trials, carrying photo-calibration marks on the nose. The extended and bulged wingtips housed electronic warfare equipment.
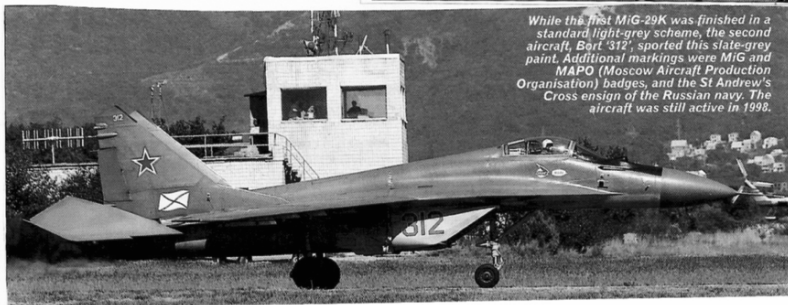
While the first MiG-29K was finished in a standard light-grey scheme, the second aircraft, Bort '312', sported this slate-grey paint. Additional markings were MiG and MAPO (Moscow Aircraft Production Organisation) badges, and the St Andrew's Cross ensign of the Russian navy. The aircraft was still active in 1998.

Plate 2.43. MiG-29K

2.16 Mikoyan MIG-29 "Fulcrum"

2.16.1 Introduction

2.16.2 Carrierborne "Fulcrum"

To provide a multi-role fighter for the Russian navy, Mikoyan expended much effort on the MiG-29K, a thorough reworking of the basic design for carrier deployment. In the event, it lost out to the Su-27K. (A reference is made to Plate No. 2.43 for this kind of aircraft.)

The origins of the MiG-29K remains shrouded in some mystery. Most sources suggest that the project was launched to provide a multi-role strike fighter to complement the single-role Su-27K interceptor, to equip the air wings of the planned four STOBAR (short take-off but arrested landing) carriers intended to enter Soviet navy service during the 1990s. A handful of analysts maintain that the MiG-29K was only ever planned as a fall-back, in case the Su-27K proved too heavy to operate from the new carriers. They believe that the Soviet carriers were planned as pure fleet air defence vessels, with no power-projection role, and thus with no requirement for fighter-bomber or strike/attack capabilities.

Trials with the hooked MiG-29KVP proved that the MiG-29 could be operated safely from a ski-jump, and that arrested landings were possible at operationally useful weights. Although the MiG-29KVP could have formed the basis of a practical carrierborne fighter, it was decided that the ideal carrierborne Mig-29 would require both additional wing area and additional thrust. Further, improved high-lift devices might produce a useful reduction in approach speed, without unacceptably raising the angle of attack on touch-down.

Since a new variant of the MiG-29 would be required, Mikoyan took the courageous decision to adapt it from the new multi-role MiG-29M, with its lightweight airframe, multi-mode/multi-role radar and PGM capability. Detail design began in 1985, one year before the MiG-29M made its maiden flight.

2.16.2.1 Uprated Engines

There was a degree of cross-fertilisation between the MiG-29M and the MiG-29K, with the uprated RD-33K engines developed for the carrier aircraft eventually being adopted for the −29 M, too. The new engine had an exceptional regime (ChR or Chrezvychainii Regim) giving 20,725 lb st (92.17 kN) thrust for a limited period, useful on launch and in the event of a missed approach or go-around. It also had FADEC (full-authority digital engine control), advanced materials and single-crystal turbine blades. They allowed the engine to operate at higher temperatures, and the basic maximum thrust figure was increased from 18,298 lb st (81.42 kN) to 19,400 lb st (86.33 kN).

When the time came to select the aircraft for Russia's one remaining carrier, the choice was made in favour of the Su-27K. This could have been largely due to Sukhoi's political influence, or perhaps the Russian navy genuinely hoped that the small batch of Su-27Ks would eventually be augmented by multi-role MiG-29s when funding permitted. The two MiG-29K prototypes remained active (though 311 was subsequently grounded, then resurrected as a MiG-29M support aircraft) and may yet contribute to the development of a new naval MiG-29, the MiG-29SMTK.

2.17 Mikoyan–Gurevich MiG-21/Chengdu J-7 "Fishbed"

2.17.1 Introduction

Produced in immense numbers, the MiG-21's success had helped to make MiG virtually a household name. In service with the Soviet Union and its client states during the Cold War, the aircraft remains on the strength of air forces worldwide.

It would be fair to claim that the MiG-21 is one of the most famous military aircraft in the world. Since the end of World War II, no other fighter has been built in such large numbers (over 10,000 in the Soviet Union and a further 2,000 in China and India), or in so many versions (and still they keep appearing). Moreover, no other fighter has ever served with so many forces (56) – the C-130 Hercules is the only military aircraft to have seen more widespread service – or been involved in so many conflicts. What is remarkable is that the MiG-21 has always been a rather small and limited aircraft, possessing equipment of no outstanding ability. Indeed, in today's conflicts, the MiG-21 has found itself outclassed by the bigger, more sophisticated and more powerful Western fighters. Nevertheless, the MiG-21 has proved popular with those who have flown it and the fact that it is easy to maintain, reliable and cheap has meant that today's air forces are still keen to operate it.

2.17.2 "Fishbed" Evolution

In 1953, the NII VVS, the scientific research institute of the Soviet air force, issued a specification for a new fighter and Mikoyan came up with a proposal for a small, supersonic aircraft, powered by a single afterburning turbojet, which would not carry heavy loads of fuel, electronics or weapons. The VVS required this new fighter purely to shoot down Century-series fighters and bombers such as the B-47, B-52 and B-58. However, it was soon accepted that this new fighter could not do everything that was asked of it and a new requirement was accordingly issued, which called for a fighter to carry out local defence in daylight, operate under close ground control and attack with guns only.

The Mikoyan OKB built two prototypes – the Ye-2 (with swept wings) and the Ye-4 (delta). Both aircraft were to be equipped with the R-11 engine, but they were designed before the engine was completed and so were fitted instead with the less powerful RD-9Ye. The Ye-2 first flew on 14 February 1955 and was well received, if considered to be a little underpowered, with the delta-winged Ye-4 flying a few days later. Over the following 2 years, a number of modifications were made to both designs and, in a final fly-off in 1957, the delta-winged variant was picked by Mikoyan and the NII VVS. The next two years saw a number of further changes to the initial design, which resulted in the Ye-6/3. Flown in December 1958, it led straight into a series of 30 production aircraft, designated MiG-21F. While the Soviets

used a Ye-6/3 to gain a number of records including the world speed record, Mikoyan was building the first true series version, the MiG-21F-13, which had new armament. Hundreds of these aircraft were constructed, including aircraft designated S-106 which were made in Czechoslovakia, and unlicensed copies in China.

2.17.3 Multi-Variant MiG

From the outset, the MiG-21 was constantly upgraded and it has gone through three generational changes which have resulted in an aircraft far removed from the prototype. After the MiG-21F-13 came the -21 P, which dispensed with the cannon and was only armed with two missiles. This was followed by the -21 PF which had a new radar, the FL for export purposes, and the PFM with a new canopy, avionics, weapons and equipment.

Later-generation models moved away from the original lightweight fighter concept, gradually becoming heavier and more sophisticated. There was the -21 R recce aircraft with reconnaissance and IR pods, TV cameras and laser sensors; the -21 S fighter variant of the R; the -21 SM with increased manoeuvrability; the -21 MF with a more powerful engine, radar and weapons fit; and the -21 SMT which was capable of carrying a greater fuel load.

The third generation MiG-21bis is by far the most advanced and capable variant, although a lack of BVR missile capability, limited radar and poor endurance limit its usefulness. It was developed as a multi-role fighter for Soviet Frontier Aviation and has a greater weapons capability than earlier variants. The bis model has served with a number of nations and, alongside earlier models, continues in front-line service although it is being replaced with more modern Western aircraft by a few countries.

The end of the Cold War did not therefore mean the end of the MiG-21, and several companies have made efforts to upgrade the surviving aircraft. IAI has produced the MiG-21-2000, Tracor has built a drone conversion named the "QMiG-21", while the Mikoyan OKB itself has constructed the MiG-21-93. A host of other companies have offered upgrades, new avionics and fresh weapons fits.

2.17.4 MiG at War

With its wide range of operators, it was inevitable that the MiG-21 would see combat. The first true conflict in which the aircraft appeared was that between India and Pakistan in 1965, its main opponents being the F-86F and F-104A. However, combat was limited and it was not until the resumption of hostilities in 1971 that the MiG-21 really found itself at war. The first kill was a PAF F-6, although F-104s were soon added to the kill lists. Other MiG-21s were used in the air-to-ground role.

The next major area of conflict for the MiG-21 was in the Middle East, where Egyptian, Syrian and Iraqi aircraft found themselves attacking Israel.
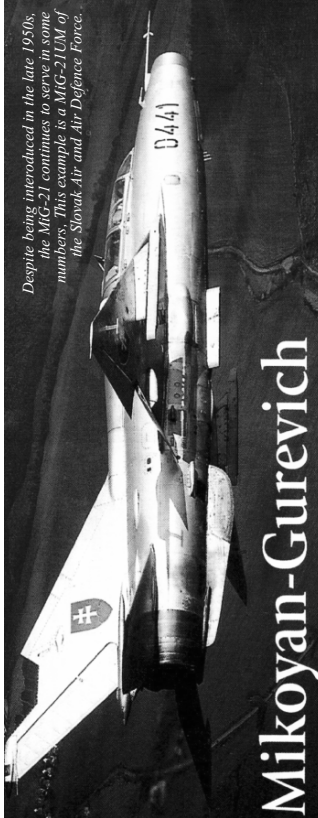
Despite being introduced in the late 1950s, the MiG-21 continues to serve in some numbers. This example is a MiG-21UM of the Slovak Air and Air Defence Force.

Mikoyan-Gurevich

China first manufactured the MiG-21 in 1961, naming its domestic aircraft J-7s, and those for its export customers F-7s. This example is an F-7MG with upgraded weapons capabilities, allowing the carriage of AIM-9 Sidewinders and R.550 Magic AAMs.
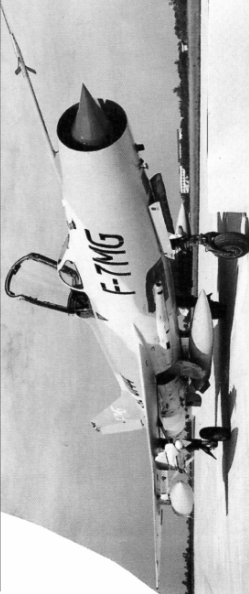
Egypt's MiG-21s saw combat against Israeli fighters during the 1960s and 1970s. They generally fared badly, scoring few kills against their better-trained opponents, although downed aircraft were soon replaced by the Soviet Union.
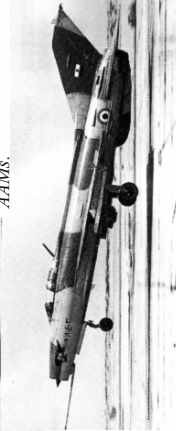
Plate 2.44. MiG-21 'Fishbed'

Here, the MiG-21 was less than successful and many fell prey to Israeli Mirage IIICJs. In the Yom Kippur war of 1973, the Arab coalition's air forces again found themselves outclassed by Israeli F-4Es, Mirages and Neshers. In Africa, Cuban-piloted Angolan MiG-21s were used against the UNITA and FNLA opposition parties, with two falling prey to South African Mirage F1s. Iraqi MiG-21s held their own against Iranian F-4s and F-5s while Somalian MiG-21s fared badly against Ethiopian F-5s.

During Vietnam, the agile MiG-21s performed well against the heavier, more sophisticated American aircraft in close combat when under tight ground control, although they suffered when fighting at greater distances. Despite American propaganda that the MiG forces were not a threat, Operation Linebacker II involved many strikes on MiG-21 bases. Since then, MiG-21s have been involved in a number of conflicts around Israel and Syria (including one over the Lebanon in 1982 in which over 80 MiG-21/23s were shot down), and in the localised conflicts across Africa. The aircraft's most recent combat appearance was during Desert Storm where the few MiG-21s that managed to get into the air were downed by the superior Coalition forces.

The MiG-21 is likely to continue in service into the next century. The air forces of poorer countries where the majority of MiG-21s remain on the frontline, regard upgrading existing aircraft as a preferred alternative to buying new machines. Types such as the F-16 or MiG-29, would be far more expensive than a MiG-21 upgrade.

It is unlikely that any fighter will ever again match the sales success of the MiG-21. In a world of shrinking defence budgets, few nations have the finances to spend great sums on squadrons of aircraft. Instead, the trend now seems to be to equip squadrons with small numbers of powerful, high-tech multi-purpose aircraft – the opposite of the original MiG-21 ideal. Plate No. 2.45–2.47 gives the layout of MiG-21MF Fishbed-J, with power plant air brakes, fuselage radom, armament with cut-away briefing and specification.

2.18 Mikoyan MiG-31 "Foxhound"

2.18.1 Introduction

Dismissed in the West as a crude, brutish adaptation of the MiG-25, the MiG-31 is in fact one of the world's most sophisticated interceptors.

Work on overhauling Soviet air defences was accorded a high priority, and development began on two new AWACS platforms (the A-50 "Mainstay" and An-74 "Madcap"), an array of new SAMs, and various new fighters. The most ambitious of these were the Mig-29 "Fulcrum" (intended as a tactical fighter for Frontal Aviation) and the Sukhoi Su-27 "Flanker" (a long-range agile interceptor and escort fighter for the IA-PVO and Frontal Aviation). Both of these aircraft were single-seaters, and neither promised to be in service before 1985, so a number of interim fighter projects were instituted.

MiG-21MF 'Fishbed-J'

Plate 2.45. MiG-21MF 'Fishbed-J'
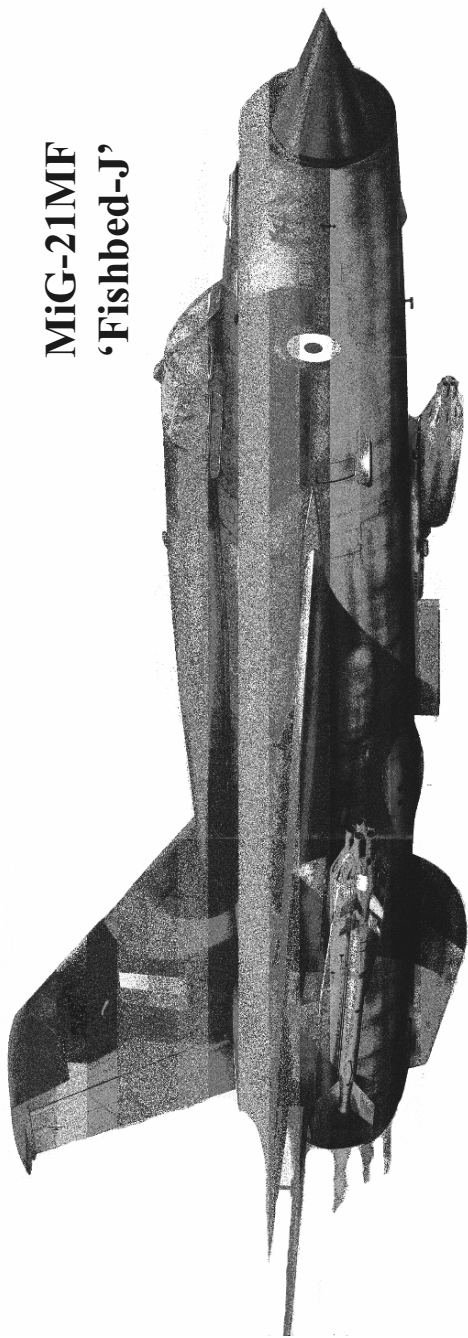
Formerly belonging to No. 7 Squadron 'Battle Axes' of the Indian Air Force, this MiG-21MF made up part of the IAF's significant MiG force. Although No. 7 Squadron now flies the Mirage 2000, two other squadrons still operate the -21MF, which was once the most numerous MiG-21 variant operated worldwide. Since the first deliveries, India has flown nearly 700 MiG-21s, either supplied from the Soviet Union built by HAL (Hindustan Aeronautics Limited) at Nasik. The M, FL and bis variants also continue to be operated.

MiG-21 'Fishbed'

Finland operated the MiG-21 between 1963 and 1998, when the final aircraft were retired. Along the way, four variants –the MiG-21F-13, U, UM and BIS – were all operated. The picture above shows the very last MiG-21 to fly, MiG-21BIS MG-138 piloted by Captain Yrjö Rantamäki, preparing to land at Rissala air base on 7 March 1998. Finland has now replaced its MiG-21s with Boeing F-18s.

A handful of MiG-21s was delivered to the West during the Cold War by means of defections from Communist countries or by other more covert methods. This example, a Soviet-built MiG-21, is seen flying over the Groom Lake/Area 51 complex and was part of the secret 4477th Test & Evaluation Squadron or 'Red Eagles'. Aircraft like these were flown, in Operation Have Doughnut, against the latest Western types to evaluate their performance, and so enable planners to formulate tactics. The obvious intense secrecy that surrounded these test flights has helped to shape the legend of Area 51 and it is entirely plausible that the supposed 'alien' aircraft are simply foreign aircraft.

SPECIFICATION

MiG-21MF 'Fishbed-J'

Dimensions

Length with probe: 51 ft 8½ in (15.76 m)
Length excluding probe: 40 ft 4 in (12.29 m)
Span: 23 ft 6 in (7.15 m)
Height: 13 ft 6 in (4.13 m)
Wing area: 247.5 sq ft (23 m²)
Wing aspect ratio: 2.23
Wheel track: 9 ft 1¼ in (2.79 m)
Wheel base: 15 ft 5½ in (4.71 m)

Powerplant

One MNPK 'Soyuz' (Tumanskii/Gavrilov) R-13-300 turbojet rated at 8,972 lb st (39.92 kN) dry and 14,037 lb st (63.66 kN) with afterburning

Weights

Empty: 11,795 lb (5350 kg)
Normal take-off with four AAMs and three 129-US gal (490-litre) drop tanks: 17,967 lb (8150 kg)
Maximum take-off: 20,723 lb (9400 kg)

Fuel and load

Internal fuel: 687 US gal (2600 litres)
External fuel: up to 387 US gal (1470 litres) in three drop tanks
Maximum ordnance: 4,409 lb (2000 kg)

Performance

Maximum rate of climb at sea level: 23,622 ft (7200 m) per minute
Service ceiling: 59,711 ft (18200 m)
Take off run: 2,625 ft (800 m)

Range

Ferry range: 971 nm (1,118 miles; 1800 km) with three drop tanks
Combat radius: 200 nm (230 miles; 370 km) on a hi-lo-hi attack mission with four 551-lb (250-kg) bombs, or 400 nm (460 miles; 740 km) on a hi-lo-hi mission with two 551-lb (250-kg) bombs and drop tanks

Armament

Standard gun is the GSh-23L, which has a calibre of 23 mm and can fire AP or HE ammunition, with 420 rounds being carried. The only guided missiles normally carried are for air-to-air use. The MF is capable of firing the K-13A (AA-2 'Atoll') and the AA-2-2 Advanced 'Atoll'. As with other MiG-21s, up to eight R-60 (AA-8 'Aphid') infra-red missils can also be caried, there is provision for various FABs (free-fall general-purpose bombs), up to 1,102 lb (500 kg) in weight. A wide range of fragmentation, chemical, cluster bombs and rocket-boosted penetrators for use against concrete can be carried, as well as 57-mm or 240-mm calibre rockets.

MIKOYAN-GUREVICH MIG-21/CHENGDU J-7 'FISHBED'   SHEET 03

Plate 2.46. Structural parts with specification

Indian MiGs

An initial batch of 12 MiG-21F-13s (illustrated), along with two PFs, was delivered to India before the 1965 war with Pakistan. Immediately afterwards, HAL began to assemble (and later build) the first of 150 MiG-21FLs. Enough MiG-21MFs to equip two squardrons were purchased directly from the USSR in 1973. Finally, 220 MiG-21bis Fighters were constructed by HAL's Nasik division between 1979 and 1987. During the conflicts with Pakisthan, Indian NiG-21s were used as escorts for HAL HF-24 Maruts and were faced in combat with PAF F-104s, Sabres, Shenyang F-6s and Dassault Mirage IIIEPS.
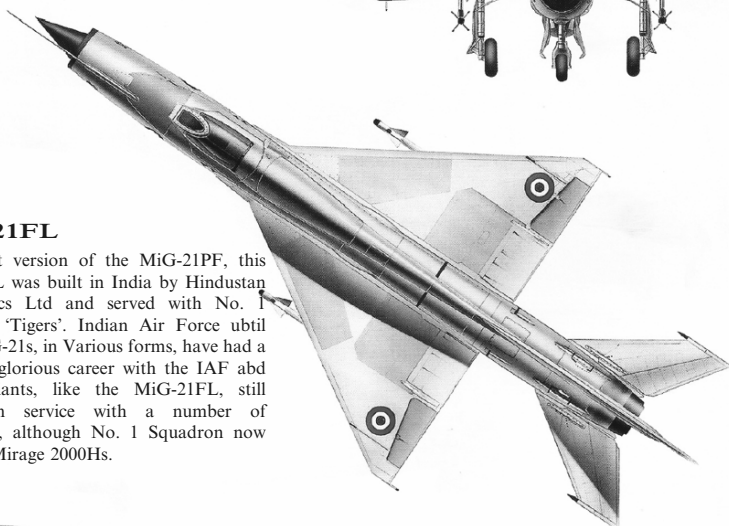
MiG-21FL

An export version of the MiG-21PF, this MiG-21FL was built in India by Hindustan Aeronautics Ltd and served with No. 1 Squadron 'Tigers'. Indian Air Force ubtil 1973. MiG-21s, in Various forms, have had a long and glorious career with the IAF abd early variants, like the MiG-21FL, still remain in service with a number of squadrons, although No. 1 Squadron now operates Mirage 2000Hs.
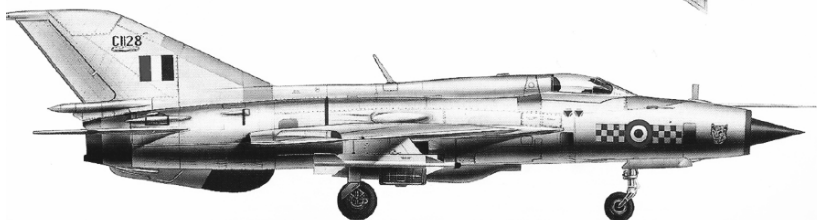
Plate 2.47. MiG-21FL

New lookdown/shootdown radar was fitted to the existing Su-15 "Flagon-F", while a similar process produced the MiG-25 "Foxbat-E". The IA-PVO also took delivery of large numbers of MiG-23 "Floggers", which had a limited lookdown/shootdown capability.

2.18.2 New Design

Although often assumed to have originated as an interim aircraft, or at best as an insurance policy in case of the failure of the Su-27, the MiG-31 actually represented an attempt to produce a long-range interceptor which would be capable of operating independently of ground control, and whose rwo crew members would also enhance mission performance in a hostile electronic warfare environment, and not just a low-risk, quick-to-develop Su-27 alternative.

The MiG-31 airframe seems to have originated from that of the Ye-155M, a research derivative of the MiG25 intended to explore ways of increasing the speed and range of the MiG-25 family. It had been intended to undertake a two-stage programme, first fitting new 29,761-Ib (132-kN) R-15BF-2-300 engines (with 7,253 Ib/32 kN more thrust than the R-15B-300 of the standard MiG-25) and then revising the aircraft structure to raise the limiting Mach number (which was then thermally limited to Mach 2.83). With the new engines, service ceiling was raised to 79,396 ft (24,200 m), and range increased to 1,193 miles (1,920 km) or 1,559 miles (2,510 km) with a 1,166-Imp gal (5,300-l) external fuel tank. Unfortunately, engine development took longer than anticipated, and the second stage of the programme, covering structural and material changes, was shelved. The two Ye-155M prototypes still had a role to play, however. They were converted to serve as testbeds for the new 34,170-Ib (152-kN) Soloviev D-30F6 dual rotor turbojets being developed for the MiG-31, after a competition between Soloviev and Tumanskii.

2.18.3 Record Breaker

Under the "cover" designation Ye-266M the re-engined Ye155M shattered a number of world records. On 17 May 1975 OKB Chief Test Pilot Alexander Fedotov set time-to-height records of 2 min 34.28 s to 8,202 ft (2,500 m), and 4 min 11.78 s to 13, 123 ft (4,000 m). His deputy, Ostapenko, took the 9,843-ft (3,000-m) record with a time of 3 min 9.8 s. On 22 July 1977, Fedotov took two more records, those for altitude (achieving 121,653 ft/37,080 m) with 2,204 and 4,409 lb (1,000 and kg) payloads. The Ye-266M's final record, set by Alexander Fedotov on 31 August 1977, was an absolute altitude of 123,524 ft (37,650 m).

The MiG-31 (which bore the internal designation Project 83) was so closely based on the experimental Ye-155M that it was originally designated Ye-155MP, and was expected to gain the service designation MiG-25MP. The first prototype, bearing the code 831 (indicating the first example of project 83), first flew on 16 September 1975, in the hands of Fedotov.

The West began to refer to the new aircraft as the MiG-31 in 1977, and began to sit up and take notice when a MiG-31 prototype was observed by a satellite destroying a target at below 200 ft (61 m), at some 12 miles (20 km) range, while itself at 20,000 ft (6,096 m). In a later test a MiG-31 at 55,000 ft

SPECIFICATION

**MiG-31B 'Foxhound-A';
MiG-31M generally similar to
MiG-31B expect where noted**

Dimensions: wing span 44 ft 2 in(13.464 m);
overall length, including probe 74 ft 5¼ in
(22.688 m); overall height 20 ft 2¼ in (6.15 m);
wing aspect ratio 2.94; wing area 663 sq ft
(61.6 m²).
Powerplant: two Aviadvigatel D-30F6
turbofans, each rated at 34,170 lb st
(151.9 kN) with afterburning.
Weights: empty 43,115 lb (21825 kg);
internal fuel 36,045 lb (16350 kg); maximum
take-off weight on internal fuel 90,390 lb
(41000 kg); maximum take-off weight with twin
underwing tanks 101,850 lb (46200 kg);
maximum take-off weight (MiG-31M)
114,640 lb (52,000 kg).
Performance: maximum permitted Mach
No. 2.3 at altitude; maximum level speed at
57,400 ft (17500 M) 1,865 mph (3000 km/h);
maximum speed at sea level 932 mph
(1500 km/h); economic cruising speed Mach
0.85; service ceiling 67,600 ft (20600 m).
Range: radius of action with maximum
internal fuel and four R-33 missiles at
Mach 2.35 447 miles (720 km); ferry range on
maximum internal fuel and without armament
2,050 miles (3300 km); maximum endurance
(unre-fuelled) 3 h 36 min.

Plate 2.48. MiG-31M "Foxhound-B"

(16,765 m) destroyed a UR-1 RPV flying at 70,000 ft (21,336 m). The reporting
name "Foxhound" was announced in mid-1982, and examples of the new type
started to be intercepted by Norwegian air force fighters from 1985. At one
stage, Western experts were happily stating that a single-seat version had
been flown, and that 24 examples of a strategic reconnaissance version were
in service. Both reports seem to have been mistaken. The West was, however,
taking the MiG-31 seriously, and some began to overestimate the new inter-
ceptor. US Assistant Secretary of State for Defense Donald Latham went as

Eurofighter demonstrates the unstable, canard configuration, 'fly-by-wire' FCS and advanced cockpit exhibited by the latest generation of fighters.
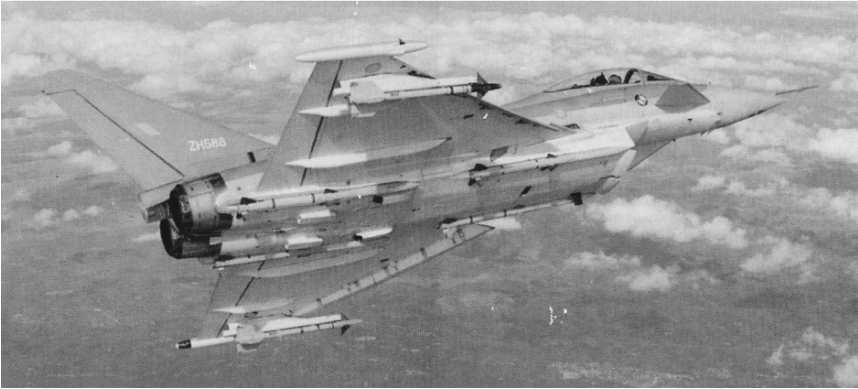
The first British development Eurofighter 2000 (previously known as EFA (European Fighter Aircraft)) demonstrates its large wing area. This gives the aircraft its excellent dog-fighting ability, while advanced radar provides beyond-visual-range (BVR) capability.

Plate 2.49. EF2000 fighter design

far as to describe the MiG-31 as being superior to any existing US fighter, including the F-15.

2.18.4 Series Production

Production of the MiG-31 commenced at Gorky (now Nizhny Novograd) in 1979, after intensive trials. These were not without incident, and numerous modifications were incorporated into the production aircraft. One of the major

Eurofighter DA.6

The first two-seat Eurofighter to fly was the second aircraft to be built – the CASA–constructed DA.6 (XCE.16-01). DA.6 took to the air on 31 August 1996. In fact, DA.6 beat both DA.4 and DA.5 (DASA's second single-seat aircraft) into the air.
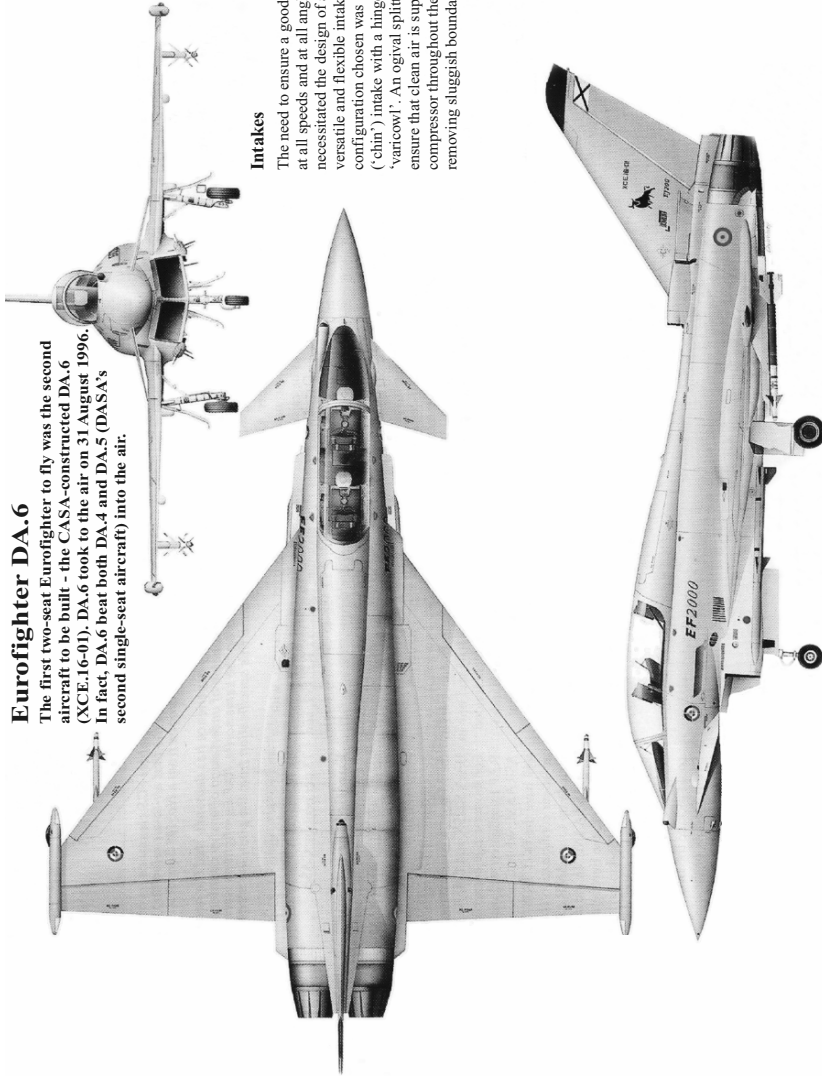
Intakes

The need to ensure a good performance at all speeds and at all angles of attack necessitated the design of an extremely versatile and flexible intake. The configuration chosen was an underfuselage ('chin') intake with a hinged lowerlip or 'varicowl'. An ogival splitter plate helps to ensure that clean air is supplied to the compressor throughout the flight envelope by removing sluggish boundary layer airflow

Plate 2.50. Eurofighter DA-6 with compliments from BAs, U.K.

improvements was the repositioning of the airbrakes underneath the intake duct, rather than on the "shoulders" of the intake ducts.

By comparison with the MiG-25, the MiG-31 has larger and more complex engine intakes, and these have been tailored to reduce airflow problems and reduce fuel consumption during missions.

2.19 EF2000 Fighter Design

2.19.1 Introduction

Designed to engage current and future airborne threats, the Eurofighter is at the cutting edge of airframe and avionics development.

The operational requirement which led to today's Eurofighter 2000 called for an aircraft with unmatched agility and long range. This demanded a novel aerodynamic approach, with low drag and high lift. Satisfying these requirements was only made possible by adoption of an unstable canard delta configuration, with "fly-by-wire" controls. To a classically trained aerodynamicist, the Eurofighter does not look as if it could fly, since the centre of lift seems to be far ahead of the centre of gravity, with massive, all-moving canard foreplanes which promise to further destablise the aircraft.

Appearances are not deceptive in this case. Eurofighter is inherently unstable, with an aerodynamic configuration which tends to force the aircraft's nose to pitch upwards away from direction of flight. The forces involved are such that no human pilot could possess reactions rapid enough to prevent the aircraft from going violently out of control and rapidly breaking up. Only the constant intervention of the aircraft's sophisticated flight control system (FCS) computers can "feed in" control inputs rapidly enough to keep the aircraft in stabilised, controlled flight at all times.

2.19.2 Flying Control System

Because the aircraft has to be flown by computer, the pilot's flying controls are not directly connected to the flying surfaces as is the case with a conventional mechanically controlled aircraft. Instead the pilot makes a control input, which is fed electrically to the FCS computers. This in turn interprets the pilot's input, and electrically feeds in appropriate deflections of elevons, rudder and canard foreplanes to fly the "requested" manoeuvre. The control surfaces can even be programmed automatically to damp out turbulence or lateral gusts, allowing more comfortable low-level flight and also reducing stresses on the aircraft structure.

This infers the use of electrical control signalling ("fly-by-wire" controls) instead of conventional hydraulic and mechanical linkages, with a significant saving in weight and a potential increase in reliability. In addition, an

automatic recovery mode (or "panic button") is incorporated into the FCS. This gives an immediate return to straight and level flight on actuation.

The Eurofighter's lack of inclination to fly along straight and level means that when the pilot does want to turn, the aircraft will turn very rapidly indeed; there is no inherent stability to keep the aircraft travelling in the direction that it was flying.

2.19.3 No Tailplane Required

The use of an unstable aerodynamic configuration and automatic flight control systems allows the control surfaces to be made smaller. Moreover, the conventional tailplane, which is used mostly to provide a down force, can be dispensed with, thus reducing drag significantly.

EF2000's FCS computers are critical to the aircraft's flight safety, that is, if they failed the aircraft would go out of control, break up and crash within seconds. Eurofighter is therefore fitted with four FCS computers, designed under the leadership of Germany's DASA (Daimler–Benz Aerospace). If one computer crashes, or malfunctions, the other three will take over its work, a system know as quadruple redundancy.

2.19.4 Direct Voice Input

Most fighter pilots have to communicate with their weapon system by clicking HOTAS (Hands On Throttle And Stick) buttons to drive menus on their display screens, or by pressing soft keys on those displays. By contrast, the Eurofighter pilot will be able to perform many cockpit "housekeeping" chores simply by DVI – Direct Voice Input – in other words, by telling his aircraft what he wants. He can request his fuel state by simply saying, "Fuel?", or can change radio frequencies, select and nominate targets and even fire his weapons simply by speaking commands.

2.20 Saab Viggen (Variants)

2.20.1 Introduction

Saab Viggen has variants such as JA37, SK37, AJ37, SH37, F6, F13, F15 and many others. Their details are given below.

(a) *Saab AJ 37 Viggen.* In the early 1960s, Saab studied a low-cost, single seat, single-engined fighter capable of supersonic flight at low altitude and Mach 2 at height, but able to take off and land in 1,640 ft (500 m) to replace the multi-role J 32. This demanding specification was necessary if the new aircraft was to operate in the SAF's STRIL 60 integrated air defence system and BASE 90 concept dispersed airstrips. For good

short-field performance, Saab pioneered the use of flap-equipped canard foreplanes with a delta-wing configuration, in conjunction with an integral thrust-reverser for the RM8 turbofan.

For reliability, the powerplant was based on the 14,771 lb st (65.7 kN) commercial Pratt & Whitney JT8D-22 turbofan, developed and built by Svenska Flygmotor for supersonic flight and with a Swedish afterburner providing a thrust increase of more than 70% to around 26,014 lb (115.7 kN) for take-off. An autoland technique for minimum landing distance involved automatic approach speed control and selection of reverse thrust in a no-flare touchdown with a 16.4 ft (5 m) per second compression of the main undercarriage oleos. The initial AJ 37 attack aircraft, soon named Viggen (Thunderbolt), incorporated many other features novel for its time, including a Saab CK-37 miniaturised digital air data and nav/attack computer, SRA head-up display for primary flight data and a Cutler-Hammer AIL microwave beam landing-guidance system. A rocket-boosted Saab ejection seat provided zero-zero escape capabilities.

(b) *JA 37 Viggen.* For the dedicated interception role, with a secondary ground attack capability, Saab developed the JA 37 Viggen. Although externally similar to the attack variant, the interceptor introduces fundamental changes under the skin, with avionics, armament, engine and structural modifications. The JA 37's primary sensor is the Ericsson PS-46/A medium-PRF multi mode X-band pulse-Doppler look down/shoot-down radar, which has four air-to-air modes and a look-down range in excess of 30 miles (48 km). New avionics include an upgraded and higher-capacity Singer-Kearfott SKC-2037 central digital computer and KT-70L INS, Decca Doppler Type 72 nav radar, Garrett AiResearch LD-5 digital air data computer, Saab-Honeywell SA07 digital AFCS, Svenska Radio integrated electronic display system, and an SRA HUD. The RM8B turbofan is uprated by Volvo to develop 16,600 lb (73.84 kN) maximum dry thrust and 28,109 lb (125 kN) with afterburning. This extra power allows the JA 37 to fly at Mach 1.2 at low altitude and to exceed Mach 2 at higher altitudes.

Airframe changes include a wing restressed for a higher load factor, a fuselage stretch of 4 in (10 cm) ahead of the wing to accommodate the modified powerplant, a fin (10 cm) fin extension similar to that of the SK 37 trainer and four instead of three elevator actuators under each wing. Four AJ 37 prototypes were modified to JA 37 standard for the development programme, the first making its initial flight on 27 September 1974, a few days after SAF orders for the first 30 production Viggen interceptors. In March 1980, the Swedish government authorised a third batch of 59 JA 37s, increasing overall production of this variant to 149 and the Viggen total to its final figure of 330. JA 37s were planned to replace Flygvapnet J 35 Drakens in the 1978–85 period and to arm at least eight of the 10 Draken air defence squadrons active at that time. Today, the JA

37 is the most numerous Viggen subtype in service and is operational in eight Divisioner (squadrons).

(c) *SK 37 Viggen*. With the Viggen fulfilling its role as the Flygvapnet's primary combat aircraft system, there was a pressing need for a trainer version. The SK 37 Viggen (Skol or School) tandem two-seat trainer was developed simultaneously with the AJ 37. This variant is somewhat unusual in having two separate cockpits for pilot and instructor. The stepped rear (instructor's) cockpit fitted with a bulged canopy and twin lateral periscopes, replaces some electronics and a forward fuel tank. Fuel capacity is partially restored by a permanently-mounted ventral fuel tank. Other changes incude a 4 in (10 cm) taller fin to restore stability following modification of the aircraft to produce the deeper forward fuselage. Because of its height, event the standard AJ 37 fin can be folded on the ground to allow clearance for the SAF's cavern based hangars. Despite its radome, the SK 37 has no radar and therefore no radar navigation capability, having to rely on Doppler and DME.

Plate No. 2.51–2.54 give the JA 37 layout with identification of zones/parts and Viggen briefing for the "cut-away" diagram and full specification.

2.21 Dassault Mirage F1

2.21.1 Introduction

Despite its suffix, the Mirage F1C was the initial production version. The private venture prototype flew on 23 December 1966 and was officially adopted in May 1967, when three service prototypes were ordered. Power was provided by a 15,873-lb st (70.61 kN) SNECMA Atar 09K50 reheated turbojet which offered good maneuverability at all speeds.

To meet the prime requirements for an all-weather interceptor, the F1C is equipped with a Thomson-CSF Cyrano IV monopulse radar operating in the I/J band. A later modification to IV-1 standards added limited look-down capability, but as ground attack is only a secondary role for the F1C there are no ground mapping or continuous target ranging options. Only single targets can be tracked, and radar performance is noticeably degraded by poor weather.

The Armée de l'Air ordered 20 F1B tandem-seat trainers for pilot conversion. Incorporation of a second cockpit adds only 12 in (30 cm) to the standard F1C's length, as remaining space is made by deleting the fuselage fuel tank and both internal cannon. Empty weight increases by 441 lb (200 kg), due partly to the installation of two French-built Martin-Baker Mk 10 zero-zero ejection seats (the C1C having Mk four seats with a forward speed limitation). Otherwise, the F1B is combat capable. Refuelling probes occasionally fitting to F1B aircraft are, in fact, dummies for training with C-135FR tankers.

SAAB VIGGEN   **SHEET 01**

Saab 37 Viggen

By comparison with the earlier Draken, the Viggen marked a massive improvement in capability, and proved to have more docile handling characteristics into the bargain.

Camouflage
All attack, reconnaissance and trainer Viggens, and many JA 37 fighters, wear a unique four-tone camouflage scheme. Consisting of three shades of green and one of brown (with undersides painted light grey) the scheme is known as the 'Fields and Meadows' camouflage, and is primarily designed to make the aircraft inconspicuous on the ground, when operating from dispersed sites. Paint for the upper surfaces is applied in hard-edged irregular slabs, whose disruptive nature tends to 'break up' the overall shape of the aircraft.

Camera nose
The SF 37, which is used for overland reconnaissance (while the SH 37 performs the maritime mission) dispenses with radar altogether, and instead has a battery of seven vertical and oblique cameras in its recontoured nose.

Windscreen
The Viggen's wraparound single-piece windscreen gives the pilot an excellent view forward, and is strengthened to withstand birdstrikes at high-speed.
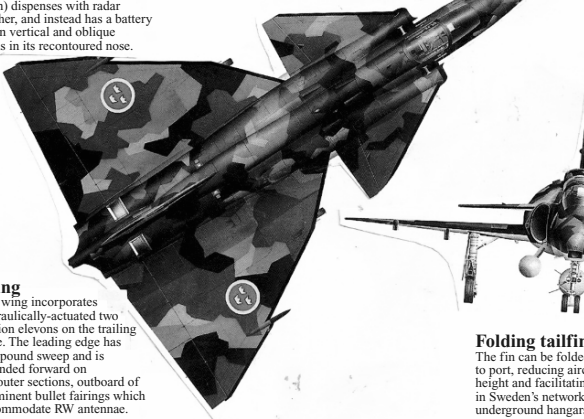
Wing
The wing incorporates hydraulically-actuated two section elevons on the trailing edge. The leading edge has compound sweep and is extended forward on the outer sections, outboard of prominent bullet fairings which accommodate RW antennae.

Folding tailfin
The fin can be folded down to port, reducing aircraft height and facilitating storage in Sweden's network of underground hangars.

Plate 2.51. Saab SF 37 Viggen

Exports of the F1C have been made to six countries, four of which went on to adopt the multi-role F1E. South Africa received the first of 16 F1CZs in 1975 for No. 3 Squadron at Waterkloof. They saw action in the confrontation with Angola.

(a)

AJ 37 Viggen

(b)

JA 37 Viggen

(c)
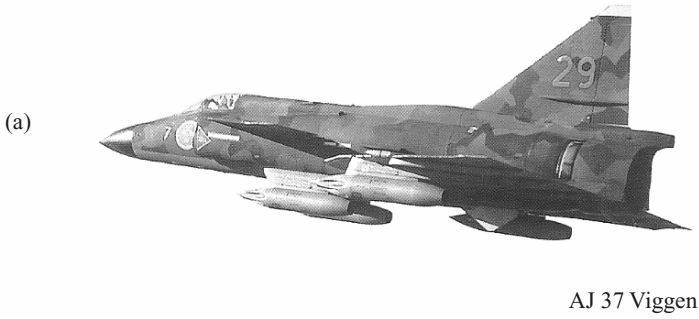
Sk 37 Viggen

Plate 2.52. Viggen variants Saab 37 Viggen

2.21.2 Reconnaissance Variant

As soon as it was clear that the Mirage F1 would support a major production run, Dassault studied a dedicated reconnaissance version, the customer being the Armée de l'Air. Designated Mirage F1CR-200, the first example flew on

JA 37 Jaktviggen

Intakes

The oval-shaped lateral intakes stand well away from the fuselage, to avoid the ingestion of sluggish boundary layer air, and are of plain, fixed type, since high supersonic speeds, where a more complex variable intake would be required, are of secondary importance.
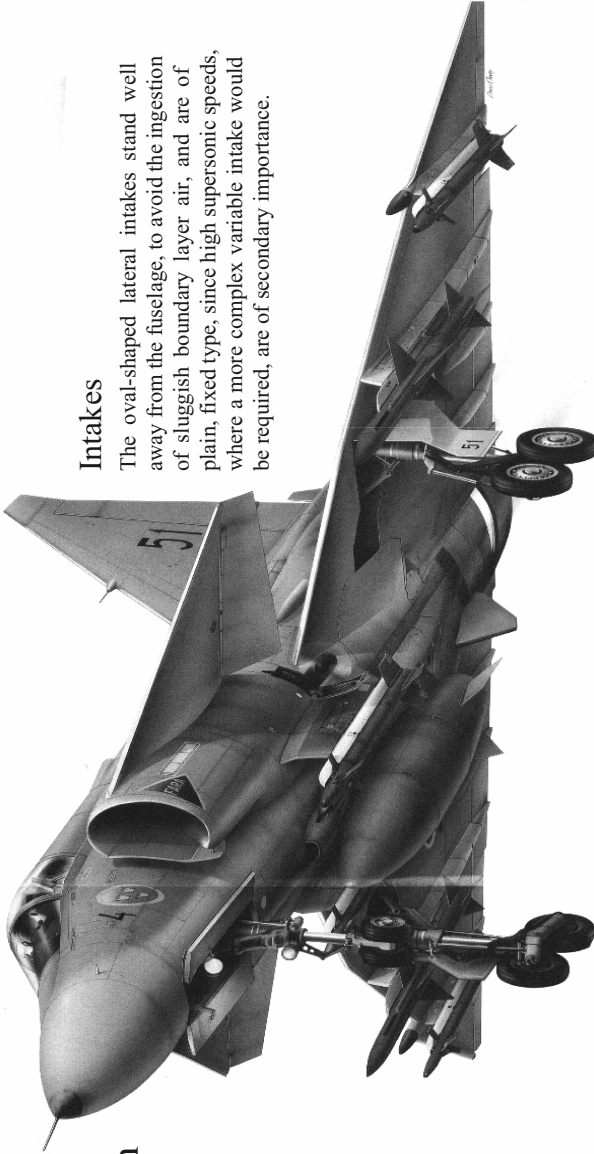
Plate 2.53. JA 37 Jaktviggen
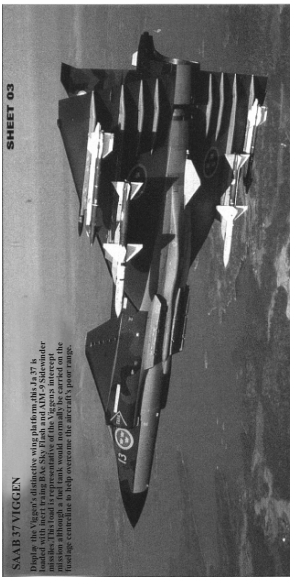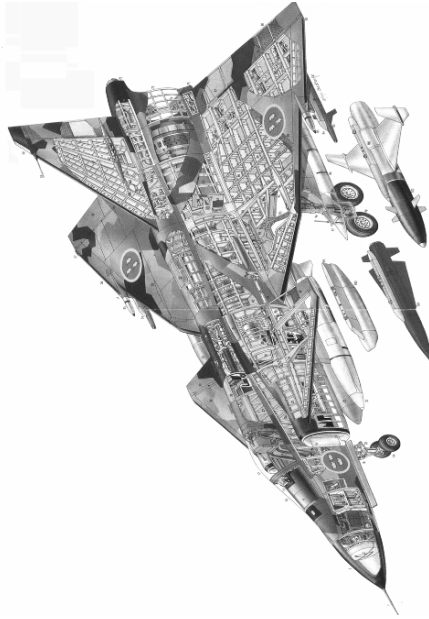
SPECIFICATION

JA 37 Viggen

Dimensions

Length: 53 ft 9¾ in (16.40 m)
Height: 19 ft 4¼ in (5.90 m)
Wingspan: 34 ft 9¼ in (10.60 m)
Wing area: 495.16 sq ft (46.00 m²)
Canard foreplane span: 17 ft 10½ in (5.45 m)
Canard foreplane area: 66.74 sq ft (6.20 m²)
Wheel base: 18 ft 8 in (5.69 m)
Wheel track: 15 ft 7½ in (4.76 m)

Powerplant

One Volvo Flygmotor RM8B turbofan (Pratt & Whitney JT8D-22 with Swedish-designed afterburner and thrust reverse) rated at 16,600 lb st (73.84 kN) maximum military dry and 28,109 lb st (125 kN) with afterburning.

Weights

Normal take off: 33,069 lb (15000 kg)
Maximum take-off interceptor: 37,478 lb (17000 kg)
Maximum take-off attack: 45,194 lb (20500 kg)

Fuel and load

Internal fuel: 1,506 US gal (5700 litres)

Performance

Maximum level speed clean at 36,000 ft (10975 m): More than 1,147 kt (1,321 mph; 2126 km/h)
Climb to 32,800 ft (10000 m): Less than 1 minute 40 seconds from brakes off with afterburning
Service ceiling: 60,000 ft (18290 m)
Take-off run at typical take-off weight: 1,312 ft (400 m)
Landing run: 1,640 ft (500 m) at normal landing weight
Combat radius on hi-lo-hi mission: 539 nm (621 miles; 1000 km)
Combat radius on lo-lo-lo mission: 270 nm (311 miles; 500 km)

Armament

Primary armament consists of six AAMs. The standard BVR weapon is the medium-range, semi-active radar guided, all-weather BAeD Rb 71 Sky Flash. Rb 74 (AIM-9L) IR-homing Sidewinders are fielded for short-range work. The JA 37 also has an integral 30-mm Oerlikon KCA revolve cannon with 150 rounds. Seven to nine pylons accommodate up to 13,000 lb (5987 kg) of external stores. These include four pods each containing six Bofors 5.3-in (13.5-cm) rockets for air-to-surface use.

SAAB 37 VIGGEN

Viggen
Briefing

Depictes the Viggen's distinctive wing platform this 1A 37 is loaded with inert firing Rbo Sky Flash and AIM-9 Sidewinder missiles. This load is representative of the Viggen's intercept mission although a fuel tank would normally be carried on the fuselage centreline to help overcome the aircraft's poor range.

SHEET 03

Plate 2.54. Structural parts and specification
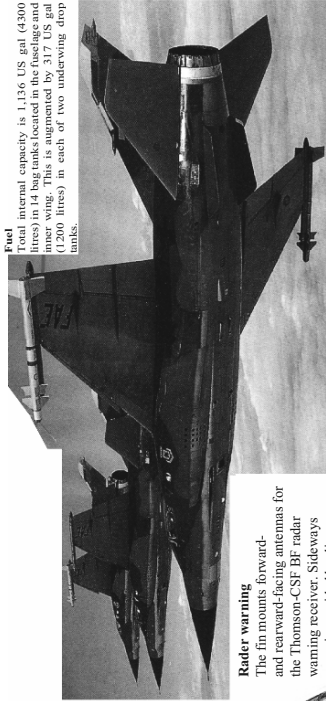
Fuel
Total internal capacity is 1,136 US gal (4300 litres) in 14 bag tanks located in the fuselage and inner wing. This is augmented by 317 US gal (1200 litres) in each of two underwing drop tanks.

Rader warning
The fin mounts forward- and rearward-facing antennas for the Thomson-CSF BF radar warning receiver. Sideways cover is provided by disc antennas flush with the fin sides.

Armament
The basic armament consists of two internal cannon with most stores carried on multiple dispensers on the centre line. Although not shown here, the F1AZ could be fitted with wingtip launch rails for the V3B Kukri or V3C Darter indigenous air-to-air missile.

Mirage F1AZ
The last South African Mirages wore this distinctive camouflage scheme. National and squadron insignia wereb often over-sprayed. This aircraft served with No. 1 Sqn, at Hoedspruit, the last SAAF Mirage F1 user before the type's retirement in last 1997.

Probe
South Africa's F1AZs had fixed refuelling probes on the starboard side for inflight refuelling.

Undernose fairing
The undernose bulge houses a Thomson-CSF TMV-360 laser rangefinder, which provides accurate distance-measuring for the ground attack role.

Ranging radar
The F1A fighter-bomber carried a small EMD Aïda 2 ranging radar in the extreme nose. The radar has a fixed antenna and provided automatic search, acquisition ranging and tracking for targets within its 16° Field of View. Data was presented to the pilot in his gyro gunsight.

Plate 2.55. Mirage F1 variants

20 November 1982. For its mission the Mirage F1CR carries a wealth of recon-naissance equipment both internally and externally. An SAT SCM2400 Super Cyclope infra-red linescan unit is installed in place of the cannon, and an undernose fairing houses either a 75-mm Thomson-TRT 40 panoramic cam-era or 150-mm Thomson-TRT 33 vertical camera. Other internal equipment includes a Cyrano IVMR radar with extra ground-mapping, blind let-down, ranging and contour-mapping modes, when compared to the fighter's radar, and provision of a navigation computer and ULISS 47 INS. Additional sen-sors are carried in various centre-line pods, these including Thomson-CSF Raphael TH side-looking airborne radar, HAROLD long-range oblique camera or Thomson-CSF ASTAC electronic intelligence pods. Various combinations of cameras can also be mounted in a pod. An inflight refuelling probe is fitted on the starboard side of the nose.

2.21.3 Latest Upgrades

The F1CT programme upgrades interceptors to a similar standard to the tactical recce F1CR. Radar changes from Cyrano IV to IVMR, with additional air-to-ground modes, and is backed by a SAGEM ULISS 47 inertial platform, Dassault Electronique M182XR central computer, Thomson VE120.

HUD, Thomson-TRT TMV630A laser rangefinder beneath the nose, Martin-Baker Mk 10 zero-zero ejection seat, improved radar warning receiver, chaff/flare dispensers and secure radio equipment.

Structurally, the cockpit is rebuilt and the wing strengthened and modified for activation of the outboard hardpoints, while the port cannon is removed to make space for the additional equipment and the whole airframe is rewired and fitted with new dielectric panels. Strengthening of the centre-line pylon permits carriage of the large, 484-Imp gal (2,200-l) tank originally developed for the Iraqi Mirage F1EQ. Externally, the blue-grey air defence camouflage is exchanged for wrap-around green and grey. The F1CT carries bombs and rocket pods for its new mission, but retains the ability to launch Super 530 and Magic 2 AAMs as a pure interceptor.

Plate No. 2.56–2.58 show the layout of Mirage F1AZ with various elements marked on it and a "cut-away" of F1 with complete briefing and specification. Weapons and stores for F1 are summarized.

2.22 Dassault Mirage 2000

2.22.1 Introduction

The latest in a long line of distinguished warplanes to bear the Mirage label, the 2000 began life as a fighter to re-equip France's interceptor squadrons, but has emerged as a true multi-role performer.
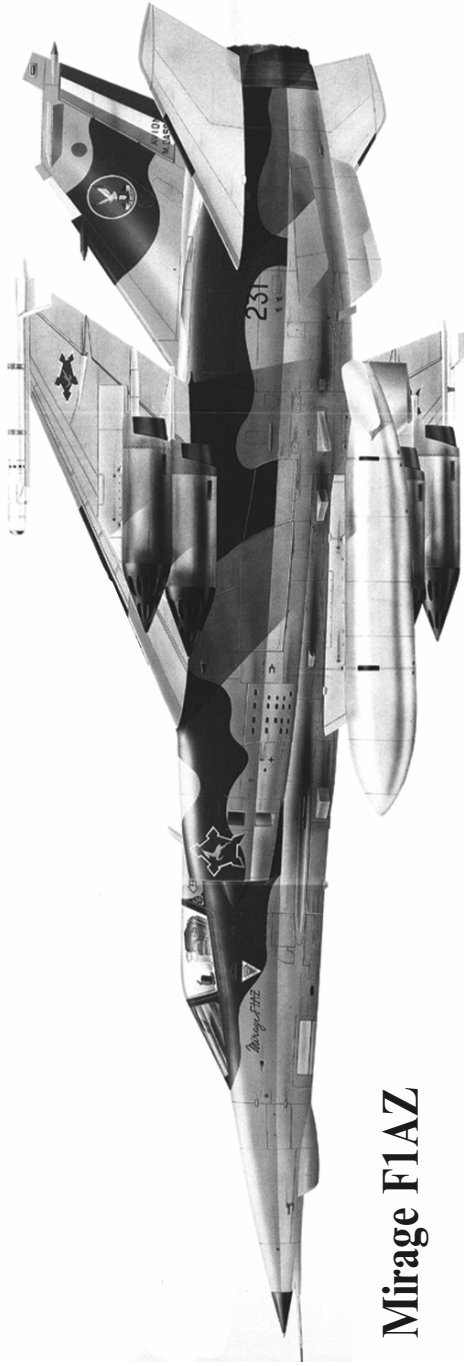
Mirage F1AZ

In the late 1990s, the only Mirage F1s remaining in French service are F1CRs (illustrated), F1CTs, F1Bs and a few F1C fighters flying operationally with EC4/33 'Vexin' stationed in Djibouti and as trainers in France. The aircraft is still an important element within the Armée de l'Air, however, and remains a key warplane in the inventories of a number of air arms.

Plate 2.56. Mirage F1AZ

Mirage F1

Possibly one of the most aesthetically pleasing combat aircraft yet designed, the Mirage F1 has demonstrated its considerable combat capability in conflicts ranging from anti-guerrilla strikes in South Africa to Desert Storm.
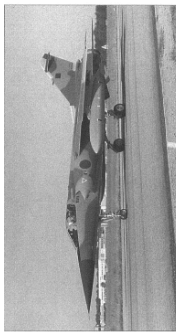
Libya ordered 38 F1s, including 16 F1EDs. The aircraft are tasked mainly with air defence, but have a limited ground-attack capability. This was practised against Chad in the 1980s, the Libyan Mirages declining to engage French F1s based in the area.

SPECIFICATION

Mirage F1C
(unless otherwise noted)

Dimensions
Wingspan without tip stores: 27 ft 6¾ in (8.40 m)
Mirage F1B: 27 ft 8   in (8.44 m)
Wingspan with tip-mounted Magic AAMs: 30 ft 6¾ in (9.32 m)
Wing aspect ratio: 2.82
Wing area: 269.11 sq ft (25.00 m²)
Length: 50 ft 2½ in (15.30 m)
Mirage F1B: 51 ft½ in (15.55 m)
Wheel track: 8 ft 2½ in (2.50 m)
Wheel base: 16 ft 4¾ in (5.00 m)
Height: 14 ft 9 in (4.50 m)
Mirage F1B: 14 ft 8½ in (4.49 m)

Powerplant
One SNECMA Atar 9K-50 turbojet rated at 11,023 lb st (49.03 kN) dry and 15,785 lb st (70.21 kN) with afterburning

Weights
Empty: 16,314 lb (7400 kg)
Operating empty (Mirage F1B including pilots): 18,078 lb (8200 kg)
Normal take-off: 24,030 lb (10900 kg)
Mirage F1B: 24,691 lb (11200 kg)
Maximum take-off: 35,715 lb (16200 kg)

Fuel and load
Internal fuel capacity: 1,134 Imp gal (4300 litres)
Mirage F1B: 1,017 Imp gal (3850 litres)
External fuel capacity: Provision for one 581-Imp gal (2200-litre) tank on centreline and two 299-Imp gal (1130-litre) tanks under the wings
Maximum weaponload: 13,889 lb (6300 kg)

Performance

Maximum level speed 'clean' at 36,090 ft (11000 m): 1,453 mph (2338 km/h)
Maximum rate of climb at sea level: 41,930 ft (12780 m) per minute
Mirage F1B (without afterburning): 13,783 ft (4200 m) per minute
Service ceiling: 65,615 ft (20000 m)
Mirage F1B (stabilised supersonic ceiling): 52,495 ft (16000 m)
Take-off run at 25,353-lb (11500-kg) weight: 1,969 ft (600 m)
Landing run at 18,739-lb (8500-kg) weight: 2,198 ft (670 m)

Range

Combat radius: 264 miles (425 km) on a hi-lo-hi attack mission with 14 551-lb (250-kg) bombs, or 373 miles (600 km) on a lo-lo-lo attack mission with six 551-lb (250-kg) bombs and two drop tanks, or 863 miles (1390 km) on a hi-lo-hi attack mission with two 551-lb (250-kg) bombs and three drop tanks
Endurance 2 hours 15 minutes on a CAP with two Super 530 AAMs and one drop tank
Mirage F1B normal training mission endurance: 2 hours

Armament

Two fixed internal DEFA 553 30-mm cannon with 135 rounds per gun; standard air-to-air load of two MATRA Magic or AIMs-9 Sidewinder missiles on wingtip rails and either one MATRA R.530 on the centreline station or two Super 530Fs underwing. A limited ground-attack capability is available using various unguided bombs, cluster munitions and rockets.

With second-hand ex-USAF F-16s complementing the F1 in Jordanian service, a number of Mirages have been sold to Spain. The F1 is a potent multirole aircraft and it is unlikely that Jordan would wish to relinquish its entire fleet.
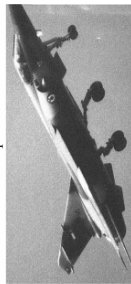
Plate 2.57. Mirage F1

F1: weapons and stores

An F1 poses with the extensive array of stores available to the aircraft. Apart from the two types of AAM in the foreground, the display includes the internal cannon and their 270 rounds of 30-mm ammunition, gun pods and their associated DEFA cannon, various dumb bombs, rockets of differing calibres and their associated pods, and an AS30 air-to-ground missile.
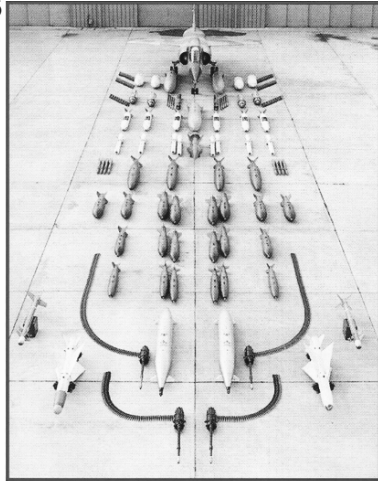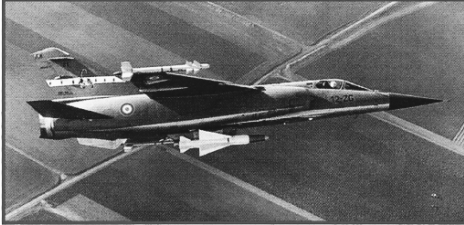
One of the standard air-to-air weaponloads of early F1Cs was that illustrated above, consisting of a centreline MATRA 530FE and two wingtip-mounted Magics. The missile was built in both semi-active radar-homing (SARH) and IR-homing versions. The latter was limited to tail-chase use only, while the missile in general had a poor combat record and was generally regarded as an inferior weapon in service.

With the 530FE providing a disappointment, its replacement was a matter of great urgency. MATRA therefore developed the Super 530-F1 from the earlier weapon, and this was to become the standard BVR missile in the F1's armoury.
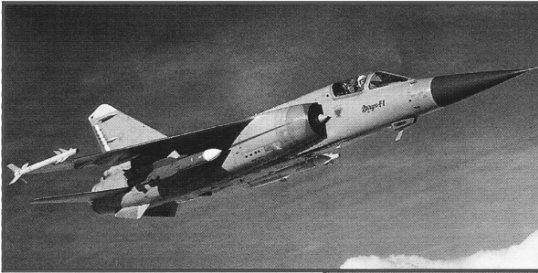
A modernised development of the anti-radar version of the Anglo-French Martel, the MATRA Armat is seen here being test-launched from a French F1. The weapon has been used in action against Iranian air defence radars by Iraqi F1EQs. The missile was available to French, Iraqi and Kuwaiti Mirage F1s.
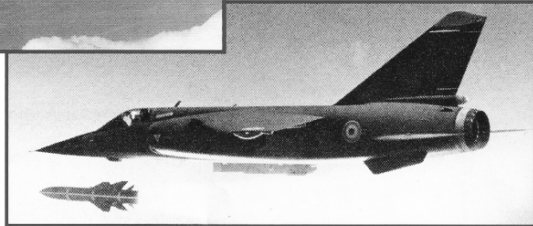
Plate 2.58. F1 Weapons and storage

One of France's principal fighter manufacturers, Dassault Aviation, has long had a policy of reusing titles which have proved successful. After the Mirage III had boldly imprinted the name of Générale Aéronautique Marcel Dassault on the map of world military aviation during the 1960s, its differently – shaped successor became the Mirage F1. During the 1980s and into the 1990s, Dassault built a third generation of Mirages, once again changed radically – in sophistication, if not in shape – from its predecessors. However, it must be said that when Mirage 2000 began life as a "back-burner" project, few ever expected it to see the light of day. Dassault's design office commenced work on its Delta 1000 project in 1972, while a far greater proportion of work was being expended on the Avion de Combat Futur (ACF) – the proposed next generation combat aircraft. But the ACF project was eventually deemed too expensive and fell away, while the Delta project now given the designation Mirage 2000, began to take shape.

For this new aircraft, Dassault returned to the delta configuration that was so successful in the Mirage III, 5 and 50 and the 2000 also shares with its predecessors the big high-lift wing and large internal volume.

2.22.2 French Operation

The Mirage 2000 is now standard equipment for the French fighter arm and is operational in a number of variants. A two-seat trainer, the Mirage 2000B flew in production form on 7 August 1983 and is only $7^1/_2$ in (19.05 cm) longer than the 2000C. French 2000Bs and Cs (standard single-set interceptor) are sometimes and confusingly known as Mirage 2000DAs (DA for "Defense Aérienne" – Air Defence). For nuclear attack missions, Dassault decided to modify a two-seater Mirage with fuselage enhancements and more accurate positioning systems. The result was the 2000N, which could carry the ASMP missile and now provides France's only aerial nuclear strike capability. Modifications to the 2000N have resulted in the Mirage 2000D, which is a conventional strike aircraft and while unable to take the ASMP, it is capable of carrying a wide range of French air-to-surface weaponry. Dassault Electronique Sabre jammers plus a Serval radar warning receiver. The aircraft could also be fitted with the MATRA Spirale integrated decoy system. Although early 2000Ns lacked Spirale as standard, since 1989 it has been fitted to all aircraft. The initial requirement was for 100 Mirage 2000Ns which would be allocated 75 ASMP missiles, some of which would have come from ex-Mirage IVP stocks. However, delays with the Dassault Rafale programme and the need for an interim replacement for the Mirage IIIE meant that a further 70 Mirages were added to the conventional attack role, with the ASMP interface deleted. Generally regarded as "non-nuclear" aircraft, they were given the designation Mirage 2000N' (N Prime). A reassessment of nuclear requirements resulted in later changes to the number of Ns and N's and to simplify the distinction between the two, the latter was designated Mirage 2000D in 1990.

It was soon realised that a single pilot could not handle the intense workload involved in nuclear interdiction missions, so the two-seat Mirage 2000B trainer was strengthened and modified to withstand the rigours of low-level attack flying.

The Mirage 2000N-01 first prototype flew initially on 3 February 1983 at lstres, and is seen here carrying an ASMP missile and the original smaller wing tanks.

Plate 2.59. Mirage 2000N France's nuclear deterrent

2.22.3 Weaponry

The first 2000Ns, with ASMP capability, were designated K1 sub-types. The ASMP, which is carried on the centerline pylon, delivers a 150 or 300 kT warhead over a maximum range of 50 miles (80 km) from a low altitude launch point. Provision is made for a pair of large, 528 US gal (2,000 l) drop tanks underwing. From the 32nd 2000N onwards, the designated K2 was used and these aircraft were capable of carrying conventional ordnance or a nuclear payload. The same weaponload is available for the 2000D, "D" standing for "Diversifié" (Diversified), the prototype of which (D01, ex-N-01) first flew on 1 January 1990. Weapons that can be carried include the Aerospatiale AS30L and MATRA BGL (Bombe Guidée Laser – laser – guided bomb), both of which are guided by the ATLIS 2 laser designator pod. The MATRA APACHE stand-off dispenser, ARMAT anti-radar missiles are also available to the 2000D.

2.22.4 Operators

At present, six Escadres de Chasse fly the Mirage 2000 in its "D" or "N" form. Mirage 2000Ds are part of the Commandement de la Force Aérienne de Combat (CFAC), France's largest command. A further Dassault modification is the Mirage 2000-5 – an upgraded 2000C with enhanced avionics incorporating a weapons management system, improved self-defence options and powerplant. French Mirage 2000Cs are currently being modified to this standard along with those of Greece and Abu Dhabi.

2.22.5 The Future

A recent modification programme has seen EC 2/2 at Dijon become the first unit to receive Mirages that have been upgraded to 2000-5F status. These fighters, equipped with MATRA/BAe Dynamics MICA air-to-air missiles are to remain in service for many years. They and the Mirage 2000Ns, will soon be joined by the superb Dassault Rafale. France's 21st century air force will be a powerful blend of high technology with indigenous aircraft that are able to hold their own worldwide.

When the Mirage 2000 was being designated one of its envisaged roles was that of a nuclear penetrator. The aircraft would be used to deliver the new tactical stand-off weapon designed by Aerospatiale and known as the ASMP (Air-Sol Moyenne Portee – Air-to-Ground Medium range) missile. Originally, this weapon was carried by the Mirage IVPs of the Strategic Air Forces and the navy's carrier based Super Etendards. The cancelled ACF (Avion de Combat Futur) had been another candidate for the ASMP. However, due to the age of the Mirage IVP, Dassault received a contract for two prototypes of an interdictor version of the new Mirage 2000, to be designated 2000P ("P" for "Penetration"). However, the designation was soon changed to 2000N ("N" for "Nucleaire") to avoid confusion with the ageing Mirage IVP.

2.22.6 Designing the 2000N

Due to the high pilot work load that would be encountered during an interdiction mission at low-level, it was decided that a WSO would be needed to undertake radar navigation, control the ECM equipment and manage the armament. The 2000N was based upon the 2000B trainer, but the airframe was strengthened to withstand the stresses of high-subsonic, low level flight. Some internal equipment was also modified from the original Mirage 2000C interceptor and this reflected the defence, conventional ground attack and tactical reconnaissance missions. Three squadrons fly from Nancy: EC1/3 "Navarre", EC 2/3 "Champagne" and EC 3/3 "Ardennes". Mirage 2000Ds are expected to serve well into the next century and they will be the last of France's current warplane fleet to be replaced by Rafale. It is estimated that, by 2015, the French air force will have a fleet of 300 Rafales ad Mirage 2000Ds.

Mirage 2000Ns operate as part of the Commandement des Forces Aériennes Strategiques (CFAS). The main mission of the strategic air forces is to provide a nuclear deterrent. Since the withdrawal of the Mirage IVP and the phase-out of the ballistic missiles at the Plateau d'Albion, the CFAS nuclear deterrent rests solely with the three Mirage 2000N units. Equipped with the ASMP missile they, together with the French navy's ballistic missile submarines, provide France with its nuclear strike capability. EC 1/4 "Dauphine" and EC 2/4 "Lafayette" from Luxeuil, while EC 3/4 "Limousin" operates from Istres. Tanker support for the 2000Ns is provided by Istres-based C-135FRs.

Plate No. 2.60–2.62 give a general profile of Mirage 2000 and 2000N with briefing and a "cut-away" marking various zones and a table of specifications.

Mirage 2000H (Vajra)

Flying for the first time on 16 April 1979, No. 03 was primarily tasked with weapons trials, being fitted with the full nine hardpoints. The aircraft became the first Mirage 2000 to fly with radar – an RDM unit on 13 November 1980. Firing trials with Super 530F and Magic missiles followed in 1982, before the delayed, but definitive, RDI radar was installed. The latter allowed the aircraft to launch the Super 530D missile for the first time on 26 October 1984. No. 03 also featured a camouflage pattern which was adopted in service, albeit with different colours chosen.

The first 15 Mirage 2000s had black radomes covering their RDM radar and, despite the carriage of the Super 530 missile, there was no illuminator for it, meaning that only the Magic missile could be fired. 2 Escadre de Chasse at Dijon-Longvic was chosen as the first Mirage 2000C operator.

Defensive systems

In addition to the RDM radar, the Mirage 2000 is extensively equipped with defensive avionics equipment. These defences include a Thomson-CSF/Dassault Electronique ECM system with VCM-65 disply and jammers housed in the leading-edge of the fin and in an extended bullet fairing at the base of the rudder. MATRA Spirale passive countermeasure systems and Thomson-CSF Serval radar warning receivers with antennas at the wingtips and the front of the fin fairing.
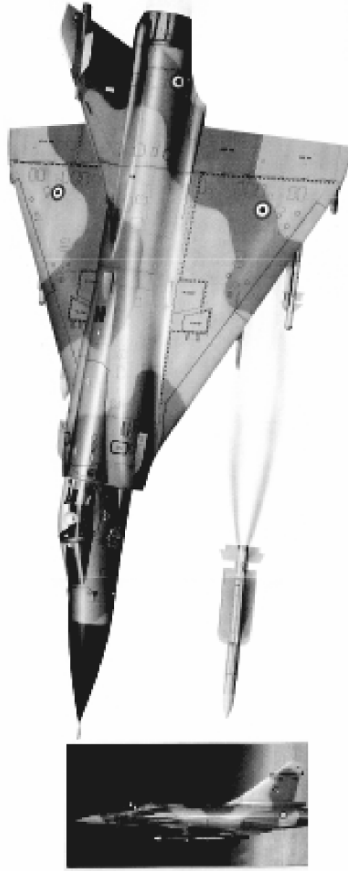
Plate 2.60. Mirage 2000H
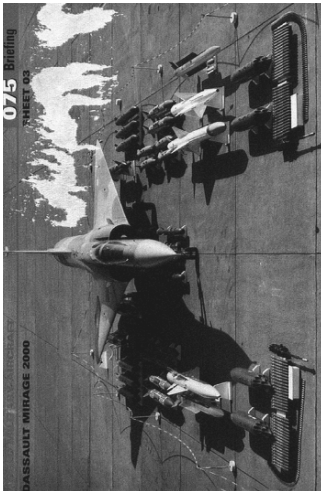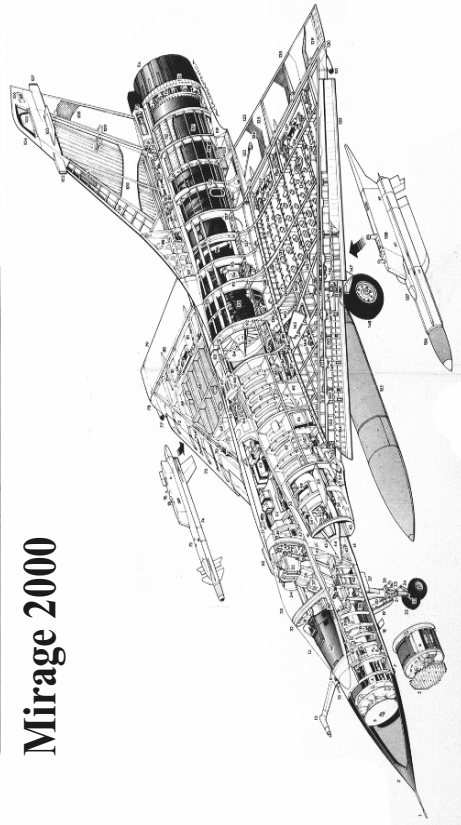
SPECIFICATION

Mirage 2000C

Dimensions

Fuselage length: 47 ft 1¼ in (9.13 m)
Wingspan: 29 ft 11½ in (9.13 m)
Wing area: 441.33 sq ft (41.00 m²)
Wing aspect ratio: 2.03
Height: 17 ft ¼ in (5.20 m)
Wheel track: 11 ft 1⅜ in (3.40 m)
Wheel base: 16 ft 4¾ in (5.00 m)

Powerplant

One SNECMA M53-P2 turbofan rated at 14,462 lb st (64.33 kN) dry and 21,384 lb st (95.12 kN) with afterburning

Weights

Empty: 16,534 lb (7500 kg)
Normal take-off: 23,534 lb (10680 kg)
Maximum take-off: 37,478 lb (17000 kg)

Fuel and load

Internal fuel: 6,966 lb (3160 kg)
External fuel: 8,201 lb (3720 kg) in one 343-US gal (1300-litre) drop tank and two 449 US-gal (1700-litter) drop tanks.
Maximum ordnance: 13,889 lb (6300 kg)

Performance

Maximum speed at high level: Mach 2.2
Maximum speed at sea level: Mach 1.2

Maximum speed in stable flight: 100 kts (115 mph; 185 km/h)
Range: Over 850 nm (979 miles; 1575 km) with 4,409 lb (2000 kg) of underwing ordnance and external fuel tanks
Service ceiling: 54,000 ft (16460 ml)
Reaction time: Under five minutes, from brakes-off to interception of Mach 3 target at 80,000 ft (24400 m)

Armament

Two internal DEFA 554 30-mm cannon with 125 rounds per gun. Total of 13,889 lb (6300 kg) of stores carried on five underfuselage and four underwing hardpoints. Standard air defence load is two MATRA Magic 2 infra-red missiles and two Super 530D radar-guided missiles. Early aircraft were only equipped to fire the Super 530F. In the ground-attack role, up to 18 551-lb (250-kg) bombs or BAP 100 anti-runway bombs, two 1,984-lb (900-kg) BGL 1000 laser-guided bombs, six Belouga cluster bombs, two AS30L laser-guided air-to-surface missiles, two ARMAT anti-radiation missiles or two AM39 Exocet anti-ship missiles are options.
Mirage 2000D/N/S: The N is dedicated to the carriage of the 1,874-lb (850-kg) ASMP stand-off nuclear missile (150 kT or 300 kT yield). The 2000D/S has provision for the MATRA APACHE, Durandal, F4 rocket pod or Dassault CC630 gun pod.

Mirage 2000

Plate 2.61. Mirage 2000 structural parts and specification

Mirage 2000 Weaponry

ATLIS 2 LASER DESIGNATION POD
ATLIS 2 is a pod-mounted laser targeting system with an automatic TV tracker, laser designator/ranger, tape recorder and interface electronics. The TV tracker and laser system reduce the pilot workload and allow single-seat aircraft to track and designate targets. The system is accurate to within 3.04 ft (1 m) at a range of 6.21 miles (10 km) and can provide a high rate of success for low- and medium-level attacks.

AM39 EXOCET ANTI-SHIP MISSILE
The Mirage 200C, 2000C-5 and, especially, the 2000D all have the ability to launch the formidable Aèrospatiale AM39 Exocet. As a medium-range missile with an HE-shaped charge warhead, the Exocet gives the Mirage 2000 a potent anti-shipping capability via a combat-proven and mature weapon. The missile entered service in 1979 with the French Navy and has been exported around the world. Iraq used the weapon against Iranian ships and oil platforms in the Iran-Iraq war and fired two missiles against USS Stark in May 1987. In addition, Exocets were launched with dramatic effect by Argentine Super Etendards against British warships during the 1982 Falklands conflict.
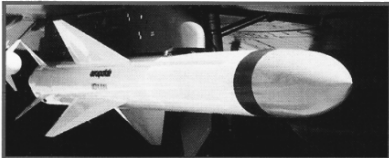
ASMP
The ASMP (Air-Sol Moyenne Portee - medium-range air-to-surface) missile is a guided nuclear stand-off weapon that was designed to replace the AN22 nuclear free-fall bomb carried by the Mirage IV. Although the Mirage IVP and Super Etendard have been cleared to carry the ASMP, it was primarily designed for carriage aboard the Mirage 2000N. The 2000N uses the Dassault Electronique / Thomson-CSF Antilope 5 radar which, when operating in ground-mapping mode, provides the ASMP with target co-ordinates and guidance information for its onboard inertial navigation systems.
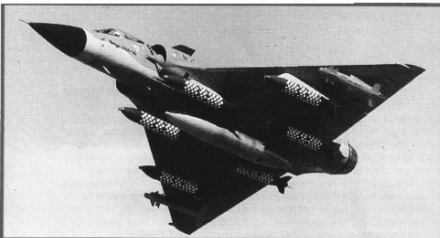
DURANDAL AIRFIELD DENIAL WEAPON
Durandal was designed in response to a l'Armèe de l'Air requirement for an airfield denial weapon capable of penetrating up to 15³/₄ in (40 cm) of concrete runway. The concrete slabs of runways and taxiways are either disturbed and/or broken as the weapon explodes beneath them, or are covered by debris. In either case, the surface is rendered unserviceable for aircraft movements. In order to generate enough kinetic energy for penetration, the bomb is accelerated by means of a rocket motor. It also strikes the surface under attack at a special angle which allows the greatest penetration and leads to the most efficient detonation of its shaped warhead in a delayed explosion. Durandal is in widespread use both in France and around the world.

SUPER 530D AIR-TO-AIR MISSILE
Third of the 530 missile family, the Super 530D ('D' for 'Doppler') was developed to counter low-flying aircraft and uses a monopulse continuous wave (CW) Doppler semi-active radar seeker. Development began in 1979 to meet a l'Armèe de l'Air requirement to arm the Mirage 2000. Firing trials of the Super 530D took place in 1984 and the system became operational four years later. The MATRA Super 530D is the current principal missile of the Mirage 2000, both with the French Air Force and with foreign operators such as India and Greece. It is able to destroy targets flying as high as 80,000 ft (24400 m).
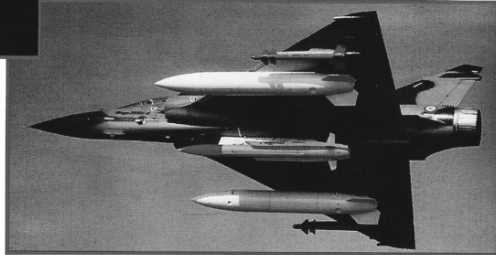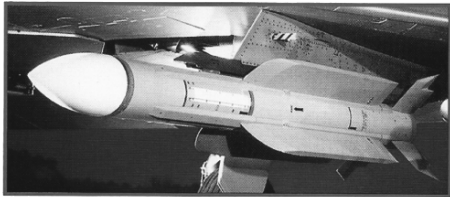
BLG 66 BELOUGA CLUSTER BOMB
With a weight of 672 Ib (305 kg), the Belouga cluster bomb contains 151 individual bomblets. These bomblets are released from the dispenser in free-fall and consist of three distinct types: fragmentation, anti-armour and area interdiction. The first is for attacks against relatively soft area targets such as dispersed aircraft, truck convoys and fuel dumps. The anti-armour bomblet is able to pierce 9.8 in (250 mm) of steel and is employed against tanks and other armoured vehicles. The interdiction munition shares many features of the fragmentation bomblet, but has time-delay fuses which cause the dispersed bomblets to explode at various times after delivery within the target area. On release from the aircraft, a parachute rapidly decelerates the weapon, allowing the launch aircraft to escape the area before the bomblets are dispensed on their own parachutes. The BLG 66 is a standard weapon of the Mirage 2000D and 2000-5.

Plate 2.62. Mirage 2000 Weaponry

2.23 Panavia Tornado

2.23.1 Introduction

With a requirement to replace its huge fleet of Starfighters, the Luftwaffe became the largest operator of the Tornado IDS. It has developed the type for

service in a number of roles, and belatedly introduced the type to operations over Bosnia.

Originally intended as a one-for-one replacement of the F-104 Starfighter, with an initial requirement for around 700 aircraft, the Tornado finally equipped four front-line Luftwaffe squadrons (and one training wing) for a total of 247 new-build aircraft. These came from production Batches 1–7. Subsequently, the Luftwaffe acquired 40 ex-Marineflieger aircraft in order to establish a tactical reconnaissance wing.

The first Luftwaffe aircraft to enter service were assigned to the Trinational Tornado Establishment at RAF Cottesmore, England which handled type conversion. Germany based JBG 38, the operational training unit at Jever, acquired its first aircraft in November 1981 (at which time it was known as the Waffenausbildungs-komponenete, or WaKo). JBG 31 at Norvenich began conversion from the F-104 in July 1983 to become the first front line unit, followed by JBG 32 at Lechfeld (July 1984), JBG 33 at Buchel (August 1985) and JBG 34 at Memmingen (October 1987). Plans to form a fifth geschwader, JBG 37, were abandoned when the Luftwaffe cancelled its 35-aircraft Batch 8 order for more ECRs. With the draw-down in forces at the end of the Cold War, a number of Luftwaffe Tornados are held in storage at MADC at Davis-Monthan AFB, Arizona.

Training began at Holloman AFB, New Mexico, in 1996 as a means of overcoming low level flying restrictions and poor weather in Germany, while the ranges around Goose Bay, Labrador, are extensively used in the summer months for low-level operational training. The initial type conversion will also be transferred to Holloman upon the closure of the TTTE in 1999.

2.23.2 Strike/Attack

When it first entered service, the Luftwaffe Tornado was dedicated to the overland strike/attack role, armed with 1,000 lb (453 kg) Mk 83 bombs or nuclear weapons – the latter being US-owned B57/B61s. the nuclear capability is retained, JBG 33 at Buchel being the strike-assigned unit. Another important weapon developed for the Tornado was the MW-1, cumbersome dispenser system carried under the fuselage which could deliver a variety of submunitions for anti-armour, anti-runway and other area denial missions.

For self defence, Luftwaffe aircraft carry a pair of AIM-9L Sidewinders on the inner wing shoulder pylon, while outboard wing pylons are used for carrying BOZ chaff/flare dispensers and Cerberus ECM jamming pods.

The Luftwaffe Tornado fleet has been gradually updated, beginning with the modification of early aircraft to Batch 5 standards with Mil Std 1553 databus and limited HARM missile capability. Thirty-five new build aircraft were completed to ECR (Electronic Combat and Reconnaissance) standard, fitted with an infra-red linescan system, forward looking infra-red and an

emitter location system. In the event, the linescan system proved troublesome and was removed, although the under fuselage fairing is retained. The ECR aircraft, which all fly with JBG 32, are now used almost exclusively in the Wild Weasel defence suppression role. For reconnaissance, the Luftwaffe has replaced its RF-4Es. A reference is made to Plate 2.63 for Tornados functional parameters.

2.24 Tupolev TU-22 Blinder/TU22M Backfire

2.24.1 Introduction

It is a part of missile carrier Regiment with a fearsome AS-4 "Kitchen Missiles". The "Blinder" is now replaced by the multi-role TU22M and has a sharp mouth like a shark.

Plate No. 2.64–2.66 give a profile of TU22M3 "Backfire-C" equipped with missiles and other armer, a cut away diagram with a briefing and abridged specification for a comparative study, a reference is made to Table 2.45.

2.25 Helicopters

Helicopters are more vulnerable than aircraft in warfare. In Peace time a helicopter may crash after losing a rotor or hitting objects such as offshore platforms, buildings, helipads or their surrounding structures. Figure 2.54 shows three types of helicopters manufactured by the Soviet Union and India. Table 2.46 gives useful data for other types of helicopters.

2.25.1 Agusta A 101G and Variants

2.25.1.1 Introduction

Agusta began the design and construction in 1958 of an aircraft to meet an Italian air force requirement for a medium sized multi-role helicopter. The programme was broadly equivalent to Sud-Aviation's Super Frelon and was initially designated AZ 101G. Under the direction of the company's chief designer, Filippo Zapatta, the design team at Cascina Costa originally devised a 16 seat helicopter which was ahead of its time both in terms of configuration and powerplant. At a time when most contemporary medium-haul transport helicopters were powered by piston engines, Agusta chose turbine power in the form of three 750 shp (559 kW) Turbomeca Turmo 3 turboshafts for a significantly increased power-to-weight ratio and performance.

In 1959, the passenger capacity was revised to 35 passengers and 1,000 shp (746 kW) Bristol Siddeley Gnome engines were specified, the machine now

Wheeling over the German forest, for which its dark 'lizard' camouflage was specifically developed, this JBG 31 Tornado lugs the bulky MW-1 dispenser. Like the JP233 employed by the RAF's Tornados, MW-1 requires the aircraft to overfly its target. This is less than ideal above today's battlefield, and development of a stand-off successor, the Taurus, is at an advanced stage.

Tornado IDS

This Tornado wears the badge of Jagdbombergeschwader 33, which consists of a Tornado plan-view superimposed on a stylised diving eagle. Based at Buchel, JBG 33 has an overland role which includes the use of B61 nuclear weapons. Most of its aircraft are from Batch 5 production. This aircraft is depicted carrying the bulky MW-1 dispenser which can be used against a variety of area targets

Defences
Active jamming is provided by the Elta/DASA Cerberus pod, the latest version being Cerberus IV. On the opposite outboard wing pylon is the BOZ-100 pod, which provides mechanical countermeasures (chaff and flares). Antennas for the Elettronica ARI 23284 radar warning receiver are mounted in the fin tip.

Radar
The AEG-Telefunken radome covers the Texas Instruments radar set. This, in effect, is two radars: one for ground mapping functions to feed the nav/attack system and one for terrain-following. The latter has a small antenna mounted below the main attack radar

Camouflage
The first Luftwaffe Tornados wore a three-tone pattern of greys and greens, but most deliveries were made in a much darker three-tone green scheme. This was ideal camouflage against enemy fighters over Central Europe. In the mid-1990s it was replaced by a light grey scheme although this has not been adopted fleet wide.

MW-1 dispenser
The MW-1 ejects its sub-munitions sideways in a variety of patterns. Sub-munition options are the MUSA fragmentation bomblet, KB 44 anti-armour bomblet, MIFF delayed action mine and the STABO

Fuel
German Tornados do not have the fin tank specified for RAF machines. Total internal capacity is 1,285 lmp gal (5842 litres), usually augmented by two 330-lmp gal (1500-litre) drop tanks on the inner wing pylons. A further pair of tanks can be carried under the fuselage.

Cannon
The IDS (and Luftwaffe reconnaissance version) has a pair of IWKA-Mauser 27-mm cannon, each armed with 180 rounds. The ECR version has the cannon removed to make room for internal equipment.

Plate 2.63. Tornados

having a design maximum loaded weight of 24,910 lb (11,299 kg). The type was subsequently revised further and given the definitive Agusta designation A 101G. Few details on the type were released until mid-1961 when an ASW version was announced.

Tu-22M3 'Backfire-C'

Plate **2.64.** Tu-22M3 Backfire

SPECIFICATION

Tu-22M3 'Backfire-C'

Dimensions

Length: 139 ft 4 in (42.46 m)
Height: 36 ft 3 in (11.05 m)
Wingspan (fully-spread):
112 ft 7 in (34.30 m)
Wingspan (fully-swept): 76
ft 11 in (23.40 m)
Weapons bay length: 22 ft
11 in (7.00 m)
Weapons bay width: 5 ft 10
in (1.80 m)

Powerplant

Two side-by-side Kuznetsov/KKBM
NK-25 turbofans in rear fuselage,
each rated at 55,115 lb st (245.2
kN) with afterburning

Weights and loads

Maximum weaponload: 52,910
lb (24000 kg)
Maximum take-off weight:
273,370 lb (124000 kg)
Maximum landing weight:
194,000 lb (88000 kg)
Fuel load: 110,230 lb (50000 kg)

Performance

Maximum level speed at
high altitude: Mach 1.88
(1,080 kt; 1,242 mph; 2000
km/h)
Maximum level speed at
low altitude: Mach 0.86
(567 kt; 652 mph; 1050 km/h)
Normal cruising speed
at height: 485 kt (560 mph;
900 km/h)
Take-off speed: 200 kt
(230 mph; 370 km/h)
Take-off run: 6,560-6,890 ft
(2000-2100 m)
Normal landing run:
3,940-4,265 ft (1200-1300 m)

Armament

Maximum offensive load is
three Kh-22 air-to-surface
missiles or 52,910 lb (24000
kg) of conventional bombs and
mines, half carried internally
and half on racks under the
wings. Internal bombs can be
replaced by-rotary launcher for
six Kh-15P short-range missiles.
Loads can include Kh-31 or
Kh-35 missiles and FAB-3000,
FAB-1500, FAB-500 or
FAB-250 bombs.

The dragon badge of the 341st TBAP (Heavy Bomber Regiment) was first worn in Afghanistan, but was retained on its Tu-22Ps in later years. As the Soviet Union dissolved, most of the 'Blinders' were stationed in Belarus. However, the Belarussians allowed the Russians to withdraw the regiments and return them to Engels air base for disbandment. As of 1997, 92 such aircraft were waiting for 'demilitarisation'.

The 'Backfire' would probably qualify as the greatest of the West's Cold War bugbears. Few aircraft have been as feared or as mocked, as overestimated or as dismissed. Soviet Military Power, the US chronicle of the USSR in the 1980s, considered the Tu-22M to be a long-range strategic aircraft. However, both it and the 'Blinder' have only ever been used in the medium-range theatre role.

Tu-22/Tu-22M

Plate 2.65. Tu-22 Fighter Aircraft

'Blinder' and 'Backfire'

Tu-22RD ™Blinder-C∏
This 'Blinder' was part of the Aviatsiya Voyenno-Morskovo Flota (Naval Defence Fleet) or AV-MF. It could be equipped for free-fall bombing. but was mostly used in the maritime reconnaissance role in support of missile-carrying Tu-22Ks.
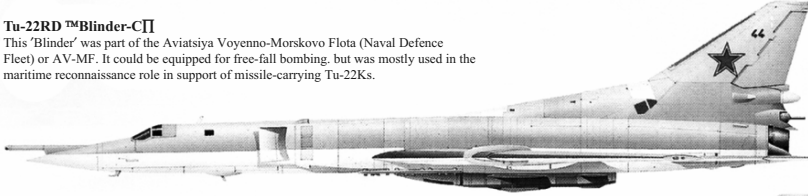
Tu-22M2 ™Backfire-B∏
Tupelov's 'Backfire' is still the primary anti-ship aircraft of the AV-MF, able to attack targets as far away as the North Atlantic. This Tu-22M carries an AS-4 ™Kitchen∏ missile under its fuselage – a total of three could be carried with the addition of wing pylons. but only at the considerable expense of range.
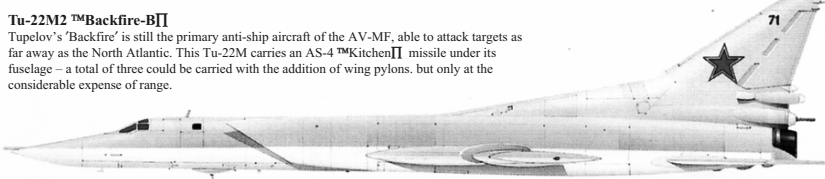
Tu-22M3 ™Backfire-C∏
The latest model of the 'Backfire', the 'C' has a number of obvious changes over previous models, most notable being the up turned nose and 'Foxbat'-style engine intakes. The aircraft first entered service with the Black Sea Fleet in 1985.

COLD WAR STRIKE

At the height of the Cold War, Soviet plans called for Kola Peninsular-based 'Backfires' to proceed to the Atlantic and, there, intercept naval vessels bringing supplies and troops to European NATO countries.

Kola Peninsular

USSR

As the Tu-22Ms rounded the Scandinavian coastline, they were regularly intercepted by Norwegian fighters. Here, a RNAF F-16A of Skv 331 escorts a Tu-22M2.

North Atlantic

NATO

WARSAW PACT

Once within range, the Tu-22M could attack targets with its devastating Kh-22 (AS-4 'Kitchen') anti-ship missiles.

Plate 2.66. Blinder and Backfire

Table 2.45. Data on the Tupolev series of aircraft

Type	Power plant	S (m)	L (m)	H (m)	A_w (m^2)	P_L (kg)	V (km/h)	w_a (kg)
TU-104	$2 \times 21{,}385$ lb (97 kN) Mikulin AM 3M500 turbojet	34.54	25.85	11.9	174.4	900	800	76,000
TU-124	$2 \times 11{,}905$ lb (54 kN) Soloviev D-20P turbofans	25.5	30.58	8.08	119	3,500	800	26,300
TU-134	$2 \times 15{,}000$ lb (66.5 kN) Soloviev D-30 turbofans	29	34.9	9	127	77,000	849	45,200
TU-144	$4 \times 44{,}000$ lb St (20,000 kg) with Kuznetsov NK-144 turbofans	28.8	65.7	12.85	438	14,000	2,500	180,000
TU-154	$3 \times 21{,}000$ lb (93.5 kN) Kuznetsov NK-8-2 turbofans	37.5	48	11.4	202	20,000	900	91,000

S, span; L, length; H, height; A_w, wing area; P_L, payload; V, speed; w_a, weight at take-off or landing
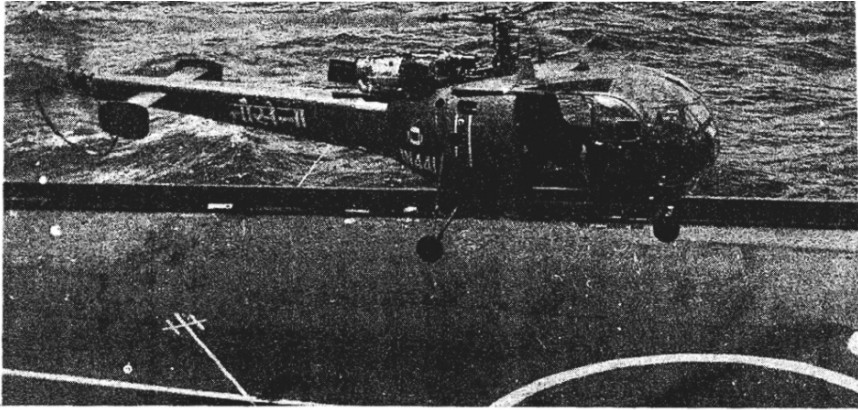
Fig. 2.54. Helicopter in service with the Indian forces (courtesy of Hindustan Aeronautics Helicopter Division)

Table 2.46. Data on helicopters

Type	Power plant	S (m)[a]	L (m)[b]	H (m)[a]	A_w (m^2)[a]	P_L (kg)	V (km h^{-1})	w_a (kg)	R (m)		
									d	t_b	h_t
Augusta A 109A MK II (Italy)		1.32	13.05	1.28	4.50	2,600	285	1,604	11.0		3.30
Augusta-Sikoysky AS-61R (HH-3F) (Italy/USA)	2 No. 1,118 kW (1,500 shp) GE: T58-GE-100 turboshafts	1.98	18.90	5.51	3.54	2,270	213	10,000	18.90	0.46	4.90
Bell 206B Jet Ranger III (USA)	1 No. 313 kW (4,205 shp) Allison 250-C20J turboshaft	1.97	11.82	2.91	4.2	1,451	216	742	10.16	0.33	2.54
Bell 206L-3 Long Ranger III (USA)	1 No. 485 kW (650 shp) Allison 250-C30P engine	1.97	13.02	3.14	2.35	1,882	246	998	11.08	0.33	2.90
Bell 212 Twin Two Twelve (USA)	Pratt and Whitney PT6 turboshafts coupled to a combined gearbox with a single output shaft producing 1,342 kW (1,800 shp)	2.86	17.46	4.53	4.5	5,080	185	2,720	14.69	0.5	3.91

Bell 412 (USA)	Pratt and Whitney PT6-3B-1 turbo twin pac (2 turboshafts) with a total 1,044 kW (1,025 shp)	2.86	17.07	4.32	7.9	5,397	230	2,935	14.02	0.29	3.29
HMZ-9A (China and Aerospatiale)	SA 365N Dauphin 2 twin turboshafts					4,100	285	2,050			
Kawasaki KV10711A-4	2 No. 1,044 kW (1,400 shp)	2.01	25.40	8.83	4.24	3,172	241	9,706	15.24	0.43	5.13
(Japan)	GE: CT58-140-1 or Ishikawajima-Harima CT58-1H1-140-1 turboshaft with max continuous rating 932 kW (1,250 shp)										
MBB-BO 105 S (Canada)	2 No. Allison 250-C28C turboshafts giving 820 kW (1,100 shp)	1.94	10.40	3.10	3.0	2,600	243	1,380	12.80	0.35	3.25
MIL-Mi-24 (Hind) MIL-Mi-25 (Hind) (USSR)	2 No. Isotov TV3-117 turboshafts each with max rating 1,640 kW (2,200 shp)	3.20	21.50	6.50		7,500	310	11,000	17.00		

Table 2.46. Continued

Type	Power plant	S (m)[a]	L (m)[b]	H (m)[a]	A_w (m^2)[a]	P_L (kg)	V (km h^{-1})	w_a (kg)	R (m)		
									d	t_b	h_t
Naras (Brantly) Model 305 (India/USA)	1 No. 227.4 kW (305 hp) Textron Lycoming IVO-540-BIA flat-6 engine	1.39	10.03	2.44	3.20	1,350	193	816	8.74	0.254	4.60
SA 332 Super Puma (Aerospatiale)	2 No. Turbomeca Makila 1A1 turboshafts each with 1,400 kW (1,877 shp)	1.55	6.05	4.92	7.80	9,300	266	4,475	15.60	0.60	4.60

[a] overall internal dimensions

[b] external rotor dimension

S, span; L, length; H, height; A_w, wing area; P_L, payload; V, speed; w_a, weight at take-off or landing; R, rotor details; d, rotor diameter; t_b, rotor blade card; h_t, overall height

A prototype was built for evaluation by the Italian air force and flew for the first time on 19 October 1964. Power was provided by three Bristol Siddeley Gnome H.1200 turboshaft engines, each developing 1,250 shp (932 kW) and driving a single five bladed main rotor system via a collective main gearbox. The tailfin mounted a six bladed anti-torque tail rotor and a large horizontal stabiliser to starboard. The A 101G incorporated a large capacity cabin with a sliding cabin door on each side as well as a large rear-loading ramp for cargo or vehicles. The helicopter could be flown with the ramp open to help accommodate bulky freight loads or for rapid unloading. Typical cabin loads included 35 passengers and 770 lb (349 kg) of baggage or the equivalent in weight of equipped troops or up to 14,330 lb (6,500 kg) of cargo or if used in the ambulance role, 18 streetcher cases with up to five attendants. The A101G was also proposed as a flying crane with loads of up to 11,023 lb (5,000 kg) carried externally on a hook mounted in the middle of the cabin floor.

As flown originally, the A 101G prototype (serial MM 80358) had quadricycle landing gear, but this was changed subsequently by the deletion of the forward pair of wheel units and their replacement by a twin wheel castoring nose unit. Only two additional prototypes were built and these featured a number of revisions including more powerful Gnome H.1400 engines, each rated at 1,400 shp (1,044 kW) a small fuselage stretch incorporating a seventh cabin window and aerodynamically refined side sponsons. All three prototypes saw limited service with the AMI (Italian air force), principally for evaluation by the AMI's RSV at Pratica di Mare. A projected civil transport version was developed by Agusta as the A 101H, which was to be powered by three 1,750 shp (1,305 kW) Bristol Siddeley Gnome H.1800 turboshaft engines. Similarly rated General Electric T58-16 turboshafts were offered as alternative powerplants.

2.25.1.2 Agusta A 104 Helicar

The Agusta A 104 Helicar two seat helicopter was a development of the single seat A 103, and was similarly intended for multi-role duties. The name Helicar ambitiously reflected the hope that, because it could be easily disassembled for stowage and re-assembled for flight by one person, some examples might be sold to private owners. The A 104 had a cabin with side-by-side seating and dual controls as an optional feature. The other major change lay in the installation of a more powerful air-cooled engine but despite the good performance of the A 104, only a single prototype was built, this flying for the first time in December 1960.

Agusta A 104 Helicar

Specification

Type: Two seat light helicopter.
Powerplant: One 138 hp (103 kW) Agusta MV A.1401V flat four piston engine,
                 derated to 120 hp (89 kW).
Performance: Maximum level speed 103 mph (165 km h^{-1}); cruising sped 84 mph
                 (135 km h^{-1}); hovering ceiling in ground effect 9,840 ft (3,000 m);
                 range 205 miles (330 km).
Weights: Empty 838 lb (380 kg) maximum take-off 1,411 lb (640 kg).
Dimensions: Main rotor diameter 26 ft 1 in (7.95 m); tail rotor diameter 4 ft $\frac{1}{4}$ in
                 (1.24 m); fuselage length 20 ft 10 in (6.35 m) height 7 ft $8\frac{1}{2}$ in; main
                 rotor disc area 534.34 sq ft (49.64 m^2).

2.25.1.3 Agusta A 105

Designed as what was hoped be a practical expression of the concept embodied in the A 104, the Agusta A 105 was intended asa two-seat utility helicopter suitable for a whole range of civil and military tasks. These included battlefield reconnaissance, liaison, supply, training, agricultural spraying and with a platform on each side of the central fuselage the transport of equipment or up to four troops over a range reduced to 62 miles (100 km).

Derived from the A 104, the A 105 was of typical light alloy construction with a pod and boom type of configuration. The boom extended rearward and slightly upward from the lower part of the pod's rear. The pod was extensively glazed with a door on each side and carried a crew of two with dual controls. The turboshaft engine was installed behind the upper part of the pod. As Bell's Italian licensee, Agusta had extensive experience of Bell-type dynamic systems and the A 105 was therefore fitted with a two bladed main rotor (complete with a Bell stabilising bar) and a two bladed tail rotor. The airframe was completed by the landing gear, which comprised a side-by-side pair of tubular steel skids with upturned fronts and two retractable ground-handling wheels toward their rears.

Agusta planned to build three prototype A 105s, and the first of these flew on 1 November 1964 but no production followed as it was quickly appreciated that the type lacked the power and payload for effective commercial or tactical use. However, further development of the A 105 led to the four seat A 105B which was proposed for essentially the same roles as those of the a 105. The A 105B had a number of modifications compared to its predecessor: the dynamic system was enlarged slightly, with small increases in the diameters of both the main and tail rotors. The cleaner lines resulting from the enlarged cabin gave the A 105B a slightly improved performance. At similar take-off weights and with the same engine power, the A 105B had a maximum level speed of 130 mph (210 km h^{-1}). A prototype A 105B was first flown in spring 1965 but like the A 105, the type did not succeed in achieving production status.

Agusta A 105

Specification

Type:	Two seat utility light helicopter.
Powerplant:	One Agusta (Turbomeca TAA.230 turboshaft engine rated at 270 shp (201 kW) for take-off and 240 shp (179 kW) for continuous running.
Performance:	Maximum speed 121 mph (195 km h^{-1}) at sea level; cruising speed 115 mph (185 km h^{-1}) at optimum altitude; initial climb rate 1,020 ft (312 m) per minute; hovering ceiling 10,170 ft (3,100 m) in ground effect ad 6,560 ft (2,000 m) out of ground effect; range 205 miles (330 km).
Weights:	Empty 1,069 lb (485 kg); normal take-off 1,984 lb (900 kg); maximum take-off 2,205 lb (1,000 kg).
Dimensions:	Main rotor diameter 27 ft $6\frac{7}{10}$ in (8.40 m); tail rotor diameter 4 ft 3 in (1.30 m); fuselage length 22 ft $\frac{1}{2}$ in (6.72 m); height 7 ft $11\frac{1}{2}$ in (2.42 m); main rotor disc area 596.53 sq ft (55.42 m^2).

Plate No. 2.67 gives the profile, layout and specification of this Agusta A101 helicopter.

2.25.2 McDonnell Douglas AH-64 Apache

2.25.2.1 Introduction

During the operation Desert Storm, 277 US Army Apaches took part in the lightning 100 h ground war. Here, one AH-64 pilot recalls those events.

2.25.2.2 Battle Commences

Plate No. 2.68 gives a typical battle profile of the Apache Helicopter.

2.25.2.3 Apache Firepower

"Hellfire is for point targets, something hard that has to be engaged with a precision munitions with a lot of penetration. This laser-guided missile will hit targets at ranges of more than 3 miles (5 km). How much further, I'm not allowed to say. The 2.75 is a good area weapon if you have a lot of vehicles or personnel in a small area and can strike from about 5 or 6 miles (8 or 9 km). Each rocket contains nine-sub-munitions, which were found to be extremely effective against trucks".

2.25.2.4 Boeing Helicopters CH-47 Chinook

The CH-47 Chinook was first committed to action in Vietnam during 1965 and quickly proved to be dependable, highly adaptable to the adverse weather conditions in Vietnam and capable of hauling tremendous loads into hostile areas, often while under fire and surviving. A reference is made to Plate No. 2.69.

Agusta A 101G

SPECIFICATION	
Agusta A 101G (definitive prototype configuration) **Type:** medium-sized multi-role helicopter **Powerplant:** three Bristol Siddeley Gnome H,1400 turboshafts, each rated at 1,400 shp (1044 KW) for continous operation **Performance:** maximum speed 143 mph (230 km/h); maximum cruising speed 114 mph (183 km/h);	service ceiling 8,530 ft (2600 m); standard range 348 miles (560 km) **Weights**: empty 14,110 lb (6400 kg); maximumtake-off 28,440 lb (12900 kg) **Dimensions:** main rotor diameter 65 ft 3 in (19.90 m); tail rotor diameter 10 ft 8 in (3.25 m); fuselage length 59 ft 1 in (18.01 m); height 16 ft 2 in (4.94 m); main rotor disc area 3,347.69 Sq ft (311.00 m^2)

Plate 2.67. Agusta A 101G
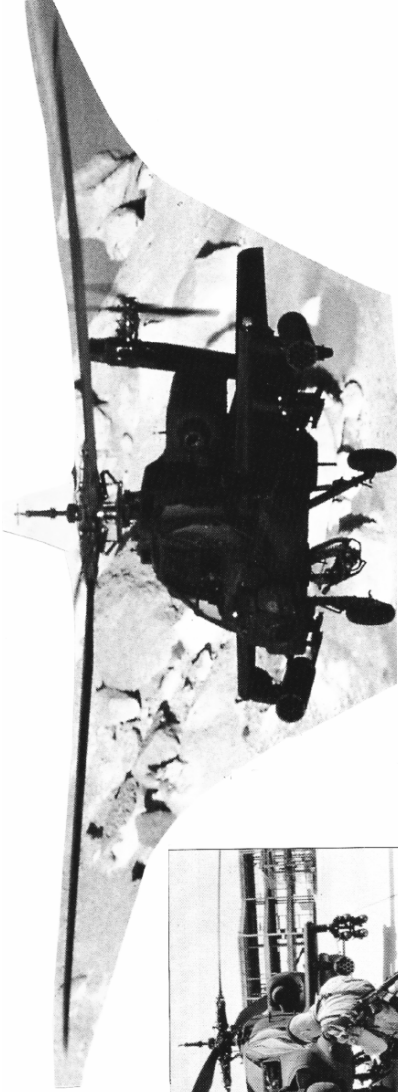
In the short, but sometimes fierce, flurry of fighting, Apaches fired 2,876 Hellfire missiles and destroyed over 1,300 Iraqi vehicles. Only one AH-64 was lost to enemy fire.
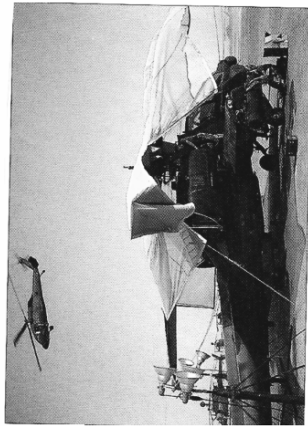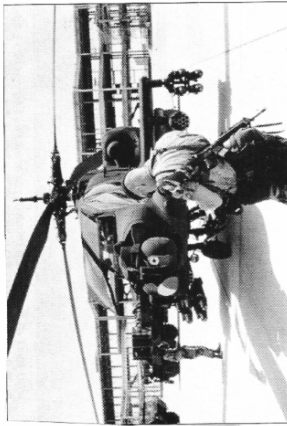
Apaches were deployed to Saudi Arabia by sea, and most came from the front-line units in Germany. Once in theatre basic maintenance was carried out in the field.

Plate 2.68. Apache

The rugged terrain of South Vietnam made the resupply of mountain-top outposts extremely difficult. In a dramatic display of the Chinook's hovering capability, a CH-47B backs into a hillside to unload equipment and ammunition. During the entire operation, only the rear wheels of the Chinook rested on the hillside.

Pictured in front of his CH-47, Lt Gary B. Roush was attached to the 242nd Assault Support Helicopter Company, known as the 'Muleskinners'. During his tour roush completed 942 combat flight-hours resulting in 3,000 landings.

Plate 2.69. Boeing Helicopters CH-47 Chinook

The traditional cargo-hauling CH-47 Chinook flew in Vietnam with a crew of four, namely two pilots, a crew chief/gunner, and an additional gunner. In the rear cabin, standard-issue windows were replaced with gun ports to enable troops on board to aim their infantry rifles. The Chinook's crew gunners were equipped with a 0.3 in (7.62 mm) M60 machine gun on a pintle on the left-hand escape hatch opening, plus a second machine gun on a swing out mounting in the right-hand forward doorway. On rare occasions, Chinook cargo helicopters were fitted with the XM41 armament package which consisted of M60 or M3 machine gun firing out of the open rear door from the ramp floor. A small number of Chinooks went to the South Vietnamese Army and some were left behind after the fall of Saigon in 1975.

An offbeat version of the Chinook was the ACH-47A gunship, of which Boeing modified four from the CH-47 for operational evaluation in Vietnam. In the ACH-47A, engineers deleted all cargo-handling equipment, soundproofing and all but five troop seats, then added 2,000 lb (907 kg) of armour plating and weapons pylons on each side of the aircraft, outboard of the front wheels. Nicknamed "Guns A Go-go", the ACH-47A model carried one 20 mm cannon,

up to five machine guns and two pylon mounted XM128 19 round pods of $2^3/_4$ in (70 mm) rockets, pus a single chin-mounted 40 mm grenade launcher. The First Air Cavalry Divison took three of the four ACH-47A gunships to Vietnam in June 1966. Eventually, development of the smaller nimbler AH-1 HueyCobra made a Chinook gunship unnecessary and the concept was not developed further.

At the height of the war in Vietnam, some 22 US Army units were in operation with the CH-47 Chinook, performing a variety of support missions. One of the most vital (known as "Pipesmoke") was the recovery vehicle – over the course of the war, CH-47s were credited with the recovery of 11,500 disabled aircraft, worth more than \$3 billion. This CH-47 is pictured transporting a sling-loaded Bell UH-1 Huey over the Vietnamese coast. Equally important was the Chinook's use in the civilian action effort (part of the "Hearts and Minds" campaign) which, often required the rapid movement of an entire village to a safe location. During one such airlift, a CH-47 Chinook lifted 147 Vietnamese and all their possessions in a single flight. Plate No. 2.69 shows the Chinook Helicopter Profile.

2.25.2.5 Boeing Vertol 234 Commercial Chinook

Introduction

The Chinook's outstanding record as a military heavylift transport prompted Boeing Vertol to develop a specialised long-range version for the civilian market. Aimed at companies flying to offshore oil rigs, the type has also served in the logging the firefighting roles. A reference is made to Plate No. 2.70 for the performance details.

Taking advantage of the substantial upgrade of the military Chinook, which was being modified into the CH-47D, Boeing announced in the summer of 1978 that it had completed the market evaluation of commercial version. The target was the growing North Sea oil business, in which drilling operations were being pushed further and further from the mainland. The availability of the Commercial Chinook was instrumental in British Airways Helicopters (BAH) obtaining a 7-year contract from Shell to service its large Brent/Cormorant oil field to the east of the Shetland Islands. In November 1978, BAH duly ordered three Model 234s at £6 million each, and later increased the contract to six. The first Commercial Chinook flew on 19 August 1980 and received Federal Aviation Administration (FAA) and UK Civil Aviation Authority (CAA) certification on 19 and 26 June 1981, respectively.

Although based on the CH-47D, the Model 234 introduced many new features. The most notable were the replacement of metal rotor blades by wide-chord glass fibre blades, redesign of the fuselage side fairings to incorporate additional fuel tanks, a lengthened nose to house the weather radar antenna, and a repositioning further forward of the front landing gear. Duplicated blind-flying instrumentation, weather radar and a dual, four-axis automatic flight

The Model 234LR
Commercial Chinook
was primarily designed
for supply flights to
oil rigs in the North Sea.
Helikopter Service of
Norway became
the second operator
to use the type in
this region, utilising
three examples from
Stavanger.

Left: Columbia Heliopters of Portland, Oregon initially acquired five
ex-BAH Model 234LRs for logging and, firefighting duties. The fairings
on the fuselage sides, which originally held additional fuel, have been
removed to allow the carriage of heavier payloads during logging operations.

Plate 2.70. 234 Chinook

control system ensure all-weather capability. The fuselage is of all-metal semi-
monocoque construction with a basically square section and a loading ramp
built into the upswept rear. Landing gear is a non-retractable quadricycle
type, with twin wheels on each forward gear, and single wheels on the rear
units. Power for the Model 234 is provided by two Avco-Lycoming AL 5512
turboshafts, pod-mounted on the sides of the rear rotor pylon. Each is rated
at 4,075 shp (3,035 kW) on take-off, and has a maximum 30 min contingency
rating of 4,355 shp (3,245 kW).

The rotor system comprises three-bladed rotors in tandem, turning in
opposite directions, driven through interconnecting shafts, which enable both
engine. The front half of each blade is made of glass fibre, and the rear half

filled with Nomex honey-comb. An aluminum screen inserted in the skin provides lightning protection by discharging strikes through the titanium leading edge. Blades also embody electric de-icing blankets. Two blades of each rotor can be folded manually. Power transmission from each engine is accomplished through individual clutches into the combiner transmission providing a single power output to the interconnecting shaft. An auxiliary transmission lubrication system ensures the flights can be completed even after a total loss of oil in the primary system.

Accommodation is provided for two pilots side-by-side on the flight deck, with dual controls, and for up to 44 passengers (depending on the variant) in the cabin, three-abreast with a central aisle. Each set has an overhead bin and underseat stowage for carry-on luggage, with large items carried in the main baggage compartment. A galley with cabin attendant's seat and toilet between the fight deck and the cabin are standard. Heating and ventilation provides a comfortable environment for pilots and passengers, and a specially turned floor construction reduces vibration. Passenger access to the cabin is via a single door on the right-hand side, while the crew has a door on each side of the flight deck. All passenger facilities can be removed and replaced by a heavy-duty floor for cargo-only service. Various arrangements of external cargo hooks are possible, including a single central hook for loads of up to 28,000 lb (12.7 tonnes); tandem hooks for better load stability in high-speed flight, and three tandem hooks for multiple loads.

The initial production versions were powered by two, 1,320 shp (984 kw) Turbomeca Turmo turboshafts, giving a maximum take-off weight of 14,109 lb (6,400 kg) and limiting speed of 151 kt (174 mph 280 $km^{-1}h^{-1}$). These early models comprised the SA 3,308 for French ALAT (Aviation Legere de I'Armee de Terre), SA 330C for military export. SA 330E as the RAF's Puma HC.Mk 1, and the civilian SA 330F. In 1974, availability of the 1,575 shp (1174 kw) Turmo equipped the Puma for "hot and high" operations, increasing its take-off weight to 16,314 lb (7,400 kg). Production in this guise concerned the civilian SA 330G and military SA 330H, although the French air force, which bought 37, used the misleading designation SA 330Ba.

Glass fibre rotor blades became available in 1977, uprating the G and H to SA 330J and SA 330L, respectively. The new blades were retrofitted to some early aircraft, including those of the RAF and 40% of ALAT's 132 SA 330Bs. The French army also bought 15 SA 330Ba versions and a few attrition replacement helicopters from the Romanian assembly line after Aerospatiale ceased production with the 686th Puma. A reference is made to Plate 2.78 for specification of the Puma.

Aerospatiale SA 315B Lama

Introduction. The Aerospatiale SA 315B Lama evolved to meet an Indian armed forces requirement of 1968 and was intended primarily for operations in "hot and high" conditions. The basic design of the Lama combines the
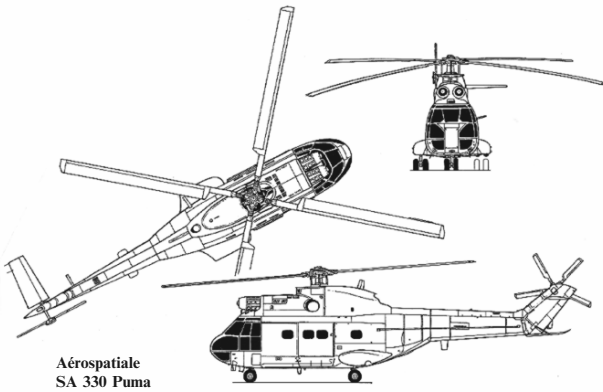
Plate 2.71. Aerospatiale SA 330 Puma

SPECIFICATION

Aérospatiale (now Eurocopter France) SA 330L Puma Powerplant: tow Turboméca Turmo IVC turboshafts each rated at 1,575 shp (1175 kW)

Performance: never-exceed speed 182 mph (204 km/h); maximum cruising speed 'clean' at optimum altitude 168 mph (271 km/h); maximum rate of climb at sea level 1,810 ft (552 m) per minute; service ceiling 19,685 ft (6000 m); hovering ceiling 14,435 ft (4400 m) in ground effect and 13,940 ft (4250 m) out of ground effect; range 355 miles (572 km)

Weights: empty 7,970 lb (3615 kg); maximum take-off 16,534 lb (7500 kg); maximum payload 7,055 lb (3200 kg)

Dimensions: main rotor diameter 49 ft 2½ in (15.00 m); length overall, rotors turning 59 ft 6½ in (18.15 m) and fuselage 46 ft 1½ in (14.06 m); height overall 16 ft 10½ in (5.14 m); main rotor disc area 1,902.20 sq ft (176.71 m^2); tail rotor disc area 78.13 sq ft (7.26 m^2)

Armament: generally unarmed, but see main text

reinforced airframe of a Sud Alouette with the dynamic components of an Aerospatiale SA 316B Alouette III, including its Artouste powerplant and rotor system. The SA 315 prototype was first flown on 17 March 1969 and
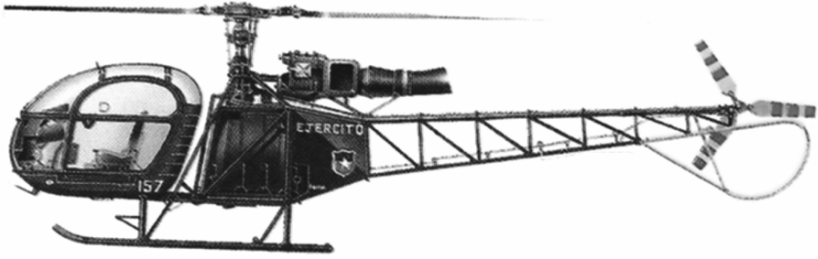
SPECIFICATION

Aérospatiale SA 315B Lama
Type: five-seat general-purpose helicopter
Powerplant: one 970-shp (649-kW) Turboméca Artouste IIIB turboshaft, derated to 550 shp (410 kW)
Performance: (at 5,070–lb/ 2300-kg take-off weight) maximum cruising speed 75 mph (120 km/h); maximum rate of climb at sea level 768 ft (234 m) per minute: service ceiling 9,840 ft (3000 m); hovering ceiling in ground effect 9,675 ft (2950 m); hovering ceiling out of ground effect 5,085 ft (1550 m); range 320 miles (515 km)
Weights: empty 2,251 lb (1021 kg); normal take-off 4,300 lb (1950 kg); maximum take-off with externally-slung cargo 5,070 lb (2300 kg)
Dimensions: main rotor diameter 36 ft 1 in (11.02 m); fuselage length 33 ft 8 in (10.26 m); height 10 ft 1 in (3.09 m); main rotor disc area 1,026.5 sq ft (95.38 m^2)

Plate 2.72. Aerospatiale SA 315B Lama

received its French Certificate of Airworthiness on 30 September 1970, the name Lama was bestowed by its manufacturers in July 1971.

From the outset, the SA 315B excelled in loading co-altitude performance. During a series of demonstration flights in the Indian Himalayas in 1969, an SA 315B carrying a crew of two and 308 lb (120 kg) of fuel, landed and took off at the highest altitude ever recoded: 24,605 ft (7,500 m). On 21 June 1972, a Lama with only a pilot aboard established a helicopter absolute height record of 40,820 ft (12,442 m). These achievements and the strong reputation for reliability established by its close relations, the Alouette II and III, ensured a good reception on the market. By 1971, arrangements had already been completed for license-production of the SA 315B by HAL at Bangalore in India. The first Indian-assembled Lama flew on 6 October 1973. The HAL produced Lama was renamed Cheetah.

The resulting HB 315B Gaviao version is operated by the Bolivian air force and the Brazilian navy.

Aerospatiale (SUD) SA 316/SA 319B Alouette III. The capability of the SA 316B soon led to the adoption of the type for military service in a two seat form for use in a variety of roles with a range of weapon options that made them suitable for light attack (typically four multiple launchers for 2.68 in/68 mm unguided rockets or for AS11 or AS12 wire guided light ASMs) or the anti-submarine task (typically two Mk 44 or Mk 46 torpedoes, reduced to one torpedo when magnetic anomaly detection equipment was installed). The SA 316B was followed by the SA 316C which entered production in 1970. Powered by an 870 shp (649 kW) Turbomeca Artouste IIID engine derated to 600 shp (447 kW), this variant was built only in limited numbers.

The SA 316A was only built in modest numbers in France before the introduction of the definitive model, the SA 316B Alouette III. This was fitted with an 870 shp (649 kW) Turbomeca Artouste IIIB turboshaft derated to 570 shp (425 kW), driving strengthened main and tail rotor transmissions. The SA 316B first flew on 27 June 1968 and its uprated powerplant enabled the Alouette III to carry an increased payload.

Aerospatiale SA 365 Dauphin. Despite its limited early sales, Aerospatiale's Dauphin series later emerged as one of the most successful helicopters ever produced. Characterised by its fenestron tail rotor, the Dauphin found particular favour as a fast executive transport.

Aerospatiale on 1 January 1970 was working on a single-engined successor. Designated the SA 360 Dauphin, the new model made its first flight on 2 June 1972, but was not seen in public until the Paris Air Show in June the following year. The first prototype (f-WSQL) was powered by the 980 shp (730 kW) Turbomeca Astazou XVI turboshaft engine and had a four bladed main rotor using Alouette blades and a fully glazed front fuselage section. But its most notable feature was the new fenestron shrouded fan in place of the conventional tail rotor, though this had already flown on the Gazelle light military utility helicopter. After 180 flights the prototype was fitted with the more powerful 1,050 shp (7,823 kW) Astazou XVIIIA along with new plastic

SPECIFICATION

Aérospatiale SA 316B Alouette III
Type: general-purpose helicopter
Powerplant: one 870-shp (649-kW) Turboméca Artouste IIIB turboshaft, derated to 570 shp (425 kW)
Performance: (standard version, at maximum take-off weight) maximum speed at sea level 130 mph (210 km/h); maximum cruising speed at sea level 115 mph (185 km/h); initial climb rate 950 ft (260 m) per minute; service ceiling 10,500 ft (3200 m); hovering ceiling in ground effect 9,450 ft (2880 m); hovering ceiling out of ground effect 5,000 ft (1520 m); range with maximum fuel at sea level 298 miles (480 km); range at optimum altitude 335 miles (540 km)
Weights: empty 2,520 lb (1143 kg); maximum take-off 4,950 lb (2200 kg)
Dimensions: main rotor diameter 36 ft 1¾ in (11.02 m); length 42 ft 1½ in (12.84 m) with rotors turning and fuselage 32 ft 10¾ in (10.03 m); height 9 ft 10 in (3.00 m); main rotor disc area 1,026.68 sq ft (95.38 m²)

SPECIFICATION

Aérospatiale SA 319B Alouette III Astazou
(generally similar to SA 316B Alouette III except in the following Parameters:)
Powerplant: one 870-shp (649-kW) Turboméca Astazou XIV turboshaft derated to 600 shp (447 kW)
Performance: maximum speed 136 mph (220 km/h) at sea level; cruising speed 122 mph (197 km/h) at sea level; initial climb rate 885 ft (270 m) per minute; hovering ceiling 10,170 ft (3100 m) in ground effect and 5,575 ft (1700 m) out of ground effect; range 375 miles (605 km) with six passengers
Weights: empty 2,513 lb (1140 kg); maximum take-off 4,960 lb (2250 kg)
Armament: generally unarmed, but see main text

Aérospatiale (Sud) SA 319B Alouette III
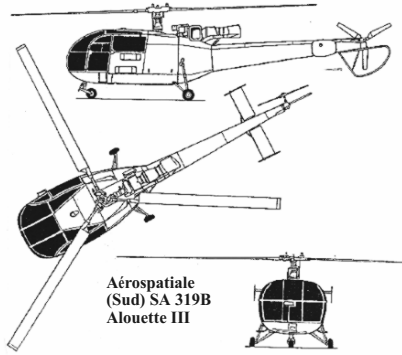
Plate 2.73. Aerospatiale (SUD) SA 316/SA 319B Alouette III

rotor blades and further modified to reduce vibration and eliminate ground resonance. It flew again in its modified form on 4 March 1973 and went to establish several closed-circuit speed records in its early career.

Production of the commercial 11 seat SA 360C Dauphin began in 1974, the French airworthiness certification was awarded on 18 December 1975, followed by American Federal Aviation Administration (FAA) certification on 31 March 1976.

Double power. The big but under-powered Dauphin proved of limited appeal in the marketplace and only 28 were built, including a single SA 360A for evaluation by France's Aeronavale. Three SA 360Cs were also converted to SA 361 models with Astazou XX turboshafts and Starflex rotor hubs, adapted as standard on later models. The prototype (F-ZWVF) for this improved variant flew for the first time on 12 July 1976. Development for military use meanwhile continued on an experimental basis, and produced the SA 361H/HCL (Hélicoptere de Combat Léger) anti-tank prototype (F-WZAK), equipped with FLIR and eight HOT missiles.

However, Aerospatiale quickly realized that the way forward was to produce a twin-engined version and this prototype, SA 365C Dauphin 2 (F-WVKE) made its maiden flight on 24 January 1975, introducing twin Arriel 1A turboshaft engines, each delivering 650 shp (485 kW) take-off power. This was followed two days later by SA 366, which differed only in having two 680 shp (507 kW) Lycoming LTS 101 engines to appeal to the American market. The first civil production model was designated SA 365C and entered service in 1978. Slight improvements in powerplants and transmissions produced the SA 365C1 with 667 shp (497 kW) Arriel 1A1 turboshafts and the SA 365C2 with 670 shp (499 kW) Arriel 1A2s.

Western Europe – Fleet Air Arm. Operating alongside their carrier-based counterparts, the "Junglies" provide aerial mobility for Commando operations around the world.

For many years, the Royal Navy's helicopter force has effectively been divided between "Pingers" (ASW) and "Junglies" (Commando). For much of the Cold War, the Commando role was of less importance than the ASW commitment, although the support of Royal Marine forces operating on NATO's northern and southern flanks was significant. In the Post-Cold War World, however, the wheel has turned full circle and the out of area and rapid deployment capabilities practiced by the Commando units have made them uniquely valuable for supporting international peacekeeping operations. Thus, while the Commando squadrons remain equipped and trained for Arctic operations and for rapid deployment to Norway, it is no coincidence that they have maintained a regular detachment in Bosnia (under UN auspices) for several years, and were heavily involved in humanitarian relief operations in Northern Iraq.

The value of the Sea King HC.Mk 4, the principal aircraft of the Commando squadrons, was conclusively demonstrated during the Falklands War of 1982, when No. 846 Squadron deployed to the South Atlantic. Since then the aircraft has been subject to a succession of useful modifications and upgrades which have dramatically expanded its capabilities. These have seen the aircraft gaining improved armour and defensive systems, together with cockpit lighting compatible with night vision goggles for improved night flying capability. In

Aérospatiale SA 365 Dauphin family
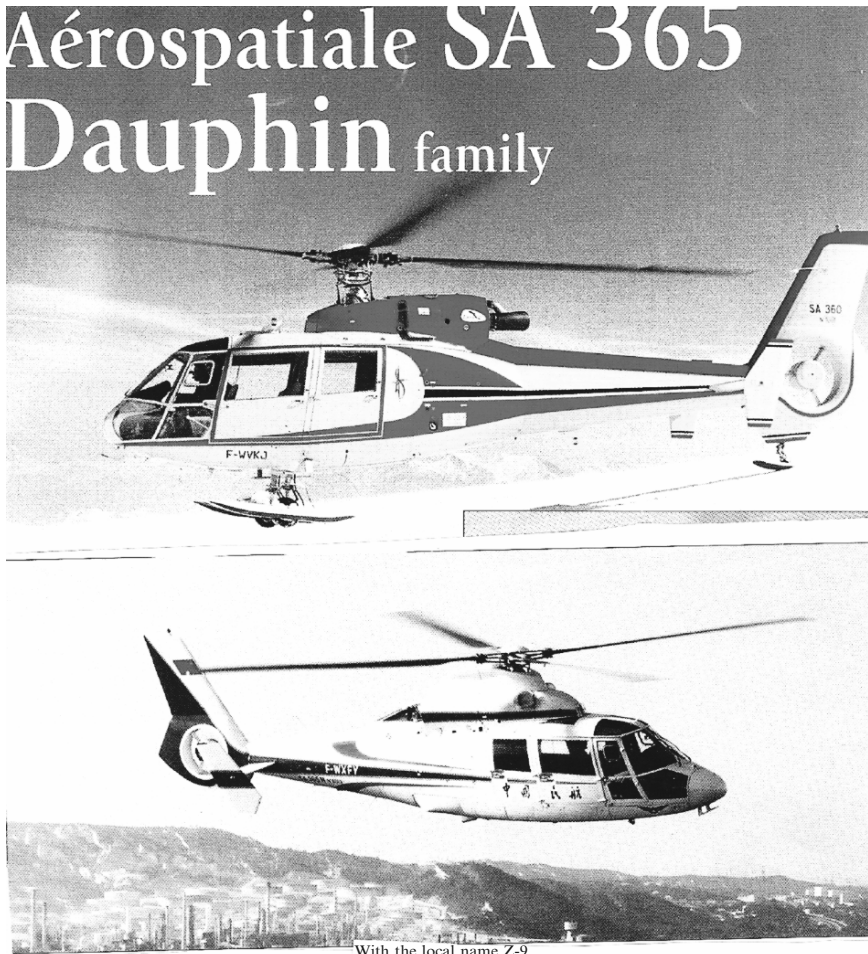
With the local name Z-9 Haitun, the Eurocopter AS 365N is built under licence by Harbin for both civil users and all three Chinese air arms. The first production batch was of 50 aircraft. The current version is the Z-9A-100, which is thought to be an anti-tank variant.

Plate 2.74. Aerospatiale SA 365

addition to three Sea King HC.Mk 4 squadrons, the Royal Navy also parents a single Royal Marine-manned unit flying a mix of Army Air Corps standard Lynx AH.Mk 7s and Gazelle AH.Mk 1s. Once known as No. 3 CBAS (commando Brigade Air Squadron), the unit today uses the No. 847 Squadron title, though its role remains the same – the support of No. 3 Commando Brigade, royal Marines. Like the Sea King HC.Mk 4 units, No. 847 Squadron is based at RNAS Yeovilton, Somerset. A reference is made to Plate No. 2.75

Sikorsky S-76 Spirit. In the early 1970s Sikorsky Aircraft turned its attention to the civil sector. After lengthy and studied evaluation of the needs of potential customers, Sikorsky chose a twin-turbine design for 12 passengers as the best way to gain a bigger share of the market. Given the designation S-76 to mark the American bicentennial, the new design was announced to the world on 19 January 1975.

From the outset, the S-76 was equipped for all weather operation and the design clearly benefited from the research and development work undertaken on the dynamic system of the S-70 military helicopter, which became known as the Black Hawk. The main rotor is a scaled down version of that of the S-70, with its four blades built around a hollow titanium spar covered in glass fibre over a Nomex honeycomb core. The leading-edge strips are made of titanium and nickel, while the blades have swept Kevlar tips. The fully-articulated rotor head has elastomeric bearings which need no lubrication and is fitted with dampers and vibration absorbers. The four bladed tail rotor to the left is of composite construction. A reference is made to Plate 2.75.

As a medium-lift helicopter, the Sea King HC.Mk 4 provides ship-to-ship and ship-to-shore support during amphibious operations by the Royal Marines.

Plate 2.75. Transport/Commando units

Sea King Mk 41

Avionics

Mk 41s were delivered with a comprehensive avionics fit which included the locally-produced Andrea AN/AIC-18 intercom, Becker ZG3M UHF homer, Honeywell GmbH AN/APN-171 radar altimeter, Siemens AN/APx-46H/M IFF/S transponder and SEL AN/ARN-52 TACAN, MITAC Micro TACAN and SETAC all-Weather landing system. HAR.Mk 3 aircraft have a similarly comprehensive, mostly UK-sourced fit, with the HAR.Mk 3A featuring new navigation and communications equipment along with a fully-coupled flight path control and full auto-hover facility.

Plate 2.76. Sea King Mk 41

SPECIFICATION

Advanced Sea King

Dimensions

Length Overall, rotors turning: 72 ft 8 in (22.15 m)
Fuselage length: 55 ft 10 in (17.02 m)
Length with main rotor blades folded: 57 ft 2 in (17.42 m)
Length with main rotor blades and tail pylon folded: 47 ft 3 in (14.40 m)
Main rotor diameter: 62 ft (18.90 m)
Tail rotor diameter: 110 ft 4 in (3.16 m)
Height overall, rotors turning: 16 ft 10 in (5.13 m)
Height overall, rotors stationary: 15 ft 11 in (4.85 m)
Height to top of rotor head: 15 ft 6 in (4.72 m)
Main rotor disc area: 3,019.07 sq ft (280.47 m²)
Tail rotor disc area: 83.86 sq ft (7.79 m²)
Wheel base: 23 ft 5 in (7.14 m)
Wheel track: 13 ft (3.96 m)

powerplant

Two Rolls-Royce Gnome H.1400-1T turboshafts each rated at 1,660 shp (1238 kW) for take-off and 1,465 shp (1092 kW) for continuous running

Weights

Basic empty with sponsons: 11,891 lb (5393 kg)
Basic empty without sponsons: 11,845 lb (5373 kg)
Empty equipped (ASW role): 16,377 lb (7428 kg)
Empty equipped (ASV role): 16,689 lb (7570 kg)
Empty equipped (AEW role): 17,143 lb (7776 kg)
Empty equipped (SAR role): 13,760 lb (6241 kg)

Empty equipped (troop transport role): 12,594 lb (5712 kg)
Empty equipped (freight role): 12,536 lb (5686 kg)
Empty equipped (VIP role): 15,917 lb (7220 kg)
Maximum take-off: 21,500 lb (9752 kg)

Fual and load

Internal fuel capacity: 817 Imp gal (3714 litres)
Auxiliary fuel: 190 Imp gal (863 litres) in an auxiliary fuselage tank
Maximum ordnance: 2,500 lb (1134 kg)

Performance

Never-exceed speed at sea level: 140 mph (226 km/h)
Maximum cruising speed at sea level: 126 mph (204 km/h)
Maximum rate of climb at sea level: 2,030 ft (919 m) per minute
Service ceiling (one engine out): 4,000 ft (1220 m)
Hovering ceiling (in ground effect): 6,500 ft (1980 m)
Hovering ceiling (out of ground effect): 4,700 ft (435 m)

Range

Ferry range with auxiliary fuel: 1,082 miles (1742 km)
Range with standard fuel: 921 miles (1482 km)

Armament

Up to four Mk 46, A244S or Sting Ray torpedoes can be carried externally, or four Mk 11 depth charges. Sea Eagle or Exocet anti-ship missiles are anti-ship option. Pintle-mounted machine-guns can be fitted to starboard door.

Since the late 1970s, the Sea King HAR.Mk 3 has been the RAF's standard SAR helicopter. An initial batch of 16 had been delivered by 1979, with a further three delivered in 1985. Six examples of the advanced HAR.Mk 3A are also now in service.

Westland Sea King

Westland achieved considerable export success with the Sea King, including the supply of the three Commando Mk 2s to Qatar (two of which are illustrated). The Commando was originally conceived as a dedicated assault version of the sea king but through a number of variants its roles now include AEW, anti-ship and VIP transport operations.

Plate 2.77. Westland Sea King Helicopter

The carefully streamlined fuselage makes extensive use of composites, comprising glass fibre, light alloy and Kevlar. The S-76's retractable tricycle landing gear has a single wheel on each leg and is hydraulically operated. The nosewheel retracts rearward and the main units inwards into the rear fuselage, all fully enclosed by doors when retracted. Non-retractable landing gear with low pressure tyres is available on the utility version. The turboshaft engines (initially the Allison 250-C30) are mounted above the cabin behind the drive shaft. The standard fuel system is comprised of a single 281 US gallon (1,064 l) fuel tank in the fuselage, although auxiliary tanks totaling another 106 gallons (401 l) for extended range operations are available as an option.

Next came the S-76C, which was similar to the S-76B, but fitted with the 723 shp (539 kW) Turbomeca Arriel 1S1. It entered service in April 1991, but has now been replaced by the S-76C+, which first flew on 30 June 1994 and obtained FAA and CAA certification in June 1996. This model is distinguished by the uprated Arriel 2S1 turboshafts, each rated at 856 shp (638 kW) for take-off, which is improved and this model offers one-genuine inoperative (OEI) performance. It also has full authority digital engine control (FADEC) and makes use of single-crystal blade technology. The −76C+ is now the only model in production – at the beginning of 1998, a total of 467 S-76s had been delivered.

Being a civil design, the helicopter never really caught on with the military. The Philippine Air Force took delivery of 12 AUH-76s configured for COIN, logistics support and medevac duties, but the dedicated armed military H-76 has found no customers since its first flight in February 1985. Six of the S-76N naval derivative have, however, been delivered to the Royal Thai Navy, equipped for maritime patrol, ship-to-shore personnel transport and search and rescue. The S-76N features a protective airframe coating, health and usage monitoring system (HUMS), strengthened landing gear, deck lock and tie down system capable of weathering Sea State 7, manually folding rotor blades, self sealing fuel system and hover-in-flight refueling (HIFR) capability.

Interesting one-offs were the S-76 SHADOW demonstrator for the US Army Rotorcraft Technology Integration (ARTI) programme, which first flew on 24 June 1985 and an H-76 fitted with the Boeing Sikorsky Fantail anti-torque system, the latter being first flown on 6 June 1990.

Sikorsky H-53 – Development. Developed from a US Marine's specification for a heavylift assault helicopter that could operate from ships, the H-53 family of helicopters has given sterling service in conflicts ranging from Vietnam to the Gulf War.

Development of the versatile H-53 family began in October 1960 when the United States Marine Corps declared a wish to replace its Sikorsky HR2S-1s with a new ship-based heavy assault helicopter. The HR2S-1 (later redesignated CH-37C) had validated the long-standing Marines conviction that helicopters were the ideal vehicles in which to bring troops and equipment ashore during amphibious raids. However, the HR2S1 was growing old and

proving difficult to maintain and so it was decided that a replacement was needed. Initially, the USMC joined the Army, Air Force and Navy in sponsoring the development of the medium-sized Tri-Service VTOL transport. However, the resulting Vought-Hiller-Ryan XC-142A programme became over-ambitious and ran late, and so the Marines decided to make their own request for a new heavylift helicopter. In a requirement issued by the Bureau of Naval Weapons on 7 March 1962, the Marines called for a ship-based helicopter capable of lifting an 8,000 lb (3,630 kg) payload over a radius of 100 nm (115 miles; 185 km) at a speed of 150 kt (172 mph; 278 km h^{-1}). Its missions would be ship-to-shore transport, downed aircraft recovery, personnel transport and aero-medical evacuation.

Three companies responded, Boeing Vertol with a redesign of its HC-1A, Kaman aircraft with a development of the British-designed Fairey Rotodyne and Sikorsky indicating its intent to develop twin-turbine S-65. Having lost a previous competition to supply the Marines with medium-lift helicopter, Sikorsky went all out to win the contract. It was selected as the winner in July 1962 when the S-65 was chosen as a result of technical, production capability and cost considerations. However, due to insufficient funds in the USMC budget, the anticipated contract for four prototypes could not be realized until Sikorsky lowered its R&D bid, and the revised number of two prototypes was ordered. This revised proposal gained acceptance and on 24 September 1962, the DoD announced that Sikorsky's helicopter had been accepted – the two YCH-53A prototypes, a static test airframe and a mock-up were built in a $9,965,635 contract.

Sikorsky's design was powered by two General Electric T64 shaft turbines and incorporated many proven features of other Sikorsky designs. There was the main transmission of the S-64 (CH-54) crane helicopter and the 72 ft (22 m) diameter, six-bladed main rotor and anti-torque rotor of the S-56 (CH-37) heavylift helicopter. The winning design itself was of similar configuration to but larger than, its S-61 (SH-3A) stablemate. First flown on 14 October 1964 and smoothly completing trials while encountering few problems, the initial production variant, the CH-53A, entered service with the Marine Corps in September 1965. The 141 "A" model Sea Stallions were followed on the production lines by three other heavylift transport variants (20 Ch-53Cs for the USAF; 126 CH-53Ds for the USMC; and two CH-53Gs for West Germany) with more powerful T64 engines and other improvements. In addition, 20 CH-53Gs were assembled in West Germany and 90 more were built under license.

Whether in combat or while undergoing trials, the heavylift transport variants of the twin-engined S-65 series proved highly satisfactory. This can be seen in the fact that, in Vietnam between 13 January 1967 and 18 May 1971, Marine Heavy Helicopter Squadron 463 (HMH-463) was credited, with recovering a total of 1,096 fixed-wing aircraft and helicopters; the dollar amount saved far exceeded the total acquisition cost of all CH-53As and Ch-53Ds. HMH-463 gained further recognition as being part of Operations Eagle Pull

and Frequent Wind which saw its helicopters being used to pull American citizens and their allies out of Phnom Penh and Saigon.

During the course of the war, the Marines lost 19 CH-53A/Ds to a variety of causes. Back in America, sea Stallions were making the headlines by establishing unofficial payload and gross weight records for a helicopter built outside the USSR. A CH-53A also became the first helicopter to be fitted with an automatic terrain clearance system.

H-53 Variants. All of these successes did not go unnoticed and the interest of the Air Force and Navy plus several foreign customers led Sikorsky to design specialised rescue and mine-countermeasure variants of its twin-engined helicopter. Development of the HH-53B, prompted by the need to provide a more powerful, better armoured and defended combat rescue aircraft, was initiated in September 1966.

Sikorsky quickly developed the Super Jolly rescue helicopter and the fist HH-53B flew on 15 March 1967. Sikorsky went on to build 44 HH-53Cs for the USAF, two S-65C-2s for Austria and 33 S-65C-3s for Israel. In Vietnam, Super Jollies proved to be highly effective combat rescue aircraft and in their first three years of combat they saved the lives of some 371 aircrew. HH-53s also gained fame for their participation in the Son Tay prison raid and the rescue of the Mayaguez crew from captivity in Cambodia. During the conflict, the USAF lost some 14 CH-53/HH-53s in combat, including one shot down by a MiG-21. After the war, the Super Jollies had their capabilities expanded when they were brought up to HH-53H Pave Low III and then Pave Low III Enhanced standard. This was partly due to the poor performance by the Navy RH-53Ds during the attempted rescue of American hostages in Iran in April 1980. In Pave Low III Enhanced form, the HH-53 is the most capable special operations helicopter in service with the Air Force Special Operations Command, and in 1986, its designation was changed to MH-53J to reflect its expanded special operations role.

Minesweepers. Experiments with minesweeping helicopters led to the conclusion that only the CH-53 was powerful enough to drag the heavy minesweeping gear. However, due to the need for CH-53As to support the Marines in Vietnam, the first experiments with minesweeping Sea Stallions did not occur until winter 1970. Fifteen helicopters were given the appropriate equipment and were redesignated RH-53As prior to their assignment to Helicopter Mine Counter-measures Squadron Twelve (HM-12). They gained notoriety during Operation Endsweep, the removal of mines from North Vietnamese waters between February and July 1972. These first RH-53A were later supplemented by 30 specially-built RH-53Ds in Navy service. They have been used since in several mine-clearance operations from Nimbus Star in 1964 to Earnest Will in the 1980s. Iran also received six essentially similar mine countermeasures helicopters before the fall of the Shah. The Iranian RH-53Ds were the last S-65s built as the success achieved with military customers did not repeat itself in the civilian world.
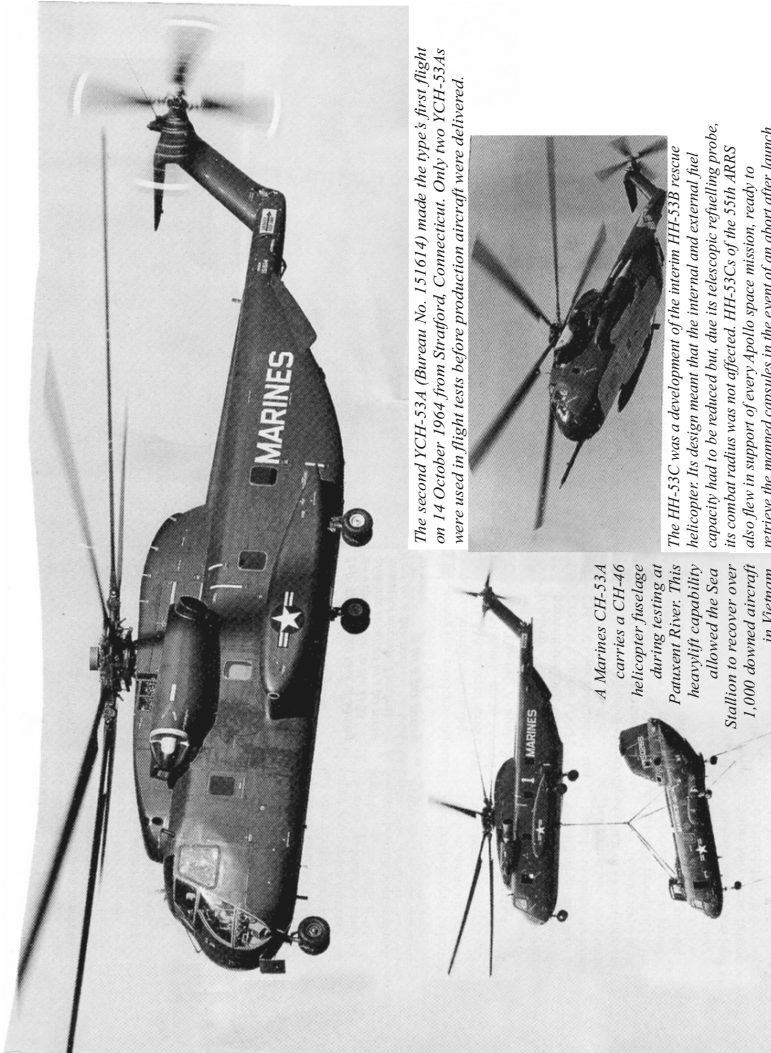
The second YCH-53A (Bureau No. 151614) made the type's first flight on 14 October 1964 from Stratford, Connecticut. Only two YCH-53As were used in flight tests before production aircraft were delivered.

The HH-53C was a development of the interim HH-53B rescue helicopter. Its design meant that the internal and external fuel capacity had to be reduced but, due its telescopic refuelling probe, its combat radius was not affected. HH-53Cs of the 55th ARRS also flew in support of every Apollo space mission, ready to retrieve the manned capsules in the event of an abort after launch.

A Marines CH-53A carries a CH-46 helicopter fuselage during testing at Patuxent River. This heavylift capability allowed the Sea Stallion to recover over 1,000 downed aircraft in Vietnam.

Plate 2.78. H-53 Development

Three-engined S-80. By autumn 1970, the USMC's experience with the CH-53A had convinced it that a helicopter was needed that could lift 1.8 times the load that could be lifted by the Sea Stallion. The first step towards acquiring such an aircraft was the approval on 24 October 1967 of a specific requirement calling for a helicopter with an 18 ton capability, but which was small enough to operate from LPH amphibious assault ships. In addition to the Marines' needs, the Navy also wanted a new vertical re-supply helicopter, and the Army a heavylift helicopter.

Sikorsky responded to this by placing a third engine inside the CH-53 upper fuselage fairing, the additional power being delivered through a beefed-up transmission to a seven-bladed main rotor. Requiring only limited airframe development; this suggestion quickly gained the interest of the Marine Corps which lent its support to the project. The Army, however, followed its own requirement which resulted in the aborted Boeing-Vertol ECH-62. The YCH-53E first flew on 1 March 1974 but, due to a more vigorous development and testing scheme than that of its predecessor, the CH-53E did not enter service until February 1981. The new helicopter proved exceedingly popular with the Marines, fulfilling all their hopes, while the Navy adopted the three-engined minesweeping derivative, the MH-53E, in April 1988. This helicopter was also delivered to the Japanese Maritime Self Defence Force as the S-80M-1 a year later. A VH-53f presidential transport derivative was also proposed, but was ultimately cancelled.

Plate No. 2.79 and 2.80 gives the helicopter profile and a cut away diagram together with specifications.

Bell AH-1 HueyCobra. Having first entered service in 1966, Bell's HueyCobra has undergone a significant number of upgrades over the years, enabling it to remain combat-capable well into the next century.

Blooded in Vietnam and proven several times since then, the diminutive AH-1 is the father of all modern gunship helicopters. Like most great aircraft, the AH-1 has been found to be irreplaceable and is still a front line type with a host of operations around the world. Although the idea of arming helicopters had been around since the 1950s, such machines were invariably modifications of existing types which in many cases were not ideally suited to the very different demands inherent in battle. There was clearly a need for a dedicated attach helicopter which married high performance with the ability to operate with a worthwhile payload, and was less vulnerable than interim types to ground fire, which had proven to be a constant hazard in operations over Vietnam.

Rush-job. Some idea of the urgency attached to this project can be gleaned from the fact that, although development was initiated only in March 1965, a Model 209 prototype was assembled in the summer of that year and few for the first time on 7 September 1965. Soon transferred to Edwards AFB, California for an exhaustive series of flight trials, the Model 209 quickly convinced army personnel that the helicopter promised a new attack capability over the battlefield. By March 1965, the Army had decided to purchase Bell's
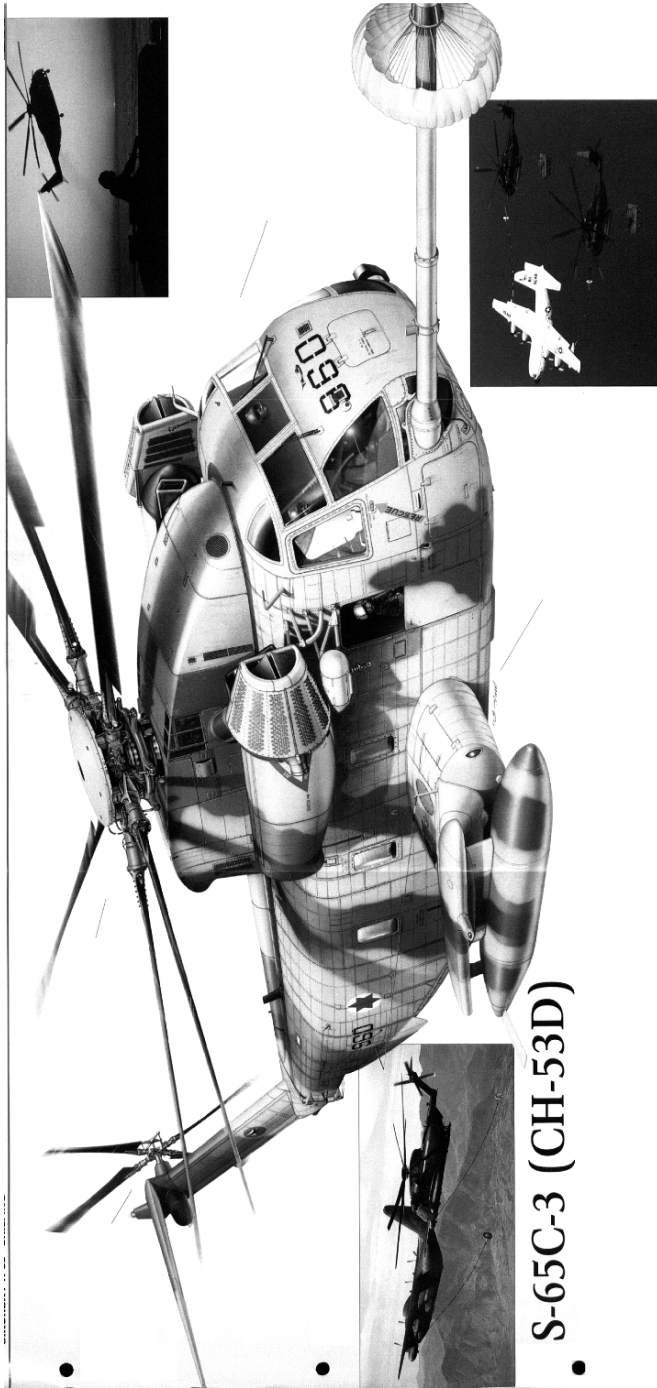
Plate 2.79. S-65C-3 Helicopter

WORLD MILITARY
SIKORSKY H-53

H-53

258 Sunday H-53
SHEET 03 Briefing

H-53 in Vietnam
It was the shortcomings of other helicopters in Vietnam that proved the impetus for the construction of the H-53. First entering service in 1967, the CH-53A, and soon after the HH-53B, proved popular for transporting supplies and rescuing downed aircrew all over the region. Two years later, in September 1969, the HH-53C made its combat debut. Outwardly similar but possessing many upgraded subfacilities the super jolly was equipped with an external cargo hook which enabled it to carry loads of up to 20,000 lb (9072 kg), while for the rescue mission it was fitted with a hoist complete with a 250-ft (76-m) cable to penetrate the tallest jungle canopy, for defence up to those 0.5-in (7.62mm) Miniguns were carried, and these could suppress enemy forces intent on reaching the downed crews before the rescue helicopters

SPECIFICATION

CH-53E Super Stallion

Dimensions
Length overall, rotors turning: 99 ft 1/2 in (30. 19 m)
Fuselage length: 73 ft 4 in (22.35 m)
Length with rotor and tail folded: 60 ft 6 in (18.44 m)
Hight overall: 29 ft 5 in (8.97 m)
Main rotor diameter: 79 ft (24.08 m)
Tail rotor diameter: 20 ft (6.10 m)
Main rotor disc area: 4,901.7 sq f (455.38 m²)
Main rotor disc area: 314.2 sq ft (29.19 m²)

Powerplant
Three General Electric T64-GE-416 engines rated at 4,380 shp (3266 kW) For ten minutes, 4,145 shp (3091 kW) For 30 minutes and 3,696 shp (2756 kW) for continuous running

Weights
Empty: 33,228 lb (15072 kg)
Maximum take-off with an internal payload: 69,750 lb (31640 kg)
Maximum take-offwith an internal payload: 73,500 lb (33340 kg)

Fuel and load
Internal fuel: 1,017 US gal (3849 litres)
External fuel: Up to two 650 US gal (2461-litres) drop tanks
Maximum payload internally over 115-mile (185-km) radius: 36,000 lb (16330 kg)
Maximum payload externally over 57.5-mile (92.5-km) radius: 32,000 lb (14515kg)

Performance
Maximum level speed 'clean' at sea level: 196 mph (315 km/h)
Cruising speed at sea level: 173 mph (278 km/h)
Maximum rate of climb at sea level with a 25,000-lb (11340-kg) payload: 2,500 ft (762 m) per minute
Service ceiling: 18,500 ft (5640 m)
Hovering ceiling: 11,500 ft (3520 m)

Range
Ferry range without aerial refuelling: 1,290 miles (2075 km)
Radius with a 20,000-lb (9072-kg) external payload: 575 miles (925 km)
Radius with a 32,000-lb (14515-kg) external payload: 57.5 miles (92.5 km)

Plate 2.80. H-53 Helicopter

The AH-1W SuperCobra has proved itself to be a truly effective weapons platform, able to carry a lethal mix of ordnance including TOW missiles, AIM-9 Sidewinders and Zuni rockets. Despite the AH-1W's performance however, it is based on an elderly design, and a replacement, such as the Apache, would be welcomed by the USMC.

Right: Viewed from above, the extremely narrow and compact fuselage of the AH-1 makes it an incredibly difficult helicopter to sight. This early AH-1G is seen on a test-flight from Bell's Fort Worth production facility in Texas.
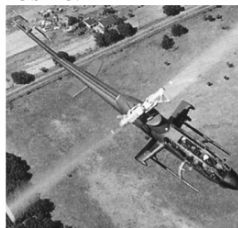
The prototype AH-1W SuperCobra was given a striking paint scheme to emphasise the Cobra name and its undoubted 'bite' for its debut in late 1983.

Plate 2.81. Bell AH-1 HueyCobra

gunship, placing an order for an initial batch of 112 production AH-1G helicopters, stipulating that they be ready at the earliest possible moment to permit deployment to Vietnam. This proved to be the forerunner of a series of contracts, procurement for the Army passing the 1,000 mark in 1972, while the US Marine Corps received 38 on loan pending the availability of that service's custom-built AH-1J SeaCobra derivative. Modest quantities were also supplied to Israel and Spain.

Battle debut. The initial production version of the HueyCobra was the AH-1G, delivery of which began in June 1967. Only 3 months later, HueyCobras arrived in South Vietnam as part of an organization known as Cobra-NETT, which was entrusted with introducing the type into combat. As the number of AH-1Gs increased, so operations were stepped up, to a point where the helicopters were undertaking daily missions such as escort, reconnaissance and fire-support – the AH-1's 0.3-in (7.62-mm) Gatling-type machine-gun devastated enemy bunkers and troop concentrations. The Gatling gun was soon supplemental by an M129 40-mm grenade-launcher; in this configuration and with wing-mounted rockets the AH-1s ranged far and wide over

South Vietnam and attack missions. The USMC received a modest number of HueyCobras from 1969 but sought a model of its own. Known as the AH-1J, the major difference was the installation of a Pratt & Whitney T400-CP-400 turboshaft engine (a military version of the PT6T-3 Turbo Twin Pac) and the deletion of the turret-mounted Gatling gun in favour of a single General Electric M197 20-mm rotary cannon. Some 84 AH-1Js were delivered between 1970 and 1977. A total of 202 AH-1Js was purchased by the Imperial Iranian army during the early 1970s, although it is thought that few remain airworthy despite covert assistance from the United States and Israel.

Missile armament. TOW missile capability first emerged around the mid-1970s when about 100 AH-1Gs were modified to carry this weapon, and was redesignated AH-1Qs. Another derivative which resulted from modernization was the AH-1R, which lacked TOW, but was equipped with a new T53-L-703 powerplant. Eventually, all AH-1Qs, AH-1Gs and AH-1Rs were brought up to improved AH-1S standard. In 1988 all survivors were redesignated AH-1F, which was the definitive US Army model. As well as procurement of the AH-1S by means of conversion, the Army also contracted for a substantial number of new machines which were initially known as Production AH-1S before adopting the designation AH-1P.

Plate No. 2.82 and 2.83 gives a complete profile of this helicopter with a cutaway and specifications.

2.26 Main Battle Tanks (MBTs) as Impactors

Main battle tanks are constantly being developed. They are always involved on the front line and are subject to impact and explosion. Table 2.47 lists data on some of the important MBTs currently in service. Figures 2.55 and 2.56 give the layouts of the 80-MBT, AMX-30 and C1-MBT with brief details of armament.

2.26.1 Marine Vessels

2.26.1.1 Light Marine Vessels

Light naval vessels are classified into cargo boats, passenger boats, lightweight sailing and fishing boats, lightweight barges, ore carriers and tankers. Table 2.48 gives specific dimensions and weights of these vessels. The maximum speed for all these vessels for impact analysis is taken as 30 knots per hour. Table 2.49 gives comprehensive data on the hovercraft illustrated in Figs. 2.57 and 2.58.

2.26.1.2 Heavy Marine Vessels

The heavy vessels are classified into ships, cruisers, aircraft carriers, mine sweepers, frigates, heavy tankers and helicopter carriers. Although they are

AH - 1F HueyCobra

Israel operates 30 AH-1F Cobras (Tzefas), most of which have undergone an extensive modification programme, involving the addition of wire strike protection system cutters positioned above and below the cockpit, a Hot-brick-type IR jammer mounted above the exhaust, and a laser spot tracker mounted in a bulge underneath the rotor head. All Israeli Cobras wear a large inverted yellow 'V' recognition marking. Despite the introduction of the Apache into the IAF, Cobras will remain in Israeli service well into the next century.
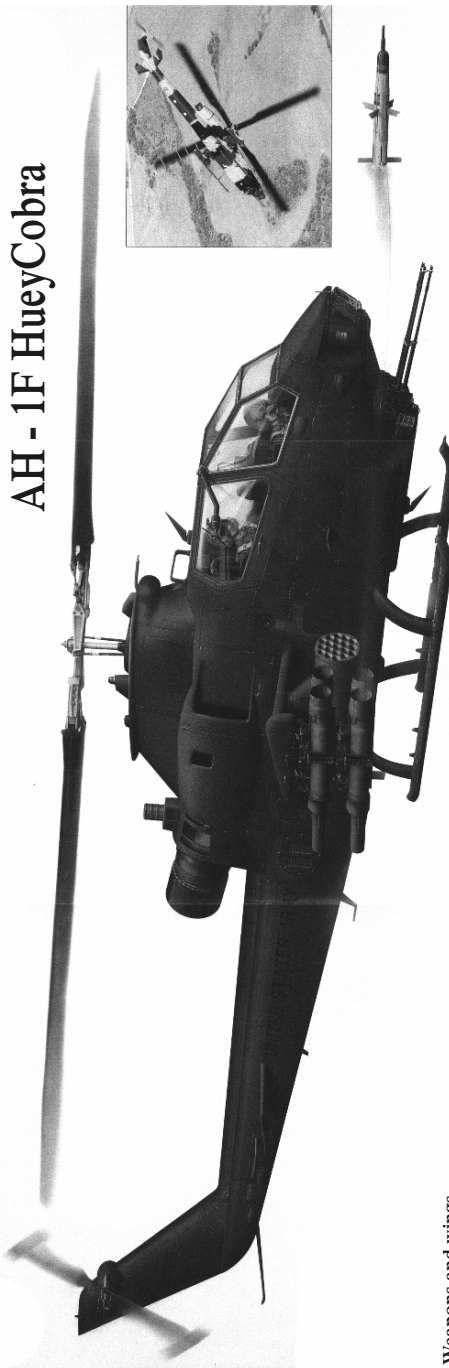
Weapons and wings

Stub wings help to off-load the main rotor and act as weapon attachment points. Late-standard AH-1F Cobras are fitted with a Baldwin Electronics M138 stores management sub-system for selection and firing of the various types of rocket pod which remain within the Cobra's inventory, despite the fitment of TOW tubes. Mounted on the two inner attachment points the M159 pod (illustrated) contains 19 FFARs (Folding-Fin Aircraft Rockets) of 2.75-in (70-mm) calibre. Each loaded pod weights 542 lb (246 kg).

Plate 2.82. AH-1F Cobra

AH-1 HueyCobra
Briefing
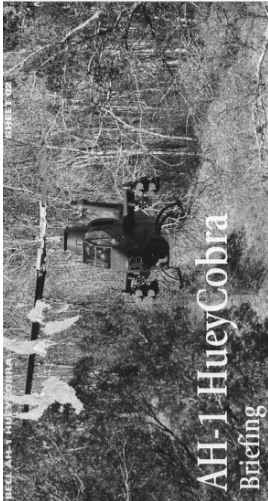
Hunting for targets at tree-top height, this production AH-1S is seen on a practice mission on one of the vast test ranges in the United States. The widespread introduction of the AH-64 Apache has resulted in the HueyCobra being withdrawn from front-line US Army operations, but for many foreign operators the Cobra remains their most important attack helicopter.
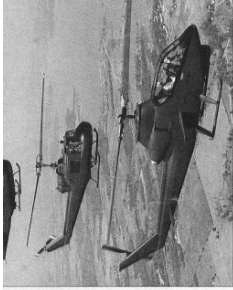
The Bell company endeared itself to the US Army with a succession of highly successful utility/transport helicopters. The AH-1G, seen in the foreground flying with a UH-1B (centre) and a UH-1D (rear), was radically different, yet used many components of the earlier UH-1 models.

74 Multi-cellular glassfibre-reinforced blade spar
75 Laminated glassfibre blade skin
76 Honeycomb trailing edge core structure
77 Kevlar trailing edge spline
78 Blade root attachment joint with provision for semi-automatic folding
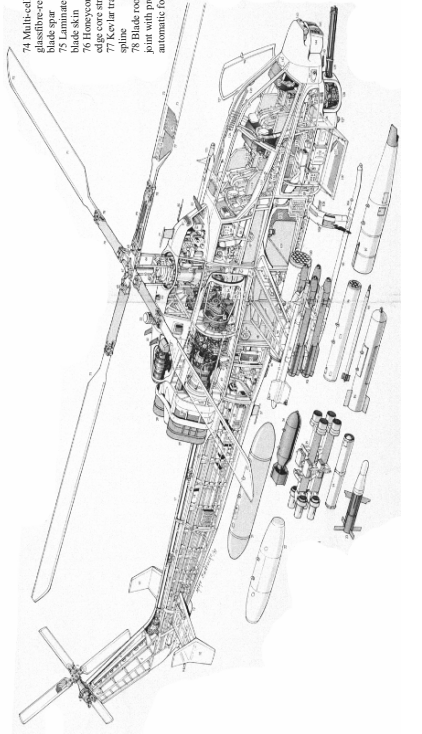
79 Upper UHF/IFF antenna
80 Pitot head
81 Cooling air grille
82 Upper cable cutter
83 Hydraulic filters
84 Avionics equipment bay, access port and starboard
85 Hydraulic equipment bay, air conditioning on port side
86 Cockpit air delivery duct
87 Gravity fuel filler
88 Stub wing attachment joints

89 Stub wing fuel cell
90 All-composite stub wing structure
91 Wingtip missile launch rail

92 AIM-9L Sidewinder or Sidearm air-to-air missile
93 AGM-114 Hellfire air-to-surface missiles

SPECIFICATION

AH-1F-HueyCobra

Dimensions
Length overall, rotors turning: 53 ft 1 in (16.18 m)
Fuselage length: 44 ft 7 in (13.59 m)
Main rotor diameter: 44 ft (13.41 m)
Tail rotor diameter: 8 ft 6 in (2.59 m)
Height to top of rotor head: 13 ft 5 in (4.09 m)
Main rotor disc area: 1,520.23 sq ft (141.26 m²)
Tail rotor disc area: 56.75 sq ft (5.27m²)
Stabiliser span: 6 ft 11 in (2.11 m)
Skid track: 7 ft (2.13 m)

Powerplant
One 1,800-shp (1342-kW) Textron Lycoming T53-L-703 turboshaft, transmission-limited to 1,290 shp (962 kW) for take-off and 1,134 shp (845 kW) for continuous running

Weights
Operating weight: 6,598 lb (2993 kg)
Normal take-off 9,975 lb (4524 kg)
Maximum take-off: 10,000 lb (4536 kg)

Performance
Never exceed speed in TOW configuration: 195 mph (315 km/h)
Maximum level speed at optimum altitude in TOW configuration: 141 mph (227 km/h)
Service ceiling: 12,200 ft (3720 m)
Range: 315 miles (507 km)

Armament
Primary armament is the TOW missile, eight of which can be carried along with 2.75-in (70-mm) FFARs with a variety of warheads. Secondary armament is the M197 triple-barrelled 20-mm cannon in a chin turret

AH-1W SuperCobra

Dimensions
Length overall, rotors turning: 58 ft (17.68 m)
Fuselage length: 45 ft 6 in (13.87 m)
Main rotor diameter: 48 ft (14.63 m)
Tail rotor diameter: 9 ft 9 in (2.97 m)
Height to top of rotor head: 13 ft 6 in (4.11 m)
Main rotor disc area: 1,809.56 sq ft (168.11 m²)
Tail rotor disc area: 74.7 sq ft (6.94 m²)
Stabiliser span: 6 ft 11 in (2.11 m)
Skid track: 7 ft (2.13 m)

Powerplant
Two 1,625-shp (1212-kW) General Electric T700-GE-401 turboshafts, transmission-limited to a total of 2,032 shp (1515 kW) for take-off and 1,725 shp (1286 kW) continuous running

Weights
Empty weight: 10,200 lb (4627 kg)
Maximum take-off: 14,750 lb (6691 kg)

Performance
Never exceed speed: 219 mph (352 km/h)
Maximum level speed 'clean' at sea level: 175 mph (282 km/h)
Service ceiling: more than 12,200 ft (3720 m)
Range: 395 miles (635 km)

Armament
Uniquely qualified to carry both TOW and Hellfire, plus up to four seven-round LAU-69A rocket pods containing 2.75-in (70-mm) Hydra 70 rockets. Self defence is provided by a single AIM-9L Sidewinder AAM mounted on a hardpoint above each wingtip

SEE OTHER FILES

027	AGM-114 Hellfire	330	Rockwell Inc.
155	Hughes/DHE Apache	341	US Army
197	AH-64A Apache	341	USMC
299	Hughes TOW missile	379	Vietnam
299	AGM-114 Hellfire	384	Desert Storm

Plate 2.83. AH-1 Cobra

Table 2.47. Tanks as impactors

Type of tank and power plant	S (m)	L (m) (hull)	H (m)	w_a (kg)	V (km h^{-1})	Max range (km)	Manufacturer and country
AMX-40 Engine: Poyand V12× 12-cylinder diesel developing 1,300 hp	3.28–3.35	6.8	2.38	43,700	55	850	Giat, France
Engesa, EE-T1 Osorio Engine: MWMTBD 234, 4-stroke, 12-cylinder water cooled turbo-charged diesel developing 1,040 hp	3.26 Track width (570 mm)	7.13	2.68	40,440	70	550	Engesa, Brazil
Leopard 2 Engine: TU MB873 Ka501, 4-stroke, 12-cylinder developing 1,500 hp	3.70	7.72	2.48	55,150	72	550	Krupp, Germany
MB-30 Tamoio Engine: Saab-Scania DS1 – 14 diesel developing 500 hp	3.22	6.5	2.50	30,000	67	550	Bernardini, Brazil
C1 MBT Engine: Fiat V-12 MTCA turbo-charged 12-cylinder diesel developing 1,200 hp	3.545	7.595	2.46	48,000	65	550	IVECO Fiat and OTTO, Italy
Challenger MBT Engine: Perkins Engines Condor 12-V 1200 12-cylinder diesel developing 1,200 hp	3.518	9.80	2.5 to 2.9	62,000	56	–	Vickers, UK
Chieftan MBT Engine: Leyland L60 2-stroke 6-cylinder NO: 4MK6A or NO: 4MK8A developing 730 bhp and 750 bhp, respectively	3.504	7.52	2.895	54,100–55,000	56	500	Vickers, UK

Type 80 MBT V-12 diesel developing 730 hp	3.372	6.325	2.874	38,000	60	430	North Industries, China
Type 88 MBT	3.594	7.477	2.248	51,000	65	500	Hyundai, South Korea
Engine: MTU 871 Ka-501 diesel developing 1,200 hp							
90 MBT	3.40	7.50	2.30	50,000	70	300	Mitsubishi, Japan
Engine: Mitsubishi 10-cylinder diesel developing 1,500 hp							
M48 MBT							
Engine: All Continental 12-cylinder							
M48 (AV-1790-5B/7/7B/7C) petrol	3.631	6.705	3.241	44,906	41.8	113	Variants, US Army, USA
M48A1 (AV-1790-7C) petrol	3.631	6.87	3.13	47,173	41.8	113	
M48A2 (AV-1790-8) petrol	3.631	6.87	3.089	47,173	48.2	258	
M48A3 (AVDS-1790-2A) diesel	3.631	6.882	3.124	47,173	48.2	463	
M48A5 (AVDS-1790-2D) diesel	3.631	6.419	3.086	48,987	48.2	499	
Note: all petrol 2,800 hp all diesel 2,400 hp							
M60 MBT, M60 A1 MBT	3.631	6.946	3.213	49,714	48.28	500	General Dynamics, USA
Engine: Continental AVDS-1790-2A 12-cylinder developing 750 bhp							
M60 A3 MBT	3.631	6.946	3.270	52,617	48.28	480	
Engine: Continental AVDS-1790-2C 12-cylinder developing 750 bhp							
Merkava 2MBT	3.70	7.45	2.64	60,000	46	400	Sibit, Israel
Engine: Teledyne Continental AVDS-1790-6A V-12 diesel developing 900 hp							

Table 2.47. (continued)

Type of tank and power plant	S (m)	L (m) (hull)	H (m)	w_a (kg)	V (km h^{-1})	Max range (km)	Manufacturer and country
MI Abrams MBT Engine: Lycoming Textron AGT 1,500 gas turbine developing 1,500 hp	3.657	7.918	2.886	57,154	67	500	General Dynamics/Lima, USA
Stridsvagn 103 MBT Engine: Rolls-Royce K60 developing 240 hp or Boeing 553 gas turbine developing 490 shp	3.63	7.04	2.43	39,700	50	390	Bofors, Sweden
T80 MBT Engine: Gas turbine developing 985 hp	3.40	7.40	2.20	42,000	75	400	China and Soviet State Arsenal, USSR
Talbot MBT Engine: Continental V-12 AVDS developing 760 hp	3.39	6.36	3.35	47,000	56	600	Peugeot, Spain
Upgraded Centurian Tank Engine: Rolls-Royce MK1VB 12-cylinder developing 650 hp	3.39	7.556	2.94	50,728			
Vickers/FMC VFM 5MBT Engine: Detroit diesel model 6V-92 TA developing 552 hp	2.69	6.20	2.62	19,750	70	483	Vickers, UK
Vijayanta MBT Engine: Leyland L60 developing 535 hp	3.168	9.788	2.711	40,000	48.3	550	Department of Defence, India

S, width; L, length; H, height; w_a, combat weight; V, speed
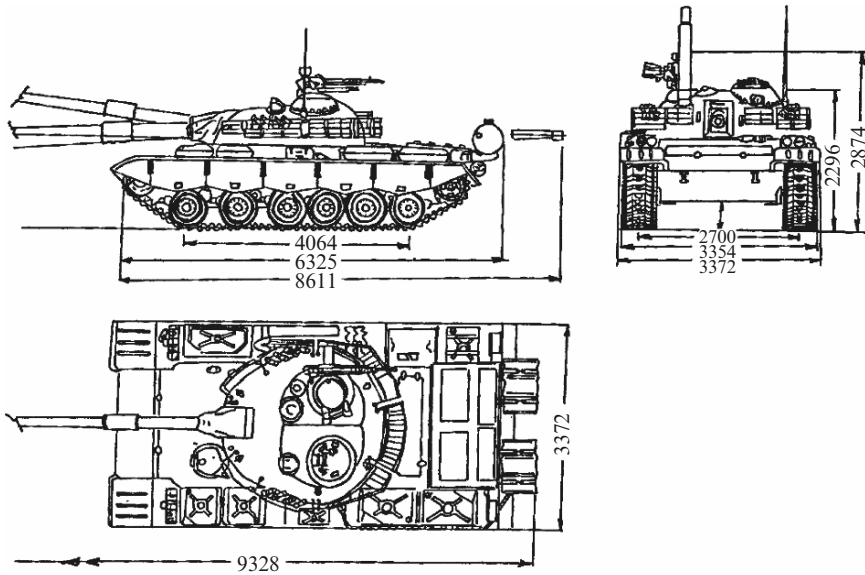
Fig. 2.55. Type 80-MBT main battle tank (courtesy of the China Government Arsenal, Beijing)

seldom involved in accidents in peace-time roles, nevertheless they are vulnerable in battle zones and are always subject to aircraft and missile attacks and terrorist attacks. Table 2.50 lists weights, basic dimensions, speeds, ranges and armament for some of the well-known naval vessels.

For other types, the analyses will require a comprehensive geometrical layout in order to assess damage due to unwarranted attacks.

2.26.2 Offshore Floating Mobile and Semi-Submersible Structures

The tension leg platform (TLP) design is a complex one. From considerations of construction and operational requirements, and because of the danger of heavy impact from sea vessels, vigorous data collection is necessary. Table 2.51 summarizes data for such a structure.

The drilling semi-submersibles can generally be characterized by the three sea conditions:

(1) Maximum drilling with significant waves of 8 m.
(2) Riser's disconnections with significant waves of 11 m.
(3) Survival conditions with significant waves of 16 m.

Based on these criteria, the basic shape and size can be directly related to the load-carrying capacity. Various drilling semi-submersibles have been designed. In Fig. 2.59, five (Aker H3, DSS 20, GVA 4000, Sonat and DSS 40) semi-submersibles are compared in terms of loadings and displacements. A typical

AMX-30 MBT

provisional three-view drawing of C1 MBT (not to 1/76th scale)

Chieftain Mk 3 MBT
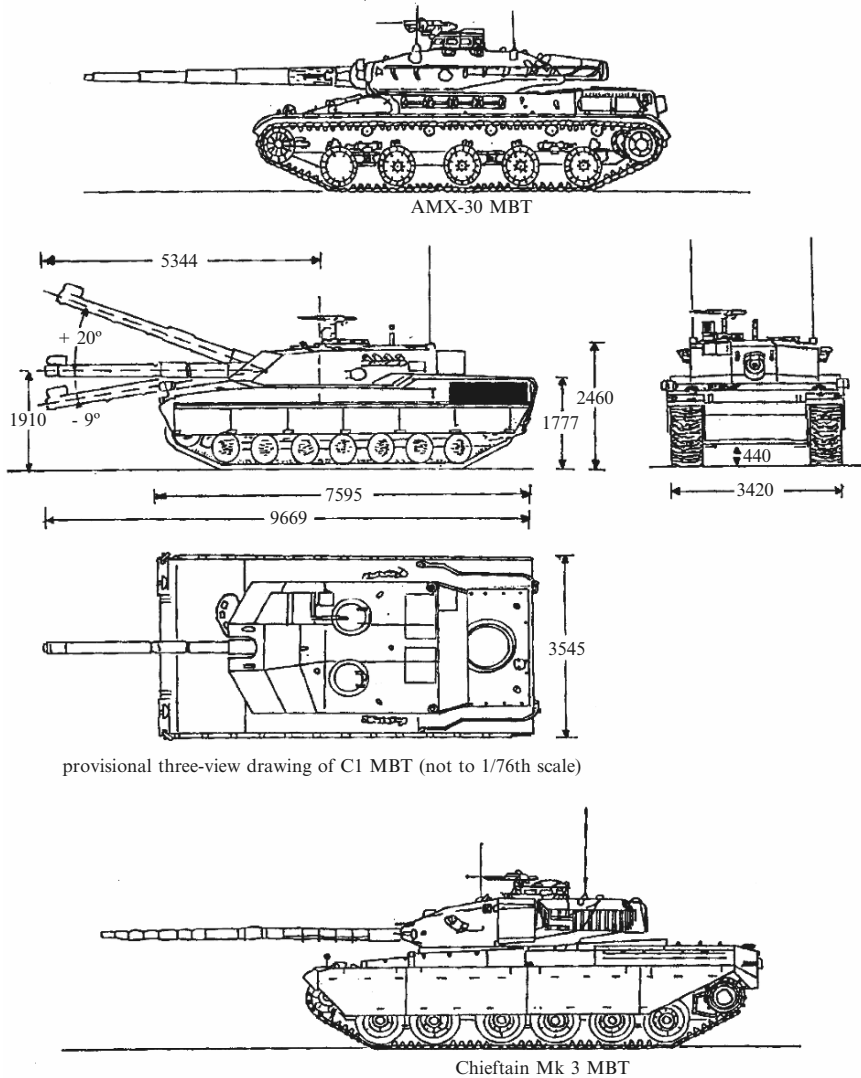
Fig. 2.56. AMX-30 and C1 Chieftan Tanks (courtesy of the Ministries of Defence, UK and France)

layout of the DSS 40 is illustrated in Fig. 2.60. It is important to consider as well the wind effects during any accident conditions. Table 2.52 gives useful data on the wind velocity profile.

For flat surfaces, all the registered companies agree to take the value of 1.0. Similarly, all take a value of 1.25 for drilling derricks. The Japanese and API take 1.3 for exposed beams and girders and 1.5 for isolated shapes. For clus-

tered deck houses or similar structures, Nippon and API take a drag coefficient of 1.1.

In addition, various dimensions are required for the semi-submersible when it is transported in a heavy lift ship. These are given in Table 2.53 for a typical case study by the Wijsmuller Transport Bureau. Taking the weights of the chains and anchors as 2.42 and 180 tonnes, respectively, the total weight is assumed to be 22.20 tonnes.

The same approach is adopted when a jack-up rig is transported. The total load is generally not more than 20 tonnes. In the absence of a specific rig, the data in Table 2.54 provided by the Wijsmuller Transport Bureau, will be adopted for impact analysis.

2.27 Types of Explosion

A comprehensive introduction is given to each type of explosion later on in Chap. 5. The purpose of this section is to provide chemical data under a specified classification for researchers and practising engineers/scientists who are familiar with the subject but wish to use it without extensive searching for materials for their individual problems. The author appreciates that many ordnance factories, munition and explosive plants and laboratories have accumulated a large amount of information which is confidential. He has therefore limited himself to data for which there is a reference available in the open literature.

Explosions may be due to bombs, shells, grenades and various explosives and also to gas leaks, nuclear detonation and fuel in chemical industries. Explosions occur in the air, on the surface, underground and underwater. They are classified in the text into:

(1) Explosions due to bombs, shells and explosives;
(2) Explosions due to gas leaks;
(3) Nuclear explosions;
(4) Dust explosions.

2.27.1 Bombs, Shells and Explosives

2.27.1.1 Bombs and Shells

Bombs and shells manufactured for military purposes are illustrated in Sect. 2.3.1 with the respective aircraft.

2.27.1.2 Explosives

During most of the period from the fourteenth to the early nineteenth century, chemistry played only a small part in the development of science. The history

Table 2.48. Lightweight vessels (weights and dimensions)

Vessel	w_a (tonnes)	L (m)	S (m)	d (m)
Barges		50	18.0	5.0
		100	20.5	5.5
		150	22.5	6.3
		200	25.0	6.6
		300	30.0	6.9
Boats	300	37	7.0	3.3
	500	43	7.8	3.8
	700	54	7.9	4.0
	1,000	61	8.9	4.5
	2,000	76	11.2	5.7
	3,000	87	12.8	6.5
	4,000	96	14.0	7.2
	5,000	103	15.1	7.8
	6,000	110	16.0	8.2
	7,000	116	16.8	8.7
	20,000	164	23.7	12.3
	25,000	176	25.5	13.3
	30,000	187	27.1	14.1
	35,000	197	28.5	14.8
	40,000	206	29.7	15.5
	50,000	222	32.0	16.7
	60,000	236	34.0	17.8
	70,000	248	35.7	18.7
	80,000	260	37.3	19.6
Cargo boats	700	52	8.3	3.8
	1,000	60	9.3	4.4
	2,000	77	11.5	5.8
	3,000	90	13.1	6.8
	4,000	100	14.3	7.7
	5,000	109	15.3	8.4
	6,000	117	16.2	9.0
	7,000	124	17.0	9.6
	8,000	130	17.7	10.1
	9,000	136	18.4	10.6
	10,000	142	19.0	11.1
	12,000	152	20.1	11.9
	15,000	165	21.6	13.0
	17,000	173	22.4	13.7
	20,000	184	23.6	14.6
Ferry boats	50	20	6.0	2.3
	100	25	7.5	2.7
	200	35	9.0	3.2
	300	42	10.0	3.5
	500	50	11.5	3.9
	1,000	64	13.0	4.4

Table 2.48. (continued)

Vessel	w_a (tonnes)	L (m)	S (m)	d (m)
Fishing boats	10,000	162.2	20.7	12.0
	17,000	189.5	23.6	12.7
	20,000	178.0	22.8	17.4
Motor and sailing boats				
Wooden boats	100	21.0	6.3	2.6
Steel boats	100	25.0	5.3	2.5
Wooden boats	200	29.0	7.4	3.4
Steel boats	200	33.0	6.6	3.3
Wooden boats	300	32.0	8.0	4.0
Steel boats	300	38.5	7.2	3.6
Ore carriers	1,000	61	8.9	4.8
	2,000	77	11.1	6.0
	3,000	88	12.7	6.8
	4,000	96	13.9	7.5
	5,000	104	14.9	8.1
	15,000	149	21.3	11.5
	20,000	164	23.4	12.7
	25,000	176	25.1	13.6
	30,000	187	26.6	14.4
	40,000	206	29.2	15.9
	50,000	222	31.4	17.1
Passenger boats	500	50	8.2	4.5
	1,000	65	10.0	5.3
	2,000	82	12.0	6.4
	3,000	95	13.5	7.3
	4,000	105	14.8	8.0
	5,000	113	15.8	8.8
	6,000	121	16.7	9.5
	7,000	127	17.5	10.2
	8,000	135	18.2	10.8
	10,000	145	19.2	12.0
	15,000	165	21.5	13.0
	20,000	180	23.0	13.8
	30,000	210	26.5	15.5
	50,000	245	30.5	18.0
	80,000	290	36.0	21.0
Trawl boats	400	53.8		7.9
	800	67.2		10.2
	1,000	76.2		10.7
	2,000	87.4		13.1
	3,000	98.6		14.2
Whaling vessels	400	53.8		8.3
	800	62.7		9.4
	1,000	68.3		10.2

w_a, gross weight; L, length; S, width; d, depth

Table 2.49. Data on the principal hovercraft

Type	Power plant	Length (ft)	Max weight (tonnes)	Max speed (mph)	General comments
					All hovercraft:
Australia					
Hovergem G-4	Two 170–200 hp aeros	30	–	65	(1) *Amphibious* Horsepower
Canada					228–565 with air
Hovergem	Three 17.5 hp JLD pistons	16	0.55	45	propeller 390–538 air jet
France					
Aerotrain 01	Lift, two 50 hp Renault auto pistons	33	2.75	215	(2) *Semi-amphibious* Horsepower
Aerotrain 02	Lift, Turbomeca air-bleed turbine	84	22.0	185	150–191
	3,000 lb thrust P&W turbojet				(3) *Non-amphibious* Horsepower 172
Aerotrain "Orleans"	400 hp Turbomeca Astazou turbine	47	11–12.5	112	
	Two 1,500 hp Turmos, one ducted ap				
Aerotrain "Cite"	Lift, 250 hp auto piston	32	5.5	50	
	Linear electric or auto wheels				
SEDAM Naviplane BC.7	Lift, 180 hp Chevrolet piston	33	4.75	62	
	Two axles, each 45 hp				
SEDAM Naviplane BC.8	Lift, 880 lb thrust Turbomeca jet	79	30.0	71	
	400 hp turbine two reversing aps				
SEDAM Naviplane N-300	Two 1,500 hp Turbomeca Turmo turbines	11	0.28	34	
	Two reversing aps				
SEDAM Naviplane Sports	Lift, 7 hp JLO piston	40	3.8	75	
	Two 4.3 hp JLO shrouded aps				
Israel					
Israel American Lady Bird 2	Lift, 230 hp auto	35	2.8	52	
	230 hp aero piston ducted ap				

Japan

Mitsui MV-PP1	Lift, 250 hp Continental 10–470	250 hp 10–470 reversing ap	53	12.0	63
Mitsui MV-PP5	1,050 hp IHI (GE LM-100) turbine	Two reversing aps	56	12.0	–

UK

BHC BH.8	Two 3,400 hp R-R Proteus turbines	Two non-swivelling aps	96	103.0	86
	Four 3,400 hp R-R Proteus turbines	Four swivelling reversing aps	130	194.0	81
BHC SR.N4	900 hp R-R Marine Gnome turbine	Fixed reversing ap	39	7.5	68
BHC SR.N5	900 hp R-R Marine Gnome turbine	Fixed reversing ap	48	11.5	60
BHC SR.N6	390 hp P&W ST6B turbine	Two low-pressure air jets	25	3.0	45
Cushioncraft CC-7	Lift, two 180 hp Caterpillar diesels	Two 400 hp diesel ms	81	34.0	31
Denny D.2	Lift, 18 hp Velocette piston	33 hp Greaves shrouded ap	13	0.35	50
Express Air Rider	Lift, 16 hp Velocette piston	Two 16 hp Velocette shrouded aps	16	0.625	34
Hover Hawk	Lift, 185 hp Cummins diesel	Two 320 hp Cummins ms	51	18.0	40
Hovermarine HM.2	Two diesels or gas turbines	Waterjets or ducted ms	160	140.0	50
Hovermarine HM.4	Lift, 46 hp Volkswagon piston	90 hp Porsche fixed ap	27	2.25	35+

Table 2.49. (continued)

Type	Power plant	Length (ft)	Max weight (tonnes)	Max speed (mph)	General comments
UK (Contd)					
Hovermarine Hovercat	Two 2,000 hp Lycoming	96	86.0	55	Two variable-pitch ms
Vosper Thorneycroft VY1	TF 20 turbines				
USA					
Aerogem 1A	Lift, 60 hp auto piston	16	0.6	60+	25 hp ducted fixed ap
Beardsley Skimmer	6 hp Chrysler piston	10	0.2	18	Air escape from fan duct
Bell SK-5 (7250)	1,000 hp GE LM-100 turbine	39	10.0	70	Fixed reversing ap
Bell SK-6 (7282)	1,250 hp GE LM-100 turbine	49	12.5	65	Fixed reversing ap
Bell SK-9	Two 1,250 hp GE LM-100 turbines	56	26.5	70	Two fixed reversing aps
Bell SK-10	Two 12,000 hp GE LM-1500 turbines	80	148.0	92	Two fixed reversing aps
Bell SES	140,000 hp (two GE 4 converted)	420	4,000.0	92	Waterjets or ducted ms
Bertelsen Aeromobile 13	Two 40–49 hp autos or aeros	21.5	1.35	50–80	Lift fans gimballed to rear
Cushionflight Airseat	45 hp Volkswagen piston	15	0.5	40	Reversing shrouded ap
Dobson Air Car D	20 hp Lloyd or similar piston	14	0.325	35	Rear vents from cushion
Gunderson Crop Sprayer	Lift, two 7 hp Tecumseh pistons	12	0.3	20	15 hp Hirth ap plus wheels

of industrial explosives began with the use of black powder for blasting in 1600. Black powder was originally used by the Arabs, Hindus and Chinese. It was a low-power explosive (LE). Its role was deflagration rather than detonation. In 1346 it was used as a gun powder in the battle of Crécy, as a propellant in wooden cannon. A safety fuse was invented in 1831.

Since an explosive is composed of a fuel and an oxidizer, a large amount of energy is given off on reaction. In the case of black powder, the sodium/potassium nitrate furnishes oxygen for the reaction which eventually combines with sulphur (S), and carbon (C). The equations of reaction are as follows:

(a) $2NaNO_3 + S + 2C = Na_2SO_4 + 2CO \uparrow N_2$ 195 kcal
$Q = \text{specific heat} = 920 \, \text{kcal kg}^{-1}$
$n = \text{number of moles of gas} = 4.7 \, \text{mole kg}^{-1}$

(b) $2NaNO_3 + 2S + \frac{3}{2}CO = 2NaSO_3 + \frac{3}{2}CO + N_2$
$Q = 620 \, \text{kcal kg}^{-1}; \; n = 6.9$

(c) $2NaNO_3 + 2S + 3C = 2NaSO_3 + 3CO + N_2$
$Q = 620 \, \text{kcal kg}^{-1}; \; n = 12.6$

(d) $2NaNO_3 + S + 2C = Na_2SO_4 + 2CO + N_2 \uparrow$
$Q = 680; \; n = 8.9$

The energy depends upon the oxygen balance and the strength depends upon the value of n.

The same principal holds for various dynamites and other high explosives (HE).

Single-compound explosives are substances such as nitroglycerin, alpha-trinitrotoluene (TNT), pentaerythrite tetra-nitrate (PETN) and others. Nitroglycerin (NG) and nitrocellulose (NC) are other substances which, when combined in a 92/8 ratio, produced a stiff gel called blasting gelantin (BG), which is a powerful explosive. The chemical formula for NG is $C_3H_5(NO_3)_3$ and it has a natural density of $1.6 \, \text{g cm}^{-3}$. Since it is oxygen positive, during detonation, the equation for the reaction is:

(e) $C_3H_5O_9N_3 = 3CO_2 + 2\frac{1}{2}H_2O + \frac{1}{2}O + 1\frac{1}{2}N_2 \uparrow$
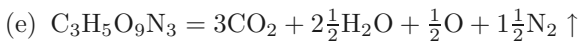
The heat of reaction is about $1,503 \, \text{cal g}^{-1}$ (298 K) and has the following mechanical properties: detonation velocity $= 7,926 \, \text{m s}^{-1}$; pressure in the detonation wave $= 25 \times 10^4 \, \text{atm}$.

Explosives may be divided according to use:

(1) *Commercial.*   Dynamites, ammonium nitrate–fuel oil (ANFO) explosives and water-based explosives.
(2) *Military.*   TNT, PETN, RDX.

Tables 2.55 and 2.56 give a useful summary of all these explosives with their individual characteristics and important parameters. Additional properties of ingredients of explosives are given in Tables 2.57 and 2.58.

Table 2.50. Heavy naval vessels data

Type of naval vessel and power plant	S (m)	L (m)	H (m)	Weight (displacement) w_a (tonnes)	V (knots)	Additional data	Range (miles)
4 × "Agosta" class Diesel electric, 2SEMT-piedstick, 16 PA 4185VG diesels, 3,600 hp, 1 electric motor, 4,600 hp (patrol submarine)	6.8	67.6	5.4	1,490–1,740	12 surface 20 diving	SSM Aerospatiale SM 39 Excocet missiles: 553 mm tube at 0.9 mach, warhead 165 kg	8,500
Ex-British "Hermes" class aircraft carrier 2 Parsons geared turbines 76,000 shp	226.9	208.8	8.7	23,900–28,700	28.0	SAM system (see Soviet)	1,200
Ex-Chinese "Huchuan" class 3 M50 diesels 3,600 hp (fast-attack hydrofoil – torpedo)	6.3	21.8	3.6		55	Guns 14.5 mm, MGS 2 No. 533 tubes, torpedoes	500
Ex-Chinese "Shanghai II" class 2M 50F diesel 2,400 hp (fast-attack craft)	5.5	39	1.7	120–155	30	4–37 mm guns, shell 1.42 kg, 8 depth charges	800
Destroyers (1) Bristol COSAG; 2 Standard Range geared, steam turbines, 30,000 shp, 2 Rolls-Royce Marine Olympus TM1A gas turbines, 30,000 shp 2 shafts, 2 boilers	16.8	154.5	5.2	7,100	30	Missiles: SAM: British Aerospace Sea Dart GWS 30 twin launcher, radar homing to 40 km (21 mm), warhead HE; 40 missiles, limited anti-ship capability Guns: 1 Vickers 4.5 in (114 mm) 55 Mk 8, 55° elevation, 25 rounds/	5,000

Table 2.50. (continued)

Type of naval vessel and power plant	S (m)	L (m)	H (m)	Weight (displacement) w_a (tonnes)	V (knots)	Additional data	Range (miles)
						minute to 22 km (11.9 nm) anti-surface, 6 km (3.3 nm) anti-aircraft weight of shell 21 kg 4 Oerlikon/BMARC 30 mm/75 GCM-A03 (2 twin); 80° elevation, 650 rounds/minute to 10 km (5.5 nm)	
(2) Birmingham, Newcastle, Glasgow, Cardiff, Exeter, Southampton, Nottingham, Liverpool COGOG; 2 Rolls-Royce Olympus TM3B gas turbines (full power), 50,000 shp: 2 Rolls-Royce Tyne RM1C gas turbines (cruising): 9,700 shp: 4 diesel generators, 4,000 kW, 2 shafts, stone manganese type XX cp propellers	14.3	119.5	5.8	3,500–4,100	29	Missiles: SAM: British Aerospace Sea Dart GWS 30 twin launcher; radar semi-active radar homing to 40 km (21 nm), warhead HE, 22 missiles limited anti-ship capability Guns: 1 Vickers 4.5 in (114 nm) 55 Mk 8, 55° elevation, 25 rounds/min to 22 km (11.9 nm) anti-surface, 6 km (3.3 nm) anti-aircraft, weight of shell 21 kg 2 Oerlikon/BMARC 20 mm GAM-BOL; 55° elevation, 1,000 rounds/minute to 2 km 2 Oerlikon 20 mm MK 9; 50° elevation; 800 rounds/minute to 2 km, weight of shell 0.24 kg 2 General Electric/General	4,000

Aircraft carriers Nimitz, Dwight D. Eisenhower, Theodore Roosevelt, Abraham Lincoln, George Washington 2 pressurized-water cooled A4W/A1G nuclear reactors: 4 geared steam turbines; 260,000 shp, 4 shafts	40.8	332.9	11.8	72,916–96,386	30+	Dynamics 20 mm Vulcan Phalanx Mk 15; 6 barrels per launcher, 3,000 rounds/minute combined to 15 km; Still to be fitted in some Torpedoes: 6–324 mm Plessey STWS Mk 2 (2 triple) tubes; Marconi Stingray, active/passive homing to 11 km (5.9 nm) at 45 knots: warhead 35 kg Honeywell/Marconi Mk 46 Mod 2; active/passive homing to 11 km (5.9 nm) at 40 knots, warhead 45 kg Missiles: SAM 3 Raytheon Sea Sparrow Mk 29 octuple launchers; semi-active radar homing to 14.6 (8 nm) at 2.5 mach Guns: 4 General Electric/General Dynamics 20 mm Vulcan Phalanx 6-barrelled Mk 15 (3 in CVN 68 and 69), 3000 rounds/minute combined to 1.5 km Countermeasures: decoys; 4 Loral Hycor SRBOC 6-barrelled fixed Mk 36: IR flares and chaff to 4 km (2.2 nm); ESM/ECM SLQ 29 (WLR 8 radar warning and SLQ 17AV jammers) Fire control: 3 Mk 91 MFCS; NTDS

Table 2.50. (continued)

Type of naval vessel and power plant	S (m)	L (m)	H (m)	Weight (displacement) w_a (tonnes)	V (knots)	Additional data	Range (miles)
French Colbert cruiser 2 sets CEM-Parsons geared turbines, 86,000 shp, 2 shafts, 4 Indrit multi-tubular boilers	20.2	180	7.7	8,500–11,300	31.5	action data automation; links 11 and 14; OE-82 satellite communications antenna, SSR 1 receiver SSM: 4 Aerospatiale MM38 Excocet missiles, range 42 km, warhead 165 kg, 2/100 mm guns	4,000
French nuclear propelled aircraft carriers (PAN) Nuclear propulsion type K15 300 MW (PWR), 82,000 hp	261.5 also deck 2.62 29.4	238 261.5 138	31.8 6.1	34,000–36,000	26	Variants, SAM 7 Thomson missiles, CSF-SAAM range 17 km at 2.5 mach	
Indian Ex-British "Majestic" class aircraft carrier 2 No. Parsons single reduction, geared turbines, 4,000 shp	24.4	231.4	7.3	16,000–19,500	24.5	7 Bofor guns, 40 mm, range 12 km, shell weight	12,000
Light aircraft carrier (Giruseppe Garibaldi) COGAG; 4 Fiat/General Electric LM 2500 gas turbines, 80,000 hp; Tosi reduction/reversing gears, 2 shafts, 5 bladed propellers, generating capacity 6–1950 kVA diesel alternators	33.4	180	6.7	13,850	30	Missiles: SSM: 4 OTO Melera/Matra Teseo Otomat launchers, inertial cruise, to active radar homing 180 km (100 nm) at 0.9 mach, warhead 200 kg, sea-skimmer SAM: 2 Selenia Elsag Albatros octuple launchers, 48 Aspide	7,000

| 4 × Meko 360
2 Rolls-Royce "Olympus" TM3B gas turbines 51,600 shp (destroyer) | 14 | 125.9 | 5.8 | 2,900–3,600 | 30.5
30.5 | 4,500 | semi-active radar homing to 13 km (7 nm) at 2.5 mach
Guns: 6 Breda 40 mm/70 (3 twin) MB, 85° elevation, 300 rounds min to 4 km (2.2 nm) anti-aircraft, weight of shell 0.96 kg
Torpedoes: 6–324 mm ILAS 3 (2 triple) tubes Whitehead A244S, anti-submarine active/ passive homing to 6 km
55M Aerospatiale MM 40 Excocet missiles: range 70 km, weight of warhead 165 kg; 1 No. OTO 40 mm guns, 8 Breda/Bofor 40 mm |

Table 2.51. Characteristics of the tension leg platform (data courtesy of Conoco, Amoco, Deep Oil Technology and International Marine Development)

Company/investigator	Hutton TLP Conoco	VMP Amoco Produce Co	Deep Oil X-1 Deep Oil Technology	Triton International Marine Development
Design environment				
Water depth (m)	150.0	264.0	61.0	182.9
Wave excitation	Irregular waves	Design wave	Design wave	Design wave
Wave height	16.6	26.0	7.6	15.2
Wave period (s)	13.9	13.0–16.0		15.0
Current velocity	$0.85\,\mathrm{m\,s^{-1}}$	$2.7\,\mathrm{m\,s^{-1}}$; lv	2.5 knots	
Wind velocity	$44.0\,\mathrm{m\,s^{-1}}$	$67\,\mathrm{m\,s^{-1}}$	60.0 knots	120.0 knots
Basic configuration				
Scale	Prototype	Model (1:60)	Model (1:3)	Model (1:6)
Deck plan	Rectangular	Square	Triangular	Rectangular
Length (m)	78.0	61.0	31.7	7.3
Breadth (m)	74.0	61.0	36.6	7.3
Depth (m)	12.0	9.1		3.2
Keel to deck (m)	69.0	64.9	20.1	13.8
Columns/cassions				
No total	6.0	4.0	6.0	6.0
No corner	4.0	$4\,\mathrm{w\,cb^{-1}}$	3.0	4.0
No interior	2.0	0	$3\,\mathrm{w\,cb^{-1}}$	$2\,\mathrm{w\,cb^{-1}}$
Corner (m)	17.7 dia	9.1–18.3 dia	3.2 dia	0.38 dia
Interior (m)	14.5 dia		0.91 dia	
Lower hull				Triangular
Length (m)	95.7	67.1	36.6	13.2
Breadth (m)	8.0	67.1	1.68 dia	1.6 dia

Height (m)	10.8			
Overall width (m)	91.7	67.1	36.6	15.2
Tendons				
Type and no	Pipe, 16	Risers, 24	Wire rope, 6	Wire rope, 6
Outside diameter (m)		0.47	0.6	0.25
Pre-tension (t)	15,000			53.0
Displacement (t)	63,000		635.0	124.0
Operating draft (m)	33.2	36.3	12.2	10.8
No. wells	32	20.0	13 risers	
Accommodation (people)	239			
Natural response periods				
Surge and sway (s)	60.0	60.0	66.0	60.0
Heave (s)	1.9	2.0	0.5	1.9
Roll and pitch (s)	1.9	2.0	2.0	1.9
Yaw (s)	43.0	60.0		43.0
Dynamic response behaviour				
Wave excitation	Irregular waves	Design wave	Random	Random
Wave height (m)	16.6	16.0	18.1	15.8
Wave period (s)	13.9	14.0	16.7	
Motion response				
Surge (m)	9.5	11.2	2.7 ha	0.34–3.06 rms
Sway (m)				
Heave (m)			0.2 da	
Roll (degrees)				
Pitch (degrees)				
Yaw (degrees)	1.7			
Tension, max (t)	300.0		0.11	0.12–0.45

Table 2.52. Wind velocity profile

Height (m)	Coefficients for wind		Drag coefficients			
	LLOYDS[a]	DNV[b]	LLOYDS	API[c]	NIPPON[d]	DNV
10	1.0	1.0	0.4	0.4	0.4	–
20	1.05	1.06	0.5	0.5	0.5	0.5
30	1.105	1.10				
50	1.14	1.16		spherical parts		
80	1.20	1.20		cylindrical parts		
100	1.22	1.23				
150	1.26	1.28				

[a] Lloyds Register, UK
[b] API, American Petroleum Institute, USA
[c] DNV, Norway
[d] Nippon, Japan

Table 2.53. Rigs and floaters

	Rigs	Floaters
L (m)	97.5	97.5
S (m)	72.5	72.5
H (m)	38.80	
x (m)	39.5	
w_a (tonnes)	19.6	
D (m)		8.5

L, length; S, width; H, height; x, distance between floaters; w_a, weight of rig; D, depth of floaters; number of columns = 8; outer diameter of columns = 11.8 m; inner diameter of columns = 9.0 m

Table 2.54. Platform dimensions

Platform
$L = 84.00$ m
$S = 90.00$ m
$D = 9.50$ m
At loading/unloading = 4.05 m

Legs
Type	Triangular lattice
Number	3
Longitudinal centres	56.80 m
Transverse centres	66.00 m
Length	156.80 m
Chord diameter	1.00 m
Chord centres	12.00 m

L, length; S, width; D, depth

Table 2.55. Data on major explosives

Explosive	Composition (%)	V_{sp} $(1\,\mathrm{kg}^{-1})$	Q_{E} $(\mathrm{kcal\,kg}^{-1})$	Temperature at explosion (°C or K)	V_{E} $(\mathrm{m\,s}^{-1})$	Properties
Abbcite (ammonia dynamite)	Ammonium nitrate (58); nitroglycerine (8); dinitrotoluene (2); sodium chloride (23); wood meal (9)					As a blasting explosive in coal mining
AG dynamite	Ammonium nitrate (45); nitroglycerine (45); ammonia gelatine wood flour dynamite (7.5); collodian cotton (2.5)	635	1,200	4,050	6,600	Mining operations, underground quarrying, tunnelling in hard rock; submarine work
Amatol (mixture of TNT and ammonium nitrate)	Ammonium nitrate (80); TNT (20); or ammonium nitrate (50); TNT (50)				5,000	As a bursting charge for high explosive shells/bombs
Ammonal	Ammonium nitrate (65); TNT (15); charcoal (33); aluminium powder (17)				7,000	Shell filler; Blasting, tunnelling
Ammonite	Potassium nitrate (10); ammonium nitrate (77); solid hydrocarbon (1); napthalene (10); gelatinized nitroglycerine (2)	860–915	938–1,020	2,310–2,600	3,500–5,100	Ammonites are the main explosive used in the USSR

Name	Composition	V_{sp}	Q_E		V_E	Description
Belgian permite	Ammonium nitrate (78); TNT (8); calcium silicide (14)					Dark-grey powder set off by service detonators
Black powder	Potassium nitrate (70–75); sulphur (10–14); charcoal (14–16)	260	588	2,615	400	Class A (pellet), class B (powder); bombs used in USA
DD 60/40 (LE)	Picric acid (60); dinitrophenol (40)					Bursting charge for shells used by the French
Gelignite	Ammonium nitrate (70); nitroglycerine (29.3); nitro cotton (0.7)	See individual components (Table 2.63)				Used for blasting
MDPC (HE)	Picric acid (55); dinitrophenol (35); trinitrocresol (10)					Bursting charge for shells used by the French
PETN	PETN (70); TNT (30)	780	1,410	4,010	8,200	High explosive charge for sea mines, drop bombs and torpedoes
Wetter-astralit	Gelatinized nitroglycerine (12); ammonium nitrate (57); wood meal (2); coal powder (2); sodium chloride (27)	See individual components (Table 2.63)				A German explosive used in many countries

V_{sp}, specific volume for explosive gases; Q_E, specific heat of explosion; V_E, velocity at explosion
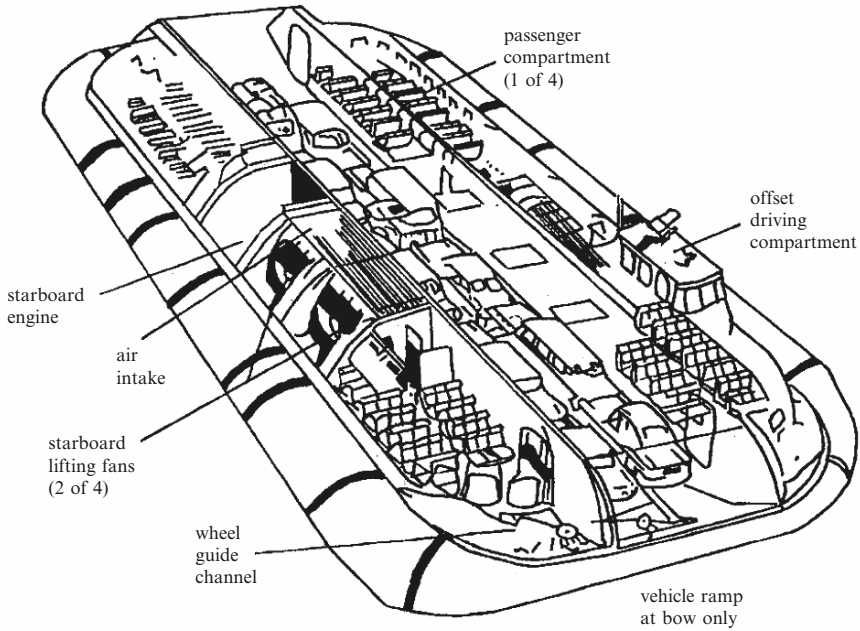
Fig. 2.57. Hovercraft layout

2.27.1.3 Explosive Types vs. Projectile Velocity of Soil/Rock Deposits and Crater Volume

A chemical charge exploding on the Earth's surface creates a shallow depression or cavity, thereby compacting the underlying medium. Most of the energy is lost into the air. When the explosive is buried, depending upon its depth a crater is produced, the size of which is directly related to the depth of the charge. When the charge depth is increased beyond the *optimum depth*, the material is ejected to a certain height only and most of it falls back in the crater. In certain cases an explosion cavity is formed due to the expansion of explosive gases. The "roof surface" is ejected and soil/rock falls into the cavity. At a certain stage a *subsidence crater* is formed. The space of *soil slip* is called the *rubble chimney*. In loose and water-saturated soils, the explosive charges produce such chimneys of the volume of the crater and if the volumes of explosive gases in the space between rubble particles are combined they will give the volume of the original explosion cavity.

Tables 2.59–2.62 show data on the performance of various explosives in creating particle and fly rock initial velocities and crater dimensions in difficult soils/rocks.

The data collected in these tables are from various sources given in the relevant references [2.144–2.185].
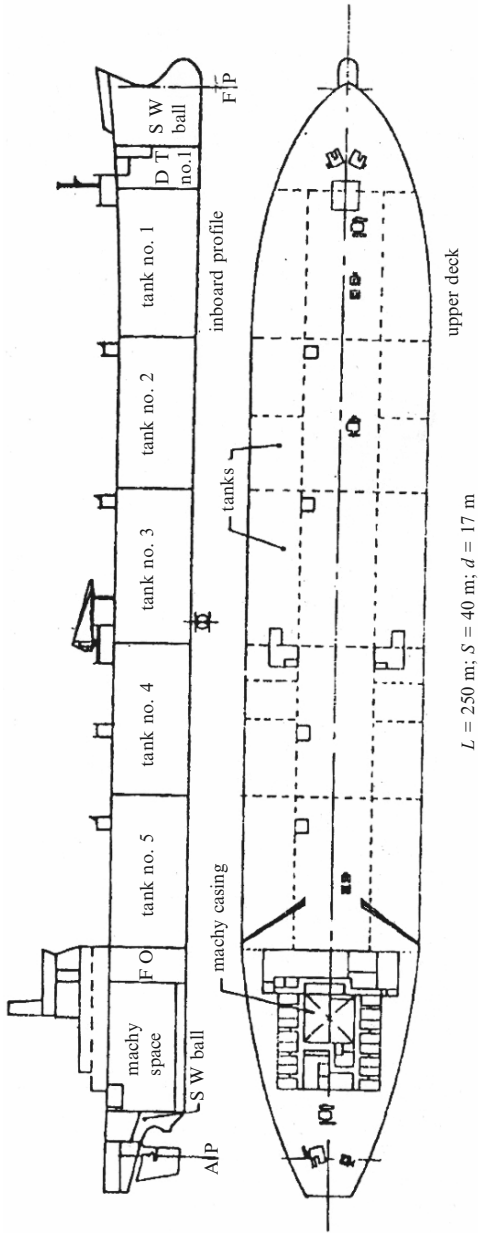
Fig. 2.58. Tanker (L, length; S, span; d, depth) [2.386]

$L = 250$ m; $S = 40$ m; $d = 17$ m

Table 2.56. Data on major explosive elements

Explosive element	Composition	Density (kg m⁻³)	V_{sp} (1 kg⁻¹)	Q_E (kcal kg⁻¹)	Temperature at explosion (°C or K)	V_E (m s⁻¹)	3 kg Load dropped at which explosions occurred / Impact sensitivity (mm)
Ammonium nitrate	NH_4NO_3	1,600		1,090			
Charcoal	Black powder or lump coal (95%) and ash (5%)	1,600	—	—	—	—	—
Dinitroglycol	$(CH_2)_2(NO_3)_2$	1,400	738	1,690	4,230	8,300	104
Dinitrophenol	$C_6H_3OH(NO_2)_2$	1,400	—	—	—	—	—
Gun cotton	Cellulose nitrate (high nitration)	300	936	810	2,640	6,300	270
Hexogen	—	1,700	908	1,500	3,850	8,300	435
Nitroglycerine	$C_3H_5(NO_3)_3$	1,600	717	1,470	4,110	8,000	60
PETN	$C(CH_2ONO_2)_4$	1,750		See Table 2.64			420
Picric acid	—	900	685	920	3,620	7,250	900
Potassium nitrate	KNO_3	—	—	—	—	—	—
Sodium nitrate	$NaNO_3$	—	—	—	—	—	—
Trinitrocresol	$C_6HCH_3(OH)(NO_2)_3CH_3$		—	—	—	—	—
Trinitrotoluene (TNT)	$C_6H_2(CH_3)(NO_2)_3$	1,600	728	1,000	2,950	6,800	2,200

V_{sp}, specific volume for explosive gases; Q_E, specific heat of explosion; V_E, velocity of explosion

Table 2.57. Ingredients of explosives and their properties

Formula	Name	(g mol^{-1})	Density (g cm^{-3})	Explosive strength (% TNT)	Gurney constant (m s^{-1})
$C_6H_6N_4O_7$	Ammonium picrate (explosive D)	246	1.72	100t, 99m, 84s, 87b, 91p, 85a	2,137
$(C_6H_7N_{2.25}O_{9.5})_n$	Nitrocellulose 12% N (NC)	263(n)	–	82b	2,189
$(C_6H_7N_{2.5}O_{10})_n$	Nitrocellulose 13.35% N (NC)	274(n)	1.67	102b, 140t	2,473
$(C_6H_7N_3O_{11})_n$	Cellulose trinitrate 14.1% N (NC)	297(n)	1.66	95s, 138b	2,966
$C_6H_8N_2O_6$	2.2 Dinitropropylacrylate (DNPA)	204	1.47	50b	1,478
$(C_6H_8N_4O_9)_n$	Cellulose dinitrate 11.1% N (NC)	252(n)	1.66	87b	2,170
$C_6H_8N_6O_{18}$	Mannitol hexanitrate	452	1.73	170t, 156b	3,451
$(C_6H_9N_3)_{11}$	Glycerol monolactate trinitrate (GLTN)	299	1.47	115m, 148b	2,952
$C_7H_3N_3O_7$	2,4,6 Trinitrobenzaldehyde	241	–	125t, 94b	2,307
$C_7H_5N_3O_6$	2,4,6 Trinitrotoluene (TNT)	227	1.65	100t, 100m, 100s, 100b	2,315
$C_7H_5N_3O_6$	2,4,6 Trinitrotoluene (liquid TNT)	227	1.447	103b	2,350
$C_7H_5N_3O_7$	2,4,6 Trinitroanisole	243	1.41	112t, 93b	2,202
$C_7H_5N_3O_7$	2,4,6 Trinitro-m	243	1.68	98t, 87b	2,131
$C_7H_5N_5O_8$	N-Methyl-N, 2,4,6 tetranitroaniline (TETRYL)cresol	287	1.73	131t, 131m, 123s, 130b, 116p	2,710
$C_{10}H_{16}N_6O_{19}$	Dipentaerythritolhexanitrate (DPEHN)	524	1.63	128t, 142m, 123s, 182b	3,268
$C_{12}H_4N_6O_{12}$	2,2′,4,4′,6,6′ Hexanitrobiphenyl (HNBP)	424	1.74	114t, 116t	2,588
$C_{12}H_4N_8O_8$	1,3,8,10 Tetranitrobenzotriazolo, (1,2a) benzotriazole (T-TACOT)	388	1.81	108b	2,655
$C_{12}H_4N_8O_8$	1,3,7,9 Tetranitrobenzotriazolo (2,1a) benzotriazole (Z-TACOT)	388	1.85	108b	2,656
$C_{12}H_4N_8O_{10}$	5,7 Dinitro-1-picrylbenzotriazole (BTX)	420	1.74	110b	2,611

Formula	Name				
$C_{12}H_4N_8O_{12}$	2,2′,4,4′,6,6′ Hexanitroazobenzene (HNAB)	452	1.78	122b	2,693
$C_{12}H_6N_8O_{12}$	Diaminohexanitrobiphenyl (dipicramide) (DIPAM)	454	1.79	105b	2,431
$C_{13}H_5N_5O_{11}$	2,2′,4,4′,6 Pentanitrobenzophenone (PENCO)	407	1.86	92b	2,352
$C_{14}H_6N_6O_{12}$	2,2′,4,4′,6,6′ Hexanitrostilbene (HNS)	450	1.74	108b	2,524
$C_{17}H_5N_{13}O_{16}$	2,6 Bis (picrylazo)-3,5-dinitro-pyridine (PADP)	647	1.86	122b	2,738
$C_{18}H_5N_9O_{18}$	2,2′,2″,4,4′,4″,6,6′,6″ Nonanitroterphenyl, (NONA)	635	1.78	113b	2,608
$C_{18}H_6N_8O_{16}$	2,2′,2″,4,4′,4″,6,6′,6″ Octanitroterphenyl (ONT)	590	1.80	106b	2,537
$C_{18}H_7N_{11}O_{18}$	1,3 Bis (picrylamino) 2,4,6 trinitrobenzene	665	1.79	101b	2,427
$C_{21}H_9N_{15}O_{18}$	2,4,6 Tris (picrylamino), s-triazine	759	1.75	86b	2,267
$C_{22}H_9N_{15}O_{20}$	2,4,6 Tris (picrylamino) s-nitropyrimidine	803	1.88	82b	2,210
$C_{23}H_9N_{15}O_{22}$	2,4,6 Tris (picrylamino) 3,5 dinitropyridine	847	1.80	98b	2,400
$C_{24}H_6N_{12}O_{24}$	2,2′,2″,2‴,4,4′,4″,4‴,6,6′,6″,6‴ Dodecanitro-m,m'-quatraphenyl	846	1.81	114b	2,625
$C_{24}H_6N_{14}O_{24}$	Azobis (2,2′,4,4′,6,6′) hexanitrobiphenyl (AHB)	874	1.78	120b	2,699
$C_{24}H_6N_{16}O_{24}$	Dodecanitro-3,3-bis (phenylazo)-biphenyl (BisHNAB)	902	1.81	127b	2,785
$C_{24}H_9N_9O_{18}$	1,3,5 Tripicrylbenzene (TPB)	711	1.67	81b	2,242
NO	Nitric oxide	30	1.30	69b	2,212

Table 2.58. Non-aluminized explosive mixtures

Name	Apparent formula	Composition	$(g\,mol^{-1})$	Density $(g\,cm^{-3})$	Explosive Strength (% TNT)	Gurney constant $(m\,s^{-1})$
Amatol	$C_{0.62}H_{4.44}N_{2.26}O_{3.53}$	80/20 Ammonium nitrate/TNT	100	1.60	143b, 130m, 123t	2,908
Anfo	$C_{0.365}H_{4.713}N_{2.000}O_{3.000}$	96/6 Ammonium nitrate/No. 2 diesel oil	85	1.63	142b, 17s, 50m, 10t	2,769
Black powder	$C_{1.25}K_{1.92}N_{5.36}O_{14.1}S_{0.31}$	75/15/10 Potassium nitrate/carbon/ sulphur	–	–	–	–
Comp A-3	$C_{1.87}H_{3.74}N_{2.46}O_{2.46}$	91/9 RDX/WAX	100	1.65	157b, 135m, 126p, 109a	2,727
Comp B-3	$C_{6.851}H_{8.740}N_{7.650}O_{9.300}$	64/36 RDX/TNT	347	1.713	133m, 130t, 132p, 149b	2,843
Comp C-4	$C_{1.82}H_{3.54}N_{2.46}O_{2.51}$	91/5.3/2.1/1.6 RDX/Di-(2-ethylhexyl) sebacate/polysiobutylene/motor oil	100	1.66	160b, 130m, 115p	2,801
Cyclotol	$C_{5.045}H_{7.461}N_{6.876}O_{7.753}$	77/23 RDX/TNT	288	1.743	159b, 112u, 133p	2,979

Name	Formula	Composition				
Dynamite (MVD)	–	75/15/10 RDX/TNT/plasticizers	–	–	105s, 122m	–
LX-14	$C_{1.52}H_{2.92}N_{2.59}O_{2.66}$	95.5/4.5 HMX/estane 5702-F1	100	1.83	167b	3,033
Octol	$C_{6.80}H_{10.00}N_{9.20}O_{10.40}$	76.3/23.7 HMX/TNT	388	1.809	115m, 158b, 160p	2,965
PBX-9011	$C_{5.696}H_{10.476}N_{8.062}O_{8.589}$	90/10 HMX/estane	329	1.767	153b, 140p	2,815
PBXC-116	$C_{1.968}H_{3.746}N_{2.356}O_{2.474}$	86/14 RDX/binder	100	1.65	117b	2,342
Pentolite	$C_{2.332}H_{2.366}N_{1.293}O_{3.219}$	50/50 TNT/PETN	100	1.65	126m, 122t, 156b, 116a, 108p	2,970
Smokeless powder	$C_6H_7N_{2.5}O_{10}$	99/1 Nitrocellulose/diphenylamine	275	–	93s	–

Table 2.59. Explosive and crater formation data

Type of soil/rock	Type of explosives	Charge data			Crater data				Charge depth (m)					Particle (a) or flyrock (b) velocity (m s^{-1})				Additional data and velocity V_E of detonation (m s^{-1}) of explosive
		Weight (kg)	Length (m)	Diameter (m)	Radius (m)	Depth (m)	Angle (degrees)	Volume (m³)	0.1	0.2	0.3	0.4	0.5	0.5	0.6	0.9	1.5	
Sandstone	*Type A* Semi-gelatine	3.632	0.22	0.132	1.25	0.400	134	0.454		b	b				b	b	b	Density = 1,153.44 kg m^{-3}
		3.632	0.25	0.132	2.44	0.700	148	4.26		60.0	60.0				30.5	15.0	2.0	V_E = 3,657.6
		3.632	0.30	0.132		no crater											1.5 / b / 2.0	
	Type A Gelatine	3.632	0.18	0.132	1.83	0.850	132	3.41									2.0	Depth 3.05 m and greater
		3.632	0.2	0.132		no crater												
	Ammonia-gelatine	3.632	0.12	0.152	0.750	0.310	130	0.176							0.6			Density = 1,361.7 kg m^{-3}
		3.632	0.152	0.152	1.83	0.920	130	3.30							b / 30.5			V_E = 6,095.7
		3.632	0.152	0.152		no crater												
	Ammonia-dynamite	3.632	0.23	0.132	1.02	0.310	142	0.937									1.5	Just broke surface
		3.632	0.23	0.132	1.0	1.700	124	0.5								b	2.0	
Granite	*Type A* Semi-gelatine	2.80	0.25	0.10	1.25	0.310	150	0.46					0.5			0.9		Density = 1,410 kg m^{-3}
		2.80	0.25	0.10	1.83	0.310	158	0.937					b			b		V_E = 2,591
		2.80	0.3048	0.10	0.75	0.1524	154	0.08					25.0			29.0		
		14.50	0.62	0.1524	1.83	0.457	105	1.306										
	Type B Semi-gelatine	1.48	0.25	0.16	0.10	1.230	152	2.90		0.2 / b / 90.0	0.3							Depth 3.15 m and greater Density = 1121.4 kg m^{-3} V_E = 1,981

Type B Gelatine	4.355	0.60	0.10	1.20	0.620	152	0.90
	14.50	0.62	0.1524	3.0	0.62	154	3.55
Marlstone *Type A* Semi-gelatine	8.62	0.47	0.128	3.20	0.40	164	5.26
	1.544	0.308	0.10	1.0	0.308	138	0.44
	1.544	0.308	0.10	1.80	0.62	118	1.58
	1.544	0.308	0.10	0.16	0.150	112	0.0044
	3.620	1.37	0.13	1.82	1.37	108	5.210
	6.130	0.32	0.13	1.82	1.22	114	5.210
Chalk *Type A* Semi-gelatine	0.908	0.22	0.08	1.01	0.4	138	0.510
	0.908	0.20	0.08	1.24	0.77	114	2.08
	2.040	0.22	0.13	2.10	1.524	106	7.39
	3.632	0.20	0.152	3.45	1.53	112	11.36
Ammonia-gelatine	3.632	0.125	0.152	1.70	0.9	130	2.70
	3.632	0.10	0.152	1.70	1.02	118	7.73
	3.632	0.152	0.152	2.10	1.52	106	8.86
	3.632	0.13	0.152	no crater			

Annotations:

Type B Gelatine — Charge depth 2 m; column values at 0.2: b, 60.0; at 0.3: b, 75.0; further 0.6, 0.9, 1.5

Marlstone *Type A* Semi-gelatine — Charge depth 1.8 m; Density = 1,153.44 kg m^{-3}; V_E = 3,657.6; values at 0.1 0.2 0.3, 0.4 0.5 0.6 0.7 0.9 1.5 3.0, 1.5, 3.0, 1.5, 1.5

Chalk *Type A* Semi-gelatine — Density = 1121.4 kg m^{-3}; V_E = 1,981; values 0.4, 1.5, 1.5

Ammonia-gelatine — Density = 1,153.44 kg m^{-3}; V_E = 3657.6; values at 0.1 0.2 0.3, 0.4 0.5 0.6 0.7 0.9 1.5 3.0, 0.6, 1.5, 3.0

Fig. 2.59. Load-carrying capacities of drilling semi-submersibles (courtesy of Aker, GVA, DSS and Sonat)

Fig. 2.60. Layout of drilling semi-submersible DSS 40 (courtesy of DSS)

2.27.2 Gas Explosions

2.27.2.1 Introduction

Gas explosion incidents involving domestic or commercial premises do occur from time to time. It is therefore necessary to have a proper understanding of the development of the pressure–pulse relationship and the way structures respond to pressure loading. Most hydrocarbon gases, when mixed with air at atmospheric pressure, can produce on ignition a maximum pressure of more than $8\,\mathrm{N\,m}^{-2}$ – a pressure unlikely to be resisted by conventional structures where explosion relief vents are not provided.

Table 2.60. Projectile weight/charge weight, horizontal distance from explosion or crater radius in soils

Ratio	Shallow soft rock		Dry clay shale		Wet clay shale		Dense rock	
Projectile weight / Charge weight	10^1		$10^{0.3}$		10^1		10^1	
		1		3		3		10
	10^0		10^0		10^0		10^0	
		2		3		8		30
	10^{-1}		10^{-1}		10^{-1}		10^{-1}	
		5		9		10		80
	10^{-2}		10^{-1}		10^{-2}		10^{-2}	
		2		10.8		20		300
	10^{-3}		10^{-3}		10^{-3}		10^{-3}	
		8		25		40		—
Distance or crater radius (m)	10^{-4}		10^{-4}		10^{-4}		10^{-4}	
		20		50		65		350

In the event of a gas explosion, the response of structures or their components must be assessed and the overpressure loadings generated as a result should be accurately evaluated. In all cases, the gas explosion loadings must not be confused with blast loadings caused by explosives. Considerable data on the full or partial venting of explosions can be gathered from the references in the text [4.176–4.180].

However, there is still uncertainty about flammable gas or vapour likely to be encountered in domestic or commercial buildings. Whether the supply to such buildings comes from natural or manufactured gas plants, the possible hazards associated with the misuse or accidental leakage are predictable. When leakage occurs, a gas layer is likely to build up near the ceiling. Eventually, with time, this layer extend downwards and explosion occurs when it reaches a source of ignition such as a pilot light, electric contact, heater, etc. The rise and rate of explosion pressure will depend on whether the volume of the room is partially or fully filled. A further complication in the domestic environment arises when there are several inter-communicating rooms or passages full of gas layers which are capable of transmitting the explosion from one compartment to the other. The passage of gas through doorways increases its turbulance and burning rate and can thus cause a violent explosion in a compartment remote from that containing the ignition source.

2.27.3 Nuclear Explosions

2.27.3.1 Introduction

A nuclear explosion, in general, results from the very rapid release of a large amount of energy associated with high temperatures and pressures. Several

Table 2.61. Particle velocity for various soils

Ratio $\dfrac{\text{Distance (m)}}{\sqrt[3]{W}\ \text{(kg)}}$	Saturated clay	Wet sandy clay	Dense sands	Sandy loam or medium sand	Dry loose sand
1	110	80	–	–	–
2	45	40	30	20	15
3	25	20	15	8	3
4	20	12	16	3	1.5
5	15	8	3	1.5	7
6	12.5	5	2	0.8	0.35
7	10	4	1.5	0.5	–
8	8	3	1	0.3	–
9	6	2.5	0.8	–	–
10	5	1.5	0.5	–	–
V_E (m s^{-1})	5	1.5	0.5	–	–

W, charge weight; V_E, particle velocity

Table 2.62. Crater dimensions in soils under the effects of high explosives

Depth of CG of charge $(m)/\sqrt[3]{W}$ (kg)	Clay				Clay and mixed soil				Mixed soil				Sand and mixed soil				Sand			
	d_w	d_d	h_w	h_d	d_w	d_d	h_w	h_d	d_w	d_d	h_w	h_d	d_w	d_d	h_w	h_d	d_w	d_d	h_w	h_d
0	4.40	3.20	1.40	1.20	3.20	2.80	1.20	0.80	2.80	2.60	0.80	0.70	2.60	2.40	0.90	0.70	2.40	2.10	0.70	0.60
0.5	5.40	4.25	2.00	1.70	4.25	3.38	1.70	1.50	3.58	3.50	1.50	1.40	3.50	3.20	1.40	1.20	3.20	2.90	1.20	1.00
1.0	5.80	5.00	2.40	1.90	5.00	4.50	1.90	1.70	4.50	4.20	1.70	1.60	4.20	3.55	1.60	1.35	3.55	3.40	1.35	1.25
1.5	6.25	5.35	2.60	2.20	5.35	4.60	2.20	1.80	4.60	4.25	1.80	1.55	4.25	4.00	1.55	1.40	4.00	3.60	1.40	1.20
2.0	6.50	5.25	2.50	2.00	5.25	4.65	2.00	1.70	4.65	4.30	1.70	1.60	4.30	3.55	1.60	1.30	3.55	3.49	1.30	1.10
2.25	6.25	5.10	2.40	1.70	5.10	4.70	1.70	1.50	4.70	4.40	1.50	1.25	4.40	3.50	1.25	0.55	3.50	3.10	0.55	0.25
3.0	5.80	4.50	1.90	1.25	4.50	4.00	1.25	0.70	4.00	3.50	0.70	0.40	3.50	2.80	–	–	2.80	2.60	–	–
3.5	5.50	3.50	1.40	0.48	3.50	3.00	–	–	–	–	–	–	–	–	–	–	–	–	–	–
4.0	4.50	3.25	0.55	0.50	–	–	–	–	–	–	–	–	–	–	–	–	–	–	–	–

d and h denote crater diameter and crater height, respectively; subscripts d and w denote dry and wet soils respectively; d_d, d_w, h_d and h_w are calculated from (crater diameter or height/$\sqrt[3]{W}$), where W is the charge weight

Table 2.63. Peak overpressure, arrival time and duration

Distance	Peak overpressure kPa (psi)		Wind speed m/s (mph)		Arrival time (s)		Duration (s)	
km (miles)	1 Mt	10 Mt	1 Mt	10 Mt	1 Mt	10 Mt	1 Mt	10 Mt
1 (0.6)	980 (140)	4,200 (660)	980 (2200)	–	0.9	–	0.9	1.0
2 (1.25)	200 (29)	1,050 (150)	400 (900)	980 (2200)	4.0	1.8	1.8	2.0
3 (1.9)	130 (18)	380 (54)	180 (400)	805 (1800)	6.0	4.7	2.3	2.4
4 (2.5)	63 (12)	220 (31)	128 (289)	490 (1100)	9.0	8.0	2.6	3.7
5 (3.1)	56 (8)	170 (24)	106 (238)	277 (620)	12	11	2.8	4.2
6 (3.8)	42 (6)	135 (19)	81 (182)	200 (450)	14	12.25	3.0	4.7
7 (4.4)	33 (4.7)	110 (16)	69 (155)	170 (380)	18	16	3.2	5.0
8 (5)	27 (3.8)	90 (13)	56 (125)	143 (320)	22	18	3.4	5.3
9 (5.6)	24 (3.4)	77 (11)	48 (108)	125 (280)	26	20	3.5	5.5
10 (6.2)	21 (3)	63 (9)	40 (90)	114 (255)	28	22	3.6	5.9
12 (7.5)	15 (2.2)	46 (6.5)	31 (70)	96 (215)	31	30	3.7	6.3
15 (9.4)	10 (1.5)	34 (4.8)	24 (53)	72 (160)	45	38	3.8	6.7
20 (12.5)	7 (1)	22 (3.3)	17 (37)	46 (103)	59	53	4.0	7.5
25 (16)	5 (0.75)	15 (2.2)	9 (20)	32 (72)	70	67	4.2	7.8

basic differences exist between nuclear explosions and explosions caused by high explosives. Some of the major differences are listed below:

(1) Nuclear explosions are many thousands of times more powerful than the conventional type of explosions.
(2) For the release of a given amount of energy, the mass of the nuclear residue is comparatively smaller and is immediately converted into hot and compressed gases.
(3) The temperatures reached in a nuclear explosion are a very much higher, thus assisting the emission of a large proportion of energy in the form of light and heat. This is known as *thermal radiation.* The remaining substances, unlike conventional explosives, emit radiation for a certain period of time.

Owing to these and many other differences, the effects of the nuclear detonations require special consideration, including their dependence on the type of burst, i.e., air, surface and subsurface. An accurate assessment is required for blast loadings in all such cases with target responses.

2.27.3.2 Air Blast Loading

It is desirable to consider in some detail the phenomena associated with waves due to air blast. A difference in the air pressure acting on different surfaces of a structure produces a force on that structure. The destructive effect will be felt due to overpressure – the maximum value of pressure at the blast wave or shock front. This maximum value is sometimes called *peak overpressure.* The other phenomena are dynamic pressure, duration and time of arrival.

A typical "fireball" associated with air burst occurs. Immediately after the formation of the "fireball" it grows in size, thus engulfing the surrounding air and decreasing its own temperature. The "fireball" rises like a hot-air balloon. The rate of rise of the radio-active cloud (from a 1-megatonne air burst) ranges from $330\,\text{miles/h}$ at $0.3\,\text{min}$ to $27\,\text{miles}\,\text{h}^{-1}$ at $3.8\,\text{min}$. The expansion of the intensely hot gases at high pressures in the fireball causes a shock wave, moving at high velocity. The pressure rises very sharply at the moving front and falls off toward the interior region of the explosion. As the blast wave travels, the overpressure decreases and the pressure behind the front falls off. After a short interval, when the shock waves have travelled a certain distance, the pressure behind the front drops below atmospheric and is known as a *negative phase* of the blast wave forms. During the negative phase, a partial vacuum is produced and the air is sucked in. The negative phase is comparatively longer, the pressure will essentially return to ambient. The peak values of the underpressure are generally small compared with the peak positive overpressures.

Since the degree of blast damage depends largely on the drag force associated with strong winds and is influenced by the shape and size of the

structure, the net pressure acting on the structure is called the *dynamic pressure* and is proportional to the square of the wind velocity and to the density of the air behind the shock front, Figure 2.61a, b shows comparisons between the overpressure and the dynamic pressure with distance and time. For very strong shocks the dynamic pressure is larger than the overpressure, but below $480 \, \mathrm{kN \, m^{-2}}$ (4.7 atmospheres) overpressure at sea level, the dynamic pressure is smaller. As shown in Fig. 2.61 the dynamic pressure decreases with increasing distance from the explosion centre. Figure 2.62 and Table 2.64 show the peak "free-air" overpressure of shock, range vs. duration.

2.27.3.3 Blast Loads From a Surface Burst

When the incident blast wave from an explosion in air strikes a more dense medium such as land or water, it is reflected. The front of the blast wave in the air will assume a hemispherical shape, as shown in Fig. 2.63. Since there is a region of regular reflection, all structures on the surface, even close to ground zero, are subjected to air blast. Some of the blast wave energy is transferred into the ground. A minor oscillation of the surface is experienced and a ground shock is produced. For large overpressures with a long positive-phase duration, the shock will penetrate some distance into the ground and will damage buried structures.

When the front of the air blast wave strikes the face of the structure, reflection occurs. As the wave front moves forward, the reflected overpressure on the face drops rapidly to that produced by the blast wave without reflection, plus an added drag force due to wind. At the same time, the air-pressure wave diffracts around the structure and is entirely engulfed by the blast. The damage caused by diffraction will be determined by the magnitude of the loading and by its duration. If the structure has openings, there will be a rapid equalization of pressure between the inside and outside of that structure. The diffraction loading of the structure as a whole will be decreased. Since large structures have openings, diffraction and drag must not be ignored.

The loads computed for the surface explosion shall be P_{so} and 2.3 P_{so} for roof/floors and walls respectively, where P_{so} is the peak incident wave pressure. Figure 2.62 and Table 2.64 show the damage–distance relationship and peak overpressure failure effects on structural components, respectively.

2.27.3.4 Shallow and Deep Underground Explosion Loadings

Shock damage to structures placed underground can be evaluated using computed codes and experiments. The degree of damage for a shallow explosion can be related to the apparent crater radius. The dependence of the crater radius and crater depth upon the depth of burst is shown in Figs. 2.64–2.67.

The Home Office gives the value of P_{so} (overpressure) as a full value for dry and high water level cases when roofs and floors are considered. For walls in dry ground, the value of P_{so} is 0.5 P_{so}. For sensitive structures above ground, the structural elements must fail under the minimum overpressures.

(a)

(b)
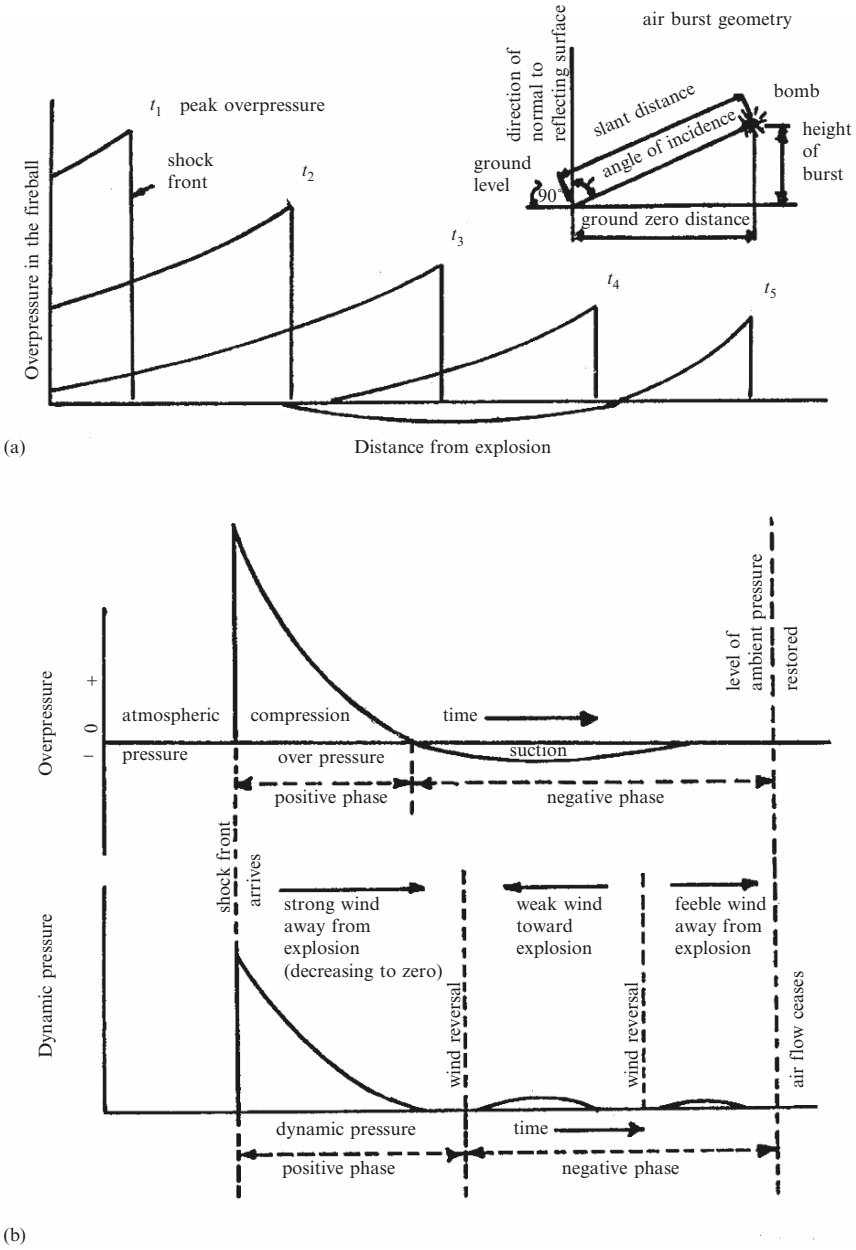
Fig. 2.61. (a) Time-dependent variation of overpressure with distance; **(b)** variation of overpressure and dynamic pressure with time
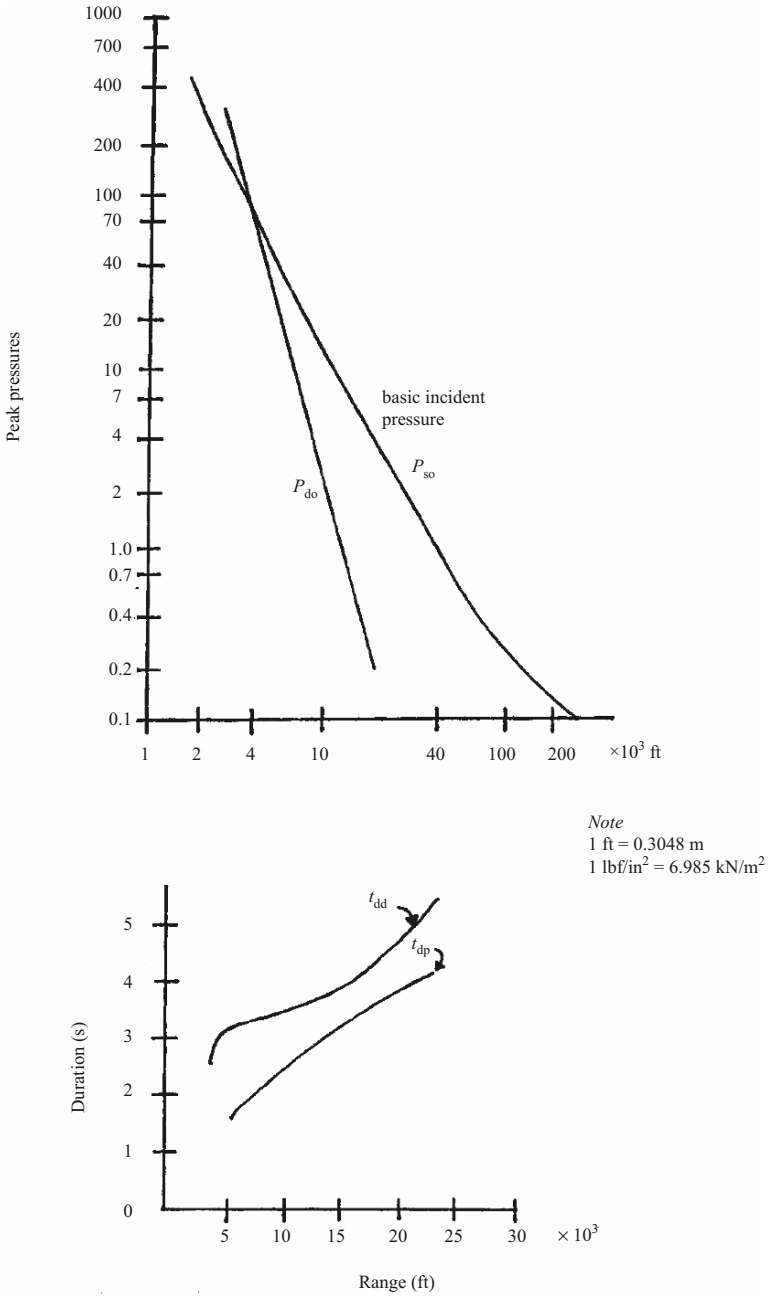
Fig. 2.62. Peak pressure, duration and range

Table 2.64. Theoretical and experimental results: a comparative study (Group 3)

Reference	Description of experiment	Explosion pressure (kN m^{-2}) obtained from experiment and theory							Reference results
		Rasbash [4.88] Theory I	Theory II	Cubbage and Simmonds [4.87] (1st Peak)	Dragosovic [4.81] (1st Peak)	Cubbage and Marshall [4.91, 4.92] (1st Peak)	Burgoyne and Wilson [4.88]	Decker [4.95] (1st Peak)	
Dragosovic	Explosion of methane-air mixtures Dimensions of building; 4 m × 2 m × 2.6 m, volume 20.8 m^3 Vent covers of hardboard, glass:								
	(1) $P_v = 0$; $K = 1$ } Hardboard	0.35	2.04	0.35	3.0	–	–	81.0	–
	(2) $P_v = 0$; $K = 1.593$	0.35	3.24	0.35	1.5–3.0	–	–	67.0	–
	(3) $P_v = 2.99$ kN m^{-2}; $K = 1.593$ (glass cover)	4.70	6.14	0.35	5.9	–	–	67.0	–
	(4) $P_v = 4.75$ kN m^{-2}; $K = 5.09$	7.48	15.10	0.35	7.75	–	–	–	–
	(5) $P_v = 21.6$ kN m^{-2}; $K = 1.7$	21.95	25.06	0.35	24.6	–	–	1.43	–
Solberg [4.88]	Explosion of propane-air mixtures Dimensions: 4.0 m × 3.5 m × 2.5 m, volume 35 m^3								
	(1) $K = 4.375$	0.35	10.83	0.35	3.0	–	–	45.3	8.98
	(2) $K = 8.75$	0.35	21.65	0.35	3.0	–	–	90.6	39.4
	(3) $K = 17.5$	0.35	43.3	0.35	3.0	–	–	181.0	60.9
Yao [4.88]	Explosion of propane-air and hydrogen-air, volume 0.765 m^3			2nd peak	2nd peak				
	(1) $K = 5.1$ C$_3$H$_8$-air	17.79	23.6	12.75	9.35	–	–	43.2	–
	(2) $K = 1.44$ C$_3$H$_8$-air	5.6	20.7	3.6	7.14	–	–	13.23	–
	(3) $K = 1.61$ C$_3$H$_8$-air (free vents)	1.28	3.99	4.38	3.09	–	–	–	–
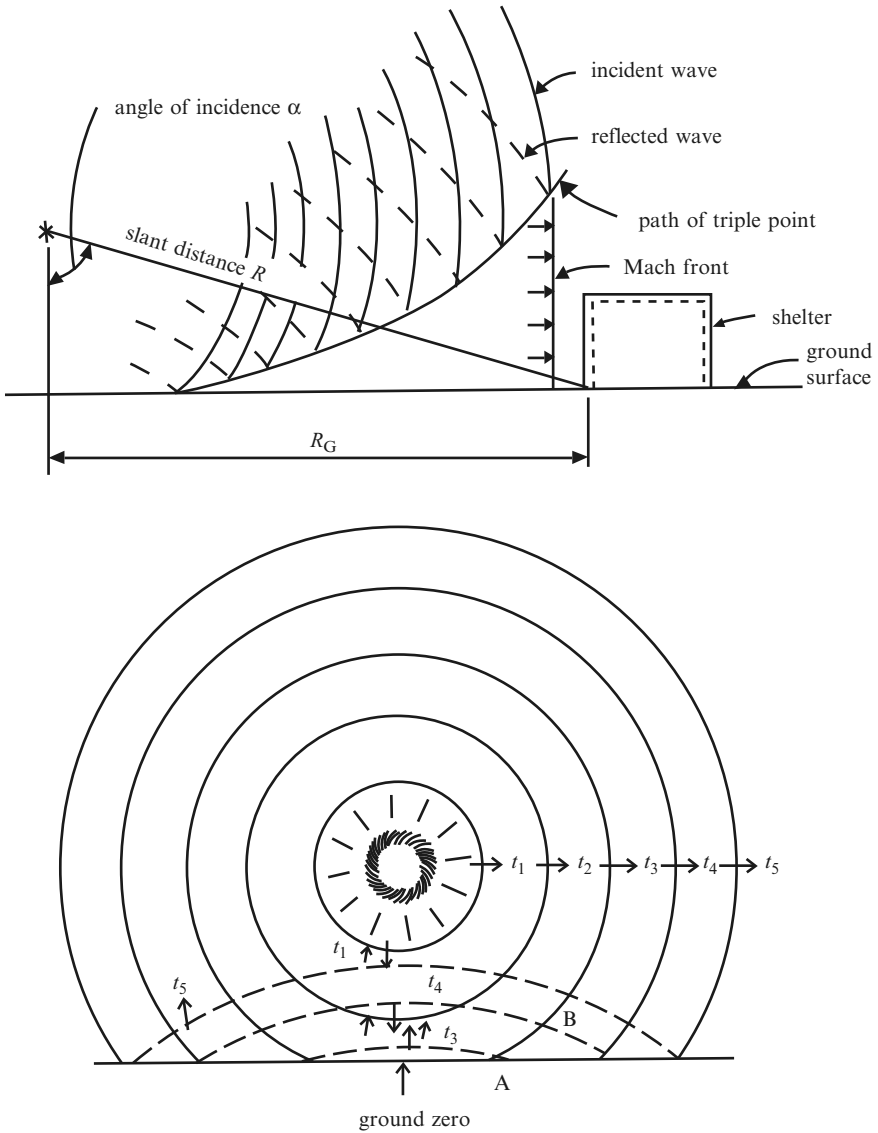
Fig. 2.63. (**a**) Air and (**b**) surface burst: incident and reflected waves meet

2.28 Dust Explosions

2.28.1 Introduction

There are similarities between dust and gas explosions when the particle size in particular is small and the turbulence level is low. The effects on the explosion pressure of a venting dust explosion are the same as with a gas explosion. The
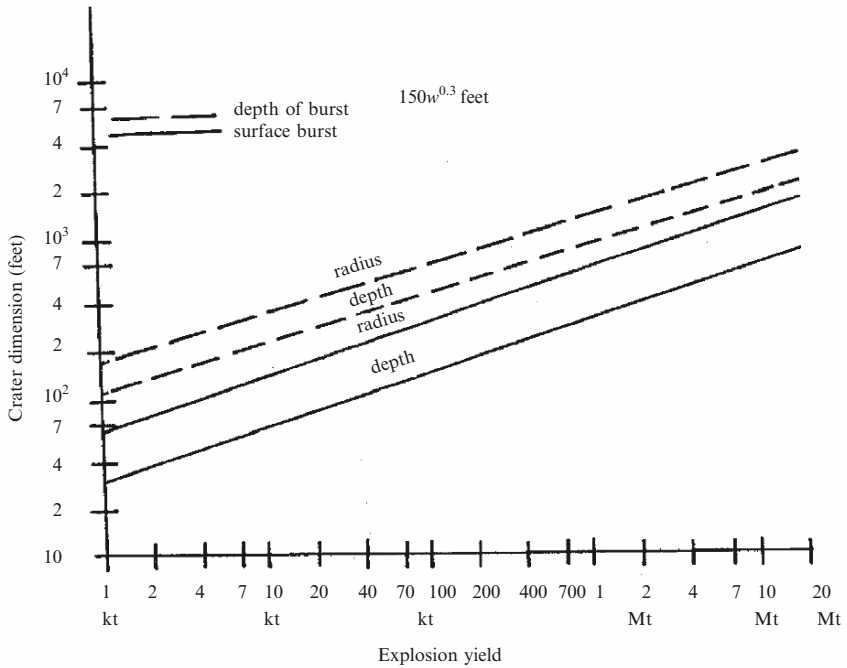
Fig. 2.64. Explosion yield vs. crater dimensions for specific yields
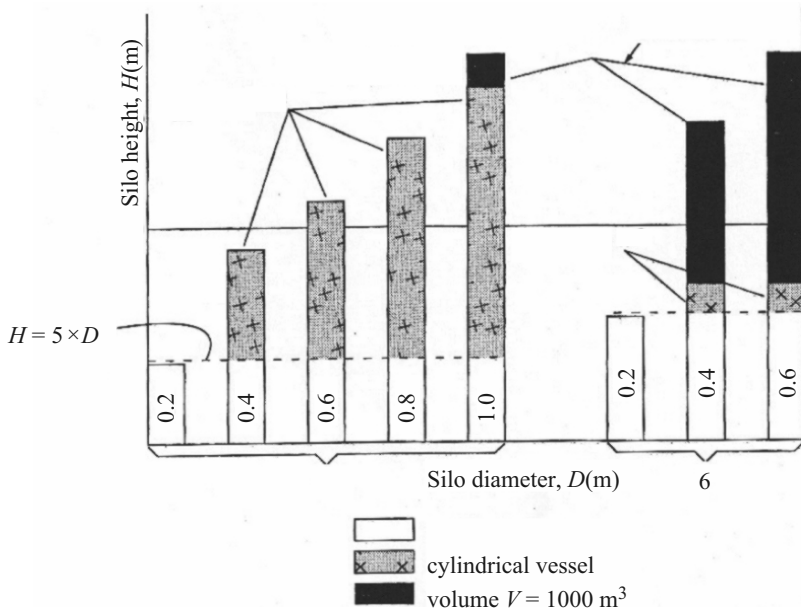
Fig. 2.65. Dusts: influence of pressure resistance (i.e. P_{red}) of silos on the allowable height, by application of the nomograms
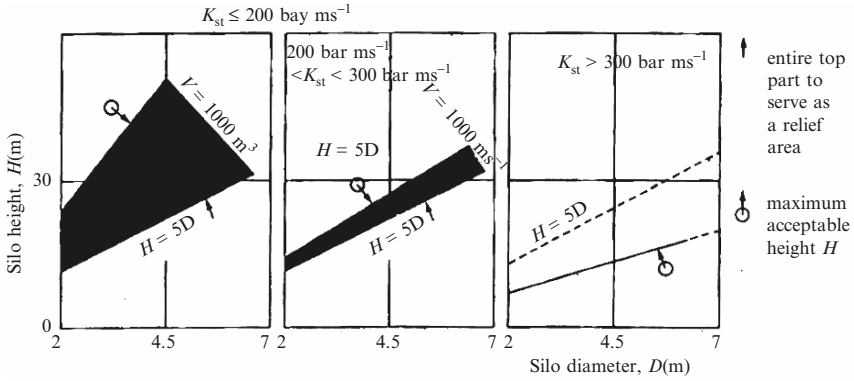
Fig. 2.66. Influence of dust explosion class on the maximum acceptable height of silos, when the nomograms are used ($P_v = 0.1\,\text{bar}, P_{max} = 0.4\,\text{bar}$)
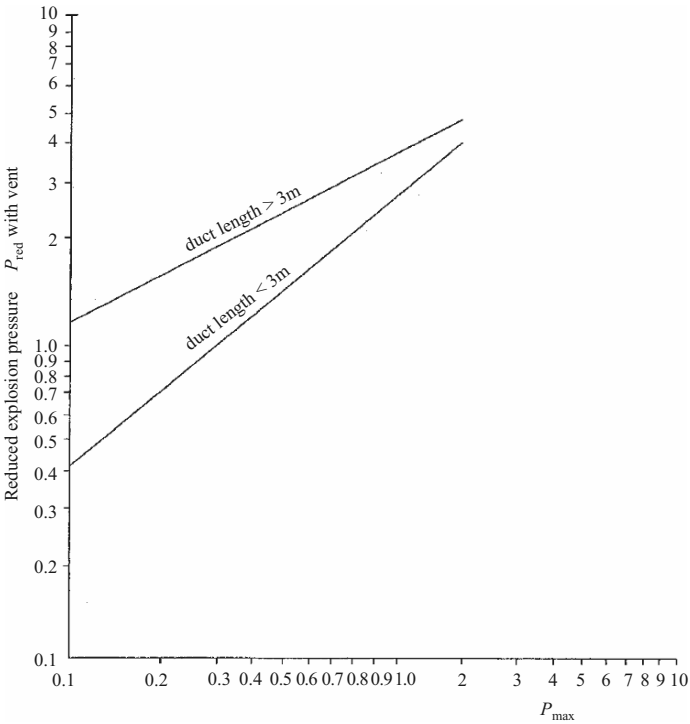
Fig. 2.67. Effect of vent ducts on vented explosion pressures

Table 2.65. Pressure-reduced time relationship of the shock wave caused by 50/50 PETN-TNT

Charge weight W (lb)	80.0	51.0	3.8
Distance R (ft)	14.0	11.9	5.0
$W^{1/3}/R\,(\text{lb}^{1/3}/\text{ft})$	0.308	0.312	0.312
Peak pressure P_m (lb/in^2)	5,910.0	6,060.0	6,040.0
Reduced time constant $\theta/W^{1/3}$ (μs/lb$^{1/3}$)	69.6	72.8	69.7
Reduced impulse $I/W^{1/3}$ (lbs/in^2/lb$^{1/3}$)	0.604	0.604	0.558
Reduced energy density $E/W^{1/3}$ (inlb/in^2/lb$^{1/3}$)	287.0	263.0	273.0

$1\,\text{lb} = 0.4536\,\text{kg}; 1\,\text{lb in}^{-2} = 15.444 \times 10^6\,\text{N m}^{-2}; 1\,\text{ft} = 0.3048\,\text{m}$
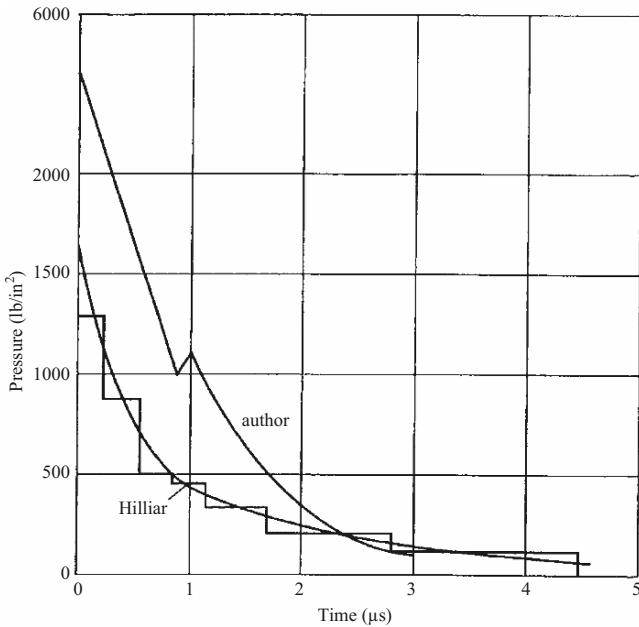
Fig. 2.68. Hilliar pressure-time curve [4.250] ($1\,\text{lb/in}^2 = 15.444 \times 10^6\,\text{N m}^{-2}$)

vented gas explosion has a number of empirical formulae for computing the explosion pressures or vent areas. In the case of dust explosions not many such formulae exist and, instead, scaling laws must be relied on.

2.29 Underwater Explosions

Underwater explosion phenomena are subject to a number of physical laws and properties, including the physical conditions at the boundary of the explosive or element of detonation and the surrounding water. A physical relationship is necessary between the detonation and the propagation of disturbances. Owing

Table 2.66. Kirkwood and Motroll results

Distance (charge radii)	Velocity $U(V_s)$ $(m s)^{-1}$	Peak pressure (kilobars)
1.00	5,710	>70
	4,885	>70
1.86	2,675	17.3
2.73	2,290	9.5
3.60	1,975	5.0
4.46	1,875	3.8
5.33	1,865	3.7
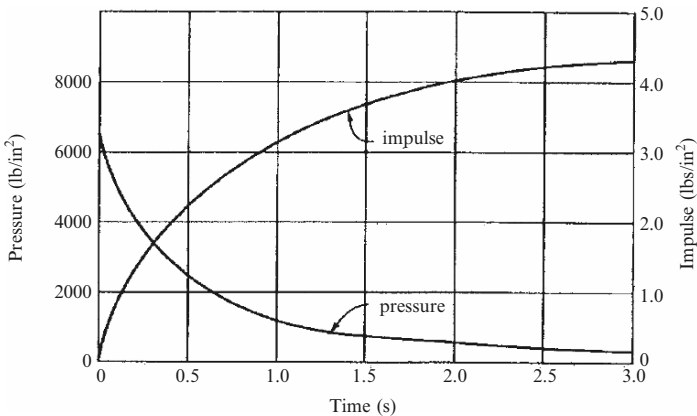
Fig. 2.69. Pressure–pulse–time relationship [4.266] ($1\,lb/in^2 = 15.444 \times 10^6\,N\,m^{-2}$)

to the dynamic properties of water (in the regions surrounding an explosion) the pressures are generally large and the wave velocities are not independent of such pressures. After detonation, secondary pressure pulses are generated. Such shock waves are dominant to certain distances and their character may be affected by factors such as viscosity and refraction by velocity gradients in the water.

Experimental pressure-time results as given by Hilliar [4.250] are shown in Fig. 2.68 together with an idealized curve. This curve was also examined at 14 ft (4.27 m) from an 80 lb (36.3 kg) 50/50 pentolite charge by the author. Despite limitations, based on a number of factors, reasonable figures were achieved for the pressure–reduced time relationship of the shock wave and they are given in Table 2.65. These results are viewed in the light of calculations produced by Kirkwood and Motroll [4.266]. Their results are given in Table 2.66 for fresh water.

Typical curves for a pressure-time impulse are given in Fig. 2.69. Table 2.67 shows peak pressures for 50 lb TNT, at detonation distances measured by the author.

Table 2.67. Peak pressures (in $\mathrm{lb\,in}^{-2} \times 10^3$, underwater of 50 lb TNT at various distances of detonation

Distance	Pressure ($\mathrm{lb\,in}^{-2} \times 10^3$)
Far end (ft)	
2	5.8
4	2.5
8	1.8
20	0.65
40	0.35
Near end (ft)	
2	5.0
4	2.3
8	1.4
20	0.5
40	0.25
Offside (ft)	
2	15
4	12
8	8
20	4
40	1.6

3

Basic Structural Dynamics for Impact, Shock and Explosion

3.1 General Introduction

Most loads acting on structures are dynamic in origin. These loads can be suddenly applied or allowed to reach full magnitude after a considerable delay. On the other hand, the structures will have various degrees of freedom with unclamped or clamped free or forced vibrations. These need to be discussed prior to the introduction of impact and explosion analysis and design.

3.2 Single-Degree-of-Freedom System

If a system is constrained such that it can vibrate in only one mode with a single co-ordinate system (geometric location of the masses within the system), then it is a single-degree-of-freedom system.

3.2.1 Unclamped Free Vibrations

A mass m is suspended by a spring with a stiffness k (force necessary to cause unit change of length). Let the mass m be displaced vertically as shown in Fig. 3.1. Then, with given restraints,

$$F - k\delta_{\mathrm{ST}} = 0, \tag{3.1}$$

where F or $W = m\mathbf{g}$, $\mathbf{g}$ = acceleration due to gravity and δ_{ST} = static deflection.

The mass is released and displaced from the equilibrium position. The coordinate x then defines the position of the mass m at any time and is taken to be positive when moving in a downward direction. Figure 3.2 shows the new positions.
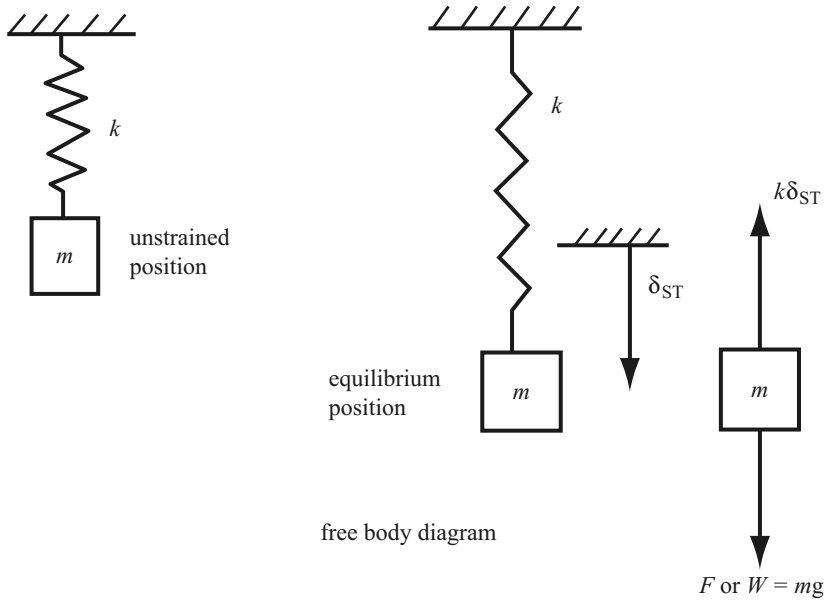
Fig. 3.1. The mass and its equilibrium position
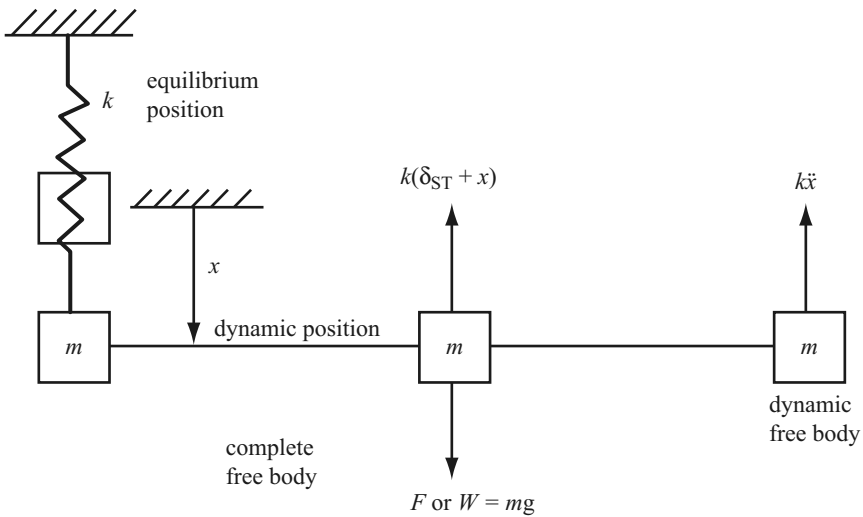
Fig. 3.2. The mass displaced from the equilibrium position

Method 1: Using Newton's Second Law of Motion

This law states that the magnitude of the acceleration of a mass is proportional to the resultant force acting upon it and has the same direction and sense as this force. The following equations are obtained:

$$m\frac{\mathrm{d}^2 x}{\mathrm{d}t^2} = -k(\delta_{\mathrm{ST}} + x) + F, \tag{3.2}$$

$$m\ddot{x} = -kx \text{ or } m\ddot{x} + kx = 0. \tag{3.3}$$

Method 2: Energy Method

For a conservative system, the total energy of the system (potential energy (PE) plus kinetic energy (KE)) is unchanged at all times. Thus

$$\mathrm{KE} + \mathrm{PE} = \text{constant; or } \frac{\mathrm{d}}{\mathrm{d}t}(\mathrm{KE} + \mathrm{PE}) = 0, \tag{3.4}$$

$$\mathrm{KE} = \frac{1}{2}m\dot{x}^2, \tag{3.5}$$

$$\mathrm{PE} = \int_x^0 [F - k(\delta_{\mathrm{ST}} + x)]\mathrm{d}x = -\int_x^0 kx\mathrm{d}x = \frac{1}{2}kx^2. \tag{3.6}$$

Using (3.5)

$$\frac{\mathrm{d}}{\mathrm{d}t}(m\dot{x}^2 + kx^2/2) = 0. \tag{3.7}$$

Hence

$$(m\ddot{x} + kx)\dot{x} = 0 \text{ or } m\ddot{x} + kx = 0. \tag{3.8}$$

Since the energy balance holds all the time, including the beginning stage, it is easy to stipulate values for x and $\dot{x}$. Assuming $x = x_0$ and $\dot{x} = 0$ at time $t = 0$ for the prescribed initial conditions, then

$$\mathrm{KE} + \mathrm{PE} = \frac{1}{2}kx_0^2, \tag{3.9}$$

$$\frac{1}{2}m\dot{x}^2 + \frac{1}{2}kx^2 = \frac{1}{2}kx_0^2. \tag{3.9a}$$

Dividing both sides by $\frac{1}{2}kx_0^2$, the following dimensionless equation results:

$$[\dot{x}/\sqrt{(k/m)}x_0]^2 + (x/x_0)^2 = 1. \tag{3.10}$$

Equation (3.10) can be plotted as a circle of radius unity. The loss or gain of the potential and kinetic energy can be estimated from this circle at various positions. This circle will also show the conversion of potential energy to kinetic energy, etc.

3.2.2 Solution of the Equation

Method 1

The value of x must be a function such that its second derivative with respect to time will be proportional to the negative value of the function itself. Cosine and sine functions have just this property. Since the equation is of order 2,

the solution must contain two arbitrary constants. Hence the value of x is written as

$$x = A \sin \omega t + B \cos \omega t, \tag{3.11}$$

where $\omega^2 = k/m$. Substitution of (3.11) into (3.3) shows that the differential equation is satisfied.

The set of arbitrary constants A, B can be replaced by another set of arbitrary constants so that

$$A = C\cos\phi,$$
$$B = C\sin\phi,$$

where ϕ is the *phase angle* or *phase*. Equation (3.11) then becomes

$$x = C(\sin \omega t \cos \phi + \cos \omega t \sin \phi), \tag{3.12}$$
$$= C \sin(\omega t + \phi),$$

where C and ϕ are the new arbitrary constants defined as

$$(C\cos\phi)^2 + (C\sin\phi)^2 = A^2 + B^2, \quad C = \sqrt{(A^2 + B^2)}, \tag{3.12a}$$
$$\tan\phi = C\sin\phi/C\cos\phi = B/A. \tag{3.12b}$$

The following solution forms can also be obtained, which all satisfy the differential equation:

$$x = C_1 \sin(\omega t - \alpha)$$
$$= C_2 \cos(\omega t + \beta) \tag{3.13}$$
$$= C_3 \cos(\omega t - \gamma).$$

The evaluation of the two arbitrary constants in (3.11) requires information such as initial conditions and that m has both initial velocity and displacement:

$$x = x_0, \quad \dot{x} = \dot{x}_0 \tag{3.14}$$

both at $t = 0$. Equation (3.11) will give

$$A = \dot{x}_0/\omega \text{ and } B = x_0. \tag{3.15}$$

The solution becomes

$$x = x_0/\omega \sin \omega t + x_0 \cos \omega t. \tag{3.16}$$

Substituting (3.15) into (3.12a and b) and then into (3.12) gives

$$x = X \sin(\omega t + \phi), \tag{3.17}$$

where the *amplitude* of the displacement is given by

$$X = \sqrt{[(\dot{x}_0/\omega)^2 + x_0^2]} \qquad (3.18)$$

and the corresponding phase angle can be written as

$$\tan \phi = x_0/(\dot{x}_0/\omega). \qquad (3.18a)$$

The motion defined by (3.16) and (3.17) is harmonic owing to its sinusoidal form. The period T, circular frequency ω and natural frequency are computed as follows:

$$T = 2\pi/\omega,$$
$$\omega = \sqrt{(k/m)} = \sqrt{(kg/W)} = \sqrt{(g/\delta_{ST})}, \qquad (3.19)$$
$$f = \omega/2\pi = \frac{1}{2}\pi\sqrt{(k/m)}.$$

The velocity $\dot{x}$ and the acceleration $\ddot{x}$ are expressed by time derivatives of (3.16) and (3.17):

Velocity

$$\begin{aligned}
\dot{x} &= \dot{x}_0 \cos \omega t - x_0 \omega \sin \omega t \\
&= X\omega \cos(\omega t + \phi) \\
&= X\omega \sin(\omega t + \phi + \pi/2) \qquad (3.20) \\
&= \dot{X} \cos(\omega t + \phi)
\end{aligned}$$

amplitude of velocity: $\dot{X} = X\omega$.

Acceleration

$$\begin{aligned}
\ddot{x} &= -\dot{x}_0 \omega \sin \omega t - x_0 \omega^2 \cos \omega t \\
&= X\omega^2 \sin(\omega t + \phi) \\
&= X\omega^2 \sin(\omega t + \phi + \pi) \qquad (3.21) \\
&= -\omega^2 x = -\ddot{X} \sin(\omega t + \phi)
\end{aligned}$$

amplitude of acceleration: $\ddot{X} = X\omega^2 = \dot{X}\omega.$ \qquad (3.21a)

The velocity is ω multiplied by the displacement, and leads it by 90°. The acceleration is ω^2 multiplied by the displacement and leads it by 180°.

Diagrams of displacement, velocity and acceleration against ωt are shown in Fig. 3.3.

The phase angle ϕ indicates the amount by which each curve is shifted ahead, with respect to an ordinary sine curve.

The rotating vector concept is evolved by looking at the displacement x from (3.12) and (3.16). Three vectors **A, B** and **C**, whose relative positions
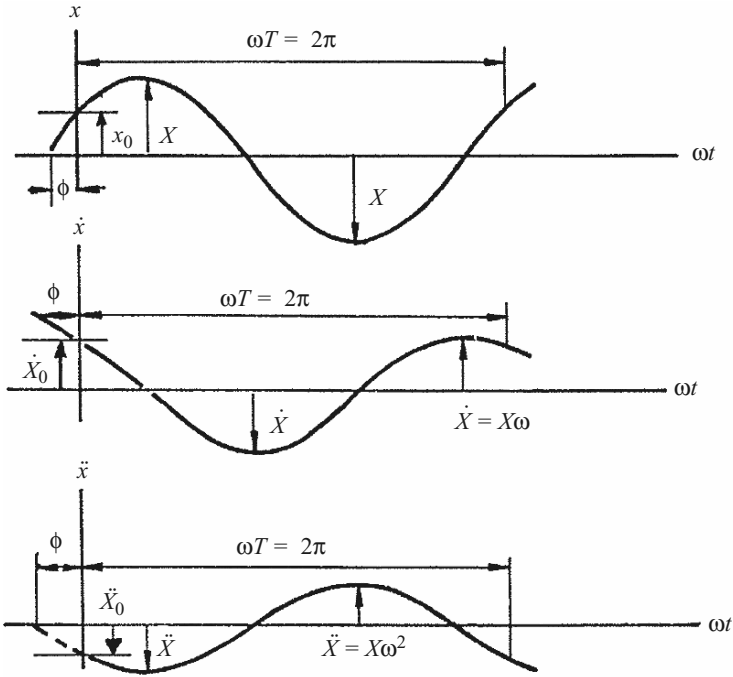
Fig. 3.3. Displacement, velocity and acceleration, with phase angles

$A = \dfrac{\dot{x}_0}{\omega}$

$B = x_0$

$C = \sqrt{(A^2 + B^2)} = X$
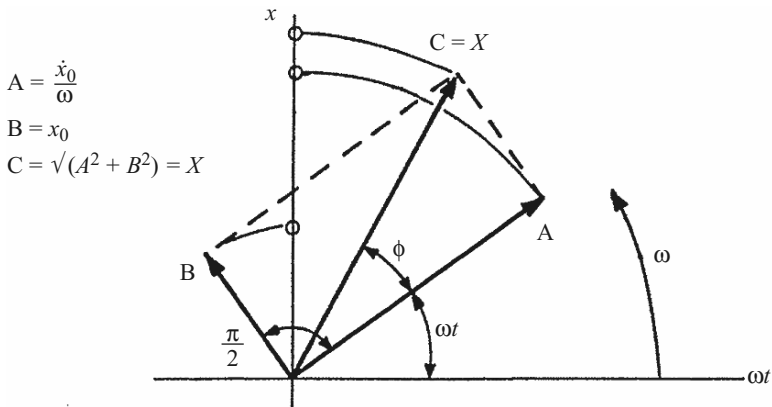
Fig. 3.4. Rotating vectors

are fixed, rotate with angular velocity ω. Their angular position at any time t is ωt. The vectors **A** and **B** are at right angles and the vector **C** leads **A** by the phase angle ϕ. A graphical representation is obtained by vertically projecting these vectors onto the graph of x against ωt shown in Fig. 3.4.
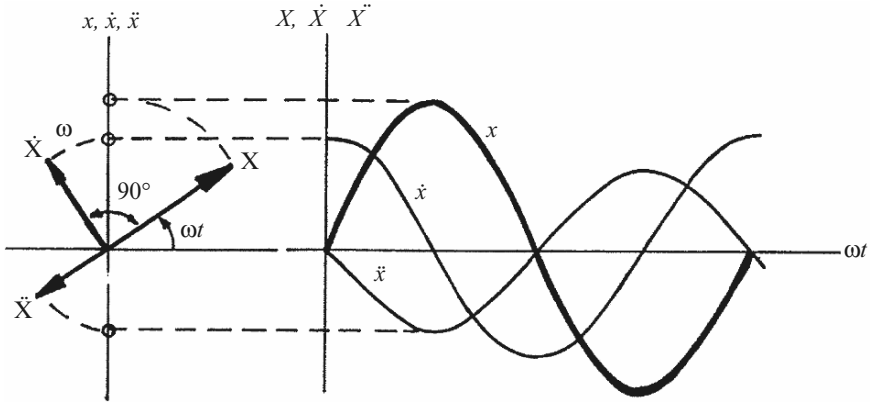
Fig. 3.5. Rotating vectors versus X, $\dot{X}$ and $\ddot{X}$

The displacement, velocity and acceleration curves can be generated in this manner, using rotating vectors $\mathbf{X}$, $\dot{\mathbf{X}}$ and $\ddot{\mathbf{X}}$. The velocity and acceleration vectors lead the displacement vector by 90° and 180°, respectively. Their relative position is fixed and they rotate with angular velocity ω. These are shown in Fig. 3.5.

The expressions for displacement, velocity and acceleration are given in (3.22).

$$x = X \sin \omega t = x_0/\omega \sin \omega t; \ x_0 = 0,$$

$$\dot{x} = X\omega \cos \omega t = \dot{X} \cos \omega t, \tag{3.22}$$

$$\ddot{x} = X\omega^2(-\sin \omega t) = \ddot{X}(-\sin \omega t).$$

Method 2

Assume an exponential function

$$x = \mathrm{Ce}^{st}, \tag{3.23}$$

where C is an arbitrary constant, but s is to be determined so that the differential equation will be satisfied.

$$(s^2 + \omega^2)\, \mathrm{Ce}^{st} = 0, \tag{3.24}$$

$$s^2 + \omega^2 = 0,$$

$$s = \pm i\omega, \tag{3.25}$$

$$x = C_1 e^{i\omega t} + C_2 e^{-i\omega t}. \tag{3.26}$$

The Euler relation is expressed as

$$e^{i\omega} = \cos\omega + i\sin\omega, \tag{3.27}$$

$$x = C_1(\cos\omega t + i\sin\omega t) + C_2(\cos\omega t - i\sin\omega t)$$
$$= (C_1 - C_2)i\sin\omega t + (C_1 + C_2)\cos\omega t$$
$$= A\sin\omega t + B\cos\omega t.$$

C_1 and C_2 are conjugate complex numbers.

$$C_1 = a + ib, \ C_2 - a - ib, \tag{3.28}$$

$$i(C_1 - C_2) = i(2ib) = -2b = A,$$

$$C_1 + C_2 = 2a = B.$$

3.2.3 Torsional Vibrations

Simple torsional vibrations are dependent on the torsional stiffness k_T, the angle of twist θ and the second moment of area I. Figure 3.6 shows a simple system. k_T is the torsional spring constant for the shaft, measured by the twisting moment per unit angle of twist. I represents the mass moment of inertia for the disk relative to its axis of rotation.

For an assumed positive angular displacement of the disk, the restoring torque acting on the disk would be

$$T = k_T \theta \tag{3.29}$$

in the direction shown in the free body diagram. The Newtonian relation for rotation about a fixed axis gives

$$I\ddot{\theta} = -k_T \theta, \tag{3.30}$$
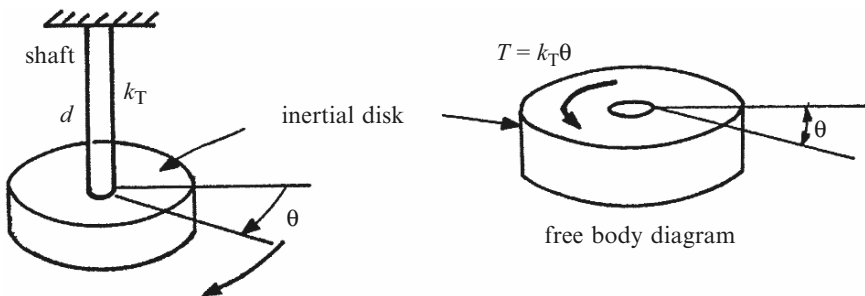
Fig. 3.6. Simple torsional vibration

hence

$$\ddot{\theta} = -k_{\mathrm{T}}\theta/I = 0. \tag{3.31}$$

This is the same form as given in (3.8) for the rectilinear case. The solution will, by analogy, be written as

$$\theta = A\sin\omega t + B\cos\omega t = C\sin(\omega t + \phi), \tag{3.32}$$

where $\omega = \sqrt{(k_{\mathrm{T}}/I)}$ depends on the physical constants of the system.

A and B or C and ϕ are determined from the initial conditions of motion.

Using the material from the previous section, and replacing x by θ, the values of θ, $\dot{\theta}$ and $\ddot{\theta}$ may be computed:

Angle of twist of shaft: $\theta = TL/GI_0$,

hence of torsional spring constant $k_{\mathrm{T}} = T = GI_0/L$,

where I_0 is the polar second moment of area and is equal to $\pi d^2/32$, G is the modulus of rigidity and L is the length of the shaft.

Using the energy method, the kinetic energy and potential energy of the system are given by

$$KE = \frac{1}{2}I\dot{\theta}^2,$$

$$PE = \frac{1}{2}k\theta^2. \tag{3.33}$$

Moreover, $\mathrm{d}/\mathrm{d}t\,(KE + PE) = 0$, which gives

$$(I\ddot{\theta}\dot{\theta} + k\theta\dot{\theta}) = 0. \tag{3.34}$$

Since $\dot{\theta}$ is always zero by virtue of

$$\dot{\theta}(I\ddot{\theta} + k\theta) = 0, \tag{3.34a}$$

hence

$$I\ddot{\theta} + k\theta = 0, \tag{3.35}$$

which is the same as (3.31).

The remaining part of the solution for amplitudes is the same as given in earlier sections.

Tables 3.1–3.6 give a limited application to the above-mentioned dynamic analysis.

Table 3.1. Undamped free vibration (single-degree system): springs

Equivalent spring stiffnesses:

(1) Springs in parallel, with equal deflections of all springs:

$$F = K_1\delta + K_2\delta + \ldots K_n\delta = \delta(\Sigma k),$$
$$F = K_{eq}\delta,$$
$$K_{eq} = \sum_{j=1}^{n} k_j = k_1 + k_2 + \ldots k_n.$$
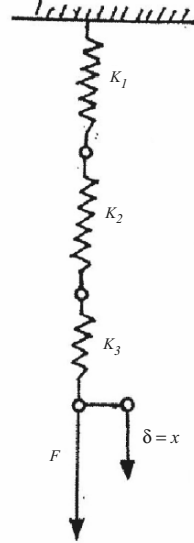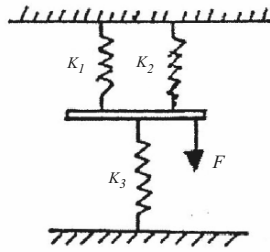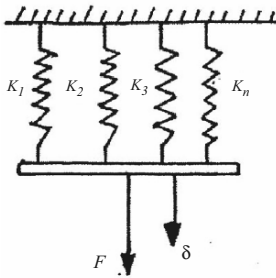
(2) Springs in series, with all springs carrying the same force:

$$F = k_1 x_1 + k_2 x_2 \ldots + k_n x_n,$$
$$F = k_{eq}\delta,$$
$$\delta = x_1 + x_2 + \ldots + x_n = \Sigma x$$
$$= F_1/k_1 + F_2/k_2 + \ldots + F_n/k_n = F/\sum_{i=1}^{n}(1/k_i),$$
$$k_{eq} = F/\delta = 1/\sum_{i=1}^{n}(1/k_i),$$
$$K = k_{eq} = 1/\sum_{i=1}^{n}(1/k_i).$$

(3) Spring mass pulley system:

Energy method
m_1 = mass of pulley,

m = mass under consideration,

$$\text{KE} = (\text{KE})_m + (\text{KE})_{m_1}$$
$$= \tfrac{1}{2}m\dot{x}^2 + \tfrac{1}{2}I_0\dot{\theta}^2 = \tfrac{1}{2}mr^2\dot{\theta}^2 + \tfrac{1}{2}I_0\dot{\theta}^2,$$
$$\text{PE} = \tfrac{1}{2}kx^2 = \tfrac{1}{2}kr^2\theta^2.$$
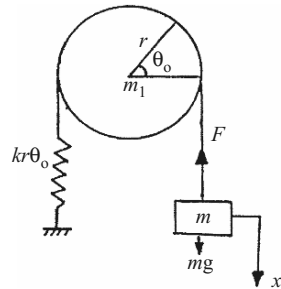
Using (3.4), the following equation of motion is derived:

$$(mr^2\ddot{\theta} + I_0\ddot{\theta} + kr^2\theta) = 0 \text{ or } \ddot{\theta} + (kr^2/I_0 + mr^2)\theta = 0,$$

but $I_0 = \tfrac{1}{2}m_1 r^2$; $I_0\ddot{\theta} = Fr - kr^2(\theta + \theta_0)$,

$$\omega = \sqrt{[k/\tfrac{1}{2}m_1 + m)]}; \quad f = \omega/2\pi.$$

Table 3.2. Undamped free vibrations: beams

(1) Simply supported beams with a single concentrated mass and a distributed mass
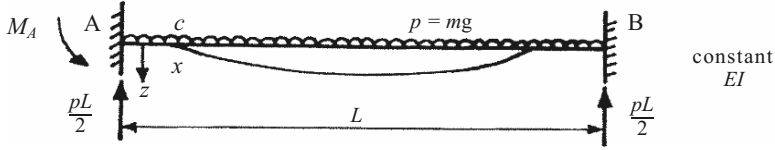
Undamped vibration of a simple beam

Assumption: The dynamic deflection curve is the same as that due to the concentrated load acting statically on the beam:

The vertical displacement $x = \dfrac{x_c}{L^3}(3zL^2 - 4x^3)$,

$\bar{F} = pL$,

$$\text{KE (distributed mass)} = 2\int_0^{L/2} \frac{\bar{F}}{2\mathbf{g}}\left(\dot{x}_c \frac{3zL^2 - 4x^3}{L^3}\right)^2 \mathrm{d}x$$

$$= \frac{17}{35}\bar{F}L\frac{x_c^2}{2\mathbf{g}},$$

$$\text{KE (concentrated mass } m) = \frac{1}{2}m\dot{x}_c^2,$$

$$\text{PE} = \frac{1}{2}kx_c^2.$$

The total energy T = KE + PE and, using (3.4), the natural frequency is given as

$$f = \omega/2\pi = \frac{1}{2\pi}\sqrt{\left(\frac{k\omega}{\bar{F} + \frac{17}{35}\bar{F}L}\right)}.$$

The total mass of the beam is put with the concentrated mass.

If the mass of the beam is negligible compared to the mass acting on it, then the maximum displacement:

$$x_c = \bar{F}L^3/48EI \qquad \text{since } k = \bar{F}/x_c = 48EI/L^3,$$

$$\omega = \sqrt{(k/m)} = \sqrt{(48EI/mL^3)}\,\mathrm{rad\,s^{-1}}.$$

(2) Simply supported beams with a continuous mass distribution and with constant *EI*:

Table 3.2. (continued)

$$EI \mathrm{d}^2 x / \mathrm{d}z^2 = M_c = pz^2/2 - pLz/2,$$

$$EIx = \frac{pz^4}{24} - \frac{pLz^3}{12} + c_1 z + c_2,$$

$$\text{when } z = 0 \quad x = 0 \quad c_2 = 0$$

$$z = L \quad x = 0 \quad c_1 = pL^3/24.$$

Hence $x = \dfrac{p}{24EI}(z^4 - 2Lz^3 + L^3 z),$

$$\omega = \sqrt{\left[\mathbf{g} \int_0^L \left(x \mathrm{d}z / \int_0^L x^2 \mathrm{d}z \right) \right]} = \sqrt{(k/m)} = \sqrt{\left(\frac{15\,120}{155} \frac{EI\mathbf{g}}{pL^4} \right)}$$

$$= 9.87 \sqrt{(EI/mL^4)} = \alpha_{\mathrm{B}} \sqrt{(EI/mL^4)},$$

$$\text{where } \alpha_{\mathrm{B}} = 9.87,$$

$$f = \omega/2\pi.$$

(3) A cantilever beam with a single concentrated mass. The static deflection x_c
of the cantilever due to the mass m is given by:

$$x_c = FL^3/3EI,$$

$$k = F/x_c = 3EI/L^3,$$

$$\omega = \sqrt{(k/m)} = \sqrt{(3EI/mL^3)},$$

$$f = \omega/2\pi.$$

Frequency of a simple cantilever beam

(4) Beams fixed at both ends with continuous mass distribution:
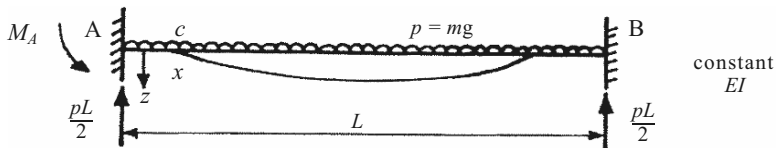
Vibration of a fixed beam

Table 3.2. (continued)

$$EI\frac{d^2x}{dz^2} = M_C = M_A + \frac{pz^2}{2} - \frac{pLz}{2},$$

$$EIx = \frac{1}{2}M_A z^2 = \frac{pz^4}{24} - \frac{pLz^3}{12} + c_1 z + c_2,$$

$$x = 0, \quad \frac{dx}{dz} = 0, \quad c_1 = 0,$$

$$x = L, \quad \frac{dx}{dz} = 0, \quad M_A = pL^2/12,$$

$$z = L, \quad x = 0, \quad c_2 = 0,$$

$$x_c = \frac{p}{24EI}(L^2 z^2 + z^4 - 2Lz^3),$$
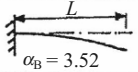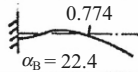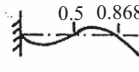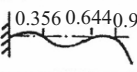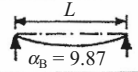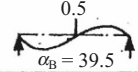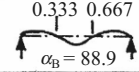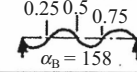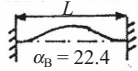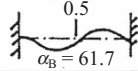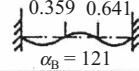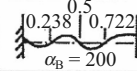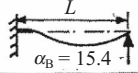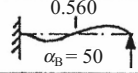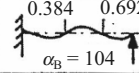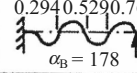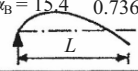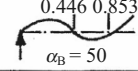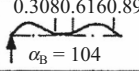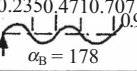
$$\omega = \sqrt{\left(\mathbf{g}\int_0^L x_c dz / \int_0^L x_c^2 dz\right)} = 22.4\sqrt{(EI/mL^4)} = \alpha_B\sqrt{(EI/mL^4)},$$
$$\text{where } \alpha_B = 22.4,$$
$$f = \omega/2\pi.$$

(5) Additional cases for the natural frequency of transverse vibration of beams with end conditions with continuous mass distribution:

$$\omega = \alpha_B\sqrt{(EI/mL^4)},$$
$$f = \omega/2\pi.$$

Type	Normal mode shapes			
Cantilever	$\alpha_B = 3.52$	0.774 $\alpha_B = 22.4$	0.5 0.868	0.356 0.644 0.906
Simply supported	$\alpha_B = 9.87$	0.5 $\alpha_B = 39.5$	0.333 0.667 $\alpha_B = 88.9$	0.25 0.5 0.75 $\alpha_B = 158$
Fixedends	$\alpha_B = 22.4$	0.5 $\alpha_B = 61.7$	0.359 0.641 $\alpha_B = 121$	0.5 0.238 0.722 $\alpha_B = 200$
Propped support	$\alpha_B = 15.4$	0.560 $\alpha_B = 50$	0.384 0.692 $\alpha_B = 104$	0.294 0.529 0.762 $\alpha_B = 178$
One end hinged other free	$\alpha_B = 15.4$ 0.736	0.446 0.853 $\alpha_B = 50$	0.308 0.616 0.898 $\alpha_B = 104$	0.235 0.471 0.707 0.922 $\alpha_B = 178$

(6) A beam vibrating vertically by both linear and torsional springs:

Table 3.2. (continued)

$$\omega = \sqrt{(6kL^2 + 3k_T)/mL^2}\ \text{rad s}^{-1},$$
$$f = \omega/2\pi \quad \omega = \theta.$$
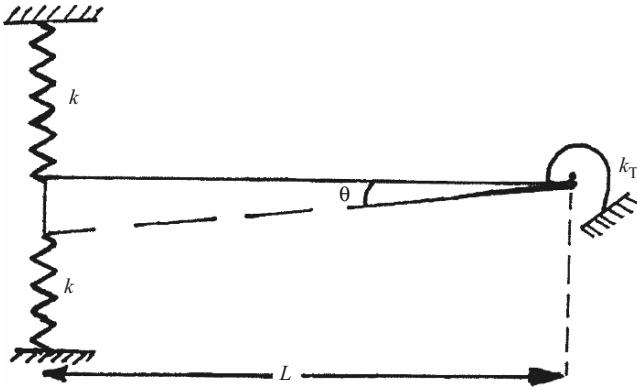
A beam with linear and torsional springs

(7) A beam/spring type of structure:

    (i) Equation of motion:

$$mL^2\ddot{\theta} + (kh^2 + mgL)\theta = 0,$$
$$\omega = \sqrt{(kh^2 + mgL)/mL^2},$$
$$f = \omega/2\pi, \quad \omega = \theta.$$
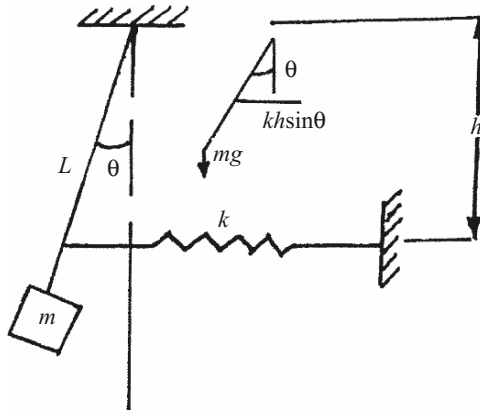
Rotating beam/mass system with a mass down

Table 3.2. (continued)

(ii) $x = L(1 - \cos\theta)$

$\approx \dfrac{1}{2}L\theta^2,$

$(\text{PE})_{\max} = \dfrac{1}{2}kh^2\theta^2 - \dfrac{1}{2}mgL\theta^2,$

$\text{KE} = \dfrac{1}{2}mL^2\theta^2,$

$\omega = \sqrt{\left[\dfrac{1}{L}(kh^2/mL - 1)\right]},$

$f = \omega/2\pi, \qquad \omega = \theta.$
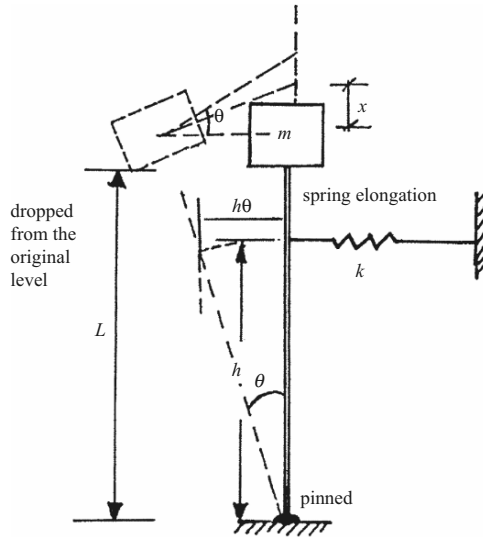
Rotating beam/mass system with a mass upward

(iii) $m_{\text{L}} = $ mass of the lever, $m_{\text{c}} = $ mass of the cylinder

$$= \rho_{\text{c}}(\tfrac{1}{4}\pi D^2 h).$$

Upward thrust on the cylinder = weight of water displaced

$T_{\text{v}} = -\rho_{\text{w}}gV$

$= -\rho_{\text{w}}g(\tfrac{1}{4}\pi D^2 x_2)$

$= -\rho_{\text{w}}g(\tfrac{1}{4}\pi D^2 L\theta),$

$F_{\text{s}} = $ spring restoring force

$= -Kx_1 = -L_1\theta x_1.$

Total restoring torque $= I_0\ddot{\theta}.$

Table 3.2. (continued)

$$D = \text{diameter}$$
$$h = \text{height}$$
$$p_c = \text{relative density of cylinder}$$
$$p_w = \text{relative density of water}$$
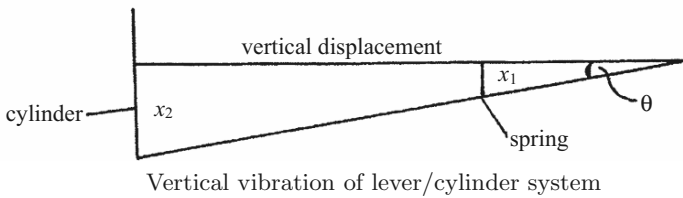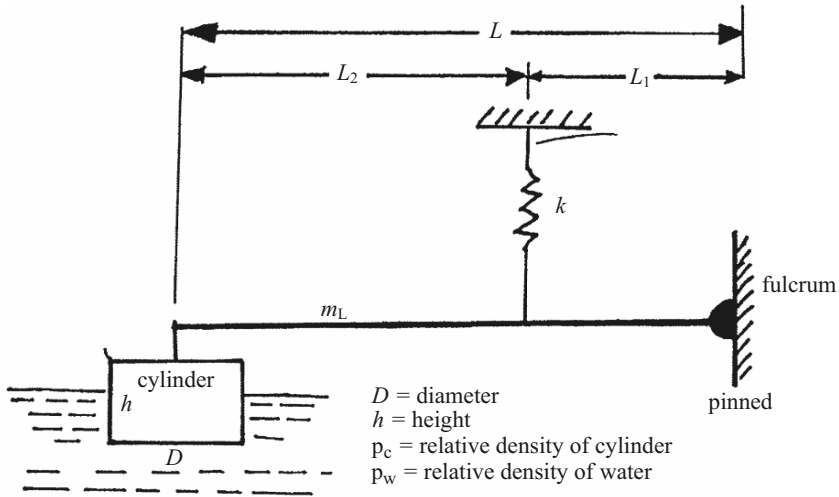
Vertical vibration of lever/cylinder system

Equation of motion:

$$T_v L + F_s L_1 = \left(m_c L^2 + \frac{L_1}{L} m_L L^2 \right) \ddot{\theta},$$

$$\theta = \left(\tfrac{1}{4} \pi D^2 L^2 \rho_w + L_1^2 x \right) / \left(\tfrac{1}{4} \pi D^2 h \rho_c L^2 + L L_1 m L \right).$$

Hence $f = \theta / 2\pi$.

Table 3.3. Natural frequency of missiles with specific cross-sectional shapes and each subject to a distributed mass

Note: circular frequency $\omega = \alpha_B \sqrt{(EI/mL^4)}$; where α_B values are as used in Table 3.2, Sect. 5. The values of I given below are substituted in the above equation with m. The values of E and L must be known; $f = \omega/2\pi$. For unit weight all expressions are multiplied by ρ.

(1) Rectangular cross-section of a missile:

$$I_{xx} = bh^3/12,$$
$$I_{yy} = hb^3/12.$$

Table 3.3. (continued)
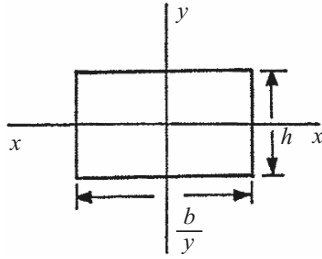
(2) Solid circular cross-section of diameter D:

$$I_{xx} = I_{yy} = \pi D^4/64.$$

(3) Hollow circular cross-section of outer diameter D and inner diameter d:

$$I_{xx} = I_{yy} = \frac{\pi}{64}(D^4 - d^4).$$

(4) Thin-walled tubular cross-section of outer diameter D and thickness t:

$$I_{xx} = I_{yy} = \pi t D^3/8.$$

(5) Elliptical type:

$$I_{xx} = \pi D d^3/64,$$
$$I_{yy} = \pi D^3 d/64.$$
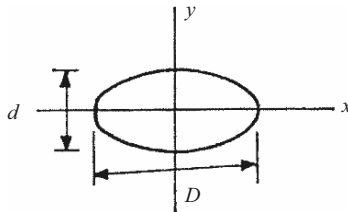
(6) Triangular cross-section with base b and height h:

$$I_{xx}(\text{parallel to } b) = bh^3/36.$$

(7) Right circular cylindrical type missile:

$$I_{zz} = \pi h R^4/2,$$
$$m = \rho \pi R^2 h.$$
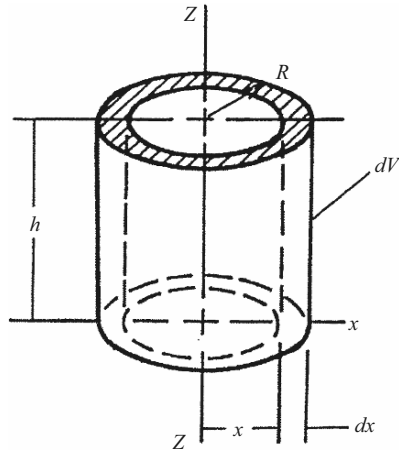
Table 3.3. (continued)

(15) Torus and spherical sector missiles:
    (i) Torus

$$I_{xx} = I_{zz} = \frac{W}{8}(4R^2 + 5r^2),$$

$$I_{yy} = \frac{W}{4}(4R^2 + 3r^2),$$

$$W = 2\pi^2 r^2 \rho,$$

$$\bar{x} = z = R + r.$$
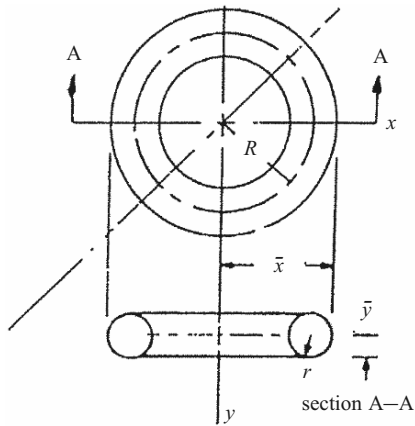
Torus-shaped missile

Table 3.3. (continued)

(ii) Spherical sector

$$I_{zz} = \frac{Wh}{5}(3R - h),$$

$$W = \frac{2}{3}\pi\rho R^2 h.$$
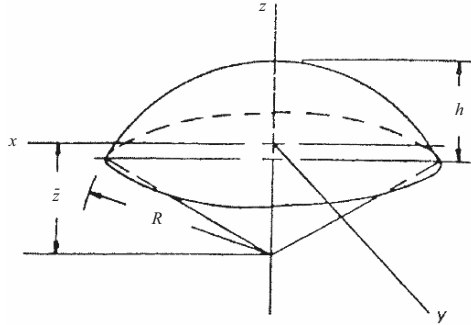
Spherical sector type missile

Table 3.4. Natural frequency of beam/column/wall system (horizontal members are infinitely stiff)

(1) Single-bay frame. Stiffnesses of vertical members:

$$k_{AB} = \frac{12EI}{L^3}; \quad k_{CD} = 12E(nI)/(nL)^3,$$

$$\Sigma k = K = \frac{12EI}{L^3}(1 + 1/n^2),$$

$$\omega = \sqrt{\left[\frac{12EI}{L^3}\left(1 + \frac{1}{n^2}\right)\right] \Big/ m},$$

$$f = \omega/2\pi.$$

n is a multiple of length L
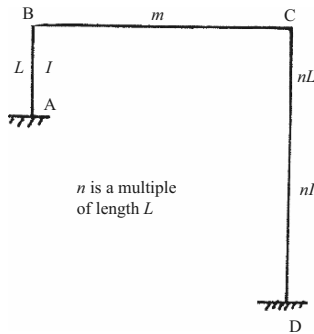
A single-bay frame

Table 3.4. (continued)

(2) Two-bay frame. Stiffnesses of vertical members:

$$k_{AB} = 12En_1I/L_1,$$

$$k_{CD} = 12En_2I/L_2,$$

$$k_{EF} = 12En_3I/L_3,$$

$$\Sigma k = K = 12EI\left(\frac{n_1}{L_1} + \frac{n_2}{L_2} + \frac{n_3}{L_3}\right),$$

$$\omega = \sqrt{(K/m)}; \quad f = \omega/2\pi.$$

n_1, n_2 and n_3 are multiples
of lengths
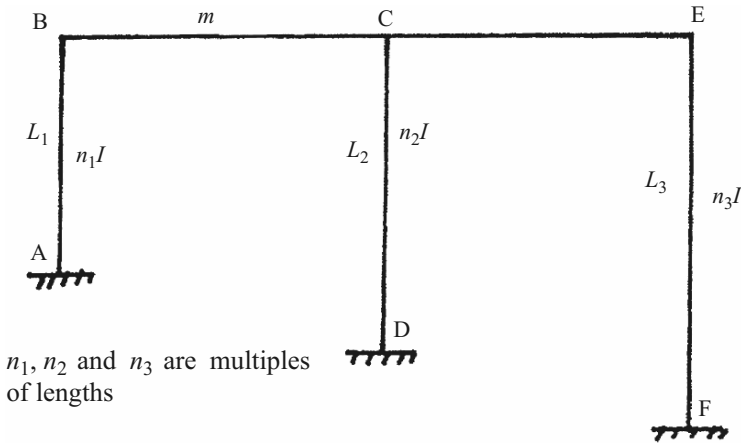
A two-bay frame

(3) Building of height h and base area $a \times b$. Equation of motion:

$$I_0\ddot{\theta} - \left(\frac{1}{2}mgh\right)\theta = -M$$

or $I_0\ddot{\theta} - \left(\frac{1}{2}mgh\right)\theta = -2\int_0^{1/2} kax^2\theta dx$

$$= kb^3a\theta/12,$$

$$\omega = \sqrt{\left[\left(\frac{kb^3a}{12} - \frac{mgh}{2}\right)\bigg/I_0\right]},$$

$$f = \omega/2\pi.$$

Table 3.4. (continued)

sectional elevation

displacement $= x\theta$

$M =$ *restoring moment due to elastic soil/foundation of stiffness k*

plan

moment at the centreline $= kadx(x\theta)x$

A single wall
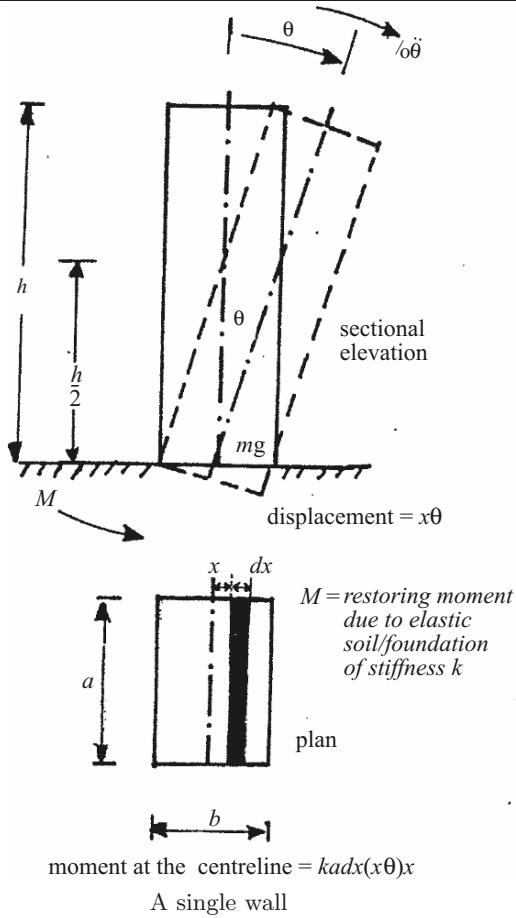
Table 3.5. Vibration of plates of uniform thickness

$$f = \frac{1}{2\pi}\alpha_{\mathrm{B}}\sqrt{[Et^2/\rho D^4(1-\nu^2)]},$$

where

f = natural frequency
ρ = density
D = diameter or length
ν = Poisson's ratio
t = thickness
α_{B} = vibration factor

Table 3.5. (continued)

Plates with boundary conditions		α_β
All edges fixed		10.4
Two edges free and two edges fixed		2.01
All edges free		4.07
All edges simply supported		5.7
Three edges simply supported and one edge fixed		6.8
Two edges simply supported and two edges fixed		8.37
Circular plates		
The rim is fixed		11.84
The rim is free		6.09
The rim is simply supported		4.35

Table 3.6. Helical springs and springs to simulate other conditions

(1) Helical springs. The following spring stiffnesses are used where springs are substituted for structure–structure and structure–foundation interactions:

Vertical direction $k_a = Gd^4/8nD^3 \times N$
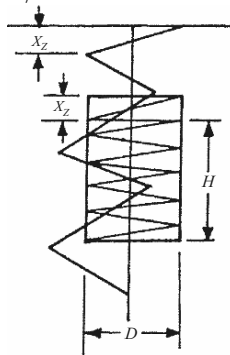
Table 3.6. (continued)

Lateral stiffness $k_\ell = k_a \left[\dfrac{1}{0.385 \; \alpha_\beta} \left(1 + \dfrac{0.77 \; H^2}{D^2} \right) \right] \times N.$

Bending stiffness $k_m = I_\ell k_a$ or $I_m k_s.$

Torsional stiffness $k_\theta = k_T = \dfrac{I_n k_\ell}{0.385 \; \alpha_\beta \; \left(1 + \frac{0.77 \; H^2}{D^2} \right)}.$

Table of α_β values

x_z/H H/D	0.10	0.20	0.30	0.40	0.50
0.10	1.00	1.00	1.00	1.00	1.00
0.25	1.00	1.03	1.03	1.03	1.03
0.50	1.08	1.08	1.08	1.08	1.08
0.55	1.08	1.10	1.10	1.17	1.20
1.00	1.08	1.10	1.15	1.25	1.34
1.25	1.08	1.15	1.30	1.45	1.60
1.50	1.09	1.20	1.43	1.70	2.03
1.55	1.10	1.40	1.50	2.10	3.00
1.75	1.15	1.45	1.60	2.50	4.40
2.00	1.20	1.55	2.00	3.04	6.00

vertical coefficients   sliding-cum-rocking coefficients   torsional coefficients
m_F = mass of foundation
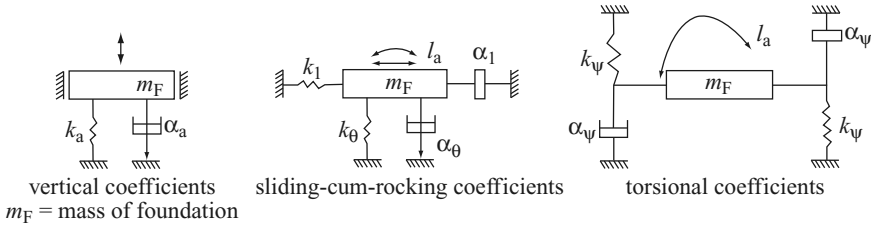
Springs representing vertical, sliding-cum-rocking and torsional effects

(2) Foundations on springs. The linear stress-strain relation demands that sub-grade reaction coefficients k_a, k_ℓ, k_θ and k_T must be determined (see table): r_a, r_ℓ and r_θ are radii of equivalent circular bases for translation, rotation and rocking modes. α_a, α_ℓ and α_ψ are given in this same table for rigid foundations, where α_ℓ, α_a = uniform compression and shear in vertical and horizontal modes, respectively; $\alpha_\psi, \alpha_\theta$ = non-uniform rocking or twisting modes, respectively.
Determination of the coefficients k_a, k_ℓ, k_θ and k_ψ

Table 3.6. (continued)

Motion	Circular foundation	
	Spring constant	References
Vertical	$k_a = \dfrac{4Gr_a}{1 - v}$	[6.73]
Lateral	$k_\ell = \dfrac{32(1 - v)Gr_a}{7 - 8v}$	[6.75]
Rocking	$k_T = \dfrac{8Gr_\psi^3}{3(1 - v)}$	[6.77]
Torsion	$k_\theta = \dfrac{16}{3}Gr_\theta^3$	[6.76]

Motion	Rectangular foundation	
	Spring constant	References
Vertical	$k_a = \dfrac{G}{1 - v}\alpha_a\sqrt{(4cd)}$	[6.74]
Lateral	$k_\ell = 4(1 + v)G\alpha_\ell\sqrt{(cd)}$	[6.74]
Rocking	$k_\psi = \dfrac{G}{1 - v}\alpha_\psi\, 8cd^2$	[6.77]

$G = E/2(1 + v)$,
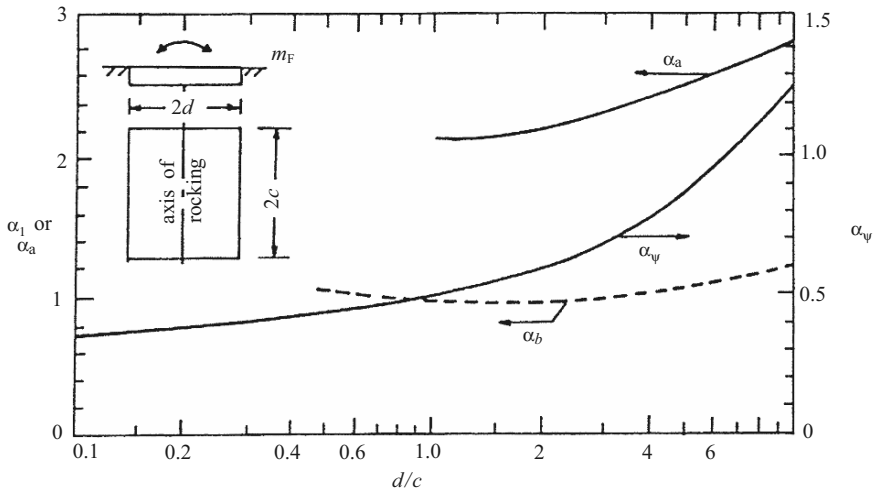
Coefficients α_a, α_ℓ and $\alpha\psi$ for rectangular footings (after Richart et al.) [6.78]

Table 3.6. (continued)

$$r_a = \sqrt{(A_F/\pi)} \text{ for translation,}$$

$$r = \sqrt[4]{4I_a/\pi} \text{ for rocking,}$$

$$r_\theta = \sqrt{[2(I_x + I_y)/\pi]} \text{ for torsion.}$$

Motion	Mass ratio α		Damping ratio
Vertical	$\alpha_a = \dfrac{(1-\nu)}{4}\dfrac{m_F}{\rho r_a^3}$		$\tau_a = \dfrac{0.425}{\sqrt{\alpha_a}}$
Horizontal (sliding)	$\alpha_\ell = \dfrac{7-8\nu}{32(1-\nu)}\dfrac{m_F}{\rho r_a^3}$		$\gamma_\ell = \dfrac{0.288}{\sqrt{\alpha_\ell}}$
Rocking	$\alpha_\psi = \dfrac{3(1-\nu)}{8}\dfrac{I_a'}{\rho r_\psi^5}$		$\gamma_\psi = \dfrac{0.15}{(1+\alpha_\psi)\sqrt{\alpha_\psi}}$
Torsional	$\alpha_\theta = \dfrac{I_{xx}+I_{yy}}{\rho r_\theta^5}$	$= \dfrac{I_a}{\rho r_\theta^5}$	$\gamma_\theta = \dfrac{0.5}{1+2\alpha_\psi}$

ρ = mass density of soil;
I_a' = mass moment of inertia about a parallel axis passing through the centroid of the foundation;
ν = 0.25–0.35 for cohesionless soils;
ν = 0.35–0.45 for cohesive soils;
γ = engineering strain;
τ = shear.

3.2.3 Free Damped Vibrations

3.2.3.1 Viscous Damping Force

Observation shows that the amplitude of free vibrations dies away slowly. A force is introduced into the mathematical model to simulate the effects of damping. A common way to do this is to postulate that the damping force is proportional to the velocity at any instant and acting in the opposite way to the displacement, i.e.

$$F = -c \times v = -c \times \dot{x}, \tag{3.36}$$

where c is the damping force per unit of velocity (damping coefficient).

The viscous type of damping is a good approximation for bodies moving at low velocities, or sliding on lubricated surfaces, or where hydraulic dashpots and shock absorbers are used.

Other types of damping may be more appropriate for structural materials, structural connections and for the entire structure. Viscous damping has
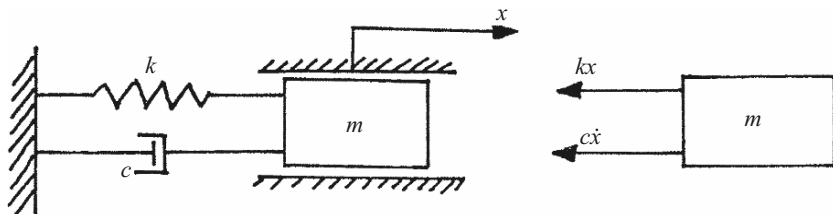
Fig. 3.7. Simple system with damping: free body

mathematical advantages because it produces a viscous force which gives the same rate of energy dissipation as the actual damping force.

Other types of damping occurring are discussed in the text later on. A typical system is shown in Fig. 3.7.

From Newton's law, the equation of motion is given by

$$m\ddot{x} = -c\dot{x} - kx, \tag{3.37}$$

$$\text{or } m\ddot{x} + c\dot{x} + kx = 0. \tag{3.38}$$

Use the trial solution $x = Ce^{\lambda t}$ $\tag{3.39}$

$$(m\lambda^2 + c\lambda + k)Ce^{\lambda t} = 0. \tag{3.40}$$

The characteristic or auxiliary equation of the system

$$m\lambda^2 + c\lambda + k = 0. \tag{3.41}$$

Therefore $\lambda_{1,2} = -c/2m \pm \sqrt{[(c/2m)^2 - k/m]}$, $\tag{3.42}$

general solution $x = C_1 e^{\lambda_1 t} + C_2 e^{\lambda_2 t}$, $\tag{3.43}$

provided that $c/2m \neq \sqrt{(k/m)}$. $\tag{3.44}$

Critical Damping

The value of the damping coefficient which causes the radical part of the exponent of (3.42) to vanish is called the *critical damping coefficient*, c_c, defined by

$$c_c/2m = \sqrt{(k/m)} = \omega,$$
$$c_c = 2\sqrt{(mk)} = 2m\omega. \tag{3.45}$$

The dimensionless parameter $\gamma = c/c_c$, called the *damping ratio*, gives a meaningful measure of the damping present in the system.

$$c/2m = \frac{c}{c_c} \times \frac{c_c}{2m} = \gamma \times \frac{2m\omega}{2m} = \gamma\omega, \tag{3.46}$$

$$\lambda_{1,2} = [-\gamma \pm \sqrt{(\gamma^2 - 1)}]\omega, \tag{3.47}$$

$$x = C_1 e^{[-\gamma + \sqrt{(\gamma^2 - 1)}]\omega t} + C_2 e^{[-\gamma - \sqrt{(\gamma^2 - 1)}]\omega t}, \tag{3.48}$$

for $\gamma \neq 1$.

First case

$\gamma > 1$ overdamping. Since $\sqrt{(\gamma^2 - 1)} < \gamma$ both exponents of (3.48) are real and negative, and the solution can be left in the form shown. This represents the sum of two decaying exponentials. The motion is called *overdamped*, it is non-periodic or aperiodic.

$$x = C_1 e^{-\alpha t} + C_2 e^{\beta t}, \tag{3.49}$$
$$\alpha = [\gamma - \sqrt{(\gamma^2 - 1)}]\omega > 0, \tag{3.50}$$
$$\beta = [\gamma + \sqrt{(\gamma^2 - 1)}]\omega > 0,$$

for
$$\beta \gg \alpha.$$

C_1 and C_2 may be positive or negative, depending on the initial conditions. Five basic types of the displacement versus time curve are possible (Fig. 3.8).

Second case

$\gamma = 1$ critical damping solution is

$$x = (C_1 + C_2 t)e^{-(c/2m)t}$$
$$= (C_1 + C_2 t)e^{-\omega t}. \tag{3.51}$$

This is the product of a linear function, $C_1 + C_2 t$, and the decaying exponential $e^{-\omega t}$, as shown in Fig. 3.9. Five different basic shapes can result, similar to those shown in Fig. 3.8.

Third case

$\gamma < 1$ underdamping. For this condition $(\gamma^2 - 1)$ is negative, and the exponential multipliers of ωt in (3.48) are conjugate complex numbers. It is therefore desirable to write

$$x = C_1 e^{[-\gamma + i\sqrt{(1-\gamma^2)}]\omega t} + C_2 e^{(-\gamma - i\sqrt{(1-\gamma^2)}]\omega t}, \tag{3.52}$$

where $i = \sqrt{-1}$. With Euler's formula:

$$e^{i\theta} = \cos\theta + i\sin\theta, \tag{3.53}$$

where $\theta = \omega$, the displacement x is given as

$$x = e^{-\gamma\omega t}[A\sin\sqrt{(1-\gamma^2)}\omega t + B\cos\sqrt{(1-\gamma^2)}\omega t]$$

or
$$x = Xe^{-\gamma\omega t}\sin[\sqrt{(1-\gamma^2)}\omega t + \phi] \tag{3.54}$$
$$= Xe^{-\gamma\omega t}\sin(\omega_d t + \phi), \quad \omega_d = \sqrt{(1-\gamma^2)}\omega, \tag{3.55}$$

where ω_d is the damped circular frequency.

The circular frequency is reduced by viscous damping. However, for the usual case of small damping, this effect is very small and it is appropriate to assume that the frequency is unaffected.
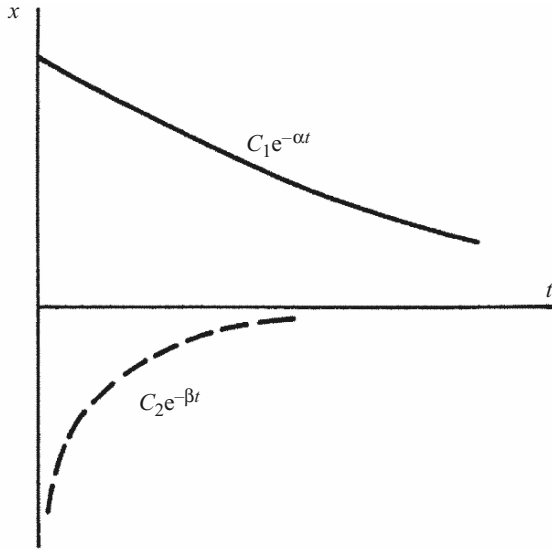
(a) $C_1 e^{-\delta t}$ and $C_2 e^{-\beta t}$ Curves
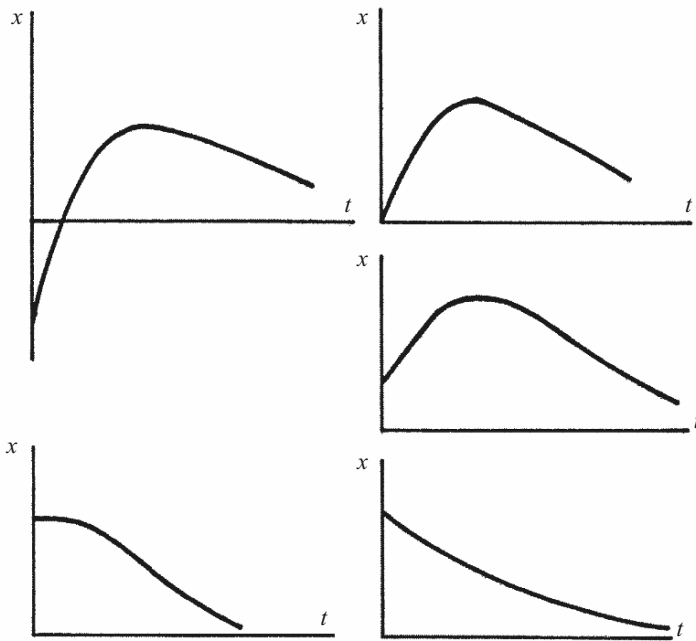
(b) x − t Curves

Fig. 3.8. Overdamping
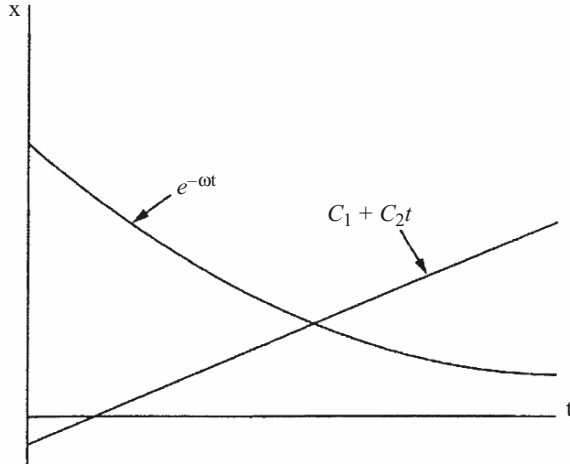
Fig. 3.9. Critical damping
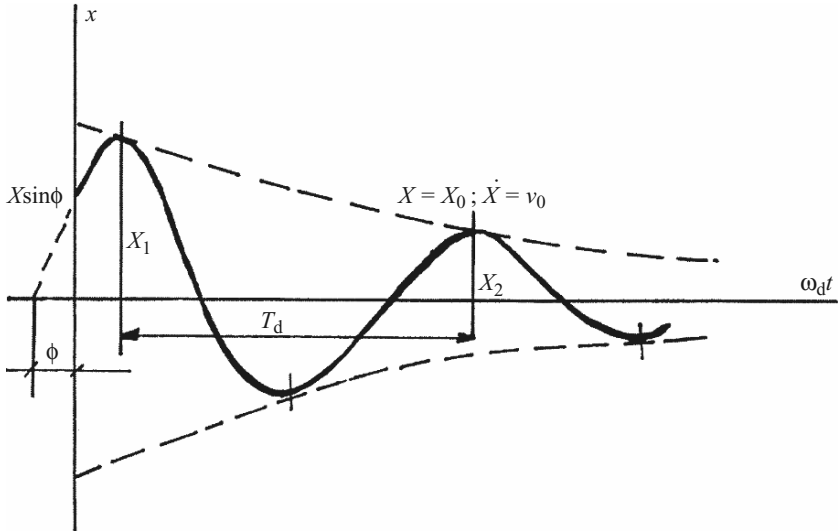
Fig. 3.10. The motion with a decaying amplitude

The successive maxima X_1 and X_2 occur with the period T_d, as shown in Fig. 3.10.

$$\omega_d T_d = 2\pi; \qquad T_d = 2\pi/\omega_d = 2\pi/\sqrt{(1-\gamma^2)}\omega. \tag{3.56}$$

The ratio of successive maximum amplitudes is equal to the ratio of the values of the exponential term $\mathrm{e}^{-\gamma\omega t}$ at the corresponding times, leading to

$$X_1/X_2 = \mathrm{e}^{-\gamma\omega t}/\mathrm{e}^{-\gamma\omega(t_1+T_\mathrm{d})} = \mathrm{e}^{\gamma\omega T_\mathrm{d}}, \tag{3.57}$$

$$X_1/X_2 = \mathrm{e}^{2\pi\gamma/\sqrt{(1-\gamma^2)}}.$$

The *logarithmic decrement*, $\bar{\delta}$, which gives the rate of attenuation, is

$$\bar{\delta} = \log X_1/X_2 = 2\pi\gamma/\sqrt{(1-\gamma^2)}. \tag{3.58}$$

For small damping this becomes

$$\bar{\delta} \doteq 2\pi\delta. \tag{3.59}$$

The logarithmic decrement $\bar{\delta}$ can be calculated from the ratio of the amplitudes several cycles apart, since for viscous damping the logarithmic decrement can be related to any pair of successive amplitudes.

$$X_0/X_n = X_0/X_1,\ X_1/X_2,\ X_2/X_3 \dots X_{n-1}/X_n \tag{3.60}$$
$$= (X_i/X_{j+1})^n,$$

$$\log(X_0/X_n) = n\log(X_j/X_{j+1}) = n\bar{\delta},$$
$$\bar{\delta} = (1/n)\log(X_0/X_n). \tag{3.61}$$

The above is the basis of the experimental determination of the damping ratio for a system.

The amplitudes are obtained by measurement of an experimental record. This gives the logarithmic decrement $\bar{\delta}$ when (3.61) is used. The damping ratio follows from (3.58) when $\bar{\delta}$ is substituted.

If the damping force is truly viscous (damping force $= c \times$ velocity), the logarithmic decrement will have a value independent of the amplitude of motion; i.e. the ratio of successive peaks in the free-vibration curve will be constant. Table 3.7 gives typical examples of damping and logarithmic decrement.

Coulomb Damping or Dry Friction Damping

Coulomb damping (Fig. 3.11) occurs when bodies slide on dry surfaces. The damping force is approximately constant provided the surfaces are uniform and the differences between the starting and moving conditions are small.

$$F_\mathrm{f} = \mu N, \tag{3.62}$$

where μ is the coefficient of kinetic friction of the materials and N is a normal force.

The equation of motion is

$$m\ddot{x} + kx \pm F_\mathrm{f} = 0. \tag{3.63}$$

If the velocity $\dot{x}$ is positive, a positive sign is normally applied to F_f. The general solutions for the displacement x and velocity $\dot{x}$ are written as

$$x = x_0\cos\omega t + F_\mathrm{f}/k(1-\cos\omega t),$$
$$\dot{x} = -\omega(x_0 - F_\mathrm{f}/k)\sin\omega t. \tag{3.64}$$

Table 3.7. Example of free damped vibration

(1) A platform is treated as a single-degree system and is deflected at mid-span by lowering the deck. The release is a sudden one. The vibration is found to decay exponentially from an amplitude of X_1 to X_2 in S cycles, such that the frequency is f_1. A vehicle with a mass m_1 is then placed at mid-span and the frequency of vibration is noted as f_2. Calculate the effective mass m_e, the effective stiffness k_e and γ for the platform.

$$f_1 = \omega/2\pi = \frac{1}{2\pi}\sqrt{\frac{k}{m}}; \qquad f_2 = \frac{1}{2\pi}\sqrt{\left(\frac{k}{m+m_e}\right)},$$

$$(f_1/f_2)^2 = (m_1 + m_e)/m_1,$$

$$m_1 = \frac{m_e}{(f_1/f_2)^2 - 1},$$

$$k_e = (2\pi f_1)^2 m_1.$$

The logarithmic decrement $\bar{\delta} = (1/S)\log(X_1/X_2)$,

$$\bar{\delta} = 2\pi\gamma/\sqrt{(1-\gamma^2)} = 1/S \ \log\ (X_1/X_2),$$

$$\gamma = \sqrt{[\tfrac{1}{4}\pi^2(1/S \ \log\ X_1/X_2)^2]/[1 + \tfrac{1}{4}\pi^2(1/S \ \log\ X_1/X_2)^2]},$$

$\gamma > 1$: overdamping, $\gamma = 1$: critical damping and $\gamma < 1$: underdamping.

(2) A structure vibrating with viscous damping makes δ_1 oscillations per second and in S_n cycles its amplitude diminishes by η per cent. Determine $\bar{\delta}$, c and γ. Assuming damping is removed, determine the decrease in proportion in the period of vibration.

$$\delta = 1/S_n \ \log[\eta/S_n \times S_1/(\eta S_1/S_n - \eta)]$$

$$= 1/S_n \ \log[\eta S_1/\eta(S_1 - S_n)],$$

$$\text{the period } T_d = 1/S_1; \qquad \omega = 2\pi/T_d = 2\pi S_1,$$

$$c = \bar{\delta}/S_1,$$

$$\gamma = \bar{\delta}/\omega = 1/(2\pi S_1)S_n \ \log\ [S_1/(S_1 - S_n)],$$

$$T/T_d = \sqrt{(1-\gamma^2)} \ \text{decrease in proportion.}$$

A diagram similar to Fig. 3.10 is drawn. The first negative peak for $t = \pi/\omega$ is

$$x = -(x_0 - 2F_f/k). \tag{3.65}$$

The amplitude is reduced by $2F_f/k$. In the second half-cycle the velocity is positive and the equation of motion is written as

$$m\ddot{x} + kx = -F_f. \tag{3.65a}$$
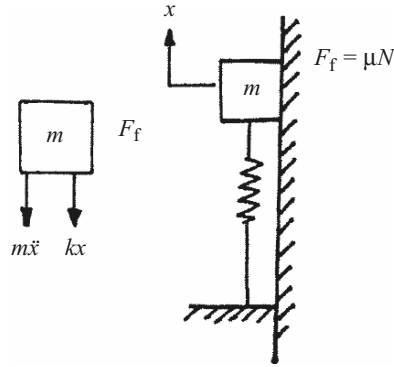
Fig. 3.11. Coulomb damping

The amplitude at the end of the next half-cycle can easily be determined by inspection. For an initial displacement of $-\bar{x}_0$ for time $t = T_d/2$, all terms in (3.65) are to be reversed, where $\bar{x}_0 = x_0 - 2F_f/k$, (3.64) is written as

$$x = -(\bar{x}_0 - F_f/k)\cos(\omega t - \pi) - (F_f/k)[1 - \cos(\omega t - \pi)] \qquad (3.66)$$
$$= -(x_0 - 3F_f/k)\cos(\omega t - \pi) - F_f/k \text{ for } T_d/2 \le t \le T_d.$$

In the second half-cycle the velocity is positive and the equation of motion becomes

$$m\ddot{x} + kx = -F_f. \qquad (3.67)$$

At the next peak value, that is at the end of the first complete cycle with $\omega = 2\pi$, the value of x becomes

$$x_1 = x_0 - 4F_f/k. \qquad (3.68)$$

The dotted line shown in Fig. 3.12 is represented by

$$x = x_0 - 4F_f/k \times t/T_d. \qquad (3.68a)$$

After n such cycles the amplitude is

$$x_n = x_0 - 4nF_f/k. \qquad (3.69)$$

For small damping at the nth cycle, the value of x_n will be larger. Eventually, with a large value of F_f or f, the vibration will cease at N cycles such that $F_f = k'x_N$. Equation (3.69) becomes

$$x_N = x_0 - 4NF_f/k'. \qquad (3.70)$$
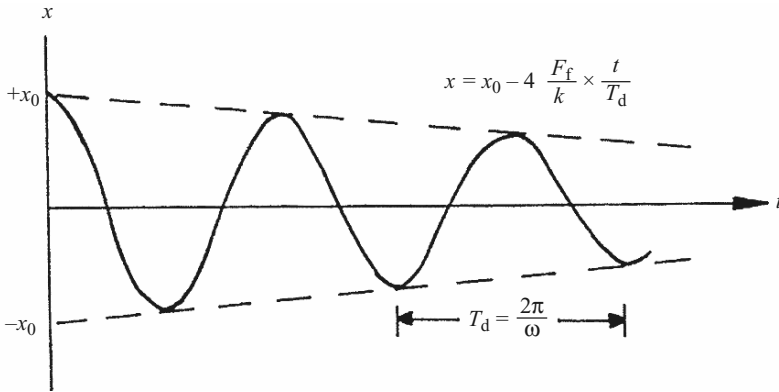
Fig. 3.12. Decay of free vibrations under Coulomb damping

This phenomenon is demonstrated in Fig. 3.12 and a typical case is examined in Table 3.8.

Structural Damping

This is due to the internal friction of the material. This type of resistance is approximately proportional to the displacement amplitude and is independent of the frequency. Suggested values for damping for steel, reinforced concrete and prestressed concrete are 2–3% without cracks and 3–5% with well disposed cracks. Table 3.9 gives damping properties of known structural materials.

3.2.4 Undamped Forced Vibrations (Harmonic Disturbing Force)

The general form of a harmonic driving or forcing function is written as

$$F = F_0 \sin(\omega_f t + \phi), \tag{3.71}$$

where F_0 is a constant presenting the amplitude of the force, ω_f is the circular frequency for the harmonic driving function and ϕ is the phase angle, which depends on the initial conditions for the force. The force is defined by

$$F = F_0 \sin \omega_f t \text{ or } F = F_0 \cos \omega_f t. \tag{3.72}$$

The model of the undamped system is shown in Fig. 3.13. Newton's law is applied and the equation of motion becomes

$$m\ddot{x} = -kx + F, \tag{3.73}$$

$$\text{or } m\ddot{x} + kx = F_0 \sin \omega_f t. \tag{3.74}$$

Table 3.8. Coulomb or dry friction damping

A bascule bridge is modelled as a single-degree of freedom system of vertical struc-
ture tied by a rotating deck with a bottom guide imposing a friction. Using the
following data find the frequency of oscillation and the number of cycles executed
prior to the ceasing of the deck motion.
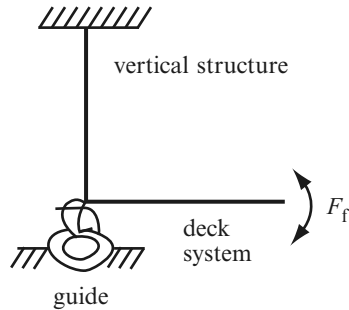
A line diagram for a bascule bridge

Stiffness of the vertical structure $= K_T$
Moment of inertia of the deck system $= I_0$
Displacement from the original position of the deck system (in radians) $= x$

$$\omega = \sqrt{(K_T/I_0)},$$

$$f = \frac{1}{2\pi}\sqrt{(K_T/I_0)}.$$

Loss in amplitude per cycle $= 4F_f/K_T$ radians, hence the number of cycles executed
prior to ceasing

$$= \frac{x}{4\ F_f/K_T} = x \times K_T/4F_f.$$

The displacement–time curve can be drawn starting at time zero for x radians to a
reduced value corresponding to $x \times K_T/4F_f$.

Table 3.9. Material damping

Material	Damping values
Aluminium	0.002
Aluminium alloy	0.0039–0.001
Cast iron	0.003–0.03
Steel	0.001–0.009
Glass	0.0006–0.002
Concrete without cracks	0.01–0.03
Concrete with cracks	0.03–0.05
Rubber	1.0
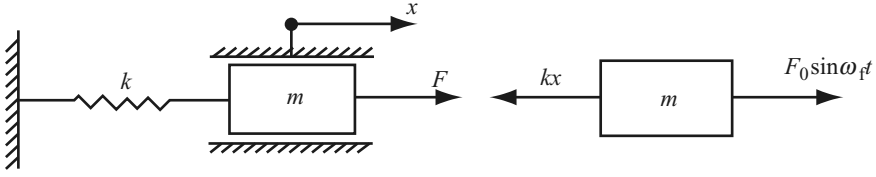
Fig. 3.13. Harmonic force excitation: free body diagram

The solution will be $x = x_{\mathrm{a}} + x_{\mathrm{b}}$, $\qquad\qquad$ (3.75)

where $x_{\mathrm{a}} = A \sin \omega_{\mathrm{f}} t + B \cos \omega_{\mathrm{f}} t$ $\qquad\qquad$ (3.76)

$\qquad$ = a complementary function
$\qquad$ = the solution of the homogeneous equation,

$\qquad x_{\mathrm{b}}$ = the particular solutions
$\qquad$ = a solution which satisfies the complete differential equation,

$\qquad x$ = the complete solution
$\qquad$ = the sum of the free-vibration and the forced-vibration
$\qquad\qquad$ components.

The particular solution for x_{b} is now considered. A particular solution of the form

$$x_{\mathrm{b}} = X \sin \omega_{\mathrm{f}} t \qquad\qquad (3.77)$$

is adopted and, upon substitution, the following equation is obtained:

$$-m\omega_{\mathrm{f}}^2 X \sin \omega_{\mathrm{f}} t + kX \sin \omega_{\mathrm{f}} t = F_0 \sin \omega_{\mathrm{f}} t, \qquad\qquad (3.78)$$

where $X = F_0/k - m\omega_{\mathrm{f}}^2$.

$$\begin{aligned}
x_{\mathrm{b}} &= [(F_0/(k - m\omega_{\mathrm{f}}^2)] \sin \omega_{\mathrm{f}} t \\
&= (F_0/k) \sin \omega_{\mathrm{f}} t / [1 - \omega_{\mathrm{f}}^2]/(k/m) \qquad\qquad (3.79) \\
&= (X_{\mathrm{ST}}/1 - \gamma_{\mathrm{f}}^2) \sin \omega_{\mathrm{f}} t \\
\text{and } x_{\mathrm{b}} &= X \sin \omega_{\mathrm{f}} t, \qquad\qquad\qquad\qquad (3.80)
\end{aligned}$$

where $\qquad \gamma_{\mathrm{f}} = \omega_{\mathrm{f}}/\omega$
$\qquad\qquad$ = the frequency ratio = $\dfrac{\text{forced frequency}}{\text{natural (free) frequency}}$,

$\qquad X_{\mathrm{ST}} = F_0/k$ = the static displacement of the spring due to a constant force F_0,

$$X = X_{\mathrm{ST}}/(1 - \gamma_{\mathrm{f}}^2) = \text{the amplitude of } x_{\mathrm{b}}. \qquad\qquad (3.81)$$
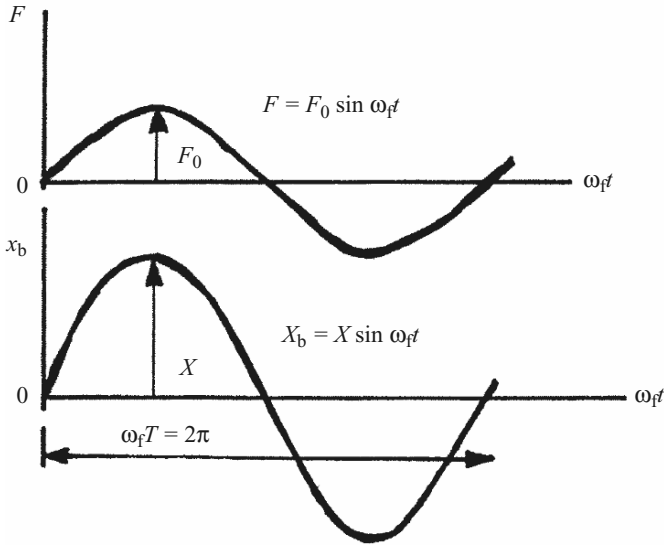
Fig. 3.14. Force and amplitude diagrams when $\gamma_f < 1$

Equation (3.80) is considered for the particular solution of x_b.

(1) $\gamma_f < 1$; $1 - \gamma_f^2 > 0$

  x_b is in phase with the force as shown in Fig. 3.14. The amplitude is given by

$$X = X_{ST}/(1 - \gamma_f^2); \qquad \gamma_f < 1. \tag{3.82}$$

(2) $\gamma_f > 1$; $1 - \gamma_f^2 < 0$

$$x_b = [X_{ST}/(\gamma_f^2 - 1)](-\sin\omega_f t) \tag{3.83}$$
$$= X(-\sin\omega_f t).$$

The positive amplitude X is given by

$$X = X_{ST}/(\gamma_f^2 - 1); \qquad \gamma_f > 1. \tag{3.84}$$

The motion is of opposite phase to the force as shown in Fig. 3.15.

(3) $\gamma_f = 1$; $\omega_f = \omega$.

  The resonant amplitude $X = X_{ST}/(1 - \gamma_f^2) \to \infty$ and resonance occurs. The solution for this case can be shown as

$$x_b = (-X_{ST}\omega_f t/2)\cos\omega_f t; \qquad \gamma_f = 1 \tag{3.85}$$

or

$$= (X_{ST}\omega_f t/2)\sin(\omega_f t - \pi/2). \tag{3.85a}$$
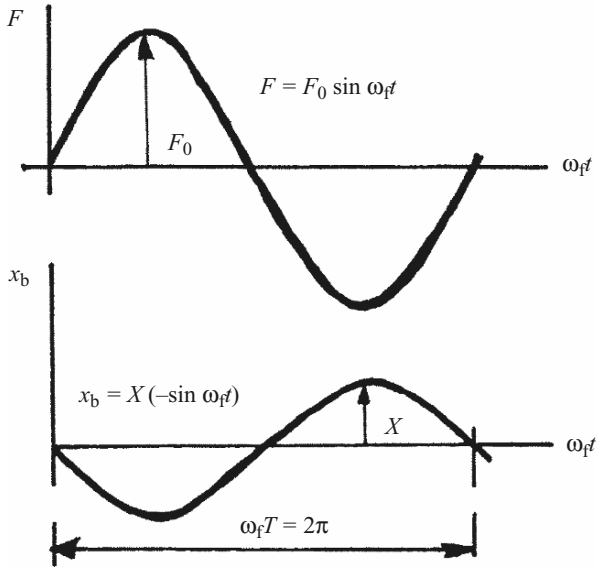
Fig. 3.15. Force and amplitude diagrams when $\gamma_f > 1$
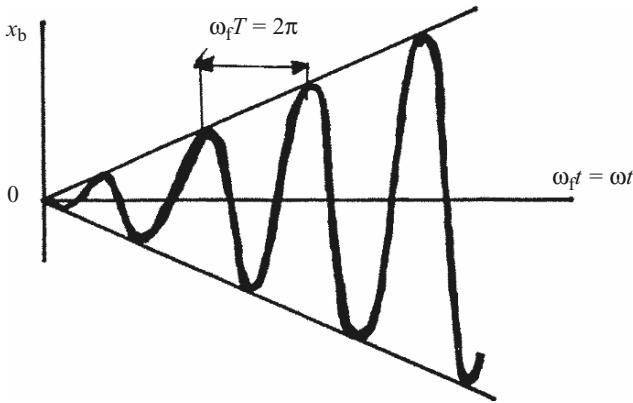
Fig. 3.16. Increase of amplitude with time

The motion is oscillating with an amplitude which increases with time, as shown in Fig. 3.16. The amplitude does not become large instantaneously but requires time to build up. The motion lags the force by 90°.

The discussion has been of the forced-motion part only of the complete solution defined by (3.75). The free-vibration part of the motion was covered in an earlier section.
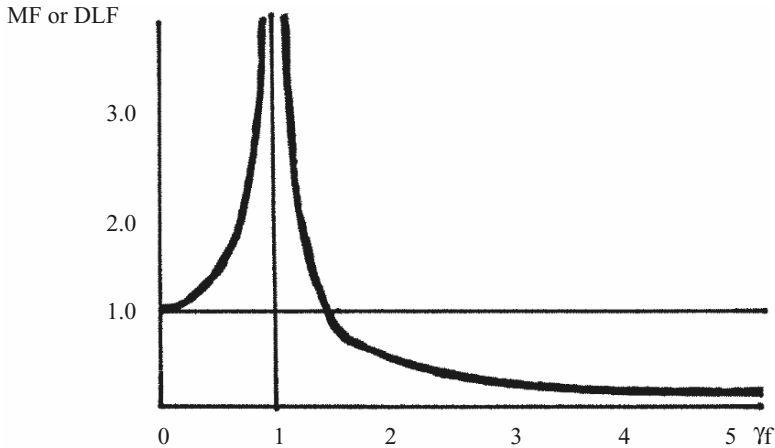
Fig. 3.17. Magnification factor (MF) vs. γ_f

(4) Forced-amplitude and magnification factor (MF):
For some purposes the amplitude of the forced motion is of great importance. The variation of the amplitude X with the frequency ratio γ_f can be studied, using the magnification factor MF (also called the dynamic load factor or DLF) defined as

$$MF = X/X_{ST} \tag{3.86}$$
$$= \text{forced amplitude/static deflection of spring,}$$
$$MF = X/X_{ST} = 1/(1 - \gamma_f^2) \qquad \gamma_f < 1$$

or

$$MF = X/X_{ST} = 1/(\gamma_f^2 - 1) \qquad \gamma_f > 1. \tag{3.87}$$

The diagram of MF against γ_f (Fig. 3.17) indicates that MF is greater than 1 in the range $\gamma_f = 0$ to $\gamma_f = 1$, approaching infinity as γ_f approaches 1. The resonant amplitude requires, however, some time to build up. The eventual large amplitude resulting from resonance is of great concern, since it may lead to the destruction of the system.

Since $\gamma_f = \omega_f/\omega$ and $\omega = \sqrt{(k/m)}$, γ_f can be changed by altering ω_f or m or k. It is proper to consider the effect on the amplitude if ω_f or m is changed; if k is altered, one should remember that not only does MF change but also X_{ST}.

(5) The complete solution and motion. The total motion is defined by $x = x_a + x_b$

$$x = X_a \sin(\omega_t + \phi) + [X_{ST}/(1 - \gamma_f^2)] \sin \omega_f t \text{ for } \gamma_f < 1, \tag{3.88}$$
$$x = X_a \sin(\omega_t + \phi) - [X_{ST}/\gamma_f^2 - 1] \sin \omega_f t \text{ for } \gamma_f > 1. \tag{3.89}$$
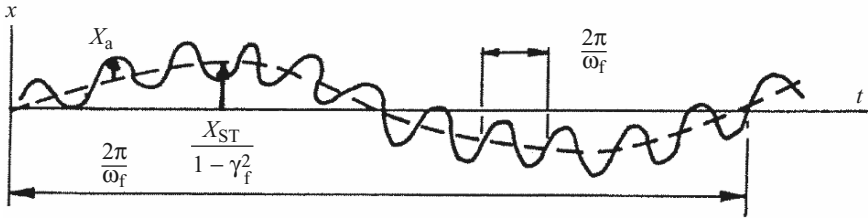
Fig. 3.18. Forced frequency smaller than natural frequency for x vs. t
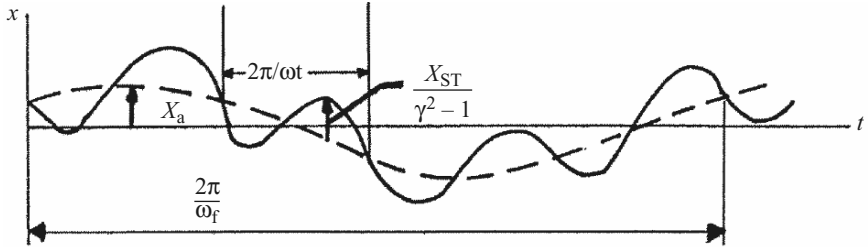
Fig. 3.19. Forced frequency greater than natural frequency for x vs. t

The complete solution is the sum of two sinusoidal curves of different frequency.

When the forced frequency is smaller than the natural frequency, the forced-motion part can be used as a basis for plotting the free-vibration part as shown in Fig. 3.18. When the forced frequency is greater than the natural frequency, the free-vibration part serves as the axis for the forced portion and is shown in Fig. 3.19.

The complete solution for the case of resonance is:

$$x = X_a \sin(\omega t + \phi) - (X_{ST}\omega_f t/2)\cos\omega_f t, \qquad \omega_f = \omega. \qquad (3.90)$$

This is the sum of a sine wave of constant amplitude and an oscillating curve having an increasing amplitude. In the early stages, the first part may be significant, but later the forced motion part becomes predominant.

Types of Pulse Load

The MFs for some common simple loading cases are discussed in this section.

Rectangular Pulse Load

A suddenly applied load F occurs with a constant duration t_{cd} and with no damping effects. The value of the displacement x is written as

$$x = F/k \, [\cos\omega(t - t_{cd})\cos\omega t]. \qquad (3.91)$$

F/k is the static deflection and x/δ_{ST} will define the value of MF.

$$\mathrm{MF} = 1 - \cos \omega t = 1 - \cos 2\pi(t/T) \text{ for } t \le t_{\mathrm{cd}},\qquad(3.92)$$
$$\mathrm{MF} = \cos 2\pi(t/T - t_{\mathrm{cd}}/T) - \cos 2\pi(t/T) \text{ for } t \ge t_{\mathrm{cd}},$$

where T is the natural period as before.

Triangular Pulse Load

Here the system is initially at rest when a load F is suddenly applied which decreases linearly to zero at time t_{cd}. The response is in two stages.

Stage 1: Response before t_{cd}
$t \le t_{\mathrm{cd}}$

$$x = \frac{F}{k}(1 - \cos \omega t) + \frac{F_1}{kt_{\mathrm{cd}}}[(\sin \omega t/\omega) - 1],\qquad(3.93)$$
$$\mathrm{MF} = 1 - \cos \omega t + (\sin \omega t/\omega t_{\mathrm{cd}}) - t/t_{\mathrm{cd}}.$$

Stage 2: Response after t_{cd}
$t \ge t_{\mathrm{cd}}$

$$x = \frac{F}{k\omega t_{\mathrm{cd}}}[\sin \omega t_{\mathrm{cd}} - \sin \omega(t - t_{\mathrm{cd}})] - \frac{F}{k} \cos \omega t,\qquad(3.94)$$
$$\mathrm{MF} = \frac{1}{\omega t_{\mathrm{cd}}}[\sin \omega t_{\mathrm{cd}} - \sin \omega(t - t_{\mathrm{cd}})] - \cos \omega t.$$

Figures 3.20 and 3.21 show design charts for rectangular and triangular pulses. The MF value is read once for a given load and the value of T is known. Table 3.10 gives a typical example with a finite time.

Constant Load with Finite Rise Time

Here is a load which has a finite rise time but remains constant thereafter. Let the rise time be t_{r}. The values of MF for two stages are given opposite.

Stage 1: Response before T_r

$$\mathrm{MF} = \frac{1}{t_{\mathrm{r}}}(t - \sin \omega t/\omega) \text{ for } t \le t_{\mathrm{r}}.\qquad(3.95)$$

Stage 2: Response after T_r

$$\mathrm{MF} = 1 + \frac{1}{\omega t_{\mathrm{r}}}[\sin \omega(t - tr) - \sin \omega t] \text{ for } t \ge t_{\mathrm{r}}.\qquad(3.96)$$
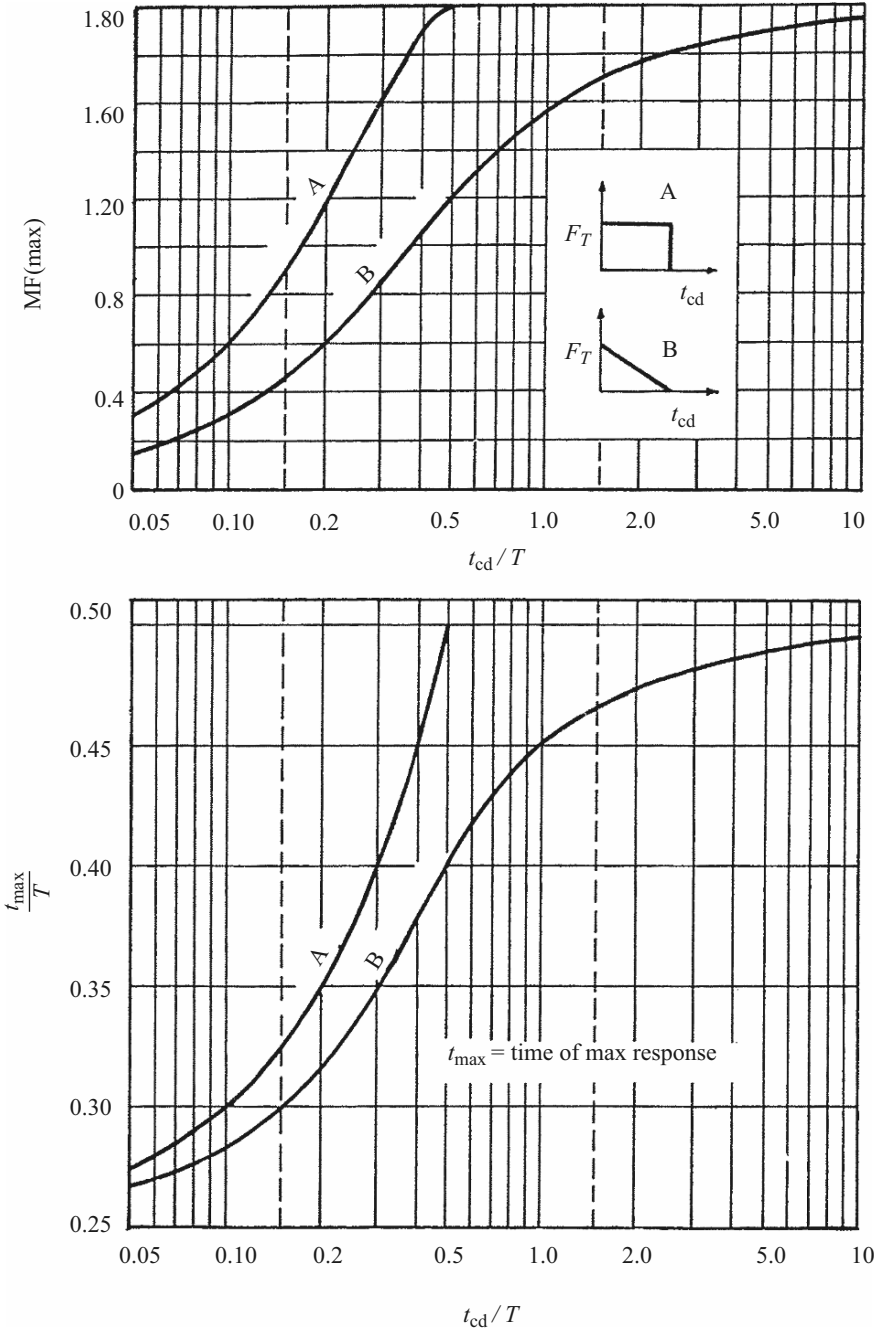
Fig. 3.20. Maximum response of single-degree elastic systems (undamped) subjected to rectangular and triangular load pulses having zero rise time (courtesy of the US Army Corps of Engineers)
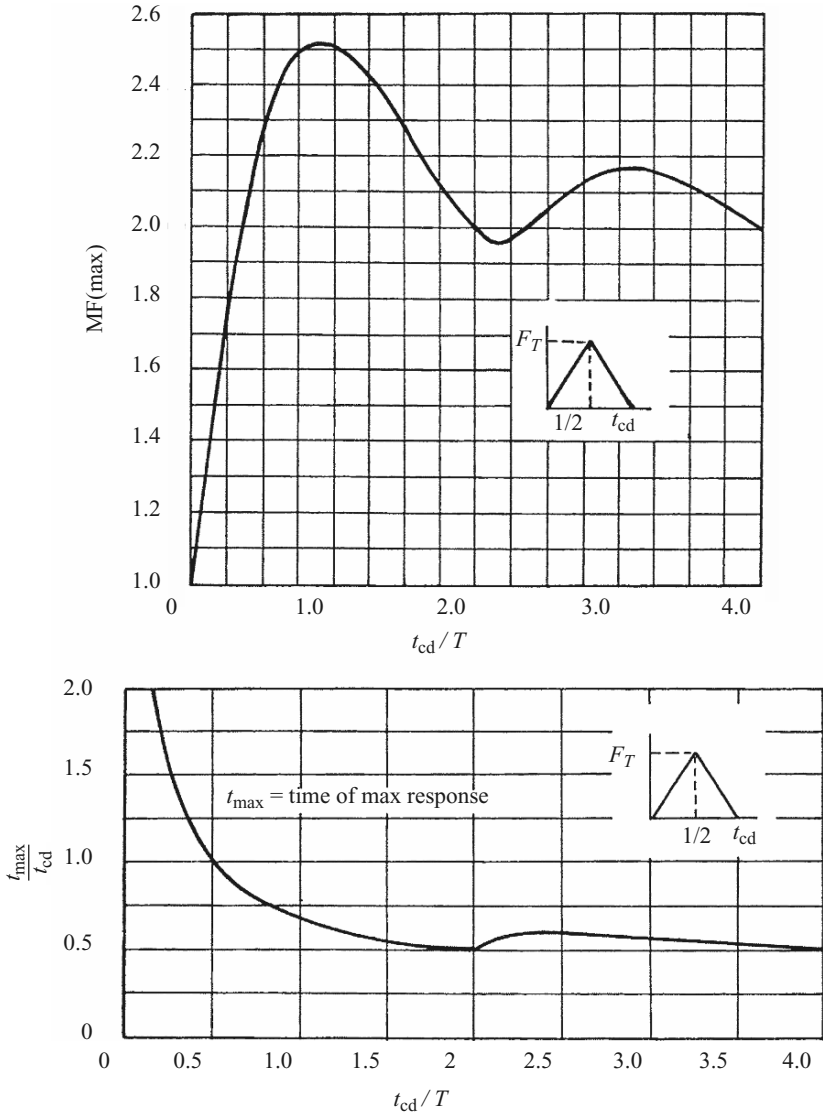
Fig. 3.21. Maximum response of single-degree elastic systems (undamped) subjected to an equilateral triangular load pulse (courtesy of US Army Corps of Engineers)

Figure 3.22 shows that when $t_r < 0.25T$, the reduction in the MF value below 2 is not significant. The loading is thus assumed to come on instantaneously. From the typical responses shown in Fig. 3.22, it can be deduced that T_r is large relative to t. Another example is that of an impulsive load of a triangular variation acting with a finite time, as shown in Table 3.11.

Table 3.10. Constant load with a finite time
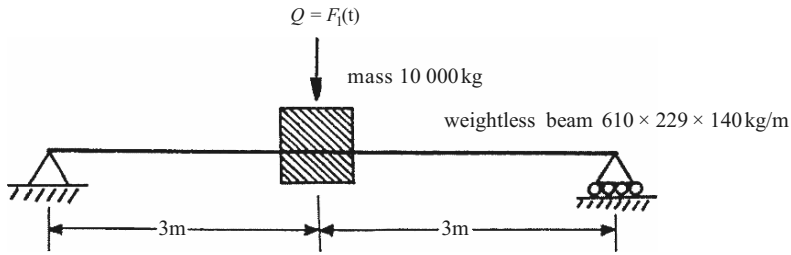
A steel beam, for which

$$L = 6\,\text{m},$$
$$t_{\text{r}} = 0.075\,\text{s},$$
$$I = 111{,}844\,\text{cm}^4,$$
$$Z_{\text{e}} = 3{,}626\,\text{cm}^3,$$
$$E = 200 \times 10^6\,\text{kN}\,\text{m}^{-2} = 200 \times 10^3\,\text{N}\,\text{mm}^{-2}$$
$$F_1 = 200\,\text{kN}.$$

The dynamic bending stress, σ_{dy}, is required.

$$
\begin{aligned}
k = \text{spring stiffness} &= 48EI/L^3 \\
&= 48 \times 200 \times 10^3 \times 111{,}844 \times 10^4/(6{,}000)^3 \\
&= 4{,}970{,}844.4\,\text{N}\,\text{mm}^{-1} \\
T = 2\pi \ \ \sqrt{(10{,}000/4{,}970{,}844.4)} &= 0.28.
\end{aligned}
$$

Using Fig. 3.22:

$$t_{\text{r}}/T = 0.075/0.28 = 0.268,$$

hence
$$t_{\text{max}}/t_{\text{r}} = 2.02,$$
$$(\text{MF})_{\text{max}} = 1.85,$$
$$
\begin{aligned}
\sigma_{\text{dy}} &= \sigma_{\text{ST}} \times (\text{MF})_{\text{max}} \\
&= M/Z (\text{MF})_{\text{max}} = [200 \times 600/(4 \times 3626)]\ (1.85) \\
&= 15.306\,\text{kN}\,\text{cm}^{-2} \\
&= 0.0015306\,\text{kN}\,\text{m}^{-2}.
\end{aligned}
$$

The time at which σ_{dy} occurs is

$$t_{\text{max}} = (t_{\text{max}}/t_{\text{r}})t_{\text{r}} = 2.02 \times 0.075 = 1.515\,\text{s} \approx 1.5\,\text{s}$$

3.2.5 Forced Vibrations with Viscous Damping (Harmonic Force)

Figure 3.23 shows a typical forced vibration system with viscous damping represented by a spring/dashpot combination. The equation of motion is written as
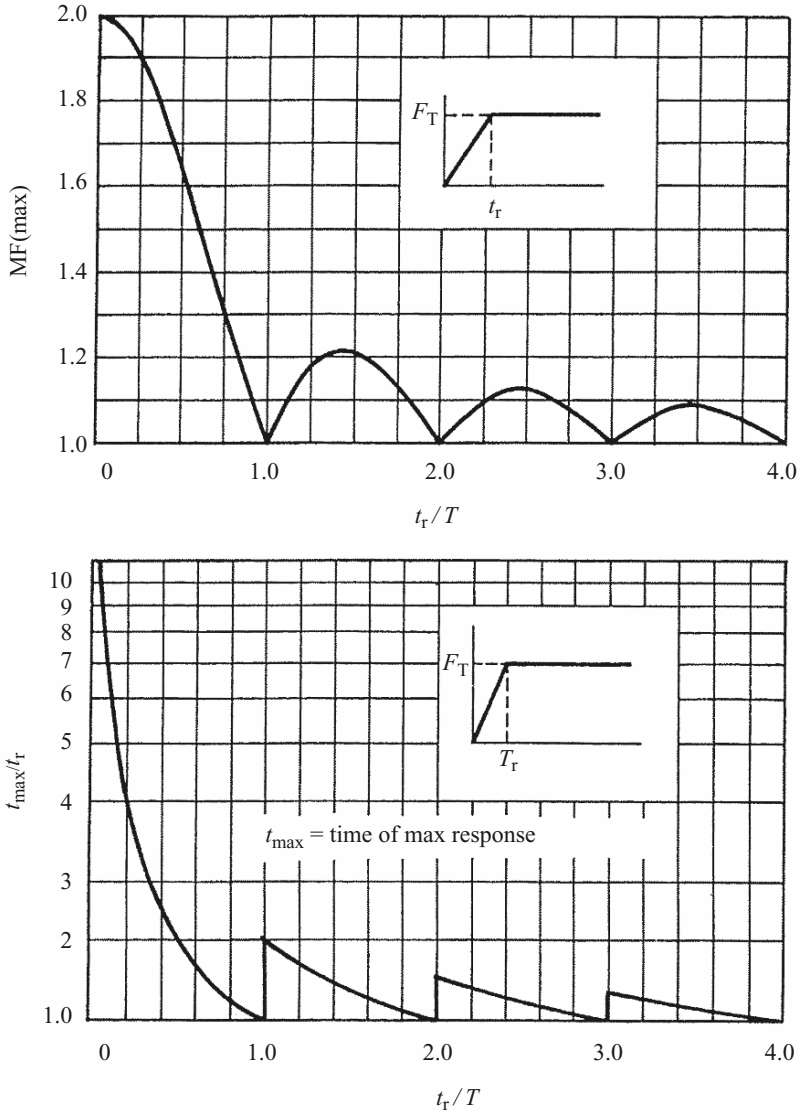
Fig. 3.22. Maximum response of single-degree elastic systems (undamped) subjected to a constant force with a finite rise time (courtesy of the US Army Corps of Engineers)

$$m\ddot{x} = -kx - c\dot{x} + F. \qquad (3.97)$$

After rearrangement of terms, the equation of motion becomes

$$m\ddot{x} + c\dot{x} + kx = F_0 \sin \omega_f t. \qquad (3.97a)$$

Table 3.11. Impulsive load with triangular variation

(a)   (b)
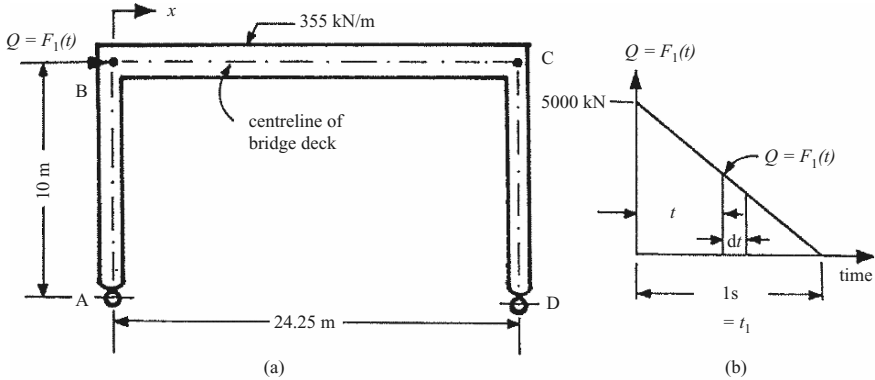
Figure (a) represents a cross-section of a concrete bridge. The bridge is subject to a time-dependent impulsive load $F(t)$ from a nearby explosion. If the impulsive load varies linearly in time, as shown in Fig. (b), determine the maximum displacement of the bridge and the dynamic shear in each pier. Use the following data:

$$I \text{ for each pier} = 1.09\,\mathrm{m}^4$$
$$E \text{ concrete} = 21\,\mathrm{GN\,m}^{-2};\ \mathbf{g} = 9.807\,\mathrm{m\,s}^{-2}$$
$$\text{Deck load} = 335\,\mathrm{kN\,m}^{-1}$$

Designation	t_0	t_1
Finite time t (s)	0.02	0.02
$F_I(t)$(kN) load	4,950	4,850
V (kN) shear resistance	100	350

$$\delta x = 1/m \int_{t=0}^{t=t_1} F(t)(t_1 - t)\mathrm{d}t.$$

The moment impulse relationship is given by

$$\delta \dot{x} = F_I(t)\frac{\mathrm{d}t}{m} - \frac{kx\mathrm{d}t}{m} = \frac{F_I(t) - V}{m} \times \delta t.$$
$$S = kx$$

Incremental impulse $[F_I(t) - V]\delta t = I_\mathrm{p}/m$

$$\dot{x} = \dot{x}_0 + \Sigma_i \delta \dot{x},$$
$$\partial x = \dot{x}\delta t,$$
$$W = 355 \times 24.25 = 8{,}532\,\mathrm{kN},$$

<div align="center">

Table 3.11. (continued)

</div>

$$\delta = FL^3/2(3EI),$$
$$\delta = 1; \ k = F = 6EI/L^3 = (6 \times 21 \times 10^6/10^3) \, (1.09) = 137{,}000 \, \mathrm{kN \, m^{-1}}$$
$$m = 8{,}532/9.872 \, \mathrm{m^2 \, s^{-1}} = 870 \, \mathrm{kN \, s^2 \, m^{-1}}.$$

Shear resistance V at $t = 0.02$
$$= 100 \, \mathrm{kN},$$
$$T = 2\pi \ \sqrt{(870/137000)} = 0.5 \, \mathrm{s},$$
$$F_\mathrm{I}(t) - S = 4950 - 100 = 4{,}850; \ \mathrm{factor} = F \times t = 4{,}850 \times 0.02 = 97,$$
$$\delta \dot{x} = 0.112; \ \dot{x} = 0.215; \ \delta x = 0.055 \times 0.02 = 0.0011,$$
$$V = 137{,}000 \times 0.0011 = 150 \, \mathrm{kN}.$$

The table gives an analysis independent of the charts
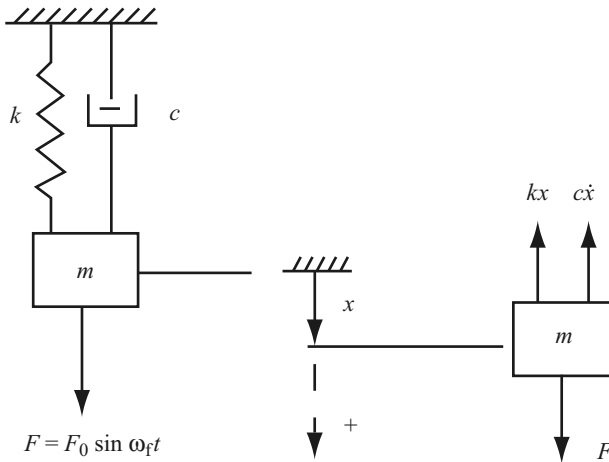
Fig. 3.23. Forced vibration with viscous damping

The solution is
$$x = x_\mathrm{a} + x_\mathrm{b},$$

where x_a is the complementary function for small damping:

$$x_\mathrm{a} = X'\mathrm{e}^{-\gamma \omega t} \sin(\omega_\mathrm{d} t + \phi)$$

decays with time to zero: *transient state*; x_b is the particular solution; the part of motion which will occur continuously, while the forcing is present; ω_f is the driving frequency: *steady state*.

Assume

$$x_b = M' \sin \omega_f t + N' \cos \omega_f t. \tag{3.98}$$

After substitution into (3.97) the following equation is derived:

$$-m\omega_f^2(M' \sin \omega_f t + N' \cos \omega_f t) + c\omega_f(M' \cos \omega_f t - N' \sin \omega_f t) +$$
$$k(M' \sin \omega_f t + N' \cos \omega_f t) = F_0 \sin \omega_f t. \tag{3.99}$$

Equating the coefficients of sine and cosine on the two sides:

$$(k - m\omega_f^2)M' - c\omega_f N' = F_0,$$
$$c\omega_f M' + (k - m\omega_f^2)N' = 0. \tag{3.100}$$

Solving for M' and N':

$$M' = (k - m\omega_f^2)F_0/[(k - m\omega_f^2)^2 + (c\omega_f)^2],$$
$$N' = -c\omega_f F_0/[k - m\omega_f^2)^2 + (c\omega_f)^2]. \tag{3.101}$$

Equation (3.98) can be written with trigonometric substitutions:

$$x_b = \sqrt{(M'^2 + N'^2)} \sin(\omega_f t - \phi),$$
$$\tan \phi = -N'/M'. \tag{3.102}$$

By substitution of (3.101) into (3.102), the values of x_b and m are obtained:

$$x_b = \{F_0/\sqrt{[(k - m\omega_f^2)^2 + (c\omega_f)^2]}\} \sin(\omega_f t - \phi),$$
$$\tan \phi = c\omega_f/(k - m\omega_f^2). \tag{3.103}$$

The following substitutions are made:

$$\frac{1}{k}(k - m\omega_f^2) = 1 - \frac{\omega_f^2}{k/m}$$
$$= 1 - \omega_f^2/\omega^2 = 1 - r_f^2,$$
$$\frac{1}{k}(c\omega_f) = [2c/2\sqrt{(mk)}][\omega_f/\sqrt{(k/m)}] = 2(c/c_c)(\omega_f/\omega) \tag{3.104}$$
$$= 2\gamma r_f.$$

Equation (3.103) can now be written as

$$x_b = X \sin(\omega_f t - \phi), \tag{3.105}$$

where

$$X = F_0/\sqrt{[(k - m\omega_f^2)^2 + (c\omega_f)^2]} \tag{3.106}$$
$$= (F_0/k)/\sqrt{[(k - m\omega_f^2/k)^2 + (c\omega_f/k)^2]}$$
$$= X_{\mathrm{ST}}/\sqrt{[(1 - r_f^2)^2 + (2\gamma r_f)^2]}$$

and

$$\tan\phi = c\omega_f/(k - m\omega_f^2) \tag{3.107}$$
$$= (c\omega_f/k)/(k - m\omega_f^2/k)$$
$$= 2\gamma r_f/(1 - r_f^2).$$

The particular solution of (3.105) is a steady-state motion of amplitude X, with the same frequency as the forcing condition, but it lags behind the force F by the phase angle ϕ, or by the time t' defined by:

$$t' = \phi/\omega_f. \tag{3.108}$$

Table 3.12 gives a typical example of a simple beam. Both the steady-state amplitude X and the phase angle m are dependent upon the damping factor γ_f and the frequency ratio r_f. The complete solution is:

$$x = X'e^{-\gamma\omega t}\sin(\omega_d t + \phi) + X\ \sin(\omega_f t - \phi), \tag{3.109}$$

where X and ϕ depend on the forcing condition as well as the physical constants of the system. The constants X' and ϕ can be determined from the initial displacement and velocity.

If the force ceases after steady-state motion has been attained, a free damped vibration will follow. Whether an immediate gain, a loss, or no change in amplitude occurs depends on when the force stops. Figure 3.24 shows force/time and displacement/time relationships.

Magnification Factor MF and Steady-State Amplitude X

The amplitude X of the steady-state motion is important in practice. The magnification factor MF is defined by:

$$\mathrm{MF} = X/X_{\mathrm{ST}} = 1/\sqrt{[(1 - r_f^2)^2 + (2\gamma r_f)^2]}. \tag{3.110}$$

MF plotted against $r_f = \omega_f/\omega$ for various damping ratios is shown in Fig. 3.25.

The maximum and minimum for MF are obtained when the derivative is set to zero:

$$\mathrm{d(MF)}/\mathrm{d}r_f = 0.$$

This results in

$$\frac{r_f(1 - r_f^2 - 2\gamma^2)}{[(1 - r_f^2)^2 + (2\gamma r_f)^2]^{3/2}} = 0, \tag{3.111}$$

Table 3.12. Forced vibrations with damping (single degree)
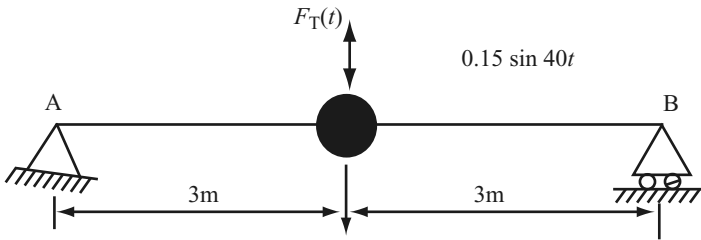
Determine the amplitude of vibration for the system shown in the diagram, for which the data are:

$$\text{length } L = 6\,\text{m},$$
$$\text{static load at mix-span} = 20\,\text{kN}$$

$$F = \text{vertical excited force} = 0.15 \sin 40t \text{ kN}$$
$$c = \text{damping coefficient} = 0.15$$
$$EI = 0.02 \times 10^6 \text{ kNm}^2,$$
$$\delta_{ST} = WL^3/48EI = 20 \times (6)^3/48 \times 0.02 \times 10^6 = 0.0045 \text{ m},$$
$$f_v = \text{vertical eigen frequency} = \frac{1}{2\pi}\sqrt{(k\,m^{-1})} = \frac{\sqrt{g}}{2\pi} \times \frac{1}{\sqrt{\delta_{ST}}},$$
$$g = 981 \text{ cm s}^{-2} = 9.81 \text{ m s}^{-2}$$
$$f_v = 5/\sqrt{\delta_{ST}} \text{ if } \delta_{ST} \text{ in cm}$$
$$\quad = 50/\sqrt{\delta_{ST}} \text{ if } \delta_{ST} \text{ in m}$$
$$\quad = 50/\sqrt{0.0045} = 745.36 \text{ cycles s}^{-1}$$
$$k = 20/0.0045 = 4444.45 \text{ kN m}^{-1}$$

Substituting in (3.106):

$$\omega_f = 2\pi(745.36) = 4685.12 \text{ cycles s}^{-1},$$
$$X = 20/4444.45 \times [1/\sqrt{\{[1 - (40)^2/(4685.12)^2]^2 + (0.15)^2/(4444.45)^2 \times (40)^2\}}$$
$$= 0.0045 \text{ m}.$$

Where the resonance $\omega_f = \omega$, for the maximum vibration case

$$X = 1.948 \text{ m}$$
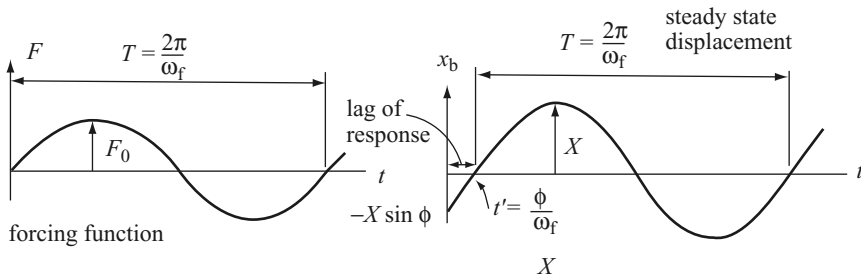
Fig. 3.24. Force/time and displacement/time diagrams
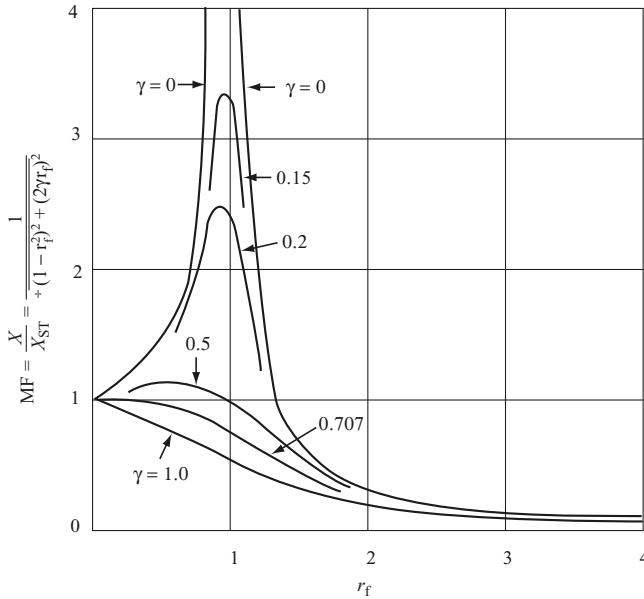
Fig. 3.25. MF versus r_{f}

which is satisfied by the following conditions:

(1) When $r_{\mathrm{f}} = 0$, this defines the starting point of the curves. This will be a minimum point provided that $\gamma < 0.707$. For $\gamma \geq 0.707$ it will be a maximum point.
(2) When $r = \infty$, this defines the final minimum point on each curve.
(3) For $(1 - r_{\mathrm{f}}^2 - 2\gamma^2) = 0$, which gives

$$r_{\mathrm{f}} = \sqrt{(1 - 2\gamma^2)}, \qquad (3.112)$$

for $1 - 2\gamma^2 > 0$, i.e. $\leq \sqrt{2}/2 = 0.707$. This last expression defines the maximum point in the *resonant* region. Since

$$r_{\mathrm{f}} = \sqrt{(1 - 2\gamma^2)} < 1, \qquad (3.113)$$

the peak of the curve occurs to the left of the resonant value of $r_{\mathrm{f}} = 1$.

The maximum amplitude can be determined by substituting (3.106) into the amplitude expression, resulting in:

$$X_{\max}/X_{\mathrm{ST}} = 1/[2\gamma\sqrt{(1 - \gamma^2)}] \qquad (3.114)$$

$$= \frac{1}{2}\gamma \quad \text{for } \gamma \ll 1. \qquad (3.115)$$

When damping occurs the maximum amplitude is limited to a finite value. For $\gamma \geq 0.707$ the maximum point occurs at $r_{\mathrm{f}} = 0$, and the curves drop continuously as r_{f} increases.

The family of curves indicates that a reduction in MF – and hence the amplitude – is obtained only in the region where r_f is large due to a high forcing frequency relative to the natural frequency of the system.

Figure 3.25 shows the effect of varying r_f upon the maximum displacement amplitude; the effect of varying r_f by changing ω_f only should be considered here. The conditions resulting from changing r_f by altering k and m (that is ω) require a separate discussion.

Phase Angle ϕ

The phase angle ϕ which is defined by (3.107), which is also related to $2Xr_f/(1 - \gamma_f^2)$, depends on the damping factor γ and the frequency ratio r_f. Plotting ϕ against r_f for various values of γ, families of curves are obtained, as shown in Fig. 3.26.
For no damping

$$\phi = 0° \text{ for } r_f = 0 \text{ to } r_f < 1,$$
$$\phi = 90° \text{ for } r_f = 1, \tag{3.116}$$
$$\phi = 180° \text{ for } r_f > 1.$$

For small values of γ, these conditions are approximated and the curves for small γ approach the curve for the zero-damping case.
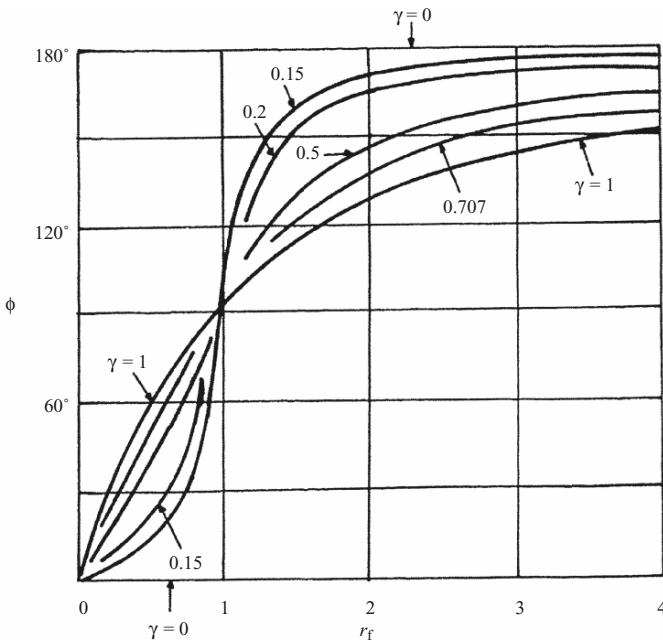
Fig. 3.26. ϕ versus r_f

Influence of Mass and Stiffness on Amplitude

In studying the effect of varying r_f upon the steady-state amplitude, recall that

$$r_f = \omega_f/\omega = \omega\,\sqrt{(m/k)}$$

and hence r_f can be varied by changing k or m as well as the driving frequency ω_f. However, if either k or m is changed, based on (3.45), this will alter γ, as

$$\gamma = c/2\sqrt{(mk)} = c/c_c$$

and distort the interpretation of Fig. 3.25, since a different γ-curve would then have to be used. In addition, altering k will change the value of the 'static' deflection X_{ST}.

While studying the effect of varying k, the amplitude relation given by (3.116) can be written in the form:

$$X = F_0/\sqrt{[(k - m\omega_f^2)^2 + (c\omega_f)^2]} \tag{3.117}$$

and X can then be plotted against k for different values of the damping coefficient c, as shown in Fig. 3.27. In this case F_0, m and ω_f are constant.

Maximum and minimum points on the curves can be obtained by setting $dX/dk = 0$. From this, it is found that the maximum point occurs for $k = m\omega_f^2$ and is defined by
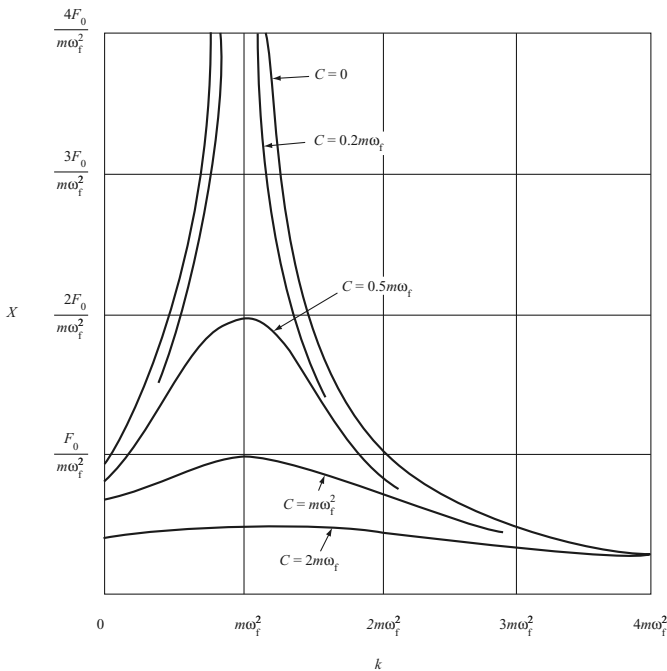
Fig. 3.27. X versus k

$$X_{\max} = F_0/c\omega_{\mathrm{f}}. \tag{3.118}$$

In addition, all the curves approach zero as k becomes large. The initial point (for $k = 0$) is given by

$$X = F_0/\sqrt{[(m\omega_{\mathrm{f}}^2)^2 + (c\omega_{\mathrm{f}})^2]}. \tag{3.119}$$

A reduction in amplitude is achieved only as k becomes large. This means that stiff springs will result in a small amplitude of motion for a given system.

The amplitude relation given by (3.133) can also be used to observe the effect of varying m upon the amplitude. In this case, X is plotted against m for various values of c, with F_0, k and ω_{f} being taken as constant. The resulting family of curves is shown in Fig. 3.28.

Maximum and minimum points on the curves can be determined by setting $\mathrm{d}X/\mathrm{d}m = 0$. The maximum point occurs at $m = k/\omega_{\mathrm{f}}^2$ and is given by

$$X_{\max} = F_0/c\omega_{\mathrm{f}}. \tag{3.120}$$

All the curves approach zero as m becomes large. The initial point (for $m = 0$) is given by

$$X = F_0/\sqrt{[k^2 + (c\omega_{\mathrm{f}})^2]}. \tag{3.121}$$

It is clearly indicated that large values of m result in a reduction in amplitude.
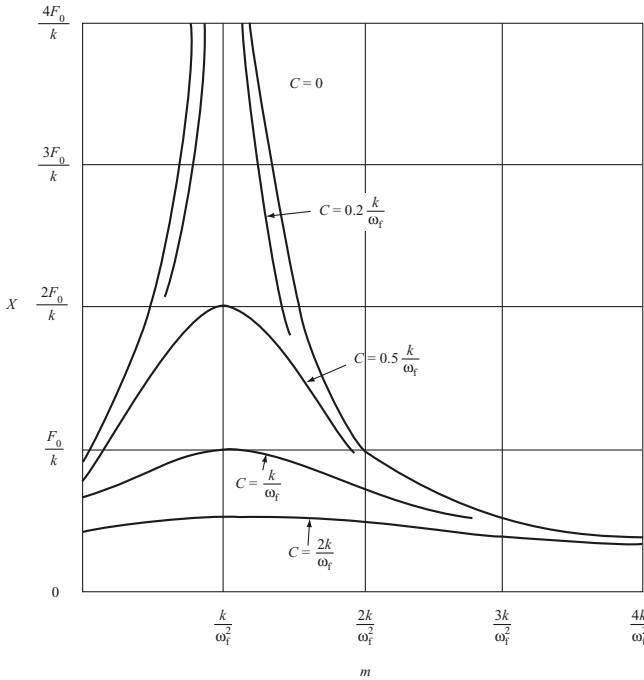
Fig. 3.28. X versus m

Mechanical Impedance Method

The equation of motion is given by (3.97). Since

$$F = F_0 e^{i\omega t} = F_0(\cos\omega_f t),\qquad(3.122)$$

then $\mathrm{Im}(F_0 e^{i\omega t})$ is the imaginary part of the solution. Let the displacement vector $X = X e^{i(\omega t - \phi)}$, the velocity and acceleration vectors will be $i\omega_f X$ and $-\omega^2 X$ respectively. Substituting these into (3.97) gives

$$(k - m\omega_f^2 + i c\omega_f)X e^{-i\phi} = F_0$$

or

$$X e^{-i\phi} = F_0/(k - m\omega_f^2 + i c\omega_f).\qquad(3.123)$$

However

$$X e^{-i\phi} = X(\cos\phi - i\sin\phi),\qquad(3.124)$$

where $\phi = \tan^{-1}\omega_f c/(k - m\omega_f^2)$. Hence (3.133) is derived, and

$$x_{\mathrm{b}} = \mathrm{Im}(X)\qquad(3.125)$$
$$= F_0 \sin(\omega_f t - \phi)/\sqrt{[(k - m\omega_f^2)^2 + (c\omega_f)^2]}.$$

The x_{a} value based on steady-state vibration is given earlier in (3.97).

3.2.5.1 Rotating Unbalance

The rotating unbalance is a common source of forced vibrations. Figure 3.29 shows such a system. The arm rotates with angular velocity $\omega_f\,\mathrm{rad\,s^{-1}}$. The angular position of the arm is defined by $\omega_f t$ with respect to the indicated horizontal datum.

Positive displacements x are assumed upwards. The horizontal motion of $(M_{\mathrm{T}} - m)$ is prevented by guides. The vertical displacement of m is $(x + e\sin\omega_f t)$. The differential equation of motion is written:

$$(M_{\mathrm{T}} - m)\frac{\mathrm{d}^2 x}{\mathrm{d}t^2} + m\frac{\mathrm{d}^2}{\mathrm{d}t^2}(x + e\sin\omega_f t)$$
$$= -kx - c\frac{\mathrm{d}x}{\mathrm{d}t}\qquad(3.126)$$

and rearranged

$$M_{\mathrm{T}}\ddot{x} + c\dot{x} + kx = me\omega_f^2\,\sin\omega_f t.\qquad(3.127)$$

Comparison with (3.97a) for motion forced by $F = F_0\sin\omega_f t$ enables the steady-state solution to be set down by analogy with (3.105) as

$$x = X\sin(\omega_f t - \phi),\qquad(3.128)$$
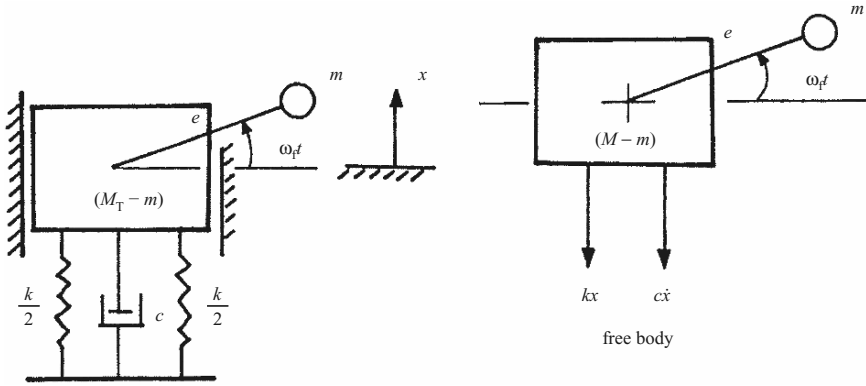
Fig. 3.29. Rotating unbalance and forced vibrations (M_T = total mass, m = eccentric mass and e = eccentricity of m)

where

$$X = \frac{me\omega_\mathrm{f}^2}{\sqrt{[(k - M_\mathrm{T}\omega_\mathrm{f}^2)^2 + (c\omega_\mathrm{f})^2}} \tag{3.129}$$

$$= \frac{\dfrac{me}{M}\omega_\mathrm{f}^2 \times \dfrac{M_\mathrm{T}}{k}}{\sqrt{[(k - M_\mathrm{T}\omega_\mathrm{f}^2/k)^2 + (c\omega_\mathrm{f}/k)^2]}} \tag{3.130}$$

$$= \frac{\dfrac{me}{M_\mathrm{T}} \times r_\mathrm{f}^2}{\sqrt{[(1 - r_\mathrm{f}^2)^2 + (2\gamma r_\mathrm{f})^2]}},$$

$$\frac{X}{me/M_\mathrm{T}} = \frac{r_\mathrm{f}^2}{\sqrt{[(1 - r_\mathrm{f}^2)2 + (2\gamma r_\mathrm{f})^2]}}, \tag{3.131}$$

$$\tan\phi = \frac{2\gamma r_\mathrm{f}}{1 - r_\mathrm{f}^2}. \tag{3.132}$$

Here $\omega = \sqrt{(k/M_\mathrm{T})}$ represents the natural circular frequency of the undamped system (including the mass m), but x defines the forced motion of the main mass $(M_T - m)$. For this case, ϕ will be represented physically by the angle of the eccentric arm relative to the horizontal datum of $\omega_\mathrm{f}t$. For a value of ϕ determined from (3.132) the arm would be at this angle when the main body is at its neutral position, moving upwards. Since the motion lags behind the driving force, the arm then leads the motion by the angle ϕ determined.

The steady-state amplitude is important, and it can be studied by plotting $X/(me/M_\mathrm{T})$ against the frequency ratio r_f for various values of the damping ratio γ, as shown in Fig. 3.30. Maximum and minimum points can be determined by setting
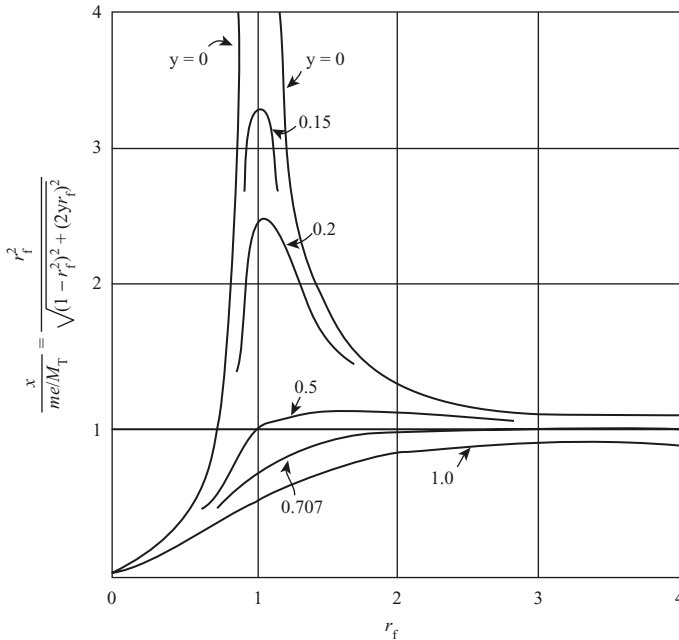
Fig. 3.30. $X/(me/M_T)$ vs. r_f values for the various values of γ

$$\frac{\mathrm{d}}{\mathrm{d}r_f}[X/(me/M)] = 0,$$

$$r_f = 1/\sqrt{(1 - 2\gamma^2)} > 1. \tag{3.133}$$

Accordingly, the peaks occur to the right of the resonance value of $r_f = 1$.

Figure 3.30 is adequate, provided that the variation in r_f is limited to changing ω_f. Note that small amplitude occurs only at low driving frequencies, as would be expected.

Since γ (as well as r_f) is dependent on k and M_T, Fig. 3.30 does not show properly the effect of varying k or M_T. The effect of varying these can be observed by writing the amplitude relation in the form given by (3.133). The amplitude X can then be plotted against either k or M_T for various values of the damping coefficient c. The resulting families of curves will be identical to those of Figs. 3.27 and 3.28, provided that m is replaced by M_T, and F_0 is replaced by $me\omega_f^2$. At resonance, (3.129) becomes:

$$X = me\omega_f/c. \tag{3.134}$$

It should be noted that the amplitude is dependent on the quantity 'em' and that if either m or e is small, the amplitude will become small. The eccentric condition should be reduced as far as possible.
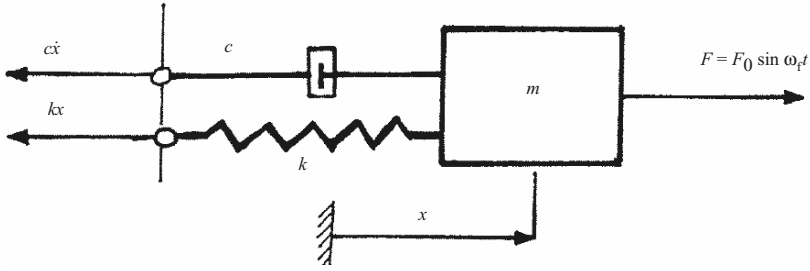
Fig. 3.31. Free-body diagram for force transmission

Force Transmission and Isolation

This section deals with the force transmitted to the support of the system. The force carried by the support is idealized by the spring and dashpot (Fig. 3.31) which are connected to it. The dynamic force F exerted on the system by the support is thus written in simple form as

$$F = kx + c\dot{x}. \tag{3.135}$$

For steady-state displacement, x and velocity $\dot{x}$ can be substituted from (3.105). This gives:

$$F = kX \sin(\omega_f t - \phi) + c\omega_f X \cos(\omega_f t - \phi), \tag{3.136}$$

where X and ϕ are defined by (3.106) and (3.107) respectively. Equation (3.136) can thus be rewritten, involving damping and frequency ratios, as

$$F = \sqrt{[kX^2 + (c\omega_f X^2)]} \ \sin(\omega_f t - \phi - \beta) \tag{3.137}$$
$$= \sqrt{[k^2 + (c\omega_f)^2]} X \sin(\omega_f t - \alpha),$$
$$\alpha = \phi + \beta \text{ and } \tan\beta = -c\omega_f/k = -2\gamma r_f. \tag{3.138}$$

The maximum force F_T, or *force amplitude*, transmitted will be

$$F_T = X\sqrt{[k^2 + (c\omega_f)^2]}$$
$$= F_0 \frac{\sqrt{[k^2 + (c\omega_f)^2]}}{\sqrt{[(k - m\omega_f^2)^2 + (c\omega_f)^2]}}. \tag{3.139}$$

Dividing numerator and denominator by k gives

$$F_T = F_0 \frac{\sqrt{[1 + (2\gamma r_f)^2]}}{\sqrt{[(1 - r_f^2)^2 + (2\gamma r_f)^2]}}. \tag{3.140}$$

The ratio F_T/F_0 is defined as the *transmissibility* or TR. Thus

$$TR = F_T/F_0 = \frac{\sqrt{[1 + (2\gamma r_f)^2]}}{\sqrt{[(1 - r_f^2)^2 + (2\gamma r_f)^2]}}. \tag{3.141}$$

Table 3.13 gives a typical example on a simple frame. The manner in which the transmitted force is influenced by the physical parameters of the system

Table 3.13. Transmissibility analysis
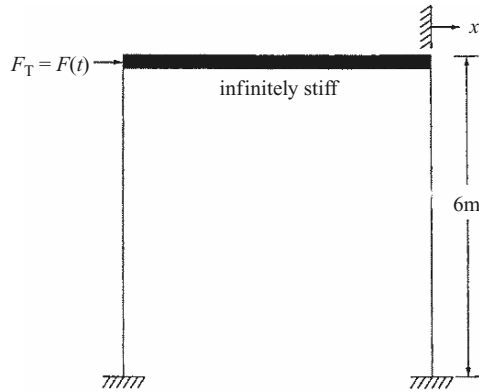
A frame shown in the figure is subjected to a sinusoidal ground motion of $250 \sin 5t$ at girder level. Calculate (1) the transmissibility of motion, (2) the maximum shear force in the columns of the frame and (3) the maximum bending stresses in the columns. Use the following data:

$$K \text{ (columns)} = 5{,}000 \,\mathrm{N\,mm^{-1}},$$
$$\gamma = 0.05,$$
$$\omega = 7.38 \,\mathrm{rad\,s^{-1}},$$
$$\omega_\mathrm{f} = 5.32 \,\mathrm{rad\,s^{-1}}$$
$$r_\mathrm{f} = 5.32/7.38 = 0.721$$
$$F_0/k = 250/5{,}000 = 0.05 \,\mathrm{mm}$$

$X = $ steady-state amplitude

$$= \frac{0.05}{\sqrt{\{[1 - (0.721)^2]^2 + (2 \times 0.05 \times 0.721)^2\}}}$$

$$= 0.103 \,\mathrm{mm}.$$

(1) $$\mathrm{TR} = \frac{\sqrt{[1 + (2\gamma r_\mathrm{f})^2]}}{\sqrt{[(1 - r_\mathrm{f}^2)^2 + (2\gamma r_\mathrm{f})^2]}}$$

$$= \frac{\sqrt{[1 + (2 \times 0.05 \times 0.721)}}{\sqrt{\{[1 - (0.721)^2]^2 + (2 \times 0.05 \times 0.721)^2\}}}$$

$$= \frac{\sqrt{(1 + 0.0051984)}}{\sqrt{0.235751}} = 2.065.$$

The relative displacement $= 0.25(0.721)^2 = 0.13 \,\mathrm{mm}$.
(2) Maximum shear force $= 5000 \times 0.13/2 = 325 \,\mathrm{N}$.
(3) Maximum bending stress $= 325 \times 6 \times 1{,}000$
$$= 195 \times 10^4 \,\mathrm{N\,mm}$$
$$= 1.95 \,\mathrm{kN\,m}.$$
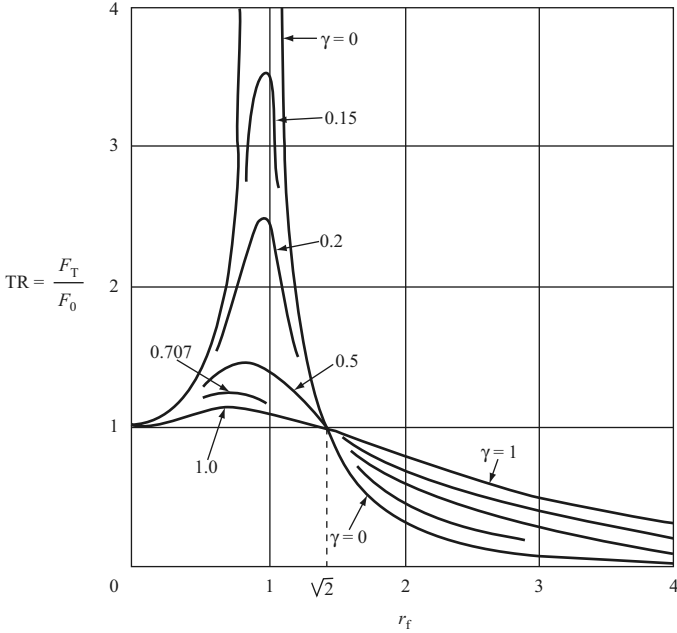
Fig. 3.32. Relationship between TR and r_f

can be shown by plotting TR against r_f for various values of the damping ratio γ, as shown in Fig. 3.32. All curves start at TR = 1 for $r_f = 0$. There is a common point, or cross-over, at $r_f = \sqrt{2}$. While damping cuts down the peak force transmitted in the resonant region, it results in greater force transmission for $r_f > \sqrt{2}$. This latter effect is opposed to the influence which the damping increase has in reducing the displacement amplitude, for larger values of r_f, as indicated by Fig. 3.25. It can be shown that the peak of the curve occurs at

$$r_f = \sqrt{[-1 + \sqrt{(1 + 8\gamma^2)}]/2\gamma} < 1. \tag{3.142}$$

Figure 3.32 should be used only in conditions in which F_0 is constant and r_f is varied by changing ω_f only.

If it is required to observe the effect of varying the spring stiffness k, (3.139) can be used to plot TR against k for various values of the damping coefficient c. The transmissibility is then expressed by

$$\begin{aligned}
\text{TR} &= F_T/F_0 \\
&= \frac{\sqrt{[k^2 + (c\omega_f)^2]}}{\sqrt{[(k - m\omega_f^2)^2 + (c\omega_f)^2]}}.
\end{aligned} \tag{3.143}$$

Several curves are drawn in Fig. 3.33 relating k and TR. The initial value of TR and cross-over point can now easily be determined, together with the
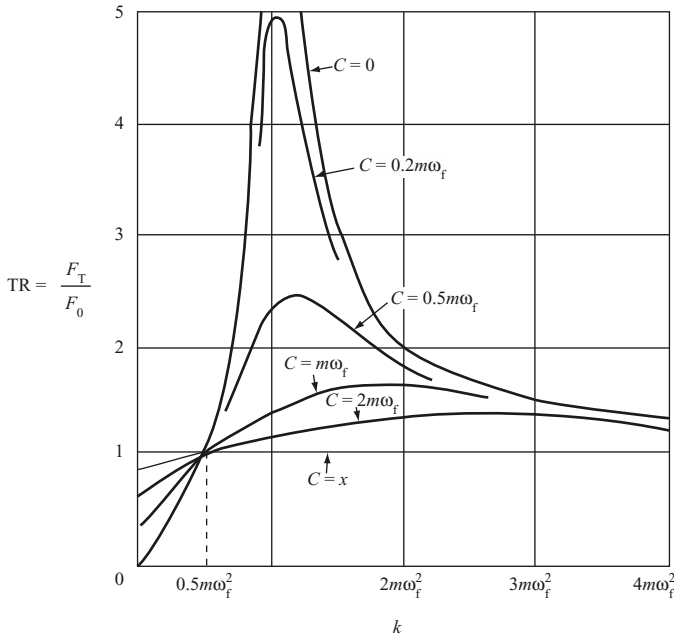
Fig. 3.33. Relationship between TR and k

trend of the curves in approaching $TR = 1$ for large values of k. The peak value from (3.145) gives the value of k:

$$k = m\omega_f^2/2 + \sqrt{[(m\omega_f^2)^2 + (c\omega_f)^2]}. \qquad (3.144)$$

This will be greater than $m\omega_f^2$ if $c \neq 0$. Therefore, the peak will occur to the right of the $k = m\omega_f^2$ value. An appreciable reduction in the transmitted force is achieved only in the region for which $k < m\omega_f^2/2$ with light damping and small spring stiffness.

The effect of varying the mass m can also be determined from (3.143) by plotting TR against m for various values of c. This is shown in Fig. 3.34. Here, the peak value occurs at $m = k/\omega_f^2$ and is written as

$$TR_{\max} = \sqrt{[k^2 + (c\omega_f)^2]}/c\omega_f. \qquad (3.145)$$

A reduction in the transmitted force occurs only in the region where m is large. This might not be expected. It is important to note that an increase in the mass m will, however, also result in an increase in the static force carried by the support.

The Force Transmitted for the Case of a Rotating Eccentric Mass m

The relation for F_T can be obtained by substituting $me\omega_f^2$ for F_0 in (3.139) and (3.140).
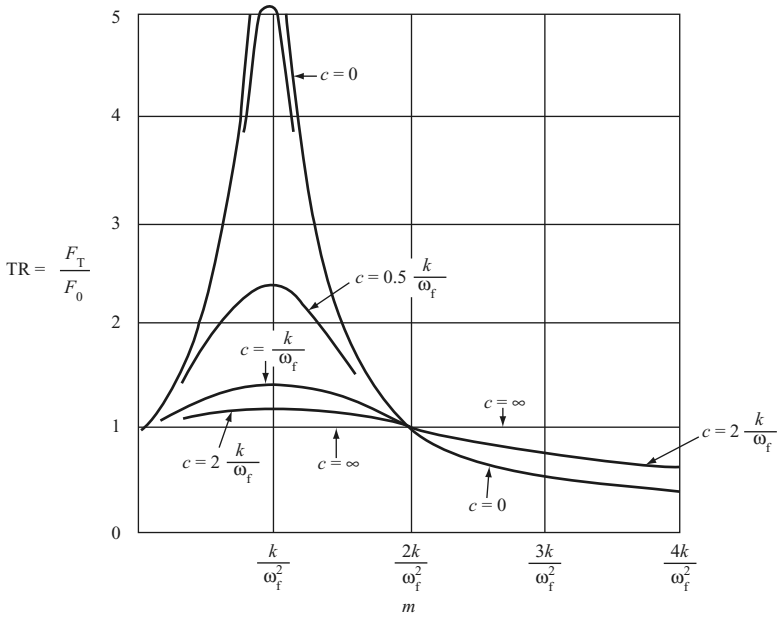
Fig. 3.34. Relationship between TR and m

$$F(t) = F_T$$

$$= me\omega_f^2 \frac{\sqrt{[k^2 + (c\omega_f)^2]}}{\sqrt{[(k - M_T\omega_f^2)^2 + (c\omega_f)^2]}} \tag{3.146}$$

$$= me\omega_f^2 \frac{\sqrt{[1 + (2\gamma r_f)^2]}}{\sqrt{[(1 - r_f^2)^2 + (2\gamma r_f)^2]}}. \tag{3.147}$$

After multiplying the numerator and denominator by k/M_T, followed by rearrangement, F_T becomes

$$F(t) = F_T = (mek/M_T) \times r_f^2 \frac{\sqrt{[1 + (2\gamma r_f)^2]}}{\sqrt{[(1 - r_f^2)^2 + (2\gamma r_f)^2]}}, \tag{3.148}$$

hence

$$F_T/(mek/M_T) = r_f^2 \frac{\sqrt{[1 + (2\gamma r_f)^2]}}{\sqrt{[(1 - r_f^2)^2 + (2\gamma r_f)^2]}}. \tag{3.149}$$

The effect of varying ω_f upon the transmitted force can be shown by plotting $F_T/(mek/M_T)$ against r_f for various values of the damping ratio γ. In so doing, k and M_T are taken as constant. The reference mek/M_T is then fixed. The curves obtained are shown in Fig. 3.35.

Damping serves to limit the transmitted force in the region of resonance. A cross-over point occurs at $r_f = \sqrt{2}$, for which $F_T/(mek/M_T)$ has a value of 2. For no damping the curve approaches a value of 1 as r_f approaches infinity.
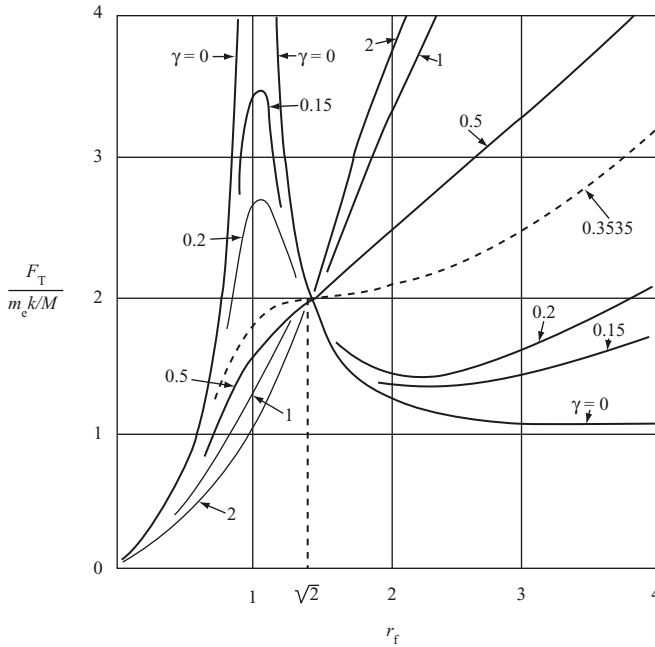
Fig. 3.35. Relationship between $F_T/(m_e k/M)$ and r_f

When damping is present, the force becomes very large as r_f increases, and the greater the damping is, the more rapidly this occurs. Even for small damping, the increase in transmitted force is significant. Since frequency ratios of 10 or more are quite common, the importance of considering damping is evident. The maximum and minimum points for the family of curves are determined by setting

$$\frac{d}{dr_f}[F_T/(m_e k/M_T)] = 0.$$

The following boundary conditions are noted:

(1) For $r_f = 0$; this defines the initial point of $F_T/(m_e k/M_T) = 0$ for all curves.
(2) By the roots of the relation

$$2\gamma^2 r_f^6 + (16\gamma^4 - 8\gamma^2)r_f^4 + (8\gamma^2 - 1)r_f^2 + 1 = 0, \qquad (3.150)$$

if $0 < \gamma < \sqrt{2}/4$ there are two positive real roots of this relation. One of these will be between $r_f = 0$ and $r_f = \sqrt{2}$, and will define a maximum point on the curve. The other will be $r_f > \sqrt{2}$ and will define a minimum point on the curve. If $\gamma > \sqrt{2}/4$ there is no maximum point on the curve.

If it is required to determine the effect of varying k and M_T upon the transmitted force, this can be done by using (3.147). After rearrangement, the following relations are established:

$$F_T/me\omega_f^2 = \frac{\sqrt{[k^2 + (c\omega_f)^2]}}{\sqrt{[(k - M_T\omega_f^2)^2 + (c\omega_f)^2]}}. \tag{3.151}$$

Since the forcing frequency ω_f, the mass m and the eccentricity e are to be held constant, this case becomes identical to those shown in Figs. 3.33 and 3.34, provided that m is replaced by M_T.

At resonance, (3.147) reduces to

$$F(t) = F_T = \frac{me\omega_f}{c} \times \sqrt{(k^2 + \omega_f^2)}$$

$$= X_{res} \sqrt{[k^2 + (c\omega_f)^2]}. \tag{3.152}$$

Oscillating Support

The oscillating support is a common cause of forced motion of a system. The following steps are taken using Fig. 3.36:

(1) Displacement of the support $y = y_0 \sin \omega_f t$. $\tag{3.153}$
(2) Displacement of the mass (assume $x > y$ and $\dot{x} > \dot{y}$).
(3) The equation of motion is written as

$$m\ddot{x} = -k(x - y) - c(\dot{x} - \dot{y}) \tag{3.153a}$$

or

$$m\ddot{x} + c\dot{x} + kx = ky + c\dot{y}$$

$$= ky_0 \sin \omega_f t + c\omega_f y_0 \cos \omega_f t \tag{3.154}$$

$$= y_0\sqrt{[k^2 + (c\omega_f)^2]} \sin(\omega_f t - \beta)$$

as before

$$\tan \beta = -c\omega_f/k = -2\gamma r_f. \tag{3.155}$$
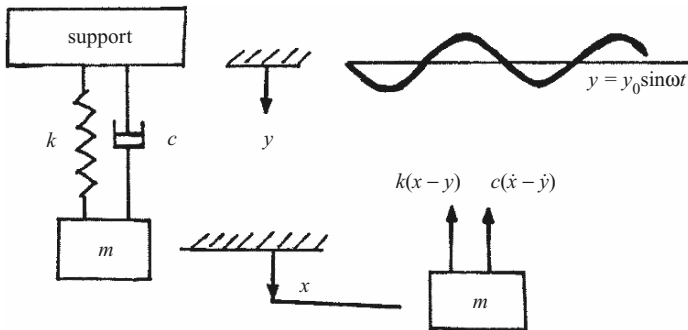
Fig. 3.36. Oscillating support

This type of force is represented by the right-hand side of (3.154); the forcing amplitude would be

$$y_0\sqrt{[k^2 + (c\omega_f)^2]}.$$

From (3.105), (3.106) and (3.107) the steady-state solution is

$$
\begin{aligned}
x &= \frac{y_0\sqrt{[k^2 + (c\omega_f)^2]}}{\sqrt{[(k - m\omega_f^2)^2 + (c\omega_f)^2]}} \times \sin(\omega_f t - \phi) \\
&= \frac{y_0\sqrt{[1 + (2\gamma r_f)^2]}}{\sqrt{[(1 - r_f^2)^2 + (2\gamma r_f)^2]}} \times \sin(\omega_f t - \phi) \qquad (3.156) \\
&= X\sin(\omega_f t - \phi),
\end{aligned}
$$

where $X = $ amplitude

$$
= \frac{y_0\sqrt{[1 + (2\gamma r_f)^2]}}{\sqrt{[(1 - r_f^2)^2 + (2\gamma r_f)^2]}}, \qquad (3.157)
$$

$$
\tan\phi = \frac{2\gamma r_f}{1 - r_f^2}. \qquad (3.158)
$$

(4) The force carried by the support is defined as

$$F = k(k - y) + c(\dot{x} - \dot{y})$$
$$\text{and } F = -m\ddot{x}.$$

Using the value of x of (3.156), the force carried by the support becomes

$$
\begin{aligned}
F &= m\omega_f^2 X\sin[\omega_f^2 - (\phi + \beta)] \qquad (3.159) \\
&= m\omega_f^2 y_0 \times \frac{\sqrt{[1 + (2\gamma r_f)^2]}}{\sqrt{[(1 - r_f^2)^2 + (2\gamma r_f)^2]}} \times \sin[\omega_f t - (\phi + \beta)] \\
&= \frac{y_0 k m\omega_f^2}{k} \times \frac{\sqrt{[1 + (2\gamma r_f)^2]}}{\sqrt{[(1 - r_f^2)^2 + (2\gamma r_f)^2]}} \times \sin[\omega_f t - (\phi + \beta)] \\
&= y_0 k \times \frac{r_f^2\sqrt{[1 + (2\gamma r_f)^2]}}{\sqrt{[(1 - r_f^2)^2 + (2\gamma r_f)^2]}} \times \sin[\omega_f t - (\phi + \beta)] \\
&= F_T\sin[\omega_f t - (\phi + \beta)], \qquad (3.160)
\end{aligned}
$$

$$
F_T = y_0 k \times \frac{\sqrt{[1 + (2\gamma r_f)^2]}}{\sqrt{[(1 - r_f^2)^2 + (2\gamma r_f)^2]}}. \qquad (3.161)
$$

This value of F_T is the amplitude of the force with a maximum value. It is in phase with m. The displacement amplitude can be studied from (3.161) arranged as

$$X/y_0 = \sqrt{[1 + (2\gamma r_f)^2]}/\sqrt{[(1 - r_f^2)^2 + (2\gamma r_f)^2]}. \qquad (3.162)$$

The transmitted force can be studied by the following arrangement:

$$F_T/y_0 k = \frac{r_f^2\sqrt{[1+(2\gamma r_f)^2]}}{\sqrt{[(1-r_f^2)^2+(2\gamma r_f)^2]}}. \tag{3.163}$$

This is the same expression as (3.149) plotted in Fig. 3.35. At resonance, (3.157) reduces to

$$X = y_0\sqrt{[1+(2\gamma)^2]}/2\gamma. \tag{3.164}$$

Energy Considerations for Forced Motion

In the case of forced motion, energy is introduced by the positive work done by the driving force during each cycle. In the case of steady-state motion, this energy is equal to the energy dissipated by damping in each cycle:

energy input = energy dissipated by viscous damping.

Energy Input for Harmonic Force Per Cycle: E_{er}

The following steps are taken:

(1) Harmonic force $F = F_0 \sin\omega_f t$
(2) Steady-state motion for viscous damping

$$x = X\sin(\omega_f t - \phi),$$

hence

$$\mathrm{d}x = X\omega_f \cos(\omega_f t - \phi)\mathrm{d}t$$

(3) Energy input/cycle $= E_{er} = \int F_T \mathrm{d}x$

$$E_{er} = \int F\mathrm{d}x$$

$$= \int_0^T F_0 \sin\omega_f t X\omega_f \cos(\omega_f t - \phi)\mathrm{d}t$$

$$= F_0 X\omega_f \int_0^{2\pi/\omega} \sin\omega_f t(\cos\omega_f t\cos\phi + \sin\phi)\mathrm{d}t$$

$$= F_0 X\omega_f \int [\cos\phi(\sin\omega_f t\cos\omega_f t + \sin\phi(\sin^2\omega_f t)]\mathrm{d}t$$

$$= F_0 X\omega_f[\cos\phi(\sin^2\omega_f t/2\omega_f) + \sin\phi t/2 - (\sin\omega_f t\cos\omega_f t/2\omega_f)]_0^{2\pi/\omega},$$

$$E_{er} = \pi F_0 X \sin\phi. \tag{3.165}$$

The maximum energy input occurs at resonance, for $\phi = 90°$

$$E_{er} = \pi F_0 X \tag{3.165a}$$

Energy Dissipated by Viscous Damping Per Cycle: E''_{VD}

The following steps are taken:

(1) Damping force $F_d = -c\dot{x}$.
(2) Steady-state motion $x = X\sin(\omega_f t - \phi)$,

$$\text{hence } dx = X\omega_f \cos(\omega_f t - \phi)dt$$
$$\text{and } \dot{x} = X\omega_f \cos(\omega_f t - \phi),$$

$$E''_{VD} = \int F_1(t)dx = \int (c\dot{x})dx$$
$$= c(\omega_f X)^2 \int_0^{2\pi/\omega} \cos^2(\omega_f t - \phi)dt$$
$$= c(\omega_f X)^2 \{(t/2) + [\sin(\omega_f t - \phi)\cos(\omega_f t - \phi)/2\omega_f]\}^{2\pi/\omega_f}$$
$$= \pi c\omega_f X^2. \tag{3.166}$$

Hence the energy dissipated per cycle is proportional to the square of the amplitude.

Boundary Conditions

The vector force diagrams give an understanding of the behaviour of the system in the three regions of the frequency ratio r_f, where

$$r_f = \omega_f/\omega = \frac{\text{forcing frequency}}{\text{natural free frequency}}.$$

(1) When $\omega_f \ll 1$, damping and inertial forces are small and the elastic forces are predominant. The elastic force is nearly equal to the disturbing force and the disturbing force is nearly in phase with the displacement. There is a small phase angle, as shown in Fig. 3.37.
(2) When $r_f = 1$, at resonance the phase angle is 90° and the inertial force is now larger. The elastic and inertial forces are balanced. The applied force is balanced by the damping force. For small damping coefficients c, the amplitude may be very large, as shown in Fig. 3.38.
(3) When $r_f \gg 1$, (Fig. 3.39) at high impressed frequencies the inertial force predominates and becomes nearly equal to the disturbing force. The latter is nearly in phase with the acceleration and the phase angle tends to be close to 180°.

Rotating Vectors and Harmonically Forced Vibrations

The differential equation of the motion equation (3.97) can be presented in the form given below when the steady-state solution and its derivatives are substituted:

$$x = X\sin(\omega_f t - \phi), \tag{3.167}$$
$$\dot{x} = \omega_f X\cos(\omega_f t - \phi) = \omega_f X\sin(\omega_f t - \phi + \pi/2), \tag{3.167a}$$
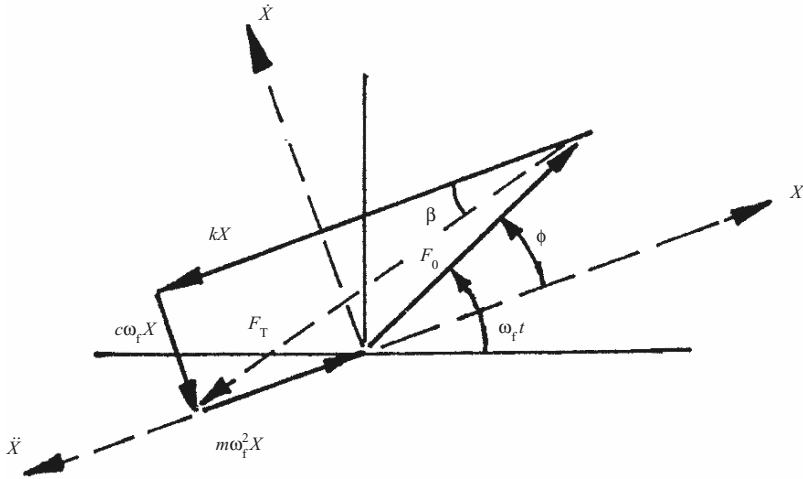
Fig. 3.37. Frequency ratio $r_f \ll 1$
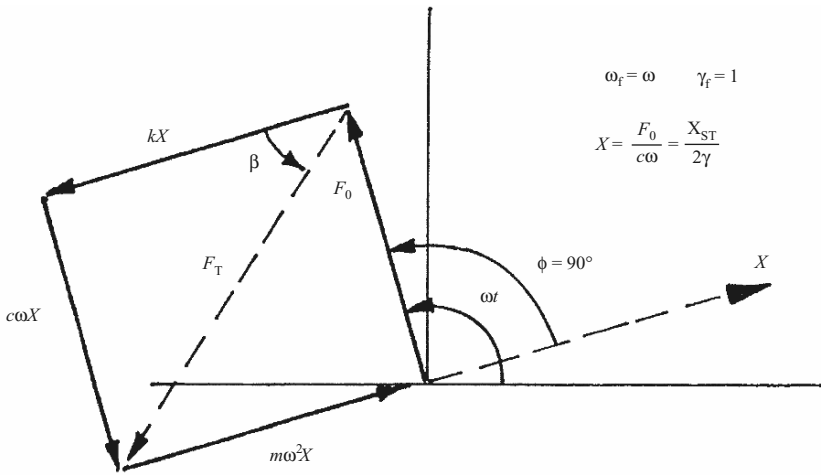
Fig. 3.38. Frequency ratio $r_f = 1$

$$\ddot{x} = -\omega_f^2 X \sin(\omega_f t - \phi) = \omega_f^2 X \sin(\omega_f t - \phi + \pi),$$
$$m\omega_f^2 X \sin(\omega_f t - \phi) - c\omega_f X \sin(\omega_f t - \phi + \pi/2) - kX \sin(\omega_f t - \phi)$$
$$+ F_0 \sin \omega_f t = 0. \tag{3.168}$$

This vector relation can be interpreted as follows:

Inertial force + damping force + restoring force + disturbing force = 0
and the vector relation is shown graphically in Fig. 3.40.
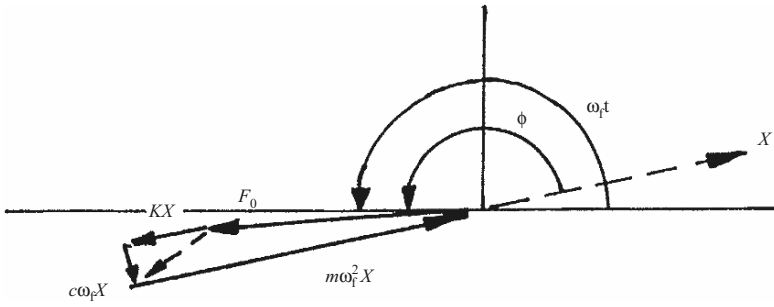
Fig. 3.39. Frequency ratio $r_f \gg 1$
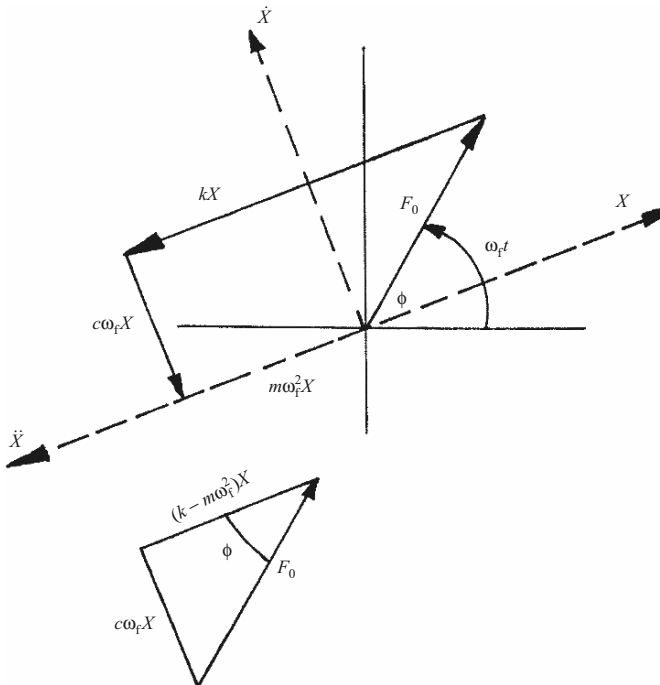
Fig. 3.40. Rotating vectors for harmonically forced vibrations

Resulting cases:

(1) The displacement lags the disturbing force by the angle ϕ, which can vary between $0°$ and $180°$.
(2) The restoration of the elastic force is always opposite in direction to the displacement.
(3) The damping force lags the displacement by $90°$ and hence is opposite in direction to the velocity.

(4) The inertial force is in phase with the displacement and opposite in direction to the acceleration.

(5) The vectors remain fixed with respect to each other and rotate together with angular velocity ω_f.

For example, the right-angled triangle in Fig. 3.40 shows:

$$X = F_0 / \sqrt{[(k - m\omega_f^2)^2 + (c\omega_f)^2]},$$
$$\tan \phi = c\omega_f / (k - m\omega_f^2). \tag{3.169}$$

This relation was put into non-dimensional form in (3.106) and (3.113) and yielded the concept of the MF given by (3.110).

3.2.6 Single-Degree Undamped Elasto-Plastic System

A single-degree undamped elasto-plastic system is assumed to have the bilinear resistance function shown in Fig. 3.41. The response solution due to a suddenly applied constant load is divided into three stages:

(1) The response up to the elastic limit x_{el}
(2) The plastic response between x_{el} and the maximum displacement
(3) The rebound after (2), when the displacement begins to decrease

Stage 1

First response $x \leq x_{el}$; the initial velocity and displacements are zero.

$$x = \delta_{ST}(1 - \cos \omega t),$$
$$\dot{x} = \delta_{ST}\omega \sin \omega t, \tag{3.170}$$

where $\delta_{ST} = F_T/k$ and $\omega = \sqrt{(k/m)}$. The time t_{el} at displacement x_{el} is obtained from (3.170).

$$\cos \omega t_{el} = 1 - x_{el}/\delta_{ST}$$
and
$$\sin \omega t_{el} = \sqrt{(1 - \cos^2 \omega t_{el})}. \tag{3.171}$$
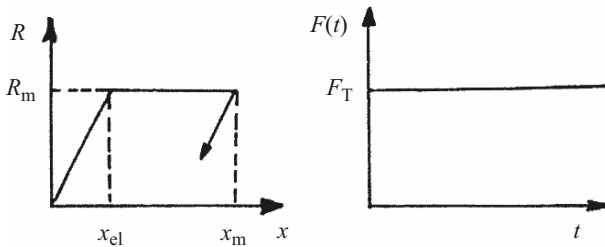
Fig. 3.41. Elasto-plastic system (R_m = maximum resistance, x_m = maximum displacement, x_{el} = elastic limit)

Stage 2

Second response $x_{\mathrm{el}} \leq x \leq x_{\mathrm{m}}$

$\quad x_0 = x_{\mathrm{el}}; \; t_2 = t - t_{\mathrm{el}}$

$$\dot{x}_0 = \delta_{\mathrm{ST}} \omega \sin \omega t_{\mathrm{el}}. \tag{3.172}$$

The equation of motion is then written as

$$m\ddot{x} + R_{\mathrm{m}} = F_{\mathrm{T}}. \tag{3.173}$$

The final solution becomes

$$x = x_{\mathrm{el}} + \frac{1}{2m}(F_{\mathrm{T}} - R_{\mathrm{m}})t_2^2 + x_{\mathrm{el}}\omega t_2 \sin \omega t_{\mathrm{el}}. \tag{3.174}$$

Differentiating (3.174) and setting the result to zero, the maximum time response $t_{2\mathrm{m}}$ is given by

$$t_{2\mathrm{m}} = [m\omega\delta_{\mathrm{ST}}/(R_{\mathrm{m}} - F_{\mathrm{T}})] \sin \omega t_{\mathrm{el}}. \tag{3.175}$$

Equation (3.175) is substituted into (3.174) for computing the maximum displacement x_{m}:

$$x_{\mathrm{m}} = x_{\mathrm{el}} + \left(\omega\delta_{\mathrm{ST}} - \frac{1}{2}\right)[m\omega\delta_{\mathrm{ST}}/(R_{\mathrm{m}} - F_{\mathrm{T}})] \sin^2 \omega t_{\mathrm{el}}. \tag{3.176}$$

Stage 3

Rebound: a similar procedure is adopted with a suitable equation of motion with initial conditions from the second stage. The easiest method is to consider a residual vibration and compute the amount by which the displacement x must decrease below x_{m}, i.e. $(R_{\mathrm{m}} - F_{\mathrm{T}})/k$, to reach the neutral position. The neutral position is given as:

$$x_{\mathrm{m}} - (R_{\mathrm{m}} - F_{\mathrm{T}})/k. \tag{3.177}$$

The response is thus

$$x = [x_{\mathrm{m}} - (R_{\mathrm{m}} - F_{\mathrm{T}})/k] + [(R_{\mathrm{m}} - F_{\mathrm{T}})/k] \cos(t - t_{2\mathrm{m}} - t_{\mathrm{el}}). \tag{3.178}$$

The maximum response charts are given in Figs. 3.42–3.45 for single-degree, undamped, elasto-plastic systems due to various load pulses.

3.3 Two-Degrees-of-Freedom System

Dynamic systems that require two independent co-ordinates to specify their positions are known as two-degrees-of-freedom systems. Typical examples are shown in Tables 3.13 and 3.14. There will be two natural frequencies from solution of the frequency equation of an undamped system or the characteristic equation of a damped system. A typical example of a spring-mass system is shown in Fig. 3.46a.
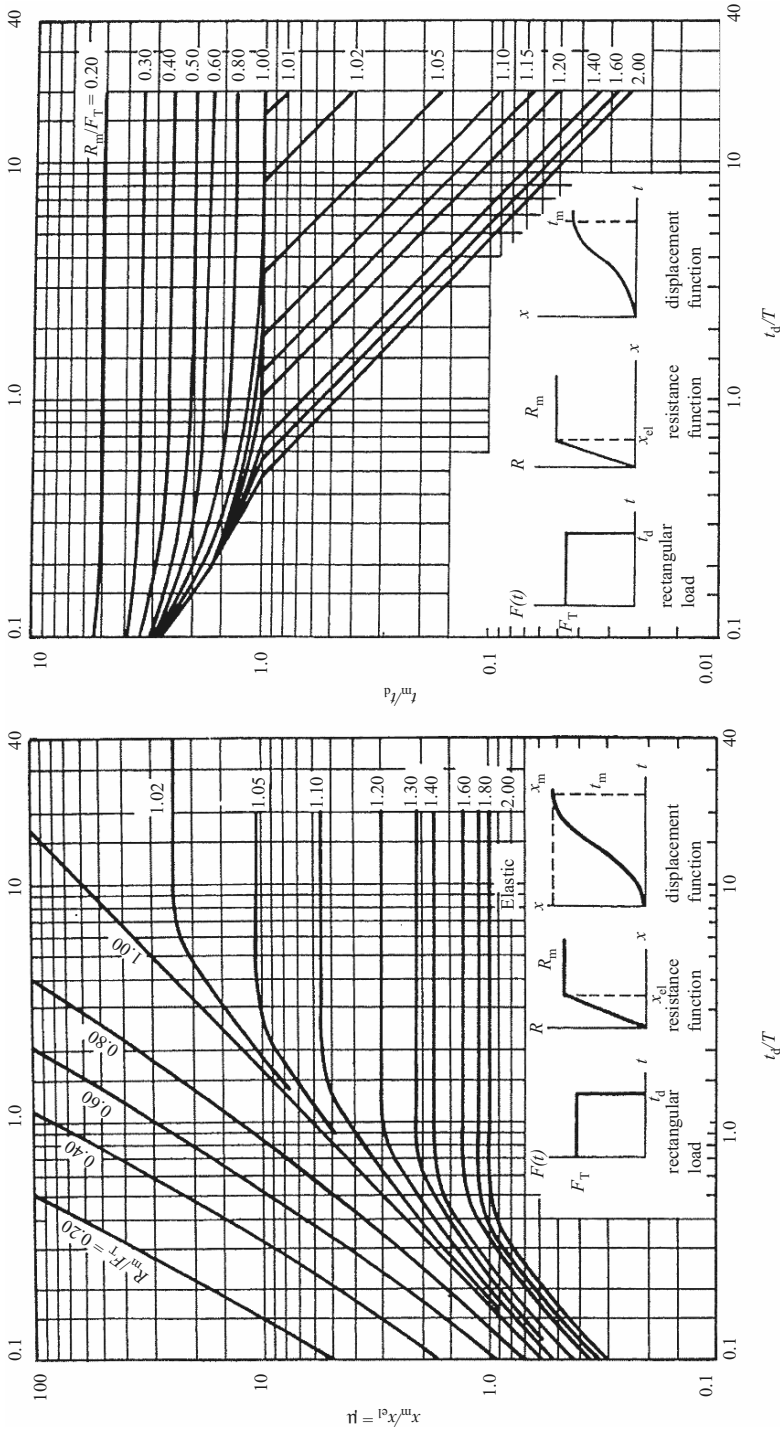
Fig. 3.42. Maximum response of elasto-plastic, single-degree, undamped systems due to rectangular load pulses (courtesy of the US Army Corps of Engineers)
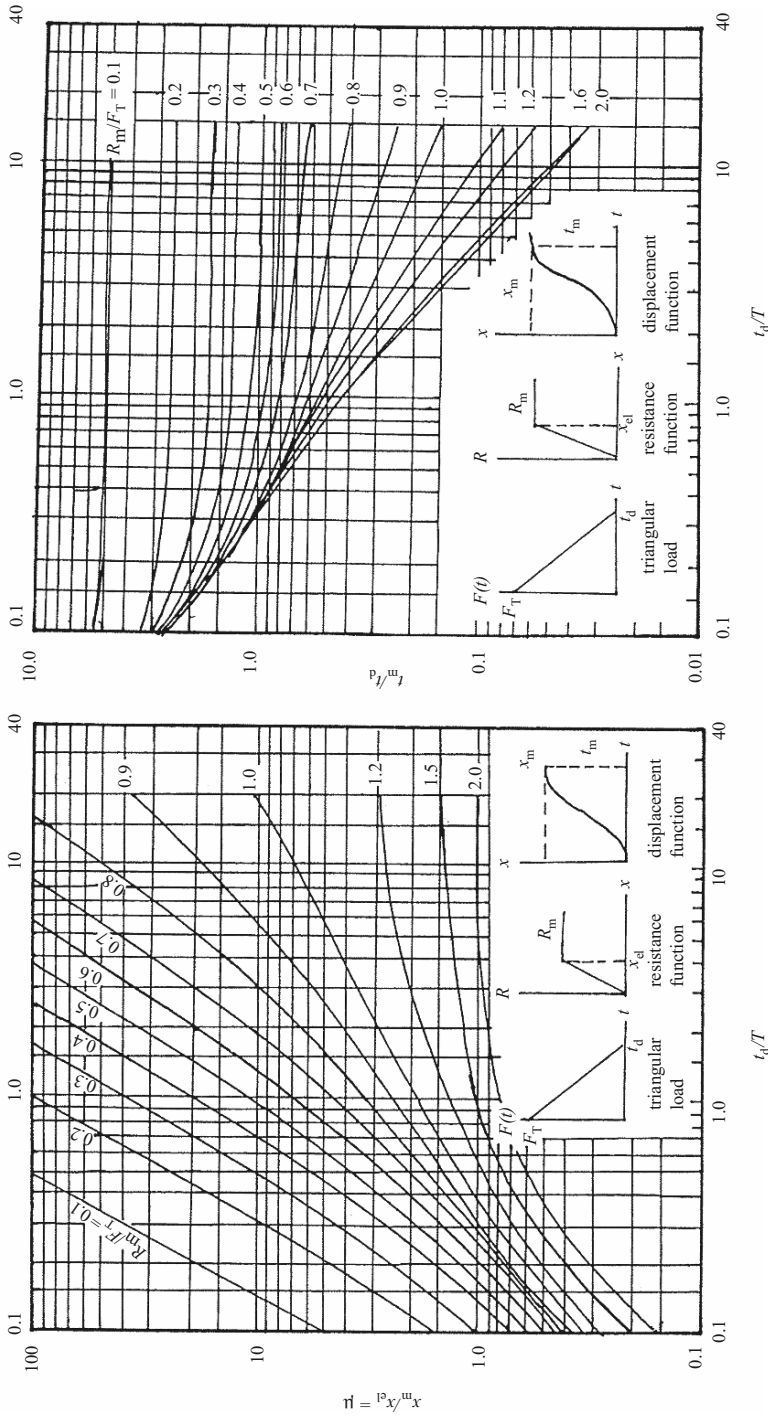
Fig. 3.43. Maximum response of elasto-plastic, single-degree, undamped systems due to triangular load pulses with zero rise time (courtesy of the US Army Corps of Engineers)
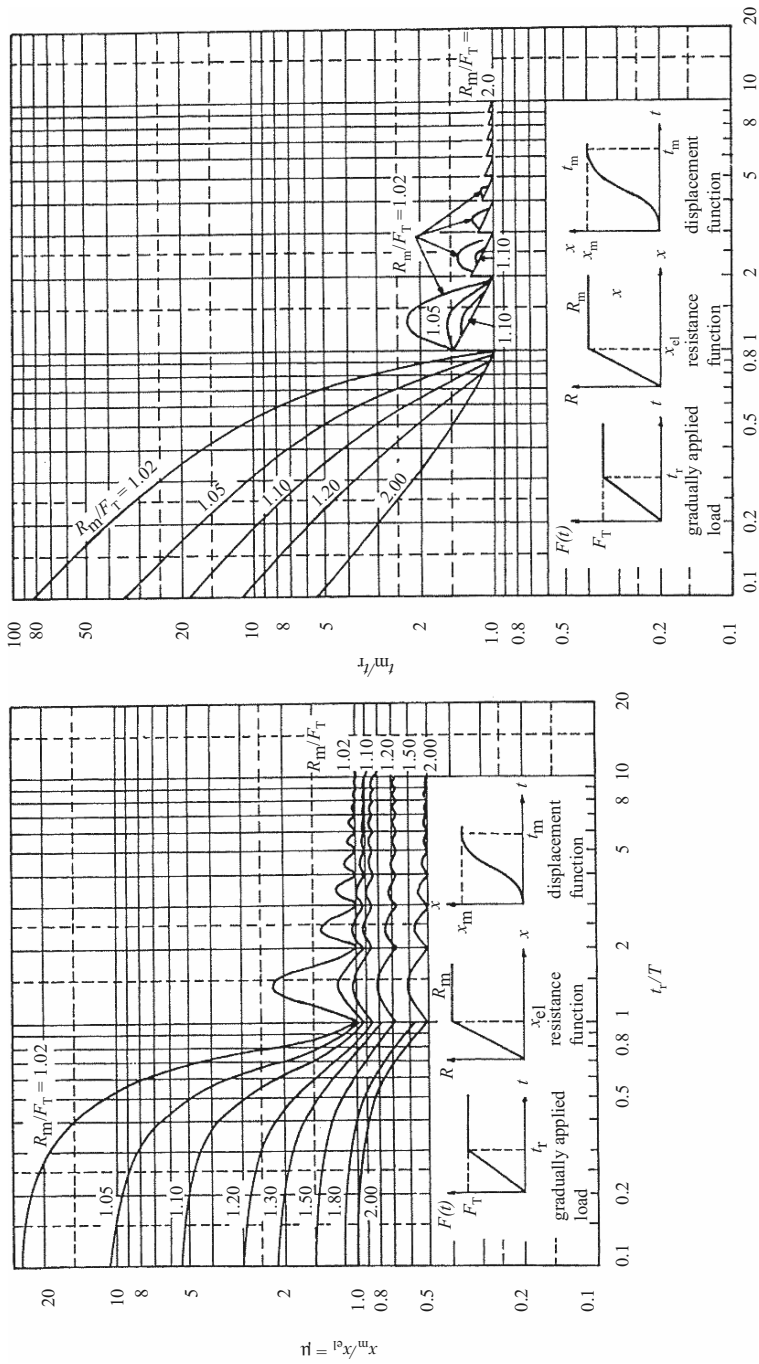
Fig. 3.44. Maximum response of elasto-plastic, single-degree, undamped systems due to a constant force with a finite rise time (courtesy of the US Army Corps of Engineers)
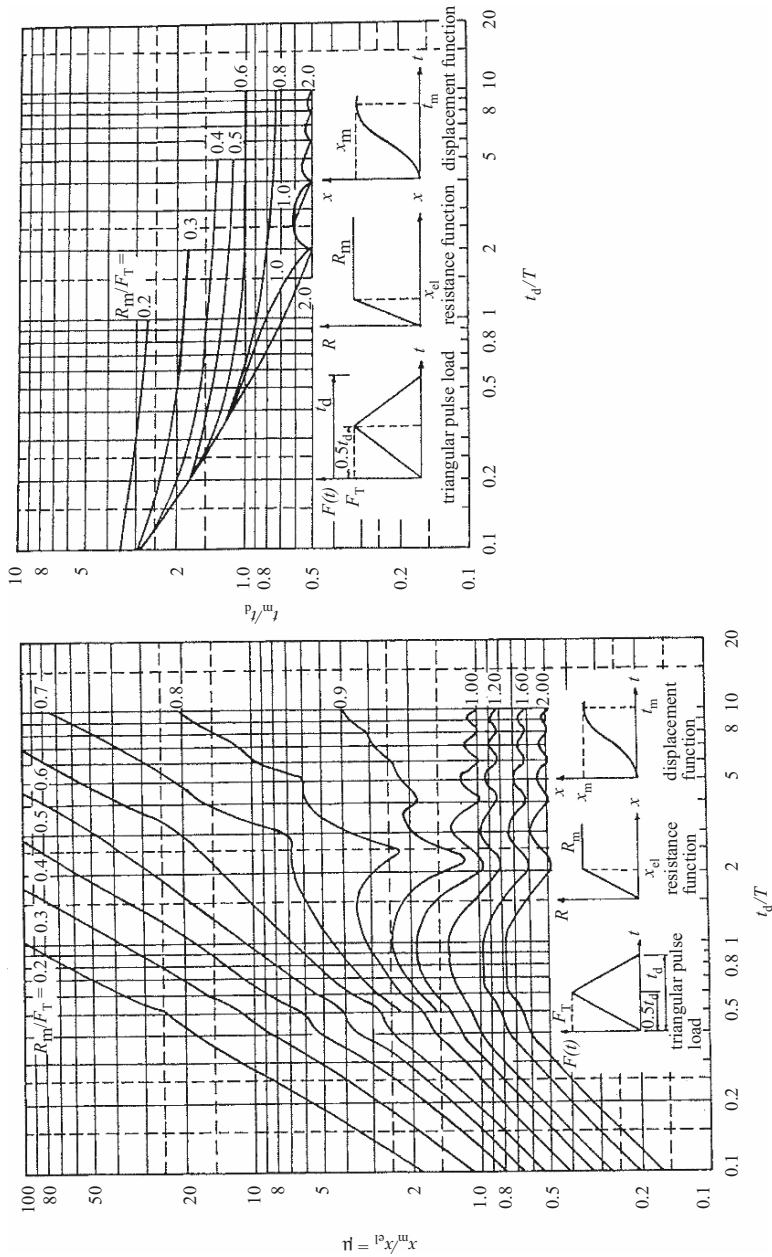
Fig. 3.45. Maximum response of elasto-plastic, single-degree, undamped systems due to equilateral triangular load pulses (courtesy of the US Army Corps of Engineers)

Table 3.14. Two-degrees-of-freedom systems (free undamped)
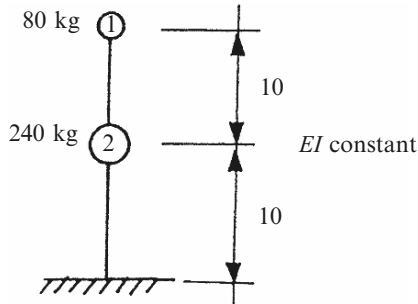
Find the frequencies and modes of vibration:

$$x = X \sin \omega t,$$

$$x_{10} = X_1 \sin \omega t, \quad \ddot{x}_{10} = -\omega^2 X_1 \sin \omega t,$$

$$x_{20} = X_2 \sin \omega t, \quad \ddot{x}_{20} = -\omega^2 X_2 \sin \omega t.$$

$$\text{Equation of motion} = -x_{10} = f_{11} m_1 \ddot{x}_{10} + f_{12} m_2 \ddot{x}_{20}, \qquad (1)$$

$$- x_{20} = f_{22} m_2 \ddot{x}_{20} + f_{21} m_1 \ddot{x}_{10}. \qquad (2)$$

Add the unit loads at points (1) and (2) and find f_{11}, f_{12}, f_{21} and f_{22}.
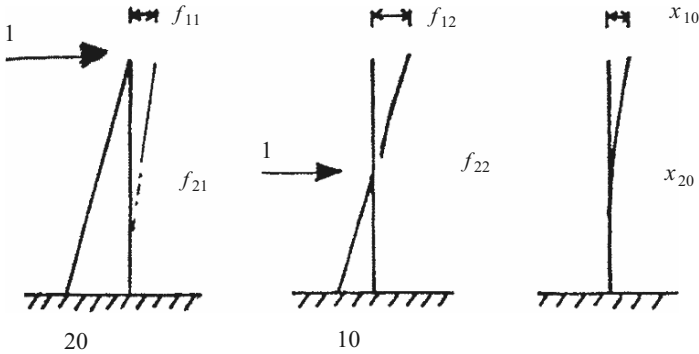
$$f_{11} = \int_0^l m_1^2/EI = \frac{20}{6EI}(2 \times 20^2) = 8{,}000/3EI,$$

$$f_{22} = \int_0^l m_2^2/EI = \frac{10}{6EI}(2 \times 10^2) = 1{,}000/3EI,$$

$$f_{12} = f_{22} = \int_0^l \frac{m_1 m_2}{EI}\, ds = \frac{10}{6EI}(2 \times 20 \times 10 + 10 \times 10)$$

$$= 2{,}500/3EI.$$

<div align="center">

Table 3.14. (continued)

</div>

Therefore, substitutions will give (*note*: x_{10}, etc. are δ_{10}, etc.)

$$- x_{10} = \ddot{x}_{10}\ 8{,}000/3EI \times 80 + 2{,}500/3EI \times 240\ \ddot{x}_{20},$$

$$- x_{20} = 1{,}000/3EI \times 240\ddot{x}_{20} + 80 \times 2{,}500/3EI \times \ddot{x}_{10},$$

$$- x_{10} = 640{,}000\omega^2 x_{10}/3EI + 200{,}000\omega^2 x_{20}/EI,$$

$$- x_{20} = 80{,}000\omega^2 x_{20}/EI + 200{,}000\omega^2 x_{10}/3EI,$$

$$x_{10}(1 + 640{,}000\omega^2/3EI) + x_{20}200{,}000\omega^2/EI = 0,$$

$$x_{10}\ 200{,}000\omega^2/3EI + x_{20}(1 + 80{,}000\omega^2/EI) = 0,$$

$$\begin{bmatrix} (1 + 640{,}000\omega^2/3EI) & (200{,}000\omega^2/EI) \\ \left(\dfrac{200{,}000\omega^2}{3EI}\right) & \left(1 + \dfrac{80{,}000\omega^2}{EI}\right) \end{bmatrix} \begin{Bmatrix} x_{10} \\ x_{20} \end{Bmatrix} = 0,$$

$$\begin{Bmatrix} x_{10} \\ x_{20} \end{Bmatrix} \neq 0, \qquad \text{therefore } \Delta = 0,$$

$$(1 + 640{,}000\omega^2/3EI)(1 + 80{,}000\omega^2/EI) - (200{,}000\omega^2/EI)^2 \times \frac{1}{3} = 0,$$

$$(1 + 880{,}000\omega^2/3EI) + (5.12 \times 10^{10}\omega^4/3EI) - (4 \times 10^{10}\omega^4/3E^2I^2) = 0,$$

$$(1 + 880{,}000k/3) + (1.12 \times 10^{10}k^2/3) = 0, \qquad \text{where } k = \omega^2/EI,$$

$$k = [-b \pm \sqrt{(b^2 - 4ac)}]/2a,$$

$$k = \{-88 \times 10^4/3 \pm \sqrt{[88 \times 10^4/3]^2}$$
$$-4 \times 1.12 \times 10^{10}/3]\}/(2 \times 1.12 \times 10^{10}/3),$$

$$k = -3.571 \times 10^{-6} \text{ or } -7.5 \times 10^{-5},$$

$$\omega = \sqrt{[(3.571 \times 10^{-6})EI]} \text{ or } \sqrt{[(7.5 \times 10^{-5})EI]},$$

$$f = \omega/2\pi,$$

$$\text{frequency} = 1.378 \times 10^{-3}\sqrt{(EI)} \text{ or } 3.01 \times 10^{-4}\sqrt{(EI)},$$

$$\text{frequency} = 3.01 \times 10^4\sqrt{(EI)}.$$

3.3.1 Undamped Free Vibrations

The equations of motion are written as

$$\Sigma F = ma,$$
$$m_1\ddot{x}_1 = -k_1 x_1 - k_2(x_1 - x_2)\ldots \text{mass } m_1, \qquad (3.179)$$
$$m_2\ddot{x}_2 = -k_2(x_2 - x_1)\ldots \text{mass } m_2.$$

Rearranging the above equations, the final equations of motion become

$$m_1\ddot{x}_1 + (k_1 + k_2)x_1 - k_2 x_2 = 0,$$
$$m_2\ddot{x}_2 - k_2 x_1 + k_2 x_2 = 0. \qquad (3.180)$$
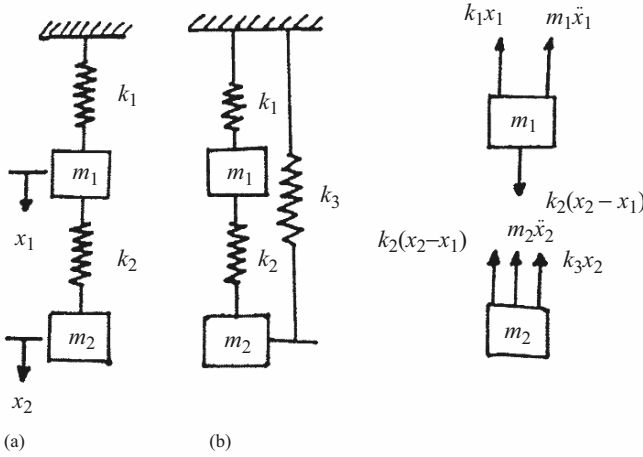
Fig. 3.46. Two-degrees-of-freedom systems

Assuming the motion is periodic and is composed of harmonic motions of various amplitudes and frequencies, then one of these components as described above may be written as

$$x_1 = X_1(\sin \omega t + \phi); \qquad \ddot{x}_1 = -X_1 \omega^2 \sin \omega (t + \phi),$$
$$x_2 = X_2(\sin \omega t + \phi); \qquad \ddot{x}_2 = -X_2 \omega^2 \sin \omega (t + \phi). \qquad (3.181)$$

When (3.181) is substituted into (3.182), which is the matrix form of (3.180),

$$\underbrace{\begin{bmatrix} m_1 & 0 \\ 0 & m_2 \end{bmatrix}}_{\substack{\text{diagonal mass} \\ \text{matrix}}} \begin{Bmatrix} \ddot{x}_1 \\ \ddot{x}_2 \end{Bmatrix} + \underbrace{\begin{bmatrix} k_1 + k_2 & -k_2 \\ -k_2 & k_2 \end{bmatrix}}_{\substack{\text{coupled stiffness} \\ \text{matrix}}} \begin{Bmatrix} x_1 \\ x_2 \end{Bmatrix} = \begin{Bmatrix} 0 \\ 0 \end{Bmatrix}, \qquad (3.182)$$

the following relationship is obtained:

$$\begin{bmatrix} (k_1 + k_2 - m_1 \omega^2) & -k_2 \\ -k^2 & (k_2 - m_2 \omega^2) \end{bmatrix} \begin{Bmatrix} X_1 \\ X_2 \end{Bmatrix} = \begin{Bmatrix} 0 \\ 0 \end{Bmatrix}. \qquad (3.183)$$

The determinant of the left-hand matrix is equal to zero since x_1 and x_2, when zero, define the equilibrium condition of the system. By expansion of the determinant the following equation is arrived at:

$$\omega^4 - [(k_1 + k_2/m_1) + k_2/m_2]\omega^2 + (k_1 k_2/m_1 m_2) = 0. \qquad (3.184)$$

The frequency equation of the system is obtained by assuming $\omega^2 = \bar{C}$ in (3.184). A quadratic equation in C is obtained and hence ω.

$$\omega^2 = \bar{C} = (k_1 + k_2/2m_1) + (k_2/2m_2) \pm \sqrt{\left\{ \frac{1}{4}[(k_1 + k_2/m_1) \right.}$$
$$\left. + (k_2/m_2)]^2 - (k_1 k_2/m_1 m_2) \right\}}. \tag{3.185}$$

If a third spring is attached with stiffness k_3, as shown in Fig. 3.46b, the determinant of the left-hand coefficient matrix of (3.183) can be written as

$$\begin{vmatrix} k_1 + k_2 - m_1\omega^2 & -k_2 \\ -k_2 & k_2 + k_3 - m_2\omega^2 \end{vmatrix} = 0$$

and (3.184) becomes

$$\omega^4 - \{[(k_1 + k_2)/m_1] + [(k_2 + k_3)/m_2]\}\omega^2 + \{[k_2(k_1 + k_2) + k_1 k_3]/m_1 m_2\} = 0. \tag{3.186}$$

Other cases are similarly analysed in Table 3.13. The natural frequency is computed as $f = \omega/2\pi$.

Assuming $k_1 = k_2 = k_3 = k$ and $m_1 = m_2$, (3.186) becomes

$$\omega^4 - (4k/m)\omega^2 + (3k^2/m^2) = 0, \quad \omega^2 = C, \tag{3.187}$$

$$C^2 - (4k/m)C + (3k^2/m^2) = 0,$$
$$C_1 = \omega_1^2 = k/m,$$
$$\omega_1 = \sqrt{(k/m)}. \tag{3.187a}$$

The other root
$$\omega_2^2 = 3k/m \text{ or } \omega_2 = 1.73\sqrt{(k/m)} \tag{3.187b}$$

The lowest frequency is $\omega_1 = \sqrt{(k/m)}$. Table 3.14 gives a standard case using the flexibility method.

3.3.2 Free Damped Vibration

The spring-mass, damped, free vibration system is shown in Fig. 3.47. The equation of motion is written as

$$m_1\ddot{x}_1 + (c_1 + c_2)\dot{x}_1 + (k_1 + k_2)x_1 - c_2\dot{x}_2 - k_2 x_2 = 0, \tag{3.188}$$
$$m_2\ddot{x}_2 + c_2\dot{x}_2 + k_2 x_2 - c_2\dot{x}_1 - k_2 x_1 = 0. \tag{3.188a}$$

Using the solution procedure given earlier, the general form of the solution will be

$$x_1 = C_1 e^{st} \text{ and } x_2 = C_2 e^{st}, \tag{3.189}$$
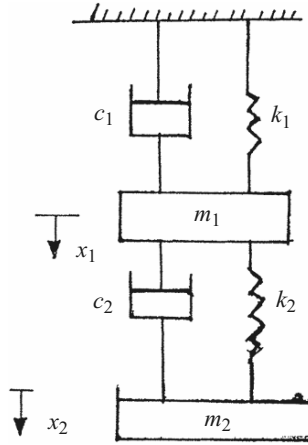
Fig. 3.47. Two-degrees, damped free system

where $s = \pm i\omega t$. Substituting (3.189) into (3.188a) and dividing the two equations throughout by e^{st}, a 2×2 matrix is formed, the determinant of which is

$$\begin{vmatrix} [m_1 s^2 + (c_1 + c_2)s + (k_1 + k_2)] & -(c_2 s + k_2) \\ -(c_2 s + k_2) & (m_2 s^2 + c_2 s + k_2) \end{vmatrix} = 0. \qquad (3.190)$$

The characteristic equation of the system after expansion of the determinant becomes

$$[m_1 s^2 + (c_1 + c_2)s + k_1 + k_2](m_2 s^2 + c_2 s + k_2) - (c_2 s + k_2)^2 = 0. \quad (3.191)$$

Since $s = \pm i\omega t$, the circular frequency ω is computed in the manner described above.

3.3.3 Forced Vibration with Damping

The system shown in Fig. 3.47 is now associated with the force $F_0 \sin \omega_f t$. The forces are acting parallel to the springs vertically and the equation of motion is

$$m_1 \ddot{x}_1 + (c_1 + c_2)\dot{x}_1 + (k_1 + k_2)x_1 - c_2 \dot{x}_2 - k_2 x_2 = F_0 \sin \omega t,$$
$$m_2 \ddot{x}_2 + c_2 \dot{x}_2 + k_2 x_2 - c_2 \dot{x}_1 - k_2 x_1 = 0. \qquad (3.192)$$

A typical example is shown in Table 3.15. If the impedance method given in "Mechanical Impedance Method" is invoked. The following shows the replacement procedure:

$$\text{Use } F_0 e^{-\omega_f t} \text{ instead of } F_0 \sin \omega_f t \qquad (3.193)$$

Table 3.15. Forced vibrations with damping (two degrees)
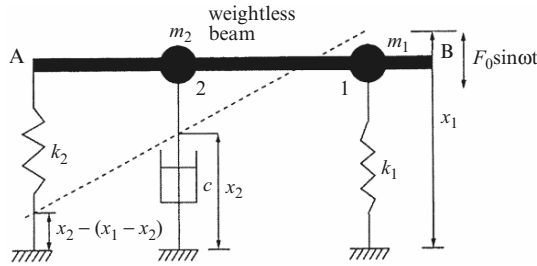
A horizontal beam with two masses is supported by springs. The location of the dashpot is shown. The force at the level of mass 1 is $F_0 \sin \omega t$ and at mass 2 is zero.

$$\text{KE} = \frac{1}{2} m_1 \dot{x}_1^2 + \frac{1}{2} m_2 \dot{x}_2^2,$$

$$\text{PE} = \frac{1}{2} k_1 x_1^2 + \frac{1}{2} k_2 [x_2 - (x_1 - x_2)]^2,$$

$$\text{DE} = \text{damping energy} = \frac{1}{2} c \dot{x}_2^2,$$

$$\frac{\mathrm{d}}{\mathrm{d}t} \left(\frac{\partial \text{KE}}{\partial \dot{x}_1} \right) - \frac{\partial \text{KE}}{\partial x_1} + \frac{\partial \text{PE}}{\partial x_1} + \frac{\partial \text{DE}}{\partial \dot{x}_1} = F_1 = F_0 \sin \omega t$$

or $$m_1 \ddot{x}_1 - 0 + k_1 x_1 - k_2 [x_2 - (x_1 - x_2)] + 0 = F_0 \sin \omega t,$$

$$\frac{\mathrm{d}}{\mathrm{d}t} \left(\frac{\partial \text{KE}}{\partial \dot{x}_2} \right) - \frac{\partial \text{KE}}{\partial x_2} + \frac{\partial \text{PE}}{\partial \dot{x}_2} + \frac{\partial \text{DE}}{\partial \dot{x}_2} = F_2 = 0,$$

$$m \ddot{x}_2 - 0 + 2 k_2 \, (2 x_2 - x_1) + c \dot{x}_2 = 0.$$

The equations of motions are written:

$$m_1 \ddot{x}_1 + (k_1 + k_2) x_1 - 2 k_2 x_2 = F_0 \sin \omega t,$$
$$m_2 \ddot{x}_2 + c \dot{x}_2 + 4 k_2 x_2 = 0.$$

They are solved for the unknown quantities using flexibility methods.

and use $X_1 \mathrm{e}^{i \omega_\mathrm{f} t}$ and $X_2 \mathrm{e}^{i \omega_\mathrm{f} t}$ instead of x_1 and x_2 respectively. By substituting (3.193) into (3.192) and dividing throughout by $\mathrm{e}^{i \omega_\mathrm{f} t}$, the following equations of motion are derived:

$$-[(k_1 + k_2) - m_1 \omega_\mathrm{f}^2 + i(c_1 + c_2) \omega_\mathrm{f}] X_1 - (k_2 + i c_2 \omega_\mathrm{f}) X_2 = F_0,$$
$$-(k_2 + i c_2 \omega_\mathrm{f}) X_1 + (k_2 - m_2 \omega_\mathrm{f}^2 + i c_2 \omega_\mathrm{f}) X_2 = 0. \qquad (3.194)$$

Using Cramer's rule:

$$X_1 = \begin{vmatrix} F_0 & -(k_2 + i c_2 \omega_\mathrm{f}) \\ 0 & (k_2 - m_2 (\omega_\mathrm{f})^2 + i c_2 \omega_\mathrm{f}) \end{vmatrix} \bigg/ \begin{array}{l} [(k_1 + k_2) - m_1 \omega_\mathrm{f}^2 \\ + i(c_1 + c_2) \omega_\mathrm{f}](k_2 - m_2 \omega_\mathrm{f}^2 + i c_2 \omega_\mathrm{f}) \\ - (k_2 + i c_2 \omega_\mathrm{f})^2. \end{array}$$

$$(3.195)$$

Using complex variables it is of the form $(a + ib)/(c + id)$, hence

$$X_1 = (a^2 + b^2)/(c^2 + d^2),$$

$$X_1 = F_0^2(k_2 - m_2\omega_f^2)^2 + c_2^2\omega_f^2/[(k_2 - m_1\omega_f^2) \times (k_2 - m_2\omega_f^2)$$
$$- m_2 k_2 \omega_f^2]^2 + \omega_f^2 c_2^2(k_1 - m_1\omega_f^2 - m_2\omega_f^2)^2. \tag{3.195a}$$

The forcing function is given by

$$F_0 \sin \omega_f t = \mathrm{Im}(F_0 e^{i\omega_f t}). \tag{3.196}$$

Also

$$X_1 = X_1 e^{i\phi_t} = F_0(\bar{g} + i\bar{h}) = X_1(\cos \phi_1 + i \sin \phi_1),$$

where $\phi_1 = \tan^{-1} \bar{g}/\bar{h}$. Hence the steady damped vibration can be given as

$$x_1 = \mathrm{Im}(X_1 e^{i\omega_f t}) = \mathrm{Im}(X_1 e^{i(\omega_f t + \phi_1)}) \tag{3.197}$$
$$= X_1 \sin(\omega_f t + \phi_1).$$

Similarly

$$X_2 = F_0(\bar{j} + i\bar{l}) = X_2 e^{i\phi_2},$$
$$x_2 = \mathrm{Im}(X_2 e^{i\omega_f t}) = \mathrm{Im}(X_2 e^{i(\omega_f t + \phi_2)}) = X_2 \sin(\omega_f t + \phi_2),$$

where $\phi_2 = \tan \bar{l}/\bar{j}$.

$$X_2 = \sqrt{F_0^2(k_2^2 + c_2^2\omega_f^2)/[(k_2 - m_1\omega_f^2)(k_2 - m_2\omega_f^2) - m_2 k_2 \omega_f^2)]^2}$$
$$+ [\omega_f^2 c_2^2(k_1 - m_1\omega_f^2 - m_2\omega_f^2)^2]. \tag{3.198}$$

If the forcing function is $F_0 \cos \omega_f t$, then

$$x_1 = X_1 \cos(\omega_f t + \phi_1),$$
$$\tag{3.199}$$
$$x_2 = X_2 \cos(\omega_f t + \phi_2).$$

3.3.4 Orthogonality Principle

The orthogonality principle is expressed as

$$\sum_{j=1}^{n} m_j X_{jr'} X_{jr''} = 0, \tag{3.200}$$

where r' and r'' identify any two normal modes, j is the jth mass out of a total of n masses and m_j is the jth mass. This principle is extremely useful in the analysis of a multi-degree system. However, in the context of two degrees of freedom, this simply means that two modes are orthogonal.

Let the vibrating system given by

$$x_1 = X_1 \sin(\omega_1 t + \phi_1) + X_2 \sin(\omega_2 t + \phi_2),$$
$$x_2 = \bar{X}_1 \sin(\omega_1 t + \phi_1) + \bar{X}_2 \sin(\omega_2 t + \phi_2), \tag{3.201}$$

where X_1, X_2, $\bar{X}_1$ and $\bar{X}_2$ are the amplitudes of vibration of the two masses and ϕ_1 and ϕ_2 are the phase angles corresponding to the two circular frequencies ω_1 and ω_2.

The kinetic energy is given by

$$(KE)_{max} = \frac{1}{2}m_1(\dot{x}_{1_{max}})^2 + \frac{1}{2}m_2(\dot{x}_{2_{max}})^2. \tag{3.202}$$

Substitution of (3.201) into (3.202) gives

$$(KE)_{max} = \frac{1}{2}m_1[(X_1\omega_1)^2 + (X_2\omega_2)^2 + (2X_1\omega_1)(X_2\omega_2)] + \frac{1}{2}m_2[\bar{X}_1\omega_1]^2$$
$$+ (\bar{X}_2\omega_2)^2 + 2(\bar{X}_1\omega_1)(\bar{X}_2\omega_2)]. \tag{3.203}$$

For the principle modes of vibration, the value of $(KE)_{max}$ is given by

$$(KE)_{max} = \frac{1}{2}[m_1(X_1\omega_1)^2 + m_2(\bar{X}_1\omega_1)^2] + \frac{1}{2}[m_1(\bar{X}_2\omega_2)^2 + m_2(\bar{X}_2\omega_2)^2]. \tag{3.204}$$

The two maximum kinetic energies must be equal, hence

$$m_1(X_1\omega_1)(X_2\omega_2) + m_2(\bar{X}_1\omega_1)(\bar{X}_2\omega_2) = 0. \tag{3.205}$$

Since ω_1 and ω_2 are not always zero

$$m_1(X_1X_2) + m_2(\bar{X}_1\bar{X}_2) = 0. \tag{3.206}$$

3.4 Multi-Degrees-of-Freedom Systems

3.4.1 Undamped Free Vibrations

The differential equations of motions for n masses and n degrees of freedom can now be written using the stiffness method.

$$m_{11}\ddot{x}_1 + m_{12}\ddot{x}_2 + \ldots m_{1n}\ddot{x}_n + k_{11}x_1 + k_{12}x_2 \ldots k_{1n}x_n = 0$$
$$m_{21}\ddot{x}_1 + m_{22}\ddot{x}_2 + \ldots m_{2n}\ddot{x}_n + k_{21}x_1 + k_{22}x_2 \ldots k_{2n}x_n = 0$$
$$\vdots \quad\quad \vdots \quad\quad\quad \vdots \quad\quad \vdots \quad\quad \vdots \quad\quad \vdots$$
$$\vdots \quad\quad \vdots \quad\quad\quad \vdots \quad\quad \vdots \quad\quad \vdots \quad\quad \vdots \tag{3.207}$$
$$\vdots \quad\quad \vdots \quad\quad\quad \vdots \quad\quad \vdots \quad\quad \vdots \quad\quad \vdots$$
$$m_{n1}\ddot{x}_1 + m_{n2}\ddot{x}_2 + \ldots m_{nn}\ddot{x}_n + k_{n1}x_1 + k_{n2}x_2 \ldots k_{nn}x_n = 0.$$

In a matrix form, (3.207) is written as

$$
\begin{bmatrix} m_{11} & m_{12} & \dots & m_{1n} \\ m_{21} & m_{22} & \dots & m_{2n} \\ \vdots & \vdots & & \vdots \\ \vdots & \vdots & & \vdots \\ m_{n1} & m_{n2} & \dots & m_{nn} \end{bmatrix} \begin{Bmatrix} \ddot{x}_1 \\ \ddot{x}_2 \\ \vdots \\ \vdots \\ \ddot{x}_n \end{Bmatrix} + \begin{bmatrix} k_{11} & k_{12} & \dots & k_{1n} \\ k_{21} & k_{22} & \dots & k_{2n} \\ \vdots & \vdots & & \vdots \\ \vdots & \vdots & & \vdots \\ k_{n1} & k_{n2} & \dots & k_{nn} \end{bmatrix} \begin{Bmatrix} x_1 \\ x_2 \\ \vdots \\ \vdots \\ x_n \end{Bmatrix} = \begin{Bmatrix} 0 \\ 0 \\ \vdots \\ \vdots \\ 0 \end{Bmatrix} \tag{3.208}
$$

$$
\text{or } [M]\{\ddot{x}\} + [K]\{x\} = 0, \tag{3.208a}
$$

where $[M]$ is the *mass* or *inertia matrix* and $[K]$ is the total or *global stiffness matrix*. Equation (3.208) can be written as:

$$
\{\ddot{x}\} + [C_D]\{x\} = 0, \tag{3.209}
$$

where $[C_D]$ (the *dynamic matrix*) $= [M]^{-1}[K]$.

Sometimes the equations for multi-degree systems given by (3.207) are written in terms of *characteristic value problems*:

$$
[K]\{X_i\} = \omega_i^2[M]\{X_i\}, \tag{3.210}
$$

where $[M]$ is a diagonal matrix and ω is a *characteristic number*. A more convenient form of (3.210) is written as

$$
([K] - \omega_i^2[M])\{X_i\} = 0. \tag{3.211}
$$

The determinant of the coefficients of X_i must be zero.

$$
|K - \omega_i^2 M| = \begin{bmatrix} (k_{11} - \omega_1^2 M_1) & k_{12} & k_{13} \dots k_{1n} \\ k_{21} & (k_{22} - \omega_1^2 M_2) & k_{23} \dots k_{2n} \\ & & \\ k_{n1} & k_{n2} & k_{n3} \dots (k_{nn} - \omega_1^2 M_n) \end{bmatrix} = 0. \tag{3.212}
$$

The determinant is expanded for the nth order equations in ω_1^2 such that for each value of ω_i^2, there will be a corresponding X_i. Table 3.15 shows typical solved examples.

3.4.2 Orthogonality Principle

For example, two characteristic vectors $\mathbf{X}_1$ and $\mathbf{X}_2$, each with n components, and their corresponding characteristic numbers (frequencies) ω_1 and ω_2 are considered. Two forms of (3.210) are written:

$$
[K]\{\mathbf{X}_1\} = \omega_1^2[M]\{\mathbf{X}_1\},
$$
$$
[K]\{\mathbf{X}_2\} = \omega_2^2[M]\{\mathbf{X}_2\}. \tag{3.213}
$$

The transposed form of (3.213) can also be written in the following way:

$$([K]\{\mathbf{X}_1\})^{\mathrm{T}}\{\mathbf{X}_2\} = \omega_1^2([M]\{\mathbf{X}_1\})^{\mathrm{T}}\{\mathbf{X}_2\},$$
$$\{\mathbf{X}_1\}^{\mathrm{T}}([K]\{\mathbf{X}_2\}) = \omega_2^2\{\mathbf{X}_1\}^{\mathrm{T}}([M]\{\mathbf{X}_2\}). \tag{3.214}$$

Since $[M]$ is a diagonal matrix $= [M]^{\mathrm{T}}$ and $[K]$ is a symmetric matrix $= [K]^{\mathrm{T}}$, the expression of (3.214) gives

$$(\omega_2^2 - \omega_1^2)\{\mathbf{X}_1\}^{\mathrm{T}}[M]\{\mathbf{X}_2\} = 0. \tag{3.215}$$

Assuming $\omega_2 = \omega_1$, (3.215) gives

$$\{\mathbf{X}_1\}^{\mathrm{T}}[M]\{\mathbf{X}_2\} = 0. \tag{3.215a}$$

As defined earlier, the principle of orthogonality with respect to the *mass matrix* $[M]$ being unity can be represented by

$$\{\mathbf{X}_1\}^{\mathrm{T}}\{\mathbf{X}_2\} = 0. \tag{3.216}$$

The condition is satisfied regardless of the value of ω. It thus follows that:

$$\{\mathbf{X}_1\}^{\mathrm{T}}[M]\{\mathbf{X}_1\} \neq 0. \tag{3.217}$$

3.4.3 Concept of Unit Vectors

The length of the vector $\mathbf{L}_v$ is given as $\sqrt{(\mathbf{X}^{\mathrm{T}}\mathbf{X})}$. The unit vector is $\mathbf{e}_i$, defined by

$$\mathbf{e}_i = \{\mathbf{X}_i\}/\sqrt{(\{\mathbf{X}_i\}^{\mathrm{T}}[M]\{\mathbf{X}_i\})}. \tag{3.218}$$

It is convenient to work in terms of $\mathbf{e}_i$ rather than $\mathbf{X}_i$, then

$$\{\mathbf{e}_i\}^{\mathrm{T}}[M]\{\mathbf{e}_i\} = [I] \tag{3.219}$$

and then n distinct values of ω_n^2, their characteristic vectors $\mathbf{X}_n$ and unit vectors $\mathbf{e}_n$ can be written as

$$[K]\,[\bar{E}] = [M][E][p], \tag{3.220}$$

$$\text{where } [\bar{E}] = \begin{bmatrix} \mathbf{e}_{11} & \mathbf{e}_{21} & \mathbf{e}_{31} & \cdots & \mathbf{e}_{n1} \\ \vdots & \vdots & \vdots & & \vdots \\ \vdots & \vdots & \vdots & & \vdots \\ \vdots & \vdots & \vdots & & \vdots \\ \mathbf{e}_{1n} & \mathbf{e}_{2n} & \mathbf{e}_{3n} & \cdots & \mathbf{e}_{nn} \end{bmatrix}, \tag{3.220a}$$

$$[\omega] = \begin{bmatrix} \omega_1^2 & 0 & 0 & \cdots & 0 \\ 0 & \omega_2^2 & 0 & \cdots & 0 \\ \vdots & \vdots & \vdots & & \vdots \\ \vdots & \vdots & \vdots & & \vdots \\ 0 & 0 & 0 & \cdots & \omega_n^2 \end{bmatrix}. \tag{3.220b}$$

Equation (3.219) is replaced by

$$[\bar{E}]^{\mathrm{T}}[M][\bar{E}] = [I], \tag{3.221}$$

where $[I]$ is the identity matrix. It is therefore easy to see that

$$[\bar{E}]^{\mathrm{T}}[K][\bar{E}] = [p]. \tag{3.222}$$

The basic equation of motion becomes

$$[M]\{\ddot{\bar{x}}_i\}_t + [K]\{\bar{x}_i\}_t = 0. \tag{3.223}$$

Equation (3.223) are converted into a set of uncoupled equations using the principle of transformation $\mathbf{x}_i = \bar{E}\mathbf{x}'_i$. The new set of basic uncoupled equations is written as

$$[\bar{E}]^{\mathrm{T}}[M][\bar{E}]\{\ddot{x}'_i\}_t + [\bar{E}]^{\mathrm{T}}[K][\bar{E}]\{x'_i\}_t = 0. \tag{3.224}$$

Using (3.221) and (3.222), (3.224) is written in n uncoupled equations

$$\{\ddot{x}'_i\}_t + \{x'_i\}_t = 0. \tag{3.225}$$

Table 3.16 illustrates the computation.

3.4.4 Undamped Forced Vibrations

If (3.223) is rewritten and equated to the forcing function $F(t)$, then following the argument given earlier, (3.224) assumes the form:

$$[\bar{E}]^{\mathrm{T}}[M][\bar{E}]\{\ddot{x}'_i\} + [\bar{E}]^{\mathrm{T}}[K][\bar{E}]\{x'_i\} = [\bar{E}]^{\mathrm{T}}F(t) \tag{3.226}$$

$$\text{or } \{\ddot{x}_i\} + [\omega]\{x'_i\} = [\bar{E}]^{\mathrm{T}}F(t). \tag{3.226a}$$

3.4.5 Non-Linear Response of Multi-Degrees-of-Freedom Systems: Incremental Method

The Wilson-θ method is suggested initially for the solution of the structures modelled by assuming that the acceleration varies linearly over the time interval from t to $t + \theta\delta t$, such that $\theta \geq 1$. For a value of $\theta \geq 1.38$, the Wilson-θ method becomes unconditionally stable. Consider the difference between the dynamic equilibrium conditions at time t_i and $t_i + \theta\delta t$. The following incremental equations are obtained on the lines suggested earlier

$$[M]\{\delta\ddot{x}'_i\} + [C]\{\dot{x}\}\{\delta\dot{x}'_i\} = [K]\{x\}\{\delta x'_i\} = \{\delta F_i(t)\}, \tag{3.227}$$

Table 3.16. Multi-degrees-of-freedom systems
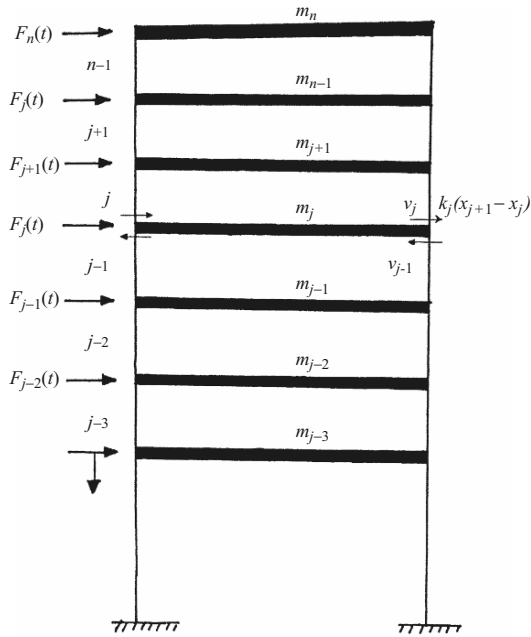
The general form of the equations of motion is given by

$$F_n(t) = m_n \ddot{x}_n + k_{n-1}\,(x_n - x_{n-1}).$$

For the applied force at level j, the above equation is written as

$$F_j(t) = m_j \ddot{x}_j + k_{j-1}\,(x_j - x_{j-1}) - k_j\,(x_{j+1} - x_j).$$

(1) Free vibrations

$$F(t) = 0.$$

The equations of motion are

$$m_2 \ddot{x}_2 + (k_2 + k_1)x_2 - k_2 x_3 = 0$$
$$m_3 \ddot{x}_3 + (k_3 + k_2)x_3 - k_3 x_4 - k_2 x_2 = 0$$
$$m_4 \ddot{x}_4 + (k_4 + k_3)x_4 - k_4 x_5 - k_3 x_3 = 0$$

$$\vdots \qquad\qquad\qquad\qquad \vdots$$

$$\vdots \qquad\qquad\qquad\qquad \vdots \qquad (1)$$

$$\vdots \qquad\qquad\qquad\qquad \vdots$$

$$m_n \ddot{x}_n + k_{n-1}(x_{n-1}) \qquad\qquad = 0,$$

(*continued*)

Table 3.16. (continued)

where $x_j = X_j \sin \omega t$. The above equations are written as

$$\{[(k_2 + k_1)/m_2] - \omega^2\}X_2 - (k_2/m_2)X_3 = 0,$$
$$- (k_2/m_3)X_2 + [(k_3 + k_2)/m_3]X_3 - (k_3/m_3)X_4 = 0, \qquad (2)$$
$$- (k_3/m_4)X_3 + \{[(k_4 + k_3)/m_4] - \omega^2\}X_4 - (k_4/m_4)X_5 = 0,$$
$$- = 0,$$
$$- = 0.$$

In general, in the above equations the values of the ks are replaced by appropriate general terms. For example, $\{[(k_2 + k_1)/m_2] - \omega^2\}$ is replaced by $\{[(k_{j+1} + k_j)/m_{j+1}] - \omega^2\}$. The determinant is solved for various values of ω and hence f, the frequencies. Associated with each value of ω, one can find the characteristic vector $\mathbf{X}$ in terms of the arbitrary constant C. The mode shapes are obtained. The associated vectors $\mathbf{L_v} = \sqrt{(\mathbf{X^T X})}$ are evaluated. The matrix $\{\mathbf{e}_i\}$ is formed such that the matrix of (3.219) becomes the identity matrix.

For a three-storey building with the following data:

j	m_j (kNs^2 m^{-1})	k_j (MN m^{-1})
1	–	10
2	15,000	9
3	15,000	8
4	15,000	

$$\{\mathbf{e}_i\} = \begin{bmatrix} 0.305 & 0.688 & 0.660 \\ 0.581 & 0.416 & -0.702 \\ 0.757 & -0.597 & 0.273 \end{bmatrix}. \qquad (3)$$

Equation (3.225) is solved using

$$\mathbf{x}_i = \bar{E}x_t'.$$

For example

$$x_{iz}' = 0.305x_{i2} + 0.581x_{i3} + 0.757x_{i4} \text{ and so on.} \qquad (4)$$

The uncoupled equations of the form for a three-storey building will be

$$\ddot{x}_2' + \omega_1^2 x_2' = 0,$$
$$\ddot{x}_3' + \omega_2^2 x_3' = 0, \qquad (5)$$
$$\ddot{x}_4' + \omega_3^2 x_4' = 0.$$

The frequencies and periods for the three-storey building are computed as

$$f_1 = 1.768 \text{ Hz}, \quad T_1 = 0.55 \text{ s},$$
$$f_2 = 4.80 \text{ Hz}, \quad T_2 = 0.22 \text{ s},$$
$$f_3 = 6.96 \text{ Hz}, \quad T_3 = 0.15 \text{ s}.$$

Table 3.16. (continued)

(2) Forced vibrations. The time interval is $0 \leq t \leq 1\,\text{s}$; $F_2(t) = 0$; $F_3(t) = 0$; $F_4(t) = 1 \times 10^5(1-t)$ kN = forcing factor in a column matrix; $F(t) = \{0,\ 0,\ 10^5(1-t)\}^\text{T}$. They are made equal to the right-hand side of (1). The uncoupled equations given in (5) are invoked. For example,

$$x_2' + \omega_1^2 x_2' = (0.305)(0) + (0.688)(0) + (0.757)\{10^5(1-t)\}$$
$$= 7.57 \times 10^4(1-t). \tag{6}$$

The procedure given above is followed:

$$\begin{aligned}
x_i' &= X_i \sin\omega_i t, \\
x_2' &= X_1 \sin\omega_1 t + 7.57 \times 10^4(1-t), \\
x_3' &= X_2 \sin\omega_2 t - 5.97 \times 10^4(1-t), \\
x_4' &= X_3 \sin\omega_3 t + 2.73 \times 10^4(1-t).
\end{aligned} \tag{7}$$

The values of x_2, x_3 and x_4 are obtained and hence the frequency f by using the text.

---

where δ is the increment associated with the extended time $\theta\delta t$. Thus

$$\begin{aligned}
\{\delta x_i'\} &= \{x(t_i + \theta\delta t)\} - \{x(t_i)\}, \quad (a) \\
\{\delta \dot{x}_i'\} &= \{\dot{x}(t_i + \theta\delta t)\} - \{\dot{x}(t_i)\}, \quad (b) \\
\{\delta \ddot{x}_i'\} &= \{\ddot{x}(t_i + \theta\delta t)\} - \{\ddot{x}(t_i)\}. \quad (c)
\end{aligned} \tag{3.228}$$

The incremental force is given by

$$\{\delta F_i(t)\} = \{F(t_i + \theta\delta t)\} - \{F(t_i)\}. \tag{3.229}$$

As shown in Fig. 3.48a, b, both stiffness and damping are obtained for each time step as the initial values of the tangent to the corresponding curves. These coefficients are given as

$$\begin{aligned}
\{k_{ij}\} &= \{\delta F_{sti}/\delta x_j\}, \\
\{c_{ij}\} &= \{\delta F_{di}/\delta x_j\}.
\end{aligned} \tag{3.230}$$

During the extended time step the linear expression for the acceleration is

$$\{\ddot{x}(t)\} = \{\ddot{x}_t\} + [\delta\ddot{x}_i'/\theta\delta t\ (t - t_i)]. \tag{3.231}$$

The value of $\delta\ddot{x}_t'$ is taken from (3.228). Integration of (3.231) gives the following equations:

$$\{\dot{x}(t)\} = \{\dot{x}_t\} + \{\ddot{x}_i(t - t_i)\} + \frac{1}{2}\left\{\frac{\delta\ddot{x}_i'}{\theta\delta t} \times (t - t_i)\right\}, \tag{3.232}$$

$$\{x(t)\} = \{x_i\} + \{\dot{x}(t - t_i) + \left\{\frac{1}{2}\ddot{x}_i(t - t_i)^2\right\} + \left\{\frac{1}{6}\frac{\delta\ddot{x}_i'}{\theta\delta t} \times (t - t_i)^2\right\}. \tag{3.233}$$
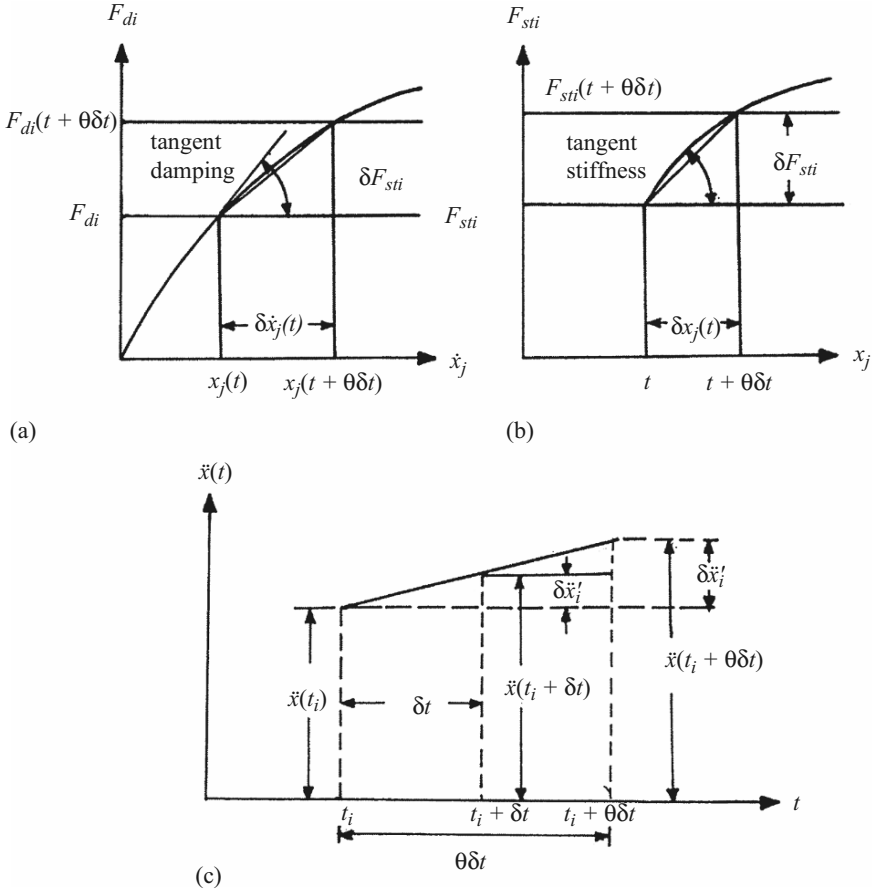
Fig. 3.48. Wilson-θ method; (**a**) values of c_{ij}; (**b**) value of k_{ij}; (**c**) linear acceleration

At the end of the extended interval $t = t_i + \theta\delta t$, (3.232) and (3.233) are reduced to

$$\delta\dot{x}_i' = \ddot{x}_i\theta\delta t + \frac{1}{2}\delta\ddot{x}_i\theta\delta t, \tag{3.234}$$

$$\delta x_i' = \dot{x}_i\theta\delta t + \frac{1}{2}\ddot{x}_i(\theta\delta t)^2 + \frac{1}{6}\delta\ddot{x}_i'(\theta\delta t)^2. \tag{3.235}$$

The values of $\delta\dot{x}_i'$ and $\delta x_i'$ are given in (3.228). By substituting the expression for $\delta x_i'$ from (3.235) into (3.234), the following equations are obtained.

$$\{\delta\ddot{x}_i'\} = \{[6/(\theta\delta t)^2]\delta\dot{x}_i'\} - \{[6/(\theta\delta t)^2]\dot{x}_i\} - \{3\ddot{x}_i\}, \tag{3.236}$$

$$\{\delta\dot{x}_i'\} = \{(3/\theta\delta t)\delta x_i\} - 3\{x_i\} - \frac{1}{2}\theta\delta t\{\ddot{x}_i\}, \tag{3.237}$$

The incremental acceleration $\delta\ddot{x}_i$ for the time interval δt can be obtained from

$$\{\delta\ddot{x}\} = \{\delta\ddot{x}'_i/\theta\}. \tag{3.238}$$

The incremental velocity and displacement for the time interval δt are given by

$$\{\delta\dot{x}_i\} = \{\ddot{x}_i\delta t\} + \frac{1}{2}\{\delta\ddot{x}_i\delta t\}, \tag{3.239}$$

$$\{\delta x_i\} = \{\dot{x}_i\delta t\} + \frac{1}{2}\{\ddot{x}_i(\delta t)^2\} + \frac{1}{6}\{\delta\ddot{x}_i(\delta t)^2\}, \tag{3.240}$$

$$\{x_{i+1}\} = \{x_i\} + \{\delta x_i\} \text{ at the end of the time step}, \tag{3.241}$$

$$\{\dot{x}_{i+1}\} = \{\dot{x}_i\} + \{\delta\dot{x}_i\}; \ t_{i+1} = t_i + \delta t. \tag{3.242}$$

When (3.236) and (3.237) are substituted into (3.227), the following results:

$$\{\delta\overline{F_i\,(t)}\} + [M]\left\{(6/\theta\delta t)\,\{\dot{x}_i\} + 3\,\{\ddot{x}_i\} + [C]_i\{3\{\dot{x}_i\} + \frac{1}{2}\theta\delta t\{\ddot{x}_i\}\right\}$$
$$= \{[K]_i + 6/\,(\theta\delta t)^2\,[M] + (3/\theta\delta t)\,[C]_i\}\,\{\delta x'_i\}. \tag{3.243}$$

Hence the initial acceleration for the next step is calculated at time $t + \delta t$ as

$$\{\ddot{x}_{i+1}\} = [M]^{-1}\,[F_{i+1}\,(t)] - \underset{\substack{\text{damping}\\\text{force}\\\text{vector}}}{[C]_{i+1}\,\{\dot{x}_{i+1}\}} - \underset{\substack{\text{stiffness}\\\text{force}\\\text{vector}}}{[K]_{i+1}\,\{x_{i+1}\}]}. \tag{3.244}$$

The procedure is repeated for t_{i+2}, etc., for the desired time.

3.4.6 Summary of the Wilson-θ Method

In order to summarize the Wilson-θ integration method, the following step-by-step solution should be considered with the dynamic, impact and explosion analysis of the structures:

(1) Assemble $[K]$, $[M]$ and $[C]$.
(2) Set the initial values of x_0, $\dot{x}_0$ and $F_0(t)$.
(3) Evaluate $\ddot{x}_0$ using

$$[M][\ddot{x}_0] = [F_0(t)] - [C]\{\dot{x}_0\} - [K]\{x_0\}.$$

(4) Select a time step δt (usually taken as 1.4) and evaluate

$$\theta\delta t, \ a_1 = 3/\,(\theta\delta t), \ a_2 = 6/\,(\theta\delta t), \ a_3 = \theta\delta t/3, \ a_4 = 6/\,(\theta\delta t)^2.$$

(5) Develop the effective stiffness matrix, $[K]_{\text{eff}}$

$$[K]_{\text{eff}} = [K] + a_4\,[M] + a_1[C],$$

where $[K] = [\bar{K}]$ or 0 for elastic and plastic respectively.

(6) Calculate $\delta \overline{F_i(t)}$ for the time interval t_i to $t_i + \theta \delta t$

$$\{\delta F_i(t)\} = \{F(t)\}_{i+1} + \left[\{F(t)\}_{i+2} - \{F(t)\}_{i+1}(\theta - 1)\right] - \{F(t)\}_i.$$

(7) Solve the incremental displacement $\{\delta x_i'\}$ ((3.230)) and the incremental acceleration $\{\delta \ddot{x}_i'\}$ ((3.232)) for the extended time interval $\theta \delta t$.
(8) Calculate $\{\delta \ddot{x}\}$ of (3.238).
(9) Calculate the incremental velocity and displacement of (3.239) and (3.240).
(10) Calculate $\{x_{i+1}\}$ and $\{\dot{x}_{i+1}\}$ for the time $t_{i+1} = t_i + \delta t$ from (3.241) and (3.242).
(11) Calculate $\{\ddot{x}_{i+1}\}$ at time $t_{i+1} = t_i + \delta t$ from the dynamic equilibrium equation (3.244).

A typical numerical example is shown in Table 3.17, where quadratic and cubic functions are considered instead of the linear function.

Table 3.17. Elasto-plastic analysis
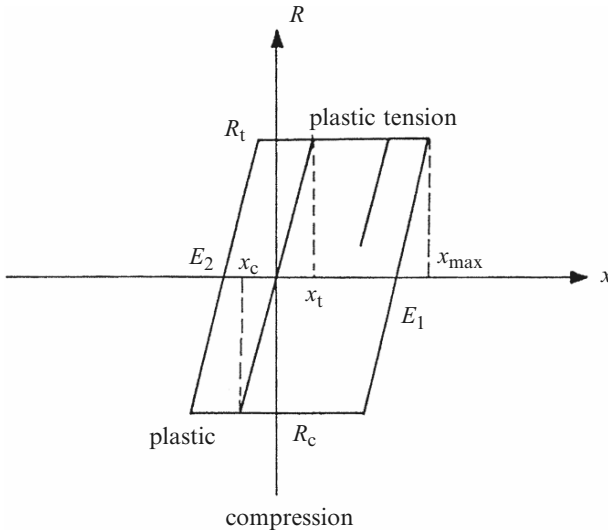
Increasing displacement $x > 0$
Decreasing displacement $x < 0$
x_t (plastic) in tension $= R_t/K$
x_c (plastic) in compression $= R_c/K$
R_t, R_c are restoring forces in tension and compression, respectively
Let $K = 3.35\,\mathrm{kN\,mm^{-1}}$; $R_t = 15\,\mathrm{kN} = R_c$; $M = 0.5\,\mathrm{kNs^2\,mm^{-1}}$
$c = $ damping coefficient $= 0.28\,\mathrm{kNs\,mm^{-1}}$
$x_0 = \dot{x}_0 = 0$ in the initial case

<div align="center">**Table 3.17.** (continued)</div>

$x_0 = 0$

$x_t = 15/3.35$ mm; $x_c = -4.48$ mm;

$T = 2\pi\sqrt{(M/K)} = 2\pi\sqrt{(0.5/3.35)} = 2.43$ s.

For convenience, $\delta t = 0.1$ s

$$[K]_{\text{eff}} = [\bar{K}] + a_4[M] + a_1[C]$$
$$= [\bar{K}]_p + (6/(0.1)^2)0.5 + (3/0.1)0.28,$$

where $[K]_p = 0$ for plastic

$$= [\bar{K}]_p + 300 + 8.4$$
$$= [\bar{K}]_p + 308.4,$$

$$\{\delta F_i(t)\} = \{\delta F(t)\} + \left(\frac{6}{\delta t}M + 3c\right)\dot{x} + \left(3M + \frac{\delta t}{2}c\right)\ddot{x}$$
$$= \{\delta F(t)\} + 3.84x + 1.514\ddot{x}.$$

The velocity increment is given by

$$\delta\dot{x} = (3/\delta t)\delta x_i - 3\dot{x}_i - (\delta t/2)\ddot{x}_i$$
$$= (3/0.1)\delta x_i - 3\dot{x}_i - (0.1/2)\ddot{x}_i$$
$$= 30\delta x_i - 3\dot{x}_i - 0.05\ddot{x}_i.$$

The results are obtained on the basis of the above two equations of force and velocity increments. The step-by-step procedure is covered in Sect. 3.4.6 and the results are tabulated as follows.

$$t \; F(t) \; x \; \dot{x} \; R \; \ddot{x} \; [\bar{K}_p] \; [K_{\text{eff}}] \; \delta F(t) \; \delta\bar{F}(t) \; \delta x \; \delta\dot{x}$$

3.5 Basic Dynamic Analysis of Sonic Booms

3.5.1 Introduction

The purpose of this section is to develop a method for estimating the time of arrival of incident and reflected sonic boom waves at any point on a building wall facing the flight track. To determine the time of arrival between bow and tail waves and their reflections, the geometric relations between wall and wave must be known for a given aircraft altitude, direction, and speed. Analytical method is developed for sonic boom and is applied to a one storey building. The results in pressures are obtained against time intervals. The analytical method is checked against finite element method and the results are fully collaborated.

3.5.2 Notation for Sonic Boom Analysis

D_{gv} horizontal distance between the vertex of the sonic boom and its ground intersection point, g

D_{pv} horizontal distance between a wall point, P, and the vertex of the sonic boom wave, at the instant P is intersected by the incident wave

m coefficient of acoustic velocity variation with altitude

S projected distance of the wave from the flight path in the YZ plane

T time for a wave to pass a point after the aircraft passes the coordinate origin (subscripts indicate incident or reflected wave; second subscript indicates the point)

ΔT_{irp} time interval between the arrival of the incident and reflected waves at a point, P, on a wall

X coordinate axis, horizontal and along the flight track on the ground

Y coordinate axis, horizontal and perpendicular to the flight track on the ground

Y_c distance along the Y-axis to the nearest corner point, c, of the wall on the ground

Z coordinate axis, vertical

B Mach angle or incident wave angle measured from the horizontal

θ angle between the wall and the Y-axis, measured clockwise from the Y-axis in the horizontal plane

τ time at which a pressure disturbance wave was emitted

Φ angle between the wall and the horizontal (XY) plane

3.5.3 Diffraction and Reflection of Sonic Boom Waves: Analytical Method

Sonic booms may be considered to act as acoustic waves, or plane weak pulses, since they are weak shock waves. The diffraction and reflection of an incident plane pulse by wedges and corners are treated and explicit, closed-form expressions are obtained in terms of elementary functions. For this geometry the solution is "conical" and independent of "radical" distance in the xyt space. This allows separation into appropriate coordinates, as is done in Busemann's conical flow method which is widely used in supersonic aerodynamics.

A solution is sought to the acoustic wave equation in the two-dimensional geometry of Plate 3.1c (subscripts represent differentiation)

$$P_{xx} + P_{yy} = \frac{1}{c^2} P_{tt} \qquad \text{for } \Phi \le \theta \le 2\pi, \qquad (3.245)$$

where

$$P = \frac{P - P_0}{P_1 - P_0},$$

$$\theta = \tan^{-1} \frac{y}{x}$$

P and P_1 are shown in Plate 3.1(c) on both side of the wave. P_0 is at point 0.
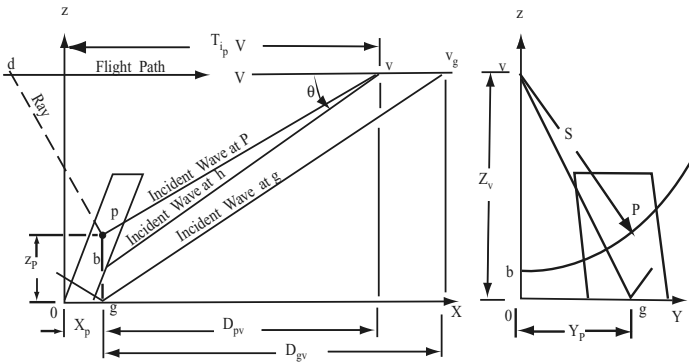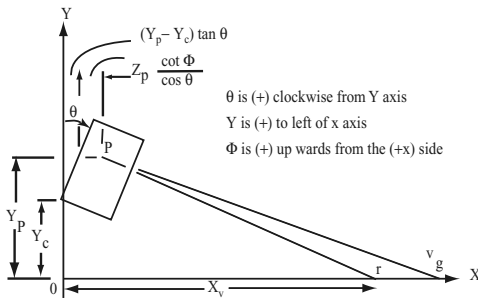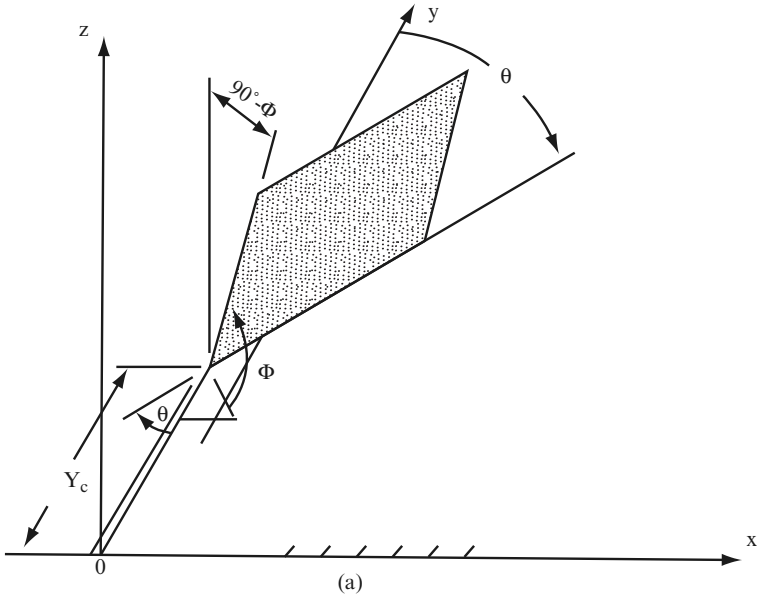
Plate 3.1. (**a**) Coordinate system for an arbitrarily oriented plane rectangular wall. (**b**) Model for the analysis of a conical wave intersecting a plane, rectangular, sloping wall. (**c**) Incident wave on a wedge

(c)
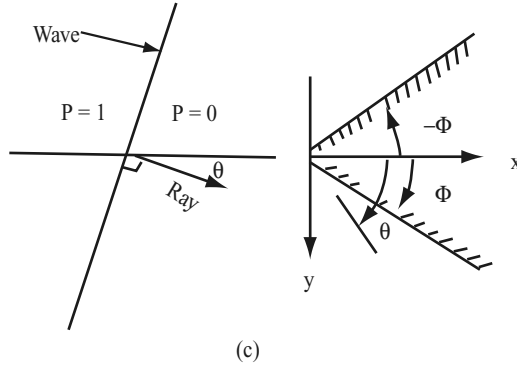
Plate 3.1. Incident waves on a wedge

By definition, the half-plane at $\theta = \pm\Phi$ form either a wedge or a corner, depending on whether Φ is less or greater than $90°$.

The solution to be considered will have jump discontinuities on a certain moving surface representing a shock wave, say $r(x, y) = ct$. It is required that r should satisfy the eiconal equation:

$$r^2_x + r^2_y = 1.$$

where c = velocity = $\dot{u} = v$ previously.

This implies that the surface can be constructed by Huygen's principle, i.e., that it moves with velocity c along its normal, and that it is reflected from the wall in accordance to the simple reflection law. A further assumption is that the reflected discontinuity value is twice the incident discontinuity value for a rigid wall. The orthogonal trajectories of a family of discontinuity surfaces S(t) are straight lines called "rays". The set of rays through a small closed curve on a discontinuity surface is called a "tube". The areas of the tubes at $S(t_o)$ and at $S(t)$, are denoted by dS_o and dS respectively. Also, the pressure discontinuities at $S(t_o)$ and $S(t)$ are denoted P_0 and P respectively. Then, for plane geometry, the magnitudes of the discontinuities must vary inversely as $\sqrt{dS}$:

$$\lim_{ds \blacktriangleright 0} \left(\frac{dS(t_0)}{dS(t)} \right)^{1/2} = \frac{P_0}{P}. \tag{3.246}$$

Equation (3.246) permits P to be computed from P_0 on the same ray, once the geometry of the discontinuity surfaces are known.

3.5.4 Method of Analysis

Looking at Plate 3.1a, b, in order to reduce computer time, dy/dz of the ray is treated constant at a value of flight altitude while the linear variation of speed of sound with altitude below the tropopause is kept constant. Its necessary to evaluate the arrival time of the incident shock wave as,

$$T_{ip} = 1/V(X_p + D_{pv}) = 1/V \left[X_p + \int_0^{S_p} \frac{dS}{\tan \beta} \right].$$ (3.247)

S is the projected distance of the wave from the flight path in YZ plane (refer to Plate 3.1b).

$$dS = \sqrt{(dY^2 + dZ^2)} = -dZ\sqrt{1 + (dY/dZ)^2}.$$ (3.248)

Flight Altitude Below the Tropopause

The assumptions and geometry give the following:

$$\left. \frac{dY}{dZ} \right|_{ray} = \text{constant} = \frac{Y - Y_v}{Z - Z_v}, \quad Y_v = 0,$$

$$dS = -dZ\sqrt{(1 + (Y/Z - Z_v)^2)},$$ (3.249)

$$c = c_g - mZ, \quad dZ = -dc/m$$

and

$$\tan \beta = \frac{1}{\sqrt{(M^2 - 1)}} = \frac{c}{\sqrt{(v_2 - c^2)}},$$

From (3.247), (3.248) and (3.249), the time interval from aircraft passage over the origin, O, when the wave arrival at point P can be calculated:

$$T_{ip} = 1/V \left[X_p + \sqrt{(1 + (Y_p/Z_p - Z_v)^2)} \int_{c^P}^{c_v} v^2 - c^2/mc.dc \right]$$

$$= 1/V \left[(Y_p - Y_c) \tan \theta + Z_p (\cot \Phi / \cos \theta) \right] + 1/mV\sqrt{1}$$
$$+ (Y_p/Z_p - Z_v)^2 \times \left[\sqrt{(v^2 - c^2{}_p)} - \sqrt{(v^2 - c^2{}_v)} \right.$$
$$\left. + V\ln \left[\frac{V + \sqrt{v^2 - c_v^2}}{V + \sqrt{v^2 - c_p^2}} \frac{c_p}{c_v} \right] \right],$$ (3.250)

$$T_{ig} = 1/V \left[(Y_p - Y_c) \tan \theta + Z_p (\cot \Phi/\cos \theta) \right] + 1/mV\sqrt{(1 + Y_p^2/Z_p)}$$
$$\times \left[\sqrt{(v^2 - c^2{}_g)} - \sqrt{(v^2 - c^2{}_v)} + V\ln \left[\frac{V + \sqrt{v^2 - c^2{}_v}}{V + \sqrt{v^2 - c^2{}_g}} \frac{c_g}{c_v} \right] \right].$$ (3.251)

Equations (3.250) and (3.251) permit T_{ip} and ΔT_{irp} to be computed.

Flight Altitude Above the Tropopause

The time of arrival of an incident wave be expressed as

$$T_{ip} = 1/V \left[X_p + \int_0^{S_p} \frac{dS}{\tan \beta} \right] = 1/V \left[X_p + \int_0^{S_t} \frac{dS}{\tan \beta} + X_p + \int_0^{S_p} \frac{dS}{\tan \beta} \right].$$ (3.252)

In view of the assumptions,

$$c = \text{constant in the region } Z_v \geq Z \geq Z_t,$$

$$\frac{Y_t}{Z_t - Z_v} = \text{Constant} = \frac{Y_p}{Z_p - Z_v}.$$

The integral terms in (3.252) become

$$\int_0^{S_t} \frac{dS}{\tan \beta} = \frac{Z_t - Z_v}{c_v} \sqrt{(v^2 - c_v^2)} \sqrt{\left(1 + (Y_t/Z_t - Z_v)^2\right)}, \qquad (3.253)$$

$$\int_{st}^{S_p} \frac{dS}{\tan \beta} = 1/m \sqrt{1 + \frac{Y_p}{Z_p - Z_v}}^2 \left[\sqrt{v^2 - c_p^2} - \sqrt{v^2 - c_v^2} \right.$$

$$\left. + V \ln \left[\frac{V + \sqrt{v^2 - c^2 v} \; c_p}{V + \sqrt{v^2 - c_p^2} \; c_v} \right] \right]. \qquad (3.254)$$

Equations (3.252), (3.253) and (3.254) are combined and the resulting expressions for T_{ip} and T_{ig} are:

$$T_{ip} = 1/V \left[(Y_p - Y_c) \; \tan \theta + Z_p (\cot \Phi / \cos \theta) \right] + 1/V \sqrt{1}$$

$$+ \frac{Y_p}{Z_p - Z_v} \left[\left[\frac{Z_v - Z_t}{c_v} \right] \times \sqrt{(v^2 - c_v^2)} \right.$$

$$\left. + \frac{\sqrt{v^2 - c_p^2}}{m} - \frac{\sqrt{v^2 - c_v^2}}{m} + \frac{V}{m} \ln \left[\frac{V + \sqrt{v^2 - c_v^2} \; c_p}{V + \sqrt{v^2 - c_p^2} \; c_v} \right] \right]. \qquad (3.255)$$

and

$$T_{ig} = 1/V \left[(Y_p - Y) \tan \theta + Z_p (\cot \Phi / \cos \theta) \right] + 1/V \sqrt{1}$$

$$+ \left[\frac{Y_p}{Z_p - Z_v} \right]^2 \left[\frac{Z_v - Z_t}{c_v} \sqrt{(v^2 - c_v^2)} + \frac{\sqrt{v^2 - c_g^2}}{m} - \frac{\sqrt{v^2 - c_v^2}}{m} \right.$$

$$\left. + \frac{V}{m} \ln \left[\frac{V + \sqrt{v^2 - c_v^2} \; c_g}{V + \sqrt{v^2 - c_g^2} \; c_v} \right] \right] \qquad (3.256)$$

From equations (3.250) and (3.251) T_{ip} and ΔT_{irp} can be computed.

Computations were performed for a vertical wall location of 30.48 m above ground level. The ground level was assumed to be at sea level, and flight altitudes of 2,1336, 10,973, and 6,096 m were used. For flight Mach numbers of 1.5, 2.0 and 3.0 and offset distances, Y_p, from O to 21,336 m, the three methods gave values of incident wave arrival time, T_{ip} and time interval between incident and reflected waves, ΔT_{irp}. The results are plotted in Figs. 3.49 and 3.50. This computational method establishes geometric relationships between the incident sonic boom bow wave and its ground reflection and a plane wall.

In (Plate 3.1c) the ray direction is normal to the discontinuity plane and is positive in the direction of motion. The angle between the ray direction and
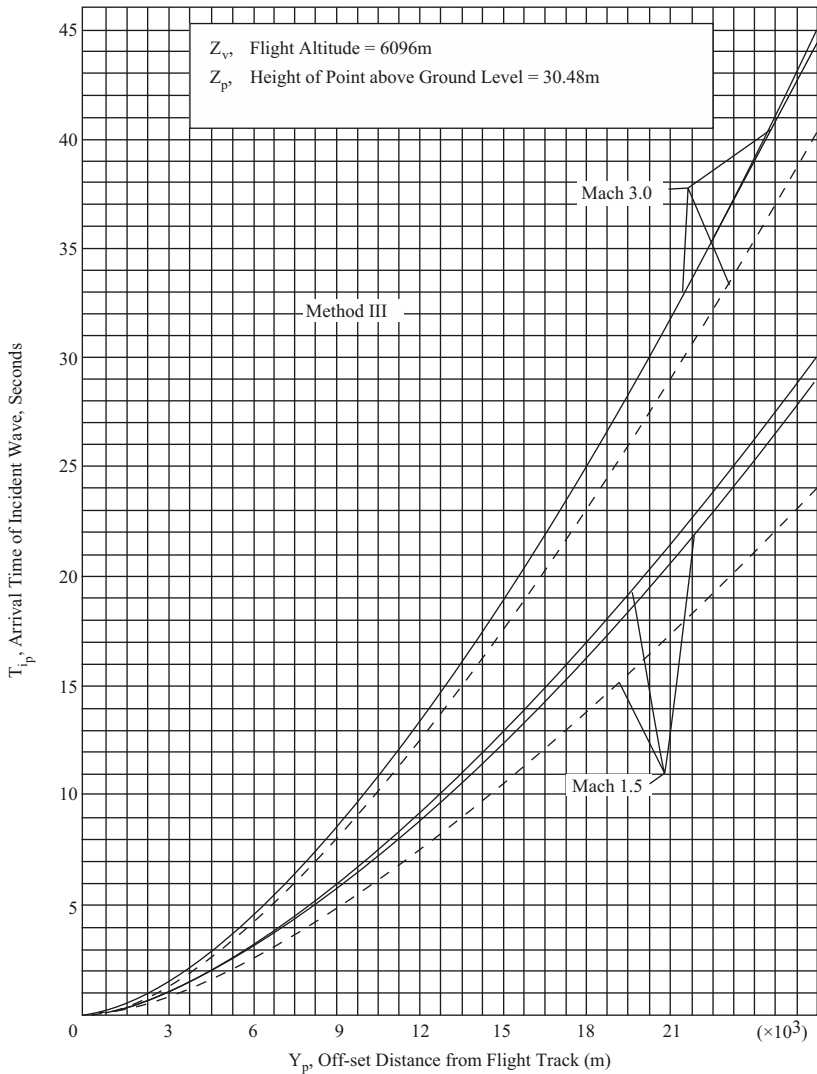
Fig. 3.49. Comparison of incident wave arrival times by the three methods

the x axis is Φ, and it is always positive. It follows that a plane discontinuity surface moves parallel to itself with velocity c along its normal and that a pressure jump, $P = 1$, across the wave does not change. This situation continues until the wave front reaches the wedge. Then reflected and diffracted discontinuity surfaces may originate. These surfaces can be obtained from the configuration at the instant of contact. Then the incident plan progresses to itself, and one (for $\geq \Phi$) or two (for $\geq \Phi$) reflected plane discontinuity surfaces,
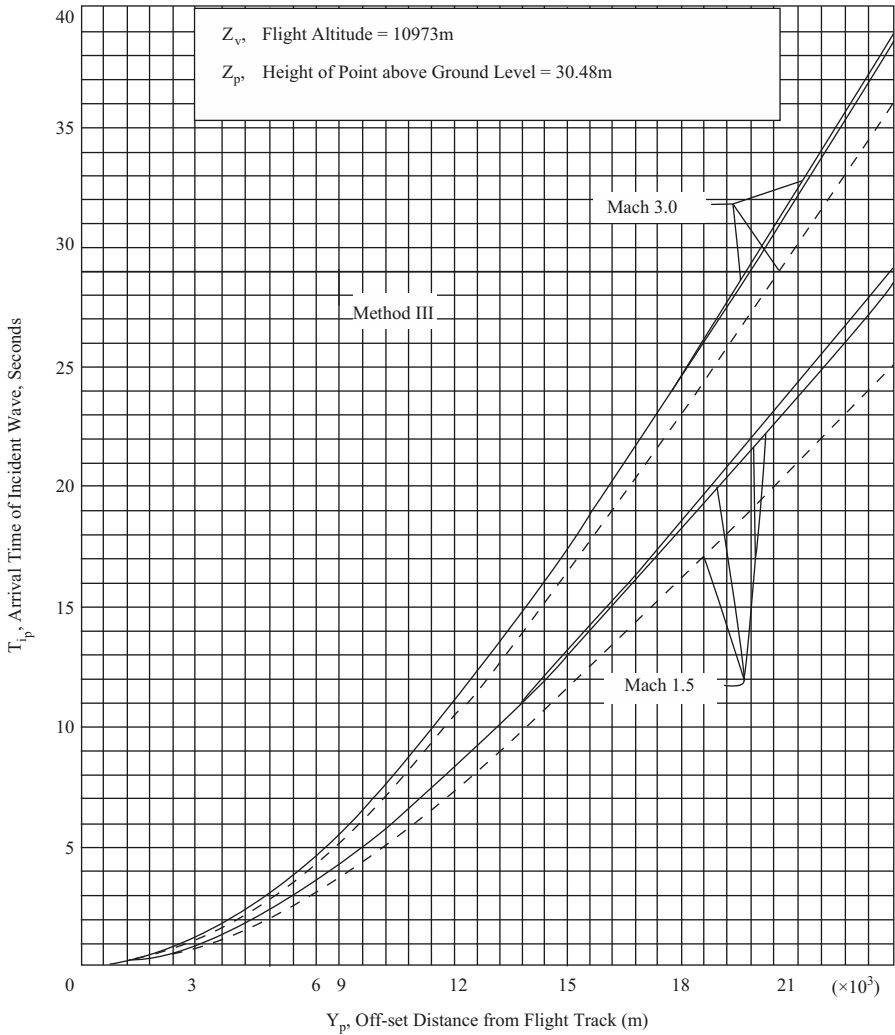
Fig. 3.49. (Continued)

plus a cylindrical surface with the wedge as its axis, are produced as Figs. 3.1a, b in Plate 3.2.

The pressure jump across the original plane is unchanged and the jump across the reflected wave is equal to that of the incident wave, making $P = 2$. The pressure jump across the cylindrical wave is zero, however, since all rays reaching it come from the axis where dS vanishes. Thus, P is not discontinuous across the cylinder. The value of P everywhere outside the cylinder is known (either 0, 1, or 2). Since $\partial p/\partial n = 0$ on the wedge and p is continuous across the circular arc, the values on the boundary are known. From these values it is possible to determine the P values within the cylinder.
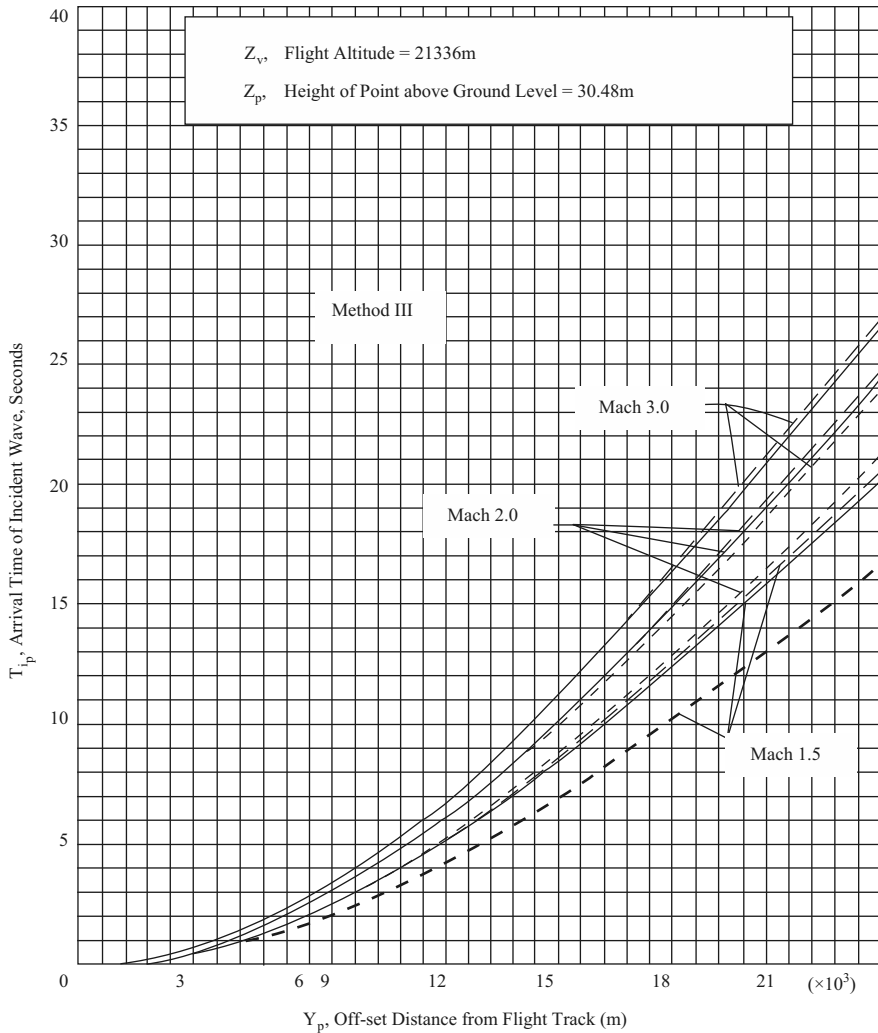
Fig. 3.49. (Continued)

The wave patterns are self-similar with respect to time, and so can be represented in x/ct and y/ct coordinates, as in Figs. 3.5a, b of Plate 3.2. Solutions are to be sought inside the circle along radial lines from the origin. A set of special coordinates in xyt space will be used for this solution. The coordinates are:

$$r = [c^2t^2 - (x^2 + y^2)]^{1/2},$$
$$s = ct/r, \qquad\qquad (3.257)$$
$$\theta = \text{arc } \tan y/x.$$

The chart's y-axis is labeled "$\Delta T_{i_r p}$, Time Interval Between Incident and Reflected Waves, Seconds" with values from 0 to .175. The x-axis is labeled "Y_p, Off-set Distance from Flight Track (m)" with values 3, 6, 9, 12, 15, 18, 21 ($\times 10^3$).

Legend box:
Z_v, Flight Altitude = 6096m
Z_p, Height of Point above Ground Level = 30.48m

Curve labels: Mach 3.0, Mach 2.0, Mach 1.5, Method III
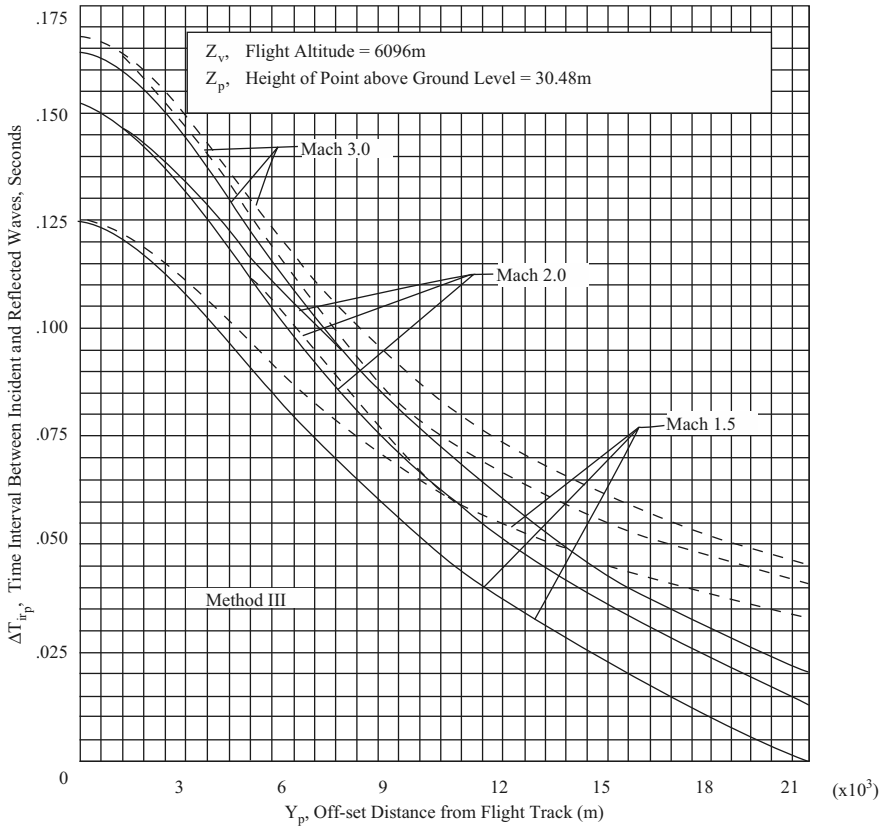
Fig. 3.50. Comparison of the time intervals between incident and reflected waves computed by the three methods

The boundary of the circle is given by r = 0 and s = ∞. Then the expression becomes as follows:

$$(r^2 P_r)_r + [(1 - s^2)p_s]_s + \frac{1}{1 - s^2}P_{\theta\theta} = 0. \tag{3.258}$$

In accordance with the assumption of similarity, $P = P(s, \theta)$, (3.258) becomes

$$[(1 - s^2)P_s]_s + \frac{1}{1 - s^2}P_{\theta\theta} = 0. \tag{3.259}$$

3.6 Pressure–Time History of a Sonic Boom Wave on Window in a Building

Plate 3.3 shows a typical Boeing aircraft used for a sonic boom test flight. The particular sonic boom was produced at a height of 11,504 m altitude at a speed of 1.4 Mach number. Orientation and distance of the aircraft course
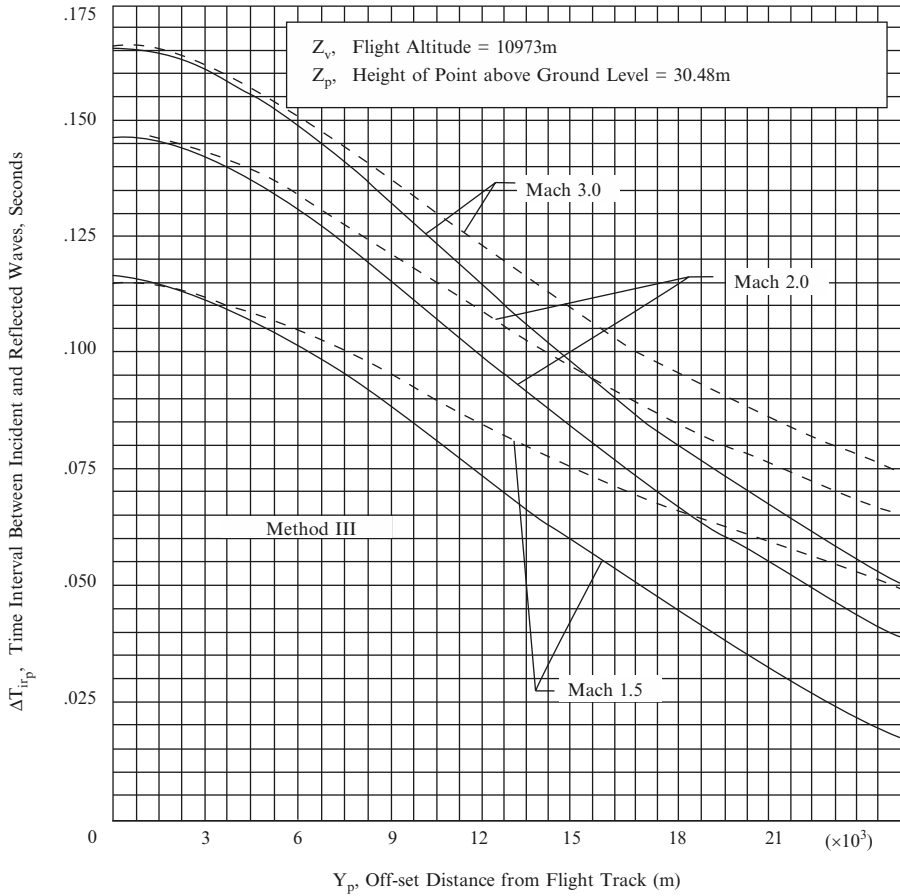
Fig. 3.50. (Continued)

with respect to the building with $2.44 \times 3.48 \times 6$ mm plate glass windows. The wave time history has been converted with the wave geometry in order to determine the angle between wave and wall in a horizontal plane, two points were chosen, T_i was computed using the above analysis. Assuming the distance between these two points is L and the points 1 and 2 with horizontal plane XY, the wave angle θ_w is computed as:

$$\tan \theta_w = \tan \theta - V/L(T_{i2} - T_{i1}) \sec \theta. \qquad (3.260)$$

Similarly two points have been chosen on a verification (upper and lower corner points) of a building, naming them 3 and 4 respectively, the vertical plane containing points 3 and 4 perpendicular to the wave line (at an angle $\theta_w + 90°$ from Y-axis plane is shown in Plate 3.5c. For a wall height H the angle Φ_w in the vertical plane is computed as:

$$\Phi_w = C/H \ (T_{i4} - T_{i3}). \qquad (3.261)$$
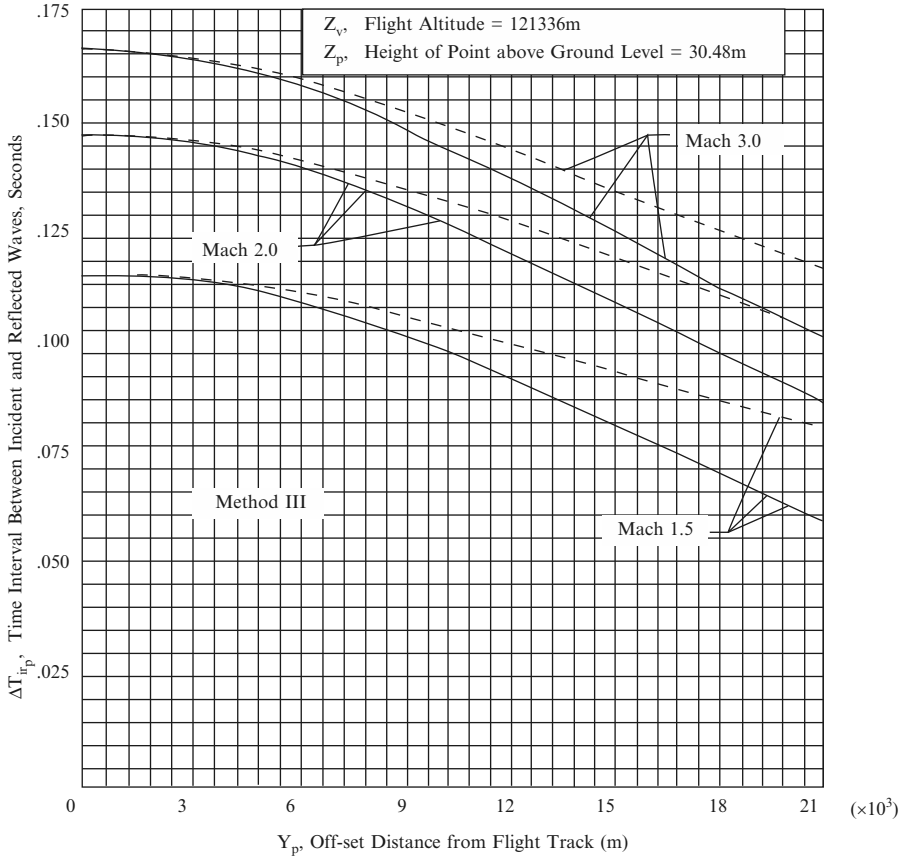
Fig. 3.50. (Continued)

Data on one-storey building (Flight Path geometry Ref: Plate 3.4)

$L = 32.0\,\text{m}, \ H = 14.0\,\text{m},$
$(T_{i2} - T_{i1}) = 0.0031\,\text{s},$
$(T_{i4} - T_{i3}) = 0.0038\,\text{s}.$
Using (3.260) and (3.261)
$\theta_w = 26.8°,$
$\Phi_w = 70.1°.$

Resulting wave building relationship is shown in Plate 3.5a with wave time positions as shown in Plate 3.5b. The value of T_{ir} – the time for a wave to pass point after it has passed the reference point at the ground level.

Using the test data of the flight Mach number, altitude and Y-distance, the bow-to-tail wave time interval is evaluated as 0.135 s. The incident ground over pressure to be $7.9\,\text{N}\,\text{m}^{-2}$.
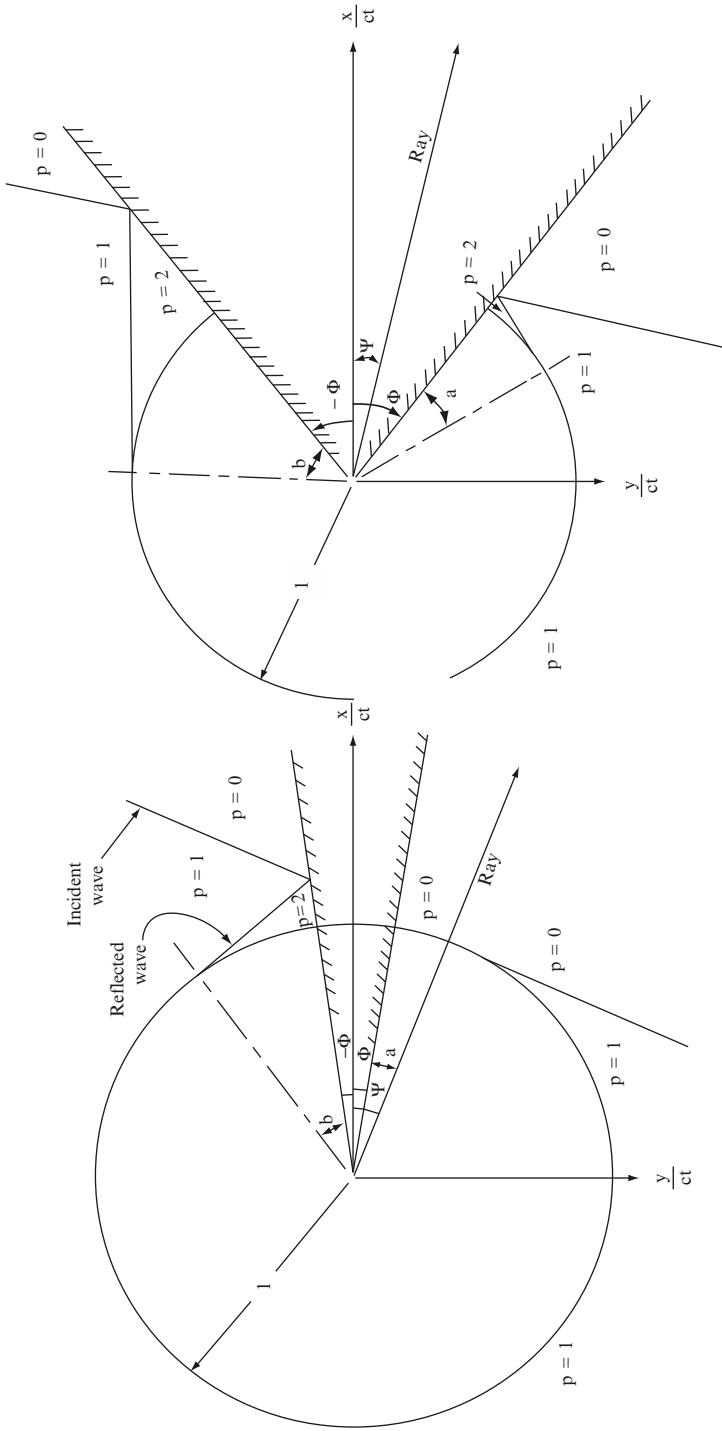
(a) $\Psi \geq \Phi$ (One Reflected Wave)

(b) $\Psi < \Phi$ (Two Reflected Waves)

Fig. 1. Diagram of a plane wave intersecting a wedge

Plate 3.2. Reflection of a plane wave
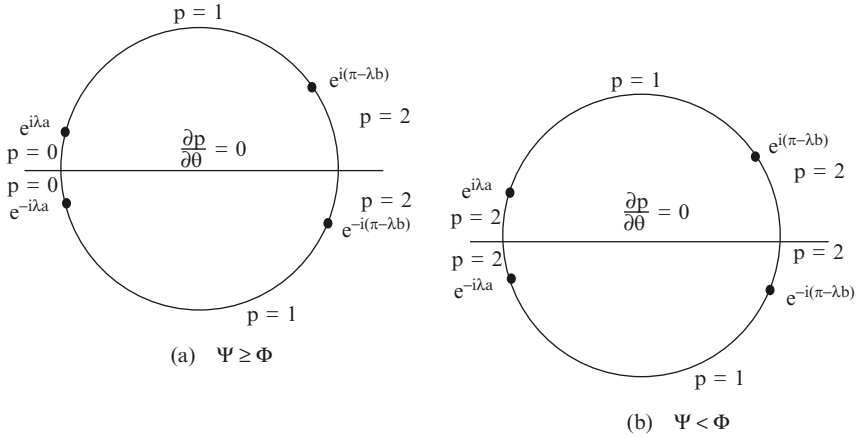
Fig. 2. Complex plane wedge/hock representation

Plate 3.2. (Continued)

Boeing 767-200ER

General Specifications

Passengers	
Typical 3-calss configuration	181
Typical 2-calss configuration	224
Typical 1-calss configuration	Up to 255
Cargo	2,875 cubic feet (81.4 cubic meters)
Engines' Maximum Thrust	
Pratt & Whitney PW4062	63,300 pounds (28,713 kilograms)
General Electric CF6-8OC287F	62,100 pounds (28,169 kilograms)
Maximum Fuel Capacity	23,980 US gaiions (90,770 liters)
Maximum Takeoff Weight	395,000 pounds (179,170 kilograms)
Maximum Range	6,600 nautical miles
Typical city pairs: New York-Beijing	12,200 kilometers
Typical Cruise Speed	0.80 Mach
at 35,000 feet	530 mph (850 km/h)
Basic Dimensions	
Wing Span	156 feet 1 inch (47.6 meters)
Overall Length	159 feet 2 inch (48.5 meters)
Tail Height	52 feet (15.8 meters)
Interior Cabin Width	15 feet 6 inches (4.7 meters)

FEDERAL EMERGENCY MANAGEMENT AGENCY

Plate 3.3. Aircraft information (FEMA, Washington) D.C. 2002
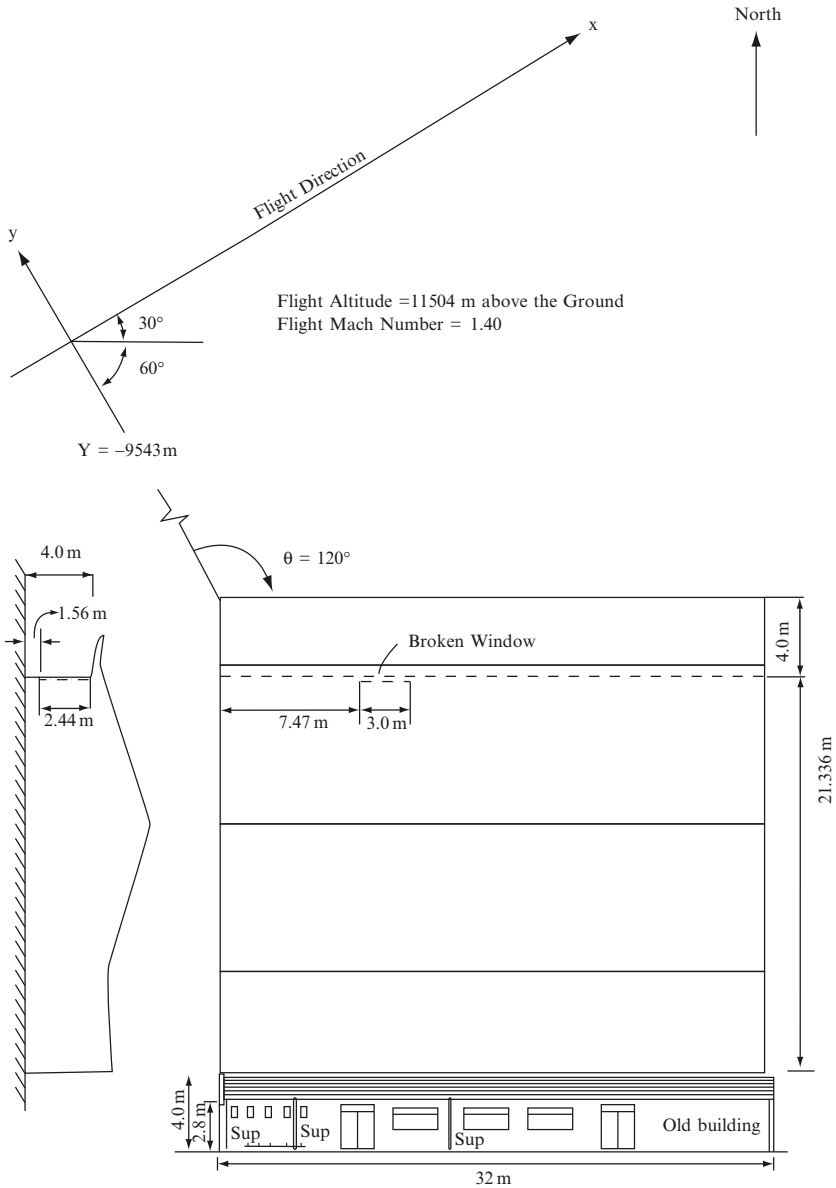
Plate 3.4. Geometry used in the arrival time

Upon computing the incident-to-reflected wave time interval, ΔT_{irp} for 2.0 m and 4.0 m heights, the pressure histories on the west wall were predicted as shown in Plate 3.6a.

Plate 3.6b shows the window on the north wall under the roof overhang and is broken. Looking at Plate 3.7a, b, the incident and reflected waves were

(a)

(c)

θ = Wall Angle
θ_w = Wave Angle

Φ_w = Wave Angle

(d)

(b)
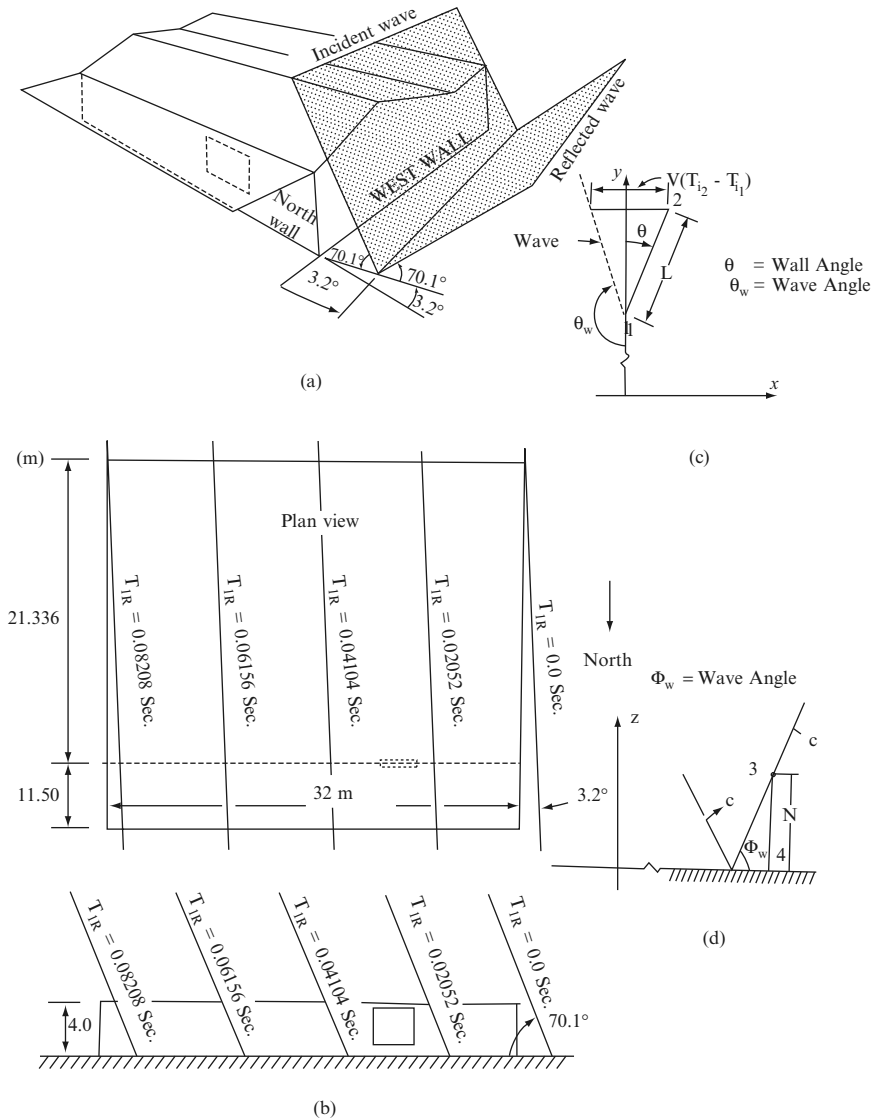
Plate 3.5. (**a**) Geometric relationship of building and wave (**b**) Arrival times of incident wave of sonic boom wave on (**c**) Wave in the horizontal plane (**d**) Wave in the vertical plane. *Note*: All Dimensions in m

defracted by the roof overhang and reflected by the ground and roof overhang. For this particular geometry $\Phi = 0$ and $\Phi = 19.9°$, when the resulting equations are obtained as shown in Table 3.18.
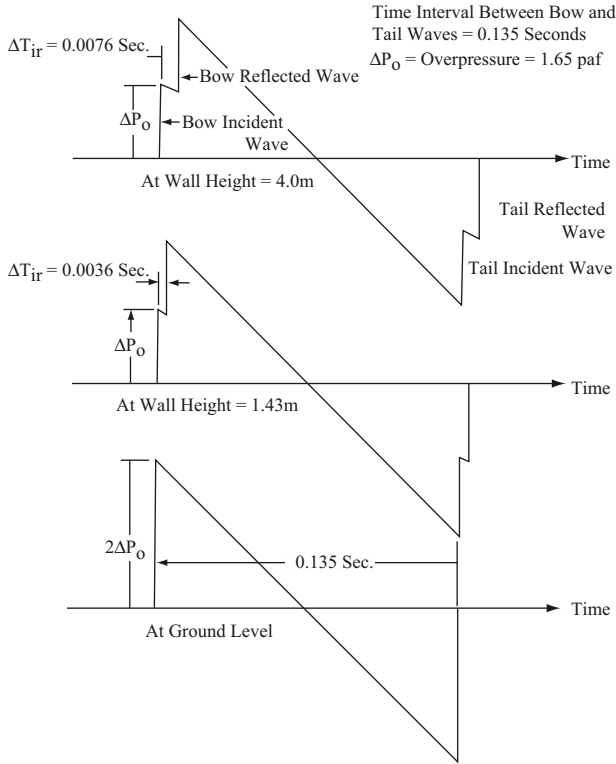
(a)
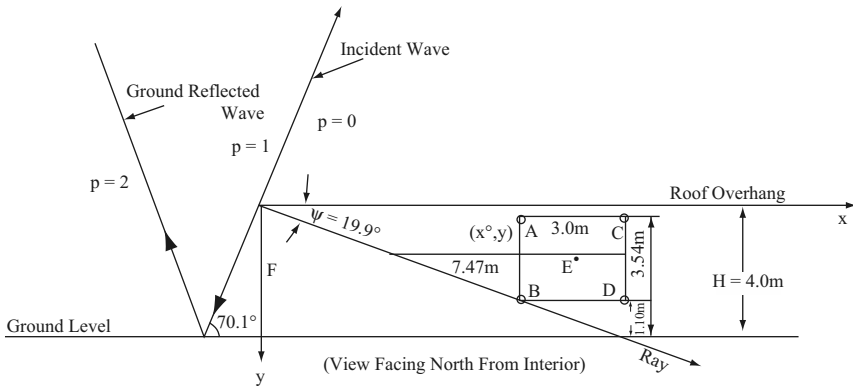
(b)

Plate 3.6. (**a**) Sonic boom wave pressure histories on the kinney shoe store west wall. (**b**) Geometry of sonic boom wave and front of the store used in the two-dimensional analysis

(View Facing North From Interior)

(a) $ct_r < \sqrt{x^2 + y^2}$

(a)

(View Facing North From Interior)
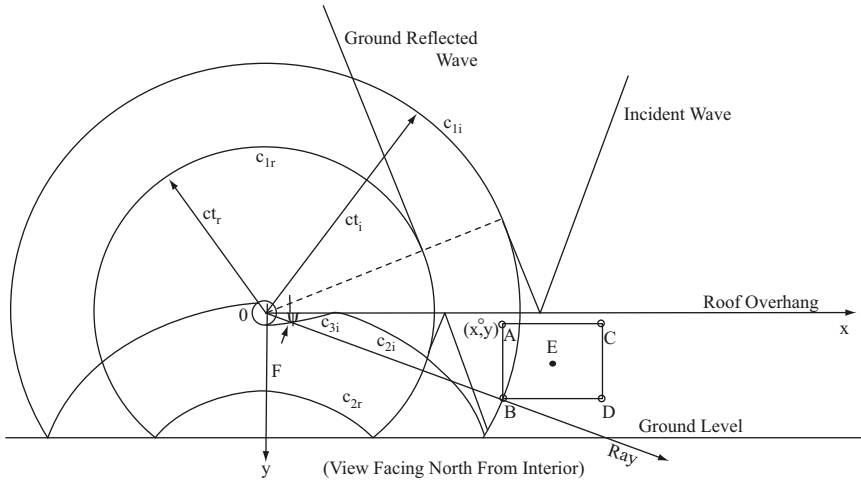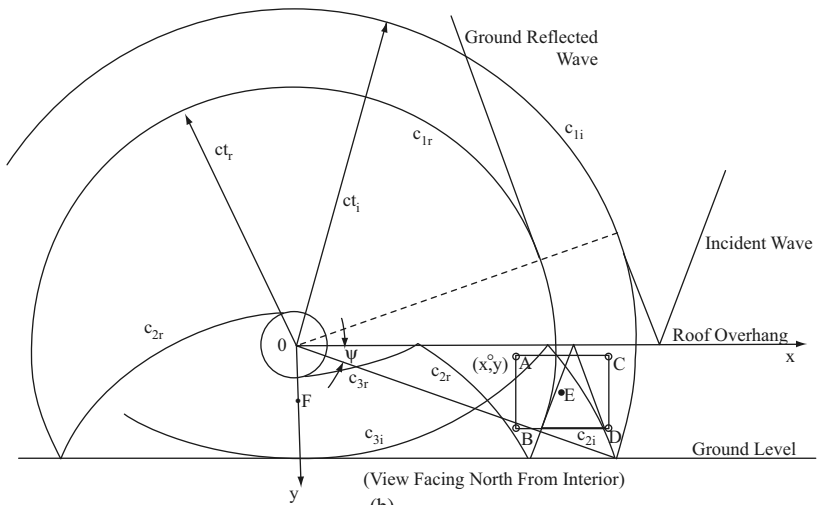
(b) $ct_r > \sqrt{x^2 + y^2}$
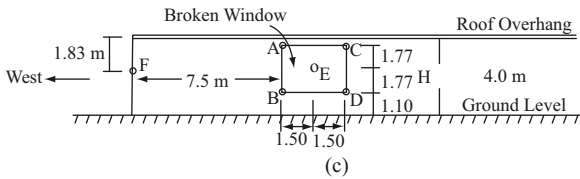
(c)

Plate 3.7. (**a**) Incident and reflected wave patterns on the north wall. (**b**) Dimensions c_{tr} and c_{2r} in x-y coordinates. (**c**) The chosen six points on the north wall of the building

Table 3.18. Expressions for overpressures due to incident and deflected waves

The value is taken in the interval between 0 and π.

Case 1, $\Phi \leq \downarrow \leq \pi/2 - \Phi$

$$\mathbf{p} = \mathbf{1} - \mathbf{1/\pi} \, \tan^{-1} \left[\frac{-(1 - \rho^{2\lambda}) \cos \lambda \, (\downarrow - \pi)}{(1 + \rho^{2\lambda}) \sin \lambda(\downarrow - \pi) - 2\rho^{\lambda} \sin \lambda(\theta - \pi)} \right]$$

$$+ \mathbf{1/\pi} \, \tan^{-1} \left[\frac{-(1 - \rho^{2\lambda}) \cos \lambda(\downarrow + \pi)}{(1 + \rho^{2\lambda}) \sin \lambda(\downarrow + \pi) - 2\rho^{\lambda} \sin \lambda(\theta - \pi)} \right]. \tag{1}$$

Case 2, $0 \leq \downarrow \leq \Phi$

$$\mathbf{p} = \mathbf{1} + \mathbf{1/\pi} \, \tan^{-1} \left[\frac{(1 - \rho^{2\lambda}) \cos \lambda(\downarrow - \pi)}{(1 + \rho^{2\lambda}) \sin \lambda(\downarrow - \pi) - 2\rho^{\lambda} \sin \lambda(\theta - \pi)} \right]$$

$$+ \mathbf{1/\pi} \, \tan^{-1} \left[\frac{-(1 - \rho^{2\lambda}) \cos \lambda(\downarrow + \pi)}{(1 + \rho^{2\lambda}) \sin \lambda \, (\downarrow + \pi) - 2\rho^{\lambda} \sin \lambda \, (\theta - \pi)} \right]. \tag{2}$$

3.6.1 Application to a Sonic Boom Wave Incident on a Building

Using (3.262) and (3.263), one can compute the pressure distribution in a circular arc of radius ct surrounding a corner of a structure struck by a sonic boom wave. The circle defines the region in which the wave is diffracted and reflected due to the pressure of the corner.

$$\lambda = \frac{\pi}{2(\pi - \Phi)} = \frac{1}{2},$$

$$\mathbf{p} = \mathbf{1} - \mathbf{1/\pi} \, \tan^{-1} \left[\frac{-(1 - \rho) \cos \frac{1}{2} \, (\downarrow - \pi)}{(1 + \rho) \sin \frac{1}{2} \, (\downarrow - \pi) - 2\sqrt{\rho} \sin \frac{1}{2} \, (\theta - \pi)} \right] \tag{3.262}$$

$$+ \mathbf{1/\pi} \, \tan^{-1} \left[\frac{-(1 - \rho) \cos \frac{1}{2} \, (\downarrow + \pi)}{(1 + \rho) \sin \frac{1}{2} \, (\downarrow + \pi) - 2\sqrt{\rho} \sin \frac{1}{2} \, (\theta - \pi)} \right].$$

Equation can be simplified to become

$$\mathbf{p} = \mathbf{1} - \mathbf{1/\pi} \, \tan^{-1} \left[\frac{(1 - \rho) \sin(\downarrow/2)}{(1 + \rho) \cos(\downarrow/2) - 2\sqrt{\rho} \cos(\theta/2)} \right]$$

$$+ \mathbf{1/\pi} \, \tan^{-1} \left[\frac{(1 - \rho) \sin(\downarrow/2)}{(1 + \rho) \cos(\downarrow/2) - 2\sqrt{\rho} \cos(\theta/2)} \right].$$

C   disturbance region

$p = \dfrac{p - p_o}{p_1 - p_o}$ dimensionless overpressure at the point x, y due to the sonic boom

p_i p at the point x, y at any time t_i due to the incident wave

p_r p at the point x, y at any time t_i due to the reflected wave

p_{np} p at the point x, y at any time t_i due to the disturbance region C_n

A computer method can be developed for the wave history at any point x,y in the coordinate system shown. The time t = 0 corresponds to the condition at which the incident wave of the sonic boom has reached the origin of the chosen coordinate axes (west edge of the roof overhang). A reference is made to program ISOPAR in the Appendix.

P_{nb} p at any time t_i at the boundary of the disturbance region at the angle θ_n

$\Delta P = P - P_o$ overpressure at the point x, y at any time t_i due to the sonic boom

$R_1 = \sqrt{(x^2 + y^2)}$ the distance of the point x, y from the origin "0"

$R_n = \sqrt{(x^2 + y_n^2)}$ the distance of the point x, y from the origin of the disturbance region C_n

t_i time elapsed since the incident wave passed over the origin "0"

t_r time elapsed since the reflected wave passed over the origin "0"

$y_n = (n - 1)H + y$, if n is odd

    $= nH - y$, if n is even; y coordinate of the disturbance region C_n.

$\theta_n = \tan^{-1}(y_n/x)$, inclination of the point x, y in the vertical plane (positive in clockwise direction from the x-axis).

A relation between t_i and t_r is established as

$$t_r = t_i - \frac{2H \tan \downarrow \cos \downarrow}{c} = t_i - \frac{2H \ \tan \downarrow}{c}. \tag{3.263}$$

The pressure history at the point x, y due to the passage of a sonic boom is a function of the geometry of the incident and reflected waves and the several disturbance regions at any time t_i. Computational procedure is presented below to predict the overpressure due to the incident and reflected wave. At any time t_i, the overpressure at the point x, y is the algebraic sum of the overpressures to the incident and reflected waves.

3.6.1.1 Computations of Overpressure due to the Incident Wave

A reference is made to PROGRAM ISOPAR
     Condition 1: $ct_i \leq R_1$

(a) If $\theta_1 \leq \downarrow$; $P_i = 0$
(b) If $\theta_1 > \downarrow$;

$$
\begin{aligned}
&\text{for } \frac{ct_i}{\cos(\theta_1 - \downarrow)} > R_1, p_i = 1, \\
&\text{and for } \frac{ct_i}{\cos(\theta_1 - \downarrow)} \leq R_1, p_i = 1.
\end{aligned}
\tag{3.264}
$$

Condition 2: $ct_i > R_1$, n was computed for

$$
R_n < ct_i \leq R_{n+1}, \tag{3.265}
$$

where

$$
R_n = (x^2 + y^2)^{1/2} \tag{3.266}
$$

and

$$
\begin{aligned}
y_n &= (n-1)H + y, \text{ if n is odd,} \\
&= nH - y, \text{ if n is even.}
\end{aligned}
\tag{3.267}
$$

Then p_i was the algebraic sum of the overpressure contributed by the regions c_{1i}, $c_{2i} \ldots c_{(n-1)i}$ and c_{ni}. So,

$$
P_i = P_{1i} + P_{2i} + P_{3i} + \ldots + P_{(n-1)i} + P_{ni}, \tag{3.268}
$$

where

$$
P_{1i} = P_{1pi}
$$

and for $n > 1$

$$
P_{ni} = P_{npi} - P_{nbi}.
$$

P_{npi} was computed and the values for ρ and θ are as follows:

$$
\rho = \frac{R_n}{R_n + \sqrt{(c^2 t_i^2 - R_n^2)}}, \tag{3.269}
$$

$$
\theta = \theta_n = \tan^{-1}(y_n/x). \tag{3.270}
$$

P_{nbi} depends on the value of θ_n and the value of always 0 or 1 or 2 depending on the geometry of the point in consideration. In this particular case, it was always 1. Hence,

$$
P_{nbi} = 1. \tag{3.271}
$$

At any time, t_i, p_i was computed by Equations (3.264) to (3.271).

3.6.1.2 Computation of Overpressures Due to the Reflected Wave

For any time t_i and t_r value was computed from (3.264) and (3.272).

Condition 1: $ct_r \leq R_1$

$$\text{If } x \geq \frac{ct_r}{\text{Cos } \theta} + y \tan \downarrow; \ P_r = 0$$

$$\text{If } x < \frac{ct_r}{\text{Cos } \theta} + y \tan \downarrow, \text{ and}$$

(a) $R_1 \geq \dfrac{ct_r}{\text{Cos}(\downarrow - \theta_1)}, \ P_r = 1$

(b) $R_1 < \dfrac{ct_r}{\text{Cos}(\downarrow - \theta_1)}, \text{ and } \theta_1 \leq \downarrow; \ P_r = 2$

(c) $R_1 < \dfrac{ct_r}{\text{Cos}(\downarrow - \theta_1)}, \text{ and } \theta_1 > \downarrow; \ P_r = 1$

Condition 2: $ct_r > R_1$, n was computed such that

$$R_n < ct_r \geq R_{n+1}. \tag{3.272}$$

Then P_r was the algebraic sum of the overpressure contributed by the regions $C_{1r}, C_{2r}, \ldots\ldots, C_{(n-1)r}$, and C_{nr}. P_r was computed by the same procedure of Condition 2 of the incident wave after replacing t_i by t_r and changing the subscripts "i" to "r" in the overpressure terms.

3.6.1.3 Computational Technique for an N-Wave

A sonic boom ordinarily will have a shape similar to an N-wave. The time interval, Δt, between the bow and tail waves of the sonic boom that caused the broken window has been estimated from related test data to be 0.135 s. An N-wave can be treated as two shocks of equal strength ($p_i = p_r = 1/2\Delta P_o$) with a series of expansion waves between them. An N-wave of strength $p_i = 1.0$ and $p_r = 1.0$ at bow and tail waves separated by 0.135 s was assumed. Then 135 small expansion waves were assumed of strength $p_i = p_r = 2/135$, each separated by a time interval of 0.001 s. Overpressure at any time t_i was then the algebraic sum of all the overpressure due to all the step waves, effective at that time. The input to the region beneath the canopy was thus an N-wave of incident pressure for a unit overpressure sonic boom wave and a period of 0.135 s. The resulting pressure at any point considered the reflection/diffraction effects and the height of the point.

3.6.1.4 Computations and Results of the Analytical Method

The pressure distribution due to the subject sonic boom was computed at six points, A through F, as shown in Plate 3.7c on the north wall of the building.

Computer programs were written both for a step input and for an N-wave utilizing the technique described above. Above 15 min were required to obtain the pressure history of each point from $t_i = 0$ to 0.16 s on an IBM 7040 computer for an N-wave. The pressure distribution at points A through D are plotted for a step input wave and for an N-Wave respectively. The dotted lines represent the input waves if there were no corner or overhang effects.

Data

Apart from data given on Plate 3.8, the following data have been used in the computations and in the finite element program ISOPAR

$T_o = 29.5\,°C$

$C = \text{constant} = c_o = 348\,\text{m s}^{-1}$

$P_o = 95.76\,\text{kN m}^{-2}$

$\rho = \text{constant} = \rho_o = 1.1052\,\text{kg m}^{-3}$

$\Delta x = h_1 = h_2\ \cot \Phi_w = 0.166\,\text{m}$

$\Delta y = h_2 = 0.457\,\text{m}$

$K = 1/c = 0.000875\,\text{s}$

$K_1 = h_1/T = K\ \sin x = 0.000824\,\text{s}$

$K_2 = h_2/T = K\ \cos x = 0.000297\,\text{s}$

$\Delta t = T = 0.000447\,\text{s}$

$\omega = 1$

$\alpha = K_{\omega c} \sin^2 x = \sin^2 x = 0.884$

$\beta = K_{\omega c} \cos^2 x = \cos^2 x = 0.114$

Computations and Results of the Numerical Method

Computer programs were written for both a step input with incident-plus-reflected wave strength of 47.88 N/m², and for an N-wave having bow-to-tail wave time interval of 0.135 s and a strength of 47.88 N/m². The initial conditions assumed for the step input in regions (0), (1), and (2) were:

$u_o = 0$

$v_o = 0$

$P_1 = 95.765\,\text{kN m}^{-2}$

$u_1 = \dfrac{c(P_1 - P_o)\sin x}{P_o}$

$v_1 = \dfrac{c(P_1 - P_o)\cos x}{P_o}$

$P_2 = 45.767$

$u_2 = 2u_2$

$v_2 = 0$

3.6.2 Analysis of Results

The N-wave was treated the same way as in the previous analysis except that here 302 expansions waves were taken so that they were spread by a distance of one field point width in the x-direction. Initial conditions in region (0) were the same as above, but in regions (1) and (2) algebraic sums of the incident and reflected compression and expansion waves were considered.

Pressure histories for the six points, A through D, were computed by interpolation of the adjacent field points for both a step input and an N-wave. Plate 3.8 shows the unbroken and broken glass with input parameters.

Loads up to elastic conditions $= 1.5\,\mathrm{kN\,m^{-2}}$ are permitted and in addition:

For window pane dimensions 1.55×1.25 m, i.e. A $= 1.934\,\mathrm{m^2}$ (8 mm toughened glass (T*) and 10 mm laminated glass (L*))

Frame loads $\times$ 2.0 (SF* $=$ safety factor) $= 50\,\mathrm{kN\,m^{-2}}$

Equivalent static yield stress $= 1.65 \times 110 = 181.5\,\mathrm{N\,mm^{-2}}$ for the frame

Deflection limitation $> 1/264$ span

The average edge reaction at edge nodes $(\mathrm{kN\,m^{-1}})$

(Equivalent ultimate static load)

$$= \frac{\text{equivalent ultimate static load} \times \text{area}}{\text{perimeter of the panel}}.$$

For example for the $1.55 \times 1.25\,\mathrm{m^2}$ pane

$$= \frac{50 \times 1.934}{2(1.55) + (1.25)}$$

$$= 17.268\,\mathrm{kN\,m^{-1}}.$$

This load is distributed in equal proportions over nodes at edges.

The analytical method presented in this section presented is compared with the finite element method based on the given geometry and data, the results obtained from both analyses are compared in figures in the form of load-time function of the sonic boom. The analytical results are compared with the finite element method in Figures 3.51 to 3.54.

Finite element mesh   *Nodes and elements*

Mode shape with glass window panel

The Window is made up of a finite element mesh:

Steel frame and fixings:

Glass: four-noded solid element isoparametric
           constant thickness and single layer   115 mm

E = 209 GN/m²

ν = 0.3

t = Varies from 0.8 mm up

Frame elements: four-noded solid element isoparametric   138 mm
                  four-noded trapezoidal   84 mm
                  four-noded triangular   84 mm
                  nodes   4300 mm

P = 7800 kg/m³

Minimum load to satisfy the protective system criteria for minimum centrally
applied load without:

(a) fracturing ———— ⎡ = 1.35kN if any length is 900 mm or over

(b) deflecting   ⎣ = 1.1kN if under 900 mm length

Plate 3.8. Finite element analysis of glass window damage
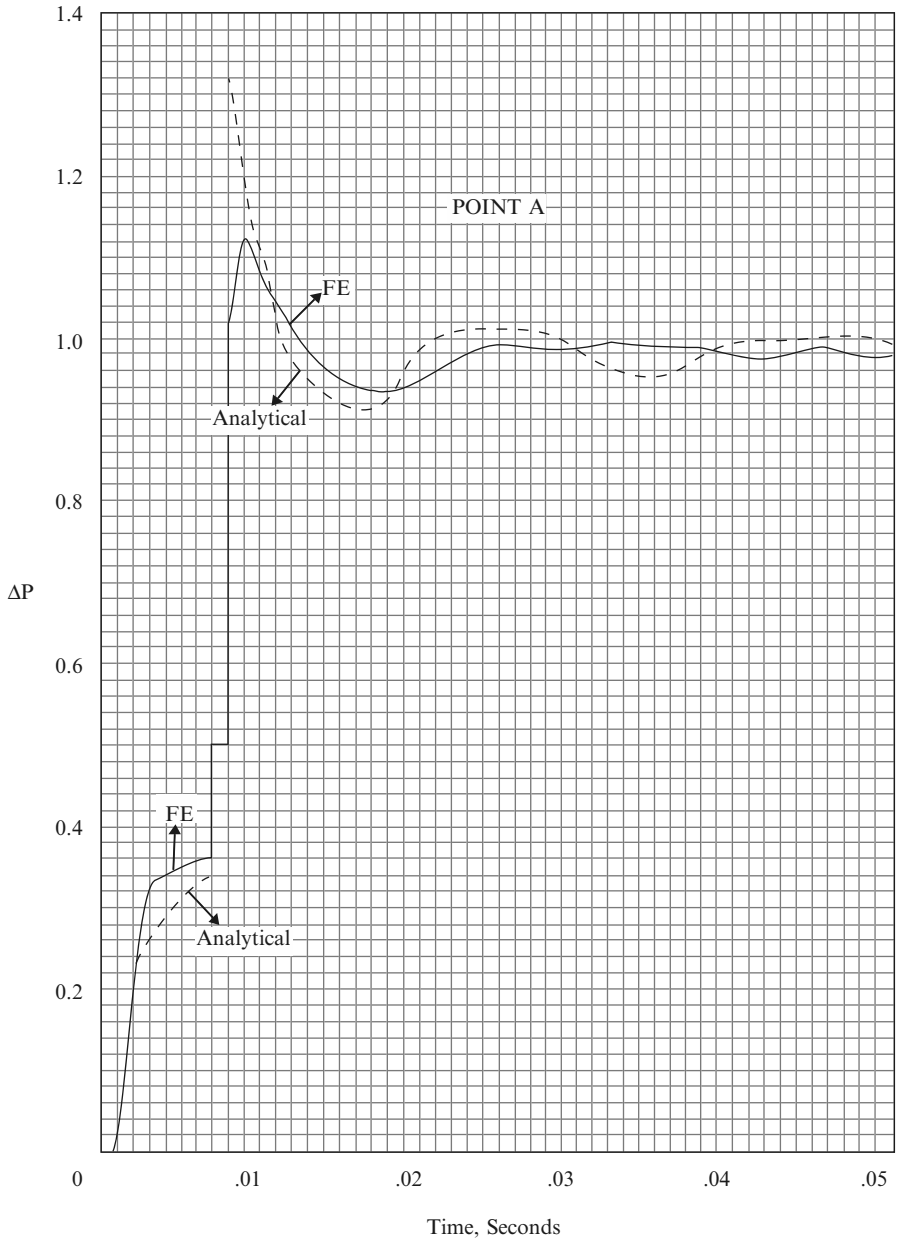
Fig. 3.51. Comparison of computed pressure histories by numerical and analytical methods for a step-wave of unit overpressure
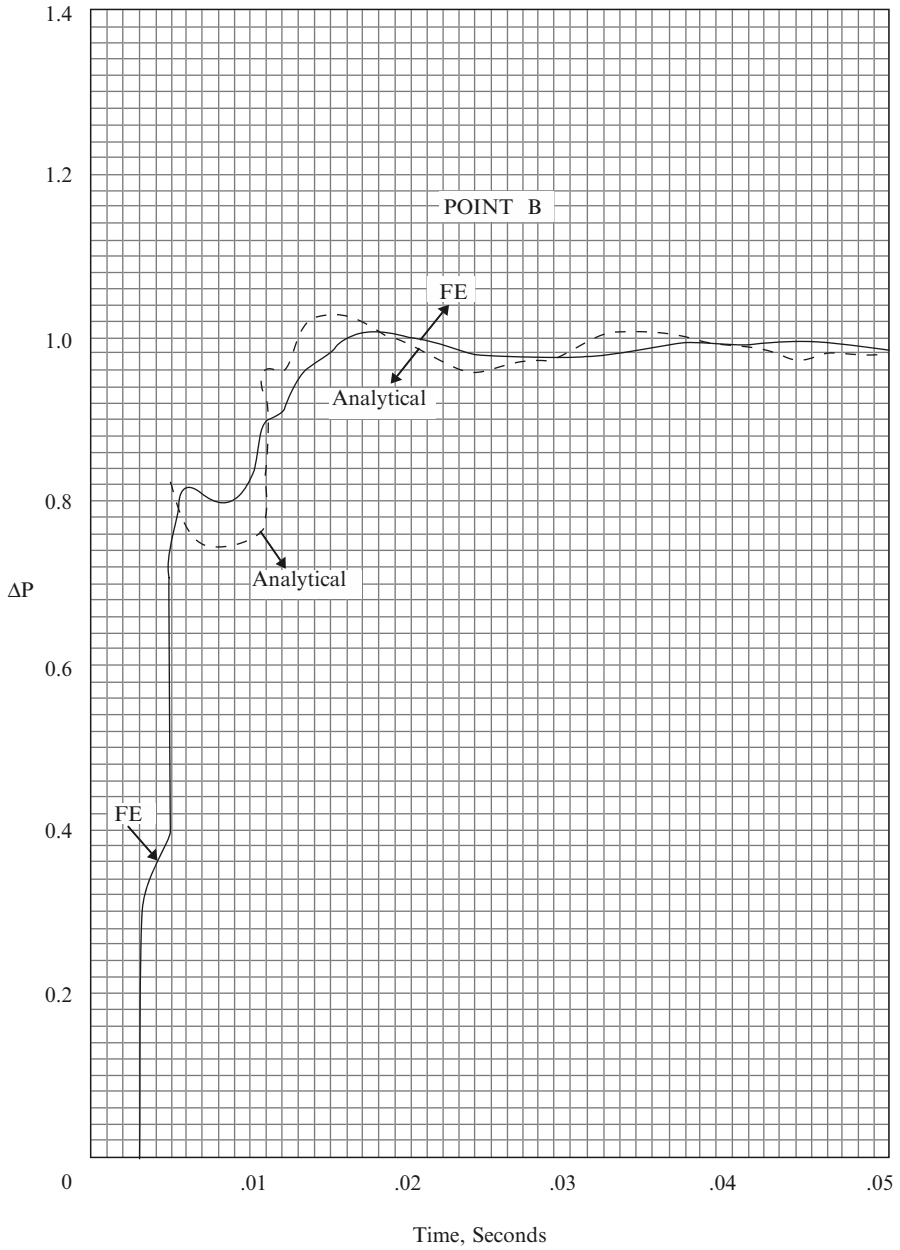
Fig. 3.52. Pressure-time relations at B
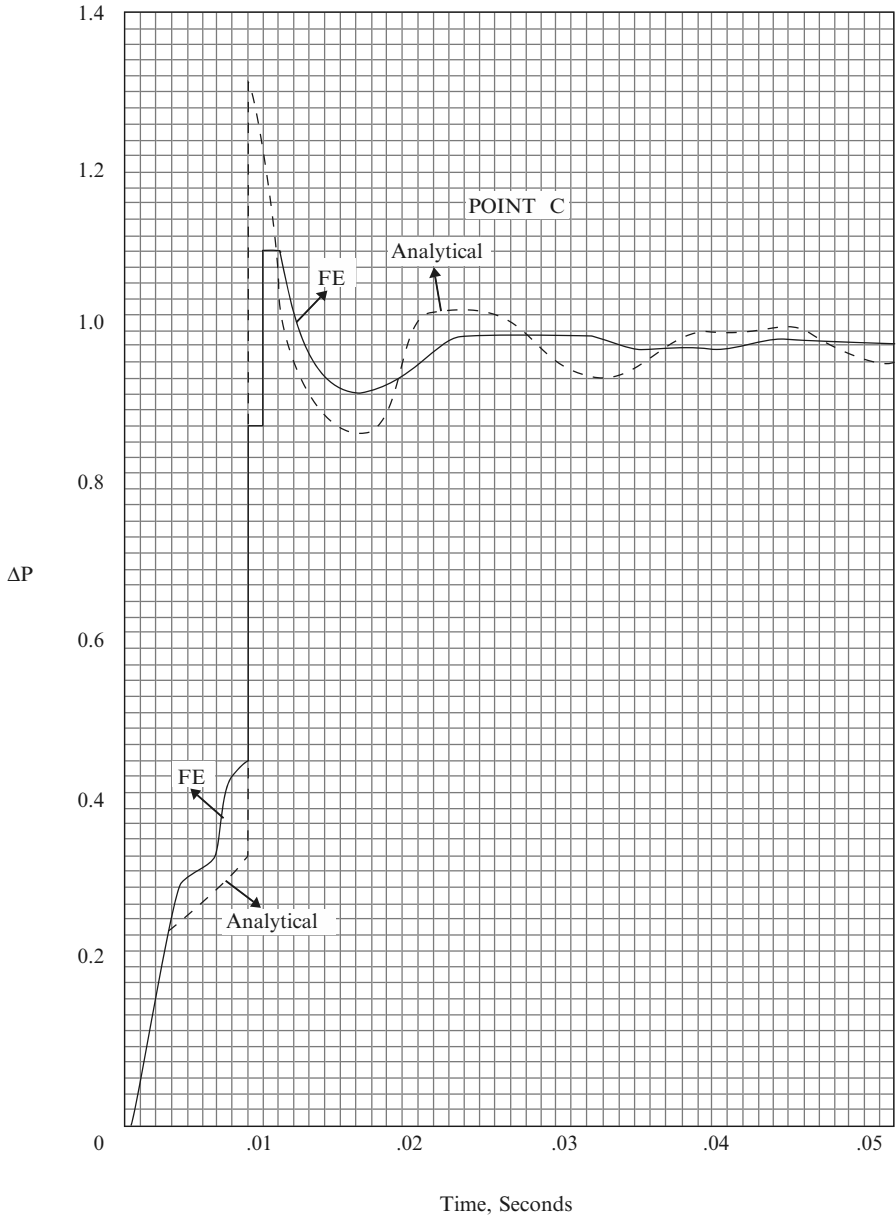
Fig. 3.53. Pressure-time relations at C
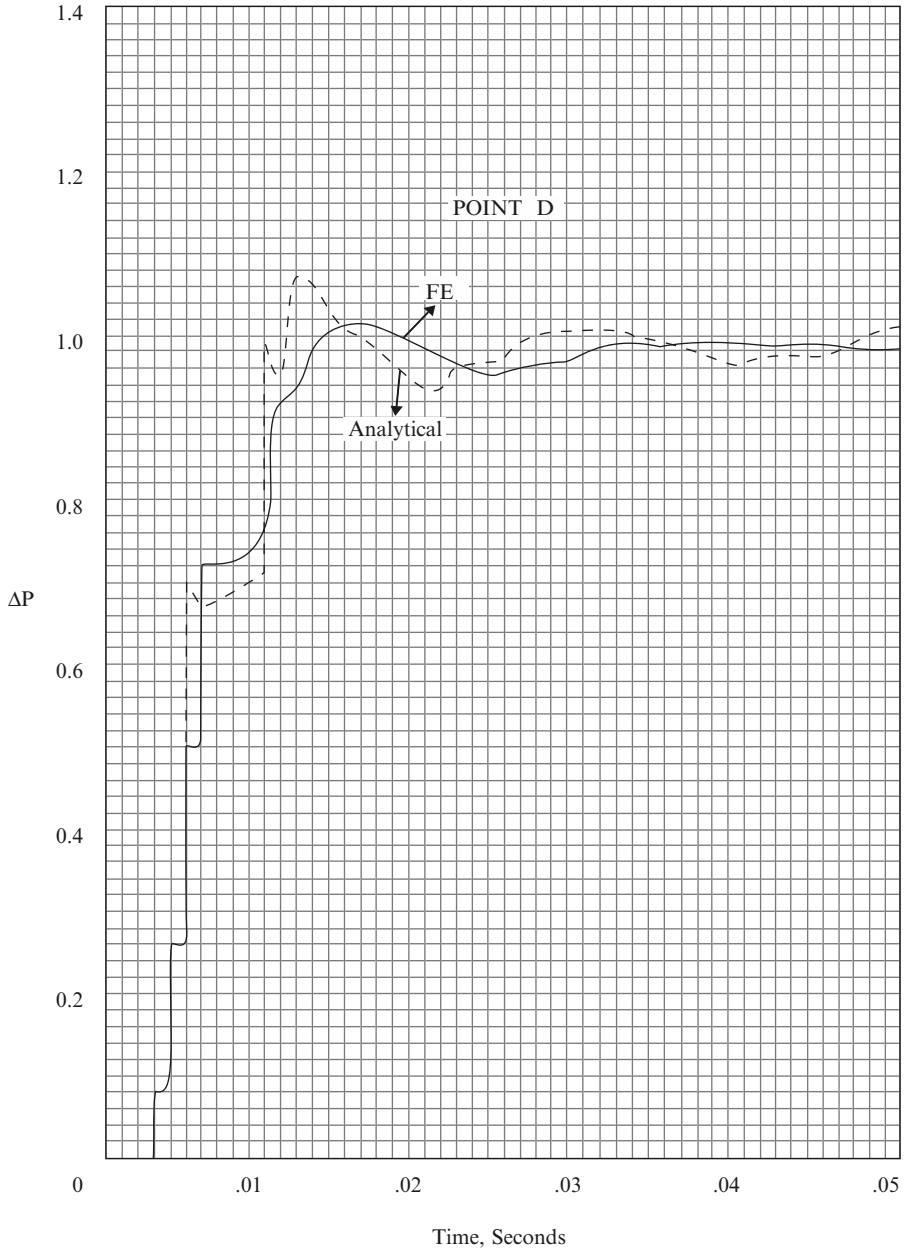
Fig. 3.54. Pressure-time relations at D

4

Shock and Impact Dynamics

4.1 Introduction

This chapter begins with basic impact dynamics. It includes impact effects due to vehicle/train collisions, aircraft/missile target interactions, drop weights and free-falling bodies and missiles on concrete and steel targets. An up-to-date impact simulation is included for jet fluids on soils and rocks. Brief numerical and experimental data are given on impacts and collisions on water surfaces. A special section is included on snow/ice impact and analysis of shock response of ceramics.

4.2 The Impactor as a Projectile

An impactor in the form of a missile is first given an initial velocity and it is then possible to assume that it is moving under the action of its own weight. If the initial velocity is not vertical, the missile will move in a curve and its flight can be evaluated in terms of horizontal and vertical components of displacement, velocity and acceleration. Some typical examples are given in Table 4.1.

4.2.1 Direct Impulse/Impact and Momentum

An impulse is defined as a force multiplied by time, such that

$$F_1(t) = \int F \, \mathrm{d}t, \tag{4.1}$$

where $F_1(t)$ is the impulse, F is the force and t is the time. The momentum of a body is the product of its mass and its velocity:

$$\text{momentum} = mv, \tag{4.2}$$

Table 4.1. Projectile statistics

(a)

(b)

(c)

Ox – horizontal
Oy – vertical
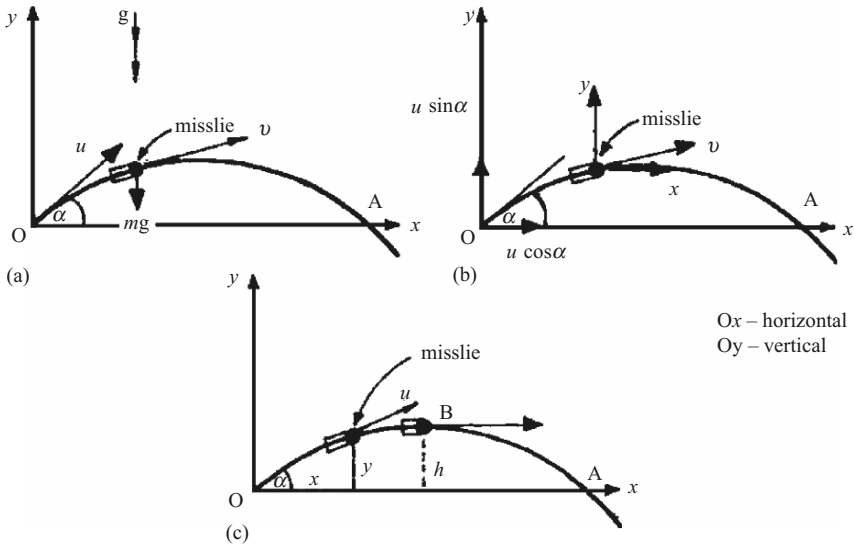
Figure (a) shows a missile projected at a velocity u from a position 0. At 0, x, $\dot{x}$ and $\ddot{x}$ are all zero. The only force on the flight is equal to $m\mathbf{g}$. Hence $\ddot{y}$, the acceleration in the vertical direction, is $-\mathbf{g}$.

The general forms of the velocity and distance equations are:

$$v = u + at, \tag{1}$$

$$s = ut + \frac{1}{2}at^2,$$

$$\dot{x} = u\cos\alpha, \qquad \dot{y} = u\sin\alpha - \mathbf{g}t \ (\text{Fig. (b)}), \tag{2}$$

$$x = (u\cos\alpha)\,t, \quad y = (u\sin\alpha)\,t - \frac{1}{2}\mathbf{g}t^2, \tag{3}$$

$$\ddot{x} = 0, \quad \ddot{y} = -\mathbf{g}. \tag{4}$$

By elimination of t from (3), the trajectory equation is written in a parabolic form as

$$y = x\tan\alpha - (\mathbf{g}x^2\sec^2\alpha/2u^2). \tag{5}$$

The velocity v of the missile during flight at any instant in time is given by

$$\mathrm{v} = \sqrt{(\dot{x}^2 + \dot{y}^2)} \quad \text{with } \alpha = \tan^{-1}(\dot{y}/\dot{x}) \tag{6}$$

since

$$\dot{y}/\dot{x} = (\mathrm{d}y/\mathrm{d}t)/(\mathrm{d}x/\mathrm{d}t) = \mathrm{d}y/\mathrm{d}x.$$

The direction of the velocity at any instant is along the tangent to the path for that particular instant. If the missile is projected from the aircraft at an

Table 4.1. (continued)

angle below its level in order to hit the target at the ground level (the aircraft level is treated as horizontal), (5) becomes

$$y = x \tan\alpha + \left(gx^2 \sec^2\alpha/2u^2\right) \tag{7}$$

and all negative signs in (2) and (3) related to **g** are *positive*.

Case 1

If the missile is projected from the aircraft at an angle of $\alpha' = 30°$, from a distance of 700 m, and hits the target at 200 m distance, the speed and the direction are computed from Fig. (d).
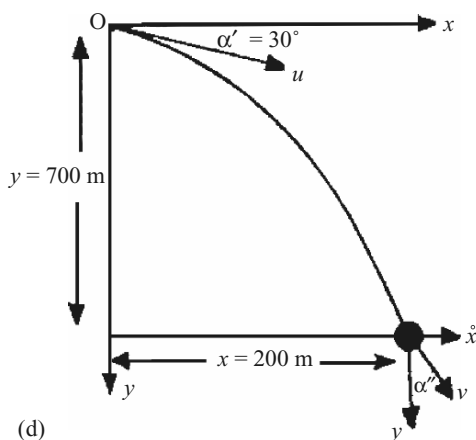
(d)

$$y = x\tan 30° + \left(gx^2/2u^2\right)\sec^2 30°$$

$$700 = (200/\sqrt{3}) + \frac{9.8 \times 200^2}{2u^2} \times 1.34$$

$$u = 21.2\,\mathrm{m\,s^{-1}}$$

$$dy/dx = \tan 30° + gx\ \sec^2 30°/u^2$$

$$= (1/\sqrt{3}) + \frac{9.8 \times 200}{21.2^2} \times 1.34$$

$$= 6.42$$

$$\alpha'' = \tan^{-1} 6.42 = 81.15°$$

Case 2

If the missile is projected 4 m above the launch level, with a velocity of $100\,\mathrm{m\,s^{-1}}$ at an angle of $45°$ to the horizontal, the horizontal distance x at

Table 4.1. (continued)

which it hits the ground is computed as follows:

$$y = x \tan \alpha - \mathbf{g}x^2 \sec^2 \alpha / 2u^2,$$
$$\text{or } -4 = x - (\mathbf{g}x^2 / 2u^2),$$
$$\text{or } -4 = x - (\mathbf{g}x^2 / 2 \times 100^2).$$

Rejecting the negative root, $x = 2{,}045\,\mathrm{m}$.

Case 3: flight time

As shown in Fig. (a), the time taken by a missile to travel along its path from 0 to A is to be computed. At any time t:

$$y = (u \sin \alpha)\, t - \frac{1}{2}\mathbf{g}t^2.$$

At A, $y = 0$

$$t = 2u \sin \alpha / \mathbf{g}. \tag{8}$$

The other value of $t = 0$ cannot be true at A, as was assumed to be the case at 0.

Case 4: maximum height and horizontal range

Reference is made to Fig. (c). At any time t, at any point B,

$$\dot{y} = 0 = u \sin \alpha - \mathbf{g}t.$$

Hence

$$t = u \sin \alpha / \mathbf{g}. \tag{9}$$

Substituting t into (3) of y

$$y = u \sin \alpha t - \frac{1}{2}\mathbf{g}t^2,$$
$$h = (u^2 \sin^2 \alpha / \mathbf{g}) - \frac{1}{2}\mathbf{g}(u \sin \alpha / \mathbf{g})^2, \tag{10}$$
$$h = u^2 \sin^2 \alpha / 2\mathbf{g}.$$

The maximum range x is obtained as

$$x = ut \cos \alpha = u\,(2u \sin \alpha / \mathbf{g})$$
$$= 2u^2 \sin \alpha \cos \alpha / \mathbf{g}$$
$$= u^2 \sin 2\alpha / \mathbf{g}.$$

Table 4.1. (continued)

When $\sin 2\alpha = 1$ or $\alpha = 45°$

$$x_{max} = u^2/\mathbf{g}. \tag{11}$$

Case 5

A missile hits the target at a distance x when travelling horizontally. The distance l at which the missile hits the ground after bouncing is computed below.

As shown in Fig. (d), by using the coefficient of restitution e, the speed after hitting the wall $= eu\cos\alpha$ in a horizontal direction. The maximum height reached is given by

$$h = u\sin\alpha/\mathbf{g}$$

(e)
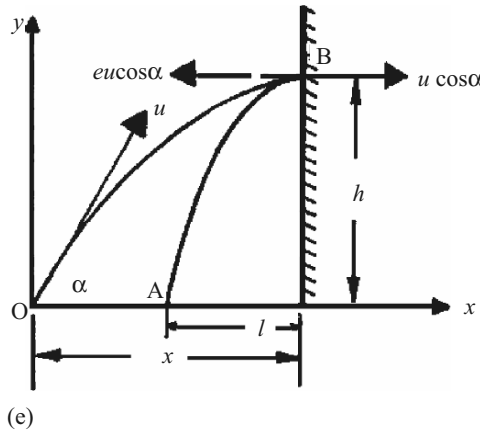
The time taken to reach ground level is calculated by

$$y = h = ut + \frac{1}{2}\mathbf{g}t^2 = 0 + \frac{1}{2}\mathbf{g}t^2,$$
$$t = \sqrt{(2h/\mathbf{g})} = \sqrt{\left(2u^2\sin^2\alpha/2\mathbf{g}^2\right)} \tag{12}$$
$$= u\sin\alpha/\mathbf{g}.$$

When the missile hits the ground level at a distance l from the wall

$$l/x = e\left(u\cos\alpha\right)/u\cos\alpha, \tag{13}$$
$$l = ex,$$

where e is the coefficient of restitution.

It can easily be proved that if the same missile hits a building floor vertically of height h with a velocity v, rebounds from there with coefficient of

(*continued*)

Table 4.1. (continued)

restitution e and rebounds to the floor with a coefficient of restitution f, then the value of v is given by

$$v = \left[2gh\left(1 - f^2 + e^2 f^2\right)\right]/e^2 f. \tag{14}$$

Case 6

Scene near O'Hare airport: an engine from a 10 ton CFM56-3C power plant of an aircraft plummets at an angle α from a height h with a speed v and hits the ground at a distance x, as shown in Fig. (f). Assuming no air resistance is offered to the parabolic flight, determine the angle at which the engine hits the ground at a distance x, using the following data:
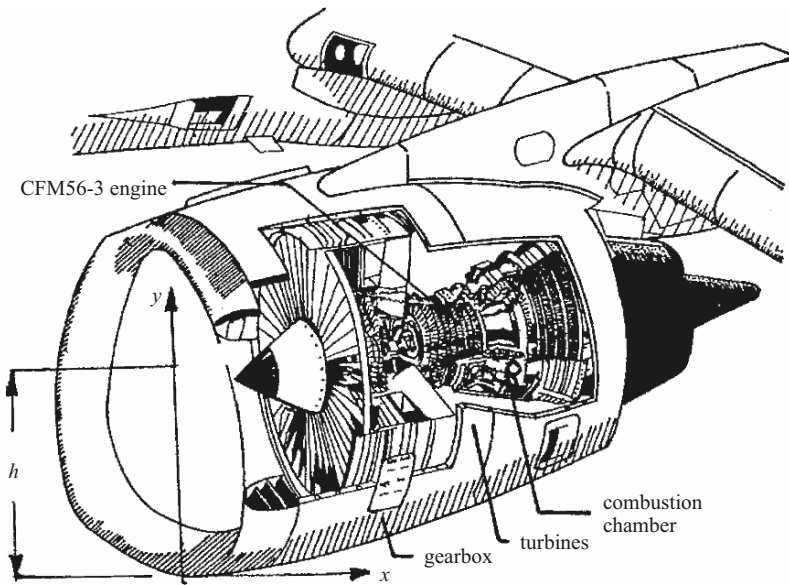
(f)

$h = 333\,\mathrm{m},\ x = 812\,\mathrm{m},\ u = 112\,\mathrm{m\,s^{-1}},\ v = 0.$

Thus

$$y = x\tan\alpha'' + (gx^2\sec^2\alpha/2u^2),$$
$$y = h = 333\,\mathrm{m},$$
$$333 = 812\tan\alpha'' + \left[9.8 \times 812^2\sec^2\alpha''/2 \times 112^2\right]$$
$$333 = 812\tan\alpha'' + 257.56(1 + \tan^2\alpha''),$$
$$\tan\alpha'' = 0.096,$$
$$\alpha'' = 5\frac{1}{2}^\circ \text{ (it was reported to be almost straight).}$$

where m is the mass and v is the velocity $=\mathrm{d}x/\mathrm{d}t$. Both velocity and momentum are vector quantities; their directions are the same. If a body is moving with a constant velocity, its momentum is constant. If velocity is to be changed, a force F must act on the body. It follows that a force F must act in order to change the momentum.

$$F = m\,\mathrm{d}v/\mathrm{d}t$$

$$\text{or} \quad F\,\mathrm{d}t = m\,\mathrm{d}v. \tag{4.2a}$$

Integrating both sides:

$$\int_{t_1}^{t_2} F\,\mathrm{d}t = \int_{u}^{v} m\,\mathrm{d}v,$$

$$F_1(t) = m\,(v - u)\,, \tag{4.3}$$

where u and v are the velocities at times t_1 and t_2 respectively. If the initial velocity $u = 0$, (4.3) becomes

$$I = mv. \tag{4.3a}$$

Thus the impulse of a force is equal to the change in momentum which it produces.

Table 4.1 gives some typical examples of elastic impulse/impact phenomena.

Impacts/Collisions of Vehicles

When two solid bodies are in contact, they exert equal and opposite forces or impulses on each other and they are in contact for the same time. If no external force affects the motion, the total momentum in the specific direction remains constant. This is known as the *principle of conservation of linear momentum.* When two bodies, m_1 and m_2, collide (Fig. 4.1), the mass ratios are then calculated from (4.1):

$$F_{11}(t) = m_1(v_1 - u_1) = \int F_1\mathrm{d}t,$$
$$F_{12}(t) = m_2\,(v_2 - u_2) = \int F_2\mathrm{d}t. \tag{4.4}$$

Since $\int F_1\mathrm{d}t + \int F_2\mathrm{d}t = 0$, the relationship between velocity change and mass becomes:

$$m_2/m_1 = (v_1 - u_1)/-(v_2 - u_2). \tag{4.5}$$

Fig. 4.1. Direct impact

Table 4.2 gives some typical examples of impulse and momentum. During the collision process, although the momentum is conserved, there is a loss of energy on impact which is determined using the concept of the *coefficient of restitution, e*, which is defined as the relative velocity of the two masses after impact divided by the relative velocity of the two masses before impact. Before impact:

$$e = (v_1 - v_2) / - (u_1 - u_2) = 0,$$

Table 4.2. Direct elastic impact

Example 1

A Fiat Panda (illustrated) with a gross laden weight of 1,190 kg and travelling at $55 \, \text{km h}^{-1}$ is brought to rest in 10 s when it strikes a buffer. Determine the constant force exerted by the buffer.
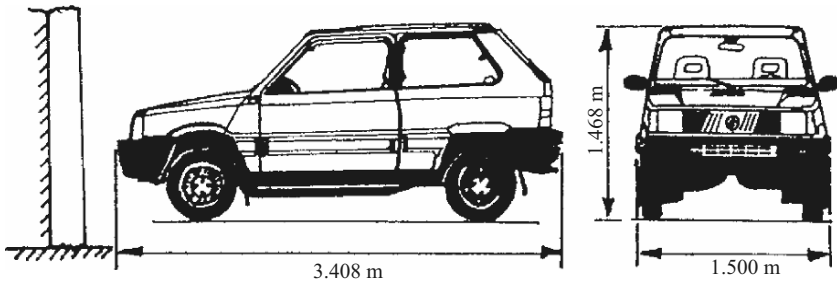
Assuming the laden weight is treated as a total mass:

$$u = 55 \, \text{km h}^{-1} = 15.28 \, \text{m s}^{-1},$$
$$F_1(\text{t}) = Ft = mv - mu$$
$$= 0 - 1,190 \, (-15.28) = 18.183 \times 10^3,$$
$$F_t = 2F = 18.183 \times 10^3 \, \text{Ns},$$
$$F = 9,091.6 \, \text{N} = 9.0916 \, \text{kN}.$$

Example 2

A car of mass 790 kg is thrown by a hurricane and hits a wall normally at a speed of $40 \, \text{m s}^{-1}$. Assuming the car acts as a missile and bounces away from the wall at right angles with a speed of $30 \, \text{m s}^{-1}$, what impulsive force does the wall exert on the car? Assume no damage occurs to the wall. Approaching the wall, $u = -40 \, \text{m s}^{-1}$; leaving the wall $v = +30 \, \text{m s}^{-1}$.

$$Ft = mv - mu = (790 \times 30 - 790 \times -40) \, 10^{-3}$$
$$= 64.39 \, \text{kN}.$$

Table 4.2. (continued)

Example 3

A windborne missile of mass m strikes a containment wall and ricochets off at $120°$ to its original direction. The speed changes from $u = 40\,\mathrm{m\,s^{-1}}$ to $v = 35\,\mathrm{m\,s^{-1}}$. Calculate the resultant impulse of the system. Assume no damage occurs.
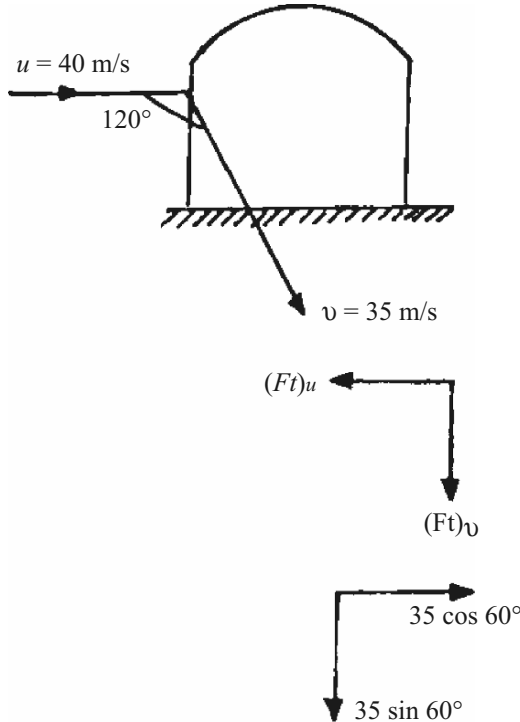
Since the direction of u and v are different before and after the impulse, the components of the impulse and the velocities in two perpendicular directions are considered.

$$(Ft)_u = m\,(+35\cos 60°) - m\,(-40)$$
$$= m\,[40 + (35/2)] = 22.5\,m, \text{ where } m = \text{mass,}$$
$$(Ft)_v = m\,(35\sin 60° - 0)$$
$$= m35\,(\sqrt{3}/2) = 30.31\,m.$$

Therefore the resultant impulse or impact

$$F_1(t) = \sqrt{\left\{[(FT)_v]^2 + [(Ft)_u]^2\right\}}$$
$$= 64.9\,m.$$

when the relative velocity vanishes, and

$$e = (v_1 - v_2) / - (u_1 - u_2) = 1, \tag{4.5a}$$

when there is no loss of relative velocity.

Where $e < 1$, it is related to the loss in kinetic energy, and where $u_2 = 0$ (refer to (4.5a))

$$m_1 (v_1 - u_1) + m_2 (v_2) = 0, \tag{4.6}$$
$$v_1 - v_2 = -eu_1,$$

hence

$$v_1 = u_1(m_1 - em_2) / (m_1 + m_2), \tag{4.6a}$$
$$v_2 = u_1[(1 + e)m_1 / (m_2 + m_1)]. \tag{4.6b}$$

The original kinetic energy $(\text{KE})' = \frac{1}{2}m_1 u_1^2$
The final kinetic energy $(\text{KE})'' = \frac{1}{2}(m_1 v_1^2 + m_2 v_2^2)$

$$(\text{KE})' - (\text{KE})'' = \frac{1}{2}m_1 u_1^2 - \frac{1}{2}\left(m_1 v_1^2 + m_2 v_2^2\right). \tag{4.7}$$

Substituting the values of v_1 and v_2:

$$(\text{KE})' - (\text{KE})'' = (\text{KE})' \left[m_1(1 - e^2)/(m_1 + m_2)\right]. \tag{4.8}$$

The displacement resulting from a short-duration (τ) impact is given by

$$x = b(t - \tau), \tag{4.9}$$

where t is the time beyond τ. Details of such analysis are dealt with in Chap. 3. For dynamic analysis, the impact time is divided into n small segments and, using (4.3a),

$$x = \frac{1}{m} \sum_0^n v_n I_n (t - \tau_n)$$

$$= \frac{1}{m} \int_0^t F(t - \tau) \, d\tau. \tag{4.10}$$

If the impact is divided into two phases such that in the first, from time t_1 to t_0, there will be compression and distortion until $(v_1 + v_2)$ are both reduced to zero (the two bodies moving together), in the second, the elastic strain energies in the bodies are restored and are separated by a negative velocity, $-V_2 = (v_1 + v_2)$. During the second phase the impulse relation between the bodies $(F_T - F_{T0})$ will be proportional to F_{T0} and the coefficient or restitution e defined above is written as

$$e = (F_T - F_{T0})/F_{T0}, \tag{4.11}$$

where F_T is the total impulse during the impact and F_{T0} is the impulse in phase one.

At time t_0

$$V_0 = v_{10} + v_{20} = v_1 + \left(\frac{F_{T0}}{m_1} + v_2 - \frac{F_{T0}}{m_2}\right) = 0, \tag{4.12}$$

hence
$$V = v_1 + v_2 = \left(\frac{1}{m_1} + \frac{1}{m_2}\right) F_{T0}. \tag{4.13}$$

Similarly, at time t_2 the relationship becomes

$$V_0 - V_2 = F_T \left(\frac{1}{m_1} + \frac{1}{m_2}\right). \tag{4.14}$$

Using (4.11), the expression given in (4.5a) may be written in the form:

$$-(V_2/V) = e. \tag{4.15}$$

Equations (4.6)–(4.6b) result from the above method. However, from (4.11) the total impulse is rewritten as

$$
\begin{aligned}
F_T &= \left(\frac{m_1 m_2}{m_1 + m_2}\right)(1+e)(v_1 + v_2) \\
&= M(1+e)V,
\end{aligned}
\tag{4.16}
$$

where M is the equivalent combined mass of the bodies.

The changes in velocity after impact of the bodies are written as

$$
\begin{aligned}
\Delta V_1 &= \frac{M}{m_1}(1+e)(v_1 + v_2) = \frac{M}{m_1}(1+e)V, \\
\Delta V_2 &= \frac{M}{m_2}(1+e)V.
\end{aligned}
\tag{4.17}
$$

4.2.2 Oblique Impact

When two bodies collide and their axes do not coincide, the problem becomes more complex. With oblique impact, as shown in Fig. 4.2, two impulses are generated: the direct impulse, F_T, and the tangential impulse, F'_T. The latter is caused by friction between the impacting surfaces and by local interlocking of the two bodies at the common surface. Let the angular velocity of the two bodies be $\dot{\theta}_1$ and $\dot{\theta}_2$ respectively. If $F'_T/F_T = \lambda'$ and the body's centre of gravity has a coordinate system X and Y, the components of the vector velocity, v_1 and u_1, normal to the impact surface may be written as follows:
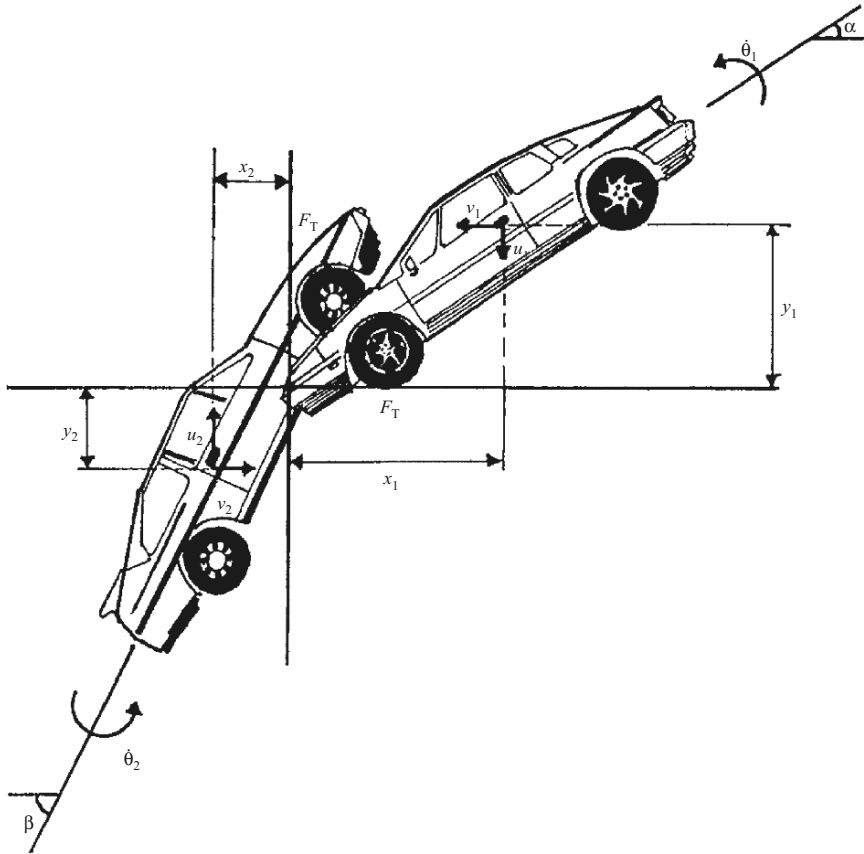
Fig. 4.2. Oblique impact

$x_1 - y_1$ system

$$v_1 = |\bar{v}_1|\cos\theta_1, \tag{4.18}$$

$$u_1 = |\bar{v}_1|\sin\theta_1, \tag{4.18a}$$

where

$$|\bar{v}_1| = \sqrt{\left(v_1^2 + u_1^2\right)},$$

$$\alpha = \tan^{-1}\left(u_1/v_1\right).$$

Similarly, v_2 is written as

$$|\bar{v}_2| = \sqrt{\left(v_2^2 + u_2^2\right)}, \tag{4.19}$$

$$\beta = \tan^{-1}\left(u_2/v_2\right). \tag{4.19a}$$

The momentum equations for the bodies are summarized below:

$$\left.\begin{aligned}
m_1 v_1' - F_{\mathrm{T}} &= m_1 v_2' \\
m_1 u_1' - \lambda' F_{\mathrm{T}} &= m_1 u_2' \\
m_1 R_1^2\, \theta_1' + F_{\mathrm{T}} y_1 - \lambda' F_{\mathrm{T}} x_1 &= m_1 R_1^2\, \dot{\theta}_2
\end{aligned}\right\} \qquad \text{body 1,} \qquad (4.20)$$

where v_1', v_2', u_1' and u_2' are for t_1 and t_2.

$x_2 - y_2$ system

$$\left.\begin{aligned}
m_2 v_1'' - F_{\mathrm{T}} &= m_2 v_2'' \\
m_2 u_1'' - F_{\mathrm{T}} &= m_2 u_2'' \\
m_2 R_2^2\, \dot{\theta}_2' + F_{\mathrm{T}} y_2 - \lambda' F_{\mathrm{T}} x_2 &= m_2 R_2^2\, \dot{\theta}_2'
\end{aligned}\right\} \qquad \text{body 2,} \qquad (4.21)$$

where mR_1^2 and mR_2^2 are the second moment of inertia about the vertical axis passing through the centre of gravity. The rate of approach and the sliding of the two surfaces at the point of contact can be written as

$$\Delta V_1 = v_1 + v_2 - \dot{\theta}_1 y_1 - \dot{\theta}_2 y_2, \qquad (4.22)$$

$$\Delta V_2 = u_1 + u_2 + \dot{\theta}_1 x_1 + \dot{\theta}_2 x_2. \qquad (4.23)$$

The addition to these equations is the restitution given by (4.15) in which, when (4.22) is substituted and then, in the final equation, (4.20) is substituted, the value of F_{T} is evaluated as

$$F_{\mathrm{T}} = \frac{V(1+e)}{c_1 - \lambda c_2}, \qquad (4.24)$$

where

$$c_1 = \frac{1}{m_1}\left(1 + \frac{y_1^2}{R_1^2}\right) + \frac{1}{m_2}\left(1 + \frac{y_2^2}{R_2^2}\right), \qquad (4.24a)$$

$$c_2 = \left(\frac{x_1 y_1}{m_1 R_1^2} + \frac{x_2 y_2}{m_2 R_2^2}\right). \qquad (4.24b)$$

Using (4.20) and (4.21):

$$\left.\begin{aligned}
v_2' &= v_1' - (F_{\mathrm{T}}/m_1), \\
u_2' &= u_1' - (\lambda' F_{\mathrm{T}}/m_1), \\
\dot{\theta}_2 &= \dot{\theta}_1 + \frac{y_1 - \lambda' x_1}{m_1 R_1^2} F_{\mathrm{T}},
\end{aligned}\right\} \qquad (4.25)$$

$$\left.\begin{aligned}
v_2'' &= v_1'' - \frac{F_{\mathrm{T}}}{m_2}, \\
u_2'' &= u_1'' - \frac{\lambda' F_{\mathrm{T}}}{m_2}, \\
\dot{\theta}_2' &= \dot{\theta}_1' + \frac{y_2 - \lambda' x_2}{m_2 R_2^2} F_{\mathrm{T}}.
\end{aligned}\right\} \qquad (4.26)$$

Figure 4.3 shows plots for (4.25) and (4.26). It is interesting to note that larger values of λ' show greater interlocking of the surfaces of the two bodies and with e reaching zero, a greater plastic deformation occurs.
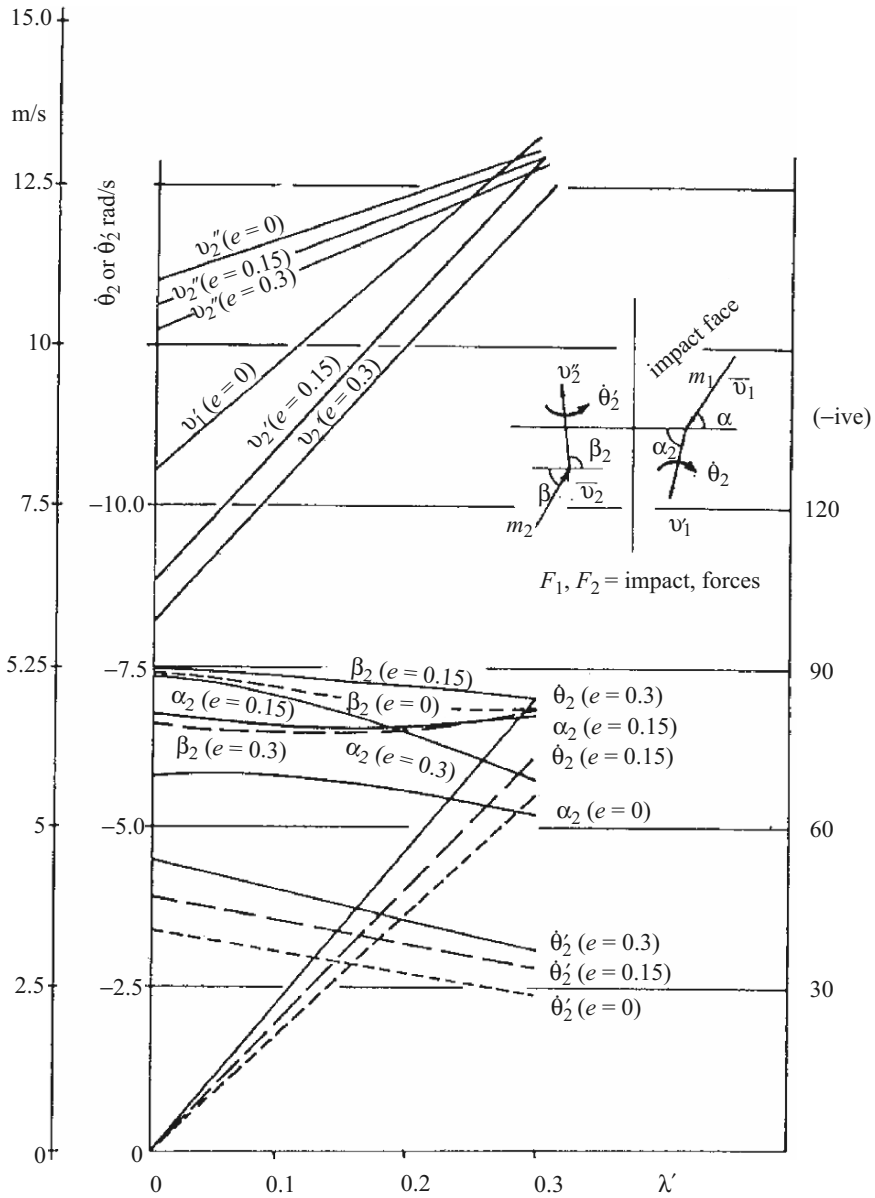
Fig. 4.3. Velocity versus λ' for oblique impact problems

Case Studies

(1) One body impacting a rigid barrier with no angular velocity

$$1/m_2 = 0; \quad v_1 = 0; \quad u_1 = 0; \quad \dot{\theta}_1 = 0 \tag{4.27}$$

$$c_1 = \frac{1}{m_1}\left(1 + \frac{y_1^2}{R_1^2}\right); \quad c_2 = \frac{x_1 y_1}{m_1 R_1^2}, \tag{4.27a}$$

$$v_2' = v_1'(y_1^2 - \lambda' x_1 y_1 - eR^2)/\bar{\lambda}, \tag{4.27b}$$

$$u_2' = u_1' - v_1'\left(\frac{\lambda'(1+e)R^2}{\bar{\lambda}}\right); \quad \dot{\theta}_1 = \frac{(1+e)(y_1 - \lambda' x_1)}{\bar{\lambda}}, \tag{4.27c}$$

where

$$\bar{\lambda} = y_1^2 - \lambda' x_1 y_1 + R^2. \tag{4.27d}$$

(2) Circular impactor with radius r_1

$$x_1 = r_1 \text{ and } y_1 = 0, \tag{4.28}$$

$$v_2' = ev_1', \tag{4.28a}$$

$$u_2' = u_1 - \lambda' v_1'(1 + e), \tag{4.28b}$$

$$\dot{\theta}_1 = -v_1'\lambda' r_1(1+e)/R^2. \tag{4.28c}$$

For a circular impactor, $R^2 = 2r_1^2/5$

$$\dot{\theta}_1 = -v_1'(5\lambda'(1+e)/2r_1). \tag{4.28d}$$

(3) Inelastic collisions. The value of $e = 0$ in the above case studies

Case study (1) $v_2' = v_1^2(y_1^2 - \lambda' x_1 y_1)/\bar{\lambda},$

$$u_2' = u_1' - v_1' \ (\lambda' R^2/\bar{\lambda}), \tag{4.29}$$

$$\dot{\theta}_1 = (y_1 - \lambda' x_1)/\bar{\lambda}.$$

Case study (2) $v_2' = 0; \quad u_2' = u_1 - \lambda' v_1',$

$$\dot{\theta}_1 = -v_1'\lambda' r_1/R^2 = -2.5 \ v_1'\lambda_1'/r_1. \tag{4.30}$$

(4) Where no interlocking exists, $\lambda' = 0$ in the above expressions

4.3 Aircraft Impact on Structures: Peak Displacement and Frequency

A great deal of work has been carried out (refer to sections 4.1 and 4.2 of the Bibliography) on the subject of missile and aircraft impact. Tall structures are more vulnerable to civilian, wide-bodied jets or multi-role combat aircraft. A great deal of work on this subject will be reported later. In this section a preliminary analysis is given for the determination of peak displacement and frequency of a tall structure when subject to an aircraft impact. As shown in Fig. 4.4, the overall dimensions of the building are given. Let A be the base area and h be the maximum height of the building. According to the principle of the conservation of momentum, if m is mass and v_1 is the
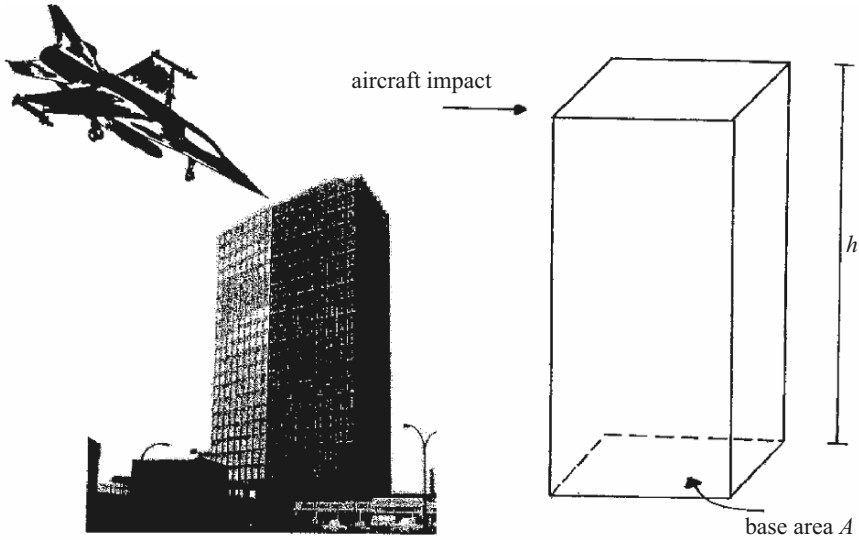
Fig. 4.4. Aircraft impact on a building

velocity of the aircraft approaching the building, then using a linear deflection profile:

$$F_1(t) = mv_1 = (\rho Ah/2\mathbf{g})\, v_{20}, \tag{4.31}$$

where ρ is the density or average specific weight and v_{20} is the velocity of the tip of the building.

The initial velocity, v_{20}, of the building can thus be evaluated from (4.31). Free vibrations studied in Chap. 3 show the time-dependent displacement $\delta(t)$ is given by

$$\delta(t) = (v_{20}/\omega)\sin\omega t \tag{4.32}$$

$$= [v_{20}/(2\pi/T)]\sin\omega t$$

$$= [v_{20}/\sqrt{(k_e/m_e)}]\sin\omega t,$$

where ω is the circular frequency and k_e and m_e are the equivalent building stiffness and mass, respectively.

Using (4.31) for v_{20} and $\sin\omega t = 1$ for $\delta_{\max}(t)$, the *peak dynamic displacement*, $\delta_{\max}(t)$, is given by

$$\delta_{\max}(t) = mv_1\mathbf{g}T/\pi\rho Ah. \tag{4.32a}$$

The equivalent point load generated for the peak dynamic displacement is given by (4.32a). If that load is $F_1(t)$, then work done is equal to the energy stored and

$$F_1(t) \times \delta_{\max}(t) = \frac{1}{2}k_e\, \delta_{\max}^2(t) \tag{4.33}$$

from which
$$F_1(t) = \frac{1}{2}k_c \, \delta_{\max}(t).$$
(4.33a)

While momentum is conserved, a portion of energy of the aircraft is lost on impact. The loss of energy E_1 is then written as

$$E_1 = \frac{1}{3}(\rho Ah/m\mathbf{g})(v_{20}/v_1)^2.$$
(4.34)

Equations in case study (1) of section "case studies" and (4.29) for inelastic collisions are applied with and without the interlocking parameter, λ'.

4.4 Aircraft Impact: Load–Time Functions

4.4.1 Introduction

Many sensitive installations are to be found in areas where heavy air traffic exists. Hence aircraft crashes cannot be entirely ruled out in such areas. Much effort is now being devoted to studies of aircraft impact with a clear aim of facilitating design to minimize damage to the aircraft and to the installations. Accident investigations, experiences and records are briefly discussed in Chap. 1. In this section some useful impact models are given which can be easily linked to both simplified and complex methods.

4.4.2 Stevenson's Direct Head-On Impact Model

Work has been carried out on the remaining undamaged length of a 45 m (150 ft) long DC-8 jet which crashed into a rigid-surface, as shown in Fig. 4.5. A simplified equation of motion is written as

$$V(\mathrm{d}V/\mathrm{d}x) \, [k(L - x_{cr}) + m_c] = F_1(t),$$
(4.35)

where V = speed of the aircraft at time t after impact, x_{cr} = crushed length, k = mass per unit length of fuselage, m_c = concentrated mass at wings including engines and others, F_1 = impact force or resistance at the crash level.
   Equation (4.35) is integrated:

$$F_1(t) = \frac{1}{2}kV_0^2 \left[\left(\frac{V}{V_0}\right)^2 - 1\right] / \log[1 - x_{cr}/(L + m_c/k)],$$
(4.36)

where V_0 is the aircraft speed prior to impact.

4.4.3 Riera Model

The response of the structure was assessed by Riera. The aircraft was replaced by an equivalent force–time function. The aircraft impinges perpendicularly
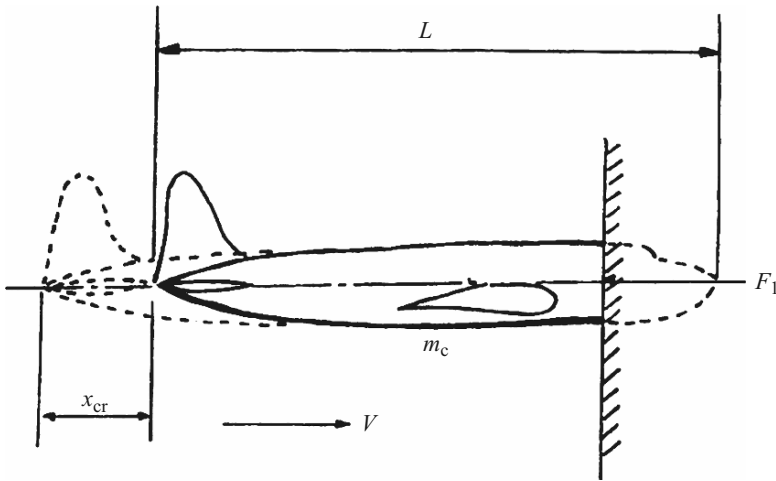
Fig. 4.5. Model aircraft impacting against a rigid surface

on a rigid target and it is assumed that it crashes only at the cross-section next to the target. The cross-sectional buckling load decelerates the remaining rigid uncrushed portion. The total impact force $F_1(t)$ is the sum of the buckling load and the force required to decelerate the mass of the impinging cross-section. Since it is a one-dimensional ideal plastic impact approach, in his model only the buckling load and the distribution of mass are needed. The equation of motion is written as:

$$F_1(t) = R_{cr}x_{cr} + m_c x_{cr}(\mathrm{d}x_{cr}/\mathrm{d}t)^2, \tag{4.37}$$

where m_c = mass per unit length of the uncrushed aircraft at impact, x_{cr} = crushed length, $\mathrm{d}x_{cr}/\mathrm{d}t = V_{un}$ = velocity of uncrushed portion, R_{cr} = resistance to crushing, i.e. crushing strength.

Non-linear equations for R_{cr} and m are set up and numerical procedures are adopted for the applied forces at discrete time steps. The deceleration of the uncrushed mass m is written as:

$$G_d = \ddot{x} = -R_{cr}\,(x_{cr})_n / \int_{(x_{cr})_n}^{L} m_c x_{cr} \mathrm{d}x_{cr}. \tag{4.38}$$

In order to determine the current acceleration, current states of $(x_{cr})_n$ and R_{cr} at time t_n can be used. Similarly, the common kinematics relationship between acceleration, velocity, displacement and time can be used to determine conditions at time $t_{n+1} = t_n + \delta t$.

$$(\dot{x}_{cr})_{n+1} = (\dot{x}_{cr})_n + \ddot{x}_n \delta t \tag{4.39}$$

$$(x_{cr})_{n+1} = (x_{cr})_n + \dot{x}_{cr}\delta t + \frac{1}{2}x_n \delta t \tag{4.40}$$

Equation (4.37) is used to calculate the current force. The force–time history can thus be determined. A typical force–time history is given in Figs. 4.6 and 4.7.
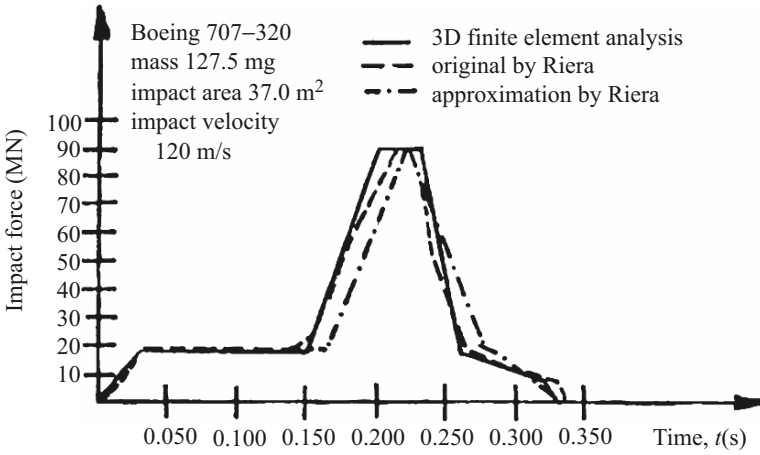
Fig. 4.6. Force as a function of time (Boeing 707–320)
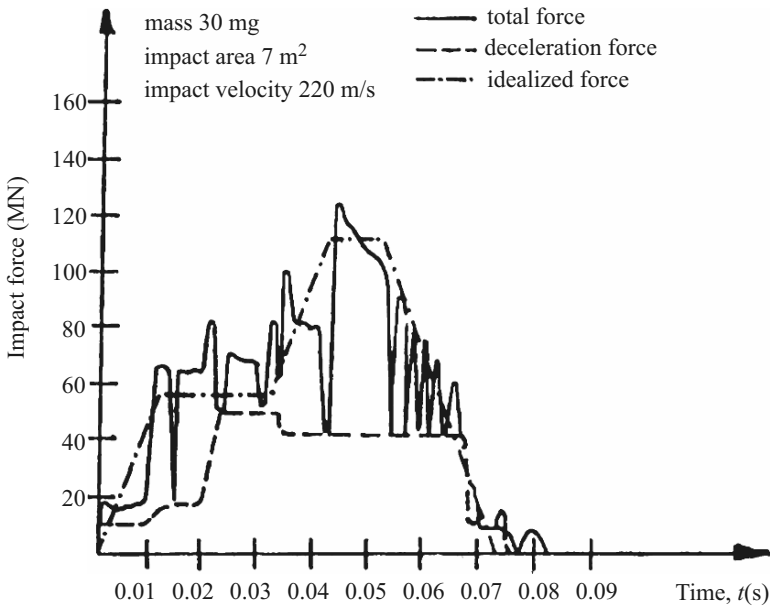
Fig. 4.7. Force as a function of time (Phantom)

4.4.4 Model of Wolf et al.

Wolf et al. developed a lumped mass, elasto-plastic model, as shown in Fig. 4.8. Just prior to impact on a target of mass m_t, Fig. 4.8a, spring stiffness k_t and damping coefficient c, the model has the mass of the fuselage which is lumped in n nodes (Fig. 4.8b). The mass m_w of the part of the wing will be assumed to break away when a certain crushing length is achieved. The nodes are connected by springs k_i of length L_i. The springs work in tension and compression. For a spring next to the target, only contact in compression is allowed. In tension, after reaching the yielding force R_{yi}, the springs ideally become plastic, with a rupturing strain ε_r. At the buckling load $R_{ti}(x)$ the springs are allowed to crush completely at $\varepsilon_i = -1$. When the spring k_j, Fig. 4.8c, reaches the value of -1, the masses m_j and m_{j+1} ideally impact plastically. Thus there is a chance for a new node to form with mass $m_j + m_{j+1}$, Fig. 4.8c. The spring stiffness k_j and its jth degree of freedom are deleted. Using the conservation of momentum, the velocity u_{j+1}^+ just after impact is computed:

$$u_{j+1}^+ = (\dot{u}_{j+1}^- m_{j+1} + \dot{u}_j^- m_j)/(m_{j+1} + m_j), \qquad (4.41)$$

where $\dot{u}_j^-$ is the displacement of the jth node, and $-$ and $+$ superscripts for before and after impact. (Note: the symbol u for displacement adopted here is the same as x, in this text.)
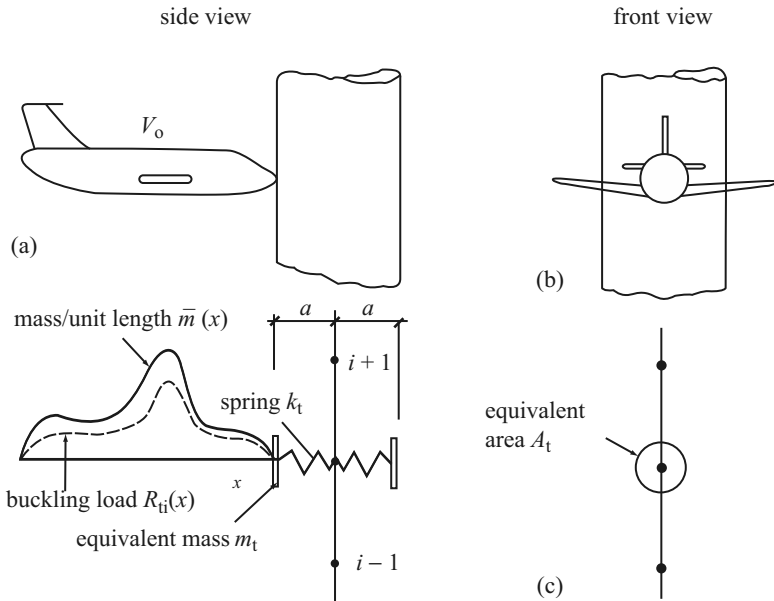
Fig. 4.8. Aircraft impact on chimney

The equations of motion with discrete time steps are adopted for the force–time relationship. The total impulse $I(t)$ from the individual mass point m_1 to the target at time t_1 is given by

$$I_1(t) = -m_\ell \, [\dot{u}_\mathrm{t}^+ - u_1^-] = (m_\mathrm{t} + m_\mathrm{b})[\dot{u}_\mathrm{t}^+ - u_\mathrm{t}^-]. \tag{4.42}$$

Since the mass m_ℓ is distributed along the axis of the aircraft, the time for the momentum transfer δt_ℓ is given by

$$\delta t_\ell = \frac{1}{2} \, (t_{\ell-1} - t_{\ell+1}), \tag{4.43}$$

where $t_{\ell-1}$ and $t_{\ell+1}$ are the times of impact of the mass points $m_{\ell-1}$ and $m_{\ell+1}$. Hence the value of $F_1(t_\ell)$ is given by

$$F_1(t_\ell) = R_\ell + I_1(t)/\delta t_\ell, \tag{4.44}$$

where R_ℓ is the force in the spring k_ℓ.

For a deformable target, as shown in Fig. 4.9,

$$F_1(t) = R_\mathrm{B}(t) + \bar{m}(t)[\dot{u}_\mathrm{a}(t) - \dot{u}_\mathrm{t}(t)]^2, \tag{4.45}$$

where
$$R_\mathrm{B}(t) = [m_\mathrm{a} - m_\mathrm{b}(t)]\ddot{u}_\mathrm{a}(t), \tag{4.46}$$

where m_a, m_b and m are the total mass of the aircraft, the mass of the crushed part of it and the mass per unit length of the crushed part next to the target, respectively and $\dot{u}_\mathrm{a}$ and $\dot{u}_\mathrm{t}$ are the velocities of the aircraft and the target respectively. The equation of motion is written as

$$[m_\mathrm{b}(t) + m_\mathrm{t}]\ddot{u}(t) = P(t) - F(t), \tag{4.47}$$

where P denotes the force in the impact spring transmitted to nodes of the target. The velocity of the new target for the ideal plastic impact is given by

$$\dot{u}_\mathrm{t} = [(m_\mathrm{b}(t) + m_\mathrm{t})\dot{u}_\mathrm{i}^- + m_\mathrm{t}\dot{u}_\mathrm{i}^-]/[m_\mathrm{b}(t) + 2m_\mathrm{t}]. \tag{4.48}$$

Again the superscripts $+$ and $-$ indicate just after and just before impact.

Wolf et al. [3.131, 3.169] tested their work on rigid and deformable targets. Data used in their work are reproduced below:

Rigid target
Boeing 707−320
$m_\mathrm{a} = 127.5\,\mathrm{Mg}$
$m_\mathrm{w} = 38.6\,\mathrm{Mg}$ included in m_a
$\varepsilon_\mathrm{y} = 2 \times 10^{-3}$; $\varepsilon_\mathrm{r} = 5 \times 10^{-2}$

Deformable target
Impact area $= 37.2\,\mathrm{m}^2$
$R_\mathrm{T} = $ yielding moment/elastic moment

Figures 4.10 and 4.11 show a comparative study for two aircraft, a Boeing 707–320 and a combat aircraft FB-111, impacting on rigid targets. Figures 4.12 and 4.13 illustrate force–time relationships for deformable targets.
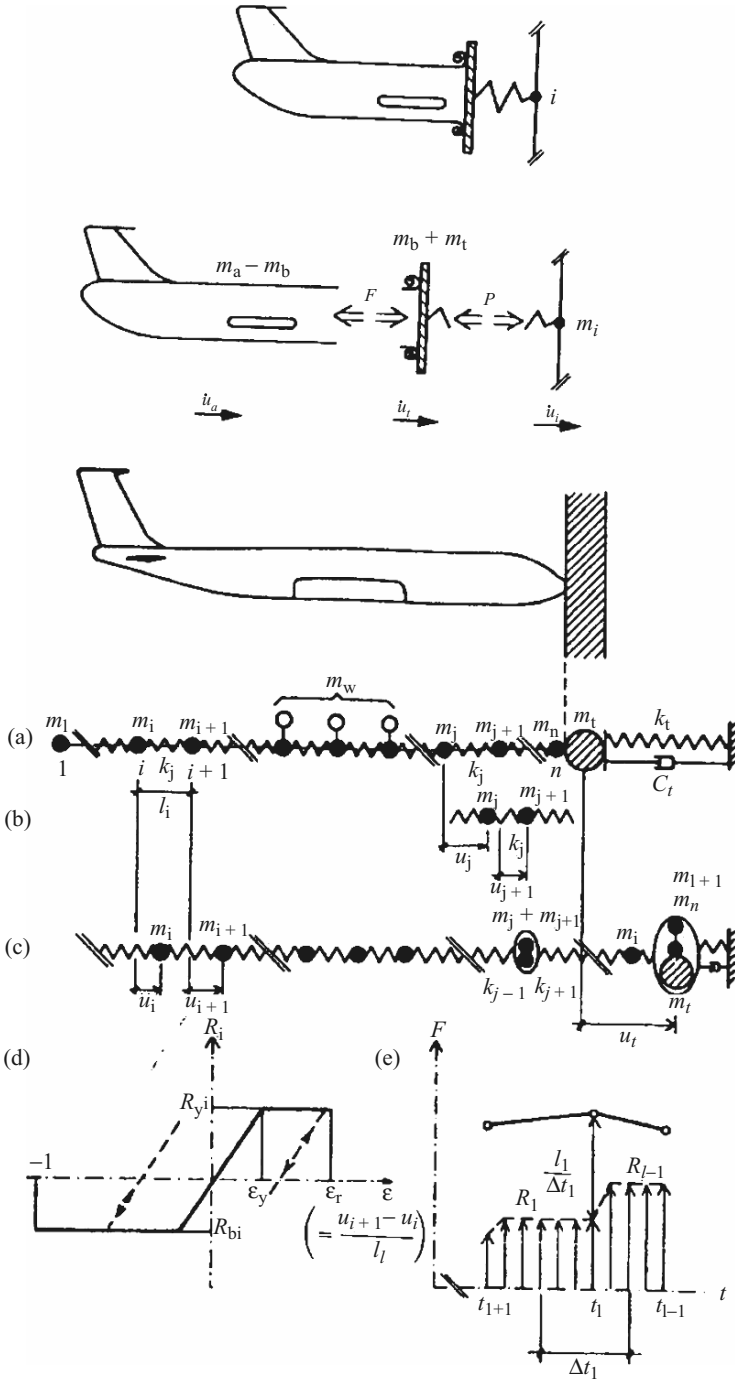
Fig. 4.9. Aircraft impact on deformable target (lumped-mass model)
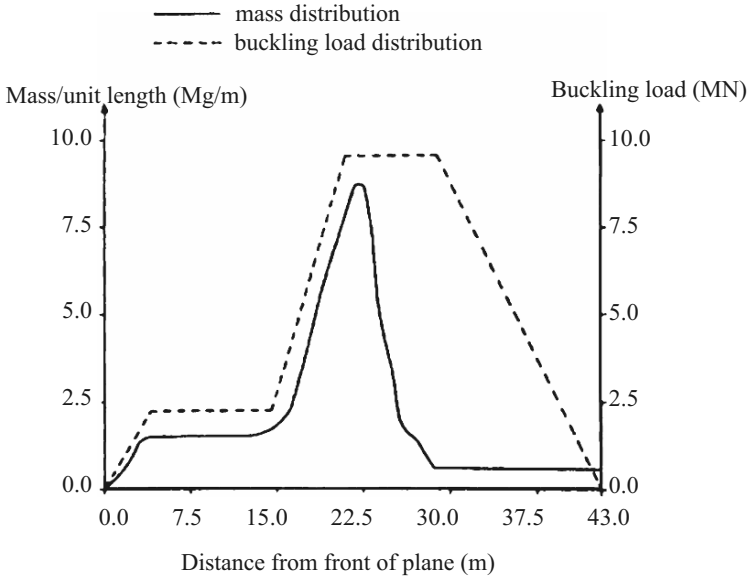
Fig. 4.10. Assumed properties of a Boeing 707–320
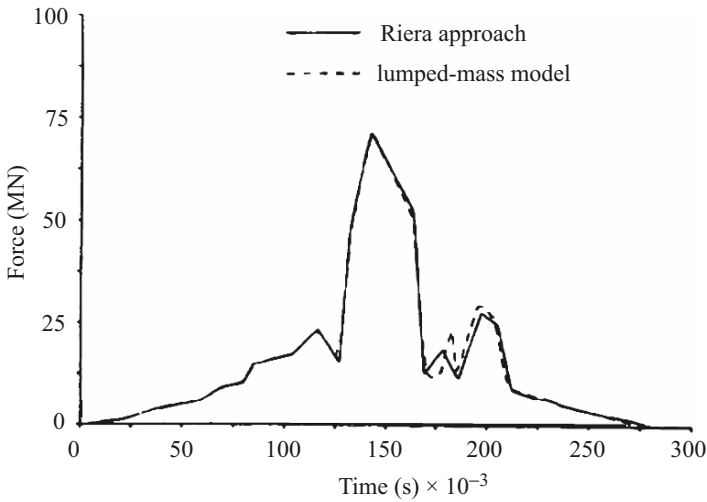
Fig. 4.11. Force–time diagrams for an FB-111

4.5 Impact Due To Dropped Weights

4.5.1 Impact on Piles and Foundations

Impact on Piles

Piles are driven into the ground using drop hammers, single and double acting hammers, diesel and vibratory hammers. It is well understood that pile driving
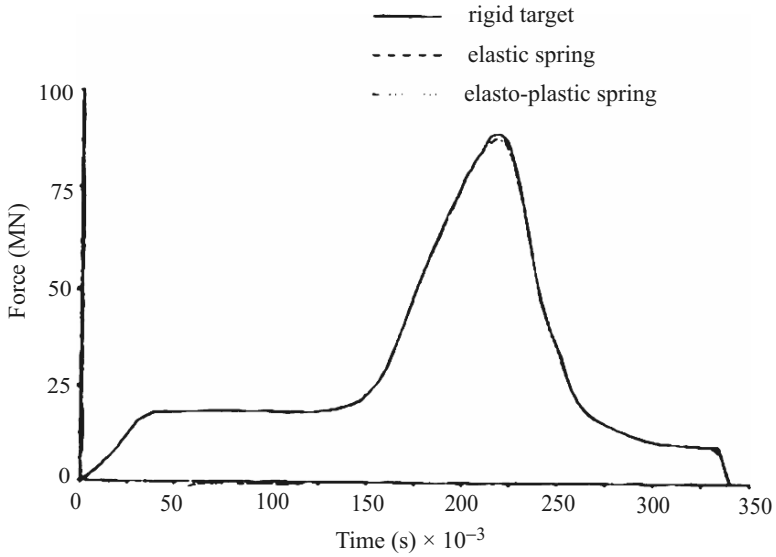
Fig. 4.12. Force–time diagram for a deformable target (frequency 50 Hz, no damping), lumped-mass model
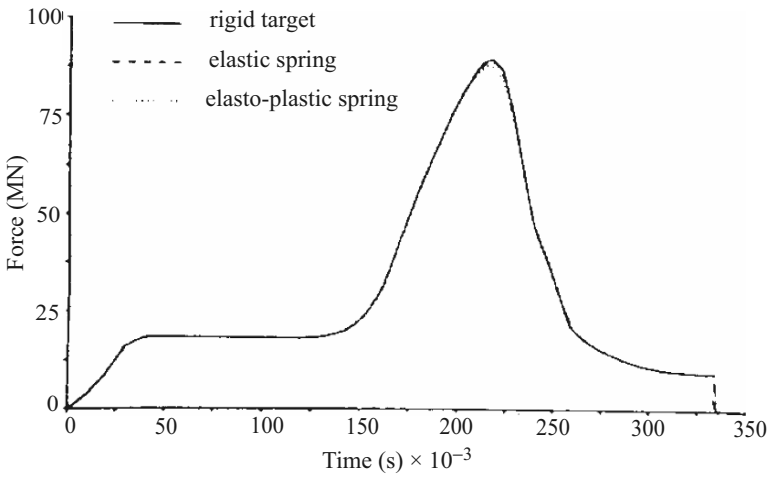
Fig. 4.13. Force–time diagram for a deformable target (frequency 50 Hz, no damping), Riera model

is not a simple case of impact which may directly be solved by Newton's law as described earlier. In fact, pile driving under impact is a case also of longitudinal compressive wave propagation and its velocity is given by

$$v_r = \sqrt{(E/\rho)}, \tag{4.49}$$

where E is the Young's modulus of the pile material and ρ is the mass density.

The one-dimensional idealization for the wave equation is given which predicts the soil load resistance, stresses in piles and ultimate load capacity at the time of driving for a particular driving resistance in bpi or blows/cm. The lumped-mass model is illustrated such that the ram and pile cap are treated as masses and the hammer cushion and optimal pile cushion are considered as springs. The series of lumped masses, with attached elasto-plastic springs and dashpots for simulating soil characteristics, are connected by springs. The time-dependent analysis is carried out on the impact load of the hammer ram striking the pile cushion at an initial specified velocity. The system shown in Fig. 4.14 is associated with a time interval δt, chosen sufficiently small that the stress wave can easily travel from any top element to the next bottom element. For a length of 2.4–3.1 m, the value of δt that gives a satisfactory answer is around 0.00025 s for steel and wood and 0.00033 s for concrete. For a shorter length, the actual value of δt is approximated as

$$\delta t = \alpha \sqrt{(W_\mathrm{m} L / \bar{A} E \mathbf{g})}, \tag{4.50}$$

where α = constant (0.5–0.75), W_m = weight of pile segment m, L = length of pile element, $\bar{A}$ = cross-sectional area of pile, E = modulus of elasticity of pile material, $\mathbf{g}$ = gravitational constant.

The current pile element displacement δ_m can be computed as

$$\delta_\mathrm{m} = 2\delta'_\mathrm{m} - \delta''_\mathrm{m} + (F_\mathrm{am} \times \mathbf{g} / W_\mathrm{m})(\delta t)^2, \tag{4.51}$$

where δ'_m = element displacement in preceding time interval δt, δ''_m = element displacement two time intervals back, F_am = unbalanced force in element causing acceleration $(F_\mathrm{am} = m\ddot{x})$.

It is not necessary to solve the equation directly. It can be done in stages. The instantaneous displacement δ_m is computed first as

$$\delta_\mathrm{m} = \delta'_\mathrm{m} + \dot{x}_\mathrm{m} \delta t, \tag{4.51a}$$

where $\dot{x}_\mathrm{m} = v_\mathrm{m}$ = velocity of the element m at δt. The relative compression or tension movement between any two adjacent elements can be written as

$$\delta_\mathrm{R} = \delta_\mathrm{m} - \delta_{\mathrm{m}+1}. \tag{4.51b}$$

The force F_m caused by the impact in segment m will become

$$F_\mathrm{m} = \delta_\mathrm{R} k_\mathrm{m} = \delta_\mathrm{R} (AE/L)_\mathrm{m}, \tag{4.51c}$$

where k_m = element stiffness. The soil springs are computed as

$$k'_\mathrm{s} = R'_\mathrm{m} / \bar{K}_\mathrm{s}, \tag{4.51d}$$
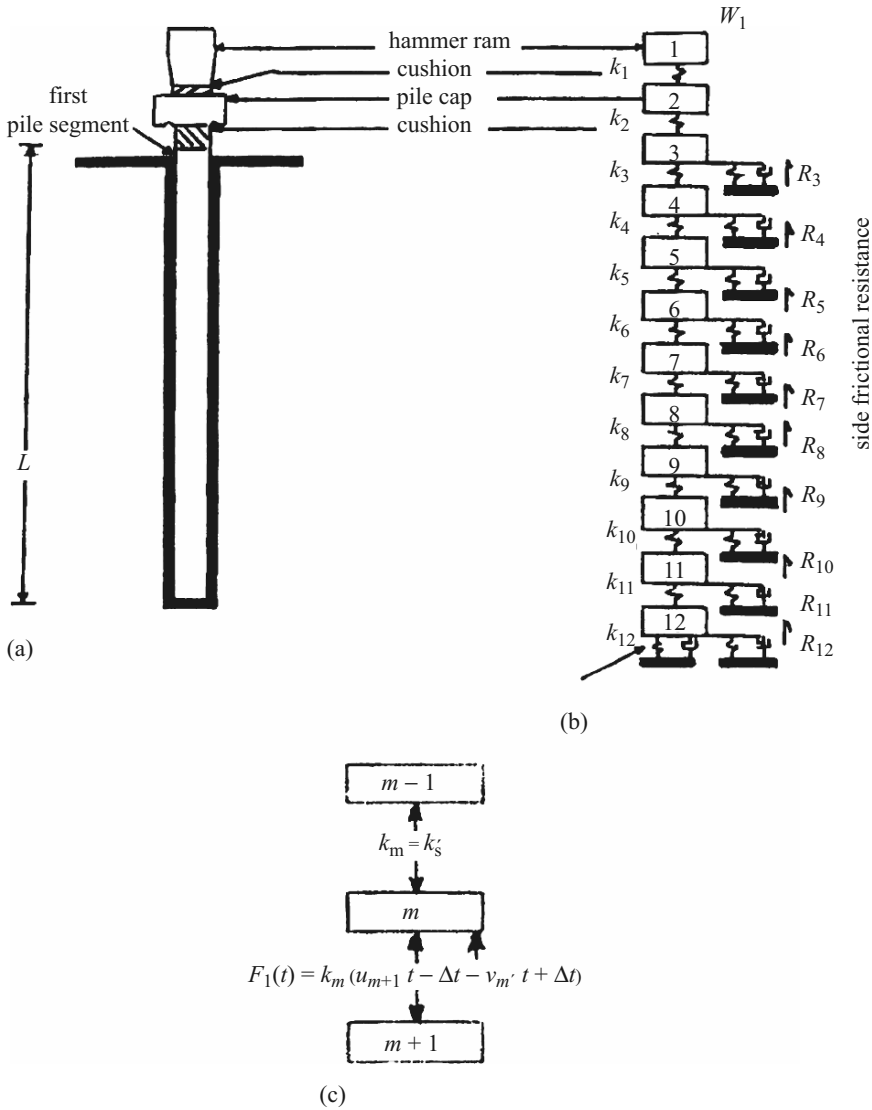
Fig. 4.14. Impact model of pile. (**a**) Actual pile; (**b**) dynamic profile of the pile; (**c**) forces on element m

where R'_m = amount of estimated ultimate pile capacity P_u on each element. $\bar{K}_s$ = the soil spring properties. $\bar{K}_s$ 1.0 to 5.0 for silt/sand 1.0 to 8.0 for clay). The side and point resistance with damping may be evaluated at the side or point values j and k respectively as

$$R_m = (\delta_m - \delta_{sm})k'_s[1 + C_s \text{ or } C_p(\dot{x}_m)], \tag{4.51e}$$

where C_s is the damping for the side point and C_p, if substituted, is for the point load. Hence the accelerating force in segment m is computed by summing forces

$$F_{am} = F_{m-1} - F_m - R_m. \tag{4.52}$$

The value of C_s is 0.33 to 0.66 s m^{-1} for sand and 1.3–3.3 for clay. The element velocity is then

$$\dot{x}_m = v_m = \dot{x}'_m + (f_{am}\mathbf{g}/W_m)\delta t, \tag{4.53}$$

where $x'_m = v'_m =$ velocity of the element m at $(\delta t - 1)$. In general, the ultimate pile capacity P_u is computed using the Bodine resonant driver (BRD) equation as

$$P_u = [\bar{A}(hp) + Br_p]/(r_p + fS_L), \tag{4.54}$$

where $\bar{A} = 550\,\text{ftlb}\,\text{s}^{-1}$ or $0.746\,\text{kJ}\,\text{s}^{-1}$
$\quad B =$ hammer weight, 22,000 lb or 89 kN (intensity of load)
$\quad r_p =$ final rate of penetration in ft/s or m s^{-1}
$\quad f =$ frequency (Hz)
$\quad S_L =$ loss factor in fts/cycle or ms/cycle
$\quad\quad = 0.244\,\text{ms}\,\text{cycle}^{-1}$ for silt, sand, gravel (loose)
$\quad\quad = 0.762\,\text{ms}\,\text{cycle}^{-1}$ for silt, sand, gravel (medium)
$\quad\quad = 2.438\,\text{ms}\,\text{cycle}^{-1}$ for silt, sand, gravel (dense)
$\quad hp =$ horsepower delivered to the pile

Note: all the above quantities are time dependent.

4.5.2 Classical or Rational Pile Formula

It is the basic dynamic pile capacity formula in which the coefficient of restitution e, discussed earlier, is included when the hammer impacts on the cap of the pile, as shown in Fig. 4.15. Let x_p be the penetration per blow at a point and h be the overall height of the ram prior to impact. The position of the pile y just as the hammer impacts on the cap will be equal to x_p plus the elastic compression of the parts. At impact the ram momentum is M_r:

$$M_r = W_r \dot{x}_i/\mathbf{g}. \tag{4.55}$$

At the end of the compression period, the value of M_r becomes

$$M_r = (W_r \dot{x}_i/\mathbf{g}) - F_1(t), \tag{4.56}$$

where $\dot{x}_i =$ velocity of the ram at the impact level, $W_r =$ weight of the ram, $F_1(t) =$ impact causing compression or a change in momentum.

The corresponding velocity $\dot{x}_{pr}$ of the ram and pile at the end of compression is given by

$$\dot{x}_{pr} = [(W_r \dot{x}_i/\mathbf{g}) - 1]\mathbf{g}/W_r. \tag{4.57}$$
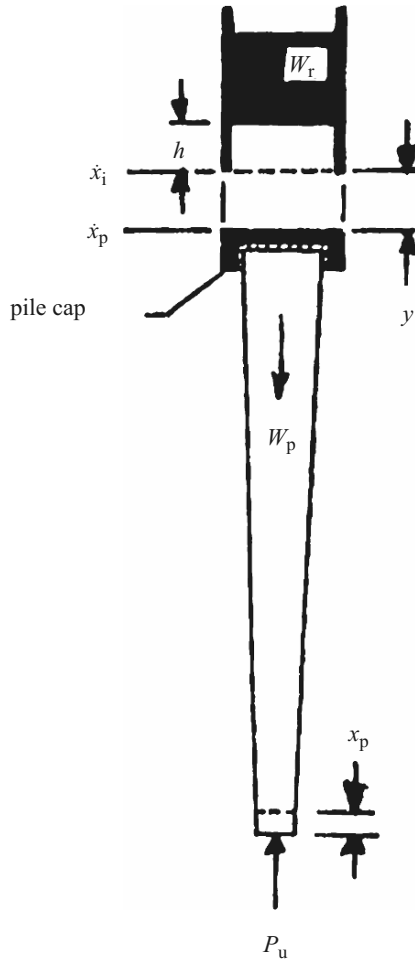
Fig. 4.15. Drop weight on piles–impact analysis

If the pile momentum $M_{\mathrm{p}} = F_1(t)$, then

$$\dot{x}_{\mathrm{pr}} = F_1(t)\mathbf{g}/W_{\mathrm{p}}. \qquad (4.58)$$

Assuming the instantaneous velocity of the pile and ram are equal and that they have not been dislocated at the end of compression, the impact value $F_1(t)$ can be written as

$$F_1(t) = \dot{x}_i \frac{W_{\mathrm{r}}W_{\mathrm{p}}}{\mathbf{g}(W_{\mathrm{r}} + W_{\mathrm{p}})}. \qquad (4.59)$$

At the end of the period of restitution e, the momentum of the pile may be computed from

$$F_1(t) + eF_1(t) = (W_{\mathrm{p}}/\mathbf{g})\dot{x}_{\mathrm{p}}. \tag{4.60}$$

Substitution of (4.59) into (4.60) gives the pile velocity $\dot{x}_{\mathrm{p}}$:

$$\dot{x}_{\mathrm{p}} = \frac{W_{\mathrm{r}} + eW_{\mathrm{r}}}{W_{\mathrm{r}} + W_{\mathrm{p}}}\, \dot{x}_i. \tag{4.61}$$

At the end of the period of restitution, the momentum of the ram becomes

$$(W_{\mathrm{r}}\dot{x}_i/\mathbf{g}) - F_1(t) - eF_1(t) = W_{\mathrm{r}}\dot{x}_{\mathrm{r}}/\mathbf{g}. \tag{4.62}$$

After substitution of the value of $F_1(t)$, the velocity of the ram, $\dot{x}_{\mathrm{r}}$, is

$$\dot{x}_{\mathrm{r}} = \frac{W_{\mathrm{r}} - eW_{\mathrm{p}}}{W_{\mathrm{r}} - W_{\mathrm{p}}}\, \dot{x}_i. \tag{4.63}$$

At the end of the period of restitution, as discussed earlier, the total energy $E_{\mathrm{p}}^{\mathrm{r}}$ of the pile and ram is written as

$$E_{\mathrm{p}}^{\mathrm{r}} = \frac{1}{2}m\,\dot{x}_{\mathrm{p}}^2 + \frac{1}{2}m\,\dot{x}_{\mathrm{r}}^2. \tag{4.64}$$

Substituting the values of $\dot{x}_{\mathrm{p}}$ and $\dot{x}_{\mathrm{r}}$ from (4.61) and (4.63):

$$E_{\mathrm{p}}^{\mathrm{r}} = \frac{1}{2}\left[m_{\mathrm{p}}\frac{W_{\mathrm{r}} + eW_{\mathrm{r}}}{W_{\mathrm{r}} + W_{\mathrm{p}}} + m_{\mathrm{r}}\frac{W_{\mathrm{r}} - eW_{\mathrm{p}}}{W_{\mathrm{r}} - W_{\mathrm{P}}}\right]\dot{x}_i, \tag{4.65}$$

where $m_{\mathrm{p}} = W_{\mathrm{p}}/\mathbf{g}$ and $m_{\mathrm{r}} = W_{\mathrm{r}}/\mathbf{g}$. The right-hand side of (4.65) is simplified to

$$E_{\mathrm{p}}^{\mathrm{r}} = \eta W_{\mathrm{r}}h\,\frac{W_{\mathrm{r}} + e^2 W_{\mathrm{p}}}{W_{\mathrm{r}} + W_{\mathrm{p}}}, \tag{4.66}$$

where η is hammer efficiency. For a 100% system, the ultimate pile capacity P_{u} is evaluated as

$$P_{\mathrm{u}} = \eta W_{\mathrm{r}}h/x_{\mathrm{p}}. \tag{4.67}$$

The pile top displacement will be

$$\begin{aligned}
\overline{\delta} &= x_{\mathrm{p}} + (P_{\mathrm{u}}L/AE)_{\mathrm{cp}} + (P_{\mathrm{u}}L/AE)_{\mathrm{ep}} + \bar{k}_{\mathrm{s}} \\
&= x_{\mathrm{p}} + C' + \bar{k}_{\mathrm{s}},
\end{aligned} \tag{4.68}$$

where the subscript cp relates to the cap block and pile cap and ep relates to elastic compression of the pile. The actual input energy to the pile system from the impact is

$$\begin{aligned}
\eta W_{\mathrm{r}}h &= P_{\mathrm{u}}[\overline{\delta} - (P_{\mathrm{u}}L/AE)_{\mathrm{ep}}] \\
&= P_{\mathrm{u}}(x_{\mathrm{p}} + C').
\end{aligned} \tag{4.69}$$

In terms of (4.66),

$$P_{\mathrm{u}} = \left(\frac{\eta W_{\mathrm{r}} h}{x_{\mathrm{p}} + C'} \right) \left(\frac{W_{\mathrm{r}} + e^2 W_{\mathrm{p}}}{W_{\mathrm{r}} + W_{\mathrm{p}}} \right). \qquad (4.70)$$

Similarly, other expressions for the pile behaviour under impact have been developed by other researchers and they are recorded in Table 4.3.

Table 4.3. Ultimate pile capacity, P_{u}, under impact loads

Canadian National Building Code (use SF = 3)

$$P_{\mathrm{u}} = \frac{\eta E_{\mathrm{h}} C_1}{x_{\mathrm{p}} + C_2 C_3}, \qquad C_1 = \frac{W_{\mathrm{r}} + e^2 \, (0.5 \, W_{\mathrm{p}})}{W_{\mathrm{r}} + W_{\mathrm{p}}},$$

$$C_2 = \frac{3 P_{\mathrm{u}}}{2 \bar{A}}, \qquad C_3 = \frac{L}{E} + 0.0001 \ (\mathrm{in.}^3 \, \mathrm{kips}^{-1}).$$

Note that the product of $C_2 C_3$ gives units of e; x_{p} = penetration distance

Danish formula [2.395] (use SF = 3 to 6)

$$P_{\mathrm{u}} = \eta E_{\mathrm{h}} / (x_{\mathrm{p}} + C_1), \qquad C_1 = \sqrt{(\eta E_{\mathrm{h}} L / 2 \bar{A} \mathrm{E})} \ (\text{units of } x_{\mathrm{p}}),$$

where E_{h} = hammer energy rating.

Eytelwein formula [2.394] (use SF = 6)

$$P_{\mathrm{u}} = \frac{\eta E_{\mathrm{h}}}{x_{\mathrm{p}} + 0.1 (W_{\mathrm{p}} / W_{\mathrm{r}})}.$$

Double-acting hammers:

$$P_{\mathrm{u}} = \left[\frac{\eta W_{\mathrm{r}} h}{x_{\mathrm{p}} + \frac{1}{2} (c' + \bar{k}_{\mathrm{s}})} \right] \left[\frac{W + e^2 W_{\mathrm{p}}}{W + W_{\mathrm{p}}} \right]$$

$c' \approx C_1$; $W = W_{\mathrm{r}} +$ weight of casing.

Gates formula [2.395] (Gates, 1957) (use SF = 3)

$$P_{\mathrm{u}} = a \sqrt{(\eta E_{\mathrm{h}})} (b - \log x_{\mathrm{p}}),$$

Where P_{u} is in kips or kN and E_{h} is in kips ft or kN m.

	x_{p}	a	b
F_{pS}	in.	27	1.0
SI	mm	104.5	2.5

$\eta = 0.75$ for drop and 0.85 for all other hammers.

Table 4.3. (continued)

Janbu [2.395] *(use SF = 3 to 6)*

$$P_u = \eta E_h / k_u x_p, \qquad C_d = 0.75 + 0.15(W_p/W_r),$$
$$k_u = C_d\{1 + \sqrt{[1 + (\lambda/C_d)]}\}, \qquad \lambda = \eta E_h L / A E x_p^2.$$

Modified ENR formula [2.395] *(use SF = 6)*

$$P_u = \left(\frac{1.25\eta E_h}{x_p + 0.1}\right) \left(\frac{W_r + e^2 W_p}{W_r + W_p}\right)$$

American Association of State Highway Officials (AASHTO) (SF = 6) (primarily for timber piles)

$$P_u = 2h(W_r + A_r p)/(x_p + 0.1)$$

For double-acting steam hammers take A_r = ram cross-sectional area and p = steam (or air) pressure. For single-acting steam hammers and gravity hammers, $A_r p = 0$. Here $\eta = 1$.

Navy-McKay formula [2.395] *(use SF = 6)*

$$P_u = \frac{\eta E_h}{x_p (1 + 0.3 C_1)}, \qquad C_1 = W_p/W_r.$$

Pacific Coast Uniform Building Code (PCUBC)

$$P_u = \frac{\eta E_h C_1}{x_p + C_2}, \qquad C_1 = \frac{W_r + k_p W_p}{W_r + W_p},$$
$$C_2 = P_u l / A E,$$

where $k_p = 0.25$ for steel piles and 0.1 for all other piles.

Coefficient of restitution e

Material	e
Broomed wood	0
Wood piles (non-deteriorated end)	0.25
Compact wood cushion on steel pile	0.32
Compact wood cushion over steel pile	0.40
Steel-on-steel anvil on either steel or concrete pile	0.50
Cast-iron hammer on concrete pile without cap	0.40

4.5.3 Impact on Foundations

Useful data are given in Table 3.6 on vibration problems related to foundations. Various machines produce an impact on foundations. An additional consideration concerns energy dissipation and absorption. Typical views of the foundation for a hammer with its frame and anvil mounted are shown in Fig. 4.16a, b. It is treated as a two-mass-spring system, as shown in Fig. 4.16c. Let m_1 and m_2 be the mass of the foundation and anvil respectively. The ks shown are the respective spring stiffnesses. The circular frequencies are given below:
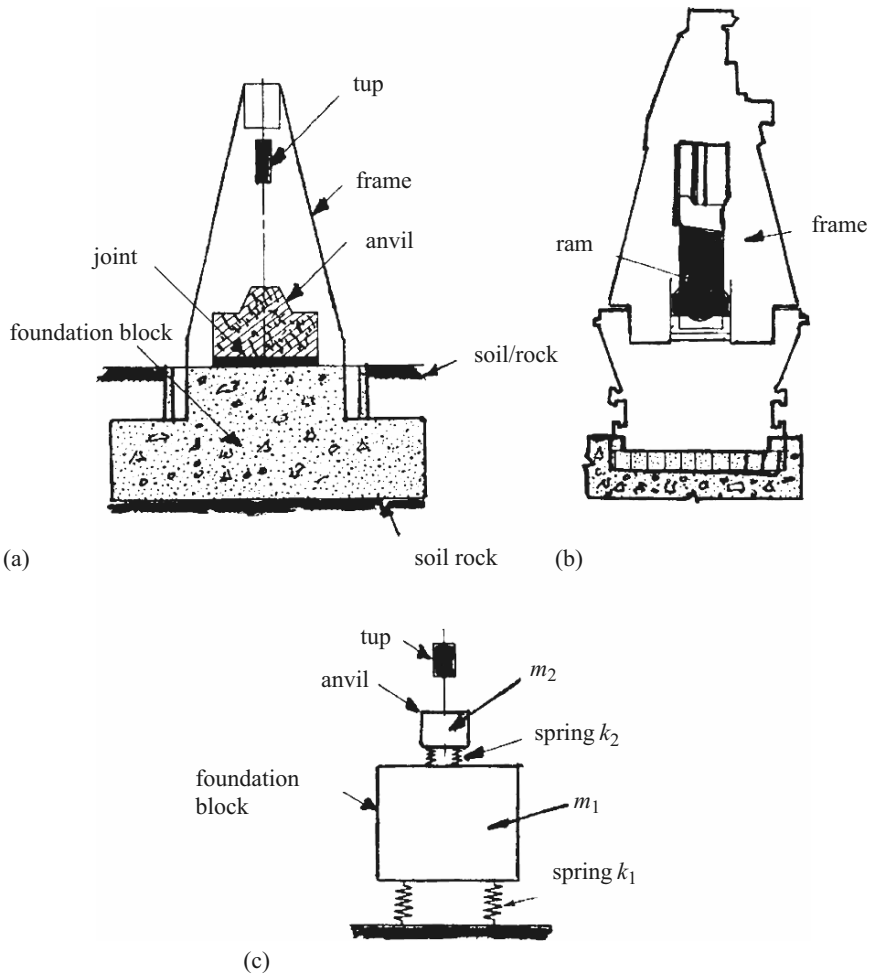
Fig. 4.16. Typical arrangement of a hammer foundation resting on soil with (**a**) a frame mounted on the foundation; (**b**) a frame mounted on the anvil; (**c**) two-mass-spring analogy for a hammer foundation

ω_{an} = foundation of the anvil on the pad

$$= \sqrt{(k_2/m_2)}, \tag{4.71}$$

ω_{ln} = the limiting circular frequency of the foundation and anvil on soil.

$$= \sqrt{\left(\frac{k_1}{m_1 + m_2}\right)}. \tag{4.72}$$

The equations of motion in free vibration are written as

$$m_1 \ddot{x}_1 + k_1 x_1 + k_2 (x_1 - x_2) = 0, \tag{4.73}$$
$$m_2 \ddot{x}_2 + k_2 (x_2 - x_1) = 0,$$

where $x_1 = A \sin \omega_{\mathrm{n}} t$ and $x_2 = B \sin \omega_{\mathrm{n}} t$. The general equation can be derived:

$$\omega_{\mathrm{n}}^4 - (1 + \alpha_{\mathrm{m}})(\omega_{\mathrm{na}}^2 + \omega_{\mathrm{n\ell}}^2) \, \omega_{\mathrm{n}}^2 + (1 + \alpha_{\mathrm{m}}) \, \omega_{\mathrm{nl}}^2 \omega_{\mathrm{na}}^2 = 0 \tag{4.74}$$

$$\text{or } \omega_{\mathrm{n1,2}}^2 = \frac{1}{2}(1 + \alpha_{\mathrm{m}})(\omega_{\mathrm{na}}^2 + \omega_{\mathrm{nl}}^2) \pm \sqrt{\{[(1 + \alpha_{\mathrm{m}})(\omega_{\mathrm{na}}^2 + \omega_{\mathrm{nl}}^2)]^2}$$
$$- 4(1 + \alpha_{\mathrm{m}})(\omega_{\mathrm{nl}}^2 \, \omega_{\mathrm{na}}^2)\}, \tag{4.75}$$

where $\alpha_{\mathrm{m}} = m_2/m_1$. The values of x_1 and x_2 are

$$x_1 = \frac{(\omega_{\mathrm{na}}^2 - \omega_{\mathrm{n1}}^2)(\omega_{\mathrm{na}}^2 - \omega_{\mathrm{n2}}^2)}{\omega_{\mathrm{na}}^2 (\omega_{\mathrm{n1}}^2 - \omega_{\mathrm{n2}}^2) \, \omega_{\mathrm{n2}}} \dot{x}_{\mathrm{a}} \tag{4.76}$$

$$\text{and } x_2 = \frac{(\omega_{\mathrm{na}}^2 - \omega_{\mathrm{n1}}^2) \, \dot{x}_{\mathrm{a}}}{(\omega_{\mathrm{n1}}^2 - \omega_{\mathrm{n2}}^2) \, \omega_{\mathrm{n2}}}. \tag{4.77}$$

The maximum values of x_1 and x_2 occur when $\sin \omega_{\mathrm{n2}} t = 1$. The value of $\dot{x}_{\mathrm{a}}$ is the anvil velocity. The initial velocity of the anvil is computed from the impact of the tup and the anvil. If h is the drop of the tup in m, $\mathbf{g}$ is the acceleration due to gravity, $\dot{x}_{\mathrm{ti}}$ is the initial velocity of the tup in $\mathrm{m\,s^{-1}}$ and η is the efficiency of the drop, then

$$\dot{x}_{\mathrm{ti}} = \sqrt{2\mathbf{g}h} \times \eta \tag{4.78}$$

if the tup is operated by a pneumatic pressure p, the area of the cylinder is A_{c} and the weight of the tup is W_0, then

$$x_{\mathrm{ti}} = \sqrt{[2\mathbf{g}(W_0 + pA_{\mathrm{c}})h/W_0]} \times \eta, \tag{4.79}$$

where η ranges between 0.45 and 0.80.

The velocity of the anvil after impact, $\dot{x}_{\mathrm{a}}$, is given by

$$\dot{x}_{\mathrm{a}} = \dot{x}_{\mathrm{ti}}(1 + e)/[1 + (W_2/W_0)], \tag{4.80}$$

where W_2 is the weight of the anvil and e is the coefficient of restitution.
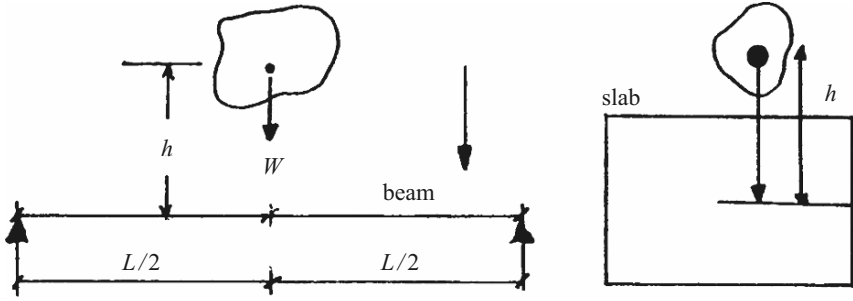
Fig. 4.17. Rock fall on a beam and slab

4.5.4 Rock Fall on Structures

Rock fall, as described in Chap. 2, Sect. 2.2.5, can cause severe damage to structures. Structural units can be beams, slabs or columns, or combinations thereof. In Fig. 4.17, a rock falls on a beam which has a peak mid-span deflection limited to $\delta_{\max}(t)$. The rock, of weight W, falls from a height h, thus the potential energy lost during the rock fall is $W[h + \delta_{\max}(t)]$ and the energy dissipated by the beam is $R_T \delta_{\max}$, where R_T is the resistance when the beam fails in the development of plastic hinges. In the ultimate case, the value of R_T is

$$R_T \delta_{\max}(t) = W(h + \delta_{\max}). \tag{4.81}$$

However,
$$R_T = 4M_p/L$$

and the ultimate moment M_u or M_p is given by

$$M_p = (WL/4)(1 + h/\delta_{\max}), \tag{4.82}$$

where M_p is the moment for the beam at collapse.

In a similar manner, a rock fall can occur on reinforcement concrete slabs and equations can be set up for the collapse moment M_p or the ultimate moment M_u.

Falling, Rolling and Bouncing of Rocks

The rock on inclined plane undergoes a gravitational force of the component in the direction of the dip, and then its value is $mg \sin \theta$ which is antagonized by a frictional force $\mu mg \cos \theta$, where θ is the slope angle, μ is the total coefficient of friction, m is the rock mass and g is the gravitational acceleration. If the volume of breadth 'B' from where the rocks are dislocated is large enough to be dominant as far as the release of motion is concerned, the rock mass in motion can be expressed by $A_i B \rho_i$ for the portion 'i'. The total impact force generated as:

$$F^R{}_i = A_i\ B\rho_i\ g\ (\operatorname{Sin}\theta_i - \mu_i \cos\theta_i), \qquad (4.83)$$

where $F^R{}_i$ = total impact force generated by A_i in the direction of dip facing the wall, if any.

There can be three coefficients of friction in the system: μ_1 in the 'back', μ_3 in the 'seat' and μ_{13} in the bend between 'back' and 'beat'. These phenomena are not included in this text which covers the final impact caused by more complicated cases which include rock-on-rock creep, release of masses with heavy precipitation, joint water pressure and rockfall and rock slides due to earthquakes and snow storm. The subject only covers the final impactive or impulsive force caused by these events. The rocks as a result may fall in any direction with and without rolling and bouncing.

Falling, Rolling and Bouncing Influencing Forces of Impact

Falling, rolling, bouncing – three mechanisms so closely linked to each other that would be difficult to separate them one and another. A single boulder sliding on steep ground will sooner or later start rolling depending upon the conditions of the terrain. Rapid rolling of an irregularly shaped rock mass is impossible without the bounces required. A bounce in the steep descent especially in the final phase is nothing but an almost perfect process of falling. It is a simplified system or process to differentiate between rock falls and rock slides. A more conservative approach is to bring about acceleration 'a' of the direction of slope and the gravitational acceleration, 'g' (Fig. 4.18). This relation is given as:

$$\underline{\frac{a}{g}} = \operatorname{Sin}\theta - \mu\cos\theta. \qquad (4.84)$$
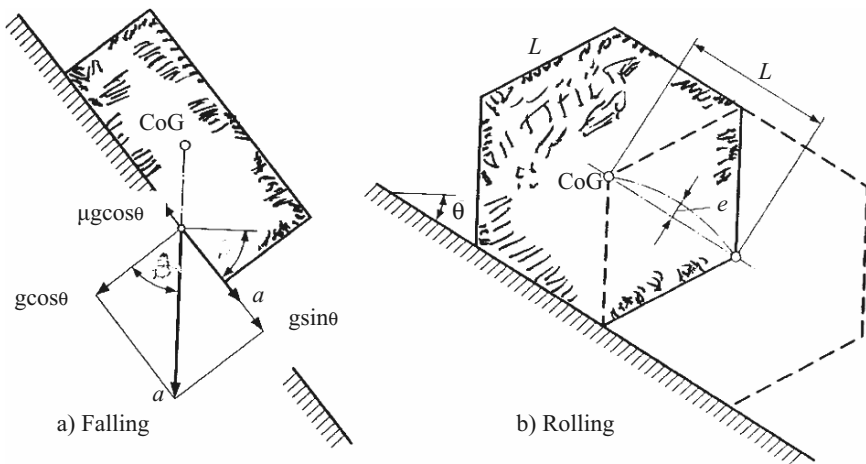
Fig. 4.18. Rock mass on the verge of falling and rolling

Table 4.4. Comparison of Acceleration with that of a free fall (A)

$\beta(°)$	45	50	55	60
a/g ($\mu = 0.2$)	0.57	0.64	0.70	0.77
a/g ($\mu = 0.4$)	0.42	0.51	0.59	0.67

Table 4.5. Rolling conditions of regular polygonal prisms on plane slopes

n	4	6	8	10	12	14	16
β	45.0	30.0	22.5	18.0	15.0	12.9	11.2
μ	1.00	0.58	0.41	0.32	0.27	0.23	0.20
e/L (%)	20.7	13.4	9.9	7.9	6.6	5.6	4.9

n: Number of sides; β: minimum slope angle required to start rolling; $\mu = \tan\beta$: minimum coefficient of friction required to start rolling on slope angle. e: deviation of centre of gravity with respect to a straight course; L: side length of polygon = longitudinal displacement when rotating from one side to the next. Parameter e/L gives an idea of the locally uneven course in slow motion

Tables 4.4 and 4.5 give useful geological data for falling and rolling of rock mass. Falling is arbitrarily defined by a > 0.6g (a: acceleration along slope; g; acceleration of gravity). In the particular case a coefficient of friction $\mu = 0.258$ and a slope angle, $\theta = 50°$ yield this critical value. Rolling is compulsively given by a non-sliding motion. In the particular case a regular hexagonal prism starts rolling on a slope angle $\theta > 30°$ provided that sliding is excluded by $\mu > 0.58$. The critical position of centre of gravity CoG is vertical above edge of contact surface. L: length of side = "step" length from one side to the next; e: deviation of CoG start rolling if slope angle θ exceeds 180/n and the coefficient of friction μ exceeds $\tan\theta$. Lower friction may lead to sliding in a similar manner as the towers (and skiers) of Fig. 4.18. Examples in the range $4 < n < 16$ are shown in Table 4.5. the limitation to $\mu > 0.20$ does not mean that, once started, a prism will not, owing to its angular kinetic energy, be able to roll on, even in spite of lower friction. In fact, as mentioned in the first paragraph of this section, an appropriately shaped single boulder on steep ground will start rolling almost inevitably: sooner or later it will encounter a local obstacle that will initiate a sufficient spin.

The last line of Table 4.5 shows the deviation e of the prism's centre of gravity in its circular motion around one of its edges. This up and down movement is referred to the side length L, identical to the horizontal travel between reposing on two consecutive sides. So e/L is an indicator for the local unevenness of slow rolling motion. Of course these figures are valid only as long as the downward acceleration remains below g. If this limit is trespassed, a short bounce is inevitable and the amount of e/L is reduced. The critical velocity of these rock masses shall be, $v = \sqrt{gR}$ where radius R is the circle circumscribed to the polygon which is size dependent.

a) Non-rotating rock mass during collision with a structure

b) Split impact
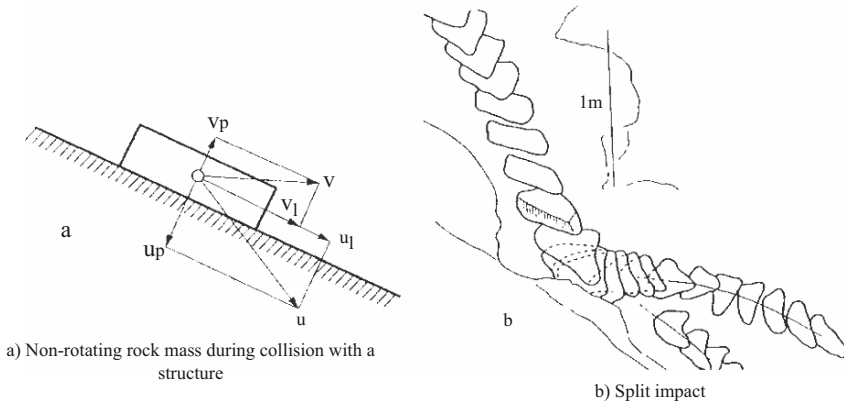
Fig. 4.19. Theoretical analysis in re-bounding

The process of rolling becomes more complicated as soon as instead of one single body a multitude of different bodies are involved. Once more, extremely idealized model will demonstrate a set of problems which, far beyond the mere didactic aspect, will reveal some fundamental physical rules of disintegrated motion.

As long as a projectile has no contact with the ground, the impact forces being reduced to gravitation and aerodynamic effects. The aerodynamic resistance or drag F_v of a bouncing body is comparatively unproblematic and is generally ignored when the final impact on structure facing is determined. Figure 4.19 indicates the u and v velocities before and after collision. They are termed u_1, u_p, v_1, and v_p as shown in the figure. The energy is lost if split occurs. The impact force would be affected. The subscript 1 and p are longitudinal and vertical components of velocity. The value of v_1 is computed as:

$$v_1 = u_1 - \mu(v_p - u_p). \tag{4.85}$$

The impact I is then written as:

$$I = m \cdot v_1,$$

where m is the mass. This shall not be less than F^R_i given in (4.83). The procedure given in Sect. 4.5.4 shall then be followed.

4.6 Impact on Concrete and Steel

4.6.1 General Introduction

When the structure receives an impact, the important consideration is to examine:

(1) local damage, which includes penetration, perforation, scabbing and/or punching shear

(2) the overall response of the structure in terms of bending and shear, etc.

These effects are defined below.

Penetration (x_p): the depth of the crater developed in the target at the zone of impact.

Perforation (t_p): full penetration of the target by the missile with and without exit velocity.

Scabbing (t_{sc}): the ejection of the target material from the opposite face of impact.

Spalling (t_{sp}): the ejection of the target material from the face at which impact occurred.

Figures 4.20–4.24 show penetration, spalling, scabbing, perforation, punching shear and overall response phenomena.

Criteria for point (1) involve the complex nature of the transient stress state. The empirical formulae developed so far, and which are described later
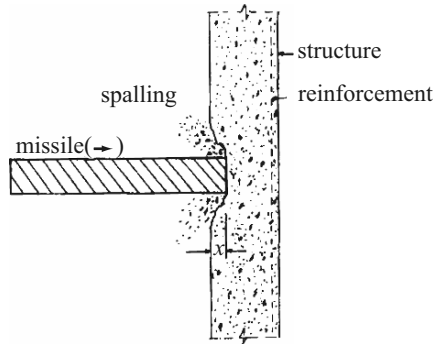
Fig. 4.20. Local effect of penetration (x) and spalling
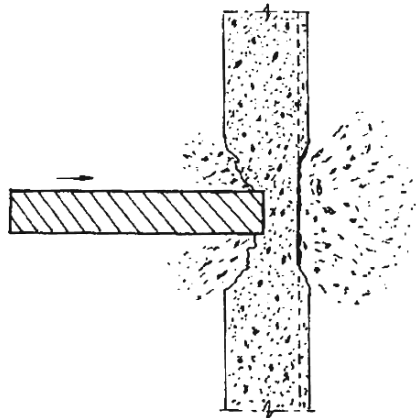
Fig. 4.21. Local effect of scabbing
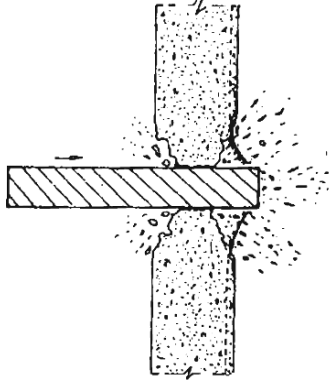
Fig. 4.22. Local effect of perforation
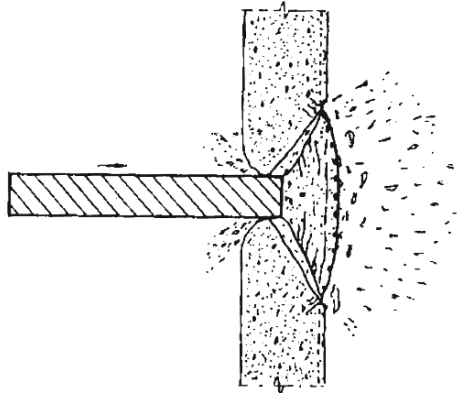
Fig. 4.23. Local effect of a punch type shear failure

on in this section, are based on available test data. They are valid for smaller missiles with limited deformation after impact. The impact conditions in section "Impacts/collisions of vehicles" are not covered by these empirical formulae since they do not penetrate the target in general. In addition to these are the interaction problems of deformable and undeformable missiles. The missile deformability lengthens the duration of impact and at the same time reduces the penetration depth x_p, but has very little effect on perforation and scabbing thicknesses. A detailed list of missiles is given in Chap. 2. In the case of soft missiles, it is generally assumed that at the level of impact a significant local deformation of the missile or target occurs. In addition, when the missile is deformable, it is imperative to develop a force-time history along the lines suggested in Sects. 4.4 and 4.5.5, while assuming the target is rigid or flexible. As explained earlier, the graphs produced are *load–time functions*. The load imposed on a rigid target is composed of both the crushing strength
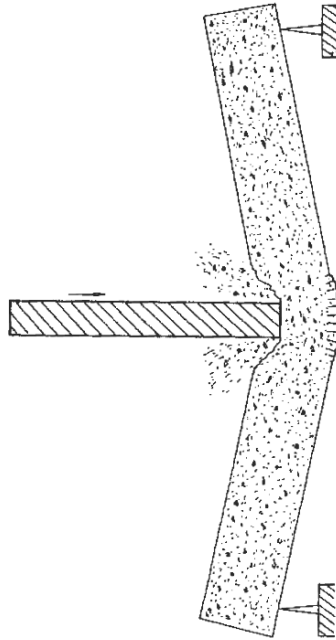
Fig. 4.24. Overall target response

and the rate of change of momentum of the missile, known as the *inertial force*. Some of this work has already been given in some detail in Sect. 4.4. It is important to include these techniques in the local and global analyses of structures subject to missile impact. Apart from the empirical formulae given in the next section, more comprehensive non-linear analyses are required to take into consideration instantaneously formed failure mechanisms, material and geometrical non-linearities, impactor-target/structure interaction and evaluation of the overall damage to the impactors and structures.

4.6.2 Available Empirical Formulae

The following sections give the empirical and derived formulae for impact on targets.

Formulae for Non-Deformable Missiles Impacting on Concrete Targets

Petry

Petry's formula is used for predicting the penetration depth x_p for infinitely thick concrete targets. This formula is derived from tests concerning high

velocity impact on infinitely thick concrete targets. Where thickness governs the failure mode or the impact response is influenced by the size and shape of the missile and the presence of the reinforcement, this formula gives very inaccurate assessments.

$$x_{\mathrm{p}} = K_{\mathrm{m}} A V' \bar{R}, \tag{4.87}$$

where x_{p} = depth of penetration in a concrete slab of thickness h, K_{m} = material property constant $(L^3/F) = 4.76 \times 10^{-3}\,\mathrm{ft^3\,lb^{-1}} = 2.97 \times 10^{-4}\,\mathrm{m^3\,kg^{-1}}$, A = sectional mass weight of the missile per unit cross-sectional area of contact (F/L^2), V' = velocity factor = $\log_{10}[1 + (v_0^2/v^{*2})]$, v_0 = initial velocity of missile at impact, v^{*2} = reference velocity equal to $215{,}000\,\mathrm{ft^2\,s^{-2}}$ $(19{,}973\,\mathrm{m^2\,s^{-2}})$, $\bar{R}$ = thickness ratio

$$x_{\mathrm{p}}/D_{\mathrm{p}} = 1 + \exp[-4(\alpha' - 2)],$$

where $\alpha' = h/D_{\mathrm{p}} = h/K_{\mathrm{m}} A V'$ and D_{p} is the penetration depth of an infinitely thick slab. The penetration depth is restricted to less than $\frac{2}{3}h$, to satisfy the inequality below, in order to prevent penetration and spalling.

$$h \geq C_1 A \times 10^{-5}\,\mathrm{ft} \text{ or an equivalent value in SI units,}$$

where C_1 is taken from Fig. 4.25. The time required for penetration is derived from the *modified Petry formula*:

$$F = m\ddot{x} = mv(\mathrm{d}v/\mathrm{d}x) = -1.15(v^{*2}/K_{\mathrm{m}} A)\exp(2.3 x_{\mathrm{p}}/K_{\mathrm{m}} A), \tag{4.88}$$

where F = the resisting force, equal to R_{m}, x_{p} = penetration at any time, v = missile velocity at any time.

Due to the non-linear nature of the equation of motion, a numerical integration is necessary to determine the velocity as a function of distance. Then:

$$\ddot{x} = -1.15(v^{*2}/K_{\mathrm{m}} A)\exp[2.3(x - \delta)/K_{\mathrm{m}} A], \tag{4.89}$$

hence
$$m\ddot{x} = m_{\mathrm{t}}\ddot{\delta} + k\delta, \tag{4.90}$$

where x = missile displacement, δ = target displacement, k = target stiffness, m, m_{t} = mass of the missile and target respectively.

When $\delta = 0$, the acceleration = $\frac{m}{m_{\mathrm{t}}} \times$ (missile acceleration). If $t = 0$; $x = \delta$; $\dot{\delta} = 0$; $\dot{x} = v_0$.

Army Corps of Engineers (ACE)

This empirical formula predicts the penetration depth x_{p} of missiles in concrete targets. Again, it is based on high velocity impact tests on targets having infinite thickness. Since the ACE formula given below for penetration depth is not velocity dependent, it gives a non-zero value for the penetration depth when the velocity is zero.
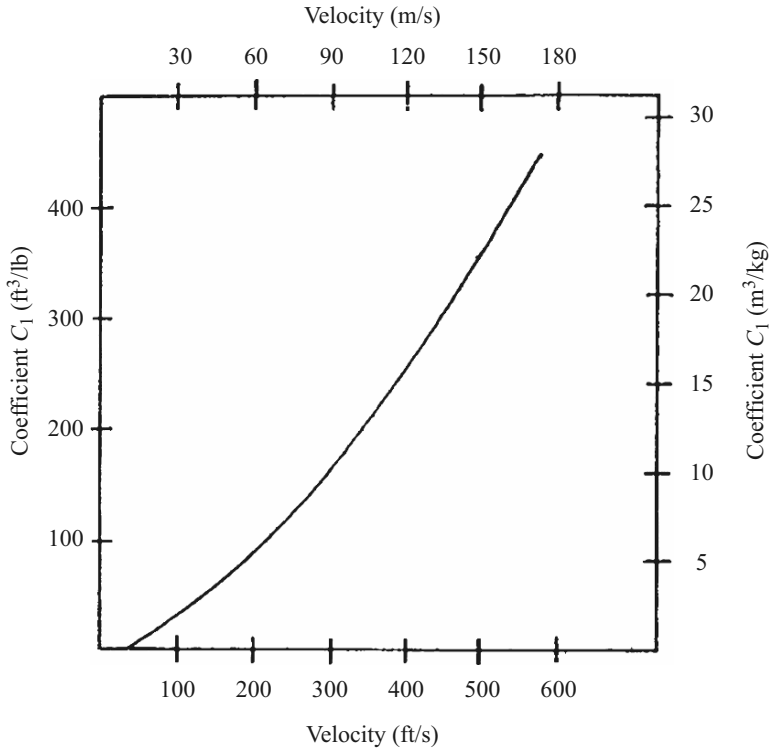
Velocity (m/s)

Fig. 4.25. Minimum thickness needed to prevent penetration and spalling

$$x_{\mathrm{p}} = 282[(Wd^{0.215})/(d^2\sqrt{f_{\mathrm{c}}'})](v/1{,}000)^{1.5} + 0.5d, \qquad (4.91)$$

where W = missile weight (lb), d = missile diameter (in), f_{c}' = concrete compressive strength (psi), v = velocity of the missile (ft s^{-1}).

When the penetration depth has been calculated, the perforation thickness t_{p} becomes

$$t_{\mathrm{p}} = 1.32d + 1.24x_{\mathrm{p}} \qquad (4.92)$$

and the spall thickness t_{sp} becomes

$$t_{\mathrm{sp}} = 2.12d + 1.36x_{\mathrm{p}}. \qquad (4.93)$$

National Defense Research Committee (NDRC)

Another empirical formula, proposed for non-deformable cylindrical missiles penetrating a massive reinforced concrete target, is the NDRC formula. The penetration depth of a solid missile given by this formula is

$$x_{\mathrm{p}} = \sqrt{[4\bar{K}_{\mathrm{p}}NWd(v/1{,}000d)^{1.8}]} \qquad \text{for } x_{\mathrm{p}}/d \le 2.0, \qquad (4.94)$$

$$x_{\mathrm{p}} = [\bar{K}_{\mathrm{p}}NW(v/1{,}000d)^{1.8}] + d \qquad \text{for } x_{\mathrm{p}}/d \le 2.0, \qquad (4.95)$$

where W = missile weight (lb), x_p = penetration depth (in), d = missile diameter (in), v = impact velocity (ft/s), f'_c = concrete cylinder compressive strength (psi), $\bar{K}_p = 180/\sqrt{f'_c}$, N = missile shape factor = 0.72 for flat-nosed bodies = 0.84 for blunt-nosed bodies = 1.00 for spherical-ended bodies = 1.14 for very sharp-nosed bodies.

(Note: $1\,\text{psi} = 6.9\,\text{kN}\,\text{m}^{-2}$; $1\,\text{fps} = 0.305\,\text{m}\,\text{s}^{-1}$; $1\,\text{in.} = 25.4\,\text{mm}$; $1\,\text{lb} = 0.453\,\text{kg}$)

The formulae for scabbing and perforation thickness, t_{sc} and t_p respectively, for a solid cylindrical steel missile and infinite thickness of the target are given below:

$$t_{sc}/d = 2.12 + 1.36 x_p/d \quad \text{for } 3 \le t_{sc}/d \le 18, \tag{4.96}$$

$$t_p/d = 1.32 + 1.24 x_p/d \quad \text{for } 3 \le t_p/d \le 18, \tag{4.97}$$

$$t_{sc}/d = 7.91(x_p/d) - 5.06(x_p/d)^2 \quad \text{for } t_{sc}/d < 3, \tag{4.98}$$

$$t_p/d = 3.19(x_p/d) - 0.718(x_p/d)^2 \quad \text{for } t_p/d < 3. \tag{4.99}$$

Modified NDRC Formula

A modification of the NDRC formula to take into account the finite thickness of a target is proposed. For large diameter missiles impacting on targets of finite thickness, the perforation and scabbing thicknesses are given below:

$$t_p/d = 3.19(x_p/d) - 0.718(x_p/d)^2 \quad \text{for } x_p/d \le 1.35, \tag{4.100}$$

$$t_{sc}/d = 7.91(x_p/d) - 5.06(x_p/d)^2 \quad \text{for } x_p/d \le 0.65.$$

Equations (4.100) and (4.101) will have a range of $0.65 \le x_p/d \le 11.75$ and $1.35 \le x_p/d \le 13.5$, respectively. In any case, $t/d \le 3$ gives comfortable results.

Modified Ballistic Research Laboratory Formula

The modified Ballistic Research Laboratory formula gives the perforation thickness of infinitely thick targets impacted by a non-deformable missile with high velocity as

$$t_p = (427\,Wd^{0.2})/(d^2\sqrt{f'_c})(v/1{,}000)^{1.33}, \tag{4.101}$$

where t_p = perforation thickness (in), W = missile weight (lb), d = missile diameter (in), f'_c = concrete compressive strength (psi), v = missile velocity ($\text{ft}\,\text{s}^{-1}$) and the spalling thickness $t_{sp} = 2t_p$.

Chalapathi, Kennedy and Wall (CKW)–BRL Formula

The penetration depth is calculated using the CKW–BRL method as

$$x_p = (6\,Wd^{0.2}/d^2)(v/1{,}000)^{4/3}, \tag{4.102}$$

where t_p = thickness to prevent perforation = $1.3x_p$. All units are imperial, as defined earlier.

Dietrich, Fürste (DF)–BRL Formula (Dietrich F., personal communication)

The formula gives the thickness to prevent perforation as

$$t_{\mathrm{p}} = (3 \times 10^{-4}/\sqrt{f_{\mathrm{ci}}})(W/d^{1.8})(v/100)^{4/3}, \tag{4.103}$$

where d and t_{p} are in m, W is in kp, f_{ci} is in $\mathrm{kp\,cm^{-2}}$ and v is in $\mathrm{km\,h^{-1}}$.

Stone and Webster

The scabbing thickness is given, as for the infinitely thick concrete targets, by

$$t_{\mathrm{sc}} = (Wv^2/c_0'), \tag{4.104}$$

where the values of W and v are in lb and $\mathrm{ft\,s^{-1}}$ respectively and c_0' is a coefficient depending upon the ratio of t_{sc}/d. The range for which this formula is considered is $3{,}000\,\mathrm{psi} \leq f_{\mathrm{c}}' \leq 4{,}500\,\mathrm{psi}$ and $1.5 \leq t_{\mathrm{s}}/d \leq 3$.

Chang Formulae

Chang has proposed two semi-analytical formulae for predicting perforation and scabbing thicknesses of concrete targets impacted by hard steel missiles of non-deformable type:

$$t_{\mathrm{p}} = (u/v)^{0.25}(mv^2/df_{\mathrm{c}}')^{0.5}, \tag{4.105}$$

$$t_{\mathrm{sc}} = 1.84(u/v)^{0.13}(f_{\mathrm{c}}')^{0.4}(d)^{-0.2}(mv^2)^{0.4}. \tag{4.106}$$

These formulae are probably validated over the following range based on random variables by Bayesian statistics:

$$16.7\,\mathrm{m\,s^{-1}} < v < 311.8\,\mathrm{m\,s^{-1}}, \tag{4.107}$$

$$0.11\,\mathrm{kg} < W < 343\,\mathrm{kg},$$

$$2.0\,\mathrm{cm} < d < 30.4\,\mathrm{cm},$$

$$232\,\mathrm{kg\,cm^{-2}} < f_{\mathrm{c}}' < 464.2\,\mathrm{kg\,cm^{-2}},$$

$$5.0\,\mathrm{cm} < h < 60.9\,\mathrm{cm},$$

where u is a reference velocity ($200\,\mathrm{ft\,s^{-1}}$ or $60.96\,\mathrm{m\,s^{-1}}$) and f_{c}', d, m and v are defined in other sections. The scabbing velocity, v_{sc} $\mathrm{ft\,s^{-1}}$, is written as:

$$v_{\mathrm{sc}} = [(1/2.469)(d^{0.2}f_{\mathrm{c}}'h/W^{0.4})]^{3/2}.$$

The IRS Formulae

The IRS formula for penetration is expressed as

$$t_{\mathrm{p}} = 1{,}183(f_{\mathrm{c}}')^{-0.5} + 1{,}038(f_{\mathrm{c}}')^{-0.18}\exp[-0.82(f_{\mathrm{c}}')^{0.18}]. \tag{4.108}$$

The IRS formula for total protection for the target against penetration, perforation and scabbing is given as

$$\mathrm{SVOLL} = 1{,}250(f_{\mathrm{c}}')^{0.5} + 1{,}673(f_{\mathrm{c}}')^{-0.18} \times \exp[-0.82(f_{\mathrm{c}}')^{0.18}], \tag{4.109}$$

where SVOLL is the minimum wall thickness to provide complete protection. The values of t_{p} and f_{c}' are in cm and $\mathrm{kgf\,cm^{-2}}$, respectively.

The Bechtel Formulae

Based on test data applicable to hard missiles impacting on nuclear power plant facilities, the two formulae for scabbing thickness are given below.
The Bechtel formula for scabbing thickness for solid steel missiles is

$$t_{sc} = (15.5/\sqrt{f'_c})(W^{0.4}v^{0.5}/d^{0.2}). \tag{4.110}$$

The Bechtel formula for steel pipe missiles (scabbing) is

$$t_{sc} = (5.42/\sqrt{f'_c})(W^{0.4}v^{0.65}/d^{0.2}). \tag{4.111}$$

The variables given above are in imperial units. The Bechtel formulae are also written for scabbing and perforation thickness in metric units using a reference velocity v^* ($60.96\,\mathrm{m\,s^{-1}}$):

$$t_{sc} = 1.75 \left(\frac{v^*}{v}\right)^{0.13} \frac{(mv^2)^{0.4}}{(d)^{0.3}(f'_c)^{0.4}}, \tag{4.112}$$

$$t_p = 0.90 \left(\frac{v^*}{v}\right)^{0.25} \frac{(mv^2)^{0.5}}{(df'_c)^{0.5}}. \tag{4.113}$$

CEA–EDF Formula

Tests were carried out for the French Atomic Energy (CEA) and Electricité de France by Berriaud, on a series of slabs subject to impactors with varying velocities (from 20 to $200\,\mathrm{m\,s^{-1}}$), thicknesses, concrete strength and reinforcement quantities. The empirical formula for a thickness to resist perforation is given by

$$t_p = 0.82(f'_c)^{-3/8}(\rho_c)^{-1/8}(W/d)^{0.5}v^{3/4}, \tag{4.114}$$

where ρ is the density of concrete, and the following ranges apply:

$$30\,\mathrm{MPa} < f'_c < 45\,\mathrm{MPa},$$
$$0.3 < t_p/d < 4,$$
$$75\,\mathrm{kg\,m^{-3}} < p < 300\,\mathrm{kg\,m^{-3}},$$

where p is the reinforcement quantity. The perforation velocity, v_p, for the target thickness is given by

$$v_p = 1.7f'_c(\rho_c)^{1/3}(dh^2/W)^{4/3} \text{ (metric)}. \tag{4.115}$$

The CEA–EDF residual velocity formula, v_r, based on several tests with a correction factor K_σ is given below, with all values in imperial units:

$$v_r = \left[\frac{1}{1 + \frac{W_t}{W}}(v^2 - v_p^2)\right]^{1/2}, \tag{4.116}$$

$$K_o v_p = \left[v_p^2 - v_r^2\left(1 + \frac{W_t}{W}\right)\right]^{1/2}, \tag{4.117}$$

where v_r, v_p, K_σ and W_t are the residual velocity of the missile, perforation velocity, correction factor and the weight of the target material removed by impact, respectively. The mean and minimum values of K_σ are 1.45 and 1.225, respectively.

Haldar, Miller and Hatami Method

The impact formula of the NDRC type associated with a non-dimensional impact factor I are presented in imperial units as

$$I = WNv^2 \, \mathbf{g} d^3 f'_c, \qquad (4.118)$$

where $\mathbf{g} = 32.2 \, \mathrm{ft \, s^{-2}}$ and, when substituted, the above equation becomes

$$I = 12 \, NW v^2 / 32.2 d^3 f'_c,$$

where N is the missile nose-shaped factor and all other notations are as defined earlier.

For various impact factors, the NDRC test results were examined using linear regression analysis for x_p/d and t_{sc}/d ratios.

$$t_{sc}/d = -0.0308 + 0.2251 \, I \quad 0.3 \le I \le 4.0, \qquad (4.119a)$$
$$t_{sc}/d = 0.6740 + 0.0567 \, I \quad \ \ 4.0 < I \le 21.0, \qquad (4.119b)$$
$$t_{sc}/d = 1.1875 + 0.0299 \, I \quad 21.0 < I \le 455, \qquad (4.119c)$$
$$t_{sc}/d = 3.3437 + 0.0342 \, I \quad 21.0 \le I \le 385. \qquad (4.119d)$$

Takeda, Tachikawa and Fujimoto Formula

Takeda et al. proposed a formula for predicting the penetration depth into reinforced concrete slabs subject to hard missiles:

$$x_p = [\alpha/(\beta + 1)](v)^{\beta+1}, \qquad (4.120)$$

where $\alpha = 2^n m^{1-n}/c'\psi$, $\beta = 1 - 2n$, x_p = maximum depth of penetration (cm), m = mass of projectile ($\mathrm{kg \, s^2 \, cm^{-1}}$), v = impact velocity ($\mathrm{cm \, s^{-1}}$), ψ = circumference of projectile (cm), c', n = constants.

Since the formula is based on the kinetic energy as input, it is valid for an energy range from $20 \times 10^2 \, \mathrm{kg \, cm}$ to $200 \times 10^5 \, \mathrm{kg \, cm}$.

Hughes Formulae

These formulae have been developed using the dimensional analysis and test analysis results of NDRC and ACE described earlier. Front and back faces are reinforced (front face 0–0.15%; back face 0.3–1.7% each way). The penetration depth calculated for a concrete barrier, assuming no scabbing or perforation occur, is given by

$$x_p/d = 0.19 \, NI/s', \qquad (4.121)$$

where N = nose-shaped coefficient = 1; 1.12; 1.26 and 1.39 for flat, blunt, spherical and very sharp noses, respectively, I = impact parameter = $(mv^2/0.63\sqrt{f'_c})\,d^3$, s' = strain-rate factor = $1 + 12.3\log(1 + 0.03\,I)$.

The thicknesses of the concrete target necessary to prevent scabbing and perforation are written as

$$t_{sc}/d = 1.74(x_p/d) + 2.3, \tag{4.122}$$
$$t_p/d = 1.58(x_p/d) + 1.4. \tag{4.123}$$

Kar Formulae

It is claimed that most of the formulae described earlier do not include dimensions, shapes of the missiles, material properties of the missiles and targets and the size of the coarse aggregate in concrete. Kar gives the penetration depth (in inches) in the concrete targets as

$$G(x_p/d) = \alpha\bar{K}_p N(W/D)(v/1{,}000d)^{1.8}, \tag{4.124}$$

where
$$G(x_p/d) = \begin{cases} (x_p/2d)^2 & \text{for } x_p/d \le 2.0, \\ (x_p/d) - 1 & \text{for } x_p/d \ge 2.0, \end{cases} \tag{4.125}$$

where D = diameter of the actual missile in the case of a circular section, or is equal to the projectile diameter d in the case of a rectangular section or is equal to the diameter of the circles inscribed within the boundary formed by joining the extremities of impacting ends of angular I or irregular sections; the minimum value of $D = d$

α = constant equal to 1.0 in imperial units
= 0.01063 if D, d, E, v, W and x_p are expressed in cm, cm, kN m^{-2}, m s^{-1}, kg and cm, respectively

N = 0.72 flat-nosed
= $0.72 + 0.25(n - 0.25)^{0.5} \le 1.17$ for spherical-nosed \hfill (4.126)

n = radius of nose/missile diameter
= $0.72 + [(D/d)^2 - 1]\,0.36 \le 1.17$ for hollow circular sections or irregular sections \hfill (4.127)

$\bar{K}_p$ = penetrability factor = $(180/\sqrt{f'_c})(E/29{,}000)^{1.25}$. \hfill (4.128)

The depth to prevent perforation or scabbing is given by

$$(t_p - a')/d = 3.19(x_p/d) - 0.718(x_p/d)^2 \quad \text{for } x_p/d \le 1.35, \tag{4.129}$$
$$(t_{sc} - a')/\text{d} = 7.91(x_p/d) - 5.06(x_p/d)^2 \quad \text{for } x_p/d \le 0.65, \tag{4.130}$$

For x_p/d larger than above, the following equations are suggested:

$$(t_p - a')/d = 1.32 + 1.24(x_p/d) \quad \text{for } 3 \le t_p/d \le 18, \tag{4.131}$$
$$\beta(t_{sc} - a')/d = 2.12 + 1.36(x_p/d) \quad \text{for } 3 \le t_{sc}/d \le 18, \tag{4.132}$$

where $\beta = (29{,}000/E)^{0.2}$, $\beta = 1$ for steel missiles, a' = maximum aggregate size in concrete.
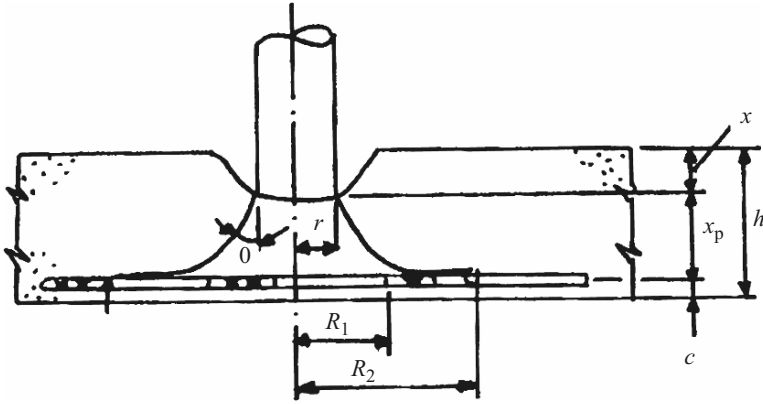
Fig. 4.26. Assumed barrier failure mechanism and derivation of hinge radius

Perry and Brown Formulae

(1) Solid hard missile on concrete targets. The penetration depth is given (Fig. 4.26) by

$$x_{\mathrm{p}}/d = 9.665\sqrt{m}[v/\sqrt{(E_{\mathrm{c}}d^3)}] + 0.06, \qquad (4.133)$$

where x_{p}, d and v are as defined earlier and m is the missile mass. If $L < 50$, the scabbing thickness does not occur; if $L > 70$, the scabbing thickness certainly occurs.

$$L = [\sqrt{m}(v/\sqrt{d})\; h(1 + h/d)]\sqrt{E_{\mathrm{c}}\sigma_{\mathrm{s}}}, \qquad (4.134)$$

where h = target thickness, E_{c} = Young's modulus, σ_{s} = maximum value of nominal shear stress before damage = $\sigma_{\mathrm{tm}}\sqrt{[1 + (\sigma_{\mathrm{cm}}/\sigma_{\mathrm{tm}})]}$, σ_{tm} = mean tensile stress in concrete, σ_{cm} = compressive stress, $\sigma_{\mathrm{cr}} = 0.9\sigma'_{\mathrm{cr}} = (0.9)[0.52[(1-v^2)/(1-v_{\mathrm{p}}^2)]^{1/2}\,(E_{\mathrm{t}}/E)^{1/2}E_{\mathrm{s}}(t^{\mathrm{p}}/r)]$, E = Young's modulus, E_{t} = tangent modulus, E_{s} = secant modulus, t^{p} = pipe thickness (in), r = pipe radius (in), v, v_{p} = Poisson ratios for elastic and plastic, respectively
Geometry:

$$\tan\theta = R_1 \times r/x = 2,$$
$$2x = R_1 \times r,$$
$$R_1 = 2(htx_{\mathrm{p}}) + r,$$
$$R_2 = C_{\mathrm{L}}t_3,$$
$$r_{\mathrm{u}} = M_{\mathrm{u}}D_{\mathrm{h}},$$

where M_{u} = ultimate curvature = eu/C_{h}, D_{h} = hinge length (or R_2R_1), $(R_2R_1)_{\mathrm{max}} = r_{\mathrm{u}}/M_{\mathrm{u}} = 0.07/0.003 = 23.3$, $(R_2)_{\mathrm{max}} = R_1 + 23$.

(2) The thickness to prevent spalling is given by

$$t_{sp} = x_p + x + c, \tag{4.135}$$

$$x(x+r)^2 > \left[\frac{6W^2V_m^2 - W}{2\mathbf{g}\pi r_u M_u}\right]\left(\frac{1,728}{\rho_c\pi}\right) - R_2^2 C, \tag{4.136}$$

where $\rho_c = 0.15\,\text{kips ft}^{-3}$, $r_u = $ ultimate rotational capacity at hinge (rad), $C = $ cover (in), $M_u = $ ultimate moment capacity at hinge (in kips in.$^{-1}$) (1 kip $= 1,000\,\text{lbf}$), $R_2 = R_1 + 23$

$$v = v_2 \qquad \text{if } v_2 > v_2',$$
$$v = v_2' \qquad \text{if } v_2 < v_2' < v_1,$$
$$\text{if } v_2' > v_1, \text{ not applicable.}$$

The spalling (4.135) and (4.136) are not applicable if $t_{sp} = h < 12$ inches.
(3) Pipe missile on concrete targets. The penetration depth is given by

$$x_p/d = 8\left[\sqrt{mv}/\sqrt{(Ed^3)}\right] + 0.24, \tag{4.137}$$

where d is the outside diameter of the pipe missile. The scabbing thickness can be achieved if $L > 60$ and is unlikely to occur if $L < 50$. The value of L in this case is expressed by

$$L = \sqrt{mdv}/\left[dh\left(1 + h/d\right)\right]\left(\sqrt{E_c}/\sigma_s\right), \tag{4.138}$$

where the various elements of the equations have been defined previously.

Barr, Carter, Howe, Neilson Winfrith Model

On the basis of a number of tests carried out on various target slabs, Winfrith modified the CEA–EDF formula to include the bending reinforcement quantity. The perforation velocity in conjunction with the CEA–EDF formula can now be written as

$$v_p = 1.3\left(\sigma_{cu}\right)^{0.5}\left(\rho_c\right)^{1/6}\left(dh^2/m\right)^{2/3} r^{0.27}, \tag{4.139}$$

where $\sigma_{cu} = f_c'$, $m = W/\mathbf{g}$, $r = $ bending reinforcement quantity in % $(0.125\% \le r \le 0.5\%)$.
All values are in metric units and $r = p$ for previous formulae.

Formulae for Deformable Missiles Impacting on Concrete Targets

McMahon, Meyers, Sen model

The model evaluates local damage including penetration and back-face spalling of reinforced concrete targets subject to the impact of deformable, tornado-generated missiles such as pipes, etc. The total penetration is given by

$$x_\rho = x_1 + x_2 + x_3, \tag{4.140}$$

where x_1 = penetration during time $t_1 = (Ft_1^2/6m) + v_0 t_1$, F = interface force = $\sigma_{cr} A$, t_1 = rise time = $3.2 \times 10^{-6} F$, A = pipe area, v_0 = missile velocity at the initial time t_0, m = mass of the missile

$$x_2 - x_1 = x_c \text{ (plastic missile deformation during } t_2 - t_1)$$
$$= \frac{m}{2F}(v_2 - v_1)^2 + \frac{mv_1}{F}$$
$$= \frac{m}{2F}(v_2^2 - v_1^2), \tag{4.140a}$$

v_1, v_2 = missile velocity at times t_1 and t_2

$$v_1 = (Ft_1/2m) + v_2; \qquad v_2 = (F/m)(t_2 - t_1) + v_1, \tag{4.140b}$$

$$x_3 = x_2 \text{ (penetration during } t_3 - t_2) = -mv_2^2/2F, \tag{4.140c}$$

$$t_2 = l/\sqrt{(E_T/\rho)} + l/\sqrt{(E/\rho)} = \text{wrinkling duration} \tag{4.140d}$$
$$\quad\text{plastic} \qquad\quad \text{elastic}$$
$$\quad\text{waves} \qquad\quad\text{waves,}$$

$$t_3 = (-mv_2/F) + t_2 = \text{final time}, \tag{4.140e}$$

where ρ is material density and l is missile length.

Rotz Damage Model

Rotz predicted scabbing thickness using Bayesian estimators as

$$t_{sp} = \overline{K}_p \left(W^{0.4} v^{0.65} / \sqrt{f_c'} d^{0.2} \right), \tag{4.141}$$

where $\overline{K}_p = 5.42$ (empirical constant), v = impact velocity (in), d = missile diameter (in), f_c' = concrete compressive strength (lb in^{-3}), t_{sp} = scabbing thickness (in), W = missile weight (lb).

Note: other soft missiles are described later on in various sections of this chapter.

PLA Damage Model for Heavy-Duty Pavements

Serviceability failure occurs in a heavy-duty pavement due to impact by either excessive vertical compressive stress in the subgrade or excessive horizontal tensile strain in the base. The allowable subgrade vertical compressive strain ε_v is given by

$$\varepsilon_v = 21{,}600/N^{-0.28}, \tag{4.142}$$

where $\overline{N}$ is the number of repetitions of impact load.

The allowable base horizontal tensile strain, ε_h, is given by

$$\varepsilon_h = \frac{993{,}500 \times f_c'}{6 \times E_b^{1.022} N^{-0.0502}}, \tag{4.143}$$

where $E_b =$ Young's modulus of the base material $(\mathrm{N\,mm^{-2}})$
$\quad\quad f'_c =$ characteristic compressive strength of the base material
$\quad\quad\quad\quad (\mathrm{N\,mm^{-2}})$
$\quad\quad\quad\quad \leq 7\,\mathrm{N\,mm^{-2}}$ then $E_b = 4 \times 10^3 f'_c$
$\quad\quad\quad\quad > 7\,\mathrm{N\,mm^{-2}}$ then $E_b = 1.68 \times 10^4 (f'_c)^{0.25}$

If these values are not met, the pavement will be damaged. Any impact formula must be assessed against these conditions. The damage effect, D_E, given below, by Heukelom and Klomp [2.382] can then be judged in the light of cracking, spalling, etc., occurring from the impact formula:

$$D_E = W^{3.75} P^{1.25},$$

where W is the wheel load with impacting factor and P is the tyre pressure $(\mathrm{N\,mm^{-2}})$.

Missiles on Steel Targets

Missiles and Targets

Missiles as projectiles with non-deformable nose shape are given in Fig. 4.27. Non-deformable projectiles are assumed to be either spherical or cylindrical (refer to Chap. 2), with a nose of one of the shapes shown in Fig. 4.28. The calibre or ballistic density ρ is generally given as W/d^3, where W is the weight of the missile and d is the diameter. Owing to changes in the value of W, a longer missile is, therefore, more dense than a short one with the same diameter and material. Metal targets are generally restricted to hard missiles of non-deformable type striking the plate.

radius

(a)   (b)   (c)   (d)
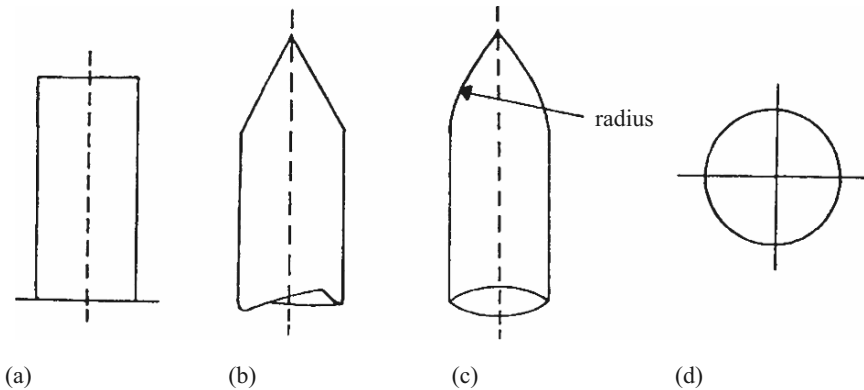
Fig. 4.27. Projectile shapes. (**a**) Flat; (**b**) conical; (**c**) ogival; (**d**) spherical
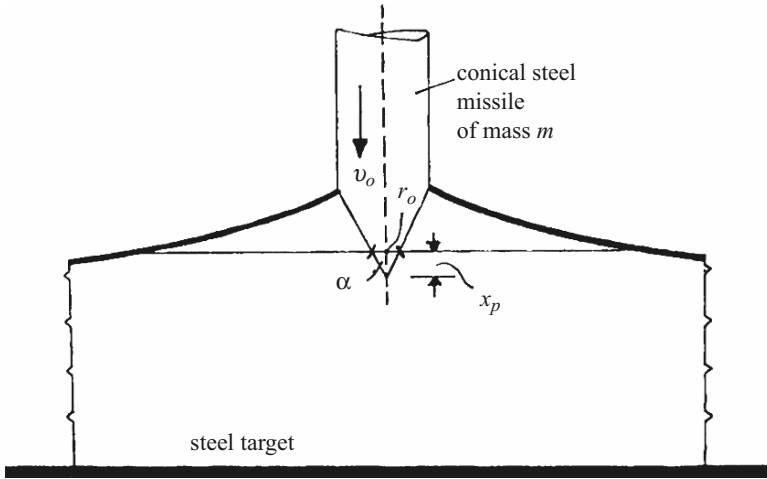
Fig. 4.28. Conical missile striking steel target

Slow Speed Indentation of Steel Targets

(1) Conical missile. Assume a conical missile is striking a steel target with a low velocity, v_0, leaving a permanent indentation of diameter d_0 (Fig. 4.28). The yield stress of the target steel $\bar{\sigma}_e = 3\sigma_t$, where σ_t is the uni-axial stress flow of the target material. The equation of motion is written as

$$m\ddot{x}_p = mv(dv/dx_p) = -\bar{\sigma}_e \pi r_0^2, \qquad (4.144)$$

where v is the missile speed after penetration x_p is achieved and r_0 is the final radius of the crater $= x_p \tan\alpha$.

After substitution of the value of r_0 into (4.144) and integration, the crater radius and depth are written as

$$r_0 = (0.4772\, m/\bar{\sigma}_e \tan^2\alpha)^{1/3} (\tan\alpha)\, v_0^{2/3}, \qquad (4.145)$$

$$x_p = 2r_0 \cot\alpha/2. \qquad (4.146)$$

(2) Spherical missile. Equation (4.144) is still applicable when x_p/d is small. It is assumed that $r_0 \approx x_p d$, the equation of motion expressed in (4.144) is integrated and the final penetration obtained as

$$x_p = \sqrt{[(m/\sigma_e)\pi d]v}, \qquad (4.147)$$

where v is the final velocity at the time of the formation of the crater.

Calder and Goldsmith Velocity Model (preliminary report, 1979)

The impact velocity at which the projectile penetrates a steel target completely, but comes to rest in the process, defines the ballistic limit. The formula

for the residual velocity, v_r, developed is based on both impact velocity and ballistic limit and is given for a *sharp-nosed* missile as

$$v_r = \sqrt{(v_0^2 + v_B^2)}, \tag{4.148}$$

where v is the initial velocity and v_B is the ballistic limit.

In (4.148) it is assumed that the missile carries no material from the steel target. The residual velocity for a *blunt-nosed* missile carrying a plug of material ejected from the steel target is given by

$$v_r = \sqrt{\left[\frac{m}{m + m_p'} \, (v_0^2 - v_B^2) \right]}, \tag{4.149}$$

where m and m_p' are the masses of the missile and the plug, respectively.

Ballistic Research Laboratory Formula (BRL)

This formula is based on the impact of small-diameter, high-calibre, high-density non-deformable missiles striking thin steel targets:

$$(t_p/d)^{3/2} = Dv^2/1{,}120{,}000 \, \bar{K}_p^2, \tag{4.150}$$

where t_p = perforation thickness (in or mm), $d = 4A_m/\pi$ = effective missile diameter (in or mm), A_m = missile area (in² or cm²), v = impact velocity (ft s⁻¹ or m s⁻¹), D = missile diameter (in or mm), W/d^3 = calibre density of missile (lb in⁻³ or kg m⁻³), from which d can be evaluated, $\bar{K}_p$ = steel penetrability constant depending upon the grade of the steel target; the value of $\bar{K}_p$ is generally taken as 1.0.

The Stanford Research Institute (SRI) Equation

Like BRL's formula, the following equation is for small-diameter, hard missile striking a thin steel target.

$$(t_p/d)^2 + (3/128)(B/d)(t_p/d) = 0.0452D_v/\sigma_{tu}, \tag{4.151}$$

where t_p, d, D and v are as defined in the BRL formula, B = width of the steel target, σ_{tu} = ultimate tensile strength of the target steel (lb in⁻² or Pascals).

The formula is based upon tests with the following range of parameters:

$$0.1 \le t_p/d \le 0.8,$$
$$2 \, \text{lb in}^{-3} \, (550 \times 10^2 \, \text{kg m}^{-3}) \le D \le 12 \, \text{lb in}^{-3} \, (3300 \times 10^2 \, \text{kg m}^{-3}),$$
$$0.062 \, \text{in} \, (1.6 \, \text{mm}) \le d \le 3.5 \, \text{in} \, (89 \, \text{mm}),$$
$$70 \, \text{ft s}^{-1} \, (21 \, \text{m s}^{-1}) \le v \le 400 \, \text{ft s}^{-1} \, (120 \, \text{m s}^{-1}),$$
$$2 \, \text{in} \, (50 \, \text{mm}) \le B \le 12 \, \text{in} \, (300 \, \text{mm}),$$
$$5 \le B/d \le 8,$$
$$8 \le B/t_p \le 100.$$

For design purposes, the design thickness due to t_p or t_{sc} must be increased by 20%.

Kar Steel Target Formula

For mid-to-medium-hard homogeneous steel plates, the barrier may have a ductile failure. When steel target Brinell hardness numbers are above 350, failure by plugging may occur. For inferior quality steel, flaking may occur on the back face of the steel targets. According to Kar, for a good quality steel, back face phenomena do not generally influence the depth of penetration. The penetration or thickness to prevent perforation is given by the following:

$$t_{\rm p} = \alpha(E/29{,}000)(0.72 + N)\ \bar{K}_{\rm p}(mv^2)^{0.667}/1{,}067(D + d), \qquad (4.152)$$

where m is the mass of the missile (lb s^2 ft^{-1}) and v (ft s^{-1}), D (in) and d (in) are as defined for (4.124) and (4.125).

The penetrability coefficient $\bar{K}_{\rm p}$ is determined from the following:

$$\bar{K}_{\rm p} = (0.632\mathrm{BHN} + 94.88)/275, \qquad (4.153)$$

where BHN is the brittle hardness number of the steel target material and is limited to between 0.37 and 1.0. The above equation is still relevant if BHN <0.37 or >1.0.

$\alpha = 1.0$ if imperial units are used
$\quad = 0.0035$ for m (kg s^2 m^{-1}), v (m s^{-1}), d (cm), E (kN m^{-2}), $t_{\rm p}$ (cm).

de Marre Modified Formula

de Marre proposed a relationship between the specific limit energy h/d and the target penetration:

$$mv_1^2/d^3 = \bar{\alpha}(h/d)^{\bar{\beta}}, \qquad (4.154)$$

where $m =$ missile mass (g), $v_1 =$ limit velocity (m s^{-1}), $d =$ missile diameter (cm), $h =$ steel target thickness (cm), $\bar{\alpha} =$ constant between 1 and 2, $\bar{\beta} =$ constant approximately 1, h is replaced by $hf(\theta)$, $\theta =$ incidence angle, $f =$ a function of obliquity, usually secant.

Taub and Curtis Model

A perceptive analysis by Taub and Curtis derived the following formula for back-face spalling or petalling type of failure:

$$mv_1^2/d^3 = \bar{\alpha}[(h/\bar{\alpha}) + \bar{\beta}] \qquad \bar{\beta} < 0. \qquad (4.154\mathrm{a})$$

Lambert Model

The development assumes back-face thickness where petalling occurs and d to be constant and β becomes complex as a quadratic function. To overcome this, Zukas replaced $\bar{\beta}$ by $\mathrm{e}^{-h/d} - 1$; d^3 by $d^{3-c}\,l^c$ and θ as stated in the case of the

de Marre formula, by $h \sec^{k'} \theta$. Both c and k′ are constants. Using Lambert's limit velocity database containing limit velocities for 200 cases involving:

range of mass	$\frac{1}{2}$ to 3,630 g
diameter	$\frac{1}{5}$ to 5 cm
l/d	4 to 30
h	$\frac{3}{5}$ to 15 cm
θ	0° to 60°
ρ_{s} (rod material density)	7.8 to 19 g cm^{-3}

$$\bar{\alpha} = 4{,}000^2; \quad c = 0.3; \quad k' = 0.75,$$

the following predicted model is established for the limit velocity v_ℓ:

$$v_\ell = u(l/d)^{0.15} \sqrt{[f(z) \, d^3/m]} \ \mathrm{m\,s}^{-1}, \tag{4.155}$$

where $z = h(\sec \theta)^{0.75}/d$, $u = 4{,}000$ for rolled homogeneous armour (RHA) and m depends on the density ρ_{s}.

$$f(z) = z + \mathrm{e}^{-z} - 1 = \Sigma_{j=2} \, (-z)^j/j, \tag{4.156}$$

$$v = \begin{cases} 0, & 0 \le v \le v_\ell, \\ \alpha(v^2 - v_\ell^2)^{1/2}, & v > v_\ell, \end{cases}$$

$$v_\ell = \max\{v: \ v_{\mathrm{r}} = 0\} = \inf\{v: \ v_{\mathrm{r}} > 0\},$$

$$v_{\mathrm{r}} = \begin{cases} 0, & 0 \le v \le v_\ell, \\ \bar{\alpha}(v^{\mathrm{p}} - v_\ell^{\mathrm{p}})^{1/p}, & v > v_\ell, \end{cases}$$

where the value of p is generally 2 and v, v_ℓ and v_{r} are striking velocity, ballistic limit and missile residual velocity, respectively.

Winfrith Perforation Energy Model

Using dimensional analysis, the perforation energy of the steel pipe is related to the geometric parameters and material properties by

$$E_{\mathrm{p}}/(\sigma_{\mathrm{u}} d^3) = \mathrm{A}(h/d)^{\mathrm{a}}(d/D)^{\mathrm{b}}, \tag{4.157}$$

where E_{p} = perforation energy, σ_{u} = characteristic strength of the material = σ_{e}, d, D = missile and pipe diameter, respectively, h = target thickness, a, b, A = constants given in Table 4.6.

Tests have been carried out on target thicknesses of 7.1 and 11 mm. For a 25 mm diameter missile the perforation energy varied as the 1.8 power of the target pipe thickness and for a 60 mm diameter missile an exponent of 1.4 was obtained. At an impact energy of 41.5 kJ, the 60 mm diameter missile displaced a shear plug in the pipe wall thickness by a distance of 3–11 mm.

Table 4.6. Permanent deformations of pipe targets

Test	a (mm)	b (mm)	A (cm^2)	d'_0 (mm)	δ (mm)	m (kg)	v (m s^{-1})	h (mm)
255	75	115	–	–	–	1.7	93	7.4
256	70	100	170	148	21	1.7	67	7.4
257	140	215	158	115	65	7.5	75	7.3
258	170	310	99	77	112	7.3	108	7.2
259	140	250	172	114	60	7.39	69	7.1
260	165	325	113	86	104	7.29	104	7.1
264	130	220	151	111	64	4.0	105	7.3
265	135	200	159	113	67	4.0	104	7.4
266	145	280	121	93	94	4.0	136	7.1
267	135	225	–	–	–	4.0	142	7.0
268	105	–	–	–	–	4.0	117	7.2
269	130	–	–	–	–	4.0	112	7.2
270	105	–	–	–	–	4.0	108	7.2
271	100	110	180	144	35	4.0	108	7.6
272	–	–	–	–	–	4.0	108	7.7
273	120	220	–	100	83	4.0	114	7.5
274	135	250	–	100	82	4.0	114	6.9
275	140	300	135	92	93	4.0	113	7.0
276	100	120	–	–	–	4.0	108	7.4
477	80	90	–		–	1.7	130	10.5
478	45	50			11	1.7	203	18.2
479	70	80	–		–	1.7	129	10.7
480	55	60			17	0.6	325	18.6
481	110	–	–	–	–	4.0	180	10.6
482	105	–	–	–	–	4.0	236	18.6
483	135	200	–	–	–	4.0	136	11.0
484	90	125			36	4.0	144	18.6
485	110	165	–	–	–	4.0	143	7.2
486	110	140	–	–	–	4.0	87	7.1
487	110	145	–	–	–	4.0	113	8.1
488	105	130	–	–		4.0	67	7.2
489	90	160			36	3.1	75	7.4
490	95	180			46	3.1	84	7.2
491	100	200			55	3.1	99	7.2
492	110	220			–	3.1	143	7.2
493		oblique impact			–	4.0	180	7.3
494						4.0	120	7.0
495	185	230			231	43.0	78	7.4
496	105	180			55	34.9	49	7.5
497	155	250			95	37.5	46	7.4
498	170	380			196	44.0	78	7.3
499	170	270			350	54.2	106	10.9
500	175	385			150	29.5	70	7.1

Courtesy of A.J. Neilson, UKAEA, Winfrith, UK
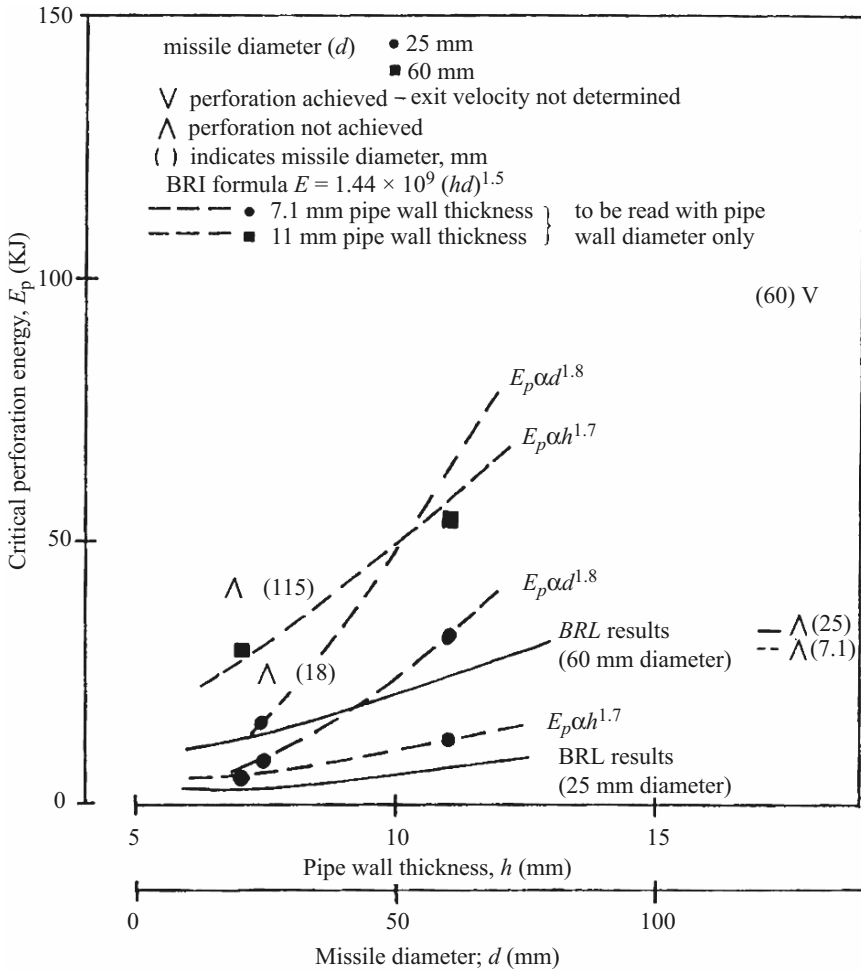
Fig. 4.29. Effect of pipe wall thickness on perforation energy of solid billet missiles (courtesy of A.J. Neilson, UKAEA, Winfrith, UK)

Figure 4.29 shows a graph of the perforation energy plotted against pipe wall thickness and the missile diameter. In the case of E_p versus d, an exponent of 1.9 is obtained for a 7.1 mm pipe wall and 1.7 for an 11 mm pipe wall thickness, averaging both sets to 1.8. Exponents ranging from 1.5 to 1.7 have been suggested for plain steel targets. The test results based on the BRL formula are also plotted. On the basis of these tests, the perforation energy is assumed to vary as

$$E_\rho = B h^{1.7} \, d^{1.8}, \tag{4.158}$$

where B is a constant.

In another expression, the exponent is given as 1.7. If this normalized perforation energy variation is imposed on the pipe perforation, the correlation as shown in Fig. 4.29 becomes

$$E_\mathrm{p}/\sigma_\mathrm{u}d^3 = A(h/d)^{1.7}(d/D)^{1.5}, \tag{4.159}$$

where the parameter $A\sigma_\mathrm{u}$ has a value of 8×10^9, if SI units are chosen for E_p, d, h and D.

Shot-Target Formula

The maximum pressure P due to the impact force $F_1(t)$ was computed by this formula by carrying out several tests on steel targets by single and multiple shots for the shot-peening process. The shots included cast steel, cut steel wires, cast iron and glass beads. Tests were carried out using cast steel with two hardness ranges – the common one is 40–50 RC. The grade number 5,240 for this research was $0.024\,\mathrm{in}$ ($0.61\,\mathrm{mm}$). The value of $F_1(t)$ when a sphere hits a flat surface is given by

$$F_1(t) = \frac{4r^{1/5}\left(\dfrac{15}{16}\pi\, mv^2\right)^{3/5}}{3\pi\left[\dfrac{(1-v_1^2)}{\pi E_1} + \dfrac{(1-v_2^2)}{\pi E_2}\right]^{2/5}}, \tag{4.160}$$

where m = mass of the shot, r = radius of the shot, v = velocity of the shot, v_1, E_1 = Poisson's ratio and Young's modulus for the target, v_2, E_2 = Poisson's ratio and Young's modulus for the shot.

The duration of impact, t, is computed as

$$t = 2.943\left[2.5\pi\rho\,\frac{(1-v^2)}{E}\right]^{\frac{2}{5}\frac{r}{v^{1/5}}}, \tag{4.161}$$

where ρ is the density of the shot,

Table 4.7 shows the relationship between the shot radius, the impact pressure P due to $F_1(t)$ and the duration of time for velocities of 30, 40, 50, 80 and $100\,\mathrm{m\,s^{-1}}$.

4.7 Impact on Soils/Rocks

4.7.1 Introduction

The problem of earth penetration by a projectile continues to be tackled by the use of numerical and experimental techniques. At present, there is a growing need for a reliable evaluation of the depth of penetration, velocity and deceleration time histories. There is no doubt that the subject is highly complex as it

Table 4.7. Impact due to shot-peening: basic data

Shot velocity $(\mathrm{m\,s^{-1}})$	Shot radius, r (mm)	Pressure, P $(\mathrm{N\,m^{-2}})$	Duration time, t (s)
30	0.990	3,920	8.80
	0.860	2,960	7.65
	0.610	2,490	5.42
	0.430	7,390	3.82
	0.304	3,700	2.70
	0.177	1,250	1.57
40	0.990	5,540	8.31
	0.860	4,180	7.22
	0.610	2,100	5.12
	0.430	5,220	3.61
	0.304	1,770	1.49
50	0.990	7,240	7.95
	0.860	5,460	6.91
	0.610	2,750	4.90
	0.430	1,370	3.45
	0.304	6,820	2.44
	0.177	2,310	1.42
80	0.990	1,270	7.24
	0.860	9,600	6.29
	0.610	4,830	4.46
	0.430	2,400	3.14
	0.304	1,200	2.22
	0.177	4,070	1.29
100	0.990	1,660	6.92
	0.860	1,250	6.01
	0.610	6,310	4.26
	0.430	3,140	3.01
	0.304	1,570	2.13
	0.177	5,310	1.24

involves the physical properties of impactors and soils/rocks, while using the acceleration time record. The study encompasses such disciplines as geology, soil mechanics, wave mechanics, dynamics of impactors and aerodynamics. An impactor can be the non-explosive type or can be generated by bombs and other detonators. Great care is taken to see that, at this stage, the reader does not confuse the two. Impact due to explosion is treated separately in this book. Figure 4.30 shows a typical earth penetrator.

4.7.2 Empirical Formulations for Earth Penetration

The depth of the penetration, x_p, and the soil resistance, R_T, are represented as functions of many parameters which are given below:

$$x_\mathrm{p} = \mathrm{f}(d, W, V_\mathrm{s}, N, E, \sigma_\mathrm{cs}), \tag{4.162}$$
$$R_\mathrm{T} = c_0 + c_1 V_\mathrm{s} + c_2 V_\mathrm{s}^2 + \ldots + c_n V_\mathrm{s}^n, \tag{4.163}$$
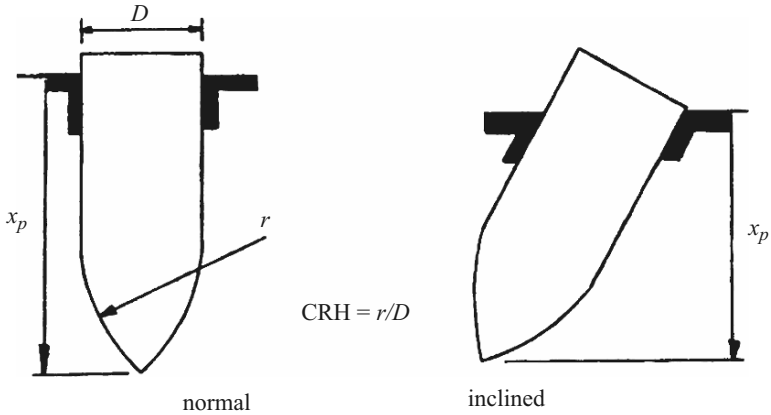
Fig. 4.30. Penetration into earth (CRH = calibre radius head)

where   f = function

d, W, V_s, N, E = impactor/missile diameter, weight, velocity, nose-shape
           factor and Young's modulus of materials, respectively

σ_{cs} = the unconfined stress of the earth material

c_n = constants

The Robin's–Euler penetration, x_p, is computed as

$$x_p = mV^2/2c_0. \tag{4.164}$$

Equation (4.164) in which m, the mass of the missile, has been modified
to include additional constant terms of (4.165) is known as the Poncelet
equation.

$$x_p = (m/2c_2) \log[1 + (c_2 V_s^2/c_0)] \tag{4.165}$$

In (4.170) the soil resistance, R_T, is given by

$$R_T = c_0 + c_2 V_s^2. \tag{4.166}$$

Sometimes the soil resistance is written as

$$R_T = c_1 V_s + c_2 V_s^2. \tag{4.167}$$

The value of x_p is then written as

$$x_p = (m/c_2) \log[1 + (c_2 V/c_1)]. \tag{4.168}$$

The values of N for various shapes are given below:

Shape	N
Flat nose	0.56
Tangent ogive (CRH[a] 2.2)	0.82
(CRH 6)	1.00
(CRH 9.25)	1.11
(CRH 12.5)	1.22
Cone $L/d = 2$	1.08
$= 3$	1.32
Cone plus cylinder	1.28

[a] CRH = the calibre radius head = the radius of curvature of the nose shape/d

For a closed impacting end, the value of N can be evaluated as follows:

$$N = 0.72 \ (\text{CRH}^{2.72}/1{,}000). \tag{4.169}$$

For a circular, hollow, pipe missile, N is written as

$$N = 0.72 + [(D/d)^2 - 1] \ (0.0306) \leq 1.0, \tag{4.170}$$

where $d = \sqrt{(D^2 - D_i^2)}$, D = outer diameter, D_i = inner diameter.

Young carried out a thorough examination of (4.162) and arrived at the following expressions for x_p, the penetration distance in feet (for various velocities in ft s^{-1}) under high- and low-velocity conditions.

Low velocity

$$x_p = f_1(N)f_6(W/A)f_5(S)c_1 \ \log(1 + 2V_s^2 \times 10^{-5}) \tag{4.171}$$

High velocity

$$x_p = f_1(N)f_6(W/A)f_5(S)c_2(V_s - 100), \tag{4.172}$$

where S is a constant dependent upon soil properties averaged over a penetration distance.

The importance of the Young's equation is felt when the effects of weight and area are included.

$$f_6(W/A) = (W/A)^{1/2} \tag{4.173}$$

The value of the soil's $f_5(S)$ is essential; however, its exact evaluation is a complicated affair. Various soil properties in this case will be related to some index of penetrability. Soil parameters are given earlier in this text. Twelve tests indicate that S lies in the range of 1–50, depending on the soil

and its depth. The maxima for the low-velocity and high-velocity types are $220\,\mathrm{ft\,s^{-1}}$ $(67\,\mathrm{m\,s^{-1}})$ and $1{,}200\,\mathrm{ft\,s^{-1}}$ $(366\,\mathrm{m\,s^{-1}})$, respectively. The maximum depth reached is $100\,\mathrm{ft}$ $(30.5\,\mathrm{m})$. The velocity effects are shown on the right-hand side of (4.171) and (4.172) respectively. The following equations give the final conclusions for (4.171) and (4.172) for x_p:

$$\left. \begin{aligned} &x_\mathrm{p} = 0.53\mathrm{S}\,N(W/A)^{1/2}\ \log(1 + 2V_\mathrm{s}^2 \times 10^{-5}), \\ &V_\mathrm{s} < 200\,\mathrm{ft\,s^{-1}}, \end{aligned} \right\} \tag{4.174}$$

$$\left. \begin{aligned} &x_\mathrm{p} = 0.0031\,\mathrm{S}N(W/A)^{1/2}(V_\mathrm{s} - 100), \\ &V_\mathrm{s} \geq 200\,\mathrm{ft\,s^{-1}}. \end{aligned} \right\} \tag{4.175}$$

For *penetration into rock*, Maurer [2.12] and Rinehart [2.13] give the penetration as

$$x_\mathrm{p} = \mathrm{K}_1(W/d)(V_\mathrm{s} - \mathrm{k}_2), \tag{4.176}$$

where all notations have already been defined and K_1 and K_2 are constants defining the rock penetration resistance and constitutive materials. Tolch and Bushkovitch [2.14] have evaluated x_p for both large and small missiles striking soft rock:

$$\left. \begin{aligned} &x_\mathrm{p} = (4.6\,W/d^{1.83})\overline{V} &&\text{small missiles,} \\ &x_\mathrm{p} = (1.4W/d^{1.53})(\overline{V})^{1.8} &&\text{large missiles,} \end{aligned} \right\} \tag{4.177}$$

where $\overline{V} = 0.001\,V_\mathrm{s}$.

Rinehart and Palmore suggest the penetrating value of the less compact soil to be

$$x_\mathrm{p} = (\mathrm{K}_1 W/d^2)\ \log_\mathrm{e}(1 + \mathrm{K}_2 V_\mathrm{s}^2), \tag{4.178}$$

where K_1 and K_2 are constants. Figure 4.31 shows the experimental data given by Rinehart and Tolch and Bushkovitch for steel spherical missiles penetrating different soils. Where the missiles are not spherical and are not made of steel an appropriate value of the nose factor N is used and an effective value of density, ρ_sc, should replace the steel density, ρ_s, by

$$\rho_\mathrm{se} = W/(\pi/6)\rho_\mathrm{s}d^3. \tag{4.178}$$

A reasonable value for x_p can be derived from

$$\left. \begin{aligned} &x_\mathrm{p} = 0.01\,d\rho_\mathrm{se}V_\mathrm{s} &&\text{for sandy soils,} \\ &x_\mathrm{p} = 0.001\,d\rho_\mathrm{sc}V_\mathrm{s} &&\text{for soft rocks,} \\ &x_\mathrm{p} = 0.004\,d\rho_\mathrm{se}V_\mathrm{s} &&\text{for hard rocks.} \end{aligned} \right\} \tag{4.179}$$

Fig. 4.31. Steel missiles penetrating different soils
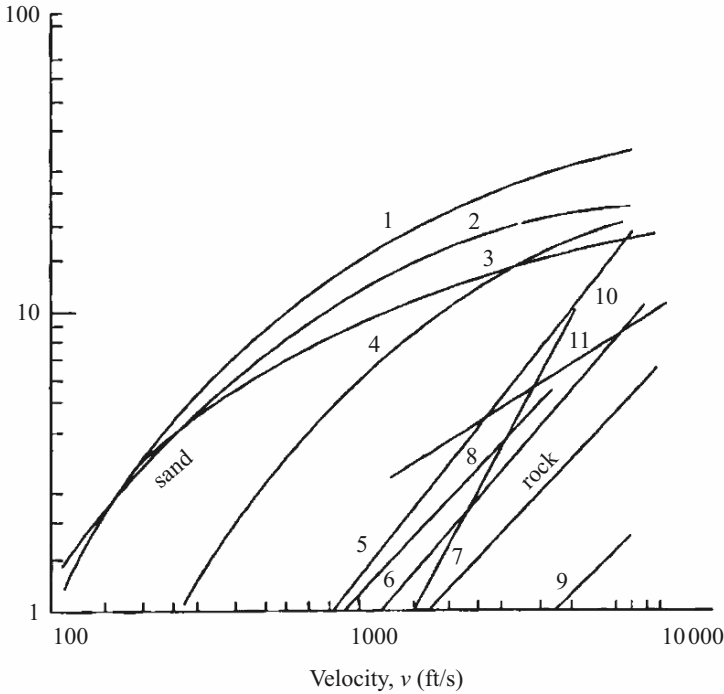
Curve	Missile	Soil model
1	4.3in cannon balls	Sand and gravel
2	Many sizes high ballistic density	Sand
3	0.356 in steel balls	Loose sand
4	0.356 in steel balls	Weakly cemented sand
5	Many	Rock–250 psi crushing strength
6	Many	Rock–2000 psi crushing strength
7	Many	Rock–10000 psi crushing strength
8	$\frac{7}{16}$ in steel balls	Red sandstone–2780 psi
9	$\frac{9}{32}$ in and $\frac{7}{16}$ in steel balls	Granite–16500 psi
10	High ballistic density	Soft rock
11	High ballistic density	Rock or sand–hypervelocity cratering

4.7.3 Velocity and Deceleration

Soils are composed of several layers. A velocity in soils depends, therefore, on the thickness and type of the constituent layers. When x_p is greater than the top-most layer, the residual velocity after this layer must be determined and used in the above equations to obtain the penetration in the

second layer, and so on. Based on the x_p/d ratios, such a residual velocity is calculated as:

$$V_{R2} = (V_s^{1.25} - \tilde{V}_{s1}^{1.25})^{1/1.25}, \qquad (4.180)$$

where V_{R2} = the velocity at the beginning of the second layer, V_s = missile velocity at the impact level, $\tilde{V}_{s1}$ = velocity to perforate the first layer.

In this way the final velocity, V_{Rn}, will be determined from

$$V_{Rn} = (V_{R(n-1)}^{1.25} - \tilde{V}_{R(n-1)}^{1.25})^{1/1.25}. \qquad (4.181)$$

Kar suggested the velocity–time history of the missile in the earth material to be

$$V = V_s \exp(-\rho_s A C_s t/m), \qquad (4.182)$$

where C_s is an impedance/damping constant and t is time.

Theoretical values of V_s may also be computed from other researchers' data. The common ones are

$$\begin{aligned}
V_s &= 1.56\,\rho_{se}fd &&\text{for sand,} \\
V_s &= 0.156\,\rho_{se}fd &&\text{for soft rock,} \qquad (4.183) \\
V_s &= 0.0624\,\rho_{se}fd &&\text{for hard rock,}
\end{aligned}$$

where f is frequency in cycles per second and V_s is in feet per second.

The deceleration is given by

$$G_a = \dot{V} = V_s \exp(-\rho_s A C_s t/m)[-\rho_s A C_s/m](\beta). \qquad (4.184)$$

Kar proposed the value of the target flexibility to be

$$\beta = 0.5924(k_{target}/k_{missile})^{0.16055} \le 1.0, \qquad (4.185)$$

where k_{target} is the stiffness of the earth under impact and $k_{missile}$ is the stiffness of the missile.

The deceleration is assumed to start at time $t = 0$ and increases linearly to a peak at time t given by

$$t = 4x_p/V_s^{1.25}. \qquad (4.186)$$

Kar used the penetration formula (developed for a concrete target) for soil. Figure 4.32 shows the experimental results for penetration.

For low-impact velocities, an average value for the deceleration can be computed as follows:

$$\begin{aligned}
(G_a)^* &= 50\,V_s/d\rho_{se} &&\text{for sand,} \\
(G_a)^* &= 500\,V_s/d\rho_{se} &&\text{for soft rock,} \qquad (4.187) \\
(G_a)^* &= 1{,}250\,V_s/d\rho_{se} &&\text{for hard rock,}
\end{aligned}$$

where $(G_a)^*$ is in $\text{ft\,s}^{-2}$.
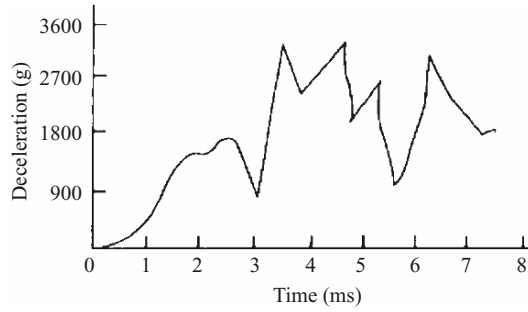
Fig. 4.32. Deceleration-time curves for penetration into limestone

The peak value of $(G_a)^*$ is given by

$$G_a = 1.5(\rho_{se}CV_s/\rho_s d\rho_{se}), \tag{4.188}$$

where C is the impedance in $\text{lb}\,\text{in}^{-2}\,\text{ft}^{-1}$ per second. For basalt the value of C is 750 and for pumice it is 124.

4.7.4 Impact on Rock Masses Due to Jet Fluids

Section 2.2.3 gives a brief introduction to the impact problems when rock masses are subject to jet fluids. Such pressures are associated with thermal hydraulic and mechanical processes. In practice there is no control over the formation of the deep underground rock masses. The water injected into the formula is done in a relatively controlled way. Many processes can be described and simulated by mathematical modelling. The finite-element, boundary-element and finite-difference processes are just some of them. In this section the fluid motion and the heat transfer associated with it are represented by suitable transport equations covering the movement of water in fissured rock masses. To begin with, a one-dimensional flow channel subject to laminar flow is considered, and the velocity v is given by

$$\begin{aligned} v &= -(TR/\mu_f)\,\partial/\partial_z\,(P + \rho\mathbf{g}x) \\ &= -\rho\mathbf{g}(TR/\mu_f)\,\partial h/\partial z. \end{aligned} \tag{4.189}$$

The momentum of the jet fluid $= \partial/\partial t\,(\rho A)$
$$= -\partial/\partial x\,(\rho Av) + i_f, \tag{4.190}$$

where TR = transmissibility of the fissure (m^2), μ_f = jet fluid viscosity $(\text{kN}\,\text{m}^{-1}\,\text{s}^{-1})$, P = jet fluid impact $(\text{kN}\,\text{m}^{-2})$, z = distance along the flow (m), x = the vertical height (m), A = the cross-sectional area = $x_p \times$ width, x_p = penetration depth (m), v = velocity, i_f = injection/extraction of the fissure $(\text{kN}\,\text{m}^{-1}\,\text{s}^{-1})$.

Differentiation of the left-hand side of (4.196) gives:

$$
\begin{aligned}
\partial(\rho A)/\partial t &= \rho(\partial A/\partial t) + A(\partial \rho/\partial t) \\
&= \rho(\partial A/\partial P)(\partial P/\partial t) + A(\partial P/\partial \rho)(\partial \rho/\partial t) \qquad\text{(4.191)} \\
&= \rho A \beta_1 (\partial P/\partial t) + \rho A \beta_2 (\partial P/\partial t) \\
&= \rho A \beta (\partial P/\partial t),
\end{aligned}
$$

$$
\begin{aligned}
\text{where } \beta &= \beta_1 + \beta_2 \\
&= (1/A)(\partial A/\partial P) + (1/\rho)(\partial f/\partial P). \qquad\text{(4.191a)}
\end{aligned}
$$

β_1 and β_2 indicate the compressibility of the fluid and the compliance of the fractures which consist of shear and normal compliance terms. The value of the transmissibility (also known as transmissivity in geology) is given by

$$
TR = x_{\mathrm{p}}^2/12 \qquad \text{for rocks with parallel edges and with}
$$
$$
\text{penetration in between,} \qquad\qquad\text{(4.191b)}
$$
$$
TR = r^2/8 \qquad \text{for rock masses of cylindrical shape with}
$$
$$
\text{hydraulic radius } r.
$$

Hopkirk and Rybach have carried out tests on several simulated holes while naming holes as RH12 and RH15. Tests were carried out for stress field directions of fissures and their spacings and geochemical information. Water was injected at the following rates:

Project I

$2.55\,\mathrm{l\,s^{-1}}$ for $2.5\,\mathrm{h}$	Total $30\,\mathrm{h}$
$3.10\,\mathrm{l\,s^{-1}}$ for a further $19.6\,\mathrm{h}$	for RH15 pressure
$1.80\,\mathrm{l\,s^{-1}}$ for a further $7.9\,\mathrm{h}$	monitored in RH12

Project II

$5.4\,\mathrm{l\,s^{-1}}$ for a period of $81\,\mathrm{h}$	Total $81\,\mathrm{h}$
	for RH12 pressure
	monitored in RH15

Figure 4.33 shows a comparative study of the pressure-time history for the two tests. These results may act as input data for more sophisticated studies.

4.8 Impact on Water Surfaces and Waves

4.8.1 Introduction

The determination of hydrodynamic forces experienced by a body entering a water surface is an extremely difficult task since the actual water surface is not planar and is constantly changing, thus making the impact parameters statistical in nature. One has to know statistical data on wave heights, wave lengths and particle velocities. Moreover, the statistical data are influenced
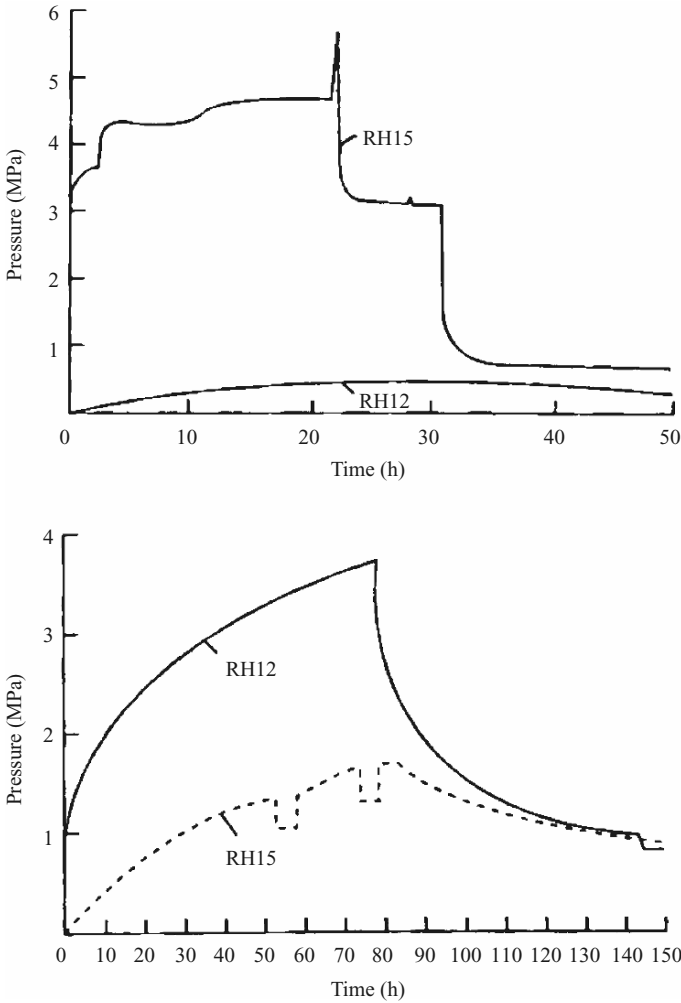
Fig. 4.33. Pressure load–time history in rock masses due to jet fluids. (**a**) Project I; (**b**) Project II

by whether the impacting body is smaller or larger than the wave dimensions. When the impacting body is smaller, the deceleration will be a function of small-scale wavelets. The shape of the water surface for impact or for vessel collision at sea may be selected which results in the highest deceleration, or it may be evaluated by adopting a statistical approach. A comprehensive body of work is reported in the text.

4.8.2 Impact on Water Surfaces

Various theories exist on the relationship between wave heights/depths and wave lengths and the wind velocities which generate the waves. Figure 4.34 shows a relationship between sustained wind speed and significant wave height in severe storms. The water surface is not always smooth, as shown in Fig. 4.35a, b. One of the popular methods for computing the wave spectrum is the JONSWAP method. The spectral density of the water surface elevation $S_{\eta\eta}(f)$ from this spectrum is given below:

$$S_{\eta\eta}(f) = (\alpha \mathbf{g}^2/(2\pi)^4 f^5) \exp[-\frac{5}{4}(f/f_\mathrm{m})^{-4}]\bar{\gamma} \qquad (4.192)$$
$$\times \exp[-(f - f_\mathrm{m})^2/2\sigma_\mathrm{s}^2 f_\mathrm{m}^2],$$
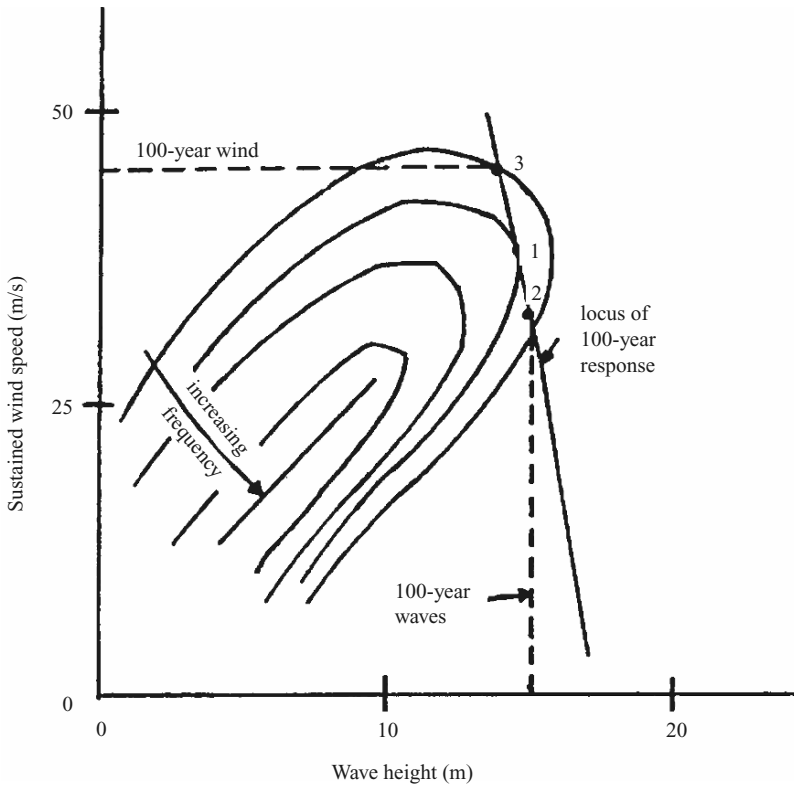
Fig. 4.34. Sustained wind speed versus significant wave heights. Joint frequency of occurrence contours for wind speed and significant wave height in severe storms are shown. Point 1 is the most likely wind/wave combination to produce the 100-year response. Point 2 is the combination of 100-year waves and associated wind producing the 100-years response. Point 3 is the combination of the 100-year wind and associated waves producing the 100-year response

(a)

(b)
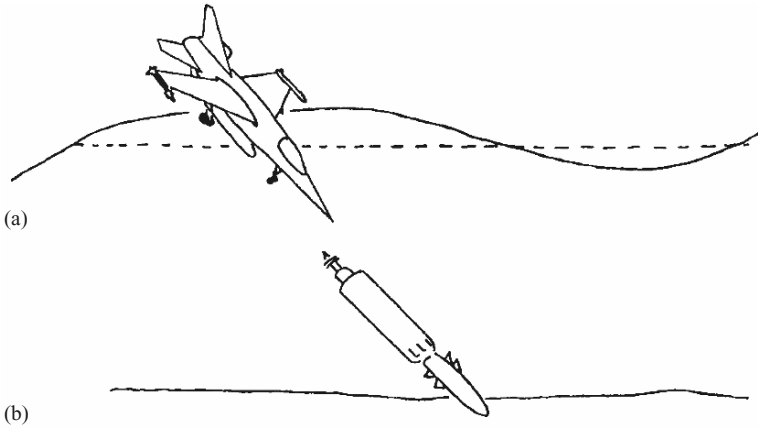
Fig. 4.35. (a) Impact of aircraft and **(b)** missile on sea surface

where $\alpha = 0.046 X_{\mathrm{f}}^{-0.22}/V_{\mathrm{w}(10)}^{2}$ or $0.0662(f_{\mathrm{m}}/2.84)^{2/3}$
$\quad\quad = $ PM constant

$\quad f_{\mathrm{m}} = 16.04/[X_{\mathrm{f}}V_{\mathrm{w}(10)}]^{0.38}$

$\quad V_{\mathrm{w}(10)} = $ wind velocity in $\mathrm{m\,s}^{-1}$ at $10\,\mathrm{m}$ above still water

$\quad\quad \bar{\gamma} \approx 3.3$ for the North Sea

$\quad\quad \sigma_{\mathrm{s}} = $ constant based on the scatter of the data for which the spectrum is derived $= \sigma_{\mathrm{a}}$ for $f \le f_{\mathrm{m}} = 0.07$

$\quad\quad\quad = \sigma_{\mathrm{b}}$ for $f > f_{\mathrm{m}} = 0.09$

$\quad X_{\mathrm{f}} = $ fetch in m

$\quad f = $ frequency in Hz around. $1.5\,\mathrm{Hz}$ (beyond it the energy is significant)

$\quad \mathbf{g} = $ acceleration due to gravity

Table 4.8 gives data on the JONSWAP spectrum for a specific $f = 1.5\,\mathrm{Hz}$.

$$\sigma_{\eta\eta} = \int_{0}^{f=1.5} S_{\eta\eta}(f)\mathrm{d}f \tag{4.193a}$$

Figure 4.36 gives the wave spectrum. Based on results from the Associated Petroleum Institute (API), typical values for the Gulf of Mexico are given in Table 4.9. The most significant finding is that the design wave shall rely on the processes such as wave motion, the probability density function of the wave height and the square of the wave period known as the Raleigh density function. Hence within each state the probability distribution functions are

$$\begin{aligned}
\mathrm{P}(H) &= 1 - \exp[-2(H/H_{\mathrm{s}})], \\
\mathrm{P}(T) &= 1 - \exp[-0.675T/\overline{T}],
\end{aligned} \tag{4.193b}$$

where H and H_{s} are the individual and significant wave heights, respectively, and T and $\overline{T}$ are the individual and mean periods, respectively.

Table 4.8. Data for the JONSWAP spectrum

Significant wave height, H_s	12.5 m
Spectral peak period, T_p	13.5–16.5 s
Wave spectrum, $S_{\eta\eta}(f)$	JONSWAP, $\bar{\gamma} = 2$
Maximum crest elevation, η	13 m
Wind speed at 40 m elevation μ_f	
1 h average	$52 \, \text{m s}^{-1}$
1 min average	$60 \, \text{m s}^{-1}$
3–5 s gust	$75 \, \text{m s}^{-1}$
Wind spectrum, $S_\mu(f)$	'blunt'
Wind speed variance, σ^2	$75 \, \text{m}^2 \, \text{s}^{-2}$
Spectral peak period, T_p	20–200 s
Wind direction	aligned with waves
Current profile	
Above 75 m depth	$1 \, \text{m s}^{-1}$
Below 75 m depth	$0.1 \, \text{m s}^{-1}$
Current direction	Aligned with wind
Storm tide	1 m
Marine growth thickness	3 cm over top 50 m
Marine growth roughness height	1.5 cm over top 50 m

The JONSWAP wave spectrum is given by (4.198)
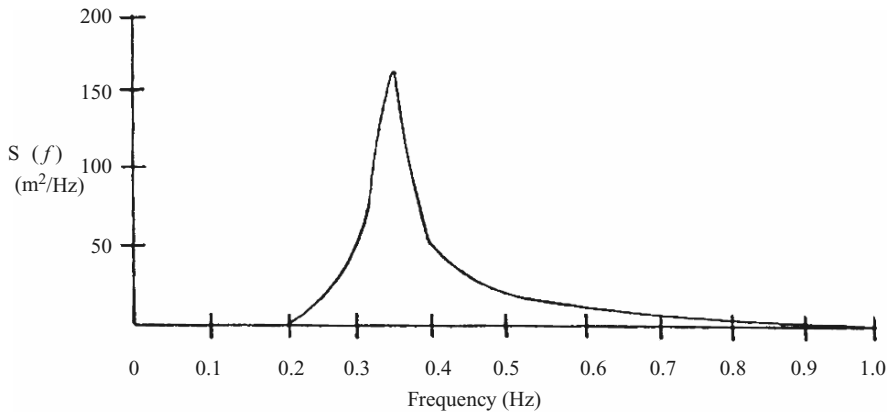
Fig. 4.36. The JONSWAP wave spectrum

Where the impact is on shallow water, Stokes and linear wave theories become numerically unstable since it becomes less and less sinusoidal. The crest becomes more pointed and troughs flatten. In this case, *solitary wave theory* is used and is independent of the wave length of the period of the wave.

$$\text{The surface profile} = H[\text{sech } \sqrt{(3H/4d^2)}x - ct]^2, \qquad (4.193c)$$

Table 4.9. Wave frequency in the North Atlantic Ocean for a whole year

Wave height (m)	Wave period (s)								Sum over all periods
	5	7	9	11	13	15	17		
0.75–	20.91	11.79	4.57	2.24	0.47	0.06	0.00	0.60	40.64
1.75–	72.78	131.08	63.08	17.26	2.39	0.33	0.11	0.77	287.80
2.75–	21.24	126.41	118.31	30.24	3.68	0.47	0.09	0.56	301.00
3.75–	3.28	49.60	92.69	32.99	5.46	0.68	0.12	0.27	185.09
4.75–	0.53	16.19	44.36	22.28	4.79	1.14	0.08	0.29	89.66
5.75–	0.12	4.34	17.30	12.89	3.13	0.56	0.13	0.04	38.51
6.75–	0.07	2.90	9.90	8.86	3.03	0.59	0.08	0.03	25.46
7.75–	0.03	1.39	4.47	5.22	1.93	0.38	0.04	0.04	13.50
8.75–	0.00	1.09	2.55	3.92	1.98	0.50	0.03	0.02	10.09
9.75–	0.00	0.54	1.36	2.26	1.54	0.68	0.20	0.04	6.62
10.75–	0.01	0.01	0.10	0.11	0.10	0.05	0.02	0.00	0.40
11.75–	0.00	0.00	0.03	0.08	0.17	0.06		0.00	0.34
12.75–		0.05	0.00	0.14	0.22	0.06	0.01		0.48
13.75–		0.02		0.07	0.09	0.03		0.01	0.22
14.75–				0.02	0.06	0.02	0.00	0.01	0.11
15.75–	0.00	0.02	0.00	0.02	0.02	0.02	0.01	0.01	0.08
Sum over all height	118.97	345.43	358.72	138.59	29.05	5.63	0.92	2.69	1,000.00

where H = wave height, d = water depth, c = wave celerity = $\sqrt{[\mathbf{g}(H+d)]}$, x = distance from crest, t = time, $\mathbf{g}$ = acceleration due to gravity.

Figure 4.37 gives a comparative study of wave heights for depths in different seas. It is important to determine the wave profile correctly prior to impact. The correct evaluation of the impact depends on whether or not the
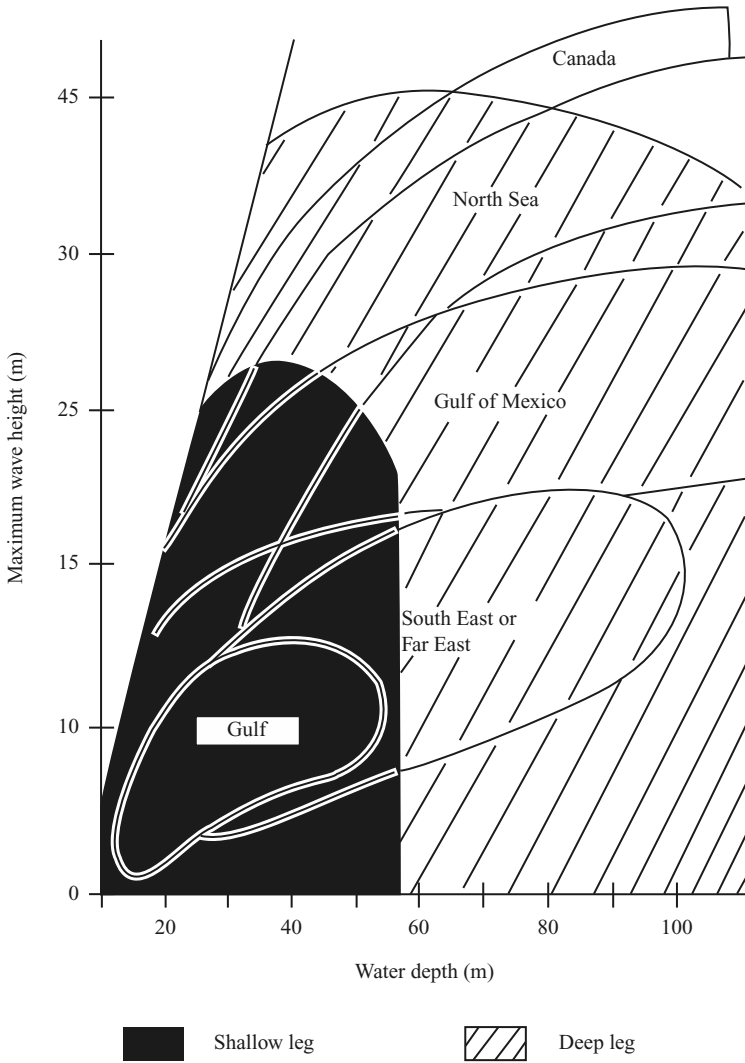
Fig. 4.37. Design conditions found in common offshore areas

surface is planar. For example, when the impact occurs due to a projectile of
any shape upon a water surface, the area of contact between body and water
surface spreads faster than the speed of sound, U_0, which is the shock wave
front velocity. The impact load causing pressure P for the impactor velocity
V is given by

$$P = \rho_\omega U_0 V, \qquad (4.194)$$

where ρ_ω is the uncompressed density of water.

By introducing a stagnating pressure of $\frac{1}{2}\rho_\omega V^2$, Kirkwood and Montroll suggest the following interface pressure for a non-rigid body:

$$P = \frac{\rho_\omega U_0 V}{1 + \dfrac{\rho_\omega V}{\rho_b U_b}}, \tag{4.195}$$

where $\rho_b U_b$ = the impedance, U_b = the stress wave front velocity.

The particle velocity in a body and interface velocity are given as follows:

$$\left.\begin{array}{ll} \text{particle velocity in body} = V_a = P/\rho_b U_b, \\ \text{interface velocity} \qquad\quad = V - V_a. \end{array}\right\} \tag{4.196}$$

For a rigid body, the pressure P (for an impact velocity) above 300 psi is given by

$$P = 2.17\rho_\omega V^2 (U_0/V)^{0.73}. \tag{4.197}$$

The shapes of the waves and of the missiles/aircraft must be taken into consideration when modifications are carried out to (4.195)–(4.197). The deceleration and velocity changes when the body enters the water have to be computed. It is important to include the shape factor known as the ballistic density factor, γ_{bd}, which is given by

$$\gamma_{bd} = \frac{\text{mass } m \text{ of the impacting body} \times \mathbf{g}}{\text{weight of sphere of water of the same radius } r} \tag{4.198}$$

$$= m\mathbf{g} / \frac{4}{3}\pi \rho_\omega r^3,$$

the initial acceleration is given by

$$\ddot{x} = 0.75\, U_0 V / r\gamma_{bd}. \tag{4.199}$$

When the rare faction (compression reflected) wave moves in from the outside, the value of the new $\ddot{x}_{ne}$ is given by

$$\ddot{x}_{n_e} = \ddot{x}[1 - (U_0 t/r)]. \tag{4.200}$$

The velocity loss ΔV is computed as

$$\Delta V = \int_{t=0}^{t=R/U_0} \frac{0.75\, U_0 V}{R\gamma_{bd}} \left(1 - \frac{U_0 t}{r}\right) \mathrm{d}t \tag{4.201}$$

$$= V(1 - \mathrm{e}^{-\gamma_{bd}/4}). \tag{4.201a}$$

Shiffman and Spencer (pers. comm.) suggest that deceleration may be calculated as

$$\ddot{x} = \frac{3}{8} C_p V^2 / r\gamma_{bd}, \tag{4.202}$$

where C_p = the drag coefficient

$$= F_1(t)/(\pi r^2)(\tfrac{1}{2}\rho_\omega V^2). \tag{4.203}$$
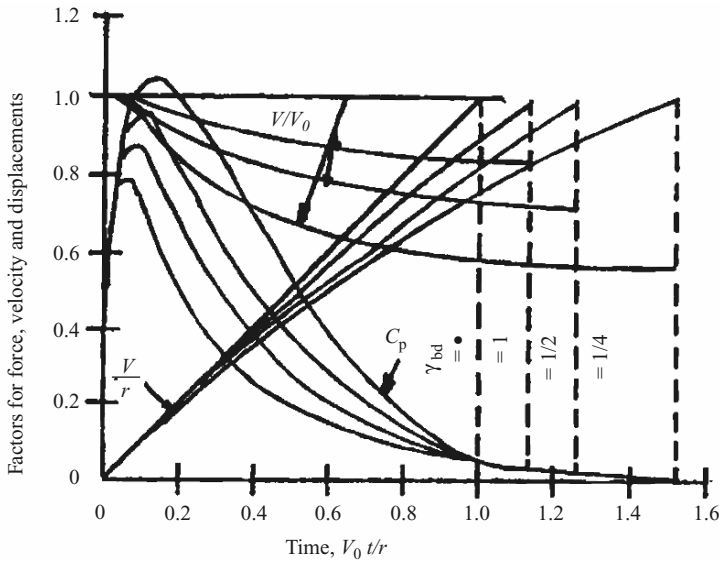
Fig. 4.38. Force, velocity and displacement versus time for spheres entering water (Shiffman and Spencer, personal communication)

Figures 4.38 and 4.39 show data for a smooth water surface subject to a spherical missile. Figures 4.40 and 4.41 illustrate data for cone-shaped missiles with the JONSWAP spectrum.

4.8.3 Impact on Ocean Surfaces

The high risk of collision between sea vessels themselves or between sea vessels and offshore installations has generated the need for accurate predictions of their responses to impact forces, F_1, which are transient in nature. When a sea vessel with speed V collides non-centrally with a platform at rest, the loss of kinetic energy is given by

$$E_K = \frac{1}{2}m_{b'}(v_{b'}\sin\theta)^2 - \frac{1}{2}(m_{a'} + m_{b'} + C_m)V^2, \qquad (4.204)$$

where C_m = added mass $0 < C_m < 1$, $m_{a'}$, $m_{b'}$ = the masses of the two ships, $v_{b'}$ = the velocity of ship b', θ = the angle of the ship b' to the horizontal where ship a' is positioned.

For the linear momentum normal to the centreline of $m_{a'}$ to be conserved

$$m_{b'}v_{b'}\sin\theta = (m_{a'} + m_{b'} + C_m)V. \qquad (4.205)$$

From (4.204) and (4.205)

$$E_K = (m_{b'}/2)K(v_{b'}\sin\theta)^2, \qquad (4.206)$$
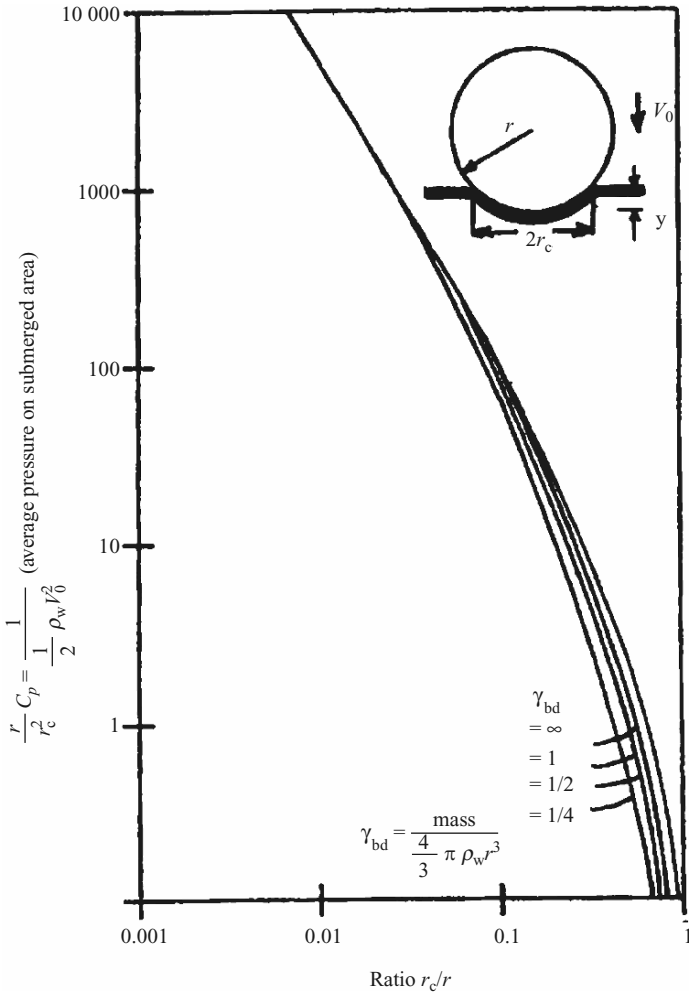
Fig. 4.39. Pressure on a sphere for normal entry into water (Shiffman and Spencer, personal communication)

where
$$K = \frac{m_a + C_m}{m_{a'} + m_{b'} + C_m} = \frac{1}{1 + M/(1 + C)},$$ (4.206a)

$$M = m_{b'}/m_{a'}.$$

If $K \to 1$ and $m_{b'} < m_{a'}$ or $M \to 0$

$M \to \infty$; $K \to 0$

If the striking ship is of relatively small mass, the energy loss would be greater and vice versa.

In terms of vessel displacements, the kinetic energy loss is given by

$$E_K = \frac{\delta_{a'} \, \delta_{b'}}{1.43\delta_{b'} + 2\delta_{a'}} (v_b \sin \theta)^2,$$ (4.207)
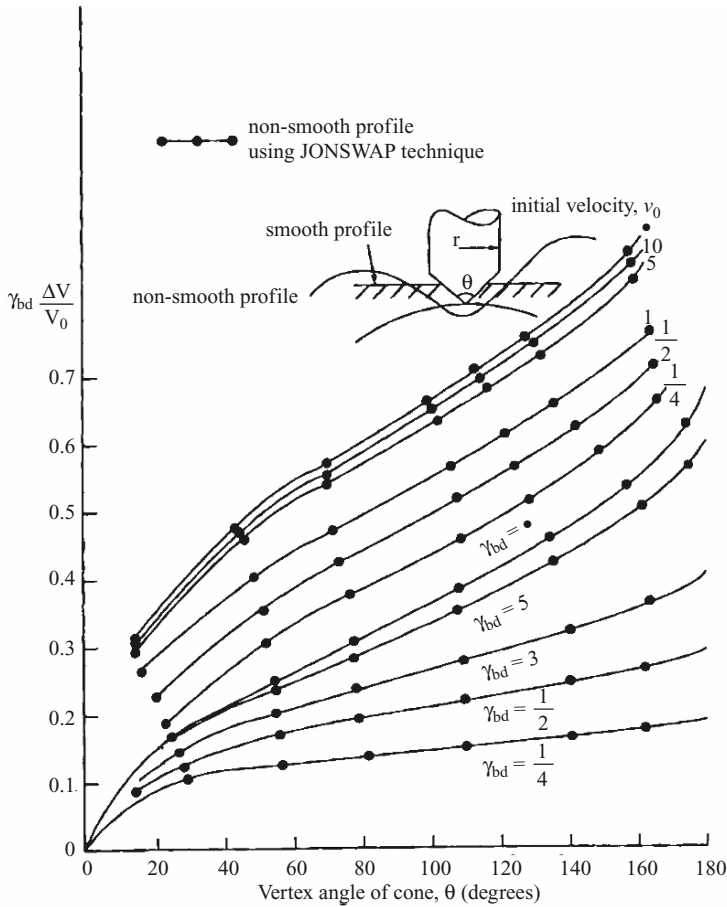
Fig. 4.40. Loss of velocity for cone-shaped missiles

where $\delta_{a'}$ and $\delta_{b'}$ are the displacements of the vessels a′ and b′, usually in tonnes, and v_b is in knots. In terms of the *resistance factor*, R_T, measured in $m^2 - mm$, Minorsky gives

$$R_T = 1.33\Sigma d_n l_n \bar{t}_n + \Sigma d_N l_N \bar{t}_N, \tag{4.208}$$

where d_n, d_N = depth of damage in the nth member of the struck vessel and the striking vessel, respectively

l_n, l_N = length of damage in the nth member of the struck vessel and the striking vessel, respectively

$\bar{t}_n, \bar{t}_N$ = thickness of the nth member of the struck vessel and the striking vessel, respectively

The energy loss can be rewritten as

$$E_K = 233.8\bar{R}_{TS} + 175.8\bar{R}_{Tb} + 124{,}000, \tag{4.209}$$
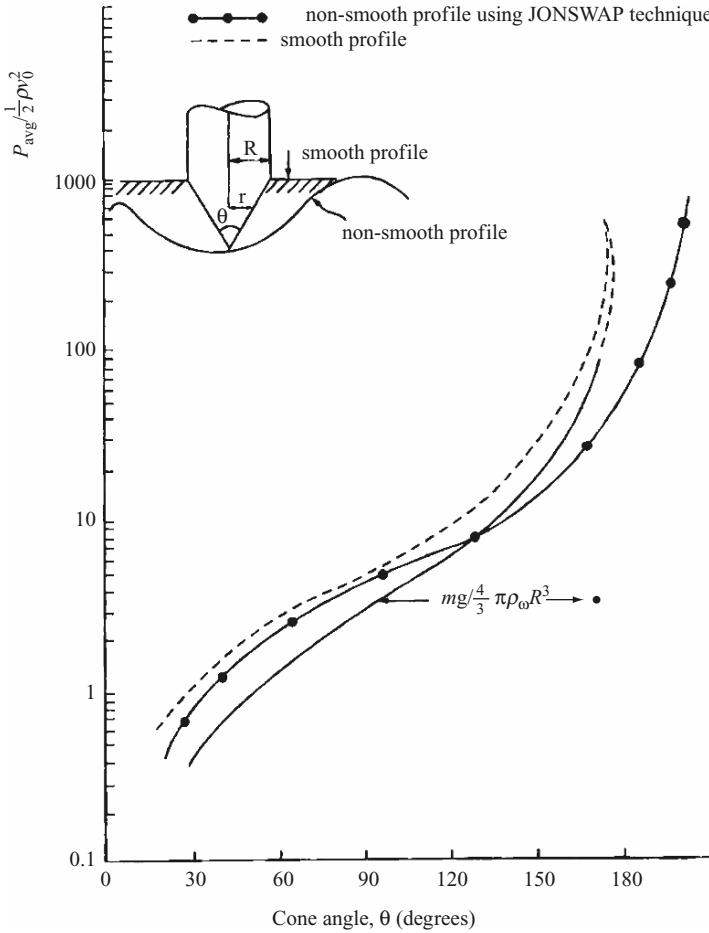
Fig. 4.41. Pressure coefficients during water entry of cones (Shiffman and Spencer, personal communication)

where $\overline{R}_{TS} = \Sigma d_n l_n \bar{t}_n$ = resistance factor for the struck ship

$\overline{R}_{Tb} = \Sigma d_N l_N \bar{t}_N$ = resistance factor for the striking ship

The added mass C_m can be determined by potential flow theory. The added mass force F_{ad} is expressed as

$$F_{ad} = \rho_\omega C_m \pi a^2 \times \ddot{x}, \tag{4.210}$$

where ρ_ω = fluid density, $\ddot{x}$ = ship acceleration, a = a dimension given for various shapes by Det Norske Veritas (DNV) in Tables 4.10 and 4.11.

Where three-dimensional dynamic final element analysis is to be carried out then wave-induced forces, the hydrodynamic reaction forces and the restoring forces should be determined for each element. Summing up these

forces and the inertia properties, the displacements, velocities and acceleration of the vessel can be determined from the equation of motion given below

$$\left[\sum_{i=1}^{n1} M_i + \sum_{j=1}^{n2} \overline{C}_m\right] \ddot{x} + \left[\sum_{j=1}^{n2} C_j\right] \dot{x}$$

$$+ \left[\sum_{j=1}^{n2} F1_j + \sum_{i=1}^{n1} F2_i\right] \bar{x} = \sum_{j=1}^{n2} \overline{F}_j \quad (4.211)$$

where i = mass point number, $n1$ = total number of mass points, j = hydro element number, $n2$ = total number of hydro elements, M_i = inertia matrix of nodal point i, C_m = added mass matrix of hydro element j, C_j = damping matrix of hydro element j, $F1_j$ = restoring force matrix (due to buoyancy force contributions) of hydro element j, $F2_i$ = restoring force matrix (due to inertia force contributions) of mass point i, $\overline{F}_j$ = wave-induced forces of hydro element j.

Tables 4.10 and 4.11 give the added mass coefficient, C_m.

Table 4.10. Added mass coefficients (C_m) for two-dimensional bodies (courtesy of Det Norske Veritas)
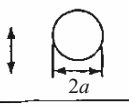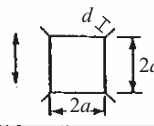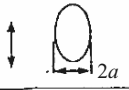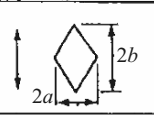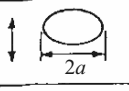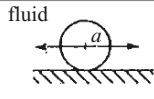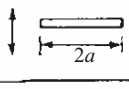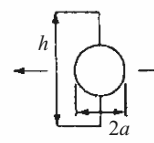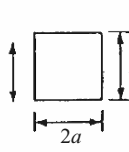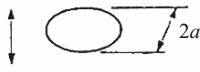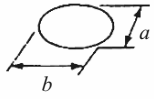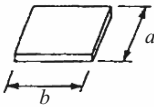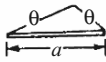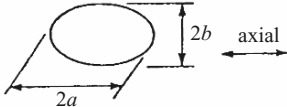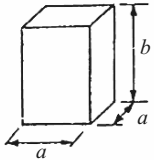
Section through body	C_m	Section through body	C_m
circle, $2a$	1.0	square d, $2a$, $d/a = 0.05$ $d/a = 0.10$ $d/a = 0.25$	1.61 1.72 2.19
$2a$	1.0	diamond $2b$, $2a$, $a/b = 2$ $a/b = 1$ $a/b = 1/2$ $a/b = 1/5$	0.89 0.76 0.67 0.61
$2a$	1.0	fluid a wall	2.29
$2a$	1.0		
$2b$, $2a$, $a/b = \infty$ $a/b = 10$ $a/b = 5$ $a/b = 2$ $a/b = 1$ $a/b = 1/2$ $a/b = 1/5$ $a/b = 1/10$	1.0 1.14 1.21 1.36 1.51 1.70 1.98 2.23	h, $2a$	$1 + \left(\dfrac{h}{2a} - \dfrac{2a}{h}\right)^2$

Table 4.11. Added mass coefficients (C_m) for three-dimensional bodies (courtesy of Det Norske Veritas)

Body shape	C_m			V
1. Flat plates Circular disc	0.64			$\dfrac{4}{3}\pi a^2$
Elliptical disc	b/a	C_m		$\dfrac{\pi}{6}a^2 b$
	∞	1.0		
	12.75	0.99		
	7.0	0.97		
	3.0	0.90		
	1.5	0.76		
	1.0	0.64		
Rectangular plates	b/a	C_m		$\dfrac{\pi}{4}a^2 b$
	1.0	0.58		
	1.5	0.69		
	2.0	0.79		
	3.0	0.83		
	∞	1.00		
Triangular plates	$\dfrac{1}{\pi}(\tan\theta)^{3/2}$			$\dfrac{a^3}{3}$
2. Bodies of revolution Spheres	0.5			$\dfrac{4}{3}\pi a^2$
Ellipsoids		C_m		$\dfrac{4}{3}\pi a^2 b$
lateral	b/a	Axial	Lateral	
	1.5	0.30	0.62	
	2.0	0.21	0.70	
	2.51	0.16	0.76	
	3.99	0.08	0.86	
	6.97	0.04	0.93	
	9.97	0.02	0.96	
3. Square prisms	b/a	C_m		$a^2 b$
	1	0.68		
	2	0.36		
	3	0.24		
	4	0.19		
	5	0.15		
	6	0.13		
	7	0.11		
	10	0.08		

4.8.4 Wave Impact on Rock Slopes and Beaches

Introduction

The wave impact phenomenon is complex as it involves, apart from the influence of the wave spectrum and storm duration discussed in Sect. 4.8.2, static and dynamic slope instability of porous and non-porous types of beaches, distortion of rubble mound revetments and the formation of a profile with damaged zones. The characteristics of rocks under impact are discussed in Chap. 2. Waves can be of plunging and surging types and can easily be influenced by parameters such as height, period and the slope angle. In this section only well known work is reported.

Wave Impact on a Dynamically Stable Profile

Prior to impact force evaluation, it is essential to define the dynamically stable profile. Power as shown in Fig. 4.42 defined the profile by two power curves. The upper curve starts at the crest and the profile defines the run-up and run-down area, up to the transition to the steep part (line with angle β). The lower curve starts at the transition and describes the step. The complete profile is then shown in the figure with a further definition of a crest height, a length for the upper curve and a depth for the lowest point of incipient motion. For evaluation of static stability, various formulae have been given in the report provided by the International Commission for the Study of Waves, PIANC Most stability formulae are in agreement, but for armour units and block revetments the buoyant mass of the stone, W' Fig. 4.43 is given by

$$W' = (\rho_a - \rho_w)d_{n50}^3, \tag{4.212}$$
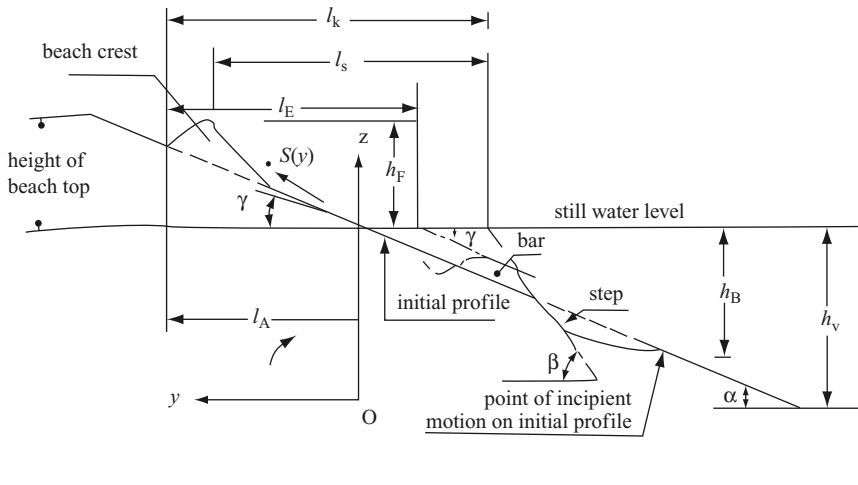
Fig. 4.42. Model for a dynamically stable profile [2.396]
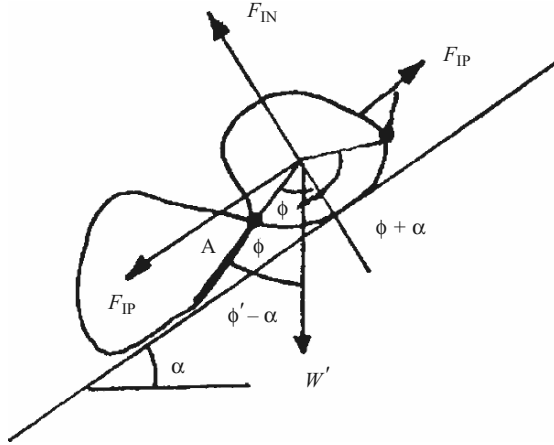
Fig. 4.43. Schematization of incipient instability

where ρ_ω = mass density of water, ρ_a = mass density of stone, d_{n50}^3 = nominal diameter with index n of 50% value of sieve curve.

The impact load $F_1(t)$ is schematized by two forces, one parallel to the slope, $F_{1P}(t)$, and the other normal to the slope, $F_{1N}(t)$. If the value of $F_1(t)$ is given by

$$F_1(t) = \rho_\omega \mathbf{g} C d^2 H, \tag{4.213}$$

where $F_1(t)$ = impact due to wave, C = coefficient, d = diameter of stone

then

$$F_{IN} \sin\phi \, \frac{d}{2} + F_{IP} \cos\phi \, \frac{d}{2} = \mathbf{g} W' \sin(\phi - \alpha) \frac{d}{2}, \tag{4.214}$$

where ϕ = angle of repose, α = angle of seaward slope.

Assuming a coefficient C_1 for the normal wave force, $F_{1N}(t)$, a coefficient C_2 for the parallel wave force, $F_{1P}(t)$, and assuming $d = K d_{n50}$ (where K is a coefficient), then

$$\rho_\omega \mathbf{g} C_1 d_{n50}^3 H \sin\phi K^3/2 + \rho_\omega \mathbf{g} C_2 d_{n50}^3 \, H \cos\phi K^3/2 = \mathbf{g}(\rho_a - \rho_\omega)d_{n50}^4$$
$$\sin(\phi - \alpha)K^4/2. \tag{4.215}$$

Equation (4.215) can be written as

$$H/\Delta d_{n50} = K \sin(\phi - \alpha)/(C_1 \sin\phi + C_2 \cos\phi), \tag{4.216}$$

where $\Delta = (\rho_a - \rho_\omega)/\rho_\omega$.

By defining the friction coefficient, μ, as $\mu = \tan\phi$, (4.216) can be finally rewritten as

$$H/\Delta d_{n50} = K(\mu\cos\alpha - \sin\alpha)/(\mu C_1 + C_2). \tag{4.217}$$

The wave steepness, S, using the deep water wave length $L = \mathbf{g}T^2/2\pi$, becomes

$$S = 2\pi H/\mathbf{g}T^2. \tag{4.218}$$

The value of S is then related to the slope angle of the slope of the stone beach by

$$S = (\tan\alpha/\bar{\bar{\xi}})^2, \tag{4.219}$$

where $\bar{\bar{\xi}}$ is a similarity parameter with the mean value $\bar{\bar{\xi}}_{\mathrm{m}}$.

The significant wave height, H_{s}, and the average period, T_{m}, can both be calculated from the spectrum as given in Sect. 4.8.2. For the *plunging wave* region, there is a functional relationship between $H_{\mathrm{s}}/\Delta d_{n50}$ and $\bar{\xi}_n$ and they are given by

$$\text{impermeable core} \quad H_{\mathrm{s}}/\Delta d_{n50} \times \sqrt{\bar{\bar{\xi}}_{\mathrm{m}}} = 4.1(S/\sqrt{N})^{0.2}, \tag{4.220}$$

$$\text{permeable core} \quad H_{\mathrm{s}}/\Delta d_{n50} \times \sqrt{\bar{\bar{\xi}}_{\mathrm{m}}} = 5.3(S/\sqrt{N})^{0.2}, \tag{4.221}$$

$$\text{homogeneous core} \quad H_{\mathrm{s}}/\Delta d_{n50} \times \sqrt{\bar{\bar{\xi}}_{\mathrm{m}}} = 5.7(S/\sqrt{N})^{0.2}, \tag{4.222}$$

where N is the number of waves.

For surging waves, equations similar to (4.226)–(4.228) have been derived:

$$\text{impermeable core} \quad H_{\mathrm{s}}/\Delta d_{n50} = 1.35(S/\sqrt{N})^{0.2}\sqrt{\cot\alpha}(\bar{\bar{\xi}}_{\mathrm{m}}^{0.1}), \tag{4.223}$$

$$\text{permeable core} \quad H_{\mathrm{s}}/\Delta d_{n50} = 1.07(S/\sqrt{N})^{0.2}\sqrt{\cot\alpha}(\bar{\bar{\xi}}_{\mathrm{m}}^{0.5}), \tag{4.224}$$

$$\text{homogenous structure} \quad H_{\mathrm{s}}/\Delta d_{n50} = 1.10(S/\sqrt{N})^{0.2}\sqrt{\cot\alpha}(\bar{\bar{\xi}}_{\mathrm{m}}^{0.6}). \tag{4.225}$$

When the permeability coefficients are included, the final $H_{\mathrm{s}}/\Delta d_{n50}$ relationships for both plunging and surging waves are written as, respectively,

$$H_{\mathrm{s}}/\Delta d_{n50} \times \sqrt{\bar{\bar{\xi}}_{\mathrm{m}}} = 6.2p^{0.18}(S/\sqrt{N})^{0.2}, \tag{4.226}$$

$$H_{\mathrm{s}}/\Delta d_{n50} = 1.0p^{-0.13}(S/\sqrt{N})^{0.2}\sqrt{\cot\alpha}(\bar{\bar{\xi}}_{\mathrm{m}})^p, \tag{4.227}$$

where p is the permeability factor.

The complete range of dynamic stability, $H_{\mathrm{s}}/\Delta d_{n50}$, can be covered by the combined wave height–period, H_0T_0, as

	Breakwater	Rock slopes and beaches
$H_{\mathrm{s}}/\Delta d_{n50}$	1–4	6–20
HT	<100	200–1,500

It is important to define various heights and lengths as they influence the impact load:

(a) Run-up length, l_r:
$$H_0 T_0 = 2.9(l_r/d_{n50} \ N^{0.05})^{1.3}$$

(b) Crest length, l_c:
$$H_0 T_0 = 21(l_c/d_{n50} \ N^{0.12})^{1.2}$$

(c) Step length, l_s:
$$H_0 T_0 = 3.8(l_s/d_{n50} \ N^{0.07})^{1.3}$$

————————————————————

(a) Crest height, h_c:
$$h_c/H_s N^{0.5} = 0.089(s_m)^{-0.5} \tag{4.228}$$

(b) Step height, h_s:
$$h_s/H_s N^{0.07} = 0.22(s_m)^{-0.3} \tag{4.229}$$

(c) Transition height, h_t:
$$h_t/H_s N^{0.04} = 0.73(s_m)^{-0.2} \tag{4.230}$$

The slope, $\tan\gamma$, is given by

$$\tan\gamma = 0.5\tan\alpha. \tag{4.231}$$

The slope, $\tan\beta$, is given by

$$\tan\beta = 1.1\tan\alpha^A, \tag{4.232}$$

where $A = 1 - 0.45\exp(-500/N)$.

For an *oblique wave* impact, all the above parameters are reduced by $\cos\phi$, except the crest length, l_c.

The number of waves impacting on the structure influence the damage. Thompson and Shuttler [5.110] produced results from five long duration tests with N up to 15,000. Table 4.11 gives the relationship between the number of waves, N, and damage, $S(N)/S(5,000)$, which means all damage is related to the final damage after 5,000 waves. The standard deviation for the ratio $S(N)/S(5,000)$ in the region $N = 1,000$–$5,000$ is about 0.1 and is independent of the number of waves. A function that meets this requirement is given by

$$f(S) = a[1 - \exp(-bN)], \tag{4.233}$$

where a and b are curve-fitting coefficients and are found to be 1.3×10^{-4} and 3×10^{-4} respectively.

Table 4.12. Relationship between the number of waves (N) and the damage $(S(N)/S(5,000))$

N	$S(N)/S(5,000)$
0	0
5,000	1
7,500	1.15
10,000	1.25
12,750	1.27
15,000	1.30

The influence of the storm duration on stability for the whole range of N is given by the following equation:

$$f(S) = S(N)/S(5,000) = 1.3[1 - \exp(-3 \times 10^{-4}N)]. \qquad (4.234)$$

The damage due to wave impact is limited to 1.3 times the damage after $N = 5,000$. Table 4.12 gives results for various waves and the corresponding damage. The influence of the wave period on the damage due to wave impact for both plunging and surging waves can be assessed using the follow equations developed by Pilarczyk and Den Boer [5.99]:

Plunging waves

$$H_\mathrm{s}/\Delta d_{n50} = 2.25(\bar{\bar{\xi}})^{-0.5}(\mu\cos\alpha + \sin\alpha) \qquad (4.235)$$

Surging waves

$$H_\mathrm{s}/\Delta d_{n50} = 0.54 \sqrt{\cot \alpha}[(\bar{\bar{\xi}})^{0.5} \ (\mathrm{H/L})^{-0.25}] \times (\mu\cos\alpha + \sin\alpha). \qquad (4.236)$$

The results of these are given in Table 4.13. The influence of permeability for various values of S is also given for homogeneous, permeable and impermeable structures for damage levels $S = 3$ and $S = 8$. For wave impact analysis, other useful parameters are given in Table 4.14.

4.9 Snow/Ice Impact

4.9.1 Introduction

At present, a great deal of controversy exists as to whether the ice-structure dynamics is the cause of a quasi-static loading or a direct impact. Nevertheless, the vibrations appear to be a complex combination of ice crushing and ice-structure actions. The records indicate that the force–time relationship is greatly dependent on the velocity of the ice floe. Some methods, mostly empirical, are available for the evaluation of impact loads. All methods quoted in this section are based on the theory of elastic plates on elastic foundations.

Table 4.13. Relationship between $H_\mathrm{s}/\Delta d_{n50}\,(\mu\cos\alpha + \sin\alpha)$ and $\tan\alpha/\sqrt{(H/L)}$

$\bar{\bar{\xi}}$	Cot α					**K**		S				
								3			8		
								H_0	P_e	I_m	H_0	P_e	I_m
	1.5	2.5	3.5	5.0	10.0								
0.6	2.80	2.80	2.80	2.80	2.80								
0.7	2.70	2.70	2.70	2.70	2.70								
0.8	2.50	2.50	2.50	2.50	2.50								
1	2.20	2.20	2.20	2.20	2.20								
2	1.65	1.65	1.65	1.80	2.25			2.25	2.20	1.60	2.70	2.60	2.00
3	1.65	1.70	1.80	2.20	3.00			1.80	1.70	1.30	2.25	2.20	1.70
4	1.68	1.80	2.10	2.30	–			1.75	1.65	1.40	2.40	2.20	1.50
5	1.69	1.80	2.20	2.50	2.80			2.30	2.00	1.25	2.60	2.40	1.55
6	1.70	2.20	2.30	–	–			–	–	1.25	–	–	1.50
7	1.80	2.30	–	–	–			–	–	1.30	–	–	1.70
8	1.90	–	–	–	–								
9	2.00	–	–	–	–								
10	–	–	–	–	–								

$\mathbf{K} = H_\mathrm{s}/\Delta d_{n50}\,(\mu\cos\alpha + \sin\alpha)$, $P_\mathrm{e} =$ permeable, $\bar{\bar{\xi}} = \tan\alpha/\sqrt{(H/L)}$, $I_\mathrm{m} =$ impermeable, $H_0 =$ homogeneous

Table 4.14. Wave impact parameters

Expression and symbol	Value	
Wave steepness $= S$ or S_m	0.01–0.06	
Similarity parameter $= \bar{\bar{\xi}}$		
Plunging	0.50–7.50	
Surging		
Collapsing	3.0	
Spilling	0.2	
Damage $S/\sqrt{N}$	<0.9	
N	250–10,000	
$H_\mathrm{s}/\Delta d_{n50}/\bar{\bar{\xi}}_\mathrm{m}$	0.533–0.61	
Damage level S	$N(1{,}000)$	$N(3{,}000)$
2	−0.5	−0.42
3	−0.54	−0.52
5	−0.57	−0.57
8	−0.50	−0.52
12	−0.42	−0.53
Permeability factor P	0.1–0.6	
The angle of wave impact ψ	0–50°	

The plasticity theory has been developed by Ralston which is in good agreement with the early model tests. Some have gone further, such as Croasdale whose published theories included ride-up on sloping beaches. A brief introduction to snow/ice impact has been given already in Chap. 2 and in this section the work is supported by analysis and empirical formulae.

4.9.2 Empirical Formulae

General Consideration

In all circumstances the force–time relationship can be characterized in terms of low and high velocities. The snow/ice strength depends greatly on strain rate. The stress–strain rate relationship begins from the left-hand side of the curve, known as *ductile failure range*, the middle zone is a *transition range* and the right-hand portion of the curve is the *brittle failure range*. The transition between the right and the left is highly complicated since both brittle and ductile failure can exist.

Figure 4.44 shows the relationship between compressive strength and the strain rate per second and the mechanical properties depend on temperature, salinity, density, grain/specimen size, loading rate and failure mode.

Sinha Model

The strain is made up of three components:

$$\epsilon = \epsilon_e + \epsilon_d + \epsilon_v, \tag{4.237}$$

where the portions of the total strain are

ϵ_e: elastic strain
ϵ_d: delayed elastic or time-dependent strain
ϵ_v: viscous or permanent strain

It is possible to estimate the onset of cracking of snow/ice on the basis of knowing ϵ_c. The value of ϵ_d is computed as

$$\epsilon_d = (c_1/E)\,(d_1/d) \sum_{i=1}^{n+1} \delta\sigma(1 - \exp\{-[a_T(n+1-i)\delta t]^b\}), \tag{4.238}$$

where E = Young's modulus ($9.5\,\text{GPa}$), d = grain diameter of the columnar crystals of ice, d_1 = unit of grain diameter (e.g. $1\,\text{mm}$ for grain sizes in mm), $a_T = 2.5 \times 10^{-4}\,\text{s}^{-1}$ at $T = -10°C$, $c_1 = 9$, $b = 0.34$, $\delta\sigma$ = stress increase per time increment, n = number of time increments, δt = time per increment.

For a columnar crystal of size $4.5\,\text{mm}$ and a temperature of $-10°C$, Sinha determined that first cracks occurred when the delayed elastic strain exceeded

$$\sigma/E \times 10^{-4}$$
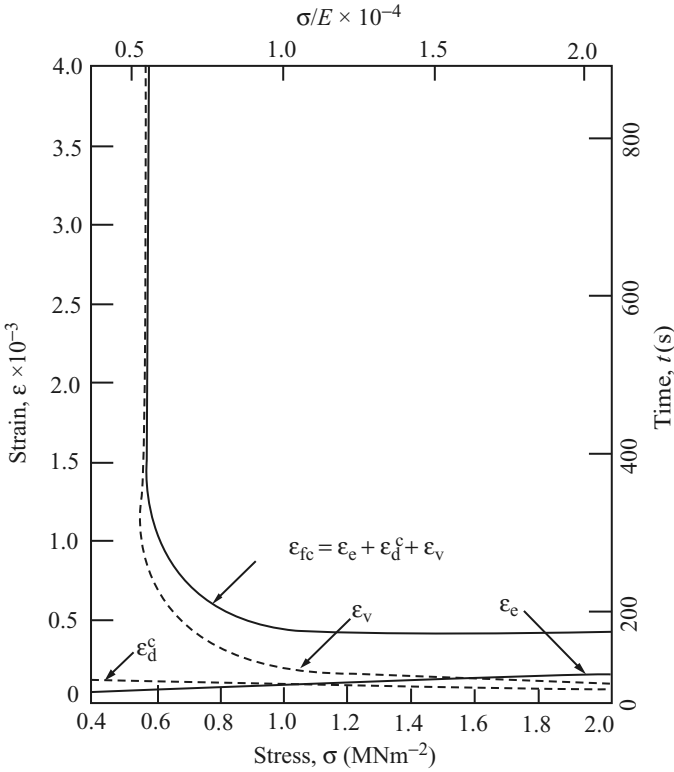
Fig. 4.44. Stress–strain at the formation of the first cracks

1.04×10^{-4}. Figure 4.45 illustrates the stress–strain time-dependent relationship at the formation of the cracks. The impact load is then computed as

$$F_1(t) = \sigma A, \tag{4.239}$$

where A is the area in m^2.

If the strain rate ranges from 1×10^{-3} to 1×10^{-5} are considered, the mean compressive strengths for -5 and $-20°C$ are $2.34 \pm 1.08\,MPa$ to $2.79 \pm 0.69\,MPa$, respectively. For circular structures the impact load is then written as

$$F_1(t) = PdT_i', \tag{4.240}$$

where d = structure diameter, T_i' = local ice thickness, P = ice failure pressure.

For impact analysis, the shape factors for circular and nose types $(60°)$ are 1.0, 0.90 and 0.59, respectively.

$$\sigma/E \times 10^{-4}$$
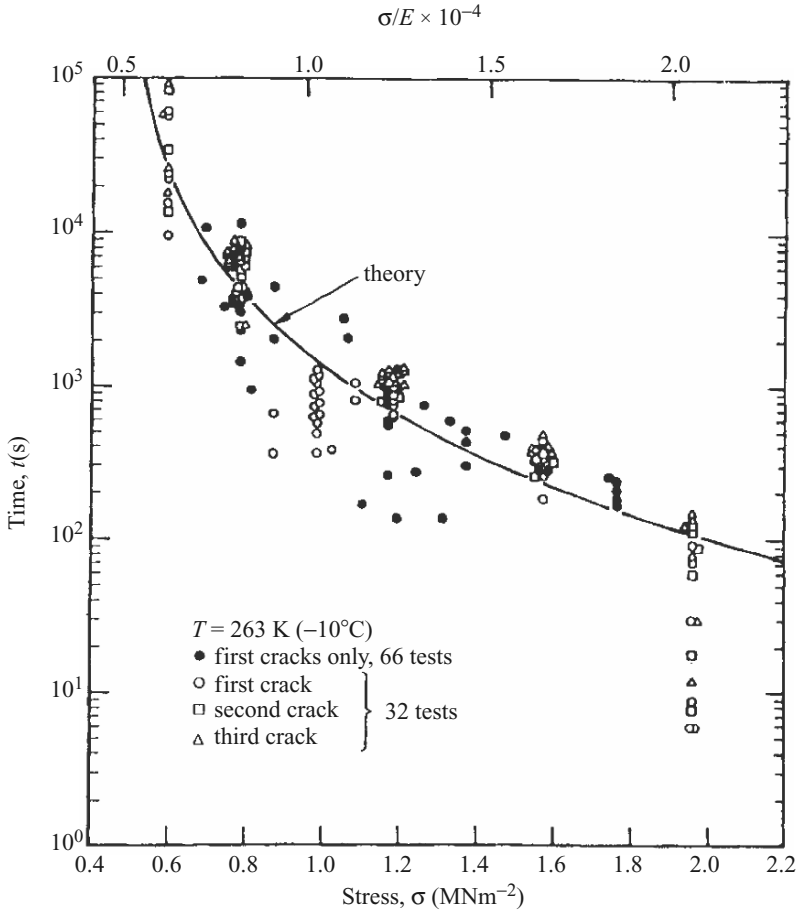
Fig. 4.45. Experimental and theoretical study of stress–time relationship at various cracks (after Sinha)

Timco Model

In the ductile mode Timco uses the following form of the Korzhavin equation:

$$F_1(t) = cS_F I dT'_i \sigma_c, \qquad (4.241)$$

where c = contact coefficient, S_F = shape coefficient, I = indentation factor, d = diameter of leg of submersible, T'_i = ice sheet thickness, σ_c = uni-axial unconfined compressive strength of ice at the strain rate $30(\dot{\epsilon})^{0.22}$ MPa, $\dot{\epsilon} = V/2d$ = strain rate.

If the width of support is considered, the following data should be used for the contact coefficient 'c' (Table 4.15).

Table 4.15. Width versus velocity of flow movement

Width of support (interaction width) (m)	Velocity of flow movement ($\mathrm{m\,s^{-1}}$)		
	0.5	1.0	2.0
3–5	0.7	0.6	0.5
6–8	0.6	0.5	0.4

Sanderson Model

This theory is known as the *reference stress method*. The impact load on a structure is determined by

$$F_1(t) = I d T_{\mathrm{i}}' [1 - (v/v_0)^{1/2}] \, [v/I \psi dA \, \exp(-\mathrm{Q}/RT)]^{1/n}, \qquad (4.242)$$

where $F_1(t)$ = total load, I = indentation factor, T_{i}' = ice sheet thickness, v = velocity in $\mathrm{m\,s^{-1}}$, ψ = angle of attack, Q = constant, R = radius, T = time, n = number of impacts, A = area, d = depth occupied on structures.

Nevel's Model

Nevel's model produces ultimate failure of the ice plates which can be applied to forces on sloping structures. On conical structures, the impact force produced by failure of a series of ice wedges (radial cracks of the ice/snow) is given as

$$F_1(t) = [1.05 + 2.0(a/l) + 0.5(a/l)^2 + 0.5 \, (a/l)^3][b_0 \sigma_{\mathrm{f}} \, (T_{\mathrm{i}}')^2 / 6], \qquad (4.243)$$

where σ_{f} = ice flexural strength $\approx 700\,\mathrm{kPa}$, T_{i}' = ice thickness, b_0 = constant defining the width of the wedge = b/x', x' = distance along the wedge, a = loaded length, l = characteristic length of the plate = $(Et^3/12\,\rho\mathbf{g})^{1/4}$.

Bercha and Danys used this theory to present an elastic analysis for the ice-breaking component of the ice-impact force on a conical structure.

Ralston Model

An approach for ice forces on a conical structure using plastic limit analysis has been proposed by Ralston. His results can be expressed as equations for H and V – the horizontal and vertical forces.

$$H = A_4[A_1 \sigma_{\mathrm{f}} (T_{\mathrm{i}}')^2 + A_2 \rho \mathbf{g}(T_{\mathrm{i}}')^2 d^2 + A_3 \rho \mathbf{g} T_{\mathrm{i}}'(d^2 - d_{\mathrm{T}}^2)] \qquad (4.244)$$
$$\text{due to ice breaking} \qquad \text{ice pieces sliding on cone}$$
$$V = B_1 H + B_2 \rho \mathbf{g} T_{\mathrm{i}}' \left(d^2 - d_{\mathrm{T}}^2\right),$$

where d_{T} is the top diameter and d is the waterline diameter. A_1 and A_2 are coefficients dependent on $\rho_w \mathbf{g} d^2 / \sigma_{\mathrm{f}} T_{\mathrm{i}}'$ and A_3, A_4, B_1 and B_2 are coefficients dependent on the cone angle α and friction μ. Values for the coefficients are reproduced in Fig. 4.46a–c; $\rho \mathbf{g} d^2 / \sigma_{\mathrm{f}} T_{\mathrm{i}}' = \bar{K}$ is taken in Fig. 4.46a.

(a)

(b)

(c)
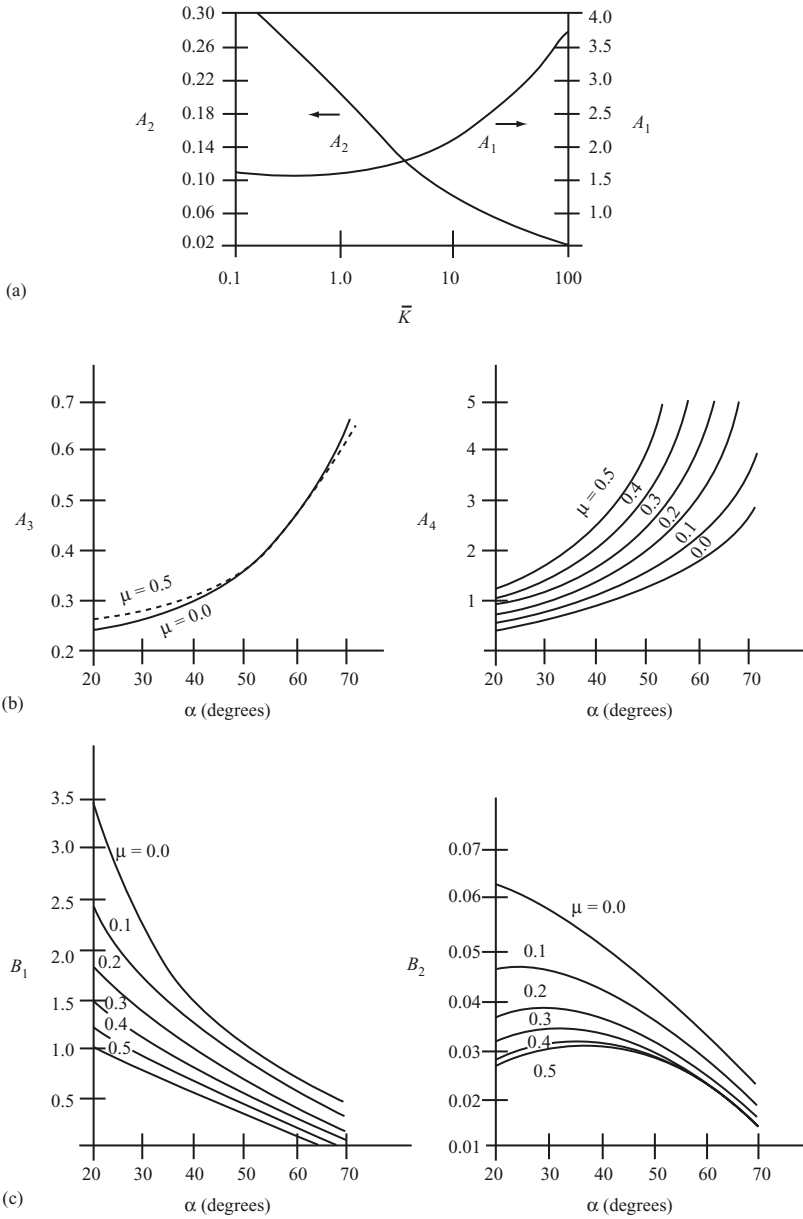
Fig. 4.46. The A and B coefficients for Ralston's plastic analysis (after Ralston [2.323–2.325])
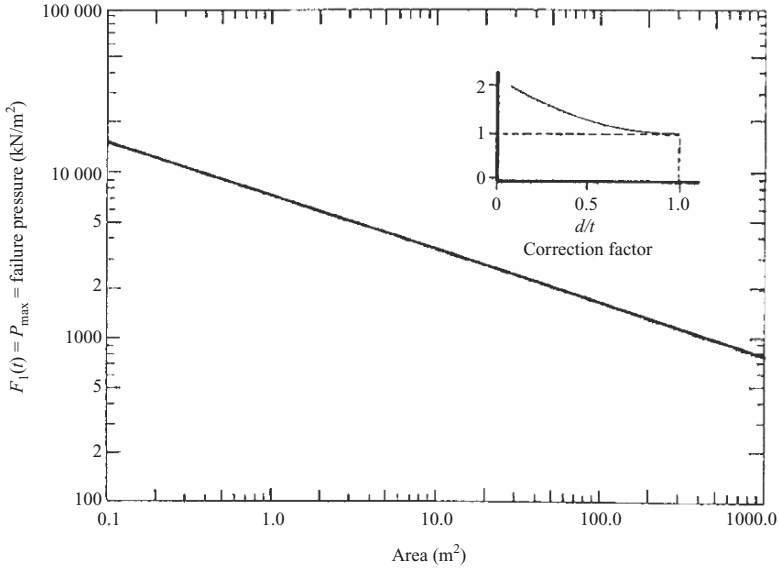
Fig. 4.47. Iyer's impact load [2.333]

Watts' Model

The numerical model is similar to the one presented by Timco in (4.241) except diameter d is not included and the shape factor S_F is defined as

$$S_F = [5(T_i'/d) + 1]^{1/2}. \tag{4.245}$$

Iyer's Model

The approach of Iyer is an empirical one and is based on the results of small indentation tests. In this approach, prior to the enveloping of the structure, contact is established locally between the ice and the structure. The local pressure will be a function of the aspect ratio d/t and the contact area. Figure 4.47 shows the curve of failure pressure versus contact area for various values of d/T_i'. An empirical relationship of the following form has been established:

$$F_1(t) = 6.8(dT_i')^{-0.3}, \tag{4.246}$$

where the product of d and T_i' is the tributary area (m) and $F_1(t)$ is the impact force in MPa.

Norwegian Model

The local impact load on the structure can be determined using the following formula:

$$F_1(t) = P_1 = 2[1 + (b_1/h)^{-0.6}][(A/A_0)^{-0.165}]\sigma_c A, \tag{4.247}$$

where b_1 = the horizontal breadth of the local load area, h = the extreme 'vertical' depth of the total area of the structure in contact with the ice, A = the local load area in cm^2, $A_0 = 1.0\,\text{cm}^2$, σ_c = the maximum uni-axial crushing strength of ice.

The effect on the pressure of the confinement of the ice or the multi-axial state of stress under which crushing takes place is represented by

$$K_\sigma = 2[1 + (b_1/h)^{-0.6}]. \tag{4.248}$$

Kato and Sodhi Model

Kato and Sodhi proposed an expression for the crushing force frequency in terms of the aspect ratio of ice contact and the speed of ice:

$$f = CV/T_i', \tag{4.249}$$

where f = frequency in cycles s^{-1}, V = ice speed in m s^{-1}, T_i' = ice sheet thickness in m, C = coefficient as a function of column diameter, d, in m, as given in Fig. 4.48b.

The impact forces measured on a single column are given below:

$$F_{\text{mean}} = \sigma_{\text{mean}} \left[5\left(T_i'/d\right) + 1\right]^{1/2} T_i' d,$$
$$F_{\text{max}} = \sigma_{\text{max}} \left[5\left(T_i'/d\right) + 1\right]^{1/2} T_i' d,$$

where T_i' = ice thickness in m, d = column diameter in m, σ_{mean} = mean crushing pressure in MN m^{-2} = $1.36\sigma_c$, σ_{max} = maximum crushing pressure in MN m^{-2} = $2.33\sigma_c$, σ_c = unconfined crushing strength of ice in MN m^{-2}.

The impact force time history is given in Fig. 4.48a.

Three-Dimensional Finite Element Method

The finite element is fully dealt with later on in this text. The following areas are to be included:

(1) Use of proper failure criteria in the model. The most appropriate to be adopted is by Frederking and Timco [2.302] and is shown in Fig. 4.49
(2) Development of finite elements with correct ice characterization, including strain rate dependence and brittle and ductile failure modes
(3) Development of ice/structure interface elements which include modelling of friction and adfreeze
(4) Incorporation of scale factor in the yield function and ice strength values
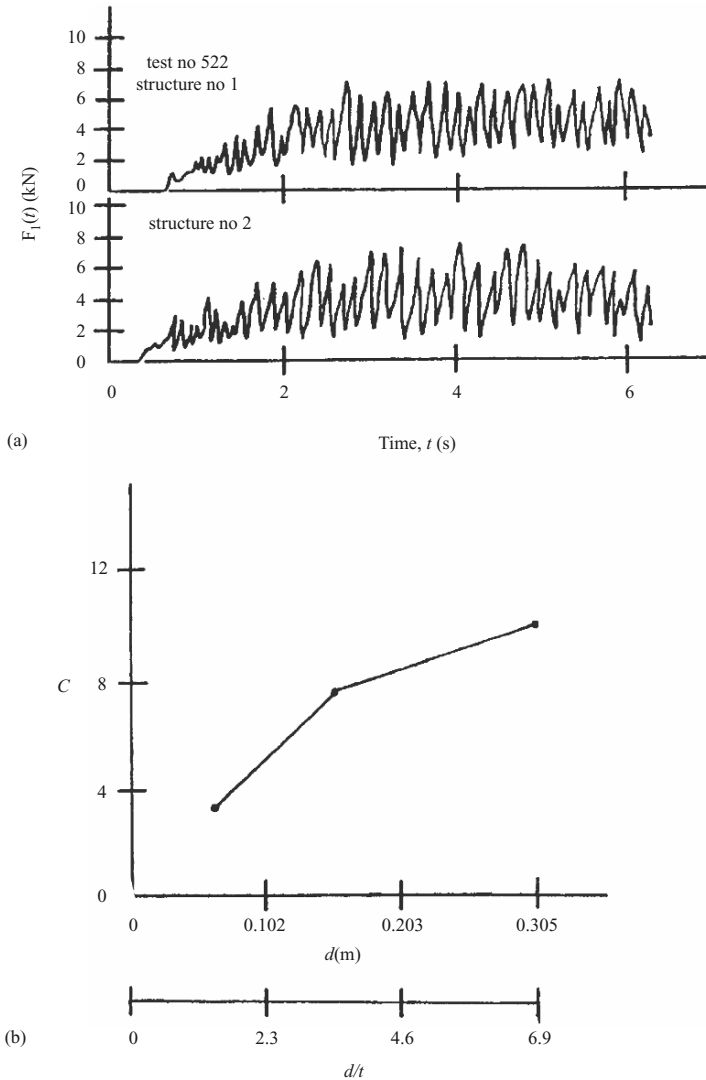
Fig. 4.48. (**a**) Typical ice-crushing force-time histories; (**b**) coefficient C versus column diameter d and aspect ratio d/t (after Kato and Sodhi [2.311])

4.10 Analysis and Modeling of Shock Response of Ceramics

4.10.1 Introduction

Ceramics are important armour materials. The high strain rate and shock response of polycrystalline ceramics is under consideration. The modeling complexity increases when the material is non-linear and the loading due to
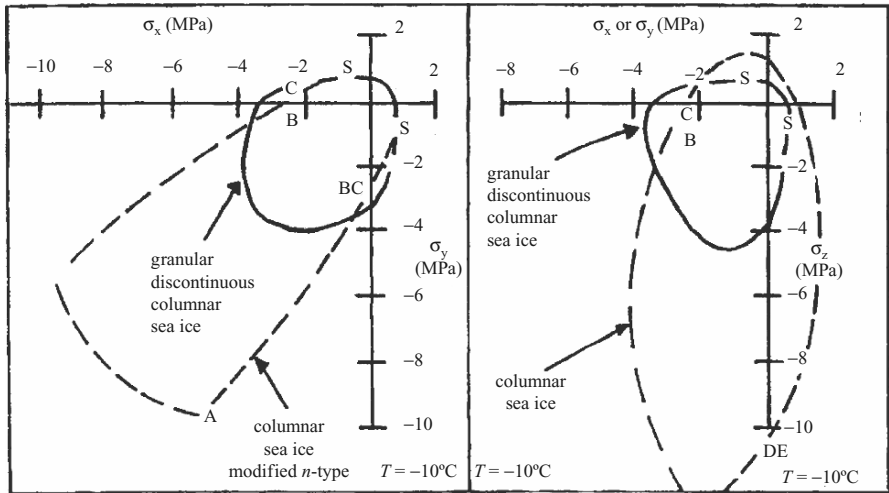
Fig. 4.49. Failure envelope for S_2 ice at two different temperatures. Outline of the failure envelope based on the present and previous tests on columnar sea ice at $\varepsilon_n = 2 \times 10^{-4}\,\mathrm{s}^{-1}$ and $T = -10°\mathrm{C}$. The *solid line* represents the extent of the failure envelope for granular/discontinuous-columnar sea ice at the same temperature and strain rate (after Frederking and Timco [2.302])

shock and impact is severe. It is important that the best ceramic model called R.G. (Rajendran-Grove) in which the following equations have been derived:

R.G. Model

(a) Elastic stress-strain for micro-cracked ceramic material

$$\sigma_{ij} = M_{ijkl}\left(\varepsilon_{kl} - \varepsilon^P{}_{kl}\right), \tag{4.250}$$

where σ_{ij} is the total stress, ε_{kl} is the total strain and $\varepsilon^P{}_{kl}$ is the plastic strain due to viscoplastic flow and pore collapse. The components of the stiffness tensor M are given by Rajendran. The elements of this stiffness matrix are degraded through a crack density parameter. The pore collapse strain components were derived from the pressure dependent yield surface of Gurson. Rajendran and Dandekar described the effect of pore collapse on the wave profiles. The strength of the intact ceramic material is described by a strain rate dependent relationship:

$$Y = A\left(1 + C\ln\varepsilon\right), \tag{4.251}$$

where A is initial yield strength, C is the strain rate sensitivity parameter and ε is the normalized equivalent plastic strain rate.

In the ceramic model, microcrack damage is defined in terms of a dimensionless microcrack density γ, where $\gamma = N^*{}_0\,a^3$. $N^*{}_0$ is the average number of microflaws per unit volume. The maximum microcrack size, a, is treated as

Table 4.16. Equation of state and material parameters

ρ (kg m^{-3})	β_1 (GPa)	β_2 (GPa)	β_3 (GPa)	G (GPa)
3,890	231	-160	2774	156

an internal state variable. Since, N^*_0 is assumed to be a constant, the increase in γ is entirely due to the increase in the crack size, a. The damage evolution law is described by:

$$a = n_1 \; C_R \left[1 - \left[\frac{G_{cr}}{G_1} \right]^{n2} \right], \qquad (4.252)$$

where C_R is the Rayleigh wave speed, G_{cr} is the critical strain energy release rate for microcrack growth, G_1 is the applied strain energy release rate, n_1 is the limiting crack growth factor and n_2 has been assumed a value of one for both tension and compression. G_{cr} is obtained from the fracture toughness K_{IC}, which is a model constant.

Recently, the following spall-parameter based tensile fracture criterion was speed introduced into the RG model: damage accumulates at the Rayleigh wave when the first principal stress exceeds the spall strength, σ_s under a triaxial tensile stress state. The modelling capability was found to substantially improve due to the inclusion of this criterion. A conventional Mie-Gruneisen equation of stat (EOS) is given in (4.253).

$$P = \left(\beta_1 \eta^1 + \beta_2 \eta^2 + \beta_3 \eta^3 \right) (1 - 0.5\Gamma\eta), \qquad (4.253)$$

where η is the volumetric strain and Γ is the Mie-Gruneisen parameter. Table 4.16 indicates the density (ρ), shear modulus (G), and EOS parameters for 99.5% alumina that were employed in the present investigation. P is a positive compressive pressure.

The RG model assumes that the ceramic material pulverizes when the γ reaches a critical value of 0.75. The strength Y_p of the pulverized material varies linearly with compressive (positive) pressure P, as $Y_p = \min [Y_{max}, \beta_p P]$, where β_p is the slope of the strength vs. pressure plot. Y_{max} is the maximum strength allowed for the confined comminuted ceramic material. An upper limit of 4 GPa was used for AD995 and β_p was assumed to be "1". This simple strength model allows the plastic strains of the pulverized elements (beneath the penetrating projectile) to build up to the critical erosion strain (150%).

4.10.2 A Comparative Study of Results

The shock response due to impact on a ceramic tile bonded with aluminum plate was modeled using spall/microcracking based damage model developed by Rajendran and Grove. The same shock model was adopted for program ISOPAR incorporating various cracking and damage criteria as stated in this

text. The data used were similar in many respects to the ones adopted by the Rajendran model. Results produced from both analyses are compared using the data given in Table 4.17. The 3D ISOPAR model adopted for the finite element analysis was carefully matched with the scanty data of Rajendran model. The results produced were plotted for axial stresses from both analyses. The other stresses along two axes could not be compared since R.G. model results were based on one dimensional model. Plate 4.1 shows relationships

Table 4.17. Finite element input data and specification

Data

– Ceramic tiles: four noded isoperimetric elements $= 210$
– Aluminum Plate: four noded isoperimetric elements $= 105$
– Bonded element is assumed to be a gap elements $= 55$, with active and passive nodes as stated in the text

Material properties:
P = density (ceramic) $= 3,890 \, \text{kg m}^{-3}$
θ = rigidity or shear modulus $= 156 \, \text{GN m}^{-2}$
n_I = limiting factor $= 1$ (tensile crack growth: RG model)
$K_{IC} > 3 \, \text{MN m}^{-2}\text{m}$
μ = dynamic coefficient of friction $= 0.45$

Aluminum plate:
Alloy ENAN 6082: T651 100 mm thick
$f_{0,2}$ = Proof strength $= 240 \, \text{N mm}^{-2}$ (0.2 proof strength)
f_u = ultimate tensile strength $= 295 \, \text{N mm}^{-2}$
A_{50} (minimum elongation) $= 7^3$

Modulus of elasticity, $E = 70,000 \, \text{N mm}^{-2}$
Shear modulus, $G = 27,000 \, \text{N mm}^{-2}$
Poisson's ratio, $v = 0,3$;
Coefficient of linear thermal expansion, $a = 23 \times 10^{-6}$ per °C
Unit mass, $\rho = 2,700 \, \text{kg m}^{-3}$

Loading projectile
A30 calibre armour (Plate 4.1)
V = Velocity $= 890 \, \text{m s}^{-1}$ (minimum time $> 3.0 \, \mu\text{s}^{-1}$)
V_{max} = maximum higher velocity $= 1.943 \, \text{km s}^{-1}$
V_{min} = minimum velocity $= 0.083 \, \text{km s}^{-1}$
No: existing flaws/volume $= 2 \times 10^{11} \, \text{m}^{-3}$ throughout

Note: A reference is made to the analysis and computer program ISOPAR given in this text. The cracking model and subroutines adopted are on 3D, completely different from the RG model based on one dimensional analysis. The ceramic target tiles $2 \, \text{m} \times 1 \, \text{m} \times 0.05 \, \text{m}$ bonded to 100 mm thick aluminum plate are subjected to the predicted R.G. shock model (Fig. 4.50a, b). Figure 4.50b, c shows the finite element mesh generation schemes based on isoperimetric approach. The following data have been used for the program ISOPAR (Table 4.17)

(a) Bonded Ceramic Plate

Aluminum plate 100 mm thick

(b) Finite Element Mesh Scheme
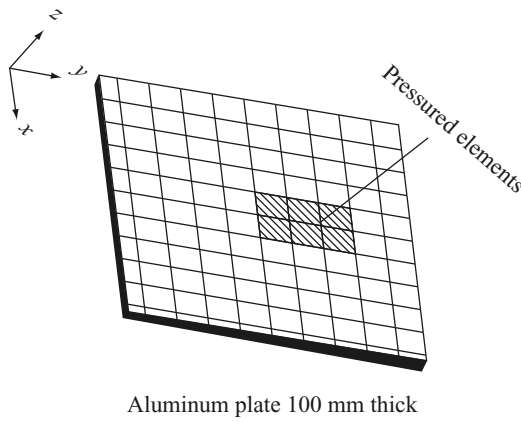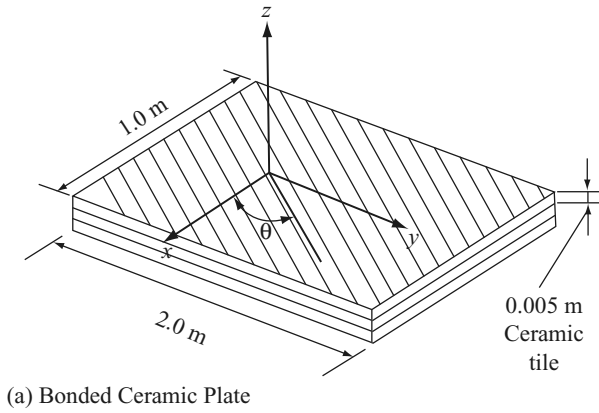
(c) Initially deformed Aluminum Plate
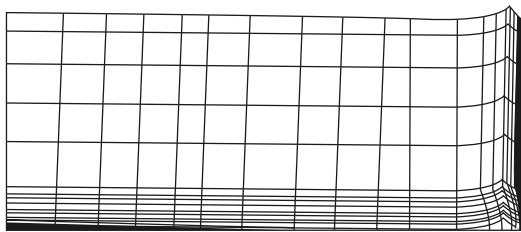
Fig. 4.50. Ceramic target tile with aluminum plate bonded

of velocity versus time and axial stresses versus time. These results were fully collaborated. The 3D finite element crack model is in full agreement with the one-dimensional model one given by the R.G. analysis.
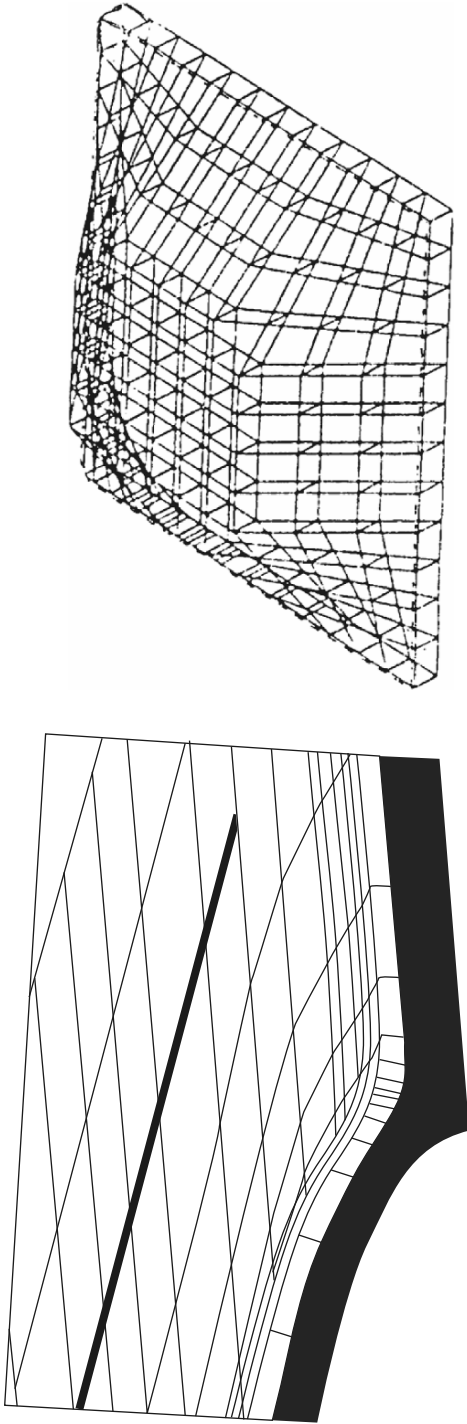
(a) Deformed aluminium bonded plate with damage profile

(b) Completed mesh deformation with damage of the ceramic plate

Fig. 4.51. Deformed and damaged plate
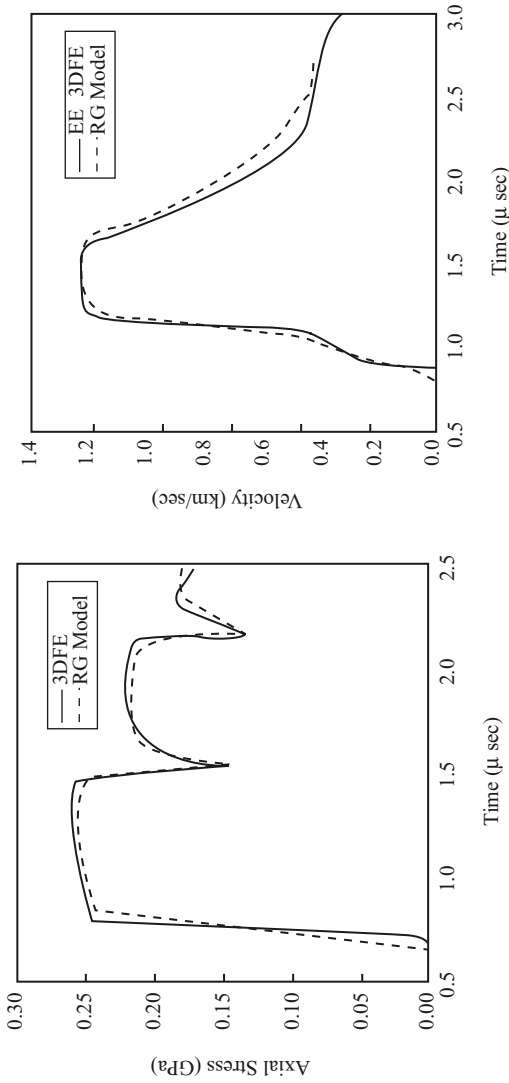
Fig. (1) Stress – Time Relation 83 m/s

Fig. (2) Velocity – Time Relation 1943 m/s

A schematic of 30 Caliber Armor – Piercing Projectile
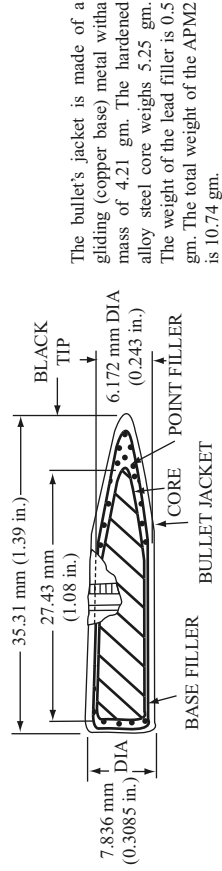
The bullet's jacket is made of a gliding (copper base) metal with a mass of 4.21 gm. The hardened alloy steel core weighs 5.25 gm. The weight of the lead filler is 0.5 gm. The total weight of the APM2 is 10.74 gm.

Plate 4.1. Stress and velocity time relations

4.11 Shock Analysis Involving Active Materials

4.11.1 Introduction

This section discusses application of active materials for shock and impact energy absorption and what methodology is needed to its control. Possibilities exist for employing piezoelectric materials in which shock and impact characteristics become controllable. The possibility is to control friction between elements of the structures or within structural elements which make it possible to control the structure of the impacting system. Alternatively shock energy can be converted into electrical energy and dissipate it into the piezomaterial with a provision that damping material may alter. Composite structures containing piezoelectric material and electrorheological materials are the relevant case for such a situation. As stated in dynamic cases, the coefficient of impact restitution "e" may be controlled by changing the phase λ of the oscillation.

4.11.2 Method of Analysis

The third method possibility is to alternate the strength of the electric field, in the systems, which are using an electromagnetic fluid for shock energy dissipation. Composite structures containing piezomaterial and electrorheological fluids here allow us to design shock and impact energy absorbing systems with self-tuning properties and functioning on internal sources of energy. The principle scheme is shown in Fig. 4.52.

The structure consists of piezomaterial and electrorheological fluid under it. The electric charge is generated at the shock tot the piezomaterial and the voltage occurs between electrodes. Under the action of the electrical field generated, the viscosity of the electrorheological fluid changes alternating the dissipation of shock energy. Additional parallel electrical circuits with variable parameters make it possible to set the necessary dissipation parameters.
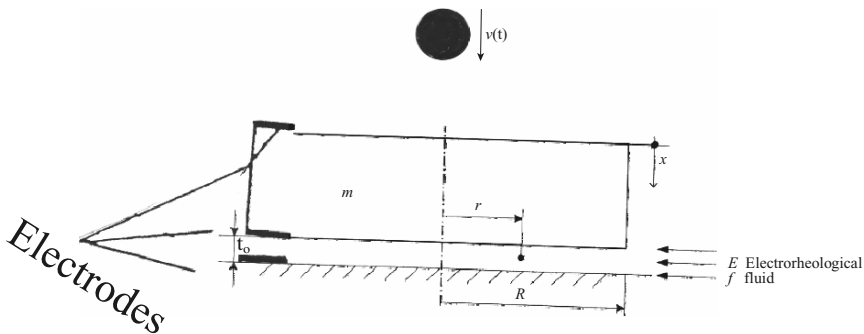
Fig. 4.52. Composite structure of active materials

Bansevicius. R and Tolocka. T presented a paper [under shock impact VIII (2004) WIT press] in which a cylindrical body is falling on to the fixed surface with radius "R". The surface is covered by a thin layer of electrorheological fluid under the action of an electrical field. Let the fluid layer have a thickness t_0. It is assumed that as soon as the body is in contact with the fluid the squeeze film damping process starts action. The fluid pressure P_f developed can be represented by

$$P = P_\eta(r) + P_1(r) + P_{ER}(r), \qquad (4.254)$$

where $P_\eta(r)$, $P_{ER}(r)$, $P_i(r)$, are pressure contributors due to viscosity, electric field effects and fluid inertia, and r is the radius. Then acting force is:

$$F = 2\pi \int_0^R P(r)dr. \qquad (4.255)$$

Viscous pressure process is described in the cylindrical coordinate system, whose centre coincides with disc centre, which is assumed fixed. The radial flow than can be approximated by the equation for laminar flow q in wide channel

$$q(r) = \frac{b(r).h(x)^3}{12\eta} \cdot \frac{\partial P_\eta}{\partial r}, \qquad (4.256)$$

where P_η is the pressure drop to the fluid viscosity η, $b(r)$ and $h(r)$ are the channel; width and height. The equation is valid when $b(r) \gg h$ for the radial squeeze flow

$$b(r) = 2\pi r; \qquad h(x) = k_o - x; \qquad q(r) = \pi r^2 x. \qquad (4.257)$$

Substituting (4.251) to (4.256) and integrating it with respect to r one obtains

$$P_\eta(r) = \frac{6\eta r^2}{(t_o - x)^3} \dot{x}. \qquad (4.258)$$

The pressure component related to the fluid inertia is equal to

$$P_i = \frac{\rho r^2}{4} \left(\frac{\ddot{x}}{(x_o - x)} + \frac{\dot{x}^2}{(x_o - x)^2} \right), \qquad (4.259)$$

where ρ is fluid density.

It is evident that P_I consists of two components, one of which is related to the fluid acceleration and second to the momentum flux.

Let the electrorheological fluid behaviour is described by Bingham plastic. Than fluid stress is equal to

$$\sigma = \alpha \overline{E}_f^2 + \eta \frac{\partial^2 u}{\partial r \partial t}, \qquad (4.260)$$

where α is the electrorheological fluid constant, $\overline{E}_f^2$-electrical fluid strength generated piezoactive material and u is the velocity of the fluid particle.

When the fluid pressure exchange due to the electrical field in radial direction is

$$\frac{\partial P_{ER}}{\partial r} = \frac{\sigma_y}{t_o - x}. \tag{4.261}$$

Substituting (4.260) into (4.261) one obtains

$$\frac{\partial P_{ER}}{\partial r} = \frac{\alpha \overline{E}_f^2}{t_o - x} + \eta \frac{1}{t_o - x} \cdot \frac{\partial^2 u}{\partial r \partial t}. \tag{4.262}$$

Neglecting second derivatives and taking into account that various properties of electrorheological fluid is defined by (4.256) and (4.258) one gets from (4.262)

$$P_{ER} = \frac{r}{t_o - x}(\alpha \overline{E}_f^2). \tag{4.263}$$

Full resistance force acting due to the falling body is defined F, substituting (2.258), (4.259) and (4.263) into (4.254)

$$F = 2\pi \int_0^r P(r) r dr = \frac{3\eta\pi\dot{x}}{(t_o - x)^3} \frac{R^4}{1} + \frac{\pi\rho}{8} \cdot R^4 \frac{1}{(t_o - x)} \left(\ddot{x} + \frac{\dot{x}^2}{t_o - x} \right)$$

$$+ \frac{2}{3} \pi \frac{R^3}{t_o - x} \cdot \alpha \overline{E}_f^2. \tag{4.264}$$

Let the falling solid body has mass m. Its motion in the fluid until it contacts with foundation is described by the equation

$$m\ddot{x} = -F + m\mathbf{g} \tag{4.265}$$

$$\left[m + \frac{\pi R^4}{8(t_o - x)}\rho \right] \ddot{x} + \frac{3\pi R^4}{(t_o - x)^3} \eta\dot{x} + \frac{\pi R^4}{8(t_o - x)^2} \rho\dot{x}^2 =$$

$$-\frac{2}{3} \pi \frac{R^3}{t_o - x} \overline{E}_f^2 + m\mathbf{g}, \tag{4.266}$$

with initial conditions $x = t_o$ and $\dot{x} = \dot{x}_o = \dot{t}_o$.

When body contacts with foundation velocity $\dot{x}_c$ it moves upwards in accordance to the equation

$$\left[m + \frac{\pi R^4}{8(t_o - x)}\rho \right] \ddot{x} + \frac{3\pi R^4}{(t_o - x)^3} \eta\dot{x} + \frac{\pi R^4}{8(t_o - x)^2} \rho\dot{x}^2 =$$

$$-\frac{2}{3} \pi \frac{R^3}{t_o - x} \overline{E}_f^2 - m\mathbf{g}, \tag{4.267}$$

with initial conditions $x = 0$ and $\dot{x} = \dot{x}_c$.

Solutions of (4.266) and (4.267) allow us to evaluate efficiency of damping by ratio:

$$K = \frac{\ddot{x}_0^r}{\ddot{x}_0},\tag{4.268}$$

where $\ddot{x}_0^r$ is the velocity of the body at the moment of leaving the electrorheological fluid after recoil.

The composite structures consisting of piezomaterials and electrorheological fluids provide a possibility to design shock and impact energy dissipation systems with self tuning properties and functioning without any external energy source.

4.11.3 Input Data

80 mm cylinder with weight 350 g with t = thickness = 0.188 mm shockwave – mach 1.2 in air Loading Ms = 1.2 shockwave force $\approx$ 400 N

$\dot{x}$ = speed 1.2, shockwave = 0.408 mm μs^{-1}

Distance x between the frontal stagnation point and the transition point ranges from 19 to 23 mm

Time t (ms) = 0 − 0.8

Pressure increment (KN m^{-2}) ranges from 0 to 150 elements (4NODED) for finite element = 350 for solid

$\qquad\qquad$ = 150 for fluid

R = 400 mm, R = 800 mm

4.11.4 Results

The existing analysis gives pressure – time curve and this curve is compared with 3D finite isoparametric (program ISOPAR) element analysis. They are shown in Fig. 4.53 and are in good agreement. The theory and results produced by Bansevicius. R and Tolacka. T. This subject has been validated using 3D finite element technique and computer program ISOPAR.

4.12 Shock Impact Load on the Container

4.12.1 Introduction

Based on BS3951, the dimension and ratings are assessed the reactions and loads in Tables 4.18 to 4.20 shall be treated as nodal loads for the finite element analysis:

Dimensions and Ratings

External dimensions

The overall external dimension and tolerance of the containers covered by this International Standard are those established in ISO 668 and ISO 1161. No part of the container shall project beyond these overall dimensions.
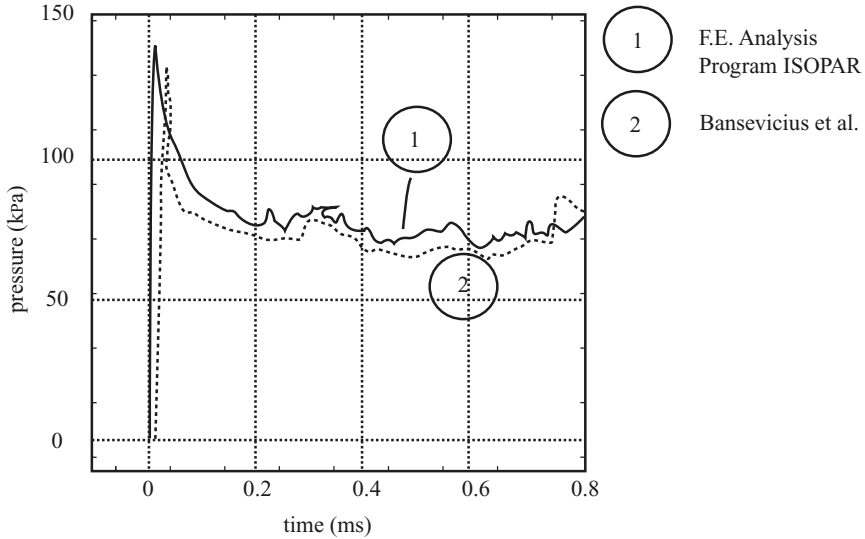
Fig. 4.53. Pressure history of individual pressure transducers

Internal dimensions

Internal dimensions are not specified.
Ratings

The value of the rating R, being the maximum operating gross weight of the container, are those given in BS 668.

$$R = P + T, \tag{4.269}$$

where P is the maximum operating payload and T is the tare weight. The symbol R denotes the maximum operating gross weight of the container.

Tables 4.18–4.20 indicate the container has to pass through several types of applied loading prior to the approval and application of the shock impact load. A reference is made to the container introduction and structural detailing in Chap. 2, with particular detail given in Tables 2.15–2.17 and Plate 4.2 the common size for the analysis of the container is maintained as $2.4 \, \text{m} \times 2.10 \, \text{m} \times 2.10 \, \text{m}$. The dimension of the fork lift pockets of the container is given in Plate 4.3. Table 4.20 gives the dimensions and ratings are given by BS3951 which are produced here for comparison.

4.12.2 Shock Impact Load Analysis of Rectangular Container

(A) Mathematical model for the rectangular container (originally developed by Borosevas. v. and Volkovas. v. reported in structures under shock and impact VI, p. 308–313).
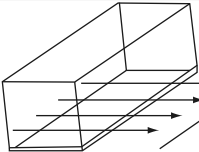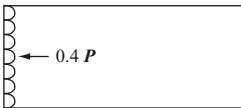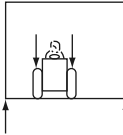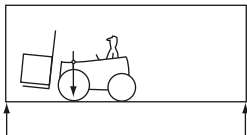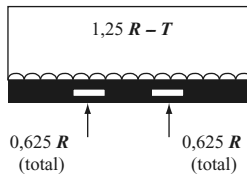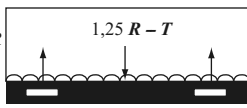
Table 4.18. Diagrammatic representation of capabilities appropriate to all containers covered by this international standard, except where otherwise stated

Notes: 1, The externally applied forces shown below are for one end or one side only. The internal loads are for the whole container. 2, The diagrams in this annex correspond to tests described in 5.2 to 5.12 only where marked

A reference is made to Plate 4.3 while assuming the container of a rectangular closed shape of a geometry Ω $(x,\ y,\ z)$. Symbols have been changed to suit the nomenclature adopted in this text to be finally used for the finite element analysis is on the lines suggested in this text throughout. The container is assumed to be filled in with solidified substance.

Table 4.19. Loads on end and side elevations

	End elevations	Side elevations
17	Roof loadings-Test No. 6 300 kg ↓ 660 lb	300 kg ↓ 660 lb
18	Internal loadings	0.6 **P**
19		Strength on end load Test No. 5 ← 0.4 **P**
20	Wheel loadings Test No. 7 2 × 2 730 kg / 2 × 6 000 lb	
21	Optional features Test No. 10 — Applicable to 1CC, 1C, 1D containers when fitted with fork pockets	1,25 **R – T** 0,625 **R** (total) 0,625 **R** (total)
22	Test No. 11 — Applicable to containers when fitted with grappler arm lift positions	0,312 5 **R** per side 1,25 **R – T** 0,312 5 **R** per side

Parameters:
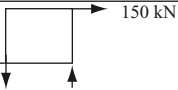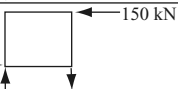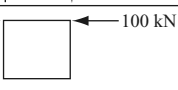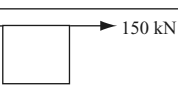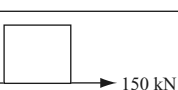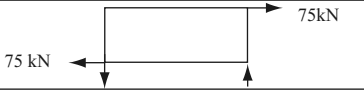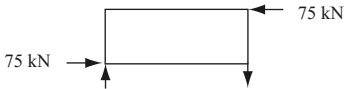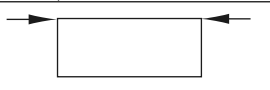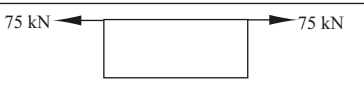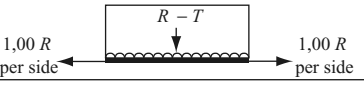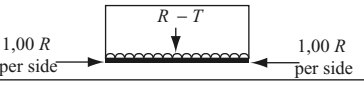
Height $= h$
Width $b = h$
Length $L = 2h$
Shear Modulus $= G$
Poisson's ration $= \nu$

Table 4.20. Additional loading cases

	End elevations	Side elevations
5	Rigidity (transverse) – Test No. 9 150 kN / 150 kN	
6	Rigidity (transverse) – Test No. 9 150 kN / 150 kN	
7	100 kN / 100 kN Lashing/securement	Applicable to 1AA, 1A, 1BB, 1B, 1CC and 1C containers only
8	150 kN / 150 kN Lashing/securement	
9	Lashing/securement 150 kN / 150 kN	
10	Lashing/securement 150 kN / 150 kN	
11	Rigidity (longitudinal) – Test No. 10	75 kN / 75kN
12	Applicable to 1AA, 1A, 1BB, 1B, 1CC and 1C containers only	75 kN / 75 kN
13	Lashing/securement (This type of loading is inadmissible except as applied in 3A)	
14	Lashing/securement	75 kN / 75 kN
15	Restraint (longitudinal) – Test No. 4 Applicable to all sizes.	$R - T$ 1,00 R per side / 1,00 R per side
16		$R - T$ 1,00 R per side / 1,00 R per side

Note: $-1\,\text{kN} \approx 100\,\text{kgf}$ (within 2%)

The theory developed here is by the authors are based on Hamilton principle.

Let u, v and w shall be the functions to suit and fit the boundary conditions of the container. The Standards Hamilton Principle is adopted to determine
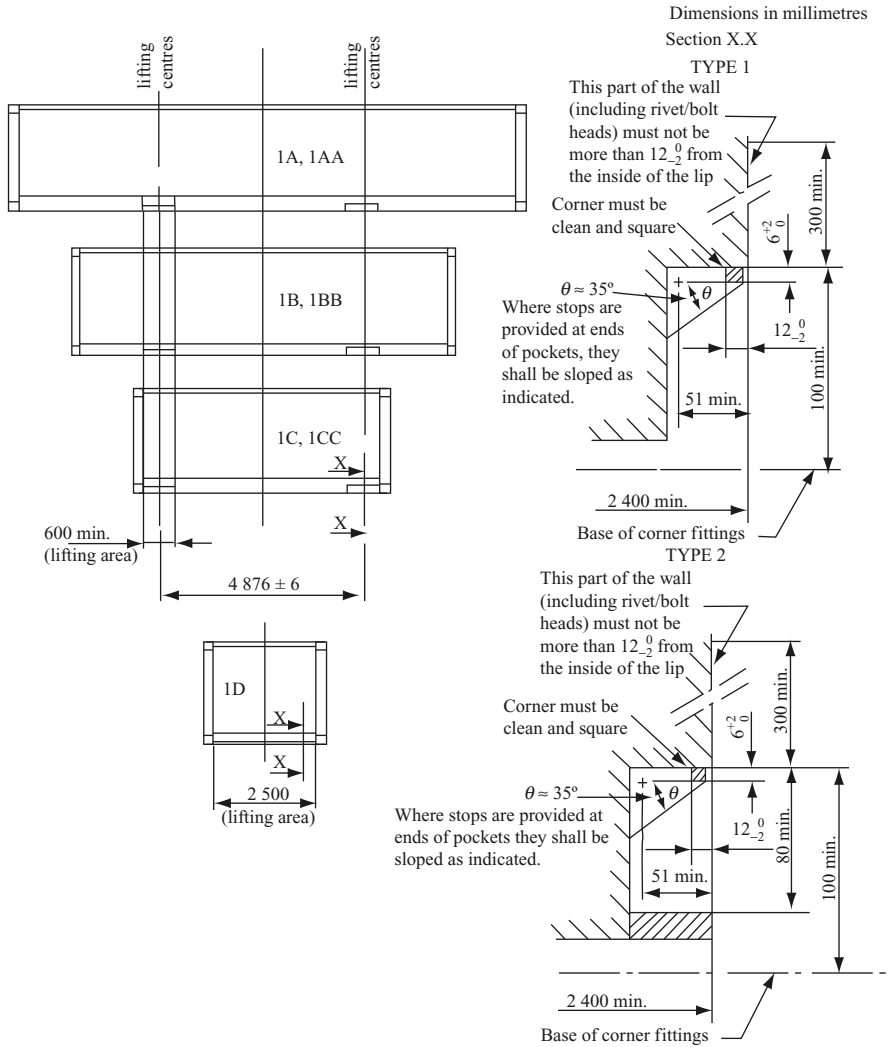
Plate 4.2. Dimensions of grappler arm lifting areas

the following shockwave from the following equation:

$$I_{F(shock)} = m\ddot{\delta} + (C_T + C_P)\,\delta. \tag{4.270}$$

Such that C_T and C_P are coefficients of elasticity and plasticity respectively. The mass "m" can be written as:

$$m = P \iiint\limits_{vol} (U^2 + V^2 + W^2)\,dxdydz. \tag{4.271}$$

Section X-X
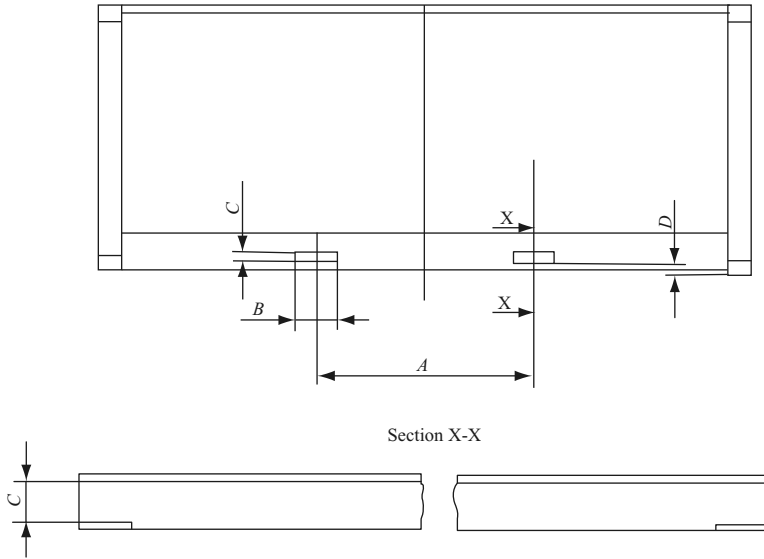
DIMENSIONS OF FORK LIFT POCKETS

Container	Dimensions							
	mm				in			
	A	B	C	D	A	B	C	D
1CC 1C	2 050 ± 50	355 min.	115 min.	20 min.	81 ± 2	14 min.	4 1/2 min.	0.8 min.
1D	980 ± 50	305 min.	102 min.	20 min.	35 1/2 ± 2	12 min.	4 min.	0.8 min.
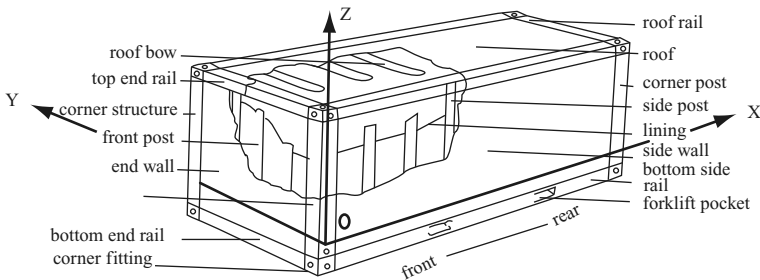
Plate 4.3. Provisions for handling by means of fork lift trucks

The values of C_T and C_P have been computed by Dorosevas. V and Voekovos (Structures and Shock and Impact, vol. VI.

The external forces on the surface part along the integration area can be computed from *Dorosevas.v and Volkovas.V*

$$I_{F(shock)} = \iint_s (F_1 U + F_2 V + F_3 V)\, ds, \tag{4.272}$$

Table 4.21. Dimensions and ratings

Ratings. For freight containers having the dimensions given in 2.1 the ratings shall be:

Designation	Ratings
	kg
A	30,480
B	25,400
C	20,320
D	10,160
E	7,110

Dimensions

Designations	Height mm	Width mm	Length mm
A	+3 2,435 −2	+3 2,435 −2	+2 200,000 −8
B	+3 2,435 −2	+3 2,435 −2	+0 9,125 −10
C	+3 2,435 −2	+3 2,435 −2	+3 6,055 −3
D	+3 2,435 −2	+3 2,435 −2	+1 2,990 −4
E	+0 2,100 −5	+0 2,100 −5	+0 2,400 −5

Note: 1. Freight containers designated A, B, C, D and E in the above table are those designation 1A, 1B, 1C and 2B respectively by the International Organisation for Standardisation

where S denotes the surface integration area. F_1, F_2 and F_3 are projections of the respective surface forces along the coordinate axes.

Analysis of the reactions of elastically plastic substance to shock impact in closed container (structures under shock and impact No VI). The shock impact load $I_{F(shock)}$ from (4.272) can occur due to explosion or direct falling. From explosion, the shock can also be directly computed by:

$$I_F = r \cdot f\left(\frac{r}{R}\right), \tag{4.273}$$

where r = radius of the charge, R = distance from the centre of the charge to the level of the object.

If the yield of the bomber charge is Wu, the value of $r = \sqrt[3]{Wu}$.   (4.274)

Using the finite element method, the external forces F_1, F_2 and F_3 as suggested by Dorosevas.V and Volkvas.V can be computed along x, y, z axes as:

Then the total pressure from shock impact P from $I_{F(shock)}$ shall be

$$P = \sqrt{P_{xn}^2 + P_{yn}^2 + P_{zn}^2}.$$ (4.275)

These values have now to be compared with the 3D finite element analysis program ISOPAR.

4.12.3 Data and Numerical Calculation (a reference is to be made to Tables 4.18 and 4.19)

Data:

L = 12.19 m

b = 2.435 m

h = 2.435 m

W = 30,480 + 2,730

　　= 33,210 kg

R = P + T = W = 33,210 kg

　　　　= 33,210 × 9.0856 × 10⁻³ KN

　　　　= 301.733 KN

h = 9 or 18 m

Table 4.22 shows the general formulation
　　　　　　　　Transverse　Longitudinal

H = horizontal force =   150 KN, 75 KN

H_1 = thrust per side = 1.0 ×R = 301.733 KN

R/2 = top lift at corners = 0.625R at support

　　　　　　　= 0.625 × 301.733

　　　　　　　= 188.5836 KN

t = thickness 87.5 mm

S = strength on end load = 0.4 P = 12,192 KN

θ = the angle of inclination to the horizontal

　= 20°, 40°, 60°, 80°

μ = coefficient of friction

Table 4.22. General formulation for simple drop weight mechanics

Here only simple drop weight mechanics for the amount of energy absorbed is discussed. The energy absorbed for a lid-edge impact is calculated. Inertia load acceleration and spigot forces are demonstrated. The spigot horizontal and vertical forces, H and V respectively, can be shown to be:

$$H = F_n \cos \alpha' + F_s \sin \alpha' \tag{a}$$
$$\overline{V} = F_n \sin \alpha' + F_s \cos \alpha'$$

Where friction is involved, $F_s/F_n = \mu$, and the relation between V and H will become

$$\overline{V} = [(\tan \alpha' - \mu)/(1 + \mu \tan \alpha')]H \tag{b}$$

The rigid body mechanics is given in this section for evaluation or rotational velocity and the energy absorbed in the knock back. Assuming the container velocity at impact is $\overline{V}_0 = \ddot{x}$, then the energy absorbed in the knock back, E_{ha}, can be evaluated for various rotational velocities and boundary condition as

$$E_{\text{ha}}[r_0^2/(r_0^2 + r^2)] \text{ with no friction} \tag{c}$$
$$E_{\text{ha}}r_0^2\{[r_0^2 + r^2 - \mu^2(r^2 + h^2)]/(r_0^2 + r^2 - \mu \, \text{rh})^2\} \text{ with sliding friction} \tag{d}$$
$$E_{\text{ha}}[(r_0^2 + h^2)/(r_0^2 + r^2 + h^2)] \text{ with no sliding} \tag{e}$$

The corresponding rational velocities are

$$\dot{x}r/(r_0^2 - r^2) \tag{f}$$
$$\dot{x}(r - \mu h)/(r_0^2 + r^2 - \mu rh) \tag{g}$$
$$\dot{x}r/(r_0^2 + r^2 + h^2) \tag{h}$$

The finite element analysis will be discussed later in this text. In addition, the classical impact mechanics is given in this chapter.

4.12.4 Drop Analysis Using 3D Dynamic Finite Element Analysis

The dropped analysis is an impact analysis of the container. The attitude for the drop is generally decided when the container has been checked for top and bottom corner fillings, stacking and top lift and lashing for securement. The altitude for the drop shall be given in which the centre of gravity of the container was over the line of impact thus ensuring that the entire energy is not dissipated in producing damage to the container. The height for the side edge and lid corner is no more than 9 and 18 m respectively. These heights are laid down by the sea - going container loaded vessels and various post authorities.

Plate 4.4 shows typical finite element mesh generation of the container the most sophisticated container mesh involving container involving container internally is also shown in Fig. (b). After the container dropped for h = 9 m,
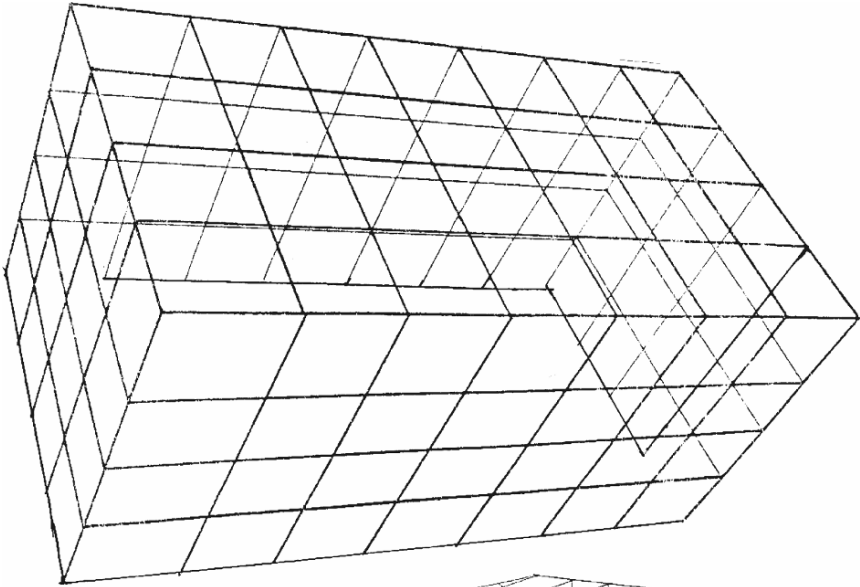
(a) Finite element mesh
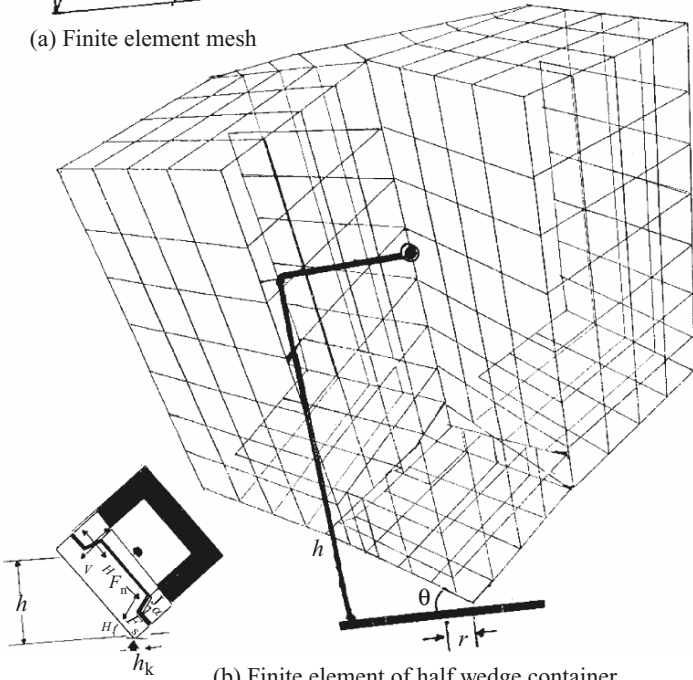
(b) Finite element of half wedge container interior

Plate 4.4. 3D dynamic finite element

(a) 3DFE Force – Time Reduction

(b) Energy absorbed versus
inclination
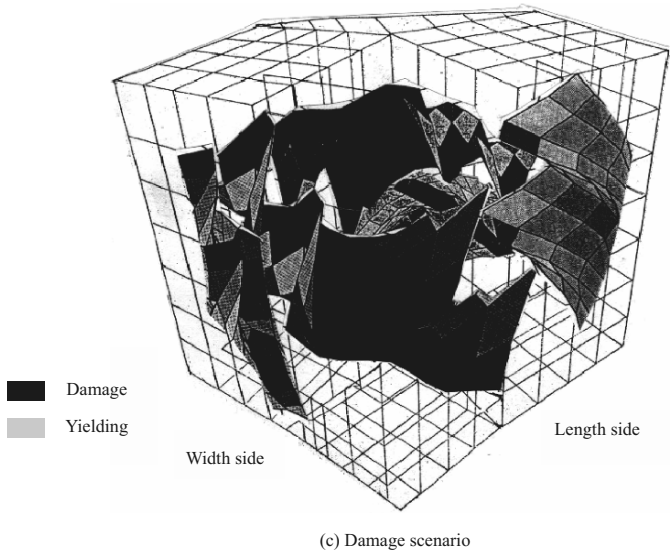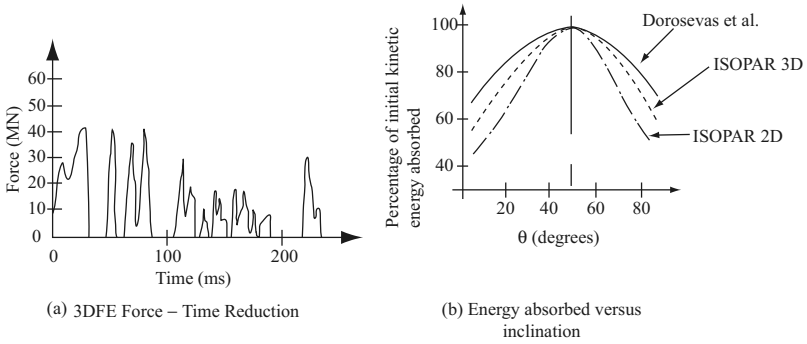
(c) Damage scenario

Plate 4.5. Container damage scenario

the results from the program ISOPAR is translated into force – time relation
is plotted in Fig. (a). Plate 4.5 from the values of F_x, F_y, F_z, computed
Dorosevas.V and Volksova.V analysis is the energy absorbed relationship
with θ is superimposed on the same figure apart from small deviations the
results are good agreement with each other. These results are plotted relating
energy absorbed against the inclined angle θ. Plate 4.5 – shows these results
together with the damage scenario given in Fig. (c) which is based on program
ISOPAR.

4.13 Shock Load Capacity of Anchor in Concrete

4.13.1 Introduction

Advances in drilling techniques have contributed significantly to the widespread use of post-installed anchors. Rotary-impact drills (rotary hammers) are most often used for anchoring applications. Diamond core drills are used less frequently, although recent advances in weight reduction, slurry-capture, and dry coring have made these systems more attractive for anchoring applications where existing reinforcement is expandable. In some cases, rock drills are used for large anchors. Details of the working principles of the metal expansion anchor are elaborated in great detail by ASCE 1997. They classified two types by Eligehausen as:

(a) Torque – controlled expansion anchors
(b) Displacement controlled expansion anchors

4.13.2 Torque Controlled Expansion Anchor

Torque-controlled expansion anchors are installed by drilling a hole, removing drilling dust and debris, inserting the anchor into the hole and securing it by applying a specified torque to the bolt head or nut with a torque wrench. Once the nut or bolt achieves bearing against the base material, the further application of the torque draws the cone at the embedded end of the anchor up into the expansion sleeve (or expansion segments), thereby expanding the expansion element(s) against the sides of the drilled hole. The ensuing frictional resistance places the bolt in tension. The compression forces acting on the concrete due to the dilatation of the expansion elements are known as the expansion forces. If the concrete around the anchor is continuous and undisrupted by cracking or proximate edge, the resulting stresses are distributed roughly symmetrically around the anchor perimeter. In the past, torque – controlled anchors were occasionally referred to as "force-controlled" expansion anchors because the torque generates a tensile force in the anchor. However, "torque-controlled" is a better descriptor for the working principle of the anchor since a prescribed torque is used to set the anchor. Torque also serves as a way of checking the installation of torque-controlled expansion anchor. An anchor that was not set correctly will rotate before achieving the prescribed torque. Rotation is normally prevented by deformations in the anchor element contacting the sides of the hole. Oversized holes or local defects in the concrete may reduce their effectiveness and allow the anchor to spin, thereby preventing attainment of the required expansion force.

4.13.3 Displacement Controlled Expansion Anchors

Displacement controlled expansion anchors usually consist of an expansion sleeve and a conical expansion plug, whereby the sleeve is internally threaded

to accept a threaded element (bolt, rod, etc.). They are set via the expansion of the sleeve as controlled by the axial displacement of the expansion plug within the sleeve. In the common displacement controlled anchor type as, known as a drop-in anchor, this is achieved by driving the expansion plug into the sleeve with a setting tool and a hammer. Like torque-controlled expansion anchors, displacement-controlled expansion anchors transfers external tension loads into the base material via friction and, in the zone of the localised deformation, some degree of mechanical interlock.

In the anchor shown in Plate 4.6, the magnitude of the expansion force depends on the degree of sleeve expansion, the gap between the anchor and the sides of the drilled hole, and the deformation resistance of the concrete. The initial expansion force generated by a fully installed displacement-controlled anchor of this type is typically considerably greater than that created by the torque-controlled expansion anchor of a similar size.
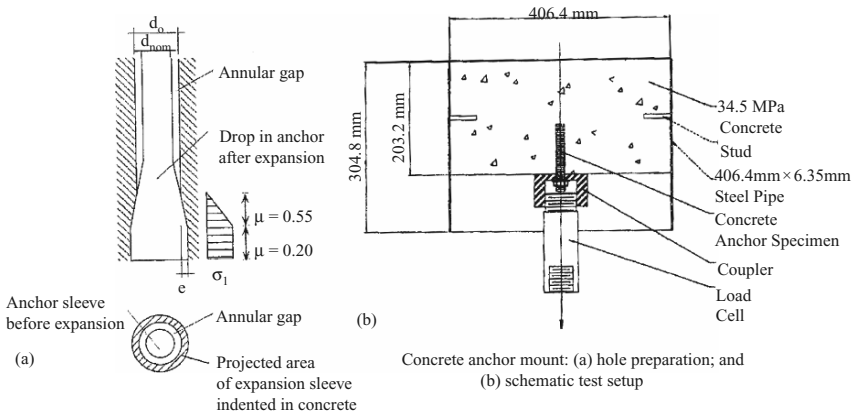
Plate 4.6 Drop in Anchors in non-cracked concrete

Drop in Data

$19\,\mathrm{mm} \times 50.8\,\mathrm{m}$ Grade B
Specified Torque $= 110\,\mathrm{Nm}$
$F_y =$ yield capacity $= 414\,\mathrm{MN/m^2}$
$F_u =$ ultimate strength $= 540\,\mathrm{MN/m^2}$
$F_{uc} =$ Concrete capacity design strength $= 58\,\mathrm{kN}$
$d_i =$ Initial Embedment depth $= 75\,\mathrm{mm}$
$f_{cu} =$ Concrete compressive strength $= 34.5\,\mathrm{MN/m^2}$

Plate 4.6. Shock analysis of drop in anchors

4.13.4 Shock Load Impact Analysis of Expansion Anchors

The proper anchoring of steel studs utilises the tensile capacity to create a high capacity for the effective blast remedial system. The Hilti HDI/9 mm dropin anchor 12 L 12 steel has a yield capacity $F_y = 414\,\mathrm{N\,mm^{-2}}$ and an ultimate limit strength $F_u = 538\,\mathrm{N\,mm^{-2}}$. Shock load-deflection time dependent analysis was carried out on the anchor shown in Plate 4.7. The input data was adopted for dropin anchor shown in Plate 4.6. The F.E static and F.E shock analysis have been compared for the time and zero time deflection against normal and shock loads. The relations indicate that these anchors have been extremely stressed due to shock loads more than the conventional loads.

4.14 Concrete Structures Subjected to Fragment Impacts: Dynamic Behaviour and Material Modelling

4.14.1 Introduction

The principle aim of this section is to improve the current knowledge of behaviour of concrete structures subjected to blast and fragment impacts. The main focus is on numerical modelling of fragment impacts on plain concrete members. In additions, experiments in combination with numerical analyses where conducted to deepen the understanding of concrete subjected to blast wave and fragment impacts. In experiments, both multiple and single fragments where shot at thick concrete blocks. To capture response of the concrete material behaviour, both the fragment impacts and the blast wave must be taken into account. The damage in the spalling zone is caused by fragment impacts, whereas the major stress wave that propagates is caused mainly by the blast wave.

To predict the penetration depth of the fragmented impacts, spalling and scabbing in concrete with numerical methods, material models that take into account the strain rate effect, large deformations and triaxail stress states are required. The depth of penetration depends mainly on compressive strength of the concrete. However, to model cracking, spalling and scabbing correctly in concrete, the tensile behaviour is very important. The bi-linear softening law and a strain rate law were implemented in the model. By parametrical studies it was shown that the tensile strength, fracture energy and the strain rate law influenced cracking and scabbing of concrete. By implementing the bi-linear softening law and modified strain rate dependent law, the results of the numerical analysis were improved for projectile and fragment impacts on concrete. The design bomb assumed is 250 kg with 50% by weight TNT that burst freely outside at a distance of 5 m during free pressure release. The detonation of the bomb, causing fragment impacts, can strike a concrete structure. Hence it is vital to examine also the dynamic behaviour of such structures subjected to blast and fragment impacts.
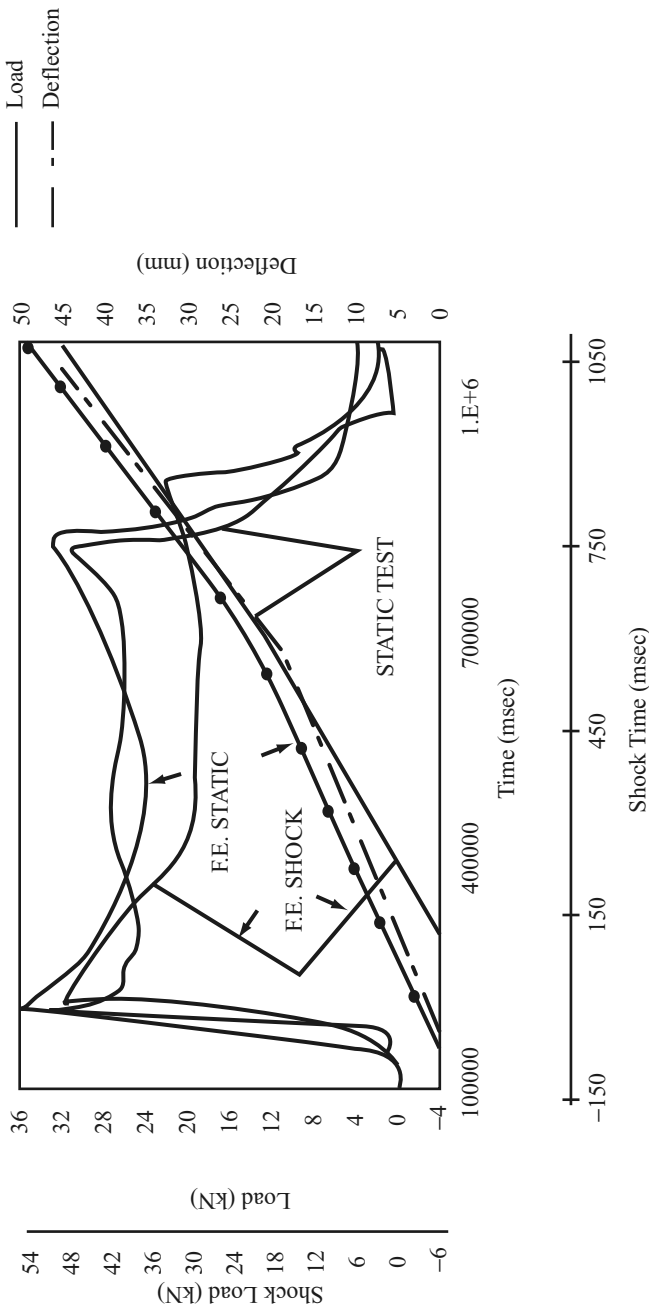
Plate 4.7. Load and deflection time histories for drop-in anchor

Pressure-Time History and Fragment Impacts

The pressure-time history expressions are given in this text, for the case, the pressure-time history is expressed as:

$$P(t) = P_0 + P(1 - \frac{t}{T_s}) \quad \text{Triangular pressure-time curve,} \tag{4.276}$$

where $P(t)$ = over pressure at time t and T_s is a positive duration and is the time for the pressure to return to the atmospheric level P_0.

When high explosives such as grenades, bombs, torpedoes, missiles or robots detonate, fragment fly out in all directions when the case is broken. The fragments from the same kind of weapon can vary in size. The fragmentation process is discussed in [4.48]; and fragment data from different types of bomb can be found, for instance in [4.38, 4.60] or [4.18]. To explain the fragmentation process Janzon [4.48] studied a cylinder. When an explosive detonates inside a cylinder, the cylinder expands and gets thinner. During the expansion, local radial tensile cracks develop from the outer surface inwards. However, the inner pressure caused by the shock wave from the detonation will delay or even stop the radial crack propagation; consequently, new radial crack can be formed. This crack formation occurs simultaneously for the whole cylinder. When the radial crack formation is completed, shear cracks form the inner surface. Again this occurs simultaneously for the whole cylinder. The crack formations are completed when the shear crack coincides with the radial cracks. This damage to the concrete from fragment impacts depends on the properties of the fragments, i.e. the striking velocity, mass and area density (kg m^{-2}). Fragment impacts causes severe cracking and crushing in the concrete, which must be supported by reinforcement to prevent failure. When fragment strike a concrete structure, they penetrate into the concrete; the impact causes spalling at the point of contact and possible scabbing on the reverse side of the wall. When 50% penetration is reached, scabbing may become a problem according to [4.54]. Furthermore the fragments can damage the reinforcement, and vibrations may reduce the bond between the concrete reinforcement. When a stress wave propagates through the concrete and reaches the inside of a structure, it is reflected as a tensile wave; as concrete is weak in tension, this lead to scabbing on the inside. The amount of reinforcement is a highly critical parameter in regards to scabbing. Experiments show that the scabbing is reduced by increasing the amount of reinforcement. To estimate the fragment velocity, empirical formulas can be found in literature, for example those proposed by von Essen [4.70], Janzon [4.48], Engberg and Karevik [4.32], ConWep [4.30], Krauthammer [4.54]. The initial velocity of the fragment is determined by the amount of explosive material and size of the casing, which can be estimated with an equation. The fragment velocity is retarded in the air, in relation to the initial fragment velocity, the fragment mass and the type of fragment. Fragments from an explosion can fly through the air over long distances, more than 1,000 m for heavy fragments, according
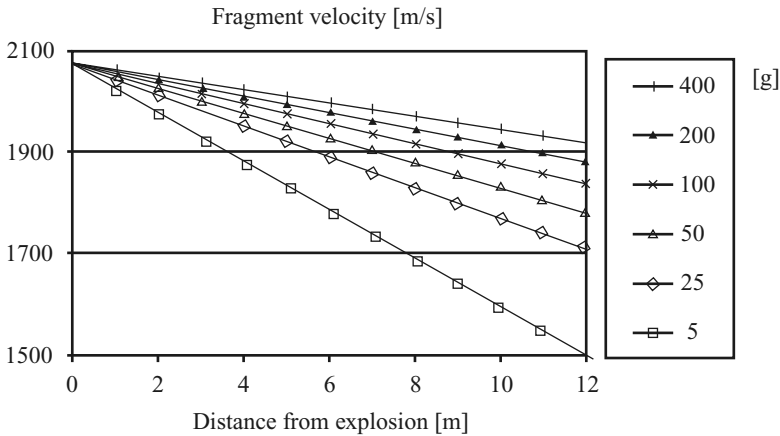
Fig. 4.54. Fragment velocity from a design bomb, for fragment weights from 5 to 400 g, based on equations from [4.32]

to [4.32]. As can be seen, the fragment velocity is highly dependent on mass: for light fragments, the velocity is retarded faster than heavy fragments. From the design bomb, the fragment weights are normally distributed from 1 to 50 g, and the impact velocity varies approximately between 1,650 and 1,950 m s^{-1}.

Fragment Velocity (Equation Used in Fig. 54)

The initial velocity of the fragment is determined by the amount of explosive material and size of casing, which can be estimated with an equation, where Q is the charge weight (kg) and M_h is the weight of the casing (kg), see [4.32]:

$$v_i = 2{,}400(1 - e^{-2Q/M_h}) \quad (\mathrm{m\,s^{-1}}). \tag{4.277}$$

The fragment velocity is retarded in the air, depending on the initial fragment velocity, the fragment mass and the type of fragment. The retardation of the velocity after a distance, r, and for steel fragments can be calculated as, see [4.70]:

$$v_r = v_i e^{-0.00456r/\sqrt[3]{m_f}} \quad (\mathrm{m\,s^{-1}}), \tag{4.278}$$

where r is the distance (m), v_i is the initial fragment velocity from (4.277) and m_f is the fragment mass (kg).

Depth of Penetration (Equation Used in Fig. 55)

By using a direct formula, [4.30], the depth of penetration, x (in inches) can be estimated for fragments penetrating massive concrete:

$$x = \frac{0.95 m_f^{0.37} v_s^{0.9}}{f_c^{0.25}} \quad \text{for } x \leq 1.4 m_f^{1/3} \tag{4.279}$$

Depth of penetration [mm]
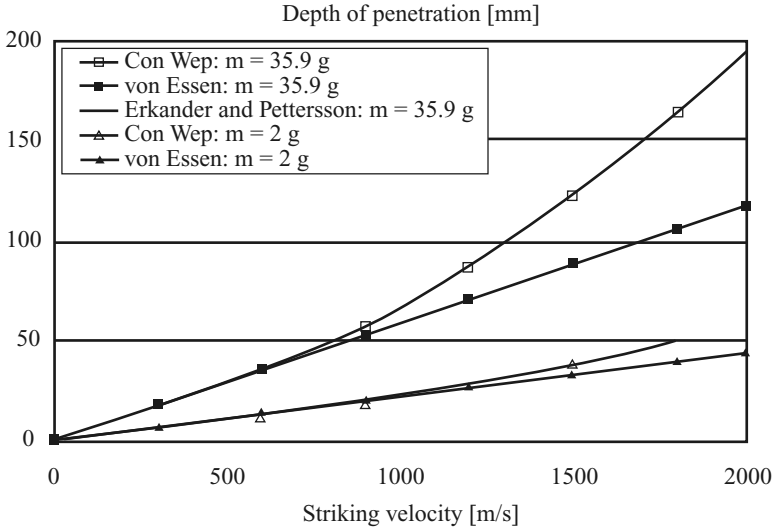
Fig. 4.55. Comparison of empirical formulations of fragment impacts [4.30, 4.33, 4.70]; with experimental data from [4.33]

Table 4.23. Conversion factors: Inch-pound to SI units (metric), according to ACI Manual of Concrete practice (2002)

To convert from	To	Multiply by
Inches	Millimetres (mm)	25.4
Feet	Metres (m)	0.3048
Kip-force/square inches (ksi)	Megapascal (MPa)	6.895
Ounces (oz)	Grams (g)	28.34

or

$$x = \frac{0.646 m_f^{0.4} v_s^{1.8}}{f_c^{0.55}} + 0.48 m_f^{1/3} \qquad \text{for } x > 1.4 m_f^{1/3}, \qquad (4.280)$$

where mf is the fragment weight (oz), v_s is the fragment striking velocity (kfps) and f_c is the concrete compressive strength (ksi). By using the conversion factors, as shown in Table 4.23 the penetration depth of the fragments can be calculated in SI units.

The depth of penetration, x, according to [4.70] can be estimated with the following equation:

$$x = 180 \cdot 10^{-6} \cdot v_r \cdot \sqrt[3]{m_f} \quad \text{(m)}, \qquad (4.281)$$

where v_r is the fragment velocity, and m_f is the fragment mass (kg). The depth penetration, x, for a spherical fragment of $35.9\,\mathrm{g}$ (i.e. $20.6\,\mathrm{mm}$ in diameter) according to [4.33] can be estimated as:

$$x = 288 \cdot 10^{-6} \cdot \sqrt[3]{m_f} \cdot (v_r - 170) \quad (\mathrm{m}), \tag{4.282}$$

where v_r is the fragment velocity, see (4.278), and m_f is the fragment mass (kg).

Thickness to Prevent Perforation

The thickness of concrete wall the just prevents perforation, d_{pf}, can be estimated with the following equation, for [4.54]:

$$d_{pf} = 1.09 x m_f^{0.033} + 0.91 m_f^{0.33} \quad \mathrm{inches}, \tag{4.283}$$

where x is the depth of penetration form (4.280) and (4.281) and m_f is the fragment weight in ounce (oz).

Equation to Determine Magnification of Factor (MF) or Dynamic Increasing Factor

The equation to determine the *MF* or *DIF* (dynamic increase factor), given by Malvar and Ross [4.57] are:

$$\frac{f_i}{f_{ts}} = \left(\frac{\dot{\varepsilon}}{\dot{\varepsilon}_s}\right)^{\delta} \qquad \text{for } \dot{\varepsilon} \leq 1 s^{-1}, \tag{4.284}$$

$$\frac{f_i}{f_{ts}} = \beta \left(\frac{\dot{\varepsilon}}{\dot{\varepsilon}_s}\right)^{1/3} \qquad \text{for } \dot{\varepsilon} > 1 s^{-1}, \tag{4.285}$$

where

f_t = tensile strength at $\dot{\varepsilon}$
f_{ts} = static tensile strength at $\dot{\varepsilon}_s$
f_t/f_{ts} = *DIF* (dynamic increase factor)
$\dot{\varepsilon}$ = strain rate in the range of 10^{-6} to $160\,\mathrm{s}^{-1}$
$\dot{\varepsilon}_s = 10^{-6}\,\mathrm{s}^{-1}$ (static strain rate)
$\mathrm{Log}\,\beta = 6\delta - 2$
$\delta = \dfrac{1}{1 + \dfrac{8 f_c'}{f_o'}}$
$f_{co}' = 10\,\mathrm{MPa}$

For comparisons of different materials, the approximate depth of penetration is given by multiples of the depth of penetration for soft steel by using a factor;

Table 4.24. Penetration depth of common materials, taken from [4.32]

Material	Factor
Armour-plate	0.75
Soft steel	1.0
Aluminium	2
Reinforced fibre-glass plastic	4
Reinforced concrete	6
Pinewood	15
Sand	18
Water	50
Wet snow	70
Dry snow	140

the factors are given in Table 4.24, taken from [4.32]. By using a direct formula, for fragments penetrating concrete, as shown in Fig. 4.55. The equation for these can be found in Appendix A. The assumptions in these formulations are not the same. The formulations in [4.33] is a curve fit to their experimental result; it will not be discussed further here. In ConWep, the depth of penetration a function of the fragment mass, the striking velocity and the concrete compressive strength. When using the equation form [4.70] the estimate the depth of penetration, the concrete strength is not taken into account; the depth of penetration is a function of fragment mass and striking velocity. Furthermore, the formulation in ConWep is designed to estimate penetration into massive concrete, while the von Essen one is for reinforced concrete. This may explain the divergence inn estimations, such as wide variations for heavy fragments in high velocity impact region. Table 4.25 gives the data.

Concrete Material Modelling Using the Modified Crack Softening Law

Program ISOPAR is having modified linear law to model the post failure response of concrete in tension. Being a brittle material, the strength is assumed decreasing rapidly after the failure initiation. Hillerborg [4.44] published a linear cracking softening law for practical use of the finite element method by using fracture mechanics. The softening slope was based on the stress-crack opening relationship. The crack opening was a function of the fracture energy and the ultimate tensile strength. Later, Hillerborg introduced a stepwise-linear crack softening law to improve the accuracy of the material response, see [4.45]. Since Hillerborg presented his work, several proposals for crack softening have appeared in the literature, for example, [4.41, 4.46]. The formulation is included in program BANG-F ISO parametric section using strain-dependency in tension.

Table 4.25. Thickness of concrete wall that just prevents perforation, compressive strength 30 MPa, for fragment weights from 5 to 400 g with striking velocities up to $3,000\,\mathrm{m\,s^{-1}}$, based on equations from [4.54]

Striking velocity $(\mathrm{m\,s^{-1}})$	Fragment mass (g)					
	5	25	50	100	200	400
300	22	39	50	65	84	108
600	30	54	70	91	118	153
900	39	74	97	127	167	220
1,200	53	101	134	177	235	312
1,500	70	135	180	239	318	424
1,800	90	175	233	312	416	556
2,100	112	220	295	394	528	707
2,400	138	271	363	487	653	877
2,700	166	327	439	590	792	1,064
3,000	196	389	522	702	943	1,268
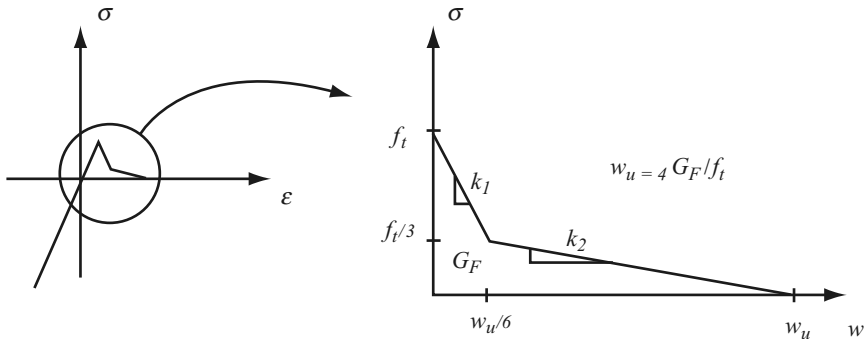
Fig. 4.56. The bi-linear uniaxial stress-crack opening relationship; based on [4.41]

4.14.2 Modified Crack Softening Law

The bi-linear softening law by Gylltoft [4.41] was implemented in the model. The softening law is based on the stress-crack opening relationship. To calculate the crack width, w_u, when the stress has fallen to zero and a real crack has formed, the fracture energy, G_F, and tensile strength, f_t, of concrete are used, as shown in Fig. 4.56. However, program BANG-F follows a smeared crack approach, and consequently the stress-strain relation is used; the maximum cracking strain is calculated from the maximum crack opening. The crack width is smeared out to a distance, l. In two-dimensional model for unreinforced concrete, the distance is normally approximated by the square root of the area of the element [4.49]. For three-dimensional models, the length is

taken to be third root of the volume of the element. The maximum cracking strain is:

$$\varepsilon_u = \frac{w_u}{l} = \frac{4G_F}{f_t l}. \tag{4.286}$$

The two slopes, k_1 and k_2 in Fig. 4.56 for the bi-linear softening are:

$$k_1 = \frac{f_t^2}{G_F} \quad \text{and} \quad k_2 = \frac{f_t^2}{10 \cdot G_F}. \tag{4.287}$$

For linear crack softening slope in the model is

$$k = \frac{f_t^2}{2 \cdot G_F}. \tag{4.288}$$

When the tensile failure stress has been reached, the slopes in (4.10), k_1 and k_2, can be described by using the slope (4.11) as:

$$k_1 = 2 \cdot k \quad \text{for} \quad \varepsilon \le \frac{1}{6}\varepsilon_u, \tag{4.289}$$

$$k_2 = \frac{2}{10} \cdot k \quad \text{for} \quad \varepsilon > \frac{1}{6}\varepsilon_u, \tag{4.290}$$

where ε is the cracking strain and ε_u is the ultimate cracking strain (when the stress has fallen to zero).

Where

G_F = Fracture energy
f_t = tensile strength
l = Length
w_u = ultimate crack opening
$k_1,\ k_2,\ k$ = crack softening slope

4.14.3 The Modified Strain Rate Law for Concrete in Tension

Concrete is very strain rate sensitive. In the CEB-FIB model code 1990 [4.28], there is a relationship for the *DIF* (dynamic increase factor) of tension as a function of strain rate. The *DIF* in the CEB is a design value, which means that the increase in strength is given at a higher strain rate than the one shown in the experiments, i.e. $30\,\text{s}^{-1}$. However, results presented in [4.57] show that the sudden increase in the *DIF* for the concrete in tension occurs at a strain rate of approximately $1\,\text{s}^{-1}$. Figure 4.57 compares a model proposed by Malvar and Ross and the CEB. The model proposed by Malvar and Ross fits the experimental data, as shown in Fig. 4.58.

DIF (Dynamic increase factor)
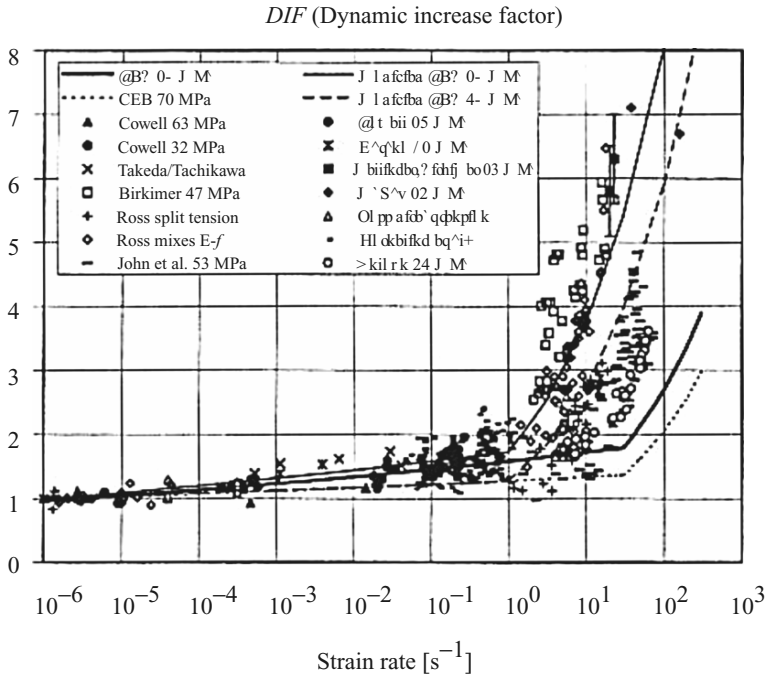
Fig. 4.57. The strain rate dependency for concrete in tension. Comparison with experimental data and modified CEB model by Malvar and Ross; recommendations according to the CEB-FIB Model Code 90. Based on [4.57]. *Note:* DIF is MF is some analysis.

Input Data for the Model

Figure (4.59) shows the finite element mesh based, is 8-noded ISO parametric element of a concrete block $4.8\,\mathrm{m} \times 2.2\,\mathrm{m} \times 1\,\mathrm{m}$.

(A) Finite element = 1,500
  No of elements = 500
  Element mesh sizes = 1–4 mm
  Strain rate is $(\mathrm{s}^{-1}) = 10^3$
  For types of loading; Impact: spherical impact with radius = $10.4\,\mathrm{mm}$
  Fragment impact; Fragment weighs = 5–$4.10\,\mathrm{g}$
  Velocity = 300–$3,000\,\mathrm{m\ s}^{-1}$
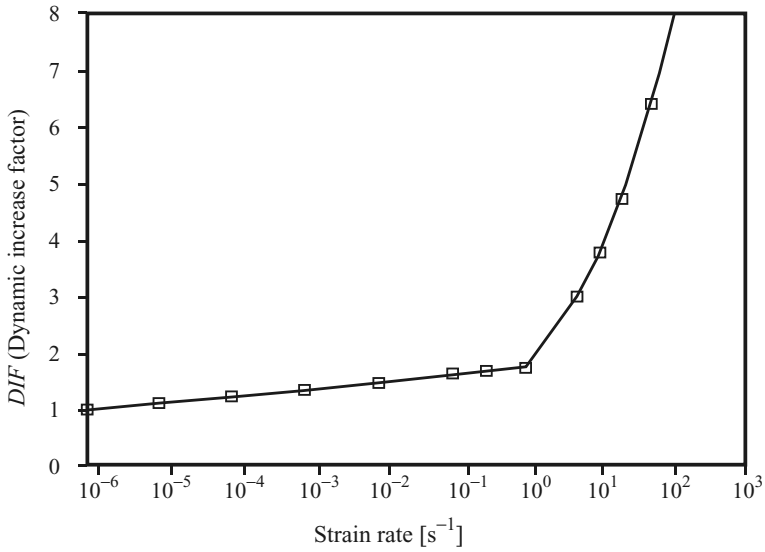
Fig. 4.58. The strain rate dependency for concrete in tension with and the modified strain rate law.

Parameters	Value
Shear modulus (kPa)	G
Compressive strength f_c (Mpa)	f_c
Tensile strength f_t/f_c	0.071–0.091
Shear strength f_s/f_c	0.18
Failure surface parameter A	2
Failure surface parameter N	0.7
Tens./compr. meridian ratio	0.685
Brittle to ductile transition	0.0105
G(elas.)/G(elas-plas.)	2
Elastic strength/f_t	0.7
Elastic strength/f_c	0.53
Residual strength const. B	1.8
Residual strength exp. M	0.7
Comp. strain rate exp. α	0.032
Tens. strain rate exp. δ	
Max. fracture strength ratio	1.10^{20}
Damage constant DI	0.04
Min. strain to failure	0.01
Residual shear modulus frac.	0.13
Tensile failure model	
Erosion strain/instantaneous	
Geometric strain (only for lagarange)	1.5

Depth of Penetration
(Variable)
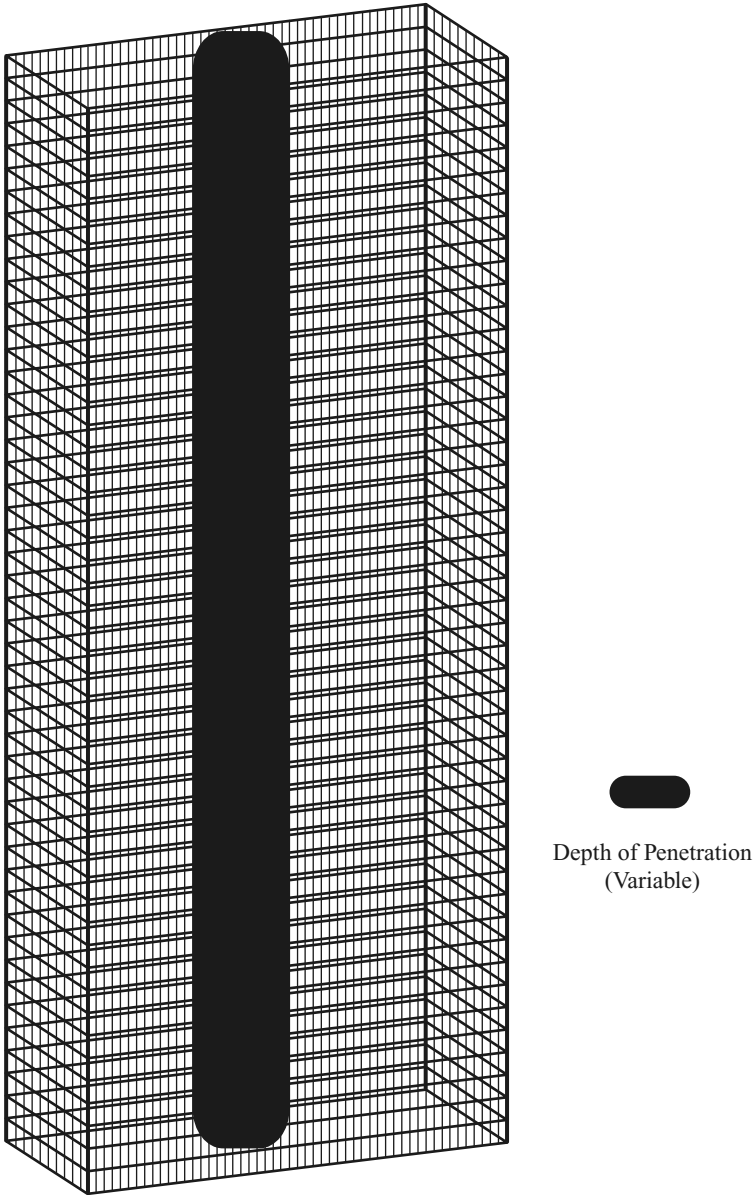
Fig. 4.59. Finite element mesh scheme for a concrete wall $4.8\,\mathrm{m} \times 2.2\,\mathrm{m} \times 1\,\mathrm{m}$ thick

Results

Element size	1 mm	Depth of penetration	90 mm; 140 mm	Crater diameter
Element size	2 mm	Depth of penetration	85 mm; 145 mm	Crater diameter
Element size	3 mm	Depth of penetration	45 mm; 130 mm	Crater diameter
Element size	4 mm	Depth of penetration	26 mm; 125 mm	Crater diameter

Figure 4.60 shows the failure and elastic stress in loading with impact time for meshes 1–4 mm sizes. A reference is made to Plate 4.8.

To study the effects of strain rate law, a comparison program ISOPAR model using isoparametric elements and the code. The results indicate 10% reduction cracking and around 12% scabbing diameter. The dynamic tensile has increased. When using the static tensile strength the crack width is on the increase. Cracking and spalling are mainly influenced by the tensile strength, fracture energy and the strain rate in tension. In case of fragment impacts spalling is caused by direct impact due crushing of the concrete. For projectile impacts, the spalling crater size depends also on the strain rate in tension. The results also show that the crack width and scabbing increase with decreasing static tensile strength. It is interesting to note that by using the *DIF* or magnification factor in tension where the sudden increase in strength occurs at lower strain rate, the scabbing is decreased.

In order to prevent perforation the program ISOPAT finite element analysis was preformed on concrete walls with concrete of $30 \, \text{MN} \, \text{m}^{-2}$ using variable fragment weights from 5 to 410 g with velocities of 300–$3{,}000 \, \text{m} \, \text{s}^{-1}$. The results are compared with those of Krauthammer equation

$$d_{pf} = 1.09 x m_f^{0.033} + 0.91 m_f^{0.33} \qquad \text{(inches)} \qquad (4.291)$$

Keeping in mind converting the answers in SI units, Table 4.26, shows the comparative study. The results are in good agreement. Both the striking velocity and the mass are vital factors in the design of this protective structure. The minimum wall thickness is 350 mm for the thickness of the massive mass concrete wall for the civil defence. The results vary with fragment mass and its velocity. Table 4.26 shows that the thickness that prevents perforation.

4.15 Impact Resistance of Fibre Concrete Beams

4.15.1 Introduction

Experimental tests have been carried out by Hibbert. A. P. and Hannat. D. J. on the impact resistance of fibre concrete at the transport and research laboratory (TRRL) in 1981. Two major test, i.e. slow fracture test and impact tests were conducted on specimen. Slow flexure tests were conducted to determine the energy absorbed in slow bending in a conventional testing machine.
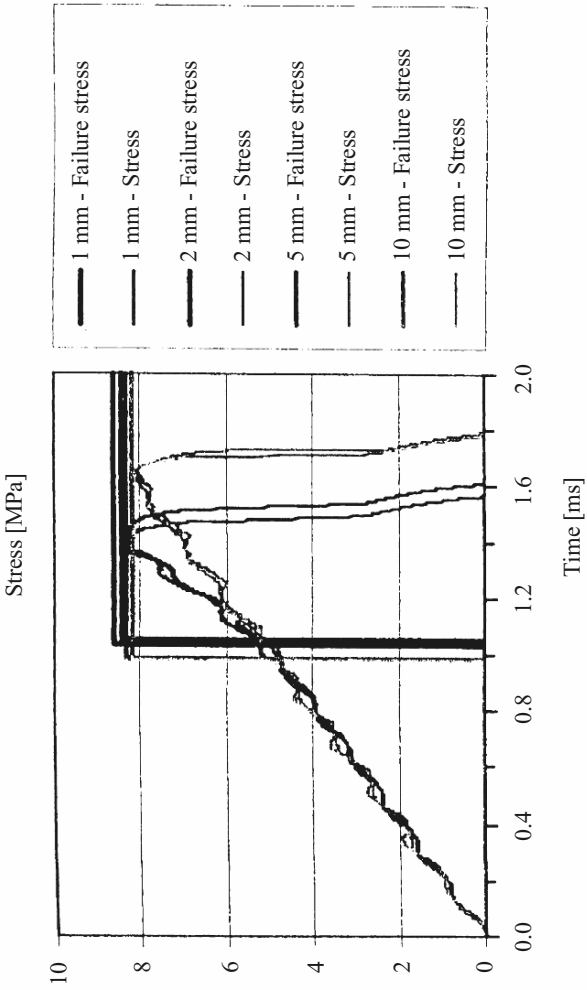
Fig. 4.60. The failure stress and axial stress in the loading direction

$v = 1.024$ m/s

149 mm

$v = 1.283$ m/s

158 mm

176 mm

Note: Dotted lines are for craters

$v = 1163$ m/s
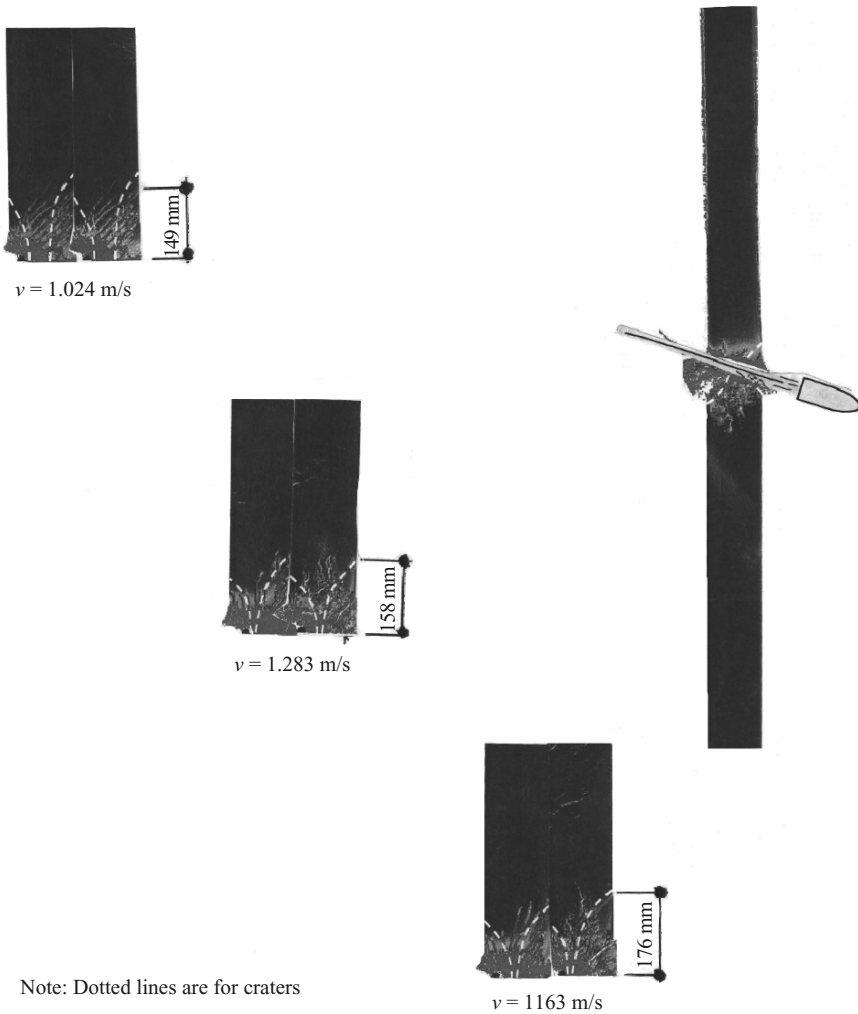
Plate 4.8. Numerical analysis of fragment penetration, spalling and scabbing

Six test beams had 60 mm electrical resistance wire gauges bonded centrally to their tensile faces. The signal was and fed to the second y-axis pen on the chart recorder. The load on the specimen was measured by a calibrated load cell between the central loading bar and the upper plate of the machine, the signal from the load cell being recorded on the y-axes of a chart recorder. The deflection was measured by two variable transformers (LVDTs) mounted (Plate 4.9). The out puts from the LVDTs being summed up before the connection to the x-axis of the chart recorder. A Denison T60 C machine was used with a constant rate cross head movement of approximately 0.05 mm s^{-1}. The load configuration (centre point loading on a simply supported span of 400 mm

Table 4.26. Thickness of concrete wall of $30\,\mathrm{MN\,m^{-2}}$ concrete to prevent perforation for fragment weights and variable velocities

Striking velocity (m s^{-1})	Fragment mass (g)					
	5	25	50	100	200	400
300	20	40	51	65	90	109
600	31	53	70	90	115	160
900	37	72	96	128	170	230
1,200	51	100	130	180	240	310
1,500	68	130	175	240	317	435
1,800	83	171	230	310	420	562
2,100	110	210	290	390	530	710
2,400	137	270	360	490	660	900
2,700	167	300	440	590	800	1,070
3,000	197	400	530	700	950	1,310

Results from Program ISOPAR

with a trowel face of the beam in tension). Was the same as in impact tests for the direct comparison of the result.

The design and construction of the instrumented Charpy impact machine used for all the impact test has been fully described elsewhere. A general view of the test shown in Plate 4.9. The machine was the pendulum type with the test beams supported near the ends and struck at the mid-span. The specimens were completely fractured in one blow and the energy to fracture was determined from the amplitude of the pendulum swing, less the kinetic energy of the broken halves, and also independently from the load-time histories obtained from the instrumented tup (or striking part) of the pendulum head. The kinetic energy of the broken halves of the specimen was determined by allowing the specimen holders to rotate after fracture against springs and a ratchet system. The tup was instrumented with electrical resistance wire gauges in such a way that it acted as a dynamic compression load-cell. The signals from this load-cell were, after suitable amplification, fed to a high speed data acquisition system, simultaneously sampled, digitised and stored in the memory of a Texas Instruments 960A minicomputer at a maximum rate of four simultaneous readings every $5\,\mu$s. Computer programs were written to enable the recorded load-time curves to be processed to provide outputs of energy and deflection of the beam with respect to time to an X-Y plotter or to the system teletypewriter. The determination of energy and deflection from load-time curves are given in detail.

The beams were tested with the trowelled face in tension, on a span of 400 mm, and the majority of tests were performed with the pendulum raised to give a velocity at impact of $2.85\,\mathrm{ms^{-1}}$ and an energy at impact of 250 Nm. A limited series of tests were performed with a pendulum energy of 500 Nm. Some test beams were instrumented with conventional 60 mm
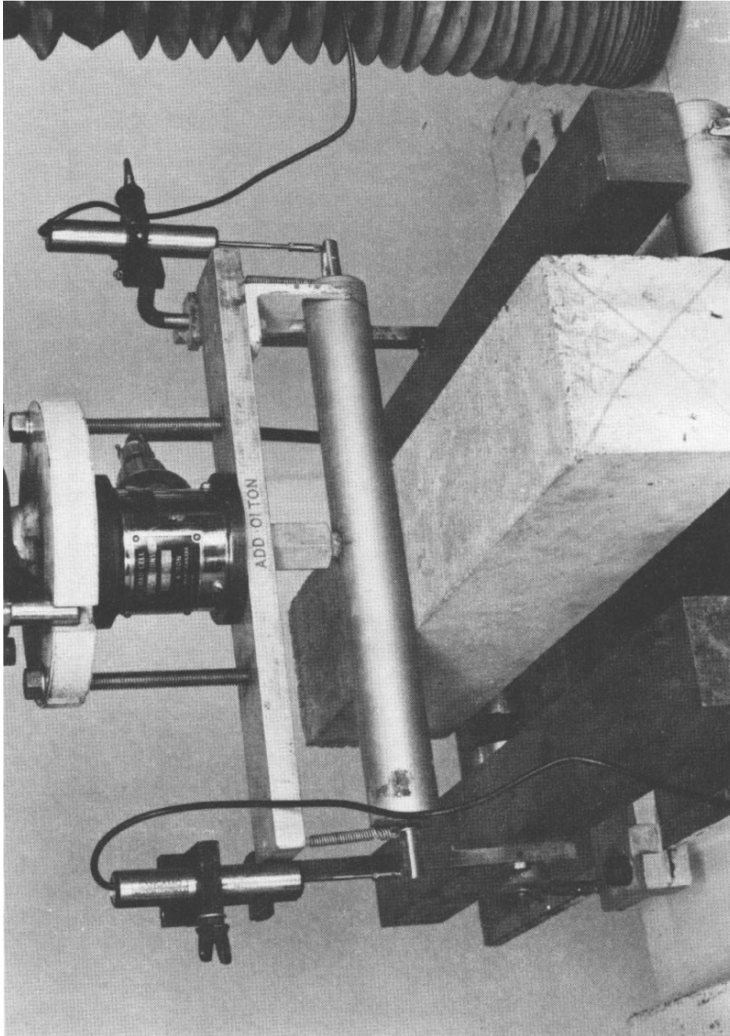
Plate 4.9. Slow flexure test arrangement showing LVDT's measuring deflection of test beam relative to the supports. Hannant DJ and Hibbert AP TRRL Supplementary report 654 (1981)

electrical resistance wire strain gauges to determine the behaviour of the beam during the impact.

Although the mechanical behaviour of fibre reinforced cementitious matrices at slow rates of loading in both tension and flexure is now quite well understood, the behaviour in impact has not received similar attention. However, it is the ability of these new materials to absorb the energy of impacts and accept the occasional overload without completely failing that are among their most attractive properties. Their toughness in comparison with the unreinforced matrix has been confirmed by many relatively crude impact tests, such as the dropping of a steel ball onto a sheet of the material and by several successful applications where impact resistance or energy absorption has been a necessary requirement. However, quantitative data on impact performance is lacking when compared with the extensive data on other properties which are less dramatically increased. Therefore it was towards the quantification of the impact resistance of fibre reinforced concretes that the work reported here was directed.

Since no standard impact test for such a material exists it was necessary to design and develop suitable equipment. The method was to determine the energy required to completely fracture $100 \times 100 \times 500$ mm test beams simply supported and struck at the mid-span by a heavy pendulum. Instrumentation of the striker – or tup – enabled the load developed during the impact to be measured and recorded. From this load record the energy absorbed with respect to central deflection of the beam was calculated and this was compared with the energy obtained from the area under the load-deflection curve in a conventional quasi-static bending test.

4.15.2 Slow Flexure Tests

A series of tests was performed on specimens similar to those tested in impact to determine the energy absorbed in slow bending in a conventional testing machine. A Denison T60C machine was used, with a constant rate of cross-head movement of approximately 0.05 mm s^{-1}. The loading configuration (centre point loading on a simply supported span of 400 mm with the trowelled face of the beam in tension) was the same as in the impact tests so that the results are directly comparable. Mean results of the slow flexure tests are given in Table 4.27. For the 3D impact finite element analysis only polypropylene data of Table 4.27 are considered.

Energy Absorbed in Fracture

The load on the specimen was measured by a calibrated cell between the centre loading bar and the upper plate of the machine (Plate 4.10), the signal from the load-cell being recorded on the Y-axis of a chart recorder. The deflection of the loading roller relative to the end supports was measured by two linear variable transformers (LVDTs) mounted as shown in Plate 4.11, the put form

Table 4.27. Mean results of slow flexure tests

Fibre type and manufacturer	Fibre size (mm) dia. × length	V_f (%)	Age at test	Maximum load (kN)[a,b]	Energy absorbed at a deflection of 5 mm	Energy absorbed at a deflection of 10 mm
—	—	—	2 mth.	9.6 (6%, 11)	2.8 (18%, 11)[c]	—
—	—	—	2½ yr.	11.6 (8%, 4)	2.1 (18%, 4)[c]	—
Steel, hooked ends DRAMIX (Bekaert Ltd)	0.5 × 50	1.2	2 mth.	13.6 (20%, 5)	53 (26%, 5)	85 (27%, 5)
Steel, hooked ends	0.5 × 50	0.6	2 mth.	11.3 (8%, 6)	35 (27%, 6)	57 (27%, 6)
Steel crimped, high C, (GKN Ltd)	0.5 × 50	1.2	2 mth.	10.8 (14%, 6)	40 (12%, 6)	66 (13%, 6)
Steel crimped, high C	0.5 × 50	1.2	2½ yr.	15.6 (12%, 6)	60 (11%, 6)	95 (16%, 6)
Steel, crimped, high C	0.5 × 50	0.6	2 mth.	12.0 (5%, 6)	33 (20%, 6)	53 (23%, 6)
Steel, crimped, low C	0.5 × 50	1.2	2½ yr.	15.9 (9%, 6)	56 (22%, 6)	80 (30%, 6)
Steel, Duoform (National Standard Ltd)	0.38 × 38	1.2	2 mth.	14.5 (6%, 6)	26 (16%, 6)	30 (19%, 6)
Steel, Duoform	0.38 × 38	1.2	2½ yr.	16.7 (6%, 6)	22 (24%, 6)	24 (23%, 6)
Steel, stainless melt-extract (National Standard Ltd)	0.7 × 25	1.2	2 mth.	11.8 (6%, 6)	30 (12%, 6)	47 (12%, 6)
Fibrillated polypropylene film, Bridon Fibres Plastics Ltd	12,000 denier × 75 mm long	1.2	2 mth.	9.8 (5%, 6)	30 (20%, 6)	43 (32%, 6)
Polypropylene	12,000 denier × 75 mm	1.2	2½ yr.	11.7 (8%, 6)	33 (21%, 6)	42 (26%, 6)
Polypropylene	12,000 denier × 35 mm	1.2	2 mth.	10.3 (9%, 6)	21 (9%, 6)	30 (11%, 6)
Polypropylene	12,000 denier × 35 mm	1.2	2½ yr.	10.7 (7%, 6)	21 (11%, 6)	28 (16%, 6)

[a] 10 kN is equivalent to a Modulus of Rupture (MOR) of 6 MNm^{-2}

[b] The first figure is the mean. The figures in parentheses are the coefficient of variation followed by the number of test results on which this is based

[c] Failure of plain concrete occurred before 5 mm deflection

10 Nm $= 1$ kJ m^{-2} apparent work of fracture based on beam cross sectional area or 10 Nm $= 0.5$ kJ m^{-2} apparent work of fracture based on nominal fracture surface area

(with compliments of TRRL, U.K.)
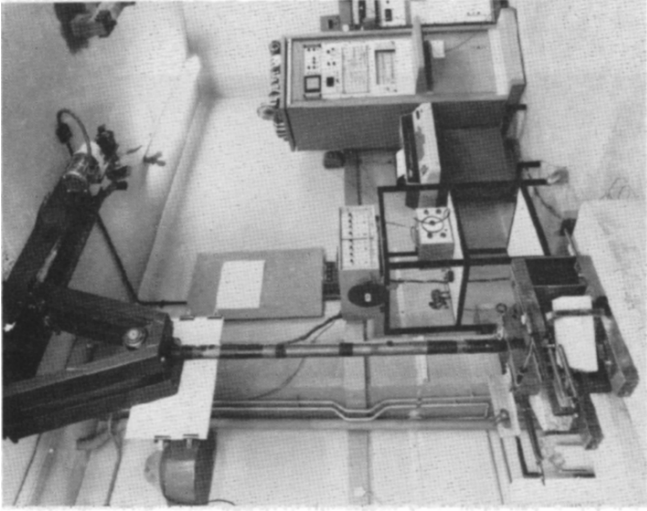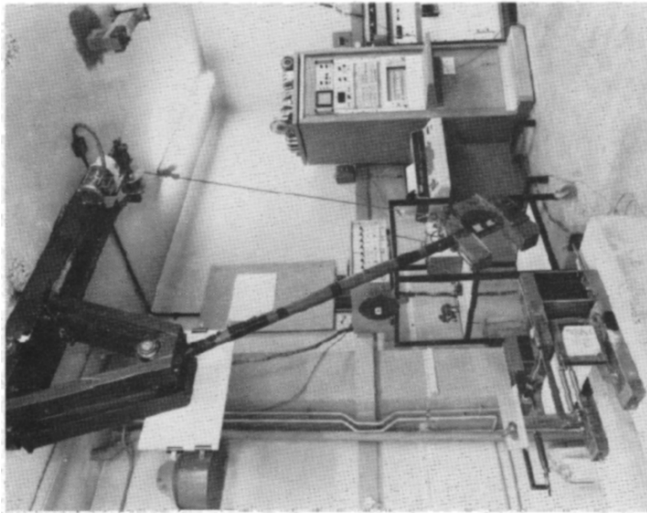
BEFORE

AFTER

Plate 4.10. General view of the instrumented impact machine and high speed data acquisition system before and after a test (with compliments Hannant D.J. and Hilbert A.P. and TRRL)

the LVDT's being summed before connection to the X-axis of the chart recorder. In this manner the load-deflection curve for each test beam was obtained and the area under the curve calculated.

Six test beams had 60 mm electrical resistance wire gauges bonded centrally to their tensile faces. The signal was amplified and fed to the second Y-axis pen on the chart recorder.

4.15.3 Impact Tests

Immediately opposite the impacted face is strained in tension. At some stage a crack is formed in the concrete and runs from the tension face to the compression face of the specimen. This results in a change both in stored elastic energy and in the compliance of the beam. During this time the specimen is accelerated from rest. If the velocity of the concrete at the point of impact becomes equal to, or greater than, the tup velocity the load on the tup falls to zero. Also, if the specimen contains no reinforcement the broken halves swing clear of the pendulum and their kinetic energy is dissipated in doing work against the springs restraining the rotating specimen holders. If, however, there are fibres across the crack the specimen is restrained from failure after the first matrix crack has occurred and, after a short deceleration period, the tup and specimen will contact again resulting in the development of a second impact, the magnitude of which will depend on the fibre type, the fibre volume and orientation.

4.15.4 Impact Analysis of Polypropylene Fibre Reinforced Concrete Beam Using Finite Element

The part data given in Table 4.27 for the polypropylene fibre reinforcement concrete beam have been considered. The impact analysis given, in general, is considered. Four noded isoparametric element as solid elements are considered for the main concrete with two noded bar elements representing polypropylene. In the finite element mesh scheme of such a beam, bars are placed in the body of the concrete as well as on the top of the solid element nodes to match the displacements. Program ISOPAR has been used to solve this impact problem.

4.15.5 Additional Data

Impact velocity $= 2.85 \, \mathrm{m \, s^{-1}}$; Impact time 0–400 μs
Impact energy $= 250 \, \mathrm{Nm}$
Impact load max $= 200 \, \mathrm{KN}$ using pendulum
Beam dimensions $= 100 \times 100 \times 500 \, \mathrm{mm}$
Concrete strength $= 60 \, \mathrm{MN \, m^{-2}}$ 28 days

Max. Concrete tension = (reference to text) = $6\,\mathrm{MN\,m^{-2}}$
Polypropylene volume = 13%
E_c (concrete) = $20\,\mathrm{GN\,m^{-2}}$
Finite elements: solid concrete element = 2,238
                 Fibre 2 noded element = 1,230

4.15.6 Results

Program ISOPAR is used to solve this beam with reinforcement of polypropylene. Figure 4.61 shows typical load deflection curves of both experimental (Hannantetal) and that given by the finite element analysis. Figure 4.62 shows the finite element mesh scheme with the damaged zones due to impact. Figure 4.63 gives the relationship between load energy absorbed versus time and deflection. The absorbed mode of failure for most of the fibre reinforcement concretes was by fibre pullout, with little evidence of fibre fracture. The exceptions were those containing either the 0.38 mm × 38 mm Duoform fibre or the 12,000 denier, 75 mm fibrillated polypropylene film fibre. In both cases there were considerable numbers of broken fibres at the crack surfaces.

The analysis indicated that if the stress developed in the fibre is insufficient to cause fibre fracture, then the fibres were debonded from the matrix and will be pulled out. The pull out is relative to the rate dependence which is in turn is related to the pull out length and the distribution of fibres across time dependent cracks. The energy is computed from the load-time curve. With some loss of energy from the load time curve will be assumed by the beam as strain energy, fracture energy and as kinetic energy. For concrete strength the five parameter method given in this text has been adopted. At 20 increment chosen was the stage of the total damage. The results are in a good agreement with these by Hannant et al.
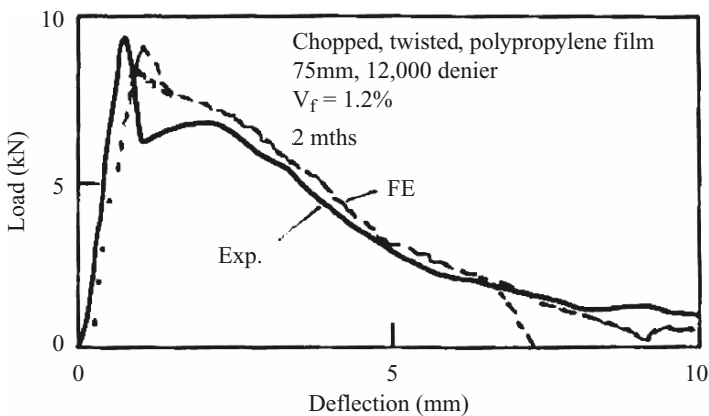
Fig. 4.61. Typical load-deflection curve for polypropylene fibre concrete in slow flexure
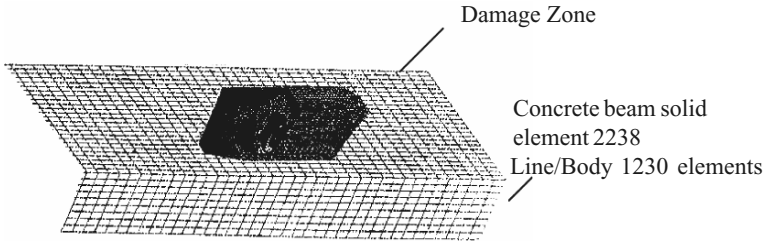
Fig. 4.62. Finite element mesh scheme of fibre reinforced concrete beam
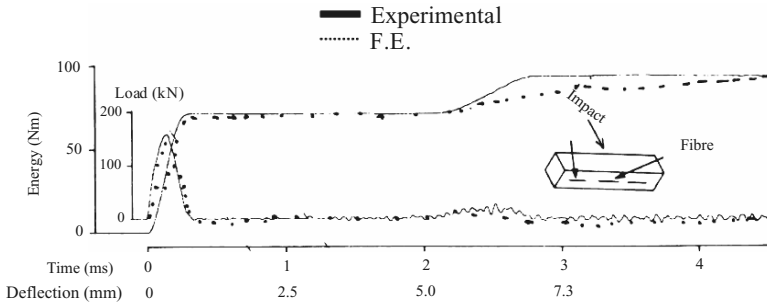
Fig. 4.63. Typical load-time, energy-time curve for chopped fibrillated polypropylene film fibre concrete in impact

4.16 Bird Impact on Aircraft

4.16.1 Introduction

The impact of a bird on an aircraft is a dangerous event for its safety. The bird impact against nacelle inlet and other parts, particularly at cockpit glass have been analysed using a proven explicit finite element in corporated in Program ISOPAR. The same sort of approach has been adopted in program such as ANSYS and L.S. DYNA and ABACUS. The external skin of the inlet is made up with composite materials. The most dangerous bird knows as *Archaeopteryx* always confronting the aircraft has been chosen for the analysis. The damage law as a material constitutive model has been adopted which is well proven in the aircraft industry. The bird is idealised with model mass and the aircraft areas are modelled as solid isopramatic elements. Hallquist gap elements as contact elements between the bird and the aircraft representing master and the slave nodes turned out to be the best for the non linear analysis. The load-time function relationship has been achieved for the impact analysis. The main purpose of this analysis of survivability is to ensure the aircraft is able to land safely after the bird impacting the aircraft. In this regard an effort is made to adhere to preventive measure while making the cockpit and the inner nacelle structure safe. The bird impact inclusive of its crashing can be modelled in order to obtain aircraft structural failure for and

finally using the data in the design of a safer aircraft. The modelling technique has incorporated a Lagrangian approach while insensitive to the F.E. mesh distortion. Moreover the bird impact against turbofan is to sustain it and to avoid damages to the engine control system which is inside the "nacelle structure". The external skin of the nacelle made in composite must have a high stiffness to weight and strength to weight ratios. The structural response is to be evaluated while including of large deformations and perforations.

4.16.2 Birds, Structures and Bird Impact

4.16.2.1 Bird Types and Their Behaviour

There are several birds that could be dangerous to the aircraft. Birds depend to a great extent on innate behaviour, responding automatically to specific visual or auditory stimuli. Even much of their feeding and reproductive behaviour is stereotyped. Feather care is vital to keep the wings and tail in condition for flying and the rest of the feathers in place were they can act as insulation. Consequently, preening, oiling, shaking, and stretching movements are well developed and regularly used. Some movements, like simultaneously stretching of one wing, one leg, and half the tail (all on the same side) are widespread if not universal among birds. Stretching both wings upward, either folded or spread, is another common movement, as is a shaking of the whole body beginning at the posterior end. Other movements have evolved in connection with bathing, either in water or in dust. Such comfort movements have frequently become ritualized as components of displays.

Many birds maintain a minimum distance between themselves and their neighbours, as can be seen in the spacing of the flock of swallows preached on a wire. In the breeding season most species maintain territories, defending areas ranging from the intermediate vicinity of the nest to extensive areas in which a pair not only nest but also forages. The frequency of the actual fighting is in birds greatly reduced by ritualized threat and appeasement displays. Birds ranging from solitary (e.g. many birds of prey) to highly gregarious, like the guanay cormorants of the Peru Current off the west coast of South America, which nest in enormous colonies of hundreds of thousands and feed in large flocks with boobies and pelicans. Auditory signals, like visual ones, are almost universal among birds.

Porosity in the bird is an important factor for impact. The skin of the bird is almost without glands. The important exception is the oil (uropygial) gland, which lies on the rump as the base of the tail. The secretion of this gland contains approximately one-half lipids (fats) and is probably important in dressing and waterproofing the plumage. In a few birds, the secretion has a strong, offensive odour. Some birds in which the oil gland is small or absent have a specialised type of feather (powder down) that grow continuously and breaks down into a fine powder, believed to be used in dressing the plumage.

The avian skeleton (Plate 4.11) is notable for its strength and lightness, achieved by fusion of elements and by pneumatization (i.e. containing air spaces). The skull represents an advance over that of reptiles in the relatively larger cranium with fusion of elements, made possible by birds having a fixed adult size. Birds differ to mammals in being able to move the upper mandible, relative to the cranium. When the mouth is opened, both lower and upper jaws move: the former by simple, hinge like articulation with the quadrate bone at the base of the jaw, the latter through flexibility provided by a hinge between the frontal and nasal bone. As the lower jaw moves downward, the quadrate rocks forward on its articulation with its cranium, transferring this motion through the bones of the palate and the bony bar below the eye to the maxilla, the main bone of the upper jaw.

The number of vertebrae various between 39 to 63, with remarkable variation (11–25) within cervical (neck) series. The principle type of vertebral articulation is heterocoelous (saddle shaped). The three to ten (usually five to eight) thoracic (chest) vertebrae each normally bear a pair of complete ribs consisting of a dorsal vertebral rib articulating with the vertebrae with the vertebral sternal rib, which in turns articulates with the sternum (breastbone). Each vertebral rib bears a flat, backward pointing spur, the uncinate process, characteristic of birds. The sternum, ribs and their articulations form the structural basis for the bellow action, by which air is moved through the lungs. Posterior to the thoracic vertebrae is a series of ten to 23 vertebrae, the synsacrum is a series of free caudal (tail) vertebrae and finally the pygostyle, which consists of several fused caudal vertebrae and supports the tail feathers. The sternum consists of a plate lying ventral to the thoracic cavity and a medial keel form the major attachment for the flight muscles. The bones of the pectoral girdle consists of the furcula (wishbone) and the paired coracoids and the scapulas (shoulder blades). The sword-shaped scapulas articulates with the coracoids and humerus (the bone of the upper "arm") and lies just dorsal to the rib basket. This explanation is necessary for the appropriate choice of elements and nodes.

The most dangerous bird is a confrontational one and that is the *Archaeopteryx* who most fly at the levels of embarication and disembarication. The nearest version is the *Hesperornis* with the teeth set in groves, not sockets. The off shoots the pigeon, the skeleton with the nearest wing raised with the far wing not shown (Plate 4.11) is taken as an example consisting of masses in thousands for the impact analysis.

4.16.3 Aircraft Vulnerable Zones for Bird Impact

(a) The impact of a bird against the structure of a modern aircraft turbofan intake is the area with the particular emphasis to the consequences of subsequent penetration. For modern turbofan nacelles, it is necessary to sustain the bird impact and avoid damage to the engine control system, which is placed inside the nacelle structure. The bird can certainly

Plate 4.11. Bird–aircraft impact – analysis for nacelle

penetrate the area. The external skin of the modern nacelle is made up of composite materials permit a light structure along with high-stiffness-weight and strength-to-weight ratios. The crash behaviour of composite materials is characterised by complex failure events (lamina bending, transverse shear and local fibre buckling) and progressive damage modes, such as inter-laminar or intra-laminar cracks. Therefore, appropriate ana-lytical models and specific Constitutive laws have to be defined and turned to predict failure/damage mechanisms and their evolution of the vulnerable parts.

(b) The aircraft's cockpit area (Plate 4.11) as a sensitive zone. The cockpit is extremely attractive to birds as it is most tempting to visualise as an area of the bird's curiosity. In the material modelling, the cylindrical cell shaped frame with glass composite material made up of carbon fibre reinforced plastic (CFRP) woven with resin volume fracture of 42%, as suggested by the aircraft industry, is to be used.

4.16.4 Material Modelling and Finite Element Analysis and Results

After careful consideration and in order to maintain air worthiness, the date for the relative material modelling must be a top priority. The data shall include both of the aircraft and impacting bird. Explicit non-linear finite ele-ment code inclusive of contact/impact problems must be adopted. Table 4.28 gives a comprehensive treatment of such a method and has been incorporated in the program ISOPAR and other well known such as ANSYS, L.S. DYNA and ABACUS. The Langrangian approach is adopted is basically insensitive to mesh distortion. Table 4.29 gives a relevant material data for the material modelling and details about the finite element.

The inlet mesh is built on the original inlet geometry. It comprises of 50,100 4-noded shell elements with 8-noded solid isoparametric elements of around 7,500. Since the mutual influence of bird impact load is of high intensity and the response of the aircraft of the relevant chosen structural component is so deep that only with the explicit finite element analysis of ISOPAR made possible to analyse this event with a degree of accuracy. The bird has been used in the analysis, Table 4.29, nodal mass model interacting with finite element. It is assumed that these masses of discrete types and have no interaction among them.

The date briefly given in Table 4.29 have been adopted for the finite ele-ment analysis. Masses are assumed for the bird with contact elements having master and slave nodes. It is noted that the finite element mesh distortion increase and both the accuracy and the time step decrease dramatically. The nodal mass model can easily be implemented with ISOPAR explicit code. Plate 4.13, shows the finite element scheme. The bird strike gives the nacelle deformation using Langrangian and nodal masses bird model. As the sim-ulation continues, the finite element mesh distortion increases. The composite

Table 4.28. Explicit finite element non-linear integration scheme

---

1. (a)	Time simulation $0 \leq t \leq t_{en}$
	Time step Δt_n where n = 1 n_{ts} = number of time steps
	t_{en} = end of simulation
	t^n = time simulation at time step n
	$u(t^n)$ = displacement at step n

1. (b)   Initial conditions
σ_0, U_0, $\dot{U}_0$, $n = 0$, $t = 0$, Compute M

2.   Calculate force F

3.   Determine acceleration $\ddot{u}^n = M^{-1}(Fn - Cu^{n-\frac{1}{2}})$, where C = damping

4.   Time update $t^{n+1} = t^n + \Delta t^{n+\frac{1}{2}}$; $t^{n+\frac{1}{2}}, = \frac{1}{2}\{t^n + t^{n+1}\}$

5.   Update nodal velocities: $u^{n+\frac{1}{2}} = u^n + \ddot{u}^n \{t^{n+\frac{1}{2}} - t^n\}$

6.   Velocity boundary conditions needed
at node m, $u_{im}^{n+\frac{1}{2}} = \bar{u}_i(x_m, t^{n+\frac{1}{2}})$

7.   Update again nodal displacement
$u^{n+1} = u^{n+\frac{1}{2}} + (t^{n+1} - t^{n+\frac{1}{2}})\ddot{u}^{n+1}$

8.   Evaluate force to come here at this stage: BANG-FORCE

9.   Compute $\ddot{u}^{n+1}$

10.   Update nodal velocities $\dot{u}^{n+1} + \dot{u}^{n+\frac{1}{2}} + (t^{n+1} - t^{n+\frac{1}{2}})\ddot{u}^{n+1}$

11.   Check energy balance from Eq. (a)

$$W_{int}^{n+1} = W_{int}^n + \frac{\Delta t^{n+\frac{1}{2}}}{2}(u^{n+\frac{1}{2}})^T(F_{int}^n + F_{int}^{n+1}) = W_{int}^n$$

$$+\frac{1}{2}\Delta u^T(F_{int}^n + F_{int}^{n+1}), \tag{a}$$

$$W_{ext}^{n+1} = W_{ext}^n + \frac{\Delta t^{n+\frac{1}{2}}}{2}(u^{n+\frac{1}{2}})^T(F_{ext}^n + F_{ext}^{n+1}) = W_{ext}^n$$

$$+\frac{1}{2}\Delta u^T(F_{ext}^n + F_{ext}^{n+1}), \tag{b}$$

where $\Delta U = U^{n+1} - U^n$. The kinetic energy is given by

$$W_{kin}^n = \frac{1}{2}(u^n)^T M_u^T.$$

The internal energies van also be computed on the element or quadrature point level by

$$W_{int}^{n+1} = W_{int}^n + \frac{1}{2}\sum_e \Delta u_e^T(F_{int}^n + F_{e,int}^{n+1}) \tag{c}$$

$$= W_{int}^n + \frac{\Delta t^{n+\frac{1}{2}}}{2}\sum_e \sum_{n_Q} w_Q \overline{U}_Q^{n+\frac{1}{2}}:(\sigma_Q^n + \sigma_Q^{n+1})J_{\xi Q}, \tag{d}$$

Table 4.28. (continued)

---

where $\sigma_Q^n = \sigma^n(\xi_Q)$, etc. Energy conversion requires that

$$|W_{kin} + W_{\text{int}} - W_{ext}| \leq \varepsilon \max(W_{ext}, W_{\text{int}}, W_{kin}), \tag{e}$$

where ε is a small tolerance, generally on the order of 10^{-2}.

If the system is very large, on the order of 10^5 nodes or larger, the energy balance should be preformed on sub domains are then treated as external forces for each sub domain

12.   Check energy balance at time step $n + 1$ from Eq. (e)

13.   Output. If simulation is incomplete go to step 4

14.   Subroutine BAMG-FORCE

14.1 $F^n = 0,\ \Delta t_{crit} = \infty$

14.2   Evaluate external forces at nodes F_{ext}^n

14.3   Over the element e LOOP

14.3.1 Element nodal displacement and velocities u and $\dot{u}$ respectively

14.3.2 $F_e^{\text{int},n} = 0$

14.3.3 Quadrature points ξ_Q loop

14.3.3.1 If $n = 0$ go to 4

14.3.3.2 Evaluate deformation $D^{n-\frac{1}{2}}(\xi_Q),\ F^n(\xi_Q)E^n(\xi_Q)$

14.3.3.3 Using constitutive equation evaluate Cauchy Stress $\sigma^n(\xi_Q)$ over quadrature points

14.3.3.4 $F_e^{\text{int},n} \leftarrow F_e^{\text{int},e} + \beta T \sigma^n \bar{w}_Q^J|_{\xi_Q}*$

14.3.3.5 Quadrature points loop END

14.4   Evaluate external forces on the element $F_e^{ext,n}$

14.4.1 $F_e^n = F_e^{ext,n} - F_e^{\text{int},n}$

14.4.2 Evaluate Δt_{crit}^e if $\Delta t_{crit}^e < \Delta t_{crit}$ then $\Delta t_{crit} = \Delta t_{crit}^e$

14.4.3 Transfer F_n^e to global F^n **

14.5   Loop over elements END

14.6 $\Delta t = \propto \Delta t_{crit}$

Note:

* Evaluate internal nodal forces by integrating the product of β matrix and the Cauchy Stress over element domain

** Nodal forces are scattered into the global array

Table 4.29. Material data and modelling

Date on aircraft

(A1): Glass fibre radome view glass. Reference:
   Chapts. 1 and 2
(A2): Nacelle area of the aircraft material and F.E data

Number of nodes

   F.E Data:
      Total 4 noded shell elements = 2,700   Inlet F.E model = 60,000
      Total 8 noded solid Isopara-
      metric elements   = 2,830
      Light alloy −5 integration points
      through thickness composite panel
      ply cockpit viewing frame:
      No: 4 noded shell element   = 50,100
      No: 8 noded solid isopara-   *Cockpit glass*
      metric element   = 7,500

E = Young's modulus   = 62,600 N mm^{-2} σ_{st} = flexural strength
                                               under impact loads

υ = Poisson's ratio   = 0.05   = 56 MN m^{-2}
G =   = 5,900 N mm^{-2} σ_{ar} = mean breaking
                                               strength
ρ_c = Density   = 1,600 kg m^{-2} = 55 MN m^{-2}
Composite shell specimen lay-ID f_{saf} = factor of safety
   [0°/45°/0°/45°/0°]-Mean force = 22.9 KN   = 2
         -Energy absorption (J) = 2,630 E_{glass} = 6 × 10^4 MN m^{-2}
         -Shortening of 150 mm υ_{glass} = Poisson's ratio
                                               = 0.25
Bird type w_g = dead weight/density
   Type Archaeopteryx type of falcon.   = 2,700 kg m^{-3}
   W = weight = 4.3 kg = 0.039076 KN
   P_{bird} = 950 kg m^{-3}
Total No. of impacting masses   = 10,100
   Each nodal mass   = 0.627 g
No. solid elements 8 noded   = 1,800
   α = bird material porosity = 0.15 ← British Animal Welfare Association

$d/l = \dfrac{Diameter}{element\ length} = 8$

$P = \text{Pressure} \dfrac{P}{P_l} = \dfrac{Density}{Initial\ Density}$ ← (Plate 4.13)

t_d = duration time (bird penetrating into = 0.004 s
      inlet structure and impacting the forward bulkhead)
t_{pen} = time of penetrating bird nacelle is empennage as well $\ngtr$ 0.002 s
u_0 = velocity at which the bird approaches nacelle = 350 kts near exhaust also
      = 139 m s^{-1}

---

proved itself to be highly effective for high velocity impacts such as bird
impacts. The stress-strain curve for the aircraft polycarbonate composite
material has been the part input for the program ISOPAR together with
the Hugoniot type pressure volume of a bird like material. Plate 4.13 shows

results of the nacelle damage curve for the light alloy zone. The response curve defining force-time-mass due to the bird impact is also shown. The axial load deformation of the aircraft composite is indicated on Plate 4.12.

4.16.5 LS-Dyna Gap/Contact Elements

The gap elements or contact elements are based on Hallquist method. Fig. (e) Plate 4.11 given in the text. The number of slave segments and number of master segments are defined by interface control cards. IREAD flag is to read additional control cards. Ties interface contact definitions are based on offset option which can be used with rigid bodies. Typical letters and numbers are given below as:

Type number (the letters 'a', 'm', 'o' and 'p' must be in col. 13)
1-sliding without penalties
p1-symmetric sliding with penalties (recommended)
2-tied, see note 1 below
02-tied with offsets permitted, see note 1 below
3-sliding, impact, friction
a3-sliding, impact, friction, no segment orientation
m3-sliding, impact, friction-metal forming option
4-single surface contact
5-discrete nodes impacting surface
a5-discrete nodes impacting surface, no segment orientation
m5-discrete nodes impacting surface-metal forming option
6-discrete nodes tied to surface, see note 1 below
06-discrete nodes tied to surface with offsets permitted
7-shell edge tied to shell surface, see note 1 below
07-shell edge tied to shell surface with offsets permitted
8-nodes spot welded to surface
9-tiebreak interface
10-one way treatment of sliding, impact, friction
a10-one way treatment, no segment orientation
m10-one way treatment of sliding, impact, friction metal forming option
11-box/material limited automatic contact for shells*
12-automatic contact for shells (no additional input required) see note 2 below
13-automatic single surface with beams and arbitrary orientations. See note 3 below
a13-like above but with extra searching for airbag contact
14-surface to surface eroding contact
15-single surface eroding contact
16-node to surface eroding contact
17-surface to surface symmetric/asymmetric constraint method
18-node to surface constraint method

(a) Cockpit with infrastrucure

(b) Bird Impact

(c) Finite Element Mesh Scheme

(e) Dynamic Displacement Response

(d) Pressure – Time function for a bird
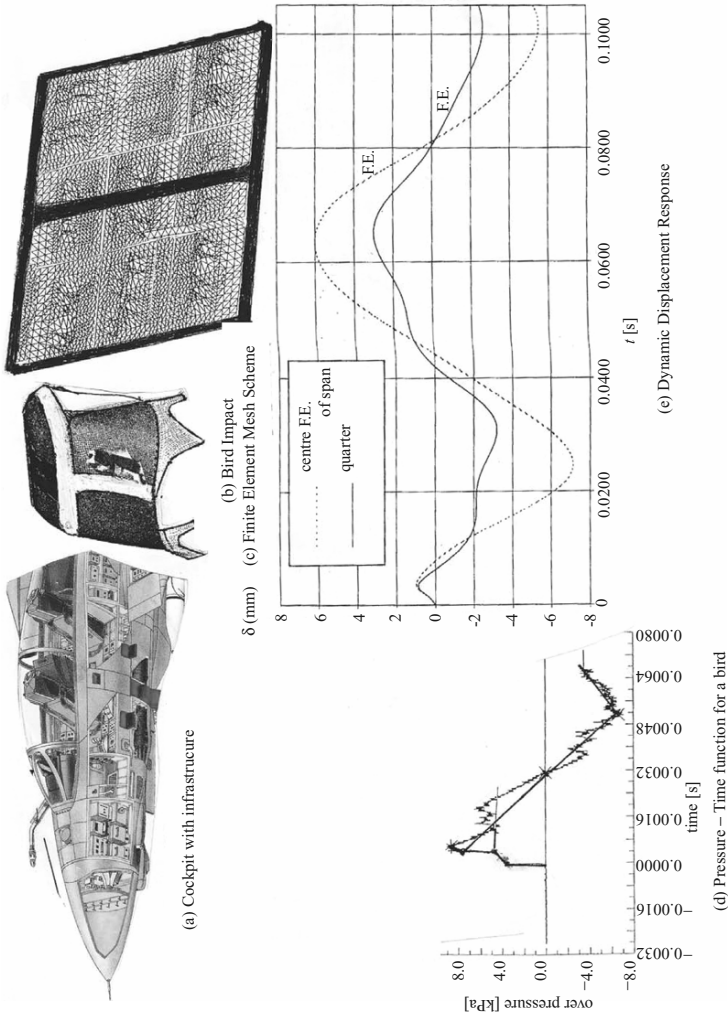
Plate 4.12. Bird impact – cockpit analysis and results

$$\sigma_r = \sigma_{r0}\left[1 + \left(\frac{\dot{\varepsilon}}{D}\right)^{1/q}\right]$$

Numerical 0.04 s^{-1}
Numerical 1600 s^{-1}

Stress-strain curve for aircraft ρdy polycarbonate composite material (Gruman, U.S.A)

Polynomial Law
Water α = 0.15

Polynomial Law for Bird
like material α = 0.15

Hugoniot water like Bird Material

Elastic-Plastic
Elastic-Plastic with Damage

Plastic strain

Damaged and stress-strain curve for light alloys in the aircraft (Gruman, U.S.A.)

Impact Load Time-dependent Impact loads versus mass with hydrodynamic response

Plate 4.13. Bird impact data and results

19-rigid body to rigid body contact with arbitrary force/deflection curve (this option may be used with deformable bodies)

20-rigid nodes to rigid body contact with arbitrary force deflection curve (this option may be used with deformable bodies)

21-rigid body to rigid body contact with arbitrary force/deflection curve. Unlike option 19 this is a one way treatment (this option may be used with deformable bodies)

22-single edge treatment for shell surface edge to edge treatment

23-simulated draw bead

25-force transducer contact for penalty based contact types. Not for types 2, 6, 7, 17 and 18

See type 27 below for the constraint type

26-automatic single surface, beams-to-beams, beam-to shell edge

27-force transducer contact for constraint based contact types. Applies to types 2, 6, 7, 17, and 18 only

Static coefficient of friction μ_s

EQ.-1: part based friction coefficients are used. Applies to contact types a 3, a5, a10 13, 15 and 26 only.

Tying will only work if the surfaces are near each other. The criteria used to determine whether a slave node is tied down is that it must be "close". For shell elements "close" is defined as distance δ, less than:

$\delta_1 = 0.60^*(\text{thickness\_slave\_node} + \text{thickness\_master\_segment})$
$\delta_2 = 0.05^* \min(\text{master\_segment\_diagonals})$
$\delta = \max(\delta_1, \ \delta_2)$

if a node is further away it will not be tied and a warning message will be printed.

For thermal control card
h_{rad} – radiation conductance
l_{gap} – length or thickness of gap between sliding surfaces
h – heat transfer conductance
$h = h_{cont}$, if the gap thickness is $0 \le l_{gap} \le l_{min}$
$h = h_{cond} + \text{hard}$, if the gap thickness is
$l_{min} \le l_{gap} \le l_{max}$
$h = 0$, if the gap thickness is $l_{gap} > l_{max}$

4.16.6 Bird Striking the Cock-Pit-Finite Element Analysis

Plate 4.12 shows the finite element mesh scheme for the cockpit framed glass. The damage scenario of the cockpit is shown on the 3D finite element mesh scheme when the heavy bird of 4.3 kg strikes the area with intensity. The impact also generated also a pressure shock wave as a shock wave function. The load-impulse of the maximum intensity shall be the sum of the pressure of incident and reflected waves on the bird impacted window surface and finally assumed to be of triangular shape or form.

The displacement response for the quarter and half of the glass (Plate 4.12) size, 1.6×1.8 m with an over pressure of 8 KN m^{-2} lasting 0.003 s. The fragment analysis given in this section can generate glass fragments ejected towards the inside of the cockpit. The extreme glass deflection, takes place under the effects of over pressure caused by the bird impact direction. The actual rotation of the glass panel in the mid plane does occur under extreme over pressures. The window frame under such an impact of great intensity not only in the basic dominant mode but also in higher vibration modes. It is interesting to observe from the shockwave, the glass failure is influenced by the rotation of the glass at mid point the results on various aspects are summarised in Plate 4.13. In conclusion it is typical, that the glass plate in initial phase of the transitional phenomenon copies practically the mode of the loading pulse if both times (dominant period and time of pressure durations are comparable) which can be observed in the displacement and stresses. The way of damage failure is based on the location of the place where ultimate location is exceeded in the dominate vibration mode. In this analysis the first cracks appear at 1/4 span of the glass. The stress strain ratio of the glass is linearly elastic and changes until the first cracks appear.

5

Shock and Explosion Dynamics

5.1 Introduction

An explosion is a rapid release of energy and can happen in air, on the Earth's surface, underground and underwater. Typical examples arise from chemical and nuclear explosives, thermal and hydroelectric sources and gas ignition. Section 2.5 of Chap. 2 gives a useful introduction to sources of explosion and also presents comprehensive data on explosions. The purpose of this chapter is to give a comprehensive treatment of explosion dynamics. The data given in Sect. 2.5 will act as input to various equations given in this chapter. The reader must now be familiar with the basis of structural dynamics given in Chap. 3. Since explosions may generate missiles, the reader is advised to have a thorough knowledge of Chap. 4. Section 3.4 of the Bibliography provides comprehensive coverage of in-depth treatment of specific areas.

5.2 Fundamental Analyses Related to an Explosion

5.2.1 Stress Waves and Blast Waves

Stress waves represent the basis of explosion in the surrounding medium, be it gaseous, liquid or solid. They are defined as moving parts of the medium, being in a state of stress such that the boundaries are *waves* and the rest of the medium consists of *wave fronts*. Stress waves are sometimes called *deformation waves*. These stress waves are divided into normal and tangential waves representing stresses in those directions. Normal waves may be divided into *pressure waves* and *tensile waves* or *rarefaction waves*. The normal waves are also known as P (longitudinal) waves and the S (tangential) waves as *transverse waves*. In geological media, the surface is the interface of individual layers of rock and soil or air and soil/rock. The interface between them is known as the *free surface*. The surface waves are then classified according to

the shape and sense of the trajectories followed by movements in a medium. The surface waves are given below:

(1) *The Rayleigh wave (R wave)*. This wave exhibits a planar elliptic motion in the medium such that its semi-axes decrease rapidly at a certain distance from a given depth.
(2) *The Love wave (Q wave)*. These waves exhibit a spatial motion in a medium and their components are parallel and normal to the plane of propagation.
(3) *The hydrodynamic wave (H wave)*. These waves are similar to R waves and propagate along the surface of the liquid and are free from shear stresses.
(4) *The composite wave (C wave)*. The surface particles exhibit a complex phenomenon when compared with others.

The R wave propagation is expressed as:

$$\delta_x = W_{E(t)}L'\{\exp(-qz) - 2q\bar{s}[(\bar{s})^2 + (L')^2 \exp(-\bar{s}z)]\} \times \sin(\omega t - L'x), \tag{5.1}$$

$$\delta_z = W_{E(t)}L'\{\exp(-qz) - 2(L')^2[(\bar{s})^2 + (L')^2 \exp(-\bar{s}z)]\} \\ \times \cos(\omega t - L'x), \tag{5.2}$$

where x, y and z are the co-ordinate axes

$L' = \omega/v_{SR}$
ω = circular frequency
v_{SR} = velocity of sine wave in the Y-direction
t = time
δ = particle displacement
$q = \omega^2 \left(v_{SZ}^2 - v_{RZ}^2\right)/v_{PZ}^2 v_{SZ}^2$
$\bar{s} = \omega^2 \left(v_{SZ}^2 - v_{RZ}^2\right)/v_{SZ}^2 v_{RZ}^2$
$W_{E(t)}$ = work done
v_{SZ} = propagation velocities of transverse waves
v_{PZ} = propagation velocities of longitudinal waves
v_{RZ} = propagation velocities of Rayleigh waves

The Q wave is generally propagating in the Y-direction if the x, y plane lies on the interface of the layer and on the mass medium. The displacement δ_y is a function of time t and the co-ordinates x and z. The Q wave is expressed as

$$\delta_y(x, z, t) = (A \cos \alpha' z + B \sin \alpha' z) \exp[L'(v_z t - x)], \tag{5.3}$$

where A, B = constants
L' = a wave number
v_z = phase velocity
$\alpha' = L'\sqrt{[v_z^2/(v_{sz}^2 - 1)]}$

The phase velocity v_z is determined from

$$v_z = \frac{G_m}{G_s L' d} \times v_{szs} \times \sqrt{\left\{ \left[\tan^{-1} \sqrt{\left(1 - \frac{v_z^2}{v_{szsn}^2}\right) \Big/ \left(\frac{v_z^2}{v_{szs}^2} - 1\right)} \right]^2 + 1 \right\}}, \quad (5.4)$$

where v_{szs} = propagation velocity of the explosion

v_{szsn} = propagation velocity in the mass half space

G_m, G_s = moduli of elasticity in shear and mass half space, respectively

Explosions and Surface Waves

Explosions can occur in different forms. The ones of note are explosions of a spherical charge and of a cylindrical charge. In blast dynamics, slab charges are popular. All these are discussed later in specific sections.

Explosion of a Spherical Charge

When a charge is located at a sufficient depth below the surface, the explosion causes vibrations to propagate in the form of spherical wave fronts in a longitudinal direction, with mass particles displaced radially. This displacement is generally calculated [4.40–4.106,4.250] as

$$\delta_r = \text{radial displacement}$$
$$= \frac{r_s^2 v_{zp} \alpha}{r_s^2 (\beta r_s - v_{zp})} \times \left\{ \frac{r_s}{v_{zp}} \left[1 - \left(t - \frac{r_s}{v_{zp}} - \frac{r_s}{\beta r_s - v_{zp}}\right) \beta \right] \right.$$
$$\left. + t - \frac{r_s}{\beta r_s - v_{zp}} \right\} e^{-\beta(t - r_s/v_{zp})}, \quad (5.5)$$

where v_{zp} = velocity in $\mathrm{m\,s^{-1}}$

r_s = radius of the cavity of the charge (sometimes known as R_w)

t = time

α, β = constants for the particular type of charge

Explosion of a Cylindrical Charge

The following gives displacements δ_R, δ_θ and δ_ϕ in cylindrical co-ordinates for a cylindrical cavity:

$$\delta_R = \frac{R_0^2 \, hp}{4 \, m_R v_{zp} R} \left(1 - \frac{2v_{zs}^2}{v_{zp}^2} \cos^2\phi\right) \frac{\partial F(t - R/v_{zp})}{\partial t}, \quad (5.6)$$

$$\delta_{\dot\theta} = 0; \; \delta_\phi = \frac{R_0^2 \, hp \sin 2\phi}{4 \, v v_{zs} R} \left[\frac{\partial F(t - R/v_{zs})}{\partial t}\right], \quad (5.7)$$

where R_0 = base of a cylinder with height h

m_R = relative mass

$\delta_R, \delta_\theta, \delta_\phi$ = displacements in cylindrical co-ordinates R, θ and ϕ, respectively

v = Poisson's ratio

t = time

Damping of Stress Waves

When a stress wave caused by an explosion propagates in a material it is damped at a certain distance, x and its amplitude $X(x)$ is given by

$$X(x) = X_0 e^{(-\gamma x)}, \tag{5.8}$$

where $X(x)$ = amplitude at a distance x
$\quad\quad X_0$ = amplitude of the wave at a source
$\quad\quad \gamma$ = damping ratio

Formation of Blast Waves from Explosives and Their Sealing Laws

Section 2.5 gives a useful introduction to blast wave formation. As stated, when the blast wave from an explosion travels outward, the volume of air included behind the shock front becomes so great that the initial volume of the explosion becomes unimportant. Positive and negative phases are predicted. In this section, blast waves occur due to explosives. The finite size of the explosive charge from chemical explosives has a different effect from that of nuclear explosives. As seen in Fig. 5.1, the effect is initially to spread out the energy with a reduction in peak overpressure over an appreciable distance from the charge source. The influence of the charge diameter on the blast wave is thus related to two volume displacements – one from a point source with no initial atmospheric change and the other from a point source in a nominal standard pressure. This is given by

$$c_f = (\rho V / \rho_{TN} V_{TN})^{1/3}, \tag{5.9}$$

where c_f = charge size factor
$\quad V, V_{TN}$ = actual and required TNT volumes, respectively
$\quad \rho, \rho_{TN}$ = actual and standard TNT atmosphere densities, respectively

For a chemical explosion, the relationships between explosion overpressure and ambient atmosphere, duration time and impact load are compared with those for a nuclear explosion in Table 5.1. Impulse or impact depends on the peak overpressure, p_{so}, in the shock front and on the duration of the wave. In some cases, the rate of decay of the overpressure can influence the impulse/impact load. The scaling principle to explosion has also been given in Sect. 2.5. The scaling law for explosion is defined for the distance for *uniform atmosphere* as

$$\text{scaled distance} = x \times \rho_{TN}^{1/3} / E_R^{1/3}. \tag{5.10}$$

For a non-uniform atmosphere the scaled distance will be different. The energy release, E_R, is almost equal to the weapon yield.

The *scaling of the overpressure* is given by

$$\text{actual pressure} = \text{overpressure} \times p_a, \tag{5.11}$$

where p_a is the atmospheric pressure.
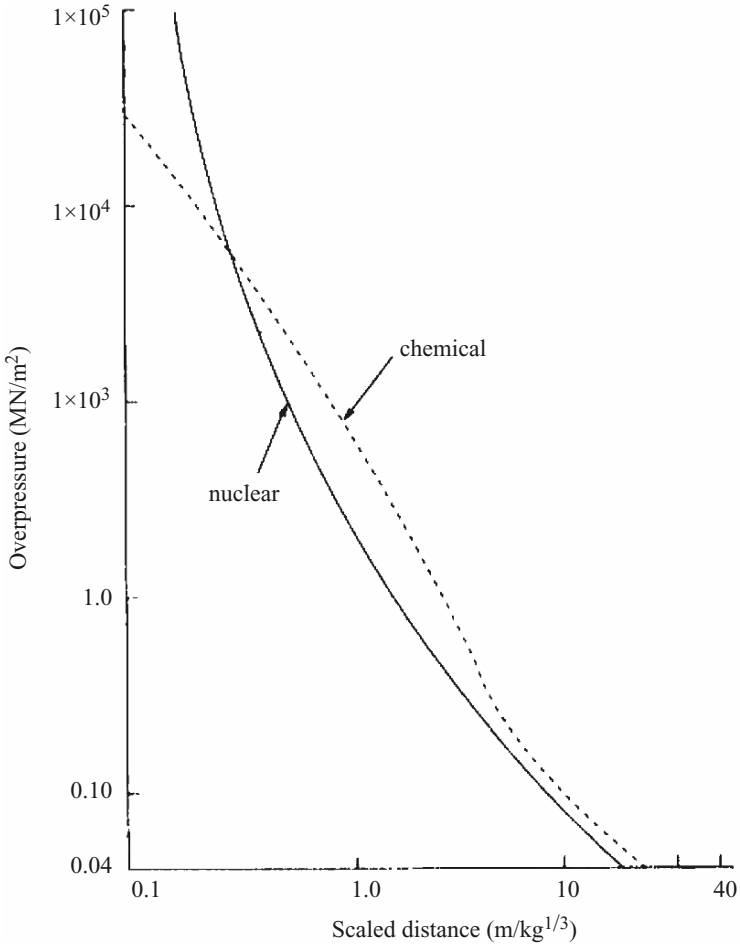
Fig. 5.1. The behaviour of chemical and nuclear explosions in terms of overpressure versus scaled distance

The *scaling time*, t_{sc}, is given by

$$t_{sc} = t_a \times f_t/Y^{1/3}, \qquad (5.12)$$

where f_t, the transmission factor for time, is given by

$$f_t = \left(\frac{\rho}{\rho_{TN}}\right)^{1/3} \left(\frac{T}{T_{TN}}\right)^{1/6} \qquad (5.13)$$

and is expressed in terms of atmospheric pressure and temperature,

where T, T_{TN} = actual and TNT temperatures, respectively
$\qquad\quad Y$ = weapon yield, W

Table 5.1. A comparison of overpressures, time duration and impact loads for chemical and nuclear explosions

Chemical	Nuclear

Chemical:

$$\frac{p_{so}}{p_a} = \frac{40.4x^2 + 810}{\sqrt{[(1 + 434x^2)(9.77x^2)(1 + 0.55x^2)]}}$$

$$\frac{t_d}{Y^{1/3}} = \frac{990 + 4.65 \times 10^5 x^{10}}{(1 + 125 \times 10^3 x^3)(1 + 6.1x^6)} \times \frac{1}{\sqrt{(1 + 0.02x^2)}}$$

$$F_I(t)/\text{unit area} = \frac{0.7}{x^2} \times \frac{\sqrt[2]{(1 + 360x^4)}}{\sqrt[3]{(1 + 0.27x^3)}}$$

t_d = duration time in seconds for 1 kilotonne TNT

x = distance in m

Example

Transmission factor for a distance = 0.7

Energy release = 100 kg TNT at a height of 12,000 m

Atmospheric pressure = 260 mbar

A point is 15 m away

Scaled distance = $0.7(15/100^{1/3}) \approx 2.30$

Peak overpressure ratio = 1.51

Transmission factor = 0.615

Scaled duration = 1.32 ms

Actual duration = $100^{1/3}(1.32/0.615) = 9.97$ ms

Overpressure = $1.52 \times 260 = 390$ mbars = 0.39 bars

Nuclear:

$$\frac{p_{so}}{p_a} = \frac{5.12}{x^2} \times \sqrt{(1 + 0.00013x^2)}$$

$$t_d/Y^{1/3} = (200\sqrt{1 + 1 \times 10^{-6}x^3})(1/Z),$$

where

$$Z = \sqrt{(1 + 0.025x)}[\sqrt[6]{(1 + 5.25 \times 10^{-13}x^5)} \times \sqrt{(1 + 2 \times 10^{-5}x)}]$$

$$F_I(t)/\text{unit area} = \frac{0.92}{x^3} \times \frac{\sqrt[2]{(1 + 1050x^4)}}{\sqrt[3]{(1 + 0.135x^3)}}$$

The *direct impulse/impact scaling* per unit area is written as

$$F_1(t)/\text{unit area} = (\text{scaled impulse/area})(p_{\text{so}}/p'_{\text{s}})(t_{\text{a}}/t_{\text{sc}}),\qquad(5.14)$$

where $p'_{\text{s}} = $ standard overpressure for reference explosion.

Transmission factors for distance and time for large explosions, with large path distances and variations in atmospheric pressure and temperature, can be written in integral form:

$$\text{scaled distance} = \frac{1}{Y^{1/3}} \int_{x_1}^{x_2} \left(\frac{\rho}{\rho_{\text{TN}}}\right)^{1/3} \, \mathrm{d}x.\qquad(5.15)$$

A *transmission factor to conform to variations of pressures and temperatures* will be given by

$$\bar{f}_{\text{d}} = \text{transmission factor for distance},$$

$$\bar{f}_{\text{d}} = \frac{1}{x} \int_{x_1}^{x_2} \left(\frac{\rho}{\rho_{\text{TN}}}\right)^{1/3} \, \mathrm{d}x,\qquad(5.16)$$

where x represents the actual distance. Similarly, the transmission for time is given by

$$f_{\text{t}}'' = \int_{x_1}^{x_2} \left(\frac{\rho}{\rho_{\text{TN}}}\right)^{1/3} \left(\frac{T}{T_{\text{TN}}}\right)^{1/2}.\qquad(5.17)$$

The subjects of open air, underground and underwater explosions are fully discussed under different headings in this chapter. The above elements are common to all of them.

5.3 Explosions in Air

Explosion characteristics, including duration, are based on the sudden release of energy. An explosion may be due to nuclear detonation, explosives, gas or dust. These have been discussed in Sect. 2.5. As stated, the magnitude of an explosion in relative values is known as the explosive yield. One generally accepted standard is the energy released in an explosion of TNT (symmetrical 2,4,6-trinitrotoluene). As stated in Sect. 2.5, the front of the shock wave is quite steep and, as a result, the pressure may be treated as instantaneous. The dynamic load is then characterized by a rapidly reached peak value which decreases as the blast wave decays. The net effect of the load depends on the structure of the blast wave and on the geometry and construction of the structure. The basic relationship for such a blast wave having a steep front is given by Rankine–Hugonist, [4.251] and is based on the conservation of mass, energy and momentum at the shock front. Using Fig. 5.2 and the above conditions together with the equation of state for air, the blast wave pressure is written as
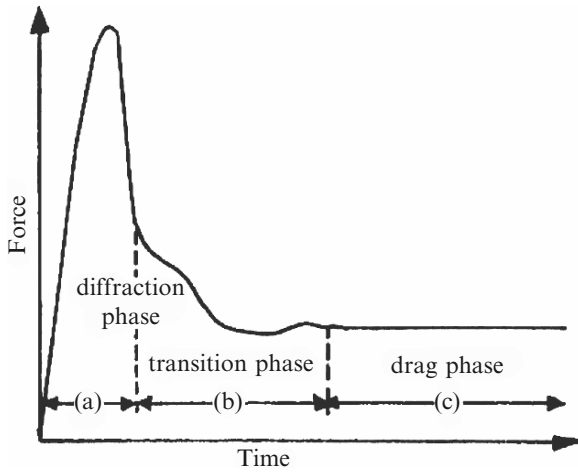
Fig. 5.2. Force–time history

$$\frac{U}{v_{\mathrm{s}}} = \left(1 + \frac{6}{7}\frac{p_{\mathrm{so}}}{p_{\mathrm{a}}}\right)^{1/2}, \tag{5.18}$$

$$\frac{u}{v_{\mathrm{s}}} = \frac{5}{7}\frac{p_{\mathrm{so}}}{p_{\mathrm{a}}}\left(1 + \frac{6}{7}\frac{p_{\mathrm{so}}}{p_{\mathrm{a}}}\right)^{1/2}, \tag{5.19}$$

$$\frac{\rho}{\rho_{\mathrm{a}}} = \frac{7 + 6p_{\mathrm{so}}/p_{\mathrm{a}}}{7 + p_{\mathrm{so}}/p_{\mathrm{a}}}, \tag{5.20}$$

$$\frac{p_{\mathrm{r}}}{p_{\mathrm{so}}} = 2\frac{7p_{\mathrm{a}} + 4p_{\mathrm{so}}}{7p_{\mathrm{a}} + p_{\mathrm{so}}}, \tag{5.21}$$

$$\frac{q}{p_{\mathrm{so}}} = \frac{5}{2}\frac{p_{\mathrm{so}}}{7p_{\mathrm{o}} + p_{\mathrm{so}}}, \tag{5.22}$$

$$\left(\frac{v_{\mathrm{so}}}{v_{\mathrm{s}}}\right)^2 = \frac{(p_{\mathrm{so}} + p_{\mathrm{a}})(p_{\mathrm{so}} + 7p_{\mathrm{a}})}{6p_{\mathrm{so}} + 7p_{\mathrm{a}}}, \tag{5.23}$$

$$M^2 = \left(\frac{u}{v_{\mathrm{so}}}\right)^2 = \frac{25}{7}\frac{p_{\mathrm{so}}^2}{(p_{\mathrm{so}} + p_{\mathrm{a}})(p_{\mathrm{so}} + 7p_{\mathrm{a}})}, \tag{5.24}$$

$$\frac{R}{R_{\mathrm{a}}} = 0.727p_{\mathrm{so}}/p_{\mathrm{a}}, \tag{5.25}$$

$$\frac{p_{\mathrm{r}}}{q_{\mathrm{do}}} = \frac{4}{5}(4 + 7p_{\mathrm{a}}/p_{\mathrm{so}}), \tag{5.26}$$

where v_{so} = speed of sound in the air behind the shock front
   v_{s} = speed of sound in ambient air
   M = Mach number
   p_{a} = pressure of ambient air
   p_{so} = overpressure
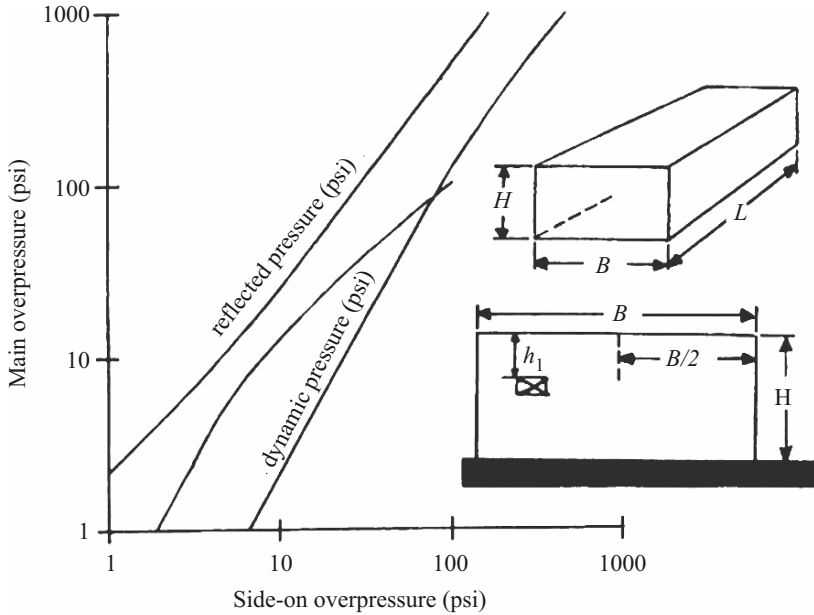
Fig. 5.3. Overpressure p_{so} versus p_r, M and q_{do} for a building

p_r = reflected pressure
p_{do} = dynamic pressure = $\frac{1}{2}\,\rho u^2$
$\overline{R}$ = Reynolds number per foot (flow behind shock front)
$\overline{R}_a$ = Reynolds number per foot for ambient air sea level (6.89×10^6)
u = particle velocity of flow behind the shock front
U = shock front velocity
ρ = density of air behind shock front
ρ_a = density of ambient air

Figure 5.3 shows reflected pressure, dynamic pressure and Mach number for side-on overpressure. When the blast wave is vertical and strikes the front face of the structure, normal reflection occurs and the entire facade of the building or structure is instantly subjected to the reflected overpressure, p_{ro}, which is greater than p_{so}, the overpressure in the immediate surroundings. As a result, the blast air flows from the region of high pressure to the one of low pressure, forming a rarefaction wave with a velocity u_{rr} over the front of the structure. It then progresses inward from the edges of the structure, moving with a velocity v_s in the reflected medium. This speed varies with time as the blast wave decays. For example, as shown in Fig. 5.3, if one takes a small panel of a structure, the wave varies at this panel with a corresponding time h_1/u_{rr}, where h_1 is the distance from the top to that panel and u_{rr} is the rarefaction velocity. Assuming this time is t_1, the relieving time, t_r, is about twice that required for the sound wave, which is $t_2 - t_1 = 2x/u_{rr}$, where t_2 is the forward
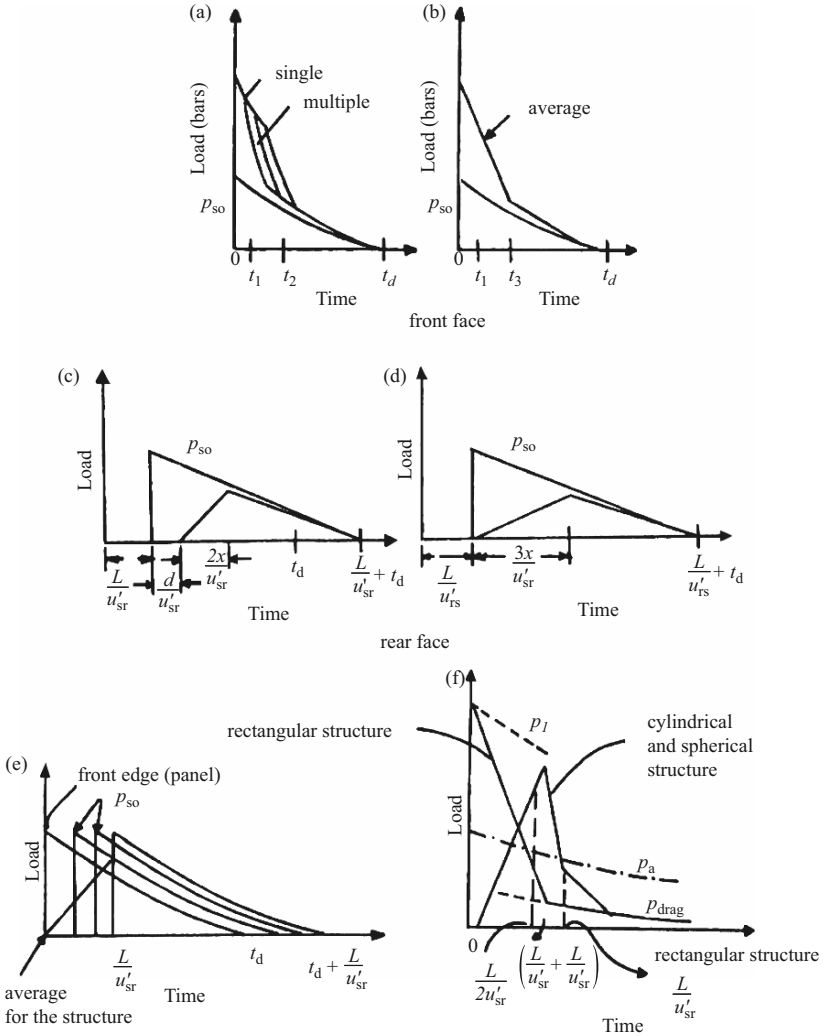
Fig. 5.4. Load–time relationships for blasts in open air. (**a**) Several panels; (**b**) average for the structure; (**c**) one panel; (**d**) average for the rear face; (**e**) side or top face; (**f**) drag type loads

time and x is the distance through which the pressure relief is obtained for the length of the structure, L, width, B, and height, H. Figure 5.4 gives load distributions on various faces against time. The peak diffraction pressure, p_{df}, and peak drag load, p_d, are given by

$$p_{df} = p_r A, \tag{5.27}$$
$$p_d = p_D C_D A, \tag{5.28}$$

where A is the projected area, C_D is the drag coefficient, p_r is the reflected pressure and p_D is the dynamic pressure $\approx p_{so}$.

The blast wind from an explosion exerts loads on structures which are quite similar to those developed by natural winds. Nevertheless, these wind load surfaces are transient in nature and of considerably greater magnitude than those developed by conventional winds. The drag coefficient is also defined as

$$
\begin{aligned}
C_D &= \text{drag energy/kinetic energy} = (p_d/\rho)/\frac{1}{2}u^2 \\
&= 2p_d/\rho u^2.
\end{aligned}
\tag{5.29}
$$

For an ideal gas explosion in air

$$
\rho = \text{density} = p_a/RT,
\tag{5.30}
$$

where R is the gas constant, T is temperature, p_d is the drag load and p_a is the pressure. The value of R is equal to $287\,\mathrm{J\,kg^{-1}\,K^{-1}}$.

The value of C_D is also written in terms of Mach numbers as

$$
C_D = 2p_d/k_r M^2 p_a.
\tag{5.31}
$$

The value of p_d is then written as

$$
p_d = \frac{1}{2}C_D\rho u^2 = \frac{1}{2}k_r M^2 C_D p_a,
\tag{5.32}
$$

where k_r = heat capacity ratio = $C_p/C_v \approx 1.4$
$\quad C_p$ = specific heat capacity at constant pressure
$\quad C_v$ = specific heat capacity at constant volume

The Mach number may be written as

$$
M = u/(kRT)^{1/2}.
\tag{5.33}
$$

An individual small panel experiences load from an explosion when the shock front has traversed the distance L, the entire length of the structure, and a compression wave has travelled a distance h_1 from the near edge into the panel. The time for the shock will be L/u'_{sr}, where u'_{sr} is the speed of the shock, a value close to U. After these times the pressure on the panel increases and becomes instantaneous pressure on the rear face equal to $p_{stag} - p_{drag}$. Figure 5.4c, d show the load–time function for the rear face for a small panel and an average for the entire rear face. Similarly, for the panels along the side or top of a structure, ignoring reflection and p_{stag} (stagnation), the overpressure diagram is as shown in Fig. 5.4e. Figure 5.4f illustrates dynamic drag type loading. To summarize, the load–time function will assume the generalized form shown in Fig. 2.72.

The stagnation pressure is an important consideration. The value of p_{stag} is computed as

$$p_{\text{stag}}/p_{\text{a}} = 1 + (k/2)M^2 + (k/8)M^4 + K/48(z-k)M^6 + \ldots \qquad (5.34)$$

$$(p_{\text{stag}} - p_{\text{a}}) - p_{\text{d}}(\text{or } q) = p_{\text{a}}(k/8)M^4 + p_{\text{a}}[k/48(z-k)]M^6 + \ldots \qquad (5.35)$$

In the case of a gas explosion in air, (5.35) shows a non-compressible fluid flow and $p_{\text{d}} = q$ represents the blast impact, but for a non-compressible fluid, with the speed of sound being infinite, all flows are at zero Mach number M. Equation (5.35) becomes

$$(p_{\text{stag}} - p_{\text{a}}) = p_{\text{d}} = q. \qquad (5.36)$$

5.3.1 Thickness of the Shock Front

The thickness of the shock wave is the ratio of the velocity jump between two points u_1 and u_2 divided by the maximum velocity gradient $(\mathrm{d}u/\mathrm{d}x)_{\text{max}}$ in a specific zone. In terms of Mach number, the thickness t_{sh} of the shock front using the Rankine–Hugonist equation is given by

$$t_{\text{sh}} = [(11 + 7M)/\rho(M-1)]10^{-8}. \qquad (5.37)$$

5.3.2 Evaluation of Stagnation Pressure, Stagnation and Post-Shock Temperatures

The stagnation pressure, p_{stag}, is given in (5.35) in terms of ambient pressure and is now defined in terms of the velocity of sound, v_{s}, and v_{so}, which is the speed of sound after the shock front. The value of p_{stag} is given by

$$p_{\text{stag}} = p_2 \left[1 + \frac{(k-1)(v_{\text{so}}/v_{\text{s}})^2}{2(T_2/T_{\text{a}})} \right]^{k/k-1}, \qquad (5.38)$$

where $p_2 = $ shock-generated pressure
$\quad T_2 = $ shock-generated temperature
$\quad T_{\text{a}} = $ ambient temperature
$\quad v_{\text{so}} = $ blast-generated velocity

The temperature known as the blast stagnation temperature obeys the relationship

$$\frac{T_{\text{stag}}}{T_{\text{o}}} = \frac{T_2}{T_{\text{a}}} + \frac{1}{2}(k-1)\left(\frac{v_{\text{so}}}{v_{\text{s}}}\right)^2. \qquad (5.39)$$

The value of k is generally taken as 1.4. The post-shock temperature T_{ps} is given for $k = 1.4$ by

$$\frac{T_{\text{ps}}}{T_{\text{a}}} = \left(\frac{v_{\text{so}}}{v_{\text{s}}}\right)^2 = \frac{(p_2/p_{\text{a}} + 6)(p_2/p_{\text{a}})^{5/7}}{6(p_2/p_{\text{a}}) + 1}, \qquad (5.40)$$

where T_{ps} is the temperature under post-shock.

5.3.3 Oblique Shock

A shock wave may occur in a plane that is oriented at an angle θ to the direction of the blast wind flow. Let that velocity be v_{so}; its components are v_1 and v_2, as shown in Fig. 5.5. In this oblique shock phenomenon, the velocity vectors are related in terms of the angle θ and the angle α of the shock plane with respect to the on-coming stream by

$$v_{so2}/v_2 = \tan(\alpha - \theta), \tag{5.41}$$

where v_{so2} and v_2 are the velocities after shock of the normal and parallel components, respectively. The Mach number is given by

$$M_1 \text{ (normal to the shock plane)} = v_{so1} \sin\alpha / v_{s1}$$
$$= M_{o1} \sin\alpha. \tag{5.42}$$

For the downstream component v_{so2}:

$$M_2 \text{ (normal to the shock plane)} = v_{so2}/v_s$$
$$= v_{so2} \sin(\alpha - \theta)/v_{s2} \tag{5.43}$$
$$= M_{o2} \sin(\alpha - \theta),$$

where v_{s1} and v_{s2} are shock velocities in planes 1 and 2.

The following equations may be derived along the same lines as (5.38)–(5.40):

$$p_2/p_a = \frac{kM_{o1}^2 \sin^2\alpha - \dfrac{k-1}{2}}{(k+1)/2}. \tag{5.44}$$
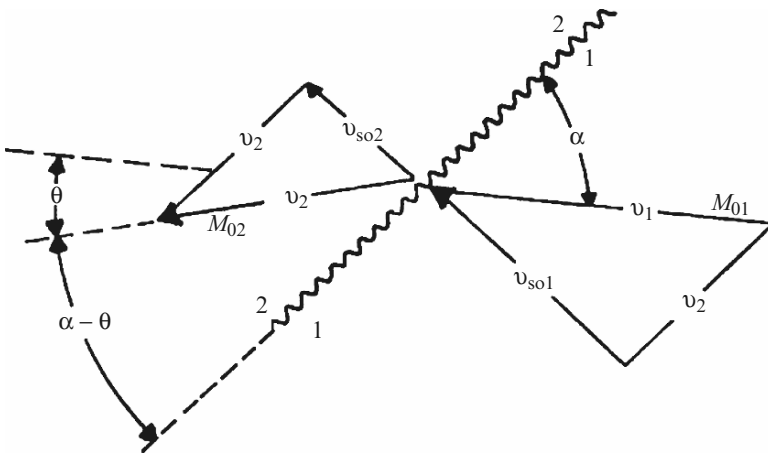
Fig. 5.5. Oblique shock

For the temperature and the speed-of-sound effects, T_2/T_a is given by

$$T_2/T_a = (v_{s2}/v_{s1})^2 = \frac{1 + \dfrac{k-1}{2}(M_{o1}^2 \sin^2 \alpha)\left(kM_{o1}^2 \sin^2 \alpha - \dfrac{k-1}{2}\right)}{\left(\dfrac{k+1}{2}\right)^2 M_{o1}^2 \sin^2 \alpha}. \quad (5.45)$$

The Mach numbers of the upstream and downstream velocities, before and after the shock, are related by

$$[M_{o2} \sin(\beta - \theta)]^2 = \frac{2 + (k-1)M_{o1}^2 \sin^2 \alpha}{2kM_{o1}^2 \sin^2 \alpha - (k-1)}. \quad (5.46)$$

The values of p_a and T_a are in plane 1, i.e. $p_a = p_2$ and $T_a = T_1$. The value of k is generally taken as 1.4.

The relation between the angle of the shock plane, α, and the angle of deflection, θ, may be found from:

$$\frac{\tan(\alpha - \theta)}{\tan \alpha} = \frac{2 + (k-1)M_{o1}^2 \sin^2 \alpha}{(k+1)M_{o1}^2 \sin^2 \alpha}. \quad (5.47)$$

The *maximum deflection* can easily be obtained from Fig. 5.6 for a given Mach number. Using the manipulated version of (5.47), the value of α is computed as

$$\sin^2 \alpha = \frac{1}{4kM_{o1}^2} \times (k+1)M_{o1}^2 - 4 + \sqrt{\{(k+1)[(k+1)M_{o1}^4 + 8(k-1)M_{o1}^2 + 16]\}}. \quad (5.48)$$

5.4 Shock Reflection

5.4.1 Normal Shock Reflection

The reflected shock front exhibits the same particle velocity as that of the incident shock. Nevertheless, the characteristics of the two shocks moving through different media are different. In a similar manner, the particle velocity ratio v_{so}/v_{so1} is related to $p_2/p_a = p_r/p_2$, using Sect. 5.3.2, by

$$(v_{so}/v_{so1})^2 = \frac{\left(\dfrac{2}{k}\right)\left(\dfrac{p_r}{p_2} - 1\right)^2}{(k+1)\left(\dfrac{p_r}{p_2}\right) + (k-1)} = \left(\frac{v_{so}}{v_{so2}}\right)\left(\frac{T_2}{T_a}\right), \quad (5.49)$$

where p_r is the absolute pressure generated in the reflected shock.
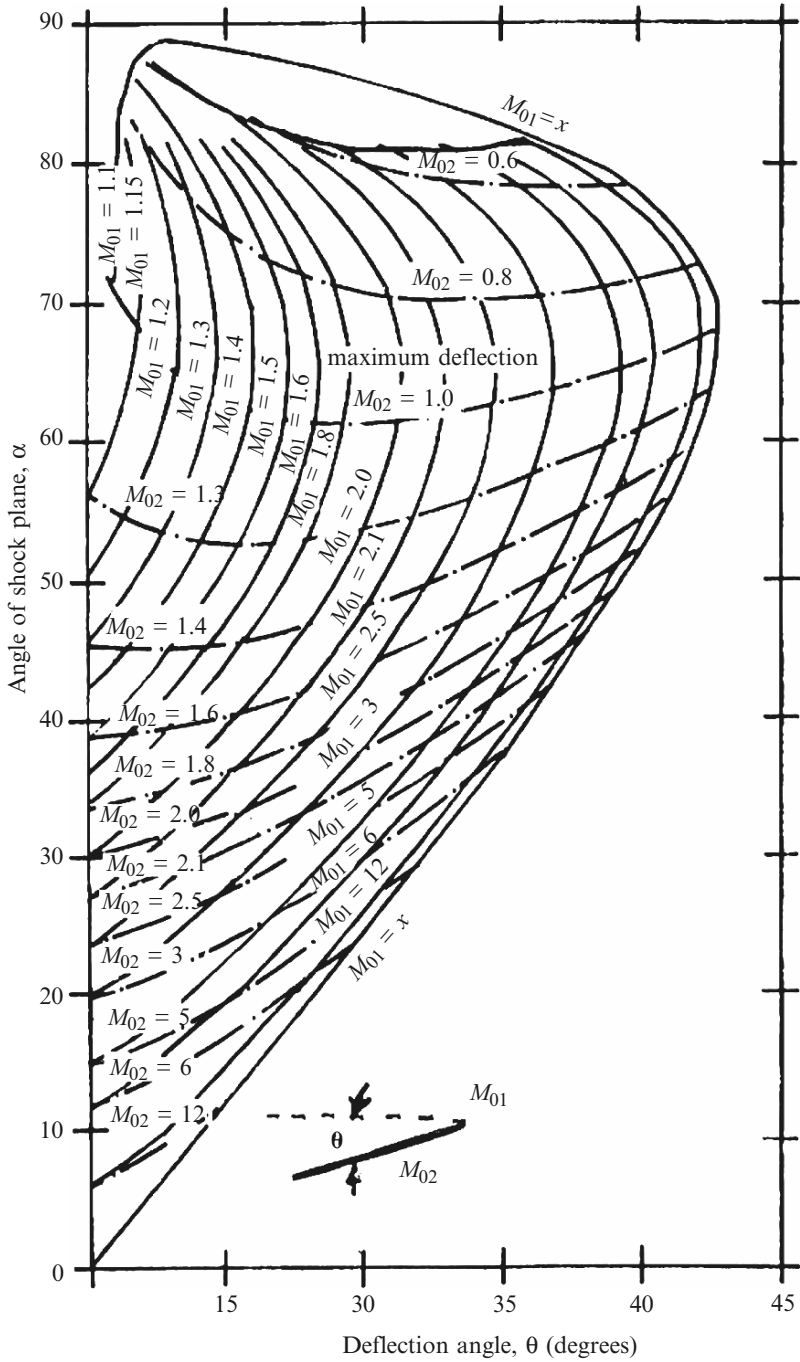
Fig. 5.6. Numerical relationships of θ and α for given values of M_{o1} and M_{o2}

Equation (5.49) can easily be written in terms of p_r/p_2 as

$$p_r/p_2 = \frac{(3k-1)(p_2/p_1) - (k-1)}{(k-1)(p_2/p_1) + (k+1)}, \tag{5.50}$$

where p_1 is the pressure of the unshocked air $\approx p_a$.

The Mach number, M_r, for the reflected shock can similarly be related to the Mach number for the incident shock, M_{o1}, by

$$M_r^2 = \frac{2kM_{o1}^2 - (k-1)}{(k-1)M_{o1}^2 + 2}. \tag{5.51}$$

The relationship between p_r and p_1, the incident shock and the Mach number can be written in the following form:

$$
\begin{aligned}
p_r/p_1 &= \frac{(p_2/p_1)[(3k-1)(p_2/p_1) - (k-1)]}{(k-1)(p_2/p_1) + (k+1)} \\
&= \frac{[(3k-1)M_1^2 - 2(k-1)][2kM_1^2 - (k-1)]}{(k^2-1)M_{o1}^2 + 2(k+1)}.
\end{aligned} \tag{5.52}
$$

Using $k = 1.4$, (5.50)–(5.52) can be modified. The resulting equations are similar to equations (5.18)–(5.26). For example, (5.51) becomes

$$M_r^2 = \frac{7M_{o1}^2 - 1}{M_{o1}^2 + 5} \tag{5.53}$$

and (5.52) becomes

$$p_r/p_1 = \frac{\left(4M_{o1}^2 - 1\right)\left(7M_{o1}^2 - 1\right)}{3(M_{o1}^2 + 5)}. \tag{5.54}$$

The temperature after the shock is greater than the ambient temperature $T_1 = T_a$. The reflected value T_r can easily be derived after algebraic manipulation similar to (5.40).

$$T_r/T_1 = T_a = \left(\frac{v_{sr}}{T_a}\right)^2 = \frac{\left[(k-1)\left(\frac{p_2}{p_1}\right) + 1\right]\left[3(k-1)\frac{p_2}{p_1} - (k-1)\right]}{k\left[(k+1)\frac{p_2}{p_1} + (k-1)\right]}. \tag{5.55}$$

The *reflection coefficient* is defined by

$$
\begin{aligned}
C_r &= \frac{p_r - p_1}{p_2 - p_1} \\
&= \frac{\text{reflected overpressure}}{\text{overpressure in the incident shock}} \\
&= \frac{(3k-1)(p_2/p_1) + (k+1)}{(k-1)(p_2/p_1) + (k+1)} \\
&= \frac{(3k-1)M_{o1}^2 + (3-k)}{(k-1)M_{o1}^2 + 2}.
\end{aligned} \tag{5.56}
$$
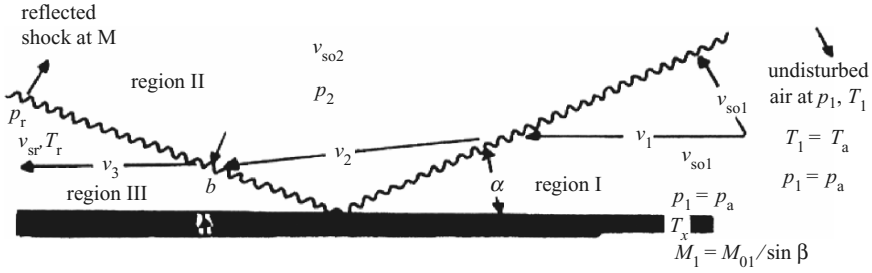
Fig. 5.7. Oblique reflection of shock waves

For $k = 1.4$

$$C_\mathrm{r} = \frac{8M_{\mathrm{o}1}^2 + 4}{M_{\mathrm{o}1}^2 + 5}. \tag{5.57}$$

5.4.2 Oblique Reflection

Figure 5.7 illustrates the basic concept of oblique reflection. An incidental shock at $M_{\mathrm{o}1}$ with an incident angle of α causes a corresponding reflected shock in Mach number:

$$M_\mathrm{r} = M_{\mathrm{o}1} \sin \alpha. \tag{5.58}$$

The angle β of this reflected shock is given by

$$\beta = (\alpha - \theta), \tag{5.59}$$

where θ is the deflection angle. From (5.54), the value of p_r/p_1 becomes

$$p_\mathrm{r}/p_1 = (7M_\mathrm{r}^2 - 1)(7M_{\mathrm{o}1}^2 - 1)/36. \tag{5.60}$$

The reflection coefficient is derived using (5.56) with $k = 1.4$:

$$\begin{aligned} C_\mathrm{r} &= \frac{p_\mathrm{r} - p_1}{p_2 - p_1} \\ &= \frac{\left(7M_\mathrm{r}^2 - 1\right)\left(7M_{\mathrm{o}1}^2 - 1\right) - 36}{42(M_{\mathrm{o}1}^2 - 1)}. \end{aligned} \tag{5.61}$$

The Mach number $M_{\mathrm{o}2}$ in region II for $k = 1.4$ will be

$$[M_{\mathrm{o}2} \sin(\alpha - \theta)]^2 = \frac{5 + M_{\mathrm{o}1}^2}{7M_{\mathrm{o}1}^2 - 1}. \tag{5.62}$$

5.5 Gas Explosions

A general introduction to explosions due to explosives and gas leaks is given in Sect. 2.5.1.2 and 2.5.2. As explained earlier in the text, the gas blast effects are in the form of a shock wave composed of a high-pressure shock front

which expands outwards from the centre of the detonation. As these waves impinge on the structure, the whole structure might be engulfed by the shock pressures. The explosion can be one of the following types:

(1) Open-air or unconfined (air-burst and surface-burst loads).
(2) Partially-confined (exterior or leakage pressure loads).
(3) Fully-vented (interior or high-pressure loads).

The open-air explosion is fully discussed in Sect. 5.4. In the case of a gas explosion, the duration of the pressure is short in comparison to its response time, the impulse rather than the pressure pulse governs. The fictitious peak pressure P_{gf} is given by

$$P_{\mathrm{gf}} = 2F_1(b)/t_{\mathrm{o}}, \tag{5.63}$$

where $F_1(b)$ = average blast impulse

t_{o} = duration time (in ms) = $(t_{\mathrm{A}})_{\mathrm{F}} - (t_{\mathrm{A}})_{\mathrm{A}} + 1.5(t_{\mathrm{o}})_{\mathrm{F}}$

$(t_{\mathrm{A}})_{\mathrm{F}}$ = time of arrival of the blast wave at structures defined by the largest slant (away from the explosion)

$(t_{\mathrm{A}})_{\mathrm{A}}$ = time of arrival of the blast wave at structures defined by the normal distance (nearest to the explosion)

$(t_{\mathrm{o}})_{\mathrm{F}}$ = duration of the blast pressure at a structure further from the explosion (for multiple reflection of the blast waves this is increased by 50%)

In partially-confined or vented cubicles (chambers), the mean pressure p_{mo} generated by a spark or charge is given by

$$p_{\mathrm{mo}} = 2{,}410(Q/V)^{0.72}, \tag{5.64}$$

where Q/V is the charge/volume ratio (lb/ft^3).

Where the structure has a small A/V ratio and the blast pressure is less than 150 psi (2316.6 MN m^{-2}), the interior pressure is calculated as

$$\Delta p_{\mathrm{i}} = C_{\mathrm{L}}(A_{\mathrm{o}}/V)\delta t, \tag{5.65}$$

where C_{L} = leakage pressure coefficient and is a function of $p - p_{\mathrm{i}}$, the pressure difference at the opening

Δp_{i} = interior pressure increment

A_{o}/V = area of the opening/volume of the structure

δt = time increment

The variation of C_{L} versus $p - p_{\mathrm{i}}$ (in psi) is given in Fig. 5.8. Table 5.2 gives a procedure for gas concentration affecting Δp_{i}. In the case of *multiple explosions* occurring several milliseconds apart, the first blast wave shall be assumed to be ahead of others. If the time delay between explosions is not
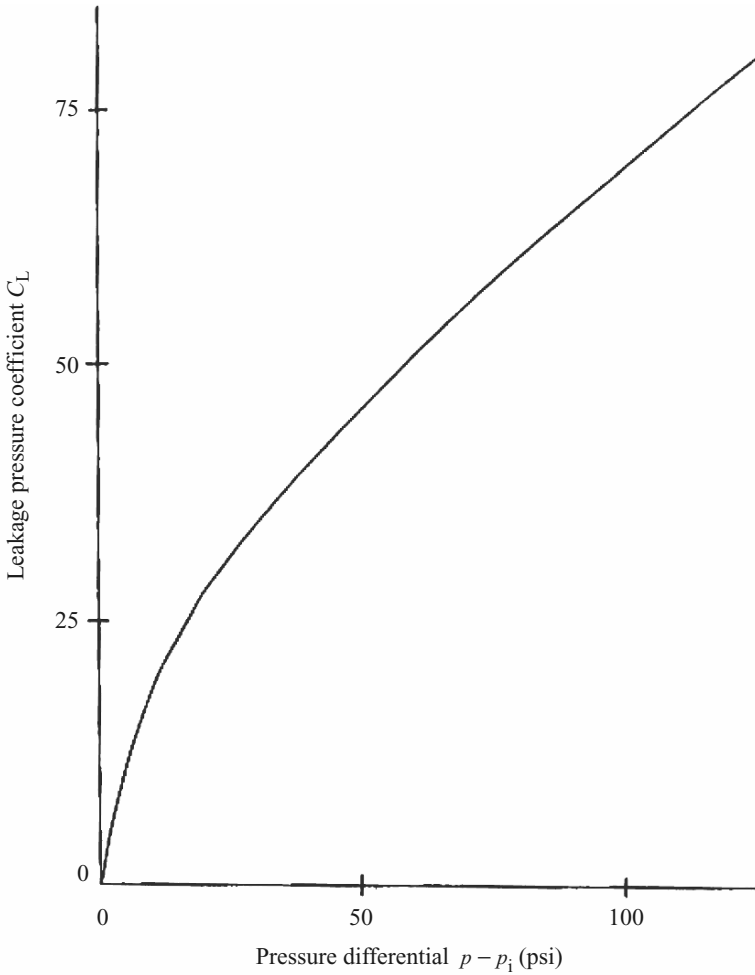
Fig. 5.8. Leakage pressure coefficient C_L versus pressure differential

too large, the subsequent blast waves will merge with the first blast wave at a distance which depends on:

(1) The magnitude of the individual explosion.
(2) The time delays between the initiations of explosions.
(3) The interference of obstructions.

The fully-vented types of explosions are discussed later on in this chapter. Reference may be made to the dynamic analysis given in Sects. 5.2 and 5.3. For a fully-confined gas explosion, the overpressure is given by

$$p_{so} = p_o \text{ (final temperature } t_f/\text{initial temperature } t_a).\qquad(5.66)$$

Table 5.2. Gas concentration and gas leakage time

Gas flow out $= (V_c/100)(V_a + V_g)dt$,	(1)
Gas flow in $= V_g dt$,	(2)
Increase in gas concentration	
$(dV_{con}/100) = [V_g - (dV_{con}/100)(V_a + V_g)dt/V]$	(3)
or $dV_{con} = [100V_g/(V_A + V_g)]\{1 - \exp[-(V_a + V_g)t/V]\}$,	(4)

where dV_{con} = percentage of gas in gas/air mixture
        = volume percentage of gas concentration
t = time
V_a, V_g = volume flow rate of air and flow rate of leaked gas rate, respectively.

Equation (4) can be used to relate dV_{con} at any time from the onset of leakage with the factors of gas leakage rate, ventilation rate and room volume.

$dV_{con}(\%)$	Time t (h)	$dV_{con}(\%)$	Time t (h)
0	0	4.00	0.42
0.50	0.10	5.00	0.50
1.00	0.15	5.50	0.53
2.0	0.2	6.00	0.55
2.50	0.21	7.00	1.25
3.00	0.25	8.00	1.50
3.50	0.30		

Gas leakage rate $= 5\,\mathrm{m^3\,h^{-1}}$; vent rate $= 55\,\mathrm{m^3\,h^{-1}}$
cubicle volume $= 30\,\mathrm{m^3}$ ($3\,\mathrm{m}$ high $\times 10\,\mathrm{m^2}$ in area)

In terms of the burning velocity v_b and the expansion ratio α_E, the pressure generated in a spherical medium of radius R is given for a fully confined case by

$$p_{so} = p_o \exp\left[\alpha_E^2(\alpha_E - 1)(v_b t/R)^3\right]. \tag{5.67}$$

The rate of pressure rise is computed by differentiating equation (5.67) with respect to time:

$$dp_{so}/dt = 3p_o/R^3 \alpha_E^3(\alpha_E - 1)v_b^3 t. \tag{5.68}$$

If the spherical assumption is excluded and $\Delta p = p_{so} - p_o$, then

$$\begin{aligned} \alpha_E^2(\alpha_E - 1) &\approx \alpha_E^3, \\ dp_{so}/dt = \Delta p &\approx (v_b \alpha_E)^3 t^3/V. \end{aligned} \tag{5.69}$$

In a vented, confined gas explosion, the pressure generated depends upon the characteristics of the gas/air mixture and the type of enclosure. From

the area of explosion relief, the overpressures generated in a vented explosion may be predicted. A number of experimental and theoretical studies on vented explosions have been carried out [4.100–4.202]. There are a number of empirically-based methods of predicting explosion overpressures. Table 5.3 gives a summary of some of the well known ones. Where volume scaling is necessary, results obtained at one scale may be transformed to another by

$$A_{v2} = A_{v1}(V_2/V_1)^{2/3}, \tag{5.70}$$

where A_{v1} is the necessary vent area of the test compartment with a volume V_1 and A_{v2} is the necessary vent area for a second compartment of volume V_2. The idea is that, in both cases, an explosion pressure exceeding a given value should be prevented. The value of v_b given in Table 5.3 is affected by the gas turbulent factor β and temperature. The value of v_b may be modified as follows:

$$v_{bt} = \text{velocity affected by turbulence} = \beta' v_b, \tag{5.71}$$

$$v_{bT} = \text{velocity affected by temperature} = v_b(T_f/T_a), \tag{5.72}$$

where T_f/T_a = final temperature/ambient temperature
= expansion ratio resulting from an increase in ambient temperature

On the basis of experiments using two inter-connected rooms, each having a volume of $28\,\text{m}^3$, Cubbage and Marshall [4.92] have produced an empirical equation which can predict an overpressure p_{so2} developed in the second compartment, following ignition in the first, as

$$p_2 = \left(ap_1 + bp_2^2\right)^{0.5}, \tag{5.73}$$

$$\text{where } a = (V_2/V_1)\left[46(KW)_{2AV}\,v_b/V_2^{0.33}\right] \tag{5.73a}$$

$$\text{and } b = (V_2/V_1)(K_2/K_{1,2}), \tag{5.73b}$$

where V_1 is the volume of room 1 in m^3, V_2 is the volume of room 2 in m^3, $(KW)_{2AV}$ is the average value of the term KW for room 2 in kg m^{-2}, $K_{1,2}$ is the vent coefficient between rooms 1 and 2 and K_2 is the vent coefficient for room 2; p_1 and p_2 are in mbar.

The Runes equation adopted by the US National Fire Protection Association [4.93] gives an explosion relief area for explosion venting:

$$A_v = KL_1L_2/(p_v)^{1/2}, \tag{5.74}$$

where A_v = vent area (m^2) to resist the overpressure p_{so} to p_v (mbar)
L_1, L_2 = smallest dimensions (m) in rectangular enclosures of rooms 1 and 2, respectively.

Table 5.3. A summary of empirical formulae and vented parameters

Author	Formulae for pressures (mbar)	Range of application
Cubbage and Simmonds	$p_1 = v_b(4.3KW + 28)/V^{1/3}$ $p_2 = 58v_b K$ $v_b(\text{m s}^{-1}) =$ the burning velocity Vent cladding can be of any material, provided that no restraining force (other than the minimum of friction) is used to maintain the vent in position	$L_{max} : L_{min} \leq 3:1$ $K \leq 5$ $W \leq 24\,\text{kg m}^{-2}$
Cubbage and Marshall	$p_m = p_v + 23(v_b^2 KW/V^{1/3})\{\ldots \ldots [f(\lambda, \lambda_o)]\}$ $v_b(\text{m s}^{-1})$ Predicts maximum pressure generated, irrespective of whether this is p_1 or p_2. For $\lambda \leq 750\,\text{kJ m}^{-3}$, and $p_v < 350$ mbar, use $f(\lambda, \lambda_o) = 1 - \exp[-(\lambda - \lambda_o)/(\lambda + \lambda_o)]$. For $\lambda \leq 750\,\text{kJ m}^{-3}$ and $p_v > 350$ mbar, use $f(\lambda, \lambda_o) = (\lambda - \lambda_o)/\lambda$. For hazard assessment use $f(\lambda, \lambda_o) = 1$ to calculate the maximum possible pressure rise.	$L_{max}:L_{min} \leq 3:1$ $K \leq 4 = A_s/A_v$ $2.4\,\text{kg m}^{-2} \leq W \leq 24\,\text{kg m}^{-2}$ $p_v \leq 490$ mbar $A_s =$ area of the enclosure in the plane of the vent
Rasbash	$p_m = 1.5p_v + 77.7v_b K$ $v_b(\text{m s}^{-1})$ Formula essentially predicts the second peak pressure, p_2; vent cladding can be any material held in place by a positive force	$L_{max}:L_{min} \leq 3:1$ $K \leq 5$ $W \leq 24\,\text{kg m}^{-2}$ venting overpressure $= p_v \leq 70$ mbar
Rasbash et al.	$p_m = 1.5p_v + \ldots v_b\{[(4.3KW + 28)/V^{1/3}] + 77.7\,K\}$ $v_b(\text{m s}^{-1})$	$L_{max}:L_{min} \leq 3:1$ $K \leq 5$ $W \leq 24\,\text{kg m}^{-2}$ $p_v \leq 70$ mbar

$K = A'_s/A_v$

A'_s = minimum area of the smallest side of the enclosure

A_v = area of the enclosure

or $K = V^{2/3}/A_v \not> 5$.

V = volume of the non-cubical vessel

Bradley and Mitcheson

Safe vent areas $\overline{A}$, the maximum $p_m \not> P_v$, the vent opening pressures

(1) Initially uncovered vents

$\overline{A}/\overline{v}_b \geq \exp[(0.64 - p_m)/2]$ for $p_m > 1$ atmosphere

and

$\overline{A}/\overline{v}_b \geq (0.7/p_m)^{0.5}$ for $p_m < 1$ atmosphere

(2) Initially covered vents

$\overline{A}/\overline{v}_b \geq (2.4/p_v)^{1.43}$ for $p_v > 1$ atmosphere

and

$\overline{A}/\overline{v}_b \geq (12.3/p_v)^{0.5}$ for $p_v < 1$ atmosphere

$\overline{A}$ = normalized vent area = $C_d(A_v/A_{ST})$

A_{ST} = surface area of the enclosure

$\overline{v}_b$ = normalized burning velocity = $(v_b/v_{so})[(\rho_{uo}/\rho_{bo}) - 1]$ $(\gamma_u p_o/\rho_{uo})^{0.5}$

v_{so} = initial laminar burning velocity

v_b = speed of sound in the unburnt gas

v_{so} = initial density of unburned gas

ρ_{uo} = density of combustion products

ρ_{bo} =

γ_u = constant = $c'_d/c_v = \dfrac{\text{discharge coefficient}}{\text{volume coefficient}}$

5.6 Dust Explosions

Section 2.6 gives an introduction to dust explosions. The well known methods introduced are the K_{st}, Schwal and Othmer, Maisey, Heinrich, Palmer and the Rust ones. There are similarities between gas and dust explosions, especially if the particle size of the dust is small and the turbulence level is low. Moreover, dust contains more volatiles. The qualitative effects on the explosion pressure of venting a dust explosion are the same as for a gas explosion. Several methods exist for estimating vent areas or explosion pressures in dust explosions. Vented gas explosions have a number of empirical relationships for calculating vent areas and explosions, as indicated in Sect. 5.5. There are not many empirical equations for dust explosions. Many just consider simple scaling methods by extrapolating results from small vessels to large vessels. There are three experimentally-based methods which are discussed below:

(1) The vent ratio method.
(2) The vent coefficient method.
(3) The K_{st} factor method.

The vent ratio method is based on the vent area divided by the volume of the vessel. For vessels greater than $1,000\,\mathrm{ft}^3$ $(283.68\,\mathrm{m}^3)$, the NFPA code 68 [4.93,4.259] recommends the following:

Volume V	Vent ratio X	
$1,000$–$25,000\,\mathrm{ft}^3$ $(28.368$–$709.2\,\mathrm{m}^3)$	$1\,\mathrm{ft}^2/30$–$50\,\mathrm{ft}^3$	
$>25,000\,\mathrm{ft}^3$ $(>709.2\,\mathrm{m}^3)$	$1\,\mathrm{ft}^2/80\,\mathrm{ft}^3$	For heavy reinforced concrete walls
	$1\,\mathrm{ft}^2/60$–$80\,\mathrm{ft}^3$	For light reinforced concrete, brick and wood wall construction
	$1\,\mathrm{ft}^2/50$–$60\,\mathrm{ft}^3$	For lightweight construction
	$1\,\mathrm{ft}^2/10$–$50\,\mathrm{ft}^3$	Large part of the volume with equipment

To convert to SI units, take $1\,\mathrm{ft}^3 = 0.028368\,\mathrm{m}^3$

The vent coefficient method is the same as used for gas. The vent coefficient K is given by

$$K = L_1 L_2/A_v, \qquad (5.75)$$

where $L_1, L_2 =$ the two smallest dimensions of the enclosure
$A_v =$ the vent area

The K_{st} factor method is the most widely used method for estimating explosion pressures and vent areas. Donat and BartKnecht's research work gives data such as shown in Fig. 2.78. The Hartmann bomb and the 20 l sphere method are the two techniques. The Hartmann bomb is a cylindrical tube of volume 1.2 l, filled with dust. The dust is dispersed by an air blast

using an ignitor. In the 20 l sphere method, the dust is injected from a pressurized container. A standard time delay between dust injection and ignition is prescribed. From the maximum rate for pressure rise, the value of K_{st} based on the cube root law is computed as

$$K_{st} = (dp/dt)V^{1/3} \, \text{bar m s}^{-1}. \tag{5.76}$$

Various nomographs produced by BartKnecht for dust explosions are shown in Fig. 5.9.

5.6.1 The Schwal and Othmer Method [4.58, 4.67, 4.75]

These authors used the Hartmann type apparatus with a volume of 1.3 l. The vented explosion pressure p_v in lb in.$^{-2}$ is given by

$$p_v = p_{max}(\text{closed})/10^{SX}, \tag{5.77}$$

where S is the slope of the semi-log plot relating the measured p_v and the vent ratio X (ft^2/100 ft^2). Figure 5.10 shows the nomograph. The pressure is given by

$$\begin{aligned} (dp/dt)_{max} = 5500/10^{2.443S} \\ (dp/dt)_{av} = 2700/10^{2.443S} \end{aligned} \tag{5.78}$$

By rearrangement of the terms of (5.78), the values of S may be derived:

$$\text{maximum } S = (1/2.443)\log[5,500/(dp/dt)_{max}]$$

or

$$\text{average } S = (1/2.443)\log[2,700/(dp/dt)_{av}]. \tag{5.79}$$

5.6.2 Maisey Method

Here similarities between gas and dust explosions are investigated by use of the equivalence coefficient method. The method relates dust explosion pressures to gas explosion pressures under similar conditions. The average rates of pressure rise and maximum explosion pressures are measured in an enclosed Hartmann bomb. The standard gas explosion medium is hexane/air. Maisey gives the following empirical relation:

$$p_v G/p_v D = \left[(dp/dt)_{av}^G \times \frac{p_{max}^D}{p_{max}^G (dp/dt)_{av}^D} \right] \times f_P f_S f_T, \tag{5.80}$$

where G and D represent gas in Maisey's Hartmann apparatus and f_P, f_S and f_T are correction factors for the initial pressure, fuel concentration and turbulence, respectively.

Table 5.4 gives an extract of the results from Maisey's Hartmann apparatus which are relevant to structural products.

Fig. 5.9. BartKnecht nomograph for dust explosions

A = max exp press (psi) (enclosed vessel)
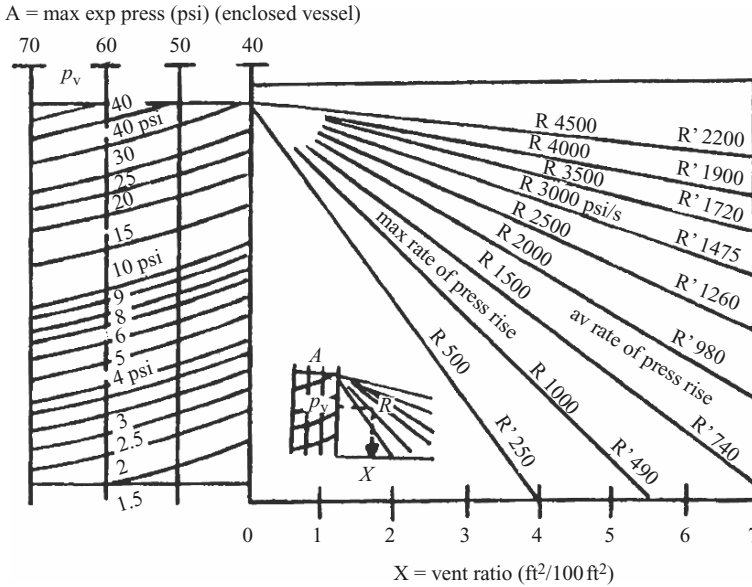
Fig. 5.10. Nomograph for pressure vent area ration (after Schwal and Othmer)

5.6.3 Heinrich Method

This is a theoretical method to predict the vented dust explosion pressure and vent areas. The effective pressure relief is given by

$$p_v - p_a = (dp/dt)_v = (dp_{ex}/dt)_v - \text{rate of pressure rise.} \tag{5.81}$$

Equation (5.81) is transformed to the following equation:

$$A_v = (V_L)^{1/3}V^{2/3}(dp_{ex}/dt)_{v,v_L}/C_d'(2RT/\overline{M})^{1/2}[p_{v_{max}}(p_{v_{max}}-p_a)]^{1/2}, \tag{5.82}$$

where C_d' = discharge coefficient
T = temperature
$\overline{M}$ = mean molecular weight
R = gas constant
p_a = ambient pressure
V_L = volume of the tested vessel

For an adiabatic process, the equation for A_v, the vent area, is given by

$$A_v = \frac{V_L^{1/3}}{\gamma'}\left(\frac{\gamma'+1}{2}\right)^{1/(\gamma'-1)}\frac{\overline{M}(\gamma'+1)}{2RT\gamma'}\frac{V^{2/3}}{C_d'p_v}\left(\frac{dp_{ex}}{dt}\right)_{max}V_L. \tag{5.83}$$

Heinrich suggests that $\overline{M}$ has the value $29\,\mathrm{g\,mole^{-1}}$ for dust/air mixtures, and C_d' has a value of 0.8. The values of γ' and R for an ideal gas are considered to be satisfactory for dust/air mixtures. The value of γ' is C_d'/C_v.

Table 5.4. Maisey's results

Material	Explosibility index	Ignition temp. (°C) cloud	Most explosive mixture			Rate of pressure rise	
			Minimum ignition energy cloud (J)	Minimum explosive concentration (oz ft^{-3})	Maximum pressure (psi g)	Average	Maximum
Thermoplastic resins							
Acetal							
Acetal, linear (polyformaldehyde)	>10.0	440	0.02	0.035	89	1,600	4,100
Acrylic							
Methyl methacrylate polymer	6.3	480	0.02	0.03	84	900	2,000
Methyl methacrylate moulding compound, cyclone fines	>10.0	440	0.015	0.02	101	450	1,800
Methyl methacrylate moulding compound, drier fines	6.1	440	0.02	0.03	80	800	1,800
Thermosetting resins							
Alkyd							
Alkyd moulding compound, mineral filter, not self-extinguishing	>0.1	500	0.12	0.155	40	150	300
Allyl							
Allyl alcohol derivative CR-39, from dust collector	>10.00	510	0.02	0.035	91	3,000	7,500
Amino							
Melamine formaldehyde, unfilled laminating type, no plasticizer	>0.1	810	0.32	0.085	81	350	800
Melamine formaldehyde, unfilled laminating type, with plasticizer	0.7	790	0.05	0.065	91	800	1,800
Urea formaldehyde, spray-dried	>0.1	530	1.28	0.135	52	200	500
Urea formaldehyde moulding compound, grade II fine	1.0	460	0.08	0.085	89	1,300	3,600
Epoxy							
Epoxy, no catalyst, modifier or additives	>10.0	540	0.015	0.02	74	2,600	8,500
Epoxy-bisphenol A mixture	1.9	510	0.035	0.03	85	1,000	2,200

Special resins and moulding compounds

Cold-moulded							
Gilsonite, from Michigan	>10.0	560	0.025	0.02	89	1,200	3,800
Petroleum resin (blown asphalt), regular	>10.0	510	0.025	0.025	94	2,200	4,600
Coumarone–indene							
Coumarone–indene, hard	>10.0	550	0.01	0.015	93	2,800	11,000
Natural							
Cashew oil phenolic, hard	>10.0	490	0.025	0.025	81	1,500	4,000
Lignin, pure	0.8	510	0.16	0.065	80	1,700	4,700
Rosin, DK	>10.0	390	0.01	0.015	87	2,800	12,000
Rosin, pine	–	440	–	0.055	82	1,900	7,500
Shellac	>10.0	400	0.01	0.02	73	1,400	3,600
Sodium resinate, dry size, plasticized	1.0	440	0.1	0.015	81	800	2,000
Rubber							
Rubber, crude, hard	7.4	350	0.05	0.025	80	1,200	3,800
Rubber, synthetic, hard, 33% sulphur	>10.0	320	0.03	0.03	93	1,100	3,100
Fillers							
Cellulose	2.8	480	0.08	0.055	119	1,800	4,500
Cellulose flock, chemical cotton, fine cut	1.4	460	0.06	0.065	87	1,300	2,900
Cork	9.7	470	0.045	0.035	80	2,300	7,000
Cotton flock, ground, filler for phenolic moulding compound	>10.0	470	0.025	0.05	94	1,800	6,000
Wood flour, filler	>10.0	450	0.04	0.04	97	2,300	7,500
Coal, Pittsburgh	1.0	610	0.06	0.055	83	800	2,300
Hexane, quiescent	1,880.0	235	0.0002	0.05	100	2,000	4,250

5.6.4 Palmer's Equation

Palmer suggests that, in enlarged containers with a large ignition source, combustion takes place throughout the entire volume of the container. Palmer gives an expression relating the mass rate, $\overline{M}_b$, of combustion products to maximum pressure, p_{max}, as

$$\frac{d\overline{M}_b}{dt} = \frac{p_{max}}{p_a} \times \frac{\rho_a}{\gamma' p_1} \left(\frac{dp}{dt}\right)_{max(enclosed)}, \tag{5.84}$$

where p_1 = pressure in a closed vessel
p_a = ambient pressure
$\gamma' = C_d'/C_v$
ρ_a = density

The following equations have been derived for low- and high-pressure cases:

Low pressure

$$p_{max} - p_a = 2.3\rho_c P_o[(V/A_v)(dP/dt)_{max}]2/C_d^2\gamma'^2 p_{max(enclosed)}^3, \tag{5.85}$$

where ρ_c is the density of an unburnt dust suspension at pressure p_a and of the combustion products at pressure $p_1 \approx 0.6p_{max}$.

High pressure

$$\frac{1}{p_{max} - p_a} = \frac{1}{p_{max(enclosed)} - p_a} + \frac{K_p A_v p_{max(enclosed)}}{0.8V\rho_c(dp/dt)_{max}}, \tag{5.86}$$

where K_p is a constant and is defined by

$$K_p = C_d'\{\gamma'(\rho_a/p_a)[2/(\gamma'+1)]^{(\gamma'+1)/(\gamma'-1)}\}^{1/2}. \tag{5.86a}$$

The derivation of (5.86) utilizes the approximation

$$(dp/dt)_{av} = 0.4(dp/dt)_{max}. \tag{5.86b}$$

Figure 5.11 shows a comparison of Palmer's results with those of Donat.

5.6.5 Rust Method

This method relies on data from closed vessels. It includes a moving flame front travelling spherically and vent panel dynamics for a pressure–time profile. Table 5.5 gives a summary of the method. The values of E_x and C_2 are functions given in Fig. 5.12.
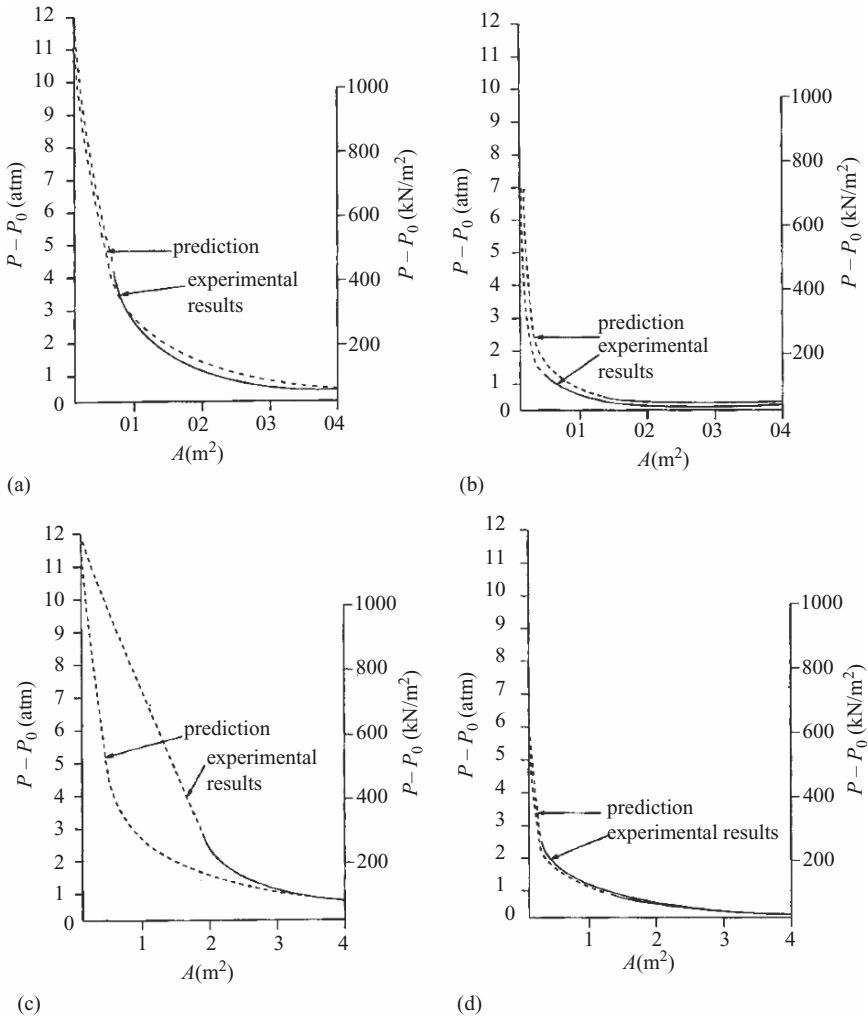
Fig. 5.11. A comparison of Palmer's and Donat's results. (**a**) Aluminium dust explosion pressures in a $1\,m^3$ vessel; (**b**) coal dust explosion pressures in a $1\,m^3$ vessel; (**c**) aluminium dust explosion pressures in a $30\,m^3$ vessel; (**d**) coal dust explosion pressures in a $30\,m^3$ vessel

5.7 Steel–Concrete Composite Structures

5.7.1 Introduction

Plastic analysis suggested by the Eurocode EN 1993-1-1 is generally recommended for steel concrete composite structures, prior to the dynamic finite element, quasi-static dynamic analysis is adopted to assess various aspects or sections.

Table 5.5. A summary of the Rust method

Steps of Calculation

(1) The explosion pressure in an enclosed vessel is given by

$$P = K_D t^3/V, \text{ where } K_D = (4/3)\pi S_u^3 P_{\max(\text{enclosed})} \tag{1}$$

(2) Differentiating:

$$dP/dt = 3K_D t^3/V \tag{2}$$

Eliminating t:

$$(3K_D/V)(PV/K_D)^3 = 3K_D^{1/3} p^{2/3}/V^{1/3}$$

where $K_D = [(dP/dt)/16]^{1/3}$ from Hartman data

(3) A_v = vent area in ft^2

$$A_v = (8.354 \times 10^{-5})F_s(P_{\max(\text{enclosed})}V)^{2/3}K_D^{1/3}/P_{\max}^{1/2}$$

where F_b = shape factor = A_F/A_{SP}
        A_F = large spherical surface of the container
        A_{SP} = surface area of the sphere which has a volume equal to
                that of the container

    The distance x or rotation θ can be calculated for the achievement of full venting
by checking the release panel dynamies

Values of x *and* θ

Horizontal translation:

$$x_t = \frac{g}{w}\left(\frac{V}{K_D}\right)^{2/3} C_2$$

Horizontal rotation around vertical shaft:

$$\theta_1 = \frac{3g}{2wb}\left(\frac{V}{K_D}\right)^{2/3} C_2$$

Vertical translation upwards:

$$X_i = g\left(\frac{V}{K_D}\right)^{2/3}\left(\frac{C_2}{w} - E_x\right)$$

w = weight of vent panel, lb ft^{-2}

Vertical rotation around horizontal shaft,
against gravity:

$$\theta_1 = \frac{3g}{2L}\left(\frac{V}{K_D}\right)^{2/3}\left(\frac{C_2}{w} - E_x\right)$$

Vertical rotation around horizontal shaft,
with gravity:

$$\theta_1 = \frac{3g}{2L}\left(\frac{V}{K_D}\right)^{2/3}\left(\frac{C_2}{w} + E_x\right)$$

In the above equations, C_2 and E_x are defined as

$$C_2 = \frac{p^{5/3}}{20} - \frac{(P_{bo})^{4/3}p^{1/3}}{4} + \frac{(P_{bo})^{5/3}}{5}$$

$$E_x = \frac{p^{2/3}}{2} - (P_{ho})^{1/3}p^{1/3} + \frac{(P_{bo})^{2/3}}{2}$$

$P_{bo} = P_v$ = vent opening pressure

Table 5.5. (continued)

Distance of panel movement to achieve full venting:
Horizontal translation:

$x = \dfrac{WL}{2(W + L)}$ L = length of vent panel W = width of ventpanel W = width of vent panel $\theta = \dfrac{W}{W + L}$ p = explosion pressure	Dust	Vessel volume (m^3)	p_{max}		dp/dt (pressure rise)	
			atm (gauge)	kN m^{-2}	atm s^{-1}	kNm^{-2} s^{-1}
		1	69	690	–	–
	Coal	30	–		27	2,700
		1	12.0	1,200	–	–
	Aluminium	30	–	–	195	19,500
		1	10.4	1,040	–	–
	Organic pigment	30	–	–	92	9,200

The global analysis covers initially the following aspect prior to the subject to explosion:

Basic Theory

(1) Action effects may be calculated by elastic global analysis, even where the resistance of a cross-section is based on its plastic or non-linear resistance.
(2) Elastic global analysis should be used for serviceability limit states, which appropriate corrections for non-linear effects such as cracking of concrete.
(3) Elastic global analysis should be used for verifications of the limit state of fatigue.
(4) The effects of shear lag and of local buckling shall be taken into account if these significantly influence the global analysis.
(5) The effects of local buckling of steel elements on the choice of method of analysis may be taken into account by the classifying cross-sections.
(6) The effects of local buckling of steel elements on stiffness may be ignored in normal composite sections. For cross-section of class 4, EN 1993-1-5, 2.2.
(7) The effects on the global analysis of slip in bolts holes and similar deformations of connecting devices should be considered.
(8) Unless non-linear analysis is used, the effects of slip and separation on calculation of internal forces and moments may be neglected at the interfaces between steel and concrete where shear connection is provided.
(9) Allowance shall be made for the flexibility of steel or concrete flanges affected by shear in their plane (shear lag) either by means of rigorous analysis, or by using effective width of flange.
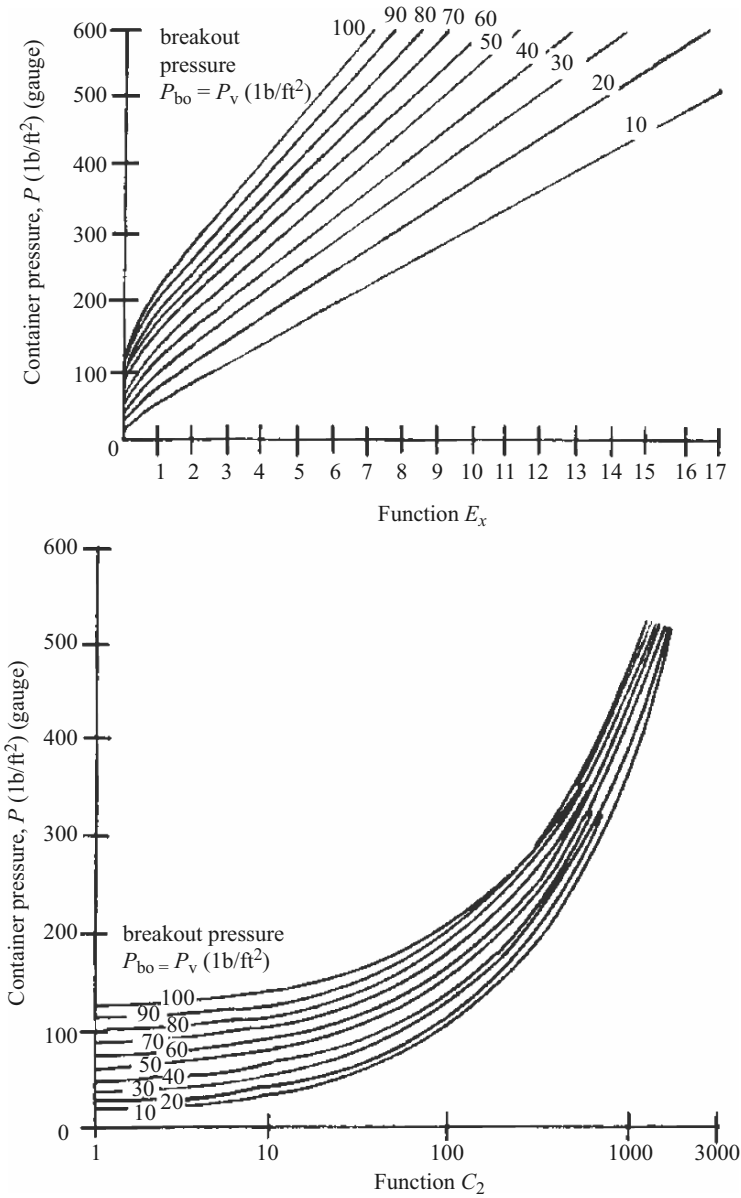
Fig. 5.12. E_x and C_2 functions

(10) The effects of shear lag in steel plate elements should be considered in accordance with EN 1993-1-1, 5.2.1(5).

(11) The effective width of the concrete flanges should be determined in accordance with the following provisions.

(12) When the elastic global analysis is used, a constant effective width may be assumed over the whole of each span. This value may be taken as the value of b_{eff} at mid-span for a span supported at both ends, or the value $b_{eff,2}$ at the support for a cantilever.

(13) At mid-span or an internal support, the total effective width b_{eff}, see Fig. 5.13, may be determined as

$$b_{eff} = b_0 + \sum,$$

where

b_0 is the distance between the centres of the outstand shear connectors

b_{ei} is the value of the effective width of the concrete flange on each side of the web and taken as $L_e/8$ but not greater than the geometric width b_i. The value b_i should be taken as the distance from the outstand shear connectors to a point mid-way between adjacent webs, measured at mid-depth of the concrete flange, except that at a free edge b_i is the distance to the free edge. The length L_e should be taken as the approximate distance between points of zero bending moment. For typical continuous composite beams, where a moment envelope from various loads arrangement governs the design, and for cantilevers, L_e may be assumed to be as shown in Fig. 5.13.

(14) The effective width at an end support may be determined as:
with:

$$\beta_i = (0,55 + 0,025\, L_e/b_{ei}) \leq 1,0,$$

where:

b_{ei} is the effective width. See (5), of the end span at mid-span and L_e is the equivalent span accordance to Fig. 5.13.

(15) The distribution of the effective width between supports and mid-span regions may be assumed to be shown in Fig. 5.13.

(16) Where in buildings the bending moment distribution is influenced by the resistance or the rational stiffness of a joint, this should be considered in the determination of the length L_e.

(17) For analysis of building structures, b_0 may be taken as zero and b_i measured from the centre of the web.

(18) Allowance should be made for the effects of cracking of concrete, creep and shrinkage of concrete, sequence of construction and pre-stressing.

(19) Non-linear analysis may be used in accordance with EN 1992-1-1, 5.7 and EN 1993-1-1, 5.4.3.

Mean bending stress
in concrete flange

(a) Effect of shear lag

(b) Effect of shear lag

(c) Variation of effective width
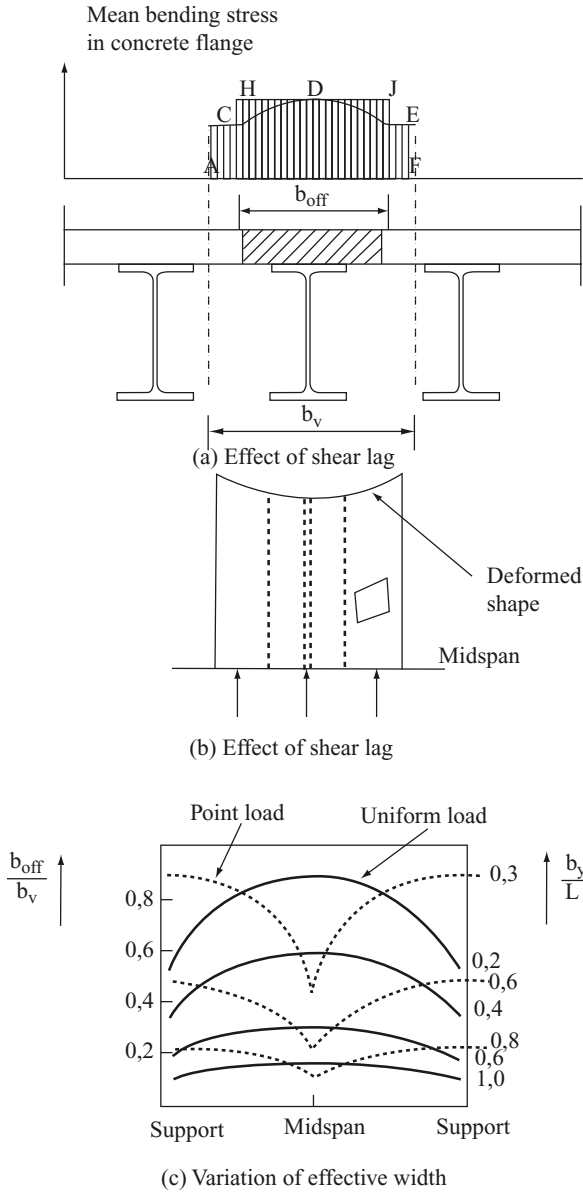
Fig. 5.13. Concrete flange

(20) The behaviour of the shear connection shall be taken into account.

(21) Effects of the deformed geometry of the structure should be taken into account in accordance with 5.2.Par44 EC2.

(22) Rigid plastic global analysis may be used for ultimate limit state verification other than fatigue, where second-order effects do not have to be considered and provide that:
  – All the members and joints pf the frame are steel or composite
  – The steel material satisfies EN 1993-1-1, 3.2.2
  – The cross-section of steel members satisfy EN 1993-1-1, 5.6
  – The joints are able to sustain their plastic resistance moments for a sufficient rotation capacity

(23) In beams and frames for building, it is not normally necessary to consider the effects of alternating plasticity.

(24) Where rigid-plastic global analysis is used, at each plastic hinge location:
  (a) The cross-section of the structural steel section shall be symmetrical about a plane parallel to the plane of the web or webs
  (b) The proportions and restraints of steel components shall be such that lateral-torsional buckling does not occur
  (c) Lateral restraint to the compression flanges shall be provided at all hinge locations at which plastic rotation may occur under any load case
  (d) The rotation capacity shall be sufficient, when account is taken of any axial compression in the member or joint, to enable the required hinge rotation to develop
  (e) Where rotation requirement are not calculated, all member containing plastic hinges shall have effective cross-sections of Class 1 at plastic hinge locations

(25) For composite beams in buildings, the rotation capacity may be assumed to be sufficient where:
  (a) The grade of structural steel does not exceed S355
  (b) The contribution of any reinforced concrete encasement in compression is neglected when calculating the design resistant moment
  (c) All effective cross-sections at plastic hinge location are in Class 1; and all other effective cross-sections are in class 1 or Class 2
  (d) Each beam-to-column joint has been shown to have sufficient design rotation capacity, or to have design resistance moment at least 1,2 times the design plastic resistance moment of the connected beam
  (e) Adjacent spans do not differ in length by more than 50% of the shorter span
  (f) End spans do not exceed 115% of the length of the adjacent span
  (g) In any span in which more than half of the total design load for that span is concentrated within length of one-fifth of the span, than any hinge location where the concrete slab is in compression, not more than 15% of the overall depth of the member should be in compression; this does not apply where it can be shown that the hinge will be the last to form in that span

   (h) The steel compression flanges at a plastic hinge location is laterally restrained
(26) Unless verified otherwise, it should be assumed that composite columns do not have rotation capacity.
(27) Where the cross-section of a steel member varies along its length. EN 1993-1-1, 5,6(3) is applicable.
(28) Where restraint is required by 17(c) or 17(h), it should be located within a distance along the member from the calculated hinge location that does not exceed half the depth of the steel section.
(29) The ratio b_{eff}/b_v depends not only on the relevant dimension of the system, but also on the type of loading, the support conditions and the cross-section considered. Figure 5.13c shows the effects of the ratio of the beam spacing to span length, b_v/L, and the type of loading, on a simply supported span.

For simply supported beams, the effective width on each side of the steel web should be taken as $l_o/8$, but not greater than half the distance to the next adjacent web, nor greater than the projection of the cantilever slab for edge beams.

The length l_o is the approximate distance between points of zero bending moment. It is equal to the span L for simply supported beams. So:

A constant effective width may be assumed over the whole of each span. This value may be taken as mid-span value for a beam.

5.7.2 Shear Connection: Full and Partial Interaction

For the steel beams and slab to act compositely and also to resist longitudinal shear, they must be structurally tied. This is normally achieved by providing shear connectors in the form of headed studs. If this is inadequate the full flexural strength of the composite beam cannot be developed. If there are sufficient connectors for the strength of the beam to be not less than that given by the plastic analysis the resulting method of design is known as *full-interaction design.* However, the most economical design is the one which the number of shear connectors is such that the degree of interaction between the slabs and the steel member is just sufficient to provide the required flexural strength. This method of design is called *partial-interaction design.* Studs may be welded either in the shop or on site using a special form of *gun.* Failure in the shear connection is more sudden and less predictable than flexural failure of composite member. For this reason design rules, aim to ensure that a properly designed beams fails in flexure at a bending moment not less than that predicted by the plastic hinge analysis of the cross-section.

For design purpose the only property that is required is slip load Q_K which can be determined from a push-out test, Tables are available to give characteristic resistances of headed studs embedded in a solid slab of normal weight concrete.

According to BS 5950, or LFRD for positive moments, the design strength, Q_p, should be taken

$$Q_\mathrm{p} = 0.8Q_\mathrm{k}. \tag{5.87}$$

For full shear connection, the total number of studs, N_p, required over half the span of a simply supported beam in order to develop the positive moment capacity of the section can be determined using the following expression:

$$N_\mathrm{p} = \frac{F_c}{Q_p}, \tag{5.88}$$

where

$F_\mathrm{c} = \mathrm{A}p_y$ (if plastic neutral axis lies in the concrete flanges)
$F_\mathrm{c} = 0.45f_{cu}B_eD_s$ (if plastic neutral axis lies in the steel beam)
$Q_P = $ Design strength of shear studs $= 0.8Q_\mathrm{k}$ (in solid slab)

5.7.3 Methods of Analysis and Design

A rigorous general analysis of the composite section demands a complete knowledge of the full stress-strain properties of the three components, steel, concrete and shear connection, over the time span being considered. By making simplified assumptions about the properties of the components materials the numerical work can be eased without significant loss of accuracy.

In this chapter, it is considered to introduce the elementary elastic theory of bending and the simple plastic theory in which the whole cross-section of a member is assumed to yield, in either tension or compression. Both theories are used for composite members, the difference being as follows:

- Concrete in tension is usually neglected in elastic theory, and always neglected in plastic theory.
- In elastic theory, concrete in compression is 'transformed' to steel by dividing its breadth by the modular ratio E_v/E_e.

Elastic Analysis

For an elastic analysis the following assumptions are generally made:

1. Full shear connection between beam and slab is provided, so that the effect of slip can be neglected and the assumption of full interaction is not affected.
2. Both steel and concrete are linearly elastic materials.
3. Concrete undergoing tensile strain is ineffective in resisting load.
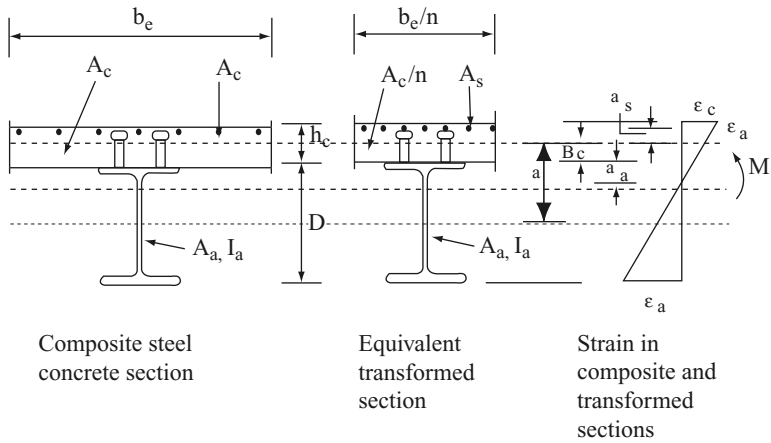
Fig. 5.14. Design for serviceability: the transformed section [74]
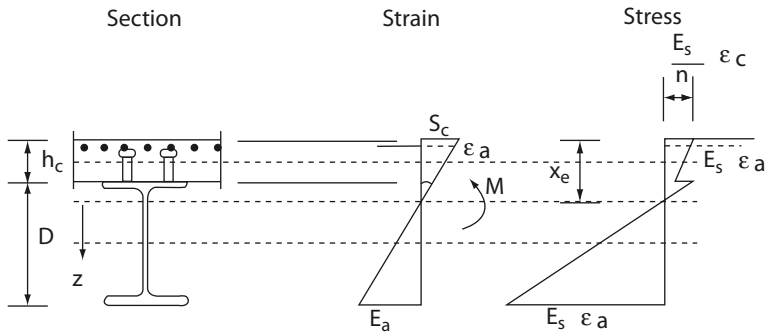
Fig. 5.15. Elastic strains and stresses in the composite section

In calculating the section properties of the composite section for serviceability checks, use is made of the concept of the transformed section. Using this concept, the steel–concrete composite section is replaced by an equivalent homogeneous section in steel. For a section subjected to positive bending, the concrete flange of area A_c is replaced with a *fictitious* steel flange of area A_c/n, where n is the modular ratio. The fictitious steel flange is of similar depth to the concrete flange, see Fig. 5.14. Geometrical properties are readily calculated for the transformed section, and strains may be obtained using the elastic modulus for steel. Use is again made of the modular ratio in calculating elastic stresses in the concrete flange of the original composite section as shown in Fig. 5.15.

Elastic Moduli

The value of the elastic modulus for structural steel, E_s, is given as $210 \times 10^3 \, \mathrm{N \, mm^{-2}}$ in Eurocode 4.

Concrete is a non-linear, non-elastic material. It does not display a unique or constant value of elastic modulus and sustains permanent deformation on removal of load. When subjected to a constant stress, concrete strains increase with time, a phenomenon known as creep. It is also subject to changes of volume caused by shrinkage (or swelling), and by temperature changes. Notwithstanding this non-linearity, it is necessary to be able to quantify the relationship between stress and strain in order to obtain a realistic estimate of deformations.

Geometrical Properties of the Section

In considering the geometric properties of the composite section for use in elastic analysis, a variety of options appear to exist, depending on:

- Whether the applied bending moment is positive or negative.
- Whether or not reinforcement is taken into account.
- The position of the neutral axis of the composite section, whether it is within the depth of the steel section or the concrete flange.

In practice, however, it is only necessary to consider a small number of options. For the uncracked section, in positive bending, the contribution of reinforcement to the section stiffness is generally ignored. If the uncracked section is being used in an area of negative bending, the reinforcement may be taken into account. In order to avoid complexity in the initial analysis, therefore, it is sometimes preferred to neglect the reinforcement in such situations. For cracked sections, however, it is common to include the area of tension reinforcement.

Second Moment of Area

The second moment of area for the sections is as follows (see Figs. 5.14 and 5.15):

(a) *The Uncracked Section – reinforcement excluded*

Taking moments of area about the neutral axis of the steel section, with $A_c = b_e \times h_c$ and with $A_t = A_a + (A_c/n)$, this simplifies to:

$$(A_c/n) \times a = A_t \times a_a \tag{5.89}$$

giving:

$$a_a = (A_c/n) \times a/A_t. \tag{5.90}$$

The second moment of area of the transformed (all-steel) section is then:

$$I = I_a + (A_c/n) \times (h_c{}^2/12) + (A_c/n) \times a_c{}^2. \tag{5.91}$$

Service Stresses

The preceding values for I are used to calculate stresses under service conditions. Thus, if $x_e = (a_c + h_c/2)$, the concrete stresses at the top (t) fibre of the uncracked section are:

$$f_t = M \times x_e/n \times I \tag{5.92}$$

while bottom (b) fibre stresses in the steel section are:

$$f_b = M \times (D + h_c - x_e)/I \tag{5.93}$$

Section Stiffnesses

Reference is made in Eurocode 4 to the following values of section stiffness:

$(EI)_I$ is the uncracked section stiffness, where: E is the E_s

I is the elastic second moment of area of the effective equivalent steel section, calculated using the short-term modular ratio.

Calculations are based on the assumption that the concrete in tension is uncracked, and taken as being unreinforced (Fig. 5.16).

I is the elastic second moment of area of the effective equivalent steel section, calculated using the long-term modular ratio. The area of concrete in tension (and its tension stiffening effect) is neglected, but account is taken of steel reinforcement.

The flexural stiffness EI_v of the uncracked cross-section and elastic neutral axis (without reinforcement):

$$EI_v = E_a I_a + E_c I_c + \frac{E_a A_a E_c A_c}{E_a A_a + E_c A_c} \alpha^2 \tag{5.94}$$

and

$$\alpha_e = \frac{E_a A_a}{E_a A_a + E_c A_c} \alpha. \tag{5.95}$$
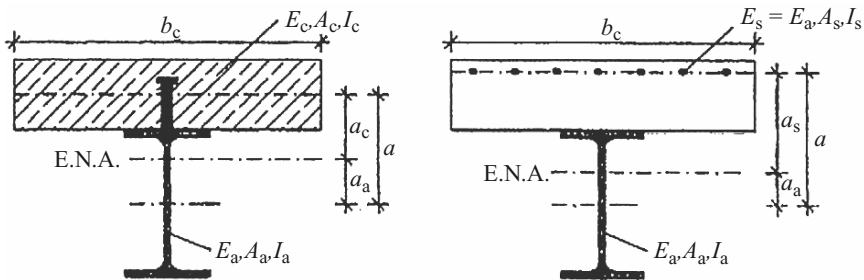
Fig. 5.16. Different positions of neural axis in reinforced and unreinforced composite beams

Plastic Analysis

Moment capacity of a composite beam is mostly appropriately calculated using plastic theory. This design method assumes that only symmetrical steel sections are used and that full shear connection between the steel and concrete exists at ultimate limit state. Special attention must be paid to the concrete slab acting as the compression flange of the composite beam.

In the case of statically determinate beams, such as simply supported single span beams, it is easy to determine the distribution of bending moments from the equilibrium conditions. To determine the stress distribution over the cross-section, plastic behaviour is assumed. The advantage of this method is that the calculation of the resistance is based on the "maximum moment at failure" condition, which is easy to understand and apply. For simply supported single spans, the concrete flange is in compression and cracking of the concrete is not relevant.

The relationship between the stresses, and the strains of steel and concrete are represented by the following diagrams, where both materials are assumed to behave in a perfectly plastic manner.

Moment Capacity

In the analysis of a composite section to determine its moment capacity based on the BS 5950, the following assumptions can be made:

(1) The stress block for concrete in compression at ultimate conditions is rectangular with a design stress of $0.45f_{cu}$.
(2) The stress block for steel in both tension and compression at ultimate conditions is rectangular with a design stress equal to p_y.
(3) The tensile strength of the concrete is zero.
(4) The ultimate moment capacity of the composite section is independent of the method of construction (propped or unpropped).

The moment capacity of a composite section depends upon the position of the plastic neutral axis within the section. There are three possibilities:

Case 1: $R_c > R_s$ **(Fig. 5.17)**

The plastic neutral axis fall within the concrete slab and since there is no resultant axial force on the section, R'_c, must equal the force in the steel beam, R_s:

$$R'_c = R_s,$$

where,

R'_c = Design stress in concrete × area of concrete in compression
  = $0.45f_{cu}B_e y_p$
R_s = Steel design strength × area of steel section
  = $p_y A$

He

Dc

Ds

t

Bs

T

0.45*vfcuBe*

Apy

py
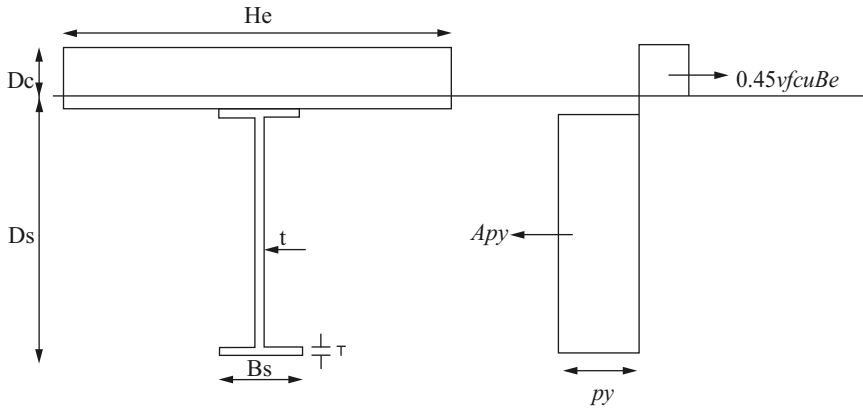
Neutral Axis in the concrete flange

Fig. 5.17. Plastic neutral axis in the concrete slab

The maximum allowable force in the concrete flange, R_c, is given by:

R_c = Design stress in concrete × area of concrete flange
$= 0.45 f_{cu} B_e D_s.$

From these two equations we end up:

$$R'_c = \frac{R_c y_p}{D_s}. \tag{5.96}$$

Hence the expression for the depth of the plastic neutral axis, y_p, is:

$$y_p = \frac{R_s}{R_c} D_s \leq D_s. \tag{5.97}$$

If the above relationship is satisfied, taking moments about the top of the concrete flange and substituting for y_p, the moment capacity of the section, M_c, can be calculated.

$$M_c = R_s \left(D_s + \frac{D}{2} \right) - \frac{R_s^2 D_s}{2 R_c}, \tag{5.98}$$

where

D = Depth of steel section
D_s = Depth of concrete flange

Case 2: $R_c < R_s$

This indicates that the neutral axis fall within the steel flange. Figure 5.18 shows the stress distribution in the section.
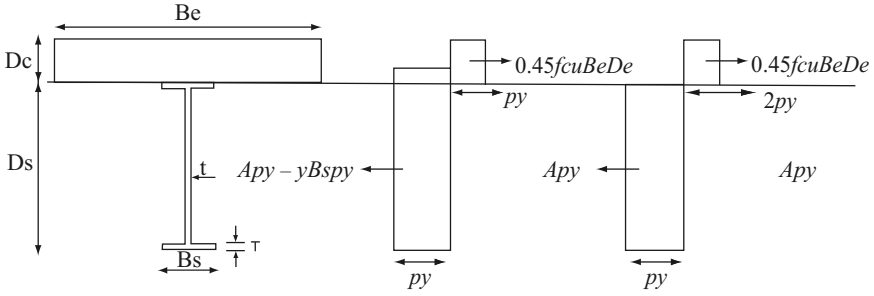
Neutral Axis in the steel flange

Fig. 5.18. Plastic neutral axis in the steel flange

By equating horizontal forces, the depth of the plastic neutral axis below the top of the steel flange, y, is obtained as follows:

$$R_c + (p_y By) = R_s - (p_y By)$$
$$y = \frac{R_s - R_c}{2Bp_y}. \tag{5.99}$$

Or using the resistance of the steel flange, R_f, which is equal to:

$$R_f = p_y BT. \tag{5.100}$$

The equation for finding the depth of the neutral axis below the top of the steel flange becomes:

$$y = \frac{R_s - R_c}{2R_f/T} \leq T. \tag{5.101}$$

The moment capacity can be found using the above diagram of the stress distribution. Taking moments about the top of the steel flange and after some alterations, M_c, is given by:

$$M_c = R_s \left(\frac{D}{2}\right) + R_c \left(\frac{D_s}{2}\right) - \frac{(R_s - R_c)^2}{4R_f} T. \tag{5.102}$$

Case 3: $R_c < R_s$

Plastic neutral axis in the steel web (Fig. 5.19)

In the case that y is larger than $T (y > T)$, the plastic neutral axis fall within the steel web. Then the resistance of clear web depth is:

$$R_v = p_y dt, \tag{5.103}$$

where

d = clear depth of the web
t = thickness of the web
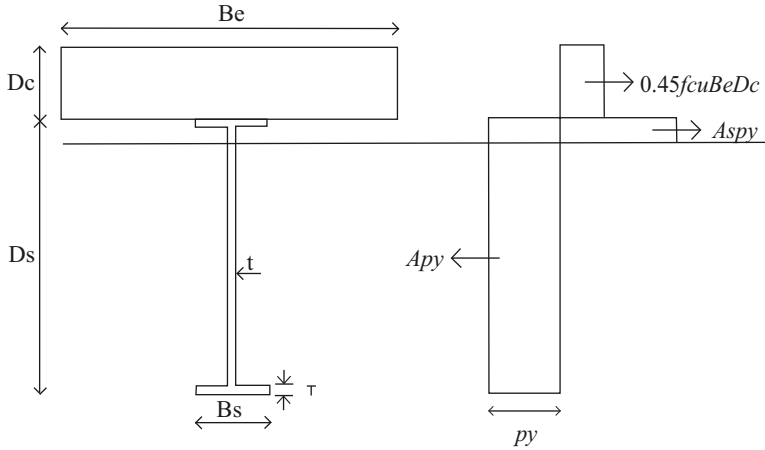
Neutral Axis in the steel web

Fig. 5.19. Plastic neutral axis in the steel web

So the plastic moment capacity using the stress blocks can be derived:

$$M_c = R_s \left(\frac{D}{2}\right) + R_c \left(\frac{D + D_s}{2}\right) - \frac{R_c^2}{R_v} \frac{d}{4}. \tag{5.104}$$

Application of Blast Loading on Composite Sections

The applied blast load is assumed to be a triangular load-time history.

The value of the plastic moment of resistance is a governing criterion for the design. The section has to withstand the moment due to the applied blast load. It should be noted that, normal 'static' design criteria should also be checked at each stage.

The member mass can be found and converted to an equivalent mass by multiplying with the load-mass factor K_{LM}, consequently the effective natural period of vibration of the element, T, is defined.

The next step is to calculate the resistance and the applied force, whose ratio plotted against the ratio of the load pulse duration and the natural period (t_d/T), shows how the ductility ratio, μ, varies with this time ratio. The maximum end rotation will determine the failure of the member.

To check if the Quasi-static/Dynamic design is valid, the ratio of the maximum response time, t_m over the duration of the applied load t_d, will demonstrate it.

(a) Loading

A vehicle is loaded by a blast bomb at a stand-off distance of 4 m. For a hemispherical charge mass of $1.8 \times 100\,\text{kg} = 180\,\text{kg}$ were $100\,\text{kg}$ is the actual mass of the equivalent TNT.

$$R' = \text{range} = 4.0\,\text{m}$$

$$Z = \text{the scaled distance} = \frac{4}{\sqrt[3]{180}} = 0.705\,\text{m}\,\text{kg}^{-1/3}. \qquad (5.105)$$

The impulse is, computed from standard charts.

$\quad i = 11{,}322\,\text{kPa-ms}$

$\quad$ and the blast load is equal to,

- $F = 390\,\text{kPa}$ for $t_\text{d} = 40\,\text{ms}$
- For 20 kg of equivalent TNT:

$$i = 6{,}299\,\text{kPa ms}$$
$$F = 217\,\text{kPa}$$
$$t_\text{d} = 40\,\text{ms}$$

- For 40 kg of equivalent TNT:

$$i = 12{,}570\,\text{kPa ms}$$
$$F = 433\,\text{kPa}$$
$$t_\text{d} = 40\,\text{ms}$$

- For 28 kg of equivalent TNT:

$$i = 8{,}709\,\text{kPa ms}$$
$$F = 300\,\text{kPa}$$
$$t_\text{d} = 40\,\text{ms}$$

These blasts loads will be applied to the composite beams for using Quasistatic/Dynamic and Impulsive design.

(b) Quasi-Static/Dynamic Loading on the Steel-Concrete Composite Beam

The same composite section as above is going to be subjected to the idealised triangular pressure–time function with $P_\text{r} = 390\,\text{kPa}$ and $t_\text{d} = 40\,\text{ms}$. The length of the beam, its strengths and its spacing are the same as in the elastic and plastic analysis.

For protection category $1, \theta \leq 2$ and $\mu \leq 10$

The required resistance per unit length is given as:

$$r_u = 390 \times 2 = 780\,\text{kN}\,\text{m}^{-1} \qquad (5.106)$$

kPa

390

40   ms
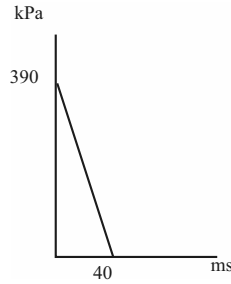
Fig. 5.19a. Blast-load time function

The required plastic moment of resistance is

$$M_p = \frac{r_u L^2}{8} = \frac{780 \times 5^2}{8} = 2{,}437.5\,\text{kN m} \tag{5.107}$$

The plastic moment of resistance of the steel-concrete composite beam, obtained from the plastic analysis, is:

$$M_\text{c} = 2{,}927.98\,\text{kN m} > M_\text{p}. \tag{5.108}$$

So the section satisfies the 'static' criterion.

The actual mass of the beam per unit length can now be found:

$$m = m_s + m_c = 197 + (2{,}400 \times 200 \times 1.25 \times 10^{-3}) = 797\,\text{kg m}^{-1}. \tag{5.109}$$

The elastic and plastic load-mass factors are 0.78 and 0.66 respectively. The K_{LM} for this particular case is assumed to be:

$$K_{LM} = \frac{0.78 + 0.66}{2} = 0.72. \tag{5.110}$$

The equivalent stiffness, K_E, using the flexural stiffness of the composite beam obtained in the elastic analysis, is

$$K_E = \frac{384EI}{5L^4} = \frac{384 \times 1.086 \times 10^{15}}{5 \times 5^4 \times 10^{12}} = 133.4\,\text{N mm}^{-1}\,\text{mm}^{-1}$$
$$= 133.4 \times 10^6\,\text{N m}^{-1}\,\text{m}^{-1}. \tag{5.111}$$

Thus, the period of oscillation of the equivalent system, T, is given by:

$$T = 2\pi\sqrt{\frac{K_{LM}m}{K_E}} = 2\pi\sqrt{\frac{0.72 \times 797}{133.4 \times 10^6}} = 0.013\,\text{s} = 13\,\text{ms}. \tag{5.112}$$

The value of, r_u, is evaluated as:

$$r_u = \frac{8M_c}{L^2} = \frac{8 \times 2927.98}{5^2} = 928.867 \times 10^3 \, \mathrm{N\,m^{-1}} \qquad (5.113)$$

and,

$$F = 390 \times 2 \times 10^3 = 780 \times 10^3 \, \mathrm{N\,m^{-1}} \qquad (5.114)$$

and so, $r_u/F = 1.19$ and $t_d/T = 3.058$. The ductility ratio $\mu = X_m/X_E = 2.34 < 3$. Since, this is less than 3 the design is acceptable.

$$
\begin{aligned}
X_m &= \mu X_E = \mu \frac{r_u}{K_E} = 2.34 \times \frac{928.867 \times 10^3}{132.28 \times 10^6} = 16.4 \, \mathrm{mm} \\
\tan\theta &= \frac{X_m}{(L/2)} = \frac{16.4}{(5 \times 10^3/2)} = 0.00656.
\end{aligned}
\qquad (5.115)
$$

Thus, $\theta = 0.374° < 2°$, which is satisfactory.

Referring to the SDOF response, $t_m/t_d = 0.32 < 3$. Therefore, pressure–time loading design is valid and the flexural capacity is adequate.

Finally, a check must be made on the performance in shear of the element. It is assumed here that the web carries the whole shear at a stress not exceeding the yield stress in shear.

The dynamic yield stress in shear, f_{dv}, is given by:

$$f_{dv} = 0.5 \times 1.3 \times 265 = 162.5 \, \mathrm{N\,mm^{-2}}, \qquad (5.116)$$

where the factor 0.5 is used to relate yield stress in tension to shear yield stress. Thus, the ultimate shear capacity is:

$$V_p = f_{dv} A_w = 162.5 \times 769.8 \times 15.6 = 1.951 \times 10^6 \, \mathrm{kN}, \qquad (5.117)$$

where A_w is the area of the web. The maximum support shear, V, based on the dynamic reaction, [16] is given by:

$$
\begin{aligned}
V &= 0.393 r_u + 0.107 F = 0.393 \times 928.867 \times 10^3 + 0.107 \times 780 \times 10^3 \\
&= 448.5 \times 10^3 \, \mathrm{kN} < V_p.
\end{aligned}
$$

Hence, the design is acceptable.

(c) Equivalent UB Steel Sections with the Same Dynamic Value of Mp

In order to compare the response of the steel-concrete composite beam with the equivalent UB section, there is a need to determine the plastic moment of resistance of this section based on the dynamic yield strength of the steel, f_{ds}. To achieve that, the appropriate plastic section modulus has to be determined from the UB steel section tables and multiplied by the dynamic yield strength of the steel, in order to find the plastic moment of resistance of this section, which is going to be approximately the same as the one of the composite

section. The use of only the plastic modulus of the section and not the average of the elastic-plastic, is providing the smallest section that will comply with the above criterion.

For the above section with the same variables ($L = 5\,\mathrm{m}, D_c = 200\,\mathrm{mm}$) it has been found that the equivalent section that satisfies the plastic moment of resistance criterion is, UB $838 \times 292 \times 226\,\mathrm{kg\,m}^{-1}$, with a plastic modulus of, $S = 9{,}155\,\mathrm{cm}^3$ (Table A.8). The static yield strength of this section is, $p_y = 265\,\mathrm{N\,mm}^{-2}$. So, the dynamic yield strength of the section is (see Chart A.5):

$$f_{\mathrm{ds}} = 1.3 p_y = 1.3 \times 265 = 344.5\,\mathrm{N\,mm}^{-2}. \tag{5.118}$$

Hence, the plastic moment of resistance of this section can be determined:

$$M_c = f_{\mathrm{ds}} S = 344.5 \times 9{,}155 \times 10^3 = 3{,}153{,}897{,}500\,\mathrm{N\,mm} = 3{,}153.9\,\mathrm{kNm} \tag{5.119}$$

Which close to the M_c of the composite section: $M_c = 2{,}927.98\,\mathrm{kNm}$

(d) Quasi-Static/Dynamic Loading on the Equivalent Steel Beam

It would be unusual to design a protective structure from steel, but steel structures are very likely to suffer 'incidental' blast loads, even though the steel structure may not be the main target.

Steel structures are categorised as either reusable, where they are required to sustain light damage, or non-reusable, where the structure sustains severe damage, but nevertheless retains its structural integrity. The maximum ductility ratios related to these categories are to be defined such that incipient failure is approached and significant deformations well into the strain-hardening range are allowed, for good energy absorption. For reusable structures, the maximum ductility ratio is 3, and for non-reusable structures, the max ductility ratio is around 6.

In this particular analysis, the beam will be designed as a reusable structure. The length of the beam, its spacing, as well as, the blast load, is the same as in the design of the composite section. ($L = 5\,\mathrm{m}$, spacing $= 2\,\mathrm{m}$, blast loading: $390\,\mathrm{kPa}$ and $t_d = 40\,\mathrm{ms}$). The dynamic increase factor for the steel is 1.3 and the yield strength is $265\,\mathrm{N\,mm}^{-2}$.

(A) Design for flexure

For protection category 1, $\theta \leq 2°$ and $\mu \leq 10$.

Since the structure is to be reusable, the dynamic load ratio, r_u/F is 1.0.

Thus, the required resistance per unit length is given as:

$$r_u = 390 \times 2 = 780\,\mathrm{kN\,m}^{-1}. \tag{5.120}$$

The required plastic moment of resistance is (see Table A.6 of the appendix):

$$M_p = \frac{r_u L^2}{8} = \frac{780 \times 5^2}{8} = 2{,}437.5\,\mathrm{kNm}. \tag{5.121}$$

The plastic moment of resistance of the steel-concrete composite beam, obtained from the plastic analysis, is:

$$M_c = 3{,}153.9\,\text{kNm} > M_p$$

So the section satisfies the 'static' criterion.

The actual mass of the beam per unit length can now be found:

$$m = m_s = 226.5\,\text{kg m}^{-1}$$

The elastic and plastic load–mass factors are 0.78 and 0.66 respectively. The K_{LM} for this particular case is assumed to be:

$$K_{LM} = \frac{0.78 + 0.66}{2} = 0.72. \tag{5.122}$$

The equivalent stiffness, K_E, using the flexural stiffness of the steel beam,

$$K_E = \frac{384EI}{5L^4} = \frac{384 \times 200 \times 10^3 \times 3397 \times 10^6}{5 \times 5^4 \times 10^{12}} = 83.49\,\text{N mm}^{-1}\,\text{mm}^{-1}$$
$$= 83.49 \times 10^6\,\text{N m}^{-1}\,\text{m}^{-1}. \tag{5.123}$$

Thus, the period of oscillation of the equivalent system, T, is given by:

$$T = 2\pi\sqrt{\frac{K_{LM}m}{K_E}} = 2\pi\sqrt{\frac{0.72 \times 226.5}{83.49 \times 10^6}} = 0.0087\,s = 8.7\,\text{ms.}$$

Then, referring to the Table A.6 of the Appendix, r_u, is evaluated:

$$r_u = \frac{8M_c}{L^2} = \frac{8 \times 3153.9}{5^2} = 1{,}009.25 \times 10^3\,\text{N m}^{-1} \tag{5.124}$$

and,

$$F = 390 \times 2 \times 10^3 = 780 \times 10^3\,\text{N m}^{-1} \tag{5.125}$$

and so, $r_u/F = 1.29$ and $t_d/T = 4.56$. The ductility ratio $\mu = X_m/X_E = 2.01 < 3$. Since, this is less than 3 the design is acceptable.

$$X_m = \mu X_E = \mu\frac{r_u}{K_E} = 2.01 \times \frac{1009.25 \times 10^3}{83.49 \times 10^6} = 24.29\,\text{mm}$$
$$\tan\theta = \frac{X_m}{(L/2)} = \frac{24.29}{(5 \times 10^3/2)} = 0.00972. \tag{5.126}$$

Thus, $\theta = 1.39° < 2°$, which is satisfactory.

Referring to the SDOF response Chart, $t_m/t_d = 0.16 < 3$. Therefore, pressure–time loading design is valid and the flexural capacity is adequate.

(B) Design for shear

Finally, a check must be made on the performance in shear of the element. It is assumed here that the web carries the whole shear at a stress not exceeding the yield stress in shear.

The dynamic yield stress in shear, f_{dv}, is given by:

$$f_{dv} = 0.5 \times 1.3 \times 265 = 162.5 \,\text{N mm}^{-2}, \tag{5.127}$$

where the factor 0.5 is used to relate yield stress in tension to shear yield stress. Thus, the ultimate shear capacity is:

$$V_p = f_{dv}A_w = 162.5 \times 769.8 \times 15.6 = 1.951 \times 10^6 \, kN = 1951 \times 10^3 \,\text{kN},$$

where A_w is the area of the web. The maximum support shear, V, based on the dynamic reaction, [16], is given by:

$$V = 0.393r_u + 0.107F = 0.393 \times 1009.25 \times 10^3 + 0.107 \times 780 \times 10^3$$
$$= 480.1 \times 10^3 \,\text{kN} < V_p.$$

Hence, the design is acceptable.

Equivalent Concrete Sections with the Same Mp

In order to compare the response of the steel-concrete composite beam with the equivalent concrete section, there is a need to determine the plastic moment of resistance of this section. To achieve that, the appropriate plastic section modulus has to be determined from the plastic analysis and multiplied by the yield strength of the concrete. The use of only the plastic modulus of the section and not the average of the elastic–plastic, is providing the smallest section that will comply with the above criterion.

For the above section with the same variables $(L - 5\,\text{m}, D_c = 200\,\text{mm})$ it has been found that:

$$M_c = 2,927.98 \,\text{kN m}.$$

The plastic moment of resistance of a rectangular section is:

$$M_c = S\sigma_y = \frac{BD^2}{4} \times 0.45 \times 35 = BD^2 \times 3.9375. \tag{5.128}$$

If B is kept constant and equal to 500 mm, then the depth of this section can be found:

$$D = \sqrt{\frac{2927.98 \times 10^6}{500 \times 3.9375}} = 1,219.52 \,\text{mm}. \tag{5.129}$$

This section is quite unrealistic for construction purposes, but is going to be used anyway for comparison reasons.

Quasi-Static/Dynamic Loading on the Equivalent Concrete Beam

Before undertaking a detailed design it must be decided what constitutes acceptable performance for the element. This means identifying the level of damage that the element may sustain. For the concrete slab of the composite beam it is assumed that it can sustain minor cracking and is classified as Type I, where, $0 < \theta < 2°$.

The aim is to provide flexural strength and ductility, in order for the strain energy developed by the member, to resist the kinetic energy delivered by the Quasi-static load.

The concrete section is the same as above, as well as the loading, the duration of the load, the length and the spacing of the beam. The beam is reinforced symmetrically with grade of 460 bars such that $\rho_s = \rho_s' = 0.35\%$, D = 1,214.245 mm and d' = 50 mm, the concrete grade is 35.

Design for Flexure

The resistance is:
$$r_u = \frac{8M_p}{L^2} \tag{5.130}$$

and
$$M_p = \frac{A_s f_{ds}}{b}(D - 0.45x), \tag{5.131}$$

where
$$x = \frac{A_s f_{ds}}{0.6b f_{dc}}. \tag{5.132}$$

For symmetrically reinforced Type I section in which the contribution of the compression reinforcement is ignored
$$f_{ds} = f_{dy} = 1.2 \times 460 = 552 \, \text{N mm}^{-2}$$

and
$$f_{dc} = f_{dcu} = 1.25 \times 40 = 50 \, \text{N mm}^{-2}.$$

Also,
$$A_s = A_s' = \frac{0.35 \times 1,000 \times (1,214.245 - 50)}{100} = 4,074.86 \, \text{mm}^{-2} \, \text{m}^{-1}.$$

Hence,
$$x = \frac{4,074.86 \times 552}{0.6 \times 1,000 \times 50} = 74.98 \, \text{mm}$$

and
$$M_p = \frac{4,074.86 \times 552}{1,000}(1,214.245 - 0.45 \times 74.98) = 2,655.33 \times 10^3 \, \text{Nm m}^{-1}$$

Therefore, r_{u}, is equal to:

$$r_u = \frac{8 \times 2{,}655.33 \times 10^3}{5^2} = 849.7 \times 10^3 \,\mathrm{N\,m^{-2}}.$$

For protection category 1, $\theta < 2°$. In the absence of stirrups, θ is taken as $1°$. Therefore, the maximum allowed deflection is:

$$X_m = L\tan\theta = 5 \times \tan 1° = 0.0873 \,\mathrm{m} = 87.3 \,\mathrm{mm}. \tag{5.133}$$

The modular ratio is taken as $m = 10$ and since $\rho_{\mathrm{s}} = 0.0035$, the second moment of area is:

$$1 = 0.026bd°. \tag{5.134}$$

Thus, the equivalent stiffness, K_{F}, is

$$K_E = \frac{384EI}{5L^4} = \frac{384 \times 20 \times 10^9 \times 0.026 \times 1 \times 1.16425^3}{5 \times 5^4}$$
$$= 100.84 \times 10^6 \,\mathrm{N\,m^{-2}\,m^{-1}}.$$

Thus, the deflection at the elastic limit, X_{E}, is given by:

$$X_E = \frac{r_u}{K_E} = \frac{849.7 \times 10^3}{100.84 \times 10^6} = 0.0084 \,\mathrm{m} = 8.4 \,\mathrm{mm}. \tag{5.135}$$

The actual mass of the beam can now be found:

$$m_c = (2{,}400 \times 1.214) = 2913.6 \,\mathrm{kg\,m^{-1}}. \tag{5.136}$$

The elastic and plastic load-mass factors are 0.78 and 0.66 respectively. The K_{LM} for this particular case is assumed to be:

$$K_{LM} = 0.72.$$

Thus, the period of oscillation of the equivalent system, T, is given by:

$$T = 2\pi\sqrt{\frac{K_{LM}m}{K_E}} = 2\pi\sqrt{\frac{0.72 \times 2913.6}{100.84 \times 10^6}} = 0.0287 \,\mathrm{s} = 28.7 \,\mathrm{ms}.$$

Also,

$$F = 390 \times 10^3 = \mathrm{N\,m^{-2}}$$

and so, $r_{\mathrm{u}}/F = 2.198$ and $t_{\mathrm{d}}/T = 1.36$. Since $r_{\mathrm{u}}/F > 2$, the section is in the elastic range, and therefore safe. So there is no need to continue the design.

5.8 Explosions in Soils

The energy of explosion is used in the fields of civil/structural engineering, mining, agriculture and forestry. Explosions in underground installations arise from explosives, plant failure or from external rockets/missiles detonating

at great depths. Nuclear explosions are adopted for finding underground resources. In mining, explosions have been adopted for tunnelling, coal mining and canal works. In agriculture and forestry, explosive methods are used to sink pils for tree planting, stump extraction and irrigation system construction. The effects of an explosion depend on the characteristics of the soils, i.e. whether hard or semi rocks, cohesive soils or cohesionless or loose soils, Table 5.6 presents a soil classification on the basis of explosions occurring underground.

The pressure of the explosive gases immediately after detonation causes the soil adjacent to the charge surface to be crushed and eventually to change into a liquid state. The zone is *highly deformed*. The size of the deformation changes as the distance from the centre of the source of detonation increases. Due to high tensile stresses, cracks/fissures are developed. From the source, the soil which looks like a brittle one is surrounded by a chamber of three zones in the order: *crushing zone, rupture zone* and *elastic zone*. Various waves, their reflections and rarefactions occur which have been described earlier. In some cases swelling occurs.

Figure 5.20 shows a typical phenomenon of the soil subject to internal explosion. Chemical and nuclear charges exploding on the Earth's surface (contact explosions) create depressions by compacting the soil beneath. Most of the explosion energy is dissipated into the air. As a result, various craters are formed. This area is discussed in detail later on in this chapter.

5.8.1 Explosion Parameters for Soils/Rocks

The wave profile in soils is dependent upon soil type, time and distance of the source. It is widely believed that up to a distance of 100–120 γ_s (γ_s being equal to R_w, the radius of the charge), the charge weight W follows the relation

$$W = \tfrac{4}{3}\pi \, \rho_w R_w^3, \tag{5.137}$$

where ρ_w is the density of the charge. Here the maximum overpressure is higher than the absolute value of the underpressure due to rarefaction. At a distance of 400–500 R_w, the overpressure is low and is of the same order as the absolute value of the underpressure of the rarefaction wave. The zone of the fissures does not exceed 5–6 R_w. Just before the fissure zone, the crushing zone generally extends from 2 to 3 R_w. The explosive wave in an unbounded rock medium obeys the law of model similarity; the overpressure duration $(t/R_w) \times 10^3$ on the relative distance $\bar{x} = x/R_w$ is written for a *spherical PETN* charge as

$$t/R_w = 10^{-3}(\alpha_0 + \alpha_1\bar{x}), \tag{5.138}$$

where $\alpha_0 = 2.51$ for diabase with $\alpha_1 = 4.56 \times 10^{-3}$
$\alpha_0 = 3.18$ for marble with $\alpha_1 = 5.30 \times 10^{-2}$
$\alpha_0 = 4.38$ for granite with $\alpha_1 = 0.135$
$\alpha_0 = 4.10$ for water-saturated limestone with $\alpha_1 = 0.192$

Table 5.6. Classification of soils under explosion effects

Soil	Density, ρ ($\mathrm{g\,cm^{-3}}$)	Propagation velocity of a longitudinal wave in a mass v_{sl} ($\mathrm{ms^{-1}} \times 10^3$)	Poisson's ratio, v	Modulus of elasticity, in tension and compression, E ($\mathrm{kN\,cm^{-2}} \times 10^5$)	Modulus of elasticity in shear, G ($\mathrm{kN\,cm^{-2}} \times 10^5$)	Bulk modulus, K ($\mathrm{kN\,cm^{-2}} \times 10^5$)
Sand	1.4–2.0	0.3–1.3	–	0.003	–	–
Clay	1.4–2.5	0.8–3.3	–	0.003	–	–
Limestone	2.42	3.43	0.26	2.17	0.85	1.71
Slate	2.45	6.92	0.24	10.22	4.13	6.50
Granite	2.60	5.20	0.22	6.20	2.54	3.77
Quartzite	2.65	6.42	0.25	9.26	3.70	7.89
Limestone	2.70	6.33	0.33	7.31	2.74	4.36
Granite ore	2.71	6.41	0.33	7.57	2.84	7.59
State	2.71	5.75	0.25	7.60	3.04	5.09
Marble white	2.73	4.42	0.20	3.84	1.60	3.32
Marble red	2.73	5.47	0.26	6.75	2.68	4.74
Marble black	2.82	5.90	0.32	5.74	2.18	7.09
Gneiss	2.85	6.08	0.28	8.35	3.26	6.38
Crystalline dolomite	2.85	6.60	0.28	9.83	3.83	7.59
Gabbrodiabase	2.85	5.40	0.26	7.40	2.88	5.58
Coal	1.25	1.20	0.36	0.18	0.07	0.09

Soil	Lame's constant (kN cm^{-2} × 10^5)	Propagation velocity of transverse wave, v_{st} (ms^{-1} × 10^3)	Compression strength, σ_c (kN cm^{-2})	Shear strength, τ (kN cm^{-2})	Tensile strength, σ_t (kN cm^{-2})
Sand	–	–	50–60	–	–
Clay	–	–	65–105	1–2	4
Limestone	0.91	1.86	450	110	70
Slate	3.75	4.06	460	70	50
Granite	2.06	3.10	1,550	–	180
Quartzite	3.70	3.70	1,480	240	–
Limestone	5.56	3.70	1,620	210	–
Granite ore	5.71	3.20	1,520	180	–
Slate	3.07	3.32	1,760	–	40
Marble white	1.06	2.80	750	–	150
Marble red	2.94	3.10	1,200	–	250
Marble black	3.85	3.28	750	–	210
Gneiss	4.18	3.37	1,175	340	–
Crystalline dolomite	5.03	3.63	1,885	1,125	340
Gabbrodiabase	3.12	3.14	1,500	–	230
Coal	0.05	0.72	80	30	5
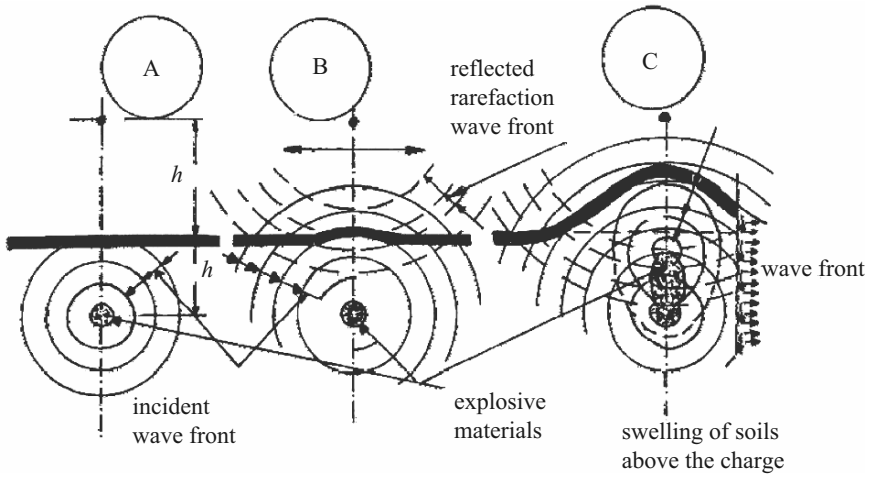
Fig. 5.20. Explosions in soils

The corresponding overpressure can be written as

$$p_{so} = \left(\frac{a_1 \times 10^3}{\bar{x}^3} + \frac{a_2 \times 10^3}{\bar{x}^2} + \frac{a_3}{\bar{x}} \right) \times 10^2. \qquad (5.139)$$

The value of a_1, a_2 and a_3 are given below:

Rock	a_1	a_2	a_3
Diabase	18.60	88.80	202.00
Marble	1.68	4.70	46.67
Granite	1.28	20.00	38.6
Saturated limestone	−1.50	21.30	−3.91

Under the same PETN charge, the maximum mass velocity, v_m, is computed as

$$v_m = \frac{\bar{\alpha}_1}{\bar{x}^3} + \frac{\bar{\alpha}_2}{\bar{x}^2} + \frac{\bar{\alpha}_3}{\bar{x}} \ \mathrm{cm\,s^{-1}}. \qquad (5.140)$$

For granite, $\bar{\alpha}_1 = 33{,}100\,\mathrm{cm\,s^{-1}}$; $\bar{\alpha}_2 = -398\,\mathrm{cm\,s^{-1}}$; $\bar{\alpha}_3 = 36.25\,\mathrm{cm\,s^{-1}}$. For other soils where $\bar{x} > 50$ all constants become equal for all kinds of explosives. The corresponding p_{so} is given by

$$p_{so} = \rho v_{pz} \times 10^2 (v_m) \ \mathrm{kN\,cm^{-2}}, \qquad (5.141)$$

where ρ = rock density, $\mathrm{kN\,cm^{-4}\,s^{-2}}$

v_{pz} = longitudinal wave velocity, $\mathrm{cm\,s^{-1}}$.

The impulse $F_1(t)$ of the pressure wave on soils is written as

$$F_1(t) = \int_0^t p_{so}(t)dt \tag{5.142}$$
$$= A_2 \sqrt[3]{W}(1/\bar{x})a_2 \, \text{kNs cm}^{-2},$$

where values of A_2 and a_2 for water-saturated sands, in particular, vary as $A_2 = 0.08\text{--}0.03$ and $a_2 = 1.05\text{--}1.50$; $\bar{x}$ is the distance from the explosion.

The time duration $t = \tau_m$ for a large number of soils from the moment of explosion to the instant at which p_{so} develops at a distance $\bar{x}$ is given by

$$t = \tau_m = 4.35 \times 10^{-3} \sqrt[3]{W}(\bar{x})^{1.6} \, \text{s} \tag{5.143}$$

For contained and contact explosions in sandy loams, the values of p_{so} ar as

$$p_{so} = 11.1(\bar{x}/\sqrt[3]{W})^{-2.7} \, \text{kN cm}^{-2} \text{ (contained explosion)}, \tag{5.144}$$
$$p_{so} = 11.1[\bar{x}/\sqrt[3]{(K_w \times W)}]^{-2.7} \, \text{kN cm}^{-2} \text{ (contact explosion)}, \tag{5.145}$$

where K_w is the reduction coefficient of the charge ≈ 0.28. The maximum mass velocity v_m for both contained and contact explosions can be written as

$$v_m(\text{contained explosion}) = 4.72[\bar{x}/(\sqrt[3]{W})^{2.06}], \tag{5.146}$$
$$v_m(\text{contact explosion}) = 1.08[\bar{x}/(\sqrt[3]{W})^{-1.65}], \tag{5.147}$$

where v_m is in m/s and $\bar{x}$ is the distance in m.

Cylindrical charges are used in earth work. Assuming, for comparison, that the cylindrical charge is W_c, then the arrival time of the wave front is computed as

$$t/\sqrt{W_c} = 0.335\bar{x}^{10.061} \text{sm}^{1/2} \, \text{kg}^{-1/2} \tag{5.148}$$

The mass velocity is written as

$$v_m = 263(\bar{x})^{-0.965} \, \text{m s}^{-1} \tag{5.149}$$

The following values are computed for $t/\sqrt{W_c}$, $\bar{x}$ and v_m:

$\bar{x}$	v_m	$t/\sqrt{W_c}$
20	9.0	4.0
40	7.0	12.5
60	5.7	22.0
80	3.9	30.0
100	3.0	40.0
120	2.5	48.0
140	2.0	58.0

Parameters for Wave Types

An underground explosion, as stated earlier, causes a surface motion of the earth medium. Some of these waves have been described in Sect. 5.2. The *P wave* is produced by the pressure wave transmitted by the first source. The value of the velocity v_{sz} (vertical) is given by

$$v_{sz} = K^P(W^{1/3}/\bar{x})$$
$$= K^P(\sqrt[3]{W})^2 \, \text{cm s}^{-1}. \tag{5.150}$$

The time t^P for the maximum growth of the motion is given by

$$t^P = K^t(\sqrt[6]{W}). \tag{5.151}$$

The amplitude X^P is given by

$$X^P = K_x[\sqrt[6]{W}(\sqrt[3]{W}/\bar{x})^2] \, \text{cm} \tag{5.152}$$
$$= 2v_{sz}(t/\pi).$$

The values of constants K^P, K^t and K_x are given below:

	K^P	K^t	K_x
Loam	1,100	0.01	75
Saturated sand	700	0.015	60
Granite	700	0.0032	15
Limestone	700	0.0032	15

The maximum soil velocity v_s^n for the *N wave*, which is transmitted by the second source – the cupola-shaped swelling of the soil surface in the epicentre region, is given by

$$v_s^n = K^n(\sqrt[3]{W}/\bar{x})^{1.7} \, \text{cm s}^{-1}. \tag{5.153}$$

The time t^n is evaluated as

$$t^n = 0.0065W^{1/6} \, \text{s (for rocks)} \tag{5.154}$$
$$= 0.06W^{0.21} \, \text{s (for clays)}.$$

The maximum amplitude X^n is given by

$$X^n = v_s^n(t^n/2\pi). \tag{5.155}$$

For saturated sands, loams, limestones and granite, the values of v_s^n are, respectively, 300–900, 1,750–3,000 and 4,200–4,500 m s^{-1}. In general form, v_s^n is given as in (5.153).

Section 5.2.1 gives a brief introduction on the formation of *R waves* and their effects on soils. The R wave is a long-period wave which is transmitted

by the second explosion source. It expands conically with moving particles departing from the radial direction towards the axis of symmetry. The maximum vertical and horizontal motion velocities, v_{szv} and v_{szh}, respectively, are given by

$$v_{\text{szv}} = 2\pi X_{\text{RZ}}/t_{\text{R}}, \tag{5.156}$$
$$v_{\text{szh}} = v_{\text{szv}}(X_{\text{RX}}/X_{\text{RZ}}), \tag{5.157}$$

where X_{RZ} and X_{RX} are the amplitudes of motion in the vertical and horizontal directions, respectively.

$$X_{\text{RZ}} = 1{,}900(x_{\text{e}}/v_{\text{sz}})\theta(d_0/x_{\text{e}})f(\bar{x}) \, \text{mm} \tag{5.158}$$

where x_{e} = the rupture zone = $4.5 \sqrt[3]{W}$ for granite
$= 3 \sqrt[3]{W}$ for limestone
$= (6/8) \sqrt[3]{W}$ for clay
$= 2.5 \sqrt[3]{W}$ for sandy clay

d_0 = depth of charge

$$f(\bar{x}) = (\bar{x})^{-0.5} e^{-1.75(\bar{x})^{0.2}} \tag{5.159}$$
$$\bar{x} = x/\sqrt[3]{W} \, \text{m kg}^{-1/3}$$

x	$f(\bar{x})$
100	1.24×10^{-3}
200	4.59×10^{-4}
500	1.025×10^{-4}
1,000	2.99×10^{-5}
2,000	7.5×10^{-6}
3,000	3.18×10^{-6}

5.8.2 Explosion Cavity

When an explosion occurs in soil, cavities are created which become filled with explosive gases of certain temperatures and pressures. These gases penetrate into the voids, expel the contained water and make the cavity dry. After a certain time, these explosive gases penetrate further into voids and fissures of the soil, the walls of the cavity eventually slide down and the soil is deformed. In waterbearing sands, the explosion cavity is distorted in a few days. In loamy-water (unsaturated) soils, the cavity happens to be stable for some years. However, in sandy-water (unsaturated) soils, the deformation occurs immediately after the detonation. The shape and size depend on the characteristics of the soil and the type of charge.

For a *spherical charge*, the cavity radius R_{vd} is given by

$$
\begin{aligned}
R_{vd} &= \overline{K}_{vd} R_w \\
&= \overline{K}_{vd}^* \sqrt[3]{W},
\end{aligned}
\tag{5.160}
$$

where R_w = charge radius of a spherical charge
  W = charge weight
  $\overline{K}_{vd}^* \approx 0.053 K_{vd}$
where K_{vd} = coefficient of proportionality $\mathrm{m\,kg^{-1/3}}$

For a *cylindrical charge*, the explosive cavity will have a cylindrical shape, except at the terminal regions.

$$
R_{vd} = \overline{K}_{vd} R_w = \overline{K}_{vd}^* \sqrt{W_c}.
\tag{5.161}
$$

	K_{vd}	$\overline{K}_{vd}$ ($\mathrm{m^{3/2}\,kg^{-1/2}}$)	$\overline{K}_{vd}^*$
Loam	11.3/13.1	28.3	0.4
Sandy soil	5.6/7.4	24.8	0.35
Limestone	3.8/4.7	19.5	0.27
Shale	1.7/2.9	10.2	0.19

For water-bearing soils, $R_{vys} = (1.2/1.3) R_{vd}$ of the above.

Dynamic Analysis for Explosion Cavity Formation

A great number of theories exist on the laws of deformation of soils. This is due to the fact that the constituent materials of soils and their characteristics vary. General reference to a crater normally means the visible crater or hole left after an explosion. The true crater is the hole actually excavated after the external body has penetrated and exploded within the soil. Debris actually falls back into the true crater. If the explosion occurs deep enough, the true cavity or crater is called a *camouflet*. This and other types are given in Fig. 5.21. Data on crater prediction in concrete and soil/rock, etc., are given in Tables 2.67–2.70. For the dynamic analysis of cratering, two Lagrange equations of motion for any medium are given:

$$
\partial p / \partial x = -\rho_{1s}[(\partial v_m / \partial t) + v_m (\partial v_m / \partial x)]
\tag{5.162}
$$

$$
\partial / \partial x [\bar{x}^2 v_m (\bar{x}, t)] = 0.
\tag{5.163}
$$

The boundary conditions for the shock wave front are formed according to the law of conservation of mass and momentum.

$$
\rho_a \dot{x}_m(x, t) = \rho_{1s}(\dot{x}_m - v_m) \quad \text{conservation of mass},
\tag{5.164}
$$

$$
p_m - p_a = \rho_a x_m v_m \quad \text{conservation of momentum},
\tag{5.165}
$$
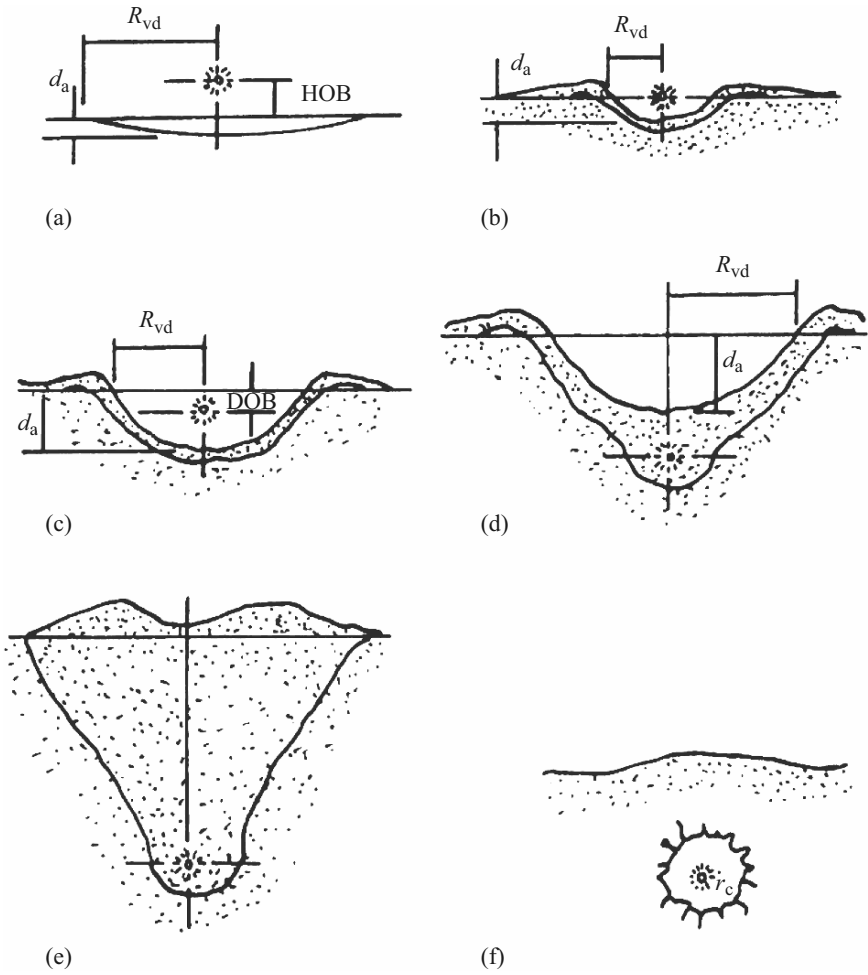
Fig. 5.21. Crater formations. (**a**) Low airburst (HOB = height of burst); (**b**) surface burst; (**c**) shallow depth of burst (DOB); (**d**) optimum DOB; (**e**) deeply buried; (**f**) camouflet

where v_m = mass velocity of soil depending on (x, t)

$\quad\quad x_m$ = distance

$\quad\quad t$ = time

$\quad\quad p_m$ = pressure dependent on (x, t)

$\quad\quad \rho_{1s}$ = density of the soil medium behind the shock front

$\quad\quad \rho_a$ = normal density at ambient temperature

On the interface of the gases and the medium, the above pressure and velocity are written as

$$p_{\text{pa}} = p(x,t) = \rho_{1\text{s}}[(f(t)/x) - (f^2(t)/2x^4)] + B(t), \tag{5.166}$$

where x is a general value of $x_{\text{m}} = R_{\text{vp}}$.

$$v_{\text{m}} = v_{\text{mp}} = f(t)/x^2. \tag{5.167}$$

From (5.167) and (5.163), the functional values of $f(t)$ and $\dot{f}(t)$ are evaluated as

$$f(t) = [1 - (\rho_{\text{a}}/\rho_{1\text{s}})]x_{\text{m}}^2 \dot{x}_{\text{m}}, \tag{5.168}$$

$$\dot{f}(t) = [1 - (\rho_{\text{a}}/\rho_{1\text{s}})]x_{\text{m}}(2\dot{x}_{\text{m}}^2 + x_{\text{m}}\ddot{x}_{\text{m}}). \tag{5.168a}$$

From equations (5.166), (5.168) and (5.178a), the following becomes the volume deformation phenomenon:

$$dV = \Delta V_{\text{vd}}/V_{\text{vd}} = (x)(x^2 \sin\phi\, d\phi\, d\psi\, dx), \tag{5.169}$$

where ϕ and ψ are geometrical parameters. The following pressure p is computed:

$$p = p_{\text{a}} + \rho_{\text{a}}\overline{D}\dot{x}_{\text{m}}^2 + \overline{D}_1(2\dot{x}_{\text{m}}^2 + x_{\text{m}}\ddot{x}_{\text{m}})[(x_{\text{m}}/x) - 1] - \tfrac{1}{2}\overline{D}_1\dot{x}_{\text{m}}^2[(x_{\text{m}}/x)^2 - 1], \tag{5.170}$$

where $\overline{D} = [1 - (\rho_{\text{a}}/\rho_{1\text{s}})]$,
$\overline{D}_1 = \rho_{1\text{s}}\overline{D}.$

The medium between the shock wave front and the explosives dictates the law of conservation of mass. Equation (5.163) indicates

$$\frac{4}{3}\pi(x_{\text{m}}^3 - x_{\text{w}})\rho_{\text{a}} = \frac{4}{3}\pi(x_{\text{m}}^3 - R_{\text{vp}}^3)\rho_{1\text{s}}. \tag{5.171}$$

Neglecting x_{w}^3 in comparison with x_{m}^3

$$R_{\text{vp}} = \overline{D}^{1/3}v_{\text{m}}, \tag{5.172}$$

where R_{vp} is the radius of the sphere of the explosive gases. By substituting x_{m} into (5.172) and taking $p = p_{\text{pa}}$ and $x = R_{\text{vp}}$, the following equation is derived:

$$P = 2(p_{\text{pa}} - p_{\text{a}})/\rho_{1\text{s}}(1 - \overline{D}^{1/3}) = 2R_{\text{vp}}\ddot{R}_{\text{vp}} + a\dot{R}_{\text{vp}}^2, \tag{5.173}$$

$$\text{where } a = 3 + \overline{D}^{1/3}(1 + \overline{D}^{1/3} + \overline{D}^{2/3}). \tag{5.174}$$

Knowing that

$$d/dR_{\text{vp}}(\dot{R}_{\text{vp}}^2 R_{\text{vp}}^a) = PR_{\text{vp}}R_{\text{vp}}^{a-1}, \tag{5.175}$$

$$v_{\text{m}}^2 = v_{\text{pv}}^2 = \frac{1}{R_{\text{vp}}^a}\int_{x=R_w}^{x=R} PR_{\text{vp}}R_{\text{vp}}^{a-1}dR_{\text{vp}}, \tag{5.176}$$

$$p_{\text{pa}} = p_{\text{w}}^*(V_{\text{w}}/V_{\text{vp}})^9, \tag{5.177}$$

the crater radius R_{vd} may be computed from

$$m_{vp} = \left\{ \frac{2p_a}{\rho_{1s}(1-\overline{D}^{1/3})a} \left[\left(\frac{R_{vd}}{R_{vp}} \right)^2 - 1 \right] \right\}^{1/2} \tag{5.178}$$

and in some cases

$$v_{pv}^2 = {}^*v_w^2$$

$$\text{as } R_{vd} = R_w \left[\frac{{}^*v_w^2 + \dfrac{2{}^*p_w}{(9-a)\rho_{1s}(1-\overline{D}^{1/3})}}{2p_a/a\rho_{1s}(1-\overline{D}^{1/3})} \right]^{1/a}. \tag{5.179}$$

Since $m_{vp} = \mathrm{d}R_{vp}/\mathrm{d}t$, by substituting into (5.178) and integrating between R_w and R_{vd}, the time t required for the creation of the explosion crater is given by

$$t = \frac{R_{vd}}{{}^*v_w} \left[\frac{\rho_{1s}{}^*v_w^2(1-\overline{D}^{1/3})a}{2p_a} \right]^{1/2} \overline{F}, \tag{5.180}$$

$$\text{where } \overline{F} = \overline{F}_1 + \frac{2}{a+2} \left(\frac{R_w}{R_{vd}} \right)^{(a+2)/2},$$

$$\overline{F}_1 = \frac{1}{a} \int z^{(2-a)/a}(1-z^a)\mathrm{d}(z^a) = \frac{\sqrt{\pi}}{a} \frac{\Gamma[(2+a)/2a]}{\Gamma[(1+a)/a]}.$$

5.8.3 Ground Shock Coupling Factor due to Weapon Penetration

The stress and ground motions will be greatly enhanced if a weapon penetrates more deeply into the soil or a protective burster layer before it detonates. The concept of an equivalent effect coupling factor is introduced to account for this effect on the ground shock parameters. The coupling factor, f_e^*, is defined as the ratio of the ground shock magnitude from a partially buried or shallow-buried weapon (Fig. 5.22) (near-surface burst) to that from a fully buried weapon (contained burst) in the same medium. It does not indicate the size of the charge, but it is a reduction factor for a contained burst, as described earlier in Sect. 5.7.1.

A single coupling factor is applicable for all ground shock parameters that depend upon the depth of burst (measured to the centre of the weapon) and the medium in which the detonation occurs, i.e. soil, concrete or a combination thereof plus air.

$$(f_c^*) = \frac{(P, V, d, I, a) \text{ near surface}}{(P, V, d, I, a) \text{ contained}}.$$

The coupling factor $(f_c^*) = 0.14$ for air is practically constant.

When a weapon penetrates into more than one material (see Fig. 5.23) for example, a long bomb that passes partially through a concrete slab, steel
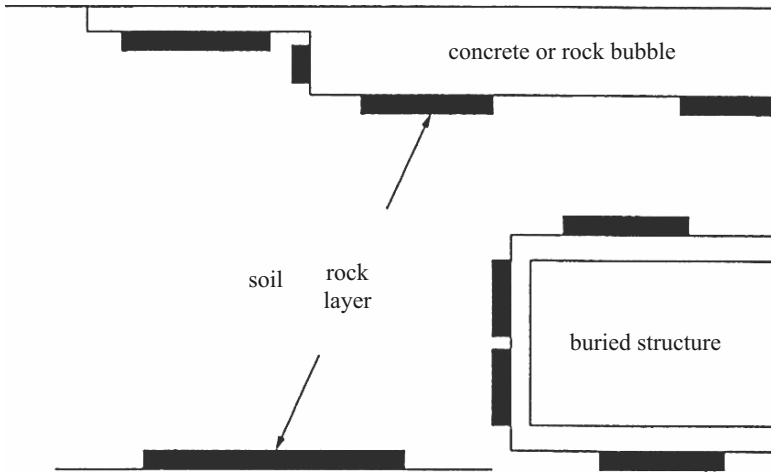
Fig. 5.22. A buried structure
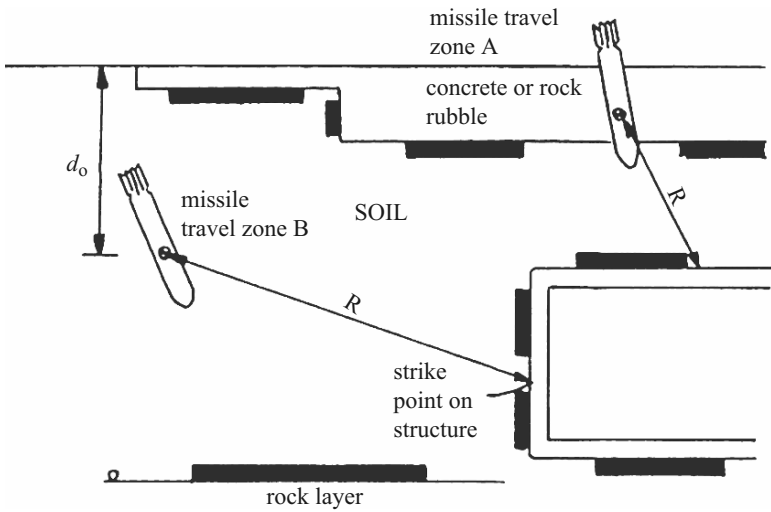
Fig. 5.23. Missile exploding on a buried structure

plates, etc., and into the soil beneath them, the coupling factor is then equal to the sum of the coupling factors for each material, weighted according to the proportion of the charge contained within each medium. The coupling factor is written as

$$(f_c^*) = \Sigma f_{ci}^*(W_i/W), \tag{5.181}$$

where f_{ci}^* = coupling factor for each component
W_i = weight of the charge in contact with each component
W = total charge weight

Since most bombs are cylindrical, the coupling factor can also be written as

$$f = \Sigma f_{ci}^{*}(L_i/L), \tag{5.182}$$

where L_i is the length of the weapon in contact and L is the total length.

The peak pressure p_{so}, velocity v_{so} and acceleration $\dot{v}_{ps}$ are written in terms of the coupling factor f_c^{*} and are given below:

$$p_{so} = f_c^{*}\rho\dot{v}_{ps}160(R/W^{1/3})^{-n}, \tag{5.183}$$

$$v_{so} = f_c^{*}160(R/W^{1/3})^{-n}, \tag{5.184}$$

$$\dot{v}_{sp}W^{1/3} = f_c^{*}50\dot{v}_{sp}(R/W^{1/3})^{-n-1}, \tag{5.185}$$

$$\delta/W^{1/3} = f_c^{*}500(1/\dot{v}_{sp})(R/W^{1/3})^{-n+1}, \tag{5.186}$$

$$F_1(t)/W^{1/3} = f_c^{*}\rho[1.1(R/W^{1/3})]^{-n+1}, \tag{5.187}$$

where p_{so} = peak pressure (psi)
$\quad f_c^{*}$ = coupling factor for near-surface detonations
$\quad v_{so}$ = seismic velocity (ft s^{-1})
$\quad R = x$ = distance to the explosion (ft)
$\quad W$ = charge weight (lb)
$\quad v_{ps}$ = peak particle velocity (ft s^{-1})
$\quad \dot{v}_{sp}$ = peak acceleration (gs)
$\quad \delta$ = peak displacement (ft)
$\quad F_1(t)$ = peak impulse (lb s in.$^{-2}$)
$\quad \rho$ = mass density (lb s^2 ft^{-4}) = 144 or equivalent
$\quad n$ = attenuation coefficient

These imperial values can be converted into SI units using standard conversions. A standard input is given in Tables 2.67–2.70.

As the weapon detonates near a structure, shock reflections from the ground surface or from layers such as a water table or rock layer can combine with the directly transmitted stress waves to cause a significant change in the magnitude and/or time t of the loading on the underground structure. Reflections from the ground surface will produce tensile waves which may combine with the incident wave to reduce the impact load $F_1(t)$ on the upper parts of the structure. Reflections from layers below the explosion will produce secondary compression waves, as stated earlier, which can combine with the incident stress to increase significantly the total loading on lower sections of the structure.

The path length travelled by the directly transmitted wave to any point on the structure is the straight line distance from the source to the point, which will be

$$x_i = \sqrt{[(d_0 - z)^2 + x^2]}. \tag{5.188}$$

The total path length of the wave reflected from the ground surface will be

$$x_r = \sqrt{[(d_0 + z)^2 + x^2]}. \tag{5.189}$$
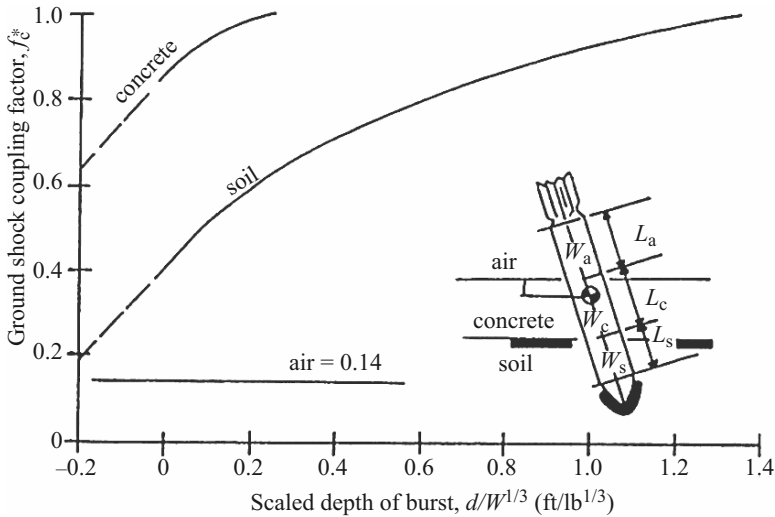
Fig. 5.24. Ground shock and scaled depth of burst

The total path length of a wave reflected from a deeper layer is then written as

$$x_\ell = \sqrt{[(2h - d_0 - z)^2 + x^2]}, \qquad (5.190)$$

where h = thickness of layer

d_0 = depth of the bomb from the ground surface

z = depth of the point on the structure from the ground surface

x = horizontal distance to the point on the structure

Figures 5.24 and 5.25 show the ground shock coupling factor (f_c^*) and the propagation paths for a burst in a layered medium.

Using (5.190) the reflected wave magnitude and the total stress-time history at the target location can be assessed from the following simple relations:

$$\sigma_d = p_{so} R_d e^{-\alpha t/t_d}, \qquad t \geq t_d = R_d/v_{su}, \qquad (5.191)$$

$$\sigma_s = -p_{so} R_s e^{-\alpha t/t_s}, \qquad t \geq t_s = R_s/v_{su}, \qquad (5.192)$$

$$\sigma_\ell = K p_{so} R_\ell e^{-\alpha t/t_\ell}, \qquad t \geq t_\ell = R_\ell/v_{su}, \qquad (5.193)$$

where v_{su} = velocity at the upper layer

σ_d = directly transmitted stress (distance R_d)

σ_s = stress reflected from the surface (distance R_s)

σ_ℓ = stress reflected from a lower layer (distance R_ℓ)

The peak stress σ_{pi} at a distance R_i is given for each by

$$\sigma_{pi} = \rho v_s 160 (R_i/W^{1/3})^{-n}. \qquad (5.194)$$
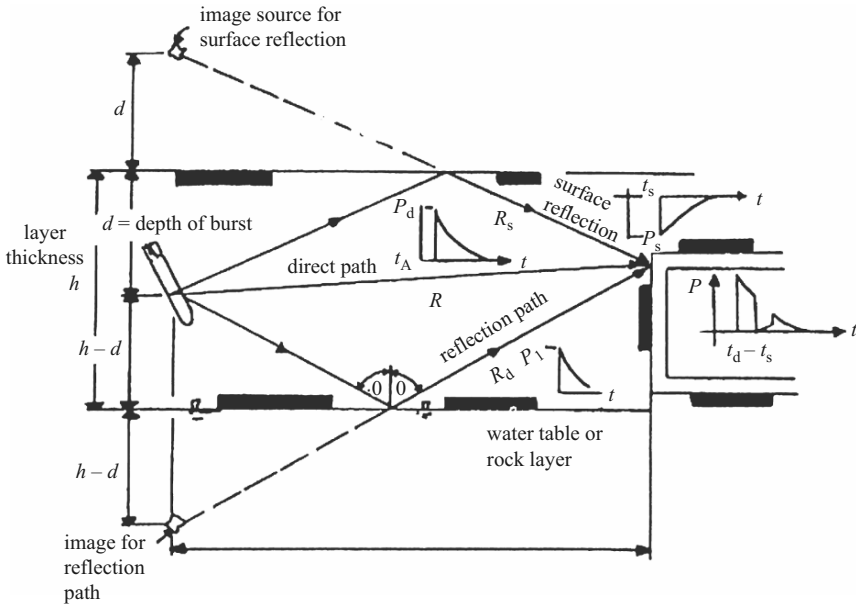
Fig. 5.25. Reflection from surface to lower layer
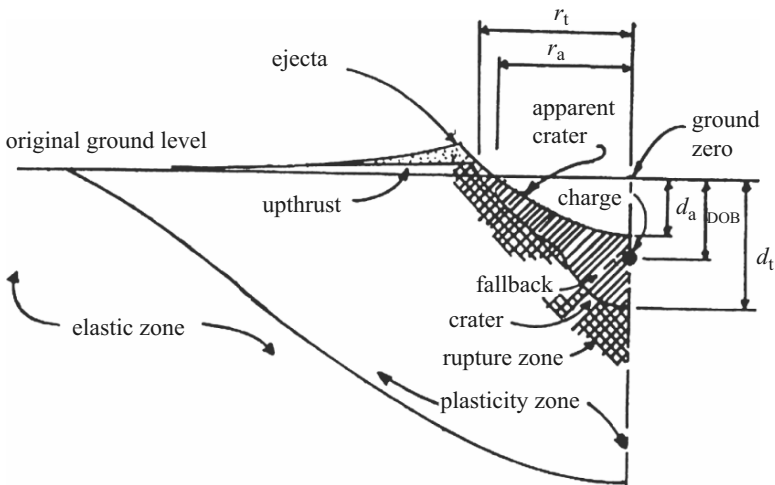
Fig. 5.26. Half-crater profile. (DOB = depth of burst; r_a = apparent radius, d_a = apparent depth; r_t = true radius; d_t = true depth.)

The reflection coefficients C_r given in (5.56) and (5.61) are applied.
    The shock load stress is given by

$$\sigma_{total} = \sigma_d + \sigma_s + \sigma_\ell. \tag{5.195}$$

A typical half-crater profile is shown in Fig. 5.26
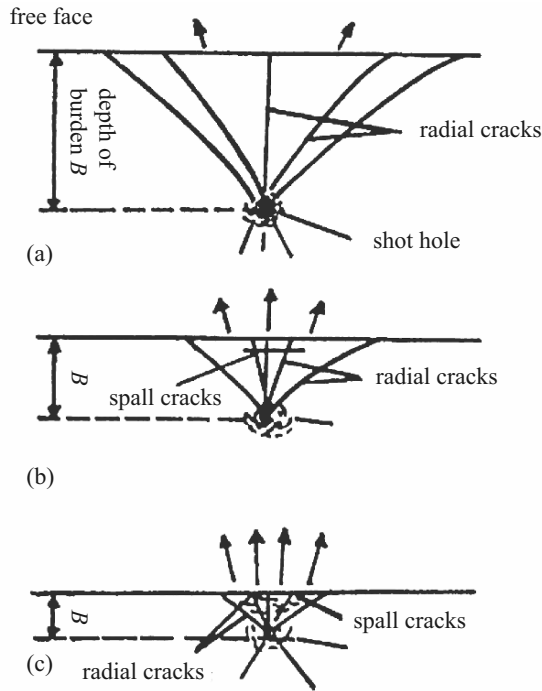
Fig. 5.27. Crack patterns at different depths. (**a**) Large burden; (**b**) intermediate burden; (**c**) small burden

5.9 Rock Blasting: Construction and Demolition

5.9.1 Rock Blasting Using Chemical Explosives of Columnar Shape and a Shot Hole

In all rock blasting work with explosives, the importance of different factors that control blasting and consequent rock fragmentation assume a priority. These factors are energy, detonation pressure, detonation velocity and explosive velocity. Although a few simple operations (drilling holes, loading of holes with explosives, detonation using a blasting cap from a distance, etc.) are needed to cause rock fragmentation, nevertheless the transient stresses and their distribution set up in the rock when an explosive detonates are complex since many variables are involved. A typical phenomenon of cracking and spalling for different types of burden is given in Fig. 5.27. The single-hole shots made in rock using PETN-based explosives produce a peak gaugehole pressure p_{gh} [4.1–4.49]:

$$p_{gh} = 764 \times \frac{2}{1 + \left(\dfrac{\rho_w v_{sd}}{\rho_r v_s}\right)\rho} \times p_D^{0.753} \times (f_{ci}^*)^{-0.715} \times \alpha_E^{0.785} \times d_g^{-1.6}, \quad (5.196)$$

where p_{gh} = peak gaugehole pressure in a water-filled hole in the rock (psi)

ρ_w = density of explosive ($\mathrm{g\,cm^{-3}}$)

v_{sd} = detonation velocity of explosive ($\mathrm{km\,s^{-1}}$)

ρ_r = density of rock

v_s = sonic velocity in rock ($5.2\,\mathrm{km\,s^{-1}}$)

p_D = detonation pressure

$$(p_D = 2.1(0.36 + \rho_w)v_{sd}^2 \text{ kilobar}) \tag{5.197}$$

f_{ci}^* = volume decoupling ratio = effective volume of shot hole:volume of explosive

α_E = calculated maximum expansion work in.$^{-1}$ of charge length, kcal in.$^{-1}$ (charge weight in g in.$^{-1}$ of charge (calculated maximum expansion in kcal g^{-1}))

d_g = distance of gaugehole from shot hole (in.)

Substitution of (5.197) into (5.196) gives the following equation for p_{gh}:

$$p_{gh} = \frac{2663}{1 + \dfrac{\rho_w v_{sd}}{\rho_r v_s}} \times (0.36 + \rho_w)^{0.573} \times v_{sd}^{1.506} \times (f_{ci}^*)^{-0.715} \times \alpha_E^{0.785} \times d_g^{-1.6}.$$

$$\tag{5.198}$$

In the case of the *loading density* ρ_L, which means bore hole filling, (5.198) is modified to

$$\rho_L = 1/\alpha_E. \tag{5.199}$$

For granite, based on the examinaton of the data from the detonation velocity series, the average fragment size plotted against the logarithm of a corrected peak gaugehole/pressure gave a reasonably straight line if the corrected peak gaugehole pressure $p_{gh,cor}$ is

$$p_{gh,cor} = p_{gh} \times \frac{1 + \dfrac{\rho_w v_{sd}}{\rho_r v_s}}{2} \times \frac{1}{1 + \dfrac{v_{sd}^2}{v_s^2} - \dfrac{v_{sd}}{v_s}}. \tag{5.200}$$

The average size, F_s, was calculated [4.248] to be

$$F_s = -2.11 \log p_{gh,cor} + 9.02,$$

$$\text{where } F_s = F_{av}\left(\frac{1}{B^3} + \frac{1}{L^3}\right)^{1/3}, \tag{5.201}$$

$$F_s = -2.11 \log \left[p_{gh} \frac{\left(1 + \dfrac{\rho_w v_{sd}}{\rho_r v_s}\right)}{2\left(1 + \dfrac{v_{sd}^2}{v_s^2} - \dfrac{v_{sd}}{v_s}\right)} \right] + 9.2,$$

where the term in square brackets defines the corrected pressure $p_{gh,cor}$ and B is the burden (in) and L is the shot-hole length. Figure 5.28 illustrates a plot of F_s versus $p_{gh,cor}$ for various series.
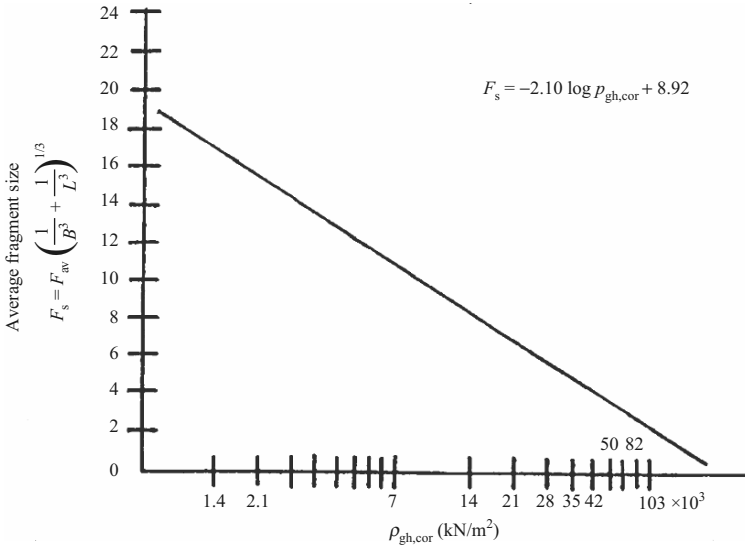
Fig. 5.28. Average fragment size versus corrected pressure for energy, pressure, detonation velocity and burden series (soils: granite; explosive: PETN)

5.9.2 Primary Fragments

Sometimes the explosion of a cased donor charge results in the creation of primary fragments. They are produced when an explosive container shatters. These fragments have small sizes and very high initial velocities which, in turn, depend on the thickness of the metal container, the shape of the explosive (spherical, cylindrical or prismatic), the shape of the end or middle of the container (conical, oval), etc. On the basis of report TM55-1300 the following expressions shall be included in the overall analysis given in this chapter.

Explosives with Cylindrical Containers: Fragment Velocity

The initial velocity v_0 (ft s^{-1}) is given by

$$v_0 = (2E')^{1/2} \left(\frac{W/W_c}{1 + W/2W_c} \right)^{1/2}, \tag{5.202}$$

where $(2E')^{1/2}$ = Gurney energy constant
$= 7{,}550$ for pentolite
$= 7{,}850\text{--}8{,}380$ for RDX/TNT
$= 6{,}940$ for TNT

$$= 7{,}460 \text{ for tetryl}$$
$$= 7{,}450 \text{ for torpex}$$
$$= 7{,}710 \text{ for H-6}$$

The explosion of a cased charge will produce a large number of fragments, N_f, with varying weights which can be obtained from the following equation:

$$\log_e N_f = \log_e \left(\frac{8W_c}{{}^*M_A^2} \right) - \frac{\sqrt{W_f}}{{}^*M_A}, \tag{5.203}$$

where N_f = number of fragments $> W_f$
$\qquad W_f$ = weight of primary fragment
$\qquad W_c$ = total weight of the cylindrical portion of the metal casing
$\qquad {}^*M_A$ = fragment distribution parameter
$$= {}^*B \, {}^*t_c^{5/6} d_i^{1/3} [1 + ({}^*t_{av}/d_i)] \tag{5.204}$$

$\qquad {}^*B$ = constant depending upon explosives and casings
$\qquad\quad = 0.24\text{–}0.35$
$\qquad t_c$ = thickness of the metal
$\qquad d_i$ = inside diameter of the casing
$\qquad {}^*t_{av}$ = average time

For a *large fragment*, $N_f = 1$ is substituted into (5.203) in order to compute its weight W_f. For other cases, reference is made to Table 5.7.

Fragment Velocity at Boundary and Uncased

The minimum boundary velocity ${}^*v_b$ at which propagation of the explosion occurs as a result of the primary fragment impact is

$$ {}^*v_b^2 = K e^{5.37 t_c / w_f^{1/3}} / W_f^{2/3} \left(1 + 3.3 t_c / W_f^{1/3} \right), \tag{5.205}$$

where K = a constant for the sensitivity of the explosive material contained
$\qquad\quad$ in the acceptor charge
$\qquad\quad = 2.78 \times 10^6$ for pentolite
$\qquad\quad = 4.10 \times 10^6$ for cyclotol (60/40)
$\qquad\quad = 3.24 \text{ to } 4.15 \times 10^6$ for RDX/TNT
$\qquad\quad = 16.30 \times 10^6$ for TNT
$\qquad\quad = 14.5 \times 10^6$ for amatol
$\qquad\quad = 3.55 \times 10^6$ for torpex
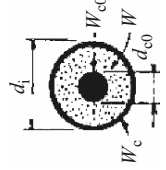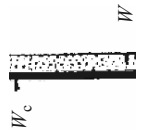
Fragment velocities v_b range between 1,200 and 4,000 ft s^{-1}. Fragment weights W_f are no more than 3 oz. Tables 2.67–2.70 give useful data for certain known cases.

Table 5.7. Initial velocity of primary fragments

Type	Cross-sectional shape	Initial fragment velocity, v_0	Maximum v_0	Remarks
Cylinder		$\sqrt{(2E')}\left[\dfrac{\frac{W}{W_c}}{1+\frac{W}{2W_c}}\right]^{1/2}$	$\sqrt{(2E')}\sqrt{2}$	
Sphere		$\sqrt{(2E')}\left[\dfrac{\frac{W}{W_c}}{1+\frac{3W}{5W_c}}\right]^{1/2}$	$\sqrt{(2E')}\sqrt{\dfrac{5}{3}}$	
Steel-cored cylinder		$\sqrt{(2E')}\left[\dfrac{\frac{W}{W_c}}{1+\frac{(3+a)W}{6(1+a)W_c}}\right]^{1/2}$ where $a = d_{c0}/1.6d_i$	$\sqrt{(2E')}\sqrt{\left[\dfrac{6(1+a)}{(3+a)}\right]}$	If the steel core is many times more massive than the explosive, this expression for the initial velocity should be modified by multiplying it by the expression: $$\sqrt{[1-(0.2W_{ct}/W)]},$$ where W_{c0} is the weight of the steel core (lb)
Plate		$\sqrt{(2E')}\left[\dfrac{\frac{3W}{5W_c}}{1+\frac{W}{5W_c}+\frac{4W_c}{5W}}\right]^{1/2}$	$\sqrt{(2E')}\sqrt{3}$	This expression applies for a rectangular explosive in contact with a metal plate having the same surface area; it is assumed that the entire system is suspended in free air and its thickness is small in comparison to its surface area, so that the resulting motions are essentially normal to the plane of the plate

Hollow cylinder		—	Although an expression to predict the velocity of fragments is not available, an upper limit of the initial velocity may be obtained using the expression for a solid cylinder and a lower limit from the expression for a single plate; the ratio of the explosive weight to the casing weight (W/W_c) of the hollow cylindrical charge is used in both expressions
Sandwich plates		If $W_{c1} \neq W_{c2}$ $$\sqrt{(2E')}\left[\frac{W}{W_{c1}+W_{c2}g+\dfrac{W}{3}(1-g+g^2)}\Big/\left(W_{c2}+\frac{W}{2}\right)\right]^{1/2}$$ where $g = \left(W_{c1}+\dfrac{W}{2}\right)\Big/\left(W_{c2}+\dfrac{W}{2}\right)$ If $W_{c1}=W_{c2}=W_c$ $$\sqrt{(2E')}\left[\frac{\dfrac{W}{2W_c}}{1+\dfrac{W}{6W_c}}\right]^{1/2}$$	$\sqrt{(2E')}\sqrt{3}$	This expression applies to a rectangular explosive sandwiched between two metal plates having the same surface area as the explosive; it is assumed that the entire system is suspended in free air and its thickness is small in comparison to its surface area, so that the resulting motions are essentially normal to the plane of the plates
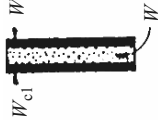
$W, W_c, W_{c0}, W_{c1}, W_{c2}$ (lb); d_1, d_{c0} (in); v_0, $\sqrt{(2E')}$ (ft s^{-1})

5.9.3 Blasting: Construction and Demolition

Much has been written about chamber charges in this text. Here distinctive features are given about the *slab charges*, which can afford an improvement in parameters of practical importance, such as directivity and accuracy of throw. The *directivity of throw* $\vec{f}_d$ is written as the volume of the debris projected in a given direction divided by the total volume removed to the free face. The other parameter is the *accuracy factor*, f_{ac}, which is written as the ratio of the volume of the rock thrown away to a predetermined area to the total volume of the rock moved to the free face. In the slab-charge system, the value of f_{ac} is higher than 90% under normal conditions.

Figures 5.29 and 5.30 explain clearly the chamber and slab systems. As seen, a chamber charge projects rock fragments in all directions. This implies a greater part of rock burden within the limits of the open pit. In the case of a sloping face, the chamber charge blast removes the rock burden of a volume contained by the angle BOC; this is dumped on the left-hand side, to be removed by bulldozers or other excavators. Thus it is not economical. The picture is totally different in the case of slab charges, the move is in a given direction in a compact form. This is due to the fact that the trajectory of the rock fragments is perpendicular to the baseline of the slab charge. The blasted rock may be removed to a desired distance by varying the angle of inclination α, as shown in Fig. 5.29. Since the fragments fly as a compact mass, air drag has much less effect on their movement than in chamber-charge blasting. The rock mass can then be easily moved to a required distance. Slab charges can be either of the layered type or the concentrated type, as shown in Fig. 5.30.

The parallel deep-hole charge is used on slopes as well. In this method, the material to be blasted in holes moves freely from a high-pressure zone to a lower-pressure zone in the depression. Since the energy is distributed in this unevenly along the slope, it is better to charge the holes area-wise and the intermediate spaces are filled with inert material. The rock blasting by slab

(a)   (b)
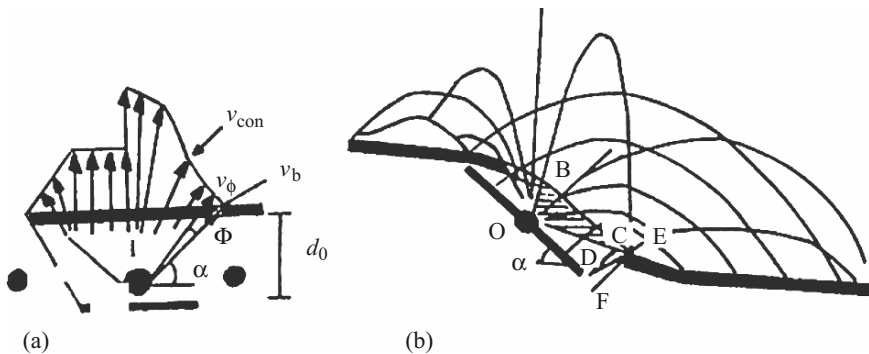
Fig. 5.29. Slab and chamber charges: initial projections, (**a**) Plain face; (**b**) sloping face
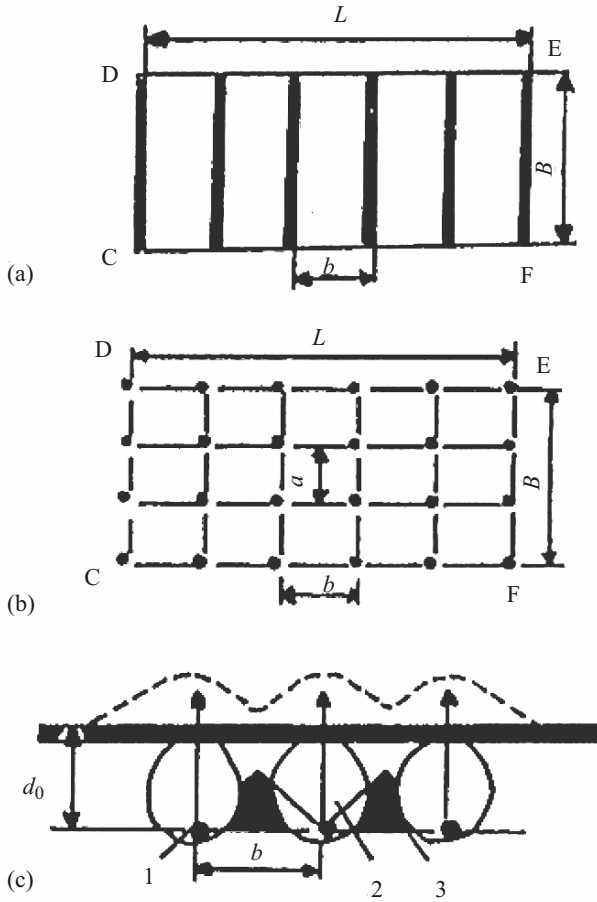
Fig. 5.30. System layout of slab charges. (**a**) Layered charges; (**b**) concentrated charges; (**c**) b = distance, 1 = charge, 2 = gas chamber, 3 = volume of undisturbed rock

charges forms trenching, and will have an even surface if the distance between consecutive rows of charges does not exceed the value of b (Fig. 5.30) where

$$b = d_0 e_f^{2/3}, \qquad (5.206)$$

where b = spaces between charges
d_0 = depth of concentrated charges
e_f = efficiency factor = R_{vd}/d_0 (see Table 5.8)
R_{vd} = crater radius, as calculated in Sect. 5.7

Table 5.8. Efficiency factor e_f versus consumption of explosive q for concentrated charges in hard rock

q (kg m^{-3})	e_f
0.5	0.20
1.0	0.35
1.5	0.42
2.0	0.50
3.0	0.60

For concentrated charges, the initial velocity v_{con} along the line of least resistance is given by

$$v_{con} = A(Q^{1/3}/d_0)^m C_f, \tag{5.207}$$

where Q = mass of concentrated charges

A, m = physio-mechanical properties of the soil, examples of which are given below:

Soil type	A	m
Loess	8	3.0
Sand	9	2.4
Loam	16	2.0
Clay	22	1.8
Hard rock	40	1.5

C_f = correction factor

$$= \sqrt{\left\{ \frac{1}{2} + \frac{1}{[(q/k_e)^{0.57} + 1]^{m+1} + [0.5(q/k_e)^{0.57} + 1]^{m+1}} \right\}}, \tag{5.208}$$

q = specific consumption of explosives

$= Q/1.047 d_0^3 \tan^2 \phi_{lim}$

k_e = computed consumption of explosives

The efficiency factor is written as

$$e_f = \frac{1}{2} \sum_0^\phi v_\phi^2 d_m / Q E_{ne}, \tag{5.209}$$

where v_ϕ = velocity at an angle ϕ

E_{nc} = specific energy of explosive

$$d_m = \tfrac{1}{3}\pi d_0^3 \tan^2 \phi \tag{5.210a}$$

$$\cos\phi_{lim} = 1/\sqrt{(\tan^2 \phi_{lim} + 1)} \tag{5.210b}$$

$$\tan\phi_{lim} = \sqrt[3]{[Q/k_c d_0^3(1 + d_0/50)]} \tag{5.210c}$$

Crushing of Fragments due to Collisions Between Themselves and Their Impact on Structures

Rock fragments are further crushed by the kinetic energy of flight and the potential energy which they impact on structures. The degree of crushing depends on the value of q, size, rock hardness, density, etc. The energy balance equation has to be developed. The text gives relevant information in earlier chapters on impact and the dynamics associated with it. The energy balance equation is formed from the following constituent relationships:

$$\text{kinetic energy (KE)} = qE_{\text{ne}}e_{\text{f}} = E_1 l_{\max}^3/k_{\text{loc}}^2, \tag{5.211}$$

where l = fragment size; $l_{\max}^3/k_{\text{loc}}^2$ = the volume
E_1 = energy in fragment

$$\text{potential energy (PE)} = l^3\rho\mathbf{g}H/k_{\text{loc}}^3,$$
$$E_{\text{crush}} = \text{crushing energy} = K_{\text{s}}(\text{KE} + \text{PE}), \tag{5.212}$$

where H = height of the rock
K_{s} = stiffness coefficient at impact, indicating that part of the energy is utilized for crushing
k_{loc} = parameter ≈ 1.3

If A_0 is the initial surface area, it is given by

$$A_0 = 6l^2/k_{\text{loc}}^2. \tag{5.213}$$

The stiffness coefficient, k_{er}, indicating the size reduction due to impact, is expressed as

$$k_{\text{er}} = 1 + (l_{\max}/6k_{\text{loc}} - e)(e_{\text{f}}qE_{\text{ne}} + \rho\mathbf{g}H), \tag{5.214}$$

where e is the energy in a unit fragment.

The values given above are assessed in the following order:

$$q = 0.5\,\text{kg}\,\text{m}^{-3};\ E_{\text{ne}} = 4 \times 10^6\,\text{J}\,\text{kg}^{-1};\ K_{\text{s}} = 0.01;\ E = 5 \times 10^{10}\,\text{N}\,\text{cm}^{-2};$$
$$\rho = 2{,}300\,\text{kg}\,\text{m}^{-3};\ H = 15\,\text{m}.$$

Wedge-Shaped Charges (for angle $0° < \alpha < 45°$)

Wedge-shaped charges are included with slab charges. The only difference is that their thickness is variable. In cross-section, their shape is trapezoidal, as shown in Figs. 5.31 and 5.32. The efficiency is written as

$$e_{\text{f}} = R_{\text{vd}}/d_{03} = \cot\beta \tag{5.215}$$
$$Q_3 = k_{\text{e}}d_{03}^3(H\ d_{03}/50)(0.4 + 0.6e_{\text{f}}^3).$$
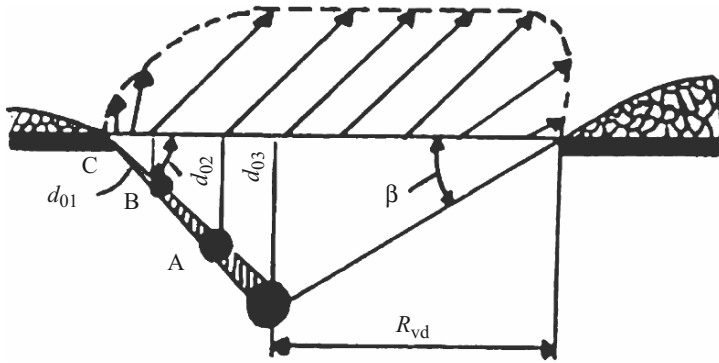
Fig. 5.31. Projection velocity for a wedge-shaped charge
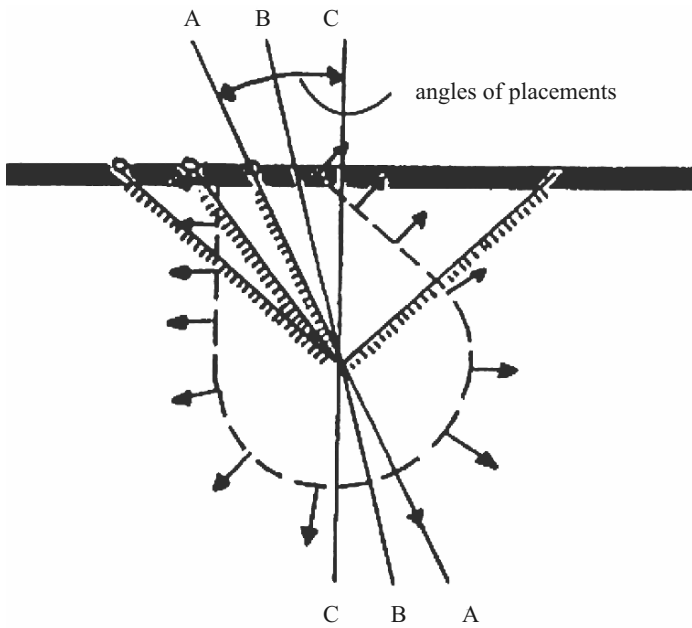
Fig. 5.32. Crater shapes for a wedge-shaped charge. (Charge placed at different angles to the vertical plane.)

For spacings and explosions, the rest of the procedure is given in Sect. 5.8.3. In the case of a multi-charge layout of a wedge shape, the specific consumption q of the explosives must ensure that the rock is projected to a distance l_x, which is given by

$$l_x = 2d_{cr}(\cot\alpha + \cot\beta), \tag{5.216}$$

where l_x is the depth of the design pit at which the next row of charges is laid. The distance between two rows (the first and second ones) is given by

$$b_1 = d_{01} \sqrt{(q/k_e)},$$

$$\text{where } d_{01} = \frac{1}{4} l_x. \tag{5.217}$$

In the same manner, the distance between the nth and the $(n+1)$th row of charges is given by

$$b_n = d_{0n} \sqrt{(q/k_e)}, \tag{5.218}$$

$$\text{where } d_{0n} = d_{0(n-1)} + b_{i-1} \tan \beta. \tag{5.219}$$

The expansion time t_{exp} between successive explosions or rows of charges is written as

$$t_{exp} = C_1 d_0 V \sqrt{(\rho q / 2E_{ne} - e_f)}, \tag{5.220}$$

where $C_1 = $ a coefficient which prevents moving rock from achieving an instant velocity of $v = \sqrt{(2E_{ne}e_f/\rho)}q \approx 1.5$

$V = \text{volume kg}^{-1} \approx 1\,\text{m}^3\,\text{kg}^{-1}$ as a unit

The optimum distance b between the rows of blast holes must obey the following relationship:

$$b \leq H(0.4/\sin 2\alpha), \tag{5.220a}$$

where H is the height of the slope being blasted.

5.10 Explosions in Water

5.10.1 Introduction

The explosive wave properties and development in water are very similar to that of an air explosion (Sects. 2.5 and 5.3). Major differences do, however, exist. The well known one is the violent compression by the surrounding water of the expansion of the explosive gases. The high pressure, the weight of water and its inertia are responsible for this phenomenon. The rate of compression depends also on the depth of the explosion. Due to the inertia of water, the explosion pressure exceeds the hydrostatic pressure. A repeated compression generates a new expansion of the gases and, as a result, pulsating spherical gas bubbles rise towards the water surface. When the bubble appears and expands, a new pressure wave is generated which is the secondary wave; the first, being the primary wave, looks very different from this one. The pressure of the secondary is around 5–20% of the primary shock wave. The pressures of the secondary waves continue to decrease as and when more and more are produced with greater and greater periods. Figure 5.33 gives a typical profile of a shock wave in water. Section 2.7 gives an introducton to the data on explosions in water.
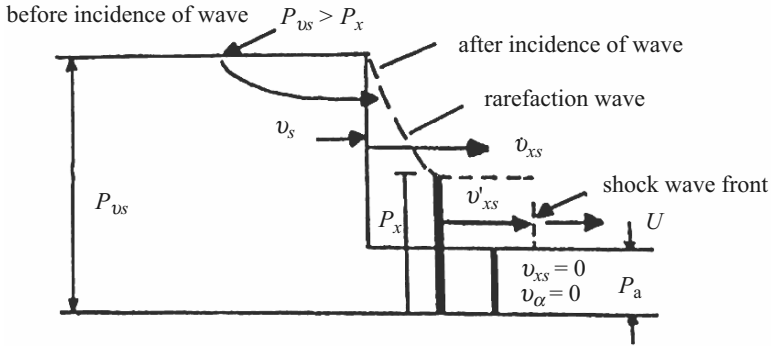
Fig. 5.33. Pressure distribution (*solid line* before incidence of wave, *dotted line* after incidence of wave)

5.10.2 Initial Parameters of Shock Waves in Water

A shock wave always propagates in a medium surrounding a charge. It is assumed that conditions at the interface are such that the pressures and velocities must be equal on both sides (Fig. 5.34). When the pressure p_{vs} is greater than p_x, the value of the velocity v'_{xs} is written as

$$
\begin{aligned}
v'_{xs} &= \frac{v_s}{k+1}\left\{1 + \frac{2k}{k-1}\left[1 - \left(\frac{P_x}{P_{vs}}\right)^{(k-1)/2k}\right]\right\} \\
&= \sqrt{[(p_x - p_a)(V_a - V_{xs})]},
\end{aligned} \tag{5.221}
$$

where the value of k lies within the range $2.54 \le k \le 3$, depending on the type of explosive; p_x, p_a, V_a and V_{xs} are pressures and volumes, respectively.

In general terms, the value of k is written as

$$
k = 2\alpha_w + 1, \tag{5.222}
$$

where α_w lies within the range $0.7 \le \alpha_w \le 1$; for TNT, α_w is equal to 0.77.

The value of $\dot{v}_{xs}$, the acceleration with which the shock wave proceeds in general from p_x, is written as

$$
\dot{v}_{xs} = -V_{xs}\sqrt{\left(\frac{p_x - p_{vs}}{V_{xs} - V}\right)} + v_s, \tag{5.223}
$$

$$
\text{again } v_s = \dot{v}_{xs}/(k+1). \tag{5.224}
$$

The value of V/V_{xs} is generally written as

$$
V/V_{xs} = \frac{(k+1)p_{vs} + (k-1)p_{vs}}{(k+1)p_x + (k-1)p_{vs}}. \tag{5.225}
$$
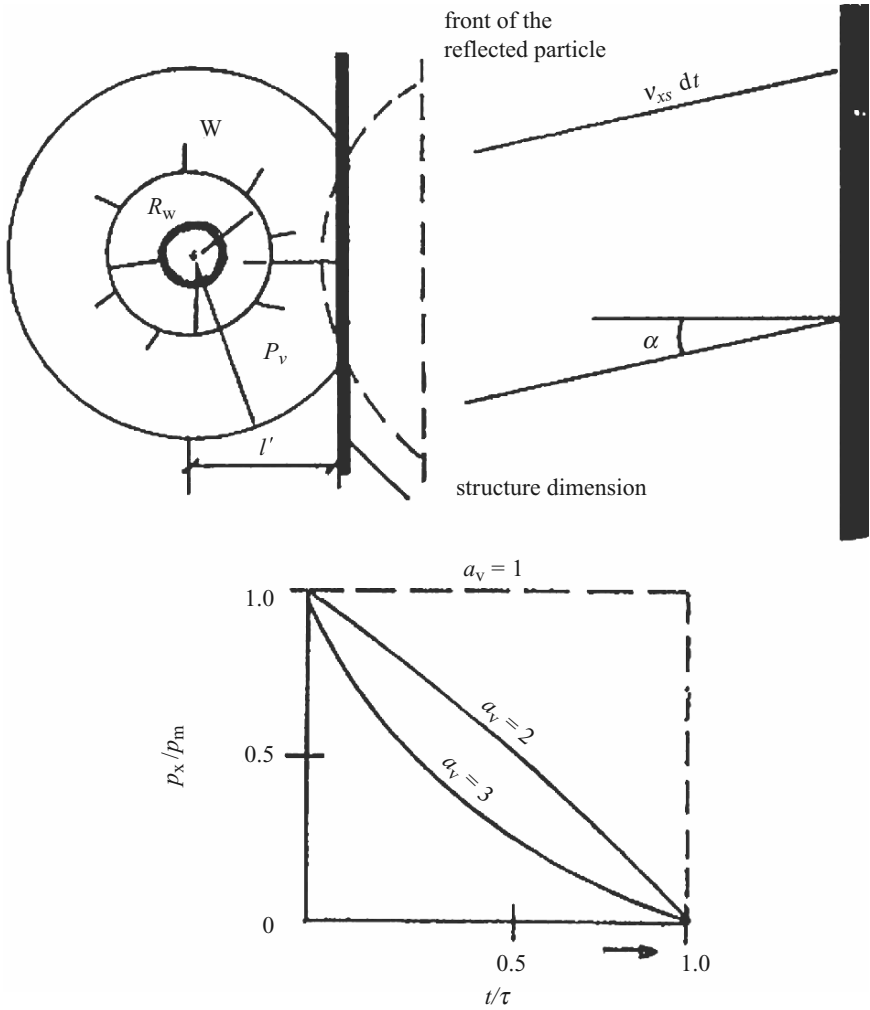
Fig. 5.34. Explosion in the vicinity of a structure

If $p_x/p_{vs} = \bar{p}$, then (5.212) is written for the respective volumes as

$$V/\dot{V}_{xs} = \frac{(k-1)\bar{p} + (k+1)}{(k+1)\bar{p} + (k-1)}. \tag{5.226}$$

The value of $\dot{v}'_{xs}$ for a typical value of p_x is written as

$$\dot{v}'_{xs} = \frac{-\dot{v}_{xs}}{(k+1)} \left\{ \left(\frac{k}{2}\right) \sqrt{[(k+1)\bar{p} + (k-1)]} - 1 \right\}, \tag{5.227}$$

for

$$
\begin{aligned}
k &= 1, \quad \bar{p} = 2.6, \quad \dot{v}'_{xs}/v_{xs} = -0.31,\\
k &= 3, \quad \bar{p} = 2.39, \quad \dot{v}'_{xs}/v_{xs} = -0.78,\\
k &= \infty, \quad \bar{p} = 2.28, \quad \dot{v}'_{xs}/v_{xs} = -1.28.
\end{aligned}
$$

In the pressure range $p \geq 5{,}000\,\mathrm{kN\,cm^{-2}}$, the adiabate of water is written as

$$
p_x = 3{,}940(\mathrm{kN\,cm^{-2}})[(\rho_{\mathrm{sw}}/\rho_{\mathrm{a}})^8 - 1], \tag{5.228}
$$

where ρ_{sw} and ρ_{a} are the densities at the shock front and under ambient conditions, respectively.

The value of v_{xs} is written as

$$
v_{xs} = \sqrt{\left\{ \left(\frac{p_x}{\rho_{\mathrm{a}}}\right)\left(1 - \frac{\rho_{\mathrm{a}}}{\rho_{\mathrm{sw}}}\right)\right\}}. \tag{5.229}
$$

For a water shock wave, p_{a} is generally neglected owing to heavy compression. However, for $p_{\mathrm{a}} < p_x$, the value of the shock $U\ (\mathrm{m\,s^{-1}})$ is written as

$$
U = v_{xs} \Big/ \left(1 - \frac{\rho_{\mathrm{a}}}{\rho_{\mathrm{sw}}}\right). \tag{5.230}
$$

The corresponding energy term is written as

$$
\Delta E = E_{nx} - E_{na} = \frac{p_x}{2}(V_{\mathrm{a}} - V_{xs}), \tag{5.231}
$$

where E_{nx} = energy for the p_x value

$\quad\ \ E_{na}$ = energy under ambient conditions

For PETN and TNT explosives, the following values for the above parameters have been reported:

	v_{xs} $(\mathrm{m\,s^{-1}})$	$\rho_{\mathrm{sw}}/\rho_{\mathrm{a}}$	$p_x \times 10^3$ $(\mathrm{kN\,cm^{-2}})$	U $(\mathrm{m\,s^{-1}})$	$U/\dot{v}_{xs}$	ΔE $(\mathrm{cal\,g^{-1}})$
PETN $(1.69\,\mathrm{g\,cm^{-3}})$	2,725	1.636	195	7,020	0.835	800
TNT $(1.60\,\mathrm{g\,cm^{-3}})$	2,185	1.557	136	6,100	0.872	570

The pressure p_{m} on a structure inside water is written as

$$
\begin{aligned}
p_{\mathrm{m}} &= [p_x/(1 - t/\tau)]^{a_{\mathrm{v}}-1}\\
&= p_{\mathrm{w}}(R_{\mathrm{w}}/R^*)^{a_{\mathrm{v}}-1}\cos^2\alpha,
\end{aligned} \tag{5.232}
$$

where $a_{\mathrm{v}} = 3$ for a spherical charge

$\quad\ \ a_{\mathrm{v}} = 2$ for a cylindrical charge

$\quad\ \ a_{\mathrm{v}} = 1$ for a flat charge

$\quad\ \ R_{\mathrm{w}}$ = radius of the charge

$\quad\ \ R^*$ = general radius of the gas sphere

$\quad\ \ \alpha$ = angle at which the pressure acts on the structure

For chemical charges, the duration time $\tau = 10^{-4}$ s. When the charge touches the underwater structures the value of t is zero. For such short periods the effect of loading on the structure does not depend on the pressure magnitude p_{m}, but on the impact $F_1(t)$. The total impact is then written as

$$
\begin{aligned}
F_1(t) &= \int_0^\tau p_x \mathrm{d}t = p_{\mathrm{m}} \int_0^\tau \left(1 - \frac{t}{\tau}\right)^{a_{\mathrm{v}}-1} \mathrm{d}t \\
&= -p_{\mathrm{m}} \int_0^\tau \left(1 - \frac{t}{\tau}\right)^{a_{\mathrm{v}}-1} \mathrm{d}\left(1 - \frac{t}{\tau}\right) \\
&= p_{\mathrm{m}} \frac{\tau}{a_{\mathrm{v}}}.
\end{aligned}
\tag{5.233}
$$

As shown in Fig. 5.34, a *nearby explosion* is effective if the distance l' (distance of the structure from the charge) is defined as $R_{\mathrm{w}} < l' \leq 10 R_{\mathrm{w}}$ if ρ_{a} and p_{a} are both zero. For spherical and cylindrical charges, respectively, the values of $F_1(t)$ are given below:

$$
F_1(t) = \frac{\overline{A}W}{(l')^2} \cos^4 \alpha,
\tag{5.234}
$$

$$
F_1(t) = \left(\frac{2\overline{A}W_{\mathrm{c}}}{l'}\right) \cos^3 \alpha,
\tag{5.235}
$$

where

$$
\overline{A} = e v_{xs}
\tag{5.236}
$$

e = coefficient of restitution
W, W_{e} = spherical and cylindrical charges (mass/unit length) respectively

For example, in an explosion occurring above a *circular structure* of radius r, assuming the explosion epicentre coincides with the centroid of the structure, the impact caused by the explosion can be written as (Fig. 5.35):

$$
\mathrm{d}(F_1'(t)) = 2\pi r \mathrm{d}r(F_1(t))
\tag{5.237}
$$

where $r = l' \tan \alpha$
$\mathrm{d}r = (l'/\cos^2 \alpha)\mathrm{d}\alpha$ (α is the angle shown on (Fig. 5.35)):

Equation (5.175) can be written as

$$
\begin{aligned}
\mathrm{d}(F_1'(t)) &= 2\pi l' \tan \alpha (l'/\cos^2 \alpha)\mathrm{d}\alpha (\overline{A}W/l') \cos^4 \alpha \mathrm{d}\alpha \\
&= 2\pi \overline{A}W \sin \alpha \cos \alpha \mathrm{d}\alpha,
\end{aligned}
\tag{5.238}
$$

$$
F_1'(t) = \int_0^{\alpha_{\mathrm{d}}} 2\pi \overline{A}W \sin \alpha \cos \alpha \mathrm{d}\alpha = \pi \overline{A}W \sin^2 \alpha_{\mathrm{d}}.
\tag{5.239}
$$

For structures of other shapes, refer to Chap. 3 on basic structural dynamics. The value of r can be any dimension L (length) and B (breadth). For an infinite circular structure, $r \to \infty$ and $\alpha_0 \approx \pi/2$, then

$$
F_1'(t) = \pi \overline{A}W.
\tag{5.240}
$$
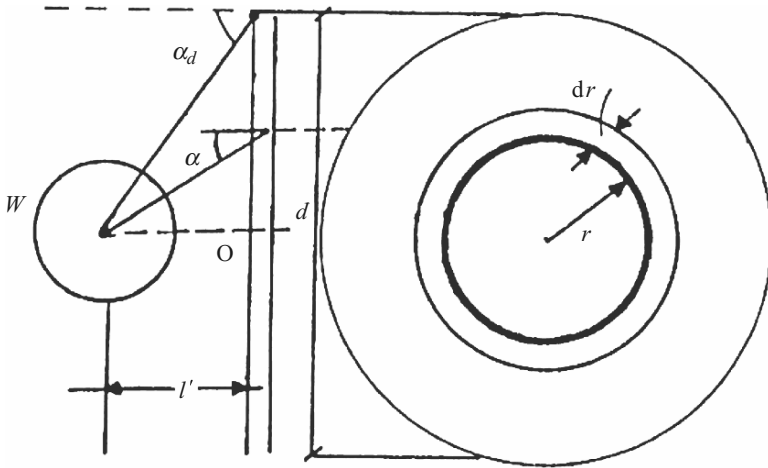
Fig. 5.35. A circular structure under an explosive load

It is important to know the *state of water*, i.e. the basic relationships of hydrostatics. The volume $V(T, p)$ and the pressure p must have a relation. The empirical equation of the state of water gives a useful relation for p and V, which in turn depend on T and p values. The Bridgman equation is written as

$$p = (109 - 93.7\,V)(T - 348) + 5{,}010\,V^{-5.58} - 4{,}310 \ (\text{kp}\,\text{cm}^{-2}). \qquad (5.241)$$

In comparison to gaseous explosions, the reactions of *solid explosives* cause greater problems owing to high temperatures and densities. Jones [4.252–4.254] developed an equation for the assumed state by fitting data from Bridgman as follows:

$$p = \alpha^* A^* e^{-\alpha^*(V/N)} - B + RTf, \qquad (5.242)$$

where $\alpha^* = 0.263\,\text{cm}^{-3}$
    $A^* = 855\,\text{kcal}\,\text{mole}^{-1}$
    $T = $ temperature
    $N = $ number of moles
    $B = 0.139\,\text{kcal}\,\text{mole}^{-1}$
    $f = 0.313\,\text{cm}^{-3}$
    $R = $ gas constant

On the basis of data for nitrogen, Jones [4.252–4.254] introduced higher temperatures and comparable densities. The total energy E_{NT} of the products of explosion becomes

$$E_{\text{NT}} = \Sigma[N_a E_a + (N - N_s)(E_a + \tfrac{3}{2}RT)], \qquad (5.243)$$

where N_a = number of moles for each molecular species (solid or gas)

$N = \Sigma N_a$

N_s = number of moles of solid products

$\frac{3}{2}RT$ = energy of interaction for the gas molecules plus vibrational energy $\frac{3}{2}RT\,\text{mole}^{-1}$

5.10.3 Major Underwater Shock Theories

Some major underwater shock theories evaluate relations between overpressure and the reduced distance. Some examples are given below.

Kirkwood–Bethe Theory

This theory covers initially a spherical shock wave in terms of kinetic enthalpy $\omega(R^*, t)$. The pressure–time curve is related by

$$p(R, t) = (a_0/R')p(\tau),$$
(5.244)

where

a_0 = initial radius of the gas sphere

R' = radius of the shock front

$p(\tau) = \rho_w(a(\tau)/a_0)\omega(a, \tau)$

a = radius of the gas sphere at any stage

(5.245)

When the shock front reaches a point R, the value of τ becomes

$$\tau = \tau_0 + (\partial\tau/\partial t)R(t - t_0) = \tau_0 + (1/\gamma_{sh})(t - t_0).$$
(5.246)

The parameter γ_{sh}, which is the measure of the time scale behind the shock front relative to the gas sphere, increases rapidly as the shock front travels outwards. Kirkwood and Bethe finally arrived at a pressure–time relationship of

$$p(r, t - t_0) = p(0)x'(a_0/R^*)e^{-(t-t_0)/\theta},$$
(5.247)

where $p(0) = (0)\omega(a_0)$

$\theta = \gamma_{sh}\theta_1.$

The value of γ_{sh} in (5.247) was taken as

$$\gamma_{sh} = 1 - \frac{1}{\beta c_0(Z_a + 1)} + \frac{2a_0}{c_0\theta_1}\frac{\beta\omega(a_0)}{c_0}\left[\log\frac{Z}{Z_a} - \frac{4(Z - Z_a)}{(Z + 1)(Z_a + 1)}\right],$$
(5.248)

where $c_0 = v_{s0}$ (initial), defined earlier

θ_1 = parameter $\theta/\gamma_{\text{sh}}$

θ = incremental time = $2(a_0/c_0)(\beta w a_0/c_0)(R^*/a_0)$

Z is a function of xa_0/R^*. The quantity Z_a is strictly a function of $xa_0/a(\tau_0)$, and is given by the relation

$$Z_a = 1 + \frac{1}{2w(a_0)x_d} + \sqrt{\left\{\frac{1}{w(a_0)x} + \left[\frac{1}{2w(a_0)x}\right]^2\right\}}, \qquad (5.249)$$

$$Z = (1 + \beta\sigma)/\beta\sigma, \qquad (5.250)$$

$$\sigma = \sum_{\rho_0}^{\rho}(1/\rho)v_s d, \qquad (5.251)$$

where $v_s = c$ = velocity of sound in water = $\sqrt{(dp/d\rho)}$

$$\beta = [(u/c_0 - 1]/\sigma,$$

$\dot{x} = u$ = particle velocity

x_d = dissipation factor

In terms of charge weight, the peak pressure p_m may then be written as an approximate value in terms of the power laws as

$$p_m = k(W^{1/3}/R^*)^\alpha. \qquad (5.252)$$

The following table gives the numerical values of some of the parameters which are given in Sect. 2.6 and below for TNT.

R^*/a_0	1.00	10	25	50	100
x	1.00	0.40	0.30	0.259	0.23
γ_{sh}	1.00	4.03	6.42	8.10	9.54
$\theta/a_0\ (10^{-5}\,\text{s cm}^{-1})$	0.345	1.40	2.20	2.80	3.30
$p_m\ (\text{lb in.}^{-2})$	537,959	20,199	6,100	26,225	1,169

The empirical value of α is around 1.16, based on the slope of the curves.

5.10.4 Penney and Dasgupta Theory

The finite amplitudes of the spherical waves involve many differential equations with a number of unknown parameters. Penney and Dasgupta have solved them for TNT, and derived the value of the peak pressure as a function of shock radius R_w^*:

$$p_m\ (\text{lb in.}^{-2}) = 103,000\ (a_0/R^*)e^{2a0/R^*}$$
$$= 14,000\ (W^{1/3}/R^*)e^{0.274w^{1/3}/R^*}, \qquad (5.253)$$

where $a_0 = R_w$.
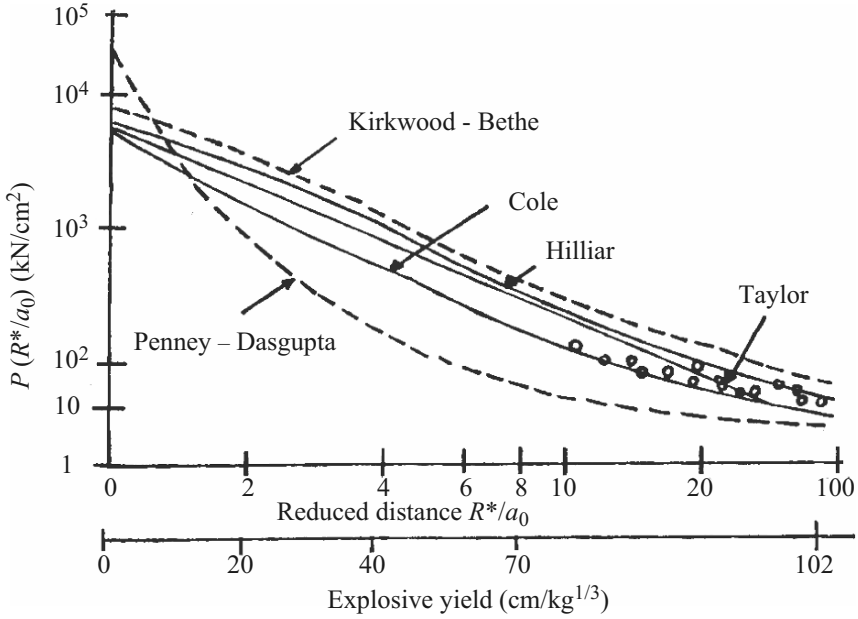
Fig. 5.36. A comparison of various underwater shock front theories

5.10.5 A Comparative Study of Underwater Shock Front Theories

It is vital to see how the above-mentioned theories and many others[1] do compare. Those of Kirkwood–Bethe, Penney–Dasgupta, Cole, Hilliar and Taylor are summarized in Fig. 5.36. The average of all these curves, using a curve-fitting approach, gives the following relationships:

$$p(\text{kN cm}^{-2}) = \frac{1}{R^*/a_0}\left[356 + \frac{114.5}{R^*/a_0} - \frac{2.45}{(R^*/a_0)^2}\right]\frac{0.05 \le R^*}{a_0 \le 10\,\text{m kg}^{-1/3}},$$

$$p(\text{kN cm}^{-2}) = \frac{1}{R^*/a_0}\left[293.5 + \frac{1{,}386.5}{R^*/a_0} - \frac{1{,}780}{(R^*/a_0)^2}\right]\frac{10 \le R^*}{a_0 \le 50\,\text{m kg}^{-1/3}},$$

$$\text{(5.254)}$$

where $R^*/a_0 = R/\sqrt[3]{W}$.
For a shock-wave impact, the value of $F_1(t)$ is given by

$$F_1(t) = \int_0^t p(t)\mathrm{d}t = p\theta^*(1 - \mathrm{e}^{-t/\theta^*})$$

$$= 604\sqrt[3]{(W)}(R^*/a_0)^{-0.86}. \tag{5.255}$$

5.10.6 Shock Wave Based on a Cylindrical Charge Explosion

Here a cylindrical column charge detonates, the wave front of which is a thin zone of chemical reaction followed by explosive gases of high pressure and temperature. If R is the distance from the charge axis, the reduced distance is adjusted in the above equations in Sect. 5.10.5 as follows:

$$R^*/a_0 = R/\sqrt{W_c}. \tag{5.256}$$

W_c is given by

$$W_c = W_{cs}Q_{sp}/Q_{WT}, \tag{5.257}$$

where W_{cs} = relative mass of the charge of the given explosive $(kg\,m^{-1})$
$\quad\quad Q_{sp}$ = explosive specific heat energy $(kcal\,kg^{-1})$
$\quad\quad Q_{WT}$ = specific energy for TNT or other explosives $\approx$ 1,000 k cal^{-1}
$\quad\quad\quad$ per kg

The peak pressure is given by

$$p_m = 720(R^*/a_0)^{-0.72}\,kg\,cm^{-2} \tag{5.258}$$

In (5.235) the value of θ^* is written as

$$\theta^* = 10^{-4}\sqrt{(W_c)}(R^*/a_0)^{0.45}\,s \tag{5.259}$$

The numerical values of p versus R^*/a_0 are given below:

$p(kN\,cm^{-2})$	$R^*/a_0(m\,kg^{-1/3})$
10^4	0.1
10^3	1
$(10^3 + 50)$	5
10^2	10
10	10^2

Figure 5.37 shows a comparison between spherical and cylindrical shock-wave effects.

5.10.7 Underwater Contact Explosions

For contact explosions, $2W$ is substituted for W in all relevant equations given in Sect. 5.10.7
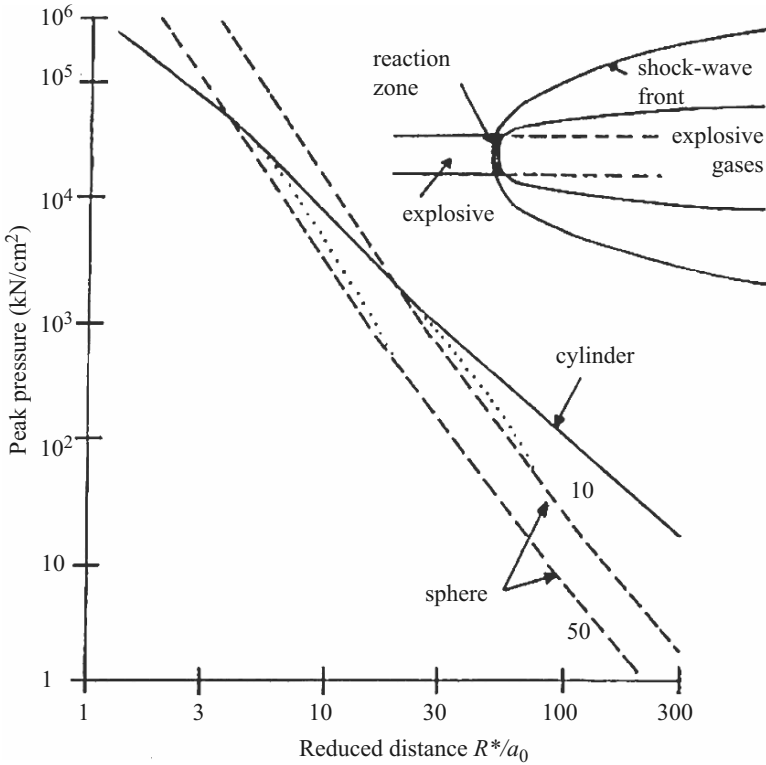
Fig. 5.37. Peak pressure versus reduced distance: a comparative study of spherical and cylindrical shock-wave effects

5.10.8 Underwater Shock-Wave Reflection

Much has been said on this subject in this chapter. The pressure acting on the underwater *static structure* due to this effect is given by

$$p_r(\mathrm{kN/cm^2}) \approx 2p(t) + \frac{2.5[p(t)]^2}{p(t) + 19{,}000}. \tag{5.260}$$

In an elastic medium, the value of $p_r(t) \approx 2p(t)$. Table 5.9 gives useful data on parameters relevant to underwater explosions (values other than those mentioned in the table should be interpolated or extrapolated). When the structure is moving in the water with a velocity $\dot{x} = v(t)$, an overpressure will exist of the value $\rho_w v_{so} v(t)$ in front of it. The value of the underpressure of the same value will have a negative sign. The procedure is shown in Fig. 5.38 $\rho_w v_{so}$ is the *characteristic impedance*. The reflected pressure $p_r(t)$ acting on the moving structure can be written as

$$p_r(t) = 2p(t) - \rho_w v_{so} u(t), \tag{5.261}$$

where $u(t) = \mathrm{d}v(t)/\mathrm{d}t$.

Table 5.9. Relationships between pressure, velocity, density and temperature in water

Pressure in the wave front, $p_m(\mathrm{kN\,cm^{-2}})$ $(\mathrm{m\,s^{-1}})$	Velocity of the wave front, $\dot{x} = v$ $(\mathrm{m\,s^{-1}})$	Velocity of water in the wave front, $u(t)$ $(\mathrm{m\,s^{-1}})$	Water density, ρ_w $(\mathrm{g\,cm^{-3}})$	Velocity of sound in the wave front, v_{s0}	Water temperature, $T(^\circ\mathrm{C})$
0	1,460	0	1.000	1,460	0
200	1,490	13	1.013	1,500	2.0
400	1,510	26	1.024	1,540	2.4
600	1,540	40	1.032	1,580	2.6
800	1,560	58	1.040	1,620	3.0
1,000	1,590	67	1.044	1,660	3.4
1,400	1,640	93	1.058	1,740	4.0
1,600	1,670	106	1.065	1,780	4.4
2,000	1,720	133	1.075	1,860	5.8
2,600	1,800	173	1.090	1,980	8.0
3,000	1,850	200	1.100	2,060	8.8
4,000	1,940	240	1.120	2,160	14.0
5,000	2,040	280	1.140	2,240	18.0
6,000	2,100	320	1.160	2,360	22.0
7,000	2,190	360	1.175	2,420	24.0
8,000	2,240	400	1.200	2,500	30.0
9,000	2,300	420	1.210	2,600	32.0
10,000	2,400	450	1.220	2,660	35.0
20,000	2,840	680	1.325	3,200	68.0
40,000	3,600	1,100	1.450	4,040	136.0
60,000	4,140	1,430	1.545	4,740	214
80,000	4,600	1,680	1.615	5,162	300
100,000	5,000	1,940	1.665	5,600	400
200,000	6,460	3,000	1.850	7,100	870
300,000	7,800	3,800	1.970	8,160	1,390

5.11 Summary of Primary Effects of Under Water Explosion; Additional Explanatory Notes on Shock Pulse and Waves

5.11.1 Detonation Process in Underwater Explosion

When a high explosion material detonates, it is converted during a very short interval of time into several constituent parts which are simpler in chemical structures, and energy is released at the same time. In the course of the detonation process, the explosive material is transformed into gaseous products which ultimately reach a temperature of the order of $3,000^\circ\mathrm{C}$ and a pressure of the order of $50,000\,\mathrm{kp\,cm^{-2}}$. The state of equilibrium of the detonation products represents an internal energy which is lower than that of the initial
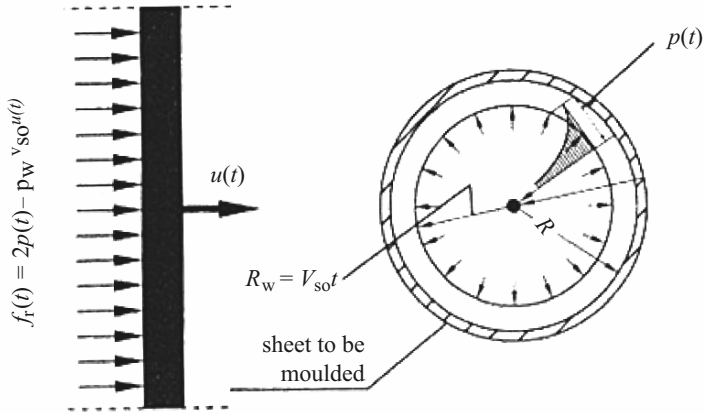
Fig. 5.38. Moving structure under shock load

explosive material. The difference is the amount of energy released, which manifests itself in an enormous increase in the pressure and the temperature of the detonation products.

If water was perfectly incompressible, the pressure developed at the surface of the products of an explosive reaction would immediately be transmitted to all parts of the body of water. Actually, however, water is compressible to a certain definite degree. Therefore, all disturbances are propagated with a certain velocity. When a shock wave front is propagated in water at 20°C and 0 atm. above atmospheric, this velocity is equal to $1,470\,\mathrm{m\,s^{-1}}$. At a pressure of $1,000$ atm. Above atmospheric, this velocity is $1,640\,\mathrm{m\,s^{-1}}$, $5,000$ atm., $2,270\,\mathrm{m\,s^{-1}}$, at $10,000$ atm., $2,710\,\mathrm{m\,s^{-1}}$ and at $50,000$ atm., $5,040\,\mathrm{m\,s^{-1}}$.

The pressure–time curve at a point situated outside the charge comprises two branches, viz., a raising pressure branch, in which the pressure increases to its maximum value in about one microsecond (one millionth part of a second), i.e. practically instantaneously, and a falling pressure branch, in which the pressure decreases approximately in accordance with an exponential law. Figure 5.39a shows this pressure–time curve for a point at a distance of $1\,\mathrm{m}$ from a $1\,\mathrm{kg}$ spherical charge. At low pressure, that is to say, up to about one atmosphere, the acoustic laws of propagation hold good:

(1) *The pressure decreases inversely as the distance.*
(2) *The duration of the pressure is independent of the distance.*

As the pressure increases, the deviations from these acoustic laws become greater. On account of energy loss, the decrease in pressure becomes greater that that expressed by the first law, and the duration increases with the distance because the higher pressure in the wave are propagated at greater velocities, Figs. 5.39b, c represent the pressure–time curves at the representative distances of $10\,\mathrm{m}$ and $100\,\mathrm{m}$ from the $1\,\mathrm{kg}$ charge. The dash-line curve shows the corresponding curves on the assumption that they can be derived from
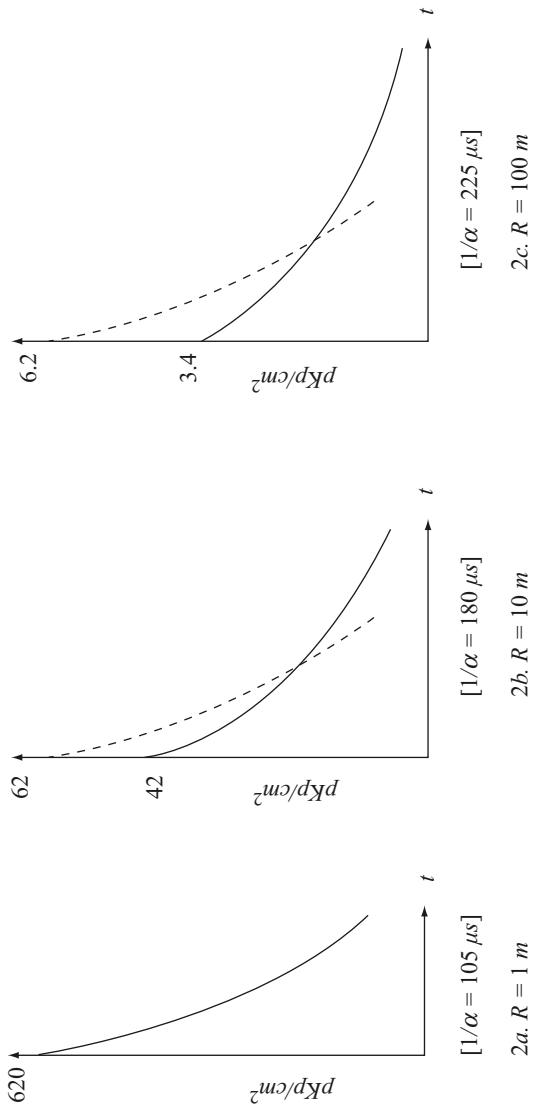
Fig. 5.39. Pressure–time curves for a shock wave originating from a 1 kg spherical charge

the pressure–time curve at the distance of 1 m in conformity with the above-mentioned acoustic laws. It is seen that the full-line curves (representing actual conditions) exhibits lower peaks and longer durations than the dash-line curves (acoustic approximations).

The disturbances represented by the pressure–time curve described in the above will be referred to as the *shock wave* in what follows. It is emitted from the charge at the instant when a pressure discontinuity is produced in the boundary surface between the charge and the water on account of the conversion of the explosive material into a gas sphere (the gas products from an explosion are also described by the term bubble and globe). In the example shown in Fig. 5.39 the duration of this shock wave can be illustrated by the values of the intervals $1/\alpha = 105, 180$, and $225\,\mu s$ (microseconds) between the maximum pressure and 37% of the maximum pressure[1]). The velocity propagation of the wave is of the order of $1,5\,\mathrm{km\,s^{-1}} = 1,5\,\mathrm{mm}\,\mu s$. consequently, in the example under consideration, the length of the wave corresponding to the interval $1/\alpha$ is of the order of 150–300 mm.

At the same times as the shock wave is emitted, the gas bubble begins to expand. As a consequence of expansion, the gas pressure decreases. When the volume of the gas bubble reaches a certain definite value, the gas pressure inside the bubble becomes equal to the external pressure. Nevertheless, the gas bubble continues to expand owing to the inertia of the body of the water. Therefore, the gas pressure drops below the external pressure, the gas bubble expands more and more slowly, and then begins to contract. This inwards motion also proceeds beyond the volume corresponding to the state of equilibrium until the pressure in the interior of the gas bubble exceeds the external pressure once more. After that, the sequence of events outlined in the above is repeated, and so forth. The result in a pulsatory motion in which the energy losses cause the equilibrium to decrease with each pulse.

The pulsation of the gas sphere is associated with the emission of the pressure waves advancing radically from the bubble. These waves are known as secondary pressure waves. If it is assumed that the water around the gas bubble is incompressible, it can be shown that the pressure emitted from the bubble varies directly as the square of the rate of bubble expansion or contraction. It is seen from Fig. 5.40 that this rate is greatest shortly before and after those points of time at which the volume of the gas bubble reaches its successive minimum values.

The scaling law for the quantities characterising the shock wave is given by the principle of similarity, which sates that if the linear dimension of the explosive charge are changes by a factor of n, the relation between the pressure and the distance and between the pressure and time remains unchanged, provided that the use is made of new time and distance scales which are n times as large as those employed before. This implies, for example, that a 1,000 kg charge produces the same pressure at a distance of 100 m as a 1 kg charge at a distance of 10 m (see Fig. 5.39b), whereas the duration and the time scale increase ten times. It can be demonstrated theoretically as well as
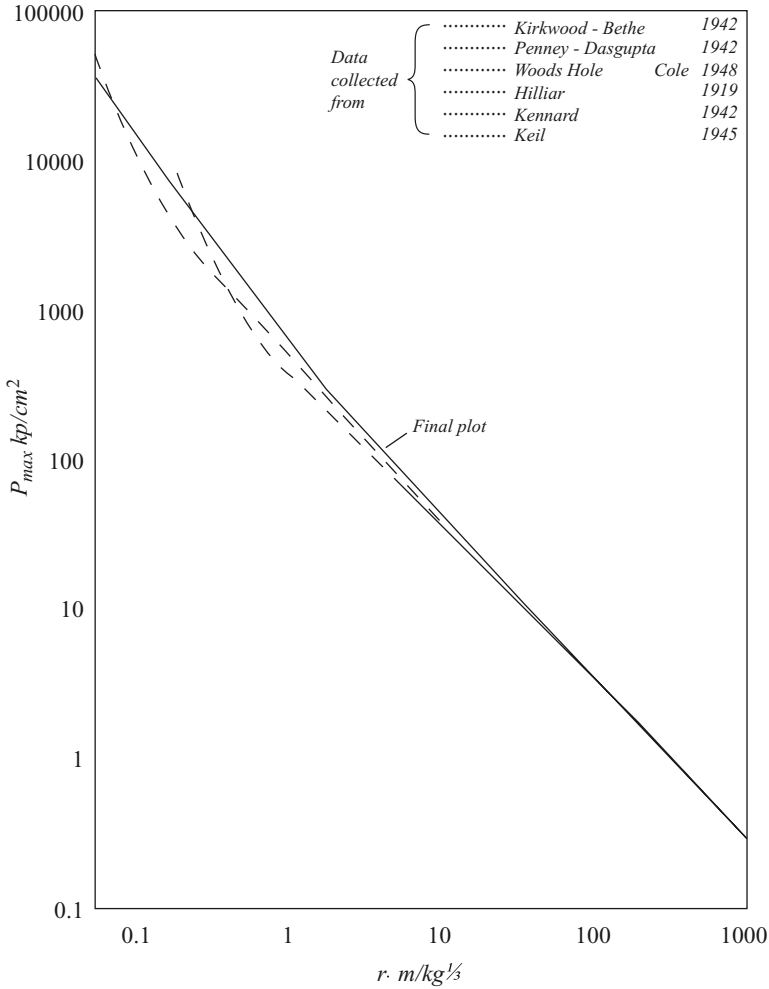
Fig. 5.40. Peak pressure $p_{\max}$. Theoretical and experimental curves final plot

experimentally [4.266] that the pressure p and the particle velocity v in the shock wave at the time t seconds at the distance R metres from a Q kg charge are equal to those at the time $n\,t$ seconds at the distance $n\,R$ metres from a $n^3 Q$ kg charge. The time function α changes into α/n in the latter case. Now if the relation between n and Q is assumed to be defined by the equation $n^3 Q = 1$, the shock wave can be described in terms of the following quantities which are independent of the model scale, but are dependent on one another,

$$p_{\max},\ \mathrm{V},\ -\frac{t}{Q^{1/3}}\quad\frac{R}{Q^{1/3}}\frac{i}{Q^{1/3}},\ \text{ and } \alpha\,.\,Q^{1/3}. \tag{5.262}$$

In what follows, $t/Q^{1/3}, R/Q^{1/3}, i/Q^{1/3}$ and $\alpha\,.\,Q^{1/3}$ will be referred to as specific time, distance, impulse, and time function quantities respectively.

5.11.2 Compression Loads due to Underwater Explosions

The first positive part of a shock wave in water can be described by the following approximative analytical expression:

$$p(r, t) = p_{\max}(r) \cdot e^{-\alpha t}, \tag{5.263}$$

where $p(r, t) =$ the pressure as a function of the time and the distance r from the charge

$p_{\max}(r) =$ the peak pressure in the wave front at the distance r

$t =$ the time reckoned from the arrival of the shock wave

$\alpha =$ a function of r

This expression approaches zero asymptotically as $t \to \infty$, whereas the actual pressure–time curve changes its sign as finite value of t, as the bubble gas expands beyond its equilibrium volume (see Figs. 5.40 and 5.41). All the same, this approximation is satisfactory for most purposes, since the pressures in the tail part of the shock wave are slight in compression with the high pressures in front part of the shock wave.
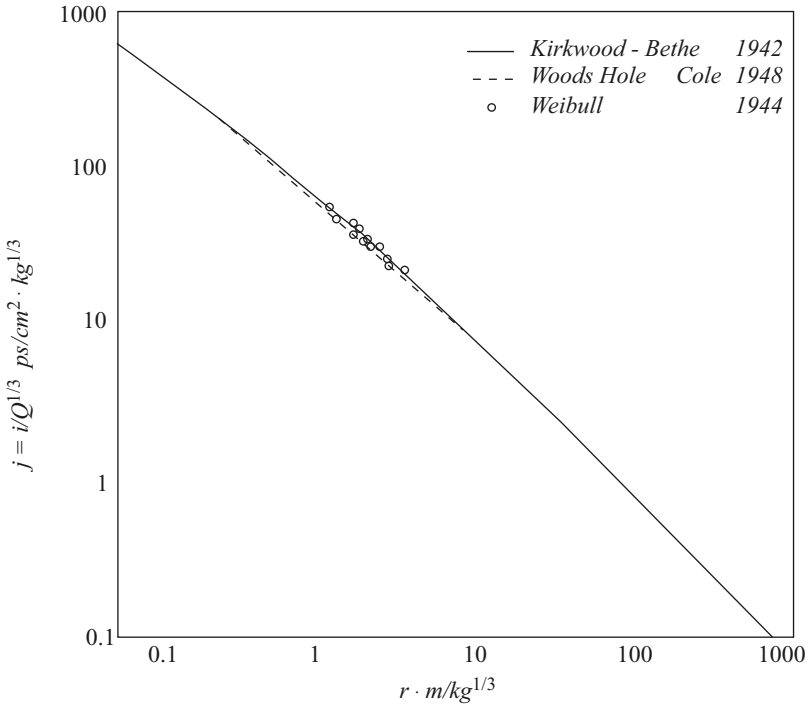
Fig. 5.41. Impulse $j = i/Q^{1/3}$. Theoretical and experimental curves

It thus appears that the following curves produced in Fig. 5.41 may be recommended for uses:

Specific Radius	CURVE
$r < 0,4$	PENNY AND DASGUPTA
$0,4 < r < 10$	WOOD HOLE
$r > 10$	KIRKWOOD AND BETHE

The test results obtained at Woods Hole can also be expressed by the formula:

$$p_{\max} = 535 \left(\frac{Q^{1/3}}{R} \right)^{1,33}. \tag{5.264}$$

6

Dynamic Finite-Element Analysis of Impact and Explosion

6.1 Introduction

A great deal of work has been published on finite-element techniques. [2.150, 3.1–3.168] This chapter presents the dynamic finite-element analysis for impact and explosion. Plasticity and cracking models are included. Solid isoparametric elements, panel and line elements represent various materials. Solution procedures are recommended. This chapter ends with some load–time functions for selected cases using finite-element analysis. There are many publications on the topic of impact and explosion which can be used for in-depth studies.

6.2 Finite-Element Equations

A three-dimensional finite-element analysis is developed in which a provision has been made for time-dependent plasticity and rupturing in steel and cracking in materials such as concrete, etc. The influence of studs, lugs and connectors is included. Concrete steel liners and studs are represented by solid isoparametric elements, shell elements and line elements with or without bond linkages. To begin with, a displacement finite element is adopted.

The displacement field within each element is defined in Fig. 6.1 as

$$\{x\} = [N]\{x\}^{\mathrm{e}} = \sum_{i=1}^{n} (N_i[I]\{x\}_i). \tag{6.1}$$

The strains and stresses can then be expressed as

$$\{\epsilon\} = \sum_{i=1}^{n} ([B_i]\{x_i\}) = [D]\{\sigma\}. \tag{6.2}$$

In order to maintain equilibrium with the element, a system of external nodal forces $\{F\}^{\mathrm{c}}$ is applied which will reduce the virtual work $(\mathrm{d}W)$ to zero. In
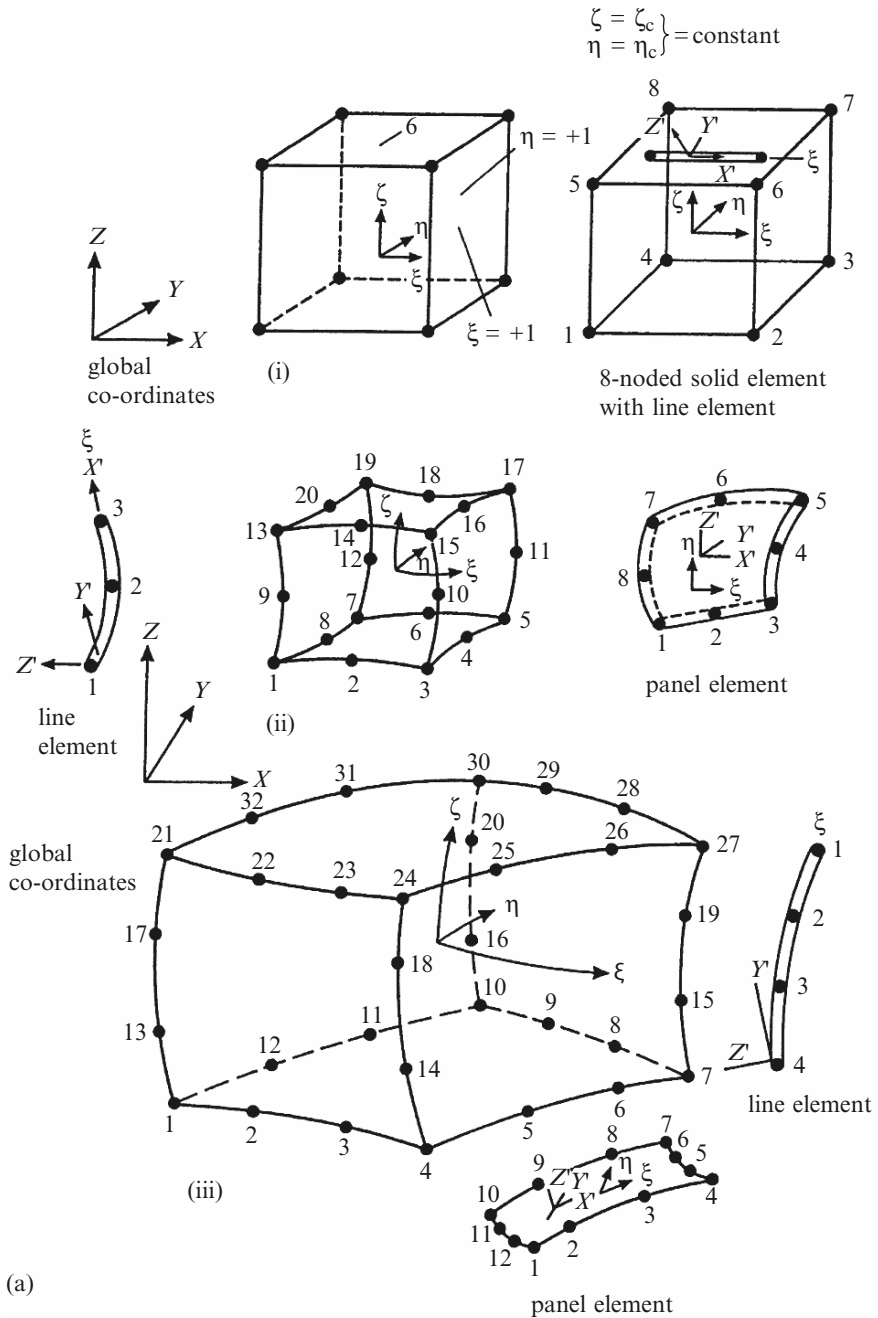
Fig. 6.1. (**a**) Isoparametric elements. (i) Parent element, three-dimensional isoparametric-derived element; (ii) solid element (20-noded); (iii) 32-noded solid element. (**b**) Line elements within the body of the solid isoparametric elements (ISS = isoparametric solid element)
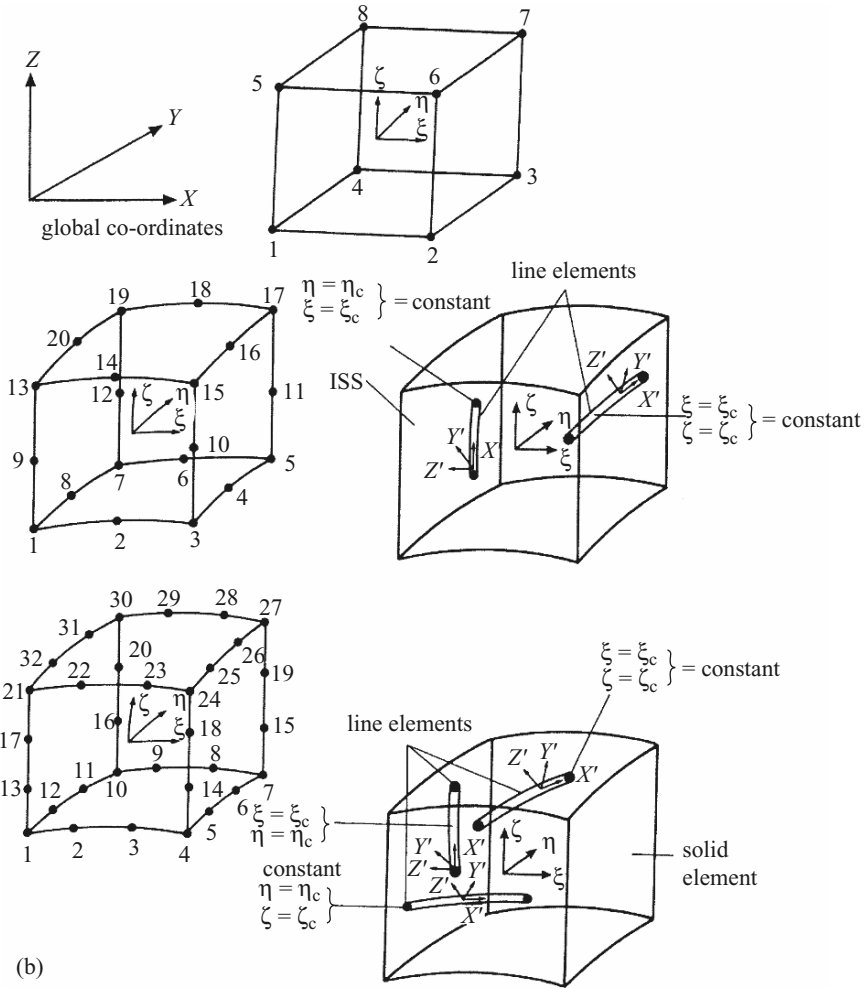
Fig. 6.1. (Continued)

the general equilibrium equation, both (6.1) and (6.2) are included. The final equation becomes

$$(\{d\delta\}^{e})^{T}\{F\}^{e} = (\{d\delta\}^{e})^{T} \int_{vol} [B]^{T}\{\sigma\}dV. \tag{6.3}$$

In terms of the local co-ordinate (ξ, η, ζ) system, (6.3) is written as

$$\{F\}^{e} = \int_{vol} [B]^{T}[D]\{\epsilon\}d\xi, d\eta, d\zeta \; \det[J]\{x\}^{e}. \tag{6.4}$$

The force–displacement relationship for each element is given by

$$\{F\}^{\mathrm{e}} = [K]^{\mathrm{e}}\{u\}^{\mathrm{e}} + \{F_{\mathrm{b}}\}^{\mathrm{e}} + \{F_{\mathrm{s}}\}^{\mathrm{e}} + \{F_{\sigma}\}_i^{\mathrm{e}} + \{F_{\epsilon}\}_c^{\mathrm{e}}, \tag{6.5}$$

where the element stiffness matrix is

$$[K_{\mathrm{c}}] = \int_{\mathrm{vol}} [B]^{\mathrm{T}}[D][B]\mathrm{d}V. \tag{6.5a}$$

The nodal force due to the body force is

$$\{F_{\mathrm{b}}\}^{\mathrm{e}} = -\int_{\mathrm{vol}} [N]^{\mathrm{T}}\{G\}\mathrm{d}V. \tag{6.5b}$$

The nodal force due to the surface force is

$$\{F_{\mathrm{s}}\}^{\mathrm{e}} = \int_{s} [N]^{\mathrm{T}}\{p\}\mathrm{d}s. \tag{6.5c}$$

The nodal force due to the initial stress is

$$\{P_{\sigma}\}_i^{\mathrm{e}} = \int_{\mathrm{vol}} [B]^{\mathrm{T}}\{\sigma_0\}\mathrm{d}V. \tag{6.5d}$$

The nodal force due to the initial strain is

$$\{P_{\epsilon}\}_i^{\mathrm{e}} = -\int_{\mathrm{vol}} [B]^{\mathrm{T}}[D]\{\epsilon_0\}\mathrm{d}V. \tag{6.5e}$$

Equations (6.4) and (6.5) represent the relationships of the nodal loads to the stiffness and displacement of the structure. These equations now require modification to include the influence of the liner and its studs. The material compliance matrices $[D]$ are given in Tables 6.1 and 6.2. The numerical values are given for various materials or their combinations in Tables 6.3–6.6. These values of the constitutive matrices are recommended in the absence of specific information.

If the stiffness matrix $[K_{\mathrm{c}}]$ for typical elements is known from (6.4) and (6.5) as

$$[K_{\mathrm{c}}] = \int_{\mathrm{vol}} [B]^{\mathrm{T}}[D][B]\mathrm{dvol}, \tag{6.6}$$

the composite stiffness matrix $[K_{\mathrm{TOT}}]$, which includes the influence of liner and stud or any other material(s) in association, can be written as

$$[K_{\mathrm{TOT}}] = [K_{\mathrm{c}}] + [K_{\ell}] + [K_{\mathrm{s}}], \tag{6.7}$$

where $[K_{\ell}]$ and $[K_{\mathrm{s}}]$ are the liner and stud or connector matrices.

If the initial and total load vectors on the liner/stud assembly and others are $[F_{\mathrm{T}}]$ and $[R_{\mathrm{T}}]$, respectively, then (6.4) is rewritten as

$$\{F\}^{\mathrm{e}} + \{F_{\mathrm{T}}\} - \{R_{\mathrm{T}}\} = [K_{\mathrm{TOT}}]\{x\}^{*}. \tag{6.8}$$

Table 6.1. Material compliance matrices $[D]$ with constant Poisson's ratio

(a) $[D]$ for steel components (isotropic). Constant Young's modulus and Poisson's ratio:

$$[D] = \frac{E}{(1+v)(1-2v)} \begin{bmatrix} 1-v & v & v & 0 & 0 & 0 \\ v & 1-v & v & 0 & 0 & 0 \\ v & v & 1-v & 0 & 0 & 0 \\ 0 & 0 & 0 & \dfrac{1-2v}{2} & 0 & 0 \\ 0 & 0 & 0 & 0 & \dfrac{1-2v}{2} & 0 \\ 0 & 0 & 0 & 0 & 0 & \dfrac{1-2v}{2} \end{bmatrix}$$

(b) $[D]$ for concrete: variable E and constant v

$$[D] = \begin{bmatrix}
D_{11} = \dfrac{E_1 (E')^3 - E_{\mathrm{cr}}}{E''} & D_{12} = \dfrac{v E_1 E_2 (E')^2 + E_{\mathrm{cr}}}{E''} & D_{13} = \dfrac{v E_1 E_3 (E')^2 + E_{\mathrm{cr}}}{E''} & D_{14} = 0 & D_{15} = 0 & D_{16} = 0 \\[2ex]
& D_{22} = \dfrac{E_2 E_3 (E')^2 + E_{\mathrm{cr}}}{E''} & D_{23} = \dfrac{v E_2 E_3 (E')^2 + E_{\mathrm{cr}}}{E''} & D_{24} = 0 & D_{25} = 0 & D_{26} = 0 \\[2ex]
& & D_{33} = \dfrac{E_3 (E')^3 - E_{\mathrm{cr}}}{E''} & D_{34} = 0 & D_{35} = 0 & D_{36} = 0 \\[2ex]
& & & D_{44} = G_{12} & D_{45} = 0 & D_{46} = 0 \\[1ex]
& & & & D_{55} = G_{23} & D_{56} = 0 \\[1ex]
& & & & & D_{66} = G_{31}
\end{bmatrix}$$

$$E_{\mathrm{cr}} = v^2 E_1 E_2 E_3 E'$$
$$E' = (E_1 + E_2 + E_3)/3$$
$$E'' = (E')^3 - 2 E_1 E_2 E_3 v^2 - E' v^2 (E_1 E_2 + E_1 E_3 + E_2 E_3)$$
$$G_{12} = E_{12}/2(1+v)$$
$$E_{12} = (E_1 + E_2)/2$$
$$G_{23} = E_{23}/2(1+v)$$
$$E_{23} = (E_2 + E_3)/2$$
$$G_{31} = E_{31}/2(1+v)$$
$$E_{31} = (E_3 + E_1)/2$$

Table 6.2. [D] with variable Young's modulus and Poisson's ratio for concrete and other materials

$$
[D] = \begin{bmatrix}
D_{11} = \dfrac{(1-v_{23}v_{32})}{\overline{E}}E_1 & D_{12} = \dfrac{(v_{12}+v_{12}v_{32})}{\overline{E}}E_2 & D_{13} = \dfrac{(v_{13}+v_{12}v_{23})}{\overline{E}}E_3 & D_{14}=0 & D_{15}=0 & D_{16}=0 \\[2ex]
D_{21} = \dfrac{(v_{21}+v_{23}v_{31})}{\overline{E}}E_1 & D_{22} = \dfrac{(1-v_{13}v_{31})}{\overline{E}}E_2 & D_{23} = \dfrac{(v_{23}+v_{13}v_{21})}{\overline{E}}E_3 & D_{24}=0 & D_{25}=0 & D_{26}=0 \\[2ex]
D_{31} = \dfrac{(v_{31}+v_{21}v_{32})}{\overline{E}}E_1 & D_{32} = \dfrac{(v_{32}+v_{12}v_{31})}{\overline{E}}E_2 & D_{33} = \dfrac{(1-v_{12}v_{21})}{\overline{E}}E_3 & D_{34}=0 & D_{35}=0 & D_{36}=0 \\[2ex]
D_{41}=0 & D_{42}=0 & D_{43}=0 & D_{44} & D_{45}=0 & D_{46}=0 \\[1ex]
D_{51}=0 & D_{52}=0 & D_{53}=0 & D_{54}=0 & D_{55} & D_{56}=0 \\[1ex]
D_{61}=0 & D_{62}=0 & D_{63}=0 & D_{64}=0 & D_{65}=0 & D_{66}
\end{bmatrix}
$$

$$\overline{E} = 1 - v_{12}v_{21} - v_{13}v_{31} - v_{23}v_{32} - v_{12}v_{23}v_{31} - v_{21}v_{13}v_{32}$$

$$
\begin{aligned}
E_1 v_{21} &= E_2 v_{12} & D_{44} &= G_{12} \\
E_2 v_{32} &= E_3 v_{23} & D_{55} &= G_{23} \\
E_3 v_{13} &= E_1 v_{31} & D_{66} &= G_{13}.
\end{aligned}
$$

The values of G_{12}, G_{23} and G_{13} are calculated in terms of the modulus of elasticity and Poisson's ratio as follows:

$$G_{12} = \frac{1}{2}\left[\frac{E_1}{2(1+v_{12})} + \frac{E_2}{2(1+v_{21})}\right] = \frac{1}{2}\left[\frac{E_1}{2(1+v_{12})} + \frac{E_1}{2\left(\frac{E_1}{E_2}+v_{12}\right)}\right],$$

$$G_{23} = \frac{1}{2}\left[\frac{E_2}{2(1+v_{23})} + \frac{E_3}{2(1+v_{32})}\right] = \frac{1}{2}\left[\frac{E_2}{2(1+v_{23})} + \frac{E_2}{2\left(\frac{E_2}{E_3}+v_{23}\right)}\right],$$

$$G_{13} = \frac{1}{2}\left[\frac{E_3}{2(1+v_{31})} + \frac{E_1}{2(1+v_{13})}\right] = \frac{1}{2}\left[\frac{E_3}{2(1+v_{31})} + \frac{E_3}{2\left(\frac{E_3}{E_1}+v_{31}\right)}\right].$$

For isotropic cases: $E_1 = E_2 = E_3 = E$, $\quad v_{12} = v_{13} = v_{23} = v_{21} = v_{31} = v_{32} = v$.

Table 6.3. Material properties of concrete, bovine, steel and composites

(1) Concrete

$\sigma_1 = \sigma_2$	$v_{13} = v_{23} = 0.2$ for any value of σ_3 up to 500 bar
$\sigma_1 < \sigma_2$	$v_{13} > v_{23}$
$\sigma_1 = 0$	$v_{13} = 0.2$ to 0.4 for any value of σ_2
	$= 0.4$ for up to $\sigma_3 = 500$ bar,

for 80°C temperature, the above values are increased by 35–50%.

$E_c(\mathrm{kN\,mm^{-2}})$	24	30	35	40
v	0.15–0.18	0.17–0.20	0.20–0.25	0.25–0.30

alternatively

$$v = 0.2 + 0.6(\sigma_2/\sigma_{cu})^4 + 0.4(\sigma_1/\sigma_{cu})^4,$$

where σ_1, σ_2 and σ_3 are the pressures/stresses along the three principle axes and σ_{cu} is an ultimate compressive stress of concrete.

(2) Bovine material

$E_1 = 11\text{–}18\,\mathrm{GPa};\ E_2 = 11\text{–}19\,\mathrm{GPa};\ E_3 = 17\text{–}20\,\mathrm{GPa}$
$G_{12} = 3.6\text{–}7.22\,\mathrm{GPa};\ G_{13} = 3.28\text{–}8.65\,\mathrm{GPa};\ G_{23} = 8.285\text{–}8.58\,\mathrm{GPa}$
$v_{12} = 0.285\text{–}0.58;\ v_{13} = 0.119\text{–}0.31;\ v_{23} = 0.142\text{–}0.31$
$v_{21} = 0.305\text{–}0.58;\ v_{31} = 0.315\text{–}0.46;\ v_{32} = 0.283\text{–}0.46$

(3) Steel

$E = 200\,\mathrm{GN\,m^{-2}};\ v = 0.3\text{–}0.33$

(4) Composite

Hot-pressed silicone nitride (HPSN) versus tungsten carbide

$\downarrow$	$\downarrow$
$E = 320\,\mathrm{GPa}$	$E = 320\,\mathrm{GPa}$
$v = 0.26$	$v = 0.24$

Carbon fibre (reinforced epoxy with 60% fibres by volume)

	Longitudinal	Transverse
Tensile strength (σ_{tu})	1,750 MPa	60 MPa
Compressive strength	1,300 MPa	–
Tensile modulus (E_t)	138 GPa	9.1 GPa
Compressive modulus (E_c')	138 GPa	9.1 GPa
Failure strain in tension $(\epsilon_{tu})\%$	1.34	0.8
Failure strain in compression $(\epsilon_{cu})\%$	0.85	2.9

Table 6.4. Material properties of additional composites

Steel indenter   versus
$\downarrow$ |
$E = 200\,\text{GN}\,\text{m}^{-2}$ |
$v = 0.3\text{--}0.33$ $\downarrow$

(1) Plexiglass

$E = 3.435\,\text{GN}\,\text{m}^{-2}$,
$v = 0.394$.

(2) Laminate: thornel 300/5,208 with fibres oriented $(0, +60, -60)$

$E_1 = 50\,\text{GN}\,\text{m}^{-2}$; $E_2 = 11.6\,\text{GN}\,\text{m}^{-2}$
$G_{11} = 19\,\text{GN}\,\text{m}^{-2}$; $G_{12} = 4.0\,\text{GN}\,\text{m}^{-2}$
$v_{11} = 0.31$; $v_{12} = 0.06$.

(3) Aluminium and FRPs

	Aluminium	BFRP[a]	GFRP[b]	CFRP[a]	CFRP[c]
$E(\text{GN}\,\text{m}^{-2})$	70	78.7	7.0	70	180
v		0.3	0.32	0.30	0.30	0.28

[a] Quasi-isotropic
[b] Random mat
[c] Unidirectional

(4) Graphite/epoxy

(Web stiffened foam sandwich panels with orthotropic facing and a number of 4 equally embedded stiffeners in a polyurethane (PU) core)
$E_1 = 120.7\,\text{GN}\,\text{m}^{-2}$; $E_2 = 7.93\,\text{GN}\,\text{m}^{-2}$,
$G_{12} = G_{23} = G_{13} = 5.52\,\text{GN}\,\text{m}^{-2}$,
$v_{12} = 0.30$.

Polyurethane foam

$E = 0.0431\,\text{GN}\,\text{m}^{-2}$; $G = 0.017\,\text{GN}\,\text{m}^{-2}$; $v = 0.267$.

(5) Boron/epoxy composites

$E_1 = 219.8\,\text{GN}\,\text{m}^{-2}$; $E_2 = 21.4\,\text{GN}\,\text{m}^{-2}$; $v = 0.208$
$E_{p1} = 2.41\,\text{GN}\,\text{m}^{-2}$; $E_{p2} = 0.04\,\text{GN}\,\text{m}^{-2}$;
$G_p = 0.008\,\text{GN}\,\text{m}^{-2}$; p at plastic level
$\sigma_{yt} = 1.1\,\text{GN}\,\text{m}^{-2}$.

(6) Layers of woven roving and chopped strand mat

$E = 14.5\,\text{GN}\,\text{m}^{-2}$; $\sigma_{yt} = 215\,\text{N}\,\text{mm}^{-2}$; $v = 0.21$

Table 6.4. (continued)

(7) Other materials

Type	E_1 (GN m^{-2})	E_2 (GN m^{-2})	G (GN m^{-2})	v_{12}
CSM/polyester	8	8	3	0.32
WR/polyester	15	15	4	0.15
Glass fibre/polyester	25	25	4	0.17
UD glass/polyester	40	10	4	0.3
UD kevlar/epoxide	76	8	3	0.34
UD carbon/epoxide	148	10	4	0.31
GY70/epoxy (celion with graphite fibre)	102	7.0	4.14	0.318
MODMORE II/epoxy				
HMS/E (with graphite fibres)	76.8	9.6	5.83	0.305
T300/E (thornel 300/epoxy with graphite fibres)	54.86	12	5.83	0.30
GL/E (glass/epoxy)	30.3	14.9	5.84	0.32

Carbon fibre (60% volume)
reinforced epoxy compound:

	Longitudinal	Transverse
E_t(GN m^{-2})	140.0	9.00
E_c(GN m^{-2})	140.0	9.00
σ_{tu}(GN m^{-2})	1.8	0.06
σ_{cu}(GN m^{-2})	1.3	0.27
v	0.3	0.02

Table 6.5. Material properties for brick and stone masonry and soil/rock

(1) Brick masonry

Brick strength $f_b = 20\text{--}70\,\text{N mm}^{-2}$ $E = 300 f_b - 2,000$
$\qquad\qquad\qquad\quad f_b > 70\,\text{N mm}^{-2}$ $E = 100 f_b + 12,750$

Brick strength (MN m^{-2})	Mortar	Mortar mean cube strength (MN M^{-2})	Wall thickness (mm)	Wall strength (MN m^{-2})
92	1:$\frac{1}{4}$:3	19.30	102.5	18.40
46	1:$\frac{1}{4}$:3	13.70	102.5	15.65
46	1:1:6	5.94	102.5	10.48

(*continued*)

Table 6.5. (continued)

(2) Stone masonry

Stone	Strength, f_b (MN m^{-2})	Mortar strength (MN m^{-2})	Failure stress (MN m^{-2})
Sandstone	112.0	0.78	2.78
Limestone	31.0	2.78	4.88
Whinstone	167.0	2.78 } 1:2:9 mix	9.86
Granite	130.6	2.78	12.32

(3) Soil/rock

	$E \times 10^2$ (MN m^{-2})	v	Density, ρ (kg m^{-3})
Fine sand	57.456	0.35	
Silty clay	48.84	0.40	
Silty sand	47.88	0.35	
Plastic clay	3.56	0.40	
Silt stone	8.4	0.30	2,622
Limestone	114.0	0.25	2,671
Alluvial clay	5.0	0.20	
Clay (embankment fill)	20.0	0.20	1,517
Saturated soil	200.0	0.30	
Jointed rock	150.0	0.25	
Sandstone	255.0	0.11	

For high plasticity, the frictional angle $\phi'_c = 18°$
For low plasticity, the frictional angle $\phi'_c = 25°$
For rocks, ϕ'_c ranges between 20° and 30°
The adhesion coefficient c is around $1 \, \text{kN m}^{-2}$

Table 6.6. Material properties of timber

Basic stresses and moduli.

Strength group	Parallel to grain (N mm^{-2})		Compression to grain (N mm^{-2})		E_{min} (N mm^{-2})
	Bending	Tension	Parallel	Perpendicular	
S$_1$	37.5	22.5	24.4	7.5	13,800
S$_2$	30.0	18.0	20.0	6.0	11,900
S$_3$	24.0	14.4	17.9	4.8	10,400
S$_4$	18.7	11.2	15.5	3.7	9,200
S$_5$	15.0	9.0	13.3	3.0	7,800

Table 6.6. (continued)

Dry grade stresses and moduli.

Grade/species	Parallel to grain $(\mathrm{N\,mm^{-2}})$		Compression to grain $(\mathrm{N\,mm^{-2}})$		$E_{\min}$ $(\mathrm{N\,mm^{-2}})$
	Bending	Tension	Parallel	Perpendicular	
SS/Douglas fir	6.2	3.7	6.6	2.4	7,000
GS/Douglas fir	4.4	2.6	5.6	2.1	6,000
SS/Redwood ⎱ Whitewood ⎰	7.5	4.5	7.9	2.1	7,000
GS/Corsican pine	5.3	3.2	6.8	1.8	5,000
GS/European pine	4.1	2.5	5.2	1.4	4,500

Plywood: all stresses and moduli are multiplied by the following factors.

Grade/glued laminated	Parallel to grain $(\mathrm{N\,mm^{-2}})$		Compression to grain $(\mathrm{N\,mm^{-2}})$		$E_{\min}$ $(\mathrm{N\,mm^{-2}})$
	Bending	Tension	Parallel	Perpendicular	
LA/4	1.85	1.85	1.15	1.33	1.0
LB/10	1.43	1.43	1.04	1.33	0.9
LB/20 or more	1.48	1.48			
LC/10	0.98	0.98	0.92	1.33	0.8
LC/20 or more	1.11	1.11			
	Permissible stresses $8\,\mathrm{N\,mm^{-2}}$		–	–	8,700
12 mm ply thickness	$5\,\mathrm{N\,mm^{-2}}$		–	–	7,400

The displacement $\{x\}^*$ is different from $\{x\}$ in (6.4), since it now includes values for both unknown displacements and restrained linear boundaries. Hence $\{x\}^*$ is defined in matrix form as

$$\{x\}^*_{x,y,z} = \begin{Bmatrix} x_{\mathrm{un}x} \\ x_{\mathrm{un}y} \\ x_{\mathrm{un}z} \\ x_{\mathrm{b}x} \\ x_{\mathrm{b}y} \\ x_{\mathrm{b}z} \end{Bmatrix} = \begin{Bmatrix} x_{\mathrm{un}} \\ x_{\mathrm{b}} \end{Bmatrix}, \tag{6.9}$$

where x_{un} and x_{b} are displacement values in unrestrained or unknown conditions and restrained conditions. Similarly, the values for $\{F_{\mathrm{T}}\}$ and $\{R_{\mathrm{T}}\}$ can

Table 6.7. Stiffness matrix and load vector for stud/liner

$$
[K_b]_{6\times6} = \pi dL
\begin{bmatrix}
(l^2E_h + pE_v + \gamma^2E_\ell) & (lmE_h + pqE_v + \gamma sE_\ell) & (lnE_h + \gamma tE_v) & (-l^2E_h - p^2E_v - \gamma^2E_\ell) & (-lmE_h - pqE_v - \gamma sE_\ell) & (-lnE_h - \gamma tE_v) \\
 & (m^2E_h + q^2E_v + s^2E_\ell) & (mnE_h + stE_v) & (-lmE_h - p^2E_v - \gamma^2E_\ell) & (-m^2E_h - q^2E_v - s^2E_\ell) & (-mnE_h - stE_v) \\
 & & (n^2E_h + t^2E_v) & (-lnE_h - \gamma tE_v) & (-mnE_h - stE_v) & (-n^2E_h - t^2E_v) \\
 & & & (l^2E_h + p^2E_v + \gamma^2E_\ell) & (lmE_h + pqE_v + \gamma sE_\ell) & (lnE_h + \gamma tE_v) \\
 & \text{symmetrical} & & & (m^2E_h + q^2E_v + s^2E_\ell) & (mnE_h + stE_v) \\
 & & & & & (n^2E_h + t^2E_v)
\end{bmatrix}
$$

Component stiffnesses using springs:

E_h = horizontal stiffness
E_v = vertical stiffness
E_ℓ = longitudinal stiffness

$$
\{\Delta P^e\}_{6\times1} = \pi dL
\begin{Bmatrix}
-l\Delta\sigma_h & -p\Delta\sigma_v & -\gamma\Delta\sigma_\ell \\
-m\Delta\sigma_h & -q\Delta\sigma_v & -s\Delta\sigma_\ell \\
-n\Delta\sigma_h & & -t\Delta\sigma_\ell \\
l\Delta\sigma_h & +p\Delta\sigma_v & +\gamma\Delta\sigma_\ell \\
m\Delta\sigma_h & +q\Delta\sigma_v & +s\Delta\sigma_\ell \\
n\Delta\sigma_h & & +t\Delta\sigma_\ell
\end{Bmatrix}
$$

πdL = perimeter of the steel

$\left.\begin{matrix} l, m, n \\ p, q, \gamma \\ s, t \end{matrix}\right\}$ = direction cosines

also be written as

$$\{F_{\mathrm{T}}\} = \left\{ \begin{matrix} F_{\mathrm{un}} \\ F_{\mathrm{b}} \end{matrix} \right\}_{x,y,z},$$

$$\{R_{\mathrm{T}}\} = \left\{ \begin{matrix} R_{\mathrm{un}} \\ R_{\mathrm{b}} \end{matrix} \right\}_{x,y,z}.$$

(6.10)

The quantities for the liner corresponding to unknown displacements can be written as

$$[K_{\ell}]\{x_{\mathrm{un}}\}_{x,y,z} = \{F_{\mathrm{un}}\}_{x,y,z}.$$

(6.11)

The shear force τ acting on studs or any other type is evaluated as

$$\{\tau\} = [K_{\mathrm{s}}]\{x_{\mathrm{un}}\}_{x,y,z}.$$

(6.12)

Table 6.7 gives the $[K_{\mathrm{s}}]$ matrix modified to include the stiffness of the liner.

6.3 Steps for Dynamic Non-Linear Analysis

The solutions of (6.6)–(6.12) require a special treatment such as under any increment of dynamic loading, stresses, strains and plasticity are obtained in steel, concrete and composites such as the liner and its anchorages and other similar materials. An additional effort is needed to evaluate the rupture of the steel or other material when cracks develop, especially in concrete beneath the liner or its anchorages.

The dynamic coupled equations are needed to solve the impact/explosion problems and to assess the response history of the structure, using the time increment δt. If $[M]$ is the mass and $[C]$ and $[K]$ are the damping and stiffness matrices, the equation of motion may be written in incremental form as

$$[M]\{\ddot{x}(t)\} + [C_{\mathrm{in}}]\{\dot{x}(t)\} + [K_{\mathrm{in}}]\{\delta(t)\} = \{R(t)\} + \{F_1(t)\},$$

(6.13)

where $F_I(t)$ is the impact/explosion load. If the load increment of $F_{\mathrm{I}}(t)$ is $\delta P_n(t)$, where n is the nth load increment, then

$$P_n(t) = P_{n-1}(t) + \delta P_n(t)$$

(6.13a)

and hence $\{R(t)\} = \{\delta P_n(t)\}$, which is the residual time-dependent load vector.

The solution of (6.13) in terms of $t + \delta t$ for a δt increment becomes

$$[M]\{\ddot{x}(t + \delta t)\} + [C_{\mathrm{in}}]\{\dot{x}(t + \delta t)\} + [K_{\mathrm{in}}]\{\delta R(t + \delta t)\} + \{\delta P(t + \delta t)\},$$

(6.14)

where 'in' denotes initial effects by iteration using the stress approach; $\delta P(t + \delta t)$ represents the non-linearity during the time increment δt and is determined by

$$\{\sigma\} = [D]\{\epsilon\} - \{\epsilon_0\} + \{\sigma_0\}. \tag{6.15}$$

The constitutive law is used with the initial stress and constant stiffness approaches throughout the non-linear and the dynamic iteration. For the iteration:

$$\{x(t + \delta t)\}_i = [K_{\mathrm{in}}]^{-1}\{R_{\mathrm{TOT}}(t + \delta t)\}_i. \tag{6.16}$$

The strains are determined using

$$\{\epsilon(t + \delta t)\}_i = [B]\{x(t + \delta t)\}_i, \tag{6.17}$$

where $[B]$ is the strain displacement. The stresses are computed as

$$\{\sigma(t + \delta t)\}_i = [D]\{\epsilon(t + \delta t)\}_i + \{\sigma_0(t + \delta t)\}_{i-1}, \tag{6.18}$$

where $\{\sigma_0(t + \delta t)\}$ is the total initial stress at the end of each iteration. All calculations for stresses and strains are performed at the Gauss points of all elements.

The initial stress vector is given by

$$\{\sigma_0(t + \delta t)\}_i = f\{\epsilon(t + \delta t)\}_i - [D]\{\epsilon(t + \delta t)\}_i. \tag{6.19}$$

Using the principle of virtual work, the change of equilibrium and nodal loads $\{\delta P(t + \delta t)\}_i$ is calculated as

$$F_1(t + \delta t) = \{\delta P(t + \delta t)\}_{i\mathrm{TOT}} \tag{6.20}$$

$$= \int_{-1}^{+1}\int_{-1}^{+1}\int_{-1}^{+1} [B]^{\mathrm{T}''}\{\delta\sigma_0(t + \delta t)\}_i \mathrm{d}\xi \mathrm{d}\eta \mathrm{d}\zeta,$$

$$\sigma_0(t) = \{\sigma_0(t + \delta t)\}_i = 0,$$

where $\mathrm{d}\xi, \mathrm{d}\eta$ and $\mathrm{d}\zeta$ are the local co-ordinates and T'' is the transpose. The integration is performed numerically at the Gauss points. The effect load vector $F_1(t)$ is given by

$$\begin{aligned}
F_1(t + \delta t) &= \{\delta P(t + \delta t)\}_{i\mathrm{TOT}} \\
&= -[\delta C(t)_{\mathrm{in}}](\{x(t + \delta t)\}_i - \{x(t)\}) \\
&\quad -[\delta C(t + \delta t)]_i\{x(t + \delta t)\}_i - [\delta K(t)_{\mathrm{in}}](\{x(t + \delta t)\}_i - \{x(t)\}_i) \\
&\quad -[\delta K(t + \delta t)]_i\{x(t + \delta t)\}_i. \tag{6.21}
\end{aligned}$$

The Von Mises criterion is used with the transitional factor f^*_{TR} to form the basis of the plastic state, such as shown in Fig. 6.2,

$$f^*_{\mathrm{TR}} = \frac{\sigma_y(t) - \sigma_{y-1}(t)}{\sigma(t + \delta t)_i - \sigma(t + \delta t)_{i-1}}. \tag{6.22}$$

The elasto-plastic stress increment will be

$$\{\delta\sigma_i\} = [D]_{\mathrm{ep}}\{\sigma(t + \delta t)\}_{i-1}(1 - f^*_{\mathrm{TR}})\{\delta\epsilon\}. \tag{6.23}$$

If $\sigma(t + \delta t)_i < \sigma_y(t)$, it is an elastic limit and the process is repeated. The equivalent stress is calculated from the current stress state where stresses are drifted; they are corrected from the equivalent stress–strain curve.

The values of $[D]_{\mathrm{ep}}$ and $[D]_{\mathrm{p}}$ are derived using plastic stress/strain increments.

In the elasto-plastic stage, the time-dependent yield function is $f(t)$. It is assumed that the strain or stress increment is normal to the plastic potential $Q(\sigma, K)$. The plastic increment, for example, is given by

$$\delta\epsilon(t + \delta t)_{\mathrm{p}} = \partial Q/\partial\sigma = \lambda b, \tag{6.24}$$

where $\lambda = $ proportionality constant > 0
$\qquad b \approx \partial Q/\partial\sigma(t + \delta t)$

When $f(t) = Q$

$$\delta\epsilon(t + \delta t)_{\mathrm{p}} = \lambda a,$$
$$a = \partial f/\partial\sigma(t + \delta t),$$
therefore, $\qquad \mathrm{d}f = [\partial f/\partial\sigma(t + \delta t)]\,\mathrm{d}\sigma(t + \delta t) + (\partial f/\mathrm{d}K)\mathrm{d}K. \tag{6.25}$

If A is the hardening plastic parameter, then

$$A = \frac{1}{\lambda}(\partial f/\mathrm{d}K)\mathrm{d}K.$$

An expression can easily be derived for the proportionality constant λ

$$\lambda = \frac{a^{\mathrm{T}''}D\delta\epsilon(t + \delta t)}{[A + a^{\mathrm{T}}Db]}, \tag{6.26}$$

hence $\delta\epsilon(t + \delta t)_{\mathrm{p}} = b\lambda$.

The value of the elasto-plastic matrix $[D]_{\mathrm{ep}}$ is given by

$$[D]_{\mathrm{ep}} = D - \frac{Dba^{\mathrm{T}''}Db}{[A + a^{\mathrm{T}''}Db]}. \tag{6.27}$$
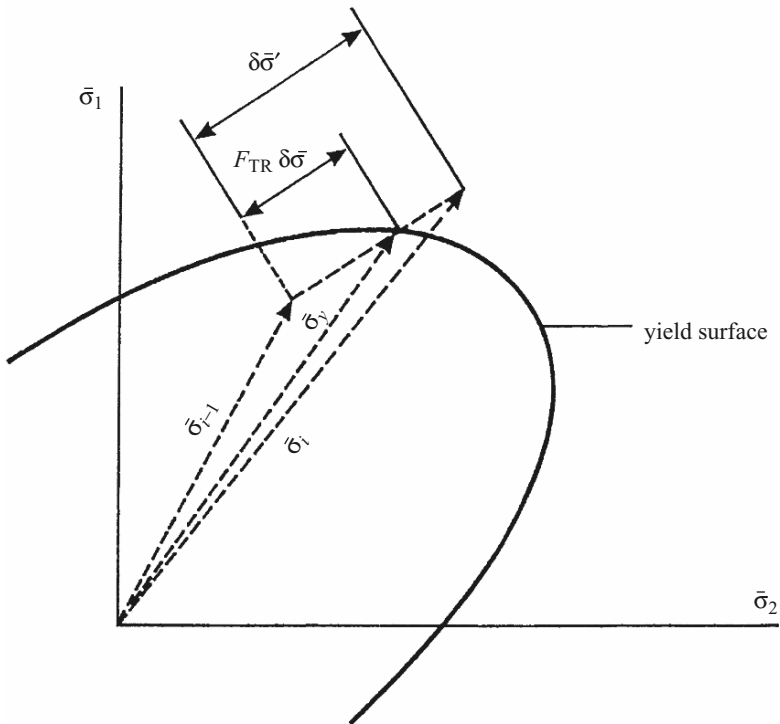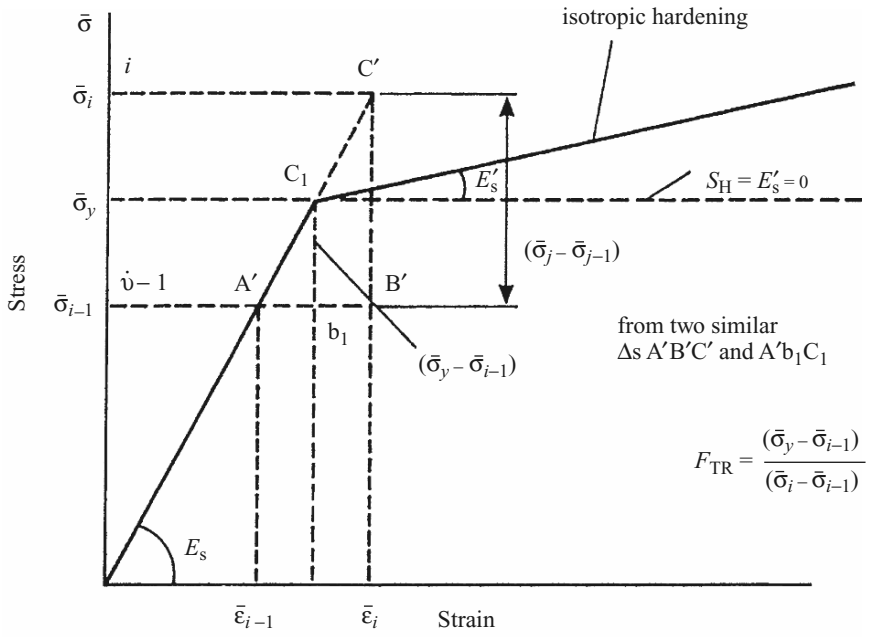
Fig. 6.2. Transitional factor and plastic point [1.149]

The value of the plastic matrix $[D]_\mathrm{p}$ is given by

$$[D]_\mathrm{p} = \left[\frac{Dba^{\mathrm{T}''}D}{A + a^{\mathrm{T}''}Db} \right],\tag{6.28}$$

where $[D]$ is the compliance matrix for the elastic case.

The elasto-plastic stress increment is given by

$$\{\delta\sigma_i\}_t = [D]_\mathrm{ep}\{\sigma_i\}_t^{Y^*}(1 - f_{\mathrm{TR}}^*)\{\delta\epsilon\}_t.\tag{6.29}$$

For the sake of brevity, $\{\delta\sigma_i\}_t = \delta\sigma(t+\delta t)$ for the ith point or increment and other symbols are as given above. The total value becomes

$$\{\sigma_i\}_{\mathrm{TOT}} = \{\sigma_i\}_t^{Y^*} + \{\delta\sigma_i\}_t.\tag{6.30}$$

If $\{\sigma_i\}_t < \sigma_{yt}$ it is an elastic point and $\{\sigma_i\}_t = \{\sigma_i'\}_t$. The process is repeated. Looking at the plastic point in the previous iteration, it is necessary to check for unloading when $\sigma \geq \sigma_y$, the unloading will bring about the total stress $\{\sigma_i\}_t = \{\sigma_{i-1}\}_t + \{\delta\sigma_i'\}_t$, and set $\{\sigma_y\}_t = \{\sigma_{i-1}\}_t$. Then loading at this point gives

$$\{\delta\sigma_i\} = [D]_\mathrm{ep}\{\sigma_{i-1}\}_t\{\delta\epsilon\}_t.\tag{6.31}$$

The total stress is then written as

$$\{\sigma_i\}_{\mathrm{TOT}} = \{\sigma_{i-1}\}_t\{\delta\sigma_i\}.\tag{6.32}$$

Stresses are calculated using the elasto-plastic material matrix, which does not drift from the yield surfaces, as shown in Fig. 6.2. Stresses are corrected from the equivalent stress–strain curve by

$$\{\sigma_{\mathrm{corr}}\} = \{\sigma_{i-1}\}_t + K\{\delta\epsilon_\mathrm{p}\}_t,\tag{6.33}$$

where $\{\delta\epsilon_\mathrm{p}\}_t = \sqrt{\frac{2}{3}}\{\sqrt{(\delta\epsilon_{ij}^\mathrm{P}\delta\epsilon_{ij}^\mathrm{P})}\}_t$ = equivalent plastic strain increment. K is the strain-hardening parameter, such that $\{\delta\epsilon_\mathrm{p}\}_t = \lambda$. The equivalent stress is calculated from the current stress state, as shown below

$$\{\sigma_i\}_{\mathrm{eq}} = f\{(\sigma_i)\}_t,\tag{6.34}$$
$$\text{the value of } \sigma_{\mathrm{corr}}/\sigma \text{ is a } factor.\tag{6.35}$$

Therefore the correct stress state on the yield surface is given by

$$\{\sigma_i\} = factor \times \{\sigma_i\}.\tag{6.36}$$

A reference is made to Fig. 6.2 for evaluating this factor as f_{TR}^*.

6.3.1 Buckling State and Slip of Layers for Composite Sections

Within the above stages, there can be a possibility of plastic buckling of the liner or any embedded anchors or layers. The buckling matrix is developed so that at appropriate stages the layer/liner/anchor system is checked against buckling. The plastic buckling matrix is given below

$$(K^i + \lambda_c K_G^i)F_T = 0, \tag{6.37}$$

where K^i is the elasto-plastic stiffness matrix as a function of the current state of plastic deformation using the above steps and K_G is the geometric stiffness matrix.

$$\lambda_c = 1 + E_{PS}, \tag{6.37a}$$

where E_{PS} represents accuracy parameters.

Where composite layers, liner and studs are involved, the incremental slips from the nodal displacements are assessed in the following manner:

$$\{\Delta S_i\}_{x,y,z} = [T'']\{d\delta_i\}, \tag{6.38}$$

where S_i is a slip at node i and T'' is the transformation matrix given in Table 6.8. The total slip at iteration is given without subscripts as

$$\{S_i\} = \{S_{i-1}\} + \{S_i\}. \tag{6.39}$$

The strains are computed as

$$\{\epsilon_i\}_t = \{\epsilon_{i-1}\}_t + \{\delta\epsilon_i\}_t. \tag{6.40}$$

The incremental stress $\{\sigma_B\}$ between the studs and concrete or between any composite materials for the ith node can then be computed as

$$\{\delta\sigma_{Bi}\}_t = [K_s]\{\sigma_{Bi-1}\}_t\{\delta S_i\}_t. \tag{6.41}$$

Table 6.8. T'' transformation matrices

$$[T_\varepsilon''] = \begin{bmatrix} l_1^2 & m_1^2 & n_1^2 & l_1 m_1 & m_1 n_1 & l_1 n_1 \\ l_2^2 & m_2^2 & n_2^2 & l_2 m_2 & m_2 n_2 & l_2 n_2 \\ l_3^2 & m_3^2 & n_3^2 & l_3 m_3 & m_3 n_3 & l_3 n_3 \\ 2l_1 l_2 & 2m_1 m_2 & 2n_1 n_2 & (l_1 m_2 + l_2 m_1) & (m_1 n_2 + m_2 n_1) & (l_1 n_2 + l_2 n_1) \\ 2l_2 l_3 & 2m_2 m_3 & 2n_2 n_3 & (l_2 m_3 + l_3 m_2) & (m_2 n_3 + n_2 m_3) & (l_2 n_3 + l_3 n_2) \\ 2l_1 l_3 & 2m_1 m_3 & 2n_1 n_3 & (l_1 m_3 + m_1 l_3) & (m_1 n_3 + m_3 n_1) & (l_1 n_3 + n_1 l_3) \end{bmatrix},$$

$$[T_\sigma''] = \begin{bmatrix} l_1^2 & m_1^2 & n_1^2 & 2l_1 m_1 & 2m_1 n_1 & 2l_1 n_1 \\ l_2^2 & m_2^2 & n_2^2 & 2l_2 m_2 & 2m_2 n_2 & 2l_2 n_2 \\ l_3^2 & m_3^2 & n_3^2 & 2l_3 m_3 & 2m_3 n_3 & 2l_3 n_3 \\ l_1 l_2 & m_1 m_2 & n_1 n_2 & (l_1 m_2 + l_2 m_1) & (m_1 n_2 + n_1 m_2) & (l_1 n_2 + l_2 n_1) \\ l_2 l_3 & m_2 m_3 & n_2 n_3 & (l_2 m_3 + l_3 m_2) & (m_2 n_3 + n_2 m_3) & (l_2 n_3 + l_3 n_2) \\ l_1 l_3 & m_1 m_3 & n_1 n_3 & (l_1 m_3 + l_3 m_1) & (m_1 n_3 + m_3 n_1) & (l_1 n_3 + n_1 l_3) \end{bmatrix}.$$

The total stresses are

$$\{\sigma_{Bi}\}_{\text{TOT}} = \{\sigma_{Bi-1}\}_t + \{\delta\sigma_{Bi}\}_t. \tag{6.42}$$

If $|S_i| > S_{\max}$ the bond between the stud and the concrete or any composite materials is broken and the pull-out occurs, i.e. $\{\sigma_{Bi}\} = 0$ and $S_{\max}$ has a value which is maximum. If $|S_i| < S_{\max}$ the value $\{S_i\}$ is calculated. The procedure is linked with the general finite element work discussed already in the non-linear dynamic cases for impact and explosion.

6.3.2 Strain Rate Effects Based on the Elastic-Viscoplastic Relationship for Earth Materials Under Impact and Explosion

It is assumed that for each dynamic loading increment, the strain rate ϵ_{ij} can be expressed as the sum of the elastic and viscoplastic components:

$$\{d\epsilon_{ij}\}_t = \{d\epsilon_{ij}\}_e + \{d\dot{\epsilon}_{ij}\}_{\text{vp}}, \tag{6.43}$$

where the subscripts e and vp denote the elastic and viscoplastic components, respectively. The elastic strains are related to the stress rate $\dot{\sigma}_{ij}$ by

$$\{d\dot{\epsilon}_{ij}\}_e = \frac{1}{9K} \times (dJ_1/dt)\delta_{ij} + \frac{1}{2G} \times dS_{ij}/dt, \tag{6.44}$$

where J_1 = deviatoric stress: first invariant
$S_{ij} = \{\sigma_{ij} - \frac{1}{3}J_1\delta_{ij}\}_t$
δ_{ij} = Knonecker delta
K = elastic bulk modulus
G = elastic shear modulus

The shear modulus is expressed in terms of the invariant J_2', where

$$J_2' = \tfrac{1}{2}S_{ij}\ S_{ij}, \tag{6.44a}$$

then
$$K = \frac{K_i}{1 - K_1}[1 - K_1 e^{-K_2 J_1}], \tag{6.44b}$$

$$G = \frac{G_i}{1 - G_1}[1 - G_1 e^{-G_2\sqrt{J_2'}}], \tag{6.44c}$$

where K_i, K_1, G_i, G_1, K_2 and G_2 are material constants. The values of J_2' and Ss are given below

$$J_2' = \tfrac{1}{2}(S_x^2 + S_y^2 + S_z^2) + \tau_{xy}^2 + \tau_{yz}^2 + \tau_{zx}^2 \text{ is the second stress invariant} \tag{6.44d}$$

$$S_x = \sigma_x - \sigma_{\text{m}}, \quad S_y = \sigma_y - \sigma_{\text{m}}, \quad S_z = \sigma_z - \sigma_{\text{m}}. \tag{6.44e}$$

The linear values of K and G are

$$K = \frac{E}{3(1 - 2v)}; \ G = \frac{E}{2(1 + v)}. \tag{6.44f}$$

Tables 6.1 and 6.2 are used for variable properties of E and v.

The components of the viscoplastic strain rate are calculated using the above-mentioned plastic flow rule for rate-sensitive material.

$$\{\dot{\epsilon}_{ij}\}_{\text{vp}} = \gamma[f(\sigma_{\text{D}}/B) \ \delta\sigma_{\text{D}}/\delta\sigma_{ij}]_t, \tag{6.45}$$

where γ = viscosity parameter
$f(\sigma_{\text{D}}/B) = f(\sigma_{\text{s}} - \beta/B)$, σ_{s} = static yield stress, B = material parameter.

$$\beta = f^{-1}\left\{\frac{1}{\gamma}\left[\frac{\frac{1}{3}(\dot{\epsilon}_{\text{KK}})_{\text{vp}} + (2\dot{e}^{-1})_{\text{vp}}^2}{3(\partial\sigma_{\text{s}}/\partial J_1)^2 + \frac{1}{2}(\partial\sigma_{\text{s}}/\partial J_2')^2}\right]\right\}, \tag{6.45a}$$

$(\dot{e}^{-1})_{\text{vp}} = [\frac{1}{2}\dot{\text{d}e}_{ij} \ \dot{\text{d}e}_{ij}]_{\text{vp}}^{1/2}$ and is the square root of the second invariant of the viscoplastic strain rate. $\tag{6.45b}$

Using this bulk modulus approach for soils, the time-dependent stress–strain relation is given in Table 6.9. With reference to *rocks*, the failure strength of the rock is defined in exactly the same way as described earlier; the values for E and v will vary. Nevertheless, the various alternative failure models given in Table 6.10 for rocks are related in terms of strain rates by

$$\bar{M} = \frac{\sigma_{\text{dyn}}}{\sigma_{\text{s}}} = 1 + \text{c} \ \log\frac{\dot{\epsilon}}{\dot{\epsilon}_{\text{s}}}, \tag{6.46}$$

Table 6.9. Bulk modulus model for earth materials under impact

$$\begin{Bmatrix} \delta\sigma_x \\ \delta\sigma_y \\ \delta\sigma_z \\ \delta\tau_{xy} \\ \delta\tau_{yz} \\ \delta\tau_{zx} \end{Bmatrix}_t = \begin{bmatrix} (K + \frac{4}{3}G) & (K - \frac{2}{3}G) & (K - \frac{2}{3}G) & 0 & 0 & 0 \\ & (K + \frac{4}{3}G) & (K - \frac{2}{3}G) & 0 & 0 & 0 \\ & & (K + \frac{4}{3}G) & 0 & 0 & 0 \\ & & & G_{12} & 0 & 0 \\ & \text{sym} & & & G_{23} & 0 \\ & & & & & G_{13} \end{bmatrix} \begin{Bmatrix} \delta\epsilon_x \\ \delta\epsilon_y \\ \delta\epsilon_z \\ \delta\epsilon_{xy} \\ \delta\epsilon_{yz} \\ \delta\epsilon_{zx} \end{Bmatrix}_t$$

or in short $\{\delta\sigma\} = [D]\{\delta\epsilon\}$,

where $[D]$ is the required material matrix

$$G_{12} = G_{23} = G_{13} = G = G_{\text{e}} - \alpha\log_{\text{e}}\frac{J_2}{J_2^{\text{e}}} \quad \text{for} \quad J_2 > J_2^{\text{e}}$$

$$G = G_{\text{e}} \quad \text{for} \quad J_2 \leq J_2^{\text{e}}$$

In the case where the soil/rock is orthotropic, the values of G_{12}, G_{23} and G_{13} are given as indicated in Table 6.2.

Table 6.10. Numerical models for rocks

---

(1) Sandstone

$$\tau = 1538 + \sigma \tan \phi, \tag{1}$$

where τ and σ = shear and compressive stresses, respectively

$$\phi = 29°\,15'$$

(2) Rupture of sandstone: Mohr failure envelope

$$\tau_{\max}/\sigma_{cu} = 0.1 + 0.76(\sigma_m/\sigma_{cu})^{0.85}, \tag{2}$$

where σ_{cu} is the uni-axial compressive stress at rupture under pure shear $\sigma_1 = -\sigma_3$.

(3) Realistic rock including friction

$$\alpha(\sigma_1 + \sigma_2 + \sigma_3) + (\sigma_1 - \sigma_2)^2 + (\sigma_2 - \sigma_3)^2 + (\sigma_3 - \sigma_1)^2 = K^*, \tag{3}$$

where $\alpha = \sqrt{(6\tan\phi)}/\sqrt{(9 + 12\tan\phi)}$ } can be obtained from

$\quad K^* = \sqrt{(6c)}/\sqrt{(9 + 12\tan\phi)}$ } Mohr envelope

$\quad \phi$ = angle of friction

$\quad c$ = cohesion

A generalized Mohr coulomb criterion is written as

$$\tau^2 = [\sqrt{(n+1)} - 1][\sigma_{tu}^2 - \sigma\sigma_{tu}], \tag{4}$$

where σ, τ = normal stress and shear stress on the fractured plane

$\quad \sigma_{tu}$ = uni-axial tensile strength

$\quad n = \sigma_{cu}/\sigma$ = brittleness

$\quad \sigma_{cu}$ = uni-axial compressive strength

Equation (4) can be expressed in terms of σ_m, mean stress, and σ_s, the maximum shear stress, by

$$\sigma_s = \sigma_{tu} - \sigma_m, \quad \text{for } \sigma_{tu} > \sigma_{m0} > \sigma_m,$$

$$\sigma_s = \tau_0\sqrt{[1 - (\sigma_m/\sigma_{tu}) - (\tau_0/2\sigma_{tu})^2]} \quad \text{for } \sigma_{m0} < \sigma_m, \tag{5}$$

where $\sigma_m = (\sigma_1 + \sigma_2)/2; \quad \sigma_s = (\sigma_1 - \sigma_2)/2$

$\quad \sigma_1, \sigma_2$ = principle stresses $(\sigma_1 > \sigma_2)$

$$\sigma_{m0} = \sigma_{tu} - \tau_0^2/2\sigma_{tu},$$

$$\tau_0 = [\sqrt{(n+1)} - 1]\sigma_{tu}. \tag{6}$$

The stress state is assessed for σ_m and σ_s from the failure surface as

$$R = \sigma_s/\sigma_{s(\text{critical})} \geq 1 \tag{7}$$

representing the failure condition. If $\sigma_s = \sigma_{s(\text{critical})}$, (5) is satisfied.

---

where σ_{dyn} = dynamic stress, σ_{s} = static stress, $\dot{\epsilon}$ = strain rate (dynamic), $\dot{\epsilon}_s$ = strain rate (static), c = constant.

The range of strain rate is $\dot{\epsilon} = 10^{-5}\,\mathrm{s}^{-1}$ up to $5 \times 10^0\,\mathrm{s}^{-1}$. The dynamic failure criterion can then be written as

$$\dot{\sigma}_{\mathrm{f}} = \tau_0 X_3 + \sigma \left[\frac{\sigma_{\mathrm{cu}}^2 X_1^2 - 4\tau_0^2 X_3^2}{4\sigma_{\mathrm{cu}} X_1 \tau X_3} \right] \quad \text{for} \quad \sigma \not< 0 \text{ compression}, \quad (6.47)$$

$$\dot{\sigma}_{\mathrm{f}}^2 = \tau_0^2 X_3^2 + \sigma \left[\frac{\tau_0^2 X_3^2 - \sigma_{\mathrm{tu}}^2 X_2^2}{\sigma_{\mathrm{tu}} X_2} \right] - \sigma^2 \text{ for} \quad \sigma \not> 0 \text{ tension}, \quad (6.48)$$

$$\not< \mathrm{A}\dot{\epsilon}^{1/3}$$

where

$$X_1 = \frac{3}{40}\overline{M} + \frac{1}{25}\overline{M}^2$$

$$X_2 = \frac{3}{100}\overline{M} + \frac{7}{1000}\overline{M}^2$$

$$X_3 = \frac{1}{40}\overline{M} + \frac{1}{100}\overline{M}^2 \qquad (6.49)$$

τ_0 = octahedral shear stress under static loads.

In the case of *brick material*, Khoo and Hendry relationships given below are used in the above failure models and strain rate simulations. The non-linear principle stress relationship (bi-axial) is given by

$$\sigma_1/\sigma_{\mathrm{cu}} = 1 + 2.91(\sigma_2/\sigma_{\mathrm{c}})^{0.805}, \qquad (6.50)$$

where σ_1 = major principle stress
σ_2 = minor principle stress
σ_{cu} = uni-axial compressive strength

The brick-failure envelope with the mortar tri-axial strength curve is given by the polynomials

$$\sigma_{\mathrm{t}}/\sigma_{\mathrm{tu}} = 0.9968 - 2.0264(\sigma/\sigma_{\mathrm{cu}}) + 1.2781(\sigma/\sigma_{\mathrm{cu}})^2 - 0.2487(\sigma/\sigma_{\mathrm{cu}})^2, \;(6.51)$$

$$\sigma_3/\sigma_{\mathrm{cu}} = -0.1620 + 0.1126(\sigma_1/\sigma_{\mathrm{cu}}) + 0.0529(\sigma_1/\sigma_{\mathrm{cu}})^2 - 0.0018(\sigma_1/\sigma_{\mathrm{cu}})^3,$$
$$(6.52)$$

where $\sigma/\sigma_{\mathrm{cu}}$ = ratio of compressive strength
$\sigma_{\mathrm{t}}/\sigma_{\mathrm{tu}}$ = ratio of tensile strength
$\sigma_{\mathrm{t}} = \alpha\sigma_3$ where $\alpha = 0.15$ and 0.40 for mortars of $1{:}\frac{1}{4}{:}3$ and $1{:}1{:}6$, respectively.

6.3.3 Finite Element of Concrete Modelling

A number of modelling methods are available for simulation into the finite-element method. [1.149, 3.1–3.168] On impact and explosion work, methods such as the endochronic, Ottoson and Blunt crack have been widely used. They are covered in this section. The bulk modulus model of Table 6.9 is reviewed to include cracking with and without aggregate interlocking. On the basis of the endochronic concept, which is widely reported, [1.28–1.30, 1.149] the following equation applies

$$\{\delta\sigma_{x,y,z}\}_t + \{\delta\sigma^{\mathrm{p}}_{x,y,z}\}_t = [D^*_{\mathrm{T}}]\{\epsilon^*_{x,y,z}\}_t, \tag{6.53}$$

where the superscript p denotes stresses in the plastic case. Table 6.11 gives details of uncracked and cracked cases for (6.52). When cracks in three directions are open the concrete loses its stiffness, then

$$[D^*_{\mathrm{T}}] = [0]. \tag{6.54}$$

Stresses $\{\sigma_i\}_t$ are checked against the cracking criteria. For example, if there is one crack normal to the X-direction, the concrete can no longer resist any tensile stress in that direction, then

$$\delta\sigma^*_x = 0.$$

Then

$$D_{11}\delta\epsilon^*_x + D_{12}\delta\epsilon^*_y + D_{13}\delta\epsilon^*_z = \delta\sigma^{\mathrm{p}^*}_x,$$

$$\delta\epsilon^*_x = \frac{\delta\sigma^{\mathrm{p}^*}_x}{D_{11}} - \frac{D_{12}}{D_{11}}\delta\epsilon^*_y - \frac{D_{13}}{D_{11}}\delta\epsilon^*_y. \tag{6.55}$$

In a similar manner, examples for shear terms can be written as

$$\delta\tau^*_{xy} + \delta\tau^{\mathrm{p}^*}_{xy} = \beta'D_{44}\gamma^*_{xy},$$
$$\delta\tau^*_{yz} + \delta\tau^{\mathrm{p}^*}_{yz} = D_{55}\delta\gamma^*_{yz}, \tag{6.56}$$
$$\delta\tau^*_{zx} + \delta\tau^{\mathrm{p}^*}_{zx} = \beta'D_{66}\delta\gamma^*_{zx}.$$

Blunt Crack Band Propagation

The smeared crack concept, rather than the isolated sharp inter-element crack concept described above, is gaining ground. Here the element topology does change. The smeared crack band of a blunt front is that in which one can easily select cracks in any direction without paying a penalty, even if the crack direction is not truly known. Bazant et al. [1.28–1.30] and Bangash [1.149] introduced the equivalent strength and energy variation which are utilized for crack propagation once it is initiated within the element. The equivalent

Table 6.11. Cracks using endochronic theory

Uncracked matrix

$$
\left\{
\begin{array}{l}
\delta\sigma_x + \delta\sigma_x^{\mathrm{P}} \\
\delta\sigma_y + \delta\sigma_y^{\mathrm{P}} \\
\delta\sigma_z + \delta\sigma_z^{\mathrm{P}} \\
\delta\tau_{xy} + \delta\tau_{xy}^{\mathrm{P}} \\
\delta\tau_{yz} + \delta\tau_{yz}^{\mathrm{P}} \\
\delta\tau_{zx} + \delta\tau_{zx}^{\mathrm{P}}
\end{array}
\right\}_t
=
\begin{bmatrix}
D_{11} & D_{12} & D_{13} & 0 & 0 & 0 \\
 & D_{21} & D_{23} & 0 & 0 & 0 \\
 & & D_{33} & 0 & 0 & 0 \\
 & & & \beta'\mathrm{D}_{44} & 0 & 0 \\
 & & & & \beta'D_{55} & 0 \\
 & & & & & \beta'D_{66}
\end{bmatrix}
\left\{
\begin{array}{l}
\delta\sigma_x \\
\delta\sigma_y \\
\delta\sigma_z \\
\delta\gamma_{xy} \\
\delta\gamma_{yz} \\
\delta\gamma_{zx}
\end{array}
\right\}_t,
$$

where $D_{11} = D_{22} = D_{33} = K + \frac{4}{3}G$ $\beta =$ aggregate inter locking $\approx \frac{1}{2}$ to $\frac{3}{4}$

$$D_{12} = D_{13} = D_{23} = K - \frac{2}{3}G$$

$$D_{44} = G_{12} = \frac{1}{2}\left[\frac{E_1}{2(1+v_{12})} + \frac{E_2}{2(1+v_{21})}\right]$$

$$D_{55} = G_{23} = \frac{1}{2}\left[\frac{E_2}{2(1+v_{23})} + \frac{E_3}{2(1+v_{32})}\right]$$

$$D_{66} = G_{13} = \frac{1}{2}\left[\frac{E_3}{2(1+v_{31})} + \frac{E_1}{2(1+v_{13})}\right]$$

The values of E and v are given in Tables 6.3–6.6

Cracked matrix

$$
\sigma_1-\text{direction:}[D]^* =
\begin{bmatrix}
0 & 0 & 0 & 0 & 0 & 0 \\
0 & \left(D_{22} - \dfrac{D_{12}^2}{D_{11}}\right) & \left(D_{23} - \dfrac{D_{12}D_{12}}{D_{11}}\right) & 0 & 0 & 0 \\
0 & \left(D_{23} - \dfrac{D_{31}D_{21}}{D_{11}}\right) & \left(D_{33} - \dfrac{D_{13}D_{13}}{D_{11}}\right) & 0 & 0 & 0 \\
0 & 0 & 0 & \beta'D_{44} & 0 & 0 \\
0 & 0 & 0 & 0 & D_{55} & 0 \\
0 & 0 & 0 & 0 & 0 & \beta'D_{66}
\end{bmatrix}
$$

$$
\sigma_2-\text{direction:}[D]^* =
\begin{bmatrix}
\left(D_{11} - \dfrac{D_{21}}{D_{22}}\right) & 0 & \left(D_{13} - \dfrac{D_{12}D_{23}}{D_{22}}\right) & 0 & 0 & 0 \\
0 & 0 & 0 & 0 & 0 & 0 \\
\left(D_{31} - \dfrac{D_{21}D_{32}}{D_{22}}\right) & 0 & \left(D_{33} - \dfrac{D_{23}^2}{D_{22}}\right) & 0 & 0 & 0 \\
0 & 0 & 0 & \beta'D_{44} & 0 & 0 \\
0 & 0 & 0 & 0 & \beta'D_{55} & 0 \\
0 & 0 & 0 & 0 & 0 & D_{66}
\end{bmatrix}
$$

$$
\sigma_3-\text{direction:}[D]^* =
\begin{bmatrix}
\left(D_{11} - \dfrac{D_{13}^2}{D_{33}}\right) & \left(D_{12} - \dfrac{D_{13}D_{23}}{D_{23}}\right) & 0 & 0 & 0 & 0 \\
\left(D_{21} - \dfrac{D_{31}D_{32}}{D_{33}}\right) & \left(D_{22} - \dfrac{D_{23}D_{23}}{D_{33}}\right) & 0 & 0 & 0 & 0 \\
0 & 0 & 0 & 0 & 0 & 0 \\
0 & 0 & 0 & D_{44} & 0 & 0 \\
0 & 0 & 0 & 0 & \beta'D_{55} & 0
\end{bmatrix}
$$

average cracking direction

$$W = \frac{A}{\Delta\alpha} = \frac{A}{r\cos\alpha}$$

definition of symbols used in crack propagation

$\theta_A = \frac{1}{3}(\theta_{n-1} + \theta_n + \theta_{n+1})$ direction of crack

$\theta_\varepsilon = \sum_1^n (\theta_{G_i} - \theta_{A_i})$ cracking error

aggregate   mortar δ_t

crack plane

$\delta_n \le (1/2) - (d + d')$

crack plane

δ_t σ_{nt}^c σ_{nn}^c δ_n

crack morphology
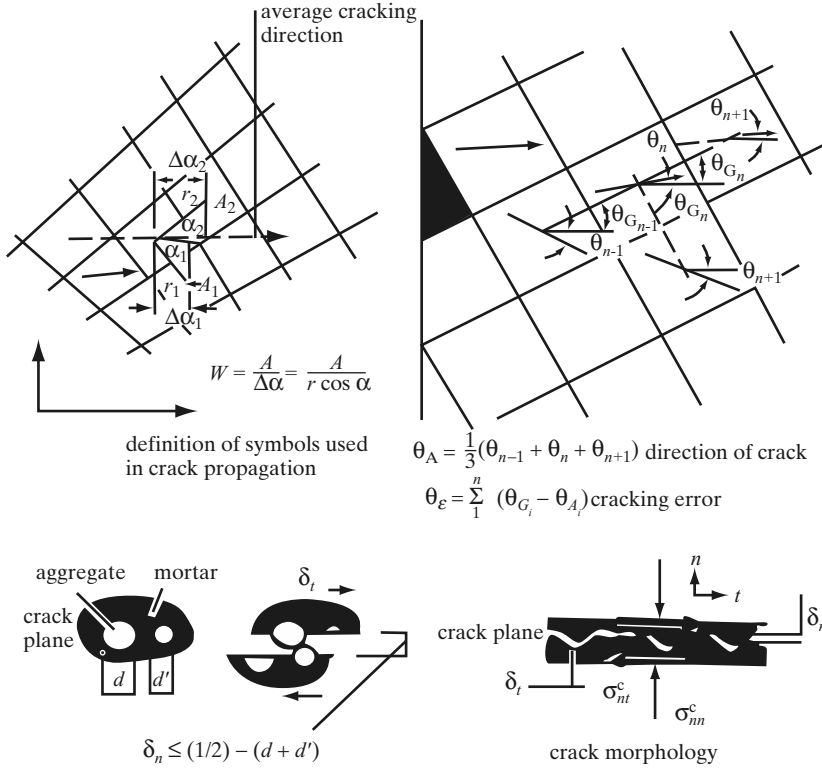
Fig. 6.3. Blunt crack propagation

strength criterion is used for crack propagation by specifying an equivalent stress within the surrounding elements of an existing crack at which cracking should be propagated. The expression for the equivalent strength σ_{eq} is given (see Fig. 6.3) as

$$\sigma_{eq} = C[EG_f/W(1 - 2v\sigma_2^0/\sigma_1^0)]^{1/2}, \tag{6.57}$$

where C = a constant dependent on the choice of elements

$\quad E$ = elastic modulus

$\quad v$ = Poisson's ratio

$\quad W = A/\delta a = A/r\cos\alpha$

$\quad A$ = area of the element at the front

$\quad r$ = centroidal distance from the last cracked elements in the front element

$\quad \alpha$ = angle measured from the established crack to the line between the centroids

$\quad G_f$ = energy release rate = $\delta E(P_i a)/\delta a = \Delta E(P_i a)/\delta a$

$\quad a$ = cracked area

$\quad P_i$ = loads

The band length is specified as $a + \Delta a/2$.

In the initial state prior to cracking, the strain energy U_0 is based on the principal stresses σ_2^0, where σ_1^0 is the largest tensile stress. After cracking, σ_1^1 becomes 0 and $\sigma_2^1 = 0$, which is used for the current value of U_1. The change of strain energy $\delta U = U_0 - U_1$ is equated to the crack length $(\Delta a \times G_f)$, where U is the total strain energy in a cracked body and δU is the energy released by the structure into the element which cracks. The crack direction within an arbitrary grid is given by

$$\theta_A = \tfrac{1}{3}(\theta_{n-1} + \theta_n + \theta_{n+1}), \tag{6.58}$$

where θ_A is the average crack direction, θ_{n-1} and θ_n are the cracking angles of the next to last cracked element, and θ_{n-1} is the impending cracking angle of the element adjacent to the crack front. Since in the arbitrary grid the cracking direction is specified by the accumulated error of the cracked direction, the accumulated cracking error θ_E is given by

$$\theta_E = \sum_i^n (\theta_{G_i} - \theta_{Ai}), \tag{6.59}$$

where n is the number of cracked elements and θ_G is the actual average crack propagation angle within each element. A better formulation by Gamborov and Karakoc, reported by Bangash, [1.149] is given of the tangent shear modulus G^{CR} whenever cracking is initiated:

$$G^{CR} = \frac{\sigma_{nt}^c}{\epsilon_{nn}^{CR}} k \frac{1}{r(a_3 + a_4|r|^3)} \tag{6.60}$$

or

$$G^{CR} = \frac{\sigma_0}{\epsilon_{nn}^{CR}} k\{1 - [2(P/D_a)\epsilon_{nn}^{CR}]^{1/2}\},$$

where

$$k = \frac{a_3 + 4a_4|\gamma|^3 - 3a_3a_4\gamma^4}{(1 + a_4\gamma^4)^2} \tag{6.61}$$

and $a_3, a_4 =$ coefficients as a function of the standard cylindrical strength f_c'
$\quad\quad \tau_0 =$ crack shear strength (ranging from 0.25 to 0.7 f_c')
$\quad\quad D_a =$ maximum aggregate size (up to 4 mm)
$\quad\quad P_c =$ large percentage of crack asperities
$\quad\quad \gamma = \delta_t/\delta_n$
$\quad\quad \delta_t, \delta_n =$ crack displacements along the normal and tangential directions
$\quad\quad\quad$ (Figs. 6.3 and 6.4)
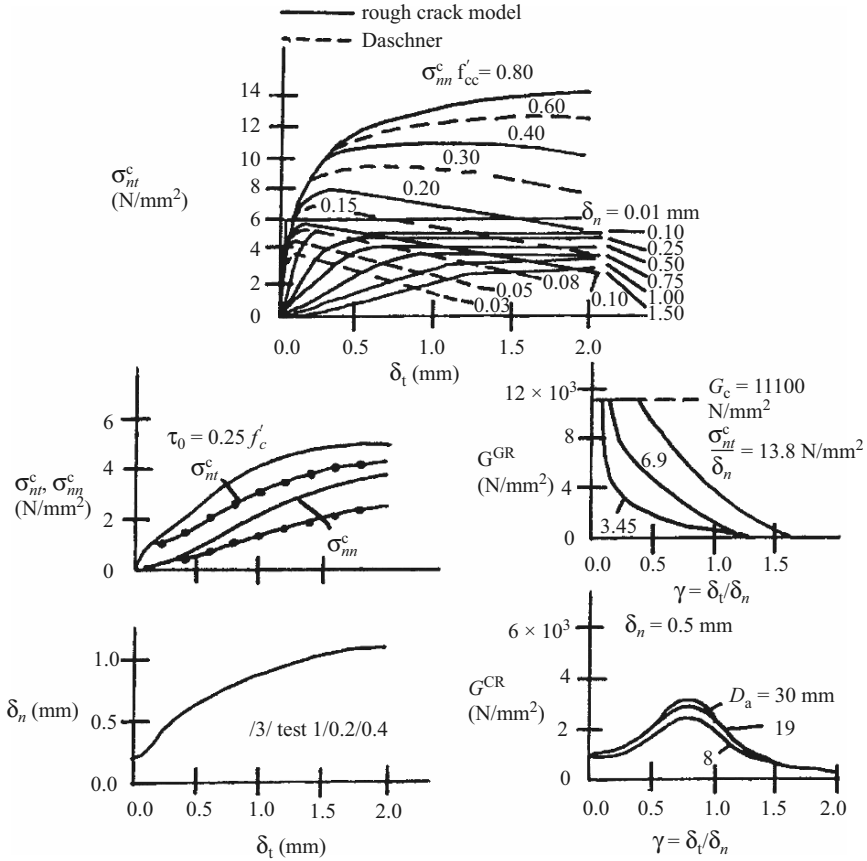
Fig. 6.4. Crack displacement versus tangent shear modulus [1.149]

Curves have been plotted showing a decrease in the value of G^{CR} when a crack opening linearly increases at increasing shear. Reference [1.149] gives a constitutive law in which a confinement stress within the rough crack model is given by

$$\sigma_{nn}^c = -a_1 a_2 \frac{\delta_t \sigma_{nt}^c}{(\delta_n^2 + \delta_t^2)^q}, \tag{6.62}$$

where σ_{nn}^c = interface normal stress

σ_{nt}^c = interface shear stress

a_1, a_2 = constant $(a_1 a_2 = 0.62)$

q = a function of the crack opening; taken to be 0.25

For different types of crack dilatancy δ_n/σ_{nt}^c (Fig. 6.3) the tangent shear modulus G^{CR} is plotted against the ratio r of the crack displacement. The value of σ_{nt}^c is given by

$$\sigma_{nt}^c = \tau_0 \left[1 - \sqrt{\left(\frac{2p}{D_a}\epsilon_{nn}^{CR}\right)}\right] r \frac{a_3 + a_4|r|^3}{1 + a_4 r^4}, \quad r = \gamma_{nt}^{CR}/\epsilon_{mn}^{CR}, \tag{6.63}$$

where p is the crack spacing and CR is cracked concrete,

$$\epsilon_{nn}^{CR} = \delta n/p = \text{strain against } \sigma_{nn}^c. \tag{6.64}$$

The σ_{nn}^c values have been computed using points common to the curves of crack opening and constant confinement stress.

Ottoson Failure Model

The Ottoson four-parameter model has a smooth but convex surface with curved meridians determined by the constants a and b [1.150].
    The analytical failure surface is defined by

$$f(I_1, J_2, J) = a\frac{J_2}{(f_c')^2} + \lambda\frac{\sqrt{J_2}}{f_c'} + b\frac{I_1}{f_c'} - 1 = 0, \tag{6.65}$$

where $I_1 = \sigma_x + \sigma_y + \sigma_z = $ the first invariant of the stress tensor   (6.65a)

$\quad J_2 = $ the second invariant of the stress deviator tensor

$\quad = \frac{1}{2}(S_x^2 + S_y^2 + S_z^2) + \tau_{xy}^2 + \tau_{yz}^2 + \tau_{zx}^2$ (6.65b)

$\quad J = \cos 3\theta = 1.5\sqrt{3}(J_3/\sqrt{J_2})$ (6.65c)

$\quad J_3 = $ the third invariant of the stress deviator tensor

$\quad = S_x S_y S_z + 2\tau_{xy}\tau_{yz}\tau_{zx} - S_x\tau_{yz}^2 - S_y\tau_{xz}^2 - S_z\tau_{xy}^2$ (6.65d)

$\quad S_x = \sigma_x - I_1/3$

$\quad S_y = \sigma_y - I_1/3$ (6.65e)

$\quad S_z = \sigma_z - I_1/3$

$\quad \lambda = \lambda(\cos 3\theta) > 0 \quad$ a and b are constant

$\quad \lambda = K_1\cos(\frac{1}{3}\cos^{-1}(K_2\cos 3\theta))$ for $\cos 3\theta > 0$

$\quad \lambda = K_1\cos(\pi/3 - \frac{1}{3}\cos^{-1}(-K_2\cos 3\theta))$ for $\cos 3\theta \leq 0$

$\quad\quad K_1, K_2, a$ and b are material parameters $(0 \leq K_2 \leq 1)$

$\quad f_c' = $ uni-axial compressive cylinder strength for concrete $= 0.87\sigma_{cu}$

$\quad \sigma_t = $ uni-axial tensile strength for concrete

Table 6.12 lists some of the relevant parameters.

Table 6.12. Ottoson's failure model for concrete [1.150]

ρ_t = tensile meridian
ρ_c = compressive meridian
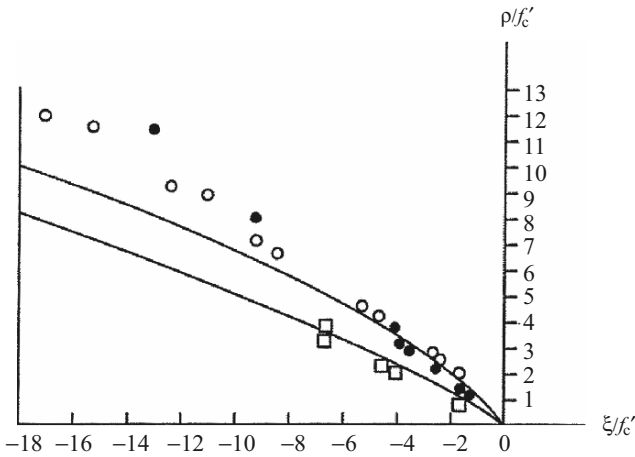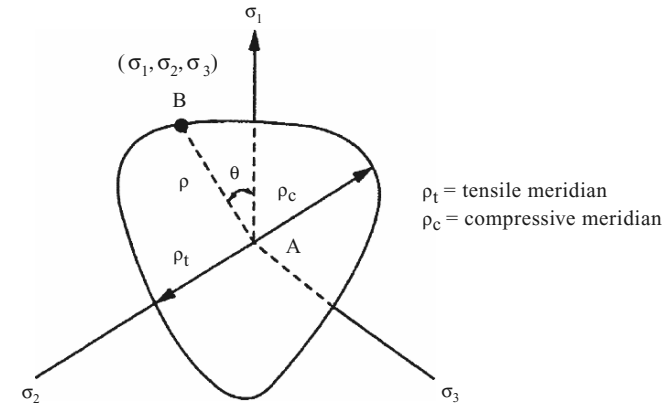
Comparison for the four-parameter model.

Four material parameters $(k = \sigma_t/\sigma_c)$

k	a	b	K_1	K_2
0.08	1.8076	4.0962	14.4863	0.9914
0.10	1.2759	3.1962	11.7365	0.9801
0.12	0.9218	2.5969	9.9110	0.9647

Values of the function $(k = \sigma_t/\sigma_c)$

k	λ_t	λ_c	$\lambda_c\lambda_t$
0.08	14.4925	7.7834	0.7378
0.1	11.7109	6.5315	0.5577
0.12	9.8720	5.6979	0.5772

(*continued*)

Table 6.12. (continued)
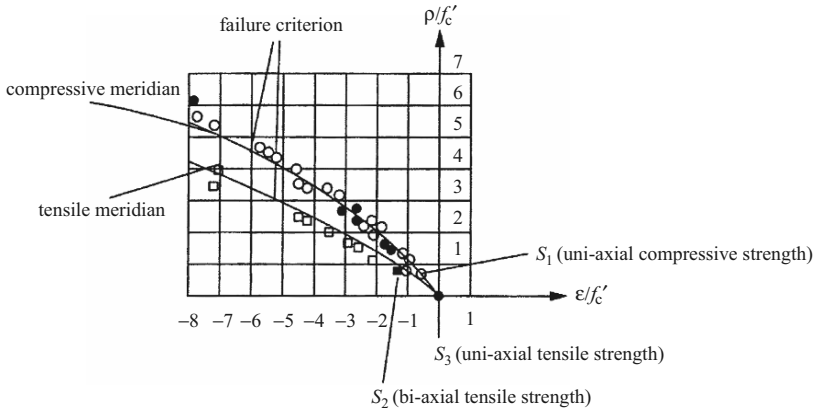
Determination of material parameters (S_1, S_2, S_3, S_4 = failure stresses).

The following three failure states were represented:

(1) Uni-axial compressive strength, $f_c'(\theta = 60°)$. Uni-axial tensile strength, $\sigma_t(\theta = 0°) = K f_c'$.
(2) Bi-axial compressive strength, $\sigma_1 = \sigma_2 = -1.16\sigma_c$; $\sigma_3 = 0(\theta = 0°)$ (test results of Kupfer) [1.16].
(3) The tri-axial state $(\xi/f_c', \rho/f_c') = (-5, 4)$ on the compressive meridian ($\theta = 60°$).

The knowledge of the mechanical properties of concrete and the reinforcement (conventional and pre-stressing steel) at high strain rates is essential for rational application of materials in those constructions where impact and explosion loadings can be expected. The usual magnitude of the strain rate ($d\epsilon/dt = \dot{\epsilon}$) for all concrete structures is of the order of $5 \times 10^5 \,\mathrm{s}^{-1}$ in the range of the ultimate load. For reinforcement, the range is between 10^5 and $10^2 \,\mathrm{s}^{-1}$. Table 6.13 gives relevant data. Figure 6.5 gives experimental stress–strain relationships for reinforcement for various strain rates. The theoretical expression in (6.46) was used.

6.4 Ice/Snow Impact

Chapter 2 gives a thorough survey on data regarding the effect of ice floes. When floating ice sheets move under the influence of strong winds and currents, a sea-going vehicle or a semi-submersible will be subject to an impact given by

$$F_1(t) = F_{1O}(t) + F_1'(t), \tag{6.66}$$

Table 6.13. Strain rate for concrete and reinforcement

The relationship between the fracture strain ϵ_f and the strain rate $\dot{\epsilon}$ is given by

$$\epsilon_f = \alpha \dot{\epsilon}^{1/3}, \tag{1}$$

for plain concrete $\alpha = 206$; for reinforced concrete $\alpha = 220$
Another expression given by DELFT for plain concrete is

$$\epsilon_f = 100 + 109 \dot{\epsilon}^{1/2}. \tag{2}$$

In (1), for say $\dot{\epsilon}/s = 35$, the value of ϵ_f for reinforced concrete will be 740×10^{-6}. For $\dot{\epsilon}/s = 30$, the value of ϵ_f for plain concrete will be 650×10^{-6}.

For fibre-reinforced concrete, the influence of the strain rate upon the tensile strength for concrete is given by

$$\sigma_t = \alpha + \beta \log_e \dot{\epsilon}, \tag{3}$$

$\alpha = 0$ for no fibres, i.e. plain concrete
$\sigma_t = 1.7 + 0.0364 \log_e \dot{\epsilon}$ for 3% fibres
$\sigma_t = 1.87 + 0.0424 \log_e \dot{\epsilon}$

For low, intermediate and high strain rate, DELFT gives an expression:

$$\sigma_t = \alpha + \beta N, \tag{4}$$

where N is the number of fibres/reinforcements

	Low	Intermediate	High
α	3.32	4.87	5.49
β	1.85×10^{-3}	2.85×10^{-3}	6.3×10^{-3}

For the fracture energy, G_f as stated in the endochronic theory will be modified as follows:

$$G_f = \alpha + \beta N$$

	Low	Intermediate	High
α	12.72	22.90	29.200
β	0.12	0.18	0.211

where $F_{1O}(t)$ and $F_1'(t)$ are constant and fluctuating values of the ice impact force, respectively. The value of $F_{1O}(t)$ is given by

$$F_{1O}(t) = S_1 S_2 S_3 f(\dot{\epsilon}) TW \times h\sigma_c \text{ (or } f_c'), \tag{6.67}$$
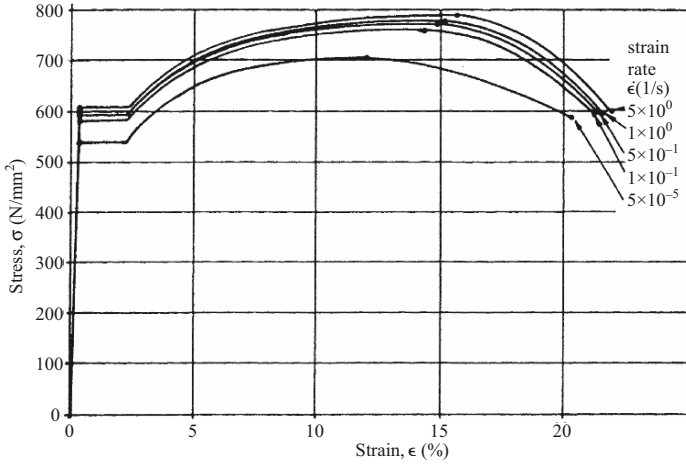
Fig. 6.5. Stress–strain relationships for various strain rates

where S_1 = contact factor around the member during crushing

S_2 = shape factor S_f of the impactor

S_3 = temperature factor which is $(1-0.012T)/(1-0.012T_s)$ $(T: 0.5°C >$ $T > -20°C)$ $(T_s = -10°C$ standard temperature)

σ_c = compressive strength of ice measured at a strain rate of $5 \times 10^{-4}\,\mathrm{s}^{-1}$ which is $\dot{\epsilon}_0$

W = transverse width of the member

h = ice sheet thickness

$$f(\dot{\epsilon}) = (\dot{\epsilon}/\dot{\epsilon}_0)^\gamma, \quad \phi = a_1 + a_2(h/W)^{1/2}, \tag{6.67a}$$

$$\dot{\epsilon} = \dot{x}/4W, \tag{6.67b}$$

where $\dot{x}$ = ice flow velocity

γ = empirical coefficient dependent on strain rate

a_1, a_2 = factors dependent on the ice thickness/diameter ratio of a member

Depending on the type of impact (direct or angular) and the stiffnesses of members and ice floes, the global equation of motion, (6.13), will be influenced by roll, pitch and yaw motions $(\theta_r, \phi_p, \psi_y)$ and surge, sway and heave motions $(\theta_s, \phi_s, \psi_h)$, respectively. Generally, the values of $\theta_r, \phi_p, \psi_y, \theta_s, \phi_s$ and ψ_h range as shown below:

$$\theta_r = -0.012\text{–}0.04 \times 10^{-3}\,\text{rad}; \; \theta_s = -0.75\text{–}6\,\text{m}$$

$$\phi_p = -0.012\text{–}0.04 \times 10^3\,\text{rad}; \; \phi_s = -1.5\text{–}3\,\text{m}$$

$$\psi_y = -0.012\text{–}0.04\,\text{rad}; \; \psi_h \approx \theta_s$$

6.5 Impact due to Missiles, Impactors and Explosions: Contact Problem Solutions

Contact problems have been introduced in Chap. 3, using the spring concept. In addition, at the time of impact constraints are imposed on global equations such as (6.13)–(6.21). Hallquist et al. [3.40] developed a useful concept of *master* and *slave nodes* sliding on each other. As shown in Fig. 6.6, slave nodes are constrained to slide on master segments after impact occurs and must remain on a master segment until a tensile interface force develops. The zone in which a slave segment exists is called a *slave zone*. A separation between the slave and the master line is known as *void*. The following basic principles apply at the interface:

(1) Update the location of each slave node by finding its closest master node or the one on which it lies.
(2) For each master segment, find out the first slave zone that overlaps.
(3) Show the existence of the tensile interface force.

Constraints are imposed on global equations by a transformation of the nodal displacement components of the slave nodes along the contact interface. Such a transformation of the displacement components of the slave nodes will eliminate their normal degrees of freedom and distribute their normal force components to the nearby master nodes. This is done using explicit time integration, as described later under solution procedures. Thereafter impact and release conditions are imposed. The slave and master nodes are shown in Fig. 6.6. Hallquist et al. [3.40] gave a useful demonstration of the identification of the 'contact point', which is the point on the master segment to the slave node n_s and which finally becomes non-trivial. As shown in Fig. 6.6, when the master segment t is given the parametric representation and $\hat{\mathbf{t}}$ is the position
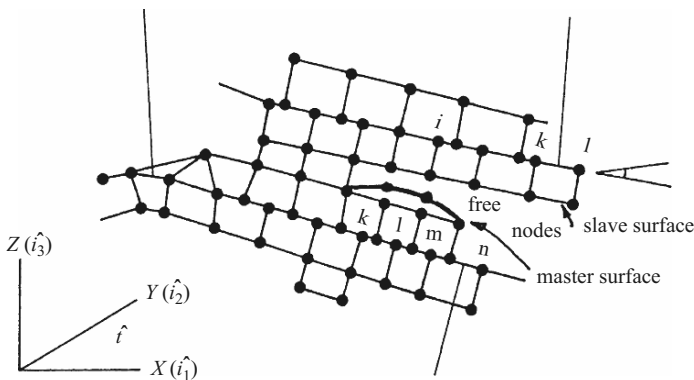
Fig. 6.6. Hallquist contact method (modified by Bangash) [1.149]

vector drawn to the slave node n_s, the contact point co-ordinate must satisfy the following equations:

$$\frac{\partial \hat{\mathbf{r}}}{\partial \xi}(\xi_c, \eta_c) \times [\hat{\mathbf{t}} - \hat{\mathbf{r}}(\xi_c, \eta_c)] = 0,$$
$$\frac{\partial \hat{\mathbf{r}}}{\partial \eta}(\xi_c, \eta_c) \times [\hat{\mathbf{t}} - \hat{\mathbf{r}}(\xi_c, \eta_c)] = 0,$$
(6.68)

where (ξ_c, η_c) are the co-ordinates on the master surface segment S_i. Where penetration through the master segment S_i occurs, the slave node n_s (containing its contact point) can be identified using the interforce vector $\mathbf{f}_s$ added, then:

$$\mathbf{f}_s = -lk_i n_i, \quad \text{if } l < 0 \tag{6.69}$$

to the degrees-of-freedom corresponding to n_s, and

$$\mathbf{f}_m^i = N_i(\xi_c, \eta_c)\mathbf{f}_s \quad \text{if } l < 0, \tag{6.70}$$

where
$$l = \hat{\mathbf{n}}_i \cdot [\hat{\mathbf{t}} - \hat{\mathbf{r}}(\xi_c, \eta_c)] < 0. \tag{6.70a}$$

A unit normal $\hat{\mathbf{n}}_i = \hat{\mathbf{n}}_i(\xi_c, \eta_c), \quad \hat{\mathbf{t}}_i = \hat{\mathbf{n}}_i \sum_{j=1}^{n} N_j (F_1)^j(t),$ (6.70b)

$$k_i = f_{si} \ K_i \ A_i^2 / V_i, \tag{6.70c}$$

where $(F_1)^j(t) =$ impact at the jth node,
$\qquad k_i =$ stiffness factor for mass segment S_i,
$K_i, V_i, A_i =$ bulk modulus, volume and face area, respectively,
$\qquad f_{si} =$ scale factor normally defaulted to 0.10,
$\qquad N_i = \frac{1}{4}(1 + \xi\xi_i)(1 + \eta\eta_i)$ for a 4-node linear surface.

Bangash extended this useful analysis for others such as 8-noded and 12-noded elements [1.149]. On the basis of this theory and owing to the non-availability of the original computer source, a new sub-program CONTACT was written in association with the program ISOPAR. CONTACT is in three-dimensions: the values of N_i for 8- and 12-noded elements are given in Table 6.14.

6.6 High Explosions

The pressure P is generally defined as a function of relative volume and internal energy. Chapters 2 and 5 present useful treatments of this subject. The evaluation of the final pressure due to explosion for various case studies is dealt with in Chap. 5. Assuming $F_1(t)$ is the final surface load, the pressure P must replace $F_1(t)$ in relevant equations by taking into consideration the surface volume on which it acts. All equations defining relevant detonation

Table 6.14. N_i for 8- and 12-noded elements [1.149]

Eight-noded membrane element

Node i	Shape functions $N_i(\xi,\eta)$	Derivatives	
		$\dfrac{\partial N_i}{\partial\xi}$	$\dfrac{\partial N_i}{\partial\eta}$
1	$\frac{1}{4}(1-\xi)(1-\eta)(-\xi-\eta-1)$	$\frac{1}{4}(1-\eta)(2\xi+\eta)$	$\frac{1}{4}(1-\xi)(2\eta+\xi)$
2	$\frac{1}{2}(1-\xi^2)(1-\eta)$	$-\xi(1-\eta)$	$-\frac{1}{2}(1-\xi^2)$
3	$\frac{1}{4}(1+\xi)(1-\eta)(\xi-\eta-1)$	$\frac{1}{4}(1-\eta)(2\xi-\eta)$	$\frac{1}{4}(1+\xi)(2\eta-\xi)$
4	$\frac{1}{2}(1-\eta^2)(1+\xi)$	$\frac{1}{2}(1-\eta^2)$	$-\eta(1+\xi)$
5	$\frac{1}{4}(1+\xi)(1+\eta)(\xi+\eta-1)$	$\frac{1}{4}(1+\eta)(2\xi+\eta)$	$\frac{1}{4}(1+\xi)(2\eta+\xi)$
6	$\frac{1}{2}(1-\xi^2)(1+\eta^2)$	$-\xi(1+\eta)$	$\frac{1}{2}(1-\xi^2)$
7	$\frac{1}{4}(1-\xi)(1+\eta)(-\xi+\eta-1)$	$\frac{1}{4}(1+\eta)(2\xi-\eta)$	$\frac{1}{4}(1-\xi)(2\eta-\xi)$
8	$\frac{1}{2}(1-\eta^2)(1-\xi)$	$-\frac{1}{2}(1-\eta^2)$	$-\eta(1-\xi)$

(continued)

Table 6.14. (continued)

Twelve-noded membrane element

Node i	Shape functions $N_i(\xi,\eta)$	Derivatives	
		$\dfrac{\partial N_i}{\partial \xi}$	$\dfrac{\partial N_i}{\partial \eta}$
1	$\frac{9}{32}(1-\xi)(1-\eta)[\xi^2+\eta^2-\frac{10}{9}]$	$\frac{9}{32}(1-\eta)[2\xi-3\xi^2-\eta^2+\frac{10}{9}]$	$\frac{9}{32}(1-\xi)[2\eta-3\eta^2-\xi^2+\frac{10}{9}]$
2	$\frac{9}{32}(1-\xi)(1-\xi^2)(1-\eta)$	$\frac{9}{32}(1-\eta)(3\xi^2-2\xi-1)$	$-\frac{9}{32}(1-\xi)(1-\xi^2)$
3	$\frac{9}{32}(1-\eta)(1-\xi^2)(1+\xi)$	$\frac{9}{32}(1-\eta)(1-2\xi-3\xi^2)$	$-\frac{9}{32}(1-\xi^2)(1+\xi)$
4	$\frac{9}{32}(1+\xi)(1-\eta)[\xi^2+\eta^2-\frac{10}{9}]$	$\frac{9}{32}(1-\eta)[2\xi+3\xi^2+\eta^2-\frac{10}{9}]$	$\frac{9}{32}(1+\xi)[2\eta-3\eta^2-\xi^2-\frac{10}{9}]$
5	$\frac{9}{32}(1+\xi)(1-\eta^2)(1-\eta)$	$\frac{9}{32}(1-\eta^2)(1-\eta)$	$\frac{9}{32}(1+\xi)(3\eta^2-2\eta-1)$
6	$\frac{9}{32}(1+\xi)(1-\eta^2)(1+\eta)$	$\frac{9}{32}(1-\eta^2)(1+\eta)$	$\frac{9}{32}(1+\xi)(1-2\eta-3\eta^2)$
7	$\frac{9}{32}(1+\xi)(1+\eta)[\xi^2+\eta^2-\frac{10}{9}]$	$\frac{9}{32}(1+\eta)[2\xi+3\xi^2+\eta^2-\frac{19}{9}]$	$\frac{9}{32}(1+\xi)[2\eta+3\eta^2+\xi^2-\frac{10}{9}]$
8	$\frac{9}{32}(1+\eta)(1-\xi^2)(1+\xi)$	$\frac{9}{32}(1+\eta)(1-2\xi-3\xi^2)$	$\frac{9}{32}(1-\xi^2)(1+\xi)$
9	$\frac{9}{32}(1+\eta)(1-\xi^2)(1-\xi)$	$\frac{9}{32}(1+\eta)(3\xi^2-3\xi-1)$	$\frac{9}{32}(1-\xi^2)(1-\xi)$
10	$\frac{9}{32}(1-\xi)(1+\eta)[\xi^2+\eta^2-\frac{10}{9}]$	$\frac{9}{32}(1+\eta)[2\xi-3\xi^2-\eta^2+\frac{10}{9}]$	$\frac{9}{32}(1-\xi)[2\eta+3\eta^2+\xi^2-\frac{10}{9}]$
11	$\frac{9}{32}(1-\xi)(1-\eta^2)(1+\eta)$	$-\frac{9}{32}(1+\eta)(1-\eta^2)$	$\frac{9}{32}(1-\xi)(1-2\eta-3\eta^2)$
12	$\frac{9}{32}(1-\xi)(1-\eta^2)(1-\eta)$	$-\frac{9}{32}(1-\eta)(1-\eta^2)$	$\frac{9}{32}(1-\xi)(3\eta^2-2\eta-1)$

pressures P must first be evaluated as shown in Chap. 5. They are then first applied as stated, in (6.13)–(6.21).

The cause of explosions can be nuclear (air burst or underground), gas, chemical, dust, bombs and explosives. The pressures, which are time-dependent, can then act as surface loads on the body of the element concerned or at nodal points of the element as concentrated loads derived on the basis of shape functions. It is essential to choose a proper time-aspect ratio as it will affect the type of solution procedure adopted. The interaction between the loads and the structure can be considered and the method shown in Sect. 6.5 must be included.

6.7 Spectrum Analysis

Spectrum analysis is an extension of the mode frequency analysis, with both base and force excitation options. The response spectrum table is generally used and includes displacements, velocities and accelerations. The force excitation is, in general, used for explosions and missile aircraft impact. The masses are assumed to be close to the reaction points on the finite element mesh rather than the master degrees of freedom. The base and forced excitations are given below. For the base excitation for wave

$$\gamma_i = \{\psi_i\}_{\mathrm{R}}^{\mathrm{T}''} [M] \{\mathbf{b}\}. \tag{6.71}$$

For the impact excitation

$$\gamma_i = \{\psi_i\}_{\mathrm{R}}^{\mathrm{T}''} \{F_1(t)\}, \tag{6.72}$$

where $\{\psi_i\}_{\mathrm{R}}$ = the slave degree of freedom vector mode,
$\quad\quad M$ = mass,
$\quad\quad \{\mathbf{b}\}$ = unit vector of the excitation direction,
$\quad\quad \{F_1(t)\}$ = an input force vector due to impact and explosion.

The values of $\{\psi\}_{\mathrm{R}}$ are normalized and the reduced displacement is calculated from the eigenvector by using a mode coefficient $\{\mathbf{M}\}$.

$$\{\mathbf{x}\}_i = [\mathbf{M}_i]\{\psi\}_i \tag{6.73}$$

where $\{\mathbf{x}\}_i$ = reduced displacement vector and $[\mathbf{M}_i]$ = mode coefficient and where

(a) for velocity spectra

$$[\mathbf{M}_i] = [\dot{x}_{\mathrm{s}i}]\{\gamma_i\}/\omega_i, \tag{6.74}$$

where $\dot{x}_{\mathrm{s}i}$ = spectral velocity for the ith mode;

(b) for force spectra

$$[\mathbf{M}_i] = [F_{\mathrm{s}i}]\{\gamma\}/\omega_{\mathrm{t}}^2, \tag{6.75}$$

where $F_{\mathrm{s}i}$ = spectral force for the ith mode;

(c) caused by explosion P or impact $F_1(t)$

$$[\mathbf{M}_i] = [\ddot{x}_{si}]\{\gamma_i\}/\omega_i^2, \tag{6.76}$$

where $\ddot{x}_{si}$ = spectral acceleration for the ith mode;

(d)

$$[\mathbf{M}_i] = [x_{si}]\{\gamma_i\}/\omega_i^2. \tag{6.77}$$

$\{x\}_i$ may be expanded to compute all the displacements, as in

$$\{\mathbf{x}_{\gamma'}\}_i = [K_{\gamma'\gamma'}]^{-1}[K_{\gamma'\gamma}]\{\mathbf{x}_i\}_R, \tag{6.78}$$

where $\{\mathbf{x}_{\gamma'}\}_i$ = slave degree of freedom vector of mode i,
$[K_{\gamma'\gamma'}], [K_{\gamma'\gamma}]$ = sub-matrix parts,
γ, γ' = retained and removed degrees of freedom.

The impact/explosion load is then equal to

$$[[K_{\gamma\gamma}] - [K_{\gamma'\gamma}][K_{\gamma\gamma'}]^{-1}[K_{\gamma'\gamma}]]\{\mathbf{x}_\gamma\} = [\{F_\gamma\} - [K_{\gamma\gamma'}][K_{\gamma\gamma'}]^{-1}\{F_{\gamma'}\}]$$
$$\text{or } [\overline{K}]\{\bar{\tilde{x}}\} = \{\bar{F}_1(t)\}, \tag{6.79}$$
$$\text{where } [\overline{K}] = [K_{\gamma\gamma}] - [K_{\gamma\gamma'}][K_{\gamma'\gamma'}]^{-1}[K_{\gamma'\gamma}], \tag{6.80}$$
$$\{\overline{F}_I(t)\} = \{F_\gamma\} - [K_{\gamma\gamma'}][K_{\gamma'\gamma'}]^{-1}\{F_{\gamma'}\}, \tag{6.81}$$
$$\{\bar{x}\} = \{\mathbf{x}_\gamma\} \tag{6.82}$$

and $[K]$ and $\{\overline{F}_1(t)\}$ are generally known as the substructure stiffness matrix and the impact load vector, respectively.

6.8 Solution Procedures

Three types of solution procedure are available for impact and explosion analysis, namely, time-domain, frequency-domain and modal analysis.

6.8.1 Time-Domain Analysis

The following steps are adopted using a direct implicit integration procedure.

Initialization

(1) The effective stiffness matrix is

$$[K_0^*] = (6/\tau^2)[M] + (3/\tau)[C_0] + [K_0] \tag{6.83}$$

(2) Triangularize $[K_0^*]$

For each time step, calculate the displacement $\{x_{t+\tau}\}$

- Constant part of the effective load vector

$$\{R^*_{t+\tau}\} = \{R_t\} + \theta(\{R_{t+\delta t}\} - \{R_t\}) + \{F_t\} + [M]$$
$$\times (6/\tau^2)\{x_t\} + (6/\tau)\{\dot{x}_t\} + 2\{\ddot{x}_t\}) + [C_0]((3/\tau)\{x_t\} + 2\{\dot{x}_t\} + (\tau/2)\{x_t\})$$
(6.84)

- Initialization, $i = 0$, $\{\delta F^i_{t \to t+\tau}\} = 0$
- Iteration
  (a) $i \to i + 1$
  (b) Effective load vector $\{R^*_{t+\tau_{\mathrm{TOT}}}\} = \{R^*_{t+\tau}\} + \{\delta F^{i-1}_{t \to t+\tau}\}$
  (c) Displacement $\{x^i_{t+\tau}\}[K^*_0]\{x^i_{t+\tau}\} = R^{*i}_{t \to t+\tau_{\mathrm{TOT}}}$
  (d) Velocity $\{\dot{x}^i_{t+\tau}\} + (3/\tau)\left(\{x^i_{t+\tau}\} - \{x_t\}\right) - 2\{\dot{x}_t\} - (\tau/2)\{\ddot{x}_t\}$
  (e) Change of initial load vector caused by non-linear behaviour of the material

$$\{\delta F^i_{t \to t+\tau}\} = -[\delta C_{o \to t}]\{\dot{x}^i_{t+\tau}\} - \{\dot{x}_t\}\omega - [\delta C^i_{t \to t+\tau}]\{\dot{x}^i_{t+\tau}\} \times [\delta K_{o \to t}]$$
$$\left(\{x^i_{t+\tau}\} - \{x_t\}\right) - [\delta K^i_{t \to t+\delta t}]\{x^i_{t+\tau}\}$$
(6.85)

  In fact, $\{\delta F^i_{t \to t+\tau}\}$ is calculated using the initial-stress method
  (f) Iteration convergence

$$\|\{\delta F^i_{t \to t+\tau}\} - \{\delta F^{i-1}_{t \to t+\tau}\}\|/\|\{\delta F^i_{t \to t+\tau}\}\| < \mathrm{tol} = 0.01 \qquad (6.86)$$

  or, analogously, on stresses

Calculation of velocity and acceleration

Calculate the new acceleration $\{\ddot{x}_{t+\delta t}\}$, velocity $(\dot{x}_{t+\delta t})$, displacement $\{x_{t+\delta t}\}$ and initial load $\{F_{t+\delta t}\}$:

$$\{\ddot{x}_{t+\delta t}\} = (6/\theta\tau^2)(\{x_{t+\tau}\} - \{x_t\}) - (6/\tau\theta)\{\dot{x}_t\} + (1 - (3/\theta))\{\ddot{x}_t\}, \quad (6.87)$$
$$\{\dot{x}_{t+\delta t}\} = \{\dot{x}_t\} + (\tau/2\theta)\{\ddot{x}_t\} + \{\ddot{x}_{t+\delta t}\}, \qquad (6.88)$$
$$\{x_{t+\delta t}\} = \{x_t\} + (\tau/\theta)\{\dot{x}_t\} + (\tau^2/6\theta^2)(2\{\ddot{x}_t\} + \{\ddot{x}_{t+\delta t}\}), \qquad (6.89)$$
$$\{F_{t+\delta t}\} = \{F_t\} + \{\delta F^i_{t \to t+\tau}\}. \qquad (6.90)$$

Calculation by quadratic integration

When the velocity varies linearly and the acceleration is constant across the time interval, appropriate substitutions are made into (6.13), giving

$$[f_1[M] + f_2[C_t] + [K'_t]]\{x_t\} = \{F_I(t)\} + \{f_3([C_t], [M], x_{t1}, x_{t2}, \ldots)\}, \quad (6.91)$$

where f_1, f_2 are functions of time. This results in an implicit time integration procedure. The only unknown is $\{x_t\}$ at each time point and this is calculated

in the same way as in static analysis. Equation (6.91) is then written as

$$
\left(\frac{2}{\delta t_0\,\delta t_0}[M] + \frac{\delta t_0 + \delta t_1}{\delta t_0\,\delta t_0}[C] + [K'_t] \right)\{x_t\} = \{F_1(t)\} + [M]\left(\frac{2}{\delta t_0\,\delta t_1}\{x_{t-1}\} \right.
$$

$$
\left. - \frac{2}{\delta t_1\,\delta t_0}\{x_{t-2}\} \right) + [C_t]\left(\frac{\delta t_0}{\delta t_0\,\delta t_1}\{x_{t-1}\} - \frac{\delta t_0}{\delta t_0\,\delta t_1}\{x_{t-2}\} \right), \qquad (6.92)
$$

where $\delta t_0 = t_0 - t_1$ and $t_0 =$ time of current iteration
$\delta t_1 = t_1 - t_2$ and $t_1 =$ time of previous iteration
$\delta t_2 = t_2 - t_3$ and $t_2 =$ time before previous iteration
$\delta t_2 = \delta t_0 + \delta t_1 = t_0 - t_2$ and $t_3 =$ time before t_2

Calculation by cubic integration

Equation (6.91) becomes cubic and hence is written as

$$
(a_1[M] + a_2[C_t] + [K'_t])\{x_t\} = \{F_1(t)\} + [M](a_3 x_{t-1}) - a_4\{x_{t-2}\}
$$

$$
+ a_5\{x_{t-3}\} + [C](a_6\{x_{t-1}\} - a_7\{x_{t-2}\} + a_8\{x_{t-3}\}), \qquad (6.93)
$$

where a_1 to a_8 are functions of the time increments; these functions are derived by inverting a 4×4 matrix.

For clear-cut solutions, the size of the time step between adjacent iterations should not be more than a factor of 10 in non-linear cases and should not be reduced by more than a factor of 2 where plasticity exists.

6.8.2 Frequency-Domain Analysis

The original equation of motion is reproduced as

$$
[M]\{\ddot{x}\} + [C]\{\dot{x}\} + [K]\{x\} = \{J_F\}\{F\}, \qquad (6.94)
$$

where $\{J_F\}$ is a vector with all components zero except the last one, which is 1. The terms $[K]$ and $[C]$ shall be frequency dependent. The value of $\{F\} = [K_N]\{x_s\}$ can be taken for solutions of rigid rock problems. If the excitation with frequency ω assumes the form e^{iwt}, then

$$
\dot{x} = i\omega x_s;\ \ddot{x}_s = -\omega^2 x_s;\ \{x\} = i\omega\{x\}\ \text{and}\ \{x\} = -\omega^2\{x\}. \qquad (6.95)
$$

Equation (6.94) can thus be written as

$$
\left([K] + i\omega[C] - \omega^2[M]\right)\{x\} = \{J_F\}K_n x_s. \qquad (6.96)
$$

For a given value of ω, a set of algebraic equation is solved using any numerical scheme. The displacement of a mass can be written as

$$
\{x\} = \left([K] + i\omega[C] - \omega^2[M]\right)^{-1}\{J_F\}K_n x_n. \qquad (6.97)
$$

From displacements, accelerations, velocities, strains and stresses can be computed. The amplification function (AF) for each frequency x_1/x_s may be derived. Repeated solutions of (6.95) are necessary for a proper definition of this function. If the fast Fourier transform is used the AF must be tabulated at each frequency interval.

Table 6.15. The Range–Kutta method

$$x^{n+1} = x^n + \frac{\delta t}{6}(f^{(1)} + 2f^{(2)} + 2f^{(3)} + f^{(4)}), \tag{a}$$

where
$$f^{(1)} = f(x^n), \ f^{(2)} = f\left(x^n + \frac{\delta t}{2}f^{(1)}\right),$$

$$f^{(3)} = f\left(x^n + \frac{\delta t}{2}f(2)\right),$$

$$f^{(4)} = f(x^n) + \delta t f^{(3)}.$$

Some computations are needed to calculate $f^{(1)}$ to $f^{(4)}$

$$f = kx. \tag{b}$$

6.8.3 Runge–Kutta Method

It is an accurate method of time integration and is explicit in nature. Table 6.15 summarises this method. This method of higher order is a robust algorithm used to solve non-linear equations but may have problems which have discontinuous coefficients which take place spatially. Some coefficients change discontinuously as the load increases strain localisation which will be difficult to produce in numerical simulation. Non-linear equations have bi-furcation. The fault problem has bifurcation. The non-linear equation of stochastic elastoplacify is more suitable for finding the most unstable solution compared with the non-linear equation of deterministic elastoplacify, since the coefficients change continuously.

6.9 Geometrically Non-Linear Problems in the Dynamic Finite Element

6.9.1 Introduction

Geometrically non-linear problems are assumed to be those associated with large displacements and strains. In the presence of large displacements the structure alters its shape so that applied loads change their distribution. Non-linearity can be mild or strong, static or dynamic. Here, one assumes unless specifically stated, that the strains are small, material stress–strain relationship is linear and problems are static.

The main feature of non-linear analysis is that equilibrium equations need to be written for deformed geometry. There is no need for complete revision or abandonment of linear analysis because non-linear problems are commonly solved as a series of linear analyses.

During deformations the coordinates are displaced and they are called "moving coordinates". A column subject to large deflections, shown in Fig. 1. is considered. Its stiffness matrix in position AB is different to that in position AC. When one writes $[K]\{\Delta D\} = \{\Delta R\}$, $\{\Delta D\}$ cannot represent displacement from AB to AC because $[K]$ is not constant for such a large step. One can treat $\{\Delta R\}$ as being effectively an array of unbalanced forces and, for the equilibrium of the nodal d.o.f. one needs $\{\Delta R\} = \{0\}$. The iterative solution will be seeking the configuration that conforms with $\{\Delta R\} = 0$.

Distortions of the element and the forces are identified in Fig. 3 where the first sketch shows undeformed element. To account for the rigid body motion separately from distortions a local axis x is introduced, such that the distorted member angle Φ can be written as

$$\phi = arctg \left[\frac{Y_L}{X_L} \right]. \tag{6.98}$$

Element distortions can be expressed in the local co-ordinate system:

$$U_2 = L - L_0 = \sqrt{x_2^2 + y_2^2} - L_0 = (x_0 + D_4 - D_1)^2 + (Y_0 + \theta_s - \theta_2)^2 - L_0, \tag{6.99}$$

$$\theta_1 = D_3 - (\phi - \phi_0) = D_3 - \left(arctg \left(\frac{Y_L}{X_L} \right) - \theta_0 \right), \tag{6.100}$$

$$\theta_2 = D_6 - (\phi - \varphi_0) = D_6 - \left(arctg \left(\frac{Y_L}{X_L} \right) - \phi_0 \right). \tag{6.101}$$

Forces $\{r\}$ applied at nodes 1 and 2 by the distorted element are

$$\{r\} = [k]\{d\}, \tag{6.102}$$

where $\{d\} = \{0\ 0\ \theta_1\ u_2\ 0\ \theta_2\}$ and $\{r\}$, $[k]$ and $\{d\}$ are expressed in local co-ordinates.

6.9.2 Criteria for the Iterative Approach

Assuming a structure that is deformed, not in equilibrium, and subject to a specified level of external load a typical iterative solution will be as follows:

1. Establish local co-ordinates by use of global displacements $\{D\}$
2. Compute element distortions, i.e. complete element nodal d.o.f $\{d\}$ in local co-ordinates
3. Establish element stiffness $[k]$ and forces $\{r\} = -[k]\{d\}$ in local co-ordinates
4. Transfer $[k]$ and $\{r\}$ to global co-ordinates
5. Repeat steps 1–4 for all elements and assemble global structural matrices $[K] = \Sigma[k]$ and $\{R_r\} = \Sigma\{r\}$

6. Compute the un-balanced loads $\{\Delta R\}$ as the vector of applied loads plus $\{R_r\}$
7. Solve structural equations $[K]\{\Delta D\} = \{\Delta R\}$ for displacement increments $\{\Delta D\}$
8. Add increments $\{\Delta D\}$ to global displacements $\{D\}$ accumulated in previous iterations (effectively update estimate of the equilibrium configuration)
9. Test for convergence, if needed return to step 1.

6.9.3 Solution Strategies

In the text and particularly several methods of solutions for material non-linearity have been discussed. The same can be used for geometric non-linearity.

Solution process for is iterative and several methods that are available will be considered with different notations:

– Direct iteration
– Newton–Raphson
– Modified Newton–Raphson
– Incremental methods, etc

Here we will consider several, standard, solution strategies that can be used for an equation of the form (6.111) which can be expressed as:

$$\psi(u) = Ku + f = 0 \text{ where } K = K(u). \tag{6.103}$$

(i) Direct Iteration

First some ignition value $u = u^0$ is assumed and an improved approximation is obtained:

$$u^{-1} = -(K^0)^{-1}f \text{ where } K^0 = K(u^0). \tag{6.104}$$

For n-th iteration one can write:

$$u^n = -(K^{n-1})^{-1}f \tag{6.105}$$

and the process is terminated when the 'error', $e = u^n - u^{n-1}$ becomes sufficiently small. This condition is usually expressed in terms of some norm such.

Graphic illustration of the procedure is shown in the figure below. Both convergent and divergent case are shown to demonstrate efficiency of the strategy. When this solution strategy is applied to FEM analysis the full set of equations is solved at each iteration.

(ii) Newton–Raphson

This strategy benefits from the Taylor expression so we have:

$$\psi(u^{n+1}) = K^{n+1}u^{n+1} - f = \psi(u^n) + \left(\frac{d\psi}{du}\right)_n \Delta u^n = 0 \tag{6.106}$$

with $u^{n+1} = u^n + \Delta u^n$

In the above, for a FEM solution, derivative represents a *tangential* matrix.

The improved value u^{n+1} is then obtained:

$$\Delta u^n = -(K_T^n)^{-1}\psi^n = -(K_T^n)^{-1}(P^n + f). \tag{6.107}$$

This strategy, often convergent, is graphically illustrated in Fig. 2 Plate 6.1.

(iii) Modified Newton–Raphson

This strategy overcomes the difficulty of having to solve a completely new system of equations at each iteration. The approximation can be introduced:

$$K_T^n = K_T^0 \tag{6.108}$$

that will modify the algorithm already shown above so that a simple resolution of the same system of equations is repeatedly used. This process is illustrated in Fig. 3 Plate 6.1.

(iv) Incremental Method

This method benefits from realization that the solution for u is known when the 'load' term is zero. Once starting point is known it is useful to study the behaviour of u as f is incremented. With suitably small increment of f convergence is highly likely and the intermediate results would provide useful information on the loading process. The method can be described as follows:

$$P(u) + \lambda f_0 = 0. \tag{6.109}$$

After differentiation with respect to λ:

$$\frac{dP}{du}\frac{du}{d\lambda} + f_0 = K_r\frac{du}{d\lambda} + f_0 = 0 \tag{6.110}$$

or

$$\frac{du}{d\lambda} = -(K_r(u))^{-1}f_0, \tag{6.111}$$
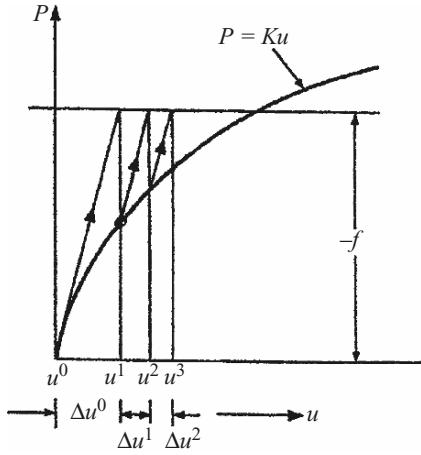
Fig. 1. Direct method
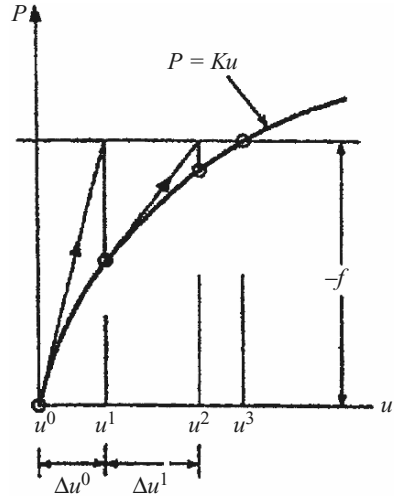
Fig. 2. Newton–Raphson method
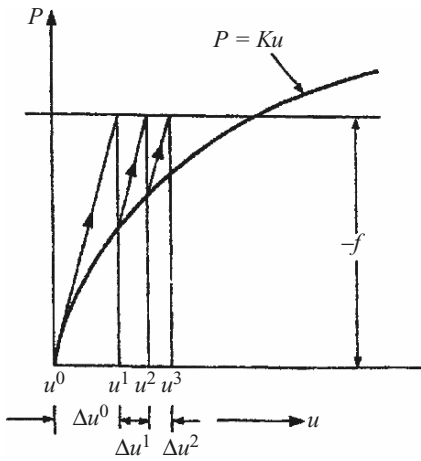
Fig. 3. Modified Newton–Raphson
method
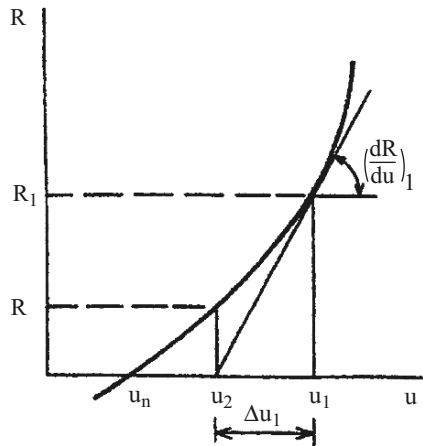
Fig. 4. Incremental method

Plate 6.1. Solution procedures

where we identify the tangential matrix as before. The simplest approximate solution for the above equation is the Euler method that states:

$$u_{m+1} - u_m = -K_r(u_m)^{-1} f_0 \Delta\lambda_m = -(K_r)^{-1}\Delta f_m, \tag{6.112}$$

where the subscript refers to increments of λ, i.e.

$$\lambda_{m+1} = \lambda_m + \Delta\lambda_m \text{ or } f_{m+1} = f_m + \Delta f_m. \tag{6.113}$$

Improved integration schemes are available and described in literature.

Implementation of the solution strategy (Newton–Raphson) is now demonstrated using the truss example.

Example (continued)

If one can assume small strains and set the problem as follows:

$$R(u) = \left(\frac{u+h}{L_0} \right) N - P = 0, \tag{6.114}$$

where R is the residual, or out of force that arises if u is such that equilibrium is not satisfied.

In this particular case the tangent stiffness is easily found as:

$$K_r = \frac{d}{du} \left(\frac{u+h}{L_0} \right) N + \left(\frac{u+h}{L_0} \right) \frac{dN}{du}. \tag{6.115}$$

Using the constitutive equations we obtain:

$$\frac{dN}{du} = \frac{EA}{L_0} \left(\frac{u+h}{L_0} \right). \tag{6.116}$$

From which we can identify

$$K_r = K_0 + K_L K_\sigma, \tag{6.117}$$

where components correspond to the linear stiffness (K_0), the initial displacement stiffness (K_L) and the initial stress stiffness (K_σ), respectively.

6.9.4 General Formulation

The total potential energy of the structure can be expressed:

$$\Pi_p = U - \{D\}^T \{R\} = U_L + U_{NL} - \{D\}^T \{R\}, \tag{6.118}$$

where U is the strain energy of the structure, U_L and U_{NL} are parts of U arising from linear and non-linear strain-displacement expressions. Providing that the system is conservative, the static equilibrium prevails when displacements satisfy the equation:

$$\left\{ \frac{\partial \Pi_p}{\partial D} \right\} = 0. \tag{6.119}$$

Thus, the material remains elastic, and loads $\{R\}$ must be independent of $\{D\}$, i.e. the changes in loads $\{R\}$ caused by virtual displacements $\{\delta D\}$ are negligible in comparison with the loads themselves.

When one differentiates

$$\left\{\frac{\partial U_L}{\partial D}\right\} = [K_L]\{D\}; \quad \left\{\frac{\partial^2 U_L}{\partial D_i \partial D_j}\right\} = K_{L_{ij}} = K_{L_{ji}}, \tag{6.120}$$

where [ ] is the conventional linear stiffness matrix. Symbolically we can write:

$$\left\{\frac{\partial^2 U_L}{\partial D_i \partial D_j}\right\} = [K_L] \quad \left\{\frac{\partial^2 U_{NL}}{\partial D_i \partial D_j}\right\} = [K_{NL}]. \tag{6.121}$$

The non-linear equilibrium equations of the structure are:

$$[K_L]\{D\} + \left\{\frac{\partial U_{NL}}{\partial D}\right\} = \{R\}. \tag{6.122}$$

Application of Newton–Raphson Solution

{R} is transferred to the left and the first order Taylor series expansion about {D}$_0$ to find {ΔD}$_1$ so that

$$f(\{D\}_0 + \{\Delta D\}_1) = 0 \tag{6.123}$$

so we have:

$$([K_L] + [K_{NL_0}])\{\Delta D\}_1 = \{R\} - [K_L]\{D\}_0 - \left\{\frac{\partial U_{NL_0}}{\partial D}\right\} \tag{6.124}$$

and

$$[k_{NL}] = \frac{AE}{L}\begin{bmatrix} 0 & \theta & 0 & -\theta \\ \theta & \theta^2 & -\theta & -\theta^2 \\ 0 & -\theta & 0 & \theta \\ -\theta & -\theta^2 & \theta & \theta^2 \end{bmatrix} + \frac{P}{L}\begin{bmatrix} 0 & 0 & 0 & 0 \\ 0 & 1 & 0 & -1 \\ 0 & 0 & 0 & 0 \\ 0 & -1 & 0 & 1 \end{bmatrix}, \tag{6.125}$$

where $P = AE\varepsilon_x = AE(e + \theta^2/2)$. The second matrix above is the initial stress stiffness matrix. When $\theta = 0$, at the initial un-rotated state [k$_{NL}$] reduces to the conventional linear stiffness matrix.

References:

(EN)	NAFEMS-Introduction to Nonlinear Finite Elements, ed. E. Hinton
(MAC)	Nonlinear Finite Element Analysis, M.A. Crisfield
(OCZ)	The Finite Element Method, O.C. Zienkiewicz
(RDC)	Concepts and applications of Finite Element Analysis

In (6.124), if $\theta = 1$, the value of K$_L$ assumes the following form:

$$[K_l] = \frac{AE}{L}\begin{bmatrix} 1 & 0 & -1 & 0 \\ 0 & 0 & 0 & 0 \\ -1 & 0 & 1 & 0 \\ 0 & 0 & 0 & 0 \end{bmatrix}. \tag{6.126}$$

Fig. 6.7. Pinned end of a member

6.9.5 Example: 6.1

Consider a pin-ended member (Fig. 6.7) element of cross sectional area A and elastic modulus E, determine $[K_{NL}]$.

The axial strain is:

$$\varepsilon_x = e + \frac{\theta^2}{2}, \quad e = \frac{d_3 - d_1}{L}, \quad \theta = \frac{d_4 - d_2}{L}. \tag{6.127}$$

The total strain energy is:

$$U_L + U_{NL} = \frac{AE}{2} \int_0^l \varepsilon_x^2 dx = \frac{AE}{2} \int_0^L e^2 dx + \frac{AE}{2} \int_0^L \left(e\theta^2 + \frac{\theta^4}{4} \right) dx. \tag{6.128}$$

On the element level, the non-linear contribution to the ith nodal force is:

$$\frac{\partial U_{NL}}{\partial d_i} = \frac{AE}{2} \int_0^L \left(\theta^2 \frac{\partial e}{\partial d_i} + 2e \frac{\partial \theta}{\partial d_i} + \theta^3 \frac{\partial \theta}{\partial d_i} \right) dx \quad i = 1, 2, 3, 4. \tag{6.129}$$

After substituting e and θ into the partial derivatives we obtain:

$$\left\{ \frac{\partial U_{NL}}{\partial d_i} \right\} = \frac{AE}{2} \left\{ \begin{array}{c} -\theta^2 \\ -2e\theta - \theta^3 \\ \theta^2 \\ 2e\theta + \theta^3 \end{array} \right\}. \tag{6.130}$$

Another differentiation and substitution of partial derivatives yields:

$$[k_{NL}] = \left[\frac{\partial^2 U_{NL}}{\partial d_i \partial d_j} \right] = \frac{AE}{L} \begin{bmatrix} 0 & \theta & 0 & -\theta \\ \theta & e + \frac{3}{2}\theta^2 & -\theta & -e - \frac{3}{2}\theta^2 \\ 0 & -\theta & 0 & \theta \\ -\theta & -e - \frac{3}{2}\theta^2 & \theta & e + \frac{3}{2}\theta^2 \end{bmatrix}. \tag{6.131}$$

A somewhat better format where the second matrix is the initial stress stiffness matrix is obtained.

6.10 Finite Element Analysis of Explosion Using the Method of Explosive Factor

In order to simulate detonation controlling of the release of chemical energy is needed. A factor is needed to multiply the equations of high explosives given in Chap. 5. The finite element method would require at the initial stage a lighting time t for each element. Assuming the detonation velocity is v_D. The value of t_{18} will be computed as:

Distance from centre line of the
detonation point to the centre of
the element divided by v_D

The Explosive Factor $f_{\exp}$ between two points 1 and 2 well be

$$f_{\exp} = \{f_{1,\exp}, f_{2,\exp}\}. \tag{6.132}$$

Such that

$$f_{1,\exp} = \frac{2(t - t_{1l})v_D}{3(v_e/A_{e_{\max}})} \qquad \text{for } t > t_{1l} \tag{6.133}$$

$$= 0 \qquad\qquad \text{for } t \leq t_{1l} \tag{6.134}$$

$$f_{2,\exp} = \frac{1 - V}{1 - V_{cj}}, \tag{6.135}$$

where v_e = velocity
$Ae_{\max}$ = area
t = current time
V_{cj} = Chapman–Jouguet relative volume
V = current volume

The value of $f_{e_{\exp}}$ has several steps towards unity and according to *Wilkins, M.L. spread the burn front over several elements.

After reaching unity f_{exp} in held constant and if exceeds 1, it is reset to 1. According to the author the high explosive material can behave as an elastic perfectly plastic solids prior to detonation. Hence it will be necessary to update the stress tensor to an elastic stress $^*s_{ij}^{n+1}$ such that

$$^*s_{ij}^{n+1} = s_{ij}^n + s_{ip}\Omega_{pi} + s_{jp}\Omega_{pi} + 2G\dot{\varepsilon}_{ij}'dt, \tag{6.136}$$

where G is the shear modulus, $\dot{\varepsilon}_{ij}'$ is the deviatoric strain rate. The von Mises yield condition is given by:

$$\phi = J_2 - \frac{\sigma_y^2}{3}, \tag{6.137}$$

---

* Wilkins, M.L., "Calculations of Elastic Plastic Flow," Meth. Comp. Phys. 3, (Academic Press), 211–263 (1964)

where the second stress invariant, J_2, is defined in terms of the deviatoric stress components as

$$J_2 = \frac{1}{2}s_{ij}s_{ij} \tag{6.138}$$

and the yield stress is σ_y. If yielding has occurred, i.e. $\Phi > 0$, the deviatoric trial stress is called to obtain the final deviatoric stress at time n+1 for detailed investigation in this field a reference is made to the following publication by the author:

"Manual of Numerical Methods In Concrete"
Thomas Telford London, 2001.

The value of s_{ij}^{n+1} can be written as:

$$s_{ij}^{n+1} = \frac{\sigma_y}{\sqrt{3J_2}} = {}^*s_{ij}^{n+1}. \tag{6.139}$$

If $\Phi \leq 0$, then

$$s_{ij}^{n+1} = {}^*s_{ij}^{n+1}. \tag{6.140}$$

Before detonation pressure is given by the expression

$$p^{n+1} = K\left(\frac{1}{V^{n+1}} - 1\right), \tag{6.141}$$

where K is the bulk modulus. Once the explosive material detonates:

$$s_{ij}^{n+1} = 0 \tag{6.142}$$

and the material behaves like a gas.

For the practical application a reference is made to the author's book on

Explosion – Resistant Buildings – Springer Verlag, 2006

And brief results obtained on Twin Towers collapse in this chapter. It will be necessary to look into the following points in order to achieve good explosive burn:

1. Where the impact occurs, the F.E. mesh must be kept constant.
2. The characteristic element dimension must be found by checking all explosive elements for the largest diagonal.
3. The detonation points, if possible, must be within or the boundary of the explosive.
4. Check always the computed lighting time for the explosive material. The lighting time in Program LS-DYNA is kept at a negative number. This is true in Program BANG F-FIRE.

In order to the line of detonation must have sufficient number of detonation points in order to visualise the line fire.

6.11 Force or Load–Time Function

6.11.1 Introduction

Chapters 2 and 3 give useful data on force or load–time functions for various cases. On the basis of the *contact* method given in Sects. 4.4.4 and 6.5 along with the proposed finite-element analysis, Fig. 6.8 illustrates a comparative study of the load–time functions of a number of aircraft decelerating at different speeds and impacting flexible targets. The analytical divisions of various manufacturers have provided details of the finite-element mesh schemes, connectivity relations and material properties of various zones of aircraft. For large problems, an IBM 4381 with a CRAY-2 front-ended has been used in this text. Both crushed and uncrushed parts together with energy release or 'take-off' were examined. The flow of material across the interface was included in order to obtain the reaction load at the damaged zone for each aircraft. The engine was treated as a hard core at the appropriate level with different material properties. The hard core was assumed to represent the engine as a hard missile. Each case study consumed 7 h cpu (central processing unit) time. It therefore becomes a useful contribution towards the analysis of structures under aircraft impact.

The United Kingdom Atomic Energy Authority at Winfrith, Dorset (UK), carries out numerous tests on impact problems. They have a missile launcher which has the following characteristics:

(1) A maximum projectile energy of 3 MJ and a mass of 2,000 kg.
(2) Two barrels with diameters of 150 and 300 mm and three barrels (horizontal impact facility) of 0.5, 1.0 and 2.0 m.
(3) A projectile velocity in the range of 10–350 m s^{-1}.

Using the computer program HONDO-II, reaction loads were computed for three hemispherically-ended steel missiles with different stiffnesses impacting a concrete face. Figure 6.9 gives the force or load–time functions for three missiles with t/R ratios of 1, 0.28 and 0.1, which were verified experimentally on concrete slabs.

Figure 6.10 gives the load–time function for a semi-submersible subject to ice-floe impact.

Figure 6.11 gives a load–time function for a pipe impacting plain concrete blocks. The pipe had a diameter of 100 mm and a wall thickness of 5 mm. the block dimensions were $500 \times 500 \times 100$ mm of normal concrete of 50 N mm^{-2}. The velocity of the pipe was 10 m s^{-1}. Both experimental results and results from the ISOPAR program are plotted on Fig. 6.11. The bulk modulus method was used as a failure model for concrete. The block was divided into 8-noded, isoparametric, solid elements. Program contact was used along with program ISOPAR for computing the load–time function. The block was treated as rigid.

Figure 6.12 shows a pressure–time forcing function for a gas explosion for both vented and unvented cases.
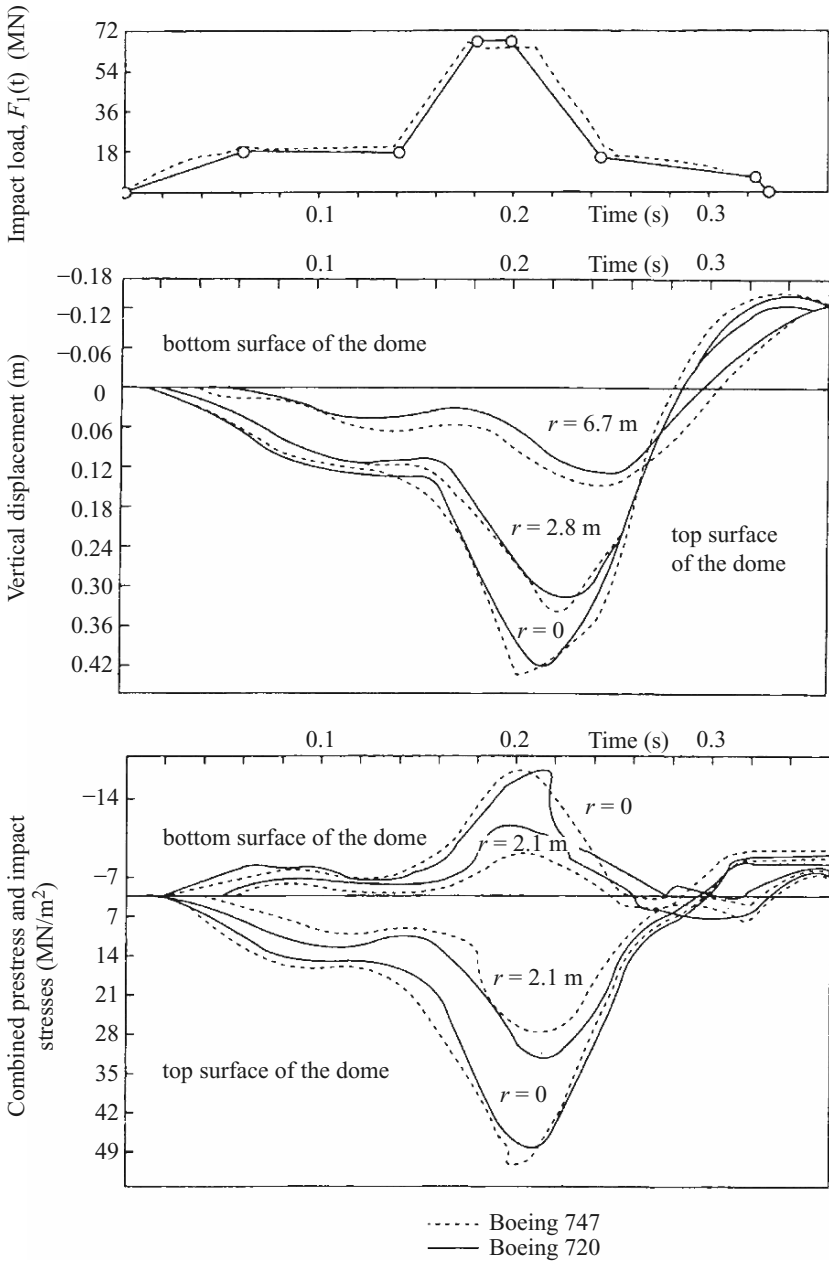
Fig. 6.8. Aircraft impact on flexible structures – a comparative study
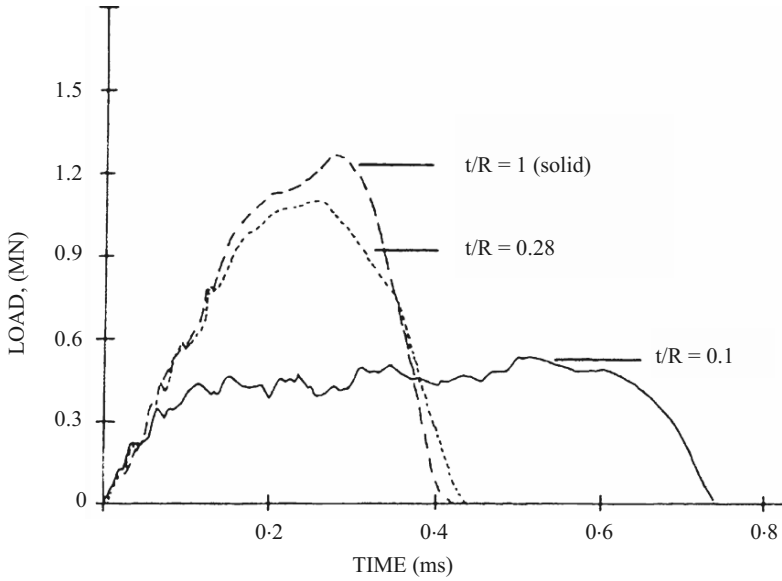
Fig. 6.9. Load–time functions for three hemispherically-ended steel missiles. $T =$ thickness, $R =$ radius. (Courtesy of A. Neilson, United Kingdon Atomic Energy Authority, Winfrith, UK)
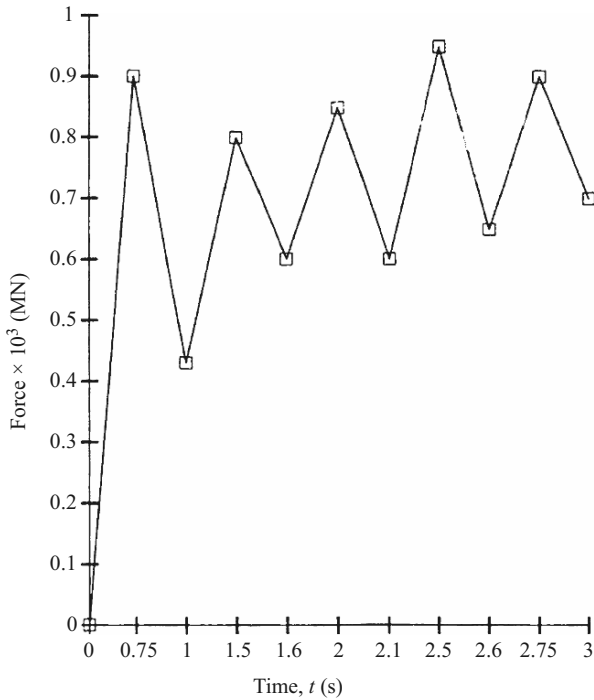
Fig. 6.10. Ice-floe impact: the load–time function for a semi-submersible
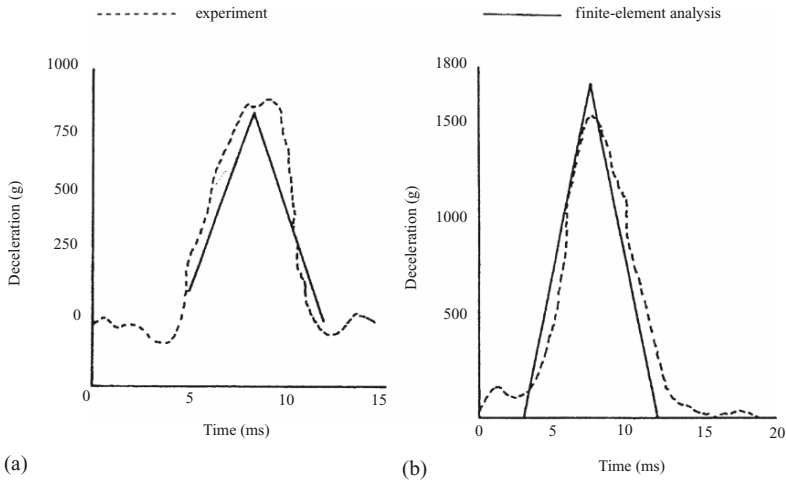
Fig. 6.11. A 100 mm diameter pipe impacting plain concrete (missile deceleration). (**a**) Direct fracture analysis; (**b**) plasticity and damage analysis
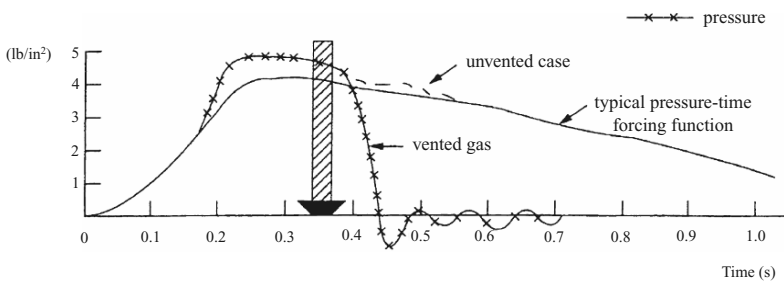
Fig. 6.12. Pressure–time relationship from a gas explosion. (courtesy of the British Ceramic Society.)

6.12 Finite-Element Mesh Schemes

A reference is made to Appendix I for Finite Element Mesh Generation Program. Finite-element analysis has been carried out for a number of case studies discussed in this book. They range from beams, slabs and panels to aircraft, ships, tanks, etc. in this section a typical finite-element mesh scheme for a battle tank is given in Fig. 6.13. This mesh scheme is used for collision and impact analyses. Where tanks have different geometric features, this standard mesh is modified to include them for the accurate prediction of damage due to impact of missiles, rockets, bombs, etc., exploding near or at the tank level.
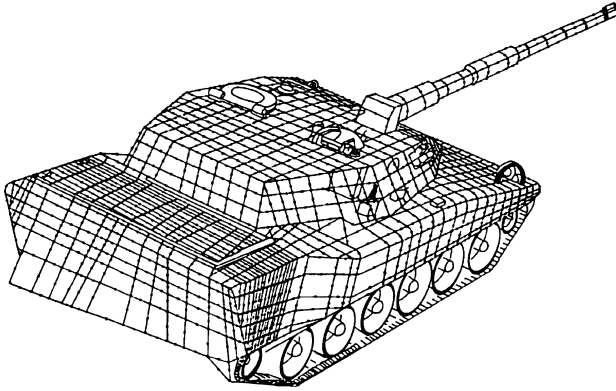
Fig. 6.13. Finite-element mesh scheme for a battle tank
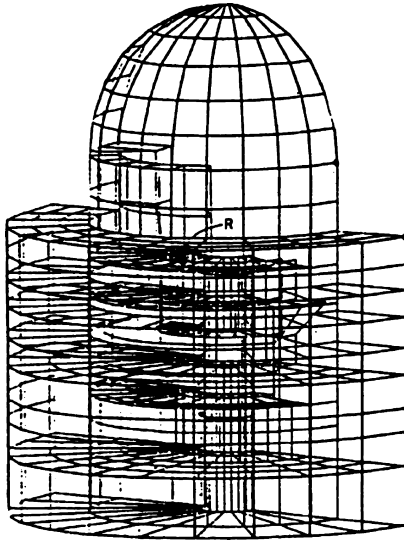
Fig. 6.14. Finite-element mesh scheme for PWR reactor vessel integrated with other buildings. (After Rebora)
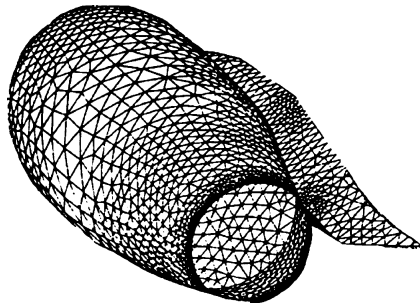
Fig. 6.15. Finite-element scheme for a fuselage of an aircraft as a dropped weight

Fig. 6.16. Finite-element mesh scheme for a chimney

Figures 6.14–6.16 show finite-element schemes for PWR reactor vessels supported by ancillary structures, aircraft fuselage for dropped weight analysis and a typical chimney for the impact analysis. Figure 6.17 gives finite-element analysis of a compartment having vents and is subject to gas explosion using
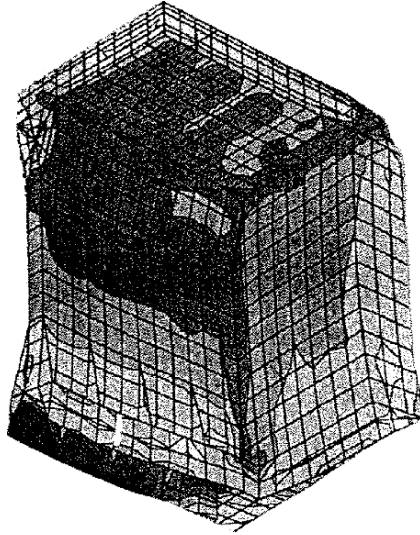
Fig. 6.17. Finite-element analysis of a gas explosion damage in a compartment with vents
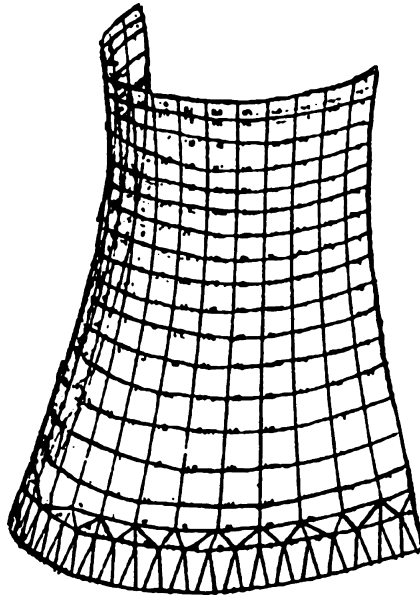
Fig. 6.18. Finite-element mesh scheme for a cooling tower

the pressure–time relationships given in Fig. 6.12. Figure 6.18 indicates a typical finite-element mesh scheme for a cooling tower discussed later in Chap. 7.

Impactzone and surface

Column
idealisation
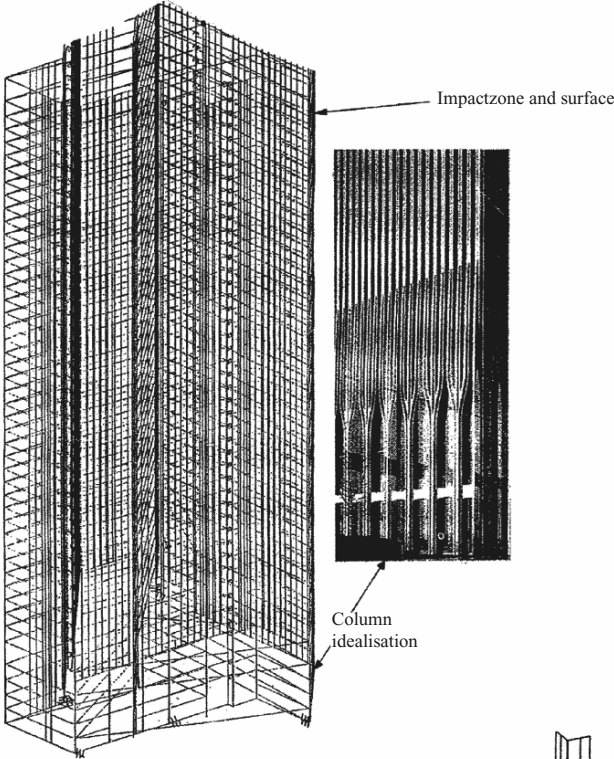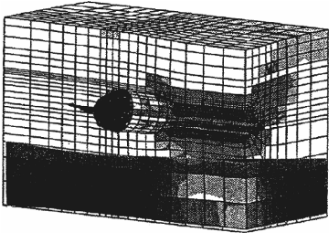
Finite element mesh scheme for the WTC-1 analysis
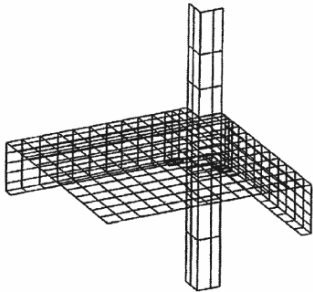
The finte element meshes

Mesh for the SID Finite Element Model

15.0 mm

Foam arm inserts, rib wrap and shoulder pads

Rubber neck, rib cushion pads and lower spine with aluminium hip bracket

Steel spine box, neck support and damper

Rib ballasts, rib bars, spine hinge, and mounting brackets

(b) Internal Componets

Ribs and damping material
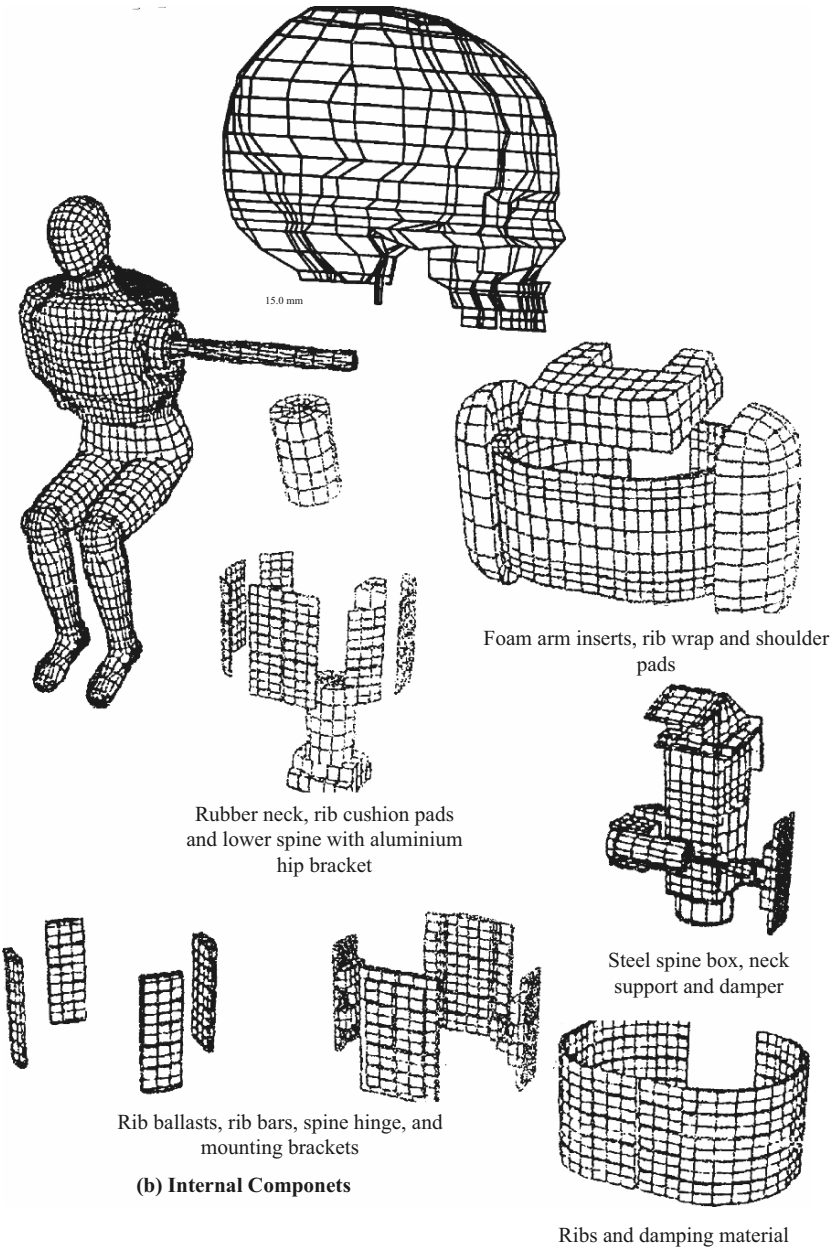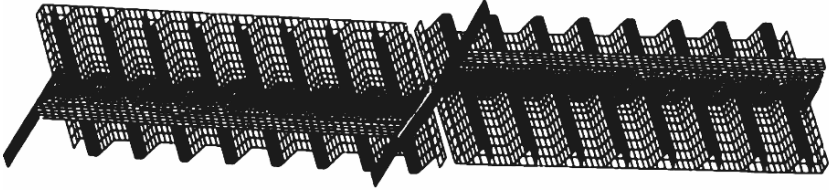
Numerical Modelling of the Orthotropic Steel Decks
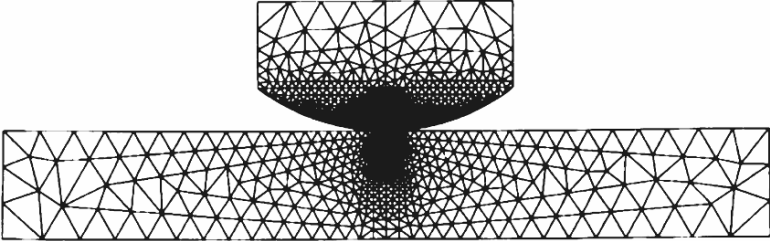
FE mesh of the global model
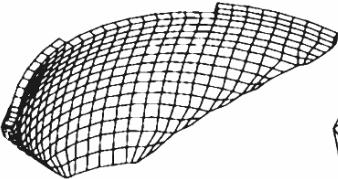
(a) Dam without foundation
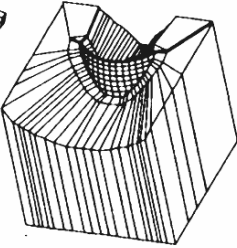
(b) Curved Dams with Foundations
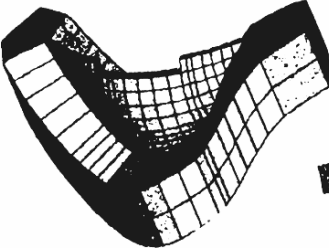
(c) Dams subject to bomb explosion impact
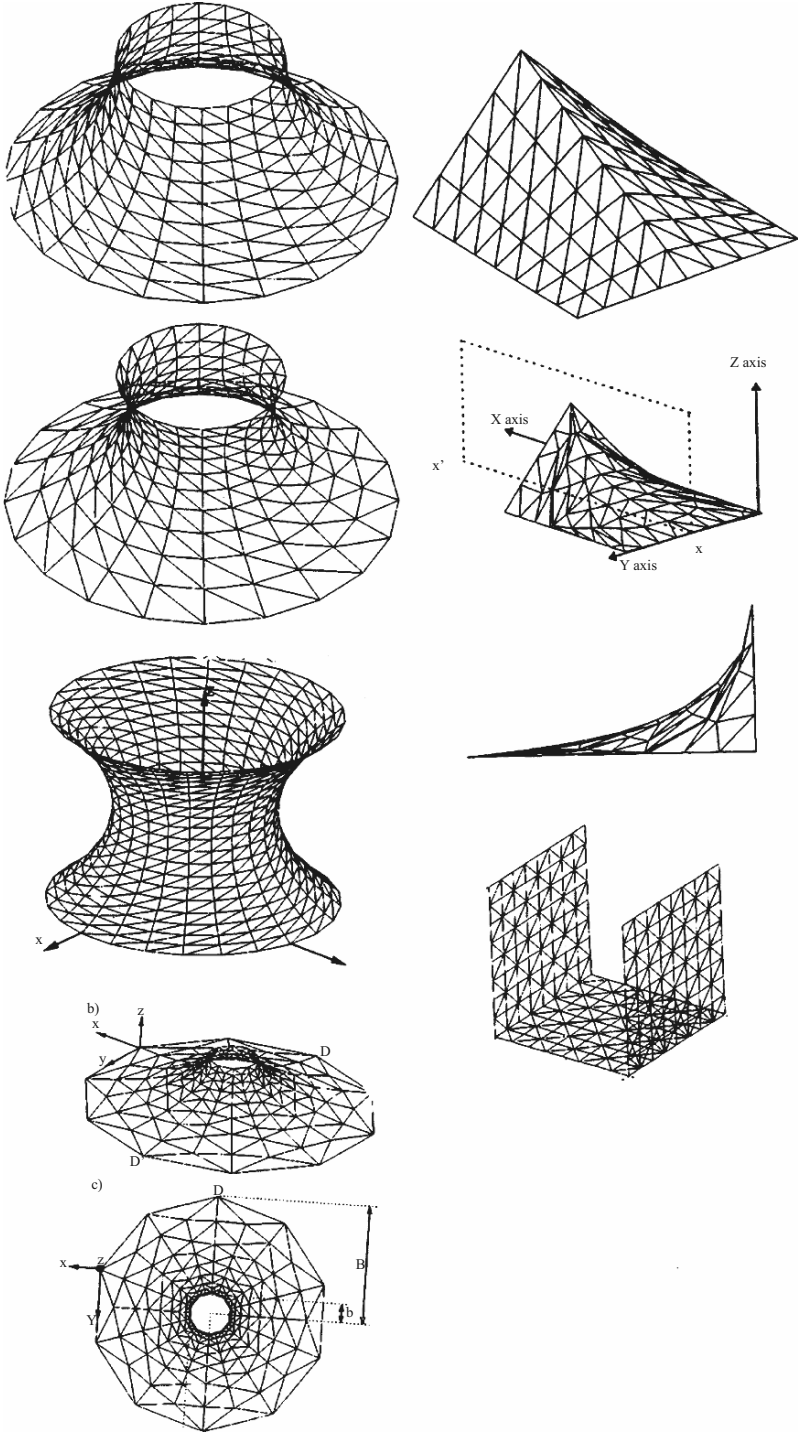
A

Steel and Composites

A.1 Steel Structures

A.1.1 Impact on Steel Beams

A number of steel beams under impact are analyzed. The beams are treated as rate-sensitive and the input energy of the impactor is assumed to be high. The strain effects (rate of strain occurring at a particular solution) for a particular state of strain are included. The impactor is assumed to strike a steel beam at mid-span. Figure A.1 shows a typical 8-node, isoparametric, finite-element mesh for a steel beam of rectangular cross-section. The material is assumed to be elastic/visco-perfectly plastic. Program ISOPAR is used to analyze the beam when subjected to a cone-shaped impactor. The following data are considered:

Plate A.1 gives the force-time relations with dominant frequency and modes. Acceleration-time relation for the beam is shown therein.

British beam

Span lengths, L: 3–10 m
Mass, M: 30–57 kg m^{-1} width
Impactor velocity, v_s: 1–25 m s^{-1}
Density of steel, ρ: 7,800 kg m^{-3} (386 kips in^{-3})
Young's modulus, E_s: 200 GN m^{-2} (30 × 10^6 lb in^{-2})
Yield stress, σ_y: 250 MN m^{-2}
Poisson's ratio, v: 0.3
Strain rate, $\dot{\varepsilon}$: 40.4 s^{-1}

American beam

$L = 30$ ft
Dead weight = 1,000 lb
MF = DLF = 1.4
$F_1(t) = 222.4$ kN (50,000 lb)

Finite elements: 8-noded isoparametric elements; 200
Assumed impact loads: triangular loads, load–time relations vary,

$$\text{typical ones } F_1(t)_{\max} = 222.4 \text{ kN } (50,000 \text{ lb})$$
$$t_r = 0.08 \text{ s}$$
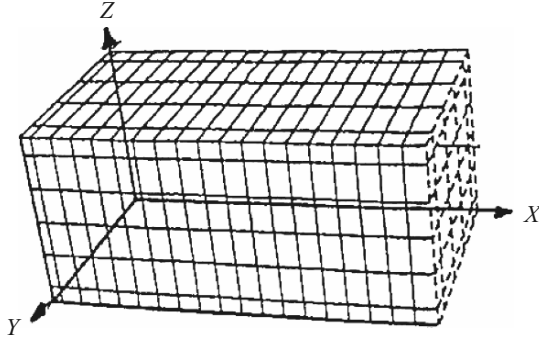
Fig. A.1. Finite-element mesh of a steel beam

The procedure for sizing up the beam using the US code for one case is as follows:

$F_1(t) + 20{,}000$ lb deadload
$L = 30$ ft; $1{,}000$ lb ft^{-1} deadload of the beam
The beam is assumed to be fixed at both ends
DLF $\not> 1.4$; $t_r/T \not< \frac{2}{3}$ (see the response chart in Chap. 3)

$$
\begin{aligned}
M_{\max} &= \frac{w_d L^2}{12} + \frac{F_D L}{8} + \frac{F_1(t)}{8}(\text{DLF}) \\
&= (1{,}000 \times 30^2/12) + (20 \times 30 \times 10^3/8) + (50{,}000 \times 30/8)1.4 \\
&= 412{,}500 \text{ in lb}
\end{aligned}
$$

$$
\begin{aligned}
Z_p &= (M \times 12)/\sigma_y = (412 \times 10^3 \times 12)/(75 \times 10^3) \\
&= 65.92 \text{ in}^3
\end{aligned}
$$

$$
\text{Section adopted } Z_p = 175.4 \text{ in}^3 \rightarrow 24\text{WF76}
$$
$$
I = 2{,}096 \text{ in}^4
$$
$$
K = 192EI/L^3 = 258{,}760 \text{ lb in}^{-1}
$$

Uniformly distributed load if treated separately (see tables in this section)

$$
K_L = 1.0
$$
$$
\text{Concentrated mass } K_M = 1.0
$$
$$
\text{Distributed mass } K_M = 0.37
$$
$$
\begin{aligned}
M_c &= \Sigma K_M M = (20{,}000 \times 1.0 + 30{,}000 \times 0.37)/(386 \times 1{,}000) \\
&= 0.081 \text{ kip s}^2 \text{ in}^{-1} \\
&= 0.081 \times 10^3 \text{ lb s}^2 \text{ in}^{-1} \\
k_e = kK_L &= 258{,}760 \times 1.0 \text{ lb in}^{-1} \\
&= 258{,}760 \text{ lb in}^{-1}
\end{aligned}
$$

$F_{cu} = 30$ MN/m^2

$230 \times 135 \times 30$
steel beam
Grade S355 UB
$P_y = 355$ MN/m^2

9.6

187.6

9.6

6.3

133.8

Typical section of an uncased
beam.

P

Lm

finite element scheme

170.9Hz
(m = 1)

207.5Hz
(m = 3)

256.3Hz
(m = 5)

305.2Hz
(m = 1)

341.8Hz
(m = 7)

683.6Hz
(m = 5)

dominant frequencies and their mode shapes.

force (kN)

600

400

200

0

0   1   2   3   4   5
time (×10^{-3} sec)

Applied impact

acceleration/P$_{max}$ (×10^{-5} G/N)

20

10

0

-10

-20

0   5   10   15   20
time (×10^{-3} sec)
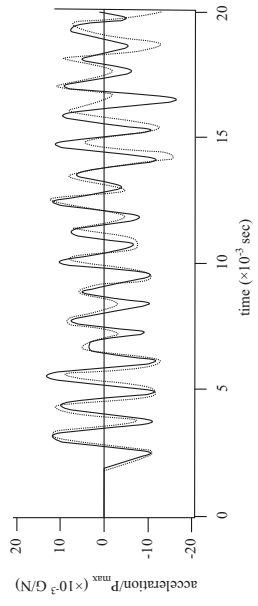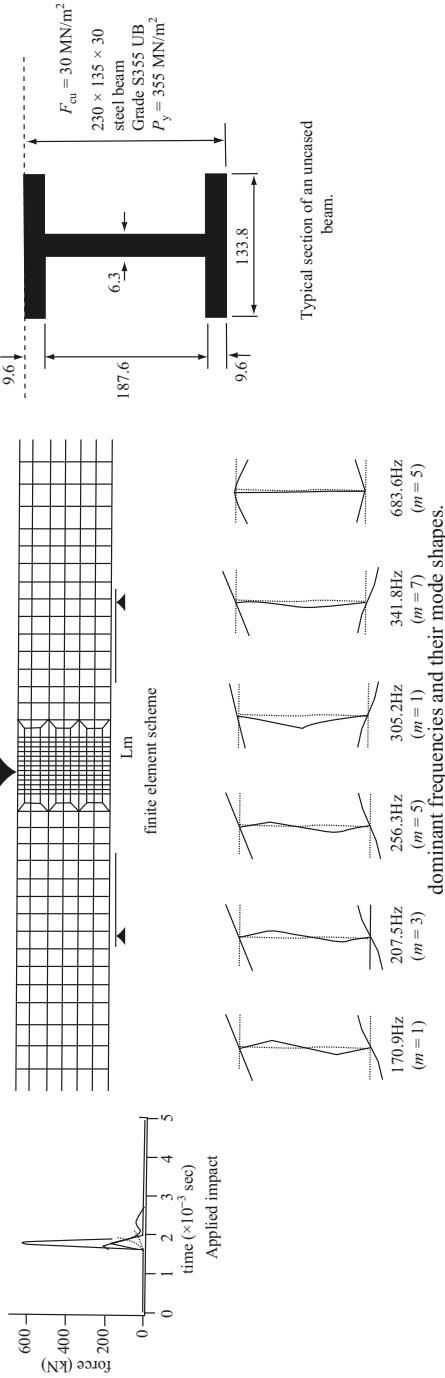
Plate A.1. Steel beam under impact

$$T = 2\pi\sqrt{(M_\mathrm{e}/K_\mathrm{e})} = 0.111\,\mathrm{s}$$
$$t_\mathrm{r}/T = 0.08/0.111 = 0.72$$
$$\mathrm{DLF} = 1.35$$
$$M_\mathrm{max}\ \text{(as above)} = \frac{1.35}{1.40} \times 412{,}500 = 397{,}767.86\,\mathrm{lb\,ft}$$
$$\sigma = M/Z_\mathrm{p} = 412{,}500/175.4 = 2351.8\,\mathrm{psi}$$

The beam size is adequate. If the rectangular size is adopted, then the depth taken is 24 in. The value of the height H varies from 1 (3 ft) to 9 m (27 ft).

For the finite-element analysis, the required depth at which the impact can occur due to a falling cone-shaped impactor can influence the failure zone. Figure A.2 gives a failure zone for the beam with a ratio of $L/H = 400$ under a triangular impact with $F_1(t) = 222.4\,\mathrm{kN}$ and $t_\mathrm{r} = 0.08\,\mathrm{s}$. In addition, various falling weights have been considered. Figure A.3 gives a relationship between δ/H and $K = M\nu_\mathrm{s}/(500 \times 10^6)H^2$ for different ratios of L/H for simple, fixed and continuous beams.
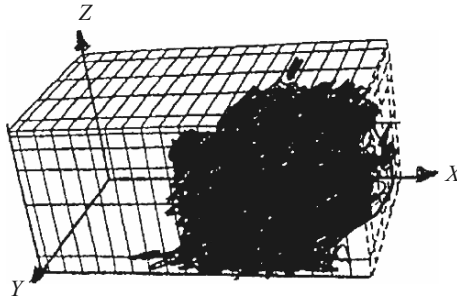
Fig. A.2. Plasticity and fracturing of a steel beam
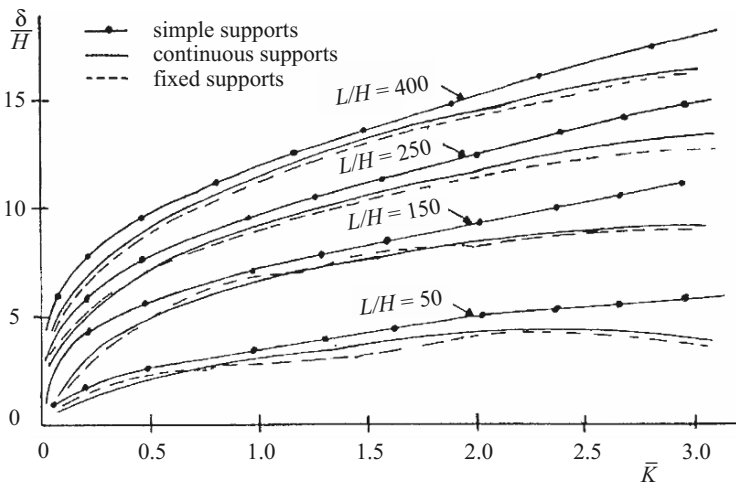
Fig. A.3. Dynamic displacement (δ = displacement; H = height)

A.1.2 Impact on Steel Plates

Plates are subject to impact and blast modes. A constant finite-element mesh scheme, suggested in Fig. A.4, has been adopted for solutions of various problems. All shapes of impactors are considered. The following summarizes the input data used in solving a number of problems:

General data

Impactors: 10 mm diameter, 35 mm length, flat-ended.
Plate thickness: rectangular and circular $20, 40, 60, 80, 100, 120, 140$ mm.
Velocity: 3–300 m s^{-1}.
Material property: yield stress 220–270 N mm^{-2}
                    failure strain 30–50%
                    ultimate tensile stress 269–414 N mm^{-2}

Perforation of Circular Steel Plates

A number of circular plates of cold-rolled mild steel were examined under the impact load. In the light of the current armoured plate thicknesses and armour chosen velocities, the finite-element analysis adopted gives useful relationships between the perforation thickness and the flat-ended impactor velocity giving bulge heights. These are given in Figs. A.5 and A.6. The displacement–time relation for these circular plates is given in Fig. A.7.

Flat Steel Plates (Square and Rectangular)

Flat plates are generally used in various armoured vehicles. Missiles and bombs are used to penetrate these plates. Finite-element analysis has been carried for the plates. Again, for the purpose of analysis, the finite-element mesh scheme shown in Fig. A.4b is adopted. A number of plate thicknesses used in the analysis are plotted against various velocities for a number of sizes and yields of bombs in Fig. A.8. The diameter, D, of the piercing bomb acts as an additional parameter in the evaluation of the perforation thickness t_p. The angle of attack ranges between $0°$ and $40°$. The pressure–time, displacement–time,

(a)   (b)
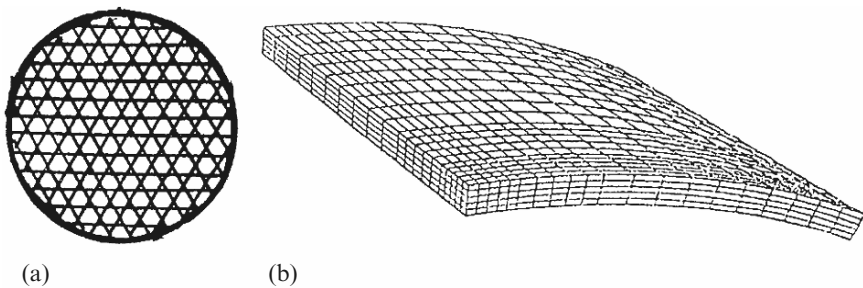
Fig. A.4. Finite-element mesh schemes for (**a**) circular plates and (**b**) rectangular plates
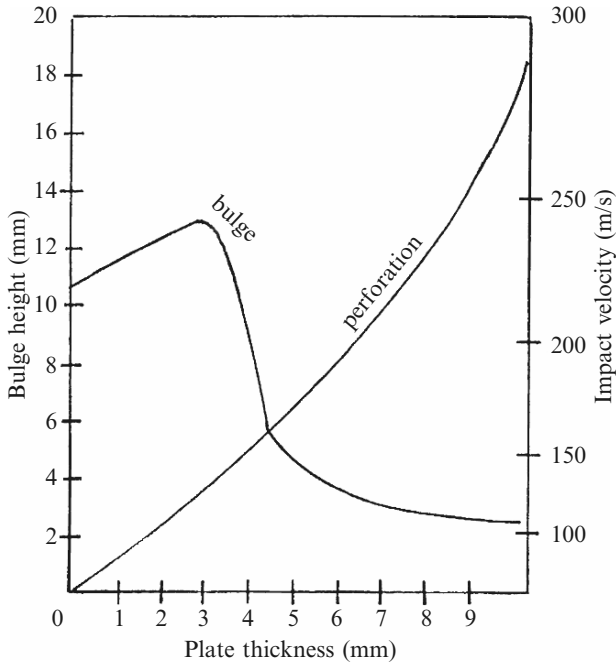
Fig. A.5. Bulge height and perforation versus plate thickness
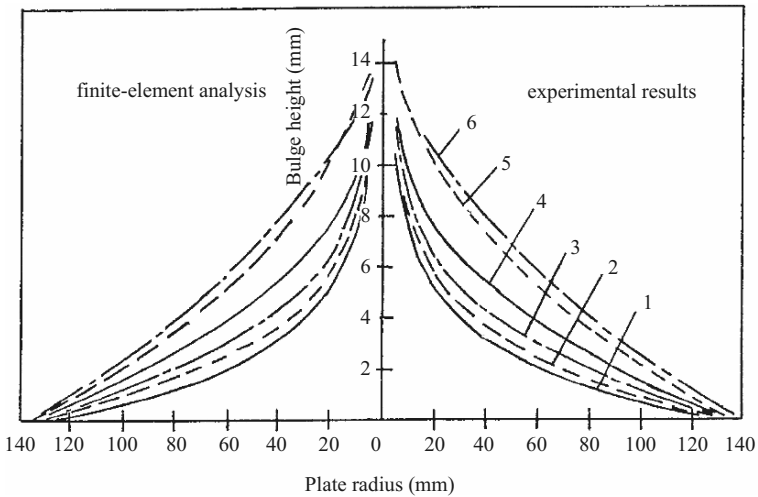
Fig. A.6. A profile of bulge height for various thicknesses and radii of plates (plate thicknesses: $1 = 2\,\text{mm}$; $2 = 3\,\text{mm}$; $3 = 4\,\text{mm}$; $4 = 5\,\text{mm}$; $5 = 6\,\text{mm}$; $6 = 8\,\text{mm}$)
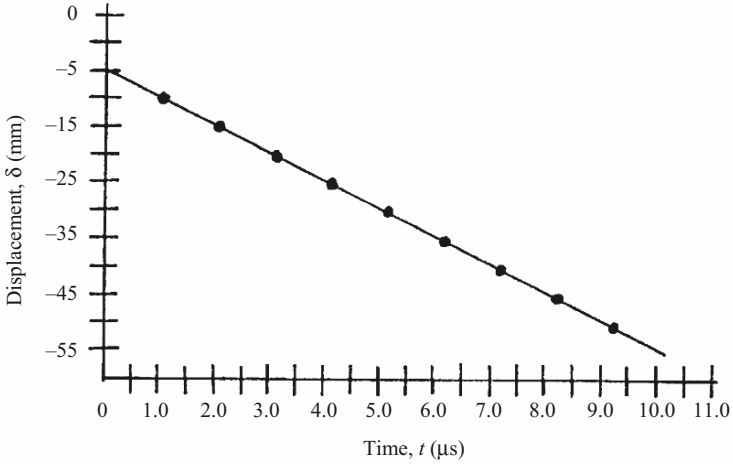
Fig. A.7. Displacement–time relationship
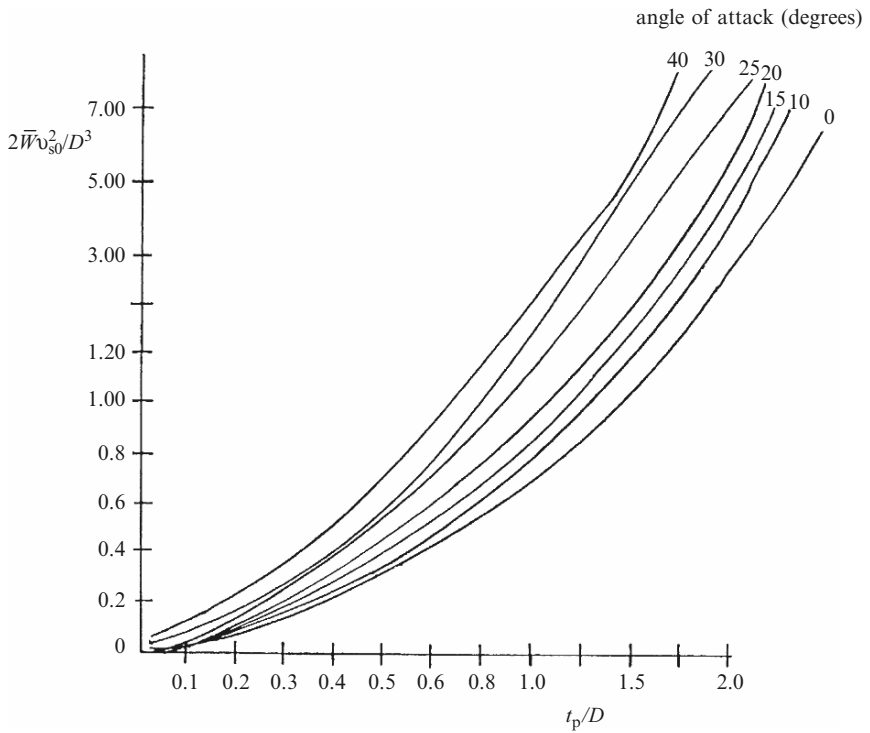
Fig. A.8. Perforation of steel armour plates by penetrating bombs

velocity–time, acceleration–time and strain–time relationships are given in
Figs. A.9–A.13. A typical three-dimensional, transient, dynamic finite-element
analysis was carried out on a steel nose cone impacting a hard steel plate
surface in a few milliseconds. The bomb is generally cone-shaped. The entire
scenario is well demonstrated in Fig. A.14.
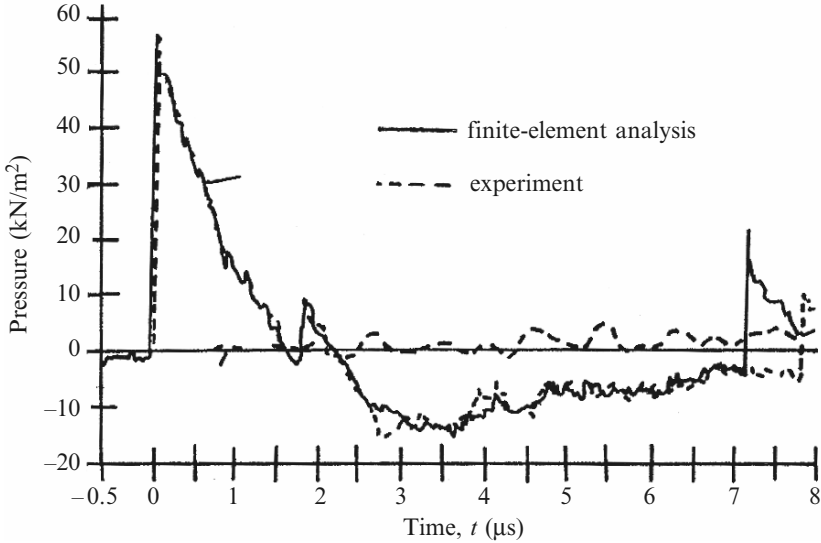
Fig. A.9. Pressure–time relationship
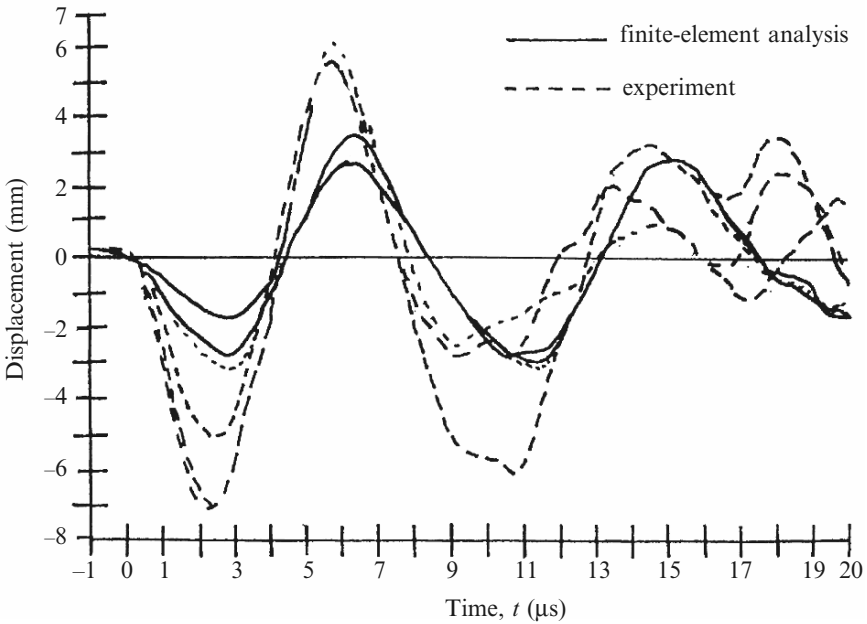
Fig. A.10. Displacement–time relationship
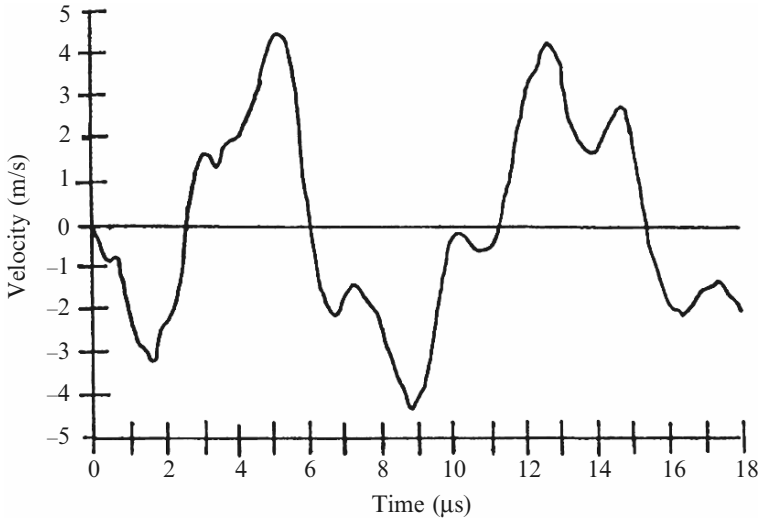
Fig. A.11. Velocity–time relationship
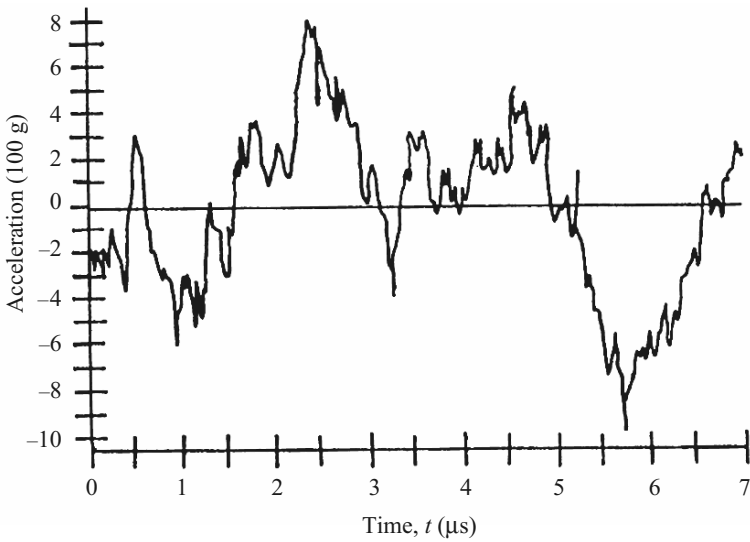
Fig. A.12. Acceleration–time relationship

Hammer Drop on Steel Plates

A simply supported rectangular flat steel plate $1.3\,\text{m} \times 1.3\,\text{m} \times 6\,\text{mm}$ thick was subject to a hammer drop at $5\,\text{m}$. The force–time relationship is given in Fig. A.15. The acceleration–time and the frequency responses are given in Figs. A.16 and A.17.
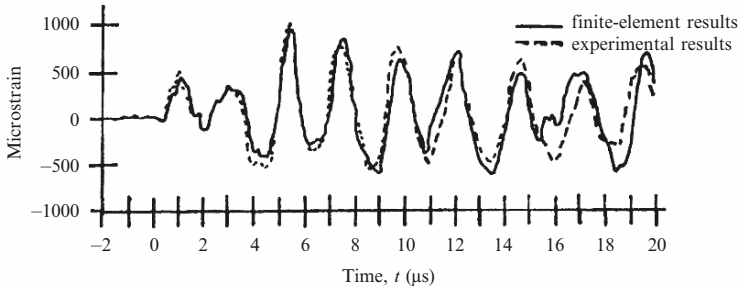
Fig. A.13. Strain–time relationship
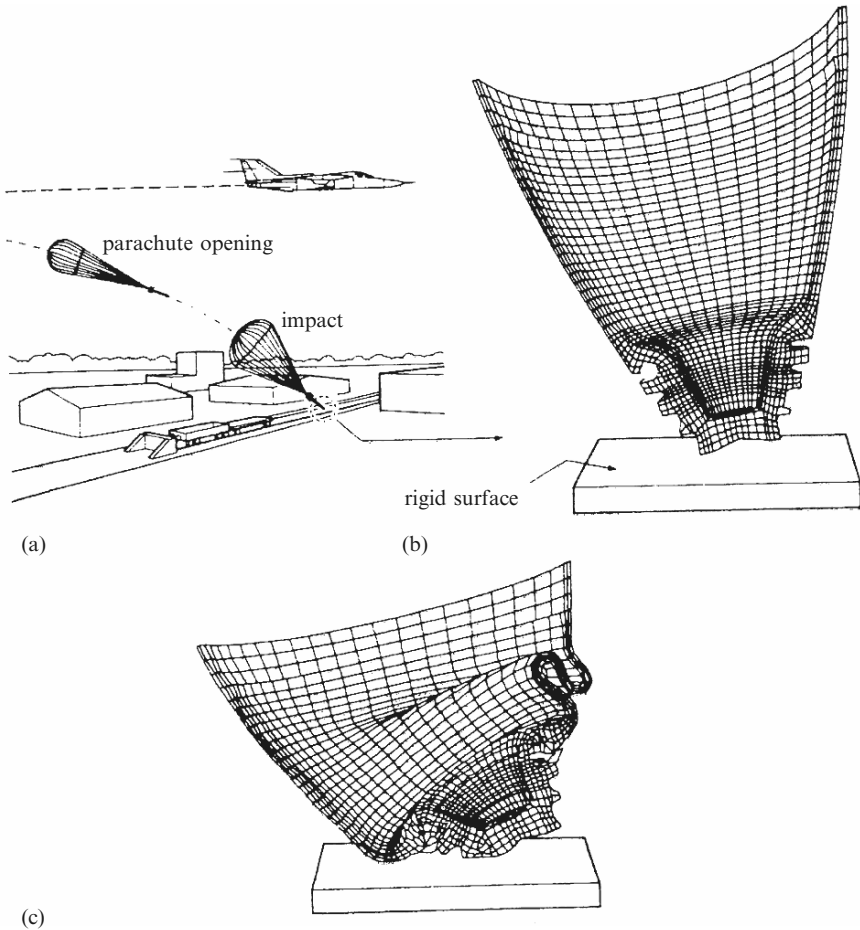
Fig. A.14. Impact crushing of a steel nose cone. (**a**) Delivery and impact of bomb; (**b**) initial mesh of nose cone (before impact); (**c**) deformed mesh (15 ms after impact) (after Chiesa and Callabressi [2.397])
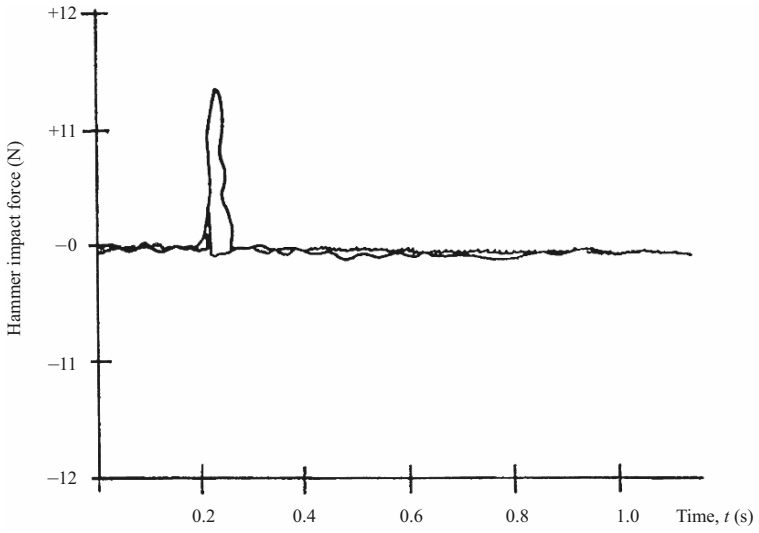
Fig. A.15. Force–time function
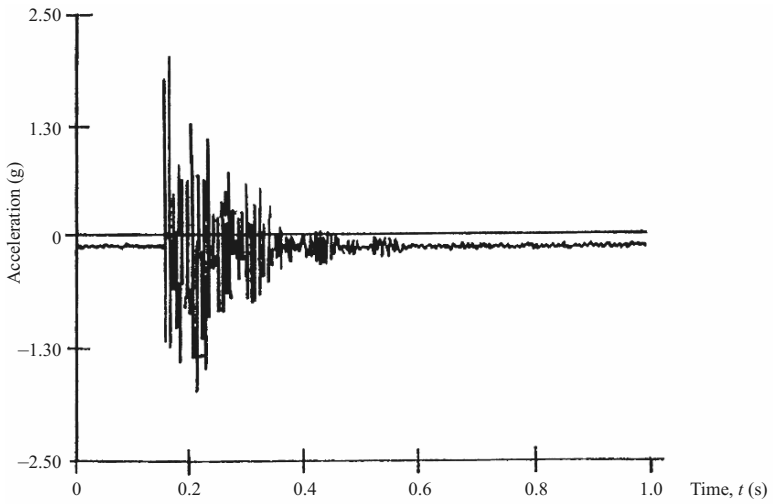
Fig. A.16. Acceleration–time response
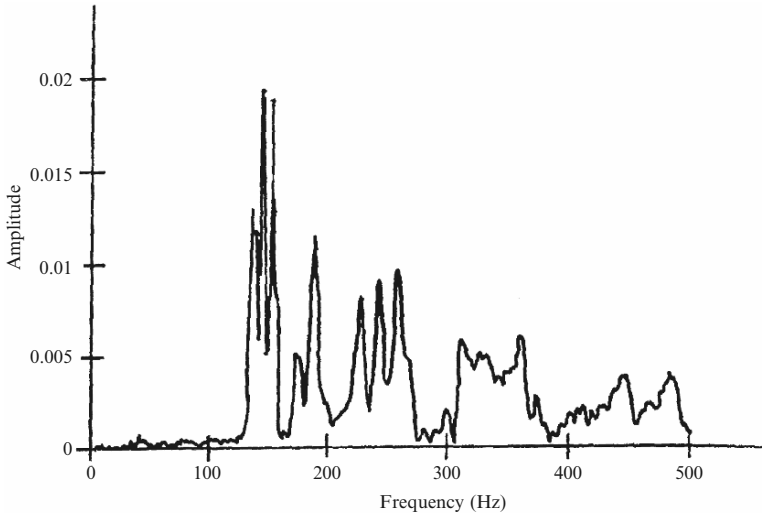
Fig. A.17. Amplitude–frequency response

Table A.1. Material properties

Material properties		Composite target
Young's modulus (tension), $kN\,m^{-2}$	6.895×10^{-6}	48.27×10^6
(compression), $kN\,m^{-2}$	5.980×10^{-6}	
Shear modulus, $kN\,m^{-2}$	2.500×10^{-6}	18.41×10^6
Tensile stress, $kN\,m^{-2}$	51.000×10^{-3}	
Compressive stress, $kN\,m^{-2}$	$13,960.000 \times 10^{-3}$	
Poisson's ratio	0.400	

A.2 Composite Structures

A.2.1 Composite Plates

Figure A.1 is considered for the finite-element analysis of composite plates. Where specific directions of fibres are suggested, these are treated as line elements either placed on the solid element nodes or in the body of the solid elements or dispersed elements.

Thornel 300 Epoxy Composite Plate

A tri-directional Thornel 300 (T300) epoxy plate is considered, subject to 50 mm diameter steel spheres with a velocity of $2\text{--}20\,m\,s^{-1}$. The plate thickness is assumed to vary from 5 to 25 mm for a circular or rectangular plate with radius or lengths 90 to 250 mm. Three fibres of the tri-directional T300 are

assumed to lie within 2 mm radius or square lengths. The following additional specifications are adopted:

Boundary conditions: plates simply supported, fixed and continuous. Figures A.18–A.20 show the relationship between impact force and impact velocity for fixed and continuous plates for various plate thicknesses. Figures A.4–A.23 show the results of the damaged plates.

Impact on a Polymethyl Methacrylate Plate (PMMA)

Shular has developed an experiment using a velocity interferometer for observing with great precision the particle velocity history of a point within PMMA material [2.398]. The PMMA projectile nose piece was 6 mm thick. The experimental results were correlated with the finite-element analysis performed by Bangash on ISOPAR [1.149].The additional finite-element data included in this analysis are

8-noded isoparametric elements: 135/spaced 800 μm
disk size: 220 mm
disk thickness: 3 mm
impact velocities: 0.06, 0.15, 0.30, 0.46, 0.64 mm μs^{-1}
shock speed: 2.834–3.349 mm μs^{-1}

These results are illustrated in Figs. A.24–A.26.
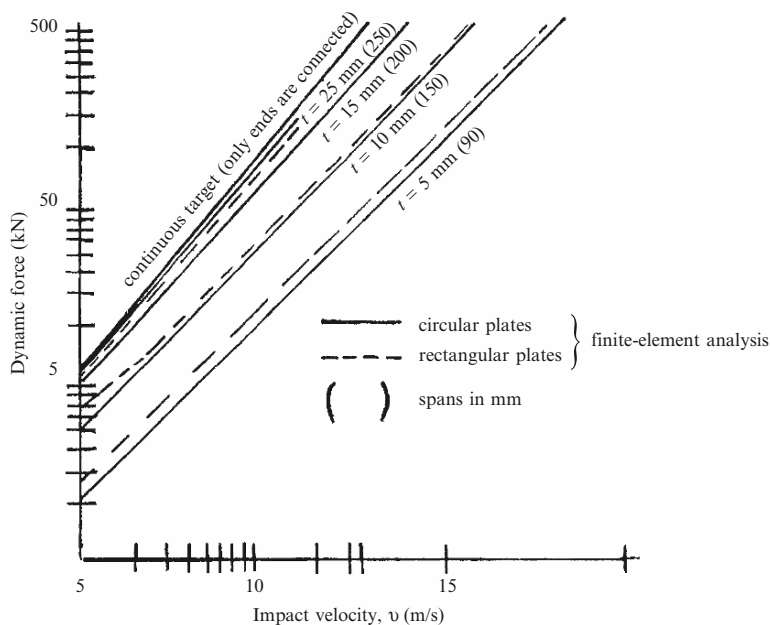
Fig. A.18. Plates fixed at boundaries
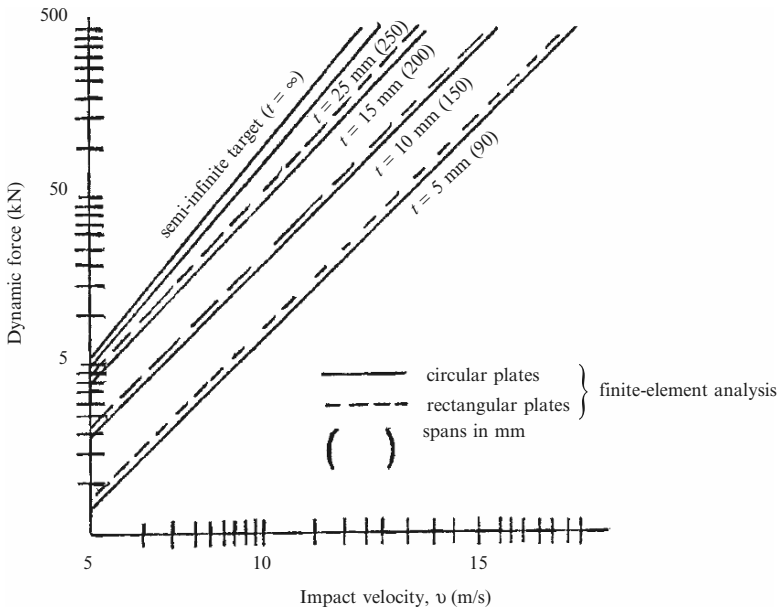
Fig. A.19. Plates fixed at boundaries
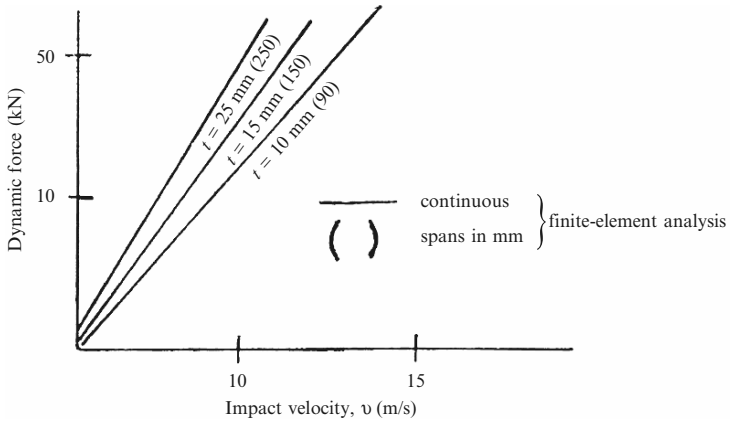
Fig. A.20. Plates fixed at boundaries
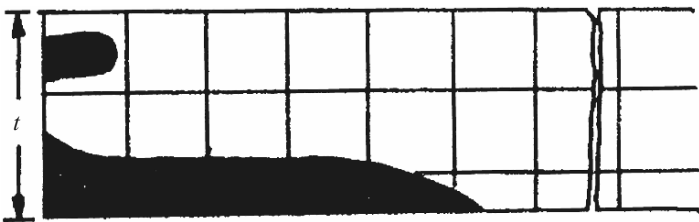
Fig. A.21. Simply supported T300 epoxy plate
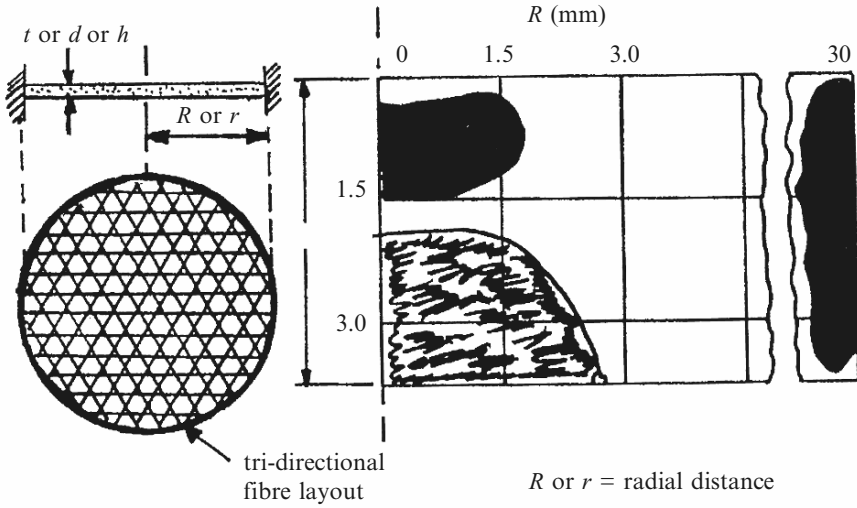
Fig. A.22. A T300 epoxy plate fixed at the edges

all dimensions in mm
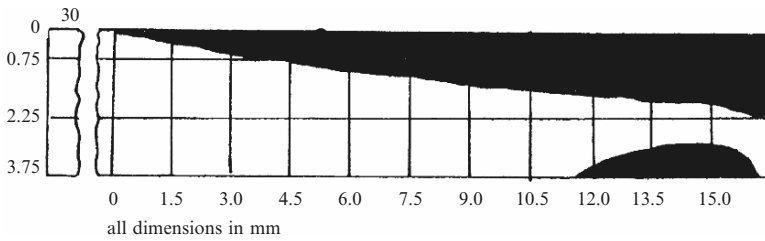
Fig. A.23. A T300 epoxy plate with continuous support
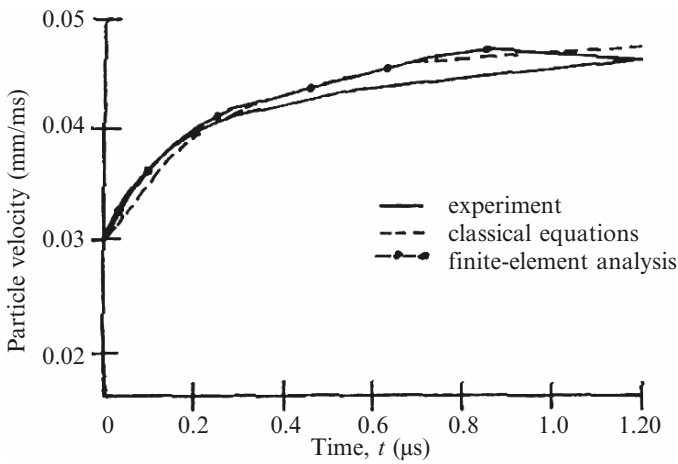
Fig. A.24. Comparison of observed and calculated particle-velocity histories for a $0.10\,\mathrm{mm\,\mu s^{-1}}$ impact (t = time after arrival)
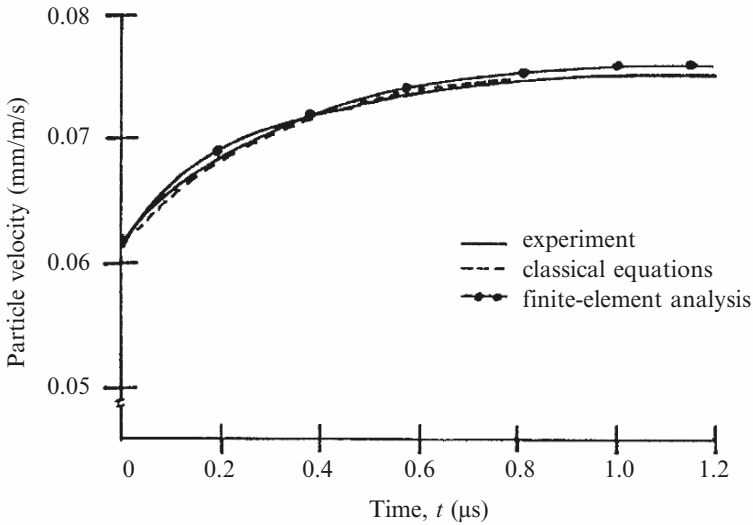
Fig. A.25. Comparison of observed and calculated particle-velocity histories for a $0.15\,\mathrm{mm\,\mu s^{-1}}$ impact ($t = $ time after arrival)
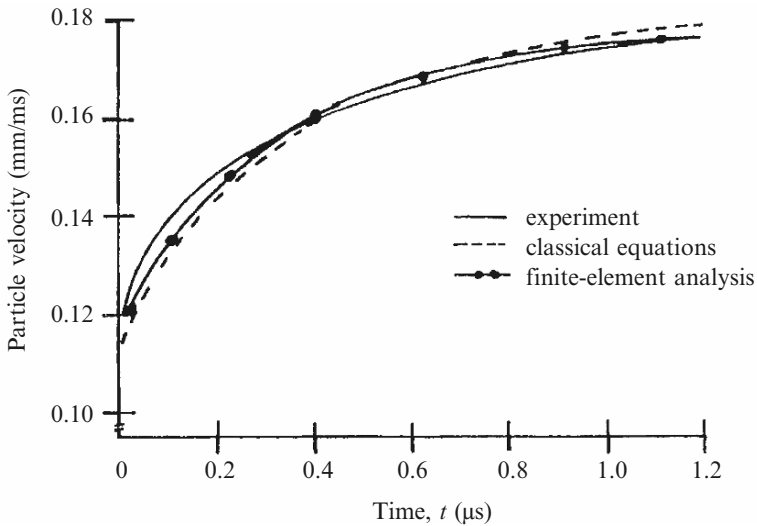
Fig. A.26. Comparison of observed and calculated particle-velocity histories for a $0.30\,\mathrm{mm\,\mu s^{-1}}$ impact ($t = $ time after arrival)

Impact on a Plexiglass Plate

A similar analysis to that used for a T300 epoxy composite plate (previous section) was carried out for plexiglass. The same number of elements were adopted, only fibres were excluded. Spherical and cone-shaped steel impactors were assumed. Impact velocities were assumed to be 2–$10\,\mathrm{m\,s^{-1}}$. Figures A.27
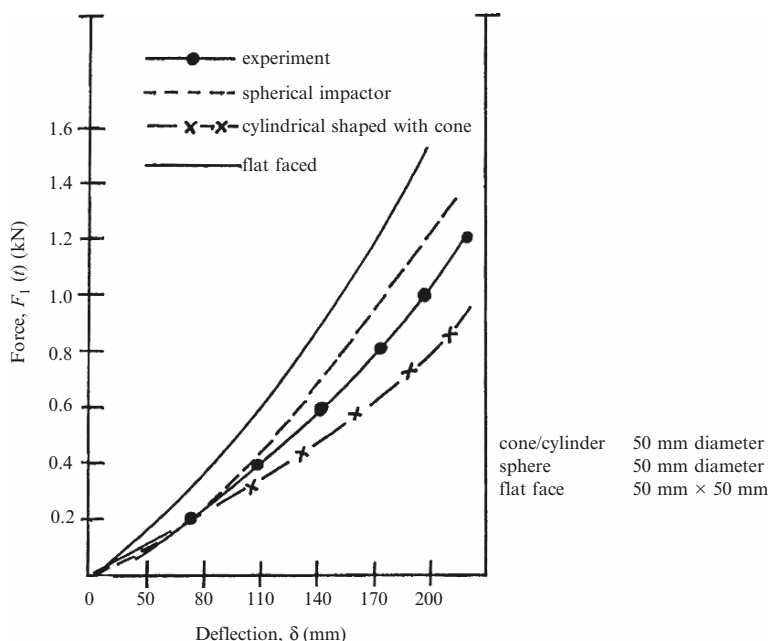
Fig. A.27. Load–deformation curve for plexiglass
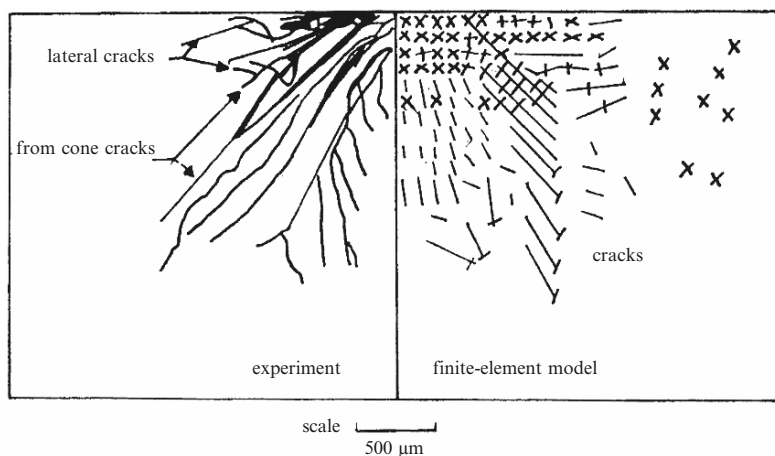
Fig. A.28. Cracking of plexiglass

and A.28 show the impact–deformation relationship and the final cracking of the plexiglass. Throughout the analysis the plate was assumed to rest on a solid support. The following additional specifications were included:

$$\text{impactor } E_{\mathrm{s}} = 200 \, \mathrm{GN \, m}^{-2}$$

$$F_{\mathrm{J}}(t) = 0.2\text{--}1.6 \, \mathrm{kN}; v_{\mathrm{s}} = 0.30$$

$$\text{plexiglass } E_{\mathrm{pg}} = 2.8 \, \mathrm{GN \, m}^{-2}; v_{\mathrm{pg}} = 0.396$$
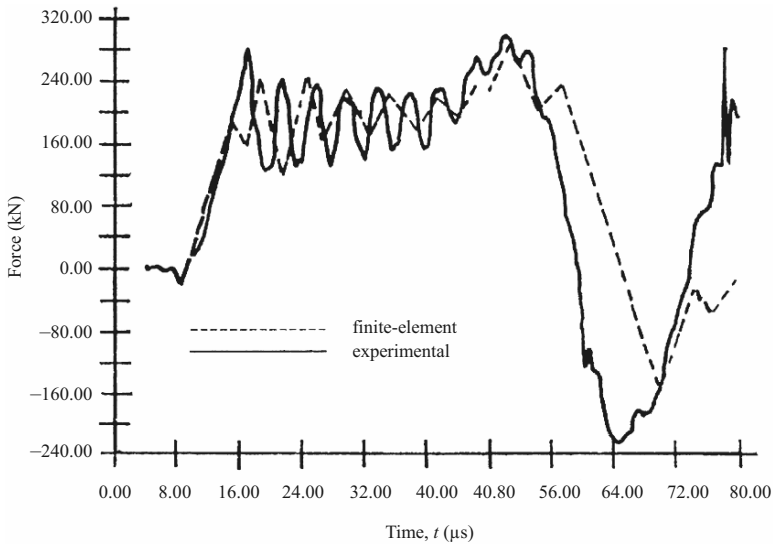
Fig. A.29. Force–time relationship for a carbon fibre/epoxy plate

Impact on a Carbon Fibre/Epoxy Plate

The effects of impact on a carbon fibre/epoxy plate depend on the type of fibre, the fibre/matrix bond strength and the fibre orientation. The purpose of this analysis is to evaluate the stress–strain behaviour of this plate and the final damage it receives under a 50 mm diameter spherical steel impactor. Carbon fibres were assumed to be of 7 μm diameter, placed in small spaces with dimensions equal to twice the fibre diameter. The plate was the same size as the plexiglass one. The force–time relationship is illustrated in Fig. A.29. The following data were considered:

Fibre modulus, E: 200 GN m^{-2}
Transverse modulus, E: 6.5 GN m^{-2}
Poisson's ratio, v: 0.32
Shear modulus, G: 4.5 GN m^{-2}
Tensile strength, σ_{yt}: 3.53×10^3 kN m^{-2}
Compressive strength, σ_c: 1.65×10^3 kN m^{-2}

The stress–strain relationship for the carbon fibre elements is shown in Fig. A.30. For various orientations of the fibres, the tension/compression strengths of the plate, displacement–time and acceleration–time relationships are shown in Figs. A.31–A.33. The crack patterns were exactly the same as shown in Fig. A.28 for plexiglass.
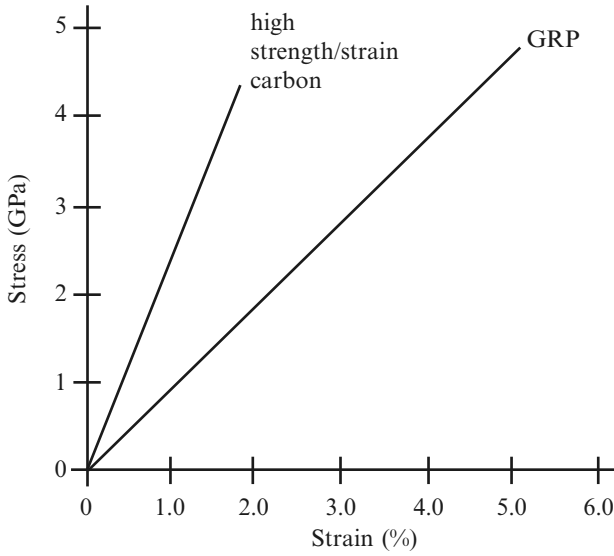
Fig. A.30. Stress–strain curves for carbon and glass reinforced plastic (GRP) plates
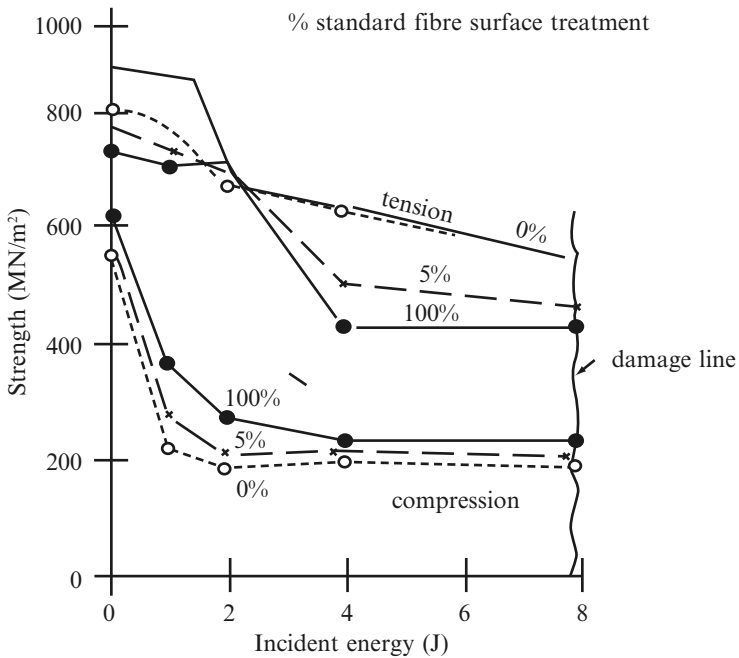
Fig. A.31. The effect of fibre surface treatment on the residual tension and compression strengths of carbon fibre epoxy $[(O_2 \pm 45)_2]_8$ laminates
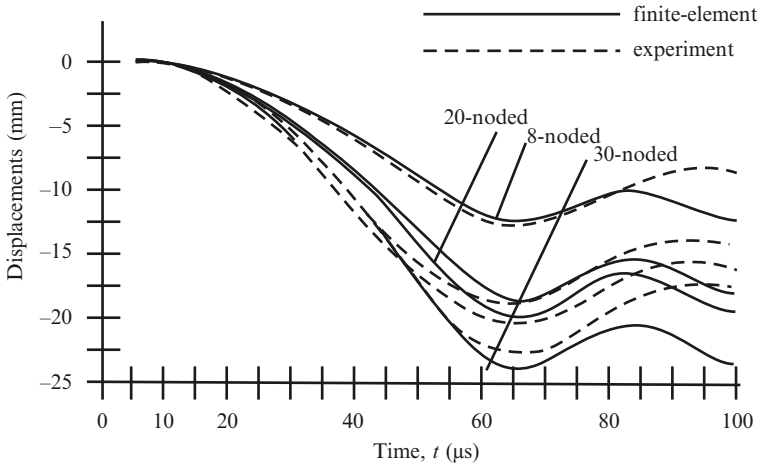
Fig. A.32. Displacement–time relationship
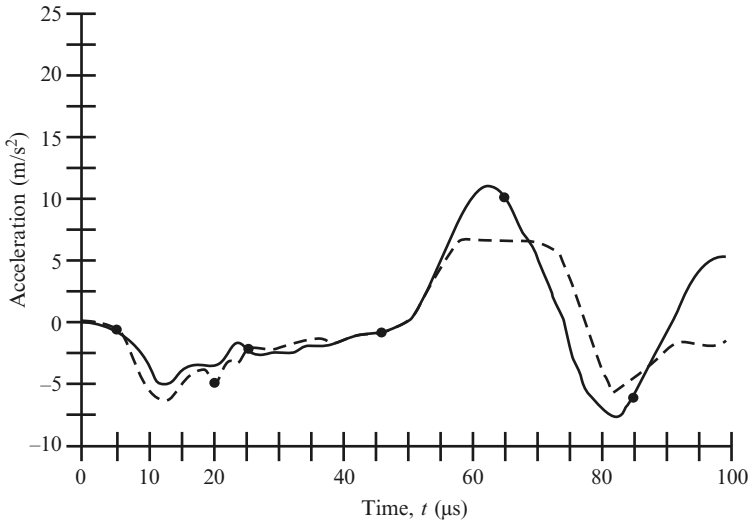
Fig. A.33. Acceleration–time relationship

Glass-Reinforced Plastic (GRP) Under Impact

The loading conditions applied to the GRP plates are similar to those applied to the carbon fibre/epoxy plates (previous section). On the basis of the loading conditions given in Fig. A.20 and the impact velocity of $9\,\mathrm{m\,s^{-1}}$, the crack pattern for a spherical impactor of $50\,\mathrm{mm^{-1}}$ was enhanced. The general distribution of the crack was similar to that of the carbon fibre/epoxy plate given in the previous section. The material is suitable for use in concrete to counter the effects of impact; this is described later in Sect. B.

A.3 Impact Analysis of Pipe Rupture

A.3.1 Experimental Data

The UK Atomic Energy Technology Centre (UKAEA) at Winfrith, Dorset, carried out tests on the response of pipes, typical of those used in the pressurized circuits of nuclear power plants, to impact by free-flying missiles from the disintegration of pressurized plants or rotating machinery. The horizontally placed target pipes were impacted by missiles imparting kinetic energies of up to $3\,\mathrm{MJ}$. All impacts occurred at the mid-span of the targets.

Data

Target pipes: length, L: $1.8\,\mathrm{m}$

   nominal bore, d: $150\,\mathrm{mm}$
   wall thickness, d_t: 11 and $18.2\,\mathrm{mm}$

Missiles: cylindrical mild steel billets with flat, conical and hemi-spherical ends.

   mass range: 1.75–$54.2\,\mathrm{kg}$
   impact velocity range: 46–$325\,\mathrm{m\,s^{-1}}$

Material property: yield stress σ_y

   Loughborough University flow stress concept $\sigma = K\epsilon^n$
   where $K = 1{,}000\,\mathrm{MPa}$; $n = 0.21$; $\epsilon = \text{strain}$
   $\sigma_\mathrm{y} = 330\,\mathrm{MPa}$

Cowper-symonds relation: $\sigma_\mathrm{y}/\sigma_\mathrm{yd} = 1 + |\dot{\epsilon}/\mathrm{D}|^{1/\mathrm{p}}$

where D and p are empirically determined constants, p = 5 and D in compression/s:

Wall	Lower yield stress	Upper yield stress
40	15,800	4,300
80	7,100	11,500

Relative perforation energies of different missile nose shapes:

flat-faced	1.0
hemi-spherically ended	0.4
90° including angle cone	0.3

Results from UKAEA Tests

Table A.2, from UKAEA, summarizes experiments on pipe targets. DYNA(3D) a three-dimensional finite-element analysis was used for pipe collapse analysis. A typical collapse analysis of the missile pipes for various time intervals is demonstrated in Fig. A.34. Pressure–time graphs and stresses/strains at different positions have been evaluated.

Table A.2. Summary of experiments on pipe targets (courtesy of UKAEA)

Test no	Missile Diameter (mm)	Mass (kg)	Impact velocity (ms⁻¹)	Target thickness (mm)	Boundary condition	Remarks
255	25.4 (flat end)	1.7	93	7.4	Clamped	Missile perforated front surface and struck rear surface at 44 ms⁻¹; deformation of missile prevented withdrawal
256	25.4 (flat end)	1.7	67	7.4	Clamped	Indentation of 21 mm on front surface
257	115 (flat end)	7.5	75	7.3	Clamped	Indentation of 65 mm on front surface; rear surface deflection 13 mm; flange weld split
258	115 (flat end)	7.37	108	7.2	Clamped	Indentation of 112 mm on front surface; rear surface deflection 26 mm; flange welds split
259	115 (flat end)	7.39	69	7.1	Suspended	Indentation of 60 mm on front surface; rear surface deflection 10 mm
260	115 (flat end)	7.29	104	7.1	Suspended	Indentation of 104 mm on front surface; rear surface deflection 30 mm
264	60 (flat end)	4.0	105	7.3	Clamped	Indentation of 64 mm on front surface; rear surface deflection 8 mm
265	60 × 4.9 wall (axial impact)	4.0	104	7.4	Clamped	Indentation of 67 mm on front surface; rear surface deflection 12 mm; missile length reduced by 13–672 mm
266	60 × 4.9 wall (axial impact)	4.0	136	7.1	Clamped	Indentation of 94 mm on front surface; missile length reduced by 20–665 mm
267	60 (flat end)	4.0	142	7.0	Clamped	Missile perforated front and rear surfaces
268	60	4.0	117	7.2	Clamped	Water-filled, 1 MPa internal pressure; missile perforated front surface forming 'keyhole'
269	60 (flat end)	4.0	112	7.2	Clamped	Water-filled, 1 MPa internal pressure; missile perforated front surface forming irregular hole

270	60 (flat end)	4.0	108	7.2	Clamped	Water-filled, 6 MPa internal pressure; missile perforated front surface forming 'keyhole'
271	60 (flat end)	4.0	108	7.6	Clamped	Water-filled, 13 MPa internal pressure; indentation of 35 mm on front surface and start of shear plug
272	60 (flat end)	4.0	108	7.7	Clamped	Water-filled, 13 MPa internal pressure; missile perforated front surface and initiated extensive crack
273	60 (flat end)	4.0	114	7.5	Clamped	Indentation of 82 mm on front surface; transient surface strains recorded
274	60 (flat end)	4.0	114	6.9	Clamped	Indentation of 82 mm on front surface; transient surface strains recorded
275	60 (flat end) (hemispherical end)	4.0	113	7.0	Clamped	Indentation of 93 mm on front surface; lateral extent of deformation zone – 150 mm
276	60 (flat end)	4.0	113	7.0	Clamped	Water-filled, 13 MPa internal pressure; missile just perforated front surface – disc wedged in hole – and was ejected from pipe at $\sim$40 ms^{-1}; transient surface deformation recorded
477	25.4 (flat end)	1.7	130	10.5	Clamped	Missile perforated front face and struck rear surface at 44 ms^{-1}; deformation of missile end ($\varnothing$ 26–27 mm) prevented withdrawal; 5 mm pimple on rear face
478	25.4 (flat end)	1.7	203	18.2	Clamped	Missile did not perforate, impact end bent through 90° and diameter increased to 35 mm; indentation of 11 mm max (6 to edge of contact mark) on pipe surface
479	25.4 (flat end)	1.7	129	10.7	Clamped	Missile perforated front face and struck rear at 51 ms^{-1}; deformation of missile end ($\varnothing$ 26 mm) prevented withdrawal; 10 mm pimple on rear face
480	25.4 (flat end)	0.6	325	18.6	Clamped	Missile did not perforate, impact end bent through 15 mm and diameter increased to $\sim$43 mm; indentation of 17 mm max (9 to edge of contact mark) on pipe surface

(*continued*)

Table A.2. (continued)

Test no	Missile Diameter (mm)	Mass (kg)	Impact velocity (ms^{-1})	Target thickness (mm)	Boundary condition	Remarks
481	60 (flat end)	4.0	180	10.6	Clamped	Missile perforated front and rear faces; residual velocity from front face ~74 ms^{-1}; impact and exit holes in line and showed clearly defined shear plug boundaries; missile diameter increased to 63 mm, residual length ~177 mm
482	60 (flat end)	4.0	236	18.6	Clamped	Missile perforated front and rear faces; impact at ~6° to normal; exit velocity not determined; missile diameter increased to 70 mm, residual length 175 mm
483	60 (flat end)	4.0	136	11.5 (nominal)	Clamped	Missile perforated front and rear faces; residual velocity from front face ~66 ms^{-1}; impact at ~7° to normal, entry and exit holes laterally displaced by ~60 mm; entry hole showed brittle tearing and cracking around whole perimeter, exit hole showed clearly defined shear plug boundary
484	60 (flat end)	4.0	144	18.6	Clamped	Missile partially penetrated front surface displacing shear plug between 3 and 11 mm (min/max); negligible missile deformation
485	60 (hemispherical end)	4.0	143	7.2 (nominal)	Clamped	Missile perforated front and rear surfaces; negligible impact end deformation; residual velocity from front face ~98 ms^{-1}
486	60 (90° conical end)	4.0	87	7.1	Clamped	Missile perforated front face and emerged 80–90 mm through rear face and wedged in; impact end flattened to ~∅8 mm
487	60	4.0	113	8.1	Clamped	Missile perforated front and rear surfaces; residual velocity from front face ~81 ms^{-1}; negligible impact end deformation; residual velocity from rear face ~60 ms^{-1}

488	60 (90° conical end)	4.0	67	7.2	Clamped	Missile perforated front surface but total penetration by conical section not obtained; missile rebounded; impact end flattened to ~Ø8 mm
489	80 × 10 (rectangle)	3.1	75	7.4	Clamped	Impact parallel to pipe axis; missile did not perforate – maximum indentation 36 mm
490	80 × 10 (rectangle)	3.1	84	7.2 (nominal)	Clamped	Impact ~5° skew to pipe axis; missile did not perforate – maximum indentation 46 mm; missile deformed to ~83 × 10 mm max
491	80 × 10 (rectangle)	3.1	99	7.2	Clamped	Impact ~10° skew to pipe axis; missile did not perforate – maximum indentation 55 mm; missile deformed to ~82 × 11 mm max
492	80 × 10 (rectangle)	3.1	143	7.2 (nominal)	Clamped	Impact parallel to pipe axis; missile perforated front face; missile deformed to 85 × 12 mm
493	60 (oblique impact)	4.0	180	7.3	Clamped	Missile perforated pipe completely; a section of wall with developed surface ~170 × 60 mm removed completely; indentation to initiation of fracture ~50 mm; knockback of missile edge ~6 mm
494	60 (oblique impact)	4.0	120	7.0	Clamped	Missile did not perforate, some surface cracks in skid mark; knockback of missile edge ~4 mm
495	150 × 18 (lateral impact)	43.0	78	7.4	Clamped	Missile did not perforate pipe; impact zone indentation 231 mm and section almost completely flattened; pull-in forces in target pipe destroyed edge support system; missile showed no apparent deformation
496	150 × 7.2 (lateral impact)	34.9	49	7.5	Clamped	Missile did not perforate pipe; impact zone indentation 55 mm; imparting pipe totally flattened and welded rear supports in good contact with it
497	150 × 11.0 (lateral impact)	37.5	46	7.4	Clamped	Missile impacted at ~20° to 'vertical' axis and did not perforate pipe; impact zone indentation 95 mm; impacting pipe flattened to Ø 125/140 mm

Table A.2. (continued)

Test no	Missile Diameter (mm)	Mass (kg)	Impact velocity (ms⁻¹)	Target thickness (mm)	Boundary condition	Remarks
498	150 × 11.0 (axial impact)	44.0	78	7.3	Clamped	Missile did not perforate pipe; maximum indentation 198 mm and no indication of plugging failure; negligible deformation of missile
499	150 × 18 (axial impact)	54.2	106	10.9	Clamped	Missile did not perforate pipe; maximum indentation 350 mm; central section under impact zone flattened and start of plugging failure visible, split formed on one portion of impact mark; negligible deformation of missile but sabot collapsed; pull-in forces sufficient to strip prepared welds on both end flanges
500	100 × 6 (axial impact)	29.5	70	7.1	Clamped	Missile did not perforate pipe; maximum indentation 150 mm; indication of plugging failure initiation; negligible deformation of missile

Time = 0.0 μs

Total collapse of missile pipe (time = 3.7 μs)
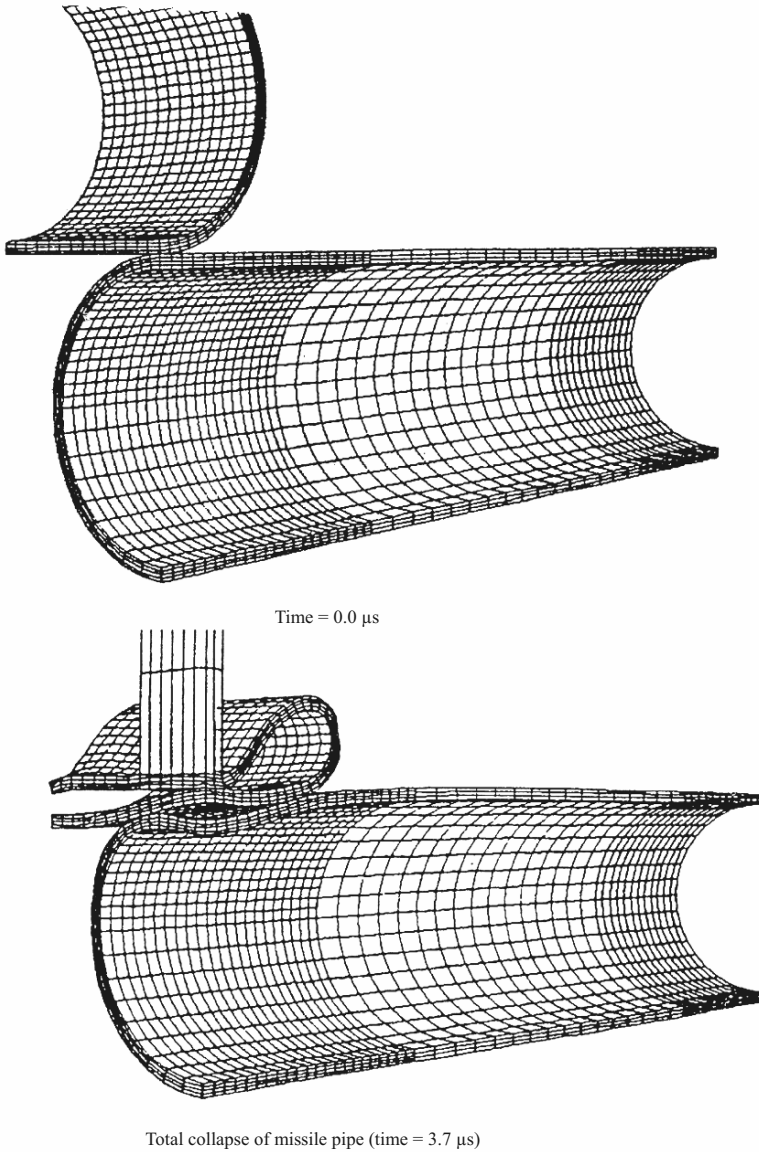
Fig. A.34. Pipe collapse analysis at various time intervals (ms = microseconds) (courtesy of the UK Atomic Energy Technology Centre, Winfrith, Dorset)

Pipe Whip Analysis

Pipe whip analysis is extremely important in areas of sensitive structures. In nuclear power plants, pipe rupture is a possibility. Impact forces are generated

at points of pipe-to-pipe and pipe-to-wall impact, as demonstrated by the UKAEA experiment/analysis (see Fig. A.34). The author has used a multi-level, sub-structuring technique in the ISOPAR program (also using material non-linearities, a plasticity model and time integration) to examine pipe whip. The following specifications were adopted:

Pipe dimensions outside: 100 mm

Thickness: 18.2 mm

Elbow radius: 143 mm

Temperature: 320° C

Maximum impact force: 750 kN

Whipping time: 10.5 μs

Velocity of impact: $32 \, \text{m/s}^{-1}$

Figure A.35 shows the finite-mesh scheme for the pipe rupture analysis at the elbow mid-point. The force–time relation is given in Fig. A.36, together with the crush.

(a)   (b)
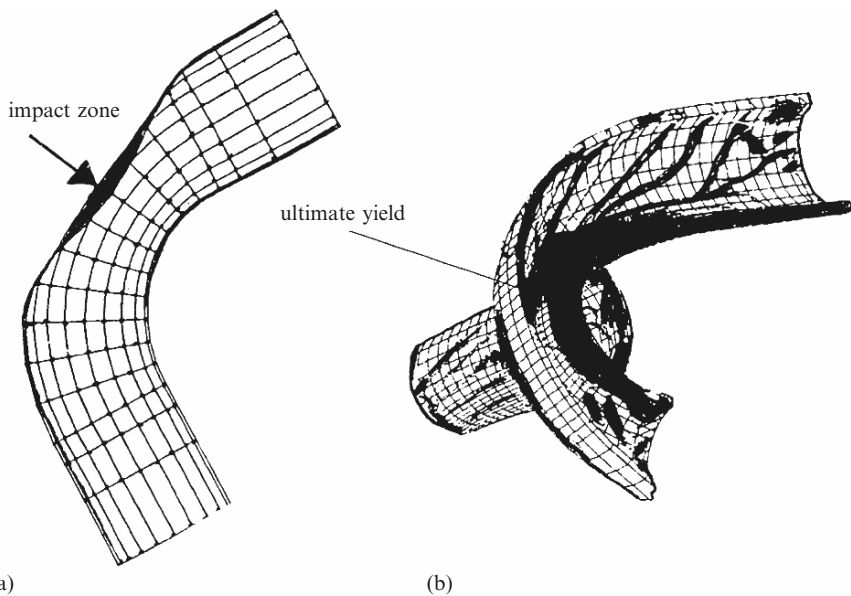
Fig. A.35. Finite-element mesh scheme and final damage. (**a**) Top pipe under impact; (**b**) top and bottom pipes whipping
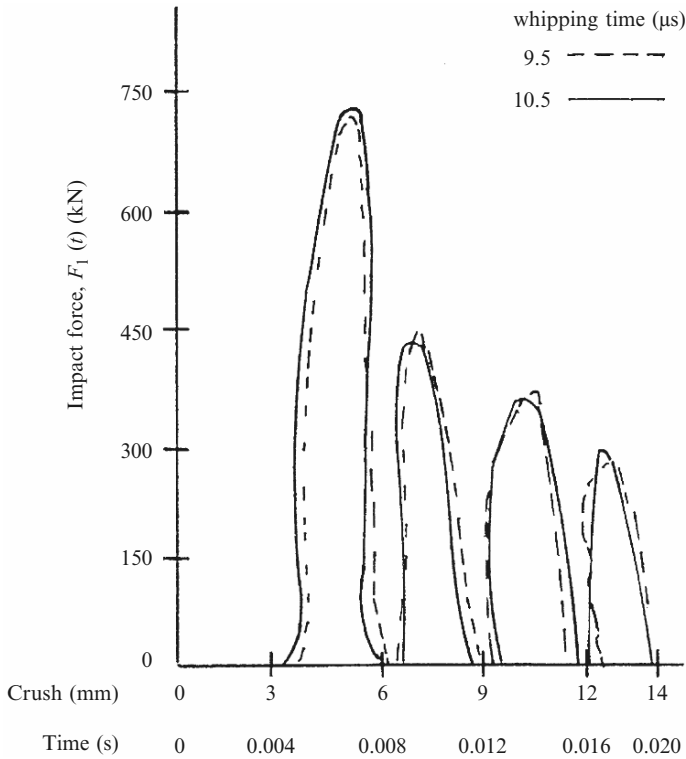
Fig. A.36. Force–time versus pipe crush

A.4 Explosions in Hollow Steel Spherical Cavities and Domes

A.4.1 Steel Spherical Cavities

Five hollow steel spheres of various cavities and thicknesses of the type shown in Fig. A.37 were examined after explosion caused by a spherical charge. The spheres were of the elastic-visco plastic type, for which the constitutive equation is:

$$\dot{\epsilon}_{ij} = (\dot{S}_{ij}/2G) + (1/2\eta)[1 - (k/I_2')]S_{ij},$$

where $\dot{\epsilon}_{ij}$ = deviator strain rate, k = strain hardening parameter, S_{ij} = deviator stress, I_2' = second invariant of stress deviator, $\dot{S}_{ij}$ = deviator stress state, G = shear modulus, η = viscosity coefficient.

The following data were used:

$$\lambda = \sqrt{[(4G + 3K)/3]} = 52.28 \times 10^{-5} \,\mathrm{mm\,s^{-1}},$$
$$\delta t = 4 \times 10^{-5} \,\mathrm{s}; E = 200 \,\mathrm{GN\,m^{-2}}; \nu = 0.3,$$
$$G/\eta = 1 \times 10^{6} \,\mathrm{s^{-1}}; r/R = 1.5, 2, 3, 5, \infty.$$
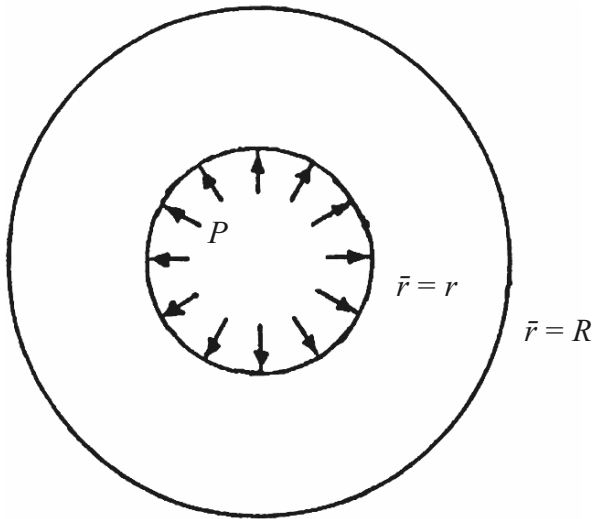
Fig. A.37. Explosion in the cavity of a sphere
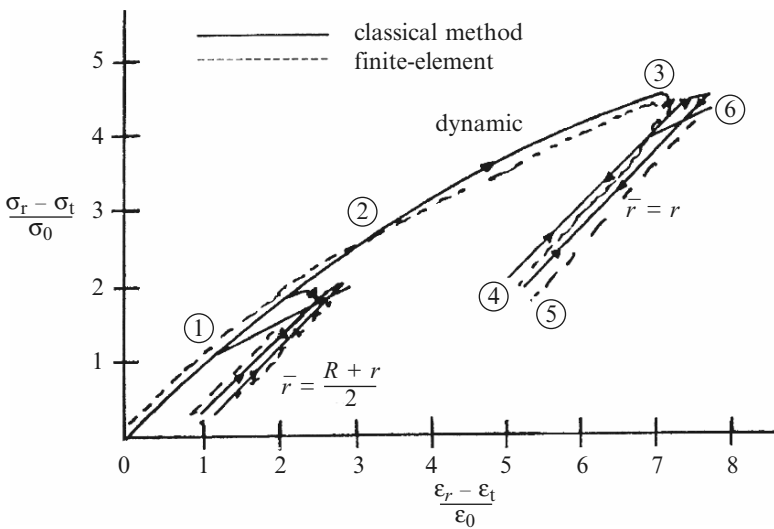
Fig. A.38. Non-dimensional stress–strain history; σ_t, σ_r = stresses in the tangential and radial directions, respectively; ϵ_t, ϵ_r = strains in the tangential and radial directions, respectively and σ_0 = average stress

Fifty pounds of explosive material with a spherical shape propagation were used. The associated flow rule and the von Mises failure criteria were adopted. A time of 2 s was considered for the total explosion duration.

Figure A.38 shows the stress–strain history from a classical approach in the radial direction at two locations based on dynamic analysis. Twenty-noded
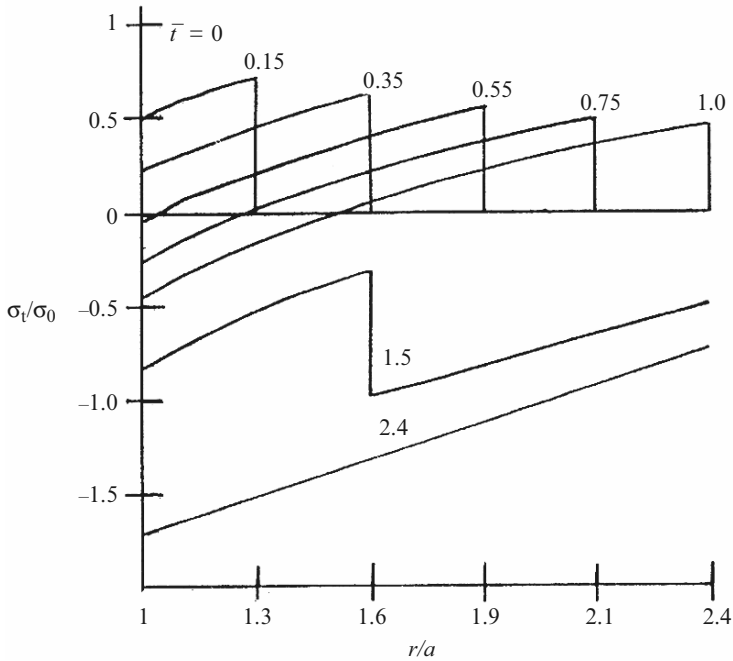
Fig. A.39. Time-dependent tangential stresses after explosion

isoparametric elements were adopted for the analysis. The total number of elements was 180. As seen, the visco-elastic strain increases along the curve 1, 2, 3. There is a shear drop at point 3 and the deformation seems to be elastic along the 3–4 line. The deformation is visco-plastic along the 3–6 line. A perfectly plastic material seems to be visco-plastic owing to the longer time for dynamic and static stress–strain curves when they intersect. The time-dependent tangential stresses which develop after the explosion are shown in Fig. A.39. Figure A.40 shows the time-history for tangential stresses at the cavity of the shell for various R/r ratios.

A.4.2 Steel Domes

Finite-element analysis was carried out on explosions in a steel spherical dome. Again, a 50 lb explosive with spherical propagation was assumed. The deformed shape for 2 s is shown in Fig. A.41, when the explosion occurs at 40 m from the centre of the dome of radius 80 m. The results of this analysis must remain classified information. The damage due to the explosion is also shown in Fig. A.41.
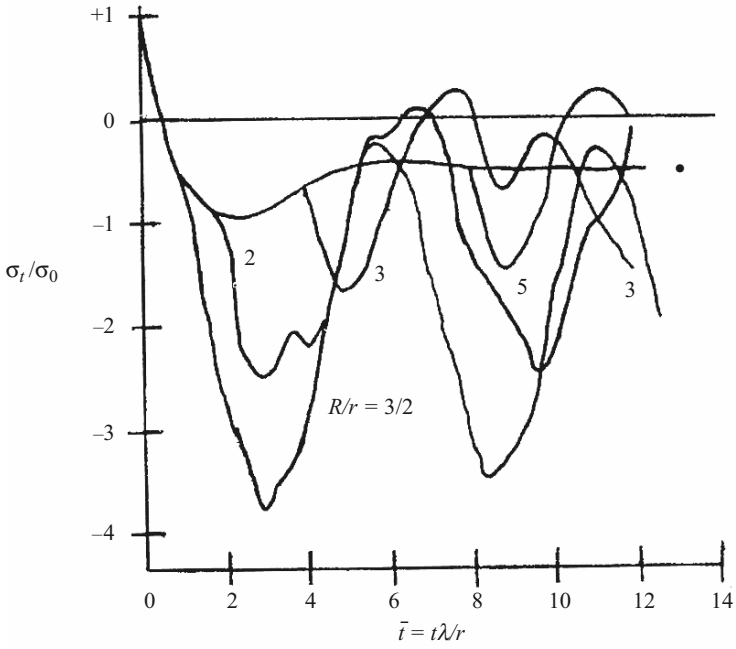
Fig. A.40. Tangential stresses at the cavity surface
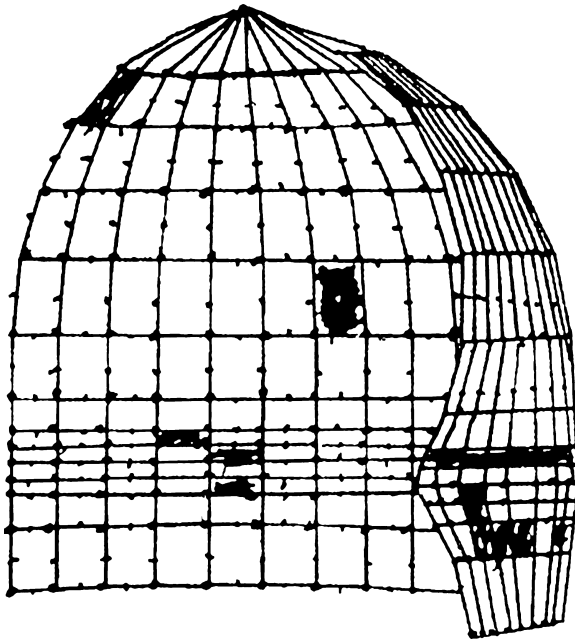
Fig. A.41. Finite-element analysis of a steel dome with an internal explosion

A.5 Car Impact and Explosion Analysis

A.5.1 General Data

Principles of impulse and momentum are frequently adopted in the study of various vehicle collisions. Rational velocity changes are included in the overall analysis. The energy loss ranges from 32 to 90% for a non-zero moment impulse with a range of restitution coefficients between -0.001 and 0.810. For a zero-moment impulse with the same range of energy loss the restitution coefficients will be between 0 and 0.4. The friction coefficients along the impact range are between -0.07 and 0.90. The collision can be at any angle, as shown in Fig. A.42. Table A.3 gives additional analytical features. Plate A.2 shows a typical picture of a crash between two cars. Plate A.3 gives a damage scenario of crash between an OZ train and a truck in Kerang, Victoria Australia bound for Melbourne.
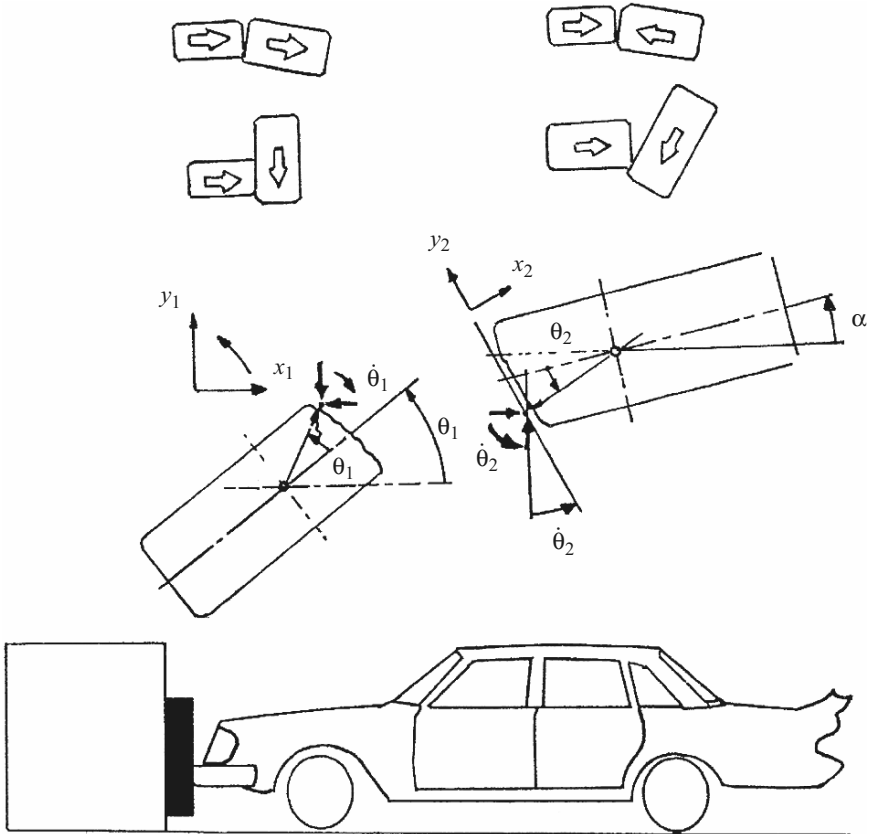
Fig. A.42. Collision phenomena of cars

Table A.3. Analysis of car rotation and dummy movement
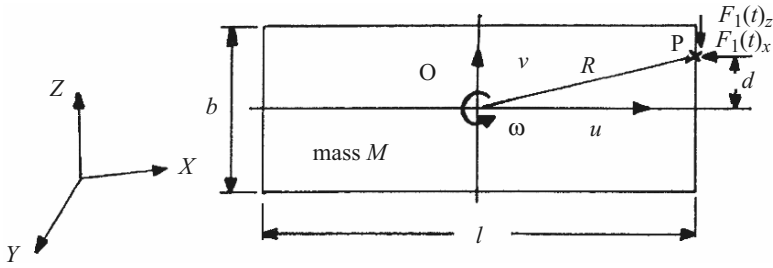
P = rotating point of a car
ω = angular velocity
    u_0, v_0 and u, v = initial and final velocities, respectively
    $u = \omega d; v = -\omega l/2; \mathrm{O}$ = centroid

$$\omega = (u_0 d)/[(I_0/M) + R^2]; I_0 = [(l^2 + b^2)/2](M/12)$$
$$= u_0(12d)/(l^2 + b^2 + 12R^2)$$

Rigid body impact: $- F_\mathrm{I}(t)_x = M(u - u_0)$
$$-F_\mathrm{I}(t)_z = Mv$$
$$I_0\omega = F_\mathrm{I}(t)_x d - F_\mathrm{I}(t)_z(l/2)$$
$$\Sigma F_{xi} = M_i(\dot{v}_{xi} + \theta_{yi}y_{zi})$$
$$\Sigma F_{zi} = M_i(\dot{v}_{zi} - \theta_{yi}v_{xi})$$
$$\Sigma M_{yi} = I_{yi}\ddot{\theta}_{yi}$$

where $\Sigma F_{xi}, \Sigma F_{zi}$ = sums of the applied forces in the X and Z directions
        ΣM_{yi} = sum of the applied moments perpendicular to the XZ plane;
        they are components of $F_\mathrm{I}(t)$
    $\dot{v}_{xi}, \dot{v}_{zi}$ = transitional accelerations in the X and Z directions
        $\ddot{\theta}_{yi}$ = angular acceleration
        I_{yi} = moment of inertia, referred to the centre of gravity

A.5.2 Finite-Element Analysis and Results

A typical finite-element mesh scheme for a car is shown in Fig. A.43. Where
the analysis includes a human body, a seat-belted dummy is added, as shown
in Fig. A.44. Bovine materials (given in the text) and steel material properties
are included in the analysis of bones and the car. Empty body and body with
packings, as dampers, for different positions in the car have been examined.
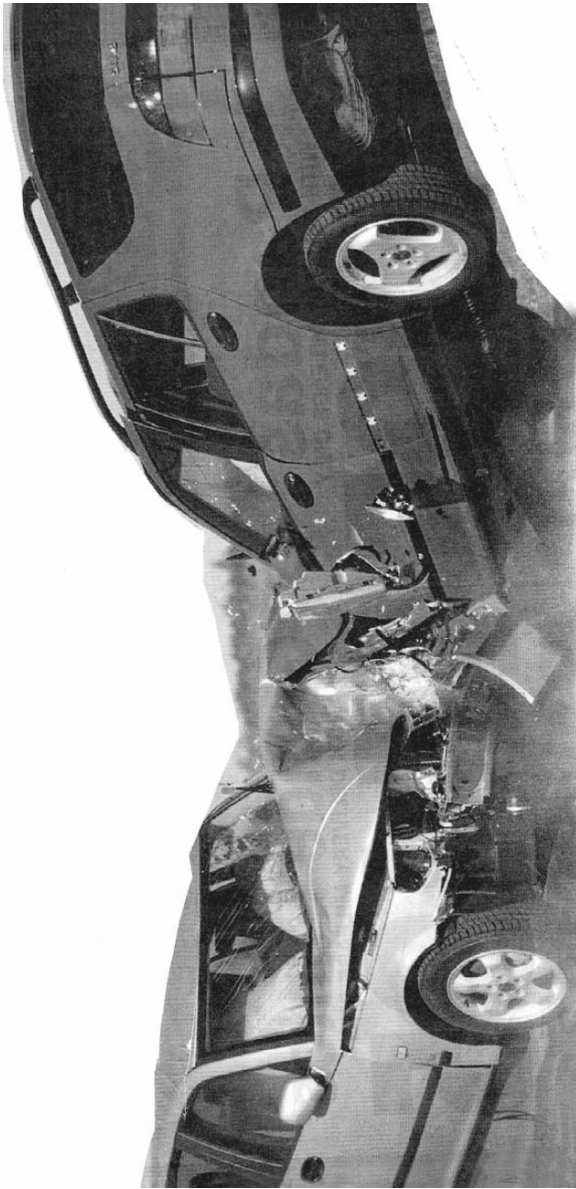
Plate A.2. Impact between two cars – A crash view
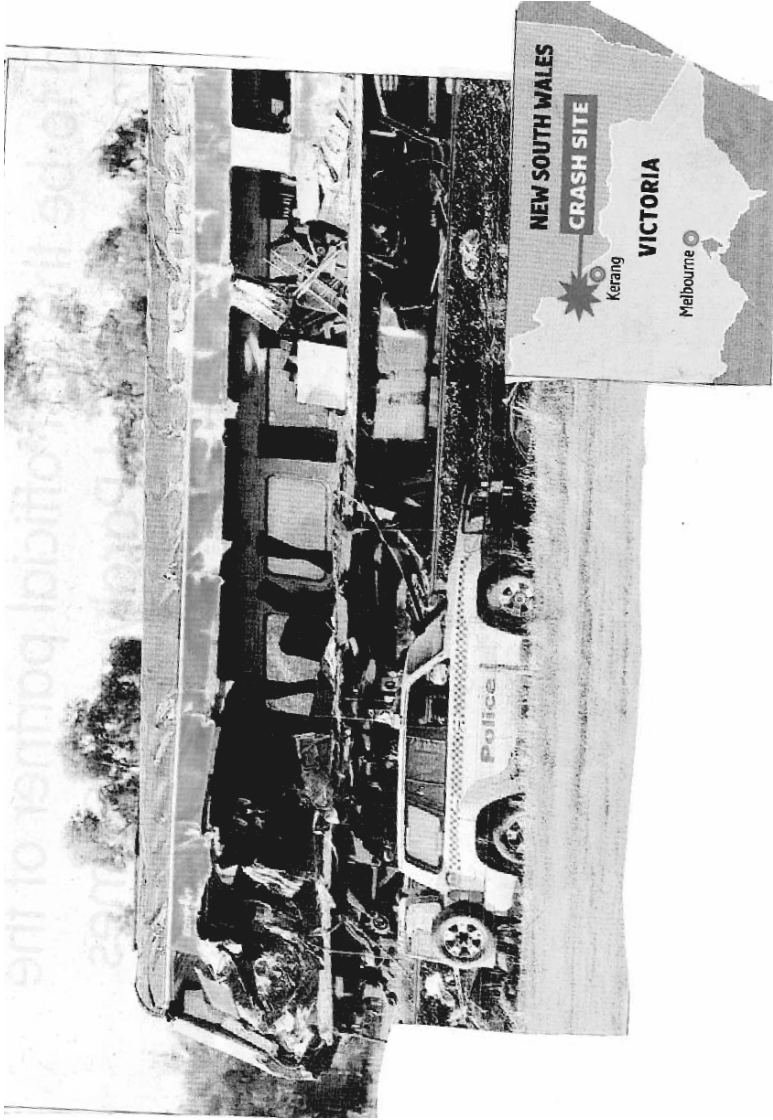
Plate A.3. A disaster scenario – Train impacting truck
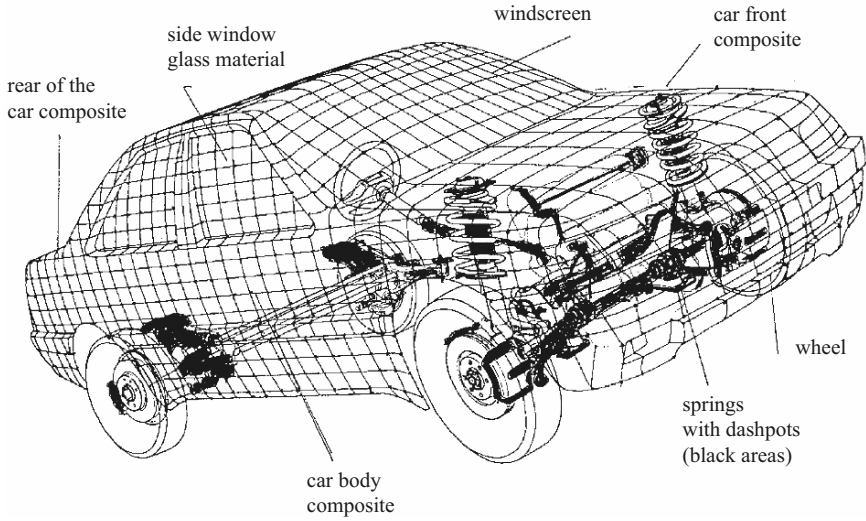
Fig. A.43. Finite-element mesh scheme for a car
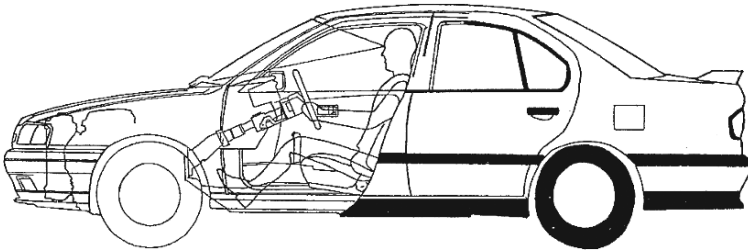
Fig. A.44. Car with a human dummy included (for mesh scheme for car see Fig. A.43)

Table A.3 is thus included in the global analysis. The Jernström model given in Table A.4 is simulated in the finite-element analysis for the crash investigation. A force–time function, given in Fig. A.45, is considered for the finite-element analysis.

The vehicles impacted the steel and aluminium barriers at velocities ranging from 30 to 50 mph. Additional input data:

Cars:	solid isoparametric elements	2,700
	(20-noded type, quadratic)	
	prism isoparametric elements	298
	(20-noded type)	
	gap elements, mixed dashpots	735
	total nodes	17,805

Table A.4. Jernström simulation data (courtesy of C. Jernström [2.399])

HEAD DECELERATION (g)

CHEST DECELERATION (g)

HIC = 1030, t_1 = 0.058, t_2 = 0.116 ---- TEST
HIC = 1027, t_1' = 0.061, t_2' = 0.135 —— SIMULATION

---- TEST
—— SIMULATION

BELT FORCE OF SEGMENT 2 AT SASH-GUIDE (kN)

BELT FORCE OF SEGMENT 5 AT SILL (kN)

---- TEST
—— SIMULATION
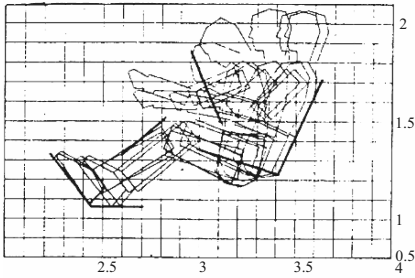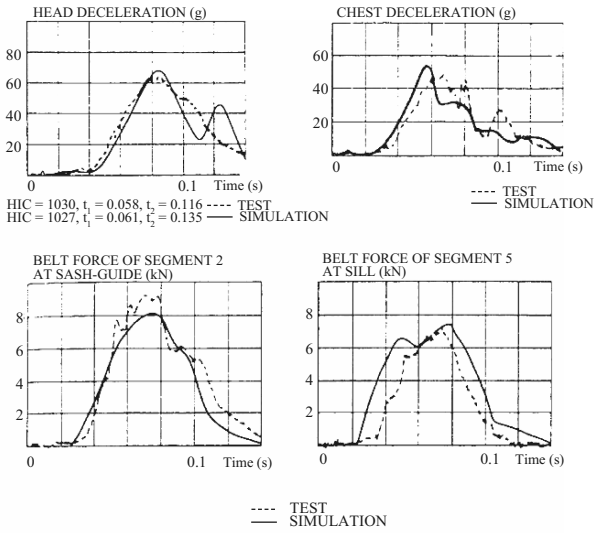
50th percentile male dummy, 10perc, 3-point belt driver's seat position, initial velocity 15.65 ms^{-1}, simulation results.
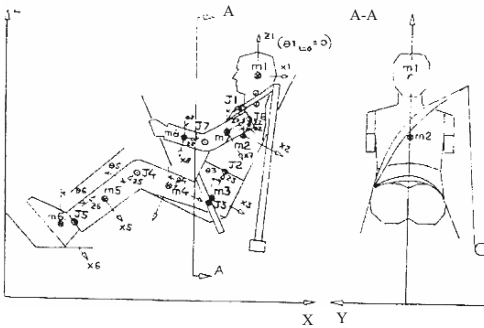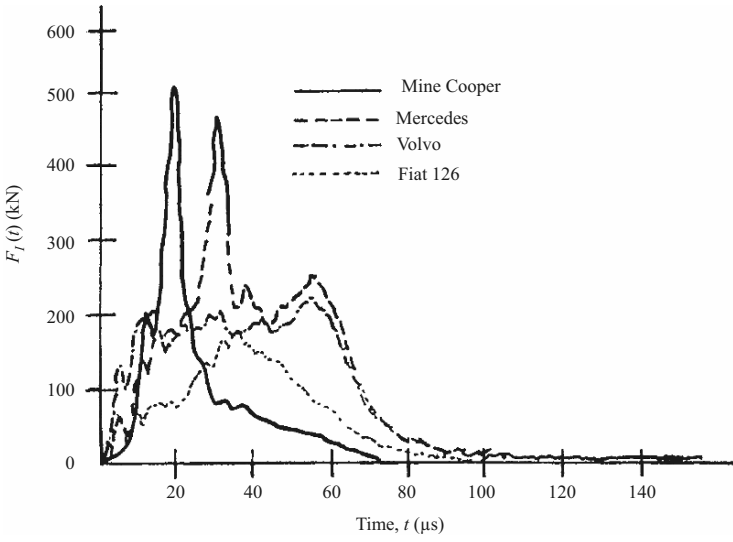
Fig. A.45. Force–time relationship
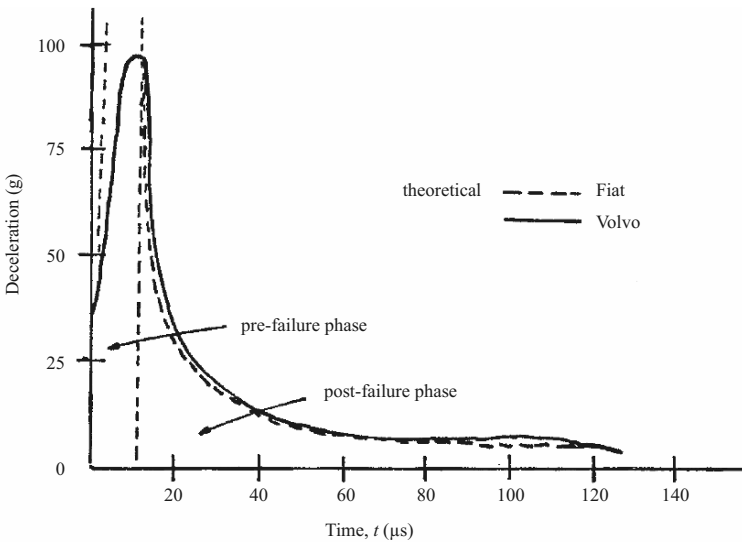
Fig. A.46. Deceleration–time relationships
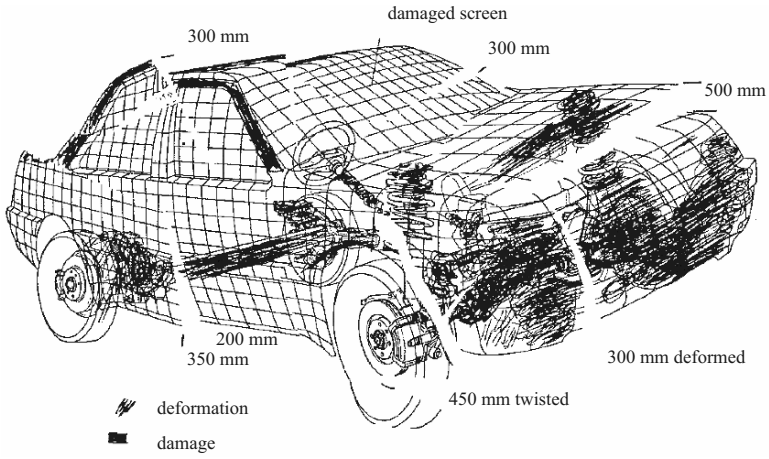
Fig. A.47. Car: post-mortem
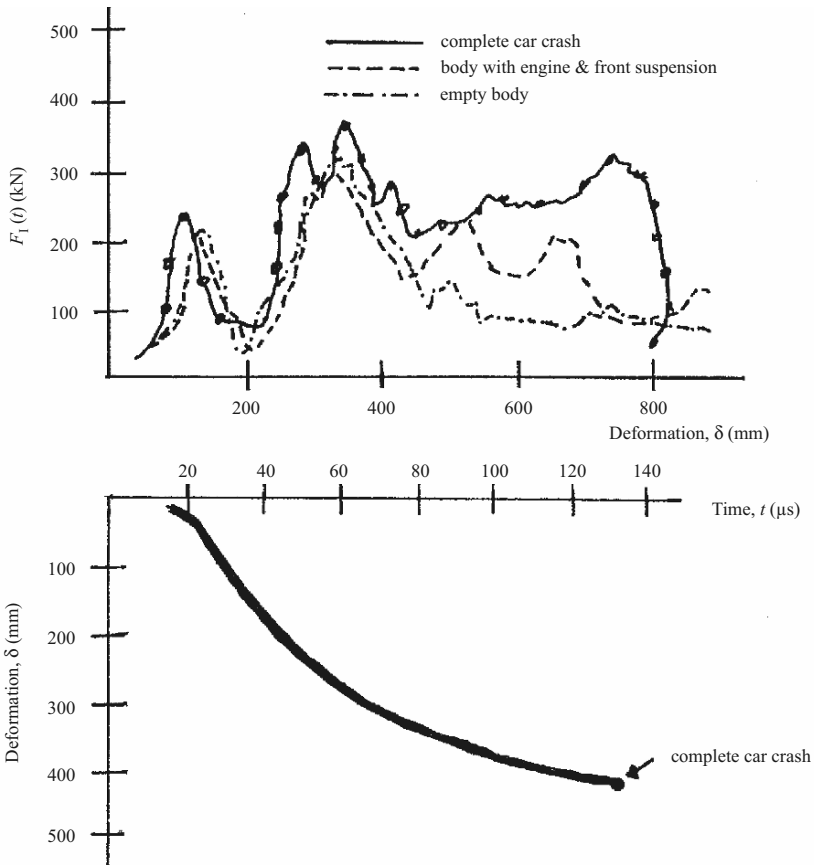
Fig. A.48. Deformation–time and car crash results
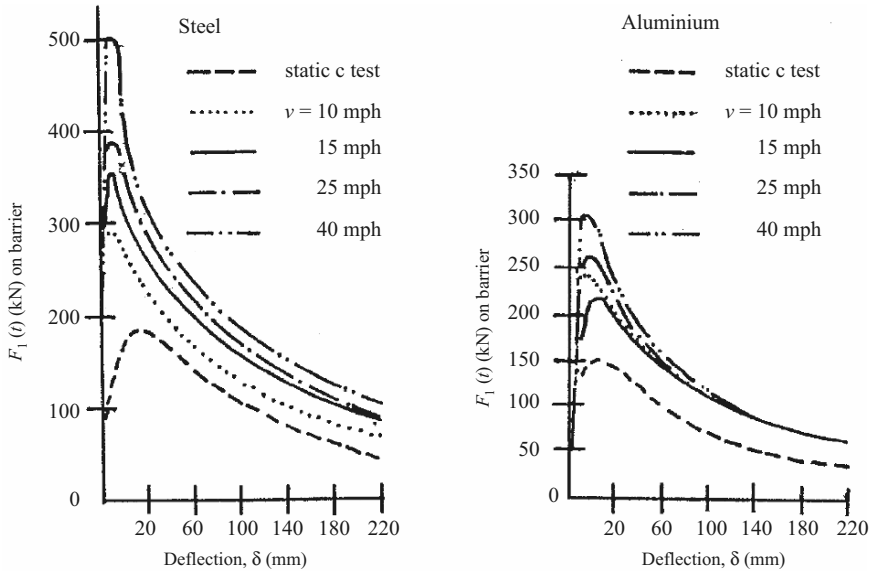
Fig. A.49. Analytical results for steel and aluminium barriers

Barriers: solid isoparametric elements   235
              (20-noded type, single layer)
              total increments   10

Total time for impact analysis $140\,\text{s}/\,\text{case}^{-1}$
t (time interval) $14\,\text{s}$
Maximum impact load $F_{\text{I}}(t)$ $500\,\text{kN}$

An IBM 4381 computer with Cray-2 front ended was used for analysis.

Figure A.46 shows the deceleration–time relationship for two types of car. The damaged car is shown in Fig. A.47. The force–deflection and the car crash with time results are shown in Fig. A.48. The barriers were examined for several impacts and various car velocities. Figure A.49 illustrates the results for flat steel and aluminium barriers braced and belted to vertical posts.

During the car crash investigation the entire dummy body was examined. The seat belts were assumed to be tension elements, each carrying 20 line nodes in total, sub-divided into 3-noded isoparametric elements. A typical damaged skull is shown in Fig. A.50. The number of finite elements representing the skull part are 350 and 210 for bones and tissues, respectively. The brain elements numbered 105. All were 20-node isoparametric elements.

displacement   8.0 μm
scale

(a)

(b)   15.0 mm
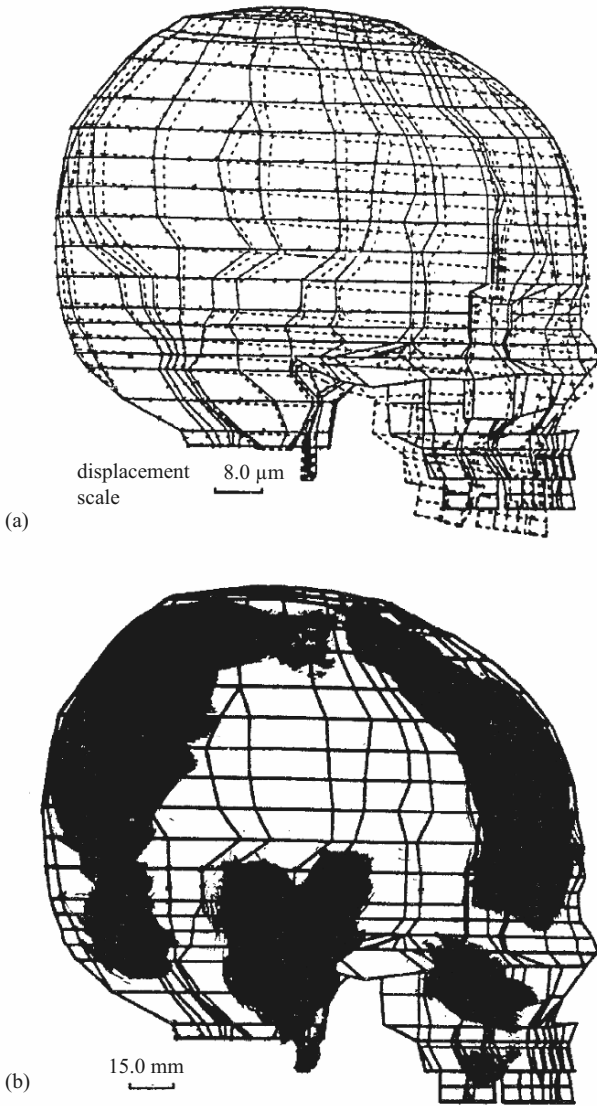
Fig. A.50. Skull damage. (**a**) Finite-element mesh and displacement due to impact; (**b**) final skull damage

B

Concrete Structures

B.1 Introduction

In this section a number of case studies in concrete are examined under impact and explosion conditions. In most cases, the results obtained from empirical formulae and finite-element analysis are compared with those available from experiments and site monitoring. Some concrete structures have been analyzed later on in other sections as well. The choice is based simply on their usage.

Impacts and explosions or blasts demand that the effects of the strain rate of concrete must be included in the global analysis of concrete structures. The text gives numerous data on this subject. Table B.1 gives the values of strain rates for concrete under compression, tension and bending conditions.

B.2 Concrete Beams

B.2.1 Reinforced Concrete Beams

A reinforced concrete beam which has already been tested in the laboratory must be analyzed so that a basis is established for the validation of the numerical tools. Ohnuma, Ito and Nomachi beams were chosen for this work; over 18 beams have been analyzed. Figure B.1 shows the impact loading system which generates impact on specimens by a high-speed striking hammer. The striking hammer is a hard steel cylinder with a diameter of $98\,\mathrm{mm}$. The weight of the hammer is $70\,\mathrm{kg}$. The maximum velocity was restricted to $50\,\mathrm{m\,s^{-1}}$. Figure B.2 shows the relationship between impact force and impact velocity. The bending failure occurred at low velocity and shearing failure occurred at high-velocity impact.

The load–time function adopted is shown in Fig. B.3. Figure B.4 shows the finite-element mesh scheme adopted for A-20, A-30 and A-50 beams. Velocities ranging from 0 to $30\,\mathrm{m\,s^{-1}}$ for the same impact were chosen. The impact forces were calculated and are plotted on Fig. B.2; a strain rate of $20\,\mathrm{s^{-1}}$

Table B.1. Strain rates for concrete under conditions of compression, tension and bending

	Test apparatus for high strain rates	Maximum strain rate (s^{-1})
Under compression		
Any type of compression	Drop weight	10.00
	Drop weight	2.00
	Drop weight	20.00
	Hydraulic	0.50
	Split Hopkinson	1,000.00
	Pressure (bar)	120
Under tension		
Uni-axial tension	Compressed air-driven loading	0.05
Splitting tension	Hydraulic	0.20
Uni-axial tension	'Pellet method' — high velocity projectile	20.00
Uni-axial tension	Split Hopkinson (bar)	0.75
Uni-axial tension with Effect of compression	Constant strain rate	0.01
Uni-axial tension with Bi-axial compression	Split Hopkinson (bar)	0.50
Under bending		
4-point bend	Instrumented Charpy impact	0.20
4-point bend	Constant displacement rate	0.01
3-point bend	Instrumented drop weight	2.00
3-point bend	Instrumented drop weight	1.00
3-point bend	Instrumented modified Charpy	0.50
2-point bend	Instrumented drop weight	0.50
3-point bend	Instrumented drop weight	1.80

was used. The damage for the A-20 beam is shown in Fig. B.5. For concrete, the endochronic theory was adopted with the tension cut-off as explained in Table B.2. The reinforcement was assumed to be 3-noded isoparametric elements and to lie on the main nodes of the solid isoparametric elements representing concrete.

The author has also carried out an experiment on a reinforced concrete beam subject to an impact load of 2,000 kN for a duration of 5 s.
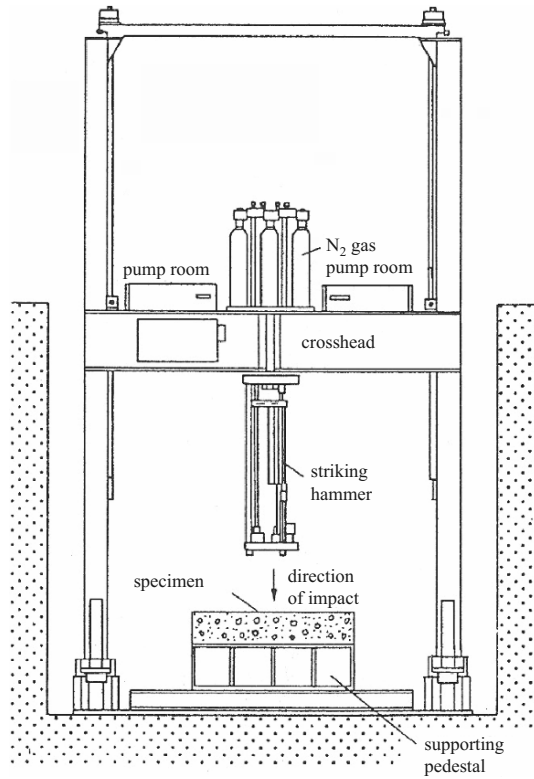
Fig. B.1. Impact testing apparatus (courtesy of Ohnuma H. & C. Ltd, Civil Engineering Laboratory, CRI EPI, Abiko 1646, Abiki-Shi, Chiba-ken, Japan and S.G. Nomachi, Hokkaido University, Japan)
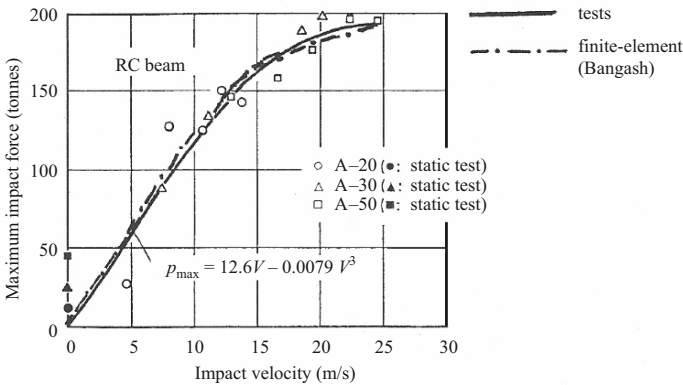
Fig. B.2. Impact force versus impact velocity for reinforced concrete (RC) beams. Dynamic response and local fracture of reinforced concrete beams/slabs under impact loading (courtesy of Ohnuma H. & C. Ltd, Civil Engineering Laboratory, CRI EPI, Abiko 1646, Abiki-Shi, Chiba-ken, Japan and S.G. Nomachi, Hokkaido University, Japan)
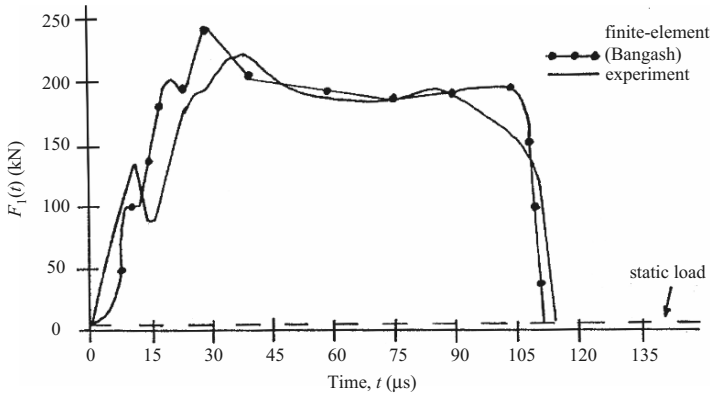
Fig. B.3. Load–time function for reinforced concrete beams
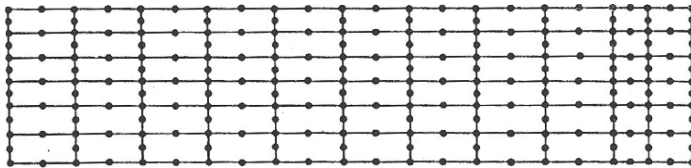
Fig. B.4. Finite-element mesh scheme, with 20-node isoparametric elements, for reinforced concrete beams of the A-20 to A-50 types
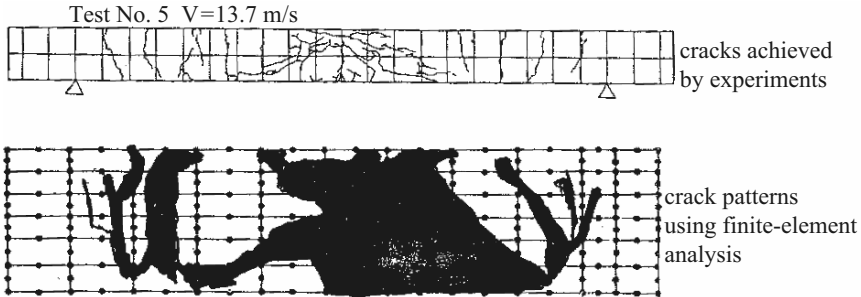
Fig. B.5. A damaged A-20 beam under a 2,000 kN impact with a $13.7\,\mathrm{m\,s}^{-1}$ velocity (courtesy of Ohnuma H. & C. Ltd, Civil Engineering Laboratory, CRI EPI, Abiko 1646, Abiki-Shi, Chiba-ken, Japan and S.G. Nomachi, Hokkaido University, Japan)

Figure B.5 shows the damaged zones obtained by finite-element analysis and these compare well with those predicted by the experiment.

The feature of high-strain loading and the propagation of stress waves from the point of explosion have been discussed in detail in the text. Such stress waves can cause non-uniform stress conditions, which ultimately cause cracks even remote from the point of explosion. Mortar bars 25 mm in diameter and 1 m long were cast vertically in 50 mm layers and compacted with a 5 mm

Table B.2. Tension cut-off and softening in concrete
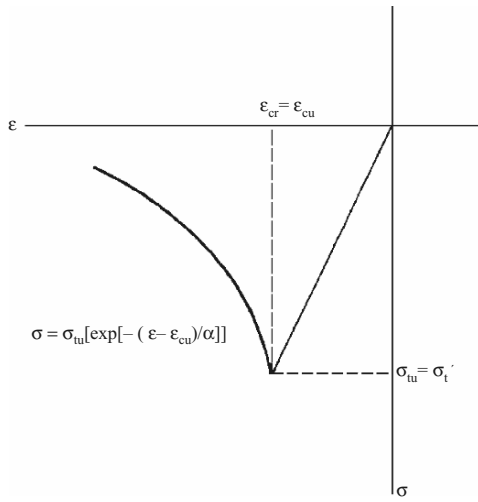
Strain softening model

$$\alpha = \text{softening parameter}$$
$$= G_r - \tfrac{1}{2}\sigma_{tu}\varepsilon_0(d\mathbf{v})^{1/3}/\sigma_{tu}(d\mathbf{v})^{1/3} > 0$$
$$d\mathbf{v} = \text{volume}$$
$$\varepsilon_0 = \varepsilon_{cr} = \text{strain at cracking}$$
$$\sigma_{tu} = \text{tensile strength of concrete}$$
$$(d\mathbf{v})^{1/3}\varepsilon_{eq} = \text{crack opening}$$
$$\varepsilon_{eq} = \text{equivalent crack strain, based on smeared crack width,}$$

where ε is the nominal tensile strain in the cracked zone, ε_{cu} is the cracking and α, the softening parameter, is given by

$$\alpha = (G_f - \tfrac{1}{2}\sigma_{tu}\varepsilon_{cu}l_c)/\sigma_{tu}l_c > 0,$$

where

$$l_c = \frac{\text{volume containing a crack}}{\text{area of crack}} = \frac{V}{A_{cs}}$$
$$\approx (dV)^{1/3}$$

and

$$dV = \text{volume of concrete represented by sample point}$$
$$G_f = \int_0^\infty \sigma(w)dw = \text{fracture energy needed to separate two cracks}$$
$$w = \text{crack width} = l_c\,\varepsilon_{cu}$$

Concrete is assumed to be elastic-brittle in tension. When a crack occurs, the stress normal to it can be immediately released and drops to zero

diameter steel tamping rod. The vibrator was attached to the mould. Electrical (resistance) strain gauges were positioned. Four gauges in each position were connected in series to form a Wheatstone bridge circuit. These bars were wrapped with 5 mm thick foam rubber at 250 mm centres and supported in a Dexion steel angle. The function of the foam rubber was to prevent any iteration between the Dexion and the mortar. A small PE4 explosive charge of 20 mm diameter with a total mass of 7 g was attached to one end of the mortar bar. A detonator was then inserted into the charge. This method was adopted by Dr. Watson of Sheffield University, UK, for his concrete block specimens. The author adopted this method for a specially cast reinforced concrete beam which is shown in Fig. B.6. The fracture pattern for 7 g gelignite attached to the underside of the beam is shown in Fig. B.7. Finite-element analysis was carried out for this beam. This time the mesh was kept coarse. The deformed mesh (20-noded isoparametric elements) and cracking are shown in Fig. B.8. A line marked XYZ (Fig. B.7) represent areas chopped off and letters A–H show

(a)

data:
concrete grade 50
tendon load
at transfer = 300kN
E_s = 200 GN/m^2
density of concrete = 2400 kg/m^3

(b)
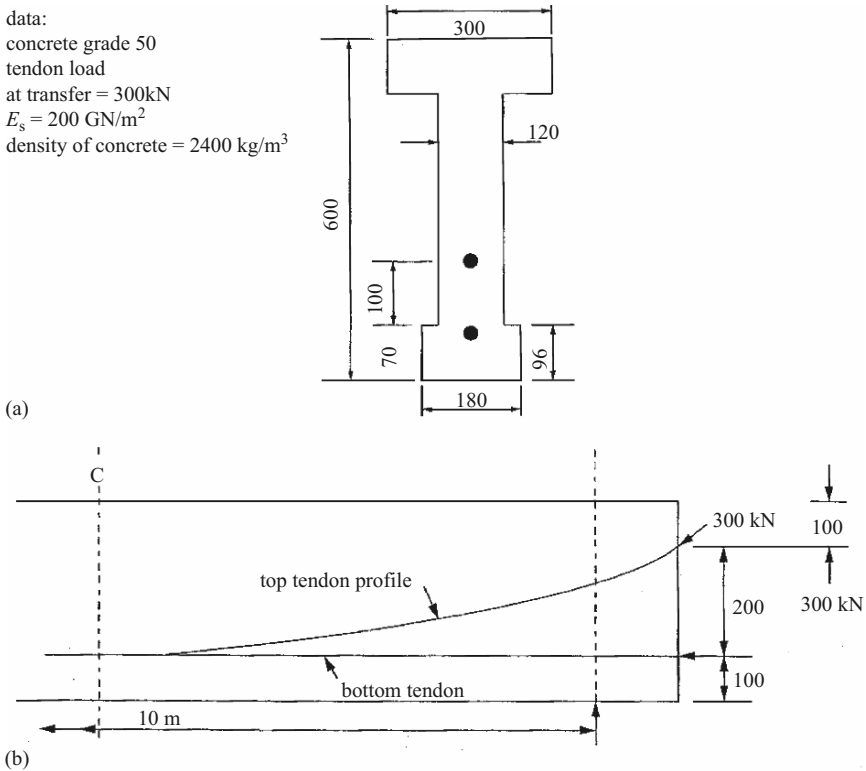
Fig. B.6. Model reinforced concrete beam: (**a**) cross-section; (**b**) longitudinal elevation

7g explosive
gelignite
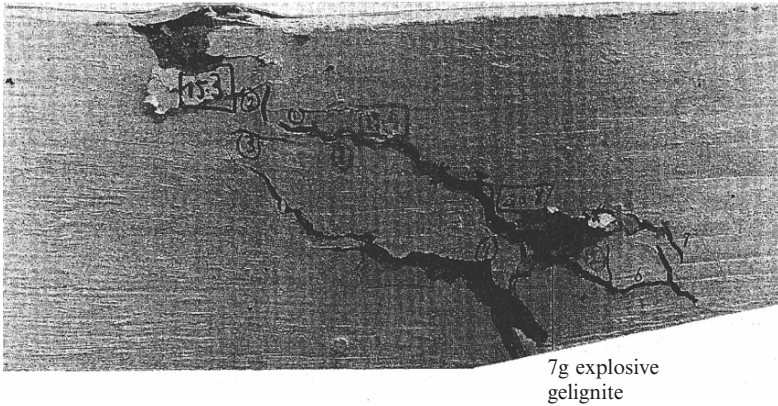
Fig. B.7. Beam failure under an internal explosion
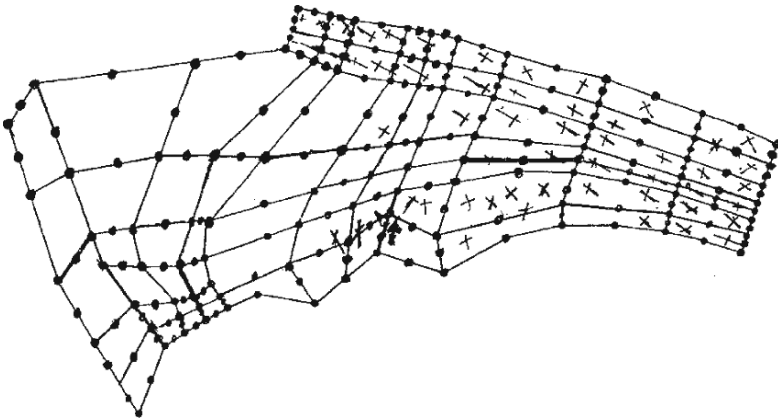
Fig. B.8. A mesh deformed by an explosion

high-level cracking zones. Again, endochronic theory was used for concrete failure with a tension cut-off. The total number of increments used was 210.

B.2.2 Pre-Stressed Concrete Beams

Twelve pre-stressed concrete beams were designed on the basis of the British Standard BS 8110. These beams were subjected to repeated impact loads of 200 kg dropped from different heights. Table B.3 gives data on these beams. The hammer was guided by a frame and the load from each impact was transmitted through a steel bearing plate. The dynamic responses were measured, particularly displacements, using a variable displacement transformer of 0–500 Hz. Using an IBM PC with special interface software, the electrical signals were transformed into displacements. Both programs, ISOPAR and ABACUS, were used, using 8-noded solid isoparametric

Table B.3. Data on pre-stressed concrete beams

P_k = characteristic pre-stressing load; e = eccentricity; h = depth; d = effective depth; L = effective length; the width of the beam is 200 mm

Beam type	L (m)	h (mm)	d (mm)	A_{sp} (mm^2)	P_K (kN)	Drop heights (mm)
[a]REC I	1.60	200	125	60	70	
II	2.50	200	122	102	123	
III	2.50	200	122	140	172	
IV	2.50	200	122	180	220	15, 30, 60, 90, 120, 160, 180, 250
V	2.50	200	124	102	123	300, 350, 400, 500, 600
VI	2.80	250	160	102	123	
VII	3.80	250	160	102	123	
VIII	4.80	300	160	102	123	
IX	5.80	300	160	102	123	
[b]BOX I	4.00	350	320	400	500	100, 150, 200, 300, 400, 500, 550, 600
II	4.00	350	320	500	600	200, 250, 300, 350, 400, 550, 600,
III	4.00	400	370	600	700	250, 300, 350, 400, 550, 600

[a] Solid rectangular beam, 200 mm wide by h deep
[b] Box beam 200 mm wide by h deep, with 60 mm thickness throughout

A_{sp}(top) = A_{sp}(bottom)
f_{cu}(concrete) = 40 N mm^{-2}
E_c(concrete) = 28–30 GN mm^{-2}
f_y(steel) = 460 N mm^{-2}
E_s(steel) = 210 GN m^{-2}

elements. Pre-stressing wires/strands were represented by 2-node elements, fully bonded. The wires/strands were placed on nodes of the 8-node isoparametric elements. In some cases, the wires/strands were placed in the body of the solid elements. The finite-element mesh of a pre-stressed concrete beam is kept as shown in Fig. B.4. The drop heights used for the experiments on these beams are given in Table B.3. Figure B.9 illustrates a comparative study
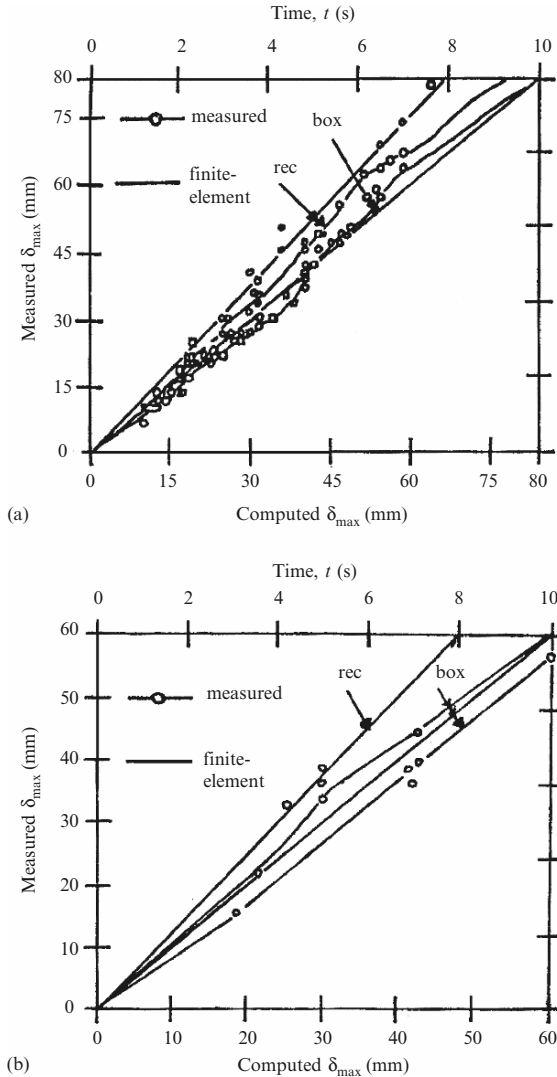
Fig. B.9. Computed and measured displacements for pre-stressed concrete beams subjected to dropped weights. (**a**) Solid beams and box beams (drop heights from 50 to 60 mm); (**b**) solid beams and box beams (drop heights 15–300 mm) (Box = box beam; rec = solid rectangular beam)
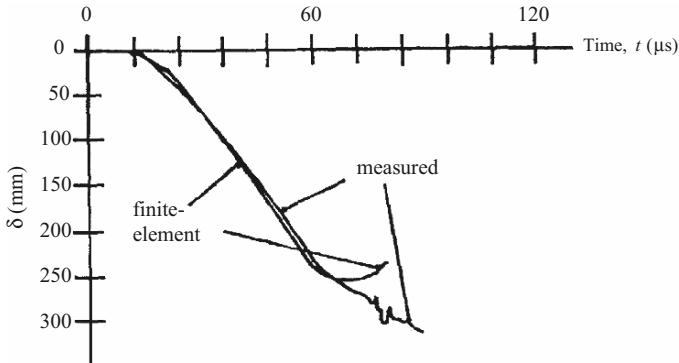
Fig. B.10. Displacement–time relationship
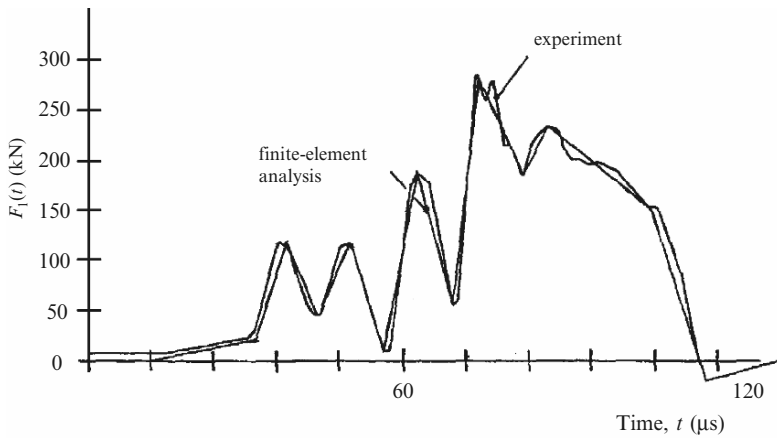
Fig. B.11. Load–time function for the pre-stressed concrete beam

of displacements produced from the experiments and finite-element analysis of the 12 beams. A typical damaged pattern of a pre-stressed solid concrete beam of 300 mm depth turned out to be as shown in Fig. B.5, when subjected to multiple impacts from a drop height of 300 mm. The displacement–time relationship is given in Fig. B.10 for the impact load–time function shown in Fig. B.11.

B.2.3 Fibre-Reinforced Concrete Beams

Introduction

References given in this text provide an in-depth study of dropped weights and projectiles impacting fibre-reinforced concrete structures. It is well known that toughness and cohesion may be greatly increased by the addition of fibres to concrete. Most of the impact work has concentrated on large masses impacting

at relatively low velocities. Table B.4 summarizes the test results on 450 mm square specimens, with various thicknesses and mix proportions, subjected to a 7.62 mm diameter, copper-sheathed, hardened steel projectile of mass 9.6–9.9 g, travelling at a speed of $800\,\mathrm{m\,s^{-1}}$. In addition, Table B.5 gives useful data on the impact tensile strength of steel-fibre concrete, much of which has already been reported in the text. Under dropped weights, the following data can be added to the existing ones: a cylindrical projectile (90 mm by 25 mm) on 200 mm cubes which are subjected to an impact load of 490 N (110.2 lb) by a hammer falling through 300 mm gives an impact energy of $60\,\mathrm{kN\,m^{-1}}$. The general proportions for fibrereinforced mortar were assumed to be 1:2:0.5. The generally recommended value for Young's modulus for mortar is $3.1 \times 10^6\,\mathrm{psi}$ or 21.4 GPa. In most cases, the recommended impact velocity was $222\,\mathrm{cm\,s^{-1}}$ for a 60 kN impact load on fibre-reinforced specimens of dimensions 5.1 mm by 10.2 mm by 50.8 mm.

For concrete steel-fibre-reinforced (mortar and others) the compressive stresses for various mixes are as recommended for a $1\,\mathrm{m\,s^{-1}}$ impact velocity.

Composite	Mix	Fibres: length × dia. (mm)	Compressive strength, σ_{cu} $(\mathrm{kN\,m^{-2}})$
Concrete steel-fibre-reinforced mortar	1:2:3,0.5	25 × 0.25	58,350
Polypropylene reinforced concrete	1:2:0:1%,0.5	6 × 0.15	58,350
Glass-fibre-reinforced concrete	1:2:0:1%,0.5	25 × 0.25	50,921

Finite-Element Analysis

For the current analysis, a concrete steel-fibre reinforcement of a concrete beam of a suitable size given was adopted. The following data analysis form the input for the analysis:

> 20-noded isoparametric elements (concrete): 84
> Steel fibres 2% by volume spread impact loads falling from a 3 m height, range: $50, 100, 200, 250, 300\,\mathrm{kN}$
> Time intervals: 0–$3.5\,\mathrm{\mu s}$
> Strain rates/s: 10^0–10^{-7}
> Concrete failure analysis: endochronic

All other data for concrete are assumed to be the same as given in Sect. B2. Figure B.12 gives the finite-element mesh scheme for solid concrete. The fibres are assumed to spread throughout the element with interlocking values of $\beta' = 0.5$. The total number of increments was 12, with a convergence factor of 0.01. The Wilson-θ method was adopted, with an implicit solution. For damage analysis, cracks occurred on the line suggested in the text.

Table B.4. Summary of main test series results

25 mm length steel fibre type	10 mm aggregate type	% fibre weight by concrete weight	Penetration path length (mm)	True crater volume (mm^3)
Melt extract	Limestone	0	76	492,000
		2.5	92	109,800
		5.0	80	150,500
		7.5	80	73,700
		10.0	66	353,000
	River gravel	0	56	280,500
		2.5	50	236,300
		5.0	86	135,200
		7.5	80	160,700
		10.0	68	147,700
	Basalt	0	87	276,900
		2.5	62	124,000
		5.0	102	83,400
		7.5	91	67,800
		10.0	101	67,200
Brass-coated circular indented	Limestone	0	83	339,500
		2.5	94	104,700
		5.0	91	125,300
		7.5	57	54,400
		10.0	74	59,100
	River gravel	0	74	346,100
		2.5	67	181,100
		5.0	93	280,500
		7.5	75	85,200
Brass-coated circular indented	Basalt	0	89	185,600
		2.5	84	147,700
		5.0	81	63,600
		7.5	84	56,800
		10.0	91	31,400
Brass-coated circular	Limestone	0	68	238,900
		2.5	87	151,300
		5.0	83	114,200
		7.5	60	62,200
		10.0	68	78,800
	River gravel	0	77	251,600
		2.5	93	149,200
		5.0	67	101,900
		7.5	71	54,100
		10.0	68	32,700
	Basalt	0	93	251,500
		2.5	85	135,500
		5.0	102	88,900
		7.5	86	48,100
		10.0	79	68,900

Table B.5. Strain-rate, energy absorption and other data

Fracture strain rate: $\epsilon_{cr} = 220\dot{\epsilon}^{1/3}$
ϵ_{cr} range: 0, 250, 500, 750 $\times 10^{-6}$
$\dot{\epsilon}(s^{-1})$ 0, 10, 20, 30, 40
Fibre volume: 0, 0.75, 1.5, 3%
Stress rate, $\dot{\sigma}$: 0.05 to 200 $N\,mm^{-2}\,s$

$E_{n_{TOT}}$ total energy per fibre $(N\,m^{-1}) = G_{TOT,f} = \alpha + \beta\log_e\dot{\delta}$
$$\dot{\delta} = 100\dot{\epsilon}\,mm\,s^{-1}$$

	Fibre volume (m^3)		
	0	1.5	3
α	198.50	8,271.8	13,690.00
β	9.31	345.5	559.10
γ^2	0.71	0.8	0.97

Strain rate	Fibre content (%)			E_n
Low	0.75	0.62	0.3	33
Intermediate	0.81	0.71	35.0	35
High	0.78	0.72	40.0	40

Concrete tensile stress, σ_{tu}: 2.85–4.22 $N\,mm^{-2}$

Specimen (%)		σ_{tu} (N mm^{-2})	δ (mm)	G_{TOT}	N
0		3.27 ± 0.46	0.013 ± 0.0025	–	–
1.5	low	3.75 ± 0.31	0.018 ± 0.0025	$7,786 \pm 3,426$	115 ± 22.6
3		3.50 ± 0.37	0.027 ± 0.011	$7,560 \pm 2,223$	190
0		4.79 ± 0.61	0.017 ± 0.001	–	–
1.5	intermediate	5.43 ± 0.52	0.022 ± 0.003	$8,457 \pm 4,235$	108 ± 43.8
3		5.36 ± 0.74	0.0368 ± 0.024	$12,772 \pm 3,880$	224 ± 24.7
0		5.57 ± 0.5	0.0165 ± 0.0026	–	–
1.5	high	6.49 ± 0.47	0.0224 ± 0.0061	$12,509 \pm 3,572$	132 ± 35
3		6.49 ± 0.96	0.022 ± 0.004	$15,656 \pm 5,413$	175 ± 46.4

δ = deformation; N = number of fibres at cross-section

Courtesy of H.A. Körmeling [2.400]
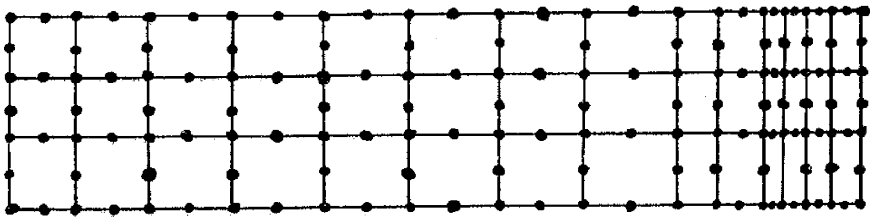
Fig. B.12. Finite-element mesh for a steel-fibre-reinforced concrete beam
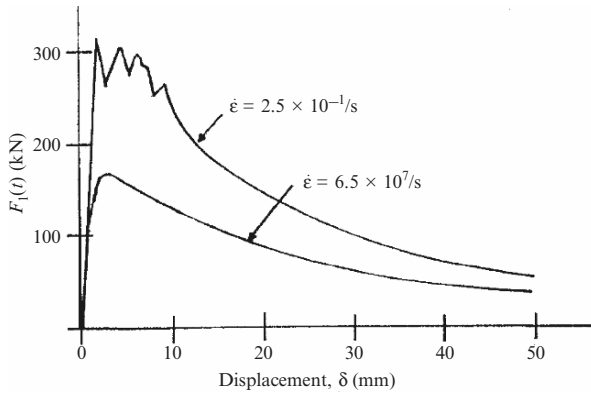
Fig. B.13. Load–displacement relationship for two selected strain rates
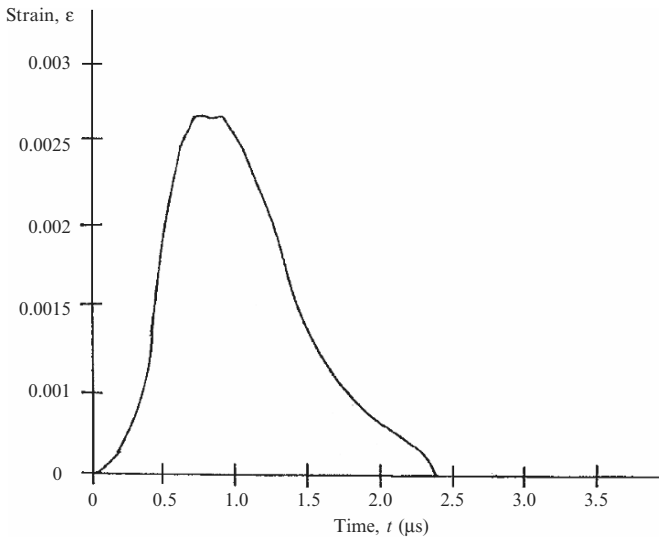
Fig. B.14. Strain–time relationship for a fibre-reinforced beam

Figure B.13 gives the impact load–displacement relationship for two chosen strain rates. Figure B.14 illustrates the strain–time relationship for this beam. The ratios of dynamic strength to static strength for various strain rate effects are shown in Fig. B.15. Prior to the damage received by this beam, the ultimate deformed shape was as shown in Fig. B.16. The final post-mortem is given in Fig. B.17. It is interesting to note that the analytical results obtained in Fig. B.15 compare well with those obtained by an experiment carried out on a totally different kind of beam.
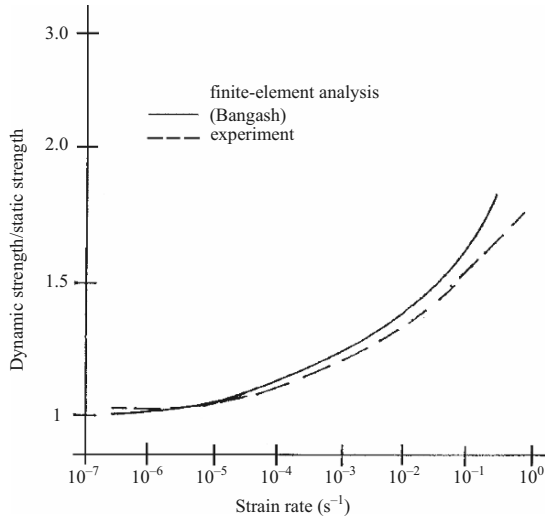
Fig. B.15. Ratios of dynamic strength to static strength for various strain rates (courtesy of W. Suaris and S.P. Shah [2.401])
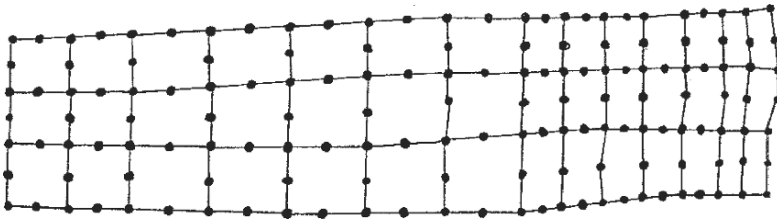
Fig. B.16. Deformed finite-element mesh
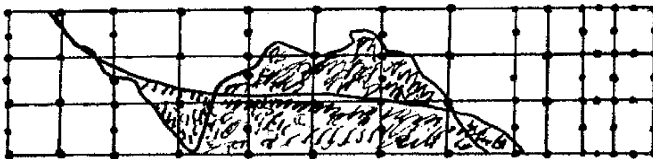
Fig. B.17. A post-mortem for a fibre-reinforced concrete beam

B.3 Reinforced Concrete Slabs and Walls

B.3.1 Introduction

A number of missile formulae are given in this text for penetration, perforation and scabbing of reinforced concrete slabs and walls. On the basis of some of these empirical formulae, computer programs have been written for rapid solution of problems. Design aids are included for preliminary manual design. In addition, finite-element analyses given in the text have been carried out on

slabs and their results compared with those obtained from empirical formulae and experimental tests. Similarly, slabs/walls subjected to explosion have been examined. Using design aids, slab reinforcements were calculated on the basis of both American and British practices.

B.3.2 Slabs and Walls Under Impact Loads

Computer Subroutines Based on Empirical Formulae

The Appendix shows the layout of the computer programs for impact on concrete structures based on empirical formulae already discussed in the text. The following examples are linked to these programs.

A slab with Clamped Edges, Using the ACI/ASCE Codes

The slab has clamped edges and measures 6.1 m by 0.76 m. The concrete data are:

$f'_c = 21$ MPa
$E_c = 21.5 \times 10^3$ MPa
Weight density $= 2320$ kg m^{-3}
Poisson's ratio for concrete $= 0.17$

The slab reinforcing steel data are:

$f_y = 280$ MPa
$E_s = 200 \times 10^3$ MPa
Depth to tensile reinforcing steel $= 0.70$ m

The missile is a flat-nosed cylinder with a concentrated impact load. It has a weight of intensity 1.8 N (Newton), a diameter of 178 mm and an impact velocity of 107 m s^{-1}.

The reinforced concrete section properties are given below.

(1) Average of cracked and uncracked moments of inertia:

$$I_a = \tfrac{1}{2}[(bt^3/12) + Fbd^3]$$

$b = 1$ cm, $t = 76$ cm, $d = 70$ cm. It is assumed that

$$\rho_1 = \rho'_1 = As/bd = 1.76 \times 10^{-3}$$
$$n = E_s/E_c = (200 \times 10^3)/(21.5 \times 10^3) = 9.3$$
$$\rho'_n = 1.76 \times 10^{-3} \times 9.3 = 0.0163$$

Using the chart in Table B.6, with values of $\rho'_n = 0.0163$ and $\rho'_1/\rho_1 = 1.0$, $F = 0.012$. Hence,

$$I_a = \tfrac{1}{2}[(1 \times 76^3/12) + (0.012 \times 1 \times 70^3)]$$
$$= 20{,}349 \,\text{cm}^4 \,\text{cm}^{-1}$$

(2) Elastic stiffness of the slab:

$$K_e = 12E_c I_a/[\alpha a^2(1 - v^2)]$$

The slab is square, therefore $a/b = 1.0$. Using Table B.6, the following values are computed:

$$\alpha = 0.0671, \nu = 0.17 \text{ for concrete}$$

$$K_e = \frac{12(21.5 \times 10^3 \times 20{,}349)}{0.0671 \times 610^2 \times (1 - 0.17^2)}$$

$$= 2.16 \times 10^9 \,\text{N}\,\text{m}^{-1}$$

$$= 2.16 \,\text{MN}\,\text{mm}^{-1}$$

(3) For a concentrated load, the load factor $K_L = 1$. The effective mass is given as

$$M_e = \int m[\varphi(x)]\mathrm{d}x$$

with a mass factor

$$K_m = M_e/M_t$$

where M_t = total mass of slab.

$$\varphi = 1 - (r/R) \quad (R = a/2)$$

$$\mathrm{d}x = \mathrm{d}A = 2\pi r \mathrm{d}r$$

$$M_e = m(2\pi) \int_{r=0}^{r=R} [1 - (r/R)]r \ \mathrm{d}r = m\pi R^2/6$$

The effective mass is one-sixth of the mass within the circular yield pattern.

$$m = \text{mass/unit area} = 2320 \times 0.76/9.81 = 179.7 \,\text{kg}\,\text{s}^2\,\text{m}^{-1}$$

$$M_c = \frac{179.7 \times \pi \times (6.1/2)^2 \times 9.81 \times 10^{-3}}{6} = 8.56 \,\text{N}\,\text{s}^2\,\text{mm}^{-1}$$

The first natural period:

$$T = 2\pi\sqrt{(M_e/K_L K_e)} = 2\pi\sqrt{(8.56/1 \times 2.16 \times 10^6)} = 0.0125$$

The Use of Empirical Formulae

The empirical formulae are based on empirical units and data and coefficients are based on them. The data shall be converted back in to SI units.

(1) National Defence Research Committee Formulae (NDRC) first formula Data conversion:

Missile weight = 400 lb
Missile diameter = 7 in
Missile velocity = 350 fps
Concrete compressive strength = 3,000 psi
Flat-nosed missile, therefore the nose-shaped factor $N = 0.72$

$$K = \text{concrete strength factor} = 180/\sqrt{f_c'} = 180/\sqrt{3{,}000}$$

$$= 3.29$$

Table B.6. Slab coefficients with cracked and uncracked conditions
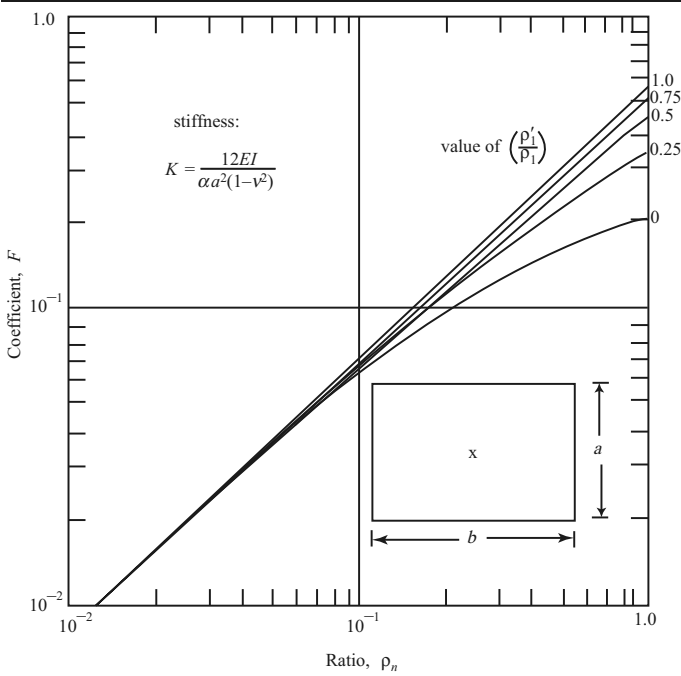
Coefficients for moment of inertia of cracked sections.

Simply supported on all four sides, with load at centre		Fixed supports on all four sides, with load at centre	
$\frac{b}{a}$	α	$\frac{b}{a}$	α
1.0	0.1390	1.0	0.0671
1.1	0.1518	1.2	0.0776
1.2	0.1624	1.4	0.0830
1.4	0.1781	1.6	0.0854
1.6	0.1884	1.8	0.0864
1.8	0.1944	2.0	0.0866
2.0	0.1981	∞	0.0871
3.0	0.2029		
∞	0.2031		

Assuming $x_p/d \leq 2.0$ and using the first formula:

$$x_p = \sqrt{[4(3.29)(0.72)(400)(7)(350/1{,}000 \times 7)^{1.8}]}$$
$$= 10.99 \, \text{in} \; (279.1 \, \text{mm})$$

Check: $x_p/d = 10.99/7 = 1.57$, OK
Check perforation and scabbing with $x_p/d = 1.57$

$$t_{\mathrm{p}}/d = 1.32 + 1.24(x_{\mathrm{p}}/d) = 3.27, \quad t_{\mathrm{p}} = 582\,\mathrm{mm}$$
$$t_{\mathrm{sc}}/d = 2.12 + 1.36(x_{\mathrm{p}}/d) = 4.25, \quad t_{\mathrm{sc}} = 757\,\mathrm{mm}$$

(2) Bechtel formulae

Solid missile:

$$t_{\mathrm{sc}} = (15.5/\sqrt{3{,}000})(400^{0.4} \times 350^{0.5}/7^{0.2})$$
$$= 39\,\mathrm{in}\,(1{,}001\,\mathrm{mm})$$

Hollow missile:

$$t_{\mathrm{sc}} = (5.42/\sqrt{3{,}000})(400^{0.4} \times 350^{0.65}/7^{0.2})$$
$$= 33\,\mathrm{in}\,(842\,\mathrm{mm})$$

(3) ACE formula

$$x_{\mathrm{p}} = \frac{282}{3{,}000}\left(\frac{400}{(7/12)^2}\right)(7/12)^{0.215}\left(\frac{350}{1{,}000}\right)^{1.5} + 0.5(7/12)$$
$$= 20.7\,\mathrm{in}\,(525\,\mathrm{mm})$$
$$t_{\mathrm{p}} = 1.23d + 1.07x_{\mathrm{p}} = 1.23(7/12) + 1.07(20.7)$$
$$= 22.9\,\mathrm{in}\,(580\,\mathrm{mm})$$

(4) CKW-BRL formula

Formula for penetration:

$$x_{\mathrm{p}} = (6 \times 400 \times 7^{0.2}/7^2)(350/1{,}000)^{4/3}$$
$$= 17.8\,\mathrm{in}\,(453\,\mathrm{mm})$$
$$t_{\mathrm{p}} = 1.3x_{\mathrm{p}} = 1.3 \times 17.8 = 23.1\,\mathrm{in}\,(588\,\mathrm{mm})$$

For example, using a rectangular pulse load characteristic where the impact load $F_1(t) = W(v_{\mathrm{s}})^2/2\mathrm{g}t_{\mathrm{p}} \approx 3.69\,\mathrm{MN}$, the duration time t_{d} is given by

$$t_{\mathrm{d}} = 2x_{\mathrm{m}}/v_{\mathrm{s}} \approx 0.00517\,\mathrm{s}.$$

On the basis of American Concrete Institute (ACI) strength reduction analysis of concrete, the collapse load of a slab is written for a circular fan failure as

$$R_{\mathrm{m}} = 4\pi\varphi[(A_{\mathrm{s}} - A_{\mathrm{s}}')f_{\mathrm{y}}(d - a/2) + A_{\mathrm{s}}'f_{\mathrm{y}}(d - d')](\mathrm{DIF})$$
$$\approx 2.949\,\mathrm{MN},$$

where φ = strength reduction factor

MF or DIF = dynamic increase factor (in this case 1.19)

$A_{\mathrm{s}}, A_{\mathrm{s}}'$ = reinforcement areas in tension and compression zones

Using Fig. B.18

$$C_{\mathrm{T}} = t_{\mathrm{d}}/T = 0.4155(R_{\mathrm{m}}/F_1) = 0.7975$$
$$x_{\mathrm{m}}/x_{\mathrm{e}} = 3.795 < \text{ductility factor } \mu = 30$$

No overall failure exists.
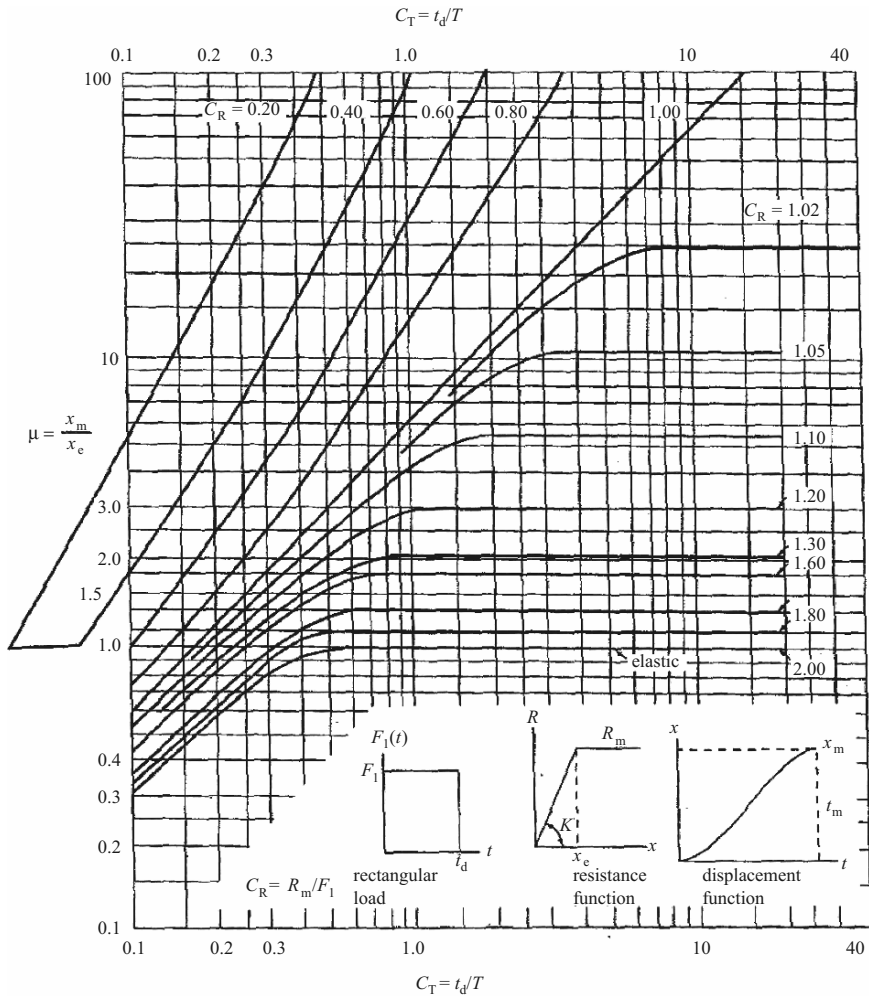
Fig. B.18. x_m/x_e curves for an elasto-plastic system based on a rectangular impulse load (courtesy of J.M. Biggs, [2.402])

Finite-Element Analysis of Reinforced Concrete Slabs/Walls

Reinforced Concrete Slabs

A typical finite-element model of a reinforced concrete slab with a damaged zone is shown in Fig. B.19. The following parameters were used:

> The slab thickness varied from 100 mm to 1,500 mm
> For a slab thickness of 100 mm, V_s ranged from 12.1 to 21 m s^{-1}
> For a slab thickness of 200 mm, V_s ranged from 20.7 to 43 m s^{-1}
> The total number of 8-noded elements was 1,584
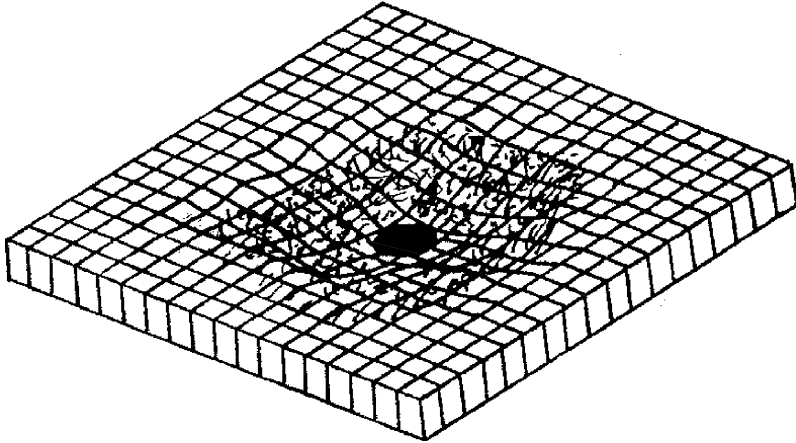
Fig. B.19. Finite-element analysis of a damaged slab

(a)   (b)

--·-- plain concrete
---- reinforced concrete, 1% steel
——— reinforced concrete, 2% steel
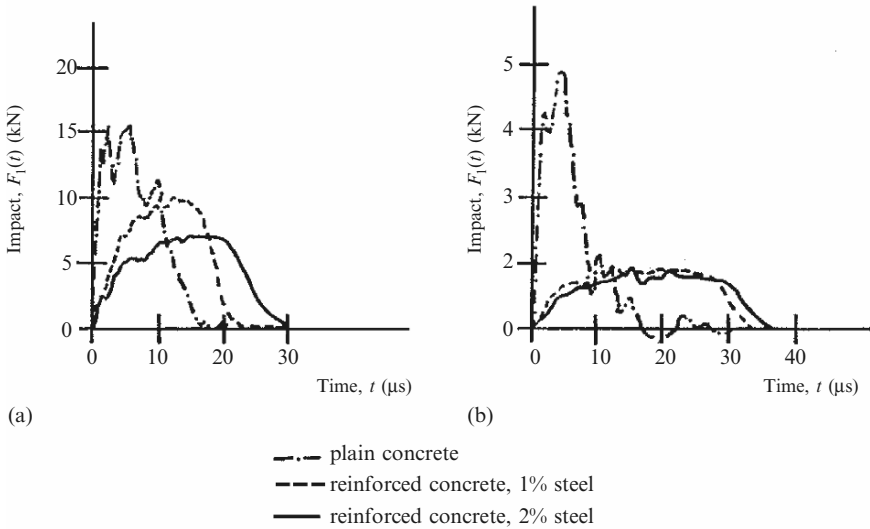
Fig. B.20. Load-time function for (**a**) a solid impactor and (**b**) a pipe impactor

The reinforcement spread was between 1 and 2%
Endochronic concrete model, $f_{cu} = 0.87 f_c'$
$$= 41.7 \, \text{N mm}^{-2}$$
Load–time function: see Fig. B.20
Drop weight of $37.8 \, \text{kg}$ at $8 \, \text{m s}^{-1}$
Nose shape for pipes: $N = 0.72$ and 1.0

Typical examples of the Ohnuma and Nomachi slabs were considered in order to test the finite-element program ISOPAR. Again, the numbers of
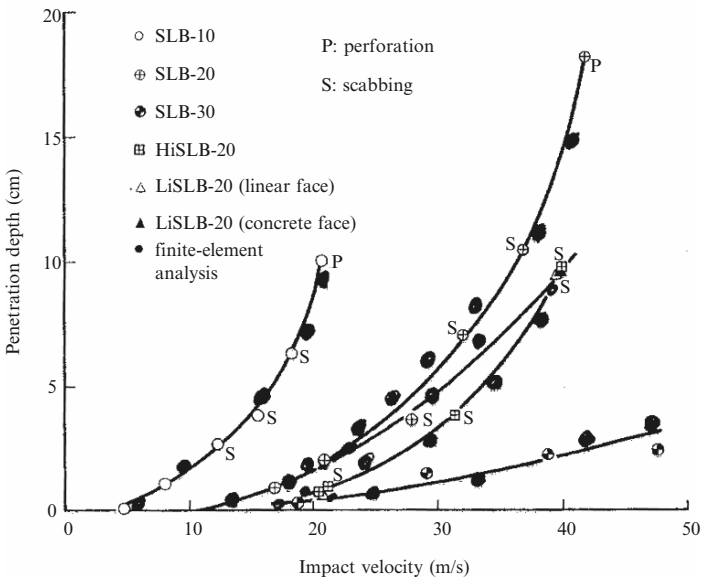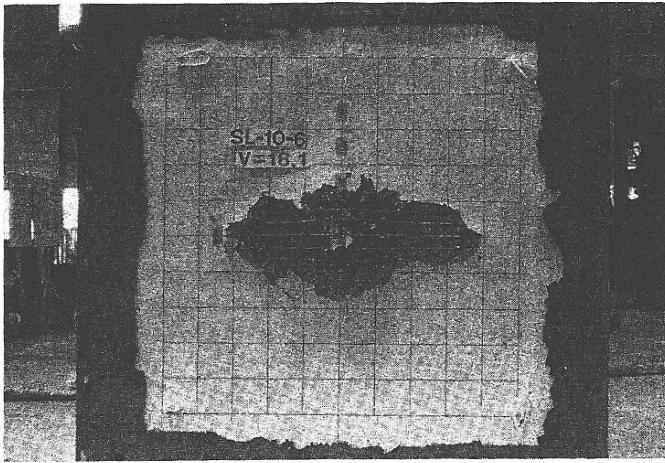
Fig. B.21. A comparative study of experimental finite-element results (H. Ohnuma, C. Ito and S.G. Nomachi, personal communication, August 1985)

elements and nodes of 8-noded isoparametric elements shown in Fig. B.19 were employed. This step was taken to reduce the computational effort and time.

Figure B.21 shows a typical scabbing phenomenon found by Ohnuma et al. (personal communication). This encouraged the author to examine their slabs when subjected to impact loads of various velocities. The loading patterns and

the slab thickness were kept the same. For a 300 mm reinforced concrete slab the impact velocity was kept at $50 \, \text{m s}^{-1}$. The penetration depths, perforations and scabbing for various impact velocities were evaluated using the ISOPAR program. Figure B.21 illustrates a comparative study of the experimental and finite-element results for slabs of 100, 200 and 300 mm thicknesses. The results of the finite-element analysis are within 5–10% of the experimental results.

Reinforced Concrete Walls

A reinforced concrete wall was subjected to impact loads caused by rods and pipes. The study was undertaken to determine the local response in terms of crushing, cratering, spalling, cracking and plug formation. The concrete constitutive model was assumed to be based on the bulk modulus approach with a tensile yield surface. The 8-noded isoparametric element was adopted. The optimum finite-element mesh for the wall was kept as shown in Fig. B.19.

Additional data for this analysis using the ISOPAR program:

Target wall: diameter $= 1 \, \text{m}$
          overall depth with a haunch $= 0.3 \, \text{m}$
          main depth $= 0.2 \, \text{m}$
          concrete grade $= 30$
          reinforcement T-25-300
Projectile: steel rods 100 mm long with a diameter of 20 mm and a
          weight of 920 g
        steel pipes 150 mm long with a diameter of 35 mm and a
          weight of 790 g
        velocity $= 22 \, \text{m s}^{-1}$

The effects of impact on a concrete wall of both steel rod and pipe projectiles at $50 \, \text{m s}^{-1}$ were examined. Figure B.22 shows the penetration–time relationships for this wall at various time intervals. Table B.7 records a comparative study of finite-element analysis and empirical formulae. The same wall was analyzed using an impact velocity of $3.3 \, \text{m s}^{-1}$. The wall was reinforced with T25. The maximum penetration was 8 mm along the entire impact line.

B.3.3 Design for Blast Resistance

General Data and Specification (BS 8110 and HMSO Guide) and TM5–1300 US Army

The ultimate load capability of a ductile structural element subjected to blast loading can be determined by considering its capacity of sustaining an external load by relatively large plastic deformation. The design rules in the guides discussed in the following sections limit the magnitude of the plastic deformation and the level of damage to the structural elements.

Table B.7. Comparative study of finite-element analysis and empirical formulae

Scabbing velocity/slabs	Formula	Empirical formulae		Finite-element analysis	
		(1) Penetration depth (m)	(2) Min thickness to prevent perforation (m)	Penetration (m)	Min thickness to prevent perforation (m)
$12.1\,\mathrm{m\,s^{-1}}$/760 mm slab	IRS	0.290	1.4	1.13	1.89
	HN-NDRC	0.2791	1.70		
	ACE	0.525	1.90		
Perforation velocity					
$12.1\,\mathrm{m\,s^{-1}}$/760 mm slab	DF-BRL	0.453	–	0.79	1.10
$43\,\mathrm{m\,s^{-1}}$/760 mm slab	BRL	0.8	1.02	0.83	1.15

N/d_p [a]	NDRC		Finite-element analysis	
	$t_\mathrm{pe}/d_\mathrm{p}$ [a]	Velocity, $V_\mathrm{s}\,(\mathrm{m\,s^{-1}})$	$t_\mathrm{pe}/d_\mathrm{p}$ [a]	Velocity, $V_\mathrm{s}\,(\mathrm{m\,s^{-1}})$
0.72/300	0	–	0	–
	0.2	1.57	0.2	1.61
	0.4	3.05	0.4	2.93
0.72/600	0.6	4.20	0.6	4.10
	0.8	6.10	0.8	5.91
	1.0	7.60	1.0	7.39
1.0/300	0	–	0	–
	0.2	2.30	0.2	2.25
	0.4	3.95	0.4	3.85
	0.6	6.10	0.6	6.05
	0.8	6.30	0.8	5.15
	1.0	–	1.0	6.75

[a] d_p = diameter of the pipe
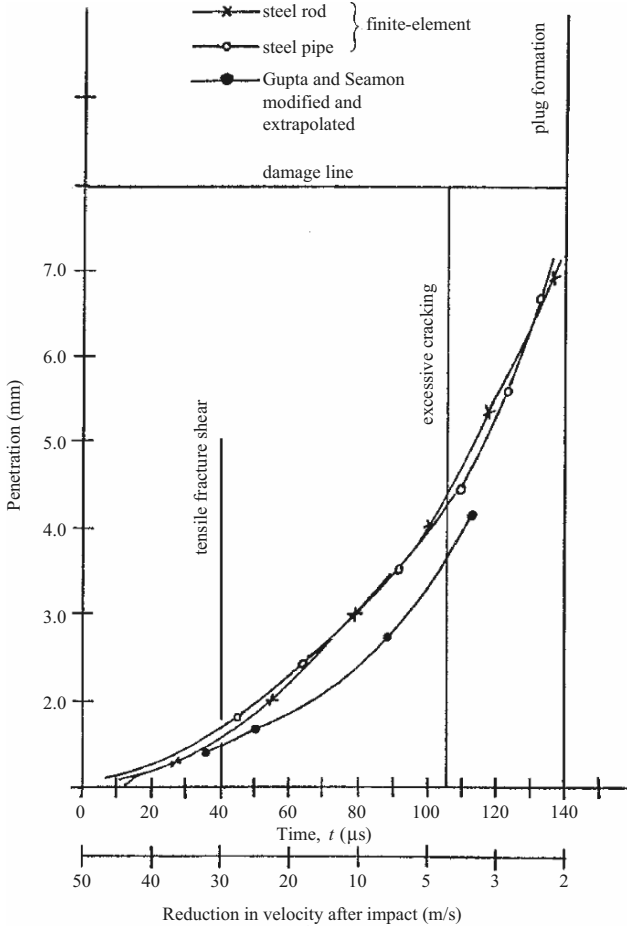
Fig. B.22. Reinforced concrete wall penetration–time–velocity relationships

General Data and Specifications: BS 8110 and HMSO Guide on Domestic Shelters

Ultimate Unit or Resistance r_u

Depending on the mass and stiffness of the concrete element, this is written as

$$r_u = F_1\{1/[1 - (1/2\,\mu)]\}.$$

The moderate damage μ is taken as 3, which gives $r_u = 1.2F_1$ and the safety factor $\gamma_1 = 1.2$. The dynamic factor MF or DIF is taken as 1.1 for bending steel and 1.25 for concrete in compression.

Ultimate Shear Capacity, Plastic Moment of Resistance and Steel Capacity

The ultimate shear stress resistance is limited to $0.4f_{cu}(0.4\sigma_{cu})$.

Edge conditions	Ultimate shear stress
Cantilever	$r = (L - d)/d$
Fixed or pinned	$r = (L/2 - d)/d$

Dynamic shear stress shall not exceed $172\,\text{N}\,\text{mm}^{-2}$

Minimum Area of Flexural Reinforcement

Reinforcement	Mild steel	High tensile steel
Main	0.25% bd	0.20% bd
Secondary	0.15% bd	0.12% bd

Connections to Concrete

The allowable dynamic stresses for bolts and welds (BS 4190) are as follows:
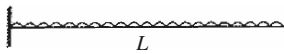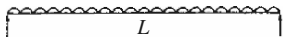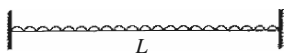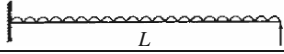
Bolts: tension $275\,\text{N}\,\text{mm}^{-2}$
shear $170\,\text{N}\,\text{mm}^{-2}$
bearing $410\,\text{N}\,\text{mm}^{-2}$
Welds: tension or compression $275\,\text{N}\,\text{mm}^{-2}$
shear $170\,\text{N}\,\text{mm}^{-2}$

Ultimate Unit Resistance for Slabs/Walls with Different Boundary Conditions

The ultimate unit resistance of a concrete element varies according to the following:

(1) Distribution of applied loads
(2) Geometry of the element
(3) Percentage of the reinforcement
(4) Type of support

Using the standard symbols, the ultimate unit resistance r_u for several one-way elements is given below:

Edge condition		Ultimate unit resistance, r_u
Cantilever	L	$2M_{HN}/L^2$
Simple support	L	$8M_{HP}/L^2$
Fixed support	L	$8(M_{HN} + M_{HP})/L^2$
Fixed simply supported	L	$4(M_{HN} + 2M_{HP})/L^2$

M_{HN} = ultimate unit negative moment capacity at support, M_{HP} = ultimate unit positive moment capacity at mid-span, L = span length

Two-way elements can be analyzed using yield line theory. The value of the ultimate unit resistance r_u for a two-way slab is given by:

$$R_m = r_u = [8(M_{HN} + M_{HP})(3L - x)]/H^2(3L - 4x) \text{ short span,}$$
$$R_m = r_u = [5(M_{HN} + M_{HP})]/x^2 \text{ long span.}$$

The ultimate unit moment capacity of a reinforced concrete element subjected to blast loading can be found by using the following equation:

$$M_u = f_y \text{ (dyn)} \times A_s \times Z,$$
$$M_u = 0.225 f_{cu} \text{ (dyn)} \times bd^2,$$
$$Z = (1 - 0.84 f_y \text{ (dyn)} \times A_s)d/(f_{cu} \text{ (dyn)} \times bd),$$
$$Z < 0.95d.$$

The ultimate unit moment capacity of other shapes of slabs with respective boundary conditions against blast loads can be evaluated using tables.

Additional Information from US Design Codes ASCE Manual 42 and TM5-1300 for Blast Loads

Ultimate Static and Dynamic Moment Capacity

The ultimate unit resisting moment, M_u, of a rectangular section of width b with tension reinforcement only is given by

$$\text{static } M_u = (A_s f_s/b)[d - (a/2)],$$

where A_s = area of tension reinforcement within the width b, f_s = static design stress for reinforcement, d = distance from extreme compression fibre to centroid of tension reinforcement, a = depth of equivalent rectangular stress block = $(A_s f_s)/(0.85 f'_c)$ static, b = width of compression face, f'_c = static ultimate compressive strength of concrete.

Dynamic f_s is replaced by $f_y(\text{dyn}) \times \varphi$. The reinforcement ratio, ρ is defined as

$$p = \rho = A_s/(bd).$$

Check on section

$$\rho_b = 0.85 K_1 \{ f'_c(\text{dyn})(87{,}000)/f_y(\text{dyn})[87{,}000 + f_y(\text{dyn})] \},$$
$$a(\text{dyn}) = [A_s f_y(\text{dyn})]/[0.85 f'_c(\text{dyn}) \times b].$$

Applied M varies for loadings and boundary conditions, and is generally equal to $r_u L^2/16$.

To ensure against sudden compression failures the reinforcement ratio ρ must not exceed 0.75 of the ratio ρ_b, which produces balanced conditions at ultimate strength and is given by

$$\rho_b = 0.85 K_1 [f'_c(87{,}000)/f_s(87{,}000 + f_s)],$$

where $K_1 = 0.85$ for f'_c up to $4{,}000\,\mathrm{psi}$ and is reduced by 0.05 for each $1{,}000\,\mathrm{psi}$ in excess of $4{,}000\,\mathrm{psi}$.

For a rectangular section of width b with compression reinforcement, the ultimate unit resistance moment is given by

$$M_\mathrm{u} = \frac{(A_\mathrm{s} - A'_\mathrm{s})}{b} f_\mathrm{s}(d - a/2) + \frac{A'_\mathrm{s} \times f_\mathrm{s}}{b}(d - d'),$$

where A'_s = area of compression reinforcement within the width b, d' = distance from the extreme compression fibre to the centroid of compression reinforcement, a = depth of equivalent rectangular stress block = $(A_\mathrm{s} - A'_\mathrm{s})f_\mathrm{s}/(0.85bf'_c)$.

The reinforcement ratio is given by

$$\rho' = A'_\mathrm{s}/(bd).$$

When the compression steel reaches the value f_s at strength,

$$\rho - \rho' = 0.85 K_1 (f'_c d'/f_\mathrm{s}d)[87{,}000/(87{,}000 - f_\mathrm{s})].$$

If $\rho - \rho'$ is less than the value given in the above equation, or when compression steel is neglected, the calculated ultimate unit resisting moment should not exceed that given by the above. The quantity $\rho - \rho'$ must not exceed 0.75 of the value of ρ_b given earlier.

Minimum Flexural Reinforcement

To ensure proper structural behaviour and also to prevent excessive cracking and deformation under conventional loadings, the minimum areas of flexural reinforcement should be as shown in the table below.

Pressure design range	Reinforcement	Two-way elements	One-way elements
Intermediate and low	Main	$A_\mathrm{s} = 0.0025bd$	$A_\mathrm{s} = 0.0025bd$
	Other	$A_\mathrm{s} = 0.0018bd$	$A_\mathrm{s} + A'_\mathrm{s} = 0.0020bT_\mathrm{c}$
High	Main	$A_\mathrm{s} = A'_\mathrm{s}$ $= 0.0025bd_\mathrm{c}$	$A_\mathrm{s} = A'_\mathrm{s}$ $= 0.0025bd_\mathrm{c}$
	Other	$A_\mathrm{s} = A'_\mathrm{s}$ $= 0.0018bd_\mathrm{c}$	$A_\mathrm{s} = A'_\mathrm{s}$ $= 0.0018bd_\mathrm{c}$

Ultimate Shear Capacity

The ultimate shear stress, v_u, is given by

$$v_\mathrm{u} = V_\mathrm{u}/(bd),$$

where V_u is the total shear.

The permitted shear stress, v_c, is given by

$$v_c = \varphi[9(f_c')^{1/2} + 2500\rho_{\max}] \leq 2.28\ \varphi(f_c')^{1/2},$$

where φ is the capacity reduction factor and is equal to 0.85.

For a dynamic case, f_c' (dyn) replaces f_c', the static value. Wherever the ultimate shear stress exceeds the shear capacity, v_c, of the concrete, shear reinforcement must be provided to carry the excess, for example stirrups or lacing.

Minimum Design Stresses

Minimum static stresses are given below and are increased by dynamic increase factors.

Material	Support rotation angle, θ	Stresses (psi)		
		f_y	f_u	f_c'
Reinforcing		40,000	70,000	–
steel A15 and	–	60,000	90,000	–
A432				
Concrete	$0° < \theta \leq 2°$	–	–	$\geq 2,500$
	$2° < \theta \leq 12°$	–	–	$\geq 3,000$

Typical Numerical Examples

Typical numerical examples are given in Tables B.8–B.20.

Design Graphs Based on the NDRC Formula and the Finite-Element Method

Using the NDRC empirical formula, the computer program developed in the Appendix has been used to calculate penetration, perforation and scabbing thicknesses, and these are given in Figs. B.24–B.26. A total of 300 slabs were analyzed with different percentages of reinforcement impactor sizes and shapes and velocities. The NDRC formula is compared with the finite-element method. Throughout the analysis, the finite-element mesh scheme adopted in Fig. B.19 was used, with 8-noded isoparametric elements and with the reinforcement lying in the body as well as on the nodes of each element. A typical example based on these graphs is given below.

Table B.8. Explosion resistance of reinforced concrete walls

Data
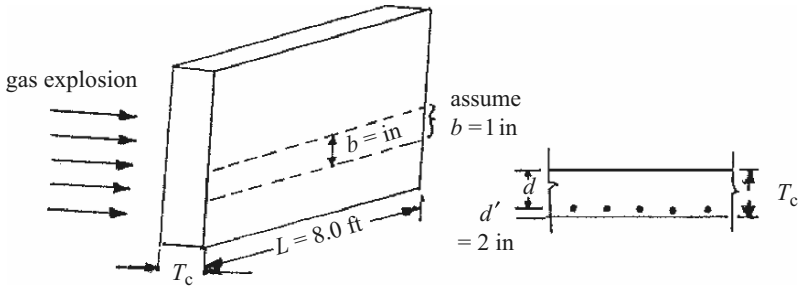
Given:

       Length of span, $L = 8.0\,\text{ft}$ (2,440 mm)

       Thickness, $T_c = 9.84\,\text{in}$ (250 mm)

       Effective depth, $d = 7.84\,\text{in}$

       Assumewidth, $b = 1\,\text{in}$

              $f_y = 60{,}000\,\text{psi}$

              $f_c' = 4{,}000\,\text{psi}$

Dynamic stresses

    $f_y(\text{dyn}) = 1.10 \times 60{,}000 = 66{,}000\,\text{psi}$

    $f_c'(\text{dyn}) = 1.25 \times 4{,}000 = 5{,}000\,\text{psi}$

Loading

    Max pressure for gas explosion $= 0.026{,}89\,\text{N}\,\text{mm}^{-2}$

    r_u for $(\text{DL} + \text{IL})$ and for soil $= 0.014{,}00\,\text{N}\,\text{mm}^{-2}$

                       Total, $r_u = 0.040{,}89\,\text{N}\,\text{mm}^{-2}$

                              $= 0.8537\,\text{kips}\,\text{ft}^{-2}$

Ultimate moment of resistance, M_u

    $M_u = (r_u \times L^2)/16 = (0.8537 \times 8^2)/16 = 3.146\,\text{ft kips}$

       $= 40.992\,\text{in kips}$

Checking capacity of section

    $\rho = \rho_{\max}$

    $f_c' = 5{,}000\,\text{psi}; K_1 = 0.80$

    $\rho_b = 0.85\,K_1(f_c'(\text{dyn})/f_y(\text{dyn})[87{,}000/(87{,}000 + f_y(\text{dyn}))]$

Substituting

    $\rho_b = 0.02929$

    $\rho_{\max} = 0.75\rho_b = 0.75 \times 0.029\,29 = 0.02197$

<div align="right">(continued)</div>

Table B.8. (continued)

Tension reinforcement

$$A_s \text{ required} = \rho_{max} \times b \times d = 0.02197(1)(7.84) = 0.172 \text{ in}^2$$
$$a = (A_s \times f_y(\text{dyn}))/(0.85 \times f'_c(\text{dyn}) \times b)$$
$$= (0.172 \times 66{,}000)/(0.85 \times 5{,}000 \times 1) = 2.67 \text{ in}$$
$$\varphi = \text{strength reduction factor} = 0.9$$
$$M_{max} = \varphi A_s \times f_y(\text{dyn})[d - (a/2)]$$
$$= 0.9(0.172)(66)[7.84 - (2.67/2)] = 66.46 \text{ in kips}$$

Since $M_{max} > M_u$, no compression steel needed

Tension steel

A_s required $= 0.172 \text{ in}^2 \text{ in}^{-1}$ run
Use no #4 bars at 8 in $\rightarrow$ (T12 − 200)
A_s provided $= 0.12 \text{ in}^2 \text{ in}^{-1}$ run

Minimum area of flexural reinforcement

$$\text{Passive design range} = \text{intermediate and low}$$
$$\text{Main reinforcement}, A_s = 0.20\% \ b \times d$$
$$= 0.002(1)(7.84)$$
$$= 0.0157 \text{ in}^2 < 0.2 \text{ in}^2 \text{ OK}$$
$$\text{Second reinforcement}, A_s = 0.12\% \ b \times T_c$$
$$= 0.0012(1)(9.84) = 0.0118 \text{ in}^2$$

Use no #3 bar at 8 in, (R10–200)
A_s provided $= 0.11 \text{ in}^2 > 0.0118 \text{ in}^2$

Checking for shear

Assume a unit area
$V = 0.5F = 0.5(0.854) = 0.427 \text{ kN}$
Ultimate shear stress

$$v_u = V/(b \times d) = 0.427/(1 \times 7.84)$$
$$= 0.0545 \text{ kips in}^{-2}$$

Permissible shear stress

$$v_c = \varphi[1.9f'_c(\text{dyn})^{1/2} + 2{,}500\rho_b]$$
$$= 0.85[1.9(5{,}000)^{1/2} + 2{,}500(0.021\,97)]$$
$$= 0.17 \text{ kips in}^{-2} > 0.0545 \text{ kips in}^{-2}$$

$v_c > v_u$, no shearing reinforcement is needed

Table B.9. Explosion resistance design of a reinforced concrete wall/slab with boundary conditions

---

Data

Required: ultimate unit resistance of a two-way element, shown below.
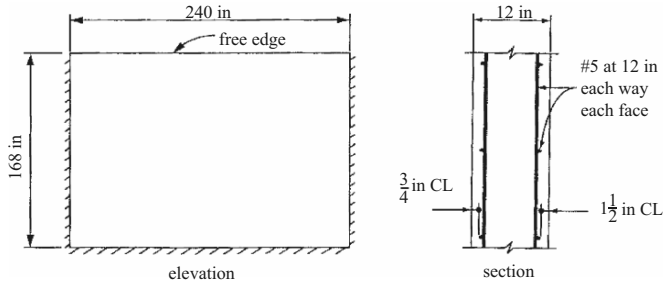
Solution

Given

$$L = 240 \, \text{in} \, (6{,}096 \, \text{mm}), \, H = 168 \, \text{in} \, (4{,}267 \, \text{mm})$$
$$T_{\text{c}} = 12 \, \text{in} \, (305 \, \text{mm})$$

Reinforcement: #5 at 12 in (T16–300) each way, each face
Three fixed supports capable of developing the moment capacity
  of the element, and one free edge
$f'_{\text{c}} = 3{,}000 \, \text{psi}$ and $f_{\text{y}} = 60{,}000 \, \text{psi}$
MF = DIF $\rightarrow$ concrete = 1.25, reinforcement = 1.10

Dynamic design strengths

$$f'_{\text{dc}} = \text{DIF} \, f'_{\text{c}} = 1.25(3{,}000) = 3750 \, \text{psi}$$
$$f'_{\text{dy}} = \text{DIF} \, f_{\text{y}} = 1.10(60{,}000) = 66{,}000 \, \text{psi}$$

Ultimate moment capacity, M_{u}

  For type **I** sections, neglecting the small effect of the compression reinforcement, the ultimate moment capacity is given by

$$M_{\text{u}} = (A_{\text{s}}/b) f'_{\text{dy}} [d - (a/2)],$$

where $a = (A_{\text{s}} \times f'_{\text{dy}})/(0.85 f'_{\text{dc}} \times b)$
For all sections, $A_{\text{s}} = 0.31 \, \text{in}^2 \, \text{ft}^{-1}$ for $b = 12 \, \text{in}$

$$a = (0.31 \times 66{,}000)/(0.85 \times 3.75 \times 12) = 0.535 \, \text{in}$$

(1) Horizontal direction
   – Negative moment, M_{HN}

$$d = 12 - (0.75 + 0.625/2) = 10.9375 \, \text{in}$$
$$M_{\text{HN}} = (0.31/12)(66{,}000)[10.9375 - (0.535/2)) = 18{,}190 \, \text{in kips}$$

Table B.9. (continued)

   – Positive moment, M_{HP}

$$d = 12 - (1.50 + 0.625/2) = 10.1875 \text{ in}$$
$$M_{HP} = (0.31/12)(66{,}000)[10.1875 - (0.535/2)) = 16{,}910 \text{ in kips}$$

(2) Vertical direction
   – Negative movement, M_{VN}

$$d = 12 - (0.75 + 0.625 + 0.625/2) = 10.3125 \text{ in}$$
$$M_{VN} = (0.31/12)(66{,}000)[10.3125 - (0.535/2)] = 17{,}130 \text{ in kips}$$

   – Positive moment, M_{VP}

$$d = 12 - (1.50 + 0.625 + 0.625/2) = 9.5625 \text{ in}$$
$$M_{VP} = (0.31/12)(66{,}000)[9.5625 - (0.535/2)] = 15{,}850 \text{ in kips}$$

Ultimate unit resistance, r_u
  The ultimate unit resistance of each sector is obtained by taking the summation of the moment about its axis of rotation (support), so that

$$M_{VN} + M_{VP} = R_c = r_u \times A_c$$

(1) Sector I

$$M_{VN} + M_{VP} = 17{,}130(120) + 2(2/3)(17{,}130)(60) + 15{,}850(120)$$
$$+ (2/3)(15{,}850)(60)$$
$$= 6.6 \times 10^6 \text{ in kips}$$
$$r_u \times A_c = r_u(240y/2)(y/3) = 40r_u \times y^2$$
$$\text{therefore,} \rightarrow r_u = (6.6 \times 10^6)/(40 \times y^2) = 164{,}900/y^2$$

(2) Sector II

$$M_{HN} + M_{HP} = 18{,}190(168 - y/2) = (2/3)(18{,}190)(y/2)$$
$$+ 16{,}190(168 - y/2) + (2/3)(16{,}910)(y/2)$$
$$= 5{,}850(1{,}008 - y)$$
$$r_u \times A_c = 4{,}800r_u(252 - y)$$
$$\text{therefore,} \rightarrow r_u = \frac{5{,}850(1{,}008 - y)}{4{,}800(252 - y)} = \frac{1.219(1{,}008 - y)}{(252 - y)}$$

Equating the ultimate unit resistance of the sectors:
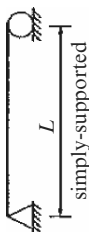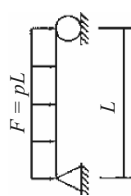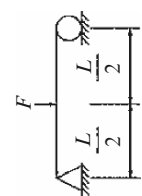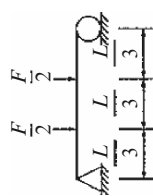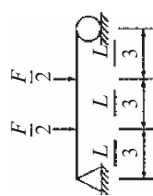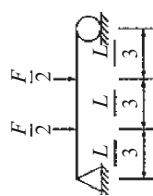
$$164{,}900/y^2 = [1.219(1{,}008 - y)]/(252 - y)$$

simplifying, $y^3 - 1{,}008y^2 - 135{,}300y + 34{,}100{,}000 = 0$ and the desired root is $y = 134.8 \text{ in}$.
  The ultimate unit resistance (Fig. B.23) is obtained by substituting the value of y into either equation obtained above, both of which yield:
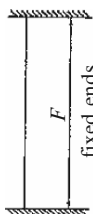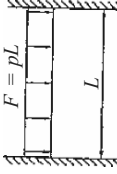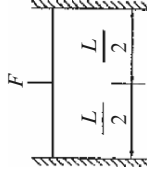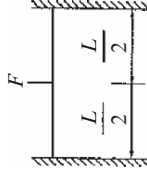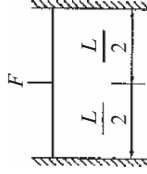
$$r_u = 9.08 \text{ psi}$$

Table B.10. Transformation factors for beams and one-way slabs (courtesy of the US Army Design Manual against Weapon Effects)

Loading diagram	Strain range	Load factor K_L	Mass factor K_M Concentrated mass[a]	Uniform mass	Load-mass factor K_{LM} Concentrated mass[a]	Uniform mass	Maximum resistance R_m	Spring constant k	Dynamic reaction V
$F = pL$ (simply-supported, uniform load over span L)	Elastic	0.64	–	0.50	–	0.78	$\dfrac{8M_P}{L}$	$\dfrac{384EI}{5L^3}$	$0.39R + 0.11F$
	Plastic	0.50	–	0.33	–	0.66	$\dfrac{8M_P}{L}$	0	$0.38R_m + 0.12F$
F (concentrated at midspan, $\frac{L}{2}$ and $\frac{L}{2}$)	Elastic	1.0	1.0	0.49	1.0	0.49	$\dfrac{4M_P}{L}$	$\dfrac{48EI}{L^3}$	$0.78R - 0.28F$
	Plastic	1.0	1.0	0.33	1.0	0.33	$\dfrac{4M_P}{L}$	0	$0.75R_m - 0.25F$
$\frac{F}{2}$, $\frac{F}{2}$ (third-point loads, $\frac{L}{3}$, $\frac{L}{3}$, $\frac{L}{3}$)	Elastic	0.87	0.76	0.52	0.87	0.60	$\dfrac{6M_P}{L}$	$\dfrac{56.4EI}{L^3}$	$0.525R - 0.025F$
	Plastic	1.0	1.0	0.56	1.0	0.56	$\dfrac{6M_P}{L}$	0	$0.52R_m - 0.02F$

[a] Concentrated mass is lumped at the concentrated load
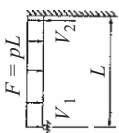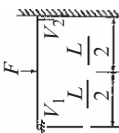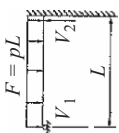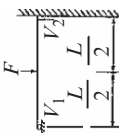
Table B.11. Transformation factors for beams and one-way slabs (courtesy of the US Army Design Manual against Weapon Effects)

Loading diagram	Strain range	Load factor K_L	Mass factor K_M		Load-mass factor K_{LM}		Maximum resistance R_m	Spring constant k	Effective spring constant k_E	Dynamic reaction V
			Concentrated mass[a]	Uniform mass	Concentrated mass[a]	Uniform mass				
	Elastic	0.53	—	0.41	—	0.77	$\dfrac{12M_{P_s}}{L}$	$\dfrac{384EI}{L^3}$	—	$0.36R + 0.14F$
	Elastic-plastic	0.64	—	0.50	—	0.78	$\dfrac{8}{L}(M_{P_s}+M_{P_m})$	$\dfrac{384EI}{5L^3}$	$\dfrac{307EI}{L^3}$	$0.39R + 0.11F$
	Plastic	0.50	—	0.33	—	0.66	$\dfrac{8}{L}(M_{P_s}+M_{P_m})$	0	—	$0.38R_m + 0.12F$
	Elastic	1.0	1.0	0.37	1.0	0.37	$\dfrac{4}{L}(M_{P_s}+M_{P_m})$	$\dfrac{192EI}{L^3}$	—	$0.71R - 0.21F$
	Plastic	1.0	1.0	0.33	1.0	0.33	$\dfrac{4}{L}(M_{P_s}+M_{P_m})$	0	—	$0.75R_m - 0.25F$

M_{P_s} = ultimate moment capacity at support, M_{P_m} = ultimate moment capacity at mid-span

[a] Concentrated mass is lumped at the concentrated load

Table B.12. Transformation factors for beams and one-way slabs (courtesy of the US Army Design Manual against Weapon Effects)

Loading diagram	Strain range	Load factor K_L	Mass factor K_M		Load-mass factor K_{LM}		Maximum resistance R_m	Spring constant k	Effective spring constant k_E	Dynamic reaction V
			Concentrated mass[a]	Uniform mass	Concentrated mass[a]	Uniform mass				
$F=pL$	Elastic	0.58	–	0.45	–	0.78	$\dfrac{8M_{P_s}}{L}$	$\dfrac{185EI}{L^3}$		$V_1=0.26R+0.12F$ $V_2=0.43R+0.19F$
	Elastic-plastic	0.64	–	0.50	–	0.78	$\dfrac{4}{L}\left(M_{P_s}+2M_{P_m}\right)$	$\dfrac{384EI}{5L^3}$	$\dfrac{160EI}{L^3}$	$V=0.39R+0.11F$ $\pm M_{P_s}/L$
	Plastic	0.50	–	0.33	–	0.66	$\dfrac{4}{L}\left(M_{P_s}+2M_{P_m}\right)$	0		$V=0.38R_m+0.12F$ $\pm M_{P_s}/L$
F	Elastic	1.0	1.0	0.43	1.0	0.43	$\dfrac{16M_{P_s}}{3L}$	$\dfrac{107EI}{L^3}$		$V_1=0.25R+0.07F$ $V_2=0.54R+0.14F$
	Elastic-plastic	1.0	1.0	0.49	1.0	0.49	$\dfrac{2}{L}\left(M_{P_s}+2M_{P_m}\right)$	$\dfrac{48EI}{L^3}$	$\dfrac{106EI}{L^3}$	$V=0.78R-0.28F$ $\pm M_{P_s}/L$
	Plastic	1.0	1.0	0.33	1.0	0.33	$\dfrac{2}{L}\left(M_{P_s}+2M_{P_m}\right)$	0		$V=0.75R_m-0.25F$ $\pm M_{P_s}/L$

Elastic	0.81	0.67	0.45	0.83	0.55	$\dfrac{6M_{P_s}}{L}$	$\dfrac{132EI}{L^3}$		$V_1 = 0.17R + 0.17F$ $V_2 = 0.33R + 0.33F$
Elastic-plastic	0.87	0.76	0.52	0.87	0.60	$\dfrac{2}{L}(M_{P_s} + 3M_{P_m})$	$\dfrac{56EI}{L^3}$	$\dfrac{122EI}{L^3}$	$V = 0.525R - 0.025F$ $\pm M_{P_s}/L$
Plastic	1.0	1.0	0.56	1.0	0.56	$\dfrac{2}{L}(M_{P_s} + 3M_{P_m})$	$-$		$V = 0.52R_m - 0.02F$ $\pm M_{P_s}/L$
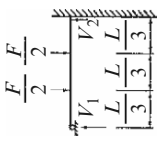
M_{P_s} = ultimate bending capacity at support. M_{P_m} = ultimate positive bending capacity
[a] Equal parts of the concentrated mass are lumped at each concentrated load

Table B.13. Transformation factors for two-way slabs: simple supports – four sides, uniform load (courtesy of the US Army Design Manual against Weapon Effects)

Strain range	a/b	Load factor K_L	Mass factor K_M	Load-mass factor K_{LM}	Maximum resistance	Spring constant k	Dynamic reactions V_A	V_B
Elastic	1.0	0.46	0.31	0.67	$\frac{12}{a}(M_{P_{fa}} + M_{P_{fb}})$	$\frac{252EI_a}{a^2}$	$0.07F + 0.18R$	$0.07F + 0.18R$
	0.9	0.47	0.33	0.70	$\frac{1}{a}(12M_{P_{fa}} + 11M_{P_{fb}})$	$\frac{230EI_a}{a^2}$	$0.06F + 0.16R$	$0.08F + 0.20R$
	0.8	0.49	0.35	0.71	$\frac{1}{a}(12M_{P_{fa}} + 10.3M_{P_{fb}})$	$\frac{212EI_a}{a^2}$	$0.06F + 0.14R$	$0.08F + 0.22R$
	0.7	0.51	0.37	0.73	$\frac{1}{a}(12M_{P_{fa}} + 9.8M_{P_{fb}})$	$\frac{201EI_a}{a^2}$	$0.05F + 0.13R$	$0.08F + 0.24R$
	0.6	0.53	0.39	0.74	$\frac{1}{a}(12M_{P_{fa}} + 9.3M_{P_{fb}})$	$\frac{197EI_a}{a^2}$	$0.04F + 0.11R$	$0.09F + 0.26R$
	0.5	0.55	0.41	0.75	$\frac{1}{a}(12M_{P_{fa}} + 9.0M_{P_{fb}})$	$\frac{201EI_a}{a^2}$	$0.04F + 0.09R$	$0.09F + 0.28R$
Plastic	1.0	0.33	0.17	0.51	$\frac{12}{a}(M_{P_{fa}} + M_{P_{fb}})$	0	$0.09F + 0.16R_m$	$0.09F + 0.16R_m$
	0.9	0.35	0.18	0.51	$\frac{1}{a}(12M_{P_{fa}} + 11M_{P_{fb}})$	0	$0.08F + 0.15R_m$	$0.09F + 0.18R_m$
	0.8	0.37	0.20	0.54	$\frac{1}{a}(12M_{P_{fa}} + 10.3M_{P_{fb}})$	0	$0.07F + 0.13R_m$	$0.10F + 0.20R_m$
	0.7	0.38	0.22	0.58	$\frac{1}{a}(12M_{P_{fa}} + 9.8M_{P_{fb}})$	0	$0.06F + 0.12R_m$	$0.10F + 0.22R_m$
	0.6	0.40	0.23	0.58	$\frac{1}{a}(12M_{P_{fa}} + 9.3M_{P_{fb}})$	0	$0.05F + 0.10R_m$	$0.10F + 0.25R_m$
	0.5	0.42	0.25	0.59	$\frac{1}{a}(12M_{P_{fa}} + 9.0M_{P_{fb}})$	0	$0.04F + 0.08R_m$	$0.11F + 0.27R_m$

V_A = total dynamic reaction along short edge; V_B = total dynamic reaction along long edge. $M_{P_{fa}}$ = total positive ultimate moment capacity along mid-span section parallel to short edge. $M_{P_{fb}}$ = total positive ultimate moment capacity along mid-span section parallel to long edge
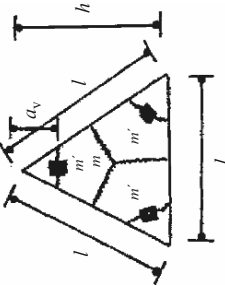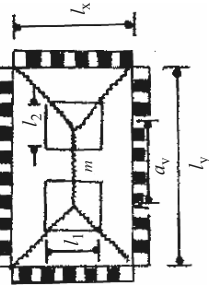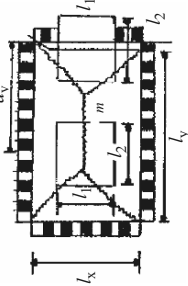
Table B.14. Transformation factors for two-way slabs: fixed four sides, uniform load (courtesy of the US Army Design Manual against Weapon Effects)

Strain range	a/b	Load factor K_L	Mass factor K_M	Load-mass factor K_{LM}	Maximum resistance	Spring constant k	Dynamic reactions V_A	V_B
Elastic	1.0	0.33	0.21	0.63	$29.2 M_{P_{sb}}^s$	$810 EI_a/a^2$	$0.10F + 0.15R$	$0.10F + 0.15R$
	0.9	0.34	0.23	0.68	$27.4 M_{P_{sb}}^s$	$742 EI_a/a^2$	$0.09F + 0.14R$	$0.10F + 0.17R$
	0.8	0.36	0.25	0.69	$26.4 M_{P_{sb}}^s$	$705 EI_a/a^2$	$0.08F + 0.12R$	$0.11F + 0.19R$
	0.7	0.38	0.27	0.71	$26.2 M_{P_{sb}}^s$	$692 EI_a/a^2$	$0.07F + 0.11R$	$0.11F + 0.21R$
	0.6	0.41	0.29	0.71	$27.3 M_{P_{sb}}^s$	$724 EI_a/a^2$	$0.06F + 0.09R$	$0.12F + 0.23R$
	0.5	0.43	0.31	0.72	$30.2 M_{P_{sb}}^s$	$806 EI_a/a^2$	$0.05F + 0.08R$	$0.12F + 0.25R$
Elastic-plastic	1.0	0.46	0.31	0.67	$(1/a)[12(M_{P_{fa}} + M_{P_{sa}}) + 12(M_{P_{fb}} + M_{P_{sb}})]$	$252 EI_a/a^2$	$0.07F + 0.18R$	$0.07F + 0.18R$
	0.9	0.47	0.33	0.70	$(1/a)[12(M_{P_{fa}} + M_{P_{sa}}) + 11(M_{P_{fb}} + M_{P_{sb}})]$	$230 EI_a/a^2$	$0.06F + 0.16R$	$0.08F + 0.20R$
	0.8	0.49	0.35	0.71	$(1/a)[12(M_{P_{fa}} + M_{P_{sa}}) + 10.3 M_{P_{fb}} + M_{P_{sb}})]$	$212 EI_a/a^2$	$0.06F + 0.14R$	$0.08F + 0.22R$
	0.7	0.51	0.37	0.73	$(1/a)[12(M_{P_{fa}} + M_{P_{sa}}) + 9.8(M_{P_{fb}} + M_{P_{sb}})]$	$201 EI_a/a^2$	$0.05F + 0.13R$	$0.08F + 0.24R$
	0.6	0.53	0.39	0.74	$(1/a)[12(M_{P_{fa}} + M_{P_{sa}}) + 9.3(M_{P_{fb}} + M_{P_{sb}})]$	$197 EI_a/a^2$	$0.04F + 0.11R$	$0.09F + 0.26R$
	0.5	0.55	0.41	0.75	$(1/a)[12(M_{P_{fa}} + M_{P_{sa}}) + 9.0(M_{P_{fb}} + M_{P_{sb}})]$	$201 EI_a/a^2$	$0.04F + 0.09R$	$0.09F + 0.28R$
Plastic	1.0	0.33	0.17	0.51	$(1/a)[12(M_{P_{fa}} + M_{P_{sa}}) + 12(M_{P_{fb}} + M_{P_{sb}})]$	0	$0.09F + 0.16R_m$	$0.09F + 0.16R_m$
	0.9	0.35	0.18	0.51	$(1/a)[12(M_{P_{fa}} + M_{P_{sa}}) + 11(M_{P_{fb}} + M_{P_{sb}})]$	0	$0.08F + 0.15R_m$	$0.09F + 0.18R_m$
	0.8	0.37	0.20	0.54	$(1/a)[12(M_{P_{fa}} + M_{P_{sa}}) + 10.3(M_{P_{fb}} + M_{P_{sb}})]$	0	$0.07F + 0.13R_m$	$0.10F + 0.20R_m$
	0.7	0.38	0.22	0.58	$(1/a)[12(M_{P_{fa}} + M_{P_{sa}}) + 9.8(M_{P_{fb}} + M_{P_{sb}})]$	0	$0.06F + 0.12R_m$	$0.10F + 0.22R_m$
	0.6	0.40	0.23	0.58	$(1/a)[12(M_{P_{fa}} + M_{P_{sa}}) + 9.3(M_{P_{fb}} + M_{P_{sb}})]$	0	$0.05F + 0.10R_m$	$0.10F + 0.25R_m$
	0.5	0.42	0.25	0.59	$(1/a)[12(M_{P_{fa}} + M_{P_{sa}}) + 9.0(M_{P_{fb}} + M_{P_{sb}})]$	0	$0.04F + 0.08R_m$	$0.11F + 0.27R_m$

$M_{P_{fa}}$ = total positive ultimate moment capacity along mid-span section parallel to short edge. $M_{P_{sa}}$ = total negative ultimate moment capacity along short edge. $M_{P_{sb}}$ = total negative ultimate moment capacity per unit width at centre of long edge. $M_{P_{fb}}$ = total positive ultimate moment capacity along mid-span section parallel to long edge. V_A = total dynamic reaction along short edge; V_B = total dynamic reaction along long edge

Table B.15. Design aids based on yield line techniques

Slab type	Load	Moment–load relationship
A1 simply-supported at 3 columns	n/unit area	$$m = \frac{n \times \text{area of triangle}}{\sqrt{3}} \left[\frac{7}{18} - \frac{a_v}{h}\right]$$ $$m' = (1/6)na_v^2$$
B1 simply-supported at 4 edges	n/unit area over two rectangles	$$m = \frac{nl_1l_2}{6} \times \frac{l_y - a_v}{2l_y - a_v} \times \frac{2l_y - l_2}{l_y} \times \frac{2l_x - 1}{l_x}$$
C1 simply-supported at 4 edges	n/unit area over two rectangles	$$m = \frac{F}{12} \times \frac{l_y + l_2 - a_v}{l_y + l_2} \times \frac{2l_y - l_2}{l_y} \times \frac{2l_x - 1}{l_x}$$ where $F = n(l_1l_2 + \frac{1}{2}l_1l_2)$

D1 Rectangular slab fixed at both edges supported on a column

$m_1' = \mu_1 m; \quad m_2' = \mu_2 m$
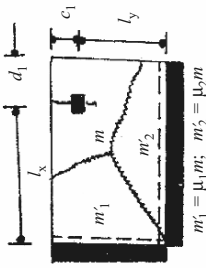
n/unit area

$$m = \left[\frac{3nl_x l_y}{8\left(2 + \dfrac{l_y}{l_x} + \dfrac{l_x}{l_y}\right)}\right] - 0.15nc_1 d_1$$

$$1 + 0.6\frac{\mu_1(c_1 + l_y) + \mu_2(l_x + d_1)}{(l_x + l_y + c_1 + d_1)}$$
$$= \bar{K}$$

V = reaction at column = $[(0.22nl_x l_y/(1+\bar{K})]$
$\quad + \frac{1}{2}n(l_y d_1 + l_x c_1) + 2.5nc_1 d_1$

E1 Rectangular slab fixed at one edge supported on two columns

$m' = \mu m$
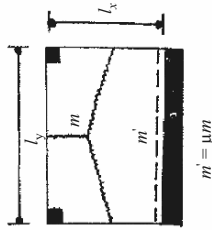
n/unit area

$$m = \frac{nl_x l_y}{18 + 12\mu}\left(\frac{5 + 2\mu}{4}\frac{l_x}{l_y} + 1\right),$$

where $(l_y/l_x) < 2 - (\mu/2)$
$\mu \le 1$

$m' = 0; \ m = \dfrac{nl_x l_y}{18}\left(\dfrac{5}{4}\dfrac{l_x}{l_y} + 1\right)$ simply supported,

where $(l_y/l_x) < 2$

for a square slab: $m' = 0; \ m = nl_x^2/8$

A2 Slab supported on four columns

n/unit area

$m_1 = (1/8)n(l_y^2 - 4c_1^2)$

$m_2 = (1/8)n(l_x^2 - 4d_1^2)$

$m_1' = (1/2)nc_1^2; \ m_2' = (1/2)nd_1^2$

(continued)

Table B.15. (continued)

Slab type	Load	Moment–load relationship
B2 Rectangular skew slabs supported at two edges and free at two edges	n/unit area	$$m = \frac{n}{8}\left\{ \frac{4l^2}{\left[\sqrt{(1+\mu_1)} + \sqrt{(1+\mu_2)}\right]^2} \right\}$$
C2 Rectangular skew slabs fixed at all edges	n/unit area	$\bar{m} = m(1.75 - \sin\psi)$ with $\psi \geq 30°$ where m in this case is the moment for a rectangular slab with sides at 90°
D2	n/unit area	$m = m[1.75 - (1/3)(\sin\psi_1 + \sin\psi_2)]$

Figure labels B2: $m'_1 = \mu_1 m$, $m'_2 = \mu_2 m$, m, m'_2, l, m'_1

Figure labels C2: $m'_1 = \mu_1 \bar{m}$, $m'_2 = \mu_2 \bar{m}$, $m'_3 = \mu_3 \bar{m}$, $m'_4 = \mu_4 \bar{m}$; m_4, m'_3, m_1, $\bar{m}$, m'_2, ψ

Figure labels D2: $m'_1 = \mu_1 \bar{m}$, $m'_2 = \mu_2 \bar{m}$, $m'_3 = \mu_3 \bar{m}$, $m'_4 = \mu_4 \bar{m}$; l_x, $l_y/2$, $l_y/2$, ψ_2, m_4, m'_3, m_3, $\bar{m}$, m'_1, m_2, ψ_1

E2   Rectangular slabs fixed at two edges and free at two edges
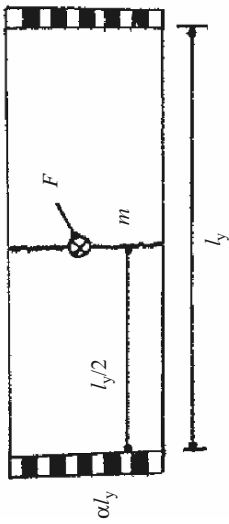
n/unit area plus F at centre $m = (nl^2/8) + (F/4\alpha)$
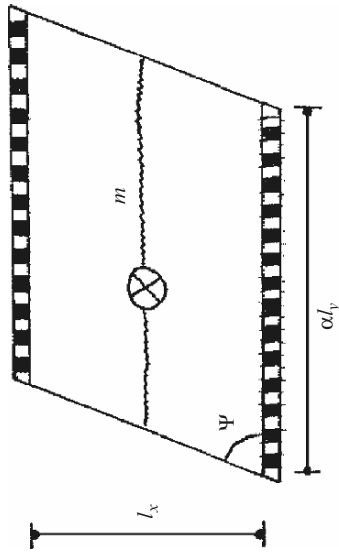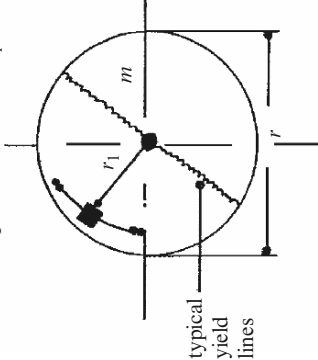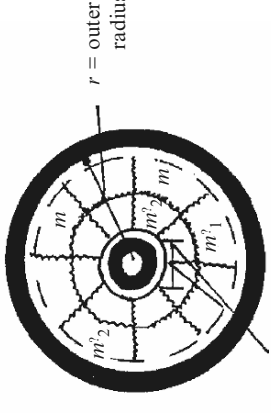
n/unit area plus F at centre $m = \dfrac{1}{\cos^2(90 - \psi)}\left(\dfrac{nl_x^2}{8} + \dfrac{F}{4\alpha}\right)$

(*continued*)

Table B.15. (continued)

Slab type	Load	Moment–load relationship
A3 Circular slab supported on n_1 number of columns placed at a radius r_1	n/unit area	$m = nr^2 \left[\dfrac{r_1}{2r} \times \dfrac{\dfrac{1}{\sin \pi/n}}{\pi/n} - \dfrac{1}{3} \right]$ for $r_1 = r$, i.e. columns at the rim $m = nr^2/6$
B3 Circular slabs rigidly supported at inner and outer circumference	n/unit area	$m_1' + m_2' + 2m = n \left[\dfrac{(a_1 - r)^2}{15} \left(\dfrac{a_1}{r} + 2.75 \right) \right]$ $a_1 = a/2;\ a = $ inner radius

typical yield lines

$r = $ outer radius

$a_1 = $ inner radius

(a)

(b)
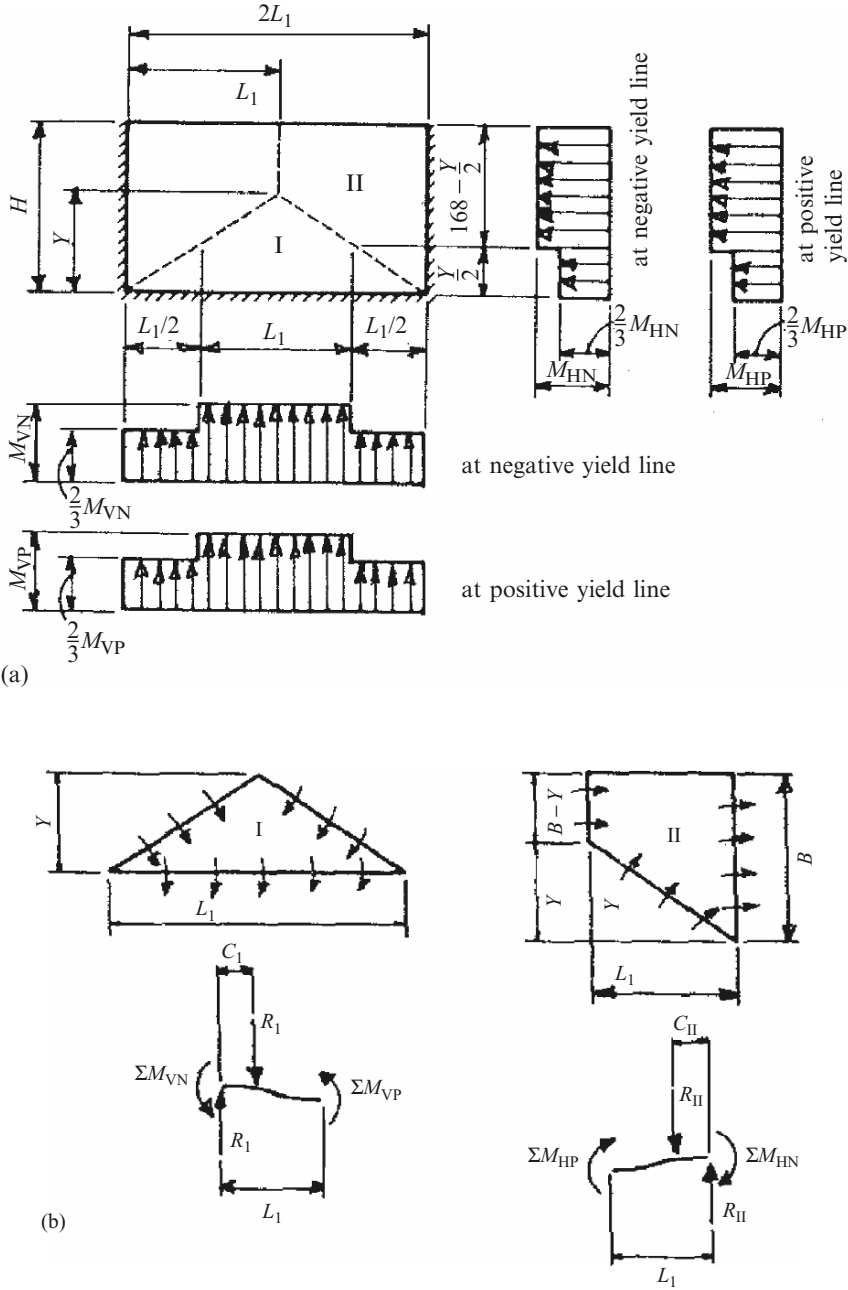
Fig. B.23. Determination of ultimate resistance. (**a**) Assumed yield lines and distribution of moments. (**b**) free-body diagrams for individual sections
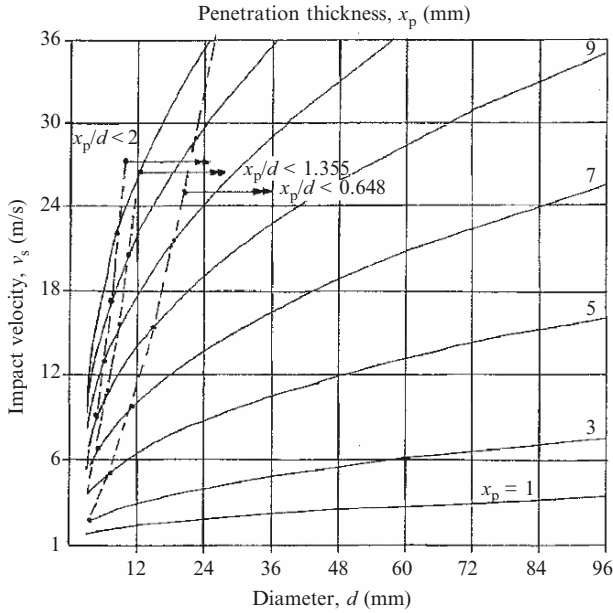
Fig. B.24. Penetration depth versus v_s and d
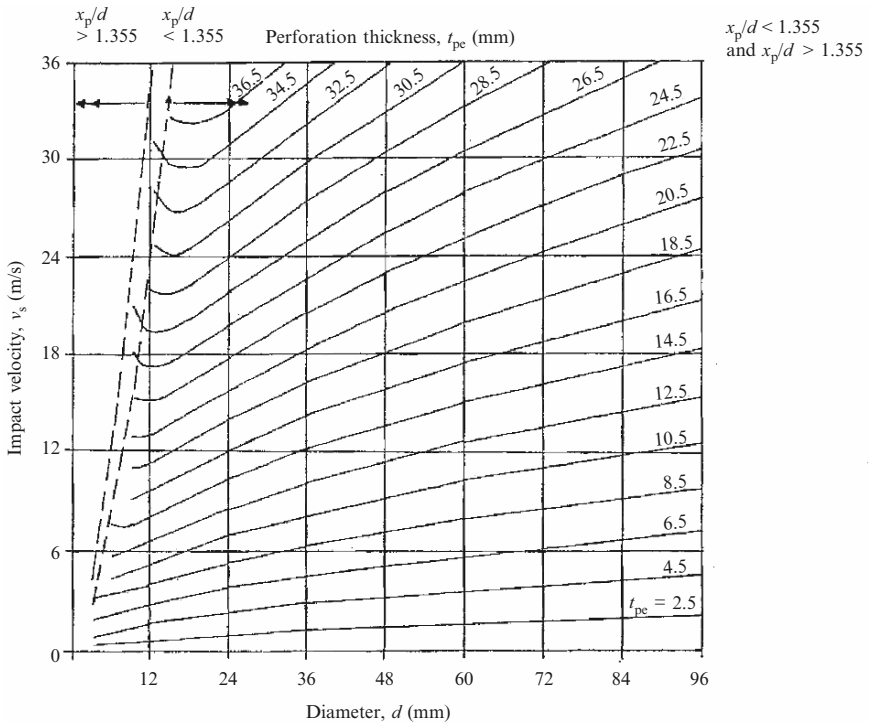
Fig. B.25. Perforation thickness versus v_s and d

Scabbing thickness, t_{sc}

for $x_p/d < 0.648$

$t_{sc}/d = 7.898\,(x_p/d)$
$\qquad -5.058\,(x_p/d)^2$

for $x_p/d < 0.648$
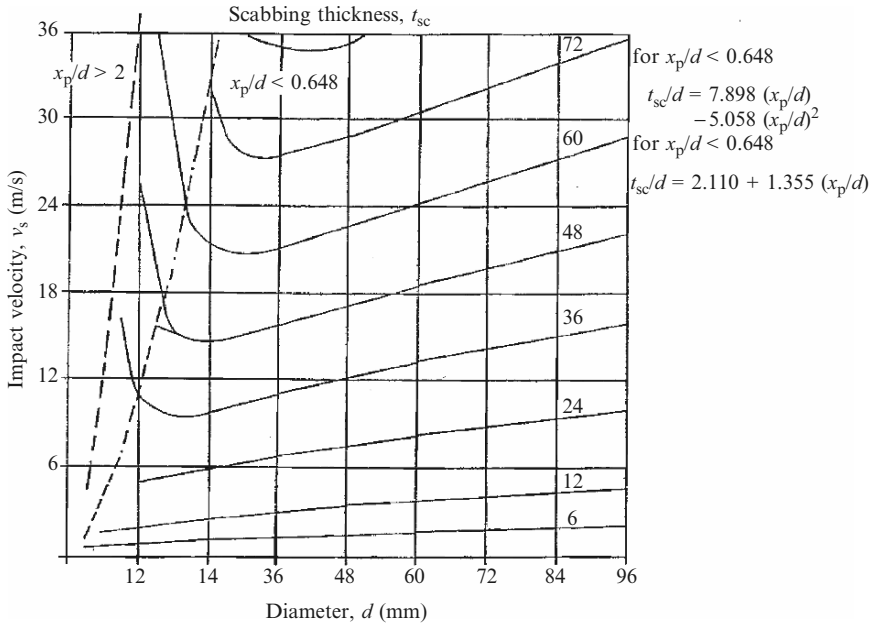
$t_{sc}/d = 2.110 + 1.355\,(x_p/d)$

Fig. B.26. Scabbing thickness versus v_s and d

Scabbing Thickness t_{sc} (mm)

Three limits are designed: $x_p/d < 0.648$, $x_p/d > 0.648$ and $x_p/d > 2$.

(1) $t_{sc}/d = 7.898(x_p/d) - 5.058(x_p/d)^2$
(2) $x_p/d > 0.648$
     $t_{sp}/d = 2.110 + 1.355(x_p/d)$

All others can be incorporated. Graphs are drawn for mass $M = 1$ kg and nose shape $N = 0.72$; modifications may be made for other values of M and N.

Penetration Thickness x_p (mm)

Two limits are defined: $x_p/d < 0.648$ and $x_p/d < 2$. Graphs are drawn for $M = 1$ kg and $N = 0.72$; again, modifications are made for other values of M and N.

$$G(x_p/d) = 9.570NM \times \sqrt{(f_c' d^{-2.8} V^{1.8})}$$
$$f_c' = 35\,\mathrm{N\,mm^{-2}}$$

Perforation Thickness t_{pe} *(mm)*

Two limits are defined: $x_p/d \lessgtr 1.349$ and $x_p/d > 2$.

$$x_p/d < 1.349 \quad t_{pe}/d = 3.18(x_p/d) + 7.18(x_p/d)^2$$
$$x_p/d > 1.349 \quad t_{pe}/d = 1.28(x_p/d) + 1.3$$

B.3.4 Steel–Concrete Composite Structures Subject to Blast/Impact Loads

Behaviour of Composite Beams Subjected to Impulsive Load (A Quasi-Static Approach Adopted)

Introduction

The results of the steel-concrete composite beams being compared will be between the composite beams under (Q-S/Dynamic load and its equivalent Universal Steel Beams with the same (approximately) plastic moment capacity as well as its equivalent rectangular concrete beam.

Procedure

First the author makes a selection of Universal Steel Beams and places on top of them a concrete slab of varying depth (100 mm–150 mm–200 mm). For demonstration purposes one of these composite beams is chosen to carry out the different analyses. This section is $762 \times 267 \times 197\,\mathrm{kg\,m}^{-1}$ with 200 m depth of concrete flange.

The next step is to perform the Elastic Analysis on this composite section, transforming it into steel, in order to determine the flexural stiffness and the steel and concrete stresses. For checking the Elastic Analysis is performed again, but this time the composite section is transformed into all concrete. The results are the same and therefore satisfactory.

The Elastic Analysis is followed by the Plastic Analysis, which will provide the author with the plastic moment of resistance. A check is made as well, for the shear capacity of the web.

After completing the static analyses of the composite section, the triangular blast load is applied. Again, because there are a variety of loads used in this thesis, the author uses for this example a pressure of 390 kPa with duration of 40 ms. The Quasi-Static/Dynamic analysis is performed.

For comparison, the equivalent UB steel section is obtained form tables with the same dynamic value of plastic moment capacity as in the composite. Again, the same blast load is applied and approached in the same way.

Finally, the author chooses an equivalent concrete section with the same plastic moment capacity as the composite and performs the blast analysis.

Table B.16. Selected sections and their geometry

Sections	Dc	Ds	Bs	T	t	d	As
914 × 305 × 224	200	910.4	304.1	23.9	15.9	824.4	28,600
914 × 305 × 224	150	910.4	304.1	23.9	15.9	824.4	28,600
914 × 305 × 224	100	910.4	304.1	23.9	15.9	824.4	28,600
838 × 292 × 194	200	840.7	292.4	21.7	14.7	761.7	24,700
838 × 292 × 194	150	840.7	292.4	21.7	14.7	761.7	24,700
838 × 292 × 194	100	840.7	292.4	21.7	14.7	761.7	24,700
762 × 267 × 197	200	769.8	268	25.4	15.6	686	25,100
762 × 267 × 197	150	769.8	268	25.4	15.6	686	25,100
762 × 267 × 197	100	769.8	268	25.4	15.6	686	25,100
686 × 254 × 170	200	692.9	255.8	23.7	14.5	615.1	21,700
686 × 254 × 170	150	692.9	255.8	23.7	14.5	615.1	21,700
686 × 254 × 170	100	692.9	255.8	23.7	14.5	615.1	21,700
610 × 305 × 238	200	635.8	311.4	31.4	18.4	540	30,300
610 × 305 × 238	150	635.8	311.4	31.4	18.4	540	30,300
610 × 305 × 238	100	635.8	311.4	31.4	18.4	540	30,300
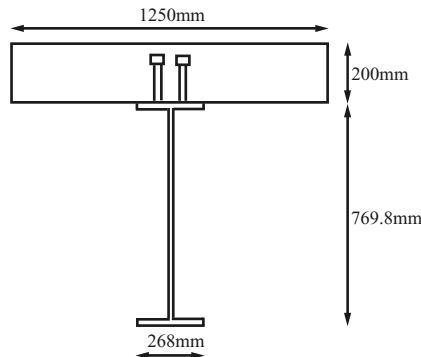
Fig. B.27. Geometry of the UB $762 \times 267 \times 197 \, \text{kg} \, \text{m}^{-1}$ section

Selection of Composite Beams

Due to the large blast loads that, later, are going to be applied on the sections, quite large beams are chosen to avoid extensive 'static' failure. All the steel sections are of grade S275 steel. The concrete slabs are 200 mm–150 mm–100 mm thick and of characteristic strength $30 \, \text{N} \, \text{mm}^{-2}$. The sections that are to be analysed are given in Table B.16.

Assumption is made, that there is no reinforcement and no cracking in the concrete slab, for simplification of the design.

Design Example Based on Elastic Analysis

First a transformation of the composite beams into equivalent steel-sections is performed. All the assumptions stated in Chap. 3 are satisfied.

The UB $762 \times 267 \times 197\,\mathrm{kg\,m^{-1}}$ is chosen from above with $200\,\mathrm{mm}$ depth of concrete flange. The elastic modulus of steel is taken $E_s = 200\,\mathrm{kN\,mm^{-2}}$ and the elastic modulus of steel $E_c = 20\,\mathrm{kN\,mm^{-2}}$. The length of the beam is $L = 5\,\mathrm{m}$ and the steel area $A_s = 25{,}100\,\mathrm{mm^2}$.

$d_c = d_t \dfrac{A_s}{A_c} = 484.9 \times \dfrac{25{,}100}{50{,}100} = 242.9\,\mathrm{mm}$, which is greater than the half of the depth of the slab, so the composite neutral axis lie in the steel beam. The total depth of the composite neutral axis from the top of the concrete slab is:

$$x_e = d_e + \left(\frac{D_c}{2}\right) = 242.9 + 100 = 342.9\,\mathrm{mm} \approx 343\,\mathrm{mm}. \qquad \text{(B.1)}$$

Having determined the depth of the neutral axis the remaining section properties can be calculated.

The second moment of area of the equivalent all-steel section, I, is:

$$I = I_s + \frac{I_c}{m} + \frac{A_c d_c^2}{m} + A_s d_s^2, \qquad \text{(B.2)}$$

where d_s is the distance between the composite neutral axis and the steel neutral axis, and is equal to:

$$d_s = h_s - \frac{D_c}{2} - d_c = 200 + \frac{769.8}{2} - 100 - 242.9 = 242\,\mathrm{mm}. \qquad \text{(B.3)}$$

Hence,

$$
\begin{aligned}
I &= I_s + \frac{I_c}{m} + \frac{A_c d_c^2}{m} + A_s d_s^2 = 240{,}000 \times 10^4 + \frac{1{,}250 \times 200^3}{12 \times 10} \\
&\quad + \frac{250{,}000 \times 241^2}{10} + 25{,}100 \times 242^2 \\
&= 5{,}428{,}299{,}926\,\mathrm{mm^4}
\end{aligned}
$$

and

$$E_s I = 200 \times 10^3 \times 5{,}428{,}299{,}926 = 1.08566 \times 10^{15}\,\mathrm{N\,mm^2}. \qquad \text{(B.4)}$$

Longitudinal stresses due to bending can be calculated. Thus, a positive bending moment causes the following maximum stresses in the steel and the concrete.

Loading:

$$
\begin{aligned}
w &= 1.4(D_s \rho_c + \text{finishes} + \text{ceiling/services})\ell + 1.6(q_k + \text{partition loading})\ell \\
&= 1.4(0.2 \times 24 + 1.2 + 1) \times 2 + 1.6(4 + 1) \times 2 = 35.6\,\mathrm{kN\,m^{-1}},
\end{aligned}
$$
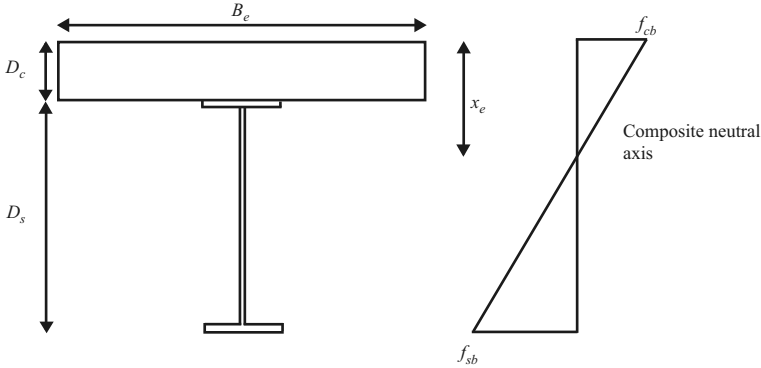
Fig. B.28. Graphical representation of the different material stresses, when the composite neutral axis falls within the steel web

where

$$\rho_c = 24 \, \text{kN} \, \text{m}^{-3}$$
$$\ell = 2 \, \text{m}$$
$$L = 5 \, \text{m}$$
$$q_k = 4 \, \text{kN} \, \text{m}^{-2}$$

So the moment due to loading is:

$$M_E = \frac{wL^2}{8} = \frac{35.6 \times 5^2}{8} = 111.25 \, \text{kN} \, \text{m} = 111{,}250 \, \text{kN} \, \text{mm} \qquad \text{(B.5)}$$

and therefore the stresses for steel and concrete, respectively, are:

$$f_{sb} = \frac{M}{I}(D_c + D_s - x_e) = \frac{111{,}250}{5{,}428{,}299{,}926}(200 + 769.8 - 343)$$
$$= 0.01284 \, \text{kN} \, \text{mm}^{-2} = 12.84 \, \text{N} \, \text{mm}^{-2} << 275 \, \text{N} \, \text{mm}^{-2} \quad \text{ok}$$
$$f_{cb} = \frac{M x_e}{mI} = \frac{111{,}250 \times 343}{10 \times 5428{,}299{,}926} = 0.0007 \, \text{kN} \, \text{mm}^{-2}$$
$$= 0.7 \, \text{N} \, \text{mm}^{-2} << 0.45 \times 35 = 15.75 \, \text{N} \, \text{mm}^{-2} \quad \text{ok}$$

Hence, both stresses are in the elastic range (see chart A.1 appendix).

Transformation of Composite Seciton to an Equivalent All-Concrete Section

The same procedure can be followed for the transformation of the composite section into an equivalent all-concrete section. But this time instead of transforming the concrete area, the transformation will occur in the steel section.

Effective breadth: $B_e = \dfrac{L}{4} = \dfrac{5{,}000}{4} = 1{,}250\,\text{mm}$ \hfill (B.6)

Modular ratio: $m = \dfrac{E_s}{E_c} = \dfrac{200 \times 10^9}{20 \times 10^9} = 10$ \hfill (B.7)

Case 1 – Composite neutral axis below the slab

Area of concrete: $A_c = B_e \times D_c = 1{,}250 \times 200 = 250{,}000\,\text{mm}^2$ \hfill (B.8)

Area of steel: $A_s = 25{,}100\,\text{mm}^2$

Transformed area: $A_s \times m = 25{,}100 \times 10 = 251{,}000\,\text{mm}^2$ \hfill (B.9)

Total composite area: $A_t = A_s \times m + A_c = 251{,}000 + 250{,}000 = 501{,}000\,\text{mm}^2$

Taking moments of area about the neutral axis of the slab,

$$A_s d_t = A_t d_c,$$

where

$$d_t = \frac{D_c + D_s}{2} = \frac{200 + 762.2}{2} = 481.1\,\text{mm}. \tag{B.10}$$

Hence,

$d_c = d_t \dfrac{A_s}{A_c} = 481.1 \times \dfrac{251{,}000}{501{,}000} = 241.03\,\text{mm}$, which is greater than the half of the depth of the slab, so the composite neutral axis lie in the steel beam. The total depth of the composite neutral axis from the top of the concrete slab is:

$$x_e = d_c + \left(\frac{D_c}{2}\right) = 241.03 + 100 = 341.03\,\text{mm} \approx 341\,\text{mm}. \tag{B.11}$$

Having determined the depth of the neutral axis the remaining section properties can be calculated.

The second moment of area of the equivalent all-steel section, I, is:

$$I = I_s \times m + I_c + A_c d_c^2 + A_s d_s^2 \times m, \tag{B.12}$$

where d_s is the distance between the composite neutral axis and the steel neutral axis, and is equal to:

$$d_s = h_s - \frac{D_c}{2} - d_c = 200 + \frac{762.2}{2} - 100 - 241 = 240.1\,\text{mm}. \tag{B.13}$$

Hence,

$$\begin{aligned}
I &= I_s m + I_c + A_c d_c^2 + A_s d_s^2 m \\
&= 240{,}000 \times 10^5 + \frac{1{,}250 \times 200^3}{12} + 250{,}000 \times 241^2 + 251{,}000 \times 341^2 \\
&= 53{,}823{,}233{,}390\,\text{mm}^4
\end{aligned}$$

and

$$E_c I = 20 \times 10^3 \times 53{,}823{,}233{,}390 = 1.0765 \times 10^{15} \,\text{Nmm}^2. \qquad (\text{B.14})$$

The stresses in steel and concrete are the same as above.

The spreadsheets in Chap. 5 summarise the procedure and identify the flexural stiffness of the different sections as well as their stresses.

Plastic Design Analysis of Composite Sections

After calculating the flexural stiffness of the beam and its longitudinal stresses, there is a need to find the plastic moment capacity of this section that will resist the moment due to the blast load, later. The same section is used, as in the elastic analysis for consistency.

Also, a check must be made of the shear capacity of the web, assuming that the web carries the whole shear at a strength not exceeding the design yield stress in shear $\left(\frac{f_y}{\sqrt{3}}\right)$. Referring to the previous chapter, the method of stress blocks is employed to obtain M_p.

The loading is the same as in the elastic analysis, and consequently, the moment due to loading.

$$w = 35.6 \,\text{kN}\,\text{m}^{-1}$$

Design moment, $M = 111.25 \,\text{kN}\,\text{m}$.

Moment Capacity

The resistance of the concrete flange, R_c, is:

$$R_c = 0.45 f_{cu} B_e D_c = 0.45 \times 35 \times 1{,}250 \times 200 \times 10^{-3} = 3{,}937.5 \,\text{kN} \quad (\text{B.15})$$

Since $T = 25.6 \,\text{mm} > 16 \,\text{mm}$ and steel grade is S275, the design strength of the beam, is $p_y = 265 \,\text{N}\,\text{mm}^{-2}$. The resistance of the steel beam, R_s, is:

$$R_s = A p_y = 25{,}100 \times 265 \times 10^{-3} = 6{,}651.5 \,\text{kN} \qquad (\text{B.16})$$
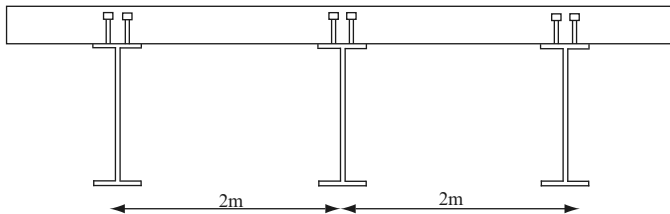
Fig. B.29. Composite floor system

Since $R_c < R_s$, the plastic neutral axis will lie in the steel beam.

$$y = \frac{R_s - R_c}{2B_s p_y} = \frac{(6{,}651.5 - 3{,}937.5) \times 10^3}{2 \times 268 \times 265} = 19.1\,\text{mm} < T = 25.6\,\text{mm}.$$
(B.17)

So the neutral axis will fall within the steel flange. The plastic moment capacity of the composite section, M_c, is:

$$M_c = R_s \frac{D_s}{2} + R_c \frac{D_c}{2} - \frac{(R_s - R_c)^2}{R_f} \frac{T}{4},$$

where

$$R_f = B_s T p_y = 268 \times 25.6 \times 265 = 1{,}797.76 \times 10^3\,\text{N}.$$

So

$$M_c = 6{,}651.5 \times 10^3 \frac{769.8}{2} + 3{,}937.5 \times 10^3 \frac{200}{2} - \frac{(6{,}651.5 - 3{,}937.5)10^3}{1{,}797.76 \times 10^3}$$
$$\times \frac{25.6}{4}$$
$$= 2{,}927.98\,\text{kN m}$$
$$M_c > M + M_{sw} = 111.25 + 1.378 = 112.628\,\text{kNm} \qquad \text{ok.}$$

Shear capacity

Shear force : $F_v = \frac{1}{2}wL = \frac{1}{2} \times 35.6 \times 5 = 89\,\text{kN}$

Shear resistance:

$$P_v = 0.6pytD_s = 0.6 \times 265 \times 10^{-3} \times 15.9 \times 769.8 = 1946\,\text{kN} > F_v \quad \text{ok.}$$

At mid-span: $F_v(=0) < 0.5P_v(=973\,\text{kN})$ and therefore the moment capacity of the section calculated above is valid.

Shear connectors

The characteristic resistance, Q_k, of the headed studs 25 mm diameter $\times$ 100 mm high is 161 kN for $f_{cu} = 35\,\text{N}\,\text{mm}^{-2}$.

Design strength of shear connectors, Q_p, is

$$Q_p = 0.8Q_k = 0.8 \times 161 = 128.8\,\text{kN}. \tag{B.18}$$

Longitudinal force that needs to be transferred, F_c, is 6,651.5 kN

$$\text{Number of studs required} = \frac{F_c}{Q_p} = \frac{6{,}651.5}{128.8} = 51.6. \tag{B.19}$$

Provide 52 studs, evenly arranged in pairs, in each half span of beam.

$$\text{Spacing} = \frac{2{,}500}{25} = 100\,\text{mm centres.} \tag{B.20}$$

B.3.5 An Office Building: Steel-Concrete Composite Slabs with R.C. Protective Walls Under Blast Loading

General Introduction

This case study is concerned with the design of an office building basically made of steel girder beams and columns rigidly connected at the top and the columns are rigidly connected to foundation slab. Concrete-Steel composite floor supported by steel girders and cross beams form the main roof. The ability of the building against blast load is being examined. Against external pressure built up by bomb explosion, reinforced concrete protective walls surrounding the steelwork have been provided in the scheme. The maximum potential of a building shown in Fig. B.30 is assessed so as to provide protection against explosive effects. Codified methods are applied to validate design calculations in respect to blast loads created by a bomb explosion with a specific yield. Program ABACUS/CAE, this time was applied, to validate the design. It was assumed that twin frame should be checked for the blast effects.

The Office Building

Figure B.30 shows a 3D orientation of the building built in complete steel-concrete composite. Figure B.31 shows the cross-section of the building. A plan view of the building is given in Fig. B.32. Figures B.33 and B.34 give purlin-to-girder and girder-to-column connections respectively. They show bolted-cum-welded details for the building frame. Based on BS 5950, the entire building frame has been checked for the conventional limit state design covering all possible design loading conditions. The frame design does have considerable ductility as well.

Particular attention needs to be given to girder to column connection design for blast enhanced structures, this is because, connection forces, relative to the size of the member being connected, will be found to be very large and also where the member becomes plastic, the connection forces will be function of the yield stress of the member.

Since ultimate-strength theory is used for both connection and member, the capacity of the former is little more than would be required to connect the same members in a conventional structure.

The building has assumed to be fully designed using British codes and is now ready to be checked against the bomb blast with a specific yield.

B.3.6 Design and Analysis of a Building Against Blast Loading

Manual Calculations

Blast Load and Modelling

The design here presented is that of a steel-frame one-story building. Against external pressure built up by bomb explosion, reinforced concrete protective
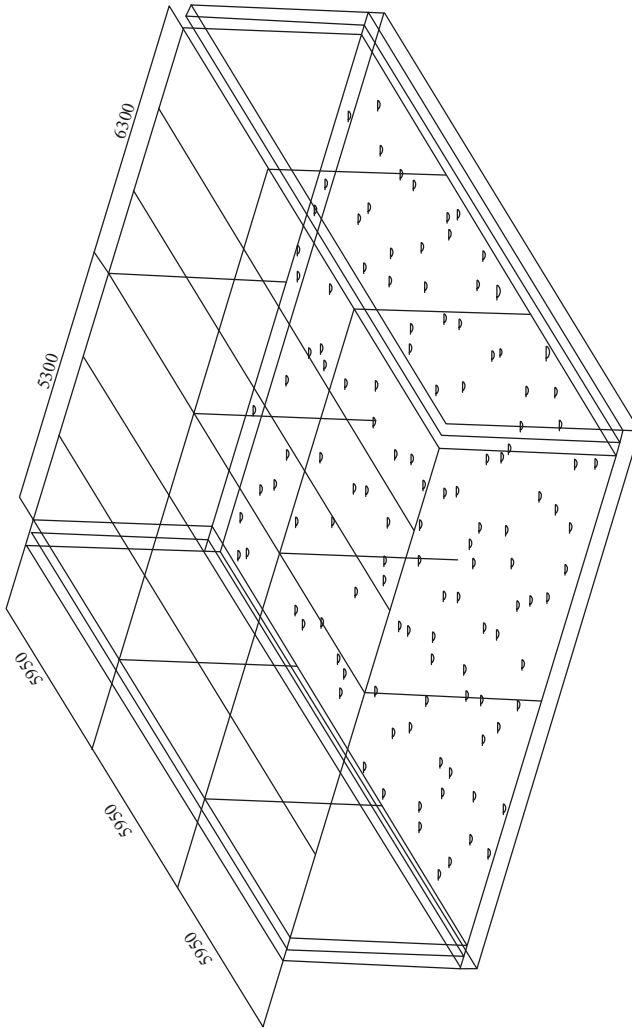
Fig. B.30. 3D Orientation of the building

walls surrounding the steelwork have been provided in the scheme. Refer to
Appendix A for the diagrams and conventional design calculations of the
building.

(A) *Blast loading*:

Use 250 kg RDX

The charge factor, $\mathrm{CF} = \dfrac{5{,}360}{4{,}520} = 1.185$

TNT equivalent $= 250 \times 1.185 = 296.25\,\mathrm{kg}$
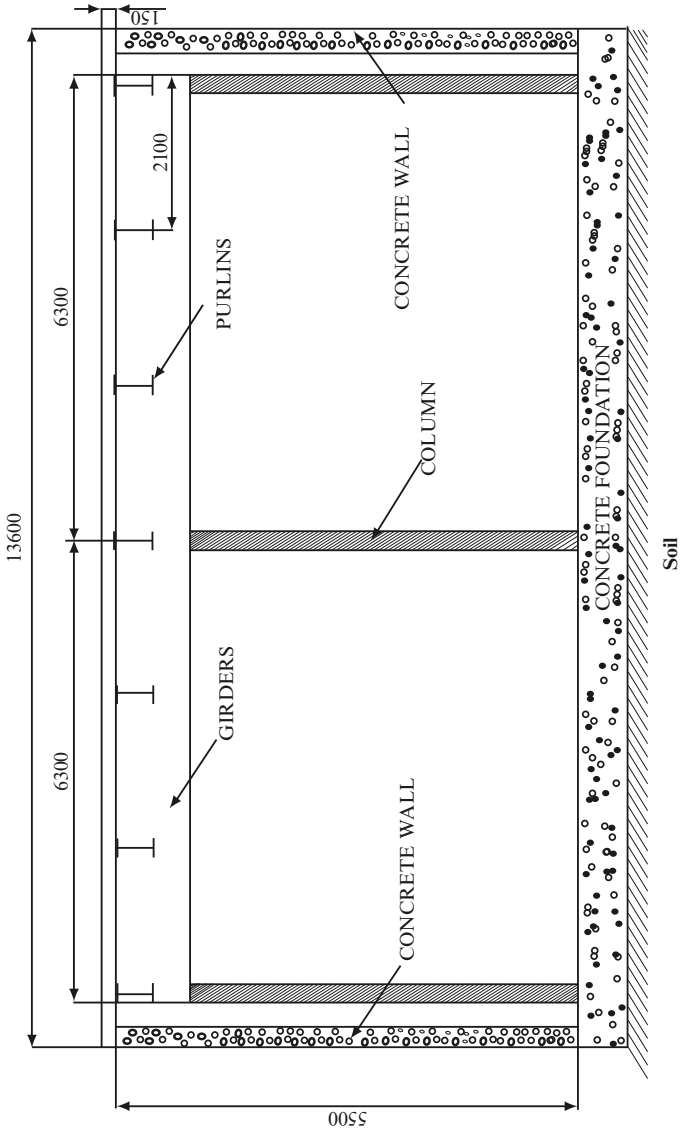
Fig. B.31. Cross section of the building

Determination of range or distance, R

$$R = \frac{KW^{0.333}}{\{1 + (3{,}175/W)^2\}^{0.1667}} = \frac{5.6 \times (296.25)^{0.333}}{\{1 + (3{,}175/296.25)^2\}^{0.1667}} = 16.9\,\text{m}$$

$$(B.21)$$
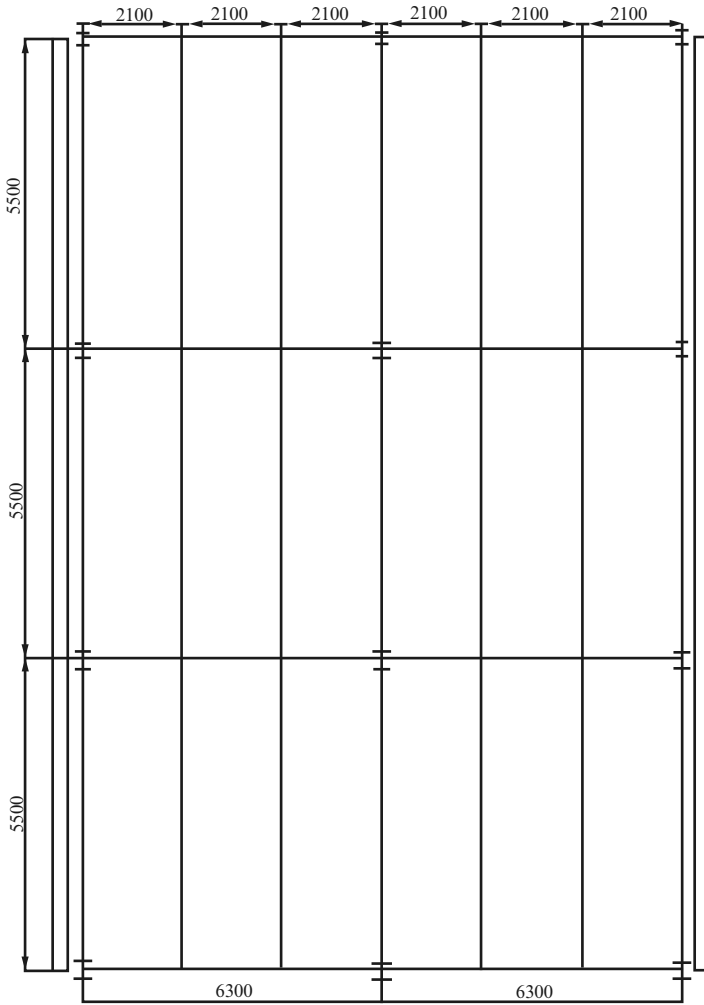
Fig. B.32. Plan of the building

R = stand off distance to the centre of detonation in metres
Blast Resistance in terms of the quantity scaled distance

$$Z = \frac{R}{W^{1/3}} = \frac{16.9}{(296.25)^{1/3}} = 2.54 \, \text{m} \, \text{kg}^{-1/3} \tag{B.22}$$

The reflected pressure or impulse i_r is found, as

$$\frac{i_r}{w^{1/3}} 10^6 = 510,000,000. \tag{B.23}$$

Therefore $i_r = 3,399.822 = 3,400 \, \text{kPa} \, \text{ms}$
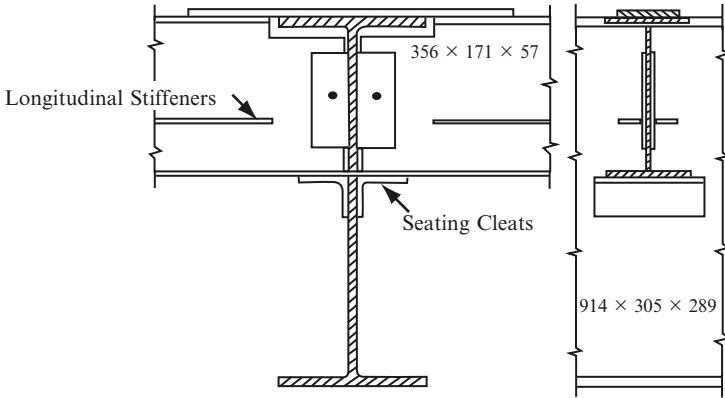
Fig. B.33. Purlin-to-girder connection
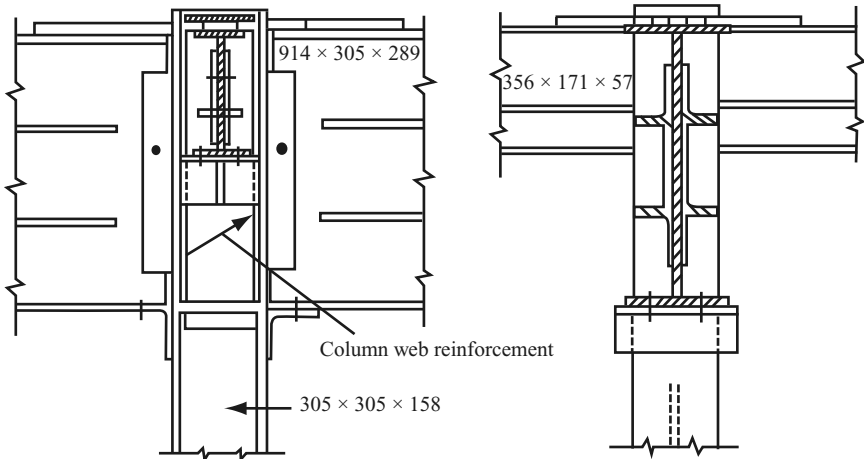
Fig. B.34. Girder-to-column connection

(B) *External blast and load modelling*

    (1) Overpressure $P_{s0} = P_B$

        The overpressure P_{s0} in its peak form in bars acting dynamically on walls of front faces of a building can be written as

$$P_{s0} = 6784\frac{W}{R^3} + 93\left(\frac{W}{R^3}\right)^{1/2}, \tag{B.24}$$

$$P_{s0} = 6784\frac{0.3}{17^3} + 93\left(\frac{0.3}{17^3}\right)^{1/2} = 0.414 + 0.73 = 1.144\,\text{bar}. \tag{B.25}$$

    Note: $1\text{bar} = 100\,\text{kN}\,\text{m}^{-2}$.

Therefore

$$P_{S0} = 114 \, \text{kN m}^{-2}$$

$$q_0 = \text{peak drag} = 2.5 C_D P_{SO}/(7 P_{SO} + P_O)$$

$$= (2.5 \times 1 \times 114)/(7 \times 114 + 100) = 0.317 \qquad (\text{B.27})$$

$$P_R = \text{Peak pressure of a reflected shock}$$

$$P_R = 2 P_O + 6/(7 P_O + P_{SO}) \quad \text{when } P_{so} < 10 \, \text{bar} \qquad (\text{B.28})$$

$$P_R = 2 \times 100 + 6/(7 \times 100 + 114) = 200 \, \text{kN m}^{-2}, \qquad (\text{B.29})$$

where P_O = ambient atmospheric pressure $\approx 1 \, \text{bar} = 100 \, \text{kN m}^{-2}$
      C_D = drag coefficient = 1.0 in general

In detail

C_{Dr} = drag coefficient for the rearface = 0.25–0.5
C_{Df} = drag coefficient for the front face = 0.8–1.6

(2) Pressure-time relation

$$T_c = \frac{3S}{U} \quad S = H_s \leq \frac{1}{2} B \quad T_C = \text{reflected pulse time} \qquad (\text{B.30})$$

S = HS when $B \geq H$
P_f = pressure at front face
P_r = pressure at rear face
B = building width
H_s = building height
t_R = time for reflected wave = $2 i_r / P_R$
i_R = total reflected pressure impulse

(C) *Duration*

$$t_B = \text{shock pulse duration} = 10,23 \frac{W^{1/3}}{\sqrt{P_{SO}}} \qquad \text{when } P_{SO} = 70 \, \text{bar} \quad (\text{B.31})$$

$$t_B = 10.23 \frac{300^{1/3}}{\sqrt{114}} = 6.41 \, \text{s}$$

$$t_R = \frac{2 i_r}{P_R} = \frac{2 \times 3{,}400}{200} = 34 \, \text{ms} \qquad (\text{B.32})$$

$$t_D = \text{time of drag} = 9.04 \left(\frac{300}{114}\right)^{1/3} \qquad \text{when } P_{SO} = 2\,\text{bar} \quad \text{(B.33)}$$

$$t_D = 9.04 \left(\frac{300}{114}\right)^{1/3} = 12.5\,\text{ms} \qquad\qquad\qquad \text{(B.34)}$$

(D) *Blast load on individual surface*

The total load acts on an area or element of a structure consists of two time-dependent components of load, which can be represented by the relationship

$$F(t) = F_{Blast}(t) + F_{Dynamics}(t) \qquad\qquad \text{(B.35)}$$

F_{blast} is the component of loading that is caused by the blast wave, while the second component $F_{Dynamics}$ is the load caused by dynamic pressure as a result of the airflow fallowing the shock wave (blast wind).

The load components F_{Blast} and $F_{Dynamic}$ are given by

$$F_{Blast} = pA_{proj} \qquad\qquad\qquad \text{(B.36)}$$

for the shock component and

$$F_{Dynamics} = q_s C_D A_{proj}, \qquad\qquad \text{(B.37)}$$

where p is the overpressure caused by the blast wave

A_{proj} is the area of structure under consideration projected onto the plane normal to the direction of approach flow

q_s is the dynamic pressure

The magnitude of the drag coefficient C_D depends on geometry of the object and on the particle velocity. For the front face of the building, C_D should be taken as +1. Therefore, the total load is

$$F(t) = F_{Blast}(t) + F_{Dynamics}(t) = pA_{proj} + q_s C_D A_{proj}, \quad \text{(B.38)}$$
$$F(t) = 114 + 48 = 162\,\text{kN}.$$

For roofs, back walls, and side walls of buildings, TM5-1300 [XX] suggest the values dependent on the pressure, as shown in Table B.17.

Table B.17. Drag coefficient C_D to be used for buildings [5]

Peak dynamic pressure (kN m^{-2})	Drag coefficient (C_D)
0–172	−0.4
172–345	−0.3
345–896	−0.2
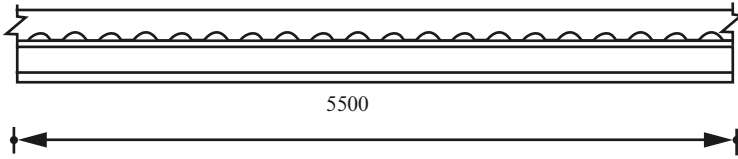
Fig. B.35. Composite floor slab
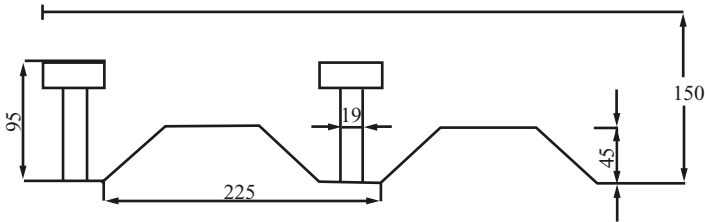
Fig. B.36. Composite section

Composite Slab Design for Floor Secondary Beams

Design data and analysis

Slab depth (taken as)	h_1	$=$	150 mm
Profile height	h_p	$=$	50 mm
Concrete slab depth	$h_c = h_1 - h_p$	$=$	90 mm
Trough spacing	b_d	$=$	150 mm
Average trough width	b_o	$=$	75 mm
Thickness of steel sheeting	t_p	$=$	1 mm

Remark: $b_o > 50$ mm: OK

Try 305 × 165 × 54 UB in S275 steel

Span $= 5.5$ m
Beam spacing $= 2.1$ m
Shear studs: 19 mm diameter, 95 mm long

Loading

(1) During construction (unpropped):

Dead load

Floor (construction slab) 0.150 m $\times 24$ kN m$^{-3} \times 2.1 = 7.56$ kN m^{-1}
Steel beam 54 kg m$^{-1} \times 9.81 \times 10^{-3}$ $= 0.53$ kN m^{-1}
Total dead load $= 8.08$ kN m^{-1}
Imposed construction loads $= 0.5$ kN m$^{-2} \times 2.1$ m $= 1.05$ kN m^{-1}

(2) Composite stage (after construction)

Tiles (screed)	$0.7\,\text{kN m}^{-2} \times 5.5\,\text{m}$	$= 3.85\,\text{kN m}^{-1}$
Slab	$0.150\,\text{m} \times 24\,\text{kN m}^{-3} \times 5.5\,\text{m}$	$= 19.8\,\text{kN m}^{-1}$
Steel (assumed)	$0.3\,\text{kN m}^{-2} \times 5.5\,\text{m}$	$= 1.65\,\text{kN m}^{-1}$
Partitions	$1.0\,\text{kN m}^{-2} \times 5.5\,\text{m}$	$= 5.5\,\text{kN m}^{-1}$
Ceiling	$0.5\,\text{kN m}^{-2} \times 5.5\,\text{m}$	$= 2.75\,\text{kN m}^{-1}$
Services	$2.0\,\text{kN m}^{-2} \times 5.5\,\text{m}$	$= 11\,\text{kN m}^{-1}$
Total dead load		$= 44.55\,\text{kN m}^{-1}$
Imposed roof load $5\,\text{kN m}^{-2} \times 5.5\,\text{m}$		$= 27.5\,\text{kN m}^{-1}$

.............in which $(1/3 \times 27.5\,\text{kN m}^{-1} = 9.2\,\text{kN m}^{-1})$ is long term loading

Serviceability deflection

Deflection of beam at the construction stage:

$$\delta = \frac{5WL^4}{384EI} = \frac{5 \times 8.08 \times 5{,}500^4}{384 \times 205{,}000 \times 11{,}700 \times 10^4} = 4.1\,\text{mm} < L/360 = 15$$

Pre-cambering for dead load is required.

Deflection of beam at the composite stage:

$\alpha_{\text{s}} = 6 \qquad \alpha_1 = 18$

$\alpha_{\text{e}} = \alpha_{\text{s}} + \rho_1(\alpha_1 - \alpha_{\text{s}})$

$\rho = \text{long term loading/total loading}$

Long term loading $=$ dead load $+ 1/3$ imposed load

$$\rho_1 = \frac{44.55 + 9.2}{44.55 + 27.5} = 0.74$$

$\alpha_{\text{e}} = 14.88$

$$I_g = I_x + \frac{B_e(D_s - D_p)^3}{12\alpha_e} + \frac{AB_E(D_s + D_p)(D + D_S + D_P)^2}{4\left[A\alpha_E + B_e(D_S - D_P)\right]}$$

$B_{\text{e}} = 2 \times 1/8 \times 5{,}500 = 1{,}375\,\text{mm}$

$A = 63.8\,\text{cm}^2 \qquad I_x = 11{,}700\,\text{cm}^4$

$D_S = 150\,\text{mm} \qquad D_p = 0 \qquad D = 310.4\,\text{mm}$

$I_g = 11{,}700 + 2{,}598 + 23{,}150 = 37{,}448\,\text{cm}^4$

$$\delta = \frac{5WL^4}{384EI_g}$$

W = Imposed load + additional dead load after construction
   = $27.5\,\text{kN m} + (44.55 - 8.08) = 64\,\text{kN m}^{-1}$

$$\delta = \frac{5 \times 64 \times 5500^4}{384 \times 205,000 \times 37,448 \times 10^4} = 9.9\,\text{mm}$$

Total deflection for fully composite beam:

Construction stage (assumed pre-cambering for 45 mm) = 0 mm
Composite stage   = 9.9 mm
Total deflection   = 9.9 mm

This is less than the allowable limit of $L/360 = 15.3\,\text{mm}$

Check for serviceability stresses

To check whether the section is cracked or uncracked.

$B_e = 2 \times 1/8 \times 5,500 = 1,375\,\text{mm}$

$A = 63.8\,\text{cm}^2 \qquad I_x = 11,700\,\text{cm}^4$

$D_s = 150\,\text{mm} \qquad D_p = 0 \qquad D = 310.4\,\text{mm}$

$$\frac{(D_s - D_p)^2 B_e}{(D + 2D_p)\alpha_E} = \frac{150^2 \times 1375}{(310.4 + 0)14.88} = 6,699\,\text{mm}^2$$

Since $A < \dfrac{(D_s - D_p)^2 B_e}{(D + 2D_P)\alpha_E}$ elastic neutral axis is in the steel member and the section is cracked.

Bending stress in steel section at construction stage:

$$M = \frac{WL^2}{8} = \frac{8.08 \times 5.5^2}{8} = 30.55\,\text{kN m}$$

Bending stress $f_{bf} = \dfrac{M}{Z_x} = \dfrac{30.55 \times 10^6}{754 \times 10^3} = 40.51\,\text{N mm}^{-2}$

Stresses in steel and concrete at composite stage

Depth of neutral axis below top of the concrete flange:

$$y_g = \frac{A\alpha_E(2D_s + D) + B_e(D_S - D_P)^2}{2[A\alpha_E + B_e(D_S - D_P)]}$$

$$y_g = \frac{63.8 \times 14.88(30.51 + 2 \times 15) + 137.5(15)^2}{2[63.8 \times 14.88 + 137.5(15)]} = 29.4\,\text{mm}$$

(1) At the lower fibre of the Steel flange

$$Z_s = \frac{I_g}{D + D_s - y_g} = \frac{37,448}{31.05 + 15 - 29.4} = 2,249\,\text{cm}^3$$

(2) At the upper surface of the concrete slab

$$Z_c = \frac{I_g \alpha_e}{y_g} = \frac{37{,}448 \times 14.88}{29.4} = 18{,}953\,\text{cm}^3$$

W = Imposed load + Additional dead load after construction

W = $64\,\text{kN}\,\text{m}^{-1}$

Bending moment, M = $\dfrac{WL^2}{8} = \dfrac{64 \times 5.5^2}{8} = 242\,\text{kN}\,\text{m}$

Bending stress in concrete $f_{bc} = \dfrac{M}{Z_c} = \dfrac{242 \times 10^6}{18.953 \times 10^3} = 12.7\,\text{N}\,\text{mm}^{-2} =$

$$< 0.5 f_{cu} = 15\,\text{N}\,\text{mm}^{-2}$$

Bending stress in steel $f_{bs} = \dfrac{M}{Z_S} = \dfrac{242 \times 10^6}{2{,}249 \times 10^3} = 107.6\,\text{N}\,\text{mm}^{-2}$

Total stress in steel: Construction stage = $7.56\,\text{N}\,\text{mm}^{-2}$

Composite stage   = $107.6\,\text{N}\,\text{mm}^{-2}$

= $115.16\,\text{N}\,\text{mm}^{-2}$

Which is less than $\rho_y = 355\,\text{N}\,\text{mm}^{-2}$

RC Cantilever Wall Design

Durability and Fire Resistance

Nominal cover: (a) severe exposure = 40 mm (b) mild = 20 mm
External cover = 40 mm   Internal cover = 20 mm
Fire resistance of 175 plain wall   1 h fire resistance ok.

Loading

Designed for wind loading W = $1.48\,\text{kN}\,\text{m}^{-2}$
Design Load   = $1.48 \times 5.5 = 8.14\,\text{kN}\,\text{m}^{-1}$

Ultimate B.M's

Maximum bending moment at free edge of the wall.

Max BM = $\dfrac{WL}{8} = \dfrac{8.14 \times 16.5 \times 5.5}{8} = 92.3\,\text{kN}\,\text{m}$

Reinforcement

$$d = 300 - 40 - 8 = 252\,\text{mm}$$

Interior mid-span and supports

$$K = \frac{M}{f_{cu}bd^2} = \frac{92.3 \times 10^6}{40 \times 10^3 \times 252^2} = 0.036$$

$$z = d\left\{0.5 + \sqrt{0.25 - \frac{K}{0.9}}\right\} = 252\left\{0.5 + \sqrt{0.25 - \frac{0.036}{0.9}}\right\} = 242$$

(but $242 > 0.95 \times 252 = 239.4$)

$$A_s = \frac{M}{0.95 f_y z} = \frac{92.3 \times 10^6}{0.95 \times 460 \times 239.4} = 883 \, \text{mm}^{-2} \, \text{m}^{-1}$$

<div align="right">

Top and Bottom
<u>T16 @ 200</u>
$1{,}005 \, \text{mm}^2 \, \text{m}^{-1}$

</div>

Check for Shear:

Table 3.10 $v = \dfrac{0.5 \times 8.14 \times 10^3}{10^3 \times 252} = 0.016 \, \text{N mm}^{-2} < v_c = 0.49$ O.K

Basic span/effective depth ratio $= 14 \, \text{max}$

Table 3.9 $\dfrac{M}{bd^2} = \dfrac{92.3 \times 10^6}{10^3 \times 252^2} = 1.43$ $f_s = \dfrac{2 \times 460 \times 883}{3 \times 1015} = 267 \, \text{N mm}^{-2}$

Table 3.10 Modification factor for tension reinforcement $= 1.5$
             Allowable span/eff. depth ratio 14×1.5 $= 21$
             Actual span/eff. depth ratio $5{,}500/525$ $= 10$

Therefore span/eff. depth ratio is ok.

Cracking

$$3d = 3 \times 252 = 761 \, \text{mm}$$

Spacing between bars $= 200 - 16 = 184 \, \text{mm} < 3 \, \text{d spacing O.K.}$

Analysis For a Walls Slab Using British Practise

Determination of Minimum Wall Thickness for Calculated Range, R

A reinforced concrete wall is loaded by a blast from a vehicle bomb of 250 actual mass. See Fig. B.37. The wall is rigidly connected at the foundation and free at the top. Using the following data, calculate the required reinforcement for the wall:

Wall heights: $5.5 \, \text{m}$
Material properties:
  Concrete grade $= \text{C40}$
  $D_C = \gamma_C = $ the density of concrete $= 24 \, \text{kg m}^{-3}$
  $f_y = $ Steel stress at yield $= 460 \, \text{N mm}^{-2}$
  $E_c = $ Young's modulus of concrete $= 28 \, \text{kN mm}^{-2} = 28 \times 10^9 \, \text{N m}^{-2}$
  $E_s = $ Young's modulus of steel $= 200 \, \text{kN mm}^{-2} = 200 \times 10^9 \, \text{N m}^{-2}$
  $\rho_s = $ The percentage of steel reinforcement 0.5%
  $f_{dy} = $ The dynamics yield stress $= 1.2 f_y$
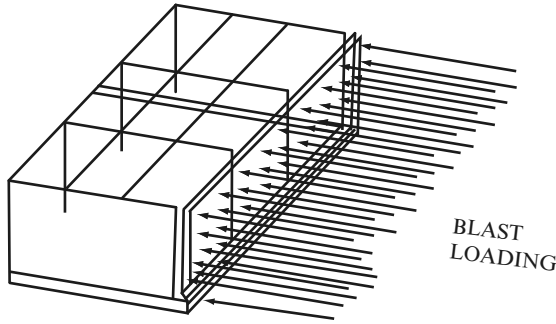
Fig. B.37. Reinforced concrete wall subjected to blast loading
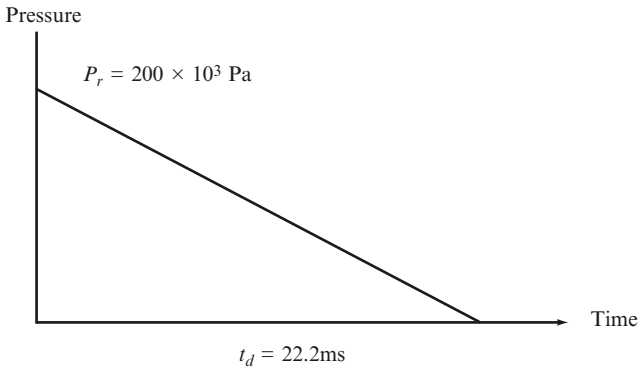
Fig. B.38. Triangular pressure pulse function

Blast loading:

Use 250 kg RDX

The charge factor, $CF = 1.185$

TNT equivalent $= 250 \times 1.185 = 296.25$ kg

$R = 16.9$ m

$$Z = \frac{R}{W^{1/3}} = \frac{16.9}{(296.25)^{1/3}} = 2.54 \, \text{m kg}^{-1/3}$$

The reflected pressure or impulse i_r is found using the chart

$$\frac{i_r}{w^{1/3}} 10^6 = 510{,}000{,}000 \tag{B.39}$$

Therefore $i_r = 3{,}399.822 = 3{,}400 \, \text{kPa ms} = 3{,}400 \, \text{N s m}^{-2}$

$f_y = $ Reinforcement yield stress $= 460 \, \text{N mm}^{-2}$ (Static Value)

$f_{dy} = 1.2 f_y = 1.2 \times 460 = 552 \, \text{MPa}$ (Dynamic Value)

$f_{du} = 1.05 f_{dy} = 1.05 \times 550 = 578 \, \text{MPa}$
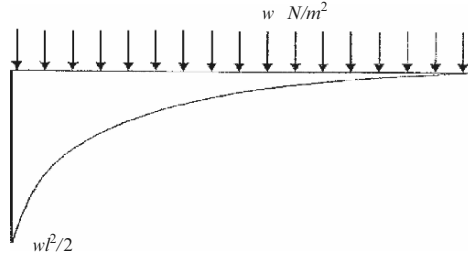
Fig. B.39. BMD for applied UDL upon a cantilever

The maximum deflection, y_m is found as

$$y_m = 4.25 \tan 4 = 0.3 \, \text{m}$$

By definition $W = r_u$

$$M = \frac{Wl^2}{2} = \frac{r_u l^2}{2}$$

Thus the ultimate load resistance, r_u

$$r_u = \frac{2M}{L^2}$$

The equivalent elastic stiffness is given by

$$K_E = \frac{8EI}{H^4} \tag{B.40}$$

The elastic deflection, y_e, is then found as

$$y_e = \frac{r_u}{K_E} = \frac{2M}{H^2} \times \frac{H^4}{4EI} = \frac{MH^2}{4EI} \tag{B.41}$$

$$I = \text{Fbd}^3$$

$$M = \rho_v f_{ds} d^2 = 0.005 \times 559 \times 10^6 d^2 = 2.795 \times 10^6 d^2 \tag{B.42}$$

Assuming, the percentage steel ρ_v to be 0.005. The coefficient, F is obtained from F chart of ASCE is found as 0.245.

Upon substituting the values into the basic impulse formulas the following equation is obtained

$$\frac{1_r^2}{2K_{IM}d_c} = \left(\frac{2}{H} \rho_v f_{ds} d_c^2\right) \tan \theta \tag{B.43}$$

$$\frac{3{,}400^2}{2 \times 0.66 \times 2{,}400d} = \frac{2M}{H^2}\left[0.3 - \frac{MH^2}{4EI}\right]$$

$$\frac{11{,}560{,}000}{3168d} = 27719d^2 - 2.84 \times 10^{-4}d$$

$$1 = 7.6d^3 - 7.78 \times 10^{-8}d^2$$

The depth subsequently found to be 0.51. d = 510.

Minimum thickness of wall required in the range of R = 16.9 m. This is now substituted to find the fallowing parameters

$$M = 2.795 \times 10^6 d^2 = 2.795 \times 10^6 \times 0.51^2 = 726{,}980 \, \text{kN m} \quad \text{(B.44)}$$

$$r_u = \frac{2 \times 726{,}980}{5.5^2} = 48{,}064$$

$$K_E = \frac{8 \times 28 \times 10^9 \times 0.245 \times 1 \times 0.51^3}{5.5^4} = 7{,}955{,}617.108 \quad \text{(B.45)}$$

$$y_e = \frac{r_u}{K_E} = \frac{48{,}064}{7{,}955{,}617.108} = 6.04 \times 10^{-3} \quad \text{(B.46)}$$

The total response time t_m is computed as

$$t_m = \frac{i}{r_u} = \frac{3{,}400}{48{,}064} = 0.07 \, \text{s} \quad \text{(B.47)}$$

$$\frac{t_m}{t_d} = \frac{0.07}{0.0221} = 3.3 > 3 \quad \text{(B.48)}$$

Hence impulse loading is valid.

Determination of Steel Reinforcement for Calculated Range, R

The required area of steel reinforcement, A_{req} is then found

$$As = 0.005 \times 510 \times 1{,}000 = 2550 \, \text{mm}^2 \, \text{m}^{-1} \, \text{width of wall.}$$

To account for design variation the principal design recommendation is to provide 20% more steel.

Therefore

$$As = (1 + 0.20)2550 = 3{,}060 \, \text{mm}^2 \, \text{m}^{-1} \, \text{width of wall,}$$
$$\text{Adopt T32-250 reinforcement } (A_s = 3{,}215 \, \text{mm}^2).$$

The shear is found using equation below:

$$v = \frac{r_u(H - d_c)}{d_c} = \frac{48{,}064(5.5 - 0.51)}{0.65 \times 10^6} = 0.37 \, \text{N mm}^{-2}.$$

From BS8110 the $v_c = 0.54$, with,

$$\frac{100 A_s}{bd} = \frac{100 \times 3{,}215}{1{,}000 \times 510} = 0.63. \quad \text{(B.49)}$$

Since $f_{cu} = 40 \, \text{N mm}^{-2}$ and is greater than 25, the fallowing correction factor from the code is applied.
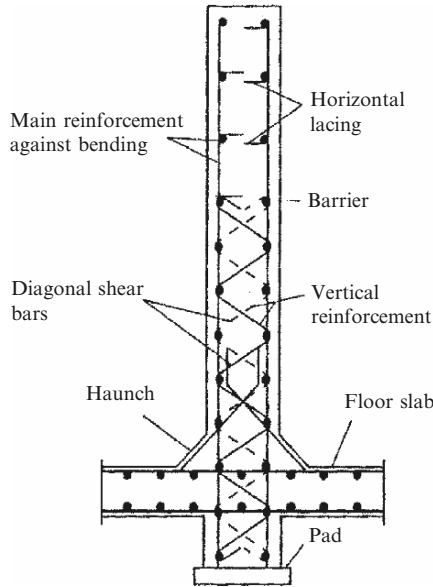
Fig. B.40. Typical laced wall

Hence

$$v_c = 0.34 \left(\frac{f_{cu}}{25} \right)^{1/3} = 0.63. \qquad (B.50)$$

Therefore the fallowing conditions applies for the provision of shear reinforcement

$$0.5v_c < v < (v_c + 0.4). \qquad (B.51)$$

The area of shear reinforcing steel assumed a link spacing of 250, is

$$A_{sv} = \frac{0.4b_v s_v}{0.87f_y} = \frac{0.4 \times 510 \times 250}{0.87 \times 460} = 127.44\,\mathrm{mm}^2.$$

Hence provide R8-200 ($A_{sv} = 393\,\mathrm{mm}^2$)

See Fig. B.40 for the typical suggested laced wall.

For the instance where a quasi-static load is applied to the wall restrained at top and bottom, it fallows:

$$r_u = \frac{8(M_{Ps} + M_{Pm})}{H^2}, \qquad (B.52)$$
$$M_P = M_{Ps} + M_{Pm},$$
$$A_S = A^I s = 2{,}550\,\mathrm{mm}^2\,\mathrm{m}^{-1},$$

x : depth of neutral axis

$$x = \frac{d-z}{0.45} = \frac{d - 0.95d}{0.45} = \frac{510 - 0.95 \times 510}{0.45} = 56.7\,\mathrm{mm}. \qquad (B.53)$$
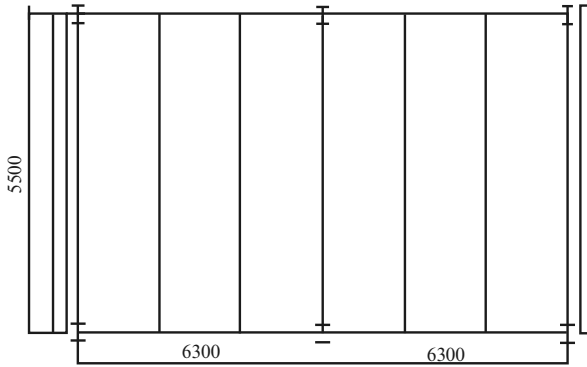
Fig. B.41. Plan of a typical bay

Ignoring the contribution of the compression reinforcement ($K = K' = 0.156$).

$$M_P = 2{,}250 \times 552(510 - 0.45 \times 56.7) \times 10^{-3} = 556\,\text{kN m m}^{-1}$$

Design of Roof Girder Against Explosion Loading

The girder is designed for elastic behaviour, even though the rest of the structure is permitted to undergo plastic deformation. This desirable since the lateral strength of the frame depend upon restraint at the top of the columns. If the plastic hinges are formed in the girders because of vertical loads, these members probably would not provide the restraint necessary for the columns to carry lateral load at he same time. Figure B.41 shows the typical plan of one bay of the building.

Thus the total stress in the girder is the sum of three effects:

1. The static purlin reactions and the of the girder itself
2. The dynamic purlin reactions
3. The dynamic moments introduced by the columns and caused by the lateral blast loads

The design criteria are that the total stress due to the maximum moment which occurs at he center column shall equal to the dynamic yield stress of $355\,\text{N mm}^{-2}$. The computations are given in some detail below.

Since the two spans of the girder are loaded almost simultaneously, and since the exterior columns are relatively slender, it is permissible to consider each span as a fixed at one end and pinned at the other. As usual one obtains the following factors:

For the concentrated mass and loads,

$$\text{K}_\text{L} = 0.81 \quad \text{K}_\text{M} = 0.67 \quad R_m = \frac{6M_p}{L} \quad k = \frac{132EI}{L^3}. \tag{B.54}$$

For the uniform mass,

$$\text{K}_\text{M} = 0.45.$$

As a preliminary-design the beam section $762 \times 267 \times 134$ will be used. We shall proceed to check the adequacy of this selection. In the case of this section not being adequate, a greater section will be selected.

Try 762 × 267 × 134 UB in S355 Steel

$\mathrm{I} = 150{,}700\,\mathrm{cm}^4$,

$\mathrm{S} = 4{,}644\,\mathrm{cm}^3$,

$M_p = f_{dy}S = 355 \times 4{,}644 \times 10^3 = 1{,}649\,\mathrm{kN\,m}$,

$$k = \frac{132EI}{L^3} = \frac{132 \times 200 \times 10^9 \times 150{,}700 \times 10^{-8}}{6.3^3} = 1.6 \times 10^5\,\mathrm{kN\,m}^{-1}. \quad \text{(B.55)}$$

Concentrated mass $= \dfrac{110}{9.81} = 11.2\,\mathrm{kN\,s^2\,m}^{-1}$.

Uniform mass $= \dfrac{1.2 \times 6.3}{9.81}(1.15) = 0.89\,\mathrm{kN\,s^2\,m}^{-1}$.

Total equivalent mass $= m_{te} = (11.2 \times 0.67) + (0.89 \times 0.45) = 7.9\,\mathrm{kN\,s^2\,m}^{-1}$ (B.56)

$$k_e = (1.6 \times 10^5 \times 0.81) = 1.296 \times 10^5\,\mathrm{kN\,m}^{-1}, \quad \text{(B.57)}$$

$$T_n = 2\pi\sqrt{\frac{m_{te}}{k_e}} = 2\pi\sqrt{\frac{7.9}{1.296 \times 10^5}} = 0.049, \quad \text{(B.58)}$$

$$\frac{T_r}{T_n} = \frac{0.034}{0.049} = 0.69. \quad \text{(B.59)}$$

As per method, the values of DLF or MF would be calculated as

$$\mathrm{MF} = \mathrm{DLF_{max}} = 1.38. \quad \text{(B.60)}$$

Maximum moment at center column due to dynamic

$$\text{purlin reaction} = \mathrm{DLF}\left(\frac{PL}{6}\right) = 1.38\frac{2{,}900 \times 6.3}{6}$$
$$= 4{,}202\,\mathrm{kN\,m}. \quad \text{(B.61)}$$

Moment due to concentrated dead loads $= \dfrac{110 \times 6.3}{6} = 116\,\mathrm{kN\,m}.$ (B.62)

Moment due to distributed dead loads $= \dfrac{0.89 \times 6.3^2}{8}(1.15) = 5.1\,\mathrm{kN\,m}.$ (B.63)

Moment due to plastic moment in column $= \dfrac{1}{2}(M_p)_{col} = 596/2 = 298\,\mathrm{kN\,m}$ (B.64)

Total moment $= (4{,}202 + 116 + 5.1 + 298) = 4{,}621.1\,\mathrm{k\,Nm} > 2{,}417$ Not Sufficient.

Try 914 × 305 × 289 UB in S355 Steel

$I = 504{,}200\,\text{cm}^4,$

$S = 12{,}570\,\text{cm}^3,$

$$M_p = f_{dy}S = 1.05 \times 355 \times 12{,}570 \times 10^3 = 4{,}686\,\text{kN m}, \tag{B.65}$$

$$k = \frac{132EI}{L^3} = \frac{132 \times 200 \times 10^9 \times 504{,}200 \times 10^{-8}}{6.3^3}$$
$$= 5.3 \times 10^5\,\text{kN m}^{-1}. \tag{B.66}$$

Concentrated mass $= \dfrac{110}{9.81} = 11.2\,\text{kN s}^2\,\text{m}^{-1}.$

Uniform mass $= \dfrac{1.2 \times 6.3}{9.81}(1.15) = 0.89\,\text{kN s}^2\,\text{m}^{-1}.$

Total equivalent mass $= m_{te} = (11.2 \times 0.67) + (0.89 \times 0.45) = 7.9\,\text{kN s}^2\,\text{m}^{-1},$
$$\tag{B.67}$$

$$k_e = (5.3 \times 10^5 \times 0.81) = 4.2 \times 10^5\,\text{kN m}^{-1}, \tag{B.68}$$

$$T_n = 2\pi\sqrt{\frac{m_{te}}{k_e}} = 2\pi\sqrt{\frac{7.9}{4.2 \times 10^5}} = 0.029, \tag{B.69}$$

$$\frac{T_r}{T_n} = \frac{0.034}{0.029} = 1.17. \tag{B.70}$$

From Fig. B.42
$$\text{DLF}_{\max} = 1.18.$$

Maximum moment at center column due to dynamic

$$\text{purlin reaction} = \text{DLF}\left(\frac{PL}{6}\right) = 1.18\frac{2{,}900 \times 6.3}{6} = 3{,}594\,\text{kN m}. \tag{B.71}$$

$$\text{Moment due to concentrated dead loads} = \frac{110 \times 6.3}{6} = 116\,\text{kN m}. \tag{B.72}$$

$$\text{Moment due to distributed dead loads} = \frac{0.89 \times 6.3^2}{8}(1.15) = 5.1\,\text{kN m}. \tag{B.73}$$

$$\text{Moment due to plastic moment in column} = \frac{1}{2}(M_p)_{col} = 596/2 = 298\,\text{kN m}. \tag{B.74}$$

$$\text{Total moment} = (3584 + 116 + 5.1 + 298) = 4{,}012.2\,\text{kN m} < 4{,}686\ \text{O.K.} \tag{B.75}$$

Thus the section is adequate for bending moment. In order to check the shear we must compute the maximum dynamic reaction.
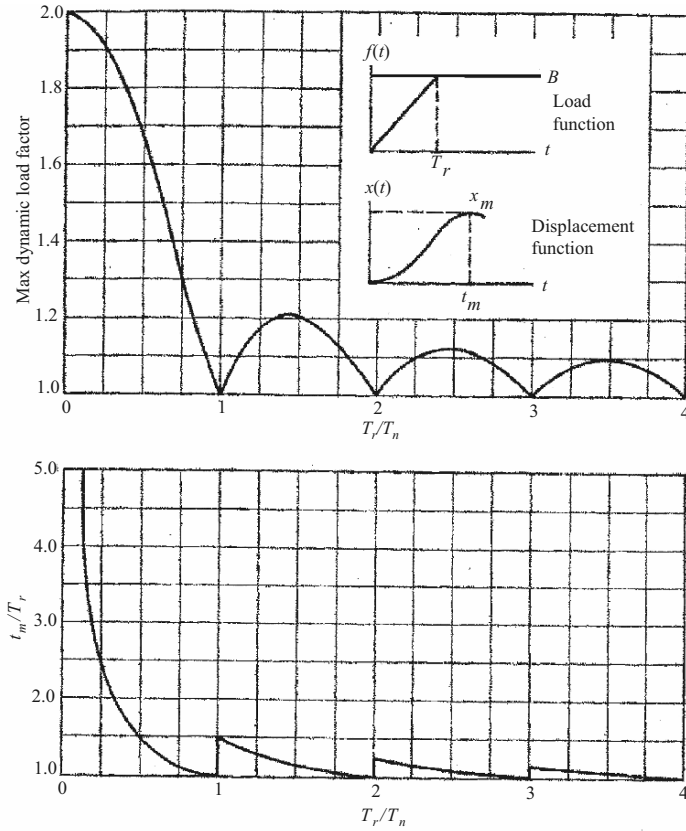
Fig. B.42. Elastic analysis of one-degree system [9]

From Fig. B.42 we note that $t_m/T_r = 1.39$; t_m is equal 0.034×1.39, or $0.047\,\mathrm{s}$. Since t_m is greater than T_r the maximum resistance and maximum load occur simultaneously and the two should be combined for maximum dynamic reaction. The value of V_2 is calculated as

$$V_2 = 0.33R + 0.33P, \tag{B.76}$$

where V_2 = shear due to dynamic load

$$R = 1.18P. \tag{B.77}$$

$$\text{Thus, } V_2 = 0.33 \times 1.18 \times 2{,}900 + 0.33 \times 2{,}900 = 2{,}086\,\mathrm{kN}. \tag{B.78}$$

Thus shear due to dead load is $92\,\mathrm{kN}$ and shear due to lateral blast load on the frame is $396\,\mathrm{kN}$. Thus the total shear stress intensity is

$$v = \frac{V}{A_w} = \frac{2{,}775}{0.914 \times 0.0195} = 155.7 \times 10^3\,\mathrm{kN\,m}^2 < 248 \times 10^3 \qquad \text{OK. (B.79)}$$

The following minimum proportions are recommended to prevent local buckling in I beams:

$$\text{Compression flange}\quad b/t_f \text{ not to exceed 17,}$$
$$\text{Web}\qquad\qquad a/t_w \text{ not to exceed 70.}$$

The criteria given above were derived for static-loading conditions and are probably conservative. This approximation is necessary because very few data on dynamic buckling are available.

When the design is completely elastic the conventional width-thickness requirements are adequate. However, in this case, we anticipate the development of the full plastic resisting moment at the center column.

$$\frac{b_f}{t_f} = \frac{307.7}{32} = 9.61 < 17$$
$$\frac{a}{t_w} = \frac{824.4}{19.5} = 42.2 < 70$$
$$\therefore\ \text{O.k} \qquad\qquad\qquad \text{(B.80)}$$

Design of Column Against Explosion Loading

The final design of the columns should be done by numerical integration because of the variety of time-varying loads involved. However, in this research it necessary to limit our discussion to an approximate solution based on curves, which are often adequate for practical purposes.

The horizontal load is equal to the dynamic reaction at the top of the side walls. The vertical-columns loads are the dead and dynamics reactions of the girders.

For this approximate analysis it may be assumed that these loads are uniform. It also assumed that three column loads are equal.

This simplifies the analysis since it enable us to consider only the total lateral resistance of the frame rather than that of the three columns separately. It does not introduce the serious error since the resulting decrease in the exterior columns is essentially balanced by the increase for the interior columns. All these columns are of the same cross section. The permissible lateral deflection of the frame is taken 220 mm, which implies plastic deformation. The frame is to be designed for protection category 1 against a specified blast-loading threat.

The total resistance when plastic hinges have formed at both ends of all three columns is equal to $3(2M_D/h)$, (B.81)

Assume $C_R = 0.2$ \qquad Required $R = 0.2 \times 5293 = 1{,}058\,\text{kN}.$

Required \qquad $M_D = \dfrac{Rh}{6} = \dfrac{1{,}058 \times 4.4}{6} = 776\,\text{kN m.}$ \qquad (B.82)

Try 254 × 254 × 132 UC in S275 Steel

$$\text{I} = 22{,}530\,\text{cm}^4 \quad \text{S} = 1{,}869\,\text{cm}^3 \quad \text{A} = 168\,\text{cm}^2$$

Check for local buckling,

$$\frac{b_f}{t_f} = \frac{261.3}{25.3} = 10.3 < 17$$
$$\frac{a}{t_w} = \frac{200.3}{15.3} = 13.1 < 43$$

$$\therefore \text{ OK}$$

Computation of M_D

$$M_P = 355 \times 1869 \times 10^3 = 664 \,\text{kN m},$$
$$P_p = 355 \times 168 \times 10^2 = 5{,}964 \,\text{kN},$$

Eq. (1) $$M_1 = \frac{f_{dy}}{3d} \left[4t_w \left(\frac{d}{2} - t_f \right)^3 + bt_f \left(3_{d^2} + 6dt_f + 4t_f^2 \right) \right]$$ (B.83)

$$M_1 = 401 \,\text{kN},$$

Eq. (2) $$P_1 = \frac{f_{dy}}{d} \left(2bt_f^2 + t_w \frac{d^2}{2} - 2t_w t_f^2 \right) = 778 \,\text{kN},$$ (B.84)

Eq. (3) $$M_D = M_P - \frac{P_D}{P_1}(M_P - M_1) \qquad P_D < P_1,$$ (B.85)

$$M_D = 664 - \frac{1{,}334}{778}(664 - 401) = 213 \,\text{kN m} \quad \text{Not Sufficient},$$ (B.86)

Try $305 \times 305 \times 158$ UC in S275 Steel

$$I = 38{,}750 \,\text{cm}^4 \qquad S = 2{,}680 \,\text{cm}^3 \qquad A = 201 \,\text{cm}^2$$

Check for local buckling according to Sec... ...

$$\frac{b_f}{t_f} = \frac{311.2}{25} = 12.3 < 17$$
$$\frac{a}{t_w} = \frac{246.7}{15.8} = 15.6 < 43$$

$$\therefore \text{ OK}$$

Compute M_D again

$$M_P = 355 \times 2680 \times 10^3 = 951 \,\text{kN m},$$
$$P_p = 355 \times 201 \times 10^2 = 7{,}136 \,\text{kN},$$

Eq. (1) $$M_1 = \frac{f_{dy}}{3d} \left[4t_w \left(\frac{d}{2} - t_f \right)^3 + bt_f \left(3_{d^2} + 6dt_f + 4t_f^2 \right) \right]$$ (B.87)

$$M_1 = 840 \,\text{kN},$$

$$\text{Eq. (2)} \quad P_1 = \frac{f_{dy}}{d}\left(2bt_f^2 + t_w\frac{d^2}{2} - 2t_w t_f^2\right) = 1{,}320\,\text{kN}, \tag{B.88}$$

$$\text{Eq. (3)} \quad M_D = M_P - \frac{P_D}{P_1}(M_P - M_1) \qquad \text{P}_\text{D} < \text{P}_1, \tag{B.89}$$

$$M_D = 951 - \frac{2{,}270}{1{,}320}(951 - 840) = 765\,\text{kN\,m} \quad \text{OK.} \tag{B.90}$$

Now check the original assumptions for CR by analysis of the equivalent system. Note that the load and mass factors are both unity.

Design and Analysis of a Building against Blast Loading

$$R_{me} = \frac{6M_D}{h} = \frac{6 \times 765}{4.4} = 1{,}043\,\text{kN}, \tag{B.91}$$

$$X_{el} = \frac{R_{me}}{k_e} = \frac{1{,}043}{2{,}0761} = 0.0502\,\text{m}, \tag{B.92}$$

$$T_n = 2\pi\sqrt{\frac{m_{te}}{k_e}} = 2\pi\sqrt{\frac{69.35}{20{,}761}} = 0.36\,\text{s}, \tag{B.93}$$

$$\frac{T}{T_n} = \frac{0.096}{0.36} = 0.26, \tag{B.94}$$

$$C_R = \frac{1{,}043}{4{,}366} = 0.24.$$

From Fig. B.43

$$\frac{X_m}{X_{el}} = 4.2, \tag{B.95}$$

$$X_m = 4.2 \times 0.0502 = 0.211\,\text{m} = 211\,\text{mm} < 220,$$

$$\tan\theta = \frac{X_m}{L/2} = 211 \times 2/12.6 \times 10^{-3}.$$

Thus, $\theta = 1.92° \le 2°$ which is satisfactory.

Having satisfied the deflection criteria, we should now check the possibility of lateral buckling of the columns.

$$\frac{K'Ld}{100bt_f} = \frac{0.14 \times 4.4 \times 327.1}{100 \times 311.2 \times 25} = 0.259 \tag{B.96}$$

$$\frac{K''L}{15r} = \frac{0.50 \times 4.4}{15 \times 0.079} = 1.86 \tag{B.97}$$

Note that the columns are assumed to be fully fixed in both directions at both ends.

$$\frac{M_D}{M_P}\left(\frac{K'Ld}{100bt_f}\right) + \frac{P_D}{P_p}\left(\frac{K''L}{15r}\right) < 1 \tag{B.98}$$

$$\therefore \text{OK}$$

$$765/951(0.259) + 2{,}270/7{,}136(1.86) = 0.79 < 1 \tag{B.99}$$
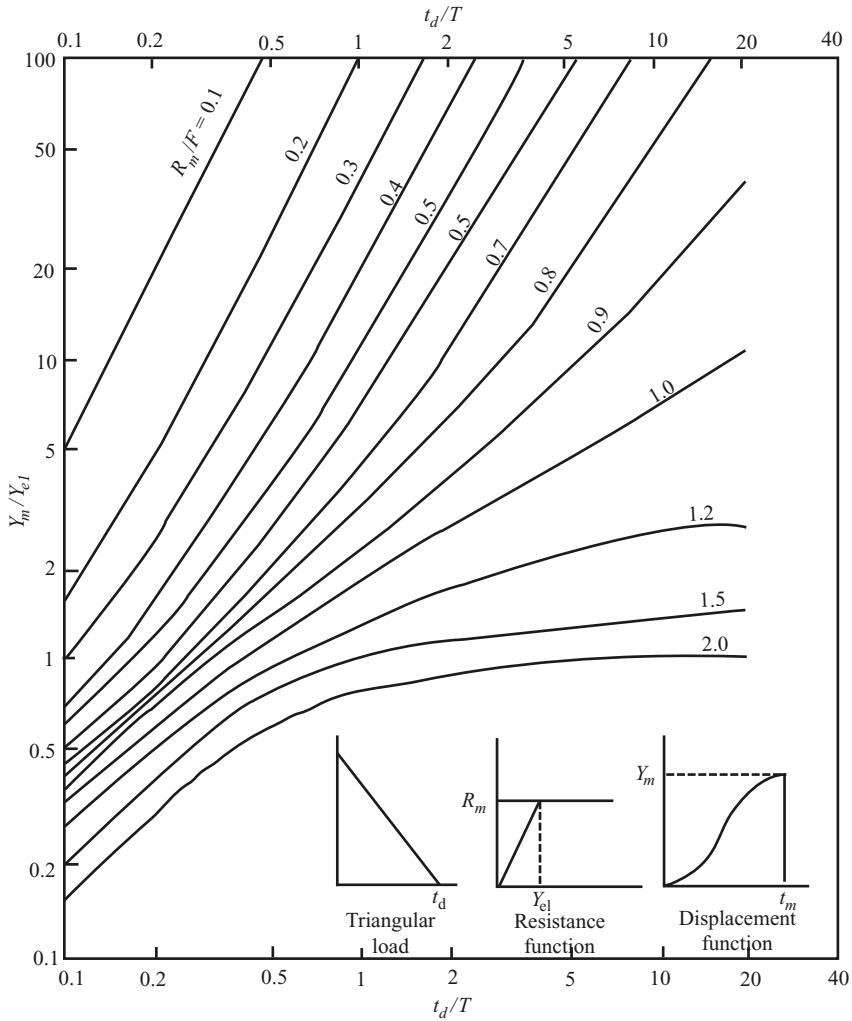
Fig. B.43. Maximum deflection of a single-degree of freedom elasto-plastic system subjected to triangular load pulse having zero rise time
(with compliments from U.S. Corp. of Engineers, U.S.A.)

Thus the *305 × 305 × 158* columns are completely satisfactory by this approximate analysis.

Design of Purlins Against Explosion Loading

Beams at 2.1 m centres

$$\frac{r_u}{F} = 1.0. \tag{B.100}$$

This value is assumed foe a new beam replacing the damaging one, i.e.

$$R_u = r_u = 162 \,\text{kN}, \tag{B.101}$$

$$M_P = \text{Plastic moment} \frac{r_u L}{8} = 162 \,\text{kN m}, \tag{B.102}$$

$$(S_x + z_e)\sigma_{dy} = 2M_p \,(\text{from the plastic analysis}), \tag{B.103}$$

$$(S_x + z_e) = \frac{2 \times 162 \times 10^3}{1.3 \times 355 \times 10^6} = 0.0158 \,\text{m}^3 = 702 \,\text{cm}^3. \tag{B.104}$$

The existing section is $305 \times 165 \times 54 \,\text{kgm}^{-1}$. Therefore:

$$(S_x + z_e) = (846 + 754) = 1{,}600 \,\text{cm}^3 > 702 \,\text{cm}^3. \tag{B.105}$$

Mass of beam + load from concrete is given by:

$$M_d = m = 54 \times 5.5 + (240 \times 5.5 \times 2.1) = 3{,}069 \,\text{kg}, \tag{B.106}$$

$$T_n = 2\pi\sqrt{\frac{K_{LM} m}{k_e}} = 2\pi\sqrt{\frac{0.72 \times 3{,}069}{0.11 \times 10^9}} = 0.016 \,\text{s or } 16 \,\text{ms}, \tag{B.107}$$

$$k_e = \frac{384 EI}{5L^3} = \frac{384 \times 200 \times 10^9 \times 11{,}700 \times 10^{-8}}{5 \times 8^3}$$
$$= 0.11 \times 10^8 \,\text{N m}^{-1}, \tag{B.108}$$

$$K_{LM} = 0.72,$$

$$\frac{t_d}{T_n} = \frac{10}{16} = 0.63,$$

$$r_u = R_u = \frac{8M_P}{L} = \frac{8 \times 1{,}600 \times 10^{-6} \times 355 \times 10^6 \times 1.3}{5.5 \times 7}$$
$$= 1.53 \times 10^5 \,\text{N}, \tag{B.109}$$

$$\frac{r_u}{F_1} = \frac{153}{162} = 0.95 \quad \text{Not Sufficient.} \tag{B.110}$$

Choose a new section Try $356 \times 171 \times 57 \,kg\,m^{-1}$

$$(S_x + z_e) = (1{,}010 + 896) = 1{,}906 \,\text{cm}^3 > 702 \,\text{cm}^3, \tag{B.111}$$

$$M_d = \bar{m} = 57 \times 5.5 + (240 \times 5.5 \times 2.1) = 3{,}086 \,\text{kg}, \tag{B.112}$$

$$T_n = 2\pi\sqrt{\frac{K_{LM} m}{k_e}} = 2\pi\sqrt{\frac{0.72 \times 3{,}086}{0.15 \times 10^9}}$$
$$= 0.024 \,\text{s or } 24 \,\text{ms}, \tag{B.113}$$

$$k_e = \frac{384 EI}{5L^3} = \frac{384 \times 200 \times 10^9 \times 16{,}040 \times 10^{-8}}{5 \times 5.5^3}$$
$$= 0.15 \times 10^8 \,\text{N m}, \tag{B.114}$$

$$K_{LM} = 0.72,$$
$$\frac{t_d}{T_n} = \frac{10}{15} = 0.63,$$
$$r_u = R_u = \frac{8M_P}{L} = \frac{8 \times 1{,}906 \times 10^{-6} \times 355 \times 10^6 \times 1.3}{5.5 \times 7}$$
$$= 1.82 \times 10^5 \,\text{N}, \tag{B.115}$$
$$\frac{r_u}{F_1} = \frac{182}{162} = 1.1 \quad \text{OK},$$
$$\frac{x_M}{x_L} = \mu = \text{ductility ratio} = 1.5 < 3.$$

This beam can be used

Check for shear:

$$V_u = \text{ultimate shear capacity} = \sigma_{dv} A_w \tag{B.116}$$
$$= 235.365 \times 2{,}900 \times 10^{-3} = 682.55 \,\text{kN}.$$

Dynamic yield stress in shear

$$\sigma_{dv} = 0.51 \times 1.3 \times 355 = 235.365 \,\text{kN}. \tag{B.117}$$

But

$$V = 0.393 r_u + 0.107 \,\text{F} \tag{B.118}$$
$$V = 0.393 \times 1.53 \times 10^2 + 0.107 \times 162 = 77.463 \,\text{kN}$$
$$V < V_u = 77.463 \,\text{kN} < 682.555 \,\text{kN}. \tag{B.119}$$

The beam is therefore adequate.

B.3.7 Impact Resistance of Steel Fibre Reinforced Concrete Panels/Slabs

Introduction

Lok. T.S. and Pei J.S. have carried out an experimental investigation on the impact resistance and ductility of simply supported steel fibre reinforced CSFR concrete panels.

Two series of panels, 50 and 75 mm thick, were manufactured with three distinct types of steel fibres. Within each series, two relatively low-volume fibre concentrations (0.5 and 1.0%) were adopted in the concrete mix. Repeated impact was provided by a free-falling hemispherical shaped steel projectile at the centre of the panels.

For a given panel thickness, an empirical formula was used to calculate the critical height that would cause perforation. However, in order to study

the influence of repeated impact, only 50% of the calculated critical height of each series of panels was used. After each impact, the deflections of the SFR panels were measured and plotted. The nominal increase in thickness does not significantly improve the damage resistance and ductility of SFR concrete panels as tested. However, the fibre concentration and fibre type influence the impact resistance and ductility of SFR concrete panels. Calculated impact ductility and support rotation compare favourably with blast design data in a US Army manual. SFR concrete panels may be categorised according to the manual. The experimental results could be utilised to assess impact resistance of SFR concrete structures. Three-dimensional eight-noded finite isoparametric elements have been chosen with sprayed steel fibres in the body of each element. The panel dimensions were the same as chosen by the authors. The results obtained form BANG-F have been fully collaborated with those produced by experimental results.

Steel Fibres in Concrete Mix

Since fibre type has an effect on the performance of SFR concrete (Soroushian and Bayasi, 1991), three types of commercially-available steel fibres with their attendant mechanical properties and characteristics were selected in the study. For each fibre type, low fibre concentrations, 0.5 and 1.0%, were used in the concrete mix to retain workability, reduced cost and minimum design effort without introducing mix design variants. Although concrete containing higher fibre concentrations in the mix may improve performance, difficulty may be experienced in mixing, placement and compaction.

Two lengths of Type A fibres were selected because it enables the effect of fibre length on damage tolerance to be investigated. Concrete incorporated with longer fibres of the same configuration have the tendency to sustain higher static loading. Type B was chosen to study the influence of fibre density on repeated impact resistance and ductility. Dense fibre distribution has been found to perform better in sustaining static concentrated central loading (Lok and Pei, 1995). Type B fibres provide a higher density of fibres per unit area for the same fibre concentration compare with their longer and thicket counterparts. The average mass of a single A1 fibre is about 0.205 gm; the fibre mass ratios of type A1 to type A2, B and C are approximately 0.84, 7.58, and 0.88 respectively. The hooked ends of Type C fibres are designed to increase pull-out resistance from the matrix (Table B.18). Details of the concrete panels are given in Table B.19.

Concrete Properties and Panel Specimens

Crushed granite aggregates, river sand and ordinary Portland cement were used in the grade 30 concrete mix design. The water/cement ratio was about 0.5 with a cement content of $400\,\mathrm{kg\,m^{-3}}$. The sand to cement ratio is 1.5, and the coarse aggregate to sand ratio is 2.2.

Table B.18. Characteristics of steel fibres

Fibre type	Fibre length (mn)	Dimensions (mm × mm)	Equiv. aspect ratio	Tensile strength $(\mathrm{N\,m^{-2}})$	Description/characteristics
A1	38	2.10 × 0.40	36.7	1,240	Corrugated cold drawn carbon steel fibre. Corrugation reduces actual length of the fibre, increases wire
A2	51	2.10 × 0.40	49.3	1,240	stiffness and bond efficiency and reduces the phenomena of "balling" during mixing. The "balling" threshold for steel fibres is about 90
B	18	0.65 × 0.35	33.4	800	Uniform short steel fibre, slightly twisted along its length and with moderately cr imped ends to increase anchorage
C	60	0.80 mm dia.	75	1,100	Uniform circular high yield steel fibre with hooked ends. Bundles are held together with water-soluble glue

Table B.19. Details of concrete panels

Fibre type/ reinforcement	Fibre conc. (%)	Panel identification			
		Series 1: 50 mm thick panels		Series 2: 75 mm thick panels	
		Set 1: static test	Set 2: impact test	Set 1: static test	Set 2: impact test
–	–	S1	S50	S2	S75
Weldmesh	–	SR1	SR50	SR2	SR75
A1	0.5	XA1	XA50	XA2	XA75
A1	1.0	XB1	XB50	XB2	XB75
A2	0.5	XC1	XC50	XC2	XC75
A2	1.0	XD1	XD50	XD2	XD75
B	0.5	EA1	EA50	EA2	EA75
B	1.0	EB1	EB50	EB2	EB75
C	0.5	DA1	DA50	DA2	DA75
C	1.0	DB1	DB50	DB2	DB75
Total no. of panels		10	10	10	10

Data:-

$\sigma_{\mathrm{cu}} = \mathrm{f_{cu}} = $ ultimate strength of concrete – 42.2 N mm^{-2} (40 N mm^{-2}adopted)

$\mathrm{f_{yc}}$ (300 × 150 mm cylinder) = 33.6 N mm^{-2}

Total No. panels = 40

$\mathrm{D_c} = \rho_{\mathrm{c}} = $ density of concrete = 2,392 kg m^{-3}

Panel dimensions or sizes = 810 mm square

Two panels each were cast without steel fibres

D = Panel thickness = 50 and 75 mm

Impactor mild steel billet of 100 mm diameter

Reinforcement: Plain concrete panels (S1, S50, S2 and S75) and panels conventionally-reinforced at mid-depth with a single layer of standard weldmesh (SR1, SR50, SR2 and SR75). The plain concrete panel was fabricated and tested because increase in the strength of other concrete panels measure against the corresponding plain concrete panel can be accounted for by either the presence of steel fibres or the weldmesh reinforcement. Relative stiffness and damage tolerance may also be compared in a similar manner. The 50 mm thick panels, SR1 and SR50, were reinforced with standard 6 mm diameter, 200 mm centre weldmesh fabric. The reinforcement represents about 0.28% of the concrete section area. For the 75 mm thick panels, SR2 and Sr5, the reinforcement ratio is 0.25% using the standard 7 mm diameter weldmesh fabric with the same spacing.

m = mass of projectile = 12.74 kg

h = target non-deformable = 6.15–8.18 m

v = impact velocity = 7.67 m s^{-1}

Nose factor = 0.65

Impactor drop height (Fig. B43) = 3.0 m

Impactor Test Results

A summary of the number of impacts on each of the panels until failure and brief comments on the response are given in Table B.20. In the majority of cases, the number of impacts on SFR shape, minimum target thickness to prevent scabbing and the effect of repeated impact. Therefore, it is not known whether meaningful results could be obtained at the preliminary stage of this investigation. The height was selected at 50% of the calculated critical level to ensure that serious damage would not occur for all the panels after the first drop and, if partially damaged, allows for repeated impact to be conducted on the same location for the SFR concrete panels until failure occurs. Figure B.44 gives the concrete target response, giving data on penetration/thickness for three cases under inputs.

B.4 Buildings and Structures Subject to Blast Loads

B.4.1 Reinforced Concrete, Single-Storey House

A single-storey house, idealized as a box-type structure, is examined under a blast load in open air. In the ISOPAR program, the distance r of a blast load is kept variable against the weapon effect W. It is assumed that the interior of the house has enclosures and the walls have openings for doors

Table B.20. Summary of number of impact to failure

Panel ID	Fibre type	Reinf't/ Fibre conc. (%)	No. of impact		Comments
			50 mm series	75 mm series	
S	–	–	1	1	Each panel was broken into several tri-angular pieces formed from fracture lines across the diagonals. However, there was no perforation
SR	Weld-mesh	0.28 or 0.25	2	3	Maximum displacements are of the same order of magnitude, and the displacement profiles are approximately the same for both panels
XA	A1	0.5	2	1	Cone shaped scabs were ejected from the 50 mm panel after the first impact. Test was stopped after the first impact for the 75 mm panel
XB	A1	1.0	3	3	Both panels were perforated on the third impact. The second impact had caused localised damage but continued to remain serviceable
XC	A2	0.5	2	2	The measured displacement on the 50 mm panel was generally about 35–40% less than the 75 mm panel.
XD	A2	1.0	3	3	After the second impact, both panels suffered localised damage and failed on the third impact. The maximum displacements were similar
EA	B	0.5	2	1	Similar behaviour to the "XA" panels. Test on the 75 mm panel was termi-nated after the first impact due to severe localised damage.
EB	B	1.0	3	3	Similar behaviour to the "XD" panels. The 75 mm panel sustained more damage after the second impact than the 50 mm panel
DA	C	0.5	3	3	Both panels sustained localised damage after the second impact. The third impact perforates them. Displacements are similar in both cases
DB	C	1.0	4	4	Both panels were able to sustain higher number of impact, as well as preventing further deterioration caused by extensive local cracking

	100mm solid Impactor	US M3A1 4.2" mortar	US M362A1 81mm mortar	US M49A4 60mm mortar
Weapon				
Mass (kg)	12.74	12.22	4.27	1.45
Nose shape factor	0.65	0.82	1.11	0.82
Impact velocity (m/s)	7.67	7.83	13.25	22.73
Equlv. mass of TNT (kg)	0	3.22	0.99	0.15

(a) Projectile penetration into massive concrete.
(b) Thickness required to prevent perforation.
(c) Thickness required to prevent spalling.
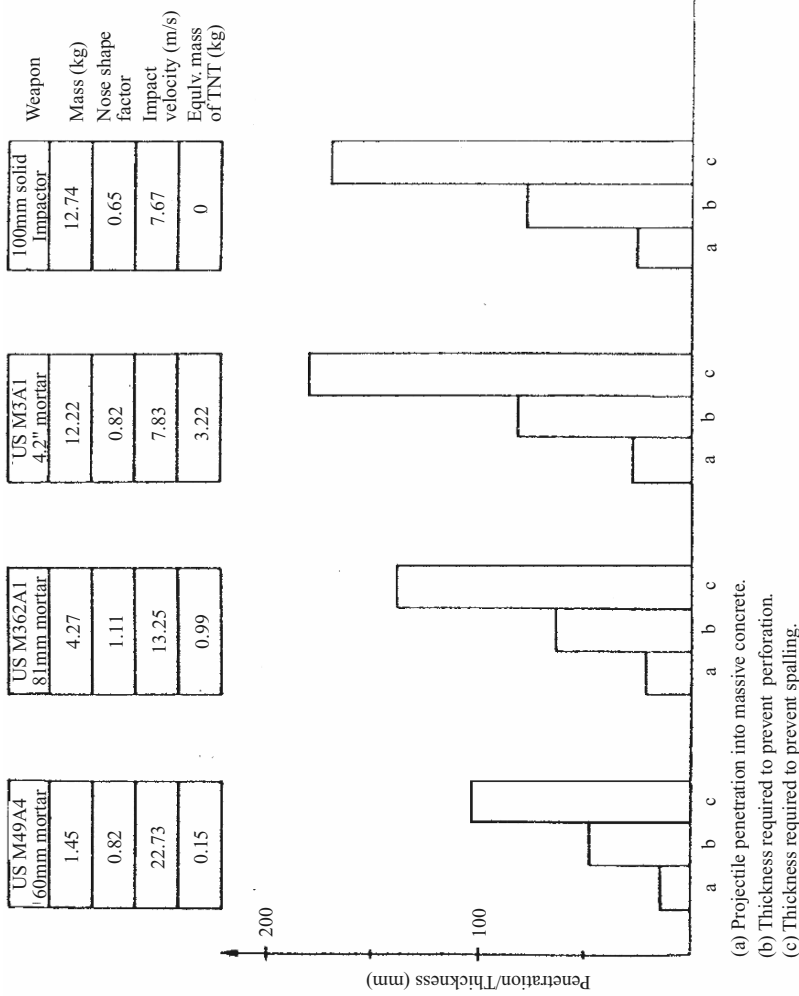
Fig. B.44. Concrete target response to same impact K.E. (compressive concrete strength $= 40\,\mathrm{N\,mm^{-2}}$)
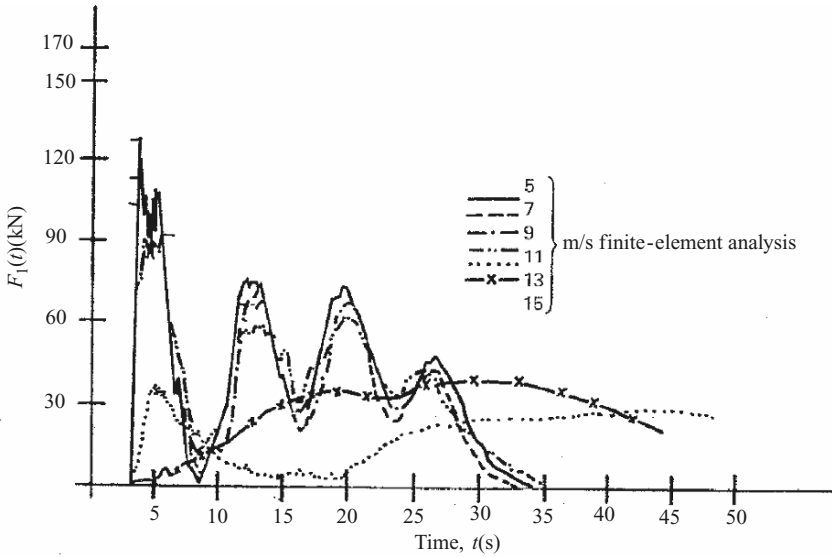
Fig. B.45. Load–time function for a 1,000 lb bomb
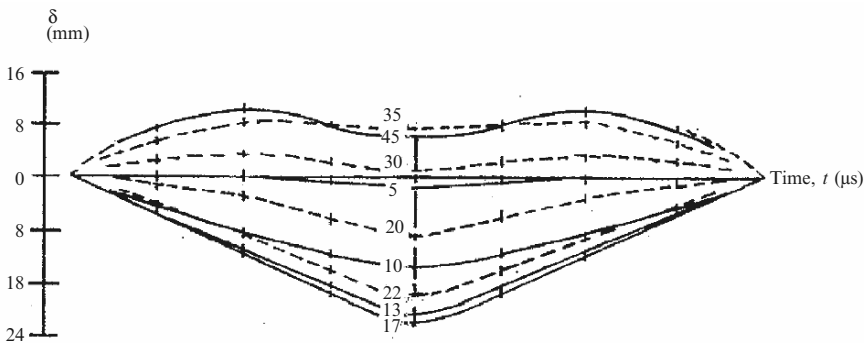
Fig. B.46. Deformation–time relationship for a runway slab

and windows. The percentage of reinforcement varies from $1\frac{1}{2}$ to 4% of the volume of concrete. The thickness T_c and the internal height h (or H) vary. The concrete strength or grade is assumed to be $50\,\mathrm{N\,mm^{-2}}$ — this strength is normally suitable for concrete under explosive effects. For economical reasons, the finite-element mesh schemes prepared for beams, walls and slabs discussed earlier are kept for this exercise. The following data support this exercise:

(1) Basic data

   Number of beams: 6

   Foundation springs with dashpots, variable soils: 300

   Saturated sand: $K = 438\,\mathrm{kN\,m^{-1}}$

   Sandy clay: $K = 292\,\mathrm{kN\,m^{-1}}$

(a)   (b)

(c)
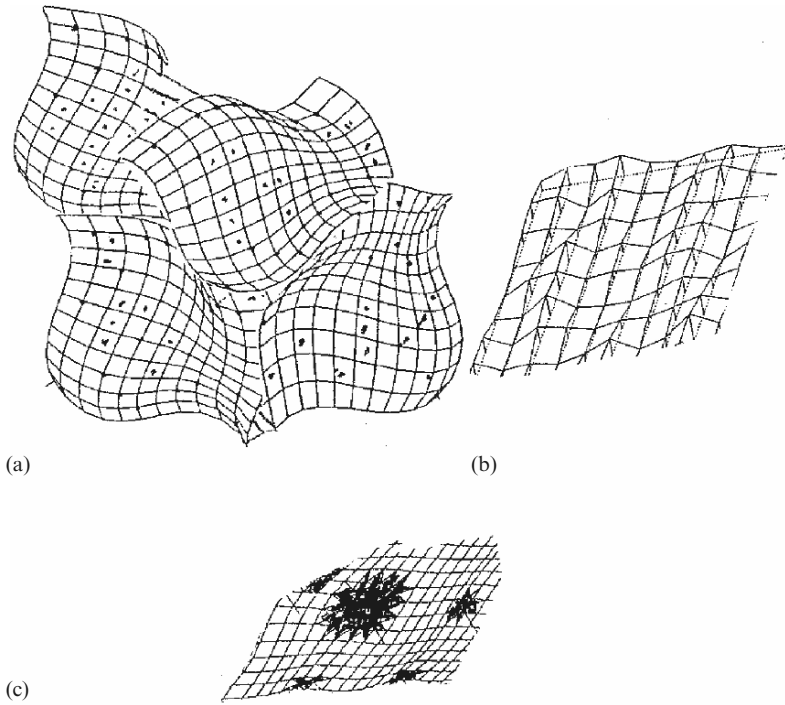
Fig. B.47. The damage scenario: (**a**) destruction phenomenon; (**b**) deformation along the thickness; (**c**) key diagram
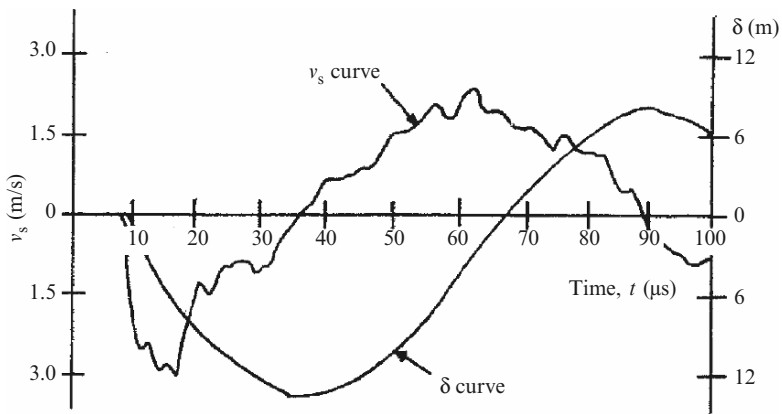
Fig. B.48. Comparative study of velocity and displacement for a runway ($v_s =$ velocity; $\delta =$ displacement)
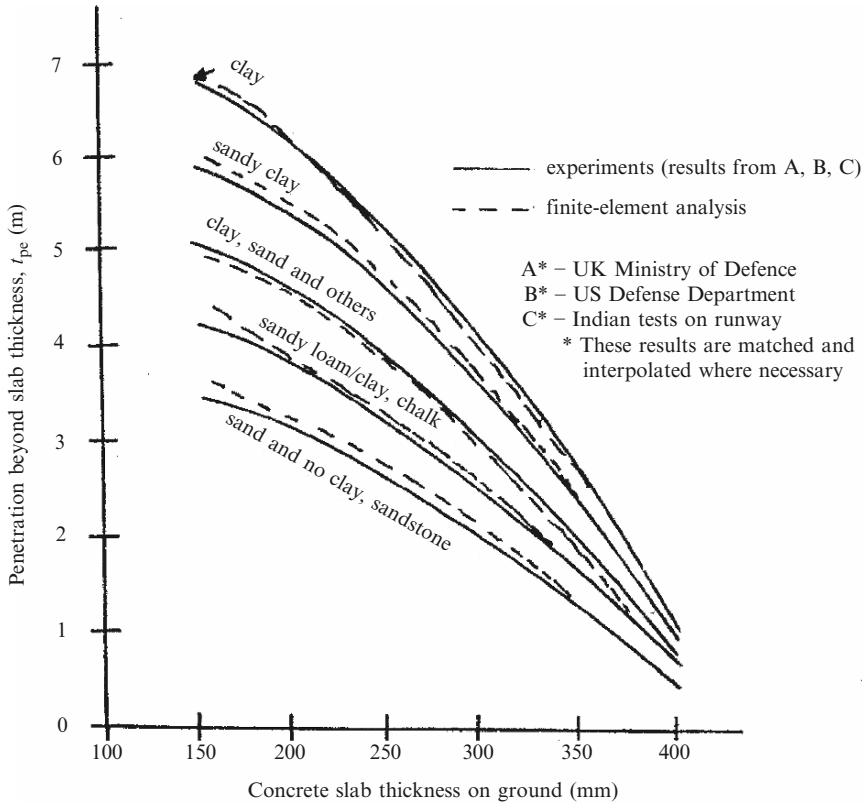
Fig. B.49. Slab thickness and penetration beyond the slab thickness (slab concrete grade ($35\,\mathrm{N\,mm^{-2}}$))

Gravelly soil: $K = 146\,\mathrm{kN\,m^{-1}}$
Distance from the explosion, r: 3, 6, 9 m
Bomb weights: 500 lb, 1,000 lb
Bomb velocity, v_{so}: $200\,\mathrm{m\,s^{-1}}$

(2) Finite-element data

8-noded isoparametric elements: $1{,}500\,\mathrm{wall^{-1}}$, $750\,\mathrm{slab^{-1}}$
Reinforcement placed 2-noded isoparametric on elemental nodes and the body of the element: 2,100/2-node
Reinforcement has lacings: 300 lacings, 2-noded
Gap elements: 300
Increments: 20
Newmark solution implicit type
Execution time: 45 min 31 s
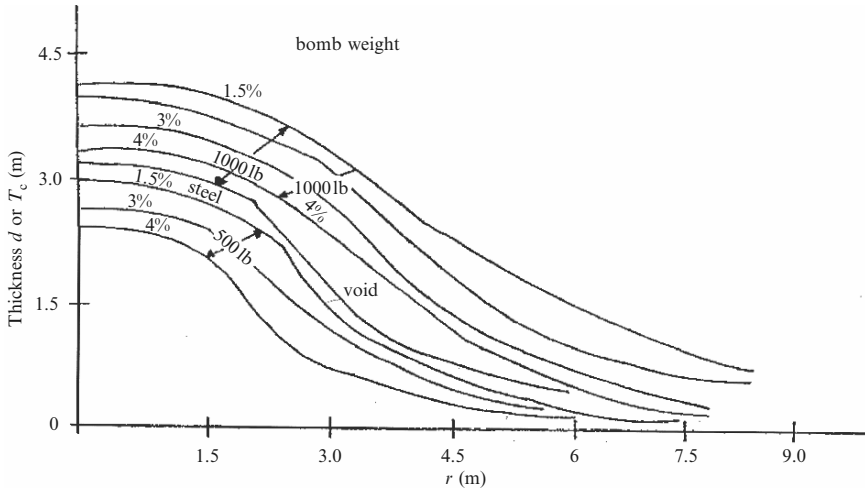
Fig. B.50. Concrete/wall slab thickness versus distance from explosion, r
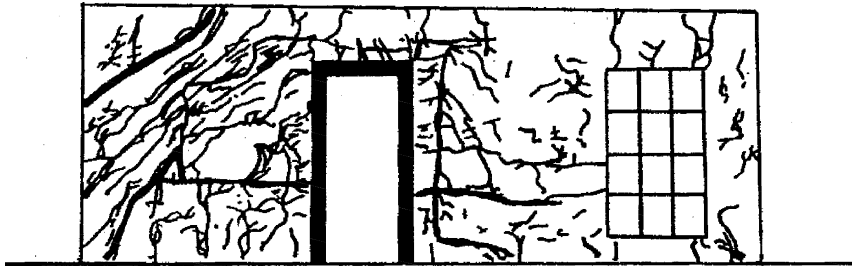
Fig. B.51. Cracking of walls with doors and windows

Figure B.50 shows the relationship between $T_{\rm c}$ and r. The wall thickness necessary to avoid damage (perforation, spalling, etc.) for various blast loads and distances, as shown in Fig. B.50, cannot easily be achieved if the point lies under the bottom curve. For example, a 1,000 lb bomb at a distance of 1.5 m and $T_{\rm c} = 1.5$ m can cause severe cracking to this wall. This is shown in Fig. B.51 for areas close to doors and windows.

B.4.2 Blast Loads in the Demolition of Buildings and Cooling Towers

This text gives a comprehensive treatment of blast loads and their effects on structures. Figure B.52 shows the finite-element mesh scheme for a high-rise, reinforced concrete building complex with 400 bombs, each containing 50 lb gelignite, placed along the perimeter. It is assumed that all the devices are detonated at the same time. Figure B.53 shows the final demolition post-mortem of this building. In practice, demolition is carried out in sequence
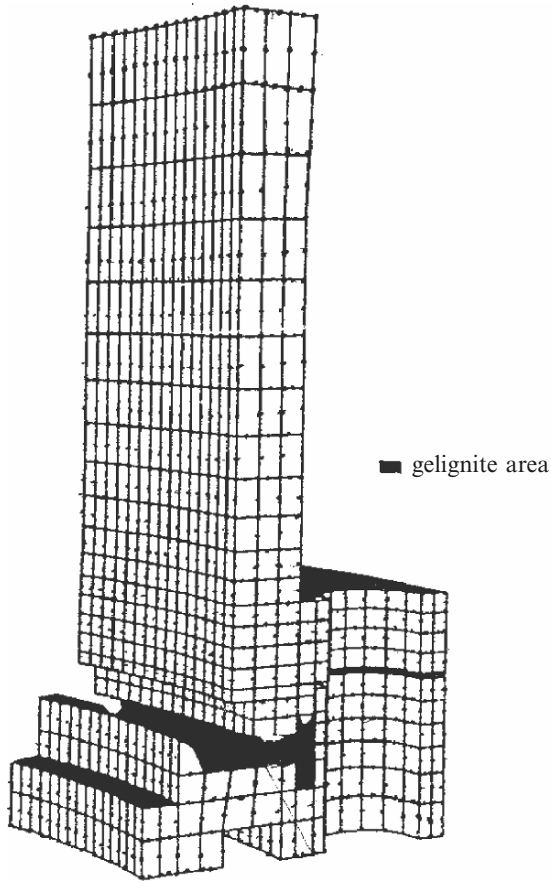
Fig. B.52. Finite-element mesh scheme of a high-rise building

at appropriate levels and in stages. This can easily be handled by the finite-element method.

B.4.3 Impact and Explosion of Cooling Towers and Chimneys

Table B.21 gives the basic data for a cooling tower or a power station. Five hundred 50 lb packages of Semtex are employed in the demolition scenario. Figure B.54 is a photograph of a cooling tower with the parameters given in Table B.21. The finite-element prediction is very similar to the one produced by the South of Scotland Electricity Board which is shown in Fig. B.55a. A comparative study is given in Fig. B.55b.

Chimneys can be dealt with in a similar manner with a modification to the finite-element mesh scheme to suit the chimneys' shape and the loads acting on them. This type of work is widely reported.

first stage
explosion

front
levels

floor

typical
damage
to five
floors

$f = 11.8\,\mathrm{Hz}$

front
displacement
in 3D

total demolition

back face
displacement
in 3D

rise 13.2 m

when
explosives are placed
here
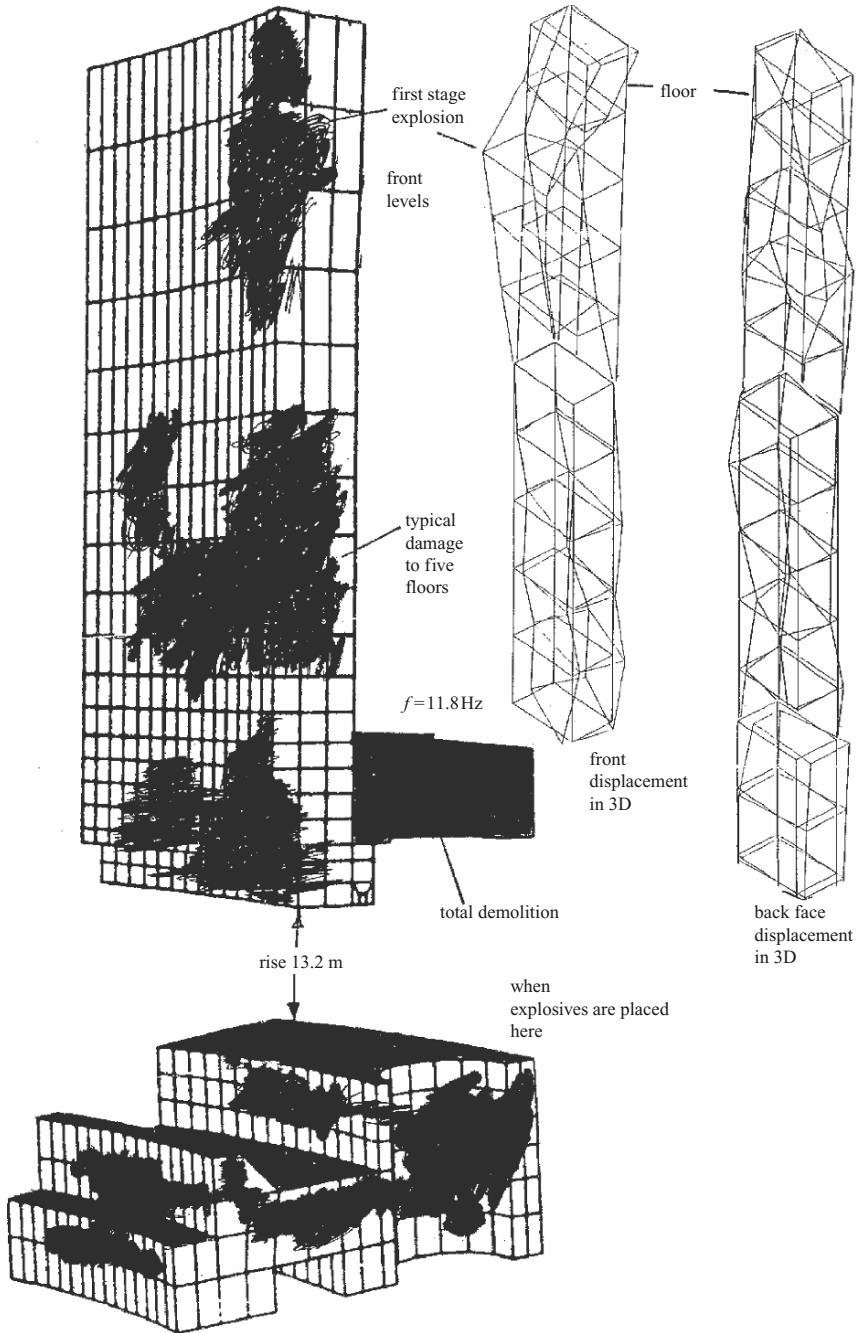
Fig. B.53. Demolished state
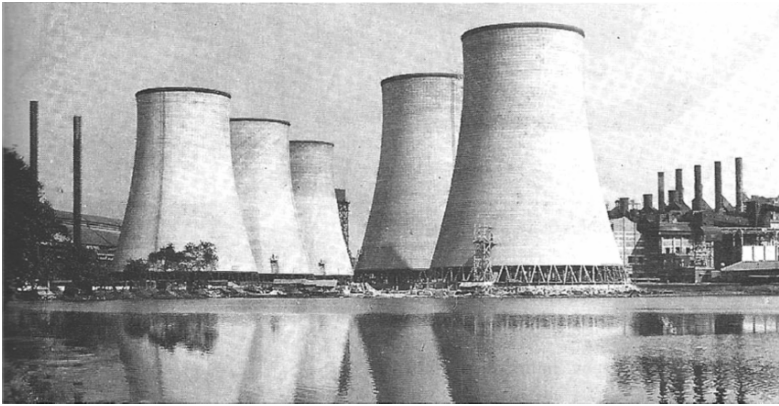
Fig. B.54. Balunpur cooling tower

Table B.21. Data for the cooling tower

Total height = 85.3 m	
Height H (m)	Diameter D (m)
0	66.4
33.7	49.2
65.4	42.6
85.3	45.4

Self-weight/unit area to be computed
Thickness: 150 mm
β values: -15, -5, 5, 15, 25, 35, 45 degrees
Number of 8-noded solid isoparametric elements: 1,900
Number of 2-noded line elements: 1,500 at nodes, 300 in the body
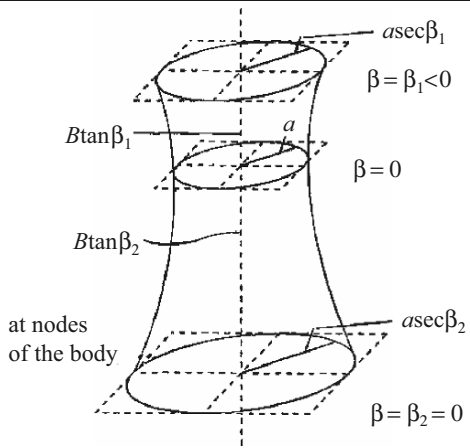
B.5 Aircraft Crashes on PWR Containment Vessels (Buildings)

Several studies have been carried out on containment vessels subjected to aircraft impact. The containments were treated both in isolation and together with surrounding buildings. The overall response with the surrounding buildings is considered. Figure B.56 shows the load–time function for a number of aircraft prepared by the author using data given in Chap. 2.

The author investigated the problems associated with the concrete containment vessels. Two existing reinforced and pre-stressed concrete containments were examined against extreme loads in elastic and cracking conditions. Figure B.57 shows a three-dimensional, finite-element mesh. The analysis
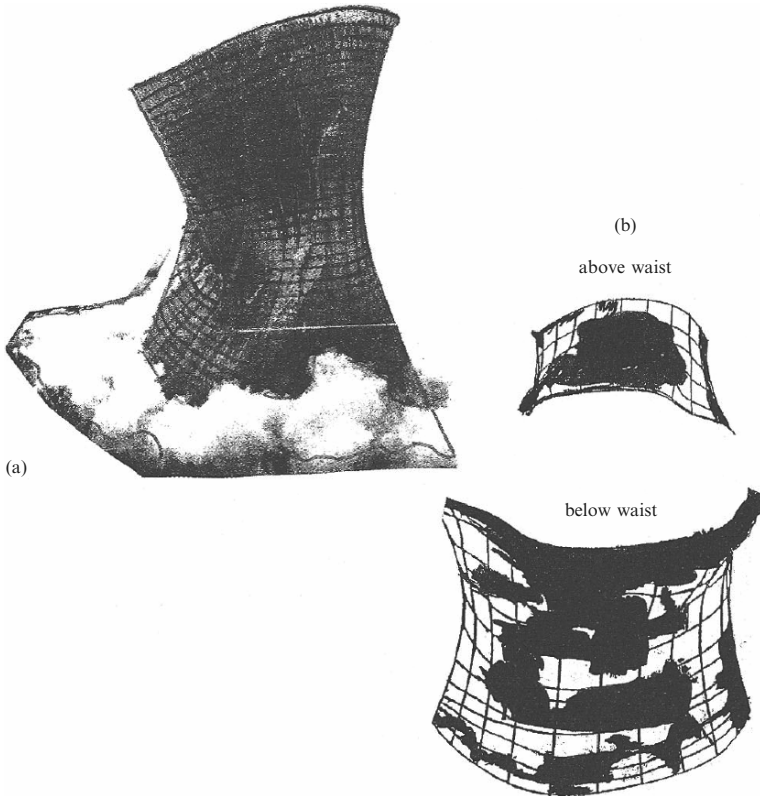
Fig. B.55. (**a**) Post-mortem of a cooling tower. (**b**) Post-mortem of a cooling tower–finite-element approach

explored the effect of an aircraft impact on the Sizewell B vessel. Figure B.58 shows crack propagations on both the interior and exterior surfaces of the vessel caused by the impact of a number of aircraft. The linear and non-linear displacements for impacts due to four aircraft are shown in Fig. B.59. Displacement–time relationships using a Tornado aircraft for the linear and non-linear cases are illustrated in Fig. B.60, for the Sizewell B vessel. Throughout the analysis, three-dimensional, 20-noded solid isoparametric elements were used for both the aircraft and the vessel concrete. The pre-stressing tendons/cables and steel liner were represented by 4- and 8-noded three-dimensional line and plate elements, respectively. Linkage elements were included at appropriate places along the tendon layouts and the anchor positions between the concrete of the vessel and the steel liner placed on the vessel interior. The vessel boundary conditions included the general building infrastructure surrounding the reactor island. The tension criteria for cracking are given earlier, together with the general endochronic theory for concrete.

Crutzen used the semi-loof shell element to examine the damage caused to the containment vessel by a Phantom RF-4E aircraft. The original and
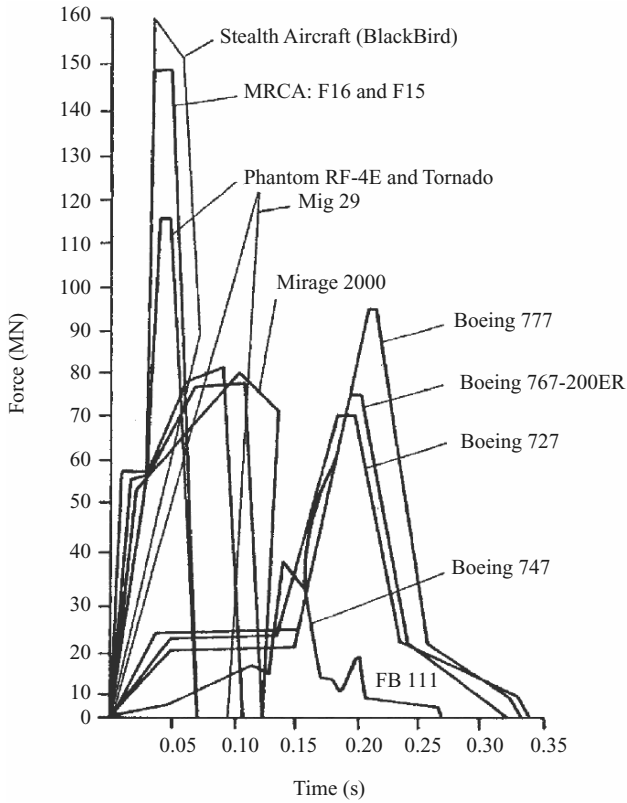
Fig. B.56. Load-time function
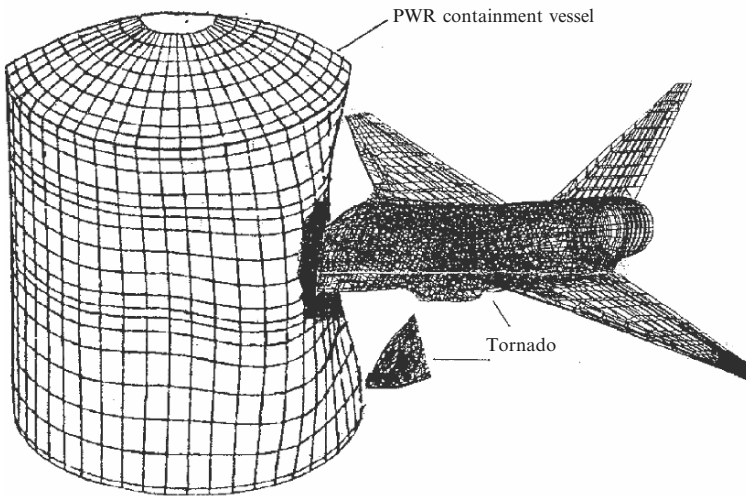
Fig. B.57. Finite-element mesh scheme for an aircraft–containment vessel impact phenomenon

interior surface   exterior surface

aircraft Tornado

scale m
0 1 2 3

interior surface   exterior surface

aircraft MRCA‑Tomcat
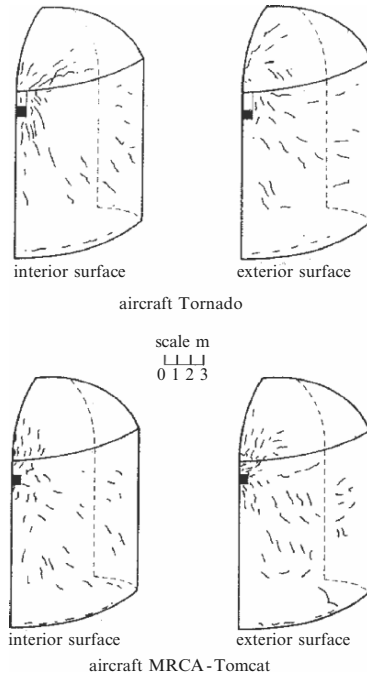
Fig. B.58. A post-mortem of the containment vessel (from Bangash [3.3])

(a) aircraft MRCA-Tomcat   (b) Boeing 747

scale in mm (×10)   .... non linear
0 2 4 6 8 10   —— linear
→ level

(c) aircraft F-16   (d) Tornado
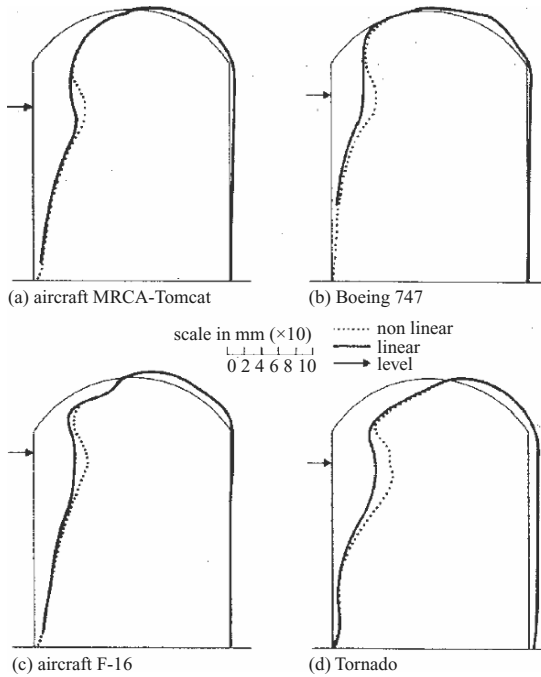
Fig. B.59. Displacements due to impact (from Bangash [3.3])
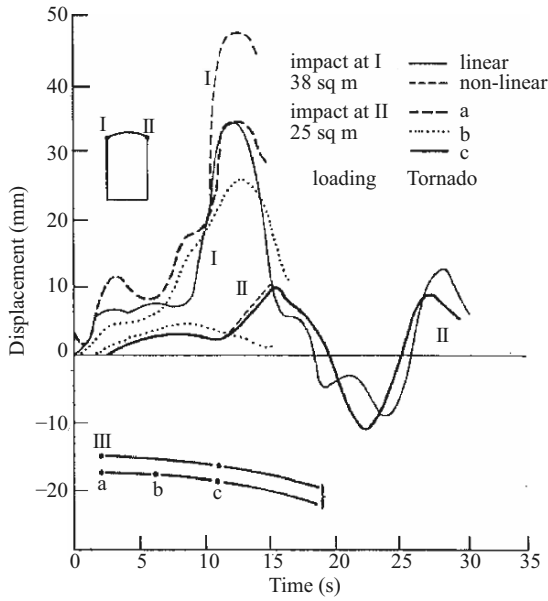
Fig. B.60. Displacement–time relationship using a Tornado aircraft
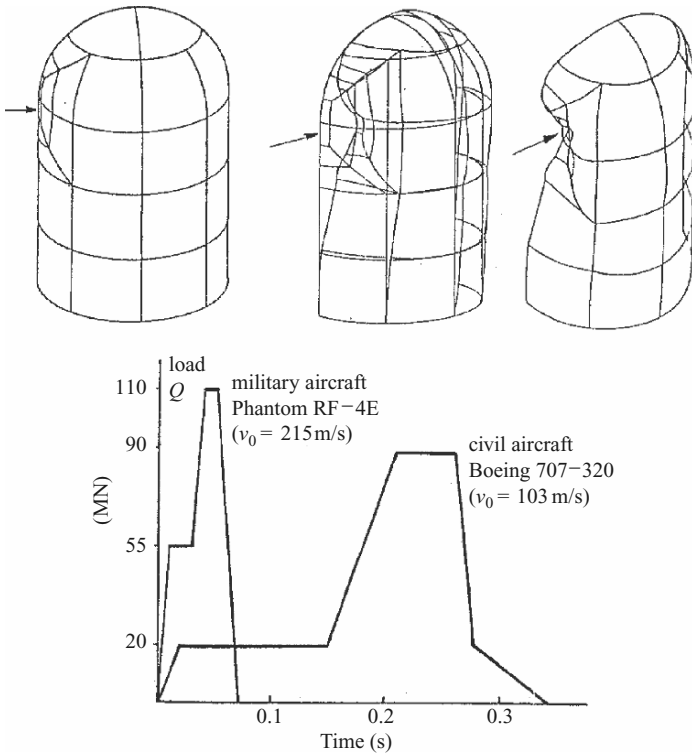
Fig. B.61. Original and deformed finite-element meshes after impact (courtesy of Kraftework Union)
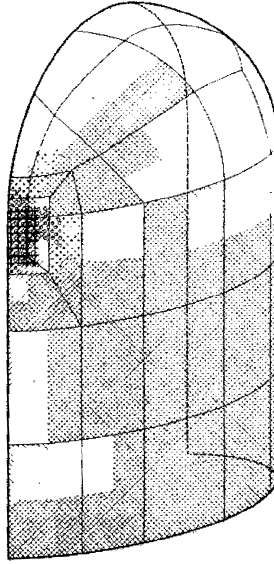
Fig. B.62. Post-mortem examination of a shell (Rebora model) (courtesy of Kraftework Union)

deformed meshes are shown in Fig. B.61. Cracking at the interior and exterior surfaces has been predicted. A similar exercise was carried out by Rebora using three-dimensional, isoparametric, 20-noded solid elements. A non-linear analysis of the vessel under the impact of a Boeing 707–320 aircraft was performed. A typical post-mortem examination of the vessel is shown in Fig. B.62.

C

Brickwork and Blockwork: Impact and Explosion

C.1 General Introduction

Gas explosions in buildings are a rare occurrence. Information on both the causes and effects of a gas explosion and some practical guidance on safe venting have already been discussed in this text. However, the importance of the structure's ability to withstand the blast load cannot be ignored. In this section, a brief analysis is given on impact and explosion in brickwork construction.

C.2 Finite-Element Analysis of Explosion

Figure C.1 shows a seven-storey building with 49 compartments. The compartments have external walls of thickness 450 mm and the thickness of the internal walls ranges between 225 and 362.5 mm. Thirteen vents are available in compartment/flat no 32. The information on a typical 3-wall cubicle, shown in Fig. C.2, is taken from flat no 32, where an explosion due to a gas leak occurs. A typical external wall of a cubicle is shown in Fig. C.3. A gas leak pressure is generated in compartment/flat no 32 using the finite-element scheme given in Fig. C.4. A pressure rise of $75.84 \, \mathrm{kN \, m^{-2}}$ was generated for a rise time of 0.2 s; various empirical expressions were used to calculate this pressure. Table C.1 lists the computer program used to evaluate such pressures. The program is linked to the finite-element ISOPAR program for the quick evaluation of pressures. The following data form part of the input for an explosion in brick buildings:

Aspect ratio of height/thickness: 1.5, 2.0, 2.5, 3.0
Openings: $1.5 \times 4, 0.4 \times 0.4, 1.0 \times 2.3 \, \mathrm{m}$
Frame stiffness, K: 11.61, 7.3, $3.69 \, \mathrm{kN \, mm^{-1}}$
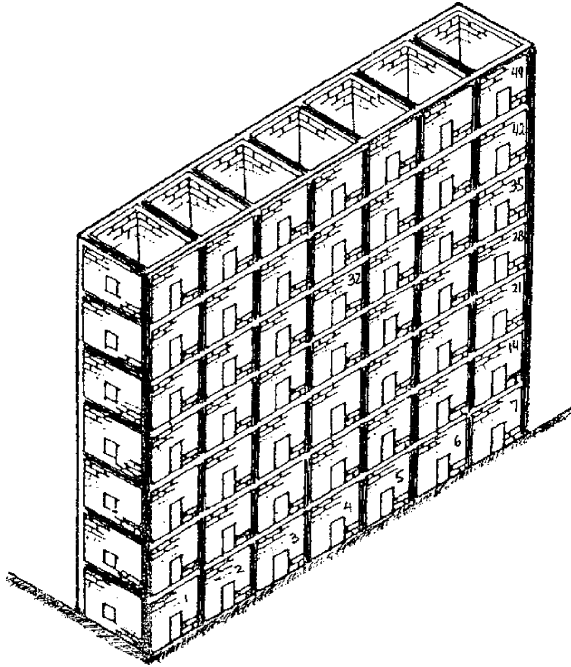
Fig. C.1. A typical 7-storey building in brickwork

Brick size: $185.9 \times 87.3 \times 87.4$ mm
   Young's modulus, E: 6.4670 kN mm^{-2}
   Poisson's ratio, v: 0.096
$224.1 \times 108 \times 67.3$ mm
   Young's modulus, E: 4.2323 kN mm^{-2}
   Poisson's ratio, v: 0.141
Number of 8-noded isoparametric elements (main building): 900
Number of 20-noded isoparametric elements (wall): 350
Mortar (cement, lime, sand): 1:1:6
   Young's modulus, E: 2.465 kN mm^{-2}
   Poisson's ratio, v: 0.244
Number of gap and 3-noded elements
   Main building: 1950
   Wall: 350

   Figure C.5 illustrates the pressure pulses for four types of explosions. The corresponding deflection type relationship is given in Fig. C.6. Figure C.7 shows the deflections for various pressures against the distance of the explosion, and Fig. C.8 shows the pressure pulse for the single wall of Fig. C.3. Figures C.9 and C.10 illustrate the post-mortems of the building and wall, respectively.

Table C.1. Pressure generated in a vented explosion

```
C     THIS IS A FORTRAN PROGRAM USED FOR THE CALCULATION OF THE
C     PREDICTION OF PRESSURE GENERATED IN A VENTED CONFINED GAS
C     EXPLOSION. A FEW METHODS OF CALCULATION WERE COMPUTED AND
C     COMPARED WITH EACH OTHER, THE HIGHEST VALUE OF THE PRESSURE
C     WAS THEN CHOSEN FOR THE DESIGN PURPOSE.
C
C        K E Y S:
C
C        P = BREAKING PRESSURE OF THE RELIEF PANEL
C        S = BURNING VELOCITY OF THE GAS INVOLVED
C        W = WEIGHT PER UNIT AREA
C        A = AREA OF RELIEF PANEL
C        B = AREA OF THE SMALLEST SECTION OF THE ROOM
C        V = VOLUME OF THE ROOM
C
C     ~~~~~~~~~~~~~~~~~~~~~~~~~~~~~~~~~~~~~~~~~~~~~~~~~~~~~~~~~~~~~~~
             REAL P, S, A, B, V, W
             WRITE (6, 10)
     10      FORMAT (2X, 'INSERT THE VALUE OF BREAKING PRESSURE, P (mbar)')
             READ (5, *)P
             WRITE (6, 20)
     20      FORMAT (2X, 'INSERT THE VALUE OF BURNING VELOCITY, S (m/s^2)')
             READ (5, *)S
             WRITE (6, 30)
     30      FORMAT (2X, 'INSERT THE AREA OF RELIEF PANEL, A (m^2)')
             READ (5, *)A
             WRITE (6, 40)
     40      FORMAT (2X, 'INSERT THE AREA OF WALL WHERE R.P LOCATED, B (m^2)')
             READ (5,*) B
             WRITE (6, 50)
     50      FORMAT (2X, 'INSERT THE VOLUME OF THE SECTION, V (m^3)')
             READ (5, *) V
             WRITE (6, 60)
     60      FORMAT (2X, 'INSERT THE WEIGHT PER UNIT AREA OF R.P, W (Kg/m^2)')
             READ (5, *)W

C  TO CALCULATE THE VALUE OF VENT COVER COEFFICIENT
C  ~~~~~~~~~~~~~~~~~~~~~~~~~~~~~~~~~~~~~~~~~~~~~
             K1 = B/A
             K2 = V**(2/3)/A

C     TO CALCULATE THE MAXIMUM PRESSURE GENERATED BY CUBBAGE & SIMMONDS
C        ~~~~~~~~~~~~~~~~~~~~~~~~~~~~~~~~~~~~~~~~~~~~~~~~~~~~~~~~~
             X1 = (S* 4.3*K1*W) + 28
             X2 = V** (1/3)
             P1 = X1/X2
             WRITE (6, 70)P1
     70      FORMAT (/, 2X, 'THE VALUE OF MAXIMUM PRESSURE BY CS IS :', F9.1)
             P12 = 58*S*K1
             WRITE (6, 70)P12
C
```

Table C.1. (continued)

```
C     TO CALCULATE THE MAXIMUM PRESSURE GENERATED BY CUBBAGE & MARSHALL
C     ~~~~~~~~~~~~~~~~~~~~~~~~~~~~~~~~~~~~~~~~~~~~~~~~~~~~~~~~~~~~~
        X1 = S**2*K1*W
        X2 = V**(1/3)
        P2 = (P + (23*(X1/X2)))
        WRITE (6, 80)P2
80      FORMAT (/, 2X, 'THE VALUE OF MAXIMUM PRESSURE BY CM IS :', F9.1)
C
C  TO CALCULATE THE MAXIMUM PRESSURE GENERATED BY RASBASH 1
C  ~~~~~~~~~~~~~~~~~~~~~~~~~~~~~~~~~~~~~~~~~~~~~~~~~~~~~~
        X1 = (1.5*P)
        X2 = (77.7*K1*S)
        P3 = (X1 + X2)
        WRITE (6, 90)P3
90      FORMAT (/, 2X, 'THE VALUE OF MAXIMUM PRESSURE BY R1 IS :', F9.1)
C
C  TO CALCULATE THE MAXIMUM PRESSURE GENERATED BY RASBASH 2
C  ~~~~~~~~~~~~~~~~~~~~~~~~~~~~~~~~~~~~~~~~~~~~~~~~~~~~~~
        X1 = 1.5*P
        X2 = (4.3*K1*W) + 28
        X3 = V**(1/3)
        X4 = 77.7*K1
        P4 = X1+S*((X2/X3)+X4)
        WRITE (6, 100)P4
100     FORMAT (/, 2X, 'THE VALUE OF MAXIMUM PRESSURE BY R2 IS :', F9.1)
C
C  TO COMPARE ALL THE VALUES OF MAXIMUM PRESSURE GENERATED AND CHOOSING
C  ~~~~~~~~~~~~~~~~~~~~~~~~~~~~~~~~~~~~~~~~~~~~~~~~~~~~~~~~~~~~~~~~~
C           THE MAXIMUM VALUE FROM THE FOUR METHOD
C           ~~~~~~~~~~~~~~~~~~~~~~~~~~~~~~~~~
        IF (P1.GT.P2.AND.P1.GT.P3.AND.P1.GT.P4) THEN
        WRITE (6, 120)P1
120     FORMAT (///, 2X, 'THE HIGHEST VALUE IS BY CS :', F9.1)
        ENDIF
        IF (P2.GT.P1.AND.P2.GT.P3.AND.P2.GT.P4) THEN
        WRITE (6, 130)P2
130     FORMAT (///, 2X, 'THE HIGHEST VALUE IS BY CM :', F9.1)
        ENDIF
        IF (P3.GT.P1.AND.P3.GT.P2.AND.P3.GT.P4) THEN
        WRITE (6, 140)P3
140     FORMAT (///, 2X, 'THE HIGHEST VALUE IS BY R1 :', F9.1)
        ENDIF
        IF (P4.GT.P1.AND.P4.GT.P2.AND.P4.GT.P3) THEN
        WRITE (6, 150)P4
150     FORMAT (///, 2X, 'THE HIGHEST VALUE IS BY R2 :', F9.1)
        ENDIF
        STOP
        END
```

Fig. C.2. Barrier and cubicle configuration and parameters (courtesy of TM 5-1300/NAVFAC P-397/AFM 88–22)
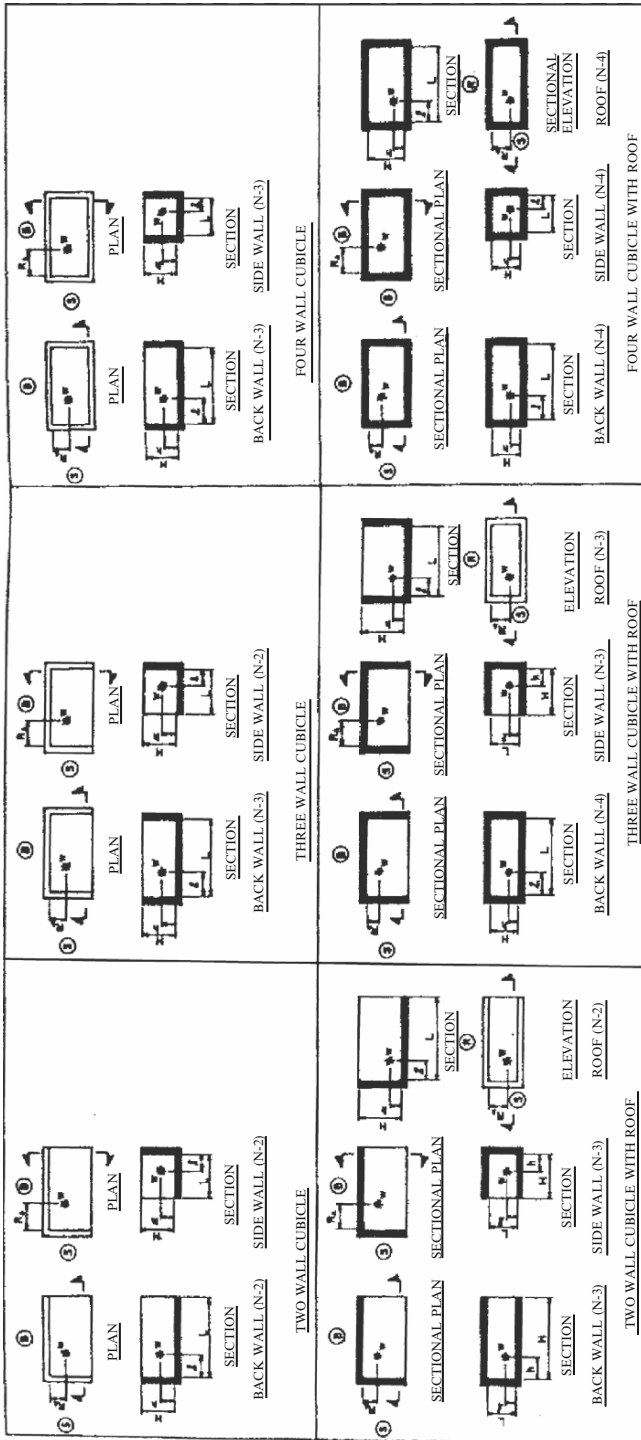
Notes

(1) B denotes back wall, S side wall and R roof.
(2) Numbers in parentheses indicate number N of reflecting surfaces adjacent to surface in question.
(3) h is always measured to the nearest reflecting surface.
(4) l is always measured to the nearest reflecting surface except for the cantilever wall where it is measured to the nearest free edge.
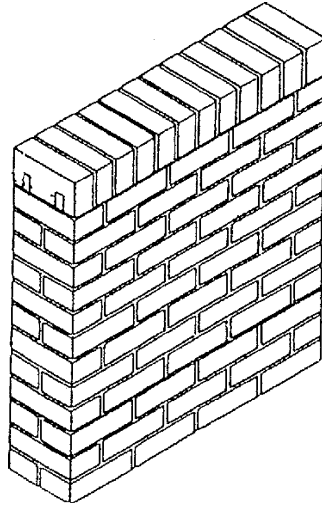
Fig. C.3. A typical external brick wall of a cubicle
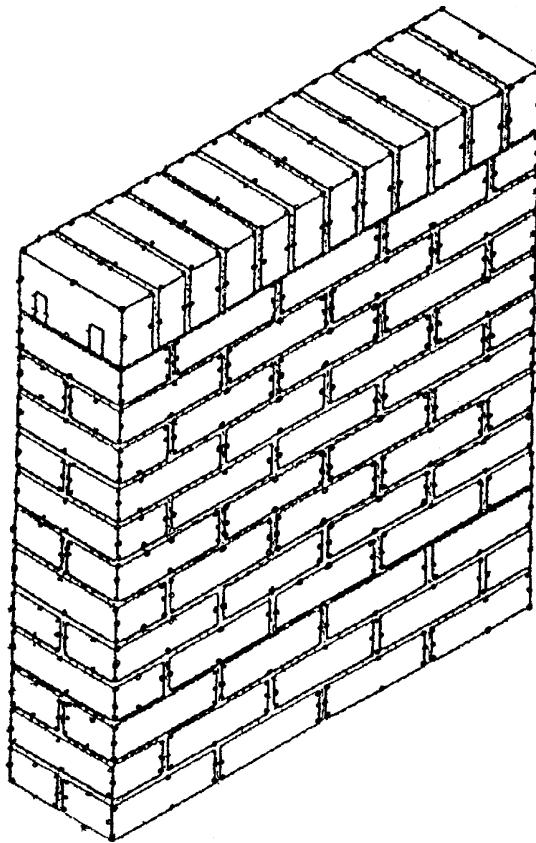
Fig. C.4. Finite-element schemes for the building walls
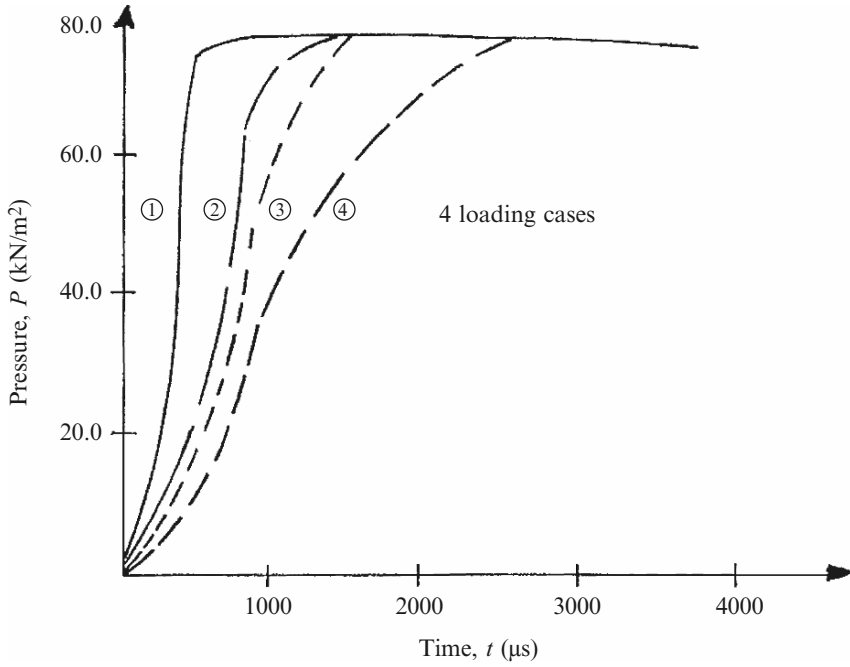
Fig. C.5. Pressure pulses for four types of explosion
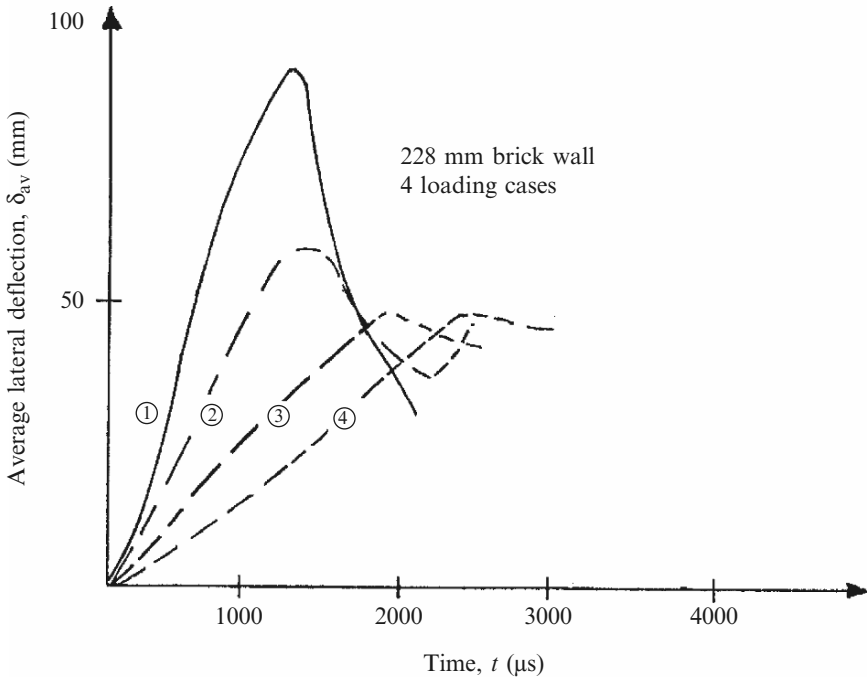
Fig. C.6. The effect of the pressure rise time on the maximum deflection
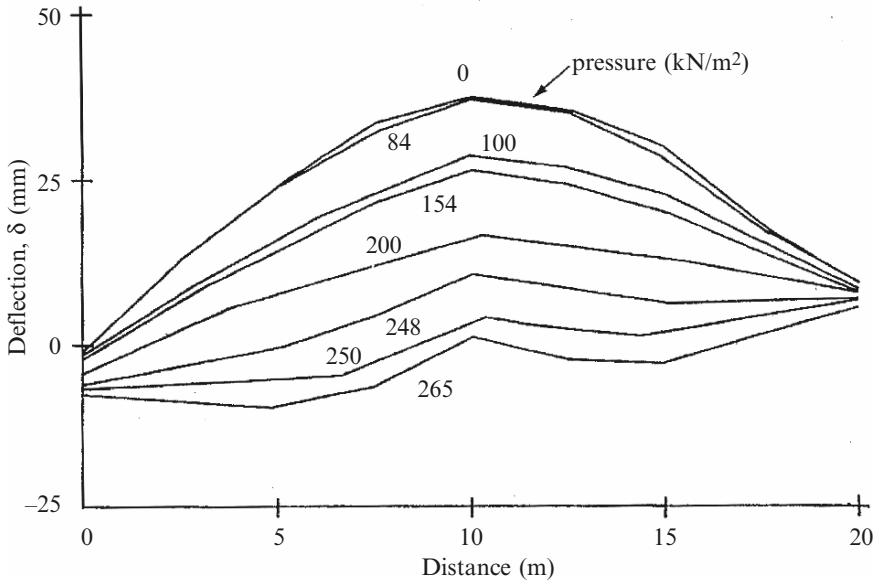
Fig. C.7. Pressure pulse versus distance of explosion for a wall
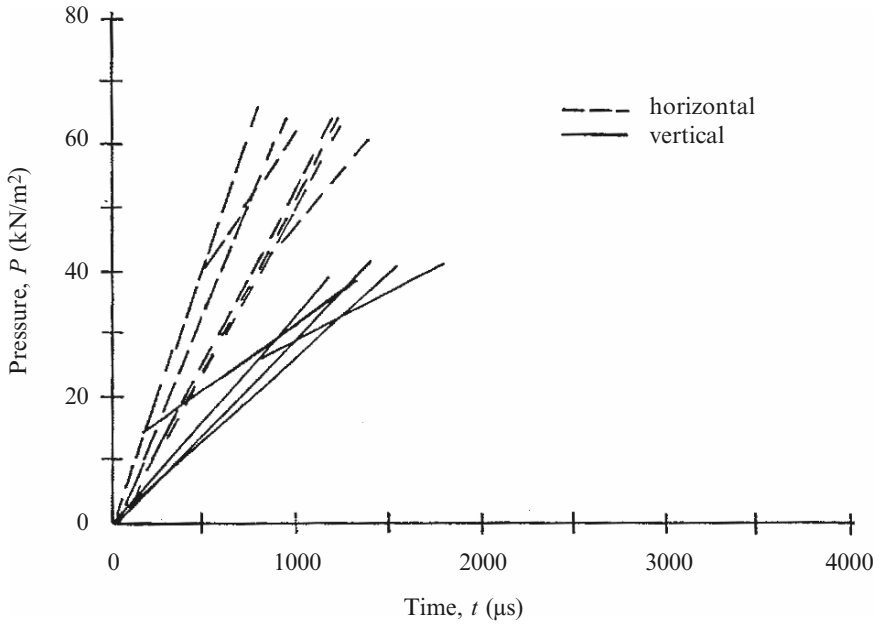
Fig. C.8. Pressure–time relationship for a wall
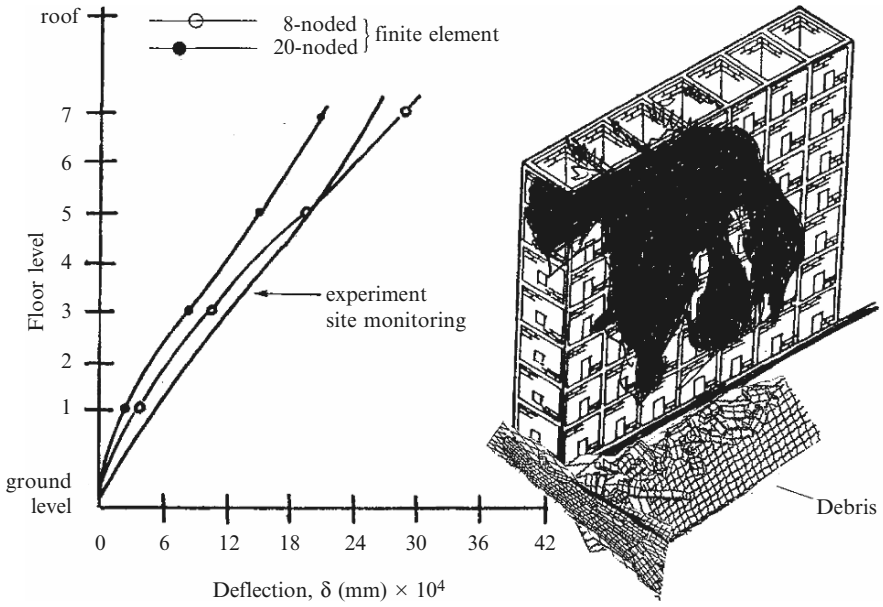
Fig. C.9. Post-mortem for the building
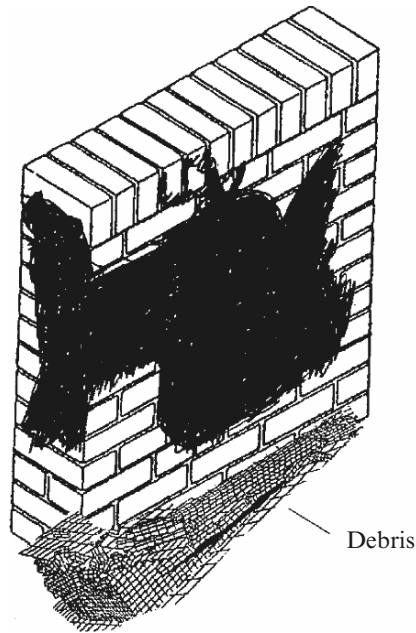
Fig. C.10. Post-mortem for the wall
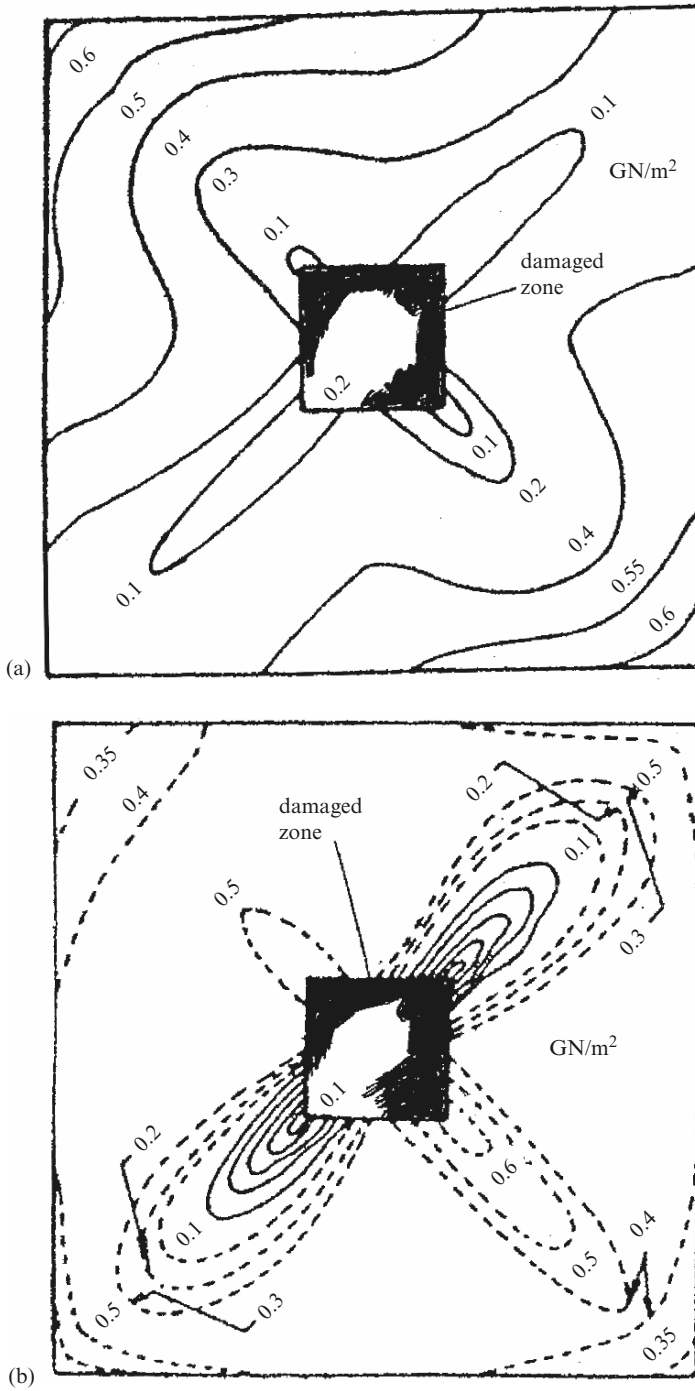
Fig. C.11. Damage to (**a**) the front of the wall and (**b**) the back of the wall

C.3 Bomb Explosion at a Wall

A $250\,\mathrm{kg}$ GP bomb is thrown by a missile at a velocity of $100\,\mathrm{m\,s^{-1}}$. The impact force is calculated by

$$F_1(t) = 0.55 \times 10^6 (mv_{\mathrm{im}}^2/u_{\mathrm{im}}),$$

where m = weapon mass (kg), v_{im} = impact velocity ($\mathrm{km\,s^{-1}}$), u_{im} = normal penetration (m) due to impact.

The finite-element analysis is carried out on a wall (Fig. C.4). The damaged zones for the front and back are indicated by Fig. C.11a, b.

D

Ice/Snow Impact

D.1 Introduction

A great deal of work has been carried out on ice impacting on ice or on structures. Major work has already been reported in this text regarding the prediction of impact loads before, during and after indentation and collapse conditions.

D.2 Finite-Element Analysis

Finite-element analysis has been carried out on a concrete platform subject to ice impact. Non-linear visco-elasticity based on the displacement method was considered. At each time step, a successive substitution-type iteration was applied to the global equations of motion, while a Newton–Raphson method combined with the α-method of numerical time integration was used in the constitutive equations at the Gauss integration points in the finite-element mesh. Variable interface conditions between the ice and the structure were simulated to limit the effects of interface adfreeze or friction. To allow the deliberate development of certain normal compressive stresses at the interface, an adaptive procedure was used to free those points at the interface. The mechanical behaviour of the sea ice was modelled as an isothropic material with creep laws. The three-dimensional yield surface was represented by Jones's tri-axial tests and is given in Fig. D.1a, b. The range of strain rates covered can be seen in Fig. D.1b. As an example, a Condeep-type platform (Fig. D.2) was assumed to lie in the ice environment and to be subjected to ice impact.

The major parameters for the iceberg impacting the platform are:

Iceberg size: 50,000 ton
Equivalent diameter: 38.2 m
Freeboard: 3.8 m
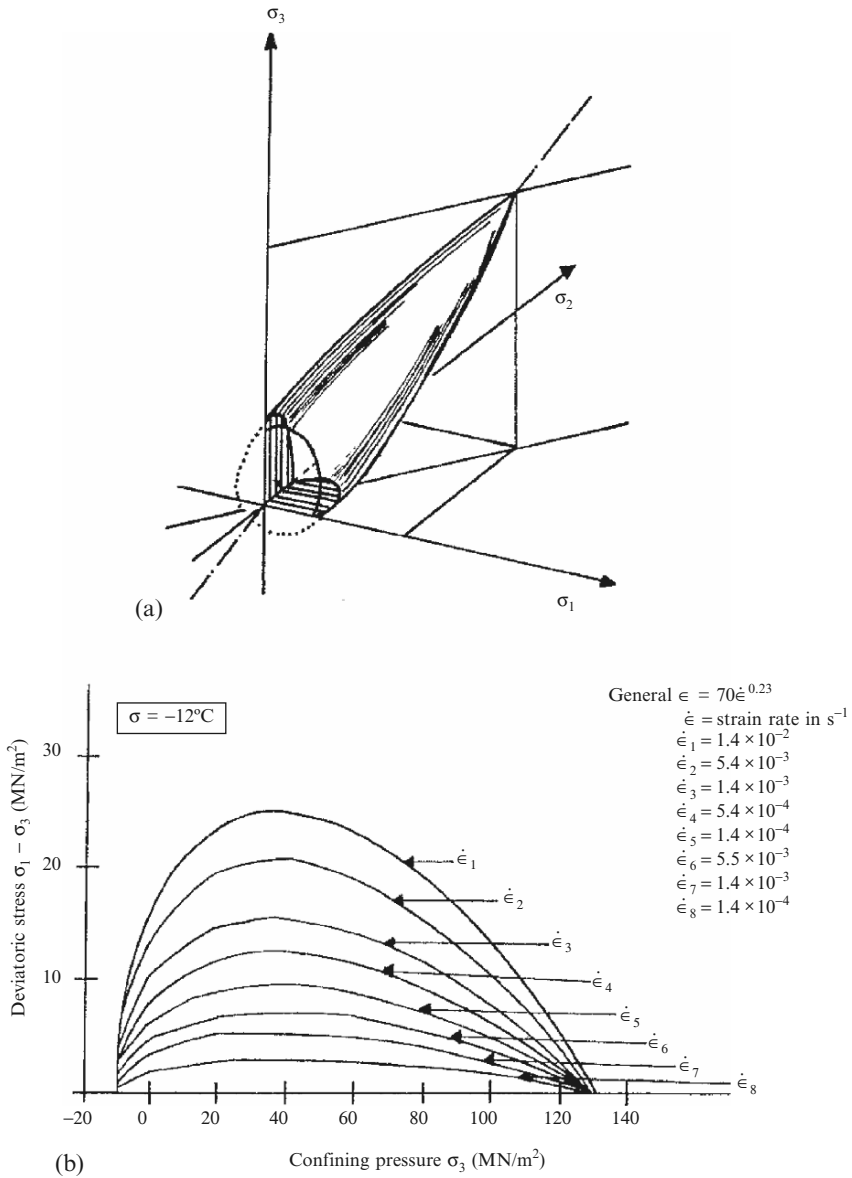
Fig. D.1. Jones's tri-axial tests. (**a**) Yield surface for isotropic ice, new formulation; (**b**) Jones's tri-axial stress

Draft: $34.4\,\mathrm{m}$
Initial velocity: $1.0\,\mathrm{m\,s^{-1}}$

$$K_{IC} = YF_1(t)/D^{1.5} = 0.08\,\mathrm{MPa}\,\sqrt{\mathrm{m}} \quad Y = 1.72(D/D_n) - 1.27,$$
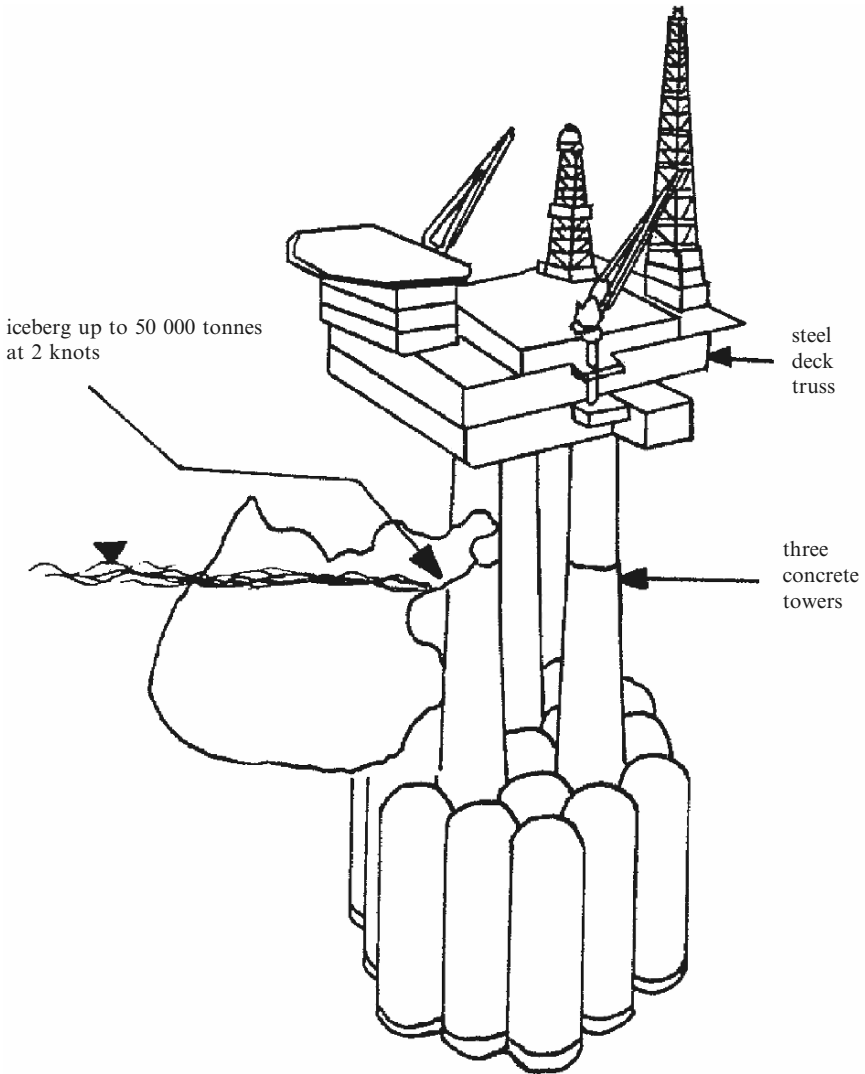
Fig. D.2. Concrete gravity platform subject to ice impact

where D, D_n = original and notch root diameters, respectively.

Data for icebergs
Added mass coefficient: 0.70
Form drag area, 50,000 ton berg: 1,315.00 m^2
Drag coefficient: 0.80
Flexural strength: 700.00 kPa
Elastic modulus, E: 3.00 GPa
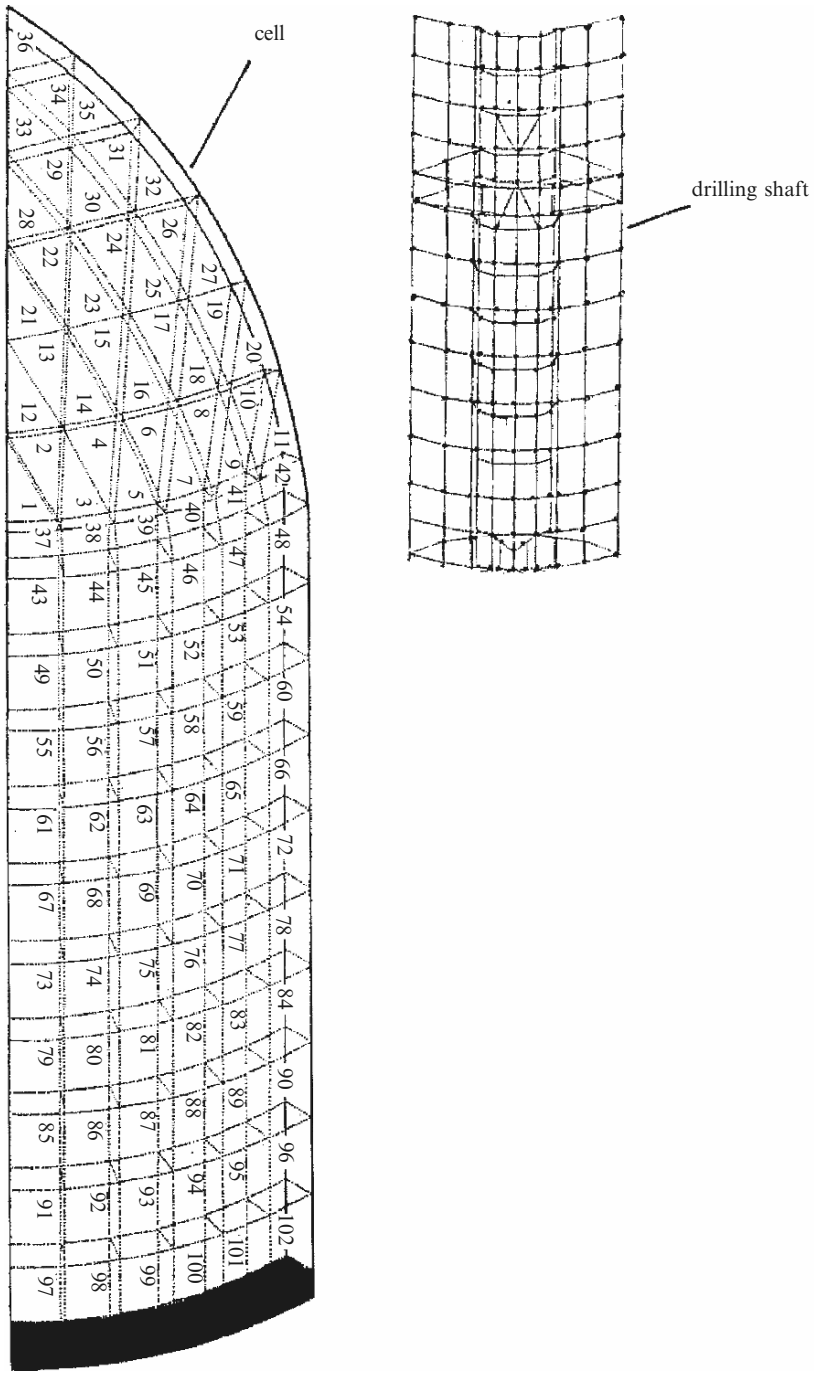
Fig. D.3. Finite-element mesh scheme for the platform concrete cell
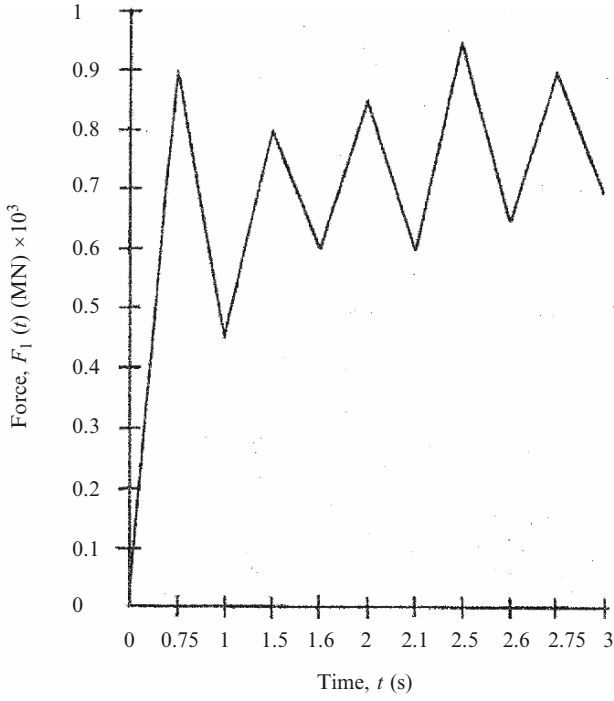
Fig. D.4. Force–time function for the iceberg
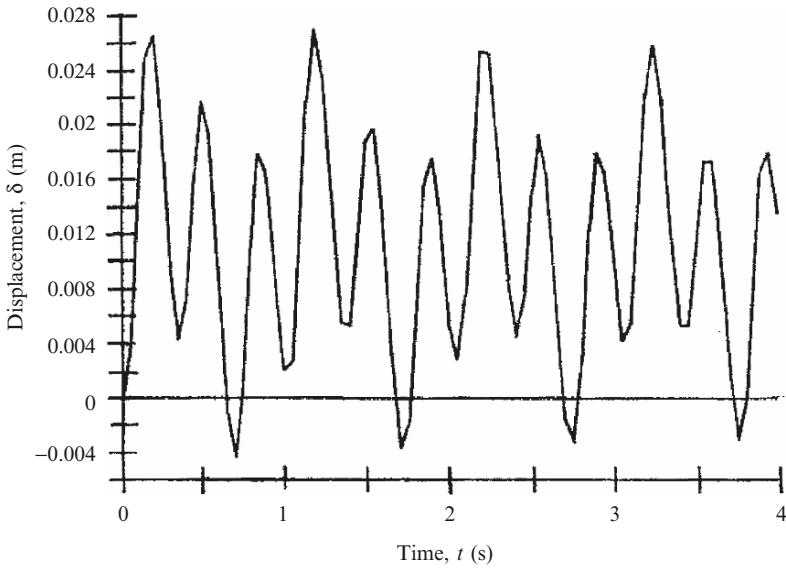
Fig. D.5. Displacement–time function
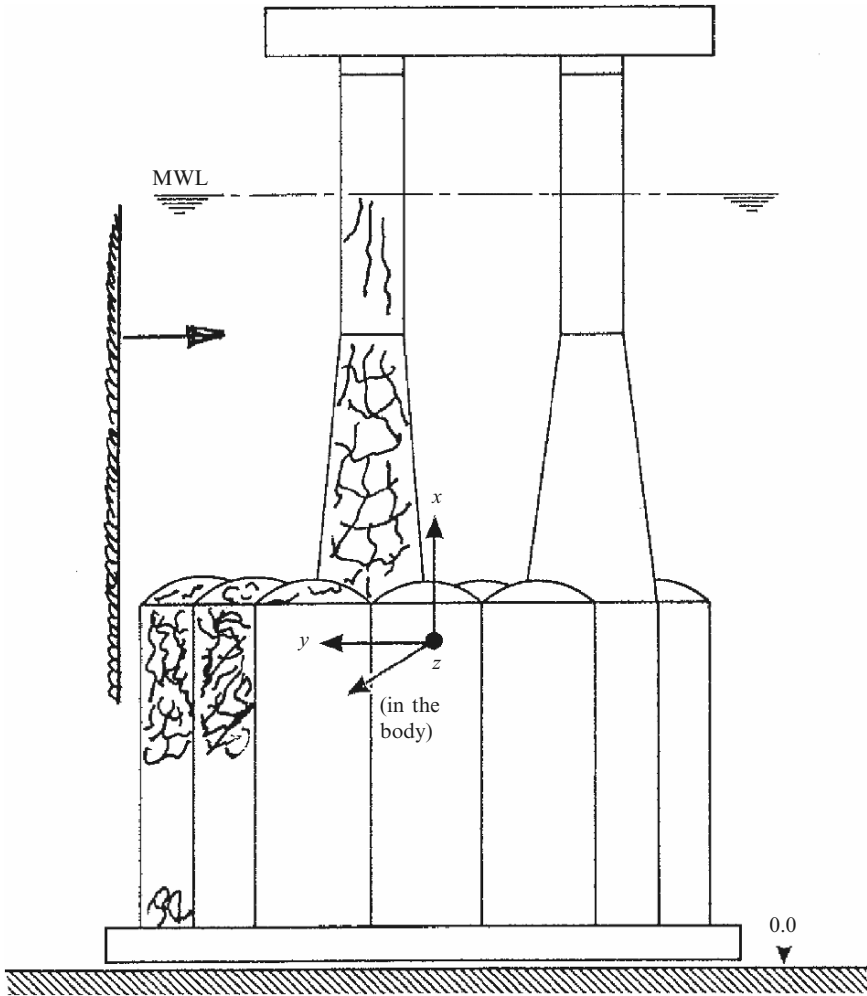
Fig. D.6. Platform post-mortem

Friction coefficient: 0.15
Adfreeze strength: 200.00 MPa
Total horizontal iceberg load: 790.00 MN
Total vertical iceberg load: 530.00 MN

   Figure D.3 shows a typical finite-element mesh scheme for the platform.
Figure D.4 gives the force–time history of the iceberg. The displacement–time
history of the platform is given in Fig. D.5. The post-mortem of the platform
is given in Fig. D.6.

E

Nuclear Reactors

E.1 PWR: Loss-of-Coolant Accident

E.1.1 Introduction to LOCA

A loss-of-coolant accident (LOCA) occurs as a result of a penetration to the main coolant boundary such that the primary circuit water is released through the break to the containment area, causing a rapid decrease in the pressure and temperature of the primary coolant. This will give an impact thermal shock load. The streamline break accident (SLBA) occurs as a result of a complete and partial rupture of a steam line inside the containment vessel. A rapid cool-down and depressurization of the primary circuit normally take place. In order to restore the reactor coolant pressure, a pressure loading unconnected with LOCA is required.

E.1.2 Description of the PWR Vessel and Its Materials

Figure E.1 shows a typical PWR vessel for Sizewell B. The vessel steel must possess high toughness and strength coupled with adequate weldability in thick sections, with generally low-alloy steels containing manganese, nickel and molybdenum. The material grade for plates is SA-533 B alloys, and SA-508 alloys for forging. Both must be in quenched and tempered conditions. The suitability of these steels rests on the mechanical properties such as yield stress, ultimate tensile strength, elongation to fracture and charpy impact energy affected by thermal aging, strain aging and neutron irradiation. The vessels are made out of thick-section plates of up to 360 mm or from ingots of over 200,000 kg. The ingots generally develop cavities of up to 3 mm in the v-segregation regions. These are healed by hot working processes. Both plates and forgings are welded. Figure E.2 shows vessel fabrications.

Table E.1 shows the data used in the three-dimensional finite-element analysis. Figures E.3 and E.4 show the finite-element mesh generation scheme
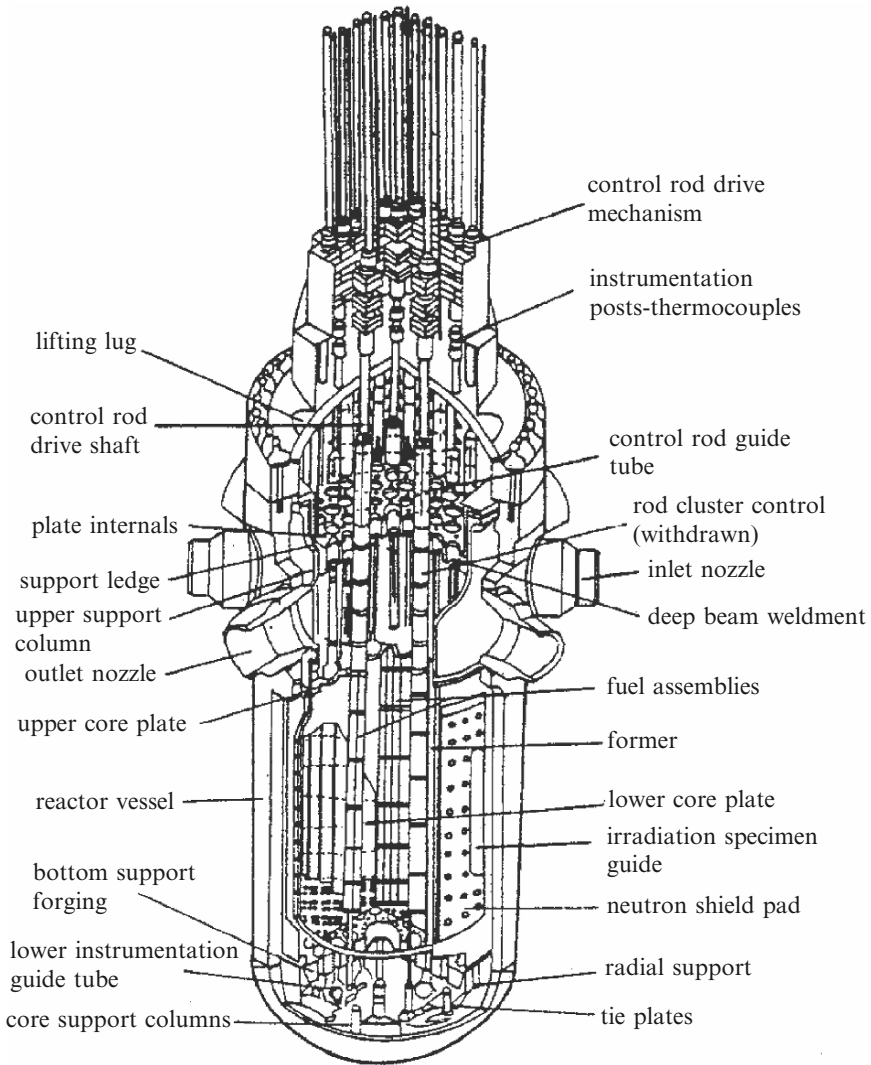
Fig. E.1. Cut-away diagram showing the PWR steel vessel and internals (former CEGB Sizewell B inquiry)

of the vessel, wall nozzles and closure heads. These are the important sections and locations in the reactor vessels from the point of view of fracture assessment. Figure E.5a and b shows the pressure–time and temperature–time relationships. Figures E.6–E.18 indicate various stresses in different zones due to a LOCA. The defect size in each region is checked using the R6 method of the former CEGB (UK) which is given in Tables E.2–E.4.
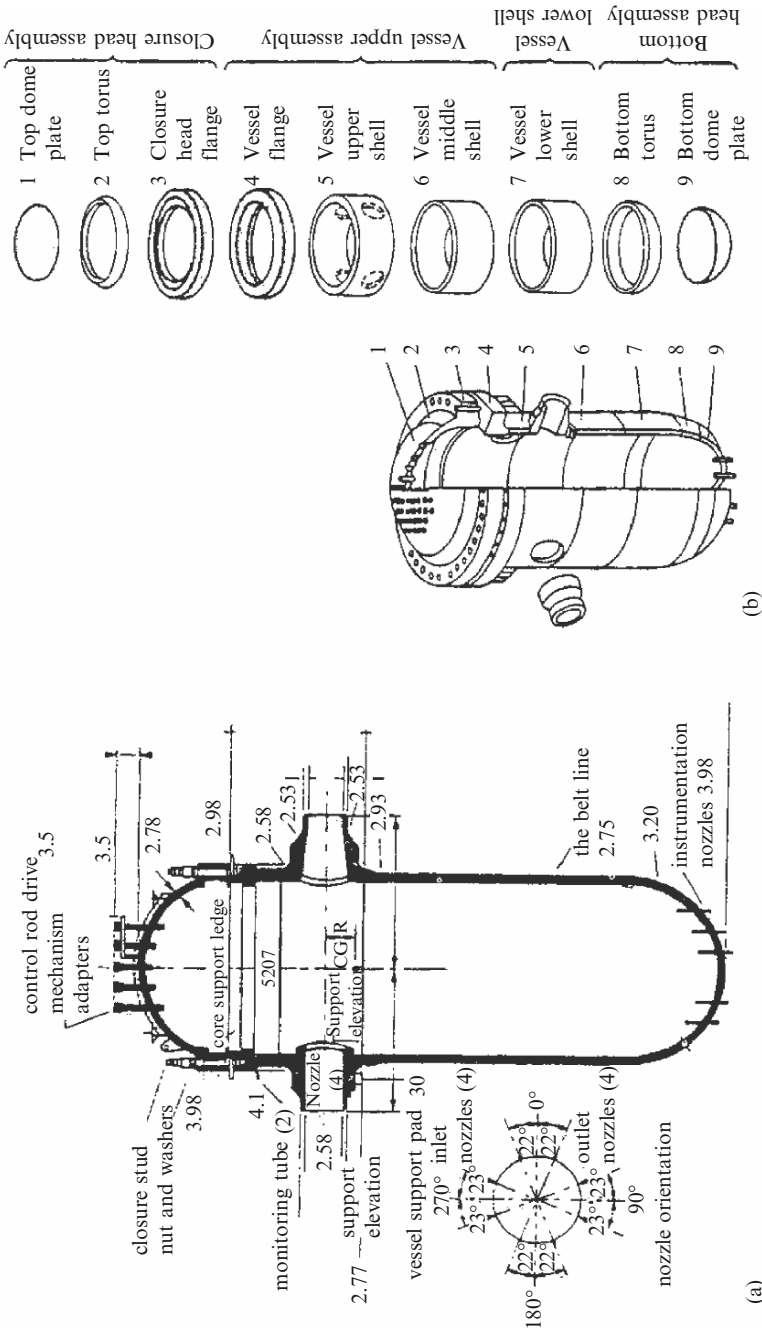
Fig. E.2. (a) The reactor vessel of a 4-loop PWR system (safety factors computed using the finite-element method). **(b)** Diagram showing sections from which the PWR vessel may be fabricated when sections are either rolled plate or forged material (shaded parts are common to both)
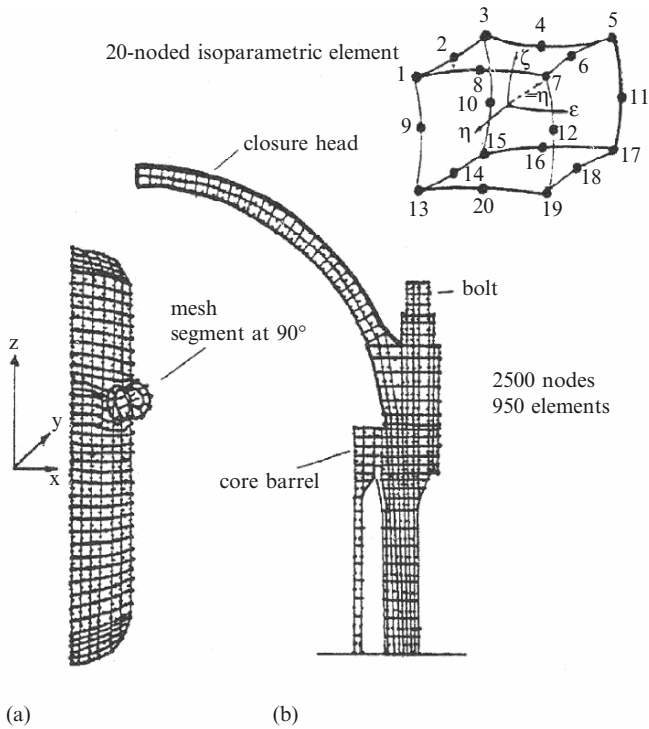
Fig. E.3. Finite-element mesh generation of the vessel (**a**) generalized vessel mesh. (**b**) Closure head–wall flange region
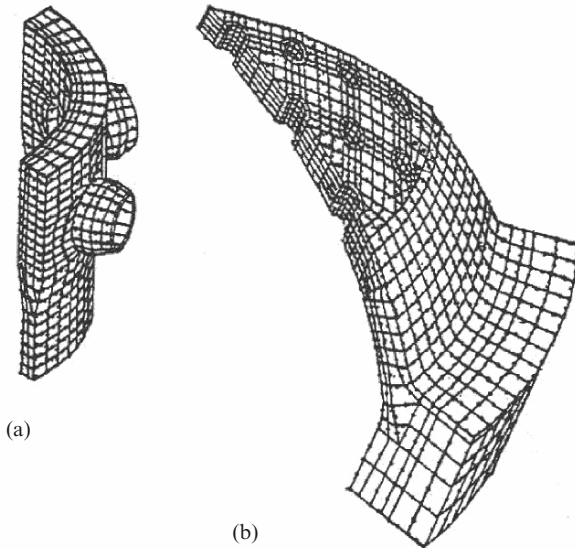
Fig. E.4. Finite-element mesh generation of (**a**) wall nozzles and (**b**) closure head (from Bangash [3.3])
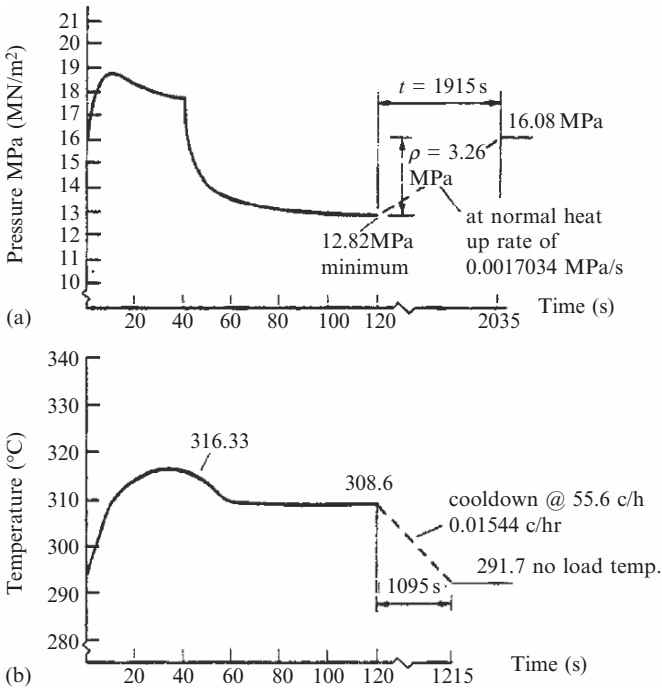
Fig. E.5. Loss of load (without immediate reactor trip) (Westinghouse revision). (**a**) Reactor coolant pressure and (**b**) temperature variations (courtesy of Marshall) (from Bangash)

E.2 Nuclear Containment Under Hydrogen Detonation

Hydrogen detonation has become an important issue after the Three-Mile-Island accident. The hydrogen burning occurred approximately 10 h into the accident. The steam reacting with the Zircaloy cladding and the oxidation of the overheated steel vessel interiors created large quantities of hydrogen. This can also occur due to interaction of the molten core. In order to predict the wall pressures due to such detonations, non-linear gas dynamics equations for the entire volume of the containment vessel have to be solved. In the current analysis of the Sizewell B containment vessel, it is assumed that the wall pressure P_o is proportional to the containment pressure P. The vessel parameters are given in Table E.1. It is assumed that the detonation starts approximately at the mid-height of the containment vessel. The spherical shock front generated obliquely converges at the dome, causing a strong reflection around the apex. The containment finite-element mesh scheme is unchanged. Bond slip and shear slip for the reinforced elements are considered. The following additional input data have been included:
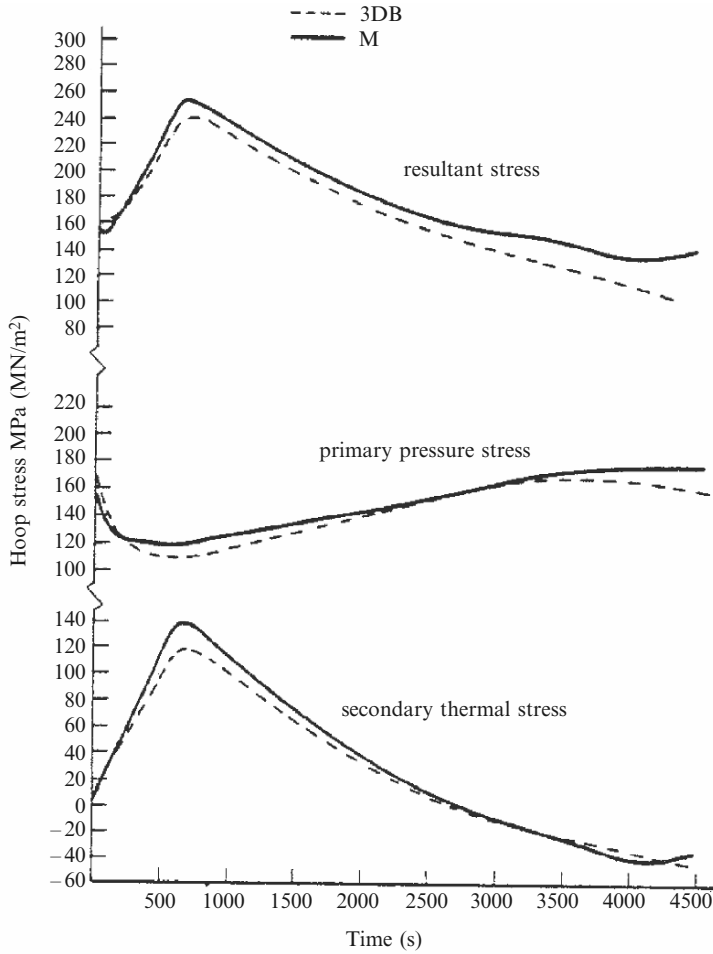
Fig. E.6. Belt-line ractor trip from full power. Time variation of hoop stress in vessel material from clad/vessel interface. 3DB: three-dimensional finite-element analysis (Bangash)

Material

Liner: $\sigma_y = 390\,\mathrm{MPa}$
Strain rate $= 0.1\,\mathrm{s}^{-1}$

Pressures and shock front

Detonation strength $q/\bar{R}T_0 = 17$ (base) and 23 (mid-height),
where $q =$ energy release/unit volume
$\qquad \bar{R} =$ gas constant $= 8.31\,\mathrm{kJ\,kg\,mole}^{-1}\,\mathrm{K}$
$\qquad T_0 =$ absolute temperature
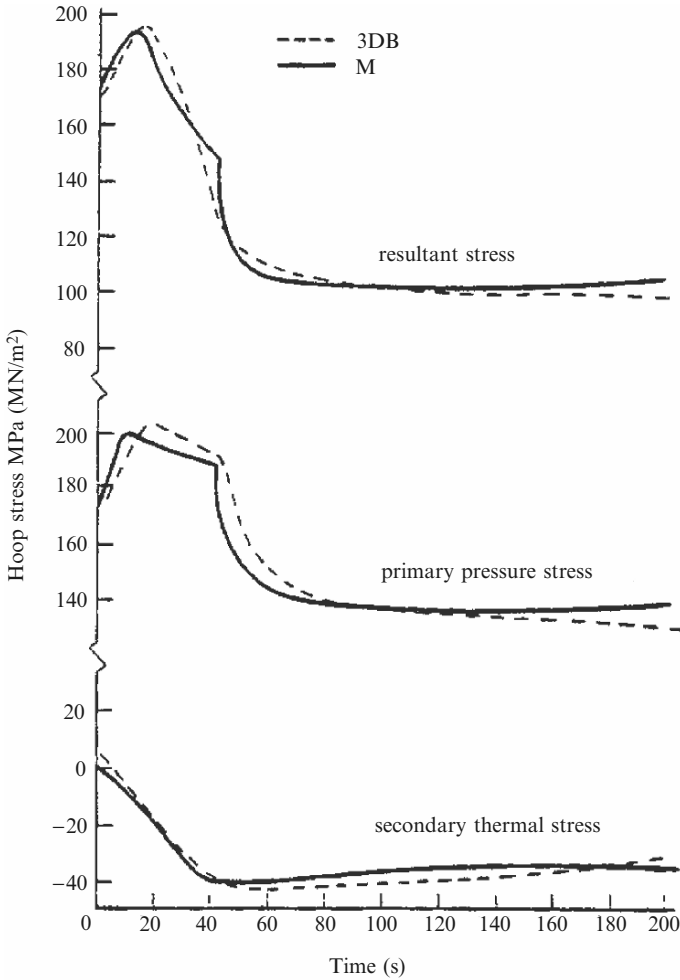
Fig. E.7. Time variation of hoop stress in vessel material from clad/vessel interface (belt-line loss of load). 3DB: Bangash

Shock front

v_{so} = shock wave velocity = $2{,}000\,\mathrm{m\,s}^{-1}$
$\quad t = 0, 50, 100, 200, 250, 300\,\mathrm{\mu s}$

Figure E.22a and b shows the non-dimensional relationship for the pressure P/P_o and $(t/R)v_{so}$ for the Sizewell B vessel at the apex of the dome and at the mid-height. The parameter R is the radius of the containment vessel. Figures E.23–E.25 illustrate the stress–time histories for the containment wall, dome springing and dome apex due to detonation.
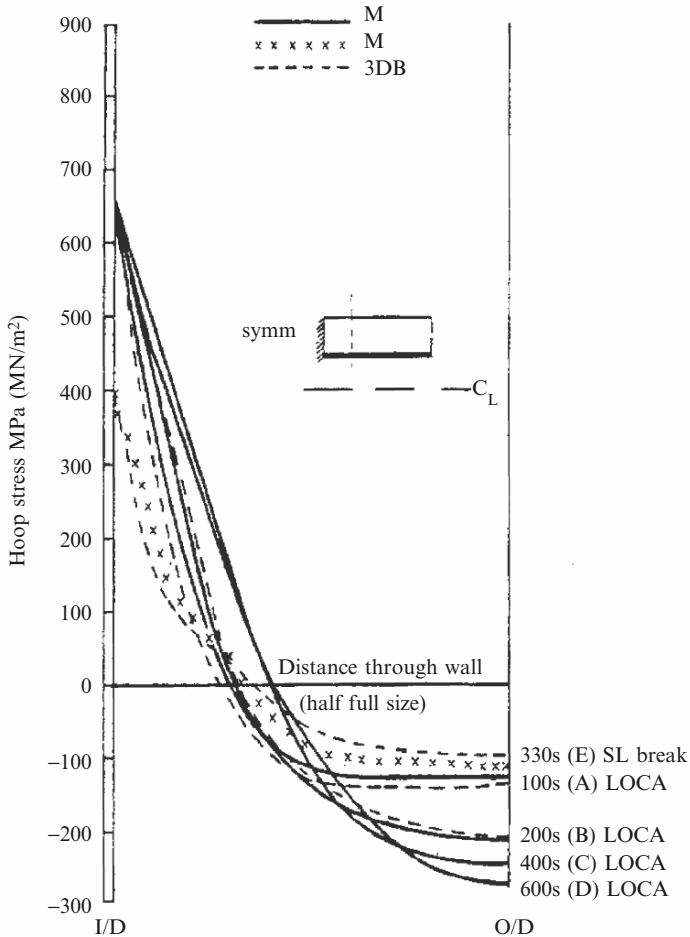
Fig. E.8. Secondary thermal stress at various durations: belt-line region, LOCA condition. 3DB: Bangash

E.3 Impact/Explosion at a Nuclear Power Station: Turbine Hall

The finite-element analysis of a concrete turbine hall is carried out for an impact/explosion caused by a Tomahawk cruise missile. The finite mesh and damaged areas of the northeast wall are examined in Fig. E.26 for the entire facility (shown in Fig. E.27). The finite-element mesh of the soil beneath such a facility is shown in Fig. E.27. Apart from the Tomahawk cruise missile data, given in Chap. 2, the following additional data have been considered:
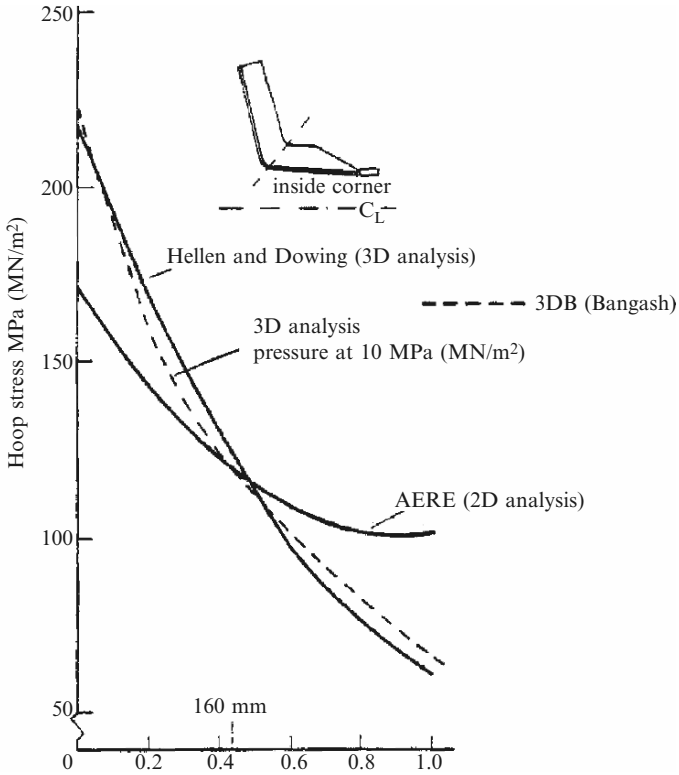
Fig. E.9. Comparative study of results for the inside corner of an inlet nozzle
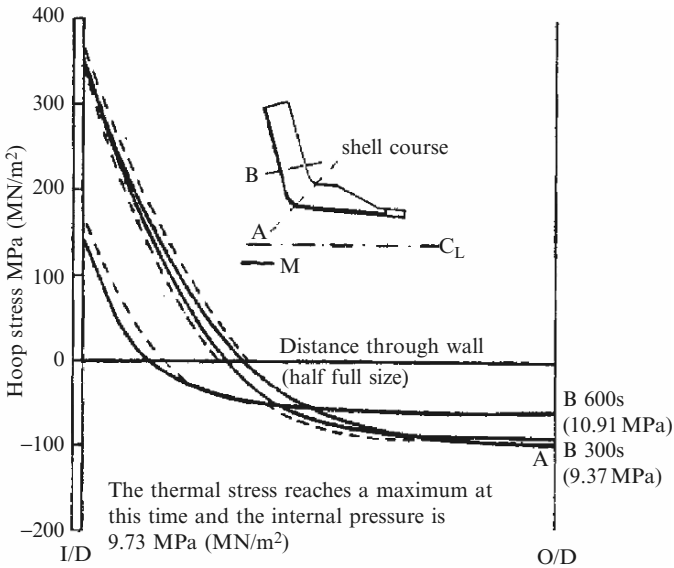
Fig. E.10. Secondary thermal stresses at various durations for an inlet nozzle shell course large streamline break
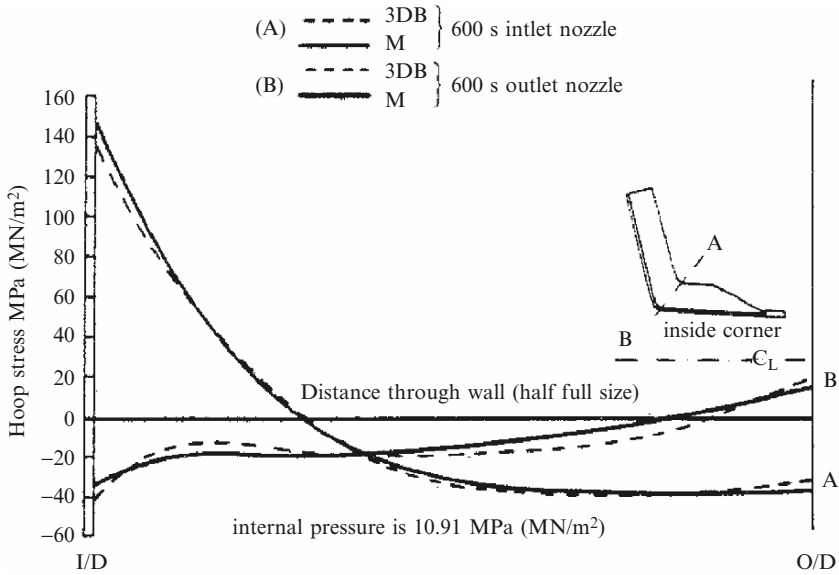
Fig. E.11. Inlet nozzle inside corner: reactor trip from full power. 3DB: Bangash
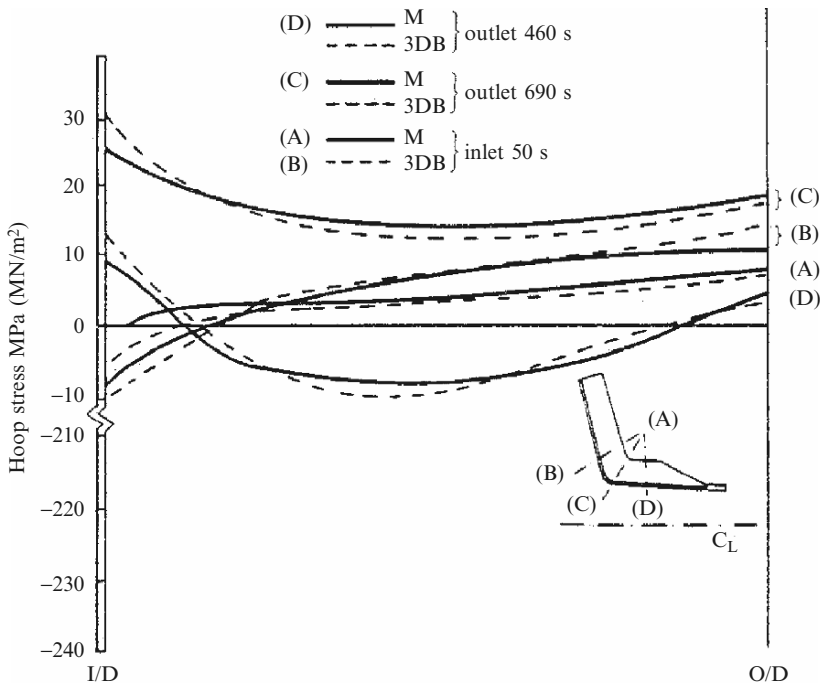
Fig. E.12. Inlet nozzle inside corner: loss of power, secondary thermal stresses. 3DB: Bangash
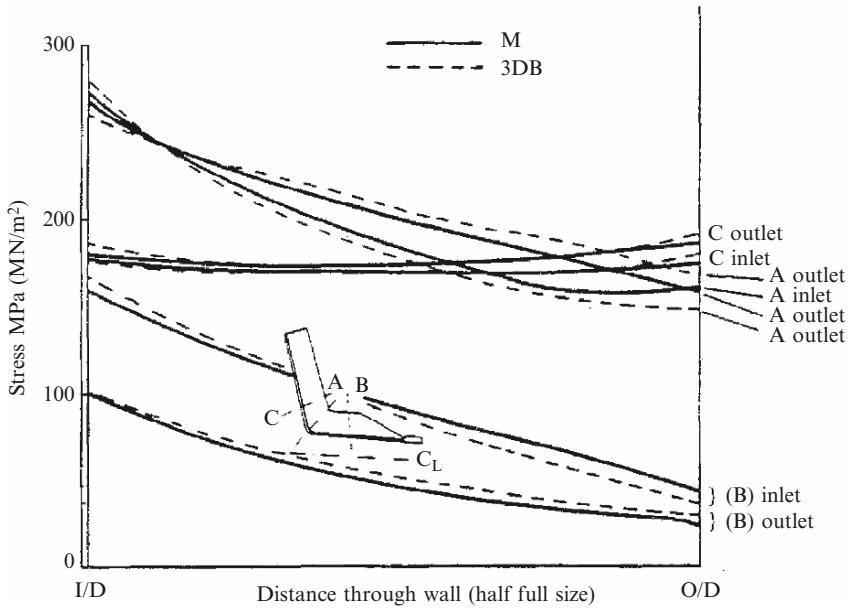
Fig. E.13. Inlet nozzle hoop stress plotted through the wall at the sections shown. Basic pressure 17.24 Mpa $(MN\,m^{-2})$
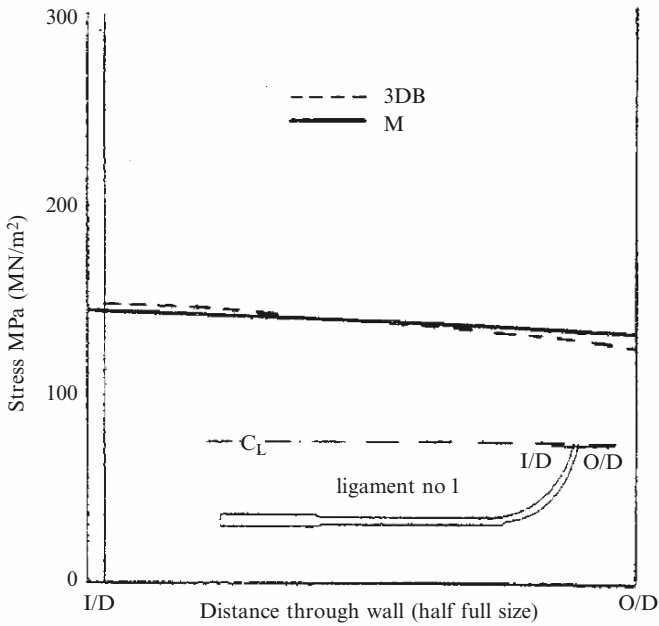
Fig. E.14. Main hoop stress plotted through the wall at the sections shown. Basic pressure load of 17.24 Mpa $(MN\,m^{-2})$
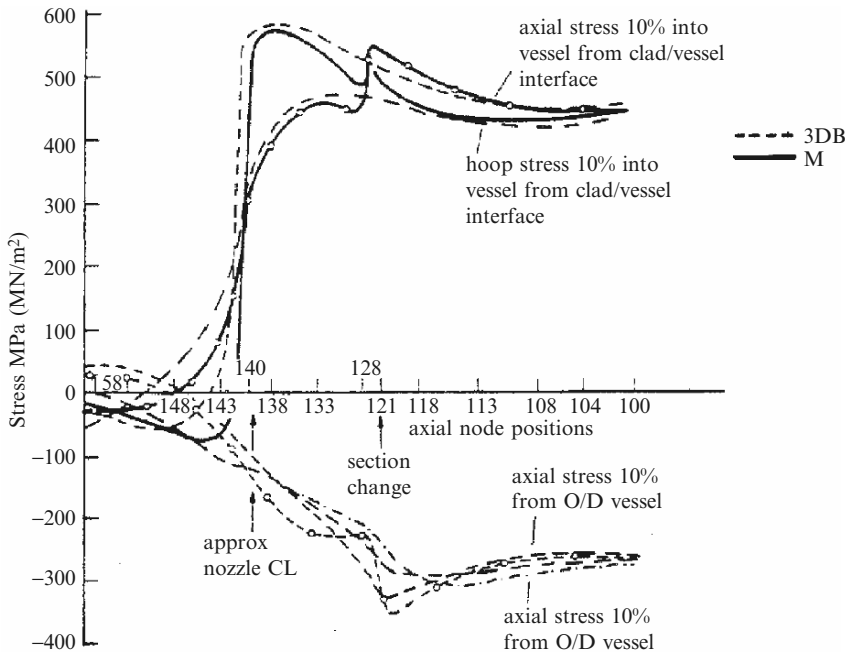
Fig. E.15. Axial and hoop stress plotted along the nozzle course and belt-line region for a large LOCA at 600 s
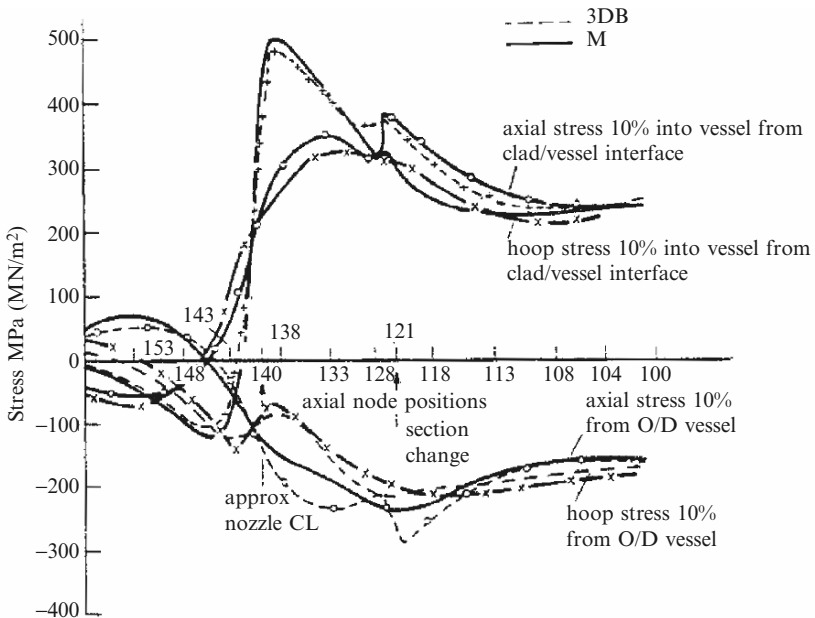
Fig. E.16. Axial and hoop stress plotted along the nozzle course and belt-line region for a large LOCA at 2,000 s
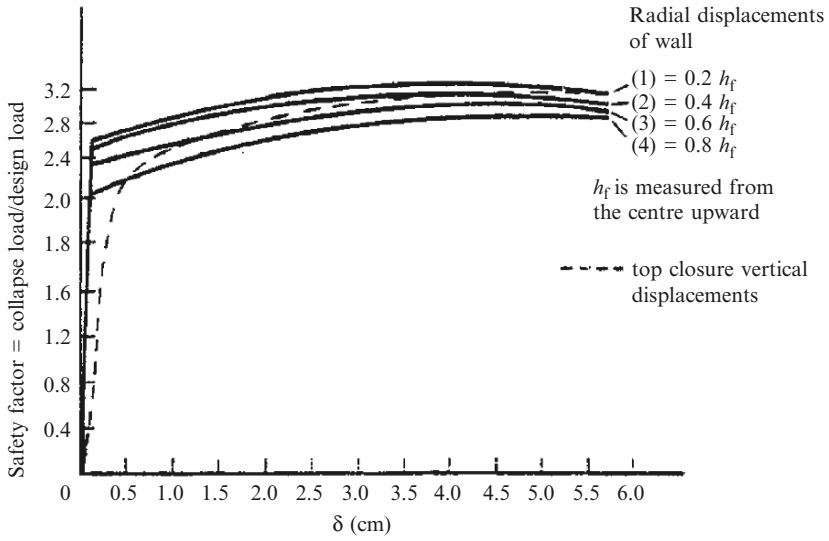
Fig. E.17. Safety factors versus displacement (δ)
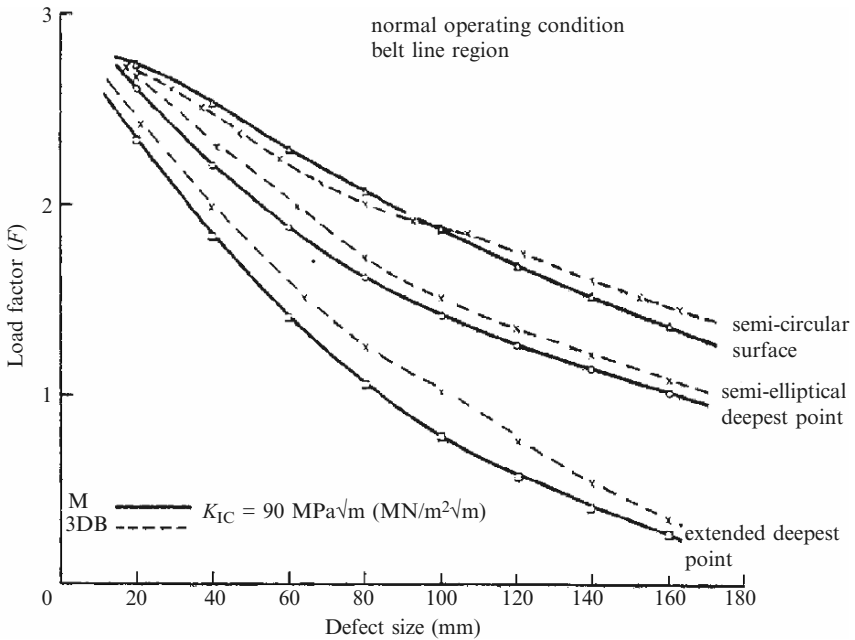
Fig. E.18. Load factor versus defect size

Table E.1. Vessel material properties and parameters

Proposed parameters for Sizewell B:

Vessel overall height	13,660 mm
Inside diameter	4,394 mm
Wall thickness opposite core	215 mm
Wall thickness at the flange	500 mm
Normal clad thickness	6 mm
Thickness of the dome top	178 mm
Thickness of the dome bottom	127 mm
Inside diameter of inlet nozzle	700 mm
Inside diameter of outlet nozzle	737 mm
Number of closure studs	54 (each 1,466 mm high)
	(nut 268 × 203)
	(washer 268 × 38)
Diameter of closure studs	173 mm
Dry weight of the pressure vessel	434.8×10^3 kg
Normal operating pressure	15.98 MPa
Design pressure	17.13 MPa
Initial hydraulic pressure	21.43 MPa
Normal operating inlet temperature	288°C
Normal operating outlet temperature	327°C
Design temperature	343°C
No load temperature	292°C
Design life	40 years at 80% load factor

$E_s = C \times E \times 10^5$ MPa C varies with temperature

(1) Material SA533B   C = 0.218, Mn = 1.367, Ni = 0.547, Mo = 0.547, Si = 0.236, Cr = 0.074,

           P = 0.009, S = 0.014

(weight per cent)   C = 0.117

(2) Submerged arc-welding (electrode wire content)

C = 0.16, Mn = 2.20, Ni = 0, Mo = 0.6, Si = 0.05, Cr = 0, P = 0.025, S = 0.035

C = 0.15

(3) Mechanical properties

	Yield stress ($N\,mm^{-2}$)		Ultimate tensile stress ($N\,mm^{-2}$)		Charpy test (minimum value)
(a) SA533B plates	at 20°C	345	at 20°C	555	
	at 400°C	280	at 400°C	520	34 J at 4.4°C
(b) SA508 forging	at 400°C	280	at 20°C	555	flanges, shell or
			at 400°C	430	rings and nozzles
(c) Weld metal		483		593	average values 150, 138, 100, respectively
(d) Stresses after 288°C irradiation unirradiated	These are given before from 3(a) to 3(c)				
	Add 2% of the above values				
(e) Fracture toughness of plates	$K_{Ic} = 106\,N\,mm^{-2}, \sqrt{m} = 153$				
(f) Bonding material	Yield = 900–1,050 $N\,mm^{-2}$; ultimate tensile stress = 1,050 $N\,mm^{-2}$; impact energy = 60.9–81.2 J				

Table E.2. R6 method of fracture assessment

The failure assessment diagram for the R6 method (courtesy of CEGB, UK).
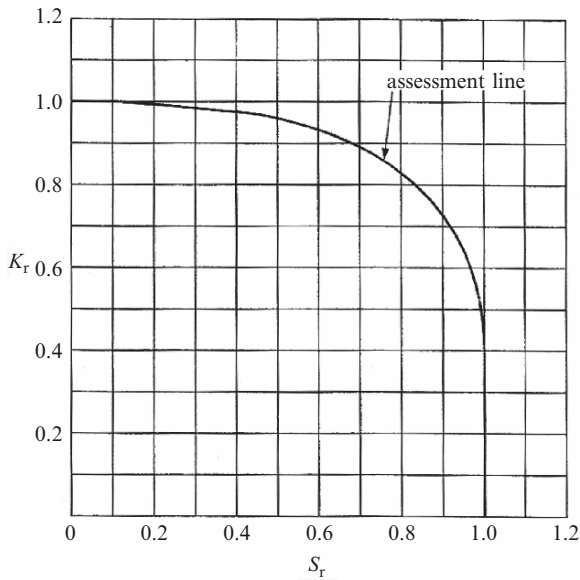
Fig. E.19. K_r–S_r diagram

$$K_r = S_r \left\{ \frac{8}{\pi^2} \log_e \sec \left(\frac{\pi}{2} S_r \right) \right\}^{-1/2}, \tag{E.1}$$

$$K_r = K_r^P / K_{IC}, \tag{E.2}$$

where K_r is a measure of how close the vessel is to linear elastic failure $= 0.59$ and K_I^P is the stress intensity factor due to σ stresses and is given by

$$K_I^P = Y\sigma\sqrt{\pi a} = 39.42\,\text{MPa}\,\sqrt{\text{m}},$$

where $Y =$ magnification factor when applying unflaw stresses obtained to postulated flawed vessel; a Y value of 1.25 has been taken

$\sigma =$ applied stress

$a =$ crack height

$K_{IC} =$ fracture toughness, with a lower limit of $170\,\text{MPa}\,\sqrt{\text{m}}$ at $288°\text{C}$

Defect length $2C$ parallel to component surface

Defect depth S distance between nearest edge of the defect and component surface (normal distance)

Table E.2. (continued)

Defect height $2a$ distance between the nearest and furthest extremities of a defect normal to the surface (buried $2a$, surface breaking a) (Figs. E.19 and E.20)
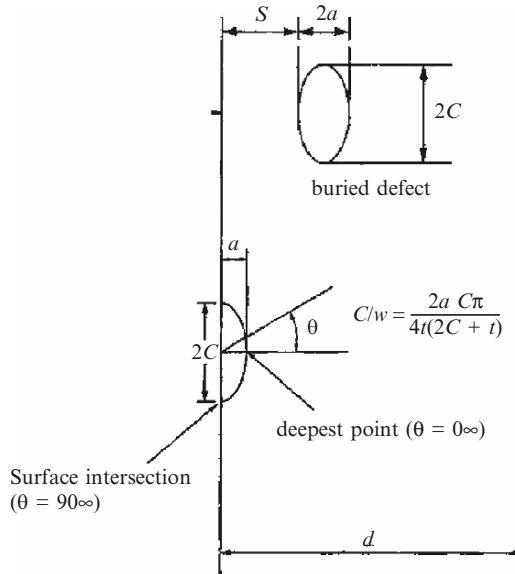
Fig. E.20. Vessel defects

Walls

$33\,\mathrm{m} \times 16\,\mathrm{m} \times 2.5\,\mathrm{m}$ reinforced concrete walls
T25: 250 bars in both ways
Impact area $5\,\mathrm{m} \times 3\,\mathrm{m}$ of centreline

Finite-element mesh scheme

360 elements, 20-noded isoparametric — concrete
2,100 elements, 3-noded isoparametric — steel bars
1,440 elements, 6-noded isoparametric — steel liners
Total number of nodes (bond slip included): 22,140
Computer used: IBM 4381 front-ended Cray-2

Material properties

Concrete grade: 43 endochronic theory adopted interlocking of aggregates ignored
Yield strength: liner $250\,\mathrm{N\,mm^{-2}}$; steel bars $410\,\mathrm{N\,mm^{-2}}$

Table E.3. Semi-elliptic surface breaking floor configuration: sample calculations

For $0.1 < a/2c < 0.5$ and $a/t \leq 0.8$. When $a/2c < 0.1$ then $c/w = a/t$ (extended crack).

Therefore the S_r value is given by

$$S_r = \{1/\bar{\sigma}(1 - c/w)^2\}\{[\sigma_{bc}/4 + \sigma_{mc}(c/w)]\}$$
$$+ [(\sigma_{bc}/4 + \sigma_{mc}(c/w))^2 + \sigma_{mc}^2(1 - c/w)^2]^{1/2}, \qquad (E.1)$$
$$a/c = \tfrac{1}{3} \text{ if } a = 70\,\text{mm}; c = 210\,\text{mm},$$
$$0.1 < 7/42 < 0.5 \text{ is satisfied.}$$

$$c/w = 2ac\pi/4t(2c + t) = 2(70)(210)\pi/4(216)(420 + 216) = 0.168, \qquad (E.2)$$
$$\sigma_{bc} = 6M/t^2 = 7.56\,\text{MPa},$$

with $a/c = \tfrac{1}{3}$, $\sigma_{mc} = 171.5\,\text{MPa}$, if $a = 70\,\text{mm}$ and $c/w = 0.168 = $ area of flaw/area of rectangle.

$$S_r = [7.56E6/4 + 171.5E6(0.168)] + [(7.56E6/4 + 171.5E6(0.168)^2$$
$$+ (171.5)^2(1 - 0.168)^2]^{1/2}/440E6(1 - 0.168)^2$$
or $S_r = 0.58$
and $K_I^P = Y\sigma_{mc}\sqrt{\pi a} = 1.25(171.5E6)\sqrt{\pi(0.07)} = 100.53\,\text{MPa}\,\sqrt{\text{m}}, \quad (E.3)$
where $K_r = K_I^P/K_{IC} = 100.53E6/170E6 = 0.59$.

$\sigma_{bc} = $ elastically calculated bending stress evaluated over the gross section containing the flaw.
$\sigma_{mc} = $ elastically calculated tensile stress evaluated over the gross section containing the flaw.

Impactor

Tomahawk cruise missile, $v_{so} = 1,200\,\text{m\,s}^{-1}$

Damaged zones (two such zones were discovered)

(1) A complete perforation size of an oval shape of $9\,\text{m}^2$. Many bars burst and buckled in this area.
(2) Outside the perforated area, cracking and crushing extended to about $10\,\text{m}$ diagonal. Crack depths ranged from $10\,\text{mm}$ to $1.35\,\text{m}$ inside to outside. Many bars yielded and bent.

E.4 Jet Impingement Forces on PWR Steel Vessel Components

The safety of nuclear installations such as the pressure vessel and its piping systems requires strict measures. In the event of steel failure, the safety rules require the assessment of the jet impinging forces on the vessel nozzle areas. In the current analysis it was assumed that the transition from the cross-section

Table E.4. Failure assessment of crack heights due to LOCA
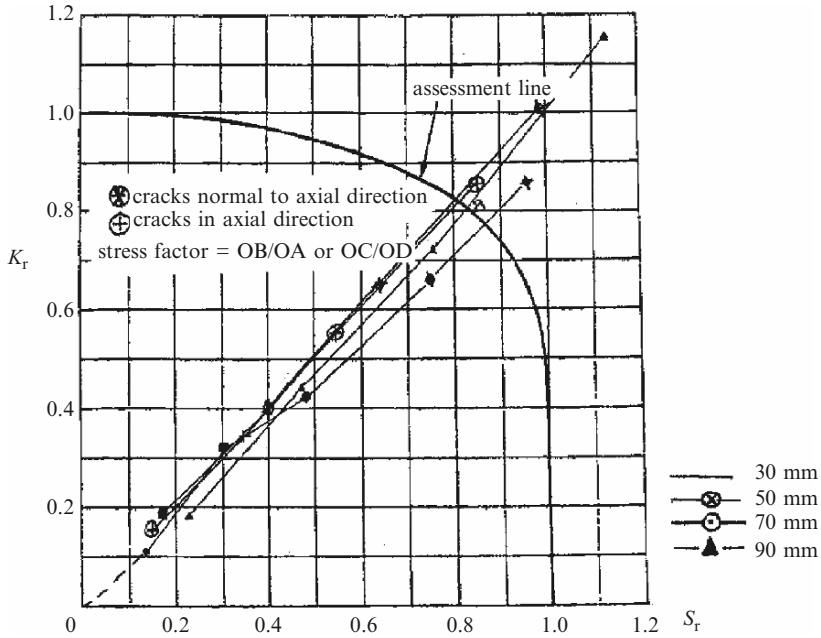
Fig. E.21. LOCA versus K_r–S_r values

Computed data: normal operating conditions, belt-line region S_r and K_r values for flaws normal to the hoop stress (Fig. E.21).

Crack height a (mm)	Effective ratio c/w	Calculated values	
		S_r	K_r
70	0.168	0.58	0.59
90	0.234	0.70	0.67
110	0.301	0.86	0.74
130	0.371	1.10	0.81

Normal operating conditions, belt-line region S_r and K_r values for flaws normal to hoop stress.

Crack height a (mm)	Effective ratio c/w	Calculated values	
		S_r	K_r
70	0.168	0.25	0.23
90	0.234	0.30	0.26
110	0.301	0.38	0.29
130	0.371	0.48	0.32
150	0.440	0.64	0.34
170	0.510	0.88	0.36
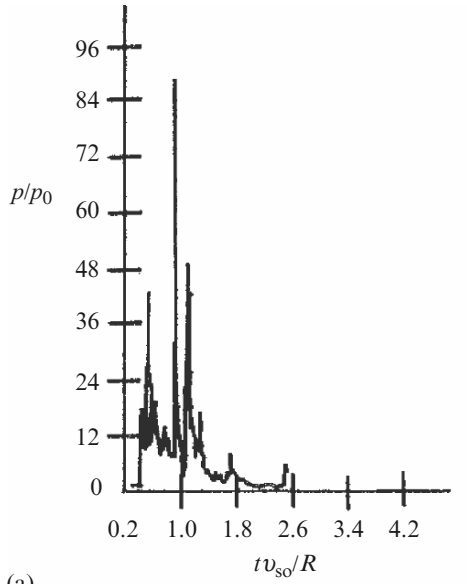
(a)
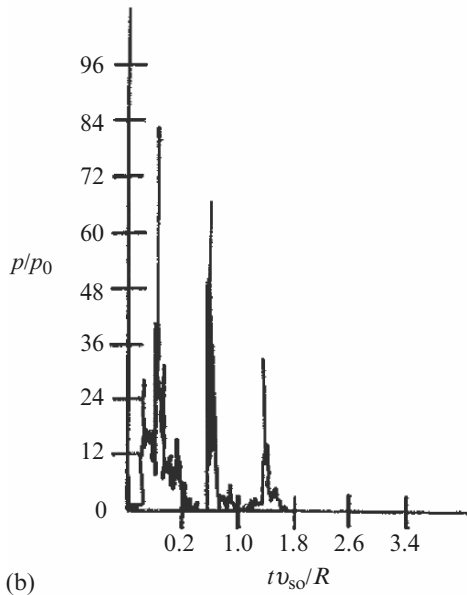
(b)

Fig. E.22. (**a**) Pressure at the mid-height; (**b**) pressure at the apex of the dome
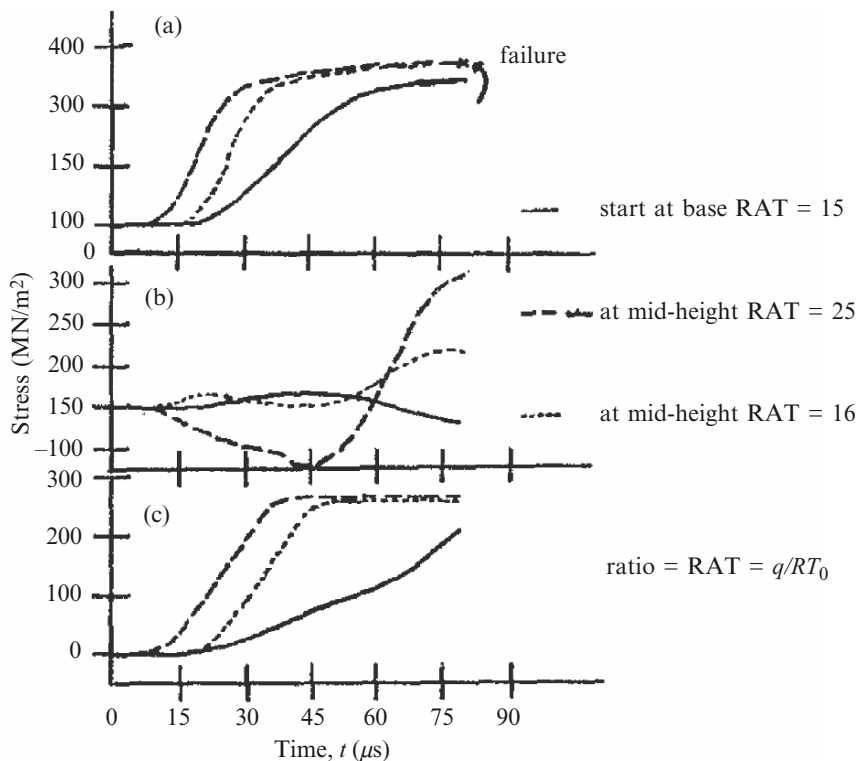
Fig. E.23. Stress histories at 40% of the cylinder, with variation of steel properties included: (**a**) inside hoop bars; (**b**) inside vertical bars; (**c**) seismic diagonal bars

of the discharging pipe to that of the outlet is abrupt. It is imperative to evaluate the structural behaviour under the jet impinging forces. The vessel chosen for this analysis was the Sizewell B PWR steel vessel. All parameters and finite-element mesh schemes are kept the same as in Sect. E.1. The following data is used:

Nozzles and pipe

$P_w = 17.13$ MPa; initial hydraulic pressure = 21.42 MPa design
Temperature: 327°C
Discharging pipe diameter: 133 mm
Outside nozzle diameter: 737 mm
Inside nozzle diameter: 730 mm
Hydraulic coefficient of resistance: 0.37–0.82
Nozzle–structure distance: 330 mm

At any height/diameter ratio ($z/D = z/737$), the pressure ratio $R'_p = p'T/P_w$ is computed, where p' is the saturation pressure at temperature T and P_w
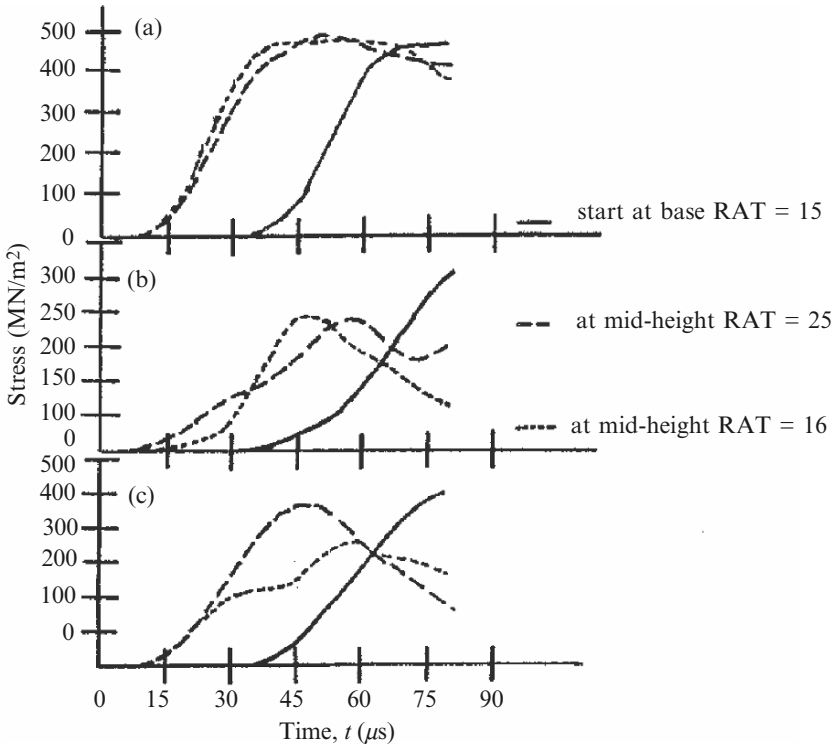
Fig. E.24. Stress histories at the dome springline, with variation of steel properties included: (**a**) inside hoop bars; (**b**) inside vertical bars; (**c**) seismic diagonal bars
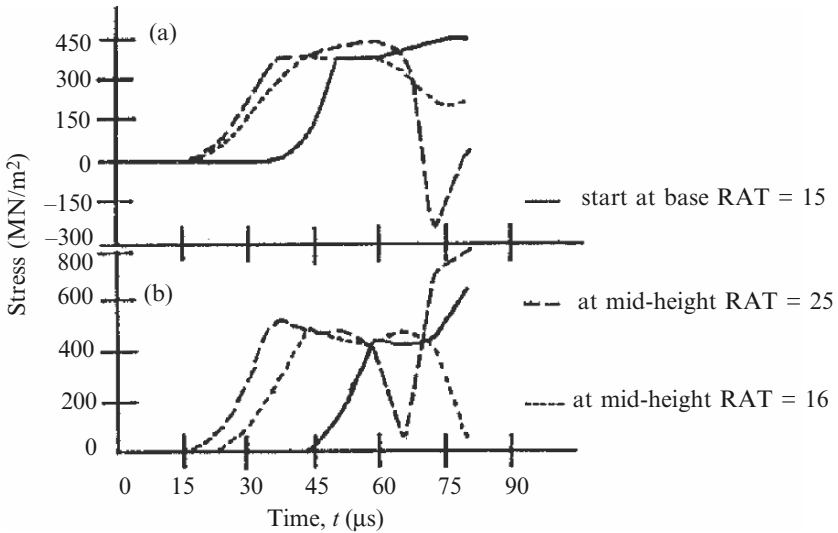
Fig. E.25. Stress histories 10° from the dome apex, with variation of steel properties included: (**a**) inside hoop bars; (**b**) inside meridional bars

impact/explosion zone
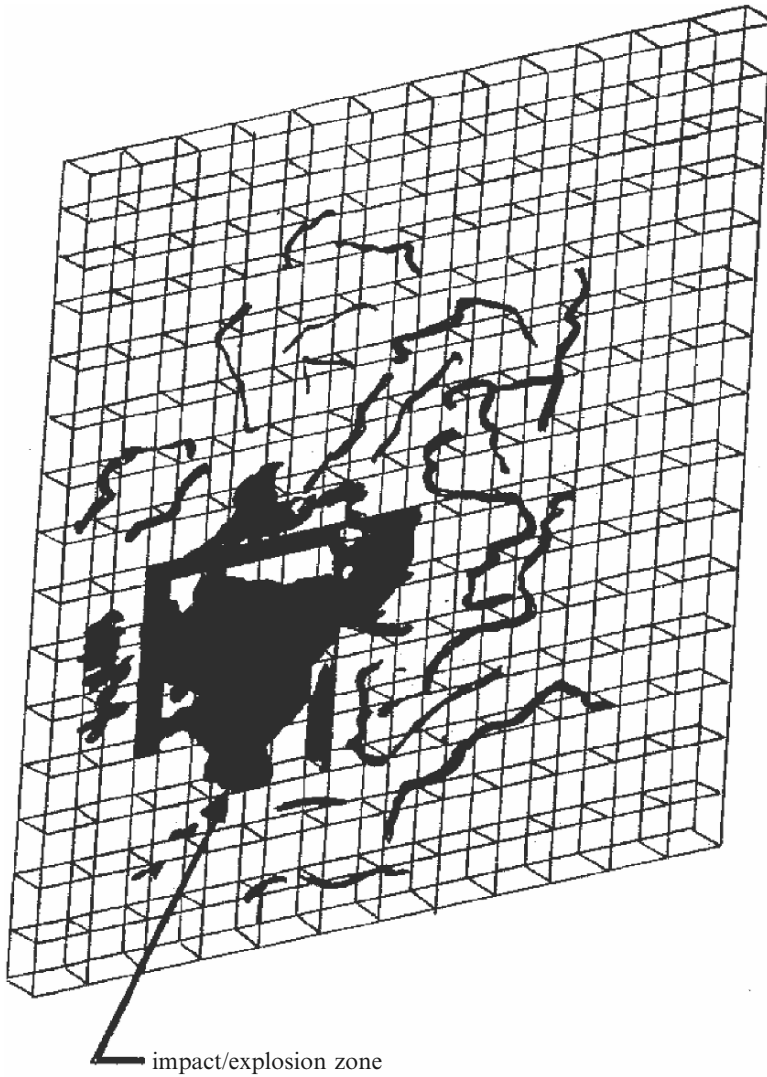
Fig. E.26. Turbine hall: Tomahawk impact/explosion

is the vessel pressure; $z/D = 0.85$, 0.95, 1, 2, 3, 4, 5 and 10; $p'T/P_w$ ranges between 0 and 1 and there is a total of 20 time steps (t), with time intervals of 0.24 s.

The jet impinging force against $p'T/P_w$ for failure conditions is given in Figs. E.28 and E.29.
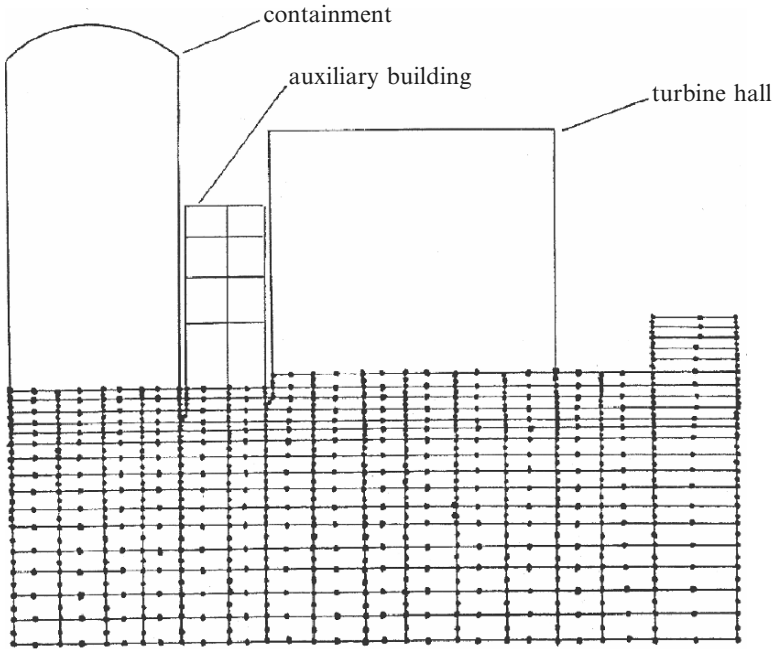
Fig. E.27. Nuclear reactor building facilities
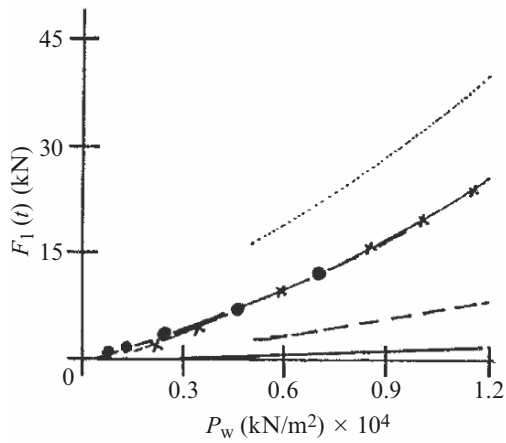
symbol	ND	z/D
⋯⋯⋯	65	0.5
━●━●━	50	0.5
✶━✶	25	1.0
━ ━ ━	10	0.5

Fig. E.28. Measurements for jet impingement forces on a flat plate due to the discharge of saturated pressurized water from circular nozzles of different diameters
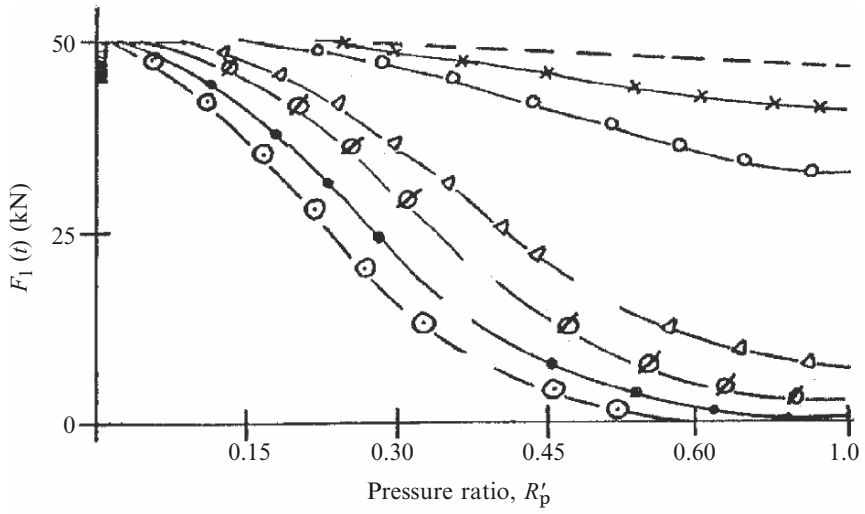
Fig. E.29. R'_p versus $F_1(t)$

F

Concrete Nuclear Shelters

F.1 Introduction

This section is devoted to the analysis and design of reinforced concrete nuclear shelters. Calculations are given for a particular study using both the British and American codes. Details are also given in this section regarding the Swedish Civil Defence Administration Code [6.79].

F.1.1 US Code Ultimate Strength Theory: General Formulae

Figure F.1 shows cracking, crushing and disengagement cases recommended in successive ACI building codes.

General Equation: Ultimate Static Moment Capacity

Cross-Section Type I

(1) The ultimate unit resisting moment M_u of a rectangular section of width b, with tension reinforcement only, is given by

$$M_u = (A_s f_s / b)(d - a/2), \qquad (F.1)$$

where A_s = area of tension reinforcement within the width b, f_s = static design stress for reinforcement, d = distance from the extreme compression fibre to the centroid of tension reinforcement, a = depth of equivalent rectangular block = $A_s f_s / 0.85 b f_c'$, b = width of compression face, f_c' = static ultimate compressive strength of concrete.
    The reinforcement ratio p is defined as

$$p = A_s / bd \qquad (F.2)$$

type *I*

no crushing
or spalling

type *II*

crushing

type *III*

spalling

$\blacksquare\blacksquare\blacksquare$ cracking

$\longrightarrow$ crushing

$\blacksquare\,\blacksquare\,\blacksquare\,\blacksquare$ disengagement
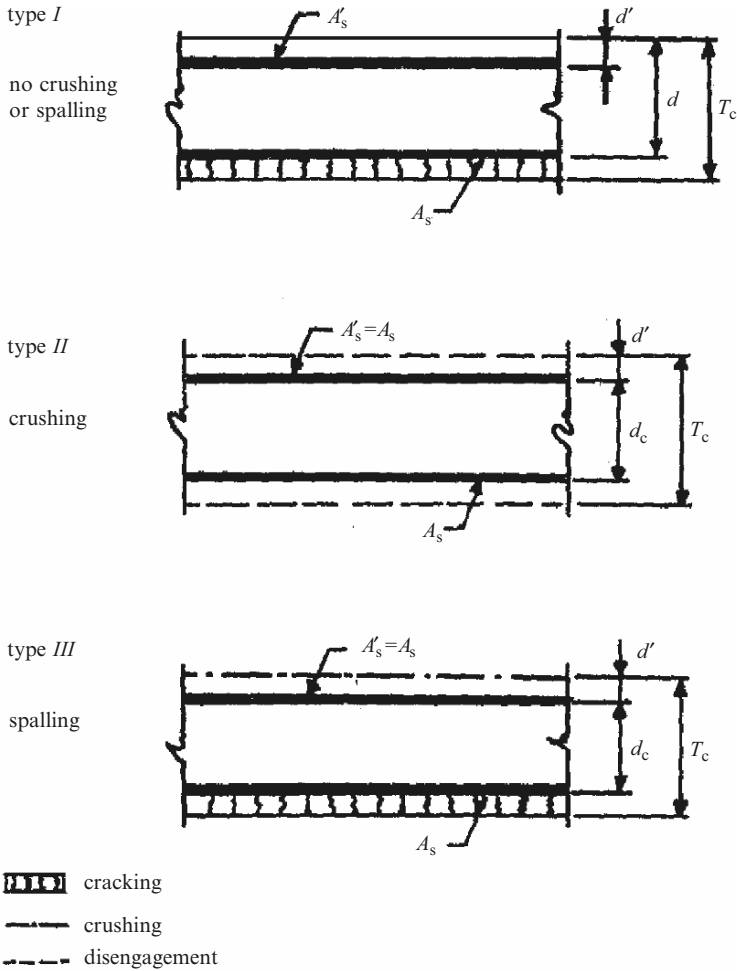
Fig. F.1. Reinforced concrete cross-sections

(2) To ensure against sudden compression failures, p must not exceed 0.75 of the ratio p_b, which produces balanced conditions at ultimate strength and is given by

$$p_b = (0.85K_1 f'_c/f_s)[87{,}000/(87{,}000 + f_s)], \qquad (\text{F.3})$$

where $K_1 = 0.85$ for f'_c up to 4,000 psi and is reduced by 0.05 for each 1,000 psi in excess of 4,000 psi.

(3) For a rectangular section of width b with compression reinforcement, the ultimate unit resisting moment is

$$M_u = [(A_s - A'_s)f_s/b](d - a/2) + [(A'_s f_s/b)(d - d')], \qquad (\text{F.4})$$

Table F.1. Reinforcement for one and two way elements

Pressure design range	Reinforcement	Two-way elements	One-way elements
Intermediate and low	Main	$A_\mathrm{s} = 0.0025bd$	$A_\mathrm{s} = 0.0025bd$
	Other	$A_\mathrm{s} = 0.0018bd$	$A_\mathrm{s} + A_\mathrm{s}' = 0.0020bT_\mathrm{c}$
High	Main	$A_\mathrm{s} = A_\mathrm{s}'$	$A_\mathrm{s} = A_\mathrm{s}'$
		$= 0.0025bd_\mathrm{c}$	$= 0.0025bd_\mathrm{c}$
	Other	$A_\mathrm{s} = A_\mathrm{s}'$	$A_\mathrm{s} = A_\mathrm{s}'$
		$= 0.0018bd_\mathrm{c}{}^\mathrm{a}$	$= 0.0018bd_\mathrm{c}{}^\mathrm{a}$

[a] But not less than $A_\mathrm{s}/4$ used in the main direction (see Fig. F.2 for coefficients)

where A_s' = area of compression reinforcement within the width b, d' = distance from the extreme compression fibre to the centroid of compression reinforcement, a = depth of the equivalent rectangular stress block = $(A_\mathrm{s} - A_\mathrm{s}')f_\mathrm{s}/0.85bf_\mathrm{c}'$.

The minimum area of flexural reinforcement is given in Table F.1.

Ultimate Static Shear Capacity

Diagonal Tension

(1) The ultimate shear stress v_u, as a measure of diagonal tension, is computed for type I sections from

$$v_\mathrm{u} = V_\mathrm{u}/bd \tag{F.5}$$

and for type II and III sections from

$$v_\mathrm{u} = V_\mathrm{u}/bd_\mathrm{c}, \tag{F.6}$$

where V_u is the total shear on a width b at the section a distance d (type I) or d_c (type II and III) from the face of the support. The shear at sections between the face of the support and the section d or d_c therefrom need not be considered critical.

(2) The shear stress permitted on an unreinforced web is limited to

$$v_\mathrm{c} = \varphi[1.9\sqrt{f_\mathrm{c}'} + 2{,}500p] \le 2.28\varphi\sqrt{f_\mathrm{c}'}, \tag{F.7}$$

where φ is the capacity reduction factor and is equal to 0.85 for all sections.

(3) When the ultimate shear capacity $v_\mathrm{u} > v_\mathrm{c}$, shear reinforcement must be provided. When stirrups are used, they should be provided for a distance d beyond the point theoretically required, and between the face of the support and the cross-section at a distance d. The required area for stirrups for type I cross-sections is calculated using

$$A_\mathrm{v} = [(v_\mathrm{u} - v_\mathrm{c})b_\mathrm{s}s_\mathrm{s}]/[\varphi f_\mathrm{s}(\sin\alpha + \cos\alpha)], \tag{F.8}$$
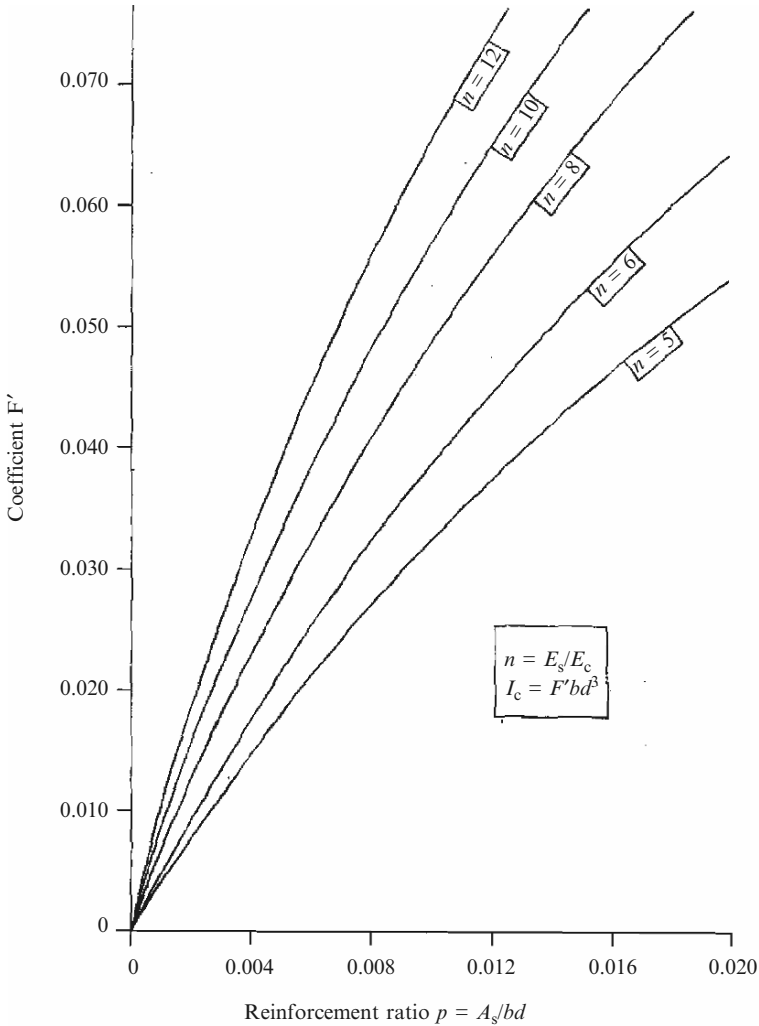
Fig. F.2. Coefficients for the moments of inertia of cracked sections with tension reinforcement only (courtesy of ACI)

while for cross-sections conforming to types I, II and III, the required area of lacing reinforcement is (see Fig. F.3):

$$A_{\mathrm{v}} = [(v_{\mathrm{u}} - v_{\mathrm{c}})b_{\ell}s_{\ell}]/[\varphi f_{\mathrm{s}}(\sin\alpha + \cos\alpha)], \qquad (\mathrm{F}.9)$$

where A_{v} = total area of stirrups or lacing reinforcement in tension within a width b_{s}, b_{ℓ} and distance s_{s} or s_{ℓ}, $(v_{\mathrm{u}} - v_{\mathrm{c}})$ = excess shear stress, b_{s} = width of concrete strip in which the diagonal tension stresses are resisted by stirrups of area A_{v}, b_{ℓ} = width of concrete strip in which the diagonal
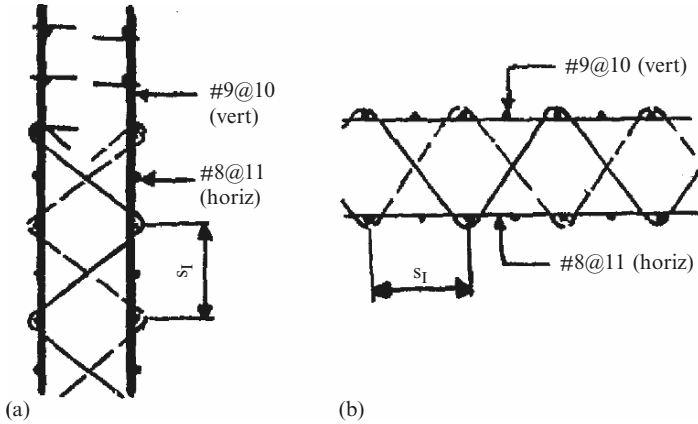
Fig. F.3. Designs of lacings: (**a**) vertical and (**b**) horizontal

tension stresses are resisted by lacing of area A_v, s_s = spacing of stirrups in the direction parallel to the longitudinal reinforcement, s_ℓ = spacing of lacing in the direction parallel to the longitudinal reinforcement, α = angle formed by the plane of the stirrups or lacing and the plane of the longitudinal reinforcement.

The excess shear stress $v_u - v_c$ is as follows.

Limits	Excess shear stress $v_u - v_c$	
	Stirrups	Lacing
$v_u \leq v_c$	0	v_c
$v_c < v_u \leq 2v_c$	$v_u - v_c$	v_c
$v_u > 2v_c$	$v_u - v_c$	$v_u - v_c$

The ultimate shear stress v_u must not exceed $10\phi\sqrt{f'_c}$ in sections using stirrups. In sections using lacing there is no restriction on v_u because of the continuity provided by this type of shear reinforcement.

Wherever stirrups are required ($v_u > v_s$), the area A_v should not be less than $0.0015bs_s$ and for type III rectangular sections of width b:

$$M_u = A_s f_s d_c / b, \tag{F.10}$$

where a_s = area of tension or compression reinforcement within the width b, d_c = distance between the centroids of the compression and the tension reinforcement.

the reinforcement ratios p and p' are given by

$$p = p' = a_s / b d_c. \tag{F.11}$$

the reinforcement ratio p' is given by

$$p' = a'_s / b d. \tag{F.12}$$

equation (F.11) is valid only when the compression steel reaches the value f_s at ultimate stress, and this condition is satisfied when

$$p - p' \geq 0.85 k_1 \frac{f_c' d'}{f_s d} \left(\frac{87{,}000}{87{,}000 - f_s} \right).$$
(F.13)

Cross-Section Types II and III

(1) The ultimate unit resisting moment of type II.

F.1.1.1 Modulus of Elasticity

Concrete

The modulus of elasticity of concrete, E_c, is given by

$$E_c = w^{1.5} \, 33\sqrt{f_c'} \text{ psi.}$$
(F.14)

The value of w, the unit weight of concrete, lies between 90 and $155 \, \text{lb} \, \text{ft}^{-2}$.

Reinforcing Steel

The modulus of elasticity of reinforcing steel, E_s, is

$$E_s = 30 \times 10^6 \, \text{psi.}$$
(F.15)

Modular Ratio

The modular ratio, n, is given by

$$n = E_s / E_c$$
(F.16)

and may be taken as the nearest whole number.

F.1.1.2 Moment of Inertia

The average moment of inertia, I_a, to be used in calculating the deflection is

$$I_a = (I_g + I_c)/2,$$
(F.17)

where I_g is the moment of inertia of the gross concrete cross-section of width b about its centroid (neglecting steel areas) and is equal to

$$I_g = bT_c^3/12$$
(F.18)

and I_c is the moment of inertia of the cracked concrete section of width b considering the compression concrete area and steel areas transformed into equivalent concrete areas and computed about the centroid of the transformed section. I_c is calculated from

$$I_c = Fbd^3.$$
(F.19)

The coefficient F varies as the modular ratio n and the amount of reinforcement used. For sections with tension reinforcement only, F is given in Fig. F.2.

F.2 Design of a Concrete Nuclear Shelter Against Explosion and Other Loads Based on the Home Office Manual

Figure F.4 shows a typical layout of a domestic nuclear shelter for a family of six.

F.2.1 Basic Data (Home Office Code [6.80])

For a 1 Mton ground burst at a distance of 1.6 km from ground zero:

Ductility ratio, μ: 5
Main reinforcement $\not< 0.25\%$ bd
Secondary reinforcement $\not< 0.15\%$ bd
Ultimate shear stress $\not> 0.04 f_{cu}$
Dynamic shear stress (mild steel) $\not> 172 \, \mathrm{N \, mm^{-2}}$
Protective factor: 4,000
Concrete f_{cu}(static): $30 \, \mathrm{N \, mm^{-2}}$ (grade 30)
Concrete f_{cu}(dynamic): $1.5 f_{cu} = 37.5 \, \mathrm{N \, mm^{-2}}$
Reinforcement f_{y}(static): $420 \, \mathrm{N \, mm^{-2}}$
Reinforcement f_{yd}(dynamic): $1.10 f_{y} = 462 \, \mathrm{N \, mm^{-2}}$
Young's modulus, E_{c}: $20 \, \mathrm{GN \, m^{-2}}$
Young's modulus, E_{s}: $200 \, \mathrm{GN \, m^{-2}}$
Clear span: 3 m
Slab thickness: 300 mm (with minimum cover 50)
Blast load: $0.17 \, \mathrm{N \, mm^{-2}}, F_{1}(t) = P_{do}$

F.2.2 Additional Data for Designs Based on US Codes

Dynamic Increase Factors (DIF)

Concrete: compression	1.25
diagonal tension	1.00
direct shear	1.10
Reinforcement: bending	1.10
shear	1.00

Dynamic stresses:

$$\text{concrete } f_{c}'(\text{cylindrical strength}) = 0.87 f_{cu}$$
$$= 3{,}000 \, \mathrm{lb \, in.^{-2}} \text{ (psi)}$$
$$\text{concrete } f_{y}(\text{static}) = 60{,}000 \, \mathrm{lb \, in.^{-2}} \text{ (psi)}$$
$$R_{m} = r_{u} = \left(\frac{1}{1 - \frac{1}{2\mu}} \right) F_{1}(t) = 1.1 F_{1}(t) = 0.187 \, \mathrm{N \, mm^{-2}}.$$
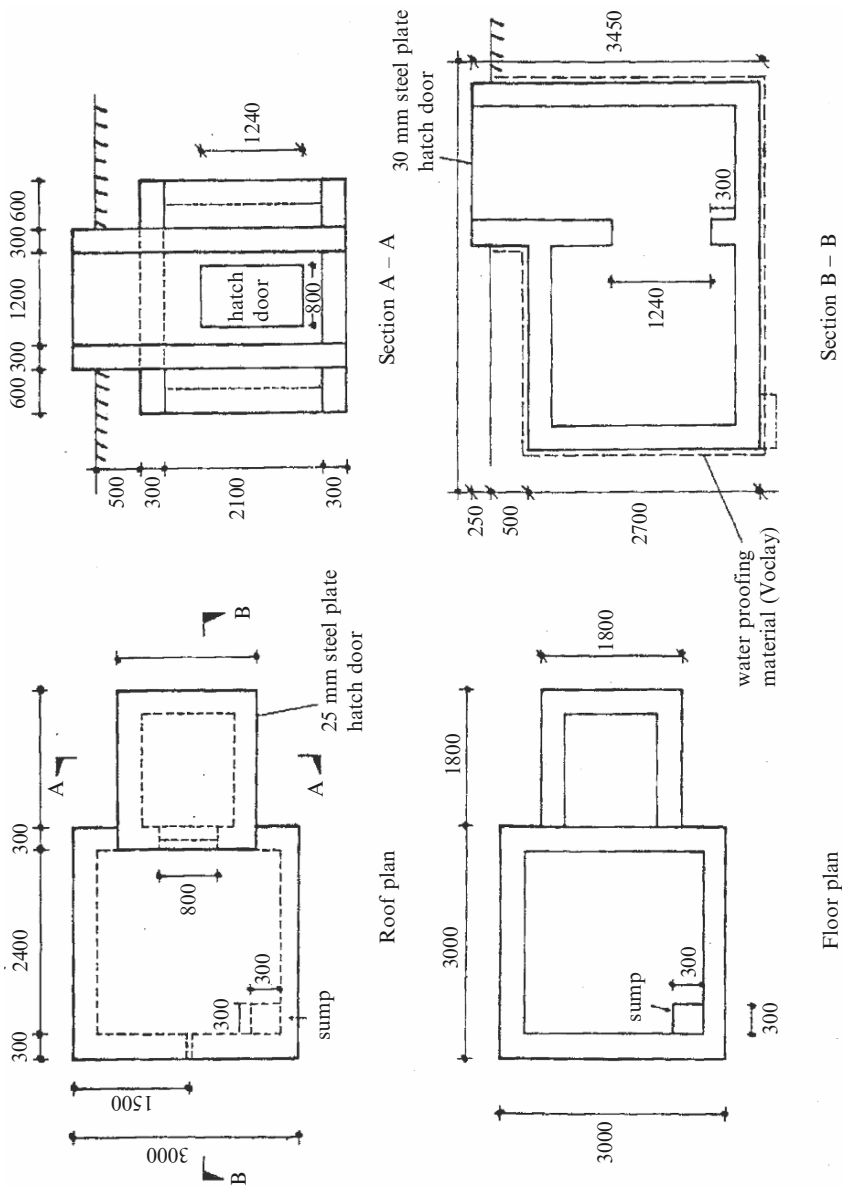
Fig. F.4. Domestic nuclear shelter: general arrangement

Deadload of concrete plus soil $= 0.014 \, \text{N mm}^{-2}$

$$r_\text{u} = 0.187 + 0.014 = 0.201 \, \text{N mm}^{-2}.$$

For a two-way slab

$$M_\text{u} = r_\text{u}L^2/16 = 0.201(3{,}000)^2/16$$
$$= 113{,}062.5 \, \text{N mm mm}^{-1}.$$

300 mm Thick Slab

T16–200 bars; $A_\text{s} = 1{,}005 \, \text{mm}^2 \, \text{m}^{-1}$; $d = 300 - 50 - 8 = 242$

$z = d - (0.84f_\text{yd}A_\text{s}/f_\text{cu}(\text{dyn})$ $\quad\rceil$ *Note*: Later on, based on
$= 242 - (0.84(462)(1{,}005)10^{-3}/37.5)$ $\,\rceil$ finite-element analysis, the
$= 231.58 \, \text{mm}$ $\qquad\qquad\qquad\qquad\rceil$ T20–200 bars adopted were checked

Area of the roof $= 9 \, \text{m}^2 = A_\text{t}$; $\sqrt{A_\text{t}} = 3 \, \text{m}$
$H - x = 2.7 - 0.3 = 2.4$ or $3.4 - 0.3 = 3.1$
$\sqrt{A_\text{t}}/(H - x) = 1.25$ and 0.97
Weight of overhead material $= 1{,}340 \, \text{kg m}^{-2}$
$R = 0.025\%$ (roof contribution)

$$\text{PF} = 100/(R + G_\text{T})$$
$$= 100/(0.025 + 0)$$
$$= 4{,}000 \quad \text{(safe)},$$

where G_T is the percentage wall contribution, ignored in the worst case.
Figure F.5 gives structural details of the reinforced concrete shelter.

Steel Blast Doors

Clear opening $800 \, \text{mm} \times 1{,}200 \, \text{mm}$.

$$F_\text{I}(t) = p_\text{do} = 2.3p_\text{so} = 2.3(0.17) = 0.39 \, \text{N mm}^{-2}$$
$$r_\text{u} = 1.1F_\text{I}(t) = 0.43 \, \text{N mm}^{-2}$$
$$M_\text{u} \text{ (simply supported)} = 0.43(800)^2/8 = 34{,}400 \, \text{N mm mm}^{-1}$$

20 mm thick steel door

$$z = bd^2/4 = 1(20^2)/4 = 100 \, \text{mm}^3$$

Also

$$z_\text{p} = M_\text{u}/1.1(265) = 118 \, \text{mm}^2$$

Calculated thickness of steel doors $= (118/100)20 = 23.6 \approx 25 \, \text{mm}$

T20−200   T20−200

T20−200

T20−200

T25−100

27T25−200

27T25−200

T20−100

T16 Ubar

T16 Ubar

T16 Ubar

T16 Ubar

T25−100

T25−100

20T25 − 100 T,B

T16 Ubar

T16 Ubar

Ubars
T16−300

15T20−200 B

3T16 Ubar

15T16−200 B

3T16−300 Ubar

T20−200 B

15T20−200 T

T20−200 T

3T16 Ubar

T16 Ubar

15T20−200 T

details of roof
Section A−A
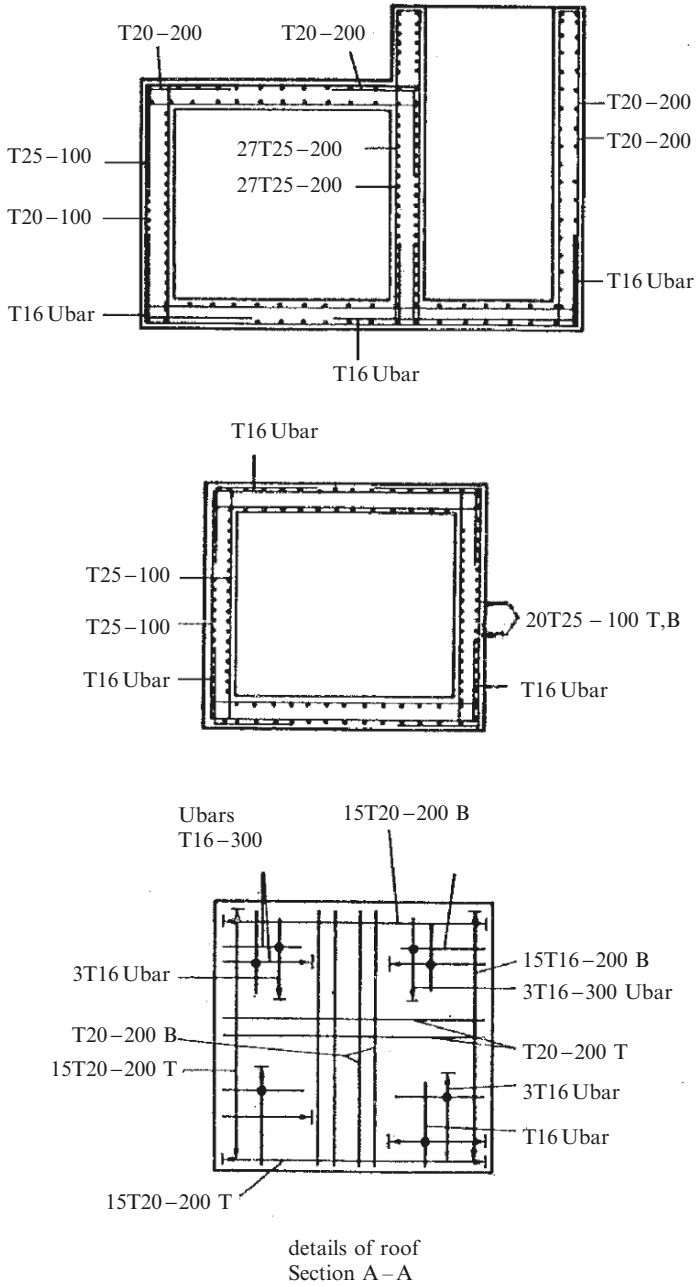
Fig. F.5. Domestic nuclear shelter (reinforced concrete): detail

A 25 mm thick door was adopted.

The thickness of the glass door may have to be increased for protection against radiation fall-out. One possibility is a steel–concrete sandwich construction. One possible steel door design is given in Fig. F.6.

$$\text{or } z = 0.95(242) = 229.9 \,\text{mm} \approx 230 \,\text{mm}$$

Walls: 300 mm Thick

Blast load on walls $= p_{\text{do}} \times 0.5 = 0.085 \,\text{N}\,\text{mm}^{-2}$
$r_{\text{u}} = 1.1 F_{\text{I}}(t) = 1.1(p_{\text{do}}) = 0.0935 \,\text{N}\,\text{mm}^{-2}$
Total (including soil) $= 0.0935 + 0.08 = 0.1735 \,\text{N}\,\text{mm}^{-2}$

F.2.2.1 Two-Way Slab

$$M_{\text{u}} = r_{\text{u}} L^2/16 = 0.1735(2{,}700)^2/16 = 79{,}050.941$$

$\left. \begin{array}{l} \text{Both walls} \\ (2{,}700 \,\text{mm and} \\ 3{,}400 \,\text{mm}) \end{array} \right\}$ also $M_{\text{u}} = [(3{,}400)^2/(2{,}700)^2](79{,}050.94)$
$$= 125{,}353.75 \,\text{N}\,\text{mm}\,\text{mm}^{-1} \text{ (adopted)}$$

$$M_{\text{u}} = 125{,}353.75 = A_{\text{s}}(230)(462)$$
$$A_{\text{s}} = 1.18 \,\text{mm}^2\,\text{mm}^{-1} = 1{,}180 \,\text{mm}^2\,\text{m}^{-1}$$

adopted T20–200 (in some critical areas T20–100 and T25–100)
Shaft wall bars: T12–200 links T16–300 U-bars
Minimum steel:

$$\text{Main} \rightarrow 0.25\% \times 1 \times 242 = 0.605 \,\text{mm}^2\,\text{mm}^{-1}(605 \,\text{mm}^2\,\text{m}^{-1})$$
$$1{,}005 \,\text{mm}^2\,\text{m}^{-1} > 605(\text{T16–200}) \text{ adopted}$$
$$\text{Secondary} \rightarrow 0.15\% \times 1 \times 242 = 0.363 \,\text{mm}^2\,\text{mm}^{-1}(363 \,\text{mm}^2\,\text{m}^{-1})$$
$$(\text{T16–200 or 300}) \text{ adopted}$$

Shear: allowable shear $= 0.04 f_{\text{cu}} = 1.2 \,\text{N}\,\text{mm}^{-2}$
$$\text{shear} = r_{\text{u}}[(L/2 - d)/d]$$
$$= (2{,}700/2 - 242)/2{,}700$$
$$= 0.41 < 1.2 \,\text{N}\,\text{mm}^{-2} \quad (\text{safe})$$
$$\text{or} = (3{,}400/2 - 242)/3{,}400$$
$$= 0.43 < 1.2 \,\text{N}\,\text{mm}^{-2}$$

Protective factor (PF) in the middle of the shelter and at 0.25–0.30 m above the floor level.
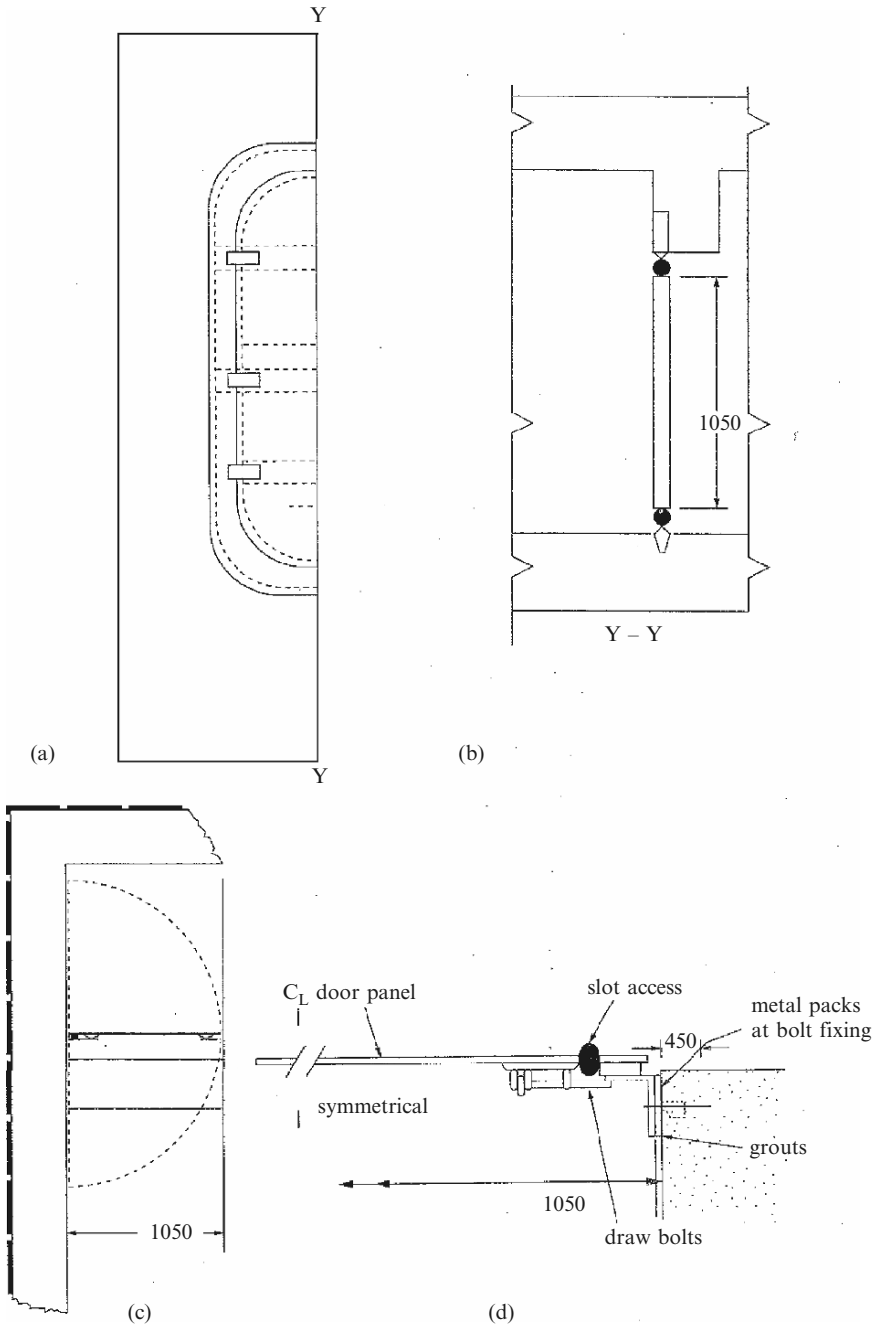
Fig. F.6. Design of steel blast doors. (**a**) Elevation; (**b**) vertical section; (**c**) door location; (**d**) horizontal section: structural details

F.3 Design of a Nuclear Shelter Based on the US Codes

F.3.1 Introduction

Many codes in the USA have empirical equations which are based on imperial units. The reader is given the conversions in SI units. However, the bulk of the calculations given here are based on imperial units (conversion factors shown below).

Conversion Factors

$1\,\mathrm{ft} = 0.3048\,\mathrm{m}$; $1\,\mathrm{lb\,ft^{-2}} = 47.88\,\mathrm{N\,m^{-2}}$;
$1\,\mathrm{lbf} = 4.448\,\mathrm{N}$; $1\,\mathrm{lb\,ft^{-2}} = 16.02\,\mathrm{kg\,m^{-2}}$;
$1\,\mathrm{lb\,in} = 0.113\,\mathrm{N\,m}$; $1\,\mathrm{kg} = 9.806\,\mathrm{N}$;
$1\,\mathrm{lb\,in^{-2}} = 6{,}895\,\mathrm{N\,m^{-2}}$; $1\,\mathrm{in} = 25.4\,\mathrm{mm}$

Dynamic Stresses

Concrete:
    Comp $- 1.25(3{,}000) = 3{,}750\,\mathrm{psi}$
    Diagonal tension $- 1.00(3{,}000) = 3{,}000\,\mathrm{psi}$
    Direct shear $- 1.10(0.18)(3{,}000) = 600\,\mathrm{psi}$

Reinforcement:
    Bending $- 1.10(60{,}000) = 66{,}000\,\mathrm{psi}$
    Shear $- 1.10(60{,}000) = 60{,}000\,\mathrm{psi}$

since $f'_c = 3{,}000\,\mathrm{psi}$ and $f_y(\text{static}) = 60{,}000\,\mathrm{psi}$.

F.3.2 Wall Design

Figure F.4 shows a one-way slab fully restrained at the supports. Wall thickness $(T_c) = 300\,\mathrm{mm}$ ($12\,\mathrm{in.}$) (see Fig. F.7). The US recommended covers are 0.75 and $1.5\,\mathrm{in.}$ ($37\,\mathrm{mm}$) rather than $50\,\mathrm{mm}$ (adopted by the Home Office).

For a negative moment, $d = 12{-}1.5{-}0.3125 = 10.1875\,\mathrm{in.}$ (assuming #5 bars). For a positive moment, $d = 12{-}0.75{-}0.3125 = 10.935\,\mathrm{in.}$

$$A_s = 0.0025 \times 12 \times 10.935 = 0.328\,\mathrm{in^2\,ft^{-1}}$$

#5 bars at $11\,\mathrm{in}$ ($275\,\mathrm{mm}$), $A_s = 0.34 > 0.328\,\mathrm{in.^2}$. The wall blast load $= 0.085\,\mathrm{N\,mm^{-2}} = 12.33\,\mathrm{lb\,in.^{-2}}$. The ultimate moment is given by

$$M_u = (A_s f_{yd}/b)(d - a/2),$$

where $a = A_s f_{yd}/0.85 b f'_c(\text{dyn}) = 0.586\,\mathrm{in.}$
    $b = 12\,\mathrm{in}$
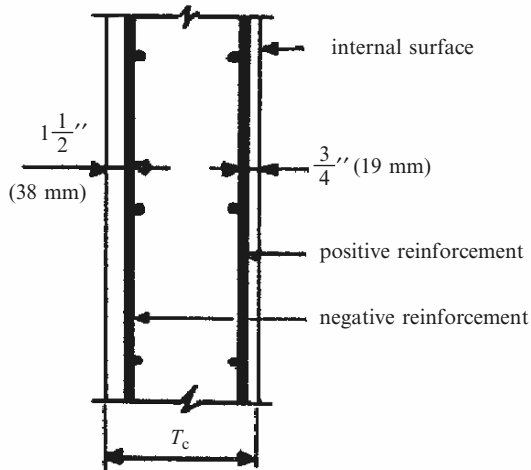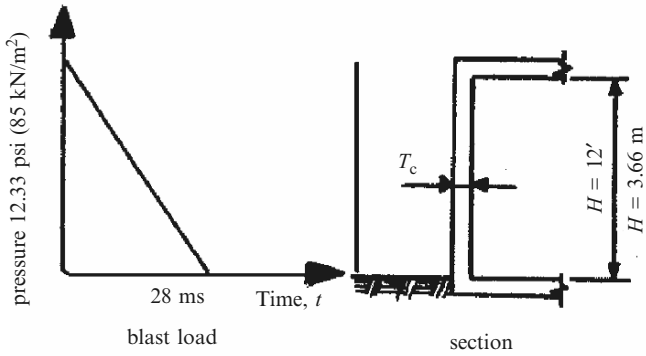
Fig. F.7. Wall analysis and design

$$M_u \text{ (positive)} = M'_P = 19{,}900 \text{ in lb in}^{-1}$$
$$M_u \text{ (negative)} = M'_N = 18{,}500 \text{ in lb in}^{-1}$$
$$E_c \text{ for concrete} = D^{1.5}33\sqrt{f'_c}$$
$$= (150 \text{ lb in}^{-3})^{1.5} \times 33(3{,}000)^2$$
$$= 3.32 \times 10^6 \text{ psi}$$
$$\rho = D = \text{density of concrete} = 150 \text{ lb in}^{-3}(23.6 \text{ kN m}^{-3})$$
$$E_s \text{ for steel} = 30 \times 10^6 \text{ psi } (200 \text{ GN m}^{-2})$$
$$n = E_s/E_c = 9.03$$

Average moment of inertia for a 1 in. strip.
$I_g \text{ (gross)} = bT_c^3/12 = 144 \text{ in.}^4$

T_c (thickness of the wall) $= d$
d (average) $= 10.5625$ in.
p (average) $= A_s/bd = 0.00268 = \rho_s$
I (cracked section)
$F' = 0.0175$; $I_{cracked} = I_c = F'bd^3 = 20.6$ in.^{4}
$I_a =$ average moment of inertia $= (I_g + I_c)/2 = 82.3$ in.^{4}

F.3.2.1 Elastic (k_e) and Elasto-Plastic (k_{ep}) Stiffness

$$k_e = (384E_cI_a)/bL^4 = 244 \text{ lb in.}^{-3}; \quad b = 1$$
$$k_{ep} = (384E_cI_a)/5bL^4 = 48.8 \text{ lb in.}^{-3}$$

F.3.2.2 Elastic and Elasto-Plastic Deflection

$$\delta_e = X_e = r_e/k_e = 10.71/244 = 0.0439 \text{ in.}$$
$$\delta_{ep} = X_p - X_e = (r_u - r_e)/k_{ep} = 0.084 \text{ in.}$$
$$X_p = 0.1279 \text{ in.}$$

Equivalent Elastic Deflection and Stiffness

$$X_E = X_e + X_p(1 - r_e/r_u)$$
$$= 0.0793 \text{ in.}$$
$$K_E = r_u/X_E = 186.8 \text{ lb in.}^{-3}$$

Load–Mass Factors and Effective Mass

Figure F.8 gives:

K_{LM}	Range
0.77	elastic
0.78	elasto-plastic
0.66	plastic

K_{LM} (elastic and elasto-plastic) $= 0.78$ (average)
K_{LM} (elastic and plastic) $= 0.72$ (average)

$$M = \rho\, T_c/\mathbf{g} = 150 \times 1 \times 10^6/32.3(1728)$$
$$= 2{,}700 \text{ lb ms}^2 \text{ in.}^{-3},$$
$$M_{effective} = K_{LM} \times M = 1{,}944 \text{ lb ms}^2 \text{ in.}^{-3},$$
$$\text{natural period} = T_N = 2\pi\sqrt{(M_e/K_E)} = 20.3 \text{ ms},$$

where $\mathbf{g} = 32.2 \text{ ft s}^{-2}$; $K_E = 186.8$.
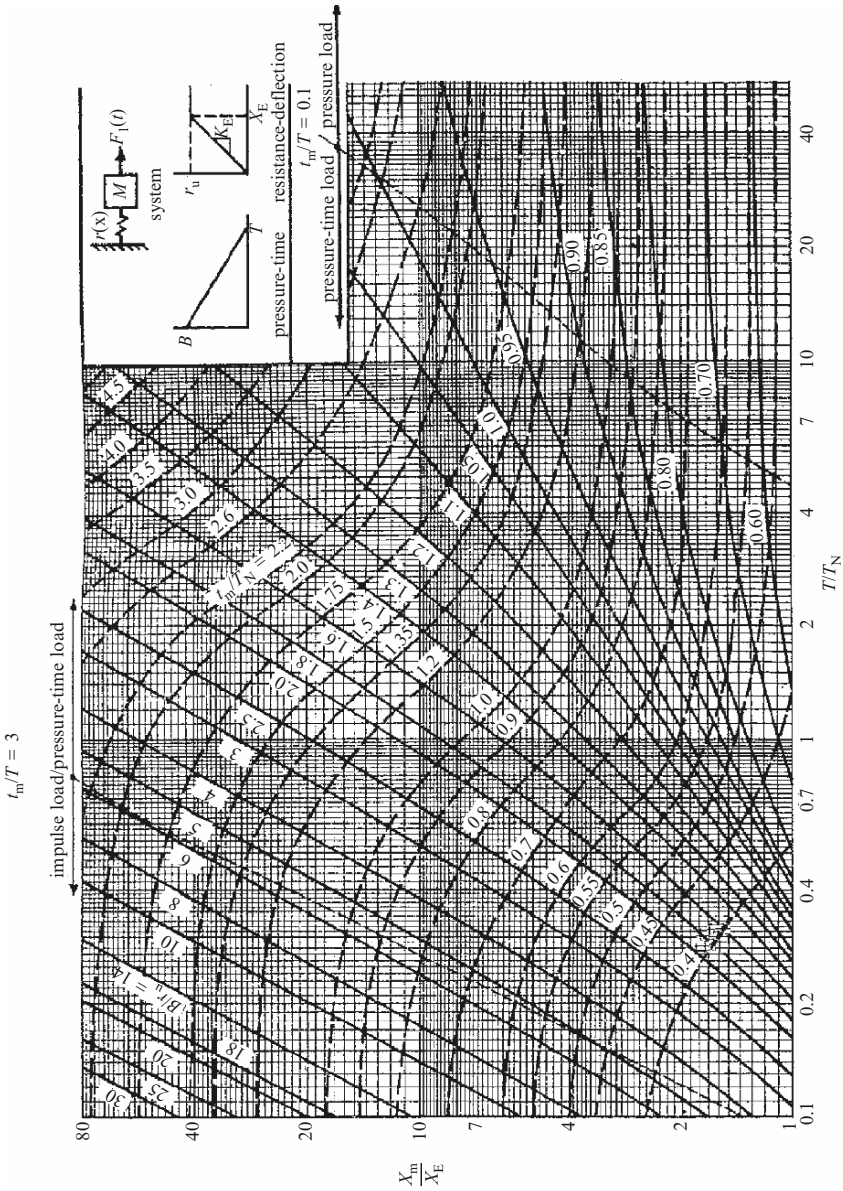
Fig. F.8. Maximum response of simple spring-mass system (with compliments of US Corp of Engineers, Washington, D.C.)

Response Chart Parameters

Reference is made to Fig. F.8.

Peak pressure $B = 12.33 \, \text{psi}$

Peak resistance $r_{\text{u}} = 14.81 \, \text{psi}$

The chart $B/r_{\text{u}} = 0.8325 \rightarrow T/T_{\text{N}} = 28/20.3 = 1.38$

$X_{\text{m}}/X_{\text{E}} = 1.50$, as this is <3 the section is safe

The corresponding $t_{\text{m}}/T_{\text{N}} = 0.50 \rightarrow t_{\text{m}}/t_{\text{o}} = t_{\text{m}}/T$

$$= (t_{\text{m}}/T_{\text{N}})/(T/T_{\text{N}}) = 0.50/1.38$$
$$= 0.3623$$

This lies within the range $3.0 > t_{\text{m}}/t_{\text{o}} > 0.1$, hence the response is satisfactory.

Diagonal Tension at a Distance d from the Support

$$v_{\text{u}} = r_{\text{u}}[(L/2) - d_{\text{e}}]/d_{\text{c}} = 14.81(72 - 10.1875)/10.1875$$
$$= 89.9 \, \text{psi}$$

The allowable shear stress, v_{c}, is given by

$$v_{\text{c}} = \varphi[1.9\sqrt{f_{\text{c}}'} + 2{,}500p] \leq 2.28\varphi\sqrt{f_{\text{c}}'},$$

where $\varphi = 0.85$

$$= 94.4 \, \text{psi, as this is} >89.9 \, \text{psi}, \ \text{OK with no stirrups}$$

Ultimate Shear

$$V_{\text{s}} = r_{\text{u}}L/2.0 = 14.81 \times 144/2.0 = 1{,}066 \, \text{lb in.}^{-1}$$

Allowable shear

$$V_{\text{d}} = 0.18f_{\text{c}}'(\text{dyn}) \, bd = 6{,}050 \, \text{lb in}^{-1} > 1{,}066 \, \text{lb in.}^{-1}$$

Hence the 300 mm (12 in.) wall designed against the same blast load in both codes (British and US) is safe. The roof slab can be checked in the same way as for the gas explosion, described earlier in the text.

F.4 Lacing Bars

When a ring forced concrete element is subject to a blast load, the element deflects far beyond the stage of well defined cracking until:

(1) The strain energy of the element is developed sufficiently to balance the kinetic energy created by the applied load when it comes to rest.
(2) Fragmentation of the concrete element results in either its partial or total collapse.

For the development of the available energy of the concrete elements, it is necessary to make changes in the reinforcement layouts and details. Each element is reinforced symmetrically. They and the intervening concrete are laced together, as shown in Figs. F.9 and F.10, with continuous bent diagonal bars. This system offers forces which will contribute to the integrity of the protective element. Where structural elements are located outside the immediate high blast intensity, they should be designed without lacing. All other types are given in Figs. F.11–F.15.

Design of Lacing Bars

Where lacing bars are needed, the following calculations will help in the design of nuclear shelters. The lacings can be in both the vertical and horizontal directions.

Vertical Lacing Bars

The wall thickness is kept the same. Data: $d_\ell = 10$ in.; $S_\ell = 22$ in.; no of bars = 6; $D_0 = 0.75$ in.

$$d_\ell = 21 + 1.13 + 2 + 0.75 = 24.88 \text{ in.}$$
$$R_{\ell_{\min}} = 3D_0$$

for $S_\ell/d_\ell = 0.884$

$$(2R_\ell + D_0)/d_\ell = 7D_0/d_\ell = 0.211$$
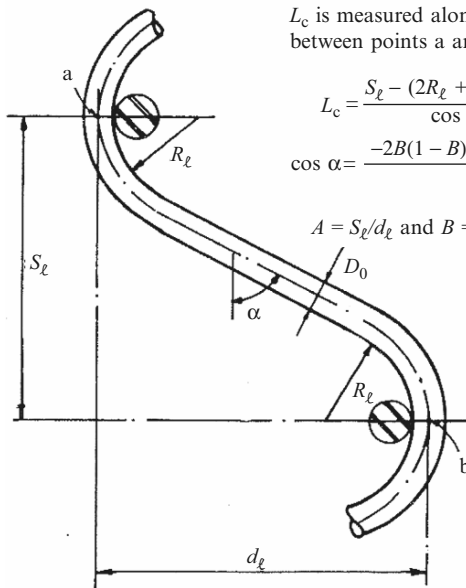
L_c is measured along the centre line of the lacing bar between points a and b.

$$L_c = \frac{S_\ell - (2R_\ell + D_0)\sin\alpha}{\cos\alpha} + \pi(2R_\ell + D_0)\left(\frac{\alpha}{180}\right) \quad \text{(F4.1)}$$

$$\cos\alpha = \frac{-2B(1-B) \pm \sqrt{\{[2B(1-B)]^2 - 4[(1-B)^2 + A^2](B^2 - A^2)\}}}{2[(1-B)^2 + A^2]}$$

$A = S_\ell/d_\ell$ and $B = \dfrac{2R + D_0}{d_\ell}$

Fig. F.9. Length of lacing bar
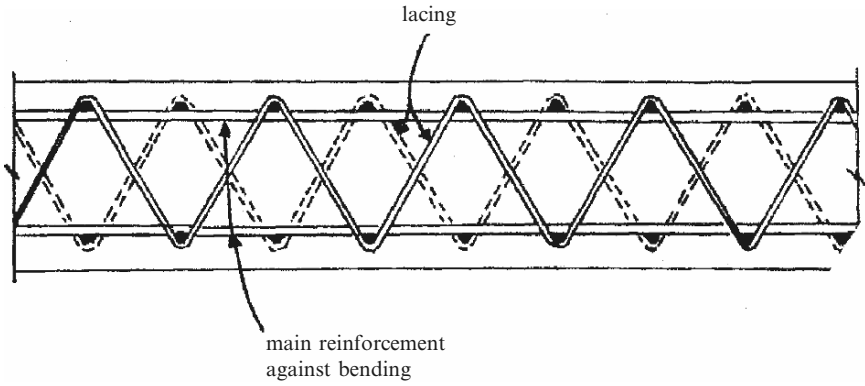
Fig. F.10. Lacing reinforcement
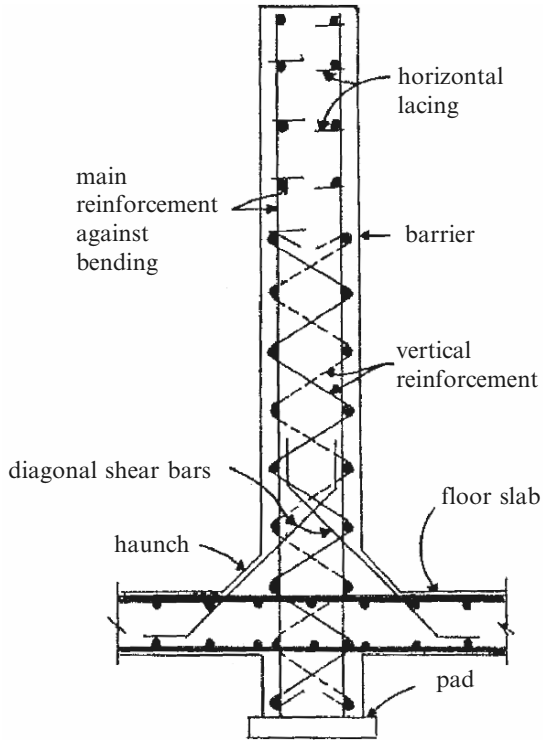
Fig. F.11. Typical laced wall

(a)

(b)
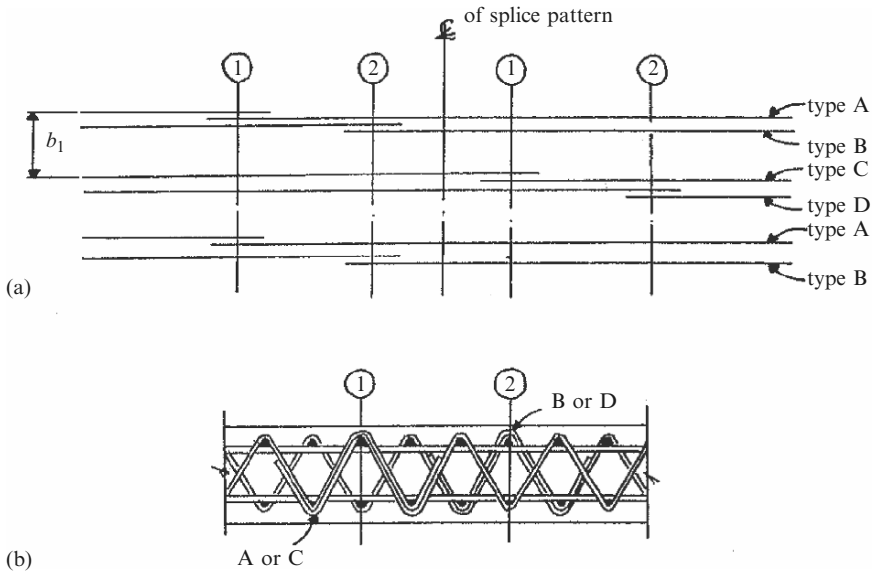
Fig. F.12. Typical details for splicing of lacing bars: (**a**) splice pattern; (**b**) lacing splice
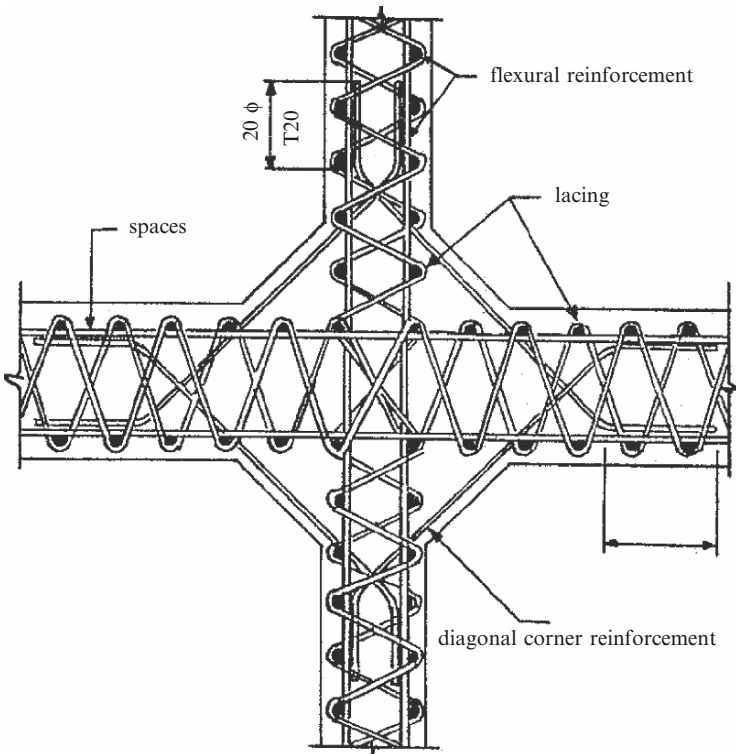
Fig. F.13. Typical detail at intersection of two continuous walls
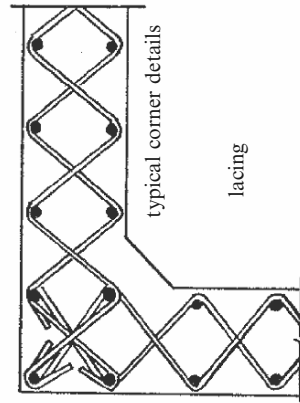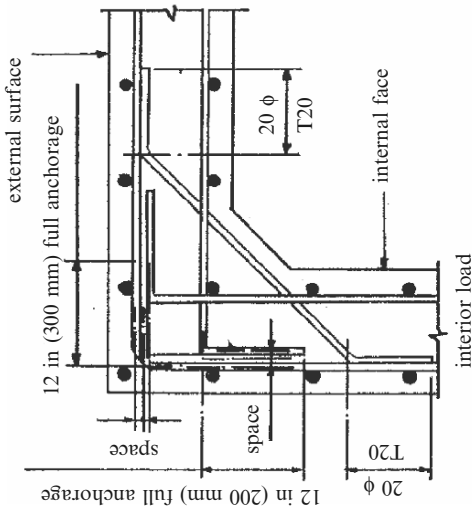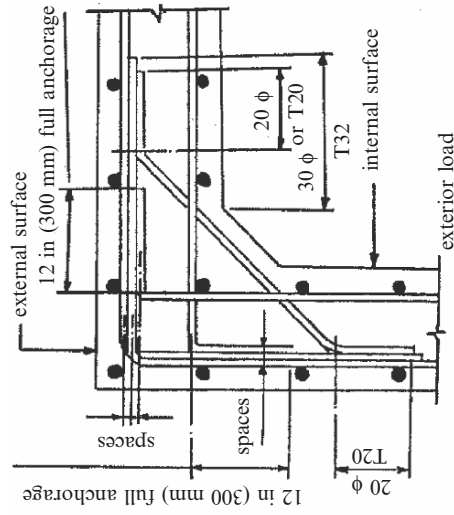
Fig. F.14. Flextural reinforcement in lacings
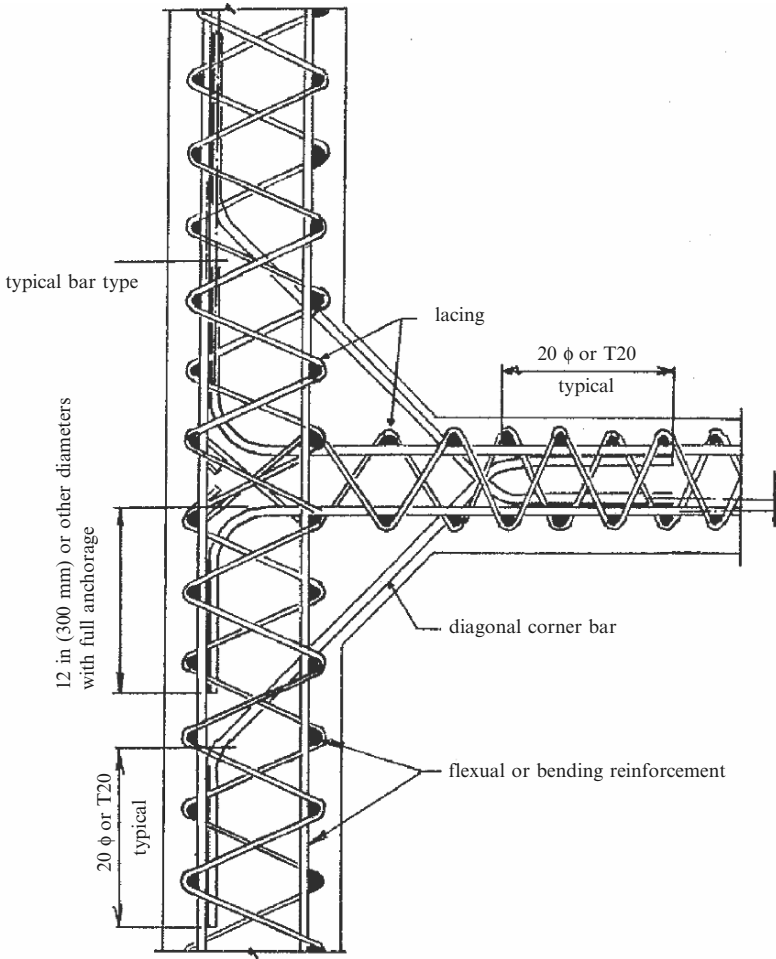
Fig. F.15. Typical detail at intersection of continuous and discontinuous walls

$\alpha = 51.5°$

$$A_v = (v_{uv} - v_c)b_\ell S_\ell / \varphi f_s (\sin\alpha + \cos\alpha) = 0.378 \, \text{in.}^2 \qquad \text{(F.1)}$$

$A_{v_{min}} = 0.0015 \, b_\ell S_\ell = 0.330 \, \text{in.}^2$; no of bars $= 6$; $A_s = 0.44 \, \text{in.}^2$, OK

Horizontal Lacing Bars

No of bars $= 6$; $D_0 = 0.75 \, \text{in.}$

$$d_\ell = 21.0 + 1.13 + 0.75 = 22.8 \, \text{in.}$$
$$R_{\ell_{min}} = 3D_0$$
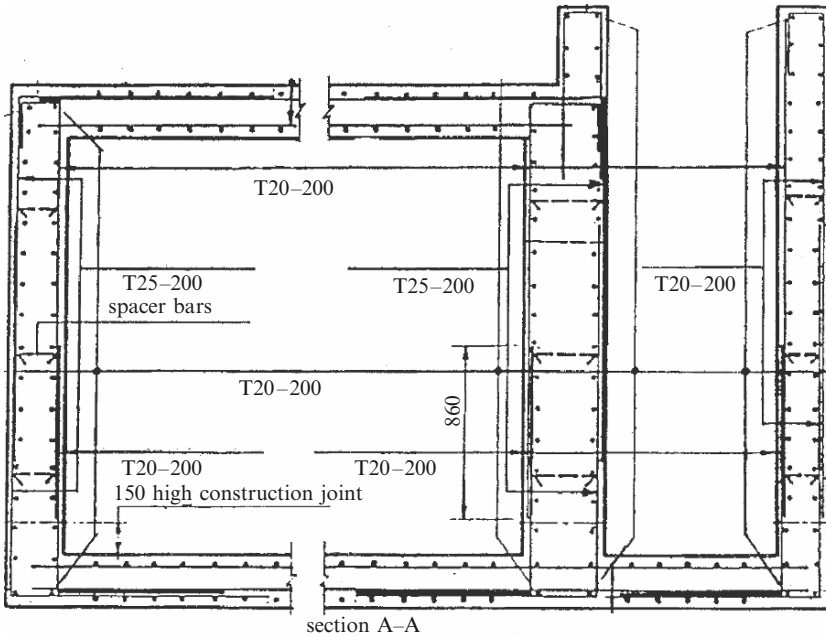
Fig. F.16. Reinforcement through section

for $S_\ell d_\ell = 20/22.88 = 0.874$

$$(2R_\ell + D_0)/d_\ell = 7D_0/d_\ell = 0.229$$

$A_v = 0.339 \text{ in.}^2$

$A_{v_{min}} = 0.0015\ b_\ell S_\ell = 0.0015 \times 11 \times 20 = 0.330 \text{ in.}^2$; no of bars $= 6$; $A_s = 0.44 \text{ in.}^2$, still OK.

Additional reinforcement details from the British code are given in Figs. F.16 and F.17.

F.5 Finite-Element Analysis

A three-dimensional isoparametric, finite-element analysis has been carried out by Bangash [1.149]. Figure F.18 shows the finite-element mesh scheme for a dynamic model for a nuclear shelter. Figure F.19 gives the relationships between pressure and time. The results are given in Fig. F.20.

F.5.1 The Swedish Design and Details

The Swedish code TB78E provides novel details of the nuclear shelter. They are presented here by courtesy of the Civil Defence Administration of Sweden. Figures F.21 and F.22 show structural details of a roof slab and sectional details illustrating various reinforcements.
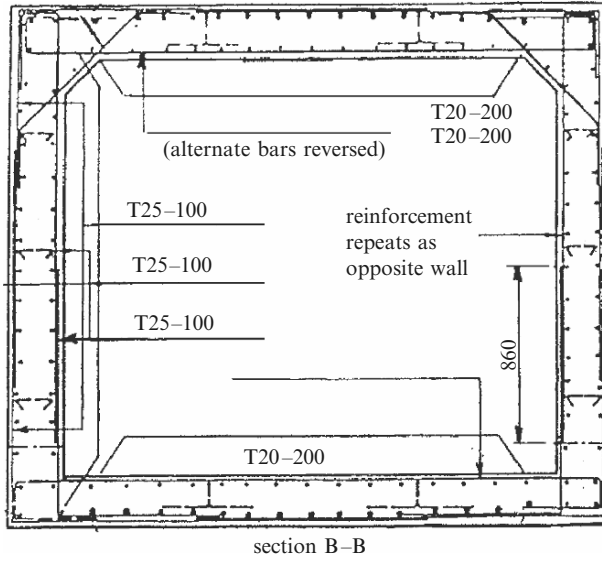
section B–B

Fig. F.17. Section B–B through shelter
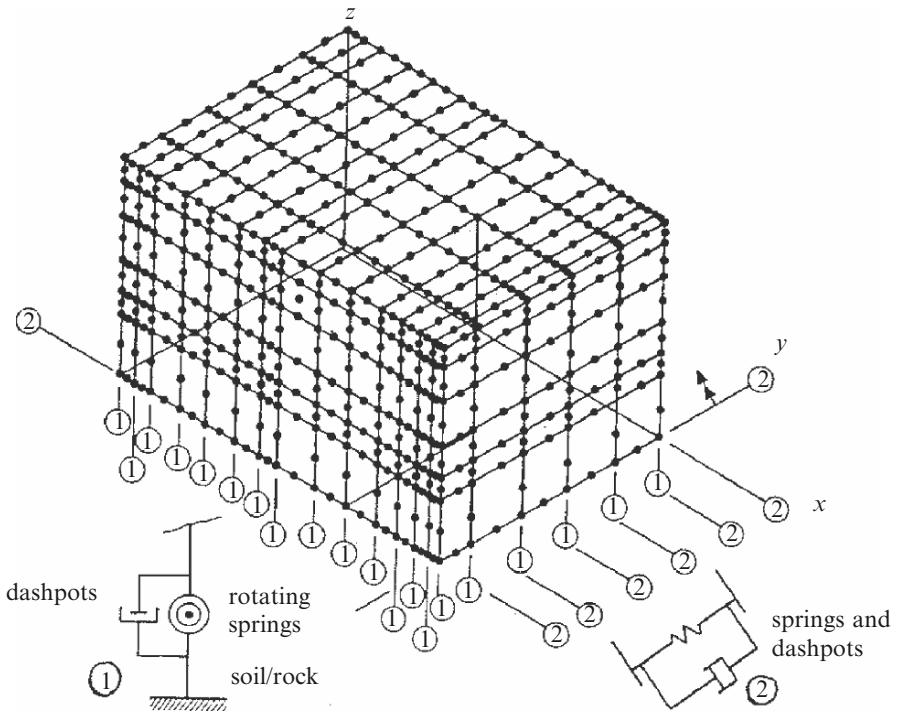
Fig. F.18. Dynamic model for a nuclear shelter
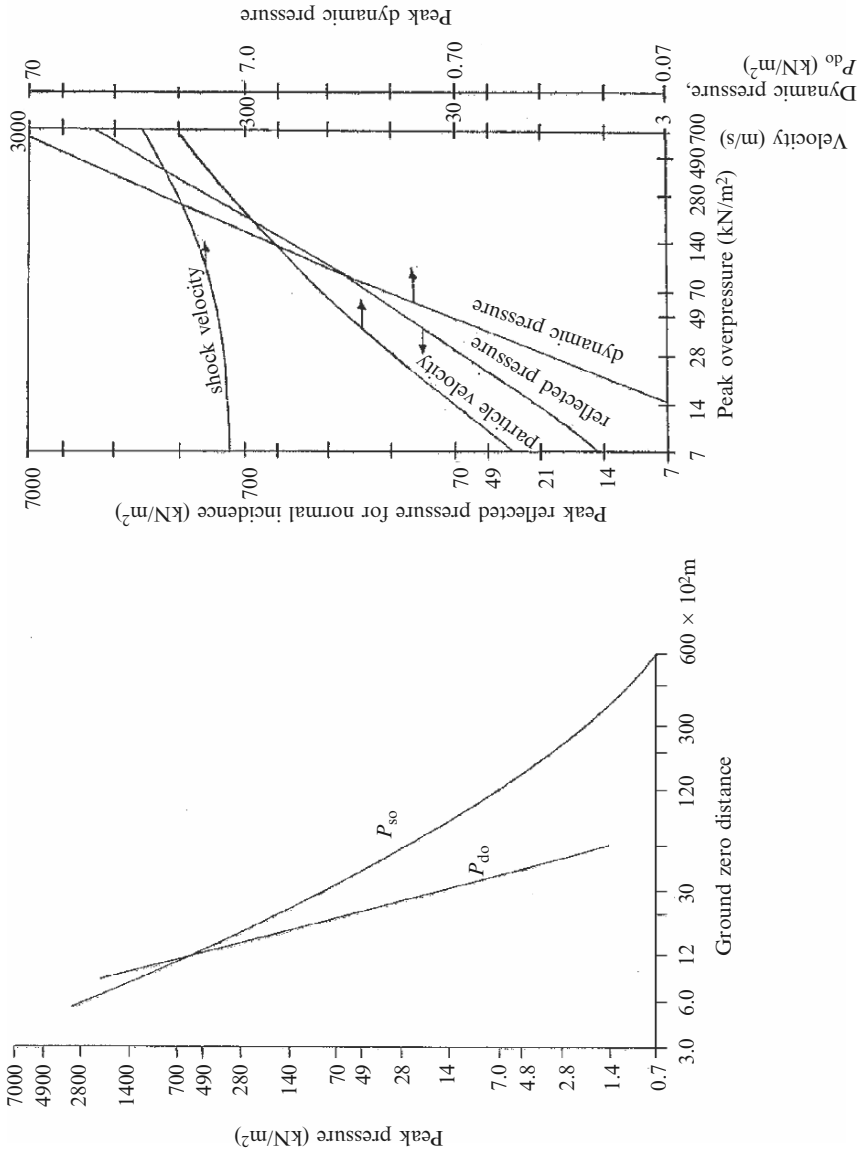
Fig. F.19. Relationships between pressures and time

cracked/crushed
scabbing with cracking
perforated

stress trajectories/cracking

cracking and scabbing
crushing and yielding
of reinforcement
crushing-cum-spalling
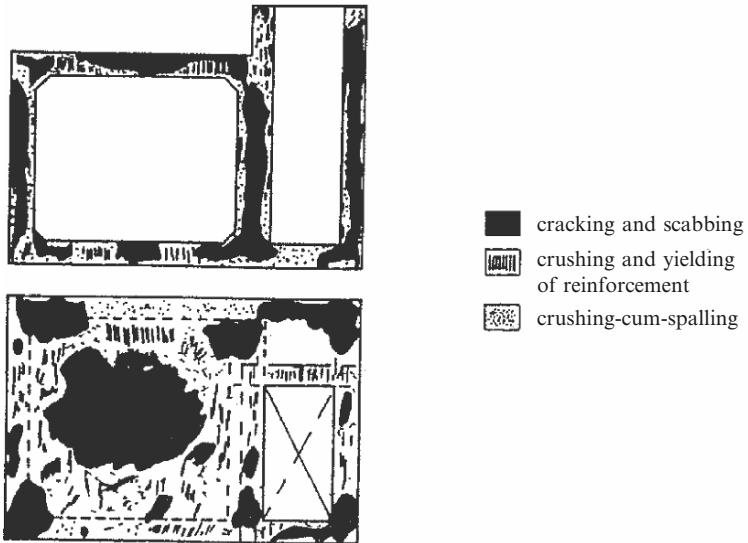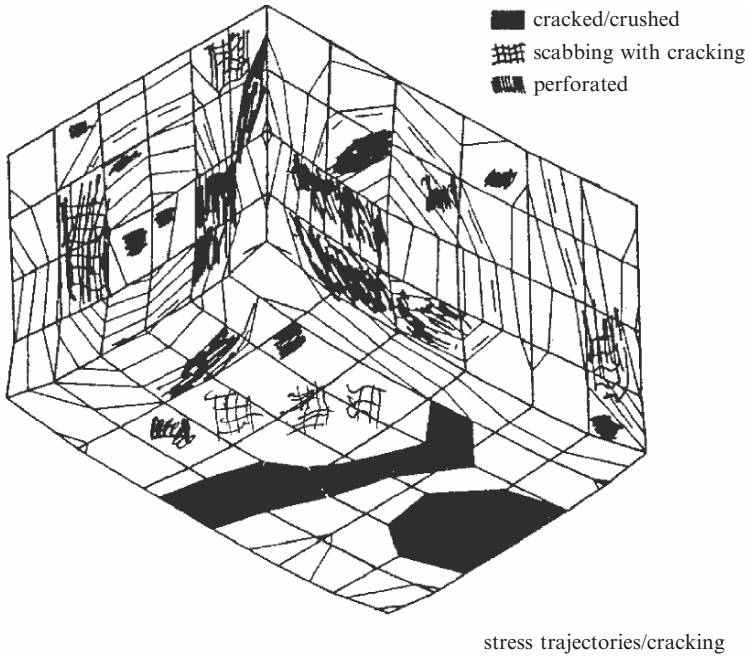
Fig. F.20. Typical results from the finite-element analysis
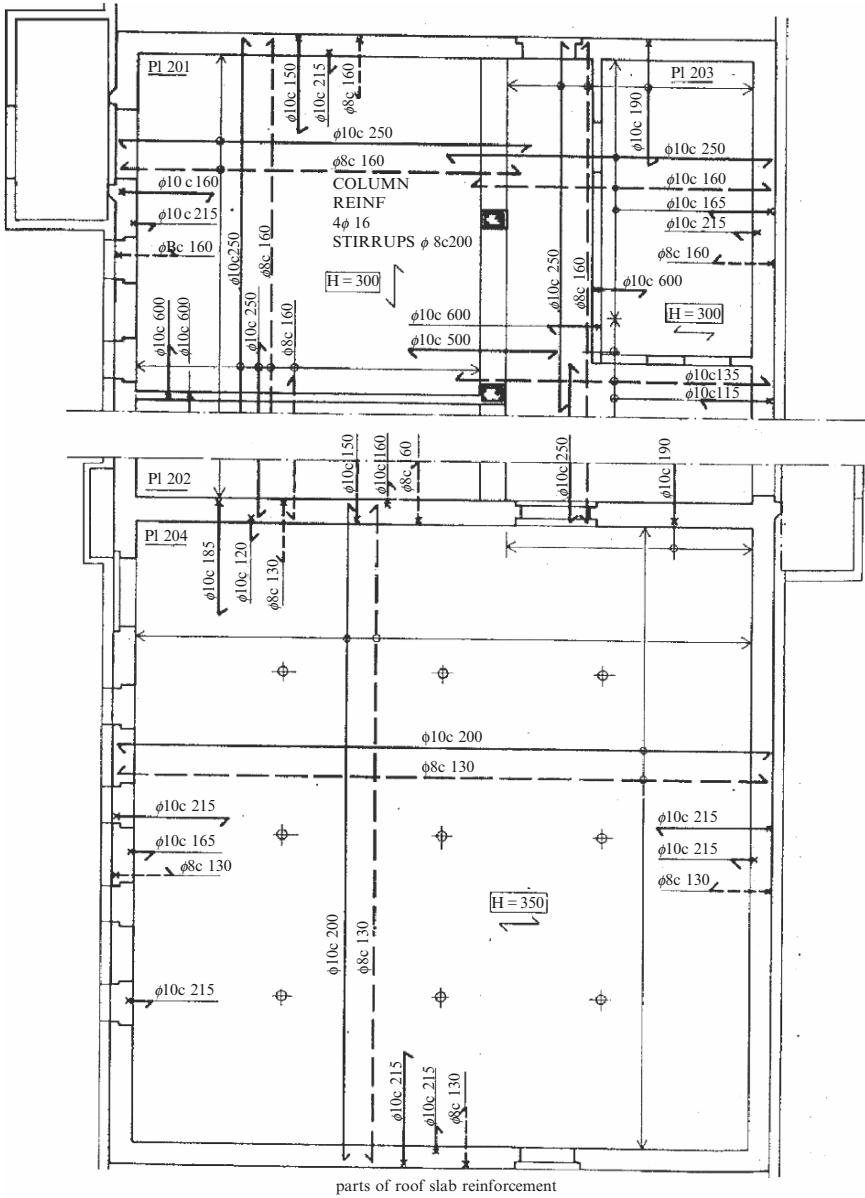
Fig. F.21. Structural details – I Swedish code TB78E

detail sections
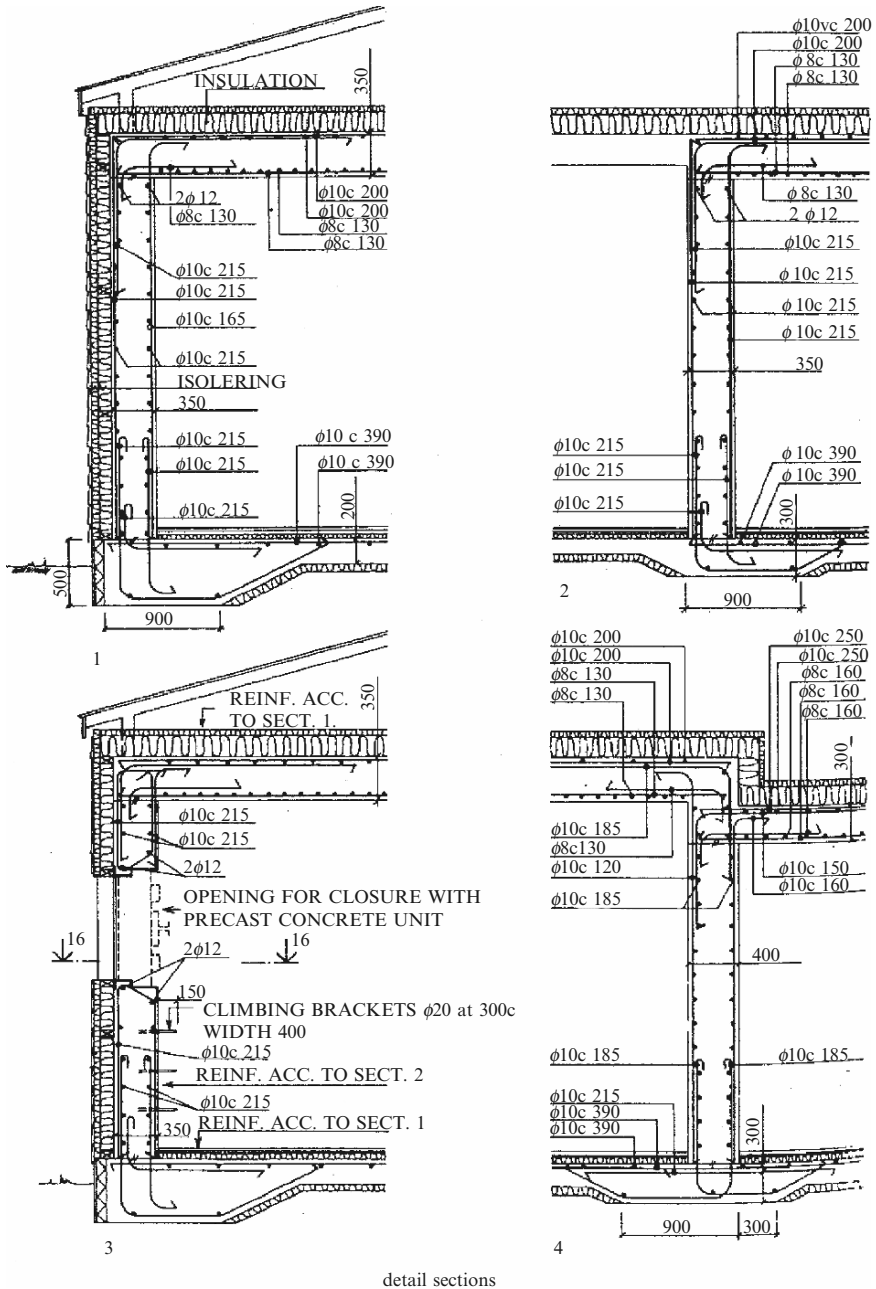
Fig. F.22. Structural details – II Swedish code TB78E

G

Sea Environment: Impact and Explosion

G.1 Multiple Wave Impact on a Beach Front

A multiple wave impact phenomenon is considered on a stone wall with a slope of 60° to the horizontal, as shown in Fig. G.1. The following are the major input parameters included in the overall impact analysis:

Wall dimensions: $10\,\text{m}$ high $\times$ $5\,\text{m}$ wide $\times$ $300\,\text{m}$ long
$E = 2.8 \times 10^7\,\text{kN m}^{-2}$
$\nu = 0.2$
ρ (density of rock) $= 2.5\,\text{Mg m}^{-3}$
Joints: $\varphi = 45°$
$\quad\quad c = \text{variable} \approx 23\,\text{kN m}^{-2}$ and at collapse $21\,\text{kN m}^{-2}$

$\quad\quad \sigma_\text{t}$ (tensile strength of joint) $= \frac{1}{10}c$

Intact rock: $\varphi = 45°$
$\quad\quad c = 5{,}600\,\text{kN m}^{-2}$

Wind associated with waves (100 waves with phase differences assumed):
$\quad$ 120 mph
Total number of 20-noded elements: 700 (size $1\,\text{m} \times 1\,\text{m} \times 1\,\text{m}$)
Total number of nodal points: 12,700
Total number of joint elements: 550 (3 mm thick)

The 20-noded, isoparametric finite-element mesh is given for the wall in Fig. G.2. After 70 continuous wave impacts, the horizontal displacement of the stone wall was as shown in Fig. G.3. At the 100th wave impact the stones were dislocated and some rocks/stones slid on the plane. Tension cracks as depicted in Fig. G.4 were developed. The total duration was 330 s and the time interval, t, was 30 s. The stress trajectory for this wall corresponding to these cracks is plotted in Fig. G.5. The associated flow rule was adopted. A gap element was considered for the slipping joint. All the rock properties given in Chap. 2 were examined. The limestone wall considered in the analysis
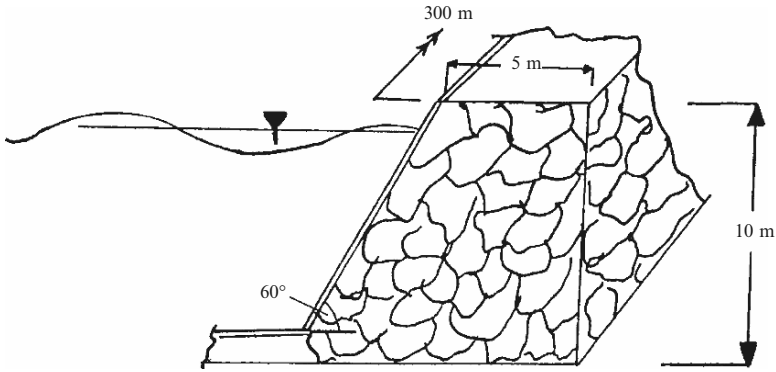
Fig. G.1. Beach front sectional elevation
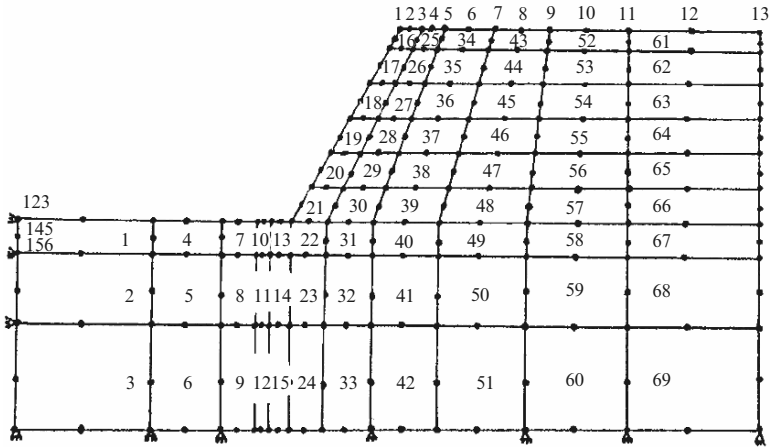
Fig. G.2. Finite-element idealization of the beach wall

was examined for its tri-axial behaviour. Endochronic theory associated with a flow rule was the main objective behind this analysis.

Another beach front was investigated against multiple wave impacts. The beach defences were formed and the armour units of tetropods and doloses were located. A specific placement of units is given in Fig. G.6 and is based on the progressive formation of a stack assembly. Since their positions are of a stochastic nature, the forces acting on the units will show a large variability. A typical formation of a breakwater is shown in Fig. G.7. It is generally accepted that the most extensive breakage occurs in the vicinity of the still water level. Wave parameters, on the other hand, determine the new bearing conditions. The finite-element mesh scheme for a dolos is shown in Fig. G.8. The following parameters are included in the finite-element analysis:
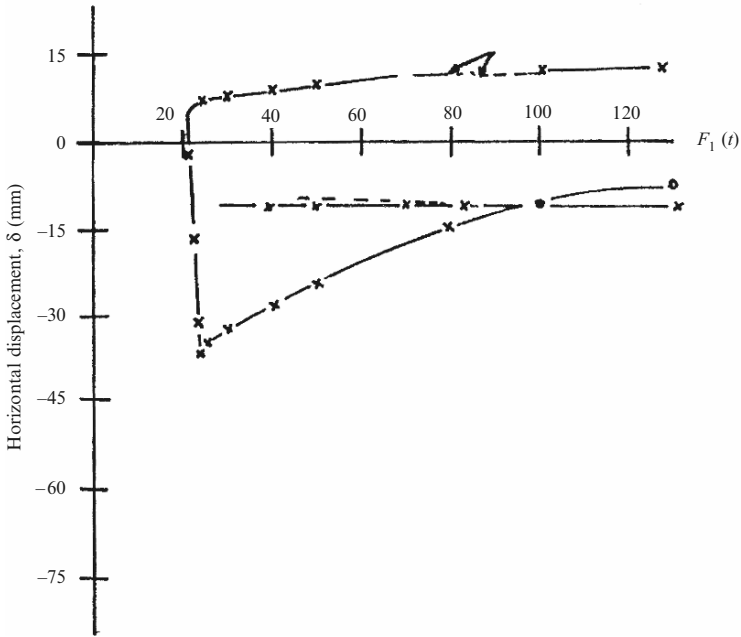
Fig. G.3. Variation of the horizontal displacement with the decreasing value of the cohesion on the joints
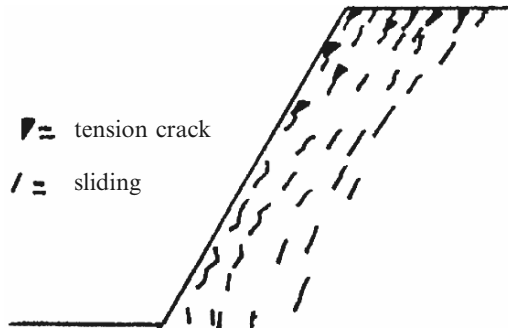
Fig. G.4. Sliding and cracking

Mass: 1,440 kg
Waist ratio: 0.329
Height: 1,660 mm
Density, ρ: 3×10^{-6} kg mm^{-3}
Dynamic modulus, E_{dy}: 4.3×10^4 N mm^{-2}
Tensile strength, σ_{tu}: 3.58 N mm^{-2}
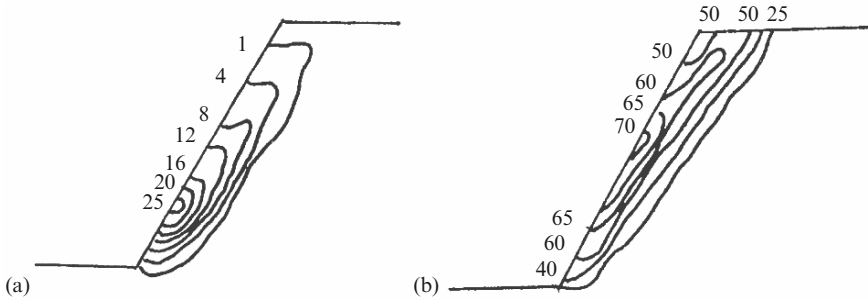
Fig. G.5. Stress contours $(\text{MN}\,\text{m}^{-2})$: (**a**) shear; (**b**) tensile
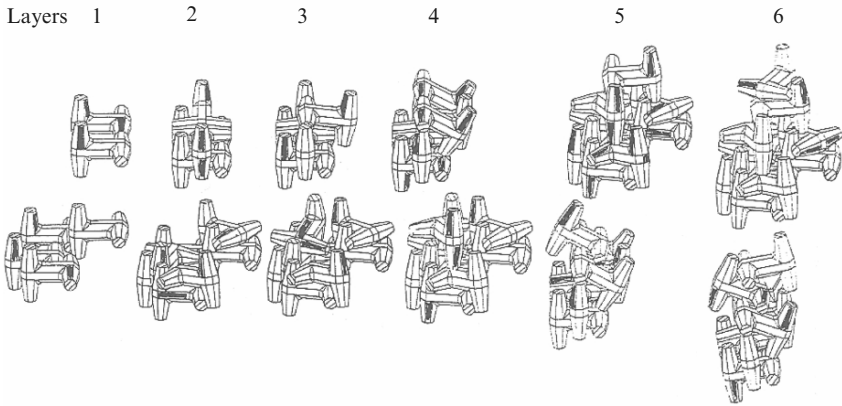
Fig. G.6. Typical placement of the armour units
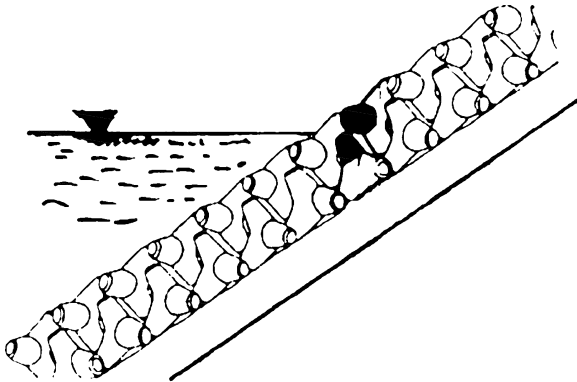
Fig. G.7. Breakwater
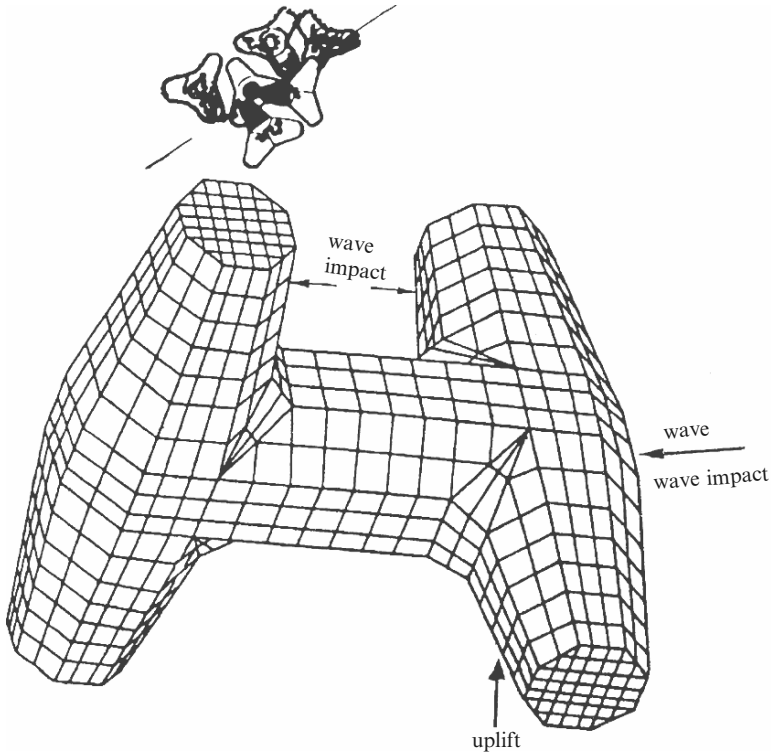
Fig. G.8. Finite-element mesh scheme of the armour unit

Number of solid isoparametric 8-node elements: $440\,\mathrm{dolos}^{-1}$
Number of prism elements: $25\,\mathrm{dolos}^{-1}$
Total number of elements for a 3-layer stack 3 m wide area/unit height:
    $1{,}450\,\mathrm{dolos}^{-1}$
Initial water depth: 2.8 m
Wave height, H: 1.4 m
Wave period, T_p: 2.5 s
Breakwater slope: 1:2.5

The Jonswap normalized spectra are given by

$$h_\mathrm{rms} = \sqrt{\left[(1/m)\sum_{i=1}^{m} h_1^2\right]},$$

where h_1 = surface elevation for a 1-h storm with a critical velocity of $2\,\mathrm{m\ s}^{-1}$.

Analysis

One hundred and fifty multiple wave impacts were considered. The analysis indicated dislocation of the front units and cracking in the middle zones.

joint failure by dislocation
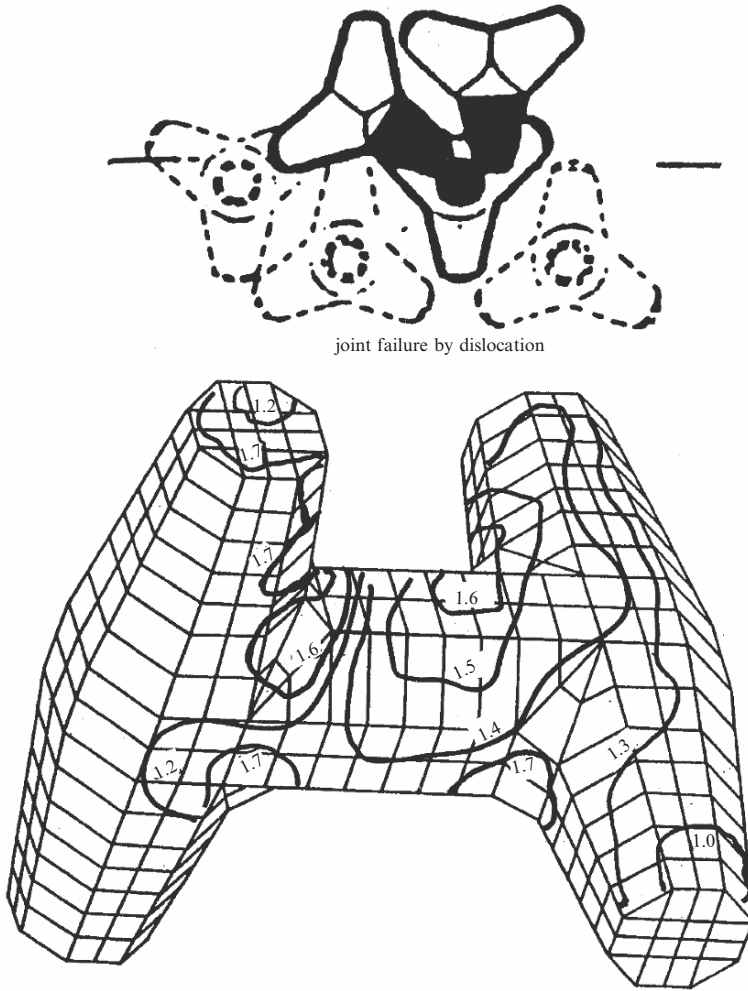
Fig. G.9. Stress-trajectory principle tensile stress (N mm^{-2})

The zone damaged by dislocation is shown in Fig. G.9. The principle stress-trajectory is given on the 150th wave impact. Dashpots were used along with the gap element to evaluate the dislocation. The main units themselves were not damaged because the tensile strains developed were below the allowable values.

G.2 Explosions Around Dams

Underwater explosions and their effects on adjacent structures are of great concern to naval architects and hydraulic/dam engineers. Typical under-ground explosion charts, shown in Figs. G.10 and G.11 give relationships for
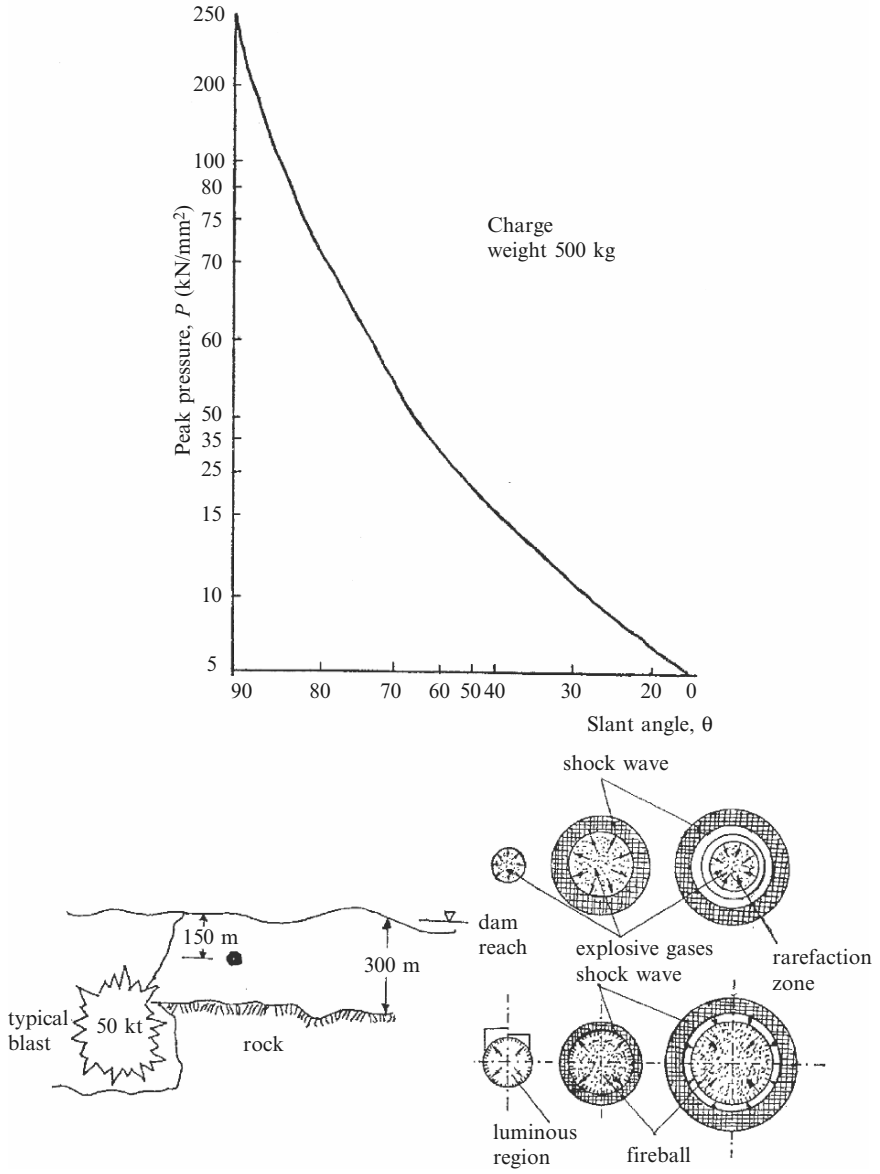
Fig. G.10. Shock wave peak pressure versus slant range

shock wave pressure versus slant range and peak pressure versus time t. A 50 kt burst in deep water was assumed at a distance of 12,000 ft (3,658 m) from a concrete arch dam. The phenomenon is given in Fig. G.10. The peak pressure $p(t)$ at 0.1 s at a slant range of 12,000 ft (3,658 m) was found to be 470 psi. The time constant θ was 0.05 s. For the normalized case $t/\tau = 2$ and thus
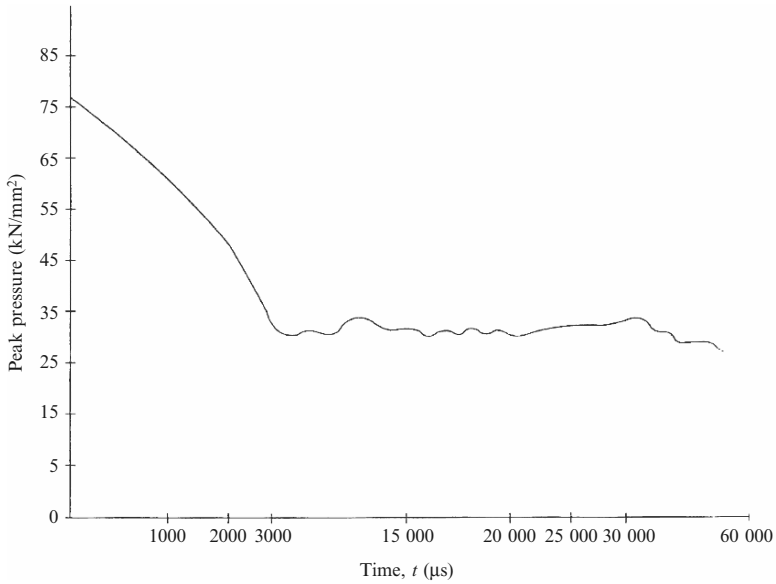
Fig. G.11. Peak pressure versus time
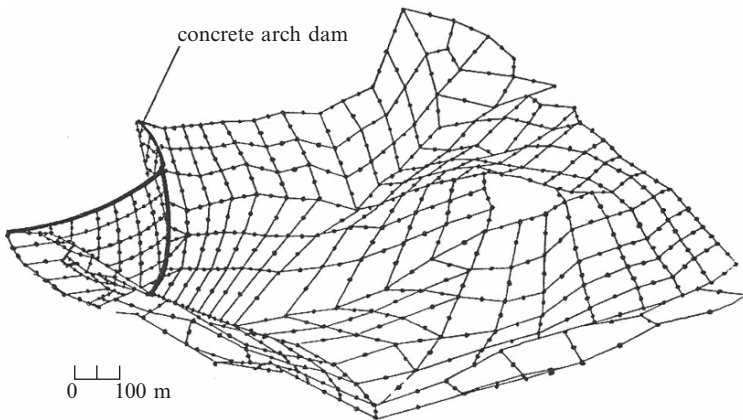
Fig. G.12. Finite-element mesh scheme for an arch dam and the surrounding medium

$p(t)/p$ is about 0.149. Therefore the $p(t)$ value will be $470 \times 0.149 \approx 70\,\text{psi}$. A mixed finite-element analysis was carried out using 20-node isoparametric brick and prism elements, as shown in Fig. G.12; $p(t)$ was applied as a dynamic load on the dam. The stress trajectories are shown in Fig. G.13. The total number of brick and prism elements was 300. The number of gap elements was 98. The frequency and modal amplitude, taking into account the hydrostatic coupling and the total displacement of the dam, were calculated

(a)

(b)   — 15 MN/m²
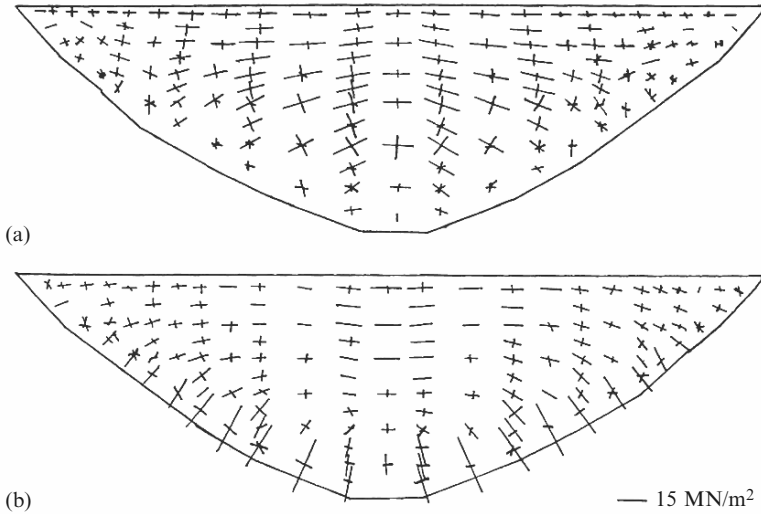
Fig. G.13. Principle stresses for the dam: (**a**) upstream face; (**b**) downstream

by recomposition. The final damaged zones are given in Fig. G.14. The vertical construction joints were cut by the tensile stresses. It is assumed that the self-weight of the dam has not changed. A frontal solution procedure mixed with the Wilson-θ method was adopted for evaluation of the results. The convergence solution was limited to 0.01. Endochronic theory was adopted for the behaviour of concrete under an explosion. Figures G.15 and G.16 illustrate the displacement–time and acceleration–time relationships, respectively.

G.3 Ship-to-Ship and Ship-to-Platform: Impact Analysis

The effects of collisions involving ships and tankers, carrying military equipment and hazardous materials in particular, are of growing public interest. Tables G.1 and G.2 give useful formulae and data for ships/aircraft carriers impacting against each other or against oil and other installations at sea. They include ship impact mechanics in the sea environment. On the basis on these data, dynamic finite-element analysis has been carried out for a cargo ship impacting an aircraft carrier. The numbers of finite elements chosen were:

  4,000 8-noded isoparametric elements for the aircraft carrier
  1,500 8-noded isoparametric elements for the cargo ship
  500 gap elements

As the impact force is quasi-static, the number of load increments was taken as 21. The Newmark β-method of the implicit type was chosen for the solution procedure. The computers used were an IBM 360/75 and an IBM
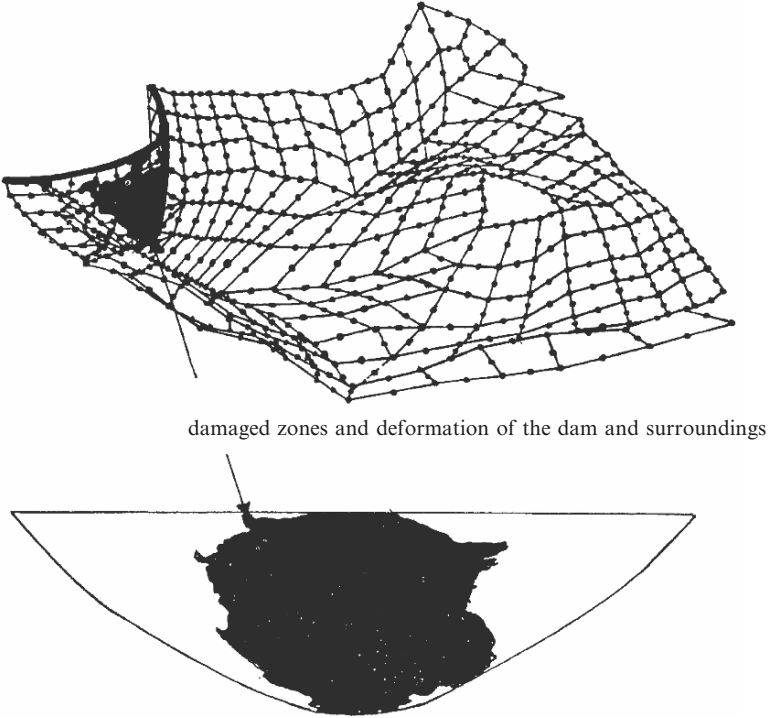
damaged zones and deformation of the dam and surroundings

Fig. G.14. Damaged zones
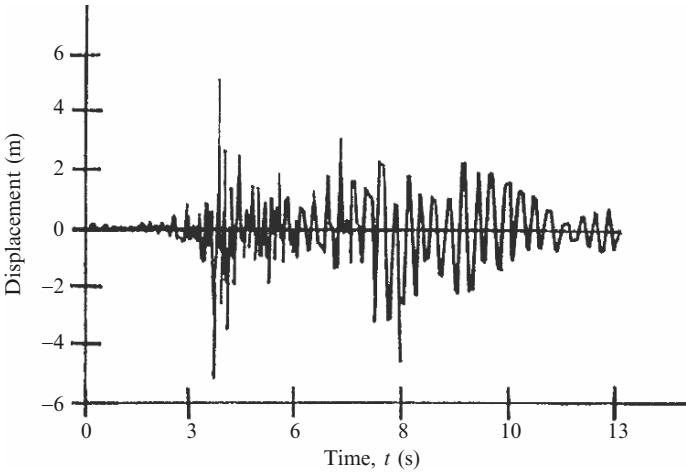
Fig. G.15. Displacement–time relationship
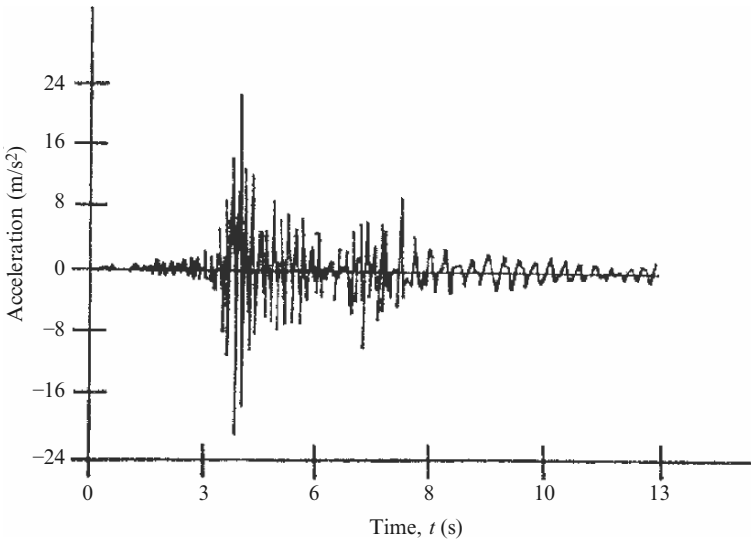
Fig. G.16. Acceleration–time relationship

4381 with front-ended Cray-2. Another sophisticated output was achieved using Cyber 72. The total time taken to analyse this impact problem was 6 h, 31 min and 31 s. Some initial work was done on VAX. Figure G.17 shows the damaged zones of both the ship and the aircraft carrier. The extent of the damaged areas can be scaled out from this figure. The time increment was 0.04 s. The material behaviour was represented by associated Prandl–Reuss, von Mises and octahedral methods. The strain rate concept was included in the overall analysis. The area parts and structural details were provided by the US Navy.

G.4 Jacket Platform: Impact and Explosion

G.4.1 Ship Impact at a Jacket Platform

Collisions between ships/tankers and platforms or other installations in offshore oil and gas fields constitute a type of accident which can have catastrophic effects. There is a growing concern about explosions caused by gas leaks and by terrorist bombs/missiles.

Figure G.18 gives a sketchy view of the type of impact which might occur at any level of the platform. Section G.3 (Tables G.1 and G.2) gives the relevant input, and if one of the objects becomes stationary the entire data can easily be modified to suit the relevant conditions. In this case the platform is assumed to be non-moveable and fixed firmly at the supports. The cargo ship of Sect. G.3

Table G.1. Ship impact mechanics

Ship/platform impact mechanics are based on two criteria, namely the conservation of momentum and the conservation of energy. For a short impact duration:

$$E_s + E_p = \tfrac{1}{2}(m_s + \Delta m_s)v_t^2\{(1 - v_t/v_s)^2/[1 + (m_s + \Delta m_s)/(m_t + \Delta m_t)]\},$$

where m_s = mass of the striking ship (m_s = added mass (40% of vessel displacement for sideways collision and 10% for bow or stern collision)), m_t = mass of the platform including the added mass or any other target, v_s = velocity of the striking ship immediately before collision, v_t = velocity of the semi-submersible platform immediately before collision, E_s = energy absorbed by the striking ship, E_p = energy absorbed by the ship/tanker or target struck.

$$F_I(t) = \text{impact force}$$
$$= E/e_t = \tfrac{1}{2}m_s v_s^2 \left[\frac{(m_s + m_t)}{m_t}/1 + \frac{(m_s + m_t)}{m_t} \right]/e_t,$$

where m_s, v_s = mass and velocity of the striking ship, respectively, m_t = equivalent added mass of the target, e_t = penetration = x_p, E = energy of deformation = $\tfrac{1}{2}m_s v_s^2 \, \varphi_1 \, \varphi_2 \, \varphi_4 + \tfrac{1}{2}m_t v_t^2 \varphi_5 - v_s v_t m_t \varphi_6$.

φ stands for the non-dimensional functions representing the colliding ship/tanker, the impact location, the angle of encounter, the speed of the target and the product of both speeds.

(1) Duration for constant collision force:

$$T = \varphi_1 \varphi_2 (m_t/F_I)v_s$$

(2) Linear collision force, duration:

$$T = (\pi/2)\sqrt{(\delta(2 - \delta)/\gamma\eta^2 \tan\,\theta)}\varphi_1\varphi_2 m_t$$

The acceleration at the time of collision is given by

$$\ddot{\delta}_{\max(x)} = F_I(t)_x/m_t; \ddot{\delta}_{(y)} = [F_I(t)_y/(m_t + m_s)] + [\delta x F_I(t)_x e/I'],$$

where δx = distance between the centre of gravity of the target and the point at which acceleration is computed, $F_I(t)_x, F_I(t)_y$ = maximum components of the collision force in the transverse and longitudinal directions, I' = mass moment of inertia of the target.

Storm tide
A maximum tide of 2.15 m is assumed and finally combined with a storm surge of 0.6 m to produce a total storm tide rise of 2.75 m.

Operating tide
A maximum tide of 2.15 m is combined with a storm surge of 0.12 m to produce a total operating tide rise of 2.27 m.

(continued)

Table G.1. (continued)

Storm current

The maximum storm current velocity varies with water depth according to the following profile:

At the water surface: $1.38 \, \text{m s}^{-1}$
Above the bottom: $0.54 \, \text{m s}^{-1}$ at $15 \, \text{m}$
At the bottom: $0.24 \, \text{m s}^{-1}$

Operating current

The maximum current velocity under the operating conditions varies with the water depth according to the following profile:

At the water surface: $1.17 \, \text{m s}^{-1}$
Above the bottom: $0.45 \, \text{m s}^{-1}$
At the bottom: $0.24 \, \text{m s}^{-1}$

Temperatures

The minimum water temperature is assumed to be $+7.0°\text{C}$. The crude oil temperature in storage is taken as $40°\text{C}$.

Wind velocities

Storm wind: the maximum wind velocity of $125 \, \text{mph}$, sustained for $1 \, \text{min}$, is used in conjunction with the storm wave.

Operating wind: a wind velocity of $60 \, \text{mph}$ is used in conjunction with the operating wave. Instantaneous gust: a maximum instantaneous gust velocity of $160 \, \text{mph}$ is used throughout.

Ship masses

Aircraft carrier 60,000 ton; impacting ship 5,000 ton.

---

is assumed to be involved in the collision. The platform, chosen for this analysis is the famous Heerema platform, shown in Fig. G.19. In addition to the data in Sect. G.3, the following are also required:

Operational impact

Maximum impact force, $F_1(t)$: $2.8 \, \text{MN}$
Total kinetic energy, KE: $0.5 \, \text{MJ}$
Velocity of the ship, v_s: $0.5 \, \text{m s}^{-1}$
Average stiffness, K: $10.0 \, \text{MN m}^{-1}$
Damping ratio: $\gamma = 0.065$

Accidental impact

Maximum impact force, $F_1(t)$: $10.3 \, \text{MN}$
Total kinetic energy, KE: $7.8 \, \text{MJ}$
Velocity, v_s: $2.0 \, \text{m s}^{-1}$

Table G.2. Additional data on ship impact mechanics. Angle of encounter versus obliquity and influence mass and eccentricity
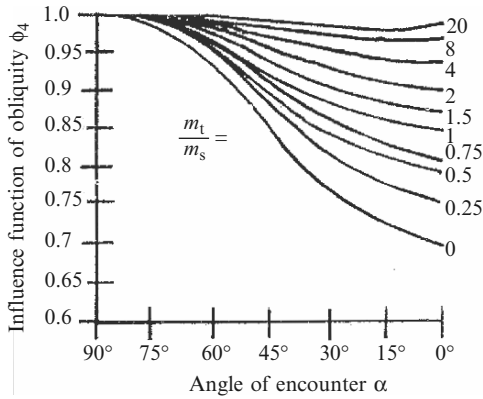
14 megajoules (MJ) for a side collision equal to 40% of added mass.
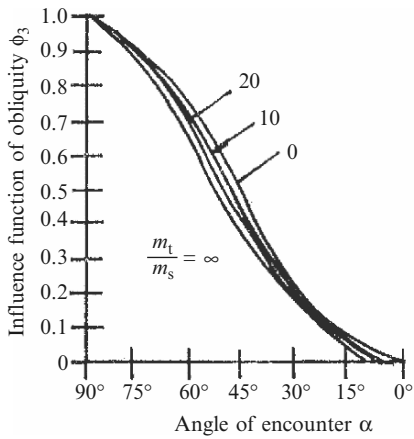
11 megajoules (MJ) for a bow or stern collision equal to 10% of added mass.
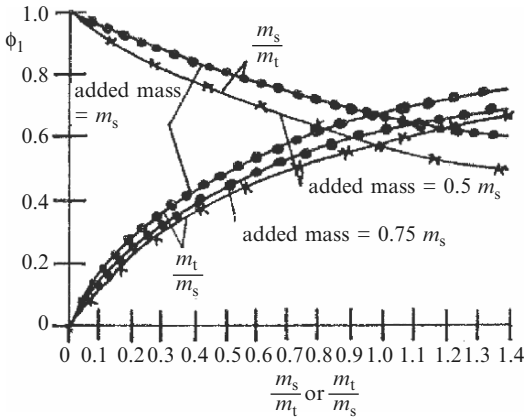
Influence of mass ratio φ_1.

Table G.2. (continued)

Influence function of eccentricity φ_2.
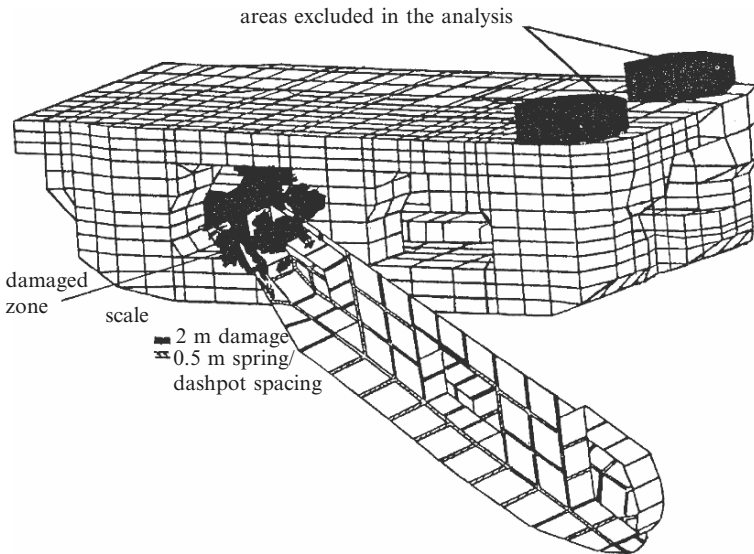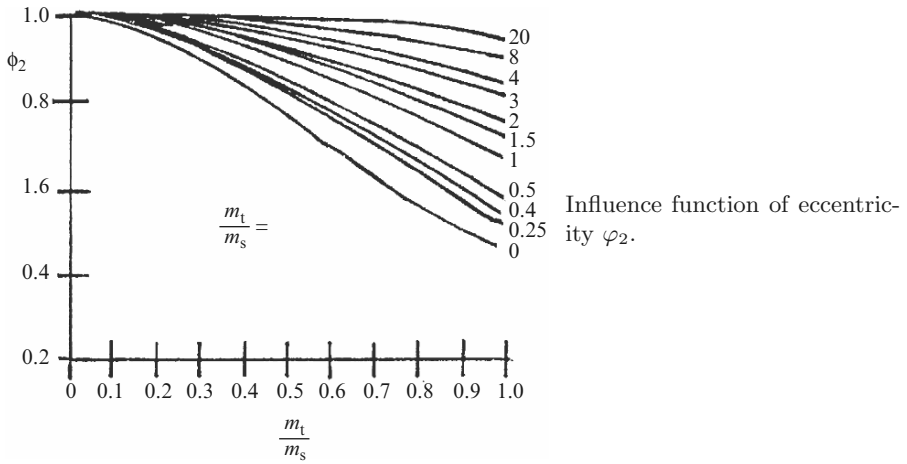
Fig. G.17. Ship/carrier impact

Material and other parameters
   Brace diameter, d_0: 2,000 mm
   Thickness, t: 80 mm
   Brace span, L: 31.6 m
   Uni-axial yield stress, f_{yi}: 360 N mm^{-2}
   Indentation depth/radius, Δ/r: 0.50
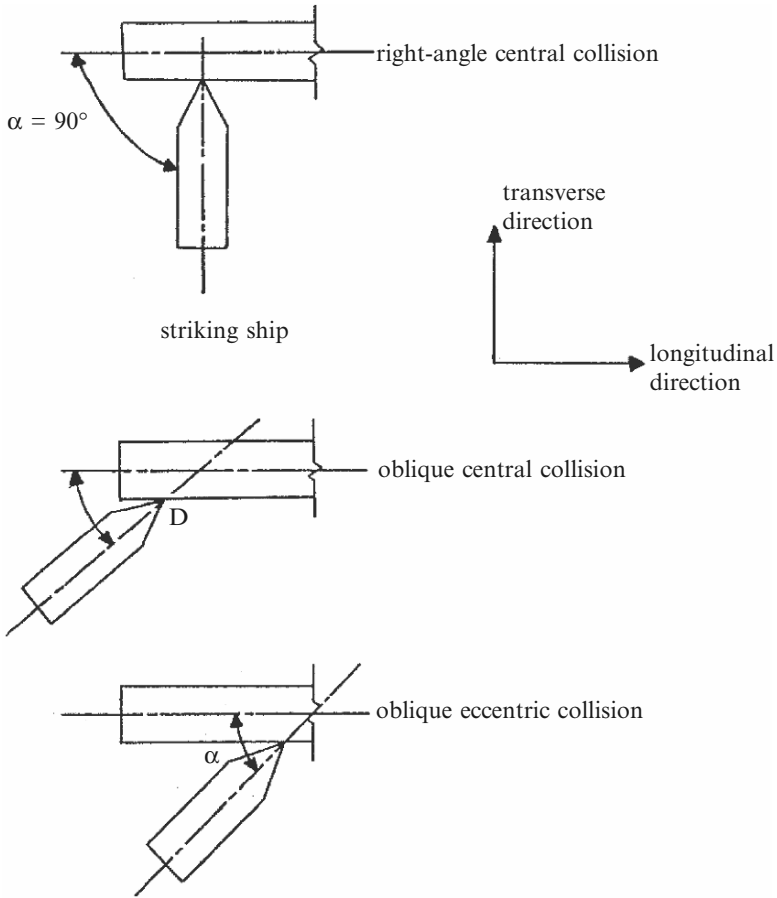
Fig. G.18. Typical types of impact at a jacket platform

T-Joint in out-of-plane bending is given by

$$K_{\mathrm{r}} = 0.0016 E R^3 (215 - 135\beta)((1/\gamma_0) - 0.02)^{(2.45 - 1.6\beta)},$$

where E = Young's modulus = $200\,\mathrm{GN\,m^{-2}}$, R = chord radius, β = brace radius/chord radius ≤ 0.6, γ_0 = chord radius/chord thickness, K_{r} = rotational spring constant.

   The deformed region $> 3.4d$.

Finite elements: 100,000 3-noded line elements of the platform match with the 20-noded elements of the ship for this problem.

   A typical damaged finite-element mesh close to the ship impact is shown in Fig. G.20. Figures G.21 and G.22 show the relationships for impact versus time and deflection versus time, respectively. Figures G.23 and G.24 give the impact load versus dent per diameter and impact versus deflection per length, respectively.
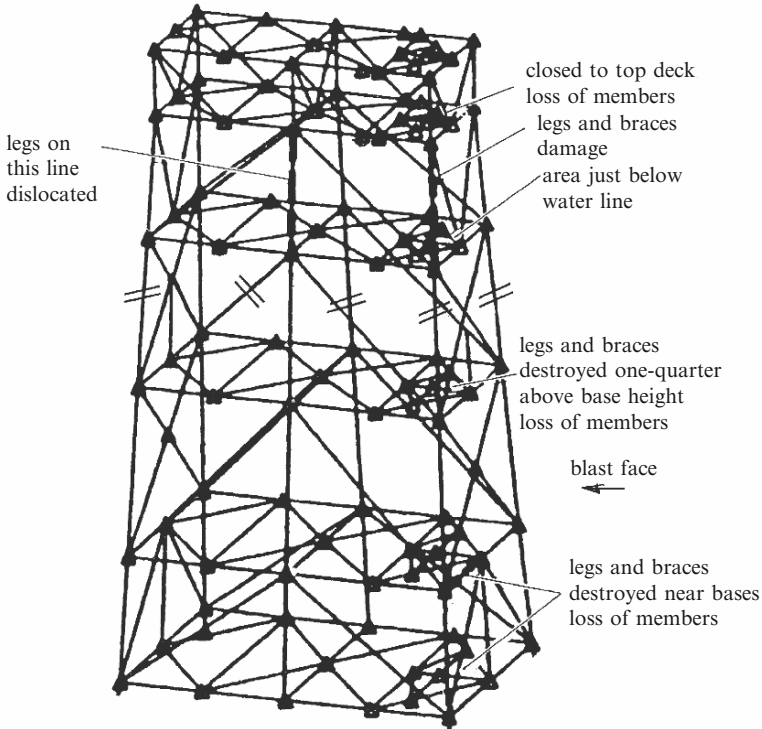
Fig. G.19. A segment of the jacket platform with damage

A 50 kg bomb was placed at a depth of 100 m at 30 m from the jacket platform. Figure G.25 gives the layout of the scheme. Figures G.26–G.28 give the pressure pulse, displacement–time and velocity–time relationships, respectively, for the platform. Figure G.29 shows the finite-element scheme of a typical joint. The damage caused by the explosion is demonstrated in Fig. G.30.

G.5 Impact of Dropped Objects on Platforms

The simultaneous drilling and production operation increases the risk of damage to completed well heads from accidentally dropped drilling equipment. In general, for the sake of protecting the platform against damage, heavy wooden mats encased in steel plate are laid out. The critical objects generally fall vertically. Heavy objects and equipment with large contact areas during impact represent severe cases for stringers and girders. For this reason, restrictions may be imposed on crane operators with regard to lifting heights and frequencies. It is essential, therefore, to evaluate initially the most critical impacted zones. Figure G.31 shows a covered impacted area determined by the extent of the crane radius. Figures G.32 and G.33 give the structural layouts of the
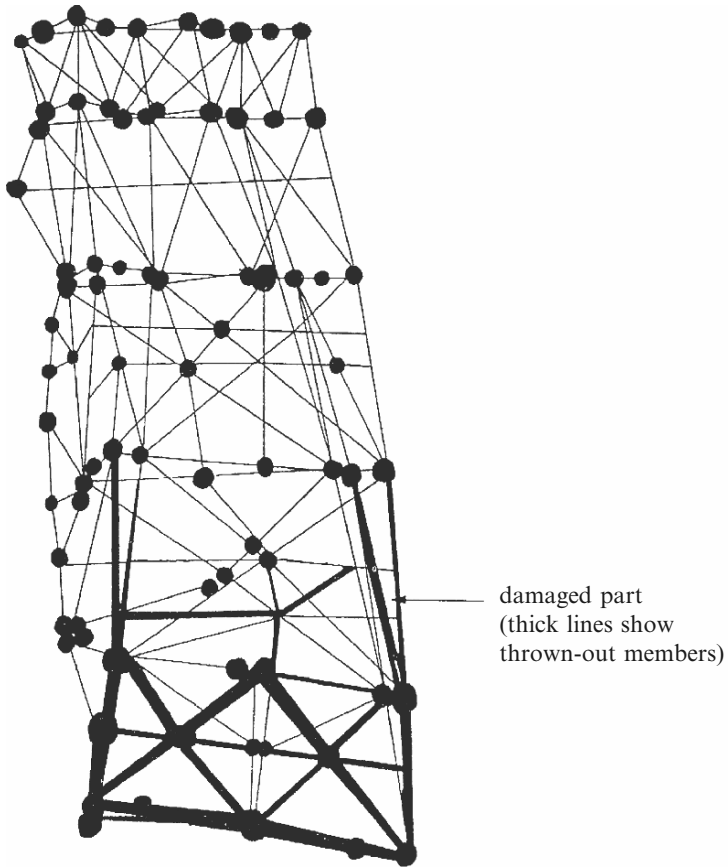
Fig. G.20. Damaged part close to the ship impact zones

zones under investigation. The following data are additional input for the finite-element analysis.

Main platform dimensions: see Figs. G.32 and G.33 for the deck.
Drop objects: see Fig. G.34
Deck plate thickness: <50 mm.

Loading and areas

$$
\left.
\begin{array}{l}
\text{80 kN dropped 2 m on to a 1 m}^2 \text{ area} \\
\text{88 kN dropped 1 m on to a 0.02 m}^2 \text{ area} \\
\text{50 kN dropped 3 m on to a 0.02 m}^2 \text{ area}
\end{array}
\right\}
\begin{array}{l}
\text{skid base lay down areas drill floor} \\
\text{pipe rack and conductor hatches} \\
\text{cantilever walkway}
\end{array}
$$

Material stresses

Minimum yield strength, f_y: 355 N mm^{-2}
Minimum ultimate strength, f_u: 510–610 N mm^{-2}
Young's modulus, E_s: 200 GN m^{-2}
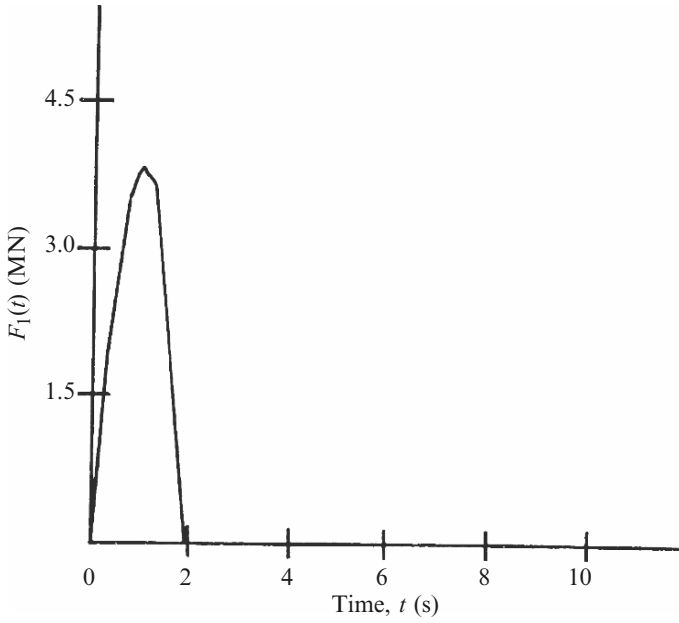
Fig. G.21. Force–time function
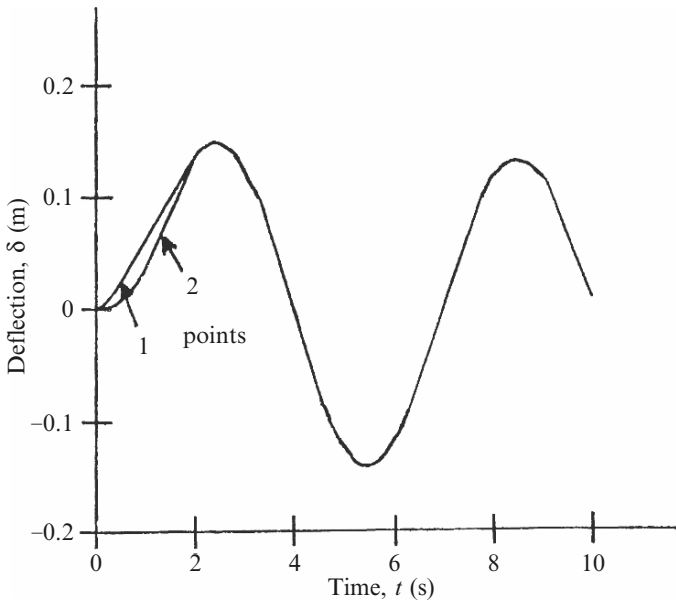
Fig. G.22. Deflection–time relationship
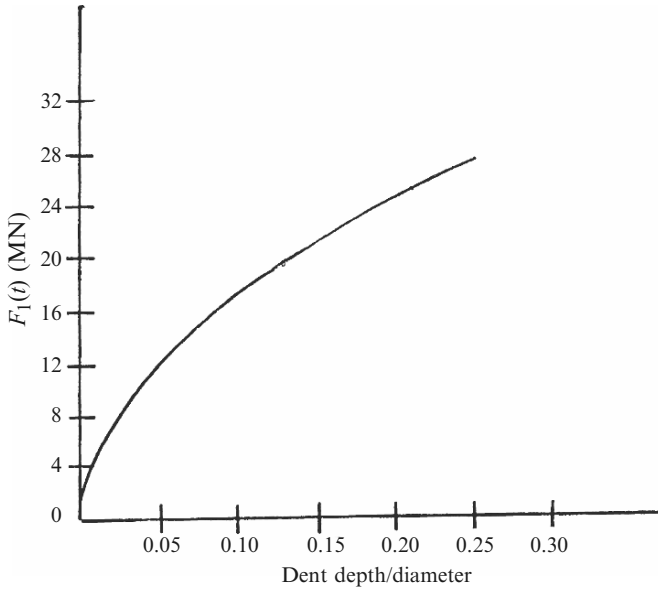
Fig. G.23. Impact versus the ratio of dent depth/diameter
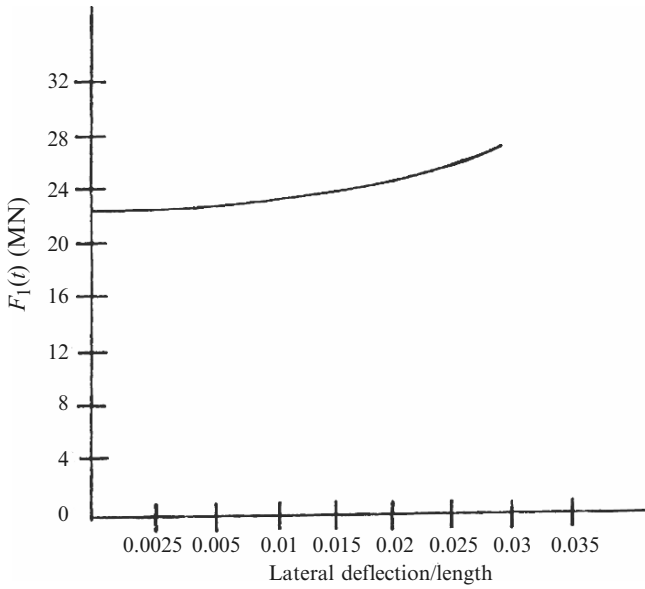
Fig. G.24. Impact versus deflection per length
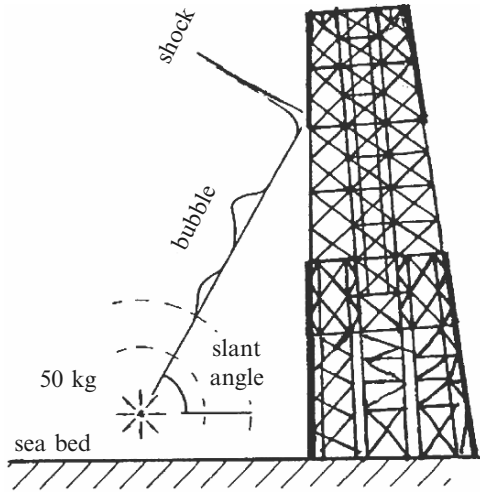
Fig. G.25. Layout of the scheme for blast load against the jack-up platform
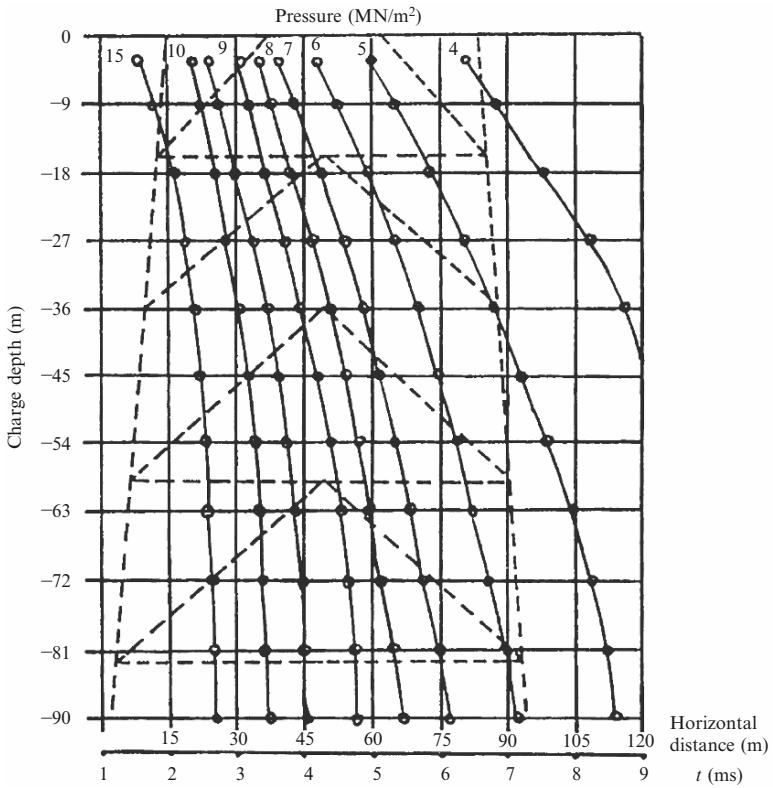
Fig. G.26. Pressure pulse
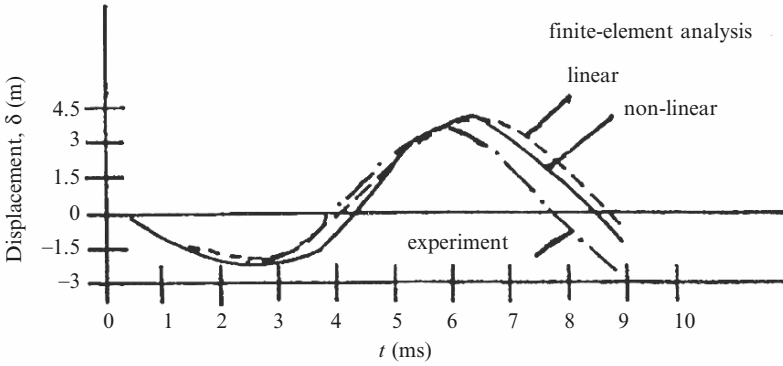
Fig. G.27. Displacement–time relationship
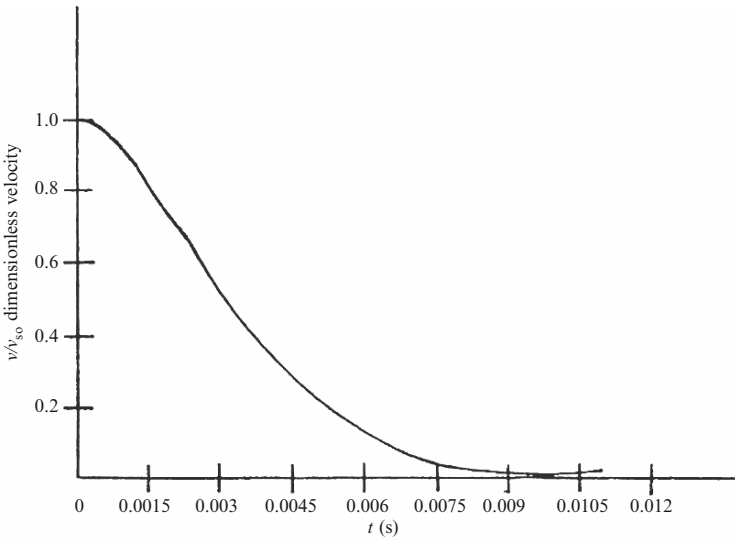
Fig. G.28. Velocity–time relationship

Finite elements
20-node isoparametric: 1,578
Gap elements: 700
3-node isoparametric line elements:
stringers: 410
girders: 200

G.5.1 Finite-Element Analysis

Dynamic finite-element analysis was carried out on the top deck of the plat-
form. The time interval was 0.04 s. The finite-element mesh scheme is based
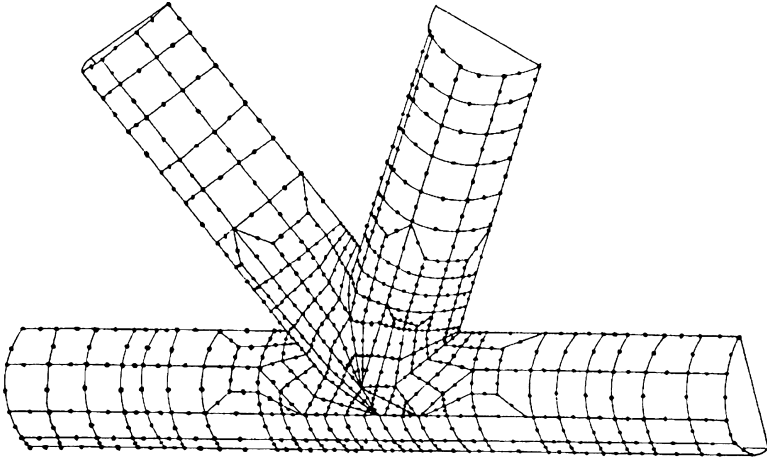
Fig. G.29. The finite-element scheme for a joint subject to explosion pressure
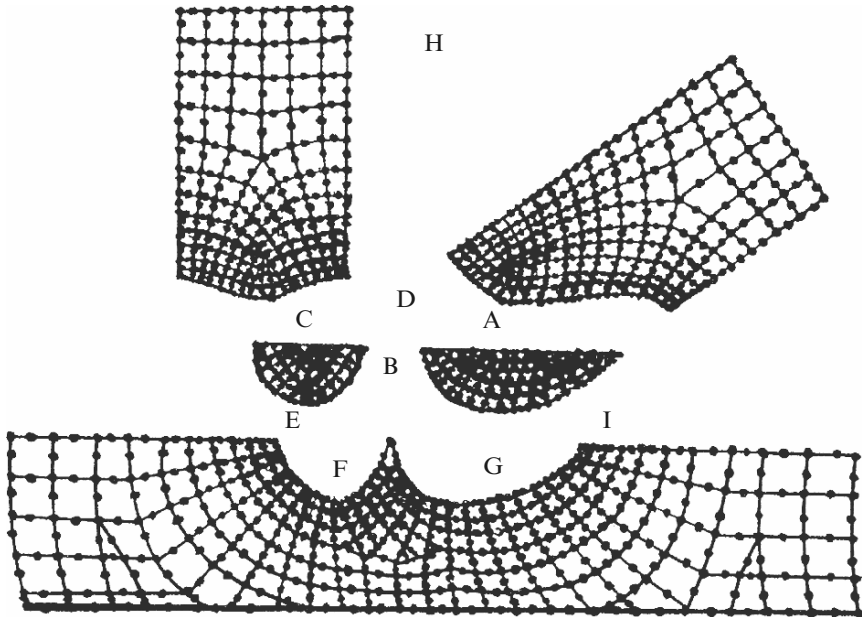
Fig. G.30. Damaged joint and maximum ejected distances (A $= 5 \times 10^6$ mm; B $= 4 \times 10^6$ mm; C $= 9 \times 10^6$ mm; D $= 8 \times 10^6$ mm; E $= 6 \times 10^6$ mm; F $= 12 \times 10^6$ mm; G $= 20 \times 10^6$ mm; H $= 50 \times 10^6$ mm; I $= 6 \times 10^6$ mm)

on the actual gridwork indicated in Fig. G.35. The total time for the execution of the job was 3 h, 15 m and 31 s on an IBM 4,381 computer using the ISOPAR program.
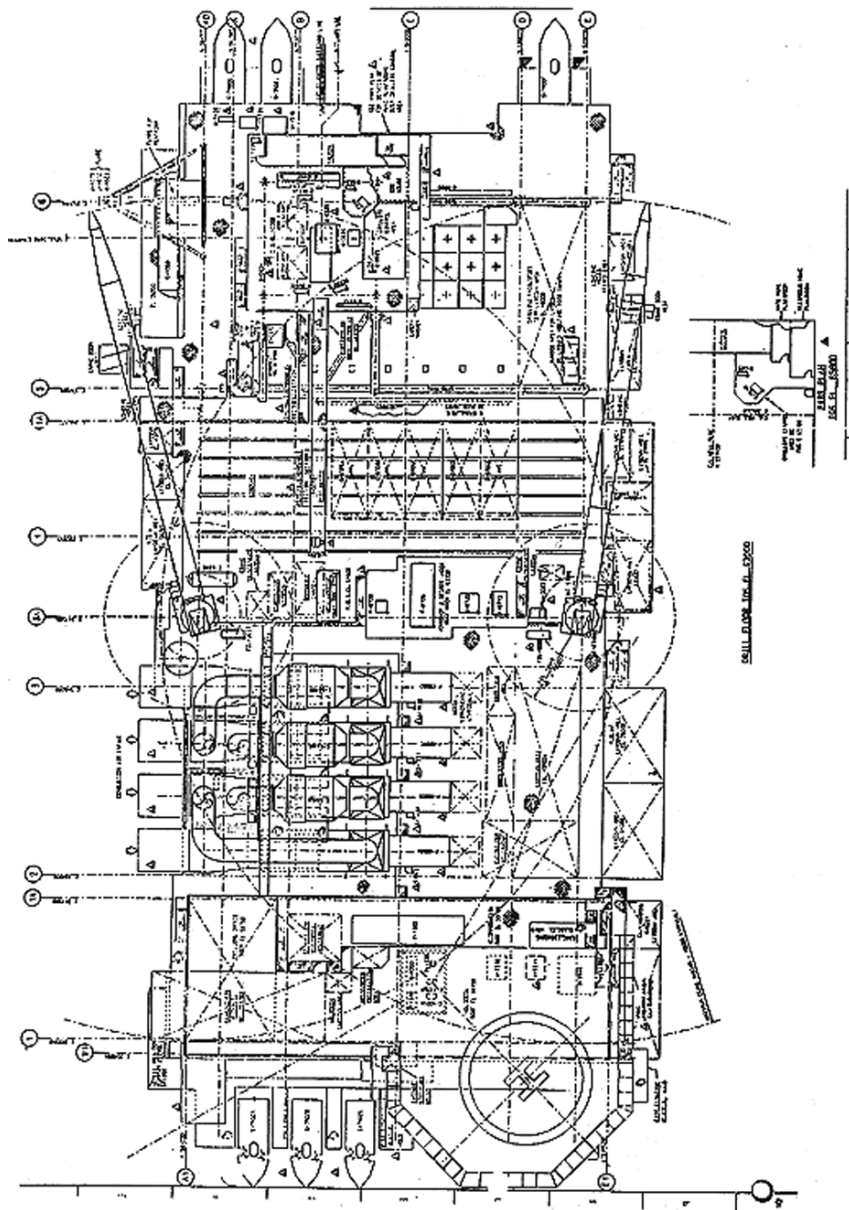
Fig. G.31. A scheme for the dropped object protection zone (courtesy of Brown and Root, Collierswood, London, UK)
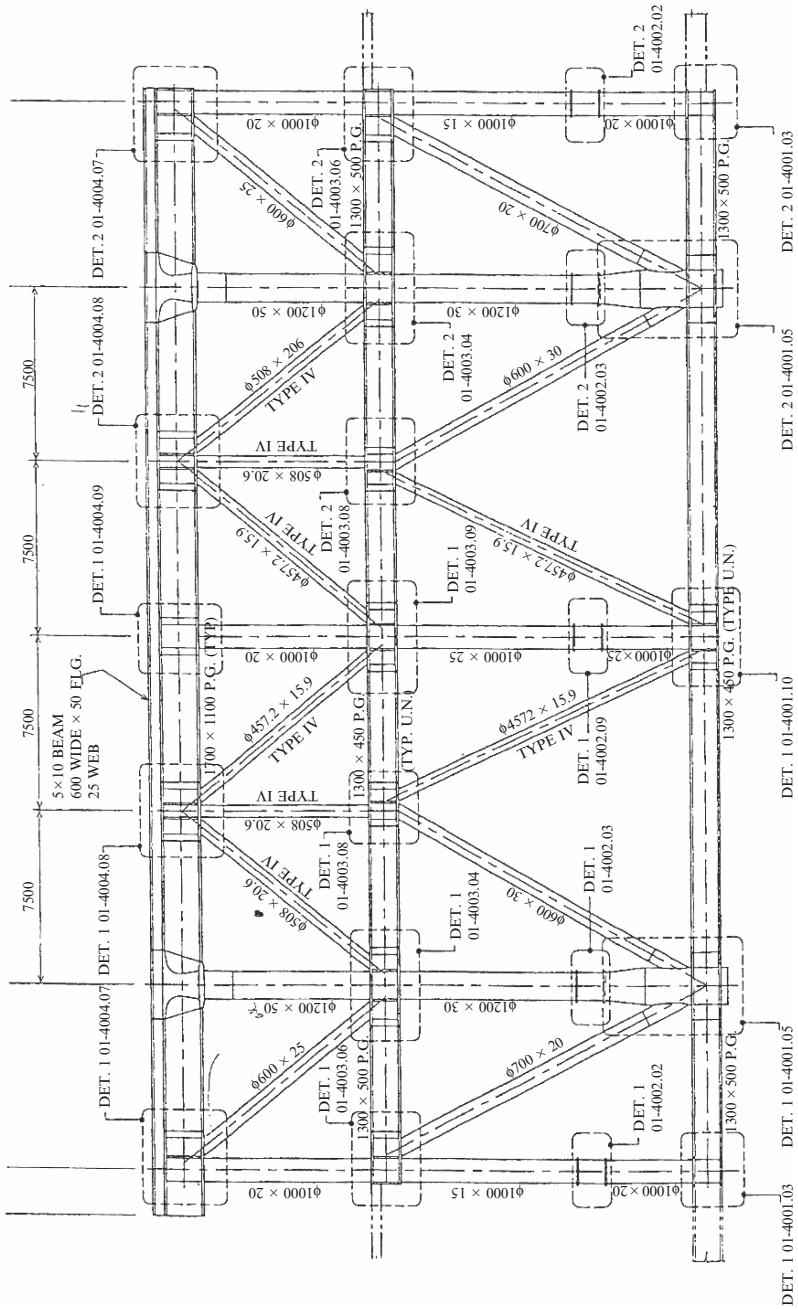
Fig. G.32. Platform truss elevation (courtesy of AGIP UK)
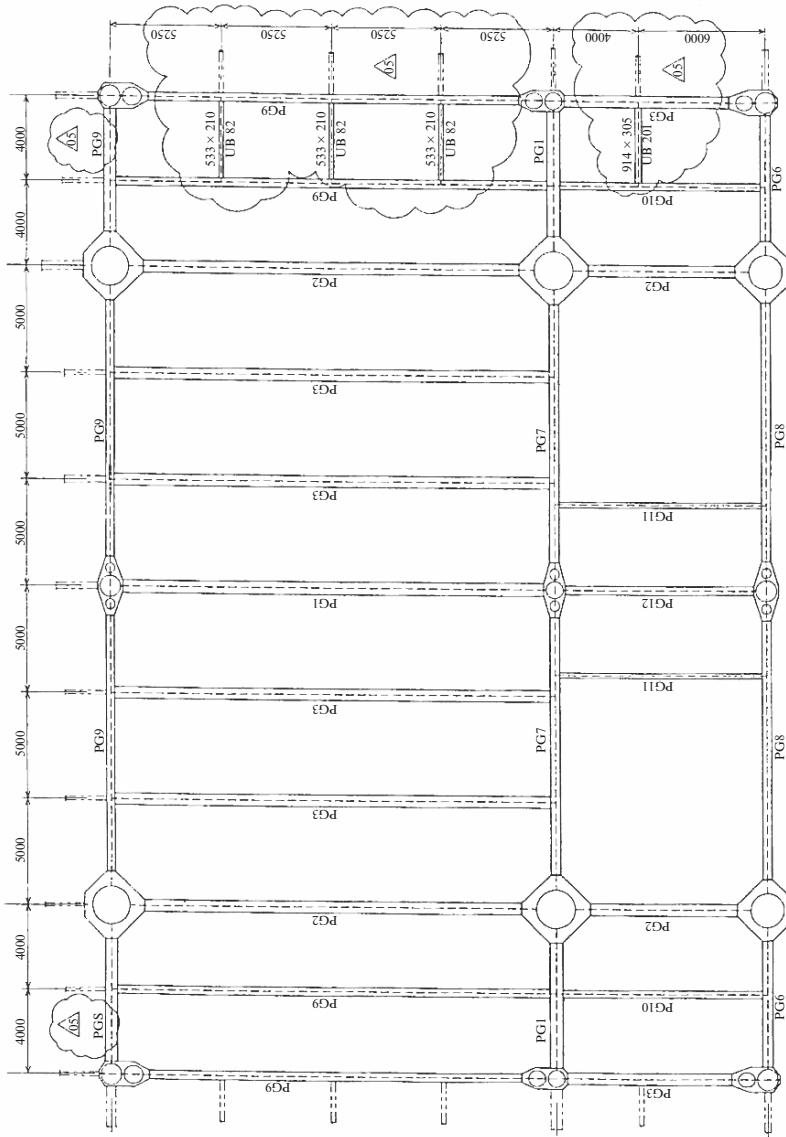
Fig. G.33. Deck framing plan (courtesy of AGIP UK)

75 mm bore

9.5 m

126 mm

drill collar

123 mm

typical slip elevator

Weight data

Diameter (in)	Weight (lb)
$6\frac{1}{2}$	2842
8	4643
$9\frac{1}{2}$	6725
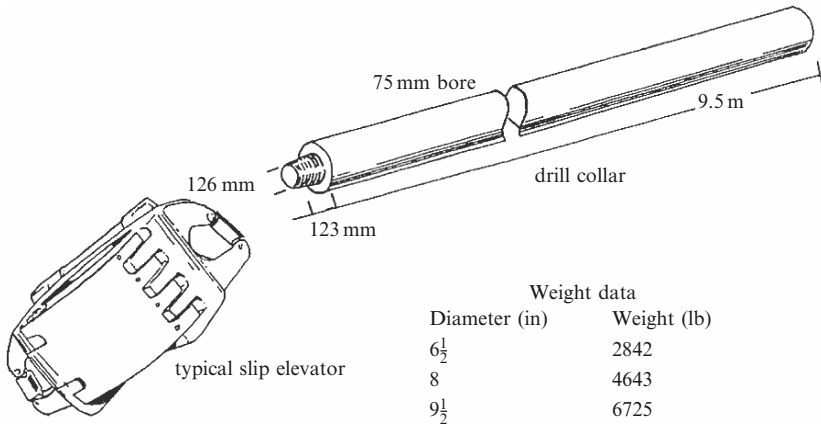
Fig. G.34. A typical drill collar as a dropped object

STIFFENED PLATE

TIMBER ON UNSTIFFENED PLATE

STIFFENED PLATE

STIFFENED REMOVABLE PANELS

ROTARY TABLE

DRAW WORKS

STIFFENED PLATE

TIMBER ON UNSTIFFENED PLATE
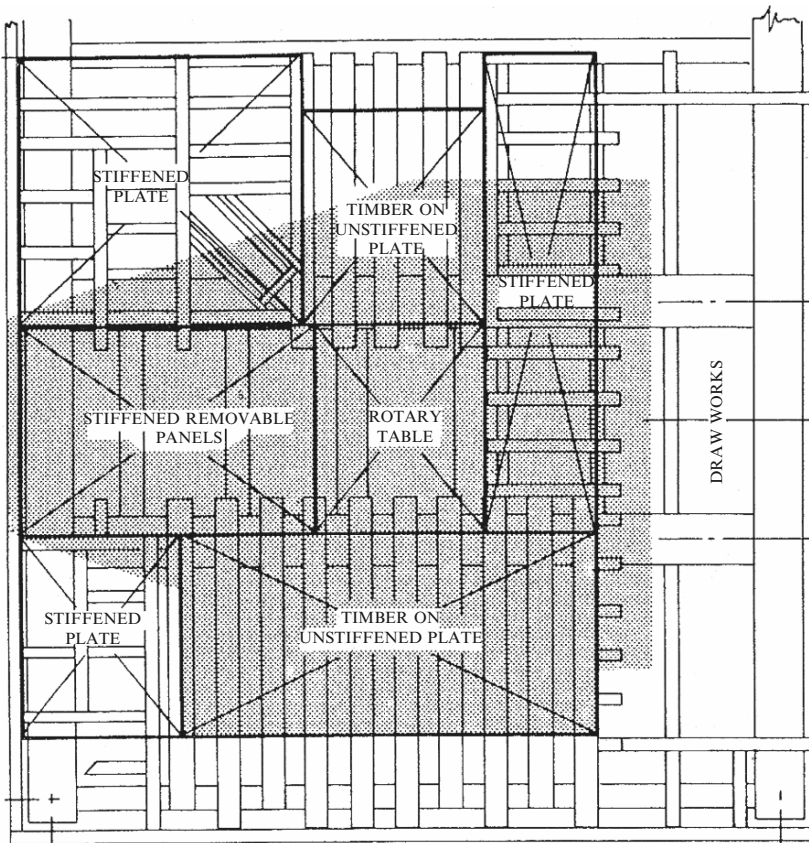
Fig. G.35. A grid for the final preparation of the finite-element mesh scheme
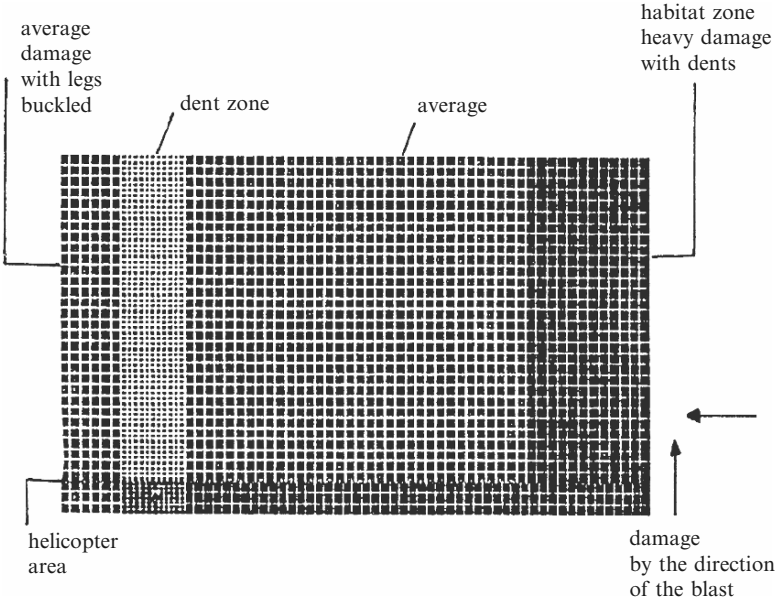
Fig. G.36. Damage zones with dents (plotted on the finite-element mesh scheme)
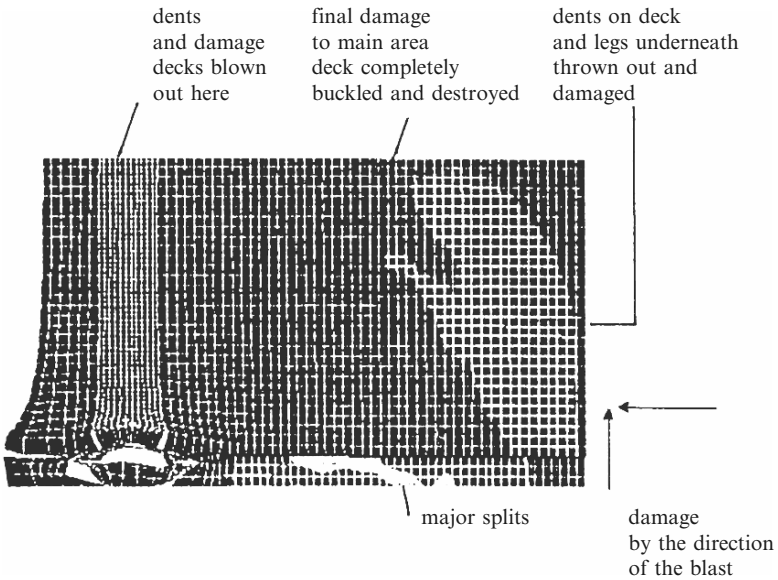
Fig. G.37. Damage location on deck under direct impact – final post-mortem

G.5.2 Results

The results are summarized as follows:

> Size of ruptured area: $175 \times 150\,\text{mm}$
> Maximum displacement: $310\,\text{mm}$ edge; $455\,\text{mm}$ edge; $726\,\text{mm}$ central; $435\,\text{mm}$ corner
> Maximum indentations: drill floor: $75\,\text{mm}$; pipe bridge: $101\,\text{mm}$; lay-down area: $98\,\text{mm}$; pipe rack: $125\,\text{mm}$

Figure G.36 illustrates the damaged zones with dents. Figure G.37 gives the damage location.

H

Soil/Rock Surface and Buried Structures

H.1 General Introduction

A great deal of information is given in this text on impact and explosion in the field of ground engineering. In this section a few examples are given on impact/explosion occurring at ground level or below, with special emphasis on the prediction of the penetration of missiles/projectiles/bombs in soil/rock media. Table H.1 lists properties and dimensions of some well known combinations of soils forming particular strata.

H.2 Soil Strata Subject to Missile Impact and Penetration

The most important objective is to model in detail both the target soil and the penetrating missile. The modelling of the soil as a target material presents a problem which stems from the fact that in situ soil/rock is a non-linear anistropic material and is further complicated by variations in the existing layered strata. A 20-node, three-dimensional, isoparametric, dynamic finite-element method was adopted for the target material, as shown in Fig. H.1. Each layer was modelled with respective material properties. Two types of expansion cavities, namely cylindrical and spherical, were modelled. Using the cylindrically-expanding cavity, the target material was assumed to move radially onwards as the missile penetrated. The radial pressure in the cylindrical cavity was then assumed to be acting normally on the penetrator surface. Where there was an angle of attack, apart from axial velocities, an angular velocity was introduced to the penetrator as and when the angular orientation of the penetrator occurs.

Where a spherical cavity is assumed, the target material was then assumed to move in a direction normal to the surface of the missile/bomb penetrator. The ISOPAR program uses both methods simultaneously in the analysis of the

Table H.1. Selected strata as targets

Target type	Soil description	Depth (m)	Soil constant
I	(a) Clayey silt, silty clay, hard and dry	0–8	5.18
	(b) Sandy silty, dense dry and well cemented	8–15	2.48
	(c) Clay, silty and soft	0–1.6	40.00
	(d) Sand, silty, clayey dense dry to damp	15–24	5.10
II	Clay, soft, wet, varied, medium to high plasticity	0–4	48.00
III	Ice glacier	0–20	4.10
IV	Silt, clayey permafrost	0–10	3.55
V	Sand loose to medium, very moist	0–22	6.70
VI	Stiff clay	0–5	9.75
VII	Sandstone	0–10	1.35
VIII	Fine grained rock	0–4	1.06
IX	Limestone	0–10	2.86

Typical density (ρ) calculation
$1\,\text{N} \approx 1\,\text{kg} \times 1\,\text{m s}^{-2}$; $1\,\text{kN} \approx 1\,\text{Mg m s}^{-2}$
Bulk density of $2\,\text{Mg m}^{-3}$; γ_w = unit weight = $\rho\mathbf{g}$ = $19.62\,\text{kN m}^{-3}$

$\rho\,(\text{Mg m}^{-3})$:

loose sand	dense sand	glacial till	soft organic clay	peat
1.44–1.79	1.75–2.08	2.11–2.32	0.68–1.43	0.09–1.091

three-dimensional behaviour of the target material. The soil/rock behaviour was assumed to follow the bulk modulus method coupled with soil plasticity and critical state. Soil constants were used for top layers and the impact velocity is taken for those layers as discussed in Chap. 2. The velocity changes as the missile/bomb penetrates through various layers. The depth of penetration at any level is computed as the missile/bomb penetrates the layer corresponding to a particular soil constant. The target I(d) of Table H.1 was chosen for the analysis.

H.2.1 Finite-Element Analysis

A dynamic finite-element analysis was carried out on target I(d) of Table H.1. The missile/bomb was assumed to be initially elastic. It was also assumed that as the penetrator struck the earth, the volumetric strain was concentrated in the first column of the element. The time step δt was originally controlled by the smallest element in the missile/bomb. As the analysis progressed, the soil elements in the first row collapsed and the time step dropped by a factor ranging between 2.5 and 4. A subroutine was added to control this aspect and to maintain the same size step throughout. An implicit solution was introduced
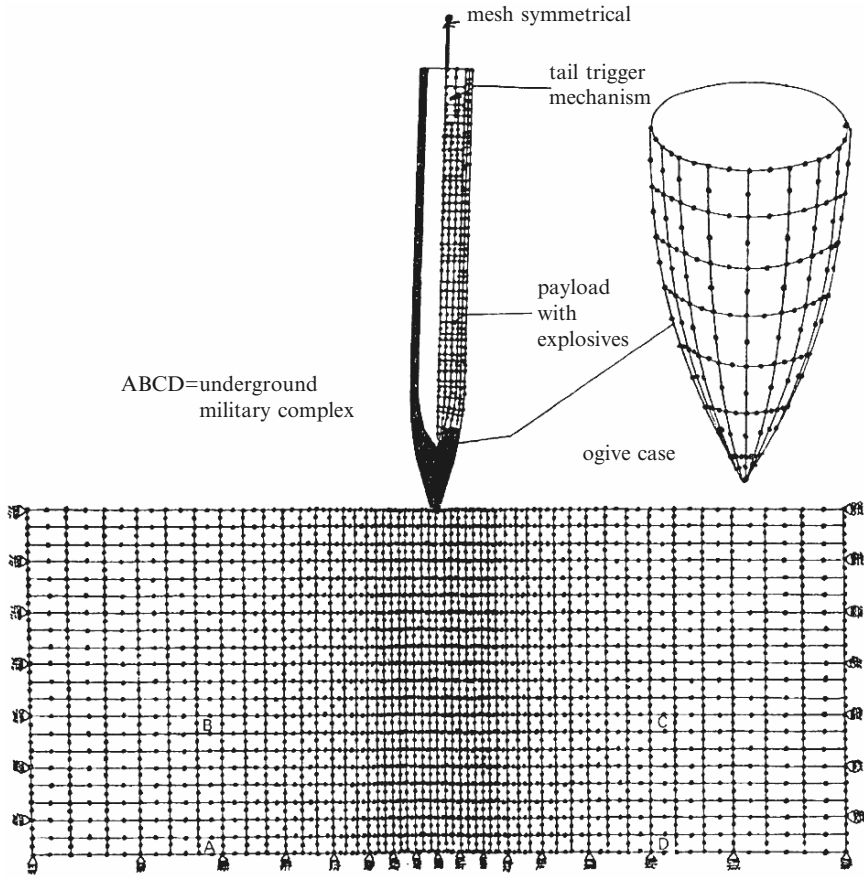
Fig. H.1. Missile with warhead penetrating soil/rock strata (20 m deep)

as well, to treat the smallest elements in particular. Manual rezoning was allowed each time a new soil element passed by the nose of the penetrator. All other large elements were advanced explicitly. The finite-element method gives a useful comparison with Petry's formula for assessing penetration depths. The following data were included in the finite-element analysis:

Number of finite elements

Target: 1,750
Scud missile: 385
Master nodes: 3,400
Slab nodes: 639
Length and width of target 100 and 35 m
Depth of target: 20 m
The material properties are as described in Chap. 2.

Additional properties

Target:
   soil/rock density varies: see Table H.2
   bulk modulus of elasticity: $7 \times 10^6 \, \text{kN m}^{-2}$
Missile:
   initial velocity: $250 \, \text{m s}^{-1}$
   weight: 500 lb (227 kg)
   inclination to vertical: 15°
   nose CRH: 6
Scud type:
   case length and diameter: 8.3 and 2.15 m

H.2.2 Results

Figures H.2 and H.3 show, for various missile velocities, the relationship between the impact force and the target sand/clay layers. As the missile penetrates through various layers at various time intervals, Fig. H.4 gives the summary, in dimensionless form, for the penetration depth and velocity against time in sand, clay and rock layers. Figure H.5 shows the missile cavity formation and the position of the gap elements in conjunction with the master and slave nodes of the elements. Figure H.6 shows the final penetration depth for a velocity of $250 \, \text{m s}^{-1}$. Figures H.7 and H.8 show the stress trajectories and the stress–time history, respectively, for a scud missile impacting the ground at an angle varying between 0° and 15°.

H.2.3 Explosions in Soil Strata

The finite-element mesh given in Fig. H.1 for soil/rock strata may also be used for other types of soils. The soils chosen are sand, clay and loam. The bomb yields considered are within the range of 45–900 kg. The altitude varies for different bombs. Figure H.9 gives the final results for all three soil strata. The depth of penetration from the ground level to the centre of the bomb was evaluated for the three soils for different bombs dropped from different heights.

H.2.4 Craters Resulting from Explosions

The plowshare program was used to predict crater dimensions when an explosive of non-yield is buried at a given depth for a specific soil stratum. This work was carried out by Lawrence Radiation Laboratory at Livermore in California [3.171]. A numerical method was developed for the calculation of crater development, including mound and cavity growth. Continuum mechanics (involving stress tensors) was the basis of the calculation. The medium was represented

Table H.2. Examples of soil profile

0.4 m

top soil

3 m   pear   GWL

0.6 m

sand

4 m

boulder clay

2 m   lacustrine clay

6 m   boulder clay

Bunterstone

(a)

3 m   compacted fill   GWL

3 m   alluvial deposit

6 m   marine clay

4 m   boulder clay

bed rock

(b)

0.2 m   top soil

2 m   sand

2 m   organic clay   GWL

8 m   clays, silts and sands

glacial fill

(c)
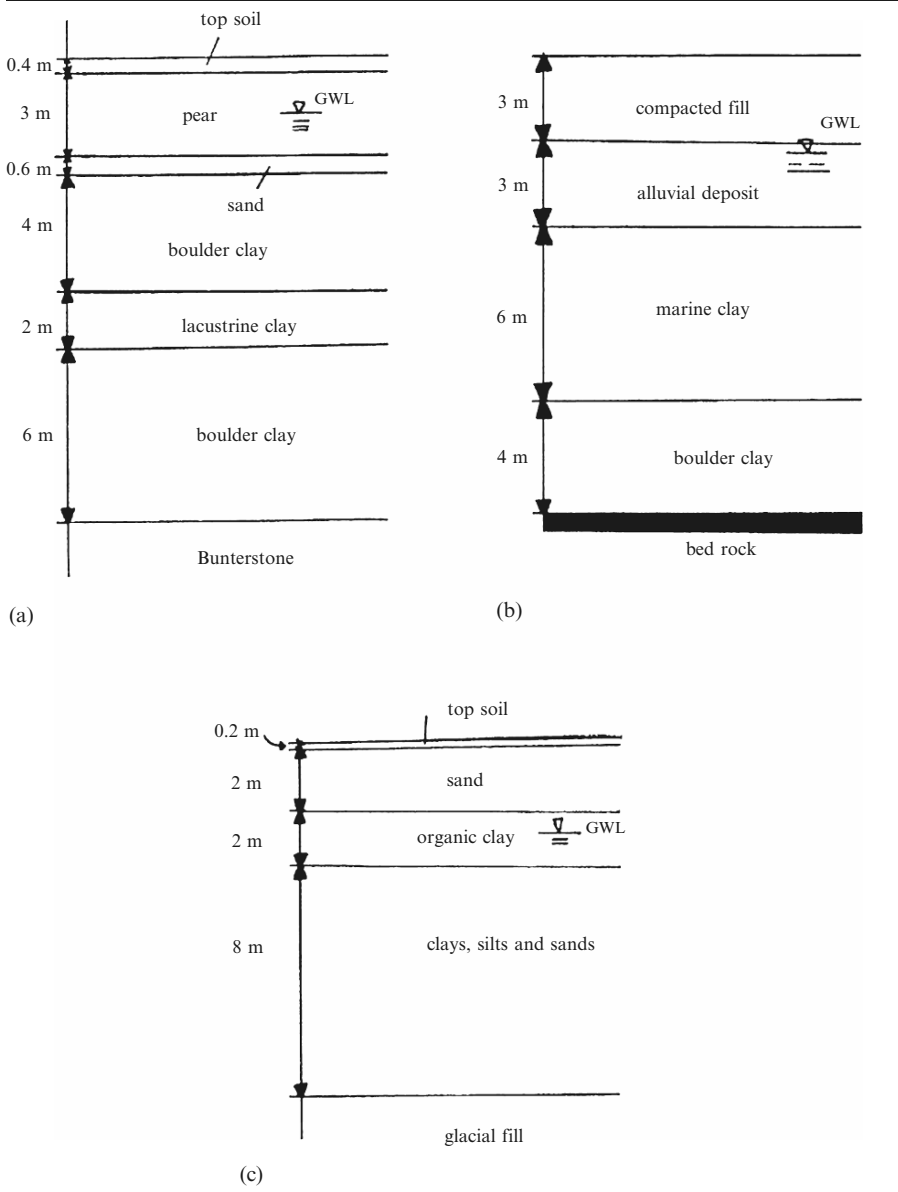
by the bulk modulus approach. Figures H.10–H.13 summarize some of the
achievements. Project Danny Boy was a nuclear cratering experiment in
basalt. A 0.4 kt device was placed 33 m below the surface, yield 1.3 m basalt.
The cavity and mound configurations at zero time are given in Fig. H.10. The
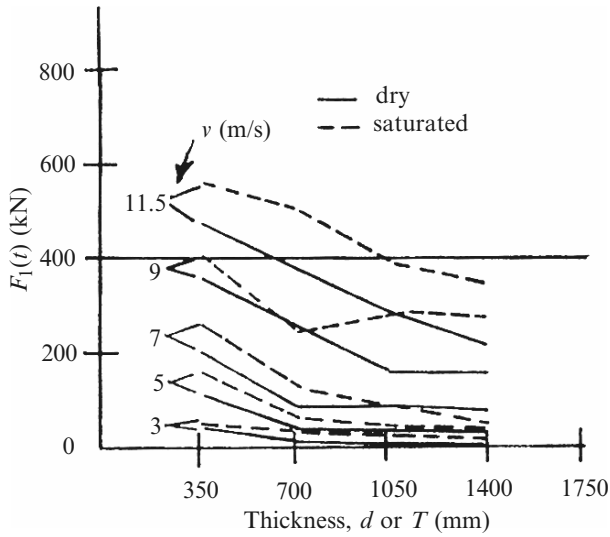
Fig. H.2. Impact force versus target layer for sand
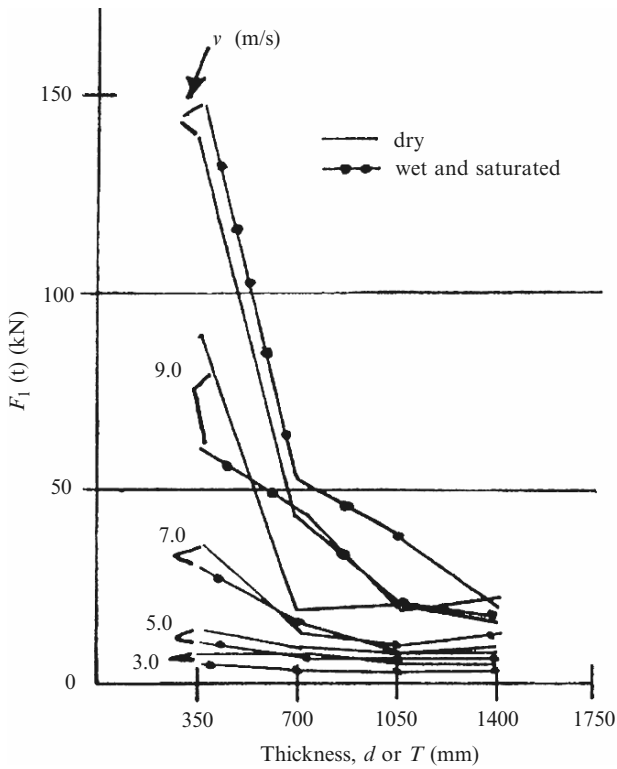
Fig. H.3. Impact force versus target layer for clay
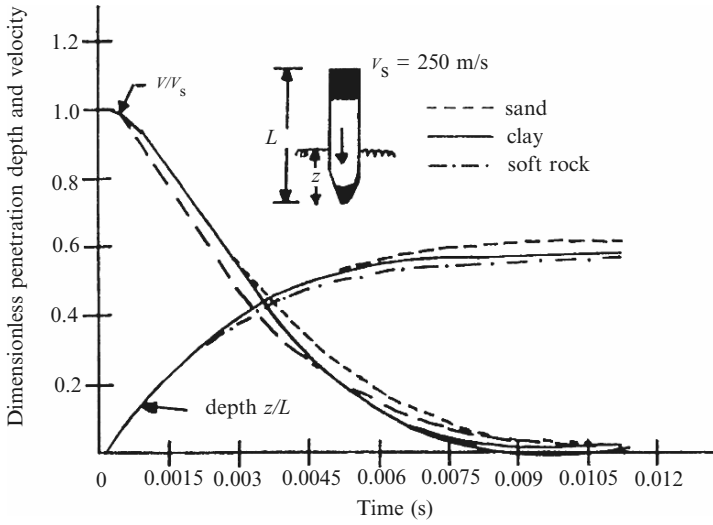
Fig. H.4. Penetration depth, velocity and time relationships for sand, clay and rock
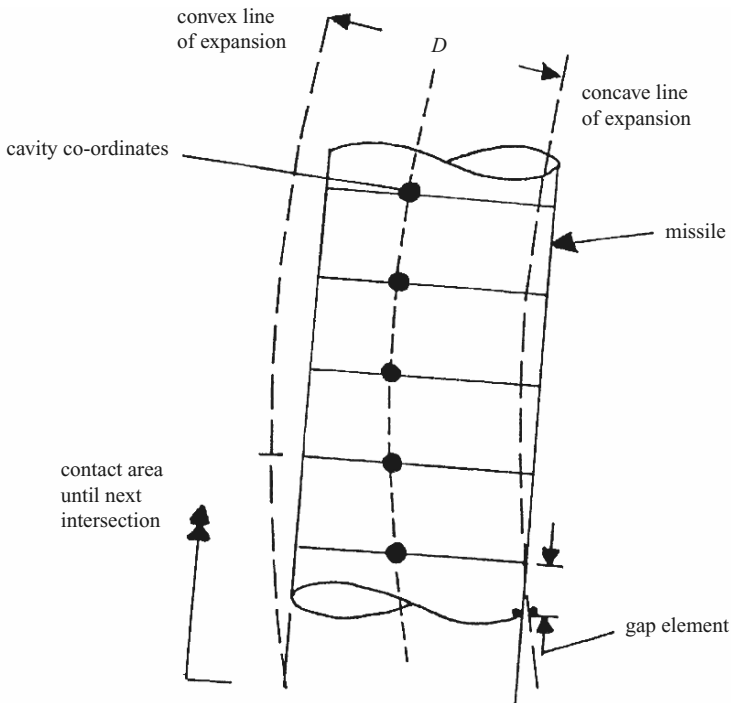
Fig. H.5. Position of the missile cavity gap elements (after Davie and Richgels [3.170])
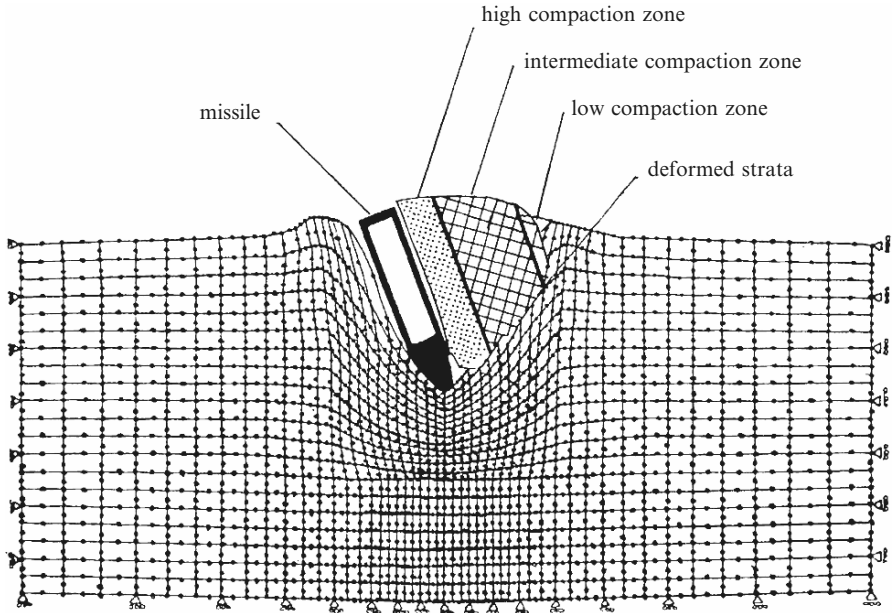
Fig. H.6. Final penetration of the target

calculated cavity and mound configurations at various time intervals are shown in Fig. H.11. For the scooter event, the tensor zoning is given in Fig. H.12. The scooter mound is finally shown in Fig. H.13.

H.2.5 Explosions in Boreholes

A typical soil stratum, as given in Table H.2, layout (c), was chosen for the finite-element analysis. The finite-element scheme given in Fig. H.1 was adopted for economic reasons. The missile line was replaced by a borehole 15 m deep. The pulse duration was maintained from 0.5 to 2 s. The burden was assumed to be 2.10 m. The velocity at the initial stage was $0.7\,\mathrm{m\ s^{-1}}$. Four different explosive pressure intensities were considered: 7, 15, 40 and $75\,\mathrm{kg\ m^{-1}}$ explosive weight per metre of the hole, thus giving explosive weights of 105, 225, 600 and 1,125 kg. The radii R ranged between 10 and 50 m. Figure H.14 gives the particle acceleration against R for various explosives. The total cavity extended by 350% laterally. The maximum frequency was 250 Hz. The maximum strain was $5,000\,\mu s$.

H.2.6 Explosions in an Underground Tunnel

Figure H.15 shows a typical tunnel layout and Fig. H.16 gives the tunnel cross-section. A typical finite-element mesh scheme is shown in Fig. H.17. A 10 kt

(a)

(b)
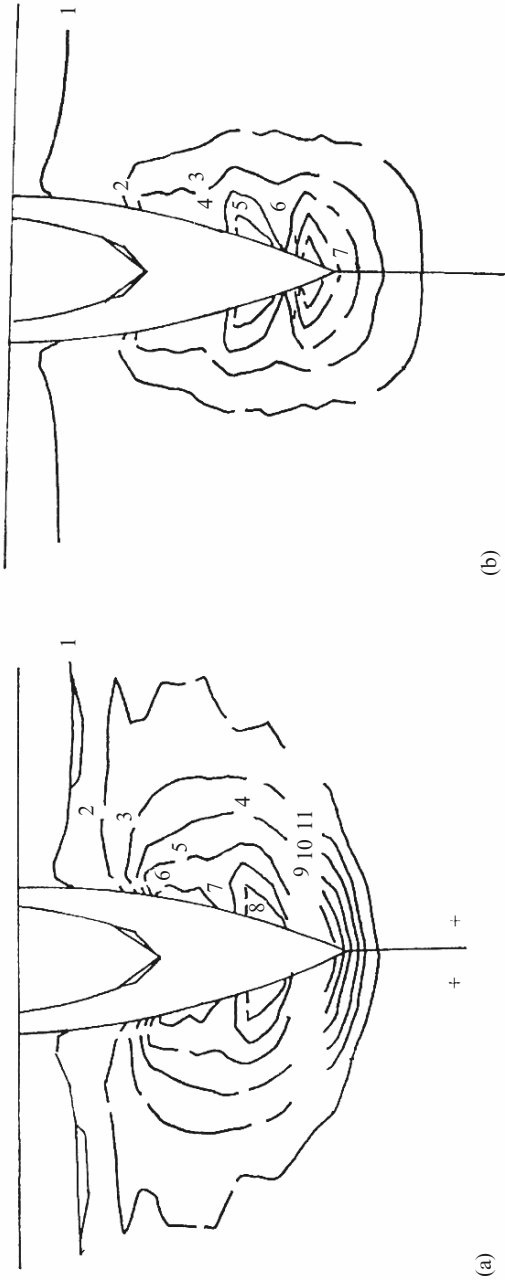
Fig. H.7. Principal stresses in (**a**) the axial and (**b**) the radial directions. (**a**) (1) 12.75, (2) 14.93, (3) 16.71, (4) 18.35, (5) 20.75, (6) 25.91, (7) 26.81, (8) 28.37 MN m^{-2}, (9), (10) and (11) tip almost plastic; (**b**) (1) 12.75, (2) 14.59, (3) 17.13, (4) 23.75, (5) 21.81, (6) 16.35 MN m^{-2}, (7) plastic
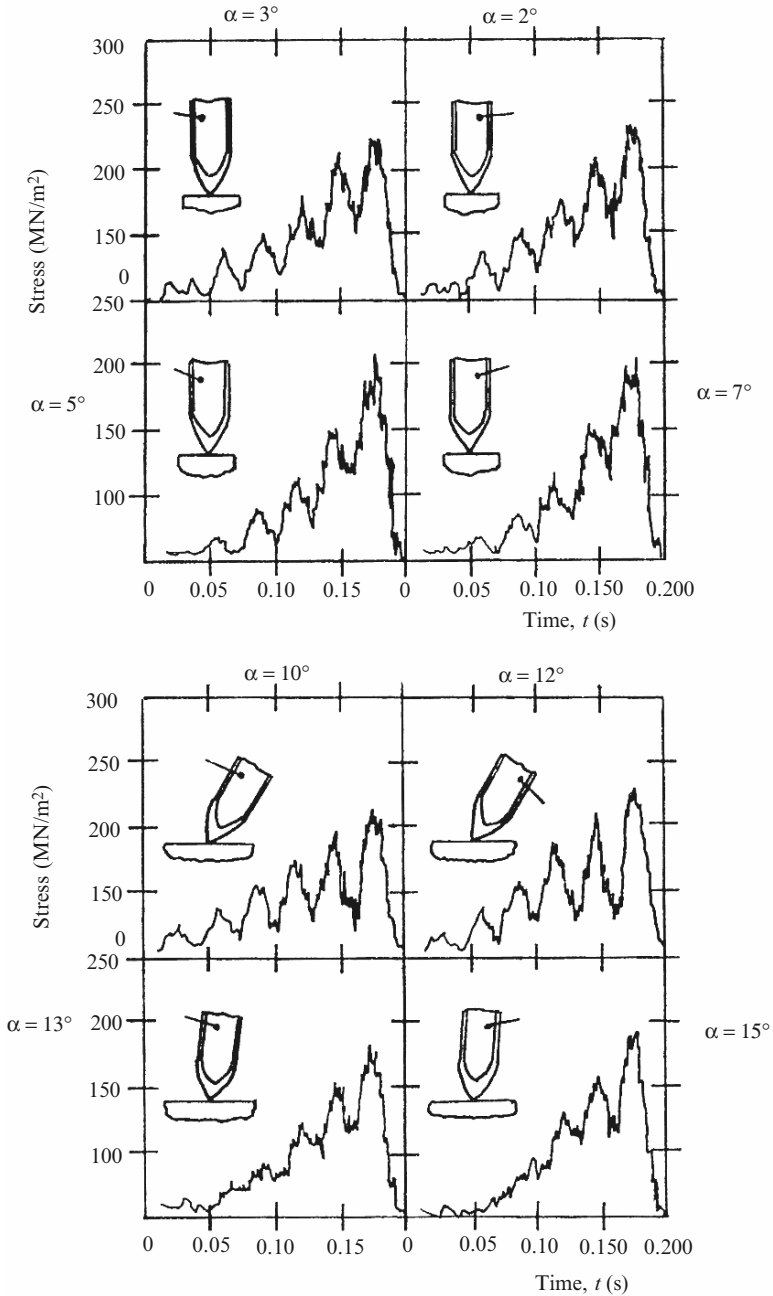
Fig. H.8. Stress–time history of the missile at various angles
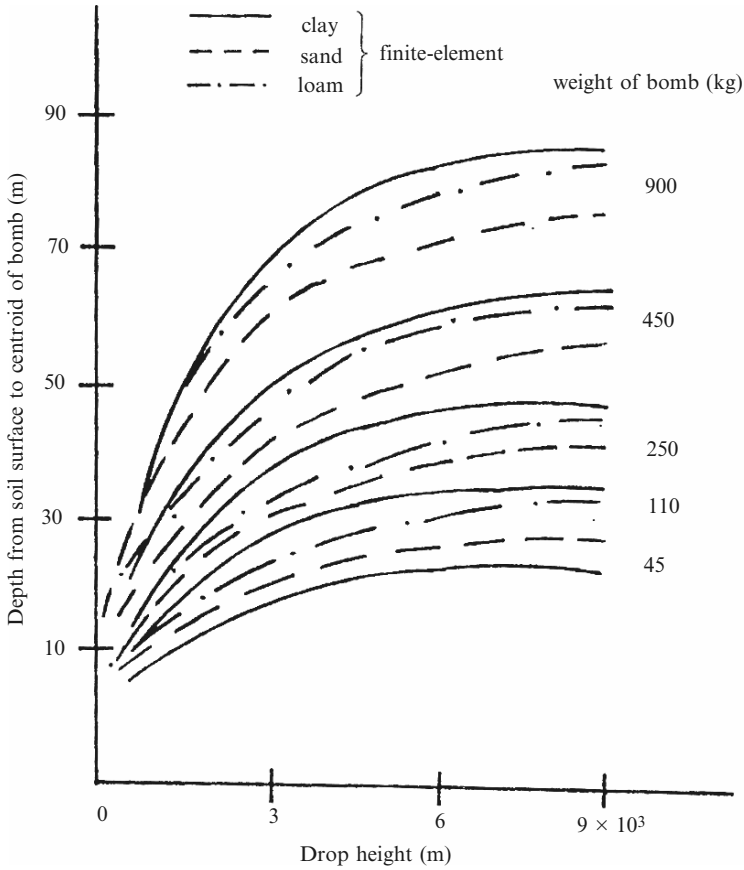
Fig. H.9. Bomb explosions in soils

nuclear explosion causing a pulse–time relationship was assumed inside the tunnel, with a rock overburden of 6 m carrying set and bedding planes. A total number of 1,180 20-node isoparametric finite elements were chosen, which gave rise to 46,230 nodes. Twenty increments were adopted. The following material properties were chosen for the finite-element input:

Maximum overburden 280 m
Intact rock
    $E = 2.8 \times 10^7$ kPa; E_m rock mass = 7,500 MPa
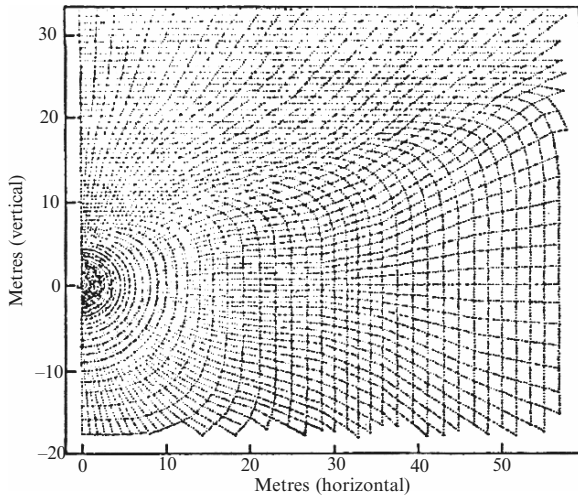
Fig. H.10. Cavity and mound configurations for the Danny Boy event at zero time (courtesy of J.T. Cherry [3.171])
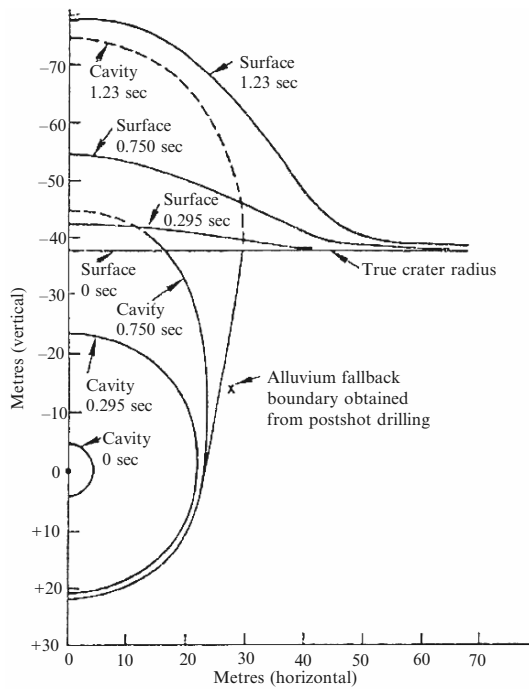
Fig. H.11. Calculated cavity and mound configurations at 0, 0.295, 0.750 and 1.23 s (courtesy of J.T. Cherry [3.171])
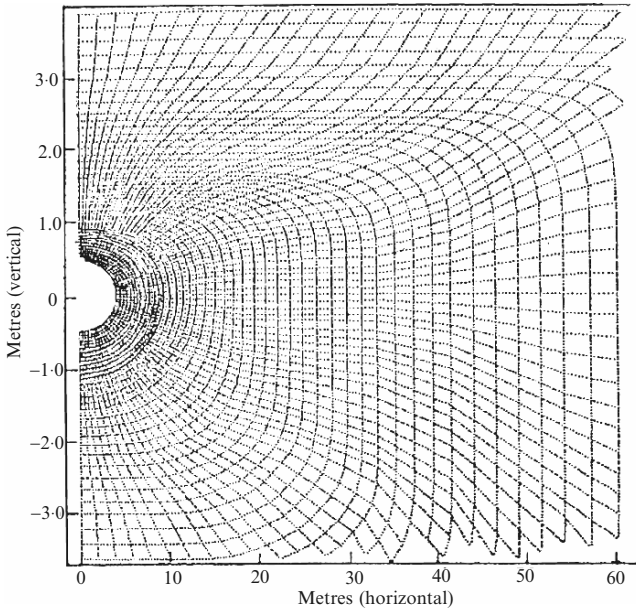
Fig. H.12. Tensor zoning for the scooter event at the start of calculation (courtesy of J.T. Cherry [3.171])
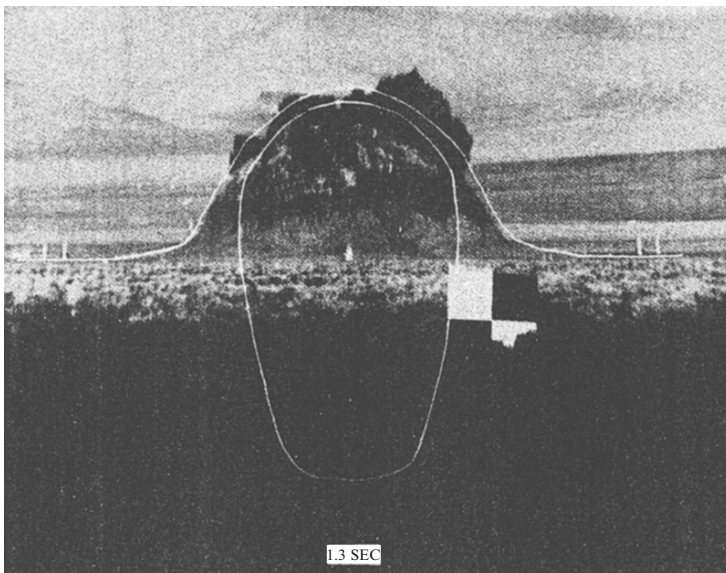
Fig. H.13. Scooter mound (compared with tensor calculations) at 1.3 s
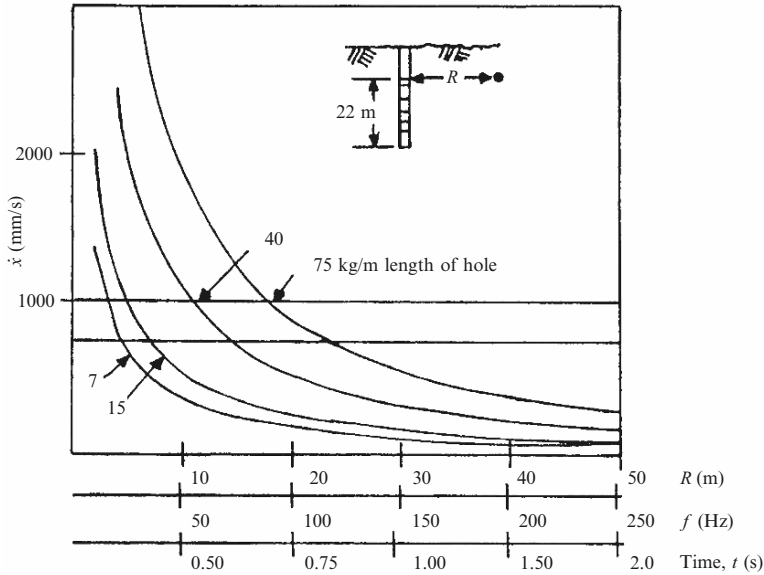
Fig. H.14. Borehole particle acceleration for various radii R and explosives

$K_{\mathrm{o}} = \frac{1}{3}$

$v = 0.2$

$\rho = 0.27\,\mathrm{kN\ m^{-3}}$

Joints

$$\left.\begin{array}{l}\text{Normal } \sigma_{\mathrm{n}} \\ \text{Oblique} \\ \text{Shear } \tau_{\mathrm{s}}\end{array}\right\}\text{compliances}\quad\left.\begin{array}{l}= 1 \times 10^{-7}\,\mathrm{m\,kPa^{-1}} \\ \\ = 2 \times 10^{-7}\,\mathrm{m\,kPa^{-1}}\end{array}\right\}\begin{array}{l}\text{bedding} \\ \\ \text{planes}\end{array}\left.\right\}\begin{array}{l}\text{N100°E/60°W} \\ \text{joint set 1 N280°E/60°W} \\ \text{joint set 2 N170°E/90°W}\end{array}$$

Cohesion, $c = 50\,\mathrm{kPa}$ or $0.05\,\mathrm{MPa}$

Friction angle, $\varphi = 45°$ and $0°$ for bedding planes

Spacing $= 1\,\mathrm{m}$

Reinforcement rock bolts

$E = 0.2 \times 10^9\,\mathrm{kPa}$

$G = 0.769 \times 10^8\,\mathrm{kPa}$

$\sigma_{\mathrm{y}} = 0.25 \times 10^6\,\mathrm{kPa}$

$p = 0.003$

The non-associated flow rule reduced the safety factor; rock bolts were included as bonded elements. The stresses were obtained at Gauss points. The properties of the joints were incorporated with the blocks into a super element of an anisotropic material, reflecting the joint directions. The failure criteria of the rock joint act as bench marks.
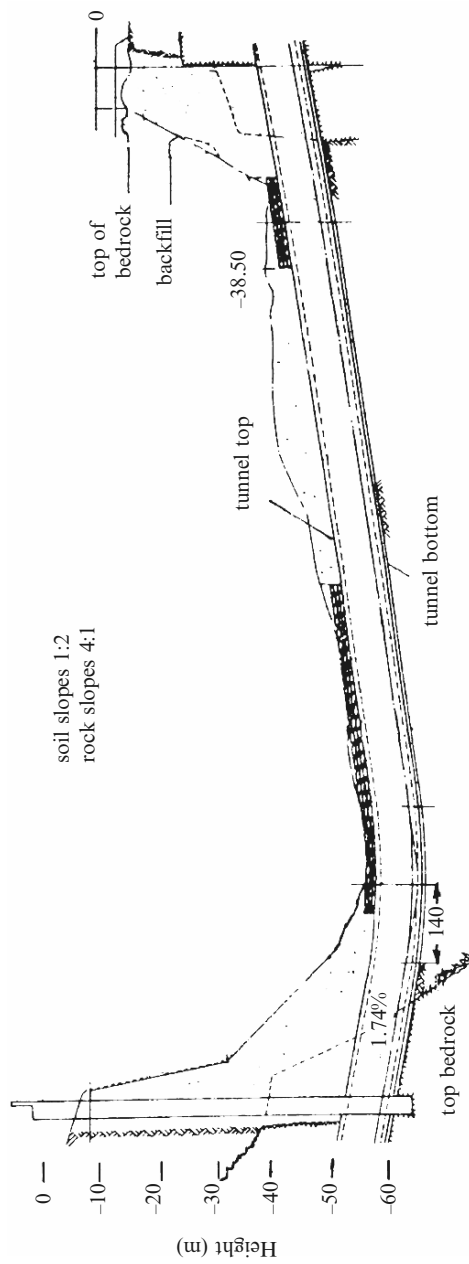
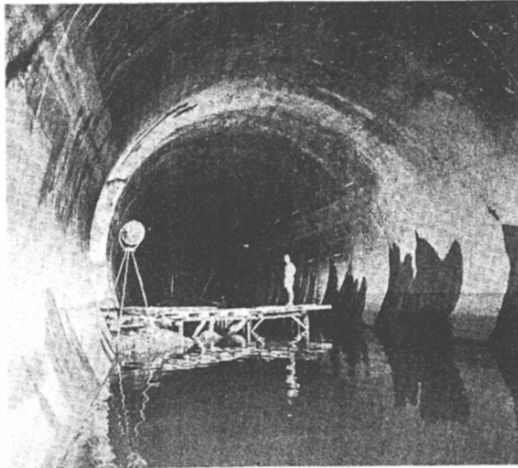**Fig. H.15.** Typical tunnel layout
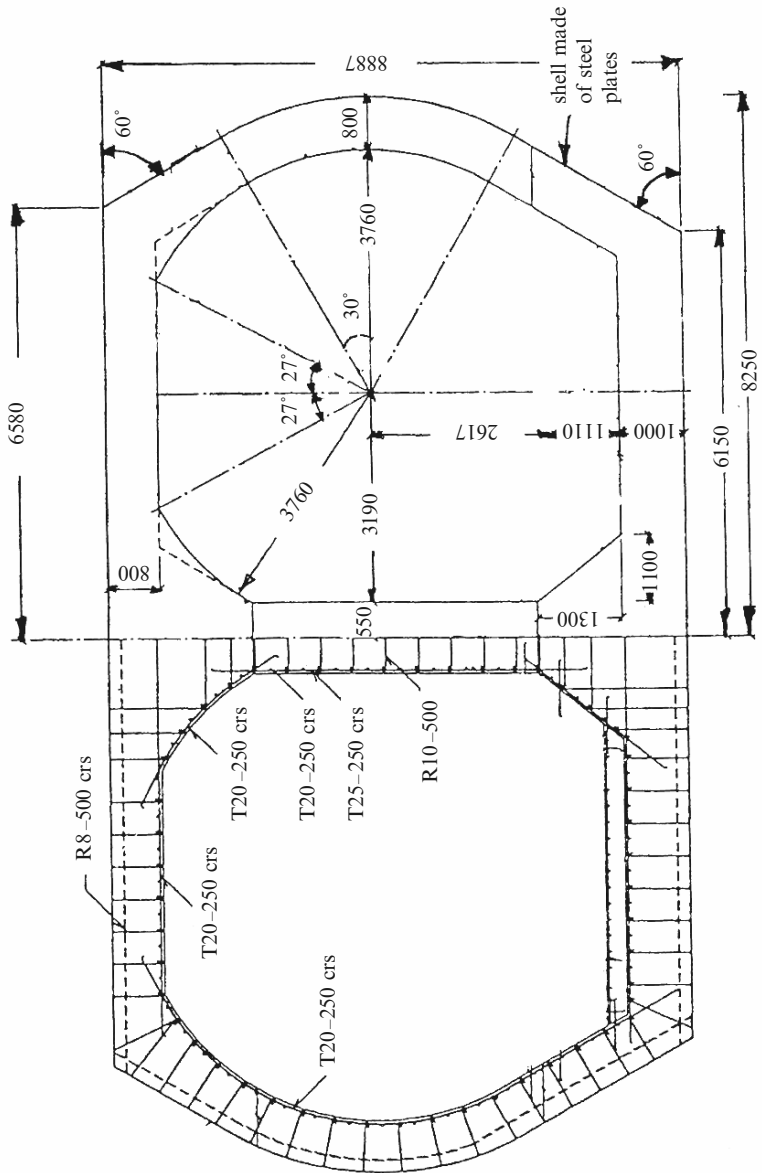
Fig. H.16. Tunnel cross-section and typical reinforcement

assumed tunnel under explosion

maximum area
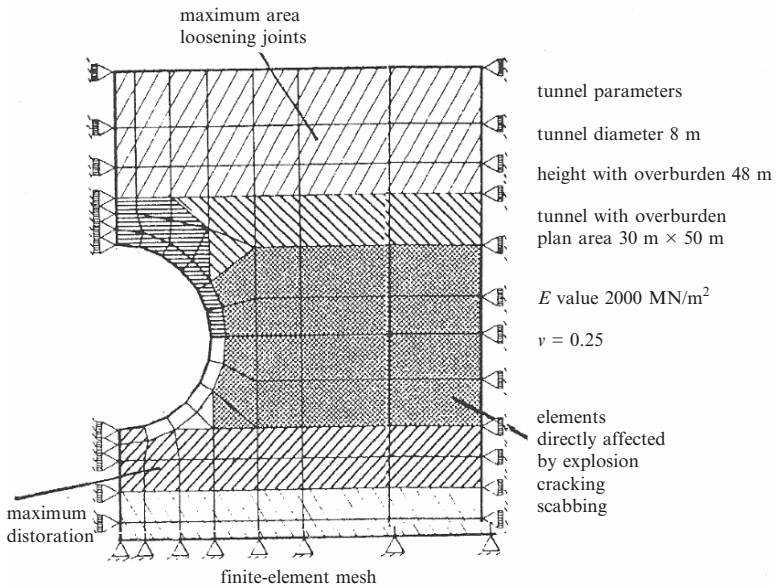loosening joints

tunnel parameters

tunnel diameter 8 m

height with overburden 48 m

tunnel with overburden
plan area 30 m × 50 m

E value 2000 MN/m^2

$v = 0.25$

elements
directly affected
by explosion
cracking
scabbing

maximum
distoration

finite-element mesh

Fig. H.17. Finite-element scheme for the tunnel

$$F = \{\tau\} + (n \tan \varphi / R_\mathrm{f}) - (c / R_\mathrm{f}) = 0,$$
$$f_\mathrm{R} = \text{flexibility ratio}$$
$$= E(1 + v)/(1/R^3)[6E_\ell I_\ell/(1 - v_1^2)],$$

where the subscript ℓ is for the liner.
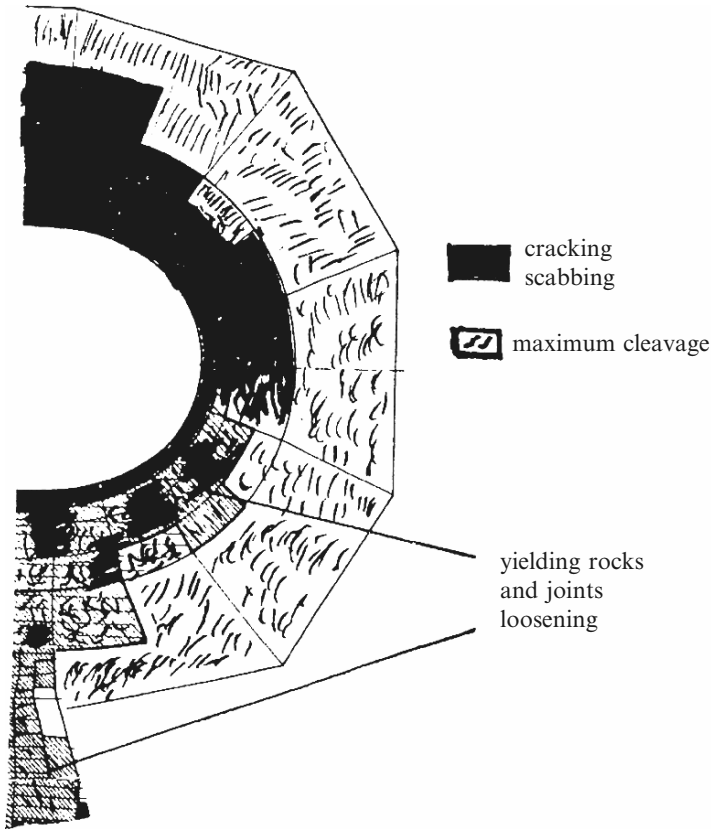
Fig. H.18. Tunnel post-mortem

Figure H.18 shows the adjacent rock tunnel failure. Figure H.19 shows displacements for various iterations.

The soil properties around the tunnel were assumed to be non-linear, visco-plastic and anisotropic. The movement between the tunnel and the surrounding medium was allowed for using the 600 gap elements between the tunnel and the surroundings. Figures H.20 and H.21 show the strain–time relationships and stress trajectories after the explosions.

H.2.7 Rock Fractures Caused by Water Jet Impact

A granite rock mass was chosen for the study of fractures produced by the shear impact of a water jet. The extreme dimensions around the granite rock, which lies in the North–West Frontier Province of Pakistan, were found to be 10.4 m by 9.3 m by 8.8 m. Four boreholes were assumed, each of diameter 300 mm and at 2.7 m distances. The chosen pressure–time pulse is shown in Fig. H.22. The injection rate given by various experts was $0.03\,\mathrm{m^3\,s^{-1}}$.

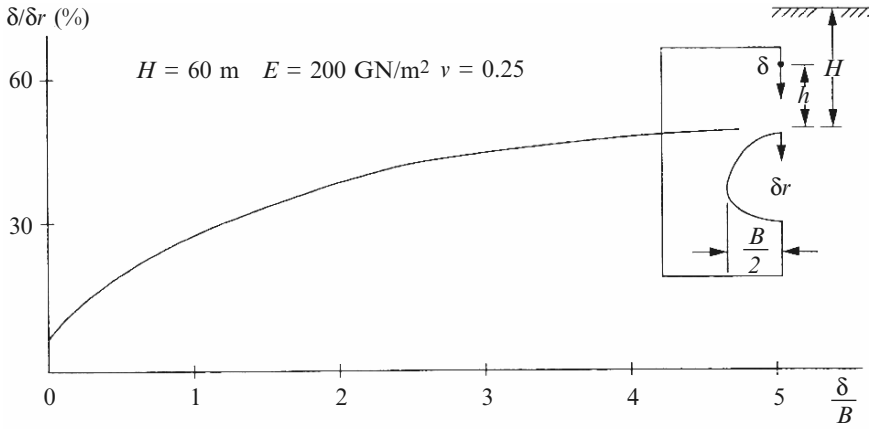δ/δr (%)

60

$H = 60$ m $E = 200$ GN/m² $v = 0.25$

δ

H

h

$δr$

$\dfrac{B}{2}$

30

0   1   2   3   4   5 $\dfrac{\delta}{B}$

distorted
original shape

without lugs

without lugs

δ (mm)

large displacements
with cracking

scale

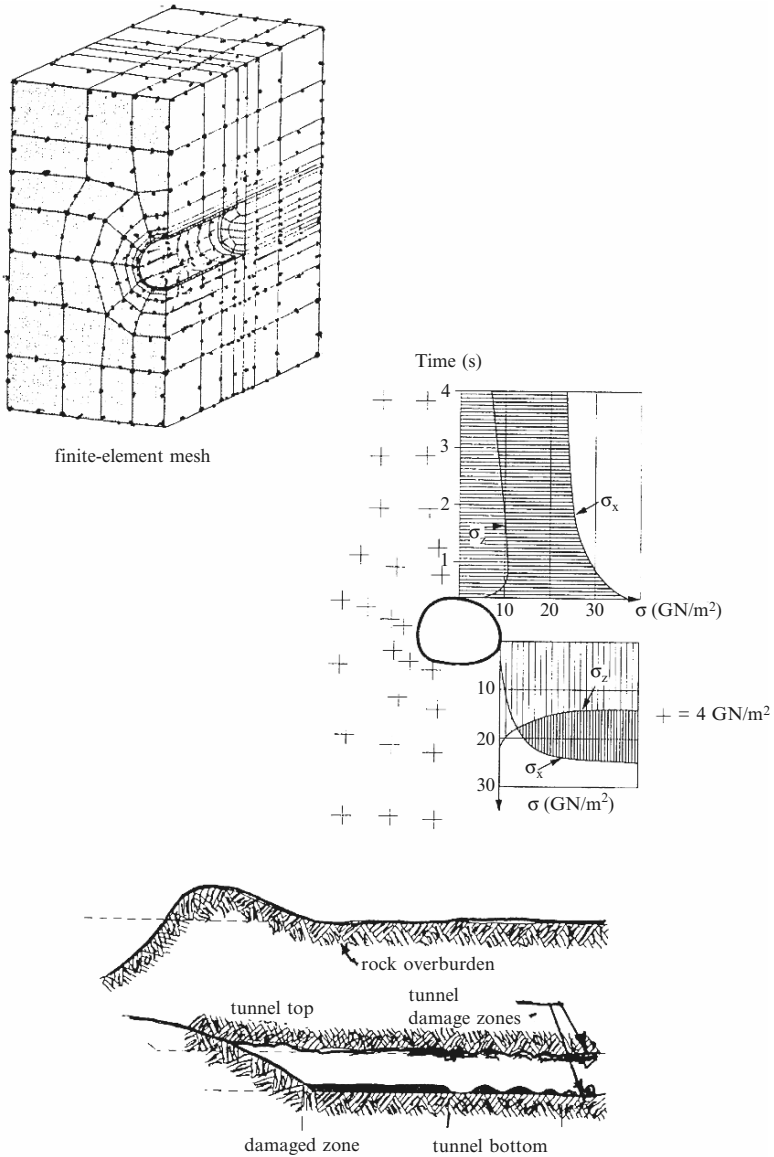20 mm
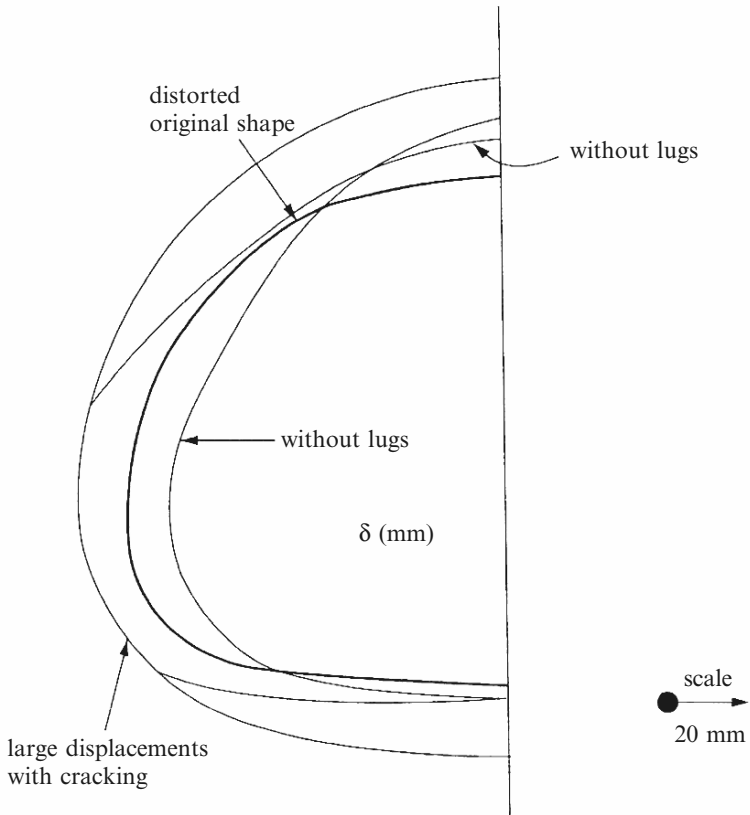
Fig. H.19. Tunnel displacements

finite-element mesh

Time (s)

Fig. H.20. Stress–time relationship after explosion

Figure H.23 gives the finite-element mesh scheme for the rock. The increase of K_{IC} with fracture size was noted. The crack tip approached zero in a number of solutions when it reached the interface. However, the non-linear fracture
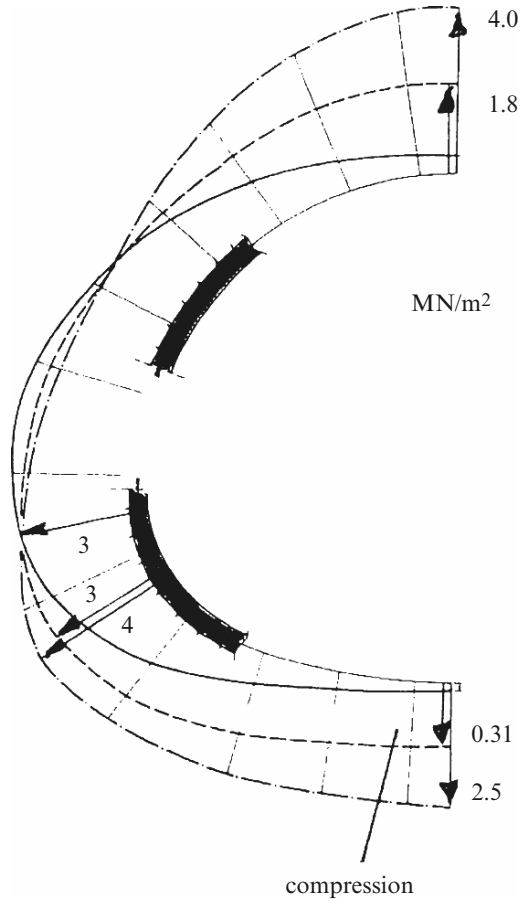
Fig. H.21. Tunnel stress trajectory after explosion
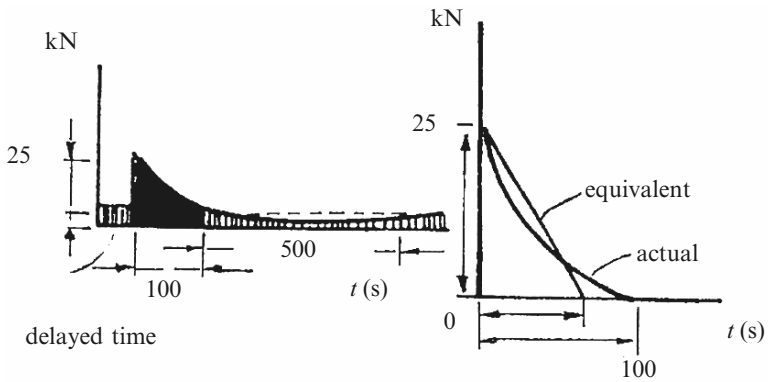
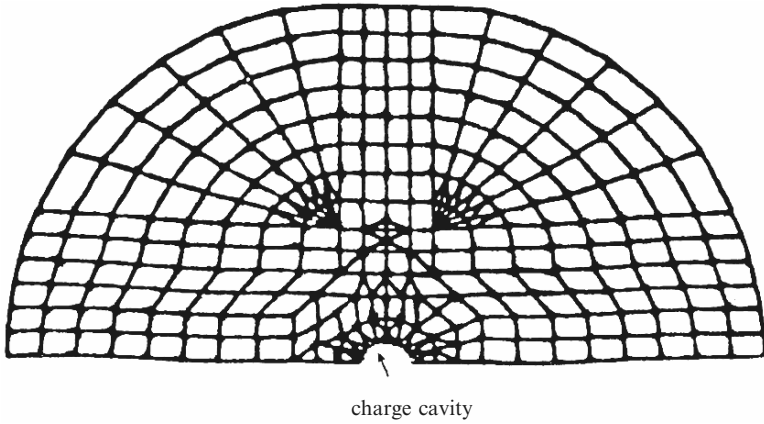**Fig. H.22.** Pressure–time pulse for fluid/rock impact

charge cavity

Fig. H.23. Finite-element mesh scheme for the granite rock

distorted
and heavy
stressed
zones

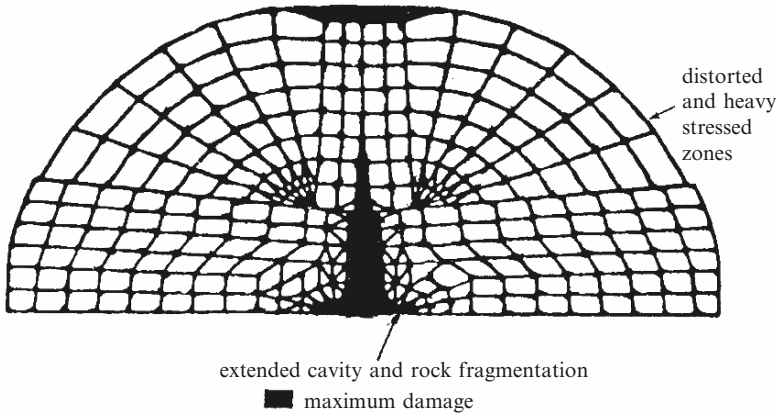extended cavity and rock fragmentation

■ maximum damage

Fig. H.24. Rock post-mortem

mechanics approach did not support this elastic analysis. The material properties, including in situ toughness, were as follows:

Young's modulus, E_{rock}: 45,000 MPa
Poisson's ratio: 0.31
Fracture toughness: 4.5 MPa $\sqrt{\text{m}}$
Confining pressure: 0–20.9 MPa
K_{1C}: 1.11–3.3 MPa $\sqrt{\text{m}}$

Figure H.24 gives a mesh plot showing the post-mortem after 10 min.

I

Underground and Underwater Explosion and Their Effects

I.1 Underground Explosion

Plowshare is the name given to the program of the US Atomic Energy Commission (USAEC) for developing peaceful uses for nuclear explosions, and it is the purpose of this paper to summarize the history of the program and describe its current status and outlook for the future. The peaceful uses of nuclear explosions can be grouped into the following three categories: underground engineering, excavation, and scientific studies. Underground engineering applications utilize the effects of completely contained nuclear explosions, while excavation applications utilize the cratering effects of less deeply buried nuclear explosives. Scientific applications make use of the extremely high density of neutrons and other unique characteristics of nuclear explosions.

In the early years of the Plowshare program almost al effort was directed toward conducting basic research on the processes and phenomena associated with nuclear explosions. This included nuclear explosion experiments such as Gnome, a scientific experiment and the first Plowshare nuclear experiment, conducted in December 1961, and Sedan, the first Plowshare nuclear cratering experiment, conducted in July 1962. In addition, many of the nuclear tests, conducted for other purposes, were studied in great detail and relevant data were integrated into the expanding Plowshare literature. This consists primarily of the investigation of underground nuclear explosion phenomenology, the design and conduct of nuclear explosion experiments, the design and testing of appropriate nuclear explosives, and related engineering. Other government agencies and private companies under contract with the USAEC provide expertise and assistance in the areas of public health, meteorology, radiological safety, seismology and structural response to ground motion. Also private industry on its own initiative has performed a great deal of research in the conventional aspects of the peaceful nuclear explosion applications now being considered, such as gas stimulation, gas storage, and in situ mineral leaching.

The use of nuclear explosions for underground engineering and excavation applications must meet three major criteria. The first is that the nuclear explosion results in an acceptable engineering product. The second is that it can be conducted safely. The third is that it must be economic. These three elements must be considered together before a decision concerning feasibility can be reached. For example each activity undertaken to assure safety involves additional cost, and this cost is part of the total cost of the application. If the safety costs are too high then, although it may be technically feasible to conduct the operation safely, the proposed use is not completely feasible since it will not be economic.

The first joint government-industry underground engineering nuclear explosion was the Gasbuggy experiment, which was conducted on 10 December 1967, by the US Government and the El Paso Natural Gas Company. Gasbuggy was designed to develop the concept of nuclear stimulation of natural gas from a host rock of low permeability. Two years of study since the detonation have shown that Gasbuggy, as an experiment, was completely successful. Re-entry and gas production testing have indicated a collapse chimney about 150 ft (46 m) in diameter extending from the 4,240 ft (1,390 m) detonation depth upward to about 3,900 ft (1,280 m) below the surface. The volumes and flow rates from the Gasbuggy chimney are encouraging when compared to the nearest conventional wells in the area. Production tests of the chimney well have resulted in a cumulative production of 213×10^6 ft^3(6.03×10^6 m^3) of hydrocarbons, and potential gas recovery over a 20 year period is estimated to be 900×10^6 ft^3(25.5×10^6 m^3), which would be an increase by a factor of at least 5 over estimated recovery from conventional field wells in this low permeability area [I.2, I.3]. Another major goal of Project Gasbuggy was to determine the gas quality with regard to contamination by radioactivity, and to evaluate various techniques for reducing this contamination. It now appears that tritium is the radionuclide which may cause the greatest difficulty if the stimulated gas is to be distributed in pipelines for normal industrial and home use [I.4].

The second underground engineering nuclear explosion, Project Rulison, also a gas stimulation experiment, was conducted on 10 September 1969. Participating in this project with the US Government is the Austral Oil Company, with the CER Geonuclear Company providing services to Austral Oil Company and acting as project manager. Production tests from the Rulison chimney have not yet begun but the rapid build-up of pressure in the cavity indicates a relatively high flow rate form the reservoir rock into the fractured zone.

Other proposals for testing possible uses for nuclear explosions have been submitted to the USAEC, and these are in various stages of implementation. These included fracturing low-grade copper deposits in preparation for in situ leaching, creating underground storage facilities for natural gas, and fracturing oil shale rock in preparation for in situ retorting [I.5–I.7]. Additional gas production stimulation experiments in differing rock types, at depths

of about 13,000 ft (3,960 m), and with varying yields are also being investigated. Another application which recently has received attention is the use of nuclear explosions for exploitation of geothermal energy sources. This application envisages the creation of a chimney and associated fracture system in a geothermal energy source with a nuclear explosion, introduction of water into the chimney-fracture system, and removal of superheated steam for the generation of electrical power. The technology for some applications such as gas stimulation has progressed more rapidly than others and is expected to be available at an earlier date.

Looking to the future, the USA plans to continue out research and development program fro developing the technologies required for practical underground engineering applications for contained nuclear explosions. Basic research will be pursued to further our understanding of the phenomenology of contained nuclear explosions, and we hope to conduct specifically designed experiments to further out knowledge in this area. Methods of both enhancing chimney height (useful for some stimulation applications) and inhibiting chimney development (in cases where overlying aquifers exist) also need to be investigated. A reference is made to the cavity method in Plate I.1.

For applications requiring rock breakage, for example for in situ ore leaching or oil shale retorting, it is very desirable and possibly and economic necessity to develop intensive permeably fracturing between chimneys. Thus detonating an array pattern with time delays between detonation of the charges might be used to cause a second charge to break toward the cavity produced by the first charge. We also need to develop related technologies necessary to permit the practical application of the decontaminate gas storage caverns and to minimize radioactive contamination of oil and various ores from in situ retorting and leaching operations.

While no nuclear explosive has yet been produced which will satisfy the specific needs of underground engineering applications, the USAEC is giving particular emphasis to the development of such an explosive. Since the principal interest at the present time is the stimulation of natural gas reservoirs, emphasis is being given to providing an explosive with characteristics suited to that purpose. Specifically, we have been working toward a small diameter explosive which will result in minimal radioactivity in the natural gas, will withstand the severe temperature and pressure environment of deep gas reservoirs, and can be made at a minimum cost. It appears that the first explosive specifically designed for gas stimulation will be approximately 27 cm in diameter, although it is hoped we may achieve diameters of approximately 20 cm for explosives of reasonable cost within a few years. Following the Gasbuggy experiment (Plate I.2) it was estimated that there were more than 4 g of tritium distributed throughout the chimney. Hopefully our first explosive specifically designed for gas stimulation will result in less that 0.2 g of tritium.
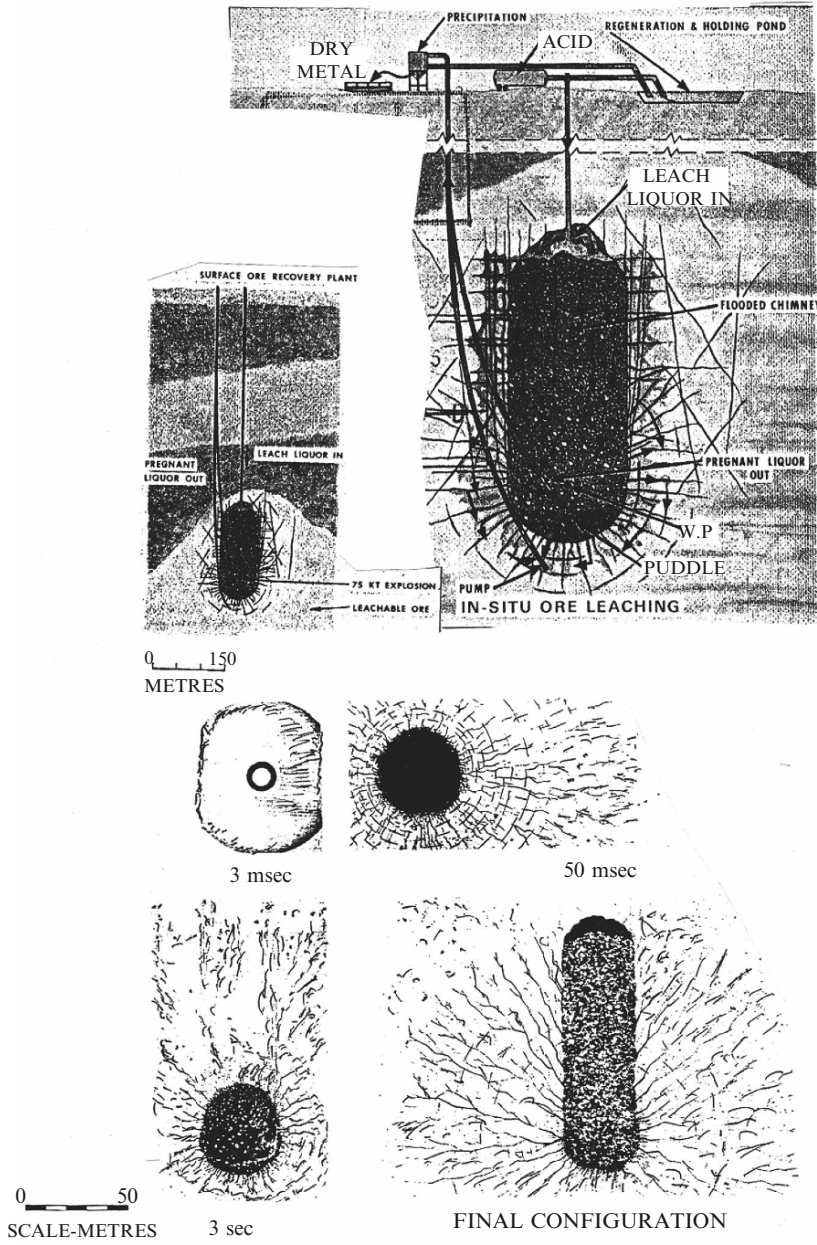
Cavity-chimney formation history for a five-kiloton explosion in granite.

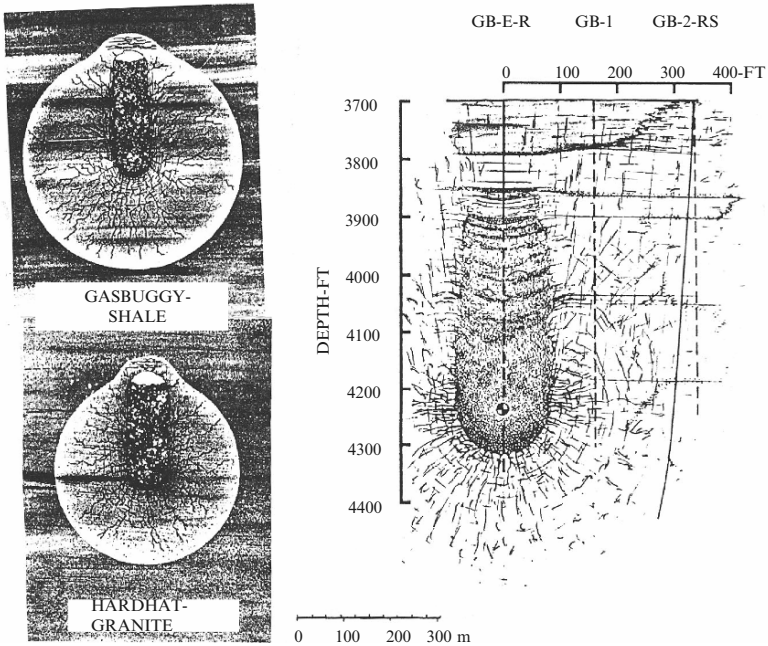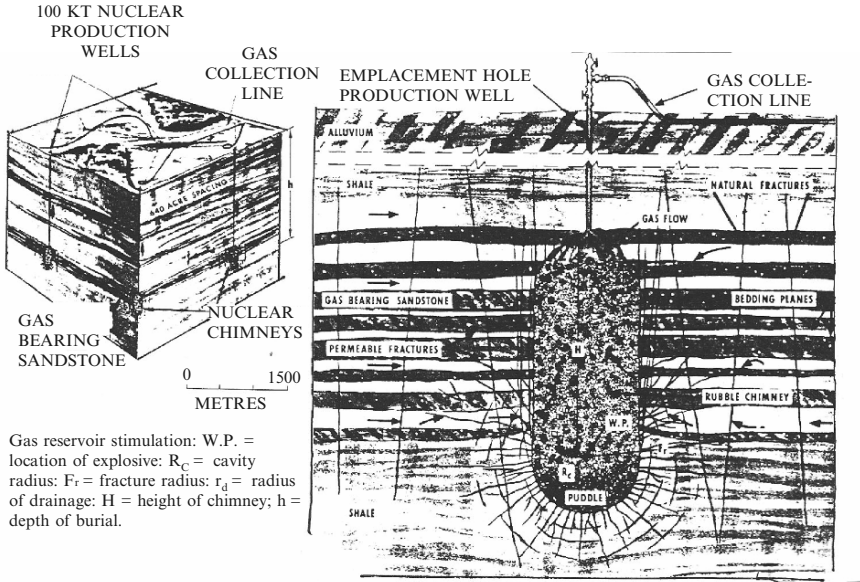**Plate I.1.** Serial-I (with compliments of IAEA, Vienna, Austria)

100 KT NUCLEAR PRODUCTION WELLS

GAS COLLECTION LINE

EMPLACEMENT HOLE PRODUCTION WELL

GAS COLLE-CTION LINE

GAS BEARING SANDSTONE

NUCLEAR CHIMNEYS

0   1500
METRES

Gas reservoir stimulation: W.P. = location of explosive: R_C = cavity radius: F_r = fracture radius: r_d = radius of drainage: H = height of chimney; h = depth of burial.

GASBUGGY-SHALE

HARDHAT-GRANITE

Plate I.2. Nuclear Explosions-Serial-II with compliments of IAEA, Vienna

From our nuclear cratering experience, computer codes have been developed to evaluate the relationship between explosive burial depth and crater dimensions for different material properties. A model of material behaviour is the first requirement for these calculations. It has been found that mound

growth during the formation of a nuclear crater results form shock, spall and gas acceleration acting sequentially. In cratering events the important equation-of-state parameters of the media in which the detonation takes place are: (1) compressibility, (2) porosity, (3) water content, and (4) strength. Additional computer codes have been developed to calculate local radioactivity deposition and to predict airborne radioactivity concentrations downwind, up to several days after the detonation.

With the calculational and the experimental evidence gathered so far we can now formulate a seven phase crater formation history:

1. Vaporisation of the explosive and a surrounding shell of earth materials
2. Melting of surrounding medium, cavity growth and an outgoing shock wave
3. Return of a rarefaction wave from the ground surface to the upper cavity surface
4. Asymmetrical growth of the upper part of the cavity as contrasted to a very slowly growing lower hemisphere at this time
5. Mound growth
6. Mound disassembly, fold-over of mound material onto the earth's surface, initiation of collapse, and release of some gaseous and fine particulate radioactivity to the atmosphere
7. Collapse, fall-back, and mass deposition beyond the point of fold-over

A reference is made to Plate I.3 for Sedan cratering and graphs drawn for the relationship between apparent crater depths and depth of burst using various experimental results in different crater conditions by various researchers.

Many potential nuclear excavation applications have been investigated and reported I.2.2.2. The most detailed investigations and studies conducted have been for the largest project contemplated, that of a sea-level canal in the Central American isthmian region. Based on information derived from recent excavation experiments, considering a greater number of possible explosive yields, and by taking advantage of the enhancement of single-charge dimensions which is inherent in multiple row charges, a recent re-evaluation of this project has led to a reduction in the explosion yields form those earlier deemed necessary. This results in a reduction of explosion effects, the most important of which is ground motion.

Another potential application which has received considerable study, and which is within the realm of existing experience, is that of harbour construction. In general, harbour construction is probably the most straightforward application of nuclear excavation in that the degree of accuracy required in crater dimensions is not overly critical and explosion yields may be kept quite low.
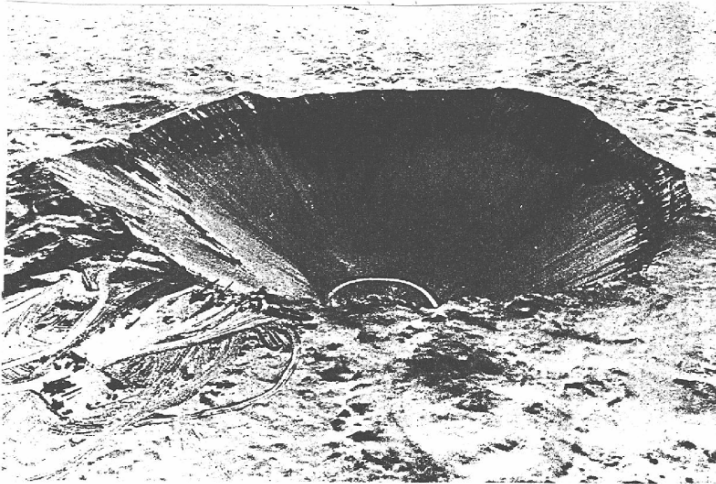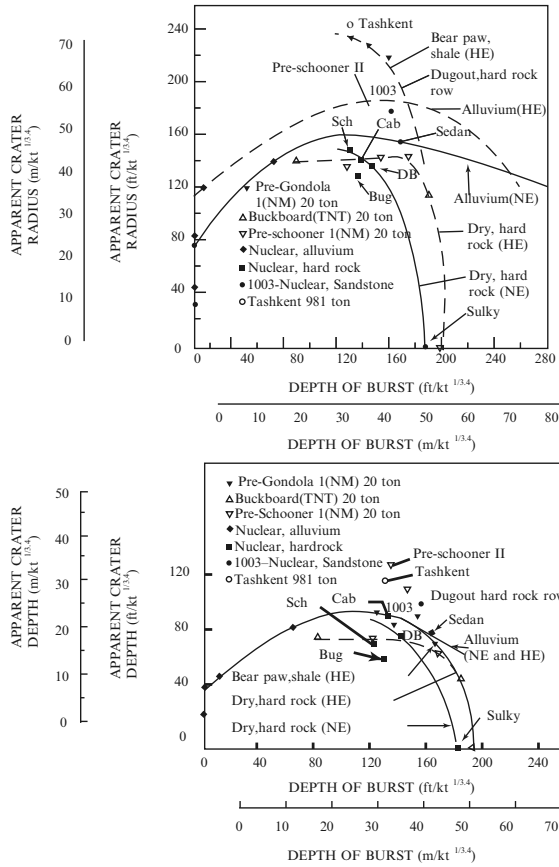
Aeriel view of the sedan crater.

Plate I.3. Depth of burst versus crater depth

An area which has recently been receiving more attention is the application of nuclear explosions to the development and management of water resources. For example, nuclear excavations might be used as surface storage reservoirs to reduce flood peaks, for irrigation water, for water based recreation, or for waste water. The rubble pile, resulting from emplacing the nuclear explosive at a depth between that required for complete containment and that required to obtain a crater, might be used as a dam structure or as a source of aggregate.

In the Hutch event of July 1969, a uranium and thorium target was exposed to a very intense neutron flux in an attempt to produce new transplutonium isotopes. Preliminary results indicate that the integrated neutron flux in the target was approximately $45\,\mathrm{mol\,cm^{-2}}$, which is better than twice the exposure in the best previous test. The heaviest isotope identified in the debris was fermium-257 which had been seen in other experiments. The search for new isotopes with mass numbers greater than 257 was unsuccessful, presumably because spontaneous fission lifetimes of these isotopes were much short than the time required to recover and analyse debris samples.

In conclusion, it should be remembered that nuclear explosions have been used to create craters, to break large amounts of rock of the type containing many natural resources, and for such scientific purposes as the production of heavy elements and making neutron cross-section measurements. Many technical, and consequently economic, questions remain to be answered, and most importantly, many refinements in the current technology must be made before it will be truly practical.

The size of the cavity thus produced can be predicted quite well on the basis of a model that assumes adiabatic expansion of the gases in the cavity until they are in equilibrium with the confining stress in the medium. This leads to an equation of the form:

$$R_c = \frac{C_1 W^{1/3}}{(K_1)^{1/3\gamma}}, \tag{I.1}$$

where R_c = cavity radius (m), W = energy released by explosion (kt), γ = adiabatic expansion coefficient, C_1 = constant characteristic of the explosion environment, and K_1 = confining stress of the medium surrounding the explosion (bars).

Higgins and Butkovich [I.7] have calculated values for γ and C_1 from laboratory and in situ measurements of rock properties. Using these values together with the assumption that K_1 is the average overburden stress (i.e. ρgZ) they have calculated values for R_c that agree quite well with US experimental data in four media. The value of γ varies somewhat with moisture content but can be well represented by the values in Table I.1. Average values for C_1 are also given in Table I.2.

On the basis of data from 13 nuclear explosions in very dry, strong granite, Michaud [I.8] has suggested that K_1 should include the strength of the medium

Table I.1. Some rock properties

Medium	Water content (%)	Density (g cm^{-3})	γ	C_1
Alluvium	12	1.9	1.125	45
Tuff	15	1.9	1.14	50
Granite	1	2.7	1.03	49
Salt $\left\{ \vphantom{\begin{array}{c}a\\b\end{array}}\right.$	4	2.3	1.11	48
	0	2.3	1.07	47
Dolomite	0	2.3	1.03	42
Shale	3.6	2.35[a]	1.06	49

[a] Average overburden density for Gasbuggy site

(i.e. $K_1 = \rho gZ + C_s$) where Z is the depth-of-burial and C_s represents the strength of the rock massif, independent of overburden stress. His analysis leads to a value for C_1 of 52 and C_s of 220.

The third type of application for nuclear explosions utilizes their unique characteristics to advance scientific knowledge. The scientific applications of nuclear explosions include the production of transplutonium elements, the measurement of neutron cross-sections, and the use of the explosion as a known energy source for seismic measurements.

In addition, apart from the above objectives the main aim is to improve the destructive power of the nuclear bombs using the means of aeroplanes on missiles.

I.2 Stress/Shock Waves Propagation: Analytical Investigations

I.2.1 Introduction

This section presents a numerical model of shock wave propagation (SWP) which uses material properties data from a preshot testing program to predict the stress-induced effects on the rock mass involved in a Plowshare application. SWP calculates stress and particle velocity history, cavity radius, extent of brittle failure, and the rock's efficiency for transmitting stress. The calculations are based on an equation of state for the rock, developed from preshot field and laboratory measurements of the rock properties. The field measurements, made by hole logging, determine in situ values of the rock's density, water content, and propagation velocity for elastic waves. These logs also are useful in judging the layering of the rock and in choosing which core samples to test in the laboratory. The laboratory analysis of rock cores includes determination of hydrostatic compressibility to 40 kb, triaxial strength data, tensile strength, Hugoniot elastic limit, and, for the rock near the point of detonation, high-pressure Hugoniot data. Equation-of-state data are presented for rock from three sites subjected to high explosive or underground nuclear shots,

including the Hardhat and Gasbuggy sites. SWP calculations of the effects of these two shots on the surrounding rock are compared with the observed effects. In both cases SWP predicts the size of the cavity quite closely. Results of the Gasbuggy calculations indicate that useful predictions of cavity size and chimney height can be made when an adequate preshot testing program is run to determine the rock's equation of state. Seismic coupling is very sensitive to the low-pressure part of the equation of state, and its successful prediction depends on agreement between the logging data and the static compressibility data. In general, it appears that enough progress has been made in calculating stress wave propagation to being looking at derived numbers, such as number of cracks per zone, for some insight into the effects on permeability. A listing of the SWP code is appended in this text using BANG-F. The paper described below was based on finite difference method, the results obtained by BANG-F which is the latest version of Program ISOPAR based on finite element method are mutually compared:

NUMERICAL SIMULATION OF STRESS WAVE PROPAGATION FROM UNDERGROUND NUCLEAR EXPLOSIONS. IAE A-PL-388/13 Peaceful used on nuclear explosion 1966.

J.T. Cherry and F.L. Petersen, Lawrence Radiation Laboratory, University of California, Livermore, CA, USA.

I.2.2 The Numerical Model

A wave is a time-dependent process that transfers energy from point to point in a medium. A wave propagates through a medium because of a feed-back loop that exists between the various physical properties of the medium that are changed by the energy deposition.

The cycle followed in calculating stress wave propagation is presented in Plate I.1. We start at the top of the loop, with the applied stress field. The equation of motion provides a functional relation between the stress field and the resulting acceleration of each point in the medium. Accelerations, when allowed to act over a small time increment Δt, produce new velocities; velocities produce displacements, displacements produce strains, and strains produce a new stress field. Time is incremented by Δt and the cycle is repeated. The analysis of this loop is provided by a computer program, SWP, which solves the equations of continuum mechanics for spherical symmetry by finite element methods. Program ISOPAR describes the complete analysis including the solution procedures.

I.2.2.1 Equation of Motion

The fundamental equations of continuum mechanics (conservation of mass, linear momentum, and angular momentum) combine to produce the following equation of motion for spherical symmetry, taken from Keller:

$$\rho \dot{u} = \left(\frac{\partial P}{\partial R} + \frac{4}{3} \frac{\partial K}{\partial R} + 4 \frac{K}{R} + g \right), \tag{I.2}$$

where ρ is the density, $\dot{u}$ is the particle acceleration, g is a body force used to include gravity effects, and the stress tensor in the spherically symmetric coordinate system is written as the sum of an isotropic tensor and a deviatoric tensor,

$$\begin{bmatrix} T_{RR} & 0 & 0 \\ 0 & T_{\theta\theta} & 0 \\ 0 & 0 & T_{\phi\phi} = T_{\theta\theta} \end{bmatrix} = \begin{bmatrix} -P & 0 & 0 \\ 0 & -P & 0 \\ 0 & 0 & -P \end{bmatrix} + \begin{bmatrix} -\frac{4}{3}K & 0 & 0 \\ 0 & \frac{2}{3}K & 0 \\ 0 & 0 & \frac{2}{3}K \end{bmatrix}. \tag{I.3}$$

We can see form (I.3) that

$$\left. \begin{aligned} P &= -\frac{1}{3}(T_{RR} + 2T_{\theta\theta}) \\ K &= \frac{T_{\theta\theta} - T_{RR}}{2} \end{aligned} \right\}. \tag{I.4}$$

Equation (I.2) is differenced by establishing a Lagrangian coordinate system (j) in the material. These coordinates move with the material and assume discrete values: $0, 1, 2, \ldots, j-1, j, j+1, \ldots$. This coordinate system divides the material into volume elements or zones, with the mass in each zone remaining constant. At zero time each Lagrangian coordinate (j) has a unique Eulerian coordinate R_j^0; after n cycles, corresponding to a time t^n, the Eulerian coordinate is R_j^n.

Equation (I.1) is transformed into the Lagrangian (j) coordinate system. Each stress component (Σ) in this equation is a scalar function of position (R) and time (t). If the Eulerian coordinate (R) is considered to be a function of j and t then we can write

$$\frac{\partial \Sigma}{\partial j} = \frac{\partial \Sigma}{\partial R} \frac{\partial R}{\partial j}. \tag{I.5}$$

Equation (I.5) is easily solved for $\partial \Sigma / \partial R$.

The time derivative of velocity simplifies considerably in the Lagrangian system since j is independent of time. In the Eulerian system we have

$$\dot{u} = \frac{\partial u}{\partial t} + \frac{dR}{dt} \frac{\partial u}{\partial R}, \tag{I.6}$$

while in the Lagrangian one has simply

$$\dot{u} = \frac{\partial u_j}{\partial t}. \tag{I.7}$$

Using (I.5) and (I.7), we obtain the following first-order difference approxima-
tion to the equation of motion (superscripts denote cycle, subscripts denote
Lagrangian coordinate, and $R_j^n - R_{j+1}^n > 0$):

$$u_j^{n+\frac{1}{2}} = u_j^{n-\frac{1}{2}} - \Delta t^n \left(\frac{\Delta P/\Delta j}{\rho(\Delta R/\Delta j)} + \frac{4}{3} \frac{\Delta K/\Delta j}{\rho(\Delta R/\Delta j)} \right) + B + g, \qquad (I.8)$$

where

$$\frac{\Delta P}{\Delta j} = P_{j-\frac{1}{2}}^n + Q_{j-\frac{1}{2}}^{n-\frac{1}{2}} - P_{j+\frac{1}{2}}^n - Q_{j+\frac{1}{2}}^{n-\frac{1}{2}},$$

$$\frac{\Delta K}{\Delta j} = K_{j-\frac{1}{2}}^n + QK_{j-\frac{1}{2}}^{n-\frac{1}{2}} - K_{j+\frac{1}{2}}^n - QK_{j+\frac{1}{2}}^{n-\frac{1}{2}},$$

$$2\rho \frac{\Delta R}{\Delta j} = \frac{M_{j-\frac{1}{2}}}{V_{j-\frac{1}{2}}^n} \left(R_{j-\frac{1}{2}}^n - R_j^n \right) + \frac{M_{j+\frac{1}{2}}}{V_{j+\frac{1}{2}}^n} \left(R_j^n - R_{j+1}^n \right),$$

$$\frac{B}{8} = \frac{K_{j+\frac{1}{2}}^n + QK_{j+\frac{1}{2}}^{n-\frac{1}{2}}}{R_j^n + R_{j+1}^n} \left(\frac{V_{j+\frac{1}{2}}^n}{M_{j+\frac{1}{2}}} \right) (1 - \xi) + \frac{K_{j-\frac{1}{2}}^n + QK_{j-\frac{1}{2}}^{n-\frac{1}{2}}}{R_{j-1}^n + R_j^n} \left(\frac{V_{j-\frac{1}{2}}^n}{M_{j-\frac{1}{2}}} \right) \xi,$$

$$\xi = \frac{R_j^n - R_{j+1}^n}{R_{j-1}^n - R_{j+1}^n}.$$

I.2.2.2 Strain Calculation

After the motion of the material under the influence of the existing stress field
has been calculated form (I.8), one must now find how this motion alters the
stress field.

   If we assume that the medium is isotropic, then the stress–strain relation
(Hooke's Law) has the following form for spherical symmetry:

$$\dot{T}_{RR} = \lambda \frac{\dot{V}}{V} + 2\mu \frac{\partial u}{\partial R}, \qquad (I.9)$$

$$\dot{T}_{\theta\theta} = \dot{T}_{\phi\phi} = \lambda \frac{\dot{V}}{V} + 2\mu \frac{u}{R}, \qquad (I.10)$$

where λ and μ are the Lamé constants and V is the volume.

   From the conservation of mass we have

$$\frac{\dot{V}}{V} = \frac{\partial u}{\partial R} + 2\frac{u}{R}. \qquad (I.11)$$

The dot represents a time derivative along a particle path. This will allow us
to write the stress–strain relation in incremental form where strain changes
will be referred to the current configuration of the element.

We use (I.4) to find $\dot{P}$ and $\dot{K}$:

$$\dot{P} = -k\frac{\dot{V}}{V} \tag{I.12}$$

(where $k = \lambda + \dfrac{2}{3}\mu$ is the bulk modulus),

$$\dot{K} = \mu\left(\frac{u}{R} - \frac{\partial u}{\partial R}\right) \tag{I.13}$$

The total volumetric strain is defined as $\left.\vphantom{\begin{array}{c}a\\b\\c\\d\end{array}}\right\}$ strain components

$$mu = \frac{V^0 - V}{V} \tag{I.14}$$

and (I.12) is replaced by

$$P = f(mu, e), \tag{I.15}$$

where e is the specific internal energy. The determination of f(mu,e) represents a major part of the equation-of-state work.

The strain components are thus calculated. Subprogram WAVE in the 3D finite element analysis given in this text simply does that. In the strain terms in the program BANG-F, the terms p^{n+1} and k^{n+1} etc. are evaluated.

I.2.2.3 Calculation of Stress (P) as σ_{3D} (Three-Dimensional Stress)

In the code the calculation of mean stress depends on the state of the material. During shock loading, (I.15) becomes

$$\sigma_{3DH}^{n+1} = f_H(mu^{n+1}), \tag{I.16}$$

where f_H is determined from hydrostatic compressibility and Hugoniot measurements on core samples.

The calculation during release depends on the maximum internal energy that has been deposited in the zone. If $e_{j+\frac{1}{2}}^{\max} > e_v^I$, then P^{n+1} is calculated using a set of gas tables, in which P is listed as a function of energy with density as the parameter. The quantity e_v^I is the vaporisation energy which is related to the difference between the shock-deposited internal energy and the area under the Hugoniot (the shaded area in Plate I.4). The vaporisation energy is obtained from the equation in Plate I.4, where P_V is the pressure value for which the shaded area is just equal to the vaporisation "waste heat" for the material (2,800 cal g^{-1} for SiO$_2$ in this case). A reference is made to Plate I.5.

I.2.2.4 Calculations for Deviatoric Stress and Crack

This procedure has been clearly underlined in many areas in Chap. 4.
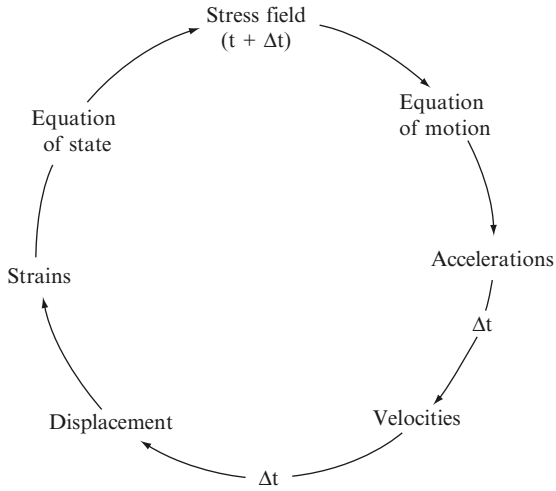
Cycle of interactions treated in calculating stress wave propagation
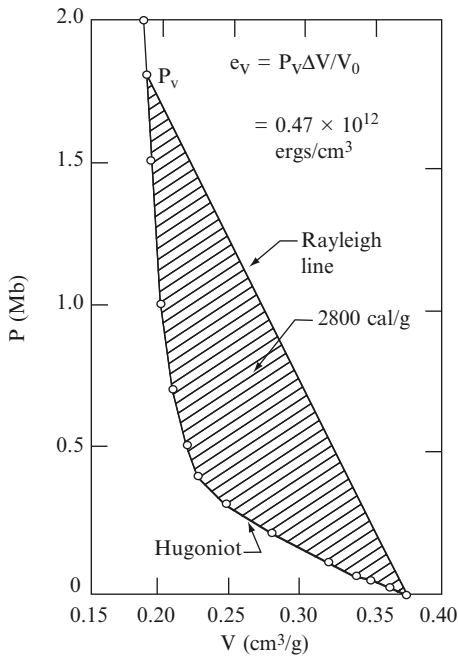
Calculation of vaporization energy

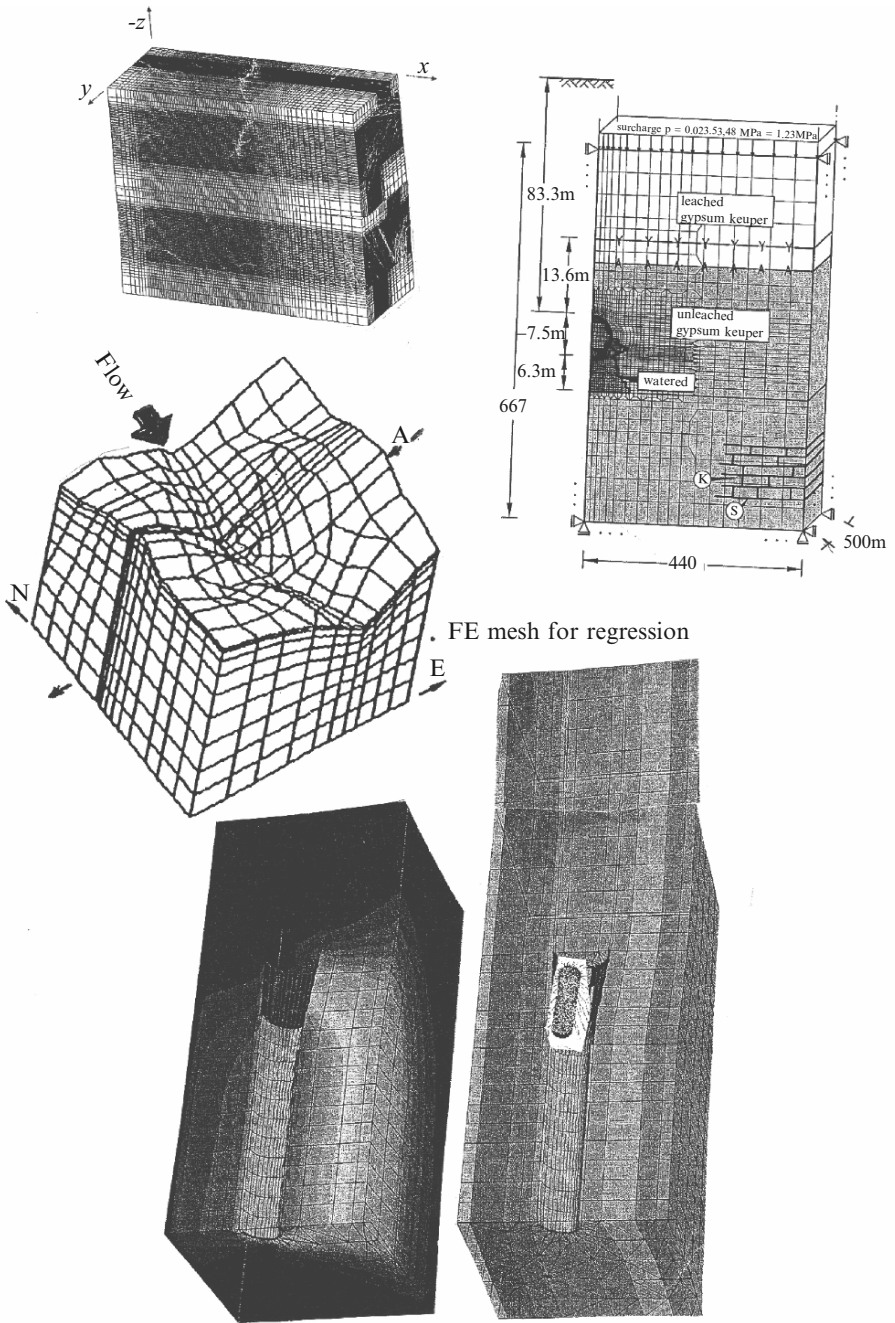**Plate I.4.** (with compliments of Cherry, J.T. et al. and IAEA-PL-388/13 1966)

Plate I.5. Finite element analysis of stress and stability

I.2.2.5 Strength Data in 3D Analysis

The rock data can act as an input since a large variety of strength tests are available for any particular site and zone in a specific country. Yield strengths $\bar{y}$ for limestone, granite, dolomite, Pyrex glass etc. do exist in literature and can be obtained in laboratory tests.

I.2.3 A Comparative Study of the Finite Element Analysis Results with Cherry and Peterson Results

I.2.3.1 Experimental Studies

Model studies were done in which a charge of high explosive and a number of pressure transducers at various distances from the charge were imbedded in a large block of grout which was allowed to set and harden. When the charge was detonated in the hardened grout, the resultant stress history was determined from the pressure transducer data.

The grout was a special mix called DF-5A, developed by the US Army Corps of Engineers. It was poured into an approximately cubical form 60 cm on a side, with the top side given a slight cylindrical curvature to facilitate study of its free surface behaviour by shadowgraph photography. A 4 cm diameter spherical charge of LX-04 high explosive was placed 14 cm below this free surface. Ten pressure transducers sensitive to radial stress were placed at distances between 4.5 and 14 cm from the charge. The transducers were all at least 10 cm below the free surface, and most of them were below the level of the charge. For the experiment, the entire form was buried in sand or gravel with only the free surface protruding.

The explosive was detonated and the free surface velocity was measure with a streaking camera in "shadowgraph" configuration. The cylindrical free surface simplified this measurement. Pressure transducers were 1.25 cm diameter 0.5 mm thick Z-cut tourmaline disks (Hearst et al. [I.9]). A characteristic of the DF-5A grout is the presence of voids due to air in the mix, a desirable feature both for transducer bonding and for producing the "locking solid" behaviour characteristic of porous rocks (Fig. I.1).

The purpose of the experiment was to compare the experimental results with the code solutions. These calculations wereperformed using the material properties furnished from laboratory tests on grout samples. Data shows the loading and unloading hydrostats measure for the grout. Figure I.2 the strength data obtained from triaxial compression tests. One regards the wet strength as the equilibrium strength and attempt to compensate for the difference between the wet and dry materials by including a strain rate term (K_2^I) of 4 kb in the equation of state. A Poisson's ratio of 0.2 was obtained from ultrasonic measurements on grout cylinders.

Figures I.3–I.5 compare calculated and measure radial stress histories at 6.5, 7.5, and 9 cm. At 7.5 and 9 cm the calculated peak radial stress is high
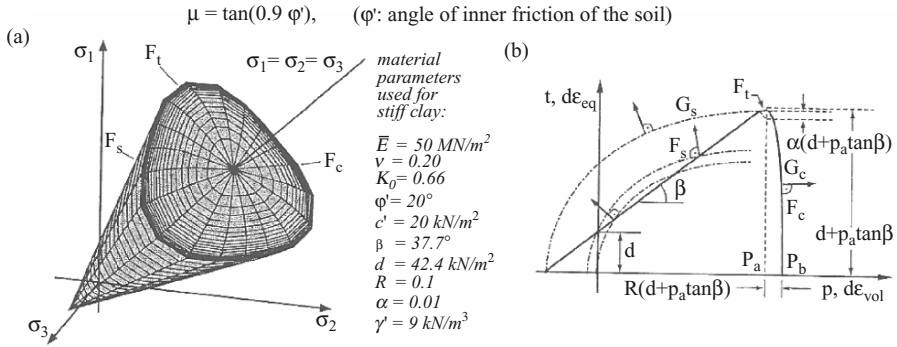
$\mu = \tan(0.9\,\varphi')$,   ($\varphi'$: angle of inner friction of the soil)

(a)

(b)

material parameters used for stiff clay:

$\bar{E} = 50\ MN/m^2$
$v = 0.20$
$K_0 = 0.66$
$\varphi' = 20°$
$c' = 20\ kN/m^2$
$\beta = 37.7°$
$d = 42.4\ kN/m^2$
$R = 0.1$
$\alpha = 0.01$
$\gamma' = 9\ kN/m^3$

Fig. I.1. Elements: Tetrahedral 4×10^6 degrees of freedom. Explosive: 5 kt and 25 kt of TNT
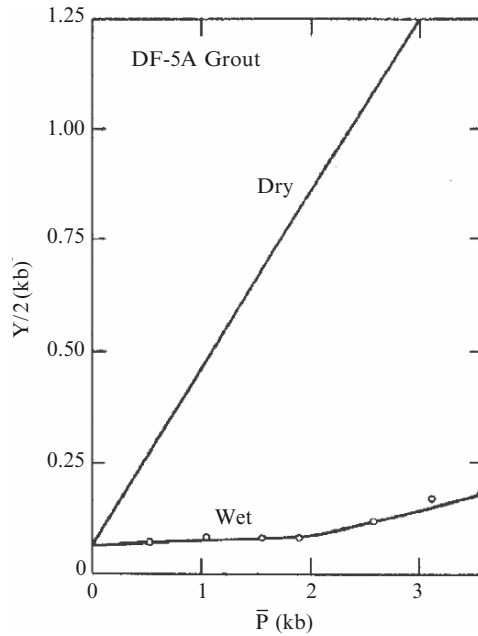
Fig. I.2. Strength of DF-5A grout

and the shock arrives too fast. Figure I.6 compares calculated and measure peak radial stress versus radial distance. Again the high calculated value is apparent. The calculated free surface (spall) velocity was $60\ \mathrm{m\ s^{-1}}$ compared to an observed value of $53\ \mathrm{m\ s^{-1}}$, rather encouraging agreement considering this measurement is the easiest to obtain and probably the most reliable part of the experimental effort.
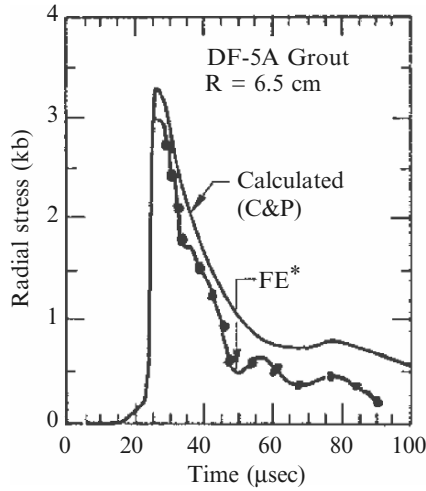
Fig. I.3. Stress history in DF-5A grout 6.5 cm from high explosive detonation.
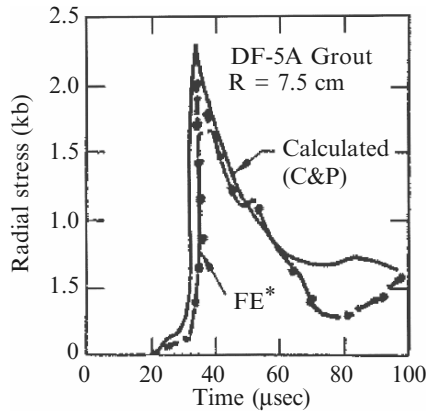NOTE: *FE mean 3D Finite Element Analysis

Fig. I.4. Stress history in DF-5A grout 7.5 cm from high explosive detonation.
NOTE: *FE mean 3D Finite Element Analysis

In view of the complexity of the grout equation of state, the agreement between calculation and experiment is considered to be good, at least encouraging enough to warrant improvement in the stress-history measurement techniques (too many gauge failures now occur) and to ask for a detailed study of the variability of the grout material properties.
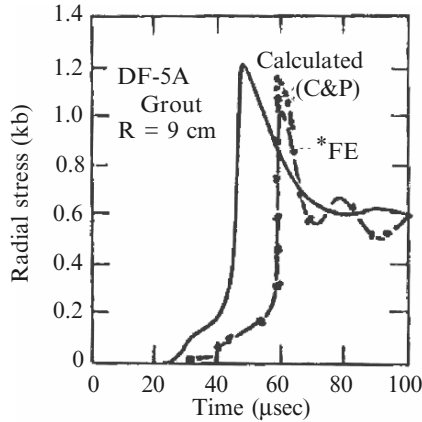
Fig. I.5. Stress history in DF-5A grout 9 cm from high explosive detonation. NOTE: *FE mean 3D Finite Element Analysis
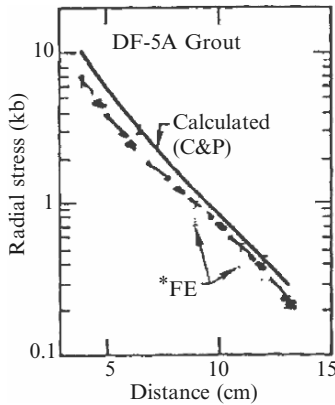

Fig. I.6. Peak radial stress in DF-5A grout versus distance from high explosive detonation. NOTE: *FE mean 3D Finite Element Analysis

I.2.3.2 Hardhat Granite

The hardhat event was a 5 kt contained nuclear explosion at a depth of 290 m in granite at NTS. The 10 kb offset between the HEL and the static isotherm is maintained for the code input. Figure I.7 gives the granite strength $(Y/2$ versus $\bar{P})$ for various states of the test sample. The strength data that gives best agreement between calculation and observation are the wet, precracked values. In order to make these strength data consistent with the HEL data, a strain term $\left(K_2^I\right)$ of 7.5 kb was included in the equation of state. This value corresponds to the 10 kb offset between the static isotherm and the HEL. A Poisson's ratio of about 0.28 was obtained from ultrasonic laboratory measurements.
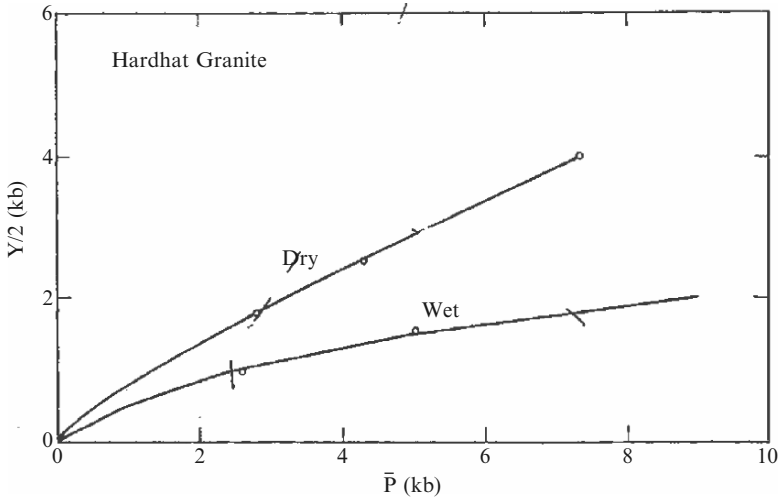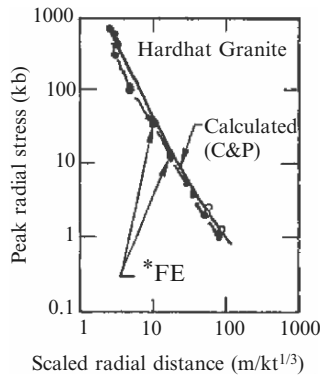
Fig. I.7. Strength of Hardhat granite

Fig. I.8. Calculated and observed peak radial stress in Hardhat granite as a function of scaled distance from a nuclear shot. NOTE: *FE mean 3D Finite Element Analysis

The calculation was begun by uniformly distributing 5 kt of internal energy in a sphere of radius 3.15 m at normal density $(2.67 \, \text{g cm}^{-3})$ and using the appropriate gas tables for this region $(SiO_2 + 1\% \, H_2O$, Butkovich [I.2]). Code calculations show that the mass of rock vaporised is proportional to the yield, and for silicate rocks approximately $70 \times 10^6 \, \text{g kt}^{-1}$ is vaporised. The value 3.15 m corresponds to the radius of vaporisation for the 5 kt source.

Figure I.8 shows calculated and observed peak radial stress versus scaled radius. Figures I.9–I.12 show calculated radial stress versus distance at 4, 16, 24 and 40 ms, A striking feature of this sequence is the emergence of the precursor (P) and the decay of the main shock.
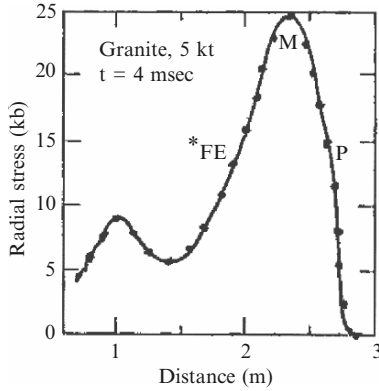
Fig. I.9. Calculated radial stress versus distance, 4 ms after a 5 kt shot in Hardhat granite. NOTE: *FE mean 3D Finite Element Analysis
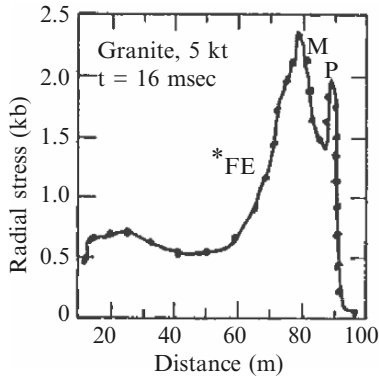

Fig. I.10. Calculated radial stress versus distance, 16 ms after a 5 kt shot in Hardhat granite. NOTE: *FE mean 3D Finite Element Analysis

Figures I.13 and I.14 show calculated and measured radial stress versus time at 62 and 120 m. The experimental stress-history data do not exhibit the strong precursor obtained from the calculations. This may be due, in part, to the weak grouting material used for an impedance match between the transducer and the granite formation.

The calculation gives a final cavity radius (corresponding to the initial gas-rock interface at 3.15 m radius) of 20.4 m. The measured Hardhat cavity radius is 19 m. Figure I.15 gives the calculated and observed reduced displacement potential (RDP) obtained from displacement versus time for a particle in the "elastic" region.

The RDP is a measure of the seismic efficiency of the medium. For a spherical outgoing elastic wave whose displacement is S_R we can write

Fig. I.11. Calculated radial stress versus distance, 24 ms after a 5 kt shot in Hardhat granite. NOTE: *FE mean 3D Finite Element Analysis
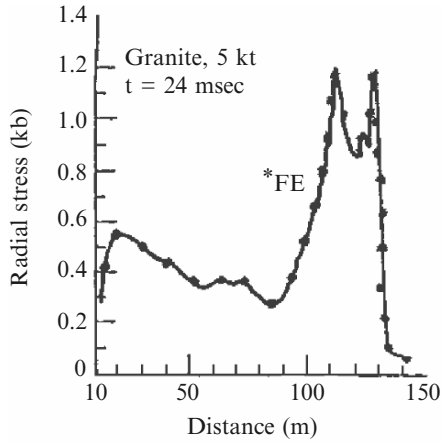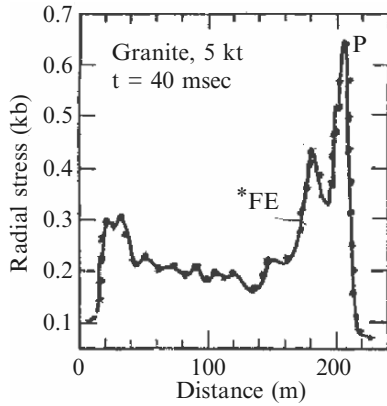

Fig. I.12. Calculated radial stress versus distance, 40 ms after a 5 kt shot in Hardhat granite. NOTE: *FE mean 3D Finite Element Analysis

$$S_R = \frac{\partial}{\partial R}\left[\frac{f(t - R/V_P)}{R}\right], \tag{I.17}$$

we define the RDP as:

$$RDP = f(t - R/V_p), \tag{I.18}$$
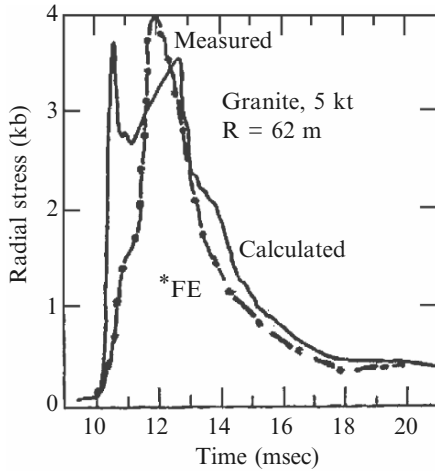
Fig. I.13. Calculated and measured stress history in Hardhat granite, 62 m from a 5 kt shot. NOTE: *FE mean 3D Finite Element Analysis
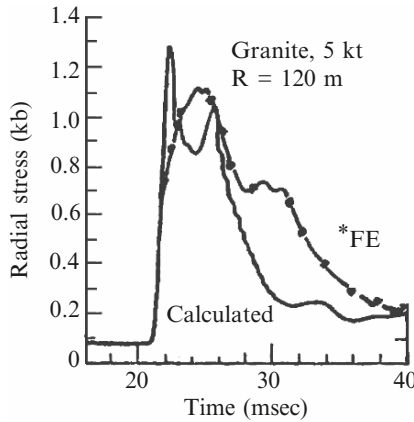
Fig. I.14. Calculated and measured stress history in Hardhat granite, 120 m from a 5 kt shot. NOTE: *FE mean 3D Finite Element Analysis

where

$$V_P = \sqrt{\frac{k + \frac{4}{3}\mu}{\rho}}. \tag{I.19}$$

The RDP, obtained by integrating (I.17), gives the source function that determines the displacement of a particle at any point in the elastic region. The source function should scale from one shot to another by multiplying the RDP by the ratio of the yields involved.

The calculated and observed steady-state values of RDP agree. The early time disagreement could be due tot eh surface reflection returning to the

Fig. I.15. Calculated and observed reduced displacement potential (RDP) for a 5 kt shot in Hardhat granite. NOTE: *FE mean 3D Finite Element Analysis

instrument 60 ms from the onset of the direct wave (Werth and Herbst [I.11]). No calculation incorporating reasonable changes in the equation of state has been able to produce the observed overshoot in RDP.

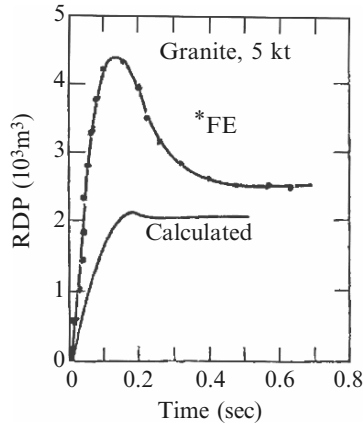Additional calculations for larger yields show that the maximum not only increases but the shape broadens. This suggests that as the yield increases the bulking of the rock, as t collapses into the cavity, should eventually become the controlling factor in determining chimney height.

The crack number, assuming it is calculated correctly, should be related to permeability changes in the medium. Apparently permeability is both difficult and expensive to measure. However, it is suggested that permeability should reach a minimum between 30 and 40 m from the cavity for 5 kt. This zone of low permeability might serve a useful purpose in some applications by helping to limit the spread of gas-borne radioactivity from the cavity; however unless it is removed by chimney collapse, it might severely limit the effectiveness of reservoir simulation.

I.2.3.3 Gasbuggy

Gasbuggy was an experiment in nuclear stimulation of a gas-bearing formation in Rio Arriba County, New Mexico, sponsored jointly by the US Atomic Energy Commission, the El Paso Natural Gas Company, and the US Bureau of Mines. A 25 kt nuclear explosive was detonated 1,280 m underground, in the Lewis shale formation 12 m below the gas-bearing Pictured Cliffs sandstone. The objective was to evaluate the effectiveness of the nuclear explosion in increasing the permeability of the Pictured Cliffs formation and thus improving the recovery of gas from it.

The best experimental measurements, in terms of stress wave propagation, were obtained by Sandia Laboratories in a deep borehole 457 m from the

emplacement hole. This part of the experiment was funded by the Advanced Research Projects Agency (ARPA).

Logging data near the emplacement hole and in the ARPA instrument hole indicate that the compressional velocity in the Lewis shale ranges from 4.75 to $3.87\,\mathrm{m\,ms^{-1}}$ and the density varies from 2.4 to $2.6\,\mathrm{g\,cm^{-3}}$. Figure I.16 shows the loading and unloading static compressibility data for the Lewis shale. The loading data gives a bulk modulus of about $160\,\mathrm{kb}$ (curve A) and an initial density of $2.61\,\mathrm{g\,cm^{-3}}$. Using a Poisson's ratio of 0.3 (obtained from the shear velocity log) we obtain a compressional velocity of about $3\,\mathrm{m\,ms^{-1}}$, a value that is not consistent with the logging data.
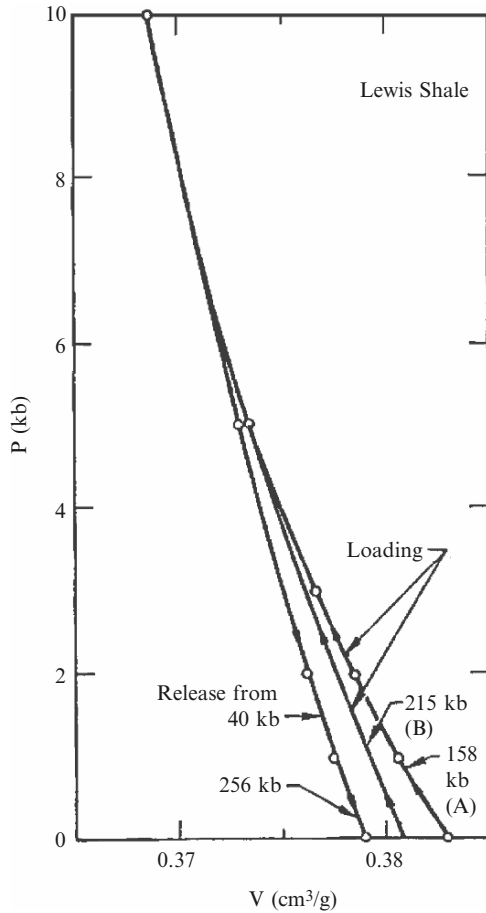

Fig. I.16. Compressibility of Lewis shale, the formation in which the Gasbuggy explosive was located
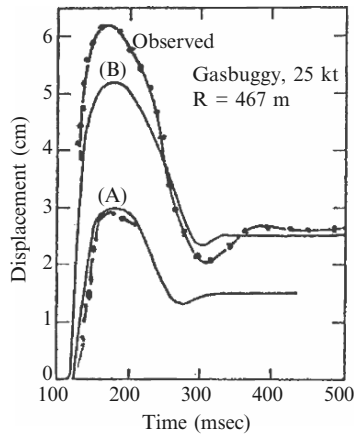
Fig. I.17. Calculated and observed reduced displacement history in Lewis shale 467 m from te 25 kt Gasbuggy shot

In order to obtain a reasonable value for the compressional velocity we have found it necessary to ignore all the loading compressibility data below 3 kb on the basis that these data are probably influenced heavily by both the release of overburden pressure (0.3 kb) on the core and the coring technique itself. The loading compressibility curve B shown in Figure I.16 was accordingly assumed for the Lewis shale. This curve, having a bulk modulus of 215 kb, gives a compressional velocity of $3.5\,\mathrm{m\,ms^{-1}}$, in fair agreement with the logging data.

This change in compressibility curves severely affects the seismic coupling. The effect is due entirely to the attenuation of the stress wave by the pressure release calculation in the code. As indicated in Fig. I.16, the measured static release path form 40 kb has a slope of 256 kb, corresponding to a rarefaction speed of about $3.7\,\mathrm{m\,ms^{-1}}$. These rarefactions overtake the slower moving $(3.0\,\mathrm{m\,ms^{-1}})$ compression front and continuously decrease its stress and particle velocity.

Figure I.17 shows measured and calculated displacement versus time at 467 m from the 25 kt source. The difference between the two calculations is obtained by changing the compressibility curve from A to B as discussed above (Fig. I.16). The sensitivity of this part of the calculation to changes in the "locking: portion of the equation of state seems dramatic until one considers the magnitude of the changes that are being made in the only material attenuation mechanism operative in the code (rarefaction velocity compared to shock velocity).

Figure I.18 gives the measured and calculated RDP corresponding to the displacement of Fig. I.17. We see that with compressibility curve B, twice as much energy is coupled into the elastic region as with curve A. These calculations indicate that a detailed equation-of-state effort is required before a seismic coupling calculation can be attempted. Even then, since the low pres-
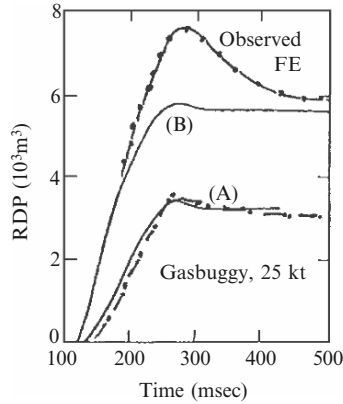
Fig. I.18. Calculated and observed reduced displacement potential (RDP) for Gasbuggy shot

sure part of the equation of state seems to control the coupling, we may not be able to predict this parameter with confidence. The key issue would seem to be obtaining agreement between the sonic logs and the static compressibility data. The Gasbuggy experiment represented the first time such severe disagreement existed between the field and laboratory data.

Calculations indicating the severity of the fracture (similar to those for Hardhat) have been performed for the Gasbuggy environment. Figure I.19 shows the compressibility curves for the Lewis shale, the Pictured Cliffs sandstone, and the Fruitland coal. Figure I.20 shows the strength curves used in the calculations.

Figure I.21 shows calculations of number of cracks per zone versus distance from the shot point for paths vertically upward through the various layers (layered calculation) and also for paths outward into the sandstone (Pictured Cliffs calculation). As noted preshot, the coal seam located between 100 and 112 m above the shot point reduces the fracturing at this distance, which corresponds to the measured height of the Gasbuggy chimney. This highly compressible coal seam also sends a rarefaction into the Pictured Cliffs formation, and the fracture number is increased accordingly. The observed postshot casing failures and gas entries are also consistent with the calculated data of Fig. I.21.

The calculated cavity radius was 26.3 m for the layered calculation and 25.8 m for the Pictured Cliffs calculation. These values compare closely with the 25.4 inferred from flow tests.

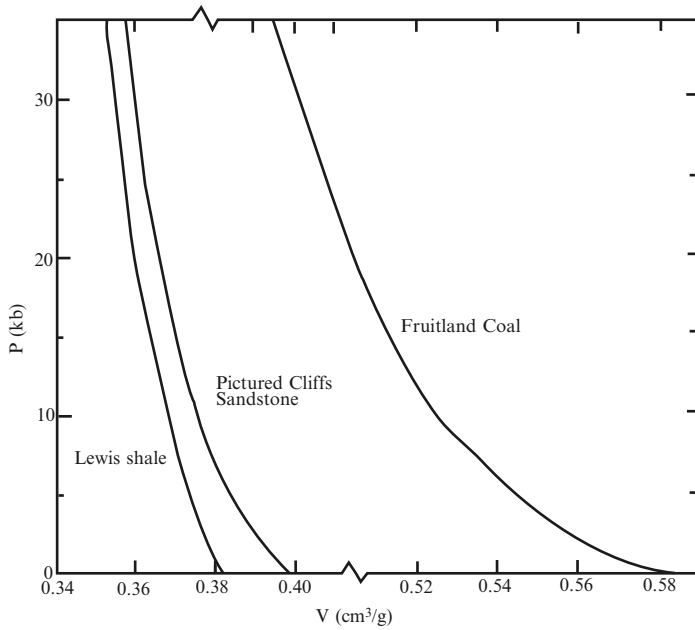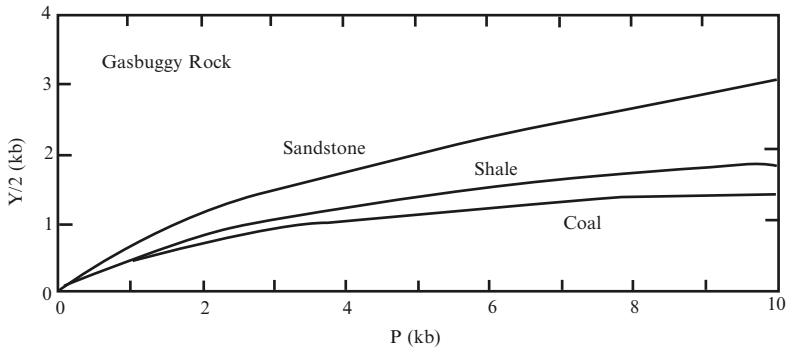**Fig. I.19.** Compressiblity of Gasbuggy rocks

Fig. I.20. Strength of Gasbuggy rocks

I.2.3.4 Data for Program BANG-F

BANG-F is a new version of Program ISOPAR which in many respects is identical to Programs ANSYS, ABACUS and MS NASTRAN etc. The following selected data used is reported:-

Rock masses: E values vary from 5,500 to 21,000 MPa
Poisson ratio: ν values vary from 0.2 to 0.28
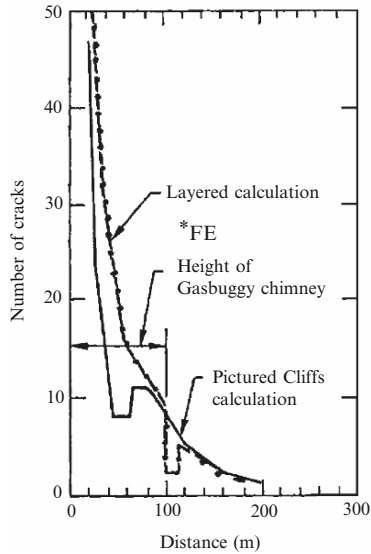
Fig. I.21. Calculated number of cracks versus distance fromt he Gasbuggy shot, for paths upward through the various layers and outward through the Pictured Cliffs sandstone. NOTE: *FE mean 3D Finite Element Analysis

Weight: γ values vary from 0.0265 to 0.0255 MPa m^{-1}
Dimensions: 3,500 m in NS direction to 500 m depth in EW.

Conclusions

A numerical model of stress wave propagation has been presented. We have included a listing of the SOC code (see Appendix) and have given a discussion of the material properties required to obtain a prediction of the stress-induced effects on the rock mass involved in an application. These effects include chimney height, seismic coupling, and permeability change. The seismic coupling parameter was shown to be primarily dependent on the low pressure part (<3 kb) of the equation of state. For high yields the controlling factor for chimney height should be cavity volume.

Future effort is required in the areas of Hugoniot release (especially for a fluid-saturated environment), laboratory strength measurements, and failure criteria. A significant improvement in the equation of state would result if the in situ rigidity modulus could be measured directly.

The preshot calculations for the Gasbuggy experiment indicate that useful predictions of cavity radius and chimney height can be made when an adequate effort is made to obtain equation-of-state data for the rock involved.

In general the code seems to be doing well enough in predicting stress wave propagation that we can begin looking at derived numbers, such as number of cracks per zone, for some insight into predicting stress-induced changes in permeability.

J

Bridges

J.1 Concrete Bridges Subject to Blast Loads

J.1.1 Introduction

A standard precast concrete bridge consists of 12 standard I-beams placed at 1.5 m c/c supporting reinforced concrete deck slab as given in Plate J.1. The deck carries three lanes and the beams are acting in composite with a 150 mm thick structural slab. The bridge deck is supported by three concrete piers placed at 5.2 m distance from each other. It is decided to design this bridge first and then it is subjected to blast loads at suitable positions.

Blast-resistant design has traditionally been considered only for essential government buildings, military structures, and petrochemical facilities. Recent terrorist threats to bridges in California and New York have demonstrated the need to evaluate the vulnerability of our transportation infrastructure. Bridge engineers, however, have not typically considered security in the design process and most of the current state of knowledge of the design of structures subjected to blast effects is based on the performance of buildings rather than bridges.

Before engineers can begin to design bridges to withstand blast loads, they need to develop an understanding of the principles of blast wave propagation and its potential effects on bridge structures. Through the use of computer-based simulation, we can gain a better understanding of blast effects on bridge components and prioritise our efforts for experimental studies of the most promising retrofit solutions.

To design bridges to withstand terrorist attacks, changes need to be incorporated into the design proves. The test gives a useful approach for security and redundancy and can be followed for bridges. During the initial stages security can be incorporated through site layout principles such as the elimination of dark hiding spaces by including additional lighting, planting protective landscaping to increase the standoff distance to piers (ensuring that overgrown vegetation will not interfere with lines of sight to critical areas), and
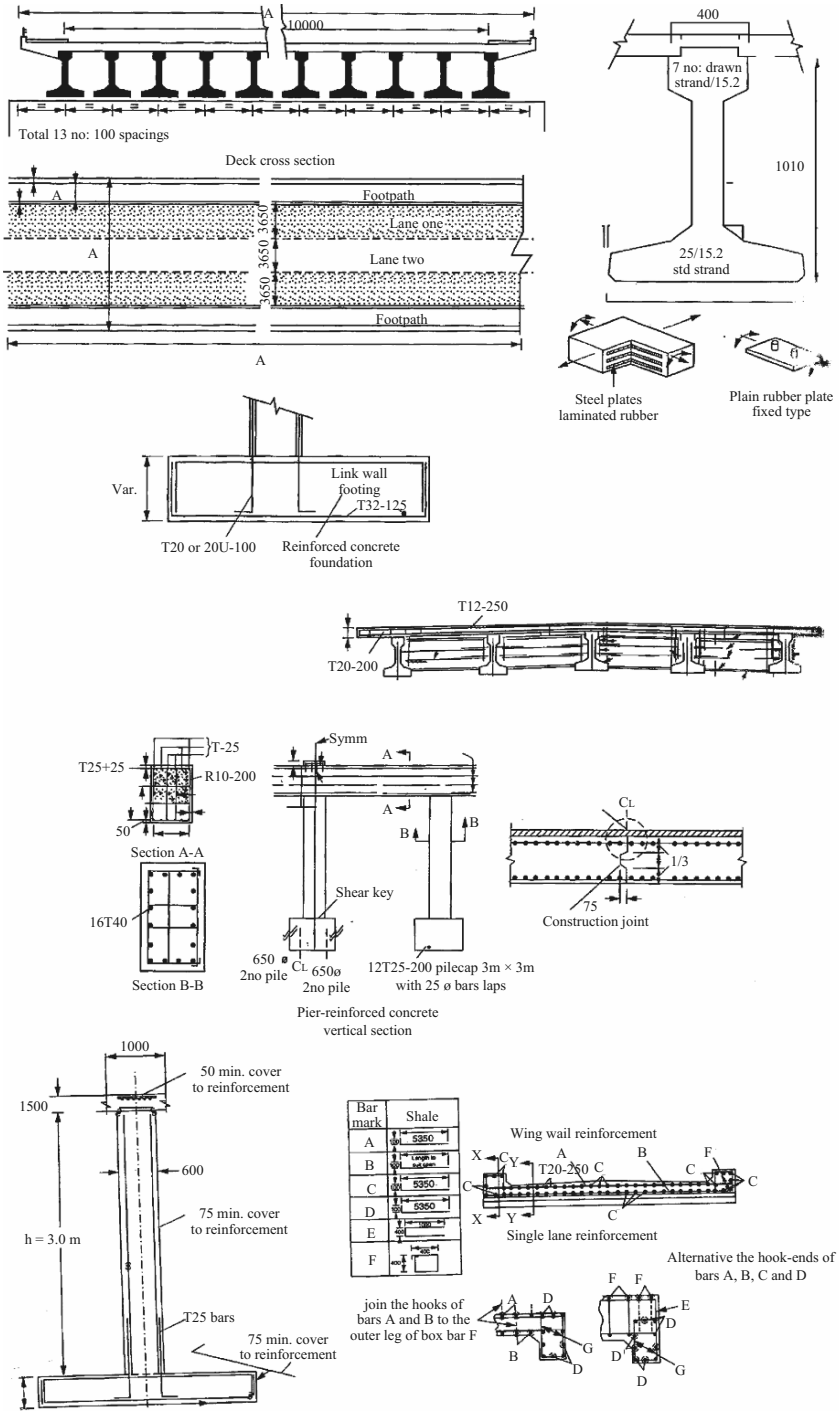
Plate J.1. Typical concrete bridge details

elimination of access to critical areas such as beneath the deck or inside towers. Parking spaces should be eliminated beneath critical bridges, and architectural features that magnify blast effects should be avoided. These features include recesses or offsets in structural members where blast effects could be amplified. A reference is also made to the principles established by the City of London Police as discussed in the text for buildings.

When an explosion occurs beneath a bridge, the deck will be subjected to large uplift forces, which may be amplified by a pressure build-up in confined regions between the girders and near the abutment. These uplift forces may cause the deck to separate from the girders if the shear connectors are incapable of resisting the loads induced by the deck response. Large explosive loads have the potential to cause shear or membrane failure of the deck. Deck failures will usually be localised and cause the blast loads to vent from confined areas, which may relieve the loads on he supporting structural elements. If shear connectors are capable of restraining (or at least partially restraining) the uplift of the deck, forces will be transferred to the floor system and girders. Without shear studs, however, it may be possible for the deck to separate form the girders with a resulting impact force after the blast loads have dissipated. In the case of above-deck explosions, shear connectors provide composite behaviour (or at least partially composite behaviour) and aid in resisting blast loads. Therefore, given the uncertainties associated with potential terrorist courses of action, and due to the fact that the deck-girder interaction varies in importance for different types of bridges (i.e. box girder bridges versus I-girder bridges), the design of shear connector details must be carefully considered for various threat scenarios and for various bridge types.

The response of the girders will depend on the loads transferred to them not only through the deck response but also by the effect of localized damage. Concrete may be removed through spalling (defined as a tension failure caused by a shock wave travelling through a structural member, reflecting off the back face, reversing direction, and creating tension forces as it travels back toward the centre of the member) or cratering (a compression crushing failure occurring on the blast face). Considering the effects of this localized damage, uplift forces may lead to significantly reduced member capacities from a loss of cover and prestress bonding.

A reference is made to the author's following books for more comprehensive analyses.

- Manual of Numerical Methods in Concrete, Thomas Telford, London, 2001
- Prototype Bridge Structures – Analysis and Design, Thomas Telford, London, 1999

For explosions below the deck, piers and columns are subjected to large lateral forces that may cause large deformations, shear, or flexure failure. If they are rigidly connected to the girders, the piers may even experience a net tensile force. Cratering and spalling may lead to the loss of cover, especially if the standoff distance is small. Preparation of explosive charges also affects loads

acting on structural components as pressure distributions and magnitudes can be changed significantly by tamping (covering and packing) the charges in the soil, placing them underwater, or cutting holes for lacing them inside a structural member.

One proposes a set of performance-based design standards for terrorist threats against bridges. The design standard for a given bridge is based on its criticality as determined by a vulnerability assessment, which dictates the performance category under which it falls. These standards establish a baseline threat level for design loads (specific charge weights are given in the texts) and define the acceptable level of damage under these loads. The design loads and acceptable damage for each category are based on a balanced assessment of the threats, acceptable risks, and available resources. The most likely threat scenarios are determined form a threat assessment, using the worst possible explosive or impact locations independently for each structural element being designed. For example, when designing the footings, blast loads are assumed to be at ground level and directed downward, while they should be directed laterally for pier design (factors such as the explosive initiation location, degree of tamping, and charge shape can significantly affect the blast environment at a given orientation from the detonation point).

As for analyses, the author suggests the following methods together with finite element solution procedures:

– Uncoupled Analysis: This provides for a simple problem, a conservative prediction for yielding and failure.
– Coupled Analysis: This accounts for coupled effects of structural response for complex models.
– Dynamic Analysis: This gives an increased accuracy taking into consideration inertia effects. With time increasing, more nodes are added beyond limit.
– SDOF Analysis: A reasonably accurate method for simple structures, but difficult to correctly model the structure. Estimate is conservative.
– MDOF Analysis: Increased accurately for complex structures for higher order response. Excessive computational time.

J.1.2 Design of the Precast Prestressed M6 Beam for the Overbridge

J.1.2.1 Introduction

Figure J.1 shows a typical M6 beam cross-section provided by the MOT and available from the British Cement Association, Crowthorne, Berkshire. Reference is made to Fig. 5.44 showing the preliminary general arrangement drawing. The total number of 11 M6 beams at 1.0 m centres with effective
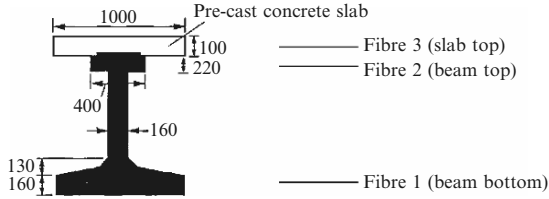
Fig. J.1. Typical M6 beam cross-section

Table J.1. Beam and composite properties

Property	Beam$_1$	Composite$_2$
Area mm^2	$A_1 = 387 \times 10^3$	$A_2 = 627 \times 10^3$
Centroid mm	$a_{1,1} = 409$	$a_{1,2} = 670$
Second moment mm^4	$I_1 = 47.6 \times 10^9$	$I_2 = 116.8 \times 10^9$
Modulus 1	$z_{1,1} = 116.2 \times 10^6$	$z_{1,2} = 174.3 \times 10^6$
Modulus 2	$z_{2,1} = 75.4 \times 10^6$	$z_{2,2} = 315.7 \times 10^6$
Modulus 3		$z_{3,2} = 233.6 \times 10^6$

span 20 m are simply supported. Additional data are detailed below and supplemented by Table J.1.

J.1.2.2 Strands

(1)   standard 15.2 mm $A_S = 139 \, \text{mm}^2$

   f_{pu} (nominal strength) $= 1{,}670 \, \text{N mm}^{-2}$

   P_u (characteristic load) $= 232 \, \text{kN}$

(2)   drawn type 15.2 mm $A_S = 165 \, \text{mm}^2$

   $$f_{pu} = 1{,}820 \, \text{N mm}^{-2}$$
   $$P_u = 300 \, \text{kN}$$

   initial load $0.8P_u, 0.7P_u = 0.8P_u$

   modulus of elasticity $(E_s) = 195 \pm 10 \, \text{kN mm}^{-2}$

(a) *Concrete grades*

$$\text{beam } f_{cu} = 50 \, \text{N mm}^{-2}$$
$$f_{ci} = 40 \, \text{N mm}^{-2} \, (\text{max})$$
$$\text{precast slab } f_{cu} = 40 \, \text{N mm}^{-2}$$

The 11 M6 beams placed at 1 m c/c with 160 mm thick precast RC slab attached to it with fully incorporated dowels have simple spans of 20 m.
   Note that:

$$\text{concrete density} = 23.6 \, \text{kN m}^{-2}$$
$$\text{surfacing material density} = 3.9 \, \text{kN m}^{-2}$$

(b) *Composite interior beam*
The properties are assessed as follows:

$$\text{depth} = 1{,}605\,\text{mm}$$
$$y_b = 901\,\text{mm}$$
$$Z_b = 233.5 \times 10^6\,\text{mm}^3$$
$$\text{area} = 616{,}880\,\text{mm}^2$$
$$Z_{\text{top precast}} = 401.59 \times 10^6\,\text{mm}^3$$
$$Z_{\text{top } in \ situ} = 298.84 \times 10^6\,\text{mm}^3$$
$$\text{second moment of area} = 210.38 \times 10^9\,\text{mm}^4$$

(c) *Composite edge beam*
The properties are assessed as follows:

$$\text{depth} = 1{,}925\,\text{mm}$$
$$y_b = 1{,}079\,\text{mm}$$
$$Z_b = 284.38 \times 10^6\,\text{mm}^3$$
$$\text{area} = 771{,}920\,\text{mm}^2$$
$$Z_{\text{top precast}} = 866.84 \times 10^6\,\text{mm}^3$$
$$Z_{\text{top } in \ situ} = 362.70 \times 10^6\,\text{mm}^3$$
$$\text{second moment of area} = 306.85 \times 10^9\,\text{mm}^4$$

(d) *In situ transverse diaphragms plus top slab*
data:

$$\text{depth} = 1{,}215\,\text{mm}$$
$$y_b = 984\,\text{mm}$$
$$Z_b = 91.65 \times 10^6\,\text{mm}^3$$
$$\text{area} = 1{,}022{,}570\,\text{mm}^2$$
$$Z_t = 390.39 \times 10^6\,\text{mm}^3$$
$$\text{second moment of area} = 90.182 \times 10^9\,\text{mm}^4$$

The loading is uniformly distributed per beam.
Pretensioned beam area cm^2

$$0.387 \times 23.6 = 9.13$$
$$0.160 \times 1.0 \times 23.6 = \underline{3.78}$$
$$12.91\,\text{kN m}^{-1}$$

and for the deck slab total dead surfacing is:

$$1 \times 3.9 = 3.90\,\text{kN m}^{-1}$$

(e) *Loading*

This considers nominal live loading on footways and future surfacing.
Nominal live load (HA + 45 units HB):

$$\text{dead load moment} = \frac{12.91 \times 20^2}{8} = 645.5\,\text{kNm}$$

$$\text{surfacing} = 3.90 \times \frac{20^2}{8} = 195.5\,\text{kNm}$$

Moments on beams 3 and 6:

	Beam 3	Beam 6
Additional superdead load (future surfacing)	68.6	9.8
Footway (live)	93.0	13.1
HB (45 units)	1,350.2	1,285.4
HA (additional) BD 37/88	186.8	391.5
HB (30 units)	900.12	856.9

(f) *SLS design moments due to superimposed dead and live loads (load combination I)(LCI)*

	γ_{fl}	Beam 3	Beam 6
Surfacing	1.2	207.0	207.0
Additional superdead	1.0	68.3	9.8
Footway (live)	1.0	93.0	13.1
HB (45 units)	1.15	1,552.71	1,928.05
HA (additional)	1.15	214.32	449.5
		2,135.33	2,607.65
HB (30 units)	1.15	1,035.2	985.5
Other loads		573.8	660.6
		1,609.0	1,646.1

(g) *Allowable stresses*

Limiting concrete stresses at transfer and during erection (due to prestress
and coexistent deadload and temporary loads during erection; see Fig. J.2.
Limits due to all other load combinations are represented by the lower
portion of Fig. J.2. Allowable stresses apply except for joints in segmental
construction. Where residual tension is not offset under service loads,
stresses are regarded as class 1.

SLS LC3 moments due to superimposed dead and live loads

	γ_{fl}	Beam 3	Beam 6
Surfacing	1.2	207.0	207.0
Additional superdead	1.0	68.3	9.8
Footway (live)	1.0	93.0	13.1
HB (45 units)	1.0	1,350.2	1,286.4
HA (additional)	1.0	186.8	391.5
		1,905.3	1,906.8
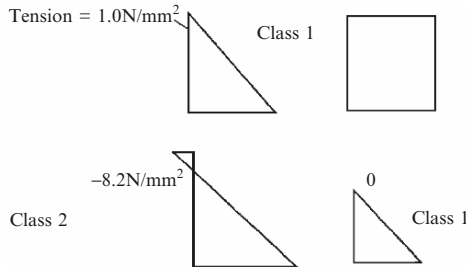
Fig. J.2. Limiting concrete stresses
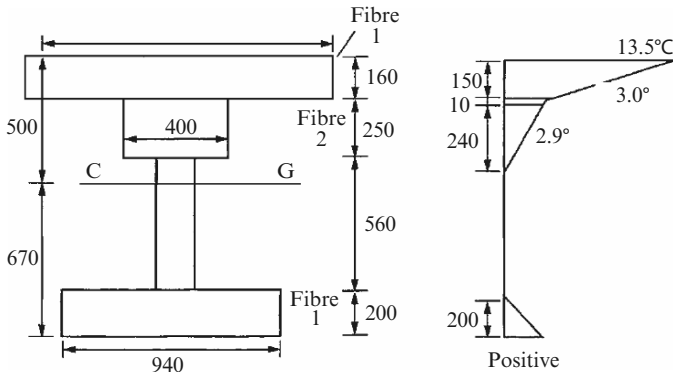
Fig. J.3. Illustration of temperature difference effects

Stresses at fibre 1

	LC1	LC1 mod	LC3
$\dfrac{M_1}{z_{1,1}}$	-4.77	4.77	-4.77
$\dfrac{M_2}{z_{1,2}}$	-14.97	9.18	-10.94
	-19.74	13.95	-15.71

Here temperature effects would be added and may become critical together with the effects of explosion

(h) *Temperature difference effects*

Simplify the beam section and apply the temperature differences given with a coefficient of thermal expansion taken as 12×10^{-6} per $°C$ (Fig. J.3). Reference is made to Table 3.2.1.3.1 of BS 5400. Take $E_c = 34\,\text{kN mm}^{-2}$ based on $f_{cu} = 50\,\text{N mm}^{-2}$ so that restrained temperature stress per $°C = 34 \times 10^3 \times 12 \times 10^{-6} = 0.408\,\text{N mm}^{-2}$.
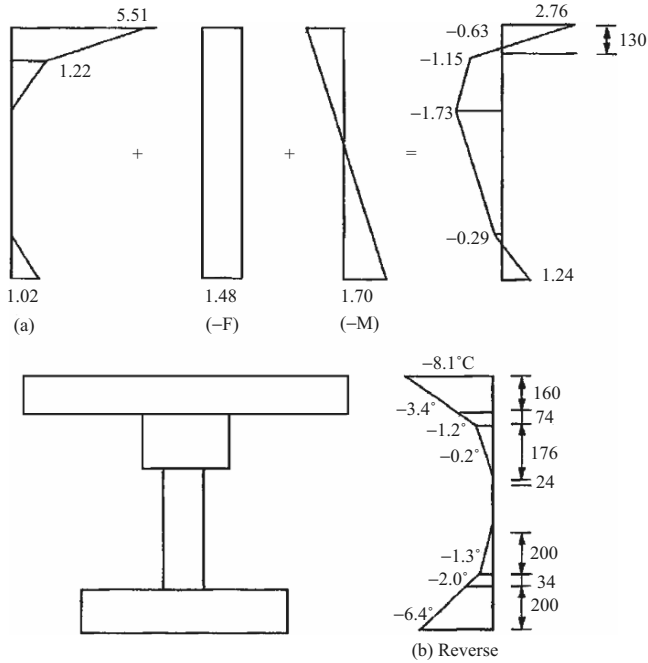
Fig. J.4. Stresses due to positive temperature difference

Force F to restrain temperature strain,

$$0.408 \times 1.5\{150(3.0 + 5.25) + 10 \times 2.95\} = 775.4\,\text{kN}$$
$$0.408(0.4 \times 240 \times 1.45 + 0.94 \times 200 \times 1.25) = \underline{152.7\,\text{kN}}$$
$$\underline{928.1\,\text{kN}}$$

Moment M about centroid of section to restrain curvature due to temperature strain (Fig. J.4):

$$0.408 \times 1.5\{150(3 \times 0.425 + 5.25 \times 0.45) + 10 \times 2.95 \times 0.345\}$$
$$+ 0.408(0.4 \times 240 \times 1.45 \times 0.260 - 0.94 \times 200 \times 1.25 \times 0.603)$$
$$= 340.15 - 43.05 - 297.1\,\text{kNm}$$

Force F to restrain temperatures strain,

$$-0.408\{1.5 \times 160(3.4 \times 2.35) + 0.4 \times 74(1.2 + 1.1)\}$$
$$-0.408\{0.4 \times 176(0.2 + 0.5) + 0.94 \times 200(2 + 2.2)\}$$
$$-0.408 \times 0.16\{34(1.3 + 0.35) + 200 \times 0.65 + 2.4 \times 0.1\}$$
$$= -5950.8 - 342.3 - 12.3 = -945.54\,\text{kN}$$
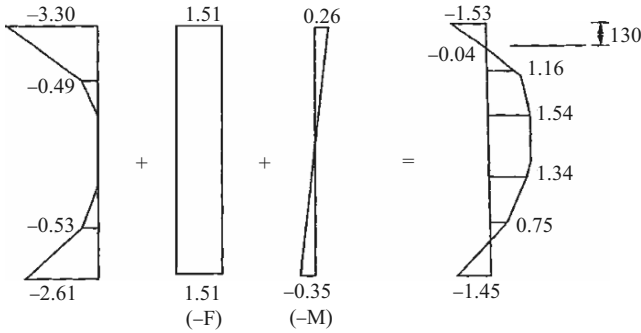
Fig. J.5. Restrain of curvature due to temperature strain

Moment M about centroid of section to restrain curvature due to temperature strain (Fig. J.5):

$$-0.408\{240(3.4 \times 0.420 + 2.35 \times 0.447)$$
$$+ 29.6(1.2 \times 0.303 + 1.1 \times 0.315)\}$$
$$-0.408\{70.4(0.2 \times 0.178 + 0.5 \times 0.207)$$
$$- 188(2 \times 0.57 + 2.2 \times 0.6037)\}$$
$$+0.065\{34(1.3 \times 0.453 + 0.35 \times 0.459)$$
$$+ 130 \times 0.369 - 2.4 \times 0.082\}$$
$$= -251.3 + 185.2 + 4.8 = -61.3 \, \text{kNm}.$$

Note that for the effects of temperature difference at the SLS (LC3), $\gamma_{\text{fl}} = 0.8$, so that the stresses shown above are to be multiplied by 0.8 and then combined with the stresses due to the design loads for LC3

(i) *Differential shrinkage effects*
Total shrinkage of in situ concrete $= 300 \times 10^{-6}$. Suppose two-thirds of this shrinkage takes place (precast concrete section) before the slab is added. The residual shrinkage is assumed to be 100×10^{-6}. The effect of residual creep strains may be considered. Let $E_{\text{c}} = 34 \, \text{kN mm}^{-2}$ for $f_{\text{cu}} = 50 \, \text{N mm}^{-2}$.

$$F = \text{force due to restraining differential shrinkage}$$
$$= -\varepsilon_{\text{diff}} E_{\text{C}} A_{\text{slab}} \phi = -200 \times 10^{-6} \times 34 \times 1{,}000 \times 160 \times 0.43$$
$$\approx -468 \, \text{kN}$$

Eccentricity given by $a_{\text{slab}} = 420 \, \text{mm}^2$.
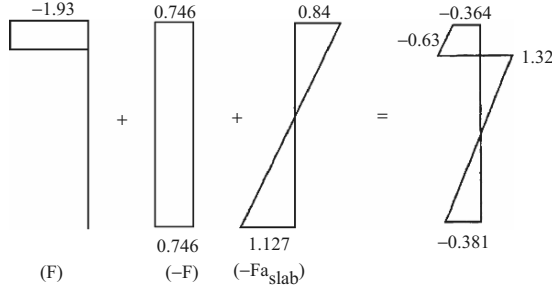
Fig. J.6. Stresses due to differential shrinkage

(j) *Maximum stress at fibre I (no prestress)*
Stress (Fig. J.6) due to design loads for SLS (LC3) plus temperature difference and differential shrinkage effects is given by:

$$f_{1,LC3} = -16.5 - 0.8 \times 1.45 - 0.364 = -18.024 \, \text{N mm}^{-2}$$

(k) *Prestressing force and eccentricity solution*
Adopting straight fully bonded tendons (constant force and eccentricity) and allowing for a 20% loss of prestress after transfer, initial prestress at fibre 1 to satisfy class 2 requirements for SLS LC3 is:

$$f_{1P} = \frac{(18.004 - 32)}{0.8} = 18.53 \, \text{N mm}^{-2} \quad (\text{say } 20 \, \text{N mm}^{-2}).$$

Critical selection at transfer occurs at the end of the transmission zone, where the moment due to the self weight of the beam is near to zero and the initial stress conditions are:

$$\frac{P}{A} + \frac{P_e}{z_1} = 18.53 \quad \text{①} \qquad \frac{P}{A} - \frac{P_e}{z_2} \geq 1 \quad \text{②}$$

Multiplying ① by z_1 ② by z_2 and adding for a maximum prestressing take ① = 20 just to give an excess prestressing force to cater for any future increase of moments

$$P \geq \left(\frac{20z_1 - 1.0z_2}{z_1 + z_2}\right) A = \left(\frac{20 \times 116.2 - 75.4}{116.2 + 75.4}\right) 387 = 4{,}542 \, \text{kN}.$$

Allowing for a 10% loss of force before and during transfer, initial force

$$P_0 = \frac{4542}{0.9}$$
$$= 5{,}046 \, \text{kN}$$

Using 29/15.2 mm standard strands with an initial force of $0.75P_u$, substituting $P = 4{,}542$ kN in ② for strand layout shown (Fig. J.7) the moment about fibre 1 is:
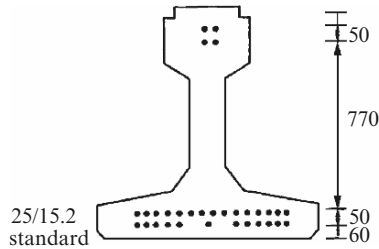
Fig. J.7. Strand layout for prestressing force and eccentricity solution

$$e \leq \frac{z_2}{A} + \frac{z_2}{P} = 211 \, \text{mm}$$

$$
\begin{aligned}
2 \; @ \; 930 &= 1{,}860 \\
2 \; @ \; 880 &= 1{,}760 \\
14 \; @ \; 110 &= 1{,}546 \\
\underline{11} \; @ \; 60 &= \underline{660} \\
29 & \; 5{,}820
\end{aligned}
$$

$$e = \frac{232 + 5{,}820}{29} = 208 \, \text{mm}.$$

Allowing for 1% relaxation loss in steel before transfer and elastic deformation of concrete at transfer, transfer force is given by.

$$
\begin{aligned}
P &= \frac{0.99 P_0}{1 + \dfrac{E_s}{E_c} \left(\dfrac{A_{\text{ps}}}{A} \right) \left(1 + \dfrac{Ae^2}{I} \right)} \\[2ex]
&= \frac{0.99 P_0}{1 + \dfrac{195}{31} \left(\dfrac{29 \times 139}{387 \times 10^3} \right) \left(1 + \dfrac{387 \times 0.208^2}{47.6} \right)} \\[2ex]
&= 0.91 P_0 = 4{,}592 \, \text{kN}
\end{aligned}
$$

Initial stresses due to prestress at end of transmission zone (Fig. J.8):

(1) $\dfrac{P}{A} \left(1 + \dfrac{Ae}{z_1} \right) = 11.87 \left(1 + \dfrac{190}{300} \right) = 20.10 \, \text{N mm}^{-2}$,

(2) $\dfrac{P}{A} \left(1 - \dfrac{Ae}{z_2} \right) = 11.87 \left(1 - \dfrac{190}{195} \right) = -0.80 \, \text{N mm}^{-2}$.

Moment due to self weight of beam at midspan:

$$w = A \times 1 \times 23.6 = 0.387 \times 1 \times 23.6 = 9.13,$$

$$M_{\text{swt}} = 9.13 \times \frac{(20)^2}{8} = 456.5.$$
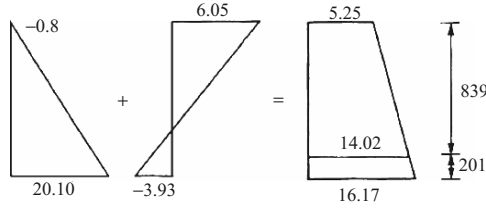
Fig. J.8. Moments for strand layout in Fig. 5.64

Stresses due to self weight of the beam at midspan:

$$f_{1,\text{swt}} = -\frac{456.3}{116.2} = -3.93 \quad f_{2,\text{swt}} = -\frac{456.5}{75.4} = 6.05\,\text{N\,mm}^{-2},$$

$$\left(> \frac{f_{\text{cr}}}{3} \right) = \frac{40}{3} = 13.33\,\text{N\,mm}^{-2}.$$

Allowing for 2% relaxation loss in the steel after transfer, concrete shrinkage $\varepsilon_{\text{cs}} = 3 \times 10^{-6}$ and concrete specific creep $c_{\text{t}} = 1.1 \times 48 \times 10^{-6}$ per $\text{N\,mm}^{-2}$, the loss of force after transfer is due to

steel relaxation $0.02 \times 5{,}046 = 107$

concrete shrinkage $(\varepsilon_{\text{cs}} E_{\text{s}} A_{\text{ps}})$

$300 \times 10^{-6} \times 195 \times 29 \times 139 = 236$

concrete creep $c_{\text{t}} f_{\text{co}} E_{\text{s}} A_{\text{ps}}$

$$1.1 \times 48 \times 10^{-6} \times 14.02 \times 195 \times 29 \times 139 = \frac{582}{919\,\text{kN}}.$$

Final force after loss of all prestress:

$$P_{\text{e}} = 4{,}592 - 919 = 3{,}673\,\text{kN} \quad \text{where} \quad \frac{P_{\text{e}}}{P} = 0.8.$$

Final stresses due to prestress after loss of all prestress:

$$f_{1,0.8\text{P}} = \frac{3{,}673}{4{,}592} \times 20.10 = 16.08 \quad f_{2,0.8\text{P}} = \frac{3{,}673}{4{,}592} \times (-0.80) = -0.64\,\text{N\,mm}^{-2}.$$

Combined stresses in final condition for worst effects of design loads, differential shrinkage and temperature difference are:

$$f_{1\text{LClmod}} = 16.08 - (14.06 + 0.381) = 1.639\,\text{N\,mm}^{-2} \quad (\geq 0),$$
$$f_{2\text{LC3}} = 16.08 - (18.024) = -1.944\,\text{N\,mm}^2 \quad (\geq -3.2),$$
$$f_{2\text{LC1}} = -0.64 + \frac{645.5}{75.4} + \frac{2{,}607.45}{315.7} + 1.32 = 17.50,$$
$$f_{3,\text{LC3}} = \frac{1{,}907}{233.6} + 0.8 \times 2.76 = 10.37\,\text{N\,mm}^{-2}.$$
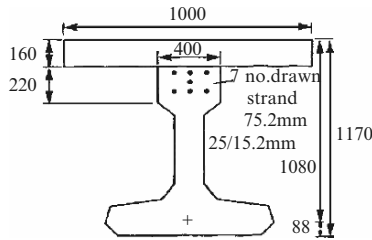
Fig. J.9. Bottom flange with 25 strands for ULS moment calculations

ULS Moment of Resistance for Solution (a)

Consider only the 25 strands in the bottom flange (see Fig. J.9).
Centroid of group occurs at

$$\frac{14 \times 110 + 11 \times 60}{14 + 11} = -88 \, \text{mm}$$

from fibre 1 so that effective depth

$$d = 1{,}170 - 88 = 1{,}080 \, \text{mm}.$$

Tensile forces in the tendons, assuming that maximum design stress is developed, are given by:

$$F_\text{p} = 25 \times 139 \times 0.87 \times 1670 \times 10^{-3} = 5{,}046 \, \text{kN}.$$

Compressive force in concrete, in the flange is:

$$F_\text{f} = 0.4 \times 40 \times 1{,}000 \times 160 \times 10^{-3} = 2{,}560 \, \text{kN}.$$

Compressive force in concrete, in the web, with $160 < x \leq 380$, where $x =$ neutral axis depth, is:

$$F_\text{w} = 0.4 \times 50 \times 400(x - 160)10^{-3} = (8x - 1{,}280) \, \text{kN}.$$

Equating forces to obtain x,

$$5{,}046 = 2{,}560 + (8x - 1{,}280)$$
$$x = 470.75 \, \text{mm}$$
$$8x = 5{,}046 - 2{,}560 + 1{,}280 = 470.75$$
$$F_\text{w} = (8 \times 470.75 - 1{,}280) = 2{,}486 \, \text{kN}$$

$$\text{prestrain } \varepsilon_\text{pe} = \frac{f_\text{pe}}{E_\text{S}} = \frac{0.55 \times 1670}{200 \times 10^3} = 0.0046,$$

$$\varepsilon_\text{pb} = \varepsilon_1 + \varepsilon_\text{pe} = \frac{609.25}{470.75} \times 0.0035 + 0.0046 = 0.00913$$

since

$$\varepsilon_{\text{pb}} \nless 0.05 + \frac{f_{\text{pu}}}{E_S \gamma_m} = 0.0123.$$

The assumptions made about design stress in the tendons is therefore justified.
Taking moments about the centroid of the tendons

$$F_f\ 2{,}560(1.08 - 0.08) = 2{,}560$$
$$F_w\ 2{,}486(1.08 - 0.235) = \underline{2{,}101}$$
$$4{,}661\,\text{kNm}$$

If all 29 strands with 4 m tops are to be taken into account the neutral axis
depth may be determined by an iterative strain compatibility analysis. Con-
sider the condition with $x = 352$ mm and determine the strains in the tendons
(see Fig. J.10): A reference is also made to Fig. J.11

$$\text{prestrain } \varepsilon_{\text{pe}} = \frac{f_{\text{pe}}}{E_S} = \frac{0.55 \times 1670}{200 \times 103} - 0.0046.$$

The strain at each level is given by:

$$\varepsilon_{\text{pb1}} = \varepsilon_1 + \varepsilon_{\text{pe}} = \frac{758}{352} \times 0.0035 + 0.0046 = 0.0121\,\text{N mm}^{-2}$$

$$\varepsilon_{\text{pb2}} = \varepsilon_2 + \varepsilon_{\text{pe}} = \frac{758}{352} \times 0.0035 + 0.0046 = 0.0116\,\text{N mm}^{-2}$$

$$\varepsilon_{\text{pb3}} = \varepsilon_3 + \varepsilon_{\text{pe}} = \frac{-87}{352} \times 0.0035 + 0.0046 = 0.0037\,\text{N mm}^{-2}$$
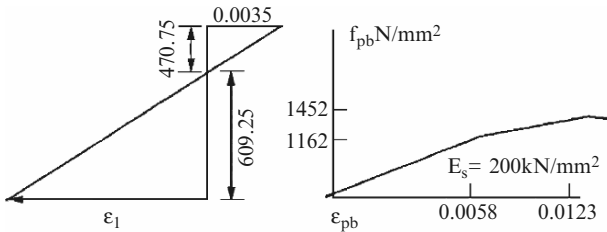
Fig. J.10. Compressive forces in the concrete flange
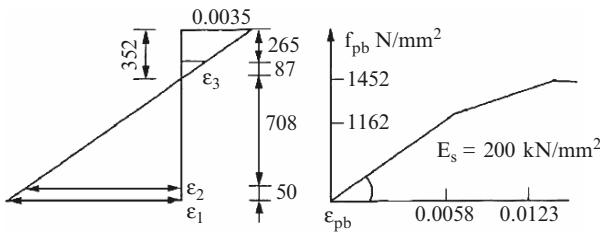
Fig. J.11. Calculating the strain in the tendons

The stress at each level is given by:

$$f_{pb1} = 1{,}162 + 290 \left(\frac{0.0063}{0.0065}\right) = 1{,}443\,\text{N}\,\text{mm}^{-2}$$

$$f_{pb2} = 1{,}162 + 290 \left(\frac{0.0058}{0.0065}\right) = 1{,}421\,\text{N}\,\text{mm}^{-2}$$

$$f_{pb3} = 0.0037 \times 200 \times 10^3 = -740\,\text{N}\,\text{mm}^{-2}$$

The tensile force in the tendons is given by:

$$F_{p1} = 11 \times 139 \times 1{,}443 \times 10^{-3} = 2{,}206$$
$$F_{p2} = 14 \times 139 \times 1{,}421 \times 10^{-3} = 2{,}765$$
$$F_{p3} = 7 \times 165 \times 740 \times 10^{-3} = \underline{-854.7}$$
$$F_t = 4{,}116.3$$

Compressive force in concrete

$$\left. \begin{array}{l} F_f = 0.4 \times 40 \times 1{,}000 \times 100 \times 10^{-3} = 2{,}560 \\ F_w = 0.4 \times 50 \times 400 \times 192 \times 10^{-3} = 1{,}536 \end{array} \right\} \quad \begin{array}{l} F_c \approx 4{,}096\,\text{kN} \\ F_t \approx F_c \end{array}$$

Details of strain, stress, tensile force and compressive force are illustrated in Fig. J.12).

Taking moments about the neutral axis

$$F_{p1}\ 2{,}206 \times 0.758 = 1{,}672$$
$$F_{p2}\ 2{,}765 \times 0.708 = 1{,}957$$
$$F_f\ 2{,}560 \times 0.272 = 696.32$$
$$F_w\ 1{,}536 \times 0.096 = 147$$
$$F_{p3}\ -854.7 \times 0.087 = \underline{-74.36}$$
$$4{,}397.6\,\text{kNm}$$

$$\frac{M_u}{M} = \frac{4{,}397.6}{3{,}770} = 1.17\ (71.15)$$

The section is therefore acceptable.

(1) *Shear in the composite member*

The vertical and longitudinal shear capacities of the composite beam are calculated using the tendon layout from solution (a) above. The stirrups arrangements have to be provided. Section properties are given on Sheet 02/3 and loads on Sheet (04/1) of the standard. Overall depth = 1,170 mm. Check shears at point B 3.7 m from the support and at the face of the diaphragm which is 0.25 m from support (thickness of the web = 160 mm; Tables J.2 and J.3).

Note that ULS analysis shows that the section is balanced if, in the upper zone, 7 drawn strands rather than 4 standard strands are provided. Thus:

$$P_{total} = \frac{31}{29} \times 3673$$
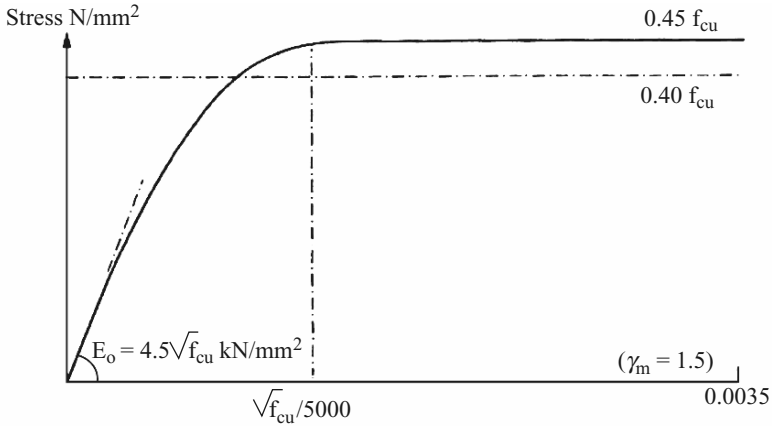
Short term design stress-strain curve for normal weight concrete
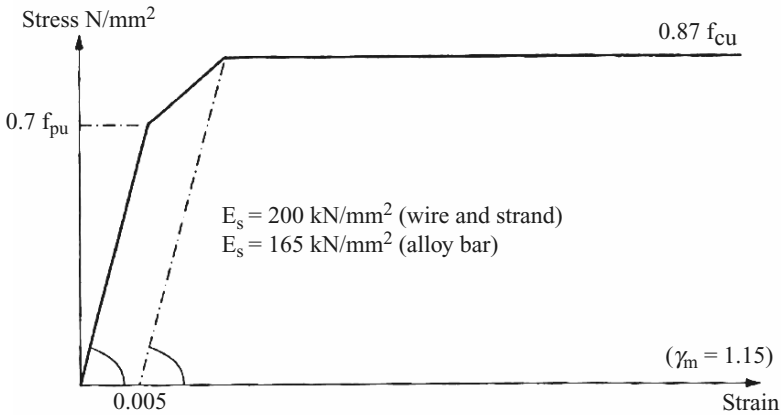
Short term design stress-strain curve for Class 1 and Class 2
relaxation prestressing tendons to B.S Specifications

Fig. J.12. Stress–strain curves for ULS (prestressed concrete)

J.1.2.3 Shears at Point B – 3.7 m from Supports (Prestress Solution A)

Shear of Section Uncracked in Flexure

Stress due to prestress at centroid of composite section:

$$f_{cr} = \frac{5{,}870{,}000}{387{,}000} - \frac{5{,}870{,}000 \times 208 \times 261}{47.6 \times 10^9}$$
$$= 15.17 - 6.70 = 8.47 \, \text{N mm}^{-2}$$

Multiply by $\gamma = 0.87$ giving $7.37 \, \text{N mm}^{-2}$

Table J.2. Loads at point B, 3.7 m from support

Loading	γ_{fL}	Shear	Shear γ_{fL}	Moment	Moment γ_{fL}
HB	1.3	308.3	400.8	920.0	1,196
HA	1.3	31.95	41.535	169.74	220.66
Footway	1.5	10.7	16.1	55.0	82.5
Super	1.75	8.0	14.0	41.0	72.3
Dead	1.2	116.6	139.9	557.19	669.4
	Total		612.335		2,240.86
	Multiply by $\gamma_{f3} = 1.1$		673.57		2,465

Table J.3. Shears at face of diaphragm ($\gamma_{fL} = 1.3$)

HB	409.4	532.2	modified
HA	36.9	47.97	HA loading
Footway	12.1	18.2	
Super	9.2	16.1	
Dead	180.4	216.5	
Total		$830.97 \times \gamma_{f3} \rightarrow 914$ kN	

$$f_{\mathrm{t}} = 0.24\sqrt{50} = 1.70$$
$$V_{\mathrm{CD}} = 0.67 \times 160 \times 1170\sqrt{1.7^2 + 1.7 \times 7.37} \times 10^{-3}$$
$$= 492.3 \,\mathrm{kN}.$$

Shear of Section Cracked in Flexure

Determine stress at extreme tension of the fibre due to prestress:

$$= 15.4117 + \frac{5{,}807{,}000 \times 208}{116.2 \times 10^6}$$
$$= 9.49 + 10.30 \approx 20.$$

Multiplying by $\gamma = 0.87$ gives $17.4\,\mathrm{N\,mm^{-2}}$.

Working to properties of composite beams

$$M_{\mathrm{cr}} = [0.37\sqrt{f_{\mathrm{cu}}} + f_{\mathrm{p1}}]\frac{I}{y} = [0.37\sqrt{50} + 17.4]174.5 \times 10^6$$
$$= 3{,}489 \,\mathrm{kNm} > 2{,}384.1.$$

Hence

$$V_{\mathrm{cr}} = 0.037b\alpha\sqrt{f_{\mathrm{cu}}} + \frac{M_{\mathrm{t}}}{M} \cdot V$$
$$= \frac{0.037 \times 160 \times 959\sqrt{50}}{10^3} + \frac{3{,}489}{2{,}384.1} \times 638.4$$
$$= 40.1 + 934.3 = 974.3 \,\mathrm{kN}.$$

Shear Reinforcement

$$\frac{A_{sv}}{S_v} = (V + 0.4bd_t - V_c)/0.87f_{yv} \cdot d_t$$

$$d_t = \text{depth to lowest tendon} = 1{,}180\,\text{mm}$$

$$\frac{A_{sv}}{S_v} = \frac{638{,}400 + 0.4 \times 160 \times 1{,}100 - 410{,}800}{0.87 \times 460 \times 1{,}100}$$

$$\frac{A_{sv}}{S_v} = 0.68$$

giving 10 mm links at 231 centres or 12 mm links at 332 centres.

Longitudinal Shear

$$\text{Longitudinal shear force } V_c = V \cdot \frac{Q}{I} = \frac{638.4 \times 10^3 \times 1{,}000 \times 160 \times 420}{116.8 \times 10^9}$$

$$= 367\,\text{N mm}^{-1}.$$

Assume surface type 2 ('rough on cast'). Width of top of precast unit = 300 mm:

$$V_c = 0.5 \quad \text{and} \quad k_1 = 0.09$$

$$\text{maximum shear} = k_1 \quad \text{for} \quad n_s = 0.09 \times 40 \times 300 = 1{,}080\,\text{N mm}^{-1}$$

$$V_e < V_e h_s + 0.7 A_c f_y$$

$$A_e = \text{area per unit length} = \frac{A_{sv}}{S_v}.$$

Hence

$$\frac{A_{sv}}{S_v} = (551 - 0.5 \times 300) \div (0.7 \times 480) = 1.25.$$

Thus requirements for longitudinal shear are greater than for vertical shear.
Requirement is 12 mm links at 180 centres.

Shears at Face of Diaphragm

Calculate length of transmission zone, for 15.2 mm standard strand:

$$l_t = \frac{k_t \phi}{\sqrt{f_{ci}}} = \frac{240 \times 15.2}{\sqrt{40}} = 576.8$$

$$\text{face of diaphragm} = 1{,}450\,\text{mm from end of beam}$$

$$\therefore \text{ tendon force} = \frac{450}{576.8} \times 5{,}870\,\text{kN} = 4{,}579.6\,\text{kN}.$$

Shear of Section Uncracked in Flexure

Stress due to prestress at centroid of composite section

$$= \frac{4{,}579{,}600}{387{,}000} - \frac{4{,}579{,}600 \times 208 \times 261}{47.6 \times 10^9}$$

$$= 11.84 - 5.23 = 6.61 \, \text{N mm}^{-2}$$

$$V_{\text{CD}} = [10.67 \times 160 \times 1{,}170 \sqrt{1.7^2 + 1.7 \times 5.75}] \times 10^{-3} = 445 \, \text{kN}.$$

Shear Reinforcement

$$\frac{A_{\text{sv}}}{S_{\text{v}}} = \frac{4{,}579{,}000 + 0.4 \times 160 \times 1{,}110 - 445{,}000}{0.87 \times 460 \times 1{,}110} = \frac{4{,}205{,}640}{444{,}222}$$

$$= 9.9670.$$

Longitudinal Shear

$$V_{\text{c}} = \frac{896.5 \times 10^3 (1{,}000 \times 160) \times 420}{116.8 \times 10^9} = 516 \, \text{N mm}^{-1}.$$

Maximum permissible $= 1{,}080 \, \text{N mm}^{-1}$ as before. Therefore value is acceptable.

Required area of steel interface is given by

$$\frac{A_{\text{sv}}}{S_{\text{v}}} = (576 - 0.5 \times 300) \div (0.7 \times 140) = 13.2.$$

A_{S} before requirements for longitudinal shear dominate. Links (required) T12-117 centres.

Check on Maximum Vertical Shear Capacity

maximum shear $= 5.3bd$

$$d = \text{distance from compression face to tendons in tension zone}$$

$$= 1{,}110 \, \text{mm}$$

$$V_{\text{max}} = 5.3 \times 160 \times 1{,}160 = 941.3 \, \text{kN}$$

applied maximum shear $= 914.1 \, \text{kN}$

Above value is permitted.

J.2 Blast Analysis of Bridges Using Finite Element

J.2.1 General Information

A comprehensive treatment is given on explosion/blast analysis using hybrid finite element with solution procedure and damage evaluation techniques.
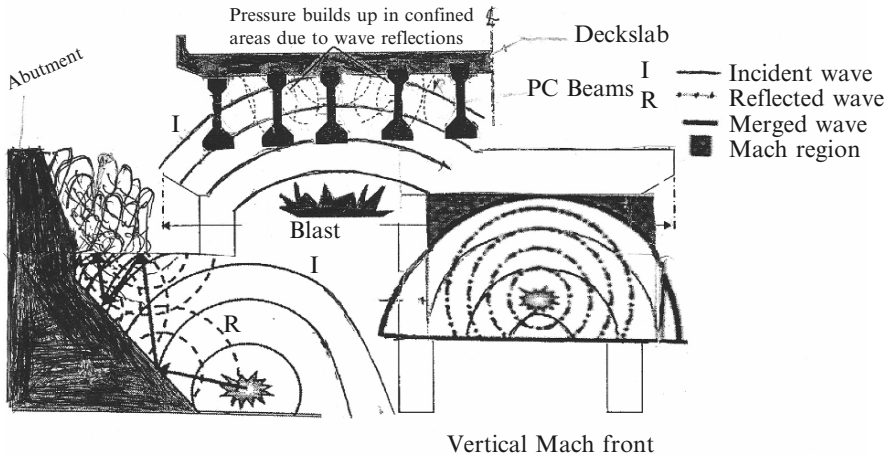
Plate J.2. Explosion at the deck level and at abutments

BANG-F has been used to carry out finite element analysis using blast load of 350 kg bomb at suitable distance equivalent of TNT of 390 kN m^{-2} as shown in the application procedures given in Plates J.2 and J.3 with specific data given in Table J.4.

Analysis programs can perform a linear analysis or consider the effects of nonlinearity due to material behaviour and large displacements. Material stress–strain nonlinearity can be accounted for in a model using a multi-linear stress–strain response for a more accurate representation of actual material properties. Due to large deformations, geometric nonlinearity has been included in the analysis to account for phenomena such as moment magnification from P-Δ effects.

Perhaps the most common analysis method used in practice is a single or multiple-degree-of-freedom, uncoupled, nonlinear dynamic analysis. The loads acting on a structure are usually determined using shock-wave propagation. BANG-F accounts for the shock waves reflected from surfaces, shock-wave addition of these reflected waves, and confinement effects. Pressure–time histories are calculated for specified "targets" on a bridge structure, and empirical data from blast tests to adjust the results. Once the loads have been determined, the structural response can be analysed using a dynamic structural analysis, accounting for the full plastic capacity of the members. Using this response, damage levels can be estimated using empirically based deformation criteria. However, because two separate analyses are performed, the blast load calculations are not couple with the structural response. This approach is normally acceptable for loads derived from shock sin air, as the impedance mismatch between air and a structure is large.

In the case where a significant number of bridge structural components fail as a result of the blast loads, thereby altering the blast environment and number of surfaces available to reflect shock waves, a ore refined analysis has

The Damage Model

390 kPa

— Pressure
-•- Impulse

under girder

7.5 10 12.5 15 17.5 20 22.5 25 27.5 30
Time, msec

PULSE-PRESSURE: CAR BOMBS

structure
reinforcement
spalling

Local effect of penetration
(x) and spalling

390 kPa

— Pressure
-•- Impulse

above girder

0 2.5 5 7.5 10 12.5 15 17.5 20 22.5 25 27.5 30
Time, msec

0   20   40   60   80   100   120
Central Displacement (cm)

Local effects of scabbing

h_2

P=11.2 kN/m²

Progression of Collapse

Blast
pressure

Δ

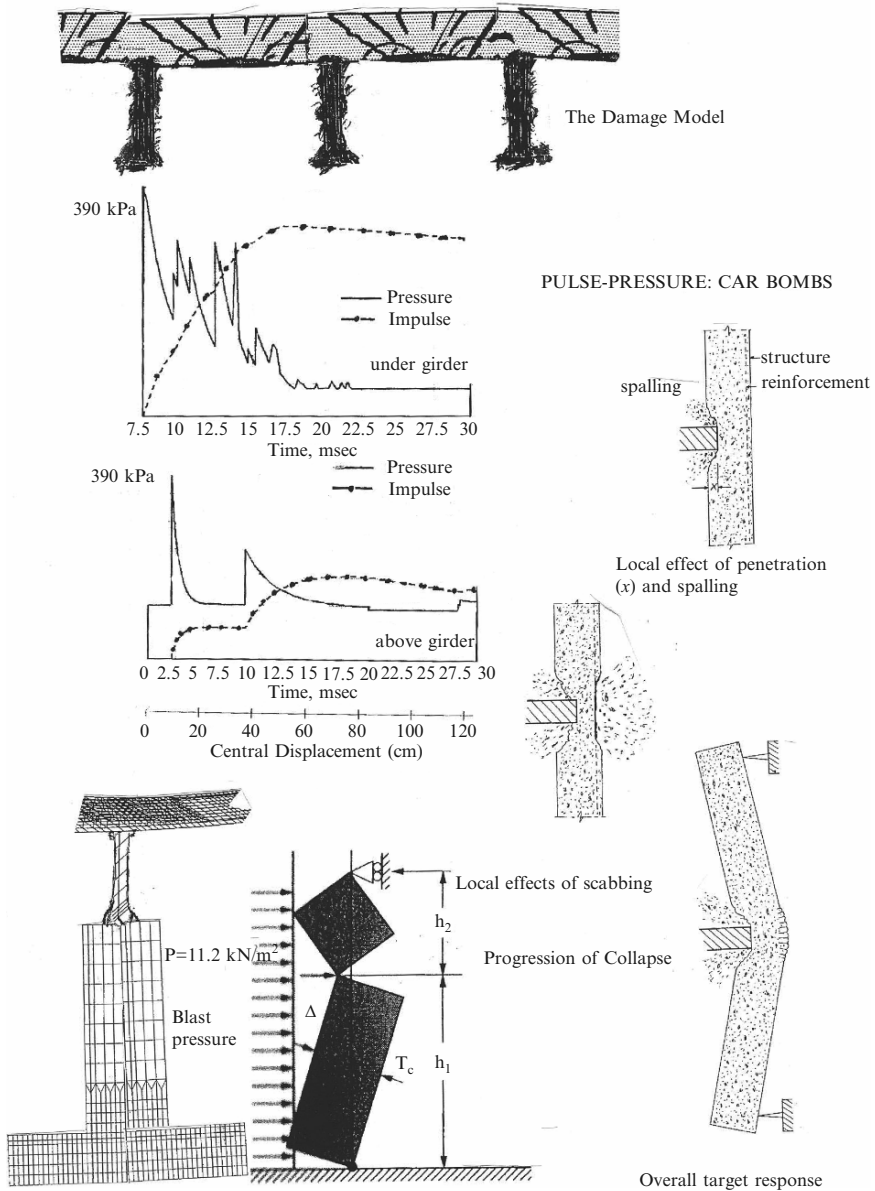T_c h_1

Overall target response

Plate J.3. Failure mode

been required. A coupled analysis performs the blast load calculations and
structural response simultaneously. This technique accounts for the motion
and response of bridge structural members as the blast wave proceeds around
(or through) them and will almost always provide a more accurate prediction

Table J.4. Data for the bridge

I.   Bridge
      A reference is made to Plates J.1–J.3 for structural details and finite element mesh generation scheme adopted. Section J.2.2 gives the limit state design of concrete deck slab and precast prestressed concrete beams.

II.   Material Properties
      Material properties for blast load analysis are given in the text and other properties are given in Sect. J.2.2.

III. Finite Element Analysis
      Throughout 8-noded isoparameter 3D hybrid elements are considered except in a small area of pier triangular isoparametric elements with a node at the centre have been adopted for smooth transitional flow of stresses due to uneven geometry.

Deck Slab: 8 noded elements	1,550 solid elements	
Precast concrete beams: single beam	720 solid elements	
gap elements	120 solid elements	
cap beam	550 solid elements	
Single pier	910 solid elements	
Single foundation	910 solid elements	
Prestressing cables/bars	1,930	2 noded
Conventional steel bars	2,150	2 noded

Note: The cables/bars are either placed in the body of the solid elements or on the surface to match with the nodes of solid concrete elements

Increments of solution procedures   12

IV.   Explosive Charge
      (a) Bomb yield $350\,kg$ TNT $- 390\,kN\ m^{-2}$ TNT of $800\,lb$
          Truck mounted or on sport utility vehicles
      (b) The charge is placed at the centre of the bridge deck – $1.25\,m$ high
          Below the deck level close to the girder – $2.5\,m$ high
      (c) Ductility factor $= 2$

---

of the structural response. Several techniques exist for performing a coupled analysis, all of which involved time scale discretisation. Couple analyses are typically used only in special circumstances due to the amount of computer resources and experience required to perform the analysis and the difficulty in interpreting the results correctly. Uncoupled analysis will usually provided conservative yet reasonable results with must less effort and are best suited to typical design cases such as those considered in the current research. These methods have been explained earlier in this section.

The BANG-F computer code provides the internal airblast environment in structures with multiple chambers for both internal and external explosions using fast-running analytical/empirical models. The code treats shockwave propagation through strings of "rooms" (i.e. defined volumes and areas to model blast transmission through multispan bridge structures.

For external explosions, BANG-F computes the pressure on external walls or on the ground surface and the shock waves and mass flow (or fill) propagated through entrances into and throughout a bridge structure. Shock waves dominate the blast environment for external explosions, while the flow of confined detonation product gases will likely also be important for explosions inside a confined area. BANG-F allows for the empty spaces and vents in bridges such that obstructions and confinement can be considered. Below deck analyses thus included the effects of multiple reflections from ground and deck surfaces as well as inside the cavities created by the deep prestressed girders and deck. The effect of reflections near the abutment could also be considered. For the above-deck calculations, obstructions and confinement are nonexistent, and those effects are not seen.

The combined effects of spall and cratering can lead to significant reductions in the cross-sectional area of the columns, or possibly even a complete breach. In addition, counterforce charges consisting of two separate hand-placed charges located on opposite sides of a target were considered. They are assumed to be primed so that they detonate simultaneously toward the centre and take advantage of the internal collision of blast waves inside the target to multiply their breaching effects.

J.2.2 Method of Analysis of Girders, Cap Beams and the Deck

Table J.3 gives the data immediately applied to bridge problems. Additional detailed analyses have been thoroughly explained in the text on which BANG-F is based.

The bridge structural system was characterised as a stack of uncoupled components or as a series of SDOF systems. The loads applied to all surfaces were attributed to supporting components according to load direction. Thus the deck response was used to determine the loads applied to the girders, and the girder response was used to determine the loads on the cap beam. A more detailed analysis could attribute factored loads and reactions from component to component, thus more accurately representing the couple response. However, the piers are extremely stiff when loaded axially by the transient cap bema reactions and would have a negligible effect on the response of the girders. Therefore, the components were left uncouple in order to simplify the analyses.

J.2.3 Analysis of Results

The load time functions for the under girder explosion and above girder explosion are given on Plate J.4 together with the damage scenario of the bridge deck with areas of spalling of concrete. The crack exceeding 3 mm, most of the prestressing cables/bars in the prestressed beams have yielded. The deck slab failed giving circumferential and radial cracks forming wedges in the slab thickness. The explosions under the bridge deck was considered for the bridge

piers. The explosion pressure underneath the deck was resolved and the lateral component of $11.2 \, \mathrm{kN \, m^{-2}}$ was finally computed as a blast pressure. Due to top fixity the failure mode shifted at the centroid a little above the centroid of the pier. The failure modes in the top slab and the pier when subjected to blast load behave as if plastic hinges occurred in areas of failure, behave as fulcrums for creating deflected shapes.

Looking at the output the girder support rotation did not exceed more than 1.04°. When the failure occurred the support rotation was around 2.06°.

Corresponding to rotation of 1.04°, the displacement achieved was 230 mm at the midspan of the girder. Failure of the girder at 2.06° rotation gave 490 mm. A reinforced concrete cap beam spanning between outside piers, the rotation for slight cap beam damage was 0.41° giving 35 mm displacement for damage conditions i.e., failure conditions, the rotation was 5° with a displacement computed to be 510 mm.

For uplift, deck sections assumed to attribute around $\frac{1}{3}$ of the loaded surface of the girders since the loss of the composite action occurred during uplift while loads in the normal downward direction contribute their entire loaded surface to the girders response. The use of $\frac{1}{3}$ rd factor is based on the expected capacity of the deck and shear connectors loaded in tension due to uplift forces from below-deck blasts. The girder reactions were accounted for.

Girder upward loads were assumed to provide no contribution to bent cap beam response due to simple bearing pad support conditions, while for the normal case, girder reactions were included in cap beam loads. Other assumptions inherent in the model include that no traffic loads will be on the bridge and that neither lateral instabilities of the girders nor seating or connection failures will occur. The following were also neglected: shear and axial deformations, lateral forces on girders from below-deck explosions (biaxial bending interaction), and rigid body translation of the deck upward for below-deck explosion. Concrete cratering and spalling from local blast damage were also neglected in the initial analysis of the girders and cap beam to simplify the analyses. Because the intent of the current research is to perform a simple analysis for numerous configurations, this level of damage resolution was not performed due to time constraints but may be included in future research.

Before determining the flexural response of the piers due to the blast pressure and reduced cross-sectional area from local damage, it was necessary to calculate an equivalent flexural capacity along the entire height of the column that accounted for the localized damage. Flexural capacities were calculated for the undamaged and damaged cross sections of the columns. For the damaged sections, the breach depth was estimated using the previously discussed, empirically based spall and breach equations given in this text. With the damaged and undamaged flexural capacities, along with the length over which damage was assumed to occur, the clearance, and assumed plastic hinge locations, an equivalent flexural capacity could be calculated using the principle of virtual work.

All along the stand off distance was considered to be 6 m.

A number of optimization case studies were considered. Results have shown that the bridge geometry can significantly affect the blast loads that develop below the deck.

For bridges with deep girders, confinement effects can greatly enhance the blast loads acting on the girders and tops of the piers and in some cases may result in more damage than an explosion occurring on top of the deck. The clearance can also have a large impact on the results, as increasing the distance from the explosion to the deck can result in more damage to the girders due to the formation of a Mach front. However, higher clearances result in lower average loads on the piers due to the larger volume of space (less confinement) under the bridge and the increased average standoff distance to a given point on the pier. Explosions occurring near sloped abutments could possibly result in more damage than an explosion at midspan due to the confinement effects at the abutments. Finally, round piers will experience lower loads due to the increased angle of incidence from he curved surface.

J.3 Barge and Ship Collision with Bridge Piers

J.3.1 Introduction to Barge and Vessel Collisions

Assessing the structural response and vulnerability of bridge piers to collisions by barges and vessels typically involve either the use of static pier analysis codes and design-specification-stipulated equivalent static loading conditions, or a lengthy model development process followed by use of general purpose finite element codes. In this section, an alternative approach is proposed that leverages the capabilities of existing nonlinear dynamic pier analysis programs by adding dynamic barge and vessel behaviour in a computationally efficient and modular manner. By coupling nonlinear barge and vessel and pier responses together through a shared collision impact force and employing numerical procedures for accelerating convergence of the couple system, dynamic barge and vessel collision analyses may be conducted for bridge piers efficiently and rapidly. The influence of impact parameters such as barge and vessel type and mass, impact speed and angle, and pier configuration can then be efficiently evaluated using dynamic collision analyses.

General-purpose contact-impact nonlinear finite-element codes may be used ot conduct vessel collision analyses. Being general purpose in nature, substantial investments of time and effort are required for the development of vessel, pier, and soil models before reliable results may be obtained. Moreover, the computational demands involved in conducting high-resolution nonlinear contact-impact vessel collision analyses often translate into the need for supercomputing resources and tens of hours of computing time. As a result, at least with respect to collision analysis of piers, such codes are typically used only in the design of major structures and in the investigation of collision initiated failures.

A number of probabilistic models exist in various European countries which can be used as test cases for the numerical models discussed here. In Sect. G.3 ship to ship and ship to platform, a numerical model for vessel collisions has been discussed.

Ships and barges colliding with each other because of the presence of a bridge, or colliding with bridge piers, is increasingly threatening the safety of people and the integrity of structures, as well as causing disruption to transport routes. It is becoming increasingly important to take into account the problem of ship collisions in the design and construction of new bridges and the protection of existing bridges over inland waterways.

J.3.2 Current Practice in Different Countries on Ship–Bridge Collision

In some countries bridge design with respect to the risk of ship–bridge collision has been included in the codes during the last decades. United States have rather extensive code provisions both with respect to sea going ship and barge traffic on inland waterways. The Swedish and Norwegian codes are mainly relevant for ships, as barge transportation is not very developed in theses countries. In Germany and in France there are some code provisions for barge traffic in rivers.

Below, some of the codes are briefly described. The text is not a complete summary of the code contents but concentrates only on the magnitude of impact forces for the sake of comparison. Particular rules on load application, load distribution and relation to other parts of the codes are left out. To use the codes one has to read the original text.

J.3.2.1 AASHTO Code USA

Code provisions for the design of bridges for vessel collision in the United States were first adopted by the American Association of State Highway and Transportation Officials (AASHTO) in 1991 in a report entitled Guide Specification and Commentary for Vessel Collision Design of Highway Bridges.

The provisions of the 1991 Guide Specification were incorporated in the recently adopted LRFD Bridge Design Code by AASHTO.

The intent of the AASHTO Code is to provide bridge components with a reasonable resistance capacity against ship and barge collisions. In navigable waterway areas where collision by merchant vessels may be anticipated, the code requires that bridge structures be designed to prevent collapse of the superstructure by considering the size and type of vessel, available water depth, vessel speed, structure response, and the risk of collision. In addition, minimum impact forces associated with drifting barges colliding with bridge structures are specified.

The code contains three alternative analysis methods for determining the appropriate vessel collision design loads for the bridge structure. Method I

is a simple to use semi-deterministic procedure; Method II is a detailed risk analysis procedure; and Method III is a relatively complex, cost effectiveness procedure (such as a benefit/cost analysis) in which the cost of bridge strengthening or bridge protection systems are compared against the benefits of risk reduction. The code requires the use of Method II for all bridges unless special circumstances described in the code for the se of Methods I and III exist (such as shallow draft inland waterways where the marine traffic consists almost exclusively of barges for Method I; and very wide waterways with many piers exposed to collision, and the retrofitting/rehabilitation of existing bridges for Method III).

The Method II acceptance criteria for vessel collision are based on the bridge importance classification as follows:

- Critical Bridges – The acceptable annual frequency of collapse, AF, of critical bridges shall be equal to, or less than, 0.0001 (a return period of 1 in 10,000 years).
- Regular Bridges – The acceptable frequency of collapse, AF, of regular bridges shall be equal to, or less than 0.001 (a return period of 1 in 1,000 years).

The vessel collision design loads for each pier or span element is chosen such that the annual frequency of collapse due to collision is less than the acceptance criterion for the element. The AASHTO model for computing the annual frequency of bridge element collapse is shown in Clause 4.2. Empirical relationship for computing an equivalent static impact force associated with a head-on (0°) collision of a ship or barge with a rigid pier is provided in the AASHTO Code.

The impact force for ships were developed from model studies and research conducted by Woisin in Germany in 1961–1976, and were found to be in relatively good agreement with research conducted by other ship collision investigators world-wide. The ship impact force used to establish design loads is computed as follows:

$$P_S = 0.98 \cdot (DWT)^{1/2} \cdot \left[\frac{\nu}{16} \right], \tag{J.1}$$

where

P_S = ship impact force (MN)
DWT = vessel dead-weight tonnage
ν = impact speed (knots).

It should be noted that the impact force in (J.1) is based on a 70% fractile force, rather than an average or median force value.

The AASHTO Code impact force for barges was developed from model studies and research conducted by Meier-Dornberg in Germany in 1983 on behalf of the Water and Shipping Directorate Southwest-Saar District. The experimental and theoretical studies performed by Meier-Dornberg were

performed to study the impact force and the deformation of the bow when barges collide with lock entrance structures and with bridge piers. A graph of typical impact forces for a European Barge Type IIa with a bow width (length dimension of 11.4) 76.3 m is shown in Fig. J.13 the Type IIa barge is very similar to the standard 35 (195 ft) hopper barge used on the inland waterway system in the United States.

J.3.2.2 Swedish Code

According to the Swedish Standard for the Design of Bridges, the bridge piers shall resist the effects of ship collision if risk for collision exists. The forces arising from ship collisions are separated into:

- Collision force in the direction transverse to the bridge alignment
- Collision force in the direction parallel to the bridge alignment

The two force directions must not be assumed to occur simultaneously.

The collision force depends on the structural properties and size of the ship, its loading condition and speed, the current direction and the point of collision against the bridge. The collision force also depends on the total mass and stiffness of the bridge.

The collision loads could be replaced, completely or partly, by collision reducing measures e.g. protection islands at the bridge piers.

If the bridge piers can be assumed to be completely rigid, so that the whole collision energy is absorbed by deformation of the vessel, the collision force
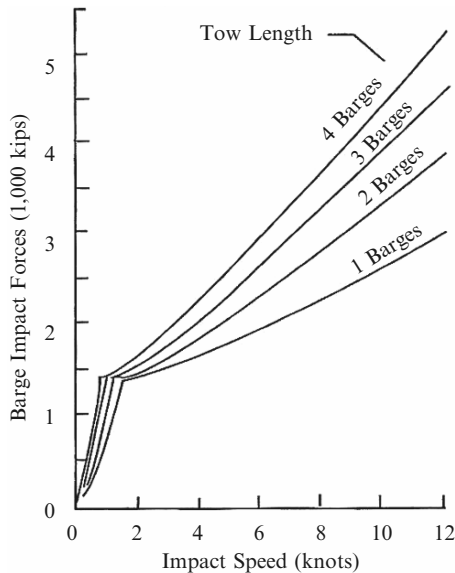

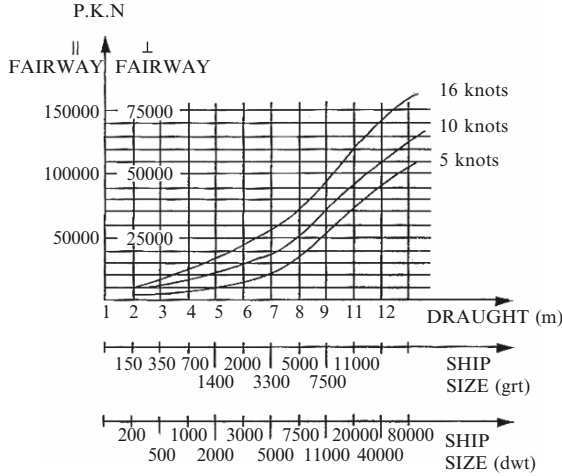**Fig. J.13.** Typical hopper barge impact forces

Fig. J.14. Vessel collision design forces (with compliments of AASHTO)

can be estimated from Fig. J.14 as a function of draught or size of ship. It is normally specified that the force perpendicular to the ship fairway is 50% of the force parallel to the ship fairway.

For vessels with draught ≥ 7 m "Fig. J.14" corresponds to Load Regulations for Road Bridges, report No.4, published by the Nordic Road Engineering Federation. For vessels with smaller draught Fig. J.14 is established on the basis of Woisin, as specified in AASHTO Code, (J.1).

The bridge superstructure shall be designed for collision forces acting in the direction parallel to the fairway if the risk of damage exists. The force shall be calculated as 1% of the force given in Fig. J.14 and shall be applied to the lower edge of the superstructure.

J.3.2.3 Norwegian Code

According to the Norwegian Rules for Loads on Bridges, all bridge elements that can be exposed to ship collision shall be design for ship impact.

In general, all relevant conditions shall be considered in the analysis of the collision forces, such as type and size of the ship, its loading and velocity, the point and direction of collision, as well as the relevant structural data of the bridge. Furthermore, a risk analysis shall be performed. The probability of occurrence of an accident depends upon several factors such as traffic density, navigation circumstances, bridge location in relation to the navigation channel, water depth, possible obstacles, marking of the waterway, supervisory systems etc.

However, the minimum design collision forces for bridges crossing coastal waterways shall be not less than the values shown in Table J.5, where $P_{\perp}$, $P_{\parallel}$ are collision forces acting perpendicularly and parallel respectively to the main axis of the bridge.

Table J.5. Minimum design collision forces

Part of bridge structure	$P_\perp$ (MN)	$P_\parallel$ (MN)
Piers off shore	1.0	0.5
Superstructure (lower edge)	0.1	

The collision loads can alternatively be computed by means of the simplified method below.

The collision forces on the bridge piers situated nearest the navigation channel; are determines by the following two expressions:

$$P_\perp = 0.9 \cdot \sqrt{DWT} \cdot \frac{\nu}{8},$$ (J.2)

which is approximately the same as the corresponding expression in the AASHTO Code, (J.1), and

$$P_\parallel = 0.5 \cdot P_\perp,$$ (J.3)

where $P_\perp$ and $P_\parallel$ are collision forces in [MN] transverse and parallel to the bridge and v is the vessel velocity in $(\mathrm{m\,s^{-1}})$.

The design vessel is selected by determining a vessel size that is exceeded by no more than 50 vessels per year.

The velocity of the vessel shall be assumed to be at least $4\,\mathrm{m\,s^{-1}}$.

If the free horizontal clearance between two piers located closest to the navigation channel is smaller than the length of the largest vessel L, the design forces above shall be increased by a factor of 2. If the free horizontal clearance is between L and 2L, the magnification factor shall be determined by linear interpolation.

The collision forces on the other piers range from $P_\perp$ for a distance L between the pier and the centre line of the navigation channel, to $1.0\,\mathrm{MN}$ for distances more than $1.5\,\mathrm{L}$.

J.3.2.4 French Code

The French code for concrete design, defines ship collision as an accidental action. The regulation is developed only for inland waterways. Quasi-static equivalent load vales are given for two collision scenarios on bridges. The values differ according to the class of waterway:

- Small waterway ($\approx$class I–III)
  Frontal impact 1.2 MN   Lateral impact 0.24 MN
- Large waterway ($\approx$class V)
  Frontal impact 10 MN   Lateral impact 2 MN

The frontal load is applied on the wall of the pier parallel to the direction of the navigation fairway. The lateral load is applied to the wall of the pier perpendicular to the direction of the navigation fairway. These values are valid assuming a rigid pier with no protection devices.

J.3.2.5 German Code

In German codes for the design of bridges the impact of ships and barges has to be considered when the bridge is crossing a waterway. Impact load values are not given. Information about the design situation should be asked for from the Waterway and Shipping Administration.

However, for the river Rhine a regulation is available and quasi-statical loads of ship impact are given as follows:

- Pier within the navigation channel
  Frontal impact 30 MN   Lateral impact 15 MN
- Pier outside the navigational channel
  Frontal impact 6 MN   Lateral impact 3 MN

For other waterways the impact loads are based on design ships, loading conditions, velocities and impact angles. The dynamic load may be based on load-indentation studies, which gives:

$$F_{dyn} = 5 \cdot \sqrt{1 + 0,128 \cdot E_{def}} \, \mathrm{MN}, \tag{J.4}$$

where E_{def} is the deformation energy in MNm. It is becoming increasingly common to employ experts to undertake a probabilistic analysis to determine the impact loads. The above design rules are not considered relevant for ship impact design for seagoing vessels.

J.3.2.6 Eurocode

The European Commission has sponsored a programme of work to make available a common set of design rules in Europe. Eurocode 1 is entitled Basis of Design and Actions on Structures, and part 2.7 of this Eurocode covers Actions on Structures: Accidental Actions. This part was agreed by the various participating countries on 22nd May 1997 and has become an ENV, which that the document is for provisional use bit does not have the status of a European standard. After a period of about three years a decision will be made as to whether the document should become a European standard.

The characteristics to be considered for collision from ships depend upon the type of waterway, the type of vessels and their impact behaviour and the type of structures and their energy dissipation characteristics. The types of vessels that can be expected should be classified according to standard ship characteristics, see Tables J.6 and J.7.

In case no more accurate calculations are carried out and the energy dissipation of the structure may be neglected, the static equivalent forces according to Tables J.6 and J.7 may be applied.

The forces given in the Tables J.6 and J.7 refer to bow impact in the main sailing direction.

In an annex to the main text in Eurocode a calculation model is suggested to take into account velocity, stiffness and mass of the vessel and also traffic intensity and probabilities of failure.

Table J.6. Ship characteristics and corresponding nominal horizontal static equivalent design forces for inland waterways

CEMT class	Length (m)	Mass (ton)	Reference mass of freight (ton)	Force (MN)
I	30–50	200–400	300	4
II	50–60	400–650	500	5
III	60–80	650–1,000	800	6
IV	80–90	1,000–1,500	1,300	7
Va	90–110	1,500–3,000	2,300	11
Vb	110–180	3,000–6,000	4,600	15
VIa	110–180	3,000–6,000	2,300	11
VIb	110–190	6,000–12,000	4,600	15
VIc	190–280	10,000–18,000	6,900	22
VII	300	14,000–27,000	6,900	22

Table J.7. Ship characteristics and corresponding nominal horizontal static equivalent design forces for sea waterways

Class	Length (m)	Mass (ton)	Force (MN)
Small	50	3,000	15
Medium	100	10,000	25
Large	200	40,000	40
Very large	300	100,000	80

Euro-Model

A probabilistic model to determine the design force for ship collision with bridges is used to calculate the design force F_d for a given probability of exceedance 10^{-4}/year.

This probability is not the probability of failure as the resistance is calculated using characteristic values which also have a certain probability of exceedance (It is worth noting that strictly speaking this is the expected annual frequency rather than a probability).

$$P(F > F_d) = N(1 - p_a) \iint \lambda(x)P[\nu_r(x,y)\sqrt{km} > F_d]f_s(y)dxdy = 10^{-4},$$
(J.5)

where

N =	the number of ships per reference period (1 year)
p_a =	the probability that a collision is avoided by human intervention
$\lambda(x)$ =	the probability of a failure per unit travelling distance at a distance x from the structure
$\nu_r(x,y)$ =	the impact velocity of the ship, given an error or mechanical failure at a point (x,y) from the structure

k =   the equivalent stiffness of the ship
m =   the mass of the ship
$f_s(y)$ =   the distribution of initial ship positions in the lateral y direction

The model assumes that the maximum force during the impact is $\nu_r(x, y)$ (km) and therefore the term inside the square brackets is P[F(x, y) > fd] where F is the impact force caused by an aberrancy at a location (x,y) from the structure.

Note that this term includes the classification of ships. This model has a higher level of sophistication when compared to the AASHTO and IABSE models. It therefore requires more detailed input data.

The λ term is similar to the PA term used in the other models, however it is a probability of failure per unit length rather than the probability per bridge passage and it does not include the probability that evasive action has been successfully undertaken; this is take into account by the pa term. Consideration should also be given to how the "geometric probability" (PG) is taken into account. In the other models the PG parameter estimates how the possible collision courses are distributed along the bridge and whether the piers are avoided by pure chance.

J.3.3 Time Integration of Barge/Vessel Equation of Motion

J.3.3.1 General Information

Time integration analysis requires due consideration of inertial forces and nonlinear structural behaviour of both piers and barges or vessels. Properly modelling structural behaviour such as inelastic force deformation response which is necessary for force development and energy dissipation during impact must be evaluated. This analysis may involve barge/vessel crushing of the barge/vessel bow. For analytical work barge/vessel crushing loading and unloading curves must be established. During barge/vessel collisions with bridge piers the analysis generally assumes that they will undergo plastic deformation. The piers can produce impact reaction depending upon their shapes whether square, circular etc. Unloading curves are obtained similarly for cyclic rather than monotonic crush analysis is required which in reality depends on repeated cycles of loading and unloading. After multiple cycles of loading and unloading, a collection of unloading/reloading curves can be obtained. A suitable choice of integration technique is necessary.

The soil-structure analysis would be included in the implementation of the proposed dynamic analysis technique can be demonstrated by coupling a barge/vessel dynamics module to the pier/soil module. A lot of such information exists in the text. The dynamic time integration exhibited in this book is primarily controlled in the soil-structure analysis by pier/soil module with a barge/vessel module determining the magnitude of impact.

In this study implicit direct time step integration using Newmark's method as discussed in this book. The overall flow of the process involved in Program

BANG-F an outer loop that controls time stepping and an inner loop that controls iteration to convergence. At the beginning of each step, the barge/vessel module is invoked to evaluate an impact force for that time step. The barge/vessel crush depth can be computed. The dynamic equation of motion is to be satisfied for barge/vessel against iterative variations. At each pass of the iteration loop the impact force is refined until convergence is achieved. Numerical damping is used to accelerate convergence of the iteration process.

J.3.4 A Case Study

The bridge problem given in this section together with the bridge profile as shown on Plate J.1 have been adopted for this case study. The mesh generations developed for the superstructure and the substructure are repeated. Material properties described, therein, are still relevant for this case study. For impact 345 piles were put to take the axial, shear and moments from the barge/vessel.

Finite elements in vessel/barge direct impact area 8-noded = 5,140
Finite elements in vessel/barge following area 8-noded = 515
Finite elements in pier = 3,140
Line elements in pier 2-noded isoparametic type placed some on surface and 50% embedded in the concrete = 15,500

J.3.4.1 Analysis of Results

Plate J.4 show results impact force time relation, impact force and crush depth and displacement time relation, among numerous results which for technical reasons could not be reported in this text. In the output, in general, displacement, velocities and accelerations in x, y and z-directions have been evaluated. The results were evaluated using 8 No-400 Mhz MIPs R12000 processors in a 20 C.P.U.SGI. supercomputer 3400. The total time of producing results was 16 h. Since the impact results from actual disaster scenario are not available, the results were checked using the method given in Sect. 4.4. The results in the current case study were identical to the results produced by Larson, O.D, when compared with his results based on current finite element analysis. Owing to nonavailability of space in this book, those results could not be published.

J.4 Highway Parapets Under Vehicle Impact

J.4.1 Introduction

The main objectives of the forms of parapets are:

(a) To provide specified levels of containment to limit vibrations by errant vehicles
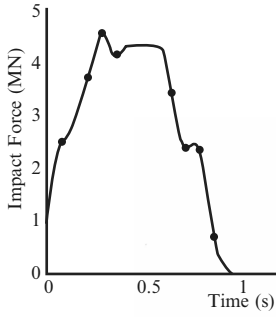
Impact force

Crush Depth (mm)

Pier displacement

Plate J.4. Impact force time relation

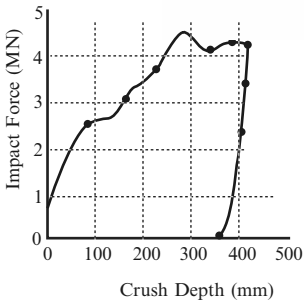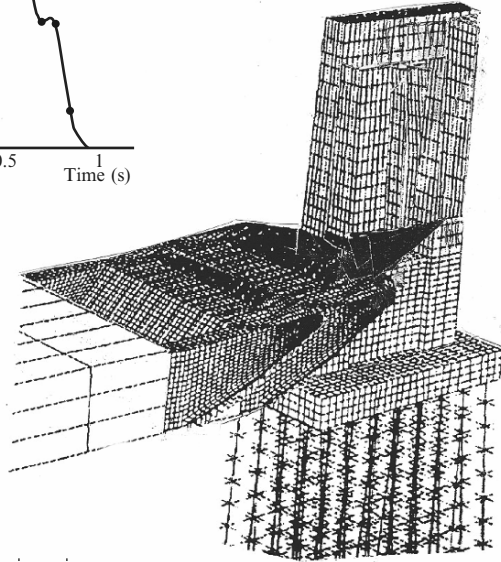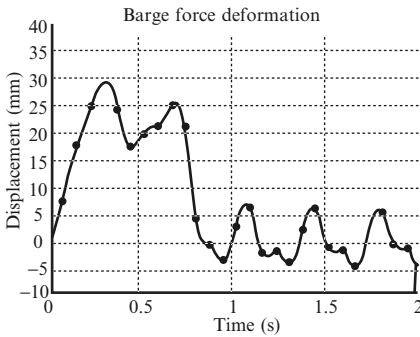(b) To protect highway users and others in the vicinity by redirecting the errant vehicles with minimum deceleration forces on to a path as close as possible to the line of the parapet and to reduce the risk of the vehicle overturning

In the UK the parapets are covered by BS6779.

J.4.2 Post, Bays and Configurations

J.4.2.1 Main structure, Anchorages, Attachment Systems, Bedding and Plinths

J.4.2.2 General

The anchorages, attachment system and the main structure, including the plinth, shall be designed to resist without damage all loads which the parapet is theoretically capable of transmitting, up to and including failure, in any one that may be induced by vehicular impact.

The design of parapet attachment systems and anchorages shall be such that removal and replacement of damaged sections of parapet may be readily achieved.

J.4.2.3 Main Structure

The local and global effects of vehicular collision with the parapets to be considered in the design of the elements of the main structure and on the superstructure, bearings and substructure shall be specified in BS 5400: Part 2.

J.4.2.4 Fixings Using Base Plates

Parapets that use base plates, such as post-and-rail systems, shall be fixed to the main structure via the base plates by stainless steel holding down bolts engaging with an anchorage.

Engagement of Holding-Down Bolts

Each holding down bolt shall have a length of engagement into the anchorage of not less that that given by the following expression:

$$0.7 \times \frac{\sigma_{\nu b}}{\sigma_{\gamma a}} \times D, \tag{J.6}$$

where

$\sigma_{\nu b}$ is the minimum ultimate tensile strength of bolt material (N mm^{-2})
$\sigma_{\gamma a}$ is the minimum yield strength of the anchorage material (N mm^{-2})
D   is the nominal bolt diameter (mm)

J.4.2.5 Levels of Containment

Normal Level of Containment

Normal level of containment shall be that required to resist penetration from the following vehicle impact characteristics:

Vehicle	Saloon car
Mass	1,500 kg
Height of centre of gravity	600 mm
Angle of impact	20°
Speed	113 km h^{-1}(70 mile h^{-1})

Note. The normal level of containment is that suitable for general use.

Low Level of Containment

Low level of containment shall be that required to resist penetration from the following vehicle impact characteristics:

Vehicle	Saloon car
Mass	1,500 kg
Height of centre of gravity	600 mm
Angle of impact	20°
Speed	80 km h^{-1} (50 mile h^{-1})

Note 1. The low level of containment using vertical infill is only suitable for use in areas where speed restrictions up to 30 mile h^{-1} apply.
Note 2. The low level of containment type of parapet, designed to redirect impacting vehicles using a post-and-horizontal rail type of parapet construction, is suitable for use in areas where speed restrictions up to 80 km h^{-1} (50 mile h^{-1}) apply.
Note 3. The 80 km h^{-1} (50 mile h^{-1}) speed adopted for the test is considered to provide the minimum acceptable level of containment.

High Level of Containment

High level of containment shall be that required to resist penetration from the following vehicle impact characteristics:

Vehicle	Four axle rigid tanker or equivalent
Mass	30,000 kg
Height of centre of gravity	1.8 mm
Angle of impact	20°
Speed	64 km h^{-1} (40 mile h^{-1})

Note. The high level of containment is for use only in extremely high risk situations.

Table J.8. Values of γ_{fL}

Element	Loading	γ_{fL}	
		Low and normal containment	High containment
Parapet components	Vehicular impact	1.0	1.0
	Wind loading	1.4	1.4
Attachment system	Parapet collapse	1.5	1.4
Anchorage	Parapet collapse	1.8	1.6

J.4.3 Design Loading Values

J.4.3.1 Design Loads

The design loads Q^* should be determined from the nominal loads Q_k according to the relationship:

$$Q^* = \gamma_{fL}Q_k,$$

where the partial load factor (Table J.8) γ_{fL} is a function of the nominal loading and element to be designed.

In the design of parapet components, the nominal load for vehicular impact with the parapet should be taken as the impact force generated by the characteristic vehicle.

J.4.3.2 Design Load Effects

The design load effects S^* should be obtained from the design loads Q^*, according to the relationship:

$$S^* = \gamma_{f3} \text{ (effects of } Q^*)$$
$$= \gamma_{f3} \text{ (effects of } \gamma_{fL}Q_k),$$

where γ_{f3} is a factor that takes account of inaccurate assessment of effects of loading and unforeseen stress distribution in the parapet. In the design of parapet components for vehicular impact, the value to be taken for γ_{f3} should be dependent on the accuracy of the loading distribution model. For wind loading, γ_{f3} should be taken as 1.1. For loading imposed by the parapet collapse, γ_{f3} should be taken as 1.0.

J.4.3.3 Design Resistance Values

The design resistance R^* may be defined as:

$$R^* = f\left(\frac{f_k}{\gamma_m}\right) \tag{J.7}$$

Table J.9. Values of f_k and γ_m

Material/component	f_k	γ_m
Steel (excluding stainless steel nuts, bolts and washers)	As given in BS 5400: Part 3	
Stainless steel nuts, bolts and washers	As given in BS 6105 or BS 1449: Part 2, as appropriate	1.2
Aluminium extrusions and plate (excluding weld affected areas)	0.2% proof stress as given in BS 1470 or BS 1474, as appropriate	1.2
Aluminium castings (excluding weld affected areas)	0.2% proof stress as given in BS 1490	1.3
Concrete plinths	As given in BS 5400: Part 4	

or, optionally for steel and aluminium

$$R^* = \frac{f(f_k)}{\gamma_m}, \tag{J.8}$$

where

f_k is the characteristic (or nominal) strength of the material
γ_m is a partial factor on material strength
Values for f_k and γ_m are given in Table J.9.

For the design of parapet components based on tested configurations, the calculated resistance may be determined from the following:

$$R^* = f(f_k), \tag{J.9}$$

J.4.3.4 Design Criteria for Components of Metal Parapets

General

The simplified expressions are derived on the basis that $\gamma_{f3} = 1.0$ and $\gamma_m = 1.0$.

(a) *Posts with other loads.* Where accommodation bridge parapet posts carry a non-effective longitudinal member above the height required for vehicle containment, such posts should be similarly designed to resist a horizontal design load Q^* of 1.4L kN, applied at the position of the top rail, where L is the distance in metres between centrelines of supports.

(b) *Strength of connection of post to base plate.* The connection between post and base plate should develop the theoretical full plastic moment of the actually post in transverse and longitudinal directions and the design load of the post in shear.

(c) *Strength of post base plate and connection of post base plate to plinth.* The post base plate and the connection between the post base plate and the

plinth should be capable of developing a moment of resistance about each axis, taken at the underside of the base plate, at least 50% greater than the theoretical full plastic moment of the actually post.

Due regard should be given to the bearing stresses developed in any grout pad or in the concrete plinth. These should not exceed $20\,\mathrm{N}\,\mathrm{mm}^{-2}$.

Strength and Continuity of Effective Longitudinal Members

Effective longitudinal members should conform to the following recommendations (a) to (c) in terms of strength and continuity.

(a) *Continuity in bending.* Longitudinal members should be structurally continuous in bending and their design strength in bending should be maintained over the whole length of the parapet where practicable.
(b) *Horizontal bending strength.* Design load Q^*, has been recommended in Table J.10, acting horizontally at the midpoint between centres of support of the longitudinal member.
(c) *Vertical bending strength.* The bending strength of the member, including all joints, about the horizontal axis should be not less than 50% of that required about the vertical axis.

Fixing of Solid Panels for High Containment

For high containment parapets the solid infilling panel should be fixed to each effective longitudinal member at 150 mm centres with stainless steel, structural, blind rivets or equivalent with an ultimate tensile and shear capacity of not less than 10.0 kN. The cladding should be fixed with the top of the panel 10 mm below the top of the top rail.

Table J.10. Design loads for parapets of tested configuration

Parapet containment level	Effective longitudinal members	Supporting posts
	Design load Q^* applied horizontally to longitudinal members at mid-point between centres of supports	Design load Q^* applied transversely to the post according to the disposition of the effective longitudinal members
	kN	kN
Low, L	$25/n$	25
Normal, N	$50/n$	50
High, H	$270/n$	270

Note. n is the number of effective longitudinal members in the parapet

J.4.3.5 Finite Element Crash Test Analysis of Parapets

Introduction

This book offers a comprehensive analysis for impact problems by using hybrid finite element technique. Program ISOPAR, recently modified to include many new features and extending case studies. This new version for impact problems is renamed as BANG-F. A typical concrete parapet is shown in Fig. J.16 is impacted using the data given in section "Normal Level of Containment" for the normal level of containment, the analysis checked also against Program ANSYS for comparison.

Finite element input data

(a) Impactor

Saloon car
Mass $= 1{,}500\,\mathrm{kg}$
Height of impact level $= 600\,\mathrm{mm}$
Impact angle $\alpha = 20°$
Vehicle speed $= 113\,\mathrm{km\,h^{-1}}$ (70 mph)

(b) Material properties of parapets/barriers

f_{cu} – concrete strength $= 50\,\mathrm{N\,mm^{-2}}$
f_{sy} = steel bar yield strength $= 460\,\mathrm{N\,mm^{-2}}$
f_y = rail yield strength $= 460\,\mathrm{N\,mm^{-2}}$
Weld length $= 600\,\mathrm{mm}$
Weld width $= 13\,\mathrm{mm}$
Throat width of the fillet weld $= 4.8\,\mathrm{mm}$
Weld angle $= 45°$

(c) Number of solid and bar elements
  – Solid isoparametric elements 20-noded $= 133{,}500$
  – Bar elements positioned to match (4-noded type) nodal points of solid isoparametric $= 65{,}000$
  – In the body of solid elements $= 35{,}500$
  – Metal connector line and plate elements $= 435$

Mesh Generation Scheme

An optimum mesh generating scheme for the parapet (barrier) is shown in Fig. J.16

Hardware: IBM 7600
Simulated time: $0.765\,\mathrm{s}$
CPU cycles: 782,333
CPU time: 2 h, 21 min

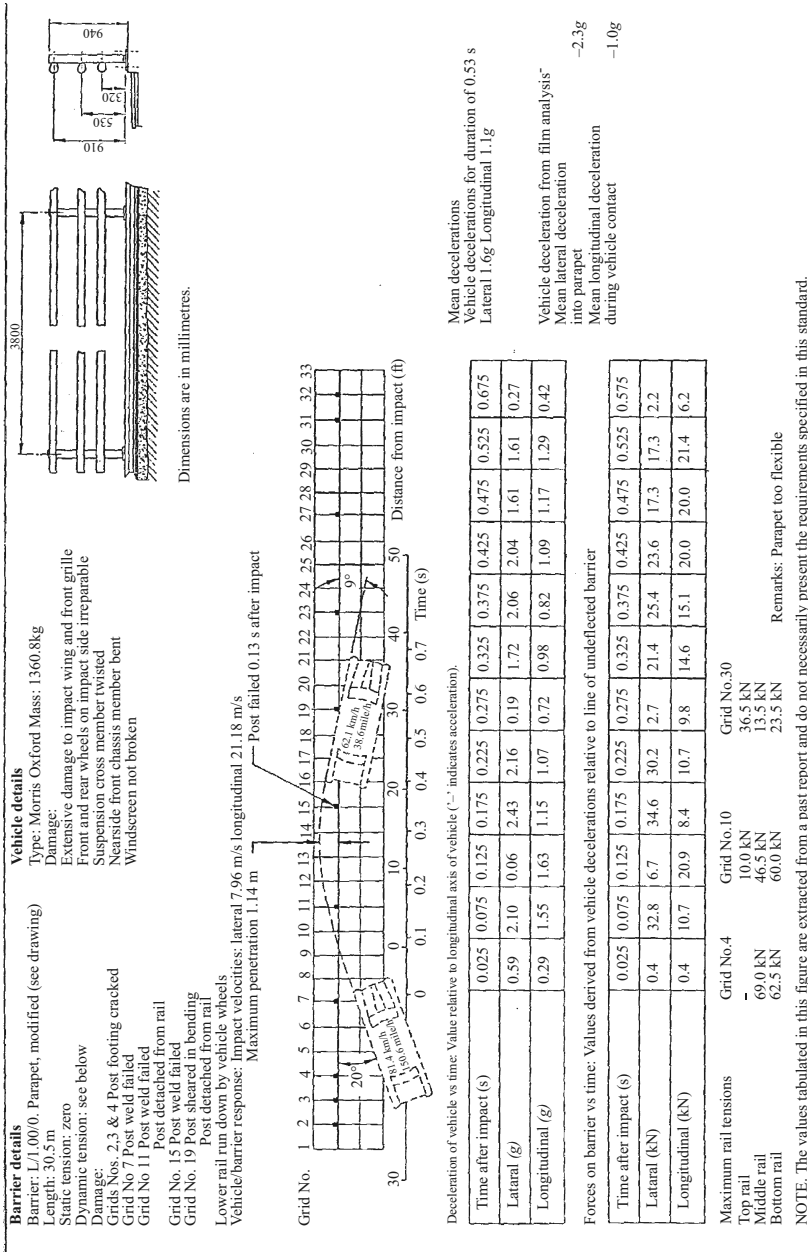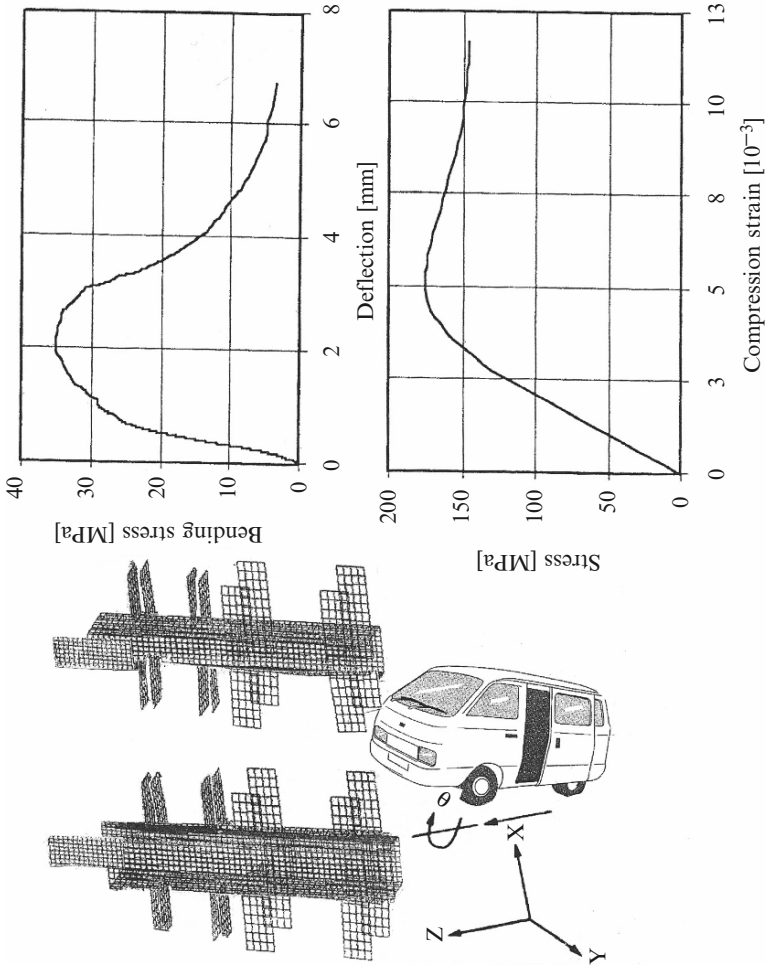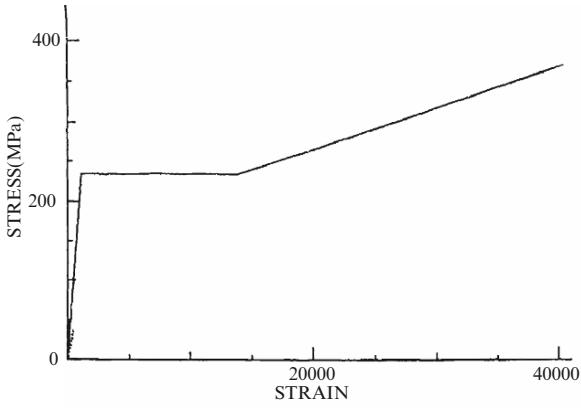**Fig. J.15.** Typical details to be included in test report with compliments from highway authority, and agency, U.K

Fig. J.16. Mesh generation scheme and typical force deformation response

Stress-strain relationship for steel rail (Input data)
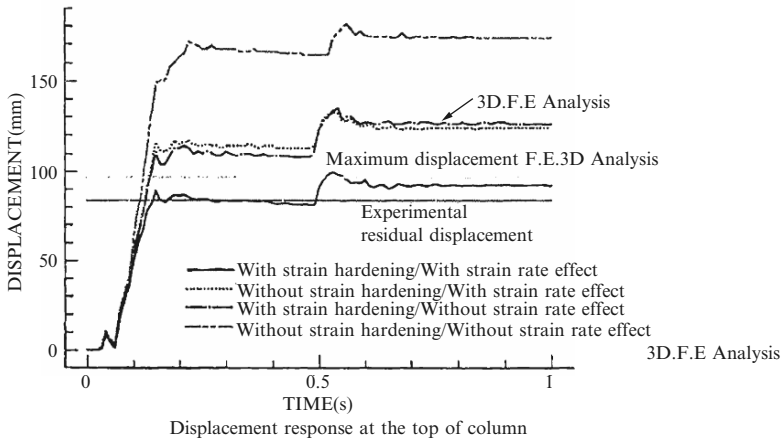

Displacement response at the top of column
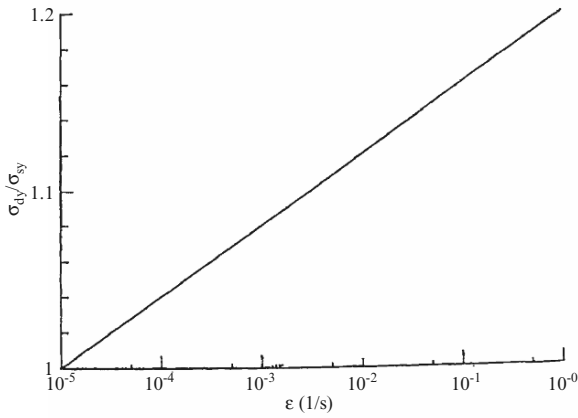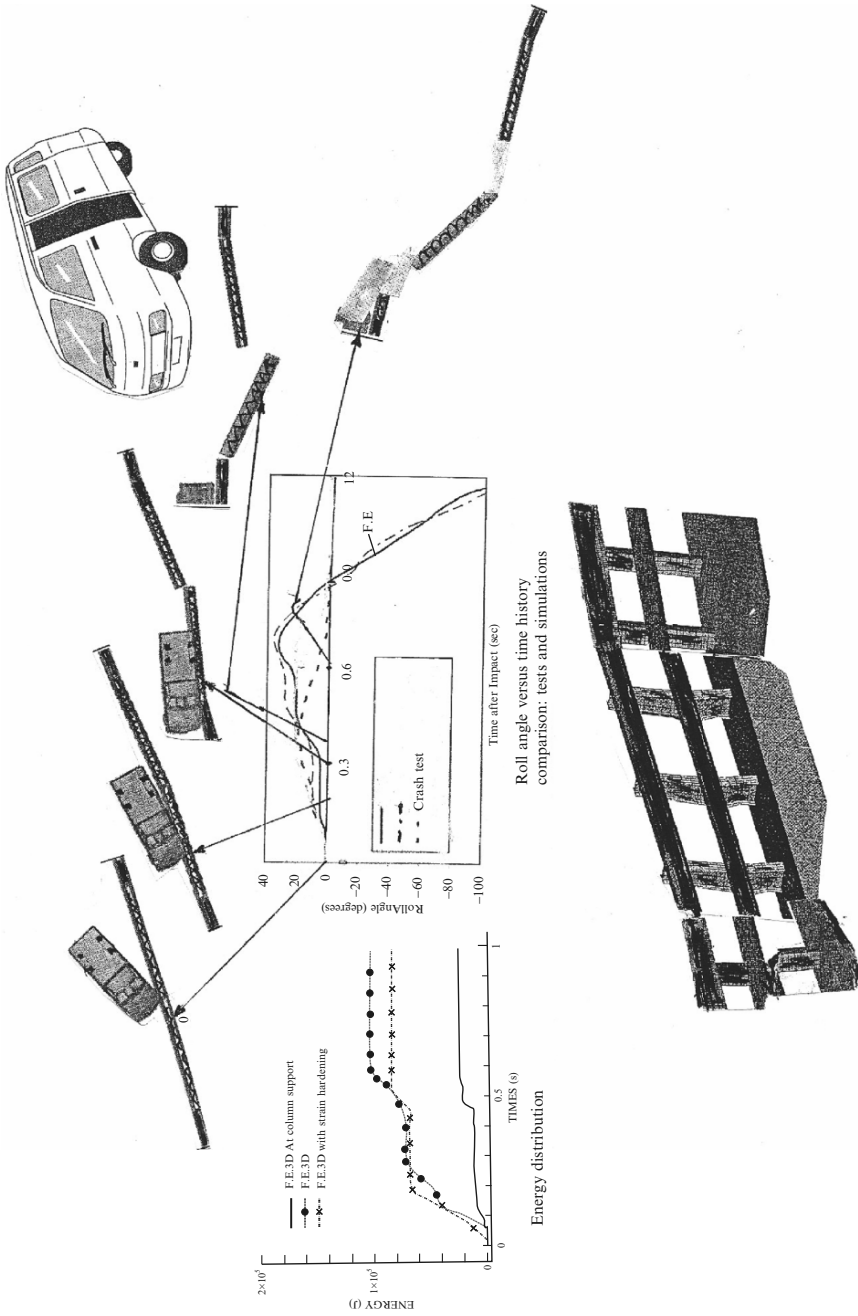
Fig. J.17.

Fig. J.18. Vehicle Impact on Parapet - A failure scenario

Table J.11. Comparison of impact performance based on BANG-F and ANSYS

S.No.	Summary: Materials and events	Net result	BANG-F		ANSYS	
			Time (s)	Speed (km h^{-1})	Time (s)	Speed (km h^{-1})
	Initial Contact		0.000 at 26.3°	98.0	0.000 at 26.3°	98
	Vehicle begins to redirect					
	2 pulls apart		0.06	96.7	0.057	97.2
	3 pulls apart		0.171	87.6	0.179	88.3
	Vehicle parallel with installation		0.218	80.9	0.225	81.6
	Impacting side rear left tire contacts PCB		0.236	77.8	0.244	78.7
	Segment 4 begins to fall over		0.251	75.7	0.26	76.4
	Vehicle exits installation		0.287	71.6	0.303	72.8
	Vehicle begins to rollover		0.467 at 13.7°	68.9	0.474 at 14.0°	70.2
					1.281	64.9
	Member post-immpact deformation or condition		DYN.BANG-F (mm)	DYN. ANSYS (mm)	DYN.BANG-F (mm)	DYN.ANSYS (mm)
	Concrete segment 2		770	890	750	880
	IJ-1		Not failed		Not failed	
	Concrete segment 3		1,160	1,270	1,140	1,260
	IJ-2		Not failed		Not failed	
	Concrete segment 4		1,170	1,280	1,130	1,270
	IJ-3		Not failed		Not failed	
	Concrete segment 5		850	920	860	930

[a]The larger of either ends.

Figure J.16 shows the details of the finite element mesh used to represent joint region. A fine mesh was developed to accurately represent the complex dynamic interactions at critical joint regions.

Analysis of Results

Figure J.16 and J.17 shows force time relation for the vehicle and the target by BANg-F. These results are then checked against the output produced by Program ANSYS. Figure J.18 shows the relationship between the roll angle in degrees and the time after impact. Table J.11 gives a summary of the crash using both BANG-F and ANSYS.

Conclusion and Recommendations

Inadequacies in the design and assumptions used in the analysis require further research and development. Full scale crash testing at the time of the analysis could not be done, although similar test results for actually testing have been carried out. Sophisticated nonlinear finite element analysis has been adopted on the lines suggested in both BANG-F and ANSYS. No full scale crash test results were available to check against the numerical models. Nevertheless a considerable amount of time and effort was spent on the details of the finite element simulation. This work has been checked by two well known programs. In order to carry out further in-depth study, the revelation of full scale crash test results must be available to check the accuracy of numerical predictions.

K

Luggage Container Subject to Internal Explosion

K.1 Introduction

The Federal Aviation Administration (FAA) of the United States has determined experimentally the explosive loading on a luggage container resulting from a bomb detonated in the luggage. Tests were based on a luggage container 50% and 75% full of luggage. The effects of venting were considered. The pressure generated within a luggage container was determined as if the environment was similar to an isotropic, porous and absorptive media which attenuates the initial shock wave produced by the blast and reduces the quasi-static pressure. The worst case would be when the explosive detonated inside an empty container. However it was found the blast attenuation would occur when the container with full luggage has an explosive device located at the centre of the container. The overpressure time relations were obtained to be used for the analysis of such containers. In addition Galaxy Scientific Corporation carried out research on the structural response and blast loading models of the luggage container. The container withstood the detonation of a bomb larger than which caused the loss of PAN AMERICAN Flight 103 over Lockerbie, Scotland 1988. The test was to increase the explosive resistance of the luggage container, which are normally located within the cargo bays of wide-body transport category of aircraft. Aluminium alloy sheets 2024-TS laminated with layers of fibreglass epoxy prepreg. Shock Pressure–time and quasi-static pressure–time relations were obtained for the analytical and design solutions of such a case study.

In this text data from these tests have been used to analyse a container and finally presented with solutions.

K.2 Data On Luggage Container

Dimensions: $1.54 \times 1.44 \times 1.475\,\text{m}$ (L $\times$ W $\times$ H)
Skin $= 50\,\text{mm}$ supported by 2 No. Stiffeners

W24 $\times$ 229 welded to its exterior in x-direction for one stiffener and deep welded in y-direction.
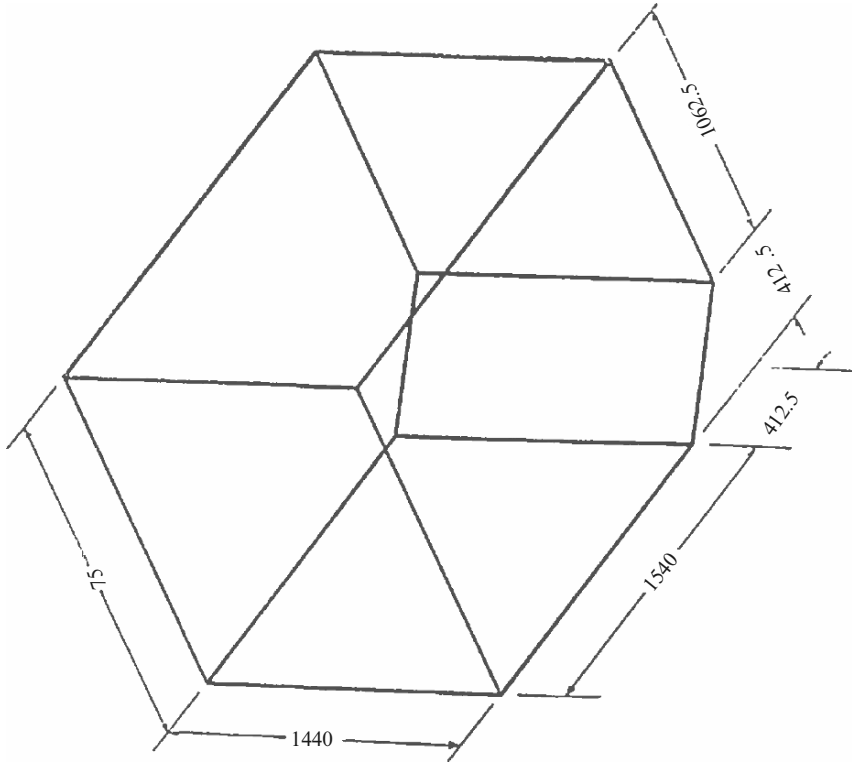
Fig. K.1. Typical luggage container. Note: All dimensions are in mm

Door = 50 mm thick M.S. bolted onto 100 mm flanges with 58 No. 30 mm bolts
A reference is made to Fig. K.1 for the luggage container.

Static internal pressure = 5.52 MN m^{-2} (5.5 N mm^{-2}) $\left. \right\}$ FAA data provided
Quasi-static pressure = 2.76 MN m^{-2} (2.76 N mm^{-2})

The quasi-static pressure-time relations is shown in Fig. K.2,
The luggage container is idealised in Fig. K.3 using the following data:

(a) Finite element
    Number of solid elements for the container = 1,480 (4-noded isoparametric
    type for the container skin)
    Doors = 450
    Flanges and stiffeners = 335
    Bolts/Nuts/Welds = 310
    This setup requires the mesh scheme to be unsymmetrical as viewed from
    any direction (Fig. K.3)
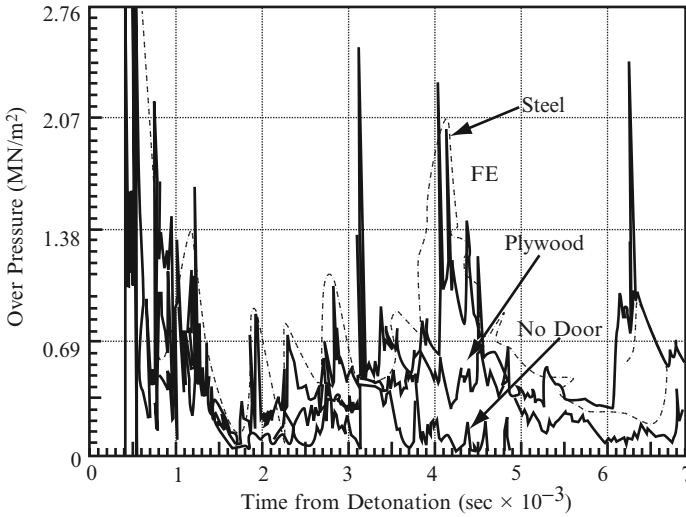
(a) Initial shock comparison with the charge in the center of an empty fixture with three venting conditions
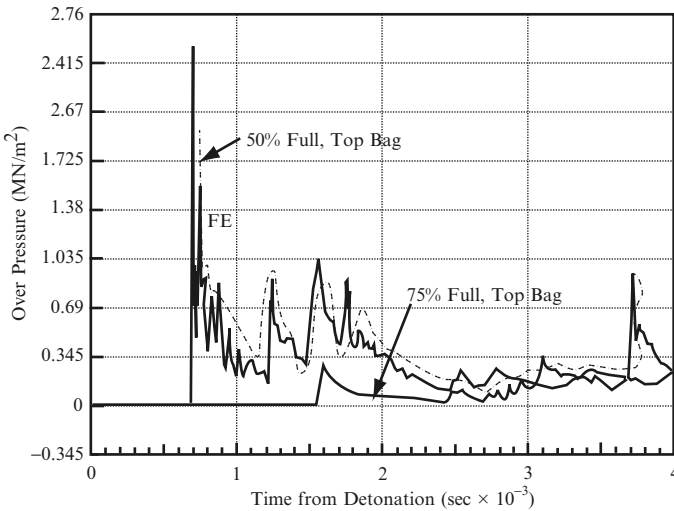
(b) Quasistatic pressure

Fig. K.2. Quasi-static pressure relations. J.A. Gatto, S. Krznaric. Office of Aviation Security Research and Development FAA Technical Centre, Atlantic City International Airport, NJ 08405, USA
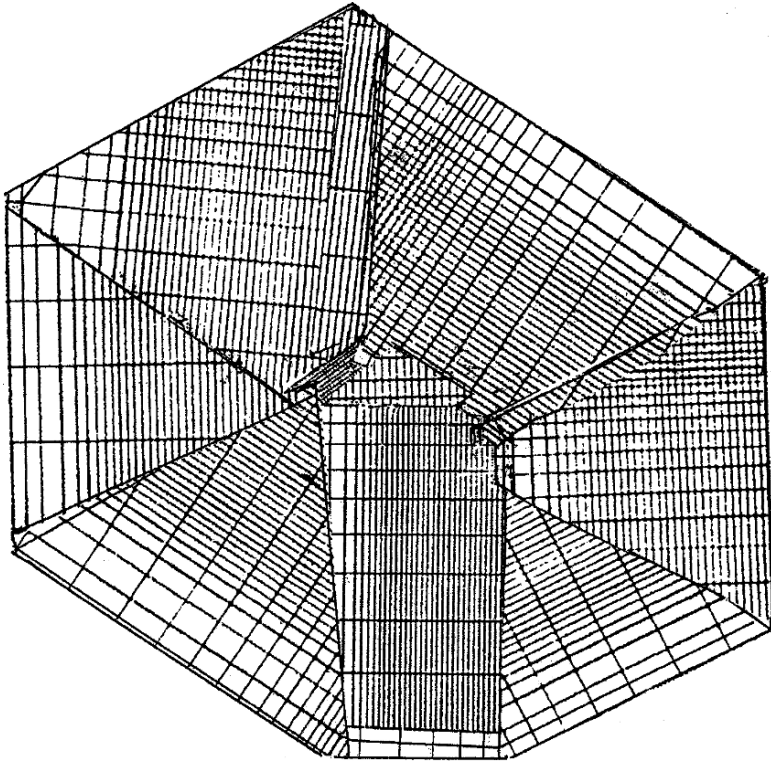
Fig. K.3. Variable finite element mesh scheme for a luggage container made with steel

(b) Material data/properties
   $f_{yt} = f_u = 460\,\text{N mm}^{-2}$ (ultimate)
   $f_y = 275\,\text{N mm}^{-2}$ (yield)
   $E_s = 210\,\text{GN m}^{-2}$ (Young's modulus of steel)
   $v = 0.35$
(c) W24 × 229 wide flange properties AISC specifications
   Total area A $= 67.2\,\text{in.}^2 = 433.56\,\text{cm}^2$
   Overall depth d $= 26\,\text{in.} = 640\,\text{mm}^2$
   Web thickness $t_w = 0.96\,\text{in.} = 24\,\text{mm}$
   Flange thickness $t_f = 1.89\,\text{in.} = 48\,\text{mm}$
   $I_{xx} = 7{,}650\,\text{in.}^4 = 318.417 \times 10^7\,\text{mm}^4$
   $S_x = Z = 588\,\text{in.}^3 = 96.4 \times 10^5\,\text{mm}^3$
   $I_{yy} = 651\,\text{in.}^4 = 27.1 \times 10^7\,\text{mm}^4$
   $S_y = Z = 99.4\,\text{in.}^3 = 16.3 \times 10^5\,\text{mm}^3$
   Estimated panel length/thickness ≥ 270

K.3 Analysis and Results

The blast resistant steel luggage container has been analysed using the best possible data obtained form IATA and Federal Aviation agency (FAA) for hardened luggage containers designed to suppress the explosive effects from the detonation of an undetectable quantity of explosives. These containers are anticipated to bridge the gap between quantities of explosives that can currently be detected and those of explosives which can destroy the aircraft. For the pressure loads generated for the internal explosion predicted one has to know the luggage pieces and the luggage environment. The FAA technical centre has carried out the total of ten tests ranging from 0 to 75% capacity with various locations. From the test matrix, the container environment assumed for the finite element analysis is based on 50 and 75% full. The input data included here for the finite element analysis are based on 50 and 75% full of the container.

The data satisfies the following four conditions:

(a) Pressure loading on a container due to internal detonation under different content conditions and charge locations.
(b) Measure of the attenuation of shockwave and the quasi-static pressure provided by the luggage.
(c) A provision of venting and the change in the pressure–time history.
(d) Additional parameters for future sophisticated testing.

The quasi-static pressure–time history chosen are selected honestly. In the analysis no temperature–time is included directly to affect the results.

The dynamic finite element analysis with implicit technique given in this text was adopted. The load–time function given by the FAA was considered. The results are summarised in Figs. J.4 and J.5. The quasi-static pressure analysis does allow for venting of the explosive products into the ambient air. Program ISOPAR has been used to evaluate the damage scenario. For each panel of the container the quasi-static pressure loading was applied. The damage scenario was achieved at t = 120 ms, allowing top panel to fly up and flip over. No evidence shows a lack of tearing or bearing failures. The design load was exceeded but the chief cause of failure was in areas between the panel and the joint. Plate K.1 shows black areas which indicate fractures 20–10 mm. Fractures in certain areas exceeded the width of 100 mm allowing the joints to blow out when the quasi-static pressure reached $2.76 \, \text{MN m}^{-2}$. The major panels rotated around $35°$ from the original boundary and displacement of 150 mm plus different panels. The door is severely fractured (multiple fractures of 15 mm in different directions along the coordinate axes in the luggage container skin. The major fractures (blown out level) were between the skin and the joints. The bolts were sheared off but no tearing and bearing failures occurred anywhere.
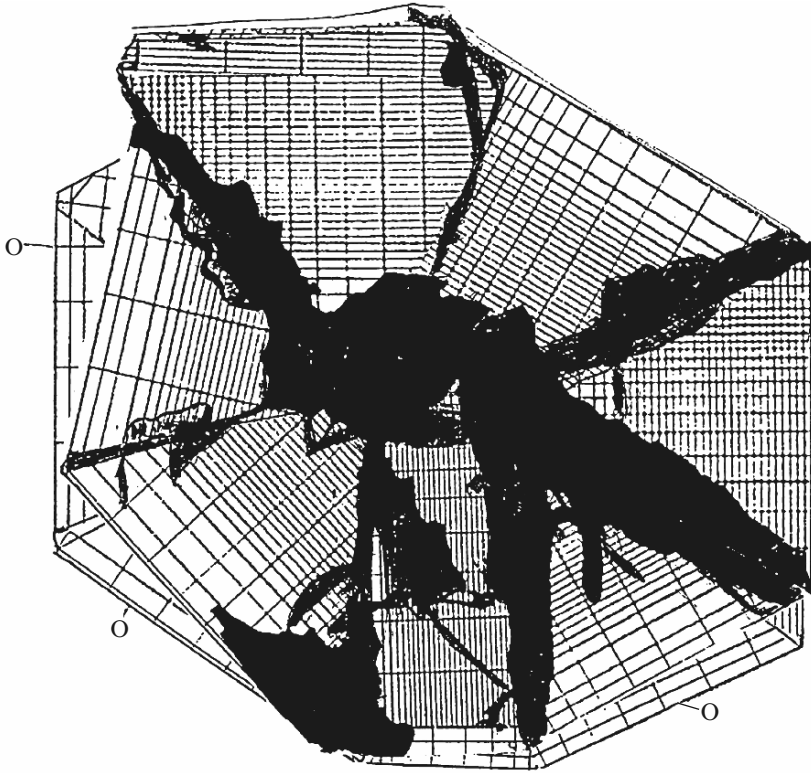
O - Original Boundary
⬛ Damage and plasticity
⬛ Elastoplasticity

Plate K.1. Damage Scenario Quasi-static Pressure @ 75% full ($2.76\,\mathrm{MN\,m^{-2}}$)

Program ISOPAR took $1\,\mathrm{h}$ and $31\,\mathrm{min}$ to complete the disaster scenario. All three solution procedures were considered and there are no appreciable differences exist in the overall rotations, displacement and bending and shear failures of the panels.

L

Blast and Impact on Buildings
due to Aircraft Crashes

L.1 Introduction

A reference is made to the following publication of the author with T. Bangash for the interaction analysis of impact and explosion-cum-fire for WTC tower collapsed under aircraft crashes:

> Explosion-Resistant Buildings
> Springer-Verlag, Heidelberg 2006

Comprehensive programs under the title of BANG-F have been developed in Fortran. A brief of this work is reposted under this section together with additional results which could not be published for technical reasons.

Aircraft/missile impact data analysis is now compiled in this book. Basic impact dynamics is initially introduced. Data on civilian and military aircraft are given in detail so that they can be useful during the inputting of various computer programs. Various equations have been developed for normal and oblique impact. Aircraft impacts on structures are introduced and analytical model is devised for the formulation of various relevant computer programs. The load–time function has been established together with impact modelling developed by a number of researchers. Military, air-force and navy missiles and impactors with their relative data are included. The damage scenario can be checked by various noted empirical formulae devised for structural perforation, penetration, scabbing, spalling and rupture. They are included in this book.

Since the collapse of the WTC towers, it is now necessary to conclude a chapter on aircraft hot fuel-structure interaction during aircraft impact conditions. A comprehensive investigation is reported in the above publication. The data on WTC towers and impactors are included in this section.

When impact, explosion along or in combination, occurs, fire is bellowed, together firing debris, as witnesses in WTC disaster scenario. Scattering flying objects are the results. This section examines the identity of the form and location of unknown elements inside a given surrounding medium. It is

proposed to measure wave reflection data in space and time. Hybrid finite
element/difference method is developed in three dimensions where scatter-
ing can be performed with time periodic or known data in the form of
short impulses. The basic mathematical tool was devised which amounts to
numerically solving the time dependent elastic wave equation with given mate-
rial coefficients. Finally the scattering phenomenon of objects was achieved
using the TIME-DOMAIN approach. Program FEMVIEW was linked to view
the damage scenario. The computerised version is identical to the actual
WTC Scenario. Global analysis with Program BANG-F (Advanced version
of PROGRAM ISOPAR) has been performed.

For the analysis the reader is referred to Sect. 4.4 for the aircraft impact
analysis and its assumptions. Here those results are included which were left
behind, when the book was published.

Boeing 767-200ER

General Specifications

Passengers	
Typical 3-class configuration	181
Typical 2-class configuration	224
Typical 1-class configuration	up to 255
Cargo	2,875 cubic feet (81.4 cubic meters)
Engines' Maximum Thrust	
Pratt & Whitney PW4062	63,300 pounds (28,713 kilograms)
General Electric CF6-80C2B7F	62,100 pounds (28,169 kilograms)
Maximum Fuel Capacity	23,980 U.S. gallons (90,770 liters)
Maximum Takeoff Weight	395,000 pounds (179,170 kilograms)
Maximum Range	6,600 nautical miles
Typical city pairs: New York-Beijing	12,200 kilometers
Typical Cruise Speed	0.80 Mach
at 35,000 feet	530 mph (850 km/h)
Basic Dimensions	
Wing Span	156 feet 1 inch (47.6 meters)
Overall Length	159 feet 2 inches (48.5 meters)
Tail Height	52 feet (15.8 meters)
Interior Cabin Width	15 feet 6 inches (4.7 meters)

FEDERAL EMERGENCY MANAGEMENT AGENCY

Plate L.1. Aircraft information

L.2 Aircraft Information and Other Tower Data

Plate L.1 gives brief information on the technical data for Boeing 767-200ER. Plate L.2 gives a comparison of high rise buildings and aircraft sizes. Plate L.3 gives a bird's eye view of WTC complex. Plate L.4 gives a disaster scenario after the aircraft Boeing 767-200ER crashes.

L.3 Input Data and Gneral Analysis of WTC-1 and WTC-2 (WORLD TRADE CENTRE)

L.3.1 Geometrical Data

The World Trade Centre and adjacent affected buildings were located on the West Side of New York, adjacent to Hudson River at the south tip of Manhattan. Here geometrical details are given for only two buildings, namely WTC-1 and WTC-2.

WTC-1:-

- (a) Up to roof height $= 1{,}368$ ft $= 417$ m
  Total main height:- Each floor height $= 12$ ft $(3.675$ m$)$
  Total floors $= 110$
  H $=$ effective height $= 402.335$ m

- (b) WTC-1
  Floor plan area:-
  Larger $- 207$ ft $(63.1$ m$) \times 207$ ft $(63.1$ m$)$
  Smaller $-$
  Regular service core $- 87$ ft $(26.517$ m$) \times 137$ ft $(41.7576$ m$)$
  $\quad = 1{,}107.31134$ m^2
  Corners chamfered $6'{-}11'$ $(2{,}108$ mm$)$

WTC-2:-

  This building was 6 ft $(1.829$ m$)$ less than WTC-1
  H $=$ effective height $= 400.072$ m
  Up to roof height $= 415.1376$ m
  Areas (same as of WTC-1)

L.3.2 Aircraft Impact Areas and Speed

L.3.2.1 American Airlines, (Flight 11) and United Airlines (Flight 175)

Boeing 767-200 ER
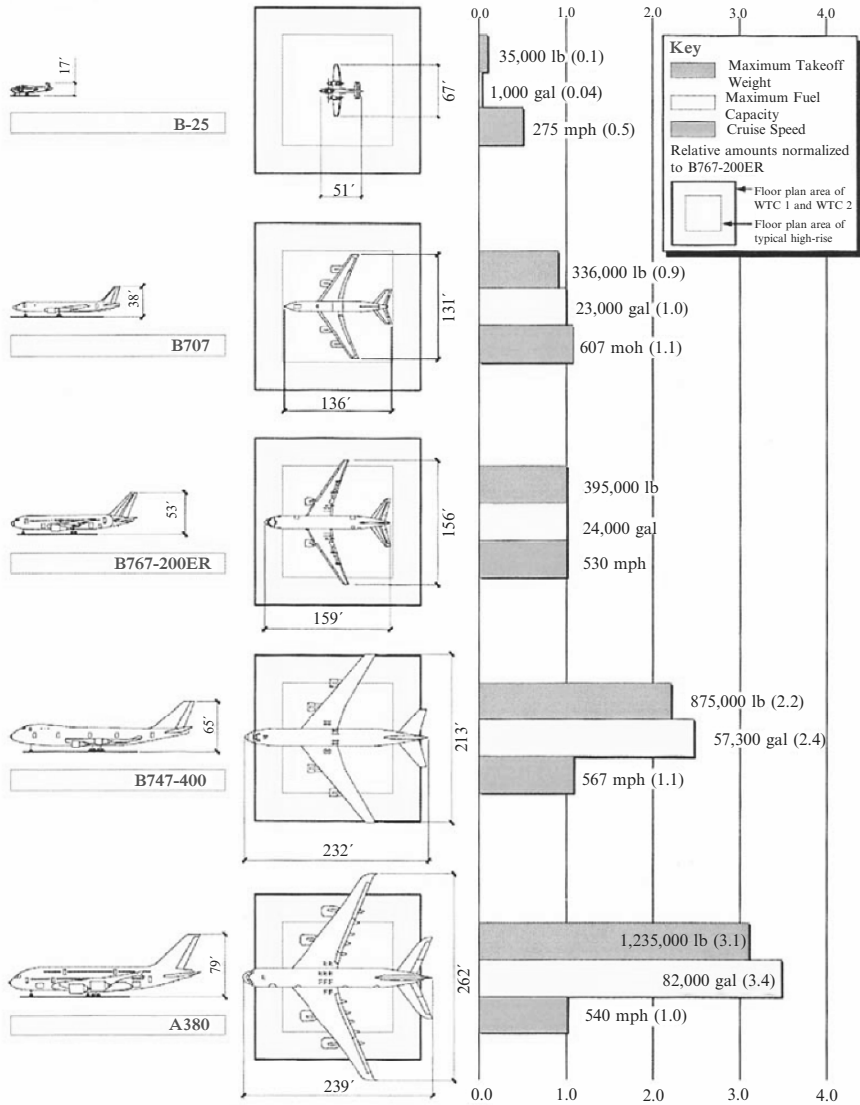
Plate L.2. Comparison of high rise building and aircraft sizes. US (FEMA) with compliments
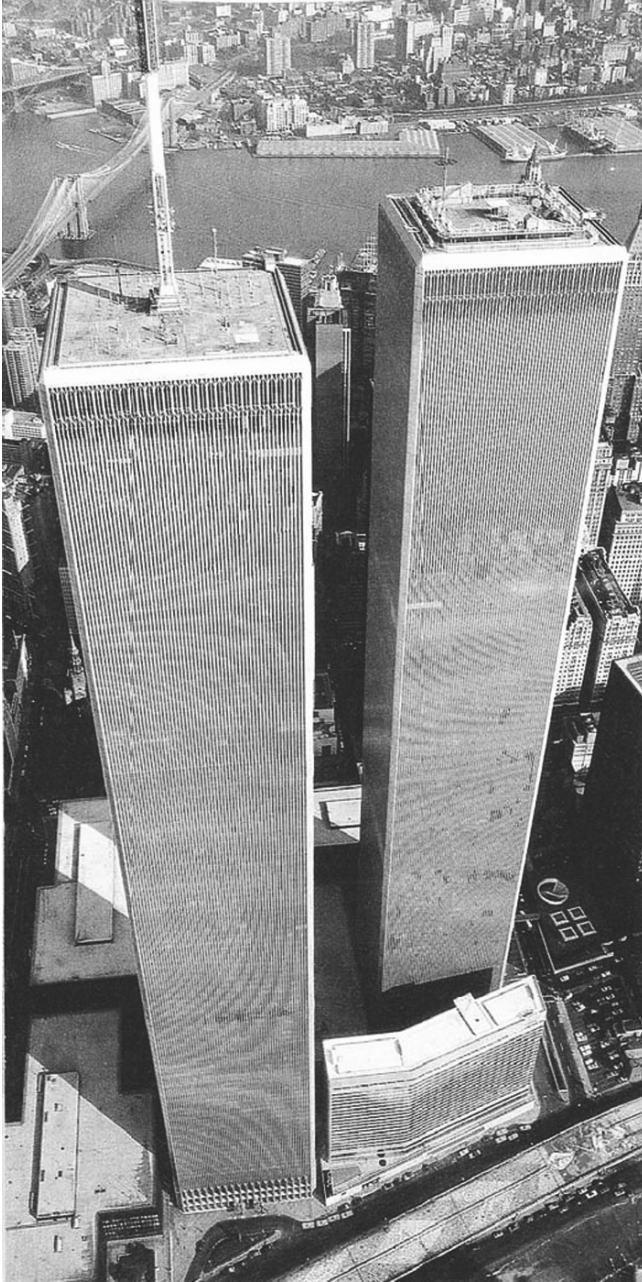
Plate L.3. A bird's eye view of the WTC complex
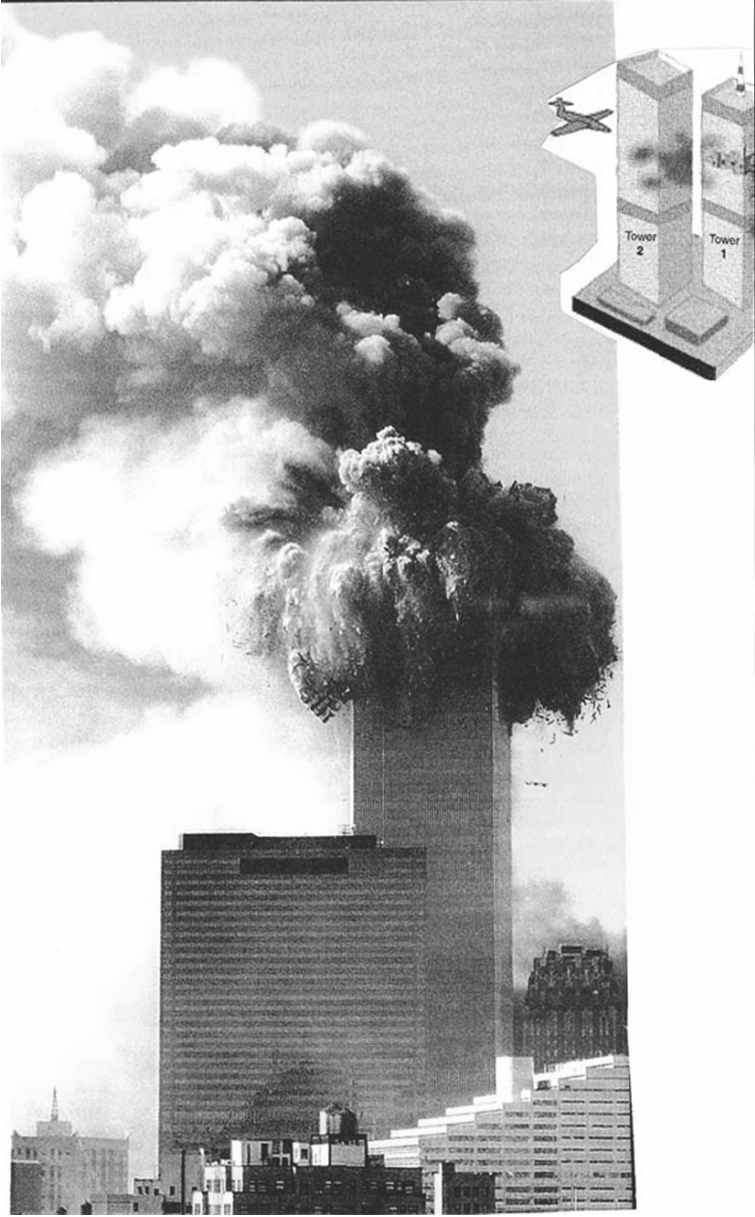
Plate L.4. WTC tower without antenna – collapsed scenario: Tower 2

Maximum take-off weight = 178,170 kg
Gross weight = 124,284.3 kg
Max range = 12,200 km
Cruise speed = 850 km h^{-1} (530 mph)
Wing span = 156′1″(47.6 m)
Overall length = 159′2″(48.5 m)
Interior cabin width = 15′6″(4.7 m)
Aircraft area = 48.5 × 47.6 = 2,308.6 m^2

Flight 11, departed time: 7.59 a.m. and crashed time 8.46 a.m.
Flight 175, departed time: 8.14 a.m. and crashed time 9.03 a.m.

L.3.2.2 Impact Areas

1. North Tower WTC-1 = 4 × 12 = 48′ (14.6304 m)
   Height: Impacted Area between
   Maximum Impact Area
   Impact between floor 98 and 94 = 30 m^2
   Centred on north face
   Speed at impact = 470 km h^{-1} = 131.6 m s^{-1}
   (taken for the analysis)
2. South Tower WTC-2
   Floors under impact = 78–84 = 6 × 12 = 72′ (21.9456 m)
   Maximum Impact Area assumed as 30 m^2
   Speed at impact = 590 km h^{-1} = 165.2 m s^{-1}
   (taken for the analysis)

L.3.2.3 Time Durations

WTC-1 – 47 min (2,820 s) collapsed at 10.29 a.m.
Time duration 10.29 − 8.46 a.m.   = 1 h 43 min
                                    = 1.717 h
                                    = 103.02 min
                                    = 6181.2 s
WTC-2 – 49 min. (2,940 s) collapsed at 56 min. after impact i.e. 9.03+56/60 = 11.223 = 9.063 a.m., time at which collapse occur.

L.3.2.4 Load–Time Function

The load–time function as explained, in Fig. L.1 is to be created with Δt, the time interval for the dynamic finite element will be the base values against impact loads Simpson rule or others can be used to develop the response of the entire structure of WTC-1 or WTC-2.

At the central zone, the impact corresponding to the air plane fuselage and engines is the worst zone. Away from the central zone, outer wing structures create also an impact zone.
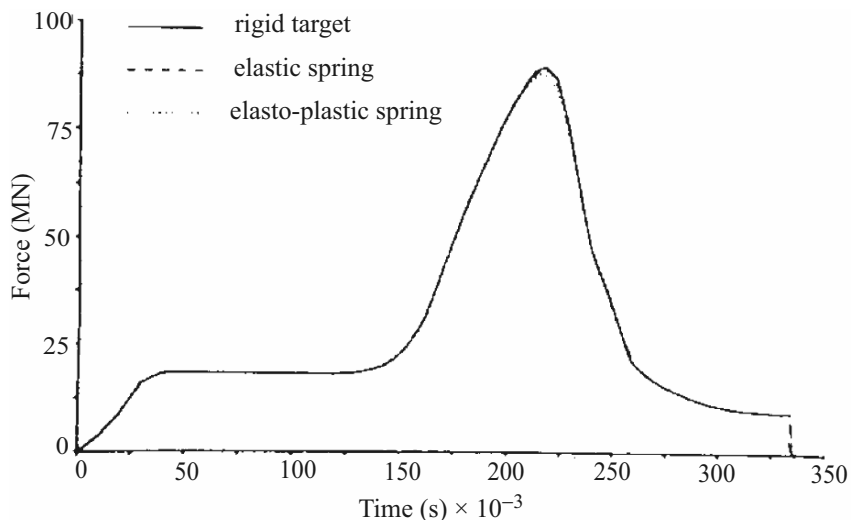
Fig. L.1.

L.3.2.5 Existing Loads on WTC-1 Apart from Those due to Aircraft Impact

The upper 55 stories of the building's exterior-wall frame were explicitly modeled using beam and column elements. This encompassed the entire structure above the zone of impact and about 20 stories below. The lower 55 stories of the exterior were modeled as a "boundary condition" consisting of a perimeter super-beam that was 52 in. deep (1,321) and about 50 in. (5,270) wide, supported on a series of springs. A base spring was provided at each column location to represent the axial stiffness of the columns from the 55th floor down to grade. The outrigger trusses at the top of the building were explicitly modeled, using truss-type elements. The interior core columns were modeled as spring elements.

An initial analysis of the building was conducted to stimulate the pre-impact condition. In addition to the weight of the floor itself (approximately 54 psf ($259 \, \mathrm{kN \, m^{-2}}$) at the building sides), a uniform floor loading of 12 psf ($0.76 \, \mathrm{kN \, m^{-2}}$) for partitions and an additional 20 psf was conservatively assumed to represent furnishings and contents.

At the impact area, all columns are damaged. The assumption is valid in the impact analysis.

L.3.2.6 Fireball and Temperature

Fireballs erupted and jet fuel across the impact floors and down interior shaft ways igniting fire. The term fireball is used to describe deflagration or ignition

of fuel vapour cloud. As a result, give raged shroud out the upper floors of
the Towers. Program BANG-FR is invoked to get necessary quantities in
terms of pressures of loads and are algebraically added to those pressures
produced from aircraft-impact specifically floors receiving hot fuel and floors
should be analysed using the above analysis. In this analysis for the jet-oil-
tower structure interaction, based on FEMA Report $-3,000$ gallons escaped
with 4,000 gallons remained on the impacted floor. The total peak rate of
fire energy per Tower is assumed as 3–5 trillion Btu h^{-1} (1–1.56 GW), with a
ceiling gas temperature 1,100°C (2,000°F). Growth of fire balls with final full
size of 200 ft (60.96 m) occur after 2 s.

L.3.2.7 Concentrated Loads

BANG-FR for fire analysis is initially concentrated on 80th floor level. The
columns above the damage area are predicted to act as tension members,
transferring around 10% of the load carried by the damaged columns upward
to outrigger trusses and this load is assumed back on core columns.

Using BANG-FR and FEMVIEW as front ended an aircraft positioning
inside the tower has been achieved in Fig. L.2 which is treated as a small chunk
of the overall mesh generation scheme of the WTC-1 in Fig. L.3.

L.3.2.8 Chunks Dismantled

As predicted on site, chunks with dimensions around 12′ (305 mm) have landed
at a distance of 15 ft (4.572 m) from the face of the building. The distance is
assumed always for the computation of forces of chunks. The maximum length
and width as observed were 40 ft (12.2 m) and 30 ft (9.144 m).

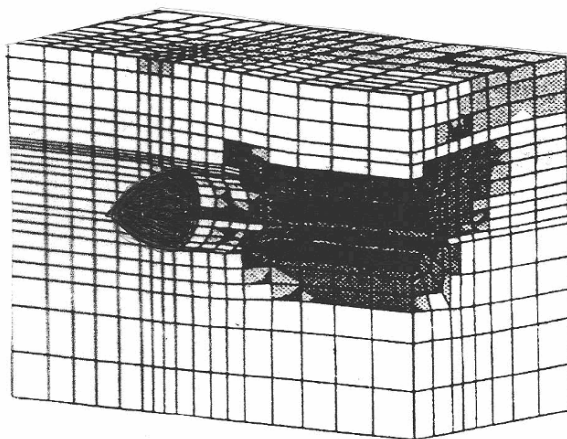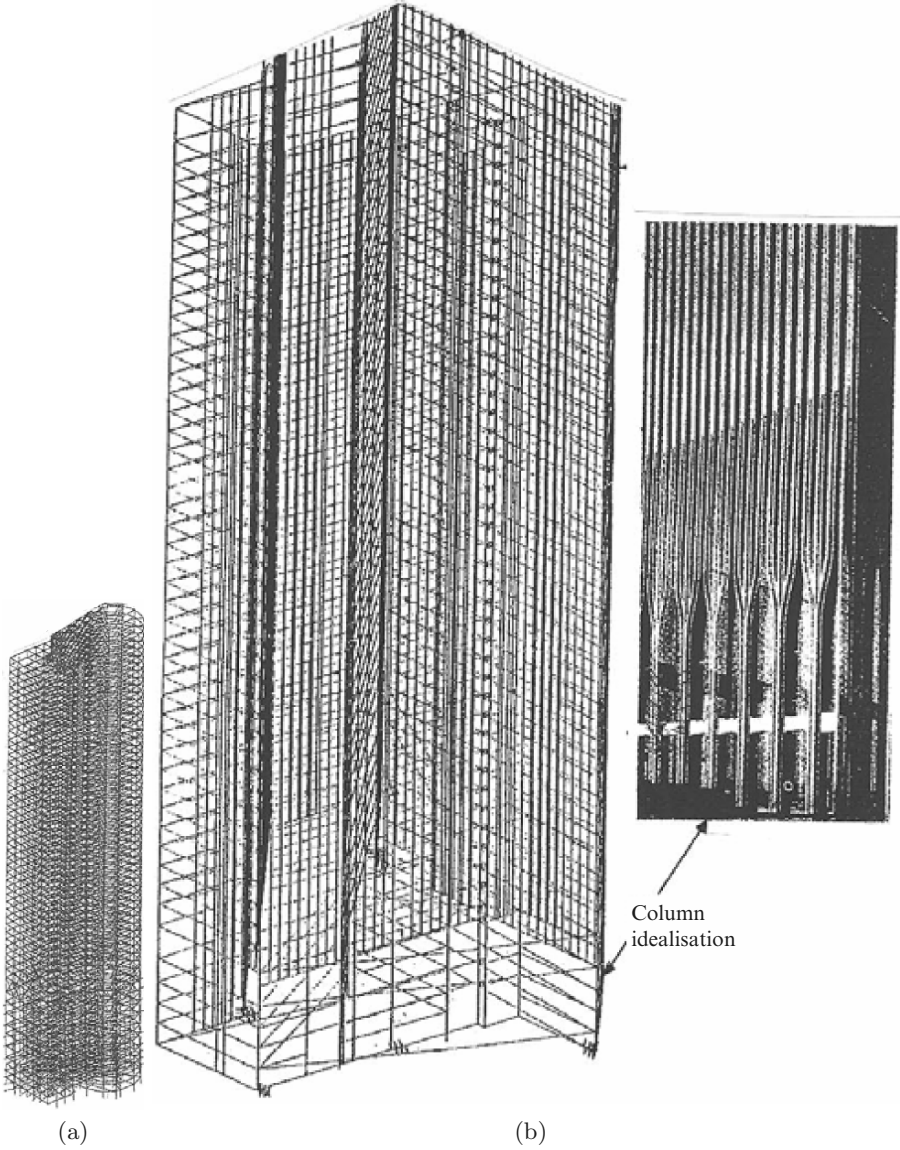**Fig. L.2.** Aircraft positioning inside tower after impact on WTC-1 tower

(a)   (b)

Fig. L.3. (**a**) Complete mesh scheme of WTC-1 tower. (**b**) Finite element mesh scheme for the WTC-1 analysis

L.3.3 Connection Details, Structural Sizes and Other Parameters

The behaviour of a typical fully rigid, partial strength wind-moment connection about the strong axis of the column was studied. The connection of the W18×50 girder to the W15×426 column between girder line 7–8 at frame line D on the 14 floor was modeled as a representative connection. The top and bottom moment plates (estimated as $5/8 \times 6 \times 24$ in. ($15.875 \times 152 \times 610$ mm) and $3/8 \times 10\text{-}1/2 \times 24$ in. ($0.56 \times 267 \times 610$ mm), respectively, were welded to girder flanges with a 1/4-in. weld. The shear plate (estimated as $5/16 \times 3 \times 12$ in.; $1.938 \times 15 \times 300$ mm) was bolted to each girder web with four 7/8 in. diameter (6.36 mm) bolts. The designs of the bolts are taken to be A 370 bolts.

Similarly, the behaviour of a typically fully rigid, partial-strength wind-moment connection about the weak axis of the column was studied. The connection of the W24 × 68 girder to the W14 × 426 column between girder line C-D at frame line 7 on the 15th floor was modeled as a representative connection. The top and bottom moment plates were estimeted as $3/8 \times 12 \times 14$ in. ($9.5 \times 300 \times 355$ mm) with a 1/4-in. (6 mm) weld with a $3/8 \times 8$ in. seat plate ($12 \times 125 \times 355$ mm). The connection capacity was estimated to be 7.500 kip in.$^{-1}$ ($8,011.5$ KNm), thus confirming that the frame design was governed by stiffness and not strength.

L.3.4 Columns, Plates and Spandrels

(a) The columns are built up by 4NO plates. $14''$ (955.6 mm) $\times 14''$ (355.6 mm) welded plates spaced $3' \, 4''$ ($1,016$ mm)

Adjacent parameter columns are interconnected at each floor level by deep spandrel plates of $52''$ ($1,320.8$ mm) depth.

In alternative stories, an additional column can be found at the centre of each of the champfered building corners.

The Sect. A, the size is $13\frac{1}{2}''$ (343 mm) with top plate $355.6 - 343 = 12.6$ mm, and the width of this section is $14''$ (350.6 mm). The base of the exterior column is assumed to be 3NO $14'' \times 14''$ (356×356 mm) welded together.

The vertical plate thickness 2 NO $\frac{1}{2}''$ (12 mm) $= 25$ total.

(b) The floor section is shown in Fig. L.5, with concrete thickness of the metal deck. The main double truss has a total width of $2,032$ mm.

(c) The estimated openings in the exterior walls of WTC1 are given in Plate I.6.

Typical 3D analysis models of flange and shear plate moment-connections in Figs. L.4 and L.5 are adopted in the FEMA report and have been re-examined in the current analysis the number of elements and nodes can be estimated from these figures for local analysis. They are given in the separate section in the text.
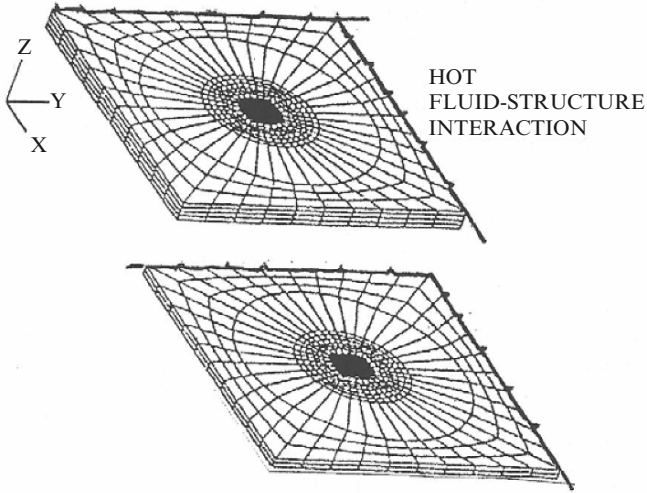
Fig. L.4. 3D concrete floor (Full degith). (a) 3D concrete plan slab (hay)
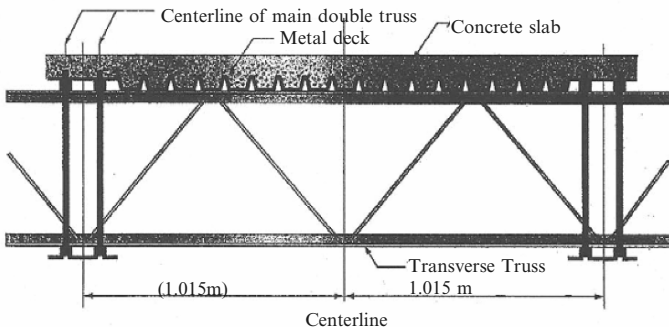
Fig. L.5. Cross-section to main double trusses supporting concrete floor

(d) Section properties (AISC Manual)
   (i) *W14 426 columns:* weight w = 426 lb
       F_y = 36 ksi; Kh with respect to r_y axial load = 2,560 kips
       F_{0y} = 50 ksi; Kh with respect to r_y axial load = 3,441 kips
       A = 125 in.^{2}; Kw = 1.875 in.
       I_x = 6,600 in.^{4}; b_f = 16.695 in.^{4}; I_y = 2,360 in.^{4}
       r_x = 4.34 in.; t_f = 3.035 in.
       $\dfrac{r_y}{r_x}$ = 1.67
       bending factor $\begin{cases} B_x = 0.177 \\ B_y = 0.442 \end{cases}$

$F'_{ex} (K_x L)^2/10^2$ kips = 547
$F'_{ey} (K_y L)^2/10^2$ kips = 195

(ii) W18 50 girders: weight w = 50 ft^{-1}

flange width = $7\,^1/_2\,''$;	A = 147 in.^{2}
L_c = 7.90 ft	d = 18 in.
L_U = 11.0 ft	t_w = 0.355
Span (ft) = 15	b_f = 7.495 in.
Span (ft) = 44	t_f = 0.570 in.

F_y = 36 ksi
Δ = 0.03''–2.64''
S_x = 88.9 in.^{3}
v = 92 kips

(iii) 14″ × 14″ Box section columns

t_w = wall inches = 0.625″ (5/8″)
area = 32.4 in.^{2}; I = 952 m^4; S = 136 in.^{3}
r = 5.42″; J = 1,530 in.^{4}; Z = 161 in.^{3}

(iv) W24 68 Columns

A = 20.1 m^2
d = 23.73 in.; t_w = 0.415; b_f = 911 in.; t_f = 0.585 in.
I_{xy} = 18.30 in.^{4}; S = 154 in.^{3}; r_x = 955 in.; I_y = 70.4 in.^{4};
S_y = 15.3 in.^{3}; r_y = 1.87
F_y = 20.2 ksi

(v) W14 193 Columns

F_y = 36 ksi
A = 56.8 in.^{2}
I_x = 2,400 in.^{4}
I_y = 931 in.^{4}
r_y = 4.05 in.
$\dfrac{r_x}{r_y}$ = 1.6
B_x = 0.183
B_y = 0.477
$F'_{ex} (k_x L_x)^2/10^2$ kips = 438
$F'_{ey} (k_y L_y)^2/10^2$ kips = 170
s = 54 in.^{3}; r_x = 955 in.; I_y = 70.4 in.^{4}; s_y = 15.3 in.^{3}; b_y = 1.89
d = 23.73 in.; t_w = 0.415; b_f = 911 in.; t_f = 0.585 in.
I_{xy} = 18.30 in.^{4}; s = 54 in.^{3}; r_x = 955 in.; I_y = 70.4 in.^{4};
s_y = 15.3 in.^{3}; b_y = 1.89

L.3.5 Typical Structural Details

Plate L.5 gives typical floor designs and Plate L.6 gives floor columns with dimensions. A damage scenario is given for WTC2 columns in Plate L.7.
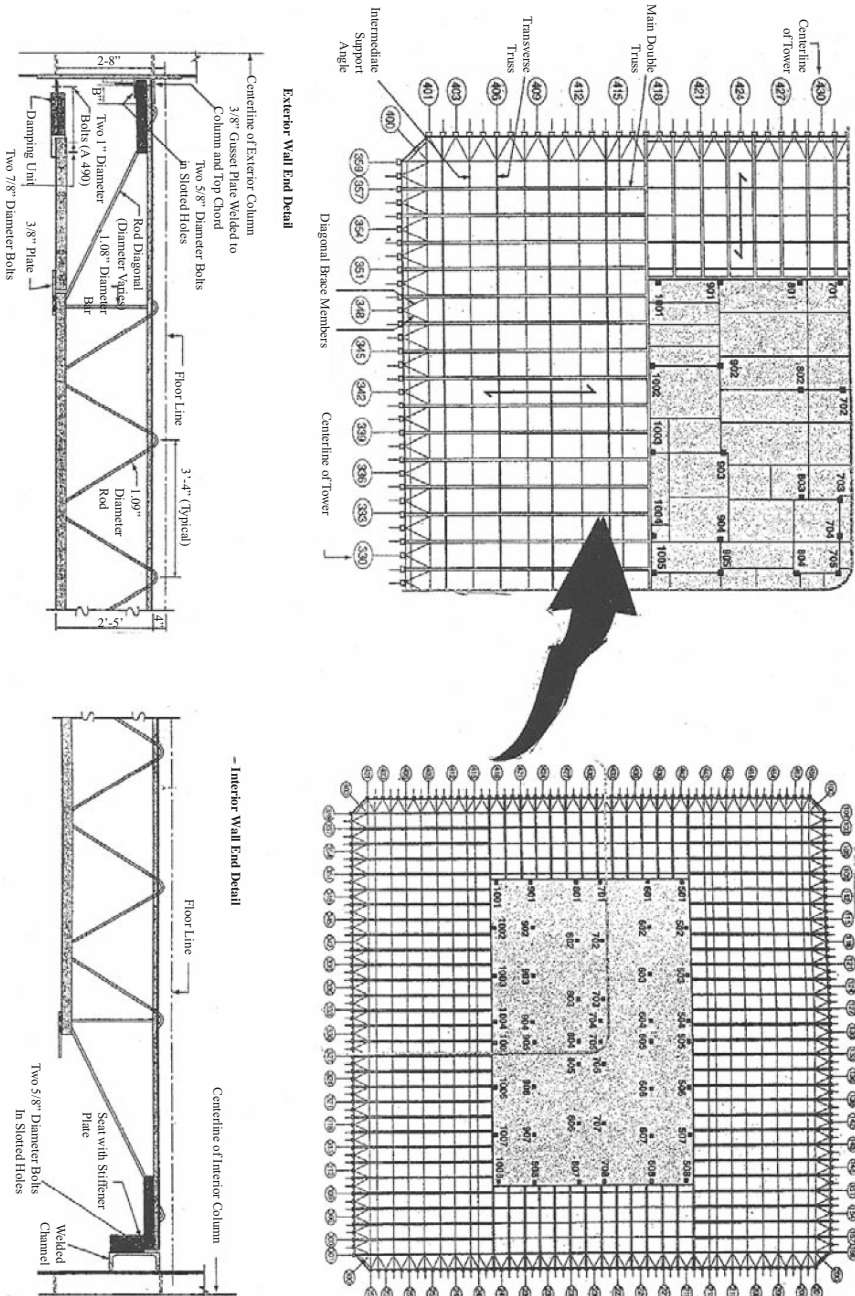
Plate L.5. WTC typical floors (FEMA)
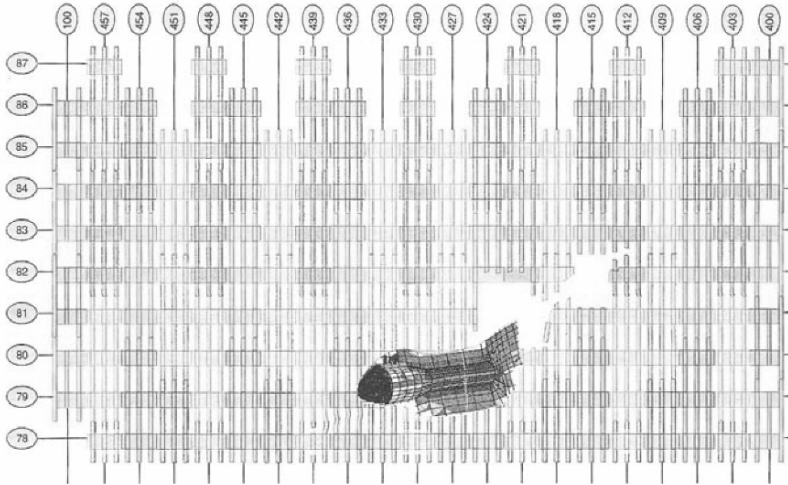
GENERAL NOTES:
(1) Column damage captured from photographs and enhanced videos.
(2) Damage to column lines 413-418 at levels 81 and 82 is estimated.
(3) There is not sufficient information to detail damage to column lines 408-411 at levels 83-84.

(a) *Impact damage to exterior columns on the south face of WTC 2.*
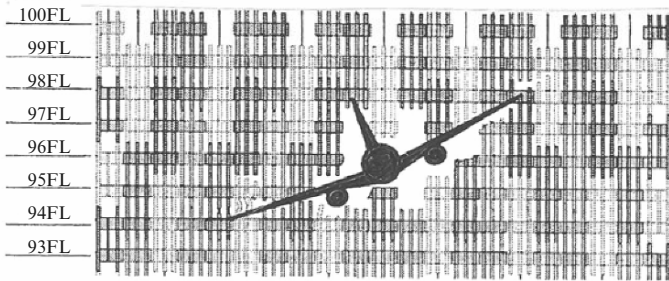
(b) Damage scenario at WTC-1
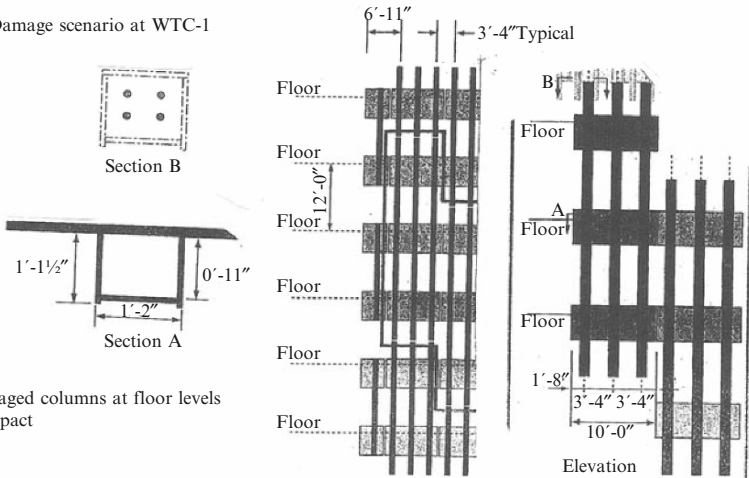
(c) Undamaged columns at floor levels prior to impact

Plate L.6. Floor columns
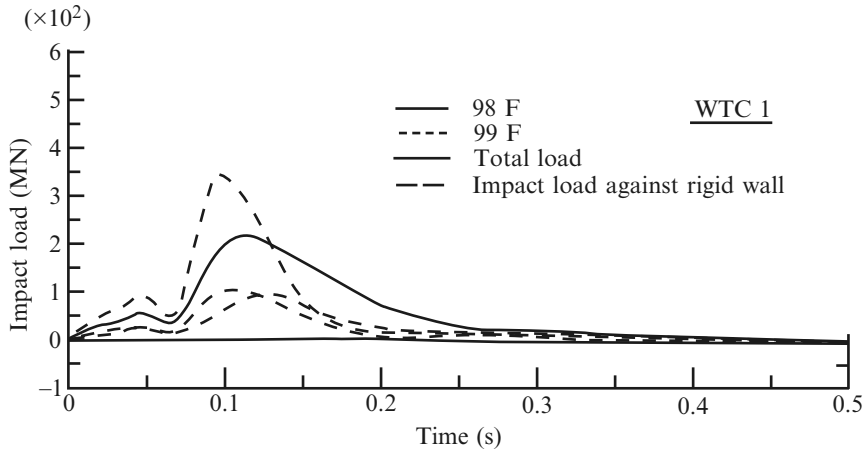
Plate L.7. Impact load time histories

L.3.6 Analysis of Results

A comprehensive treatment of WTC towers and various analytical methods and damage scenarios are given in the author's book on

Explosion-Resistant Buildings
(Springer Verlag, Heidelberg, January 2006)

Note: *Here the additional results left over are given which could not be published at the time of the publication of the above book.*

The towers were 417 and 415 m high with a typical storey height of 3.676 m. They were 63.1 m square in plan with bevelled corners and a rectangular core measuring 26.5 m wide and 41.8 m long. The tubular building comprised of 240 box columns located along the perimeter at intervals of 1.016 m with steel spandrel beams carrying the horizontal design wind. The core was comprised of 47 columns connected by small beams made of W-shape steel members as given in Sect. L.3.4. The total building weight above ground evaluated for the finite element analysis was estimated at 3,631 MN. The dead and the live loads were 2,900 and 741 MN respectively giving a mean weight per unit floor area to be evaluated as 8.31 kN/m^{-2}.

The aircraft crash gives an impact load versus time history for 93–99th floor in WTC-1 and 78–85th floors in WTC-2. Plate L.7 shows the impact load–time histories for both the tower.

The time of 0.4 s was considered for the nose of the aircraft to perforate the building. The impact load duration was 0.25 s. For WTC-1, the aircraft took 0.5 s for the aircraft nose to perforate the building. The duration of the impact load was prolonged to 0.5 s as the aircraft loses strength. The velocity–time curve has been evaluated in Plate L.8 for both the towers. They show velocity reduction values till the total aircraft collapse occurred
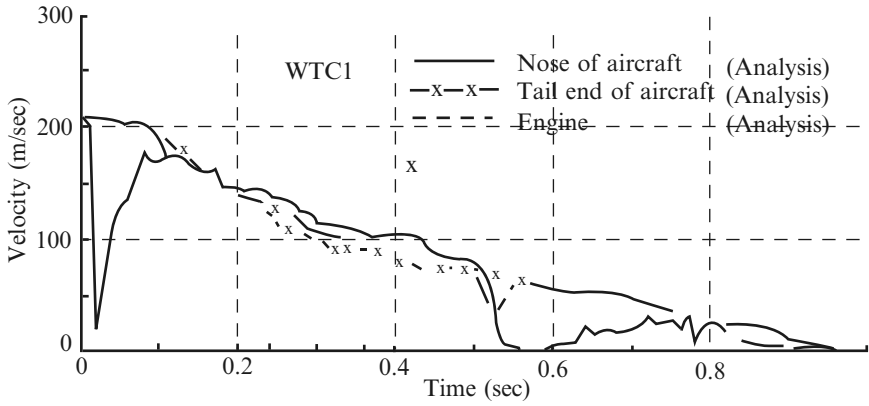
Plate L.8. Velocity reduction curve of aircraft
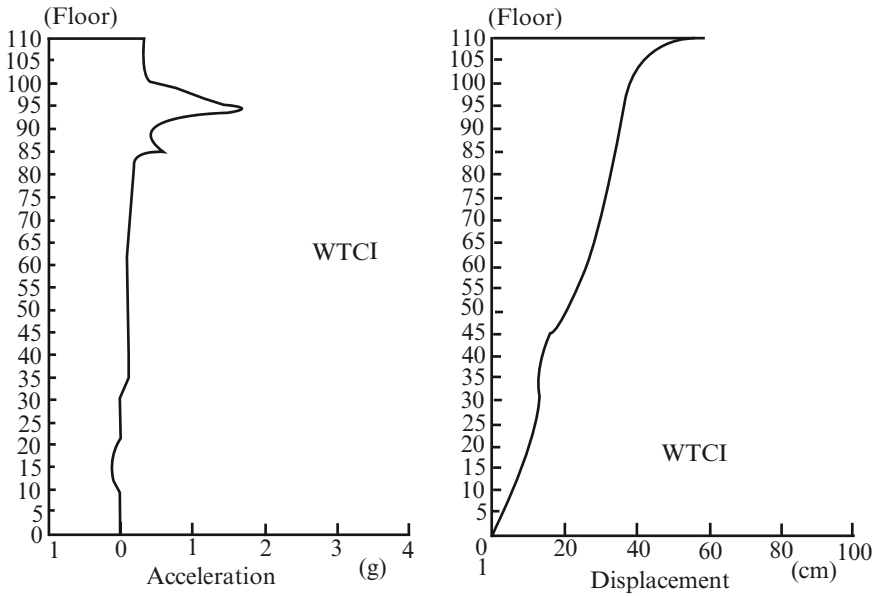
Plate L.9. Maximum response acceleration and displacement

and finally destroyed in each tower case. Plate L.9 indicates the results of maximum response acceleration and displacement for both towers. Program BANG-F which is the advanced version of Program ISOPAR, was used to calculate the displacement-time histories for each floor. These curve are shown in Plate L.10.
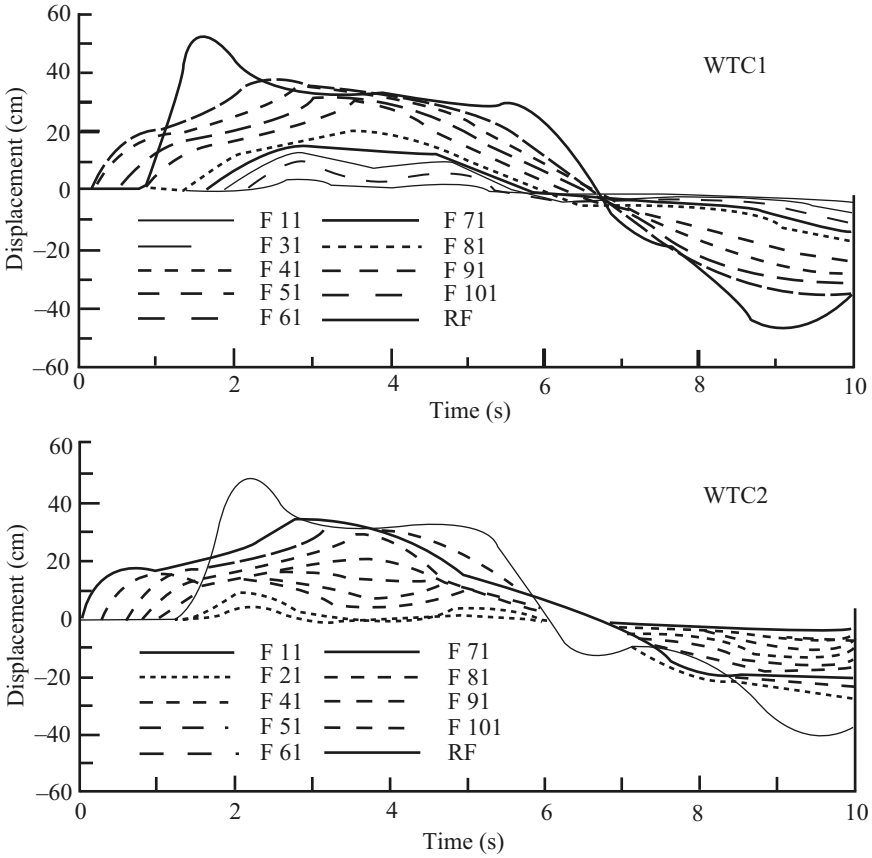
Plate L.10. Displacement time histories of each floor. F-Floor

Plate L.11 shows the impact force damage for the WTC 1. Plates L.11 and L.12 indicate the damage scenarios for WTC 1 towers using Program PATRAN. The computer versions of the damage scenarios are given in Plates L.13 and L.14. It is to be reminded that fire generated is combined with impact due to aircraft and the fire generated by air gushing through holes.
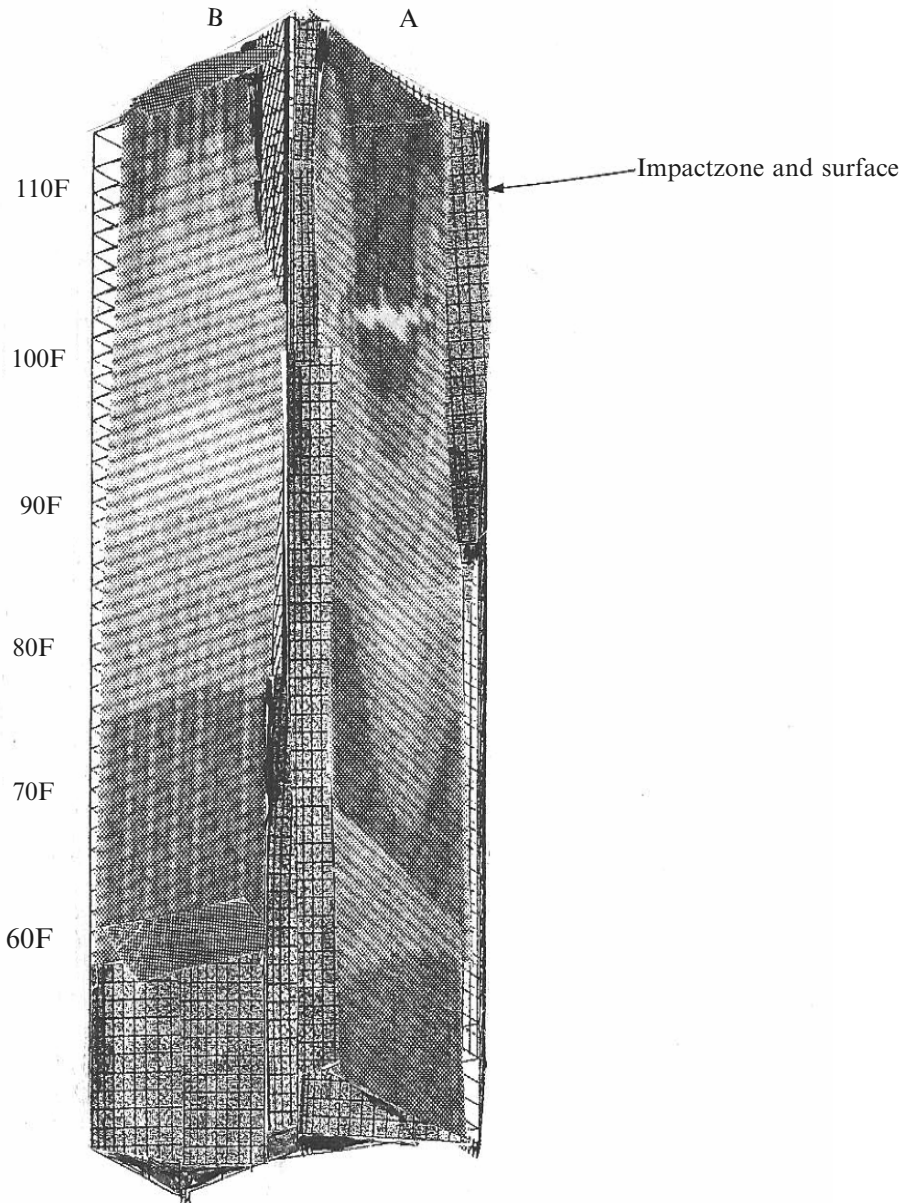
Finite element mesh scheme for the WTC-1 analysis

Plate L.11. A damage scenario of WTC-1
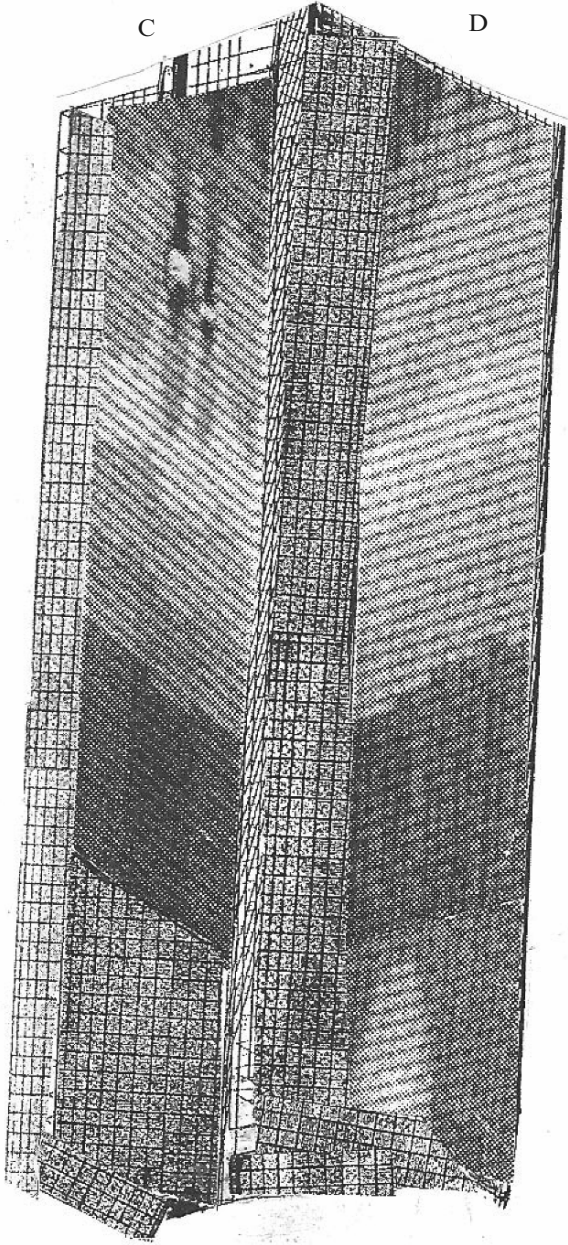
Plate L.12. A damage scenario of WTC-1
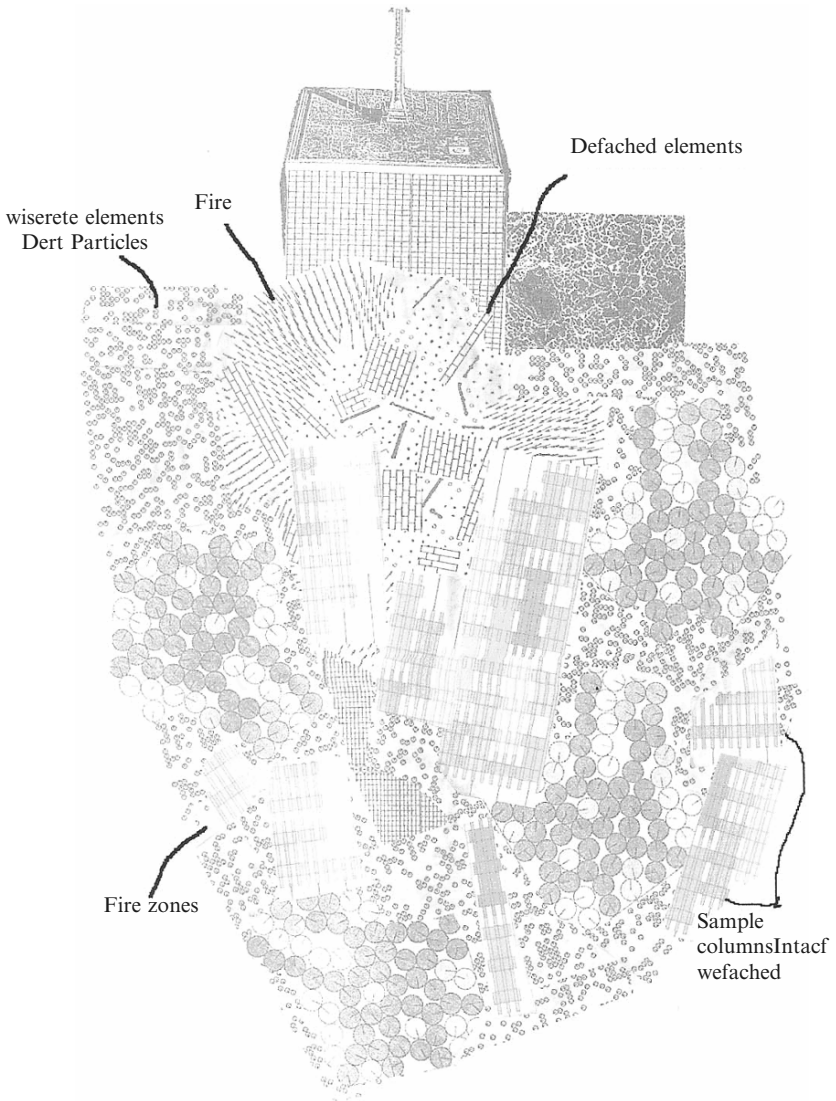
Plate L.13. Computed damage senario using finite element scannine

Plate L.14. W.T.C.1 on fire

Bibliography

1 Material Properties

1.1. Richart F.E., Brandzaeg A. and Brown R.L. (1928) A study of the failure of concrete under combined compressive stresses. *Bulletin No. 185*, Vol. 26. Engineering Experiment Station, University of Illinois.

1.2. Mazars J. and Bazant Z.P. (1989) *Cracking and Damage (Strain Localization and Size Effect)*. Elsevier, Amsterdam.

1.3. Hannant D.J. and Frederick C.D. (1968) Failure for concrete in compression. *Magazine of Concrete Research*, **20**, 137–44.

1.4. Link J. (1975) Numerical analysis oriented biaxial stress–strain relation and failure criterion of plain concrete. Third International Conference on Structural Mechanics in Reactor Technology (SMiRT), London, September 1975, Paper H1/2.

1.5. Chinn J. and Zimmerman R.M. (1965) Behaviour of plain concrete under various high triaxial compression loading conditions. *Technical Report No. WL TR 64–163 (AD468460)*. Air Force Weapon Laboratory, New Mexico.

1.6. Reimann H. (1965) *Kritische Spannungszustande der Betons bei mehrachsiger, ruhender Kurzzeitbelastung*. Deutscher Ausschuss für Stahlbeton, Berlin, Heft 175.

1.7. Willam K.J. (1974) Constitutive model for the trixial behaviour of concrete. IABSE Seminar, ISMES, Bergamo, Italy.

1.8. York G.P., Kennedy T.W. and Perry E.S. (1971) An experimental approach to the study of the creep behaviour of plain concrete subjected to triaxial stresses and elevated temperatures. *Union Carbide, Report No. 28642*. The University of Texas, Austin.

1.9. Linse D., Aschl H. and Stockl S. (1975) Concrete for PCRV's strength of concrete under triaxial loading and creep at elevated temperatures. Third International Conference on Structural Mechanics in Reactor Technology (SMiRT), London, September 1975, Paper H1/3.

1.10. Gardner J.J. (1969) Triaxial behaviour of concrete. *Proc. Am. Concr. Inst.*, no. 2, 136–47.

1.11. Kasami H. (1975) Properties of concrete exposed to sustained elevated temperature. Third International Conference on Structural Mechanics in Reactor Technology (SMiRT), London, September 1975, Vol. 3, Paper H1/5.

1.12. Browne R.D. (1958) Properties of concrete in reactor vessels. *ICE Conference on Prestressed Concrete Pressure Vessels*, pp. 131–51. Institution of Civil Engineers, London.

1.13. England G.L. and Jardaan I.J. (1975) Time-dependent and steady state stresses in concrete structures with steel reinforcement at normal and raised temperatures. *Magazine of Concrete Research*, **27**, 131–42.

1.14. Bangash Y. and England G.L. (1980) The influence of thermal creep on the operational behaviour of complex structures. International Conference on Fundamental Creep and Shrinkage, Lausanne, Switzerland.

1.15. Mohr O. (1914) *Abhandlungen aus dem Gebiet der Technischen Mechanik*, 2nd edn, p. 192. Wilhelm Ernst und Sohn, Berlin.

1.16. Kupfer H. (1973) Das Verhalten des Betons Unter Mehrachsigen Kurzzeitbelastung der Zweiachsigen Beanspruchung. Deutscher Ausschuss für Stahlbeton, Berlin, Heft 229.

1.17. Evans R.J. and Pister K.S. (1966) Constitutive equations for a class of on-linear elastic solids. *Int. J. Solids Struct.*, **2**, 427–5.

1.18. Chinn J. and Zimmerman R.M. (1965) Behaviour of plain concrete under various high triaxial compression loading conditions. *Technical Report No. WL TR 64–163 (AD4684460)*. Air Force Laboratory, New Mexico.

1.19. Mills L.L. and Zimmerman R.M. (1970) Compressive strength of plain concrete under multiaxial loading conditions. *ACI J.*, **67**, 802–7.

1.20. Chen E.S. and Buyulozturk O. (1983) *Damage Model for Concrete in Multiaxial Cyclic Stress*. Department of Civil Engineering, MIT, Cambridge, MA.

1.21. Bangash Y. (1985) PWR steel pressure vessel design and practice. *Prog. Nucl. Energ.*, **16**, 1–40.

1.22. Hobbs D.W. (1977) Design stresses for concrete structures subjected to multiaxial stresses. *Struct. Eng.*, **55**, 157–64.

1.23. Kotsovos M. (1974) *Failure Criteria for Concrete Under Generalised Stress States*, p. 284. PhD Thesis, University of London.

1.24. Chen, A.C.T. and Chen W.F. (1975) Constitutive relations for concrete. *J. Eng. Mech. Div., ASCE*, **101**, 465–81.

1.25. Chen W.F. et al. (1983) *Constitutive Equations for Engineering Materials*. Wiley, New York.

1.26. Bazant Z.P. (1978) Endochronic inelasticity and incremental plasticity. *Int. J. Solids Struct.*, **14**, 691–714.

1.27. Cedolin L., Crutzen Y.R.J. and Dei Foli S. (1977) Triaxial stress–strain relationships for concrete. *J. Eng. Mech. Div., ASCE*, **103**, 423–39, no. EM3, Proc. Paper 12969.

1.28. Bazant Z.P. and Bhat P.D. (1976) Endochronic theory of inelasticity and failure of concrete. *J. Eng. Mech. Div., ASCE*, **102**, 701–21.

1.29. Bazant Z.P. and Shieh H. (1978) Endoelectronic model for non-linear triaxial behaviour of concrete. *Nucl. Eng. Des.*, **47**, 305–15.

1.30. Pfiffer P.A. et al. (1983) Blunt crack propagation in finite element analysis for concrete structures. Seventh International Conference on Structural Mechanics in Reactor Technology (SMiRT), Amsterdam, North Holland, Paper H/2.

1.31. Johnson W. (1972) *Impact Strength of Materials*. Edward Arnold, London.

1.32. Ford H. and Alexander J.M. (1977) *Advanced Mechanics of Materials*, 2nd edn. Ellis Norwood Chichester, UK.

1.33. Achenbach J.D. (1973) *Wave Propagation in Elastic Solids.* North Holland/ American Elsevier.

1.34. Freakley P.K. and Payne A.R. (1978) *Theory and Practice of Engineering with Rubber.* Applied Science Publishers, Barking.

1.35. Williams D.J. (1971) *Polymer Science and Engineering.* Prentice-Hall, Englewood eliffs, NJ.

1.36. Campbell J.D. (1970) *Dynamic Plasticity of Metals.* Springer Verlag, Berlin.

1.37. Knott J.F. (1973) *Fundamentals of Fracture Mechanics.* Butterworths, London.

1.38. Lawn B.R. and Wilshire T.R. (1975) *Fracture of Brittle Solids.* Cambridge University Press.

1.39. François D. (Ed.) (1981) Advances in fracture research. In *Proceedings of Fifth International Conference on Fracture*, Vols. 1 and 2. Pergamon, New York.

1.40. Cottrell A.H. (1957) Deformation of solids at high rates of strain. In *The Properties of Materials at High Rates of Strain.* Institution of Mechanical Engineering.

1.41. Grundy J.D. et al. (1985) Assessment of crash-worthy car materials. *Chartered Mech. Eng.*, April, 31–5.

1.42. Oxley P.L.B. (1974) Rate effects in metal working processes. In *Mechanical Properties at High Rates of Strain.* Institute of Physics, London.

1.43. Radon J.C. and Fitzpatrick N.P. (1973) Deformation of PMMA at high rates of strain. In *Dynamic Crack Propagation* (Ed. by G.C. Sih). Noordhoff, Gronigen, Holland.

1.44. Vigness I. et al. (1957) Effect of loading history upon the yield strength of a plain carbon steel. In *The Properties of Materials at High Rates of Strain.* Institution of Mechanical Engineers, London.

1.45. Wigley D.A. (1971) *Mechanical Properties at Low Temperatures.* Plenum Press, New York.

1.46. Al-Haidary J.T., Petch M.J. and De Los Rios E. (1983) The plastic deformation of polycrystalline aluminum. In *Yields, Flow and Fracture of Polycrystals* (Ed. by T.N. Baker), p. 33. Applied Science Publishers, London.

1.47. Armstrong J.T. (1983) The yield and flow stress dependence on polycrystal grain size. In *Yield Flow and Fracture of Polycrystals* (Ed. by T.N. Baker), p. 1. Applied Science Publishers, London.

1.48. Bloom T.A., Kocks U.F. and Nash P. (1985) Deformation behaviour of Ni–Mo alloys. *Acta Metall.*, **33**, 265.

1.49. Conrad H. (1964) Thermally activated deformation in metals. *J. Metals*, **16**, 582.

1.50. Duffy J. (1983) Strain-rate history effects and dislocation structure. In *Material Behavior Under High Stress and Ultrahigh Loading Rates* (Ed. by J. Mescall and V. Weiss), p. 21. Plenum Press, New York.

1.51. Hart E.W. (1970) A phenomenological theory for plastic deformation of polycrystalline metals. *Acta Metall*, **18**, 599.

1.52. Klepaczko J.R. (1968) Thermally activated flow and strain rate history effects for polycrystalline aluminum and theory of intersections. *J. Mech. Phys. Solids*, **16**, 255.

1.53. Klepaczko J.R. (1975) Thermally activated flow and strain rate history effects for some polycrystalline F.C.C. metals. *Mater. Sci. Eng.*, **18**, 121.

1.54. Klepaczko J.R. and Duffy J. (1982) Strain rate history effects in body-centered-cubic metals. In *Proceedings of the Conference on Mechanical Testing for Deformation Model Development* (Ed. by R.W. Rhode and J.C. Swearengen), p. 251. ASTM STP no. 765, Philadelphia.

1.55. Klepaczko J.R. (1986) Constitutive modelling of strain rate and temperature effects in F.C.C. metals. In *Proceedings of International Symposium, Beijing, China, Intense Dynamic Loading and its Effects*, p. 670. Pergamon Press, Oxford.

1.56. Klopp R.W. and Clifton R.J. (1984) Pressure-shear impact and the dynamic viscoelastic response of metals. In *Proceedings of the Workshop on Inelastic Deformation and Failure Modes*. Northwestern University, Evanston.

1.57. Rybin V.V. (1986) Large plastic deformations and fracturing of metals. *Metallurgy, Moscow* (in Russian). MIR, Georgia (former USSR).

1.58. Swearengen J.C. and Holbrook J.H. (1985) Internal variable models for rate-dependent plasticity: analysis of theory and experiment. *Res. Mechanica*, **13**, 93.

1.59. Shah S.P. (Ed.) (1985) Application of fracture mechanics to cementitious composites. In *Proceedings, NATO Advanced Research Workshop*. Martinus Nijhoff, The Hague.

1.60. Wittman F.H. (Ed.) (1986) *Fracture Toughness and Fracture Energy of Concrete*. Elsevier, The Netherlands.

1.61. Suaris W. and Shah S.P. (1982) Mechanical properties of materials under impact and impulsive loading. In *Introductory Report for the Interassociation (RILEM, CEB, IABSE, IASS) Symposium on Concrete Structures Under Impact and Impulsive Loading*. Berlin (West), BAM 33–62.

1.62. Banthia N.P. (1987) *Impact Resistance of Concrete*. PhD thesis, University of British Columbia, Canada.

1.63. Mindess S. (1985) Rate of loading effects on the fracture of cementitious materials. In *Application of Fracture Mechanics to Cementitious Composites* (Ed. by S.P. Shah), pp. 617–36. Martinus, Nijhoff, The Hague.

1.64. Mayrhofer A.S. and Thor S. (1982) Dynamic response of fibre and steel reinforced concrete plates under simulated blast load, in concrete structures under impact and impulsive loading. In *Proceedings, RILEM-CEB-IABSE-IASS Interassociation Symposium*, pp. 279–88. BAM, Berlin (West).

1.65. Gopalaratnam V.S. and Shan S.P. (1985) Properties of steel fiber reinforced concrete subjected to impact loading. *ACI J.*, **83**(8), 117–26.

1.66. Naaman A.E. and Gopalaratnam V.S. (1983) Impact properties of steel fiber reinforced concrete in bending. *International Journal of Cement Composites and Lightweight Concrete*, **5**(4), 225–33.

1.67. Tinic C. and Bruhwiler E. (1985) Effects of compressive loads on the tensile strength of concrete at high strain rates. *International Journal of Cement Composites and Lightweight Concrete*, **7**(2), 103–8.

1.68. Wecharatna M. and Roland E. (1987) Strain rate effects as properties of cement-based composites under impact loading. Engineering Mechanics Sixth Conference, ASCE, Buffalo, NY, USA.

1.69. Takeda J. and Tachikawa H. (1971) Deformations and fracture of concrete subjected to dynamic load. In *Proceedings, International Conference on Mechanical Behaviour of Materials, Vol. IV, Concrete and Cement Paste, Glass and Ceramics*, pp. 267–77, Kyoto, Japan.

1.70. Takeda J., Tachikawa H. and Fujimoto L. (1982) Mechanical properties of concrete and steel in reinforced concrete structures subjected to impact or impulsive loads. In *Proceedings of RILEM-CEB-IABSE-IASS Interassociation Symposium*, pp. 83–91. BAM, Berlin (West).

1.71. Evans A.G. (1974) Slow crack growth in brittle materials under dynamic loading conditions. *Int. J. Fract.*, **10**(2), 251–9.

1.72. Charles R.J. (1958) Dynamic fatigue of glass. *J. Appl. Phys.*, **29**(12), 1657–62.

1.73. Mihashi H. and Wittmann F.H. (1980) Stochastic approach to study the influence of rate of loading on strength of concrete. The Netherlands, *Heron*, **25**(3).

1.74. Jenq Y.S. and Shah S.P. (1986) Crack propagation resistance of fiber reinforced concrete. *J. Struct. Eng., ASCE*, **112**(10), 19–34.

1.75. Jenq Y.S. (1987) *Fracture Mechanics of Cementitious Composites*. PhD Dissertation, Northwestern University, Evanston, IL, USA.

1.76. Goldsmith W., Polivka M. and Yang T. (1966) Dynamic behavior of concrete. *Experimental Mechanics*, February, pp. 65–79.

1.77. Read H.E. and Maiden C.J. (1971) *The Dynamic Behavior of Concrete*. National Technical Information Service, Springfield, Va, no. AD894240, August.

1.78. Bazant Z.P. and Oh B.H. (1982) Strain-rate in rapid triaxial loading of concrete. *Proceedings, ASCE*, **108**(EM5), 764–82.

1.79. Oh B.H. (1987) Behaviour of concrete under dynamic loads. *ACI Mat. J.*, **84**(1), 8–13.

1.80. Loland K.E. (1980) Continuous damage model for load response estimation of concrete. *Cement Concrete Res.*, **10**, 395–402.

1.81. Mould J.C. and Levine H. (1987) A three invariant visco-plastic concrete model. In *Constitutive Laws for Engineering Materials: Theory and Applications* (Ed. by C.S. Desai et al.), pp. 707–16. Elsevier Science, New York.

1.82. Brook N. (1977) The use of irregular specimens for rock strength tests. *Int. J. Rock Mech. Min. Sci.*, **14**, 193–202.

1.83. Clark G.B. (1981) Geotechnical centrifuges for model studies and physical property testing of rock structures. *Colo. School Mines Q.*, **76**(4).

1.84. Haller H.F., Pattison H.C. and Baldonado O.C. (1973) Interrelationship of in-situ rock properties, excavation method and muck characteristics. *Technical Report HN-8121.2*. Holmes and Narver.

1.85. Kreimer G.S. (1968) *Strength of Hard Alloys*. Consultant's Bureau, New York.

1.86. Protodiakonov M.M. (1962) Mechanical properties and drillability of rock. In *Proceedings of the Fifth Symposium on Rock Mechanics, University of Minnesota*, pp. 103–18.

1.87. Somerton W.H., Esfandari F. and Singhal A. (1957) Further studies of the relation of physical properties of rock to drillability. Fourth Conference on Drilling and Rock Mechanics, University of Texas, Austin.

1.88. Sandia Corp (1957) Energy-absorbing characteristics of several materials. *Technical Memorandum no. SCRM 284–57(51)*. California, USA.

1.89. Seed H.B. and Idriss I.M. (1970) Soil moduli and damping factors for dynamic response analyses. *Report no. EERC 70–10*. University of California Earthquake Eng. Research Centre.

1.90. Hardin B.O. and Drnevich V.P. (1972) Shear modulus and damping soils: measurement and parameter effects. *J. Soil Mech. Found. Div., ASCE*, **98**, no. SM6, Proc. Paper 8977, pp. 603–24.

1.91. Matsukawa E. and Hunter A.M. (1956) The variation of sound velocity with stress in sand. *Proceedings of the Physical Society (London) Series B*, vol. 69, no. 8, pp. 847–8.

1.92. Theirs G.R. and Seed H.B. (1968) Cyclic stress–strain characteristics of clay. *J. Soil Mech. Found. Div., ASCE*, **94**, no. SM2, Proc. Paper 5871, pp. 555–69.

1.93. Swain R.J. (1962) Recent techniques for determination of in-situ properties and measurement of motion amplification in layered media. *Geophysics*, **27**(2), 237–41.

1.94. Maxwell A.A. and Fry Z.B. (1967) A procedure for determining elastic moduli of *in-situ* soils by dynamic technique. In *Proceedings, International Symposium on Wave Propagation and Dynamic Properties of Earth Materials*, pp. 913–19. University of New Mexico Press.

1.95. Seed H.B. and Lee K.L. (1966) Liquefaction of saturated sands during cyclic loading. *J. Soil Mech. Found. Div., ASCE*, **92**, no. SM6, Proc. Paper 4972, pp. 105–34.

1.96. Kovacs W.D., Seed H.B. and Chan C.K. (1971) Dynamic moduli and damping ratios for a soft clay. *J. Soil Mech. Found. Div., ASCE*, **97**, no SM1, Proc. Paper 7813, 59–75.

1.97. Zeevaert L. (1967) Free vibrations torsion tests to determine the shear modulus of elasticity on soils. In *Proceedings, Third Pan-American Conference on Soil Mechanics and Foundation Engineering*, Vol. 1, pp. 111–29. Caracas.

1.98. Florin V.A. and Ivanov, P.L. (1961) Liquefaction of saturated sandy soils. In *Proceedings, Fifth International Conference on Soil Mechanics and Foundation Engineering*, Vol. 1, pp. 107–11. Paris, France.

1.99. Prakash S. and Mathur J.N. (1965) Liquefaction of fine sand under dynamic loads. In *Proceedings, Fifth Symposium of the Civil and Hydraulic Engineering Department*. Indian Institute of Science, Bangalore.

1.100. Rocker K. (1968) The liquefaction behavior of sands subjected to cyclic loading. *Progress Report no. 3*. Repeated load and vibration tests upon sand. *Research Report R68-36, Soils Pub. no. 221*. Department of Civil Engineering, Massachusetts Institute of Technology, Cambridge.

1.101. Seed H.B. and Peacock W.H. (1971) Test procedure for measuring soil liquefaction characteristics. *J. Soil Mech. Found. Div., ASCE*, **97**, no. SM8, Proc. Paper 8330, 1099–119.

1.102. Schnable P.B., Lysmer J. and Seed H.B. (1972) SHAKE – a computer program for earthquake response analysis of horizontally layered sites. *Report no. EERC 72–12*. Earthquake Engineering Research Center, University of California, Berkeley.

1.103. Wilson E.L. (1968) A computer program for the dynamic stress analysis of underground structures. *Report no. 68–1*. Structural Engineering Laboratory, University of California, Berkeley.

1.104. Dibaj M. and Penzien, J. (1969) Nonlinear seismic response of earth structures. *Report no. EERC 69–2*. Earthquake Engineering Research Center, University of California, Berkeley.

1.105. Konder R.L. (1963) Hyperbolic stress–strain response: cohesive soils. *J. Soil Mech. Found. Div., ASCE*, **89**, no. SM1, Proc. Paper 3429, pp. 115–53.

1.106. Konder R.L. and Zelasko J.S. (1963) A hyperbolic stress–strain formulation for sands. In *Proceedings, Second Pan-American Conference on Soil Mechanics and Foundation Engineering*, Vol. 1, pp. 289–324. Brazil.

1.107. Singh A. and Mitchell J.K. (1968) General stress–strain time function for soils. *J. Soil Mech. Found. Div., ASCE*, **94**, no. SM1, Proc. Paper 5728, pp. 21–46.

1.108. Miller R.P., Troncoso J.H. and Brown F.R. Jr. (1975) In-situ impulse test for dynamic shear modulus of soils. In *Proceedings, Conference on In-Situ Measurement of Soil Properties, ASCE*. Vol. 1, pp. 319–35. North Carolina State University, Raleigh NC.

1.109. DeAlba P., Chan C.K. and Seed H.B. (1975) Determination of soil liquefaction characteristics by large-scale laboratory tests. *Report no. EERC 75–14*. Earthquake Engineering Research Center, University of California, Berkeley.

1.110. Kipp M.E., Grady D.E. and Chen E.P. (1980) Strain-rate dependent fracture initiation. *Int. J. Fract.*, **16**, 471–8.

1.111. Carroll M.M. and Holt A.C. (1972) Static and dynamic pore-collapse relations for ductile porous materials. *J. Appl. Phys*, **43**, 1626–36.

1.112. Davison L., Stevens A.L. and Kipp M.E. (1977) Theory of spall damage accumulation in ductile metals. *J. Mech. Phys. Solids*, **25**, 11–28.

1.113. Zlatin N.A. and Ioffe B.S. (1973) Time dependence of the resistance to spalling. *Sov. Phys.–Tech. Phys.*, **17**, 1390–93. (English translation.)

1.114. Shockey D.A., Curran D.R., Seaman L., Rosenberg J.T. and Peterson C.F. (1974) Fragmentation of rock under dynamic loads. *Int. J. Rock Mech. Sci.*, **11**, 303–17.

1.115. Birkimer D.L. (1971) A possible fracture criterion for the dynamic tensile strength of rock. In *Dynamic Rock Mechanics* (Ed. by G.B., Clark), pp. 573–90. Balkema, Holland.

1.116. Johnson J.N. (1983) Ductile fracture of rapidly expanding rings. *J. Appl. Mech.*, **50**, 593–600.

1.117. Regazzoni G., Johnson J.N. and Follansbee P.S. (1986) Theoretical study of the dynamic tensile test. *J. Appl. Mech.*, **53**, 519–28.

1.118. Johnson G.R. and Cook W.H. (1985) Fracture characteristics of three metals subjected to various. strains, strain rates, temperature and pressures. *Eng. Fract. Mech.*, **21**, 31–48.

1.119. Kinloch A.J. and Young R.J. (1983) *Fracture Behaviour of Polymers*. Applied Science Publishers, London and New York.

1.120. Samuelides E. and Frieze P.A. (1983) Rigid bow impacts on ship-hull models. In *Proceedings of the IABSE Colloquium on Ship Collision with Bridges and Offshore Structures, Preliminary Report*, pp. 263–70. Copenhagen.

1.121. Lorenz R.A. (1982) The vaporization of structural materials in severe accidents. In *Proceedings of the International Meeting on Thermal Nuclear Reactor Safety, NUREG/CP-0027*, Vol. 2, p. 1090. Chicago.

1.122. Atchley B.L. and Furr H.L. (1967) Strength and energy absorption capacity of plain concrete under dynamic and static loading. *J. Am. Concrete Inst.*, 745–56.

1.123. Birkimer D.L. (1971) A possible fracture criterion for the dynamic tensile strength of rock. In *Proceedings of the Twelfth Symposium on Rock Mechanics*, pp. 573–89.

1.124. Birkimer D.L. and Lindeman R. (1971) Dynamic tensile strength of concrete materials. *J. Am. Concrete Inst.*, **68**, 47–9.

1.125. Banthia N. and Ohama Y. (1989) Dynamic tensile fracture of carbon fibre reinforced cements. *Int. Conf. Recent Developments in Fibre Reinforced Cements and Concretes, Cardiff September 1989.*

1.126. Alford N. McN. (1982) Dynamic considerations for fracture of mortars. *J. Mater. Sci.*, **56**(3), 279–87.

1.127. John R. and Shah S.P. (1986) Fracture of concrete subjected to impact loading. *Cement Concrete Aggregates*, **8**(1), 24–32.

1.128. Mindess S., Banthia N. and Cheng Y. (1987) The fracture toughness of concrete under impact loading. *Cement Concrete Res.*, **1**(17), 231–41.

1.129. ASCE (1964) Design of structures to resist nuclear weapons effects. *ASCE, Manual of Engineering Practice*, no. 42. American Society of Civil Engineers, New York.

1.130. Crawford R.E., Higgins O.H. and Bultmann E.H. (1974) *The Air Force Manual for Design and Analysis of Hardened Structures.* AFWL TR 74–102, Air Force Weapons Laboratory, Kirtland AFB, New Mexico.

1.131. Meunier Y., Sangoy L. and Pont G. (1988) Dynamic behaviour of armoured steels. In *International Conference on Ballistics* (Ed. by East China Institute of Technology), pp. IV/74–IV/81. In *Proceedings of the International Conference on Ballistics.* Nanjing, China, 25–28 October 1988. ECIT, Nanjing.

1.132. Schulz J., Heimdahl E. and Finnegan S. (1987) Computer characterisation of debris clouds resulting from hypervelocity impact. *Int. J. Impact Eng.*, **5**, 577–84.

1.133. Meyers M.A. and Aimone C.T. (1983) Dynamic fracture (spalling) of metals. *Prog. Mat. Sci.*, **28**, 1–96.

1.134. Buchar J., Bilek Z. and Dusek F. (1986) *Mechanical Behaviour of Materials at Extremely High Strain Rates.* Trans Tech Publications, Switzerland.

1.135. Davison L., Stevens A.L. and Kipp M.E. (1977) Theory of spall damage accumulation in ductile metals. *J. Mech. Phys. Solids*, **25**, 11–28.

1.136. Johnson J.N. (1981) Dynamic fracture and spallation in ductile solids. *J. Appl. Phys.*, **52**, 2812–25.

1.137. Seaman L., Curran D.R. and Shockey D.A. (1976) Computational models for ductile and brittle fracture. *J. Appl. Phys.*, **47**, 4814–26.

1.138. British Standards Institution (BSI) (1985) *BS 8110: The Structural Use of Concrete, Part 1: Code of Practice for Design and Construction.* BSI, London.

1.139. British Standards Institution (BSI) (1985) *BS 5950: Part 1 Structural Use of Steelwork in Buildings. Code of Practice for Design in Simple and Continuous Construction: Hot Rolled Sections.* BSI, London.

1.140. UCCS, European Convention for Constructional Steelwork (1981) *European Recommendation for Steel Construction.* The Construction Press, London.

1.141. British Construction Steelwork Association (BCSA) (1983) *International Structural Steelwork Handbook.* Chameleon Press, UK.

1.142. CONSTRADO *Steelwork Design Guides to BS 5950: Part 1* (1985), Vol. I, Constructional Steel Research and Development Organisation, London. (1986) Vol. II, The Steel Construction Institute, London.

1.143. Gran J.K., Florence A.L. and Colton J.D. (1987) Dynamic triaxial compression experiments on high-strength concrete. In *Proceedings of the ASCE Sixth Annual Structures Congress.* Orlando, Florida.

1.144. Malvern L.E., Tang D., Jenkins D.A. and Gong J.C. (1986) Dynamic compressive strength of cementitious materials. *Mat. Res. Soc. Symp.*, **64**, 119–38.

1.145. Frantziskonis G. and Desai C.S. (1987) Elastoplastic model with damage for strain softening geomaterials. *Acta Mech.*, **68**, 151–70.

1.146. Pijaudier-Cabot G. and Bazant Z.P. (1987) Nonlocal damage theory. *Report No. 86–8/428n.* Center for Concrete and Geomaterials, Northwestern Univ., Il.

1.147. Schreyer H.L. and Bean J.E. (1987). Plasticity models for soils, rock and concrete. Report to the New Mexico Engineering Research Institute, Albuquerque, NM.

1.148. Soroushian P. and Ghoi K.B. (1987) Steel mechanical properties at different strain rates. *J. Struct. Eng., ASCE*, **113**(4), 663–72.

1.149. Bangash M.Y.H. (1989) *Concrete and Concrete Structures–Numerical Modelling and Applications.* Elsevier, Barking, UK.

1.150. Ottoson N.S. (1979) Constitutive model for short-time loading of concrete. *J. Eng. Mech. Div., ASCE*, **105**, EM1 Proc. Paper 14375.

1.151. Pietruszczak S. and Pande C.N. (1989) *Numerical Models in Geomechanics NUMOG III.* Elsevier, Barking, UK.

1.152. Stokes et al. Private Communications, BC Canada 1990.

2 Shock and Impact Dynamics

2.1. Davie T.N. and Richgels A.M. (1983) An earth penetrator code. *Sandia Report (SAND-82-2358).* Sandia National Laboratories, Livermore, CA.

2.2. Kar A.K. (1978) Projectile penetration into buried structures. *J. Struct. Div., ASCE*, Paper 13479STI.

2.3. Henrych J. (1979) *The Dynamics of Explosion and its Use.* Elsevier, Amsterdam.

2.4. Glasstone S. and Dolan P.J. (1977) *The Effects of Nuclear Weapons.* US Department of Defense, Washington.

2.5. Jones N. and Wierzbicki T. (1983) *Structural Crash Worthiness.* Butterworths, London.

2.6. Morrow C.T. and Smith M.R. (1961) Ballistic missile and aerospace technology. *Proc. Sixth Symposium.* Academic Press, New York.

2.7. FIP (1987) Concrete for hazard protection. *First International Conference on Concrete Society*, Edinburgh.

2.8. Abaham L.M. (1962) *Structural Design of Missiles and Space-Craft.* McGraw Hill, New York.

2.9. BAM (1982) *Concrete Structures Under Impact and Impulsive Loading.* Bundesanstalt für Materialprüfung, Berlin.

2.10. Macmillan R.H. (1983) *Dynamics of Vehicle Collisions. Special Publications SP5.* Inderscience Enterprises, Jersey, UK.

2.11. Taylor D.W. and Whitman R.V. (1953) The behaviour of soils under dynamic loadings. 2. Interim report on wave propagation and strain-rate effect. *MIT Report AFSWP-117.*

2.12. Maurer W.C. (1959) *Impact Crater Formation in Sandstone and Granite.* Master's thesis submitted to Colorado School of Mines.

2.13. Rinehart J.S. (1980) Stresses associated with lunar landings. *Contribution no. 11.* Mining Research Laboratory Colorado School of Mines.

2.14. Tolch N.A. and Bushkovitch A.V. (1947) Penetration and crater volume in various kinds of rocks as dependent on caliber, mass and striking velocity of projectile. *BRL Report no. 641.* UK.

2.15. NDRC (1946) Effects of impact and explosion. Summary Technical Report of Div. 2, National Design and Research Corporation (NDRC), Vol. 1. Washington DC.

2.16. Lang H.A. (1956) Lunar instrument carrier – landing factors. *Rand RM-1725, ASTIA Doc. no. AD 112403.*

2.17. Palmore J.I. (1961) Lunar impact probe. *ARS J.*, 1066–73.

2.18. Rinehart J.S. (1960) Portions of traite de balistique experimentale which deal with terminal ballistics. Chapters III, IV, V and XIV, Félix Hélie, Paris (1884), Naval Ordnance Test Station TM RRB-75.

2.19. Dennington R.J. (1958) Terminal ballistics studies. *Proj. Doan Brook Tech. Memo. no. 20 Case Inst.*, ASTIA AD 146 913.

2.20. Kornhauser M. (1958) Prediction of cratering caused by meteoroid impacts. *J. Astron. Sci.*, **V**, no. 3–4.

2.21. Rinehart J.S. and Pearson J. (1954) *Behaviour of Metals Under Impulsive Loads.* American Society for Metals, Cleveland.

2.22. Rinehart J.S. (1950) Some observations on high-speed impact. Naval Ordnance Test Station RRB-50. Félix Hélie, Paris, France.

2.23. Rinehart J.S. and White W.C. (1952) Shapes of craters formed in plaster-of-paris by ultra-speed pellets. *Am. J. Phys.*, **20**(1).

2.24. Gazley C. Jr. (1957) Deceleration and heating of a body entering a planetary atmosphere from space. *RAND Corporation Report P-955.* USA.

2.25. Lees L., Hartwig F.W. and Cohen C.B. (1959) Use of aerodynamic lift during entry into the earth's atmosphere. *ARS J.*, 633–41.

2.26. Lowe R.E. and Gervais R.L. (1961) Manned entry missions to Mars and Venus. In *ARS Space Flight Report to the Nation*, Paper 2158–61. New York.

2.27. Turnacliff R.D. and Hartnett J.P. (1957) Generalized trajectories for free-falling bodies of high drag. ARS Paper 543–57, 12th annual meeting, New York, 2–5 December 1957.

2.28. Creighton D.C. (1982) Non-normal projectile penetration in soil and rock: user's guide for computer code PENCO2D. *Technical Report SL-82-7.* US Army Engineering Waterways Experiment Station, Vicksburg, Miss.

2.29. Young C.W. (1972) Empirical equations for predicting penetration performance in layered earth materials for complex penetrator configurations. *Development Report No. SC-DR-72–0523.* Sandia National Laboratory, Albuquerque, NM.

2.30. Young C.W. (1985) Simplified analytical model of penetration with lateral loading. *SAND84–1635.* Sandia National Laboratory, Albuquerque, NM.

2.31. Matuska D., Durrett R.E. and Osborn J.J. (1982) Hull user's guide for three-dimensional linking with EPIC 3. *ARBRL-CR-00484.* Orlando Technology, Shalimar, Fl.

2.32. Ito Y.M., Nelson R.B. and Ross-Perry F.W. (1979) Three-dimensional numerical analysis of earth penetration dynamics. *Report DNA 5404F.* Defense Nuclear Agency, Washington DC, USA.

2.33. Johnson G.R. and Stryk R.A. (1986) Dynamic-Lagrangian computations for solids, with variable nodal connectivity for severe distortions. *Int. J. Num. Methods Eng*, **23**, 509–22.

2.34. Hallquist J.O. (1984) User's manual for DYNA2D – an explicit two-dimensional hydrodynamic finite element code with interactive rezoning. *Report UCID-18756, Revision 2.* University of California, Lawrence Livermore National Laboratory, USA.

2.35. Hallquist J.O. and Benson D.J. (1986) DYNA3D user's manual (nonlinear dynamic analysis of structures in three dimensions). *Report UCID-19592, Revision 2.* University of California, Lawrence Livermore National Laboratory.

2.36. Carr H.H. (1948) Analysis of head failure in aircraft torpedoes. *NOTS Navord Report 1019*, Patent Office Library, London.

2.37. Reissner E. (1946; 1947) Stresses and small displacements of shallow spherical shells. *J. Math. Phys*, **XXV**, 1 and 4.

2.38. Friedrichs K.O. (1941) On the minimum buckling load for spherical shells. In *Theodore von Kàrmàn Anniversary Volume*, pp. 258–72. CIT, Pasadena, USA.

2.39. Tsein H.S. (1942) A theory for the buckling of thin shells. *J. Aero. Sci.*, **9**, 373–84.

2.40. Payton R.G. (1962) Initial bending stresses in elastic shells impacting into compressible fluids. *Quart. J. Mech. Appl. Math.*, **15**, 77–90.

2.41. Office of the Scientific Research and Development (1946) Aircraft torpedo development and water entry ballistics, *OSRD Report 2550.* CIT, Pasadena, USA.

2.42. Kornhauser M. (1958) Impact protection for the human structure. Am. Astron. Soc., Western Regional Meeting, 18–19 August 1958, Palo Alto, CA.

2.43. Kornhauser M. (1960) Structural limitations on the impulsiveness of astronautical maneuvers. ARS Conference on Structural Design of Space Vehicles, 6 April 1960, Santa Barbara, CA.

2.44. ANC-5; Depts of Air Force, Navy and Commerce (1955) *Strength of Metal Aircraft Elements.* Republican Press, Hamilton, OH.

2.45. Coppa A. (1960) On the mechanics of buckling of a cylindrical shell under longitudinal impact. Tenth International Congress App. Mech., September 1960, Stressa, Italy.

2.46. Polentz L.M. (1959) Linear energy absorbers. *Machine Design.*

2.47. Martin E.D. (1961) A design study of the inflated sphere landing vehicle, including the landing performance and the effects of deviations from design conditions. *NASA TN D-692.*

2.48. Esgar J.B. and Morgan W.C. (1960) Analytical study of soft landings on gas-fill bags. *NASA TR R-75.*

2.49. Fisher L.J. Jr. (1961) Landing–impact–dissipation systems. *NASA TN D-975.*

2.50. Schrader C.D. (1962) Lunar and planetary soft landings by means of gas-filled balloons. ARS Lunar Missions Meeting, Cleveland, 17–19 July 1962, Paper 2480–62.

2.51. Bethe H.A. (1941) Attempt of a theory of armor penetration. Frankford Arsenal Rep., Philadelphia.

2.52. Taylor G.I. (1941) Notes on H.A. Bethe's theory of armor penetration, II. Enlargement of a hole in a flat sheet at high speeds. Home Ministry Security Report, R.C. 280 UK.

2.53. Taylor G.I. (1948) The formation and enlargement of a circular hole in a thin plastic sheet. *Quart. J. Mech. Appl. Math.*, **1**.

2.54. Kineke J.H. and Vitali R. (1963) Transient observations of crater formation in semiinfinite targets. In *Proceedings of the Sixth Symposium on Hypervelocity Impact*, Vol. II, part 2. Springer Verlag, Berlin, Germany.

2.55. Eichelberger R.J. and Kineke J.H. (1967) Hypervelocity impact. In *High Speed Physics* (Ed. by K. Vollrath and G. Thomer). Springer-Verlag Wien, New York.

2.56. Turpin W.C. and Carson J.M. (1970) Hole growth in thin plates perforated by hypervelocity pellets. *Air Force Materials Lab. Rep. 70–83.* Wright-Patterson AFB, OH.

2.57. Holloway L.S. (1963) Observations of crater growth in wax. *BRL Rep., USABRL-M-1526.*

2.58. Freiberger W. (1952) A problem in dynamic plasticity: the enlargement of a circular hole in a flat sheet. *Proc. Cambridge Phil. Soc.*, **48**.

2.59. Fraiser J.T., Karpov B.G. and Holloway L.S. (1965) The behavior of wax targets subjected to hypervelocity impact. In *Proceedings of the Seventh Hypervelocity Impact Symposium*, Vol. V. Springer Verlag, Berlin, Germany.

2.60. Rolsten R.F., Wellnitz J.N. and Hunt H.H. (1964) An example of hole diameter in thin plates due to hypervelocity impact. *J. Appl. Phys.*, **35**.

2.61. Allison F.E. (1965) Mechanics of hypervelocity impact. In *Proceedings of the Seventh Hypervelocity Impact Symposium*, Vol. I. Springer Verlag, Berlin, Germany.

2.62. Wilkins M. and Guinan M. (1973) Impact of cylinders on a rigid boundary. *J. Appl. Phys.*, **44**.

2.63. Whiffin A.C. (1948) The use of flat-ended projectiles for determining dynamic yield stress, II, tests on various metallic materials. *Proc. R. Soc. London Ser. A*, **194**.

2.64. Goldsmith W. (1960) *Impact, The Theory and Physical Behaviour of Colliding Solids.* Edward Arnold, London.

2.65. Johnson W. (1972) *Impact Strength of Materials.* Edward Arnold, New York.

2.66. Walters W. (1979) Influence of material viscosity on the theory of shaped-charge jet formation. *BRL Rep., BRL-MR-02941.*

2.67. Chhabildas L.C. and Asay J.R. (1979) Rise-time measurements of shock transitions in aluminum, copper and steel. *J. Appl. Phys.*, **50**.

2.68. Birkhoff G., MacDougall D., Pugh E. and Taylor G. (1948) Explosives with lined cavities. *J. Appl. Phys.*, **19**.

2.69. Scott B. and Walters W. (1984) A model of the crater growth-rate under ballistic impact conditions. In *Proceedings of the Southeastern Conference on Theoretical and Applied Mechanics*, Georgia.

2.70. Rohani B. (1975) Analysis of projectile penetration into concrete and rock targets. *S-75–25.* US Army Engineer Waterways Experimental Station.

2.71. Housen K., Schmidt R. and Holsapple K. (1983) Crater ejecta scaling laws: fundamental forms based on dimensional analysis. *J. Geophys. Res.*, **88**.

2.72. Glass J. and Bruchey W. (1982) Internal deformation and energy absorption during penetration of semi-infinite targets. In *Proceedings of the Eighth International Symposium on Ballistics*, NASA, Langely, USA.

2.73. Wang W.L. (1971) Low velocity projectile penetration. *J. Soil Mech. Found. Div.*, ASCE **97**, no. SM12, Proc. Paper 8592.

2.74. Young C.W. (1969) Depth prediction for earth-penetrating projectiles. *J. Soil Mech. Found. Div., ASCE*, **95**, no. SM3, Proc. Paper 6558.

2.75. Petry L. (1910) *Monographies de Systèmes d'Artillerie*. Brussels.

2.76. Hakala W.W. (1965) *Resistance of a Granular Medium to Normal Impact of a Rigid Projectile*. Thesis presented to the Virginia Polytechnic Institute, Blacksburg, VA, in partial fulfilment of the requirements for the degree of doctor of Philosophy.

2.77. Thigpen L. (1974) Projectile penetration of elastic-plastic earth-media. *J. Geotech. Eng. Div., ASCE*, **100**, no. GT3, Proc. Paper 10414.

2.78. Butler D.K. (1975) An analytical study of projectile penetration into rock. *Technical Report S-75–7*. Soils and Pavements Laboratory, US Army Engineer Waterways Experiment Station, Vicksburg, MO.

2.79. Butler D.K. (1975) Pretest penetration for DNA rock penetration experiments at a sandstone site near San Ysidro, New Mexico. Soils and Pavements Laboratory, US Army Engineer Waterways Experiment Station, Vicksburg, MO.

2.80. Butler D.K. (1975) Development of high-velocity powder gun and analysis of fragment penetration tests into sand. *Misc. Paper S-75–27*. Soils and Pavements Laboratory, US Army Engineer Waterways Experiment Station, Vicksburg, Miss.

2.81. Bernard R.S. and Hanagud S.V. (1975) Development of a projectile penetration theory, Report 1, Penetration theory for shallow to moderate depths. *Technical Report S-75–9*. Soils and Pavements Laboratory, US Army Engineer Waterways Experiment Station, Vicksburg, MO.

2.82. Bernard R.S. (1976) Development of a projectile penetration theory, Report 2, Deep penetration theory of homogeneous and layered targets. *Technical Report S-75–9*. Soils and Pavements Laboratory, US Army Engineer Waterways Experiment Station, Vicksburg, MO.

2.83. Hammel J. (1979) Impact loading on a spherical shell. Fifth International Conference on Structural Mechanics in Reactor Technology (SMiRT), Berlin.

2.84. Barber E.M. et al. (1972) A study of air distribution in survival shelters using a small-scale modelling technique. *Report 10689*, USA National Bureau of Standards.

2.85. Barneby H.L. et al. (1963) Toxic gas protection. Paper to ASHRAE Symposium on Survival Shelters, 1962.

2.86. Barthel R. (1965) Research on the climate in an underground shelter. *Ingenieur*, 77, 143–7 (in Dutch).

2.87. Barthel R. (1965) Theoretical and experimental research regarding the indoor climate in an underground shelter. *Ingenieur*, **77**, 6143–7 (in Dutch).

2.88. Cooper J. (1980) After the bomb. *J. Chartered Inst. Building Services*, **2**, 48–9.

2.89. Dasler A.R. and Minrad D. (1965) Environmental physiology of shelter habitation. *ASHRAE Trans.*, **71**, 115–24.

2.90. Drucker E.E. and Cheng H.S. (1963) Analogue study of heating in survival shelters. ASHRAE Symposium on Survival Shelters, 1962. ASHRAE.

2.91. Bigg J.M. (1964) *Introduction to Structural Dynamics*. McGraw Hill, New York.

2.92. Gates A.S. (1963) Air revitalization in sealed shelters. ASHRAE Symposium on Survival Shelters, 1962. ASHRAE.

2.93. Gessner H. (1961) The ventilation of air-raid shelters. *Schweizerische Blätter für Heizung and Luftung*, **28**, 1–12 (in German).

2.94. Hanna G.M. (1962) Ventilation design for fallout and blast shelters. *Air Eng.*, **4**, 19–21.

2.95. Home Office (1981) *Domestic Nuclear Shelters (DNS) – Technical Guidance.* HMSO.

2.96. Home Office (1981) *Domestic Nuclear Shelters.* HMSO.

2.97. Eibl J. (1982) Behaviour of critical regions under soft missile impact and impulsive loading. *IBAM*, June.

2.98. Hughes G. and Speirs D. (1982) An investigation of the beam impact problem. *Technical Report 546*, C & CA, UK (now British Cement Association).

2.99. Bate S. (1961) The effect of impact loading on prestressed and ordinary reinforced concrete beams. *National Building Studies Research Paper 35*.

2.100. Billing I. (1960) *Structure Concrete.* Macmillan, London.

2.101. Watson A. and Ang T. (1982) Impact resistance of reinforced concrete structures. In *Designs for Dynamic Loading.* Construction Press, London, UK.

2.102. Watson A. and Ang T. (1984) Impact response and post-impact residual strength of reinforced concrete structures. International Conference and Exposition of Structural Impact and Crashworthiness, Imperial College, London, UK.

2.103. Perry S. and Brown I. (1982) Model prestressed slabs subjected to hard missile loading. In *Design for Dynamic Loading.* Construction Press, London, UK.

2.104. Perry S., Brown I. and Dinic G. (1984) Factors influencing the response of concrete slabs to impact. International Conference and Exposition of Structural Impact and Crashworthiness, Imperial College, London, UK.

2.105. Kufuor K. and Perry S. (1984) Hard impact of shallow reinforced concrete domes. International Conference and Exposition of Structural Impact and Crashworthiness, Imperial College, London, UK.

2.106. Burgess W. and Campbell-Allen D. (1974) Impact resistance of reinforced concrete as a problem of containment. *Research Report no. R251*. School of Civil Engineering, University of Sydney.

2.107. Stephenson A. (1976) Tornado-generated missile full-scale testing. In *Proceedings of the Symposium on Tornadoes, Assessment of Knowledge and Implications for Man.* Texas University.

2.108. Jankov Z., Turnham J. and White M. (1976) Missile tests of quarter-scale reinforced concrete barriers. In *Proceedings of the Symposium on Tornadoes, Assessment of Knowledge and Implications for Man.* Texas University, June 1976.

2.109. Stephen A. and Silter G. (1977) Full-scale tornado-missile impact tests. Fourth International Conference on Structural Mechanics in Reactor Technology (SMiRT), Berlin, 1977, Paper J10/1.

2.110. Jonas W. and Rudiger E. (1977) Experimental and analytical research on the behaviour of reinforced concrete slabs subjected to impact loads. Fourth International Conference on Structural Mechanics in Reactor Technology (SMiRT), Berlin, Paper J7/6.

2.111. Beriaud C. et al. (1977) Local behaviour of reinforced concrete walls under hard missile impact. Fourth International Conference on Structural Mechanics in Reactor Technology (SMiRT), Berlin, 1977, Paper J7/9.

2.112. Gupta Y. and Seaman L. (1977) Local response of reinforced concrete to missile impacts. Fourth International Conference on Structural Mechanics in Reactor Technology (SMiRT), Berlin, 1977, Paper J10/4.

2.113. Barr P. et al. (1982) An experimental investigation of scaling of reinforced concrete structures under impact loading. In *Design for Dynamic Loading*. Construction Press, London, UK.

2.114. Barr P. et al. (1983) Experimental studies of the impact resistance of steel faced concrete composition. Seventh International Conference on Structural Mechanics in Reactor Technology (SMiRT), 1983, Paper J8/4, Chicago, USA.

2.115. Det Norske Veritas (1981) *Rules for Classification of Mobile Offshore Units*.

2.116. Minorsky V.V. (1959) An analysis of ship collisions with reference to nuclear power plants. *J. Ship Res.*, **3**, 1–4.

2.117. Soreide T.H. (1981) *Ultimate Load Analysis of Marine Structures*. Tapir, Trondheim.

2.118. JABSF (1983) Ship collision with an offshore structure. IABSE Colloquium, Copenhagen.

2.119. Woisin G. (1977) Conclusion from collision examinations for nuclear merchant ships in the FRG. In *Proceedings of the Symposium on Naval Submarines*. Hamburg.

2.120. Reckling K.A. (1977) On the collision protection of ships. PRADS Symposium, Tokyo.

2.121. Nagasawa H., Arita K., Tani M. and Oka S. (1977) A study on the collapse of ship structure in collision with bridge piers. *J. Soc. Nav. Arch. Jpn.*, **142**.

2.122. Macaulay M.A. and Macmillan R.H. (1968) Impact testing of vehicle structures. In *Proceedings of the Twelfth FISITA Congress*. Barcelona.

2.123. Emori R.I. (1968) Analytical approach to automobile collisions. *SAE Paper 680016*. Society of Automobile Engineers, USA.

2.124. Neilson I.D. et al. (1968) Controlled impact investigations. *TRRL Report LR 132*. Transport Road Research Laboratory, Crowthorne, UK.

2.125. Grime G. and Jones I.S. (1969) Car collisions – the movement of cars and their occupants. *Proc. I. Mech. Eng.*, **184**, no. 5.

2.126. Emori R.I. and Tani M. (1970) Vehicle trajectories after intersection collision impact. *SAE Paper 700176*. Society of Automobile Engineers.

2.127. Wall J.G. et al. (1970) Comparative head-on impact tests. *TRRL Report LR 155*. Transport Road Research Laboratory, Crowthorne, UK.

2.128. Jones I.S. (1975) Mechanics of roll-over as the result of curb impact. *SAE Paper 750461*. Society of Automobile Engineers.

2.129. Wagner R. (1978) Compatibility in frontal collisions. In *Proceedings of the 17th FISITA Congress*, Budapest.

2.130. Rouse H. and Howe J.W. (1953) *Basic Mechanics of Fluids*. Wiley, New York.

2.131. Kinslow R. (Ed.) (1970) *High Velocity Impact Phenomena*. Academic Press, New York.

2.132. Nowacki W.K. (1978) *Stress Waves in Non-Elastic Solids*. Pergamon, New York.

2.133. Hurty W.C. and Rubinstein M.F. (1964) *Dynamics of Structures*. Prentice-Hall, Englewood cliffs, NJ.

2.134. Morrow C.T. (1963) *Shock and Vibration Engineering*. Wiley, New York.

2.135. Biggs J.M. (1964) *Introduction to Structural Dynamics*, chapter 2. McGraw-Hill, New York.

2.136. Snowdon J.C. (1968) *Vibration and Shock in Damped Mechanical Systems*. Wiley, New York.

2.137. Craig R.R. (1981) *Structural Dynamics: An Introduction to Computer Methods*. Wiley, New York.

2.138. Davies G.A. (1984) *Structural Impact and Crashworthiness*, Vol. 1, chapter 7. Elsevier, Amsterdam.

2.139. Andrews K.P.F. et al. (1983) Classification of the axial collapse of cylindrical tubes under quasi-static loading. *Int. J. Mech. Sci.*, **25**, 678–96.

2.140. Bodner S.R. and Symonds P.S. (1972) Experimental and theoretical investigation of the plastic deformation of cantilever beams subjected to impulsive loading. *J. Appl. Mech.*, December, 719–28.

2.141. Conway M.D. and Jakubowski M. (1969) Axial impact of short cylindrical bars. *J. Appl. Mech.*, **36**, 809.

2.142. Hagiwara K. et al. (1983) A proposed method of predicting ship collision damage. *Int. J. Impact Eng.*, **1**, 257–80.

2.143. Lee E.H. and Morrison J.A. (1956) A comparison of the propagation of longitudinal waves in rods of viscoelastic materials. *J. Polym. Sci.*, **19**, 93–110.

2.144. Samuelides E. and Frieze P.A. (1983) Strip model simulation for low energy impacts on flat-plated structures. *Int. J. Mech. Sci.*, **25**, 669–86.

2.145. Backman M.E. and Goldsmith W. (1978) The mechanics of penetration of projectiles into targets. *Int. J. Eng. Sci.*, **16**, 1–99.

2.146. Bernard R.S. and Hanagud S.V. (1975) Development of a projectile penetration theory. *Technical Report S-75–9*. US Army Waterways Experiment Station.

2.147. Bernard R.S. (1976) Development of a projectile penetration theory report 2: deep penetration theory for homogeneous and layered targets. *Technical Report S-75–9*. US Army Waterways Experiment Station, Virginia, USA.

2.148. Byers R.K. and Chabai A.J. (1977) Penetration calculations and measurements for a layered soil target. *Int. J. Numer. Anal. Methods Geomech.*, **1**, 107–38.

2.149. Bjork R.L. (1975) Calculations of earth penetrators impacting soils. *AD-AO46 236*. Pacifica Technology Hawaii, USA.

2.150. DNA/SANDIA (1975) Soil penetration experiment at DRES: results and analysis. *SAND.75.0001*. Sandia Laboratories, Albuquerque.

2.151. Hadala P.F. (1975) Evaluation of empirical and analytical procedures used for predicting the rigid body motion of an earth penetrator. *Technical Report S-75–15*. US Army Waterways Experiment Station, Virginia, USA.

2.152. Norwood F.R. and Sears M.P. (1982) A nonlinear model for the dynamics of penetration into geological targets. *J. Appl. Mech.*, **49**, 26–30.

2.153. Rohani B. (1972) High velocity fragment penetration of a soil target. In *Proceedings of the Conference on Rapid Penetration of Terrestrial Materials*. Texas A & M University.

2.154. Triandafilidis G.E. (1976) State of the art of earth penetration technology, 2 volumes. *Technical Report CE-42(76) DNA-297*. The University of New Mexico.

2.155. Wagner M.H., Kreyenhagen K.N. and Goerke W.S. (1975) Numerical analysis of projectile impact and deep penetration into earth media. *WES Contract Report S-75–4*. California Research and Technology, Inc.

2.156. Yankelevsky D.Z. (1979) Normal penetration into geomaterials. *Research Report 30*. Faculty of Civil Engineering, Technion, Israel.

2.157. Yankelevsky D.Z. (1983) The optimal shape of an earth penetrating projectile. *Int. J. Solids Struct.*, **19**, 25–31.

2.158. Yankelevsky, D.Z. (1985) Cavitation phenomena in soil projectile interaction. *Int. J. Imp. Eng.*, **3**, 167–78.

2.159. Young C.W. and Ozanne G.M. (1966) Low velocity penetration study. *SC-RR-66–118*. Sandia Laboratories, USA.

2.160. Young C.W. (1969) Depth prediction for earth penetrating projectiles. *J. Soil Mech. Found. Div., Proc. Am. Soc. Civ. Eng.*, **95**, 803–17.

2.161. Young C.W. (1976) Status report on high velocity soil penetration. *SAND 76–0291*. Sandia Laboratories, USA.

2.162. Yarrington P. (1977) A one dimensional approximate technique for earth penetration calculations. *SAND 77–1126*. Sandia Laboratories, USA.

2.163. Alekseevskii V.P. (1966) Penetration of a rod into a target at high velocity. *Comb. Expl. Shock Waves*, **2**, 99–106 (English translation).

2.164. Backman M.E. & Goldsmith W. (1978) The mechanics of penetration of projectiles into targets. *Int. J. Eng. Sci.*, **16**, 1–99.

2.165. Forrestal M.J., Rosenberg Z., Luk V.K. and Bless S.J. (1986) Perforation of aluminum plates with conical-nosed rods. *SAND 86–0292J*. Sandia National Laboratory, Albuquerque, USA.

2.166. Frank K. and Zook J. (1986) Energy-efficient penetration and perforation of targets in the hyper-velocity regime. Hypervelocity Impact Symposium, San Antonio, 1986.

2.167. Levy N. and Goldsmith W. (1984) Normal impact and perforation of thin plates by hemispherically-tipped projectiles – I. Analytical considerations. *Int. J. Impact Eng.*, **2**, 209–29.

2.168. Pidsley P.H. (1984) A numerical study of long rod impact onto a large target. *J. Mech. Phys. Sol.*, **32**, 315–34.

2.169. Tate A. (1986) Long rod penetration models – part I. A flow field model for high speed–long rod penetration. *Int. J. Mech. Sci.*, **28**, 525–48.

2.170. Zukas J.A., Jones G.H., Kinsey K.D. and Sherrick T.M. (1981) Three-dimensional impact simulations: resources and results. In *Computer Analysis of Large Scale Structures* (Ed. by K.C. Park and R.F. Jones) AMD-49, pp. 35–68. New York.

2.171. Asay J.R. and Kerley G.I. (1987) The response of materials to dynamic loading. *Int. J. Impact Eng.*, **5**(1–4), 69–99.

2.172. Holian K.S. and Burkett M.W. (1987) Sensitivity to hypervelocity impact simulation to equation of state. *Int. J. Impact Eng.*, **5**(1–4), 333–41.

2.173. Maiden C.J. (1963) Experimental and theoretical results concerning the protective ability of a thin shield against hypervelocity projectiles. In *Proceedings of the Sixth Symposium on Hypervelocity Impact*, III, pp. 69–156. Springer Verlag, Berlin.

2.174. Ravid M., Bodner S.R. and Holeman I. (1987) Analysis of very high speed impact. *Int. J. Eng. Sci.*, **25**(4), 473–82.

2.175. Tillotson J.H. (1962) *Metallic Equations of State for Hypervelocity Impact*. General Atomic, Division of General Dynamics, GA-3216, San Diego.

2.176. Chen J.K. and Sun C.T. (1985) On the impact of initially stressed composite laminates. *J. Comp. Mat.*, **19**, 490–504.

2.177. Tsai S.W. and Hahn H.T. (1980) *Introduction to Composite Materials*. Technical Publishing Company, Pennsylvania.

2.178. Brook N. and Summers D.A. (1969) The penetration of rock by high-speed water jets. *Int. J. Rock Mech. Mining Sci.*, **6**, 249–58.

2.179. Haimson B. (1965) *High Velocity, Low Velocity, and Static Bit Penetration Characteristics in Tennessee Marble*. Master's thesis, University of Minnesota.

2.180. Haimson B.C. and Fairhurst C. (1970) Some bit penetration characteristics in pink Tennessee marble. In *Proceedings of the Twelfth Symposium of Rock Mechanics*, pp. 547–59. University of Missouri School of Mines, USA.

2.181. Simon R. (1963) Digital machine computations of the stress waves produced by striker impact in percussive drilling machines. In *Fifth Symposium on Rock Mechanics*. Pergamon, Oxford.

2.182. Vijay M.M. and Brierly W.H. (1980) Drilling of rocks with rotating high pressure water jets: an assessment of nozzles. In *Proceedings of the Fifth International Symposium on Jet Cutting Technology*. Hanover.

2.183. Watson R.W. (1973) Card-gap and projectile impact sensitivity measurements, a compilation. *US Bureau of Mines Information Circular No. 8605*.

2.184. Wells E.S. (1949) Penetration speed of percussion drill bits. *Chem. Eng. Miner. Rev.*, **41**(10), 362–4.

2.185. Winzer R.R. and Ritter A.P. (1980) Effect of delays in fragmentation in large limestone blocks. *Report No. MML TR 80–25*. Martin Marietta Laboratories, USA.

2.186. O'Connell W.J. and Fortney R.A. (1974) Turbine missile impact analysis: a detailed treatment. *Transactions of the American Nuclear Society*, **19**, 31; EDS Nuclear Inc. Report, 27 October 1974.

2.187. Moody F.J. (1969) Prediction of blowdown thrust and jet forces. *ASME Transaction 69-HT-31*. American Society of Mechanical Engineers.

2.188. Norris C.H. et al. (1959) *Structural Design for Dynamic Loads*. McGraw-Hill, New York.

2.189. Emori R.I. (1968) Analytical approach to automobile collisions. Automotive Engineering Congress, Detroit, Michigan, Paper no. 680016.

2.190. Ivey D.L., Ruth E. and Hirsch T.J. (1970) Feasibility of lightweight cellular concrete for vehicle crash cushions. Paper Presented at the Annual Meeting of the Highway Research Board, Washington DC.

2.191. Chen E.P. and Sih G.C. (1977) Transient response of cracks to impact loads. In *Elasto-Dynamic Crack Problems*, Vol. 4. Noordhoff, Gröningen, Leyden.

2.192. Davison L. and Graham R.A. (1979) Shock compression of solids. *Phys. Rep.*, **55**, 255–379.

2.193. Meyer M.A. and Aimone C.T. (1983) Dynamic fracture (spalling) of metals. *Prog. Mat. Sci.*, **28**, 1–96.

2.194. Grady D.E. (1981) Fragmentation of solids under impulsive stress loading. *J. Geophys. Res.*, **86**, 1047–54.

2.195. Grady D.E. (1981) Application of survival statistics to the impulsive fragmentation of ductile rings. In *Shock Waves and High-Strain-Rate Phenomena in Metals* (Ed. by M.A. Meyers and L.E. Murr), pp. 181–92. Plenum, New York.

2.196. Grady D.E., Bergstresser T.K. and Taylor J.M. (1985) Impact fragmentation of lead and uranium plates. *SAND85–1545 (technical report)*. Sandia Laboratories.

2.197. Grady D.E. and Kipp M.E. (1979) The micromechanics of impact fracture of rock. *Int. J. Rock Mech. Min. Sci.*, **16**, 293–302.

2.198. Cour-Palais B.G. (1987) Hypervelocity impact in metals, glass and composites. *Int. J. Impact Eng.*, **5**, 221–38.

2.199. Holsapple K.A. (1987) The scaling of impact phenomena. *Int. J. Impact Eng.*, **5**, 343–56.

2.200. Johns Hopkins University (1961) The resistance of various metallic materials to perforation by steel fragments; empirical relationships for fragment residual velocity and residual weight. Ballistic Res. Lab. Proj. Thor TR no. 47. Johns Hopkins University, Baltimore, MD.

2.201. Johns Hopkins University (1961) The resistance of various non-metallic materials to perforation by steel fragments; empirical relationships for fragment residual velocity and residual weight. Ballistic Res. Lab. Proj. Thor TR no 47. Johns Hopkins University, Baltimore, MD.

2.202. Yatteau J.D. (1982) High velocity penetration model. NSWU TR, 82–123. New South Wales University, Australia.

2.203. Piekutowski A.J. (1987) Debris clouds generated by hypervelocity impact of cylindrical projectiles with thin aluminum plates. *Int. J. Impact Eng.*, **5**, 509–18.

2.204. Rinehart J.S. and Pearson J. (1965) *Behaviour of Metals under Impulsive Loading.* Dover, New York.

2.205. Al-Hassani S.T.S., Johnson W. and Nasim M. (1972) Fracture of triangular plates due to contact explosive pressure. *J. Mech. Eng. Sci.*, **14**(3), 173–83.

2.206. Al-Hassani S.T.S. and Silva-Gomes J.F. (1979) Internal fracture paraboloids of revolution due to stress wave focussing. *Conf. Ser. – Inst. Phys.*, **47**, 187–96.

2.207. Al-Hassani S.T.S. and Silva-Gomes J.F. (1986) Internal fractures in solids of revolution due to stress wave focussing. In *Shock Waves and High-Strain-Rate Phenomena in Metals* (Ed. by M.A. Meyers and L.E. Murr), chapter 10. Plenum, New York.

2.208. Al-Hassani S.T.S. (1986) Fracturing of explosively loaded solids. In *Metal Forming and Impact Mechanics* (Ed. by S.R. Reid), chapter 18. Pergamon, Oxford.

2.209. Swain M.V. and Lawn B.R. (1976) Indentation fracture in brittle rocks and glasses. *Int. J. Rock Mech. Min. Sci. Geomech. Abstr.*, **13**, 311–19.

2.210. Jones N. and Liu J.H. (1988) Local impact loading of beams. In *Intense Dynamic Loading and its Effects*, pp. 444–9. Science Press, Beijing, and Pergamon Press.

2.211. Liu J.H. and Jones N. (1988) Dynamic response of a rigid plastic clamped beam struck by a mass at any point on the span. *Int. J. Solids Struct.*, **24**, 251–70.

2.212. Liu J.H. and Jones N. (1987) Experimental investigation of clamped beams struck transversely by a mass. *Int. J. Impact Eng.*, **6**, 303–35.

2.213. Líu J.H. and Jones N. (1987) Plastic failure of a clamped beam struck transversely by a mass. Report ES/31/87. Department of Mechanical Engineering, University of Liverpool.

2.214. Jones N. (1979) Response of structures to dynamic loading. *Conf. Ser. – Inst. Phys.*, **47**, 254–76.

2.215. Recht R.F. and Ipson T.W. (1963) Ballistic perforation dynamics. *J. Appl. Mech.*, **30**, 384–90.

2.216. Lindholm U.S., Yeakley L.M. and Davidson D.L. (1974) Biaxial strength tests on beryllium and titanium alloys. *AFML-TR-74-172*. Air Force Systems Command, Wright-Patterson Air Force Base, Oh.

2.217. Jones N. (1970) The influence of large deflections on the behavior of rigid-plastic cylindrical shells loaded impulsively. *J. Appl. Mech.*, **37**, 416–25.

2.218. Lindberg, H.E., Anderson D.L., Firth R.D. and Parker L.V. (1965) Response of re-entry vehicle-type shells to blast loads. *SRI project FGD-5228*. Stanford Research Institute, Menlo Park, CA.

2.219. Cronkhite J.D. and Berry V.L. (1983) Investigation of the crash impact characteristics of helicopter composite structure. *USA AVRADCOM-TR-82 D-14*.

2.220. Farley G.L. (1987) Energy absorption of composite materials and structures. Forty-Third American Helicopter Society Annual Forum, New York.

2.221. Hull D. (1983) Axial crushing of fibre reinforced composite tubes. In *Structural Crashworthiness* (Ed. by N. Jones and T. Wierzbider), pp. 118–35. Butterworths, London.

2.222. Schmeuser D.W. and Wickliffe L.E. (1987) Impact energy absorption of continuous fibre composite tubes. *Trans. ASME*, **109**, 72–7.

2.223. Thornton P.H. and Edwards P.J. (1982) Energy absorption in composite tubes. *J. Comp. Mat.*, **16**, 521–45.

2.224. Hull D. (1982) Energy absorption of composite materials under crush conditions. In *Progress in Science and Engineering of Composites* (Ed. by T. Hayashi, K. Kawata and S. Umekawa), Vol. 1, ICCM-IV, pp. 861–70. Tokyo University.

2.225. Fairfull A.H. (1986) *Scaling Effects in the Energy Absorption of Axially Crushed Composite Tubes*. PhD thesis, University of Liverpool.

2.226. Price J.N. and Hull D. (1987) The crush performance of composite structures. In *Composite Structures* (Ed. by I.H. Marshall), pp. 2.32–2.44. Elsevier, Amsterdam.

2.227. Price J.N. and Hull D. (1987) Axial crushing of glass fibre-polyster composite cones. *Comp. Sci. Technol.*, **28**, 211–30.

2.228. Berry J.P. (1984) *Energy Absorption and Failure Mechanisms of Axially Crushed GRP tubes*. PhD thesis. University of Liverpool.

2.229. de Runtz J.A. and Hodge P.G. (1963) Crushing of tubes between rigid plates. *J. Appl. Mech.*, **30**, 381–95.

2.230. Abramowicz W. and Jones N. (1984) Dynamic axial crushing of square tubes. *Int. J. Impact Eng.*, **2**(2), 179–208.

2.231. Soreide T.H. and Amdahl J. (1982) Deformation characteristics of tubular members with reference to impact loads from collisions and dropped objects. *Norw. Marit. Res.*, **10**, 3–12.

2.232. Soreide T.H. and Kavlie D. (1985) Collision damage and residual strength of tubular members in steel offshore structures. In *Shell Structures Stability and Strength* (Ed. by R. Narayanan), pp. 185–220. Elsevier, London.

2.233. Taby J. and Moan T. (1985) Collapse and residual strength of damaged tubular members. BOSS '85, Paper B8.

2.234. Durkin S. (1987) An analytical method for predicting the ultimate capacity of a dented tubular member. *Int. J. Mech. Sci.*, **29**, 449–67.

2.235. Ellinas C.O. and Valsgård S. (1985) Collisions and damage of offshore structure: a state-of-the art. In *Proc. Int. Symp. OMAE, Fourth.* Organisation of Motor Association for Engineering, USA.

2.236. de Oliveira J.G. (1981) Design of steel offshore structures against impact loads due to dropped objects. *Report No. 81–6.* Department of Ocean Engineering, Massachusetts Institute of Technology, Cambridge, MA.

2.237. Adamchak J. (1984) An approximate method for estimating the collapse of a ship's hull in preliminary design. In *Proc. Ship Struct. Symp., SNAME.* Arlington, VA.

2.238. Furnes O. and Amdahl J. (1979) Computer simulation study of offshore collisions and analysis of ship platform impacts. Paper presented at The Second International Symposium on Offshore Structures, Brazil, October 1979 (also in *Applied Ocean Research*, **2**, no. 3, 119–27, 1980).

2.239. Furness O. and Amdahl J. (1980) Ship collisions with offshore platforms. DnV Paper 80-P080, presented at Intermaritec '80 Conference, Hamburg, September 1980.

2.240. Brown and Root Incorp (1990) Design of steel offshore structures against impact loads due to dropped objects. Private Communication, 1990.

2.241. Knapp A.E., Green D.J. and Etie R.S. (1984) Collision of a tanker with a platform. OTC Paper 4734, presented at the Sixteenth Annual Offshore Technology Conference, Houston, Texas.

2.242. Kochler P.E. and Jorgensen L. (1985) Ship impact ice analysis. In *Proceedings of the Fourth Symposium on Offshore Mechanics and Arctic Engineering, ASME-Omae*, pp. 344–50. Dallas, TX, February 1985.

2.243. Guttman S.I., Pushar F.J. and Bea R.G. (1984) Analysis of offshore structures subject to arctic ice impacts. In *Proceedings of the Third Symposium on Offshore Mechanics and Arctic in Engineering*, pp. 238–45. New Orleans, LA.

2.244. Hamza H. and Muggeridge D.B. (1984) A theoretical fracture analysis of the impact of a large ice flow with a large offshore structure. In *Proceedings of the Third Symposium on Offshore Mechanics and Arctic Engineering*, pp. 291–7. New Orleans, LA.

2.245. Roland B., Olsen T. and Skaare T. (1982) Ship impact on concrete shafts. Paper EUR 305, presented at the Third European Petroleum Conference, London.

2.246. Hetherington W.G. (1979) Floating jetties – construction, damage and repair. Paper no. 3 from the Concrete Ships and Floating Structures Convention.

2.247. Larsen C.M. and Engseth A.G. (1978) Ship collision and fendering of offshore concrete structures. Paper EUR 17, presented at The First European Petroleum Conference, London.

2.248. Hjelde E., Nottveit A. and Amdahl J. (1978) Impacts and collisions offshore report no. 2 — pilot tests with pendulum impacts on fendered/unfendered concrete cylinders. *DnV Report No. 78–106.*

2.249. Carlin B. and Ronning B. (1979) Impacts and collisions, offshore report no. 9: punching shear tests on concrete shells state-of-the-art. *DnV Report No. 79–0690.*

2.250. Birdy J.N., Bhula D.N., Smith J.R. and Wicks S.J. (1985) Punching resistance of slabs and shells used for arctic concrete platforms. OTC Paper 4855, presented at the Annual Offshore Technology Conference, Houston, TX.

2.251. Jiang C.W. (1984) Dynamic interaction of ship–fender system. In *Proceedings of the Fourth OMAE Symposium*, pp. 192–7. New Orleans, LA.

2.252. Hunter S.C. (1957) Energy absorbed by elastic waves during impact. *J. Mech. Phys. Sol.*, **5**, 162–71.

2.253. de Oliveira J.G. (1982) Beams under lateral projectile impact. In *Proc. ASCE J. Eng. Mech Div.*, **108**, no. EM1, 51–71.

2.254. Jenssen T.K. (1978) Structural damage from ship collision. *Det Norske Veritas Report 78–063*.

2.255. Van Mater P.R. (1979) Critical evaluation of low energy ship collision damage theories and design methodologies. Vol. 1, evaluation and recommendations. *Ship Structure Committee Paper SSC-284*.

2.256. IABSE (1983) Ship collisions with bridges and offshore structures. In *Proceedings of the IABSE Colloquium Copenhagen*, Vol. 42.

2.257. Sorensen K.A. (1976) Behaviour of reinforced and presented concrete tubes under static and impact loading. First International BOSS Conference, Trondheim.

2.258. Jakobsen B., Olsen T.O., Roland B. and Skare E. (1983) Ship impact on the shaft of a concrete gravity platform. In *Proceedings of the IABSE Colloquium Copenhagen*, Vol. 42, pp. 235–43.

2.259. Blok J.J. and Dekker J.N. (1983) Hydrodynamic aspects of ships colliding with fixed structures. In *Proceedings of the IABSE Colloquium Copenhagen*, Vol. 42, pp. 175–85.

2.260. Haywood J.H. (1978) Ship collisions with fixed offshore structures. *Technical Memo TM 78282*. Admiralty Marine Technology Establishment (Dunfermline).

2.261. Corneliussen C. and Laheld P. (1982) Risk for collisions with oil and gas installations on the Norwegian Shelf — collection and preparation of data. *DnV Technical Note 200–002–92*. Norway.

2.262. Laheld P. (1982) Risk for collisions with oil and gas installations on the Norwegian Continental Shelf. Collection and preparation of data. Part report no. 4a. Reports on incidents of drifting ships, barges, anchor buoys and other objects. *DnV Report No. 20–003–92*. Norway.

2.263. Laheld P. (1982) Risk for collisions with oil and gas installations on the Norwegian Continental Shelf. Collection and preparation of data. Part report no. 4b. Incidents of drifting vessels. *DnV Report FDIV/20–82–018*. Norway.

2.264. Laheld P. (1982) Risk for collisions with oil and gas installations on the Norwegian Continental shelf. Collection and preparation of data. Part report no. 7. Reported ship impacts with fixed and mobile offshore platforms. *DnV Report FDIV/20–82–021*.

2.265. Brink-Kjoer O. et al. (1983) Modelling of ship collision against protected structures. In *Proceedings IABSE Colloquium Copenhagen*, Vol. 42, pp. 147–64.

2.266. Veritec A.S. (1984) Worldwide Offshore Accident Databank (WOAD). *Annual Statistical Report 83*. Government of Norway, Oslo, Norway.

2.267. Low H.Y. and Morley C.T. (1983) Indentation tests of simplified models of ships' structures. In *Proceedings of the IABSE Colloquium on Ship Collision*

with Bridges and Offshore Structures, pp. 213–20. Preliminary Report, Copenhagen.

2.268. Chang P.T. et al. (1980) A rational methodology for the prediction of structural response due to collisions of ships. SNAME Annual Meeting, New York, 13–15, Paper no. 6.

2.269. Wierzbicki T. et al. (1982) Crushing analysis of ship structures with particular reference to bow collisions. *Det Norske Veritas, Progress Report No. 16 on Impacts and Collisions Offshore, Report No. 82–079.*

2.270. Blok J.J. and Dekker J.N. (1979) On hydrodynamic aspects of ship collision with rigid or non-rigid structures. OTC Paper 3664, presented at the Eleventh Annual Offshore Technology Conference, Houston, TX.

2.271. Acres International Ltd (1983) Influence of small icebergs on semi-submersibles. Report prepared for the Petroleum Directorate, Government of Newfoundland.

2.272. 'Acres International Ltd (1987) Northumberland Strait Bridge: ice forces report, draft copy of Acres International Ltd. Report prepared for Public Works, Canada.

2.273. Afanasev V.P., Dolgopolov Y.V. and Shvaishstein Z.I. (1973) Ice pressure on individual marine structures. In *Ice Physics and Ice Engineering* (Ed. by G.N. Yakovlev). Leningrad. (Translated by the Israel Program for Scientific Translation, Jerusalem.)

2.274. Alaska Oil and Gas Association Project 309 (1986) Computer software to analyze ice interaction with semi-submersibles. Alaskan Government, USA.

2.275. Allyn M. (1986) Keynote address on global and local ice loads including dynamic effects. Ice/Structure Interaction State-of-the-art Research Needs Workshop, Calgary.

2.276. Arctic Petroleum Operators Association (1975) Preliminary modeling of the process of penetration of pressure ridges by conical structures. APOA Project no. 86.

2.277. Arctic Petroleum Operators Association (1975) Computer program to evaluate the forces generated by a moving ice field encountering a conical structure. APOA Project no. 87.

2.278. Ashby M.F., Palmer A.C., Thouless M., Goodman D.J., Howard M., Hallam S.D., Murrell S.A.F., Jones N., Sanderson T.J.O. and Ponter A.R.S. (1986) Nonsimultaneous failure and ice loads on arctic structures. In *Proceedings of the Eighteenth Annual Offshore Technology Conference*, Paper no. OTC 5127. Houston, TX.

2.279. Bass D., Gaskill H. and Riggs N. (1985) Analysis of iceberg impacts with gravity based structures at Hibernia. In *Proceedings of the Fourth International Conference on Offshore Mechanics and Arctic Engineering (OMAE 1985).* Dallas, TX.

2.280. Bercha F.G. and Danys J.V. (1977) On forces generated by ice acting against bridge piers. In *Proceedings of the Third National Hydrotechnical Conference.* Canadian Society for Civil Engineering, L'Université Laval, Quebec City, 26–7.

2.281. Bercha F.G., Brown T.G. and Cheung M.S. (1985) Local pressure in ice-structure interactions. In *Proceedings ARCTIC '85.* pp. 1243–51. American Society of Civil Engineers, San Francisco.

2.282. Bruen F.J. and Vivitrat V. (1984) Ice force prediction based on strain-rate field. In *Third International Offshore Mechanics and Arctic Engineering Symposium OMAE '84*, Vol. 3, pp. 275–81.

2.283. Cammaert A.B. and Tsinker G.B. (1981) Impact of large ice floes and icebergs on marine structures. In *Proceedings of the Sixth International Conference on Port and Ocean Engineering Under Arctic conditions*, Vol. II, pp. 653–67. Quebec City, Canada.

2.284. Cammaert A.B., Wong T.T. and Curtis D.D. (1983) Impact of icebergs on offshore gravity and floating platforms. In *Proceedings of the Seventh International Conference on Port and Ocean Engineering Under Arctic Conditions (POAC '83)*. Helsinki, Finland.

2.285. Colbeck S.C. (Ed.) (1980) *Dynamics of Snow and Ice Masses.* Academic Press, New York.

2.286. Cox J., Lewis J., Abdelnour R. and Behnke D. (1983) Assessment of ice ride-up/pile-up on slopes and beaches. In *Proceedings of the Seventh International Conference on Port and Ocean Engineering under Arctic Conditions (POAC '83)*, Vol. II, pp. 971–81. Helsinki, Finland.

2.287. Croasdale K.R. (1975) Review of ice forces on offshore structures. Third International Ice Symposium, International Association of Hydraulic Research, Hanover, New Hampshire.

2.288. Croasdale K.R. (1980) Ice forces on fixed rigid structures. In *Working Group on Ice Forces on Structures: A State of the Art Report* (Ed. by T. Carstens). USA CRREL Special Report 80–26, ADA-089674, Hanover, New Hampshire.

2.289. Croasdale K.R. (1985) Recent developments in ice mechanics and ice loads. In *Behaviour of Offshore Structures*, pp. 53–74. Elsevier, Amsterdam.

2.290. Croasdale K.R. (1986) Ice investigations at Beaufort Sea Caisson, 1985. K.R. Croasdale and Associates report prepared for the National Research Council of Canada and the US Department of the Interior.

2.291. Croasdale K.R. and Marcellus R.W. (1978) Ice and wave action on artificial islands in the Beaufort Sea. *Can. J. Civil Eng.*, **5**(1), 98–113.

2.292. Croteau P., Rojansky M. and Gerwick B.C. (1984) Summer ice floe impacts against Caisson-Type exploratory and production platforms. In *Third International Offshore Mechanics and Arctic Engineering Symposium OMAE '84*, Vol. 3, pp. 228–37.

2.293. Daoud N. and Lee F.C. (1986) Ice-induced dynamic loads on offshore structures. In *Proceedings of the Fifth Offshore Mechanics and Arctic Engineering Symposium, OMAE '86*, Vol. 4, pp. 212–18.

2.294. Danielewicz B.W., Metge M. and Dunwoody A.B. (1983) On estimating large scale ice forces from deceleration of ice floes. In *Proceedings of the Seventh International Conference on Port and Ocean Engineering, POAC '83*, Vol. 4, pp. 537–46, Helsinki, Finland.

2.295. Dickins D.F. (1981) Ice conditions along arctic tanker routes. D.F. Dickens and Associates Ltd, report prepared for Dome Petroleum Ltd.

2.296. Edwards R.Y., Wallace W.G. and Abdelnour R. (1974) Model experiments to determine the forces exerted on structures by moving ice fields (comparison with small prototype test results). Arctic Canada Limited APOA project no. 77.

2.297. Edwards R.Y. and Croasdale K.R. (1976) Model experiments to determine ice forces on conical structures. Symposium of Applied Glaciology, International Glaciological Society, Cambridge, UK, 12–17 September 1976.

2.298. El-Tahan H., Swamidas A.S.J., Arockiasary M. and Reddy D.V. (1984) Strength of iceberg and artificial snow ice under high strain rates and impact loads. In *Proceedings of the Third Offshore Mechanics and Arctic Engineering Symposium*, Vol. 3, pp. 158–65.

2.299. El-Tahan H., Swamidas A.S.J. and Arockiasary M. (1985) Response of semi-submersible models to bergy-bit impact. In *Proceedings of the Eighth International Conference on Port and Ocean Engineering under Arctic Conditions, POAC '85*. Narssarssuaq, Kalaallitt Nunaat.

2.300. Eranti E., Hayes F., Maattanen M. and Soong T. (1981) Dynamic ice–structure interaction analysis for narrow vertical structures. *Proceedings of the Sixth International Conference on Port and Ocean Engineering under Arctic Conditions, POAC '81*. Quebec City.

2.301. Frederking R.M.W. (1979) Dynamic ice forces on an inclined structure. In *Physics and Mechanics of Ice* (Ed. by P. Tryde), pp. 104–16. International Union of Theoretical and Applied Mechanics Symposium at the Technical University of Denmark, August 1979. Springer Verlag, New York.

2.302. Frederking R.M.W. and Timco G.W. (1983) On measuring flexural properties of ice using cantilever beams. *Ann. Glaciol.*, **4**, 58–65.

2.303. Frederking R.M.W. and Nakawo M. (1984) Ice action on Nanisivik Wharf, Winter 1979–1980. *Can. J. Civil Eng.*, **11**(4), 996–1003.

2.304. Guttman S.I., Puskar F.J. and Bea R.G. (1984) Analysis of offshore structures subject to Arctic ice impacts. In *Third International Offshore Mechanics and Arctic Engineering Symposium OMAE '84*, Vol. 3, pp. 228–45.

2.305. Hocking G., Mustoe G.G.W. and Williams J.R. (1985) Validation of CICE code for ice ride-up and ice ridge cone interaction. In *Proceedings, ARCTIC '85*, pp. 962–70. American Society of Civil Engineers, San Francisco.

2.306. Hocking G., Mustoe G.G.W. and Williams J.R. (1985) Dynamic global forces on an offshore structure from Multi-Year Floe Impacts. In *Proceedings, ARCTIC '85*, pp. 202–10. American Society of Civil Engineers, San Francisco.

2.307. Johansson P. (1981) Ice-induced vibration of fixed offshore structures. Part 1: review of dynamic response analysis. Marine structures – ice. *Norwegian Research Project, Report No. 81–061*.

2.308. Jordaan I., Lanthos S. and Nessim M. (1985) A probabilistic approach to the estimation of environmental driving forces acting upon arctic offshore structures. Det Norske Veritas (Canada) Ltd.

2.309. Jordann I.J. (1986) Numerical and finite element techniques in calculation of ice–structure interaction. Third State-of-the-Art Report on Ice Forces, IAHR Ice Symposium, Iowa City.

2.310. Kashteljan V.I., Poznjak I.I. and Ryvlin A.Ja. (1968) *Ice Resistance to Motion of a Ship*. (Translated from Russian by Marine Computer Applications Corp, USA.)

2.311. Kato K. and Sodhi D.S. (1983) Ice action on pairs of cylinders and conical structures. *CRREL Report 83–25*. Californian Regional Research Engineering Laboratory, California, USA.

2.312. Kitami E., Fujishima K., Taguchi Y., Nawata T., Kawasaki T. and Sakai F. (1984) Iceberg collision with semi-submersible drilling unit. In *Proceedings of the International Association of Hydraulic. Research Symposium on Ice*. Hamburg, Germany.

2.313. Koehler P.E. and Jorgensen L. (1985) Ship ice impact analysis. In *Proceedings of the Fourth Offshore Mechanics and Arctic Engineering Symposium, OAME '85.*

2.314. Kry P.R. (1978) A statistical prediction of effective ice crushing stresses on wide structures. In *IAHR International Symposium on Ice Problems (IAHR 1978).* Lulea, Sweden, part I, pp. 33–47.

2.315. Kry P.R. (1980) Implications of structure width for design ice forces. In *Physics and Mechanics of Ice* (Ed. by P. Tryde), pp. 179–93. International Union of Theoretical and Applied Mechanics Symposium at the Technical University of Denmark, August 1979. Springer Verlag, New York.

2.316. Maattanen M. (1977) Stability of self-excited ice-induced structure vibrations. In *Proceeding of the Fourth International Conference on Port and Ocean Engineering under Arctic Conditions POAC '77.* Vol. 2, pp. 684–94. St. John's, Newfoundland.

2.317. Maattanen M. (1979) Laboratory tests for dynamic ice–structure interaction. In *Proceedings of the Fifth International Conference on Port and Ocean Engineering under Arctic Conditions, POAC '79.* Trondheim, Norway.

2.318. Maattanen M. (1981) Ice structure – dynamic interaction. In *Proceedings of the International Association of Hydraulic Research Symposium on Ice.* Quebec City.

2.319. Matlock H. and Panak J. (1969) A model for the prediction of ice–structure interaction. Offshore Technology Conference, Paper no. 1066.

2.320. Matsuishi M. and Ettama R. (1986) Model tests on the dynamic behaviour of a floating, cable-moored platform impacted by floes of annual ice. Fifth Offshore Mechanics and Arctic Engineering Symposium, Houston, USA.

2.321. Neill C. (1976) Dynamic ice forces on piers and piles. An assessment of design guidelines in the light of recent research. *Can. J. Civil Eng.*, **3**(2), 305–41.

2.322. Nevel D.E. (1972) The ultimate failure of a floating ice sheet. In *Proceedings of the IAHR Symposium on Ice and its Action on Hydraulic Structures*, pp. 17–23. The Netherlands.

2.323. Ralston T. (1977) Ice force design considerations for conical offshore structures. In *Proceedings of the Fourth International Conference on Port and Ocean Engineering under Arctic Conditions, POAC '77.* Memorial University of Newfoundland, St. John's, Newfoundland.

2.324. Ralston T. (1979) Ice force design considerations for conical offshore structures. In *Proceedings of the Fifth International Conference on Port and Ocean Engineering under Arctic Conditions, POAC '79.* Trondheim, Norway.

2.325. Ralston T. (1980) Plastic limit analysis of sheet ice loads on conical structures. In *Physics and Mechanics of Ice* (Ed. by P. Tryde), pp. 289–308. International Union of Theoretical and Applied Mechanics Symposium at the Technical University of Denmark, August 1979. Springer Verlag, New York.

2.326. Reinicke K.M. (1980) Analytical approach for the determination of ice forces using plasticity theory. In *Physics and Mechanics of Ice* (Ed. by P. Tryde), pp. 325–41. International Union of Theoretical and Applied Mechanics Symposium at the Technical University of Denmark, August 1979. Springer Verlag, New York.

2.327. Saeki B. et al. (1981) Mechanical properties of adhesion strength to pile structures. In *Proceedings of the International Association for Hydraulic Research Symposium*, Vol. 2, pp. 641–9. Quebec City.

2.328. Saeki H., Hamanika K. and Ozaki A. (1969) Experimental study on ice force on a pile. Offshore Technology Conference, Houston, TX.

2.329. Sanderson T.J.O. and Child A.J. (1986) Ice loads on offshore structures: the transition from creep to fracture. *Cold Regions Sci. Technol.*, **12**, 157–61.

2.330. Semeniuk A. (1975) Computer program to evaluate the forces generated by a moving ice field encountering a conical structure. APOA project no. 87. Association of Petroleum in Antarctica, San Diego, CA.

2.331. Sinha N.K. (1982) Delayed elastic strain criterion for first cracks in ice. In *Proceedings of the International Union Theoretical and Applied Mechanics Symposium on Deformation and Failure of Granular Materials*, pp. 323–30. Delft, The Netherlands.

2.332. Sinha N.K. (1982) Acoustic emission and microcracking in ice. In *Proceedings of the 1982 SESA/Japan Society for Mechanical Engineers*, part II, pp. 767–72. Honolulu/Maui, Hawaii.

2.333. Sinha N.K. (1986) Young arctic frazil sea ice: field and laboratory strength tests. *J. Mater. Sci.*, **21**(5), 1533–46.

2.334. Timco G.W. (1984) Ice forces on structures: physical modeling techniques. In *Proceedings of the IAHR International Ice Symposium*, Vol. IV, pp. 117–50. Hamburg, West Germany.

2.335. Timco G.W. (1986) Ice forces on multi-legged structures. Third state-of-the-art report on ice forces. In *Proceedings of the IAHR Ice Symposium.* Iowa City, IO.

2.336. Timco G.W. and Pratte B.D. (1985) The force of a moving ice cover on a row of vertical piles. Canadian Coastal Conference, Quebec.

2.337. Tsuchiya M., Kanie S., Ikejiri K., Yoshida A. and Saeki H. (1985) An experimental study of ice–structure interaction. Offshore Technology Conference, Houston, TX.

2.338. Vaudrey K.D. (1977) Ice engineering: study of related properties of floating sea-ice sheets and a summary of elastic and viscoelastic analyses. *Technical Report R860*, p. 79. US Navy Civil Engineering Laboratory.

2.339. Vaudrey K.D. and Potter R.E. (1981) Ice defense for natural barrier islands during freeze up. In *Proceedings of the Sixth International Conference on Port and Ocean Engineering under Arctic conditions, POAC '81.* Quebec City, Quebec.

2.340. Wang Y. (1984) Analysis and model tests of pressure ridges failing against conical structures. In *Proceedings of the International Ice Symposium.* International Association of Hydrological Research, Hamburg.

2.341. Wierzbicki T., Chryssostomidis C. and Wiernicki C. (1984) Rupture analysis of ship plating due to hydrodynamic wave impact. Society of Naval Architects and Mechanical Engineers Ship Structure Symposium '84.

2.342. Zayas V.A., Dao B.V. and Hammett D.S. (1985) Experimental and analytical comparisons of semi-sumbersible offshore rig damage resulting from a ship collision. Offshore Technology Conference, Houston, TX.

2.343. Banthia N. (1987) *Impact Resistance of Concrete.* PhD thesis, University of British Columbia, Vancouver.

2.344. Banthia N., Mindess S. and Bentur A. (1987) Impact behaviour of concrete beams. *Mater. Struct.*, **20**, 293–302.

2.345. Ravid M. and Bodner S.R. (1983) Dynamic perforation of viscoplastic plates by rigid projectiles. *Int. J. Eng. Sci.*, **21**, 577–91.

2.346. Curran D.R., Seaman L. and Shockey D.A. (1987) Dynamic failure of solids. *Phys. Rep.*, **147**, 254–387.

2.347. Anderson C.E. and Bodner S.R. (1988) Ballistic impact: the status of analytical and numerical modeling. *Int. J. Impact Eng.*, **7**, 9–35.

2.348. Goldsmith W. and Finnegan S.A. (1986) Normal and oblique impact of cylindro-conical and cylindrical projectiles on metallics plates. *Int. J. Impact Eng.*, **4**, 83–105.

2.349. Lambert J.P. (1978) *ARBRL-TR-02033*. Ballistic Research Laboratory, Alabama, USA.

2.350. Meunier Y., Sangoy L. and Pont G. (1989) Steels for ballistic protection. In *Proceedings of the Fourth Israel Materials Engineering Conference* (Ed. by J. Baram and D. Eliezer). Beer-Sheva, Israel, 7–8 December 1988.

2.351. Wilkins M.L. and Guinan M.W. (1973) Impact of cylinders on a rigid boundary. *J. Appl. Phys.*, **44**(3), 1200–6.

2.352. Yatteau J. and Recht R. (1970) High speed penetration of spaced plates by computer fragments. In *Proceedings of the Ninth International Symposium on Ballistics 2*, pp. 365–74. Shrivenham.

2.353. Naz P. (1987) Spaced plated penetration by spherical high density fragments at high velocity. In *Proceedings of the Tenth International Symposium on Ballistics 2*. San Diego.

2.354. Richards A. and Bowden A. (1987) The development of a projectile velocity measuring system for the RARDE No. 2 Hypervelocity Launcher. *Int. J. Impact Eng*, **5**, 519–32.

2.355. Zhong Z.H. (1988) *On Contact–Impact Problems*. Dissertation no. 178, Linköping University, Sweden.

2.356. Zhong Z.H. and Nilsson L.A. (1988) A contact searching algorithm for general contact problems. *Comput. Struct.*

2.357. Zhong Z.H. (1988) New algorithms for numerical treatments of general contact–impact interfaces. In *Proceedings of the Fourth SAS–World Conference FEMCAD*, Vol. 1. China.

2.358. Chaudhary A.B. and Bathe K.J. (1986) A solution method for static and dynamic analysis of three-dimensional contact problems with friction. *Compute. Struct.*, **24**.

2.359. Zhong Z.H. (1989) Evaluation of friction in general contact–impact interfaces. *Communi. Appl. Numer. Methods.*

2.360. Zhong Z.H. (1989) Recent developments of the HITA and DENA contact–impact algorithms. *Publication LiTH.IKP.R.547*. Linköping University, Sweden.

2.361. Michie J.D. (1981) Collision risk assessment based on occupant flail-space model. *Transportation Research Record No. 796*. Transportation Research Board, Washington DC.

2.362. Ray M.H. and Carney J.F. III (1989) *An Improved Method for Determining Vehicle and Occupant Kinematics in Full-scale Crash Tests*. Transportation Research Board, Washington DC.

2.363. Hargrave M.W., Hansen A.G. and Hinch J.A. (1989) A summary of recent side impact research conducted by the Federal Highway Administration. *SAE Technical Paper No. 890377*. Society of Automotive Engineers, Warrendale, PA.

2.364. Ray M.H., Mayer J.B. and Michie J.D. (1987) Replacing the 4500-lb passenger sedan in report 230 tests, evaluation of design analysis procedures and

acceptance criteria for roadside hardware. Final Report, Federal Highway Administration, Washington DC.

2.365. Shadbolt P.J. (1981) *Impact Loading of Plates*. DPhil Thesis, Oxford University.

2.366. Salvatorelli F. and Rollins M.A. (1988) *Some Applications of ABAQUS*, ABAQUS User's Conference, pp. 377–96. HKS, Inc. Newport, Rhode Island.

2.367. Xia Y.R. and Ruiz C. (1989) Response of layered plates to projectile impact. In *Proceedings of the Fourth International Conference on Mechanical Properties of Materials at High Rates of Strain*. Institute of Physics, Oxford.

2.368. Xia, Y.R. and Ruiz C. (1989) Shear effects between the layers of laminated beams under impact loading. *Proceedings of the Institute of Mechanical Engineers*, London, 87–92.

2.369. Winter R. and Pifko A.B. (1988) Finite element crash analysis of automobiles and helicopters. In *Structural Impact and Crash Worthiness* (Ed. by J. Morton), Vol. II, pp. 278–309. Conference Papers. Elsevier.

2.370. Chan A.S.L. and Li F-N (1989) Impact of thin-walled shells using a simplified finite element model. Private communication.

2.371. Chan A.S.L. (1989) Reinforcements in the impact analysis of thin-walled shells using a simplified finite element model. Private communication.

2.372. Varpason P. and Kentalla J. (1981) The analysis of the containment building for global effects of an aircraft crash. Sixth International Conference, SMiRT, Paper J9/10, 1981. Paris.

2.373. Ohnuma H. (1985) Dynamic response and local rupture of reinforced concrete beam and slab under impact loading. Eighth International SMiRT Conference, Brussels, 1985, Paper J5/3.

2.374. Crutzen Y. (1979) *Non-Linear Transient Dynamic Analysis of Thin Shells Using the SEMILOOF Finite Element*. PhD thesis, University of Brussels.

2.375. NDRC (1946) *Effects of Impact and Explosion, Summary Technical Report of Division 2*, Vol. 1. National Defense Research Committee, Washington DC.

2.376. Jenkov Z.D. et al. (1976) Missile tests of quarter-scale reinforced concrete barriers. Prepared for Stone & Webster, Inc. by Texas Technical University.

2.377. BPC (1974) Design of structures for missile impact. *Topical Report BC-TOP-9-A*. Bechtel Power Corporation.

2.378. Haldav A. Hatami M. and Miller F. (1983) Penetration and spalling depth estimation for concrete structures. Seventh International Conference on Structural Mechanics in Reactor Technology (SMiRT), Paper J7/2. (Also Turbine missile – a critical review. *Nucl. Eng Des.*, **55**, 1979.)

2.379. Takeda J. et al. (1982) *Proc. Inst. Assoc. Symp. Concrete Structures Under Impact and Impulsive Loading*, pp. 289–95. BAM, Berlin.

2.380. Kar A.K. (1979) Impactive effects of tornado missiles and aircraft. *Trans. ASCE*, **105**, ST2, 2243–60. (Also Loading time – history for tornado generated missiles. *Nucl. Eng Des.*, **51**, 487–93, 1979.)

2.381. Rotz J. (1976) Evaluation of tornado missile impact effects on structures. In *Proceedings of the Symposium on Tornadoes, Assessment of Knowledge and Implications for Man*. USA.

2.382. PLA (1989) *Design Manual for Concrete Pavements*. Port of London Authority.

2.383. Kar A. (1979) Projectile penetration into steel. *J. Struct. Div., ASCE*.

2.384. ACE (1946) Fundamentals of protective design. *Report AT 1207821*. Army Corps of Engineers, USA.

2.385. Rinaldi L.J. (1972) *Containerization: the New Method of Intermodal Transport.* Stirling Publishing.

2.386. D'Arcangelo A.M. (Ed.) (1975) *Ship Design and Construction.* The Society of Naval Architects and Marine Engineers, New York.

2.387. Petry S. and Brown I. (1982) *Model Prestressed Concrete Slab Subjected to Hard Missile Loading. Design for Dynamic Loading.* Construction Press.

2.388. International Conference: *Structural Impact and Crash Worthiness*, July 1984, Imperial College, London. Elsevier, Vols. 1, 2, 3.

2.389. Stevenson J. (Ed.) (1976) *Design for Nuclear Power Plant Facilities.* ASCE, New York.

2.390. Behaviour of reinforced concrete barriers subject to the impact of turbine missiles. Fifth Int. Conf. Struct. Mech. in Reactor Technology (SMiRT), Berlin, 1979, Paper J7/5.

2.391. SRI (1960) *Report No. 361.* Stanford Research Institute, California, USA.

2.392. Neilson A.J. (1985) Winfrith perforation energy model. *UK Atomic Energy Report No. 31.* Winfrith, Dorset, UK.

2.393. Neilson A.J. (1980) Missile impact on metal structures. *Nucl. Energy*, **19**(3), 191–8.

2.394. Chellis R.D. (1961) *Pile Foundations.* McGraw Hill, New York.

2.395. Chandrasekaran V. (1974) *Analysis of Pile Foundations Under Static and Dynamic Loads.* PhD Thesis, University of Roorkee, India.

2.396. Van der Meer J.W. and Pilarczyk K.W. (1984) Stability of rubble mound slopes under random wave attack. In *Proceedings of the 19th ICCE*, chapter 176. Houston, USA.

2.397. Chiesa M.L. and Callabressi M.L. (1981) Non-linear analysis of a mitigating steel nose cone. In *Computational Methods in Non-Linear Structural and Solid Mechanics* (Ed. by A.K. Noor and H.G. McComb, Jr.), pp. 295–300. Pergamon, New York.

2.398. Shular W. (1970) Propagation of study shockwaves in polymethyl methocrylate. *J. Mech. Phys. Solids*, **18**, 277–93.

2.399. Jernström C. (1983) Computer simulation of a motor vehicle crash dummy and use of simulation in the design/analysis process. *Int. J. Vehicle Design*, **4**(2), 136–49.

2.400. Körmeling H.A. (1984) Impact tensile strength of steel fibre concrete. *Report 1.5–84–8.* Department of Civil Engineering, The Delft University of Technology.

2.401. Suaris W. and Shah S.P. (1982) Properties of concrete subjected to impact. *ASCE St. Div.*, **109**(7), 1727–41.

2.402. Biggs J.M. (1964) *Introduction to Structural Dynamics.* McGraw-Hill, Berkeley, CA.

3 Finite-Element and Other Numerical Methods

3.1. Hussain M. and Saugy S. (1970) Elevation of the influence of some concrete characteristics on non-linear behaviour of a prestressed concrete reactor vessel. Concrete for Nuclear Reactors, American Concrete Institute, Detroit, Michigan, paper SP-34-8.

3.2. Zienkiewicz O. and Watson M. (1966) Some creep effects in stress analysis with particular reference to concrete pressure vessels. *Nucl. Eng Des.*, no. 4.

3.3. Bangash Y. (1982) Reactor pressure vessel design and practice. *Prog. Nucl. Energy*, **10**, 69–124.

3.4. Saugy B. (1973) Three-dimensional rupture analysis of a prestressed concrete pressure vessel including creep effects. Second International Conference on Structural Mechanics in Reactor Technology (SMiRT), Berlin.

3.5. Saouma V. (1981) *Automated nonlinear finite element analysis of reinforced concrete: a fracture mechanics approach.* Thesis presented to Cornell University, Ithaca, NY, in partial fulfilment of the requirements for the degree of Doctor of Philosophy.

3.6. Phillips D.V. and Zienkiewicz O.C. (1976) Finite element non-linear analysis of concrete structures. *Proc. Inst. Civ. Eng Res. Theory*, **61**.

3.7. Cook R.D. (1981) *Concepts and Applications of Finite Element Analysis*, 2nd edn. Wiley, New York.

3.8. Zienkiewicz O.C. (1977) *The Finite Element in Engineering Science.* McGraw Hill, London.

3.9. Martin H.C. and Carrey G.F. (1973) *Introduction to Finite Element Analysis.* McGraw Hill, New York.

3.10. Bathe K.J. and Wilson E.L. (1972) *Numerical Methods in Finite Element Analysis.* Prentice-Hall, Englewood Cliffs, NJ.

3.11. Desai C.S. and Abel J.F. (1972) *Introduction to the Finite Element Method.* Van Nostrand Reinhold, New York.

3.12. Ahmed S. (1969) *Curved Finite Element in the Analysis of Solid Shell and Plate Structures.* PhD Thesis, University of Wales, Swansea.

3.13. Marcal P.V. (1972) Finite element analysis with material non-linearities – theory and practice. In *Conference on Finite Element Methods in Civil Engineering*, pp. 71–113. Montreal, 1972.

3.14. Rashid Y.R. (1966) Analysis of concrete composite structures by the finite element method. *Nucl. Eng Des.*, 3.

3.15. Rashid Y.R. and Rockenhauser W. (1968) Pressure vessel analysis by finite element techniques. In *Conference on Prestressed Concrete Pressure Vessels.* Institute of Civil Engineers, London.

3.16. Akyuz F.A. and Merwin J.A. (1968) Solution of non-linear problems of elastoplasticity by finite element method. *AIAA J.*, **6**.

3.17. Argyris J.H. (1965) Three-dimensional anisotropic and inhomogenous elastic media, matrix analysis for small and large displacements. *Ingenieur Archiv.*, **34**.

3.18. Dupuis G.A. (1971) Incremental finite element analysis of large elastic deformation problems. Brown University, USA.

3.19. Bangash Y. (1981) The structural integrity of concrete containment vessels under external impacts. In *Proceedings of the Sixth International Conference on Structural Mechanics in Reactor Technology (SMiRT)*, Paper J7/6. Paris.

3.20. Bangash Y. (1981) The automated three-dimensional cracking analysis of prestressed concrete vessels. In *Proceedings of the Sixth International Conference on Structural Mechanics in Reactor Technology (SMiRT)*, Paper H3/2. Paris.

3.21. Bathe K.J. and Wilson E.L. (1971) Stability and accuracy analysis of direct integration method. *Int. J. Earthquake Eng. Struct. Dyn.*, **1**, 283–91.

3.22. Ahmed M. (1983) *Bond Strength History in Prestressed Concrete Reactor Vessels.* PhD Thesis (CNAA), R-84, Thames Polytechnic.

3.23. Bicanic N. and Zienkeiwicz O.C. (1983) Constitutive models for concrete under dynamic loading. *Earthquake Eng. and Struct. Dyn.*, **11**, 689–720.

3.24. Gunasekera J.S. et al. (1972) Matrix analysis of the large deformation of an elasticplastic axially symmetric continuum. In *Proceedings of the Symposium on Foundations of Plasticity.* Warsaw.

3.25. Martin H.C. (1965) Derivation of stiffness matrices for the analysis of large deflection and stability problems. In *Proceedings of the First Conference on Matrix Methods in Structural Mechanics.* Ohio.

3.26. Washizu K. (1968) *Variational Methods in Elasticity and Plasticity.* Pergamon Press, Oxford.

3.27. Murray D.W. et al. (1969) An approximate non-linear analysis of thin-plates. In *Proceedings of the Second Conference on Matrix Methods in Structural Mechanics.* Berlin, Germany.

3.28. Bechtel Corporation (1972) *Containment Building Liner Plate Design Report.* San Francisco.

3.29. Mutzl J. et al. (1975) Buckling analysis of the hot liner of the Austrian PCRV Concept. In *Third International Conference on Structural Mechanics in Reactor Technology*, Paper H3/9. London.

3.30. Koiter W.T. (1963) The effect of axisymmetric imperfections on the buckling of cylindrical shells under axial compression. *Proc. Koninkl. Nederl. Akademie van Wenschappen* (Series B) **66**.

3.31. Yaghmai S. (1969) *Incremental Analysis of Large Deformations in Mechanics of Solids with Applications to Axisymmetric Shells of Revolution.* PhD thesis, University of California, Berkeley.

3.32. Bangash Y. (1972) Prestressed concrete reactor vessel. Time-saving ultimate load analysis. *J. Inst. Nucl. Eng.*, **13**.

3.33. Bangash Y. (1972) A basis for the design of bonded reinforcement in the prestressed concrete reactor vessels. *Inst. Civ. Eng.*, Paper 7478S, supplement (8).

3.34. Smee D.J. (1967) The effect of aggregate size and concrete strength on the failure of concrete under multiaxial compression. *Civil Engineering Trans.*, Institute of Engineers, Australia, **CE9** (2) 339–44.

3.35. Bangash Y. (1987) The simulation of endochronic model in the cracking analysis of PCPV. In *Proceedings of the Ninth International Conference on Structural Mechanics in Reactor Technology (SMiRT)*, Vol. 4, pp. 333–40. Lausanne.

3.36. Al-Noury S.I. and Bangash Y. (1987) Prestressed concrete containment structures – circumferential hoop tendon calculation. In *Proceedings of the Ninth International Conference on Structural Mechanics in Reactor Technology (SMiRT)*, Vol. 4, pp. 395–401. Lausanne.

3.37. Belytschko T., Yen H.J. and Mullen R. (1979) Mixed methods for time integration. *Computer Methods in Applied Mechanics and Engineering*, **17**, 259–75.

3.38. Belytschko T. (1980) Nonlinear finite element analysis in structural mechanics. In *Partitioned and Adaptive Algorithms for Explicit Time Integration* (Ed. by W. Wunderlich et al.), pp. 572–84.

3.39. Belytschko T. and Lin J.I. (1987) A three-dimensional impact-penetration algorithm with erosion. *Comput. Struct.*, **25**(1), 95–104.

3.40. Hallquist J.O., Gondreau G.L. and Benson D.J. (1985) Sliding interfaces with contact–impact in large-scale Lagrangian computations. *Comput. Methods Appl. Mech. Eng.*, **51**, 107–37.

3.41. Oden J.T. and Martin J.A.C. (1985) Models and computational methods for dynamic friction phenomena. *Comput. Methods Appl. Mech. Eng.*, **52**, 527–634.

3.42. Hallquist J.O. (1984) NIKE3D: an implicit, finite deformation, finite element code for analyzing the static and dynamic response of three-dimensional solids. *UCID-18822, Rev. 1.*, University of California.

3.43. Hallquist J.O. (1986) NIKE2D: A vectorized, implicit, finite deformation, finite element code for analyzing the static and dynamic response of 2-D solids. *UCID-19677, Rev. 1.* University of California.

3.44. Hughes T.J.R., Pister K.S. and Taylor R.L. (1979) Implicit-explicit finite elements in nonlinear transient analysis. *Comput. Methods Appl. Mech. Eng.*, **17/18**, 159–82.

3.45. Hughes T.J.R., Levit I. and Winget J.M. (1983) An element-by-element solution algorithm for problems of structural and solid mechanics. *Methods Appl. Mech. Eng.*, **36**, 241–54.

3.46. Hughes T.J.R., Raefsky A., Muller A., Winget J.M. and Levit I. (1984) A progress report on EBE solution procedures in solid mechanics. In *Numerical Methods for Nonlinear Problems* (Ed. by C. Taylor et al.), Vol. 2, pp. 18–26. Pineridge Press, Swansea, UK.

3.47. Belytschko T.B. and Millen R. (1988) Two-dimensional fluid-structure impact computations with regularization. *Comput. Methods Appl. Mech. Eng.*, **27**, 139–54.

3.48. Key S.W. (1985) A comparison of recent results from HONDO III with JSME nuclear shipping cask benchmark calculations. *Nucl. Eng Des.*, **85**, 15–23.

3.49. Kulak R.F. (1984) A finite element quasi-eulerian method for three-dimensional fluid-structure interactions. *Comput. Struct.*, **18**, 319–32.

3.50. Kulak R.F. (1985) Adaptive contact elements for three-dimensional fluid-structure interfaces. In *Fluid–Structure Dynamics. PVP-98-7*, (Ed. by D.C. Ma and F.J. Moody), and pp. 159–66, American Society of Mechanical Engineers, New York.

3.51. Kulak R.F. (1985) Three-dimensional fluid–structure coupling in transient analysis. *Comput. Struct.*, **21(3)**, 529–542.

3.52. Nichols B.D. and Hirt C.W. (1978) Numerical simulations of hydro-dynamic impact loads on cylinders. *EPRI NP-824 Interim Report.* Electric Power Research Institute, Palo Alto, CA.

3.53. Hughes T.J.R. (1978) A simple scheme for developing upwind finite elements. *Int. J. Numer. Methods Eng.*, **12**, 1359–65.

3.54. Hughes T.J.R. and Mallat M. (1986) A new finite element formulation for computational fluid dynamics: III. The generalized streamline operator for multidimensional advective diffuse systems. *Comput. Methods Appl. Mech. Eng.*, **58**, 305–28.

3.55. Amdsden A.A., Ruppel H.M. and Hirt C.W. (1980) *SALE: A Simplified ALE Computer Program for Fluid Flow at All Speeds.* Los Almos Scientific Laboratory.

3.56. Donea J. (1983) Arbitrary Lagrangian-Eulerian finite element methods. In *Computational Methods for Transient Analysis* (Ed. by T. Belytschko and T.J.R. Hughes), pp. 473–516. Elsevier, Amsterdam.

3.57. Hughes T.J.R., Liu W.K. and Zimmerman T.K. (1981) Lagrangian–Eulerian finite element formulation for incompressible viscous flows. *Comput. Methods Appl. Mech. Eng.*, **29**, 329–49.

3.58. Bathe K.J. and Wilson E.L. (1976) *Numerical Methods in Finite Element Analysis*. Prentice-Hall, New Jersey.

3.59. Belytschki Y. and Engelmann B.E. (1987) On flexurally superconvergent four-node quadrilaterals. *Comput. Struct.*, **25**, 909–18.

3.60. Belytschko T., Ong J.S.-J., Liu W.K. and Kennedy J.M. (1984) Hourglass control in linear and non-linear problems. *Comput. Methods Appl. Mechanics and Engineering*, **43**, 251–76.

3.61. Sun C.T. and Huang S.N. (1975) Transverse impact problems by higher order beam finite element. *Comput. Struct.*, **5**, 297–303.

3.62. Tan T.M. and Sun C.T. (1985) Use of statical indentation laws in the impact analysis of laminated composite plates. *J. Appl. Mech.*, **107**, 6–12.

3.63. Zienkiewicz O.C., Irons B. and Nath B. (1965) Natural frequencies of complex free or submerged structures by the finite element method. Symposium on Vibrations in Civil Engineering, London.

3.64. Bathe K.J., Wilson E.L. and Peterson F.E. (1973) SAPIV – a structural analysis program for static and dynamic response of linear systems. *EERC Report No. 73–11*. University of California, Berkeley.

3.65. NASA (1970) The NASTRAN theoretical manual. *Report SP-221*. National Aeronautics and Space Administration.

3.66. Swanson J.A. (1971) *ANSYS-Engineering Analysis System User's Manual*. Swanson Analysis Systems, Inc., Pittsburgh, PA, USA.

3.67. Johnston P.R. and Weaver W. (1984) *Finite Elements for Structural Analysis*. Prentice-Hall, Englewood Cliffs, NJ.

3.68. Johnston P.R. and Weaver W. Jr. (1987) *Structural Dynamics by Finite Elements*. Prentice-Hall, Englewood Cliffs, NJ.

3.69. Derbalian G., Fowler G. and Thomas J. (1984) Three-dimensional finite element analysis of a scale model nuclear containment vessel. *Am. Soc. Mech. Eng.*, Paper 84-PVP-55.

3.70. Margolin L.G. and Adams T.F. (1982) Numerical simulation of fracture. In *Issues in Rock Mechanics* (Ed. by R.E. Goodman and F.E. Heuze), pp. 637–44.

3.71. Kipp M.E. and Stevens A.L. (1976) Numerical integration of a spall-damage viscoplastic constitutive model in a one-dimensional wave propagation code. *SAND76-0061*. Sandia Lab. (technical report).

3.72. Fredriksson B. and Mackerle J. (1983) *Structural Mechanics Finite Element Computer Programs*, 4th edn. Advanced Engineering Corporation, Linköping, Sweden.

3.73. Noor A.K. (1981) Survey of computer programs for solution of nonlinear structural and solid mechanics problems. *Comput. Struct.*, **13**, 425–65.

3.74. Yagawa G., Ohtsubo H., Takeda H., Toi Y., Aizawa T. and Ikushima T. (1984) A round robin on numerical analyses for impact problems. *Nucl. Eng. Des.*, **78**, 377–87.

3.75. de Roevray A., Haug E. and Dubois J. (1983) Failure mechanisms and strength reduction in composite laminates with cut-outs – a 3-D finite element numerical autopsy. In *Composite Structures* (Ed. by I.H. Marshall). Applied Science, London and New York.

3.76. Bhat S. (1985) *Analysis of Large Plastic Shape Distortion of Shells*. PhD thesis, Massachusetts Institute of Technology, Cambridge.

3.77. ADINA Engineering (1984) *Automatic Incremental Nonlinear Analysis: Users Manual*. ADINA Engineering Inc., MIT, MA, USA.

3.78. Dyhrkopp F. (1984) Inspection of floating offshore platforms. *Proc. Int. Symp. Role Des., Inspect. Redundancy Mar. Struct. Reliabil*. National Academic Press, Washington, DC.

3.79. Engseth A. (1984) *Finite Element Collapse Analysis of Tubular Steel Offshore Structures*. Doctoral Thesis, Report UR-85-46, Div. Marine Structures Norw. Inst. Technol., Trondheim.

3.80. Marshall P.W., Gates W.E. and Anagnostopoulos S. (1977) Inelastic dynamic analysis of tubular offshore structures. *Proceedings of Offshore Technology Conference*, Paper no. 2908.

3.81. Bergen P.G. and Arnesen A. (1983) FENRIS – a general purpose finite element program. In *Proceedings of the Fourth International Conference on Finite Element Systems*. Southampton.

3.82. Plesha M.E. (1987) Eigenvalue estimation for dynamic contact problems. *J. Eng. Mech., ASCE*, **113**, 457–62.

3.83. Isaacson E. and Keller H.B. (1966) *Analysis of Numerical Methods*. Wiley, New York.

3.84. Kulak R.F. and Fiala C. (1983) NEPTUNE: a system of finite element programs for three-dimensional non-linear analysis. *Nucl. Eng. Des.*, **106**, 47–68.

3.85. Kulak R.F. (1989) Adaptive contact elements for three-dimensional explicit transient analysis. *Comput. Meth. Appl. Mech. Eng.*, **72**, 125–51.

3.86. Madsen N. (1984) Numerically efficient procedures for dynamic contact problems. *Int. J. Num. Meth. Eng.*, **20**, 1–14.

3.87. Kanto Y. and Yagawa G. (1980) Finite element analysis of dynamic buckling with contact. *Trans. Jpn. Soc. Mech. Eng., Ser. A*, **51**, 2747–56.

3.88. Pascoe S.K. and Mottershead J.E. (1988) Linear elastic problems using curved elements and including dynamic friction. *Int. J. Num. Methods Eng.*, **26**, 1631–42.

3.89. Bronlund O.E. (1969) Eigenvalues of large matrices. Symposium on Finite Element Techniques, University of Stuttgart, 10–12 June 1969.

3.90. Clint M. and Jennings A. (1970) The evaluation of Eigenvalues and Eigenvectors of real symmetric matrices by simultaneous iteration. *Comput. J.*, **13**(1).

3.91. Bathe K.J. (1971) Solution methods for large generalized Eigenvalue problems in structural engineering. *SESM Rep. 71–20*. Civil Engineering Department, University of California, Berkeley.

3.92. Truesdell C. and Noll W. (1965) The non-linear field theories of mechanics. In *Encyclopedia of Physics* (Ed. by S. Flugge), Vol. III, Art. 3. Springer-Verlag, Berlin.

3.93. Murakawa H. and Atluri S.N. (1978) Finite elasticity solutions using hybrid finite elements based on a complementary energy principle. *J. Appl. Mech., Trans. ASME*, **45**, 539–48.

3.94. Atluri S.N. (1979) On rate principles for finite strain analysis of elastic and inelastic non-linear solids. In *Recent Research on Mechanic Behavior of Solids* (Miyamoto Anniversary Volume), pp. 79–107. University of Tokyo Press, Tokyo.

3.95. Drucker D.C. (1951) A more fundamental approach to plastic stress strain relations. *Proceedings of the First US National Congress on Applied Mechanics*, pp. 487–91. Pasadena, USA.

3.96. Atluri S.N. (1984) On constitutive relations at finite strain: hypoelasticity and elastoplasticity with isotropic or kinematic hardening. *Comput. Meth. Appl. Mech. Eng.*, **43**, 137–71.

3.97. Watanabe O. and Atluri S.N. (1985) A new endochronic approach to computational elastoplasticity: example of a cyclically loaded cracked plate. *J. Appl. Mech.*, **52**, 857–64.

3.98. Reed K.W. and Atluri S.N. (1983) Analysis of large quasistatic deformations of inelastic bodies by a new hybrid-stress finite element algorithm. *Comp. Meth. Appl. Mech. Eng.*, **39**, 245–95; II. Applications. **40**, 171–98.

3.99. Surana K.S. (1983) *FINESSE (Finite Element System for Nonlinear Analysis) Theoretical Manual*. McDonnell Douglas Automation Company, St. Louis.

3.100. Moan T. (1974) A note on the convergence of finite element approximations for problems formulated in curvilinear coordinate systems. *Comp. Meth. Appl. Mech.*, **3**, 209–35.

3.101. Fried I. (1971) Basic computational problems in the finite element analysis of shells. *Int. J. Solids Struct.*, **7**, 1705–15.

3.102. Noor A.K. and Peters J.M. (1981) Mixed models and reduced/selective integration displacement models for non-linear analysis of curved beams. *Int. J. Num. Meth. Eng.*, **17**, 615–31.

3.103. Cantin G. (1970) Rigid body motions in curved finite elements. *AIAA J.*, **8**, 1252–5.

3.104. Elias Z.M. (1972) Mixed finite element method for axisymmetric shells. *Int. J. Num. Meth. Eng.*, **4**, 261–77.

3.105. Ahmad S., Irons B.M. and Zienkiewicz O.C. (1970) Analysis of thick and thin shell structures by curved finite elements. *Int. J. Num. Meth. Eng.*, **2**, 419–51.

3.106. Pugh E.D.L., Hinton E. and Zienkiewicz O.C. (1978) A study of quadrilateral plate bending elements with reduced integration. *Int. J. Num. Meth. Eng.*, **12**, 1059–79.

3.107. Argyris J.H. and Scharpf D. (1968) The SHEBA family of shell elements for the matrix displacement method. *Aeronaut. J.*, **72**, 873–83.

3.108. Sander G. and Idelsohn S. (1982) A family of conforming finite elements for deep shell analysis. *Int. J. Num. Meth. Eng.*, **18**, 363–80.

3.109. Irons B.M. (1976) The semiloof shell element. In *Finite Elements for Thin Shells and Curved Members* (Ed. by D.G Ashwell and R.H. Gallagher). Wiley, London.

3.110. Belytschko T., Liu W.K. and Ong J.S.J. (1984) Nine node Lagrange shell elements with spurious mode control. Twenty-fifth Structures, Structural Dynamics and Materials Conference, AIAA/ASME/AHS, Palm Springs, California.

3.111. Szabo B.A. and Mehta A.K. (1978) P-convergent finite element approximations in fracture mechanics. *Int. J. Num. Meth. Eng.*, **12**, 551–60.

3.112. Babuska I. and Szabo B.A. (1982) On the rates of convergence of the finite element method. *Int. Num. Meth. Eng.*, **18**, 323–41.

3.113. Babuska I. and Miller A. (1984) The post-processing approach in the finite element method: part I calculation of displacements, stresses and other higher derivatives of the displacements. *Int. Num. Meth. Eng.*, **20**, 1085–109.

3.114. Babuska I. and Miller A. (1984) The post-processing approach in the finite element method: part 2 the calculation of stress intensity factors. *Int. J. Num. Meth. Eng.*, **20**, 1111–29.

3.115. Babuska I. and Miller A. (1984) The post-processing approach in the finite element method: part 3 error estimates and adaptive mesh selection. *Int. J. Num. Meth. Eng.*, **20**, 2311–24.

3.116. Parks D.M. (1975) *Some Problems in Elastic–Plastic Finite Element Analysis of Cracks.* PhD Thesis, Brown University, Providence, RI.

3.117. Barsoum R.S. (1976) On the use of isoparametric finite elements in linear fracture mechanics. *Int. J. Num. Meth. Eng.*, **10**, 25–37.

3.118. *MARC User's Manuals, Version J.2.* MARC Analysis Research Corp, Palo Alto, California. (Published annually.)

3.119. Schulz J.C. (1978) Finite element analysis of a kinetic energy warhead penetrating concrete. In *Proceedings of the Fourth International Symposium on Ballistics.* Monterey, CA.

3.120. Key S.W., Beising Z.E. and Krieg R.D. (1978) *HONDO II, A Finite Element Computer Program for the Large Deformation Dynamic of Axisymmetric Solids.* Sandia Laboratories, Albuquerque.

3.121. Levy A. (1979) Development of the PLANS computer program for elastic–plastic creep analysis of nuclear reactor structural components. *Grumman Research Department Report RE-567, ORNL-Sub4485-2.* Grumman Aerospace Corporation, Bethpage, New York.

3.122. Felippa C.A. and Park K.C. (1978) Direct time integration methods in non-linear structural dynamics. PENOMECH 1978 Conference, University of Stuttgart.

3.123. Underwood P.G. and Park K.C. (1980) A variable step central difference method for structural dynamic analysis: implementation and performance evaluation. *Comput. Meth. Appl. Mech. Eng.*, **23**, 259–79.

3.124. Geradin M., Hogge M. and Idelsohn S. (1983) In *Implicit Element Methods. Computational Methods for Transient Analysis* (Ed. by T. Belytschko and T. Hughes), pp. 417–71. North-Holland, Amsterdam.

3.125. Mathies H. and Strang G. (1979) The solution of non-linear finite element equations. *Int. J. Num. Meth. Eng.*, **14**, 1613–26.

3.126. Batoz J.L. and Dhatt G. (1971) Une évaluation des méthodes du type Newton-Raphson implicit l'accroissement d'un déplacement. Rapport Université Technologique de Compiègne.

3.127. Belytschko T. and Rughes T.J.R. (Eds) (1983) *Computational Methods for Transient Analysis.* Elsevier, New York.

3.128. Beckers P. and Sander G. (1979) Improvement of the frontal solution technique. *LTAS Report SA-72.* University of Liège, Belgium.

3.129. Ericsson T. and Ruhe A. (1980) The spectral transformation Lanczos method for the numerical solution of large sparse generalized symmetric Eigenvalue problems. *Math. Comput.*, **35**, 152.

3.130. Atkinson K.E. (1978) *An Introduction to Numerical Analysis*, 1st edn. Wiley, New York.

3.131. Wolf M.A. (1978) *Numerical Methods for Unconstrained Optimization – An Introduction.* Van Nostrand Rheinhold, New York.

3.132. Pian T.H.H. and Tong P. (1970) Variational formulations of finite displacement analysis. *IUTAM Symposium, High Speed Computing of Elastic Structures*, pp. 43–63. Liège, Belgium.

3.133. Riks E. (1979) An incremental approach to the solution of snapping and buckling problems. *Int. J. Solids Struct.*, **15**, 529–51.

3.134. Geradin M. and Fleury C. (1982) Unconstrained and linearly constrained minimization. In *Foundation of Structural Optimization: A Unified Approach* (Ed. by A.J. Morris), chapter 8. Wiley, New York.

3.135. Gerardin M. and Carnoy E. (1979) On the practical use of Eigenvalue bracketing in finite element applications to vibration and stability problems. *Euromech 112*, pp. 151–71. Hungarian Academy of Science.

3.136. Wolfshtein M. (1967) *Conviction Processes in Turbulent Impinging Jet.* PhD Thesis, University of London.

3.137. Baker A.J. (1983) *Finite Element Computational Fluid Mechanics.* Hemisphere/McGraw-Hill, New York.

3.138. Chung T.J. (1978) *Finite Element Analysis of Fluid Dynamics.* McGraw-Hill, New York.

3.139. Norrie D.H. and de Vries G. (1980) Admissibility requirements and the least squares finite element solution for potential flow. In *Proceedings of the Seventh Australasian Hydraulics and Fluid Mechanics Conference*, pp. 115–18. Nat. Conf. Pub. 80/4, Institution of Engineers (Australia).

3.140. Argyris J.H., Mareczek G. and Scharpf D.W. (1969) Two and three dimensional flow using finite elements. *Aero. J.R. Aero. Soc.*, **73**, 961–4.

3.141. Zienkiewicz O.C. and Heinrich J.C. (1978) The finite element method and convection potential fluid mechanics. In *Finite Elements in Fluids* (Ed. by R.H. Gallagher et al.) Vol. 3, pp. 1–23. Wiley, New York.

3.142. Seto H. (1982) New hybrid element approach to wave hydrodynamic loadings on off-shore structures. In *Finite Element Flow Analysis* (Ed. by T. Kawai), pp. 435–42. University of Tokyo Press, Tokyo.

3.143. Sakai F. (1981) Vibration analysis of fluid–solids systems. In *Interdisciplinary Finite Element Analysis* (Ed. by J.F. Abel, T. Kawai and S.F. Shen), pp. 453–77. Cornell University Press, Ithaca, NY.

3.144. Bettess P. and Zienkiewicz O.C. (1977) Diffraction and refraction of surface waves using finite and infinite elements. *Int. J. Num. Meth. Eng.*, **11**, 1271–90.

3.145. Ganeba M.B., Wellford L.C. Jr. and Lee J.J. (1982) Dissipative finite element model for harbour resonance problems. In *Finite Element Flow Analysis* (Ed. by T. Kawai) pp. 451–9. University of Tokyo Press, Tokyo.

3.146. Kawahara M. (1980) On finite element methods in shallow water long wave flow analysis. In *Computational Methods in Non-Linear Mechanics* (Ed. by J.T. Oden), pp. 261–87. North Holland, Amsterdam.

3.147. Kawahara M. (1978) Finite element method in two layer and multi-leveled flow analysis. In *Finite Elements in Water Resources* (Ed. by S.Y. Wang et al.), pp. 5.3–5.19. University of Mississippi Press.

3.148. Kawahara M. and Hasegawa K. (1978) Periodic galerkin finite element method of tidalflow. *Int. Num. Meth. Eng.*, **12**, 115–27.

3.149. Kawahara M., Hasegawa K. and Kawanago Y. (1977) Periodic tidal flow analysis by finite element perturbation method. *Comput. Fluid.*, **5**, 175–89.

3.150. Agnntaru V. and Spraggs L. (1982) A time integration technique for modelling of small amplitude tidal waves. In *Finite Elements in Water Resources* (Ed. by K.P. Holz et al.), pp. 5.17–5.25. Springer-Verlag, Hanover.

3.151. Partridge P.W. and Brebbia C.A. (1976) Quadratic finite elements in shallow water problems. *Proc. ASCE 102 (HY9)*, 1299–1313.

3.152. Wong I.P. and Norton W.R. (1978) Recent application of RMA's finite element models for two dimensional hydrodynamics and water quality. In *Proceedings of the Second Conference on Finite Element Water Resources*, pp. 2.81–2.99.

3.153. Tanaka T., Ono Y., Ishise T. and Nakata K. (1982) Simulation analysis for diffusion of discharged warm water in the bay by finite elements. In *Finite Elements in Water Resources* (Ed. by K.P. Holz et al.), pp. 15.31–15.41. Springer-Verlag.

3.154. Zienkiewicz O.C., Bettess P. and Kelly D.W. (1978) The finite element method for determining fluid loading on rigid structures – two- and three-dimensional formulations. In *Numerical Methods in Offshore Engineering* (Ed. by O.C. Zienkiewicz et al.), pp. 141–83. Wiley, New York.

3.155. Austin D.I. and Bettess P. (1982) Longshore boundary conditions for numerical wave models. *Int. J. Num. Meth. Fluids*, **2**, 263–76.

3.156. Taylor C., Patil B.S. and Zienkiewicz O.C. (1969) Harbour oscillation – a numerical treatment for undamped natural modes. *Proc. Inst. Civ. Eng.*, **43**, 141–56.

3.157. Connor J.J. and Brebbia C.A. (1976) *Finite Element Techniques for Fluid Flow*. Newnes, Butterworth, London.

3.158. Zienkiewicz O.C and Heinrich J.C. (1979) A unified treatment of steady-state shallow water and two-dimensional Navier–Stokes equations – finite element penalty function approach. *Comput. Mech. Appl. Mech. Eng.*, **17/18**, 673–98.

3.159. Byrne P.M. and Janzen W. (1981) SOILSTRESS: a computer program for non-linear analysis of stress and deformation in soil. *Soil Mech. Ser.*, no. 52, University of British Columbia.

3.160. Duncan J.M. and Chang C.Y. (1970) Non-linear analysis of stress and strain in soils. *J. Soil. Mech. Found. Div., ASCE*, **96**(SM5), 1629–51.

3.161. Duncan J.M., Byrne P.M., Wong K.S. and Mabry P. (1980) Strength stress–strain and bulk modulus parameters for finite element analyses of stresses and movements in soil masses. *Report No. UCB/GT/78–02*. Department of Civil Engineering, University of California, Berkeley.

3.162. Duncan J.M., D'Orazio T.B., Chang C.S., Wong K.S. and Namiq L.I. (1981) CON2D: a finite element computer program for analysis of consolidation. *Report No. UCB/GT/81–01*. US Army Engineers Waterways Experiment Station, Vicksburg, MS, USA.

3.163. Lee M.K.W. and Liam Finn W.D. (1978) DESRA-2: dynamic effective stress response analysis soil deposits with energy transmitting boundary including assessment of liquefaction parameters. *Report No. 38, Soil Mech. Ser.* Department of Civil Engineering, University of British Colombia, Vancouver.

3.164. Martin P.P. (1975) *Non-Linear Methods for Dynamic Analysis of Ground Response*. PhD Thesis, Department of Civil Engineering, University of California, Berkeley.

3.165. Princeton University Computer Centre (1981) DYNAFLOW – a nonlinear transient finite element analysis program. Princeton University, Princeton, NJ.

3.166. Ungless R.F. (1973) *An infinite element*. MSc Thesis, Department of Civil Engineering, University of British Columbia, Vancouver.

3.167. Stevenson J. (1980) Current-summary of international extreme load design requirements for nuclear power plant facilities. *Nucl. Eng Des.*, **60**.

3.168. Riera J. (1980) A critical reappraisal of nuclear power plant safety against accidental aircraft impact. *Nucl. Eng Des.*, **57**.

3.169. Ribora B., Zimmermann Th. and Wolf J.P. (1976) Dynamic Rupture Analysis of R.C. Shells. *Nucl. Eng Des.*, **37**, 269–77.

3.170. Davie N.T. and Richgels M.A. (1983) GNOME: an earth penetrator code. *Sandia Report 82–2358*. Sandia Laboratories, USA.

3.171. Cherry J.T. (1967) Explosion in soils. *Int. J. Rock Mech.*, **4**, 1–22.

4 Blasts and Explosion Dynamics

4.1. Whitney C.S., Anderson B.G. and Cohen E. (1955) Design of blast construction for atomic explosions. *J. Am. Concrete Inst.*, **26**(7), 589–695.

4.2. Glasstone S. (Ed.) (1962) The effects of nuclear weapons. United States Atomic Energy Commissions, revised edition.

4.3. Azo K. (1966) *Phenomenon Involved in Presplitting by Blasting*. Doctoral dissertation, Stanford University, Palo Alto, USA.

4.4. Banks D.C. (1968) Selected methods for analyzing the stability of crater slopes. *Miscellaneous Paper S-68-8*. USA Waterways Experiment Station.

4.5. Barker D.B., Fourney W.L. and Holloway D.C. (1979) Photoelastic investigation of flaw initiated cracks and their contribution to the mechanisms of fragmentation. 21st Symposium on Rock Mechanics, Austin, TX, June 1979.

4.6. Bickel J.O. and Kuesel T.R. (Eds) (1982) *Tunnel Engineering Handbook*. Van Nostrand Reinhold, New York.

4.7. Blindheim O.T. (1976) Preinvestigations resistance to blasting and drillability predictions in hard rock tunnelling, mechanical boring or drill and blast tunnelling. First US – Swedish Underground Workshop, Stockholm, pp. 81–97.

4.8. Bowden F.P. and Yoffe A.D. (1962) *Initiation and Growth of Explosions in Liquid and Solids*. Cambridge University Press, Cambridge, UK.

4.9. Brown F.W. (1941) Theoretical calculations for explosives. *US Bureau of Mines Technical Publication No. 632*.

4.10. Bullock R.L. (1975) Technological review of all-hydraulic rock drills. *Transactions of the American Institute of Mining, Metallurgical, and Petroleum Engineers – Society of Mining Engineers*, preprint no. 75-Au-42.

4.11. Bullock R.L. (1976) An update of hydraulic drilling performance. *American Institute of Mining, Metallurgical, and Petroleum Engineers, Rapid Excavation and Tunnelling Conference*, pp. 627–48. Las Vegas.

4.12. Clark G.B. (1959) Mathematics of explosives calculations. Fourth Symposium on Mining Research. *University of Missouri School of Mines and Metallurgy Bulletin Technical Series No. 97.32–80.*

4.13. Clark G.B. (1979) Principles of rock drilling. *Colo. School Mines Q.*, **74**(2).

4.14. Clark G.B., Bruzewski R.F., Yancik J.J., Lyons J.E. and Hopler R. (1961) Particle characteristics of ammonium nitrate and blasting agent performance. *Colo. School Mines Q.*, **56**, 183–98.

4.15. Clark G.B. and Maleki H. (1978) Basic operational parameters of an automated plug and feather rock splitter. Sponsored by National Science Foundation, NSF Ap73-07486-A02, Colorado School of Mines, USA.

4.16. Cook M.A. (1958) *The Science of High Explosives*. Reinhold, New York.

4.17. Crow S.C. and Hurlburt G.H. (1974) The mechanics of hydraulic rock cutting. Second International Symposium on Jet Cutting Technology, Cambridge, UK, Paper E1.

4.18. Cunningham C. (1983) The Kuz-Ram model for prediction of fragmentation from blasting. *First International Symposium on Rock Fragmentation by Blasting*, Vol. 2, pp. 439–52. Lulea, Sweden.

4.19. Dick R.A. and Gletcher L.R. (1973) A study of fragmentation from bench blasting in limestone at reduced scale. *US Bureau of Mines Report of Investigations No. 7704.*

4.20. Dinsdale J.R. (1940) Ground failure around excavations. *Trans. Inst. Min. Metall. L.*

4.21. Ditson J.D. (1948) Determining blow energy of rock drills. *Compressed Air Magazine*, **53**(1), 15–16.

4.22. Duvall W.I. (1953) Strain wave shapes in rock near explosions. *Geophysics*, **18**, 310–23.

4.23. Duvall W.I. and Atchison T.C. (1957) Rock breakage by explosives. *US Bureau of Mines Report of Investigations No. 5356.*

4.24. Fairhurst C. (1961) Wave mechanics in precursive drilling. *Mining Quarry Eng.*, **27**.

4.25. Fairhurst C. and Lacabanne W.D. (1957) Hard rock drilling techniques. *Mining Quarry Eng.*, **23**, 157–74.

4.26. Field J.E. and Ladegaarde-Pedersen A. (1971) The importance of the reflected wave in blasting. *Int. J. Rock Mech. Mining Sci.*, **8**, 213–26.

4.27. Fogelson D.E., Duvall W.I. and Atchison T.C. (1959) Strain energy in explosive-generated strain pulses. *US Bureau of Mines Report of Investigations No. 5514.*

4.28. Hino K. (1959) *Theory and Practice of Blasting.* Nippon Kayaku Co, Japan.

4.29. Hornsey E.E. and Clark G.B. (1968) Comparison of spherical elastic viogt and observed wave forms for large underground explosions. Tenth Symposium on Rock Mechanics, Austin, TX.

4.30. Jost W. (1946) *Explosion and Combustion Processes in Gases.* McGraw-Hill, New York.

4.31. Kutter H.K. and Fairhurst C. (1971) On the fracture process in blasting. *Int. J. Rock Mech. Min. Sci.*, **8**, 181–202.

4.32. Lean D.J. and Paine G.G. (1981) Preliminary blasting for a bucket wheel excavator operation at COCA Coonyella Mine, Central Queensland. Australian Mineral Foundation Workshop Course, No. 152/81.

4.33. Lee H.B. and Akre R.L. (1981) Blasting process (patent). *US Patent 2,703,528.* US Patent-Office, Washington.

4.34. Lounds C.M. (1986) Computer modelling of fragmentation from an array of shotholes. *First International Symposium on Rock Fragmentation by Blasting*, Vol. 2, pp. 455–68. Lulea, Sweden.

4.35. Lundquist R.G. and Anderson C.F. (1969) Energetics of percussive drills – longitudinal strain energy. *US Bureau of Mines Report of Investigation No. 7329.*

4.36. Mason C.M. and Aiken E.G. (1972) Methods of evaluating explosives and hazardous materials. *US Bureau of Mines Information Circular No. 8541.*

4.37. Morrell J.R. and Larsen D.A. (1974) Disk cutter experiments in metamorphic and igneous rocks – tunnel boring technology: *US Bureau of Mines Report of Investigations No. 7691.*

4.38. National Fire Protection Association (1962) Blasting agents. In *Code for the Manufacture, Transportation, Storage and Use of Explosive and Blasting Agents*, no. 495, pp. 25–9.

4.39. Nikonov G.P. and Goldin Y.A. (1972) Coal and rock penetration by fine, continuous high pressure water jets. First International Symposium on Jet Cutting Technology, BHRA, Coventry, UK, paper E2.

4.40. Obert L. and Duvall W.I. (1950) Generation and propagation of strain waves in rock. Part 1. *US Bureau of Mines Report of Investigations No. 4683*.

4.41. Peele R. and Church J.H. (1941) *Mining Engineers Handbook*. Wiley, New York.

4.42. Pons L. et al. (1962) Sur la fragilisation superficielle au cours de frottement de carbures de tungstens frittes. *Academie des Sciences, Paris*, **225**, 2100.

4.43. Rad P.F. and Olson R.C. (1974) Tunneling machine research: size distribution of rock fragments produced by rolling disc cutters. *US Bureau of Mines Report of Investigations No. 7882*.

4.44. Roxborough F.F. and Rispin A. (1972) Rock excavation by disc cutter. Report to Transport and Road Research Laboratory of the Department of Environment, University of Newcastle-upon-Tyne, UK.

4.45. Roxborough F.F. and Phillips H.R. (1975) Rock excavation by disc cutter. *Int. J. Rock Mech. Min. Sci.*, **12**, 361–6.

4.46. Ryd E. and Holdo J. (1953) Percussive rock drills. In *Manual on Rock Blasting*. Atlas Deisel and Saudvikens, Stockholm.

4.47. Sharpe J.A. (1942) The production of elastic waves by explosion pressure. I. Theory and empirical field observation. *Geophysics*, **17**(3), 144–55.

4.48. Tarkoy P.J.J. (1973) Predicting TBM penetration rates in selected rock types. In *Proceedings, Ninth Canadian Rock Mechanics Symposium*, pp. 263–74. Montreal.

4.49. Van Dolah R.W. and Malesky J.S. (1962) Fire and explosion in a blasting agent mix building, Norton Virginia. *US Bureau of Mines Report of Investigations No. 6015*.

4.50. Van Dolah R.W., Gibson F.C. and Murphy J.N. (1966) Sympathetic detonation of ammonium nitrate and ammonium nitrate – fuel oil. *US Bureau of Mines Report of Investigations No. 6746*.

4.51. Van Dolah R.W., Mason C.M., Perzak F.J.P. and Forshey D.R. (1966) Explosion hazards of ammonium nitrate under fire hazard. *US Bureau of Mines Report of Investigations No. 6773*.

4.52. (1965) Structures to Resist the Effects of Accidental Explosions. *TM 5–1300*. Department of the Army, Washington DC.

4.53. Okamoto S., Tamura C., Kato K. and Hamada M. (1973) Behaviors of submerged tunnels during earthquakes. *Proceedings, Fifth World Conference on Earthquake Engineering*, Vol. 1, pp. 544–53. Rome, Italy.

4.54. Wyllie L.A., McClure F.E. and Degenkolb H.J. (1973) Performance of underground structures at the Joseph Jensen Filtration Plant. *Proceedings, Fifth World Conference on Earthquake Engineering*. Rome, Italy.

4.55. Lewis B. and Von Elbe G. (1961) *Combustion, Flames and Explosions of Gases*. Academic Press, USA.

4.56. Bradley J.N. (1969) *Flame and Combustion Phenomena*. Chapman & Hall, London.

4.57. Andrews G.E. and Bradley D. (1972) Determination of burning velocities, a critical review. *Combust. Flame*, **18**, 133. See also The burning velocity of methane–air mixtures. *Combust. Flame*, **19**, 275.

4.58. Perry R.H. and Chilton C.H. (1973) *Chemical Engineers' Handbook*, 5th edn. McGraw-Hill, New York, USA.

4.59. Zabetakis M.G. (1965) Flammability characteristics of combustible gases and vapours. *US Bureau of Mines Bulletin 627*.

4.60. Gibbs G.J. and Calcote H.F. (1959) Effect of molecular structure on burning velocity. *J. Chem. Eng. Data*, **5**, 226.

4.61. Egerton A. and Lefebvre A.H. (1954) The effect of pressure variation on burning velocities. *Proc. R. Soc. A222*, 206.

4.62. Dugger G.L. (1962) Effect of initial mixture temperature on flame speed of methane air, propane air and ethylene air mixtures. *NASA Report 1061*. National Aeronautics and Space Administration, USA.

4.63. Cubbage P.A. (1959) Flame traps for use with town gas air mixtures. *Inst. Gas Engineers, Communication GC 63*.

4.64. Cubbage P.A. (1963) The protection by flame traps of pipes conveying combustible mixtures. *Second Symposium on Chemical Process Hazards, I. Chem. E.*

4.65. Rasbash D.J. and Rogowski Z.W. (1960) Gaseous explosions in vented ducts. *Combust. Flame*, **4**, 301.

4.66. Rasbash D.J. and Rogowski Z.W. (1961) Relief of explosions in duct systems. *First Symposium on Chemical Process Hazards, I. Chem. E.*, 58.

4.67. Rasbash D.J. and Rogoswki Z.W. (1963) Relief of explosions in propane air mixtures moving in a straight unobstructed duct. *Second Symposium on Chemical Process Hazards, I. Chem. E.*

4.68. Leach S.J. and Bloomfield D.P. (1973) Ventilation in relation to toxic and flammable gases in buildings. *Building Sci.*, **8**, 289.

4.69. *British Standard 5925, Code of Practice for Design of Buildings. Ventilation Principles and Designing for Natural Ventilation.* (Formerly CP3 Chapter 1(c).) British Standards Institute (1980).

4.70. British Gas Engineering Standard PS/SHAI, Code of Practice for hazardous Area Classification, part 1 – Natural Gas. (Draft, 1981).

4.71. Jost W. (1946) *Explosion and Combustion Processes in Gases*. McGraw Hill, New York, USA.

4.72. Bradley D. and Metcheson A. (1976) Mathematical solutions for explosions in spherical vessels. *Combust. Flame*, **26**, 201.

4.73. Nagy J., Conn W.J. and Verakis H.C. (1969) Explosion development in a spherical vessel. *US Bureau of Mines Report of Investigations 727*.

4.74. Donat C. (1977) Pressure relief as used in explosion protection. *Loss Prevention II*, p. 86. American Institute of Chemical Engineers.

4.75. Heinrich H.J. and Kowall R. (1971) Results of recent pressure relief experiments in connection with dust explosions. *Staub Reinhalting der Luft 31*, no. 4.

4.76. Bartknecht W. (1981) *Explosions, Course Prevention, Protection*. Springer Verlag, Berlin.

4.77. Maisey H.R. (1965) Gaseous and dust explosion venting – a critical review of the literature. *Chem. Process. Eng.*, **46**, 527.

4.78. Lee J.H.S. and Guirao C.M. (1982) Pressure development in closed and vented vessels. *Plant/Oper. Prog.*, **1**, 2, 75.

4.79. Harris G.F.P. and Briscoe P.G. (1967) The venting of pentane vapour air explosion, in a large vessel. *Combust. Flame*, **11**, 329.

4.80. Zalosh R.G. (1979) Gas explosion tests in roomlike vented enclosures. *Thirteenth Loss Prevention Symposium, A. I. Chem. E.*

4.81. Dragosavic M. (1972) Structural measures to prevent explosions of natural gas in multi-storey domestic structures. *Institute TNO (Delft) Report No. B1–72–604302520.*

4.82. Zeeuwen J.P. (1982) Review of current research at TNO into gas and dust explosions. *Proceedings of the International Conference on Fuel-Air Explosions.* McGill University, Montreal, Canada. University of Waterloo Press.

4.83. Palmer H.N. (1956) Progress review no. 38. A review of information on selected aspects of gas and vapour explosions. *J. Inst. Fuel*, **29**, 293.

4.84. Butlin R.N. (1975) A review of information on experiments concerning the venting of gas explosions in buildings. *Fire Research Note No. 1026.*

4.85. Bradley D. and Mitcheson A. (1978) The venting of gaseous explosions in spherical vessels I – theory. *Combust. Flame*, **32**, 221.

4.86. Bradley D. & Mitcheson A. (1978) The venting of gaseous explosions in spherical vessels II – theory and experiment. *Combust. Flame*, **32**, 237.

4.87. Cubbage P.A. and Simmonds W.A. (1957) An investigation of explosion reliefs for industrial drying ovens – II Back reliefs in box ovens, relief in conveyor ovens. *Trans. Inst. Gas Eng.*, **107**.

4.88. Rasbash D.J. (1969) The relief of gas and vapour explosions in domestic structures. *Fire Research Note No. 759.*

4.89. Rasbash D.J., Drysdale D.D. and Kemp N. (1976) Design of an explosion relief system for a building handling liquefied fuel gases. *I. Chem. E. Symp. Ser. No. 47.*

4.90. Marshall M.R. (1977) Calculation of gas explosion relief requirements. The use of empirical equations. *I. Chem. E. Symp. Ser. No. 49.*

4.91. Cubbage P.A. and Marshall M.R. (1972) Pressure generated in combustion chambers by the ignition of gas–air mixtures. *I. Chem. E. Symp. Ser. No. 33.*

4.92. Cubbage P.A. and Marshall M.R. (1974) Explosion relief protection for industrial plant of intermediate strength. *I. Chem. E. Symp. Ser. No. 39a.*

4.93. National Fire Protection Association (1974, revised 1978) *Booklet No. 68 – Guide for Explosive Venting.*

4.94. Department of Employment (1972) *Health and Safety at Work Booklet No. 22, Dust Explosion in Factories.* HMSO, London.

4.95. Runes E. (1972) Explosive venting. *A. I. Chem. E., Sixth Loss Prevention Symposium*, p. 63.

4.96. Yao C. (1973) Explosion venting of low strength equipment and structures. *A. I. Chem. E., Eighth Loss Prevention Symposium*, p. 1.

4.97. Rust A.E. (1979) Explosion venting for low pressure equipment. *Chem. Eng.*, p. 102.

4.98. Fairweather M. and Vasey M.W. (1982) A mathematical model for the prediction of overpressures generated in totally confined and vented explosions. *Nineteenth Symposium (International) on Combustion*, p. 645. The Combustion Institute.

4.99. Kinney G.F. (1962) *Explosive Shocks in Air.* Macmillan.

4.100. Glasstone S. and Dolan P.J. (1977) *The Effects of Nuclear Weapons*, 3rd edn. United States Department of Defense and United States Department of Energy.

4.101. Pritchard D.K. (1981) Breakage of glass windows by explosions. *J. Occ. Accidents*, **3**, 69.

4.102. Astbury N.F., West H.W.H., Hodgkinson H.R., Cubbage P.A. and Clare R. (1970) Explosions in load bearing brick structures. *British Ceramic Research Association Special Publication No. 68*.

4.103. Astbury N.F., West H.W.H. and Hodgkinson H.R. (1972) Experimental gas explosions report of further tests at Potters Marston. *British Ceramic Research Association Special Publication No. 74*.

4.104. Harris R.J., Marshall M.R. and Moppett D.J. (1977) The response of glass windows to explosion pressures. *I. Chem. E. Symp. Seri. No. 49*.

4.105. Thomas M., Wachob H.F. and Osteraas J.D. (1984) Investigation of bellows failure in coal gasification plant. *Failure Anal. Assoc. Rep. FaAA-84–3–7*.

4.106. Grady D.E. and Kipp M.E. (1987) Dynamic rock fragmentation. In *Fracture Mechanics of Rock* (Ed. by B.K. Atkinson), pp. 429–75. Academic Press, London.

4.107. Chou P.C. and Carleone J. (1977) The stability of shaped-charge jets. *J. Appl. Phys.*, **48**, 4187–95.

4.108. Grady D.F. (1982) Local inertia effects in dynamic fragmentation. *J. Appl. Phys.*, **53**, 322–5.

4.109. Kiang T. (1966) Random fragmentation in two and three dimensions. *Z. Astrophys.*, **64**, 433–9.

4.110. Silva-Gomes J.F., Al-Hassani S.T.S. and Johnson W. (1976) A note on times to fracture in solid perspex spheres due to point explosive loading. *Int. J. Mech. Sci.*, **18**, 543.

4.111. Lovall E., Al-Hassani S.T.S. and Johnson W. (1974) Fracture of spheres and circular discs due to explosive pressure. *Int. J. Mech. Sci.*, **16**, 193.

4.112. Al-Hassani S.T.S. and Johnson W. (1969) The dynamics of the fragmentation process for spherical shells containing explosives. *Int. J. Mech. Sci.*, **11**, 811.

4.113. Al-Hassani S.T.S. (1986) Explosive requirements and structural safety aspects in offshore decommissioning applications. Offshore Decommissioning Conference ODC86, Heathrow Penta.

4.114. Proctor J.F. (1970) Containment of explosions in water-filled right-circular cylinders. *Exp. Mech.*, **10**, 458.

4.115. McNaught L.W. (1984) *Nuclear Weapons and Their Effects*. Brasseys Defence Publishers, London.

4.116. Baker W.E., Cox P.A., Westine P.S., Kulesz J.J. and Strehlow A. (1983) *Explosion Hazards and Evaluation*. Fundamental Study in Engineering. Elsevier, Amsterdam.

4.117. Theofanous T.G., Nourkbakshs H.P. and Lee C.H. (1984) Natural circulation phenomena and primary system failure in station blackout accidents. Sixth Information Exchange Meeting on Debris Coolability, UCLA.

4.118. Butland A.T.D., Turland B.D. and Young R.L.D. (1985) The UKAEA PWR Severe Accident Containment Study. Thirteenth Water Reactor Safety Research Information Exchange Meeting, Washington DC.

4.119. Wooton R.O. and Avci H.I. (1980) MARCH (Meltdown Accident Response Characteristics) code description and users manual. *NUREG/CR-1711*. Nuclear Regulatory Agency, Washington DC, USA.

4.120. Allison C.M. et al. (1981) Severe core damage analysis package (SCDAP). *Code Conceptual Design Report EEG-CDAP-5397*. USA.

4.121. Wright R.V., Silberberg M. and Marino G.P. (1984) Status of the joint program of severe fuel damage research of the USNRC and foreign partners. Fifth International Meeting on Thermal Reactor Safety, Karlsruhe, Germany.

4.122. Butland A.T.D., Haller J.P., Johns N.A., Roberts G.J. and Williams D.A. (1984) Theoretical studies of primary system retention in PWR severe accidents. In *Proceedings of the ANS Topical Meeting on Fission Product Behaviour and Source Term Research*. Snowbird, Utah.

4.123. Wooton R.O., Cybulskis P. and Quayle S.F. (1984) MARCH2 (Meltdown Accident Response Characteristics) Code Description and Users Manual. *NUREG/CR-3988*. Nuclear Regulatory Agency, Washington DC, USA.

4.124. Butland A.T.D., Turland B.D. and Young R.L.D. (1985) The UKAEA PWR Severe Accident Containment Study. Thirteenth Water Reactor Safety Research Information Exchange Meeting, Washington, USA.

4.125. Yue D.D. and Cole T.E. (1982) BWR 4/MARK I Accident Sequence Assessment. *NUREG/CR-2825*. Nuclear Regulatory Agency, Washington DC, USA.

4.126. Cook D.H. et al. (1981) Station Blackout at Brown's Ferry Unit One – Accident Sequence Analysis. *NUREG/CR-2182*. Nuclear Regulatory Agency, Washington DC, USA.

4.127. Cook D.H. et al. (1983) Loss of DHR Sequence at Brown's Ferry Unit One – Accident Sequence Analysis. *NUREG/CR-2973*. Nuclear Regulatory Agency, Washington DC, USA.

4.128. Silberberg M. (1984) Completion of BWR MARK I, MARK II Standard Problems. NCR Memorandum. Nuclear Commission and Regulation, Washington DC, USA.

4.129. Speis T.P. et al. (1985) Estimates of early containment loads from core melt accidents. *NUREG/1079* (draft). Nuclear Regulatory Agency, Washington DC, USA.

4.130. Muir J.F., Cole R.K., Corradini M.L. and Ellis M.A. (1981) An improved model for molten core–concrete interactions. *SAND 80–2415*. Sandia Laboratory, California, USA.

4.131. Harrington R.M. and Ott L.J. (1983) MARCH 1.1 Code Improvements for BWR Degraded Core Studies. *NUREG/CR-3179*, B. Nuclear Regulatory Agency, Washington DC, USA.

4.132. Ghorbani A. (1990) *Three Dimensional Finite Element Analysis of Loss-of-Coolant Accident in PWR*. MPhil thesis, CNAA, UK.

4.133. Murfin W.B. (1977) A preliminary model for core/concrete interactions. *SAND-77/0370*. Sandia Laboratory, California, USA.

4.134. Industry Degraded Core Rulemaking, Nuclear Power Plant Response to Severe Accidents. Final Technical Summary, 1984. Sandia Laboratory, California, USA.

4.135. Berthion Y., Lhiaubet G. and Gauvin J. (1985) Aerosol behavior in the reactor containment building during a severe accident. Fission Product Behavior and source Term research (Proc. ANS Topical Meeting Snowbird, Utah, 1984), Electric Power Research Institute Report NP-4113-SR.

4.136. Bergeron K.D. et al. (1985) User's manual for CONTAIN 1.0. *Sandia Laboratories Reports, NUREG/CR-4085, SAND84–1204*. Nuclear Regulatory Agency, Washington DC, USA.

4.137. Fermandjian J., Bunz H., Dunbar I.H., Gauvin J. and Ricchena R. (1986) Comparison of computer codes relative to the aerosol behavior in the reactor containment building during severe core damage accidents in a PWR. Presented at the International Conference of the American Nuclear Society/ European Nuclear Society ANS/ENS Topical Meeting on Thermal Reactor Safety, San Diego.

4.138. Braun W., Hassmann K., Hennies H.H. and Hosemann J.P. (1984) The reactor containment of Federal German PWRs of standard design. International Conference on Containment Design, Toronto.

4.139. Alysmeyer H., Reimann M. and Hosemann J.P. (1984) Preliminary results of the KFK molten core concrete experimental BETA facility. Transactions of the 12th Water Reactor Safety Research Information Meeting, United States Nuclear Regulatory Commission Report NUREG/CP-0057. Nuclear Regulatory Agency, Washington DC, USA.

4.140. Henrt R.E. and Fauske H.K. (1981) Required initial conditions for energetic steam explosions. *Proceedings of the ASME Winter Meeting.* Washington DC.

4.141. Corrandini M.L. and Moses G.A. (1983) A dynamic model for fuel–coolant mixing. *Proceedings of the International Meeting on LWR Severe Accident Evaluation.* Cambridge, MA, 6.3–1.

4.142. Berman M. (1984) Molten core–coolant interactions program. *Proceedings of the Twelfth Water Reactor Safety Research Information Meeting.*

4.143. Corradini M.L. et al. (1984) Ex vessel steam explosions in the Mark II containment. University of Wisconsin Research Staff Report 7321.

4.144. Haskin F.E., Behr V.L. and Smith L.N. (1984) Combustion-induced loads in large-dry PWR containments. *Proceedings of the Second Containment Integrity Workshop.* Crystal City, VA.

4.145. Pong L., Corradine M.L. and Moses G.A. (1985) HMC: A containment code for severe accident sequence analysis. University of Wisconsin. Private communication.

4.146. Evans N.A. (1983) Status of core-melt programs, July–August 1983 (M. Berman and R.K. Cole, memorandum to T.J. Walker and S.B. Burson USNRC). US Nuclear Regulatory Commission).

4.147. Green G. (1984) Corium/concrete interaction in the Mark I containment drywell and local liner failure. *NUREG-1079*, appendix II. Nuclear Regulatory Agency, Washington DC, USA.

4.148. Gasser R.D. et al. (1984) MARCON Results for Mark I and II Containment Standard Problems, Letter to T. Pratt, Brookhaven National Laboratory, Sandia National Laboratories, USA.

4.149. Clauss D.B. (1985) Comparison of analytical predictions and experimental results for a 1:8-scale containment model pressurized to failure. NUREG/CR-4209, SAND85–0679 Nuclear Regulatory Agency, Washington, DC, USA and Sandia Laboratory, California, USA.

4.150. The Reactor Safety Study (1975) WASH 1400 (NUREG 75/014). Nuclear Regulatory Agency, Washington DC, USA.

4.151. Hillary J.J. et al. (1966) Iodine removal by a scale model of the S.G.H.W. Reactor Vented Steam Suppression System. TRG Report 1256. UK Atomic Energy Commission, Winfrith, Dorset, UK.

4.152. Hobbs B., Watson A.J. and Wright S.J. (1989) Explosive tests on model concrete bridge elements. Fourth International Symposium on the Interaction of Conventional Munitions with Protective Structures, Florida.

4.153. Baker W.E., Cox P.A., Westine P.S., Kulesz J.J. and Strehlow R.A. (1983) *Explosion Hazards and Evaluation*, chapter 2. Elsevier, Amsterdam, Oxford, New York.

4.154. Fleischer C.C. (1983) A study of explosive demolition techniques for heavy reinforced and prestressed concrete structures. *CEC Report No. EUR 9862 EN.*

4.155. Sheridan A.J. (1987) Response of concrete to high explosive detonation. In *Proceedings of the International Symposium on the Interaction of Non-Nuclear Munitions with Structures.* Mannheim.

4.156. Weerheijm J., van Zantyoort P.J.H. and Opschoor G. (1988) The applicability of the FE-technique to dynamic failure analysis of concrete structures. Twenty-third DoD Explosives Safety Seminar, Atlanta, Georgia, USA.

4.157. Cullis I. and Nash M. (1986) The use of fracture models in the theoretical study of explosive, metal interactions. In *Ninth International Symposium on Ballistics 2*, pp. 285–92. Shrivenham, UK.

4.158. Baylot J.T. et al. (1985) Fundamentals of protective design for conventional weapons. Structures Laboratory, US Army Engineer Waterways Experiment Station, Vicksburg, MS.

4.159. Crawford R.E. et al. (1971) Protection from nonnuclear weapons. *Technical Report No. AFWL-TR-70–127.* Air Force Weapons Laboratory, Kirtland AFB, NM, USA.

4.160. Whitney M.G. et al. (1986) Structures to resist the effects of accidental explosions Vol. II, blast, fragment and shock loads. *Special Publication ARLCD-SP-84001.* US Armament Research, Development and Engineering Center, Dover, NJ.

4.161. Baker W.E. et al. (1982) Manual for the prediction of blast and fragment loadings on structures. *DOE/TIC-11268.* US Department of Energy, Pantex Plant, Amarillo, TX, USA.

4.162. Marchand K.A. et al. (1986) Impulsive loading of special doors: flyer plate impact of heavily reinforced concrete blast doors test program results. Southwest Research Institute.

4.163. Coltharp D.R. et al. (1985) Blast response tests of reinforced concrete box structures – methods for reducing spall. *Proceedings of the Second Symposium on the Interaction of Nonnuclear Munitions with Structures.* Washington DC, USA.

4.164. Baylot J.T., Kiger S.A., Marchand K.A. and Painter K.T. (1985) Response of buried structures to earth-penetrating conventional weapons. *ESL-TR-85–09.* Engineering & Services Laboratory, Tyndall AFB, FL.

4.165. Marchand K.A. et al. (1988) Development of an alternate munition storage barrier system, phase II report tests of the barrier concepts. *Contract Report No. DACA88–86D-0017.* Delivery Order Nos. 002 002, 004 and 010. US Army Construction Engineering Research Laboratory. Vicksburg, MS, USA.

4.166. Marchand K.A. and Garza L.R. (1988) Countering explosive threats – analysis report, SWRI project 06–1473–090, Tecolote Research Inc., Santa Barbara, CA (subcontract TR187–107, NCEL prime contract no. 00123–86–D-0299).

4.167. Cockcroit F. (1982) The circumstances of sea collisions. *J. Navigation*, **35**, 100.

4.168. Marine Board (1983) Shop collisions with bridges: the nature of the accidents, their prevention and mitigation. Commission on Engineering and Technical Systems, National Research Council, Washington, DC.

4.169. Frandsen P. (1982) Accidents involving bridges. IABSE Colloquium on Ship Collision with Bridges and Offshore Structures – Copenhagen. *Proceedings IABSE*, **41**, 11.

4.170. United States Coast Guard (1980–83) Statistics of casualties. In *Proceedings of the Marine Safety Council*.

4.171. Standing and Brendling (1985) *Collisions of Attendant Vessels with Offshore Installations*, parts 1 and 2. National Maritime Institute Ltd, London.

4.172. Sibul K. (1954) Laboratory studies of the motion of freely floating bodies in non-uniform and uniform long crested waves. In *Proceedings of the First Conference on Ships and Waves*. Hoboken, NJ.

4.173. Bradford G. (1971) A preliminary report of the observation of sea ice pressure and its effect on merchant vessels under icebreaker escort. In *Proceedings of International Conference on Sea Ice*. Reykjavik, Iceland.

4.174. Yankelevsky D.Z. (1985) Elasto-plastic blast response of rectangular plates. *Int. J. Impact Eng.*, **3**(2), 107–19.

4.175. Gürke G., Bücking P. et al. (1987) Elasto-plastic response of steel plates to blast loads. In *Proceeding of the Tenth International Symposium on Military Application of Blast Simulation*, pp. 382–94. Bad Reichenhall, Federal Republic of Germany.

4.176. Forsén R. (1987) Increase of in-plane compressive forces due to inertia in wall panels subjected to air-blast loading. In *Proceedings of the Tenth International Symposium on Military Applications of Blast Simulation*, pp. 369–80. Bad Reichenhall, Federal Republic of Germany.

4.177. Bishop V.J. and Rowe R.D. (1967) The interaction of a long Friedlander shaped blast wave with an infinitely long circular cylinder. *AWRE Report 0–38/67*. Atomic Weapons Research Establishment, Aldermaston, Berkshire.

4.178. Salvatorelli-D'Angelo F. (1988) *Structural Stability Under Dynamic Loading of LNG Tanks*. PhD thesis, Oxford University.

4.179. Ross G.A., Strickland W.S. and Sierakowski R.L. (1977) Response and failure of simple structural elements subjected to blast loadings. *The Shock and Vibration Digest*, **9**(12).

4.180. Hall S.F., Martin D. and Mackenzie J. (1984) Gas cloud explosions and their effects on nuclear power plants, FLARE User Manual. EUR, first edition, EUR 8955EN, 1984.

4.181. Thompson V.K. (1985) *Structural Integrity of Liquid Natural Gas Storage Tanks*. PhD Thesis, Oxford University.

4.182. Dobratz B.M. (1981) LLNL Explosives Handbook. Properties of Chemical Explosives and Explosive Simulants. *LLNL Report UCRL-52997*. University of California Research Laboratory, Berkeley, CA, USA.

4.183. Bulson P.S. (1966) Stability of buried tubes under static and dynamic overpressure, part 1: circular tubes in compacted sand. *Research Report RES 47.5/7*. Military Engineering Experimental Establishment, Aldermaston, UK.

4.184. Marino R.L. and Riley W.F. (1964) Response of buried structures to static and dynamic overpressures. In *Proceedings of the Symposium on Soil–Structure Interaction*. University of Arizona, Tucson.

4.185. Albritton G.E., Kirkland J.L., Kennedy T.E. and Dorris A.F. (1966) The elastic response of buried cylinders. *Technical Report 1–750*. US Army Waterways Experiment Station, USA.

4.186. Dunns C.S. and Butterfield R. (1971) Flexible buried cylinders – part II: dynamic response. *Int. J. Rock Mech. Min. Sci.*, **8**, 601–12.

4.187. Gumbel J.E., O'Reilly M.P., Lake L.M. and Carder D.R. (1982) The development of a new design method for buried pipes. In *Proceedings of the Europipe Conference*, pp. 87–98. Basle.

4.188. Drake J.L., Frank R.A. and Rochefort M.A. (1987) A simplified method for the prediction of the ground shock loads on buried structures. In *Proceedings of the International Symposium on the Interaction of Conventional Munitions with Protective Structures*. Mannheim, West Germany.

4.189. Hinman E. (1989) Interaction of deformation and shock response for buried structures subject to explosions. In *Proceedings of the International Symposium on the Interaction of Non-Nuclear Munitions With Structures*. Panama City, FL.

4.190. Hinman E. (1989) Shock response of buried structures subject to explosions. In *Proceedings of the ASCE Speciality Conference on Structures for Enhanced Safety and Physical Security*. Arlington, VA.

4.191. Hinman E. (1988) Shock response of underground structures to explosions. Presented at the Eighth International Colloquium on Vibration and Shock, 14–16 June 1988, Ecole Centrale de Lyon, Ecully, France.

4.192. Weidlinger P. and Hinman, E. (1988) Analysis of underground protective structures. *J. Struct. Eng., ASCE*, **114**(7), 1658–73.

4.193. Wong F.S. and Weidlinger P. (1979) Design of underground protective structures. *J. Struct. Eng., ASCE*, **109**(8), 1972–1979.

4.194. Mazzá G., Minasola R., Molinaro P. and Papa A. (1987) Dynamic structural response of steel slab doors to blast loadings. *Proceedings of the International Conference on Computational Plasticity*. Barcelona, Spain.

4.195. Adushkin V.V. (1961) On the formation of a shock wave and the outburst of explosion products. IIMTφ, no. 5, AH CCCP, Mockba.

4.196. Alekseenko V.D. (1963) Experimental investigation of a dynamic stress field in soft soil produced by an explosion. IIMTφ, no. 5, AH CCCP, Mockba.

4.197. Alekseev N.A., Rakhmatulin KhA. and Sagomonyan A.Ya. (1963) On the fundamental equations of soil dynamics. IIMTΦ, no. 2, AH CCCP, Mockba.

4.198. Andreev K.K. and Belyaev A.F. (1960) Theory of explosives. No. 3, AH CCCP, Mockba.

4.199. Assonov V.A (1953) Blasting. No. 1, AH CCCP, Mockba.

4.200. Barkan D.D. (1948) Dynamics of Soils and Foundations. Mockba.

4.201. Brode H.L. (1959) Blast wave from a spherical charge. *The Physics of Fluids*, no. 2.

4.202. Enhamre R. (1954) The effects of underwater explosion on elastic structures in water. *Transactions of the Royal Institute of Technology*, bulletin no. 42. The Institution Hydraulics, Stockholm.

4.203. Hauptman L. (1954) *Handbook for Blasters*. SNTL, Prague, Hungary.

4.204. Heer J.E. (1965) *Response of Inelastic Systems to Ground Shock*. PhD Thesis, University of Illinois.

4.205. Henrych J. (1966) Plastická deformace oblouku pri dynamickém zatizeni (plastic deformation of arches subjected to a dynamic load). *Stavebnicky casopis SAV*, **XIV**, no. 6, Bratislava.

4.206. Henrych J. (1966) Plastická deformace kopuli pri dynamickém zatizeni (plastic deformation of domes subjected to a dynamic load). *Stavebnicky casopis SAV*, **XIV**, Bratislava.

4.207. Henrych J. (1966) Intenzivni dynamické zatizeni kruhovych desek (intensive dynamic loading of circular plates). *Strojnicky casopis*, **XVII**, no. 2, Bratislava.

4.208. Ivanov P.L. (1967) Consolidation of cohensionless soils by explosion, no. 3, AH CCCP, Mockba.

4.209. Yakolev Yu S. (1961) Hydrodynamics of explosion. No. 6, AH CCCP, Mockba.

4.210. Pokrovskil G.I. and Fedorov I.S. (1957) Effect on shock and explosion in deformable media. Mockba.

4.211. Salamakhin T.M. (1969) Effect of explosion on structure elements. Mockba.

4.212. Seismology and Explosion Craters of Underground Explosions. Collection of Essays, Mockba 1968.

4.213. Chou P., Karpp R.R. and Huang S.L. (1967) Numerical calculation of blast waves by the method of characteristics. *AIAA J.*, **5**(4), 618–23.

4.214. Cowan G. et al. (1970) The present status of scientific application of nuclear explosives. *Proceedings of a Symposium on Engineering with Nuclear Explosives*, Las Vegas, Nevada p. 216.

4.215. Vlasov O.E. (1965) Principles of explosion dynamics. Mockba.

4.216. Butkovich T.R. (1965) Calculation of the shock wave from an underground nuclear explosion granite. *J. Geophys. Res.*, **70**, 885–92.

4.217. Johnson G.W. and Higgins G.H. (1965) Engineering applications of nuclear explosives: project plowshare. *Rev. Geophys.*, **13**(3), 365–85.

4.218. Johnson G.W. (1964) Excavating with nuclear explosives. *Discovery*, **25**(11), 16.

4.219. Kestenbolm KH.S., Roslyakov G.S. and Chudov L.A. (1974) Point explosion. Hayka, Mockba.

4.220. Kirkwood J.G. and Bethe H.A. (1967) In *John Gamble Kirkwood Collected Works – Shock and Detonation Wayes* (Ed. by W.W. Wood et al.), p. 1. Wiley, New York.

4.221. Knox J. (1969) Nuclear excavation, theory and applications. *Nucl. Appl. Technol.*, **7**(3), 189–231.

4.222. Kot C.A. (1970) *Point Source Underwater Explosions*. PhD Thesis, Illinois Institute of Technology.

4.223. Kyrpin A.V., Solovev V.Ya., Sheftel N.I. and Kobelev A.G. (1975) Deformation of metals by explosion. MCCCP 6, Mockba.

4.224. Le Mehaute B. (1971) Theory of explosions-generated water waves. *Adv. Hydrosci.*, **7**, 1.

4.225. Lorenz H. (1955) *Dynamik im Grundbau*. Grundbau Taschenbuch, B.I. Berlin.

4.226. Mueller R.A. (1969) Prediction of seismic motion from contained and excavation nuclear detonations. In *Proc. Symp. Eng. Nucl. Explosives, US Atomic Energy Commission.*

4.227. Mueller R.A. (1969) Seismic energy efficiency of underground nuclear detonations. *Bull. Soc. Am.*, **59**, 2311–23.

4.228. Parkin B.R., Gilmore F.R. and Brode H.L. (1961) Shock waves in bubbly water. Memorandum RM-2795-PR (abridged). US Atomic Energy, Washington DC, USA.

4.229. Sternberg H.M. and Walker W.A. (1970) Artificial viscosity method calculation of an underwater detonation. Fifth Symp. (Intl) on Detonation, ONR Report DR-163.

4.230. Shurvalov L.V. (1971) Calculation of large underwater explosions. MCCCP No. 5, Mockba.

4.231. Newmark N.M. (1956) An engineering approach to blast-resistant design. *Trans. ASCE*, 2786.

4.232. Taylor J. (1952) *Detonation in Condensed Explosives*. Clarendon Press, Oxford.

4.233. Cook M.-A. (1958) *The Science of High Explosives*. Reinhold, New York.

4.234. Duvall W.I. and Atchison T.C. (1957) Rock breakage by explosives. *Bureau of Mines Report No. 5356*.

4.235. Atchison T.C. and Tournay W.E. (1959) Comparative studies of explosives in granite. *Bureau of Mines Report No. 5509*.

4.236. Atchison T.C., Duvall W.I. and Pugliese J.P. (1964) Effect of decoupling on explosion-generated strain pulses in rocks. *Bureau of Mines Report No. 6333*.

4.237. Bur T.R., Colburn L.W. and Slykhouse T.E. (1967) Comparison of two methods for studying relative performance of explosives in rock. *Bureau of Mines Report No. 6888*. USA.

4.238. Livingston C.W. (1956) Fundamental concepts of rock failure. *Colorado School of Mines Q*, **51**, no. 3. USA.

4.239. Bauer A. (1984) Crater method formulas – a criticism. *E. M. J.*, **166**, no. 7.

4.240. Grant C.N. (1964) Simplified explanation of crater method. *E. M. J.*, **165**, no. 11, 86–9.

4.241. Slykhouse T.E. (1965) Empirical methods of correlating explosive cratering results. *Seventh Symposium on Rock Mechanics*, Vol. 1, pp. 22–47. The Pennsylvania State University, University Park, PA, 14–16 June 1968.

4.242. Hino K. (1956) Fragmentation of rock through blasting and shock wave theory of blasting. *Quarterly Colorado School of Mines*, **51**, no. 3.

4.243. Pearse G.E. (1955) Rock blasting – some aspects on theory and practice. *Mines Quarry Eng.*, **21**, 25–30.

4.244. Noren C.H. (1956) Blasting experiments in granite rock. *Quart. Colorado School Mines*, **51**(3), 210–25.

4.245. Clay R.B., Cook M.A., Cook V.O., Keyes R.T. and Udy L.L. (1965) Behaviour of rock during blasting. *Seventh Symposium on Rock Mechanics*, Vol. 2, pp. 438–61. The Pennsylvania State University, University Park, PA.

4.246. Langefors U. and Kihlström K. (1963) *The Modern Technique of Rock Blasting*. Wiley, New York.

4.247. Langefors U. (1965) Fragmentation in rock blasting. *Seventh Symposium on Rock Mechanics*, Vol. 1, pp. 1–21.

4.248. Johnson J.B. (1962) Small-scale blasting in mortar. *Bureau of Mines, Report No. 6012*.

4.249. Bergmann O.R., Riggle J.W. and Wu F.C. (1973) Model rock blasting – effectiveness of explosive properties and other variables on blasting results. *Int. J. Rock Mech. Min. Sci. Geomech. Abstr.*, **10**, 585–612.

4.250. Hilliar H.W. (1949) *Report R.E. 142/119*. British Scientific Research, UK.

4.251. Hudson G.E. (1943) TMB Report 509, 1943, United Kingdom.

4.252. Jones H. Report RC-166 1941, United Kingdom.

4.253. Jones H. Report RC-212 1941, United Kingdom.

4.254. Jones H. Report RC-383 1943, United Kingdom.

4.255. Kirkwood J.G. et al. The pressure wave produced by an underwater explosion:
   (a) Basic Propagation Theory. *OSRD*, 588, 1942.
   (b) Properties of Pure Water at a Shock Front. *OSRD*, 676, 1942.
   (c) Properties of Salt Water at a Shock Front. *OSRD*, 813, 1942.
   (d) Calculations of initial conditions, superseded by V and *OSRD*, 3949, 1942.
   (e) Calculations for thirty explosives. *OSRD*, 2022, 1943.
   (f) Calculations for cylindrical symmetry. *OSRD* 2023, 1943.
   (g) Final report on propagation theory for cylindrical symmetry. *OSRD*, 3950, 1944.

4.256. Kirkwood J.G. and Brinkley S.R. Jr. (1945) Theory of propagation of shock waves from explosive sources in air and water. *OSRD*, 4814.

4.257. Kirkwood J.G. and Richardson J.M. (1944) The plastic deformation of circular diaphragms under dynamic loading by an underwater explosion wave. *OSRD*, 4200 1944. Plastic deformation of marine structures by an underwater explosion. *OSRD*, 793, 1115.

4.258. Penney W.G. and Dasgupta H.K. (1942) *British Report RC-333*.

4.259. The NFPA Fire Code 68, National Fire Protection Association, USA, 1981.

4.260. The NFPA Fire Code 70, National Fire Protection Association, USA, 1983.

4.261. *Report TM55–1300*. Nuclear Regulatory Agency, USA, 1983.

4.262. Coles J.S. (1946) *Report OSRD 6240*.

4.263. Coles J.S. (1946) *Report OSRD 6241*.

4.264. Taylor G.I. (1946) The air wave surrounding an expanding sphere. *Proc. Roy. Soc. A.*, **186**, 273.

4.265. Cole R.H. and Coles J.S. (1947) Propagation of spherical shock waves in water. *Phys. Rev.*, **71**, 128.

4.266. Cole R.H. (1948) *Underwater Explosions*. Princeton University Press, USA.

4.267. Terzaghi K. (1943) *Theoretical Soil Mechanics*. Wiley, New York.

4.268. Kiger S.A., Eagles P.S. and Baylot J.T. (1984) Response of earth-covered slabs in clay and sand backfills. Technical Report SL-84-18, AD-A149296, Waterways Experiment Station, Structures Laboratory, Vicksburg, MS, October 1984.

4.269. Weidlinger P. and Hinman E. (1988) Analysis of underground protective structures. *ASCE, J. Struct. Eng.*, **114**(7).

4.270. Drake J.L. Walker R.E. and Slawson T. (1989) Backfill effect on buried structure response. Proc. of the Fourth International Symposium on the Interaction of Non-Nuclear Munitions with Structures, Vol. 2, Panama City Beach, FL, April, 1989.

4.271. Kiger S.A. and Getchell J.V. (1980) Vulnerability of shallow-buried flat roof structures; Report 1, Foam HEST 1 and 2. Technical Report SL-80-7, Waterways Experiment Station, Structures Laboratory, Vicksburg, MS, September 1980.

4.272. Chen H.L. (1988) *Dynamic response of embedded structures*. Ph.D. Thesis, Department of Civil Engineering, Northwestern University, Evanston, IL.

4.273. Chen H.L., Shah S.P. and Keer L.M. (1990) Dynamic response of shallow-buried cylindrical structures. *J Eng. Mech.*, **116**(1).

4.274. Dancygier A.N. (1991) *Response of shallow-embedded structures to surface impact loading.* Ph.D. Thesis, Department of Civil Engineering, Northwestern University, Evanston, IL, 1991.

4.275. Taylor E.S. (1974) *Dimensional Analysis for Engineers.* Clarendon Press, Oxford.

4.276. Rudeen D.K. and Rath J.S. (1986) SAMSON2, A Nonlinear Two-Dimensional Structure-Media Interaction Computer Code: User's Manual (Revised). New Mexico Engineering Research Institute, University of New Mexico, Albuquerque, New Mexico, September, 1986.

4.277. Galiev U. (1996) Experimental observations and discussion of counterintuitive behavior of plates and shallow shells subjected to blast loading. *Int. J. Impact Eng.*, **18**(7–8), 783–802.

4.278. Krauthammer T. and Ku C. (1996) A hybrid computational approach for the analysis of blast resistant connections. *Comput. Struct.*, **61**(5), 831–43.

4.279. Smith P., Rose T. and Saotonglang E. (1999) Clearing of blast waves from building facades. Proceedings of Institution of Civil Engineers: Structures and Buildings, Vol. 134, pp. 193–199.

4.280. Pan. Y. and Louca, L. (1999) Experimental and numerical studies on the response of stiffened plates subjected to gas explosions. *J. Construct. Steel Res.*, **52**, 171–93.

4.281. Louca L., Boh J. and Choo Y. (2004) Design and analysis of stainless steel profiled blast barriers. *J. Construct. Steel Res.*, **60**, 1699–1723.

4.282. Boh J., Louca L. and Choo Y. (2004) Numerical assessment of explosion resistant profiled barriers. Marine Struct., **17**, 139–160.

4.283. ABAQUS/Standard 5.7-3: User's Manual, 1997.

4.284. Davis Robert N. (2003) Modeling of high-speed friction using multi-step incrementation of the coefficient of sliding friction, A1AA 54th Annual Southeastern Regional Student Conference, Kill Devil Hills, NC, March 27–28, 2003.

4.285. Davis Robert N. Jones, S.E. and Hughes, Mary L. (2003) High-speed penetration of concrete using a new analytical model of velocity-dependent friction, *Thermal-Hydraulic Problems, Sloshing Phenomena, and Extreme Loads on Structures, ASME-PVP* (to appear).

4.286. Davis Robert N., Neely Amanda M. and Jones S.E. (2003) Mass loss and blunting during high-speed penetration, *J. Mech. Eng. Sci., Proceedings of the Institution of Mechanical Engineers, Part C* (submitted for publication).

4.287. Kragelskii I.V. (1965) *Friction and Wear*, Butterworths, Inc., Washington, DC.

4.288. Jones S.E., Davis Robert N., Hughes Mary L., Toness Odin A. (2002) Penetration with high-speed friction, *Thermal-Hydraulic Problems, Sloshing Phenomena, and Extreme Loads on Structures, PVP-Vol. 435*, F.J. Moody, ed., pp. 255–262.

4.289. Jerome D.M., Tynon R.T., Wilson L.L. and Osborn J.J. (2000) Experimental observations of the stability and survivability of ogive-nosed, high-strength steel alloy projectiles in cementious materials at striking velocities from 800–1800 m/sec. Third Joint Classified Ballistics Symposium, San Diego, CA, May 1–4, 2000.

4.290. Davie T.N. and Richgels A.M. (1983) An earth penetrator code. Sandia Report – (SAND-82-2358), Sandia National Laboratories, Livermore, CA.

4.291. Kar A.K. (1978) Projectile penetration into buried structures. *J. Struct. Div.*, ASCE, Paper 13479STI.

4.292. Henrych J. (1979) *The Dynamic of Explosion and Its Use.* Elsevier, Amsterdam.

4.293. Glasstone S. and Dolan P.J. *The Effects of Nuclear Weapons.* US Department of Defense, Washington.

4.294. Jones N. and Wierzbicki T. (1961) Structural crash worthiness. Butterworths, London Morrow C.T., Smith M.R. (1961) *Ballistic Missile and Aerospace Technology. Proc. 6th Symp.*, Academic Press, New York.

4.295. FIP Concrete for hazard protection. First International Conference on Concrete Society, Edinburgh.

4.296. Abaham L.M. Structural design of missiles and space-craft. McGraw Hill, New York.

4.297. BAM (1982) *Concrete Structures Under Impact and Impulsive Loading.* Bundesanstalt für Materialprüfung, Berlin.

4.298. Macmillan R.H. Dynamics of vehicle collisions. Special Publications SP5, Interscience Enterprises, Jersey, UK.

4.299. Taylor D.W. and Whitman R.V. (1953) The behaviour of soils under dynamic loadings. 2. Interim report on wave propagation and strain-rate effect, MIT Report AFSWP-117.

4.300. Maurer W.C. (1959) Impact crater formation in sandstone and granite. Master's thesis submitted to Colorado School of Mines, Colorado, U.S.A.

4.301. Rinehart J.S. (1980) Stresses associated with lunar landings. Contribution no. 11, Mining Research Laboratory Colorado School of Mines.

4.302. Tolch N.A. and Bushkovitch A.V. (1947) Penetration and crater volume in various kinds of rocks as dependent on caliber, mass and striking velocity of projectile. BRL Report No. 641, UK.

4.303. NDRC (1946) Effects of impact and explosion. Summary Technical Report of Div. 2, National Design and Research Corporation (NDRC), Vol. 1. Washington DC.

4.304. Lang H.A. (1956) Lunar instrument carrier – landing factors. Rand RM-1725, ASTIA Doc. no. AD 112403.

4.305. Palmore J.I. (1961) Lunar impact probe. *ARS J.*:1066–1073.

4.306. Rinehart J.S. (1960) Portions of traite de balistique experimentale which deal with terminal ballistics. Chapters III, IV, V and XIV, Félix Hélie, Paris (1884), Naval Ordnance Test Station TM RRB-75.

4.307. Dennington R.J. (1958) Terminal ballistics studies. Proj. Doan Brook Tech. Memo. no. 20 Case Inst., ASTIA AD 146 913.

4.308. Kornhauser M. (1958) Prediction of cratering caused by meteoroid impacts. *J. Astron. Sci.* **V**(3–4).

4.309. Rinehart J.S. and Pearson J. (1954) Behaviour of metals under impulsive loads. American Society for Metals, Cleveland.

4.310. Rinehart J.S. and White W.C. (1952) Shapes of craters formed in plaster-of-paris by ultra-speed pellets. *Am. J. Phys.*, **20**(1).

4.311. Gazley C. Jr. (1957) Deceleration and heating of a body entering a planetary atmosphere from space. RAND Corporation Report P-955, USA.

4.312. Lees L., Hartwig F.W. and Cohen C.B. (1959) Use of aerodynamic lift during entry into the earth's atmosphere. *ARS J.*, 633–41.

4.313. Lowe R.E. and Gervais R.L. (1961) Manned entry missions to Mars and Venus. In: *ARS Space Flight Report to the Nation*, Paper 2158–61, New York.

4.314. Turnacliff R.D. and Hartnett J.P. (1957) Generalized trajectories for free-falling bodies of high drag. ARS Paper 543-57, 12th Annual Meeting, New York, 2–5 December 1957.

4.315. Creighton D.C. (1982) Non-normal projectile penetration in soil and rock: User's guide for computercode PENCO2D. Technical Report SL-82-7, US Army Engineering Waterways Experiment Station, Vicksburg, MS.

4.316. Young C.W. (1972) Empirical equations for predicting penetration performance in layered earth materials for complex penetrator configurations. Development Report No. SC-DR-72-0523, Sandia National Laboratory, Albuquerque, NM.

4.317. Young C.W. (1985) Simplified analytical model of penetration with lateral loading. SAND84-1635, Sandia National Laboratory, Albuquerque N.M., Matuska D., Durrett R.E. and Osborn J.J. (1982) Hull User's Guide for Three-Dimensional linking with EPIC 3. ARBRL-CR-00484, Orlando Technology, Shalimar, FL.

4.318. Ito Y.M., Nelson R.B. and Ross-Perry, F.W. (1979) Three-dimensional numerical analysis of earth penetration dynamics. Report DNA 5404F, Defense Nuclear Agency, Washington DC, USA.

4.319. Johnson G.R. and Stryk R.A. (1986) Dynamic-Lagrangian computations for solids, with variable nodal connectivity for severe distortions. *Int. Num. Methods Eng.*, **23**, 509–22.

4.320. Hallquist J.O. (1984) User's manual fur DYNAW – An explicit two-dimensional hydrodynamic finite element code with interactive rezoning. Report UCID-18756, Revision 2, University of California, Lawrence Livermore National Laboratory, USA.

4.321. Hallquist J.O. and Benson D.J. (1986) DYNA3D user's manual (nonlinear dynamic analysis of structures in three dimensions). Report UCID-19592, Revision 2, University of California, Lawrence Livermore National Laboratory.

4.322. Carr H.H. (1948) Analysis of head failure in aircraft torpedoes. NOTS Navord Report 1019, Patent Office Library, London.

4.323. Reissner E. (1946, 1947) Stresses and small displacements of shallow spherical shells. *J. Math. Phys.*, XXV 1 and 4.

4.324. Friedrichs K.O. (1941) On the minimum buckling load for spherical shells. In: *Theodore von Kàrmàn Anniversary Volume*, CIT, Pasadena, USA, pp. 258–272.

4.325. Tsein H.S. (1942) A theory for the buckling of thin shells. *J. Aero. Sci.*, 9:373–384.

4.326. Scott B. and Walters W. (1984) A model of the crater growth-rate under ballistic impact conditions. In: Proceedings Southeastern Conference on Theoretical and Applied Mechanics, Georgia.

4.327. Rohani B. (1975) Analysis of projectile penetration into concrete and rock targets. S-75-25. US Army Engineer Waterways Experimental Station.

4.328. Housen K., Schmidt R. and Holsapple K. (1983) Crater eject a scaling laws: Fundamental forms based on dimensional analysis. *J. Geophys. Res.* **88**.

4.329. Glass J. and Bruchey W. (1982) Internal deformation and energy absorption during penetration of semi-infinitec targets. In: Proceedings Eigth International Symposium Ballistics, NASA, Langely, USA.

4.330. Wang W.L. (1971) Low velocity projectile penetration. *J. Soil Mech. Found. Div.*, ASCE 97, no. SM12, Proc. Paper 8592.

4.331. Young C.W. (1969) Depth prediction for earth-penetrating projectiles. *J. Soil Mech. Found. Div.*, ASCE 95, no. SM3, Proc. Paper 6558.

4.332. Petry L. (1910) Monographies de systèmes d'artillerie. Brussels.

4.333. Hakala W.W. (1965) Resistance of a granular medium to normal impact of a rigid projectile. Thesis presented to the Virginia Polytechnic Institute, Blacksburg, VA, in partial fulfilment of the requirements for the degree of doctor of Philosophy.

4.334. Thigpen L. (1974) Projectile penetration of elastic–plastic earth-media. *J. Geotech. Eng. Div.*, ASCE 100, no. GT3, Proc. Paper 10414.

4.335. Butler D.K. (1975) An analytical study of projectile penetration into rock. Technical Report S-75-7, Soils and Pavements Laboratory, US Army Engineer Waterways Experiment Station, Vicksburg, MS.

4.336. Butler D.K. (1975) Pretest penetration for DNA rock penetration experiments at a sandstone site near San Ysidro. New Mexico. Soils and Pavements Laboratory, US Army Engineer Waterways Experiment Station, Vicksburg, MS.

4.337. Bernard R.S. and Hanagud S.V. (1975) Development of a projectile penetration theory. Technical Report S-75-9, US Army Waterways Experiment Station.

4.338. Bernard R.S. (1976) Development of a projectile penetration theory report 2: Deep penetration theory for homogeneous and layered targets. Technical Report S-75-9, US Army Waterways Experiment Station, VI, USA.

4.339. Byers R.K. and Chabai A.J. (1977) Penetration calculations and measurements for a layered soil target. *Int. J. Numer. Anal. Meth. Geomech.*, **1**, 107–138.

4.340. Bjork R.L. (1975) Calculations of earth penetrators impacting soils. AD-AO46 236, Pacifica Technology Hawaii, USA.

4.341. DNA/SANDIA (1975) Soil penetration experiment at DRES: results and analysis. SAND.75.0001, Sandia Laboraturics, Albuquerque.

4.342. Hadala P.F. (1975) Evaluation of empirical and analytical procedures used for predicting the rigid body motion of an earth penetrator. Technical Report S-75-15, US Army Waterways Experiment Station, Virginia, USA.

4.343. Norwood F.R. and Sears M.P. (1982) A nonlinear model for the dynamics of penetration into geological targets. *J. Appl. Mech.*, **49**, 26–30.

4.344. Rohani B. (1972) High velocity fragment penetration of a soil target. In: Proceedings of Conference on Rapid Penetration of Terrestrial Materials, Texas A & M University.

4.345. Triandafilidis G.E. (1976) State of the art of earth penetration technology, 2 volumes, Technical Report CE-42(76) DNA-297, The University of New Mexico.

4.346. Wagner M.H., Kreyenhagen K.N. and Goerke W.S. (1975) Numerical analysis of projectile impact and deep penetration into earth media. WES Contract Report S-75-4, California Research and Technology, Inc.

4.347. Yankelevsky D.Z. (1979) Normal penetration into geomaterials. Research Report 30, Faculty of Civil Engineering, Technion, Israel.

4.348. Yankelevsky D.Z. (1983) The optimal shape of an earth penetrating projectile. *Int. J. Solids Struct.* **19**, 25–31.

4.349. Yankelevsky D.Z. (1985) Cavitation phenomena in soil projectile interaction. *Int. J. Imp. Eng.* **3**, 167–78.

4.350. Young C.W. and Ozanne G.M. (1966) Low velocity penetration study. SC-RR-66-118, Sandia Laboratories, USA.

4.351. Young C.W. (1969) Depth prediction for earth penetrating projectiles. *J. Soil Mech. Found. Div., Proc. Am. Soc. Civ. Eng.* **95**, 803–17.

4.352. Young C.W. (1976) Status report on high velocity soil penetration. SAND 76-0291, Sandia Laboratories, USA.

4.353. Yarrington P. (1977) A one dimensional approximate technique for earth penetration calculations. SAND 77-1126, Sandia Laboratories, USA.

4.354. Alekseevskii V.P. (1966) Penetration of a rod into a target at high velocity. *Comb. Expl. Shock Waves*, **2**, 99–106 (English translation).

4.355. Backman M.E. and Goldsmith W. (1978) The mechanics of penetration of projectiles into targets. *Int. J. Eng Sci.*, **16**, 1–99.

4.356. Forrestal M.J., Rosenberg Z., Luk V.K. and Bless S.J. (1986) Perforation of aluminum plates with conical-nosed rods. SAND 86-02921, Sandia National Laboratory, Albuquerque, USA.

4.357. Frank K. and Zook J. (1986) Energy-efficient penetration and perforation of targets in the hyper-velocity regime. Hypervelocity Impact Symp., San Antonio, 1986.

4.358. Levy N. and Goldsmith W. (1984) Normal impact and perforation of thin plates by hemispherically-tipped projectiles – I. Analytical considerations. *Int. J. Impact Eng.*, **2**, 209–29.

4.359. Pidsley P.H. (1984) A numerical study of long rod impact onto a large target. *J. Mech. Phys. Sol.*, **32**, 315–34.

4.360. Tate A. (1986) Long rod penetration models - part I. A flow field model for high speed-long rod penetration. *Int. J. Mech. Sci.*, **28**, 525–48.

4.361. Zukas J.A., Jones G.H., Kinsey K.D. and Sherrick T.M. (1981) Three-dimensional impact simulations: resources and results. In: Park K.C. and Jones R.F. (eds.) Computer Analysis of Large Scale Structures, AMD-49, New York, pp. 35–68.

4.362. Asay J.R. and Kerley G.I. (1987) The response of materials to dynamic loading. *Int. J. Impact Eng.*, **5**(1–4), 69–99.

4.363. Holian K.S. and Burkett M.W. (1987) Sensitivity to hypervelocity impact simulation to equation of state. *Int. J. Impact Eng.*, **5**(1–4), 333–41.

4.364. Maiden C.J. (1963) Experimental and theoretical results concerning the protective ability of a thin shield against hypervelocity projectiles. In: Proceedings of the Sixth Symposium on Hypervelocity Impact, III, Springer-Verlag, Berlin, pp. 69–156.

4.365. Ravid M., Bodner S.R. and Holeman I. (1987) Analysis of very high speed impact. *Int. J. Eng Sci.*, **25**(4), 473–82.

4.366. Tillotson J.H. (1962) Metallic equations of state for hypervelocity impact. General Atomic, Division of General Dynamics, GA-3216, San Diego.

4.367. Chen J.K. and Sun C.T. (1985) On the impact of initially stressed composite laminates. *J. Camp. Mat.*, **19**, 490–504.

4.368. Tsai S.W. and Hahn H.T. (1980) Introduction to composite materials. Technical Publishing Company, Pennsylvania.

4.369. Brook N. and Summers D.A. (1969) The penetration of rock by high-speed water jets. *Int. J. Rock Mech. Mining Sci.*, **6**, 249–258.

4.370. Haimson B. (1965) High velocity, low velocity, and static bit penetration characteristics in Tennessee marble, Master's Thesis, University of Minnesota.

4.371. Haimson B.C. and Fairhurst C. (1970) Some bit penetration characteristics in pink Tennessee marble. In: Proceedings of the 12th Symposium on Rock Mechanics, University of Missouri School of Mines, USA, pp. 547–59.

4.372. Rajendran A.M. (1994) Modeling the impact behavior of AD85 ceramic under multiaxial loading. *Int. J. Impact Eng.*, **15**(6), 749–768.

4.373. Rajendran A.M. and Grove D.J. (1996) Modeling the shock response of silicon carbide, boron carbide, and titanium diboride. *Int. J. Impact Eng.*, **18**(6), 611–631.

4.374. Rajendran A.M. and Grove D.J. (1998) Modeling of shock and impact behaviors of aluminum oxide. *Structures Under Shock and Impact V* (Ed. by N. Jones, D.G. Talaslidis, C.A. Brebbia, and G.D. Manolis), pp. 447–460, Computational Mechanics Publications.

4.375. Gurson A.L. (1977) Continuum theory of ductile rupture by void nucleation and growth; Part I: Yield criterion and flow rules for porous ductile materials. *J. Eng. Mater. Technol.*, **99**, 2–15.

4.376. Rajendran A.M. and Dandekar D.P. (1995) Inelastic response of alumina. *Int. J. Impact Eng.*, **17**, 649–659.

4.377. Margolin L.G. (1984) A generalized griffith criterion for crack propagation. *Eng. Fract. Mec.*, **19**, 539–543.

4.378. Dandekar D.P. and Bartkowski P. (1994) Shock response of AD995 alumina, *High-Pressure Science and Technology - 1993, Part 2*, AIP Press, pp. 733–736.

4.379. Grady D.E. and Moody R.L. (1996) *Shock Compression Profiles in Ceramics*, Sandia Report, SAND96-0551, March.

4.380. Johnson G.R., Stryk R.A., Petersen E.H., Holmquist T.J., Schonhardt J.A. and Burns C.R. (1994) *User Instructions for the 1995 Version of the EPIC Code*, Alliant Techsystems Inc., Brooklyn Park, Minnesota, November.

4.381. Woolsey P. (1991) unpublished work at AMTL, Watertown, MA.

4.382. American Concrete Institute (ACI) (2002). Building code requirements for structural concrete (*ACI 318-02*) and commentary (*ACI 318R-02*). Farmington Hills, Mich.

4.383. Collins D.M., Klingner R.E. and Polyzois D. (1989) Load-deflection behavior of cast-in-place and retrofit concrete anchors subjected to static, fatigue, and impact tensile loads. *Res. Rep. No. 1126-1*, Center for Transportation Research

4.384. Dinan R. Salim H., Ashbery W., Lane J. and Townsend P.T. (2003) Recent experience using steel studs to construct blast resistant walls in reinforced concrete buildings. *Proc., 11th Int. Symp. on Interaction of the Effects of Munitions with Structures (11th ISIEMS)*, Streit-krafteamt, Germany and Defense Threat Reduction Agency.

4.385. DiPaolo B., Salim H., Townsend T. and Davis J. (2003) A study on static and dynamic responses of exterior cold-formed steel-stud framing walls for enhanced blast resistance. *Proc. 16th Engineering Mechanics Conf.*, ASCE, Reston, VA.

4.386. Fuchs W., Eligehausen R. and Breen J.E. (1995) Concrete capacity design approach for fastening to concrete. *ACI Struct. J.*, **92**(1), 73–94.

4.387. Hilti (2002). *Systems and Solutions Customer Catalogue* (brochure), Tulsa, Okla.

4.388. Hunziker P. (1999) Shock testing of concrete anchor bolts for shock.

4.389. Andersson A., Axelsson H. and Holmström S. (1989) *Splitter från flygbomber. Sprängningar med 250 kg mb m/50 och 500 kg mb m/56* (In Swedish). Försvarets Forskningsanstalt, FOA Rapport, C 20744-2.3, Stockholm, Sweden, January, 37 pp.

4.390. Ansari F. and Li Q.B. (1998) High-strength concrete subjected to triaxial compression. *ACI Mater. J.*, **95**(6), 747–755.

4.391. Attard M.M. and Setunge S. (1996) Stress-strain relationship of confined and unconfined concrete. *ACI Mater. J.*, **93**(5), 432–442.

4.392. AUTODYN Manuals (2004) *AUTODYN Manuals.* Version 5, Century Dynamics, Inc., Concord, CA, USA.

4.393. Baker W.E. (1973) *Explosions in Air.* Univ. of Texas Press. Austin, TX, USA, 268 pp.

4.394. Bažant Z.P., Xiang Y.Y., Adley M.D., Prat P.C. and Akers, S.A. (1996) Microplane model for concrete: II: data delocalization and verification. *J. Eng. Mech.*, **122**(3), 255–262.

4.395. Benson D.J. (1992) Computational methods in Lagrangian and Eulerian hydrocodes. *Comput. Methods Appl. Mech. Eng.*, **99**(2–3), 235–394.

4.396. Bischoff P.H. and Perry S.H. (1991) Compressive behaviour of concrete at high strain rates. *Mater. Struct.*, **24**, 425–450.

4.397. Bryntse A. (1997) *Penetration av stålsplitter vid 1 500 m/s mot armerad betong (Förstudie)* (In Swedish). Försvarets Forskningsanstalt, FOA-D–97-00304-311-SE, Stockholm, Sweden, January, 9 pp.

4.398. Bulson P.S. (1997) *Explosive Loading of Engineering Structures.* E& FN Spon. London, UK, 233 pp.

4.399. CEB-FIB Model Code 1990 (1993): *CEB-FIB Model Code 1990.* Design Code, Thomas Telford, Lausanne, Switzerland, 437 pp.

4.400. Clegg R.A., Sheridan J., Hayhurst C.J. and Francis N.J. (1997) The application of SPH techniques in AUTODYN-2D to kinetic energy penetrator impacts on multi-layered soil and concrete targets. *8th International Symposium on Interaction of the Effects of Munitions with Structures*, Virginia, USA, 22–25 April, 9 pp.

4.401. ConWep (1992) *ConWep.* Collection of conventional weapons effects calculations based on TM 5-855-1, Fundamentals of Protective Design for Conventional Weapons, U. S. Army Engineer Waterways Experiment Station, Vicksburg, VA, USA.

4.402. Ekengren B. (2003) *Skyddsrumsregler SR* (Shelter Regulations, In Swedish). Swedish Rescue Services Agency, Publication B54-141/03, Karlstad, Sweden, 126 pp.

4.403. Engberg T. and Karevik S. (1987) *Fortifikationshandbok del 1, FortH 1.* Försvarets läromedelscentral (FLC), Stockholm, Sweden, 50 pp.

4.404. Erkander Å. and Pettersson L. (1985) *Betong som splitterskydd: Skjutförsök på plattor av olika betongmaterial* (Concrete as protective material against fragment impacts: Fragment impacts on concrete plates of different types of concrete, In Swedish). Försvarets Forskningsanstalt, C 20574-D6(D4), Stockholm, Sweden, May, 66 pp.

4.405. Forsén R. (1989) *Initialverkan, verkan på byggnader av inneslutna explosioner* (In Swedish). Forsvarets Forskningsanstalt, FOA rapport C 20747-2.6, Stockholm, Sweden, February, 37 pp.

4.406. Forsén R. (1997) *Belastning av betongplattor med tryck och splitter från 250 kg minbomber* (In Swedish). Försvarets Forskningsanstalt, FOA-R–97-00418-311-SE, Tumba, Sweden, February, 50 pp.

4.407. Forsén R. and Edin K. (1991) *Vapenverkan mot flervånings betongbyggnad III. Bestämning av skador från splitterladdningar mot husfasad i skala 1:4* (In Swedish). Försvarets Forskningsanstalt, FOA rapport C 20860-2.3, Sundbyberg, Sweden, December, 40 pp.

4.408. Forsén R. and Nordström M. (1992) *Damage to Reinforced Concrete Slabs Due to the Combination of Blast and Fragment Loading* (In Swedish). National Defence Research Establishment (FOA), FOA Report B 20101-2.6, Tumba, Sweden, September, 12 pp.

4.409. Forsén R. and Sten G. (1994) *Utredning om splitterverkan/splitterskydd. Jämförelse mellan två 250 kg minbomber* (In Swedish). Försvarets Forskningsanstalt, FOA dnr 94-2502/S, Sundbyberg, Sweden, April, 76 pp.

4.410. Gebbeken N. (2001) Determination of shock equation of state properties of concrete using full-scale experiments and flyer-plate impact tests. *Trends in Computational Structural Mechanics*, Barcelona, Spain, pp. 109–117.

4.411. Grady D. (1996) Shock equation of state properties of concrete. *Structures Under Shock and Impact IV*, Udine, Italy, pp. 405–414.

4.412. Gylltoft K. (1983) *Fracture Mechanics Models for Fatigue in Concrete Structures*. Doctoral Thesis. Division of Structural Engineering, Luleå University of Technology, Luleå, Sweden, 210 pp.

4.413. Hansson H. (1998) *Numerical Simulation of Concrete Penetration*. FOA-R, Defence Research Establishment, FOA-R–98-00816-311–SE, Tumba, Sweden, 17 pp.

4.414. Hayhurst C.J., Clegg R.A., Livingstone I.A. and Francis N.J. (1996) The application of SPH techniques in AUTODYN-2D to ballistic impact problems. *16th International Symposium on Ballistics*, San Francisco, CA, USA, 23–28 September, 9 pp.

4.415. Hillerborg A. (1976) Analysis of crack formation and crack growth in concrete by means of fracture mechanics and finite elements. *Cement Concrete Res.*, **6**, 773–782.

4.416. Hillerborg A. (1980) Analysis of fracture by means of the fictitious crack model, particularly for fibre reinforced concrete. *Int. J. Cement Compos.*, **2**(4), 177–184.

4.417. Hillerborg A. (1985) The theoretical basis of a method to determine the fracture energy GF of concrete. *Rilem Tech. Committees*, **18**(106), 291–296.

4.418. Imran I. and Pantazopoulou S.J. (2001) Plasticity model for concrete under triaxial compression. *J. Eng. Mech.*, **127**(3), 281–290.

4.419. Janzon B. (1978) *Grundläggande Stridsdelsfysik* (In Swedish). Försvarets Forskningsanstalt, FOA Rapport C 20261-D4, Stockholm, Sweden, September, 164 pp.

4.420. Johansson M. (2000) *Structural Behaviour in Concrete Frame Corners of Civil Defence Shelters, Non-linear Finite Element Analyses and Experiments*. Doctoral Thesis. Department of Structural Engineering, Concrete Structures, Chalmers University of Technology, Publication no. 00:2, Göteborg, Sweden, 204 pp.

4.421. Johnson G.R., Stryk R.A., Beissel S.R. and Holmquist T.J. (2002) An algorithm to automatically convert distorted finite elements into meshless particles during dynamic deformation. *Int. J. Impact Eng.*, **27**(10), 997–1013.

4.422. Jonasson T. (1990) *Kontaktverkan I, Sprängladdningars kontaktverkan på armerade betongplattor* (In Swedish). Försvarets Forskningsanstalt, FOA-R, C 20809-2.6, Sundbyberg, August, 58 pp.

4.423. Kim D.S. and McCarter M.K. (1998) Quantitative assessment of extrinsic damage in rock materials. *Rock Mech. Rock Eng.*, **31**(1), 43–62.

4.424. Krauthammer T. (1999) Blast-resistant structural concrete and steel connections. *Int. J. Impact Eng.*, **22**(9–10), 887–910.

4.425. Krauthammer T. (2000) *Modern Protective Structures, Design, Analysis and Evaluation*. Course notes. The Pennsylvania State University, 358 pp.

4.426. Leppänen J. (2002) *Dynamic Behaviour of Concrete Structures subjected to Blast and Fragment Impacts*. Licentiate Thesis. Department of Structural Engineering, Concrete Structures, Chalmers University of Technology, Publication no. 02:4, Archive no. 31, Göteborg, Sweden, 71 pp.

4.427. Leppänen J. (2003) *Splitterbelastad betong - Experiment och numeriska analyser* (Fragment Impacts into Concrete - Experiments and Numerical analyses, In Swedish). Department of Structural Engineering and Mechanics, Concrete Structures, Chalmers University of Technology, Report no. 03:6, Göteborg, Sweden, August, 76 pp.

4.428. Malvar L.J. and Ross C.A. (1998) Review of Strain Rate Effects for Concrete in Tension. *ACI Mater. J.*, **95**(6), 735–739.

4.429. Nordström M. (1992) *Splitterbelastning av betongplattor 1, Metodik för bestämning av energiupptagande förmåga hos armerade betongplattor belastade med olika splittertätheter* (In Swedish). Försvarets Forskningsanstalt, FOA rapport, D 20209-2.3, Sundbyberg, October, 54 pp.

4.430. Nordström M. (1993) *Splitterbelastning av betongplattor II. Energiupptagande förmåga hos armerade betongplattor belastade med olika splittertätheter* (In Swedish). Försvarets Forskningsanstalt, FOA rapport, D 20226-2.3, Sundbyberg, June, 30 pp.

4.431. Nordström M. (1995) *Försök med experimentladdningar för simulering av splitterlast från spränggranater och minbomber* (In Swedish). Försvarets Forskningsanstalt, FOA-R–95-00109-7(6,2.6)–SE, Stockholm, Sweden, March, 54 pp.

4.432. Nordström M. (1995) *Splitterbelastning av betongplattor III, Energiupptagande förmåga hos armerade betongplattor belastade med olika kombinationer av splitterhastigheter, splittertätheter och splitterstorlekar* (In Swedish). Försvarets Forskningsanstalt, FOA-R–95-00094-7(6,2.6)–SE, Stockholm, Sweden, March, 101 pp.

4.433. Papados P.P. (2000) A reinforced concrete structure under impact: Response to high rate loads. *Sixth International Conference on Structures Under Shock and Impact*, Cambridge, UK, July, pp. 501–510.

4.434. Plos M. (1995) *Application of fracture mechanics to concrete bridges, Finite Element Analyses and Experiments*. Doctoral Thesis. Department of Structural Engineering, Division of Concrete Structures, Chalmers University of Technology, Göteborg, Sweden, 57 pp.

4.435. Rempling R. (2004) *Concrete wall subjected to fragment impacts - Numerical analyses of perforation and scabbing*. Master's Thesis. Department of

Structural Engineering and Mechanics, Concrete Structures, Chalmers University of Technology, 04:1, Göteborg, Sweden, 54 pp.

4.436. Richart F.E., Brandtzaeg A. and Brown R.L. (1928) *A Study of the Failure of Concrete under Combined Compressive Stresses*. Bulletin No.185, University of Illinois, Engineering Experimental Station, Urbana, Illinois, USA.

4.437. Riedel W. (2000) *Beton unter dynamischen Lasten Meso- und makromechanische Modelle und ihre Parameter*. In German, Doctoral Thesis. Institut Kurzzeitdynamik, Ernst-Mach-Institut, der Bundeswehr Munchen, Freiburg, 210 pp.

4.438. Rinehart E.J. and Welch C.R. (1995) Material properties testing using high explosives. *Int. J. Impact Eng.*, **17**(4–6), 673–684.

4.439. Ross C.A., Jerome D.M., Tedesco J.W. and Hughes M.L. (1996) Moisture and strain rate effects on concrete strength. *ACI Mater. J.*, **93**(3), 293–300.

4.440. Svahn P.O. (2003) *Impact-Loaded Concrete Piles – Theoretical and Experimental Study of Load Effects and Capacity*. Licentiate Thesis. Department of Structural Engineering, Concrete Structures, Chalmers University of Technology, Publication no. 02:4, Archive no. 38, Göteborg, Sweden, 51 pp.

4.441. von Essen W. (1973) *Provisoriska anvisningar för dimensionering av armerade betongkonstruktioner som skydd mot verkan av konventionella vapen inom närmissområde. Kommentarer* (In Swedish). Fortifikationsförvaltningen, Publ. 25:2, May, 34 pp.

4.442. Weerheijm J. (1992) *Concrete Under Impact Tensile Loading and Lateral Compression*. Doctoral Thesis. Delft University of Technology, The Netherlands, 157 pp.

4.443. Zukas J.A. and Scheffler D.R. (2000) Practical aspects of numerical simulations of dynamic events: Effects of meshing. *Int. J. Impact Eng.*, **24**(9), 925–945.

4.444. Ågårdh L. (1997) Fe-modeling of fibre reinforced concrete slabs subjected to blast load. *J. Phys. IV*, **7**(C3), 723–728.

4.445. Ågårdh L. and Laine L. (1999) 3D FE-simulation of high-velocity fragment perforation of reinforced concrete slabs: *Int. J. Impact Eng.*, **22**(9), 911–922.

4.446. Hibbert A.P. (1979) Impact Resistance of Fibre Concrete. PhD Thesis. University of Surrey.

4.447. Hibbert A.P. and Hannant D.J. (1978) The design of an instrumented impact test machine for fibre concretes. Testing and Test Methods of Fibre Cement Composites. *RILEM Symposium, Sheffield*, pp. 107–120. The Construction Press.

4.448. Edgington J., Hannant D.J. and Williams R.I.T. (1974) Steel fibre reinforced concrete. *Building Research Establishment Current Paper*, CP69/74. July, (1970) (Building Research Establishment).

4.449. British Standards Institution (1970) Methods of testing concrete. BS 1881. London (British Standards Institution).

4.450. Cottrell A.H. (1964) Strong solids. *Proc. Roy. Soc., A* **282**(2).

4.451. De Vekey R.C. and Majumdar A.J. (1968). Determining bond strength in fibre reinforced composites. *Mag. Concrete Res.*, **20**(65), 229–234.

4.452. Hughes B.P. and Fattuhi N.I. (1975) Fibre bond strengths in cement and concrete. *Mag. Concrete Res.*, **27**(92), 161–166.

4.453. Aveston J., Mercer R.A. and Sillwood J.M. (1975) The mechanism of fibre reinforcement of cement and concrete. *Nat. Phys Laboratory Rep* No. 90/11/98, Part 1. January (National Physical Laboratory).

5 Related Studies on Shock/Impact in the Sea Environment

5.1. Forrestal M.J. et al. (1980) An explosive loading technique for the uniform of 304 stainless steel cylinders at high strain rates. *J. Appl. Mech.*, **47**, 17.

5.2. Kuznetsov V.M. (1973) The mean diameter of the fragments formed by blasting rock. *Soviet Mining Sci.*, **9**, 144–8.

5.3. Lyakhav G.M. (1964) Principles of explosion dynamics in soils and in liquid media. Nera, Mockba.

5.4. *Underwater Explosion Research*, Vol. 1, p. 273. Office of Naval Research, Department of the Navy, Washington 1950.

5.5. Department of Energy (1985) *Offshore Installations Guidance on Design and Construction*, 4th edn. HMSO, London.

5.6. Onoufriou A., Harding J.E. and Dowling P.J. (1987) Impact damage on ring-stiffened cylinders. In *Proceedings of the International Colloquium on Stability of Plate and Shell Structures*. Ghent, Belgium.

5.7. Onoufriou A. and Harding J.E. (1985) Residual strength of damaged ring-stiffened cylinders. In *Proceedings of the Fourth OMAE Symposium*. ASME, Dallas.

5.8. Ronalds B.F. and Dowling P.J. (1987) Residual compressive strength of damaged orthogonally stiffened cylinders. In *Proceedings of the International Colloquium on Stability of Plate and Shell Structures*, p. 503. Ghent, Belgium.

5.9. Onoufriou A., Elnashai A.S., Harding J.E. and Dowling P.J. (1987) Numerical modelling of damage to ring stiffened cylinders. In *Proceedings of the Sixth OMAE Symposium*. ASME, Houston.

5.10. Department of Energy (1987) *Study on Offshore Installation Protection Against Impact. Offshore Technology Report*. HMSO, London.

5.11. Det Norske Veritas (1984) *Rules for Classification of Mobile Offshore Units*.

5.12. Det Norske Veritas (1981) Impact loads from boats. *Technical Note TNA 202*.

5.13. Williams K.A.J. and Ellinas C.P. (1987) Design guidelines and developments in collision and damage of offshore structures. In *Proceedings of the International Conference on Steel and Aluminium Structures*. University College, Cardiff.

5.14. NMI Ltd, Collision of attendant vessels with offshore installations. Part 1: General Description and Principal Results. *Offshore Technology Report, OTH 84 208*. HMSO London.

5.15. NMI Ltd (1985) Collisions of attendant vessels with offshore installations. Part 2: detailed calculations. *Offshore Technology Report OTH 84 209*. HMSO, London.

5.16. UNO (1990) Code for the construction and equipment of mobile offshore drilling units (MODU CODE). Inter-Government Maritime Consultative Organisation (IMCO).

5.17. Atwood (1796) Disquisition on the stability of ships. *Philosophical Transactions of the Royal Society of London*.

5.18. Moseley C. (1850) On the dynamical stability and oscillation of floating bodies. *Philosophical Transactions of the Royal Society of London*.

5.19. Harrori Y., Ishihama T., Matsumoto K., Sakata N. and Ando A. (1982) Full scale measurement of natural frequency and damping ratio of jack-up rigs and some theoretical considerations. OTC Conference, Paper no. 4287.

5.20. Trickey J.C. (1981) A simplified approach to the dynamic analysis of self-elevating drilling units. *Noble Denton Report L8292/NDA/JCT*. USA.

5.21. Wordsworth A.C. and Smedley G.P. (1978) Stress concentrations at unstiffened tubular joints. Presented at the European Offshore Steels Research Seminar, Cambridge, UK.

5.22. Kinnaman S.C. (1986) The workover task impact on subsea well servicing and workover vessels. Norwegian Petroleum Society (NPF) Conference, Kristiansand.

5.23. Standing R.G. (1987) The sensitivity of structure loads and responses to environmental modelling. Conference on Modelling the Offshore Environment, Society for Underwater Technology, London.

5.24. Takagi M., Arai S.I., Takezawa S., Tanaka K. and Takarada N. (1985) A comparison of methods for calculating the motion of a semi-submersible. *Ocean Eng.*, **12**(1), 45–97.

5.25. Eatok Taylor T. and Jefferys E.R. (1986) Variability of hydrodynamic load predictions for a tension leg platform. *Ocean Eng.*, **13**(5), 449–90.

5.26. Standing R.G., Rowe S.J. and Brendling W.J. (1986) Jacket transportation analysis in multi-directional waves. Offshore Technology Conference, Houston, 1986, Paper no. OTC 5283.

5.27. Rowe S.J., Brendling W.J. and Davies M.E. (1984) Dynamic wind loading of semi-submersible platforms. International Symposium on Developments in Floating Production Systems, RINA, London.

5.28. Ikegami K., Watenabe Y. and Matsuura M. (1986) Study on dynamic response of semi-submersible platform under fluctuating wind. Third International Conference on Stability of Ships and Ocean Vehicles (STAB '86), Gdansk.

5.29. Standing R.G. and Dacunha N.M.C. (1982) Slowly-varying and mean second-order wave forces on ships and offshore structures. In *Proceedings of the Fourteenth ONR Symposium on Naval Hydrodynamics*. Ann Arbor.

5.30. Pinkster J.A. (1980) Low frequency second order wave exciting forces on floating structures. NSMB, Wageningen, report no. 650. Germany.

5.31. Huse E. (1977) Wave induced mean force on platforms in direction opposite to wave propagation. *Norwegian Maritime Res.*, **5**(1), 2–5.

5.32. Pinkster J.A. and Wichers J.E.W. (1987) The statistical properties of low-frequency motions of nonlinearly moored tankers. Offshore Technology Conference, Paper no. OTC 5457, Houston.

5.33. McClelland B., Young A.G. and Remmes B.D. (1981) Avoiding jack-up rig foundation failures. In *Proceedings of the Symposium on Geotechnical Aspects of Offshore and Nearshore Structures*, Bangkok.

5.34. Young A.G., Remmes B.D. and Meyer B.J. (1984) Foundation performance of offshore jack-up drilling rigs. *J. Geotech. Eng.*, **110**(7), 841–59.

5.35. Davie J.R. and Sutherland H.B. (1977) Uplift resistance of cohesive soils. *ASCE J. Geotech. Eng. Div.*, 935–53.

5.36. Rapoport V. and Young A.G. (1985) Uplift capacity of shallow offshore foundations. In *Proceedings of a Session on Uplift Behavior of Anchor Foundations in Soil, ASCE Convention*, pp. 73–85. Detroit, Michigan.

5.37. Smith C.S., Davidson P.C., Chapman J.C. and Dowling P.J. (1988) Strength and stiffness of ships plating under in-plane compression and tension. *Trans. R. Inst. Naval Arch.*, **130**.

5.38. Akita Y. (1982) Lessons learned from failure and damage of ships. Jt. Sess. 1, Eight ISSC, Gdansk.

5.39. Amdahl J. (1980) Impact capacity of steel platforms and tests on large deformations of tubes under transverse loading. *Det Norske Veritas, Prog. Rep. No. 10, Rep. No. 80–0036.*

5.40. Taby J. and Moan T. (1987) Ultimate behaviour of circular tubular members with large initial imperfections. In *Proceedings of the Annual SSRC Conference.*

5.41. Marshall P.W. (1984) Connections for welded tubular structures. In *Welding of Tubular Structures.* International Institute of Welding, Pergamon, Oxford.

5.42. Hoadley P.W. et al. (1985) Ultimate strength of tubular joints subjected to combined loads. *Proceedings of Offshore Technology Conference*, Paper no. 4854.

5.43. Mahinom Y., Kurobane Y., Takizawa S. and Yamamoto N. (1986) Behaviour of tubular T- and K-joints under combined loads. *Proceedings of Offshore Technology Conference*, Paper no. 5133.

5.44. *Risk Assessment of Buoyancy Loss, Ship Model Collision Frequency.* Technica, London, 1987.

5.45. Norwegian Petroleum Directorate (NPD) (1981) *Guidelines for Safety Evaluation of Platform Conceptual Design.* NPD, Stavanger.

5.46. American Petroleum Institute (API) (1985) *Planning, Designing and Constructing Fixed Offshore Platforms*, 15th edn. API RP2A, Washington DC.

5.47. Det Norske Veritas (1983) *Classification Note 31.5, Strength Analysis of Main Structures of Self Elevating Units.* Hovik, Norway.

5.48. Barratt M.J. (1981) Collision risk estimates in the English Channel and western approaches. *Offshore Technology Report OT-R-8144 to Department of Energy.* HMSO.

5.49. Hathaway R.S. and Rowe S.J. (1981) Collision velocities between offshore supply vessels and fixed platforms. *Offshore Technology Report OT-R-8201 to Department of Energy.* HMSO, UK.

5.50. NMI (1985) Collision of attendant vessels with offshore installations. Part 2: detailed calculations. *Offshore Technology Report OTH 84 209.*

5.51. Borse E. (1979) Design basis accidents and accident analysis with particular reference to offshore platforms. *J. Occupational Accidents*, **2**, 227–43.

5.52. Amdahl J. and Heldor E. (1978) Impacts and collisions offshore. Progress report no. 1. Simulation applied to analysis of the probability of collision between ships and offshore structures. *DnV Report 78–037.* Norway.

5.53. Amdahl J. and Anderson R. (1979) Impacts and collisions offshore. Progress report no. 5. Computer simulation analysis of the collision probability offshore. *DnV Report 78–624.*

5.54. Amdahl J. and Anderson E. (1979) Impacts and collisions offshore. Progress report no. 6. Computer simulation study of collision probability between tanker/platform. *DnV Report 79–0192.* Norway.

5.55. Heldor E. and Amdahl J. (1979) Impacts and collisions offshore. Progress report no. 7. Collision accidents occurred to offshore structures during the period 1970–1978. *DnV Report 79–0538.* Norway.

5.56. Tviet O.J. and Evandt O. (1981) Experiences with failures and accidents of offshore structures. Third International Conference on Structural Safety and Reliability (ICOSSAR '81), Trondheim, Norway, June 1981 (also published as *DnV Paper 81-P038*), Norway.

5.57. Macduff T. (1974) Probability of collision – a note on encounters between ships, terra firma and offshore structures. *Fairplay International Shipping Weekly*, 21 March 1974, 28–32.

5.58. Kjeoy H. (1982) Impacts and collisions offshore, phase II. Progress report no. 12. Overall deformation of braced offshore structures subjected to ship impact loads. Part 1. *DnV Report 81–1213*.

5.59. Frieze P.A. and Samuelides E. (1982) Summary of research on collisions and other impacts on ships and offshore platforms. University of Glasgow, Department of Naval Architecture of Ocean Engineering *Report No. NAOE-82–15*.

5.60. Jones N. (1971) A theoretical study of the dynamic plastic behaviour of beams and plates with finite deflections. *Int. J. Solids Struct.*, **7**, 1007–29.

5.61. Haskell D.F. (1970) Large impact deformation response of spherical shells. *AIAA J.*, **8**, 2128–9.

5.62. Updike D.P. (1972) On the large deformation of a rigid plastic spherical shell compressed by a rigid plate. *J. Eng. Industry*, 949–55.

5.63. Minorsky V.U. (1983) An analysis of ship collisions with reference to protection of nuclear power plants. *J. Ship Res.*, 1–4.

5.64. Taby J., Moan T. and Rashed S.M. (1981) Theoretical and experimental study of the behaviour of damaged tubular members in offshore structures. *J. Norwegian Maritime Res.* no. 2, 26–33.

5.65. Ronalds B.F. and Dowling P.J. (1986) Finite deformations of stringer stiffened plates and shells under knife edge loading. Fifth OMAE Symposium, Tokyo.

5.66. Walker A.C. and Kwok M. (1986) Process of damage in thin-walled cylindrical shells. Fifth OMAE Symposium, Tokyo.

5.67. Walker A.C. and McCall S. (1985) Combined loading of damaged cylinders. Appendices 3–8. University of Surrey.

5.68. Cho S.R. and Frieze P.A. (1985) Lateral impact tests on unstiffened cylinders. Final Report, University of Glasgow.

5.69. Rhodes P.S. (1974) The structural assessment of buildings subjected to bomb damage. *Struct. Eng.*, **52**, 329–39.

5.70. Hopkirk R.J. and Rybach L. (1989) Modelling pressure behaviour in artificially stimulated rock masses – matching field pressure records. *Int. J. Rock Mech. Min. Sci. Geomech. Abstr.*, **26**, no. 314, 341–9.

5.71. Kirkwood J.G. and Montroll E. (1942) Properties of pure water at a shock. *Report OSRD*, 676.

5.72. Powel K.A. (1986) *The Hydraulic Behaviour of Shingle Beaches Under Regular Waves of Normal Incidence.* Doctoral thesis, University of Southampton.

5.73. PIANC (1976) Final report of the International Commission for the Study of Waves, second part. *Bulletin No. 25*, Vol. III (annex).

5.74. PIANC (1980) Final report of the International Commission for the Study of Waves, third part. *Bulletin No. 36*, Vol. II (annex).

5.75. Burcharth H.F. (1981) A design method for impact-loaded slender armour units *Bulletin H2 18*. Aalborg University Center, Denmark.

5.76. Coastal Engineering Research Center (1984) *Shore Protection Manual*. US Army Corps of Engineers, USA.

5.77. Dai Y.B. and Kamel A.M. (1969) Scale effect tests for rubble-mound breakwaters. *Research Report H-69–2*. WES, USA.

5.78. Delft Hydraulics-ENDEC (1986) *ENDEC, Wave Propagation Model. User's Manual.*

5.79. Delft Hydraulics-H24 (1987) Golfoverslag Afsluitdijk. Verslag modelonderzoek (Wave overtopping at the Afsluitdijk. Report on model investigation) (in Dutch).

5.80. Delft Hydraulics-M1216 (1974) Grindstranden. Evenwichtsprofiel bij loodrechte regelmatige golfaanval. Verslag modelonderzoek, deel I. (Gravel beaches. Equilibrium profile under monochromatic and perpendicular wave attack. Report on model investigation, Part I) (in Dutch).

5.81. Delft Hydraulics-M1216 (1975) Grindstranden. Evenwichtsprofiel bij loodrechte regelmatige golfaanval. Verslag modelonderzoek, deel II. (Gravel beaches. Equilibrium profile under monochromatic and perpendicular wave attack. Report on model investigation, Part II) (in Dutch).

5.82. Delft Hydraulics-M1216 (1979) Grindstranden. Evenwichtsprofiel bij loodrechte onregelmatige golfaanval. Verslag modelonderzoek, deel II. (Gravel beaches. Equilibrium profile under irregular and perpendicular wave attack. Report on model investigation, Part III) (in Dutch).

5.83. Delft Hydraulics-M1216 (1981) Grindstranden. Evenwichtsprofiel en langstransport bij scheve onregelmatige golfaanval. Verslag modelonderzoek, deel IV. (Gravel beaches. Equilibrium profile under irregular and oblique wave attack. Report on model investigation, Part IV) (in Dutch).

5.84. Delft Hydraulics-M1968 (1983) Golfbrekers. Sterkte betonnen afdekelmenten – Belastingen. (Breakwaters. Strength of concrete armour units – loads) (confidential report in Dutch).

5.85. Delft Hydraulics-M1968 (1983) Golfbrekers. Sterkte betonnen afdekelementen – Bloksterkte. (Breakwaters. Strength of concrete armour units – strength of block) (confidential report in Dutch).

5.86. Delft Hydraulics-M1809 (1984) Taluds van losgestorte materialen. Hydraulische aspecten van stortsteen, grind en zandtaluds onder golfaanval. Verslag literatuurstudie. (Slopes of loose materials. Hydraulic aspects of rock, gravel and sand slopes under wave attack. Report on literature) (in Dutch).

5.87. Delft Hydraulics-M2006 (1986) Taluds van losgestorte materialen. Stabiliteit van stortsteen-bermen en teenkonstrukties. Verslag literatuurstudie en modelonderzoek. (Slopes of loose materials. Stability of rubble mound berm and toe structures. Report on literature and model investigation) (in Dutch).

5.88. Delft Hydraulics-M1983 (1988) Taluds van losgestorte materialen. Statische stabiliteit van stortsteen taluds onder golfaanval. Onwerp formules. Verslag modelonderzoek, deel I (Slopes of loose materials. Static stability of rubble mound slopes under wave attack. Design formulae. Report on model investigation, part I) (in Dutch).

5.89. Delft Hydraulics-M1983 (1988) Taluds van losgestorte materialen. Dynamische stabiliteit van grind-en stortsteen taluds onder golfaanval. Model voor profielvorming. Verslag modelonderzoek, deel II. (Slopes of loose materials. Dynamic stability of gravel beaches and rubble mound slopes under wave

attack. Model for profile formation. Report on model investigation, part II), (in Dutch).

5.90. Gravesen H., Jensen O.J. and Sörensen T. (1979) Stability of rubble mound breakwaters II. Conference on Coastal Structures 79, Virginia, USA.

5.91. IAHR/PIANC (1986) List of sea state parameters. *Bulletin No. 52* (suppl).

5.92. Kobayashi N. and Jacobs B.K. (1985) Riprap stability under wave action. *Proc. ASCE, J. WPC OE*, **111**, no. 3.

5.93. Kobayashi N. and Jacobs B.K. (1985) Stability of armor units on composite slopes. *Proc. ASCE, J. WPC OE*, **111**, no. 5.

5.94. Kobayashi N., Roy I. and Otta A.K. (1986) Numerical simulation of wave runup and armor stability. In *Proceedings of the Eighteenth Annual OTC*, pp. 51–60. Houston, USA.

5.95. Kobayashi N. and Otta A.K. (1987) Hydraulic stability analysis of armor units. *Proc. ASCE, J. WPC OE,* **113**, no. 2.

5.96. Kobayashi N., Otta A.K. and Roy I. (1987) Wave reflection and run-up on rough slopes. *Proc. ASCE, J. WPC OE*, **113**, no. 3.

5.97. Losada M.A. and Giménez-Curto L.A. (1981) Flow characteristics on rough, permeable slopes under wave action. *Coastal Eng.*, **4**, 187–206.

5.98. Losada M.A. and Giménez-Curto L.A. (1982) Mound breakwaters under oblique wave attack; a working hypothesis. *Coastal Eng.*, **6**, 83–92.

5.99. Pilarczyk K.W. and Den Boer K. (1983) Stability and profile development of coarse materials and their application in coastal engineering. In *Proceedings of the International Conference on Coastal and Port Engineering in Developing Countries*. Colombo, Sri Lanka.

5.100. Popov I.J. (1960) Experimental research in formation by waves of stable profiles of upstream faces of earth dams and reservoir shores. In *Proceedings of the Seventh ICCE*, chapter 16. The Hague, The Netherlands.

5.101. Ryu C.R. and Sawaragi T. (1986) Wave control functions and design principles of composite slope rubble mound structures. *Coastal Eng. Jpn*, **29**, 227–40.

5.102. Sawaragi T., Ryu C.R. and Kusumi M. (1985) Destruction mechanism and design of rubble mound structures by irregular waves. *Coastal Eng. Jpn*, **28**, 173–89.

5.103. Siggurdson G. (1962) Wave forces on breakwater capstones. *Proc. ASCE, J. WHC CED*, **88**, no. WW3.

5.104. Tautenhain E., Kohlhase S. and Partenscky H.W. (1982) Wave run-up at sea dikes under oblique wave approach. In *Proceedings of the Eighteenth ICCE*, chapter 50. Cape Town, South Africa.

5.105. Thompson D.M. and Shuttler R.M. (1975) Riprap design for wind wave attack. A laboratory study in random waves. *Report EX 707*. Hydraulic Research Station, Wallingford, UK.

5.106. Van der Meer J.W. (1985) Stability of rubble mound revetments and breakwaters under random wave attack. In *Development in Breakwaters, ICE, Proceedings of the Breakwaters '85 Conference*. London, UK.

5.107. Van der Meer J.W. and Pilarczyk K.W. (1986) Dynamic stability of rock slopes and gravel beaches. In *Proceedings of the Twentieth ICCE*, chapter 125. Taipei, Taiwan.

5.108. Walton I.L. and Weggel J.R. (1981) Stability of rubble-mound breakwaters. *Proc. ASCE, J. WPC OE*, **107**, no WW3, 195–201.

5.109. Whillock A.F. and Price W.A. (1976) Armour blocks as slope protection. In *Proceedings of the Fifteenth ICCE*, chapter 147. Honolulu, Hawaii.

5.110. Thompson D.M. and Shuttler R.M. (1976) Design of riprap slope protection against wind waves. *CIRIA Report 61*. Hydraulic Research Station, Wallingford.

5.111. The Gas Council (1960) *Industrial Gas Handbook*.

5.112. Chappell W.G. (1973) Pressure time diagrams for explosion vented spaces. *A.I. Chem. E., Eighth Loss Prevention Symposium*, p. 76.

5.113. Harvey J.F. (1985) *Theory and Design of Pressure Vessels*. Van Nostrand-Reinhold, New York.

5.114. Haug E., Dowlatyari P. and de Rouvray A. (1986) Numerical calculation of damage tolerance and admissible stress in composite materials using the PAM-FISS Bi-PHASE material model. *ESA SP-238*. European Space Agency (special publication). Belgium.

5.115. de Rouvray A., Vogel F. and Haug E. (1986) Investigation of micromechanics for composites, Phase 1 Rep. Vol. 2, *ESI Rep. ED/84–477/RD/MS* (under ESA/ESTEC contract). Eng. Sys. Int., Rungis-Cedex, France.

5.116. de Rouvray A., Dowlatyari P. and Haug E. (1987) Investigation of micromechanics for composites, Phase 2a Rep. *WP2, ESI Rep. ED/85–521/RD/MS* (under SEA/ASTEC contract). *Eng. Syst. Int.*, Rungis-Cedex, France.

5.117. Magee C.L. and Thornton P.H. (1978) Design considerations in energy absorption by structural collapse. *SAE Trans.*, **87**, 2041–55.

5.118. Thornton P.H., Mahmood H.F. and Magee C.L. (1983) Energy absorption by structural collapse. In *Structural Crashworthiness* (Ed. by M. Jones and T. Wierzbicki). pp. 96–117. Butterworth, London.

5.119. Dye L.C. and Lankford B.W. (1966) A simplified method of designing ship structure for air blast. *Nav. Eng. J.*, **693**.

5.120. JCSS (1981) General principles on reliability for structural design. *Jt. Comm. Struct. Saf.*, **35**, part II.

5.121. Bach-Gansmo O. et al. (1985) Design against accidental loads in mobile platforms. *Project Summary Report, Rep. No. 15, Veritec Rep. 85–3094*. Veritec/Otter, Oslo, Norway.

5.122. Amdahl J. et al. (1987) Progressive collapse analysis of mobile platforms. *Proc. Int. Symp. PRADS, 3rd.*

5.123. Fjeld S. (1983) Design for explosion pressure/structural response. *Seminar, Gas Explosions – Consequences and Measures*. Norw. Soc. Char. Eng., Geilo.

5.124. Ellis G.R. and Perret K.R. (1980) The design of an impact resistant roof for platform wellhead modules. In *Proceedings of the OTC, Paper no. 3907*. Houston, USA.

5.125. Bach-Gansmo O. (1982) Selection of relevant accidental loads based on reported rig accidents. Project report no. 3. Design against accidental loads on mobile platforms. *DnV Report 82–0764*. Norway.

5.126. Kjeoy H. and Amdahl J. (1979) Impacts and collisions offshore. Progress report no. 8. Ship impact forces in collision with platform legs. *DnV Report 79–0691.*

5.127. de Oliveira J.G. and Mavrikios Y. (1983) Design against collision for offshore structures. *Report M1TSG 83–7*. Massachusetts Institute of Technology, USA.

5.128. Wenger A., Edvardsen G., Olafssen S. and Alvestad T. (1983) Design for impact of dropped objects. Fifteenth Annual Offshore Technology Conference, Houston, Texas, May 1983, OTC Paper 4471.

5.129. Blok J.J., Brozius L.H. and Dekker J.N. (1983) The impact loads of ships colliding with fixed structures. Fifteenth Annual Offshore Technology Conference, Houston, Texas, May 1983, OTC Paper 4469.

5.130. Foss G. and Evardsen G. (1982) Energy absorption during ship-impact on offshore steel structures. Fourteenth Annual Offshore Technology Conference, Houston, Texas, May 1982, OTC Paper 4217.

5.131. Chryssanthopoulos M. and Skjerven E. (1983) Progressive collapse analysis of a jack-up platform in intact and damaged condition. Project report 9 in design against accidental loads on mobile platforms. *DnV Technical Report 83–1026*. Norway.

5.132. Valsgard S. (1982) Design against accidental loads on mobile platforms. Presented at Closure Conference of Safety Offshore Project, Stavanger, Norway, November 1982. (Also issued as *DnV Paper 82–P080*.)

5.133. Hagiwara K., Tahanabe H. and Kawano H. (1983) A proposed method of predicting ship collision damage. *Int. J. Impact Eng.*, **1**, 257–79.

5.134. Richards D.M. and Andronicou A. (1985) Residual strength of dented tubulars impact energy correlation. In *Proceedings of the Fourth International Symposium of Offshore Mechanics and Arctic Engineering*, pp. 1–10. OMAE-ASME, Dallas, Texas.

5.135. Jones N., Jouri W.S. and Birch R.S. (1984) On the scaling of ship collision damage. In *Proceedings of the Third International Congress*. Athens, Greece.

5.136. Ronalds B.F. and Dowling P.J. (1985) Damage of orthogonally stiffened shells. In *Proceedings of the BOSS 85 Conference*. Delft.

5.137. Griffiths D.R. and Wickens H.G. (1984) The effects of damage on circular tubular compression members. In *Proceedings of the Third International Space Structures Conference*. University of Surrey.

5.138. Ellingwood B. (1981) Treatment of accidental loads and progressive failures in design standards. In *Proceedings of the Third International Conference on Structural Safety and Reliability (ICOSSAR 3)*, pp. 649–65. Trondheim, Norway.

5.139. Davies I.L. (1980) A method for the determination of the reaction forces and structural damage arising in ship collisions. In *Proceedings of the European Offshore Petroleum Conference and Exhibition*, Paper EUR237, pp. 245–54. London, 1980. (Also in *J. Petroleum Technology*, 2006–14, 1981.)

5.140. Valsgard S. and Pettersen E. (1983) Simplified non-linear analysis of ship/ship collisions. *Norwegian Maritime Research*, **10**, 2–17.

5.141. Woisin G. (1979) Design against collision. In *International Symposium on Advances in Marine Technology*, Vol. 2, pp. 309–36. Trondheim.

5.142. Faulkner D. (1979) Design against collapse for marine structures. In *International Symposium on Advances in Marine Technology*, pp. 275–308. Trondheim.

5.143. Braun P. (1983) Mooring and fendering rational principles in design. *Eighth International Harbour Congress*, paper 2/21. Antwerp. Belgium.

5.144. Donegan E. (1982) New platform designs minimise ship collision damage. *Petroleum Engineer International*, February, 79–88.

5.145. Soreide T. (1985) Ultimate load analysis of marine structures. Tapir, University of Denmark.

5.146. Pettersen E. (1981) Assessment of impact damage by means of a simplified non-linear approach. *Second International Symposium on Integrity of Offshore Structures*, p. 317. Glasgow.

5.147. Donegan E.M. (1982) Appraisal of accidental impact loadings on steel piled North Sea structures. Fourteenth Annual Offshore Technology Conference, OTC Paper 4193. Houston, Texas.

5.148. *Suppressive Shields, Structural Design and Analysis Handbook.* (1977) US Army Corps of Engineers, Huntsville Division, HNDM-1110–1–2 (AD A049 017).

5.149. Dobbs N. and Caltigirone J.P. (1987) Structures to resist the effects of accidental explosions. Vol. 1 Introduction. *Special Publication ARLCD-SP-84001.* Government Printing Press, Washington DC, USA.

5.150. Dobbs N. et al. (1986) Structures to resist the effects of accidental explosions. Vol. II Blast, fragment and shock loads. *Special Publication ARLCD-SP-84001.* Government Printing Press, Washington DC, USA.

5.151. Dobbs N. et al. (1984) Structures to resist the effects of accidental explosions. Volume III Principles of dynamic analysis. *Special Publication ARLCD-SP-84001.* Government Printing Press, Washington DC, USA.

5.152. Dobbs N. et al. (1987) Structures to resist the effects of accidental explosions. Volume IV Reinforced concrete design. *Special Publication ARLCD-SP-84001.* Government Printing Press, Washington DC, USA.

5.153. Dobbs N. et al. (1987) Structures to resist the effects of accidental explosions. Volume V Structural steel design. *Special Publication ARLCD-SP-84001.* Government Printing Press, Washington DC, USA.

5.154. Dobbs N. et al. (1985) Structures to resist the effects of accidental explosions. Vol. VI Special considerations in explosive facility design. *Special Publication ARLCD-SP-84001.* Government Printing Press, Washington DC, USA.

5.155. Marshall W. (1982) An assessment of the integrity of PWR pressure vessels. Report of the Study Group of UKAEA, Risley, Cheshire.

5.156. Andrews Associates Inc and Hudgins, Thompson, Ball and Associates Inc "Final Report on Studies of Structural Response to Sonic Boom", for the Federal Aviation Agency, Vol. 1, February 1965.

5.157. Simpson J.D. (1966) The transient response of a Helmholtz resonator with application to sonic boom response studies. Ph.D. Thesis, Oklahoma State University, May 1966.

5.158. Whitehouse G.D. (1967) Coupled and Uncoupled Panel Response to Sonic Boom Type Inputs Ph.D. Thesis, Oklahoma State University, May 1967.

5.159. Reddy N.N. (1967) Response spectra of coupled acoustical resonators to transient excitations, Ph.D. Thesis, Oklahoma State University, May 1967.

5.160. Rusanov V.V. (1961) The Calculation of the Interaction of Non-Stationary Shock Waves and Obstacles. National Research Council of Canada Library, Ottawa, Canada, Technical Translation 1027 by D.A. Sinclair 1962. Translated from: Zhurnal Vychislitelnoi Fiziki, Akademiya Nauk, SSSR 1, Vol. 1, No. 2, 1961, p. 267.

5.161. Randall D.G. (1967) Methods for estimating distributions and intensities of sonic bangs. British Aeronautical Research Council, Report and Memoranda No. 3113, August 1967.

5.162. Lasing D.L. (1964) Application of acoustic theory to prediction of sonic-Boom ground patterns from maneuvering aircraft. National Aeronautics and Space Administration, TN-D-1860, October 1964.

5.163. Tyler L.D. (1965) Numerical solutions of the flow field produced by a plane shock wave emerging into a crossflow, Ph.D. Thesis, Oklahoma State University, May 1965; Published as Engineering Research Report SBW-10 by Tyler, L.D. and G.W. Zumwalt.

5.164. Walker W.F. and Tyler L.D. (1965) Literature survey on shock wave interactions with shocks and bodies. Oklahoma State University Research Report SBW-7.

5.165. Walker W.F. (1966) A numerical solution for the interactions of a moving shock wave with a turbulent mixing region, Ph.D. Thesis, Oklahoma State University, May 1966.

5.166. Busemann A. (1943) "Infinitesimale Kegelige Uberschallstromung" Schriften der Deutschen Akademie for Luftfahrshung, Vol. 7B, No. 3, P105, 1943 (Translation NACA TM 110).

5.167. Luneberg R.K. (1944) Mathematical theory of optics, Brown University Lectures.

5.168. Keller J.B. (1949–1950) Mechanics of continuous media, New York University Lectures.

5.169. Keller J.B. and Blank A. (1951) Diffraction and reflection of pulses by wedges and corners, Comm. Pure Appl. Math., Vol. IV, No. 1.

5.170. Von Neumann J. (1963) Oblique reflection of shocks, John Von Neumann Collected Works, Vol. VI, Macmillan, New York, p. 238.

5.171. Ting L. (1953) Diffraction and reflection of weak shocks by structures. *J. Math.* Phys., **XXXII**(2–3), 102.

5.172. Whitham G.B. (1956) On the propagation of weak shocks, *J. Fluid Mech.*, **1**, 290.

5.173. Ting L. (1957) Diffraction of disturbance around a convex right corner with applications in acoustics and wing-body interference. *J Aero. Sci.*, **24**, 281.

5.174. Filippov I.G. (1963) On the theory of diffraction of weak shock waves round contours of arbitrary shape, PMM, **27**(1), 309.

5.175. Reines F. and Von Neumann J. (1963) The Mach Effect and height of burst. John Von Neumann Collected Works, Vol. VI. Macmillan, New York, p. 309.

5.176. Lax P. (1953) On discontinuous initial value problems for nonlinear equations and finite difference schemes. LAMS – 1332.

5.177. Lax P. and Wendroff B. (1960) Systems of conservation laws. *Comm. Pure Appl. Math.*, **XIII**, 217.

5.178. Lax P. (1957) Hyperbolic systems of conservation of laws. *Comm. Pure Appl. Math.*, **X**, 537.

5.179. Von Neumann J. and Richtmeyer R.D. (1950) A method for the numerical calculation of hydrodynamic shocks. *J. Appl. Phys.*, **21**, 232.

5.180. Holf E. The partial differential equation $U_t + UU_x = \mu U$. *Comm. Pure Appl. Math.*, **III**, P201.

5.181. Oleninik A.O. (1963) Construction of a generalized solution of the cauchy problems for a quasi-linear equation of first order by the introduction of vanishing viscosity. American Mathematical Society Translations, **33**, Series 2m, 1963, 277.

5.182. Burstein S.Z. Numerical methods in multidimensional shocked flows, AIAA, **2**(12), 2111.

5.183. Richtmeyer R.D. (1957) Difference methods for initial-value problems, Interscience, New York.

5.184. Fox L. (1962) Numerical solution of ordinary and partial difference equations. Addison Wesley, Reading, MA.

6 Design for Impact and Explosion Including Gas Explosion

6.1. Getzler F., Komomek A. and Mazwicks A. (1968) Model study on arching above buried structures. *J. Soil Mech. Found., ASCE.*

6.2. Simiu E. (1975) Probabilistic models of extreme wind speeds: uncertainties and limitation. In *Proceedings of the Fourth International Conference on Wind Effect on Structures and Buildings*, pp. 53–62. London, UK.

6.3. Tryggvason B.V., Surry D. and Davenport A.G. (1976) Predicting wind-induced response in hurricane zones. *J. Struct. Div., ASCE*, **102**, no. ST12, 2333–51.

6.4. Sklarin J. (1977) *Probabilities of Hurricanes.* Research Report, Department of Civil Engineering, MIT, Cambridge, MA.

6.5. Fujita T.T. (1970) Estimates of a real probability of tornadoes from inflationary reporting of their frequencies. *SMRP Research Paper No. 89*, Satellite and Mesometeorology Research Project, University of Chicago.

6.6. Thom H.C.S. (1963) Tornado probabilities. *Monthly Weather Review*, October–December, pp. 73–736.

6.7. Pautz M.E. (Ed.) (1969) Severe local storm occurrences 1955–1967. *ESSA Tech. Memo. WBTM FCST 12*, US Department of Commerce, Environmental Science Services Administration, Washington DC, USA.

6.8. Markee E.H. jr, Beckerley J.G. and Sanders K.E. (1964) *Technical Basis for Interim Regional Tornado Criteria.* US Atomic Energy Commission, Office of Regulation, WASH 1300.

6.9. Fujita T.T. (1972) F-scale classification of 1971 tornadoes. *SMRP Research Paper No. 100*. University of Chicago.

6.10. Singh M.P., Morcos A. and Chu S.L. (1973) Probabilistic treatment of problems in nuclear power plant design. In *Proceedings of the Speciality Conference on Structural Design of Nuclear Plant Facilities*, Vol. 1, pp. 263–89. Chicago, IL.

6.11. Garson R.C., Catalan J.M. and Cornell C.A. (1975) Tornado design winds based on risk. *J. Struct. Div., ASCE*, **101**, no. ST9, 1883–97.

6.12. Hoecker W.H. Jr. (1960) Wind speed and air flow patterns in the Dallas tornado of April 2, 1957. *Monthly Weather Review*, **88**, no. 5, 167–80.

6.13. Hoecker W.H. Jr. (1961) Three dimensional pressure patterns of the Dallas tornado and some resultant implications. *Monthly Weather Review*, **89**, no. 12, 533–42.

6.14. Wen Y.K. (1975) Dynamic wind loads on tall buildings. *J. Struct. Div., ASCE*, **101**, no. ST1, 169–85.

6.15. McDonald J.R., Minor J.E. and Mehta K.C. (1973) Tornado generated missiles. In *Proceedings of the Speciality Conference on Structural Design of Nuclear Power Plant Facilities*, Vol. II, pp. 543–56. Chicago, IL.

6.16. Abbey R.F. and Fujita T.T. (1975) Use of tornado path length and gradations of damage to assess tornado intensity probability. Ninth Conference on Severe Local Storms, Norman, Oklahoma.

6.17. VanDorn W.G. (1965) Tsunamis. In *Advances in Hydroscience*, Vol. 2. Academic Press, New York.

6.18. Johnson B. (1976) Tornado missile risk analysis. Study conducted for Boston Edison Power Company by Science Applications Inc. Private communication.

6.19. Bush S.H. (1973) Probability of damage to nuclear components due to turbine failure. *Nucl. Safety*, **14**(3), 187–201.

6.20. Rankin A.W. and Seguin B.R. (1973) Report of the investigation of the turbine-wheel fracture at Tanners Creek, *Nucl. Safety*, **14**(3), 47.

6.21. Kalderton D. (1972) Steam turbine failure at Hinkley Point 'A'. *Proc. Inst. Mech. Eng.*, **186**, 341.

6.22. Gray J.L. (1972) Investigation into the consequences of the failure of a turbine-generator at Hinkley Point 'A' Power Station. *Proc. Inst. Mech. Eng.*, **186**, 379.

6.23. Downs J.E. (1973) Hypothetical turbine missiles – probability of occurrence. Memo report, General Eletric Co.

6.24. Hagg A.C. and Sankey G.O. (1974) The containment of disk burst fragments by cylindrical shells. *Transactions of the ASME, J. Eng. Power*, **96**, 114–23.

6.25. Semanderes S.N. (1972) Method of determining missile impact probability. *Trans. Am. Nucl. Soc.*, **15**, no. 1, 401.

6.26. Bhattacharyya A.K. and Chaudhuri S.K. (1976) The probability of a turbine missile hitting a particular region of a nuclear power plant. *Nucl. Technol.*, **28**, 194–8.

6.27. Johnson B. et al. (1976) Analysis of the turbine missile hazard to the nuclear thermal power plant at Pebble Springs, Oregon. Science Applications Inc. Report to the Portland General Electric Company, PGE-2012.

6.28. USNRC (1975) *Standard Review Plan, Section 3.5.1.6., Aircraft Hazards*. US Nuclear Regulatory Commission, Office of Nuclear Reactor Regulation.

6.29. Chalapathi C.V., Kennedy R.P. and Wall I.B. (1972) Probabilistic assessment of aircraft hazard for nuclear power plants. *Nucl. Eng. Des.*, **19**, 333–64.

6.30. Chalapathi C.V. and Wall I.B. (1970) Probabilistic assessment of aircraft hazard for nuclear power plants – II. *Trans. Am. Nucl. Soc.*, **13**, 218.

6.31. Wall I.B. (1974) Probabilistic assessment of aircraft risk for nuclear power plants. *Nuclear Safety*, **15**(3).

6.32. Hornyik K. (1973) Airplane crash probability near a flight target. *Trans. Am. Nucl. Soc.*, **16**, 209.

6.33. Hornyik K. and Grund J.E. (1974) Evaluation of air traffic hazards at nuclear power plants. *Nucl. Technol.*, **23**, 28–37.

6.34. USNRC (1975) *NRC Regulatory Guide 1.70, Standard Format and Content of Safety Analysis Reports for Nuclear Power Plants*, LWR edn, revn 3, NUREG-75/094. US Nuclear Regulatory Commisssion, Office of Standards Development.

6.35. Anon (1976) Aircraft crash probabilities. *Nucl. Saf.*, **17**, 312–14.

6.36. Stevenson J.D. (1973) Containment structures for pressurized water reactor systems, past, present and future – state of the art. Second International Conference on Structural Mechanics in Reactor Technology, Berlin, September 1973, Paper 72/1.

6.37. ACI–ASME Joint Technical Committee (1975) Code for concrete vessels and containments, ASME boiler and pressure vessel code section III – division 2 and ACI standard, 359–74.

6.38. US Atomic Energy Commission (1973) Regulatory guide 1.57. Design limits and loading combinations for metal primary reactor components. US Atomic Energy Commission, Directorate of Regulatory Standards.

6.39. US Atomic Energy Commission (1976) Standard review plan, section 3.8.2. Steel containment. US Atomic Energy Commission, Directorate of Licensing.

6.40. American Concrete Institute (ACI) (1976) ACI standard 349–76. Code requirements for nuclear safety related concrete and structures.

6.41. US Atomic Energy Commission (1976) Standard review plan, section 3.8.3. Concrete and steel internal structures of steel or concrete containments. US Atomic Energy Commission, Directorate of Licensing.

6.42. American Concrete Institute (1975) Proposed code requirements for nuclear safety-related concrete structures, draft of section C.3.3.3., rotational limits. American Concrete Institute, Committee 349.

6.43. ASCE (1961) Design of structures to resist nuclear weapons effects. *American Society of Civil Engineers Manual No. 42*.

6.44. American Concrete Institute (1975) Proposed code requirements for nuclear safety-related concrete structures. Report by the American Concrete Institute, Committee 349.

6.45. Amirikian A. (1950) Design of protective structures. *Report NT-3726*. Bureau of Yards and Docks, Department of the Navy Washington DC, USA.

6.46. Gwaltney R.C. (1968) Missile generation and protection in light-water-cooled power reactor plants. *ORNL NSIC-22*. Oak Ridge National Laboratory, Oak Ridge, Tennessee, for the US Atomic Energy Commission.

6.47. Kennedy R.P. (1966) *Effects of an Aircraft Crash into a Concrete Building.* Holmes & Narver Inc, Anaheim, CA.

6.48. Vassalo F.A. (1975) Missile impact testing of reinforced concrete panels. *HC-5609-D-1*. Calspan Corporation, Buffalo, New York, prepared for Bechtel Power Corporation.

6.49. United Engineers and Constructors Inc (1975) Seabrook Station aircraft impact analysis. *Docket Nos. 50–433/444*. Prepared for Public Service Company of New Hampshire, Seabrook, New Hampshire.

6.50. United Engineers and Constructors Inc (1975) Supplemental information to Seabrook Station aircraft impact analysis. *Docket Nos. 5–443/444*. Prepared for Public Service Company of New Hamsphire, Seabrook, New Hampshire.

6.51. Lorenz H. (1970) Aircraft impact design. *Power Eng.*, November, 44–6.

6.52. Gilbert Associates Inc (1968) Three-Mile Island preliminary safety analysis report. *Docket No. 50–289*, supplement W5. Report prepared for Metropolitan Edison Company.

6.53. Stevenson A.E. (1975) Tornado vulnerability of nuclear production facilities. Sandia Laboratories Los Angeles, California, USA.

6.54. Chalapathi C.V. (1970) Probability of perforation of a reactor building due to an aircraft crash. *HN-212*. Holmes & Narver, Anaheim, CA.

6.55. White R.W. & Botsford N.B. (1963) Containment of fragments for a runaway reactor. *Report SRIA-113*. Stanford Research Institute, USA.

6.56. American Society of Mechanical Engineers (1974) Rules for construction of nuclear power plant components, ASME boiler and pressure vessel code section III division 1.

6.57. US Atomic Energy Commission (1974) Reactor safety study, an assessment of accident risks in the US commercial nuclear power plants. *WASH-1400*. Washington, USA.

6.58. 1976 Quality assurance criteria for nuclear power plants and fuel reprocessing plants. Federal Regulation 10 CFR 50 appendix B.

6.59. American National Standards Institute (1978) Status report of projects under the Nuclear Standards Management Board. *NSMB SR-15*.

6.60. Anthony E.J. (1977/8) The use of venting formulae in the design and protection of buildings and industrial plant from damage by gas or vapour explosions. *J. Hazardous Mater.*, **2**, 23.

6.61. West H.W.H., Hodgkinson H.R. and Webb W.F. (1973) The resistance of brick walls to lateral loading. *Proc. Brit. Ceramic Soc.*, **21**, 141.

6.62. Hendry A.W., Sinha B.P. and Maurenbracher A.H.P. (1971) Full scale tests on the lateral strength of brick cavity walls with precompression. *Proc. Brit. Ceramic Soc.*, 33.

6.63. Astbury N.F. and Vaughan G.N. (1972) Motion of a brickwork structure under certain assumed conditions. *British Ceramic Research Association Technical Note No. 191*.

6.64. Mainstone R.J. (1971) The breakage of glass windows by gas explosions. *Building Research Station Current Paper 26/71*.

6.65. West H.W.H. (1973) A note on the resistance of glass windows to pressures generated by gaseous explosions. *Proc. Brit. Ceramic Soc.*, **21**, 213.

6.66. British Gas Corporation (1977) Code of practice for the use of gas in atmosphere gas generators and associated plant, parts 1, 2 and 3. *Publication IM/9*.

6.67. British Gas Corporation (1982) Code of practice for the use of gas in low temperature plant (includes aspects of dual fuel burners previously covered by *IM/7*). *Publication IM/18*.

6.68. Marshall M.R. (1980) Gaseous and dust explosion venting: determination of explosion relief requirements. Third International Symposium on Loss Prevention and Safety Promotion in the Process Industries, Basle, Switzerland.

6.69. Howard W.B. and Karabinis A.H. (1980) Tests of explosion venting of buildings. Third International Symposium on Loss Prevention and Safety Promotion in the Process Industries, Basle, Switzerland.

6.70. Hattwig M. (1977) Selected aspects of explosion venting. Second International Symposium on Loss Prevention and Safety Promotion in the Process Industries, Heidelberg.

6.71. Croft W.M. (1981) Fires involving explosion – a literature review. *Fire Safety J.*, **3**, 21.

6.72. Butlin R.N. and Tonkin P.S. (1974) Pressures produced by gas explosions in a vented compartment. *Fire Research Note No. 1019*.

6.73. Timoshenko S. and Goodier G.N. (1951) *Theory of Elasticity*, 2nd edn. McGraw-Hill.

6.74. Barkan D.D. (1962) *Dynamics of Bases and Foundations*, McGraw Hill, New York.

6.75. Bycroft G.N. (1956) Forced vibration of a rigid circular plate on a semi-infinite elastic space and on an elastic stratum. *Phil. Trans R. Soc. London, Ser. A*, **248**, 327–68.

6.76. Reissner E. (1936) Stationare Axial Symmetricke durch eine schuttiond massive Erregt schwingiuingen eines Homogenen Blastischen Halbraumes. *Ingenieur–Archiev*, **7**, no. 6, Berlin, 381–96.

6.77. Nowaki W. (1961) *Dynamika Budowli*. Arkady, Warsaw.

6.78. Richart F.E. et al. (1970) *Vibrations of Soils and Foundations*. Prentice Hall, New Jersey, USA.

6.79. Technical Regulations for Shelters TB78I. Publication no. 6.06. Swedish Government Press, Stockholm, Sweden.

6.80. Home Office (1975) *Home Office Manual: Domestic Nuclear Shelters*. HMSO, UK.

6.81. Butler D.K. (1975) Development of high-velocity powder gun and analysis of fragment penetration tests into sand. Misc. paper S-75-27, Soils and Pavements Laboratory, US Army Engineer Waterways Experiment Station, Vicksburg, MS.

6.82. Bernard R.S. and Hanagud S.V. (1975) Development of a projectile penetration theory, Report I, Penetration theory for shallow to moderate depths. Technical Report S-75-9, Soils and Pavements Laboratory, US Army Engineer Waterways Experiment Station, Vicksburg, MS.

6.83. Bernard R.S. (1976) Development of a projectile penetration theory, Report 2, Deep penetration theory of homogeneous and layered targets. Technical Report S-75-9, Soils and Pavements Laboratory. US Army Engineer Waterways Experiment Station, Vicksburg, MS.

6.84. Hammel J. (1979) Impact loading on a spherical shell. Fifth International Conference on Structural Mechanics in Reactor Technology (SMiRT), Berlin.

6.85. Barber E.M. et al. (1972) A study of air distribution in survival shelters using a small-scale modelling technique. Report 10689, USA National Bureau of Standards.

6.86. Barneby H.L. et al. (1963) Toxic gas protection. Paper to ASHRAE Symp. Survival Shelters, 1962.

6.87. Barthel R. (1965) Research on the climate in an underground shelter. Ingenieur **77**, 143–7 (in Dutch).

6.88. Barthel R. (1965) Theoretical and experimental research regarding the in-door climate in an underground shelter. Ingenieur, **77**, 6143–7 (in Dutch).

6.89. Cooper J. (1980) After the bomb. *J. Chartered Insti. Building Services*, **2**, 48–9.

6.90. Dasler A.R. and Minrad D. (1965) Environmental physiology of shelter habitation. ASHRAE Trans. **71**, 115–24.

6.91. Drucker E.E. and Cheng H.S. (1963) Analogue study of heating in survival shelters. ASHRAE Symp. Survival Shelters, 1962, ASHRAE.

6.92. Bigg J.M. (1964) Introduction to structural dynamics. McGraw Hill, New York.

6.93. Gates A.S. (1963) Air revitalization in sealed shelters. ASHRAE Symp. Survival Shelters, 1962, ASHRAE.

6.94. Gessner H. (1961) The ventilation of air-raid shelters. Schweizerische Blätter für Heizung und Lüftung, **28**, 1–12 (in German).

6.95. Hanna G.M. (1962) Ventilation design for fallout and blast shelters. Air Engineering, **4**, 19–21.

6.96. Home Office (1981) Domestic nuclear shelters (DNS) – Technical guidance. HMSO.

6.97. Home Office (1981) Domestic nuclear shelters. HMSO.

6.98. Eibl J. (1982) Behaviour of critical regions under soft missile impact and impulsive loading. IBAM, June.

6.99. Hughes G. and Speirs D. (1982) An investigation of the beam impact problem. Technical Report 546, C & CA, UK (now British Cement Association).

6.100. Bate S. (1961) The effect of impact loading on prestressed and ordinary reinforced concrete beams. National Building Studies Research Paper 35.

6.101. Billing I. (1960) Structure concrete. Macmillan, London.

6.102. Watson A. and Ang T. (1982) Impact resistance of reinforced concrete structures. In: Design of Dynamic Loading, Construction Press, U.K.

6.103. Watson A. and Ang T. (1984) Impact response and post-impact residual strength of reinforced concrete structures. Int. Conf. and Exposition of Structural Impact and Crashworthiness, Imperial College, London, UK.

6.104. Perry S. and Brown I. (1982) Model prestressed slabs subjected to hard missile loading. In: Design for dynamic loading, Construction Press, London, UK.

6.105. Perry S. Brown I. and Dinic G. (1984) Factors influencing the response of concrete slabs to impact. International Conference on and Exposition of Structural Impact and Crashworthiness, Imperial College, London, UK.

6.106. Kufuor K. and Perry S. (1984) Hard impact of shallow reinforced concrete domes. Int. Conf. and Exposition of Structural Impact and Crashworthiness, Imperial College, London, UK.

6.107. Burgess W. and Campbell-Allen D. (1974) Impact resistance of reinforced concrete as a problem of containment. Research Report no. R251, School of Civil Engineering, University of Sydney.

6.108. Stephenson A. (1976) Tornado-generated missile full-scale testing. In: Proc Symp. Tornadoes, Assessment of Knowledge and Implications for Man. Texas University.

6.109. Jankov Z., Turnham J. and While M. (1976) Missile tests of quarter-scale reinforced concrete barriers. In: Proc. Symp. Tornadoes, Assessment of Knowledge and Implications for Man, Texas University, June 1976.

6.110. Stephen A. and Silter G. (1977) Full-scale tornado-missile impact tests. Fifth International Conference on Structural Mechanics in Reactor Technology (SMiRT), Berlin, 1977, Paper J10/1.

6.111. Jonas W. and Rudiger E. (1977) Experimental and analytical research on the behaviour of reinforced concrete slabs subjected to impact loads. Fifth International Conference on Structural Mechanics in Reactor Technology (SMiRT), Berlin, Paper J7/6.

6.112. Beriaud C. et al. (1977) Local behaviour of reinforced concrete walls under hard missile impact. Fifth International Conference on Structural Mecbanics in Reactor Technology (SMiRT), Berlin, 1977, Paper J7/9.

6.113. Gupta Y. and Seaman L. (1977) Local response of reinforced concrete to missile impacts. Fifth International Conference on Structural Mechanics in Reactor Technology (SMiRT), Berlin, 1977, Paper J10/4.

6.114. Barr P. et al. (1982) An experimental investigation of scaling of reinforced concrete structures under impact loading. In: Design for dynamic loading, Construction Press, London, UK.

6.115. Barr P. et al. (1983) Experimental studies of the impact resistance of steel faced concrete composition. Seventh International Conference on Structural Mechanics in Reactor Technology (SMiRT), 1983, paper J8/4, Chicago, USA.

7 Collision, Fragmentation and Materials

7.1. Al-Hassani S.T.S. and Silva-Gomes J.F. (1979) Internal fracture paraboloids of revolution due to stress wave focussing. Conf. Ser. – Inst. Phys. 47, 187–96.

7.2. Al-Hassani S.T.S. and Silva-Gomes J.F. (1986) Internal fractures in solids of revolution due to stress wave focussing. In: Shock Waves and High-strain-rate Phenomena in Metals (Ed. by M.A. Meyers and. L.E. Murr), chapter 10. Plenum, New York.

7.3. Al-Hassani S.T.S. (1986) Fracturing of explosively loaded solids. In: Reid S.R. (ed.) Metal Forming and Impact Mechanics, Chap. 18, Pergamon, Oxford.

7.4. Swain M.V. and Lawn B.R. (1976) Indentation fracture in brittle rocks and glasses. *Int. J. Rock Mech. Min. Sci. Geomech. Abstr.*, 13, 311–319.

7.5. Jones N. and Liu J.H. (1988) Local impact loading of beams. In: Intense dynamic loading and its effects, Science Press, Beijing, and Pergamon Press, pp. 444–449.

7.6. Liu J.H. and Jones N. (1988) Dynamic response of a rigid plastic clamped beam struck by a mass at any point on the span. *Int. J. Solids Struct.*, **24**, 251–270.

7.7. Liu J.H. and Jones N. (1987) Experimental investigation of clamped beams struck transversely by a mass. *Int. J. Impact Eng.*, **6**, 303–335.

7.8. Liu J.H. and Jones N. (1987) Plastic failure of a clamped beam struck transversely by a mass. Report ES/31/87. Department of Mechanical Engineering, University of Liverpool.

7.9. Jones N. (1979) Response of structures to dynamic loading. *Conf. Ser. – Inst. Phys.* **47**, 254–276.

7.10. Recht R.F. and Ipson T.W. (1963) Ballistic perforation dynamics. *J. Appl. Mech.*, **30**, 384–390.

7.11. Lindholm U.S., Yeakley L.M. and Davidson D.L. (1974) Biaxial strength tests on beryllium and titanium alloys. AFML-TR-74–172, Air Force Systems Command, Wright-Patterson Air Force Base, OH.

7.12. Jones N. (1970) The influence of large deflections on the behavior of rigid-plastic cylindrical shells loaded impulsively. *J. Appl. Mech.* **37**, 416–425.

7.13. Lindberg H.E., Anderson D.L., Firth R.D. and Parker L.V. (1965) Response of reentry vehicle-type shells to blast loads. SRI project FGD-5228, Stanford Research Institute, Menlo Park, CA.

7.14. Cronkhite J.D. and Berry V.L. (1983) Investigation of the crash impact characteristics of helicopter composite structure. USA AVRADCDM-TR-82 D.14.

7.15. Farley G.L. (1987) Energy absorption of composite materials and structures. 43rd American Helicopter Society Annual Forum, New York.

7.16. Hull D. (1983) Axial crushing of fibre reinforced composite tubes. In: Jones N., Wierzbider T. (eds.) Structural crashworthiness, Butterworth, London, pp. 118–135.

7.17. Schmeuser D.W. and Wickliffe L.E. (1987) Impact energy absorption of continuous fibre composite tubes. Trans ASME 109:72–77.

7.18. Thornton P.H. and Edwards P.J. (1982) Energy absorption in composite tubes. J. Comp. Mat. 16:521–45

7.19. Hull D. (1982) Energy absorption of composite materials under crush conditions. In: Hayashi T., Kawata K., Umekawa S. (eds.) Progress in science and engineering of composites, Vol. I, ICCM-IV, Tokyo University.

7.20. O'Connell W.J. and Fortney R.A. (1974) Turbine missile impact analysis: A detailed treatment. Transactions of the American Nuclear Society 19, 31; EDS Nuclear Inc. Report, 27 October 1974.

7.21. Moody F.J. (1969) Prediction of blowdown thrust and jet forces. ASME Transaction 69-HT-31, American Society of Mechanical Engineers.

7.22. Norris C.H. et al. (1959) Structural design for dynamic loads. McGraw-Hill, New York.

7.23. Emori R.I. (1968) Analytical approach to automobile collisions. Automotive Engineering Congress, Detroit, Michigan, Paper no. 680016.

7.24. Ivey D.L., Ruth E. and Hirsch T.J. (1970) Feasibility of lightweight cellular concrete for vehicle crash cushions. Paper presented at the Annual Meeting of the Highway Research Board, Washington DC.

7.25. Chen E.P. and Sih G.C. (J977) Transient response of cracks to impact loads. In: Elasto-dynamic crack problems. Vol. 4. Noordhoff, Gröningen, Leyden.

7.26. Davison L. and Graham R.A. (1979) Shock compression of solids. *Phys. Rep.* **55**, 255–379.

7.27. Meyer M.A. and Aimonc C.T. (1983) Dynamic fracture (spalling) of metals. *Prog. Mat. Sci.* **28**, 1–96.

7.28. Reckling K.A. (1977) On the collision protection of ships. PRADS Symp., Tokyo.

7.29. Nagasawa H., Arita K., Tani M. and Oka S. (1977) A study on the collapse of ship structure in collision with bridge piers. *J. Soc. Nav. Arch. Japan*, **142**.

7.30. Macaulay M.A. and Macmillan R.H. (1968) Impact testing of vehicle structures. In: Proc. 12th FISITA Congress, Barcelona.

7.31. Emori R.I. (1968) Analytical approach to automobile collisions. SAE Paper 680016, Society of Automobile Engineers, USA.

7.32. Neilson I.D. et al. (1968) Controlled impact investigations. TRRL Report LR 132, Transport Road Research Laboratory, Crowthome, UK.

7.33. Grime G. and Jones I.S. (1969) Car collisions – The movement of cars and their occupants. *Proc. I. Mech. Eng.* **184**(5).

7.34. Emori R.I. and Tani M. (1970) Vechicle trajectories after intersection collision impact. SAE Paper 700176, Society of Automobile Engineers.

7.35. Wall J.G. et al. (1970) Comparative head-on impact tests. TRRL Report LR 155, Transport Road Research Laboratory, Crowthome, UK.

7.36. Jones I.S. (1975) Mechanics of roll-over as the result of curb impact. SAE Paper 750461, Society of Automobile Engineers.

7.37. Wagner R. (1978) Compatibility in frontal collisions. In: Proc. 17th FISITA Congress, Budapest.

7.38. Rouse H. and Howe J.W. (1953) Basic mechanics of fluids. Wiley, New York.

7.39. Kinslow R. (ed.) (1970) High velocity impact phenomena. Academic Press,

7.40. Nowacki W.K. (1978) Stress waves in non-elastic solids. Pergamon, Oxford.

7.41. Hurty W.C. and Rubinstein M.F. (1964) Dynamics of structures. Prentice-Hall,

7.42. Morrow C.T. (1963) Shock and vibration engineering. Wiley, New York.

7.43. Biggs J.M. (1964) Introduction to structural dynamics, Chapter 2, McGraw-Hill, New York.

7.44. Snowdon I.C. (1968) Vibration and Shock in Damped Mechanical Systems. Wiley, New York.

7.45. Craig R.R. (1981) Structural dynamics: An introduction to computer methods. Wiley, New York.

7.46. Davies G.A. (1984) Structural impact and crashworthiness. Vol. I, Chapter 7, Elsevier, Amsterdam.

7.47. Andrews K.P.F. et al. (1983) Classification of the axial collapse of cylindrical tubes under quasi-static loading. *Int. J. Mech. Sci.* **25**, 678–96.

7.48. Bodner S.R. and Symonds P.S. (1972) Experimental and theoretical investigation of the plastic deformation of cantilever beams subjected to impulsive loading. *J. Appl. Mech.* (December):719–28.

7.49. Conway M.D. and Jakubowski M. (1969) Axial impact of short cylindrical bars. *J. Appl. Mech.* **36**, 809.

7.50. Hagiwara K. et al. (1983) A proposed method of predicting ship collision damage. *Int. J. Impact Eng.* **1**, 257–80.

7.51. Lee E.H. and Morrison J.A. (1956) A comparison of the propagation of longitudinal waves in rods of viscoelastic materials. *J. Polymer Science* **19**, 93–110.

7.52. Samuelides E. and Frieze P.A. (1983) Strip model simulation for low energy impacts on flat-plated structures. *Int. J. Mech. Sci.* **25**, 669–86.

7.53. Grady D.E. (1981) Fragmentation of solids under impulsive stress loading. *J. Geophys. Res.* **86**, 1047–54.

7.54. Grady D.E. (1981) Application of survival statistics to the impulsive fragmentation of ductile rings. In: Meyers M.A., Murr L.E. (eds.) Shock waves and high-strain-rate phenomena in metals, Plenum, New York, pp. 181–192.

7.55. Grady D.E., Bergstresser T.K. and Taylor J.M. (1985) Impact fragmentation of lead and uranium plates. SAND85–1545 (technical report), Sandia Laboratories.

7.56. Grady D.E. and Kipp M.E. (1979) The micromechanics of impact fracture of rock. *Int. J. Rock Mech. Min. Sci.* **16**, 293–302.

7.57. Cour-Palais B.G. (1987) Hypervelocity impact in metals, glass and composites. *Int. J. Impact Eng.* **5**, 221–38.

7.58. Holsapple K.A. (1987) The scaling of impact phenomena. *Int. J. Impact Eng.* **5**, 343–56.

7.59. Johns Hopkins University (1961) The resistance of various metallic materials to perforation by steel fragments, Empirical relationships for fragment residual velocity and residual weight. Ballistic Res. Lab. Proj. Thor T.R. no. 47, Johns Hopkins University, Baltimore, MD.

7.60. Johns Hopkins University (1961) The resistance of various non-metallic materials to perforation by steel fragments, Empirical relationships for fragment residual velocity and residual weight. Ballistic Res. Lab. Proj. Thor T.R. no. **47**, Johns Hopkins University, Baltimore, MD.

7.61. Fairfull A.H. (1986) Scaling effects in the energy absorption of axially crushed composite tubes. PhD thesis, University of Liverpool.

7.62. Price J.N. and Hull D. (1987) The crush performance of composite structures. In: Marshall IH (ed.) Composite Structures, Elsevier, Amsterdam, pp. 2.32–2.44.

7.63. Price J.N. and Hull D. (1987) Axial crushing of glass fibre-polyster oomposite cones. *Comp. Sci. Technol.* **28**, 211–30.

7.64. Berry J.P. (1984) Energy absorption und failure mechanisms of axially crushed GRP tubes. PhD thesis. University of Liverpool.

7.65. de Runtz J.A. and Hodge P.G. (1963) Crushing of tubes between rigid plates. *J. Appl. Mech.* **30**, 381–95.

7.66. Abramowicz W. and Jones N. (1984) Dynamic axial crushing of square tubes. *Int. J. Impact Eng.* **2**(2), 179–208.

7.67. Soreide T.H. and Amdahl J. (1982) Deformation characteristics of tubular members with reference to impact loads from collisions and dropped objects. Norw. *Marit. Res.* **10**, 3–12.

7.68. Soreide T.H. and Kavlie D. (1985) Collision damage and residual strength of tubular members in steel offshore structures. In: Narayanan R. (ed.) Shell structures stability and strength, Elsevier, London, pp. 185–220.

7.69. Taby J. and Moan T. (1985) Collapse and residual strength of damaged tubular members. BOSS '85, Paper B8.

7.70. Durkin S. (1987) An analytical method for predicting the ultimate capacity of a dented tubular member. *Int. J. Mech. Sci.* **29**, 449–67.

7.71. Ellinas C.O. and Valsgård S. (1985) Collisions and damage of offshore structure: A state-of-the art. In: Proc. Fourth Int. Symp. OMAE, Organisation of Motor Association for Engineering, USA.

7.72. de Oliveira J.G. (1981) Design of steel offshore structures against impact loads due to dropped objects. Report No. 81–6, Department of Ocean Engineering, Massachusetts Institute of Technology, Cambridge, MA.

7.73. Adamchak J. (1984) An approximate method for estimating the collapse of a ship's hull in preliminary design. In: Proc. Ship Struct. Symp., SNAME, Arlington, VA.

7.74. Furness O. and Amdahl J. (1979) Computer simulation study of offshore collisions and analysis of ship platform impacts. Paper presented at The 2nd Int. Symp. Offshore Structures, Brazil, October 1979; also In: Applied Ocean Research **2**(3), 119–27.

7.75. Furness O. and Amdahl J. (1980) Ship collisions with offshore platforms. DnV Paper 80-PO80, presented at Intermaritee '80 Conf., Hamburg, September 1980.

7.76. Brown and Root Incorp. (1990) Design of steel offshore structures against impact loads due to dropped objects. Private communication.

7.77. Knapp A.E., Green D.J. and Etie R.S. (1984) Collision of a tanker with a platform. OTC Paper 4734, Presented at the 16th Annual Offshore Technology Conference, Houston, TX.

7.78. Kochler P.E. and Jorgensen L. (1985) Ship impact ice analysis. In: Proceedings of the Fourth Symp. Offshore Mechanics and Arctic Engineering, ASME-Omae, Dallas, Texas, February 1985, pp. 344–50.

7.79. Jones S.E. and Rule W.K. (2000) On the Optimal Nose Geometry for a Rigid Penetrator, Including the Effects of Pressure-Dependent Friction, *Int. J. Impact Eng.*, **24**, 403–15.

7.80. Jones S.E., Toness O., Jerome D.M. and Rule William K. (2001) Normal Penetration of Semi-Infinite Targets by Ogive-Nose Projectiles, Including the Effects of Blunting and Erosion, *Thermal Hydraulics, Liquid Sloshing, Extreme Loads, and Structural Response, PVP-Vol. 421*, F.J. Moody, ed., pp. 53–9.

7.81. Jones S.E., Foster J.C. Jr., Toness O.A., DeAngelis R.J., Rule W.K. (2002) An estimate for mass loss from high velocity steel penetrators, *Thermal-Hydraulic Problems, Sloshing Phenomena, and Extreme Loads on Structures, PVP-Vol. 435*, F.J. Moody, ed., pp. 227–237.

7.82. Klepaczko and Janusz R. (2001) Surface layer thermomechanics of steel penetrators at high and very high sliding velocities, Technical Report, University of Florida, GERC, Shalimar, FL.

7.83. Tate A. (1967) A theory for the deceleration of long rods after impact, *J. Mech. Phys. Solids*, **15**, 387–99.

7.84. JABSF (1983) Ship collision with an offshore structure. IABSE Colloquium, Copenhagen.

7.85. Woisin G. (1977) Conclusion from collision examinations for nuclear merchant ships in the FRG. In: Proc. Symp. Naval Submarines, Hamburg.

8 Impact and Explosion related to Bridges, Barges and Barriers

8.1. AASHTO (1998). LRFD bridge design specifications, 2nd Edition. Washington, D.C.

8.2. Abramson H.N. et al. (1999). Improving surface transportation security: A research and development strategy. Committee on R & D Strategies to Improve Surface Transportation Security, National Research Council, National Academy Press, Washington D.C.

8.3. AT Blast version 2.0 (2000). Applied Research Associates, Inc. Vicksburg, MS.

8.4. BlastX version 4.2.3.0 (2001). Science Applications International Corp. San Diego, Calif. (distribution limited to U.S. government agencies and their contractors).

8.5. Bounds W. ed. (1998). Concrete and Blast Effects. Special Publication SP-175, American Concrete Institute, Farmington Hills, MI.

8.6. California Department of Transportation (CALTRANS). (2002). Seismic Retrofit Program Fact Sheet. (www.dot.ca.gov/hq/paffairs/about/retrofit.htm).

8.7. Conrath E.J., Krauthammer, T., Marchand, K.A. and Mlakar P.F. (1999). Structural design for physical security: State of the practice ASCE, Reston, VA.

8.8. Defense Threat Reduction Agency (DTRA) (1997). Design and analysis of hardened structures to conventional weapons effects, Washington D.C. (distribution restricted to U.S. Government agencies and their contractors).

8.9. Department of the Army (1992). Explosives and Demolitions. FM 5-250, U.S. Government Printing Office (distribution restriction to US Government agencies only), Washington D.C.

8.10. Federal Highway Administration (FHWA). (2003). Recommendations for bridge and tunnel security. Rep. prepared by the Blue Ribbon Panel on Bridge and Tunnel Security for AASHTO Transportation Security Task Force. (www.fhwa.dot.gov/bridge/security/brptoc.htm)

8.11. Jenkins B.M. (2001). Protecting public surface transportation against terrorism and serious crime: An Executive overview. MTI Rep. 01–14, Mineta Transportation Institute, San Jose, CA.

8.12. Marchand, K. and Plenge, B. (1998). Concrete hard target spall and breach model'. AFRL-MN-EG-TR-1998-7032, Technical Rep. Prepared for the

Munitions Directorate of the Air Force Research Laboratory. Eglin Air Force Base, Fla (Distribution limited to U.S. Government agencies and their contractors).

8.13. NONLIN version 6.01 (1996). Advanced Structural Concepts, Golden, Colo.

8.14. Science Applications International Corporation (SAIC). (2002). A guide to highway vulnerability assessment for critical asset identification and protection. Rep. prepared for American Association of State Highway and Transportation Officials' Security Task Force. (http://security.transportation.org/community/security/doc/guide-VA_FinalReport.pdf)

8.15. SPAn32 version 1.2.6.9 (2002). U.S. Army Corps of Engineers Omaha District, Omaha, Neb (distribution limited to U.S. Govermnet agencies and their contractors).

8.16. AASHTO (1991). Guide Specification and commentary for vessel collision design of Highway bridges, Washington D.C.

8.17. Arroyo J.R. and Ebeling R.B. (2004). A numerical method for computing barge impact forces based on ultimate strength of the lashings between barges. United States Army Corps of Engineers Rep. ERDC/ITL TR-04-2, August.

8.18. Brown D.A., O'Neill W.M., Hoit M., McVay M., El Naggar M.H. and Chakraborty S. (2001). Static and dynamic lateral loading of pile groups. Rep. 461, National Cooperative Highway Research Program, Transportation Research Board, Washington D.C.

8.19. Consolazio G.R., Cook R.A., Biggs A.E., Cowan D.R. and Bollmann H.T. (2003). Barge impact testing of the St. George Island Causeway Bridge Phase II: Design of instrumentation systems. Structures Research Rep. No. 883, Engineering and Industrial Experiment station, University of Florida, Gainesville, Fla., April.

8.20. Consolazio G.R. and Cowan D.R. (2003). Nonlinear analysis of barge crush behavior and its relationship to impact resistant bridge design. *Comput. Struct.* **81**(8–11), 547–557.

8.21. Consolazio G.R., Hendrix J.L. McVay M.C. Williams M.E. and Bollmann H.T. (2004a). Prediction of pier response to barge impacts using design-oriented dynamic finite element analysis. Transportation Research Record. 1868, Transportation Research Board, Washington, D.C. 177–189.

8.22. Consolazio G.R., Lehr G.B. and McVay M.C. (2004b). Dynamic finite element analysis of vessel-pier-soil interaction during barge impact events. Transportation Research Record. 1849, Transportation Research Board, Washington D.C. 81–90.

8.23. FB-PIER User's Manual (2003). Florida Bridge Software Institute, University of Florida, Gainesville, Fla.

8.24. Fernandez C. Jr. (1999) Nonlinear dynamic analysis of bridge piers. PhD dissertation, Department of Civil and Coastal Engineering, University of Florida, Gainesville, Fla.

8.25. Abu-Odeh A.Y., Albin R.B. and Bullard D.L. (2002). Finite element simulations and testing of Washington State precast concrete barrier. Proc. 7th International LS-DYNA User's Conference, Paper No. 7–23, Dearborn, MI.

8.26. Abu-Odeh A.Y., Bligh R.P. and Hamilton M.H. (2003). Analysis and design of the Texas T6 breakaway bridge railing system using finite element methodology. TRB Paper No. 03–2219, Transportation Research Board, Washington D.C.

8.27. Atahan A.O. and Cansiz O.F. (2005). Impact analysis of a vertical flared back bridge rail to guardrail transition structure using simulation. Finite Element *Anal. Design.* **41**(4), 371–96.

8.28. Bligh R.P., Mak K.K. and Menges W.L. (2003). Work zone appurtenances tested to NCHRP Report 350. Report No. FHWA-RD-03-038, Federal Highway Administration, Washington D.C.

8.29. Consolazio G., Chung J. and Gurley K. (2003). Impact simulation and full scale crash testing of a low profile concrete work zone barrier. *Comput. Struct.* **81**(13), 1359–374.

8.30. Graham J.L., Loumiet J.R. and Migletz, J. (1987). Portable concrete barrier connections. Report No. FHWA-TS-88-006, Federal Highway Administration, Washington D.C.

8.31. Hallquist J.O. (1998). LS-DYNA theoretical manual, Livermore Software Technology Corporation, Livermore, CA.

8.32. Hamilton, M.E. (1999). Simulation of T6 bridge rail system using LS-DYN£D. MS Thesis, Texas A&M Univ. College Station, TX.

8.33. Livermore Software Technology Corporation (LSTC). (2000). A general purpose dynamic finite element analysis program: LS-DYNA version 960 user's manual, Livermore software Technology Corporation, Livermore, CA.

8.34. Japan Road Association. *The standard of setting up guard fences and explanation of it*, Maruzen Press, 1999 (in Japanese).

8.35. Public Works Research Institute. *A Study on the Steel Guard Fences*, Research Report No. 74, Tsukuba, 1992 (in Japanese).

8.36. Public Works Research Institute. *A Study on the High Performance Aluminum Alloy Guard Fence*, Research Report No. 74, Tsukuba, 1990 (in Japanese).

8.37. NCHRP Report *350 Recommended Procedures for the Safety Performance Evaluation of Highway Features*: National Cooperative Highway Research Program, National Academy Press, 1993.

8.38. Paul Miller, and John F. Camey III. (1997). Computer Simulation of Roadside Crash Cushion Impacts, *J. Transport. Eng.*, Vol. 123, No. 5, pp. 370–76.

8.39. John D. Reid, Dean L. Sicking, Gene W. Paulsen. (1996). Design and Analysis of Approach Terminal Sections Using Simulation, *J. Transport. Eng.*, **123**(5), 399–405.

8.40. Itoh Y., Ohno T., and Mori M. (1998). Numerical analysis on behavior of steel columns subjected to vehicle collection impact, *J. Struct. Eng.*, JSCE, **40A**, 1531–42, (in Japanese).

8.41. Itoh Y., Mori M., and Liu C. (1999). Numerical analysis on high capacity steel guard fences subjected to vehicle collision impact, The Fourth International Conference on Steel and Aluminum Structures, Espoo, Finland, pp. 53–60, 1999.

8.42. Takahashi Y., Ohno T., and Ohta T., and Hino S. Strain-Rate effects on elasto-plastic behaviors of reinforced concrete beams under impact loadings, J. Struct. Eng., JSCE, 37A, 1567–1580, 1991 (in Japanese).

8.43. Itoh Y., Sasada T., and Ohno T. (1996). Nonlinear impact behavior considering strain rate, Steel Construction Engineering. **3**(11), 47–58, (in Japanese).

9 Aircraft Impact, Collision and Fire: Buildings

9.1. NFP A Codes, Standards, Recommended Practices and Manuals (see the latest
9.2. NFP A Codes and Standards Catalog for availability of currents editions of the following documents).
9.3. NFPA 12 A, Standard on Halon 1301 Fire Extinguishing Systems.
9.4. NFPA 12 B, Standard on Halon 1211 Fire Extinguishing Systems.
9.5. NFPA 70, National Electrical Code.
9.6. NFPA 101, Code for Safety to Life for Fire in Buildings and Structures.
9.7. NFPA 403, Manual for Aircraft Rescue and Fire Fighting Operational Procedures.
9.8. NFPA 407, Standard for Aircraft Fuel Servicing.
9.9. NFPA 408, Standard for Aircraft Hand Fire Extinguishers.
9.10. NFPA 409, Standard on Aircraft Hangars.
9.11. NFPA 410, Standard on Aircraft Maintenance.
9.12. NFPA 412, Standard for Evaluating Foam Fire Fighting Equipment on Aircraft Rescue and Fire Fighting Vehicles.
9.13. NFPA 414, Standard for Aircraft rescue and Fire Fighting Vehicles.
9.14. NFPA 415, Standard on Aircraft Fueling Ramp Drainage.
9.15. NFPA 416, Standard on Construction and Protection of Airport Terminal Buildings.
9.16. NFPA 417, Standard on Construction and Protection of Aircraft Loading Walkways.
9.17. NFPA 418, Standard on Roof-top Heliport Construction and Protection.
9.18. NFPA 419, Guide for Master Planning Airport Water Supply Systems for Fire Protection.
9.19. NFPA 421, Recommended Practice on Aircraft Interior Fire Protection Systems.
9.20. NFPA 422M, Manual for Aircraft and Explosion Fire Investigators.
9.21. NFPA 424, Recommended Practice for Airport/Community Emergency Planning.
9.22. NFPA 1003, Standard for Airport Fire Fighter Professional Qualifications.
9.23. Aeronautics and Space, Code of Federal Regulations, Title 14, Washington, D.C. (under continuous revision).
9.24. Federal Aviation Administration Advisory Circulars, U.S. Department of Transportation, Washington, D.C. (with the following designations and titles):
9.25. Aircraft Fire and Rescue Communications, 150/5210-7A, Mar. 16, 1972.
9.26. Aircraft Fire and Rescue Facilities and Extinguishing Agents, 150/5210-6B, Jan. 25, 1973.
9.27. Airport Fire and Rescue Vehicle Specification Guide, 150/5220-14, Mar. 15, 1979.
9.28. Airport Fire Department Operating Procedures During Period of Low Visibility, 150/5210-0, Oct. 27, 1967.
9.29. Airport Operations Manual, 150/5280-1, June 16, 1972.
9.30. Fire and Rescue Service for Certificated Airports, 150/5210-12, Mar. 2, 1972.
9.31. Fire Department Responsibility in Protecting Evidence at the Scene of an Aircraft Accident, 150/5200-12, Aug. 8, 1969.

9.32. Fire Fighting Exemptions under the 1976 Amendement to the Federal Aviation Act, 150/5200-12, Aug. 8, 1969.

9.33. Fire Fighting Exemptions under the 1976 Amendement to the Federal Aviation Act, 150/5280-3, Feb. 4, 1977.

9.34. Fire Prevention During Aircraft Fueling Operations, 150/5230-3, Apr. 8, 1969.

9.35. Hand Fire Extinguishers for Use on Aircraft, 150/5210-13, May 4, 1972.

9.36. ECCS (1983) Calculation of the fire resistance for composite concrete slabs with profiles steel sheet exposed to the standard fire. Publication No. 32, European Commission for Constructional Steelwork, Brussels, Belgium.

9.37. ECCS (1985) Design manual on the European recommendations for the fire safety of steel structures. European Commission for Constructional Steelwork, Brussels, Belgium.

9.38. ECCS (1988) Calculation of the fire resistance of centrally-loaded composite steel-concrete columns exposed to the standard fire. Technical Note No. 55, European Commission for Constructional Steelwork, Brussels, Belgium.

9.39. ECCS (1995) Fire resistance of steel structures. ECCS Technical Note No. 89, Technical Committee 3, European Commission for Constructional Steelwork, Brussels, Belgium.

9.40. Ellinwood B.R. and Corotis R.B. (1991) Load combinations for buildings exposed to fires. Eng. J., Am. Inst. Steel Construct. **28**(1), 37–44.

9.41. El-Rimawi J.A., Burgess I.W. and Plank R.J. (1996) The treatment of strain reversal in structural members during the cooling phase of a fire. J. Construct. Steel Res. **37**(2), 115–135.

9.42. England J.P., Young S.A., Hui M.C. and Kurban N. (2000) Guide for the design of fire resistant barriers and structures. Building Control Commission, Melbourne, Australia.

9.43. FCRC (1996) Fire engineering guidelines. Fire Code Reform Centre, Sydney, Australia.

9.44. Feasey R. and Buchanan A.H. (1999) Post-flashover design fires. Fire Engineering Research Report 99/6, University of Canterbury, New Zealand.

9.45. Feasey R. and Buchanan A.H. (2000) Post-flashover fires for structural design, submitted to *Fire Safety Journal*.

9.46. FIP/CEB (1975) Guides to good practice. FIP/CEB recommendations for the design of reinforced and prestressed concrete structural members for fire resistance. FIP/1/1. Fédération Internationale de la Précontrainte. Wexham Springs, Slough, UK.

9.47. Fleischmann C.M. (1995) Analytical methods for determining fire resistance of concrete members. In: SFPE Handbook of Fire Protection Engineering. 2nd edn, Society of Fire Protection Engineers, USA, Chap. 4.10.

9.48. Skinner P. and Wallace M. (2002) World Trade Center. The giants that defied the sky. White Star s.r.l., p. 123.

9.49. The Daily Telegraph/The Independent (London)/The Times (London) (2001) Extract from features on WTC. September 16, 30 pp.

9.50. Hopkison J. (2001) Fire-safety engineering: the consultant's view. *J. Instruct. E* **79**(19), 22–23, London, Oct. 2.

9.51. Subramanian N. (2002) Collapse of WTC. Its impact on skyscraper construction. *J. Indian Concrete* (March):165–169.

9.52. Baker W.E., Cox P.A., Westine P.S. and Kulesz J.J. (eds.) (1982) Explosion hazards and evaluation. Fundamental studies in engineering. Elsevier Scientific, New York.

9.53. Bangash M. (1993) Impact and explosion, analysis and design. CRC Press, *Sect. 4.3.*

9.54. Council on Tall Buildings and Urban Habitat (1978) Monograph on planning and design of tall buildings. Vol CB: Structural design of tall concrete and masonry buildings. American Society of Civil Engineers.

9.55. Council on Tall Buildings and Urban Habitat (1978) Monograph on planning and design of tall buildings. Vol. SB: Structural design of tall steel buildings. American Society of Civil Engineers.

9.56. Council on Tall Buildings and Urban Habitat (1978) Monograph on planning and design of tall buildings. Vol. SC: Structural buildings systems and concepts. American Society of Civil Engineers.

9.57. Council on Tall Buildings and Urban Habitat (1978) Monograph on planning and design of tall buildings. Vol. CB: Structural design of tall concrete and masonry buildings. American Society of Civil Engineers.

9.58. Croll J.G.A. and Walker A.C. (1972) Elements of structural stability. Macmillan, London.

9.59. Csonka P. (1956) Über proportionierte Rahmen. Die Bautechnik **33**, 19–20.

9.60. Csonka P. (1956) Simple procedure for multistory frameworks under wind load. Az MTA VI Oszt. Közl., Budapest, **35**, 209–19 (in Hungarian).

9.61. Ellis R.B. (1986) The significance of dynamic soil-structure interaction in tall buildings. Proc. ICE, Part 2, **81**, 221–42.

9.62. Ellis R.B. and Ji T. (1996) Dynamic testing and numerical modelling of the Cardington Steel Framed Building from construction to completion. The Structural Engineer **74**(11), 186–92.

9.63. Asztalos Z. (1972) Buckling analysis of multistorey, one-bay frameworks using the continuum model, taking the axial deformations of the columns into account. Magyar Epítöipar: 471–474 (in Hungarian).

9.64. Barbero E. and Tomblin J. (1993) Euler buckling of thin-walled composite columns. Thin-Walled Struct. **17**, 237–58.

9.65. Barkan D.D. (1962) Dynamics of bases and foundations. McGraw-Hill, London.

9.66. Beck H. (1956) Ein neues Berechungsverfahren für gegliederte Scheiben, dargestellt am Beispiel des Vierendeel-Trägers. Der Bauingenieur **31**, 436–443.

9.67. Beck H., Konig G. and Reech H. (1968) Kenngrössen zur Beurteilung der Torsionssteifigkeit von Hochhäusern. Beton und Stahlbetonbau **63**, 268–77.

9.68. Beck H. and Shafer H.G. (1969) Die Berechnung von Hochhäusern durch Zusammenfassung aller aussteinenden Bauteile zu einem Balken. Der Bauingenieur **44**, 80–7.

9.69. National Fire Protection Association (1999) Standard methods of fire tests of building construction and materials. NFPA 251, Quincy, MA.

9.70. U.S. Department of Energy (1996) Accident analysis for aircraft crash into hazardous facilities. DOE Standard 3014–96, October.

9.71. Zalosh R.G. (2002) Explosion protection. In: SFPE Handbook of Fire Protection Engineering. 3rd edn, Quincy, MA.

9.72. Bangash T. (2003) PhD. Thesis, London University.

9.73. Allen L.W. (1970) Fire endurance of selected non-loadbearing concrete masonry, DBR Fire Study No. 25, Division of Building Research, National Research Cou, Canada, Ottawa, Canada.

9.74. Almand K. (1989) The role of passive systems in fire safety design in buildings. Fire and Engineering – International Symposium Papers, The Warren University of Sydney, Australia, pp. 103–29.

9.75. Anderberg Y. (1986) Measured and predicted behaviour of steel beams and columns in fire. Lund Institute of Technology, Lund, Sweden. Anderberg Y. (1988) Modeling and steel behaviour: Fire Safety J.

9.76. Corley W.G. et al. (1996) The Oklahoma City bombing, improving building performance through multi-hazard mitigation. FEMA Bull 277, ASCE Press.

9.77. Corley W.G. et al. (2001) Effects of structural integrity on damage from the Oklahoma City, USA bombing. Forensic Engineering, Thomas Telford, London.

9.78. Corley W.G. et al. (1997) Using forensic engineering techniques to obtain data from the Oklahoma City bombing. In: Proc. First Forensic Engineering Congress, Reston, VA, ASCE Press.

9.79. Corley W.G. et al. (1995): Blast loading and response of the Murrah Building. J. Performance of Constructed Facilities, ASCE Press **12**(3), 100–112.

9.80. Hinmann E. (1997) Lessons from the Oklahoma City bombing-defensive design techniques. ASCE Press.

9.81. Hinman E.E. (1995) Explosion and collapse: Disaster in milliseconds. *Fire Eng.* (Oct.)

9.82. Construction News (1995) Oklahoma blast forces unsettling design questions (May 1).

9.83. Times international index. Volumes from 1961–1997. Westminster Research Library, London.

9.84. Holzer T.L. et al. (1995): Interpretation of seismographs of April 19 1995 Oklahoma City bombing. US Geological Survey, Menlo Pk, CA.

9.85. Norville H.S. et al. (1995) Glass related injuries in the Oklahoma City bombing. *J. Perf. Constr. Fac.* **13**(3), 100–12, ASCE Press.

9.86. ENR News (1995) Weighing future safety of Federal Buildings. McGraw-Hill Companies (May 8).

9.87. Ettouney M. et al. (1996) Blast resistant design of commercial buildings. Practice Periodical on Struct. Design Construct. **1**(1) (Feb.) ASCE.

9.88. Longinow A. et al. (1996) Protecting vehicles against vehicle bomb attacks. Practice Periodical on Struct. Design and Construct. **1**(1) (Feb.) ASCE.

9.89. O'Connell J. (1995) Supporting a fractured building. Fire Eng. (Nov.)

9.90. Brown M.G. (1995) The work of a task force: Dismantling a dying building. Fire Engineering (Nov.)

9.91. Carrl T. (1995) USAR task force logistics. Fire Eng. (Nov.)

9.92. Massa R. (1995) Vulnerability of buildings to bombs: Additional thoughts after Oklahoma City. Fire Eng. (Nov.)

9.93. Hammond D.J. (1995) Engineering the collapse: making the structure safe. Fire Eng. (Nov.)

9.94. Kirkpatrick Engineering Company (KEC) (2001) Engineering drawings of the Oklahoma Building, received by the Author.

9.95. Bangash, T. (2004) The combined finite/discrete element method in transient dynamics of reinforced concrete structures under blast loading. PhD Thesis, University of London.

9.96. Robinson J.H. and Nolen A.M. (1995) Investigation of metal matrix composites as shields for hypervelocity orbital debris impacts. *Int. J. Impact Eng.*, **17**(4), 685–96.

9.97. Chang F.K. and Chang K.Y. (1987) Post-failure analysis of bolted composite joints in tension or shear concentration. J. of composite materials., **21**, 809–833.

9.98. Chang F.K. and Chang K.Y. (1987) A progressive damage model for laminates composites containing stress concentration. J. Compos. Mater., **21**, 834–55.

9.99. Lee W.S. and Sue W.C. (2000) Dynamic impact and fracture behaviour of carbon fiber reinforced 7075 Al metal matrix composite. *J. Compos. Mater.*, **1**.

9.100. Batra R.C. and Wright T.W. (1986) Steady state penetration of rigid perfectly plastic targets. *Int. J. Eng. Sci.*, **24**(1), 41–45.

9.101. Virostek S.P., Dual P. and Goldsmith W. (1987) Direct force measurement in normal and oblique impact of plates by projectiles. *Int. J. Impact Eng.*, **6**(4), 247–269.

9.102. Johnson W., Sengupta A.K. and Ghosh S.K. (1982) High velocity oblique impact and ricochet mainly of long rod projectile: an overview. *Int. J. Mech. Sci.*, **24**(7), 425–436.

9.103. Corbett G.G., Reid S.R. and Johnson W. (1996). Impact loading of plates and shells by free-flying projectiles: a review *Int. J. Impact Eng.*, **18**(2), 141–230.

9.104. Vaziri R., Delfosse D., Pageau G. and Poursartip, A. (1993). High speed impact response of particulate metal matrix composite materials – an experimental and theoretical investigation. *Int. J. Impact Eng.*, **13**(2), 329–352.

9.105. Christman T., Needleman A. and Suresh, S. (1989). An experimental and numerical study of deformation in metal-matrix composites. *Acta Metall.*, **37**(11), 3029–3050.

9.106. Simon R. (1963) Digital machine computations of the stress waves produced by striker impact in percussive drilling machines. In: Fifth Symp. Rock Mechanics, Pergamon, Oxford.

9.107. Vijay M.M. and Brierly W.H. (1980) Drilling of rocks with rotating high pressure water jets: An assessment of nozzles. In: Proceedings of the Symp. Jet Cutting Technology, Hanover.

9.108. Watson R.W. (1973) Card-gap and projectile impact sensitivity measurements, a compilation. US Bureau of Miles Information Circular No. 8605.

9.109. Wells E.S. (1949) Penetration speed of percussion drill bits. *Chem. Eng. Miner. Rev.* **41**(10), 362–64.

9.110. Winzer R.R. and Ritter A.P. (1980) Effect of delays in fragmentation in large limestone blocks. Report No. MML TR 80-25, Martin Marietta Laboratory, U.S.A.

9.111. Allison F.E. (1965) Mechanics of hypervelocity impact. In: Proceedings of the Seventh Hypervelocity Impact Symp., Vol. I. Springer Verlag, Berlin, Germany.

9.112. Wilkins M. and Guinan M. (1973) Impact of cylinders on a rigid boundary. *J. Appl. Phys.*, **44**.

9.113. Whiffin A.C. (1948) The use of flat-ended projectiles for determining dynamic yield stress, II, Tests on various metallic materials. *Proc. R. Soc. London Ser.* A, **194**.

9.114. Goldsmith W. (1960) Impact. The theory and physical behaviour of solliding solids. Edward Arnold, London.

9.115. Johnson W. (1972) Impact Strength of Materials. Edward Arnold, New York.

9.116. Walters W. (1979) Influence of material viscosity on the theory of shaped-charge jet formation. BRL Rep., BRL-MR-02941.

9.117. Chhabildas L.C. and Asay J.R. (1979) Rise-time measurements of shock transitions in aluminum, copper and steel. *J. Appl. Phys.*, **50**.

9.118. Birkhoff G., MacDougall D., Pugh E. and Taylor G. (1948) Explosives with lined cavities. *J. Appl. Phys.* **19**.
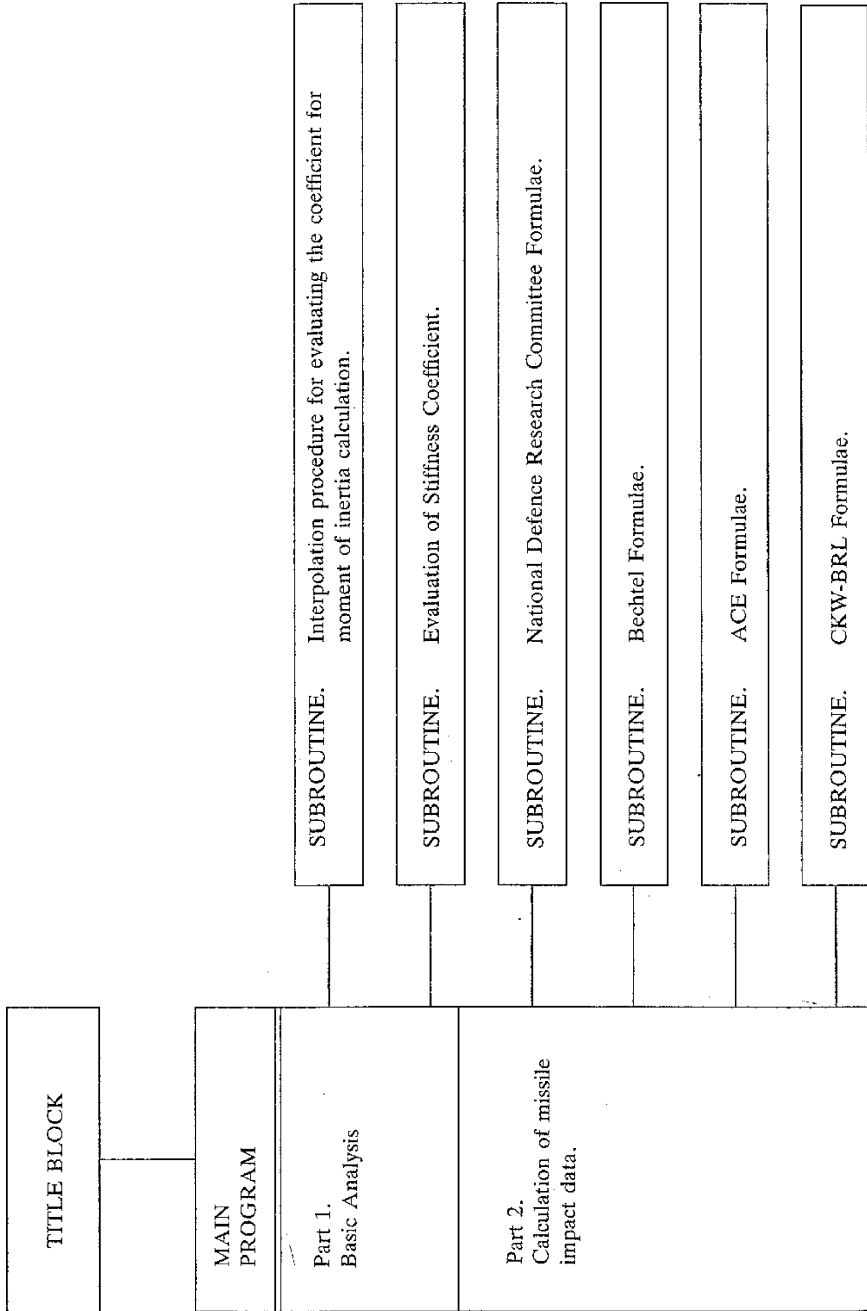
I. Underground and Underwater Explosion and Their Effects

I.1. Keller, J. B. (1954) Geometrical acoustics, I. The theory of weak shock waves. *J. Appl. Phys.* **25**, 938.

I.2. Butkovich, T. R. (1966) *The Gas Equation of State of Natural Materials*, Lawrence Radiation Laboratory, Llvennore, Rep. UCRL-14729.

I.3. Bienlawaski, Z. T. (1968) Fracture dynamics of rocks. *Int. J. Fract. Mech.* **4**, 415.

I.4. Byerlee, J. D. (1967) Frictional characteristics of granite under high confining pressures. *J. Geophys. Res.* **72**, 3639.

I.5. Ahrens, T. J. and Duvall, G. E. (1966) Stress relaxation behind elastic shock waves in rocks. J. Geophys. Res. **71**, 4349.

I.6. Cherry, J. T. (1967) Computer calculations of explosion produced craters. *Int. J. Rock Mech. Mining Sci.* **4**, 1.

I.7. Handin, J., Heard, H. C., Magouirk, J. N. (1967) Effects of the intermediate principal stress on the failure of limestone, dolomite, and glass at different temperatures and strain rates. *J. Geophys. Res.* **72**, 611.

I.8. Mogi, K. (1967) Effect of the intermediate principal stress on rock failure. *J. Geophys. Res.* **72**, 5117.

I.9. Hearst, J. R., Irani, G. B., and Geesaman, L. B. (1965) Piezoelectric response of Z-cut tourmaline to shocks up to 21 kilobars. *J. Appl. Phys.* **36**, 3440.

I.10. Wilkins, M., Squier, B., and Halperin, B., *The Equation of State of PBX 9404 and LX 04-01*, Lawrence Radiation Laboratory, Livermore, Rep. UCRL-7797 (1964).

I.11. Werth, G. C. and Herbst, R. F. (1962) *Comparison of Amplitudes of Seismic Waves from Nuclear Explosions in Four Media*, Lawrence Radiation Laboratory, Livermore, Rep. UCRL-6962.

I.12. Perret, W. R. (1969) *Gasbuggy Seismic Source and Surface Motion*, Sandia Laboratories, Albuquerque, Rep. PNE-1002.

Appendix 1

Subroutines for Program Isopar and Program F-Bang

Program Structural Layout

Andrew Watson main programmer (supervised by M.Y.H. Bangash)

TITLE BLOCK

MAIN PROGRAM

Part 1.
Basic Analysis

Part 2.
Calculation of missile impact data.

SUBROUTINE.   Interpolation procedure for evaluating the coefficient for moment of inertia calculation.

SUBROUTINE.   Evaluation of Stiffness Coefficient.

SUBROUTINE.   National Defence Research Committee Formulae.

SUBROUTINE.   Bechtel Formulae.

SUBROUTINE.   ACE Formulae.

SUBROUTINE.   CKW-BRL Formulae.

```
     REAL I,B,T,F,D,K,V,P,N,PN,PT,AY,AX,EC,ES,X,Y,Q,Q1,S,ME,MPUA,C
     REAL NTP,KL,NSF,FC,W,DIA,VEL,FCI,KCPFI,WI,DIAI,VELI,PENEI
     REAL PENET,RAT,PERF,SCAB,SSCAB,HSCAB,ACEP,ACPER,CKPEN,CKPER
     WRITE (6,1)
 1   FORMAT (1H/,'Put in your values of B(cm),T(cm),D(cm)'/
     +        1H/,'B (Unit width of slab ,cm)'/
     +        1H/,'T (Overall depth of slab ,cm)'/
     +        1H/,'D (Depth to reinforcing steel ,cm)')
     READ (5,*) B,T,D
     CALL INTN (F)
     I=0.5000*(((B*(T*T*T))/12)+F*B*(D*D*D))
     WRITE (6,2)
 2   FORMAT (1H/,'The average moment of inertia,Ia(cm4/cm) ,is')
     WRITE (6,3) I
 3   FORMAT (1H/,F30.2)
     CALL INT (Q)
     WRITE (6,17)
17   FORMAT (1H/,'Key in the value of Q that corresponds to'/
     +        1H/,'your calculated value of X/Y. This is the '/
     +        1H/,'required Stiffness Coefficient')
     READ (5,*) Q
     WRITE (6,12)
12   FORMAT (1H/,'Put in your values of V,EC(MPa),Y(m)'/
     +        1H/,'V (Poissons Ratio for concrete ,usually 0.17'/
     +        1H/,'EC (Elastic modulus of concrete ,MPa)       '/
     +        1H/,'Y (Length of slab ,m)                       ')
     READ (5,*) V,EC,Y
     K=((12*EC*I)/((((Q*Y*Y)*(1-(V*V)))*1000000000))
     WRITE (6,5)
 5   FORMAT (1H/,'The value of K (MN/mm) is')
     WRITE (6,6) K
 6   FORMAT (1H/, F30.2)
     WRITE (6,7)
 7   FORMAT (1H/,'Input the following data :           '/
     +        1H/,'WD (The Weight Density of the concrete ,Kg/m3)'/
     +        1H/,'T (The overall depth of the slab ,m)'/
     +        1H/,'X (The width of the slab ,m)')
     READ (5,*) WD,T,X
     MPUA=((WD*T)/9.81)
     WRITE (6,8)
 8   FORMAT (1H/,'The mass per unit area of the slab is, (Kg.sec2/m3')
     WRITE (6,9) MPUA
 9   FORMAT (1H/,F5.1)
     ME=((MPUA*3.142*X*X*9.81)/(6*4*1000))
     WRITE (6,10)
10   FORMAT (1H/,'The effective mass is one sixth of the mass'/
     +        1H/,'within the circular yield pattern.          '/
     +        1H/,'Effective mass is ,N.sec2/mm')
     WRITE (6,11) ME
11   FORMAT (1H/,F4.2)
450  FORMAT(1H/,'Key in the corresponding F value')
     READ (5,*) Y1
     WRITE (6,500)
```

```
 500  FORMAT (1H/,'Key in the value of PN from the table that is'/
      +        1H/,'just higher than your calculated value of PN')
      READ (5,*) X3
      WRITE (6,550)
 550  FORMAT(1H/,'Key in the corresponding F value')
      READ (5,*) Y2
      WRITE (6,600)
 600  FORMAT (1H/,'Key in your calculated value of PN')
      READ (5,*) X2
      F=((((X2-X1)/(X3-X1))* (Y2-Y1))+Y1)
      WRITE (6,700)
 700  FORMAT(1H/,'The value of F you require is')
      WRITE (6,800) F
 800  FORMAT(1H/,F8.5)
      RETURN
      END
      SUBROUTINE INT (Q)
      WRITE (6,1000)
1000  FORMAT (1H/,'Key in the length,X (m),& width,Y (m) ,of the slab')
      READ (5,*) X,Y
      Q1=X/Y
      WRITE (6,1100)
1100  FORMAT (1H/,'You require a Q value that corresponds with this'/
      +        1H/,'calculated value of X/Y')
      WRITE (6,1200) Q1
1200  FORMAT (1H/,F4.2)
      WRITE (6,1300)
1300  FORMAT (1H/,'The table you use is dependant on support'/
      +        1H/,'conditions at the sides')
      WRITE (6,1400)
1400  FORMAT (1H/,'SIMPLY SUPPORTED ON      FULLY FIXED ON ALL  '/
      +        1H/,'ALL FOUR SIDES            FOUR SIDES'/
      +        1H/,'X/Y VALUES |Q VALUES     X/Y VALUES |Q VALUES'/
      +        1H/,'==========|========     ==========|========'/
      +        1H/,'   1.0     | 0.1391         1.0     | 0.0671 '/
      +        1H/,'   1.1     | 0.1518         1.2     | 0.0776 '/
      +        1H/,'   1.2     | 0.1624         1.4     | 0.0830 '/
      +        1H/,'   1.4     | 0.1781         1.6     | 0.0854 '/
      +        1H/,'   1.6     | 0.1884         1.8     | 0.0864 '/
      +        1H/,'   1.8     | 0.1944         2.0     | 0.0866 '/
      +        1H/,'   2.0     | 0.1981      INFINATE | 0.0871 '/
      +        1H/,'   3.0     | 0.2029                       '/
      +        1H/,'  INFINATE | 0.2031                       ')
      RETURN
      END
      SUBROUTINE NDRC (PENET,PERF,SCAB)
      REAL NSF,KCPFI,FC,W,DIA,VEL,FCI,WI,DIAI,VELI,PENET,PENET,RAT,T
      WRITE (6,1998)
1998  FORMAT (1H/,'Input,T,the overall depth ,mm')
      READ (5,*) T
      WRITE (6,2000)
2000  FORMAT (1H/,'Input the relevant missile shape factor ,NSF'/
      +        1H/,'For flat nosed missiles, NSF=0.72'/
      +        1H/,'For blunt nosed missiles, NSF=0.84'/
```

```
     +         1H/,'For sperical nosed missiles, NSF=1.00'/
     +         1H/,'For very sharp nosed missiles, NSF=1.14')
      READ (5,*) NSF
      WRITE (6,2100)
2100  FORMAT (1H/,'Input the following :'/
     +         1H/,'FC The ultimate concrete compressive strength,N/mm2'/
     +         1H/,'W (The weight of the missile, N)'/
     +         1H/,'DIA (The circular section diameter, mm)'/
     +         1H/,'VEL (The impact velocity, m/sec)')
      READ (5,*) FC,W,DIA,VEL
      FCI=(FC/0.007)
      KCPFI=(180/SQRT(FCI))
      WI=((2*W)/9)
      DIAI=(DIA/25.4)
      VELI=(VEL/0.3048)
      PENEI=(SQRT((4*KCPFI*NSF*WI*DIAI)*((VELI/(1000*DIAI))**1.8)))
      PENET=(PENEI*25.4)
      RAT=(PENET/DIA)
      IF (RAT.LT.2.0) THEN
      GO TO 2200
      ELSE IF (RAT.GT.2.0) THEN
      GO TO 2400
      END IF
2200  WRITE (6,2300)
2300  FORMAT (1H/,'The missile penetration using the NDRC (National'/
     +         1H/,'Defence Research Committee) Formula for'/
     +         1H/,'''x/d'' less than or equal to 2.0 is ,(mm)')
      WRITE (6,2350) PENET
2350  FORMAT (1H/,F6.1)
      GO TO 2700
2400  PENEI=(((KCPFI*NSF*WI)*((VELI/(1000*DIAI))**1.8))+DIAI)
      PENET=(PENEI*25.4)
      WRITE (6,2450)
2450  FORMAT (1H/, 'The missile penetration using the NDRC (National'/
     +         1H/,'Defence Research Committee) Formula for'/
     +         1H/,'''x/d'' greater than 2.0 is ,(mm)')
      WRITE (6,2470) PENET
2470  FORMAT (1H/,F6.1)
2700  WRITE (6,2710)
2710  FORMAT (1H/,'The ''x/d''ratio is')
      WRITE (6,2720) RAT
2720  FORMAT (1H/,F5.3)
      IF (RAT.LT.1.35) THEN
      GO TO 2800
      ELSE IF (RAT.GT.1.35) THEN
      GO TO 2900
      END IF
2800  PERF=(DIA*((3.19*RAT)-(0.718*RAT*RAT)))
      GO TO 3000
2900  PERF=(DIA*(1.32+(1.24*RAT)))
3000  WRITE (6,3100)
3100  FORMAT (1H/,'The Perforation,calculated using the NDRC, is ,mm')
      WRITE (6,3200) PERF
```

```
3200  FORMAT (1H/,F5.1)
      IF (PERF.LT.T) THEN
      GO TO 3300
      ELSE IF (PERF.GT.T) THEN
      GO TO 3400
      END IF
3300  WRITE (6,3350)
3350  FORMAT (1H/,'This value is less than the overall depth.The'/
     +         1H/,'slab adequately resists collapse due to perforation')
      GO TO 3500
3400  WRITE (6,3450)
3450  FORMAT (1H/,'This value is greater than the overall depth.The'/
     +         1H/,'slab will collapse due to perforation')
3500  IF (RAT.LT.0.65) THEN
      GO TO 3600
      ELSE IF (RAT.GT.0.65) THEN
      GO TO 3700
      END IF
3600  SCAB=(DIA*((7.91*RAT)-(5.06*RAT*RAT)))
      GO TO 3800
3700  SCAB=(DIA*(2.12+(1.36*RAT)))
3800  WRITE (6,3850)
3850  FORMAT (1H/,'The Scabbing thickness,calculated using NDRC, is ,mm')
      WRITE (6,3860) SCAB
3860  FORMAT (1H/,F5.1)
      IF (SCAB.LT.T) THEN
      GO TO 3900
      ELSE IF (SCAB.GT.T) THEN
      GO TO 4000
      END IF
3900  WRITE (6,3950)
3950  FORMAT (1H/,'This value is less than the overall depth.The'/
     +         1H/,'slab will not collapse due to scabbing')
      GO TO 4100
4000  WRITE (6,4050)
4050  FORMAT (1H/,'This value is greater than the overall depth.The'/
     +         1H/,'slab will collapse due to scabbing')
4100  RETURN
      END
      SUBROUTINE BTEL (SSCAB, HSCAB)
      REAL W,VEL,DIA,FC,FCI,WI,DIAI,VELI,SSCI,HSCI,SSCAB,HSCAB
      WRITE (6,5000).
5000  FORMAT (1H/,'Input the following:'/
     +         1H/,'W (The weight of the missile,N)'/
     +         1H/,'VEL (The impact velocity of the missile,m/sec)'/
     +         1H/,'DIA (The diameter of the missile,mm)'/
     +         1H/,'FC (The concrete compressive strength,N/mm2)')
      READ (5,*) W,VEL,DIA,FC
      FCI=(FC/0.007)
      WI=((2*W)/9)
      DIAI=(DIA/25.4)
      VELI=(VEL/0.3048)
      SSCI=((15.5*(WI**0.4)*(VELI**0.5))/(SQRT(FCI)*(DIAI**0.2)))
      HSCI=((5.42*(WI**0.4)*(VELI**0.65))/(SQRT(FCI)*(DIAI**0.2)))
```

```
       SSCAB=(SSCI*25.4)
       HSCAB=(HSCI*25.4)
       WRITE (6,5100)
5100   FORMAT (1H/,'Using the BECHTEL formula the slab thickness'/
      +         1H/,'to prevent scabbing from a solid missile is,mm')
       WRITE (6,5200) SSCAB
5200   FORMAT (1H/,F6.1)
       WRITE (6,5300)
5300   FORMAT (1H/,'Using the BECHTEL formula the slab thickness to'/
      +         1H/,'prevent scabbing from a hollow missile is,mm')
       WRITE (6,5400) HSCAB
5400   FORMAT (1H/,F5.1)
       RETURN
       END
       SUBROUTINE ACE (ACEP,ACPER)
       REAL W,DIA,VEL,FC,FCI,DIAI,WI,VELI,ACEPI,APFI,ACEP,ACPER,EPI
       WRITE (6,6000)
6000   FORMAT (1H/,'Input the following:'/
      +         1H/,'W (The weight of the missile,N)'/
      +         1H/,'DIA (The diameter of the missile,mm)'/
      +         1H/,'VEL (The impact velocity of the missile,m/sec)'/
      +         1H/,'FC (The concrete compressive strength,N/mm2)')
       READ (5,*) W,DIA,VEL,FC
       FCI=(FC/0.007)
       WI=((2*W)/9)
       DIAI=(DIA/304.8)
       VELI=(VEL/0.3048)
       ACPI=((282*WI*(DIAI**0.215)*((VELI/1000)**1.5))/(FCI*DIAI**2))
       EPI=(0.5*DIAI)
       ACEPI=(ACPI+EPI)
       APFI=((1.23*DIAI)+(1.07*ACEPI))
       ACEP=(ACEPI*25.4)
       ACPER=(APFI*25.4)
       WRITE (6,6100)
6100   FORMAT (1H/,'The penetration depth using the ACE formula is,mm')
       WRITE (6,6200) ACEP
6200   FORMAT (1H/,F5.1)
       WRITE (6,6300)
6300   FORMAT (1H/,'Thickness to prevent perforation using ACE is,mm')
       WRITE (6,6400) ACPER
6400   FORMAT (1H/,F5.1)
       RETURN
       END
       SUBROUTINE CKW (CKPEN,CKPER)
       REAL W,DIA,VEL,WI,DIAI,VELI,CKPEI,CKPRI,CKPEN,CKPER
       WRITE (6,7000)
7000   FORMAT (1H/,'Input the following:'/
      +         1H/,'W (The weight of the missile,N)'/
      +         1H/,'DIA (The diameter of the missile,mm)'/
      +         1H/,'VEL (The impact velocity of the missile,m/sec)')
       READ (5,*) W,DIA,VEL
       WI=((2*W)/9)
       DIAI=(DIA/25.4)
       VELI=(VEL/0.3048)
```

```
      CKPEI=((6*WI*(DIAI**0.2)*((VELI/1000)**1.333333))/(DIAI**2))
      CKPRI=(1.3*CKPEI)
      CKPEN=(CKPEI*25.4)
      CKPER=(CKPRI*25.4)
      WRITE (6,7100)
7100  FORMAT (1H/,'The penetration using the CKW-BRL formula is,mm')
      WRITE (6,7200) CKPEN
7200  FORMAT (1H/,F5.1)
      WRITE (6,7300)
7300  FORMAT (1H/,'Thickness to prevent perforation using CKW-BRL,mm')
      WRITE (6,7400) CKPER
7400  FORMAT (1H/,F5.1)
      RETURN
      END
```

Blast Loading Program

```
>LIST10.410
    10 REM ''INITIALIZE PRINTER''
    20 VDU2,1,27,1,64,3
    30 REM ''DISABLE PAPER END DETECTOR''
    40 VDU2,1,27,1,56,3
    50 REM ''SELECT PRINT STYLE 24''
    60 VDU2,1,27,1,33,1,56,3
    70 REM ''SET LEFT MARGIN - 4 SPACES''
    80 VDU2,1,27,1,108,1,4,3
    90 REM ''SET LINE SPACING - 35/216INCHES''
   100 VDU2,1,27,1,51,1,38
   110 PRINT:VDU3:INPUT ''DO YOU REQUIRE PRINT-OUT ON PAPER? ENTER Y FOR Y
ES AND N FOR NO '':A1$:IF A1$=''Y'' THEN VDU2
   120 PRINT ''BLAST LOADING PROGRAM:''
   130 VDU2,1,27,1,33,1,53,3:IF A1$=''Y'' THEN VDU2
   140 PRINT ''BY N.M. ALAM (1987)''
   150 VDU2,1,27,1,106,1,10,3:IF A1$=''Y'' THEN VDU2
   160 PRINT ''----------------------------'':PRINT:GOTO 180
   170 PRINT:VDU3:INPUT ''DO YOU REQUIRE PRINT-OUT ON PAPER? ENTER Y FOR Y
ES AND N FOR NO '';A1$
   180 VDU2,1,27,1,33,1,0,3:VDU2,1,27,1,108,1,8,3:IF A1$=''Y'' THEN VDU2
   190 PRINT ''-----------------------------------------------------------
----------'':VDU2:PRINT:VDU2,1,27,1,106,1,18,3
   200 INPUT ''OPERATOR'S NAME'';N$;''RUN NUMBER'';N1:INPUT ''DATE'';N1$
   210 IF A1$=''Y'' THEN VDU2:VDU21:PRINT ''OPERATOR'S NAME: '';N$;TAB(36);''R
UN NUMBER: '';N1;TAB(52);''DATE: '';N1$:VDU6
   220 VDU2,1,27,1,106,1,15,3:IF A1$=''Y'' THEN VDU2
   230 PRINT ''-----------------------------------------------------------
----------'': PRINT:IF A1$=''Y'' THEN VDU2
   240 PRINT ''DESIGN OF A WALL, IN A HIGH EXPLOSIVE ENVIRONMENT. THE DESI
GN AIM IS''
   250 PRINT ''TO LIMIT THE DAMAGE RESULTING FROM BLAST LOADS IN CONNECTIO
N WITH AN''
   260 PRINT ''ACCIDENTAL EXPLOSION.''
   270 PRINT:VDU2:PRINT:VDU3:IF A1$=''Y'' THEN VDU2
```

```
    280 REM DETERMINE THE WORST CASE LOADING ON THE WALL. THE WALL WILL
    290 REM BE LOADED BY BLAST WAVES AND BY THE BUILD-UP OF QUASI-STATIC
    300 REM PRESSURE WITHIN THE ENCLOSED VOLUME.
    310 PRINT ''B L A S T  W A V E  LOADING:''
    320 VDU2,1,27,1,106,1,20,3:IF A1$=''Y'' THEN VDU2
    330 PRINT ''----------------------------''
    340 PRINT
    350 REM LOADING FROM THE BLAST WAVE IS INFLUENCED BY THE CHARGE
    360 REM LOCATION. A CHARGE LOCATED ADJACENT TO A SIDE WALL WILL
    370 REM GIVE A REFLECTION OFF THE SIDE WALL AS WELL AS THE FLOOR
    380 REM AND PRODUCE HIGHER LOADS.
    390 PRINT ''FOR  W O R S T  CASE LOADING A CHARGE REFLECTION FACTOR O
F  2,''
    400 PRINT ''FROM BOTH FLOOR AND WALL SHOULD BE USED.''
    410 PRINT
>LIST420,860
    420 VDU2,1,27,1,106,1,15,3
    430 INPUT ''CHARGE REFLECTION FACTOR (WALL) '';C1
    440 INPUT ''CHARGE REFLECTION FACTOR (FLOOR)'';C2
    450 INPUT ''CHARGE WEIGHT (kg of TNT)'';W
    460 IF A1$=''Y'' THEN VDU2
    470 VDU21:PRINT ''CHARGE REFLECTION FACTOR (WALL) ? '';C1
    480 PRINT ''CHARGE REFLECTION FACTOR (FLOOR)? '';C2
    490 PRINT ''CHARGE WEIGHT (kg of TNT)? '';W:VDU6
    500 LET W1=C1*C2*W
    510 PRINT
    520 VDU2,1,27,1,106,1,15,3:IF A1$=''Y'' THEN VDU2
    530 PRINT ''EFFECTIVE CHARGE WEIGHT = '';W1;''kg of TNT''
    540 PRINT:PRINT
    550 PRINT ''*** CALCULATION OF CHARGE STAND OFF ***''
    560 PRINT
    570 PRINT ''CHARGE STANDOFF IS THE DISTANCE FROM THE WALL BEING DESIGNE
D  TO THE''
    580 PRINT ''EDGE OF THE HIGH EXPLOSIVE AREA, PLUS THE CHARGE RADIUS.''
    590 PRINT
    600 VDU2,1,27,1,106,1,15,3
    610 INPUT ''DISTANCE FROM WALL TO EDGE OF HIGH EXPLOSIVE AREA (m)'';D
    620 INPUT ''SPHERICAL CHARGE RADIUS (m)'';D1
    630 IF A1$=''Y'' THEN VDU2
    640 VDU21:PRINT ''DISTANCE FROM WALL TO EDGE OF HIGH EXPLOSIVE AREA (m)
?  '';D
    650 PRINT ''SPHERICAL CHARGE RADIUS (m)? '';D1:VDU6
    660 LET R=D+D1
    670 PRINT
    680 VDU2,1,27,1,106,1,15,3:IF A1$=''Y'' THEN VDU2
    690 PRINT ''STANDOFF DISTANCE = '';R;''m''
    700 PRINT:PRINT
    710 PRINT ''*** SCALED STANDOFF DISTANCE ***''
    720 PRINT
    730 LET R1=R/(W1^(1/3))
    740 LET R7=INT(R1*1000+0.5)/1000
    750 PRINT ''SCALED STANDOFF DISTANCE = '';R7;''m/kg'';
    760 VDU2,1,27,1,83,1,0,3:IF A1$=''Y'' THEN VDU2
    770 PRINT ''1/3'':VDU2,1,27,1,84,3:IF A1$=''Y'' THEN VDU2
```

```
   780 PRINT
   790 VDU2,1,27,1,106,1,15,3:IF A1$=''Y'' THEN VDU2
   800 PRINT ''FOR THIS SCALED STANDOFF DISTANCE-REFER TO FIGURE 4 FOR THE
REFLECTED''
   810 PRINT ''PRESSURE AND REFLECTED IMPULSE VALUES.''
   820 PRINT
   830 VDU2,1,27,1,106,1,15,3
   840 INPUT ''REFLECTED PRESSURE Pr (kPa) '';P
   850 INPUT ''VALUE FOR ir/W∧1/3 (kPa.sec/kg∧1/3) '';I
   860 IF A1$=''Y'' THEN VDU2
>LIST870.1340
   870 VDU21:PRINT ''REFLECTED PRESSURE Pr (kPa)? '';P
   880 PRINT ''VALUE FOR ir/W'';
   890 VDU6:VDU2,1,27,1,83,1,0,3:IF A1$=''Y'' THEN VDU2
   900 VDU21:PRINT ''1/3'';
   910 VDU6:VDU2,1,27,1,84,3:IF A1$=''Y'' THEN VDU2
   920 VDU21:PRINT '' (kPa.sec/kg'';
   930 VDU6:VDU2,1,27,1,83,1,0,3:IF A1$=''Y'' THEN VDU2
   940 VDU21:PRINT ''1/3'';
   950 VDU6:VDU2,1,27,1,84,3:IF A1$=''Y'' THEN VDU2
   960 VDU21:PRINT '')? '';I:VDU6
   970 LET I1=W1∧(1/3)∗I
   980 LET I2=INT(I1∗1000+0.5)/1000
   990 PRINT
  1000 VDU2,1,27,1,106,1,15,3:IF A1$=''Y'' THEN VDU2
  1010 PRINT ''REFLECTED IMPULSE ON WALL ir = '';I2;''kPa.sec''
  1020 PRINT
  1030 PRINT ''BLAST WAVE LOADING IS IDEALIZED AS A TRIANGULAR PULSE WITH
ZERO RISE''
  1040 PRINT ''TIME.''
  1050 PRINT
  1060 PRINT ''*** LOAD DURATION ***''
  1070 PRINT
  1080 LET T=2∗I1/P
  1090 LET T5=INT (T∗1E5+0.5)/1E5
  1100 PRINT ''LOAD DURATION = '';T5;''sec''
  1110 VDU2,1,27,1,51,1,210,3:IF A1$=''Y'' THEN VDU2
  1120 PRINT:PRINT
  1130 VDU2,1,27,1,51,1,42,3:IF A1$=''Y'' THEN VDU2
  1140 PRINT ''QUASI-STATIC LOADING:''
  1150 VDU2,1,27,1,106,1,27,3:IF A1$=''Y'' THEN VDU2
  1160 PRINT ''----------------------------''
  1170 PRINT
  1180 PRINT ''*** VOLUME OF ROOM ***''
  1190 PRINT:VDU3
  1200 INPUT ''LENGTH OF ROOM (m)'';L
  1210 INPUT ''WIDTH OF ROOM (m)'';L1
  1220 INPUT ''FLOOR TO CEILING HEIGHT (m)'';L2
  1230 IF A1$=''Y'' THEN VDU2
  1240 VDU21:PRINT ''LENGTH OF ROOM (m)? '';L
  1250 PRINT ''WIDTH OF ROOM (m)? '';L1
  1260 PRINT ''FLOOR TO CEILING HEIGHT (m)? '';L2:VDU6
  1270 LET V=L∗L1∗L2
  1280 LET V1=INT(V∗1000+0.5)/1000
```

```
  1290 PRINT
  1300 VDU2,1,27,1,106,1,15,3:IF A1$=''Y'' THEN VDU2
  1310 PRINT ''VOLUME OF ROOM = '';V1;''m'';
  1320 VDU2,1,27,1,83,1,0,3:IF A1$=''Y'' THEN VDU2
  1330 PRINT ''3'':VDU2,1,27,1,84,3:IF A1$=''Y'' THEN VDU2
  1340 LET D3=W/V
>LIST3600,3990
  3600 LET T6=INT(T3*1E5+0.5)/1E5
  3610 PRINT ''PERIOD OF THE SYSTEM = '';T6;''sec''
  3620 PRINT
  3630 PROCdisplay
  3640 VDU2,1,27,1,51,1,210,3:IF A1$=''Y'' THEN VDU2
  3650 PRINT:PRINT:VDU2,1,27,1,106,1,20,3:IF A1$=''Y'' THEN VDU2
  3660 VDU2,1,27,1,51,1,31,3:IF A1$=''Y'' THEN VDU2
  3670 PRINT ''*** NUMERICAL INTEGRATION ***''
  3680 PRINT ''*** FOR ONE DEGREE OF FREEDOM SPRING-MASS SYSTEM ***''
  3700 PRINT
  3720 PRINT ''TO INTEGRATE THE EQUATION OF MOTION, A TIME STEP LESS THAN
OR EQUAL''
  3730 PRINT ''TO ONE-TENTH OF THE FUNDAMENTAL PERIOD IS ADEQUATE IN MOST
INSTANCES.''
  3740 PRINT:PRINT
  3750 VDU2,1,27,1,106,1,25,3
  3760 INPUT ''CHOSEN VALUE FOR TIME STEP (sec)'';T4
  3770 IF A1$=''Y'' THEN VDU2
  3780 VDU21:PRINT ''CHOSEN VALUE FOR TIME STEP (sec)? '';T4:VDU6
  3790 PRINT
  3800 VDU2,1,27,1,106,1,10,3
  3810 INPUT ''SPECIFY TIME AT WHICH CALCULATIONS SHOULD TERMINATE (sec) ''
;N
  3820 IF A1$=''Y'' THEN VDU2
  3830 VDU21:PRINT ''SPECIFY TIME AT WHICH CALCULATIONS SHOULD TERMINATE (
sec)? '';N:VDU6
  3840 VDU2,1,27,1,33,1,15:VDU2,1,27,1,108,1,10,3:IF A1$=''Y'' THEN VDU2:PR
INT:PRINT:VDU2,1,27,1,106,1,20,3:IF A1$=''Y'' THEN VDU2
  3850 PRINT TAB(1);''COL 1'';TAB(14);''COL 2'';TAB(27);''COL 3'';TAB(41);''COL
4'';TAB(55);''COL 5'';TAB(66);''COL 6'';TAB(76);''COL 7''
  3860 PRINT
  3870 VDU2,1,27,1,106,1,15,3:IF A1$=''Y'' THEN VDU2
  3880 PRINT TAB(1);''TIME:'';TAB(55);''ACC.:'';TAB(66);''VEL.:'';TAB(76);
''DISP .:''
  3890 VDU2,1,27,1,106,1,20,3:IF A1$=''Y'' THEN VDU2:PRINT ''-------------
----------------------------------------------------------------------''
  3900 PRINT:VDU2,1,27,1,106,1,15,3:IF A1$=''Y'' THEN VDU2
  3910 LET E1=0
  3920 LET E2=0
  3930 FOR S=0 TO N STEP 14
  3940 LET E=F4*1000-((F4*1000/T)*S)
  3950 IF E<0 THEN LET E=0
  3960 IF S=0 THEN LET Q=0:Q1=0:Q2=0
  3970 LET U=K1*1000*(Q+T4*Q1+((T4^2/4)*Q2))
  3980 LET U1=E-U
  3990 LET U2=U1/(0.66*M7+0.25*K1*1000*T4^2)
```
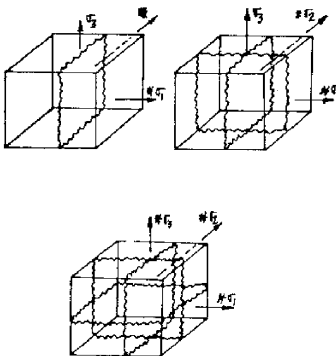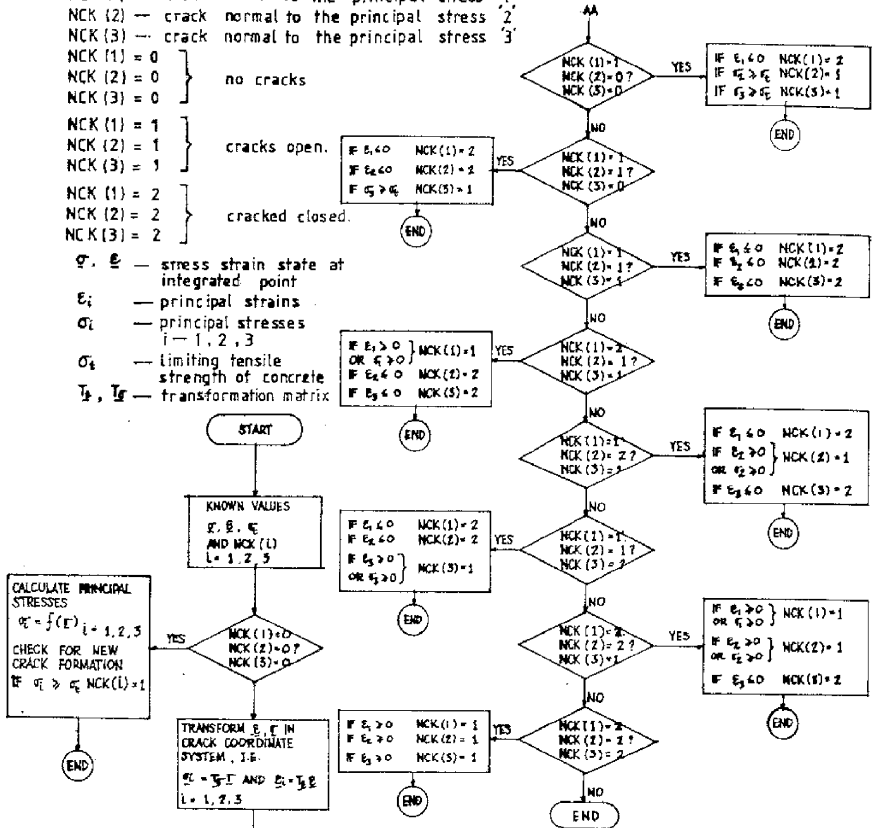
```
>LIST4000,4460
  4000 LET U3=Q1+0.5*(U2+Q2)*T4
  4010 LET U4=Q+0.5*(U3+Q1)*T4
  4020 IF S=0 THEN LET U3=0:U4=0
  4030 LET O1=INT(S*1E5+0.5)/1E5
  4040 LET O2=INT(E*100+0.5)/100
  4050 LET O3=INT(U*100+0.5)/100
  4060 LET O4=INT(U1*100+0.5)/100
  4070 LET O5=INT(U2*1000+0.5)/1000
  4080 LET O6=INT(U3*1E4+0.5)/1E4
  4090 LET O7=INT(U4*1E5+0.5)/1E5
  4100 LET G=O1:PROCtable:PRINT TAB(2−G1);G;
  4110 LET G=O2:PROCtable:PRINT TAB(19−G1);G;
  4120 LET G=O3:PROCtable:PRINT TAB(32−G1);G;
  4130 LET G=O4:PROCtable:PRINT TAB(46−G1);G;
  4140 LET G=O5:PROCtable:PRINT TAB(57−G1);G;
  4150 LET G=O6:PROCtable:PRINT TAB(66−G1);G;
  4160 LET G=O7:PROCtable:PRINT TAB(76−G1);G
  4170 LET Q=U4
  4180 LET Q1=U3
  4190 LET Q2=U2
  4200 LET E1=U4
  4210 IF E2<E1 THEN LET E2=E1
  4220 NEXT S
  4230 VDU2,1,27,1,51,1,210,3:IF A1$=''Y'' THEN VDU2
  4240 PRINT:PRINT
  4250 VDU2,1,27,1,51,1,40,3:IF A1$=''Y'' THEN VDU2
  4260 PRINT
  4270 VDU2,1,27,1,33,1,0,3:IF A1$=''Y'' THEN VDU2
  4280 VDU2,1,27,1,108,1,8,3:IF A1$=''Y'' THEN VDU2
  4290 PRINT ''*** MAXIMUM DISPLACEMENT OBTAINED FROM INTEGRATION PROCEDURE
***''
  4300 LET E3=E2*1000
  4310 LET E4=INT (E3*100+0.5)/100
  4320 PRINT
  4330 VDU2,1,27,1,106,1,15,3:IF A1$=''Y'' THEN VDU2
  4340 PRINT ''MAXIMUM CENTRE DISPLACEMENT OF WALL = '';E4;''mm''
  4350 PRINT:PRINT
  4360 PRINT ''*** DUCTILITY RATIO ***''
  4370 LET H=E2/(R5/K)
  4380 LET H4=INT(H*100+0.5)/100
  4390 PRINT
  4400 VDU2,1,27,1,106,1,15,3:IF A1$=''Y'' THEN VDU2
  4410 PRINT ''DUCTILITY RATIO = '';H4
  4420 PRINT:PRINT
  4430 PRINT ''*** MAXIMUM HINGE ROTATION AT THE SUPPORT ***''
  4440 PRINT
  4450 VDU2,1,27,1,106,1,15,3:IF A1$=''Y'' THEN VDU2
  4460 LET H1=E2/(L2/2)
>LIST4470,4900
  4470 LET H2=ATN(H1)
  4480 LET H3=H2*360/(2*3141592654)
  4490 LET H5=INT (H3*100+0.5)/100
  4500 PRINT ''MAXIMUM HINGE ROTATION AT THE SUPPORT = '';H5;'' DEGREES''
```

Program ISOPAR

Crack indicators   NCK (1), NCK (2), NCK (3)
NCK (1) — crack normal to the principal stress '1'
NCK (2) — crack normal to the principal stress '2'
NCK (3) — crack normal to the principal stress '3'

$$
\left.\begin{array}{l}
NCK (1) = 0 \\
NCK (2) = 0 \\
NCK (3) = 0
\end{array}\right\} \text{ no cracks}
$$

$$
\left.\begin{array}{l}
NCK (1) = 1 \\
NCK (2) = 1 \\
NCK (3) = 1
\end{array}\right\} \text{ cracks open.}
$$

$$
\left.\begin{array}{l}
NCK (1) = 2 \\
NCK (2) = 2 \\
NCK (3) = 2
\end{array}\right\} \text{ cracked closed.}
$$

σ, ε — stress strain state at integrated point
ε_i — principal strains
σ_i — principal stresses   i — 1, 2, 3
σ_t — limiting tensile strength of concrete
T_ε, T_σ — transformation matrix

START

KNOWN VALUES
σ, ε, ε_t
AND NCK (L)
L = 1, 2, 3

CALCULATE PRINCIPAL STRESSES
$\sigma_i = f(\varepsilon)$ i = 1, 2, 3
CHECK FOR NEW CRACK FORMATION
IF $\sigma_i \geq \sigma_t$ NCK(L) = 1

NCK (1) = 0
NCK (2) = 0 ?   YES
NCK (3) = 0

TRANSFORM ε, σ IN CRACK COORDINATE SYSTEM, I.E.
$\sigma_i = T_\sigma \sigma$ AND $\varepsilon_i = T_\varepsilon \varepsilon$
i = 1, 2, 3

END

AA

NCK (1) = 1
NCK (2) = 0 ?   YES
NCK (3) = 0

IF $\varepsilon_1 < 0$ NCK(1) = 2
IF $\varepsilon_2 > \varepsilon_t$ NCK(2) = 1
IF $\varepsilon_3 > \varepsilon_t$ NCK(3) = 1

END

NCK (1) = 1
NCK (2) = 1 ?   YES
NCK (3) = 0

IF $\varepsilon_1 < 0$ NCK(1) = 2
IF $\varepsilon_2 < 0$ NCK(2) = 2
IF $\varepsilon_3 > \varepsilon_t$ NCK(3) = 1

END

NCK (1) = 1
NCK (2) = 1 ?   YES
NCK (3) = 1

IF $\varepsilon_1 < 0$ NCK(1) = 2
IF $\varepsilon_2 < 0$ NCK(2) = 2
IF $\varepsilon_3 < 0$ NCK(3) = 2

END

NCK (1) = 2
NCK (2) = 1 ?   YES
NCK (3) = 1

IF $\varepsilon_1 > 0$ OR $\varepsilon_t > 0$ } NCK(1) = 1
IF $\varepsilon_2 < 0$ NCK(2) = 2
IF $\varepsilon_3 < 0$ NCK(3) = 2

END

NCK (1) = 1
NCK (2) = 2 ?   YES
NCK (3) = 1

IF $\varepsilon_1 < 0$ NCK(1) = 2
IF $\varepsilon_2 > 0$ OR $\varepsilon_t > 0$ } NCK(2) = 1
IF $\varepsilon_3 < 0$ NCK(3) = 2

END

NCK (1) = 2
NCK (2) = 1 ?   YES
NCK (3) = 2

IF $\varepsilon_1 < 0$ NCK(1) = 2
IF $\varepsilon_2 < 0$ NCK(2) = 2
IF $\varepsilon_3 > 0$ OR $\varepsilon_t > 0$ } NCK(3) = 1

END

NCK (1) = 2
NCK (2) = 2 ?   YES
NCK (3) = 1

IF $\varepsilon_1 > 0$ OR $\varepsilon_t > 0$ } NCK(1) = 1
IF $\varepsilon_2 > 0$ OR $\varepsilon_t > 0$ } NCK(2) = 1
IF $\varepsilon_3 < 0$ NCK(3) = 2

END

NCK (1) = 2
NCK (2) = 2 ?
NCK (3) = 2

END

AA

CRACK IN PRINCIPAL DIRECTIONS THREE AND ONE

$$D_{11}^{**} = D_{33}^{**} = D_{12}^{**} = D_{21}^{**} = 0$$

$$D_{13}^{**} = D_{31}^{**} = D_{23}^{**} = D_{31}^{**} = 0$$

$$D_{22}^{**} \quad D_{22} - D_{12}\frac{D_{12}}{D_{11}} - D_{23}\frac{D_{23}}{D_{33}}$$

$$D_{44}^{**} = \beta D_{44}$$

$$D_{55}^{**} = \beta D_{55}$$

$$D_{66}^{**} = \beta D_{66}$$

CRACKS IN ALL THREE PRINCIPAL DIRECTIONS

$$[D^{**}] = [0]$$
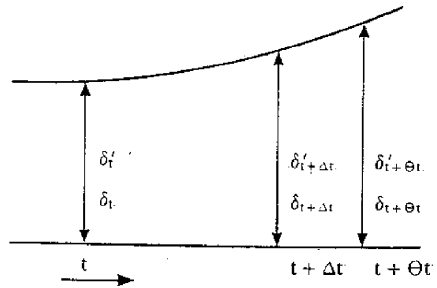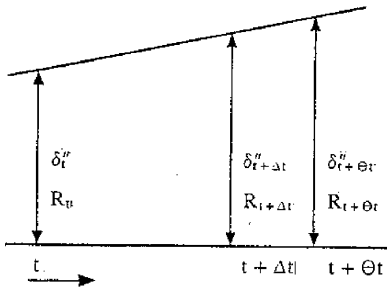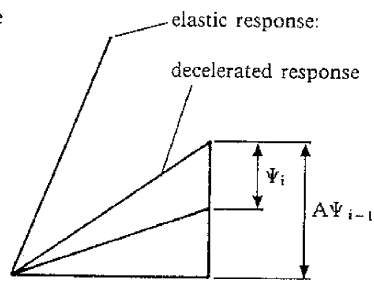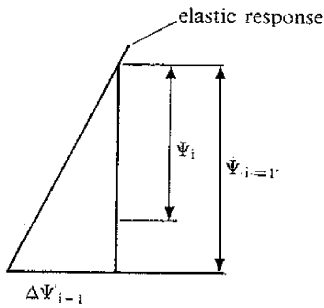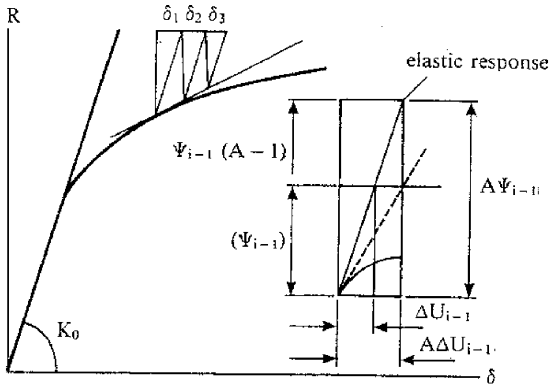
```
4510 PRINT:PRINT:PRINT
4520 VDU3
4530 INPUT ''DO YOU WANT TO RUN THE INTEGRATION PROCEDURE AGAIN? ENTER Y
FOR YES AND N FOR NO '';Z1$
4540 IF A1$=''Y'' THEN VDU2
4550 VDU21:PRINT ''DO YOU WANT TO RUN THE INTEGRATION PROCEDURE AGAIN? ''
;Z1$:VDU6
4560 IF Z1$=''Y'' THEN GOTO 3650
4570 PRINT:PRINT
4580 VDU3
```

```
  4590 INPUT ''DO YOU WANT TO RUN THE PROGRAMME AGAIN FROM THE START? ENTER
Y FOR YES AND N FOR NO '';Z$
  4600 IF A1$=''Y'' THEN VDU2
  4610 VDU21:PRINT ''DO YOU WANT TO RUN THE PROGRAMME AGAIN FROM THE START
? '';Z$:VDU6
  4620 IF Z$=''Y'' THEN GOTO 170
  4630 PRINT:PRINT
  4640 PRINT ''                       ***  E  N  D  *** ''
  4650 VDU3
  4660 END
  4670 DEF PROCtable
  4680 LET G$=STR$(G)
  4690 LET J=0
  4700 LET J=J+1
  4710 LET G1$=RIGHT$(G$,J)
  4720 LET G2$=LEFT$(G1$,1)
  4730 LET G7$=LEFT$(G$,1)
  4740 LET G3$=MID$(G$,2,1)
  4750 IF G7$=''−'' THEN LET G3$=MID$(G$,3,1)
  4760 IF G2$=''.'' THEN GOTO 4790
  4770 IF LEN(G1$)=LEN(G$) THEN GOTO 4810
  4780 GOTO 4700
  4790 LET G1=LEN(G$)-LEN(G1$)
  4800 IF G2$=''.'' THEN GOTO 4820
  4810 LET G1=LEN(G$)
  4820 IF G3$=''E'' THEN LET G1=G1−3
  4830 ENDPROC
  4840 DEF PROCdisplay
  4850 VDU3
  4860 PRINT ''PRESS ANY KEY TO CONTINUE(EXCEPT CONTROL KEYS SUCH AS >BREA
K<, >ESCAPE<, ETC.''
  4870 key$=GET$
  4880 CLS
  4890 IF A1$=''Y'' THEN VDU2
  4900 ENDPROC
```

Ottosen Model

```
      IMPLICIT REAL*8(A−H,O−Z)
      COMMON/MTMD3D/DEP(6,6),STRESS(6),STRAIN(6),IPT,NEL
      DIMENSION PAR(3,5),FS(6,6),FSTPOS(6,6),PROP(1),SIG(1),
      @        DVI1DS(6),DVJ2DS(6),DVJ3DS(6),DVTHDS(6)
      OPEN (UNIT=5,FILE='PARAMETERS',STATUS='OLD')
      READ (5,*,END=3700)((PAR(IF,JF),JF=1,5),IF=1,3)
3700  CLOSE (5)
      PK = PROP(3)/PROP(4)
      IP = 0
      JP = 0
      IF (PK .LE. 0.08) IP = 1
      IF (PK .EQ. 0.10) IP = 2
      IF (PK .GE. 0.12) IP = 3
      IF (PK .LT. 0.10) JP = 1
```

```
      IF (PK .GT. 0.10) JP = 2
      IF (IP .EQ. 0) GOTO 3800
      A = PAR(IP,2)
      B = PAR(IP,3)
      PK1 = PAR(IP,4)
      PK2 = PAR(IP,5)
      GOTO 3909
3800  SUB1 = PK−PAR(JP,1)
      SUB2 = PAR(JP + 1,1)−PAR(JP,1)
      A = SUB1*(PAR(JP*1,2)−PAR(JP,2))/SUB2+PAR(JP,2)
      B = SUB1*(PAR(JP*1,3)−PAR(JP,3))/SUB2+PAR(JP,3)
      PK1 = SUB1*(PAR(JP*1,4)−PAR(JP,4))/SUB2+PAR(JP,4)
      PK2 = SUB1*(PAR(JP*1,5)−PAR(JP,5))/SUB2+PAR(JP,5)
3900  VARI1 = SIG(1)+SIG(2)+SIG(3)
      VARJ2 = 1.0/6.0*((SIG(1)−SIG(2))**2+(SIG(2)−SIG(3))**2+
      @      (SIG(3)−SIG(1))**2)+SIG(4)**2+SIG(5)**2+SIG(6)**2
      VARI13 = VARI1/3.0
      VI131 = SIG(1)−VARI13
      VI132 = SIG(2)−VARI13
      VI133 = SIG(3)−VARI13
      VARJ3 = VI131*(VI132*VI133−SIG(5)**2)−SIG(4)*(SIG(4)*VI133
      @       −SIG(5)*SIG(5))+SIG(6)*(SIG(4)*SIG(5)−SIG(6)*VI132)
      VAR3TH = 1.5*3.0**(0.5)*VARJ3/VARJ2**1.5
      IF (VAR3TH .GE. 0.0) GOTO 4000
      ALAM = 22.0/21.0−1.0/3.0*ACOS(−PK2*VAR3TH)
      TOTLAM = PK1*COS(ALAM)
      DFD3TH = PK1*PK2*VARJ2**0.5*SIN(ALAM)/(3.0*PROP(4)*
      @         SIN(ACOS(−PK2*VAR3TH)))
      GOTO 4100
4000  ALAM = 1.0/3.0*ACOS(PK2*VAR3TH)
      TOTLAM = PK1*COS(ALAM)
      DFD3TH = PK1*PK2*VARJ2**0.5*SIN(ALAM)/(3.0*PROP(4)*
      @         SIN(ACOS(PK2*VAR3TH)))
4100  DFDI1 = B/PROP(4)
      DFDJ2 = A/PROP(4)**2+TOTLAM/(PROP(4)*VARJ2**0.5)
      DVI1DS(1) = 1.0
      DVI1DS(2) = 1.0
      DVI1DS(3) = 1.0
      DVI1DS(4) = 0.0
      DVI1DS(5) = 0.0
      DVI1DS(6) = 0.0
      DVJ2DS(1) = 1.0/3.0*(2.0*SIG(1)−SIG(2)−SIG(3))
      DVJ2DS(2) = 1.0/3.0*(2.0*SIG(2)−SIG(1)−SIG(3))
      DVJ2DS(3) = 1.0/3.0*(2.0*SIG(3)−SIG(1)−SIG(2))
      DVJ2DS(4) = 2.0*SIG(4)
      DVJ2DS(5) = 2.0*SIG(5)
      DVJ2DS(6) = 2.0*SIG(6)
      DVJ3DS(1) = 1.0/3.0*(VI131*(−VI132−VI133))+2.0*VI132*VI131−
      @           2.0*SIG(5)**2*SIG(4)**2*SIG(6)**2
      DVJ3DS(2) = 1.0/3.0*(VI132*(−VI131−VI133))+2.0*VI131*VI133−
      @           2.0*SIG(6)**2*SIG(4)**2*SIG(5)**2
      DVJ3DS(3) = 1.0/3.0*(VI133*(−VI131−VI132))+2.0*VI131*VI132−
      @           2.0*SIG(4)**2*SIG(5)**2*SIG(6)**2
      DVJ3DS(4) = −2.0*VI133*SIG(4)+2.0*SIG(5)*SIG(6)
```

```
      DVJ3DS(5) = −2.0*VI131*SIG(5)+2.0*SIG(4)*SIG(6)
      DVJ3DS(6) = −2.0*VI132*SIG(6)+2.0*SIG(4)*SIG(5)
      CONVJ2 = 3.0*3.0**0.5/(2.0*VARJ*1.2)
      VJ3J2 = VARJ3/VARJ2**0.5
      DVTHDS(1) = CONVJ2*(−0.5*VJ3J2*(2.0*SIG(1)−SIG(2)−SIG(3))+
     @           DVJ3DS(1))
      DVTHDS(2) = CONVJ2*(−0.5*VJ3J2*(2.0*SIG(2)−SIG(1)−SIG(3))+
     @           DVJ3DS(2))
      DVTHDS(3) = CONVJ2*(−0.5*VJ3J2*(2.0*SIG(3)−SIG(1)−SIG(2))+
     @           DVJ3DS(3))
      DVTHDS(4) = CONVJ2*(−3.0*VJ3J2*SIG(4)+DVJ3DS(4))
      DVTHDS(5) = CONVJ2*(−3.0*VJ3J2*SIG(5)+DVJ3DS(5))
      DVTHDS(6) = CONVJ2*(−3.0*VJ3J2*SIG(6)+DVJ3DS(6))
      DO 4200 IS = 1,6
      FS(IS,1) = DFDI1*DVI1DS(IS)+DFDJ2*DVJ2DS(IS)*
                 DFD3TH*DVTHDS(IS)
4200  FSTPDS(1,IS) = FS(IS,1)
      RETURN
      END
```

Main Program for Non-Linear Analysis

```
C
        SUBROUTINE NONSTR(TEL,IGAUS,TEM)
C------------          THIS SUBR. CALC. THE INCREMENTAL
C------------          AND UPDATED STRESS, LOADING AND UNLOADING
C------------          AND CRACK FORMATION
C
£INSERT COMMON.FF
C
C-----       IF POINT IS ALREADY CRUSHED DO NOT DO ANY CALCULATION
        IF(NCRK(IGAUS,IEL).EQ.999)GO TO 555
C
C
C          CRACK INDICATOR
        NCR=NCRK(IGAUS,IEL)
C              LOADING − UNLOADING INDICATOR
        IUNL=IUNLOD(IGAUS,IEL)
C
C--------          CRACK WIDTH(IN TERMS OF STRAINS)
C        DO 5 J=1,3
C        CRW(J)=CWI(J,IGAUS)
C5      CONTINUE
C
C----------          COPY ANGL INTO DC
        DO 7 J=1,9
        DO(J)=ANGL(J,IGAUS,IEL)
7       CONTINUE
C
        CALL RZERO(CET,6)
C
C---------------          STRESSES CURRENT AND TOTAL
```

```
         DO 10 J=1,6
         STG(J)=SIGT(J,IGAUS,IEL)
         STB(J)=STG(J)+SIG(J)
10       CONTINUE
C
         IF(NCR.EQ.0)GO TO 30
C
C----------               TRANSFORMATION MATRIX IN CRACK DIRECTIONS
         DO 20 J=1,3
         DC1(J)=ANGL(J,IGAUS,IEL)
         DC2(J)=ANGL(J+3,IGAUS,IEL)
         DC3(J)=ANGL(J+6,IGAUS,IEL)
20       CONTINUE
C
         CALL TRANSF (3)
C---------------         TRANSFORM STB STRESS IN CRACK DIRECTION
C---------------         ALSO INCREMENTAL STRESS SIG
         CALL MVECT(QM,STB,CET,6,6)
C
          CALL MVECT(QM,SIG,STC,6,6)
C
C---------------               TRANSF. TOTAL STRAIN IN CRACK DIR.
C
         CALL TRANSF(1)
         DO 21 J=1,6
         AJ(J)=ECT(J,IGAUS)
21       CONTINUE
C
         CALL MVECT(QM,AJ,ECA,6,6)
C
C
         GO TO 50
C
30       CONTINUE
C------------                CALC. PRINCIPAL STRESSES DUE TO STB
         CALL PRINCL(2,IGAUS,STB)
         CET(1)=PS1(IGAUS)
         CET(2)=PS2(IGAUS)
         CET(3)=PS3(IGAUS)
         KKOO=1
         IF(KKOO.EQ.1)GO TO 40
C----------          PRINCIPAL STRAINS
         DO 38 J=1,6
         ECB(J)=ECT(J,IGAUS)
38       CONTINUE
C
         CALL PRINCL (1,IGAUS, ECB)
         ECA(1)=EP1(IGAUS)
         ECA(2)=EP2(IGAUS)
         ECA(3)=EP3(IGAUS)
40       CONTINUE
C
C
C-----          CALCULATE EQUIVALENT STRAIN
```

```
C
        EQSTN=SIGEFF(ECB)
C---------------             CHECK FOR CONCRETE CRUSHING
C        EC1=ECA(1)+ECU
C        EC2=ECA(2)+ECU
C        EC3=ECA(3)+ECU
C        IF(EC1.LT.0.0 .OR. EC2.LT.0.0 .OR. EC3.LT.0.0)GO TO 888
C
        CRUSH=EQSTN − ECU
        IF(CRUSH .GT. 0.0) GO TO 888
C
   50   CONTINUE
C
C-----       CALC. AND UPDATE CRACK INDICATOR
C
C
        CALL CRACK(CET,ECA,NCR,CRW)
C
C----------             STORE UPDATED VALUES IN ARRAYS
        NCRK (IGAUS,IEL)=NCR
        DO 41 J=1,9
        ANGL(J,IGAUS,IEL)=DC(J)
   41   CONTINUE
C
C        DO 42 J=1,3
C        CWI(J,IGAUS)=CRW(J)
C  42      CONTINUE
C
        IF(NCR.EQ.0)GO TO 110
        DO 105 J=1,3
        DC1(J)=ANGL(J,IGAUS,IEL)
        DC2(J)=ANGL(J+3,IGAUS,IEL)
        DC3(J)=ANGL(J+6,IGAUS,IEL)
  105   CONTINUE
        CALL TRANSF(1)
        DO 106 J=1,6
        ECB(J)=EC(J)
  106   CONTINUE
C
        CALL MVECT (QM,ECB,EC,6,6)
C
C
  110   CONTINUE
C--------           GO TO APPROPRIATE CONCRETE COMPRESSION CRITERION
        IF (ICOMP.EQ.1)GO TO 98
C---------             CALC. UNIAXIAL STRAINS
        DO 308 J=1,3
        IF (ENU(J).LT.1.E−15)GO TO 306
        EIU(J)=SIG(J)/ENU(J)
        GO TO 308
  306   CONTINUE
        EIU(J)=0.0
  308   CONTINUE
C---------------                 EQUIV. STRESS AT PREVIOUS UNLOADED POINT
```

```
      SEQ=SIGY(IGAUS,IEL)
C--------------                    CALC. EFFECTIVE STRESS DUE TO CURRENT
C------------                      AND TOTAL STRESS
      SIGEF2=SIGEFF(ECT(1,IGAUS))
       DO 109 J=1,6
      ECB(J)=ECT(J,IGAUS)-ECRT(J)
  109 CONTINUE
      SIGEF1=SIGEFF (ECB)
      FLOA=SIGEF2-SIGEF1
      IF(IUNL .EQ. 1) GO TO 60
C         IUNL=0 --- ON THE EQUIV. CURVE
C
      IF(SIGEF2 .GE. SEQ)GO TO 43
C--------------               UNLOADING AT THIS POINT
      RFACT=(SEG-SIGEF1)/FLOA
C--------------               NON-LINEAR STRAIN
      DO 35 J=1,6
      ECB (J)=RFACT*EC(J)
  35    CONTINUE
C-----        MEAN NON-LINEAR STRAIN
      DO 201 J=1,3
      ETU(J,IGAUS)=ETU(J,IGAUS)+0.5*RFACT*EIU(J)
  201    CONTINUE
      CALL DMATL(STB,IEL,IGAUS,TEM)
C--------------                       INCREMENTAL STRESS ASSOCIATED WITH -ECB
      CALL MVECT (DDS,ECB,AJ,6,6)
C--------------                ELASTIC STRAIN
      DO 36 J=1,6
      ECB(J)=(1.0-RFACT)*EC(J)
  36    CONTINUE
      IUNLOD(IGAUS,IEL)=1
C-------------          ELASTIC STRESS INCR.
      CALL DMATL(CET,IEL,IGAUS,TEM)
      CALL MVECT(DOS,ECB,STA,6,6)
C---------- TOTAL STRESS INCREMENT
      DO 37 J=1,6
      SIG(J)=STA(J)+AJ(J)
  37    CONTINUE
C
       DO 202 J=1,3
       ETU(J,IGAUS)=ETU(J,IGAUS)+EIU(J)-0.5*RFACT*EIU(J)
  202    CONTINUE
      GO TO 99
  43    CONTINUE
C--------------         LOADING AT THIS POINT
C-----        MEAN UNIAXIAL STRAIN
      DO 203 J=1,3
      ETU(J,IGAUS)=ETU(J,IGAUS)+EIU(J)*0.5
  203    CONTINUE
      CALL DMATL(STB,IEL,IGAUS,TEM)
C--------------              STRESS INCREMENT
C
      CALL MVECT(DDS,EC,SIG,6,6)
C
```

```
C-----            ACCUMULATE TOTAL UNIAXIAL STRAIN
      DO 205 J=1,3
        ETU(J,IGAUS)=ETU(J,IGAUS)+EIU(J)*0.5
  205    CONTINUE
      GO TO 99
C
   60    CONTINUE
C-------------          NOT ON THE EQUIV. CURVE
      IF(SIGEF2 .GT. SEQ)GO TO 70
C-----------          ELASTIC UNLOADING
      CALL DMATL(CET,IEL,IGAUS,TEM)
C-------------          ELASTIC STRESS
      CALL MVECT(DOS,EC,SIG,6,6)
C-----            ACCUMULATE UNIAXIAL STRAIN
        DO 206 J=1,3
      ETU(J,IGAUS)=ETU(J,IGAUS)+EIU(J)
  206    CONTINUE
      GO TO 99
   70    CONTINUE
C-----------          LOADING PARTLY ELASTIC PARTLY NON-LINEAR
      FRAC=(SEQ-SIGEF1)/FLOA
C-----------          ELASTIC STRAIN
      DO 71 J=1,6
      ECB(J)=FRAC*EC(J)
   71    CONTINUE
      CALL DMATL(CET,IEL,IGAUS,TEM)
      CALL MVECT(DDS,ECB,STA,6,6)
C---------------          STRESS AT THE CURVE
      DO 72 J=1,6
      AJ(J)=STG(J)+STA(J)
   72    CONTINUE
C-----          MEAN UNIAXIAL STRAIN
        DO 207 J=1,3
      ETU(J,IGAUS)=ETU(J,IGAUS)+0.5*EIU(J)*(1.+FRAC)
  207     CONTINUE
C
      IUNLOD(IGAUS,IEL)=0
C-----------          STRAIN ASSOCIATED WITH NON-LINEAR CURVE
      DO 73 J=1,6
      ECB(J)=(1.0-FRAC)*EC(J)
   73    CONTINUE
      CALL DMATL(AJ,IEL,IGAUS,TEM)
C-------          STRESS INCR.
      CALL MVECT(DDS,ECB,STB,6,6)
C-----------------          TOTAL INCREMENTAL STRESS
      DO 74 J=1,6
      SIG(J)=STA(J)+STB(J)
   74    CONTINUE
C
      DO 208 J=1,3
        ETU(J,IGAUS)=ETU(J,IGAUS)+0.5*EIU(J)*(1.-FRAC)
  208    CONTINUE
      GO TO 99
   98    CONTINUE
```

```
C--------            STRESS INCREMENT ON THE BASIS OF ENDOCHRONIC THEORY
C
       DO 1223 J=1,6
       SIGG(J)=SIG(J)
       ECC(J)=EC(J)
  1223 CONTINUE
       CALL ENDOST(IEL,IGAUS,SIGG,ECC)
C
   99  CONTINUE
       IF(NCR.EQ.0)GO TO 50
       DO 91 J=1,6
       AJ(J)=SIGT(J,IGAUS,IEL)
   91    CONTINUE
       CALL TRANSF(3)
       CALL MVECT(QM,AJ,STG,6,6)
C----------            TRANSFORM LOCAL STRESSES IN GLOBAL DIRN
       CALL TRANSF(2)
       DO 92 J=1,6
       STG(J)=STG(J)+SIG(J)
   92  CONTINUE
C----------            RELEASE STRESSES ACROSS THE OPEN CRACKS
       CALL GETNCK (NCR,NCK)
       IF(NCK(1).EQ.1)STG(1)=0.0
       IF(NCK(2).EQ.1)STG(2)=0.0
       IF(NCK(3).EQ.1)STG(3)=0.0
       CALL MVECT(QM,STG,STA,6,6)
C
       DO 94 J=1,6
       SIGT(J,IGAUS,IEL)=STA(J)
   94    CONTINUE
C
       GO TO 999
90       CONTINUE
       DO 100 J=1,6
       SIGT(J,IGAUS,IEL)=SIGT(J,IGAUS,IEL)+SIG(J)
100      CONTINUE
       GO TO 999
888      CONTINUE
C-----------            CRUSHING OF CONCRETE
       NCRK(IGAUS,IEL)=999
C---------            RELEASE STRESSES
       DO 101 J=1,6
       SIGT(J,IGAUS,IEL)=0.0
101      CONTINUE
C
       GO TO 555
999      CONTINUE
C-----        CHECK THAT THE CURRENT STATE OF STRESS IS
C-----          INSIDE THE FAILURE SURFACE
       CALL PRINCL(2,IGAUS,SIGT(1,IGAUS,IEL))
       CET(1)=PS1(IGAUS)
       CET(2)=PS2(IGAUS)
       CET(3)=PS3(IGAUS)
       IF(CET(1).GT.0.0 .OR.CET(2).GT.0.0 .OR.CET(3).GT.0.0)
```

```
         1                                           GO TO 555
         CALL CONCR1(CET)
C         IF(ICOMP.EQ.2)     CALL CONCR3(CET)
         BRING=1.0
         IF(FF.GT.1.0001)BRING=BRING/FF
         DO 553 J=1,6
         SIGT(J,IGAUS,IEL)=BRING*SIGT(J,IGAUS,IEL)
   553   CONTINUE
C
   555   CONTINUE
         RETURN
         END
C
         SUBROUTINE ASSLOD(IEL,NER,ELOD)
£INSERT COMMON.FF
C
C-----------              TO ASSEMBLE LOAD VECTOR
C
         DO 95 J=1,NER
         M1=(MCODE(J,IEL)-1)*NDF
C------              ELASTO-PLASTIC STRAIN INCR.
         DO 88 J=1,3
         ECM(J)=FPROP*ECM(J)
    88   CONTINUE
         CALL SBINST (ECM,NSUB,SGMT(1,IGAUS,I1))
C-----    ADD ELASTIC STRESS INCR
         DO 94 J=1-3
         SGMT(J,1GAUS,I1)=SGMT(J.IGAUS,I1)+SGM(J)
    94   CONTINUE
         NYM(IGAUS,I1)=2
99       CONTINUE
         RETURN
         END
C
         SUBROUTINE MEMDAT(I1,IGAUS,STD)
£INSERT COMMON.FF
C
C------------                 TO CALC. ELAS TO - PLASTIC MATERIAL MATRIX
C-----------                  AT STRESS LEVEL,STD FOR MEMBRANE ELEMENTS
C
C
C------------                 CALC. ELASTIC MATERIAL MATRIX
C
         CALL DMEMB
C-----------                 CHECK WHETHER CURRENT POINT IS PLASTIC
         IF(NYM(IGAUS,I1).NE.1)GO TO 50
C
C
         EFF=ZMISE(STD)
         SX=(2.*STD(1)-STD(2))/3.
         SY=(2.*STD(2)-STD(1))/3.
         FAC=EFF/1.5
C
C------------                    CALC. (DF/D(STD) = AJ
```

```
      AJ(1)=SX/FAC
      AJ(2)=SY/FAC
      AJ(3)=2.*STD(3)/FAC
C
C------------                  CALC. DENOMINATOR OF PLASTIC MATRIX
C                    DENOM=AJ(T)*DJ*AJ + HARDG
C
      CALL MVECT(DJ,AJ,STC,3,3)
C
      DENOM=0.0
      DO 10 J=1,3
      DENOM=DENOM+AJ(J)*STC(J)
10       CONTINUE
C
      DENOM=DENOM+HARDG
C
C-----------                  CALC. ELASTO-PLASTIC MATERIAL MATRIX AND
C-----------                  STORE IT INTO DJ
      DO 30 J=1,3
      DO 20 K=1,3
      DJ(J,K)=DJ(J,K)-STC(J)*STC(K)/DENOM
20       CONTINUE
30       CONTINUE
C
50       CONTINUE
C
      RETURN
      END
C
C
      SUBROUTINE SBINST(ECL,NSUB,STA)
C-----      STRESS INCR IS CALCULATED USING SUB-INCREMENTAL
C-----      METHOD,ALSO STRESS STA IS UPDATED
£INSERT COMMON.FF
      DIMENSION ECL(1)
      RSUB=NSUB
      DO 3 J=1,3
      ECB(J)=ECL(J)/RSUB
  3    CONTINUE
      SIGY1=ZMISE(STA)
C-----      LOOP OVER SUB-INCREMENTS
      DO 70 ISUB=1,NSUB
C------------                  CALC. ELASTO-PLASTIC MATERIAL MATRIX -DJ
C
      SX=(2.*STA(1)-STA(2))/3.
      SY=(2.*STA(2)-STA(1))/3.
      FAC=SIGY1/1.5
C
C-----------                  CALC. (DF/D(STA) = AJ
      AJ(1)=SX/FAC
      AJ(2)=SY/FAC
      AJ(3)=2.*STA(3)/FAC
C
C------------                  CALC. DENOMINATOR OF PLASTIC MATRIX
```

```
C                             DENOM=AJ(T)*DJ*AJ + HARDG
C
        CALL MVECT(DJ,AJ,STC,3,3)
C
        DENOM=0.0
        DO 10 J=1,3
        DENOM=DENOM+AJ(J)*STC(J)
10        CONTINUE
C
        DENOM=DENOM+HARDG
C-----------           CALC. ELASTO-PLASTIC MATERIAL MATRIX AND
C-----------           STORE IT INTO DJ
        DO 30 J=1,3
        DO 20 K=1,3
        DJ(J.K)=DJ(J,K)-STC(J)*STC(K)/DENOM
20      CONTINUE
30       CONTINUE
C-----        CALC. DLAMB AND EQUIV. PLASTIC STRAIN INCREMENT
        DLAMB=0.0
        DO 64 J=1,3
        DLAMB=DLAMB+STC(J)*ECB(J)
    64    CONTINUE
        DLAMB=DLAMB/DENOM
C-----        UNLOADING IS PLASTIC INSIDE A SUBINCREMENTS
C       IF(DLAMB.LT.0.0)CLAMB=0.0
        BB=0.0
        DO 65 J=1,3
        BB=BB+AJ(J)*STA(J)
    65    CONTINUE
        EQSTN=DLAMB*BB/SIGY1
        CALL MVECT(DJ,ECB,STB,3,3)
        DO 60 J=1,3
        STA(J)=STA(J)+STB(J)
    60    CONTINUE
C-----        CALC. UPDATED YIELD SURFACE
        SIGY2=ZMISE(STA)
        SIGY1=SIGY1+HARDG*EQSTN
        FACT=1.0
        IF(SIGY2.GT.SIGY1)FACT=SIGY1/SIGY2
C-----        UPDATE STRESS VECTOR
        DO 62 J=1,3
        STA(J)=STA(J)*FACT
    62    CONTINUE
C
    70    CONTINUE
        RETURN
        END
C
        SUBROUTINE STELST(I)
£INSERT COMMON.FF
C
C---------           CALC. ELASTO-PLASTIC STRESS INCR AND UDATE
C---------           CURRENT STRESS AND PLASTIC INDICATOR
            N=LRF(I)
```

```
C
      I1=I−(NTE1+NTE2)
C
      T1=SIGGT(I1)
      T2=T1+STRV
      T1=RABS(T1)
      T2=RABS(T2)
C
      FACL=T2−T1
      IF(FACL.EQ.0.0)GO TO 99
C----------              CHECK FOR LOADING OR UNLOADING AT THIS POINT
C
       IF(ISPL(I1).EQ.1)GO TO 40
C-----        POINT ELASTIC BEFORE
      IF(T2.LT.YIELST(I1))GO TO 50
C-----        TRANSITION ZONE - LOADING
C----------           FRACTION OF ELASTIC STRAIN INCR.
      FRAC=(YIELST(I1)−T1)/FACL
C
      ISPL(I1)=1
C*--------        ELASTIC STRESS INCREMENT
      STRV=STRV+FRAC
C*--------        STRESS AT YIELD SURFACE
      SIGGT(I1)=SIGGT(I1)+STRV
C*--------         PLASTIC STRAIN INCR.
      STRNV=(1.0−FRAC)*STRNV
      GO TO 45
C
  40  CONTINUE
C-----       POINT PLASTIC BEFORE
      IF(T2.GT.YIELST(I1))GO TO 45
      GO TO 50
  45  CONTINUE
      EPSMOD=ZESBAR(I)
C--------         CALC. PLASTIC STRESS INCR. AND UPDATE STRESS
      STRVPL=STRNV*EPSMOD
      STRV=STRV+STRVPL
      SIGGT(I1)=SIGGT(I1)+STRVPL
C
      GO TO 99
C
  50    CONTINUE
C---------              UNLOADING AT THIS POINT
C
C-------        CHECK IF POINT WAS PLASTIC IN PREVIOUS ITERATION
      IF(ISPL(I1).EQ.1)GO TO 55
      SIGGT(I1)=SIGGT(I1)+STRV
      GO TO 99
  55  CONTINUE
C-----       CHECK THAT THE UNLOADING IS REAL
      STRV=ZESBAR(I)*STRNV
      T2=SIGGT(I1)+STRV
      T2=RABS(T2)
      IF(T2.GT.YIELST(I1))GO TO 45
```

```
        FACL=T2−T1
        IF(FACL.EQ.0.0)GO TO 99
        FRAC=(YIELST(I1)−T1)/FACL
C--------------                  PLASTIC STRESS INCR.
        STRPL=FRAC*STRV
        ISPL(I1)=2
C
C--------------                  ELASTIC STRESS INCR.
        STREL=ZESBAR(I)*(1.0−FRAC)*STRNV
        STRV=STRPL+STREL
C
        SIGGT(I1)=SIGGT(I1)+STRV
99       CONTINUE
        RETURN
        END
C
        SUBROUTINE INCLNE(I,NER)
£INSERT COMMON.FF
C-----------------------------------------------------------------
C
        IF(JRADL.NE.0)GO TO 10
        IF(NBC.GT.0)GO TO 188
   10   CONTINUE
        JP=NER*NDF
        I1=I−(NTE1+NTE2)
        LET=IDENT(I)
        DO 13 J=1,NER
        IJ=MCODE(J,I)
        IF(LET.GT.2)IJ=LCODE(J,I1)
13      LC(J)=IJ
        DO 3 J=1,3
        DO 3 K=1,3
3       C(J,K)=0.0
        IF(JRADL.NE.0)GO TO 31
        C(1,1)=RCOS(SHY)
        C(2,2)=RCOS(SHY)
        C(3.3)=1.0
        C(1,2)= −RSIM(SHY)
        C(2,1)=RSIN(SHY)
31      DO 132 J=1,NER
        M1=LC(J)
        IF(JRADL.NE.0)GO TO 17
        M1=(M1−1)*NDF
        JS=0
        DO 26 K=1,6
        Q(K,J)=QM(J,K)
26      CONTINUE
C
        CALL MPPODT(Q,0,OOS,6,6,6)
25      CONTINUE
        RETURN
        END
C
        SUBROUTINE PRINCL(NEP,M,CET)
```

```
£INSERT COMMON.FF
C
C-------------------------------------------------------------------------------
C                            THIS SUBROUTINE CALCULATES THE PRINCIPAL STRAINS
C                            PRINCIPAL STRESSES AND DIRECTION COSINES
C                       NEP=2 — PRINCIPAL STRESS AND D.C.
C                            NEP=1 — PRINCIPAL STRAINS ONLY
        LL=0
        DO 10 J=1,6
        IF(RABS(CET(J)).GT.1.OE—15)LL=1
10      CONTINUE
C
        IF(NEP.EO.1)GO TO 20
        PS1(M)=0.0
        PS2(M)=0.0
        PS3(M)=0.0
        GO TO 30
20      CONTINUE
        EP1(M)=0.0
        EP2(M)=0.0
        EP3(M)=0.0
30      CONTINUE
C
        IF(LL.EQ.0)GO TO 999
C
        G1= CET(1)
        G2= CET(2)
        G3= CET(3)
        G4= CET(4)
        G5= CET(5)
        G6= CET(6)
        ZNV1 = G1 + G2 + G3
        ZNV2 = G1*G2 + G2*G3 + G3*G1 — G4*G4 — G5*G5 — G6*G6
        ZNV3 = G1+G2*G3+2.0 *G4*G5*G6 —G1*G5*G5 — G2*G5* G6
     1          — G3*G4*G4
        BB = — ZNV1
        CW = ZNV2
        CD = — ZNV3
C       FIND ALL ROOTS OF CUBIC EQUATION AA*X*3 + BB*X*2 + CC*X + DD
C       FIRST ROOT (X5) IS FOUND BY NEWTON'S METHOD USING 0 AS
C       FIRST APPROX. THEN SOLVE QUADRATIC BY STANDARD FORMULA
C       ERR IS THE ACCUR ACY REQUIRED FOR ROOT X5
        ERR = 1E—6
        X1 = 0.0
        CORT=2.0*ERR
        MGG=0
1000    B1 = BB + X1
        MGG=MGG+1
        IF(MGG.GT.35)GO TO 2000
        B2 = CW + X1*B1
        IF(RABS(CORT).LT. ERR)GO TO 2000
        B3 = CD+ X1 * B2
        C3 = ( X1 + B1) * X1 + B2
        IF( RABS(C3) .LT. 1E—30) C3 = 1.0
```

```
         CORT=B3/C3
         X1=X1−CORT
         GO TO 1000
2000     X5 = X1
C
C        SECOND PART - FIND ROOTS OF QUADRATIC
C                       X**2 + B1*X + B2 = 0.0
C
         DIP = B1*B1 - 4.0*B2
         IF(DIP .LT. 0.0) GO TO 3000
         SD = RSORT (DIP)
         X6 = (SD − B1) * 0.5
         X7 = − (SD + B1) * 0.5
         GO TO 335
3000     X6 = − 0.5 * B1
         X7 = 0.5 * RSQRT (−DIP)
         WRITE(JOUT, 800) I,M
800      FORMAT(/,15X, 9HCONJUGATE, 215)
335      CONTINUE
C                       PRINCIPAL STRESSES AND DIRECTION COSINES
C           DC1,DC2,DC3 ARE THE DIRECTION COSINES OF
C           PRINCIPAL STRESSES PS1, PS2, PS3
         IF (X5 .GE. X6 .AND. X6 .GE. X7) GO TO 430
         IF(X5 .GE. X7 .AND. X7 .GE. X6) GO TO 431
         IF(X6 .GE. X6 .AND. X5 .GE. X7) GO TO 432
         IF(X6 .GE. X7 .AND. X7 .GE. X5) GO TO 433
         IF(X7 .GE. X5 .AND. X5 .GE. X6) GO TO 434
         IF(X7 .GE. X6 .AND. X6 .GE. X5) GO TO 435
430      X1 = X5
         X2 = X6
         X3 = X7
         GO TO 438
431      X1 = X5
          X2 = X7
         X3 = X6
         GO TO 438
432      X1 = X6
         X2 = X5
         X3 = X7
         GO TO 438
433      X1 = X6
         X2 = X7
         X3 = X5
         GO TO 438
434       X1 = X7
         X2 = X5
         X3 = X6
         GO TO 438
435      X1 = X7
         X2 = X6
         X3 = X5
438      CONTINUE
         IF(NEP.EQ.1)GO TO 99
C----------           PRINCIPAL STRESSES
```

```
        PS1(M)=X1
        PS2(M)=X2
        PS3(M)=X3
        DO 440 IS = 1,3
        GO TO (443 , 445 ,447) ,IS
443     AS1 = G1 — X1
        AS2 = G2 — X1
        AS3 = G3 — X1
        GO TO 444
445     AS1 = G1 — X2
        AS2 = G2 — X2
        AS3 = G3 — X2
        GO TO 444
447     AS1 = G1 — X3
        AS2 = G2 — X3
        AS3 = G3 — X3
444     CONTINUE
        AK=G4
        BK= G5
        CK= G6
        YAP1=AS2*CK—BK*AK
        YAP2=AK*AK—AS1*AS2
        IF(YAP1 .EQ. 0.0 ) YAP1=1.0
        IF(YAP2 .EQ. 0.0 ) YAP2=1.0
        BJM1=    (BK*BK—AS2*AS3)/YAP1
        BJM2= (AS1*BK—AK*CK) /YAP2
        BJ1 = BJM1*BJM1
        BJ2 = BJM2*BJM2
        ZIP = RSQRT( BJ1 + BJ2 + 1.0)
         IF ( ZIP .LT. 0.0 ) ZIP=1.0
        DC3(IS)= 1.0 / ZIP
        DC1(IS)= BJM1 * DC3(IS)
        DC2(IS)= BJM2 * DC3(IS)
440     CONTINUE
        GO TO 999
  99    CONTINUE
C-----------          PRINCIPAL STRAINS
        EP1(M)=X1
        EP2(M)=X2
        EP3(M)=X3
  999 CONTINUE
        RETURN


        SUBROUTINE RESIDL(1)
        DIMENSION XJ(6)
        COMMON/MEM/SP(20),SJ(3,3)
        DIMENSION TF(60)
        COMMON/TOR/ SV(146),TE(20),CET(6),CTE,DTIME,TIME
        COMMON/REL/ U(438),P(438),PP(438),UU(438)
        COMMON/AAA/ NEL,NNP,NEQ,NHBD,NBC,NTE1,NTE2,NTE3,NTE4,
     1 NNE1,NNE2,NNE3,NNE4,NDF,NRF,NRS,DET3,NGP,INCORE,JRADL
        COMMON/BBB/ D(6,6),D1(6,6),E(12,3),POIS(12,6),MCODE(128,8),
     1        EK(24,24) ,H(6,24),LRF(128),IDENT(128)
```

```
      COMMON/CCC/ X(146),Y(146),Z(146),NZN(438),NFIX(10)
     1 ,AST(12),EST(12),DIA(12),SIGT(1,8,6),ECR(1,1,1)
      COMMON/CAP/ GE1(27),GE2(27),GE3(27),WE(4),W(14),NG1
      COMMON/ABC/ PS1(14),PS2(14),PS3(14),SIG(14,6),EC(14,6)
C-------------------    THIS SUBR. CALCULATES RESIDUAL FORCE DUE TO CREEP
      JP=NNE1*NDF
      CALL DMAT(1)
      DO 13 J=1,JP
13    TF(J)=0.0
      M=0
      DO 28 J1=1,NG1
      DO 28 J2=1,NG1
      DO 28 J3=1,NG1
      M=M+1
      CALL ISOP2(1,J1,J2,J3,3,4)
      DOS=DETJ*WE(J1)*WE(J2)*WE(J3)
      DO 18 J=1,6
      SUM=0.
      DO 17 K=1,6
17    SUM=SUM+D1(J,K)*ECP(M,K)
18    XJ(J)=SUM
      DO 20 J=1,JP
      SUM=0.
      DO 19 JK=1,6
19    SUM=SUM+H(JK,J)*XJ(JK)
20    TF(J)=TF(J)+SUM*DOS
28    CONTINUE
C
      DO 35 J=1,NNE1
      M1=(MCODE(1,J)-1)*NDF
      JJ=(J-1)*NDF
      DO 35 K=1,NDF
      JJ=JJ+1
      M1=M1+1
35    P(M1)=P(M1)+TF(JJ)
      RETURN
      END




      SUBROUTINE ROTATE(NK)
      COMMON/AAA/ NEL,NNP,NEQ,NHBD,NBC,NTE1,NTE2,NTE3,NTE4,
1    1 NNE1,NNE2,NNE3,NNE4,NDF,NRF,NRS,DETJ,NGP,INCORE,JRADL
      COMMON/CCC/ X(146),Y(146),Z(146),NZN(438),NFIX(10)
     1 ,AST(12),EST(12),DIA(12),SIGT(1,8,6),ECR(1,1,1)
      COMMON/REL/ O(438),P(438),PP(438),UU(438)
C-------    MULTIPLY BY ROTATION MATRIX IN LOAD VECTOR
      SHY=22.5/57.29
      CS=COS(SHY)
      SN=SIN(SHY)
      DO 1 JI=1,NNP
      IF(JRADL.EQ.1)GO TO 81
      LK=(JI-1)*NDF
      DO 2 KL=1,NDF
```

```
         LK=LK+1
         IF(NZN(LK).LT.0)GO TO 4
2        CONTINUE
         GO TO 1
81       RR=SQRT(X(JI)*X(JI)+Y(JI)*Y(JI))
         CS=X(JI)/RR
         SN=Y(JI)/RR
4        JJ=(JI-1)*NDF
         IF(NK.EQ.2)GO TO 50
         S1=P(JJ+1)*CS+P(JJ+2)*SN
         S2=P(JJ+2)*CS-P(JJ+1)*SN
         P(JJ+1)=S1
         P(JJ+2)=S2
         GO TO 1
50       CONTINUE
         S1=U(JJ+1)*CS-U(JJ+2)*SN
         S2=U(JJ+2)*CS+U(JJ+1)*SN
         U(JJ+1)=S1
         U(JJ+2)=S2
1        CONTINUE
         RETURN
         END



         SUBROUTINE DMAT(I)
         COMMON/BBB/ D(6,6),D1(6,6),E(12,3),POIS(12,6),MCODE(128,8),
        1           EK(24,24) ,H(6,24),LRF(128),IDENT(128)
         N= LRF(I)
         IF(DIME.EQ.N) RETURN
         LIME=N
C        DUE TO SYMMETRY OF THE COMPLIANCES, THREE RELATION EXIST
         POIS(N,4) = POIS(N,1)* E(N,2)/ E(N,1)
         POIS(N,5) = POIS(N,2)* E(N,3)/ E(N,2)
         POIS(N,6) =POIS(N,3)* E(N,3)/ E(N,1)
         RAT = 1- POIS(N ,1)* POIS(N,4)-POIS(N,3)* POIS(N,6)-POIS(N,2)
        1*POIS(N,5) -POIS(N,1) * POIS(N,2)*POIS(N,3) -
        2    POIS(N,4) * POIS(N,5) * POIS(N,6)
13       D1(1,1)= (1 -POIS(N,2) * POIS(N,5))* E(N,1)/ RAT
         D1(1,2)= (POIS(N,1) + POIS(N,3) * POIS(N,5))*E(N,2)/RAT
         D1(1,3)= (POIS(N,3) + POIS(N,1) * POIS(N,2))*E(N,3)/RAT
         D1(2,2)= (1- POIS(N,3)* POIS(N,6))*E(N,2)/RAT
         D1(2,3)= (POIS(N,2) + POIS(N,3)*POIS(N,4))*E(N,3)/RAT
         D1(2,1)    = D1(1,2)
         D1(3,1) =D1(1,3)
         D1(3,2) = D1(2,3)
         D1(3,3)= (1-POIS(N,1)*POIS(N,4))* E(N,3)/RAT
         E11 = 0.5 *(E(N,1)/ (1+ POIS(N,1)))
         E22 = 0.5 *(E(N,1)/ (   POIS(N,1) + E(N,1)/E(N,2)))
         D1(4,4)=   0.5 * (E11 +E22)
         E31 = 0.5 * (E(N,2)/(1+ POIS(N,2)))
         E32 = 0.5 * (E(N,2)/(E(N,2)/ E(N,3) + POIS(N,2)))
         D1(5,5)= 0.5 * (E31+ E32)
         E42 = 0.5 *(E(N,3) /(1+ POIS(N,6)))
```

```
      E43 = 0.5 * (E(N,3)/(E(N,3)/E(N,1) + POIS(N,6)))
      D1(6,6) = 0.5 * (E42 +E43)
      RETURN
      END




      SUBROUTINE GAUSS
      COMMON/CAP/ GE1(27),GE2(27),GE3(27),WE(4),W(14),NG1
      COMMON/AAA/ NEL,NNP,NEQ,NHBD,NBC,NTE1,NTE2,NTE3,NTE4,
     1  NNE1,NNE2,NNE3,NNE4,NDF,NRF,NRS,DETJ,NGP,INCORE,JRADL
      IF(NGP.EQ.8)GO TO 25
      NG1=3
      GE1(1)=0.77459666924
      GE2(1)=GE1(1)
      GE3(1)=GE1(1)
      GE1(3)= -GE1(1)
      GE2(3)= -GE1(1)
      GE3(3)= -GE1(1)
      GE1(2)=0.0
      GE2(2)=0.0
      GE3(2)=0.0
      WE(1)=0.55555555555556
      WE(2)=0.88888888888889
      WE(3)=WE(1)
      GO TO 33
25    CONTINUE
      NG1=2
      WE(1)=1.0
      WE(2)=1.0
      WE(3)=1.0
      GE1(1)=0.57735026918
      GE1(2)= -GE1(1)
      GE2(1)=GE1(1)
      GE2(2)= -GE1(1)
      GE3(1)=GE1(1)
      GE3(2)= -GE1(1)
33    CONTINUE
      RETURN
      END




      SUBROUTINE  ELSTIF(1)
      COMMON/AAA/ NEL,NNP,NEQ,NHBD,NBC,NTE1,NTE2,NTE3,NTE4,
     1  NNE1,NNE2,NNE3,NNE4,NDF,NRF,NRS,DETJ,NGP,INCORE,JRADL
      COMMON/CAP/ GE1(27),GE2(27),GE3(27),WE(4),W(14),NG1
      COMMON/BBB/ D(6,6),D1(6,6),E(12,3),POIS(12,6),MCODE(128,8),
     1        EK(24,24) ,H(6,24),LRF(128),IDENT(128)
      COMMON/CCC/ X(146),Y(146),Z(146),NZN(438),NFIX(10)
     1  ,AST(12),EST(12),DIA(12),SIGT(1,8,6),ECR(1,1,1)
      DIMENSION ES(3,24),S(3,3),C(3,3)
      SHY=22.5
      SHY=(3.14/180.)*SHY
```

```
        JP=NDF*NNE1
        DO 12 IS =1,24
        DO 12 JS =1,24
12      EK(IS,JS) =0.0
        CALL DMAT(I)
        IF( NGP .EQ. 14 ) GO TO 23
C
C                     (2×2×2) AND (3×3×3) GAUSS INTEGRATION
C
        DO 39   J1 = 1 , NG1
        DO  39   J2 = 1 , NG1
        DO  39   J3 = 1, NG1
        CALL ISOP2(I,J1,J2,J3,3,1)
        DOS = WE(J1)*WE(J2)*WE(J3)*DETJ
        DO 17 N1=1,6
        DO 17 N2 =1,6
17      D(N1,N2)=DOS*D1(N1,N2)
        DO 38 II=1, JP
        DO 38 JJ=1, JP
        IF (II.GT.JJ)GO TO 2522
        EIKJ = 0.0
        DO 37 IJ=1,6
        HTDIK = 0.0
        DO 36 JI=1,6
        HTDIK = HTDIK + H(JI,II) * D(JI,IJ)
36      CONTINUE
        EIKJ = EIKJ + HTDIK * H(IJ,JJ)
37      CONTINUE
        EK(II,JJ) = EK(II,JJ) + EIKJ
2522    CONTINUE
38      CONTINUE
39      CONTINUE
        GO TO 333
23      CONTINUE
        DO21 M=1, NGP
         CALL ISOP2(I,M,M,M,3,1)
C
C   MATERIAL PROPERTY MATRIX ^D^, ^D^ IS MULTIPLIED BY
C   WEIGHTING COEFFICIENTS AND DET. OF JACOBIAN DETJ
C
        DOS= W(M)*DETJ
        DO 18 N1=1,6
        DO 18 N2=1,6
18       D(N1,N2)=DOS*D1(N1,N2)
        DO 6  II= 1,24
        DO 5 JJ =1, 24
        IF(II .GT. JJ) GO TO 5
        EIKJ =0.0
        DO 4 IJ =1,6
        HTDIK =0.0
        DO 3 JI = 1, 6
        HTDIK = HTDIK + H( JI, II)*D(JI,IJ)
C
C            H(JI,II)= TRANSPOSE OF  H(II,JI)
```

```
C
3       CONTINUE
        EIKJ =EIKJ +HTDIK *H(IJ,JJ)
4       CONTINUE
        EK(II,JJ) = EK(II,JJ) +EIKJ
5       CONTINUE
6       CONTINUE
21      CONTINUE
333     CONTINUE
        DO 2523 II=1,JP
        DO 2523 JJ=1,JP
2523    EK(JJ,II)=EK(II,JJ)
C       CALL BOUNDC(JP,NNE1 ,I)
        RETURN
        C(1,1)=COS(SHY)
          C(2,2)=COS(SHY)
          C(1,2)= −SIN(SHY)
        C(2,1)=SIN(SHY)
        C(3,3)=1.0
        C(1,3)=0.
        C(3,1)=0.
        C(2,3)=0.
        C(3,2)=0.
        DO 132J=1,NNE1
        M1=(MCODE(I,J)−1)*NDF
        JS=0
        DO 110K=1,NDF
        M1=M1+1
        IF(NZN(M1).LT.0)JS=1
110     CONTINUE
        IF(JS.EQ.0)GO TO 132
        IS=(J−1)*NDF
        DO 116JI=1,NNE1
        JN=(JI−1)*NDF
        DO 112N=1,NDF
        DO 112NN=1,NDF
        IJ=JN+NN
        SUM=0.
        DO 111NJ=1,NDF
        IN=IS+NJ
111     SUM=SUM+C(NJ,N)*EK(IN,IJ)
112     ES(N,IJ)=SUM
116     CONTINUE
        DO 122N=1,NDF
        DO122NN=1,NDF
        SUM=0.
        DO 123NJ=1,NDF
        IN=IS+NJ
123     SUM=SUM+ES(N,IN)*C(NJ,NN)
122     S(N,NN)=SUM
        DO124N=1,NDF
        DO124NN=1,NDF
        IN=IS+NN
124     ES(N,IN)=S(N,NN)
```

```
      DO 125KJ=1,NDF
      JM=IS+KJ
      DO 125JK=1,JP
125   EK(JM,JK)=ES(KJ,JK)
132   CONTINUE
      RETURN
      END


      SUBROUTINE ISOP2(1,J1,J2,J3,NEJ,NF)
      COMMON/AAA/ NEL,NNP,NEQ,NHBD,NBC,NTE1,NTE2,NTE3,NTE4,
     1 NNE1,NNE2,NNE3,NNE4,NDF,NRF,NRS,DETJ,NGP,INCORE,JRADG
      COMMON/DGE/S(20,3),CC(3,20),C(3,3)
      COMMON/BBB/ D(6,6),D1(6,6),E(12,3),POIS(12,6),MCODE(128,8),
     1         EK(24,24) ,H(6,24),LRF(128),IDENT(128)
      COMMON/MEM/ SP(20),SJ(3,3)
      COMMON/CCC/ X(146),Y(146),Z(146),NZN(438),NFIX(10)
     1 ,AST(12),EST(12),DIA(12),SIGT(1,8,6),ECR(1,1,1)
      COMMON/CAP/ GE1(27),GE2(27),GE3(27),WE(4),W(14),NG1
C
      JP=NNE1*NDF
      DO 80 J=1,6
      DO 80 K=1,JP
80    H(J,K)=0.0
      S1= 1.0 + GE1(J1)
      S2= 1.0 - GE1(J1)
      S3= 1.0 + GE2(J2)
      S4= 1.0 - GE2(J2)
      S5= 1.0 + GE3(J3)
      S6= 1.0 - GE3(J3)
      IF(NNE1 .EQ. 20 .OR.NNE1.EQ.32 ) GO TO 34
C
      A=0.125
      IF(NEJ .GT. 2 )GO TO 81
      SP(1)=A*S2*S4*S6
      SP(2) = A*S1*S4*S6
      SP(3)=A*S1*S3*S6
      SP(4)=A* S2*S3*S6
      SP(5)=A*S2*S4*S5
      SP(6)=A*S1*S4*S5
      SP(7)=A*S1*S3*S5
      SP(8)=A*S2*S3*S5
      IF(NEJ .EQ. 1) RETURN
81    CONTINUE
      S(1,1) = - A * S4 * S6
      S(1,2) =  -A * S2 * S6
      S(1,3) =  -A * S4 * S2
      S(2,1) =   A * S4 * S6
      S(2,2) =    -A * S1 * S6
      S(2,3) = - A * S1 * S4
      S(3,1) =   A * S3 * S6
      S(3,2)  =  A * S1 * S6
      S(3,3)  = - A * S1 * S3
      S(4,1)  = -A * S3 * S6
```

```
       S(4,2)   =    A * S2 * S6
       S(4,3)   =  - A * S2 * S3
       S(5,1)   =  - A * S4 * S5
       S(5,2)   =    -A * S2 * S5
       S(5,3)   =    A * S2 * S4
       S(6,1)   =    A * S4 * S5
       S(6,2)   =    -A * S1 * S5
       S(6,3)   =    A * S1 * S4
       S(7,1) =       A * S3 * S5
       S(7,2) =     A * S1 * S5
       S(7,3) =       A * S1 * S3
       S(8,1) =     - A * S3 * S5
       S(8,2) =     A * S2 * S5
       S(8,3) =       A * S2 * S3
       GO TO 38
34     CONTINUE
       S7= S1*S2
       S8 = S3*S4
       S9 = S5*S6
       S11 = GE1(J1)
       S12 = GE2(J2)
       S13 = GE3(J3)
       IF (NNE3 .EQ. 32 ) GO TO 36
       IF (NEJ .GT. 2 )GO TO 82
C
C         SHAPE FUNCTIONS FOR 20-NODE ELEMENT
       SP(1)  = A* S2* S3 *S6 *(−S11+ S12− S13−2)
       SP(2)  = 2*A* S7* S3*S6
       SP(3)  = A* S1* S3* S6*(S11 +S12−S13 −2)
       SP(4)  = A*2*S1*S8* S6
       SP(5)  = A*S1*S4* S6* (S11−S12 −S13 −2)
       SP(6)= 2*A*S7* S4* S6
       SP(7)=   A* S2*S4* S6*(−S11− S12−S13−2)
       SP(8)= 2*A*S2* S8 *S6
       SP(9)=   2*A*S2*S3* S9
       SP(10)  = 2*A*S1* S3* S9
       SP(11)= 2*A*S1* S4*S9
       SP(12)= 2*A*S2*S4* S9
       SP(13)  =   A* S2* S3* S5*(−S11 +S12 +S13−2)
       SP(14)  =   2*A * S7* S3* S5
       SP(15)  = A* S1* S3 *S5* (S11+S12+ S13−2)
       SP(16)  = 2*A*S1* S8*S5
       SP(17)  = A*S1* S4*S5 * ( S11−S12+S13 −2)
       SP(18)  =   2*A* S7* S3*S5
       SP(19)=   A*S2*S4 *S5*(−S11−S12 +S13−2)
       SP(20)  = 2*A* S2* S8* S5
C-------------------------------------------------------
B2     CONTINUE
       IF(NEJ .EQ. 1) RETURN
       S(1,1)  = 0.125 * S3 * S6 *(2.0*S11+1.0−(S12−S13))
       S(1,2)  = 0.125 * S2 * S6*(2.0*S12−1.0−S11−S13)
       S(1,3)  = 0.125* S2*S3*(2.0*S13+1.0−S12 + S11)
       S(2,1)  = −0.5*S11*S3*S6
       S(2,2)  = 0.25* S7*S6
```

```
S(2,3)  = −0.25*S7*S3
S(3,1)  = 0.125*S3*S6*(2.0*S11−1.0+S12 − S13)
S(3,2)  = 0.125*S1*S6*(2.0*S12−1.0+S11−S13)
S(3,3)  = 0.125*S1*S3*(2*S13 + 1.0− S11−S12)
S(4,1)  = 0.25*S6*S8
S(4,2)  = −0.5*S12*S1*S6
S(4,3)  = − 0.25*S1*S8
S(5,2)  = 0.125*S1*S6*(2*S12 +1.0−S11+S13)
S(5,3)  = 0.125*S1*S4*(2*S13+1.0−S11+S12)
S(5,1)  = 0.125*S4*S6*(2*S11−1.0−S12−S13)
S(6,1)  = −0.5*S4*S6*S11
S(6,2)  = −0.25*S7*S6
S(6,3)  = −0.25 * S7*S4
S(7,1)  = 0.125*S4*S6*(2*S11+1.0+S12+S13)
S(7,2)  = 0.125*S2*S6*(2.0*S12+1.0+S11+S13)
S(7,3)  = 0.125*S2*S4*(2.0*S13+1.0+S11+S12)
S(8,1)   = − 0.25*S8*S6
S(8,2)  =−0.50*S12*S2*S6
S(8,3)   = − 0.25* S2 * S8
S(9,1)   = − 0.25*S3*S9
S(9,2)   =  0.25*S2*S9
S(9,3)  = −0.5*S13*S2*S3
S(10,1) =   0.25*S3*S9
S(10,2) =   0.25*S1*S9
S(10,3)=−0.5*S13*S1*S3
S(11,1) =   0.25*S4*S9
S(11,2) = −0.25*S1*S9
S(11,3)=−0.5*S1*S4*S13
S(12,1) = −0.25*S4*S9
S(12,2) = −0.25*S2*S9
S(12,3)=−0.5*S13*S2*S4
S(13,1)=0.125*S3*S5*(2*S11+1.0− S12−S13)
S(13,2)= 0.125*S2*S5*(2*S12−1.0+S13−S11)
S(13,3)=0.125*S2*S3*(2.0*S13−1.0+S12−S11)
S(14,1)= −0.5*S11*S3*S5
S(14,2) = 0.25*S7*S5
S(14,3)= 0.25*S7*S3
S(15,1)=0.125*S3*S5*(2.0*S11+S12+S13−1.0)
S(15,2)=0.125*S1*S5*(2.0*S12+S11+S13−1.0)
S(15,3)=0.125*S1*S3*(2.0*S13+S11+S12−1.0)
S(16,1) = 0.25*S8*S5
S(16,2)= −0.5*S12*S1*S5
S(16,3) = 0.25*S8*S1
S(17,1)=0.125*S4*S5*(2 *S11+S13−S12 −1.0)
S(17,2) =0.125*S1*S5*(2.0*S12−S11 −S13+1.0)
S(17,3) =0.125*S1*S4*(2.0*S13 +S11−S12−1.0)
S(18,1)=−0.5*S4*S5*S11
S(18,2)= −0.25*S7*S5
S(18,3)= 0.25*S7*S4
S(19,1)= 0.125*S4*S5*(2.0*S11+S12−S13+1.0)
S(19,2)=0.125*S2*S5*(2.0*S12+S11−S13+1.0)
S(19,3)=0.125*S2*S4*(2.0* S13−S11−S12−1.0)
S(20,1)= − 0.25*S8*S5
S(20,2)= −0.5*S12*S2*S5
```

```
          S(20,3) = 0.25*S2*S8
          GO TO 38
36        CONTINUE
38        CONTINUE
          P1=0.0
          P2=0.0
          P3=0.0
          P4=0.0
          P5=0.0
          P6=0.0
          P7=0.0
          P8=0.0
          P9=0.0
          DO 44 J = 1,NNE1
          M1 = MCODE(I,J)
           P1 = P1 + S(J,2)*Y(M1)
          P2 = P2 + S(J,3)*Z(M1)
          P3 = P3 + S(J,2)*Z(M1)
          P4 = P4 + S(J,3)*Y(M1)
          P5 = P5 + S(J,1)*Z(M1)
          P6 = P6 + S(J,1)*Y(M1)
          P7 = P7 + S(J,3)*X(M1)
          P8 = P8 + S(J,2)*X(M1)
          P9 = P9 + S(J,1)*X(M1)
44        CONTINUE
          SJ(1,1) = P1*P2−P3*P4
          SJ(1,2)= P3*P7 −P8* P2
          SJ(1,3) = P8*P4 −P1*P7
          SJ(2,1)= P4*P5− P2*P6
          SJ(2,2) =P2*P9−P5*P7
          SJ(2,3)= P7*P6−P4*P9
          SJ(3,1)= P6*P3 − P5*P1
          SJ(3,2) = P5*P8−P9*P3
          SJ(3,3) = P9*P1 − P6*P8
          IF(NEJ .EQ. 2) RETURN
C   DETERMINANT  OF  JACOBIAN
C
          DETJ = (P9 * (P1* P2 − P3 * P4 ) + P8 * ( P4 * P5 − P2 * P6)
     1          + P7 * ( P3 * P6 − P1 * P5))
          IF(DETJ .LE. 0.0) WRITE(3,133) 1
C
C   JACOBIAN    INVERSION
C
          DO 75 N1=1,3
          DO 75 N2 =1,3
75        C(N2,N1)=SJ(N1,N2)/DETJ
C
          DO 45 K=1,3
          DO 45 J=1,NNE1
          CC(K,J)=0.0
45        CONTINUE
C
          DO 47 K=1,3
          DO 47 J=1,NNE1
```

```
      DO 46 N1=1,3
46    CC(K,J) = CC(K,J) + C(K,N1)*S(J,N1)
47    CONTINUE
C
C                     STRAIN-DISPLACEMENT MATRIX
      DO 54 N1=1,NNE1
      N2 = (N1-1)*NDF
      L1 = N2+1
      L2 = N2+2
      L3=N2+3
      H(1,L1)=CC(1,N1)
      H(4,L1+1)=CC(1,N1)
      H(6,L1+2)=CC(1,N1)
      H(2,L2)=CC(2,N1)
      H(4,L2-1)=CC(2,N1)
      H(5,L2+1)=CC(2,N1)
      H(3,L3)=CC(3,N1)
      H(5,L3-1)=CC(3,N1)
      H(6,L3-2)=CC(3,N1)
54    CONTINUE
      IF(NF .EQ. 4) RETURN
C
C     ---------- MODIFY ^H^ MATRIX FOR INCLINED BOUNDARY CONDITIONS
C
      PHI=22.5*3.14155/180.0
      CS=COS(PHI)
      SN=SIN(PHI)
      DO 68 J=1,NNE1
      IF(JRADL.EQ.1)GO TO 63
      JH=(MCODE(I,J)-1)*NDF
      DO 332KP=1,NDF
      JH=JH+1
      IF(NZN(JH).LT.0)GO TO 64
332   CONTINUE
      GO TO 68
63    M1=MCODE(I,J)
      RR=SQRT(X(M1)*X(M1)+Y(M1)*Y(M1))
      CS=X(M1)/RR
      SN=Y(M1)/RR
64    NJ=J
      N2=(NJ-1)*NDF
      L1=N2+1
      L2=N2+2
      L3=N2+3
      C1=CC(1,NJ)
      C2=CC(2,NJ)
      C3=CC(3,NJ)
C
      H(1,L1)=CS*C1
      H(1,L2)=-SN*C1
      H(2,L1)=SN*C2
      H(2,L2)=CS*C2
      H(3,L3)=C3
      H(4,L1)=CS*C2+SN*C1
```

```
      H(4,L2)=CS*C1−SN*C2
      H(5,L1)=SN*C3
      H(5,L2)=CS*C3
      COMMON/FF/ SIGG1(110),SIGG2(110)
      COMMON/TOR/ SV(146),TE(20),CET(6),CTE,DTIME,TIME
      COMMON/BBB/ D(6,6),D1(6,6),E(12,3),POIS(12,6),MCODE(128,8),
     1            EK(24,24),H(6,24),LRF(128),IDENT(128)
      COMMON/ABC/ PSI(14),PS2(14),PS3(14),SIG(14,6),EC(14,6)
     1,DC1(14,3), DC2(14,3), DC3(14,3),ECP(14,6)
      COMMON/LID/ SK(438,84)
      COMMON/BON/ NNODE, NEUB,NETB,NBLOK, NDISK1,NDISK2,NDISK3
      COMMON/REL/ U(438),P(438),PP(438),UU(438)
      COMMON/CCC/ X(146),Y(146),Z(146),NZN(438),NFIX(10)
     1,AST(12),EST(12),DIA(12),SIGT(1,8,6),ECR(1,1,1)
      COMMON/AAA/ NEL,NNP,NEQ,NHBD,NBC,NTE1,NTE2,NTE3,NTE4,
     1 NNE1,NNE2,NNE3,NNE4,NDF,NRF,NRS,DEIJ,NGP,INCORE,JRADL
      COMMON/CAP/ GE1(27),GE2(27),GE3(27),WE(4),W(14),NG1
C   ISOPARAMETRIC ELEMENTS REPRESENT         CONCRETE OF THE VESSEL
C
C   LINE ELEMENTS REPRESENT PRESTRESSING CABLES AND REINFORCEMENTS
C   LINKAGE ELEMENTS REPRESENT NON-LINEAR BOND
      OPEN(UNIT=20,DEVICE='DSK',ACCESS='SEQINOUT',FILE='NSA20.TMP',
     1  DISPOSE='DELETE',PROTECTION=''011)
      OPEN(UNIT=21,DEVICE='DSK',ACCESS='SEQINOUT'
     1 ,FILE='NSAR21.TMP',  DISPOSE='DELETE',PROTECTION=''011)
      OPEN(UNIT=22,DEVICE='DSK',ACCESS='SEQINOUT',FILE='NSAR22.TMP',
     1 DISPOSE='DELETE',PROTECTION=''011)
      IELST=1
      IELST=0
      CALL INPUT
      DO 500 I=1,NTE1
       DO 500 J=1,NGP
      DO 500 K=1,6
      SIGT(I,J,K)=0.0
      ECR(1,J,K)=0.
500   CONTINUE
      DO 501 J=1,NGP
      PS1(J)=0.
      PS2(J)=0.
      PS3(J)=0.
      DO501K=1,6
      SIG(J,K)=0.
      EC(J,K)=0.0
501    CONTINUE
      CALL GAUSS
      CALL ASSEMB
      CALL DECOMP
       DO 1000 NPR=1,1
      CALL LOAD
      CALL ROTATE(1)
      DO 3 JJ=1,NEQ
      IF( NZN(JJ) .NE. 0 ) P(JJ)=0.0
3     CONTINUE
      NLI=0
```

```
502     CONTINUE
        NLI=NLI+1
        TIME=0.
        IF(NGI.EQ.1)GO TO 612
        IF(IELST.EQ.0)GO TO 612
C-------------SPECIFY A TIME INCREMENT IN DAYS
C-------------DTIME=0.777 TO TERMINATE THE ITERATION
        READ(1,507)DTIME
        IF(DTIME-0.777)549,550,549
507     FORMAT(F0.0)
549     CONTINUE
        WRITE(3,508)DTIME
508     FORMAT(///,40X,'TIME INCREMENT(IN DAYS)=',F12.5)
        TIME=TIME+DTIME
        TT=TIME
        DT=DTIME
        DO 509 I=1,NTE1
        CALL CREEP(I,DT,TT,2)
C       DO 510J=1,NGP
C       DO 510 K=1,6
C510    ECR(I,J,K)=ECR(I,J,K)+ECP(J,K)
        CALL RESIDL(I)
509     CONTINUE
        CALL ROTATE(1)
612     CONTINUE
        CALL RHVECT
        CALL RESOLV
C-------        TRANSFORM INCLINED DISPL. IN GLOBAL SYSTEM----------------
        CALL ROTATE(2)
        DO 503 J=1,NEQ
        P(J)=0.
503     UU(J)=UU(J)+U(J)
        DO 504 I=1,NEL

        CALL STRESS(I,NLI)
        GO TO (515,515,516)IDENT(I)
515     CONTINUE
        DO 505 J=1,NGP
        DO 505 K=1,6
        SIGT(1,J,K)=SIGT(1,J,K)+SIG(J,K)
505     CONTINUE
        GO TO 504
516     CONTINUE
        SIGG2(I)=SIGG2(I)+SIGG1(I)
504     CONTINUE
        CALL OUTPUT
        IF (IELST.EQ.0)GO TO 550
        GO TO 502
550     CONTINUE
1000    CONTINUE
        CLOSE(UNIT=20)
        CLOSE(UNIT=21)
        CLOSE(UNIT=22)
        STOP
```

```
        END
        COMMON/FF/ SIGG1(110),SIGG2(110)
        COMMON/TOR/ SV(146),TE(20),CET(6),CTE,DTIME,TIME
        COMMON/BBB/ D(6,6),D1(6,6),E(12,3),PDIS(12,6),MCODE(128,8),
       1          EK(24,24) ,H(6,24),LRF(128),IDENT(128)
        COMMON/ABC/ PS1(14),PS2(14),PS3(14),SIG(14,6),EC(14,6)
       1,DC1(14,3), DC2(14,3), DC3(14,3),ECP(14,6)
        COMMON/LID/ SK(438,84)
        COMMON/BON/ NNODE, NEUB,NETB,NBLOK, NDISK1,NDISK2,NDISK3
        COMMON/REL/ U(438),P(438),PP(438),UU(438)
        COMMON/CCC/ X(146),Y(146),Z(146),NZN(438),NFIX(10)
       1 ,AST(12),EST(12),DIA(12),SIGT(1,8,6),ECR(1,1,1)
        COMMON/AAA/ NEL,NNP,NEQ,NHBD,NBC,NTE1,NTE2,NTE3,NTE4,
       1 NNE1,NNE2,NNE3,NNE4,NDF,NRF,NRS,DETJ,NGP,INCORE,JRADL
        COMMON/CAP/ GE1(27J,GE2(27),GE3(27),WE(4),W(14),NG1
C   ISOPARAMETRIC ELEMENTS REPRESENT  CONCRETE OF THE VESSEL
C
C   LINE ELEMENTS REPRESENT PRESTRESSING CABLES AND REINFORCEMENTS
C   LINKAGE ELEMENTS REPRESENT NON-LINEAR BOND
          OPEN(UNIT=20,DEVICE='DSK',ACCESS='SEQINOUT',FILE='NSA20.TMP',
       1  DISPOSE='DELETE',PROTECTION=''011)
          OPEN(UNIT=21,DEVICE='DSK',ACCESS='SEQINOUT'
       1 ,FILE='NSAR21.TMP', DISPOSE='DELETE',PROTECTION=''011)
          OPEN(UNIT=22,DEVICE='DSK',ACCESS='SEQINOUT',FILE='NSAR22.TMP',
       1  DISPOSE='DELETE',PROTECTION=''011)
        IELST=1
        IELST=0
        CALL INPUT
        DO 500 I=1,NTE1
         DO500 J=1,NGP
        DO 500 K=1,6
        SIGT(I,J,K)=0.0
        ECR(1,J,K)=0.
500     CONTINUE
        DO 501 J=1,NGP
        PS1(J)=0.
        PS2(J)=0.
        PS3(J)=0.
        DO501K=1,6
        SIG(J,K)=0.
        EC(J,K)=0.0
501      CONTINUE
        CALL GAUSS
        CALL ASSEMB
        CALL DECOMP
         DO 1000 NPR=1,1
        CALL LOAD
        CALL ROTATE(1)
        DO 3 JJ=1,NEQ
        IF( NZN(JJ) .NE. 0 ) P(JJ)=0.0
3       CONTINUE
        NLI=0
502     CONTINUE
        NLI=NLI+1
```

```
       TIME=0.
       IF(NLI.EQ.1)GO TO 612
       IF(IELST.EQ.0)GO TO 612
C--------------SPECIFY A TIME INCREMENT IN DAYS
C--------------DTIME=0.777 TO TERMINATE THE ITERATION
       READ(1,507)DTIME
       IF(DTIME-0.777)549,550,549
507    FORMAT(F0.0)
549    CONTINUE
       WRITE(3,508)DTIME
508    FORMAT(///,40X,'TIME INCREMENT(IN DAYS)=',F12.5)
       TIME=TIME+DTIME
       TT=TIME
       DT=DTIME
       DO 509 I=1,NTE1
       CALL CREEP(I,DT,TT,2)
C      DO 510J=1,NGP
C      DO 510 K=1,6
C510   ECR(I,J,K)=ECR(I,J,K)+ECP(J,K)
       CALL RESIDL(I)
509    CONTINUE
       CALL ROTATE(1)
612    CONTINUE
       CALL RHVECT
       CALL RESOLV
C-------        TRANSFORM INCLINED DISPL. IN GLOBAL SYSTEM-----
       CALL ROTATE(2)
       DO 503 J=1,NEQ
       P(J)=0.
503    UU(J)=UU(J)+U(J)
       DO 504 I=1,NEL

       CALL STRESS(I,NLI)
       GO TO(515,515,516)IDENT(1)
515    CONTINUE
       DO 505 J=1,NGP
       DO 505 K=1,6
       SIGT(1,J,K)=SIGT(1,J,K)+SIG(J,K)
505    CONTINUE
       GO TO 504
516    CONTINUE
       SIGG2(I)=SIGG2(I)+SIGG1(I)
504    CONTINUE
       CALL OUTPUT
       IF(IELST.EQ.0)GO TO 550
       GO TO 502
550    CONTINUE
1000   CONTINUE
       CLOSE(UNIT=20)
       CLOSE(UNIT=21)
       CLOSE(UNIT=22)
       STOP
       END
```

```
      SUBROUTINE FLOW(FF ,A1)
      COMMON/JJ/ELE(100)
      DIMENSION        AA1(6) , AA2(6) , AA3(6) , A1(6) ,A2(6)
      COMMON/AAA/ NEL,NNP,NEQ,NHBD,NBC,NTE1,NTE2,NTE3,NTE4,CCC,CCT,
     1 NNE1,NNE2,NNE3,NNE4,NDF,NRF,NRS,DETJ,NITER,NLY,NTYPE,YY1,YY2
       CCY=0.7*CCC
      AKF = CCT/CCC
      IF( AKF .EQ. 0.08) GO TO 41
      IF( AKF .EQ. 0.10) GO TO 42
      IF( AKF .EQ. 0.12) GO TO 43
41    AMM = 1.8076
      BMM = 4.0962
      CMM = 14.4863
      DMM = 0.9914
      GO TO 44
42    AMM = 1.2759
      BMM = 3.1962
      CMM = 11.7365
      DMM = 0.9801
      GO TO 44
43    AMM = 0.9218
      BMM = 2.5969
      CMM = 9.9110
      DMM = 0.9647
44    CONTINUE
      ZNZ2= A1(1)+A1(2)+A1(3)
      ZNZ1=0.33333334*ZNZ2
      SS1 = A1(1) −ZNZ1
      SS2 = A1(2) −ZNZ1
      SS3 = A1(3) −ZNZ1
C
C         ZNY2, ZNY3 ARE SECOND AND THIRD INVARIANTS OF
C         DEVIATORIC STRESSES
C
      ZNY2 = 0.5 * ( SS1 * SS1 + SS2 * SS2 + SS3*SS3) + A1(4)*A1(4)
     1        + A1(5)* A1(5) + A1(6) * A1(6)
       IF(ZNY2 .EQ. 0.0 > ZNY2=1.0
      ZNY3 = SS1*SS2*SS3 + 2.0*A1(4)*A1(5)*A1(6)
     1           − SS1*A1(5) * A1(5) − SS2*A1(6)*A1(6)
     1           − SS3 *A1(4) * A1(4)
       QOS3 = 1.50*1.732 * ZNY3 / (ZNY2**1.50)
       IF(QOS3 .GE. 0.0) GO TO 46
      LAMD = CMM * COS(1.047 − ACOS(−DMM*QOS3)*0.3334)
      GO TO 47
46    LAMD = CMM * COS(0.3334* ACOS(DMM * QOS3))
47    FF = AMM*ZNY2/(CCY*CCY ) *LAMD*SQRT(ZNY2)/CCY+ BMM*ZNZ2/CCY−1.0
      GO TO 17
2     CONTINUE
C-------------- MOHR COULOMB YIELD CRITERIA-----
C
      AJ1=A1(1)+A1(2)+A1(3)
      AJ=AJ1/3.0
      SX=A1(1)−AJ
      SY=A1(2)−AJ
```

```
      SZ=A1(3)−AJ
      AJ2=0.5*(SX*SX+SY*SY+SZ*SZ)+A1(4)+A1(4)+A1(5)*A1(5)+A1(6)*A1(6)
100   FORMAT(//,5X,5F12.3)
      WRITE(2.100)AJ1,SX,SY,SZ,AJ2
      FF=3.0*AJ2+CCY*AJ1+0.2*AJ1*AJ1
      FF=3.0*FF
       FF=FF−CCY**2
       AJ2=SQRT(AJ2)
       FF=SQRT(3)*AJ2−CCY
17    CONTINUE
      RETURN
      END


         SUBROUTINE INPUT
         COMMON/GSS/ ZETA(27), ETA(27), ZI(27), W(27), NGP
         COMMON/AAA/ NEL,NNP,NEQ,NHBD,NBC,NTE1,NTE2,NTE3,NTE4,CCC,CCT,
     1   NNE1,NNE2,NNE3,NNE4,NDF,NRF,NRS,DETJ,NITER,NLI,NTYPE,YY1,YY2
         COMMON/CCC/ X(125),Y(125),Z(125),NFIX(55),NZN(55),
     1   AST(12),EST(12),DIA(12),ELINE(6,6),ELINK(6,6)
         COMMON/BBB/ D(6,6),D1(6,6),E(12,3),POIS(12,6),MCODE(20,8),
     1        EK(24,24),H(6,24),LRF(20),IDENT(20)
         COMMON/BPP/    BS1(20),BS2(20),BS3(20),SL1(20),SL2(20),SL3(20)
         COMMON/BIR/ SLOPH,SLOPV,SLOPS,NPOINTS,ELE(20)
         COMMON/OOO/ FF,ECU,BETA
C  INPUT  DATAS FOR ISOPARAMETRIC ELEMENT
C
C        READ  AND PRINT NODAL CO-ORDINATES
C
         READ(1, 10)NNP,NTE1,NTE2,NTE3,NNE1,NNE2,NNE3,NRF,NBC,NDF,NGP,NRS,
     1   NNE4 ,NTE4
         NEL = NTE1+NTE2+NTE3+NTE4
         WRITE (2,15) NEL,NNP,NTE1,NTE2,NTE3,NNE1,NNE2,NNE3,NRF,NBC,NDF,NGP
     1,  NRS
         WRITE(2,30)
         DO  8  I= 1,NNP
         READ(1,40) X(I), Y(I),Z(I)
B        WRITE(2,50) I, X(I),Y(I),Z(I)
C
C  READ AND PRINT CONNECTIVITY ARRAYS
C
         WRITE(2,60)
         NEXT =NTE1+1
         NUMB = NTE1 + NTE2
         JNUMB = NUMB + 1
         MAMP = NTE1 + NTE2+NTE3
         JMAM = MAMP + 1
         IF(NTE1 .EQ. 0)GO TO 312
         DO 3 I = 1, NTE1
         READ(1,65) (MCODE(I,J),J=1,NNE1),LRF(I),IDENT(I)
3        WRITE(2,66)I, (MCODE(I,J),J=1,NNE1),LRF(I),IDENT(I)
312      CONTINUE
         IF(NTE2 .EQ. 0) GO TO 313
         DO 7 I = NEXT, NUMB
```

```
          READ(1,106)(MODDE(I,J),J=1,NNE2),LRF(I),IDENT(I)
7         WRITE(2,107)I,(MCODE(I,J),J = 1,NNE2),LRF(I), IDENT(I)
313       CONTINUE
          IF(NTE3 .EQ. 0) GO TO 57
          DO  56  I = JNUMB , MAMP
          READ(1,67) (MCODE(I,J),J=1,NNE3),LRF(I), IDENT(I)
56        WRITE(2,68) I, (MCODE(I, J),J=1,NNE3), LRF(I),IDENT(I)
57        CONTINUE
          IF(NTE4 .EQ. 0) GO TO 311
          DO  13  I = JMAM, NEL
          READ(1,69) (MCODE(I,J),J=1,NNE4), LRF(I),IDENT(I)
13        WRITE(2,70)I, (MCODE(I,J),J=1,NNE4), LRF(I),IDENT(I)
311       CONTINUE
C
C             CALCULATE  HALF - BANDWIDTH
C
          JHBD = 1
          DO  266  I = 1, NEL
          LET = IDENT(I)
          GO TO (256,257,258,260) LET
256       NER = NNE1
          GO TO 259
257       NER = NNE2
          GO TO 259
258       NER = NNE3
          GO TO 259
260       NER=NNE4
259       MET = 10000
          JET = 1
          DO 266 J = 1, NER
          IF (MCODE(I , J) .LT. MET)  MET = MCODE(I,J)
          IF (MCODE(I, J) .GT. JET)   JET = MCODE(I,J)
          IF ((JET - MET). GT. JHBD)  JHBD = (JET - MET )
266       CONTINUE
          NHBD = (JHBD + 1)*NDF
          WRITE(2,207) NHBD
          WRITE(2,75)
          DO 11 I = 1, NRF
          READ(1, 80)    ( E(I, J), J=1,3),(POIS(I,M),M=1,3)
11        WRITE(2,85)I,( E(I,J), J=1,3),(POIS(I,M),M=1,3)
          WRITE(2, 90)
          DO 12 I = 1, NBC
          READ(1,95)NZN(I) , NFIX(I)
12        WRITE(2,100) NZN(I),NFIX(I)
C
C   READ  YOUNG'S  MODULUS  FOR  PRESTRESSING  STEEL
          WRITE (2,81)
          DO 14 I =1 , NRS
          READ(1, 71) EST(I), DIA(I)
    14    WRITE(2,72)  I , EST(I), DIA(I)
C
C                              READ PLASTIC CONSTANTS
C
          READ(1,31) CCC,CCT,YY1,YY2,BETA,ECU,NLI,NTYPE
```

```
31         FORMAT(6F0.0,2I0)
           WRITE(2,32)CCC,CCT,YY1,YY2,BETA,ECU,NLI,NTYPE
C---------------    READ DATAS OF BOND LINKAGE ELEMENTS------------------
C
           READ(1,211) NPOINTS
           IF(NPOINTS.EQ.0)GO TO 307
           WRITE(2,216)
           DO 356 I=1,NPOINTS
           READ(1, 217) BS1(I), SL1(I)
356        WRITE(2,218) I,BS1(I),SL1(I)
           WRITE(2,212)
           DO 358 I=1,NTE4
           READ(1,213) ELE(I)
358        WRITE(2,214)I, ELE(I)
           SLOPS=8.0**10
           SLOPV =8.0**10
           SLOPH=(BS1(2)-BS1(1))/(SL1(2)-SL1(1))
307        CONTINUE
211        FORMAT(I0)
212        FORMAT(//////,5X,15HLINKAGE ELEMENT,5X,14HAVERAGE LENGTH)
213        FORMAT(F0.0)
214        FORMAT(5X, I5,14X,F12.4)
216        FORMAT(//////,25X,12HCURVE POINTS,5X,11HBOND STRESS,11HSLIP VALUES)
217        FORMAT(2F0.0)
218        FORMAT(25X,I5,10X,F10.4,10X,F10. 9)
32         FORMAT(1H1,20X,33H CONCRETE COMPRESSIVE STRENGTH  =, F12.4//
          1  20X, 32H CONCRETE TENSILE STRENGTH     =,F12.4//
          1  20X, 35H YIELD STRESS OF PRESTRESSING WIRE  =,F12.4//
          1  20X, 34H YIELD STRESS OF REINFORCEMENT     =,F12.4//
          1   20X, 33H    SHEAR FACTOR              =, F5.3//
          1  20X, 33H    CONCRETE FAILURE STRAIN       =, F6.5//
          1  20X, 34H     NO. OF LOAD INCREMENTS     =, I5//
          1  20X, 34H  NO. OF TYPE-1 STEEL ELEMENTS   =,I5)
C
C
C
C
10         FORMAT(14I0)
15         FORMAT(1H1,20X,37HNUMBER OF ELEMENTS                     =, I5//
          1         20X, 37HNO OF NODAL POINTS              =,I5//
          2         20X, 37HNO OF TYPE 1 ELEMENT            =,I5//
          3         20X, 37HNO OF TYPE 2 ELEMENT            =,I5//
          4         20X, 37HNO OF TYPE 3 ELEMENT            =,I5//
          5         20X, 37HNO OF NODESIN TYPE1 ELEMENT     =,I5//
          6         20X, 37HNO OF NODESIN TYPE2 ELEMENT     =,I5//
          7         20X, 37HNO OF NODESIN TYPE3 ELEMENT     =,I5//
          8         20X, 36HSECTION REFERENCE FOR TYPE1 ELEMENT =,I5//
          9         20X, 37HNO OF BOUNDARY CONDITIONS       =,I5//
          1         20X, 35H NO OF DEGREES OF FREEDOM PER NODE  =,I5//
          1         20X, 37HNO OF GASS POINTS FOR INTEGRATION   =,I5//
          1         20X, 38HSECTION REFERENCE FOR TYPE3 ELEMENT  =,I5////)
30         FORMAT(5X,5HNODES,10X,12HX-COORDINATE,10X,12HY-COORDINATE,
          1         10X,12HZ-COORDINATE)
40         FORMAT(3F0.0)
```

```
50         FORMAT(5X, 15, 13X, F10.4,12X, F10.4, 12X,F10.4)
60         FORMAT(1H1,5X,11HELEMENT NO.,10X,33HCONNECTIVITY   ARRAYS (NODE N
           10S),
           1      10X, 17HSECTION REFERENCE,3X,17HEL IDENTIFICATION)
65          FORMAT(1010)
66         FORMAT(5X,15,5X,815,18X,13,14X,15)
67         FORMAT(410)
68         FORMAT(5X,15,12X,216,39X,13,14X,15)
69         FORMAT(410)
70         FORMAT(5X,15,12X,216,12X,15,28X,15)
71         FORMAT(2F0.0)
72         FORMAT(8X,15,11X,F12.3,12X,F10.6)
75         FORMAT(1H1, 3X,17HSECTION REFERENCE,5X,38H ELASTIC MODULUS OF
           1  CONCRETE   ,27H*****POISSION'S RATIOS ****)
80         FORMAT(6F0.0)
81         FORMAT(/////////, 5X,11HSECTION REF,8X,14HYOUNGS MODULUS,BX,
           1   13HDIA. OF STEEL)
85         FORMAT(8X,13, 12X, F10.2,2X,F10.2,2X,F10.2,4X,F4.3,2X,F4.3,2X,F4.3
           1,2X,F4.3,2X,F4.3,2X,F4.3)
90         FORMAT(1H1, 5X, 10HZERO NODES, 10X,11HCONSTRAINTS)
95         FORMAT(210)
100        FORMAT(5X,15,14X,16)
105        FORMAT(F15.4)
106        FORMAT(810)
107        FORMAT(5X,15, 5X, 615,28X,13,14X,15)
207         FORMAT(////////,15X,20HHALF BANDWIDTH IS =, 5X,15)
           RETURN
           END
```

SOC LISTING

```
*     LIST 8
*     CARCS COLUMN
*     FCRIRAN NCRM
C     VERSION CURRENT OCTOBER 1969
      CLICHE COMMON
COMMON WHICH CAN VARY WITH TIME
       COMMON NC, JN, LN, TT, IR, LX, ENI, RN(12C2), DRMX(1202), VMX(1202
     1), PX(1202), QMX(1202), SIGR(1202), SIGT(1202), XMU(1202), AM(1202
     2), C1(1202), CR(1202), DV(1202), DVC(1202), EC(1202), ISV(1202),
     3 P(1202), Q(1202), CK(1202), TK(1202), VN(1202), VO(1202), AMU(120
     42), E(1202), I(1202), R(1202), V(1202), TC(12), TIC(12), RPL(25),
     5 CT, DTH, DTN, DTPR, EPP, ETOT, FDT, HDTI, IL, IPI, IPU, ITCX,
     6 IBANK, NCD, PJM, PTS, CXT, RJH, STR, SXN, TPR, HDTH, TTS
COMMON WHICH REMAINS THE SAME FOR DURATION OF PROBLEM
       COMMON CPLOT, IEPLOT, IRPLOT, IHEAC(8), GR, DXT, PLOD(100), GAS(27
     128), PT(400), FMU(400), DPM(400), PTC(200), FMC(200), DPC(200),
     2 EK(200), EP(200), DEK(200), CK(200), CP(200), CKP(200), AK(10),
     3 VI(10), RM(10), AMZ(10), AM1(10), AM2(10), GXK(10), PZO(10), P1(1
     40), P2(10), GSL(10), GCT(10), SE(0), EF(10), EV(10), GSI(10),
     5 IT(10), ITT(10), IP(10), RB(11), RHO(11), GK(10), CF, CCN, HCCN,
     6 IRZ, REZF, IWRT(4), PPR(61), TP(61), IVR, IALF
```

```
COMMON WHICH IS USED FOR GENERAL CALCULATION BUT NOT SAVEC
      COMMON ABF(4004), ABA(4004), ABB(4004), BF(200), EN(11), OCH(11),
    1 ENC(11), EDP(6), FDT(6), EDTL(6), ING(25), FNG(25), IDN(4), PRI,
    2 IC(2), MC(2), ID(8), A, ABS, AMC, AME, AMPI, B, BARK, C, CKL, CRC
    3 CIC, CZC, CAVR, CRTI, CVEL, CVRC, D, DP, CU, CEC, DRI, CR2, DRH,
    4 CRS, DIV, DV1, DVK, EW, EDV, EKL, ETA, ETW, EJTW, ERCU, FA, FST,
    5 FSTM, FSTR, G1, G2, GAM, GLN, GMI, GMU, IBX, III, IIJ, IPB, IPDT,
    6 ITER, ITOT, ITIME, ITOTL, ITSTP, J, K, L, LL, LP, M, N, NN, NP,
    7 NCYC, CFF, PCT, PL3, PL4, PQ1, PC2, PBAR, CO, CS, QKS, QSAV, R21,
    8 R22, RDR, RH1, RH2, ROR, RZI, RACT, RII21, RH22, RMV1, RMV2, SK,
    9 SLC, SLE, SLP, SMU, SDSP, SLP1, STAB, TV, TAR, TBR, TFR, TK1
      COMMON TK2, TO1, TQ2, TRR, TERK, VCC, VDV, VM1, VM2, VN1, VNH,
    1 VOL1, VOL2, WT, YN1, RIX(10), GW, F, S, AD, AF, CA, CB, DC, CD,
    2 KIM, ZETA, LIL
      COMMON CT(1202), EKS(1202)
      EQUIVALENCE (YN1, RIX(1))
      EQUIVALENCE (ION(4),PRI)
      EQUIVALENCE (ING,FNG)
      END CLICHE
      USE COMMON
C     READ 68 AND WRITE 6A
      CALL REGST
      N=.LOC.ABF(1)
      J=.LOC.ZETA
      N=J-N
      DC 1 LIL=1,N
      ABF(LIL)=C.
    1 CONTINUE
      CALL REWIND (16)
      CALL CLOCK (MO(1), MO(2))
      CRTI=1.
      NCYC=J=5
      L=16
    2 BLFFER IN (16,1) (DPLOT,IALF)
    3 IF (UNIT,16,M) 3, ,219,219
      CALL RECEOF (16)
      J=5
    4 BUFFER IN (16,1) (NC,TTS)
    5 IF (UNIT,16,M) 5, ,22C,220
      BACKSPACE FILE 16
      CALL BSPACE (16)
      CALL FSPACE (16)
      READ INPUT TAPE 2, 95C, (ID(J), J=1,8)
      READ INPUT TAPE 2, 951, GW, ITIME, A, STR
      STR=100,*STR
      CALL ASSIGN (7,0,10HSCCPLOTBUF,4020C)
      SET UP RUNNING TIME
      IF (ITIME) ,7,7
      IF (IBANK) 6, ,6
      IBANK=-ITIME
    6 ITIME=IBANK
    7 IBX=1
      TTS=MAX1F(GW*1000.,TTS)
 ECK  FOR RIGHT TAPE
```

```
      DC 8 J=1,8
      IF (IHEAD(J)-ID(J)) ,8,
      WRITE OUTPUT TAPE 3, 954, (IHEAD(J), J=1,8)
      CALL ERROR (0.)
    8 CONTINUE
      K=6
      IF (A) , ,9
      CALL WRSO
      GO TO 1C
    9 CALL RECEOF (6)
      CALL BSPACE (6)
   10 CALL WRST
      CALL WRTEOF (6)
      CALL BSPACE (6)
      CALL BANDP (ICN(1), ICN(3))
      B=ICN(2)
      B=B/PRI
      A=B-40.
      ICN(1)=A
      IF (ITIME) , ,11
      ITIME=ION(1)
      GO TO 12
   11 ITIME=XMINOF(ION(1), ITIME)
   12 ITOTL=8
      IF (NC) 13, ,13
CLE   1 CONSTANTS INITIALIZED
      CALL BANDP (ION(1), ION(3))
      A=ION(2)
      A=A/PRI
      ITOT=A
      ITCT=ITCTL-ITOT
      GO TO 15
CHECK CLOCK FOR TIME STOP -- INCREMENT COUNTER
C     EVERY 20 CYCLES GOES TO 10 INSTEAC OF 11
   13 ITSTP=0
      CALL BANDP (ICN(1), ICN(3))
      A=ION(2)
      A=A/PRI
      ITCT=A
      ITCT=ITOTL-ITCT
   14 ITSTP=ITSTP+1
CALCULATE DELTA T
      A=1.1*DTH
      B=(SQRTI(SXN))/3.
      B=MINIF(B, A)
      DT=.5*(B+DTH)
      DTH=B
CHECK FOR PRESSURE PROFILE
   15 IF (IPO-2) 20,16,
C     OUTER PRESSURE PROFILE
      L=1
      GO TO 17
C     INNER PRESSURE PROFILE
   16 L=LX
```

```
      17 TK(L)=0.
      18 A=DIMF (TP(IPI+1),TT)
         IF (A) 19, ,19
         IPI=IPI+1
         IF (TP(IPI+1)) , ,18
         IPO=1
         GO TO 20
      19 A=TT-TP(IPI)
         B=TP(IPI+1)-TP(IPI)
         P(L)=PPR(IPI)+(PPR(IPI+1)-PPR(IPI))*A/B
         EPP=EPP+(PJM*HDT1+P(L)*DTN)*V(L-1)*CCN*(3.*RJH*RJH+FDT*V(L-1)*V(
         11))
         ETOT=EPP+ENI
CYCLE CONSTANT INITIALIZATION
      20 PCT=BARK=0.
         TT=TT+DTH
         HDTI=.5*DT
         HDTH=.5*DTH
         DTN=DTH-HDTI
         FDT=HDTP*HDTH
         L=IR
         SXN=DXT
         QXT=ABSF(QXT)
         VCC=1.0E-3*QXT/SQRTI(AK(L)*RHC(L+1))
         VCC=MINIF(VCC,1.0E-8)
         QXT=1.
         PC1=P(JN)+Q(JN)
         TC1=TK(JN)+CK(JN)
         IF (I(JN)) ,21,
         DR1=DR(JN-1)-CR(JN)+RN(JN-1)-RN(JN)
         R21=DR(JN-1)+CR(JN)+RN(JN-1)+RN(JN)
         VCL1=VN(JN)-DVO(JN)
         VM1=(VOL1-DV(JN))/AM(JN)
         TK1=TQ1*VM1/R21
         RMV1=DR1/VM1
         RH1=R(JN-1)+V(JN-1)*HDTH
         RH21=RH1*RH1*V(JN-1)
CALCULATION OF J-LINES BEGINS HERE
      21 CC 144 J=JN,LN
         GAM=0.
         III=(I(J)-1)/10C+1
         EC(J)=E(J)
         VC(J)=V(J)
CALCULATE EQUATIONS OF MOTION
         IF (R(J)) 218,27,
         PC2=P(J+1)+Q(J+1)
         TC2=TK(J+1)+QK(J+1)
         IF (I(J+1)) ,28,
         CR2=CR(J)-DR(J+1)+RN(J)-RN(J+1)
         R22=DR(J)+DR(J+1)+RN(J)+RN(J+1)
         VCL2=VN(J+1)-DVC(J+1)
         VM2=(VOL2-DV(J+1))/AM(J+1)
         TK2=TQ2*VM2/R22
         RMV2=DR2/VM2
```

```
      IF (I(J)) ,29,
      ROR=(TK2*DR1+TK1*DR2)/(DR1+DR2)
      RCR=.5*(RMV1+RMV2)
   22 A=(PQ1-PQ2)/RDR
      IF (V(J)) ,23,
      VCC=1.E-2C
   23 DV1=DT*(1.333333333*(TQ1-TQ2)/RDR+A+8.*RCR+GR)
      V(J)=V(J)-DV1
      IF (ABSF(V(J))-VCC) 30,30,
   24 C=DTH*V(J)
      RH2=R(J)+.5*C
      RH22=RH2*RH2*V(J)
      DR(J)=DR(J)+C
      R(J)=RN(J)+DR(J)
      CRS=R(J-1)-R(J)
      IF (I(J)) ,113,
   25 C=(V(J)-V(J-1))*(V(J)*(V(J-1)+V(J))+V(J-1)*V(J-1))
      C=DTH*(3.*(RH22-RH21)+FDT*C)
      DV(J)=DV(J)+C
      VN1=VOL1-DV(J)
      VNH=VN1+.5*C
      D=(DV(J)+DVC(J))/VN1
      AMP1=D+1.
      EDV=C/VN(J)
      DVK=C/VNH
      FTA=VN(J)/VNH
      VCV=VN(J)*C/(VN1*(VN1+C))
      DU=V(J-1)-V(J)
      DRH=RH1-RH2
      IF (CU) ,26,26
      ERCU=ETA*DU*RHO(L+1)
      QSAV=ERCU*DU
    6 TER=3.*CTH*CU/DRH
      TERK=DVK+TER
      IF (III-3) 31,31,
      IF (I(J)-40C) 116,125,125
CALCULATE BOUNDARY CONDITIONS
    7 RH2=RH22=0.
      GO TO 25
    8 RCR=.5*RMV1
      ROR=TK1
      GO TO 22
    9 RDR=.5*RMV2
      ROR=TK2
      GO TO 22
CALCULATIONS MADE WHEN LITTLE OR NO ACTIVITY EXISTS
   10 V(J)=0.
      IF (V(J-1)) 24, ,24
      RH2=R(J)
      RH22=0.
      IF (III-3) 113,113,
      IF (III-4) ,24,
      C=DR1*(R(J-1)*R21+R(J)*R(J))
      PCT=C*P(J)+PCT
```

```
        GO TO 113
CALCULATE SLOPE AND PRESSLRE FOR I LESS THAN 300
   11 N=IT(L)+1
      NP=IP(L)+1
      PL3=SLP=SMU=0.
      IF (XMU(J)-2.*GCT(L)*AM2(L)) ,47,47
      IF (XMU(J)) 56, ,
      IF (D-XMU(J)) 32, ,
      XMU(J)=C
      GO TO 42
      IF (XMU(J)-AM1(L)) 42,42,
      IF (III-2) 34, ,
      IF (P(J)) , ,34
      IF (XMU(J)-AM2(L)) 33, ,
      XMU(J)=.98*AM2(L)
      XMU(J)= -XMU(J)
      GO TO 56
      IF (XMU(J)-AM2(L)) ,48,48
      IF (D-.95*XMU(J)) ,42,42
  PECIAL UNLOAdING SCHEME - A -
      IF (D-AM1(L)) , ,35
      SLP=AK(L)
      GO TO 41
   35 CC 36 K=NP,NP+38
      IF (P(J)-PT(K)) 37,37,
      IF (FMU(K+1)-FMU(K)) 37,37,
   36 CONTINUE
      K=NP+38
   37 SLE=DPM(K)
      DO 38 K=N,N+18
      IF (P(J)-PTC(K)) 39,39,
      IF (FMC(K+1)-FMC(K)) , ,38
      SLC=SLE
      GO TO 40
   38 CONTINUE
      K=N+18
   39 SLC=DPC(K)
   40 SLP1=SLE+XML(J)*(SLC-SLE)/AM2(L)
      SLP=SLP1-AM1(L)*(SLP1-AK(L))/C
   41 PL3=P(J)+SLP*VDV
      GO TO 65
CALCULATE ELASTIC P-MU TABLE - B -
   42 ABS=D
      CALL PSUB
      GO TO 65
      ENTRY PSUB
      DO 44 K=NP,NP+38
      IF (ABS-FMU(K)) ,45,43
      PL3=PT(K-1)+(ABS-FML(K-1))*DPM(K)
      GO TO 46
   43 IF (FMU(K+1)-FMU(K)) 45,45,
   44 CONTINUE
      K=NP+38
   45 PL3=PT(K)+(ABS-FMU(K))*DPM(K)
```

```
   46 SLP=DPM(K)
      RETURN PSUB
CALCULATE CRUSHED P-MU TABLE
   47 XMU(J)=MAX1F(D, XMU(J))
   48 SLP=AK(L)*.C1
      ABS=D
      DC 51 K=N−1,N+18
      IF (D−FMC(K)) 49, ,50
      PL3=PTC(K)
      SLP=DPC(K)
      GO TO 52
   49 IF (K−N) 52, ,
      PL3=PTC(K−1)+(D−FMC(K−1))*DPC(K)
      SLP=DPC(K)
      GO TO 52
   50 IF (FMC(K+1)−FMC(K)) , ,51
      CALL PSUB
      GO TO 52
   51 CONTINUE
      CALL PSUB
   52 IF (D−.985*XMU(J)) ,65,65
      ABS=XMU(J)
      PL4=PL3
      SLP1=SLP
      CALL PSUB
      GAM=.5*PL3*XMU(J)/(1.+XMU(J))
      GAM=GXK(L)*(GAM−EF(L))/(EV(L)−EF(L))
      IF (GAM), ,53
      PL3=PL4
      SLP=SLP1
      GO TO 65
   53 GAM=MIN1F(GAM,GXK(L))
      ABS=C
      IF (D) , ,54
      PL4=GSL(L)*C
      PL3=SLP=0.
      SLP1=GSL(L)
      GO TO 55
   54 CALL PSUB
   55 DP=GAM*(E(J)−.5*PL3*D/AMP1)
      PL4=PL4+DP
      SLP=SLP1+.5*GAM*((PL4+P(J))/ETA−(.5*(B+AMU(J))*SLP+PL3/ETA))/ETA
      PL3=PL4
      IF (SLP) ,65,65
      SLP=.01*AK(L)
      GO TO 65
CALCULATE S.L.S.
   56 IF (D−AMZ(L)) , ,57
      PL3=0.
      SLP=AK(L)
      GO TO 65
   57 DO 58 K=N,N+18
      IF (P(J)−PTC(K)) 62, ,
      IF (FMC(K+1)−FMC(K)) 59,59,
```

```
 58 CONTINUE
 59 DO 60 K=NP,NP+38
    IF (P(J)−PT(K)) 61, ,
    IF (FMU(K+1)−FMU(K)) 61,61,
 60 CONTINUE
    K=NP+38
 61 ABS=FMU(K−1)+(P(J)−PT(K−1))/DPM(K)
    SLP=DPM(K)
    GO TO 63
 62 ABS=FMC(K−1)+(P(J)−PTC(K−1))/CPC(K)
    SLP=DPC(K)
 63 IF (D−ABS) ,64,64
    IF (ABS−AMZ(L)) ,64,
    SLP=(D−AMZ(L))*SLP/(ABS−AMZ(L))
 64 PL3=P(J)+SLP*VDV
    IF (PL3) ,65,65
    PL3=0.
 - EXIT -
 65 IF (E(J)−EF(L)) ,66,66
    ABF(IBX+1)=V(J)
    A=ISV(J)
    ABF(IBX+2)=SIGNF(C1(J),A)
    ABF(IBX+3)=AMU(J)
    ABF(IBX+4)=P(J)
    ABF(IBX+5)=TK(J)
    IBX=IBX+7
209 CONTINUE
    IF (IEPLOT) 211,211,
    ABF(IBX−1)= −100.
    ABF(IBX)=ETCT
    DC 210 N=1,6
    ABF(IBX+1)=EDTL(N)
    IBX=IBX+1
210 CONTINUE
    IBX=IBX+1
    GO TO 212
211 ABF(IBX−1)= −10.
212 IF (ITSTP−2C) 14,13,13
213 L=2
CALCULATE BALANCE OF REAL TIME IN ACCOUNT (NEG. RUNNING TIME) AND RESET
214 IF (IBANK) 215,215,
    IBANK=IBANK−ITOT
215 III=2
C - EMPTY PLOT BUFFER ONTO 68 BEFORE TERMINATICN
    IF (DPLCT) 216,216,
    CALL PLTOUT
C - WRITE FINAL DUMP ON 68
216 K=16
    CALL WRST
    K=6
    CALL PLOTE
    CALL WRST
    CALL WRTEOF (6)
    CALL UNLOAD (6)
```

```
      CALL CLCCK (IC(1),IC(2))
      WRITE OUTPUT TAPE 3, 966, ITOT, IC(1),IC(2)
      WRITE OUTPUT TAPE 3, 967
      CALL OOND3A(3)
      CALL OOND3A(61)
      IF (L−1) ,217,
      READ INPUT TAPE 2, 971, L
      IF (L−8) 217, ,217
C - CALL PLOT
      CALL CHAIN (5,5)
C - UNLOAD TAPES − CALL EXIT − NO PLOT
  217 CALL UNLOAD (16)
      CALL EXIT
CREATE IF RADIUS NEGATIVE
        OUTPUT TAPE 3, 968, J−1
        ERROR (1.)
        ROUTINES
  219 CALL TSTR
      GO TO (221,2,2,2), J
  220 CALL TSTR
      GO TO (221,4,4,4), J
  221 WRITE OUTPUT TAPE 3, 972
      PRINT 972
      CALL OOND3A(3)
      CALL OOND3A(61)
      CALL EXIT
C     MAIN CODE TAPE SUBRCUTINES
      ENTRY TSTO
      CALL BSPACE (K)
      DO 900 M=1, (5−N)
      CALL WRBLNK (K)
  900 CONTINUE
      N=N−1
      RETURN TSTO
      ENTRY WRSC
      N=5
  901 BUFFER OUT (K, 1) (DPLOT,IALF)
  902 IF (UNIT, K, M) 902,904, ,
      CALL TSTO
      IF (N−1) 901, ,901
      WRITE OUTPUT TAPE 3, 908, K
      IF (K−6) 903, ,903
      RETURN WRSO
  903 CALL OOND3A(3)
      CALL OOND3A(61)
      CALL EXIT
  904 CALL WRTEOF (K)
      RETURN WRSO
      ENTRY WRST
      N=5
  905 BUFFER CUT (K,1) (NC,TTS)
  906 IF (UNIT,K,M) 906,907, ,
      N=N−1
      IF (N−1) 905, ,905
```

```
907 RETURN WRST
    ENTRY TSTR
    CALL BSPACE (L)
    J=J−1
    RETURN TSTR
    FORMAT STATEMENTS
908 FORMAT ( 7H1 TAPE ,13,38H IS BAD, PLEASE REPLACE IT AND RESTART)
950 FORMAT (8A1C)
951 FORMAT (E7.C,17,2E7.0)
952 FORMAT (///35H ENERGY TOTALS PER ORIGINAL REGIONS)
953 FORMAT (///33H ENERGY TOTALS PER MATERIAL STATE)
954 FORMAT (60H TAPE 68 AND CARD I.D. ARE NOT THE SAME, PROBLEM TERMIN
    1IATED///22H TAPE IS FOR PROBLEM ,8A10)
956 FORMAT (1H1/8H SOC II ,7A10,4A10//, 9H STARTED ,1A8, 4H ON ,1A8/)
957 FORMAT (1H1/8A1C,4A10)
958 FORMAT (///43H N CYCLE  DELTA T(N)  DELTA T(N+.5)   TIME//1X,16,
    11X,3E14.5//42H   DELTA T CONTROLLED BY ZONE WITH RADIUS =,E14.5)
960 FORMAT (//69H     KINETIC ENERGY    INTERNAL ENERGY     GRAVITY
    1   TOTAL ENERGY//(4E18.10))
961 FORMAT (///17H ENERGY INPUT IS ,E18.10)
962 FORMAT (///35H THIS IS A PRESSURE PROFILE PROBLEM)
963 FORMAT (///36H VOLUME WEIGHTED CAVITY PRESSURE IS ,E12.5)
964 FORMAT (18H BAD ENERGY CHECK/)
966 FORMAT (26H PROBLEM TERMINATED AFTER ,16,8H SECONDS///13H THE TIME
    1 IS ,1A8,13H THE MACHINE ,1A8)
967 FORMAT (1H1)
968 FORMAT (1H1///19H NEGATIVE R AT J = ,14,14H CHECK PROBLEM)
971 FORMAT (11)
972 FORMAT (65H 3 BAD READS OF 68, CHECK TAPE AND UNIT, THEN RESTART
    1THIS JOB )
973 FORMAT (60H ERROR IN THIS PROBLEM.  DO NOT TRY TO CONTINUE OR RES
    1TART.)
974 FORMAT (1H1///47H SLOPE LESS THAN OR EQUAL TO ZERO. CHECK INPUT//)
    1//117H CYCLE DELTA T(N) DELTA T(N+.5) J STATE P(N+1)
    2SLOPE     MU(N+1)     P(N)     MU(N)     MU MAX//1X,16,
    32E12.5,216,5E13.5,E12.5)
975 FORMAT (1H1///30H MU−E/SLOPE GREATER THAN 1.501///60H     MU−E
    1    SLOPE     MU N+1     PRESSURE     LOC.//4E14.5,11)
976 FORMAT (1H1///30H MU−C/SLOPE GREATER THAN 1.501///60H     MU−C
    1    SLOPE     MU N+1     PRESSURE     //4E14.5)
977 FORMAT (45H END OF TAPE SENSED - DUMP TAKEN - RECORD = ,13)
    END
*   LIST8
*   CARDS COLUMN
*   FORTRAN    PLTC
    SUBROUTINE PLIOUT
    USE COMMON
    CALL REWIND (7)
    BUFFER IN (7,1) (ABA(1),ABA(4C04))
    M=4005
    J=1
    DO 7 N=1,IPB
  1 IF (UNIT,7,K) 1,2,,100
    WRITE OUTPUT TAPE 3, 103, N, IPB
```

```
103 FORMAT (20H END TAPE ERROR − N=,I3,6H I PB =,I3)
    GO TO 2
100 IF (IO CHECK,7) ,102
    WRITE OUTPUT TAPE 3, 101, N, IPB
101 FORMAT (20H PARAITY ERROR − N =,I3,6H I PB =,I3)
    GO TO 2
102 WRITE OUTPUT TAPE 3, 104, N, IPB
104 FORMAT (20H WORD COUNT ERROR,N=,I3,6H IPB =,I3)
  2 IF (N−IPB) ,3,3
    BUFFER IN (7,1) (ABA(M),ABA(M+4003))
  3 BUFFER OUT (16,1) (ABA(J),ABA(J+4003))
  4 IF (UNIT,16,K) 4,5,,
    WRITE OUTPUT TAPE 3, 900
    IF (M−1) , ,6
    M=4005
    J=1
    GO TO 7
  6 M=1
    J=4005
  7 CONTINUE
  8 CALL REWIND (7)
    BUFFER OUT (16,1) (ABF(1), ABF(4004))
  9 IF (UNIT,16,K) 9,10,,
    WRITE OUTPUT TAPE 3, 900
 10 CALL WRTEOF (16)
    RETURN
900 FORMAT (51H BAD TAPE READ/WRITE, PLOT MAY HAVE SOME BAD POINTS)
    END
*   LIST 8
*   CARDS COLUMN
*   FORTRAN    RPLOT
    SUBROUTINE RPLOT
    USE COMMON
    A=R(JN)
    DO I J=JN,LN
    IF (I(J)-390) 1, ,
    B=R(J−1)
    LP=J−1
    GO TO 2
  1 CONTINUE
    B=R(LN)
    LP=LN
  2 YN1=GW=V(J)
    F=S=P(JN)
    AD=AF=TK(JN)
    DA=CB=EO(JN)=P(JN)+1.3333333*TK(JN)
    DC=CD=VO(JN)=P(JN)−.66666667*TK(JN)
    DC 3 J=JN+1,LP
    YN1=MAX1F(YN1,V(J))
    Gh=MIN1F(GW,V(J))
    F=MAX1F(F,P(J))
    S=MIN1F(S,P(J))
    AD=MAX1F(AD,TK(J))
    AF=MIN1F(AF,TK(J))
```

```
      VO(J)=P(J)−.66666667*TK(J)
      EO(J)=P(J)+1.3333333*TK(J)
      DA=MAX1F(DA,EO(J))
      DB=MIN1F(DB,EO(J))
      DO=MAX1F(DC,VO(J))
      DD=MIN1F(DD,VO(J))
    3 CONTINUE
      K=LP−JN+1
      DO 12 J=1,10, 2
      IF (RIX(J)−RIX(J+1)) 12,12,
      CALL SETCH (10.,2.,0, 0, 0, 0)
      GO TO (4,5,6,8,9), J/2+1
    4 WRITE OUTPUT TAPE 100, 450, (IHEAD(N), N=1,8), TT
      L=JN+12020
      GO TO 7
    5 WRITE OUTPUT TAPE 100, 451, (IHEAD(N), N=1,8), TT
      L=JN
      GO TO 7
    6 WRITE OUTPUT TAPE 100, 452, (IHEAD(N), N=1,8), TT
      L=JN+3606
    7 CALL MAPG(B, A, RIX(J+1), RIX(J))
      CALL TRACE (R(JN), P(L), K)
      GO TO 11
    8 WRITE OUTPUT TAPE 100, 453, (IHEAD(N), N=1,8), TT
      L=JN
      GO TO 10
    9 WRITE OUTPUT TAPE 100, 454, (IHEAD(N), N=1,8), TT
      L=JN+8414
   10 CALL MAPG (B, A, RIX(J+1), RIX(J))
      CALL TRACE (R(JN), EOIL), K)
   11 CALL FRAME
   12 CONTINUE
      RETURN
  450 FORMAT (8A1C/30H VELOCITY VERSUS RADIUS AT T = ,E12.5)
  451 FORMAT (8A1C/30H PRESSURE VERSUS RADIUS AT T = ,E12.5)
  452 FORMAT (8A1C/31H K−R THETA VERSUS RADIUS AT T = ,E12.5)
  453 FORMAT (8A1C/30H RADIAL STRESS VERSUS R AT T = ,E12.5)
  454 FORMAT (8A1C/34H TANGENTIAL STRESS VERSUS R AT T = ,E12.5)
      END
*        LIST 8
*        CARDS COLUMN
*        FORTRAN
         SUBROUTINE BANDP (IBA,ITL)
         USE COMMON
C
C        CALL BANDP(A,B)
C        STORES ASCII USER NUMBER IN A(1)
C        STORES NUMBER OF SECONDS IN BANK ACCOUNT IN A(2) INTEGER
C        STORES TL IN B(1) INTEGER SECONDS
C        STORES PRIORITY IN B(2) FLOATING PT
C
         COMMON /GOBCOM/ GCOM
         ADDRESS ZETA
         DIMENSION IBA(2), ITL(2)
```

```
          ZETA=0
          KIM = (2401B.SHL.48).LN.((.LOC.ERROR) .SHL.30) .UN.(.LOC.IBA(1))
          GCOM=(1004B.SHL.18).UN.(.LOC.KIM)
          GO TO ZETA
ERROR     GO TO OK
          GO TO ERROR
OK        IBA(2) =IBA(2) / 1000000
          KIM =(2403B.SHL.48).UN.((.LOC.ERR) .SHL.30 ) .UN.(.LOC.ITL(1))
          GCOM=(1004B.SHL.18).UN.(.LOC.KIM)
          GO TO ZETA
ERR        GO TO THRU
          GO TO ERR
THRU      ITL(1)= ITL(1) / 1000000
          RETURN
          END
*     LIST 8
*     CARDS COLUMN
*     FORTRAN     ERRCR
      SUBROUTINE ERROR (ERR)
      USE COMMON
      CALL UNLOAD (16)
      CALL UNLOAD (6)
      IF (CRTI) 1, ,1
      CALL PLOTE
    1 IF (ERR) 3,3,
      WRITE OUTPUT TAPE 3, 100, NC, DT, DTH, TT, RADT
      DO 2 J=JN,LN
      I(J)=XSIGNF(I(J),ISV(J))
    2 CONTINUE
      WRITE OUTPUT TAPE 3, 101, (J-1, DR(J), R(J), V(J), AMU(J), P(J),
     1 Q(J), TK(J), QK(J), E(J), I(J), J=JN,LN+1)
    3 CALL OOND3A (3)
      CALL OOND3A (61)
      CALL EXIT
  100 FORMAT (18H1 ERROR PRINTOUT///43H N CYCLE   DELTA T(N) DELTA T
     1(N+.5) TIME///X,I6,1X,3E14.5//42H DELTA T CONTROLLED BY ZONE WIT
     2H RADIUS =,E14.5)
  101 FORMAT (///120H   J   DELTA R     RADIUS    VELOCITY    MU
     1 PRESSURE   SHOCK   k R-THETA   K SHOCK    ENERGY    ST
     2 ATE//(1X,14,9E12.5,17))
        END
```

Index